

Advances in Isotope Geochemistry

Mark Baskaran *Editor*

Handbook of Environmental Isotope Geochemistry

 Springer

Mark Baskaran
Editor

Handbook of Environmental Isotope Geochemistry

 Springer

Editor

Dr. Mark Baskaran
Wayne State University
Dept. Geology
Detroit Michigan
0224 Old Main Bldg
USA
Baskaran@wayne.edu

ISBN 978-3-642-10636-1 (Printed in 2 volumes)
DOI 10.1007/978-3-642-10637-8
Springer Heidelberg Dordrecht London New York

e-ISBN 978-3-642-10637-8

Library of Congress Control Number: 2011935432

© Springer-Verlag Berlin Heidelberg 2011

This work is subject to copyright. All rights are reserved, whether the whole or part of the material is concerned, specifically the rights of translation, reprinting, reuse of illustrations, recitation, broadcasting, reproduction on microfilm or in any other way, and storage in data banks. Duplication of this publication or parts thereof is permitted only under the provisions of the German Copyright Law of September 9, 1965, in its current version, and permission for use must always be obtained from Springer. Violations are liable to prosecution under the German Copyright Law.

The use of general descriptive names, registered names, trademarks, etc. in this publication does not imply, even in the absence of a specific statement, that such names are exempt from the relevant protective laws and regulations and therefore free for general use.

Printed on acid-free paper

Springer is part of Springer Science+Business Media (www.springer.com)

To
The Founders, Architects and Builders
Of
Yesterday, Today and Tomorrow
Of
The Field "Isotope Geochemistry"

Endorsement from Prof. Gerald J. Wasserburg

“Environmental Science is concerned with chemical compounds that effect the well being of society-where they come from, how they are transported & where they are deposited. Isotopic geochemistry plays a key role in deciphering this code. The approaches given in this “Hand Book” give a clear view of answers, potential answers & approaches in this field.”

G.J. Wasserburg, Caltech
Crafoord Laureate and John D. MacArthur Professor of Geology
and Geophysics, Emeritus

Endorsement from Prof. Alex Halliday

“The environment has never before been the focus of such fascination, challenge and global engagement. Yet trying to comprehend it or predict how it might evolve is difficult because of the complexities of the systems. This is a volume of immense scope that provides up to date information on the range of new isotopic tools that are being developed and utilised to assail this issue. It is an invaluable reference work that explains the range of techniques, the archives and the discoveries, and should be of interest to any environmental scientist who wants to explore and understand these same critical parts of Earth’s surface.”

Alex N. Halliday FRS
Head, Mathematical, Physical and Life Sciences Division
University of Oxford

Preface

Applications of concepts and methods of physics and chemistry to geology resulted in the field of *Isotope Geochemistry* which has revolutionized our understanding of our Earth system and our environment. When isotope techniques applied to understanding environmental changes that have taken place in the anthropocene, the resultant field can be defined as *Environmental Isotope Geochemistry*. The applications of isotopes as tracers and chronometers have permeated not only every sub-branch of geosciences, but also archaeology, anthropology and environmental forensics.

Over the past three to four decades major developments in instrumentation have resulted in high precision and sensitivity in the measurement of a large number of radioactive and stable isotopes that are widely utilized as powerful tools in earth and environmental science. These developments have opened-up new areas of research, resulting in even widening and deepening knowledge of geochemical processes and new discoveries.

The purpose of this two-set volume is to bring together the more recent applications of a much larger number of radioactive and stable isotopes in earth and environmental science, compared to the previous efforts (detailed in Chap. 1), which is necessitated by the rapid developments in the field from the broad expansion of elements studied now and novel applications that have emerged. In this first most-comprehensive edited volume, the 40 chapters that follow cover applications of 115 isotopes from $Z = 1$ to $Z = 95$ (hydrogen to americium; radioactive isotopes of 30 elements, stable isotopes of 27 elements, and both radioactive and stable nuclides of 9 elements) as environmental tracers and chronometers. The topics covered in this Handbook include: the cycling, transport and scavenging of atmospheric constituents; the biogeochemical cycling of inorganic and organic substances in aqueous systems; redox processes; the sources, fate, and transport of organic and inorganic pollutants in the environment; material transport in various Earth's sub-systems (viz., lithosphere, hydrosphere, atmosphere and biosphere); weathering and erosion studies; effective surface exposure ages; sediment dynamics; the chronology of inorganic and organic substances; reconstruction of paleoclimate and paleoenvironment; water mass mixing; tracing both the production and origin of food; tracing the sources of pollutant metals in the human body; archaeology; and anthropology. We anticipate that this handbook will serve as an excellent resource for veteran researchers, graduate students, applied scientists in environmental companies, and regulators in public agencies, reviewing many tried and tested techniques as well as presenting state of the art advances in *Environmental Isotope Geochemistry*.

The field of *Environmental Isotope Geochemistry* is so vast that it is not possible to cover every aspect of this field. The audience in this field includes atmospheric scientists, geologists, hydrologists, oceanographers, limnologists, glaciologists, geochemists, biogeochemists, soil scientists, radiation and health physicists and it is our hope that we have included in-depth chapters in this Handbook that are relevant to everyone of this group.

This idea of editing this handbook was conceived in 2008 and the proposal was submitted to the publisher in 2009 during my sabbatical leave as a *Plummer Visiting Research Fellow* at St. Anne's College, University of Oxford. I owe a special thanks to Don Porcelli for inviting me to Oxford and for the countless discussions we have had during my pleasant stay there. An advisory committee comprised of the following scientists was formed to advise the editor in selecting topics and authors: Per Andersson (Sweden), Joel Blum (USA), Thure Cerling (USA), Brian Gulson (Australia), Kastsumi Hirose (Japan), Gi-Hoon Hong (South Korea), Carol Kendall (USA), Devendra Lal (USA), Don Porcelli (UK), R. Ramesh (India), Henry Schwarcz (Canada), Peter Swarzenski (USA), and Jing Zhang (China). I would like to thank the Editorial Advisory Board members for thoughtful suggestions at various stages of this Handbook. I would like to specially thank Carol Kendall, Gi-Hoon Hong, Henry Schwarcz and Peter Swarzenski for suggesting some key chapters for inclusion in this Handbook that enhanced the overall breadth of coverage. S. Krishnaswami has been very helpful in looking through the original list of topics and came forth with many good suggestions to improve the content of this handbook. My association with him over the past 28 years (first as one of my early advisors in graduate school at the Physical Research Laboratory (PRL), in Ahmedabad, India) has been very enjoyable. I thank student assistant Vineeth Mohan of my department for his editorial assistance with the manuscripts. We thank all of the 82 external reviewers who gave up their time for reviewing all the manuscripts. Finally, I am deeply indebted to all the authors for their relentless efforts in collectively producing a thorough comprehensive two-set volume of articles with breadth and depth for a variety of audiences and their efforts will be highly appreciated by students of yesterday, today and tomorrow.

Wayne State University
Detroit, Michigan, USA

Mark Baskaran

Contents

Volume I

Part I Introductory Chapters

- 1 “Environmental Isotope Geochemistry”:
Past, Present and Future 3
Mark Baskaran
- 2 An Overview of Isotope Geochemistry in Environmental Studies 11
D. Porcelli and M. Baskaran
- 3 Humans and Isotopes: Impacts and Tracers of Human
Interactions with the Environment 33
Karl K. Turekian

Part II Isotopes as Tracers of Continental and Aquatic Processes

- 4 Lithium Isotopes as Tracers in Marine and Terrestrial
Environments 41
K.W. Burton and N. Vigier
- 5 Meteoric ^7Be and ^{10}Be as Process Tracers in the Environment 61
James M. Kaste and Mark Baskaran
- 6 Silicon Isotopes as Tracers of Terrestrial Processes 87
B. Reynolds
- 7 Calcium Isotopes as Tracers of Biogeochemical Processes 105
Laura C. Nielsen, Jennifer L. Druhan, Wenbo Yang,
Shaun T. Brown, and Donald J. DePaolo
- 8 Natural and Anthropogenic Cd Isotope Variations 125
M. Rehkämper, F. Wombacher, T.J. Horner, and Z. Xue
- 9 Stable Isotopes of Cr and Se as Tracers of Redox Processes
in Earth Surface Environments 155
Thomas M. Johnson
- 10 Stable Isotopes of Transition and Post-Transition Metals
as Tracers in Environmental Studies 177
Thomas D. Bullen

11 Applications of Osmium and Iridium as Biogeochemical Tracers in the Environment	205
Mukul Sharma	
12 Applications of Stable Mercury Isotopes to Biogeochemistry	229
Joel D. Blum	
13 Thallium Isotopes and Their Application to Problems in Earth and Environmental Science	247
Sune G. Nielsen and Mark Rehkämper	
14 Po-210 in the Environment: Biogeochemical Cycling and Bioavailability	271
Guebuem Kim, Tae-Hoon Kim, and Thomas M. Church	
15 Applications of Groundwater Helium	285
J.T. Kulongoski and D.R. Hilton	
16 Applications of Short-Lived Radionuclides (^7Be, ^{210}Pb, ^{210}Po, ^{137}Cs and ^{234}Th) to Trace the Sources, Transport Pathways and Deposition of Particles/Sediments in Rivers, Estuaries and Coasts	305
J.Z. Du, J. Zhang, and M. Baskaran	
17 Radium Isotope Tracers to Evaluate Coastal Ocean Mixing and Residence Times	331
L. Zhang, J. Zhang, P.W. Swarzenski, and Z. Liu	
18 Natural Radium and Radon Tracers to Quantify Water Exchange and Movement in Reservoirs	345
C.G. Smith, P.W. Swarzenski, N.T. Dimova, and J. Zhang	
19 Applications of Anthropogenic Radionuclides as Tracers to Investigate Marine Environmental Processes	367
G.-H. Hong, T.F. Hamilton, M. Baskaran, and T.C. Kenna	
20 Applications of Transuranics as Tracers and Chronometers in the Environment	395
Michael E. Ketterer, Jian Zheng, and Masatoshi Yamada	
21 Tracing the Sources and Biogeochemical Cycling of Phosphorus in Aquatic Systems Using Isotopes of Oxygen in Phosphate	419
Adina Paytan and Karen McLaughlin	
22 Isotopic Tracing of Perchlorate in the Environment	437
Neil C. Sturchio, John Karl Böhlke, Baohua Gu, Paul B. Hatzinger, and W. Andrew Jackson	
23 The Isotopomers of Nitrous Oxide: Analytical Considerations and Application to Resolution of Microbial Production Pathways	453
Nathaniel E. Ostrom and Peggy H. Ostrom	

24 Using Cosmogenic Radionuclides for the Determination of Effective Surface Exposure Age and Time-Averaged Erosion Rates	477
D. Lal	
25 Measuring Soil Erosion Rates Using Natural (^7Be, ^{210}Pb) and Anthropogenic (^{137}Cs, $^{239,240}\text{Pu}$) Radionuclides	487
Gerald Matisoff and Peter J. Whiting	
26 Sr and Nd Isotopes as Tracers of Chemical and Physical Erosion	521
Gyana Ranjan Tripathy, Sunil Kumar Singh, and S. Krishnaswami	
27 Constraining Rates of Chemical and Physical Erosion Using U-Series Radionuclides	553
Nathalie Vigier and Bernard Bourdon	

Volume II

Part III Isotopes as Tracers of Atmospheric Processes

28 Applications of Cosmogenic Isotopes as Atmospheric Tracers	575
D. Lal and M. Baskaran	
29 Uranium, Thorium and Anthropogenic Radionuclides as Atmospheric Tracers	591
K. Hirose	
30 Oxygen Isotope Dynamics of Atmospheric Nitrate and Its Precursor Molecules	613
Greg Michalski, S.K. Bhattacharya, and David F. Mase	

Part IV Isotopes as Tracers of Environmental Forensics

31 Applications of Stable Isotopes in Hydrocarbon Exploration and Environmental Forensics	639
R. Paul Philp and Guillermo Lo Monaco	
32 Utility of Stable Isotopes of Hydrogen and Carbon as Tracers of POPs and Related Polyhalogenated Compounds in the Environment	679
W. Vetter	

Part V Isotopes as Tracers in Archaeology and Anthropology

33 Light-Element Isotopes (H, C, N, and O) as Tracers of Human Diet: A Case Study on Fast Food Meals	707
Lesley A. Chesson, James R. Ehleringer, and Thure E. Cerling	
34 Stable Isotopes of Carbon and Nitrogen as Tracers for Paleo-Diet Reconstruction	725
H.P. Schwarcz and M.J. Schoeninger	

35 Applications of Sr Isotopes in Archaeology	743
N.M. Slovak and A. Paytan	
36 Sources of Lead and Its Mobility in the Human Body Inferred from Lead Isotopes	769
Brian L. Gulson	
Part VI Isotopes as Tracers of Paleoclimate and Paleoenvironments	
37 Dating of Biogenic and Inorganic Carbonates Using ^{210}Pb-^{226}Ra Disequilibrium Method: A Review	789
Mark Baskaran	
38 Isotope Dendroclimatology: A Review with a Special Emphasis on Tropics	811
S.R. Managave and R. Ramesh	
39 The N, O, S Isotopes of Oxy-Anions in Ice Cores and Polar Environments	835
Joël Savarino and Samuel Morin	
40 Stable Isotopes of N and Ar as Tracers to Retrieve Past Air Temperature from Air Trapped in Ice Cores	865
A. Landais	
Author Index	887
Subject Index	939

Contributors

W. Andrew Jackson Texas Tech University, Lubbock, TX 79409, USA

M. Baskaran Department of Geology, Wayne State University, Detroit, MI 48202, USA, baskaran@wayne.edu

S.K. Bhattacharya Physical Research Laboratory, Navrangpura, Ahmedabad, India, bhatta@prl.res.in

Joel D. Blum Department of Geological Sciences, University of Michigan, 1100 North University Avenue, Ann Arbor, MI 48109, USA, jdblum@umich.edu

Bernard Bourdon Institute of Geochemistry and Petrology, Clausiusstrasse 25 ETH Zurich, Zurich 8092, Switzerland, Bernard.bourdon@erdw.ethz.ch

Shaun T. Brown Earth Sciences Division, Lawrence Berkeley National Laboratory, Berkeley, CA 94720, USA

Thomas D. Bullen U.S. Geological Survey, MS 420, 345 Middlefield Road, Menlo Park, CA 94025, USA, tbullen@usgs.gov

K.W. Burton Department of Earth Sciences, Durham University, Science Labs, Durham, DH1 3LE, UK, kevin.burton@durham.ac.uk

Thure E. Cerling IsoForensics Inc, Salt Lake City, UT 84108, USA; Department of Biology, University of Utah, Salt Lake City, UT 84112, USA; Department of Geology and Geophysics University of Utah, Salt Lake City, UT 84112, USA, thure.cerling@utah.edu

Lesley A. Chesson IsoForensics Inc, Salt Lake City, UT 84108, USA; Department of Biology University of Utah, Salt Lake City, UT 84112, USA, lesley@isoforensics.com

Thomas M. Church College of Earth, Ocean, and Environment, University of Delaware, Newark, DE, USA, tchurch@udel.edu

Donald J. DePaolo Department of Earth and Planetary Science, University of California, Berkeley, CA 94720, USA; Earth Sciences Division Lawrence Berkeley National Laboratory, Berkeley, CA 94720, USA, depaolo@eps.berkeley.edu

N. Dimova UC-Santa Cruz/US Geological Survey, 400 Natural Bridges Drive, Santa Cruz, CA, USA, ndimova@usgs.gov

Jennifer L. Druhan Department of Earth and Planetary Science, University of California, Berkeley, CA 94720, USA; Earth Sciences Division Lawrence Berkeley National Laboratory, Berkeley, CA 94720, USA

J.Z. Du State Key Laboratory of Estuarine and Coastal Research, East China Normal University, Shanghai 200062, China, jzdu@sklec.ecnu.edu.cn

James R. Ehleringer IsoForensics Inc, Salt Lake City, UT 84108, USA; Department of Biology University of Utah, Salt Lake City, UT 84112, USA, ehleringer@biology.utah.edu

Baohua Gu Oak Ridge National Laboratory, Oak Ridge, TN 37831, USA

Brian L. Gulson Graduate School of the Environment, Macquarie University, Sydney, NSW 2109, Australia, bgulson@gse.mq.edu.au

T.F. Hamilton Center for Accelerator Mass Spectrometry, Lawrence Livermore National Laboratory, Livermore, CA 94551-0808, USA, hamilton18@llnl.gov

Paul B. Hatzinger Shaw Environmental, Inc., Lawrenceville, NJ 08648, USA

D.R. Hilton Scripps Institution of Oceanography, University of California, San Diego, La Jolla, CA 92093-0244, USA, drhilton@ucsd.edu

K. Hirose Department of Materials and Life Sciences, Sophia University, 7-1 Kioicho, Chiyodaku, Tokyo 102-8554, Japan, hirose45037@mail2.accsnet.ne.jp

G.-H Hong Korea Ocean Research and Development Institute, Ansan P.O.Box 29 Kyonggi 425-600, South Korea, ghhong@kordi.re.kr

T.J. Horner Department of Earth Sciences, University of Oxford, Oxford OX1 3AN, UK, Tristan.Horner@earth.ox.ac.uk

Thomas M. Johnson Department of Geology, University of Illinois at Urbana-Champaign, Urbana, IL 61801, USA, tmjohnsn@illinois.edu

John Karl Böhlke U.S. Geological Survey, Reston, VA 20192, USA, jkbohlke@usgs.gov

James M. Kaste Department of Geology, The College of William & Mary, Williamsburg, VA 23187, USA, jmkaste@wm.edu

T.C. Kenna Lamont-Doherty Earth Observatory, Columbia University, Palisades, NY 10964, USA, tkenna@ldeo.columbia.edu

Michael E. Ketterer Department of Chemistry and Biochemistry, Box 5698, Northern Arizona University, Flagstaff, AZ 86011-5698, USA, Michael.Ketterer@nau.edu

Guebuem Kim School of Earth and Environmental Sciences, Seoul National University, Seoul, South Korea, gkim@snu.ac.kr

Tae-Hoon Kim School of Earth and Environmental Sciences, Seoul National University, Seoul, South Korea, esutaiki@snu.ac.kr

S Krishnaswami Geosciences Division, Physical Research Laboratory, Ahmedabad 380009, India, swami@prl.res.in

J.T. Kulongoski California Water Science Center, U.S. Geological Survey, San Diego, CA 92101, USA, kulongos@usgs.gov

D. Lal Geosciences Research Division, Scripps Institution of Oceanography, 9500 Gilman Drive, La Jolla, CA 92093-0244, USA; Scripps Institution of Oceanography University of California, San Diego, CA 92093, USA, dlal@ucsd.edu

A. Landais Institut Pierre Simon Laplace/Laboratoire des Sciences du Climat et de l'Environnement, CEA/CNRS/UVSQ, Orme des Merisiers, 91191 Gif sur Yvette, France, amaelle.landais@lscce.ipsl.fr

Z. Liu Key Laboratory of Marine Environment and Ecology (Ocean University of China), Ministry of Education, 238 Songling Road, Qingdao 266003, P.R. China, liuzhe_ecnu@yahoo.com.cn

Guillermo Lo Monaco School of Geology and Geophysics, University of Oklahoma, Norman, OK 73019, USA

S.R. Managave Presently at Department of Earth Sciences, Pondicherry University, R.V. Nagar, Kalapet, Puducherry 605014, shreyasman@gmail.com

David F. Mase Purdue University, 550 Stadium Mall Drive, West Lafayette, IN 47907-1210, USA, dmase@purdue.edu

Gerald Matisoff Department of Geological Sciences, Case Western Reserve University, Cleveland, OH 44106-7216, USA, gerald.matisoff@case.edu

Karen McLaughlin Southern California Coastal Water Research Project, Costa Mesa, CA 92626, USA, karenm@sccwrp.org

Greg Michalski Purdue University, 550 Stadium Mall Drive, West Lafayette, IN 47907-1210, USA, gmichals@purdue.edu

Samuel Morin Institut National des Sciences de l'Univers, CNRS, Grenoble, France; Météo-France CNRM-GAME, Centre d'Études de la Neige, St Martin d'Hères, France, morin.samuel@gmail.com

Sune G. Nielsen Woods Hole Oceanographic Institution, Dept. Geology and Geophysics, 02543 Woods Hole, MA, USA, snielsen@whoi.edu

Laura C. Nielsen Department of Earth and Planetary Science, University of California, Berkeley, CA 94720, USA; Earth Sciences Division, Lawrence Berkeley National Laboratory, Berkeley, CA 94720, USA, lnielsen@berkeley.edu

Nathaniel E. Ostrom Department of Zoology, Michigan State University, 204 Natural Sciences Building, East Lansing, MI 48824, USA, ostromn@msu.edu

Peggy H. Ostrom Department of Zoology, Michigan State University, 204 Natural Sciences Building, East Lansing, MI 48824, USA, ostrom@msu.edu

Adina Paytan University of California, Santa Cruz, CA 95064, USA, apaytan@ucsc.edu

R. Paul Philp School of Geology and Geophysics, University of Oklahoma, Norman, OK 73019, USA, pphilp@ou.edu

D. Porcelli Department of Earth Sciences, Oxford University, South Parks Road, Oxford OX1 3AN, UK, Don.Porcelli@earth.ox.ac.uk

R. Ramesh Geosciences Division, Physical Research Laboratory, Navrangpura, Ahmedabad 380009, India, rramesh@prl.res.in

Mark Rehkämper Department of Earth Science and Engineering, Imperial College, London SW7 2AZ, UK, markrehk@imperial.ac.uk

B. Reynolds Institute for Geochemistry and Petrology, ETH Zurich, Switzerland, reynolds@erdw.ethz.ch

Joël Savarino Laboratoire de Glaciologie et Géophysique de l'Environnement, Université Joseph Fourier, St Martin d'Hères, France; Institut National des Sciences de l'Univers CNRS, Grenoble, France, jsavarino@lgge.obs.ujf-grenoble.fr

M.J. Schoeninger University of California at San Diego, 9500 Gillman Drive, La Jolla, CA 92093, USA, mjschoen@ucsd.edu

H.P. Schwarcz School of Geography and Earth Sciences, McMaster University, Hamilton ON L8S 4K1, Canada, schwarcz@mcmaster.ca

Mukul Sharma Radiogenic Isotope Geochemistry Laboratory, Department of Earth Sciences, Dartmouth College, 6105 Fairchild Hall, Hanover, NH 03755, USA, Mukul.Sharma@Dartmouth.edu

Sunil Kumar Singh Geosciences Division, Physical Research Laboratory, Ahmedabad 380009, India, sunil@prl.res.in

N.M. Slovak Department of Behavioral Sciences, Santa Rosa Junior College, 1501 Mendocino Avenue, Santa Rosa, CA, USA, nmslovak@yahoo.com

C.G. Smith US Geological Survey, 600 4th Street South, St. Petersburg, FL, USA, cgsmith@usgs.gov

Neil C. Sturchio University of Illinois at Chicago, Chicago, IL 60607, USA, sturchio@uic.edu

P.W. Swarzenski US Geological Survey, 400 Natural Bridges Drive, Santa Cruz, CA 95060, USA, pswarzen@usgs.gov

Gyana Ranjan Tripathy Geosciences Division, Physical Research Laboratory, Ahmedabad 380009, India, gyana@prl.res.in

Karl K. Turekian Department of Geology and Geophysics, Yale University, New Haven, CT 06511, USA, karl.turekian@yale.edu

W. Vetter University of Hohenheim, Institute of Food Chemistry, Garbenstrasse 28, 70599 Stuttgart, Germany, walter.vetter@uni-hohenheim.de

Nathalie Vigier CRPG-CNRS, Nancy Université, 15 rue Notre Dame des Pauvres, 54500 Vandoeuvre les Nancy, France, nvigier@crpg.cnrs-nancy.fr

Peter J. Whiting Department of Geological Sciences, Case Western Reserve University, Cleveland, OH 44106-7216, USA, peter.whiting@case.edu

F. Wombacher Institut für Geologie und Mineralogie, Universität zu Köln, Zùlpicher Straße 49b 50674, Köln, Germany, fwombach@uni-koeln.de

Z. Xue Department of Earth Science and Engineering, Imperial College London, London SW7 2AZ, UK, z.xue07@imperial.ac.uk

Masatoshi Yamada Environmental Radiation Effects Research Group, National Institute of Radiological Sciences, 4-9-1 Anagawa, Inage, Chiba 263-8555, Japan

Wenbo Yang Department of Earth and Planetary Science, University of California, Berkeley, CA 94720, USA; Earth Sciences Division, Lawrence Berkeley National Laboratory, Berkeley, CA 94720, USA

J. Zhang State Key Laboratory of Estuarine and Coastal Research, East China Normal University, Shanghai 200062, China, jzhang@sklec.ecnu.edu.cn

Jian Zheng Environmental Radiation Effects Research Group, National Institute of Radiological Sciences, 4-9-1 Anagawa, Inage, Chiba 263-8555, Japan, jzheng@nirs.go.jp

Part I
Introductory Chapters

Chapter 1

“Environmental Isotope Geochemistry”: Past, Present and Future

Mark Baskaran

1.1 Introduction and Early History

A large number of radioactive and stable isotopes of the first 95 elements in the periodic table that occur in the environment have provided a tremendous wealth of information towards unraveling many secrets of our Earth and its environmental health. These isotopes, because of their suitable geochemical and nuclear properties, serve as tracers and chronometers to investigate a variety of topics that include chronology of rocks and minerals, reconstruction of sea-level changes, paleoclimates, and paleoenvironments, erosion and weathering rates of rocks and minerals, rock-water interactions, material transport within and between various reservoirs of earth, and magmatic processes. Isotopic data have also provided information on time scales of mixing processes in the oceans and atmosphere, as well as residence times of oceanic constituents and gases in the atmosphere. Arguably the most important milestone on the application of isotopes to earth science is the determination of the age of the Earth and our solar system. Isotope-based dating methods serve as the *gold-standard* and are routinely used to validate other non-isotope-based dating methods. Dating of hominid fossils provides a handle to understand the evolution and migration pattern of humans and stable isotope analyses of organic matter, as well as phosphate in bones and teeth in recovered fossils provide evidence for food sources consumed by humans and other animals (e.g., Abelson 1988; Schwarcz and Schoeninger 2011). To put it succinctly,

our current understanding of the chronological evolution of the earth, its exterior and interior processes occurring on time scales of minutes to billions of years and the reconstruction of the evolution of human civilization has been developed in great part by the measurement of isotopic ratios.

The field of isotope geochemistry started taking its roots shortly after the discovery of “radioactivity” (term coined by Marie Curie) in 1896 by Henri Becquerel (Becquerel 1896; Curie 1898). Within a few years of this remarkable discovery, Rutherford reported an exponential decrease of activity of a radioactive substance with time and introduced the concept of half-lives opening the door for age determination of natural substances containing radioactive elements (Rutherford 1900). The term *isotope* was introduced by Soddy in 1913 (Soddy 1913). The rules governing the transmutation of elements during radioactive decay was simultaneously established by Soddy (1913) and Fajans (1913). Secular equilibrium between radioactive parent and daughter was first described by Rutherford and Soddy (1902). The first radiometric age determination of a geologic sample was made on a sample of pitchblende in 1905 by Rutherford and ages of a variety of other minerals were subsequently made by Strutt (1905) and Boltwood (1907) using the U-He and U-Pb systems. The complete ^{238}U and ^{232}Th chain was established by 1913 and is similar to the one that is in use today (e.g., Ivanovich and Harmon 1992; Henderson 2003). The disequilibria between the members of the U-Th series resulting from differences in geochemical properties of different elements within the chain opened a new field of research to investigate aqueous geochemical processes, rock-water interaction, dating of inorganic precipitates, detrital and biogenic sediments and archaeological objects (e.g., Ivanovich and Harmon

M. Baskaran (✉)
Department of Geology, Wayne State University, Detroit, MI
48202, USA
e-mail: Baskaran@wayne.edu

1992; Bourdon et al. 2003; Krishnaswami and Cochran 2008). One of the key discoveries in this field was made when large fractionations of ^{238}U and ^{234}U were observed in rocks, leachates of rocks and natural waters (Cherdynstev 1955; Thurber 1962). This disequilibrium is caused by a *nuclear* effect resulting from the displacement of ^{234}U (in some cases release into the surrounding aqueous phase from mineral grain surfaces) by recoil during alpha decay (^{238}U decays to ^{234}Th which is displaced from the original position of ^{238}U due to recoil), in contrast to the fractionation caused by differences in the *geochemical* properties between different members of the decay chain.

Soon after the discovery of radioactivity, Victor Hess (1912) measured the radiation levels in the atmosphere at various altitudes using a Geiger counter (developed in 1908) and reported that the radiation levels increased with altitude. He attributed this to radiation coming from outer space called *cosmic radiation* and now commonly called *cosmic rays*. Cosmic rays comprise of charged particles (including high-energy charged particles) such as protons, alpha particles, electrons, helium, nuclei of other elements and subatomic particles. The high-energy charged particles entering the atmosphere interact with atmospheric constituents (N, O, Ar, etc) and produce a suite of cosmogenic radioactive isotopes, whose half-lives range from less than an hour to millions of years (Lal and Peters 1967; Krishnaswami and Lal 2008; Lal and Baskaran 2011). Some of the cosmogenic isotopes (^{14}C , ^{10}Be , ^7Be) have found extensive applications in quantifying processes in earth surface reservoirs such as air-sea exchange, atmospheric mixing, ocean circulation and mixing, scavenging, sediment accumulation and mixing rates in aqueous systems, erosion rates, exposure ages, changes in cosmic ray production rates, and history of human civilization. Among these, ^{14}C has been used universally as the most-robust dating tool and has contributed tremendously to our understanding of human civilization.

The field of stable isotope geochemistry started taking roots with the first set of stable isotope measurements of terrestrial samples made by Murphy and Urey (1932), Nier and Gulbransen (1939), Dole and Slobod (1940) and Urey (1948), much before the discovery of cosmogenic isotopes such as ^7Be , ^{10}Be , and ^{14}C . The theoretical foundation of isotopic

fractionation was later provided by Urey (1947) and Bigeleisen and Mayer (1947) using the methods of statistical quantum mechanics and statistical thermodynamics. Of the 54 elements (first 82 elements are stable of which promethium and technetium are radioactive; 26 are monoisotopic elements) that have two or more stable isotopes, only six of them (H, C, N, O, S and Si) have been extensively studied, with >10,000 published papers, abstracts and theses published on C and O isotope variations since late 1930s for investigating various near earth and earth-surface processes. Fractionations caused by mass-dependent processes such as isotope-exchange reactions, physical and biological reactions result in variations in the isotopic ratios of these elements. All of these elements form chemical bonds that have a high degree of covalent character and some are found in multiple oxidation states in the environment. In contrast, variations in radiogenic stable isotope ratios, such as Pb ($^{206}\text{Pb}/^{204}\text{Pb}$, $^{207}\text{Pb}/^{204}\text{Pb}$ and $^{208}\text{Pb}/^{204}\text{Pb}$), Sr ($^{87}\text{Sr}/^{86}\text{Sr}$), Ce ($^{138}\text{Ce}/^{142}\text{Ce}$), Nd ($^{143}\text{Nd}/^{144}\text{Nd}$), Os ($^{187}\text{Os}/^{186}\text{Os}$) and Hf ($^{176}\text{Hf}/^{177}\text{Hf}$) in natural materials depend on the differences of their initial ratios, the parent concentrations, decay constants, and time elapsed since the solid material was formed.

A natural progression of the light-element stable isotope research is to look for stable isotope fractionation of transition and post-transition elements. Sporadic attempts were made to look for them during 1970's and 1980's, and the initial results appeared to be encouraging. Nonetheless, because of the existing technology at that time and the preconceived notion that mass-dependent fractionations among heavy elements are expected to be negligible, there was no real progress in this area of research (O'Neil 1986). Indeed, mass-dependent isotopic fractionation in transition and post-transition elements are small compared to those in light-elements. However, as will be discussed later, these inferences and conclusions have been challenged and the occurrence of isotope fractionation in transition elements is more of a rule than exception.

The radiogenic isotopes (Pb ($^{206}\text{Pb}/^{204}\text{Pb}$, $^{207}\text{Pb}/^{204}\text{Pb}$ and $^{208}\text{Pb}/^{204}\text{Pb}$), Sr ($^{87}\text{Sr}/^{86}\text{Sr}$), Ce ($^{138}\text{Ce}/^{142}\text{Ce}$), Nd ($^{143}\text{Nd}/^{144}\text{Nd}$), Hf ($^{176}\text{Hf}/^{177}\text{Hf}$) and Os ($^{187}\text{Os}/^{186}\text{Os}$) have been widely used as tracers and stratigraphic chronometers in the environment. Pb isotopes have been utilized to trace the sources of transboundary atmospheric pollution (e.g., Bollhöfer

and Rosman 2001; Komárek et al. 2008), the sources of local and global Pb pollution in a variety of natural reservoirs that include lake and coastal sediments, snow and ice samples, peat deposits, tree rings, lichens and grasses (e.g., Komárek et al. 2008) and to trace the pathways of lead from the environment in to human bodies (e.g., Gulson 2011).

The dawn of the Atomic Age started with the detonation of the first nuclear weapon in 1945. Subsequent nuclear weapon tests during 1950's (started in 1952) and early 1960's (implementation of Nuclear Test Ban Treaty in 1963) released a large amount of radioactive isotopes, mainly ^{137}Cs , ^{90}Sr , Pu and ^{14}C to the environment. These isotopes have been extensively utilized to investigate environmental processes that have occurred since the 1950's, a period of time that witnessed considerable environmental changes due to anthropogenic activities. Although over 70% of the fission products ^{137}Cs and ^{90}Sr derived from global nuclear weapons tests have already decayed away, several of the long-lived isotopes (^{14}C and transuranics) continue to serve as effective tracers and chronometers in environmental studies.

In this present Anthropocene Era, elements of economic value are mobilized from their respective sources into various Earth's subsystems of the lithosphere, hydrosphere, atmosphere and biosphere. With the increases in population and the spectacular sustained growth of emerging economies over the past 2–3 decades, the demand for Earth's resources have increased exponentially. While several hundreds of millions of people are taken out of poverty as a result of global economic growth, rapid industrialization has resulted in sustained environmental degradation in many developed and emerging economies. For example, in Detroit, Michigan, USA, the average Pb concentration in soil is more than an order of magnitude higher than the average upper crustal value. The Environmental Protection Agency in the USA and many regulatory agencies in the United States and elsewhere have listed the following ten elements as priority pollutants: Cd, Cr, Cu, Pb, Hg, Ni, Se, Ag, Tl and Zn. Except for Pb, high precision measurements of the isotopes of these elements given above for environmental studies are relatively new (<15 years old), and thus, the isotopic ratios of these pollutant elements offer exciting opportunities for future research.

The twentieth century witnessed an explosion of the applications of radioactive and stable isotopes

in studies of earth system science. Many of these studies, particularly those made prior to 1980 were discussed in some detail in the first two published volumes entitled *Environmental Isotope Geochemistry* edited by P. Fritz and J.Ch. Fontes (Volume-I, 1980 and Volume-II, 1986). These volumes focused primarily on stable isotopes of light elements (H,C,O,N, and S), Pb, Sr, Cl, U-series, and a suite of noble gases and provided state-of-the-art reviews of their applications in selected areas of earth sciences. In the last 25 years since the second volume was published, there have been major advances in instrumentation for high precision isotope measurements of several elements that include U-Th-series radionuclides (^{238}U , ^{234}U , ^{232}Th , ^{230}Th , ^{231}Pa , ^{226}Ra) using thermal ionization mass spectrometer (TIMS), platinum group elements using negative thermal ionization mass spectrometer (NTIMS) and multiple-collector inductively-coupled plasma mass spectrometer (MC-ICPMS). These developments have opened new areas of research in different areas of earth and environmental science.

The purpose of this volume is to bring together recent applications of a much larger number of radioactive and stable isotopes in earth and environmental sciences. There are a few earlier published volumes wherein selected aspects of these applications pertaining to particular processes or environment were discussed. The earlier edited volumes include: *Reviews in Mineralogy and Geochemistry* Volumes 16, 33, 38, 43, 50, and 52 (16: *Stable Isotopes in High Temperature Geological Processes*; 33: *Boron: Mineralogy Petrology and Geochemistry*; 38: *Uranium: Mineralogy, Geochemistry and the Environment*; 43: *Stable Isotope Geochemistry*; 50: *Beryllium: Mineralogy, Petrology, and Geochemistry*; and 52: *Uranium Series Geochemistry*); similarly, there are volumes on application of U-Th series and fallout isotopes in aqueous systems (e.g., Ivanovich and Harmon 1992; Livingston 2004; Krishnaswami and Cochran 2008). The scope of the present volume is much wider. New applications have become possible because of new understandings of isotope fractionation processes, improvements in chemical separation and purification techniques (in particular developments of actinide-specific resins) and development of high sensitivity instruments for measurements of isotopic ratios. Some of these are briefly discussed below.

1.2 Mass Independent Fractionation

The discovery of chemically-produced mass-independent isotope fractionation opened a new variety of applications, including investigations in paleoclimatology, biologic primary productivity, origin and evolution of life in Earth's earliest environment, and atmospheric chemistry (Young et al. 2002; Thiemens 2006). On the surface of Earth, the kinetic and equilibrium fractionations as well as isotopic exchange reactions result in fractionations that are mass-dependent. For example, when CaCO_3 precipitates from a solution, $^{18}\text{O}/^{16}\text{O}$ fractionation is twice as that of $^{17}\text{O}/^{16}\text{O}$ fractionation. However, in meteorites, mass-independent isotopic fractionation was observed and was attributed to nucleosynthetic processes (Clayton et al. 1973). Subsequently, it was shown that a chemically produced, mass-independent fractionation of oxygen is possible (Thiemens and Heidenreich 1983). Mass-independent fractionation appears to be caused by a molecular symmetry effect and the asymmetric molecule (e.g., O_3 in the form of $^{16}\text{O}^{17}\text{O}^{18}\text{O}$) undergoes mass-independent fractionation and is enriched in heavy isotopes while O_3 in the form of $^{18}\text{O}^{18}\text{O}^{18}\text{O}$ or $^{16}\text{O}^{16}\text{O}^{16}\text{O}$ is not (Heidenreich and Thiemens 1986). Recent results on Hg indicate that Hg displays mass-independent isotope fractionation during photochemical radical pair reactions, wherein the reactivity of odd and even mass number isotopes differs (summarized in Blum 2011).

1.3 Developments in Instrumentation

It took 30 years since the first publication of ^{14}C dating with beta counting method (Anderson et al. 1947) to achieve the first break-through in instrumentation with the use of cyclotron and tandem accelerators as a high-energy mass spectrometer (commonly denoted as accelerated mass spectrometers, AMS), for the measurement of ^{14}C (cyclotron, Muller 1977; tandem accelerators, Bennett et al. 1977; Nelson et al. 1977), resulting in an order of magnitude higher precision than the beta counting method which in turn resulted in three to four orders of magnitude reduction in the sample size (e.g., Trumbore 2002). Subsequently, AMS has been extensively used for high precision

measurements of other cosmogenic radionuclides including ^{10}Be , ^{26}Al , ^{36}Cl and ^{129}I . The second major break-through came in the measurements of U-Th series radionuclides (^{238}U , ^{235}U , ^{234}U , ^{232}Th , ^{230}Th , ^{231}Pa , ^{226}Ra), using thermal ionization mass spectrometer (TIMS) starting from mid 1980's, and was mainly due to high ionization efficiency achieved on U,Th,Pa, Ra and other elements when the samples were prepared by the graphite-sandwich technique on a single Re filament and the ionization efficiency improved from 10^{-4} to few percent (U and Th isotopes: Chen et al. 1986; Edwards et al. 1987; ^{231}Pa : Pickett et al. 1994; ^{226}Ra : Volpe et al. 1991; Cohen and O'Nions 1991). Concentrations as low as 0.1 μg of ^{238}U and ^{232}Th can now be measured with better than 1–3‰ precision (summarized in Goldstein and Stirling 2003). Such high precision and sensitivity resulted in the possibility of dating very young corals (< 500 years) with $^{230}\text{Th}/^{234}\text{U}$ dating method, as well as extending the dating limit of $^{230}\text{Th}/^{234}\text{U}$ method to ~500 kyr (Edwards et al. 1987, 1988). The third major break-through came in the measurement of some of the platinum group elements (PGE, specifically Os, Re, and Ir), using the negatively charged oxides of these elements. Conventional TIMS had a low precision for PGE due to poor ionization efficiency, as these elements have high ionization potential (Os: 8.7 eV, Re: 7.9 eV and Ir: 9.1 eV). The principal ion species of Os, Re, and Ir are negative oxides and negative thermal ionization mass-spectrometry resulted in high ionization efficiencies (2–6% for Os, >20% for Re; Creaser et al. 1991). A higher precision of $\pm 2\%$ (2σ) on the isotopic composition of Os with 4 ng Os have been reported. The fourth major break-through in the mass spectrometry, Inductively Coupled Plasma Mass Spectrometer (ICPMS) came in 1980's, most of them in the initial generation were conventional ICPMS, comprised of quadrupole ICPMS, high-resolution sector field ICPMS (HR-ICPMS), and time of flight ICPMS (TOF-ICPMS). Very high ionization (>90%) is obtained with ICPMS for all elements at high temperature (~6,000°K), including those that have high first ionization potentials (such as the PGE elements listed above). The sample throughput is faster and sample preparation time is significantly less in ICPMS compared to TIMS. It was not until the use of multiple-collector ICPMS (MC-ICPMS) in mid 1990s that combined sector-field ICPMS with a multiple collector detector system, major strides have been made in

obtaining high precision measurements of U-Th series radionuclides as well as other transitional and post-transitional elements. This technique emerged as an alternative or in some cases superior to TIMS method (a comparison of the sample size, precision, and sensitivity of TIMS, SIMS and ICPMS (multiple-collector, laser ablation and laser ablation-multiple collector) are given in Goldstein and Stirling (2003)). Although the first U measurements with ICPMS was made nearly 20 years ago (Walder and Freedman 1992; Taylor et al. 1995), only recently high precision measurements have been achieved. High precision measurements of Cu and Zn isotopes were made for the first time in late 1990s using ICPMS equipped with multiple collectors and magnetic sector, although earlier attempt to measure differences in Zn isotopes in environmental samples were not successful due to lack of sensitivity and precision (Rosman 1972; Maréchal et al. 1999). High-precision Tl isotopic measurement was made in 1999 for the first time with MC- ICPMS, with a precision of 0.1–0.2‰ (Rehkämper and Halliday 1999), although earlier attempts with TIMS resulted in relatively large errors (>2‰). It has been assumed all along that the $^{238}\text{U}/^{235}\text{U}$ atomic ratio to be constant, 137.88, except for uranium in the Oklo natural nuclear fission reactor discovered in 1972 in Gabon, Africa. Measurements of unprecedented high precision were made recently of $^{238}\text{U}/^{235}\text{U}$ ratios on up to 40 ppm (0.040‰) precision in seawater and other aqueous systems (Stirling et al. 2007). With the advent of MC-ICPMS and improvements in the preparation of gases for introduction into gas-source mass spectrometers, the precision for a large number of isotopes is getting better than 0.050‰.

In radioactive counting, some of the short-lived radionuclides can be measured at very low levels. With a delayed-coincidence counting system, ~3,000 atoms of ^{224}Ra corresponding to 1.1×10^{-18} g of ^{224}Ra (half-life = 3.66 days) or 5.0×10^{-21} mole of ^{224}Ra , can be measured with a precision of ~10% (1σ) (Moore 2008). This technique can be employed to measure some other short-lived radionuclides such as ^{223}Ra (half-life = 11.435 days) and ^{228}Th (half-life = 1.913 year). The precision and sensitivity for some of the short-lived U-Th series (^{210}Po , ^{234}Th , ^{228}Th and ^{227}Th) with radioactive counting methods (in particular with alpha and beta counting instruments) are excellent (Baskaran 2011; Baskaran et al. 2009) and most likely counting instruments will be the method of choice in the foreseeable future.

1.4 Future Forecast for 25 Years from Now

We have come a long way over the past ~100 years in improving the precision of isotopic analyses. In the first stable isotope paper (Murphy and Urey 1932), the relative abundances of the nitrogen and oxygen isotopes on natural samples had a precision of about 10% and now we are at the threshold of reaching a precision of ~10 ppm (10,000 times better precision). Technological advances will continue to drive the new and innovative application of the tracer techniques. For example, 1% uncertainties in ^{14}C measurements in the late 1970's with AMS was considered to be major advance (compared to the beta counting), but over the last 10 years, 3‰ has been the state-of-the-art. Attempts have been made to achieve a precision below 2‰, while reaching 1‰ still remains a challenge (Synal and Wacker 2010). This is probably applicable to other key cosmogenic radionuclides including ^{10}Be , ^{26}Al , ^{36}Cl , and ^{129}I . The conventional paradigm that no significant mass-dependent isotopic fractionations is expected in alkali and alkaline earth elements that commonly bond ionically or elements that are heavy where the mass difference between the heavier and lighter isotope is small is undergoing a major shift. Now the accepted view is that chemical, physical and biological processes that take place at normal environmental conditions result in measurable variations in the isotopic ratios of heavy elements. It behooves us to ask the question: Will the instrumental developments be in the *driver-seat* for the scientific breakthroughs in the applications of isotopes (both radioactive and stable) for earth and environmental studies?

Although the foundations for mass-dependent isotope fractionation resulting from kinetic and equilibrium processes were established in 1940's, the refinements in those theoretical foundations over the past 6 decades are minor. It is likely that when the precision improves by a factor of 5–10 (to 10 ppm level), better understanding of the fractionation mechanisms could result in multiple fractionation laws and could result in the reevaluation of the reference mass fractionation line for lighter stable isotope ratios (e.g., C, O, N). In the case of environmental forensics for organic pollutants, the future research in the source identification and fate and

transport of pesticides, herbicides and other POPs, VOCs, and other organic pollutants appears to depend on the analysis of molecular compounds at a higher precision. Compound-specific stable carbon isotope measurements of dissolved chlorinated ethane (PCE and TCE) in groundwater provide evidence for reductive dechlorination of chlorinated hydrocarbons. For example, the $\delta^{13}\text{C}$ values were found to be more positive (-18.0‰) in down-gradient wells compared to those in the source region (-25.0 to -26.0‰), paving the way for the quantification of extent of biodegradation between the zones of the contaminant plume (Sherwood Lollar et al. 2001). Multiple compound-specific isotopic analyses ($\delta^{37}\text{Cl}$, $\delta^{81}\text{Br}$, $\delta^{13}\text{C}$, δD) on chlorinated compounds with gas chromatography interfaced to ICPMS with much improved precision and sensitivity could provide a powerful tool in source(s) identification, fate and transport of organic pollutants including emerging contaminants, in aqueous systems.

When the biological fractionation is well understood and the precision is significantly improved from the present limit, then, isotopes of Zn and Cd and certain redox-sensitive elements such as Cr, Cu, Fe, Se, Hg, Tl, and U could provide insight on the biogeochemical processes in marine and lacustrine environments. One of the major concerns in the surface waters is the ever-increasing temporal and spatial extent of harmful algal blooms (HAB). The isotopes of macro- and micro-nutrient elements [macro- (N and P) and micro-(Fe, Cr, Mn, Se, Zn, Mo, I); for P, oxygen isotope ratios in phosphate can be used] could serve as effective tracers to investigate the factors and processes that lead to the formation and sustenance of HAB. Fractionation of these transition and post-transition elements caused during smelting operation could result in isotopically light elements in the vapor phase and when the condensation of the vapor phase takes place in the environment, gradient in the isotopic ratios of elements from the source of release to farther distances is expected and the isotopic ratios could provide a tool for tracing industrial sources of these elements (Weiss et al. 2008).

In conclusion, if we were to plot the sheer number of publications or the total funding made available for conducting isotope-related research in earth and environmental science versus time since the 1930's, the slope would suggest that we have every reason to be optimistic. We eagerly await the ground-breaking

research that will be made in this field in the next 25 years!

Acknowledgments I thank S. Krishnaswami, Jim O'Neil and Peter Swarzenski for their in-depth reviews which resulted in considerable improvement of this chapter. Some of their suggestions on the past and present status of the work are also included in this revised version.

References

- Abelson PH (1988) Isotopes in earth science. *Science* 242:1357
- Anderson EC, Libby WF, Weinhouse S, Reid AF et al (1947) Radiocarbon from cosmic radiation. *Nature* 105:576–577
- Baskaran M (2011) Dating of biogenic and inorganic carbonates using ^{210}Pb - ^{226}Ra disequilibrium method – a review. In: *Handbook of environmental isotope geochemistry*. Springer, Berlin
- Baskaran M, Hong GH, Santschi PH (2009) Radionuclide analyses in seawater. In: Wurl O (ed) *Practical guidelines for the analysis of seawater*. CRC Press, Boca Raton, pp 259–304
- Becquerel AH (1896) On the rays emitted by phosphorescent bodies. *Comptes Rendus de Seances de l'Academie de Sciences* 122:501–503
- Bennett RP, Beukens RP, Clover HE, Gove RB et al (1977) Radiocarbon dating using electrostatic accelerators: negative ions provide the key. *Science* 198:508–510
- Bigeleisen J, Mayer M (1947) Calculation of equilibrium constant for isotope exchange reactions. *J Chem Phys* 15:261–167
- Blum JD (2011) Applications of stable mercury isotopes to biogeochemistry. In: *Advances in isotope geochemistry*. Springer, Heidelberg
- Bollhofer A, Rosman K (2001) Isotopic source signatures for atmospheric lead; the Northern hemisphere. *Geochim Cosmochim Acta* 65:1727–1740
- Boltwood BB (1907) Note on a new radioactive element. *Am J Sci* 24:370–372
- Bourdon B, Henderson GM, Lundstrom CC, Turner SP (2003) Uranium-series geochemistry (eds) vol 52. *Geochemical Society – Mineralogical Society of America*, Washington, DC, pp. 656
- Chen JH, Edwards RL, Wasserburg GJ (1986) ^{238}U , ^{234}U , and ^{232}Th in seawater. *Earth Planet Sci Lett* 80:241–251
- Cherdyntsev VV (1955) On isotopic composition of radioelements in natural objects, and problems of geochronology. *Izv Akad Nauk SSR* 175
- Clayton RN, Grossman L, Mayeda TK (1973) A component of primitive nuclear composition in carbonaceous meteorites. *Science* 182:485–488
- Cohen AS, O'Nions RK (1991) Precise determination of femto-gram quantities of radium by thermal ionization mass spectrometry. *Anal Chem* 63:2705–2708
- Creaser RA, Papanastassiou DA, Wasserburg GJ (1991) Negative thermal ion mass-spectrometry of osmium, rhenium and iridium. *Geochim Cosmochim Acta* 55:397–401

- Curie M (1898) Rays emitted by compounds of uranium and thorium. *Comptes Rendus de Seances de l'Academie de Sciences* 126:1101–1103
- Dole M, Slobod RL (1940) Isotopic composition of oxygen in carbonate rocks and iron oxide ores. *J Am Chem Soc* 62:471–479
- Edwards RL, Chen JH, Wasserburg GJ (1987) ^{238}U – ^{234}U – ^{230}Th – ^{232}Th systematic and the precise measurement of time over the past 500,000 years. *Earth Planet Sci Lett* 81:175–192
- Edwards RL, Chen JH, Wasserburg GJ (1988) Dating earthquakes with high-precision thorium-230 ages of very young corals. *Earth Planet Sci Lett* 90:371–381
- Fajans K (1913) Radioactive transformations and the periodic system of the elements. *Berichte der Deutschen Chemischen Gesellschaft* 46:422–439
- Goldstein SJ, Stirling CH (2003) Techniques for measuring uranium-series nuclides: 1992–2002. *Rev Mineral Geochem* 52:23–57
- Gulson B (2011) Sources of lead and its mobility in the human body Inferred from Lead Isotopes. In: *Advances in isotope geochemistry* Springer, Heidelberg
- Heidenreich BC III, Thiemens MH (1986) A non-mass-dependent oxygen isotope effect in the production of ozone from molecular oxygen: the role of symmetry in isotope chemistry. *J Chem Phys* 84:2129–2136
- Henderson GM (2003) One hundred years ago: the birth of uranium-series science. *Rev Mineral Geochem* 52:v–x
- Ivanovich M, Harmon RS (eds) (1992) Uranium-series disequilibrium. Applications to earth, marine, and environmental sciences, 2nd edn. Clarendon Press, Oxford, p 909
- Komárek M, Ettler V, Chrástný V, Mihaljevič M (2008) Lead isotopes in environmental sciences: a review. *Environ Int* 34:562–577
- Krishnaswami S, Cochran JK (2008) U-Th series nuclides in aquatic systems, Vol 13 (Radioactivity in the Environment). Elsevier, Amsterdam, pp. 458
- Krishnaswami S, Lal D (2008) Cosmogenic nuclides in the environment: a brief review of their applications. In: Gupta H, Fareeduddin (eds) *Recent Advances in Earth System Sciences*. Geol Soc India Golden Jubilee Volume pp 559–600
- Lal D, Baskaran M (2011) Applications of cosmogenic-isotopes as atmospheric tracers. In: *Advances in isotope geochemistry*. Springer, Heidelberg
- Lal D, Peters B (1967) Cosmic-ray produced radioactivities on the earth. *Handbuch Phys.* 46. Springer, Berlin, p 551
- Livingston HD (2004) Marine Radioactivity (In: *Radioactivity in the Environment Series*), 6. Elsevier, Amsterdam, pp. 310.
- Maréchal C, Télouk P, Albarède F (1999) Precise analysis of copper and zinc isotope compositions by plasma-source mass spectrometry. *Chem Geol* 156:251–273
- Moore WS (2008) Fifteen years experience in measuring ^{224}Ra and ^{223}Ra by delayed-coincidence counting. *Mar Chem* 109:188–197
- Muller RA (1977) Radioisotope dating with a Cyclotron. *Science* 196:489–494
- Murphy GM, Urey HC (1932) On the relative abundances of the nitrogen and oxygen isotopes. *Phys Rev* 41:921–924
- Nelson DE, Koertling RG, Stott WR (1977) Carbon-14: direct detection at natural concentrations. *Science* 198:507–508
- Nier AO, Gulbransen EA (1939) Variations in the relative abundance of the carbon isotopes. *J Am Chem Soc* 61:697–698
- O'Neil JR (1986) Theoretical and experimental aspects of isotopic fractionation. *Rev Mineral* 16:1–40
- Pickett DA, Murrell MT, Williams RW (1994) Determination of femtogram quantities of protactinium in geologic samples by thermal ionization mass spectrometry. *Anal Chem* 66:1044–1049
- Rehkämper M, Halliday AN (1999) The precise measurement of Ti isotopic compositions by MC-ICPMS: application to the analysis of geological materials and meteorites. *Geochim Cosmochim Acta* 63:935–944
- Rosman KJR (1972) A survey of the isotopic and elemental abundances of zinc. *Geochim Cosmochim Acta* 36:801–819
- Rutherford E (1900) A radioactive substance emitted from thorium compounds. *Philos Mag* 49:1–14
- Rutherford E, Soddy F (1902) The cause and nature of radioactivity Part 1. *Philos Trans R Soc* 4:370–396
- Schwarz HP, Schoeninger MJ (2011) Stable isotopes of carbon and nitrogen as tracers for paleo-diet reconstruction. In: *Advances in isotope geochemistry*. Springer, Heidelberg
- Sherwood Lollar B, Slater GF, Sleep B, Witt M et al (2001) Stable carbon isotope evidence for intrinsic bioremediation of tetrachloroethene and trichloroethene at Area 6, Dover Air Force Base. *Environ Sci Technol* 35:261–269
- Soddy F (1913) Radioactivity. In: *Annual Reports on the Progress of Chemistry*. The Chemical Society, London, pp 262–288
- Stirling CH, Andersen MB, Potter E-K, Halliday AN (2007) Low-temperature isotopic fractionation of uranium. *Earth Planet Sci Lett* 264:208–225
- Strutt RJ (1905) On the radio-active minerals. *Proc R Soc London* 76:88–101
- Synal H-A, Wacker L (2010) AMS Measurement technique after 30 years: possibilities and limitations of low energy systems. *Nucl Inst Meth Phys Res B* 268:701–707
- Taylor PDP, De Bievre P, Walder AJ, Entwistle A (1995) Validation of the analytical linearity and mass discrimination correction model exhibited by a Multiple Collector Inductively Coupled Plasma Mass Spectrometer by means of a set of synthetic uranium isotope mixtures. *J Anal At Spectrom* 10:395–398
- Thiemens MH (2006) History and applications of mass-independent isotope effects. *Annu Rev Earth Planet Sci* 34:217–262
- Thiemens MH, Heidenreich JE (1983) The mass-independent fractionation of oxygen: a novel isotope effect and its possible cosmochemical implications. *Science* 219:1073–1075
- Thurber DL (1962) Anomalous $^{234}\text{U}/^{238}\text{U}$ in nature. *J Geophys Res* 67:4518–1523
- Trumbore SE (2002) Radiocarbon chronology. In: Noller JS, Sowers JM, Lettis WR (eds) *Quaternary geochronology: methods and applications*, AGU Reference Shelf 4, pp 41–60
- Urey HC (1947) The thermodynamic properties of isotopic substances. *J Chem Soc Lond* 562–581
- Urey HC (1948) Oxygen isotopes in nature and in the laboratory. *Science* 108:489–496
- Volpe AM, Olivares JA, Murrell MT (1991) Determination of radium isotope ratios and abundances in geologic samples by thermal ionization mass spectrometry. *Anal Chem* 63:913–916

- Walder AJ, Freedman PA (1992) Isotopic ratio measurement using a double focusing magnetic-sector mass analyzer with an inductively coupled plasma as an ion-source. *J Anal Atom Spec* 7:571–575
- Weiss DJ, Rehkämper M, Schoenberg R, McLaughlin M et al (2008) Application of nontraditional stable-isotope systems to the study of sources and fate of metals in the environment. *Environ Sci Technol* 42:655–664
- Young ED, Gay A, Nagahara H (2002) Kinetic and equilibrium mass-dependent isotope fractionation laws in nature and their geochemical and cosmochemical significance. *Geochim Cosmochim Acta* 66:1095–1104

Chapter 2

An Overview of Isotope Geochemistry in Environmental Studies

D. Porcelli and M. Baskaran

Abstract Isotopes of many elements have been used in terrestrial, atmospheric, and aqueous environmental studies, providing powerful tracers and rate monitors. Short-lived nuclides that can be used to measure time are continuously produced from nuclear reactions involving cosmic rays, both within the atmosphere and exposed surfaces, and from decay of long-lived isotopes. Nuclear activities have produced various isotopes that can be used as atmospheric and ocean circulation tracers. Production of radiogenic nuclides from decay of long-lived nuclides generates widespread distinctive isotopic compositions in rocks and soils that can be used to identify the sources of ores and trace water circulation patterns. Variations in isotope ratios are also generated as isotopes are fractionated between chemical species, and the extent of fractionation can be used to identify the specific chemical processes involved. A number of different techniques are used to separate and measure isotopes of interest depending upon the half-life of the isotopes, the ratios of the stable isotopes of the element, and the overall abundance of the isotopes available for analysis. Future progress in the field will follow developments in analytical instrumentation and in the creative exploitation of isotopic tools to new applications.

2.1 Introduction

Isotope geochemistry is a discipline central to environmental studies, providing dating methods, tracers, rate information, and fingerprints for chemical processes in almost every setting. There are 75 elements that have useful isotopes in this respect, and so there is a large array of isotopic methods potentially available. The field has grown dramatically as the technological means have been developed for measuring small variations in the abundance of specific isotopes, and the ratios of isotopes with increasing precision.

Most elements have several naturally occurring isotopes, as the number of neutrons that can form a stable or long-lived nucleus can vary, and the relative abundances of these isotopes can be very different. Every element also has isotopes that contain neutrons in a quantity that render them unstable. While most have exceedingly short half-lives and are only seen under artificial conditions (>80% of the 2,500 nuclides), there are many that are produced by naturally-occurring processes and have sufficiently long half-lives to be present in the environment in measurable quantities. Such production involves nuclear reactions, either the decay of parent isotopes, the interactions of stable nuclides with natural fluxes of subatomic particles in the environment, or the reactions occurring in nuclear reactors or nuclear detonations. The isotopes thus produced provide the basis for most methods for obtaining absolute ages and information on the rates of environmental processes. Their decay follows the well-known radioactive decay law (first-order kinetics), where the fraction of atoms, λ (the decay constant), that decay over a period of time is fixed and an intrinsic characteristic of the isotope:

D. Porcelli (✉)
Department of Earth Sciences, Oxford University, South Parks Road, Oxford OX1 3AN, UK
e-mail: Don.Porcelli@earth.ox.ac.uk
M. Baskaran
Department of Geology, Wayne State University, Detroit, MI 48202, USA
e-mail: Baskaran@wayne.edu

$$\frac{dN}{dt} = -\lambda N. \quad (2.1)$$

When an isotope is incorporated and subsequently isolated in an environmental material with no exchange with surroundings and no additional production, the abundance changes only due to radioactive decay, and (2.1) can be integrated to describe the resulting isotope abundance with time;

$$N = N_0 e^{-\lambda t}. \quad (2.2)$$

The decay constant is related to the well-known half-life ($t_{1/2}$) by the relationship:

$$\lambda = \frac{\ln 2}{t_{1/2}} = \frac{0.693}{t_{1/2}}. \quad (2.3)$$

This equation provides the basis for all absolute dating methodologies. However, individual methods may involve considering further factors, such as continuing production within the material, open system behaviour, or the accumulation of daughter isotopes. The radionuclides undergo radioactive decay by alpha, beta (negatron and positron) or electron capture. The elements that have radioactive isotopes, or isotopic variations due to radioactive decay, are shown in Fig. 2.1.

Variations in stable isotopes also occur, as the slight differences in mass between the different isotopes lead to slightly different bond strengths that

affect the partitioning between different chemical species and the adsorption of ions. Isotope variations therefore provide a fingerprint of the processes that have affected an element. While the isotope variations of H, O, and C have been widely used to understand the cycles of water and carbon, relatively recent advances in instrumentation has made it possible to precisely measure the variations in other elements, and the potential information that can be obtained has yet to be fully exploited. The full range of elements with multiple isotopes is shown in Fig. 2.2.

One consideration for assessing the feasibility of obtaining isotopic measurements is the amount of an element available. Note that it is not necessarily the concentrations that are a limitation, but the absolute amount, since elements can be concentrated from whatever mass is necessary- although of course there are considerations of difficulty of separation, sample availability and blanks. For example, it is not difficult to filter very large volumes of air, or to concentrate constituents from relatively large amounts of water, but the dissolution of large silicate rock samples is more involved. In response to difficulties in present methods or the challenges of new applications, new methods for the separation of the elements of interest from different materials are being constantly developed. Overall, analyses can be performed not only on major elements, but even elements that are trace constituents; e.g. very pure materials (99.999% pure) still contain constituents in concentrations of micrograms

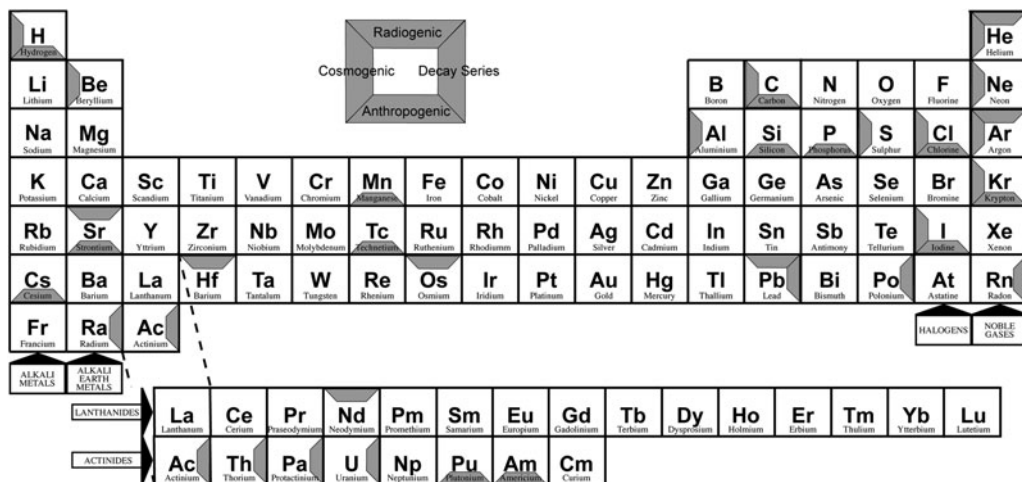


Fig. 2.1 Elements with isotopes that can be used in environmental studies and are anthropogenic, cosmogenic (produced either in the atmosphere or within exposed materials), radiogenic

(from production of long-lived isotopes), or that are part of the U- or Th-decay series

The figure shows a periodic table with the following annotations:

- Circled elements:** H, Li, Be, B, C, N, O, F, Ne, Na, Mg, Al, Si, P, S, Cl, Ar, K, Ca, Sc, Ti, V, Cr, Mn, Fe, Co, Ni, Cu, Zn, Ga, Ge, As, Se, Br, Kr, Rb, Sr, Y, Zr, Nb, Mo, Tc, Ru, Rh, Pd, Ag, Cd, In, Sn, Sb, Te, I, Xe, Cs, Ba, La, Hf, Ta, W, Re, Os, Ir, Pt, Au, Hg, Tl, Pb, Bi, Po, At, Rn, Fr, Ra, Ac.
- Shaded elements:** K, Ca, Sc, Ti, V, Cr, Mn, Fe, Co, Ni, Cu, Zn, Ga, Ge, As, Se, Br, Kr, Rb, Sr, Y, Zr, Nb, Mo, Tc, Ru, Rh, Pd, Ag, Cd, In, Sn, Sb, Te, I, Xe, Cs, Ba, La, Hf, Ta, W, Re, Os, Ir, Pt, Au, Hg, Tl, Pb, Bi, Po, At, Rn, Fr, Ra, Ac.
- Other elements:** H, He, Li, Be, B, C, N, O, F, Ne, Na, Mg, Al, Si, P, S, Cl, Ar, K, Ca, Sc, Ti, V, Cr, Mn, Fe, Co, Ni, Cu, Zn, Ga, Ge, As, Se, Br, Kr, Rb, Sr, Y, Zr, Nb, Mo, Tc, Ru, Rh, Pd, Ag, Cd, In, Sn, Sb, Te, I, Xe, Cs, Ba, La, Hf, Ta, W, Re, Os, Ir, Pt, Au, Hg, Tl, Pb, Bi, Po, At, Rn, Fr, Ra, Ac.

Fig. 2.2 The elements that have stable isotope variations useful for environmental studies. The shaded elements do not have more than one isotope that is stable and not radiogenic. While

all others potentially can display stable isotope variations, significant isotopic variations in the environment have been documented for the circled elements

per gram (ppm) and so are amenable to analysis. Further considerations of the abundances that can be measured are discussed below.

The following sections provide a general guide to the range of isotopes available, and the most widespread uses in the terrestrial environment. It is not meant to be exhaustive, as there are many innovative uses of isotopes, but rather indicative of the sorts of problems that can be approached, and what isotopic tools are available for particular questions. More details about the most commonly used methods, as well as the most innovative new applications, are reported elsewhere in this volume. Section 2.3 provides a brief survey of the analytical methods available.

2.2 Applications of Isotopes in the Environment

In the following sections, applications of isotopes to environmental problems are presented according to the different sources of radioactive isotopes and causes of variations in stable isotopes.

2.2.1 Atmospheric Short-Lived Nuclides

A range of isotopes is produced from reactions involving cosmic rays, largely neutrons, which bombard the

Earth from space. The interactions between these cosmic rays and atmospheric gases produce a suite of radionuclides with half-lives ranging from less than a second to more than a million years (see list in Lal and Baskaran 2011). There are a number of nuclides that have sufficiently long half-lives to then enter into environmental cycles in various ways (see Table 2.1). The best-known nuclide is ^{14}C , which forms CO_2 after its production and then is incorporated into organic matter or dissolves into the oceans. With a half-life of 5730a, it can be used to date material that incorporates this $^{14}\text{CO}_2$, from plant material, calcium carbonate (including corals), to circulating ocean waters. Information can also be obtained regarding rates of exchange between reservoirs with different $^{14}\text{C}/^{12}\text{C}$ ratios, and biogeochemical cycling of C and associated elements. Other nuclides are removed from the atmosphere by scavenging onto aerosols and removed by precipitation, and can provide information on the rates of atmospheric removal. By entering into surface waters and sediments, these nuclides also serve as environmental tracers. For example, there are two isotopes produced of the particle-reactive element Be, ^7Be ($t_{1/2} = 53.3$ days) and ^{10}Be (1.4Ma). The distribution of $^7\text{Be}/^{10}\text{Be}$ ratios, combined with data on the spatial variations in the flux of Be isotopes to the Earth's surface, can be used to quantify processes such as stratospheric-tropospheric exchange of air masses, atmospheric circulation, and the removal rate

Table 2.1 Atmospheric radionuclides

Isotope	Half-life	Common applications
³ H	12.32a	Dating of groundwater, mixing of water masses, diffusion rates
⁷ Be	53.3 day	Atmospheric scavenging, atmospheric circulation, vertical mixing of water, soil erosion studies
¹⁰ Be	1.4 × 10 ⁶ a	Dating of sediments, growth rates of Mn nodules, soil erosion study, stratosphere-troposphere exchange, residence time of aerosols
¹⁴ C	5730a	Atmospheric circulation, dating of sediments, tracing of C cycling in reservoirs, dating groundwater
³² Si	140a	Atmospheric circulation, Si cycling in the ocean
³² P	25.3 day	Atmospheric circulation, tracing oceanic
³³ P	14.3 day	P pool
³⁵ S	87 day	Cycling of S in the atmosphere
³⁹ Ar	268a	Atmospheric circulation and air-sea exchange
⁸¹ Kr	2.3 × 10 ⁵ a	Dating of groundwater
¹²⁹ I	1.6 × 10 ⁷ a	Dating of groundwater
²¹⁰ Pb	22.3a	Dating, deposition velocity of aerosols, sources of air masses, soil erosion, sediment focusing

Selected isotopes generated within the atmosphere that have been used for environmental studies, along with some common applications. All isotopes are produced by nuclear reactions in the atmosphere induced by cosmic radiation, with the exception of ²¹⁰Pb, which is produced by decay of ²²²Rn released from the surface

of aerosols (see Lal and Baskaran 2011). The record of Be in ice cores and sediments on the continents can be used to determine past Be fluxes as well as to quantify sources of sediments, rates of sediment accumulation and mixing (see Du et al. 2011; Kaste and Baskaran 2011). Other isotopes, with different half-lives or different scavenging characteristics, provide complementary constraints on atmospheric and sedimentary processes (Table 2.1).

A number of isotopes are produced in the atmosphere from the decay of ²²²Rn, which is produced within rocks and soils from decay of ²²⁶Ra, and then released into the atmosphere. The daughter products of ²²²Rn (mainly ²¹⁰Pb (22.3a) and ²¹⁰Po (138 days)) that are produced in the atmosphere have been used as tracers to identify the sources of aerosols and their residence times in the atmosphere (Kim et al. 2011; Baskaran 2011). Furthermore, ²¹⁰Pb adheres to particles that are delivered to the Earth's surface at a relatively constant rate and are deposited in sediments,

and its subsequent decay provides a widely used method for determining the age of sediments and so the rates of sedimentation.

A number of isotopes are incorporated into the hydrologic cycle and so provide means for dating groundwaters. This includes the noble gases ³⁹Ar ($t_{1/2} = 268a$), ⁸¹Kr (230ka) and ³H (Kulongoski and Hilton 2011) which dissolve into waters and then provide ideal tracers that do not interact with aquifer rocks and so travel conservatively with groundwater, but are present in such low concentrations that their measurement has proven to be difficult. The isotope ¹²⁹I (16Ma) readily dissolves and also behaves conservatively: with such a long half-life, however, it is only useful for very old groundwater systems. The readily analyzed ¹⁴C also has been used for dating groundwater, but the ¹⁴C/¹²C ratio changes not only because of decay of ¹⁴C, but also through a number of other processes such as interaction with C-bearing minerals such as calcium carbonate; therefore, more detailed modelling is required to obtain a reliable age.

General reviews on the use of isotopes produced in the atmosphere for determining soil erosion and sedimentation rates, and for providing constraints in hydrological studies, are provided by Lal (1991, 1999) and Phillips and Castro (2003).

2.2.2 Cosmogenic Nuclides in Solids

Cosmogenic nuclides are formed not just within the atmosphere, but also in solids at the Earth's surface, and so can be used to date materials based only upon exposure history, rather than reflecting the time of formation or of specific chemical interactions. The cosmic particles that have escaped interaction within the atmosphere penetrate into rocks for up to a few meters, and interact with a range of target elements to generate nuclear reactions through neutron capture, muon capture, and spallation (emission of various fragments). From the present concentration and the production rate, an age for the exposure of that surface to cosmic rays can be readily calculated (Lal 1991). A wide range of nuclides is produced, although only a few are produced in detectable amounts, are sufficiently long-lived, and are not naturally present in concentrations that overwhelm additions from cosmic ray interactions. An additional complexity in

obtaining ages from this method is that production rates must be well known, and considerable research has been devoted to their determination. These are dependent upon target characteristics, including the concentration of target isotopes, the depth of burial, and the angle of exposure, as well as factors affecting the intensity of the incident cosmic radiation, including altitude and geomagnetic latitude. Also, development

of these methods has been coupled to advances in analytical capabilities that have made it possible to measure the small number of atoms involved. It is the high resolution available from accelerator mass spectrometry (see Sect. 2.3.2) that has made it possible to do this in the presence of other isotopes of the same element that are present in quantities that are many orders of magnitude greater.

Table 2.2 Widely used cosmogenic nuclides in solids

Isotope	Primary targets	Half-life	Commonly dated materials
¹⁰ Be	O, Mg, Fe	1.4Ma	Quartz, olivine, magnetite
²⁶ Al	Si, Al, Fe	705ka	Quartz, olivine
³⁶ Cl	Ca, K, Cl	301ka	Quartz
³ He	O, Mg, Si, Ca, Fe, Al	Stable	Olivine, pyroxene
²¹ Ne	Mg, Na, Al, Fe, Si	Stable	Quartz, olivine, pyroxene

The most commonly used isotopes that are produced by interaction of cosmic rays the primary target elements listed

The most commonly used cosmogenic nuclides are listed in Table 2.2 (see also Fig. 2.3). These include several stable isotopes, ³He and ²¹Ne, which accumulate continuously within materials. In contrast, the radioactive isotopes ¹⁰Be, ¹⁴C, ²⁶Al, and ³⁶Cl will continue to increase until a steady state concentration is reached in which the constant production rate is matched by the decay rate (which is proportional to the concentration). While this state is approached asymptotically, in practice within ~5 half-lives concentration changes are no longer resolvable. At this

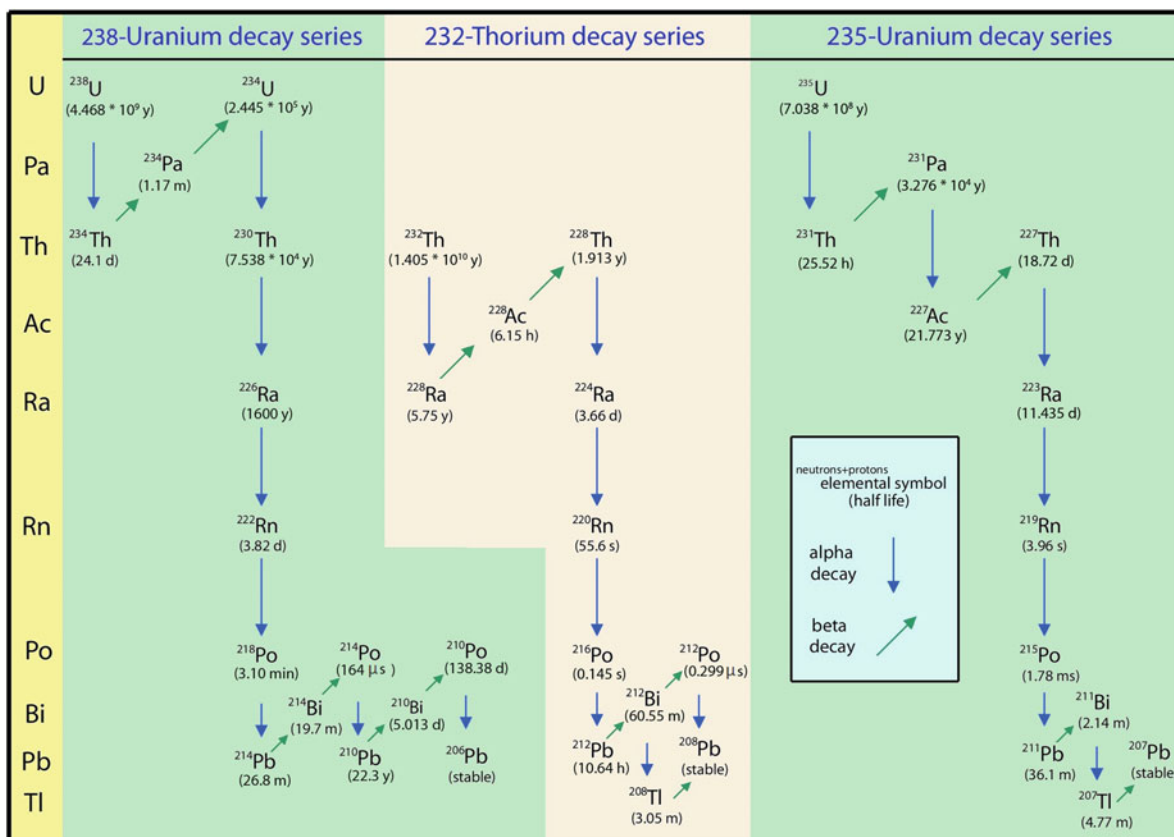


Fig. 2.3 The ²³⁸U, ²³⁵U, and ²³²Th decay series. The presence of the series of short-lived nuclides throughout the environment is due to their continuous production by long-lived parents

point, no further time information is gained; such samples can then be assigned only a minimum age.

There have been a considerable number of applications of these methods, which have proven invaluable to the understanding of recent surface events. There are a number of reviews available, including those by Niedermann (2002), which focuses on ^3He and ^{21}Ne , and Gosse and Phillips (2001). A full description of the methods and applications is given by Dunai (2010). Some of the obvious targets for obtaining simple exposure ages are lava flows, material exposed by landslides, and archaeological surfaces. Meteorite impacts have been dated by obtaining exposure ages of excavated material, and the timing of glacial retreats has been constrained by dating boulders in glacial moraines and glacial erratics. The ages of the oldest surfaces in dry environments where little erosion occurs have also been obtained. Movement on faults has been studied by measuring samples along fault scarps to obtain the rate at which the fault face was exposed.

Cosmogenic nuclides have also been used for understanding landscape evolution (see review by Cockburn and Summerfield 2004) and erosion rates (Lal 1991). In this case, the production rate with depth must be known and coupled with an erosion history, usually assumed to occur at a constant rate. The concentrations of samples at the surface (or any depth) are then the result of the production rate over the time that the sample has approached the surface due to erosion and was subjected to progressively increasing production. The calculations are somewhat involved, since production rates due to neutron capture, muon reactions, and spallation have different depth dependencies, and the use of several different cosmogenic nuclides can provide better constraints (Lal 2011). Overall, plausible rates have been obtained for erosion, which had hitherto been very difficult to constrain. The same principle has been applied to studies of regional rates of erosion by measuring ^{10}Be in surface material that has been gathered in rivers (Schaller et al. 2001), and this has provided key data for regional landscape evolution studies (Willenbring and von Blanckenburg 2010).

2.2.3 Decay Series Nuclides

The very long-lived nuclides ^{238}U , ^{235}U , and ^{232}Th decay to sequences of short-lived nuclides that

eventually lead to stable Pb isotopes (see Fig. 2.3 and Table 2.3). The decay of these parents thus supports a continuous definable supply of short-lived nuclides in the environment that can be exploited for environmental studies, especially for determining ages and rates over a range of timescales from days to hundreds of thousands of years. The abundance of each isotope is controlled by that of its parent, and since this dependence continues up the chain, the connections between the isotopes can lead to considerable complexity in calculating the evolution of some daughters. However, since the isotopes represent a wide range of elements with very different geochemical behaviours, such connections also present a wealth of opportunities for short-term geochronology and

Table 2.3 Decay series nuclides used in environmental studies

Isotope	Half-life	Common applications
^{238}U	$4.468 \times 10^9\text{a}$	Dating, tracing sources of U
^{234}U	$2.445 \times 10^4\text{a}$	Dating of carbonates, tracing sources of water
^{232}Th	$1.405 \times 10^{10}\text{a}$	Quantifying lithogenic component in aqueous system, atmosphere
^{230}Th	$7.538 \times 10^4\text{a}$	Dating, scavenging, ventilation of water mass
^{234}Th	24.1 day	Particle cycling, POC export, rates of sediment mixing
^{228}Th	1.913a	Particle scavenging and tracer for other particulate pollutants
^{227}Th	18.72 day	Particle tracer
^{231}Pa	$3.276 \times 10^4\text{a}$	Dating, sedimentation rates, scavenging
^{228}Ra	5.75a	Tracing water masses, vertical and horizontal mixing rates
^{226}Ra	1600a	Dating, water mass tracing, rates of mixing
^{224}Ra	3.66 day	Residence time of coastal waters, mixing of shallow waters
^{223}Ra	11.435 day	Residence time of coastal waters, mixing of shallow waters
^{227}Ac	21.773a	Dating, scavenging
^{222}Rn	3.82 day	Gas exchange, vertical and horizontal diffusion
^{210}Pb	22.3a	Dating (e.g. carbonates, sediments, ice cores, aerosols, artwork); sediment mixing, focusing and erosion; scavenging; resuspension
^{210}Po	138 day	Carbon export, remineralization, particle cycling in marine environment

Radioactive isotopes within the ^{238}U , ^{235}U , and ^{232}Th decay series that have been directly applied to environmental studies. The remaining isotopes within the decay series are generally too short-lived to provide useful environmental information and are simply present in activities equal to those of their parents

environmental rate studies (see several papers in Ivanovich and Harmon 1992; Baskaran 2011).

The abundance of a short-lived nuclide is conveniently reported as an activity ($= N\lambda$, i.e. the abundance times the decay constant), which is equal to the decay rate (dN/dt). In any sample that has been undisturbed for a long period ($> \sim 1.5$ Ma), the activities of all of the isotopes in each decay chain are equal to that of the long-lived parent element, in what is referred to as secular equilibrium. In this case, the ratios of the abundances of all the daughter isotopes are clearly defined, and the distribution of all the isotopes in a decay chain is controlled by the distribution of the long-lived parent. Unweathered bedrock provides an example where secular equilibrium could be expected to occur. However, the different isotopes can be separated by a number of processes. The different chemical properties of the elements can lead to different mobilities under different environmental conditions. Uranium is relatively soluble under oxidizing conditions, and so is readily transported in groundwaters and surface waters. Thorium, Pa and Pb are insoluble and highly reactive with surfaces of soil grains and aquifer rocks, and adsorb onto particles in the water column. Radium is also readily adsorbed in freshwaters, but not in highly saline waters where it is displaced by competing ions. Radon is a noble gas, and so is not surface-reactive and is the most mobile.

Isotopes in the decay series can also be separated from one another by the physical process of recoil. During alpha decay, a sufficient amount of energy is released to propel alpha particles a considerable distance, while the daughter isotope is recoiled in the opposite direction several hundred Angstroms (depending upon the decay energy and the matrix). When this recoil sends an atom across a material's surface, it leads to the release of the atom. This is the dominant process releasing short-lived nuclides into groundwater, as well as releasing Rn from source rocks. This mechanism therefore can separate short-lived daughter nuclides from the long-lived parent of the decay series. It can also separate the products of alpha decay from those of beta decay, which is not sufficiently energetic to result in substantial recoil. For example, waters typically have ($^{234}\text{U}/^{238}\text{U}$) activity ratios that are greater than the secular equilibrium ratio of that found in crustal rocks, due to the preferential release of ^{234}U by recoil.

A more detailed discussion of the equations describing the production and decay of the intermedi-

ate daughters of the decay series is included in Appendix 2. In general, where an intermediate isotope is isolated from its parent, it decays according to (2.2). Where the activity ratio of daughter to parent is shifted from the secular equilibrium value of 1, the ratio will evolve back to the same activity as its parent through either decay of the excess daughter, or grow-in of the daughter back to secular equilibrium (Baskaran 2011). These features form the basis for dating recently produced materials. In addition, U- and Th- series systematics can be used to understand dynamic processes, where the isotopes are continuously supplied and removed by physical or chemical processes as well as by decay (e.g. Vigier and Bourdon 2011).

The U-Th series radionuclides have a wide range of applications throughout the environmental sciences. Recent reviews cover those related to nuclides in the atmosphere (Church and Sarin 2008; Baskaran 2010; Hirose 2011), in weathering profiles and surface waters (Chabaux et al. 2003; Cochran and Masque 2003; Swarzenski et al. 2003), and in groundwater (Porcelli and Swarzenski 2003; Porcelli 2008). Recent materials that incorporate nuclides in ratios that do not reflect secular equilibrium (due either to discrimination during uptake or availability of the nuclides) can be dated, including biogenic and inorganic carbonates from marine and terrestrial environments that readily take up U and Ra but not Th or Pb, and sediments from marine and lacustrine systems that accumulate sinking sediments enriched in particle-reactive elements like Th and Pb (Baskaran 2011). The migration rates of U-Th-series radionuclides can be constrained where continuing fractionation between parent and daughter isotopes occurs. These rates can then be related to broader processes, such as physical and chemical erosion rates as well as water-rock interaction in groundwater systems, where soluble from insoluble nuclides are separated (Vigier and Bourdon 2011). Also, the effects of particles in the atmosphere and water column can be assessed from the removal rates of particle-reactive nuclides (Kim et al. 2011).

2.2.4 Anthropogenic Isotopes

Anthropogenic isotopes are generated through nuclear reactions created under the unusual circumstances of high energies and high atomic particle fluxes, either within nuclear reactors or during nuclear weapons

explosions. These are certainly of concern as contaminants in the environment, but also provide tools for environmental studies, often representing clear signals from defined sources. These include radionuclides not otherwise present in the environment that can therefore be clearly traced at low concentrations (e.g. ^{137}Cs , $^{239,240}\text{Pu}$; Hong et al. 2011; Ketterer et al. 2011), as well as distinct pulses of otherwise naturally-occurring species (e.g. ^{14}C). There is a very wide range of isotopes that have been produced by such sources, but many of these are too short-lived or do not provide a sufficiently large signal over natural background concentrations to be of widespread use in environmental studies. Those that have found broader application are listed in Table 2.4.

The release of radioactive nuclides into the environment from reactors, as well as from nuclear waste reprocessing and storage facilities, can occur in a number of ways. Discharges through airborne effluents can widely disperse the isotopes over a large area and enter soils and the hydrological cycle through fallout, as observed for the Chernobyl release in 1986. Discharges of water effluents, including cooling and process waters, can be followed from these point sources in circulating waters, such as from the Sellafield nuclear processing and power plant, which released radionuclides (e.g. ^{137}Cs , ^{134}Cs , ^{129}I) from the western coast of England into the Irish Sea and

which can be traced high into the Arctic Ocean (discussed in Hong et al. 2011). Leaks into the ground from storage and processing facilities can also release radionuclides that are transported in groundwater, at locations such as the Hanford nuclear production facility in Washington State. At the Nevada Test Site, Pu was found to have migrated >1 km, facilitated by transport on colloids. Releases by all of these mechanisms at lower levels have been documented around many reactor facilities. Even where levels are too low to pose a health concern, the isotopes can be readily measured and their sources identified. Transuranics are also utilized as tracers for investigating soil erosion, transport and deposition in the environment (Ketterer et al. 2011; Matisoff and Whiting 2011).

As discussed above, cosmic rays entering the atmosphere cause nuclear reactions that produce a number of radioisotopes. Atmospheric bomb testing, which peaked in the late 1950s and diminished dramatically after 1963, produced a spike in the production of some of these radionuclides (e.g. ^{14}C), and high atmospheric concentrations have persisted due to long atmospheric residence times or continuing fluxes from nuclear activities. These higher concentrations can then be used as markers to identify younger materials. The most widely used isotopes in this category are ^3H and ^{14}C . There are a number of others, including ^{85}Kr (10.72a), ^{129}I (15.7Ma), and ^{36}Cl ($3.0 \times 10^5\text{a}$)

Table 2.4 Anthropogenic isotopes most commonly used in environmental studies

Isotope	Half-life	Main sources	Examples of major uses	Notes
^3H	12.32a	Bomb testing	Tracing rainwater from time of bomb peak in ground waters and seawater	Background cosmogenic ^3H
		Reactors	Ages determined using ^3H - ^3He	
^{14}C	5730a	Bomb testing	Identifying organic and inorganic carbonate materials produced in last 60 years	Background cosmogenic ^{14}C
^{54}Mn	312 day	Bomb testing	Trophic transfer in organisms	No background
^{137}Cs , ^{134}Cs	30.14a	bomb testing, reactors, reprocessing plants	Tracing seawater, soil erosion, sediment dating and mixing, sources of aerosols	No background
^{90}Sr	28.6a	Reactors, bomb testing	Tracing seawater, sources of dust	No background
^{239}Pu , ^{240}Pu	24100a 6560a	Reactors, bomb testing	Tracing seawater, identifying sources of Pu, sediment dating, soil erosion, tracing	No naturally-occurring Pu
^{241}Pu	14.4a		atmospheric dust	
^{131}I	8.02 day			
^{129}I	$1.57 \times 10^7\text{a}$	Bomb testing, reactors	Dating groundwater, water mass movements	Background cosmogenic ^{129}I
^{85}Kr	10.72a	Bomb testing	Dating groundwater	
^{36}Cl	$3.0 \times 10^5\text{a}$	Bomb testing	Dating groundwater	Background cosmogenic ^{36}Cl
^{241}Am	432.2a	Reactors	Tracing sources of Am	No naturally-occurring Am

The anthropogenic isotopes that can be used as point source tracers, or provide global markers of the time of formation of environmental materials

that have not been as widely applied, partly because they require difficult analyses. For a discussion of a number of applications, see Phillips and Castro (2003).

For the anthropogenic radionuclides that have half-lives that are long compared to the times since their release, time information can be derived from knowing the time of nuclide production, e.g. the present distribution of an isotope provides information on the rate of transport since production or discharge. An exception to this is ^3H , which has a half-life of only 12.3 years and decays to the rare stable isotope ^3He . By measuring both of these isotopes, time information can be obtained, e.g. ^3H - ^3He ages for groundwaters, which measure the time since rainwater incorporating atmospheric ^3H has entered the aquifer (Kulongoski and Hilton 2011).

2.2.5 Radiogenic Isotopes

There are a number of radioactive isotopes with half-lives that are useful for understanding geological time-scales, but do not change significantly over periods of interest in environmental studies. However, these isotopes have produced substantial variations in the isotopes of the elements that have daughter isotopes. The resulting isotopic signatures in rocks, sediments, and ores have been exploited in environmental studies. An example is the Rb-Sr system, which is the most commonly used. The long-term decay of ^{87}Rb produces ^{87}Sr , and so the abundance of this isotope, relative to a stable isotope of Sr such as ^{86}Sr , varies according to the equation:

$$\frac{^{87}\text{Sr}}{^{86}\text{Sr}} = \left(\frac{^{87}\text{Sr}}{^{86}\text{Sr}} \right)_0 + \frac{^{87}\text{Rb}}{^{86}\text{Sr}} (e^{\lambda_{87}t} - 1), \quad (2.4)$$

where the $(^{87}\text{Sr}/^{86}\text{Sr})_0$ ratio is the initial isotope ratio and λ_{87} is the decay constant of ^{87}Rb . Clearly, the present $^{87}\text{Sr}/^{86}\text{Sr}$ ratio is greater for samples that have greater ages, t , and samples with larger Rb/Sr ratios. The $^{87}\text{Sr}/^{86}\text{Sr}$ ratio therefore varies between different rock types and formations. Since Rb is an alkali metal and Sr is an alkaline earth, these elements behave differently in geological processes, creating large variations in Rb/Sr, and so large variations in $^{87}\text{Sr}/^{86}\text{Sr}$. The $^{87}\text{Sr}/^{86}\text{Sr}$ ratio has been shown to vary widely in surface rocks, and so any Sr released into soils, rivers, and groundwaters has an isotopic signature that reflects

its source. Changes in local sources can also be identified; for example, Keller et al. (2010) identified thawing of permafrost from the changes in stream water $^{87}\text{Sr}/^{86}\text{Sr}$ ratio as tills with greater amounts of carbonate deeper in soil profiles were weathered. Strontium isotopes have been used as tracers for identifying populations of migratory birds and fish in streams and rivers (Kennedy et al. 1997; Chamberlain et al. 1997) as well as in archaeology (Slovak and Paytan 2011). Sr isotopes have also been used to trace agricultural products, which have incorporated Sr, along with Ca, from soils incorporating Sr isotope ratios of the underlying rocks. The sources and transport of dust across the globe have been traced using the isotopic compositions of Sr, Nd, and Pb (Grousset and Biscaye 2005). Variations in the Pb isotopic ratios between environmental samples (soil, aerosols, household paint, household dust, and water samples in house) and children's blood have been utilized to identify and quantify the sources of blood Pb in children (Gulson 2011).

Other isotope systems that can be used for similar purposes are listed in Table 2.5. In each case, chemical differences between the chemical behaviour of the parent and daughter isotopes have led to variations in their ratio over geological timescales, and so identifiable variations in the environment can be exploited for tracing. The most obvious differences are often regional, as reflected in the isotopic compositions in rivers, especially for Sr and Nd. More local studies can identify different rocks, or even separate minerals, involved in weathering or contributing to waters (Tripathy et al. 2011). Using this information, groundwater flow paths and the sources of inorganic constituents can be deduced.

2.2.6 Stable Isotopes

In addition to variations in isotope ratios produced by the production or decay of nuclides due to nuclear processes, there are variations in the distribution of other isotopes between different phases or chemical species. These are subtle, as isotopes of an element still behave in fundamentally the same way, but the slight variations in atomic mass result in differences in bonding and kinetics. This is due to differences in vibrational energies reflecting differences in the masses of atoms, since the vibrational frequency of a

Table 2.5 Radiogenic isotopes commonly used in environmental studies

Decay scheme	Half-life	Isotope ratio	Comments
$^{87}\text{Rb} \rightarrow ^{87}\text{Sr}$	$4.88 \times 10^{10}\text{a}$	$^{87}\text{Sr}/^{86}\text{Sr}$	Bioarchaeology, erosion rates
$^{147}\text{Sm} \rightarrow ^{143}\text{Nd}$	$1.06 \times 10^{11}\text{a}$	$^{143}\text{Nd}/^{144}\text{Nd}$	Regional variations due to age, rates of weathering, source tracking of sediments
$^{238}\text{U} \rightarrow ^{206}\text{Pb}$	$4.468 \times 10^9\text{a}$	$^{206}\text{Pb}/^{204}\text{Pb}$	Distinguish sources of Pb ores and sources of Pb; tracing sources of Pb to human body
$^{235}\text{U} \rightarrow ^{207}\text{Pb}$	$7.038 \times 10^8\text{a}$	$^{207}\text{Pb}/^{204}\text{Pb}$	
$^{232}\text{Th} \rightarrow ^{208}\text{Pb}$	$1.405 \times 10^{10}\text{a}$	$^{208}\text{Pb}/^{204}\text{Pb}$	Complements Nd/Sm
$^{176}\text{Lu} \rightarrow ^{176}\text{Hf}$	$3.71 \times 10^{10}\text{a}$	$^{176}\text{Hf}/^{177}\text{Hf}$	
$^{187}\text{Re} \rightarrow ^{187}\text{Os}$	$4.6 \times 10^{10}\text{a}$	$^{187}\text{Os}/^{188}\text{Os}$	Organic-rich sources have distinctly high Re/Os
$^{238}\text{U}, ^{235}\text{U}, ^{232}\text{Th} \rightarrow ^4\text{He}$	As above	$^3\text{He}/^4\text{He}$	Dating by ^4He accumulation
$^{40}\text{K} \rightarrow ^{40}\text{Ar}$	$1.397 \times 10^9\text{a}$	$^{40}\text{Ar}/^{36}\text{Ar}$	Tracing deep sources of volatiles
			Dating

The isotopes that are produced by long-lived parents and so exhibit variations in geological materials that can be used as tracers in environmental studies

molecule is directly proportional to the forces that hold atoms together, such as electron arrangements, nuclear charges and the positions of the atoms in the molecule, and inversely proportional to the masses of the atoms. The result is stable isotope fractionation, which is generally considered only for isotopes that are neither radioactive nor radiogenic, since variations in these isotopes often cannot be readily separated from decay effects. While studies of such fractionations were originally confined to light elements (e.g. H, O, N, S), isotopic variations have now been found even in the heavy stable elements Tl (Rehkamper and Halliday 1999) and U (Stirling et al. 2007), and so across the entire periodic table.

The difference in the ratio of two isotopes of the same element in species or phases A (R_A) and B (R_B) can be described by a fractionation factor α

$$\alpha = \frac{R_A}{R_B}. \quad (2.5)$$

Fractionation between isotopes of the same element generally appear to be linear; e.g. the ratio of isotopes two mass units apart will be fractionated twice as much as the ratio of elements one mass unit apart (mass dependent fractionation). Since the changes in isotopic values are generally very small, values are typically given as parts per thousand (permil) deviations from a standard; e.g. for example, for O,

$$\delta^{18}\text{O}_{\text{sample}} = \frac{(^{18}\text{O}/^{16}\text{O})_{\text{sample}} - (^{18}\text{O}/^{16}\text{O})_{\text{standard}}}{(^{18}\text{O}/^{16}\text{O})_{\text{standard}}} \times 10^3. \quad (2.6)$$

Therefore, results are reported relative to a standard. In some cases, however, several standards are in use, especially when analytical procedures are being developed, making comparisons between datasets difficult. In those cases where smaller variations can be measured precisely, values are given in parts per 10^4 (as ϵ values). When the isotopic composition of two phases in equilibrium are measured, the difference between them can be related to the fractionation factor by

$$\delta^{18}\text{O}_A - \delta^{18}\text{O}_B \approx (\alpha - 1) \times 10^3. \quad (2.7)$$

Therefore, the fractionation factor between two phases can be obtained by measuring the difference in isotopic composition between phases in equilibrium.

Schauble (2004) provides a summary of the general patterns seen in equilibrium isotope fractionation. Fractionation effects are largest for low mass elements, and scale according to the difference in atomic masses of two isotopes relative to the average mass of the element squared, i.e. $\Delta m/m^2$. Heavy isotopes will favour species in which the element has the stiffest bonds. In environmental systems, this includes bonds of metals with the highest oxidation state, those with a bond partner with a high oxidation state, and bonds with anions with low atomic number (including organic ligands).

Fractionation can occur not only by equilibrium partitioning, but also due to kinetic processes. This includes transport phenomena such as diffusion, where lighter isotopes have higher velocities (inversely proportional to the square root of atomic/

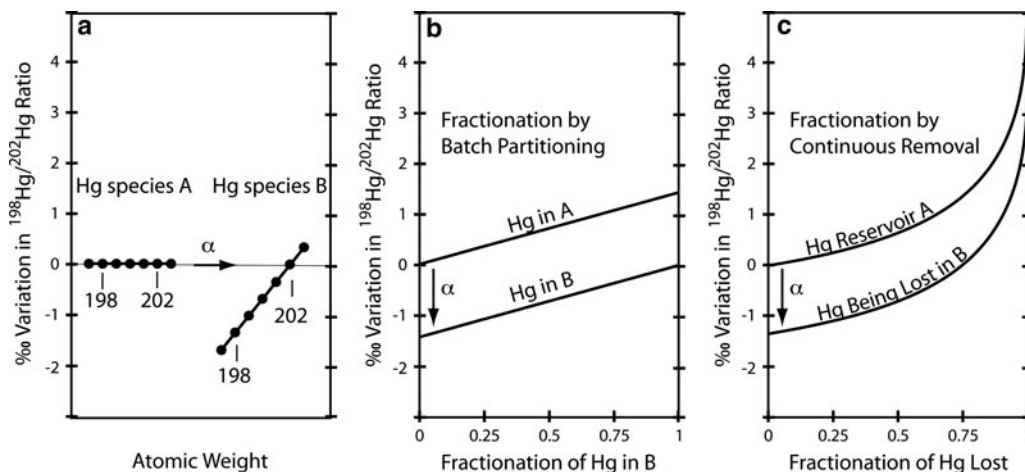


Fig. 2.4 An example of stable isotope fractionation. (a) When Hg is partitioned between two phases, isotopic fractionation can occur; the heavier isotopes are preferentially incorporated into phase B, so that $\alpha(^{198}\text{Hg}/^{202}\text{Hg})_A = (^{198}\text{Hg}/^{202}\text{Hg})_B$. Fractionation between all the isotopes is generally linear, i.e. the extent of fractionation between any two isotopes is proportional to the mass difference between them. (b) If there is equilibrium batch partitioning between A and B, then there is a difference of α

between both phases, and the specific composition of each depends upon mass balance; e.g. if there is very little of phase A, then the ratio of phase B is about equal to the bulk value, while phase A has a value that is α times higher. (c) If there is continuous removal of phase B, so that only each increment being removed is in equilibrium with phase A, then this process of Rayleigh distillation will drive the isotopic composition of A to more extreme compositions than a batch process

molecular weight) that generate fractionation over diffusive gradients. This can also be due to reaction kinetics related to the strength of bonding, where lighter isotopes have bonds that can be broken more readily and so can be enriched in reactants. This can be seen in many biological processes, where uptake of elements can involve pathways involving multiple reactions and so considerable fractionation. It is important to note that it is not always possible to determine if equilibrium or kinetic fractionation is occurring; while laboratory experiments often endeavour to ensure equilibrium is reached, it is not always clear in the natural environment. Also, where kinetic fractionation is produced in a regular fashion, for example due to microbial reduction, it may not be easily distinguished from inorganic equilibrium fractionation processes

When the isotopes of an element are distributed between two separate phases or species in equilibrium, then the difference in isotope ratio is determined by (2.7). However, the absolute ratio of each is determined by mass balance according to the simple mixing equation

$$R_{\text{Total}} = R_A f_A + R_B (1 - f_A). \quad (2.8)$$

For example, as shown in Fig. 2.4, if an element is partitioned between two phases, and the mixture is almost entirely composed of phase A, then that phase will have the ratio close to that of the total mixture, while the ratio of phase B will be offset by the fractionation factor. If the mixture is almost entirely composed of phase B, it is the composition of phase A that will be offset from the bulk. Intermediate values of R for each phase will reflect the balance between the two phases according to (2.8). Such batch partitioning is more likely to apply where both forms are entirely open to chemical exchange, e.g. two different species in solution.

Often equilibrium is not maintained between a chemical species or phase and the source reservoir. In this case, the isotopic composition of the source evolves according to Rayleigh distillation, in which a small increment of a phase or species is formed in equilibrium with the source, but is immediately removed from further interaction, and so does not remain in equilibrium with the changing source. For example, crystals precipitating from solution are unlikely to continue reacting with the solution. If the source originally had an isotope ratio R_0 , and the isotopes of an element of interest are fractionated with material being removed according to

a fractionation factor α , then when in total a fraction f of the element has been removed, the integrated effect will be to generate a ratio R_A in the source according to the equation:

$$\frac{R_A}{R_0} = f^{(\alpha-1)}. \quad (2.9)$$

This is illustrated in Fig. 2.4; once a significant amount of an element has been removed, the ratio of the source has changed to a greater degree than by batch partitioning, and more extreme ratios can be obtained when f approaches 1 (most of the element has been removed). As long as the same fractionation factor affects each increment, (2.9) will describe the evolution of the solution, whether the fractionation is due to equilibrium or kinetic fractionation. Such evolution is likely to apply where solid phases are formed from solution, where water-rock interaction occurs, and where biological uptake occurs.

While fractionation between isotopes of an element is generally mass dependent, i.e. proportional to the mass difference between any two isotopes, there are a few circumstances where mass-independent fractionation is observed and a number of theories have been proposed to explain this phenomenon. Examples include O isotopes in stratospheric and tropospheric ozone (due to rotational energies of asymmetric molecules; Gao and Marcus 2001), S in Archean sediments (possibly from S photo-dissociated in the early atmosphere; Farquhar et al. 2000), and Hg isotopes involved in photochemical reactions in the environment (due to nuclear volume and magnetic isotope effects; see Blum 2011). These provide an added dimension for diagnosing the processes affecting these elements.

A wide range of applications has been explored for stable isotope fractionations. Oxygen isotopes vary in precipitation, and have been used as a hydrological tracer, while C, S, and N have been used to trace biogeochemical cycles (see e.g. reviews in Kendall and McDonnell 1998) and tracers of human diet (Chesson et al. 2011; Schwarcz and Schoeninger 2011). Isotopic variations in Li, Mg, and Sr have been related to adsorption and incorporation in clays, and so can be used to understand weathering and trace element migration (Burton and Vigier 2011; Reynolds 2011). Various metals with multiple redox states, including Fe, Cr, U, Mo, Ni, Cu, Zn, Cd, Hg, Se, and Tl, have isotopic variations that have been used to understand redox processes in present and past environments (see the

four papers by Bullen 2011; Johnson 2011; Nielsen and Rehkämper 2011; Rehkämper et al. 2011).

Stable isotopes can also be used in understanding environmental contamination. Chemical processing can generate isotopic differences in industrial products that provide a means for identifying sources. For example, C and Cl isotope differences have been found between different manufacturers of chlorinated solvents (van Warmerdam et al. 1995) and this can be used to trace contaminant migration. It has also been shown that degradation of these compounds can fractionate Cl isotopes, so that the extent of degradation can be determined (Sturchio et al. 1998, 2011). As another example, Cr isotopes are fractionated in groundwaters when Cr is reduced to a less soluble species, and so decreases in concentrations due to dilution can be distinguished from decreases due to precipitation (Ellis et al. 2002).

Other examples of documented isotope variations that have been used to understand environmental processes are listed in Table 2.6. Measurements are all made using mass spectrometry. Samples are corrected for instrumental fractionation using either comparison with standards in gas-source mass spectrometry and ICPMS, or using a double spike and TIMS and ICPMS (see below).

2.3 Measurement Techniques

There are two fundamental approaches to measuring the abundance of isotopes. Radioactive isotopes can be measured by quantifying the radiation resulting from decay, and then relating the decay rate to the abundance using (2.1). A number of these counting methods are widely used, especially for short-lived nuclides. Alternatively, atoms of any isotope can be directly measured by mass spectrometry, which separates ions according to mass followed by direct counting. These methods typically involve greater investment in instrumentation, but can often detect more subtle variations. The techniques are discussed further in the following sections.

2.3.1 Counting Methods

There are a number of techniques available for the detection of alpha, beta, and gamma radiation that

Table 2.6 Commonly used stable isotopes

Element	Typical reported ratio	Examples of applications
H	$^2\text{H}/^1\text{H}$ (D/H)	Tracing both production and origin of food, groundwater sources
Li	$^6\text{Li}/^7\text{Li}$	Weathering processes, adsorption of Li in aquifers
B	$^{10}\text{B}/^9\text{B}$	
C	$^{13}\text{C}/^{12}\text{C}$	Tracing both production and origin of food, paleodiet reconstruction, hydrocarbon exploration, environmental forensics
N	$^{15}\text{N}/^{14}\text{N}$	N cycling, tracing both production and origin of food
O	$^{18}\text{O}/^{16}\text{O}$	Tracing both production and origin of food, sulphate and nitrate cycle in the atmosphere and aqueous system, oxidation pathways of compounds, paleoclimate (air temperature, humidity and amounts of precipitation), sources of groundwater
Mg	$^{26}\text{Mg}/^{24}\text{Mg}$	Lithological studies, adsorption of Mg in aquifers
Si	$^{30}\text{Si}/^{28}\text{Si}$	Global Si cycle, weathering rates, biogeochemical cycling of Si
S	$^{34}\text{S}/^{32}\text{S}$	Sulfur cycling in the atmosphere, sources of S in the environment
Cl	$^{37}\text{Cl}/^{35}\text{Cl}$	Forensics, source tracking of organochlorine and inorganic chlorate, fractionation in deep brines
Ca	$^{44}\text{Ca}/^{40}\text{Ca}$	Vertebrate paleodiet tracer, biogeochemical pathways of Ca
Cr	$^{53}\text{Cr}/^{52}\text{Cr}$	Source tracking of Cr contamination, Cr reduction
Fe	$^{56}\text{Fe}/^{54}\text{Fe}$	Fe redox cycling, Fe incorporation in aquifers
Ni	$^{60}\text{Ni}/^{58}\text{Ni}$	Sources and transport of Ni; methanogenesis
Cu	$^{65}\text{Cu}/^{63}\text{Cu}$	Sources and transport of Cu; partitioning of Cu between ligand-bound dissolved and particulate phases
Zn	$^{66}\text{Zn}/^{64}\text{Zn}$	Transport of Zn along cell walls of xylem; micronutrient transport in plants; pathways of anthropogenic Zn
Se	$^{80}\text{Se}/^{76}\text{Se}$	Redox reactions
Sr	$^{88}\text{Sr}/^{86}\text{Sr}$	Sr adsorption in aquifers

(continued)

Table 2.6 (continued)

Element	Typical reported ratio	Examples of applications
Mo	$^{97}\text{Mo}/^{94}\text{Mo}$	Sources, transport of Mo, paleo-redox changes in aqueous system
Cd	$^{114}\text{Cd}/^{110}\text{Cd}$, $^{112}\text{Cd}/^{110}\text{Cd}$	Paleo-ocenoigraphy, reconstruction of past nutrient levels in seawater
Os	$^{187}\text{Os}/^{188}\text{Os}$	Tracking anthropogenic and weathering sources of Os
Mo	$^{97}\text{Mo}/^{95}\text{Mo}$	Redox reactions
Hg	$^{202}\text{Hg}/^{198}\text{Hg}$, $^{199}\text{Hg}/^{198}\text{Hg}$, $^{201}\text{Hg}/^{198}\text{Hg}$	Forensics, sources tracking, reaction pathways of Hg using both mass-dependent and mass-independent fractionation
Tl	$^{205}\text{Tl}/^{203}\text{Tl}$	Paleoinput of Fe and Mn, hydrothermal fluid flux
Pb	$^{206}\text{Pb}/^{204}\text{Pb}$, $^{207}\text{Pb}/^{204}\text{Pb}$, $^{208}\text{Pb}/^{204}\text{Pb}$	Source identification of Pb in metals, tracing pathways of Pb to human system, tracing dust
Po	^{210}Po	POC export, remineralization of particles, biogenic particle cycling
U	$^{238}\text{U}/^{235}\text{U}$	Depleted/enriched uranium identification, redox

can be applied depending upon the mode and energy of decay, as well as the emission spectrum that is produced. In some circumstances, an isotope will decay to another short-lived isotope that can be more readily measured and then related to the abundance of the parent (e.g. ^{210}Pb using ^{210}Po measured by alpha spectrometry or ^{226}Ra using ^{214}Pb or ^{214}Bi measured by gamma spectrometry).

Following is a brief description of the different analytical methods available. For many isotopes, there are several measurement options, and the best method is determined by the type of sample, the abundance of the isotope of interest, and the precision required. A more extensive review is given by Hou and Roos (2008).

2.3.1.1 Alpha Spectrometry

Isotopes that are subject to alpha decay can be measured by detecting and counting the emitted alpha particles. Contributions from the decay of other

isotopes can be distinguished by alpha particle energy, although there is overlap between alpha energies emitted by some of the nuclides. However, practical difficulties arise due to the interaction of alpha particles with atoms of other species that are loaded in the source along with the sample. This can cause a spread in particle energies and so reduce the energy resolution of the alpha spectrum, making the data often unusable. Therefore, good chemical separation and purification from other elements is critical, and the isotope of interest must be then deposited as a thin layer to minimize adsorption by the element of interest itself (self-shielding). This is done by electroplating onto metal discs or by sorbing onto thin MnO_2 layers. Accurate determination of the concentration of these isotopes requires careful control of chemical yields during processing as well as of counter efficiency. A detailed review of the chemical procedures adopted for measuring alpha-emitting radionuclides in the U-Th-series is given in Lally (1992).

A number of detectors have been utilized for alpha measurements that include ionization chambers, proportional counters, scintillation detectors (plastic and liquid), and semiconductor detectors. Of these, the semiconductors (in particular, surface barrier and ion-implanted silicon detectors) have been the most widely used detectors due to their superior energy resolution and relatively high counting efficiency (typically 30% for a 450-mm^2 surface-barrier detector). More detailed comparison of the various types of detector material is given in Hou and Roos (2008).

The very low background of alpha detectors (0.8–2 counts for a particular isotope per day), relatively high efficiency (~30% for 450 mm^2 surface area detectors) and very good energy resolution (about 17–20 keV for 5.1 MeV) lead to detection limits of 0.010–0.025 mBq (where Bq, a Becquerel, is a decay per second); this can be related to an abundance using (2.1), so that, e.g. for a 1×10^5 year half-life radionuclide this corresponds to as little as 0.08 femtomoles. While the long preparation times associated with chemical separation, purification, electroplating and counting impose a practical constraint on sample throughput, the relatively low-cost of alpha spectrometers and their maintenance is an advantage.

2.3.1.2 Beta Spectrometry

For isotopes that are subject to beta decay, abundances can be measured by detecting and counting the beta particles (electrons) that are emitted. The most common detector is a Geiger-Müller (GM) counter, which employs a gas-filled tube where atoms are ionized by each intercepted beta particle, and this is converted into an electrical pulse. Background signals from cosmic rays are reduced through shielding and anti-coincidence counters, which subtract counts that correspond to detections of high-energy particles entering the counting chamber.

Although adsorption by surrounding atoms is not as efficient as for alpha particles, it is still significant, and so samples are often deposited as thin sources onto a metal disc to increase counting efficiencies. Also, filters that contain particles collected from air and water samples can be measured directly. Dissolved species of particle-reactive elements (e.g. Th) can be concentrated from large water volumes by scavenging onto precipitated Fe or Mn oxides that are then collected onto filters. These filters can be analyzed directly (Rutgers van der Loeff and Moore 1999).

It should be noted that GM counters do not distinguish between beta particles by energy, and so cannot separate contributions from different isotopes through the energy spectrum. While isotopes can often be isolated by chemical separation, some elements have several isotopes and some isotopes have short-lived beta-emitting daughter isotopes that are continuously produced. In these cases, multiple counting can be done to identify and quantify different isotopes based upon their different half-lives. Also, selective absorbers of various thicknesses between the source and counter can be used to suppress interference from isotopes that produce lower energy beta particles.

The counting efficiency of a GM counter varies depending on the thickness of the source and on counter properties. One of the commonly used GM counters, the Risø Counter (Risø National Laboratory, Roskilde, Denmark), has a typical efficiency of ~40% for most commonly occurring beta-emitting radionuclides. A typical background of this anti-coincidence counter, with 10 cm of lead shielding, is 0.15–0.20 counts per minute, corresponding to ~0.8 mBq. This can be compared to the detection limit for an alpha-emitting radionuclide; the background of a new

alpha detector is 0.03–0.09 counts per hour, which corresponds to 0.03–0.08 mBq (at ~30% counting efficiency). Thus, the detection limit in alpha spectrometry is more than an order of magnitude higher than that of beta spectrometry.

The GM counter is not suitable for analyzing isotopes such as ^3H and ^{14}C that emit low-energy (~200 keV) electrons, which are adsorbed in the detector window. For these nuclides, a liquid scintillation counter (LSC) is used, in which a sample is dissolved in a solvent solution containing compounds that convert energy received from each beta particle into light, and the resulting pulses are counted. This method has minimal self-adsorption and relatively easy sample preparation, and can be used for all beta-emitters. However, background count rates are substantially higher than in GM counters.

2.3.1.3 Gamma Spectrometry

Alpha and beta-emitting radionuclides often decay to atoms in excited energy states, which then reach the ground state by emitting gamma radiation at discrete characteristic energies. Gamma rays can be detected when they ionize target atoms, so that the resulting charge can be measured. Gamma rays can penetrate a considerable distance in solid material, so that isotopes of interest do not need to be separated from sample material before counting, unless preconcentration from large volumes is required. Therefore, the method has the advantage of being non-destructive and easy to use.

A number of detectors have been used for the detection and quantification of gamma rays emitted from radionuclides of interest. Lithium-doped Ge (Ge(Li)) and Si (Si(Li)) semiconductor detectors have been widely used due to their high-energy resolution. For example, using large-volume Ge crystals with relatively high efficiencies, absolute efficiencies of ~70% have been achieved in Ge-well detectors for small samples (1–2 mL volume) at energies of 46.5 keV (^{210}Pb) and 63 keV (^{234}Th). This efficiency decreases to about 24–30% for 10 mL geometries due to the wider solid angle between the counting vial and Ge-crystal (Jweda 2007). However, the counting efficiency of gamma spectrometry with planar or co-axial detectors is generally quite low (<10%), and is dependent upon detector geometry and gamma energy. An advantage of the gamma counting method is that

energy spectra are obtained, so that a number of gamma-emitting radionuclides can be measured simultaneously. The typical energy resolution for the Ge-well detector is high, ~1.3 keV at 46 keV and ~2.2 keV at 1.33 MeV.

The backgrounds in gamma-ray detectors are high compared to alpha and beta detectors, mainly due to cosmic-ray muons and Earth's natural radioactivity. Graded shields (of Cu, Cd, Perspex, etc) have considerably reduced the background mainly arising from environmental radioactivity surrounding the detector, and anti-coincidence techniques have helped to cut down background from muons. Ultra-low background cryostats have also helped to reduce the overall background of the gamma-ray detector. Nonetheless, the detection limit is typically several orders of magnitude higher than for beta and alpha counting.

2.3.2 Mass Spectrometry

For measuring stable isotopes, or as an alternative to counting decays of atoms, it is possible to count the atoms directly. This requires a separation of atoms and this can be achieved by utilizing the fact that the path of charged particles travelling through a magnetic field is diverted along a radius of curvature r that is dependent upon mass and energy:

$$r = \left(\frac{2V}{e H^2} \right)^{1/2} (m/z)^{1/2}, \quad (2.10)$$

where V is accelerating potential, z is charge of the ion, e is the magnitude of electronic charge, and H is the intensity of the magnetic field. The accelerated ions will traverse a semi-circular path of radius r while within the magnetic field. When all ions of an element have the same charge and subject to the same magnetic field, they are accelerated to the same velocity, so that the path radii are only a function of mass. Ions will therefore exit the magnetic field sorted in beams according to mass. This property therefore dictates the basic features of a mass spectrometer: a source where the element of interest is ionized to the same degree and the atoms are accelerated with as little spread in energy as possible; a magnet with a field that is homogeneous throughout the ion paths; detectors located where each beam can be collected separately; and a flight tube that

maintains a vacuum along the ion paths, reducing energy-scattering collisions. These methods generally require separation of the element of interest from other constituents that may produce isobaric interferences (either as separate ions or as molecular species) or interfere with the generation of ions. More sophisticated instruments are equipped with further filters, including energy filters that discriminate between ions based on their energy and so separate ions that otherwise interfere due to scattering.

Mass spectrometers can provide high sensitivity measurements of element concentrations as well. While comparisons with standards to calibrate the instrument are needed, these measurements can be limited by variations between sample and standard analysis. In this case, higher precisions can be obtained using isotope dilution, in which a spike that has the relative abundance of at least one isotope artificially enhanced is mixed with the sample once the sample is dissolved. The resulting isotope composition reflects the ratio of spike to sample, and if the amount of spike that is added is known, then the amount of sample can be calculated with high precision directly from measurement of the isotope composition. A further advantage of this approach is that this isotope composition is not affected by losses during chemical separation or analysis. Spikes can also be used to correct for isotope fractionation that occurs within the instrument. In this case, a double spike, which is enriched in two isotopes, is added. The measured ratio of these two isotopes can then be used to calculate the instrument fractionation, and this correction can be applied to the ratios of other measured stable isotopes to obtain corrected sample values.

There are many designs of magnet geometries, as well as electric fields, in order to improve focusing and resolution. However, for isotope geochemistry there are a number of basic, widely used approaches, as discussed below and in the review articles by Goldstein and Stirling (2003) and Albarede and Beard (2004).

2.3.2.1 Thermal Ionization Mass Spectrometry (TIMS)

In this design, samples are manually loaded onto metal filaments installed within the source. Under vacuum, the

metal is resistance-heated, and atoms are evaporated. Some atoms are ionized, and are then accelerated down the flight tube and into the magnetic field. The proportion of atoms that are ionized can be very low depending upon the element, but can be enhanced using various techniques, including the use of different filament metals, loading the sample in a mixture that raises the evaporation temperature, and using a second filament held at much higher temperature to ionize atoms vaporized from the evaporation filament. While TIMS can produce ion beams with a narrow range of energies and generate high precision data, it is time-consuming and the proportion of vaporizing atoms that ionize can be low for elements with high ionization potentials. However, it is the analytical tool of choice for high precision data for some elements. Due to signal variability between samples, concentration data must be obtained using isotope dilution. Also, variable isotope fractionation during analysis is usually corrected for by assuming that the ratio of stable, nonradiogenic isotopes is equal to a standard value and so that there is no natural isotope fractionation. Therefore, detection of natural stable isotope fractionation in the samples requires the use of a double spike.

2.3.2.2 Inductively-Coupled Plasma Source Mass Spectrometry (ICP-MS)

In ICP-MS, samples in solution are introduced into an Ar plasma where ions are efficiently ionized. An ion extraction system then transfers ions from the high-pressure plasma source to the vacuum system of the mass analyzer. However, ions exit the source with a much greater energy spread than in TIMS sources, and precise measurements require additional correction of ion beams. The most recent generation of instruments, with electrostatic fields and additional magnets to focus beams, and techniques such as collision cells to decrease interferences, have achieved high sensitivity and high precision data. These instruments have been found to be versatile and have been used for a wide range of elements. Isotopic fractionation within the instrument can be quite consistent and so corrected for by alternating analyses of samples with those of standards. Corrections can also be made using other elements within the sample with similar masses, which exhibit comparable fractionations. Therefore, it is this

method that has been used to document stable isotope variations in many elements. Also, sample throughput is considerably greater than for the TIMS method. Methods for high spatial resolution analyses are advancing using laser ablation for in situ sampling, which is coupled to an ICPMS for on-line analysis. For further information, see Albarede and Beard (2004).

2.3.2.3 Gas Source Mass Spectrometry

Volatile elements, including H, O, S, and the noble gases, are measured using a mass spectrometer that has a gas source, where samples are introduced as a gas phase and are then ionized by bombardment of electrons emitted from a heated metal filament. Fractionation of the sample during introduction, ionization, and analysis is corrected for by monitoring a standard, which is introduced and analyzed under identical conditions and run between samples.

2.3.2.4 Accelerator Mass Spectrometry (AMS)

There are a number of isotopes that have such low concentrations that they are difficult to measure precisely by mass spectrometry. C has a $^{14}\text{C}/^{12}\text{C}$ ratio of $<1 \times 10^{12}$, and measurement precision is limited by isobaric interferences. The problem is similar for other cosmogenic nuclides such as ^{10}Be , ^{26}Al , ^{36}Cl , and ^{129}I . The development of accelerator mass spectrometry has made it possible to precisely measure as few as 10^4 atoms of ^{14}C , and so has extended the time scale of high precision ^{14}C age dating on substantially smaller samples than by counting methods, as well as making it possible to obtain accurate measurements on the longer-lived cosmogenic nuclides. In accelerator mass spectrometry, negative ions are accelerated to extremely high energies using a tandem accelerator and then passed through a stripper of low pressure gas or a foil, where several electrons are stripped off to produce highly charged positive ions and where molecules are dissociated, thereby eliminating molecular interferences. Subsequent mass discrimination involves the use of an analyzing magnet, with further separation of interfering ions made possible using an electrostatic analyzer (which separates ions by kinetic energy per charge) and a velocity filter. Detection is made by counters that allow determination of the rate

of energy loss of the ion, which is dependent upon the element, and so allows further separation of interfering ions. There are a number of AMS facilities worldwide, and each is generally optimally configured for a particular set of isotopes. A more extended review is provided by Muzikar et al. (2003).

Comparison Between Alpha Spectrometry and Mass Spectrometry

Techniques for decay counting as well as for mass spectrometry have been continuously evolving over more than 60 years, with progressively improving precision and sensitivity. For measuring radioactive isotopes, both approaches can be used, although often to different levels of precision. For measuring the abundance of any radioactive isotope, the precision possible by mass spectrometry can be compared to that achievable by decay counting. Considering only the uncertainty, or relative standard deviation, due to counting (Poisson) statistics, then for a total number of atoms N of a nuclide with a decay constant of λ that are counted by a mass spectrometer with an ionization efficiency of η_i and where there is a fraction F of ions counted, the uncertainty is

$$P_{\text{ms}} = (N F \eta_i)^{-1/2}. \quad (2.11)$$

A reasonable value for F is 20%; the ionization can differ by orders of magnitude between elements. Alternatively, if the decay rate of these atoms is measured in a counting system of counting efficiency η_c and over a time t , then

$$P_c = (N \lambda t \eta_c)^{-1/2}. \quad (2.12)$$

A reasonable maximum value for t is 5 days, and a typical counting efficiency for alpha counting is 30%. The precision for counting is better as the decay constant increases, and so as the half-life decreases. For an ionization efficiency during mass spectrometry of $\eta_c = 1 \times 10^{-3}$, counting is equally precise for nuclides with $\lambda = 0.02 \text{ year}^{-1}$ ($t_{1/2} = 30$ years). Nuclides with longer half-lives would be more precisely measured by mass spectrometry. While the values of the other parameters may vary, and precisions are often somewhat worse due to factors other than counting statistics, in general isotopes with half-lives of less than $\sim 10^2$ years are more effectively

measured by decay counting methods (Chen et al. 1992; Baskaran et al. 2009).

2.4 The Future of Isotope Geochemistry in the Environmental Sciences

Isotope geochemistry has become an essential tool for the environmental sciences, providing clearly defined tracers of sources, quantitative information on mixing, identification of physical and chemical processes, and information on the rates of environmental processes. Clearly, this tool will continue to be important in all aspects of the field, including studies of contamination, resource management, climate change, biogeochemistry, exploration geochemistry, archaeology, and ecology. In addition to further utilization of established methods, new applications will continue to be developed. These will likely include discovering new isotope and trace element characteristics of materials, and defining isotope variations that are diagnostic of different processes. One particular area of great potential is in understanding the role of microbial activity in geochemical cycles and transport.

There will certainly be further development of new isotope systems as isotopic variations in elements other than those now widely studied are discovered. Advances in instrumentation and analytical techniques will continue to improve precision and sensitivity, so that it will be possible to identify and interpret more subtle variations. Methods for greater spatial resolution will also improve with better sample preparation and probe techniques, so that time-dependent variations could be resolved in sequentially-deposited precipitate layers and biological growth bands in corals and plants. New applications will follow the development of new methods for extraction of target elements, greater understanding of controls on particular isotopes, and certainly new ideas for isotope tracers. Isotope variations of new elements, in particular stable isotope variations, will be explored, further widening the scope of isotope geochemistry.

Overall, it is inevitable that there will be increasing integration of isotopic tools in environmental studies.

Appendix 1: Decay Energies of Decay Series Isotopes

Table 2.7 Commonly measured isotopes of the ^{238}U decay series data taken from Firestone and Shirley (1999)

Isotope	Half-life	Decay	Emission energy (MeV) ^a	Yield (%)
^{238}U	$4.468 \times 10^9 \text{ a}$	α	4.198 (α_0)	77
			4.151 (α_1)	23
			4.038 (α_2)	0.23
^{234}Th	24.1 day	β^-	0.199	70.3
		β^-	0.104	19
		γ	0.093	5.58
^{234}Pa	1.17 m	γ	0.063	4.85
		β^-	2.290	98.2
^{234}U	$2.445 \times 10^5 \text{ a}$	β^-	1.500	1.8
		α	4.775 (α_0)	72.5
^{230}Th	$7.538 \times 10^4 \text{ a}$	α	4.722 (α_1)	27.5
		γ	0.014	10.4
		α	4.687 (α_0)	76.3
^{226}Ra	$1.6 \times 10^3 \text{ a}$	α	4.621 (α_1)	23.4
		α	4.784 (α_0)	94.55
^{226}Rn	3.82 day	α	4.601 (α_1)	5.45
		γ	0.186	3.51
^{222}Rn	3.82 day	α	5.489 (α_0)	~100
^{218}Po	3.10 min	α	6.002 (α_0)	~100
^{214}Pb	26.8 min	β^-	1.023 (β_0)	~100
		γ	0.3519	35.9
		γ	0.2952	18.5
^{214}Bi	19.7 min	γ	0.2420	7.5
		α	5.621 (α_0)	0.021
		β^-	3.272	~100
		γ	~100	0.609
^{214}Po	164 μs	γ	1.120	15.0
		γ	1.764	15.9
^{214}Po	164 μs	α	7.687 (α_0)	~100
^{210}Pb	22.3 year	β^-	0.0635 (β_0)	16
		γ	0.0465	4.25
^{210}Bi	5.013 day	β^-	1.163 (β_0)	100
^{210}Po	138.38 day	α	5.304 (α_0)	100
		Stable	—	—
^{206}Pb	138.38 day	α	5.304 (α_0)	100

^aEnergies of beta decay are maxima

Table 2.8 Commonly measured isotopes of the ^{235}U decay series data taken from Firestone and Shirley (1999)

Isotope	Half-life	Decay	Emission energy (MeV) ^a	Yield (%)
^{235}U	$7.038 \times 10^8 \text{ a}$	α	4.215–4.4596	93.4
		γ	0.1857	57.3
		γ	0.1438	10.96

(continued)

Table 2.8 (continued)

Isotope	Half-life	Decay	Emission energy (MeV) ^a	Yield (%)
²³¹ Th	25.52 h	β ⁻	0.3895	100
		γ	0.0256	14.5
		γ	0.0842	6.6
²³¹ Pa	3.276 × 10 ⁴ a	α	4.934–5.059	86.5
		α	4.681–4.853	12.3
		γ	0.0274	10.3
		γ	0.300–0.303	4.7
²²⁷ Ac	21.773a	α (1.38%)	4.941–4.953	87.3
		β (98.62%)	0.0449	~100
²²⁷ Th	18.72 day	α	5.960–6.038	50.6
			5.701–5.757	37.2
		γ	0.236	12.3
²²³ Ra	11.435 day	α	0.256	7.0
		α	5.539–5.747	96.8
²¹⁹ Rn	3.96 s	γ	0.2695	13.7
		α	6.819 (α ₀)	79.4
²¹⁵ Po	1.78 ms		6.553 (α ₁)	12.9
			6.425 (α ₂)	7.6
			7.386 (α ₀)	100
²¹¹ Pb	36.1 min	β ⁻	1.373	100
²¹¹ Bi	2.14 min	α (99.72%)	6.623	83.8
			6.278	16.2
		β ⁻ (0.28%)	0.579	100
²⁰⁷ Tl	4.77 min	γ	0.351	13.0
		β ⁻	1.423	100
²⁰⁷ Pb	Stable	–	–	–

^aEnergies of beta decay are maxima**Table 2.9** Commonly measured isotopes of the ²³²Th decay series data taken from Firestone and Shirley (1999)

Isotope	Half-life	Decay	Emission energy (MeV) ^a	Yield (%)
²³² Th	1.405 × 10 ¹⁰ a	α	4.013	77.9
			3.954	22.1
²²⁸ Ra	5.75a	β ⁻	0.046	100
²²⁸ Ac	6.15 h	β ⁻	2.127	100
		γ	0.9112	26.6
			0.9690	16.2
			0.3383	11.3
²²⁸ Th	1.913a	α	5.423	71.1
			5.340	28.2
²²⁴ Ra	3.66 day	α	5.685 (α ₀)	94.9
			5.449 (α ₁)	5.1
		γ	0.2410	3.97
²²⁰ Rn	55.6 s	α	6.288 (α ₀)	99.89
			5.747 (α ₁)	0.11
			6.778 (α ₀)	~100
²¹⁶ Po	0.145 s	α	6.778 (α ₀)	~100
²¹² Pb	10.64 h	β ⁻	0.574	100
		γ	0.2386	43.3
			0.3001	3.28

(continued)

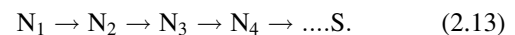
Table 2.9 (continued)

Isotope	Half-life	Decay	Emission energy (MeV) ^a	Yield (%)
²¹² Bi	60.55	α (35.94%)	6.051	69.9
			6.090	27.1
		β ⁻	2.254	100
²¹² Po	0.299 μs	γ		
²⁰⁸ Tl	3.05 min	α	8.784 (α ₀)	100
		β ⁻	1.372	100
²⁰⁷ Pb	Stable	γ	0.405	3
			0.832	2.8
		–	–	–

^aEnergies of beta decay are maxima

Appendix 2: Decay Series Systematics

Within a decay series, the evolution of the abundance of a daughter radioactive isotope is dependent upon its decay rate as well as production from its radioactive parent. Since the abundance of the parent is in turn dependent upon that of its parent, and so on up the decay chain, the systematics can become complicated, although for most applications simplifying circumstances can be found. The evolution of the abundances of isotopes within a decay series is described by the Bateman equations (see Bourdon et al. 2003 for derivations). For a decay series starting from the long-lived parent N_1 and ending with a stable isotope S ,



The long-lived parent evolves according to the basic decay equation:

$$(N_1) = (N_1)_0 e^{-\lambda_1 t}. \quad (2.14)$$

(N_1) is the activity, so that

$$(N_1) = \frac{dN_1}{dt} = \lambda_1 N_1. \quad (2.15)$$

The next two nuclides in the decay series evolves according to the equations

$$(N_2) = \frac{\lambda_2}{\lambda_2 - \lambda_1} (N_1)_0 (e^{-\lambda_1 t} - e^{-\lambda_2 t}) + (N_2)_0 e^{-\lambda_2 t} \quad (2.16)$$

$$\begin{aligned}
 (N_3) = & \frac{(N_1)_0 \lambda_2 \lambda_3}{\lambda_2 - \lambda_1} \left(\frac{e^{-\lambda_1 t}}{(\lambda_2 - \lambda_1)(\lambda_3 - \lambda_1)} \right. \\
 & \left. + \frac{e^{-\lambda_2 t}}{(\lambda_1 - \lambda_2)(\lambda_3 - \lambda_2)} + \frac{e^{-\lambda_3 t}}{(\lambda_1 - \lambda_3)(\lambda_2 - \lambda_3)} \right) \\
 & + \frac{(N_2)_0 \lambda_3}{(\lambda_3 - \lambda_2)} (e^{-\lambda_2 t} - e^{-\lambda_3 t}) + (N_3)_0 e^{-\lambda_3 t}.
 \end{aligned} \tag{2.17}$$

The equations become increasingly complex, but are rarely necessary for environmental applications. Further, these equations can be greatly simplified under most circumstances.

- For all environmental timescales, the abundance of the long-lived parent (N_1) of the chain is constant, and $e^{-\lambda_1 t} \approx 1$. Further, $\lambda_2 - \lambda_1 \approx \lambda_2$ and $\lambda_3 - \lambda_1 \approx \lambda_3$.
- When a system has been closed for a long time, i.e. when $e^{-\lambda_2 t} \approx e^{-\lambda_3 t} \approx 0$, the above equations reduce to $(N_1 \lambda_1) = (N_2 \lambda_2) = (N_3 \lambda_3)$, so that all the nuclides have the same activity as their parents, i.e. are in secular equilibrium, and the entire chain has the same activity as that of the long-lived parent. This is the state within very long-lived materials, such as unweathered rocks, and is the state all systems evolve towards when nuclides are redistributed.
- The activity of the daughter evolves towards secular equilibrium with its parent according to its half-life (and *not* that of the half life of its parent). This could be grow-in, where the daughter starts with a lower activity, or decay when the daughter starts with a higher activity; in either case it is the difference in the activities that declines at a rate determined by the half-life of the daughter. Therefore, the half-life of the daughter dictates the time-scale for which it is useful.

The linking of all the isotopes in the chain can lead to considerable complexity, since the parent concentration of each nuclide is changing, and so potentially the concentrations of the entire chain must be considered. However, for most applications, this can be greatly simplified by the following considerations:

- When a nuclide is isolated from its parent, then it becomes the head of the decay chain and simply decays away according to the decay equation (2.1); that is, it becomes the top of the chain. An example

is ^{210}Pb , which is generated in the atmosphere from ^{222}Rn and then transferred to sediments in fallout, where its activity simply diminishes according to (2.14) with a 22.3a half-life.

- Where the time scale of interest is short compared to the half-life of an isotope, the abundance of that isotope can be considered to be constant. In this case, this nuclide can be considered the head of the decay chain, and the influence of all nuclides higher in the decay series, can be ignored. For example, over periods of several 1,000 years, ^{230}Th ($t_{1/2} = 75\text{ka}$) remains essentially constant, while ^{226}Ra ($t_{1/2} = 1.6\text{ka}$) will grow into secular equilibrium according to (2.16).
- Where the time scale of interest is long compared to the half-life of an isotope, the activity of that isotope can be considered to be equal to that of the parent. For example, in a closed mineral, the ^{222}Rn activity will be equal to that of parent ^{226}Ra after several weeks, and so while the activity of ^{210}Pb will grow-in towards that of its parent ^{222}Rn , this can be represented by measurements of ^{226}Ra . Therefore, shorter-lived intermediate isotopes can be ignored.
- The most common circumstance when (2.17) is required is dating materials that have incorporated U from waters. Since the ($^{234}\text{U}/^{238}\text{U}$) ratio of waters is often above that of secular equilibrium, obtaining an age from the grow-in of ^{230}Th requires considering the chain $^{238}\text{U} \rightarrow ^{234}\text{U} \rightarrow ^{230}\text{Th} \rightarrow \dots$

References

- Albarede F, Beard B (2004) Analytical methods for non-traditional isotopes. *Rev Mineral Geochem* 55:113–152
- Baskaran M (2011) Po-210 and Pb-210 as atmospheric tracers and global atmospheric Pb-210 fallout: a Review. *J Environ Radioact* 102:500–513
- Baskaran M (2011) Dating of biogenic and inorganic carbonates using ^{210}Pb - ^{226}Ra disequilibrium method – a review. In: Baskaran M (ed) *Handbook of environmental isotope geochemistry*. Springer, Berlin
- Baskaran M, Hong G.-H, Santschi PH (2009) Radionuclide analysis in seawater. In: Oliver Wurl (ed) *Practical guidelines for the analysis of seawater*. CRC Press, Boca Raton, FL, pp 259–304
- Blum J (2011) Applications of stable mercury isotopes to biogeochemistry. In: Baskaran M (ed) *Handbook of environmental isotope geochemistry*. Springer, Berlin
- Bourdon B, Turner S, Henderson GM, Lundstrom CC (2003) Introduction to U-series geochemistry. *Rev Mineral Geochem* 52:1–21

- Bullen TD (2011) Stable isotopes of transition and post-transition metals as tracers in environmental studies. In: Baskaran M (ed) Handbook of environmental isotope geochemistry. Springer, Berlin
- Burton KW, Vigier N (2011) Lithium isotopes as tracers in marine and terrestrial environment. In: Baskaran M (ed) Handbook of environmental isotope geochemistry. Springer, Berlin
- Chabaux F, Riotte J, Dequincey O (2003) U-Th-Ra fractionation during weathering and river transport. *Rev Mineral Geochem* 52:533–576
- Chamberlain CP, Blum JD, Holmes RT, Feng X et al (1997) The use of isotope tracers for identifying populations of migratory birds. *Oecologia* 109:132–141
- Chen JM, Edwards RL, Wasserburg GJ (1992) Mass spectrometry and application to uranium-series disequilibrium. In: Ivanovich M, Harmon RS (eds) Uranium-series disequilibrium. Applications to Earth, Marine, and Environmental Sciences. 2nd Ed. Clarendon Press, Oxford, pp. 174–206
- Chesson LA, Ehleringer JR, Cerling TE (2011) Light-element isotopes (H, C, N, and O) as tracers of human diet: a case study on fast food meals. In: Baskaran M (ed) Handbook of environmental isotope geochemistry. Springer, Berlin
- Church T, Sarin MM (2008) U and Th series nuclides in the atmosphere: supply, exchange, scavenging, and applications to aquatic processes. In: Krishnaswami S, Cochran JK (eds) U/Th series radionuclides in aquatic systems. Elsevier, Amsterdam, pp 105–153
- Cochran JK, Masque P (2003) Short-lived U/Th series radionuclides in the ocean: tracers for scavenging rates, export fluxes and particle dynamics. *Rev Mineral Geochem* 52:461–492
- Cockburn HAP, Summerfield MA (2004) Geomorphological applications of cosmogenic isotope analysis. *Prog Phys Geogr* 28:1–42
- Du JZ, Zhang J, Baskaran M (2011) Applications of short-lived radionuclides (^7Be , ^{210}Pb , ^{210}Po , ^{137}Cs and ^{234}Th) to trace the sources, transport pathways and deposition of particles/sediments in rivers, estuaries and coasts. In: Baskaran M (ed) Handbook of environmental isotope geochemistry. Springer, Berlin
- Dunai TJ (2010) Cosmogenic nuclides: principles, concepts, and applications in the earth surface sciences. Cambridge University Press, Cambridge
- Ellis AS, Johnson TM, Bullen TD (2002) Chromium isotopes and the fate of hexavalent chromium in the environment. *Science* 295:2060–2062
- Farquhar JB, Bao H, Thieme M (2000) Atmospheric influence of Earth's earliest sulfur cycle. *Science* 289:756–758
- Firestone RB, Shirley VS (1999) Table of isotopes, 8th edn. Update with CD-ROM, Wiley-Interscience
- Gao YQ, Marcus RA (2001) Strange and unconventional isotope effects in ozone formation. *Science* 293:259–263
- Goldstein SJ, Stirling CH (2003) Techniques for measuring uranium-series nuclides: 1992–2002. *Rev Mineral Geochem* 52:23–57
- Gosse JC, Phillips FM (2001) Terrestrial in situ cosmogenic nuclides: theory and application. *Quatern Sci Rev* 20: 1475–1560
- Grousset FE, Biscaye PE (2005) Tracing dust sources and transport patterns using Sr, Nd, and Pb isotopes. *Chem Geol* 222:149–167
- Gulson B (2011) Sources of lead and its mobility in the human body using lead isotopes. In: Baskaran M (ed) Handbook of environmental isotope geochemistry. Springer, Berlin
- Hirose K (2011) Uranium, thorium and anthropogenic radionuclides as atmospheric tracers. In: Baskaran M (ed) Handbook of environmental isotope geochemistry. Springer, Berlin
- Hong G-H, Hamilton TF, Baskaran M, Kenna TC (2011) Applications of anthropogenic radionuclides as tracers to investigate marine environmental processes. In: Baskaran M (ed) Handbook of environmental isotope geochemistry. Springer, Berlin
- Hou X, Roos P (2008) Critical comparison of radiometric and mass spectrometric methods for the determination of radionuclides in environmental, biological and nuclear waste samples. *Anal Chim Acta* 608:105–139
- Ivanovich M, Harmon RS (1992) Uranium-series disequilibrium. In: Ivanovich M, Harmon RS (eds) Applications to Earth, Marine, and Environmental Sciences. 2nd Ed. Clarendon Press, Oxford, pp. 909
- Johnson TM (2011) Stable isotopes of Cr and Se as tracers of redox processes in Earth surface environments. In: Baskaran M (ed) Handbook of environmental isotope geochemistry. Springer, Berlin
- Jweda J (2007) Short-lived radionuclides (^{210}Pb and ^7Be) as tracers of particle dynamics and chronometers for sediment accumulation and mixing rates in a river system in Southeast Michigan. M.S. Thesis, Department of Geology, Wayne State University, Detroit, Michigan, pp. 167
- Kaste JM, Baskaran M (2011) Meteoric ^7Be and ^{10}Be as process tracers in the environment. In: Baskaran M (ed) Handbook of environmental isotope geochemistry. Springer, Berlin
- Keller K, Blum JD, Kling GW (2010) Stream geochemistry as an indicator of increasing permafrost thaw depth in an arctic watershed. *Chem Geol* 273:76–81
- Kendall C, McDonnell JJ (1998) Isotope tracers in catchment hydrology (edited volume), Elsevier Science B.V., Amsterdam, pp. 839
- Kennedy BP, Folt CL, Blum JD, Chamberlain CP (1997) Natural isotope markers in salmon. *Nature* 387:766–767
- Ketterer ME, Zheng J, Yamada M (2011) Source tracing of transuranics using their isotopes. In: Baskaran M (ed) Handbook of environmental isotope geochemistry. Springer, Berlin
- Kim G, Kim T-H, Church TM (2011) Po-210 in the environment: biogeochemical cycling and bioavailability. In: Baskaran M (ed) Handbook of environmental isotope geochemistry. Springer, Berlin
- Kulongoski JT, Hilton DR (2011) Helium isotope studies of ground waters. In: Baskaran M (ed) Handbook of environmental isotope geochemistry. Springer, Berlin
- Lal D (1991) Cosmic ray tagging of erosion surfaces: in situ production rates and erosion models. *Earth Planet Sci Lett* 104:424–439
- Lal D (1999) An overview of five decades of studies of cosmic ray produced nuclides in oceans. *Sci Total Environ* 237/ 238:3–13

- Lal D (2011) Using cosmogenic radionuclides for the determination of effective surface exposure age and time-averaged erosion rates. In: Baskaran M (ed) Handbook of environmental isotope geochemistry. Springer, Berlin
- Lal D, Baskaran M (2011) Applications of cosmogenic isotopes as atmospheric tracers. In: Baskaran M (ed) Handbook of environmental isotope geochemistry. Springer, Berlin
- Lally AE (1992) Chemical procedures. In: Ivanovich M, Harmon RS (eds) Uranium-series disequilibrium. Applications to Earth, Marine, and Environmental Sciences. 2nd Ed. Clarendon Press, Oxford, pp. 95–126
- Matisoff G, Whiting PJ (2011) Measuring soil erosion rates using natural (^7Be , ^{210}Pb) and anthropogenic (^{137}Cs , $^{239,240}\text{Pu}$) radionuclides. In: Baskaran M (ed) Handbook of environmental isotope geochemistry. Springer, Berlin
- Muzikar P, Elmore D, Granger DE (2003) Accelerator mass spectrometry in geologic research. *Geol Soc Am Bull* 115:643–654
- Niedermann S (2002) Cosmic-ray-produced noble gases in terrestrial rocks: dating tools for surface processes. *Rev Mineral Geochem* 47:731–784
- Nielsen SG, Rehkämper M (2011) Thallium isotopes and their application to problems in earth and environmental science. In: Baskaran M (ed) Handbook of environmental isotope geochemistry. Springer, Berlin
- Phillips FM, Castro MC (2003) Groundwater dating and residence time measurements: in *Treatise on Geochemistry* (Holland, H.D., and Turekian, K.K., eds.), Vol. 5, Surface and Ground Water, Weathering, and Soils (Drever, J.I., ed.), Oxford University Press, Oxford, p. 451–497
- Porcelli D (2008) Investigating groundwater processes using U- and Th-series nuclides. In: Krishnaswami S, Cochran JK (eds) U-Th series nuclides in aquatic systems, Elsevier, London, pp 105–154
- Porcelli D, Swarzenski PW (2003) The behavior of U- and Th-series nuclides in groundwater. *Rev Mineral Geochem* 52:317–362
- Rehkämper M, Halliday A (1999) The precise measurement of Tl isotopic compositions by MC-ICPMS: application to the analysis of geological materials and meteorites- reading the isotopic code. *Geochim Cosmochim Acta* 63(63):935–944
- Rehkämper M, Wombacher F, Horner TJ, Xue Z (2011) Natural and anthropogenic Cd isotope variations. In: Baskaran M (ed) Handbook of environmental isotope geochemistry. Springer, Berlin
- Reynolds B (2011) Silicon isotopes as tracers of terrestrial process. In: Baskaran M (ed) Handbook of environmental isotope geochemistry. Springer, Berlin
- Rutgers van der Loeff M, Moore WS (1999) Determination of natural radioactive tracers. In: Grasshoff K, Ehrardt M, Kremling K (eds), Weinheim, Germany: Wiley-VCH, pp. 365–397
- Schaller M, von Blanckenburg F, Hovius N, Kubik PW (2001) Large-scale erosion rates from in situ-produced cosmogenic nuclides in European river sediments. *Earth Planet Sci Lett* 188:441–458
- Schauble EA (2004) Applying stable isotope fractionation theory to new systems. *Rev Mineral Geochem* 55:65–111
- Schwarcz HP, Schoeninger MJ (2011) Stable isotopes of carbon and nitrogen as tracers for paleo-diet reconstruction. In: Baskaran M (ed) Handbook of environmental isotope geochemistry. Springer, Berlin
- Slovak NM, Paytan A (2011) Applications of Sr isotopes in archaeology. In: Baskaran M (ed) Handbook of environmental isotope geochemistry. Springer, Berlin
- Stirling CH, Andersen MB, Potter E-K, Halliday AN (2007) Low-temperature isotopic fractionation of uranium. *Earth Planet Sci Lett* 264:208–225
- Sturchio NC, Clausen JL, Heraty LJ, Huang L, Holt BD, Abrajano A Jr (1998) Chlorine isotope investigation of natural attenuation of trichloroethene in an aerobic aquifer. *Environ Sci Tech* 32:3037–3042
- Sturchio NC, Bohlke JK, Gu B, Hatzinger PB, Jackson WA (2011) Isotopic tracing of perchlorate in the environment. In: Baskaran M (ed) Handbook of environmental isotope geochemistry. Springer, Berlin
- Swarzenski PW, Porcelli D, Andersson PS, Smoak JM (2003) The behavior of U- and Th-series nuclides in the estuarine environment. *Rev Mineral Geochem* 52:577–606
- Tripathy GR, Singh SK, Krishnaswami S (2011) Sr and Nd isotopes as tracers of chemical and physical erosion. In: Baskaran M (ed) Handbook of environmental isotope geochemistry. Springer, Berlin
- van Warmerdam EM, Frape SK, Aravena R, Drimmie RJ, Flatt H, Cherry JA (1995) Stable chlorine and carbon isotope measurements of selected chlorinated organic solvents. *Appl Geochem* 10:547–552
- Vigier N, Bourdon B (2011) Constraining rates of chemical and physical erosion using U-series radionuclides. In: Baskaran M (ed) Handbook of environmental isotope geochemistry. Springer, Berlin
- Willenbring JK, von Blanckenburg F (2010) Meteoric cosmogenic beryllium-10 adsorbed to river sediment and soil: applications for Earth-surface dynamics. *Earth Sci Rev* 98:105–122

Chapter 3

Humans and Isotopes: Impacts and Tracers of Human Interactions with the Environment

Karl K. Turekian

Abstract Radioactive, radiogenic and light stable isotopes have been useful adjuncts in addressing matters of concern to humans including human health, environmental tracers, radioactive geochronometry of the history of humans and forensic uses including reconstructing diets of the past.

3.1 Introduction

Humans are influenced by radioactive and stable isotopes both by affecting them directly and as tracers of processes that affect their well. Some radioactive isotopes have been injected into the environment from human activity such as nuclear warfare, testing and accidents. Most are naturally produced both from the initial composition of Earth and the subsequent continual production by cosmic rays. The former include U isotopes and Th that produce a range of radioactive daughters as well as ^{40}K accompanying potassium in biological systems and the environment. The latter include radiocarbon as well as a host of other radioactive species discussed in Chaps. 7 and 33. The aim of this chapter is to discuss in narrative fashion the salient ways in which these isotopes from various sources affect human health and the environmental processes that influence human activities.

K.K. Turekian (✉)
Department of Geology and Geophysics, Yale University,
New Haven, CT 06511, USA
e-mail: karl.turekian@yale.edu

3.2 Human Health

After Ra was discovered by Marie Curie its various properties as a radiation emitter were utilized mainly for the production of watch faces with luminescent figures and arms. The radiation dose for the wearers was certainly present but the greatest impact was on the workers (mainly women) who painted on the radium solution on the watch faces. Many of these workers eventually came down with radiation-produced diseases (as did Marie Curie) and the mortality rate among watch factory workers became high. The practice continued from 1917 to 1926.

As the result of the increased need for uranium during World War II and thereafter in connection with the nuclear weapons program followed by more peaceful uses, mines developed to obtain uranium ore. One of the daughters of uranium, radon, produced a range of energetic alpha emitting daughters that were adsorbed onto mine dust or cigarette smoke. The inhalation of these aerosols caused an increase in lung cancer rates among uranium miners.

These two processes have been replicated in other situations that arose from related activities. The detonation of nuclear devices into the atmosphere usually penetrated into the stratosphere. As a result long-lived fission isotopes of Sr (^{90}Sr) and Cs (^{137}Cs) made their way slowly into the troposphere and ultimately into the human food chain. After World War II with the increased atmospheric testing lasting until 1962 there was concern about ^{90}Sr entering the human body and lodging in the bone just as Ra had been shown to do. This resulted in an Atomic Energy Commission program called “Project Sunshine” (1953) that was classified for a while. Among the institutions involved in the project was Columbia University and part of my

thesis on the geochemistry and biogeochemistry of Sr was supported by this project to obtain the initial estimate of the expected body burden of ^{90}Sr , with a paucity of bone ^{90}Sr data, based on the distribution of Sr in human bones (Turekian and Kulp 1956).

The concern about the perils of cigarette smoking was pursued by Edward Martell of NCAR. He at first reasoned that tobacco leaves stored in curing barns scavenged Rn daughters that were then inhaled by smoking the tobacco. He soon realized rather that smoking produced aerosols that adsorbed short lived and energetically intense Rn daughters in closed environs such as basements (Martell 1983). This was analogous to the lung cancer associated with U miners. Subsequently basements of houses were checked for Rn seeping in from soils through their foundations. The capture by aerosols and especially smoke from cigarettes would burden the lung with radiation and be one additional contributor to the health hazards of smoking.

As a footnote one of the last things that Martell was working on just before he died was on directly estimating the effects of alpha radiation on genetic variation. Feeding fruit flies free of the lethal gene on food laced with ^{228}Th he determined that the lethal gene was generated over time. Rather than concluding that he had discovered the cause of alpha decay cancer formation instead he concluded that the bombardment of skin surfaces by alpha radiation eliminated many cells to allow reformation to eradicate cells that might be altered by chemical and ultraviolet exposure. Although these results have not been confirmed yet by others it provides an interesting possibility of the possible benefits of some radiation.

Lethality and medical harm caused by extreme radiation as during a nuclear blast or accidental exposure around a nuclear facility is the concern for all involved in nuclear activities. Care in the operation of nuclear power plants is exercised with great diligence because of these concerns and the proper disposal of nuclear waste remains a primary consideration in the exploitation of nuclear energy.

3.3 Natural and Artificially Produced Radionuclides as Environmental Tracers

The properties of the atmosphere and oceans and freshwater system of importance to human activities can be studied using the radionuclides discussed

above. Specifically the following applications have been made:

- (a) The mean residence time of air in the stratosphere was initially determined by heat balance in the atmosphere but confirmed by measurements of the fluxes of the bomb produced nuclides ^{90}Sr and ^{137}Cs each with half lives of about three decades. The concentration in stratospheric air and the flux to Earth's surface provided such information (Peirson et al. 1966). This measurement can also be made using the cosmogenic isotopes such as ^{10}Be . The mean residence time of stratospheric air also provides a method of determining the flux of tropospheric pollutants to the stratosphere. These fluxes provide a measure of the rate of destruction of stratospheric ozone. They also can be used to determine the rate of supply of water responsible for the formation of stratospheric and upper tropospheric cirrus clouds, important as a component of tropospheric heating.
- (b) The mean residence time of aerosols in the troposphere has been determined using ^{210}Pb and its daughters, ^{210}Bi and ^{210}Po . The ^{210}Pb is produced in the decay chain of ^{222}Rn which is supplied to the atmosphere from soils (Turekian and Graustein 2003 – This reference will be used in several places in the following discussion because it is a summary paper with appropriate references contained therein). The value obtained for the troposphere is about 5 days based on the standing crop of ^{210}Pb in the troposphere and the precipitation flux of ^{210}Pb . The application of this residence time to aerosols injected into the troposphere from pollution sources and natural elevation of submicron aerosols from fires and dust storms provides a way of determining the extent of transport of those aerosols from point sources.
- (c) Sources of potential pollutants can be tracked by using both atmospheric ^{210}Pb and cosmogenic ^7Be . The former has its highest concentration near Earth's surface, decreasing with elevation and the latter increases with elevation. Thus the ratio of ^7Be to ^{210}Pb provides a unique indication of the source of other components of tropospheric air. Using this property it was discovered that in the free troposphere in the Canary Islands the source of both ozone and nitrate was the upper troposphere and was not related to either biomass burning in Africa or pollution from high population centers in Europe (Turekian and Graustein 2003).

- (d) The short-lived isotopes, ^{210}Pb , ^{90}Sr and ^{137}Cs have been used to determine time in salt marsh deposits and lake sediments to track the pollution history of various environments. ^{210}Pb has also been used in salt marshes to determine the rate of rise of sea level over the past 100 years due to global warming and the associated increase in the volume of the oceans because of valley glacial melting, ground water exploitation and thermal expansion. These are clearly ways of monitoring the impact of humans on the environment (Von Damm et al. 1979; McCaffrey and Thomson 1980; Cochran et al. 1998).
- (e) Bomb produced tritium in the atmosphere reach the marine environment as water molecules exchange with the surface ocean. In the North Atlantic, where the deep water has its origin at high latitudes, the use of ^3H - ^3He dating to determine the rate of formation of North Atlantic Deep Water and the rate of its transport meridionally has been done using mass spectrometric measurements of ^3He (Jenkins 2008). This type of information feeds directly into the understanding of the oceanic “conveyor belt” some consider a critical component in understanding the effects of global warming and fresh water fluxes to the high latitude oceans.
- (f) The transport of chemicals in ground waters can be traced using the emission and adsorption properties of members of uranium and thorium decay series. Using the Rn flux to the ground water as a measure of other recoil fluxes of alpha emitters in the uranium and thorium decay chains the retardation factors for a number of elements can be determined. These include Pb, Ra, Th and U. By analogy to these elements responsive to oxidation-reduction conditions as well as acidity and salinity the result can be extended to a range of ionic species including those associated with nuclear materials that might be stored underground and subject to accidental release to ground water (Krishnaswami et al. 1982).

3.4 Radioactive Geochronometry of Human Development

- (a) The history of human evolution has been documented using principally the radioactive isotope ^{40}K that decays to ^{40}Ar . Potassium in volcanic

materials can be dated using this technique. In some cases the dates can be backed up with U-Pb dating of zircons but the main tool for determining the time scale of hominid evolution especially in east Africa is via the ^{40}K - ^{40}Ar dating method. A current chronology of hominid evolution in east Africa and its relation to climate change is reported in a National Research Council report entitled “Understanding climate’s influence on human evolution” (2010).

In addition to this method, which has been useful over a five million year time period, travertine deposits (and in some cases bones) have been dated using the ^{234}U - ^{238}U - ^{230}Th decay chain. This method has been found useful for about 300,000 years (Shen et al. 2004; Shen et al. 2007).

- (b) Dating using radiocarbon (^{14}C) with a half-life of 5,730 years has provided important chronological data for human migration and development. Once it had been discovered that the $^{14}\text{C}/^{12}\text{C}$ ratio in the atmosphere had not remained constant over time efforts were made to calibrate the time dependent variation using tree rings. These results were only useful to about 10,000 years before present. The problem of extending the information on variability over a longer period of time was resolved by the use of coral, specifically those in a section undergoing submergence off Barbados, for precise dating using the ^{234}U - ^{238}U - ^{230}Th dating technique alluded to above. Precise dates of corals matched with the radiocarbon content of the synchronously dated coral provided accurate information on the history of variability of atmospheric $^{14}\text{C}/^{12}\text{C}$ over the past 50,000 years (Fairbanks et al. 2005).

One of the greatest triumphs of this approach was to determine the migration time scale of *Homo sapiens* along the European side of the Mediterranean Sea as humans migrated from the near east beginning 49,000 years BP to Spain, reaching there at about 41,000 years BP (Mellars 2006). This migration was accomplished in the interstadial of the last major glaciation when Europe, especially the southern part, was relatively more ice free than during peak glaciation. The rate of migration was about a kilometer a year. Curiously this is the same rate as the spread of agriculture from the near east to northwestern Europe about 7,000 years ago!

3.5 The Forensic Uses of Radiative and Stable Isotopes

- (a) Tracing human diets using carbon isotopes has proven to be a valuable pursuit in anthropology and human history. The ratio of ^{13}C to ^{12}C usually expressed as variations relative to a standard as delta values ($\delta^{13}\text{C}$) is different for different food sources used by humans over time and place. For example, the value for C3 plants and animals feeding on them has a $\delta^{13}\text{C}$ value of -25 . C4 plants such as maize, sorghum and cane sugar have $\delta^{13}\text{C}$ values of about -12.5 . Sea food generally is also on the less negative side. By using these differences, carbon in fossil human bones can be used to determine the source of food and how it changed over time. For example it was shown that the ancestors of the Viking in Denmark shifted from eating marine animals to agriculture-based products composed of C3 plants about 5,000 BP. In North America the southwestern native population survived on a maize food base seen as a $\delta^{13}\text{C}$ value of -12.5 in carbon in their bones. The native populations of the Midwest and to the east were dependent on C3 plants and animals using these plants for nourishment until about 1,000 BP when maize was introduced. This radically change the culture of the Midwest and the northeast and this transition can be seen in the carbon isotopes of fossil human bones where there is a shift in $\delta^{13}\text{C}$ from -25 to -12.5 .
- (b) Oxygen and hydrogen isotopes in textiles and related materials will record the isotopic composition of the water from which the fibers were formed whether vegetable or animal. For example, the paper used in American currency is uniquely made of cotton from Texas fields grown with irrigated water from the Ogallala formation and has a unique oxygen and hydrogen isotopic composition (commonly expressed as $\delta^{18}\text{O}$ and δD) (Ehleringer, personal communication). Similarly textiles from the Aswan region of the Nile River has been shown to be partitioned into early locally grown cotton and later imported flax from the Nile delta region because of the diagnostic water isotopic compositions of the upper Nile water source and the modified water at the delta region (Judith Schwartz, personal communication).
- (c) A similar use of oxygen and hydrogen isotopes has been used to identify the sources of bacteria in the study of epidemiology (Kreuzer-Martin et al. 2003). Also these isotopes provide definite markers for the sources of drugs such as marijuana which may be important in tracking down the sources in drug trafficking.
- (d) There are some times when the issue of authenticity of human artifacts is in question. In those cases it is possible that some of the information contained in radioactive isotopes can be of assistance. One example is the establishment of the true antiquity of an iron object. Before about 1789 all iron was made using charcoal and the carbon alloyed or occluded with the iron would have a radiocarbon signature that actually could be used in chronometric studies (van der Merwe 1969). Any iron artifact manufactured using coke would not have radiocarbon in it thereby distinguishing it from the older material. If there were any question about the authenticity of an iron object purportedly made before the eighteenth century it could be verified with a radiocarbon measurement (Turekian 1977).
- Also most contemporarily available lead has been processed from recycled lead exposed to rainfall and therefore impacted by atmospherically derived ^{210}Pb . This was discovered when lead from bombed cathedrals in England during World War II were assayed for radioactivity with the prospect of using “old” lead for radioactive shielding in the Manhattan Project. Since ^{210}Pb has a half-life of 22 years any object made of lead, whether it contained ^{210}Pb or not from any source, would have decayed away whereas any object made using contemporary commercially available lead would be high in ^{210}Pb . This difference has been used to establish the authenticity of lead bearing artifacts of questionable chronological authenticity found in museums. In principle the method can be applied to white lead oxide used in paintings as well as in assaying lead containing alloys in testing for authenticity (Keisch 1968).
- (e) Another use of forensics involving isotopes is the tracking of nuclear proliferation, nuclear bomb testing and nuclear fuel processing. These provide important constraints on treaties and environmental considerations. For example each nuclear blast has characteristic plutonium isotope signatures as

well as xenon isotope signatures. The measurement of contemporary atmospheric gas samples and aerosols can determine if there has been clandestine testing of a nuclear device. A record of past nuclear activity from a variety of sources can be determined from the Pu isotope signature observed in such historical records as ice cores and sediments. Where spent nuclear fuel has been processed ^{129}I (half-life of 17 million years) is commonly released and if this release is adjacent to the oceans it can act as a tracer for surface ocean circulation (Edmonds et al. 2001).

3.6 Conclusions and Future Directions

Radioactive and stable isotopes have served as hazards, tracers and forensic tools for a number of human encounters. The capacity to make refined measurement of a variety of radioactive and stable isotopes on ever smaller sample sizes will allow the tracing of organic compounds as well as small quantities of pollutants for effective evaluation of human involvement with the environment. Clearly the study of the presence and distribution of these various isotopes has and will continue to have significance for every aspect of human life. The continued exploration for these applications is certain to be made in the future.

References

- Cochran JK, Frignani M, Salamanca M et al (1998) Lead-210 as a tracer of atmospheric input of heavy metals in the northern Venice Lagoon. *Mar Chem* 62:15–29
- Edmonds HN, Zhou ZQ, Raisbeck G et al (2001) The distribution and behavior of anthropogenic ^{129}I in water masses ventilating the North Atlantic. *J Geophys Res* 106: 6881–6894
- Fairbanks RG, Mortlock RA, Chiu T-C et al (2005) Radiocarbon calibration curve spanning 0 to 50,000 years BP based on paired ^{230}Th / ^{234}U / ^{238}U and ^{14}C dates on pristine corals. *Quat Sci Res* 24:1781–1796
- Jenkins WJ (2008) Tritium-helium dating. *Encyclopedia of Ocean Sciences* (Second Edition) doi:10.1016/B978-012374473-9.00164-8 Elsevier, Editor-in-Chief: John H. Steele, Karl K. Turekian, and Steve A. Thorpe, London
- Keisch B (1968) Dating works of art through their natural radioactivity: Improvements and applications. *Science* 160: 413–415
- Kreuzer-Martin HW, Lott MJ, Dorigan J, Ehleringer JR (2003) Microbe forensics: Oxygen and hydrogen stable isotope ratios in *Bacillus subtilis* cells and spores. *Proc Nat Acad Sci* 100:815–819
- Krishnaswami S, Graustein WC, Turekian KK, Dowd JW (1982) Radium, thorium and radioactive lead isotopes in groundwaters: application to the in situ determination of adsorption-desorption constants and retardation factors. *Water Resources Res* 18:1663–1675
- Martell EA (1983) a-radiation dose at bronchial bifurcations of smokers from indoor exposure to radon progeny. *Proc Nat Acad Sci* 30:1285–1289
- McCaffrey RJ, Thomson J (1980) A record of the accumulation of sediment and trace metals in a Connecticut salt marsh. In: Saltzman, B., Ed., *Estuarine physics and chemistry: studies in long island sound*. *Adv Geophys* 22:129–164
- Mellars P (2006) A new radiocarbon revolution and the dispersal of modern humans in Eurasia. *Nature* 434:931–934
- National Research Council (2010) *Understanding climate's influence on human evolution*. The National Academies Press, Washington, p 115
- Peirson DH, Cambray RS, Spicer GS (1966) Lead-210 and polonium-210 in the atmosphere. *Tellus XVIII* 2:427–433
- Project Sunshine (1953) *Worldwide effects of atomic weapons*. R-251-AEC (amended) 112 pp. Rand Corporation, copyright 1956
- Shen GJ, Cheng H, Edwards RL (2004) Mass spectrometric U-series dating of New Cave at Zhoukoudian, China. *J Arch Sci* 31:337–342
- Shen GJ, Wang W, Cheng H, Edwards RL (2007) Mass spectrometric U-series dating of Laibin hominid site in Guangxi, southern China. *J Arch Sci* 34:2109–2114
- Turekian KK (1977) Physical and chemical approaches to the study of archaeological materials. *Discovery (Yale Peabody Museum)* 12(2):52–64
- Turekian KK and Graustein WC (2003) Natural radionuclides in the atmosphere. In: *The Atmosphere* (ed. RF Keeling) Vol.4 *Treatise on Geochemistry* (eds HD Holland and KK Turekian). Elsevier-Pergamon, Oxford, pp 261–279
- Turekian KK, Kulp JL (1956) Strontium content of human bones. *Science* 124:405–407
- van der Merwe NJ (1969) *The carbon-14 dating of iron*. University of Chicago Press, Chicago
- Von Damm KL, Benninger LK, Turekian KK (1979) The ^{210}Pb chronology of a core from Mirror Lake, New Hampshire. *Limnol Oceanogr* 24:434–439

Part II
**Isotopes as Tracers of Continental
and Aquatic Processes**

Chapter 4

Lithium Isotopes as Tracers in Marine and Terrestrial Environments

K.W. Burton and N. Vigier

Abstract The investigation and the use of lithium isotopes as tracers of water-rock interactions at low and high temperature have significantly developed over the last 10 years. This chapter relates our current understanding of lithium isotope and elemental behaviour in the Earth's surface environment. In the introduction, we provide information on the chemical properties and behaviour of lithium, its occurrence and applications. The first section reviews the techniques used for the measurement of Li isotopes. The second section outlines the primary sources of Li in the environment and their potential impact on the hydrological cycle. The third and fourth sections investigate the impact of chemical weathering of continental rocks and oceanic crust, respectively. Finally, the last section assesses marine records of lithium.

4.1 Introduction

Naturally occurring lithium (Li) has two stable isotopes, ${}^6\text{Li}$ and ${}^7\text{Li}$, (7.52% ${}^6\text{Li}$ and 92.48% ${}^7\text{Li}$), which have the largest relative mass difference of any isotope pair (~16%) aside from hydrogen and deuterium. Lithium is fluid-mobile, moderately incompatible, and like other alkali metals is only present on Earth in the +1 valence state, so the isotope composition is not directly influenced by redox reactions. Moreover,

unlike more established light isotope systems (such as C, O and S), lithium is a trace element and does not form an integral part of hydrological, atmospheric or biological cycles.

Nevertheless, there is significant potential for mass-dependent fractionation, demonstrated by the early experiments of Taylor and Urey (1938) who separated ${}^6\text{Li}$ from ${}^7\text{Li}$ using ion exchange chromatography, suggesting natural chemical exchange processes, such as water-rock interaction, have the potential to generate distinct isotope reservoirs on Earth.

4.1.1 Occurrence of Lithium

In the solar system: Lithium was one of the few elements produced during Big Bang nucleosynthesis, within the first 3 min of the beginning of the Universe (e.g. Spite and Spite 1982; Burles et al. 2001). Lithium is also produced during stellar nucleosynthesis, however, stellar processes tend to destroy lithium, along with beryllium and boron, so their abundances in the solar system are lower than might be expected by comparison with elements with either lower or higher atomic numbers. Stars that achieve temperatures necessary for fusing hydrogen (2.5×10^6 K) rapidly lose their Li through collision of ${}^7\text{Li}$ and a proton, producing two ${}^4\text{He}$ nuclei. Convection in low mass stars mixes the Li into the hotter interior where it will be destroyed (e.g. Korn et al. 2006). Therefore the presence of Li in a star's spectrum is a good indication that it is sub-stellar (that is, a Brown dwarf too low in mass to sustain hydrogen fusion). As a consequence of these stellar processes most of the lithium, and beryllium and boron, in the solar system was formed through cosmic ray (mostly high energy proton) mediated break-up

K.W. Burton (✉)

Department of Earth Sciences, Durham University, Science Labs, Durham, DH1 3LE, UK
e-mail: kevin.burton@durham.ac.uk

N. Vigier

CRPG-CNRS, Nancy Université, 15 rue Notre Dame des Pauvres, 54500 Vandoeuvre-les-Nancy, France

(spallation) of heavier elements residing in interstellar gas and dust (e.g. Olive and Schramm 1992).

On Earth: Lithium is widely distributed on Earth, but does not occur naturally in elemental form due to its very high reactivity. Lithium abundances in mantle rocks range from 0.1 to 7.7 ppm by weight, whereas crustal rocks range from 1 to 80 ppm, with an average abundance of 22 ppm, making Li the 25th most abundant element in the Earth's crust. Lithium is incompatible in most minerals but is preferentially incorporated into biotite, cordierite and alkali-feldspar, and forms a major element in spodumene ($\text{LiAl}[\text{Si}_2\text{O}_6]$) and petalite ($\text{Li}[\text{AlSi}_4\text{O}_{10}]$) characteristic minerals in Li-rich granitic pegmatites, both of which are, at present, the most commercially viable sources of Li. The world's largest reserve base of lithium is located in brines under salt flats, in the Salar de Uyuni area of Bolivia, which are estimated to hold at least 5.4 million tons of Li (US Geological Survey 2009).

4.1.2 Applications of Lithium

High temperature lubricant: Because of its high specific heat capacity, the highest of all solids, lithium is often used as a coolant for heat transfer applications. Thus, the first major application of lithium was as a high temperature lubricant for aircraft engines, and lithium stearate is still used at the present day.

Thermonuclear weapons: Lithium deuteride (${}^6\text{Li}^2\text{H}$) is the fusion fuel used in thermonuclear weapons of the Teller-Ulam design. The lithium deuteride is bombarded with neutrons, heated and compressed, producing tritium from the lithium, which then triggers a reaction between deuterium and helium nucleons.

Nuclear energy: Lithium fluoride (enriched in ${}^7\text{Li}$) also forms a constituent of the fluoride salt mixture (LiF-BeF_2) into which uranium and thorium are introduced in liquid-fluoride nuclear reactors.

Medical use: Lithium is used medically for the treatment of bipolar disorders (e.g. Schou 1988). How Li^+ works remains a matter of debate – but it is known to elevate levels of serotonin – however, therapeutic levels of Li are only slightly lower than toxic amounts, which affect the muscular and renal system. Lithium isotopes potentially offer a means of quantifying Li dosage, and ${}^6\text{Li}$ and ${}^7\text{Li}$ have a differential effect on kidney health (Stoll et al. 2001).

The enrichment of lithium for the nuclear industry has used: (1) ion exchange (Colex separation) of a lithium-mercury amalgam and lithium hydroxide solution, where ${}^6\text{Li}$ has a greater affinity for mercury than ${}^7\text{Li}$ (Palko et al. 1976); (2) vacuum distillation, where lithium is heated in a vacuum and gaseous isotopes diffuse at different speeds because of their different atomic weights, and are collected preferentially on a cold surface; (3) electrochemical separation (Umeda et al. 2001). Enrichment factors for ${}^6\text{Li}$ of 1–8% are typical of these techniques (Symons 1985). One interesting side effect of these industrial enrichment processes is that some commercial standards possess highly anomalous isotope compositions with over 300% enrichment in ${}^7\text{Li}$ relative to natural terrestrial materials (Qi et al. 1997).

Lithium and its compounds also have a number of industrial applications including high-resistance glass and ceramics, and high strength to weight alloys in aircraft (see also Bach 1985). Of increasing importance is the use of lithium as an anode material in rechargeable batteries, because of the low atomic mass of Li such batteries have a high charge and power-to-weight ratio.

4.2 Analytical Methods

The sampling procedures used for Li isotope analyses of environmental materials, such as river or soil pore waters and particles, are essentially the same as those used for trace element analyses. In brief, waters are filtered at 0.2 or 0.45 μm using frontal filtration techniques and stored in acid pre-cleaned polyethylene or polypropylene bottles. After acidification to a pH of 2, bottles are stored at 4°C (see e.g. Witherow et al. 2010; Kisakurek et al. 2005; Millot et al. 2010a, b, c). River particles, soils and sediments are dissolved in a mixture of concentrated acids (usually HF, HNO_3 , HCl, and sometimes HClO_4) (e.g. Vigier et al. 2009). Lithium isotopes in such samples are analysed either using TIMS (James and Palmer 2000a), QUAD-ICP-MS (Kosler et al. 2001; Vigier et al. 2008) or MC-ICP-

MS (Millot et al. 2004; Jeffcoate et al. 2004; Hathorne and James 2006). Analysis using MC-ICP-MS enables the measurement of lower level samples, such as carbonates (<1 ppm) and waters (ppb level), with better precisions (<1‰). All of these techniques require the pre-separation of Li from the rest of the sample matrix, in order to avoid interference and matrix effects that are difficult to correct for at the level of precision required. All of these separation techniques use chromatography and cation exchange resins (in particular, the AGW 50X8 resin). Two types of eluant used in recent studies can be found in recent literature: organic based eluant (using a mixture of ethanol or methanol with nitric or hydrochloric acid) (Moriguti and Nakamura 1998; Tomascak et al. 1999; Marriott et al. 2004a; Rosner et al. 2007; Witherow et al. 2010; Nishio et al. 2010), and dilute HCl (Chan 1987; You and Chan 1996; James and Palmer 2000a; Hall et al. 2005; Millot et al. 2004). Since Li isotopes significantly fractionate during the elution, a yield of 100% is necessary. This yield can be confirmed by measuring Li content in the sample before and after column elution. However, it is important to note that even a small percentage loss of Li may bias the $\delta^7\text{Li}$ value by a few per mil. The analysis of a well-characterised secondary standard, having a similar matrix to the sample, provides another means of establishing the accuracy of the entire chemical and analytical procedure. Seawater, rock reference materials and Li solutions doped with various elements are generally used. A review of published $\delta^7\text{Li}$ values for these reference materials can be found in Carignan et al. (2007) and Jeffcoate et al. (2004).

Lithium isotope analysis using Quad and MC-ICPMS techniques are undertaken following the standard-bracketing method, using L-SVEC as the bracketing standard. This allows the instrumental mass bias and its variation as a function of time to be corrected for. For analyses, the Li fraction is dissolved in highly diluted nitric acid (typically from 0.05 to 0.5 M HNO_3), and passed through either a dual cyclonic/Scott spray chamber or a desolvating system before being injected in the Ar-plasma of the mass spectrometer (see e.g. Millot et al. 2004; Rosner et al. 2007; Hathorne and James 2006). Using MC-ICP-MS, the long-term reproducibility of pure Li solutions is better than 0.3‰ at the 2σ level (Millot et al. 2010a). For reference materials, that additionally need

to go through the chromatographic separation procedure, this reproducibility is estimated to be 0.4–0.5‰ for seawater (Millot et al. 2010a, 2004), and 0.6‰ for JB-2 (a basalt standard from Geological Survey of Japan) (see Carignan et al. 2007 for a compilation).

Recently, Li isotopes have also been measured in situ in low level environmental samples (such as carbonates), using the 1270 Ion Microprobe (Chaussidon and Robert 1998; Kasemann et al. 2005; Vigier et al. 2007; Rollion-Bard et al. 2009). The estimated reproducibility of this technique for the analyses of corals and foraminifera tests is $\sim 2\%$ (2σ). The instrumental mass bias is corrected for using a carbonate standard having the same matrix and being isotopically homogeneous, and for which the $\delta^7\text{Li}$ value has been measured with a MC-ICP-MS technique (Vigier et al. 2007; Rollion-Bard et al. 2009).

4.3 Primary Sources of Li in the Environment

4.3.1 $\delta^7\text{Li}$ of the Oceanic and the Continental Crust

Most of the Li of the silicate Earth is located in the mantle (91.8%). Since Li is incompatible during magmatic processes, the continental crust is enriched in Li compared to the oceanic crust, which contain 7 and 1% of the global Li budget respectively (Teng et al. 2004). Inorganic and biogenic carbonates are particularly depleted in Li (usually 1 ppm in pure carbonate) and this reservoir is minor in the overall Li budget (Hoefs and Sywall 1997).

The average $\delta^7\text{Li}$ value for MORB estimated by Tomascak et al. (2008) is $3.7 \pm 1.9\%$ close to that estimated for the undepleted upper mantle (3.5‰; Jeffcoate et al. 2007) (Fig. 4.1). The range of $\delta^7\text{Li}$ values in MORB is relatively narrow, between 1.5 and 5.6‰, but still significantly larger than that for mantle peridotite (displaying a 1‰ range), considered to represent the residual source of MORB melts. The cause of the measured heterogeneity displayed by MORB remains a matter of debate (cf. Elliott et al. 2006; Tomascak et al. 2008). Crystal fractionation induces only minor Li isotope fractionation

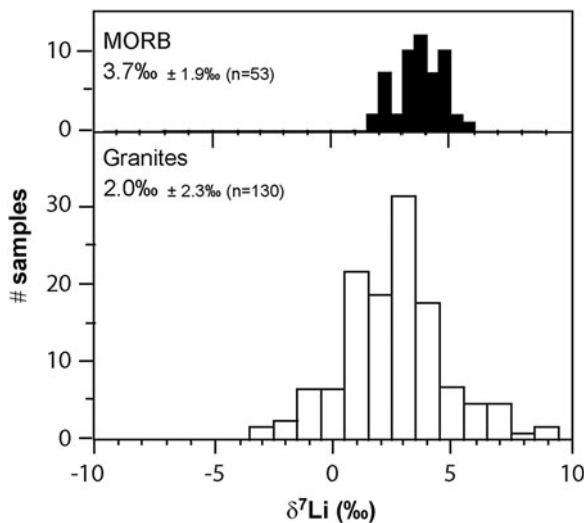


Fig. 4.1 Li isotope compositions of pristine MORB (Tomascak et al. 2008), and granites from the continental crust (Teng et al. 2004, 2008, 2009)

(Tomascak et al. 1999), and diffusion effects may be difficult to preserve in ridge magma chambers with high melt to rock ratio. Incorporation of recycled subduction-metasomatized upper mantle in the MORB source may explain the correlations highlighted with radiogenic isotopes from two localities on the East Pacific Rise (EPR) (Elliott et al. 2006). Alternatively the incorporation of seawater altered components in shallow level magma chambers may explain some of the highest MORB $\delta^7\text{Li}$ values (Tomascak et al. 2008).

Continental granites of various types (I, A, S) display an average $\delta^7\text{Li}$ value slightly lighter than that of the mantle (Teng et al. 2008). The Li isotope composition for the continental crust has recently been estimated to be $2.0 \pm 2.3\text{‰}$, and the corresponding range is large (-3.1 to $+8.1\text{‰}$) compared to MORB. This lighter composition is best explained by weathering and water-rock interactions, that have, over geological timescales, successively removed “heavy” lithium from the continents, which has been carried away by river and ground waters to the ocean (see following sections). However, even if shales are significantly enriched in clay minerals and in Li, they display a similar range of $\delta^7\text{Li}$ to loess and granites (Teng et al. 2004), and the overall role of weathering on the isotope composition of the present-day continental crust still remains to be investigated.

4.3.2 Li Isotope Composition of Natural Waters

The best evidence of fractionation of Li isotopes during low temperature weathering is the systematic enrichment of natural waters in ^7Li (river, groundwaters and the ocean), when compared to the drained bedrocks. In rivers, the $\delta^7\text{Li}$ value of the dissolved phase is systematically higher than the $\delta^7\text{Li}$ value of suspended or bed sediments (see Fig. 4.2). This contrasted feature is observed everywhere, in mixed lithology basins, but also in small monolithologic basins, such as the basaltic basins of Iceland (Vigier et al. 2009) and the granitic sub-basins of the Orinoco and the Mackenzie (Huh et al. 2001; Millot et al. 2010b). In addition, for all mixed lithology basins studied thus far, most of the dissolved Li (>80%) is estimated to derive from the weathering of silicate lithologies present within the basin (Kisakurek et al. 2005; Millot et al. 2010b).

Atmospheric precipitation (rain and snow) possesses low Li contents, but highly variable $\delta^7\text{Li}$ values (Millot et al. 2010b, c). The range displayed by rainwaters collected in France is 3–96‰. The highest values are explained by a significant contribution of anthropogenic lithium potentially derived from fertilizers in agricultural areas, suggesting that such pollution may significantly impact the lithium isotope signatures in some rivers, an aspect yet to be investigated.

A recent compilation of $\delta^7\text{Li}$ values measured in filtered seawater highlighted significant dispersion of the data (28.9–33.4‰) (Carignan et al. 2004). This was surprising since the ocean is expected to be isotopically homogenous as the residence time of lithium in the ocean is long (~ 1 Ma) (Stoffyn-Egli and Mackenzie 1984; Huh et al. 1998). More recently, improved chemical purification and new generation of MC-ICP-MS instrumentation have enabled a much improved precision, and the most recent estimate of $\delta^7\text{Li}$ for North Atlantic seawater is $31.2 \pm 0.4\text{‰}$ (e.g. Millot et al. 2010a; Jeffcoate et al. 2004), which corresponds well to the mean value obtained when considering all published data for the ocean. This value for seawater is significantly higher than the $\delta^7\text{Li}$ values determined for its principal Li sources: the average $\delta^7\text{Li}$ for oceanic hydrothermal fluids is 9‰, and for river waters is 23.4‰ (Huh et al. 1998). This offset might be partly accounted for a better estimate of Li sources to the

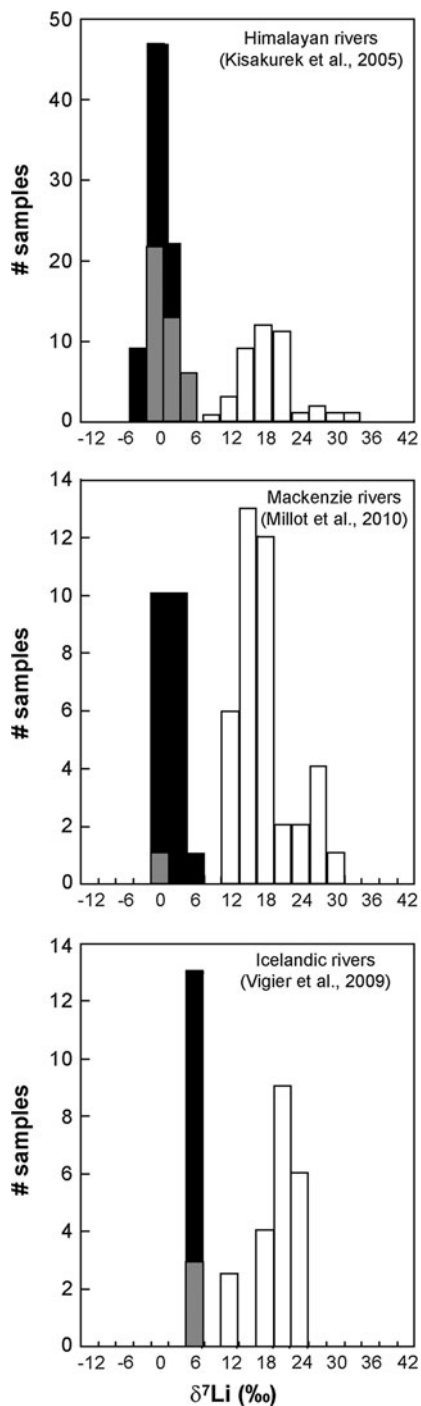


Fig. 4.2 Histograms showing the Li isotope composition of selected river waters (in white), suspended sediments (in grey) and bedload sands (in black). River water $\delta^7\text{Li}$ values are systematically higher than those measured for river particles and sediments, for both mixed lithology basins (Himalaya, Canada) and monolithologic basins (in Iceland). The range of values measured in river solid phases is narrow and close to the average of the source rocks (see Fig. 4.1)

ocean and their isotope compositions. Also, low temperature seafloor weathering and the formation of ^6Li -rich oceanic clays are thought to play a key role in the Li ocean cycle (see the following sections).

4.4 Using Li Isotopes as Tracers of Continental Weathering

Lithium is relatively mobile in the weathering environment, as a result of its low ionic charge, relatively small ionic radius (approximately 0.068 nm; Shannon 1976) and high degree of covalency. Stable isotopes, such as those of lithium, will not be affected by variations in rock and mineral composition that result from the decay of the parent isotope over time, such as for example, for the rubidium-strontium (^{87}Rb - ^{86}Sr) or lutetium-hafnium (^{176}Lu - ^{176}Hf) isotope systems (e.g. Blum and Erel 1995; Bayon et al. 2006). Nevertheless, there are a number of processes that may lead to the fractionation of ^6Li and ^7Li during weathering, including:

Primary mineral dissolution: The composition and mineralogy of the parent bedrock determines the initial isotope composition of the waters during mineral dissolution. The primary mineralogy also partly determines which elements are available in solution to form secondary minerals. Previous studies suggest that there is little fractionation of Li isotopes at magmatic temperatures (e.g. Tomascak et al. 1999) and little variation in the composition of coexisting minerals (Chan and Frey 2003). Hence under normal circumstances the preferential weathering of a primary mineral phase should not generate significant differences in the Li isotope composition of waters. Nevertheless, in principle, during diffusion or the incongruent dissolution of primary phases small differences in the bond energies of ions of a different mass may result in isotope fractionation (O'Neil 1986). For lithium breaking the higher energy bonds of ^6Li is energetically favourable, potentially enriching any solution with the lighter isotope.

Secondary mineral formation: Lithium is highly hydrated in aqueous solutions relative to most other alkali metals, and ordinarily assumes tetrahedral hydrated coordination (Olsher et al. 1991). In most minerals lithium occupies either tetrahedrally- or octahedrally coordinated sites (Olsher et al. 1991; Wenger and

Armbruster 1991). During the process of crystallization isotope fractionation can occur when an energetic advantage is gained by the incorporation of one isotope over another into a crystallographic site (O'Neil 1986). On the basis of ab initio calculations, ^6Li is preferentially incorporated into octahedral crystallographic sites of minerals from aqueous solution (Yamaji et al. 2001).

Adsorption onto minerals: Adsorption of aqueous ions onto mineral surface sites is another mechanism that can potentially lead to isotope fractionation. Sorption of Li onto minerals from aqueous solutions at ambient temperatures has been seen in a range of minerals (Taylor and Urey 1938; Anderson et al. 1989) despite early predictions that Li would tend to be the least sorbed of the alkalis, due to its high degree of hydration (Heier and Billings 1970). Sorption and retention of ions from solution depends upon both mineral surface chemistry and the composition of the solution. Early experiments were taken to indicate that the magnitude of mass fractionation on desorption is equivalent to that of adsorption (Taylor and Urey 1938) however, empirical data suggest that this fractionation is not reversible (Comans et al. 1991; James and Palmer 2000a, b). The irreversibility of this process has been attributed to physical adsorption into crystallographic surface sites rather than surface ion exchange sites, in which case the magnitude of this effect will vary among minerals.

The actual secondary minerals formed depends upon elemental supply (saturating solutions in their constituent elements), the stability of those phases (principally controlled by pH and temperature), and their formation kinetics. Lithium is not a nutrient element, and there appears to be little Li isotope fractionation accompanying incorporation into biomass (Lemarchand et al. 2010). Nevertheless, the depletion of other elements, such as K and Mg, due to their incorporation into biomass may inhibit the formation of secondary minerals, indirectly affecting the isotope behaviour of Li (Pogge von Strandmann et al. 2010).

In this section we review how experimental work and studies of soils and rivers yield key information on the influence of weathering processes on Li isotopes, and highlight the utility of Li isotopes as a weathering tracer. Also, studies of Li in the estuarine environment illustrate how the continental weathering signal is transferred to the oceans.

4.4.1 Experimental Work

Primary mineral dissolution: Partial dissolution of basalt in dilute HNO_3 does not result in fractionation of Li isotopes (Pistiner and Henderson 2003) although similar dissolution of granite did result in significant apparent fractionation of Li isotopes. This was attributed to the dissolution of secondary phases in the granite or differences in the isotope composition of primary igneous minerals in this more evolved rock (Pistiner and Henderson 2003). More recently controlled experimental dissolution of basalt glass and olivine at pH and temperatures appropriate to natural conditions (pH 2–4; $T = 25^\circ\text{C}$) indicates that there is no resolvable Li isotope fractionation accompanying dissolution of single phases (Wimpenny et al. 2010b). These experimental observations suggest that primary mineral dissolution does not result in significant fractionation of Li isotopes.

Secondary mineral formation: On the basis of natural observations and experiments the formation of clays, both at high and low temperatures, is thought to be the major process responsible for the fractionation of Li isotopes at the Earth's surface and the high $\delta^7\text{Li}$ found in waters (see Sect. 4.3). However, there are few experimental studies where Li isotope behaviour has been quantified for the crystallisation of a single phase. Clays are not systematically enriched in Li and the type of clay may influence water isotope signatures. Past work has shown that Li behaviour in soils and waters is strongly linked to that of magnesium (e.g. Huh et al. 1998), suggesting that Mg-bearing primary and secondary phases play a key role in the Li cycle.

Williams and Hervig (2005) studied the Li isotope fractionation of experimentally synthesized illite and smectite under controlled P-T and fluid conditions. It was found that during illitization, Li substitutes into the octahedral sites. The elemental concentration and isotope composition were found to reach a steady state with the onset of nearest neighbour (R1) ordering. However, isotope fractionation for Li of between -5 and -11‰ varied systematically with crystal size, suggesting that kinetic effects may influence Li uptake by clays. More recently tri-octahedral Mg-Li smectites (hectorites) were synthesized at temperatures ranging between 25 and 250°C (Vigier et al. 2008). The Li isotope fractionation factors linked to the incorporation of Li into the octahedral sites, in substitution for

Mg^{2+} , were determined. Experimental $\Delta^7\text{Li}_{\text{clay-solution}}$ correlates inversely with temperature, as theory predicts, and ranges between $-1.6 \pm 1.3\text{‰}$ at 250°C and $-10.0 \pm 1.3\text{‰}$ at 90°C , and then stays relatively constant down to 25°C . The relatively constant isotope fractionation below 90°C was attributed to high concentrations of edge octahedra in low crystallinity smectites. It was also found that the fractionation factor does not depend on the solution composition, nor on the amount of Li incorporated into the clay, at a given temperature. Experimental precipitation of chrysotile from olivine dissolution also results in a significant Li isotope fractionation of the residual fluids (Wimpenny et al. 2010b) although there was insufficient chrysotile for measurement and quantification of the fractionation into the solid phase.

Adsorption: Zhang et al. (1998) found a similar degree of Li isotope fractionation during Li sorption from seawater onto kaolinite and vermiculite, $\alpha = 0.979$ and 0.971 , respectively. Pistiner and Henderson (2003) undertook Li sorption experiments on a variety of minerals and found that isotope fractionation does not occur when Li is not structurally incorporated into the solid (physical sorption) for example during outer sphere sorption of Li onto smectite. By contrast, when Li is incorporated by stronger bonds (chemical sorption), an isotope fractionation is observed that is dependent on the chemical structure of the minerals (Anghel et al. 2002). For example, some fractionation was seen to accompany sorption onto ferrihydrate, and significant fractionation occurred during the formation of inner sphere complexes on the surface of gibbsite ($\alpha = 0.986$) (Pistiner and Henderson 2003).

Taken together, these experimental results suggest that secondary mineral formation and adsorption onto secondary minerals are the major processes controlling isotope fractionation during continental weathering. Moreover, while different minerals have variable fractionation factors, the sense of fractionation is always the same, where the lighter isotope ^6Li is preferentially incorporated into the solid phase.

4.4.2 Lithium Behavior Accompanying Soil Formation

Soils represent complex biogeochemical systems, however, given that Li is not significantly fractionated

by incorporation into biomass, it can be anticipated that this element will respond primarily to the formation of secondary phases in response to the breakdown of the parent rock and/or external inputs (aeolian or groundwater).

However, early work on soils developed on Hawaiian basalts gave unexpected results. Huh et al. (2004) reported increases in Li concentration, and variable but heavy Li isotope compositions for soils, attributed to the uptake of aerosol lithium from seawater. Whereas, Pistiner and Henderson (2003) found little elemental or isotope variation in a soil developed on a similar basalt, and it was suggested that atmospheric deposits with high $\delta^7\text{Li}$ may have counterbalanced the preferential release of ^7Li . A laterite soil developed on the Deccan basalt was found to possess Li isotope compositions that were, in general, light relative to the composition of the parent basalt (Kisakurek et al. 2004). However, Li isotopes displayed a strong negative covariation with Li concentration which was best explained by mixing of precursor basalt and aeolian material, rather than simply being due to the presence of Li-enriched secondary phases.

Work on saprolite sequences developed on igneous rocks in South Carolina (USA), a granite and a diabase, demonstrated that the soils can consistently possess a much lighter Li isotope composition than the igneous rocks from which they formed (Rudnick et al. 2004). More recently Lemarchand et al. (2010) studied soils and soil solutions (pore waters) developed on a granite bedrock in the Strengbach catchment (Vosges, France). While there was little variation of the Li isotope composition of the soils with depth, there is a significant variation in the isotope composition of the pore waters, with deep waters possessing heavy isotope compositions and shallow waters light isotope compositions relative to the parent rock (Fig. 4.3). These variations were attributed to dissolution and precipitation processes. In the deepest horizons the precipitation of secondary minerals results in the preferential incorporation of light isotopes, driving the pore waters to heavy values. Whereas in the shallower soil horizons the data suggest that those secondary minerals as well as residual primary phases are actively dissolving shifting the composition of the pore waters to light values.

Overall, soil studies are broadly consistent with the prediction that secondary mineral formation during weathering releases heavy lithium to the hydrosphere,

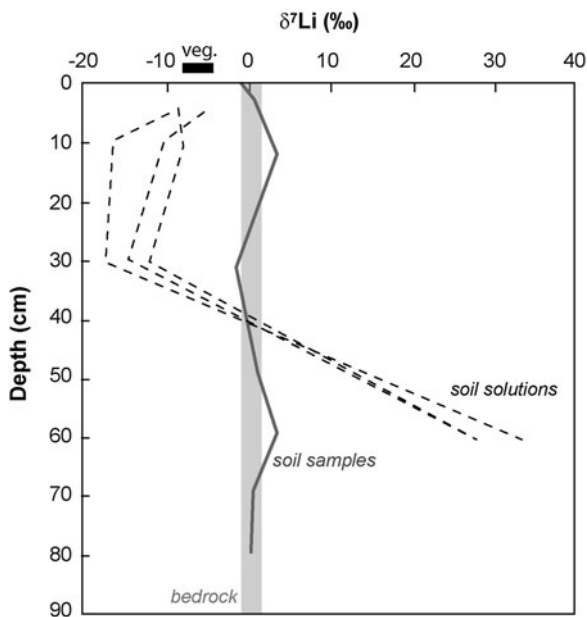


Fig. 4.3 Lithium isotope systematics for an experimental ecosystem located in the Strengbach catchment (Vosges mountains, NE France). The range of $\delta^7\text{Li}$ values obtained for the local vegetation (spruce needle, root, branches) is shown by the *black bar*. Soil solutions have been sampled at various times of the year (*dashed lines*) and show a similar pattern with depth. Solid phases have $\delta^7\text{Li}$ values close to those of the bedrock. Modified from Lemarchand et al. (2010)

leaving isotopically light Li behind in the solid phases. However, many of these studies also point to the influence of externally derived Li either from atmospheric input or groundwater, and the breakdown of early formed secondary minerals may also impart a light isotope signal to the pore waters.

4.4.3 Lithium Isotopes in Rivers

Rivers represent the principal means by which the products of continental weathering are transported to the oceans, and exert an important control on the Li isotope composition of seawater. In a study of major rivers (comprising some 30% of the global river discharge) Huh et al. (1998) found that the dissolved phase (filtered to $<0.45\ \mu\text{m}$) possessed a wide range of Li isotope compositions in accord with earlier studies (e.g. Chan et al. 1992; Falkner et al. 1997). No clear relationship between isotope composition and catchment rock type was observed, consistent with a decoupling of $\delta^7\text{Li}$ and $^{87}\text{Sr}/^{86}\text{Sr}$ in the same samples,

although Li concentrations did show a relationship with the weathering susceptibility of the parent rock type. Lithium concentrations were also found to covary with Mg, but rarely with Si and K, even though both are sourced by the weathering of silicates, in accord with the tendency of Li to be retained in secondary clays, substituting for Mg^{2+} . These results were taken to indicate that the dominant effects on river chemistry are isotope fractionation between waters and secondary minerals and the degree of chemical erosion.

River data for the Orinoco basin shows a conspicuous difference in the $\delta^7\text{Li}$ of the dissolved load between rivers draining the young Andean mountains (31.0–37.5‰) compared to the shield terrains (13.5–22.8‰) even though the $\delta^7\text{Li}$ composition of the suspended load is similar between the two (Huh et al. 2001). These differences were attributed not to variations in lithology, but to distinctions in the weathering regimes. In the high-relief Andean mountains weathering is reaction-limited and the dissolved load is high in Li and isotopically heavy. Whereas, in the low-relief stable shield areas weathering is transport limited, Li concentrations in waters are low and isotopically light in proportion to the increasing degree of weathering.

In a study of carbonate and silicate catchments in the Himalayas it was found that most of the dissolved Li is sourced by the dissolution of silicate minerals even in carbonate dominated terrains (Kisakurek et al. 2005). A distinct difference was also found in the $\delta^7\text{Li}$ isotope composition of both bedload and suspended load reflecting the different composition of the bedrock. However, the isotope composition of the suspended load is nearly always lighter than the corresponding bedload probably reflecting the presence of secondary phases. There is considerable overlap in the $\delta^7\text{Li}$ composition of the dissolved load from the carbonate-silicate catchments, suggesting that the main control on the Li isotope chemistry of the dissolved load is not the bedrock lithology, but rather weathering reactions involving the formation of secondary minerals.

For rivers in the Mackenzie basin, Canada, it was also found that the Li in the dissolved load is dominated by the weathering of silicates, and that the Li isotope composition is inversely correlated with the relative mobility of Li (when compared with Na) (Millot et al. 2010b). Surprisingly, the most significant ^7Li enrichment in the dissolved phase of the rivers

accompanied incipient weathering in the Rocky Mountain and shield areas. The fractionation was not considered to be accounted for by the formation of clays, and was rather attributed to the formation of Fe-oxyhydroxides. By comparison, rivers in the lowland areas are the most depleted in Li, with lower $\delta^7\text{Li}$ values (although still enriched in ^7Li compared to the bedrock) and this was attributed to equilibrium with clay minerals in aquifers which contribute to the dissolved load of rivers.

Small monolithologic catchments provide a means of understanding and quantifying the effects of weathering processes alone, because there is little variation due to differences in rock type. Over recent years there have been several studies of Li isotope behaviour in rivers draining basalt terrains (Pogge von Strandmann et al. 2006, 2010; Vigier et al. 2009) where the controls on water chemistry are better understood through both natural observations and experimental work. Rivers in Iceland display a wide range of $\delta^7\text{Li}$ isotope compositions (10.1–43.7‰) that are always heavier than the basalt bedrock and bedload sand (3.1–8.9‰). Whereas, the suspended load in these rivers are invariably lighter than their corresponding bedload ($\delta^7\text{Li} = -1.3$ – 6.0 ‰) likely due to the presence of secondary phases enriched in ^6Li (Fig. 4.2). Simple mixing between basalt weathering ($\delta^7\text{Li} = 3.9$ ‰), precipitation (rain/snow) which is dominated by seawater aerosols ($\delta^7\text{Li} = 33.3$ ‰) and hydrothermal springs ($\delta^7\text{Li} = 5.5$ – 10.9 ‰) cannot account for these variations, rather they are better explained by uptake in secondary minerals.

The Li isotope composition of the dissolved phase in the rivers in Iceland shows a dependence upon the weathering regime. In the older basaltic terrains (largely non-glacial) weathering tends to be more reaction-limited, and result in waters with low $\text{K}/(\text{K} + \text{Na})$ ratios (relative to the parent basalt) and heavy Li isotope compositions. This has been explained by preferential Li and K incorporation into secondary minerals and biomass (K) relative to mobile elements such as Na. Whereas, in the younger, largely glacial catchments, weathering is relatively transport-limited and $\text{K}/(\text{K} + \text{Na})$ ratios and Li isotope compositions are closer to those of the parent basalt. Moreover, for many rivers in Iceland discharge rates are monitored and chemical erosion rates can be calculated. For these terrains at least Li isotope behaviour can be explained by a simple empirical relationship

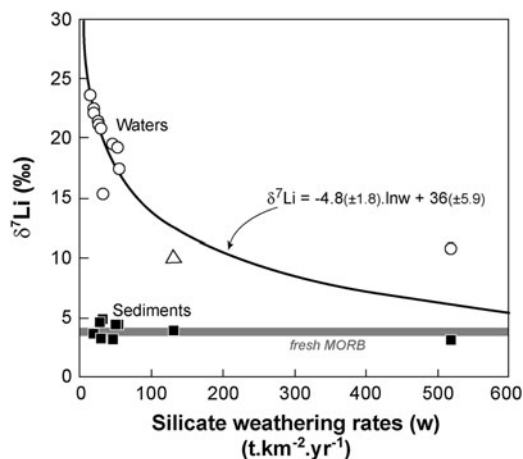


Fig. 4.4 $\delta^7\text{Li}$ of the dissolved phase (in white) and sediments (in black) of Icelandic rivers, as a function of weathering or chemical erosion rate, estimated independently from major and trace elements concentrations measured in the dissolved loads (Vigier et al. 2009)

with erosion rate (Fig. 4.4) (cf. Vigier et al. 2009). Put simply, the Li concentrations and isotope compositions reflect the balance of Li derived from the parent rock against that affected by incorporation into secondary phases. When weathering rates are high, Li concentrations of the waters are also high and Li isotope compositions are closer to those of the parent rock, whereas when weathering rates are low, the isotope composition of the waters more strongly reflects incorporation into secondary phases. Finally, Wimpenny et al. (2010a) found that significant fractionation of Li occurs during glacial weathering despite little evidence for the formation of clays in the chemistry of the glacial waters. This was attributed to sub-glacial weathering of sulphide and other Fe-bearing minerals, resulting in the formation of Fe-oxyhydroxides (e.g. Tranter 2003; Raiswell et al. 2006). Leaching experiments suggested that some 65% of the Li in the suspended load is hosted by such Fe-oxyhydroxides, and that this has a light Li isotope composition (relative to the dissolved phases) indicating that this mineral preferentially incorporates ^6Li relative to ^7Li (Wimpenny et al. 2010a).

4.4.4 Estuarine Behaviour of Lithium

Dissolved lithium exhibits conservative behaviour in estuaries, including the well-mixed estuary of the St

Lawrence river, the partially mixed Scheldt (Stoffyn-Egli 1982) and the salt-wedge Mississippi rivers (Colten and Hanor 1984). Lithium also behaves conservatively in the Gulf of Papua, where particulate Li is trapped in aluminosilicate muds on the shelf (Brunskill et al. 2003). Similarly, dissolved Li in estuaries draining dominantly basaltic terrains in Iceland and the Azores show simple elemental and isotopic mixing trends indicating that the Li elemental and isotope signature is transferred to seawater without modification in the estuarine mixing zone (Pogge von Strandmann et al. 2008) (Fig. 4.5).

The Li concentration of suspended particles in the estuary at Borgarfjordur in Iceland is within the range of source basalt, however, remarkably the Li content of the particles and $\delta^7\text{Li}$ both increase with increasing salinity. This relationship was taken to indicate continued weathering (and precipitation of secondary clays) in the estuarine environment. The particulate data suggests a fractionation factor $\alpha_{\text{mineral-fluid}}$ of 0.981 ± 0.003 for the clay-seawater in the estuary, similar to the value of 0.981 reported by Chan et al. (1992) for weathered sea-floor basalts. Moreover, it was concluded that the weathering of such particles in the estuarine environment may significantly impact the Li flux to the oceans, reducing the global riverine flux by between 15 and 25%.

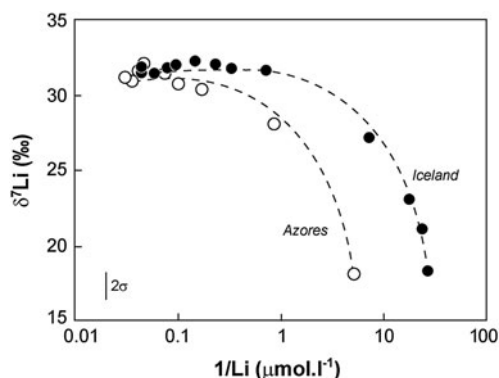


Fig. 4.5 $\delta^7\text{Li}$ measured in the dissolved phase of two small estuaries on basaltic islands (in the Azores in white, and in Iceland in black) (Pogge von Strandmann et al. 2008). In both cases, mixing lines between fresh and sea waters strongly suggest a conservative behaviour of lithium within the studied estuaries

4.5 Li Isotopes as Tracers of Hydrothermal Processes and Ocean Floor Weathering

The isotope and elemental budget of Li in the oceans is controlled by: *input* from continental weathering (via rivers, groundwater and aeolian dust) and from high-temperature hydrothermal fluids; and *removal* through sea-floor alteration, high temperature (hydrothermal) recrystallisation and adsorption. Precipitation of marine carbonates and biogenic silica are minor sinks of Li (<5% total) given their low Li concentrations, and the diffusive flux from sediments is also small (see Table 4.1).

4.5.1 Li Mobility During Ocean-Floor Weathering

During weathering (or alteration) of oceanic basalt Li from seawater is incorporated into secondary phases (in much the same way as during continental weathering) (Fig. 4.6). Data for altered sea-floor basalts indicates that the variations cannot be simply attributed to mixing between pristine basalt and seawater. Rather seawater Li enters the secondary weathering phases with an apparent fractionation

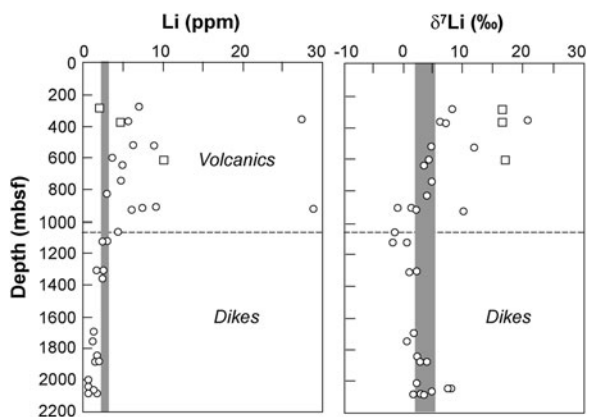


Fig. 4.6 Variation of Li concentration, and $\delta^7\text{Li}$ values with depth for whole rocks (white circles) and smectites (white squares) from DSDP/ODP Site 504B (modified from Chan et al. 2002). The range for pristine MORB is shown for comparison (in light grey). The uppermost volcanic section is enriched in Li with high $\delta^7\text{Li}$ values. In contrast, Li is lost from the dyke complex through extraction by hydrothermal fluids with less isotope fractionation

factor $\alpha \sim 0.981$ (Chan et al. 1992, 2002) indistinguishable from the fractionation factor observed during the weathering of basaltic suspended material in estuaries (Pogge von Strandmann et al. 2008). The relative uniformity of this fractionation at a range of localities suggests either that Li uptake is dominated by a single phase, or else that the phases involved possess similar fractionation factors for Li incorporation. The principal secondary phases in highly weathered basalts are clays, Fe-oxyhydroxides and smectites. Experiments suggest that the fractionation factor accompanying smectite precipitation is <0.990 , however, the low-T experiments need to be refined (Vigier et al. 2008). The fractionation factor associated with the precipitation of Fe-oxyhydroxides ranges from 0.978 to 0.999 (Pistiner and Henderson 2003; Chan and Hein 2007; Wimpenny et al. 2010a), although the fractionation factor for zeolite has not yet been determined. Lithium uptake may also be partly controlled by adsorption processes, in a study of Li uptake from seawater onto kaolinite and vermiculite fractionation factors of 0.979 and 0.971, respectively, were determined (Zhang et al. 1998).

4.5.2 Lithium in Hydrothermal Fluids

Seawater circulates through ocean crust of all ages, driven by temperature induced pressure gradients. At mid-ocean ridges the convective flow of seawater is driven by crystallisation and cooling of the magma that upwells from the mantle to form oceanic crust. High-T hydrothermal exchange between basalt and seawater is a significant source of Li to the oceans, although the magnitude of the hydrothermal flux remains poorly quantified, in particular at the ridge flanks (Elderfield and Schultz 1996).

Lithium is enriched in high temperature ($>350^\circ\text{C}$) vent fluids by a factor of 20–50 times that of seawater, and the $\delta^7\text{Li}$ compositions of fluids from vents in a range of settings yield values ranging from those of MORB to several per mil heavier (Chan and Edmond 1988; Chan et al. 1993, 1994). There is no correlation between $\delta^7\text{Li}$ and seafloor spreading rate suggesting that mid-ocean ridge hydrothermal fluids derive most of their Li from young, unaltered, basaltic crust, rather than older basalts (Chan et al. 1993). Sediment cover appears to have little effect on the isotope and

elemental composition of hydrothermal fluids, suggesting that the isotope signal is sourced by deep processes not linked to surface sediments enriched in Li that is highly susceptible to hydrothermal alteration (Chan et al. 1994).

It has been suggested that oceanic crust preserving a record of the interaction with high-temperature hydrothermal fluids may be uncommon, because of the prevalence of low-temperature weathering. Nevertheless, observations suggest that such hydrothermal alteration preferentially removes heavy Li from the rock, leaving the residual, altered oceanic crustal rock with a lower Li concentration and lighter isotope composition than the parent material (Chan et al. 1992, 1994; You et al. 1995; James et al. 1999).

4.5.3 Lithium in Abyssal Peridotite and Mantle Rocks

In oceanic fracture zones and actively-upwelling mud volcanoes seawater reacts directly with mantle rocks (Decitre et al. 2002; Savov et al. 2005; Benton et al. 2004). Serpentinites (altered mantle rocks) from these studies are enriched in Li relative to unaltered mantle rocks, but possess highly variable $\delta^7\text{Li}$ isotope compositions, both heavier and lighter than unaltered mantle rocks, although the mean $\delta^7\text{Li}$ ($=+7 \pm 5\%$) is similar to that of average seafloor vent fluids ($+8 \pm 4\%$). The Li isotope composition of Indian ocean serpentinites has been attributed to the recycling of Li derived from basaltic oceanic crust, rather than from seawater (Decitre et al. 2002). Where the variable isotope compositions of serpentinites result from the interaction of mantle rocks with a hydrothermal fluid, as it cools and reacts along its flow path towards heavier Li isotope compositions (Vils et al. 2009).

4.5.4 Lithium in Marine Pore-Fluids

During diagenesis (compaction and mineral dehydration) pore waters, carrying a chemical signature of fluid-sediment interaction, may be released from marine sediments to seawater. A number of studies have measured the Li isotope and elemental composition

of both pore waters and host sediments (e.g. Zhang et al. 1998; Chan and Kastner 2000; James et al. 1999; James and Palmer 2000b) and these data indicate that the pore fluids possess a wide range of Li isotope compositions ($\delta^7\text{Li}$ values range from less than 20 to $>40\text{‰}$), almost always having a heavier Li isotope composition than their host sediment. Zhang et al. (1998) recognised the importance of NH_4^+ (produced by the breakdown of organic matter) in pore fluids as a counterion for exchange with Li adsorbed on sediments. It was observed that the peak in NH_4^+ concentrations coincided with Li isotope compositions lighter than seawater, suggesting that Li desorbed from sediments is isotopically lighter than the seawater starting composition. Chan and Kastner (2000) documented an inverse correlation between Li concentration and $\delta^7\text{Li}$ values that was considered to reflect the superimposed effects of the alteration of volcanic ash, taking up Li from the fluids through the formation of smectite, and ion exchange (between Li^+ and NH_4^+).

In a study of active hydrothermal venting through a thick sediment sequence close to the Gorda ridge (James et al. 1999) Li isotope variations were interpreted in terms of initial hydrothermal removal of Li from sediments, followed by uptake of dissolved Li accompanying the crystallisation of secondary minerals, and dilution with seawater. At another site on the Gorda ridge, the Li in pore fluids was estimated to be substantially derived ($>65\%$) from Li initially adsorbed on particles in the water column (James and Palmer 2000a, b). On the basis of comparison between experimental results and natural data it was inferred that the upwelling rate was also a critical control on the Li isotope composition of pore waters, where slow rates of upwelling favour increased fluid-sediment interaction (James et al. 2003).

4.5.5 Lithium Isotope Fractionation During Laboratory Experiments

Laboratory experiments have also been undertaken to quantify Li isotope behaviour during interactions of high temperature fluids with basalt, altered basalts and sediments (Chan et al. 1994; Seyfried et al. 1998; James et al. 2003). All of these studies show that Li is extracted from these rock types even at temperatures $<100^\circ\text{C}$. At temperatures up to 150°C Li is

incorporated into clays (such as smectite and illite) during basalt alteration (Seyfried et al. 1998; James et al. 2003) with an affinity that is proportional to the fluid/rock ratio, such that Li is simultaneously added to and removed from fluids. Whereas at higher temperature hydrothermal conditions ($\sim 350^\circ\text{C}$) Li is largely removed from solids, and kept in solution rather than in secondary alteration minerals (Seyfried et al. 1998).

Natural studies of the interaction between seawater and basalts suggest that there is a fractionation of Li isotopes that is strongly temperature dependent (Chan and Edmond 1988; Chan et al. 1992, 1993, 1994; James et al. 1999). High temperature experiments between clinopyroxene and aqueous fluids ($500\text{--}900^\circ\text{C}$) also show a temperature dependent isotope fractionation (Wunder et al. 2006). More recent low temperature ($25\text{--}250^\circ\text{C}$) experiments have also quantified the temperature dependent fractionation of Li isotopes accompanying seawater-basalt interaction (Millot et al. 2010c), deriving the following relationship between isotope fractionation and temperature:

$$\Delta_{\text{solution-solid}} = 7,847/T - 8.093$$

(temperature in Kelvin)

These experiments were taken to indicate that the Li isotope and elemental composition of fluids derived from seawater-basalt interaction are controlled by (1) mixing between Li in seawater, and Li released from the basalt and (2) uptake of Li into secondary minerals (Millot et al. 2010c).

4.6 Marine Li Records

Due mainly to analytical difficulties linked to the particularly low levels of Li in carbonates (<1 ppm), and, in contrast, the high levels of Li ($\gg 10$ ppm) in potential contaminants (marine clays and oxides), there are very few published data for $\delta^7\text{Li}$ in marine carbonates, and data for only two marine records (recorded by foraminifera) have been published thus far. In parallel, experimental studies allow the isotope fractionation during formation of various types of carbonates to be constrained, and some controlling factors to be identified. In parallel, other proxy substrates are investigated, but are not yet fully understood (see Sect. 4.6.3).

Table 4.1 Main marine lithium inputs and outputs

	Li flux (10^{10} g year $^{-1}$)	$\delta^7\text{Li}$ (‰)	References
Li inputs to the ocean			
Rivers	5.6	+23.5	Huh et al. (1998)
Hydrothermal fluids	4.2 (2–20)	+8.5	Chan et al. (1993), Elderfield and Schultz (1996), and Vigier et al. (2008)
Fluid expulsion at convergent margins	0.06–0.4	+20 to >+40	Zhang et al. (1998), You et al. (1995), Chan and Kastner (2000), and Scholz et al. (2010)
Mud volcanoes	0.2 (0.003–0.5)	+12 to +31	Vanneste et al. (2010), You et al. (2004), and Scholz et al. (2009)
Li outputs			
Uptake by clays	0.7–25	+1 to +14	Stoffyn-Egli and Mackenzie (1984), Chan et al. (1992, 2002, 2006), and Wheat and Mottle (2000)
Carbonate formation	0.2–0.6	+27 to +31	Hoefs and Sywall (1997), Milliman (1993), and Hathorne and James (2006)
Biogenic silica	0.06–1	–1 to +8	Chan et al. (2006)

4.6.1 Foraminiferal Records

The first studies appeared to indicate highly variable Li isotope compositions for foraminifera through time, with $\delta^7\text{Li}$ values ranging from less than 10‰ up to 40‰ (Kosler et al. 2001; Hoefs and Sywall 1997). However, more recent work indicates that foraminifera preserve a much narrower range of $\delta^7\text{Li}$ values for the Cenozoic, for a number of different species (Hall et al. 2005; Hathorne and James 2006) (Fig. 4.7). These contrasting results are partly explained by the use of more sensitive MC-ICP-MS, but also

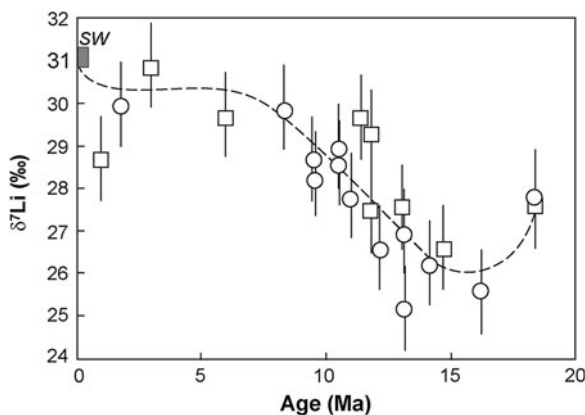


Fig. 4.7 Record of planktic foraminiferal $\delta^7\text{Li}$ for the past 18 million years (after Hathorne and James 2006). This record is based on different species of foraminifera. Note that there appears to be little difference in the $\delta^7\text{Li}$ value of samples recovered from the Pacific (squares) and Atlantic (circles) oceans

by improved cleaning techniques for foraminifera. Marriott et al. (2004a, b) and Vigier et al. (2007) have shown that the cleaning procedure strongly affects both the Li content and isotope composition of the foraminifera. This is because the foraminiferal calcite possesses very low Li contents relative to contaminant phases such as Fe-Mn oxyhydroxides and silicate grains, and there is also a significant difference between the $\delta^7\text{Li}$ value of foraminiferal calcite and the contaminant phases. It has recently been shown that ion microprobe and laser techniques could be used to avoid contaminant phases, but other difficulties then arise, such as requirement for large shells with thick chamber walls, as well as appropriate calcite standards (Hathorne et al. 2009; Vigier et al. 2007).

The 0.4–35.8 kyr record obtained by TIMS by Hall et al. (2005) suggests that *O. universa* (planktic foraminifera) have $\delta^7\text{Li}$ values that are close to seawater. Glacial and interglacial samples display similar $\delta^7\text{Li}$ values to surface sediment samples. This is consistent with the long residence time of Li in the ocean (>1 Myr, Huh et al. 1998), implying that changes in Li sources and sinks in the ocean cannot be resolved in the $\delta^7\text{Li}$ record over short timescales.

The 0–18 Ma record of Hathorne and James (2006) is based on analysis of several species of planktic foraminifera, separated from sediments from both the Atlantic and the Pacific oceans. The data are globally consistent, and they suggest that the seawater $\delta^7\text{Li}$ value has been constant for the last 10 Ma. In contrast, the interval from 10 to 18 Ma is marked by a significant decrease in planktic foraminifera $\delta^7\text{Li}$. This

decrease was attributed to a change in seawater $\delta^7\text{Li}$, due to a change in the rate of continental weathering. Overall, this study illustrates that the Li isotope signature of the ocean may be affected by a change of the isotope signature of river waters. If the river water signature is mainly due to chemical weathering of silicates, then records of past oceanic $\delta^7\text{Li}$ may yield precious information on the link between climate and silicate weathering.

The same study also highlights the need of constraining, in parallel, changes in the continental Li flux. In principle, the Li flux can be estimated from the Li/Ca ratio measured in foraminifera, although a strong species effect has been demonstrated and must be corrected for (Hathorne and James 2006). This species effect may, at least in part, explain discrepancies between different studies. Significant glacial/interglacial variation in the Li/Ca ratio preserved by planktonic and benthic foraminifera (Hall and Chan 2004; Lear and Rosenthal 2006) has been taken to suggest a role for temperature and/or calcite saturation state on the amount of Li incorporated by these species. In contrast, Delaney and Boyle (1986) found constant Li/Ca ratios for mixed planktonic foraminifera over the last 40 Myr.

4.6.2 Influence of Environmental Parameters on Li Isotope Fractionation

The interpretation of Li isotope signatures measured in foraminifera or other types of carbonates requires knowledge of the isotope fractionation accompanying Li incorporation into the carbonate matrix. Indeed, in order to calculate the ocean $\delta^7\text{Li}$ from a value measured for an inorganic or a biogenic carbonate, it is necessary first to constrain the isotope fractionation that has occurred during its formation, and second to identify the parameters controlling this fractionation (e.g. T, pH, calcification rate).

The inverse-correlation between Li/Ca and $\delta^7\text{Li}$ obtained by Hathorne and James (2006) for recent planktonic foraminifera strongly suggests that “species effects” and biomineralization mechanisms are likely to influence both Li isotope fractionation and Li concentration. The influence of environmental parameters on the Li isotope fractionation and Li/Ca

ratios has been evaluated for inorganic calcite and aragonite experimentally grown in the laboratory (Marriott et al. 2004a, b). Depending on the experimental conditions, measured Li isotope fractionation between the precipitated calcite and solution is not the same. Despite this discrepancy, no dependency on temperature is found for this fractionation at least between 5 and 30°C (Fig. 4.8). In contrast, Li/Ca inversely correlates with temperature. The Li/Ca ratio recorded by a tropical coral (aragonitic) from the Pacific Ocean varies over the course of the year and displays the same pattern as $\delta^{18}\text{O}$, but $\delta^7\text{Li}$ values remain constant. Marriott et al. (2004a, b) also showed that salinity has no influence on the Li isotope fractionation during experimental formation of calcite and aragonite. The main difference between these forms of calcium carbonate lies in the magnitude of the Li isotope fractionation (relative to the parent solution). Inorganic and biogenic calcite display $\delta^7\text{Li}$ values that are often close to that of the solution, while aragonite

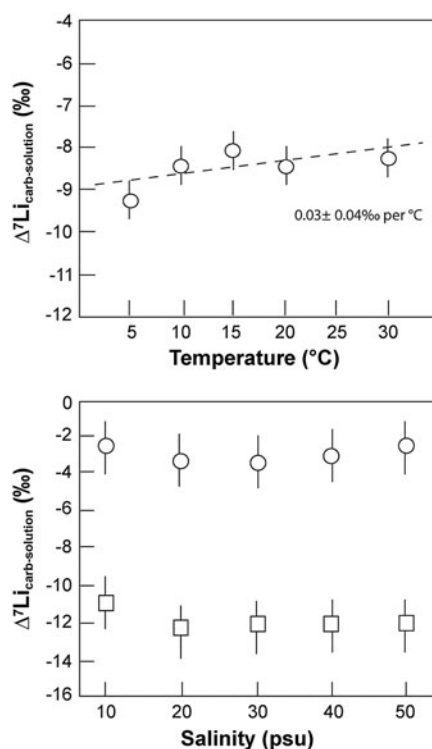


Fig. 4.8 Temperature and salinity dependency on $\delta^7\text{Li}$ measured in calcite (circles) and aragonite (squares) grown experimentally (Marriott et al. 2004a, b). In both cases the solution $\delta^7\text{Li}$ remains constant, at its initial value (0‰)

samples are significantly enriched in the light isotope (generally by more than 10‰).

In brief, thus far, the Li isotope signatures of carbonates seem to be little affected by environmental factors and therefore may be appropriate for determining the evolution of the isotope signature of seawater on geological timescales. However, some parameters still need to be tested such as the calcification rate and/or the role of dissolved CO_3^{2-} .

4.6.3 Other Marine Archives in Development

Two other marine substrates have recently been assessed as potential recorders of the Li and Li isotope composition of seawater: corals and oceanic ferromanganese deposits.

In situ measurements of Li isotopes in calcite and aragonite matrices have recently been developed (Vigier et al. 2007; Rollion-Bard et al. 2009). These studies show first that in situ isotope analyses of aragonitic corals are easier than that of foraminifera tests. They also find that shallow water and deep sea corals, either natural or grown in the laboratory, are isotopically homogeneous at the micron scale (within the 1.1‰ uncertainty of the technique). This implies that the biomineralization process, which is thought to be different for the different skeletal components of the coral (e.g. centres of calcification (COC or EMZ, Early Mineralization Zone) vs. the fibrous parts) does not influence the Li isotope fractionation during skeletal formation. It is also shown that corals grown under highly different pCO_2 and pH conditions display similar isotope signatures. This absence of dependency on environmental conditions strongly suggests that corals can record the evolution of oceanic $\delta^7\text{Li}$, with limited disturbance. However, several present-day species display different isotope fractionation relative to seawater, and this aspect remains to be investigated since it is difficult to estimate long term oceanic paleovariations based on a single species.

Recently formed Fe-Mn crusts display highly variable Li contents. In fact, the Li content of Fe-Mn deposits can be used to discriminate among the various types of deposits, because hydrothermal and diagenetic

crusts are highly enriched in Li ($\gg 100$ ppm) whereas hydrogenetic Fe-Mn crust that form from seawater on the seafloor display low Li levels (generally < 2 ppm) (Chan and Hein 2007; Jiang et al. 2007). Only a few Li isotope data have been published thus far for Fe-Mn crusts. It appears that the crusts incorporate at least two types of Li: loosely bound Li having an isotope signature close to that of seawater (31‰), and more tightly bound Li which can be significantly lighter than the seawater value (Chan and Hein 2007). However, diffusion effects may be significant for Li (Henderson and Burton 1999), and ancient Fe-Mn crusts are unlikely to provide a direct record of the isotope signature of seawater at the time of their formation. More data are certainly needed for confirming these recent observations.

4.7 Conclusion and Future Directions

Studies involving Li isotopes have increased almost exponentially over the past few years. Both experimental and field studies show that significant isotope fractionation of Li occurs during water-rock interactions. Both low and high temperature fluids display $\delta^7\text{Li}$ values that are significantly different from those of primary or secondary minerals. The major role of silicate lithologies and clay formation in the Li budget has been assessed, both at a regional scale, and at a continental scale. In order to bring more quantitative constraints on present-day and past chemical erosion rates of silicates, using Li isotopes, a better calibration of this fractionation in natural systems is required, in particular during low-temperature rock weathering. Also, materials that record the Li isotope composition of seawater need to be investigated and understood in more detail. The recent developments in mass spectrometry, and in particular the advent of MC-ICP-MS technology, should help the expansion of the use of this promising tool for the study of chemical weathering and erosional processes.

Acknowledgements We thank the two reviewers, an anonymous reviewer and Rachael James, for their constructive comments on this chapter. We are also grateful for the detailed comments of the Editor, Mark Baskaran.

References

- Anderson MA, Bertsch PM, Miller WP (1989) Exchange and apparent fixation of lithium in selected soils and clay minerals. *Soil Sci* 148:46–52
- Anghel I, Turin HJ, Reimus PW (2002) Lithium sorption to Yucca Mountain tuffs. *Appl Geochem* 17:819–824
- Bach RO (ed) (1985) *Lithium – current applications in science, medicine and technology*. Wiley, New York
- Bayon G, Vigier N, Burton KW, Brenot A, Carignan J, Chu N-C, Etoubleau J (2006) The control of weathering process on riverine and seawater hafnium isotope ratios. *Geology* 34:433–436
- Benton LD, Ryan JG, Savov IP (2004) Lithium abundance and isotope systematics of forearc serpentinites, conical seamount, Mariana forearc: insights into the mechanics of slab-mantle exchange during subduction. *Geochem Geophys Geosyst* 8. doi:10.1029/2004GC000708
- Blum JD, Erel Y (1995) A silicate weathering mechanism linking increase in marine $^{87}\text{Sr}/^{86}\text{Sr}$ with global glaciation. *Nature* 373:415–418
- Brunskill GJ, Zagorskis I, Pfitzner J (2003) Geochemical mass balance for lithium, boron, and strontium in the Gulf of Papua, Papua New Guinea (Project TROPICS). *Geochim Cosmochim Acta* 67:3365–3383
- Burles S, Nollett KM, Turner MS (2001) Big bang nucleosynthesis predictions for precise cosmology. *Astrophys J* 552: L1–L5
- Carignan J, Cardinal D, Eisenhauer A, Galy A, Rehkämper M, Wombacher F, Vigier N (2004) A reflection on Mg, Ca, Cd, Li and Si isotopic measurements and related reference materials. *Geostand Geoanal Res* 28:139–148
- Carignan J, Vigier N, Millot R (2007) Three secondary reference materials for Li isotopic measurements: $^7\text{Li-N}$, $^6\text{Li-N}$ and LiCl-N . *Geostand Geoanal Res* 31:7–12
- Chan LH (1987) Lithium isotope analysis by thermal ionization mass spectrometry of lithium tetraborate. *Anal Chem* 59:2662–2665
- Chan L-H, Edmond JM (1988) Variation of lithium isotope composition in the marine environment: a preliminary report. *Geochim Cosmochim Acta* 52:1711–1717
- Chan L-H, Frey FA (2003) Lithium isotope geochemistry of the Hawaiian plume: results from the Hawaiian Scientific Drilling Project and Koolau Volcano. *Geochem Geophys Geosyst* 4:8707
- Chan L-H, Hein JR (2007) Lithium contents and isotopic compositions of ferromanganese deposits from the global ocean. *Deep Sea Res I Top Stud Oceanogr* 54:1147–1162
- Chan LH, Kastner M (2000) Lithium isotopic composition of pore fluids and sediments in the Costa Rica subduction zone: implications for fluid processes and sediment contribution to the arc volcanoes. *Earth Planet Sci Lett* 183:275–290
- Chan L-H, Edmond JM, Thompson G, Gillis K (1992) Lithium isotopic composition of submarine basalts: implications for the lithium cycle in the oceans. *Earth Planet Sci Lett* 108:151–160
- Chan L-H, Edmond JM, Thompson G (1993) A lithium isotope study of hot springs and metabasalts from Mid-Ocean ridge hydrothermal systems. *J Geophys Res* 98:9653–9659
- Chan L-H, Gieskes JM, You C-F, Edmond JM (1994) Lithium isotope geochemistry of sediments and hydrothermal fluids of the Guyamas Basin, Gulf of California. *Geochim Cosmochim Acta* 58:4443–4454
- Chan L-H, Alt JC, Teagle DAH (2002) Lithium and lithium isotope profiles through the upper oceanic crust: a study of seawater-basalt exchange at ODP Sites 504B and 896A. *Earth Planet Sci Lett* 201:187–201
- Chan LH, Leeman WP, Plank T (2006) Lithium isotopic composition of marine sediments. *Geochem Geophys Geosyst* 7: Q06005. doi:10.1029/2005GC001202
- Chaussidon M, Robert F (1998) $^7\text{Li}/^6\text{Li}$ and $^{11}\text{B}/^{10}\text{B}$ variations in chondrules from the Semarkona unequilibrated chondrite. *Earth Planet Sci Lett* 164:577–589
- Colten VA, Hanor JS (1984) Variations in dissolved lithium in the Mississippi River and Mississippi River Estuary, Louisiana, USA, during Low River stage. *Chem Geol* 47:85–96
- Comans RNJ, Haller M, De Preter P (1991) Sorption of cesium on illite: non-equilibrium behaviour and reversibility. *Geochim Cosmochim Acta* 55:433–440
- Decitre S, Deloule E, Resiberg L, James R, Agrinier P, Mével C (2002) Behaviour of Li and its isotopes during serpentinization of oceanic peridotites. *Geochem Geophys Geosyst* 3. doi:10.1029/2001GC000178
- Delaney ML, Boyle EA (1986) Lithium in foraminiferal shells: implications for high-temperature hydrothermal circulation fluxes and oceanic crustal generation rates. *Earth Planet Sci Lett* 80:91–105
- Elderfield H, Schultz A (1996) Mid-ocean ridge hydrothermal fluxes and the chemical composition of the ocean. *Annu Rev Earth Planet Sci* 24:191–224
- Elliott T, Thomas A, Jeffcoate A, Niu Y (2006) Lithium isotope evidence for subduction enriched mantle in the source of mid-ocean-ridge basalts. *Nature* 443:565–568
- Falkner KK, Chrucho M, Measures CI, LeBaron G, Thouron D, Jeandel C, Strodal MC, Gill GA, Mortlock R, Froelich P, Chan LH (1997) Minor and trace element chemistry of Lake Baikal, its tributaries, and surrounding hot springs. *Limnol Oceanogr* 42:329–345
- Hall JM, Chan L-H (2004) Li/Ca in multiple species of benthic and planktonic foraminifera: thermocline, latitudinal, and glacial-interglacial variation. *Geochim Cosmochim Acta* 68:529–545
- Hall JM, Chan L-H, McDonough WF, Turekian KK (2005) Determination of the lithium isotopic composition of planktonic foraminifera and its application as a paleo-seawater proxy. *Mar Geol* 217:255–265
- Hathorne EC, James RH (2006) Temporal record of lithium in seawater: a tracer for silicate weathering? *Earth Planet Sci Lett* 246:393–406
- Hathorne EC, James RH, Lampitt RS (2009) Environmental versus biomineralization controls on the intratest variation in the trace element composition of the planktonic foraminifera *G. inflata* and *G. scitula*. *Paleoceanography* 24: PA4204. doi:10.1029/2009PA001742
- Heier KS, Billings GK (1970) Lithium. In: Wedepohl KH (ed) *Handbook of geochemistry*, vol II-1. Springer, Berlin, pp 3-A-1–3-O-1
- Henderson GM, Burton KW (1999) Using $(^{234}\text{U}/^{238}\text{U})$ to assess diffusion rates of isotope tracers in ferromanganese crusts. *Earth Planet Sci Lett* 170:169–179

- Hoefs J, Sywall M (1997) Lithium isotope composition of quaternary and tertiary biogenic carbonates and a global lithium isotope balance. *Geochim Cosmochim Acta* 61:2679–2690
- Huh Y, Chan LH, Zhang L, Edmond JM (1998) Lithium and its isotopes in major world rivers: implications for weathering and the oceanic budget. *Geochim Cosmochim Acta* 62:2039–2051
- Huh Y, Chan L-H, Edmond JM (2001) Lithium isotopes as a probe of weathering processes: Orinoco River. *Earth Planet Sci Lett* 194:189–199
- Huh Y, Chan L-H, Chadwick O (2004) Behaviour of lithium and its isotopes during weathering of Hawaiian basalts. *Geochim Geophys Geosyst* 5. doi:10.1029/2004GC000729
- James RH, Palmer MR (2000a) The lithium isotope composition of international rock standards. *Chem Geol* 166:319–326
- James RH, Palmer MR (2000b) Marine geochemical cycles of the alkali elements and boron: the role of sediments. *Geochim Cosmochim Acta* 63:3111–3122
- James RH, Rudnicki MD, Palmer MR (1999) The alkali element and boron geochemistry of the Escanaba Trough sediment-hosted hydrothermal system: the role of sediments. *Earth Planet Sci Lett* 171:157–169
- James RH, Allen DE, Seyfried WE Jr (2003) An experimental study of alteration of oceanic crust and terrigenous sediments at moderate temperatures (51 to 350°C): insights as to chemical processes in near-shore ridge-flank hydrothermal systems. *Geochim Cosmochim Acta* 67:681–691
- Jeffcoate AB, Elliott T, Thomas A, Bouman C (2004) Precise, small sample size determinations of lithium isotopic compositions of geological reference materials and modern seawater by MC-ICP-MS. *Geostand Geoanal Res* 28:161–172
- Jeffcoate AB, Elliott T, Kasemann SA, Ionov D, Cooper K, Brooker R (2007) Li isotope fractionation in peridotites and mafic melts. *Geochim Cosmochim Acta* 71:202–218
- Jiang X, Lin X, Yao D, Zhai S, Guo W (2007) Geochemistry of lithium in marine ferromanganese oxide deposits. *Deep Sea Res I* 54:85–98
- Kasemann SA, Jeffcoate AB, Elliott T (2005) Lithium isotope composition of basalt glass reference material. *Ann Chem* 77:5251–5257
- Kisakurek B, Widdowson M, James RH (2004) Behaviour of Li isotopes during continental weathering: the Bidar laterite profile. *India Chem Geol* 212:27–44
- Kisakurek B, James RH, Harris NBW (2005) Li and delta Li-7 in Himalayan rivers: proxies for silicate weathering? *Earth Planet Sci Lett* 237:387–401
- Korn AJ, Grundahl F, Richard O, Barklem PS, Mashonkina L, Collet R, Piskunov N, Gustafsson (2006) A probable stellar solution to the cosmological lithium discrepancy. *Nature* 442:657–659
- Kosler J, Kucera M, Sylvester P (2001) Precise measurement of Li isotopes in planktonic foraminiferal tests by quadrupole ICPMS. *Chem Geol* 181:169–179
- Lear CH, Rosenthal Y (2006) Benthic foraminiferal Li/Ca: insights into Cenozoic seawater carbonate saturation state. *Geology* 34:985–988
- Lemarchand E, Chabaux F, Vigier N, Millot R, Pierret M-C (2010) Lithium isotope systematics in a forested granitic catchment (Strengbach, Vosges Mountains, France). *Geochim Cosmochim Acta* 74:4612–4628
- Marriott CS, Henderson GM, Belshaw NS, Tudhope AW (2004a) Temperature dependence of $\delta^7\text{Li}$, $\delta^{44}\text{Ca}$ and Li/Ca incorporation into calcium carbonate. *Earth Planet Sci Lett* 222:615–624
- Marriott CS, Henderson GM, Crompton R, Staubwasser M, Shaw S (2004b) Effect of mineralogy, salinity, and temperature on Li/Ca and Li isotope composition of calcium carbonate. *Chem Geol* 212:5–15
- Milliman JD (1993) Production and accumulation of calcium carbonate in the ocean: budget of a nonsteady state. *Glob Biogeochem Cycles* 7:927–957
- Millot R, Guerrot C, Vigier N (2004) Accurate and high-precision measurement of lithium isotopes in two reference materials by MC-ICP-MS. *Geostand Geoanal Res* 28:153–159
- Millot R, Petelet-Giraud E, Guerrot C, Négrel P (2010a) Multi-isotopic composition ($\delta^7\text{Li}$ – $\delta^{11}\text{B}$ – δD – $\delta^{18}\text{O}$) of rainwaters in France: origin and spatio-temporal characterization. *Appl Geochem* 25:1510–1524
- Millot R, Vigier N, Gaillardet J (2010b) Behaviour of lithium and its isotopes during weathering in the Mackenzie Basin, Canada. *Geochim Cosmochim Acta* 74:3897–3912
- Millot R, Scaillet B, Sanjuan B (2010c) Lithium isotopes in island arc geothermal systems: Guadeloupe, Martinique (French West Indies) and experimental approach. *Geochim Cosmochim Acta* 74:1852–1871
- Moriguti T, Nakamura E (1998) High-yield lithium separation and precise isotopic analysis for natural rock and aqueous samples. *Chem Geol* 145:91–104
- Nishio Y, Okamura K, Tanimizu M, Ishikawa T, Sano Y (2010) Lithium and strontium isotopic systematics of waters around Ontake volcano, Japan: implications for deep-seated fluids and earthquake swarms. *Earth Planet Sci Lett* 297:567–576
- O’Neil JR (1986) Theoretical and experimental aspects of isotopic fractionation. *Rev Mineral* 16:1–40
- Olive KA, Schramm DN (1992) Astrophysical ^7Li as a product of Big Bang nucleosynthesis and galactic cosmic-ray spallation. *Nature* 360:439–442
- Olsher U, Izatt RM, Bradshaw JS, Dalley NK (1991) Coordination chemistry of lithium ion: a crystal and molecular structure review. *Chem Rev* 91:137–164
- Palko AA, Drury JS, Begun GM (1976) Lithium isotope separation factors of some two-phase equilibrium systems. *J Chem Phys* 64:1828–1837
- Pistiner JS, Henderson GM (2003) Lithium-isotope fractionation during continental weathering processes. *Earth Planet Sci Lett* 214:327–339
- Pogge von Strandmann PAE, Burton KW, James RH, van Calsteren P, Gíslason SR, Mokadem F (2006) Riverine behaviour of uranium and lithium isotopes in an actively glaciated basaltic terrain. *Earth Planet Sci Lett* 251:134–147
- Pogge von Strandmann PAE, James RH, van Calsteren P, Gíslason SR, Burton KW (2008) Lithium, magnesium and uranium isotope behaviour in the estuarine environment of basaltic islands. *Earth Planet Sci Lett* 274:462–471
- Pogge von Strandmann PAE, Burton KW, James RH, van Calsteren P, Gíslason SR (2010) Assessing the role of climate on uranium and lithium isotope behaviour in rivers draining a basaltic terrain. *Chem Geol* 270:227–239
- Qi HP, Coplen TB, Wang QZ, Wang YH (1997) Unnatural isotopic composition of lithium reagents. *Anal Chem* 69:4076–4078

- Raiswell R, Tranter M, Benning LG, Siegert M, De'ath R, Huybrechts P, Payne T (2006) Contributions from glacially derived sediment to the global iron (oxyhydr)oxide cycle: implications for iron delivery to the oceans. *Geochim Cosmochim Acta* 70:2765–2780
- Rollion-Bard C, Vigier N, Meibom A, Blamart D, Reynaud S, Rodolfo-Metalpa R, Martin S, Gattuso J-P (2009) Effect of environmental conditions and skeletal ultrastructure on the Li isotopic composition of scleractinian corals, *Earth Planet. Sci Lett* 286:63–70. doi:[10.1016/j.epsl.2009.06.015](https://doi.org/10.1016/j.epsl.2009.06.015)
- Rosner M, Ball L, Peucker-Ehrenbrink B, Blusztajn J, Bach W, Erzinger J (2007) A simplified, accurate and fast method for lithium isotope analysis of rocks and fluids, and $\delta^7\text{Li}$ values of seawater and rock reference materials. *Geostand Geoanal Res* 31:77–88
- Rudnick RL, Tomascak PB, Njo HB, Gardner LR (2004) Extreme lithium isotopic fractionation during continental weathering revealed in saprolites from South Carolina. *Chem Geol* 212:45–57
- Savov IP, Ryan JG, D'Antonio M, Kelley K, Mattie P (2005) Geochemistry of serpentinized peridotites from the Mariana Forearc Conical Seamount, ODP Leg 125: implications for the elemental recycling at subduction zones. *Geochem Geophys Geosyst* 6:Q04J15. doi:[10.1029/2004GC000777](https://doi.org/10.1029/2004GC000777)
- Scholz F, Hensen C, Reitz A, Romer RL, Liebetau V, Meixner A, Weise SM, Haeckel M (2009) Isotopic evidence ($^{87}\text{Sr}/^{86}\text{Sr}$, $\delta^7\text{Li}$) for alteration of the oceanic crust at deep-rooted mud volcanoes in the Gulf of Cadiz, NE Atlantic Ocean original research. *Geochim Cosmochim Acta* 73:5444–5459
- Scholz F, Hensen C, DeLange GJ, Haeckel M, Liebetau V, Meixner A, Reitz A, Romer RL (2010) Lithium isotope geochemistry of marine pore waters – insights from cold seep fluids. *Geochim Cosmochim Acta* 74:3459–3475
- Shou M (1988) Lithium treatment of manic-depressive illness – past, present and perspectives. *J Am Med Assoc* 259:1834–1836
- Seyfried WE Jr, Chen X, Chan L-H (1998) Trace element mobility and lithium isotopic exchange during hydrothermal alteration of seafloor weathered basalt: an experimental study at 350°C, 500 bars. *Geochim Cosmochim Acta* 62:949–960
- Shannon RD (1976) Revised effective ionic-radii and systematic studies of interatomic distances in halides and chalcogenides. *Acta Cryst A* 32:751–767
- Spite M, Spite F (1982) Lithium abundance at the formation of the galaxy. *Nature* 297:483–485
- Stoffyn-Egli P (1982) Conservative behaviour of dissolved lithium in estuarine waters. *Estuar Coast Shelf Sci* 14:577–587
- Stoffyn-Egli P, Mackenzie FT (1984) Mass balance of dissolved lithium in the oceans. *Geochim Cosmochim Acta* 48:859–872
- Stoll PM, Stokes PE, Okamoto M (2001) Lithium isotopes: differential effects on renal function and histology. *Bipolar Disord* 3:174–180
- Symons EA (1985) Lithium isotope separation: a review of possible techniques. *Sep Sci Tech* 20:633–651
- Taylor TI, Urey HC (1938) Fractionation of the lithium and potassium isotopes by chemical exchange with zeolites. *J Chem Phys* 6:429–438
- Teng F-Z, McDonough WF, Rudnick RL, Dalpé C, Tomascak PB, Chappell BW, Gao S (2004) Lithium isotopic composition and concentration of the upper continental crust. *Geochim Cosmochim Acta* 68:4167–4178
- Teng F-Z, Rudnick RL, McDonough WF, Gao S, Tomascak PB, Liu Y (2008) Lithium isotopic composition and concentration of the deep continental crust. *Chem Geol* 255:47–59
- Teng F-Z, Rudnick RL, McDonough WF, Wu F-Y (2009) Lithium isotopic systematics of A-type granites and their mafic enclaves: further constraints on the Li isotopic composition of the continental crust. *Chem Geol* 262:370–379
- Tomascak PB, Tera F, Helz RT, Walker RJ (1999) The absence of lithium isotope fractionation during basalt differentiation: new measurements by multi-collector sector ICP-MS. *Geochim Cosmochim Acta* 63:907–910
- Tomascak PB, Langmuir CH, le Roux P, Shirey SB (2008) Lithium isotopes in global mid-ocean ridge basalts. *Geochim Cosmochim Acta* 72:1626–1637
- Tranter M (2003) Geochemical weathering in glacial and proglacial environments. In: Holland HD, Turekian KK (eds) *Treatise on geochemistry*. Pergamon, Oxford, pp 189–205
- Umeda M, Tuchiya K, Kawamura H, Hasegawa Y, Nanjo Y (2001) Preliminary characterization on Li isotope separation with Li ionic conductors. *Fusion Technol* 39:654–658
- US Geological survey (2009) Mineral commodity summaries 2009. U.S. Geological Survey, 195pp
- Vanneste H, Kelly-Gerreyn BA, Connelly DP, James RRH, Haeckel M, Fisher RE, Heeschen K, Mills RA (2010) Spatial variation in fluid flow and geochemical fluxes across the sediment-seawater interface at the Carlos Ribeiro mud volcano (Gulf of Cadiz). *Geochim Cosmochim Acta* 75(4):1124–1144
- Vigier N, Rollion-Bard C, Spezzaferri S, Brunet F (2007) In-situ measurements of Li isotopes in foraminifera. *Geochem Geophys Geosyst* Q01003. doi:[10.1029/2006GC001432](https://doi.org/10.1029/2006GC001432)
- Vigier N, Decarreau A, Millot R, Carignan J, Petit S, France-Lanord C (2008) Quantifying Li isotope fractionation during smectite formation and implications for the Li cycle. *Geochim Cosmochim Acta* 72:780–792
- Vigier N, Gislason SR, Burton KW, Millot R, Mokadem F (2009) The relationship between riverine lithium isotope composition and silicate weathering rates in Iceland. *Earth Planet Sci Lett* 287:434–441
- Vils F, Tonarini S, Kalt A, Seitz H-M (2009) Boron, lithium and strontium isotopes as tracers of seawater–serpentinite interaction at Mid-Atlantic ridge, ODP Leg 209, *Earth Planet. Sci Lett* 286:414–425
- Wenger M, Armbruster T (1991) Crystal chemistry of lithium: oxygen coordination and bonding. *Eur J Mineral* 3:387–399
- Wheat CG, Mottl MJ (2000) Composition of pore and spring waters from Baby Bare: Global implications of geochemical fluxes from a ridge flank hydrothermal system. *Geochim Cosmochim Acta* 64:629–642
- Williams LB, Hervig RL (2005) Lithium and boron isotopes in illite-smectite: the importance of crystal size. *Geochim Cosmochim Acta* 24:5705–5716
- Wimpenny J, James RH, Burton KW, Gannoun A, Mokadem F, Gislason SR (2010a) Glacial effects on weathering processes: new insights from the elemental and lithium isotopic composition of West Greenland rivers. *Earth Planet Sci Lett* 290:427–437

- Wimpenny J, Gisalason SR, James RH, Gannoun A, Pogge von Strandmann PAE, Burton KW (2010b) The behaviour of Li and Mg isotopes during primary phase dissolution and secondary mineral formation in basalt. *Geochim Cosmochim Acta* 74:5259–5279
- Witherow RA, Lyons WB, Henderson GM (2010) Lithium isotopic composition of the McMurdo Dry Valleys aquatic systems. *Chem Geol* 275:139–147
- Wunder B, Meixner A, Romer RL, Heinrich W (2006) Temperature-dependent isotopic fractionation of lithium between clinopyroxene and high-pressure hydrous fluids. *Contrib Mineral Petrol* 151:112–120
- Yamaji K, Makita Y, Watanabe H, Sonoda A, Kanoh H, Hirotsu T, Ooi K (2001) Theoretical estimation of lithium reduced partition function ratio for lithium ions in aqueous solution. *J Phys Chem A* 105:602–613
- You C-F, Chan L-H (1996) Precise determination of lithium isotopic composition in low concentration natural samples. *Geochim Cosmochim Acta* 60:909–915
- You C-F, Chan L-H, Spivack AJ, Gieskes JM (1995) Lithium, boron and their isotopes in sediments and pore waters of Ocean Drilling Program Site 808, Nankai Trough: implications for fluid expulsion in accretionary prisms. *Geology* 23:37–40
- You CF, Gieskes JM, Lee T, Yui TF, Chen HW (2004) Geochemistry of mud volcano fluids in the Taiwan accretionary prism. *Appl Geochem* 19:695–707
- Zhang L, Chan LH, Gieskes JM (1998) Lithium isotope geochemistry of pore waters from Ocean Drilling Program Sites 918 and 919, Irminger Basin. *Geochim Cosmochim Acta* 62:2437–2450

Chapter 5

Meteoric ^7Be and ^{10}Be as Process Tracers in the Environment

James M. Kaste and Mark Baskaran

Abstract ^7Be ($T_{1/2} = 53$ days) and ^{10}Be ($T_{1/2} = 1.4$ Ma) form via natural cosmogenic reactions in the atmosphere and are delivered to Earth's surface by wet and dry deposition. The distinct source term and near-constant fallout of these radionuclides onto soils, vegetation, waters, ice, and sediments makes them valuable tracers of a wide range of environmental processes operating over timescales from weeks to millions of years. Beryllium tends to form strong bonds with oxygen atoms, so ^7Be and ^{10}Be adsorb rapidly to organic and inorganic solid phases in the terrestrial and marine environment. Thus, cosmogenic isotopes of beryllium can be used to quantify surface age, sediment source, mixing rates, and particle residence and transit times in soils, streams, lakes, and the oceans. A number of caveats exist, however, for the general application of these radionuclides as tracers in the environment, as steady deposition and geochemical immobility are not guaranteed in all systems. Here we synthesize and review scientific literature documenting the deposition and behavior of these nuclides at the Earth's surface, focusing on current and potential applications for Earth scientists working to quantify terrestrial and marine processes.

5.1 Introduction

Cosmogenic isotopes of beryllium (Be) form when neutrons and protons spallate oxygen and nitrogen atoms (Fig. 5.1; Lal et al. 1958). The two naturally

J.M. Kaste (✉)
Department of Geology, The College of William & Mary,
Williamsburg, VA 23187, USA
e-mail: jmkaste@wm.edu

M. Baskaran
Department of Geology, Wayne State University, Detroit, MI
48202, USA
e-mail: Baskaran@wayne.edu

occurring Be isotopes of use to Earth scientists are the short-lived ^7Be ($T_{1/2} = 53.1$ days) and the longer-lived ^{10}Be ($T_{1/2} = 1.4$ Ma; Nishiizumi et al. 2007). Because cosmic rays that cause the initial cascade of neutrons and protons in the upper atmosphere responsible for the spallation reactions are attenuated by the mass of the atmosphere itself, production rates of cosmogenic Be are three orders of magnitude higher in the stratosphere than they are at sea-level (Masarik and Beer 1999, 2009). Most of the production of cosmogenic Be therefore occurs in the upper atmosphere (5–30 km), although there is trace, but measurable production as oxygen atoms in minerals at the Earth's surface are spallated (in situ produced; see Lal 2011, Chap. 24). After cosmogenic Be is formed in the atmosphere, it is removed by rain, snow, and dry deposition. The near-constant production rate of cosmogenic Be isotopes in the atmosphere (Leya et al. 2000; Vonmoos et al. 2006) and the particle-reactive nature of the Be atom (You et al. 1989) make *meteoric* cosmogenic Be nuclides (sometimes referred to as “garden variety” to differentiate from in situ) a valuable tracer of a wide range of chemical, physical, and biogeochemical processes. Here we focus on the current and potential applications of meteoric ^7Be and ^{10}Be for quantifying and tracing natural processes occurring in soil, fluvial, lacustrine, and marine environments.

5.1.1 Production and Deposition of Meteoric ^7Be and ^{10}Be

The delivery of meteoric ^7Be and ^{10}Be to a particular point on the Earth's surface is controlled by the nuclide production rate in the atmosphere, the region's air mass source, amounts of precipitation, and the

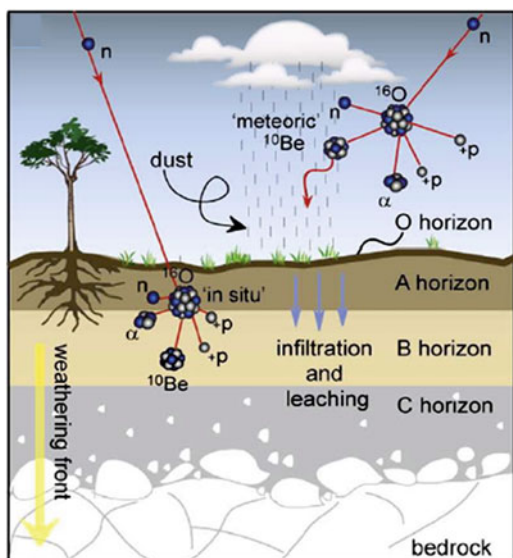


Fig. 5.1 Schematic of cosmogenic ^{10}Be production (^7Be forms in a similar manner). Meteoric ^7Be and ^{10}Be form in the atmosphere, and are delivered to the Earth's surface by wet and dry deposition. Most cosmogenic ^7Be is found on vegetation surfaces and in the O horizon or uppermost 2-cm of soil. Because of its longer half-life, ^{10}Be is commonly found on the surface, throughout the soil profile, and occasionally in saprolite. Reprinted from Willenbring and von Blanckenburg (2010a), Copyright (2010), with permission from Elsevier

efficiency of wet and dry depositional processes. Production rates of cosmogenic Be vary inversely with solar activity, because increased solar output strengthens the Earth's magnetic field which deflects cosmic rays. On timescales of decades, production rates vary by approximately 25% with the 11 year solar cycle, but over the course of hundreds of years, production rates may vary by a factor of two or more due to longer timescale modulations in the activity of the sun (Koch and Mann 1996; Vonmoos et al. 2006; Berggren et al. 2009). Because cosmic rays are deflected towards the poles, production rates of cosmogenic Be are a factor of 3–5 higher in polar air than in equatorial air (Harvey and Matthews 1989; Masarik and Beer 1999), depending on altitude. Polar air masses therefore have higher amounts of cosmogenic Be available for scavenging, but precipitation rates are generally very low here, which ultimately limits the meteoric radionuclide fluxes to the Earth's surface at high latitudes. The strong production gradient of cosmogenic Be with elevation in the atmosphere causes seasonal variability (at least in some latitude belts) in ^7Be and ^{10}Be deposition. This has been evident at mid-latitudes, as

injections of stratospheric air into the troposphere during the spring season of each year result in higher concentrations of cosmogenic Be in meteoric waters (Husain et al. 1977). Stronger convection in the troposphere during summer months also increases ^7Be and ^{10}Be in rainfall as higher air is tapped (Baskaran 1995). Typically, fluxes of meteoric ^7Be and ^{10}Be to the Earth's surface scale with precipitation rates more than with latitude, and dry deposition generally is of lesser importance (Olsen et al. 1985; Brown et al. 1989; Wallbrink and Murray 1994; Whiting et al. 2005; Zhu and Olsen 2009), particularly for the shorter-lived ^7Be .

While the concentrations of cosmogenic Be in precipitation can vary by a factor of 20 between different storm events at one location, and are strongly dependent on latitude, amounts in rain and snow for each nuclide are commonly on the order of 10^4 atoms g^{-1} , with $^7\text{Be}/^{10}\text{Be}$ atomic ratios falling between 0.41 and 0.61 in the Southern hemisphere and 0.67 and 0.85 in the Northern hemisphere (Brown et al. 1989; Knies et al. 1994). The production ratio of $^7\text{Be}/^{10}\text{Be}$ in the atmosphere is projected to be 1.9 (Nishiizumi et al. 1996; Masarik and Beer 1999); $^7\text{Be}/^{10}\text{Be}$ ratios measured in precipitation will be controlled by residence time in the atmosphere as ^7Be decays during air mass or aerosol transport. Snow commonly has higher concentrations of cosmogenic Be isotopes than rain, possibly because of the higher surface area of snowflakes compared with rain droplets (McNeary and Baskaran 2003). Concentrations of cosmogenic Be in precipitation compared from storm to storm are usually inversely proportional to rainfall amount, as aerosols are scavenged during the initial stages of a storm event and larger storms are simply more diluted (Olsen et al. 1985; Todd et al. 1989; Baskaran et al. 1993). For example, Ishikawa et al. (1995) documented a sharp reduction in the concentration of ^7Be in precipitation measured over the course of 2-day storm in Japan. During the first ~ 6 h of the storm, the ^7Be content of snowfall was approximately $10^{4.4}$ atoms g^{-1} (4 Bq L^{-1}), but this dropped to $<10^{3.8}$ atoms g^{-1} ($<1 \text{ Bq L}^{-1}$) during the latter stages of the event. Resuspended dust can be a significant source of ^{10}Be in rain (Monaghan et al. 1986; Graham et al. 2003; Lal and Baskaran 2011), but is probably a minor source of ^7Be to meteoric waters because of its shorter half-life. The ^{10}Be content of continental dust is near that of the average concentrations in regional surface soil, which

indicates that topsoil erosion is the likely source of dust over continents (Gu et al. 1996). Lal (2007) estimated the global average value of atmospheric dust to be $2.12(\pm 0.04) \times 10^9$ ^{10}Be atoms g^{-1} dust.

It is presumed that once ^7Be or ^{10}Be is produced, it combines with atmospheric oxygen or hydroxyl to form Be oxide (BeO) or hydroxide (BeOH_x^{2-x}), molecules that are scavenged by atmospheric moisture. Equilibrium thermodynamics can be used to predict that in slightly acidic cloudwater or rainfall ($\text{pH} < 6$), Be speciation will be dominated by Be^{2+} (Vesely et al. 1989; Takahashi et al. 1999). After rainfall hits the surface of the Earth, precipitation having a pH of < 6 is usually neutralized rapidly, and cosmogenic Be quickly adsorbs to vegetation and the uppermost layer of soils and sediments (Pavich et al. 1984; Wallbrink and Murray 1996; Kaste et al. 2007). Because of the wide variability in the concentrations of cosmogenic Be isotopes in rainfall within storms, between storms, between seasons, and from year to year, and the potential of dust deposition being significant particularly for ^{10}Be , it takes several years worth of input measurements to accurately generalize deposition rates for a single location (Brown et al. 1989; Baskaran 1995). Furthermore, care must be taken to acidify samples because Be^{2+} can adsorb to plastic sampling funnels or collection bottles (Baskaran et al. 1993). A summary of the volume-weighted ^7Be concentrations measured in rainfall and calculated wet deposition fluxes is given in Table 5.1.

5.1.2 General Abundances of ^7Be and ^{10}Be at the Earth's Surface

Inventories of meteoric cosmogenic Be on the Earth's surface (in units of atoms $(n) \text{m}^{-2}$ or activity $(\text{Bq} = n\lambda) \text{m}^{-2}$) at a particular location are a function of atmospheric deposition rates, exposure age, and soluble (from leaching or "desorption") and particulate (from erosion or sediment deposition) losses or gains. Soluble losses of cosmogenic Be from soils are thought to be negligible in watersheds of near-neutral pH , but can be appreciable in acidic systems (Pavich et al. 1985; Brown et al. 1992b). In most soils on gentle slopes, erosional losses of ^7Be are minimal because of its short half-life compared to the residence time of particle-reactive radionuclides in watersheds (or the timescale

needed for significant erosion), but ^{10}Be inventory deficiencies are used to calculate steady-state erosion rates (Brown et al. 1995). ^7Be in soils may thus be in an approximate radioactive equilibrium with atmospheric deposition, such that decay rates roughly equal deposition rates on a Bq m^{-2} basis (Olsen et al. 1985). However, in areas where there is very strong seasonal variations of precipitation (such as San Francisco, CA and other areas controlled by seasonal monsoons such as East Asia, Southeast Asia, etc.), very high precipitation during certain months may result in transient equilibrium with much higher inventories in soils during wetter periods (Walling et al. 2009).

Generally, concentrations of ^7Be and ^{10}Be in soils and sediments near the Earth's surface are in the range of 10^3 – 10^5 atoms g^{-1} (0.15 – 15 Bq kg^{-1}), and 10^7 – 10^9 atoms g^{-1} , respectively (Fig. 5.2). Because of its short half-life, ^7Be is confined to vegetation and just the upper few cm of regolith and typically has an exponential decrease of concentration with depth in soils (Wallbrink and Murray 1996; Blake et al. 1999; Whiting et al. 2001; Wilson et al. 2003; Kaste et al. 2007). However, it may be found deeper than 10 cm in sedimentary environments with high deposition rates or where sediment mixing by bioturbation and/or physical mixing is significant (Canuel et al. 1990) or when there are flood events (Sommerfield et al. 1999). Vegetation plays a significant role in scavenging radionuclides from the atmosphere (Russell et al. 1981). A large fraction of the ^7Be surface inventory can reside in grasses or the forest canopy (Monaghan et al. 1983; Wallbrink and Murray 1996; Kaste et al. 2002) and decays before it can reach the top of the soil profile or enter into the hydrologic cycle. Surface ^7Be inventories typically range between $10^{8.8}$ and $10^{9.8}$ atoms m^{-2} (100 – $1,000$ Bq m^{-2} ; Table 5.1) and show some scaling with precipitation patterns (Whiting et al. 2005). Salisbury and Cartwright (2005) took a creative approach in quantifying ^7Be deposition along a precipitation gradient by showing that sheep feces sampled on a transect from sea-level to approximately 1,000 m in North Wales had approximately a fivefold gradient in ^7Be concentrations. They projected that rainfall rates increased by a factor of approximately three to four along this transect, and because much of the ^7Be was deposited directly on vegetation that the sheep ate, fresh feces recorded the deposition signal. An advantage of this technique is that it averages some of the spatial

Table 5.1 Compilation of ^7Be fallout fluxes and terrestrial surface inventories

Location	Latitude	Period of collection (month year ⁻¹)	Annual precipitation (cm) ^a	Average monthly ^7Be flux (Bq m ⁻² month ⁻¹) ^a	Volume-weighted ^7Be activity (Bq L ⁻¹) ^a	References
Precipitation-based collectors						
Bombay (India)	29° 0' N	1955–1961, 1963–1965, 1968, 1970	230	106	0.55	Lal et al. (1979)
Galveston, TX	29° 18' N	12/1988–2/1992	117 (97–150)	204 (124–322)	1.45–2.58 (2.03)	Baskaran et al. (1993)
College Station, TX	30° 35' N	6/1989–2/1992	122 (98–146)	192 (174–208)	1.73–2.07 (1.90)	Baskaran et al. (1993)
Bermuda	32° 20' N	9/1977–8/1978	170	238	1.57	Turekian et al. (1983)
Oak Ridge, TN	35° 58' N	9/1982–8/1984	127 (110–143)	169 (142–196)	1.60 (1.55–1.65)	Olsen et al. (1986)
Norfolk, VA	36° 53' N	1/1983–12/1984	136 (132–141)	173 (167–179)	1.58 (1.50–1.67)	Todd et al. (1989)
Ansan, S. Korea	37° 17' N	1/1992–6/1993	112 (106–117)	142	1.08	Kim et al. (1998)
Solomon, MD	38° 19' N	3/1986–11/1987	96	189	2.36	Dibb and Rice (1989b)
Onagawa, Japan	38° 26' N	4/1987–3/1989	115 (88–142)	150 (118–181)	1.57 (1.54–1.60)	Ishikawa et al. (1995)
Thessaloniki, Greece	40° 38' N	1/1987–4/1990	48 (33–65)	51(40–70)	1.29 (1.10–1.48)	Papastefanou and Ioannidou (1991)
Westwood, NJ	40° 59' N	12/1960–8/1961	78	60	0.92	Walton and Fried (1962)
New Haven, CT	41° 31' N	3/1977–6/1978	148	315	2.63	Turekian et al. (1983)
Detroit, MI	42° 25' N	9/1999–2/2001	76	181	2.87	McNeary and Baskaran (2003)
Geneva, Switzerland	46° 16' N	11/1997–11/1998	97	174	2.16	Caillet et al. (2001)
Lake Geneva, Switzerland	46° 30' N		120	230	2.30	Dominik et al. (1987)
Lake Zurich, Switzerland	47° 22' N		110	223	2.43	Schuler et al. (1991)
Quillayute, Wash.	47° 57' N	2/1976–1/1977	270	113	0.50	Creelius (1981)
Chilton, England	51° 26' N	10/1959–9/1960	68	76	1.35	Peirson (1963)
Milford, England	51° 42' N	10/1959–9/1960	63	72	1.38	Peirson (1963)
Rijswijk, Netherlands	52° 01' N	11/1960–10/1961	93	132	1.70	Bleichrodt and Van Abkoude (1963)
Terrestrial surface inventories						
		Collection date (month/year)	Median surface inventory (Bq m ⁻²)	^7Be flux (Bq m ⁻² month ⁻¹) ^b	Surface type	
SE Queensland, AU	28° 01' S	5/2003	440	175	Soil	Doering et al. (2006)
Black Mtn, Australia	35° 15' S	9/1988	200	79	Soil + overlying grass	Wallbrink and Murray (1996)
Black Mtn, Australia	35° 15' S	9/1988	130	52	Alluvial bare soil	Wallbrink and Murray (1996)
Black Mtn, Australia	35° 15' S	5/1989	400	159	Soil + overlying grass	Wallbrink and Murray (1996)
Black Mtn, Australia	35° 15' S	5/1989	155	61	Alluvial bare soil	Wallbrink and Murray (1996)
Oak Ridge, TN	35° 58' N	7/1984	673	267	Soil + overlying grass	Olsen et al. (1985)
Owens Valley, CA	37° 22' N	10/2006	85	34	Soil + grass	Elmore et al. (2008)
Wallops Island, VA	37° 55' N	1/1985	673	267	Marsh + overlying grass	Olsen et al. (1985)
Wallops Island, VA	37° 55' N	1/1985	107	42	Unvegetated marsh	Olsen et al. (1985)
Mendocino, CA	39° 18' N	6/1980	700	278	Above-ground vegetation and litter	Monaghan et al. (1983)
Delaware Marsh	39° 27' N	7/1982	207	82	Marsh + overlying grass	Olsen et al. (1985)
Valdivia, Chile	39° 44' S	9/2003	573	227	Soil	Schuller et al. (2006)
Valdivia Chile	39° 49' S	4/2006	522	207	Recently harvested forest soil	Walling et al. (2009)
Valdivia Chile	39° 49' S	10/2006	1,139	452	Recently harvested forest soil	Walling et al. (2009)
Central Idaho	44° 50' N	5/1996	139	55	Soil + overlying vegetation	Bonniwell et al. (1999)
Central Maine	44° 50' N	12/98	554	220	Bog core + overlying vegetation	Kaste (1999)
Cooke City, MT	45° 01' N	6/2000	449	178	Soil	Whiting et al. (2005)
Devon, UK	50° 47' N	2/1998	512	203	Soil	Blake et al. (1999)

^aNumbers in parenthesis denote the range when data are reported for ≥ 2 years

^bAssumes steady-state between surface and atmospheric flux: calculated by multiplying the median surface inventory (Bq m⁻²) by 0.3966 month⁻¹

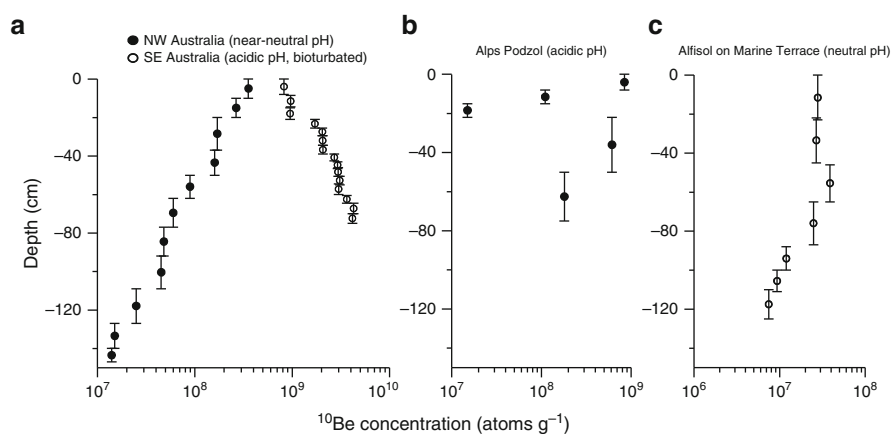


Fig. 5.2 Concentrations of meteoric ^{10}Be with depth in (a) a neutral pH soil profile in NW Australia and an acidic soil that was strongly bioturbated in SE Australia (Fifield et al. 2010), (b)

an acidic Podzol from the Alps (Egli et al. 2010), and (c) a near-neutral pH soil developed on a marine terrace in California (Monaghan et al. 1992)

heterogeneity associated with atmospheric deposition on vegetated terrain. Because the half-life of ^{10}Be is ~ 8 orders of magnitude larger than the residence time of aerosols in the atmosphere, in temperate to tropical regions where the air is stripped of cosmogenic Be isotopes in the initial part of storms, ^{10}Be inventories may not be controlled by rainfall rate as higher rainfall amounts simply dilute concentrations but do not add to the flux (Willenbring and von Blanckenburg 2010a). The fact that small changes in amount of precipitation for a region may not significantly alter depositional fluxes makes it slightly simpler to project steady-state ^{10}Be inventories for a landform.

5.2 Background

5.2.1 General Geochemical Behavior of Be in the Environment

Beryllium has the smallest ionic radius (0.31 Å) of all the metal cations, and exists only in the +2 valence state in natural aqueous solutions (Baes and Mesmer 1976). Its first hydrolysis constant $\{[\text{H}^+][\text{BeOH}^+]/[\text{Be}^{2+}]\}$ is $10^{-5.7}$; hence in meteoric waters where pH is controlled by atmospheric CO_2 , there should be a near equal distribution of the divalent cation $[\text{Be}^{2+}]$ and its first hydrolysis product $[\text{BeOH}^+]$. In acidic precipitation where anthropogenic acids have depressed the

pH of rainfall to < 5.5 , much of the meteoric cosmogenic Be may exist as Be^{2+} , whereas in regions where rainfall pH is buffered by calcite-bearing dust, cosmogenic Be may be in the BeOH^+ form. Given the typical pH range of natural waters of 5–9, equilibrium-based thermodynamic models would predict that the relative Be species abundances and the partitioning of cosmogenic Be may vary by orders of magnitude between slightly acidic systems and more alkaline systems. Indeed, experimental studies demonstrate that the partitioning of Be from the aqueous phase to an adsorbed phase on a range of materials is strongly pH dependent (Bloom and Crecelius 1983; Hawley et al. 1986; You et al. 1989). Using 3-week equilibration periods, You et al. (1989) showed a > 100 -fold variation in the solid-phase partitioning coefficient (K_d in kg L^{-1}) over the pH range of 4–8 for different substrate types (Fig. 5.3).

In freshwater rivers, amounts of dissolved ^7Be in the water column are commonly below detection limits (Dominik et al. 1987; Bonniwell et al. 1999), but in marine environments, Be may be characterized as having a limited affinity for suspended matter, as large fraction of the ^7Be and ^{10}Be appears to be dissolved (Merrill et al. 1960; Bloom and Crecelius 1983; Kusakabe et al. 1987; Dibb and Rice 1989a; Measures et al. 1996). The mechanism of Be adsorption onto inorganic minerals, including primary silicate minerals, secondary silicates, and iron and aluminum oxyhydroxides is typically considered to be via the formation of a complex between the Be atom and oxygen on

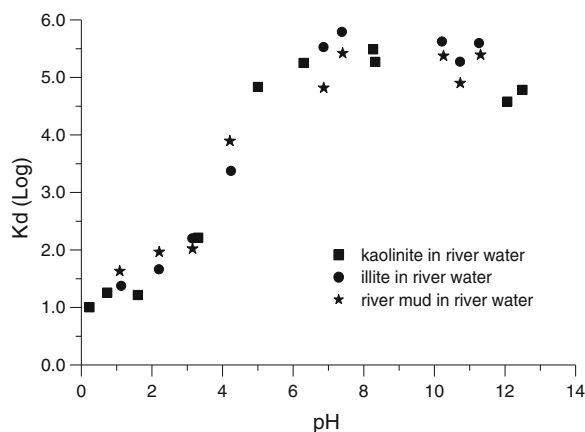


Fig. 5.3 The dependence of the K_D of Be for different materials over varying pH, using equilibration times of 3 weeks and suspended solids concentrations of 0.2 g L^{-1} . Reprinted from You et al. (1989), Copyright (1989), with permission from Elsevier

the surfaces or corners of minerals (“inner sphere adsorption”). The K_d may increase on timescales of weeks to months as adsorption-desorption equilibrium is followed by cationic lattice substitution (Nyffeler et al. 1984; Dibb and Rice 1989a). Like other particle-reactive metals, the K_d varies inversely with suspended solids concentrations below 30 mg L^{-1} (Hawley et al. 1986). While Be can form complexes with organic matter functional groups (daSilva et al. 1996), its partitioning coefficients seem to be significantly higher for inorganic materials compared with algae or seston (Bloom and Crecelius 1983; Dibb and Rice 1989a). Selective chemical extractions of marine sediments (Bourles et al. 1989) and soils (Barg et al. 1997) show that most of the meteoric Be is associated with authigenic phases (secondary Al, Fe, and Mn minerals) and organic matter coatings. Beryllium forms strong complexes with fluoride and humate, which could theoretically affect the strength and rate of aqueous to solid-phase partitioning (Nyffeler et al. 1984; Vesely et al. 1989; Takahashi et al. 1999).

The depth to which meteoric Be penetrates in soils and sediments will be controlled by advection (leaching or percolation) and diffusion-like (mixing) processes. The short half-life and tendency to adsorb to the solid phase causes ^7Be to generally be fixed in the vegetation and upper 2-cm of soil (Wallbrink and Murray 1996; Walling et al. 2009), but meteoric ^{10}Be is usually detectable from the soil surface to the C horizon, and in some cases through saprolite (Pavich et al. 1985). In high pH soils that are not intensively mixed, fallout Be exhibit an exponential decline in

concentrations with depth (Fig. 5.2a, NW Australia Site) as the affinity of the Be atom for the surface of almost any material (layered clays, secondary oxide minerals, organic matter, etc.) will be very strong. In acidic soil profiles, however, the Be atom may be highly enriched in specific layers that have the most favorable surface sites for adsorption (Fig. 5.2a, b). In most near-neutral pH soils, the concentration of meteoric ^{10}Be in soils has a subsurface concentration maximum in the B horizon layer where iron and aluminum accumulate (Barg et al. 1997; Jungers et al. 2009; Egli et al. 2010); beneath this there is often a general exponential decrease with depth (Fig. 5.2c). Physical soil mixing by organisms, wetting-drying cycles, or freeze-thaw cycles appears to create a layer of homogenized ^{10}Be concentrations (Fifield et al. 2010) as seen in the SE Australia ^{10}Be profile given in Fig. 5.2a.

5.2.1.1 Cosmogenic ^7Be and ^{10}Be in Freshwater Environments

The few watershed-scale studies that measure ^7Be and/or ^{10}Be in soils and waters have demonstrated that the actual distribution of Be between the solid and aqueous phase is broadly consistent with the thermodynamic predictions described above. In a survey of tropical watersheds in the Orinoco and Amazon basin, Brown et al. (1992b) found that acidic drainage waters had nearly the same concentration of dissolved ^{10}Be as incoming precipitation, indicating very little adsorption to soils and sediments. In more neutral to alkaline waters, concentrations of dissolved ^{10}Be in streamwater are often orders of magnitude smaller than meteoric waters because of adsorption to aluminum and iron oxide coatings on soils and sediments (Brown et al. 1992b; Barg et al. 1997) (Fig. 5.3).

Because of its shorter half-life and tendency to adsorb, the vast majority of ^7Be is retained by the vegetation and upper soils of a watershed (Olsen et al. 1986; Cooper et al. 1991; Wallbrink and Murray 1996; Bonniwell et al. 1999). Even during snowmelt events when the storm hydrograph is dominated by new water, most ^7Be never reaches the stream (Cooper et al. 1991). There are no reports of ^7Be in groundwater above typical detection limits ($<10 \text{ atoms g}^{-1}$ or 1.5 mBq L^{-1}). Due to the short half-life and high K_d s of ^7Be , it is not expected to penetrate very far beyond soil-air interface and hence it is not expected to be present in groundwater. In freshwater rivers,

concentrations of dissolved ($<0.45\ \mu\text{m}$) ^7Be are usually on the order of undetectable to $10^2\ \text{atoms g}^{-1}$ ($15\ \text{mBq L}^{-1}$), which is orders of magnitude lower than levels usually found in precipitation. Suspended sediments in streams however can have ^7Be concentrations on the order of $10^6\ \text{atoms g}^{-1}$ ($100\text{--}200\ \text{Bq kg}^{-1}$) (Dominik et al. 1987; Bonniwell et al. 1999); export of ^7Be from watersheds is evidently dominated by erosion and particulate losses. The concentration of dissolved ^7Be in lakes can vary by an order of magnitude over the course of a year as biological productivity varies with seasons. A sub-alpine lake in Bodensee had dissolved concentrations of ^7Be fluctuating from approximately $10^{0.8}\text{--}10^{1.8}\ \text{atoms g}^{-1}$ ($1\text{--}10\ \text{mBq L}^{-1}$) over the course of the year, which appeared to be controlled by the availability of particulates that are ultimately regulated by biological processes (Vogler et al. 1996).

Cosmogenic ^{10}Be in groundwater has been reported to range from 10^2 to $10^3\ \text{atoms g}^{-1}$ (Pavich et al. 1985; McHargue and Damon 1991). Pavich et al. (1985) calculated that the groundwater losses of ^{10}Be from a watershed in Virginia were three orders of magnitude lower than meteoric inputs. In a general survey of North American rivers and the Pearl River Basin in China, Kusakabe et al. (1991) reported dissolved concentrations of ^{10}Be to range from approximately

$10^3\text{--}10^{3.7}\ \text{atoms g}^{-1}$, which was slightly less than the ^{10}Be content of rainfall, but an order of magnitude higher than the amounts found in estuaries. However, dissolved ^{10}Be in the slightly acidic Orinoco River was found to be nearly equivalent to concentrations measured in local precipitation (Brown et al. 1992b). It seems that in acidic watersheds, the exchange sites on mineral surfaces may be dominated by other ions (H^+ , Al , etc.), which may inhibit Be adsorption. McHargue and Damon (1991) used an average ^{10}Be concentration of $10^3\ \text{atoms g}^{-1}$ for freshwaters, the volume of water in the world's rivers and lakes, and the global annual runoff flux to calculate that the residence time of ^{10}Be in the world's freshwaters is approximately 3 years.

5.2.1.2 Cosmogenic ^7Be and ^{10}Be in the Marine Environments

After Be radionuclides are delivered to the air-water interface via wet and dry fallout, the ions are removed from the water column primarily by adsorption onto particulate matter. While the removal rate is strongly dependent on the concentration and composition of suspended particulate matter (Dibb and Rice 1989a), the residence time of dissolved Be above the thermocline is on the order of 0.5 years (Fig. 5.4), which

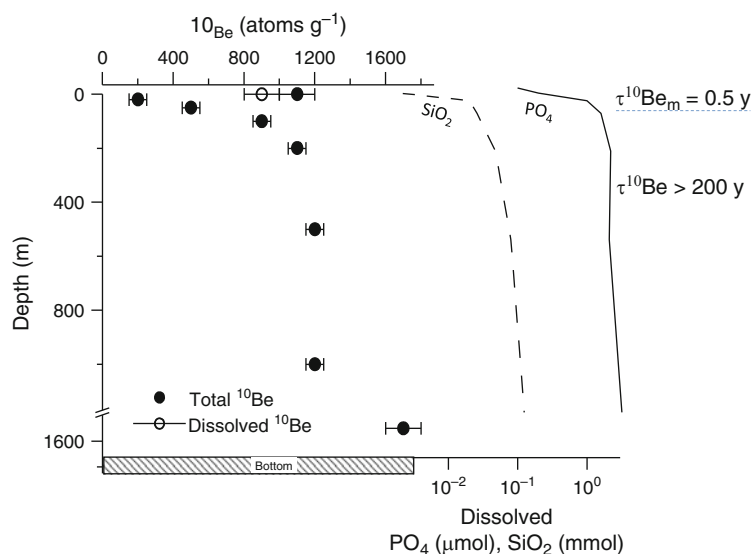


Fig. 5.4 ^{10}Be , phosphate, and silica concentrations in the water column in the San Nicolas Basin (Kusakabe et al. 1982). Above the thermocline in the “mixed layer” (upper $\sim 100\ \text{m}$), high concentrations of suspended particles cause rapid removal of

dissolved Be from the water column. As the particles dissolve beneath the thermocline, ^{10}Be is recycled back into the water column where it has a residence time of hundreds of years

is similar to the residence times reported for other particle-reactive atoms like Th and Pb (Kusakabe et al. 1982). The first measurement of ^7Be in seawater from the Indian Ocean was reported by Lal et al. (1960). Silker et al. (1968) later demonstrated that ^7Be had relatively uniform dissolved concentrations in surface waters of the Atlantic Ocean ($5^\circ 48' - 25^\circ 38' \text{N}$, $n = 7$ samples), ranging from $10^{1.4}$ to $10^{1.7}$ atoms $^7\text{Be g}^{-1}$ ($40\text{--}70 \text{ mBq L}^{-1}$), with a particulate fraction ranging between 7.4 and 14.9% of the total. Kusakabe et al. (1982) found that concentrations of ^{10}Be measured in unfiltered water samples collected from the surface of San Nicolas Basin were indistinguishable from the ^{10}Be measured in filtered water samples (Nucleopore $0.4 \mu\text{m}$ filter), and concluded that most ^{10}Be was in dissolved form (Fig. 5.4).

Although the monthly depositional fluxes of ^7Be have been reported to vary by a factor of ~ 10 , in the water column of the ocean, activities (Bq L^{-1}) vary much less, as the water column integrates the activities over its mean life. The amount of precipitation on the ocean varies with latitude and season, which will affect the depositional fluxes of ^7Be and thus their water column inventories. Concentrations of particulate and dissolved ^7Be within an estuarine system vary spatially and temporally. For example, the particulate and total (total = dissolved + particulate) ^7Be activities in June 2003 in Tampa Bay, Florida varied between $10^{-0.5}$ and $10^{0.4}$ atoms g^{-1} (0.05 and 0.39 mBq L^{-1}) and 10 and $10^{2.5}$ atoms g^{-1} (1.7 and 49 mBq L^{-1}), respectively while the corresponding values varied between $10^{0.3}$ and $10^{1.4}$ atoms g^{-1} (0.3 and 3.7 mBq L^{-1}) and $10^{1.1}$ and $10^{2.3}$ atoms g^{-1} (2 and 28 mBq L^{-1}), respectively in August 2003 (Baskaran and Swarzenski 2007). Particulate ^7Be concentrations are generally higher in the spring compared with summer, mainly due to higher amounts of water discharge and precipitation in late spring and early summer months, which results in higher particulate fluxes, resuspension, and scavenging during that time. The total residence time of ^7Be (τ_{Be}) is calculated using a simple approach, assuming that the water column is uniformly-mixed:

$$\tau_{\text{Be}} = \ln 2 \times A_{\text{Be}} \times h / I_{\text{Be}} \quad (5.1)$$

where A_{Be} is the total activity of ^7Be (Bq m^{-3}), I_{Be} is the atmospheric input rate of ^7Be ($\text{Bq m}^{-2} \text{ day}^{-1}$), and h is the mean depth (m) of the well-mixed sampling area. The residence time of dissolved Be in coastal

Table 5.2 Residence time of dissolved ^7Be in various coastal waters

Location	Residence time of ^7Be (d)	References
New York Harbor	8–17	Olsen et al. (1986)
James River Estuary	2–4	Olsen et al. (1986)
Raritan Bay	7–17	Olsen et al. (1986)
Chesapeake Bay	5–52	Dibb and Rice (1989a)
Galveston Bay	0.9–1.8	Baskaran and Santschi (1993)
Sabine-Neches estuary	0.8–10.5	Baskaran et al. (1997)
Tampa Bay	1.6–58.7	Baskaran and Swarzenski (2007)
Clinton River	1.0–60.3	Jweda et al. (2008)
Hudson River Estuary	0.7–9.5	Feng et al. (1999)

waters varies over an order of magnitude, from < 1 to 60 days, depending on the depth of the coastal/estuarine waters and concentrations of suspended particulate matter (Table 5.2). The K_d values in coastal waters may vary over two orders of magnitude, between 7×10^3 and 1.2×10^6 (Olsen et al. 1986; Baskaran and Santschi 1993; Baskaran et al. 1997; Kaste et al. 2002; Jweda et al. 2008). The K_d values are reported to be higher in June than in August, which is related to the variations in the amount of freshwater discharge and the amounts of precipitation that control the extent of resuspension of bottom sediments.

The concentration of dissolved ^{10}Be in marine surface waters typically varies between $10^{2.6}$ and $10^{3.2}$ atoms g^{-1} , and the residence time of Be has been generally reported to be shorter than the mixing time of the oceans (Merrill et al. 1960; Frank et al. 2009). Meltwaters from glaciers (both polar and high-altitude) could have higher concentrations of ^{10}Be compared with surrounding waters (e.g., Antarctic ice contains about $10^{4.7}$ atom g^{-1} of ^{10}Be , Raisbeck et al. 1978b). With the exception of one dataset, all data indicate that the water column inventory of ^{10}Be , in the Pacific is higher than that in the Atlantic (Table 5.3), perhaps a result of lower suspended matter concentrations in the Pacific. The transfer of ^{10}Be from the dissolved phase to the solid (adsorbed) phase may be regulated by the recycling of biogenic particles in the oceans (Fig. 5.4).

A wide range of dissolved residence times of ^{10}Be in the open ocean have been reported in the literature. Several approaches have been used to obtain residence times that include the inventories of ^{10}Be and annual

removal or depositional input of ^{10}Be , and from the Fe-Mn crust and Mn-nodule measurements (Raisbeck et al. 1978a, 1980; Kusakabe et al. 1982, 1987; Segl et al. 1987; Anderson et al. 1990; Ku et al. 1990; Brown et al. 1992a; Measures et al. 1996; von Blanckenburg et al. 1996; Frank et al. 2002, 2009). A large range of residence time values, if real, has major implications on the changing geochemical processes that lead to varying removal rates of Be^{2+} from the water column. In order to assess the variations, the data from all the open ocean sites were recalculated to determine the inventories of ^{10}Be in the water column (a standard depth of 3,600 m was used for all the basins) and the inventories are given in Table 5.3. Except the Arctic Ocean, where we compared the residence times of ^{10}Be in all four major basins (Nansen, Amundsen, Makarov and Canada Basins), we used the same depositional flux for each of the sites. The vertical profiles of dissolved ^{10}Be from these four basins are given in Fig. 5.5. The errors associated with the concentrations of ^{10}Be in individual depths reported in the publications are propagated to obtain the error associated with the inventory, which we use in the calculation of the errors associated with the residence times. The residence time of ^{10}Be in these major deep basins of the Arctic Ocean ranged from 680 to 830 years (Table 5.3), and given the propagated errors, there is no discernable difference in the residence time of ^{10}Be between the four basins of the Arctic. This observation can be compared to another particle-reactive radionuclide, Th in these major basins. A compilation of ^{230}Th data from these four basins clearly showed that the residence time of Th in the Makarov Basin is the longest (45 ± 1 years) compared to Canada Basin (22 ± 2 years), Amundsen Basin (19 ± 1 years) and Nansen Basin (17 ± 2 years; Trimble et al. 2004). The lack of difference we observe with ^{10}Be could be real or due to using the same atmospheric depositional input of $0.25 \times 10^6 \text{ atoms cm}^{-2} \text{ year}^{-1}$ (Frank et al. 2009) for all four basins. Since the annual removal rate and annual depositional flux data are sparse, we do not know whether there is a real difference between the residence times, but there are real differences between the particle concentrations and particle fluxes between these basins (Trimble et al. 2004).

Our calculated residence time given in Table 5.3 varies by a factor of 2.4 (between 236 and 505 years) between the Atlantic (western North Atlantic, South Atlantic) and Pacific Ocean. Thus, it appears that the

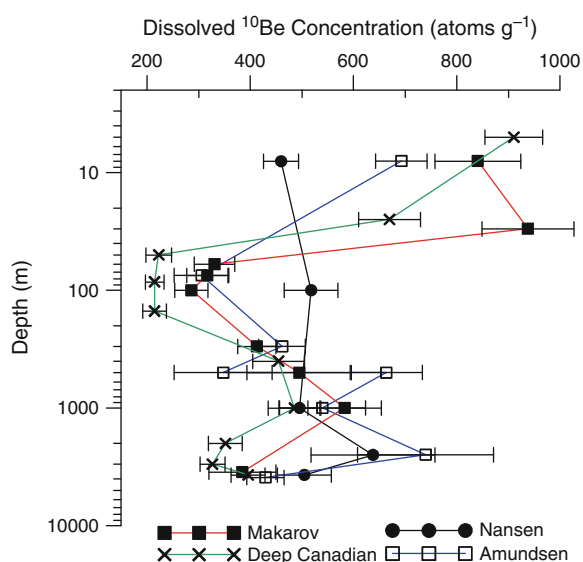


Fig. 5.5 Vertical profiles of dissolved ^{10}Be concentrations from all four major deep basins of the Arctic Ocean. Data are plotted from Frank et al. (2009)

wider range of residence times reported by various authors in the past (factor of ~ 10) may be due to poorly constrained input term used in their calculations. Lao et al. (1992a) estimated the deposition rate of ^{10}Be for the entire Pacific Ocean to be $1.5 \times 10^6 \text{ atoms cm}^{-2} \text{ year}^{-1}$, during the Holocene based on dated sediment cores. While the inventories can be measured precisely (with better than 10% precision), the annual depositional (input) flux is more difficult to constrain, as it can significantly vary depending on the amount of precipitation. Multi-year depositional flux measurement could reduce the uncertainty in the depositional flux. Perhaps by quantifying the relationship between ^{10}Be and another fallout isotope that is easier to measure in rainfall or has longer term datasets available (e.g., ^{210}Pb , Preiss et al. 1996; Sheets and Lawrence 1999), the depositional fluxes of ^{10}Be could be better constrained for residence time calculations.

5.2.2 Measuring ^7Be and ^{10}Be in Environmental Samples

5.2.2.1 Preconcentration Methods

The concentrations of ^7Be in surface water samples are so dilute a preconcentration method is usually needed.

Table 5.3 Concentrations, inventories and residences times of dissolved ^{10}Be in the major world oceans

Sample code	Coordinates	Depth (m)	Surface water ^{10}Be (atoms g^{-1})	^{10}Be inventory (10^8 atoms cm^{-2})	Residence time (years)	References
Arctic ocean						
Nansen Basin	84°16.87'N; 33°39.81'E	4,039	460	1.98 ± 0.30	790 ± 120	Frank et al. (2009) ¹
Amundsen Basin	88°24.48'N; 95°22.78'E	4,400	693	2.08 ± 0.38	830 ± 150	Frank et al. (2009) ¹
Makarov Basin	87°54.97'N; 154°22.50'E	3,985	841	1.70 ± 0.15	680 ± 60	Frank et al. (2009) ¹
Canada Basin	75°12.5'N; 149°57.0'W	3,850	911	1.72 ± 0.24	690 ± 96	Frank et al. (2009) ¹
Atlantic ocean						
Transect at 25°N	25°N; 60°W	>4,500	1,407	4.50 ± 0.22	372 ± 18	Segl et al. (1987) ²
Transect at 25°N	26°N; 50°W	>4,500	1,671	6.80 ± 0.78	562 ± 64	Segl et al. (1987) ²
Transect at 25°N	27°N; 44–45°W	>3,319	1,310	5.98 ± 0.70	494 ± 58	Segl et al. (1987) ²
Transect at 25°N	27°N; 35°W	>4,500	1,416	4.57 ± 0.59	378 ± 49	Segl et al. (1987) ²
Western North A.	41°32'N; 63°37'W	>3,411	430	2.85 ± 0.18	236 ± 15	Ku et al. (1990) ³
Western North A.	34°1'N; 63°0'W	>5,178	640	2.94 ± 0.22	243 ± 18	Ku et al. (1990) ³
South Atlantic	24°40'S; 38°21'W	>3,830	930	3.35 ± 0.14	279 ± 12	Measures et al. (1990) ⁴
South Atlantic	24°55'S; 01°00'W	>4,152	585	3.66 ± 0.16	305 ± 13	Measures et al. (1990) ⁴
South Atlantic	01°59'S; 04°02'W	>4,850	671	3.12 ± 0.13	260 ± 13	Measures et al. (1990) ⁴
Drake Passage	57–63°S; 66–69°W	>3,700	1,400	4.97 ± 0.41	49 ± 12 ^a (279 ± 12) ^a	Kusakabe et al. (1982)
Pacific Ocean	25°00'N; 169°59'E	6,013	1,060	5.74 ± 0.36	879 ± 54 ^b (475 ± 29) ^b	Kusakabe et al. (1987)
Pacific Ocean	17°28'N; 117°58'W	3,950	610	5.74 ± 0.33	870 ± 50 ^b (475 ± 27) ^b	Kusakabe et al. (1987)
Pacific Ocean	2°46'S; 117°02'W	4,200	810	6.11 ± 0.27	926 ± 41 ^b (505 ± 22) ^b	Kusakabe et al. (1987)

The following atmospheric inputs were assumed: 1: 2.5×10^5 atoms cm^{-2} year^{-1} (Frank et al. 2009); 2: 1.21×10^6 atoms cm^{-2} year^{-1} (Segl et al. 1987); 3: 1.21×10^6 atoms cm^{-2} year^{-1} (Monaghan et al. 1986); 4: 1.21×10^6 atoms cm^{-2} year^{-1} was assumed

^aDownward flux of 6.9×10^6 atoms cm^{-2} year^{-1} calculated using concentration gradient in ^{10}Be and assuming a vertical diffusivity (Kusakabe et al. 1982); the number in parenthesis is calculated assuming 1.21×10^6 atoms cm^{-2} year^{-1} (Monaghan et al. 1986)

^bInflux value of 6.6×10^5 atoms cm^{-2} year^{-1} was assumed (Kusakabe et al. 1987); the number in parenthesis is calculated assuming 1.21×10^6 atoms cm^{-2} year^{-1} (Monaghan et al. 1986)

This is particularly important for partitioning studies in lakes, rivers and marine system which require precise measurements in the particulate and dissolved phases. For the extraction of particulate matter, filter cartridges have been widely employed (Silker 1972; Baskaran et al. 1997, 2009b; Feng et al. 1999; Baskaran and Swarzenski 2007). When the dissolved phase (<pore-size of the filter, either absolute cut-off or nominal) is passed through a prefilter, it is possible that some of the dissolved phase may sorb onto the polypropylene/acrylic/glass filters. So far, no studies have been made to quantify this, although recent work indicates that a finite fraction of the dissolved Th is

removed by the prefilter (Baskaran et al. 2009b). For preconcentrating the dissolved phase, three common methods are employed that include: (1) evaporation; (2) co-precipitation; and (3) ion-extraction or extraction onto sorbents. Of these three methods, very low ionic strength solutions, including rainwater and freshwaters can be evaporated to reduce the volume (as low as 5–10 mL) that can be directly gamma-counted in Ge-well detectors. Evaporation of seawater samples will result in large amount of salts (~ 35 g L^{-1} of seawater) and hence it is not the suitable method for seawaters and other waters with high total dissolved solids. Co-precipitation with FeCl_3 is one of the most

common methods employed to preconcentrate; detailed procedures are given in Baskaran et al. (2009b). Stable Be carrier is added as yield monitor. Sorbents that have been utilized to extract dissolved radionuclides include $\text{Fe}(\text{OH})_3$ -impregnated fibers and a bed of aluminum oxide (Lee et al. 1991; Kadko and Olson 1996). Silker (1972) demonstrated that a flow rate of 35 L min^{-1} through a 6.4 mm thick alumina bed removed 70% of the ^7Be from seawater. Kadko and Olson (1996) assumed a constant efficiency of $69 \pm 3\%$, although most cartridge methods for particle-reactive radionuclides (such as Th, Pb, etc.) have been found to have variable extraction efficiencies (Baskaran et al. 2009a). The constant efficiency assumption for Be removal needs to be rigorously tested. Concentrations of ^{10}Be in surface waters of the global ocean vary between 10^2 and $10^3 \text{ atoms g}^{-1}$ (Raisbeck et al. 1978a; Kusakabe et al. 1982, 1990; Ku et al. 1990; Frank et al. 2009) and hence preconcentration is required. A minimum of a 2-L water sample ($\sim 0.4\text{--}2 \times 10^7$ atoms) is needed and details on chemical separation and purification are given in Baskaran et al. (2009b). For ^{10}Be analysis, sediments and aerosol samples are digested with concentrated HF, HNO_3 , HCl and brought to solution with the addition of ^9Be carrier. Beryllium from this digested solution can be separated and purified following the procedure summarized in Baskaran et al. (2009b). The purified Be in the form of $\text{Be}(\text{OH})_2$ is mixed with a small amount of AgNO_3 powder and then ashed at 850°C for 6 h and the ashed BeO powder is to prepare the target for the AMS analysis. Although the separation and purification of ^{10}Be is straight forward, isobaric interference from boron isotopes (^{10}B) could affect the measurements of ^{10}Be by AMS and hence care must be exercised in the purification of Be to eliminate B. Earlier studies added ^7Be spike (obtained from a commercial company) for the measurements of ^{10}Be in seawater as a yield monitor which had a high blank levels of ^{10}Be and hence caution needs to be exercised in utilizing ^7Be spike as a yield monitor (Kusakabe et al. 1982).

5.2.2.2 Measurement of ^7Be and ^{10}Be Concentrations

^7Be is most commonly measured in environmental samples using low-background decay counting techniques (Arnold and Al-Salih 1955; Larsen and

Cutshall 1981). ^7Be decays to ^7Li via electron capture, with 89.6% of the decays emitting a very low energy x-ray as they go directly to the ground state, and 10.4% of the decays first going to an excited state, which is the fraction that emits the 477.6 keV gamma. Gamma measurements are usually done using shielded scintillation detectors (e.g., NaI crystals) or semiconductor detectors made of Ge(Li) or pure (intrinsic) germanium (Arnold and Al-Salih 1955; Silker 1972; Larsen and Cutshall 1981; Krishnaswami et al. 1982; Murray et al. 1987; Baskaran et al. 1997; Baskaran and Shaw 2001). The absolute detection efficiency of NaI detectors for gamma rays is typically higher than the efficiency of Ge detectors, but NaI detectors have poor energy resolution. The width of the peak at half of the maximum value (full width at half maximum, FWHM of the Gaussian curve) for NaI detectors at 478 keV is commonly $\geq 30 \text{ keV}$, which is inadequate for resolving the ^7Be gamma from possible emissions from U and Th series isotopes. Most notably, ^{228}Ac (^{232}Th series) has a strong emission (4.74% yield) at 463 keV (Dalmasso et al. 1987), and radon progeny have low yield emissions at 480 and 487 keV (Morel et al. 2004) which can be significant when counting samples high in ^{226}Ra . Separation and purification of the Be atom is therefore necessary when using scintillation detectors, but Ge(Li) and intrinsic Ge detectors have high enough resolution ($\sim 1\text{--}2 \text{ keV}$ FWHM) in the 478 keV region which allows for the direct analysis of soils, sediments, waters, or filter papers for the ^7Be gamma.

One of the most important considerations that must be made when analyzing for ^7Be is the background of the gamma spectrum, which can control the detection limits. Compton scattering occurs when high energy gammas eject an electron with only a fraction of their full energy, which can create a “count” on the detector’s spectrum and a newer lower energy gamma ray that can also create counts on the detector. Thus, high energy photons ($>500 \text{ keV}$) from the U and Th decay series, ^{40}K , and cosmic rays thus generate random noise in the region of the gamma spectrum where ^7Be decays. By completely surrounding the scintillation or Ge detectors with 4” of lead and using detector hardware (preamplifier, wires, etc.) made of ultra-low-background materials, the Compton scattering effect from gammas originating from external sources (the ground, the walls, and the atmosphere) can be minimized. As a general rule, if the detector is completely

surrounded by 4'' of lead, external gammas from the ^{238}U , ^{235}U , and ^{232}Th decay series and ^{40}K are effectively attenuated. To minimize the Compton scattering effect from cosmic rays, detectors should be housed in basements of buildings or below ground. A thin copper liner is often used to separate the detector (and sample) from X-rays generated by the lead shielding itself.

In general, the larger the scintillation or Ge Detector (in thickness and surface area), the higher the efficiency for the ^7Be detection process, but larger detectors require the thickest shielding. The efficiency of the detector type for absorbing the full energy of the 478 keV ^7Be gamma is a function of the detector and the counting geometry. The relationship between efficiency and energy for each detector and counting geometry must be defined to calculate accurate ^7Be concentrations. This is commonly done by counting a synthesized mixture of radionuclides that decay over a wide range of energies (40–1,400 keV) in the exact geometry that the unknown samples will be analyzed in, which allows the analyst to construct a relationship between energy (keV) and detection efficiency. Alternatively, if certified ^7Be Standard Reference Material can be obtained, then, the detector can be calibrated for well-defined geometries and dpm/cpm ratios can be obtained for different geometries and these ratios can be directly used to obtain the activities of samples. Detectors can be planar in form for petri-dish style counting geometries, but large well detectors have the highest efficiencies for small geometry samples (a Ge well detector has an absolute detection efficiency at 478 keV of $21.9 \pm 0.3\%$ for 1-mL geometry; Jweda et al. 2008). There have been successful measurements of ^7Be in environmental samples by accelerator mass spectrometry, which has a detection limit of $\sim 10^4$ atoms (corresponding to 0.09 dpm or 1.5 mBq) which is at least an order of magnitude more sensitive than the counting methods (Nagai et al. 2004). Details on calculation of activities and calibration methods are given in Baskaran et al. (2009b).

A number of accelerators (e.g., Tandem Van De Graaff and other high-voltage Tandem accelerators, cyclotron, etc.) have been utilized to measure ^{10}Be (Raisbeck et al. 1978b; Turekian et al. 1979; Galindo-Uribarri et al. 2007). Details on the differences between these accelerated mass spectrometers are beyond the scope of this article. A detailed methodology on how the Tandem Van De Graaff accelera-

tor is set-up and used for the ^{10}Be measurements is given in Turekian et al. (1979).

5.3 Applications

The near-steady input of ^7Be and ^{10}Be and the particle-reactive nature of the Be atom makes meteoric Be nuclides a very useful tracer for quantifying a range of environmental processes operating on timescales from weeks to millennia. Both nuclides can be used to study atmospheric transport and depositional processes (see Lal and Baskaran 2011, Chap. 28). ^7Be can be used to quantify a number of short-timescale processes, including the infiltration of particle-reactive elements in soils, overland flow processes, and topsoil erosion (see Matisoff and Whiting 2011, Chap. 25). In lakes, streams, and marine environments, ^7Be is a valuable tracer of colloid and particulate dynamics, recent sediment deposition, mixing and focusing, and particle resuspension and transport. Meteoric ^{10}Be has been used to quantify landform age, creep rates, erosion rates, loess accumulation, and it has potential for dating authigenic mineral formation.

5.3.1 Using ^7Be and ^{10}Be to Trace Hillslope and Soil Processes

The short half-life of ^7Be makes it a valuable tracer of event-scale transport in soil profiles and on hillslopes. Given that ^7Be is usually deposited during rainfall events, especially intense rains and thunderstorms, the vertical distribution of this nuclide in soils can be used to infer the initial depth-penetration of other particle-reactive radionuclides and contaminants from a single deposition event. The initial conditions for an advection-diffusion transport model of other fallout isotopes (e.g., ^{210}Pb) can be constrained using the vertical distribution of ^7Be (Kaste et al. 2007). Measurements of ^7Be in stormwater, for example, can be used to study the fate of atmospherically-deposited particle reactive contaminants (Hg, Pb, etc.) released from a melting snowpack (Cooper et al. 1991). The spatial distribution of ^7Be on hillslopes measured after a significant storm can also be used to trace

event-scale soil sediment redistribution. If the ^7Be distribution is compared with the distribution of other sediment tracers that track longer timescales (e. g., ^{137}Cs), the contribution of single, intense storms to soil movement can be put into perspective with processes operating over the course of years to decades (Walling et al. 1999).

Because of its longer half-life, meteoric ^{10}Be has great potential for quantifying soil and sediment transport processes and authigenic mineral formation rates on soil-mantled hillslopes (Willenbring and von Blanckenburg 2010a). The inventory of meteoric ^{10}Be (I , in units of atoms area^{-1}) at a point on Earth can be expressed as:

$$I = \int_{-z}^0 C\rho dz \quad (5.2)$$

where $-z$ is the depth in the soil to which meteoric ^{10}Be has penetrated, 0 is the soil surface, C is the concentration of meteoric ^{10}Be (in atoms mass^{-1}), and ρ is the soil density (mass volume^{-1}). In practice, this is measured by collecting samples with sampling depth resolution (dz) on the order of 20 cm to up to a meter (Pavich et al. 1985; McKean et al. 1993; Jungers et al. 2009). The inventory I at a location is governed by ^{10}Be deposition, which is a function of production in the atmosphere and wet + dry depositional processes, age, radioactive decay, particulate losses, and solute losses. Inventories are used to find the age of stable, non-eroding surfaces if the nuclear production rates in the atmosphere and deposition varies around some mean value that can be constrained for time period of interest (Tsai et al. 2008; Willenbring and von Blanckenburg 2010a). However, at many sites, solution and/or erosional losses limit the ^{10}Be inventories (Monaghan et al. 1983). Given an eroding surface where weathering, soil formation, and soil loss are in equilibrium, inventories can be used to calculate steady-state erosion rates (Pavich et al. 1986; Brown et al. 1988). This technique can be extended to study the fate of other particle-reactive elements on landscapes. For example, the loss and accumulation of ^{10}Be over different points of a landform can be used to study how sediment transport processes control the fate and storage of carbon on a hillslope (Harden et al. 2002).

Inventories of meteoric ^{10}Be along points on soil-mantled hillslope profiles often increase with distance from the divide (McKean et al. 1993). This gradient results because points farthest from the divide have traveled the longest distance and resided on the hillslope for a longer duration and thus received more of a ^{10}Be dose. By constructing a linear regression between I values measured for points on a hillslope profile and projected soil particle paths, Jungers et al. (2009) used the rate of inventory change (dI/dx) and an average ^{10}Be input assumption to calculate virtual soil velocities for a hillslope in the Great Smoky Mountains, NC. Downslope soil transport velocities calculated using ^{10}Be inventories can be used to test assumptions about landscape equilibrium. McKean et al. (1993) used this technique to show that the soil creep flux was related to slope, which supported G.K. Gilbert's hypothesis (1877) that hillslopes exist in a dynamic equilibrium with a uniform soil production rate.

Meteoric ^{10}Be may be useful for dating authigenic minerals in soils, which was first suggested by Lal et al. (1991). Dating of secondary minerals in soil profiles could be extremely valuable for quantifying the rate of soil formation, and, using additional information, can be used for putting formation rates into context with erosion rates. Secondary minerals have, for the most part, defied traditional isotopic dating methods, such as U-Th series chronology, because of large uncertainties in defining the initially inherited isotopic composition (Cornu et al. 2009).

Barg et al. (1997) developed a "closed system" model which relied on the $^{10}\text{Be}/^9\text{Be}$ ratio as a chronometer for modeling the age of clays and iron and aluminum hydroxide minerals. In this model, cosmogenic ^{10}Be and bedrock-derived ^9Be equilibrate in the upper soil horizons, and slowly move down the profile by adsorption-desorption reactions. It is assumed that secondary minerals form primarily in the C-horizon, and, at the time of formation $^{10}\text{Be}/^9\text{Be}$ is locked in, and will change as a function of time. Indeed, the $^{10}\text{Be}/^9\text{Be}$ values were found to be in a narrower range than the ^{10}Be concentration, and, by using selective chemical extractions that targeted secondary minerals, they found that the highest $^{10}\text{Be}/^9\text{Be}$ values were found at the soil-bedrock interface, where authigenic mineral formation is projected to take place. This technique needs considerably more development, to account for secondary mineral dissolution and illuviation processes.

5.3.2 Using ^7Be as a Tracer in Lake and River Systems

5.3.2.1 ^7Be as a Tracer of Metal Scavenging, Colloidal, and Particulate Dynamics in Lakes

When dissolved metals are introduced into lake waters via atmospheric deposition, they can be scavenged by colloids, a process that greatly reduces their potential toxicity to the lake's ecosystem. Honeyman and Santschi (1989) describe a "colloidal pumping" process by which metals are removed from waters in three stages: (1) in the first stage, dissolved trace metals and radionuclides are released into the water column, either from atmospheric deposition or through production from the parents and these species are removed quickly onto colloidal particles through sorption reactions; (2) colloidal-bound trace metals and radionuclides undergo coagulation relatively slowly with the small particle pool and (3) the particles move in the particle size spectrum and are then eventually removed from the water column. In this, the coagulation of colloids is the rate controlling step in trace metals and radionuclide scavenging. Steinmann et al. (1999) modified a steady-state particle scavenging model (Honeyman and Santschi 1989) so that ($\lambda = 0.013 \text{ d}^{-1}$, the decay constant of ^7Be) ^7Be could be applied to study mechanisms and rates of metal scavenging from the waters of Lake Lugano (Switzerland, Italy):

$$\begin{aligned} Be_d \lambda_{ads} &= Be_c \lambda + Be_c \lambda_{coag} \\ Be_c \lambda_{coag} &= Be_p \lambda + Be_p \lambda_{sed} \\ F_{sed}^{Be} &= Be_p \lambda_{sed} \end{aligned} \quad (5.3-5.5)$$

By directly measuring the concentrations (in Bq m^{-3}) of dissolved ^7Be (Be_d ; $<10 \text{ kD}$), colloidal ^7Be (Be_c ; $10 \text{ kD} - 1 \mu\text{m}$), particulate ^7Be (Be_p ; $>1 \mu\text{m}$), and the sedimentary flux of ^7Be (F_{sed}^{Be} ; in $\text{Bq m}^{-3} \text{ day}^{-1}$), the adsorption rate (λ_{ads}) of ^7Be onto colloids was calculated to be approximately $0.02 - 0.005 \text{ day}^{-1}$, corresponding to a dissolved ^7Be residence time of 50–200 days. The residence time of colloids ($1/\lambda_{coag}$) ranged from a few days to a few weeks, while the residence time of particulates ($1/\lambda_{sed}$) was typically less than a week. The authors suggested that colloids $<10 \text{ kD}$ containing ^7Be could be affecting the calcu-

lated residence times, and thus adsorption rates of ^7Be , and that perhaps the rate limiting step for the removal of ^7Be from the water column was in fact the coagulation of small colloids $<10 \text{ kD}$. This application of ^7Be was also useful for quantifying the effect of biological processes on trace metal scavenging, as the highest coagulation rates (λ_{coag}) followed algal blooms. While true steady-steady conditions may not be possible on timescales of weeks because of the episodic nature of ^7Be deposition, the quantitative modeling approach described above is still useful for constraining the rates of metal adsorption, colloidal coagulation, and particle sedimentation in natural systems (Dominik et al. 1989).

^7Be can also be used to identify sources of particulates to the water column in lakes and to examine mixing processes. In Lake Michigan, under isothermal conditions that persist from December to May, the concentration of ^7Be on suspended matter is nearly constant with depth (Robbins and Eadie 1991), indicating that the waters are mixed vertically on short timescales.

However, in early summer, the ^7Be content of suspended sediments reaches a maxima near the surface of the lake ($<20 \text{ m}$) as lake stratification limits the settling of sediment (Robbins and Eadie 1991). A similar stratification effect on the vertical distribution of ^7Be has been observed in waters of Lake Zurich (Schuler et al. 1991). In the summer, calcite formation and/or algal blooms can effectively scavenge ^7Be from the upper fraction of the water column, reducing ^7Be in the epilimnion (Robbins and Eadie 1991; Vogler et al. 1996). In the late fall, lake turnover recharges the suspended sediment pool to lake water again, as ^7Be increases again in the epilimnion (Robbins and Eadie 1991; Vogler et al. 1996). These tracer studies have demonstrated how the dissolved to particulate ^7Be varies seasonally, and that the scavenging of metals from surface waters can be controlled by biological productivity and/or authigenic mineral formation.

5.3.2.2 ^7Be as a Tracer of Sediment Source, Focusing, Resuspension, and Transport in Rivers

Sediment can directly and indirectly degrade river ecosystems, and humans have altered landscapes and sediment fluxes and dynamics in nearly every river system on Earth. The focusing of fine sediment deposition from land use change, in particular, can degrade

spawning gravels, and, in some cases, sediments contain particle-reactive contaminants such as Pb, Hg, and PCBs that directly impact organisms. Cosmogenic ^7Be can be a useful tracer in fluvial systems, and has been successfully used to trace sediment sources in rivers, residence times, resuspension rates, transit times, and the fate of recently contaminated sediments. In many cases the use of ^7Be in fluvial systems relies on the fact that sediments that are buried for a period of more than 6 months will have undetectable ^7Be . This “old” sediment can be separated from recently exposed sediment by doing end-member mixing analysis (Bonniwell et al. 1999; Matisoff et al. 2005). In rivers, sediment deposition and resuspension rates can be calculated by projecting the inventories present in bed sediments present from atmospheric deposition, and quantifying depletion from resuspension, or excess, from deposition (Jweda et al. 2008). This technique was used in the Fox River, in Wisconsin, to determine the fate and dynamics of a PCB-contaminated sediment layer (Fitzgerald et al. 2001), much of which was resuspended during high flow despite the impounded nature of the river.

Humans have profoundly altered the flow regimes and sediment supplies of rivers through urbanization, logging, the construction of dams, and the engineering of stream banks (Croke et al. 1999; Magilligan et al. 2003). In recent years, the use of ^7Be as a tracer of fine sediment deposition, resuspension, and transport has been expanded to study processes in a wide range of fluvial environments, and to quantify how sediment dynamics might respond to different forcings. The enrichment of the upper few cm of topsoil with ^7Be makes it a valuable tracer of sediments derived from surface erosion (Blake et al. 1999, 2002; Wallbrink et al. 1999) and enables a quantitative partitioning of runoff processes between sheetwash and rilling (Whiting et al. 2001). Sediment transport rates within a fluvial system can also be calculated using ^7Be . Salant et al. (2007) repeatedly measured point bar and streambed sands in a regulated river immediately downstream of a dam in Vermont, U.S.A. During the winter months, sediment stored behind the dam became depleted in ^7Be , and when the gates were opened in the early spring the pulse of depleted “new” sediment was discernable from the surrounding sediments that were supplied by tributaries and previously exposed bars. Sediment transport rates of 30–80 m day⁻¹ were calculated using the known starting point of the sands and monthly sampling at fixed

points to monitor the pulse of sediment as it moved down river. The ^7Be content of bedload sediment in a single river varies by more than a factor of two over the course of a single year, as seasonal changes in ^7Be delivery (Olsen et al. 1985) and flow regimes regulate sediment source, grain size, and transport processes. Cosmogenic ^7Be may trace sediment substrates and nutrients that are favorable for certain aquatic insects. Svendsen et al. (2009) reported a significant correlation between ^7Be concentrations in transitional bed load sediment and benthic community structure at tributary junctions along a mainstem river in Vermont.

There is a strong dependence of grain size on the adsorption of ^7Be , and, in rivers, grain size will vary with flow regime which can make the relationship between ^7Be and age difficult to reconstruct. To normalize for grain-size effects on ^7Be values, models have been developed that utilize the $^7\text{Be}/^{210}\text{Pb}_{\text{ex}}$ ratio for calculating sediment age or fraction of new sediment in suspension. This relies on the fact that $^{210}\text{Pb}_{\text{ex}}$, which is the atmospherically-delivered portion of ^{210}Pb in sediments (^{210}Pb in “excess” of that projected to be supported by in situ ^{222}Rn decay) also adsorbs strongly to sediment and organic matter surfaces, and is reported to have partitioning coefficients (K_d) at least as high as Be (Sauve et al. 2000a, b). The change in the $^7\text{Be}/^{210}\text{Pb}_{\text{ex}}$ can thus be a more sensitive indicator of age, since ^7Be decays much faster than ^{210}Pb . Others have found a very strong correlation with $^7\text{Be}/^{210}\text{Pb}$ values and ^7Be divided by grain surface area (Fisher et al. 2010). In a study of a coastal plain river in Maine, U.S.A., Fisher et al. (2010) used a constant initial $^7\text{Be}/^{210}\text{Pb}$ model to measure the time-scale of sediment storage behind large woody debris and boulders. They found that in independently-assessed “transport-limited” reaches of the Ducktrap River, sediment sequestration behind in-stream obstructions was >100 days, but in supply limited reaches sediment was replenished more quickly.

5.3.3 Applications of Meteoric ^7Be and ^{10}Be as Process Tracers in the Marine Environment

From the time the ^7Be and ^{10}Be are produced in the atmosphere until its ultimate disposal, either through radioactive decay or their permanent incorporation into

the bottom sediments in oceans, these nuclides often pass through a number of transient reservoirs, such as various layers of atmosphere, precipitation and surface waters. The half-life of ^7Be is suitable for studying the vertical eddy diffusion coefficients and associated vertical transport rates in the upper layers of the thermocline (Silker 1972; Kadko and Olson 1996). Silker (1972) utilized the vertical concentration gradients of ^7Be in the Atlantic water column to determine the vertical eddy diffusion coefficients within the thermocline, assuming that atmospheric input of ^7Be is constant and the horizontal advective transport is negligible. Due to its short mean-life (76.9 days) and the lack of biological removal of Be, the effects of long-range advective transport on the vertical distribution is likely negligible and hence it is reasonable to assume that ^7Be will be effective in tracing diffusion at the top of the thermocline. Since ^7Be is delivered at the air-water interface, that layer is “tagged” with ^7Be constantly and when this layer undergoes sinking, the vertical profiles of ^7Be can be utilized to retrieve the record of the seasonal changes in the mixed layer depth (Kadko 2000).

5.3.3.1 Measuring Sediment Accumulation, Mixing Rates, and Sediment Focusing with ^7Be

A large number of studies have been conducted utilizing ^7Be to identify and quantify flood deposits (Corbett et al. 2007; more discussion are given in Du et al. 2011, Chap. 16). ^7Be is also utilized to quantify recent sediment accumulation and mixing rates (Krishnaswami et al. 1980; Clifton et al. 1995; Corbett et al. 2007). The sediment mixing involves both advective (physical particle transport) and diffusive mixing components. A combined effect of advective and diffusive mixing is analogous to eddy diffusion and has been modeled to determine eddy mixing coefficients. In coastal areas, the ^7Be profiles in sediments are not often in steady-state due to seasonal variations in the riverine discharge which delivers relatively large amount of ^7Be . In marine and lacustrine environments, the sediment inventories at selected sites are often far excessive compared to what is expected and this elevated levels is often caused by physical transport processes of sediments (such as sediment focusing by bottom currents and gravity flows, e.g., slumps and gravity flows). A comparison

of the measured sediment inventories (I_{sed} , Bq m^{-2}) to the measured depositional fluxes (or expected) of ^7Be (I_{dep}) will yield information on sediment focusing ($I_{\text{sed}}/I_{\text{dep}} > 1$) or erosion ($I_{\text{sed}}/I_{\text{dep}} < 1$).

5.3.3.2 Boundary Scavenging and Long-Range Transport of ^{10}Be in Marine Systems

Advective transport of dissolved nuclides to regions of high productivity waters in the margins results in higher suspended particle concentrations and fluxes which result in enhanced scavenging of ^{10}Be and other particle-reactive nuclides (e.g., ^{230}Th , ^{231}Pa , ^{210}Pb , etc.). In ocean margin sediments, the ^{10}Be concentrations were found to be much higher than that expected from the direct atmospheric deposition and this was attributed to boundary scavenging. The deposition rates of ^{10}Be in pelagic red clays were reported to be much less than its global average production rate, whereas in ocean-margin sediments, the ^{10}Be deposition rate exceeds its global average production rate (Brown et al. 1985; Anderson et al. 1990; Lao et al. 1992b). Particle composition (such as opal Si, Fe-Mn oxides, carbonate, terrigenous material such as clays; Luo and Ku 2004a, b; Chase et al. 2003) also plays a significant role on the scavenging of dissolved ^{10}Be . Sharma et al. (1987) reported strong correlation between ^{10}Be and Al in the sediment trap and attributed the aluminosilicate to be the major carrier phase for the scavenging of dissolved ^{10}Be .

Deposition rates of ^{10}Be at margin sites calculated from sedimentary records (= sediment accumulation rates ($\text{g cm}^{-2} \text{ year}^{-1}$) \times concentration of ^{10}Be in surficial sediments (atoms g^{-1})) have been found to be significantly higher than the rate of ^{10}Be supply at the Earth's surface at sites far away from the margins (such as off Northwest Africa and off California, equatorial Pacific off Ecuador, margins in North Atlantic, Brown et al. 1985; Anderson et al. 1990) and is attributed to boundary scavenging. Boundary scavenging exerts influence when the dissolved residence time of Be is greater than the time required for the advective transport to move the water from the center of the basin to the margins. Physical transport processes such as bottom currents and gravity flows (turbidities and slumps) also could lead to increased rates of ^{10}Be accumulation rates, resulting in higher ocean-wide average ^{10}Be deposition rates.

There are limited data on the temporal and spatial variations of ^{10}Be and ^7Be isotopes in oceanic particulate matter. Depositional fluxes measured in sediment traps deployed at two sites in the eastern equatorial North Pacific Ocean show that the ^{10}Be flux at traps deployed 50 m above the bottom of the sediment-water interface were up to an order of magnitude higher than that at mid-depth in the water depth column (at 1,565 and 1,465 m with total water depth of 3,100 and 3,600 m). The flux in the bottom trap (4.6×10^6 and 2.4×10^6 atoms $\text{cm}^{-2} \text{year}^{-1}$) was significantly higher than the average global depositional flux of 1.2×10^6 atoms $\text{cm}^{-2} \text{year}^{-1}$ while at intermediate depth the ^{10}Be flux was lower (0.9×10^6 and 0.4×10^6 atoms $\text{cm}^{-2} \text{year}^{-1}$) than the global depositional flux (Sharma et al. 1987). This difference was attributed to contribution from lateral input as well as from the resuspended material in the bottom nepheloid layers. A strong correlation between ^{10}Be concentration and Al suggest that aluminosilicate is the major carrier phase of ^{10}Be . Variations in atmospheric dust input may result in variations in the scavenging of ^{10}Be from the water column and thus, the variations in particle fluxes can be linked to the depositional fluxes in the traps.

5.3.3.3 ^7Be as a Tracer of Ice Rafted Sediments (IRS) in the Oceans

Concentrations of ^7Be in ice-rafted sediments (IRS) in the seasonal ice-cover of the Arctic Ocean have been reported to be relatively high (Masque et al. 2007). When sea ice is formed mostly in shallow waters in the marginal seas of the Arctic Ocean (such as Siberian margins of the Laptev, Kara and Barents Seas), large amounts of fine-grained sediments get incorporated into the sea ice during formation of new ice mainly through suspension freezing of bottom sediments and river-borne sediments (Barnes et al. 1982; Reimnitz et al. 1992; Nurnberg et al. 1994) and are subsequently transported to different parts of the Arctic. During its transit, atmospherically-delivered ^7Be is intercepted by the ice cover and the ^7Be is added to the IRS during freezing-thawing cycles (Baskaran 2005). The activities of ^7Be in IRS have been reported to be highly variable, with values ranging between $10^{4.9}$ and $10^{6.2}$ atoms g^{-1} (13 and 212 Bq kg^{-1}), which is 1–2 orders of magnitude higher than those reported in the coastal sediments. The dissolved ^7Be activities in melt ponds

were also reported to be much higher (30–60 mBq L^{-1}) than the surface waters in the Arctic (0.6–2.3 mBq L^{-1}) as well as surface water samples collected between 1.0 and 2.0 m from the air-sea interface (2.6 mBq L^{-1}) (Eicken et al. 2002; Kadko and Swart 2004). The concentrations of ^7Be in sea ice also were reported to be ~2 orders of magnitude higher than that in the ocean mixed layer below the sea ice and this was attributed to dilution of ^7Be with longer depths of the mixed layer compared with the <1 m thick seasonal ice (Cooper et al. 1991). During summer, the snow and upper 0.3–0.7 m of the ice melt off the ice surface. Tracer studies indicate that meltwaters disperse over distances of tens of meters on time scales of days, with much of the meltwater pooling in depressions at the surface (Eicken et al. 2002). IRS accumulates at the surface and in melt pools and are subjected to meltwater flushing (Nurnberg et al. 1994). During this process, the IRS released from melting comes in contact with seawater in meltponds and additional scavenging may take place. It has been estimated that ~60% of the ^7Be inventory is found in the water column from the sea ice melt and the remaining ~40% is found in sea ice (Eicken et al. 2002). Based on controlled experiments, it has been estimated that ~15% of the total sediment load is released to the water column during melt (Eicken et al. 2002). During multiple freezing-thawing cycles, the IRS is often pelletized and thus, can undergo sinking very quickly. Cooper et al. (2005) reported ^7Be in benthic surface sediments collected as deep as 945 m in Barrow Canyon in the Arctic, but it has not been reported from any other ocean basins. The activities of ^7Be in benthic sediments at different water column depths will be useful to quantify the amount of sediments released from melting of sea ice.

5.3.3.4 Using Meteoric ^{10}Be as a Chronological Tool in Marine Sediments

^{10}Be has been extensively utilized to date marine sediments, Mn-nodules, and other authigenic minerals. Prior to the development of AMS techniques, dating of Mn-nodules and deep-sea sediment cores were dated by conventional beta counting technique (Somayajulu 1967; Sharma and Somayajulu 1982). The concentration of ^{10}Be in Mn-nodules is very high ($\sim 10^{10}$ atoms g^{-1}) and hence a very small amount of sample is required (<10 mg). The first measurement of

^{10}Be by AMS basically confirmed the slow growth rates of Mn-nodules observed by conventional counting method (Somayajulu 1967; Turekian et al. 1979). Based on the exponential decay of ^{10}Be with depth on manganese crusts over a period of past 7 Ma, Ku et al. (1982) suggested that the $^{10}\text{Be}/^9\text{Be}$ ratio has remained constant over this time period. The ^{10}Be concentrations in Mn-nodules extrapolated to zero depth indicate that there is wide range of ^{10}Be values in nodules collected at different basins and varied between 1.5×10^{10} and 6.5×10^{10} atoms g^{-1} (Kusakabe and Ku 1984; Segl et al. 1984a, b; Mangini et al. 1986). The $^{10}\text{Be}/^9\text{Be}$ ratios in nodules from Atlantic and Pacific only ranged between 1.1×10^{-7} and 1.6×10^{-7} . A comparison of the extrapolated to the surface value (corresponding to present time) of $^{10}\text{Be}/^9\text{Be}$ ratio to that in the deep waters suggesting that the dissolved Be are well mixed in the bottom waters and that the ratio is well-preserved in authigenic minerals formed out of seawater (Kusakabe et al. 1987). Sediment cores have been dated using certain assumptions that include constant supply of ^{10}Be to the seafloor over the time interval of interest. It has been shown that the flux of ^{10}Be is largely dependent on the sedimentation rate (Tanaka et al. 1982; Mangini et al. 1984). Sediment focusing and boundary scavenging, however, make the assumption of constant supply of ^{10}Be questionable. In the Arctic, the variations in the particle flux (due to variations in the release of ice-rafted sediments) have resulted in highly varying concentrations of ^{10}Be in a vertical profile (Eisenhauer et al. 1994; Aldahan et al. 1997). The authigenic minerals seems to be better candidates for ^{10}Be dating compared to deep sea sediments, as the chemical link between deep seawater and authigenic minerals make this method work well for authigenic minerals. By measuring the ^{10}Be in deep-ocean Fe-Mn crusts, the decay corrected $^{10}\text{Be}/^9\text{Be}$ ratio was found to be constant over the past 12 Myr and this was attributed to constant global chemical weathering flux over this time period (Willenbring and von Blanckenburg 2010b).

5.3.3.5 Case Study: Dating of Marine Particulate Matter Using $^7\text{Be}/^{10}\text{Be}$ Ratios as Tracer

As was discussed earlier, once ^7Be and ^{10}Be are delivered at the air-sea interface primarily through wet precipitation, during their life-span in the water column, they are scavenged by suspended particulate matter and

eventually reach the ocean floor. Due to the short mean-life of ^7Be , most of the ^7Be undergoes radioactive decay while virtually no ^{10}Be undergoes radioactive decay. Although there are more than an order of magnitude variations on the monthly depositional fluxes of these nuclides, the variations on the $^7\text{Be}/^{10}\text{Be}$ ratios is very narrow, within a factor of ~ 2 (Brown et al. 1989; Graham et al. 2003; Heikkila et al. 2008; Lal and Baskaran 2011). When marine particulate matter leaves the surface layer with a finite $^7\text{Be}/^{10}\text{Be}$ ratio, as it sinks the ratio values will decrease and the rate of decrease can, in principle, be used to date the marine particulate matter, provided additional scavenging of ^7Be and ^{10}Be in subsurface layers does not alter the $^7\text{Be}/^{10}\text{Be}$ ratio. With the detection limit of ^7Be of 10^4 atoms using AMS (Raisbeck and Yiou 1988), one can measure $^7\text{Be}/^{10}\text{Be}$ ratios in particulate matter collected from ~ 20 L water sample assuming that 0.2 Bq/100 L of ^7Be (2.65×10^5 atoms), the average value for a six coastal water systems along the Gulf coast (Baskaran and Santschi 1993; Baskaran et al. 1997; Baskaran and Swarzenski 2007) and ^{10}Be abundance of ~ 500 atoms g^{-1} (corresponding to $\sim 10^7$ atoms of in 20-L sample), particulate matter can be reliably dated.

When particles leave the mixed layer with $^7\text{Be}/^{10}\text{Be}$ ratio (R_0), at any depth below mixed-layer, the measured ratio is R_d , then the time of transit (or residence time) of particulate matter is given by:

$$t = \tau \ln(R_0/R_d) \quad (5.6)$$

where τ is the mean-life of ^7Be . If we assume that the particles are fresh in the mixed-layer, then, t can be considered as the age of the particulate matter. At depth “ d ,” if there is equilibrium between the particulate matter and dissolved phase, then, the dissolved phase will likely have the same $^7\text{Be}/^{10}\text{Be}$ ratio as the particulate matter and hence by measuring $^7\text{Be}/^{10}\text{Be}$ ratio in the dissolved phase, we will be able to determine the “age” of the particulate matter.

5.3.4 Other Applications of Meteoric ^7Be and ^{10}Be at the Earth's Surface

The unique source term of the ^7Be and ^{10}Be nuclides make them particularly useful for tracing deposition and examining whether minerals are formed from elements derived from the atmosphere or the lithosphere.

Recently, these nuclides were used to study how rock varnish accumulates elements (Moore et al. 2001). Rock varnish specimens shielded from rainfall accumulate detectable ^7Be , presumably from dew or dry deposition, but specimens exposed to precipitation accumulate considerably higher doses of ^7Be . It was calculated that rock varnish accumulates a few percent of the total deposition of cosmogenic Be nuclides; ultraviolet radiation did not inhibit ^7Be accumulation in rock varnish, which suggests that varnish may be formed abiotically (Moore et al. 2001). The use of cosmogenic Be isotopes in conjunction with other fallout radionuclides (^{137}Cs , ^{210}Pb) may be useful for understanding the rates and mechanisms by which atmospheric elements are incorporated into mineral structures (Fleisher et al. 1999; Moore et al. 2001).

5.4 Other Future Directions

5.4.1 Deposition

There is considerable uncertainty on how cosmogenic Be deposition varies spatially over the Earth's surface and how climate might control fluxes to points on land and sea. The meteoric input uncertainty appears to be limiting our ability to quantify and compare the residence time of dissolved Be radionuclides in the oceans (Table 5.3). Climate change will likely result in the global redistribution of rainfall, and changes in the frequency and intensity of rainfall may affect the seasonal depositional fluxes of meteoric Be. However, input functions need to be well constrained in order to effectively use ^7Be and ^{10}Be as tracers in the environment, and, in particular, to apply ^{10}Be to quantify ages or steady-state erosion rates on timescales of thousands to millions of years. While there is often an inverse relationship between ^7Be and ^{10}Be concentrations in rainfall and storm duration at many sites (Baskaran et al. 1993; Baskaran 1995; Ishikawa et al. 1995), the dependence of annual cosmogenic Be fluxes on precipitation rates has not been well described. If cosmogenic Be is removed from an air mass during the initial parts of a storm, as most datasets indicate, a question remains as to whether or not additional rainfall over some threshold has an additive effect on fluxes. A number of studies have demon-

strated that rainfall rates ultimately control the total amounts of tropospheric contaminants and weapons-derived atmospheric ^{137}Cs delivered to the surface (Kiss et al. 1988; Simon et al. 2004). However, Willenbring and Von Blanckenburg (2010a) suggested that at coastal and island settings where the atmospheric transport time is fast and ^{10}Be and ^7Be concentrations in rain have a strongly inverse relationship with precipitation rate, annual fluxes should remain constant even if climate were to vary. The controls that climate and annual precipitation have on cosmogenic Be nuclide deposition should be studied further.

There are essentially two methods by which annual atmospheric fluxes can be determined for a region: direct monitoring of wet + dry atmospheric deposition on a weekly to monthly basis, or indirect determination using soil, sediment, and/or ice inventories. Long-term monitoring of cosmogenic Be wet depositional fluxes on landscapes can be costly, and it can be difficult assessing dry fluxes. The use of stable surfaces that record cosmogenic Be inventories has some advantages for calculating fluxes if surface age is known or if steady-state can be assumed. Relating ^{10}Be inventories to atmospheric fluxes would be complex given that surface age, and solute and particulate losses would be difficult to constrain in everything but perhaps ice records, but the use of ^7Be for this purpose does not suffer from these complications. The advantage of using surface inventory measurements of ^7Be for calculating fluxes is that a single measurement can integrate months of deposition, which works particularly well in temperate climates where rainfall is generally evenly distributed throughout the year. At sites where there is a distinct wet and dry season, multiple samples may be necessary to calculate annual atmospheric fluxes. There is an order of magnitude range of ^7Be soil inventories reported for stable soils around the world (Table 5.1). While many of the sites measured for ^7Be inventories are of temperate climate, the one arid region dataset falls in the low end of the range, reporting approximately 85 Bq m^{-2} for Owens Valley, CA (Elmore et al. 2008). Salisbury and Cartwright (2005) used ^7Be measurements of sheep feces to infer that vegetation along an elevation gradient in North Wales had higher concentrations of ^7Be . While they could not calculate atmospheric fluxes from their measurements, their data indicate some relationship between wet precipitation amounts and cosmogenic Be deposition. It would be valuable to have surface ^7Be inventory data available

for a range of climates so that that processes controlling atmospheric fluxes could be better understood.

5.4.2 Species and Geochemical Behavior

The geochemical behavior of Be is complex, yet simplifications are often made in order to extend the use of ^7Be and ^{10}Be as process tracers. It is evident from experimental work that partitioning strength is generally high ($K_d > 5,000$), but dissolved meteoric Be is commonly measurable or even dominates over particle-bound Be in the water columns of lakes and oceans (Silker et al. 1968; Kusakabe et al. 1982, 1987, 1990; Bloom and Crecelius 1983; Sharma et al. 1987; Dibb and Rice 1989a; Dominik et al. 1989; Steinmann et al. 1999). It appears that the availability of particles in a water column may limit the scavenging of meteoric Be radionuclides, but the effects of salinity, time, and particle composition (e.g., algae, organic detritus, Al/Fe/Mn phases) on partitioning strength and kinetics need to be better quantified.

In neutral to alkaline soil environments, Be is expected to form complexes with oxygen on surfaces of secondary clays and oxides and organic matter (Nyffeler et al. 1984; You et al. 1989). However, it is possible that soluble Be complexes could form, inhibiting adsorption and increasing the geochemical mobility of ^7Be and ^{10}Be in the environment. Equilibrium thermodynamic approach has been used to predict that Be forms soluble complexes with humic and fulvic acids and fluoride (Vesely et al. 1989; Takahashi et al. 1999) but there are no field-based studies documenting enhanced mobility in the environment from these species. It is also possible that cosmogenic Be could adsorb to very small colloids formed at soils through the breakdown of organic matter and Be could migrate vertically downward. Steinmann et al. (1999) used continuous flow centrifugation and tangential flow ultrafiltration to separate dissolved, colloidal, and particulate ^7Be phases in lake water. Despite their substantial efforts to separate truly dissolved ^7Be from other phases, they concluded that ^7Be might be adsorbed to very fine colloids (<10 kD) that are not easily separated from other phases or size fractions. More theoretical, experimental, and field-based data need to be collected on the distribution of Be species in the environment, and to identify the

various mechanisms by which cosmogenic Be can be transported in different systems.

5.4.3 "Dating" of Suspended Particulate Matter with $^7\text{Be}/^{10}\text{Be}$

Particulate matter at the air-sea interface is tagged with a finite $^7\text{Be}/^{10}\text{Be}$ ratio which is likely to remain constant at any season and as the particles undergo sinking, ^7Be undergoes radioactive decay. Typical settling rates of a terrigenous particle (density = 2.6 g cm^{-3}) of 4 mm diameter is $\sim 1 \text{ m day}^{-1}$ (for 16 mm diameter $\sim 19 \text{ m day}^{-1}$, corresponding to reaching a depth of $\sim 1,460 \text{ m}$ over the mean-life of ^7Be). Particulate matter from a sediment trap deployed at $\sim 1,500 \text{ m}$ can be utilized to determine the settling velocity of particulate matter. $^7\text{Be}/^{10}\text{Be}$ measurements on size-fractionated particulate matter could provide differences in the settling velocity of particulate matter. The deposition velocities could provide insight on the particle aggregation-disaggregation processes that are taking place in marine environment. It is known that beryllium is biologically inactive and hence could serve as an ideal tracer for the settling of terrigenous particulate matter. In the Arctic, $^7\text{Be}/^{10}\text{Be}$ ratios in sediment traps from seasonally ice-covered areas could provide insight on the amount of sediments released from sea ice during seasonal melting-freezing cycles. While ^7Be in sea ice sediments records the history of the material for <1 year, ^{10}Be data would record a much longer history, and hence the $^7\text{Be}/^{10}\text{Be}$ ratio may provide information on the time scale and extent of recycling of IRS. There are currently no ^{10}Be data available for sea ice sediments, so more work is needed to develop this potentially valuable tracing tool.

5.5 Concluding Remarks

Meteoric ^7Be and ^{10}Be are valuable tracers that can be used to characterize an incredibly wide range of environmental processes. While ^7Be can be used to quantify short-timescale processes, including the scavenging of metals and particles from waters, and the origin and fate of fine grained sediments in terrestrial and marine systems, meteoric ^{10}Be can be used to date

geomorphic surfaces and authigenic minerals, test quantitative theories about landscape evolution, and study boundary scavenging processes. However, a considerable amount of fundamental work still needs to be done to effectively use these isotopes of beryllium as tools to study Earth systems processes. The atmospheric fluxes of these nuclides and the processes that control deposition need to be characterized better, and the biogeochemical behavior of these isotopes in a wide range of environments needs to be described. We are optimistic that new studies will shed further light on the dynamics of ⁷Be and ¹⁰Be in the environment, and that these tracers will continue to help scientists solve complex environmental problems in the future.

Acknowledgements We thank Jane Willenbring for a thoughtful and thorough review of the earlier version of this manuscript.

References

- Aldahan AA, Ning S, Possnert G et al (1997) Be-10 records from sediments of the Arctic Ocean covering the past 350 ka. *Mar Geol* 144:147–162
- Anderson RF, Lao Y, Broecker WS et al (1990) Boundary scavenging in the Pacific Ocean – a comparison of Be-10 and Pa-231. *Earth Planet Sci Lett* 96:287–304
- Arnold JR, Al-Salih H (1955) Beryllium-7 produced by cosmic rays. *Science* 121:451–453
- Baes CF, Mesmer RE (1976) *The hydrolysis of cations*. Wiley, New York
- Barg E, Lal D, Pavich MJ et al (1997) Beryllium geochemistry in soils: evaluation of Be-10/Be-9 ratios in authigenic minerals as a basis for age models. *Chem Geol* 140:237–258
- Barnes PW, Reimnitz E, Fox D (1982) Ice rafting of fine-grained sediment: a sorting and transport mechanism, Beaufort Sea, Alaska. *J Sediment Petrol* 52:493–502
- Baskaran M (1995) A search for the seasonal variability on the depositional fluxes of Be-7 and Pb-210. *J Geophys Res Atmos* 100:2833–2840
- Baskaran M (2005) Interaction of sea ice sediments and surface sea water in the Arctic Ocean: evidence from excess Pb-210. *Geophys Res Lett* 32:4
- Baskaran M, Santschi PH (1993) The role of particles and colloids in the transport of radionuclides in coastal environments of Texas. *Mar Chem* 43:95–114
- Baskaran M, Shaw GE (2001) Residence time of arctic haze aerosols using the concentrations and activity ratios of Po-210, Pb-210 and Be-7. *J Aerosol Sci* 32:443–452
- Baskaran M, Swarzenski PW (2007) Seasonal variations on the residence times and partitioning of short-lived radionuclides (Th-234, Be-7 and Pb-210) and depositional fluxes of Be-7 and Pb-210 in Tampa Bay, Florida. *Mar Chem* 104:27–42
- Baskaran M, Coleman CH, Santschi PH (1993) Atmospheric depositional fluxes of Be-7 and Pb-210 at Galveston and College Station, Texas. *J Geophys Res Atmos* 98:20555–20571
- Baskaran M, Ravichandran M, Bianchi TS (1997) Cycling of Be-7 and Pb-210 in a high DOC, shallow, turbid estuary of south-east Texas. *Estuar Coast Shelf Sci* 45:165–176
- Baskaran M, Swarzenski PW, Biddanda BA (2009a) Constraints on the utility of MnO₂ cartridge method for the extraction of radionuclides: a case study using Th-234. *Geochem Geophys Geosyst* 10:9
- Baskaran M, Hong GH, Santschi PH (2009b) Radionuclide analysis in seawater. In: Wurl O (ed) *Practical guidelines for the analysis of seawater*. CRC Press, Boca Raton
- Berggren AM, Beer J, Possnert G et al (2009) A 600-year annual Be-10 record from the NGRIP ice core, Greenland. *Geophys Res Lett* 36:5
- Blake WH, Walling DE, He Q (1999) Fallout beryllium-7 as a tracer in soil erosion investigations. *Appl Radiat Isot* 51:599–605
- Blake WH, Walling DE, He Q (2002) Using cosmogenic beryllium-7 as a tracer in sediment budget investigations. *Geogr Ann Ser A Phys Geogr* 84A:89–102
- Bleichrodt JF, Van Abkoude ER (1963) On the deposition of cosmic-ray-produced ⁷Be. *J Geophys Res* 68:5283–5288
- Bloom N, Creelius EA (1983) Solubility behavior of atmospheric Be-7 in the marine environment. *Mar Chem* 12:323–331
- Bonniwell EC, Matisoff G, Whiting PJ (1999) Determining the times and distances of particle transit in a mountain stream using fallout radionuclides. *Geomorphology* 27:75–92
- Bourles D, Raisbeck GM, Yiou F (1989) Be-10 and Be-9 in marine-sediments and their potential for dating. *Geochim Cosmochim Acta* 53:443–452
- Brown L, Klein J, Middleton R (1985) Anomalous isotopic concentrations in the sea off Southern-California. *Geochim Cosmochim Acta* 49:153–157
- Brown L, Pavich MJ, Hickman RE et al (1988) Erosion of the Eastern United States observed with ¹⁰Be. *Earth Surf Process Landforms* 13:441–457
- Brown L, Stensland GJ, Klein J et al (1989) Atmospheric deposition of Be-7 and Be-10. *Geochim Cosmochim Acta* 53:135–142
- Brown ET, Measures CI, Edmond JM et al (1992a) Continental inputs of beryllium to the oceans. *Earth Planet Sci Lett* 114:101–111
- Brown ET, Edmond JM, Raisbeck GM et al (1992b) Beryllium isotope geochemistry in tropical river basins. *Geochim Cosmochim Acta* 56:1607–1624
- Brown ET, Stallard RF, Larsen MC et al (1995) Denudation rates determined from the accumulation of in-situ produced Be-10 in the Luquillo experimental forest, Puerto-Rico. *Earth Planet Sci Lett* 129:193–202
- Caillet S, Arpagaus P, Monna F et al (2001) Factors controlling Be-7 and Pb-210 atmospheric deposition as revealed by sampling individual rain events in the region of Geneva, Switzerland. *J Environ Radioact* 53:241–256
- Canuel EA, Martens CS, Benninger LK (1990) Seasonal-variations in Be-7 activity in the sediments of Cape Lookout-Bight, North Carolina. *Geochim Cosmochim Acta* 54:237–245
- Chase Z, Anderson RF, Fleisher MQ, Kubik PW (2003) Scavenging of ²³⁰Th, ²³¹Pa, and ¹⁰Be in the Southern Ocean (SW Pacific sector): the importance of particle flux, particle composition, and advection. *Deep Sea Res Part II* 50:739–768

- Clifton RJ, Watson PG, Davey JT et al (1995) A study of processes affecting the uptake of contaminants by intertidal sediments, using the radioactive tracers Be-7, Cs-137, and unsupported Pb-210. *Estuar Coast Shelf Sci* 41:459–474
- Cooper LW, Olsen CR, Solomon DK et al (1991) Stable isotopes of oxygen and natural and fallout radionuclides used for tracing runoff during snowmelt in an arctic watershed. *Water Resour Res* 27:2171–2179
- Cooper LW, Larsen IL, Grebmeier JM et al (2005) Detection of rapid deposition of sea ice-rafted material to the Arctic Ocean benthos using the cosmogenic tracer Be-7. *Deep Sea Res* 52:3452–3461
- Corbett DR, Dail M, McKee B (2007) High-frequency time-series of the dynamic sedimentation processes on the western shelf of the Mississippi River Delta. *Cont Shelf Res* 27:1600–1615
- Cornu S, Montagne D, Vasconcelos PM (2009) Dating constituent formation in soils to determine rates of soil processes: a review. *Geoderma* 153:293–303
- Crecelius EA (1981) Prediction of marine atmospheric deposition rates using total Be-7 deposition velocities. *Atmos Environ* 15:579–582
- Croke J, Hairsine P, Fogarty P (1999) Sediment transport, redistribution and storage on logged forest hillslopes in south-eastern Australia. *Hydrol Process* 13:2705–2720
- Dalmasso J, Maria H, Ardisson G (1987) Th-228 nuclear-states fed in Ac-228 decay. *Phys Rev C* 36:2510–2527
- daSilva J, Machado A, Ramos MA et al (1996) Quantitative study of Be(II) complexation by soil fulvic acids by molecular fluorescence spectroscopy. *Environ Sci Technol* 30:3155–3160
- Dibb JE, Rice DL (1989a) The geochemistry of beryllium-7 in Chesapeake Bay. *Estuar Coast Shelf Sci* 28:379–394
- Dibb JE, Rice DL (1989b) Temporal and spatial-distribution of beryllium-7 in the sediments of Chesapeake Bay. *Estuar Coast Shelf Sci* 28:395–406
- Doering C, Akker R, Heijnis H (2006) Vertical distributions of ^{210}Pb excess, ^7Be and ^{137}Cs in selected grass covered soils in Southeast Queensland, Australia. *J Environ Radioact* 87:135–147
- Dominik J, Burrus D, Vernet J-P (1987) Transport of the environmental radionuclides in an alpine watershed. *Earth Planet Sci Lett* 84:165–180
- Dominik J, Schuler C, Santschi PH (1989) Residence times of ^{234}Th and ^7Be in Lake Geneva. *Earth Planet Sci Lett* 93:345–358
- Du JZ, Zhang J, Baskaran M (2011) Applications of short-lived radionuclides (^7Be , ^{210}Pb , ^{210}Po , ^{137}Cs and ^{234}Th) to trace the sources, transport pathways and deposition of particles/sediments in rivers estuaries and coasts. In: Baskaran M (ed) *Handbook of environmental isotope geochemistry*. Springer, Heidelberg
- Egli M, Brandova D, Bohlert R et al (2010) Be-10 inventories in Alpine soils and their potential for dating land surfaces. *Geomorphology* 121:378
- Eicken H, Krouse HR, Kadko D et al (2002) Tracer studies of pathways and rates of meltwater transport through Arctic summer sea ice. *J Geophys Res Oceans* 107:20
- Eisenhauer A, Spielhagen RF, Frank M et al (1994) Be-10 records of sediment cores from high northern latitudes – implications for environmental and climatic changes. *Earth Planet Sci Lett* 124:171–184
- Elmore AJ, Kaste JM, Okin GS et al (2008) Groundwater influences on atmospheric dust generation in deserts. *J Arid Environ* 72:1753–1765
- Feng H, Cochran JK, Hirschberg DJ (1999) Th-234 and Be-7 as tracers for the sources of particles to the turbidity maximum of the Hudson River estuary. *Estuar Coast Shelf Sci* 49:629–645
- Fifield LK, Wasson RJ, Pillars B et al (2010) The longevity of hillslope soil in SE and NW Australia. *Catena* 81:32–42
- Fisher GB, Magilligan FJ, Kaste JM et al (2010) Constraining the timescale of sediment sequestration associated with large woody debris using cosmogenic ^7Be . *J Geophys Res Earth Surf* 115:F01013
- Fitzgerald SA, Klump JV, Swarzenski PW et al (2001) Beryllium-7 as a tracer of short-term sediment deposition and resuspension in the Fox River, Wisconsin. *Environ Sci Technol* 35:300–305
- Fleisher M, Liu TZ, Broecker WS et al (1999) A clue regarding the origin of rock varnish. *Geophys Res Lett* 26:103–106
- Frank M, van der Loeff MMR, Kubik PW et al (2002) Quasi-conservative behaviour of Be-10 in deep waters of the Weddell Sea and the Atlantic sector of the Antarctic Circumpolar Current. *Earth Planet Sci Lett* 201:171–186
- Frank M, Porcelli D, Andersson P et al (2009) The dissolved beryllium isotope composition of the Arctic Ocean. *Geochim Cosmochim Acta* 73:6114–6133
- Galindo-Uribarri A, Beene JR, Danchev M et al. (2007) Pushing the limits of accelerator mass spectrometry. *Nucl Instrum Meth Phys Res Sect B Beam Interact Mater Atoms* 259:123–130
- Graham I, Ditchburn R, Barry B (2003) Atmospheric deposition of Be-7 and Be-10 in New Zealand rain (1996–98). *Geochim Cosmochim Acta* 67:361–373
- Gu ZY, Lal D, Liu TS et al (1996) Five million year Be-10 record in Chinese loess and red-clay: climate and weathering relationships. *Earth Planet Sci Lett* 144:273–287
- Harden JW, Fries TL, Pavich MJ (2002) Cycling of beryllium and carbon through hillslope soils in Iowa. *Biogeochemistry* 60:317–335
- Harvey MJ, Matthews KM (1989) ^7Be deposition in a high-rainfall area of New Zealand. *J Atmos Chem* 8:299–306
- Hawley N, Robbins JA, Eadie BJ (1986) The partitioning of beryllium-7 in fresh-water. *Geochim Cosmochim Acta* 50:1127–1131
- Heikkila U, Beer J, Alifimov V (2008) Beryllium-10 and beryllium-7 in precipitation in Dubendorf (440 m) and at Jungfraujoch (3580 m), Switzerland (1998-2005). *J Geophys Res Atmos* 113:10
- Honeyman BD, Santschi PH (1989) A brownian-pumping model for oceanic trace-metal scavenging – evidence from Th-isotopes. *J Mar Res* 47:951–992
- Husain L, Coffey PE, Meyers RE et al (1977) Ozone transport from stratosphere to troposphere. *Geophys Res Lett* 4:363–365
- Ishikawa Y, Murakami H, Sekine T et al (1995) Precipitation scavenging studies of radionuclides in air using cosmogenic Be-7. *J Environ Radioact* 26:19–36
- Jungers MC, Bierman PR, Matmon A et al (2009) Tracing hillslope sediment production and transport with in situ and meteoric Be-10. *J Geophys Res Earth Surf* 114:16
- Jweda J, Baskaran M, van Hees E et al (2008) Short-lived radionuclides (Be-7 and Pb-210) as tracers of particle

- dynamics in a river system in southeast Michigan. *Limnol Oceanogr* 53:1934–1944
- Kadko D (2000) Modeling the evolution of the Arctic mixed layer during the fall 1997 Surface Heat Budget of the Arctic Ocean (SHEBA) project using measurements of Be-7. *J Geophys Res Oceans* 105:3369–3378
- Kadko D, Olson D (1996) Beryllium-7 as a tracer of surface water subduction and mixed-layer history. *Deep Sea Res Part I Oceanogr Res Pap* 43:89–116
- Kadko D, Swart P (2004) The source of the high heat and freshwater content of the upper ocean at the SHEBA site in the Beaufort Sea in 1997. *J Geophys Res Oceans* 109:10
- Kaste JM (1999) Dynamics of cosmogenic and bedrock-derived beryllium nuclides in forested ecosystems in Maine, USA. MSc Thesis, University of Maine
- Kaste JM, Norton SA, Hess CT (2002) Environmental chemistry of beryllium-7. In: Grew E (ed) *Beryllium: mineralogy, petrology, and geochemistry*. Mineralogical Society of America, Washington
- Kaste JM, Heimsath AM, Bostick BC (2007) Short-term soil mixing quantified with fallout radionuclides. *Geology* 35: 243–246
- Kim SH, Hong GH, Baskaran M, Park KM, Chung CS, Kim KH (1998) Wet removal of atmospheric ⁷Be and ²¹⁰Pb at the Korean Yellow Sea Coast. *The Yellow Sea* 4:58–68
- Kiss JJ, De Jong E, Martz LW (1988) The distribution of fallout Cs-137 in Southern Saskatchewan, Canada. *J Environ Qual* 17:445–452
- Knies DL, Elmore D, Sharma P et al (1994) Be-7, Be-10, and Cl-36 in precipitation. *Nucl Instrum Meth Phys Res* 92:340–344
- Koch DM, Mann ME (1996) Spatial and temporal variability of Be-7 surface concentrations. *Tellus Ser B Chem Phys Meteorol* 48:387–396
- Krishnaswami S, Benninger LK, Aller RC et al (1980) Atmospherically-derived radionuclides as tracers of sediment mixing and accumulation in near-shore marine and lake-sediments – evidence from Be-7, Pb-210, and Pu-239, Pu-240. *Earth Planet Sci Lett* 47:307–318
- Krishnaswami S, Mangini A, Thomas JH et al (1982) Be-10 and Th isotopes in manganese nodules and adjacent sediments – nodule growth histories and nuclide behavior. *Earth Planet Sci Lett* 59:217–234
- Ku TL, Kusakabe M, Nelson DE et al (1982) Constancy of oceanic deposition of Be-10 as recorded in manganese crusts. *Nature* 299:240–242
- Ku TL, Kusakabe M, Measures CI et al (1990) Beryllium isotope distribution in the Western North-Atlantic – a comparison to the Pacific. *Deep Sea Res Part I* 37:795–808
- Kusakabe M, Ku TL (1984) Incorporation of Be isotopes and other trace-metals into marine ferromanganese deposits. *Geochim Cosmochim Acta* 48:2187–2193
- Kusakabe M, Ku TL, Vogel J et al (1982) Be-10 profiles in seawater. *Nature* 299:712–714
- Kusakabe M, Ku TL, Southon JR et al (1987) Distribution of Be-10 and Be-9 in the Pacific Ocean. *Earth Planet Sci Lett* 82:231–240
- Kusakabe M, Ku TL, Southon JR et al (1990) Beryllium isotopes in the ocean. *Geochem J* 24:263–272
- Kusakabe M, Ku TL, Southon JR et al (1991) Be isotopes in river estuaries and their oceanic budgets. *Earth Planet Sci Lett* 102:265–276
- Lal D (2007) Recycling of cosmogenic nuclides after their removal from the atmosphere; special case of appreciable transport of Be-10 to polar regions by aeolian dust. *Earth Planet Sci Lett* 264:177–187
- Lal D (2011) Using cosmogenic radionuclides for the determination of effective surface exposure age and time-averaged erosion rates. In: Baskaran M (ed) *Handbook of environmental isotope geochemistry*. Springer, Heidelberg
- Lal D, Baskaran M (2011) Applications of cosmogenic-isotopes as atmospheric tracers. In: Baskaran M (ed) *Handbook of environmental isotope geochemistry*. Springer, Heidelberg
- Lal D, Malhotra PK, Peters B (1958) On the production of radioisotopes in the atmosphere by cosmic radiation and their application to meteorology. *J Atmos Terr Phys* 12:306–328
- Lal D, Nijampurkar VN, Rajagopalan G, Somayajulu BLK (1979) Annual fallout of Si-32, Pb-210, Na-22, S-35 and Be-7 in rains in India. *Proc Indian Natl Sci Acad* 88:29–40
- Lal D, Rama T, Zutshi PK (1960) Radioisotopes P-32, Be-7, and S-35 in the atmosphere. *J Geophys Res* 65:669–674
- Lal D, Barg E, Pavich M (1991) Development of cosmogenic nuclear methods for the study of soil-erosion and formation rates. *Curr Sci* 61:636–640
- Lao Y, Anderson RF, Broecker WS et al (1992a) Transport and burial rates of Be-10 and Pa-231 in the Pacific-Ocean during the Holocene period. *Earth Planet Sci Lett* 113:173–189
- Lao Y, Anderson RF, Broecker WS et al (1992b) Increased production of cosmogenic Be-10 during the last glacial maximum. *Nature* 357:576–578
- Larsen IL, Cutshall NH (1981) Direct determination of ⁷Be in sediments. *Earth Planet Sci Lett* 54:379–384
- Lee T, Barg E, Lal D (1991) Studies of vertical mixing in the southern California Bight with cosmogenic radionuclides P-32 and Be-7. *Limnol Oceanogr* 36:1044–1053
- Leya I, Lange HJ, Neumann S et al (2000) The production of cosmogenic nuclides in stony meteoroids by galactic cosmic-ray particles. *Meteor Planet Sci* 35:259–286
- Luo SD, Ku TL (2004a) On the importance of opal, carbonate, and lithogenic clays in scavenging and fractionating ²³⁰Th, ²³¹Pa and ¹⁰Be in the ocean. *Earth Planet Sci Lett* 220:201–211
- Luo SD, Ku TL (2004b) Reply to comment on “On the importance of opal, carbonate, and lithogenic clays in scavenging and fractionating ²³⁰Th, ²³¹Pa and ¹⁰Be in the ocean”. *Earth Planet Sci Lett* 220:223–229
- Magilligan FJ, Nislow KH, Graber BE (2003) Scale-independent assessment of discharge reduction and riparian disconnectivity following flow regulation by dams. *Geology* 31:569–572
- Mangini A, Segl M, Bonani G et al (1984) Mass spectrometric Be-10 dating of deep-sea sediments applying the Zurich tandem accelerator. *Nucl Instrum Meth Phys Res Sect B Beam Interact Mater Atoms* 5:353–358
- Mangini A, Segl M, Kudrass H et al (1986) Diffusion and supply rates of Be-10 and Th-230 radioisotopes in 2 manganese encrustations from the South China Sea. *Geochim Cosmochim Acta* 50:149–156
- Masarik J, Beer J (1999) Simulation of particle fluxes and cosmogenic nuclide production in the Earth’s atmosphere. *J Geophys Res Atmos* 104:12099–12111
- Masarik J, Beer J (2009) An updated simulation of particle fluxes and cosmogenic nuclide production in the Earth’s atmosphere. *J Geophys Res Atmos* 114:9

- Masque P, Cochran JK, Hirschberg DJ et al (2007) Radionuclides in Arctic sea ice: tracers of sources, fates and ice transit time scales. *Deep Sea Res Part I* 54:1289–1310
- Matisoff G, Whiting PJ (2011) Measuring soil erosion rates using natural (^7Be , ^{210}Pb) and anthropogenic (^{137}Cs , $^{239,240}\text{Pu}$) radionuclides. In: Baskaran M (ed) *Handbook of environmental isotope geochemistry*. Springer, Heidelberg
- Matisoff G, Wilson CG, Whiting PJ (2005) The Be-7/Pb-210 (xs) ratio as an indicator of suspended sediment age or fraction new sediment in suspension. *Earth Surf Process Landforms* 30:1191–1201
- McHargue LR, Damon PE (1991) The global beryllium 10 cycle. *Rev Geophys* 29:141–158
- McKean JA, Dietrich WE, Finkel RC et al (1993) Quantification of soil production and downslope creep rates from cosmogenic Be-10 accumulations on a hillslope profile. *Geology* 21:343–346
- McNeary D, Baskaran M (2003) Depositional characteristics of Be-7 and Pb-210 in southeastern Michigan. *J Geophys Res Atmos* 108:15
- Measures CI, Ku TL, Luo S et al (1996) The distribution of Be-10 and Be-9 in the South Atlantic. *Deep Sea Res Part I Oceanogr Res Pap* 43:987–1009
- Merrill JR, Lyden EFX, Honda M et al (1960) The sedimentary geochemistry of the beryllium isotopes. *Geochim Cosmochim Acta* 18:108–129
- Monaghan MC, Krishnaswami S, Thomas JH (1983) Be-10 concentrations and the long-term fate of particle-reactive nuclides in 5 soil profiles from California. *Earth Planet Sci Lett* 65:51–60
- Monaghan MC, Krishnaswami S, Turekian K (1986) The global-average production rate of ^{10}Be . *Earth Planet Sci Lett* 76:279–287
- Monaghan MC, McKean J, Dietrich W et al (1992) Be-10 chronometry of bedrock-to-soil conversion rates. *Earth Planet Sci Lett* 111:483–492
- Moore WS, Liu TZ, Broecker WS et al (2001) Factors influencing Be-7 accumulation on rock varnish. *Geophys Res Lett* 28:4475–4478
- Morel J, Sepman S, Rasko M et al (2004) Precise determination of photon emission probabilities for main X- and gamma-rays of Ra-226 in equilibrium with daughters. *Appl Radiat Isot* 60:341–346
- Murray AS, Marten R, Johnston A et al (1987) Analysis for naturally-occurring radionuclides at environmental concentrations by gamma spectrometry. *J Radioanal Nucl Chem Artic* 115:263–288
- Nagai H, Tada W, Matsumura H et al (2004) Measurement of Be-7 at MALT. *Nucl Instrum Meth Phys Res Sect B Beam Interact Mater Atoms* 223:237–241
- Nishiizumi K, Finkel RC, Klein J et al (1996) Cosmogenic production of Be-7 and Be-10 in water targets. *J Geophys Res Solid Earth* 101:22225–22232
- Nishiizumi K, Imamura M, Caffee MW et al (2007) Absolute calibration of Be-10 AMS standards. *Nucl Instrum Meth Phys Res Sect B Beam Interact Mater Atoms* 258:403–413
- Nurnberg D, Wollenburg I, Dethleff D et al (1994) Sediments in arctic sea ice-implications for entrainment, transport, and release. *Mar Geol* 119:185–214
- Nyffeler UP, Li YH, Santschi PH (1984) A kinetic approach to describe trace-element distribution between particles and solution in natural aquatic systems. *Geochim Cosmochim Acta* 48:1513–1522
- Olsen CR, Larsen IL, Lowry PD et al (1985) Atmospheric fluxes and marsh soil inventories of ^7Be and ^{210}Pb . *J Geophys Res* 90:10487–10495
- Olsen CR, Larsen IL, Lowry PD et al (1986) Geochemistry and deposition of ^7Be in river-estuarine and coastal waters. *J Geophys Res* 91:896–908
- Papastefanou C, Ioannidou A (1991) Depositional fluxes and other physical characteristics of atmospheric beryllium-7 in the temperate zones (40-degrees N) with a dry (precipitation-free) climate. *Atmos Environ A Gen Topics* 25:2335–2343
- Pavich MJ, Brown L, Klein J et al (1984) Be-10 accumulation in a soil chronosequence. *Earth Planet Sci Lett* 68:198–204
- Peirson DA (1963) ^7Be in air and rain. *J Geophys Res* 68:3831–3832
- Pavich MJ, Brown L, Valetsilver N et al (1985) ^{10}Be analysis of a quaternary weathering profile in the Virginia Piedmont. *Geology* 13:39–41
- Pavich M, Brown L, Harden JW et al (1986) ^{10}Be distribution in soils from Merced river terraces, California. *Geology* 50:1727–1735
- Preiss N, Melieres MA, Pourchet M (1996) A compilation of data on lead 210 concentration in surface air and fluxes at the air-surface and water-sediment interfaces. *J Geophys Res Atmos* 101:28847–28862
- Raisbeck GM, Yiou F (1988) Measurement of Be-7 by accelerator mass-spectrometry. *Earth Planet Sci Lett* 89:103–108
- Raisbeck GM, Yiou F, Fruneau M et al (1978a) Be-10 mass spectrometry with a cyclotron. *Science* 202:215–217
- Raisbeck GM, Yiou F, Fruneau M et al (1978b) Measurement of Be-10 in 1,000 year-old and 5,000 year old antarctic ice. *Nature* 275:731–733
- Raisbeck GM, Yiou F, Fruneau M et al (1980) ^{10}Be concentration and residence time in the deep ocean. *Earth Planet Sci Lett* 51:275–278
- Reimnitz E, Marincovich L, McCormick M et al (1992) Suspension freezing of bottom sediment and biota in the northwest passage and implications for arctic-ocean sedimentation. *Can J Earth Sci* 29:693–703
- Robbins JA, Eadie BJ (1991) Seasonal cycling of trace-elements Cs-137, Be-7, and Pu-239+240 in Lake Michigan. *J Geophys Res Oceans* 96:17081–17104
- Russell IJ, Choquette CE, Fang SL et al (1981) Forest vegetation as a sink for atmospheric particulates – quantitative studies in rain and dry deposition. *J Geophys Res* 86:5247–5363
- Salant NL, Renshaw CE, Magilligan FJ et al (2007) The use of short-lived radionuclides to quantify transitional bed material transport in a regulated river. *Earth Surf Process Landforms* 32:509–524
- Salisbury RT, Cartwright J (2005) Cosmogenic Be-7 deposition in North Wales: Be-7 concentrations in sheep faeces in relation to altitude and precipitation. *J Environ Radioact* 78:353–361
- Sauve S, Hendershot W, Allen HE (2000a) Solid-solution partitioning of metals in contaminated soils: dependence on pH, total metal burden, and organic matter. *Environ Sci Technol* 34:1125–1131
- Sauve S, Martinez CE, McBride M et al (2000b) Adsorption of free lead (Pb²⁺) by pedogenic oxides, ferrihydrite, and leaf compost. *Soil Sci Soc Am J* 64:595–599

- Schuler C, Wieland E, Santschi PH et al (1991) A multitracer study of radionuclides in Lake Zurich, Switzerland. 1. Comparison of atmospheric and sedimentary fluxes of Be-7, Be-10, Pb-210, Po-210, and Cs-137. *J Geophys Res Oceans* 96:17051–17065
- Schuller P, Iroume A, Walling DE et al (2006) Use of beryllium-7 to document soil redistribution following forest harvest operations. *J Environ Qual* 35:1756–1763
- Segl M, Mangini A, Bonani G et al (1984a) Be-10 dating of the inner structure of Mn-encrustations applying the Zurich tandem accelerator. *Nucl Instrum Meth Phys Res Sect B Beam Interact Mater Atoms* 5:359–364
- Segl M, Mangini A, Bonani G et al (1984b) Be-10 dating of a manganese crust from central North Pacific and implications for ocean paleocirculation. *Nature* 309:540–543
- Segl M, Magini A, Beer J et al (1987) ¹⁰Be in the Atlantic Ocean, a transect at 25 deg N. *Nucl Instr Meth Phys Res B* 29:332–334
- Sharma P, Somayajulu BLK (1982) Be-10 dating of large manganese nodules from world oceans. *Earth Planet Sci Lett* 59:235–244
- Sharma P, Mahannah R, Moore WS et al (1987) Transport of Be-10 and Be-9 in the ocean. *Earth Planet Sci Lett* 86:69–76
- Sheets RW, Lawrence AE (1999) Temporal dynamics of airborne lead-210 in Missouri (USA): implications for geochronological methods. *Environ Geol* 38:343–348
- Silker WB (1972) Horizontal and vertical distributions of radionuclides in North Pacific ocean. *J Geophys Res* 77:1061
- Silker WB, Robertson DE, Rieck HG et al (1968) Beryllium-7 in ocean water. *Science* 161:879–880
- Simon SL, Bouville A, Beck HL (2004) The geographic distribution of radionuclide deposition across the continental US from atmospheric nuclear testing. *J Environ Radioact* 74:91–105
- Somayajulu BLK (1967) Beryllium-10 in a manganese nodule. *Science* 156:1219
- Sommerfield CK, Nittrouer CA, Alexander CR (1999) Be-7 as a tracer of flood sedimentation on the northern California continental margin. *Cont Shelf Res* 19:335–361
- Steinmann P, Billen T, Loizeau JI et al (1999) Beryllium-7 as a tracer to study mechanisms and rates of metal scavenging from lake surface waters. *Geochim Cosmochim Acta* 63:1621–1633
- Svendsen KM, Renshaw CE, Magilligan FJ et al (2009) Flow and sediment regimes at tributary junctions on a regulated river: impact on sediment residence time and benthic macroinvertebrate communities. *Hydrol Process* 23:284–296
- Takahashi Y, Minai Y, Ambe S et al (1999) Comparison of adsorption behavior of multiple inorganic ions on kaolinite and silica in the presence of humic acid using the multitracer technique. *Geochim Cosmochim Acta* 63:815–836
- Tanaka S, Inoue T, Huang ZY (1982) Be-10 and Be-10/Be-9 in near Antarctica sediment cores. *Geochem J* 16:321–325
- Todd JF, Wong GTF, Olsen CR et al (1989) Atmospheric depositional characteristics of beryllium-7 and lead-210 along the southeastern Virginia coast. *J Geophys Res Atmos* 94:11106–11116
- Trimble SM, Baskaran M, Porcelli D (2004) Scavenging of thorium isotopes in the Canada basin of the Arctic Ocean. *Earth Planet Sci Lett* 222:915–932
- Tsai H, Maejima Y, Hseu ZY (2008) Meteoric Be-10 dating of highly weathered soils from fluvial terraces in Taiwan. *Quat Int* 188:185–196
- Turekian KK, Cochran JK, Krishnaswami S et al (1979) Measurement of Be-10 in manganese nodules using a tandem vandergraaff accelerator. *Geophys Res Lett* 6:417–420
- Turekian KK, Benninger LK, Dion EP (1983) Be-7 and Pb-210 total deposition fluxes at New Haven, Connecticut and at Bermuda. *J Geophys Res* 88:5411–5415
- Vesely J, Benes P, Sevcik K (1989) Occurrence and speciation of beryllium in acidified freshwaters. *Water Res* 23:711–717
- Vogler S, Jung M, Mangini A (1996) Scavenging of Th-234 and Be-7 in Lake Constance. *Limnol Oceanogr* 41:1384–1393
- von Blanckenburg F, O’Nions RK, Belshaw NS et al (1996) Global distribution of beryllium isotopes in deep ocean water as derived from Fe-Mn crusts. *Earth Planet Sci Lett* 141:213–226
- Vonmoos M, Beer J, Muscheler R (2006) Large variations in Holocene solar activity: constraints from Be-10 in the Greenland Ice Core Project ice core. *J Geophys Res Space Phys* 111:A10105
- Wallbrink PJ, Murray AS (1994) Fallout of Be-7 in South Eastern Australia. *J Environ Radioact* 25:213–228
- Wallbrink PJ, Murray AS (1996) Distribution and variability of Be-7 in soils under different surface cover conditions and its potential for describing soil redistribution processes. *Water Resour Res* 32:467–476
- Wallbrink PJ, Murray AS, Olley JM (1999) Relating suspended sediment to its original soil depth using fallout radionuclides. *Soil Sci Soc Am J* 63:369–378
- Walling DE, He Q, Blake W (1999) Use of Be-7 and Cs-137 measurements to document short- and medium-term rates of water-induced soil erosion on agricultural land. *Water Resour Res* 35:3865–3874
- Walling DE, Schuller P, Zhang Y et al (2009) Extending the timescale for using beryllium 7 measurements to document soil redistribution by erosion. *Water Resour Res* 45:13
- Walton A, Fried RE (1962) The deposition of ⁷Be and ³²P in precipitation at north temperate latitudes. *J Geophys Res* 67:5335–5340
- Whiting PJ, Bonniwell EC, Matisoff G (2001) Depth and areal extent of sheet and rill erosion based on radionuclides in soils and suspended sediment. *Geology* 29:1131–1134
- Whiting PJ, Matisoff G, Fornes W (2005) Suspended sediment sources and transport distances in the Yellowstone River basin. *Geol Soc Am Bull* 117:515–529
- Willenbring JK, von Blanckenburg F (2010a) Meteoric cosmogenic Beryllium-10 adsorbed to river sediment and soil: applications for earth-surface dynamics. *Earth Sci Rev* 98:105–122
- Willenbring JK, von Blanckenburg F (2010b) Long-term stability of global erosion rates and weathering during late-Cenozoic cooling. *Nature* 465:211–214
- Wilson CG, Matisoff G, Whiting PJ (2003) Short-term erosion rates from a Be-7 inventory balance. *Earth Surf Process Landforms* 28:967–977
- You CF, Lee T, Li YH (1989) The partitioning of Be between soil and water. *Chem Geol* 77:105–118
- Zhu J, Olsen CR (2009) Beryllium-7 atmospheric deposition and sediment inventories in the Neponset River estuary, Massachusetts, USA. *J Environ Radioact* 100:192–197

Chapter 6

Silicon Isotopes as Tracers of Terrestrial Processes

B. Reynolds

Abstract Chemical weathering of silicate rocks consumes carbon dioxide during the breakdown of minerals and liberates ions and silicic acid. Weathering reactions can lead to the fractionation of stable silicon (Si) isotopes, which allows variations in Si isotopic ratios to be used to quantify the global Si cycle. Here, I detail the methods and applications of assessing variations in continental Si stable isotope compositions, and show how such studies can elucidate the processes that affect the terrestrial Si cycle. The global Si cycle and its stable isotope variations are strongly affected by biology, with Si uptake by phytoplankton in oceans and lakes, and biological uptake by terrestrial plants, especially modern crops, on land. This biological uptake and subsequent release often leads to a strong seasonal cycle overprinted onto the underlying weathering reactions. Nevertheless, it can be shown that weathering reactions lead to the fractionation of Si into a light Si reservoir stored in soils and sedimentary basins, and a heavy Si reservoir in rivers, lakes and the oceans.

6.1 Introduction

Silicon (Si) is the most abundant element at the Earth's surface after oxygen, with the continental crust containing 25.7 wt% Si. Chemical weathering of silicate rocks leads to the consumption of CO₂. Hence the Si biogeochemical cycle is linked to the global carbon cycle, and chemical weathering can influence the

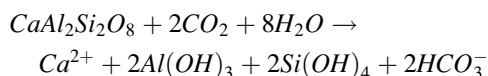
global climate over geological timescales via the greenhouse effect and the carbon cycle.

Global weathering rates or intensities may potentially be quantified using isotope systems, both classical radiogenic isotopes, like Sr, and novel stable isotope variations, like Li (Vigier et al. 2009; Burton and Vigier 2011). Indeed, the enrichment of radiogenic Sr over the Cenozoic, as recorded in marine sediments, has been considered to reflect an increase in continental weathering rates, and a draw-down of CO₂, leading to global cooling via a weakened greenhouse effect (Raymo and Ruddiman 1992). Stable isotope compositions of divalent cations, such as Ca, Mg and Sr, represent relatively new tools for investigating global biogeochemical cycles and variations in weathering intensities over geological timescales (Farkas et al. 2007; Tipper et al. 2008; de Souza et al. 2010). Although the draw-down of CO₂ is primarily due to the weathering of divalent cations (Mg²⁺ and Ca²⁺) and their subsequent precipitation as carbonates, the weathering reactions also lead to the release of Si. Hence, similarly to the studies of Mg and Ca isotopes, stable Si isotopes may also potentially be used to quantify chemical weathering reactions or processes, as shown here.

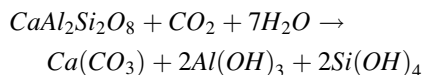
The term “weathering” can imply a number of processes. Weathering involves the physical and chemical breakdown of rocks and minerals through numerous processes, but here we focus on the chemical weathering of primary minerals. Two basic approaches for investigating chemical weathering are discussed here: (i) studying the material removed by weathering via quantification of dissolved ions drained from a catchment, and (ii) studying the remnants of weathering retained during soil formation. The chemical reactions of weathering can be simplified and written as various reactions:

B. Reynolds (✉)
Institute for Geochemistry and Petrology, ETH Zurich,
Switzerland
e-mail: reynolds@erdw.ethz.ch

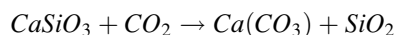
Dissolution reaction:



Hydration reaction:



Or silicate to carbonate exchange reactions:



These reactions neglect the fact that weathering of primary minerals is often accompanied by the formation of secondary minerals such as oxides and clay minerals, or the leaching of cations from interlayer crystallographic sites. Furthermore, the presence of organic ligands or microbial action can strongly affect the weathering reactions in terms of both the rate and extent of reaction. Thus, in natural systems “chemical weathering” may involve numerous reactions, which overall release dissolved ions and Si.

Dissolved Si released from weathering reactions forms silicic acid, which can be written as $\text{Si}(\text{OH})_4$ or H_4SiO_4 . As silicic acid is fully hydrated, unlike carbonic acid, H_2CO_3 , it does not form a meta-stable ion, and remains predominantly an uncharged species at most naturally occurring pHs, shown in Fig. 6.1. However, silicic acid can adsorb to surfaces, due to the presence of charged species (e.g. Hiemstra et al. 2007). Silicic acid also polymerizes, especially at higher concentrations and higher pH, converting mono-silicic acid to polymeric silica, or even larger

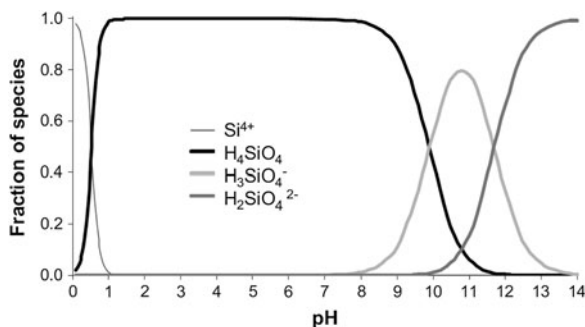


Fig. 6.1 The relative composition of each silicic acid species with variable pH

colloidal silica particles (see Iler 1979). Polymeric silica can remain truly dissolved, passing through colloidal-size filtration. Although polymeric silica does not react with molybdate ions to form coloured complexes (Boltz et al. 1978; Strickland 1952), it can be detected by the difference of sample concentrations between samples left untreated and samples reacted to enhanced dissolution using NaOH or hydrofluoric acid (Iler 1979). The solubility of mono-silicic acid is strongly dependent on the concentration of other ions, with additional salt increasing the solubility of Si (Icopini et al. 2005). The solubility of mono-silicic acid in “pure” water is close to that of quartz (~3 ppm Si (Morey et al. 1962)), but Si concentrations in natural waters are often in much higher, with a solubility close to that of amorphous silica (~100 ppm Si, see Iler (1979)).

It is important to appreciate how observations of stable Si isotope variations can be used to evaluate the terrestrial Si geochemical cycle, and hence the role chemical weathering plays on the release of silicic acid. The terrestrial Si cycle is also strongly affected by biology, with Si uptake and precipitation of biogenic opal (phytoliths) by plants, which can equally lead to stable isotope fractionation. Hence in order to understand the role of chemical weathering, we must also address how biological cycling can influence the terrestrial cycle of Si and its isotopes.

6.1.1 Nomenclature

Variations in the stable isotope compositions are usually given as relative variations in isotope ratios, scaled and expressed with a δ -notation. In terms of quoting stable isotope variations, this standard definition leads to several potential problems in comparing different data. Firstly, the variation given in permil depends upon the isotope ratio used. Secondly, the standard δ definition is actually non-linear (Miller 2002) and a slightly different definition, the linearized form δ' (Hulston and Thode 1965), is mathematically more exact to describe mass-dependent fractionation. This linearization becomes critical when considering correlations between three isotopes with a large range in fractionation (Miller 2002). Thirdly, the scale is only relative and an arbitrary zero point must be defined and the scale calibrated.

Silicon has three stable isotopes: ^{28}Si (92.22%), ^{29}Si (4.69%) and ^{30}Si (3.09%). Variations in stable Si isotopes are given relative to the zero reference standard, NBS28 (SRM 8546) (Coplen et al. 2002), and expressed using the standard δ - (and linearized δ' -) notation, in units of permil (‰):

$$\delta^x\text{Si} = 10^3 \left[\frac{({}^x\text{Si}/{}^{28}\text{Si})_{\text{sample}}}{({}^x\text{Si}/{}^{28}\text{Si})_{\text{NBS28}}} - 1 \right] \cong \delta'^x\text{Si}$$

$$\delta'^x\text{Si} = 10^3 \ln \left[\frac{({}^x\text{Si}/{}^{28}\text{Si})_{\text{sample}}}{({}^x\text{Si}/{}^{28}\text{Si})_{\text{NBS28}}} \right]$$

where x is either of the heavier isotopes, 29 or 30. In order to ensure a scale calibration, secondary reference materials of Diatomite and Big Batch were used to inter-compare laboratories and measurement techniques (Reynolds et al. 2007). All terrestrial Si isotope fractionations are mass-dependent, with $\delta^{30}\text{Si}$ values approximately twice those of $\delta^{29}\text{Si}$, hence datasets of $\delta^{29}\text{Si}$ and $\delta^{30}\text{Si}$ can be compared assuming $\delta^{29}\text{Si} = 0.51 \delta^{30}\text{Si}$ (Reynolds et al. 2007), as shown in Fig. 6.2. Higher $\delta^{30}\text{Si}$ values reflect an increase in the $^{30}\text{Si}/^{28}\text{Si}$ ratio, or enrichment in heavier isotopes making Si heavier; a $\delta^{30}\text{Si}$ value 1‰ higher is equivalent to an increase in the atomic weight of Si by 2.8 ppm ($79 \mu\text{g mol}^{-1}$). Current precision does not allow for the determination of differences in the

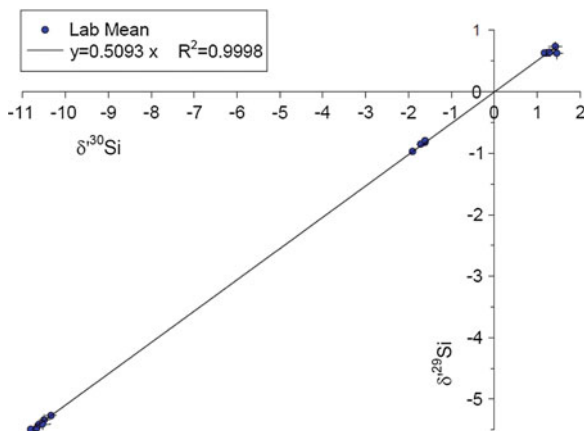


Fig. 6.2 Three isotope plot of $\delta^{29}\text{Si}$ versus $\delta^{30}\text{Si}$ (error bars are $1 \sigma_{\text{SD}}$) for the standard reference materials measured by several international laboratories, adapted from Reynolds et al. (2007). All data fall along a mass-dependent fractionation array with a slope of 0.5093 ± 0.0016 , in agreement with kinetic isotope fractionation of Si of 0.5092

mass-dependent fractionation laws between kinetic and equilibrium fractionation (see Young et al. 2002) to be adequately resolved for the small fractionations ($<2\text{‰}$ $\delta^{30}\text{Si}$) and the $<0.02\text{‰}$ difference between the standard and linearized forms of the δ -notation is hence immaterial.

In order to define the degree of isotope fractionation of a process, the isotope fractionation factor (α , or ϵ in permil) between two substances, A and B, is defined as:

$$\alpha_{\text{A-B}} = \frac{({}^{30}\text{Si}/{}^{28}\text{Si})_{\text{A}}}{({}^{30}\text{Si}/{}^{28}\text{Si})_{\text{B}}} = \frac{1 + 1000(\delta^{30}\text{Si})_{\text{A}}}{1 + 1000(\delta^{30}\text{Si})_{\text{B}}}$$

$$= 1 + \frac{{}^{30}\epsilon_{\text{A-B}}}{10^3}$$

It should be noted that the fractionation factor written as α depends upon the ratio pair used, just like the δ notation, although the distinction is not commonly stated for α . If using a linearized form of the δ -notation (δ'), the fractionation factor in permil can also be written in a number of other ways:

$$10^3 \ln(\alpha_{\text{A-B}}) = 10^3 \ln \left[\frac{({}^{30}\text{Si}/{}^{28}\text{Si})_{\text{A}}}{({}^{30}\text{Si}/{}^{28}\text{Si})_{\text{B}}} \right]$$

$$\cong {}^{30}\epsilon_{\text{A-B}}$$

$$= 10^3 \ln ({}^{30}\text{Si}/{}^{28}\text{Si})_{\text{A}} - 10^3 \ln ({}^{30}\text{Si}/{}^{28}\text{Si})_{\text{B}}$$

$$= \delta'^{30}\text{Si}_{\text{A}} - \delta'^{30}\text{Si}_{\text{B}}$$

$$\cong \delta^{30}\text{Si}_{\text{A}} - \delta^{30}\text{Si}_{\text{B}} = \Delta^{30}\text{Si}_{\text{A-B}}$$

So the fractionation factor, expressed in permil, is almost equivalent to the difference between the two δ -values, typically written as $\Delta_{\text{A-B}}$. Unfortunately, expressing fractionation as either ϵ or Δ can lead to confusion as both are also used to in isotope geochemistry to denote isotopic anomalies: either radiogenic anomalies such as $\epsilon^{143}\text{Nd}$, or variations from an equilibrium mass-dependent fractionation line such as $\Delta^{17}\text{O}$. It is high time that a new standardization is employed such that these confusions can be avoided, and that values given for an element are not dependent upon the isotope ratio used. For example, fractionation could be given as variations in the atomic weight or as variations in ppm per amu, such that data can be easily compared across the mass-spectrum:

$$\text{ppm per amu}' = \varphi = \frac{10^6}{m_1 - m_2} \ln \left[\frac{R_{\text{A}}}{R_{\text{B}}} \right]$$

where $m_1 - m_2$ denotes the mass difference in amu between the two masses used in the isotope ratio, R (Rudge et al. 2009).

6.2 Materials and Methods

The natural stable isotope variations of Si have been measured for over 50 years, but terrestrial Si isotope variations have been inadequately investigated mainly due to analytical difficulties and poor reproducibility. Conventional analyses involved measurement of gaseous fluorinated silicon (SiF_3^+) in a Nier-type mass spectrometer, using either direct fluorination of purified SiO_2 (Allenby 1954) or by the thermal decomposition of Ba_2SiF_2 (Reynolds and Verhoogen 1953). Careful early studies of silicon in meteorites and lunar material could not resolve any Si isotopic anomalies due to non-mass-dependent processes, with all of the measured Si isotope compositions falling close to a single mass-dependent fractionation line (e.g. Epstein and Taylor 1970). The measured variations in the stable isotope compositions of Si in igneous rocks were small, 1.1‰ (Douthitt 1982). Whilst the $^{30}\text{Si}/^{28}\text{Si}$ ratios of biogenic opal have a larger range of 6‰ compared to the range for silicate rocks of 3.5‰, assessing the fractionation related to aqueous or biological processes was limited by the inability to measure dissolved Si isotope compositions. Hence, in the following decades little work was done to further investigate Si isotope variations (see Ding 2004).

Recently, there has been a renewed interest in the measurement of silicon isotope variations in natural samples because of the importance of Si in terrestrial and marine biogeochemical cycles (Basile-Doelsch 2006; Brzezinski et al. 2002), and its importance as the most abundant non-volatile element in the solar system (Fitoussi et al. 2009; Georg et al. 2007a). The application of Si isotope variations to the investigation of geochemical cycles has been facilitated by two separate developments. Firstly, the development of new chemical preparation techniques to measure the Si isotope composition of a wide range of samples: dissolved and biogenic Si from marine and freshwater environments (Alleman et al. 2005; André et al. 2006; Cardinal et al. 2005; De La Rocha et al. 2000; Engström et al. 2006; Georg et al. 2006a, b; Reynolds

et al. 2006b; Varela et al. 2004), plants and organic-rich soils (Ding et al. 2005; Opfergelt et al. 2006a, b); as well as altered rocks and mineral soils (André et al. 2006; Basile-Doelsch et al. 2005; Georg et al. 2006b; van den Boorn et al. 2006; Ziegler et al. 2005a, b). Secondly, the advancement of Multi-Collector Inductively-Coupled-Plasma Mass-Spectrometry (MC-ICPMS) (Cardinal et al. 2003; De La Rocha 2002; Reynolds et al. 2006c), and recently improved gas source isotope ratio mass spectrometer (IRMS) techniques (Brzezinski et al. 2006), now provide the precision required to better quantify biogeochemical Si isotope fractionations. It has been shown by inter-laboratory comparison that various analytical techniques do not bias the measured stable isotope variations (Reynolds et al. 2007), and there are now several reference materials with well-known $\delta^{30}\text{Si}$ values with which to compare datasets, as shown in Table 6.1.

The MC-ICPMS offers two distinct advantages compared to analysis using the IRMS. Firstly, analytical protocols are faster (both chemical processing and analysis time), including repeated analyses; and secondly, much smaller sample sizes are required. Some types of sample preparation for IRMS are complicated, time consuming, and require the use of extremely hazardous chemicals such as BrF_5 or F_2 (De La Rocha et al. 1996; Ding 2004). The MC-ICPMS also has some significant disadvantages that must be addressed. The plasma source induces a much larger mass-dependent fractionation than dual-inlet IRMS, and this fractionation must be corrected for by standard-sample bracketing which can be highly sensitive to “matrix effects” that can induce systematic offsets between samples and standards. Furthermore, the plasma source can produce significant polyatomic isobaric interferences. However, these drawbacks can be addressed with the correct analytical protocols, as discussed below.

Table 6.1 The Si isotope composition of silica reference materials determined by several laboratories with errors indicating 95% confidence limits (Hendry et al. 2010; Reynolds et al. 2007; Savage et al. 2010)

Reference material	$\delta^{30}\text{Si}$ value (in ‰)
NBS 28	0.0
Diatomite	+1.25 ± 0.02
Big batch	-10.48 ± 0.04
Terrestrial basalts (e.g. BHVO-1 or -2)	-0.29 ± 0.03
Sponge (LMG08)	-3.35 ± 0.06

6.2.1 Multi-Collector ICP-MS Methods

On MC-ICPMS instruments, all three Si ion beams are measured simultaneously in static mode with Faraday collectors, typically equipped with $10^{11} \Omega$ resistors. In order to ionize Si in an ICP source, the Si must be introduced into the plasma as a dilute aerosol, which is typically done by volatilization of a silicic acid solution. The analyte (sample solution) is turned into small droplets in a nebulizer. This wet aerosol is often then dried by a desolvating unit before being introduced into the plasma in an Ar carrier flow. The transfer of ions from the plasma operating at atmospheric pressure into the high vacuum analyzer of the MS results in considerable loss of ions (>99%) and significant mass-fractionation, which results in a measurement bias towards the heavier isotopes (termed mass-bias). This mass-bias can be corrected for by external doping of another element with a known isotope composition (known as external doping), and/or *relative* Si isotope variations can be measured using a standard-sample-standard bracketing technique that requires identical conditions between samples and standards, and minimal drift in the instrumental mass-bias with time. External doping with Mg isotopes has been demonstrated to be valid for external mass-bias correction for Si isotopes (Cardinal et al. 2003). Failure to ensure identical conditions of samples and standards for the bracketing protocol can easily lead to variations in the mass-bias and thus erroneous determination of relative isotopic compositions. Such mass-bias effects are often referred to as “matrix-effects”, although “plasma loading effects” may be a more accurate description since these are usually caused by the presence of additional ions in the sample solutions. Although such effects may be quantified, they may also be dependent upon specific tuning conditions and cannot be easily corrected for. External doping can help determine significant “matrix effects”, but it also may also induce effects itself, and may not adequately correct for variable mass-bias at the *sub*-permil level. Thus, in order to directly compare standard and samples without inducing “matrix effects” during ICP-MS analysis, challenging requirements exist for sample purity.

Initially, measurements of Si isotopes using MC-ICPMS used a “wet-plasma” sample introduction technique, with 0.25 M HF (De La Rocha 2002). The analytical precision was poor, because of very low

sensitivity, poor temporal stability of instrumental mass-bias and severe memory effects. A refined analytical technique was developed by Cardinal et al. (2003), with a “dry-plasma” sample introduction using a desolvating nebulization system and Mg external doping for mass bias correction. This technique introduced very dilute acids, with HF below 0.01 M, in order to increase sensitivity and stabilize instrumental mass-bias over time. However, the presence of HF can lead to the loss of Si as volatile SiF_4 within the desolvating unit, and it degrades analytical reproducibility (Georg et al. 2006b). Thus, if a desolvating nebulization system is used to increase sensitivity and minimize polyatomic interferences, sample and standard preparation techniques must avoid significantly large amounts of HF within the final analyte solutions.

Under normal operating conditions, in addition to the efficient ionization of Si, interfering polyatomic ions may be produced either within the plasma or in the interface region of the MC-ICPMS where the pressure drops by twelve orders of magnitude. Assuming a typical $^{28}\text{Si}^+$ intensity of 60 pA on an instrument equipped with a desolvating nebulizer (Cardinal et al. 2003; Georg et al. 2006b), the polyatomic species $^{14}\text{N}_2^+$, $^{14}\text{N}_2\text{H}^+$ and $^{14}\text{N}^{16}\text{O}^+$ would typically result in signals corresponding to at least 1, 0.7 and 5% of the $^{28}\text{Si}^+$, $^{29}\text{Si}^+$ and $^{30}\text{Si}^+$ ion beams, respectively (see Fig. 6.3). So, even though the $^{14}\text{N}_2^+$ is the largest ion beam, it is the $^{14}\text{N}^{16}\text{O}^+$ ion beam that results in the largest interference for determination of the Si isotope compositions. For instruments using conventional “wet-plasma” sample introduction systems (Engström et al. 2006), the magnitude of these spectral interferences on the silicon isotopes would be even more pronounced. Although some of these interferences can be corrected for (Reynolds et al. 2006c), the polyatomic interference on mass 30 prevented the accurate measurement of $^{30}\text{Si}/^{28}\text{Si}$ on the standard MC-ICPMS instruments initially used. However, as polyatomic ions are slightly heavier than atomic ions of the same nominal mass (below 60 amu), the slight difference in mass can be exploited using a higher mass-resolution to separate the Si^+ ion beams from potential polyatomic interferences, as shown in Fig. 6.3. This requires the ability to resolve ion beams that differ by less than 1% in mass (usually expressed as requiring a mass-resolution ($m/\Delta m$) in excess of 1,000). Since all polyatomic interferences are heavier than the isobaric Si^+ ion, it is not necessary to “fully resolve” all the ion beams.

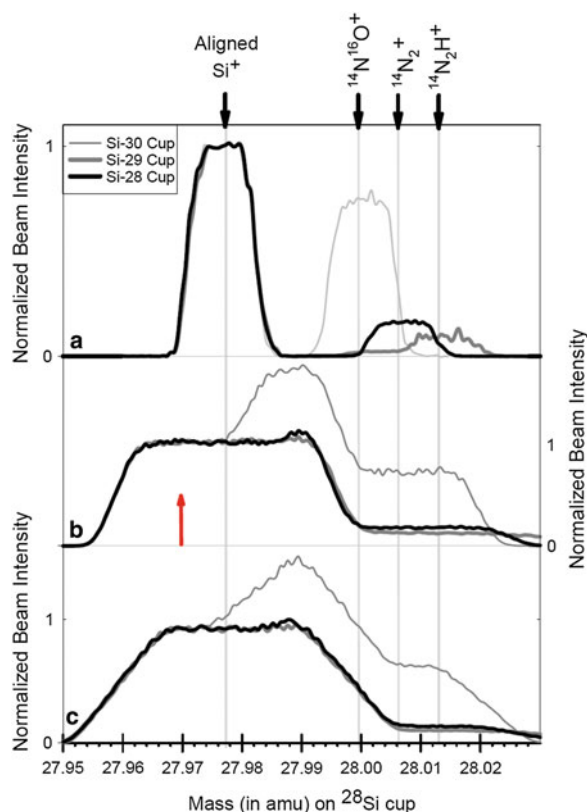


Fig. 6.3 Peak scans for silicon isotopes ^{28}Si (black line), ^{29}Si (thick grey line) and ^{30}Si (thin grey line) using a multi-collector ICP-MS in (a) high mass-resolution (b) pseudo high mass-resolution, and (c) low mass-resolution. Position of Si^+ beams and polyatomic interferences are shown relative to m/z on the Si-28 cup. Mass-resolutions shown (full peak width, $m/\Delta m$) are approximately 2,000, 600 and 500, with resolving powers (slope width, $m/\Delta m$) of 6,000, 4,000 and 1,800 for (a, b and c) respectively. In pseudo-high resolution mode, the measurements were carried out on the left side of the peak plateau (indicated by the arrow) to avoid the interferences. Interference from SiH^+ ions cannot be observed on peak-scans

Instead instruments can be run using a “pseudo” high-resolution mode (Engström et al. 2006), where all the Si ion beams are positioned towards the high mass-side of the collector, such that heavier polyatomic interferences do not enter the Faraday cup collector, as shown schematically in Fig. 6.3.

6.2.2 IRMS Methods

Traditional gas-source mass-spectrometry measures Si ions as SiF_3^+ ions, generated from the electron

bombardment of gaseous SiF_4 . The details of this IRMS technique, which has been used for over 50 years, can be found in numerous books and articles (e.g. Taylor 2004), and will not be fully detailed here. Whilst many preparation methods have used hazardous techniques for the fluorination of silica samples (Allenby 1954; De La Rocha et al. 1996; Ding 2004), relatively pure SiF_4 can be produced from the thermal decomposition of BaSiF_6 (Debievre et al. 1995; Reynolds and Verhooghen 1953) or acidic decomposition of Cs_2SiF_6 (Brzezinski et al. 2006). Purity is important as volatile fluorides and oxyfluorides are hard to separate from SiF_4 (Ding 2004), such as COF_3^+ leading to isobaric interferences on masses 85, 86 and 87. As F has only one isotope, no further corrections are required. The use of a dual-inlet system optimizes the standard-sample-standard bracketing technique, with fast switching between samples and standards through a switch-over valve. Typical analytical precisions obtained range from 0.06 to 0.2‰ ($2\sigma_{\text{SD}}$) (Ding 2004), and are thus directly comparable to MC-ICPMS.

6.3 Applications

The geochemical cycle of Si is explicitly linked to chemical weathering, but weathering studies often focus on dissolved cations. For the terrestrial and biological cycling of elements, there is extensive literature on Si, but this chapter focuses on Si isotopes, rather than Si per se, and will not review the wealth of information about Si within various sub-disciplines that has been reviewed elsewhere (e.g. Sommer et al. 2006; Struyf et al. 2009). Here is shown how the use of Si isotope can be useful in quantifying the terrestrial Si biogeochemical cycle.

It has been known for a long time that the processes controlling the Si cycle have a measurable impact on the Si isotope composition at the Earth’s surface (as reviewed by Douthitt (1982) and shown in Fig. 6.4). Although samples precipitated from solution were shown to be highly fractionated (Douthitt 1982), it was not until the truly dissolved $\delta^{30}\text{Si}$ was measured from natural waters (De La Rocha et al. 2000), that the importance of aqueous chemistry on $\delta^{30}\text{Si}$ values was finally realized. This pioneering work showed that “marine and riverine $\delta^{30}\text{Si}$ are more positive than

$\delta^{30}\text{Si}$ of igneous rocks, suggesting isotopic fractionation during weathering and clay formation and/or biomineralization” (De La Rocha et al. 2000). Although some work has been done to quantify the global Si isotopic mass-balance (Basile-Doelsch et al. 2005), there has been almost no discussion of the clear difference in $\delta^{30}\text{Si}$ between mafic (-0.3‰) (Savage et al. 2010) and granitic rocks (0.0‰), shown in Fig. 6.4. This difference would imply that either there is a fractionation during partial melting and crystallization, or

that the progressive recycling of silicate material over Earth’s history has lead to the enrichment of the upper continental crust in heavier Si isotopes. That the continental crust has a higher $\delta^{30}\text{Si}$ value is counterintuitive given that Si in recycled material, such as secondary clay and biogenic opal, is isotopically lighter, as detailed below. Such a scenario would suggest a preferential loss of light Si back into the mantle during crustal recycling, although the nature of this process remains to be explored.

It is important to consider that Si is a nutrient for plants and that the interactions between chemical and biological processes largely occur within soils. In soils Si mainly exists within minerals, including primary minerals, secondary minerals developed through soil formation, and as biogenically precipitated opal (either phytogenic, microbial or protozoic Si precipitates, as shown in Fig. 6.5). In general, knowledge about size, properties, and transformation of these biogenic pools is very scarce for almost all soils (Sommer et al. 2006). However, it has been long recognized that the recycling of Si by plants within soils can be much larger than fluxes associated with chemical weathering (Alexandre et al. 1997). Thus the formation of phytoliths within plants and subsequent dissolution during litter degradation can be a major source of dissolved Si (Farmer et al. 2005). We thus need to assess isotope fractionation in plants to

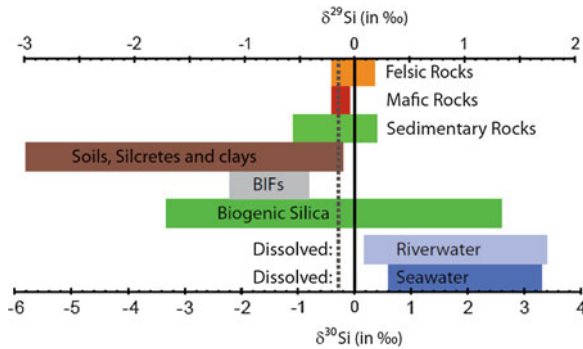


Fig. 6.4 Reported Si isotopic composition of terrestrial samples, expressed as $\delta^{29}\text{Si}$ and $\delta^{30}\text{Si}$. Dissolved Si reservoirs are enriched in the heavier Si isotopes, and secondary precipitated reservoir such as clays and biogenic Si contain light Si (sources: André et al. 2006; Ding et al. 1996; Douthitt 1982; Reynolds et al. 2007; Savage et al. 2010). The vertical dashed line represents the estimate of the Bulk Silicate Earth (Savage et al. 2010)

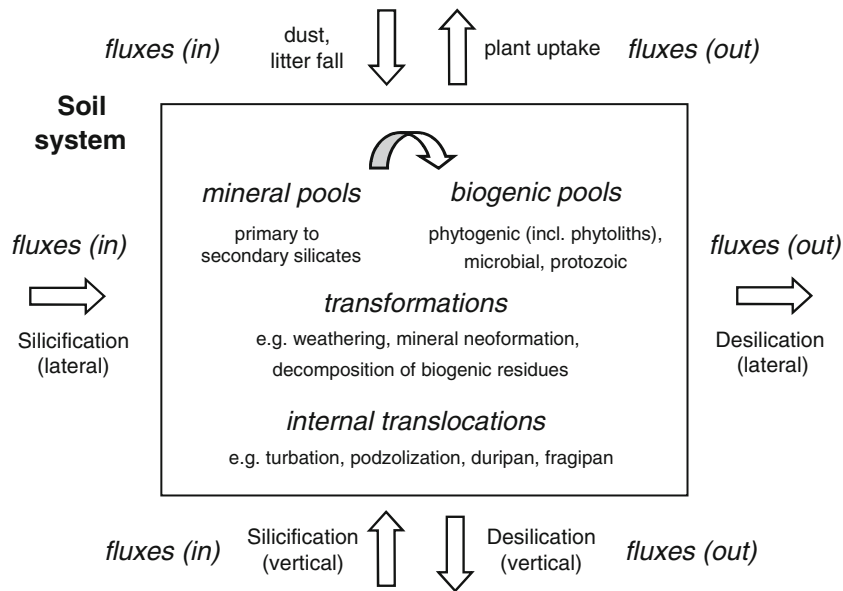


Fig. 6.5 Schematic representation of the reservoirs, transformation, fluxes of Si in soils (without erosion/deposition), from Sommer et al. (2006). Copyright Wiley-VCH Verlag GmbH & Co. KGaA. Reproduced with permission

quantify their impact on the Si isotope compositions of soils, before looking at larger scale catchment-scale studies aimed at quantifying the global Si biogeochemical cycle.

6.3.1 Si Uptake by Plants

Silicon is often one of the most abundant mineral elements in vegetation (besides Ca, Mg, K and P), but is not generally considered as an essential element for higher plants (Marschner 1995) as terrestrial plants rarely experience Si deficiency. The uptake of Si by plants is often passive, but some plants are able to actively enhance or via Si rejection lower Si uptake compared to that of water (Cornelis et al. 2010b; Raven 1983). It has long been recognized that plant uptake and formation of biogenic silica leads to Si isotope fractionation (Douthitt 1982), and these initial studies open interesting applications of isotope geochemistry tools to agricultural or plant sciences. It has been shown that Si is an important nutrient for vascular plants, with beneficial effects for crop growth (Epstein 2003; Mitani and Ma 2005), including crops, such as rice, cereals, and bananas. Silicon helps create the rigidity of cell walls and can increase resistance to pathogens, water stress, and grazing (Ma 2004; Sangster and Hodson 2007).

Within the plant the transpirational loss of water results in the concentration of silicic acid to the saturation value and the subsequent irreversible precipitation of silica, mainly in cell walls (Raven 1983, 2001).

Rice requires high levels of Si for healthy growth, and Si is actively transported against a concentration gradient into the cortical cells and then into the xylem (Ma et al. 2004). Experiments with rice plants grown hydroponically determined the Si uptake and fractionation during growth (Ding et al. 2008a; Sun et al. 2008). Dissolved Si not taken up by the plants evolved to high $\delta^{30}\text{Si}$ values ($>1.4\text{‰}$) as the plants preferentially incorporated lighter Si isotopes during active Si uptake (Ding et al. 2008a; Sun et al. 2008). However, this evolution to higher $\delta^{30}\text{Si}$ values with decreasing Si concentrations in the nutrient solutions does not follow a simple Rayleigh-type fractionation curve expected from irreversible uptake with a constant fractionation factor. Instead the data fits a model with a continuous variation in fractionation between the rice plant and nutrient supply between -1.7 and -0.5‰ $\delta^{30}\text{Si}$ (Ding et al. 2008a). Alternatively, the data could fit an equilibrium fractionation reaction, as shown in Fig. 6.6, with a fractionation of -1.6‰ $\delta^{30}\text{Si}$ (or -2‰ if fractionation only occurs after about one third of the available Si is taken up, when there is sufficient evapotranspiration through the leaves). However, the equilibrium modeling of the fractionation

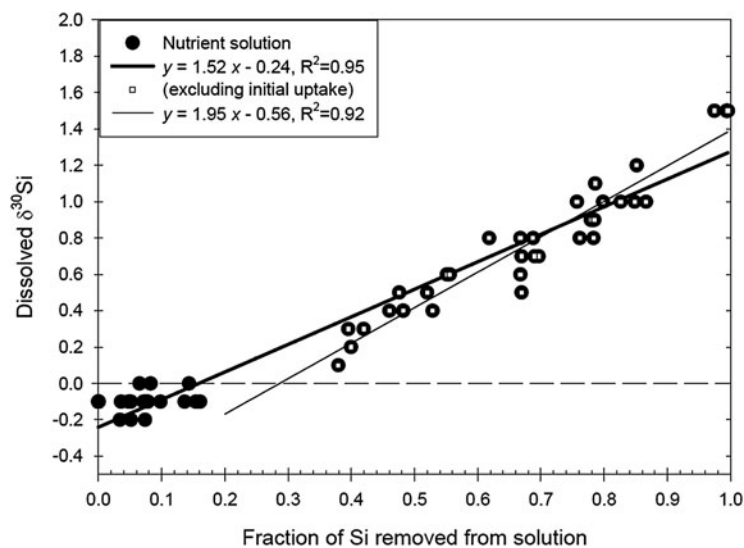


Fig. 6.6 The $\delta^{30}\text{Si}$ variations for silicic acid in the nutrient solution as a function of the fraction of silicon removed from the solution by the uptake of rice plants grown under hydroponic conditions (Ding et al. 2008a). The apparent linear fit to the data

shown here could imply a reversible exchange of Si between plant and solution within uniform fractionation factor. However, such reversible exchange may not be considered appropriate given the active Si uptake by rice plants

presented here would require Si transport from the xylem to the soil solution as well as the active uptake of Si, which is counter to views held by many plant physiologists.

An investigation of the Si isotope composition in Chinese rice plants showed that the Si concentrations and $\delta^{30}\text{Si}$ values increased within the plants from the soil and roots through the stems and leaves to the husks (Ding et al. 2005), reaching over 10 wt% silica and an increase in $\delta^{30}\text{Si}$ of 0.9‰. Within the rice grains, silica content is low, typically between 0.02 and 0.05%, but the measured $\delta^{30}\text{Si}$ values are exceptionally high, ranging from +1.3 to +6.1‰ (Ding et al. 2005). The increasing $\delta^{30}\text{Si}$ values are shown to fit a simple model of Rayleigh-type fractionation within the plants as Si is transported from the roots to the grains (Ding et al. 2005). The distribution of $\delta^{30}\text{Si}$ values within the plant reflects both a temporal increase in the $\delta^{30}\text{Si}$ values of the bulk plant, but also the larger intra-plant fractionation, with $\delta^{30}\text{Si}$ variations of 3.5‰ between low values in roots and high values of rice grains (Ding et al. 2008a).

In order to determine the fractionation factor between bulk banana plantlets and source solutions, plants were grown in hydroponics (Opfergelt et al. 2006b), as the exact nature of fractionation during Si uptake by banana plants cannot be understood from field studies. The fractionation factor $^{30}\epsilon_{\text{plantlet-solution}}$ ranged from -0.6 to -1.1‰, with larger differences observed for samples with higher Si uptake (Opfergelt et al. 2006b). It was further shown that there are large variations within each plant in both the Si concentration and $\delta^{30}\text{Si}$ value, as observed for rice, with values increasing from the roots, through the midrib to the lamina of the leaves, for both in situ and in vitro plants (Opfergelt et al. 2006a, b). The larger Si isotope fractionation between the external dissolved Si pool and that of the xylem indicates that an active transport mechanism exists that preferentially transport the lighter isotopes, as above.

Despite the large $\delta^{30}\text{Si}$ variations within plants, similar plant organs collected from different plant individuals at similar times in the growth cycle should have experienced equivalent Si mass fractionation, thus any differences between these plants may potentially reflect differences in the source $\delta^{30}\text{Si}$ composition in the soils (Opfergelt et al. 2008). Variation of $\delta^{30}\text{Si}$ values observed in mature banana plants should reflect variations in the $\delta^{30}\text{Si}$ values of the nutrient Si,

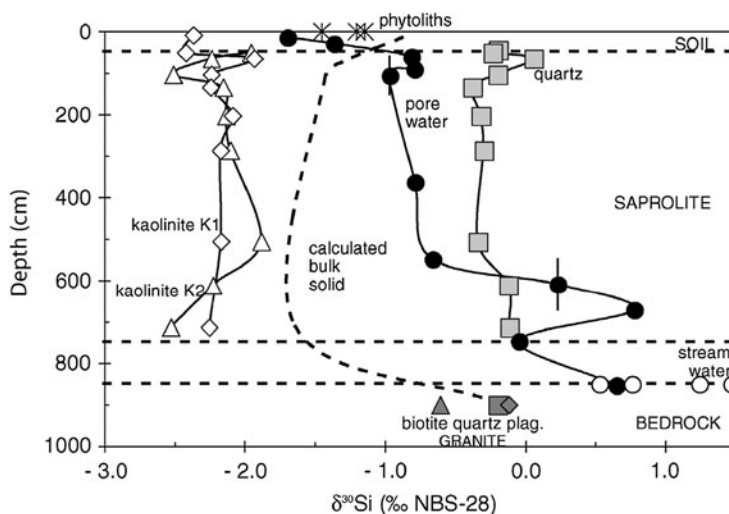
which may be related to the degree of soil weathering (Opfergelt et al. 2008, 2009). Variations of $\delta^{30}\text{Si}$ values between bamboo plants in China have also been inferred to reflect variations in the soil, with higher plant $\delta^{30}\text{Si}$ values associated with more organic rich soils (Ding et al. 2008b).

6.3.2 Si in Soils

As reviewed by Sommer et al. (2006), the Si cycle within soil systems is complex, with transfer of Si via the dissolved phase between primary minerals, secondary precipitates and plants, as shown in Fig. 6.5. Dissolved Si in the soil is lost via four main pathways: (1) as discussed above, dissolved Si that is taken up by plants is precipitated and return to the soil predominantly as phytoliths, (2) dissolved Si is precipitated as secondary mineral or amorphous complexes, (3) dissolved Si is absorbed to surfaces, like Fe oxyhydroxides, and (4) dissolved Si is washed out of the soils into the river systems. Only the flux of dissolved Si out of the soil is not associated with a Si isotope fractionation, with the other pathways leading to Si isotope fractionation during the development of soils. In addition, Si isotope fractionation within the soils may be induced during dissolution (Demarest et al. 2009; Ziegler et al. 2005b) and by adsorption/desorption reactions (Opfergelt et al. 2009). Initial studies of Si isotope fractionation during soil development (Ziegler et al. 2005a, b), investigated granitic and basaltic soils in tropical climates, where weathering rates are high (White et al. 1998). For the Hawaiian Islands variable lava ages allowed for the construction of a chronosequence of basaltic soil development, and assessment of the processes affecting the Si isotope composition during basaltic weathering (Ziegler et al. 2005b).

On Hawaii, primary minerals are replaced by allophane, a metastable clay which slowly converts to kaolinite. Primary volcanic minerals are almost completely weathered within the first 20,000 years, whilst conversion of allophane to kaolinite requires millions of years, and is thus only seen in the oldest soil profiles (Bern et al. 2010; Ziegler et al. 2005b). During progressive mineral weathering the Si isotope composition of the soil (<2 mm size fraction) changes from the initial -0.5‰ $\delta^{30}\text{Si}$ of the unweathered basalt to lower $\delta^{30}\text{Si}$ values, down to -2.5‰ $\delta^{30}\text{Si}$ in the

Fig. 6.7 Depth plot of $\delta^{30}\text{Si}$ values of different Si phases (vertical bars on pore-water data indicates depth interval sampled; horizontal dotted lines separate soil, saprolite, and bedrock zones), from Ziegler et al. (2005a)



oldest samples with >20 wt% kaolinite. It has been shown that this progressive enrichment in lighter isotopes is correlated to the net mass loss of Si in the lower soil horizons. It was also noted that the topmost soil may be shifted to lower $\delta^{30}\text{Si}$ values due to the recycling of biogenic Si from plants (phytoliths) (Ziegler et al. 2005b). The slightly lower $\delta^{30}\text{Si}$ value for the unweathered Hawaiian basalt (-0.5‰ (Ziegler et al. 2005b)) compared to other basalts analyzed (-0.3‰ (Savage et al. 2010)) may indicate some alteration of the unweathered basalt, or simply reflect errors in external reproducibility between groups (Reynolds et al. 2007). Regardless, the development of a clay-rich soil leads to the progressive reduction in bulk soil $\delta^{30}\text{Si}$ values (Ziegler et al. 2005b).

The Si isotope compositions of soils have also been investigated for basaltic soils in Cameroon, western Africa (Opfergelt et al. 2009). Just as for the Hawaiian soils, soil $\delta^{30}\text{Si}$ values varies from the initial basaltic pumice value of -0.3 to -2.6‰ in the clay rich samples. However, in Cameroon amorphous Si phases were observed, which have higher $\delta^{30}\text{Si}$ values, ranging from -0.5 to $+0.6\text{‰}$, and were derived from volcanic ashes and biogenic silica (Opfergelt et al. 2010).

In Puerto Rico, rapid weathering of a quartz diorite intrusion produces a saprolite that has minimal loss of quartz and biotite, but near complete dissolution of plagioclase and hornblende, and formation of secondary clay minerals. It was shown that secondary kaolinites, which precipitated from either transformation via epitax-

ial overgrowth of biotite or by re-precipitation after dissolution of plagioclase feldspars, have constant $\delta^{30}\text{Si}$ values around -2.2‰ (Ziegler et al. 2005b). This is distinctly lower than any primary silicates including biotite (-0.6‰), plagioclase (-0.1‰), and quartz (-0.2‰) in the host diorite, as shown in Fig. 6.7. The mass-fractionation during formation of the kaolinite was calculated to be -2.1‰ from the re-precipitation after dissolution of plagioclase feldspars, and -1.6‰ from the transformation via epitaxial overgrowth of biotite (Ziegler et al. 2005a). However, the $\delta^{30}\text{Si}$ difference between co-existing biotite and plagioclase is hard to reconcile with the small potential mass-fractionation between different minerals at higher temperatures of crystallization. Potentially the lower $\delta^{30}\text{Si}$ value measured for biotite may be due to some partial alteration of the biotite since crystallization. Unfortunately no systematic studies of the Si isotope fractionation factor between silicic acid and clay minerals have been completed.

Although the mineral soil pool may evolve, and clays incorporate lower $\delta^{30}\text{Si}$ values, it has been argued that there are feedback reactions between the elemental cycling by plants and soil mineralogical properties (Lucas 2001; Sommer et al. 2006), such that Si cycling through plants has consequences for soil development itself. It has also been shown that in terrestrial systems the internal recycling of the phytolith pool is larger than the overall Si weathering rate (Conley 2002). As well as the temporal development of soils, it is important to consider their vertical

development. Silicon recycling by plants results in the active transport of dissolved Si at depth to biogenic Si at the surface. Furthermore, humic acids from plants can lead to distinctly acidic conditions that can result in the dissolution of clay minerals (Viers et al. 1997). It has been proposed for organic-rich swampy soils in the Congo Basin (Cardinal et al. 2010), that although clays with light Si may be formed at the weathering front at the bottom of the soil profile, the dissolution of clays near the top can provide a source of light Si, resulting in little overall mass-fractionation between the primary minerals and dissolved riverine compositions.

As the Si isotope fractionation associated with plant uptake and mineral precipitation is similar, Si isotopes alone cannot be used to uniquely distinguish between biotic and abiotic cycling. Difficulties in assessing the recycling by plants arise because it is hard to determine the average Si isotope composition of the Si source within the soil for the plant biomass, and the efficiency of recycling of biogenic Si between the soil and plants. However, the behaviour of Si and germanium (Ge), a chemical analog of Si, are different between the two processes, and can be used to constrain the Si pathways within the soil-plant system (Cornelis et al. 2010a). During uptake by plants, Ge/Si ratios are fractionated; phytoliths contain low Ge/Si ratios, whilst clay minerals contain high Ge/Si ratios, compared to the bedrocks.

The importance of plant-soil recycling compared to the total weathering input and hydrological output may thus be quantified by examining the Ge/Si ratios. Data from an initial Hawaiian study (Derry et al. 2005) was used to infer that most of the hydrological Si flux out of the watershed had passed through the biogenic Si pool, rather than being directly weathered. It was further suggested that “other systems exhibiting strong Si depletion of the mineral soils and/or high Si uptake rates by biomass will also have strong biological control on silica cycling and export” (Derry et al. 2005). Thus it is crucial to evaluate the role of vegetation on the Si biogeochemical cycle.

Within the African soils, higher $\delta^{30}\text{Si}$ values were associated with lower Ge/Si ratios (Opfergelt et al. 2010). The low Ge/Si found in the soils must reflect the recycling of phytoliths from banana plants with low Ge/Si at the studied sites, which have also resulted in higher $\delta^{30}\text{Si}$ values. Hence, plant material can have a significant impact on the Si isotope composition of soils. It should be noted that there may be mass-fractionation

during further dissolution, with preferential dissolution of lighter isotopes (Demarest et al. 2009; Ziegler et al. 2005b).

Mass balance considerations imply that without the build-up of a fractionated Si reservoir, the recycling of Si by plants could not have a large impact on the Si isotope composition supplied to the oceans from the terrestrial cycle, even though they may dominate the fluxes in the global Si cycle. However, the production of particulate Si by plants could strongly affect the difference between the Si isotope composition of dissolved and particulate matter at the global scale. Within the Anthropocene, human cultivation could have an extreme effect on the global Si cycle and the dissolved Si isotope composition supplied to seawater (Conley 2002). For example, the annual discharge of Si from the Yangtze River in China is estimated to be almost 100 Gmol Si (Ding et al. 2004), about 2% of the global riverine discharge of silicic acid, but the amount of Si in rice plants within this catchment is ~500 Gmol (Ding et al. 2004), about 5 times the annual riverine discharge. Thus, most Si must be cycled through the rice plants several times, strongly affecting the seasonal cycle of Si. The annually removal of harvested rice grains contain ~5 Gmol Si, so rice export should have a small effect on the Si budget and the overall Si isotope composition. In summary, it is clear from these early studies that the seasonal growth and uptake by plants and the seasonal degradation of litter should add a strong seasonality to the cycling of Si and the Si isotope composition of soil waters.

6.3.3 Dissolved Si and Catchment-Scale Studies

Assuming that the recycling of Si by plants is at a steady-state, where the inputs to the soil-plant cycle are equal to the outputs, then the recycling of Si by plants will not impact the riverine Si flux, or its Si isotope composition at larger temporal and spatial scales. The total riverine flux is then a function of the silicate weathering within the catchment, and the riverine Si isotope composition should largely reflect abiotic processes. For example, Cardinal et al. (2010) showed that a typical stable phytolith pool does not impact the $\delta^{30}\text{Si}$ value of water exported, despite

a significant contribution to the recycling of Si in the soil. However, we must consider whether the assumption of steady-state recycling of Si between plants and soils is applicable to catchment scale studies, or the global Si budget. Studies of dissolved Si isotopic composition do indeed show dramatic $\delta^{30}\text{Si}$ variations, both spatially and temporally (Alleman et al. 2005; Engström et al. 2010; Georg et al. 2006a), but often the cause of the fractionation could not be resolved.

As discussed above, the large uptake of Si by rice plants and bamboo in China could influence the dissolved Si composition of Chinese rivers. An early study of the Yangtze (Changjiang) River (Ding et al. 2004) documented dissolved $\delta^{30}\text{Si}$ values ranging from +0.7‰ in the uppermost reaches to >3.0‰ in the middle and lower reaches of the river. Such high $\delta^{30}\text{Si}$ values are hard to reconcile with other published dissolved $\delta^{30}\text{Si}$ values (+0.8 ± 0.5‰ (De La Rocha et al. 2000)), without invoking large influences of biologically induced fractionation, or a counterbalancing build-up of a light Si reservoir in the Chinese soils (Ding et al. 2004). A weak inverse correlation between Si concentrations and $\delta^{30}\text{Si}$ values of the Yangtze samples was interpreted to indicate that isotope fractionation must have occurred during removal of dissolved Si by grass and rice plants (Ding et al. 2004). Unfortunately, seasonal data are not yet available to quantify the effect of seasonal uptake by plants on the $\delta^{30}\text{Si}$ values within this river system.

An investigation of Swiss rivers (Georg et al. 2006a) draining a variety of lithologies showed seasonal variations in Si concentrations and $\delta^{30}\text{Si}$ values. The $\delta^{30}\text{Si}$ values ranged from +0.5 to +1.3‰, lower values being associated with high discharge rates, but no obvious differences in the mean $\delta^{30}\text{Si}$ value between the four rivers studied, despite the difference in sizes and lithologies of their catchments (Georg et al. 2006a). Within one mountainous catchment in the Alps, there is a direct relationship between Si concentration and $\delta^{30}\text{Si}$ values, with an inverse relationship between Si flux and $\delta^{30}\text{Si}$ values. This direct relationship between Si concentration and $\delta^{30}\text{Si}$ values contrasts to the Yangtze River study (Ding et al. 2004), and cannot be driven by the removal of isotopically light dissolved Si. For the small Alpine catchment, it was argued that two distinct components, or reservoirs, of dissolved Si supply the silicic acid to the river: high

$\delta^{30}\text{Si}$ values with high Si concentrations are supplied as a base hydraulic flow from the seepage of soil and/or groundwaters, and low $\delta^{30}\text{Si}$ values in more Si dilute waters are associated with higher dissolved cation loads, which indicate higher mineral dissolution and less Si fractionation from either clay formation or biological utilization (Georg et al. 2006a).

From the development of the Si isotope composition of Hawaiian soils with age (Ziegler et al. 2005b), there should be a relationship between the age of the catchment and the Si isotope composition of the river waters. However, a catchment scale study of the rivers in Iceland (Georg et al. 2007b) failed to find such a correlation despite the same basaltic bedrock lithology. The biggest difference between Hawaii and Iceland is the climate and vegetation. The colder climate of Iceland does not allow for lush vegetation, and much thinner soils develop. The dissolved $\delta^{30}\text{Si}$ values of the rivers were found to correlate with the dissolved Ca/Si ratio, which is elevated compared to the basaltic source rocks. It was proposed that, since Ca is not supplied by carbonate weathering on Iceland and is not strongly incorporated into secondary precipitates, increases in the Ca/Si ratio result from the preferential loss of Si. Thus, the Ca/Si ratio can be used to estimate the fraction of Si lost from the dissolved phase. Estimates of Si re-precipitated ranged from 33 to 66%, although in three glacially-fed rivers it appeared that some Ca must have been derived from carbonate weathering. Furthermore, the correlation between $\delta^{30}\text{Si}$ values and the estimated amount of Si lost could be used to derive an average fractionation factor of -1.6‰ for the processes driving this loss, as shown in Fig. 6.8. This loss was considered to be secondary mineral precipitation and is in agreement with the fractionation factor between water and clays estimated from theoretical and field studies (Méheut et al. 2007, 2009; Ziegler et al. 2005b). However, as all sampling occurred in the summer, the influence of seasonal variations in $\delta^{30}\text{Si}$ values could not be evaluated, and thus the influence of vegetation and soils could not be assessed.

Large seasonal variations in $\delta^{30}\text{Si}$ values have now been observed in another catchment scale study from the same latitude, in Northern Sweden (Engström et al. 2010). In this granitic catchment of pristine boreal forests, the discharge from the Kalix River is highly seasonal, with minimal flow during the winter due to freezing, and a short period of very high discharge due to the snow melt in the spring. The chemical denudation

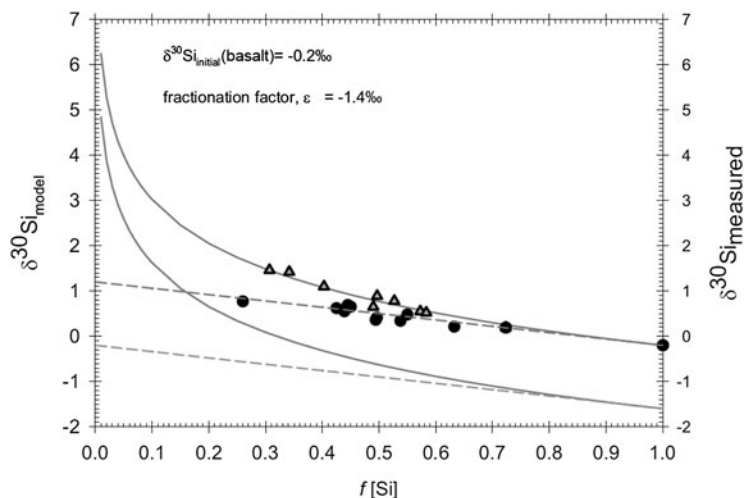


Fig. 6.8 The relation between the riverine Si isotope composition and the fraction dissolved remaining in solution, f_{Si} , computed using the Ca/Si ratios, can be described by open and closed system fractionation behaviour. It appears that rivers

collected on the western part of Iceland (*triangles*) follow rather a Rayleigh-type model, whereas rivers collected from eastern and central Iceland (*black dots*) follow an steady-state system fractionation kinetics, from Georg et al. (2007b)

is highest during the high discharge period, with dissolved K, Al and Si concentrations elevated compared to Mg, which can be used to normalize the effect of dilution by snow melt. The $\delta^{30}\text{Si}$ values are lowest during this period ($\sim -0.7\text{‰}$), but are still elevated compared to the underlying granitic rocks. However, in late summer, especially in sub-catchments within the Kalix watershed, the $\delta^{30}\text{Si}$ values are relatively high ($>1.2\text{‰}$) and associated with a depletion of Si relative to Mg, which was interpreted as a loss of Si and isotope fractionation during the summer due to plant growth, either terrestrial plants or aquatic diatoms. Thus, active Si uptake by plants and algae may influence the seasonal Si isotope composition of rivers. It was argued that lower $\delta^{30}\text{Si}$ values could not be due to less secondary clay formation as hypothesized for the Icelandic rivers, given the changes in Al content of the river and the Si/Al ratio of clays (Engström et al. 2010). Potentially, the breakdown of plant material and phytoliths in spring influences the seasonal Si isotope composition of the rivers, as the lowest $\delta^{30}\text{Si}$ values are associated with high dissolved organic carbon (DOC) (Engström et al. 2010) as the snow melt leaches the upper, organic-rich soil horizons, and stream waters are dominantly fed from soil water (Land et al. 2000).

The seasonal pattern of chemical weathering observed in the granitic catchment of the Kalix River is also

seen in basaltic Siberian rivers (Pokrovsky et al. 2005). Large changes in $\delta^{30}\text{Si}$ values are observed, with lowest values during the spring snow melt ($\sim -0.7\text{‰}$) and highest values in the fall ($>2\text{‰}$) (Reynolds et al. 2006a). The lowest $\delta^{30}\text{Si}$ values are associated with high DOC, and thus light Si may be supplied from the dissolution of phytoliths, or the leaching of light Si from the soil. However, light Si may also be supplied inorganically from absorption-desorption reactions (Delstanche et al. 2009; Opfergelt et al. 2009), or from precipitation due to freezing (Dietzel 2005). During freezing of water in winter, mono-silicic acid can become super-saturated and fractionate during precipitation, leading to the formation of amorphous opal (Dietzel 2005), similar to phytoliths. The degree to which this phenomenon occurs in nature has yet to be evaluated, so it is impossible to fully quantify the relative roles of organic and inorganic cycling of Si on the isotope composition of Si in rivers.

6.3.4 Si in Groundwater Systems

Since most deep groundwaters systems are fed from the infiltration of surface water, the isotope composition of dissolved Si in groundwaters should have positive $\delta^{30}\text{Si}$

values similar to rivers or soil waters. However, measured groundwaters exhibit strongly negative $\delta^{30}\text{Si}$ values. Indeed, it has been shown that the $\delta^{30}\text{Si}$ values of dissolved Si in groundwater flowing through an artesian basin appear to evolve to lower values during flow (Georg et al. 2009a). The shift towards negative $\delta^{30}\text{Si}$ values as Si concentrations increase can readily be explained by the dissolution of previously precipitated clay minerals or silcretes with very negative $\delta^{30}\text{Si}$ values ($< -3\text{‰}$) (Basile-Doelsch et al. 2005; Georg et al. 2009a). Further evolution to lower $\delta^{30}\text{Si}$ values without increasing Si concentrations were explained by the existence of different silcretes within the aquifer with more extreme negative $\delta^{30}\text{Si}$ values. Alternatively, continuous precipitation-dissolution or exchange reactions between water and clay minerals within the aquifer system and that potential conversions between kaolinite and smectite result in isotope exchange and re-equilibration between minerals and dissolved species for both Si and Li isotopes.

Since groundwaters have lower $\delta^{30}\text{Si}$ values than rivers, an under-estimation of the global subterranean groundwater discharge to the oceans would lead to a bias in the estimated average $\delta^{30}\text{Si}$ value supplied to

the oceans (Georg et al. 2009b). Since solute concentrations, including silicic acid, are higher in groundwater, it has been estimated that groundwater discharge may constitute up to 40% of the Si flux to the oceans from the Bay of Bengal (Georg et al. 2009b), and thus chemical denudation rates based upon river fluxes alone may dramatically underestimate the total global denudations rates.

6.3.5 Modeling the Si Biogeochemical Cycle

There have now been some attempts at developing models of the Si cycle and its isotope composition for the continental and marine environments (Basile-Doelsch 2006; Basile-Doelsch et al. 2005), as shown in Fig. 6.9, and the oceans themselves (De La Rocha and Bickle 2005; Reynolds 2009; Wischmeyer et al. 2003). Following the observation that river waters and the oceans have higher $\delta^{30}\text{Si}$ values than igneous rocks, it was argued that there must be a counterbalancing “negative” reservoir of light Si which

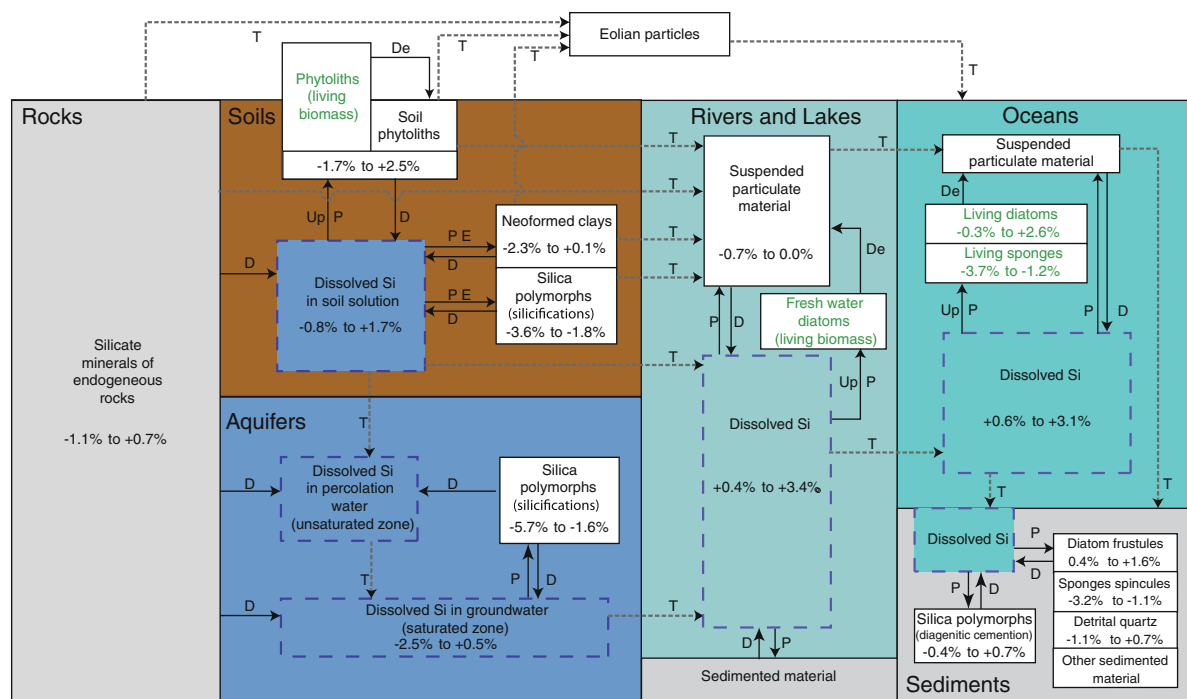


Fig. 6.9 Biogeochemical cycle of Si in continental and marine environments. *D* dissolution; *P* precipitation; *T* transport; *E* exchange; *Up* uptake; *De* death. $\delta^{30}\text{Si}$ ranges are from the literature and taken from Basile-Doelsch (2006)

develops during weathering, which was initially identified as continental silcretes (Basile-Doelsch et al. 2005). However, this counter-balancing light Si may also be in other continental Si pools, such as phytoliths, clays or biological material (Basile-Doelsch 2006). Above-ground biomass cannot be the light Si counter-balance despite its importance as a Si pool because it does not generally contain light Si. It would appear that the counter-balance must be secondary precipitates stored up in soils and sedimentary basins in the form of clays (Ziegler et al. 2005b) or silcretes (Basile-Doelsch et al. 2005), or adsorption onto Fe oxides (Delstanche et al. 2009).

From modeling the oceanographic Si cycle (Reynolds 2009), it was estimated that the mean $\delta^{30}\text{Si}$ value supplied to the ocean was about +0.8‰. Assuming a simple model of isotope fractionation during Si removal with a fractionation factor of -1.6‰ (Georg et al. 2007b), this mean $\delta^{30}\text{Si}$ value would imply that about half of the primary weathered Si (with a mean $\delta^{30}\text{Si}$ value around zero) is removed from solution and stored on the continents, as estimated for weathering on Iceland (Georg et al. 2007b). This calculation would imply that the continental crust is being enriched in light Si by about 6 Tmol Si per year with a $\delta^{30}\text{Si}$ value -0.8‰, which would be equivalent to ~800 million tons of kaolinite per year with a $\delta^{30}\text{Si}$ value -2.2‰. This amount of material is the same order of magnitude as the amount of sediment carried by the Mississippi into the Gulf of Mexico per year.

Interestingly, the estimated increase of light Si in the continental crust is in marked contrast to the heavier Si isotopic composition of the granitic continental crust compared to the basaltic mantle. Thus the difference between granitic and basaltic $\delta^{30}\text{Si}$ values cannot be due to the continuous recycling of Si via the rock cycle over Earth's history, and the actual cause of the difference is currently enigmatic.

6.4 Future Directions

It seems that the biogeochemical Si cycle is more complex than previously fathomed, with published studies pointing to an intense terrestrial biogeochemical cycling of Si (Struyf et al. 2009). Thus, considerable work is required to assess the terrestrial cycling of

Si and its isotopes, in particular the role of plants and siliceous algae. Future field studies will allow the natural cycling of Si to be assessed in more detail, and most importantly, careful laboratory experiments will determine the mechanisms of biogenic silica and mineral silicate formation and associated Si isotope fractionation. Regrettably, the application of Si isotope studies in terrestrial environments is still somewhat hampered by the limited development of sample preparation techniques and the analytical requirements that are still far from routine. Here, I would like to suggest a number of potential research avenues which would help develop this exciting field in the near future.

- For the measurement of Si isotopes by MC-ICPMS, there is currently no technique for separation of silicic acid from anions, without conversion to SiF_6 in hydrofluoric acid. As anions, like sulphur, can cause large "matrix effects" (van den Boorn et al. 2009), a fast and efficient separation of silicic acid from other anions is greatly needed, with existing methods either requiring extensive preparation steps or significant amounts of HF (Engström et al. 2006). If HF cannot be eliminated, a change in the introduction system, with removal of a desolvating unit may be advantageous.
- A change in biomass could lead to significant alteration of the terrestrial Si cycle, such as the anthropogenic transformation from forests to pasture (Conley 2002). Sudden disruption of the plant biomass, like harvesting and forest fires, could also have significant impact on the Si fluxes and isotope composition. As Si is beneficial to plants, we need to understand the molecular mechanism of biogenic opal mineralization and associated isotope fractionation, and the way in which different plants adapt and respond to changes in Si availability.
- Lastly, more studies of river and groundwater systems are required in order to better constrain the global dissolved Si budget, and the role that lithology, climate and vegetation can have on global biogeochemical cycles. However, we should perhaps no longer consider that the global biogeochemical cycles can be accurately assessed from modern observations because, within the modern Anthropocene, human activity now moves more material across the globe than rivers do.

Acknowledgments I would like to thank Mark Baskaran and two anonymous reviewers for their great help in improving this manuscript.

References

- Alexandre A, Meunier J-D, Colin F, Koud J-M (1997) Plant impact on the biogeochemical cycle of silicon and related weathering processes. *Geochim Cosmochim Acta* 61(3): 677–682
- Alleman LY, Cardinal D, Cocquyt C, Plisnier P-D, Descy J-P, Kimirei I, Sinyinza D, André L (2005) Silicon isotopic fractionation in Lake Tanganyika and its main tributaries. *J Great Lakes Res* 31(4):509–519
- Allenby RJ (1954) Determination of the isotopic ratios of silicon in rocks. *Geochim Cosmochim Acta* 5(1):40–48
- André L, Cardinal D, Alleman LY, Moorbath S (2006) Silicon isotopes in 3.8 Ga West Greenland rocks as clues to the Eoarchean supracrustal Si cycle. *Earth Planet Sci Lett* 245(1–2):162–173
- Basile-Doelsch I (2006) Si stable isotopes in the Earth's surface: a review. *J Geochem Explor* 88(1–3):252–256
- Basile-Doelsch I, Meunier JD, Parron C (2005) Another continental pool in the terrestrial silicon cycle. *Nature* 433(7024): 399–402
- Bern CR, Brzezinski MA, Beucher C, Ziegler K, Chadwick OA (2010) Weathering, dust, and biocycling effects on soil silicon isotope ratios. *Geochim Cosmochim Acta* 74(3): 876–889
- Boltz DF, Trudell LA, Potter GV (1978) Silicon. In: Boltz DF, Trudell LA (eds) *Colorimetric determination of nonmetals*. Wiley, New York, pp 421–462
- Brzezinski MA, Pride CJ, Franck VM, Sigman DM, Sarmiento JL, Matsumoto K, Gruber N, Rau GH, Coale KH (2002) A switch from $\text{Si}(\text{OH})_4$ to NO_3^- depletion in the glacial Southern Ocean. *Geophys Res Lett* 29(12):1564. doi:1510.1029/2001GL014349
- Brzezinski MA, Jones JL, Beucher CP, Demarest MS, Berg HL (2006) Automated determination of silicon isotope natural abundance by the acid decomposition of cesium hexafluosilicate. *Anal Chem* 78(17):6109–6114
- Burton KW, Vigier N (2011) Lithium Isotopes as Tracers in Marine and Terrestrial Environments. In: Baskaran M (ed) *Handbook of Environmental Isotope Geochemistry*. Springer, Heidelberg
- Cardinal D, Alleman LY, de Jong J, Ziegler K, André L (2003) Isotopic composition of silicon measured by multicollector plasma source mass spectrometry in dry plasma mode. *J Anal At Spectrom* 18(3):213–218
- Cardinal D, Alleman LY, Dehairs F, Savoye N, Trull TW, André L (2005) Relevance of silicon isotopes to Si-nutrient utilization and Si-source assessment in Antarctic waters. *Global Biogeochem Cycles* 19:2007. doi:10.1029/2004GB002364
- Cardinal D, Gaillardet J, Hughes HJ, Opfergelt S, André L (2010) Contrasting silicon isotope signatures in rivers from the Congo Basin and the specific behaviour of organic-rich waters. *Geophys Res Lett* 37(12):L12403
- Conley DJ (2002) Terrestrial ecosystems and the global biogeochemical silica cycle. *Global Biogeochem Cycles* 16(4): 1121
- Coplen TB, Bohlke JK, De Bievre P, Ding T, Holden NE, Hopple JA, Krouse HR, Lamberty A, Peiser HS, Revesz K, Rieder SE, Rosman KJR, Roth E, Taylor PDP, Vocke RD, Xiao YK (2002) Isotope-abundance variations of selected elements – (IUPAC Technical Report). *Pure Appl Chem* 74(10):1987–2017
- Cornelis JT, Delvaux B, Georg RB, Lucas Y, Ranger J, Opfergelt S (2010a) Tracing the origin of dissolved silicon transferred from various soil-plant systems towards rivers: a review. *Biogeosci Discuss* 7(4):5873–5930
- Cornelis JT, Delvaux B, Cardinal D, André L, Ranger J, Opfergelt S (2010b) Tracing mechanisms controlling the release of dissolved silicon in forest soil solutions using Si isotopes and Ge/Si ratios. *Geochim Cosmochim Acta* 74(14): 3913–3924
- De La Rocha CL (2002) Measurement of silicon stable isotope natural abundances via multicollector inductively coupled plasma mass spectrometry (MC-ICP-MS). *Geochem Geophys Geosyst* 3(8):art. no.-1045
- De La Rocha CL, Bickle MJ (2005) Sensitivity of silicon isotopes to whole-ocean changes in the silica cycle. *Mar Geol* 217(3–4):267–282
- De La Rocha CL, Brzezinski MA, DeNiro MJ (1996) Purification, recovery, and laser-driven fluorination of silicon from dissolved and particulate silica for the measurement of natural stable isotope abundances. *Anal Chem* 68(21): 3746–3750
- De La Rocha CL, Brzezinski MA, DeNiro MJ (2000) A first look at the distribution of the stable isotopes of silicon in natural waters. *Geochim Cosmochim Acta* 64(14): 2467–2477
- de Souza GF, Reynolds BC, Kiczka M, Bourdon B (2010) Evidence for mass-dependent isotopic fractionation of strontium in a glaciated granitic watershed. *Geochim Cosmochim Acta* 74(9):2596–2614
- Debievre P, Lenaers G, Murphy TJ, Peiser HS, Valkiers S (1995) The chemical preparation and characterization of specimens for absolute measurements of the molar-mass of an element, exemplified by silicon, for redeterminations of the Avogadro constant. *Metrologia* 32(2):103–110
- Delstanche S, Opfergelt S, Cardinal D, Elsass F, André L, Delvaux B (2009) Silicon isotopic fractionation during adsorption of aqueous monosilicic acid onto iron oxide. *Geochim Cosmochim Acta* 73(4):923–934
- Demarest MS, Brzezinski MA, Beucher CP (2009) Fractionation of silicon isotopes during biogenic silica dissolution. *Geochim Et Cosmochim Acta* 73(19):5572–5583
- Derry LA, Kurtz AC, Ziegler K, Chadwick OA (2005) Biological control of terrestrial silica cycling and export fluxes to watersheds. *Nature* 433(7027):728–731
- Dietzel M (2005) Impact of cyclic freezing on precipitation of silica in Me-SiO₂-H₂O systems and geochemical implications for cryosols and -sediments. *Chem Geol* 216(1–2): 79–88
- Ding T (2004) Analytical methods for silicon isotope determination. In: de Groot PA (ed) *Handbook of stable isotope analytical techniques*, vol 1. Elsevier, Amsterdam, pp 523–537

- Ding T, Jiang S, Wan D, Li Y, Li J, Song H, Liu Z, Yao X (1996) Silicon Isotope Geochemistry. Geological Publishing House, Beijing, China, p 125
- Ding T, Wan D, Wang C, Zhang F (2004) Silicon isotope compositions of dissolved silicon and suspended matter in the Yangtze River, China. *Geochim Cosmochim Acta* 68(2): 205–216
- Ding TP, Ma GR, Shui MX, Wan DF, Li RH (2005) Silicon isotope study on rice plants from the Zhejiang province, China. *Chem Geol* 218(1–2):41–50
- Ding TP, Tian SH, Sun L, Wu LH, Zhou JX, Chen ZY (2008a) Silicon isotope fractionation between rice plants and nutrient solution and its significance to the study of the silicon cycle. *Geochim Cosmochim Acta* 72(23):5600–5615
- Ding TP, Zhou JX, Wan DF, Chen ZY, Wang CY, Zhang F (2008b) Silicon isotope fractionation in bamboo and its significance to the biogeochemical cycle of silicon. *Geochim Cosmochim Acta* 72(5):1381–1395
- Douthitt CB (1982) The geochemistry of the stable isotopes of silicon. *Geochim Cosmochim Acta* 46(8):1449–1458
- Engström E, Rodushkin I, Baxter DC, Ohlander B (2006) Chromatographic purification for the determination of dissolved silicon isotopic compositions in natural waters by high-resolution multicollector inductively coupled plasma mass spectrometry. *Anal Chem* 78(1):250–257
- Engström E, Rodushkin I, Ingri J, Baxter DC, Ecke F, Österlund H, Ohlander B (2010) Temporal isotopic variations of dissolved silicon in a pristine boreal river. *Chem Geol* 271(3–4):142–152
- Epstein E (2003) SILICON. *Annu Rev Plant Physiol Plant Mol Biol* 50(1):641–664
- Epstein S, Taylor HP Jr (1970) $^{18}\text{O}/^{16}\text{O}$, $^{30}\text{Si}/^{28}\text{Si}$, D/H, and $^{13}\text{C}/^{12}\text{C}$ studies of lunar rocks and minerals. *Science* 167(3918, The Moon Issue):533–535
- Farkas J, Bohm F, Wallmann K, Blenkinsop J, Eisenhauer A, van Geldern R, Munnecke A, Voigt S, Veizer J (2007) Calcium isotope record of Phanerozoic oceans: implications for chemical evolution of seawater and its causative mechanisms. *Geochim Cosmochim Acta* 71(21):5117–5134
- Farmer VC, Delbos E, Miller JD (2005) The role of phytolith formation and dissolution in controlling concentrations of silica in soil solutions and streams. *Geoderma* 127(1–2):71–79
- Fitoussi C, Bourdon B, Kleine T, Oberli F, Reynolds BC (2009) Si isotope systematics of meteorites and terrestrial peridotites: implications for Mg/Si fractionation in the solar nebula and for Si in the Earth's core. *Earth Planet Sci Lett* 287(1–2): 77–85
- Georg RB, Reynolds BC, Frank M, Halliday AN (2006a) Mechanisms controlling the silicon isotopic compositions of river waters. *Earth Planet Sci Lett* 249(3–4):290–306
- Georg RB, Reynolds BC, Frank M, Halliday AN (2006b) New sample preparation techniques for determination of Si isotope composition using MC-ICPMS. *Chem Geol* 235(1–2): 95–104
- Georg RB, Halliday AN, Schauble EA, Reynolds BC (2007a) Silicon in the Earth's core. *Nature* 447(7148):1102–1106
- Georg RB, Reynolds BC, West AJ, Burton KW, Halliday AN (2007b) Silicon isotope variations accompanying basalt weathering in Iceland. *Earth Planet Sci Lett* 261(3–4): 476–490
- Georg RB, Zhu C, Reynolds BC, Halliday AN (2009a) Stable silicon isotopes of groundwater, feldspars, and clay coatings in the Navajo Sandstone aquifer, Black Mesa, Arizona, USA. *Geochim Cosmochim Acta* 73(8):2229–2241
- Georg RB, West AJ, Basu AR, Halliday AN (2009b) Silicon fluxes and isotope composition of direct groundwater discharge into the Bay of Bengal and the effect on the global ocean silicon isotope budget. *Earth Planet Sci Lett* 283(1–4): 67–74
- Hendry KR, Leng MJ, Robinson LF, Sloane HJ, Blusztjan J, Rickaby REM, Georg RB, Halliday AN (2010) Silicon isotopes in Antarctic sponges: an interlaboratory comparison. *Antarctic Sci* 23(1):34–42
- Hiemstra T, Barnett MO, van Riemsdijk WH (2007) Interaction of silicic acid with goethite. *J Colloid Interface Sci* 310(1): 8–17
- Hulston JR, Thode HG (1965) Variations in the S^{33} , S^{34} , and S^{36} contents of meteorites and their relation to chemical and nuclear effects. *J Geophys Res* 70:3475–3584
- Icopini GA, Brantley SL, Heaney PJ (2005) Kinetics of silica oligomerization and nanocolloid formation as a function of pH and ionic strength at 25 degrees C. *Geochim Cosmochim Acta* 69(2):293–303
- Iler RK (1979) The Chemistry of silica – solubility, polymerization, colloid and surface properties and biochemistry. Wiley, New York, p 1026
- Land M, Ingri J, Andersson PS, Ohlander B (2000) Ba/Sr, Ca/Sr and $^{87}\text{Sr}/^{86}\text{Sr}$ ratios in soil water and groundwater: implications for relative contributions to stream water discharge. *Appl Geochem* 15(3):311–325
- Lucas Y (2001) The role of plants in controlling rates and products of weathering: importance of biological pumping. *Annu Rev Earth Planet Sci* 29:135–163
- Ma JF (2004) Role of silicon in enhancing the resistance of plants to biotic and abiotic stresses. *Soil Sci Plant Nutr* 50(1): 11–18
- Ma JF, Mitani N, Nagao S, Konishi S, Tamai K, Iwashita T, Yano M (2004) Characterization of the silicon uptake system and molecular mapping of the silicon transporter gene in rice. *Plant Physiol* 136(2):3284–3289
- Marschner H (1995) Beneficial mineral elements. In: Mineral nutrition of higher plants, 2nd edn. Academic, London, pp 405–435
- Méheut M, Lazzeri M, Balan E, Mauri F (2007) Equilibrium isotopic fractionation in the kaolinite, quartz, water system: prediction from first-principles density-functional theory. *Geochim Cosmochim Acta* 71(13):3170–3181
- Méheut M, Lazzeri M, Balan E, Mauri F (2009) Structural control over equilibrium silicon and oxygen isotopic fractionation: a first-principles density-functional theory study. *Chem Geol* 258(1–2):28–37
- Miller MF (2002) Isotopic fractionation and the quantification of O-17 anomalies in the oxygen three-isotope system: an appraisal and geochemical significance. *Geochim Cosmochim Acta* 66(11):1881–1889
- Mitani N, Ma JF (2005) Uptake system of silicon in different plant species. *J Exp Bot* 56(414):1255–1261
- Morey GW, Fournier RO, Rowe JJ (1962) The solubility of quartz in water in the temperature interval from 25° to 300° C. *Geochim Cosmochim Acta* 26(10):1029–1040, IN1011, 1041–1043

- Opfergelt S, Cardinal D, Henriët C, André L, Delvaux B (2006a) Silicon isotope fractionation between plant parts in banana: in situ vs. in vitro. *J Geochem Explor* 88 (1–3):224–227
- Opfergelt S, Cardinal D, Henriët C, Draye X, André L, Delvaux B (2006b) Silicon isotopic fractionation by banana (*Musa* spp.) grown in a continuous nutrient flow device. *Plant Soil* V285(1):333–345
- Opfergelt S, Delvaux B, André L, Cardinal D (2008) Plant silicon isotopic signature might reflect soil weathering degree. *Biogeochemistry* 91(2):163–175
- Opfergelt S, de Bournonville G, Cardinal D, André L, Delstanche S, Delvaux B (2009) Impact of soil weathering degree on silicon isotopic fractionation during adsorption onto iron oxides in basaltic ash soils, Cameroon. *Geochim Cosmochim Acta* 73(24):7226–7240
- Opfergelt S, Cardinal D, André L, Delvigne C, Bremond L, Delvaux B (2010) Variations of $\delta^{30}\text{Si}$ and Ge/Si with weathering and biogenic input in tropical basaltic ash soils under monoculture. *Geochim Cosmochim Acta* 74(1):225–240
- Pokrovsky OS, Schott J, Kudryavtzev DI, Dupre B (2005) Basalt weathering in Central Siberia under permafrost conditions. *Geochim Cosmochim Acta* 69(24):5659–5680
- Raven JA (1983) The transport and function of silicon in plants. *Biol Rev* 58(2):179–207
- Raven JA (2001) Chapter 3 Silicon transport at the cell and tissue level. In: Datnoff LE, Snyder GH, Korndörfer GH (eds) *Studies in plant science*, vol 8. Elsevier, Amsterdam, pp 41–55
- Raymo ME, Ruddiman WF (1992) Tectonic forcing of late Cenozoic climate. *Nature* 359(6391):117–122
- Reynolds BC (2009) Modeling the modern marine $\delta^{30}\text{Si}$ distribution. *Global Biogeochem Cycles* 23:GB2015. doi:10.1029/2008GB003266
- Reynolds JH, Verhoogen J (1953) Natural variations in the isotopic constitution of silicon. *Geochim Cosmochim Acta* 3(5):224–234
- Reynolds BC, Pokrovsky OS, Schott J (2006a) Si isotopes for tracing basalt weathering in Central Siberia. *Geochim Cosmochim Acta* 70(18 suppl 1):A528
- Reynolds BC, Frank M, Halliday AN (2006b) Silicon isotope fractionation during nutrient utilization in the North Pacific. *Earth Planet Sci Lett* 244(1–2):431–443
- Reynolds BC, Georg RB, Oberli F, Wiechert UH, Halliday AN (2006c) Re-assessment of silicon isotope reference materials using high-resolution multi-collector ICP-MS. *J Anal At Spectrom* 21(3):266–269
- Reynolds BC, Aggarwal J, Andre L, Baxter D, Beucher C, Brzezinski MA, Engstrom E, Georg RB, Land M, Leng MJ, Opfergelt S, Rodushkin I, Sloane HJ, van den Boorn S, Vroon PZ, Cardinal D (2007) An inter-laboratory comparison of Si isotope reference materials. *J Anal At Spectrom* 22(5):561–568
- Rudge J, Reynolds BC, Bourdon B (2009) The double spike toolbox. *Chem Geol* 265:420–431
- Sangster AG, Hodson MJ (2007) Silica in higher plants. In: Evered D, O'Connor M (eds) *Ciba Foundation Symposium 121 – silicon biochemistry*. Wiley, Chichester, pp 90–111
- Savage PS, Georg RB, Armytage RMG, Williams HM, Halliday AN (2010) Silicon isotope homogeneity in the mantle. *Earth Planet Sci Lett* 295(1–2):139–146
- Sommer M, Kaczorek D, Kuzyakov Y, Breuer J (2006) Silicon pools and fluxes in soils and landscapes – a review. *J Plant Nutr Soil Sci* 169(3):310–329
- Strickland JDH (1952) The preparation and properties of silicomolybdic acid III. The combination of silicate and molybdate. *J Am Chem Soc* 74(4):872–876
- Struyf E, Smis A, Van Damme S, Meire P, Conley D (2009) Global Biogeochem Silicon Cycle. *SILICON* 1(4):207–213. doi:10.1007/s12633-010-9035-x
- Sun L, Wu L, Ding T, Tian S (2008) Silicon isotope fractionation in rice plants, an experimental study on rice growth under hydroponic conditions. *Plant Soil* 304(1):291–300
- Taylor BE (2004) Fluorination methods in stable isotope analysis. In: de Groot PA (ed) *Handbook of stable isotope analytical techniques*, vol 1. Elsevier, Amsterdam, pp 400–472
- Tipper ET, Galy A, Bickle MJ (2008) Calcium and magnesium isotope systematics in rivers draining the Himalaya-Tibetan-Plateau region: lithological or fractionation control? *Geochim Cosmochim Acta* 72(4):1057–1075
- van den Boorn SHJM, Vroon PZ, van Belle CC, van der Wagt B, Schwieters J, van Bergen MJ (2006) Determination of silicon isotope ratios in silicate materials by high-resolution MC-ICP-MS using a sodium hydroxide sample digestion method. *J Anal At Spectrom* 21:734–742
- van den Boorn SHJM, Vroon PZ, van Bergen MJ (2009) Sulfur-induced offsets in MC-ICP-MS silicon-isotope measurements. *J Anal At Spectrom* 24:1111–1114
- Varela DE, Pride CJ, Brzezinski MA (2004) Biological fractionation of silicon isotopes in Southern Ocean surface waters. *Global Biogeochem Cycles* 18:GB1047. doi:10.1029/2003GB002140
- Viers J, Dupré B, Polvé M, Schott J, Dandurand J-L, Braun J-J (1997) Chemical weathering in the drainage basin of a tropical watershed (Nsimi-Zoetele site, Cameroon): comparison between organic-poor and organic-rich waters. *Chem Geol* 140(3–4):181–206
- Vigier N, Gislason SR, Burton KW, Millot R, Mokadem F (2009) The relationship between riverine lithium isotope composition and silicate weathering rates in Iceland. *Earth Planet Sci Lett* 287(3–4):434–441
- White AF, Blum AE, Schulz MS, Vivit DV, Stonestrom DA, Larsen M, Murphy SF, Eberl D (1998) Chemical weathering in a tropical watershed, Luquillo mountains, Puerto Rico: I. Long-term versus short-term weathering fluxes. *Geochim Cosmochim Acta* 62(2):209–226
- Wischmeyer A, DelaRocha CL, Maier-Reimer E, Wolf-Gladrow DA (2003) Control mechanisms for the oceanic distribution of silicon isotopes. *Global Biogeochem Cycles* 17(3):1083. doi:10.1029/2002GB002022
- Young ED, Galy A, Nagahara H (2002) Kinetic and equilibrium mass-dependent isotope fractionation laws in nature and their geochemical and cosmochemical significance. *Geochim Cosmochim Acta* 66(6):1095–1104
- Ziegler K, Chadwick OA, White AF, Brzezinski MA (2005a) $\delta^{30}\text{Si}$ systematics in a granitic saprolite, Puerto Rico. *Geology* 33(10):817–820
- Ziegler K, Chadwick OA, Brzezinski MA, Kelly EF (2005b) Natural variations of $\delta^{30}\text{Si}$ ratios during progressive basalt weathering, Hawaiian Islands. *Geochim Cosmochim Acta* 69(19):4597–4610

Chapter 7

Calcium Isotopes as Tracers of Biogeochemical Processes

Laura C. Nielsen, Jennifer L. Druhan, Wenbo Yang, Shaun T. Brown, and Donald J. DePaolo

Abstract The prevalence of calcium as a major cation in surface and oceanic environments, the necessity of calcium in the functioning of living cells and bone growth, and the large spread in mass between calcium isotopes all suggest that calcium isotope biogeochemistry can be an important avenue of insight into past and present biogeochemical cycling processes. In the following chapter, we review the main areas of research where Ca isotope studies have been pursued and detail recent research results in biogeochemical applications. In marine environments, biogenic fractionation of Ca isotopes during biomineralization produces predictable offsets in some organisms, which facilitate the reconstruction of seawater $\delta^{44/40}\text{Ca}$ over geologic timescales. In terrestrial studies, observed Ca isotope fractionation between soil and various components of vegetation enables the construction of a local Ca budget and provides a partial explanation for the scale of Ca isotopic variability within a single watershed. The research reviewed in this chapter provides a foundation for future investigations into the macro- and microscopic processes and biochemical pathways dictating the distribution of this essential nutrient using stable Ca isotope ratios.

7.1 Introduction

Calcium is an alkaline earth metal with six naturally occurring isotopes: ^{40}Ca (96.941%), ^{41}Ca , ^{42}Ca (0.647%), ^{43}Ca (0.135%), ^{44}Ca (2.086%), ^{46}Ca (0.004%) and ^{48}Ca (0.187%). By mass, calcium is the fifth most abundant element in both the earth's crust and seawater. The prevalence of calcium as a major cation in surface and oceanic environments, the necessity of calcium in the functioning of living cells and bone growth and the large spread in mass between calcium isotopes all suggest calcium isotope biogeochemistry can be an important avenue of insight into past and present biogeochemical cycling processes. In the following subsections, we review the main research areas where biogeochemical Ca isotope studies have been pursued, and in later sections more details are provided regarding recent research results. Throughout this paper we have renormalized all $\delta^{44/40}\text{Ca}$ values to a bulk silicate Earth (BSE) standard, which we describe in Section II.

7.1.1 Ca Isotopes and the Marine Calcium Cycle

Calcium isotopes provide a promising means to constrain the global Ca budget over geologic timescales and to identify the causes of variability in the marine calcium cycle (e.g. Zhu and MacDougall 1998; DePaolo 2004; Farkaš et al. 2007). Seawater has a globally homogeneous $\delta^{44/40}\text{Ca}$ ($0.91 \pm 0.04\text{‰}$; Hippler et al. 2003; Farkaš et al. 2007) that is uniform with water depth, due to the long oceanic Ca residence time (~1 million years) relative to oceanic turnover

L.C. Nielsen (✉), J.L. Druhan, W. Yang, and D.J. DePaolo
Department of Earth and Planetary Science, University
of California, Berkeley, CA 94720, USA
Earth Sciences Division, Lawrence Berkeley National
Laboratory, Berkeley, CA 94720, USA
e-mail: lnielsen@berkeley.edu
S.T. Brown
Earth Sciences Division, Lawrence Berkeley National
Laboratory, Berkeley, CA 94720, USA

time (1,500 years; Broecker and Peng 1982). The heavy Ca isotopic composition of seawater relative to global rocks (0.0‰; Simon and DePaolo 2010) and continental water (−0.2‰; Schmitt et al. 2003b) is primarily maintained by biogenic isotope fractionation during calcium carbonate precipitation, where ^{40}Ca is preferentially removed from solution relative to ^{44}Ca .

The concentration and isotopic composition of marine Ca depends upon the balance between the Ca input and output fluxes (e.g. De La Rocha and DePaolo 2000). Calcium enters the ocean as a solute transported by rivers due to continental weathering, by hydrothermal fluids due to metasomatism (Schmitt et al. 2003b; Amini et al. 2008), and by Ca replacement by Mg during dolomitization (Heuser et al. 2005; Böhm et al. 2005; Farkaš et al. 2007; Holmden 2009). These sources are isotopically similar to within ~1‰ (Schmitt et al. 2003b; Fig. 7.1). Riverine input is variable in isotopic composition and unrelated to the source watershed lithology or climate (Zhu and MacDougall 1998; Schmitt et al. 2003b). The magnitude of watershed-scale variability in $\delta^{44/40}\text{Ca}$ resembles global variability due to mass fractionation during Ca transport through the environment (Tipper et al. 2006). Calcium carbonate precipitation causes the majority of continental Ca isotope fractionation, while preferential uptake of light Ca by vegetation in terrestrial ecosystems also plays a role. Precipitation of carbonate (and minor phosphate) minerals

removes Ca from seawater at a rate similar to the input weathering flux (Berner et al. 1983; DePaolo 2004). Average calcium isotopic compositions of pelagic calcite (Skulan et al. 1997; Gussone et al. 2003, 2005) and aragonite differ by over ~0.5‰ due primarily to precipitate mineralogy: biogenic and inorganic aragonite are typically lighter than calcite (Gussone et al. 2003, 2005). Coccolithophores and modern scleractinian corals constitute an important exception to this rule, with average Ca isotopic compositions straddling the calcite and aragonite end members (Böhm et al. 2006). Sources of minor variability in modern marine biogenic carbonate $\delta^{44/40}\text{Ca}$ include species-dependent as well as systematic intra-species temperature-dependent Ca isotope fractionation (Nägler et al. 2000; Gussone et al. 2003).

Variability in the ratio of Ca weathering to sedimentation fluxes and isotope compositions can affect seawater $\delta^{44/40}\text{Ca}$ (δ_{sw}) over geologic timescales. Though δ_{sw} can vary with time, the ocean is thought to be currently at steady state with respect to Ca, indicating that the concentration and isotopic composition of Ca are stable over timescales smaller than the Ca oceanic residence time ($\tau = 10^6$ years) (Skulan et al. 1997; De La Rocha and DePaolo 2000; Schmitt et al. 2003a, b). De La Rocha and DePaolo (2000) constructed a simplified model for Ca mass balance in the ocean based on the relative fluxes of Ca into the ocean via continental weathering and out of the ocean via biogenic carbonate sedimentation, where F_w and

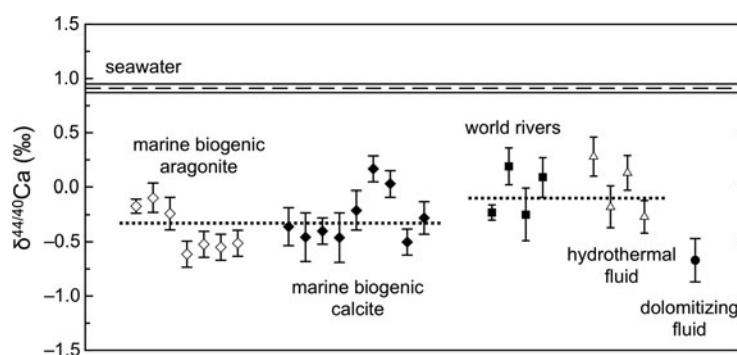


Fig. 7.1 $\delta^{44/40}\text{Ca}$ of Ca fluxes into and out of seawater. *Dashed line* denotes the average seawater Ca isotopic composition ($0.91 \pm 0.4\text{‰}$), with 2σ errors marked as lines above and below. Species average marine biogenic aragonite (Holmden 2005; Gussone et al. 2005; Böhm et al. 2006) and calcite (Gussone et al. 2005; Farkaš et al. 2007; Griffith et al. 2008b; Hippler et al. 2009) $\delta^{44/40}\text{Ca}$ data are depicted with a *dotted line*

through both data sets approximating the average δ_{sed} . Calcium isotopic data for aqueous Ca from major world-rivers, hydrothermal fluids and dolomitizing fluids (Schmitt et al. 2003b; Farkaš et al. 2007) are shown with a *dotted line* approximating the current average δ_w . Ca fluxes into and out of seawater are similar in $\delta^{44/40}\text{Ca}$ indicating that the ocean is at steady state with respect to Ca

F_{sed} represent weathering and sedimentation fluxes respectively, and δ_w and δ_{sed} represent weathered Ca and sediment Ca isotopic compositions:

$$N_{Ca} \frac{d\delta^{44/40}Ca_{sw}}{dt} = F_w \left(\delta^{44/40}Ca_w - \delta^{44/40}Ca_{sw} \right) - F_{sed} \Delta_{sed},$$

where N_{Ca} is the amount of Ca in the ocean and $\Delta_{sed} = \delta_{sed} - \delta_{sw}$ is average Ca isotope separation (‰) during $CaCO_3$ precipitation. At steady state, $F_w = F_{sed}$ and δ_{sw} is constant in time, so:

$$\delta_{sw} = \delta_w - \Delta_{sed},$$

and

$$\delta_w = \delta_{sed}.$$

Current estimates of δ_{sed} and δ_w are $-0.3 \pm 0.2\%$ and $-0.2 \pm 0.2\%$ relative to BSE, supporting the theory that the ocean is close to steady state with respect to Ca (De La Rocha and DePaolo 2000; Farkaš et al. 2007).

Reconstructions of past δ_{sw} based on marine carbonate oozes (De La Rocha and DePaolo 2000; Fantle and DePaolo 2005, 2007), brachiopod shells, belemnites (Farkaš et al. 2007), rudists (Steuber and Buhl 2006), and foraminifera (Sime et al. 2007; Heuser et al. 2005) form a coherent record of oceanic Ca isotopes throughout the Phanerozoic (Fig. 7.2). Additional reconstructions based on phosphate minerals (Schmitt et al. 2003a; Soudry et al. 2004) are inconsistent with carbonate reconstructions, while those based on marine pelagic barite roughly correspond with carbonate data (Griffith et al. 2008a). A better understanding of marine biogenic and inorganic Ca isotope

fractionation during $CaCO_3$ precipitation is necessary to reduce scatter in the reconstructed δ_{sw} record as it currently stands.

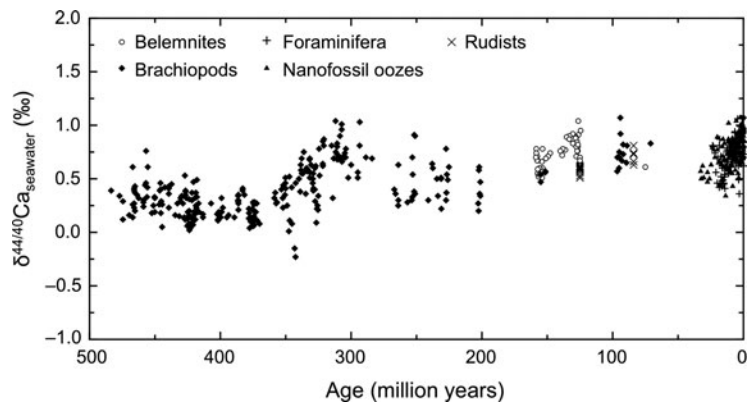
Despite a $\sim 0.5\%$ spread in the reconstruction, δ_{sw} variability within a given sample type can shed light upon the causes of Ca isotopic shifts with time. Observed long-timescale variation in δ_{sw} could be caused by changes in the ratio of sedimentation to weathering fluxes (De La Rocha and DePaolo 2000; Fantle and DePaolo 2005) or by changes in the Ca isotopic composition of these fluxes (Farkaš et al. 2007). In the first case, inequality of F_w and F_s over a period longer than the residence time of Ca in the ocean (~ 1 Ma) will result in a quasi steady state δ_{sw} :

$$\delta_{sw}(t) \approx \delta_w(t) - \frac{F_{sed}}{F_w}(t) \Delta_{sed}.$$

The ratio of sedimentation to weathering fluxes (F_{sed}/F_w) approximately ranges between 0.7 and 1.3 (Lasaga et al. 1985), which would cause a $\sim 0.8\%$ shift in δ_{sw} (De La Rocha and DePaolo 2000). Observed δ_{sw} variability of $\sim 0.9\%$ in fossil oozes of Cretaceous age and younger is consistent with this hypothesis; however, additional analyses of marine biogenic carbonates encompass a range closer to 1.5% (Fig. 7.2).

Farkaš et al. (2007) present an alternative hypothesis to explain long-term shifts in the oceanic Ca isotopic composition. They argue that the isotopic composition of the sedimentation flux, δ_{sed} , changes due to transitions in oceanic carbonate mineralogy. Throughout the Phanerozoic, variations in global tectonic activity caused long term alterations in oceanic major element chemistry, specifically Mg/Ca. Periods of enhanced tectonism raised oceanic Mg/Ca, facilitating the precipitation of aragonite relative to

Fig. 7.2 $\delta^{44/40}Ca$ of seawater throughout the Phanerozoic from various carbonate data sets (Heuser et al. 2005; Steuber and Buhl 2006; Fantle and DePaolo 2005, 2007; Sime et al. 2007; Farkaš et al. 2007). Seawater Ca isotopic compositions were calculated based on published fractionation factors between the given sediment type and seawater (Fantle and DePaolo 2005; Farkaš et al. 2007). Fantle and DePaolo (2005, 2007) values were first calculated relative to the NIST standard based on their measurement of seawater $\delta^{44/40}Ca$ ($0.95 \pm 0.10\%$)



calcite. Based on this hypothesis, “aragonite seas” should correspond with heavy δ_{sw} and “calcite seas” should correspond with light δ_{sw} . Paleozoic, early Mesozoic and Neogene shifts in δ_{sw} are in phase with oscillating “calcite-aragonite seas,” as predicted. The relationship between δ_{sw} and dominant mineralogy breaks down in the later Mesozoic and Cenozoic, probably due to the expansion of coccolithophores and scleractinian corals, whose Ca isotopic compositions are decoupled from mineralogy (Farkaš et al. 2007). A third possible explanation for the long-term variability in δ_{sw} , changing δ_{w} , is still being debated. While some consider major changes in the isotopic composition of the weathering flux to be unlikely based on the current narrow range in riverine $\delta^{44/40}\text{Ca}$ values (De La Rocha and DePaolo 2000; Tipper et al. 2006), others have not ruled out this possibility (Griffith et al. 2008a; Fantle 2010).

Short-term changes in the calcium isotopic composition of the ocean, those occurring on sub-Ma time-scales, are smaller in magnitude and likely caused by different processes than previously discussed. Enhanced silicate weathering due to a period of active volcanism, for example, could cause transient drops in δ_{sw} (Farkaš et al. 2007), as could enhanced carbonate dissolution due to ocean acidification (Payne et al. 2010). Analysis of complementary isotope systems such as sulfur and carbon could confirm or contest proposed mechanisms of these short-term excursions.

Marine Ca isotopic budgets may be applied to paleoclimate reconstructions to investigate aspects of the global carbon cycle. Kasemann et al. (2005) use boron and calcium isotopic analyses of carbonate sediments harboring evidence of Neoproterozoic glaciation in Namibia to refute the snowball earth hypothesis, a hotly debated topic in the Earth sciences. When applied in concert with indicators of paleoseawater pH such as boron isotopes ($\delta^{11}\text{B}$), calcium isotopic variability in marine carbonate sediment can highlight excursions in atmospheric pCO_2 (Kasemann et al. 2005). $\delta^{44/40}\text{Ca}$ variations are used to estimate seawater $[\text{Ca}]$, which in turn may be used to estimate $[\text{CO}_3^{2-}]$. With the additional pH indicator provided by B isotopes, the carbonic acid system is fully constrained, and atmospheric pCO_2 may be estimated. The major weakness in this methodology is that absolute Ca fluxes to and from the ocean (F_{w} and F_{sed}) cannot be fully constrained by calcium isotopic mass balance alone. Additional determinations such

as carbonate sedimentation rate are required to generate a more robust estimate of seawater calcium concentrations with time.

Though our understanding of the mechanisms and environmental sensitivity of Ca isotope fractionation during inorganic and biogenic CaCO_3 precipitation is still in its infancy, much has already been learned about the global marine Ca budget. As discussed in a later section, investigations into the pathways of Ca transport during biomineralization are beginning to reveal the causes of inter-species variability in $\Delta^{44/40}\text{Ca}_{\text{seawater}-\text{CaCO}_3}$. Constraints on Ca isotopic sensitivity to environmental controls such as T, pH and $[\text{CO}_3^{2-}]$ suggest proxy possibilities beyond reconstructing past oceanic δ_{sw} . Non-traditional metal stable isotope systems such as Ca promise to expand typical isotope geochemistry applications and explain the underlying chemical mechanisms of myriad processes observed in nature.

7.1.2 Ca Isotopes and the Terrestrial Calcium Cycle

Although it has already been shown that biological Ca isotope fractionation is an important process within marine biogeochemical Ca cycles, the current understanding of biological influences on terrestrial biogenic Ca isotope fractionation is still under development. From a broad perspective, the flux weighted mean discharge $\delta^{44/40}\text{Ca}$ value of the largest rivers in the world is -0.2% relative to BSE (Fig. 7.1; Schmitt et al. 2003b). In comparison, the total range of values reported for igneous rock is -0.12 to 0.58% (Richter et al. 2003). This discrepancy indicates fractionation during the translocation of calcium from primary rock to soil and sedimentary rock to aqueous systems on the continents (e.g. DePaolo 2004). An important component of this isotope separation may be biogenic cycling in higher-order plants, which require calcium as a major nutrient.

Calcium is required to stabilize cell walls, promote enzyme activity, and act as an intracellular messenger and as a counter-cation in the vacuoles of plant cells (Marschner 1995). Unlike other macronutrients incorporated into organic compounds like nitrogen and phosphorous, calcium remains in its elementary

cationic form throughout its residence in plants (Amtmann and Blatt 2009). Calcium from the soil solution enters the plant via fine root ends where it is transported through the xylem to shoots, stems and leaves. Uptake from the soil into the xylem can occur at high rates through both apoplastic and symplastic transport protein mediated pathways (White and Broadley 2003). Once taken into the root, the majority of calcium is directly adsorbed to cell walls. The remainder is taken into the cytoplasm where it may be transported to stem and leaf cells, though once incorporated in the phloem it is trapped and cannot undergo recirculation in the plant (von Blanckenburg et al. 2009). Retention of calcium in older growth has direct implications for the calcium signature of surrounding leaf litter and topsoil. Calcium isotope fractionation associated with movement of calcium through a plant will eventually affect the isotopic ratio of the detritus and soil of the ecosystem, suggesting a link between soil $\delta^{44/40}\text{Ca}$ and ecosystem evolution.

In the past 5 years, substantial progress has been made in quantifying the isotopic fractionation of calcium associated with uptake, translocation and redeposition by higher-order plants (von Blanckenburg et al. 2009). To date only a few studies directly address the influence of plants and ecosystem dynamics on calcium isotope fractionation (Wiegand et al. 2005; Perakis et al. 2006; Schmitt and Stille 2005; Page et al. 2008; Cenki-Tok et al. 2009; Holmden and Bélanger 2010). Results suggest that fractionation by higher-

order plants exhibits a 4‰ range in $\delta^{44/40}\text{Ca}$ (Holmden and Bélanger 2010), representing one of the largest terrestrial sources of calcium isotopic variation. In the sections to follow, these studies will be discussed in further detail, and an example of the use of $\delta^{44/40}\text{Ca}$ to discern the vital effects in tree rings of phreatophytes in Death Valley, California (Yang et al. 1996), will be presented to illustrate the diversity of applications for calcium stable isotopes in the study of higher-order plants.

7.1.3 Calcium Isotopes in Food Chains

Skulan et al. (1997) were the first to report a systematic trend towards lighter $\delta^{44/40}\text{Ca}$ values with increasing trophic level in a marine ecosystem (Fig. 7.3a), and similar trends were subsequently observed in terrestrial systems (Fig. 7.3b; Skulan and DePaolo 1999; Skulan 1999). The marine system shows a $\Delta^{44/40}\text{Ca}$ of 3.2‰ between seawater and an orca, separated by four trophic levels. The terrestrial $\Delta^{44/40}\text{Ca}$ is slightly larger at 3.5‰ between total soil calcium and a cougar, with three trophic levels of separation. The clear loss of heavy ^{44}Ca relative to light ^{40}Ca across both food chains indicates preferential incorporation of the lighter isotope in the bone structure relative to that available in the organism's diet (Clementz et al. 2003; DePaolo 2004).

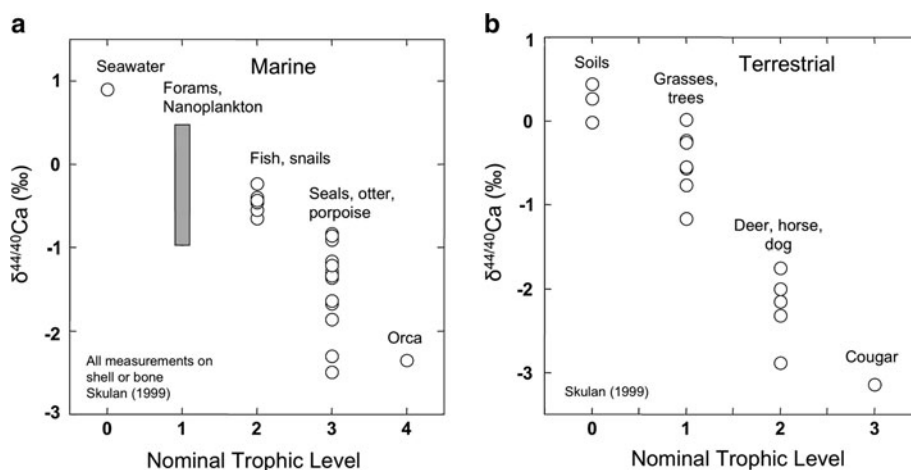


Fig. 7.3 Calcium isotopic composition of materials as a function of marine (a) and terrestrial (b) trophic levels from DePaolo (2004). $\delta^{44/40}\text{Ca}$ of calcium reported relative to the Skulan et al. (1997) reference material. Data represent values reported in

Skulan et al. (1997), Skulan and DePaolo (1999) and Skulan (1999). More recent data may be found in Reynard et al. (2010). Reprinted with permission from the author

The fractionation between dietary and bone $\delta^{44/40}\text{Ca}$ has several important applications. First, Skulan and DePaolo (1999) present a model for $\delta^{44/40}\text{Ca}$ fractionation in organisms based on observations suggesting that the $\delta^{44/40}\text{Ca}$ of living tissue is much more transient and responsive to recent diet than bone, which is generally $\sim 1.3\%$ lighter. The model incorporates the availability of calcium in the diet and the rate of bone growth and bone loss and indicates healthy adults should have a near constant bone $\delta^{44/40}\text{Ca}$ value, while healthy juveniles should show $\delta^{44/40}\text{Ca}$ $\sim 1.5\%$ lower than the diet source. These findings have led to subsequent research regarding calcium isotopes as a proxy for calcium availability in vertebrates (Chu et al. 2006; Hirata et al. 2008; Bullen and Walczyk 2009; Heuser and Eisenhauer 2010; Reynard et al. 2010). Second, Clementz et al. (2003) reported similar systematic variation between trophic levels, and showed preservation of this fractionation in bones as old as 15 million years, presenting a novel means of tracking vertebrate paleodiets. Recent developments built upon these studies will be addressed in subsequent sections.

7.2 Analytical Methods and Standards

Ca isotope fractionation can be measured by a variety of techniques including thermal ionization mass spectrometry (TIMS), multi-collector inductively coupled plasma-mass spectrometry (MC-ICP-MS), and in situ by ion microprobe secondary ion mass spectrometry (SIMS; Rollion-Bard et al. 2007). The large spread in Ca isotopic abundances and the large relative mass difference ($\sim 20\%$) make measurement of Ca isotopes complex. Precise determinations of mass dependent Ca isotope composition by TIMS requires the use of a double spike (a tracer solution enriched in two minor isotopes), typically $^{42}\text{Ca}/^{48}\text{Ca}$ (Russell et al. 1978; Zhu and Macdougall 1998; Skulan et al. 1997), $^{43}\text{Ca}/^{48}\text{Ca}$ (Nägler et al. 2000; Heuser et al. 2002; Gussone et al. 2003; Hippler et al. 2003) or $^{43}\text{Ca}/^{46}\text{Ca}$ (Fletcher et al. 1997) to correct for isotopic fractionation in the mass spectrometer. Early TIMS methods employed “peak jumping” or magnetic field stepping, measuring the four masses required for spike subtraction (typically 40, 42, 44 and 48) in sequence on a single collector (Russell et al. 1978; Skulan et al. 1997). This

method provided superior external precision compared to the previous generation of multicollector mass spectrometers, but required a long-lived, stable ion beam (Skulan et al. 1997). Discrepancies between the analytical precision based on counting statistics and the external reproducibility of samples and standards were commonly attributed to inter-block focusing. Most researchers now measure Ca isotopes using the new generation TIMS instruments such as the Thermo Triton. The current generation ($\sim 1998\text{--}2009$) of Triton TIMS instruments are only capable of measuring $\sim 17\%$ relative mass difference and thus do not allow for simultaneous measurement of all Ca isotopes. To circumvent this problem most labs measure multiple sequences with a “low mass” scan that measures $^{40}\text{Ca}\text{--}^{44}\text{Ca}$ and a second “high mass” sequence that measures $^{42}\text{Ca}\text{--}^{48}\text{Ca}$. An alternate approach is to avoid measuring either ^{40}Ca or ^{48}Ca (Fantle and Bullen 2009; Holmden 2005). Fantle and Bullen (2009) provide a detailed summary of commonly used cup configurations and double spike compositions. Approximately 50–200 cycles are collected during the course of a sample run, and post-run processing is used to correct data for mass fractionation during analysis. Typical 2σ external reproducibility using TIMS is 0.1–0.2‰ (DePaolo 2004), which is worse than the internal errors generated from counting statistics (0.02–0.05‰). The source of additional error in Ca isotope measurements is still attributed to poor focusing (DePaolo 2004) and reservoir mixing during sample ionization (Fantle and Bullen 2009) though the effect has been minimized in recent years. Despite some shortcomings TIMS is the preferred and most common technique for Ca isotope analysis.

MC-ICP-MS is another widely used method in measuring calcium isotope fractionation. The technique may be employed using either the “cool plasma technique” (CPT; Fietzke et al. 2004) or the “hot plasma technique” (HPT; Halicz et al. 1999). Isobaric interferences from $^{40}\text{Ar}^+$ and numerous other sources undermine the utility of MC-ICP-MS for Ca isotope measurements, and the original hot plasma technique required a thorough accounting of and correction for interferences (Halicz et al. 1999). These effects can be greatly diminished by lowering the plasma RF power to $\sim 400\text{ W}$ (Fietzke et al. 2004). MC-ICP-MS analyses enable the simultaneous measurement of various Ca isotope masses as well as sample-standard bracketing, rendering the use of a double spike unnecessary. This

method yields poorer precision than TIMS, with 2σ uncertainty in $\delta^{44/40}\text{Ca}$ of 0.2–0.3‰ (Fietzke et al. 2004; Hippler et al. 2007) and in $\delta^{44/42}\text{Ca}$ of 0.09‰ (Tipper et al. 2006).

A novel ion microprobe technique has recently been developed to measure Ca isotope ratios via SIMS in situ with high (15–20 μm) spatial resolution (Rollion-Bard et al. 2007; Kasemann et al. 2008). Secondary $^{40}\text{Ca}^+$ and $^{44}\text{Ca}^+$ ions are simultaneously measured on two Faraday cups, providing good internal reproducibility. Interferences from $^{40}\text{K}^+$ and $^{88}\text{Sr}^{2+}$ on $^{40}\text{Ca}^+$ and $^{44}\text{Ca}^+$ respectively cannot currently be resolved but must be monitored on mass 41 and 43.5 to ensure no corrections are needed. Uncertainties up to 0.3‰ (2σ) are reported for in situ sample analyses (Rollion-Bard et al. 2007; Kasemann et al. 2008), meaning this method must be further refined for application in systems where minor isotopic variability is expected.

Isotopic analyses of most Ca carbonate minerals require minimal chemical preparation. Other materials with increased concentrations of matrix elements require more extensive separation procedures, which are detailed in the literature (e.g. Skulan and DePaolo 1999). For the TIMS technique, carbonate samples are first dissolved in 2N to 4N ultrapure nitric acid or HCl and centrifuged if detrital material is present. One M acetic acid is more commonly used in lieu of the stronger HCl or HNO_3 to avoid extraction of Ca from any associated detrital clay minerals (Ewing et al. 2008). The Ca double spike is added to an aliquot of sample to correct for mass discrimination during analysis. Optimal spike-sample ratios are discussed elsewhere (Rudge et al. 2009 and references therein). Samples are then dried and re-dissolved in acid. Purification of Ca from the sample matrix may be achieved using a variety of ion chromatography techniques such as cation exchange (Russell et al. 1978; Fantle and DePaolo 2007); and MCI gel (Heuser et al. 2002). Recently the Berkeley lab has started using DGA resin (Eichrom Technologies, normal variety), which efficiently separates Ca from matrix elements in a similar fashion to the better-known Sr-spec resin (Horwitz et al. 2005). Sufficiently pure carbonates may not require chemical purification (Eisenhauer et al. 2004). Purified Ca is dissolved in a small volume of 3N HNO_3 and a few micrograms of dissolved Ca are loaded onto degassed, zone-refined Re filaments and subsequently capped with phosphoric acid.

An alternate technique uses approximately 300 ng of Ca loaded with a Ta_2O_5 activator using the “sandwich technique” for analysis on single Re filaments (activator-sample-activator; Gussone et al. 2003). Sample throughput of ~6–12 per day is possible with this method. Cleaning and preparation of Ca bearing samples is similar for the MC-ICP-MS technique, and ion chromatography is often used to prevent matrix effects and isobaric interferences (Halicz et al. 1999). Once dissolved in acid, samples are diluted with nitric acid solution and introduced into the plasma source through a nebulizer (Halicz et al. 1999; Fietzke et al. 2004). Sample preparation for analysis on the ion microprobe requires that samples be mounted in epoxy, polished to 1 μm using a diamond paste, and coated in gold (Rollion-Bard et al. 2007).

7.2.1 Calcium Isotope Standards: A Proposal

Calcium isotopes are reported in delta notation (‰) as the ratio of the heavy ^{44}Ca over the abundant ^{40}Ca isotope with reference to a known standard value, consistent with the convention of other stable isotope systems (Skulan et al. 1997):

$$\delta^{44/40}\text{Ca} = \left(\frac{\left[\frac{^{44}\text{Ca}}{^{40}\text{Ca}} \right]_{\text{sample}}}{\left[\frac{^{44}\text{Ca}}{^{40}\text{Ca}} \right]_{\text{std}}} - 1 \right) \times 1,000.$$

Isotope compositions may also be presented in the $^{44/42}\text{Ca}$ notation, which may be converted to $\delta^{44/40}\text{Ca}$ to avoid discrepancies due to radiogenic ingrowth of ^{40}Ca (Hippler et al. 2003):

$$\delta^{44/40}\text{Ca} = \delta^{44/42}\text{Ca} \times \frac{43.956 - 39.963}{43.956 - 41.959}.$$

At the time of writing the most widely used standard reference material for calcium measurements is the NIST synthetic carbonate, SRM 915a (Hippler et al. 2003). The original material, SRM 915a is no longer available and has been superseded by a new reference material SRM 915b, which is $0.72 \pm 0.04\%$ heavier in $\delta^{44/40}\text{Ca}$ than SRM 915a (Heuser and Eisenhauer 2008). Other common standard reference materials include purified calcium salts such as CaF_2

(Russell et al. 1978; Nägler et al. 2000; Gussone et al. 2003) and CaCO_3 (Skulan et al. 1997) and seawater (Zhu and Macdougall 1998; Schmitt et al. 2001; Hippler et al. 2003). NIST SRM 915a has a $\delta^{44/40}\text{Ca}$ of $-1.88 \pm 0.04\%$ relative to seawater (Hippler et al. 2003) and $\delta^{44/40}\text{Ca}$ of -1.21% relative to the Skulan et al. (1997) standard. Stable Ca isotope fractionation between two phases (e.g. i, j) is expressed as a fractionation factor,

$$\alpha_{i-j} = \frac{{}^{44}\text{Ca}/{}^{40}\text{Ca}_i}{{}^{40}\text{Ca}/{}^{40}\text{Ca}_j},$$

or as isotope separation,

$$\Delta^{44}\text{Ca}_{i-j} = \delta^{44}\text{Ca}_i - \delta^{44}\text{Ca}_j \approx 1000\ln(\alpha_{i-j}).$$

Though SRM 915a provides the most reliable inter-lab working reference standard, it can be argued that the most desirable reference standard for reporting $\delta^{44/40}\text{Ca}$ values is bulk silicate Earth (BSE). Unlike seawater, this value does not shift through Earth history, except for very small effects due to radioactive decay of ${}^{40}\text{K}$, and because it represents the overall bulk composition of the Earth, all deviations from the BSE value have geochemical significance. While SRM 915a is the most widely used laboratory standard, laboratory standards are not the same as standard values used for referencing the delta values for most stable isotope systems. In the case of O isotopes, for example, there are multiple laboratory standards and multiple reference materials. Simon and DePaolo 2010 have reported analyses of silicate materials from the Earth, Mars, and the Moon, and have determined that the bulk silicate value for these three planetary bodies is indistinguishable and identical to that of ordinary chondritic meteorites. Relative to this Bulk Planetary or Chondritic value (BSE), the SRM 915a standard is reported to have $\delta^{44/40}\text{Ca} = -0.97 \pm 0.04$. Values for mantle clinopyroxene reported by Huang et al. (2010) are consistent with the Simon and DePaolo (2010) results. Thus we will henceforth report all $\delta^{44/40}\text{Ca}$ values relative to the BSE value, and we propose that the convention be that the standard BSE value of ${}^{44}\text{Ca}/{}^{40}\text{Ca}$ is exactly 1.00100 times the value of ${}^{44}\text{Ca}/{}^{40}\text{Ca}$ in SRM 915a. In general practice, it will be sufficiently accurate to convert $\delta^{44/40}\text{Ca}$ relative to SRM 915a to $\delta^{44/40}\text{Ca}$ relative to BSE

by simply subtracting 1.00 from the former. In this chapter we report all $\delta^{44/40}\text{Ca}$ values relative to BSE. These $\delta^{44/40}\text{Ca}$ values differ from those reported by the U.C. Berkeley group through 2010 by 0.2 units of $\delta^{44/40}\text{Ca}$.

7.3 Current Research

7.3.1 Calcium Isotopes and Marine Biomineralization

The calcium isotopic composition of carbonate-secreting marine organisms constitutes a promising tool for paleoclimatologic research, because the shells of certain species preserve paleoenvironmental information such as seawater temperature at the time of formation (e.g. Nägler et al. 2000; Hippler et al. 2009). Some species of planktonic foraminifera such as *Globigerinoides sacculifer* (*G. sacculifer*) and *Neogloboquadrina pachyderma* (sinistral) appear to exhibit strong $\delta^{44/40}\text{Ca}$ temperature sensitivity on order 0.2‰ per 1°C (Nägler et al. 2000; Gussone et al. 2004; Hippler et al. 2006, 2009); however, this sensitivity in *G. sacculifer* is widely contested (Chang et al. 2004; Sime et al. 2005; Griffith et al. 2008b). Most species of marine organisms, including corals (Böhm et al. 2006), dinoflagellates (Gussone et al. 2010), and foraminifera (Skulan et al. 1997; Gussone et al. 2003; Griffith et al. 2008b) are effectively independent of temperature in calcium isotopic composition, providing a robust means of determining oceanic $\delta^{44/40}\text{Ca}$ variability over geologic timescales. Understanding the temporal variability in oceanic Ca stable isotope composition has helped to constrain the global Ca budget. Recent research on Ca isotopes in marine calcifying organisms focuses on small but significant vital effects and variability in $\delta^{44/40}\text{Ca}$ not explained by temperature dependence or inorganic control, because they may contain additional information about the biological pathways of calcification (e.g. Eisenhauer et al. 2009).

Biological mechanisms of calcification vary widely among marine organisms. Corals secreting aragonitic skeletons follow a biocalcification pathway much different from that of foraminifera, resulting in a distinct relationship between $\delta^{44/40}\text{Ca}$ and growth environment. Though the Ca fractionation behavior of both

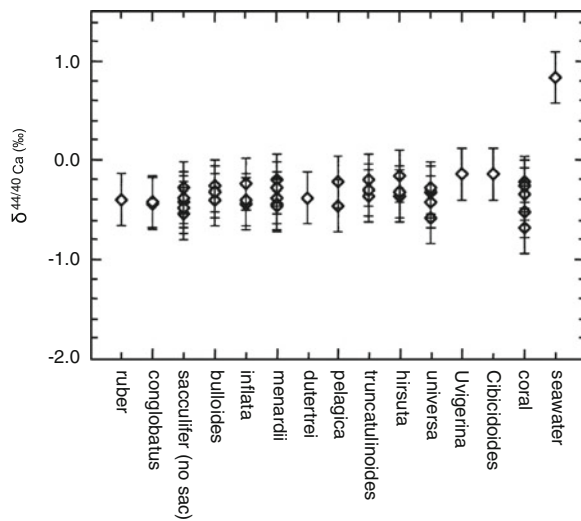


Fig. 7.4 Ca isotopic composition of seawater, corals and foraminifera from Holocene sediments distributed worldwide (Chang et al. 2004). Minimal intra-species variability in the magnitude of $\delta^{44/40}\text{Ca}$ suggests a similar Ca stable isotope fractionation mechanism between organisms. Reprinted from Chang et al. (2004), Copyright (2004), with permission from Elsevier

foraminifera and corals has been shown to resemble abiotic Ca isotope fractionation during CaCO_3 precipitation (Gussone et al. 2003; Lemarchand et al. 2004; Marriott et al. 2004; Böhm et al. 2006; Tang et al. 2008), coral Ca is likely biologically fractionated by active transport through tissues (Böhm et al. 2006), while foraminifera appear to precipitate their shells directly from pH-modified seawater entrained in vacuoles (Erez 2003). Care should be taken when deducing biological Ca isotope fractionation mechanisms based on the experiments of Lemarchand et al. (2004) and Tang et al. (2008), because these groups report directly opposite relationships between $\Delta^{44/40}\text{Ca}$ and precipitation rate. Despite inter-species differences and the challenge of interpretation, the overall homogeneity in average $\delta^{44/40}\text{Ca}$ across Holocene marine calcifying organisms (Fig. 7.4) suggests that a universal mechanism may control marine biogenic Ca isotope fractionation.

7.3.1.1 Calcium Isotopes in Coral Skeletons

Though the details of coral calcification are still a major subject of debate, corals are currently thought to actively transport calcium from seawater to the site of calcification by a multi-step process requiring

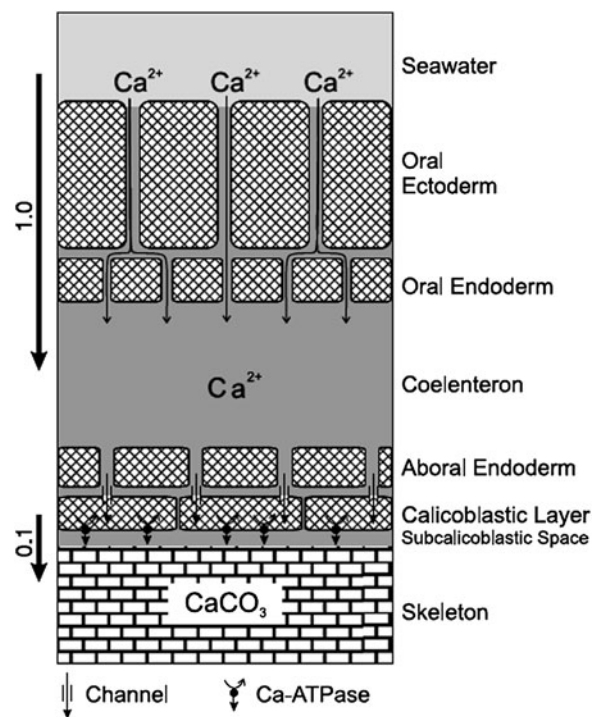


Fig. 7.5 Schematic of calcium transport and skeletal growth in corals. Numbered arrows on the left of the diagram indicate relative rates of Ca transport; calcium flows into the coelenteron an order of magnitude more quickly than into the calcifying fluid. Reprinted from Böhm et al. (2006), Copyright (2006), with permission from Elsevier

active Ca pumping through numerous tissues (Böhm et al. 2006; Fig. 7.5). Ca^{2+} ions first diffuse from seawater into coral tissue, through the oral ectoderm and endoderm into the coelenteron. There, they are sealed during the day while calcification takes place. Ca then passes from the coelenteron through the aboral endoderm to the calicoblastic layer, where it is actively transported via Ca-ATPase either to the calcifying subcalicoblastic space or possibly from the cell to the skeleton via an organic matrix (Allemand et al. 2004; Cuif and Dauphin 2005). Neither the existence of a subcalicoblastic space (Tambutté et al. 2007; Holbrèque et al. 2009) nor the role of the organic matrix in directing the transport and deposition of Ca ions (Allemand et al. 2004) has definitively been established. From its final reservoir, Ca^{2+} is incorporated into skeletal material (Clode and Marshall 2003; Böhm et al. 2006).

Each step in the coral biogeochemical Ca transport pathway may fractionate stable calcium isotopes, resulting in the preferential incorporation of ^{40}Ca

over ^{44}Ca into skeletal material. Unlike inorganic CaCO_3 growth, Ca isotope fractionation likely does not occur at the carbonate mineral surface. Instead, it has been suggested that the kinetics of solvated Ca^{2+} dehydration at the cell membrane and of Ca^{2+} ion attachment to proteins such as Ca-ATPase causes the preferential incorporation of light calcium in coral skeletons (Gussone et al. 2006; Böhm et al. 2006). Dehydration kinetics of solvated Ca^{2+} ions is also a possible cause of kinetic, surface-controlled Ca isotope fractionation during inorganic calcite and aragonite precipitation (DePaolo 2011), so it is not surprising that the fractionation factor generated by these very different processes is similar.

The $\delta^{44/40}\text{Ca}$ of both cultured and open-ocean coral skeletal material is relatively insensitive to seawater temperature, with a T-dependence similar to marine biogenic calcite and aragonite (Fig. 7.6; Böhm et al. 2006):

$$\delta^{44/40}\text{Ca} (\text{BSE}) = 0.020(\pm 0.015) \times T(^{\circ}\text{C}) - 0.7(\pm 0.4).$$

Despite the morphological similarity between coral skeletal aragonite and synthetic aragonite precipitated under controlled growth conditions (Holcomb et al.

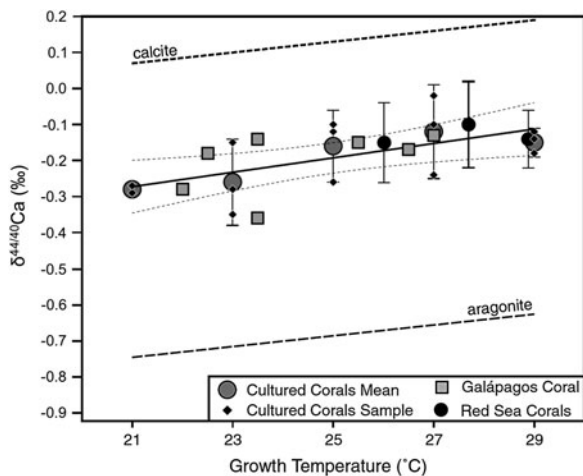


Fig. 7.6 Cultured and open-ocean coral skeletal $\delta^{44/40}\text{Ca}$ plotted as a function of temperature, compared with similar linear regressions of marine biogenic calcite (brachiopods, sclerosponges, and red alga) and aragonite (sclerosponges and pteropods; Böhm et al. 2006). The slope of the T dependence of these organisms is very similar to other marine biogenic calcite and aragonite, but the magnitude of fractionation is offset by $\sim 0.5\%$ from each. Reprinted from Böhm et al. (2006), Copyright (2006), with permission from Elsevier

2009), coral $\delta^{44/40}\text{Ca}$ values are offset by 0.5‰ from inorganic precipitates and other marine biogenic aragonite (Böhm et al. 2006). The magnitude of Ca isotope fractionation in coral skeletal material, then, is primarily controlled by biological mechanisms, while the T-dependence of fractionation is likely due to geochemical processes that are mechanistically similar in both inorganic and biological systems.

7.3.1.2 Calcium Isotopes in Foraminiferal Biomineralization

Most species of marine calcifying foraminifera exhibit a $\delta^{44/40}\text{Ca}$ T-dependence similar to that of corals and inorganic calcite and aragonite. Because the calcification mechanism of foraminifera more closely resembles inorganic CaCO_3 precipitation (e.g. Erez 2003), it may be more appropriate to consider the rate dependence of Ca isotope fractionation during foraminiferal calcification than during coral skeletal growth. The growth of calcite skeletal material in foraminifera is a two-stage process producing two distinct phases, primary and secondary calcite. These phases differ in both trace element (Erez 2003) and Ca isotopic (Rollion-Bard et al. 2007; Kasemann et al. 2008) composition due to mechanistic differences in the calcification process. Erez (2003) summarizes a working hypothesis of the foraminiferal calcification process as follows. Primary calcite formation is initiated by Ca concentration in a highly soluble mineral phase (also rich in Mg, P and likely S) embedded in the cellular membrane of the endoplasm. These soluble granules provide Ca for the primary calcite crystals, which precipitate as a wall of spherulites directly over an organic matrix. Primary calcite spherulites are Mg-rich, and may reflect the formation of an amorphous calcium carbonate (ACC) precursor (Bentov and Erez 2006). Secondary calcite precipitates adjacent to the primary layer as a low-Mg, crystallographically oriented mineral phase (*c*-axis perpendicular to skeletal wall). Vacuoles of seawater provide calcium for the secondary phase, so unlike in corals, Ca is not actively transported through cellular membranes and fractionation cannot be attributed to biological pumping. This phase constitutes the bulk of foraminiferal skeletal material, and secondary calcite precipitation resembles inorganic, surface-controlled calcite

precipitation. Alternating layers of primary and secondary calcite are deposited onto the skeletal wall, causing heterogeneity of both trace elements (Erez 2003) and possibly stable Ca isotopes (Rollion-Bard et al. 2007) within a single shell.

The $\delta^{44/40}\text{Ca}$ temperature dependence of most studied foraminiferal shell material resembles that of inorganic calcite (Marriott et al. 2004) and aragonite (Gussone et al. 2003). The skeletal Ca isotopic composition typically increases approximately 0.02‰ per 1°C increase in seawater temperature (e.g. Skulan 1997; Gussone et al. 2003; Griffith et al. 2008b). Two exceptions are *N. pachyderma* (sin.) and *G. sacculifer*, which have temperature sensitive Ca isotopic compositions. Linear regression of the temperature sensitivity of Ca isotopic composition for *N. pachyderma* (sin.) for sea surface temperatures greater than $2.0 \pm 0.5^\circ\text{C}$ can be expressed as (Hippler et al. 2009):

$$\delta^{44/40}\text{Ca}(\text{BSE}) = 0.15(\pm 0.01) \times \text{SST}(\text{°C}) - 1.12(\pm 0.06).$$

The $\delta^{44/40}\text{Ca}$ -temperature relationship for surface water *G. sacculifer* has similarly been expressed as follows (Hippler et al. 2006):

$$\delta^{44/40}\text{Ca}(\text{BSE}) = 0.22(\pm 0.05) \times \text{SST}(\text{°C}) - 5.85,$$

which is very similar to the regression generated by Nägler et al. (2000) for cultured samples. Despite the apparent strength of the temperature signal, the temperature sensitivity of $\delta^{44/40}\text{Ca}$ in *G. sacculifer* is not agreed upon in the literature. Attempts at T calibration of this species from core-top samples have resulted in a range of interpretations from no T dependence (Sime et al. 2005, 2007), to a weak dependence similar to other foraminifera (Griffith et al. 2008b). Ca isotope fractionation in low-salinity cultures of *G. sacculifer* also appears to be only weakly temperature dependent (Gussone et al. 2009). In general, plankton tow samples exhibit a stronger T dependence than the same species collected from core-top samples (e.g. Griffith et al. 2008b), which may reflect the averaged sampling of organisms accumulated from throughout the water column. This ambiguity calls into question the utility of down-core samples of *G. sacculifer* as a paleotemperature proxy.

7.3.1.3 Marine Calcification, Ca Isotope Fractionation and Precipitation Rate

The temperature dependence of Ca isotope fractionation during inorganic and marine biogenic CaCO_3 precipitation is likely caused by the T sensitivity of mineral growth rates due to changing oversaturation (Lemarchand et al. 2004; Gussone et al. 2005; Steuber and Buhl 2006). Increasing temperature alters carbonic acid speciation, shifting phase equilibrium towards the CO_3^{2-} endmember and increasing precipitation rate (e.g. Millero 1995). The rate dependence of Ca isotope fractionation during calcite precipitation is not well understood, and is a subject of recent debate. At issue is whether Ca isotope fractionation during CaCO_3 precipitation is equilibrium- (e.g. Marriott et al. 2004; Lemarchand et al. 2004) or kinetically-controlled. Lemarchand et al. (2004) found that the Ca isotopic fractionation factor increases (approaches $\alpha = 1.000$) with increasing rate, while more recent calcite precipitation experiments performed by Tang et al. (2008) generated the opposite relationship at similar growth rates (Fig. 7.7). Both groups argue that the low-rate limit fractionation factor ($-1.5 \pm 0.25\%$ for Lemarchand et al., $\sim 0\%$ for Tang et al.) approaches the equilibrium fractionation between calcite and aqueous Ca^{2+} . An equilibrium fractionation factor close to 0‰ is supported by calcite equilibrated with pore fluid Ca^{2+} over tens of millions of years (Fantle and DePaolo 2007), so it follows that marine biogenic Ca isotope fractionation must be kinetically controlled.

Calculated precipitation rates and ranges for marine biogenic calcite and aragonite fall within experimental inorganic Ca carbonate growth rate ranges. A comparison of associated Ca fractionation factors reveals that most biogenic carbonates are consistent with inorganic experimental data, with the exception of *Acopora* coral skeletal material (Fig. 7.7). The range of both surface area normalized growth rates and fractionation factors of an additional foraminiferan, *G. sacculifer*, fall within the experimental region ($1.5\text{--}3.3 \mu\text{mol}/\text{m}^2/\text{h}$, -0.81 to -1.64% ; Carpenter and Lohmann 1992; Erez 1982), but the fractionation factor as a function of growth rate cannot yet be determined for this species. Differences in the Ca coordination environment between CaCO_3 polymorphs likely explains the additional offset in magnitude of $\sim 0.6\%$ between calcite and aragonite $\delta^{44/40}\text{Ca}$. Better constraint of surface-area normalized marine biocalcification rates

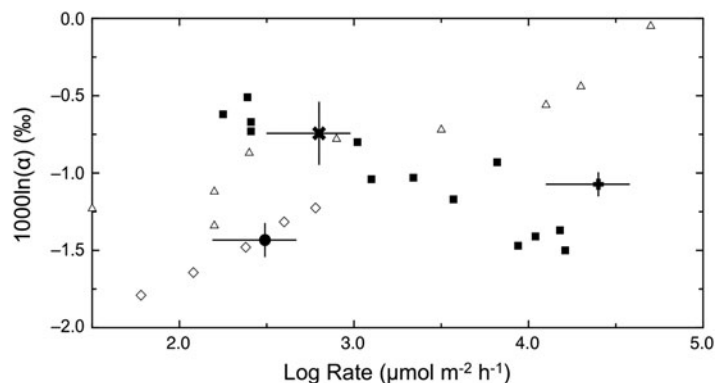


Fig. 7.7 CaCO_3 fractionation ($1000\ln(\alpha)$) as a function of precipitation rate for inorganic and marine biogenic calcite and aragonite. Tang et al. (2008) data (filled squares) suggest that experimentally precipitated inorganic calcite becomes lighter at faster growth rates, while Lemarchand et al. (2004) data (open triangles) follow the opposite trend. Inorganic aragonite (open diamonds) appears to follow a similar rate vs. fraction-

ation trend as the latter. Marine biogenic carbonate skeletons from *Ceratoporella nicholsoni* (aragonite; filled circle) and *Acanthochaetetes wellsi* (calcite; \times symbol) (Gussone et al. 2005) are consistent with inorganic precipitates, while the shells of cultured *Acropora* coral (aragonite; + symbol; Böhm et al. 2006) fall off of the expected trends. Error bars signify 2σ uncertainty in $1000\ln(\alpha)$ and $\pm 50\%$ in rate

is necessary before the relationship between shell growth rate and Ca isotope fractionation can be established. Because the growth rates of foraminiferal shells have been shown to depend upon environmental conditions (Kisakürek et al. 2008), vital effects in calcium isotopic composition may eventually provide proxy information for rate-controlling environmental conditions such as seawater pH.

7.3.2 Calcium Isotopes in Bone

Since Skulan et al. (1997) first published evidence for a systematic decrease in $\delta^{44/40}\text{Ca}$ with increasing trophic level, subsequent studies have broadly fallen into two groups, (1) fractionation between tissue and bone in living and fossilized samples for use as a paleo-proxy, and (2) development of $\delta^{44/40}\text{Ca}$ tests to assess calcium consumption and bone composition in living subjects. Within the first group, Clementz et al. (2003) built upon the studies of Skulan et al. (1997), Skulan and DePaolo (1999) and Skulan (1999), extending analysis to a 15 Ma fossil record of marine species with similar evidence of isotopic enrichment across trophic levels. Fossilized embryos of *Megaclonophycus onustus* and *Parapandorina raphospissa* from as early as the Neoproterozoic have since been analyzed by Komiya et al. (2008) and show a 0.1–0.5‰ depletion in $\delta^{44/40}\text{Ca}$ relative to host phosphorite and dolostone

values, a finding the authors attribute to preservation of the dietary $\delta^{44/40}\text{Ca}$ signal.

To date the most comprehensive study of fossilized calcium isotopes, and the first to report the $\delta^{44/40}\text{Ca}$ of human bones, is Reynard et al. (2010). Building upon the techniques outlined in Chu et al. (2006) and work done by Skulan et al. (2007), the Reynard et al. (2010) study reports a survey of $\delta^{44/40}\text{Ca}$ in both a herd of modern sheep and a variety of fossilized herbivores and humans at five locations ranging in age from ~11 to 3 ka. Results of modern sheep bone show female $\delta^{44/40}\text{Ca}$ values are higher than males by an average of $0.14 \pm 0.08\%$. The study presents a modified version of the Skulan and DePaolo (1999) model showing this difference may be attributed to a combination of calcium loss due to lactation and additional bone growth during pregnancy. Fossil data illustrate significant variation between sites as a result of variation in the source values of $\delta^{44/40}\text{Ca}$ between regions. At all sites, human bone values are lower than those of herbivores (Fig. 7.8) by an average of 0.2‰. The absence of systematic variation between sites pre-dating and post-dating herbivore domestication suggests dairy consumption cannot account for the wider variation in $\delta^{44/40}\text{Ca}$ of human bones relative to those of local fauna. The authors conclude that substantial variation in the bone $\delta^{44/40}\text{Ca}$ of individuals due to unique physiology may impede the use of calcium isotopes as an archeological tool, but support their use in dietary studies of living organisms. In the study of living

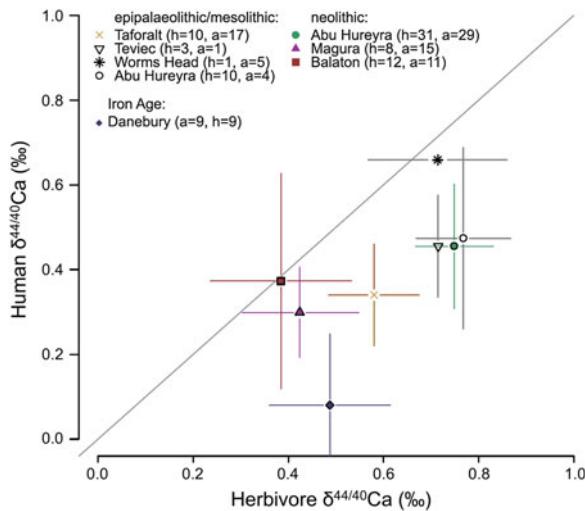


Fig. 7.8 $\delta^{44/40}\text{Ca}$ for herbivore and human bones from common archeological sites. Error bars show 1σ standard deviation and line represents 1:1 ratio of herbivore to human values. Site locations are listed in the key with corresponding numbers of human (h) and animal (a) samples. Reprinted from Reynard et al. (2010), Copyright (2010), with permission from Elsevier

organisms, calcium isotopes are currently under development as a proxy for internal calcium balance. At the risk of deviating too far from the topic of calcium isotopes in biogeochemistry, we will refer the reader to Skulan et al. (2007), Hirata et al. (2008) and Heuser and Eisenhauer (2010) for further information.

7.3.3 Calcium Isotopes and Higher-Order Plants

The first study to report systematic lowering of $\delta^{44/40}\text{Ca}$ values between calcium bound in plant material and associated exchangeable soil calcium was conducted in tropical ecosystems of Hawaii (Wiegand et al. 2005). The authors reported fractionation between basaltic soils and ohia trees (*Metrosideros polymorpha*) in forests ranging in soil age from 0.2 to 4.0 Ma (Fig. 7.9). Significant results of this study include (1) evidence for a systematic decrease in $\delta^{44/40}\text{Ca}$ from roots to leaves, and (2) evidence that younger soils exhibit exchangeable soil pools with high ^{40}Ca , whereas older, more developed soils have higher ^{44}Ca pools, indicating previous recycling of plant material in the upper soil layers. Complementary to this research, studies by Schmitt et al. (2003b) and

Schmitt and Stille (2005) reported values of riverine and precipitation $\delta^{44/40}\text{Ca}$ suggesting that at local scales forests might influence the calcium isotopic value of precipitation by incorporation of canopy calcium sources such as leaf excretions.

Temperate hardwood forests of the Oregon coast range (Perakis et al. 2006), Adirondack Mountains of New York (Page et al. 2008) and Northeastern France (Cenki-Tok et al. 2009) exhibit similar systematic lowering of the $\delta^{44/40}\text{Ca}$ ratio in trees relative to adjacent exchangeable soil calcium (Fig. 7.9). Soils measured by Perakis et al. (2006) show lower $\delta^{44/40}\text{Ca}$ values in surface soils relative to soils at 60 cm depth. The authors suggest Douglas fir (*Pseudotsuga menziesii*) growing on this soil add leaf litter with light $\delta^{44/40}\text{Ca}$ to the upper soil layers, thus recycling calcium to meet nutrient needs and creating a gradient in the soil isotope profile. Page et al. (2008) report similar results in species such as sugar maples, American beech, white ash, American basswood and yellow birch, where again extractable soil calcium $\delta^{44/40}\text{Ca}$ is lighter in forest floor samples ($-1.55 \pm 0.61\%$ BSE) than soils at depth ($-0.14 \pm 0.7\%$ BSE at 75 cm depth). The study also shows the lowest $\delta^{44/40}\text{Ca}$ value in both sugar maples and beech are found in the roots, followed by progressive enrichment of ^{44}Ca from stems to leaves. Cenki-Tok et al. (2009) used calcium isotope measurement of stream water, springs, soil solutions, precipitation and vegetation to show that both water-rock interaction and biologic cycling influence aqueous calcium isotopic signatures.

These studies result in the following observations:

1. ^{40}Ca is preferentially removed from the soil solution and incorporated into the plant roots, leaving the adjacent residual soil calcium pool enriched in ^{44}Ca relative to the plant.
2. Once taken into the plant, calcium is fractionated during translocation from root to stems to leaves such that the isotopic value of the leaf has the highest $\delta^{44/40}\text{Ca}$ value.
3. Soil profiles in well developed forests typically show a gradient in $\delta^{44/40}\text{Ca}$ with depth from lower values at the surface to greater values at depth, indicating recycling of isotopically light leaf and wood matter in the upper soil layers.

The points listed above are illustrated (Fig. 7.10) by data collected on a simplified system of aspen seedlings grown in a container of mixed basalt and

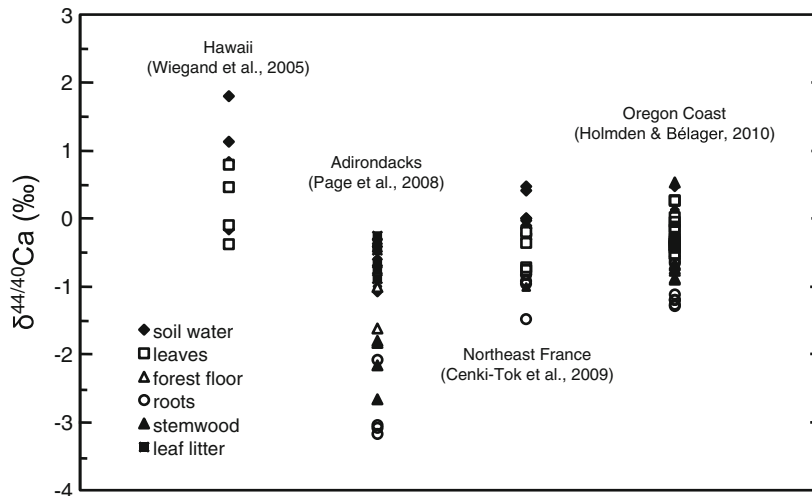


Fig. 7.9 $\delta^{44/40}\text{Ca}$ of terrestrial material from four recent studies on ecosystem calcium isotope fractionation. Wiegand et al. (2005) report total soil values, exchangeable soil Ca values using a 0.1 N ammonium acetate extraction (shown above as soil water), and digested leaf values (shown). Page et al. (2008) report values from two adjacent catchments on a calcium rich rhyolite bedrock including an exchangeable soil Ca value using 0.1 N ammonium acetate (shown above as soil water), separate values of forest floor soil and leaf litter, roots, stems and leaves

from sugar maple, beech, white ash and basswood (shown above as root, stemwood and leaves). Cenki-Tok et al. (2009) report values along a hill slope transect including soil solutions obtained from lysimeters, roots, stems and leaves from beech and spruce varieties. Holmden and Bélanger (2010) report values from two toposequences including soil water collected in lysimeters, root, stemwood and foliage from a variety of species. Values for jack pine, trembling aspen, and black spruce are shown above

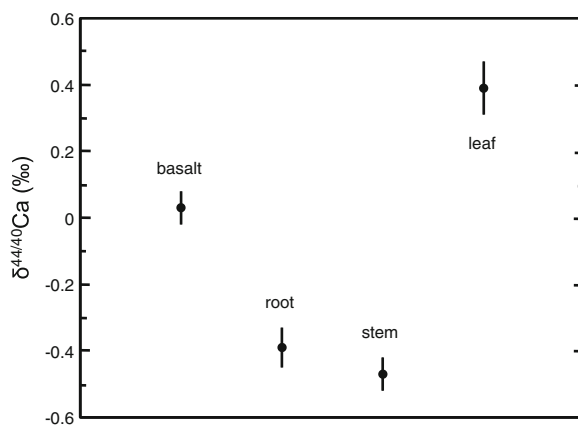


Fig. 7.10 $\delta^{44/40}\text{Ca}$ for an aspen seedling grown in a potted mixture of basalt and quartz (data reproduced from Holmden and Bélanger 2010)

quartz (Holmden and Bélanger 2010). After 2 months of growth the seedlings were harvested for analysis. Between the basalt mixture and the root the $\Delta^{44/40}\text{Ca}_{\text{basalt-root}}$ is 0.42‰, illustrating preferential incorporation of the lighter ^{40}Ca isotope (observation 1). The values of the root and stem are within error of one another, but between the root and leaf $\Delta^{44/40}\text{Ca}_{\text{root-leaf}}$ is -0.78% , indicating fractionation

during translocation within the plant (observation 2). As described by Wiegand et al. (2005), on fresh parent rock a high ^{40}Ca flux is noted from the soil to the root, but presumably if a soil profile were allowed to develop as this aspen “forest” matured, the $\delta^{44/40}\text{Ca}$ would show decreasing values from the basalt end-member to surface soil incorporating leaf and wood debris (observation 3).

Holmden and Bélanger (2010) have developed a model based on their study of a forested catchment in Saskatchewan, Canada (Fig. 7.11) towards a more quantitative analysis of the information calcium isotopes contain regarding interaction between vegetation, soil development and rock weathering. The model incorporates two available calcium pools, (1) the exchangeable calcium in the forest floor down to 10 cm, and (2) the exchangeable calcium in the B soil horizon from 10 to 25 cm depth. Fluxes in and out of these pools are soil mineral weathering, atmospheric deposition, leached plant litter, plant uptake, exchange between reservoirs and removal to the groundwater. The atmospheric calcium flux is adjusted to match independent calcium flux data based on $^{87}\text{Sr}/^{86}\text{Sr}$ measurements and 80% of annual tree calcium is derived from recycled leaf litter. The steady state solution for

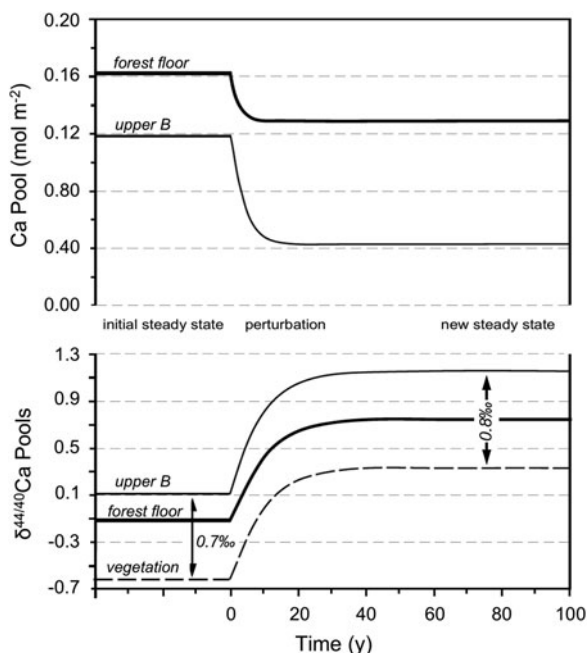


Fig. 7.11 Model calcium concentrations and $\delta^{44/40}\text{Ca}$ in exchangeable pools. Initial steady state values are shown prior to time = 0, at which point calcium uptake flux by trees is increased 50%. This increase alters the balance of calcium input fluxes from mineral weathering, atmospheric deposition and leaf litter with uptake flux by the trees, leading to a change in the isotopic composition of all exchangeable pools. Reprinted from Holmden and Bélanger (2010), Copyright (2010), with permission from Elsevier

the Boreal forest yields values in agreement with those obtained from independent measurement and soil models. Using the time-dependent form of the model, the authors show an increase in calcium uptake by plants depletes soil calcium concentrations and causes a shift to higher $\delta^{44/40}\text{Ca}$ values in the vegetation and soil pools (Fig. 7.11), illustrating a relationship between soil isotopic signature and the balance between calcium input (mineral weathering and leaf litter) and removal (root) fluxes. These results illustrate the potential for calcium isotopes as a tracer of water-rock-vegetation interactions and overall ecosystem health.

7.3.4 Case Study: Desert Environments and Vital Effects in Tree Rings

We determined $\delta^{44/40}\text{Ca}$ variation in the tree rings of exotic phreatophytes in the desert climate of Death Valley, California. These results provide an indication

of the behavior of biologically mediated Ca in a desert environment, the variability of Ca isotope fractionation during Ca uptake over several decades of growth, and the relationship between Ca, S, and C isotopes and precipitation variations.

The distribution of the two major types of desert plant species in Death Valley correlate with geology and soil hydrology. Xerophytes dominate on the alluvial fan gravels and have ephemeral water supplies in the vadose zone. The less-abundant phreatophytes grow at the toes of the alluvial fan gravels where their roots can reach the water table to provide a perennial water supply. On the valley floor, the salt-pan is devoid of plants. These desert plants constitute a potential source of information regarding hydrological, ecological and biogeochemical processes in Death Valley (Yang et al. 1996), complementary to abiotic effects observed in the Ca isotopes of arid environments (Ewing et al. 2008).

Among the larger phreatophytes in Death Valley is an exotic perennial, *Tamarix aphylla*, which serves as a dune stabilizer and windbreak (Robinson 1965; Baum 1978). Its taproots can reach down to 30 m depths and sub-superficial side roots may reach 50 m horizontally; the species can store large amounts of water in its roots and undergoes high evapotranspiration. Salt secretion is another typical feature of this tree, which leads to desalinization of deeper soil and increase of salinity in the upper layers. Since *Tamarix aphylla* is a perennial tree growing in desert environments and its roots extend to the water table, it can be a good proxy for modeling the biological calcium isotope fractionation in desert ecological and hydrologic systems.

Chemical analyses of *Tamarix aphylla* show high sulfur concentrations in the tree-rings (4–6 wt%, expressed as sulfate) and X-ray diffraction analyses show that the dominant sulfur compound is CaSO_4 (0.15–0.62 H_2O) (Yang et al. 1996). The $\delta^{34}\text{S}$ values of soluble sulfate increase from +13.5 to +18‰ VCDT from the core to the bark of the trunk, which are interpreted as reflecting deeper sulfate sources as the tree grew (Fig. 7.12). The $\delta^{13}\text{C}$ variations of the tree-ring cellulose (–27.6 to –24.0‰ VPDB) reflect changes in local precipitation, and show that *Tamarix aphylla* undergoes C_3 photosynthesis (Yang et al. 1996).

Calcium isotopes were measured in the soluble fraction of 12 tree ring samples from a 50-year-old specimen growing on an alluvial fan in Death Valley (Yang et al. 1996). The $\delta^{44/40}\text{Ca}$ for the soluble calcium sulfates through the tree-ring section, which

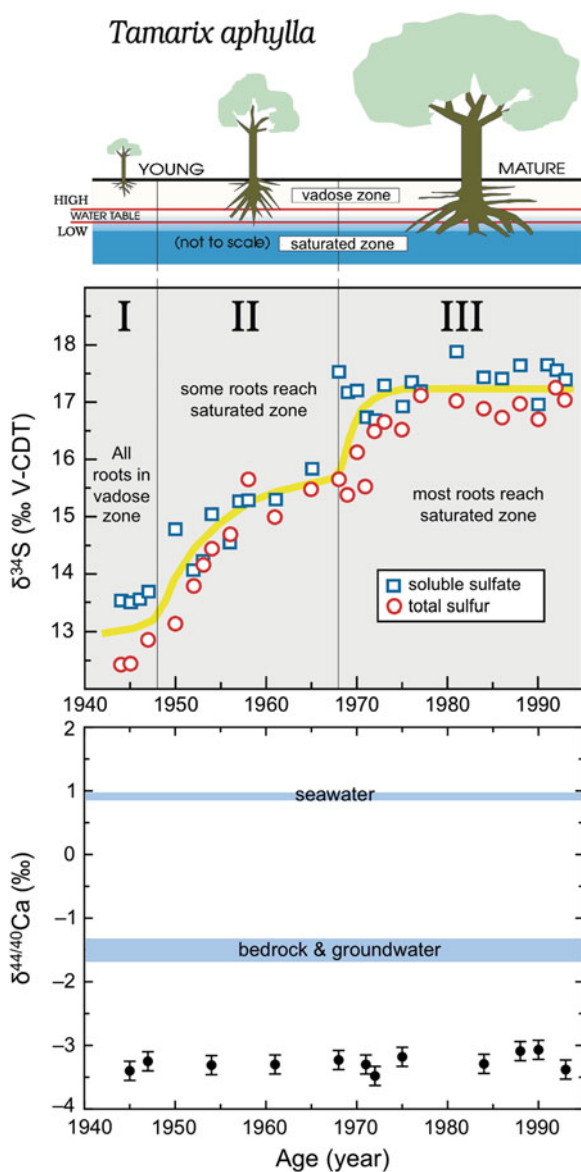


Fig. 7.12 $\delta^{34}\text{S}$ and $\delta^{44/40}\text{Ca}$ variation with time as recorded in the tree rings of *Tamarix aphylla* from Death Valley, California

cover a time period from 1945 to 1993, have an average value of $\delta^{44/40}\text{Ca} = -3.3\text{‰}$ (Fig. 7.12). Small variations are observed, from -3.46 to -3.05‰ ; the highest value (for 1990) occurs near the end of an extended drought. The low $\delta^{44/40}\text{Ca}$ values are similar to previous measurements of stems from a temperate forest (Page et al. 2008; Fig. 7.9). Our current limited data for the Death Valley hydro-ecological systems indicate that the tree has only one calcium source ($\delta^{44/40}\text{Ca} \approx -1.6\text{‰}$) from Nevares Spring water,

which is isotopically uniform and similar to both local rainfall and limestones ($\delta^{44/40}\text{Ca} \approx -1.4\text{‰}$). The calcium isotopic fractionation between trunk and source is $\Delta^{44/40}\text{Ca}_{\text{trunk-water}} = -1.7\text{‰}$. This fractionation must be due to transport processes during root uptake of calcium. The slight increase in $\delta^{44/40}\text{Ca}$ under drought conditions suggests that when the tree is stressed, there may be less calcium isotope fractionation, either (1) because the calcium is held more tightly in small pores in the soil, or (2) the available calcium pool shrinks such that soil calcium starts to shift to more positive $\delta^{44/40}\text{Ca}$ values due to depletion of light calcium by the plant. The accumulating database on calcium isotopes in plants continues to suggest that systematic calcium isotope studies may be fruitful for understanding cation transport in plants, and soil ecological conditions in general.

7.4 Conclusions and Future Directions

In this chapter, we have shown that studies of Ca isotope fractionation shed light on the biogeochemical cycling of Ca isotopes in diverse natural ecosystems spanning oceanic and terrestrial environments. Biogenic fractionation of Ca isotopes during biomineralization produces predictable offsets in some marine organisms, which facilitate the reconstruction of seawater $\delta^{44/40}\text{Ca}$ over geologic timescales. Minor variability in Ca isotope fractionation both among and between marine calcifying organisms has begun to shed light on microscopic biomineralization pathways and their sensitivity to environmental change. Ca cycling in terrestrial ecosystems is similarly informed by studies of calcium isotopic fractionation. Observed Ca isotope fractionation between soil and various components of vegetation enables the construction of a local Ca soil budget which complements other data and provides a partial explanation for the scale of Ca isotopic variability within a single watershed. Watershed-scale variability is in turn similar in magnitude to variability on the global scale. The dependence of Ca isotopic composition on trophic level suggests the utility of this isotope system as a tracer of both food source and calcium balance within individual organisms. The research reviewed in this paper provides a foundation for future investigations into the macro- and microscopic processes and biogeochemical pathways dictating the distribution of this essential nutrient.

Potential future applications of Ca isotopes as biogeochemical tracers are diverse. To better constrain variability in the global marine Ca cycle, seawater $\delta^{44/40}\text{Ca}$ reconstructions may be coupled with other isotopic and trace element indicators to explain short- and long-term excursions (e.g. Farkaš 2007; Payne et al. 2010). The relationship between CaCO_3 precipitation rate and microscopic mechanisms of Ca isotope partitioning remains unresolved, so future researchers must constrain the rates of biogenic calcification and determine the sensitivity of both Ca isotopic and trace element compositions to growth rates and environmental variables. An associated challenge will be to improve the small-scale resolution of Ca isotopic analyses and to improve upon the ion probe methods developed by Rollion-Bard et al. (2007) and Kasemann et al. (2008). The development of such a tool may elucidate the microscopic effects of mineralization pathway and perturbations in growth conditions on biomineral Ca isotope composition, which will in turn control global Ca isotopic signatures. Associated investigations of inorganic CaCO_3 precipitation to determine surface-controlled kinetic Ca isotope fractionation mechanisms may provide a basis for comparison with biogenic growth to constrain biological Ca transport pathways and biomineralization mechanisms. Studies of metal stable isotopes including calcium embody the cutting edge of research in isotope geochemistry, providing a framework for understanding the mechanisms and pathways controlling biogeochemical processes.

Acknowledgements Research on the biogeochemistry of Ca isotopes by the authors has been supported by the National Science Foundation (NSF EAR-9526997; NSF EAR-9909639; NSF EAR-0838168), a NASA Astrobiology Institute grant (BioMARS; NAI02-0024-0006), and by the Director, Office of Science, Office of Basic Energy Sciences, of the U.S. Department of Energy under Contract No. DEAC02-05CH11231 to the Lawrence Berkeley National Laboratory.

References

- Allemand D, Ferrier-Pagès C, Furla P et al (2004) Biomineralization in reef-building corals: from molecular mechanisms to environmental control. *C R Palevol* 3:453–467
- Amini M, Eisenhauer A, Böhm F et al (2008) Calcium isotope ($\delta^{44/40}\text{Ca}$) fractionation along hydrothermal pathways, Logatchev field (Mid-Atlantic Ridge, 14°45'N). *Geochim Cosmochim Acta* 72:4107–4122
- Amtmann A, Blatt M (2009) Regulation of macronutrient transport. *New Phytol* 181:35–52
- Baum BR (1978) The genus *Tamarix*. The Israel Academy of Sciences and Humanities, Jerusalem
- Bentov S, Erez J (2006) Impact of biomineralization processes on the Mg content of foraminiferal shells: a biological perspective. *Geochem Geophys Geosyst* 7:1–11
- Berner R, Lasaga A, Garrels R (1983) The carbonate-silicate geochemical cycle and its effect on atmospheric carbon dioxide over the past 100 million years. *Am J Sci* 283: 641–683
- Böhm F, Eisenhauer A, Heuser A, Kiessling W, Wallmann K (2005) Calcium isotope fractionation during dolomitization. *GeoErlangen, Schriften Deutscher Ges Geowissensch* 39.
- Böhm F, Gussone N, Eisenhauer A et al (2006) Calcium isotope fractionation in modern scleractinian corals. *Geochim Cosmochim Acta* 70:4452–4462
- Broecker W, Peng T (1982) Tracers in the sea. Eldigo Press, New York
- Bullen T, Walczyk T (2009) Environmental and biomedical applications of natural metal stable isotope variations. *Elements* 5:381–385
- Carpenter S, Lohmann K (1992) Sr/Mg ratios of modern marine calcite: empirical indicators of ocean chemistry and precipitation rate. *Geochim Cosmochim Acta* 56:1837–1849
- Centi-Tok B, Chabaux F, Lemarchand D et al (2009) The impact of water-rock interaction and vegetation on calcium isotope fractionation in soil- and stream waters of a small, forested catchment (the Strengbach case). *Geochim Cosmochim Acta* 73:2215–2228
- Chang V, Williams R, Makishima A et al (2004) Mg and Ca isotope fractionation during CaCO_3 biomineralisation. *Biochem Biophys Res Commun* 323:79–85
- Chu N, Henderson G, Belshaw N et al (2006) Establishing the potential of Ca isotopes as proxy for consumption of dairy products. *Appl Geochem* 21:1656–1667
- Clement M, Holden P, Koch P (2003) Are calcium isotopes a reliable monitor of trophic level in marine settings? *Int J Osteoarchaeol* 13:29–36
- Clode P, Marshall A (2003) Calcium associated with fibrillar organic matrix in the scleractinian coral *Galaxea fascicularis*. *Protoplasma* 220:153–161
- Cuif J, Dauphin Y (2005) The environment recording unit in coral skeletons – a synthesis of structural and chemical evidences for a biochemically driven, stepping-growth process in fibers. *Biogeoscience* 2:61–73
- De La Rocha C, DePaolo D (2000) Isotopic evidence for variations in the marine calcium cycle over the Cenozoic. *Science* 289:1176–1178
- DePaolo D (2004) Calcium isotope variations produced by biological, kinetic, radiogenic and nucleosynthetic processes. In: Johnson C, Beard B, Albarede F (eds) *Reviews in mineralogy and geochemistry: geochemistry of the non-traditional stable isotopes*, 52. Mineralogical Society of America, Washington
- DePaolo D (2011) Theory of isotopic and trace element fractionation during precipitation of carbonate minerals from aqueous solutions: surface reaction control limit. *Geochim Cosmochim Acta* 75:1039–1056
- Eisenhauer A, Nägler T, Stille P et al (2004) Proposal for international agreement on Ca notation resulting from

- discussions at workshops on stable isotope measurements held in Davos (Goldschmidt 2002) and Nice (EGS-AGU-EUG 2003). *Geostand Geoanal Res* 28:149–151
- Eisenhauer A, Kisakürek B, Böhm F (2009) Marine calcification: an alkali earth metal isotope perspective. *Elements* 5: 365–368
- Erez J (1982) Calcification rates, photosynthesis and light in planktonic foraminifera. In: Westbroek P, De Jong E (eds) *Biomineralization and biological metal accumulation*. Reidel, Dordrecht
- Erez J (2003) The source of ions for biomineralization in foraminifera and their implications for paleoceanographic proxies. In: Dove P, De Yoreo J, Weiner S (eds) *Reviews in mineralogy and geochemistry: biomineralization*, vol 54. Mineralogical Society of America, Washington
- Ewing S, Yang W, DePaolo D et al (2008) Non-biological fractionation of stable Ca isotopes in soils of the Atacama desert, Chile. *Geochim Cosmochim Acta* 72:1096–1110
- Fantle M (2010) Evaluating the Ca isotope proxy. *Am J Sci* 310:194–230
- Fantle M, DePaolo D (2005) Variations in the marine Ca cycle over the past 20 millino years. *Earth Planet Sci Lett* 237: 102–117
- Fantle M, DePaolo D (2007) Ca isotopes in carbonate sediment and pore fluid from ODP site 807A: the $\text{Ca}^{2+}(\text{aq})$ -calcite equilibrium fractionation factor and calcite recrystallization rates in Pleistocene sediments. *Geochim Cosmochim Acta* 71:2524–2546
- Fantle M, Bullen T (2009) Essentials of iron, chromium, and calcium isotope analysis of natural materials by thermal ionization mass spectrometry. *Chem Geol* 258:50–64
- Farkaš J, Böhm F, Wallmann K et al (2007) Calcium isotope record of Phanerozoic oceans: implications for chemical evolution of seawater and its causative mechanisms. *Geochim Cosmochim Acta* 71:5117–5134
- Fietzke J, Eisenhauer A, Gussone N et al (2004) Direct measurement of $^{44}\text{Ca}/^{40}\text{Ca}$ ratios by MC-ICP-MS using the cool plasma technique. *Chem Geol* 206:11–20
- Fletcher I, Maggi A, Rosman K et al (1997) Isotopic abundance measurements of K and Ca using a wide-dispersion multicollector mass spectrometer and low-fractionation ionisation techniques. *Int J Mass Spectrom Ion Process* 163:1–17
- Griffith E, Paytan A, Caldeira K et al (2008a) A dynamic marine calcium cycle during the past 28 million years. *Science* 322: 1671–1674
- Griffith E, Paytan A, Kozdon R et al (2008b) Influences on the fractionation of calcium isotopes in planktonic foraminifera. *Earth Planet Sci Lett* 268:124–136
- Gussone N, Eisenhauer A, Heuser A et al (2003) Model for kinetic effects on calcium isotope fractionation ($\delta^{44}\text{Ca}$) in inorganic aragonite and cultured planktonic foraminifera. *Geochim Cosmochim Acta* 67:1375–1382
- Gussone N, Eisenhauer A, Tiedemann R et al (2004) $\delta^{44}\text{Ca}$, $\delta^{18}\text{O}$ and Mg/Ca reveal Caribbean Sea surface temperature and salinity fluctuations during the pliocene closure of the Central-American gateway. *Earth Planet Sci Lett* 227: 201–214
- Gussone N, Böhm F, Eisenhauer A et al (2005) Calcium isotope fractionation in calcite and aragonite. *Geochim Cosmochim Acta* 69:4485–4494
- Gussone N, Langer G, Thoms S et al (2006) Cellular calcium pathways and isotope fractionation in *Emiliania huxleyi*. *Geology* 34:625–628
- Gussone N, Hönisch B, Heuser A et al (2009) A critical evaluation of calcium isotope ratios in tests of planktonic foraminifers. *Geochim Cosmochim Acta* 73:7241–7255
- Gussone M, Zonneveld K, Kuhnert H (2010) Minor element and Ca isotope composition of calcareous dinoflagellate cysts of cultured *Thoracosphaera heimii*. *Earth Planet Sci Lett* 289: 180–188
- Halicz L, Galy A, Belshaw N et al (1999) High-precision measurement of calcium isotopes in carbonates and related materials by multiple collector inductively coupled plasma mass spectrometry (MC-ICP-MS). *J Anal At Spectrom* 14: 1835–1838
- Heuser A, Eisenhauer A, Gussone N et al (2002) Measurement of calcium isotopes ($\delta^{44}\text{Ca}$) using a multicollector TIMS technique. *Int J Mass Spec* 220:385–397
- Heuser A, Eisenhauer A (2008) The calcium isotope composition ($\delta^{44/40}\text{Ca}$) of NIST SRM 915b and NIST SRM 1486. *Geostand Newsl J Geostand Geoanal* 32:311–315
- Heuser A, Eisenhauer A (2010) A pilot study on the use of natural calcium isotope ($^{44}\text{Ca}/^{40}\text{Ca}$) fractionation in urine as a proxy for the human body calcium balance. *Bone* 45:889–896
- Heuser A, Eisenhauer A, Böhm F et al (2005) Calcium isotope ($\delta^{44/40}\text{Ca}$) variations of Neogene planktonic foraminifera. *Paleoceanography* 20:1–13
- Hippler D, Schmidt A, Gussone N et al (2003) Calcium isotopic composition of various reference materials and seawater. *Geostand Newsl J Geostand Geoanal* 27:13–19
- Hippler D, Eisenhauer A, Nägler T (2006) Tropical Atlantic SST history inferred from Ca isotope thermometry over the last 140ka. *Geochim Cosmochim Acta* 70(90):100
- Hippler D, Kozdon R, Darling K et al (2007) Calcium isotope composition of high-latitude proxy carrier *Neogloboquadrina pachyderma* (sin.). *Biogeosci Discuss* 4: 3301–3330
- Hippler D, Kozdon R, Darling K et al (2009) Calcium isotopic composition of high-latitude proxy carrier *Neogloboquadrina pachyderma* (sin.). *Biogeosci Discuss* 4:3301–3330
- Hirata T, Tanoshima M, Suga A et al (2008) Isotopic analysis of calcium in blood plasma and bone from mouse samples by multiple collector-ICP-mass spectrometry. *Anal Sci* 24: 1501–1507
- Holbrèque F, Meibom A, Cuif J-P et al (2009) Strontium-86 labeling experiments show spatially heterogeneous skeletal formation in the scleractinian coral *Porites porites*. *Geophys Res Lett* 36:L04604
- Holcomb M, Cohen A, Gabitov R et al (2009) Compositional and morphological features of aragonite precipitated experimentally from seawater and biogenically by corals. *Geochim Cosmochim Acta* 73:4166–4179
- Holmden C (2005) Measurement of $\delta^{44}\text{Ca}$ using a ^{42}Ca - ^{43}Ca double-spike TIMS technique: summary of investigations. In: Saskatchewan Geological Survey, Sask Industry Resources, Misc Rep 1:A-4
- Holmden C (2009) Ca isotope study of Ordovician dolomite, limestone, and anhydrite in the Williston Basin: implications

- for subsurface dolomitization and local Ca cycling. *Chem Geol* 268:180–188
- Holmden C, Bélanger N (2010) Ca isotope cycling in a forested ecosystem. *Geochim Cosmochim Acta* 74:995–1015
- Horwitz E, McAlister D, Bond A et al (2005) Novel extraction of chromatographic resins based on Tetraalkyldiglycolamides: characterization and potential applications. *Solvent Extr Ion Exch* 23:319–344
- Huang S, Farkaš J, Jacobsen S (2010) Calcium isotopic fractionation between clinopyroxene and orthopyroxene from mantle peridotites. *Earth Planet Sci Lett* 292:337–344
- Kasemann S, Hawkesworth C, Pravec A et al (2005) Boron and calcium isotope composition in Neoproterozoic carbonate rocks from Namibia: evidence for extreme environmental change. *Earth Planet Sci Lett* 231:73–86
- Kasemann S, Schmidt D, Pearson P et al (2008) Biological and ecological insights into Ca isotopes in planktic foraminifers as a paleotemperature proxy. *Earth Planet Sci Lett* 271:292–302
- Kisakürek B, Eisenhauer A, Böhm F et al (2008) Controls on shell Mg/Ca and Sr/Ca in cultured planktonic foraminiferan, *Globigerinoides ruber* (white). *Earth Planet Sci Lett* 273:260–269
- Komiya T, Suga A, Ohno T et al (2008) Ca isotopic compositions of dolomite, phosphorite and the oldest animal embryo fossils from the Neoproterozoic in Weng'an. *S China Gondwana Res* 14:209–218
- Lasaga A, Berner R, Garrels R (1985) An improved geochemical model of atmospheric CO₂ fluctuations over the past 100 million years. In: Sundquist E, Broecker W (eds) *The carbon cycle and atmospheric CO₂: natural variations archean to present*. American Geophysical Union, Washington
- Lemarchand D, Wasserburg G, Papanastassiou D (2004) Rate-controlled calcium isotope fractionation in synthetic calcite. *Geochim Cosmochim Acta* 68:4665–4678
- Marschner H (1995) *Mineral nutrition of higher plants*, 2nd edn. Academic, London
- Marriott C, Henderson G, Belshaw N et al (2004) Temperature dependence of $\delta^7\text{Li}$, $\delta^{44}\text{Ca}$ and Li/Ca during growth of calcium carbonate. *Earth Planet Sci Lett* 222:615–624
- Millero F (1995) Thermodynamics of the carbon dioxide system in the oceans. *Geochim Cosmochim Acta* 59:661–677
- Nägler T, Eisenhauer A, Müller A et al (2000) $\delta^{44}\text{Ca}$ -temperature calibration on fossil and cultured *Globigerinoides sacculifer*: new tool for reconstruction of past sea surface temperatures. *Geochem Geophys Geosyst* 1:2000GC000091
- Page B, Bullen T, Mitchell M (2008) Influences of calcium availability and tree species on Ca isotope fractionation in soil and vegetation. *Biogeochemistry* 88:1–13
- Payne J, Turchyn A, Paytan A et al (2010) Calcium isotope constraints on the end-Permian mass extinction. *Proc Natl Acad Sci USA* 107:8543–8548
- Perakis S, Maguire D, Bullen T et al (2006) Coupled nitrogen and calcium cycles in forests of the Oregon coast range. *Ecosystems* 9:63–74
- Reynard L, Henderson G, Hedges R (2010) Calcium isotope ratios in animal and human bone. *Geochim Cosmochim Acta* 74:3735–3750
- Richter F, Davis A, DePaolo D (2003) Isotope fractionation by chemical diffusion between molten basalt and rhyolite. *Geochim Cosmochim Acta* 67:3905–3923
- Robinson T (1965) Geological Survey Professional Paper 491-A: introduction, spread and areal extent of saltcedar (*Tamarix*) in the Western States. United States Government Printing Office, Washington
- Rollion-Bard C, Vigier N, Spezzaferri S (2007) In situ measurements of calcium isotopes by ion microprobe in carbonates and application to foraminifera. *Chem Geol* 244:679–690
- Rudge J, Reynolds B, Bourdon B (2009) The double spike toolbox. *Chem Geol* 265:420–431
- Russell W, Papanastassiou D, Tombrello T (1978) Ca isotope fractionation on the Earth and other solar system materials. *Geochim Cosmochim Acta* 42:1075–1090
- Schmitt A, Stille P (2005) The source of calcium in wet atmospheric deposits: Ca-Sr isotope evidence. *Geochim Cosmochim Acta* 69:3463–3468
- Schmitt A, Bracke G, Stille P et al (2001) The calcium isotope composition of modern seawater determined by thermal ionisation mass spectrometry. *Geostand Newsl J Geostand Geoanal* 25:267–275
- Schmitt A, Stille P, Vennemann T (2003a) Variations of the $^{44}\text{Ca}/^{40}\text{Ca}$ ratio in seawater during the past 24 million years: evidence from $\delta^{44}\text{Ca}$ and $\delta^{18}\text{O}$ values of Miocene phosphates. *Geochim Cosmochim Acta* 67:2607–2614
- Schmitt A, Chabaux F, Stille P (2003b) The calcium riverine and hydrothermal isotopic fluxes and the oceanic calcium mass balance. *Earth Planet Sci Lett* 213:503–518
- Sime N, De La Rocha C, Galy A (2005) Negligible temperature dependence of calcium isotope fractionation in 12 species of planktonic foraminifera. *Earth Planet Sci Lett* 232:51–66
- Sime N, De La Rocha C, Tipper E et al (2007) Interpreting the Ca isotope record of marine biogenic carbonates. *Geochim Cosmochim Acta* 71:3979–3989
- Simon J, DePaolo D (2010) Stable calcium isotopic composition of meteorites and rocky planets. *Earth Planet Sci Lett* 289:457–466
- Skulan J (1999) Calcium isotopes and the evolution of terrestrial reproduction in vertebrates. PhD Dissertation, University of California, Berkeley
- Skulan J, DePaolo D (1999) Calcium isotope fractionation between soft and mineralized tissues as a monitor of calcium use in vertebrates. *Proc Natl Acad Sci USA* 96:13709–13713
- Skulan J, DePaolo D, Owens T (1997) Biological control of calcium isotopic abundances in the global calcium cycle. *Geochim Cosmochim Acta* 61:2505–2510
- Skulan J, Bullen T, Anbar A et al (2007) Natural calcium isotopic composition of urine as a marker of bone mineral balance. *Clin Chem* 53:1155–1158
- Soudry D, Segal I, Nathan Y et al (2004) $^{44}\text{Ca}/^{42}\text{Ca}$ and $^{143}\text{Nd}/^{144}\text{Nd}$ isotope variations in Cretaceous-Eocene Tethyan francolites and their bearings on phosphogenesis in the southern Tethys. *Geology* 32:389–392
- Steuber T, Buhl D (2006) Calcium-isotope fractionation in selected modern and ancient marine carbonates. *Geochim Cosmochim Acta* 70:5507–5521
- Tambutté E, Allemant D, Zoccola D et al (2007) Observations of the tissue-skeleton interface in the scleractinian coral *Stylophora pistillata*. *Coral Reefs* 26:517–529
- Tang J, Dietzel M, Böhm F et al (2008) Sr²⁺/Ca²⁺ and $^{44}\text{Ca}/^{40}\text{Ca}$ fractionation during inorganic calcite formation: II. Ca isotopes. *Geochim Cosmochim Acta* 72:3733–3745

- Tipper E, Galy A, Bickle M (2006) Riverine evidence for a fractionated reservoir of Ca and Mg on the continents: implications for the oceanic Ca cycle. *Earth Planet Sci Lett* 247:267–279
- von Blanckenburg F, Wiren N, Guelke M et al (2009) Fractionation of metal stable isotopes by higher plants. *Elements* 5:375–380
- White P, Broadley M (2003) Calcium in plants. *Ann Bot* 92: 487–511
- Wiegand B, Chadwick O, Vitousek P et al (2005) Ca cycling and isotopic fluxes in forested ecosystems in Hawaii. *Geophys Res Lett* 32:L11404. doi:[10.1029/2005GL022746](https://doi.org/10.1029/2005GL022746)
- Yang W, Spencer R, Krouse H (1996) Stable sulfur isotope hydrogeochemical studies using desert shrubs and tree rings, Death Valley, California, USA. *Geochim Cosmochim Acta* 60:3015–3022
- Zhu P, Macdougall J (1998) Calcium isotopes in the marine environment and the oceanic calcium cycle. *Geochim Cosmochim Acta* 62:1691–1698

Chapter 8

Natural and Anthropogenic Cd Isotope Variations

M. Rehkämper, F. Wombacher, T.J. Horner, and Z. Xue

Abstract Cadmium is a transition metal with eight naturally occurring isotopes that have atomic mass numbers of between 106 and 116. The large Cd isotope anomalies of meteorites have been subject to investigation since the 1970s, but improvements in instrumentation and techniques have more recently enabled routine studies of the smaller stable Cd isotope fractionations that characterize various natural and anthropogenic terrestrial materials. Whilst the current database is still comparatively small, pilot studies have identified two predominant mechanisms that routinely generate Cd isotope effects – partial evaporation/condensation and biological utilization. Processes that involve evaporation and condensation appear to be largely responsible for the Cd isotope fractionations of up to 1‰ (for $^{114}\text{Cd}/^{110}\text{Cd}$) that have been determined for industrial Cd emissions, for example from ore refineries. Cadmium isotope measurements hence hold significant promise for tracing anthropogenic sources of this highly toxic metal in the environment. The even larger Cd isotope fractionations that have been identified in the oceans (up to 4‰ for $^{114}\text{Cd}/^{110}\text{Cd}$) are due to biological uptake and utilization of dissolved seawater Cd. This finding confirms previous work, which identified Cd as

an essential marine micronutrient that exhibits a phosphate-like distribution in the oceans. The marine Cd isotope fractionations are of particular interest, as they can be used to study micronutrient cycling and its impact on ocean productivity. In addition, they may also inform on past changes in marine nutrient utilization and how these are linked to global climate, if suitable archives of seawater Cd isotope compositions can be identified.

8.1 Introduction

8.1.1 The Element Cd

The element cadmium (Cd) was discovered in 1817 by Friedrich Strohmeyer of Göttingen (Germany), whilst analyzing a brownish, Cd-rich Zn-oxide or carbonate. The association of Cd with Zn is common in nature and the scarce mineral deposits of greenockite (CdS) and otavite (CdCO_3) are generally found in association with more abundant sphalerite (ZnS) and smithsonite (ZnCO_3). Hence, industrial recovery of Cd occurs as a by-product of processing Zn and also Pb ores, as galena (PbS) is commonly associated with sphalerite. Zinc metal is first produced from these ores and Cd metal is then isolated from Zn by either distillation or electrolysis. Ultra-pure Cd (99.9999%) is prepared by zone refining (Chizhikov 1966; Aylett 1973; Holleman et al. 1985; Cotton and Wilkinson 1988).

Some key chemical and physical properties of Cd, which is a Group 12 element along with Zn and Hg, are summarized in Table 8.1. Cadmium is a soft, silvery-blue lustrous metal that tarnishes in air but is otherwise stable at room temperature. Cadmium metal is comparatively volatile and produces a monoatomic

M. Rehkämper (✉) and Z. Xue
Department of Earth Science and Engineering, Imperial College
London, London SW7 2AZ, UK
e-mail: markrehk@imperial.ac.uk

F. Wombacher
Institut für Geologie und Mineralogie, Universität zu Köln,
Zùlpicher Straße 49b 50674, Köln, Germany

T.J. Horner
Department of Earth Sciences, University of Oxford, Oxford
OX1 3AN, UK

Table 8.1 Chemical and physical properties of Cd

Property	
Atomic number	48
Standard atomic weight (g/mol) (Wieser 2006)	112.411
Electron configuration of Cd ⁰	[Kr] 4d ¹⁰ 5s ²
Melting point (°C)	320.9
Boiling point (°C)	767.3
Density of solid at 25°C (g/cm ³)	8.642
Density of liquid at m.p. (g/cm ³)	8.02
Oxidation states	+2, +1 (rare)
Electronegativity ^a	1.69
E ⁰ for Cd ²⁺ + 2e ⁻ = Cd (V)	-0.402
First ionization energy (kJ/mol)	867
Second ionization energy (kJ/mol)	1,625
Atomic radius (pm) (Slater 1964)	155
Ionic radius of Cd ²⁺ (pm) (Shannon 1976)	95
Mohrs hardness	2.0

All other data from Chizhikov (1966), Aylett (1973), Holleman et al. (1985) and Cotton and Wilkinson (1988)

^aPauling's scale

vapor. The metal also forms many alloys, burns to CdO on heating, and reacts readily with both oxidizing and non-oxidizing acids. Cadmium displays chemical similarities to Zn, with both elements showing a strong preference for the +2 oxidation state but Cd has a more diverse complex chemistry in solution. The electronegativity of Cd (1.69 on Pauling's scale) is similar to V, Cr and Tl, and most Cd compounds (e.g., chlorides, nitrates, sulfates, etc.) therefore have a predominant ionic character. Cadmium and many of its compounds are highly toxic and carcinogenic. This is particularly problematic because Cd accumulates in organisms and is difficult to flush out (Nriagu 1981).

The production of rechargeable Ni-Cd batteries constitutes the most important industrial use of Cd. Other important applications include its use as a corrosion resistant coating for metals, and in the production of pigments and plastic stabilizers. Overall, industrial use of Cd has been decreasing, in account of its toxicity and legislation that governs handling and application of the metal (Chizhikov 1966; Aylett 1973; Holleman et al. 1985; Cotton and Wilkinson 1988).

8.1.2 Cadmium Isotopes and Natural Isotope Variations

The identity of the eight stable or quasi-stable isotopes of Cd with mass numbers of between 106 and 116 was first confirmed in the 1930s, based on the pioneering

mass spectrometric analyses of Aston (1935), Nier (1936), and others (Table 8.2). The isotopic abundances that were published by Leland and Nier (1948) are remarkably precise and already identical, within uncertainty, to the most recent reference values published by IUPAC (Böhlke et al. 2005) (Table 8.1). The latter compilation lists the results of Rosman et al. (1980) as the best measurement from a single source.

On Earth, the only significant natural source of Cd isotope variations are stable isotope fractionations. The isotopes ¹¹³Cd and ¹¹⁶Cd are long-lived radioactive isotopes that transform to ¹¹³In and ¹¹⁶Sn by β⁻-decay. Both nuclides have extremely long half-lives (of ~9 × 10¹⁵ a and ~2.6 × 10¹⁹ a, respectively), however, such that they are considered to be quasi-stable isotopes with essentially constant abundances (Pfennig et al. 1998).

In extraterrestrial materials, Cd isotope compositions can be altered as a result of neutron capture reactions, which are induced by secondary neutrons generated by cosmic rays. The isotope ¹¹³Cd has a large neutron capture cross section of 20,600 barns for (epithermal) neutrons with energies of less than about 0.5 eV and produces ¹¹⁴Cd by a (n, γ) reaction (Pfennig et al. 1998). Consequently, the ¹¹³Cd/¹¹⁴Cd ratios of lunar soils and surface rocks were observed to differ from the terrestrial value by up to 5% (Sands et al. 2001; Schediwiy et al. 2006; Wombacher et al. 2008). Such cosmogenic Cd isotope effects are not significant for terrestrial samples (Wombacher et al. 2008), as the Earth's surface completely shields the interior from cosmic rays, whilst the atmosphere severely attenuates the cosmic ray flux to the surface.

As is common in geochemistry, variations in Cd stable isotope compositions are reported using a relative notation and both ε- and δ-values are currently in use. For the ¹¹⁴Cd/¹¹⁰Cd isotope ratio, these are calculated as:

$$\varepsilon^{114/110}\text{Cd} = \left[\frac{\left(\frac{^{114}\text{Cd}}{^{110}\text{Cd}} \right)_{\text{sample}}}{\left(\frac{^{114}\text{Cd}}{^{110}\text{Cd}} \right)_{\text{std}}} - 1 \right] \times 10,000 \quad (8.1)$$

$$\delta^{114/110}\text{Cd} = \left[\frac{\left(\frac{^{114}\text{Cd}}{^{110}\text{Cd}} \right)_{\text{sample}}}{\left(\frac{^{114}\text{Cd}}{^{110}\text{Cd}} \right)_{\text{std}}} - 1 \right] \times 1,000. \quad (8.2)$$

Both notations provide the relative deviation of the isotope composition of a sample from a standard

Table 8.2 Isotope ratios and abundances of Cd

Mass number	106	107	108	109	110	111	112	113	114	115	116	117	118
Cadmium isotope ratios $^x\text{Cd}/^{114}\text{Cd}$													
Rosman et al. (1980) ^a	0.044247		0.031374		0.438564	0.44845	0.84324	0.42605			0.259629		
Wombacher et al. (2004) ^a	0.044206		0.031364		0.438564	0.448848	0.843259	0.42645			0.259661		
Prizkow et al. (2007) ^b	0.043314		0.030907		0.433845	0.445155	0.838821	0.425395			0.261562		
Isotope abundances (in %) of Cd and isobaric elements (Böhlke et al. 2005)													
Cd (Böhlke et al. 2005)	1.25		0.89		12.49	12.80	24.13	12.22	28.73		7.49		
Cd (Prizkow et al. 2007)	1.25		0.89		12.47	12.80	24.11	12.23	28.74		7.52		
Pd	27.3		26.5		11.7								
Ag		51.8		48.2									
In								4.3	0.65	95.7	14.5	7.68	24.2
Sn										0.36			
Isotope abundances (in %) of major molecular interferences (Böhlke et al. 2005)													
M ⁴⁰ Ar ⁺	⁶⁶ Zn 27.9	⁶⁷ Zn 4.1	⁶⁸ Zn 18.8	⁶⁹ Ga 60.1	⁷⁰ Ge 20.5	⁷¹ Ga 39.9	⁷² Ge 27.4	⁷³ Ge 7.8	⁷⁴ Ge 36.5	⁷⁵ As 100	⁷⁶ Ge 7.8	⁷⁷ Se 7.6	⁷⁸ Se 23.6
					⁷⁰ Zn 0.6						⁷⁶ Se 9.0	⁷⁸ Kr 0.35	
M ¹⁶ O ⁺	⁹⁰ Zr 51.5	⁹¹ Zr 11.2	⁹² Zr 17.2	⁹³ Nb 100	⁹⁴ Zr 17.4	⁹⁵ Mo 15.9	⁹⁶ Zr 2.80	⁹⁷ Mo 9.55	⁹⁸ Mo 24.1	⁹⁹ Ru 12.7	¹⁰⁰ Mo 9.63	¹⁰² Ru	¹⁰¹ Ru 31.6
		⁹² Mo 14.8	⁹⁴ Mo 9.25		⁹⁴ Mo 16.7	⁹⁸ Ru 1.88	⁹⁶ Mo 16.7	⁹⁸ Ru 5.52		¹⁰⁰ Ru 12.6	¹⁰² Pd 1.02		

Also shown are the isotopic abundances of other elements with isotopes that can produce major isobaric and molecular interferences on Cd

^aThe isotopic analyses utilized internal normalization relative to $^{110}\text{Cd}/^{114}\text{Cd} = 0.438564$ for mass bias correction

^bThe results are based on an absolute measurement of atomic weight; the mass bias correction is based on analyses of gravimetric mixtures of seven enriched Cd isotope materials

reference material (std) but they differ in sensitivity by a factor of 10.

A number of recent studies have investigated Cd stable isotope variations in various terrestrial materials and environments. Large Cd isotope effects were detected (1) in seawater, which features $\epsilon^{114/110}\text{Cd}$ values as high as +40, presumably as a result of preferential biological uptake of isotopically light Cd by plankton (see Sect. 8.4.4); (2) dust and other products of Cd refining as well as polluted soils from the vicinity of ore processing plants, which feature $\epsilon^{114/110}\text{Cd}$ values as low as about -8 , probably due to Cd isotope fractionation during partial evaporation/condensation (Sect. 8.4.1). Very large Cd isotope effects from thermal processing were also detected in primitive meteorites (chondrites) with $\epsilon^{114/110}\text{Cd}$ values of between about -80 and $+160$ (Sect. 8.4.2), and even larger fractionations were observed in industrial Cd metal samples, which remained after Cd loss by evaporation (Sect. 8.4.1).

Overall, these results demonstrate that significant Cd isotope variations, of more than 0.5% for $^{114}\text{Cd}/^{110}\text{Cd}$, exist in various terrestrial environments. These appear to be generated primarily by either biological uptake of Cd or partial evaporation and/or condensation of volatile Cd. Hence, this indicates that Cd isotopes can be applied as a tracer of materials that have been affected by such processes. Such applications are further presented and discussed in Sect. 8.4. However, in many environments, such as the silicate Earth (Sect. 8.4.3), Cd isotope variations are commonly very small at less than 0.5 ϵ for $^{114}\text{Cd}/^{110}\text{Cd}$. The reliable resolution of Cd isotope variations at this level is particularly challenging, as Cd is a trace metal with concentrations of less than 1 $\mu\text{g/g}$ in most terrestrial environments. Hence, highly sensitive and precise techniques of Cd isotope analysis are necessary and these invariably require that Cd is efficiently separated from the sample matrix prior to analysis. Such procedures are discussed in Sect. 8.2.

8.2 Cadmium Isotope Analyses

8.2.1 Chemical Separation of Cd

The acquisition of accurate and precise Cd stable isotope data for geological samples necessitates that

Cd is separated from the sample matrix prior to mass spectrometric analysis. Ideally, the separation procedure should provide both highly purified Cd separates and essentially perfect (100%) yields, to ensure the best possible conditions for the isotopic measurements. Near quantitative yields are particularly important, to prevent analytical artifacts that may result from the isotope fractionation that is known to occur during incomplete elution of Cd from columns that utilize anion exchange or Eichrom resins (Wombacher et al. 2003; Cloquet et al. 2005b; Schmitt et al. 2009b). Application of the double spike methodology largely bypasses the latter problem but high yields are nevertheless desirable for optimum sensitivity, because Cd is a trace element in most relevant materials.

All recently published Cd isotope studies apply anion exchange chromatography to affect the separation of Cd from a wide range of natural materials, including meteorites, silicate rocks, sediments, minerals, seawater, and industrial samples. Such methods are particularly advantageous, as Cd is strongly retained on various types of strongly basic anion-exchange resin from (generally dilute) solutions of HCl (Kraus and Nelson 1955), HBr (Andersen and Knutsen 1962; StreLOW 1978), and HBr-HNO₃ mixtures (StreLOW 1978). For examples, Cd displays $D_{S/L}$ values (solid/liquid distribution coefficients) of >100 for anion exchange resin at HCl concentrations from 0.05 to 8 M (Korkisch 1989). Such media, applied at appropriate concentrations, are also suitable for the effective elution of relevant matrix elements, including the major elements of common geological samples (e.g., Na, Mg, Ca, Fe, Al) and problematic trace elements, which can produce isobaric or molecular interferences on Cd during the isotopic analyses (Table 8.2). Following elution of the matrix, Cd can be readily rinsed from the resin columns using mineral acid media that generate low $D_{S/L}$ values, such as (dilute) HNO₃ (Faris and Buchanan 1964) or suitable HBr-HNO₃ mixtures (StreLOW 1978).

Most studies have found that a single pass of the sample through a column with about 1–2 mL of anion-exchange resin is generally adequate to obtain Cd separates, which are sufficiently pure for mass spectrometry (Wombacher et al. 2003; Cloquet et al. 2005b; Shiel et al. 2009). A second pass, using smaller columns with less resin (~ 100 μL), has been used for further purification of Cd separated from seawater samples, which exhibit particularly low Cd contents

and unfavorable Cd/matrix ratios (Ripperger and Rehkämper 2007). Prior to isotopic analyses by MC-ICPMS (multiple collector inductively coupled plasma mass spectrometry) a number of workers have further purified the Cd obtained from the anion exchange separation using columns filled with ~100 μL Eichrom TRU resin (Wombacher et al. 2003; Ripperger and Rehkämper 2007). This procedure serves to effectively isolate Cd from Sn as well as any possible traces of Zr and Mo, which can produce isobaric/molecular interferences on isotopes of Cd (Table 8.2). The Cd purification protocol of Schmitt et al. (2009b) also employs an additional separation step. This is carried out prior to the anion-exchange procedure and removes Fe from the 6 M HCl sample solutions by liquid-liquid extraction into an organic phase.

8.2.2 Cd Isotope Ratio Measurements

8.2.2.1 Thermal-Ionization Mass Spectrometry (TIMS)

The pioneering Cd isotope studies of Rosman and de Laeter (1975) first investigated terrestrial minerals but subsequent work, which revealed the first natural variations in Cd stable isotope compositions focused exclusively on extraterrestrial samples (Rosman and

de Laeter 1976, 1978). These analyses were accomplished by TIMS, using a silica gel activator to enhance ionization and an electron multiplier for detection. To correct for the effects of instrumental mass fractionation, the sample data were initially compared to results obtained for a pure Cd standard, whilst all measurements applied the same, rigorous data acquisition protocol (Rosman and de Laeter 1975, 1978). The precision of these data was limited (Table 8.3), however, and subsequent analyses therefore applied a ^{106}Cd - ^{111}Cd double spike to correct for instrumental mass fractionation. Application of the double spike improved reproducibility to about ± 4 ϵ/amu (2sd; Table 8.3), for analyses in which Cd ion beams with a total intensity of about 0.1 pA were monitored for several hours using a single electron multiplier (Rosman and de Laeter 1978). More recent Cd isotope measurements from the same laboratory also utilized a ^{106}Cd - ^{111}Cd double spike but the application of multiple Faraday cups for data acquisition provided improved reproducibilities of about ± 2 ϵ/amu (Schediwy et al. 2006) (Table 8.3).

The so far most precise method for Cd stable isotope measurements was published by Schmitt et al. (2009b). These workers applied a ^{106}Cd - ^{108}Cd double spike and a Thermo Scientific Triton TIMS instrument equipped with Faraday cups, to achieve external reproducibilities of about ± 0.07 ϵ/amu (2sd) for multiple standard measurements (Table 8.3). Analyses of ~100 ng Cd loads typically yielded total Cd ion

Table 8.3 Reproducibility of Cd isotope measurements by various laboratories

Analysts	Method	Instrument	$\pm 2\text{sd } \epsilon\text{Cd}/\text{amu}$
Rosman and de Laeter (1975, 1978)	Constant run conditions	TIMS	8–16
Rosman and de Laeter (1978)	^{106}Cd - ^{111}Cd DS	TIMS	≤ 4
Wombacher et al. (2004)	SSB	MC-ICPMS	1.0–1.5
Wombacher et al. (2003)	Ag-, Sb-normalization	MC-ICPMS	0.2–0.8
Cloquet et al. (2005b)	SSB	MC-ICPMS	0.1–0.5
Schediwy et al. (2006)	^{106}Cd - ^{111}Cd DS	TIMS	2 ^a
Lacan et al. (2006)	Ag normalization	MC-ICPMS	0.1–0.5
Ripperger and Rehkämper (2007)	Ag normalization	MC-ICPMS	0.4
Ripperger and Rehkämper (2007)	^{110}Cd - ^{111}Cd DS	MC-ICPMS	0.2–0.3
Gao et al. (2008)	SSB	MC-ICPMS	0.2–0.3
Schmitt et al. (2009b)	^{106}Cd - ^{108}Cd DS	TIMS	0.07
Shiel et al. (2009)	Ag normalization	MC-ICPMS	0.2–0.8
Horner et al. (2010)	^{111}Cd - ^{113}Cd DS	MC-ICPMS	0.2–0.3
Xue and Rehkämper, unpublished results obtained using techniques adapted from Horner et al. (2010)	^{111}Cd - ^{113}Cd DS	MC-ICPMS	0.1–0.2

The reproducibilities are based on the 2sd values obtained for multiple analyses of pure Cd standard solutions and are quoted in units of $\epsilon\text{Cd}/\text{amu}$ (modified from Schmitt et al. 2009b). Methods: DS double spike; SSB standard-sample bracketing

^aUncertainty quoted for multiple analyses of the USGS rock standard BCR-1

beam intensities of about 240 pA for ~30 min, equivalent to an ionization efficiency of approximately 0.3% (Schmitt et al. 2009b).

8.2.2.2 Multiple Collector Inductively Coupled Plasma Mass Spectrometry (MC-ICPMS)

The study of Wombacher et al. (2003) was the first to apply MC-ICPMS to Cd isotope measurements. The success of this and subsequent MC-ICPMS investigations spurred further interest in Cd isotope research, and established MC-ICPMS as the dominant instrumental technique for such analyses (Tables 8.3 and 8.4).

In principle, Cd isotope measurements are more straightforward by MC-ICPMS than TIMS, because the high first ionization potential of Cd (Table 8.1) is readily overcome by plasma ionization (Rehkämper et al. 2001). There are other factors, however, which render the acquisition of precise and, in particular, accurate Cd stable isotope data by MC-ICPMS challenging. First, the high ionization efficiency of the plasma source implies that the numerous possible spectral interferences on the isotopes of Cd from both isobars and molecular species (see Table 8.2) must be either avoided or reduced to tolerable levels by chemical separation. Second, the instrumental mass bias correction for natural samples, which invariably contain some residual matrix (including remains of ion exchange resin), is readily affected by non-spectral interferences (matrix effects), if carried out by the commonly applied methods of either (1) standard sample bracketing (SSB), whereby the $\epsilon^{114/110}\text{Cd}$ values are calculated directly from the “raw” (unprocessed) isotope data of samples, by referencing these to results obtained for “bracketing” analyses of a Cd standard; or (2) “external” normalization, whereby a suitable fractionation law or empirical correlation is applied for mass bias correction, based on the fractionation observed for a constant isotope ratio of an admixed (dopant) element (Rehkämper et al. 2001). In particular, it has been shown for Cd that even very low matrix levels in sample solutions can generate unsystematic mass bias behavior that is not corrected by either of the above techniques, and which can thus lead to poor precision and/or inaccurate results (Wombacher et al. 2003; Shiel et al. 2009).

Problems from both spectral and non-spectral interferences can be avoided through appropriate analytical

Table 8.4 Summary of Cd isotopic data obtained for various intercalibration standards by different laboratories and techniques

Analysts	Method and instrument	BAM-I012 Cd	Münster Cd	Alfa Cd Zürich	MPI JMC Cd	Nancy Spex Cd	NIST 3108 Cd
Wombacher and Rehkämper (2004)	Ag-n, MC-ICPMS	-10.8 ± 1.5	46.5 ± 0.5				
Cloquet et al. (2005b)	SSB, MC-ICPMS		44.3 ± 0.4			-0.5 ± 1.2	
Lacan et al. (2006)	Ag-n, MC-ICPMS		44.3 ± 2.0				
Ripperger and Rehkämper (2007)	DS, MC-ICPMS	-12.4 ± 1.1	46.4 ± 1.2	0.0 ± 0.5			
Ripperger and Rehkämper (2007)	Ag-n, MC-ICPMS	-11.4 ± 1.5	46.0 ± 1.5				
Schmitt et al. (2009a, b)	DS, TIMS	-12.3 ± 0.3	44.8 ± 0.2		2.2 ± 0.2	0.0 ± 0.4	
Gao et al. (2008)	SSB, MC-ICPMS	-12.0 ± 1.2	45.9 ± 1.2			0.1 ± 1.2	
Shiel et al. (2009)	Ag-n, MC-ICPMS	-13.7 ± 2.5	45.0 ± 0.3				
Horner et al. (2010)	DS, MC-ICPMS			0.5 ± 0.4			
Wombacher, unpublished results	Ag-n, MC-ICPMS				2.6 ± 0.4		0.8 ± 0.5
Xue and Rehkämper, unpublished results	DS, MC-ICPMS	-12.2 ± 0.4					1.0 ± 0.4

All results are reported as $\epsilon^{114/110}\text{Cd}$ values ($\pm 2\text{sd}$) relative to the JMC Cd Münster zero-epsilon standard
Methods: SSB standard-sample bracketing; Ag-n Ag normalization; DS double spike

protocols including rigorous purification of the samples prior to mass spectrometry. This is not straightforward, however, as the separation of Cd must provide essentially quantitative yields. Any significant loss of Cd during chromatography will result in Cd isotope fractionations (Wombacher et al. 2003; Cloquet et al. 2005b; Schmitt et al. 2009b) and thus generate analytical artifacts. A number of Cd isotope studies have shown that such problems can be overcome successfully either by careful Cd purification and/or the use of double spiking.

The majority of the published MC-ICPMS Cd isotope data were obtained using external normalization to admixed Ag (and in one case Sb) for the correction of mass fractionation (Table 8.3). These investigations quote typical external reproducibilities ($\pm 2\text{sd}$) for multiple standard analyses of about 0.2–0.8 ϵ/amu (Table 8.3). Using a Nu Plasma MC-ICPMS instrument, Wombacher et al. (2003) reported instrumental sensitivities of about 125×10^{-11} A/ppm (125 V/ppm), equivalent to a transmission efficiency of about 0.09%.

It was also shown that the application of standard sample bracketing for correction of instrumental mass bias yields reproducibilities of about 0.2–1.0 ϵ/amu for pure Cd standards, similar to the results obtained with external normalization (Table 8.3). Comparative studies have demonstrated, however, that the standard sample bracketing approach is clearly more susceptible to matrix effects that produce inaccurate isotopic data for natural samples than various techniques of external normalization (Wombacher et al. 2003; Lacan et al. 2006; Shiel et al. 2009).

In order to avoid problems associated with matrix effects and to ensure accurate data acquisition even for challenging seawater samples, Ripperger and Rehkämper (2007) employed the double spike approach for mass bias correction in conjunction with analyses by MC-ICPMS. Using a ^{110}Cd - ^{111}Cd double spike, they were able to achieve reproducibilities ($\pm 2\text{sd}$) of about 0.2–0.3 ϵ/amu for multiple standard and sample analyses, which consumed about 40–60 ng of natural Cd (Table 8.3). More recent measurements (Xue and Rehkämper, unpublished results) applied a more favorable ^{111}Cd - ^{113}Cd spike and routinely provided an external precision ($\pm 2\text{sd}$) of about 0.1–0.2 ϵ/amu , which is only slightly worse than the best reported TIMS results (Table 8.3). The latter analyses, conducted with a Nu Plasma MC-ICPMS instrument, consumed about 30 ng of

natural Cd at typical sensitivities of about 250–350 V/ppm, equivalent to a transmission efficiency of up to 0.25%.

8.2.2.3 Double Spike Methodology

The double spike methodology involves spiking of samples with a well-characterized solution that is enriched in two isotopes of the target element, relative to the natural isotope abundances. The isotopic fractionation of the natural sample is then determined from mass spectrometric data, which are collected for three isotope ratios (sharing a common denominator) of the sample-spike mixture (Dodson 1963; Wetherill 1964; Hofmann 1971; Galer 1999; Rudge et al. 2009). Double spiking of Cd (and other elements) offers three principle advantages. (1) The procedure of mass bias correction is, in essence, similar to the method of “internal” normalization commonly employed in radiogenic isotope geochemistry. Importantly, internal normalization is known to be more robust towards the generation of analytical artifacts from matrix effects than either standard sample bracketing or external normalization (Rehkämper et al. 2001); (2) If the double spike is added to and equilibrated with a sample prior to the chemical separation of Cd, the approach can accurately correct for the effects of both instrumental and laboratory-induced mass fractionations; (3) As a byproduct of double spiking, precise Cd concentrations can be determined. The main disadvantage of double spiking is that it requires (at least) four non-radiogenic isotopes, which must all be free from spectral interferences (Dodson 1963; Wetherill 1964; Hofmann 1971; Galer 1999; Rudge et al. 2009).

Cadmium has eight stable isotopes (Table 8.2) and a multitude of double spike compositions are thus available, in principle, for the acquisition of stable isotope data. A quantitative evaluation of the most suitable spike composition(s) for precise Cd isotope analyses of natural samples is not straightforward but has been carried out using numerical methods. To this end, both Galer (1999) and Rudge et al. (2009) applied somewhat distinct error propagation models to identify double spike compositions and associated spike/sample ratios, which yield the most favorable uncertainties for the determination of natural isotope fractionations, following the correction of instrumental

mass bias. Both analyses focus on the propagation of uncertainties that are scaled to the relative ion beam intensities. A systematic investigation of how the choice of double spike may effect the accuracy of the stable isotope data that are acquired has yet to be carried out, however. This will be difficult in any case, given the numerous sources of systematic error that need to be considered.

However, there are number of well know issues that should be factored into the decision to adopt a particular Cd double spike composition: (1) problematic isobaric and molecular interferences (Table 8.2); (2) possible isotopic variations from sources other than mass dependent isotope fractionation, such as cosmogenic isotope anomalies for samples (Sands et al. 2001; Wombacher et al. 2008) or magnetic odd-even isotope effects during TIMS analyses that apply a silica gel activator (Manhès and Göpel 2003, 2007; Schmitt et al. 2009b); note that such non-mass dependent instrumental fractionations have hitherto not been reported for MC-ICPMS measurements; (3) limitations imposed by the collector configuration and the maximum mass dispersion that can be accommodated by the collectors.

Based on a comprehensive consideration of these factors, Schmitt et al. (2009b) chose a ^{106}Cd - ^{108}Cd double spike (measured in conjunction with ^{110}Cd , ^{112}Cd) for TIMS analyses, instead of the ^{106}Cd - ^{111}Cd spike that was applied in previous TIMS studies (Rosman and de Laeter 1978; Schediwy et al. 2006) (Table 8.3). A particular advantage of the former composition is that it avoids uncertainties, which are related to the apparent mass independent fractionation behavior of odd-mass isotopes of Cd during TIMS analyses (Manhès and Göpel 2003, 2007; Schmitt et al. 2009b). The error propagation model of Rudge et al. (2009) does not consider such effects and predicts that an optimized ^{106}Cd - ^{111}Cd double spike should provide the most precise Cd stable isotope results, with uncertainties that are more than a factor of 2 better than to those obtainable with a ^{106}Cd - ^{108}Cd spike.

The ^{110}Cd - ^{111}Cd double spike that was used by Ripperger and Rehkämper (2007) with MC-ICPMS, fares even worse in the evaluation of Rudge et al. (2009), but its application to seawater analyses was most severely compromised by isobaric interferences from ^{110}Pd (Table 8.2), which required correction in a separate (and hence undesirable) measurement sequence. More recently, a ^{111}Cd - ^{113}Cd double spike (in conjunction with ^{112}Cd , ^{114}Cd) was therefore used

for MC-ICPMS analyses (Baker et al. 2010; Horner et al. 2010), as this (1) avoids problematic isobaric interferences from Sn and Pd on ^{116}Cd and ^{110}Cd , respectively, and (2) should provide approximately the same measurement precision (Rudge et al. 2009) as the ^{106}Cd - ^{108}Cd double spike of Schmitt et al. (2009b).

8.3 Cadmium Isotope Data

8.3.1 Cadmium Isotope Reference Materials

A straightforward comparison of the ϵ or δ values obtained for samples by different laboratories is only possible if all data are presented relative to the same “zero-epsilon” or “zero-delta” reference material. Unfortunately, this has not been the case for most published Cd analyses. In fact, many laboratories have utilized different commercially available 1,000 $\mu\text{g/g}$ Cd solutions (generally sold for the calibration of ICP-MS/OES concentration analyses) as in-house zero-epsilon reference standards. Typically, these are designated based on the name of the manufacturer and/or laboratory location, e.g., JMC Cd Münster, Alfa Cd Zürich, MPI JMC Cd (Wombacher et al. 2003; Ripperger and Rehkämper 2007; Schmitt et al. 2009b).

It is obvious that the renormalization of sample data requires a precise cross-calibration between different zero-epsilon standards. Until recently such data were not available, in part because it was assumed that various shelf standards would not exhibit significant Cd isotope variability (Wombacher and Rehkämper 2004). However, a number of analyses have now revealed differences of more than 2 $\epsilon^{114/110}\text{Cd}$ for different batches of Cd shelf standards obtained from Alfa Aesar/JMC (e.g., Table 8.4). These differences are probably due to stable isotope fractionation of Cd during the industrial separation and purification of the element. This interpretation is supported by the observation that highly purified samples of Cd metal, which have presumably been processed by zone refining in addition to electrolysis and/or distillation, appear to commonly feature distinctly light Cd isotope compositions. Examples of this are the BAM-I012 reference material (Table 8.4) and Alfa Aesar/JMC Puratronic grade Cd metal (99.9999% purity). Analyses of two

different batches of the latter yielded $\varepsilon^{114/110}\text{Cd}$ values of -14.7 (MPI JMC metal; Schmitt et al. 2009b) and -17.0 (JMC Cd metal Zürich; Ripperger and Rehkämper 2007) relative to the JMC Cd Münster standard.

Due to the significant isotopic variability of commercially available Cd metal and Cd solutions, it would be advantageous for all laboratories to adopt a single zero-epsilon Cd isotope reference material. A suitable material for this purpose should fulfill a number of criteria including: (1) storage and distribution in solution form to ensure isotopic homogeneity; (2) long-term availability; (3) high purity, such that elemental impurities do not generate significant interferences during isotopic analyses; (4) an isotope composition, which closely resembles the bulk silicate Earth (BSE).

The JMC Cd Münster solution, introduced by Wombacher et al. (2003), was used in a number of studies and laboratories (Table 8.4) as zero-epsilon standard with an isotope composition that is essentially identical to the BSE. However, the availability of this material is limited, such that it is not suitable as a long-term reference material. The BAM-I012 Cd isotope standard was produced by the German Federal Institute for Materials Research and Testing (BAM) to address the lack of a suitable zero-epsilon reference material. Subsequent analyses, however, revealed an isotopic composition that is far removed from the BSE value (Tables 8.4 and 8.5) and BAM-I012 Cd was therefore not adopted as zero-epsilon standard by the geochemical community. The continued need for a common zero-epsilon reference led to a concerted search effort by various Cd isotope laboratories, and the NIST SRM 3108 Cd solution was identified as a potentially suitable material (Abouchami et al. 2010b). An inter-laboratory calibration exercise to characterize the isotopic offset between NIST 3108 Cd and other previously applied in-house zero-epsilon reference materials is currently ongoing (Abouchami et al. 2010b).

Recent Cd isotope studies relied on data for additional secondary “fractionated” reference materials, to enable the comparison of results obtained by different laboratories. Such analyses will continue to be of importance for quality control, even if a common zero-epsilon reference is adopted (Abouchami et al. 2010b). The use of the same secondary reference materials by all laboratories is furthermore desirable,

to facilitate the inter-laboratory comparison of results obtained with different instruments and techniques. Two particularly suitable materials with fractionated Cd isotope compositions are already available for this purpose – the isotopically heavy Münster Cd solution (aliquots available from F. Wombacher and J. Carignan at CRPG-CNRS in Nancy, France) and BAM-I012 Cd, which is characterized by a light isotope composition (Table 8.4). Both standards have already been analyzed by a number of laboratories and the measurements have yielded remarkably consistent results (Table 8.4), which can serve as benchmarks for future analyses.

8.3.2 Notation and Conversion of Cd Isotope Data

The majority of recent studies reported Cd stable isotope compositions using either an ε - or δ -notation for a specific isotope ratio (8.1) and (8.2). The δ -notation is most commonly applied for many classical and non-traditional stable isotope systems elements but the use of ε values provides a higher sensitivity, which is advantageous for terrestrial Cd isotope studies, as the isotopic variations are often smaller than 0.1‰. Fortunately, the conversion between ε - and δ -values is very straightforward.

In addition, a number of Cd isotope studies have reported fractionations using a ε/amu , δ/amu or even $\%/\text{amu}$ notation (Rosman and de Laeter 1976; Wombacher et al. 2003; Lacan et al. 2006; Schediwy et al. 2006). With this technique, the fractionation (δ or ε value) calculated for any isotope ratio is normalized to a mass difference of one amu. As an example, the calculation of ε/amu values from $^{114}\text{Cd}/^{110}\text{Cd}$ utilizes:

$$\varepsilon_{\text{Cd}/\text{amu}} = \left[\frac{(^{114}\text{Cd}/^{110}\text{Cd})_{\text{sample}}}{(^{114}\text{Cd}/^{110}\text{Cd})_{\text{std}}} - 1 \right] \times 10,000 / (m_{114} - m_{110})$$

where m_{114} and m_{110} denote the (exact) atomic masses of the Cd isotopes. The advantage of this approach is that $\varepsilon_{\text{Cd}/\text{amu}}$ (or $\delta_{\text{Cd}/\text{amu}}$) can be determined from multiple isotope ratios. Data from multiple isotope ratios or different laboratories (which measure

Table 8.5 Selected Cd concentrations and isotope compositions (reported as $\epsilon^{114/110}\text{Cd}$ relative to NIST 3108 Cd) for important meteorite types, Earth reservoirs and terrestrial samples

Sample type or reservoir	Typical concentrations or calculated mean values ^a	References	$\epsilon^{114/110}\text{Cd}$ range or mean ^a	References
Chondritic meteorites				
Carbonaceous chondrites	ng/g 650–710 (CI); ~370 (CM, CV)	Wasson and Kallemeyn (1988), Palme and O'Neill (2005), McDonough and Sun (1995), Lodders (2003)	–4.4 to 5.1 ^b 3.0 ± 1.4 ^b	Baker et al. (2010)
Ordinary chondrites (H,L, LL groups)	ng/g ~10–40; total range of [Cd]: 0.1–1,000	Wasson and Kallemeyn (1988), Wombacher et al. (2008)	–78 to 159	Wombacher et al. (2008)
Bulk silicate Earth (BSE)	ng/g 64; 40; 35 ± 7; 18	Palme and O'Neill (2005), McDonough and Sun (1995), Witt-Eickschen et al. (2009), Yi et al. (2000)	–0.3 ± 0.5	Schmitt et al. (2009a)
Mantle and mantle-derived rocks				
Peridotites	ng/g 40 ± 28; 41 ± 14; 10–40	Heinrichs et al. (1980), McDonough (1990), Witt-Eickschen et al. (2009)		
Mid-ocean ridge basalts (MORB)	ng/g 119 ± 22	Yi et al. (2000)	0.0 ± 0.3	Schmitt et al. (2009a)
Ocean island basalts (OIB)	ng/g 100 ^c ; 100–160	Heinrichs et al. (1980), Yi et al. (2000)	–0.7 ± 0.3	Schmitt et al. (2009a)
Continental crust and crustal rocks				
Bulk continental crust	ng/g 102; 98; 90	Wedepohl (1995), Taylor and McLennan (1985), Rudnick and Gao (2005)	(–0.1 ± 0.4 ^d)	Schmitt et al. (2009a)
Upper continental crust	ng/g 100; 100; 80	Wedepohl (1995), Taylor and McLennan (1985), Rudnick and Gao (2005)	–0.1 ± 0.4 ^d 0.5 ± 1.0 ^e	Schmitt et al. (2009a)
Andesites	ng/g 58	Heinrichs et al. (1980)		
Granites/granodiorites	ng/g 60–130	Heinrichs et al. (1980)		
Gneisses and granulites	ng/g 95–115	Heinrichs et al. (1980)		
Clastic river and shelf sediments	ng/g ~100–200	Heinrichs et al. (1980)	–4 to +4	Wombacher et al. (2003), Gao et al. (2008)
Loess	ng/g 110–130	Schmitt et al. (2009a)	–0.1 ± 0.4	Schmitt et al. (2009a)
Cd and Cd-rich minerals			–2 to +3	Schmitt et al. (2009a), Wombacher et al. (2003), Shiel et al. (2010)
Marine environment				
Surface ocean (dissolved Cd)	nmol/L ~0.001–0.5	Bruland (1983), de Baar et al. (1994)	~0 to +38	Ripperger et al. (2007), Lacan et al. (2006)
Oceans ≥1 km (dissolved Cd)	nmol/L ~0.2–1.1	Bruland (1983), de Baar et al. (1994)	2.9 ± 0.5	Ripperger et al. (2007)
Cd/Ca ratios of foraminiferal tests	μmol/mol <0.01 to >0.25	Boyle (1988), Ripperger et al. (2008)		
Pelagic clays	ng/g 100–350; 420	Heinrichs et al. (1980), Li and Schoonmaker (2005)		
Hydrogenetic Fe-Mn crusts	μg/g 1–20	Horner et al. (2010), Hein et al. (1997)	2.5 ± 1.0	Horner et al. (2010)
Hydrogenetic Fe-Mn nodules	μg/g 1–20	Schmitt et al. (2009a), Hein et al. (1997)	2.2 ± 1.1	Schmitt et al. (2009a)

(continued)

Table 8.5 (continued)

Sample type or reservoir	Typical concentrations or calculated mean values ^a	References	$\epsilon^{114/110}\text{Cd}$ range or mean ^a	References
Hydrothermal Fe-Mn crusts	$\mu\text{g/g}$ 3–20	Schmitt et al. (2009a), Hein et al. (1997)	0.6–1.1	Schmitt et al. (2009a)
Hydrothermal sulfides	$\mu\text{g/g}$ ~100–400	Schmitt et al. (2009a)	–4.5 to 3.9	Schmitt et al. (2009a)
Anthropogenic samples				
Purified Cd and Cd metal			–17 to 4	Shiel et al. (2010), This study, Table 8.3, Ripperger and Rehkämper (2007)
Samples from of Pb-Zn refinery			–7 to +5	Shiel et al. (2010), Cloquet et al. (2006)
Soils polluted by Pb-Zn refinery			–7 to +3	Gao et al. (2008), Cloquet et al. (2006)

^aRanges in concentration and $\epsilon^{114/110}\text{Cd}$, based on published data, are given in normal font; calculated or published mean concentrations or $\epsilon^{114/110}\text{Cd}$ values are given in *italics* and are quoted with 1sd, if available

^bExcludes the anomalous samples Colony, Leoville and Kainsaz, which are characterized by $\epsilon^{114/110}\text{Cd} \approx 10\text{--}40$

^cIncludes continental basalts

^dBased on analyses of upper crustal loess

^eBased on ten high-precision analyses of continental sulfides

different Cd isotopes) can therefore be readily compared and applied to calculate, presumably more reliable, averages. A detailed evaluation demonstrates, however, that various Cd isotope ratios (e.g., $^{110}\text{Cd}/^{111}\text{Cd}$ and $^{113}\text{Cd}/^{114}\text{Cd}$) will yield slightly different $\epsilon\text{Cd}/\text{amu}$ results. These differences reflect: (1) variations in the relative mass difference of the isotopes (e.g., 0.91% for ^{110}Cd and ^{111}Cd and 0.89% for ^{113}Cd and ^{114}Cd), (2) the mechanism and hence mass dependence of mass fractionation (equilibrium vs. kinetic effects), and (3) the absolute extent of isotope fractionation, whereby larger fractionations produce greater differences (Wombacher and Rehkämper 2004). For example, assuming that kinetic mass fractionation is relevant, a value of $\epsilon\text{Cd}/\text{amu} = 10.0$ determined from $^{114}\text{Cd}/^{110}\text{Cd}$ corresponds to $\epsilon\text{Cd}/\text{amu} = 9.9$ for $^{114}\text{Cd}/^{112}\text{Cd}$. This difference is small, but it is an inherent drawback of the methodology that may become more serious with future improvements in analytical precision. We suggest that the “per amu” notation is therefore best avoided in the future.

Given that Cd has eight stable isotopes, of which five have relative abundances of more than 10% (Table 8.2), it is not surprising that various studies report stable isotope fractionations using different Cd isotope ratios. Most commonly, ϵ or δ values are

reported for $^{114}\text{Cd}/^{110}\text{Cd}$ (Cloquet et al. 2005b; Ripperger et al. 2007; Wombacher et al. 2008; Shiel et al. 2009) or $^{112}\text{Cd}/^{110}\text{Cd}$ (Schmitt et al. 2009a). The former approach yields larger numerical values, which can be advantageous to differentiate between results that differ only slightly, whilst the latter features a 2-amu mass difference that is also commonly applied for the notation of other elements (e.g., Mg, Fe, Cu, Zn).

An accurate comparison of ϵ -values calculated for different Cd isotope ratios is possible but this requires that the results are recalculated using a suitable mass fractionation law (Wombacher and Rehkämper 2004). In many cases, particularly where the Cd isotope fractionations are large (e.g., from evaporation and biological utilization), the kinetic law (Young et al. 2002) may be most suitable. The $\epsilon^{k/m}\text{Cd}$ value for one isotope ratio $R_{k/m} = {}^k\text{Cd}/{}^m\text{Cd}$ is related to the $\epsilon^{l/m}\text{Cd}$ value of a second isotope ratio $R^{l/m} = {}^l\text{Cd}/{}^m\text{Cd}$ by:

$$\epsilon^{k/m}\text{Cd} = \left[\left(e^{l/m}\text{Cd}/10,000 + 1 \right)^\beta - 1 \right] \times 10,000. \quad (8.4)$$

For the kinetic law, β is defined as:

$$\beta = \ln(m_k/m_m) / \ln(m_l/m_m), \quad (8.5)$$

where m_k , m_l and m_m refer to the exact atomic masses of the Cd isotopes k , l , and m (Wombacher and Rehkämper 2003). Note that a simplified equation can be used in many instances, whereby

$$\varepsilon^{k/m}\text{Cd} \approx \varepsilon^{l/m}\text{Cd} \times \beta. \quad (8.6)$$

This simplified technique is accurate to better than $\pm 0.01 \varepsilon$ ($=1$ ppm) for the conversion between $\varepsilon^{114/110}\text{Cd}$ and $\varepsilon^{112/110}\text{Cd}$, for $\varepsilon^{114/110}\text{Cd}$ values of 0 ± 50 .

8.3.3 Renormalization of Cd Isotope Data

The $\varepsilon^{114/110}\text{Cd}$ values that are determined for a sample relative to an in-house zero-epsilon standard can be renormalized to a second reference material using the standard conversion identity (Criss 1999). The relevant equation is formulated here (as an example) for the conversion of an ε value originally determined for a sample (S) relative to JMC Münster Cd, to an ε value relative to NIST 3108 Cd:

$$\begin{aligned} \varepsilon^{114/110}\text{Cd}_{\text{S-NIST}} &= \varepsilon^{114/110}\text{Cd}_{\text{S-JMC}} + \varepsilon^{114/110}\text{Cd}_{\text{JMC-NIST}} \\ &+ \frac{(\varepsilon^{114/110}\text{Cd}_{\text{S-JMC}})(\varepsilon^{114/110}\text{Cd}_{\text{JMC-NIST}})}{10,000}. \end{aligned} \quad (8.7)$$

In practice, the conversion is often carried out using the approximation:

$$\varepsilon^{114/110}\text{Cd}_{\text{S-NIST}} \approx \varepsilon^{114/110}\text{Cd}_{\text{S-JMC}} + \varepsilon^{114/110}\text{Cd}_{\text{JMC-NIST}}. \quad (8.8)$$

The application of this simplified approach is justified in many cases because it introduces systematic errors that are much smaller than the analytical uncertainties.

8.3.4 Conventions Adopted in this Study

In order to directly compare the results obtained by different laboratories in this manuscript, it was useful to (1) adopt a common method of Cd isotope notation

and (2) renormalize published isotopic data to a common zero-epsilon reference standard. To this end, results quoted in the present paper are reported using an $\varepsilon^{114/110}\text{Cd}$ notation, relative to the NIST SRM 3108 Cd solution (except when otherwise stated). This approach was taken in anticipation of the future adoption of NIST SRM 3108 Cd as the commonly accepted zero-epsilon reference standard (Abouchami et al. 2010b).

The renormalization was carried out based on preliminary results that were obtained for analyses of NIST SRM 3108 Cd, JMC Münster Cd, Alfa Cd Zurich, MPI JMC Cd, BAM-I012 Cd and Münster Cd as part of a current intercalibration effort (Abouchami et al. 2010b). Furthermore utilized were published differences between the in-house zero-epsilon materials of various laboratories and secondary Cd isotope standards. Such data are fortunately available in all recently published Cd isotope studies (Table 8.4). Based on the preliminary results compiled by Abouchami et al. (2010b), the following isotopic differences were adopted in this manuscript for the $\varepsilon^{114/110}\text{Cd}$ values of zero-epsilon standards *relative* to NIST SRM 3108 Cd: JMC Münster Cd: -0.8 ; Alfa Cd Zürich: -0.4 ; MPI JMC Cd: $+1.5$; Nancy Spex Cd: -0.8 ; PCIGR-1 Cd: -0.5 . Note that these isotopic differences are preliminary results that are subject to (slight) future revisions, which may be adopted once the current intercalibration effort is finalized (Abouchami et al. 2010b). The renormalization of the data was carried out using the standard conversion identity (8.7).

8.4 Cadmium Isotopes: Applications and Results

8.4.1 Industrial and Anthropogenic Samples

8.4.1.1 Cadmium Stable Isotope Fractionation During Evaporation

The variability of Cd isotope compositions in different pure Cd metal samples and standard solutions was mentioned previously (Table 8.4) and this is likely to reflect isotopic fractionations from the purification of

Cd by either (non-quantitative) distillation or zone refining. For the evaporation of volatile Cd (Table 8.1), kinetic theory predicts an isotope fractionation factor α that can be calculated from the square root of the masses (m) of the relevant isotopes or isotopologues. Given that Cd generally appears to evaporate as a monoatomic gas (Chizhikov 1966), the relevant equation is $\alpha_{\text{kin}} = ({}^{114}\text{Cd}/{}^{110}\text{Cd})_{\text{residue}} / ({}^{114}\text{Cd}/{}^{110}\text{Cd})_{\text{vapor}} = (m_2/m_1)^{0.5} \approx (114/110)^{0.5} = 1.018$. This is equivalent to a fractionation of $\Delta \approx 18\%$ for ${}^{114}\text{Cd}/{}^{110}\text{Cd}$ during kinetic evaporation, where the “big delta” is given by $\Delta \approx 1,000 \ln \alpha$ (Criss 1999).

Cadmium isotope fractionation during evaporation and condensation processes were investigated by Wombacher et al. (2004) using three Cd metal samples that were residues from evaporation of molten Cd in a vacuum chamber at about 10^{-4} mbar. At these conditions, Cd has a boiling point of $\sim 180^\circ\text{C}$. The samples were obtained from an industrial process, in which Cd vapor is used to coat metal parts with a thin layer of Cd for a high level of corrosion protection. In detail, the analyzed metals (Samples C, D, E of Fig. 8.1) were residues, which remained after about 90–99.5% of the initial Cd had been lost to evaporation, such that they featured highly fractionated (heavy) Cd isotope compositions that differed from the starting material (Sample A of Fig. 8.1) by up to 4.8% for ${}^{110}\text{Cd}/{}^{114}\text{Cd}$ and almost 10% for ${}^{106}\text{Cd}/{}^{114}\text{Cd}$ (Wombacher et al. 2004). At such large absolute fractionations, the isotopic compositions that are expected for pure equilibrium and kinetic evaporation processes (Young et al. 2002) are sufficiently different in three isotope plots (e.g., ${}^{106}\text{Cd}/{}^{114}\text{Cd}$ vs. ${}^{110}\text{Cd}/{}^{114}\text{Cd}$; Fig. 8.1) to be resolved by mass spectrometry. In principle, this approach is, therefore, able to provide fundamental constraints on fractionation mechanisms.

Wombacher et al. (2004) utilized the generalized power law of Maréchal et al. (1999) to evaluate the Cd isotope data obtained for the metal samples and they determined that the evaporation residues displayed a mass dependence intermediate between that expected for equilibrium and kinetic isotope fractionation (Fig. 8.1). They also found that the evaporation process yielded smaller fractionations than expected from $\alpha_{\text{kin}} = (m_2/m_1)^{0.5}$. Taken together, these observations were interpreted to reflect hybrid evaporation with kinetic isotope fractionation characterized by $\alpha_{\text{kin}} = (m_2/m_1)^{0.5}$ and limited, but still significant, equilibrium isotope partitioning between the vapor phase

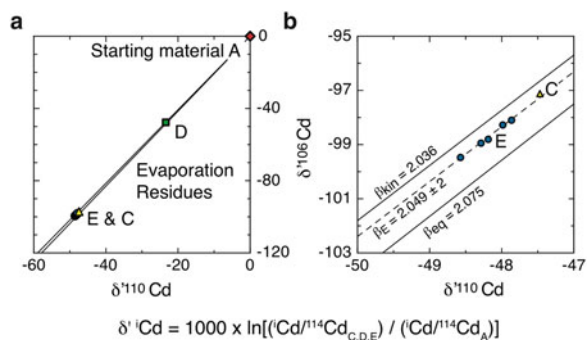


Fig. 8.1 Three isotope plot of Cd data for industrial Cd metal samples (Wombacher et al. 2004). Results are shown in the δ' notation, as defined below the figure (Hulston and Thode 1965), because this produces linear fractionation lines rather than curved trends, which would result from the use of conventional δ or ε values. Note that the δ' values of the fractionated evaporation residues C, D, E are calculated relative to the starting material A. (a) Samples C, D, E and the starting material A define a fractionation line in $\delta'^{106}\text{Cd}$ vs. $\delta'^{110}\text{Cd}$ isotope space. (b) Close-up of (a) that shows the results obtained for samples C and E. Shown in (b) are reference lines for mass-dependent isotope fractionation according to the kinetic and equilibrium fractionation laws, with slopes β_{kin} and β_{equil} calculated as described by Young et al. (2002). Also denoted in (b) is the best-fit fractionation line inferred for sample E with slope $\beta_{\text{E}} = \delta'^{106}\text{Cd}/\delta'^{110}\text{Cd}$. The inferred β values for samples E and C (not shown) are intermediate between those expected for equilibrium and kinetic fractionation. The drift of the instrumental mass discrimination, which is apparent for the repeated measurements of sample E, is negligible compared to the overall magnitude of the isotope fractionation from evaporation

and melt. More recent data have shown, however, that evaporation of Mg also produces an intermediate mass dependence, albeit at very high temperatures (Davis et al. 2005). Given that equilibrium isotope partitioning is temperature sensitive, Wombacher et al. (2008) concluded that equilibrium partitioning of Cd isotopes between vapor and melt (α_{equil}) were overestimated by Wombacher et al. (2004), because evaporation into a vacuum under kinetic conditions is not necessarily characterized by kinetic mass scaling (Young et al. 2002) and $\alpha_{\text{kin}} = (m_2/m_1)^{0.5}$. Unidirectional evaporation processes which display (1) fractionations that are about 50% lower than predicted by $\alpha_{\text{kin}} = (m_2/m_1)^{0.5}$ and (2) mass-dependencies intermediate between those expected for equilibrium and kinetic isotope effects, are therefore probably the result of chemical interactions in the melt phase (Simon and Young 2007) and/or the melt-vacuum interface (Richter et al. 2002).

8.4.1.2 Metallurgy and Anthropogenic Emissions

The large Cd isotope fractionations that can be produced by evaporation, suggest that isotopic analyses may be useful for tracing Cd pollution, which is released by anthropogenic emissions, including smelting/refining processes that are associated with the recovery of Cd from ores, waste incineration and the burning of coal. Such studies are of particular interest, because Cd is highly toxic and commonly enriched (to levels of up to a few percent) in sulfide ores, which are processed for the recovery of Pb and Zn. So far, the combustion of coal and other fossil fuels have not been investigated using Cd isotope methods, even though they represent the most important anthropogenic source of Cd to the environment (Nriagu and Pacyna 1988). Furthermore, only preliminary results are available for a Cd isotope study of waste incineration. Importantly, this investigation identified variations of up to 10 ϵ for $^{114}\text{Cd}/^{110}\text{Cd}$, in bulk, leachate and leachate residue samples of fly ash from an urban waste combustor (Cloquet et al. 2005a). These large isotope effects were thought to reflect modification of the Cd isotope composition in the residual gas phase by progressive kinetic condensation.

Three published studies have looked for and identified significant Cd isotope fractionations in various samples from Pb-Zn smelters and refineries, as well as the immediate environments of such plants (Cloquet et al. 2006; Gao et al. 2008; Shiel et al. 2010). Cloquet et al. (2006) investigated the Cd and Pb isotope compositions of soils collected in the vicinity of a Pb-Zn refinery, at distances of up to 4.5 km. Also analyzed were dust from exhaust filters and a slag produced in the plant furnace. The isotopic analyses showed that two dust samples from the refinery exhibited Cd isotope compositions that were lighter in $^{114}\text{Cd}/^{110}\text{Cd}$ by $\sim 10 \epsilon$ compared to the slag (Fig. 8.2). This difference in Cd isotope composition was interpreted to reflect progressive evaporation of Cd, under equilibrium conditions, to form a gas phase enriched in light isotopes, from which the dust condensed on cooling. As the $\epsilon^{114/110}\text{Cd}$ value of the slag was thought to represent the last fraction of evaporated Cd in the refinery, an equilibrium solid-gas fractionation factor α of only 1.0001 was derived for the system (Cloquet et al. 2006). This result is significantly lower than the fractionation predicted for

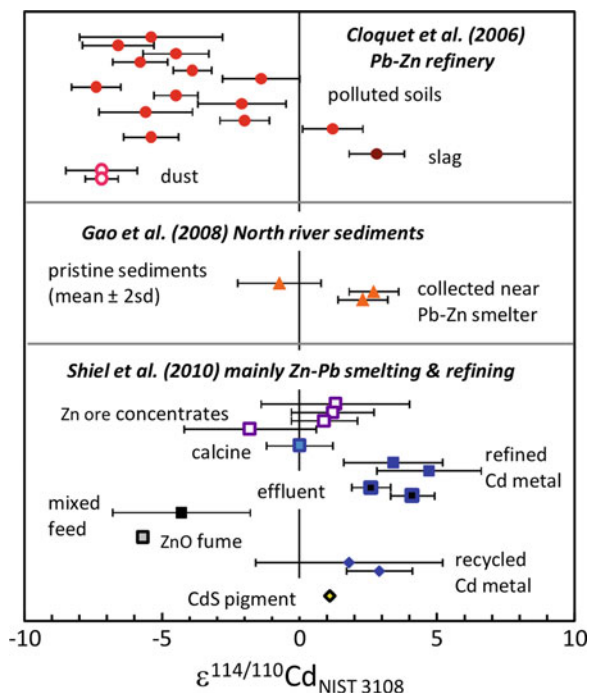


Fig. 8.2 Cadmium isotope data (reported as $\epsilon^{114/110}\text{Cd}$ relative to NIST 3108 Cd) for samples from Zn-Pb smelting/refining plants and environmental samples that were affected by emissions from such plants (Cloquet et al. 2006; Gao et al. 2008; Shiel et al. 2010). The uncertainties are shown as reported in the original publications, except for the average calculated for five unpolluted river sediments (Gao et al. 2008)

kinetic evaporation ($\alpha_{\text{kin}} = 1.0018$) and the (presumably overestimated) fractionation factor of $\alpha_{\text{equil}} = 1.0007$ that was inferred for equilibrium evaporation at 180°C (Wombacher et al. 2004). The origin of the low observed α value is not well constrained but may be due to either negligible equilibrium isotope fractionation at high temperature (Cloquet et al. 2006) and/or a lack of isotopic homogenization in the residual materials during the evaporation process.

Cloquet et al. (2006) also found that soil samples from the vicinity of the refinery plant were characterized by high Cd contents and clear differences in Cd isotope compositions with $\epsilon^{114/110}\text{Cd}$ ranging from -7.4 to $+1.2$ (Fig. 8.2, Table 8.5). Soils from locations close to the refinery exhibited the lowest $\epsilon^{114/110}\text{Cd}$ values and the isotopic variability was thought to reflect contamination of the soils by variable mixtures of dust- and slag-derived Cd. The viability of tracing anthropogenic emissions of Cd to the environment was further corroborated by the work of Gao et al. (2008), who carried out a combined Cd-Pb isotope study of

sediments from the North River in China. This investigation found that two samples from the vicinity of a Pb-Zn smelter displayed elevated Cd concentrations and higher $\epsilon^{114/110}\text{Cd}$ values (of +2.3 and +2.7) compared to five pristine river sediments, which exhibited $\epsilon^{114/110}\text{Cd} \approx 0$ (Fig. 8.2). The clear difference in Cd isotope compositions was interpreted to reflect isotope fractionation from processing of Cd in the Pb-Zn smelter (Gao et al. 2008).

Shiel et al. (2010) investigated the Cd, Zn and Pb isotope compositions of samples from a Pb-Zn smelter and refining plant in Canada. Cadmium isotope data were obtained for (1) four Zn ore concentrates (primarily sphalerite); (2) calcine (mainly ZnO, obtained from roasting of the sulfide ores); (3) the Pb smelter feed (comprised of Pb ore concentrates and residues from the extraction of Zn from the calcine); (4) CdO-rich ZnO fumes produced during Pb purification; (5) effluents (Zn and Cd-rich waste products from the Zn plant that are recycled to the smelter); and (6) the final refined Cd metal (Fig. 8.2). The Zn ore concentrate samples exhibited Cd isotope compositions ($\epsilon^{114/110}\text{Cd} \approx -2$ to +1) similar to those observed for other continental and oceanic sulfides (Fig. 8.3, Table 8.5). The calcine sample also falls within this range, probably due to the near-quantitative Cd yield of the roasting process (Fig. 8.2). The Zn and Cd-rich effluent and the refined Cd metal displayed similar and distinctly positive $\epsilon^{114/110}\text{Cd}$ values (of between about +3 and +5), whilst the ZnO fume and the Pb smelter feed are enriched in isotopically light Cd ($\epsilon^{114/110}\text{Cd} \approx -4$ to -6). The origin of these distinct differences, which should essentially balance out to yield the Cd isotope composition of the original ore concentrate, is difficult to trace due to the unknown yields of various production stages. Based on a careful assessment of mass balances, Shiel et al. (2010) concluded that the isotopic fractionation is mainly (but not solely) related to differences in the Cd isotope compositions of various mineralogical phases that are formed during roasting, and which are separated from one another, as they display distinct reactivities during further processing. Shiel et al. (2010) also analyzed Cd metal that was thermally recovered from Ni-Cd batteries and a CdS pigment sample. These materials had inconspicuous Cd isotope compositions that were identical to the range of values determined for Zn ore concentrates and refined Cd metal (Fig. 8.2).

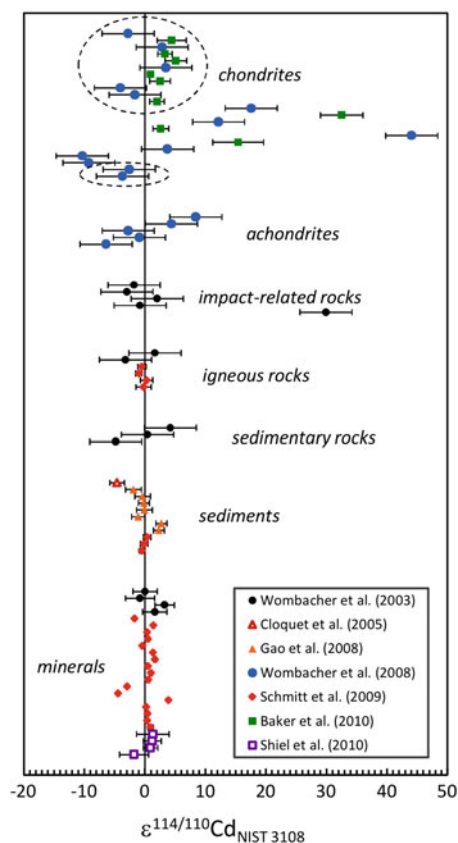


Fig. 8.3 Cadmium stable isotope data (reported as $\epsilon^{114/110}\text{Cd}$ relative to NIST 3108 Cd) for various terrestrial sediments and rocks (including a tektite and other samples related to impact events), Zn and Cd minerals, and selected meteorites. The meteorite data are limited to carbonaceous chondrites, enstatite chondrites (of type EH) and selected achondrites (eucrites and SNC meteorites from Mars). The chondrite data encircled by the hashed line, denote results for unfractionated carbonaceous chondrites which have not been overprinted by strong parent body metamorphism (Wombacher et al. 2003, 2008)

In summary, it should be considered significant that these pioneering studies of Cd isotope fractionations in industrial and polluted environmental samples were all able to resolve clear differences in $\epsilon^{114/110}\text{Cd}$ that are primarily of anthropogenic origin. Importantly, these differences were identified even though individual industrial processes are unlikely to be associated with fractionation factors that exceed values of $\Delta \approx 10 \epsilon$. It was also shown that the isotopic signatures can be applied to interrogate the behavior of Cd during industrial processes. Furthermore, they show significant promise for tracing anthropogenic emissions to and cycling of Cd in polluted environments.

The power of such applications is essentially limited by the precision of the analytical data relative to the observed isotopic variability.

8.4.2 Extraterrestrial Materials

The first systematic studies of Cd isotope compositions, which led to the identification of natural Cd isotope fractionations were carried out by Rosman and de Laeter on meteorite samples in the 1970s (Rosman and de Laeter 1976, 1978) and such investigations continue to draw significant interest. A thorough review of this literature is outside the scope of this contribution but a short synopsis of key results is nonetheless provided, as a reference for the study of terrestrial Cd isotope variations.

Chondrites are primitive meteorites that formed in the early solar system and amongst these, some carbonaceous chondrites feature elemental abundances that most closely resemble the bulk solar system. The majority of carbonaceous chondrites have relatively constant Cd isotope compositions (Baker et al. 2010) with an average of $\epsilon^{114/110}\text{Cd} = +3.0 \pm 2.8$ (2sd). This indicates that the depletion of Cd and other volatile elements in inner solar system bodies did not generate large isotopic fractionations and hence probably did not involve partial kinetic evaporation. In contrast, large Cd stable isotope effects, with $\epsilon^{114/110}\text{Cd}$ values ranging from -78 to $+159$ are recorded in ordinary and many enstatite chondrites (Fig. 8.3, Table 8.5). The Cd isotope fractionations in these meteorites are thought to be caused by redistribution of Cd during thermal metamorphism in the interiors of the asteroidal parent bodies (Wombacher et al. 2003, 2008). However, there are also many extraterrestrial samples that display Cd isotope compositions, which are very similar or identical to the (unfractionated) carbonaceous chondrites (Fig. 8.3). In particular, this includes achondrites, which are derived from differentiated (and hence formerly molten) parent asteroids. Also essentially indistinguishable from unfractionated carbonaceous chondrites are most terrestrial rocks (Fig. 8.3, Table 8.5) and two samples from the Moon (Wombacher et al. 2003, 2008; Schediwy et al. 2006). Taken together, these results demonstrate that Cd isotope heterogeneities are homogenized within planetary bodies during differentiation and that large

stable isotope fractionations do not occur as a consequence of volatile element depletion and parent body differentiation.

8.4.3 Reservoirs and Samples of the Silicate Earth

In solid Earth geochemistry, Cd is generally classified as a trace element that exhibits both lithophile and chalcophile characteristics. High concentrations of Cd are typically found in continental igneous sulfide ore deposits, particularly as greenockite (CdS) associated with sphalerite (ZnS). In silicate rocks, Cd preferentially partitions into Mg-Fe silicate minerals such as biotite, chlorite, pyroxene and amphibole (Heinrichs et al. 1980; Witt-Eickschen et al. 2009). In most igneous, sedimentary and metamorphic rocks of the continental crust and the mantle, Cd furthermore typically exhibits relatively uniform concentrations of about 20–200 ng/g (Table 8.5). This uniformity reflects, in part, that Cd is only moderately incompatible during mantle melting with a partition coefficient that resembles the rare earth elements dysprosium (Dy) or ytterbium (Yb) (Yi et al. 2000; Witt-Eickschen et al. 2009).

Most compositional estimates for the continental crust and its sub-reservoirs (of upper, middle, and lower crust) provide Cd concentrations of ~ 100 ng/g, with only limited intra-crustal differences (Table 8.5). A notable exception is the recent study of Hu and Gao (2008), which suggests a relatively low Cd content of 60 ng/g for the upper continental crust. For the BSE, four abundance estimates derive mean Cd concentrations of between 18 and 64 ng/g (Table 8.5). Based on the geochemical similarity of Cd to Dy and Yb during mantle melting, Cd should be moderately enriched, by about a factor of 5, in the continental crust (CC) relative to the BSE (McDonough and Sun 1995; Palme and O'Neill 2005). Taken at face value, this conclusion is in accord with only some of the published Cd abundance estimates for silicate Earth reservoirs, whilst the majority of the data are more suggestive of $[\text{Cd}]_{\text{CC}} \approx (2.5 \pm 1) \times [\text{Cd}]_{\text{BSE}}$ (Table 8.5). Similarly, the geochemical similarity of Cd to Dy and Yb can also be used to infer the Cd concentration of the depleted MORB source mantle (DMM) as

$[\text{Cd}]_{\text{DMM}} \approx (0.80 \pm 0.05) \times [\text{Cd}]_{\text{BSE}}$ (Workman and Hart 2005), which is equivalent to $[\text{Cd}]_{\text{DMM}} \approx 15\text{--}50$ ng/g.

Despite of the large uncertainty of the BSE estimates, the available data suggest that the silicate Earth is depleted in Cd relative to carbonaceous chondrites (Table 8.5), as a consequence of volatile depletion and potentially also core partitioning. Estimates for the Cd content of the Earth's core are highly speculative, however, due to our limited understanding of Cd partitioning between silicate, metal, and sulfide phases during terrestrial accretion (Lagos et al. 2008). Based on mass balance, McDonough (2005) estimated that about 60–65% of the bulk Earth's Cd resides in the core, to support a concentration of ~ 150 ng/g in the metal.

At present, only very limited Cd isotope data are available, which characterizes the silicate Earth and explores Cd isotope variations amongst and within its reservoirs. Overall, the variability of $\epsilon^{114/110}\text{Cd}$ in rocks and minerals from the crust and mantle is limited with values between -4 and $+4$ (Fig. 8.3, Table 8.5). This excludes all polluted and industrially processed samples, as well as marine sediments and minerals, which show larger Cd isotope variations. Also excluded is a tektite analyzed by Wombacher et al. (2003), which features a heavy isotope composition ($\epsilon^{114/110}\text{Cd} = 30$) and low Cd content, presumably due to loss Cd by evaporation (Fig. 8.3). Additional analyses of other impact-related rocks did not reveal any significant Cd isotope variations, however (Wombacher et al. 2003).

Apart from the tektite and the marine sediments (which are discussed in Sect. 8.4.4.3), the only samples from the solid Earth to exhibit clearly resolvable Cd isotope variations are some continental mineral deposits (Fig. 8.3, Table 8.5). In particular, no significant variability in Cd isotope compositions is apparent for loess and clastic sediments from rivers and continental margins as well as igneous rocks derived from the crust and mantle (Fig. 8.3, Table 8.5). As such, the present dataset does not provide evidence for systematic Cd isotope fractionations between or within the major reservoirs of the silicate Earth. At present, the isotope compositions of the Earth's mantle and continental crust are therefore best characterized by the limited but precise double spike TIMS data of Schmitt et al. (2009a). These workers analyzed three samples of loess (representative of the continental crust) and two samples each of MORB (mid ocean ridge basalts)

and OIB (ocean island basalts) to characterize the mantle (Table 8.5). The results obtained suggest that both the continental crust and the mantle display essentially identical $\epsilon^{114/110}\text{Cd}$ values of -0.1 and -0.4 , respectively (Table 8.5). These data can be combined (Schmitt et al. 2009a) to derive a precise estimate for the mean isotope composition of the BSE of $\epsilon^{114/110}\text{Cd} = -0.3 \pm 1.0$ (2sd; Table 8.5).

The conclusion that Cd isotopes were not fractionated during the formation of the continental crust by the extraction of partial melts from the (originally primitive) mantle (Schmitt et al. 2009a) is reasonable given that high temperature processes are generally not expected to generate large Cd isotope effects. However, further high-precision analyses for additional samples, particularly mantle peridotites, are required to fully address this issue. This is of particular relevance because preliminary data obtained by Schönbacher et al. (2009) hint at a minor difference between the Cd isotope compositions of mantle-derived basalts and ultramafic komatiites/peridotites. Such analyses are furthermore of interest, to resolve whether there is indeed a small but resolvable fractionation in $\epsilon^{114/110}\text{Cd}$ between the BSE and chondritic meteorites (Schönbacher et al. 2009). The current Cd isotope database for terrestrial rocks is too imprecise and limited in size to adequately address this question.

8.4.4 Marine Environments

8.4.4.1 Cadmium in the Oceans and Marine Sediments

The geochemistry of Cd in the oceans and marine sediments has attracted significant scientific interest for more than 30 years. This interest is primarily based on the observation that the dissolved Cd concentrations of seawater show a nutrient-like distribution (Fig. 8.4), which very closely resembles the distribution of the marine macronutrient phosphate (Boyle et al. 1976; Bruland 1980). Both Cd and P display low concentrations in surface waters, due to the uptake by marine organisms (Fig. 8.4). After the organisms cease, the organic material sinks through the water column and is subsequently decomposed at depth, so that Cd and P are remineralized into the

dissolved form (Bender and Gagner 1976; Boyle et al. 1976; Bruland 1980). Whilst it has been suggested in the past that the nutrient-like behavior of Cd may also reflect passive adsorption of Cd onto (deceased) organic matter (Collier and Edmond 1984; Yee and Fein 2001; Dixon et al. 2006), it has been demonstrated by a number of recent studies that Cd is a marine micronutrient with an important biological function. In particular, it has been shown that Cd can substitute for Zn in the enzyme carbonic anhydrase, which plays an important role in the process of inorganic carbon acquisition (Price and Morel 1990; Cullen et al. 1999; Sunda and Huntsman 2000; Lane et al. 2005; Xu et al. 2008).

Oceanic circulation modifies this simple one-dimensional pattern of Cd and phosphate distribution (Fig. 8.4) to create water masses with distinct chemical signatures. A key feature is that Pacific deepwater, which is characterized by older ventilation ages, has significantly higher Cd and P concentrations than comparatively young Atlantic deepwater (Fig. 8.4). This difference reflects the progressive accumulation of remineralized nutrients, as deepwater masses pass from the Atlantic through the Southern to the Pacific Ocean (Donat and Bruland 1995). Despite of this complexity, the Cd and phosphate data for seawater correlate remarkably well for a large global dataset (Fig. 8.5). A particular feature of this largely linear

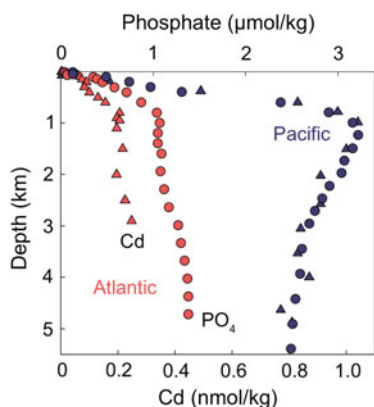


Fig. 8.4 Depth profiles of Cd and phosphate concentrations (shown as *triangles* and *circles*, respectively) for stations in the Atlantic Ocean (in *red*) and Pacific Ocean (in *blue*) (Bruland 1983). The Cd and P contents are well correlated with extremely low surface water abundances and a rapid increase of concentrations at depths of 0–1 km. The higher Cd and phosphate contents of the Pacific deep water are a typical feature of macro- and micronutrient elements

correlation is the “kink” at intermediate Cd and phosphate abundances, which has been described by some as a consequence of a slightly curved [Cd]-[PO₄] trend (Elderfield and Rickaby 2000). The origin of this feature has been the subject of numerous investigations and its interpretation continues to be contentious (Frew and Hunter 1992; de Baar et al. 1994; Elderfield and Rickaby 2000; Cullen 2006).

The particular interest of paleoceanographers in the element Cd is based on the [Cd]-[PO₄] correlation of seawater (Fig. 8.5) coupled with the finding that past seawater phosphate contents are generally not recorded in marine sediments (Henderson 2002). In contrast, it was observed that Cd is incorporated into the tests of foraminifera, in proportion to the Cd (and hence phosphate) concentration of the surrounding seawater (Boyle 1981; Ripperger et al. 2008). Subsequent studies have further refined this understanding and developed (1) empirical depth-dependent distribution coefficients for Cd between benthic foraminifera and seawater (Boyle 1992) and (2) temperature dependent corrections for the tests of planktonic foraminifera from surface waters (Rickaby and Elderfield 1999). On this basis, the Cd/Ca data of foraminifera have become an important tool in paleoceanography as proxy of past marine nutrient (phosphate) distribution and utilization (Henderson 2002; Lynch-Stieglitz 2006). Paleoceanographic studies that aim to reconstruct past changes in the marine distribution of Cd

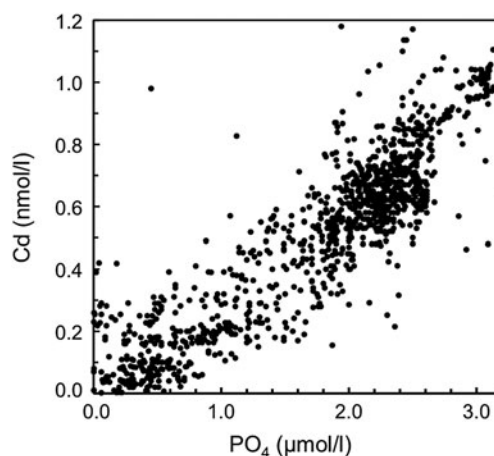


Fig. 8.5 Cadmium vs. phosphate concentrations for a global dataset of open ocean samples. The dataset is essentially identical to that used by (Hendry et al. 2008). The “kink” or slight curvature in the well-defined positive correlation is apparent

have two principal aims. (1) Cadmium is applied as a non-conservative tracer of water masses to trace temporal changes in ocean circulation patterns. (2) The seawater concentration of Cd is a nutrient- and thus carbon-linked property, which can be used to infer variations in both deep and surface water nutrient levels (Boyle 1988, 1992; Rickaby and Elderfield 1999; Elderfield and Rickaby 2000). The Cd data for sedimentary archives thus provides constraints on past changes in ocean productivity and the processes, which drive atmospheric CO₂ variability (Elderfield and Rickaby 2000; Sigman and Boyle 2000).

8.4.4.2 Cadmium Isotopes in the Oceans

At present, the published Cd isotope database for seawater samples is limited to results from only two studies (Lacan et al. 2006; Ripperger et al. 2007). However, there are a number of recent conference abstracts that announce further results from ongoing work, and this highlights the significant current interest in this field of Cd isotope research (Abouchami et al. 2009; Gault-Ringold et al. 2009; Abouchami et al. 2010a, b; Xue et al. 2010a, b).

The study of Ripperger et al. (2007) currently provides the most comprehensive and precise Cd isotope dataset for seawater, with results for 22 samples, representing both surface waters and depth profiles, from eight locations in all major ocean basins. This

investigation found large variations in Cd isotope compositions, with $\epsilon^{114/110}\text{Cd}$ ranging from ~ 0 to values as high as $+38 \pm 6$ (Fig. 8.6). The isotopic variability of Cd was found to be restricted almost exclusively to the upper level of the water column (at depths ≤ 500 m) and the largest fractionations were observed for highly Cd depleted surface water samples from the Pacific, which featured Cd contents as low as ~ 5 pmol/kg (Fig. 8.6). In contrast, nearly uniform isotope compositions were determined for samples from ≥ 900 m depth (Fig. 8.6). The majority of the samples from the study of Ripperger et al. (2007) were furthermore seen to display an inverse relationship between dissolved Cd contents and isotope compositions (Fig. 8.7). A few samples, however, do not follow this broad trend because they exhibit both low Cd contents and nearly unfractionated Cd isotope compositions (Fig. 8.7).

The Cd isotope data of Lacan et al. (2006) are less precise and 28 samples from two depth profiles (in the northwest Pacific Ocean and Mediterranean Sea) display a much smaller range in Cd concentrations and isotope compositions, with $\epsilon^{114/110}\text{Cd}$ values between about -4 and $+2$ (with an uncertainty of $\pm 3 \epsilon$, 2sd). Despite the limited variation, the samples are in accord with the $\epsilon^{114/110}\text{Cd}$ vs. [Cd] trend observed by Ripperger et al. (2007), as the data for the Pacific Ocean depth profile also exhibit a statistically significant correlation between Cd isotope composition and concentration (Lacan et al. 2006). Importantly,

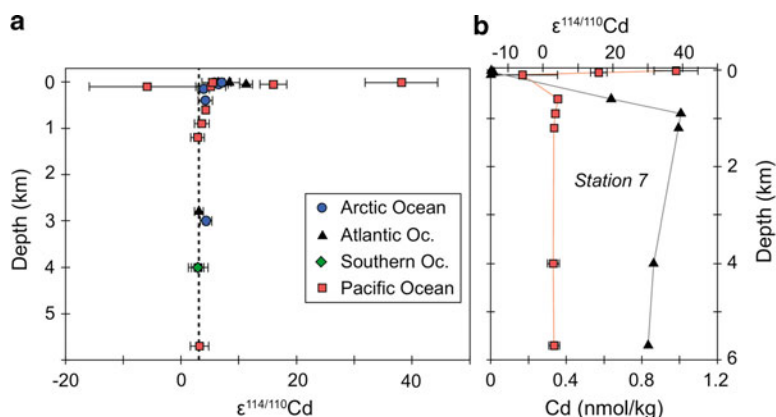


Fig. 8.6 Cd concentrations and isotope data (reported as $\epsilon^{114/110}\text{Cd}$ relative to NIST 3108 Cd) for seawater samples, plotted a function of depth. (a) Shows the results for all 22 samples analyzed by Ripperger et al. (2007). Seawater from depths of ≤ 150 m in the photic zone exhibits the largest Cd isotope fractionations, presumably due to isotope fractionation

from biological utilization. (b) Vertical distribution of [Cd] (triangles) and $\epsilon^{114/110}\text{Cd}$ (squares) in the central North Pacific Ocean (Ripperger et al. 2007). Note that the samples with the lowest Cd contents exhibit the largest isotopic variability. The uncertainties (2sd) are shown as reported in the original publication

Lacan et al. (2006) also presented Cd isotope data for cultured freshwater phytoplankton and found that the organisms were systematically enriched in isotopically light Cd, presumably due to the kinetic isotope fractionation that results from biological uptake of dissolved seawater Cd.

Based on these findings, Ripperger et al. (2007) concluded that the large Cd isotope variations that were observed in the upper water column are most reasonably accounted for by biological utilization of Cd and associated isotope fractionation. This interpretation is supported by the observation that the seawater Cd data are in accord with closed system Rayleigh fractionation trends for fractionation factors of $\alpha \approx 1.0002$ – 1.0006 (Fig. 8.7). This result is in general agreement with the isotope fractionation factor of 1.0014 ± 0.0006 (2sd) that was determined for Cd uptake by cultured phytoplankton (Lacan et al. 2006). The small but significant difference in the fractionation factors inferred from seawater and the culturing experiments may reflect vital effects or additional uncharacterized marine processes, which have an impact on Cd isotope compositions (Ripperger

et al. 2007). Water mass mixing in particular, may be able to generate large deviations from the main fractionation trend if this involves both Cd-rich and Cd-depleted endmembers, a scenario that may be appropriate for the upwelling of deep waters to the surface ocean. In this case, mixing would generate distinct downward deviations from the main $\epsilon^{114/110}\text{Cd}$ vs. [Cd] trend (as highlighted by the green curve of Fig. 8.7). Mixing processes may hence be responsible for the unusual compositions of samples, which feature both low Cd contents and $\epsilon^{114/110}\text{Cd}$ values of about 0 to +5 (Ripperger et al. 2007).

For the Cd-rich seawater samples obtained from depths ≥ 900 m in the Arctic, Atlantic, Southern and Pacific Oceans, Ripperger et al. (2007) observed nearly constant and unfractionated Cd isotope compositions, which define a mean deep water value of $\epsilon^{114/110}\text{Cd} = +2.9 \pm 1.0$ (2sd; Fig. 8.8). The sample data of Lacan et al. (2006) are less precise (at about $\pm 3 \epsilon$) but this study also reports very similar Cd isotope data for seven Pacific water samples, obtained from depths ≥ 1 km at a single station, with a slightly lower (but statistically identical) mean value of $\epsilon^{114/110}\text{Cd} = +0.7 \pm 1.4$. The constant Cd isotope compositions of the deep water samples stand in contrast to the Cd contents, which increase systematically along the global deep water pathway, from concentrations of ~ 0.2 – 0.3 nM in the Arctic and Atlantic Oceans to values of ~ 0.8 – 1.0 nM in the Pacific (Fig. 8.8). These observations are most readily reconciled if the organic matter, which increases the Cd contents of deep water masses by remineralization, also features a nearly constant Cd isotope composition of $\epsilon^{114/110}\text{Cd} \approx +3$. It was, therefore, concluded by Ripperger et al. (2007) that such biomass is most readily produced if the distribution of Cd in surface water is dominated by near-quantitative closed system uptake of Cd by phytoplankton. This interpretation is in accord with the results of previous investigations of marine nutrient cycling (De La Rocha et al. 1998; Elderfield and Rickaby 2000) and the extremely low Cd contents of open ocean surface waters.

Taken together, the currently published Cd isotope database for seawater, which encompasses only 50 samples, shows interesting systematics, including a broad correlation of increasing Cd isotope fractionation with decreasing [Cd]. These results are of particular interest as they provide a tentative foundation for two important applications of Cd isotopes in marine

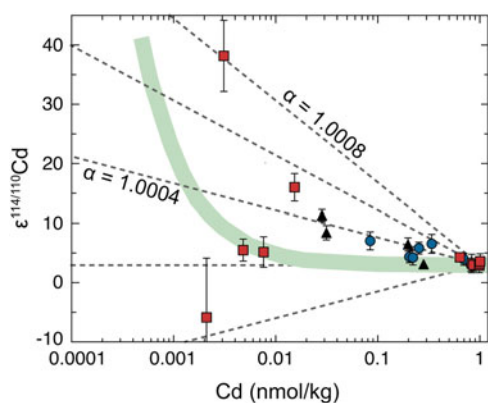


Fig. 8.7 Plot of Cd isotope compositions (reported as $\epsilon^{114/110}\text{Cd}$ relative to NIST 3108 Cd) vs. Cd concentrations for seawater samples (Ripperger et al. 2007). Samples from different ocean basins are denoted by distinct symbols (see legend of Fig. 8.6). The dashed lines denote calculated isotope fractionation trends for dissolved seawater Cd, assuming that biological uptake of Cd occurs by closed-system Rayleigh fractionation with fractionation factors α of between 0.9998 and 1.0008. The broad green line is the mixing trend expected for addition of Cd-rich deep water ($\epsilon^{114/110}\text{Cd} = 3$, [Cd] = 1 nmol/kg) to Cd-depleted surface water ($\epsilon^{114/110}\text{Cd} = 40$, [Cd] = 0.5 pmol/kg). Note that such mixing produces downward deviations from the main fractionation trend that is exhibited by the majority of the seawater samples. The uncertainties (2sd) are shown as reported in the original publication

research. (1) The Cd isotope data reveal more detail and complexity in the marine distribution of Cd than can be discerned from concentration data alone. Hence, Cd isotope compositions have the potential to provide new insights into the biogeochemical processes, which govern the cycling of Cd in the oceans. (2) The $\epsilon^{114/110}\text{Cd}$ -[Cd] correlation observed for seawater suggests that Cd isotopes could be used in paleoceanography, as a proxy of nutrient utilization. The scarcity of seawater data currently renders such an application premature, however. In addition, it also requires the identification of suitable archives that reliably record the Cd isotope composition of seawater over periods of ka to Ma.

8.4.4.3 Cadmium Isotopes in Marine Sediments

At present, only a limited number of marine deposits have been analyzed for Cd isotope compositions, with a database that encompasses ten samples related to sub-seafloor hydrothermal activity at spreading centers and 50 hydrogenetic ferromanganese nodules and crusts (Fig. 8.9).

The set of hydrothermal samples (Schmitt et al. 2009a) includes seven sulfides with high Cd concentrations (>100 ppm Cd; Table 8.5) from the vent

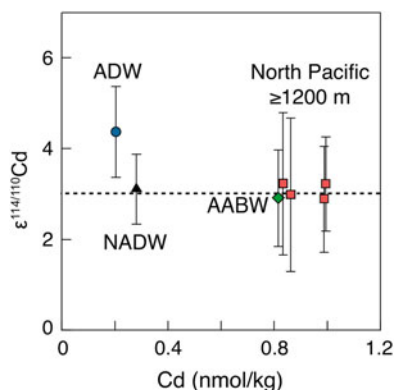


Fig. 8.8 Cd isotope data (reported as $\epsilon^{114/110}\text{Cd}$ relative to NIST 3108 Cd) plotted vs. Cd concentrations for water samples from depths of ≥ 900 m: Arctic deep water (ADW); North Atlantic deep water (NADW); Antarctic bottom water (AABW); and North Pacific water masses from depths $\geq 1,200$ m (Ripperger et al. 2007). These samples display little isotopic variation and define a mean isotope composition, denoted by the hashed line, of $\epsilon^{114/110}\text{Cd} = +2.9 \pm 1.0$ (2sd) (Ripperger et al. 2007). The uncertainties (2sd) are shown as reported in the original publication

chimneys of either hot black smokers or slightly cooler grey smokers. Furthermore analyzed were three hydrothermal ferromanganese (Fe-Mn) crusts with Cd contents of about 3–20 $\mu\text{g/g}$ (Table 8.5). Such crusts are typically deposited from cool ($< 100^\circ\text{C}$) diffuse flows of vent fluids in the distal parts of hydrothermal systems (Hein et al. 1997). With the exception of a single black smoker sulfide from the Lau Basin (a back-arc spreading center), all hydrothermal deposits are from a narrow region at $\sim 10^\circ\text{N}$ of the East Pacific Rise (EPR).

The Cd isotope data for the four black smoker sulfides cluster around a value of $\epsilon^{114/110}\text{Cd} \approx 0.5$ (Fig. 8.9) and were thought to record the isotope composition of the pristine hydrothermal fluids, from

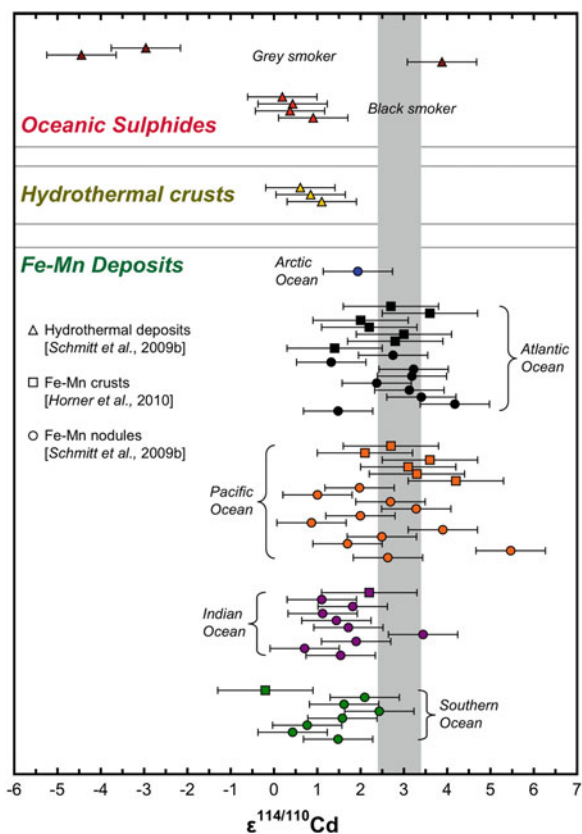


Fig. 8.9 Compilation of Cd isotope data (reported as $\epsilon^{114/110}\text{Cd}$ relative to NIST 3108 Cd) for marine sediments and deposits (Schmitt et al. 2009a; Horner et al. 2010). The samples are grouped by deposit type and location (for the hydrogenetic ferromanganese Fe-Mn deposits). The mean Cd isotopic composition of oceanic deep water (Ripperger et al. 2007) of $\epsilon^{114/110}\text{Cd} = 2.9 \pm 1.0$, is denoted by the grey band. The uncertainties (2sd) are shown as reported in the original publications

which the deposits were precipitated (Schmitt et al. 2009a). The $\epsilon^{114/110}\text{Cd}$ values of the chimney sulfides are lower than the average oceanic deep water value derived by Ripperger et al. (2007) ($\epsilon^{114/110}\text{Cd} \approx 2.9$, Fig. 8.8, Table 8.5) but similar to the bulk silicate Earth estimate of $\epsilon^{114/110}\text{Cd} \approx -0.3$ (Fig. 8.9, Table 8.5). This may indicate that the isotopic signature of pristine hydrothermal fluids is primarily inherited from Cd that is leached from the basaltic ocean crust, without significant isotope fractionation. The three hydrothermal Fe-Mn crusts display $\epsilon^{114/110}\text{Cd}$ values akin to those of the black smoker sulfides and hence these samples were also thought to record the Cd isotope composition of the (pristine) vent fluids, without large fractionation effects (Schmitt et al. 2009a).

The sulfides from a grey smoker ($T \approx 200^\circ\text{C}$) at the EPR displayed the largest Cd isotope variations of the hydrothermal deposits (Fig. 8.9). These samples displayed $\epsilon^{114/110}\text{Cd}$ values that varied between -4.5 and $+3.9$ and furthermore showed a good (negative) linear correlation with $1/[\text{Cd}]$. This correlation was speculated to be a consequence of sulfide precipitation in the vent system and associated isotope fractionation (Schmitt et al. 2009a). Similar processes were previously inferred to be responsible for the Zn isotope variability of these samples (John et al. 2008).

Investigations of hydrogenetic Fe-Mn deposits are of particular interest and such samples hence dominate the current Cd isotope database for marine sediments (Fig. 8.9). This interest is based on the observation that the surface layers of hydrogenetic Fe-Mn crusts and nodules faithfully record the isotopic composition of seawater for numerous trace metals. Consequently, time series data obtained for older deposits have been used in paleoceanographic studies, to interrogate temporal changes in the radiogenic (e.g., Nd, Pb) and stable (e.g., Tl, Mo) isotope composition of seawater (Frank 2002; Rehkämper et al. 2002, 2004; Siebert et al. 2003).

The compendium of presently available Cd isotope data encompasses 15 Fe-Mn crusts (Horner et al. 2010) and 37 Fe-Mn nodules (Schmitt et al. 2009a). These two types of deposits differ in that Fe-Mn crusts form on basaltic substrates whereas nodules are precipitated on pelagic sediments. Despite this difference, both crusts and nodules were observed to display similar Cd contents (of about 1–20 $\mu\text{g/g}$) and isotope compositions, with $\epsilon^{114/110}\text{Cd}$ values of between about 0 and $+5.5$ (Fig. 8.9, Table 8.5). In particular,

essentially all hydrogenetic Fe-Mn deposits are characterized by Cd isotope composition that are identical, within error, to the oceanic deep water average of $\epsilon^{114/110}\text{Cd} = 2.9 \pm 1.0$ (Ripperger et al. 2007). This result is significant because it implies that Fe-Mn crusts and nodules record the Cd isotope composition of seawater without significant isotopic fractionation (Schmitt et al. 2009a; Horner et al. 2010). This observation is surprising because it contrasts with the behavior of Zn, an element that generally exhibits similar marine biogeochemical characteristics to Cd (de Baar and La Roche 2002). The Zn isotope composition of deep ocean seawater (Bermin et al. 2006) appears to be offset from isotopically heavier Zn in Fe-Mn nodules (Maréchal et al. 2000) by about 5ϵ for $^{66}\text{Zn}/^{64}\text{Zn}$. This fractionation has been corroborated by laboratory studies, which have shown that “heavy” Zn isotopes are preferentially scavenged from solutions by (oxy)hydroxide precipitates (Pokrovsky et al. 2005; Balistrieri et al. 2008; Juillot et al. 2008). Offsets in stable isotope compositions between seawater and hydrogenetic Fe-Mn deposits are also common for other elements, including Mo (Barling et al. 2001) and Tl (Rehkämper et al. 2002; Rehkämper et al. 2004), although the mechanisms of isotopic fractionation are still the subject of ongoing research and may be different for each element.

The absence of isotopic effects during the incorporation of Cd into hydrogenetic Fe-Mn crusts and nodules is a promising result because this simplifies the interpretation of Cd isotope time series data that are obtained for such samples. Based on this finding, it may be possible to interpret temporal variations in $\epsilon^{114/110}\text{Cd}$ that are identified for Fe-Mn deposits, as reflecting changes in the Cd isotope composition of seawater, rather than differences in the isotopic fractionation between seawater and the Fe-Mn minerals. Preliminary time-resolved Cd isotope data were obtained for a Fe-Mn nodule from the Atlantic Ocean by Schmitt et al. (2009a). Six samples with ages of between 0 and 8 Ma were analyzed and no significant change in $\epsilon^{114/110}\text{Cd}$ was detected. This suggests that long-term temporal variations in the Cd isotope composition of oceanic deep water are likely to be small (Schmitt et al. 2009a). However, it is possible that the stable Cd isotope systematics of this nodule were altered by diagenetic processes, such as isotopic equilibration with Cd from pore fluids (Rehkämper et al. 2002).

The time series data for the nodules also do not preclude short-term fluctuations in the Cd isotope composition of the oceans and these may be best recorded in marine carbonates. This conclusion follows from the observation that the carbonate records of Cd/Ca (Boyle and Keigwin 1982; Boyle 1992) and other trace metal isotope systems (Lea 2006; Lynch-Stieglitz 2006) show significant variability on glacial/interglacial timescales. Cadmium isotope results are, however, currently not available for carbonate samples that are commonly employed in paleoclimate studies. This lack of data reflects the challenging nature of the analyses, which are rendered particularly difficult by the low Cd contents of such materials (e.g., foraminiferal tests; Table 8.5). This necessitates that large samples (typically >1 g) are processed for analysis, as at least 1–10 ng of Cd are required for a reasonably precise isotopic measurement. The only carbonates for which Cd isotope data are currently available, are aragonites from laboratory precipitation experiments. These samples were observed to exhibit consistently light Cd isotope signatures, with a fractionation of $-6.4 \pm 0.9 \text{ } \epsilon^{114/110}\text{Cd}$ ($\pm 2\text{sd}$) relative to the growth solution. It is possible but currently unconstrained whether natural biogenic carbonates exhibit similar Cd isotope effects.

8.4.5 Mass Independent Cd Isotope Fractionations

Most natural stable isotope fractionations scale with the mass differences of the isotopes involved. The ability to acquire more precise isotopic data as a consequence of advances in mass spectrometric techniques and instrumentation has, however, also enabled the identification of stable isotope effects that clearly do not scale with differences in nuclide mass. Such mass independent stable isotope effects were first documented for the light elements O and S (Thiemens 1999, 2006). More recently, the importance of mass independent fractionation for heavier elements was recognized based on results acquired for both natural samples (particularly Hg, Tl and U; Rehkämper et al. 2004; Smith et al. 2005; Xie et al. 2005; Schauble 2007; Stirling et al. 2007; Weyer et al. 2008; Blum 2011; Nielsen and Rehkämper 2011) and laboratory experiments (Hg, U and many other elements;

Biegeleisen 1996; Estrade et al. 2009; Fujii et al. 2009a).

For heavier elements, non-mass dependent isotope fractionations are generally thought to be a consequence of either nuclear volume (Biegeleisen 1996; Schauble 2007; Fujii et al. 2009a) or magnetic isotope effects (Buchachenko 2001). Nuclear volume fractionations are also known as nuclear field shift effects and are a consequence of non-mass dependent differences in nuclear volume and shape. Nuclear volume (or the nuclear charge radius) increases with the number of neutrons and this increase is generally slightly smaller for isotopes with odd mass numbers as compared to even mass numbers. Hence, nuclear volume effects are typically expected to generate odd-even isotope fractionation patterns (Biegeleisen 1996; Schauble 2007; Fujii et al. 2009a). In the case of Cd, ^{116}Cd is an exception, however (Fig. 8.10), as the nuclear volume of this even mass isotope displays a relative deficit similar to that observed for the odd mass isotopes ^{111}Cd and ^{113}Cd (Angeli 2004). Nuclear volume effects are most significant for heavier elements but smaller, yet resolvable, effects were also deemed to be reasonable, based on theoretical considerations, for elements that have atomic masses similar to those of Cd, such as Ru and Sn (Knyazev and Myasoedov 2001; Schauble 2007; Fujii et al. 2009a). Magnetic isotope effects stringently distinguish between isotopes with odd and even mass numbers, as they result from hyperfine coupling between the non-zero nuclear spins of odd nuclei and the magnetic moments of electrons (Buchachenko 2001).

Both nuclear volume and magnetic isotope fractionations have been suggested to affect Cd under certain conditions. Magnetic isotope effects, however, only appear to play a role during Cd isotope analyses by TIMS when silica gel is used as an activator. In particular, it was shown for such TIMS measurements that Cd isotope ratios with the odd mass nuclides ^{111}Cd and ^{113}Cd do not display a mass dependent instrumental fractionation relative to ratios that feature only the even mass isotopes ^{110}Cd , ^{112}Cd , ^{114}Cd and ^{116}Cd (Manhès and Göpel 2003, 2007; Schmitt et al. 2009b). Such odd-even isotope anomalies were also observed for Pb and Zn isotope analyses by TIMS (Thirlwall 2000; Doucelance and Manhès 2001; Manhès and Göpel 2003) and ascribed to a magnetic isotope effect because (1) nuclear volume fractionations would also generate anomalies for ^{116}Cd and (2)

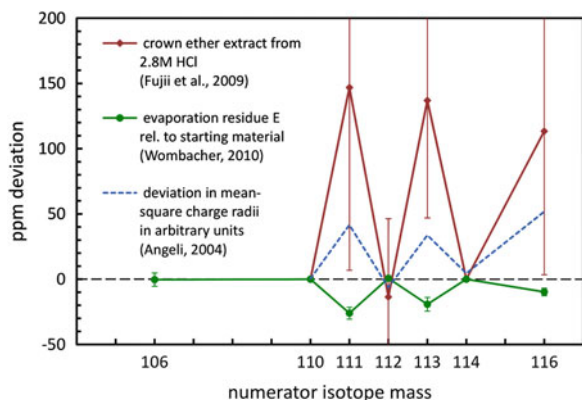


Fig. 8.10 Experimental evidence for nuclear volume Cd isotope effects that was obtained for a crown ether extraction experiment (Fujii et al. 2009b) and an evaporation residue (Wombacher 2010). The relative deviation of a Cd isotope ratio in parts per million (ppm) from the value expected for purely mass dependent stable isotope fractionation is shown on the y-axis. Results are depicted for all Cd isotope ratios from $^{106}\text{Cd}/^{114}\text{Cd}$ to $^{116}\text{Cd}/^{114}\text{Cd}$. The data for the odd mass isotopes ^{111}Cd and ^{113}Cd and the even isotope ^{116}Cd deviate from mass dependent behavior. This is in accord with the pattern expected for non-mass dependent nuclear volume effects, which reflect differences in nuclear charge radii (Angeli 2004). The results for the crown ether extract (Fujii et al. 2009b) were recalculated, such that ^{114}Cd is the common denominator; the uncertainties were assessed based on the reported δ -values and are likely to be overestimated. The data for the Cd evaporation residue E (see Fig. 8.1; Wombacher 2010) were obtained with a Neptune MC-ICPMS instrument (Universität Bonn) in 30 min analyses at high ion beam intensities. Shown are the average results ($\pm 2\text{sd}$ uncertainties) of three analyses conducted using two different collector settings and sample introduction systems. The generalized power law (with exponent $n = -0.353$) was applied to correct for the large mass dependent fractionation of the Cd, as described in (Wombacher et al. 2004)

comparatively large (permil-level) non-mass dependent effects were observed for ^{111}Cd and ^{113}Cd .

In order to investigate potential nuclear volume isotope effects for Cd, Fujii et al. (2009b) conducted an experimental study of isotope fractionation during extraction of Cd from aqueous HCl solutions using a crown ether dissolved in an immiscible organic solvent. Large Cd isotope fractionations of up to about 50‰ $^{114}/^{110}\text{Cd}$ were generated and resolvable non-mass dependent isotope effects were observed for ^{111}Cd , ^{113}Cd , and ^{116}Cd as a consequence of nuclear field shifts (Fig. 8.10). Fujii et al. (2009b) concluded that between 5 and 30% of the measured Cd isotope fractionations (depending on the isotope ratio evaluated) were contributions from nuclear field shift effects.

Further evidence for non-mass dependent Cd isotope effects was provided by analyses of highly fractionated Cd metal samples that were produced as residues of evaporation (Fig. 8.1, Sect. 8.4.1.1). Inspection of the original measurement results suggests that the isotope fractionation, which is recorded by ratios that include ^{111}Cd and ^{113}Cd , may indeed exhibit ppm level deviations from the trends defined by ^{106}Cd , ^{108}Cd , ^{110}Cd , ^{112}Cd and ^{114}Cd (Wombacher et al. 2004). These differences are, however, barely resolvable given the quoted analytical uncertainties. Wombacher (2010) reanalyzed these Cd metal samples with improved precision and determined small but clearly resolvable non-mass dependent isotope anomalies of -26 ± 5 , -19 ± 5 and -10 ± 3 ppm (parts per million) for $^{111}\text{Cd}/^{114}\text{Cd}$, $^{113}\text{Cd}/^{114}\text{Cd}$ and $^{116}\text{Cd}/^{114}\text{Cd}$, respectively (Fig. 8.10). Importantly, the relative magnitude of the measured effects is in accord with, or similar to, the fractionation pattern that is predicted based on published nuclear charge radius data (Fig. 8.10). The interpretation that the observed anomalies indeed reflect nuclear field shift effects from evaporation is furthermore supported by the observation of similar nuclear volume isotope effects for evaporation residues of Hg (Estrade et al. 2009).

The nuclear field shift effects determined for the evaporation of Cd are very small, however, as they contribute only about 0.5% to the total observed isotope fractionation from evaporation of Cd (Wombacher 2010). Hence, these non-mass dependent effects (Fig. 8.10) were only detectable because the absolute extent of mass dependent isotope fractionation from evaporation was extremely large, at up to almost 50‰ for $^{110}\text{Cd}/^{114}\text{Cd}$ (Fig. 8.1). The mass independent Cd isotope effects determined for TIMS analyses and crown ether extractions are much larger but these results may not be relevant for the generation of isotope anomalies in natural systems. Biological uptake of Cd has been shown to create large isotope fractionations (Figs. 8.6 and 8.7, Sect. 8.4.4.2) and thus provides an alternative pathway for the generation of mass-independent Cd isotope effects. Biological processes, however, are likely to involve bonding environments for Cd that exhibit significant covalent contributions (due to electron sharing) and such conditions are thought to greatly reduce the importance of nuclear field shift effects (Knyazev and Myasoedov 2001; Schauble 2007).

In summary, these observations suggest that mass independent Cd isotope effects may not be significant in nature. It will be important, however, to verify this somewhat speculative conclusion by further high-precision Cd isotope analyses of suitable, highly fractionated samples without use of a double spike. This is particularly significant as (1) non-mass dependent Cd isotope fractionations may enable novel tracer applications and (2) the current techniques of Cd double spike data reduction explicitly assume that any differences Cd isotope compositions arise only from mass dependent effects.

8.5 Future Directions and Outlook

The first targeted search for natural differences in the Cd isotope composition of terrestrial materials was conducted in the 1970s (Rosman and de Laeter 1975). However, no variability could be resolved until more precise mass spectrometric techniques were developed less than a decade ago (Wombacher et al. 2003; Ripperger and Rehkämper 2007; Schmitt et al. 2009b). The current Cd isotope database for terrestrial materials is still relatively small, compared to that available for other non-traditional stable isotope systems, such as Fe, Zn, or Mo (Johnson et al. 2004). However, small natural Cd isotope variations have been identified even for samples of the silicate Earth, such as rocks and minerals from the continental crust (Figs. 8.2 and 8.3). Furthermore, two specific mechanisms have been identified, which routinely generate larger Cd isotope fractionations in nature – these are partial evaporation/condensation (Wombacher et al. 2004; Cloquet et al. 2006) and biological utilization (Lacan et al. 2006; Ripperger et al. 2007). These findings have recently stirred significant interest in Cd isotope studies and an increasing number of laboratories are currently acquiring results.

Due to this interest, it is of particular importance to quickly establish a new zero- ϵ (or zero- δ) reference material that is universally adopted by all laboratories. This development is needed, to ensure that the results of different laboratories do not feature systematic offsets (which can result from poor intercalibration) but are accurate at the current level of analytical precision (about ± 0.1 to $0.3 \text{ } \epsilon\text{Cd/amu}$; Table 8.3). The currently ongoing intercalibration of NIST SRM 3108 Cd

(Abouchami et al. 2010b) is promising in this respect and will hopefully lead to the adoption of this standard as a universally accepted zero- ϵ reference material for Cd isotopes in the near future.

Given the current scarcity of Cd isotope data, it will be important for future studies to expand this database in a systematic manner. Of particular interest will be data acquired at high precision and accuracy, and these are probably best obtained using a double spike approach with either TIMS or MC-ICPMS (Tables 8.3 and 8.4). Additional analyses that are conducted without a double spike also will be important, however, to search for non-mass dependent Cd isotope anomalies. In any case, the samples for such analyses will need to be carefully chosen, as the methods are time-consuming and it is unclear whether future improvements in instrumentation or techniques will be able to significantly increase sample throughput. Regardless of such limitations, there are a number of interesting problems and potential applications, which should (and are very likely to be) investigated in the near future.

Fractionation mechanisms. A striking advantage of the Cd stable isotope system is that essentially all larger isotopic effects are known to be due to either evaporation/condensation or biological utilization. This observation is backed up by a few experimental studies, which clearly demonstrate the effect of these processes on Cd isotope compositions (Wombacher et al. 2004; Lacan et al. 2006). However, in detail, there are many questions that should be addressed. For example, Cd isotope fractionation by biological utilization has only been investigated in experiments with freshwater phytoplankton (Lacan et al. 2006), but such effects are most common and scientifically interesting in marine (seawater) environments. Hence, laboratory studies of Cd uptake by various marine organisms, which characterize potential vital effects and fractionation pathways are particularly desirable. Similarly, it has been observed that isotope fractionations for Cd (and other elements) from partial evaporation are typically much smaller (by about a factor of two) than expected from kinetic theory, which predicts a fractionation factor of $\alpha_{\text{kin}} = (m_2/m_1)^{0.5}$ (Wombacher et al. 2004, 2008). The origin of this behavior is currently not understood and should hence be investigated.

Anthropogenic Cd isotope fractionations. An improved understanding of Cd isotope effects from

evaporation and condensation is of particular interest, as a number of important anthropogenic fluxes of Cd to the environment involve volatilization. This includes, for example, the burning of coal and urban waste as well as the smelting and refining processes that are applied in the industrial production of Cd. Based on the results obtained to date (Fig. 8.2), combined Cd isotope and concentration measurements hold significant promise for the tracing and quantification of anthropogenic inputs and such studies are of particular relevance due to the high toxicity of Cd (Nriagu 1981). The isotopic tracing approach furthermore appears promising, given (1) the high volatility of Cd, which should aid in the generation of fractionation effects that are larger compared to those observed for the geochemically similar but less volatile element Zn; and (2) the lack of other significant (abiotic) fractionation pathways for Cd isotopes.

Cd isotope fractionation in the silicate Earth. Only few high precision isotopic data are currently available for samples of the Earth's continental crust and mantle. These results indicate very limited natural variability in Cd isotope compositions (Figs. 8.2 and 8.3, Table 8.5) but this may be an artifact of the small number of samples analyzed. Hence, additional high precision measurements are important that target diverse environments, lithologies and samples types, to confirm or revise the present observations. For example, preliminary results obtained for ultramafic samples may indicate that these differ in Cd isotope composition from mafic and felsic rocks, potentially as a result of magmatic processes (Schönbächler et al. 2009).

The primary aim of such analyses will be to better establish the extent of Cd isotope variability in the silicate Earth. Such data will be of importance to environmental scientists, as isotopic tracing of anthropogenic Cd is not feasible without a detailed understanding natural Cd isotope variations in the silicate Earth. Furthermore, the larger database will also provide more robust constraints on the Cd isotope composition of the silicate Earth. Notably, the best current estimate of $\epsilon^{114/110}\text{Cd}$ for the bulk silicate Earth (Table 8.5) is based on results for only seven silicate rock samples (Schmitt et al. 2009a). A comparison of the mean terrestrial $\epsilon^{114/110}\text{Cd}$ value with meteorite data is important, as this may provide new insights into the processes responsible for the volatile depleted

nature of the Earth and other planetary bodies (Palme et al. 1988; Wombacher et al. 2008).

Cd isotopes in marine environments. The small database for Cd isotopes in seawater is currently growing rapidly, as samples from the GEOTRACES research program (Measures 2007) are analyzed. The availability of such data for a wider range of marine locations and conditions is desirable, as this will enhance our understanding of the cycling and biological role of Cd in the oceans.

Further interest will focus on the question whether this larger dataset still exhibits a robust co-variation between Cd concentrations and isotope compositions (Fig. 8.7). Confirmation of this trend is desirable because this would provide a solid basis for paleoceanographic applications. Specifically, a robust $\epsilon^{114/110}\text{Cd}$ -[Cd] relationship for seawater would imply that marine records of Cd isotope compositions could be used, either alone or in combination with foraminiferal Cd/Ca ratios, to study past changes in ocean circulation and marine nutrient utilization (Boyle and Keigwin 1982; Boyle 1988; Rickaby and Elderfield 1999). Potential archives that warrant further investigation are Fe-Mn crusts and nodules (Schmitt et al. 2009a; Horner et al. 2010), the hydrogenetic components of pelagic sediments, and marine carbonates. The latter archives are of particular interest, as they can be sampled at sufficient resolution to resolve glacial-interglacial cycles. Hence, they can be used to further interrogate the role of the marine carbon cycle in driving changes in atmospheric CO_2 levels and global climate conditions (Elderfield and Rickaby 2000; Sigman and Boyle 2000). Cadmium isotope analyses of marine carbonates will be very challenging, however, as the low Cd contents of such phases necessitate that relatively large samples are processed for isotopic analyses. Typically, a precise Cd isotope analysis will require about 100–1,000 times more Cd than are necessary for Cd/Ca measurements of carbonates. Nonetheless, such analyses will be of great interest, if they can provide robust records for a marine $\epsilon^{114/110}\text{Cd}$ proxy that can be applied to study changes in marine nutrient levels.

The development of such paleoceanographic applications also requires, however, that any isotopic fractionation from incorporation of Cd into the archive is well characterized, ideally by studies of both natural

and experimental systems. The presently published data indicate that the incorporation of Cd into marine Fe-Mn oxyhydroxide phases is probably not accompanied by significant Cd isotope fractionations (Schmitt et al. 2009a; Horner et al. 2010), whilst such effects have been detected for carbonate phases (Wombacher et al. 2003). These first results, however, need to be thoroughly verified in further studies. An investigation of the dependence of carbonate mineral fractionation factors on temperature, precipitation rate and other parameters will be particularly important because the Cd/Ca ratios of planktonic foraminiferal tests have been shown to vary strongly with seawater temperature (Rickaby and Elderfield 1999).

Of general interest is, furthermore, an isotopic investigation of the sources and sinks of Cd in the oceans. For the sources, the analyses should ideally encompass rivers and estuarine systems, hydrothermal fluids and atmospheric inputs, including volcanic emissions, which might be expected to exhibit large Cd isotope effects from volatilization. Marine sedimentary deposits represent the main sink of Cd in the oceans, and relatively high Cd concentrations (of >100 ng/g) are commonly found in pelagic clays (Table 8.5) and C-rich sediments from continental margins (Heinrichs et al. 1980). Of particular importance is the application of these data to carry out an independent review of previously published mass balance estimates for the input and output fluxes of marine Cd. In addition, the isotopic results will also provide new constraints on the marine residence time of Cd, which has been estimated at about 18,000–180,000 a by previous investigations (Balistrieri et al. 1981; Martin and Whitfield 1983; Boyle 1988). These results will furthermore be of relevance for paleoceanography, as they inform on whether processes other than nutrient utilization are able to alter the Cd isotope composition of the oceans.

Acknowledgments Wafa Abouchami and Steve Galer from the Max Planck Institute for Chemistry in Mainz (Germany) are thanked for their efforts to identify a suitable common Cd isotope reference material and their encouragement to present data relative to the NIST standard in this manuscript. Constructive formal reviews by Tom Bullen and an anonymous referee as well as the editorial efforts of Mark Baskaran are gratefully acknowledged. F.W. thanks Carsten Münker, Stefan Weyer and Ambre Luguët for support of additional Cd isotope analyses of reference materials and Cd metal samples in the Neptune lab in Bonn and Steve Galer for discussions. M.R. is grateful for helpful advice and contributions provided by Maria Schönbacher.

References

- Abouchami W et al (2009) The Cd isotope signature of the Southern Ocean. *Eos Trans. AGU* 90, Fall Meet. Suppl: Abstract PP13A-1376
- Abouchami W et al (2010a) Cd isotopes, a proxy for water mass and nutrient uptake in the Southern Ocean. *Eos Trans. AGU* 91, Ocean Sci. Meet. Suppl: Abstract CO13A-03
- Abouchami W et al (2010b) In search of a common reference material for cadmium isotope studies. 2010 Goldschmidt Conference A2
- Andersen T, Knutsen AB (1962) Anion-exchange study. I. Adsorption of some elements in HBr-solutions. *Acta Chem Scand* 16:849–854
- Angeli I (2004) A consistent set of nuclear rms charge radii: properties of the radius surface $R(N, Z)$. *At Data Nucl Data* 87:185–206
- Aston FW (1935) The isotopic constitution and atomic weights of hafnium, thorium, rhodium, titanium, zirconium, calcium, gallium, silver, carbon, nickel, cadmium, iron and indium. *Proc R Soc Lond A* 149:396–405
- Aylett BJ (1973) Group IIB – cadmium. In: Trotman-Dickenson AF (ed) *Comprehensive inorganic chemistry*. Pergamon, Oxford
- Baker RGA et al (2010) The thallium isotope composition of carbonaceous chondrites – new evidence for live ^{205}Pb in the early solar system. *Earth Planet Sci Lett* 291:39–47
- Balistreri L, Brewer PG, Murray JW (1981) Scavenging residence times of trace metals and surface chemistry of sinking particles in the deep sea. *Deep Sea Res* 28:101–121
- Balistreri LS et al (2008) Fractionation of Cu and Zn isotopes during adsorption onto amorphous Fe(III) oxyhydroxide: experimental mixing of acid rock drainage and ambient river water. *Geochim Cosmochim Acta* 72:311–328
- Barling J, Arnold GL, Anbar AD (2001) Natural mass-dependent variations in the isotopic composition of molybdenum. *Earth Planet Sci Lett* 193:447–457
- Bender ML, Gagner CL (1976) Dissolved copper, nickel, and cadmium in the Sargasso Sea. *J Mar Res* 34:327–339
- Bermin J et al (2006) The determination of the isotopic composition of Cu and Zn in seawater. *Chem Geol* 226:280–297
- Biegeleisen J (1996) Nuclear size and shape effects in chemical reactions. *Isotope chemistry of the heavy elements*. *J Am Chem Soc* 118:3676–3680
- Blum JD (2011) Chapter 12 Applications of stable mercury isotopes to biogeochemistry. In: Baskaran MM (ed) *Handbook of environmental isotope geochemistry*. Springer, Berlin
- Böhlke JK et al (2005) Isotopic compositions of the elements, 2001. *J Phys Chem Ref Data* 34:57–67
- Boyle EA, Sclater F, Edmond JM (1976) On the marine geochemistry of cadmium. *Nature* 263:42–44
- Boyle EA (1981) Cadmium, zinc, copper, and barium in foraminifera tests. *Earth Planet Sci Lett* 53:11–35
- Boyle EA, Keigwin LD (1982) Deep circulation of the North Atlantic over the last 200,000 years: geochemical evidence. *Science* 218:784–787
- Boyle EA (1988) Cadmium: chemical tracer of deepwater paleoceanography. *Paleoceanography* 3:471–489
- Boyle EA (1992) Cadmium and $\delta^{13}\text{C}$ paleochemical ocean distributions during the Stage 2 glacial maximum. *Annu Rev Earth Planet Sci* 20:245–287

- Bruland KW (1980) Oceanographic distributions of cadmium, zinc, nickel, and copper in the North Pacific. *Earth Planet Sci Lett* 47:176–198
- Bruland KW (1983) Trace elements in sea-water. In: Ripley JP, Chester R (eds) *Chemical oceanography*. Academic Press, London
- Buchachenko AL (2001) Magnetic isotope effect: nuclear spin control of chemical reactions. *J Phys Chem A* 105:9995–10011
- Chizhikov DM (1966) *Cadmium*. Pergamon, Oxford
- Cloquet C, Carignan J, Libourel G (2005a) Kinetic isotope fractionation of Cd and Zn during condensation. *Eos Trans. AGU 86 Fall Meet. Suppl:Abstract V41F-1523*
- Cloquet C et al (2005b) Natural cadmium isotopic variations in eight geological reference materials (NIST SRM 2711, BCR 176, GSS-1, GXR-1, GXR-2, GSD-12, Nod-P-1, Nod-A-1) and anthropogenic samples, measured by MC-ICP-MS. *Geostand Geoanalyst Res* 29:95–106
- Cloquet C et al (2006) Tracing source pollution in soils using cadmium and lead isotopes. *Environ Sci Technol* 40:2525–2530
- Collier R, Edmond JM (1984) The trace element geochemistry of marine biogenic particulate matter. *Prog Oceanogr* 13:113–199
- Cotton FA, Wilkinson G (1988) *Advanced inorganic chemistry*. Wiley, New York
- Criss RE (1999) *Principles of stable isotope distribution*. Oxford University Press, Oxford
- Cullen JT et al (1999) Modulation of cadmium uptake in phytoplankton by seawater CO₂ concentration. *Nature* 402:165–167
- Cullen JT (2006) On the nonlinear relationship between dissolved cadmium and phosphate in the modern global ocean: could chronic iron limitation of phytoplankton growth cause the kink? *Limnol Oceanogr* 51:1369–1380
- Davis AM et al (2005) Isotopic mass-fractionation laws and the initial solar system ²⁶Al/²⁷Al ratio. *Lunar Planet Sci Conf XXXVI Abstract No:2334*
- de Baar HJW et al (1994) Cadmium versus phosphate in the world ocean. *Mar Chem* 46:261–281
- de Baar HJW, La Roche J (2002) Trace metals in the oceans: evolution, biology and global change. In: Wefer G, Lamy F, Mantoura F (eds) *Marine science frontiers for Europe*. Springer, Berlin
- De La Rocha CL et al (1998) Silicon-isotope composition of diatoms as an indicator of past oceanic change. *Nature* 395:680–683
- Dixon JL et al (2006) Cadmium uptake by marine micro-organisms in the English Channel and Celtic Sea. *Aquat Microb Ecol* 44:31–43
- Dodson MH (1963) A theoretical study of the use of internal standards for precise isotopic analysis by the surface ionization technique: part I – General first-order algebraic solutions. *J Sci Instrum* 40:289–295
- Donat JR, Bruland KW (1995) Trace elements in the oceans. In: Salbu B, Steinnes E (eds) *Trace elements in natural waters*. CRC Press, Boca Raton
- Doucelance R, Manhès G (2001) Reevaluation of precise lead isotope measurements by thermal ionization mass spectrometry: comparison with determinations by plasma source mass spectrometry. *Chem Geol* 176:361–377
- Elderfield H, Rickaby REM (2000) Oceanic Cd/P ratio and nutrient utilization in the glacial Southern Ocean. *Nature* 405:305–310
- Estrade N et al (2009) Mercury isotope fractionation during liquid-vapor evaporation experiments. *Geochim Cosmochim Acta* 73:2693–2711
- Faris JP, Buchanan RF (1964) Anion exchange characteristics of elements in nitric acid medium. *Anal Chem* 36:1157–1158
- Frank M (2002) Radiogenic isotopes: tracers of past ocean circulation and erosional input. *Rev Geophys* 40:1–38
- Frew RD, Hunter KA (1992) Influence of Southern Ocean waters on the cadmium–phosphate properties of the global ocean. *Nature* 360:144–146
- Fujii T, Moynier F, Albarède F (2009a) The nuclear field shift effect in chemical exchange reactions. *Chem Geol* 267:139–156
- Fujii T et al (2009b) Nuclear field shift effect in the isotope exchange reaction of cadmium using a crown ether. *Chem Geol* 267:157–163
- Galer SJG (1999) Optimal double and triple spiking for high precision lead isotopic measurements. *Chem Geol* 157:255–274
- Gao B et al (2008) Precise determination of cadmium and lead isotopic compositions in river sediments. *Anal Chim Acta* 612:114–120
- Gault-Ringold M et al (2009) Cadmium isotopic compositions and nutrient cycling in the Southern Ocean. *Goldschmidt Conference A418*
- Hein JR et al (1997) Iron and manganese oxide mineralization in the Pacific. In: Nicholson K, Hein JR, Bühn B, Dasgupta S (eds) *Manganese mineralization: geochemistry and mineralogy of terrestrial and marine deposits*. Special Publications, London
- Heinrichs H, Schulz-Dobrick B, Wedepohl KH (1980) Terrestrial geochemistry of Cd, Bi, Tl, Pb, Zn, and Rb. *Geochim Cosmochim Acta* 44:1519–1533
- Henderson GM (2002) New oceanic proxies for paleoclimate. *Earth Planet Sci Lett* 203:1–13
- Hendry KR et al (2008) Cadmium and phosphate in coastal Antarctic seawater: implications for Southern Ocean nutrient cycling. *Mar Chem* 112:149–157
- Hofmann A (1971) Fractionation correction for mixed-isotope spikes of Sr, K, and Pb. *Earth Planet Sci Lett* 10:397–402
- Holleman AF, Wiberg E, Wiberg N (1985) *Lehrbuch der Anorganischen Chemie* (91–100 ed). de Gruyter, Berlin
- Horner TJ et al (2010) Ferromanganese crusts as archives of deep water Cd isotope compositions. *Geochem Geophys Geosys* 11:Q04001. doi:10.1029/2009GC002987
- Hu Z, Gao S (2008) Upper crustal abundances of trace elements: a revision and update. *Chem Geol* 253:205–221
- Hulston JR, Thode HG (1965) Variations in the S³³, S³⁴, and S³⁶ contents of meteorites and their relation to chemical and nuclear effects. *J Geophys Res* 70:3475–3484
- John SG et al (2008) Zinc stable isotopes in seafloor hydrothermal vent fluids and chimneys. *Earth Planet Sci Lett* 269:17–28
- Johnson CM, Beard BL, Albarède F (Eds.) (2004) *Geochemistry of Non-Traditional Stable Isotopes*, 454 pp., Mineralogical Society, Washington, DC
- Juillot F et al (2008) Zn isotopic fractionation caused by sorption on goethite and 2-lines ferrihydrite. *Geochim Cosmochim Acta* 72:4886–4900
- Knyazev DA, Myasoedov NF (2001) Specific effects of heavy nuclei in chemical equilibrium. *Separ Sci Technol* 36:1677–1696

- Korkisch J (1989) Handbook of ion exchange resins: their application to inorganic analytical chemistry. CRC Press, Boca Raton
- Kraus KA, Nelson F (1955) Anion Exchange Studies of the Fission Products, paper presented at International Conference on the Peaceful Uses of Atomic Energy, United Nations, New York, Geneva, 1956
- Lacan F et al (2006) Cadmium isotopic composition in the ocean. *Geochim Cosmochim Acta* 70:5104–5118
- Lagos M et al (2008) The Earth's missing lead may not be in the core. *Nature* 456:89–92
- Lane TW et al (2005) A cadmium enzyme from a marine diatom. *Nature* 435:42
- Lea DW (2006) Elemental and isotopic proxies of past ocean temperatures. In: Elderfield H (ed) *The oceans and marine geochemistry*. Elsevier, Amsterdam
- Leland WT, Nier AO (1948) The relative abundances of the zinc and cadmium isotopes. *Phys Rev* 73:1206
- Li Y-H, Schoonmaker JE (2005) Chemical composition and mineralogy of marine sediments. In: Mackenzie FT (ed) *Sediments, diagenesis, and sedimentary rocks*. Elsevier, Amsterdam
- Lodders K (2003) Solar system abundances and condensation temperatures of the elements. *Astrophys J* 591:1220–1247
- Lynch-Stieglitz J (2006) Tracers of past ocean circulation. In: Elderfield H (ed) *The oceans and marine geochemistry*. Elsevier, Amsterdam
- Manhès G, Göpel C (2003) Heavy stable isotope measurements with thermal ionization mass spectrometry: non mass-dependent fractionation effects between even and uneven isotopes. *Geophys Res Abstr* 5:10936
- Manhès G, Göpel C (2007) Mass-independent fractionation during TIMS measurements: evidence of nuclear shift effect? *Geochim Cosmochim Acta* 71:A618
- Maréchal CN, Télouk P, Albarède F (1999) Precise analysis of copper and zinc isotopic compositions by plasma-source mass spectrometry. *Chem Geol* 156:251–273
- Maréchal CN et al (2000) Abundance of zinc isotopes as a marine biogeochemical tracer. *Geochem Geophys Geosys* 1:1999GC000029
- Martin JM, Whitfield M (1983) River input of chemical elements to the ocean. In: Wong CS, Boyle EA, Bruland KW, Burton JD, Goldberg ED (eds) *Trace metals in seawater*. Plenum, New York
- McDonough WF (1990) Constraints on the composition of the continental lithospheric mantle. *Earth Planet Sci Lett* 101:1–18
- McDonough WF, Sun S-s (1995) The composition of the Earth. *Chem Geol* 120:223–253
- McDonough WF (2005) Compositional model for the Earth's core. In: Davis AM (ed) *Meteorites, comets, and planets*. Elsevier, Amsterdam
- Measures C (2007) GEOTRACES – an international study of the global marine biogeochemical cycles of trace elements and their isotopes. *Chem d Erde Geochem* 67:85–131
- Nielsen SG, Rehkämper M (2011) Chapter 13 Thallium isotopes and their application to problems in earth and environmental science. In: Baskaran MM (ed) *Handbook of environmental isotope geochemistry*. Springer, Berlin
- Nier AO (1936) A mass-spectrographic study of the isotopes of argon, potassium, rubidium, zinc and cadmium. *Phys Rev* 50:1041–1045
- Nriagu JO (Ed.) (1981) *Cadmium in the Environment. Part II: Health Effects*, 908 pp., Wiley & Sons, New York
- Nriagu JO, Pacyna JM (1988) Quantitative assessment of worldwide contamination of air, water and soils by trace metals. *Nature* 333:134–139
- Palme H, Larimer JW, Lipschutz ME (1988) Moderately volatile elements. In: Kerridge JF, Matthews MS (eds) *Meteorites and the early solar system*. University of Arizona Press, Tucson
- Palme H, O'Neill HStC (2005) Cosmochemical estimates of mantle composition. In: Carlson RW (ed) *The mantle and core*. Elsevier, Amsterdam
- Pfennig G, Klewe-Nebenius H, Seelmann-Eggebert W (1998) Chart of the nuclides. Forschungszentrum Karlsruhe, Karlsruhe
- Pokrovsky OS, Viers J, Freydier R (2005) Zinc stable isotope fractionation during its adsorption on oxides and hydroxides. *J Coll Interf Sci* 291:192–200
- Price NM, Morel FMM (1990) Cadmium and cobalt substitution for zinc in marine diatom. *Nature* 344:658–660
- Prizkow W et al (2007) The isotope abundances and the atomic weight of cadmium by a metrological approach. *Int J Mass Spectrom* 261:74–85
- Rehkämper M, Schönbacher M, Stirling CH (2001) Multiple collector ICP-MS: introduction to instrumentation, measurement techniques and analytical capabilities. *Geostand Newslett* 25:23–40
- Rehkämper M et al (2002) Thallium isotope variations in seawater and hydrogenetic, diagenetic, and hydrothermal ferromanganese deposits. *Earth Planet Sci Lett* 197:65–81
- Rehkämper M et al (2004) Cenozoic marine geochemistry of thallium deduced from isotopic studies of ferromanganese crusts. *Earth Planet Sci Lett* 219:77–91
- Richter FM et al (2002) Elemental and isotopic fractionation of type B calcium-, aluminum-rich inclusions: experiments, theoretical considerations, and constraints on their thermal evolution. *Geochim Cosmochim Acta* 66:521–540
- Rickaby REM, Elderfield H (1999) Planktonic foraminiferal Cd/Ca: paleonutrients or paleotemperature? *Paleoceanography* 14:293–303
- Ripperger S, Rehkämper M (2007) Precise determination of cadmium isotope fractionation in seawater by double-spike MC-ICPMS. *Geochim Cosmochim Acta* 71:631–642
- Ripperger S et al (2007) Cadmium isotope fractionation in seawater – a signature of biological activity. *Earth Planet Sci Lett* 261:670–684
- Ripperger S et al (2008) Cd/Ca ratios of in situ collected planktonic foraminiferal tests. *Paleoceanography* 23:PA3209
- Rosman KJR, de Laeter JR (1975) The isotopic composition of cadmium in terrestrial minerals. *Int J Mass Spectrom Ion Phys* 16:385–394
- Rosman KJR, de Laeter JR (1976) Isotopic fractionation in meteoritic cadmium. *Nature* 261:216–218
- Rosman KJR, de Laeter JR (1978) A survey of cadmium isotopic abundances. *J Geophys Res* 83:1279–1287
- Rosman KJR et al (1980) Isotope composition of Cd, Ca, Mg in the Brownfield chondrite. *Geochem J* 14:269–277
- Rudge JF, Reynolds BC, Bourdon B (2009) The double spike toolbox. *Chem Geol* 265:420–431
- Rudnick RL, Gao S (2005) Composition of the continental crust. In: Rudnick RL (ed) *The crust*. Elsevier, Amsterdam
- Sands DG, de Laeter JR, Rosman KJR (2001) Measurements of neutron capture effects on Cd, Sm and Gd in lunar samples

- with implications for the neutron energy spectrum. *Earth Planet Sci Lett* 186:335–346
- Schauble EA (2007) Role of nuclear volume in driving equilibrium stable isotope fractionation of mercury, thallium, and other very heavy elements. *Geochim Cosmochim Acta* 71: 2170–2189
- Schediwy S, Rosman KJR, de Laeter JR (2006) Isotope fractionation of cadmium in lunar material. *Earth Planet Sci Lett* 243:326–335
- Schmitt A-D, Galer SJG, Abouchami W (2009a) Mass-dependent cadmium isotopic variations in nature with emphasis on the marine environment. *Earth Planet Sci Lett* 277:262–272
- Schmitt A-D, Galer SJG, Abouchami W (2009b) High-precision cadmium stable isotope measurements by double spike thermal ionisation mass spectrometry. *J Anal At Spectrom* 24: 1079–1088
- Schönbächler M et al (2009) The cadmium isotope composition of the Earth. *Geochim Cosmochim Acta* 73:A1183
- Shannon RD (1976) Revised effective ionic radii and systematic studies of interatomic distances in halides and chalcogenides. *Acta Cryst* A32:751–767
- Shiel AE et al (2009) Matrix effects on the multi-collector inductively coupled plasma mass spectrometric analysis of high-precision cadmium and zinc isotope ratios. *Anal Chim Acta* 633:29–37
- Shiel AE, Weiss D, Oriens KJ (2010) Evaluation of zinc, cadmium and lead isotope fractionation during smelting and refining. *Sci Total Environ* 408:2357–2368
- Siebert C et al (2003) Molybdenum isotope records as a potential new proxy for paleoceanography. *Earth Planet Sci Lett* 211:159–171
- Sigman DM, Boyle EA (2000) Glacial/interglacial variations in atmospheric carbon dioxide. *Nature* 407:859–869
- Simon JI, Young ED (2007) Evaporation and Mg isotope fractionation: model constraints for CAIs. *Lunar Planet Sci XXXVIII Abstract No:2426*
- Slater JC (1964) Atomic radii in crystals. *J Chem Phys* 41: 3199–3204
- Smith CN et al (2005) Mercury isotope fractionation in fossil hydrothermal systems. *Geology* 33:825–828
- Stirling CH et al (2007) Low-temperature isotopic fractionation of uranium. *Earth Planet Sci Lett* 264:208–225
- Strelow FWE (1978) Distribution coefficients and anion exchange behavior of some elements in hydrobromic-nitric acid mixtures. *Anal Chem* 50:1359–1361
- Sunda WG, Huntsman SA (2000) Effect of Zn, Mn, and Fe on Cd accumulation in phytoplankton: implications for oceanic Cd cycling. *Limnol Oceanogr* 45:1501–1516
- Taylor SR, McLennan SM (1985) *The continental crust: its composition and evolution*. Blackwell Scientific, Oxford
- Thiemens MH (1999) Mass independent isotope effects in planetary atmospheres and the early solar system. *Science* 283: 341–345
- Thiemens MH (2006) History and applications of mass-independent isotope effects. *Annu Rev Earth Planet Sci* 34: 217–262
- Thirlwall MF (2000) Inter-laboratory and other errors in Pb isotope analyses investigated using a ^{207}Pb - ^{204}Pb double spike. *Chem Geol* 163:299–322
- Wasson JT, Kallemeyn GW (1988) Compositions of chondrites. *Phil Trans R Soc Lond Ser A* 325:535–544
- Wedepohl KH (1995) The composition of the continental crust. *Geochim Cosmochim Acta* 59:1217–1232
- Wetherill GW (1964) Isotopic composition and concentration of molybdenum in iron meteorites. *J Geophys Res* 69: 4403–4408
- Weyer S et al (2008) Natural fractionation of $^{238}\text{U}/^{235}\text{U}$. *Geochim Cosmochim Acta* 72:345–359
- Wieser ME (2006) Atomic weights of the elements (IUPAC technical report). *Pure Appl Chem* 78:2051–2066
- Witt-Eickchen G et al (2009) The geochemistry of the volatile trace elements As, Cd, Ga, In and Sn in the Earth's mantle: new evidence from in situ analyses of mantle xenoliths. *Geochim Cosmochim Acta* 73:1755–1778
- Wombacher F, Rehkämper M (2003) Investigation of the mass discrimination of multiple collector ICP-MS using neodymium isotopes and the generalised power law. *J Anal At Spectrom* 18:1371–1375
- Wombacher F et al (2003) Stable isotope compositions of cadmium in geological materials and meteorites determined by multiple collector-ICPMS. *Geochim Cosmochim Acta* 67: 4639–4654
- Wombacher F, Rehkämper M (2004) Problems and suggestions concerning the notation of Cd stable isotope compositions and the use of reference materials. *Geostand Geoanal Res* 28:173–178
- Wombacher F et al (2004) Determination of the mass-dependence of cadmium isotope fractionation during evaporation. *Geochim Cosmochim Acta* 68:2349–2357
- Wombacher F et al (2008) Cadmium stable isotope cosmochemistry. *Geochim Cosmochim Acta* 72:646–667
- Wombacher F (2010) Mass-independent cadmium isotope fractionation during evaporation. 88th Ann. Meet. German Mineral. Soc. p 65
- Workman RK, Hart SR (2005) Major and trace element composition of the depleted MORB mantle (DMM). *Earth Planet Sci Lett* 231:53–72
- Xie Q et al (2005) High precision Hg isotope analysis of environmental samples using gold trap-MC-ICP-MS. *J Anal At Spectrom* 20:515–522
- Xu Y et al (2008) Structure and metal exchange in the cadmium carbonic anhydrase of marine diatoms. *Nature* 452:56–62
- Xue Z et al (2010a) Cadmium isotope constraints on nutrient cycling in the Peruvian oxygen minimum zone. *Goldschmidt 2010 Conference* A1166
- Xue Z et al (2010b) Cadmium isotope fractionation in the Southern Ocean. *Eos Trans. AGU* 91, Ocean Sci Meet Suppl:Abstract CO15C-12
- Yee N, Fein J (2001) Cd adsorption onto bacterial surfaces: a universal adsorption edge. *Geochim Cosmochim Acta* 65:2037–2042
- Yi W et al (2000) Cadmium, indium, tin, tellurium, and sulfur in oceanic basalts: implications for chalcophile element fractionation in the Earth. *J Geophys Res* 105:18927–18948
- Young ED, Galy A, Nagahara H (2002) Kinetic and equilibrium mass-dependent isotope fractionation laws in nature and their geochemical and cosmochemical significance. *Geochim Cosmochim Acta* 66:1095–1104

Chapter 9

Stable Isotopes of Cr and Se as Tracers of Redox Processes in Earth Surface Environments

Thomas M. Johnson

Abstract Redox reactions play a central role in the environmental geochemistry of chromium (Cr) and selenium (Se). A small but growing body of research shows that the stable isotope abundances of both elements are altered by these redox reactions. As is observed with nitrate and sulfate, reduction of the higher valence oxoanions to lower valence forms induces isotopic fractionation, with the reaction product enriched in lighter isotopes. The magnitudes of isotope ratio shifts range up to 4.5‰ for $^{53}\text{Cr}/^{52}\text{Cr}$ during Cr(VI) reduction, and up to 18‰ for $^{82}\text{Se}/^{76}\text{Se}$ during Se(VI) or Se(IV) reduction, but they vary with reaction mechanism and can be much smaller for environmentally relevant conditions. Other chemical processes generally produce lesser fractionation. Accordingly, Cr and Se isotope ratios have potential as indicators of reduction. Application of Cr isotope data as a quantitative indicator of natural reduction of hexavalent Cr in groundwater appears to be successful. Application of Se isotope data to constrain selenate reduction in wetlands has not been successful because effective fractionations induced by redox reactions are small, but recent studies suggest that reduction in groundwater produces significant fractionation and may be detected using Se isotope measurements.

9.1 Introduction

Chromium and selenium each have multiple valence states in environmental systems, and reduction and oxidation (redox) reactions are of central importance in their geochemistry. These reactions alter the two elements' chemical behavior markedly and can provide energy for biological activity relevant to environmental processes. Redox reactions have the potential to induce large isotopic fractionations because they greatly alter the atoms' bond energies. Decades of C, N, and S isotope studies have exploited redox-related isotope ratio shifts (e.g., Valley and Cole 2001). More recent research has revealed that many heavier elements exhibit similar redox-driven isotopic fractionation. In this chapter, we review research on Cr and Se isotopes together, because of similarities in their isotope systematics and applications.

Decades of theoretical studies of isotopic fractionation, mostly focused on lighter elements, provide some general systematic concepts that aid in understanding redox-driven isotopic fractionation in the Cr and Se isotope systems. We provide only a brief review here; more complete reviews exist, and those treat these concepts in detail (e.g., Valley and Cole 2001). Many studies have predicted equilibrium isotope fractionation, using chemical bond energies derived from spectroscopic data and molecular models (Chacko et al. 2001; Schauble et al. 2004). The most general prediction is that, at isotopic equilibrium, heavier isotopes of an element tend to partition into sites with greater bonding energies (Criss 1999). Greater valence number generally leads to shorter bonds with greater energies, so heavier isotopes tend to be enriched in phases containing higher valence states, relative to

T.M. Johnson
Department of Geology, University of Illinois at Urbana-Champaign, Urbana, IL 61801, USA
e-mail: tmjohnsn@illinois.edu

phases containing lower valence states with which they are in isotopic equilibrium.

At earth surface conditions, however, redox reactions are often far from equilibrium and proceed dominantly in one direction with little back reaction. This absence of chemical equilibrium is often accompanied by an absence of isotopic equilibrium. The most important C and S isotope effects at earth surface temperatures arise from reduction reactions (photosynthesis and sulfate reduction) operating far from equilibrium (Canfield 2001; Hayes 2001). In these cases, *kinetic isotope effects* may occur. In the simplest form of kinetic isotope fractionation, bonds of lighter isotopes are effectively weaker, so their reaction rates tend to be greater than those of heavier isotopes (Bigeleisen 1949; Criss 1999). For example, during sulfate reduction, the weaker bonds in ^{32}S -bearing sulfate cause it to have a greater reaction rate compared to ^{34}S -bearing sulfate (Canfield 2001).

Kinetic isotope fractionation can be complex, and the fractionation factor for a given reaction varies, depending on the reaction mechanism and/or the relative rates of steps within a multi-step reaction. For example, the magnitude of S isotope fractionation induced by microbial sulfate reduction depends on the type of microbial metabolism and, for a single species, on the electron donor availability and other environmental variables (Kaplan and Rittenberg 1964; Detmers et al. 2001). Furthermore, individual steps within a multi-step reaction can be close to isotopic equilibrium while the overall reaction is not (Hayes 2001). This leads to complex and variable kinetic

isotopic effects observed for the overall reaction. A basic understanding of this variability is essential in applying Se and Cr isotopes in geochemical studies.

9.1.1 Chromium Geochemistry and Stable Isotopes

The aqueous geochemistry of Cr was reviewed recently by Ball and Nordstrom (1998); an Eh-pH diagram is presented in Fig. 9.1. Chromium is a group 6 element; the +6 valence is stable under oxidizing conditions. This is also true of S, and thus some insight into Cr isotope geochemistry can be gained from understanding that of S. The chromate (CrO_4^{2-}) and hydrochromate (HCrO_4^-) ions, together referred to as Cr(VI), are generally soluble, weakly adsorbing, and mobile (Davis and Olsen 1995). Under weakly to strongly reducing conditions, Cr(VI) tends to reduce to the +3 valence, or Cr(III), which is geochemically similar to ferric iron. It readily precipitates and/or adsorbs to solid surfaces. Importantly, Cr is mobile and bioavailable in its oxidized forms, but generally immobile and non-bioavailable in its reduced forms. Cr(III) can be oxidized to Cr(VI), but oxidation by dissolved oxygen is slow. MnO_2 minerals are thought to be required for rapid oxidation of Cr(III) (Fendorf et al. 1993).

Cr(VI) has been used in several common industrial processes (U.S. Department of Health 2000); groundwater Cr(VI) plumes are present in most industrial

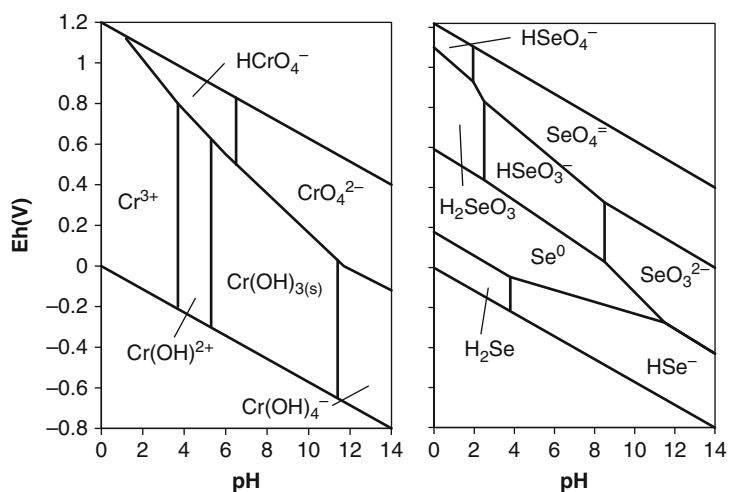


Fig. 9.1 Thermodynamic stability diagrams for Cr and Se after Ball and Nordstrom (1998) and Séby et al. (2001), respectively. Total Cr and Se concentrations are 10^{-6} and 10^{-8} M, respectively

centers of developed countries and occasionally at rural industrial installations. Cr(VI) also occurs naturally, where weathering of ultramafic rocks occurs (Oze et al. 2007; Izbicki et al. 2008). Cr(VI) is known to have various negative health effects whereas Cr(III) is relatively non-toxic (Katz and Salem 1994). The U.S. Environmental Protection Agency's drinking water maximum contaminant level for chromium is 0.10 mg/L (U.S. Environmental Protection Agency 2009). Cr(VI) reduction is often an attractive remediation strategy, as it immobilizes and detoxifies the Cr. In some cases, natural reduction occurs, whereas in other cases, active remediation is attempted by emplacement of reducing agents or stimulation of microbial action (Blowes 2002).

Cr has four stable isotopes, ^{50}Cr , ^{52}Cr , ^{53}Cr , ^{54}Cr , with natural abundances 4.3, 83.8, 9.5, and 2.4%, respectively. All studies to date have measured the $^{53}\text{Cr}/^{52}\text{Cr}$ ratio, which provides a mass difference of about 2%.

9.1.2 Selenium Geochemistry and Stable Isotopes

The aqueous geochemistry of Se is reviewed in a recent article (Seby et al. 2001); an Eh-pH diagram is presented in Fig. 9.1. Se is a group 16 element, with valence electron configurations and geochemical properties similar to those of S. Like S, Se is stable in the +6 and -2 valence states. Selenate (SeO_4^{2-}) and selenide (Se^{2-}) species, which are geochemically similar to sulfate and sulfide, are formed. However, Se geochemistry departs from that of S in that the +4 and 0 valences can be thermodynamically stable (Seby et al. 2001). The +4 valence forms SeO_3^{2-} and HSeO_3^- ions, together referred to as Se(IV), which are highly soluble like Se(VI), but more prone to sorption. The 0 valence state readily forms a solid Se^0 precipitate, even at sub-micromolar concentrations (McNeal and Balistrieri 1989; Seby et al. 2001). Like Cr, Se is highly mobile and bioavailable in its oxidized forms, but is often reduced to insoluble Se(0) and precipitated in moderately reducing environments. Alternatively, under moderately to strongly reducing conditions, metal selenides (e.g., HgSe , CuSe , Ag_2Se , FeSe) may form. In Se-contaminated

modern environments, reduction may sequester soluble Se in insoluble reduced forms.

Like S, Se is utilized in biological activity. But whereas most systems contain inorganic S well in excess of biological uptake, Se is much less abundant and much of the bioavailable Se in a given system may cycle like a nutrient (Cutter and Cutter 2001), with organic forms more abundant than inorganic forms in some waters and many sediments (Clark and Johnson 2010). The strong organic cycling of Se, combined with the stability of the +4 and 0 valences, causes the environmental geochemistry of Se to differ greatly from that of sulfur.

Se is used by organisms as a nutrient, but at concentrations only one to two orders of magnitude above optimal levels, Se may be toxic and has caused disease, deformity, and/or death among certain animals and, in very rare cases, among humans (Lemly 1998; Skorupa 1998; Zhu et al. 2004). In most cases, Se contamination arises from weathering of Se-rich sedimentary rocks, with human land and water management playing an important role (Presser 1994). Mining activities can release problematic masses of Se in some cases (Stilling and Amacher 2010). The drinking water maximum contaminant level for selenium is 0.050 mg/L (U.S. Environmental Protection Agency 2009).

Se has six stable isotopes, ^{74}Se , ^{76}Se , ^{77}Se , ^{78}Se , ^{80}Se , and ^{82}Se , with natural abundances 0.89, 9.4, 7.6, 23.8, 49.6, and 8.7%, respectively. Although Se is a somewhat heavy element, the mass of ^{82}Se is nearly 8% greater than that of ^{76}Se in the commonly measured $^{82}\text{Se}/^{76}\text{Se}$ ratio. This large difference amplifies isotopic fractionation.

9.2 Methods

9.2.1 Notation and the Rayleigh Fractionation Equation

This chapter focuses on mass-dependent fractionation of isotopes, in which chemical processes shift the relative abundances of heavy isotopes of an element relative to its lighter isotopes. These shifts are expressed as ratios of abundances, and by convention that of the heavier isotope is the numerator. For example:

$$R = \frac{{}^{53}\text{Cr}}{{}^{52}\text{Cr}} \quad (9.1)$$

Because meaningful variations in R are much less than one percent, it is inconvenient to write ratios explicitly (e.g., 0.11338 and 0.11339 may be significantly different ratios). Measured ratios are thus expressed as relative deviations of a measured ratio from that of a standard reference material:

$$\delta^{53}\text{Cr} = \frac{R_{\text{Sample}}}{R_{\text{Standard}}} - 1. \quad (9.2)$$

Typically, delta is expressed in parts per thousand, or per mil. For example, if the measured ratio is greater than that of the standard by a factor of 1.002, then $\delta^{53}\text{Cr} = 0.002$, which typically is written as “+2‰.” Alternatively, this result can be expressed in parts per million, i.e., “+2,000 ppm.” Some workers have used the symbol ε in place of δ to express “parts per 10,000” deviation. This can lead to confusion, as ε has long been used to conveniently express the magnitude of an isotopic fractionation (see below).

It is essential to have a parameter that expresses quantitatively the degree to which isotopes are fractionated by a chemical process. This is done by defining a fractionation factor, which compares the isotope ratio of a reactant to that of a product, or compares two phases in equilibrium:

$$\alpha = \frac{R_{\text{Reactant}}}{R_{\text{Product}}} \quad (9.3)$$

or

$$\alpha = \frac{R_{\text{Product}}}{R_{\text{Reactant}}} \quad (9.4)$$

One can choose either of these two definitions of alpha. The latter may seem a natural choice, but the former has been used for decades by the carbon and sulfur isotope communities because it is more convenient (see below). Both have been used in the Cr and Se isotope literature.

Just as it is more convenient to express measurement results using δ rather than R , the parameter ε is defined to conveniently quantify isotopic fractionation:

$$\varepsilon = \alpha - 1, \quad (9.5)$$

ε is expressed in per mil form, and is a convenient quantity because it is very close to the difference in delta values between the reactant and the product flux:

$$\varepsilon \approx \delta_{\text{reactant}} - \delta_{\text{product}}, \quad (9.6)$$

when (9.3) is used to define α . For example, if R_{reactant} is greater than R_{product} by a factor of 1.002, we write $\varepsilon = +2\text{‰}$.

For normal kinetic isotope effects, $R_{\text{reactant}} > R_{\text{product}}$ and thus ε is a positive quantity when (9.3) is used to define α . When (9.4) is used to define α , simple kinetic effects lead to ε values that are equal in magnitude but negative in sign. This leads to confusing language, because greater (stronger) isotopic fractionation corresponds to lesser (more negative) ε values. For this reason, studies focusing on “normal” kinetic effects, in which reaction products are depleted in heavy isotopes relative to reactants (Canfield 2001; Hayes 2001) often choose (9.3) as the definition of α . This approach is followed in this chapter.

The magnitude of equilibrium isotope fractionation is often expressed using Δ :

$$\Delta \equiv \delta_A - \delta_B, \quad (9.7)$$

where A and B are the two phases in equilibrium. Like ε , Δ is more convenient than α for routine use.

When kinetic isotope effects occur, the Rayleigh distillation equation is often invoked to provide quantitative relationships between the extent of the reaction and the isotope ratios of the reactant and product. This concept applies rigorously to a closed, well-mixed system in which the reaction products do not interact with the reactant pool (e.g, no back-reaction occurs). When α is defined as $R_{\text{reactant}}/R_{\text{product}}$, the Rayleigh equation giving the isotopic composition of the remaining reactant is:

$$\delta = (\delta_0 + 1000)f^{\frac{1}{\alpha} - 1} - 1000, \quad (9.8)$$

where f is the fraction of reactant remaining. An example of a Rayleigh model is plotted in Fig. 9.2, along with an equilibrium fractionation model, in which the product and reactant remain in full isotopic equilibrium as a reaction proceeds.

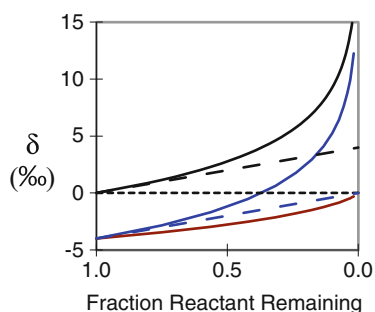


Fig. 9.2 Models for isotopic fractionation as a function of the extent of a reaction. *Solid lines* give values for a Rayleigh model with $\epsilon = 4\%$; *dashed lines* for an equilibrium model with $\Delta = 4\%$. For both models, black lines give the isotopic composition of the reactant; blue lines give that of the accumulated reaction product. The *red line* gives the isotopic composition of the product flux (the incremental product produced at one instant in time) for the Rayleigh model

9.2.2 Sampling

Water samples must be treated carefully to maintain species in solution and avoid isotopic fractionation during transport and storage. In all cases, samples must be filtered to avoid microbial redox reactions and resulting isotopic shifts. Even after filtration, Cr (VI) may be reduced by abiotic reducing agents such as dissolved organic molecules. Reduction to Cr(III), which causes loss of Cr from solution and alters isotope ratios, is promoted by acidic conditions, so acidification of samples should be avoided (Stollenwerk and Grove 1985). Se(VI) is relatively insensitive to abiotic reduction and acidification of waters to $\text{pH} < 2$ has been recommended for preservation of dissolved speciation (Cheam and Agemian 1980). However, Se(IV) is more prone to reduction via abiotic reduction, and Se(IV) oxidation has been reported for some HCl-bearing solutions (Heninger et al. 1997). It is wise to monitor Se(IV) concentrations, if possible, during sample storage. Refrigeration of samples is highly advantageous for both Se and Cr, as it slows these reactions (Heninger et al. 1997). Storage in the dark is also advisable, to avoid photochemical reactions.

Samples of solid materials can be similarly unstable, as microbial action and ongoing abiotic reactions can greatly change redox speciation and alter isotope ratios during transport and storage. Immediate processing of samples and/or refrigeration, and/or careful exclusion of air may be required.

9.2.3 Mass Spectrometry

Methods for Cr and Se isotope measurements are rather specialized, and a number of analytical issues affect how studies are planned and carried out (e.g., choices of analytical hardware and method dictate minimum usable sample size). For this reason, the major analytical issues are reviewed here with the goal of providing a guide for non-specialists to navigate the analytical choices involved. Sample preparation methods are described after this section, as those methods are determined by the details of mass spectrometry reviewed here.

9.2.3.1 Hardware Choices and Double Spike Methods

Most recent Cr and Se isotope studies employ multi-collector inductively coupled plasma mass spectrometry (MC-ICP-MS), in which the analyte is ionized in a plasma, the ion beam passes through a magnetic sector to separate the isotopes, and the individual ions beams are measured simultaneously in an array of Faraday collectors (Albarède and Beard 2004). Single collector ICP-MS instruments do not provide the required precision for the vast majority of Cr and Se applications. Thermal ionization mass spectrometry (TIMS) is a viable option for both elements. Well-developed methods exist, though they generally have lesser sample throughput, compared to MC-ICP-MS.

Both TIMS and MC-ICP-MS instruments exhibit “mass bias.” MC-ICP-MS instruments have a strong bias in favor of heavier isotopes (See reviews by Albarède and Beard 2004; Weiss et al. 2008). For example, measured $^{53}\text{Cr}/^{52}\text{Cr}$ ratios are a few percent larger than true values. With TIMS, the bias is roughly an order of magnitude smaller, but changes over time during analysis. With MC-ICP-MS, the bias is nearly constant over time, and can be determined by analyzing standards before and after each sample (Albarède and Beard 2004). However, this “sample-standard bracketing” approach can lose precision if mass bias variation between standards does not vary smoothly because of instrumental noise or sample matrix effects.

Some Cr and Se MC-ICP-MS studies, and all of the TIMS studies, have employed double isotope tracer, or “double spike” methods to determine instrumental

mass bias (Johnson and Beard 1999; Johnson et al. 1999; Clark and Johnson 2008; Schoenberg et al. 2008; Berna et al. 2010). A “spike” solution containing two stable isotopes (e.g., for Cr, ^{54}Cr and ^{50}Cr are used) in a known ratio is mixed thoroughly with each sample (i.e., care must be taken to assure complete isotopic equilibration between spike and sample). The measured ratio of the spike isotopes is then used to monitor mass bias. Although this ratio is partially determined by the sample’s contributions to the spike isotope signals, the relative proportions of spike and sample are precisely determined, and the spike and sample contributions to measured signals are separated mathematically. Calculation routines to carry this out are complex, but they are described in the literature and, once implemented, require little effort per sample (Johnson and Beard 1999; Johnson et al. 1999; Schoenberg et al. 2008).

The double spike approach has important advantages: It monitors mass bias during, not before and after, sample measurements and thus can accommodate sample matrix effects and non-systematic shifts in mass bias. Also, it can correct for isotopic fractionation that may occur during sample preparation, provided the spike is mixed with the sample prior to sample preparation steps. Finally, it can provide highly precise concentration measurements if the spike solution’s concentration is carefully calibrated. The double spike approach also has some disadvantages: At least four isotopes must be measured rather than two, and this may increase the number of interferences that must be addressed. Furthermore, many elements (e.g., Li, Mg, Si, Cu, Sb, Tl) have fewer than 4 stable isotopes.

A third approach used to correct for MC-ICP-MS mass bias drift is the “elemental spike” approach. In this case, a second element is doped into the analyzed solution; drift in the mass bias is monitored by measuring drift in an isotope ratio of the spike element. For example, Cu can be used as an elemental spike for Fe analyses, with the $^{65}\text{Cu}/^{63}\text{Cu}$ ratio monitored to detect mass bias drift (Albarède and Beard 2004). There has been minor use of Sr as an elemental spike for Se (Rouxel et al. 2002), but overall, this approach has not been used for Cr and Se.

9.2.3.2 Cr Mass Spectrometry Methods

Methods used for Cr isotope analysis are closely similar to those used for Fe, with most of the methods

development occurring first for Fe measurements, with later adaptation to Cr. A double spike TIMS method for Cr (Ellis et al. 2002) was used in a few studies and, though its usage seems to be waning, it remains a viable option. MC-ICP-MS analysis offers faster sample throughput but is more prone to interfering species with masses close to those of the Cr isotopes. ArC^+ , ArN^+ , ClO^+ , and SO^+ interferences can be avoided using high resolution methods (Halicz et al. 2008; Schoenberg et al. 2008) that closely follow methods used for Fe (Weyer and Schwieters 2003). Recent methods and mass spectrometers are capable of resolving small differences in mass, thereby measuring the Cr isotopes while excluding interfering ArC^+ and ArN^+ ions, which have slightly greater masses. This approach, first developed for Fe isotope ratios (Weyer and Schwieters 2003) requires special instrumentation; not all MC-ICP-MS instruments have the required narrow ion source slit and precise ion optics. Furthermore, the narrow slit decreases signal intensity, so the mass of Cr required for analysis is increased roughly tenfold.

An alternative to this high-resolution approach measures the combined intensity of the Cr and interfering beams, then subtracts the interferences. The interference intensities are determined by measurements on blank solutions. This approach has been used for Fe isotope measurements (Anbar et al. 2000; Belshaw et al. 2000), but so far, no Cr isotope publications have used it. Desolvating nebulizers are often used to reduce Ar-based interferences and increase signal strength (Anbar et al. 2000). Some mass spectrometers are equipped with collision cells that greatly decrease ArN^+ and ArO^+ intensities (Albarède and Beard 2004).

MC-ICP-MS measurements of Cr isotope ratios can be done with either double spike methods (Schoenberg et al. 2008) or sample-standard bracketing (Halicz et al. 2008). When the $^{54}\text{Cr} + ^{50}\text{Cr}$ double spike approach is used, interferences from ^{54}Fe and ^{50}Ti must be dealt with. Clean sample preparation methods can reduce these to small levels, but traces of Fe and Ti usually remain. The masses of the interfering isotopes are so close to those of the Cr isotopes that high mass resolution methods are of no help. Thus, small corrections, calculated using, for example, ^{56}Fe and ^{49}Ti beam intensities, are usually applied. Sample standard bracketing methods also require almost complete purification of the sample’s Cr, as any matrix components found in the sample could cause its mass bias to differ relative to that of the more pure bracketing standard solution.

Precision reported in the literature ranges from 0.04 to 0.2‰ (Ellis et al. 2002; Halicz et al. 2008; Schoenberg et al. 2008; Berna et al. 2010). The more precise measurements require about one microgram Cr. With less Cr, analyses can be carried out with diminishing precision as signal strength decreases.

Results are generally reported relative to IRMM-012 or NIST SRM-979. These materials should be isotopically identical, as IRMM-012 is a solution made from SRM-979 material. NIST SRM-3112a may be a useful secondary standard; its $\delta^{53}\text{Cr}$ value is -0.07‰ relative to IRMM-012 (Schoenberg et al. 2008). Analyses of basaltic rocks, ultramafic rocks, and Cr ores (Schoenberg et al. 2008) fall within a very narrow range close to SRM-979 ($-0.124 \pm 0.101\text{‰}$), so all three of these standards are reasonably close to the bulk-earth value.

9.2.3.3 Se Mass Spectrometry Methods

The most effective method for Se isotope analysis at present is MC-ICP-MS, though other methods have been used in the past. Early methods used gas-source mass spectrometry of SeF_6 (Krouse and Thode 1962), but that method requires relatively large amount of Se per analysis and fluorination of the purified Se. It is not currently in use. More recent work successfully employed TIMS methods (Johnson et al. 1999), but that method also requires a relatively large mass of Se (500 ng per analysis) and has slower sample throughput relative to MC-ICP-MS methods.

MC-ICP-MS methods exploit hydride generation, whereby Se(IV) in solution is converted to H_2Se via reaction with a reducing agent and injected into the plasma as a gas. This approach, developed for Se isotopic measurements by Rouxel et al. (2002) has the advantage of delivering nearly 100% of the Se to the plasma, along with only a few other elements and minor amounts of H_2O , H_2 , and HCl vapor. This efficient delivery and lack of sample matrix loading in the plasma enables high sensitivity and precise analyses that consume as little as 20 ng Se (Rouxel et al. 2002; Clark and Johnson 2008). This small sample size requirement is essential to the success of many studies, as Se concentrations in many waters and solids are small.

MC-ICP-MS methods for Se must address a large array of interferences; every Se isotope is affected

(Rouxel et al. 2002; Clark and Johnson 2008). These include ArAr^+ , Kr^+ , Ge^+ , ArCl^+ , SeH^+ , BrH^+ , and AsH^+ . Although most elements do not follow Se through the hydride generation process into the plasma, Ge and As do. Specific strategies used to address interferences are given in recent publications (Rouxel et al. 2002; Clark and Johnson 2008). High-resolution methods have not been successful to date, in part because they decrease signal strength and thus require more Se per analysis.

Mass bias correction has been accomplished through either sample-standard bracketing (Rouxel et al. 2002; Carignan and Wen 2007) or double spike methods, which include $^{82}\text{Se}+^{74}\text{Se}$ and $^{77}\text{Se}+^{74}\text{Se}$ spikes (Johnson et al. 1999; Clark and Johnson 2008). Reported precision for sample-standard bracketing and $^{77}\text{Se}+^{74}\text{Se}$ double spike methods is ± 0.25 per mil on the $^{82}\text{Se}/^{76}\text{Se}$ ratio. The $^{82}\text{Se}+^{74}\text{Se}$ double spike approach produces precision of 0.15‰ on the $^{78}\text{Se}/^{76}\text{Se}$ ratio (Clark and Johnson 2008). Various in-house standards have been used in Se isotope studies, but a recent publication proposes that the readily available NIST SRM-3149 solution is a suitable interlaboratory standard with an isotopic composition close to that of the bulk earth (Carignan and Wen 2007). Analyses reported relative to the “Merck” and “MH-495” in-house standards used in some early publications can be converted to the SRM-3149 scale using the results of Carignan and Wen (2007).

9.2.4 Separation/Purification Prior to Mass Spectrometry

Sample preparation methods differ greatly between Cr and Se, but in both cases the goal is to separate the analyte from the sample matrix and purify the analyte prior to mass spectrometry. Choice of analytical method dictates the type and amount of impurities that can be tolerated. TIMS methods are usually very sensitive to contaminants; small amounts of organic compounds, for example, can greatly inhibit signal strength. With MC-ICP-MS methods, mass bias can be greatly shifted by contaminants. Double spike methods, and, to a lesser extent, elemental spike methods can often correct for such mass bias shifts. Simple sample-standard bracketing methods cannot.

9.2.4.1 Cr Sample Preparation

Two different ion exchange methods have been used to purify Cr for mass spectrometry. The first approach exploits redox manipulation, which shifts Cr from an anionic form to a cationic form (Ball and Bassett 2000; Ellis et al. 2002; Schoenberg et al. 2008). The sample's Cr, in the form of the Cr(VI) anion, is adsorbed onto anion exchange resin, the sample matrix is flushed from the resin, and the Cr(VI) is reduced to Cr(III), which is then easily eluted. Incomplete recovery of sample Cr, and thus the potential for isotopic fractionation, has been reported for this approach (Schoenberg et al. 2008). Hence, the procedures published to date should not be used if mass spectrometry utilizes the sample-standard bracketing method. However, if a double isotope spike is used, and is added prior to sample preparation, this fractionation is readily removed along with the mass bias (see above). The second approach (Halicz et al. 2008) similarly adsorbs Cr(VI) onto anion exchange resin, elutes it with 2 M HNO₃, converts it to Cr(III), adsorbs the Cr(III) onto cation exchange resin, and finally elutes it in 5 M HNO₃. This method recovers essentially all of the Cr and does not fractionate isotopes (Halicz et al. 2008). However, it is more time consuming, with the second ion exchange step involving passage of a large volume (180 mL) of solution through the exchange column.

9.2.4.2 Se Sample Preparation

Because the hydride generation method that delivers Se to the plasma is selective, many matrix components (e.g., Na, K, Mg, Ca, Cl⁻, SO₄²⁻) can be tolerated in large concentrations. Unfortunately, Ge and As are delivered to the plasma, so they must be removed. ⁷⁴Ge and ⁷⁶Ge are isobaric interferences, so only trace amounts of Ge can be tolerated (Rouxel et al. 2002). ⁷⁵As is not itself an interference, but a small fraction of As forms ⁷⁵AsH⁺ ions, which interfere with ⁷⁶Se when large amounts of As are present (Rouxel et al. 2002). Also, oxidants like HNO₃ and H₂O₂, and metals like Hg or Cu that form selenide precipitates, can interfere with formation and delivery of H₂Se.

Selenium can be extracted and purified from a variety of aqueous matrices using cotton with thiol functional groups attached (Rouxel et al. 2002). The thiol groups extract Se(IV) from aqueous solutions;

most matrix components pass through. This method affords excellent separation of Se from Ge, but somewhat incomplete separation from As. Separation of Se (VI) and Se(IV) species, or pre-concentration of both species from dilute solutions, can be done by anion exchange (Clark and Johnson 2008). This method can be effective with large-volume sample of fresh water, and Se is efficiently separated from Ge and As. However, high concentrations of sulfate and other anions can overwhelm the resin's capacity; this method is therefore ineffective for seawater and other saline waters.

9.3 Chromium Isotope Systematics and Applications

9.3.1 Cr Isotope Systematics

9.3.1.1 Equilibrium vs. Kinetic Isotopic Fractionation

A few experiments and some theoretical considerations suggest that isotopic equilibration between Cr (VI) and Cr(III) species is slow in environmental systems. Recent experiments (Zink and Schoenberg 2009) indicate negligible exchange between aqueous Cr(VI) and Cr(III) over a time scale of weeks. It thus appears chromium is somewhat similar to sulfur, in that chemical and isotopic disequilibrium between the dominant natural species is common, and the most important isotopic fractionations are kinetically controlled. Possibly, this arises from the fact that multiple electrons must be transferred, and unstable, rare intermediates must react, as the redox transformations occur. This contrasts strongly with the situation with Fe isotopes, where a single electron transfer amounts to an isotopic exchange reaction between the dominant Fe(III) and Fe(II). The issue of Cr isotopic equilibration is not fully settled, though, as Cr(VI) and Cr(III) often coexist for decades or longer, in the presence of solid phases and dissolved constituents that might catalyze reactions. Knowledge of the degree to which isotopic equilibrium occurs in various types of system is needed to choose appropriate models with which data can be quantitatively interpreted. Figure 9.2 shows a pure Rayleigh model (no reactant-product

interaction), along with a pure equilibrium model (full reactant-product equilibrium); in a real system partial equilibrium could lead to intermediate relationships between these extremes.

Although isotopic equilibrium may not occur in most Cr isotope studies, equilibrium fractionation factors provide important guidance toward understanding Cr isotope systematics. One study (Schauble et al. 2004) provides estimates of equilibrium $^{53}\text{Cr}/^{52}\text{Cr}$ isotope fractionation factors using measured vibrational spectra of various Cr species and models derived from both empirical and ab initio force field methods. Reported values of Δ for equilibrium between CrO_4^{2-} and $\{\text{Cr}(\text{H}_2\text{O})_6\}^{3+}$ complexes are 7‰ at 0°C and 6‰ at 30°C, with the $^{53}\text{Cr}/^{52}\text{Cr}$ ratio being greater for CrO_4^{2-} . Substitution of Cl^- for O^{2-} ligands in $\{\text{Cr}(\text{H}_2\text{O})_6\}^{3+}$ complexes leads to additional fractionation; Δ is about 4‰ for $\text{Cr}(\text{H}_2\text{O})_6^{3+}$ - CrCl_6^{3-} equilibrium, with the $^{53}\text{Cr}/^{52}\text{Cr}$ ratio being lesser in CrCl_6^{3+} . This fractionation is fairly large but will not be observed in most practical settings, where Cr(III) does not normally include more than one or two Cl^- ligands in its first coordination sphere. In general we expect potential Cr isotopic fractionation up to several per mil when Cr redox reactions occur, with much smaller fractionations occurring if ligands are exchanged.

9.3.1.2 Cr(VI) Reduction

Because Cr(VI) reduction is a critically important process in contaminated groundwater settings, this reaction has been the focus of most research on Cr isotope systematics. Unlike nitrate and sulfate reduction, Cr(VI) reduction may proceed via a variety of abiotic processes in addition to microbial ones. All reduction mechanisms studied to date have been found to induce Cr isotope fractionation, with the lighter isotopes enriched in the product. The magnitude of fractionation varies considerably; results of the studies done to date are given in Table 9.1. In the microbial reduction study, weaker isotopic fractionation was observed when the cells were supplied with a greater concentration of electron donor and reduced Cr(VI) more rapidly. Sulfate reducing bacteria have similar variability in ϵ (Canfield 2001). Abiotic and

microbial reduction have overlapping ranges of the isotopic fractionation factor.

9.3.1.3 Cr(III) Oxidation

Cr(III) oxidation is a key step in the natural generation of mobile Cr(VI) from Cr-rich minerals, in which Cr occurs predominantly as Cr(III) (Oze et al. 2007; Izbicki et al. 2008). Similarly, Cr(III) generated by remediation of Cr(VI) contamination could later be remobilized if subsurface conditions become more oxidizing. To date, a few determinations of isotopic fractionation induced by oxidation of aqueous Cr(III) by Mn oxides have been reported. Bain and Bullen (2005) reported, in a conference abstract, variable ϵ values during this process, with the Cr(VI) product being enriched in the lighter isotope at times, but evolving toward enrichment in heavier isotopes over time. A second study, also presented only in a conference abstract (Villalobos-Aragon et al. 2008) reported a consistent fractionation, with the product enriched in the heavier isotope by +1.1‰. This result cannot be explained as a simple kinetic isotope effect, which would yield isotopically light reaction products. The multi-step oxidation of Cr(III) must include considerable back-reaction or partial approach toward isotopic equilibrium at one or more of the steps. For example, if isotopic equilibrium between Cr(III) and an ephemeral Cr(IV) intermediate species were to occur within the overall reaction chain, the more oxidized Cr(IV) should be enriched in the heavier isotope. This could cause the final Cr(VI) product to be enriched in the heavier isotope as observed. This issue is not settled, but at present preliminary evidence suggests Cr(III) oxidation involves isotopic fractionation, probably with enrichment of the heavier isotope in the Cr(VI) product.

9.3.1.4 Precipitation and Adsorption

Adsorption of Cr(VI) onto Al_2O_3 or Geothite does not induce significant fractionation (Ellis et al. 2004), presumably because Cr(VI)-O bonds within the tetrahedral CrO_4^{2-} complex are not affected much. Similarly, little isotopic fractionation occurs during

Table 9.1 Isotopic fractionation caused by Cr transformations

Study	Reaction	Mechanism or reactant	ϵ (‰) ^a $\delta^{53}\text{Cr}/\delta^{52}\text{Cr}$
Ellis et al. (2002)	Cr(VI) to Cr(III)	Magnetite	3.5
Kitchen et al. (2004)	“	Fe(II)	4.3 ^b
Kitchen et al. (2004)	“	Fulvic, humic, mandelic acids	3.0
Sikora et al. (2008)	“	<i>Shewanella oneidensis</i> MR-1	1.8–4.5
Ellis et al. (2002)	“	Pond and estuary sediment	3.3, 3.5
Berna et al. (2010)	“	Aquifer sediment	2.4, 3.1
Bain and Bullen (2005)	Cr(III) oxidation	Mn oxides	2.5 to –0.7
Villalobos-Aragon et al. (2008)	“	Mn oxides	–1.1
Ellis et al. (2004)	Cr(VI) adsorption	Goethite, alumina	<0.04

^aThe fractionation factor is defined here so that a positive value indicates enrichment of the reaction product in the lighter isotope

^bTwo of these experiments were flawed, and the reported pH-dependence reported was incorrect (unpublished results demonstrate this)

precipitation of PbCrO_4 , which has $\delta^{53}\text{Cr}$ only 0.1‰ greater than the parent solution (Schoenberg et al. 2008). Based on studies presently available, it appears redox reactions will control $\delta^{53}\text{Cr}$ values, whereas non-redox processes will not affect them much. This follows the general pattern observed with redox-sensitive elements; redox reactions cause large changes in the local bonding environments, whereas non-redox reactions tend to have much smaller effects (Kendall 1998; Canfield 2001; Hayes 2001; Beard and Johnson 2004; Asael et al. 2009).

9.3.2 Cr Isotope Ratios in Rocks, Natural Dissolved Cr(VI), and Anthropogenic Contaminant Sources

Recent analyses of an array of mantle rocks, mafic igneous rocks, and one granite revealed a very narrow range of $\delta^{53}\text{Cr}$ values, with a mean of -0.12‰ and a standard deviation of 0.05‰ (Schoenberg et al. 2008). This provides a good estimate for the composition of the bulk earth, as Cr-rich mantle rocks are the major Cr reservoir on earth. An array of 9 marine sediments analyzed in the same study yielded slightly greater values (-0.06 ± 0.05 1σ). A study focusing on 0.55–3.75 billion-year-old banded iron formation rocks found that most of their $\delta^{53}\text{Cr}$ values clustered around bulk-earth values, but during some time periods, they shifted upward, scattering between bulk-earth values and 4.96‰ (Frei et al. 2009). The authors interpreted these excursions as a response to increases

in atmospheric oxygen about 2.4 and 0.75 billion years ago. Although a complete survey of rock values does not yet exist, it appears that most rocks cluster close to bulk-earth values, with notable exceptions related to Cr redox processes.

Cr isotope data on naturally produced Cr(VI) in groundwater are consistent with enrichment of the heavier isotope in the Cr(VI) released by weathering. Cr(VI) released from ultramafic rocks into groundwater in certain areas of the Mojave desert, USA has $\delta^{53}\text{Cr}$ values of 0.7‰ to about 3.1‰ , whereas the source rocks are close to 0.0‰ (Izbicki et al. 2008). Values $>3.1\text{‰}$ are also found in the area, but are most likely related to Cr(VI) reduction (see below). Naturally sourced Cr(VI) in the eastern Snake River Plain aquifer of Idaho, USA has a $\delta^{53}\text{Cr}$ range of $0.79\text{--}2.45\text{‰}$ (Raddatz et al. 2011). The emerging pattern is of mildly elevated $\delta^{53}\text{Cr}$ values in natural Cr(VI) in groundwater, but the data are still sparse.

Industrial Cr supplies and reagent Cr appear to be restricted to near-zero values (Ellis et al. 2002; Schoenberg et al. 2008; Berna et al. 2010). This is expected, as Cr ores are usually igneous in origin and little Cr is lost during processing of the ore. Cr plating bath solutions, a common source of Cr contamination, appear to be slightly positive (Ellis et al. 2002; Berna et al. 2010), with solutions sampled at three facilities ranging from 0.29 to 0.83‰ . There may be some potential to distinguish natural dissolved Cr(VI), with its tendency toward positive $\delta^{53}\text{Cr}$ values, from industrial contamination with near-zero values (Izbicki et al. 2008), but one would need to consider potential overlap in the values and possible elevation of $\delta^{53}\text{Cr}$ by Cr(VI) reduction.

9.3.3 Cr Isotope Applications

9.3.3.1 Detection of Chromate Reduction: Berkeley Example

Detection and quantification of groundwater Cr(VI) reduction has been the major environmental application of Cr isotopes to date. Because reduction renders the contaminant immobile and nearly non-toxic, reduction, either naturally driven or artificial, is commonly used to remediate Cr(VI) plumes (Blowes 2002). Given the complexity of groundwater systems, with sorption, dilution, and advection processes operating, it is often difficult, slow, and expensive to detect slow natural reduction via Cr(VI) concentration measurements alone.

Cr isotope data can provide a more direct indication of Cr(VI) reduction that is unaffected by sorption, dilution, and advection (Ellis et al. 2002; Berna et al. 2010). Qualitatively, if $\delta^{53}\text{Cr}$ of Cr(VI) in a groundwater plume is greater than that of the contaminant source, partial reduction of the Cr(VI) must have occurred. Quantitatively, one can invoke the Rayleigh model (9.8) to approximate the evolution of $\delta^{53}\text{Cr}$ as a function of the extent of reduction. However, the classic Rayleigh model is built upon an assumption of a closed system, whereas a “packet” of groundwater seeping from a contaminant source area to a sampled well is not closed and exchanges mass with neighboring packets via hydrodynamic dispersion and diffusion. The effects of longitudinal dispersion have been shown to affect interpretation of isotopic data to a minor or moderate extent (Abe and Hunkeler 2006). If Cr(VI) reduction is restricted to fine-grained lenses within a more permeable matrix, a large decrease in the effective value of ϵ is expected (Berna et al. 2010). Rayleigh models thus have known flaws, but can provide good approximations if properly applied and/or modified.

A recent study of an urban Cr(VI) plume in Berkeley, CA, USA (Berna et al. 2010) provides a good example of the use of $\delta^{53}\text{Cr}$ to quantify Cr(VI) reduction. $\delta^{53}\text{Cr}$ was measured over several years’ time on dissolved Cr(VI) from an array of 15 monitoring wells and a few temporary “direct push” sampling points. The original contaminant Cr(VI), released decades ago, was assumed to have a $\delta^{53}\text{Cr}$ value close to 0.83‰, the value of the present-day Cr plating bath on site. All groundwater

$\delta^{53}\text{Cr}$ measurements were greater than that, ranging from 1.26 to 6.27‰ (Fig. 9.3). The values are lowest close to the plume source and increase consistently with distance traveled from it. This indicates reduction occurs as Cr(VI) migrates through the aquifer, and the extent of reduction increases with distance traveled.

A quantitative interpretation of these data was developed using a modified Rayleigh fractionation model (Berna et al. 2010). Two laboratory experiments with Cr(VI) reduction by aquifer materials from the site yielded ϵ values of -2.4 and -3.1% respectively. Other experiments revealed that reduction is restricted to greenish lenses of fine-grained reduced material, whereas the dominant coarser, brownish materials did not reduce Cr(VI). In light of that finding, a modified Rayleigh model was constructed with $\epsilon = -1.37\%$, one half the mean value of the two experiments. This smaller value was used to account for a presumed diffusive barrier between reduction sites in the greenish layers and the main mass of Cr(VI) in the coarser layers. The resulting model is reasonably close to the $\delta^{53}\text{Cr}$ vs. Cr(VI) concentration trend defined by samples along the plume axis (Fig. 9.4). Samples from the lateral fringes of the plume have lower concentrations relative to this trend. This is expected, as transverse dispersion dilutes contaminant Cr(VI) in those areas.

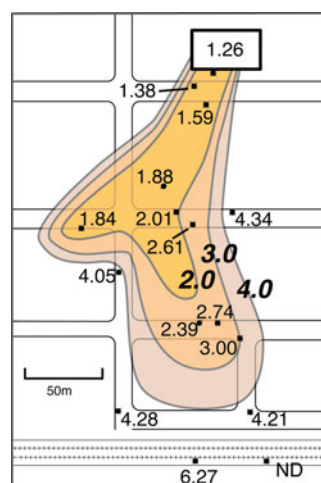


Fig. 9.3 Map view of $\delta^{53}\text{Cr}$ (per mil, relative to SRM-979) in a groundwater Cr(VI) plume in Berkeley, California, USA (Berna et al. 2010). Large bold numbers give per mil values of the contour lines

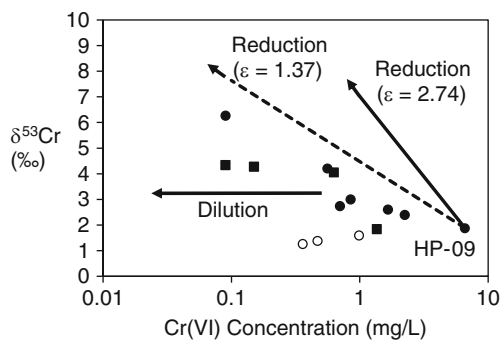


Fig. 9.4 Relationship between $\delta^{53}\text{Cr}$ and Cr concentration for the Berkeley Cr(VI) plume. *Solid circles* represent locations close to the plume axis. *Squares* represent locations toward the lateral fringes, where dilution is strong. *Open circles* represent locations in an upgradient area where concentrations are decreasing because the contaminant source has been removed. Rayleigh fractionation models follow straight lines as shown; dilution (e.g., transverse dispersion) shifts waters to the left. The data do not conform to a Rayleigh model constructed using the mean ϵ value derived from experiments with site sediments. Data from samples taken near the plume axis are close to a modified Rayleigh model with an ϵ value equal to 1.37‰, one half the experimental value

The results of this study lead to important implications for the fate of Cr(VI) in the system. The estimated extent of Cr(VI) reduction at the most distal sampling point, using the Rayleigh model with $\epsilon = 1.37\%$, was 98%. This indicates that the down-gradient fringe of the plume was not an advancing contaminant front, but rather the location where Cr(VI) reduction reached completion. This suggests remediation via natural attenuation is an effective strategy at the site. Furthermore, $\delta^{53}\text{Cr}$ of most of the monitoring wells were shown to be invariant over several years' time, suggesting that the extents of reduction at these points are stable and the Cr(VI)-reducing power of the aquifer is not waning (Berna et al. 2010).

9.3.3.2 Detection of Chromate Reduction and/or Source Identification when Multiple Sources are Present

Two other studies have used Cr isotope data to detect reduction in groundwater systems. One investigated the fate of dissolved Cr(VI) in parts of the Mojave desert, USA (Izbicki et al. 2008), where both natural and industrial sources exist. In uncontaminated areas,

the $\delta^{53}\text{Cr}$ values of native dissolved Cr(VI) are invariably greater than those inferred for the parent rocks: Values in waters where Cr(VI) reduction is thought to be negligible ranged from 0.7 to 3.1‰, with a mean of 1.7‰ and a standard deviation of 0.4‰. Despite the potential for elevated $\delta^{53}\text{Cr}$ values in the natural background Cr, Cr(VI) reduction could be inferred in some areas. Trends of increasing $\delta^{53}\text{Cr}$ and decreasing Cr(VI) concentration along groundwater flow paths were strongly suggestive of reduction, with up to half the originally present Cr(VI) lost from solution.

The Izbicki et al. (2008) study was also successful in distinguishing sources of Cr contamination. Monitoring wells near a facility where chemical milling of metal parts was conducted contained elevated Cr(VI) concentrations and low $\delta^{53}\text{Cr}$ values suggestive of contamination by industrial Cr with near-zero values. One well yielded $\delta^{53}\text{Cr}$ values of -0.1% , which is clearly outside the range of native Cr and within the expected range for industrial Cr. However, for several other wells, $\delta^{53}\text{Cr}$ values were not so low and data interpretation was not so simple because of the presence of native Cr(VI) in the aquifer. A mixing model was constructed to calculate Cr(VI) concentrations and $\delta^{53}\text{Cr}$ values for mixtures between the native Cr(VI) and the inferred range of contaminant Cr(VI). Waters from some of the wells conform to this mixing model, with varying fractions of the sampled Cr(VI) sourced from the facility. As an alternative interpretation, $\delta^{53}\text{Cr}$ and Cr(VI) concentration data from most wells in the vicinity of the facility conformed to a model where most Cr(VI) was sourced from the facility and was subject to variable amounts of Cr(VI) reduction. Overall, this study demonstrated the potential to distinguish anthropogenic Cr from naturally occurring Cr, at least in the study area. But it also revealed the complexity that arises when mixing of two sources and Cr(VI) reduction are both potentially involved.

The second study investigated Cr(VI) in the eastern Snake River Plain aquifer of Idaho, USA (Raddatz et al. 2011). Results for naturally sourced Cr(VI) were similar to those of the Mojave desert study: Mean $\delta^{53}\text{Cr}$ was 1.15‰; standard deviation was 0.46. Once again, it appears that Cr(VI) released by weathering is enriched in the heavier isotope relative to the parent material, which in this case is the basaltic host rock of the aquifer. Contaminant Cr(VI) had near-zero $\delta^{53}\text{Cr}$ values. The main goal of the study was to detect any reduction of the contaminant. Some

contaminated wells showed near-zero $\delta^{53}\text{Cr}$ values indicative of negligible Cr(VI) reduction along some flow paths. Other contaminated wells showed elevated $\delta^{53}\text{Cr}$ values ranging from 0.78 to 1.79‰. Interpretation of these data was complicated by the presumed presence of naturally sourced Cr(VI) with similar $\delta^{53}\text{Cr}$ values in the waters. A mixing model was used to define possible combinations of Cr(VI) and $\delta^{53}\text{Cr}$ in mixtures of contaminant and natural Cr(VI), without reduction. Comparison with the data revealed that several contaminated wells had $\delta^{53}\text{Cr}$ values greater than plausible mixtures of contaminant and natural Cr(VI). This indicated that small amounts of reduction occurred, but only along the shallowest flow paths in the aquifer.

9.3.4 Outlook for Environmental Applications of Cr Isotope Data

The studies published to date strongly suggest that $\delta^{53}\text{Cr}$ data can provide an effective means of detecting Cr(VI) reduction. In systems where contaminant Cr(VI) concentrations are much greater than the natural background, elevated $\delta^{53}\text{Cr}$ values relative to contaminant source values are indicative of Cr(VI) reduction. At present, this approach seems quite robust, barring the unlikely discovery of some unforeseen phenomenon other than Cr(VI) reduction that causes large increases in $\delta^{53}\text{Cr}$. However, one must be aware that in waters where the contaminant does not completely overwhelm the natural background, interpretation is more complicated. One should determine the $\delta^{53}\text{Cr}$ range of the background, then use mixing calculations to determine if elevated $\delta^{53}\text{Cr}$ values are indeed indicative of reduction rather than mixing alone.

Quantitative determination of reduction using $\delta^{53}\text{Cr}$ data is more challenging, and more research must be done to address certain issues. The fractionation factor for Cr(VI) reduction depends on the reduction mechanism and environmental conditions, and a full understanding of its variability does not yet exist. Rayleigh fractionation calculations provide an imperfect model of reaction within groundwater systems, and it appears this can greatly affect the calibration of $\delta^{53}\text{Cr}$ increase as a function of the extent of reduction.

The use of $\delta^{53}\text{Cr}$ data as source indicators is less well developed, but the emerging picture suggests that anthropogenic Cr(VI) tends to have lower $\delta^{53}\text{Cr}$ values than that of natural background Cr(VI). This tendency is based on few studies at present and must be explored in future work. If indeed such a contrast exists at a particular site, one must be careful to consider that reduction of the contaminant Cr(VI) can increase its $\delta^{53}\text{Cr}$ and render the source contrast useless. If the goal is to “fingerprint” Cr from multiple anthropogenic plumes, one should not expect them to have distinct “signatures” a priori because industrial Cr contamination seems to have near-zero $\delta^{53}\text{Cr}$ values as a general rule. However, there are likely processes, such as Cr(VI) reduction in soils prior to release into groundwater, that could generate distinctive $\delta^{53}\text{Cr}$ values that can be traced. Such usage of Cr isotope analyses would necessarily be developed on a site-by-site basis and has been explored little at this time.

9.4 Selenium Isotope Systematics and Applications

9.4.1 Se Isotope Systematics

Selenium has 4 stable valence states in natural systems, so its isotopic systematics are more complex than those of Cr. However, the general pattern of isotopic fractionation, with the greatest fractionation induced by reduction and smaller effects due to oxidation and non-redox processes such as adsorption, is similar. Here we discuss the magnitude of fractionation for the $^{82}\text{Se}/^{76}\text{Se}$ ratio (Table 9.2), as it is the most commonly reported ratio with the newer analytical methods and will likely be the one used in most future studies. Some of the fractionation factors have been converted from other originally reported ratios, such as $^{80}\text{Se}/^{76}\text{Se}$.

9.4.1.1 Equilibrium Isotope Fractionation

Attainment of isotopic equilibrium in Se redox reactions is probably extremely slow under most

Table 9.2 Kinetic isotopic fractionation caused by Se transformations

Study	Reaction	Mechanism	ϵ (‰) ^{82/76} Se/ ⁷⁶ Se
Rees and Thode (1966)	Se(VI) to Se(IV)	8 M HCl, 25°C	18
Johnson and Bullen (2003)	“	“Green rust”	11.1 ^a
Ellis et al. (2003)	“	Sediment slurry (microbial)	3.9–4.7 ^a
Clark and Johnson (2008)	“	”	1.8
Kirk et al. (2009)	“	<i>Dechloromonas sp.</i>	2.4
Herbel et al. (2000)	“	Bacterial cultures	1.7–7.2 ^a
Krouse and Thode (1962), Rees and Thode (1966), Webster (1972), Rashid and Krouse (1985)	Se(IV) to Se(0)	NH ₂ OH or ascorbic acid	15.0–19.2
Ellis et al. (2003)	“	Sediment slurry (microbial)	8.4 ^a
Herbel et al. (2000)	“	Bacterial cultures	9.0–13.7 ^a
Johnson (2004)	Se(IV) to Se(VI)	NaOH + H ₂ O ₂	< 0.5 ^a
Johnson et al. (1999)	Se(0) oxidation	Incubated soil	< 0.5 ^a
Herbel et al. (2002)	Plant uptake	Wetland plants	< 1.5 ^a
Hagiwara (2000)	Algal uptake	<i>C. reinhardtii</i>	1.5–3.9 ^a
Johnson et al. (1999)	Se volatilization	Cyanobacteria	< 1.7 ^a
“	“	Soil (microbes)	< 0.9 ^a
Schilling et al. (2010)	“	Fungi	1.0–4.0
“	Se(IV) adsorption	Fe(OH) ₃ •nH ₂ O	0.8 ^a

^aConverted from original measured ratio using $\epsilon_{82/76} = 1.48 \epsilon_{80/76}$

environmental conditions, because chemical disequilibrium is observed in nature (White et al. 1991) and, as with Cr, redox reactions involve multiple electron transfers. Furthermore, the similarities between Se and S suggest that the predominantly kinetic interpretation used for S isotope studies at environmental temperatures should apply to Se also. However, experiments have not yet been done to measure rates of Se isotopic equilibration.

Although isotopic equilibrium may not be relevant in most Se isotope studies, equilibrium fractionation factors provide guidance toward understanding Se isotope systematics. Krouse and Thode (1962) used vibrational spectra and theoretical calculations to estimate fractionation factors for several Se species. Their estimate for Δ for SeO₄²⁻–H₂Se equilibrium at 25°C is 33‰. In comparison, Tudge and Thode (1950) estimated $\Delta = 75$ ‰ for SO₄²⁻–H₂S equilibrium. These results suggest the potential for significant Se isotope fractionation, but it also indicates fractionation for a given Se redox reaction will tend to be much smaller than that of an analogous S redox reaction. Furthermore, because the +4 and 0 valences of Se are stable, reactions involving the entire eight-electron difference between +6 and –2 valences are not relevant. The actual relevant reactions involve two or four electrons transferred, have less bonding contrast, and exhibit lesser isotopic fractionation.

9.4.1.2 Se(VI) Reduction to Se(IV)

As with sulfate, abiotic reduction of Se(VI) is kinetically sluggish at environmental temperatures. One environmentally relevant abiotic Se(VI) reduction process is known; Se(VI) can be reduced to Se(IV) and ultimately to Se(0) by “green rust,” a layered ferric+ferrous oxide with anions occupying interlayer spaces (Myneni et al. 1997). Johnson and Bullen (2003) performed room-temperature laboratory experiments to obtain an ϵ value of 11.1‰ ± 0.3‰ for the Se(VI) reduction reaction. Less relevant experiments have been carried out which use 8 N HCl as the reductant of Se(VI) (Table 9.2).

Selenate can be reduced readily by certain microbes, and generally proceeds stepwise, with Se(IV) as a potentially stable product. This differs from sulfate reduction, where a single microbe may convert sulfate to sulfide. Se isotope fractionation factors were reported by Herbel et al. (2000) for Se(VI) reduction by growing, anaerobic batch cultures of *Bacillus arsenicoselenatis* strain E1H, a haloalkaliphile, and *Sulfurospirillum barnesii* strain SES-3, a freshwater bacterium. Fractionation factors varied in these experiments. In the *S. barnesii* experiment, isotopic fractionation was nearly nonexistent in the earliest stages, then increased to $\epsilon \approx 6$ ‰, whereas with *B. arsenicoselenatis* $\epsilon \approx 7$ ‰. Washed cell suspensions

of *S. barnesii* yielded $\epsilon \approx 1.6\%$. In all the experiments, high initial concentrations of electron donor (e.g., 20 mmol/L lactate) and Se(VI) (e.g., 10 mmol/L) were used. So although the results clearly indicate microbial Se(VI) reduction can induce isotopic fractionation, they cannot be directly applied to natural settings. Furthermore, the variability observed in the fractionation factor suggests that environmental conditions will to some extent control the magnitude of fractionation, as is observed with sulfate reduction (Canfield 2001).

In an attempt to obtain fractionation factors relevant to natural settings, Ellis et al. (2003) performed batch incubation experiments with unamended, anaerobic sediments from three different Se-impacted surface water systems in California, USA. Starting Se(VI) concentrations were environmentally relevant, ranging from 230 nmol/L to 100 $\mu\text{mol/L}$. The results yielded a narrow range in the fractionation factor, with ϵ ranging from 3.9 to 4.7%. Clark and Johnson (2008) performed a similar incubation of sediment from a Se-impacted wetland at Sweitzer Lake in Colorado, USA, with 30 $\mu\text{mol/L}$ initial Se(VI), and obtained a much smaller value (1.8%). Kirk et al. (2009) also reported a relatively small value of 2.4% for incubations of phosphate mine waste rock from Idaho, USA, inoculated with an enrichment culture of native microbes and supplied with 150 $\mu\text{mol/L}$ initial Se(VI). In all of these studies, Se(VI) reduction was microbially mediated. In general, the results suggest that microbial Se(VI) reduction in natural settings induces little isotopic fractionation, relative to that observed for the abiotic reaction. This raises the possibility of distinguishing microbial Se(VI) reduction from abiotic reduction using observed fractionation factors in a field setting, but such an approach would require detailed knowledge of the factors relevant for each site. For example, a large fractionation generated by a reaction may be manifested as a relatively small apparent fractionation if the measured Se is separated from the reduction sites by a diffusive barrier (see below).

9.4.1.3 Se(IV) Reduction

Abiotic Se(IV) reduction is not kinetically inhibited as are selenate and sulfate reduction. For example, the strong reducing agent BH_4^- instantaneously reduces

Se(IV) to H_2Se at room temperature but does not react with Se(VI) quickly. Se(IV) can be reduced by several reducing agents such as dissolved ascorbic acid or SO_2 , and presumably a variety of naturally occurring organic reductants can reduce Se(IV) to Se(0) in nature. Microbes may also reduce Se(IV) (Blum et al. 1998).

Several studies have explored Se isotope fractionation during abiotic Se(IV) reduction. Krouse and Thode (1962), Rees and Thode (1966), and Rashid and Krouse (1985) reported ϵ values ranging from 15.0 to 19.2%, for reduction by ascorbic acid and hydroxylamine. The latter authors noted that their data were not consistent with a simple Rayleigh-type fractionation process; they modeled the reaction as a two step process, with the rate constant of the second step two orders of magnitude smaller than the first, and kinetic isotope effects of 4.8 and 13.2% for the first and second steps. Data from all three studies were fit. This highlights the need to consider the potential variability of fractionation factors for kinetic processes, even ones that are abiotic and apparently simple.

Se isotope fractionation induced by microbial reduction of Se(IV) to Se(0) appears to be somewhat smaller than that induced by abiotic reduction. Herbel et al. (2000) reported fractionation factors for pure cultures of selenate respiring bacteria *B. arsenicosele-natis* and *S. Barnesii* and also *B. selenitireducens*, which grows with Se(IV) as an electron acceptor but not with Se(VI). The cultures were actively growing during the experiments, and initial concentrations were 10 mmol/L Se(IV) and lactate. Results yielded a range of ϵ from 9.0 to 13.7%. These experiments demonstrate the potential for relatively large isotopic fractionation, but were conducted rather far from natural conditions. The Ellis et al. (2003) study described above obtained a slightly smaller value, 8.4%, for two unamended sediment slurry experiments, with Se(IV) concentrations ranging from 0.24 to 100 $\mu\text{mol/L}$. Overall, it appears that Se(IV) reduction imparts a much larger isotopic fractionation than does reduction of Se(VI) to Se(IV).

9.4.1.4 Se Oxidation and Adsorption

Isotopic effects induced by Se oxidation reactions have not yet been studied fully. The only experiments

reported so far are oxidation of Se(IV) to Se(VI) in a 0.8-M NaOH + 3% H₂O₂ solution. No isotopic shift was detected within the 0.2‰ uncertainty of the ⁸⁰Se/⁷⁶Se measurements (Johnson 2004). As with Cr (III) oxidation, a simple kinetic isotope effect is not observed, presumably because of the competing tendencies of simple kinetic effects, which lead to enrichment of lighter isotopes in the oxidized product, and back reaction or equilibrium effects, which promote enrichment of the product in heavier isotopes. Oxidation of Se(0) and Se(-II) have not yet been studied isotopically. However, S isotopic fractionation induced by sulfide oxidation is relatively weak (Canfield 2001) and it is likely that Se follows suit.

In one adsorption experiment, Johnson et al. (1999) found Se(IV) adsorbed onto hydrous ferric oxides to be slightly (0.8‰) enriched in the lighter isotope relative to the coexisting solution. Apparently, Se(IV) adsorption, at least with this surface, does not change the local bonding environment of Se(IV) much. This fits the general pattern set by adsorption of sulfate (Van Stempvoort et al. 1990) and chromate (Ellis et al. 2004), which both show small or unmeasurable effects.

9.4.1.5 Se in Biota

Assimilation of Se(VI) and Se(IV) by algae induces minor Se isotope fractionation. Hagiwara (2000) found that the fresh water alga, *Chlamydomonas reinhardtii*, grown in Se(VI)- and Se(IV)-bearing media, was enriched in the lighter isotope by 1.7–3.9‰. Clark and Johnson (2010) reported a much smaller offset (mean of 0.59‰ in the same direction) for phytoplankton recovered from Sweitzer Lake, Colorado, relative to the mean composition of waters in the lake. This result is consistent with the minor S isotopic fractionation (0.9–2.8‰) induced by algal assimilation of sulfate (Kaplan et al. 1963).

Uptake of Se into higher plants also induces generally small but significant Se isotope fractionations. Herbel et al. (2002) determined the isotopic compositions of Se in five macrophytes from an artificial wetland receiving water with ca. 320 nmol/L Se(VI). The plants' Se isotope ratios varied little and the mean value was slightly (1.1‰) less than that of the surface waters. In a more extensive survey of roots, stems, and leaves from several plants in a Se(VI)-impacted

wetland, plant tissues' $\delta^{82}\text{Se}$ values generally ranged from identical to the median wetland water Se(VI) value to 1.8‰ less than that, with a few outliers up to 4.2‰ less (Clark and Johnson 2010). Once again, Se isotope systematics are similar to those of sulfur; Trust and Fry (1992) found higher plants to be an average of 1.5‰ enriched in the lighter isotope relative to the sulfate assimilated.

Se can be methylated and volatilized by algae, plants, and fungi. Johnson et al. (1999) reported that volatile Se generated by cyanobacterial mats and incubated soils was enriched in the lighter isotope by 0.0–1.7‰ relative to the supplied selenate. Volatile Se species recovered from four water samples from a Se-impacted lake in Colorado, USA were enriched in the lighter isotope by 0.0–1.5‰ (Clark and Johnson 2010) relative to the lake's selenate. In contrast to those results, pure cultures of the fungus *Alternaria alternata* have been reported to produce volatile Se species enriched in the lighter isotope by as much as 4.0‰ (Schilling et al. 2011).

Se isotope ratios in zooplankton and fish have been studied at the Sweitzer Lake field site (Clark and Johnson 2010). Two zooplankton samples had $\delta^{82}\text{Se}$ values 0.2‰ and 0.5‰ less than coexisting phytoplankton. Livers and muscle tissue from four fish were, respectively, 0.5 and 1.3‰ less than coexisting phytoplankton. This limited data set suggests that animals largely reflect their food sources, with only minor Se isotopic offsets.

9.4.2 Se Isotope Ratios in Rocks and Waters

Rouxel et al. (2002) reported $\delta^{82}\text{Se}$ for several igneous rocks and four iron meteorites. These all lie within 0.6‰ of SRM-3149. An array of recent marine and estuarine sediments, and unweathered sedimentary rocks from a variety of geologic time periods fall within 1.6‰ of zero (Hagiwara 2000; Rouxel et al. 2002; Zhu et al. 2008; Clark and Johnson 2010; Mitchell et al. 2010). Weathered organic-rich shale exhibits greater variation, with values spanning the range –13‰ to +13‰ in a single outcrop (Hagiwara 2000; Wen et al. 2011; Zhu et al. 2008). This variation is thought to reflect near-surface redox cycling during the weathering process.

Se in water appears to be somewhat more variable and weakly positive in $\delta^{82}\text{Se}$, but few studies have been published to date. Several analyses of surface waters generated by agricultural activities in the San Joaquin Valley, California, USA range from 0.9 to 2.9‰ (Herbel et al. 2002), 4 water samples from the northern arm of the San Francisco estuary, California ranged from 0.5 to 3.3‰ (Johnson et al. 2000), and surface waters from the Sweitzer Lake site in western Colorado, USA range from 0.6 to 4.4‰ (Clark and Johnson 2010). Wastewaters from four oil refineries near the northern reach of San Francisco bay range from 1.2 to 4.5‰ (Johnson et al. 2000).

9.4.3 Se Isotope Applications

Most Se-related environmental research has focused on wetland environments, where the greatest environmental impacts have occurred (Presser 1994). Se isotope research followed this emphasis, with the goal of providing a new means to detect and perhaps quantify selenate reduction in wetlands and other surface water environments. This reaction is of primary importance, as it leads to sequestration of the contaminant. Se isotope studies in groundwater or vadose zone settings have developed more slowly.

9.4.3.1 Detection of Selenate Reduction in Wetlands and Lakes

Early studies of isotopic fractionation by Se(VI) and Se(IV) reduction led to a working hypothesis that these reactions would produce strong Se isotope ratio shifts and would thus be readily detected via isotopic analyses. Johnson et al. (2000) reported that $\delta^{82}\text{Se}$ values of reduced Se found in estuarine sediments of the northern arm of San Francisco Bay, California, USA, were only about 3‰ less than the overlying waters. Herbel et al. (2002) found a similar offset of less than 2.0‰ in an artificial wetland receiving selenate-rich agricultural drain waters in the San Joaquin Valley of California, USA. More importantly, although about 75% of the selenate input to the wetland was removed by biogeochemical processes, the outlet water was not enriched in the heavier isotopes relative to the inflow.

This lack of significant isotopic fractionation was interpreted to be the result of an absence of direct Se (VI) or Se(IV) reduction and dominance of Se cycling via plant uptake, but more recent research suggests that the isotopic contrasts generated by reduction reactions may be quite small in surface water systems. Clark and Johnson (2008) investigated isotopic fractionation in sediments from the Sweitzer Lake site (Fig. 9.5). Unamended site sediment incubated with Se(VI)-spiked site water showed rather small isotopic fractionation for microbial Se(VI) reduction ($\epsilon = 1.8\text{‰}$).

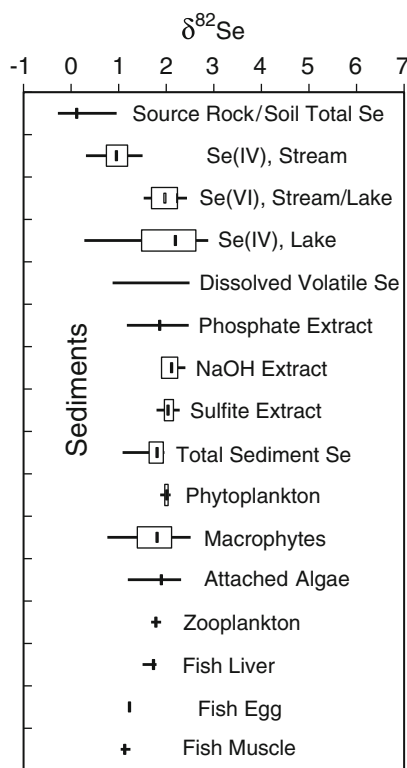


Fig. 9.5 Se isotope data from Sweitzer Lake, Colorado, USA (Clark and Johnson 2010). Mean values are given by the vertical tick marks. Boxes indicate the 25th and 75th quartiles of measurements, when sufficient data are available. The horizontal lines indicate the total range of measurements. The observed range in the isotopic composition of dissolved Se(VI) and the other major Se reservoirs in the system, is narrow. Se(VI) released into the environment is slightly enriched in heavier isotopes relative to the parent rock, but little isotope fractionation is manifested within the lake/wetland system, despite the presence of reducing sediments. Phosphate, NaOH, and sulfite extracts are designed to recover adsorbed Se, labile organic compounds, and elemental Se, respectively

Additional experimental results and theory presented by Clark and Johnson (2008) reveal a phenomenon that diminishes the isotopic shifts generated by reactions in surface water-sediment systems. This phenomenon applies whenever any isotope ratios in surface waters are used to detect reactions hosted by sediments, not just those of selenium. Here we review the concept briefly. Figure 9.6 provides concentration and isotopic profiles for a simple case. When reduction occurs inside sediments, isotopic fractionation occurring at the sites of reduction is not fully manifested in the surface waters above. The cause of this can be described as a “reservoir effect”; in the pore spaces of the sediment, reduction causes the dissolved Se(VI) to become enriched in the heavier isotopes (Fig. 9.6). This counteracts the tendency for the reaction to enrich the product in lighter isotopes. Although the pore space is connected by diffusion to surface water above by, diffusion is generally not fast enough to erase the reservoir effect. Bender (1990) and Brandes and Devol (1997) developed mathematical models for

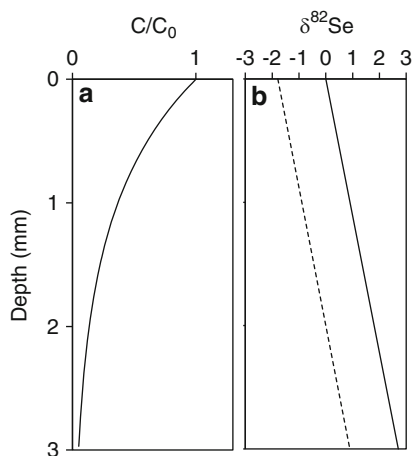


Fig. 9.6 Illustration of reservoir effects in a sediment-water system (Bender 1990; Clark and Johnson 2008). Concentration (a) and isotopic composition (b) of dissolved Se(VI) are given as a function of depth below the sediment/water interface. C_0 is the concentration in the overlying water. The *solid* and *dashed* lines in (b) give the isotopic compositions of Se(VI) in pore water and of reduced Se accumulating in the sediment, respectively. $\delta^{82}\text{Se}$ increases with increasing depth because isotopic fractionation enriches pore water Se(VI) in heavier isotopes. The magnitude of isotopic fractionation (ϵ) at any given point is 1.8‰. However, the average $\delta^{82}\text{Se}$ value of the accumulated reduced Se is offset from the overlying water by much less than 1.8‰, and thus the effective isotopic fractionation ($\epsilon = 0.9\text{‰}$ for this particular model) is much smaller than the intrinsic fractionation

this phenomenon, and found that the isotopic effect observed in the surface water can be described using an effective fractionation factor. For a given system, the effective ϵ value is smaller than the intrinsic ϵ value (the micro-scale fractionation induced by the reaction itself) by a factor of two or more, depending on diffusive communication between water and sediment. Clark and Johnson (2008) performed a series of laboratory experiments that confirmed the predictions of these models and yielded an effective ϵ value of only 0.6‰ for an intact Sweitzer lake core.

It thus appears that Se isotope data may not provide a simple indicator of Se(VI) reduction in wetlands and other surface systems. The effective fractionation is small in the Sweitzer Lake case and is no greater than that occurring with plant and phytoplankton uptake. This may be the case elsewhere. For example, the lack of large isotopic contrast between reduced Se in sediments and that in the overlying water in the San Francisco Bay and artificial wetland settings (Johnson et al. 2000; Herbel et al. 2002) may reflect small effective fractionation for Se(VI) reduction and not a lack of dissimilatory microbial reduction as the original studies concluded.

The data from Sweitzer Lake (Clark and Johnson 2010) provide additional support for the view that effective fractionation is small (Fig. 9.5). The study provided a comprehensive survey of Se isotope data in the wetland/lake system and found a remarkably small range of Se isotope ratios. $\delta^{82}\text{Se}$ values for the vast majority of samples, including dissolved Se(VI) and Se(IV), extracted sediment components, plants, phytoplankton and higher plants, fall between 1.5 and 4.1‰ (relative to NIST SRM-3149); the Se(VI) input had a consistent 3.4‰ value. Incubations of site sediment showed that Se(VI) reduction was rapid (Clark and Johnson 2008), suggesting that it occurs in the system, but the associated effective fractionation is small.

9.4.3.2 Reduction of Se in Subsurface Waters

There are few published Se isotope data from groundwater or vadose systems at this time. Whole-rock samples from an outcrop in Hubei Province, China that contains extremely high Se concentrations causing human Se poisoning decades ago (Zhu et al. 2004) have been analyzed for Se isotope ratios (Wen et al. 2011; Zhu et al. 2008). In contrast to the lack of

significant isotopic variation in surface water settings, $\delta^{82}\text{Se}$ values vary strongly, ranging from -13.2 to $+11.4\%$ over a short distance in the outcrop. Wen et al. (2011) concluded that redox reactions, and potential repeated redox cycling of Se must have occurred at the site and caused the Se enrichment. Zhu et al. (2008) reported a relative lack of Se isotope variation in drill core samples from greater than 50 m depth, confirming that the isotopic variability was indeed caused by near-surface processes. This demonstrates that Se redox reactions occurring in shallow groundwater or vadose zone water can impart large isotopic fractionation.

Data from soil and weathered Mancos shale of western Colorado, USA, along with surface waters derived from the same rock unit, also suggest Se isotope ratios are shifted by subsurface redox reactions (Clark and Johnson 2010). Se(VI) in surface water was enriched in heavier isotopes by about 3‰ relative to the rock (Fig. 9.5). This is suggestive of redox reactions causing some fractionation during weathering.

9.4.4 Outlook for Environmental Applications of Se Isotope Data

At present, it appears that Se isotope ratios are not likely to provide a robust indicator of Se redox reactions in wetlands and other surface water systems. Despite the potential for large Se isotope variations to be induced by Se(VI) and Se(IV) reduction reactions in general, the intrinsic fractionations of the actual reduction mechanisms operating in wetland and lake sediments appear to be small. Additionally, when reduction is restricted to underlying sediments, the effective fractionation observed in surface waters is even smaller. We suggest the outlook for tracing Se redox reactions in these systems is poor, because the small redox-driven isotopic variations are no larger than those caused by a variety of other processes, such as assimilation of Se by plants. However, the lack of large isotopic fractionations observed in surface water systems suggests the possibility that Se from different sources may be traced in surface water systems, as their isotopic “signatures” may be affected little by redox reactions.

The outlook for groundwater applications appears much better. Data are sparse at this time, but it appears

Se isotopic fractionation can be large in subsurface systems. Se isotope data could possibly be used to detect reduction of contaminant Se(VI) or Se(IV) in groundwater just as Cr isotope data are used to detect Cr(VI) reduction. For example, Se released from mine wastes or fly ash may be immobilized in the subsurface by microbial reduction (Kirk et al. 2009). It is likely that $\delta^{82}\text{Se}$ measurements of dissolved Se(VI) will provide a means to detect and possibly quantify reductive immobilization of the Se.

References

- Abe Y, Hunkeler D (2006) Does the Rayleigh equation apply to evaluate field isotope data in contaminant hydrogeology? *Environ Sci Technol* 40:1588–1596
- Albarède F, Beard BL (2004) Analytical methods for non-traditional isotopes. In: Johnson CM, Beard BL, Albarede F (eds) *Geochemistry of non-traditional stable isotopes*. Mineralogical Society of America, Washington
- Anbar AD, Roe JE, Holman ES, Barling J, Nealson KH (2000) Non-biological fractionation of iron isotopes. *Science* 288:126–128
- Asael D, Matthews A, Oszczepalski S, Bar-Matthews M, Halicz L (2009) Fluid speciation controls of low temperature copper isotope fractionation applied to the Kupferschiefer and Timna ore deposits. *Chem Geol* 262:147–158
- Bain DJ, Bullen TD (2005) Chromium isotope fractionation during oxidation of Cr(III) by manganese oxides. *Geochim Cosmochim Acta* 69(10) Suppl. 1:A212
- Ball JW, Bassett RL (2000) Ion exchange separation of chromium from natural water matrix for stable isotope mass spectrometric analysis. *Chem Geol* 168:123–134
- Ball JW, Nordstrom DK (1998) Critical evaluation and selection of standard state thermodynamic properties for chromium metal and its aqueous ions, hydrolysis species, oxides, and hydroxides. *J Chem Eng Data* 43:895–918
- Beard BL, Johnson CM (2004) Fe isotope variations in the modern and ancient earth and other planetary bodies. In: Johnson CM, Beard BL, Albarede F (eds) *Geochemistry of non-traditional stable isotopes*. Mineralogical Society of America, Washington
- Belshaw NS, Zhu XK, Guo Y, O’Nions RK (2000) High precision measurement of iron isotopes by plasma source mass spectrometry. *Int J Mass Spectrom* 197:191–195
- Bender ML (1990) The $\delta^{18}\text{O}$ of dissolved O_2 in seawater: a unique tracer of circulation and respiration in the deep sea. *J Geophys Res* 95:22243–22252
- Berna EC, Johnson TM, Makhisi RS, Basu A (2010) Cr stable isotopes as indicators of Cr(VI) reduction in groundwater: a detailed time-series study of a point-source plume. *Environ Sci Technol* 44:1043–1048
- Bigeleisen J (1949) The relative reaction velocities of isotopic molecules. *J Chem Phys* 17:675–678
- Blowes DW (2002) Tracking hexavalent Cr in groundwater. *Science* 295:2024–2025

- Blum JS, Bindi AB, Buzzelli J, Stolz J, Oremland RS (1998) *Bacillus arsenicoselenatis*, sp. nov., and *Bacillus selenitireducens*, sp. nov.: two haloalkaliphiles from Mono Lake, California that respire oxyanions of selenium and arsenic. *Arch Microbiol* 171:19–30
- Brandes JA, Devol AH (1997) Isotopic fractionation of oxygen and nitrogen in coastal marine sediments. *Geochim Cosmochim Acta* 61:1793–1801
- Canfield DE (2001) Biogeochemistry of sulfur isotopes. In: Valley JW, Cole DR (eds) *Stable isotope geochemistry*. Mineralogical Society of America, Washington
- Carignan J, Wen HJ (2007) Scaling NIST SRM 3149 for Se isotope analysis and isotopic variations of natural samples. *Chem Geol* 242:347–350
- Chacko T, Cole DR, Horita J (2001) Equilibrium oxygen, hydrogen, and carbon isotope fractionation factors applicable to geologic systems. In: Valley JW, Cole DR (eds) *Stable isotope geochemistry*. Mineralogical Society of America, Washington
- Cheam V, Aagemian H (1980) Preservation and stability of inorganic selenium-compounds at ppb levels in water samples. *Analyt Chim Acta* 113:237–245
- Clark SK, Johnson TM (2008) Effective isotopic fractionation factors for solute removal by reactive sediments: a laboratory microcosm and slurry study. *Environ Sci Technol* 42:7850–7855
- Clark SK, Johnson TM (2010) Selenium stable isotope investigation into selenium biogeochemical cycling in a lacustrine environment: Sweitzer lake, Colorado. *J Environ Qual* 39:2200–2210
- Criss RE (1999) *Principles of stable isotope distribution*. Oxford University press, New York, 254 pp
- Cutter GA, Cutter LS (2001) Sources and cycling of selenium in the western and equatorial Atlantic Ocean. *Deep-Sea Res Part II* 48:2917–2931
- Davis A, Olsen RL (1995) The geochemistry of chromium migration and remediation in the subsurface. *Ground Water* 33:759–768
- Detmers J, Brüchert V, Habicht KS, Kuever J (2001) Diversity of sulfur isotope fractionations by sulfate-reducing prokaryotes. *Appl Environ Microbiol* 67:888–894
- Ellis AS, Johnson TM, Bullen TD (2002) Cr isotopes and the fate of hexavalent chromium in the environment. *Science* 295:2060–2062
- Ellis AS, Johnson TM, Bullen TD, Herbel MJ (2003) Stable isotope fractionation of selenium by natural microbial consortia. *Chem Geol* 195:119–129
- Ellis AS, Johnson TM, Bullen TD (2004) Using chromium stable isotope ratios to quantify Cr(VI) reduction: lack of sorption effects. *Environ Sci Technol* 38:3604–3607
- U.S. Environmental Protection Agency (2009) National Primary Drinking Water Regulations. <http://water.epa.gov/drink/contaminants/index.cfm> Accessed 23 Nov 2010
- Fendorf SE, Zasoski RJ, Burau RG (1993) Competing metal ion influences on chromium(III) oxidation by birnessite. *Soil Sci Soc Am J* 57:1508–1515
- Frei R, Gaucher C, Poulton SW, Canfield DE (2009) Fluctuations in Precambrian atmospheric oxygenation recorded by chromium isotopes. *Nature* 461:250–253
- Hagiwara Y (2000) Selenium isotope ratios in marine sediments and algae – a reconnaissance study. M.S. Thesis, University of Illinois at Urbana-Champaign, Urbana, IL
- Halicz L, Yang L, Teplyakov N, Burg A, Sturgeon R, Kolodny Y (2008) High precision determination of chromium isotope ratios in geological samples by MC-ICP-MS. *J Anal Chem* 23:1622–1627
- Hayes JM (2001) Fractionation of carbon and hydrogen isotopes in biosynthetic processes. In: Valley JW, Cole DR (eds) *Stable isotope geochemistry*. Mineralogical Society of America, Washington
- Heninger I, PotinGautier M, deGregori I, Pinochet H (1997) Storage of aqueous solutions of selenium for speciation at trace level. *Fresenius J Anal Chem* 357:600–610
- Herbel MJ, Johnson TM, Oremland RS, Bullen TD (2000) Selenium stable isotope fractionation during bacterial dissimilatory reduction of selenium oxyanions. *Geochim Cosmochim Acta* 64:3701–3709
- Herbel MJ, Johnson TM, Tanji KK, Gao S, Bullen TD (2002) Selenium stable isotope ratios in agricultural drainage water systems of the western San Joaquin Valley, CA. *J Environ Qual* 31:1146–1156
- Izbicki JA, Ball JW, Bullen TD, Sutley SJ (2008) Chromium, chromium isotopes and selected trace elements, western Mojave Desert, USA. *Appl Geochem* 23:1325–1352
- Johnson TM (2004) A review of mass-dependent fractionation of selenium isotopes and implications for other heavy stable isotopes. *Chem Geol* 204:201–214
- Johnson CM, Beard BL (1999) Correction of instrumentally produced mass fractionation during isotopic analysis of Fe by thermal ionization mass spectrometry. *Int J Mass Spectrom* 193:87–99
- Johnson TM, Bullen TD (2003) Selenium isotope fractionation during reduction by Fe(II)-Fe(III) hydroxide-sulfate (green rust). *Geochim Cosmochim Acta* 67:413–419
- Johnson TM, Herbel MJ, Bullen TD, Zawislanski PT (1999) Selenium isotope ratios as indicators of selenium sources and oxyanion reduction. *Geochim Cosmochim Acta* 63:2775–2783
- Johnson TM, Bullen TD, Zawislanski PT (2000) Selenium stable isotope ratios as indicators of sources and cycling of selenium: Results from the northern reach of San Francisco Bay. *Environ Sci Tech* 34:2075–2079
- Kaplan IR, Rittenberg SC (1964) Microbial fractionation of sulfur isotopes. *Gen Microbiol* 43:195–212
- Kaplan IR, Emery KO, Rittenberg SC (1963) The distribution and isotopic abundance of sulphur in recent marine sediments off southern California. *Geochim Cosmochim Acta* 27:297–331
- Katz SA, Salem H (1994) *The biological and environmental chemistry of chromium*. VCH Publishers, New York
- Kendall C (1998) Tracing nitrogen sources and cycling in catchments. In: Kendall C, McDonnell JJ (eds) *Isotope tracers in catchment hydrology*. Elsevier, Amsterdam
- Kirk LB, Childers SE, Peyton B, McDermott T, Gerlach R, Johnson TM (2009) Geomicrobiological control of selenium solubility in subsurface phosphate overburden deposits. *Geochim Cosmochim Acta* 73(13) Suppl. 1:A661
- Kitchen JW, Johnson TM, Bullen TD (2004) Chromium Stable Isotope Fractionation During Abiotic Reduction of Hexavalent Chromium. *Eos Trans AGU* 85(47) Fall Meet. Suppl.: Abstract V51A-0519
- Krouse HR, Thode HC (1962) Thermodynamic properties and geochemistry of isotopic compounds of selenium. *Can J Chem* 40:367–375

- Lemly AD (1998) Pathology of selenium poisoning in fish. In: Frankenberger WT Jr, Engberg RA (eds) Environmental chemistry of selenium. Marcel Dekker, New York
- McNeal JM, Balistreri LS (1989) Geochemistry and occurrence of selenium; an overview. In: Jacobs LW (ed) Selenium in agriculture and the environment. SSSA Special Publication. Soil Science Society of America, Madison, WI
- Mitchell K, Mason PRD, Johnson TM, Lyons TW, Van Cappellen P (2010) Selenium isotope variation during oceanic anoxic events. *Geochim Cosmochim Acta* 74(12) Suppl. 1:A714
- Myneni SCB, Tokunaga TK, Brown GE Jr (1997) Abiotic selenium redox transformations in the presence of Fe (II, III) oxides. *Science* 278:1106–1109
- Oze C, Bird DK, Fendorf S (2007) Genesis of hexavalent chromium from natural sources in soil and groundwater. *Proc Natl Acad Sci USA* 104:6544–6549
- Presser TS (1994) The Kesterson effect. *Environ Manage* 18:437–454
- Raddatz AL, Johnson TM, McLing TL (2011) Cr stable isotopes in Snake River Plain aquifer groundwater: evidence for natural reduction of dissolved Cr(VI). *Environ Sci Technol* 45:502–507
- Rashid K, Krouse HR (1985) Selenium isotopic fractionation during SeO_3^{2-} reduction to Se^0 and H_2Se . *Can J Chem* 63:3195–3199
- Rees CB, Thode HG (1966) Selenium isotope effects in the reduction of sodium selenite and of sodium selenate. *Can J Chem* 44:419–427
- Rouxel O, Ludden J, Carginan J, Marin L, Fouquet Y (2002) Natural variations of Se isotopic composition determined by hydride generation multiple collector inductively coupled plasma mass spectrometry. *Geochim Cosmochim Acta* 66: 3191–3199
- Schauble E, Rossman GR, Taylor HP (2004) Theoretical estimates of equilibrium chromium-isotope fractionations. *Chem Geol* 205:99–114
- Schilling K, Johnson TM, Wilcke W (2011) Isotope fractionation of selenium during fungal biomethylation by *Alternaria alternata*. *Environ Sci Technol* 45:2670–2676
- Schoenberg R, Zink S, Staubwasser M, von Blanckenburg F (2008) The stable Cr isotope inventory of solid earth reservoirs determined by double spike MC-ICP-MS. *Chem Geol* 249:294–306
- Seby F, Potin-Gautier M, Giffaut E, Borge G, Donard OFX (2001) A critical review of thermodynamic data for selenium species at 25 degrees C. *Chem Geol* 171:173–194
- Sikora ER, Johnson TM, Bullen TD (2008) Microbial mass-dependent fractionation of chromium isotopes. *Geochim Cosmochim Acta* 72:3631–3641
- Skorupa JP (1998) Selenium poisoning of fish and wildlife in nature: lessons from twelve real-world-examples. In: Frankenberger WT Jr, Engberg RA (eds) Environmental chemistry of selenium. Marcel Dekker, New York
- Stilling LL, Amacher MC (2010) Kinetics of selenium release in mine waste from the Meade Peak Phosphatic Shale, Phosphoria Formation, Wooley Valley, Idaho, USA. *Chem Geol* 269:113–123
- Stollenwerk KG, Grove DB (1985) Reduction of hexavalent chromium in water samples acidified for preservation. *J Environ Qual* 14:396–399
- Trust BA, Fry B (1992) Stable sulphur isotopes in plants: a review. *Plant Cell Environ* 15:1105–1110
- Tudge AP, Thode HG (1950) Thermodynamic properties of isotopic compounds of sulfur. *Can J Res B28:567–578*
- U.S. Department of Health (2000) Toxicological Profile for Chromium. U.S. Department of Health and Human Services, Atlanta
- Valley JW, Cole DR (eds) (2001) Stable isotope geochemistry. Mineralogical Society of America, Washington
- Van Stempvoort DR, Reardon EJ, Fritz P (1990) Fractionation of sulfur and oxygen isotopes in sulfate by soil sorption. *Geochim Cosmochim Acta* 54:2817–2826
- Villalobos-Aragon A, Ellis AS, Johnson TM, Bullen TD, Glessner JJ (2008) Chromium stable isotope fractionation during transport: sorption and oxidation experiments. 2008 Geological Society of America Annual Meeting abstracts, p. 239
- Webster CL (1972) Selenium isotope analysis and geochemical applications. Ph.D Dissertation, Colorado State University, Fort Collins, CO
- Weiss DJ et al (2008) Application of nontraditional stable-isotope systems to the study of sources and fate of metals in the environment. *Environ Sci Technol* 42:655–664
- Wen HJ, Carignan J (2011) Selenium isotopes trace the source and redox processes in the black shale-hosted Se-rich deposits in China. *Geochim Cosmochim Acta* 75:1411–1427
- Weyer S, Schwieters JB (2003) High precision Fe isotope measurements with high mass resolution MC-ICPMS. *Int J Mass Spectrom Ion Processes* 226:355–368
- White AF, Benson SM, Yee AW, Wollenberg HA, Flexser S (1991) Groundwater contamination at the Kesterson reservoir, California.2. Geochemical parameters influencing selenium mobility. *Water Resour Res* 27:1085–1098
- Zhu J, Zuo W, Liang X, Li S, Zheng B (2004) Occurrence of native selenium in Yutangba and its environmental implications. *Appl Geochem* 19:461–467
- Zhu JM, Johnson TM, Clark SK (2008) Selenium isotope variations in weathering zones of Se-rich carbonaceous rocks at Yutangba, China. *Geochim Cosmochim Acta* 72(12) Suppl. 1:A1102
- Zink S, Schoenberg R, Staubwasser M (2010) Isotopic fractionation and reaction kinetics between Cr(III) and Cr(VI) in aqueous media. *Geochim Cosmochim Acta* 74:5729–5745

Chapter 10

Stable Isotopes of Transition and Post-Transition Metals as Tracers in Environmental Studies

Thomas D. Bullen

Abstract The transition and post-transition metals, which include the elements in Groups 3–12 of the Periodic Table, have a broad range of geological and biological roles as well as industrial applications and thus are widespread in the environment. Interdisciplinary research over the past decade has resulted in a broad understanding of the isotope systematics of this important group of elements and revealed largely unexpected variability in isotope composition for natural materials. Significant kinetic and equilibrium isotope fractionation has been observed for redox sensitive metals such as iron, chromium, copper, molybdenum and mercury, and for metals that are not redox sensitive in nature such as cadmium and zinc. In the environmental sciences, the isotopes are increasingly being used to understand important issues such as tracing of metal contaminant sources and fates, unraveling metal redox cycles, deciphering metal nutrient pathways and cycles, and developing isotope biosignatures that can indicate the role of biological activity in ancient and modern planetary systems.

10.1 Introduction

The transition metals form a geochemically and isotopically complex and interesting group of elements clustered in the center of the periodic table. The term *transition metal*, according to the International Union of Pure and Applied Chemistry (IUPAC), refers to an element whose atom has an incomplete d sub-shell or which can give rise to cations with an incomplete d

sub-shell. As shown in Fig. 10.1, according to this definition transition metals occur in Groups 1B and 3B–8B of the periodic table, and the transition metals across the periodic table have progressively increasing d-shell electron occupancy up to a maximum of 9. A characteristic of transition metals is that they generally exhibit two or more oxidation states, which as a consequence often leads to differences in the stable isotope composition of the chemical compounds and aqueous species they form. Transition metals for which significant variation of stable isotope composition in natural materials has been demonstrated include chromium (Cr), iron (Fe), nickel (Ni), copper (Cu), molybdenum (Mo) and silver (Ag).

The above definition of *transition metal* specifically excludes the Group 2B elements zinc (Zn), cadmium (Cd) and mercury (Hg), which are often referred to as *post-transition metals*. These metals have the d shell filled and thus generally occur as cations only in the +2 oxidation state. However, it is useful to include the post-transition metals in any discussion of transition metals, as they provide interesting similarities and contrasts in chemical behavior, are subject to change in redox state either naturally (e.g. Hg) or under anthropogenic influence (e.g. Zn, Cd) and display significant variation of stable isotope composition in natural materials.

Given this broad perspective, a description of the isotope systematics of the transition and post-transition metals is given here, including general isotopic distribution, examples of processes leading to stable isotope fractionation, and chemical properties pertinent to the discussion of stable isotope variability observed in natural materials. Rather than providing a comprehensive treatment of these issues, the intent here is to provide a general understanding of how the transition metal stable isotopes behave in Earth's hydrosphere

T.D. Bullen (✉)
U.S. Geological Survey, MS 420, 345 Middlefield Road,
Menlo Park, CA 94025, USA

3B	4B	5B	6B	7B	8B	1B	2B		
Sc scandium	Ti titanium	V vanadium	Cr chromium	Mn manganese	Fe iron	Co cobalt	Ni nickel	Cu copper	Zn zinc
Y yttrium	Zr zirconium	Nb niobium	Mo molybdenum	Tc technetium	Ru ruthenium	Rh rhodium	Pd palladium	Ag silver	Cd cadmium
(La) lanthanum	Hf hafnium	Ta tantalum	W tungsten	Re rhenium	Os osmium	Ir iridium	Pt platinum	Au gold	Hg mercury

Fig. 10.1 A portion of the Periodic Table of the Elements, showing the transition and post-transition metals. Elements with *green borders* are those for which significant variability of stable isotope composition has been observed in natural materials. Elements with *red borders* have only one stable isotope (no stable isotope in the case of Tc)

and atmosphere that are the venue of environmental research. Familiarity with the material in this section will help readers who are not well versed in stable isotope geochemistry to better appreciate the specific applications discussed in the later part of the chapter.

10.1.1 Chromium (Cr)

Chromium is an important trace element, particularly in ultramafic and mafic rock minerals, and is a major element in several minerals such as chromite (FeCr_2O_4) of the spinel group, uvarovite ($\text{Ca}_3\text{Cr}_2(\text{SiO}_4)_3$) of the garnet group, and crocoite (PbCrO_4). Chromium has numerous industrial applications, including use in electroplating, in leather tanning, as pigment in paint, and as an anticorrosion agent. Chromium is stable at the Earth's surface in two oxidation states: Cr^{6+} (Cr(VI)), commonly referred to as hexavalent Cr, and Cr^{3+} (Cr(III)), commonly referred to as trivalent Cr. Cr(VI) is a strong oxidant, and occurs mainly as the toxic, water-soluble oxyanions chromate (CrO_4^{2-}) and bichromate ($\text{HCr}_2\text{O}_7^{1-}$). Cr(III) is nontoxic and is insoluble in water.

Chromium has four stable isotopes: ^{50}Cr (4.35%), ^{52}Cr (83.79%), ^{53}Cr (9.50%) and ^{54}Cr (2.37%); note that for Cr and other elements discussed below that relative percentages of the isotopes are the values

more than one stable isotope and thus the potential to have variability of stable isotope composition in natural materials, but such variability has yet to be rigorously demonstrated. Elements with *red borders* have only one stable isotope (no stable isotope in the case of Tc)

recommended by IUPAC to represent average terrestrial abundances. Igneous rocks have a very restricted range of $^{53}\text{Cr}/^{52}\text{Cr}$ which on average is about 0.12‰ (parts per thousand) less than that of NIST (National Institute of Standards and Technology) 979 Cr metal (Schoenberg et al. 2008). Presently the measured range of $^{53}\text{Cr}/^{52}\text{Cr}$ in natural materials is ~6‰, essentially reflecting the range measured for naturally occurring Cr(VI) in groundwater (Izbicki et al. 2008). Both inorganic and microbially mediated reduction of Cr (VI) to Cr(III) have been shown to result in isotope fractionation, with breakage of the strong Cr-O bond in chromate and bichromate appearing to be the rate limiting step (Ellis et al. 2002; Sikora et al. 2008). During reduction of Cr(VI), the product Cr(III) formed at any step of the process is 3–4‰ lighter than co-existing remnant Cr(VI). The fact that the oxidized species, Cr(VI), is heavier than the reduced species, Cr(III), is consistent with observations for other redox-sensitive elements such as selenium (Johnson et al. 2000; Johnson 2011) and mercury (Bergquist and Blum 2009; Blum 2011). While oxidation of Cr(III) to Cr(VI) is also likely to cause stable isotope fractionation (Schauble 2004), this phenomenon has yet to be rigorously demonstrated. Sorption of chromate and bichromate on Fe- and Al-oxyhydroxides has only a negligible instantaneous effect on the distribution of Cr isotopes, with preferential partitioning of light Cr isotopes onto sorption sites. Sorption effects may be

magnified at reaction fronts such as the leading edge of a Cr contaminant plume in groundwater (Ellis et al. 2004).

10.1.2 Iron (Fe)

Iron is the most abundant element on Earth and the fourth most abundant element in the Earth's crust. Iron is the most widely used metal in industry, and thus is pervasive in the environment. Iron is stable at the Earth's surface in two oxidation states: Fe^{2+} (Fe(II)), commonly referred to as ferrous Fe, and Fe^{3+} (Fe(III)), commonly referred to as ferric Fe. Fe(II) is a strong reductant, is water-soluble, and is an important constituent of Fe minerals formed under reducing conditions (e.g. magnetite, siderite, pyrite). Fe(III) is only sparingly water-soluble and is an important constituent of Fe minerals formed under oxidizing conditions (e.g. ferrihydrite, goethite, hematite). Iron metal has a wide variety of applications in metallurgy such as construction of automobiles and ships, structural components of buildings, and machinery in general. Iron compounds such as Fe(III)-chloride and Fe(II)-sulfate are likewise widely used in industry for a variety of purposes. Iron plays an important role in biology and is an essential nutrient for nearly all living organisms. For example, Fe combines with oxygen to form hemoglobin and myoglobin, the two main oxygen transport proteins in vertebrates. Iron can serve as both electron donor and electron acceptor for a wide range of microorganisms, and thus Fe redox reactions have the potential to support substantial microbial populations in soil and sedimentary environments (Weber et al. 2006). Iron has been viewed as a limiting nutrient for phytoplankton growth in the oceans (Martin and Fitzwater 1988). Iron transformations and cycling processes are critical determinants of plant, forest and agricultural ecosystem function. Iron itself is generally non-toxic, but dissolved Fe(II) does impart an unpleasant taste to water and Fe(III) staining of plumbing fixtures can be a nuisance.

Like Cr, Fe has four stable isotopes: ^{54}Fe (5.58%), ^{56}Fe (91.95%), ^{57}Fe (2.18%) and ^{58}Fe (0.30%). Igneous rocks have a very restricted range of $^{56}\text{Fe}/^{54}\text{Fe}$. Presently the measured range of $^{56}\text{Fe}/^{54}\text{Fe}$ in natural materials is $\sim 5\%$, with pyrites from Precambrian black shales spanning this range (-3.6 to $+1.2\%$ rela-

tive to igneous rocks; Severmann and Anbar 2009). Both inorganic and microbially-mediated oxidation of Fe(II) to Fe(III) and microbial reduction of Fe(III) to Fe(II) have been shown to result in stable isotope fractionation (Bullen et al. 2001; Balci et al. 2006; Beard et al. 1999). Perhaps most important in this regard is the experimentally and theoretically well-established isotope exchange equilibrium between Fe(II)- and Fe(III)-hexaquo complexes of $\sim 3\%$ (Johnson et al. 2002; Anbar et al. 2005), in which the oxidized species, Fe(III), is heavier than the reduced species, Fe(II), as is the case for Cr. In addition, an important role for sorption of Fe onto mineral surfaces has been recognized, with heavy Fe species observed to populate the sorption sites after equilibrium is attained (Beard et al. 2010).

10.1.3 Nickel (Ni)

Nickel is used in many industrial and consumer products, including stainless steel and other metal alloys, coins, rechargeable batteries, and electroplating. Nickel is an important trace element in ultramafic and mafic rocks. Nickel is stable at the Earth's surface in three oxidation states: primarily as Ni^{2+} (Ni(II)), but also as Ni^{1+} (Ni(I)) and Ni^{3+} (Ni(III)). Nickel is an important enzyme cofactor, for example in urease, which assists in the hydrolysis of urea.

Nickel has five stable isotopes: ^{58}Ni (68.1%), ^{60}Ni (26.2%), ^{61}Ni (1.1%), ^{62}Ni (3.6%) and ^{64}Ni (0.9%). In a recent study of Ni stable isotope variations related to methanogenesis, Cameron et al. (2009) found that methanogens cultured in the laboratory preferentially assimilated light Ni from the media, leaving the residue enriched in heavy Ni isotopes. Fractionation of as much as 1.6‰ for $^{60}\text{Ni}/^{58}\text{Ni}$ was observed. In contrast, little variability was observed among meteorites, basalts and continental sediments, suggesting a lithologic baseline for comparison of this potential biomarker of methanogenesis.

10.1.4 Copper (Cu)

Copper has a wide range of industrial applications, including use for electrical wires, in metal alloys, in

boat paint to prevent biologic fouling, in water and gas supply pipes, and in coins. Copper is stable at the Earth's surface in two oxidation states: Cu^{1+} (Cu(I)), which is the common form in sulfide minerals such as chalcopyrite (CuFeS_2), chalcocite (Cu_2S), and enargite (Cu_3AsS_4); and Cu^{2+} (Cu(II)), which is the common form in aqueous solution. Copper can be toxic to animals, due in large part to its ability to accept and donate single electrons readily as it changes between oxidation states. This is thought to catalyze the production of reactive radical ions leading to the condition known as oxidative stress.

Cu has two stable isotopes: ^{63}Cu (69.17%) and ^{65}Cu (30.83%). In natural materials, the measured range of $^{65}\text{Cu}/^{63}\text{Cu}$ is approximately 9‰ for solid samples and 3‰ for water samples (Larson et al. 2003; Borrok et al. 2008). In one study of possible Cu stable isotope fractionation processes, abiotic oxidative dissolution of Cu-bearing sulfide minerals resulted in the product aqueous Cu(II) being ~1.4‰ heavier in terms of the $^{65}\text{Cu}/^{63}\text{Cu}$ ratio than Cu in chalcopyrite and ~3.0‰ heavier than Cu in chalcocite. Involving the microbe *Acidithiobacillus ferrooxidans* in the dissolution process reduced the fractionation observed in both cases (Mathur et al. 2005).

Copper isotopes are beginning to provide important new insights into how Cu behaves in Earth's rivers and oceans, as well as how the isotopes may be fractionated. Vance et al. (2008) reported $^{65}\text{Cu}/^{63}\text{Cu}$ ratios for riverine water, estuarine water and particulates, and open ocean water samples. They observed that dissolved Cu in rivers had $^{65}\text{Cu}/^{63}\text{Cu}$ of from 0.02 to 1.45‰ greater than that of the NIST 976 Cu standard, and for the most part greater than that of Cu in crustal rocks (+0.16‰ relative to NIST 976). In the estuarine samples, $^{65}\text{Cu}/^{63}\text{Cu}$ of dissolved Cu was 0.8–1.5‰ greater than that of Cu associated with particulate material. Vance et al. (2008) interpreted this isotopic contrast to reflect isotopic partitioning of the weathered pool of Cu between a light fraction adsorbed to particulates and a heavy dissolved fraction dominated by Cu bound to strong organic complexes, providing a mechanism to deliver heavy dissolved Cu to the oceans. Dissolved Cu in open ocean water samples was even heavier than that in the river waters, suggesting a continuation of the fractionation between dissolved and particulate Cu fractions particularly in the surface ocean.

10.1.5 Zinc (Zn)

The post-transition metal Zn is used in electroplating, metal alloys, pigment in paint, agricultural fertilizers and pesticides, galvanized roofing material, and television-screen phosphors. Zinc is stable at the Earth's surface in one oxidation state, Zn^{2+} (Zn(II)). The large pool of Zn^0 metal produced industrially is manufactured specifically for purposes that take advantage of its high oxidation potential relative to other metals (e.g. as an anti-fouling and anti-corrosive agent on the submerged portion of ship hulls and propeller shafts). Zinc is an important enzyme cofactor, for example in alcohol dehydrogenase in humans, and is generally thought to be non-toxic.

Zinc has five stable isotopes: ^{64}Zn (48.63%), ^{66}Zn (27.90%), ^{67}Zn (4.10%), ^{68}Zn (18.75%) and ^{70}Zn (0.62%). In natural materials, the measured range of $^{66}\text{Zn}/^{64}\text{Zn}$ is approximately 2‰ (Cloquet et al. 2008). Maréchal et al. (1999) published the first high-quality measurements of zinc and copper isotope compositions in a variety of minerals and biological materials. Since this pioneering work the field of Zn isotope biogeochemistry has rapidly expanded into a variety of environmental applications. For example, Zn has a relatively low boiling point (~910°C) compared with that of Cr or Cu, within the operating temperature range of ore smelters. Thus Zn can evaporate from ore during smelting, which would favor escape of light Zn isotopes in the exhaust as demonstrated by Mattielli et al. (2009), and retention of heavy Zn isotopes in the slag residue as shown by Sivry et al. (2009). Kavner et al. (2008) demonstrated that electroplated Zn, reduced to metallic state from a large pool of aqueous Zn(II), is isotopically light compared to the parent solution, potentially resulting in a large pool of isotopically light electroplated Zn in the environment. In addition, Weiss et al. (2007) demonstrated that Zn adsorption due to complexation by organic compounds is selective for the heavy Zn isotopes, resulting for example in peat samples that have heavier Zn isotope compositions than any potential natural source. On the other hand, Borrok et al. (2008) pointed out that Zn uptake by microorganisms is selective for the light Zn isotopes. Thus there are several fractionation processes for Zn that might modify its isotope composition in the environment.

10.1.6 Molybdenum (Mo)

Molybdenum is used in the production of high-strength steel alloys, as pigments and catalysts, and in a variety of high temperature applications such as lubricants, electrical contacts and industrial motors. Molybdenum is stable at the Earth's surface in several oxidation states, the most stable being Mo^{4+} (Mo(IV)) and Mo^{6+} (Mo(VI)). Molybdenum is an essential enzyme cofactor in nearly all organisms, with particular importance for nitrogen fixation, nitrate reduction and sulfite oxidation. Molybdenum is soluble in strongly alkaline water such as seawater, forming molybdates (MoO_4^{2-}). Molybdates bear structural similarities to chromates, yet are weaker oxidants. In fact, although Mo lies directly below Cr in the periodic table, Mo compounds show more similarity to those of tungsten (W), which lies directly below Mo in the periodic table.

Molybdenum has seven stable isotopes: ^{92}Mo (14.84%), ^{94}Mo (9.25%), ^{95}Mo (15.92%), ^{96}Mo (16.68%), ^{97}Mo (9.55%), ^{98}Mo (24.13%) and ^{100}Mo (9.63%). In natural materials, the measured range of $^{97}\text{Mo}/^{95}\text{Mo}$ is $\sim 3\text{‰}$, with pelagic clays extending to -1‰ and suboxic sediment pore fluids extending to $+2\text{‰}$ relative to a modeled "bulk earth" composition as defined by Mo ores (Barling et al. 2001; Siebert et al. 2003; Anbar 2004; Arnold et al. 2004). Molybdenum isotopes are fractionated during adsorption to ferromanganese oxides in oxidizing environments (Barling et al. 2001; Barling and Anbar 2004) and precipitation of Fe-Mo-S solids in reducing environments (Poulson et al. 2006; Neubert et al. 2008), and the extent of fractionation differs in these two extreme conditions. Thus Mo isotopes can provide information about local redox conditions.

10.1.7 Cadmium (Cd)

The post-transition metal Cd is used primarily in Ni-Cd batteries, metal alloys, electroplating, pigment in paint, and electronic components. Cadmium is stable at the Earth's surface primarily in the Cd^{2+} (Cd(II)) oxidation state. Cadmium has a strong geological affinity to Zn, but unlike Zn can be toxic to humans due to its effective substitution for calcium in bone and

its tendency to concentrate in the kidneys and liver where it may become carcinogenic.

Cadmium has eight stable isotopes: ^{106}Cd (1.25%), ^{108}Cd (0.89%), ^{110}Cd (12.49%), ^{111}Cd (12.80%), ^{112}Cd (24.13%), ^{113}Cd (12.22%), ^{114}Cd (28.73%) and ^{116}Cd (7.49%). In terrestrial materials, the measured range of $^{114}\text{Cd}/^{110}\text{Cd}$ is approximately 0.5‰; considering anthropogenically influenced materials extends that range to $\sim 1.5\text{‰}$ (Ripperger and Rehkämper 2007; Schmitt et al. 2009a, b; Shiel et al. 2010). Cadmium has an even lower boiling point ($\sim 760^\circ\text{C}$) than Zn, and like Zn, Cd in ores likely evaporates during smelting favoring escape of light Cd isotopes in the exhaust, as recently demonstrated by Cloquet et al. (2006a). Cadmium behaves like Zn during electroplating (Kavner et al. 2008), potentially resulting in a large pool of isotopically light Cd in the environment. Although Cd is discussed in this chapter mainly in a multi-tracer context, Rehkämper et al. (2011) provide a thorough discussion of the application of Cd isotopes in environmental studies.

10.1.8 Mercury (Hg)

The post-transition metal Hg is used in thermometers and other scientific apparatus, amalgam for dental restoration, Hg vapor lamps, cosmetics, and liquid mirror telescopes. Historically, Hg has been widely used in gold mining operations. Mercury is stable at the Earth's surface as soluble Hg^{2+} (Hg(II)) and as Hg^+ (Hg(I)) in the form of monomethylmercury (CH_3Hg^+). In addition, and unlike the other transition and post-transition metals, Hg has a stable gaseous form (Hg^0) at environmental temperatures with a residence time in the atmosphere of approximately 1 year (Schroeder and Munthe 1998). Mercury and its compounds (e.g. monomethylmercury (MeHg), mercuric chloride) are extremely toxic and can be readily ingested through inhalation or absorption through the skin and mucous membranes.

Mercury has seven stable isotopes: ^{196}Hg (0.15%), ^{198}Hg (9.97%), ^{199}Hg (16.87%), ^{200}Hg (23.10%), ^{201}Hg (13.18%), ^{202}Hg (29.86%) and ^{204}Hg (6.87%). Based on the compilation of existing high-precision Hg isotope data reported by Bergquist and Blum (2009), the measured range of $^{202}\text{Hg}/^{198}\text{Hg}$ in natural

materials resulting from *mass dependent fractionation* (MDF) between coexisting Hg pools is approximately 7‰. This is remarkable, considering that measurable fractionation of Hg isotopes was generally thought to be non-existent as late as the 1990s. In addition, Hg stable isotopes exhibit considerable *mass independent fractionation* (MIF), in which the odd-numbered isotopes ^{199}Hg and ^{201}Hg behave differently than the even-numbered isotopes in certain chemical reactions such as photochemical reduction (Bergquist and Blum 2007), leading to significant enrichments and depletions of the odd-numbered isotopes relative to the even-numbered isotopes in environmental Hg pools.

Although Hg is included in the discussion here, Blum (2011) provides a thorough discussion of the theory and application of Hg isotopes in environmental studies. In his chapter, Blum (2011) points out that most environmental applications of Hg isotopes are concerned with either (1) interpreting the isotopic composition of MeHg occurring in sediments and organisms, or (2) interpreting the isotopic composition of Hg(II) associated with sediments or deposited onto the land surface or into a water body. In addition, the author stresses the importance of redox reactions as the main cause of isotope fractionation in the Hg system and the role that the isotopes can play in helping to increase our understanding of the chemical bonding environments that lead to various Hg fractions in sediments and other natural materials.

10.1.9 Other Transition Metals Potentially Having Useful Isotopic Variability

There are several other transition metals, outlined in blue in Fig. 10.1, that have multiple stable isotopes and thus the potential for stable isotope variability in nature, but which have yet to be rigorously explored in terms of isotope systematics. Examples of these elements that would be especially useful in environmental studies are titanium (Ti), vanadium (V), silver (Ag), tungsten (W) and rhenium (Re). For example, as pointed out by Severman and Anbar (2009), Re (^{185}Re (37.4%), ^{187}Re (62.6%); common oxidation states Re^{2+} , Re^{4+} , Re^{6+} , Re^{7+}) is removed from solution into sediments only under anoxic or suboxic conditions,

making it a suitable tracer for moderately reducing conditions. In contrast, V (^{50}V (0.25%), ^{51}V (99.75%); common oxidation states V^{2+} , V^{3+} , V^{4+} , V^{5+}) is scavenged from solution by manganese oxides and Fe-oxhydroxides, making it a suitable tracer for oxic conditions. Both potential redox-tracing applications assume that sedimentation promotes isotope fractionation between sediment and residual aqueous pools of Re or V, but such fractionation has yet to be demonstrated.

Silver, in addition to its historic value as a precious metal, is widely used in dentistry, photographic materials, mirrors and optics, control rods in nuclear reactors, clothing (as an anti-fungal agent) and in certain medicines. Silver has the highest electrical conductivity of any element and the highest thermal conductivity of any metal and thus is widely used in electrical contacts and conductors. Silver is stable at the Earth's surface primarily in three oxidation states: Ag^0 or native silver, and Ag^{1+} and Ag^{2+} , the common forms in a wide variety of Ag-containing compounds and minerals. Silver has two stable isotopes: ^{107}Ag (51.84%) and ^{109}Ag (48.16%). In an initial study of Ag stable isotope variation in sediment and domestic and industrial sludge samples, Luo et al. (2010) reported a small but significant range of variation in $^{109}\text{Ag}/^{107}\text{Ag}$ of 0.1‰ that bracketed the value for their standard. They found a different value for Ag from a fish liver (+0.28‰ relative to their standard) that may indicate a biological influence. However, at this stage Ag is only beginning to be explored in terms of stable isotope variability.

Tungsten provides an especially intriguing but as yet untested candidate for stable isotope variation in natural materials at the Earth's surface. Tungsten is used in many high-temperature applications, such as light bulbs and welding processes, and in lubricants, abrasives, ceramic glazes, and heavy metal alloys. The most common oxidation state of W at the Earth's surface is W^{6+} , but W exhibits all oxidation states from W^{2+} to W^{6+} . Tungsten has five stable isotopes: ^{180}W (0.12%), ^{182}W (26.50%), ^{183}W (14.31%), ^{184}W (30.64%) and ^{186}W (28.43%); ^{180}W is radioactive, but with a half-life of 1.8×10^{18} years it is essentially stable. While there is substantial literature describing ^{182}W variations in meteorites, there have been essentially no published systematic studies of low-temperature processes involving W. However, Irisawa and Hirata (2006) reported that W isotope ratios for

sediment reference materials differed significantly from values for igneous rocks, hinting at the possibility that low-temperature redox and/or sorption processes may fractionate the W isotopes.

The potential for Ti to have significant variability of stable isotope composition in natural materials at the Earth's surface is probably less than that for W, V and Re. This is due to the fact that the geochemistry of Ti is dominated by the Ti^{4+} oxidation state, and Ti is not known to play a large role in biological processes such as enzyme stabilization. Regardless, titanium has five stable isotopes spanning a large mass range: ^{46}Ti (8.0%), ^{47}Ti (7.3%), ^{48}Ti (73.8%), ^{49}Ti (5.5%) and ^{50}Ti (5.4%). If our experience with exploration of stable isotope variability of other elements dominated by a single oxidation state may serve as a guide, it is not unrealistic that a thorough reconnaissance study of Ti or other unexplored transition metal stable isotope systematics in environmental materials (e.g. nanoparticles, pigments, electroplated steel) would reveal unexpected surprises.

10.2 Methodology

Although the transition and post-transition metals represent a geochemically diverse group of elements, the details of the analytical procedures required for measurement of their isotope compositions are quite uniform. Once a laboratory establishes a protocol for analysis of one of these metals, it can be relatively straightforward to add more of the remaining metals to the repertoire. On the other hand, transition and post-transition metals are everywhere, in field and laboratory equipment, and care must be taken to maintain strict cleanliness during sample collection, processing and measurement.

10.2.1 Sampling Protocols

As a general rule, the sampling protocol for transition or post-transition metal isotope analysis of water is identical to that for standard dissolved cation analysis. The sample is collected using plastic tubing for pumps or plastic containers for dipping and placed into plastic containers that have been rinsed several times with the

water being collected. Pre-cleaning of the plastic containers with nitric acid may be required if container "blanks", obtained by allowing distilled water to sit in the container for an extended period of time, reveal significant metal content. The sample needs to be filtered, the pore-size of the filter being determined by the question being asked (e.g. is there isotopic fractionation between colloidal and non-colloidal size fractions?). Generally an in-line filter with 0.1 μm pore size provides sufficient filtration, but this may cause retention of some of the colloidal fraction as well (size: 1 nm–1 μm). Alternatively, the sample can be filtered after initial collection using a plastic syringe fitted with a disposable filter cartridge. Care must be taken to prevent possible redox changes of the redox-sensitive species in the oxic environment. Use of an in-line filter minimizes potential formation of Fe- and Mn-oxyhydroxides that can scavenge the metals from solution. Additionally, collection and filtration can be carried out in a portable nitrogen-atmosphere glove box. The sample should be acidified with exceptionally clean nitric or hydrochloric acid, to a pH of approximately 2.0. Additional precautions such as wearing ultra-clean over-garments, gloves and boots may be required, particularly when metal concentrations are expected to be extremely small.

Knowledge of metal concentrations in the sample prior to collection for isotope analysis is useful in order to ensure that sufficient metal is collected to meet the requirements of the analytical technique. As a general rule of thumb, sufficient material to provide 1–10 μg of the target metal should be collected when possible. The amount of metal required for isotope analysis ranges from as little as 5 ng to as much as 1 μg , depending on factors such as ionization efficiency in the mass spectrometer and resolution mode employed (see below). Moreover, knowledge of procedural blank levels is useful for deciding what kinds of plastic tubing and containers to use and what protective measures to take. A worthwhile exercise is to take a supply of the cleanest distilled laboratory water available to the field site and to treat the distilled water as a sample, using all intended plastic tubing and containers, filters and other collection equipment, and techniques. One or two field blanks should be collected during each sampling session, and the blank should be measured for concentration of the metal of interest prior to investing time in sample preparation and mass spectrometry.

Collection of solid samples such as soils, plant tissues and landfill materials requires common sense more than anything. Solid samples should be collected into plastic bags, and care should be taken to ensure that sampling equipment (e.g. shovels, augers, stem-wood borers) do not contain the metal of interest. Particular care should be taken to avoid sampling equipment with painted surfaces as the paint is likely to have transition or post-transition metals as pigments.

10.2.2 Sample Preparation

Prior to mass spectrometry, the metal of interest must be isolated from the rest of the sample matrix and particularly from elements that would produce isobaric interferences on the target masses for analysis. For example, in preparing a sample for Cr isotope analysis, all Ti, V and Fe must be removed, as each of these metals has an isotope at the same mass as a Cr isotope. Similarly, some elements form double-charged ions in the mass spectrometer that are detected at $\frac{1}{2}$ of their mass due to the direct dependence of ion flight path through the magnetic sector of the mass spectrometer on mass:charge ratio of the ion. For example, Ba^{2+} ions can be formed in both multi-collector inductively coupled plasma mass spectrometry (MC-ICP-MS) and thermal ionization mass spectrometry (TIMS), the two common methods for analysis of metal stable isotope composition. $^{132}\text{Ba}^{2+}$ would be detected at mass 66, $^{134}\text{Ba}^{2+}$ would be detected at mass 67, and $^{136}\text{Ba}^{2+}$ would be detected at mass 68, all directly overlapping the Zn isotopes of the same masses. Thus, a goal of the chemistry is to produce as pure a target metal fraction as possible, preferably if not assuredly with quantitative recovery.

Most chemical procedures for purification of the transition and post-transition metals involve some form of ion exchange chromatography, making use of different affinities of the metals for the ion exchange resins in different strengths of acid media. For example, Wombacher et al. (2003) developed a method to purify Cd from geological materials and meteorites. The digested sample is dissolved in 3 M HCl and loaded directly onto an exchange column containing AG1-X8 strong acid anion exchange resin. The column is rinsed with set volumes of 0.5, 1, 2 and finally

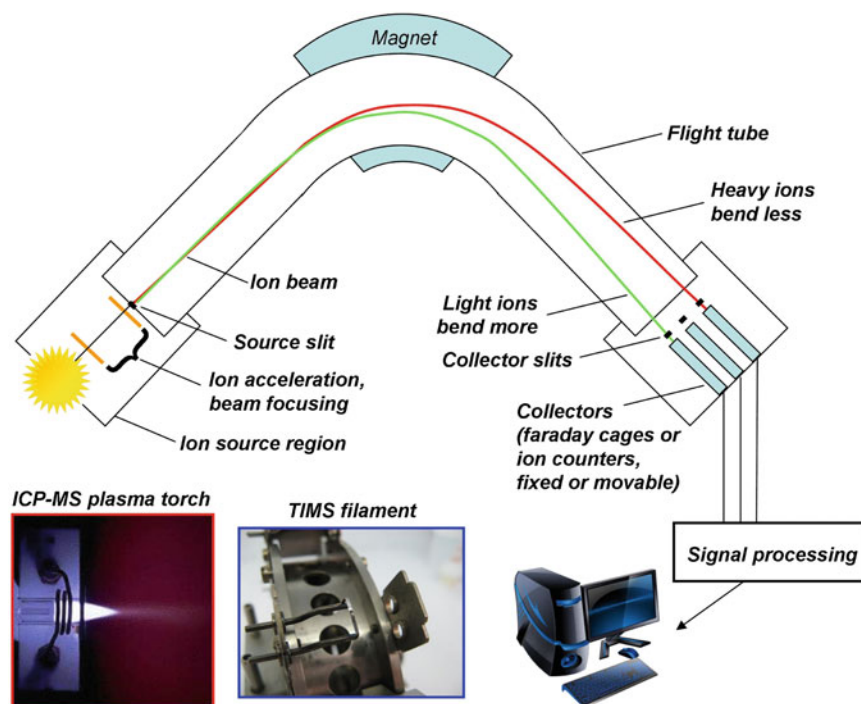
8 M HCl in order to remove the majority of matrix elements. Following this series of rinses, all that remains on the resin are Ag, Zn, tin (Sn) and Cd. Additional rinsing with 8 M HCl removes the Ag, which can be retained for isotope analysis if desired (although quantitative recovery must be demonstrated). The rinse solution is then changed to a 0.5 M HNO_3 –0.1 M HBr mixture, which removes Zn and some of the Sn from the column; this fraction can be retained for further processing for Zn isotope analysis, if desired. The rinse solution is then changed to 2 M HNO_3 , which removes the Cd and the remainder of the Sn. This product solution is then taken to dryness, re-dissolved in 6 M HCl and loaded onto a small column containing a resin (TRU Spec, Eichrom Industries) that retains the Sn but not the Cd, which is collected in a beaker. The product solution contains only Cd, and is ready for isotopic determination. This example demonstrates the versatility of the ion exchange resin method, and new element-specific resins are continually being developed as the need for new applications is encountered.

Procedures for chemical purification of the other transition and post-transition metals follow a similar logic and most are able to achieve quantitative recovery, thereby avoiding isotope fractionation on the resin column which has been demonstrated to occur for several elements such as Fe (Anbar et al. 2000). References providing detailed descriptions of purification techniques for the transition and post-transition metals discussed here include: Cr, Ellis et al. (2002; supplementary material); Fe, Beard and Johnson (1999); Ni, Cameron et al. (2009); Cu and Zn, Borrokar et al. (2007); Mo, Barling et al. (2001); Cd, Wombacher et al. (2003); Ag, Luo et al. (2010); Ti, Das and Pobi (1990); V, Pelly et al. (1970); W, Sahoo et al. (2006); Re, Liu et al. (1998). Note that sample preparation of Hg for isotope analysis requires an entirely different approach, as discussed in Blum (2011).

10.2.3 Instrumentation

As mentioned above, the stable isotope composition of the transition and post-transition metals is measured using either MC-ICP-MS or TIMS. A generalized schematic of these mass spectrometers is given in Fig. 10.2, which illustrates essential aspects of their

Fig. 10.2 Generalized schematic of the important aspects of multi-collector mass spectrometers used for determination of metal stable isotope compositions. Key features are discussed in the text. Modified after Bullen and Eisenhauer (2009)



function (Bullen and Eisenhauer 2009). All instruments consist of three main components: ion source, ion optics (ion acceleration, ion beam focusing, isotope mass separation) and ion collection. Ions are produced by thermal processes in the source region: in MC-ICP-MS, the sample is injected into the source region either as a nebulized liquid aerosol or as ablated solid particulate in a gaseous stream which passes through a high-temperature plasma (up to 10,000°K; see photo insert in Fig. 10.2) at near-atmospheric pressure. At this high temperature, atoms of the sample material are very efficiently ionized. In TIMS, the sample is deposited on a wire filament (see photo insert in Fig. 10.2), placed in a high vacuum ($\sim 10^{-8}$ torr), and the filament is heated to the temperature required for ion production of the particular element (typically 800–1,700°C). The ions produced in either instrument then enter the optics region, where they are accelerated through a large potential (up to 10 kV) and focused electronically to create a discrete ion beam. In MC-ICP-MS, the vacuum must be substantially improved over this short optics region via efficient mechanical and electrical “ion getter” vacuum pumps. Beyond the ion optics region, an exceptional vacuum ($\sim 10^{-8}$ torr) must be maintained in both instruments.

The accelerated and focused ion beam then passes through a slit into the flight tube where the different isotopes of the element are dispersed by mass using an electromagnet. The width of the slit determines the ability of the mass spectrometer to partially resolve sample ions and extraneous molecules of nearly similar mass (“isobaric interferences”). For example, since the plasma in ICP-source instruments is predominantly composed of Ar, a narrow slit must be used to resolve ^{56}Fe from $^{40}\text{Ar}^{16}\text{O}$. In TIMS instruments, ^{56}Fe must be resolved from organic molecules with mass ~ 56 atomic mass units. In general, a narrower slit provides greater resolving power but reduced signal intensity.

The fundamental power of MC-ICP-MS and TIMS instruments to disperse the isotopes of an element rests in the ability of the magnet to differentially divert the flight paths of the various isotopes according to their individual energies. The ion flight paths are bent along the axis of the flight tube depending on the ratio of ion mass to charge: light ions are bent more (green path in diagram), heavy ions are bent less (red path in diagram). For any particular isotope, a restricted range of ion energies leaving the magnetic sector is required to create a concentrated, flat-topped signal that is ideal

for detection and measurement. In TIMS, ions of a particular isotope produced at the source filament are essentially mono-energetic, and once the ion beam is focused in the source region mass (i.e. energy) dispersion can be effectively achieved in the magnetic sector. In contrast, in MC-ICP-MS ions of a particular isotope leave the source region having a fairly wide energy distribution due to numerous processes occurring in the source region. Thus in most MC-ICP-MS instruments, the poly-energetic ion beam must first pass through an electrostatic discriminator (not shown) which disperses the ion beam in exactly the opposite sense to that which follows in the magnetic sector. As a result of exacting electromechanical design, the ion beam that ultimately passes out of the magnetic sector has a balanced and much smaller energy spread that allows the flat-topped signal to develop. In a few MC-ICP-MS instruments, the ion beam first passes through a “collision cell” containing molecules of a gas such as Ar where collisions of the metal ions with the gas molecules substantially reduce the kinetic energies of those ions, which can then be reaccelerated in a nearly mono-energetic condition for passage through the magnetic field as in TIMS.

Ion detection collectors are configured to perfectly intersect the resulting flight paths of the component isotope ion beams of the element. In some instruments, collectors can be moved perpendicularly to the ion paths until desired coincidence is achieved for a particular element. In other instruments, the collector positions are fixed and the trajectories of the ion beams themselves are adjusted along the final section of the flight tube by further electronic focusing in order to achieve coincidence. Collectors are either Faraday cages, credit-card sized, thin rectangular boxes open on one narrow end to receive and trap ions on the internal surfaces resulting in a measurable total ion current on the internal surfaces, or ion counters that record individual ion collisions with the counter surfaces. Faraday cages may have slits positioned along the ion flight path prior to the point of ion entry into the cage in order to better shape the ion beam for optimum signal detection. Channel-specific total ion currents detected over a certain period of time are then processed through a series of electronic conversions into signals that can be interpreted by computer software as relative isotope abundances for the element.

Each instrument has its advantages in certain applications, but as a general rule the stable isotope

composition of all the transition and post-transition metals discussed in this chapter can be most efficiently determined using MC-ICP-MS. The high ionization efficiency of the plasma source used to generate ions in MC-ICP-MS compared to that of the metal filament source used in TIMS results in improved isotope measurement of very small quantities (i.e. tens of nanograms) of elements with high ionization potentials, such as Zn (e.g. Chen et al. 2008), Mo (e.g. Barling and Anbar 2004), and Hg (e.g. Blum and Bergquist 2007). In addition, MC-ICP-MS instruments typically have the capability to sufficiently resolve measureable portions of metal ion beams from “isobaric” polyatomic interfering species having nearly the same mass (e.g. ^{56}Fe vs. $^{40}\text{Ar}^{16}\text{O}$ generated in the Ar plasma). Some interfering species, primarily oxides, can also be removed from the ion stream to a large extent by desolvating the sample prior to introduction to the plasma. Alternatively, in some instruments polyatomic molecules can be disaggregated in the collision cell apparatus described above due to collisions of the molecules with atoms of the gas supplied to the cell. In MC-ICP-MS, uncertainty due to signal noise resulting from the inherent instability of the plasma source is eliminated by measuring all ion beams simultaneously with the multicollector array. An additional strength of MC-ICP-MS is that samples can be introduced using laser ablation equipment, in which layers of atoms are sputtered off the surface of a solid material and transported by a gas stream to the plasma for ionization. Excellent references on the general topic of isotope analysis by MC-ICP-MS are Albarède and Beard (2004), Rehkämper et al. (2004) and Wieser and Schwieters (2005).

On the other hand, TIMS has been used for more than 50 years and has long been the workhorse for metal isotope research. TIMS provided much of the data on transition and post-transition metal stable isotope systematics prior to the proliferation of MC-ICP-MS in research labs and continues to provide excellent isotope measurements for more readily ionized elements such as Cr (e.g. Ellis et al. 2002) and Fe (Bullen and Amundson 2010) and even for elements that are difficult to ionize such as Cd (Schmitt et al. 2009a, b). TIMS is less affected by isobaric interferences than MC-ICP-MS because there is no need for the Ar gas and because the sample is ionized under high vacuum rather than in an aqueous solution or gas stream at atmospheric pressure. TIMS likewise benefits from

simultaneous multicollector ion beam detection (Fantle and Bullen 2009). Typical external precision (i.e. comparison of total procedural replicates for natural samples) is at the 0.1‰ level for both TIMS and MC-ICP-MS. A disadvantage of both instruments is a sizable footprint in the laboratory and high costs for purchase and maintenance.

10.2.4 Data: Acquisition, Reduction, Accuracy, and Standard Reference Materials

Isotope fractionation of the ion beam produced in both TIMS and MC-ICP-MS, which is an unavoidable characteristic of both analytical platforms, means that the relative proportion of isotopes of an element reaching the detectors in the mass spectrometer is not identical to that of the sample. This instrument-induced fractionation, or “mass bias”, is often larger than the isotopic variation between samples. In MC-ICP-MS, light ions of any element are preferentially discriminated against and removed from the ion stream at the sampling cones situated just beyond the plasma source, resulting in relatively heavy raw measured ratios that tend to stay very constant over the course of a measurement. In TIMS, light ions of any element are preferentially ionized off the filament surface, causing the raw measured ratio to be light at the outset and progressively heavier over the course of a measurement. Thus it is essential to provide some means to correct for isotope discrimination so that measured isotope compositions of samples can be compared to those of standards and other samples.

The classic approach to correct for isotope discrimination in TIMS is referred to as the *double spike technique*. An excellent treatment of the theoretical aspects of the double spike technique is given by Johnson and Beard (1999), and a practical overview of the technique is provided by Rudge et al. (2009). This technique requires that the element have at least four naturally-occurring isotopes, two that can be used as isotopes for the double spike and two that can be used to calculate a ratio that provides information on the relative natural isotope composition of a sample. The double spike is a mixture of two typically minor isotopes of the element that have each been

industrially enriched in their proportion relative to the other isotopes. There are now several commercial suppliers of highly enriched (i.e. typically >90% pure) stable isotopes of most multi-isotopic elements, and thus it is relatively straightforward to create a double spike using any combination of two isotopes of an element. The double spike mixture, which has been carefully characterized for isotope composition and concentration, is added to a sample prior to analysis thus imparting an unnatural isotope composition to the sample-double spike mixture. Following analysis, the measured ratio of the two isotopes used to create the double spike can be compared to the known, carefully characterized value to obtain a “mass bias factor” that quantifies isotope fractionation that has occurred during analysis. The measured isotope composition of the sample-double spike mixture can then be corrected based on this mass bias factor, and the double spike component of the mixture can be mathematically subtracted from the fractionation-corrected composition to reveal the natural ratios of the two or more isotopes not used for the double spike as the residual.

For example, the $^{53}\text{Cr}/^{52}\text{Cr}$ natural isotope ratio of a sample can be determined using a double spike consisting of a mixture of nearly pure ^{50}Cr and ^{54}Cr , the two minor isotopes of Cr. Of the elements discussed here, Cr, Fe, Ni, Zn, Cd, Mo, Hg, Ti, and W are suitable for analysis by the double spike technique while Ag, Re and V are not. An important advantage of the double spike technique is that the double spike solution can be added to the sample prior to purification chemistry, and thus, without any additional effort, can be used to correct for isotope fractionation that might occur during chemical purification prior to analysis (e.g. due to non-quantitative recovery of the metal from the resin).

The nature of MC-ICP-MS allows application of two additional techniques for correction of isotope discrimination in the instrument during analysis, *standard-sample-standard bracketing* and *internal standardization*. As the name implies, in standard-sample-standard bracketing a standard solution is analyzed directly before and after a sample, and the interpolated isotope ratio of the standard at the time of the sample analysis is taken as the reference value. This is an incredibly straightforward approach, but assumes that the sample and standard behave similarly in the plasma (e.g. have identical matrices). With internal standardization, an element with a known

isotope composition and similar fractionation behavior to the element being analyzed is added to the sample solution prior to aspiration into the plasma (e.g. Zr as an internal standard for Mo isotope analysis, Cu as an internal standard for Fe or Zn isotope analysis). The isotope ratio measured for the internal standard can be compared to its known value to quantify machine-induced fractionation and a correction can then be applied to the isotope ratio of the target element on a scan by scan basis. Using internal standardization, a plot of the measured isotope ratios of the target element vs. those of the internal standard element typically defines a mass dependent fractionation relationship that provides the basis for the correction (Longerich et al. (1987); Maréchal et al. (1999)).

The power of the standard-sample-standard bracketing and internal standardization techniques is that they can be used for isotopic analysis of any element having two or more isotopes. On the other hand, the double spike technique required for TIMS stable isotope analysis can likewise be used for MC-ICP-MS isotope analysis of elements having four or more isotopes, and is in essence a special case of internal standardization. The advantage of using a double spike for MC-ICP-MS analysis is that quantitative yield during sample purification is not required as it is for standard-sample-standard bracketing and internal standardization approaches (Siebert et al. 2001).

Differences in transition and post-transition metal stable isotope composition between materials tend to be small, a few parts per thousand at most, so that differences in absolute isotope ratio are difficult to conceptualize. For example, say that the $^{53}\text{Cr}/^{52}\text{Cr}$ ratio determined by TIMS for a native groundwater sample is 0.114000, while the value for the Cr isotope standard is 0.113392. To better visualize this small difference, most researchers in the field have adopted the delta notation used for gas isotope ratio comparison so that ratios can be compared on a per mil (‰) basis. Using the Cr example:

$$\begin{aligned} \delta^{53/52}\text{Cr} &= 1000 * \left(\frac{^{53}\text{Cr}/^{52}\text{Cr}_{\text{groundwater}}}{^{53}\text{Cr}/^{52}\text{Cr}_{\text{standard}}} \right) / \left(\frac{^{53}\text{Cr}}{^{52}\text{Cr}_{\text{standard}}} \right) \\ &= 1000 * (0.114000 - 0.113392) / 0.113392 \\ &= +5.36. \end{aligned}$$

δ values are preceded by a plus or minus sign to denote ratios that are, respectively, heavier or lighter

than the reference material, which in this case is NIST 979 Cr metal. There are two important variants of the δ notation: (1) Δ_{A-B} may be used to represent the difference in δ values between two samples, A and B; and (2) workers may use the ϵ notation, equal to 10 times δ , or parts per 10,000, in cases where differences in isotope composition between samples are extremely small. Caution is advised as there are additional uses of both Δ and ϵ in isotope science terminology, and some researchers report isotope ratio variations on a per atomic mass unit basis.

Standard reference materials (SRM) provide the basis for inter- and intra-laboratory comparison of isotope ratio measurements. While the mass spectrometers used in different laboratories might produce different absolute values for an SRM, the ratios obtained on samples are comparable through use of the delta scale described above, calculated relative to the SRM. Most standards used in metal stable isotope research are supplied by two sources: the Institute for Reference Materials and Measurements (IRMM, Belgium) and the National Institute for Standards and Technology (NIST, USA). Both organizations have gone to great lengths to produce large quantities of metal isotope SRM, which have been rigorously assessed through round-robin analyses at a number of isotope laboratories. A good SRM must (1) be in abundant supply and available for distribution, (2) be homogeneous in isotopic composition across the supply, (3) have an isotopic composition similar to or bordering the range to be measured in samples, and (4) have an agreed-upon value. Ideally, for a given metal it is preferable to have at least two well-characterized SRM that bracket the range of isotope ratios anticipated in samples. This is rarely the case, and thus most researchers rely on a single SRM that is used widely by other laboratories, together with routinely analyzed internal standards used to monitor consistency of laboratory processing and mass spectrometer function. An important point is that all isotope research should be conducted using widely available SRM in order to allow other laboratories to make a check of accuracy.

Commonly used SRM include: Cr, NIST 979; Fe, IRMM-014; Ni, NIST 986; Cu, NIST 976; Zn, JMC (Johnson Matthey Corporation) 3-0749-L and IRMM-3702; Mo, NIST 3134 (proposed; presently there is no internationally accepted SRM (Wen et al. 2010), but acceptance by the isotope community requires a period of inter-laboratory comparison to validate the

choice); Cd, JMC lot 502552A and NIST 3108; Ag, NIST 978a. Note that there are currently no internationally accepted or proposed SRM for Ti, V, W or Re isotope analysis.

IRMM and NIST typically supply an SRM for metal stable isotope analysis in the form of a purified metal or salt, both of which are easy to dissolve and use routinely. However, some researchers choose to use natural samples as standards, provided those samples meet the criteria listed above. The advantage of using a natural material as an SRM is that it must follow the same chemical purification steps as samples, thus assuring integrity of the chemical procedures. For some metals, there are both natural and synthetic SRM. For Fe stable isotope research, for example, there are two widely available SRM: specific basalts and other igneous rocks, which have been shown to have uniform isotope composition (Beard et al. 2003), and IRMM-014, a synthetic iron standard. The isotope composition of IRMM-014 is now generally considered to be the zero point for the delta scale; on this basis, igneous rocks have on average a $\delta^{56/54}\text{Fe}$ value of +0.09‰. Unfortunately, Fe lacks SRM having isotope compositions at the light and heavy extremes of the natural spectrum.

10.3 Metal Stable Isotope Fractionation Processes

Isotope fractionation is a set of processes which can divide an isotopically homogeneous pool of an element into multiple fractions that have different complementary isotope compositions. For a given element, observed fractionation may be either mass dependent, scaling approximately as the mass difference between isotope pairs, or mass independent, where one isotope behaves non-systematically with respect to the others. By far, most of the stable isotope variability of the transition and post-transition metals observed to date has resulted from mass dependent processes.

There are two main categories of isotope fractionation processes that affect the transition and post-transition metals, kinetic isotope effects and equilibrium isotope exchange. Kinetic isotope effects result from uni-directional physical and chemical reactions, during which the light isotope is always

favored in the product phase. Examples of processes resulting in kinetic isotope effects are evaporation, where light isotopes of metals such as Zn and Cd escape more efficiently at the liquid-air interface than heavy isotopes (e.g. Cloquet et al. 2006a, b), electroplating, where light isotopes of metals from the plating bath are preferentially deposited onto a metal substrate (Kavner et al. 2008), and diffusion (Richter et al. 2009). A special class of kinetic isotope effects arises for elements having differences in specific isotope reaction rates, for example where the odd-numbered isotopes of Hg behave non-systematically with respect to the even-numbered isotopes (Bergquist and Blum 2009; Blum 2011). Isotope equilibrium results from protracted exchange between reaction products and reactants, and at equilibrium the products may be either lighter or heavier than the reactants depending on factors such as metal ion coordination, packing density and bond strength. Examples of processes resulting in isotope equilibrium are the partitioning of relatively heavy Fe into $[\text{Fe(III)(H}_2\text{O)}_6]_{(\text{aq})}^{3+}$ compared to Fe in coexisting $[\text{Fe(II)(H}_2\text{O)}_6]_{(\text{aq})}^{2+}$ (Johnson et al. 2002; Welch et al. 2003), and the exchange of Fe between hematite and $[\text{Fe(III)(H}_2\text{O)}_6]_{(\text{aq})}^{3+}$ leading to identical Fe isotope compositions of these two phases (i.e. no isotope fractionation). This latter example is interesting in that hematite formed initially in synthesis experiments has light Fe relative to coexisting $[\text{Fe(III)(H}_2\text{O)}_6]_{(\text{aq})}^{3+}$ due to kinetic isotope effects that are subsequently reversed (Skulan et al. 2002). Note that isotope equilibrium between liquid and vapor is likewise possible, as in the case of Hg (Estrade et al. 2009). Excellent discussions of the topic of kinetic and equilibrium isotope fractionation, with examples pertinent to environmental studies, are provided by Clark and Fritz (1997) and Kendall and McDonnell (1998).

Redox reactions, whether strictly inorganic or microbially mediated, consistently result in significant metal stable isotope fractionation, and the reduced species of the metal redox pair is generally isotopically lighter than the oxidized species. Thus, determination of the isotope composition of redox-sensitive metals has proven useful for understanding redox dynamics in paleo- and present-day environmental systems (Severmann and Anbar 2009; Bergquist and Blum 2009; Bullen and Walczyk 2009). On the other hand, the stable isotope composition of metals which occur naturally in only one redox state (e.g. Cd, Zn)

but which may fractionate during complexation with redox-sensitive species such as sulfur (Schauble 2003) or with organic matter (Weiss et al. 2007) can likewise be indicative of redox conditions.

Sorption of metals onto the surfaces of minerals in sediments and soils is an environmentally important process that can help to moderate aqueous concentrations of those metals and aid in metal contaminant remediation. Isotope fractionation associated with sorption has been recognized for several of the transition and post-transition metals, but is highly element specific. For example, sorption of isotopically light Mo onto ferromanganese oxides in the oxic oceans is viewed as having been an important isotope fractionation process for Mo over much of Earth history (Wasylenki et al. 2008). In contrast, sorbed Fe(II) on goethite was found to be isotopically heavy compared to $[\text{Fe(II)(H}_2\text{O)}_6]_{(\text{aq})}^{3+}$ in a series of carefully conducted equilibrium isotope exchange experiments reported by Beard et al. (2010). In the case of Cr, only a negligible isotope fractionation was observed between sorbed and aqueous CrO_4^{2-} and HCr_2O_7^- when either $\gamma\text{-Al}_2\text{O}_3$ or goethite was used as the sorption substrate (Ellis et al. 2004).

Coordination environment of the metals in liquids and solids is an additional important determinant of stable isotope fractionation. In general, for a given system chemistry, higher coordination favors the lighter isotopes. Using the system Fe-O as an example, Fe in hematite (Fe_2O_3) is in octahedral coordination while Fe in magnetite (Fe_3O_4) is in both octahedral and tetrahedral coordination within their respective oxygen framework. The result is a higher average coordination number for Fe in hematite than for Fe in magnetite. As expected, when the two phases coexist at or near equilibrium, Fe in hematite is isotopically lighter than Fe in magnetite by approximately 3‰, as has been reported for coexisting magnetite-hematite pairs in banded iron formations (Johnson et al. 2003). The difference in metal ion coordination environment in coexisting solid-liquid pairs is likewise an important determinant of stable isotope fractionation. For example, theoretical calculations of equilibrium isotope fractionation predict that aqueous Fe(II), which is in octahedral coordination within a “hexaquo” inner hydration sphere ($[\text{Fe(II)(H}_2\text{O)}_6]_{(\text{aq})}^{2+}$), should be heavier than Fe(II) in coexisting siderite (FeCO_3), in which the Fe(II) is in more open octahedral coordination with oxygen of the carbonate groups (Polyakov

and Mineev 2000; Schauble 2004). Siderite synthesis experiments confirm the sense of this theoretical fractionation, but observed magnitudes are less than those predicted by theory (Wiesli et al. 2004). Gaining a better understanding of aqueous metal coordination environments and the implications for stable isotope fractionation is one of the major challenges facing the field.

10.4 Applications of Metal Isotopes to Environmental Studies

The transition and post-transition metals are subject to numerous potential isotope fractionation processes over a wide range of environmental conditions, and thus their isotope compositions may provide a unique record of those processes that can be used to understand present-day and paleo-environmental systems. In this section, several examples are given that illustrate the spectrum of environmental issues that can be addressed using these novel stable isotope tracers as process recorders. These include using the isotopes to trace metal contaminants, to identify metal redox processes, to assess plant nutrition cycles and understand processes within plants, and to serve as biomarkers. Although familiarity with the general topic of stable isotope biogeochemistry will help the reader to appreciate the details of the following examples, the introductory material and references in this and other chapters of this book should help those not familiar with the field to better understand why the isotopes are useful and how they work in these specific cases.

10.4.1 Tracing Metal Contaminant Sources and Sinks

The ability of isotope signatures to trace the sources of and processes affecting metal contaminants in groundwater and the atmosphere appears to be receiving the most attention from research groups focused on environmental applications of transition and post-transition metal stable isotopes. Of metal contaminants in groundwater, Cr(VI) is arguably the best understood in terms of isotope systematics based on laboratory

experiments, and Cr stable isotopes have been used to study the fate of toxic Cr contamination at numerous field sites. Of the potential metal contaminants in the atmosphere, the most progress has been made in understanding Hg sources and sinks as discussed by Blum (2011), but Zn, Cd and Cr are likewise receiving considerable attention and are discussed here.

10.4.1.1 Tracing Sources of Chromium in Groundwater

As described above in the overview of Cr, reduction of Cr(VI) to Cr(III) is accompanied by a large isotope fractionation. Thus, Cr stable isotopes should be useful for monitoring Cr(VI) reduction in a contaminant plume, for distinguishing between Cr(VI) reduction and advective mixing with Cr-free groundwater (two mechanisms that can decrease Cr(VI) concentrations in the contaminant plume), and potentially for distinguishing between industrial and natural sources of Cr (VI). Sources of Cr used for industrial purposes are likely to be Cr ore deposits and minerals, which consistently have $\delta^{53/52}\text{Cr}$ values close to 0‰ relative to NIST 979 (Ellis et al. 2002; Schoenberg et al. 2008). In contrast, naturally occurring Cr in groundwater displays a range of values ($\delta^{53/52}\text{Cr}$: +1.0 to +5.8‰; Ellis et al. 2002; Izbicki et al. 2008). These values likely reflect fractionation during oxidation of Cr(III) on manganese oxides and fractionation during subsequent reduction of Cr(VI) along groundwater flowpaths following mobilization of the highly soluble Cr(VI) from mineral surface sorption sites. Thus under favorable conditions the natural and industrial Cr pools at a contaminated site may have different $\delta^{53/52}\text{Cr}$ values.

In order to test the usefulness of Cr stable isotopes for Cr contamination source assessment and process identification at a well-studied contaminated site, a pilot study (CH2MHill 2007) was carried out at the Pacific Gas & Electric (PG&E) Compressor Facility in Hinkley, California, made famous in the movie “Erin Brockovich.” From 1952 to 1966, waste water containing Cr(VI) used as an anti-corrosive in the cooling towers leaked into the underlying sandy aquifer, creating a plume of Cr(VI)-contaminated groundwater that by 2000 had migrated nearly 2 miles downgradient from the facility. Groundwater samples from immediately adjacent to the facility, from within the plume, and of regional groundwater

collected well away from the plume were analyzed for Cr stable isotope composition (Bullen 2007). As shown in Fig. 10.3, the data plot along a well-organized trend, with near-facility (contaminant) and regional groundwaters defining the extremes, while samples from the contaminant plume plot in between. There is no question that in this particular case, the Cr stable isotopes clearly distinguish the natural and anthropogenic Cr(VI) end-members.

It is less clear how the samples collected from the contaminant plume obtained their compositions in $\delta^{53/52}\text{Cr}$ -Cr concentration space. For example, as shown in Fig. 10.3 the plume sample data all lie well to the low-Cr side of model trends describing both abiotic and microbially-mediated Cr(VI) reduction (Ellis et al. 2002; Sikora et al. 2008) and well to the high- $\delta^{53/52}\text{Cr}$ side of the model trend for advective mixing between near-facility contaminant and regional groundwaters, suggesting that neither Cr(VI) reduction nor advective mixing alone is able to account for those compositions. However, some combination of Cr(VI) reduction and advective mixing could account for the plume sample compositions, and a scenario that is at least consistent with field relations (Bullen 2007) is shown in Fig. 10.3. In this scenario, Cr(VI) at the front and margins of the migrating contaminant plume would come into contact with the limited reductant (e.g. ferrous iron, organic matter) in this aquifer, allowing small amounts of Cr(VI) reduction to occur and driving remnant Cr(VI) compositions along the model Cr(VI) reduction vectors. At the same time, advective mixing with regional groundwaters at the plume front and margins would shift remnant Cr(VI) compositions to the low-Cr side of the model Cr(VI) reduction vectors (e.g. along trajectories similar to the lines labeled “plume front Cr(VI) reduction-mixing” in Fig. 10.3). After 40 years of plume migration, one could imagine an array of developed plume front and margin groundwater compositions similar to region “FM” in Fig. 10.3. This range of plume front and margin groundwater compositions would result from specific evolutionary trends that depend on the relative amount of Cr(VI) reduction and advective mixing with regional groundwater that occurred at any particular position along the plume front or margin. In this scenario, the actual plume sample array would develop by advective mixing between these hypothesized plume front and margin groundwaters and the contaminated groundwater

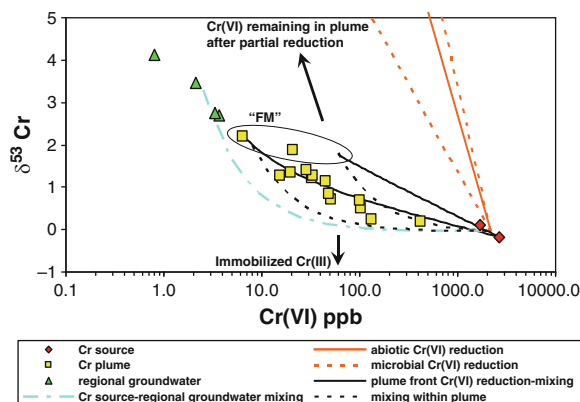


Fig. 10.3 $\delta^{53/52}\text{Cr}$ and Cr(VI) concentration data for groundwater at the Hinkley, CA site “Cr source” samples were collected at the PG&E compressor facility, “Cr plume” samples were collected downgradient of the compressor facility within the Cr(VI) plume. “Regional groundwater” samples were collected just upgradient, just down gradient, and well away from the plume. The “Cr source-regional groundwater mixing” curve shows mixing between Cr source and average regional groundwater. The “abiotic Cr(VI) reduction vector” is from Ellis et al. (2002); the “microbial Cr(VI) reduction” vectors are from Sikora et al. (2008), and show the range of fractionation observed in their experiments. The field labeled “FM” represents plume Front and Margin samples produced through combined Cr(VI) reduction and advective mixing with regional groundwater as described in the text. The “mixing within plume” curves show mixing between “FM”-type and “Cr source” groundwaters. The arrow labeled “Cr(VI) remaining in plume following partial reduction” shows the direction that homogeneous Cr(VI) reduction within the plume will move residual Cr(VI) compositions on this diagram. The arrow labeled “immobilized Cr(III)” shows that Cr(III) produced during Cr(VI) reduction will have negative $\delta^{53/52}\text{Cr}$. The uncertainty of the data for all samples is less than the size of the symbol

within the plume body itself. Note that extremely careful, discrete depth sampling at the plume front and margins would be necessary to confirm the existence and determine the exact shape of the “FM” region hypothesized in Fig. 10.3, but such an effort would be useful for supporting the validity of this proposed scenario.

In their detailed time-series study of a point-source Cr contamination plume emanating from a Cr plating facility in Berkeley, California, Berna et al. (2010) observed a similar trend for plume groundwater samples in $\delta^{53/52}\text{Cr}$ -Cr concentration space, such that the plume samples had intermediate compositions between vectors describing Cr(VI) reduction and advective mixing with Cr-free groundwater. Although

they concluded that Cr(VI) reduction and advective mixing were important processes determining the composition of the plume groundwater samples, they likewise pointed to the potential importance of heterogeneous Cr(VI) reduction in the aquifer. Their laboratory incubation experiments had demonstrated that Cr(VI) reduction was limited to greenish, fine-grained lenses that are embedded in non-reducing aquifer materials. They proposed that total reduction of small pools of Cr(VI) in the greenish lenses would decrease the amount of Cr(VI) measured in a down-gradient sampling well, but would not change the $\delta^{53/52}\text{Cr}$ value of the remaining Cr(VI) transported through the non-reducing aquifer materials. As a result, the $\delta^{53/52}\text{Cr}$ value of groundwater sampled along the plume is not as high and the $\delta^{53/52}\text{Cr}$ value of Cr(III) immobilized on the aquifer sediment is not as low as would be predicted for a system where reduction occurs homogeneously throughout the aquifer. As at Hinkley, careful discrete depth sampling would help to determine the influence of aquifer heterogeneity on Cr(VI) reduction effectiveness and measured $\delta^{53/52}\text{Cr}$ values.

10.4.1.2 Sources of Zinc in River Water

As described above in the overview on Zn, there are several processes that may result in Zn stable isotope fractionation including biological incorporation, abiotic adsorption, chemical diffusion and industrial processing. Although Zn is not a highly toxic metal it does provide a useful index of environmental contamination because it is commonly associated with toxic metals such as Cd and Pb. Thus Zn stable isotopes may be useful for distinguishing natural and anthropogenic sources of metals in both hydrologic and atmospheric systems.

An interesting example of the usefulness of Zn isotopes to trace contaminant sources is the work of Chen et al. (2008, 2009) who studied Zn isotope systematics of the Seine River of France. The Seine River is one of the most anthropogenically impacted rivers in Europe, with high relative concentrations of metals (Zn, Cu, Pb, Ni, etc.) in dissolved and suspended loads compared to large rivers of the world (Chen et al. 2009). For their study, these workers sampled both the dissolved and suspended particulate matter (SPM) fractions of Seine River waters along the length

of the river and, during both high and low flow periods, in the center of the city of Paris. This sampling strategy allowed these workers to test for a Zn isotope signal of industrial and urban activity, since most industry is concentrated in and downstream of Paris.

Chen et al. (2009) observed an overall negative correlation between $\delta^{66/64}\text{Zn}$ of SPM and the Zn enrichment factor (EF), which describes the enrichment of Zn in a sample relative to the natural background and is defined as:

$$\text{EF} = (\text{Zn}/\text{Al})_{\text{sample}} / (\text{Zn}/\text{Al})_{\text{background}}$$

where $(\text{Zn}/\text{Al})_{\text{background}}$ was estimated using average concentrations of Zn and Al in uncontaminated forest sediments and pre-historical deposits as assessed by Thevenot et al. (2007). Specifically, as shown in Fig. 10.4a, SPM samples with lesser $\delta^{66/64}\text{Zn}$ and greater Zn EF were those collected within Paris during the low flow periods and from downstream of Paris. Chen et al. (2009) identified two potential anthropogenic contaminant sources, Zn in roof runoff from buildings in Paris and waste water treatment plant effluent, each having low $\delta^{66/64}\text{Zn}$ and high Zn EF that could explain the low flow Zn isotope signal. In contrast, background Zn from upstream sources was determined to have elevated $\delta^{66/64}\text{Zn}$ and low Zn EF based on analyses of bedrock from the region (the composition for bedrock granite from the region is shown in Fig. 10.4a) and the compositions of SPM from upstream of Paris.

Chen et al. (2009) observed additional complexity when they considered $\delta^{66/64}\text{Zn}$ of SPM and $\delta^{66/64}\text{Zn}$ of dissolved Zn together (Fig. 10.4b). Seine Basin transect and Paris low flow samples defined a linear array that could be explained by mixing between natural and anthropogenic end-members. The natural end-member (Zn_{nat}) was inferred to have $\delta^{66/64}\text{Zn}$ of SPM similar to that of bedrock granite (+0.33‰) and $\delta^{66/64}\text{Zn}$ of dissolved Zn similar to that of Cretaceous chalk from the region (+0.90‰), highlighting the fact that Zn in SPM and the dissolved phase can come from different sources. Some Paris high flow samples required an additional component, again having $\delta^{66/64}\text{Zn}$ of SPM similar to that of bedrock granite, but having $\delta^{66/64}\text{Zn}$ of dissolved Zn reflecting a mix-

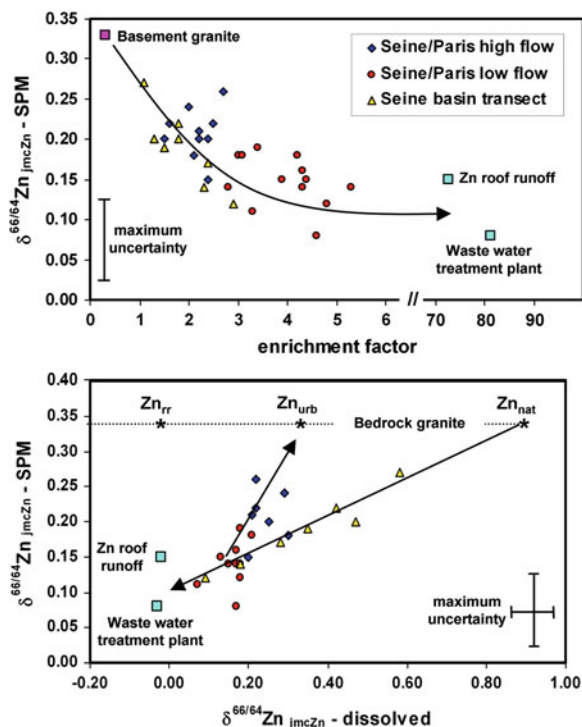


Fig. 10.4 Zn isotope systematics of the Seine River, modified after Chen et al. (2008, 2009). (a) $\delta^{66/64}\text{Zn}$ of suspended particulate matter (SPM) vs. the Zn enrichment factor (defined in text). Curved vector describes mixing between a natural end-member, basement granite, and likely anthropogenic end-members, Zn roof runoff and waste water treatment plant effluent. Note break in enrichment factor scale. (b) $\delta^{66/64}\text{Zn}$ of SPM vs. $\delta^{66/64}\text{Zn}$ of dissolved Zn. Symbols are the same as in Fig. 10.4a. Zn isotope compositions of basin transect and Paris low flow samples can be explained as mixtures of a natural end-member (Zn_{nat} , having $\delta^{66/64}\text{Zn}$ of SPM dominated by bedrock granite and $\delta^{66/64}\text{Zn}$ of dissolved Zn dominated by Cretaceous chalk), and an anthropogenic end-member having Zn isotope composition similar to that of Zn roof runoff and waste water treatment plant effluent. Paris high flow samples require an additional “urban” end-member (Zn_{urb} , having $\delta^{66/64}\text{Zn}$ of SPM dominated by bedrock granite and $\delta^{66/64}\text{Zn}$ of dissolved Zn reflecting a mixture of Cretaceous chalk Zn and Zn from roof runoff (Zn_{rr}). Errors are equal to or less than maximum uncertainty bars shown

ture of Zn from Cretaceous chalk (the dissolved component of Zn_{nat}) and the dissolved component of Zn from roof runoff (Zn_{rr}). Chen et al. (2009) suggested that urban Zn storm runoff (Zn_{urb}) adds considerable dissolved Zn but only minor SPM associated with zinc roofing materials to the river.

10.4.1.3 Tracing Sources of Metals in Dust Using a Multi-Tracer Approach

Inhalation of dust particles is potentially a primary delivery mechanism of toxic metals to humans. Moreover, incorporation of deposited dust in soil can allow the metals to become available to plants, providing an additional source of metal loading to crops. There are many possible sources of transition and post-transition metals that could supply the metal content of dust. The major contributors are likely to include metal refining and smelting, coal combustion fly ash and residues, petroleum burning and particularly vehicle emissions, municipal waste incineration, scrap metal deterioration, and wood burning. Early approaches for identifying dust sources relied on tracers such as concentration ratios of metals and surrogates such as strontium isotopes that might be able to tie the dust back to specific geologic or regional sources. While there have been numerous examples of success with this approach, environmental isotope scientists have been exploring whether the stable isotope composition of the transition and post-transition metals might be more directly useful for fingerprinting the sources of the metals in dust.

Of the potential sources for these metals listed above, metal refining and smelting have received the most attention, mainly for Zn and Cd, pointing to the unique physical characteristics of these two post-transition metals. As noted above in the overview on these elements, their boiling points are sufficiently low that they can both be evaporated in the smelter furnace, resulting in a kinetic isotope fractionation that partitions light metal into the vapor that escapes the factory stack. For Zn, light compositions in refinery stack emissions have been documented by Mattielli et al. (2009), while heavy compositions in residual slag compositions have been documented by Sivry et al. (2009). For Cd, the same sense of isotope fractionation was observed for smelter exhaust and slag by Cloquet et al. (2006a). Mercury similarly has a low boiling point within the range of smelter and waste incinerator furnace temperatures, and partitioning of light Hg into stack emissions has been proposed (Estrade et al. 2010). Thus the association of light Zn, Cd, and Hg, along with unfractionated compositions relative to the ore sources for other metals having far greater boiling points (such as Cr and Cu) could implicate a metal refining smelter exhaust stack source for those metals in dust samples.

The Zn and Cd stable isotope compositions of the other potential sources of metals in dust listed above are less constrained, although some reconnaissance values for Zn are available in the literature. Cloquet et al. (2006b) reported $\delta^{66/64}\text{Zn}$ values for particulates trapped on bus air filters and emitted in urban waste incinerator flue gas from Metz, France, which spanned a small range from +0.04 to +0.19‰ relative to the JMC-Lyon Zn standard. On the other hand, lichens collected from around Metz that had high Pb concentrations and Pb isotope signatures consistent with a leaded gasoline source likewise had high Zn concentrations and negative $\delta^{66/64}\text{Zn}$ (to -0.2‰), suggesting that light Zn might be associated with road traffic circulation. Sivry et al. (2008) reported $\delta^{66/64}\text{Zn}$ of +0.72‰ for a coal ash from southwest France, which is consistent with the association of heavy Zn with organic materials recognized by Weiss et al. (2007).

In their study of sources of metals observed in dust samples collected in Paris, France, Widory et al. (2010) have expanded this emerging isotope database for the sources and specifically have measured Zn, Cd, and Cr stable isotope compositions for each of their samples. Important aspects of their data, shown in Fig. 10.5a and b, include: (1) a broad range of $\delta^{114/110}\text{Cd}$ for particulates in vehicle exhaust; (2) the tendency of organic-associated materials such as fuel oil and coal to have positive $\delta^{66/64}\text{Zn}$; and (3) the positive $\delta^{53/52}\text{Cr}$ values of the coal combustion samples, perhaps reflecting the particular redox history of the coal deposit. These data highlight the potential variability of the anthropogenic signal and show the utility of the multi-isotope approach.

Although the influence of dust from deteriorating metal in scrapyards has yet to be rigorously quantified in terms of either metal flux or stable isotope composition, there is potentially an important isotope signal resulting from electroplating as noted above. Electroplating is a ubiquitous process that can produce an isotopically light pool for all the transition and post-transition metals (e.g. Kavner et al. 2008), and recognition of light isotope compositions for a suite of metals such as Zn, Cd and Cr in a set of dust samples may point to such sources. Cadmium and Zn isotope compositions of an electroplated metal nut and Cr and Zn isotope compositions of an electroplated metal bolt, measured by the author, are included in Fig. 10.5a and b to illustrate the potential signal.

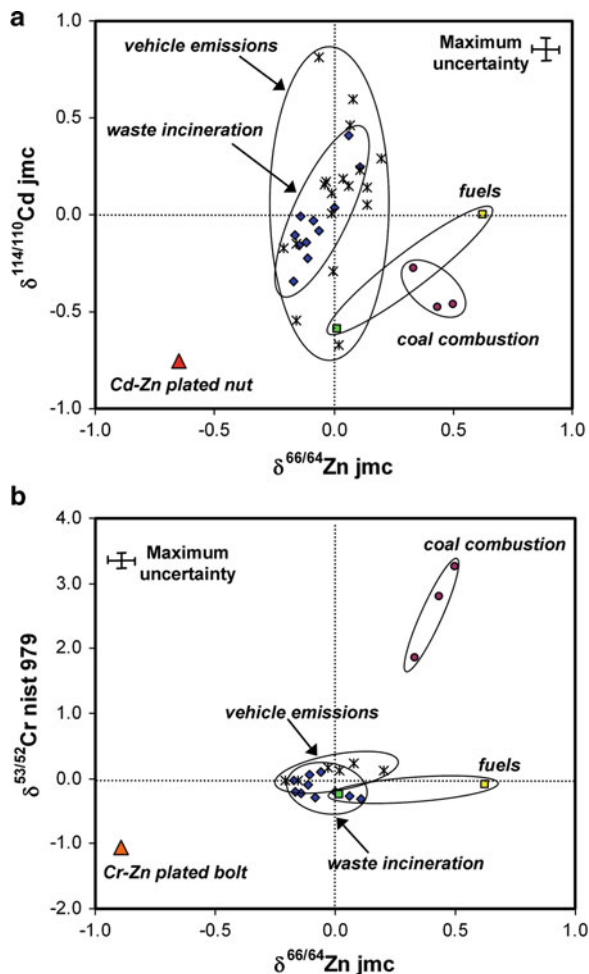


Fig. 10.5 (a) Cd-Zn and (b) Cr-Zn isotope systematics of suspected sources of metals in dust from northern France. Measurements were made on acid leachates of particles collected at municipal waste incinerators and coal combustion plants, from vehicle exhaust pipe filters, on acid leachates of plated nuts and bolts, and on total digests of fuels. Modified from Widory et al. (2010) with additional unpublished data from author

The obvious need to understand the potential influence of deteriorating electroplated metal stockpiles on the isotope composition of atmospheric dust, perhaps mostly to monitor the global transport of potentially toxic metals, makes this an important avenue for future research.

10.4.2 Metal Redox Cycles

The common association of changes in redox status of the transition and post-transition metals with isotope

fractionation between oxidized and reduced states points to the potentially powerful application of the isotopes as tracers of redox cycles in natural systems. Isotopes can be used, for example, to distinguish between biological and geochemical processes, such as microbial reduction and inorganic oxidation, and physical processes, such as advective mixing and diffusion, to explain chemical and isotopic composition gradients in hydrologic systems.

Teutsch et al. (2009) used Fe isotopes to study the Fe cycle across the oxic-anoxic boundary of meromictic Lake Nyos, Cameroon, the site of a sudden catastrophic release of CO_2 in 1986 that killed about 1,700 people. To avoid the recurrence of catastrophic outgassing of CO_2 that is supplied by groundwater to the lake bottom, the lake is now artificially degassed by a tube that drains deep water to the surface (Kling et al. 2005). The degassing system spreads deep water with concentrations of dissolved Fe(II) in a high jet over the lake, causing immediate oxidation of the Fe(II) to Fe(III)-oxyhydroxide particulate which then settles into the lake. Concentrations of dissolved Fe(II) in the oxic surface waters are negligible, but sharply increase as particles settle across the oxic-anoxic boundary at depth. Partial reduction of the Fe(III)-rich particles at this boundary releases Fe(II) to solution, which then diffuses upwards into the oxic zone where it is re-oxidized to form Fe(III)-oxyhydroxides which settle back to the oxic-anoxic boundary, and the cycle continues.

Depth profiles sampled in the lake revealed a sharp increase in both dissolved Fe(II) concentrations and $\delta^{57/54}\text{Fe}$ values in a thin zone across the oxic-anoxic boundary. Using a calibrated one dimensional reaction-transport model that considered the isotopic signatures of dissolved Fe(II) and the settling of Fe(III)-rich particles, the settling fluxes of the particles and the dissolved Fe(II) concentration profiles, Teutsch et al. (2009) showed that the sharp increase in $\delta^{57/54}\text{Fe}$ values is caused by isotopic fractionation associated with dissimilatory Fe(III) reduction across the oxic-anoxic boundary. They further showed that the continued shift toward even greater $\delta^{57/54}\text{Fe}$ values below the oxic-anoxic boundary is due to vertical mixing of Fe-rich lake bottom water that has high- $\delta^{57/54}\text{Fe}$ values, perhaps due to precipitation of siderite. In this study, isotopic analyses coupled to modeling proved invaluable for identifying the

processes responsible for the broad range of $\delta^{57/54}\text{Fe}$ values observed in this lake.

Isotopes can likewise be used to assess paleoredox conditions in water bodies, for example by looking at variations of the redox-sensitive Mo isotope composition of sediments. In oxic settings, Mo isotopes are fractionated during adsorption of Mo to ferromanganese oxides, with light isotopes preferentially associated with the solids. Experimental work under oxidizing conditions has shown that $\delta^{97/95}\text{Mo}$ of aqueous Mo in seawater is 2.7‰ greater than that of adsorbed Mo on sediment (Barling et al. 2001; Barling and Anbar 2004; Wasylenki et al. 2008). As waters progress from oxic to suboxic to anoxic to euxinic (i.e. sulfidic) conditions, MoO_4^{2-} is converted to MoS_4^{2-} which readily adsorbs to particles allowing aqueous Mo to be more effectively removed to the sediment (Poulson et al. 2006; Neubert et al. 2008). The net result is that the isotopic contrast between aqueous and sorbed Mo is greatest at slightly reducing conditions and low sedimentation rates, but decreases with increasingly reducing and sulfidic conditions due to increasingly more quantitative removal of Mo from solution.

This concept was used by Siebert et al. (2006) to account for differences in the average Mo isotope composition of sediment profiles from continental margin settings. These workers recognized a co-variation between the Mo isotope composition of the sediments and the rate of both authigenic Mo accumulation and organic carbon oxidation and burial under reducing conditions. Malinovsky et al. (2007) tried the same approach to understand paleoredox cycles in lakes from northern Sweden and northwestern Russia, where variations of Mo isotope composition in the sediments could be attributed to both redox status of the water column and isotopically variable input of Mo into the lakes due to Mo isotopic heterogeneity of bedrock in the drainage basins. This latter study points to the need for rigorous source term characterization, particularly as study site size decreases from global to local scale.

An area of applied research where transition and post-transition metal stable isotopes are increasingly being used is to understand sedimentary and low temperature hydrothermal metal redox cycling, where both inorganic and biological redox processes can cause isotope fractionation. For example, Asael et al. (2007) used Cu stable isotopes to understand Cu redox cycling and mass transfer functions during sequential

cycles of low temperature alteration of igneous copper porphyries, marine sedimentary diagenesis and epigenetic mobilization of Cu in sandstones at a site of historic Cu mining in southern Israel. As predicted by theory and experiment, they found that $\delta^{65/63}\text{Cu}$ values of Cu(I)-sulfides in the stratiform sediment-hosted Cu deposits are significantly lower than those of coexisting Cu(II)-carbonates and hydroxides. Coupling the Cu isotope composition of the minerals to a mass balance model revealed that the main Cu reservoir of the ore body is a sandstone-shale sequence and that the importance of Cu-sulfide reservoirs is small, consistent with field observations. Thus most of the Cu transport occurred in relatively oxidized conditions, the knowledge of which provides a novel tool for exploration in the future.

10.4.3 Plant Nutrition and Processes Within Plants

Numerous transition and post-transition metals play important chemical roles in plant nutrition (Marschner 1995). For example, of the metals discussed in this chapter, Fe is essential for chlorophyll development and function, assists in energy transfer functions and redox reactions, is an important constituent of enzymes and participates in nitrogen fixation. Zinc is important for carbohydrate and protein metabolism, pollen formation, and general disease resistance, and is a structural constituent or regulatory co-factor of numerous plant enzymes. Molybdenum, Cu and Ni each play additional important physiological roles in plant nutrition, while excesses can lead to a variety of toxic effects on plant vitality. Using the stable isotopes of these metals as indicators of metal sources and cycling processes, and perhaps to reveal the onset of metal toxicity, is an emerging field in isotope biogeoscience.

As pointed out by von Blanckenburg et al. (2009), the metabolic processes that control the behavior of metals in plants can be envisaged as a gigantic geochemical pump that continuously moves metals between reservoirs. As plants move metals from soils into roots and along the transpiration stream, the metals are cycled through a variety of chemical species via processes that can lead to isotope

fractionation. During the past several years, for the metals discussed here stable isotope fractionation in higher plants has been demonstrated for Fe and Zn (Weiss et al. 2005; Guelke and von Blanckenburg 2007; Viers et al. 2007; Moynier et al. 2008; Kiczka et al. 2010). This is an intriguing pair of metals to consider, as the isotope fractionations observed in plants are largely controlled by redox status for Fe, and by complexation chemistry for Zn.

Plants have developed two different strategies for transporting Fe from soils into roots. Roots of dicotyledons and nongraminaceous monocotyledons (“strategy I plants”, e.g. pea, bean) release protons into the rhizosphere, promoting dissolution of Fe(III) precipitates, and activating membrane-bound enzymes that reduce chelate-bound Fe(III). The reduced Fe is then transported across the root plasma membrane by unspecific metal transporters (Briat et al. 2007). Partial reduction of an Fe(III)-solid produces aqueous Fe(II) with an $^{56}\text{Fe}/^{54}\text{Fe}$ ratio that is approximately 1–1.5‰ less than that in the remaining Fe(III)-solid (Johnson et al. 2004). As a consequence, the Fe(II) that crosses the root plasma membrane, and thus the pool of Fe in a strategy I plant, is lighter than the soil Fe pool. In contrast, roots of graminaceous plant species (“strategy II plants”, e.g. maize, wheat) can release phytosiderophores into the rhizosphere, which form complexes with Fe(III) (Romheld and Marschner 1986; Kraemer et al. 2006). These Fe(III)-complexes are then transported across the root plasma membrane by a specialized class of transport proteins, but due to

lack of reduction, the pool of Fe(III) in a strategy II plant has the same Fe isotope composition as the soil Fe pool.

The results of two studies of Fe isotope variability in plants are shown in Fig. 10.6. In a variety of strategy I plants studied by Guelke and von Blanckenburg (2007), $\delta^{56/54}\text{Fe}$ values of tissues decreased from soils to stems, from stems to leaves and from leaves to seeds. In contrast, all tissues in their strategy II plants had similar $\delta^{56/54}\text{Fe}$ values, which they attributed to differences in the way that Fe is translocated in the two plant types. These results are consistent with the different Fe uptake and transport processes proposed above for strategy I and strategy II plants. Kiczka et al. (2010), working with strategy I and II plants collected from a recently deglaciated site, identified several reaction points along the translocation stream of both plant types where Fe(III) reduction and thus isotope fractionation might occur, including between the root symplast and apoplast, between the leaf cytoplasm and the xylem, and between the phloem and the leaf cytoplasm, at each step moving lighter Fe along the transpiration stream. However, in contrast to the results of Guelke and von Blanckenburg (2007), Kiczka et al. (2010) observed similar Fe isotope patterns in their strategy I and II plants, with $\delta^{56/54}\text{Fe}$ values generally increasing from root stele to stem to leaf. To explain this discrepancy, they pointed to previous studies suggesting that release of siderophores by strategy II plants into the rhizosphere is suppressed under Fe-rich soil conditions similar to

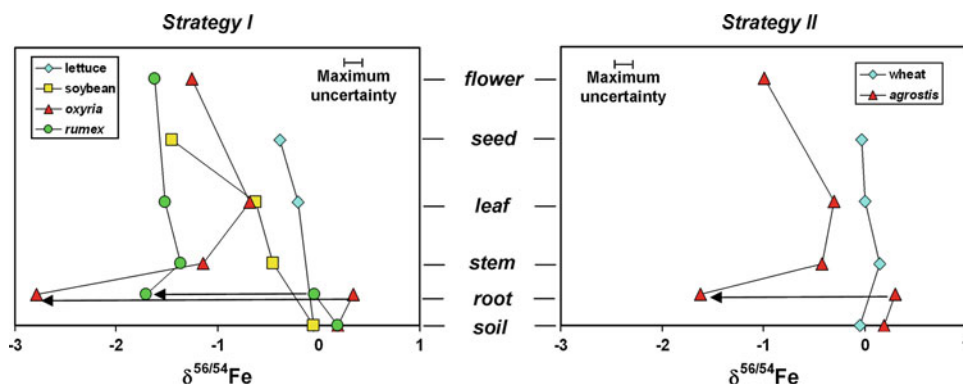


Fig. 10.6 $\delta^{56/54}\text{Fe}$ values for a variety of plant tissues. Values for lettuce and soybean (Strategy I) and wheat (Strategy II) are from Guelke and von Blanckenburg (2007), values for *oxyria digyna* and *rumex scutatus* (Strategy I) and *agrostis givantea* (Strategy II) are from Kiczka et al. (2010). In each diagram, the arrows between root tissues point from cortex to stele, and

demonstrate the large Fe isotope fractionation that occurs across the plasma membrane. Complex Fe isotope variations within individual plants result from a variety of possible isotope fractionation processes which can occur along the transpiration stream

those at their field site (Marschner 1995), and suggesting that strategy I and II plants mobilize and transport Fe similarly under such conditions (Charlson and Shoemaker 2006).

In the case of Zn, dissolution of Fe(III) solids in the soil by protons released from plant roots results in release of Zn that is adsorbed on the Fe(III) solids. Subsequent uptake of Zn by roots depends only on the induction of specific Zn transporters, which belong to the same protein family as the Fe transporters (Kramer et al. 2007). Likewise, the release of phytosiderophores benefits the acquisition of Zn (Suzuki et al. 2006). Apparently the transport of Fe and Zn to plant roots is closely linked. Zn isotope variability within plants appears to be fairly straightforward and similar for strategy I and strategy II plants, based on several laboratory and field based studies (Weiss et al. 2005; Viers et al. 2007; Moynier et al. 2008). Roots tend to have the heaviest Zn, probably reflecting the preferential adsorption of heavy Zn onto the root and plaque surfaces. However it should be noted that the possibility of Zn isotope contrast between the root cortex and stele of plants has yet to be explored, as has been done for Fe isotopes (Kiczka et al. 2010). Shoots have similar to lesser $\delta^{66/64}\text{Zn}$ values than bulk roots, and leaves invariably contain the lightest Zn in the plants. These observations are consistent with light Zn isotopes being transported preferentially during nutrient exchange along the cell walls of the xylem although it is unclear at this stage whether this is a kinetic or an equilibrium process (von Blanckenburg et al. 2009).

There clearly remains much to be done to understand the causes of transition and post-transition metal stable isotope fractionation in plants, and certainly the remaining metals deserve at least a thorough reconnaissance for a variety of plant species and field situations. To date, much of the work has aimed at explaining observed variations of isotope composition in terms of known plant processes. With greater understanding, future work will gradually shift toward using the isotopes to identify as yet unknown or unconstrained processes in plants.

10.4.4 Biosignatures

One of the most enduring hopes and goals of metal stable isotope biogeochemistry is to be able to use the isotopes as biosignatures, by developing either single

or multi-tracer tests that could be applied to a natural system to decipher a biological influence on its origins. A recurring theme in metal stable isotope studies of biological systems is that biological activities that result in significant isotope fractionation generally involve preferential processing of lighter isotopes from the metal source pool into and within the biological materials (e.g. Zhu et al. 2002; Bermin et al. 2006; Johnson et al. 2008; Eisenhauer et al. 2009). Indeed, in the early days of the transition and post-transition metal stable isotope data explosion (i.e. the late 1990s), the general thinking was that most metal stable isotope fractionation observed in nature would be due to biological processing (e.g. Beard and Johnson 1999). This thinking led to pioneering attempts to constrain experimentally an Fe isotope biosignature (Beard et al. 1999), but likewise inspired early attempts to demonstrate the importance of inorganic processes that could fractionate Fe isotopes both in the laboratory (e.g. Anbar et al. 2000) and in natural settings (e.g. Bullen et al. 2001). We now realize that ranges of metal stable isotope fractionation caused by inorganic processes can exceed and overlap those produced by biological processing, making development of robust metal stable isotope biosignature tools a challenge but also an exceptional research opportunity.

Given the early and persistent focus on the isotope systematics of Fe, it is not surprising that the greatest progress toward development of a metal stable isotope biosignature has been for Fe, at least for early Earth environments. As stressed by Johnson et al. (2008), the fluxes of mobilized Fe must have been far greater in the Archean and early Proterozoic because of the enormous amount of Fe-rich sediments (e.g. banded iron formations) that were deposited in that time span. The Fe isotope composition of those sediments is highly variable compared to igneous rocks, implying that the processes responsible for fractionating Fe must have been especially active and variable in extent during that time span. Because microbial dissimilatory Fe reduction (DIR) appears to be the most important process capable of producing large quantities of isotopically light Fe, by an order of magnitude or more compared to inorganic processes, DIR is likely to have been the dominant process affecting Fe during that time span.

In this case, the effectiveness of the Fe isotope biosignature depended on knowledge of the relative sizes of the reduced and oxidized Fe pools during early

Earth history. If we are going to be able to use Fe isotopes to detect a record of DIR in other environments (e.g. in the search for life on Mars and other planetary bodies), we must be able to assess the size of those pools in those environments as well. Confidence in the approach will increase as more terrestrial field sites are studied. A promising example from modern Earth comes from the work of Severmann et al. (2008), who used Fe isotopes to support their contention that DIR coupled to Fe(II) oxidation in oxic shelf sediments can account for the large amount of isotopically light Fe produced on the shelf and shuttled to the euxinic basin of the Black Sea.

Biosignatures based on the other transition and post-transition metal isotope systems have yet to be explored as deeply as that based on Fe, but there are promising signs for success. For example, Borrok et al. (2008) documented a diel cycle for dissolved Zn concentrations and $\delta^{66/64}\text{Zn}$ values in Prickly Pear Creek, which drains a former mining district in the Boulder Batholith, Montana, USA. They found that dissolved Zn concentrations and $\delta^{66/64}\text{Zn}$ values were inversely correlated, with Zn at low concentrations in the daytime having elevated $\delta^{66/64}\text{Zn}$ due to sequestration of light Zn in bed sediments. Biological uptake of light Zn was invoked to explain this relationship, since adsorption of Zn onto amorphous Fe(III) oxides prevalent in bed sediments preferentially concentrates heavy Zn onto sorption sites (Balistrieri et al. 2008). As discussed above, Cameron et al. (2009) demonstrated that methanogenic bacteria cultured in the laboratory preferentially assimilate and retain isotopically light Ni, while a wide range of geologic materials have uniform Ni isotope composition. Nickel isotopes are thus likely to become an important biosignature of methanogenesis. And, as pointed out by von Blanckenburg et al. (2009), plant tissues recycled into soil generally have different metal stable isotope composition than the growth medium, thus the upper soil may retain a time-integrated metal isotope fingerprint of plant activity. New biosignatures are likely to emerge as well understood biological systems are studied.

10.5 Future Directions

As pointed out by Severmann and Anbar (2009), the field of metal stable isotope biogeochemistry emerged primarily as an analytical pursuit driven by advances in mass spectrometry applied to interesting geological

materials. Arguably, much of the work that has been done to date with the transition and post-transition metal stable isotopes has resulted in a better understanding of the isotope systems themselves rather than the materials that have been measured. Many observed variations in isotope composition have been explained in terms of well understood physical, chemical and biological processes, but isotope analyses have so far rarely revealed some unanticipated or poorly understood set of processes. On the other hand, useful applications pertinent to environmental studies are beginning to emerge: isotopic characteristics of plant homeostasis are being established, multi-tracer approaches for identifying metal sources are being developed, biosignatures are being rigorously constrained through analysis of well understood geological and biological materials, and the isotopic signatures of redox reactions are being characterized. As understanding of metal stable isotope systematics increases, it will become easier to think of novel ways that isotopes can enhance understanding of complex processes in environmental systems.

What should be clear from this chapter is that the field of transition and post-transition metal stable isotope biogeochemistry is really just beginning to mature, and that opportunities are abundant. Major advances over the next several years are likely to include: improving the routine precision and reproducibility of total procedural replicate measurements of samples to the few hundredths of a per mil level; developing robust multi-tracer approaches to identify metal sources and pathways for forensic purposes; looking for the unexpected isotope fractionation of metals such as Ti and Ni in environmental systems; expanding the list of robust biosignatures, including the fingerprint of anthropogenic activities; exploring the metal stable isotope signals of global climate change. This is only a partial list, but one where success is likely to be realized through well-crafted interdisciplinary efforts, careful selection of field sites, and clever laboratory- and field-based experiments.

References

- Albarède F, Beard B (2004) Analytical methods for non-traditional isotopes. In: Johnson CM, Beard BL, Albarède F (eds) *Geochemistry of non-traditional stable isotopes*.

- Reviews of Mineralogy and Geochemistry, vol 55. Mineralogical Society of America, Washington, pp 113–152
- Anbar AD (2004) Molybdenum stable isotopes: observations, interpretations and directions. *Rev Mineral Geochem* 55: 425–454
- Anbar AD, Roe JE, Barling J, Nealon KH (2000) Nonbiological fractionation of iron isotopes. *Science* 288:126–128
- Anbar AD, Jarzecki AA, Spiro TG (2005) Theoretical investigation of iron isotope fractionation between $\text{Fe}(\text{H}_2\text{O})_6^{3+}$ and $\text{Fe}(\text{H}_2\text{O})_6^{2+}$: implications for iron stable isotope geochemistry. *Geochim Cosmochim Acta* 69:825–837
- Arnold GL, Anbar AD, Barling J, Lyons TW (2004) Molybdenum isotope evidence for widespread anoxia in mid-Proterozoic oceans. *Science* 304:87–90
- Asael D, Matthews Bar-Matthews M, Halicz L (2007) Copper isotope fractionation in sedimentary copper mineralization (Timna Valley, Israel). *Chem Geol* 243:238–254
- Balci N, Bullen TD, Witte-Lien K, Shanks WC, Motelica M, Mandernack KW (2006) Iron isotope fractionation during microbially stimulated Fe(II) oxidation and Fe(II) precipitation. *Geochim Cosmochim Acta* 70:622–639
- Balistreri LS, Borrok DM, Wanty RB, Ridley WI (2008) Fractionation of Cu and Zn isotopes during adsorption onto amorphous Fe(III) oxides: experimental mixing of acid rock drainage and pristine river water. *Geochim Cosmochim Acta* 72:311–328
- Barling J, Anbar AD (2004) Molybdenum isotope fractionation during adsorption by manganese oxides. *Earth Planet Sci Lett* 217:315–329
- Barling J, Arnold GL, Anbar AD (2001) Natural mass-dependent variations in the isotopic composition of molybdenum. *Earth Planet Sci Lett* 193:447–457
- Beard BL, Johnson CM (1999) High precision iron isotope measurements of terrestrial and lunar materials. *Geochim Cosmochim Acta* 63:1653–1660
- Beard BL, Johnson CM, Cox L, Sun H, Nealon KH, Aguilar C (1999) Iron isotope biosignatures. *Science* 285:1889–1892
- Beard BL, Johnson CM, Skulan JL, Nealon KH, Cox L, Sun H (2003) Application of Fe isotopes to tracing the geochemical and biological cycling of Fe. *Chem Geol* 195:87–117
- Beard BL, Handler RM, Scherer MM, Wu L, Czaja AD, Heimann A, Johnson CM (2010) Iron isotope fractionation between aqueous ferrous iron and goethite. *Earth Planet Sci Lett* 295:241–250
- Bergquist BA, Blum JD (2007) Mass-dependent and -independent fractionation of Hg isotopes by photoreduction in aquatic systems. *Science* 318:417–420
- Bergquist BA, Blum JD (2009) The odds and evens of mercury isotopes: applications of mass-dependent and mass-independent isotope fractionation. *Elements* 5:353–357
- Bermin J, Vance D, Archer C, Statham PJ (2006) The determination of the isotopic composition of Cu and Zn in seawater. *Chem Geol* 226:280–297
- Berna EC, Johnson TM, Makdisi RS, Basu A (2010) Cr stable isotopes as indicators of Cr(VI) reduction in groundwater: a detailed time-series study of a point-source plume. *Environ Sci Technol* 44:1043–1048
- Blum JD (2011) Applications of stable mercury isotopes to biogeochemistry. In: Baskaran M (ed) *Handbook of Environmental Isotope Geochemistry, Advances in Isotope Geochemistry*, DOI:10.1007/978-3-642-10637-8_10, © Springer-Verlag Berlin Heidelberg 2011
- Blum JD, Bergquist BA (2007) Reporting of variations in the natural isotopic composition of mercury. *Anal Bioanal Chem* 388:353–359
- Borrok DM, Wanty RB, Ridley WI, Wolf R, Lamothe PJ, Adams M (2007) Separation of copper, iron and zinc from complex aqueous solutions for isotopic measurement. *Chem Geol* 242:400–414
- Borrok DM, Nimick DA, Wanty RB, Ridley WI (2008) Isotopic variations of dissolved copper and zinc in stream waters affected by historical mining. *Geochim Cosmochim Acta* 72:329–344
- Briat JF, Curie C, Gaymard F (2007) Iron utilization and metabolism in plants. *Curr Opin Plant Biol* 10:276–282
- Bullen TD (2007) Chromium stable isotopes as a new tool for forensic hydrology at sites contaminated with anthropogenic chromium. In: Bullen TD, Wang Y (eds) *Water-rock interaction: proceedings of the 12th international symposium on water-rock interaction*, vol 1. Taylor & Francis, London, pp 699–702
- Bullen TD, Amundson R (2010) Interpreting Ca and Fe stable isotope signals in carbonates: a new perspective. *Proceedings of the 13th International Symposium on Water-Rock Interaction (WRI-13)*, Guanajuato, Mexico. Taylor & Francis, London
- Bullen TD, Eisenhauer AE (2009) Metal stable isotopes in low-temperature systems: a primer. *Elements* 5:349–352
- Bullen TD, Walczyk T (2009) Environmental and biomedical applications of natural metal stable isotope variations. *Elements* 5:381–385
- Bullen TD, White AF, Childs CW, Vivit DV, Schulz MS (2001) Demonstration of significant abiotic iron isotope fractionation in nature. *Geology* 29:699–702
- Cameron V, Vance D, Archer C, House C (2009) A biomarker based on the stable isotopes of nickel. *Proc Natl Acad Sci* 106:10944–10948
- CH2MHill (2007) Groundwater background study report, Hinkley Compressor Station, Hinkley, California. Internal Report to Pacific Gas & Electric Corporation, February 2007
- Charlson DV, Shoemaker RC (2006) Evolution of iron acquisition in higher plants. *J Plant Nutr* 29:1109–1125
- Chen JB, Gaillardet J, Louvat P (2008) Zinc isotopes in the Seine River waters, France: a probe of anthropogenic contamination. *Environ Sci Technol* 42:6494–6501
- Chen JB, Gaillardet J, Louvat P, Huon S (2009) Zinc isotopes in the suspended load of the Seine River, France; isotopic variations and source determination. *Geochim Cosmochim Acta* 73:4060–4076
- Clark I, Fritz P (1997) *Environmental isotopes in hydrogeology*. Lewis Publishers, Boca Raton, 328p
- Cloquet C, Carignan J, Libourel G, Sterckeman T, Perdrix E (2006a) Tracing source pollution in soils using cadmium and lead isotopes. *Environ Sci Technol* 40:2525–2530
- Cloquet C, Carignan J, Libourel G (2006b) Isotopic composition of Zn and Pb atmospheric depositions in an urban/periurban area of northeastern France. *Environ Sci Technol* 40: 6594–6600
- Cloquet C, Carignan J, Lehmann MF, Vanhaecke F (2008) Variation in the isotopic composition of zinc in the natural

- environment and the use of zinc isotopes in biogeosciences: a review. *Anal Bioanal Chem* 390:451–463
- Das J, Pobi M (1990) Separation of titanium, iron and aluminum on a chelating resin with benzoylphenylhydroxylamine group and application to bauxite and clay. *Fresenius' J Anal Chem* 336:578–581
- Eisenhauer A, Kisakurek B, Bohm F (2009) Marine calcification: an alkali earth metal isotope perspective. *Elements* 5: 365–368
- Ellis A, Johnson TM, Bullen TD (2002) Chromium isotopes and the fate of hexavalent chromium in the environment. *Science* 295:2060–2062
- Ellis A, Johnson TM, Bullen TD (2004) Using chromium stable isotope ratios to quantify Cr(VI) reduction: lack of sorption effects. *Environ Sci Technol* 38:3604–3607
- Estrade N, Carignan J, Sonke JE, Donard OFX (2009) Mercury isotope fractionation during liquid-vapor evaporation experiments. *Geochim Cosmochim Acta* 73:2693–2711
- Estrade N, Carignan J, Donard OFX (2010) Isotope tracing of atmospheric mercury sources in an urban area of northeastern France. *Environ Sci Technol* 44:6062–6067
- Fantle MS, Bullen TD (2009) Essentials of iron, chromium and calcium isotope analysis of natural materials by thermal ionization mass spectrometry. *Chem Geol* 258:50–64
- Geulke M, von Blanckenburg F (2007) Fractionation of stable iron isotopes in higher plants. *Environ Sci Technol* 41: 1896–1901
- Irisawa K, Hirata T (2006) Tungsten isotopic analysis of six geochemical reference materials using multiple collector-ICP-mass spectrometry coupled with rhenium-external correction technique. *Geochim Cosmochim Acta* 70:A279
- Izbicki JA, Ball JW, Bullen TD, Sutley SJ (2008) Chromium, chromium isotopes and selected trace elements, western Mojave Desert, USA. *Appl Geochim* 23:1325–1352
- Johnson TM (2011) Stable isotopes of Cr and Se as tracers of redox processes in earth surface environments. In: Baskaran M (ed) *Handbook of environmental isotope geochemistry*. Springer, Heidelberg
- Johnson CM, Beard BL (1999) Correction of instrumentally produced mass fractionation during isotopic analysis of Fe by thermal ionization mass spectrometry. *Int J Mass Spectrom* 193:87–99
- Johnson TM, Bullen TD, Zawislanski PT (2000) Selenium stable isotope ratios as indicators of sources and cycling of selenium: results from the northern reach of San Francisco Bay. *Environ Sci Technol* 34:2075–2079
- Johnson CM, Skulan JL, Beard BL, Sun H, Neelson KH, Brateman PS (2002) Isotopic fractionation between Fe(III) and Fe(II) in aqueous solutions. *Earth Planet Sci Lett* 195:141–153
- Johnson CM, Beard BL, Beukes NJ, Klein C, O'Leary JM (2003) Ancient geochemical cycling in the Earth as inferred from Fe isotope studies of banded iron formations from the Transvaal Craton. *Contrib Mineralog Petrol* 144: 523–547
- Johnson CM, Beard BL, Roden EE, Newman DK, Neelson KH (2004) Isotopic constraints on biogeochemical cycling of Fe. In: Johnson CM, Beard BL, Albarède F (eds) *Geochemistry of non-traditional stable isotopes*. Mineralogical Society of America *Reviews in Mineralogy & Geochemistry* 55: 359–408
- Johnson CM, Beard BL, Roden EE (2008) The iron isotope fingerprints of redox and biogeochemical cycling in modern and ancient Earth. *Annu Rev Earth Planet Sci* 36:457–493
- Kavner A, John SG, Sass S, Boyle EA (2008) Redox-driven stable isotope fractionation in transition metals: Application to Zn electroplating. *Geochim Cosmochim Acta* 72: 1731–1741
- Kendall C, McDonnell JJ (1998) *Isotope tracers in catchment hydrology*. Elsevier, Amsterdam, 839p
- Kiczka M, Wiederhold JG, Kraemer SM, Bourdon B, Kretzschmar R (2010) Iron isotope fractionation during Fe uptake and translocation in alpine plants. *Environ Sci Technol* 44: 6144–6150
- Kling GW, Evans WC, Tanyileke G, Kusakabe M, Ohba T, Yoshida Y, Hell JV (2005) Degassing Lakes Nyos and Nonoun: defusing certain disaster. *Proc Natl Acad Sci USA* 102:14185–14190
- Kraemer SM, Crowley DE, Kretzschmar R (2006) Geochemical aspects of phytosiderophore-promoted iron acquisition by plants. *Adv Agron* 91:1–46
- Kramer U, Talke IN, Hanikenne M (2007) Transition metal transport. *FEBS Lett* 581:2263–2272
- Larson PB, Maher K, Ramos FC, Chang Z, Gaspar M, Meinert LD (2003) Copper isotope ratios in magmatic and hydrothermal ore-forming environments. *Chem Geol* 201:337–350
- Liu Y, Huang M, Masuda A, Inoue M (1998) High-precision determination of osmium and rhenium isotope ratios by in situ oxygen isotope ratio correction using negative thermal ionization mass spectrometry. *Int J Mass Spectrom Ion Processes* 173:163–175
- Longerich HP, Fryer BJ, Strong DF (1987) Determination of lead isotope ratios by inductively coupled plasma-mass spectrometry (ICP-MS). *Spectrochimica Acta* 42B:39–48
- Luo Y, Dabek-Zlotorzynska E, Celo V, Muir DCG, Yang L (2010) Accurate and precise determination of silver isotope fractionation in environmental samples by multi-collector-ICPMS. *Anal Chem* 82:3922–3928
- Malinovsky D, Hammarlund D, Ilyashuk B, Martinsson O, Gelting J (2007) Variations in the isotopic composition of molybdenum in freshwater lake systems. *Chem Geol* 236: 181–198
- Maréchal CN, Télouk P, Albarède F (1999) Precise analysis of copper and zinc isotopic compositions by plasma-source mass spectrometry. *Chem Geol* 156:251–273
- Marschner H (1995) *Mineral nutrition of higher plants*, 2nd edn. Academic, London, p 889
- Martin JH and Fitzwater SE (1988) Iron-deficiency limits phytoplankton growth in the Northeast Pacific Subarctic. *Nature* 331:341–343
- Mathur R, Ruiz J, Tittley S, Liermann L, Buss H, Brantley SL (2005) Cu isotopic fractionation in the supergene environment with and without bacteria. *Geochim Cosmochim Acta* 69:5233–5246
- Mattielli N, Petit JCY, Deboudt K, Flament P, Perdrix E, Taillez A, Rimetz-Planchon J, Weis D (2009) Zn isotope study of atmospheric emissions and dry depositions within a 5 km radius of a Pb–Zn refinery. *Atmos Environ* 43:1265–1272
- Moynier F, Pichat S, Pons M-L, Fike D, Balter V, Albarède F (2008) Isotopic fractionation and transport mechanisms of Zn in plants. *Chem Geol* 267:125–130

- Neubert N, Nägler TF, Böttcher ME (2008) Sulfidity controls molybdenum isotope fractionation into euxinic sediments: evidence from the modern Black Sea. *Geology* 36:775–778
- Pelly IZ, Lipschutz ME, Balsiger H (1970) Vanadium isotopic composition and contents in chondrites. *Geochim Cosmochim Acta* 34:1033–1036
- Polyakov VB, Mineev SD (2000) The use of Mossbauer spectroscopy in stable isotope geochemistry. *Geochim Cosmochim Acta* 64:849–865
- Poulson RL, Siebert C, McManus J, Berelson WM (2006) Authigenic molybdenum isotope signatures in marine sediments. *Geology* 34:617–620
- Rehkämper M, Wombacher F, Aggarwal JK (2004) Stable isotope analysis by multiple collector ICP-MS. In: de Groot PA (ed) *Handbook of stable isotope analytical techniques*. Elsevier, Amsterdam, pp 692–725
- Rehkämper M, Wombacher F, Horner TJ, Xue Z (2011) Natural and anthropogenic Cd isotope variations. In: Baskaran M (ed) *Handbook of Environmental Isotope Geochemistry, Advances in Isotope Geochemistry*, DOI 10.1007/978-3-642-10637-8_10, © Springer-Verlag Berlin Heidelberg 2011
- Richter FM, Dauphas N, Teng F-Z (2009) Non-traditional fractionation of non-traditional isotopes: Evaporation, chemical diffusion and Soret diffusion. *Chem Geol* 258:92–103
- Ripperger S, Rehkämper M (2007) Precise determination of cadmium isotope fractionation in seawater by double-spike MC-ICPMS. *Geochim Cosmochim Acta* 71:631–642
- Romheld V, Marschner H (1986) Evidence for a specific uptake system for iron phytosiderophores in roots of grasses. *Plant Physiol* 80:175–180
- Rudge JF, Reynolds BC, Bourdon B (2009) The double spike toolbox. *Chem Geol* 265:420–431
- Sahoo YV, Nakai S, Ali A (2006) Modified ion exchange separation for tungsten isotopic measurements from kimberlite samples using multi-collector inductively coupled plasma mass spectrometry. *Analyst* 131:434–439
- Schauble EA (2003) Modeling zinc isotope fractionations. *EOS Trans AGU* 84:F232
- Schauble EA (2004) Applying stable isotope fractionation theory to new systems. In: Johnson CM, Beard BL, Albarède F (eds) *Geochemistry of non-traditional stable isotopes, reviews in mineralogy and geochemistry*, vol 55. Mineralogical Society of America and Geochemical Society, Washington, D.C., pp 65–111
- Schmitt A-D, Galer SJG, Abouchami W (2009a) High-precision cadmium stable isotope measurements by double spike thermal ionization mass spectrometry. *J Anal At Spectrom* 24:1079–1088
- Schmitt A-D, Galer SJG, Abouchami W (2009b) Mass-dependent cadmium isotopic variations in nature with emphasis on the marine environment. *Earth Planet Sci Lett* 277:262–272
- Schoenberg R, Zink S, Staubwasser M, von Blanckenburg F (2008) The stable Cr isotope inventory of solid Earth reservoirs determined by double spike MC-ICP-MS. *Chem Geol* 249:294–306
- Schroeder WH, Munthe J (1998) Atmospheric mercury – an overview. *Atmos Environ* 32:809–822
- Severmann S, Anbar AD (2009) Reconstructing paleoredox conditions through a multitracer approach: the key to the past is the present. *Elements* 5:359–364
- Severmann S, Lyons TW, Anbar A, McManus J, Gordon G (2008) Modern iron isotope perspective on the benthic iron shuttle and the redox evolution of ancient oceans. *Geology* 36:487–490
- Shiel AE, Weiss D, Orians KJ (2010) Evaluation of zinc, cadmium and lead isotope fractionation during smelting and refining. *Sci Total Environ* 408:2357–2368
- Siebert C, Nägler TF, Kramers JD (2001) Determination of molybdenum isotope fractionation by double-spike multi-collector inductively coupled plasma mass spectrometry. *Geochem Geophys, Geosyst* 2:1032
- Siebert C, Nägler TF, von Blanckenburg F, Kramers JD (2003) Molybdenum isotope records as a potential new proxy for paleoceanography. *Earth Planet Sci Lett* 211:159–171
- Siebert C, McManus J, Bice A, Poulson R, Berelson WM (2006) Molybdenum isotope signatures in continental margin marine sediments. *Earth Planet Sci Lett* 241:723–733
- Sikora ER, Johnson TM, Bullen TD (2008) Microbial mass-dependent fractionation of chromium isotopes. *Geochim Cosmochim Acta* 72:3631–3641
- Sivry Y, Riotte J, Sonke JE, Audry S, Schäfer J, Viers J, Blanc G, Freydier R, Dupré B (2008) Zn isotopes as tracers of anthropogenic pollution from Zn-ore smelters: the Riu Mort–Lot River system. *Chem Geol* 255:295–304
- Skulan JL, Beard BL, Johnson CM (2002) Kinetic and equilibrium Fe isotope fractionation between aqueous Fe(III) and hematite. *Geochim Cosmochim Acta* 66:2995–3015
- Suzuki M et al (2006) Biosynthesis and secretion of mugineic acid family phytosiderophores in zinc-deficient barley. *Plant J* 48:85–97
- Teutsch N, Schmid M, Muller B, Halliday AN, Burgmann H, Wehrli B (2009) Large iron isotope fractionation at the oxic-anoxic boundary in Lake Nyos. *Earth Planet Sci Lett* 285:52–60
- Thevenot DR, Moilleron R, Lestel L, Gromaire MC, Rocher V, Cambier P, Bonte P, Colin JL, de Ponteves C, Maybeck M (2007) Critical budget of metal sources and pathways in the Seine River basin (1994–2003) for Cd, Cr, Cu, Hg, Ni, Pb and Zn. *Sci Total Environ* 375:180–203
- Vance D, Archer C, Bermin J, Perkins J, Statham PJ, Lohan MC, Elwood MJ, Mills RA (2008) The copper isotope geochemistry of rivers and the oceans. *Earth Planet Sci Lett* 274:204–213
- Viers J, Oliva P, Nonell A, Gélabert A, Sonke JE, Freydier R, Gainville R, Dupré B (2007) Evidence of Zn isotopic fractionation in a soil plant system of a pristine tropical watershed (Nsimi, Cameroon). *Chem Geol* 239:124–137
- Von Blanckenburg F, von Wirén N, Guelke M, Weiss DJ, Bullen TD (2009) Fractionation of metal stable isotopes by higher plants. *Elements* 5:375–380
- Wasylenki LE, Rolfe BA, Weeks CL, Spiro TG, Anbar AD (2008) Experimental investigation of the effects of temperature and ionic strength on Mo isotope fractionation during adsorption to manganese oxides. *Geochim Cosmochim Acta* 72:5997–6005
- Weber KA, Achenbach LA, Coates JD (2006) Microorganisms pumping iron: anaerobic microbial oxidation and reduction. *Nat Rev Microbiol* 4:752–764
- Weiss DJ, Mason TFD, Zhao FJ, Kirk GJD, Coles BJ, Horstwood MSA (2005) Isotopic discrimination of zinc in higher plants. *New Phytol* 165:703–710

- Weiss DJ, Rausch N, Mason TFD, Coles BJ, Wilkinson JJ, Ukonmaanaho L, Arnold T, Nieminen TM (2007) Atmospheric deposition and isotope biogeochemistry of zinc in ombrotrophic peat. *Geochim Cosmochim Acta* 71: 3498–3517
- Welch SA, Beard BL, Johnson CM, Braterman PS (2003) Kinetic and equilibrium Fe isotope fractionation between aqueous Fe(II) and Fe(III). *Geochim Cosmochim Acta* 67:4231–4250
- Wen H, Carignan J, Cloquet C, Zhu X, Zhang Y (2010) Isotopic delta values of molybdenum standard reference and prepared solutions measured by MC-ICP-MS: proposition for delta zero and secondary references. *J Anal At Spectrom* 25: 716–721
- Widory D, Petelet-Giraud E, LeBihan O, LeMoulllec Y, Quétel C, Snell J, Van Bocxstaele M, Hure A, Canard E, Joos E, Forti L, Bullen T, Johnson T, Fiani E (2010) Metals in atmospheric particles: can isotopes help discriminate potential sources? *Atmospheric Pollution, Special Edition*:75–82
- Wieser ME, Schwieters JB (2005) The development of multiple collector mass spectrometry for isotope ratio measurements. *Int J Mass Spectrom* 242:97–115
- Wiesli RA, Beard BL, Johnson CM (2004) Experimental determination of Fe isotope fractionation between aqueous Fe(II), siderite and “green rust” in abiotic systems. *Chem Geol* 211:343–362
- Wombacher F, Rehkamper M, Mezger K, Munker C (2003) Stable isotope compositions of cadmium in geological materials and meteorites determined by multiple-collector ICPMS. *Geochim Cosmochim Acta* 67:4639–4654
- Zhu XK, Guo Y, Williams RJP, O’Nions RK, Matthews A, Belshaw NS, Canters GW, deWaal EC, Weser U, Burgess BK, Salvato B (2002) Mass fractionation processes of transition metal isotopes. *Earth Planet Sci Lett* 200:47–62

Chapter 11

Applications of Osmium and Iridium as Biogeochemical Tracers in the Environment

Mukul Sharma

Abstract Osmium (Os) and Iridium (Ir) and are among the rarest elements on the surface of the earth and ones whose applications in modern industry are quite limited. However, their environmental burden has been increasing as they occur in nature with other platinum group elements, which have a wide variety of industrial, chemical, electrical and pharmaceutical applications. This review traces the development of the analytical techniques used to precisely measure Os and Ir concentrations and Os isotope composition in the environmental samples from their roots in geochemical and cosmochemical investigations. We then examine the distribution of Os and Ir in natural samples and review recent literature applying these elements as biogeochemical tracers. The primary environmental applications of Os and Ir arise from the fact that these elements are extremely rare on the surface of the earth and their introduction into the environment leads to an increase in their concentration in surface materials. In addition, a unique isotope fingerprint is present for Os introduced into the environment in that it comes from ores mined primarily in South Africa and Russia. In particular, we examine studies where (a) Os isotopes have been utilized to track the dispersal of platinum group elements from automobile catalysts and also to assess dispersal of Os itself and (b) Ir has been introduced as an intentional tracer to evaluate soot contribution from burning of fossil fuels.

11.1 Introduction

The intent of this paper is to outline advances over the last 20 years in the detection and accurate measurements of Os and Ir concentrations and Os isotopes in natural samples and their applications to environmental issues. Development of environmental applications for these elements has followed cosmo- and geochemical applications. This paper gives a brief outline of the studies done in these collateral areas of research and then presents a review of the analytical techniques used to measure Os and Ir. Following this we discuss distribution of Os and Ir in natural samples and their environmental applications. Os and Ir are highly siderophile or chalcophile, i.e., they strongly prefer metal or sulfide phases over silicate minerals. During the formation of the earth's core these elements were extracted nearly quantitatively from the mantle into the core. Moreover, during mantle melting and magma formation, both Os and Ir are highly compatible. Consequently, while Os and Ir are highly enriched in meteorites/cosmic dust (average ~600 ng/g; Os/Ir ~ 1, Barker and Anders 1968; Chen et al. 2005; Walker et al. 2002a) they are depleted in the upper continental crust (average ~30 pg/g; Os/Ir ~ 1, Esser and Turekian 1993b; Peucker-Ehrenbrink and Jahn 2001). They are among the rarest elements in seawater with concentrations of 6–14 and 0.08–3.6 pg/kg for Os and Ir, respectively.

Osmium has seven naturally occurring isotopes: ^{184}Os (0.02%), ^{186}Os (1.56%), ^{187}Os (1.6%), ^{188}Os (13.3%), ^{190}Os (26.4%) and ^{192}Os (41.0%). The molar abundances given are nominal as ^{187}Os and ^{186}Os are radiogenic and produced from the decay of ^{187}Re (β -decay, $t_{1/2} = 41.2$ billion years) and ^{190}Pt (α -decay, $t_{1/2} = 494.4$ billion years), respectively.

M. Sharma (✉)
Radiogenic Isotope Geochemistry Laboratory, Department of
Earth Sciences, Dartmouth College, 6105 Fairchild Hall,
Hanover, NH 03755, USA
e-mail: Mukul.Sharma@Dartmouth.edu

Early interest in the ^{187}Re - ^{187}Os isotope system stemmed from using it as a geochronometer for dating of Re-bearing ore-minerals (Hintenberger et al. 1954) and iron meteorites (Herr et al. 1961) and as a cosmochronometer in evaluating the age of the Universe (Clayton 1964; Truran 1998). The ^{187}Re - ^{187}Os isotope system is unique among long-lived geochronometers as both parent and daughter are siderophile-chalcophile. This has permitted dating of geological samples that could not be dated using traditional isotope systems (^{87}Rb - ^{87}Sr , ^{147}Sm - ^{143}Nd , U-Th-Pb) that involve lithophile elements. The ^{187}Re - ^{187}Os isotope system has been successfully utilized in numerous studies dating meteorites and terrestrial rocks and mineral deposits (e.g., Shen et al. 1996; Stein et al. 2004; Yang et al. 2009; Walker et al. 2002a). It has also been used in assessing the evolution of the planetary mantles (see e.g., Walker 2009). The environmental applications of the ^{187}Re - ^{187}Os isotope system are based on using the $^{187}\text{Os}/^{188}\text{Os}$ ratio as a tracer of mantle derived Os and other platinum group elements (PGE). The fundamental systematics for such applications has been worked out in studies that have attempted to assess meteorite impacts and changes in continental weathering. It is based on the large Os isotope ratio difference between meteorites ($^{187}\text{Os}/^{188}\text{Os} = 0.13$) and continental crustal rocks ($^{187}\text{Os}/^{188}\text{Os} = 1.3$), which makes Os isotopes a highly sensitive tracer of extraterrestrial and/or continental material.

A number of investigations have utilized Os isotopes to trace bolide impacts throughout geological time (Gordon et al. 2009; Koeberl et al. 2004; Lee et al. 2003; Luck and Turekian 1983; Meisel et al. 1995; Paquay et al. 2009; Peucker-Ehrenbrink et al. 1995; Schmitz et al. 2001) and to evaluate the size of the impactor (Paquay et al. 2008) and also to assess the temporal variations in the cosmic dust flux (Dalai and Ravizza 2006; Dalai et al. 2006; Esser and Turekian 1988; Marcantonio et al. 1999; Peucker-Ehrenbrink 1996; Peucker-Ehrenbrink and Ravizza 2000a). Another set of studies has utilized Os isotopes to determine the extent to which the meteorite component is present in target rocks (Frei and Frei 2002; Gelinas et al. 2004; Koeberl et al. 1994a, b, c; Lee et al. 2006; McDonald et al. 2007) or in distal ejecta (e.g., tektites) from the impact (Koeberl and Shirey 1993, 1997).

Variations in the $^{187}\text{Os}/^{188}\text{Os}$ ratios in the oceans have been used to infer changes in continental weathering resulting from the uplift of mountain

ranges (Pegram et al. 1992; Pegram and Turekian 1999; Peucker-Ehrenbrink 1996; Sharma et al. 1999) and waxing and waning of ice ages (Burton et al. 2010; Oxburgh 1998; Oxburgh et al. 2007). They have also been used to trace flood basalt volcanism (Ravizza and Peucker-Ehrenbrink 2003; Robinson et al. 2009).

The environmental studies of ^{187}Re - ^{187}Os isotope system began with the discovery of anthropogenic Os in estuarine sediments from Long Island Sound that was inferred to be derived from effluents from hospitals where OsO_4 is used as a fixative for electron microscopy (Esser and Turekian 1993a; Williams and Turekian 2002). High concentrations of anthropogenic Os were also found in sewage discharge from Boston suggesting that Os isotopes could be used to assess municipal sewage dispersal from major cities adjoining estuaries (Ravizza and Bothner 1996). Recent environmental studies have focused on the role of automobile catalytic converters and industrial refining of ores as sources of anthropogenic osmium (Chen et al. 2009; Poirier and Garipey 2005; Rauch et al. 2004, 2005, 2006, 2010; Rodushkin et al. 2007a, b). Pre-historic refining of sulfide ores in the Iberian Peninsula, Spain has also been traced using Os isotopes (Rauch et al. 2010).

The production of ^{186}Os over geologic time is minor as ^{190}Pt is a minor isotope of Pt (0.013%) with an extremely long half-life (Walker et al. 1997). The ^{190}Pt - ^{186}Os system has been successfully utilized to date meteorites and old terrestrial rocks (e.g., Cook et al. 2004; Puchtel et al. 2009). It has also been used to study core-mantle interaction (see Walker 2009 and references therein). Variations of the order of a few tens of parts per million in $^{186}\text{Os}/^{188}\text{Os}$ ratios have been observed between different lithologies (ultramafic rocks and black shales) that upon erosion contribute Os to the oceans (McDaniel et al. 2004). The ^{190}Pt - ^{186}Os system has not been developed for environmental applications so far.

Iridium has two naturally occurring stable isotopes: ^{191}Ir (37.3%) and ^{193}Ir (62.7%). So far, no variations in $^{193}\text{Ir}/^{191}\text{Ir}$ ratios have been documented in nature; the expected variations in this ratio are about 1‰ or less (E. Schauble, personal communication). Due to its low abundance on the earth's surface and high concentration in meteorites Ir concentrations in marine sediments and ice cores have been utilized to assess bolide impacts (Alvarez et al. 1980) and long term accretion of cosmic dust (Gabielli et al. 2004a; Karner et al. 2003; Kyte and Wasson 1986). It has

also been used to examine fall out from volcanic eruptions (Gabrielli et al. 2008). In environmental studies Ir has been introduced as an intentional tracer to track soot emissions from coal fired plants, public buses and diesel sanitation truck fleets (Heller-Zeisler et al. 2000; Suarez et al. 1998; Wu et al. 1998). Introduction of Ir in latest automobile catalytic converters has led to a study of its abundance in urban areas (Iavicoli et al. 2008).

and Meisel (2002). Here we will concentrate only on the determination of Os and Ir. Table 11.1 provides a comparison of the detection limits of various procedures used in estimating the concentrations of Os and Ir in sediments, rocks, and waters; with the exception of the study by Meisel and Moser (2004) all studies that have measured Os concentration have also measured Os isotope composition.

11.2 Analytical Techniques

Several excellent reviews have appeared over the years dealing with different aspects of chemical separation and measurements of the PGEs. These include: Barefoot and Van Loon (1999), Meisel and Moser (2004), Pearson and Woodland (2000) and Reisberg

11.2.1 Osmium

11.2.1.1 Determination of Os in Solid Samples

Early osmium concentration measurements were made using Neutron Activation Analysis (NAA; Barker and Anders 1968; Bate and Huizenga 1963;

Table 11.1 Comparison of various procedures used to measure Os and Ir

Sample	Element	Preconc. procedure	Measurement	Detection limit (pg)	References
Sediments	Os	NiS/distillation	ID-N-TIMS	13.4	Ravizza and Pyle (1997)
Rocks	Os	Carius tube/solvent extraction	ID-N-TIMS	≤5	Cohen and Waters (1996) and Shen et al. (1996) and Shirey and Walker (1996)
Rocks	Os	Carius tube/sparging	ID-ICP-MS	<2	Meisel and Moser (2004)
Rocks	Os	HF + HCl + EtOH/distill.	SIMS	<5	Walker (1988)
Rocks	Os	HF + HBr/CrO ₃ + Br ₂	N-TIMS	0.06	Birck et al. (1997)
Seawater	Os	CrO ₃ + Br ₂ /microdistill	N-TIMS	0.022	Levasseur et al. (1998)
Seawater	Os	H ₂ SO ₄ + H ₂ O ₂ distill	N-TIMS	0.120	Woodhouse et al. (1999)
Seawater	Os	Carius tube/distillation	N-TIMS	0.0027	Chen and Sharma (2009)
Groundwater	Os	Carius tube/Br ₂ extract.	N-TIMS	0.069	Paul et al. (2009)
Rain	Os	CrO ₃ + Br ₂ /microdistill	N-TIMS	0.0203	Levasseur et al. (1999)
Rain and snow	Os	Carius tube/distillation	N-TIMS	0.0027	Chen and Sharma (2009)
Sediments and rocks	Ir	Na-peroxide/anion exch.	GFAAS	30	Hodge et al. (1986)
sediments	Ir	Acid digest/anion exch.	ICP-MS	6	Colodner et al. (1993)
Rocks	Ir	Na-peroxide/Te-ppt	RNAA	4	Morcelli and Figueiredo (2000)
Rocks	Ir	Na peroxide/Te-ppt	ICP-MS	300	Enzweiler et al. (1995)
Rocks	Ir	NiS digestion	INAA	790	Tanaka et al. (2008)
Rocks	Ir	NiS digestion	ID-ICP-MS	15.6	Ravizza and Pyle (1997)
Rocks	Ir	NiS-anion exch.	ID-ICP-MS	<1,565	Rehkamper and Halliday (1997)
Rocks	Ir	Carius/anion exch.	ID-ICP-MS	<3	Rehkamper et al. (1998)
Rocks	Ir	Carius/sparging	ID-ICP-MS	<2	Meisel and Moser (2004)
Rocks	Ir	NiS digest/Te-ppt	ICP-MS	40	Pattou et al. (1996)
Aerosols	Ir	None	INAA	0.06	Heller-Zeisler et al. (2000)
Aerosols	Ir	Acid digest/anion exch.	RNAA	0.09	Heller-Zeisler et al. (2000)
Aerosols	Ir	Acid digest/anion exch.	ID-N-TIMS	0.3	Heller-Zeisler et al. (2000)
Ice-core dust	Ir	Filtration from water	INAA	<0.001	Karner et al. (2003)
Snow	Ir	Evaporation	ICP-MS	<0.001	Gabrielli et al. (2004a, b)
Seawater	Ir	Anion exch.	INAA	0.2	Li et al. (2007)
Seawater	Ir	Anion exch.	ID-N-TIMS	0.005	Anbar et al. (1997)

Morgan 1965), which utilized γ -ray detection of ^{185}Os (646 keV) and ^{191}Os (130 keV) and permitted Os concentration determination in nanogram-sized samples. Interest in the geochemical and cosmochemical applications of the ^{187}Re - ^{187}Os isotope system required precise measurements of Os isotopes in samples containing 10^{-9} – 10^{-12} g/g of Os. However, a high ionization potential of Os (8.7 eV) meant that it could not be analyzed using conventional positive Thermal Ionization Mass Spectrometry. This difficulty led to the development of isotope ratio measurement techniques using secondary ion mass spectrometry (SIMS, Luck and Allegre 1983), resonance ionization mass spectrometry (RIMS, Walker and Fassett 1986), and accelerator mass spectrometry (AMS, Fehn et al. 1986; Teng et al. 1987). The SIMS and AMS techniques involved generation of Os ions by sputtering of a target containing Os with high energy molecular ion beams and required specialized equipment (ion probe and accelerator mass spectrometer, respectively). The RIMS technique involved resonance ionization of evaporated Os atoms with laser and had the advantage of utilizing a thermal ionization mass spectrometer platform for ion detection and measurement. These techniques have been supplanted by the development of Inductively Coupled Plasma-Mass Spectrometry (ICP-MS) and negative Thermal Ionization Mass Spectrometry (N-TIMS).

Routine ICP-MS measurements for Os isotopes involve introducing the sample in solution into plasma through a nebulizer and spray chamber assembly and suffer from low sensitivity. The most sensitive of ICP-MS techniques for Os isotope measurement involve generating volatile osmium tetroxide (OsO_4) from sample and introducing (“sparging”) it directly into the plasma (Hassler et al. 2000; Russ and Bazan 1987a, b). This procedure has the significant advantage of not requiring prior chemical separation of Os. The preferred method for Os isotope analysis is N-TIMS using OsO_3^- (Creaser et al. 1991; Volkening et al. 1991). This technique can analyze very small amounts of Os to a high precision but requires Os pre-concentration and purification (Table 11.1). Purified Os in solution is loaded and dried on high purity Pt filaments following which Ba-hydroxide is loaded and dried; the latter provides electrons needed for negative thermal ionization.

Advances in the chemical separation of Os from solids and its purification have gone hand in hand with the development of mass spectrometry. For SIMS

measurements high level Os samples (Laurite $\text{Ru}(\text{Os}, \text{Ir})\text{S}_2$, Fe-Mn nodules) were dissolved in Ni vessels, the resulting OsO_4 was distilled and purified using ion exchange chromatography and loaded on an Al disc (Luck and Allegre 1983; Palmer and Turekian 1986; Turekian and Luck 1984). RIMS measurements were conducted with Os separated by dissolving powdered rock samples in Teflon bombs with $\text{HF} + \text{HCl} + \text{ethanol}$. Ethanol was used to keep Os from getting oxidized to volatile OsO_4 during this stage. After dissolution, Os was oxidized and purified by distillation (Walker 1988). This technique was also used for N-TIMS work. Ravizza and Bothner (1996) used the NiS fire assay method in combination with isotope dilution N-TIMS to measure Os concentration and isotope composition in marine sediments. The NiS method was initially developed for neutron activation analysis to permit PGE concentration determination in large samples (Hoffman et al. 1978). This method takes advantage of the chalcophile character of the PGEs and the immiscibility of a sulfide melt to separate the PGEs from the silicate rocks. Powdered solid samples are mixed with a flux containing sodium tetraborate, sodium carbonate, Ni powder, sulfur powder and silica and fused at $1,000^\circ\text{C}$. The PGEs are concentrated into NiS beads, which are then dissolved in hydrochloric acid, leaving Ni into the solution and isolating insoluble sulfide compounds of the PGEs (Hoffman et al. 1978; Tanaka et al. 2008). Ravizza and Bothner (1996) filtered the PGE sulfides and then dissolved them in a combination of $\text{H}_2\text{SO}_4 + \text{Cr}^{\text{VI}}\text{O}_3$. The resulting volatile OsO_4 was distilled and further purified using ion exchange. Birck et al. (1997) pioneered a technique in which a powdered sample with tracer is attacked first by HF and HBr in a Teflon vessel. The resulting solution is dried and further dissolved using HNO_3 in the presence of $\text{Cr}^{\text{VI}}\text{O}_3$ and $\text{Br}_2(\text{liq})$. The resulting OsO_4 is extracted in $\text{Br}_2(\text{liq})$, reduced in HBr and further purified using microdistillation.

Memory effects caused by OsO_4 diffused into Teflon at high temperature can be severe. This observation and the requirement that dissolution procedure has to be carried out in a closed-system to achieve sample-tracer equilibration provided the basic incentive to develop the Carius tube technique (Cohen and Waters 1996; Shen et al. 1996; Shirey and Walker 1995) in which samples are dissolved in sealed thick-walled glass vessels (Carius tubes). Typical

digestion temperatures used in the Carius tube method range from 200 to 240°C and are dictated by the bursting pressure of the glass tube, which depends on the glass thickness and internal diameter of the tube. This technique has been subsequently modified to use a high pressure asher (HPA-S), where a confining pressure is applied with dry nitrogen and the operating temperature can be raised to 300°C for a relatively thin-walled and higher-capacity quartz glass tube. During high temperature attack with Lefort aqua regia, Os is leached out from the sample and Os-tracer equilibrate as they get converted to OsO₄, which can then be distilled or extracted using CCl₄ or CHCl₃ or Br₂ (liq). No further purification is needed if Os isotopes are measured using an ICP-MS (see e.g., Meisel and Moser 2004). For N-TIMS, Os is further purified using microdistillation, which essentially removes all organics from the sample (Birck et al. 1997). Removal of organics is required to achieve a high ionization efficiency of 10–20%, which has permitted precise isotope ratio measurements samples containing as little as 100×10^{-15} g of Os (see below).

11.2.1.2 Determination of Os in Natural Waters

Suzuki et al. (1998) used an aqueous solution of an Os-thiourea complex with GFAAS to measure Os concentrations in waste water from electron microscopy laboratories, which use OsO₄(aq) to fix cells for microscopy. A number of attempts have been made to determine the osmium concentration and isotope composition of seawater. Its low abundance in seawater and possible multiple oxidation states frustrated initial efforts to precisely measure its concentration and isotope composition. Koide et al. (1996) used isotope dilution RIMS to obtain the osmium concentration and isotope composition of seawater. A 25 L sample of seawater was spiked with ¹⁹⁰Os tracer and Os was separated using anion exchange chromatography and purified using distillation. Sharma et al. (1997) reduced seawater and tracer Os by bubbling SO₂(g) and then coprecipitated Os with iron oxyhydroxide in 4–10 L samples. Os was extracted from iron oxyhydroxide using the carius tube technique followed by CCl₄ extraction, microdistillation, and measurement using N-TIMS. These techniques were found to not provide a quantitative yield for Os leading to the development of three new techniques. Levasseur et al.

(1998) oxidized seawater and tracer Os by heating 50 g samples at 80°C with a mixture of Cr^{VI}O₃ and Br₂(liq); the resulting OsO₄ was extracted with Br₂(liq) and purified. Woodhouse et al. (1999) oxidized Os in 1.5-L seawater samples by adding a mixture of H₂SO₄ and H₂O₂ and distilling OsO₄, which was trapped in HBr and further purified. Os isotopes were measured using N-TIMS. Sharma et al. (1999) modified the Carius tube technique to remove Os from 50 to 70 g of seawater. The samples with tracer and Cr^{VI}O₃ were heated at 180°C for more than 40 h; the resulting OsO₄ was distilled and trapped in HBr. It was further purified and measured using N-TIMS. A recent study by Chen and Sharma (2009) has, however, demonstrated that oxidation of all species of Os present in seawater requires much higher temperatures (300°C). In fact as much as 30% of Os in seawater is not extracted by any of the previous techniques. That Os occurring in other natural waters (such as groundwaters) is present in multiple oxidation states has also been inferred in a recent study by Paul et al. (2009) who oxidize waters in a HPA-S using a mixture of H₂O₂ and H₂SO₄ and extract the resulting OsO₄ using Br₂(liq). High temperature oxidation of Os seems to be the only way to provide quantitative estimates of the Os concentrations in waters.

11.2.2 Iridium

11.2.2.1 Determination of Ir in Solid Samples

The classical technique to determine Ir is NAA. Despite the development of other more sensitive methods (see below) the NAA continues to be extensively used on its own (Instrumental Neutron Activation Analysis, INAA) or in combination with chemical purification of Ir from a pre-irradiated sample (Radiochemical Neutron Activation Analysis, RNAA). Neutron irradiation of ¹⁹¹Ir results in the production of ¹⁹²Ir, which has a half life of 73.83 days and decays via emitting γ rays with energies of 295, 308, 316.51 and 468.07 keV; the last two rays are more intense than the first two and are usually used for concentration determination. The γ rays are detected by high purity Ge-detectors and Ir amounts estimated using sensitivities obtained from concurrently irradiated Ir-standards. Background interference from samples

depends on the type of sample being analyzed (rock, water, etc.). It may come mainly from ^{46}Sc , ^{51}Cr , ^{60}Co , ^{65}Zn , ^{76}Se , and ^{124}Sb . Different approaches have been employed to remove the background and to improve detection limit:

1. Electronic suppression of background: This technique involves essentially reducing the background by simultaneously detecting 316.51 and 468.07 keV rays, whose emission is near-coincident, by a pair of detectors; background interference is substantially reduced except from that produced from Compton interactions of high energy coincident pairs of gamma rays from ^{46}Sc and ^{60}Co . This background can also be removed by independent detection of Compton-gamma-rays (Karner et al. 2003; Michel et al. 1990).
2. Preconcentration of Ir using the NiS fire assay method (see previous section for description) followed by neutron irradiation and measurement. The PGE sulfides are then filtered, irradiated and analyzed.
3. Chemical purification following irradiation and after adding Ir carrier:
 - (a) Irradiated sample with Ir carrier is sintered with sodium peroxide and then dissolved in HCl. The resulting solution is filtered and Ir co-precipitated with Te metal and analyzed (Morcelli and Figueiredo 2000; Nogueira and Figueiredo 1995).
 - (b) Iridium separation using anion exchange chromatography. During the ion exchange chromatography advantage is taken of extremely high affinity of Ir^{IV} to anion exchange resin AG-1 in dilute HCl. Dissolved sample mixed with Ir carrier is loaded on to a column of pre-cleaned AG-1 resin. The interfering nuclides are removed by eluting the column in dilute HCl and water. Since Ir^{IV} can be reduced on the column and mobilized an oxidizing reagent (Ce^{4+}) is mixed with the sample to ensure quantitative retention of Ir on the column. Following this Ir can be retained on the column and resin separated and analyzed or eluted and further purified before analysis (Heller-Zeisler et al. 2000; Keays et al. 1974).

Iridium separated from marine sediments and organisms has been measured using Graphite Furnace Atomic absorption Spectrometry (GFAAS) (Hodge

et al. 1986). Samples were sintered with sodium peroxide and then dissolved in HCl and spiked with ^{192}Ir tracer. Chlorine gas was bubbled through the solution, which was then passed through a column of AG-1X8 resin. Iridium retained on the column was recovered using hot nitric acid and further purified prior to analysis. Iridium was determined with the spectrometer's monochromator set on 266.5 nm. Measured Ir concentrations were corrected for loss during separation and purification by determining the loss of ^{192}Ir activity in the final solution.

With the development of Inductively Couple Plasma-Mass Spectrometry (ICP-MS) external calibration or isotope dilution techniques have been successfully employed to accurately and precisely measure Ir concentrations in geochemical samples (Colodner et al. 1993; Date et al. 1987; Gregoire 1988; Gros et al. 2002; Jackson et al. 1990; Meisel and Moser 2004; Sengupta and Gregoire 1989). The ICP-MS technique appears to have successfully replaced atomic absorption spectrometry for the determination of Ir. The technique involves generation of ions by introducing solution carrying elements of interest in to plasma using by means of a nebulizer and spray chamber, followed by acceleration of ions through a Quadrupole filter/magnetic sector and their detection. The technique usually requires pre-concentration of Ir. A procedure involving sintering the sample with sodium peroxide followed by co-precipitation of tracer (enriched ^{191}Ir) and sample Ir with Te and subsequent measurement using ICP-MS was developed in the mid 1990s (Enzweiler et al. 1995). Ir precipitation is not quantitative but not required for this method as it uses isotope dilution to determine the concentration. For any isotope dilution method it is imperative that the sample and tracer fully equilibrate so that losses during subsequent processing do not impact the result. It was found that reproducible results are obtained when spike solution is mixed to strongly alkaline solution resulting from the dissolution of fusion cake.

As NiS fire assay method provides nearly quantitative recovery of Ir (e.g., Hoffman et al. 1978), it has been used as a pre-concentration technique prior to ICP-MS determination (Gros et al. 2002; Plessen and Erzinger 1998). A variation of this technique involves isotope dilution analysis in which Ir-tracer is mixed to the sample prior to the fire assay (Ravizza and Pyle 1997). This permits achievement of isotopic

equilibrium between the sample and tracer Ir within the immiscible NiS melt needed to obtain accurate concentration determination. While NiS fire assay is simple and can be used with a large volume of samples, it suffers from high procedural blanks owing to the large amounts of reagents needed (Table 11.1; see also Pearson and Woodland 2000) and its Re yield is not quantitative. These issues along with the desire to measure other PGE and especially Re and Os isotopes in the same sample aliquots (see above) have led to the development of a digestion procedure in which samples mixed with tracers are decomposed with aqua-regia at high temperature in Carius tubes (Rehkamper et al. 1998). Under these conditions Ir leached from the sample equilibrates with the tracer. It can then be separated from other elements using anion exchange column chromatography and solvent extraction and measured on an ICP-MS. The procedural blanks for the Carius tube/HPA-S methods are low permitting precise determination in samples with pg/g of Ir (Meisel and Moser 2004; Pearson and Woodland 2000; Rehkamper and Halliday 1997; Rehkamper et al. 1998; Shinotsuka and Suzuki 2007; Table 11.1).

11.2.2.2 Determination of Ir in Natural Waters

Gabrielli et al. (2004a, b) measured Ir concentrations in an ice core from Greenland using external calibration with a high resolution magnetic sector ICP-MS. This procedure involved pre-concentration of Ir by sub-boiling evaporation of water followed by mass spectrometry. Seawater and river water have complex matrices and require pre-concentration procedures. Fresco et al. (1985) removed Ir from 1.5 L sea-water by reducing it with magnesium and then used neutron activation to measure Ir concentration. Hodge et al. (1986) used anion exchange chromatography and GFAAS to measure Ir in seawater. This method required 100 L of seawater for a single measurement. Chlorine gas was bubbled in samples spiked with ^{192}Ir tracer to convert any Ir^{III} to Ir^{IV} (cf. Yi and Masuda 1996a, b). The water was then passed through a column of AG1-X8 resin. Iridium was removed with hot nitric acid and further purified and measured using GFAAS as described above. Anbar et al. (1996, 1997) used highly sensitive isotope dilution Negative Thermal Ionization Mass Spectrometry (ID-NTIMS) to determine Ir in seawater and river water. This pro-

cedure requires 2–4 L of sample and involves equilibrating tracer and water Ir by bubbling Cl_2 gas into water. Ir is then separated from water by (1) using anion exchange chromatography or (2) co-precipitation with ferric hydroxide followed by ion exchange chromatography. It is further purified and measured as IrO_2^- ions in a thermal ionization mass spectrometer (cf. Creaser et al. 1991; Walczyk and Heumann 1993). Recently, Li et al. (2007) have determined Ir concentrations in 1–2 L of seawater using anion exchange chromatography and NAA. Seawater samples were loaded on to a column of pre-cleaned AG-1 resin. The interfering nuclides were removed by eluting the column in dilute HCl and water. To ensure quantitative retention Ir^{IV} on the column Cl_2 was bubbled in the sample and eluting solutions (Li et al. 2007). Following this, the resin containing Ir was ashed, irradiated, and analyzed.

11.3 Distributions Among Natural Samples

Here I briefly give the distribution of Os and Ir in solid earth, meteorites, ores, waters and marine sediments and discuss the resulting systematics that form the basis of the environmental applications in Sect. 11.4.

11.3.1 Distribution in Solid Earth and Meteorites

The distribution of Os and Ir in rocks reflects their siderophile and chalcophile character (Table 11.2). They are highly enriched in iron meteorites over stony meteorites. Metal-silicate equilibrium partitioning data suggest that differentiation of earth into a metal core and silicate mantle depleted these elements in the mantle as they were quantitatively sequestered in the core (see Shirey and Walker 1998 and references therein). The higher than expected PGE concentrations in the mantle suggest that following the core formation some PGE (including Os and Ir) were accreted as a “late veneer”. The $^{187}\text{Os}/^{188}\text{Os}$ ratio of the primitive upper mantle indicates that the late veneer was likely either ordinary or enstatite

Table 11.2 Os and Ir concentrations, Os/Ir ratios, and $^{187}\text{Os}/^{188}\text{Os}$ ratios in natural samples

	[Os] ^a	[Ir] ^a	Os/Ir	$^{187}\text{Os}/^{188}\text{Os}$	References
Iron meteorites (IVB)	27.3 µg/g	24.1 µg/g	1.1	0.1240	Walker et al. (2008)
Carbonaceous chondrite	636 ng/g	599 ng/g	1.1	0.1257	Horan et al. (2003)
Ordinary chondrite	685 ng/g	617 ng/g	1.1	0.1281	Horan et al. (2003)
Cosmic dust	1,060 ng/g	–	~1	0.125	Measurement of a single unmelted 21 µg sample of a micrometeorite (Chen and Sharma, unpublished data)
Primitive mantle	3.4 ng/g	3.2 ng/g	1.1	0.1290	McDonough and Sun (1995)
Continental mineral aerosol (upper continental crust)	0.031 ng/g	0.022 ng/g	1.4	1.26	Esser and Turekian (1993b) and Peucker-Ehrenbrink and Jahn (2001)
PGE-sulfide ores	4.6 µg/g	6.3 µg/g	0.7	0.15–0.20	Chen et al. (2009) and Naldrett (2004)
Base-metal sulfide ores	0.17 µg/g	0.15 µg/g	0.8	0.15 to >2	Chen et al. (2009) and Naldrett (2004)
Chromite ores	0.049 µg/g	0.041 µg/g	1.2	0.12–0.14	Ahmed and Arai (2002, 2009), Büchl et al. (2004), Chen et al. (2009), Economou-Eliopoulos (1996), Pedersen et al. (1993), Prichard and Lord (1993), Prichard et al. (2008), and Zaccarini et al. (2004)
Pelagic sediment	0.16 ng/g	0.40 ng/g	0.4		Koide et al. (1991)
Fe-Mn nodules/crusts	0.80 ng/g	1.8 ng/g	0.3		Koide et al. (1991)
Pelagic carbonate	0.065 ng/g	0.022 ng/g	3		Ravizza and Dalai (2006)
Black shale	4 ng/g	1 ng/g	5		Jiang et al. (2007), Paquay et al. (2009), and Pasava (1993)
Seawater	6–14 fg/g	0.08–3.6 fg/g	68	1.05 (deep) < 1.05 (surface)	Chen and Sharma (2009)
River water	3–84 fg/g	0.56–3	7–14	1.45	Anbar et al. (1996), Chen et al. (2006), Gannoun et al. (2006), Levasseur et al. (1999), Martin et al. (2001), Sharma et al. (1999, 2007a), Sharma and Wasserburg (1997), and Turekian et al. (2007)
Groundwater	20–191 fg/g	–	?	0.96–2.8	Paul et al. (2010)
Rainwater/snow	0.3–23 fg/g	0.1–5 fg/g	?	0.16–0.40	Chen et al. (2009) and Gabrielli et al. (2004a)

^aConcentrations in the table vary about 11 orders of magnitude.

Note: 1 µg/g = 10⁻⁶ g/g, 1 ng/g = 10⁻⁹ g/g, and 1 fg/g = 10⁻¹⁵ g/g = pg/kg

chondrites (Meisel et al. 1996). Os and Ir are highly compatible elements during melting of the earth's mantle, i.e., they do not partition into the melts that form the crust. As a result, these elements are extremely depleted in the continental crust. Also, the Os/Ir ratio of the continental crust is about the same as the mantle and meteorites (~1). However, during mantle melting Re is incompatible resulting in an average $^{187}\text{Re}/^{188}\text{Os}$ ratio of the continental material of ~48, which is much higher than that of the mantle and meteorites (~0.36). As a consequence, the time-integrated average $^{187}\text{Os}/^{188}\text{Os}$ ratio of continental crust is about ten times higher than that of the mantle and meteorites (Table 11.2).

Osmium and Ir are highly enriched in cosmic dust, which is produced as a result of collision of asteroids in the asteroidal belt and travels toward the sun due to the Poynting-Robertson light effect. Approximately, 40×10^6 kg of cosmic dust accretes annually on earth (Love and Brownlee 1993) providing a nearly constant background flux of Os and Ir. Lal and Jull (2003) have pointed out that a relatively large flux of the PGE also comes from the fragmentation and vaporization of meteorites as they enter the earth's atmosphere. This "meteoric smoke" likely gets concentrated in the polar-regions leading to an enhanced apparent flux of the PGE in polar ice (Gabrielli et al. 2006). Osmium and Ir concentrations and Os isotopes in deep marine sediments have been used to assess

cosmic dust flux and its variations over long-term (Peucker-Ehrenbrink and Ravizza 2000a and references therein).

11.3.1.1 Distribution in Ore Deposits

Relatively high concentrations of Os and Ir in PGE-sulfide and chromitite ores (Table 11.2) reflect enrichment during crystallization in magma chambers. An excellent recent review of the literature on the PGE bearing magmatic sulfide deposits is by Naldrett (2004). The largest PGE deposits are in the 2 Ga Bushveld Complex of South Africa, where mixing of two magmas engendered nearly simultaneous chromite crystallization and segregation of an immiscible sulfide-rich melt. Scavenging of the PGE by sulfide melts and also by chromites led to unusually high concentrations of the PGEs, which are found in the Merensky Reef and UG-2 ore bodies (Naldrett 2004). Noril'sk Ni-Cu sulfide ore deposits in Russia are the second largest source of PGE (Jones 1999). They are associated with 251 Ma Siberian Flood Basalt Province. Here magma contamination and consequent segregation of immiscible sulfide melts along dykes that fed lavas to the surface has led to crystallization of PGE-enriched Ni-Cu sulfide ores (Naldrett 2004). Modest enrichments of the PGE are always associated with magmatic sulfides (Table 11.2) and quite possibly with other types of sulfide deposits (sedimentary-exhalative deposits, Cu and Mo porphyry deposits; see e.g., Sotnikov et al. 2001). The Re/Os ratios of sulfide ores are quite variable and as a result depending on their age, the $^{187}\text{Os}/^{188}\text{Os}$ ratios of the ores also vary from ~ 0.15 to >2 (Chen et al. 2009).

Relatively modest PGE-enrichments are also found all over the world in podiform chromitite bodies associated with ultramafic rocks within ophiolite complexes (e.g., Ahmed and Arai 2002; Ahmed et al. 2009; Büchl et al. 2004; Economou-Eliopoulos 1996; Pedersen et al. 1993; Prichard and Lord 1993; Prichard et al. 2008; Zaccarini et al. 2004). Here chromite encloses primarily laurite and also metal clusters of Ru-Os-Ir alloys. The Re/Os ratios of chromites are extremely low and therefore their $^{187}\text{Os}/^{188}\text{Os}$ ratios reflect the time when these ores were derived from the mantle (Walker et al. 2002b).

11.3.2 Distribution in Natural Waters

The speciation and oxidation states of Os and Ir in waters are not well constrained. Thermodynamic data predicts that Os should exist as either OsO_4^0 (Byrne 2002) or H_3OsO_6^- (Palmer et al. 1988) in seawater, both of which are in the fully oxidized (Os^{VIII}) state. However, experimental observations indicate that Os in seawater does not solely reside in its fully oxidized state because great effort is required to fully oxidize seawater Os. The rich organometallic chemistry of Os suggests that it may also be present in a reduced inert organic form in seawater (Chen and Sharma 2009; Levasseur et al. 1998). Os is abundant in both oxidizing and reducing marine sediments (see Table 11.2) and its redox behavior seems to impact its distribution in seawater-sediment system. A recent X-ray absorption near-edge structure (XANES) study shows that Os incorporated in reducing sediment is mainly trivalent and that removed in oxic sediment is tetravalent (Yamashita et al. 2007). In comparison, the speciation of Ir in seawater is dominated by Ir^{III} oxidation state forming anionic chloro-complex IrCl_6^{3-} (Anbar 1996 and references therein). Recent work suggests that Ir^{III} in seawater may form mixed ligand complexes (Byrne 2002). The principal species of Ir^{III} in seawater is tentatively assigned to be $\text{IrCl}_a(\text{OH})_b^{3-(a+b)}$. Iridium may also be stabilized in seawater by the formation of stable organic complexes (Anbar et al. 1996). Iridium also has a large first hydroxide binding constant and is thus likely to be very reactive toward Fe-Mn oxyhydroxides and clays (Anbar 1996). Oxidation of Ir from trivalent to tetravalent state may occur during mineral formation (Hodge et al. 1986).

The differences in the redox behavior and particle reactivity appear to control the removal and fractionation of Os and Ir in the oceans. These elements are concentrated in anoxic black shales as well as oxic chemical precipitates (Fe-Mn nodules/crusts) (Table 11.2). Remarkably, however, there is a substantial fractionation between Os and Ir in these sediments, i.e., the average Os/Ir ratio of black shales is ~ 15 times higher than that of the Fe-Mn nodules/crusts. This suggests that geochemical behaviors of these elements in seawater column are vastly different and much unlike their behaviors during planetary formation and differentiation! This observation can be further examined by

calculating the ratio of the dissolved to suspended particulate fluxes entering the oceans via rivers. Assuming that the concentrations in pelagic sediments are the same as those transported by rivers and the suspended particulate flow rate from rivers is $15.5 \times 10^{15} \text{ g year}^{-1}$ (Martin and Meybeck 1979), the ratio of dissolved to suspended particulates fluxes to the oceans are 0.1 and 0.01 for Os and Ir, respectively. Note that there is a large uncertainty in the riverine Ir flux as only three rivers have been analyzed so far (Anbar et al. 1996). Nonetheless we can infer that only a small fraction of continental Os and Ir are transported to the oceans in dissolved form and that subtle changes in the Ir concentrations of oceanic sediments (e.g., by reduction of oxic marine sediments, which would release Ir) could potentially impact its seawater concentrations, potentially providing a flux that is significant compared to the riverine Ir flux.

The Os concentration ($=[\text{Os}]$) in seawater varies from 6 to 14 of fg/g (Table 11.2; Fig. 11.1). As discussed above, only the latest analytical technique

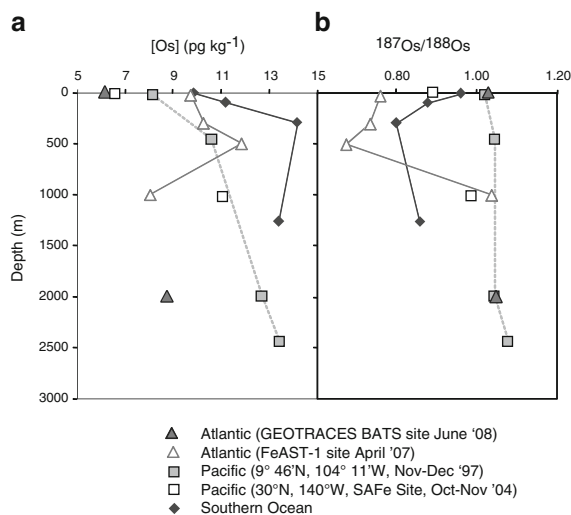


Fig. 11.1 Seawater profiles of Os isotopic compositions and concentrations from the Atlantic, Pacific, and Southern Oceans. Os concentrations are variable across ocean basins and are lowest at the surface and becoming enriched at ~ 500 m depth (a). At a depth of 2,000 m, the eastern North Pacific has a much higher concentration than the Atlantic. While the GEOTRACES sample collected at 2,000 m has an $^{187}\text{Os}/^{188}\text{Os}$ ratio of 1.052 ± 0.004 ($N = 8$) and confirms earlier results from the Sargasso Sea, the Os isotope compositions of samples at shallower levels vary between basins and with depth (b). Moreover, surface samples seem to have lower $^{187}\text{Os}/^{188}\text{Os}$ ratios than those for deeper waters. Figure modified from Chen and Sharma (2009)

appears to provide a quantitative yield of the Os concentration in seawater. Using these limited data we can infer that the behavior of Os in the oceans is non-conservative (Fig. 11.1a). The surface water of the Atlantic, the Pacific, and the Southern Ocean is less concentrated in Os than the deep oceans. At a depth of 2,000 m the water in the eastern Pacific is more concentrated in Os than the Atlantic. Depth profiles suggest a nutrient like behavior: Os is depleted near the surface and becomes enriched at ~ 500 m; at depths of 700–1,000 m it seems to decrease.

The Atlantic and Pacific waters from a depth of 2,000 m have a $^{187}\text{Os}/^{188}\text{Os}$ ratio of 1.05, which is identical to a previously established ratio of 1.05 ± 0.01 for the deep oceans (Levasseur et al. 1998; Sharma et al. 1997; Woodhouse et al. 1999). However, deeper water, in the eastern Pacific is even more radiogenic, $^{187}\text{Os}/^{188}\text{Os} = 1.08 \pm 0.01$ (2,440 m, Chen and Sharma 2009) and 1.09 ± 0.02 (2,778 m, Woodhouse et al. 1999). While these studies suggest that the deep oceans do not have a homogeneous $^{187}\text{Os}/^{188}\text{Os}$ ratio, a lot more data from the deep oceans are needed to confirm this observation. The $^{187}\text{Os}/^{188}\text{Os}$ ratio of the waters from surface to a depth of about 1,000 m appears to be quite variable and always lower than the deep waters (Fig. 11.1b). Os isotopic composition of seawater is therefore not homogeneous. Chen et al. (2009) have surmised that the Os isotope composition of surface waters is impacted by recent anthropogenic Os contributions (see below). More detailed depth profiles are needed to confirm this behavior.

The Ir concentration ($=[\text{Ir}]$) in seawater varies from 0.1 to ~ 3.5 of fg/g (Table 11.2; Fig. 11.2), with the exception of a sample from the Pacific coast (Point Loma, San Diego, CA) that yielded $[\text{Ir}]$ of ~ 10 fg/g ($N = 6$, Fresco et al. 1985). Hodge et al. (1986) analyzed a sample from the Pier at Scripps Institution of Oceanography (La Jolla, CA) and found $[\text{Ir}]$ to be 1.3 fg/g ($N = 4$). Whether the observed large variations in the concentration are real or analytical issues is not clear as no cross-calibrations have been performed. Since the samples analyzed by the above two studies came from within a few km of each other a concentration difference of a factor of ~ 8 by natural variations is hard to imagine. To examine this issue further depth profiles from two more recent studies are plotted in Fig. 11.2. It is intriguing that seawater analyzed using RNAA (Arctic and Bering Sea,

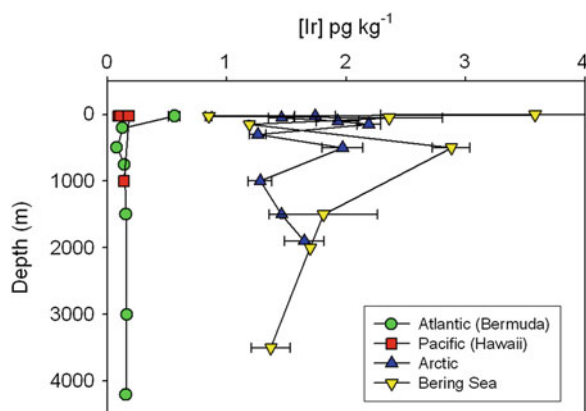


Fig. 11.2 Seawater profiles of Ir concentrations from the Atlantic, Pacific, Arctic and Bering Sea. The Ir concentrations from (a) the Atlantic and the Pacific Oceans were measured using negative thermal ionization mass spectrometry (Anbar et al. 1996, 1997) and (b) the Arctic Ocean and Bering Sea were measured using neutron activation analysis (Li et al. 2007)

$N = 17$) yields Ir concentrations that are, on average, ~ 1.8 fg/g and about ten times more than those obtained using isotope dilution (Pacific and Atlantic, $N = 11$). Since all of the analyzed samples come from open oceans the data indicate a large variability in the Ir concentration in different ocean basins. Alternatively, there are unresolved analytical issues with either or both techniques. These issues will need to be investigated in future. For the discussion below we will assume that the data are accurate.

Only three seawater samples from depths of 25, 500 and 3,000 m in the Sargasso Sea have been analyzed for both Os and Ir concentrations in the oceans (Os data: M. Sharma unpublished data; Ir data from Anbar et al. 1997). These yield Os/Ir ratios of 10, 81 and 41, respectively. The Os concentrations were analyzed by heating seawater with tracer and $\text{Cr}^{\text{IV}}\text{O}_3$ to 180°C for more than 40 h (see above). Since this method systematically underestimates Os concentration (Chen and Sharma 2009) it is possible to estimate the “true” Os/Ir ratios, which yields an average Os/Ir ratio of ~ 68 for the Sargasso Sea. An average Os/Ir ratio for the Arctic can also be estimated. Average Os concentration of four samples from the Arctic (86°N , 85°E , Edmonds et al. 2003) is ~ 7 fg/g (M. Sharma, unpublished data). Combined with Ir concentration data by Li et al. (2007) gives an Os/Ir ratio for the Arctic to be ~ 4 . This ratio is likely higher as the Os concentration data were obtained by heating the samples at 180°C instead

of 300°C . We estimate that the Os/Ir ratio of the Arctic Ocean is ~ 6 . The Os/Ir ratios in the seawater thus appear to be variable and remarkably fractionated, compared to the three main sources of these elements (continents, mantle and cosmic dust/meteoric smoke; Table 11.2). As discussed above, there is a large fractionation of Os and Ir between oxic and anoxic sediments, with Os/Ir ratio of anoxic sediments being much higher than the oxic sediments. Evidence of a recent (last 50 years) large-scale increase in reducing conditions has been found in all major Arctic Ocean basin sediments (Gobeil et al. 2001) suggesting that during this time the rainout rate of Ir in the Arctic has been significantly reduced. Moreover if there is reduction of oxidized sediments taking place, it would release Ir as shown by Colodner et al. (1992). That Os/Ir ratios are rather high in the oxic waters of the Sargasso Sea and low in the Arctic thus appears consistent with the fractionation observed in the sediments.

11.3.2.1 Mass Balance

Details of Os and Ir mass balances have been discussed in a number of papers (Os: Burton et al. 2010; Levasseur et al. 1999; Peucker-Ehrenbrink 2002; Peucker-Ehrenbrink and Ravizza 2000b; Sharma et al. 1997, 2007b, Ir: Anbar et al. 1996). The $^{187}\text{Os}/^{188}\text{Os}$ ratio of the deep oceans is thought to reflect a balance between inputs from the continents ($^{187}\text{Os}/^{188}\text{Os}$ ratio ~ 1.26) and from a combination of the mantle and cosmic sources ($^{187}\text{Os}/^{188}\text{Os}$ ratio ~ 0.13). Assuming that the $^{187}\text{Os}/^{188}\text{Os}$ ratio of the deep oceans is rather homogeneous ($=1.05$), the continents currently supply 81% of Os dissolved in the oceans. Using the available data that represent approximately 39% of the annual river flux, the estimated average riverine $[\text{Os}] = 8.5$ fg/g ($=45$ fmol/kg) and $^{187}\text{Os}/^{188}\text{Os} = 1.45$. Assuming that the estuaries trap about 15% of riverine Os (Turekian et al. 2007), we find that the rivers supply about 270 kg ($=1,423$ mol) of Os annually to the oceans. The groundwater and the continental mineral aerosol are also assumed to provide continental Os to the oceans. However, a recent study finds that the Os groundwater flux from Bangladesh delta is negligible (Paul et al. 2010). Approximately, 450×10^{12} g of continental mineral dust, which is generated primarily in the Sahara and Gobi

deserts, is deposited on the ocean surface (Jickells et al. 2005). Its dissolution in the waters is critical in providing essentially micro-nutrients (such as Fe) to the oceans. Assuming that the dust contains about 31 pg g^{-1} of Os, its *complete* dissolution would provide $\sim 5\%$ of riverine Os flux to the oceans. The leachable Os associated with continent-derived dust to the oceans would be smaller still (cf. Williams and Turekian 2004).

The isotope mass balance of the deep oceans dictates that 19% of Os must come from mantle and/or cosmic sources. The low and high temperature hydrothermal alteration, and cosmic dust/meteoric smoke have been postulated to provide Os to the oceans. Detailed studies of high and low temperature alteration along and away from the Juan de Fuca ridge have indicated a negligible mantle contribution via hydrothermal alteration of sea floor basalt (Sharma et al. 2000, 2007b). The extent to which dissolution of cosmic dust/meteoric smoke contributes Os to the seawater could be large but remains un-quantified (Sharma et al. 2007b). Additional sources of mantle derived Os include volcanic dust and submarine alteration of abyssal peridotites. Analyses of rain from around the world, however, indicate a large anthropogenic Os source and no (or negligible) input of volcanic Os to the oceans (Chen et al. 2009). Alteration of peridotites in the oceans could potentially deliver a large amount of mantle derived Os to the oceans, provided that Os is mobilized during the alteration (see Burton et al. 2010; Sharma et al. 2007b; Cave et al. 2003).

The mean residence time of Os in the oceans ($\bar{\tau}_{Os}^{SW}$) is given as: $\bar{\tau}_{Os}^{SW} = \frac{N_{Os}^{SW}}{(1-f_{Os}^E)(QC_{Os}^C/f_{Os}^C)}$ where N_{Os}^{SW} is the total amount of Os in the oceans ($=66 \times 10^6 \text{ mol}$), f_{Os}^E is the fraction of Os trapped in estuaries ($=0.15$), Q is the annual run-off ($=3.74 \times 10^{16} \text{ kg year}^{-1}$), C_{Os}^C is the average concentration of Os in rivers ($=45 \times 10^{-15} \text{ mol kg}^{-1}$) and $f_{Os}^C = 0.81$, is the fraction of continent-derived Os in the oceans. These yield a $\bar{\tau}_{Os}^{SW} = 37 \pm 14(2\sigma) \text{ kyr}$ (Sharma et al. 2007a). This is much longer than the ocean mixing time scale of $\sim 1,500$ years.

The $\bar{\tau}_{Os}^{SW}$ can also be estimated from the relaxation time, which can be determined from the recovery rate of $^{187}\text{Os}/^{188}\text{Os}$ ratio following an excursion. Excursions to lower $^{187}\text{Os}/^{188}\text{Os}$ ratios associated with glacial maxima have been observed in the rapidly

accumulating Fe-Mn sediments on the flanks of the East Pacific Rise (EPR) and in the anoxic sediments from the Cariaco Basin (Oxburgh 1998, 2001). They are also found in sub-oxic to anoxic sediments from the Santa Barbara Basin (Williams and Turekian 2002) and Japan Sea (Dalai et al. 2005). Finally, these excursions have been found in the planktic foraminifera recovered from ODP site 758 in the northern Indian Ocean (Burton et al. 2010). Excursions to lower $^{187}\text{Os}/^{188}\text{Os}$ ratios associated with glacial maxima followed by upswing to higher $^{187}\text{Os}/^{188}\text{Os}$ ratios during the interglacials were used to estimate $\bar{\tau}_{Os}^{SW}$. The estimated relaxation time for the EPR sediments = 8–12 kyr (Oxburgh 1998) and for the Cariaco Basin = 3–4 kyr (Oxburgh 2001). The $\bar{\tau}_{Os}^{SW}$ thus estimated is much less than that determined from mass balance considerations, However, not *all* high resolution Os records display the glacial-interglacial variations: no excursion in $^{187}\text{Os}/^{188}\text{Os}$ ratios has been observed in a deep sea core from the Cape Basin for the past 100,000 years (core: TNO57-21, Zylberberg et al. 2006), in sediments containing dominantly hydrogeneous Os from ODP Site 806 on the Ontong Java plateau (Dalai and Ravizza 2006), and in early Pleistocene sediments from ODP Site 849 in the eastern equatorial Pacific (Dalai and Ravizza 2010). These observations suggests that the observed glacial-interglacial variations in the marine Os isotope ratios are not global and that the residence times calculated using relaxation times likely reflect different rain-out rates of Os in different basins (see Sharma et al. 2007a).

All of the above-mentioned sources of Os could also be the sources for Ir. In addition, reduction of oxic sediments could also be a source of Ir. However, a detailed understanding of Ir budget in the oceans is not yet possible due to lack of data. Direct measurements of a relatively small river in Sweden (Kalixälven) that is unperturbed by human activities, transport of water through the Baltic Sea, the Ir concentration in the Pacific and Atlantic oceans and its burial in sediments have been used to obtain a rough picture of the Ir budget of the oceans (Anbar et al. 1996). Average Kalixälven concentration is 0.63 fg/g . Assuming this is the concentration in all the rivers gives an annual riverine input of $23.5 \text{ kg year}^{-1}$ ($=122 \text{ mol year}^{-1}$). Following analogy from the Baltic Sea about 75% of riverine Ir input gets trapped in the estuaries (Anbar et al. 1996). This indicates that the riverine input to the

deep oceans is only $\sim 5.9 \text{ kg year}^{-1}$. The Os/Ir ratio of this input is likely between 24 and 48. In comparison, the Ir input from cosmic dust/meteoritic smoke to the oceans is between 7 and 61 kg year^{-1} (Sharma et al. 2007b). The extent to which Ir from cosmic dust is dissolved in the oceans is unknown. Similarly, dissolution of continental mineral dust could supply up to 9.9 kg year^{-1} . The hydrothermal contribution of Ir is unknown and is likely small primarily due to removal by sulfide precipitation (see Sharma et al. 2001). The amount of Ir released due to reduction of oxic sediments is also unknown. Anbar et al. (1996) estimated lower and upper limits for the mean residence time of ($\text{Ir} = \bar{\tau}_{\text{Ir}}^{\text{SW}}$) in the oceans to be between 2,500 and 21,000 years.

Assuming that amount of Ir released due to reduction of oxic sediments is negligible we can estimate $\bar{\tau}_{\text{Ir}}^{\text{SW}}$ using $\bar{\tau}_{\text{Os}}^{\text{SW}}$ and Os/Ir ratios of the inputs and ocean. Defining $\rho^k = \left(\text{Ir}/^{188}\text{Os}\right)^k$ for the ratio of dissolved Ir and ^{188}Os provided by source “k”, the ratio of the residence times of Os and Ir in seawater (SW) can be given as (see Sharma et al. 1997):

$$\frac{\bar{\tau}_{\text{Os}}^{\text{SW}}}{\bar{\tau}_{\text{Ir}}^{\text{SW}}} = \frac{\rho^C}{\rho^{\text{SW}}} f_{^{188}\text{Os}}^C + \frac{\rho^H}{\rho^{\text{SW}}} f_{^{188}\text{Os}}^H + \frac{\rho^D}{\rho^{\text{SW}}} f_{^{188}\text{Os}}^D \quad (11.1)$$

where $f_{^{188}\text{Os}}^k$ denotes fractional contributions of ^{188}Os from continents (C), hydrothermal fluids (H), and cosmic dust/meteoritic smoke (D). As $\rho^H \approx \rho^D$, using the data given in Table 11.2 the above equation gives:

$\bar{\tau}_{\text{Ir}}^{\text{SW}} = \frac{\rho^{\text{SW}} \bar{\tau}_{\text{Os}}^{\text{SW}}}{f_{^{188}\text{Os}}^C \rho^C + 0.19} = \frac{0.124 \times (37,000 \pm 14,000)}{0.81 \rho^C + 0.19}$. Using the Os/Ir input of the riverine source to be either 24 or 48, we find that $9 \text{ kyr} < \bar{\tau}_{\text{Ir}}^{\text{SW}} < 14 \text{ kyr}$.

11.4 Applications

The primary environmental applications of Os and Ir arise from the fact that these elements are extremely rare on the surface of the earth and their introduction into the environment leads to an increase in their concentration in surface materials. In addition, a unique isotope fingerprint is present for Os introduced into the environment in that it comes from ores mined primarily in South Africa and Russia. The following are examples of environmental applications of Os and Ir.

11.4.1 Platinum Group Element Dispersal Due to Ore Processing and Use in Automobiles

As mentioned above, the PGEs are highly siderophile and therefore concentrated in sulfide ores. They are also quite abundant in chromite ores where they may exist as minerals (such as laurite, osmiridium, etc.). Industrial refining of ores to obtain PGEs and their usage in a wide variety of industrial, chemical, electrical and pharmaceutical applications has increased their burden on the environment. In particular, the production of Pt, Pd, and Rh, has increased exponentially over the last 40 years following the requirement in the US and other countries that all new automobiles have to be equipped with catalytic converters that reduce SO_2 , CO and NO_x emissions. There are over 500 million automobiles operating around the world and a majority of them has catalytic converters containing (depending on the make and size) 2–15 g of Pt and lesser amounts of Ru and Rh. The catalytic converters have a ceramic substrate with a honeycomb structure to permit the passage and reaction of exhaust gases with the PGEs that are impregnated on the honeycomb with the help of the washcoat, which is a highly porous alumina coating providing high surface area for the catalytic reactions. During the life-time of an automobile physical and chemical stresses on the catalytic converters cause small quantities of the PGEs, including Os, Ir, and Ru that are present as impurities, to emit together with particles from the washcoat. So while the urban air quality has substantially improved following the introduction of automobile catalytic converters, the PGE concentrations in the environment have also increased. Indeed several studies have documented elevated levels of PGEs in air, street dust, soil, vegetation, and organisms (see reviews by Ravindra et al. 2004 and Wiseman and Zereini 2009). In addition, snow from relatively pristine central Greenland has registered an increase in the PGE concentrations, which have been attributed to the large scale atmospheric contamination of these elements by catalytic converters (Barbante et al. 2001).

Osmium isotopes have been utilized to (a) track the dispersal of the PGEs associated with particulates and (b) assess dispersal of Os *itself* from either direct utilization of OsO_4 in a unique research application or indirect spreading of this compound due to industrial

processing and refining of PGE and other ores. Approximately 92% of the PGEs produced in the world come from the Merensky reef in South Africa and from the intrusions in the Noril'sk region, Russia (Jones 1999). The $^{187}\text{Os}/^{188}\text{Os}$ ratios of ores from these deposits lie between 0.15 and 0.20 (see references in Chen et al. 2009; Table 11.2). In comparison, the Os isotope ratios of dominant natural sources of Os on the earth surface are much more radiogenic: the average $^{187}\text{Os}/^{188}\text{Os}$ ratio of the continental mineral dust examined so far is 1.05 ± 0.23 (Esser and Turekian 1993b; Peucker-Ehrenbrink and Jahn 2001; Table 11.2). If the Os isotope composition (Γ) of a given environmental sample is assumed to be a binary mixture of a lithogenic and an anthropogenic end-member, fractional anthropogenic contribution of Os ($f_{\text{Os}}^{\text{Anthropogenic}}$) in the sample can be computed as follows:

$$f_{\text{Os}}^{\text{Anthropogenic}} = \frac{\Gamma_{\text{sample}} - \Gamma_{\text{lithogenic}}}{\Gamma_{\text{Anthropogenic}} - \Gamma_{\text{lithogenic}}}. \quad (11.2)$$

Moreover, assuming that the ratio of Os to other PGEs is similar to that in the continental mineral dust, fractional anthropogenic contribution of the PGEs ($f_{\text{Anthropogenic}}^{\text{PGE}}$) in the sample can also be estimated from:

$$f_{\text{Anthropogenic}}^{\text{PGE}} = 1 - \frac{[\text{PGE}]_{\text{UCC}} / [\text{PGE}]_{\text{Sample}}}{[\text{Os}]_{\text{UCC}} / [\text{Os}]_{\text{Sample}} (1 - f_{\text{Anthropogenic}}^{\text{Os}})}. \quad (11.3)$$

Here the subscript UCC = Upper Continental Crust. Utilizing this approach Rauch et al. (2004) analyzed a set of samples from an ombrotrophic peat bog (Thoreau's bog) in Concord, Massachusetts for Os, Ir, Pt, Pd, Rh, and Al concentrations and Os isotopes. The samples were dated using ^{210}Pb and were found to have accumulated from 1980 through 2002. Rauch et al. (2004) determined that in all samples the PGEs were enriched over those estimated from PGE/Al ratios and inferred that almost all (i.e., >99%) Pt, Pd, Rh, and Ir and ~94% of Os were of non-lithogenic origin. Assuming that non-lithogenic Os fraction in the peat samples was derived from catalytic converter

exhaust and rainwater and that the rain Os isotope composition was similar to that of the continental mineral dust or ocean (~1.05), Rauch et al. (2004) estimated that the anthropogenic and rainwater fractions represent, on average, 43 and 57% of non-lithogenic Os, respectively. That is, a total of 96.5% of Os (=94% + 43% of the remaining 6%) in Thoreau's bog was derived from catalytic exhaust and the rest from the rain.

A recent study, however, shows that the rainwater on the US eastern seaboard has an $^{187}\text{Os}/^{188}\text{Os}$ ratio of ~0.2 (Chen et al. 2009). Since the average $^{187}\text{Os}/^{188}\text{Os}$ ratio of the Thoreau's bog samples is ~0.6 an alternative explanation using (11.1) would be that only ~53% Os is rain and catalytic converter derived and the rest comes from lithogenic sources with an average $^{187}\text{Os}/^{188}\text{Os}$ ratio of 1.05. What fraction of rain and catalytic converter derived Os can be attributed to coming as particulates with Pt, Pd and Rh? It is likely negligible! This is because (1) Os is present only as an impurity in Pt, Pd and Rh and (2) under the oxidizing conditions present in a section of the catalytic converter Os would be lost as OsO_4 . It is therefore likely that that bulk of Os in Thoreau's bog comes from atmospheric precipitation and does not provide any insight into the concentration of Pt, Pd and Rh that are automobile exhaust derived. If true, (11.2) cannot be used as the source of anthropogenic Os in the sample is decoupled from that of the other PGEs.

The above interpretation is consistent with another study done by Rauch et al. (2005) where they analyzed Pt, Pd, Rh, and Os concentrations and Os isotope compositions in samples of 10 μm diameter airborne particles (PM_{10}) collected from various sites in the city of Boston. They found significant correlations between Pt, Pd and Rh concentrations that also showed no correlation with Os. In fact the Pt/Os ratio varies widely from 9 to 12,000 with a median of 1,000. The Os isotope compositions of all 28 samples analyzed are highly radiogenic ($^{187}\text{Os}/^{188}\text{Os} = 0.3\text{--}2.8$; median = 1.12). Intriguingly, there are four samples with Pt/Os ratios ranging from 9 to 40 that yield $^{187}\text{Os}/^{188}\text{Os}$ ratios with an average of 0.5 ± 0.2 (2σ , $N = 4$). Since the average Pt/Os ratio of PGE ores is about 50, such low Pt/Os ratios are not expected for the catalytic converters, which use purified Pt. The isotope ratio in these samples nonetheless indicates a source that is quite different from the lithogenic source. These observations suggest that catalytic converters

provide little Os to the PM₁₀ particles in Boston and possibly elsewhere. Nonetheless further studies are needed to evaluate the relationship between Pt, Pd, and Rh and Os isotopes for different size fractions in urban air.

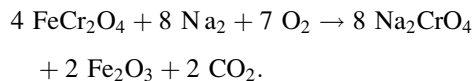
Attempts to use osmium isotopes in identifying and tracing anthropogenic Os pollution have been more successful. While examining the estuarine sediments of New Haven Harbor and the Long Island Sound (LIS) for Os Esser and Turekian (1993a) discovered that the top 15 cm of the sediments had Os isotope compositions that were identical to those of the ores from South Africa. They then traced the source of the anthropogenic Os to the New Haven sewage sludge and suggested that the primary source of anthropogenic Os was fixative solutions used to stain tissue for electron microscopy in medical laboratories. Williams et al. (1997) and Turekian et al. (2007) further extended this study to examine the anthropogenic Os from New York City medical facilities transported by the East River, which is the western source of water to the LIS. They found that there is a net transport of about 0.4–1 mol of anthropogenic Os per year from the East River into the LIS and that bulk of anthropogenic Os coming into the sound is retained there.

Studies in other estuaries have also been promising suggesting that osmium isotopes may track the influence of particle-borne contaminants, delivered by sewage, on sediments in estuarine environments. Ravizza and Bothner (1996) compared Os isotopes and Ag concentrations in sediments collected from Boston Harbor, Massachusetts Bay, and Cape Cod Bay and found that discharge of sewage into Boston Harbor has affected sediments in Cape Cod Bay, about 70 km away! Helz et al. (2000) examined sediments from a number of sites in the Chesapeake Bay region, including the sewage discharge sites from the city of Baltimore. They observed anthropogenic Os in sludge from the city's principal wastewater treatment plant and inferred it to be derived from medical facilities in the city. Baltimore was a major world supplier of chromium compounds and Isaac Tyson's Baltimore Chrome Works operated from 1827 through 1986. However, Helz et al. (2000) did not find any anthropogenic Os derived from processing of chromite ores to extract Cr. This is actually not an unexpected result as the first step in extraction of chromium from chromite involves high temperature oxidation of Cr^{III} to Cr^{VI}. This process would convert all Os present in the ore to

OsO₄, which would then be released in the air and transported to long distances (see below).

Helz et al. (2000) also found that a site in the mid-Chesapeake Bay region at a distance of >50 km from any known anthropogenic sources displays the strongest anthropogenic Os signal in their data set. They noted that the transport of particles to this site overrode the northward flowing bottom currents in the estuary and that finding anthropogenic Os at this site would suggest that other particle-borne substances, including hazardous ones, could be dispersed broadly in this estuary. Interestingly this site received anthropogenic Os as early as 1949. Could this come from chromium industry? A more detailed analysis of several sediment cores especially in the northern part of the Bay combined with an understanding of chromium production rates in Baltimore, past wind trajectories and also water circulation would be needed to assess the distribution of Os derived from roasting of chromite ores.

Osmium bearing PGE minerals and nuggets reside within chromites, which can have tens of ng of Os per g. Consideration of the primary reaction involved in the extraction of Cr from chromite ores (e.g., Burke et al. 1991) shows that it would also release OsO₄.



Here insoluble chromite (FeCr₂O₄) containing trivalent Cr is converted to water soluble sodium chromate (Na₂CrO₄) containing hexavalent Cr. To fully oxidize Cr(III) finely crushed chromite ore is mixed with soda ash and lime and roasted in rotary kilns at 1,100–1,150°C. The mix does not fuse but the molten soda ash reacts with the chromite to form sodium chromate. That chromite hosted Os minerals released as a result of the breakdown of the chromite lattice would also be attacked under highly oxidizing conditions and volatile OsO₄ produced has been indicated by recent experimental data from Yokoyama et al. (2010). Since the kiln does not trap evolving CO₂ it is likely that OsO₄ would be carried away with CO₂ escaping from the kiln.

In a pioneering study examining the Os isotopes in humus, plants, mushrooms, mosses and lichens as well as soils Rodushkin et al. (2007a, b) demonstrated the impact of OsO₄ transport to the region surrounding a

chromium producing plant. They found that mosses and lichens collected in rural northern Sweden had Os concentrations that were tenfold higher than those reported for particulate Os in dust samples from urban centers in the US. In addition, they also noted that from southwest to northeast transect of the sampling area along Sweden's eastern coastline the Os concentrations were increasing with decreasing $^{187}\text{Os}/^{188}\text{Os}$ ratios indicating a local anthropogenic source in the northeast. They were then able to trace the source to Kemi chromite ore, which is being processed to obtain chromium and ferrochromium in Torneå, Finland. From the data it appears that OsO_4 from Torneå smelter was transported to a distance of 100+ km southwest in Sweden. An important outcome of this study is the demonstration of the utility of using mosses and lichens in absorbing OsO_4 from the ambient atmosphere. Lichens have been used in the past to distinguish between local natural, local anthropogenic and background sources of lead (Simonetti et al. 2003). Their utilization to assess the extent of OsO_4 deposition in major urban centers should shed light on the issue of atmospheric Os loading from catalytic converters.

During the industrial processing and refining of sulfide ores of base metals (Cu, Ni, Pb, Zn) and PGE, OsO_4 is generated during the converting phase, where sulfur is removed as SO_2 by blasting hot air/oxygen through the molten (900–1,250°C) matte that contains mainly metal plus sulfur. The processing of sulfide ores would therefore constitute the single largest source of worldwide OsO_4 emission. However, environmental laws restricting the release of SO_2 from base metal smelters appear to have inadvertently eliminated a large fraction of OsO_4 from the environment (Chen et al. 2009). This is because a majority of nations requires that the base metal sulfide industry scrubs the SO_2 produced from exhaust stream. Scrubbing appears to nearly quantitatively remove OsO_4 (Abisheva et al. 2001). In the first stage of scrubbing the SO_2 is cleaned off any dust. Most of OsO_4 is trapped either by the wash sulfuric acid or the slime produced. Any remaining OsO_4 in the washed SO_2 is likely sequestered during subsequent treatments that attempt to recover sulfur as (1) sulfuric acid, (2) gypsum, (3) liquefied SO_2 , or (4) elemental sulfur.

High concentrations of SO_2 in the flue gas stream are needed to make sulfur recovery economically feasible, which is typically possible with modern arc

furnace technology used by base-metal industry (Goonan 2005). In contrast, the PGE ore processing facilities do not scrub SO_2 as its low concentration in furnace gases and intermittent production from the converter make scrubbing technically challenging and uneconomical. Instead the SO_2 is discharged into the atmosphere using tall stacks (Jones 1999). So it seems likely only PGE ore processing plants release OsO_4 into the environment. Indeed the Os isotope composition of snow and rain collected worldwide implicates OsO_4 released from PGE ore processing as providing the single largest Os burden to the atmosphere (Chen et al. 2009). Moreover, the deposition of anthropogenic Os over the last several decades has lowered the Os isotopic composition of oceans surface by about 10% compared to that of the deep oceans (Chen et al. 2009; Chen and Sharma 2009).

11.4.2 Distribution of Soot from Diesel Engines

This novel application uses Ir as an intentional tracer to track soot particles generated during burning of fossil fuel. Soot particles contain poly-aromatic hydrocarbons (PAH), which are known mutagenic and carcinogenic agents. Soot emissions from motor vehicles especially those employing diesel engines constitute the single largest source of PAHs in the US. The key issue then is the extent to which urban and surrounding rural areas are affected by such emissions. The answer depends on the aerodynamic size of the soot particles generated and its evolution with time. Since soot in a given location may be derived from multiple sources (power plants, cars and trucks, barbecues, etc.) the basic problem is how to trace soot from a given source. Iridium as an intentional particulate tracer was shown to be useful in studies of soot transport, deposition, and source attribution in two studies (Suarez et al. 1998; Wu et al. 1998). Advantage was taken of the fact an inexpensive commercially available Ir compound (2,4-pentanedionate containing 38.07% of Ir) is readily soluble in organic solvents (i.e., toluene) that in turn are miscible in diesel fuel.

In the first study, diesel fuel used by the sanitation trucks in the city of Baltimore was tagged with Ir^{III} octahedral pentanedionate dissolved in toluene

(Suarez et al. 1998). Size sorted aerosol samples were collected from several sites in the city and surrounding areas. Samples were also collected from a sanitation vehicle's tail-pipe. The samples were analyzed for Ir and Fe concentrations using neutron activation analysis. Iridium concentrations over the background and Iridium to iron ratios were used to assess the extent to which Ir introduced in the diesel fuel was associated with the soot particles. It was found that the tracer Ir concentration in the tail-pipe emission of single sanitation truck showed a skewed distribution with particle size, peaking between 0.1 and 0.2 μm – 50% of Ir was found to lie between 0.1 and 0.2 μm and the remainder on larger particles. The peak in Ir also corresponded to the peak in organic carbon confirming that Ir is a good surrogate for soot emitting from diesel engines. The Ir concentration – particle size distribution spectra for aerosol samples collected on days when the sanitation trucks were running was found to be distinctly different from that of the single truck and also from the background: a large proportion of Ir was found associated with 2.4 μm . The authors concluded that the ambient spectra probably reflected aerosol particle populations from a range of new and old diesel sanitation trucks operating over a wide range of on-road conditions.

In the second study another important question examined was that of the soot loading by public bus exhausts on school-going children who live in urban areas as opposed to those living in suburbs (Wu et al. 1998). Diesel supplies for the public buses in the city of Baltimore were spiked with Ir^{III} octahedral penta-nedionate dissolved in toluene and student exposure to soot emitted from the buses evaluated by analyzing Ir concentrations on the filters borne by individuals. It was found that the highest exposure of diesel soot occurred when an individual was getting on and off the vehicle. However, the Ir data demonstrate that the public bus derived soot contributed only 2–10% of the total carbon exposure to an individual.

11.5 Future Directions

These are exciting times to understand environmental transport of Os and Ir. Improvements in clean laboratory chemistry and measurement techniques are opening new avenues to examine increasingly lower level samples for Os and Ir concentrations and Os isotope composition. Although much has been learned at the

observational level about the dispersal of Os and Ir, many unsolved problems exist and much remains to be discovered. First of all the natural distributions of Os and Ir especially their mass balances in modern oceans need to be worked out in detail. In spite of the mostly phenomenological studies to date, there remains a dearth of information about fundamental mechanisms underlying the transport of Os and Ir nature and in environment. The basic issue of whether Ir isotopes fractionate should be resolved with the help of modern mass spectrometry. A lot more work is also needed to assess the atmospheric burden of Os from base-metal sulfide smelting beginning from the industrial revolution to about 1980s when modern SO_2 scrubbing techniques began to be employed. Utilization of the PGEs is expected to continue to increase through this century and consequently the environmental burden of Os and Ir is also slated to rise. The processes that make these elements bioavailable and the extent to which they are toxic to life are topics of immediate importance (e.g., Ravindra et al. 2004; Smith et al. 1974; Wiseman and Zereini 2009). For example, recent work with rats shows that ingestion of soluble Ir could impact immune system (Iavicoli et al. 2010). Perhaps the biggest unknown in the assessment of transport and bioavailability of anthropogenic Os and Ir is the extent to which these elements occur as nanoparticles in automobile exhausts. It will be important in future studies to seek answers to the following questions related to environmental dispersal of the PGE:

1. How are Pt, Pd and Rh dispersals from catalytic converters related to the distributions of anthropogenic Ir and Os? In particular, analysis of size-segregated aerosol samples collected from major urban areas would be useful and so would be the data obtained directly from automobile exhausts.
2. What is the residence time of Os in the atmosphere? What are the scavenging mechanisms that remove Os from the atmosphere? Of interest here would be to investigate the observed/inferred differences between the path lengths of OsO_4 emitted by chromite smelters and PGE-ore processing plants.
3. What is the role of local sources in impacting the Os isotope composition of snow and rain?
4. Beginning from the industrial revolution what was the impact of the base metal sulfide ore refining on the atmospheric burden of the atmosphere? Both ice-core records and ombrotrophic peat records will be useful to address this question.

Acknowledgements I would like to thank Mark Baskaran for inviting me to write this review. I gratefully acknowledge reviews from Karl Turekian, Mark Baskaran, and an anonymous reviewer that led to considerable improvement of this paper. Over the years I have benefited from discussions with several individuals on various aspects of the geochemistry of Ir and Os. These span from professors, when I was a graduate student and a post doc, to my own graduate students and fellow researchers in the field. I would like to thank them all for generously giving me insights into this fascinating field, and into the art of making and evaluating the challenging measurements involved. I am especially grateful to Ariel Anbar, Gerhard Brueggemann, Cynthia Chen, Udo Fehn, Dimitri Papanastassiou, Bernhard Peucker-Ehrenbrink, Matthieu Roy-Barman, Mark Rehkamper, Karl Turekian, Rich Walker, and G.J. Wasserburg.

References

- Abisheva ZS, Zagorognyaya AN, Bukurov TN (2001) Recovery of radiogenic osmium-187 from sulfide copper ores in Kazakhstan. *Platinum Met Rev* 45:132–135
- Ahmed AH, Arai S (2002) Unexpectedly high-PGE chromitite from the deeper mantle section of the northern Oman ophiolite and its tectonic implications. *Contrib Mineralog Petrol* 143:263–278
- Ahmed AH, Arai S, Abdel-Aziz YM et al (2009) Platinum-group elements distribution and spinel composition in podiform chromitites and associated rocks from the upper mantle section of the neoproterozoic Bou Azzer ophiolite, Anti-Atlas, Morocco. *J Afr Earth Sci* 55:92–104
- Alvarez LW, Alvarez W, Asaro F et al (1980) Extraterrestrial cause for the Cretaceous-tertiary extinction – experimental results and theoretical interpretation. *Science* 208:1095–1108
- Anbar AD (1996) I. Rhenium and Iridium in natural waters. II. Methyl bromide: ocean sources, ocean sinks, and climate sensitivity. III. CO₂ stability and heterogeneous chemistry in the atmosphere of Mars. Division of Geological and Planetary Sciences, California Institute of Technology, Pasadena
- Anbar AD, Wasserburg GJ, Papanastassiou DA et al (1996) Iridium in natural waters. *Science* 273:1524–1528
- Anbar AD, Papanastassiou DA, Wasserburg GJ (1997) Determination of iridium in natural waters by clean chemical extraction and negative thermal ionization mass spectrometry. *Anal Chem* 69:2444–2450
- Barbante C, Veysseyre A, Ferrari C et al (2001) Greenland snow evidence of large scale atmospheric contamination for platinum, palladium, and rhodium. *Environ Sci Technol* 35:835–839
- Barefoot RR, Van Loon JC (1999) Recent advances in the determination of the platinum group elements and gold. *Talanta* 49:1–14
- Barker JL, Anders E (1968) Accretion rate of cosmic matter from iridium and osmium contents of deep-sea sediments. *Geochim Cosmochim Acta* 32:627
- Bate GL, Huizenga JR (1963) Abundances of ruthenium, osmium and uranium in some cosmic and terrestrial sources. *Geochim Cosmochim Acta* 27:345–360
- Birck JL, Roy Barman M, Capmas F (1997) Re-Os isotopic measurements at the femtomole level in natural samples. *Geostandards News* 20:19–27
- Büchl A, Brugmann G, Batanova VG (2004) Formation of podiform chromitite deposits: Implications from PGE abundances and Os isotopic compositions of chromites from the Troodos complex, Cyprus. *Chem Geol* 208:217–232
- Burke T, Fagliano J, Goldoft M et al (1991) Chromite ore processing residue in Hudson County, New-Jersey. *Environ Health Perspect* 92:131–137
- Burton KW, Gannoun A, Parkinson IJ (2010) Climate driven glacial-interglacial variations in the osmium isotope composition of seawater recorded by planktic foraminifera. *Earth Planet Sci Lett* 295:58–68
- Byrne RH (2002) Inorganic speciation of dissolved elements in seawater: the influence of pH on concentration ratios. *Geochem Trans* 3:11–16
- Cave RR, Ravizza GE, German CR et al. (2003) Deposition of osmium and other platinum-group elements beneath the ultramafic-hosted rainbow hydrothermal plume. *Earth Planet Sci Lett* 210:65–79
- Chen C, Sharma M (2009) High precision and high sensitivity measurements of osmium in seawater. *Anal Chem* 81:5400–5406
- Chen C, Taylor S, Sharma M (2005) Iron and osmium isotopes from stony micrometeorites and implications for the Os budget of the ocean. In: Lunar planetary science conference XXXVI. LPI, Houston
- Chen C, Sharma M, Bostick BC (2006) Lithologic controls on osmium isotopes in the rio orinoco. *Earth Planet Sci Lett* 252:138–151
- Chen C, Sedwick PN, Sharma M (2009) Anthropogenic osmium in rain and snow reveals global-scale atmospheric contamination. *Proc Natl Acad Sci U S A* 106:7724–7728
- Clayton DD (1964) Cosmoradiogenic chronologies of nucleosynthesis. *Astrophys J* 139:637–663
- Cohen AS, Waters FG (1996) Separation of osmium from geological materials by solvent extraction for analysis by thermal ionisation mass spectrometry. *Anal Chim Acta* 332:269–275
- Colodner DC, Boyle EA, Edmond JM et al (1992) Postdepositional mobility of platinum, iridium and rhenium in marine-sediments. *Nature* 358:402–404
- Colodner DC, Boyle EA, Edmond JM (1993) Determination of rhenium and platinum in natural-waters and sediments, and iridium in sediments by flow-injection isotope-dilution inductively coupled plasma-mass spectrometry. *Anal Chem* 65:1419–1425
- Cook DL, Walker RJ, Horan MF et al (2004) Pt-Re-Os systematics of group IIAB and IIIAB iron meteorites. *Geochim Cosmochim Acta* 68:1413–1431
- Creaser RA, Papanastassiou DA, Wasserburg GJ (1991) Negative thermal ion mass-spectrometry of osmium, rhenium, and iridium. *Geochim Cosmochim Acta* 55:397–401
- Dalai TK, Ravizza G (2006) Evaluation of osmium isotopes and iridium as paleoflux tracers in pelagic carbonates. *Geochim Cosmochim Acta* 70:3928–3942
- Dalai TK, Ravizza G (2010) Investigation of an early Pleistocene marine osmium isotope record from the eastern equatorial Pacific. *Geochim Cosmochim Acta* 74:4332–4345
- Dalai TK, Suzuki K, Minagawa M et al (2005) Variations in seawater osmium isotope composition since the last glacial

- maximum: a case study from the Japan Sea. *Chem Geol* 220:303–314
- Dalai TK, Ravizza GE, Peucker-Ehrenbrink B (2006) The late Eocene Os-187/Os-188 excursion: chemostratigraphy, cosmic dust flux and the early Oligocene glaciation. *Earth Planet Sci Lett* 241:477–492
- Date AR, Davis AE, Cheung YY (1987) The potential of fire assay and inductively coupled plasma source-mass spectrometry for the determination of platinum group elements in geological-materials. *Analyst* 112:1217–1222
- Economou-Eliopoulos M (1996) Platinum-group element distribution in chromite ores from ophiolite complexes: implications for their exploration. *Ore Geol Rev* 11:363–381
- Edmonds HN, Michael PJ, Baker ET et al (2003) Discovery of abundant hydrothermal venting on the ultraslow-spreading Gakkel Ridge in the Arctic. *Nature* 421:252–256
- Enzweiler J, Potts PJ, Jarvis KE (1995) Determination of platinum, palladium, ruthenium and iridium in geological samples by isotope-dilution inductively-coupled plasma-mass spectrometry using a sodium peroxide fusion and tellurium coprecipitation. *Analyst* 120:1391–1396
- Esser BK, Turekian KK (1988) Accretion rate of extraterrestrial particles determined from osmium isotope systematics of pacific pelagic clay and manganese nodules. *Geochim Cosmochim Acta* 52:1383–1388
- Esser BK, Turekian KK (1993a) Anthropogenic osmium in coastal deposits. *Environ Sci Technol* 27:2719–2724
- Esser BK, Turekian KK (1993b) The osmium isotopic composition of the continental-crust. *Geochim Cosmochim Acta* 57:3093–3104
- Fehn U, Teng R, Elmoro D et al (1986) Isotopic composition of osmium in terrestrial samples determined by accelerator mass-spectrometry. *Nature* 323:707–710
- Frei R, Frei KM (2002) A multi-isotopic and trace element investigation of the cretaceous-tertiary boundary layer at Stevns Klint, Denmark – inferences for the origin and nature of siderophile and lithophile element geochemical anomalies. *Earth Planet Sci Lett* 203:691–708
- Fresco J, Weiss HV, Phillips RB et al (1985) Iridium in seawater. *Talanta* 32:830–831
- Gabrielli P, Barbante C, Plane JMC et al (2004a) Meteoric smoke fallout over the Holocene epoch revealed by iridium and platinum in Greenland ice. *Nature* 432:1011–1014
- Gabrielli P, Varga A, Barbante C et al (2004b) Determination of Ir and Pt down to the sub-femtogram per gram level in polar ice by ICP-SFMS using preconcentration and a desolvation system (vol 19, pg 831, 2004). *J Anal At Spectrom* 19: 831–837
- Gabrielli P, Plane JMC, Boutron CF et al (2006) A climatic control on the accretion of meteoric and super-chondritic iridium-platinum to the Antarctic ice cap. *Earth Planet Sci Lett* 250:459–469
- Gabrielli P, Barbante C, Plane JMC et al (2008) Siderophile metal fallout to Greenland from the 1991 winter eruption of Hekla (Iceland) and during the global atmospheric perturbation of Pinatubo. *Chem Geol* 255:78–86
- Gannoun A, Burton KW, Vigier N et al (2006) The influence of weathering process on riverine osmium isotopes in a basaltic terrain. *Earth Planet Sci Lett* 243:732–748
- Gelin A, Kring DA, Zurcher L et al (2004) Osmium isotope constraints on the proportion of bolide component in Chicxulub impact melt rocks. *Meteorit Planet Sci* 39:1003–1008
- Gobeil C, Sundby B, Macdonald RW et al (2001) Recent change in organic carbon flux to arctic ocean deep basins: evidence from acid volatile sulfide, manganese and rhenium discord in sediments. *Geophys Res Lett* 28:1743–1746
- Goonan TG (2005) Flows of selected materials associated with world copper smelting. In: USGS Open-File Report 2004-1395, Reston
- Gordon GW, Rockman M, Turekian KK et al (2009) Osmium isotopic evidence against an impact at the Frasnian-Famennian boundary. *Am J Sci* 309:420–430
- Gregoire DC (1988) Determination of platinum, palladium, ruthenium and iridium geological-materials by inductively coupled plasma mass-spectrometry with sample introduction by electrothermal vaporization. *J Anal At Spectrom* 3: 309–314
- Gros M, Lorand JP, Luguet A (2002) Analysis of platinum group elements and gold in geological materials using NiS fire assay and Te coprecipitation; the NiS dissolution step revisited. *Chem Geol* 185:179–190
- Hassler DR, Peucker-Ehrenbrink B, Ravizza GE (2000) Rapid determination of Os isotopic composition by sparging OsO₄ into a magnetic-sector icp-ms. *Chem Geol* 166:1–14
- Heller-Zeisler SF, Borgoul PV, Moore RR et al (2000) Comparison of INAA and RNAA methods with thermal-ionization mass spectrometry for iridium determinations in atmospheric tracer studies. *J Radioanal Nucl Chem* 244: 93–96
- Helz GR, Adelson JM, Miller CV et al (2000) Osmium isotopes demonstrate distal transport of contaminated sediments in Chesapeake Bay. *Environ Sci Technol* 34:2528–2534
- Herr W, Hoffmeister W, Hirt B et al (1961) Versuch zur datierung von eisenmeteoriten nach der rhenium-osmium-methode. *Z Naturforsch* 16:1053–1058
- Hintenberger H, Herr W, Voshage H (1954) Radiogenic osmium from rhenium-containing molybdenite. *Phys Rev* 95: 1690–1691
- Hodge V, Stallard M, Koide M et al (1986) Determination of platinum and iridium in marine waters, sediments, and organisms. *Anal Chem* 58:616–620
- Hoffman EL, Naldrett AJ, Vanloon JC et al (1978) Determination of all platinum group elements and gold in rocks and ore by neutron-activation analysis after preconcentration by a nickel sulfide fire-assay technique on large samples. *Anal Chim Acta* 102:157–166
- Horan MF, Walker RJ, Morgan JW et al (2003) Highly siderophile elements in chondrites. *Chem Geol* 196:5–20
- Iavicoli I, Carelli G, Bocca B et al (2008) Environmental and biological monitoring of iridium in the city of Rome. *Chemosphere* 71:568–573
- Iavicoli I, Fontana L, Marinaccio A et al (2010) Iridium alters immune balance between T helper 1 and T helper 2 responses. *Hum Exp Toxicol* 29:213–219
- Jackson SE, Fryer BJ, Gosse W et al (1990) Determination of the precious metals in geological-materials by inductively coupled plasma mass-spectrometry (ICP-MS) with nickel sulfide fire-assay collection and tellurium coprecipitation. *Chem Geol* 83:119–132

- Jiang SY, Yang JH, Ling HF et al (2007) Extreme enrichment of polymetallic Ni-Mo-PGE-Au in lower Cambrian black shales of south China: an Os isotope and PGE geochemical investigation. *Palaeogeogr Palaeoclimatol Palaeoecol* 254: 217–228
- Jickells TD, An ZS, Andersen KK et al (2005) Global iron connections between desert dust, ocean biogeochemistry, and climate. *Science* 308:67–71
- Jones RT (1999) Platinum smelting in South Africa. *S Afr J Sci* 95:525–534
- Karner DB, Levine J, Muller RA et al (2003) Extraterrestrial accretion from the GISP2 ice core. *Geochim Cosmochim Acta* 67:751–763
- Keays RR, Ganapath R, Laul JC et al (1974) Simultaneous determination of 20 trace-elements in terrestrial, lunar and meteoritic material by radio-chemical neutron-activation analysis. *Anal Chim Acta* 72:1–29
- Koerberl C, Shirey SB (1993) Detection of a meteoritic component in Ivory-Coast tektites with Rhenium-Osmium isotopes. *Science* 261:595–598
- Koerberl C, Shirey SB (1997) Re-Os isotope systematics as a diagnostic tool for the study of impact craters and distal ejecta. *Palaeogeogr Palaeoclimatol Palaeoecol* 132:25–46
- Koerberl C, Reimold WU, Shirey SB (1994a) Saltpan impact crater, South-Africa – geochemistry of target rocks, breccias, and impact glasses, and osmium isotope systematics. *Geochim Cosmochim Acta* 58:2893–2910
- Koerberl C, Reimold WU, Shirey SB et al (1994b) Kalkkop crater, Cape Province, South-Africa – confirmation of impact origin using osmium isotope systematics. *Geochim Cosmochim Acta* 58:1229–1234
- Koerberl C, Sharpton VL, Schuraytz BC et al (1994c) Evidence for a meteoritic component in impact melt rock from the Chicxulub structure. *Geochim Cosmochim Acta* 58: 1679–1684
- Koerberl C, Farley KA, Peucker-Ehrenbrink B et al (2004) Geochemistry of the end-permian extinction event in Austria and Italy: no evidence for an extraterrestrial component. *Geology* 32:1053–1056
- Koide M, Goldberg ED, Niemeyer S et al (1991) Osmium in marine-sediments. *Geochim Cosmochim Acta* 55: 1641–1648
- Koide M, Goldberg ED, Walker R (1996) The analysis of seawater osmium. *Deep Sea Res II* 43:53–55
- Kyte FT, Wasson JT (1986) Accretion rate of extraterrestrial matter – iridium deposited 33 to 67 million years ago. *Science* 232:1225–1229
- Lal D, Jull AJT (2003) Extra-terrestrial influx rates of cosmogenic isotopes and platinum group elements: realizable geochemical effects. *Geochim Cosmochim Acta* 67:4925–4933
- Lee CTA, Wasserburg GJ, Kyte FT (2003) Platinum-group elements (PGE) and rhenium in marine sediments across the cretaceous-tertiary boundary: constraints on Re-PGE transport in the marine environment. *Geochim Cosmochim Acta* 67:655–670
- Lee SR, Horton JW, Walker RJ (2006) Confirmation of a meteoritic component in impact-melt rocks of the Chesapeake Bay impact structure, Virginia, USA – evidence from osmium isotopic and PGE systematics. *Meteorit Planet Sci* 41:819–833
- Levasseur S, Birck JL, Allegre CJ (1998) Direct measurement of femtomoles of osmium and the Os-187/Os-186 ratio in seawater. *Science* 282:272–274
- Levasseur S, Birck JL, Allegre CJ (1999) The osmium riverine flux and the oceanic mass balance of osmium. *Earth Planet Sci Lett* 174:7–23
- Li SH, Chai ZF, Mao XY (2007) Iridium in the Bering Sea and Arctic Ocean studied by neutron activation analysis. *J Radioanal Nucl Chem* 271:125–128
- Love SG, Brownlee DE (1993) A direct measurement of the terrestrial mass accretion rate of cosmic dust. *Science* 262:550–553
- Luck JM, Allegre CJ (1983) Re-187-Os-187 systematics in meteorites and cosmochemical consequences. *Nature* 302: 130–132
- Luck JM, Turekian KK (1983) Os-187/Os-186 in manganese nodules and the cretaceous-tertiary boundary. *Science* 222:613–615
- Marcantonio F, Turekian KK, Higgins S et al (1999) The accretion rate of extraterrestrial He-3 based on oceanic Th-230 flux and the relation to Os isotope variation over the past 200,000 years in an Indian ocean core. *Earth Planet Sci Lett* 170:157–168
- Martin JM, Meybeck M (1979) Elemental mass-balance of material carried by major world rivers. *Mar Chem* 7: 173–206
- Martin CE, Peucker-Ehrenbrink B, Brunskill G et al (2001) Osmium isotope geochemistry of a tropical estuary. *Geochim Cosmochim Acta* 65:3193–3200
- McDaniel DK, Walker RJ, Hemming SR et al (2004) Sources of osmium to the modern oceans: new evidence from the Pt-190-Os-186 system. *Geochim Cosmochim Acta* 68: 1243–1252
- McDonald I, Peucker-Ehrenbrink B, Coney L et al (2007) Search for a meteoritic component in drill cores from the Bosumtwi impact structure, Ghana: platinum group element contents and osmium isotopic characteristics. *Meteorit Planet Sci* 42:743–753
- McDonough WF, Sun S-S (1995) Composition of the earth. *Chem Geol* 120:223–253
- Meisel T, Moser J (2004) Reference materials for geochemical PGE analysis: new analytical data for Ru, Rh, Pd, Os, Ir, Pt and Re by isotope dilution ICP-MS in 11 geological reference materials. *Chem Geol* 208:319–338
- Meisel T, Krahenbuhl U, Nazarov MA (1995) Combined osmium and strontium isotopic study of the cretaceous-tertiary boundary at Sumbar, Turkmenistan – a test for an impact vs a volcanic hypothesis. *Geology* 23: 313–316
- Meisel T, Walker RJ, Morgan JW (1996) The osmium isotopic composition of the earth's primitive upper mantle. *Nature* 383:517–520
- Michel HV, Alvarez LW (1990) Geochemical studies of the cretaceous-tertiary boundary in ODP holes 689b and 690c. In: Scientific results, Proceedings of the ocean drilling program. *Scientific Results, Proc Ocean Drill Prog* 113:159–168
- Morcelli CPR, Figueiredo AMG (2000) Determination of iridium at sub ng levels in geological materials by RNAA. *J Radioanal Nucl Chem* 244:619–621

- Morgan JW (1965) Simultaneous determination of rhenium and osmium in rocks by neutron activation analysis. *Anal Chim Acta* 32:8
- Naldrett AJ (2004) Magmatic sulfide deposits. Springer, Berlin, p 727
- Nogueira CA, Figueiredo AMG (1995) Determination of platinum, palladium, iridium and gold in selected geological reference materials by radiochemical neutron-activation analysis – comparison of procedures based on aqua regia leaching and sodium peroxide sintering. *Analyst* 120: 1441–1443
- Oxburgh R (1998) Variations in the osmium isotope composition of sea-water over the past 200,000 years. *Earth Planet Sci Lett* 159:183–191
- Oxburgh R (2001) Residence time of osmium in the oceans. *Geochem Geophys Geosyst* 2:2000GC000104
- Oxburgh R, Pierson-Wickmann AC, Reisberg L et al (2007) Climate-correlated variations in seawater Os-187/Os-188 over the past 200,000 yr: evidence from the Cariaco basin, Venezuela. *Earth Planet Sci Lett* 263:246–258
- Palmer MR, Turekian KK (1986) Os-187/Os-186 in marine manganese nodules and the constraints on the crustal geochemistries of rhenium and osmium. *Nature* 319: 216–220
- Palmer MR, Falkner KK, Turekian KK et al (1988) Sources of osmium isotopes in manganese nodules. *Geochim Cosmochim Acta* 52:1197–1202
- Paquay FS, Ravizza GE, Dalai TK et al (2008) Determining chondritic impactor size from the marine osmium isotope record. *Science* 320:214–218
- Paquay FS, Goderis S, Ravizza G et al (2009) Absence of geochemical evidence for an impact event at the Bolling-Allerød/Younger Dryas transition. *Proc Natl Acad Sci U S A* 106:21505–21510
- Pasava J (1993) Anoxic sediments an important environment for PGE; an overview. *Ore Geol Rev* 8:425–445
- Pattou L, Lorand JP, Gros M (1996) Non-chondritic platinum-group element ratios in the earth's mantle. *Nature* 379:712–715
- Paul M, Reisberg L, Vigier N (2009) A new method for analysis of osmium isotopes and concentrations in surface and subsurface water samples. *Chem Geol* 258:136–144
- Paul M, Reisberg L, Vigier N et al (2010) Dissolved osmium in Bengal plain groundwater: implications for the marine Os budget. *Geochim Cosmochim Acta* 74:3432–3448
- Pearson DG, Woodland SJ (2000) Solvent extraction/anion exchange separation and determination of PGEs (Os, Ir, Pt, Pd, Ru) and Re-Os isotopes in geological samples by isotope dilution ICP-MS. *Chem Geol* 165:87–107
- Pedersen RB, Johannesen GM, Boyd R (1993) Stratiform platinum-group element mineralizations in the ultramafic cumulates of the Leka ophiolite complex, central Norway. *Econ Geol Bull Soc Econ Geol* 88:782–803
- Pegram WJ, Turekian KK (1999) The osmium isotopic composition change of Cenozoic sea water as inferred from a deep-sea core corrected for meteoritic contributions. *Geochim Cosmochim Acta* 63:4053–4058
- Pegram WJ, Krishnaswami S, Ravizza GE et al (1992) The record of sea-water Os-187/Os-186 variation through the Cenozoic. *Earth Planet Sci Lett* 113:569–576
- Peucker-Ehrenbrink B (1996) Accretion of extraterrestrial matter during the last 80-million-years and. *Geochim Cosmochim Acta* 60:3187–3196
- Peucker-Ehrenbrink B (2002) Comment on “residence time of osmium in the oceans” by Rachel Oxburgh. *Geochem Geophys Geosyst* 3:1
- Peucker-Ehrenbrink B, Jahn BM (2001) Rhenium-osmium isotope systematics and platinum group element concentrations: loess and the upper continental crust. *Geochem Geophys Geosyst* 2:26
- Peucker-Ehrenbrink B, Ravizza G (2000a) The effects of sampling artifacts on cosmic dust flux estimates: a reevaluation of nonvolatile tracers (Os, Ir). *Geochim Cosmochim Acta* 64:1965–1970
- Peucker-Ehrenbrink B, Ravizza G (2000b) The marine osmium isotope record. *Terra Nova* 12:205–219
- Peucker-Ehrenbrink B, Ravizza G, Hofmann AW (1995) The marine Os-187/Os-186 record of the past 80-million years. *Earth Planet Sci Lett* 130:155–167
- Plessen HG, Erzinger J (1998) Determination of the platinum-group elements and gold in twenty rock reference materials by inductively coupled plasma-mass spectrometry (ICP-MS) after pre-concentration by nickel sulfide fire assay. *Geostandards News* 22:187–194
- Poirier A, Gariepy C (2005) Isotopic signature and impact of car catalysts on the anthropogenic osmium budget. *Environ Sci Technol* 39:4431–4434
- Prichard HM, Lord RA (1993) An overview of the PGE concentrations in the Shetland ophiolite complex. In: Prichard HM, Alabaster T, Harris NBW, Neary CR (eds) *Magmatic processes and plate tectonics*, vol 76. Geological Society, London
- Prichard HM, Neary CR, Fisher PC et al (2008) PGE-rich podiform chromitites in the Al'ays ophiolite complex, Saudi Arabia: an example of critical mantle melting to extract and concentrate PGE. *Econ Geol* 103:1507–1529
- Puchtel IS, Walker RJ, Brandon AD et al (2009) Pt-Re-Os and Sm-Nd isotope and HSE and REE systematics of the 2.7 Ga Belingwe and Abitibi komatiites. *Geochim Cosmochim Acta* 73:6367–6389
- Rauch S, Hemond HF, Peucker-Ehrenbrink B (2004) Source characterisation of atmospheric platinum group element deposition into an ombrotrophic peat bog. *J Environ Monit* 6:335–343
- Rauch S, Hemond HF, Peucker-Ehrenbrink B et al (2005) Platinum group element concentrations and osmium isotopic composition in urban airborne particles from Boston. *Massachusetts Environ Sci Technol* 39:9464–9470
- Rauch S, Peucker-Ehrenbrink B, Molina LT et al (2006) Platinum group elements in airborne particles in Mexico city. *Environ Sci Technol* 40:7554–7560
- Rauch S, Peucker-Ehrenbrink B, Kylander ME et al (2010) Anthropogenic forcings on the surficial osmium cycle. *Environ Sci Technol* 44:881–887
- Ravindra K, Bencs L, Van Grieken R (2004) Platinum group elements in the environment and their health risk. *Sci Total Environ* 318:1–43
- Ravizza GE, Bothner MH (1996) Osmium isotopes and silver as tracers of anthropogenic metals in sediments from Massachusetts and Cape Cod Bays. *Geochim Cosmochim Acta* 60:2753–2763

- Ravizza G, Dalai TK (2006) The potential of Ir and Os isotopes as point paleoflux tracers. *Geochim Cosmochim Acta* 70:A520
- Ravizza G, Peucker-Ehrenbrink B (2003) Chemostratigraphic evidence of Deccan volcanism from the marine osmium isotope record. *Science* 302:1392–1395
- Ravizza G, Pyle D (1997) PGE and Os isotopic analyses of single sample aliquots with NiS fire assay preconcentration. *Chem Geol* 141:251–268
- Rehkamper M, Halliday AN (1997) Development and application of new ion-exchange techniques for the separation of the platinum group and other siderophile elements from geological samples. *Talanta* 44:663–672
- Rehkamper M, Halliday AN, Wentz RF (1998) Low-blank digestion of geological samples for platinum-group element analysis using a modified carius tube design. *Fresenius J Anal Chem* 361:217–219
- Reisberg L, Meisel T (2002) The Re-Os isotopic system: a review of analytical techniques. *Geostandards News* 26:249–267
- Robinson N, Ravizza G, Coccioni R et al (2009) A high-resolution marine Os-187/Os-188 record for the late Maastrichtian: distinguishing the chemical fingerprints of Deccan volcanism and the K-Pg impact event. *Earth Planet Sci Lett* 281:159–168
- Rodushkin I, Engstrom E, Sorlin D et al (2007a) Osmium in environmental samples from northeast Sweden. Part II. Identification of anthropogenic sources. *Sci Total Environ* 386:159–168
- Rodushkin I, Engstrom E, Sorlin D et al (2007b) Osmium. In environmental samples from northeast Sweden – part I. Evaluation of background status. *Sci Total Environ* 386:145–158
- Russ GP, Bazan JM (1987a) Isotopic ratio measurements with an inductively coupled plasma source-mass spectrometer. *Spectrochim Acta B* 42:49–62
- Russ GP, Bazan JM (1987b) Osmium isotopic ratio measurements by inductively coupled plasma source-mass spectrometry. *Anal Chem* 59:984–989
- Schmitz B, Tassinari M, Peucker-Ehrenbrink B (2001) A rain of ordinary chondritic meteorites in the early Ordovician. *Earth Planet Sci Lett* 194:1–15
- Sengupta JG, Gregoire DC (1989) Determination of ruthenium, palladium and iridium in 27 international reference silicate and iron-formation rocks, ores and related materials by isotope-dilution inductively-coupled plasma mass-spectrometry. *Geostandards News* 13:197–204
- Sharma M, Wasserburg GJ (1997) Osmium in the rivers. *Geochim Cosmochim Acta* 61:5411–5416
- Sharma M, Papanastassiou DA, Wasserburg GJ (1997) The concentration and isotopic composition of osmium in the oceans. *Geochim Cosmochim Acta* 61:3287–3299
- Sharma M, Wasserburg GJ, Hofmann AW et al (1999) Himalayan uplift and osmium isotopes in oceans and rivers. *Geochim Cosmochim Acta* 63:4005–4012
- Sharma M, Wasserburg GJ, Hofmann AW et al (2000) Osmium isotopes in hydrothermal fluids from the Juan de Fuca ridge. *Earth Planet Sci Lett* 179:139–152
- Sharma M, Polizzotto M, Anbar AD (2001) Iron isotopes in hot springs along the Juan de Fuca ridge. *Earth Planet Sci Lett* 194:39–51
- Sharma M, Balakrishna K, Hofmann AW et al (2007a) The transport of osmium and strontium isotopes through a tropical estuary. *Geochim Cosmochim Acta* 71:4856–4867
- Sharma M, Rosenberg EJ, Butterfield DA (2007b) Search for the proverbial mantle osmium sources to the oceans: hydrothermal alteration of mid-ocean ridge basalt. *Geochim Cosmochim Acta* 71:4655–4667
- Shen JJ, Papanastassiou DA, Wasserburg GJ (1996) Precise Re-Os determinations and systematics of iron meteorites. *Geochim Cosmochim Acta* 60:2887–2900
- Shinotsuka K, Suzuki K (2007) Simultaneous determination of platinum group elements and rhenium in rock samples using isotope dilution inductively coupled plasma mass spectrometry after cation exchange separation followed by solvent extraction. *Anal Chim Acta* 603:129–139
- Shirey SB, Walker RJ (1995) Carius tube digestion for low-blank rhenium-osmium analysis. *Anal Chem* 67:2136–2141
- Shirey SB, Walker RJ (1998) The Re-Os isotope system in cosmochemistry and high-temperature geochemistry. *Annu Rev Earth Planet Sci* 26:423–500
- Simonetti A, Garipey C, Carignan J (2003) Tracing sources of atmospheric pollution in western Canada using the Pb isotopic composition and heavy metal abundances of epiphytic lichens. *Atmospheric Environment* 37:2853–2865
- Smith IC, Carson BL, Ferguson TL (1974) Osmium: an appraisal of environmental exposure. *Environ Health Perspect* 8:201–213
- Sotnikov VI, Berzina AN, Economou-Eliopoulos M et al (2001) Palladium, platinum and gold distribution in porphyry Cu +/- Mo deposits of Russia and Mongolia. *Ore Geol Rev* 18:95–111
- Stein HJ, Hannah JL, Zimmerman A et al. (2004) A 2.5 Ga porphyry Cu-Mo-Au deposit at Malanjkhand, central India: Implications for late Archean continental assembly. *Precambrian Research* 134:189–226
- Suarez AE, Caffrey PF, Borgoul PV et al (1998) Use of an iridium tracer to determine the size distribution of aerosol emitted from a fleet of diesel sanitation trucks. *Environ Sci Technol* 32:1522–1529
- Suzuki T, Miyada M, Ohta K et al (1998) Determination of osmium in waste water by graphite furnace atomic absorption spectrometry. *Mikrochim Acta* 129:259–263
- Tanaka N, Oura Y, Ebihara M (2008) Determination of iridium and gold in rock samples by using pre-concentration neutron activation analysis. *J Radioanal Nucl Chem* 278:603–606
- Teng RTD, Fehn U, Elmore D et al (1987) Determination of Os isotopes and Re/Os ratios using AMS. *Nucl Instrum Meth Phys Res B* 29:281–285
- Truran JW (1998) The age of the universe from nuclear chronometers. *Proc Natl Acad Sci U S A* 95:18–21
- Turekian KK, Luck JM (1984) Estimation of continental Os-187/Os-186 values by using Os-187/Os-186 and Nd-143/Nd-144 ratios in marine manganese nodules. *Proc Natl Acad Sci U S A Phys Sci* 81:8032–8034
- Turekian KK, Sharma M, Gordon GW (2007) The behavior of natural and anthropogenic osmium in the Hudson river-Long Island Sound estuarine system. *Geochim Cosmochim Acta* 71:4135–4140
- Volkening J, Walczyk T, Heumann KG (1991) Osmium isotope ratio determinations by negative thermal ionization mass-spectrometry. *Int J Mass Spectrom Ion Process* 105:147–159

- Walczyk T, Heumann KG (1993) Iridium isotope ratio measurements by negative thermal ionization mass-spectrometry and atomic-weight of iridium. *Int J Mass Spectrom Ion Process* 123:139–147
- Walker RJ (1988) Low-blank chemical-separation of rhenium and osmium from gram quantities of silicate rock for measurement by resonance ionization mass-spectrometry. *Anal Chem* 60:1231–1234
- Walker RJ (2009) Highly siderophile elements in the Earth, Moon and Mars: update and implications for planetary accretion and differentiation. *Chem Erde Geochem* 69:101–125
- Walker RJ, Fassett JD (1986) Isotopic measurement of subnanogram quantities of rhenium and osmium by resonance ionization mass-spectrometry. *Anal Chem* 58:2923–2927
- Walker RJ, Morgan JW, Beary ES et al (1997) Applications of the Pt-190-Os-186 isotope system to geochemistry and cosmochemistry. *Geochim Cosmochim Acta* 61:4799–4807
- Walker RJ, Horan MF, Morgan JW et al (2002a) Comparative Re-187-Os-187 systematics of chondrites: implications regarding early solar system processes. *Geochim Cosmochim Acta* 66:4187–4201
- Walker RJ, Prichard HM, Ishiwatari A et al (2002b) The osmium isotopic composition of convecting upper mantle deduced from ophiolite chromites. *Geochim Cosmochim Acta* 66:329–345
- Walker RJ, McDonough WF, Honesto J et al (2008) Modeling fractional crystallization of group IVB iron meteorites. *Geochim Cosmochim Acta* 72:2198–2216
- Williams GA, Turekian KK (2002) Atmospheric supply of osmium to the oceans. *Geochim Cosmochim Acta* 66:3789–3791
- Williams GA, Turekian KK (2004) The glacial-interglacial variation of seawater osmium isotopes as recorded in Santa Barbara basin. *Earth Planet Sci Lett* 228:379–389
- Williams G, Marcantonio F, Turekian KK (1997) The behavior of natural and anthropogenic osmium in long island sound, an urban estuary in the eastern US. *Earth Planet Sci Lett* 148:341–347
- Wiseman CLS, Zereini F (2009) Airborne particulate matter, platinum group elements and human health: a review of recent evidence. *Sci Total Environ* 407:2493–2500
- Woodhouse OB, Ravizza G, Kenison-Falkner K et al (1999) Osmium in seawater: vertical profiles of concentration and isotopic composition in the eastern Pacific Ocean. *Earth Planet Sci Lett* 173:223–233
- Wu CC, Suarez AE, Lin ZB et al (1998) Application of an Ir tracer to determine soot exposure to students commuting to school on Baltimore public buses. *Atmos Environ* 32:1911–1919
- Yamashita Y, Takahashi Y, Haba H et al (2007) Comparison of reductive accumulation of Re and Os in seawater – sediment systems. *Geochim Cosmochim Acta* 71:3458–3475
- Yang G, Hannah JL, Zimmerman A et al. (2009) Re-Os depositional age for Archean carbonaceous slates from the southwestern superior province: Challenges and insights. *Earth Planet Sci Lett* 280:83–92
- Yi YV, Masuda A (1996a) Isotopic homogenization of iridium for high sensitivity determination by isotope dilution inductively coupled plasma mass spectrometry. *Anal Sci* 12:7–12
- Yi YV, Masuda A (1996b) Simultaneous determination of ruthenium, palladium, iridium, and platinum at ultratrace levels by isotope dilution inductively coupled plasma mass spectrometry in geological samples. *Anal Chem* 68:1444–1450
- Yokoyama T, Alexander CMO, Walker RJ (2010) Osmium isotope anomalies in chondrites: results for acid residues and related leachates. *Earth Planet Sci Lett* 291:48–59
- Zaccarini F, Pushkarev EV, Fershtater GB et al (2004) Composition and mineralogy of PGE -rich chromitites in the Nurali lherzolite-gabbro complex, southern Urals, Russia. *Can Mineralog* 42:545–562
- Zylberberg DR, Goldstein SL, Sharma M (2006) A 100ky record of the osmium isotopic composition of seawater. In: *Eos transactions*, vol 87(52), Fall meeting supplement, American Geophysical Union

Chapter 12

Applications of Stable Mercury Isotopes to Biogeochemistry

Joel D. Blum

Abstract The application of mercury (Hg) stable isotopes to problems in environmental chemistry is relatively new, but is a rapidly expanding field of investigation. Interest in this isotope system has been stimulated by concerns regarding the global distribution of mercury, its tendency to be methylated and bioaccumulated in the environment, and the severe health affects associated with this toxic metal. Mercury displays mass-dependent isotope fractionation during most biotic and abiotic chemical transformations. Additionally, mercury displays mass-independent fractionation, mainly during photochemical radical pair reactions, wherein the reactivity of odd and even mass number isotopes differs. The combination of mass-dependent and mass-independent fractionation provides a new and much needed probe into the reaction pathways and history of mercury in biogeochemical systems, and also provides an isotopic fingerprint of various mercury sources to the environment.

12.1 Introduction

Mercury is a geochemically unique element that has attracted a large amount of research interest because it is globally distributed and forms methylmercury (MeHg), which is a potent neurotoxin, in the environment. Once formed, MeHg is highly bioaccumulative and poses a significant health risk to humans and to a wide variety of wildlife. The speciation of Hg in the environment is controlled by microbial activity, dark

abiotic reactions, and photochemical reactions. Hg speciation dramatically affects its mobility, which ranges from stable solid phases (e.g., HgS) to a globally distributed atmospheric gas [Hg(0)]. Speciation also strongly affects Hg toxicity and bioaccumulation, which are greatly enhanced when Hg is in the methylated form (e.g., Morel et al. 1998).

Mercury biogeochemistry is of great importance in both atmospheric and aqueous systems. It is estimated that present-day anthropogenic atmospheric emissions of Hg are about 3 times higher than natural emissions (Mason et al. 1994). Anthropogenic emissions are dominated by coal combustion, cement production and waste incineration, whereas primary natural emissions are dominated by volcanic and hydrothermal systems (US EPA 1997). There is also a growing amount of previously deposited natural and anthropogenically-derived Hg that can be re-emitted due to biomass burning and reduction to Hg(0) in both aquatic and terrestrial systems (Gustin et al. 2008).

Details of the speciation of Hg in the atmosphere are not well known, but Hg speciation is generally reported as three operationally defined forms: gaseous elemental mercury [Hg(0)_{gas}], reactive gaseous mercury [Hg(II)_{gas}] and particulate mercury [Hg(II)_{part}]. Hg(0)_{gas} has a relatively long atmospheric residence time of ~1 year, but once it is photochemically oxidized to Hg(II)_{gas} it becomes extremely reactive and is rapidly deposited in precipitation or attached to particles and deposited as Hg(II)_{part} (Schroeder and Munthe 1998). Hg is distributed and deposited globally even to remote and otherwise pristine areas including the Arctic (e.g., Lindberg et al. 2002; Douglas et al. 2008).

In aqueous solutions Hg can exist in the reduced form as dissolved Hg(0)_{aq}, or in the oxidized Hg(II) and MeHg(II) forms associated with a wide range of dissolved inorganic and organic ligands and with

J.D. Blum (✉)
Department of Geological Sciences, University of Michigan,
1100 North University Avenue, Ann Arbor, MI 48109, USA
e-mail: jdblum@umich.edu

particle surfaces. Microbial, photochemical, and dark abiotic reactions are known to reduce Hg(II) in solution to Hg(0)_{aq}. In reducing environments some sulfate and iron-reducing bacteria can methylate Hg(II) to MeHg. Microbial and photochemical processes can also degrade MeHg back to Hg(II) or Hg(0)_{aq} (e.g., Fitzgerald and Lamborg 2003). Once it is produced, MeHg can enter both aquatic and terrestrial foodwebs. It is strongly bio-accumulated and can reach toxic levels in piscivorous fish, mammals and birds as well as insectivorous birds (Evers et al. 2007). The main pathway for human mercury exposure is through the consumption of piscivorous marine and fresh water fish (Sunderland 2007). To present a graphical picture of environmental Hg isotope fractionations associated with transitions in Hg speciation, several of these transitions are shown as a flow-chart in Fig. 12.1. The small but rapidly growing literature on Hg isotope fractionation along these pathways is keyed to the diagram and will be discussed below.

Mercury has seven stable isotopes with the following approximate abundances for the National Institute of Standards and Technology (NIST) Standard Reference Material (SRM)-3133: ¹⁹⁶Hg = 0.155%, ¹⁹⁸Hg = 10.04%, ¹⁹⁹Hg = 16.94%, ²⁰⁰Hg = 23.14%, ²⁰¹Hg = 13.17%, ²⁰²Hg = 29.73%, ²⁰⁴Hg = 6.83% (Blum and Bergquist 2007; Fig. 12.2a). These abundances are referenced to the certified ²⁰⁵Tl/²⁰³Tl ratio of 2.38714 for the NIST SRM-997 because absolute abundances for the Hg isotopes in NIST SRM-3133 have not been accurately determined. Institute for National Measurement Standards of the National Research Council Canada reference material NIMS-1 was recently certified for isotopic abundances at nearly indistinguishable values to those reported above (Meija et al. 2010). Because ¹⁹⁶Hg has a very low abundance and ²⁰⁴Hg suffers from an isobaric interference with ²⁰⁴Pb, the ²⁰²Hg/¹⁹⁸Hg ratio is used to describe mass-dependent stable isotope fractionation (MDF) relative to the NIST SRM-3133. Hg isotopic compositions relative to NIST SRM-3133 are reported as:

$$\delta^{xxx}\text{Hg}(\text{‰}) = \left\{ \left[\frac{(^{xxx}\text{Hg}/^{198}\text{Hg})_{\text{unknown}}}{(^{xxx}\text{Hg}/^{198}\text{Hg})_{\text{SRM3133}}} - 1 \right] \times 1,000 \right\}$$

Mass-independent isotope fractionation (MIF) has also been observed for the odd isotopes of Hg and is reported as $\Delta^{199}\text{Hg}$ and $\Delta^{201}\text{Hg}$. These values are the differences between the measured $\delta^{199}\text{Hg}$ and $\delta^{201}\text{Hg}$

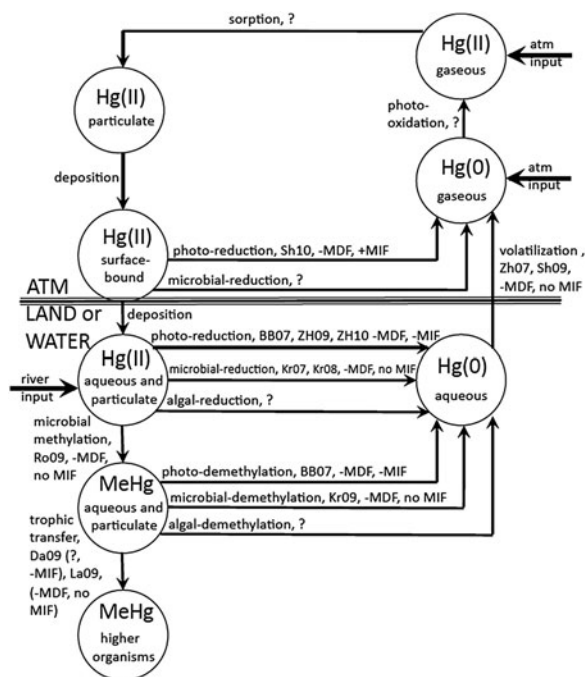


Fig. 12.1 Flow-chart showing some of the major biogeochemical transformations of Hg speciation in the environment and their associated Hg isotope fractionations. Atmospheric and riverine inputs of Hg to the global biogeochemical system are shown as *input arrows*. For those transformations where experimental fractionation studies have been carried out, the positive (+) or negative (–) mass dependent (MDF) and mass independent (MIF) fractionation of the product relative to the reactant is indicated. References to the publications relevant to each transformation are also given with the following abbreviations: BB07 = Bergquist and Blum (2007); Da09 = Das et al. (2009); Kr07,08,09 = Kritee et al. (2007, 2008, 2009); La09 = Laffont et al. (2009); Ro09 = Rodriguez-Gonzalez et al. (2009); Sh09,10 = Sherman et al. (2009, 2010); Zh07 = Zheng et al. (2007); ZH09,10 = Zheng and Hintelmann (2009, 2010b)

values and those predicted based on the measured $\delta^{202}\text{Hg}$ and the kinetic mass-dependent fractionation law derived from transition state theory. For variations of less than ~10‰, these values were approximated by Blum and Bergquist (2007) to be:

$$\Delta^{199}\text{Hg} = \delta^{199}\text{Hg} - (\delta^{202}\text{Hg} \times 0.2520)$$

$$\Delta^{200}\text{Hg} = \delta^{200}\text{Hg} - (\delta^{202}\text{Hg} \times 0.5024)$$

$$\Delta^{201}\text{Hg} = \delta^{201}\text{Hg} - (\delta^{202}\text{Hg} \times 0.7520)$$

$$\Delta^{204}\text{Hg} = \delta^{204}\text{Hg} - (\delta^{202}\text{Hg} \times 1.493)$$

The magnitude of mass-dependent and mass-independent fractionation will be described in this

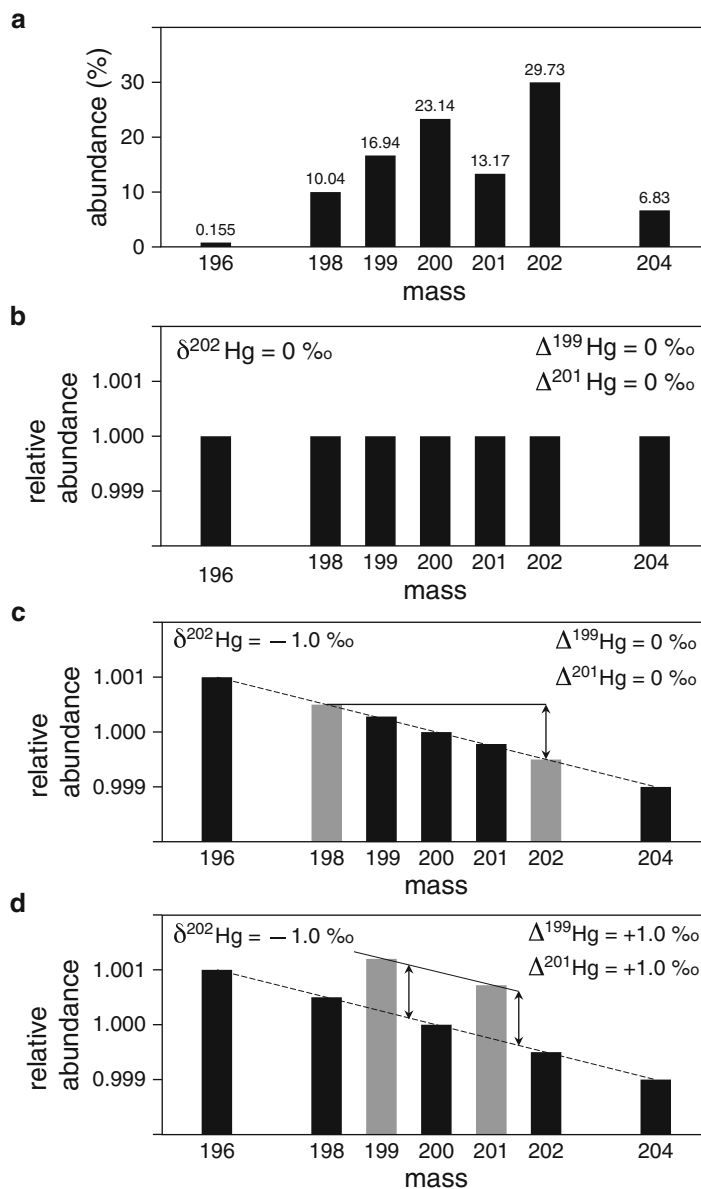


Fig. 12.2 Schematic diagrams illustrating (a) the average abundance of the Hg isotopes, (b) the abundance of the Hg isotopes relative to a standard reference material with no frac-

tionation, (c) with negative mass-dependent fractionation, and (d) with negative mass-dependent and positive mass-independent fractionation

chapter primarily with $\delta^{202}\text{Hg}$ and $\Delta^{201}\text{Hg}$ (Fig. 12.2b–d). In addition to variations in the magnitude of these isotope ratios, trends in the ratios of the isotope ratios have been shown to be diagnostic of certain chemical transformation mechanisms (Bergquist and Blum 2007). The most diagnostic “ratio of ratios” that have been described in the literature are the $\Delta^{199}\text{Hg}/\Delta^{201}\text{Hg}$ and $\Delta^{201}\text{Hg}/\delta^{202}\text{Hg}$ ratios and these will be discussed extensively below.

12.2 Materials and Methods

12.2.1 Sampling and Sample Size

The unusual chemistry of mercury and the low concentration of this element in many environmental samples of interest necessitates special attention to sampling protocols. Sampling must be done under

trace metal clean conditions and sample bottles must be acid leached in a multi-step cleaning procedure (e.g., Johnson et al. 2008). Unlike other trace metal clean preparations, to obtain low Hg blank levels, it is necessary to leach materials in the strong oxidant BrCl rather than just HCl and HNO₃. Sample sizes needed for Hg isotopic analysis scale with concentration, which can vary by over eight orders of magnitude in environmental samples. The total amount of Hg that is needed for a high-precision isotope measurement varies according to specific sample introduction systems and mass spectrometer sensitivities. Nevertheless the range typically quoted is 10 and 20 ng. With smaller amounts of Hg than 10–20 ng the precision of isotope ratio measurements can be considerably compromised.

12.2.2 Pre-Treatment

A variety of sample preservation protocols are needed and these differ depending on the material that is sampled. In general, solid samples such as rock and sediment can be stored at room temperature in clean plastic or glass containers. Vegetation, fish tissues and other organic samples should be stored in clean plastic or glass containers and either kept frozen or freeze-dried and refrigerated. Water samples require the most specialized attention and must be stored in either glass, Teflon or fluorinated polyethylene bottles. Traditional polyethylene and polypropylene bottles used for other trace elements are much more porous to Hg(0)_{vapor} than Teflon or fluorinated polyethylene bottles and storage of water samples in these containers can result in Hg loss from the sample or gain from the ambient atmosphere. Depending on what fraction of Hg in water is of interest to a particular study, water samples are often filtered prior to further treatment. Samples are then acidified and oxidized typically with 1% BrCl to keep Hg stable in solution as Hg(II). Trace-metal clean reagents must be purged with Hg-free N or Ar to achieve the lowest Hg blank levels.

For the highest precision isotope analyses Hg should be quantitatively separated from samples and concentrated to produce ~4 g of a solution with ~4 ng/g Hg(II) for analysis by mass spectrometry. Liquid samples can be reduced with SnCl₂ and the produced Hg(0) can be sparged into an oxidizing solu-

tion of KMnO₄ or amalgamated onto gold by passing it through a gold-coated bead trap. Solid samples can be digested in acids and then diluted as long as Hg is kept fully oxidized in solution to avoid loss of Hg as Hg(0). Alternatively, solid samples can be combusted in a two-stage furnace to fully volatilize Hg as Hg(0) (Smith et al 2005; Biswas et al 2008) and the Hg(0) can be collected by bubbling into an oxidizing solution of KMnO₄ or by amalgamation onto gold. Hg(II) in KMnO₄ or diluted acidic solutions can then be reduced with SnCl₂, sparged from solution and bubbled into a smaller volume of KMnO₄ solution to purify and concentrate the Hg. Similarly, gold traps can be slowly heated in a flow of Hg-free N or Ar and bubbled into KMnO₄ solution to yield a solution of ~4 ng/g Hg. It is essential to measure the yield of the Hg extraction and concentration procedure for each sample, because incomplete yield (<90%) can produce significant levels of mass-dependent Hg isotope fractionation.

12.2.3 Instrument Used for Analyses

High precision stable Hg isotope analysis of environmental samples was made possible by two developments. The first was the advent of multiple collector inductively coupled plasma mass spectrometry (MC-ICP-MS) and the second was the development of continuous flow cold vapor introduction systems for MC-ICP-MS. The first study to combine these features and obtain high precision isotope ratios was Lauretta et al. (2001), who used a continuous flow cold vapor generator (CFCVG; Klaue and Blum 1999) fed directly into a VG P-54 MC-ICP-MS. Evans et al (2001), Hintelmann and Ogrinc (2003), Hintelmann and Lu (2003), Xie et al. (2005), Krupp and Donard (2005), Epov et al. (2008) and Sonke et al. (2008) developed methods for measurement of transient signals on MC-ICP-MS but the precision of this approach has not attained the level of performance of CFCVG. Jackson et al. (2004) coupled CFCVG to a Finnigan Neptune MC-ICP-MS but lacked optimal correction for instrumental mass bias. The continuous flow method was adapted to the Nu-Plasma MC-ICP-MS (e.g., Smith et al. 2005; Bergquist and Blum 2007) and the Thermo Neptune MC-ICP-MS (e.g., Foucher and Hintelmann 2006; Zheng et al. 2007; Zambardi et al. 2009; Estrade et al. 2010) with optimal mass bias

correction to achieve the current high precision capabilities of the method.

12.2.4 Detection Limit, Precision and Accuracy of the Method

The accuracy of Hg isotope ratio measurement is optimized by measuring isotope ratios relative to a standard reference material, which is analyzed before and after each unknown sample. Sample-standard bracketing alone can achieve good mass bias correction, but for the most precise Hg isotope measurements Tl is introduced to the Hg vapor stream as a dry aerosol and the $^{205}\text{Tl}/^{203}\text{Tl}$ ratio of NIST SRM-997 is first used for mass bias correction of the Hg isotope ratios, followed by sample-standard bracketing. The optimal conditions for analysis include complete separation of Hg from sample matrix, analysis of bracketing standards at the same concentration and in the same matrix solution as samples, careful monitoring of background signals, and performance of on-peak blank corrections. Under these conditions analytical precision of $\pm 0.08\text{‰}$ (2SD) for $\delta^{202}\text{Hg}$ and $\pm 0.05\text{‰}$ (2SD) for $\Delta^{201}\text{Hg}$ and $\Delta^{199}\text{Hg}$ are achievable (e.g., Blum and Bergquist 2007).

12.3 Discussion and Applications

The environmental isotope geochemistry of Hg is a topic of widespread interest because Hg contamination is globally pervasive and found in virtually all ecosystems and their various components. The integration of Hg isotopes into Hg research is in its earliest stages, but is growing at a very rapid rate. Published studies generally fall into one or more of the following three categories: (1) laboratory experimental studies to measure Hg isotope fractionation during biotic and abiotic chemical transformations of Hg, (2) measurements of Hg isotopic compositions in the environment to gain insight into biogeochemical transformations that are occurring or (3) measurements of Hg isotopic compositions in the environment and their use to fingerprint Hg sources. For the purpose of organizing this chapter I will discuss the published literature on experimental investigations first and then delve into applications of

Hg isotopes to provide insight into environmental processes and sources of environmental Hg contamination. Like any rapidly developing field there are numerous meeting abstracts with important developments appearing on a monthly basis. In this review I have restricted discussion to only peer-reviewed articles published in research journals. I have also focused this review on applications of Hg isotope measurements to environmental problems rather than on the physical chemistry of Hg isotope fractionation or the characterization of geological reservoirs for Hg isotopes. These topics were recently reviewed by Bergquist and Blum (2009). In an attempt to organize the growing and somewhat complex literature on experimental Hg fractionation studies I have summarized study results that are relevant to environmental systems on a diagram showing important biogeochemical transformation of Hg in the atmosphere, on land and in aquatic systems (Fig. 12.1).

12.3.1 Experimental Studies

12.3.1.1 Mechanisms of Hg Isotope Fractionation

The environmental isotope geochemistry of Hg is a very rich topic owing to the widespread occurrence of both MDF and MIF. MDF is fractionation of isotopes in proportion to the differences in the masses of the isotopes and this has been observed to occur for Hg in most equilibrium and kinetic processes that have been studied. MIF is fractionation of isotopes that is not in proportion to the differences in the masses of the isotopes and MIF of Hg appears to be associated with two different mechanisms, the nuclear volume effect (NVE) and the magnetic isotope effect (MIE). The nuclear volume effect is an isotope fractionation caused because nuclear volume and nuclear charge radius do not scale linearly with mass. This isotope effect has been predicted by quantum mechanical calculations (Schauble 2007) and was recently observed in laboratory experiments (Estrade et al. 2009; Zheng and Hintelmann 2010a). The magnitude of the observed MIF due to the NVE is generally quite small ($< 0.2\text{‰}$ for $\Delta^{199}\text{Hg}$ and $\Delta^{201}\text{Hg}$) and results in $\Delta^{199}\text{Hg}/\Delta^{201}\text{Hg}$ ratios of $\sim 1.5\text{--}2$ (Estrade et al. 2009; Zheng and Hintelmann 2010a). The MIE is

a kinetic fractionation that appears to occur primarily during photochemical radical pair reactions (e.g., Buchachenko 2009). The magnetic spin of the odd isotopes enhances triplet to singlet and singlet to triplet intersystem crossing. As a result, reaction products can be either enriched or depleted in the odd isotopes of Hg depending on whether singlet or triplet radical pairs are produced photochemically. In laboratory experiments with natural sunlight, photochemical reduction/degradation of Hg(II) and MeHg in aqueous solution with natural DOC have been shown to produce reduced Hg reaction products with depletions of odd isotopes (–MIF; Bergquist and Blum 2007) whereas photochemical reduction of Hg-halogen compounds in snow have been shown to produce reduced Hg with enrichments of odd isotopes (+MIF; Sherman et al. 2010).

12.3.1.2 Biotic Experiments

Experimental studies of fractionation by higher organisms have not yet been performed, but experimental investigations have been carried out to quantify fractionation factors for some of the most important microbially mediated Hg transformations. Kritee et al. (2007, 2008, 2009) determined fractionation factors for Hg transformations mediated by organisms that express the mer-A and mer-B enzymes that reduce Hg(II) and demethylate MeHg, respectively. In both cases the Hg(0) that was produced had lower $\delta^{202}\text{Hg}$ than the starting Hg(II) or MeHg. Fractionation factors varied depending on the organisms, temperature, growth rate, and other experimental conditions. In no case did any of the microbial experiments produce detectable levels of MIF. A recent study of fermentative methylation by a sulphate reducing bacteria (Rodriguez-Gonzalez et al. 2009) showed that the MeHg product had lower $\delta^{202}\text{Hg}$ than the Hg(II) starting material (–MDF) and also found no evidence for biotic MIF during methylation.

12.3.1.3 Abiotic Experiments

The first abiotic Hg isotope fractionation experiments used natural sunlight to reduce Hg(II) and MeHg from aqueous solutions in the presence of DOC in the form of Suwannee River fulvic acid (Bergquist and Blum

2007). These experiments were, however, carried out at Hg/DOC ratios much higher than those observed in natural waters. The product, Hg(0), was found to have lower $\delta^{202}\text{Hg}$ than the reactant (–MDF), as in the case of microbial reduction, but unlike microbial reduction it was also depleted in the odd isotopes of Hg (–MIF). The isotopic trends with increasing amounts of reduction were different for Hg(II) reduction vs. MeHg reduction. The ratio of MDF/MIF ($\Delta^{201}\text{Hg}/\delta^{202}\text{Hg}$) was ~1.5 for Hg(II) reduction and ~3.0 for MeHg reduction. Additionally, the $\Delta^{199}\text{Hg}/\Delta^{201}\text{Hg}$ ratio was 1.00 for Hg(II) reduction and 1.36 for MeHg reduction (Bergquist and Blum 2007). Yang and Sturgeon (2009) studied Hg(II) photoreduction using formic acid and a UV light-source and observed –MDF but did not observe significant MIF. The experimental conditions were quite different, but the specific factor(s) responsible for the lack of MIF during this study is not clear.

Photoreduction of Hg(II) was explored in detail in a series of laboratory experiments that tested the importance of the Hg/DOC ratio and the effect of different ligands on Hg isotope fractionation (Zheng and Hintelmann 2009, 2010b). The experiments of Zheng and Hintelmann (2009) differed from those of Bergquist and Blum (2007) in several ways, including the use of a filtered Xe lamp instead of natural sunlight, the use of natural lake water as the source of DOC, and the use of a range of Hg/DOC ratios that approached values found in natural systems. These experiments showed –MDF and –MIF, but also demonstrated a range of $\Delta^{199}\text{Hg}/\Delta^{201}\text{Hg}$ ratios from 1.31 at high Hg/DOC, to a lower value of 1.19 at lower and more realistic values of Hg/DOC. The authors suggested that this range represented differing behavior of Hg bonded predominantly to reduced sulfur groups at low Hg/DOC and to oxygen groups at higher Hg/DOC.

Zheng and Hintelmann (2010b) expanded upon earlier work by studying fractionation during photochemical reduction of Hg(II) by individual low molecular weight organic acids that either contained, or did not contain, reduced sulfur groups. When reduced sulfur groups (e.g., cysteine) were present the authors observed fractionation similar to that observed using natural DOC (–MDF and –MIF). However, in the absence of reduced sulfur groups (e.g., serine) the reduction products were enriched in odd isotopes (+MIF), suggesting that opposite magnetic isotope

effects were operating. This +MIF behavior is similar to that observed during the photochemical reduction of Hg(II) associated with halogens in Arctic snow (Sherman et al. 2010, see below).

Based on studies of Hg isotopes in natural hydrothermal systems, Smith et al. (2005) and Sherman et al. (2009) suggested that aqueous Hg(0) released from hydrothermal solutions would have lower $\delta^{202}\text{Hg}$ than Hg in solution (−MDF). This was demonstrated experimentally and quantified by Zheng et al. (2007) who showed that Hg(0) volatilization from an aqueous phase to a gas phase resulted in −MDF and no MIF. Yang and Sturgeon (2009) also showed that reduction of Hg(II) with SnCl_2 and sodium tetraethylborate (NaBH_4) resulted in −MDF and no MIF. In addition, Yang and Sturgeon (2009) inorganically ethylated Hg (II) using NaBH_4 and found −MDF but no MIF.

Estrade et al. (2009) showed that evaporation of $\text{Hg}(0)_{\text{vapor}}$ from pure metallic Hg(0) caused −MDF and a small degree of +MIF (<0.2‰). The $\Delta^{199}\text{Hg}/\Delta^{201}\text{Hg}$ ratio for this MIF was ~2, suggesting that it was the result of the nuclear volume effect rather than the magnetic isotope effect (Estrade et al. 2009). Zheng and Hintelmann (2010a) studied the abiotic dark reduction of Hg(II) by DOC and SnCl_2 and found evidence for −MDF and a small (<−0.4‰) amount of −MIF in the reactant with a $\Delta^{199}\text{Hg}/\Delta^{201}\text{Hg}$ ratio of 1.5–1.6. They also attributed this small amount of MIF to the nuclear volume effect.

12.3.1.4 Summary of Experimental Studies

As a way of organizing and summarizing the many results of experimental Hg fractionation experiments I have compiled some of the most important results on Fig. 12.3. Figure 12.3a is a plot of MDF vs. MIF ($\delta^{202}\text{Hg}$ vs. $\Delta^{201}\text{Hg}$) with the value for SRM-3133 at the origin. In most environmental applications of Hg isotopes investigators are interested in either (1) interpreting the isotopic composition of MeHg occurring in sediments or organisms, or (2) interpreting the isotopic composition of Hg(II) associated with sediments or deposited onto the land surface or into a water body. Thus I have designed Fig. 12.3 to show the direction of the evolution of the isotopic composition of Hg as it might be expected to move through the biogeochemical cycle. If we begin with Hg(II) with an isotopic composition of SRM-3133, the arrows dis-

play the trajectory of isotopic evolution of the residual Hg(II) in the system during microbial reduction, microbial methylation, and photochemical reduction. If we begin with MeHg with an isotopic composition of SRM-3133, the arrows display the trajectory of isotopic evolution of the residual MeHg in the system during microbial and photochemical reduction (Fig. 12.3a). Thus if a set of samples have been affected by the same process, but to varying degrees, we might expect the sample analyses to plot along a line approximated by the lines shown on Fig. 12.3a.

In those processes where MIF occurs, the $\Delta^{199}\text{Hg}/\Delta^{201}\text{Hg}$ ratio may be indicative of the reaction mechanism(s) that have affected Hg(II) or MeHg. As in Fig. 12.3a, b shows the direction of evolution of the isotopic composition of Hg as it might be expected to move through the biogeochemical cycle. If we begin with Hg(II) or MeHg with an isotopic composition of SRM-3133, the arrows display the trajectory of isotopic evolution of the residual Hg(II) or MeHg in the system during photochemical reduction (Fig. 12.3b). Thus, as in Fig. 12.3a, if a set of samples have been affected by the same photochemical process, but to varying degrees, we might expect them to plot along a line approximated by those shown on Fig. 12.3b.

12.3.2 Studies in the Environment

12.3.2.1 Fresh Water Sediments and Food Webs

Mercury isotope research on fresh water fisheries began inauspiciously with the publication of stable isotope ratios for sediments and food web animals measured using a quadrupole ICP-MS (Jackson 2001a). Unfortunately the data were not of high enough precision to draw conclusions regarding natural Hg isotope variation and this fact was soon pointed out in a comment by Hintelmann et al. (2001) for which there was also a reply (Jackson 2001b). A subsequent paper by Jackson et al. (2004) used MC-ICP-MS to analyze Hg isotopes in a sediment core from an Arctic lake and documented mass-dependent changes in the Hg isotopic composition with depth. These variations were attributed to microbial activities linked to oxidation–reduction reactions in the lake.

Bergquist and Blum (2007) measured Hg isotopes in fish from small New England lakes and from Lake Michigan with previously unprecedented analytical

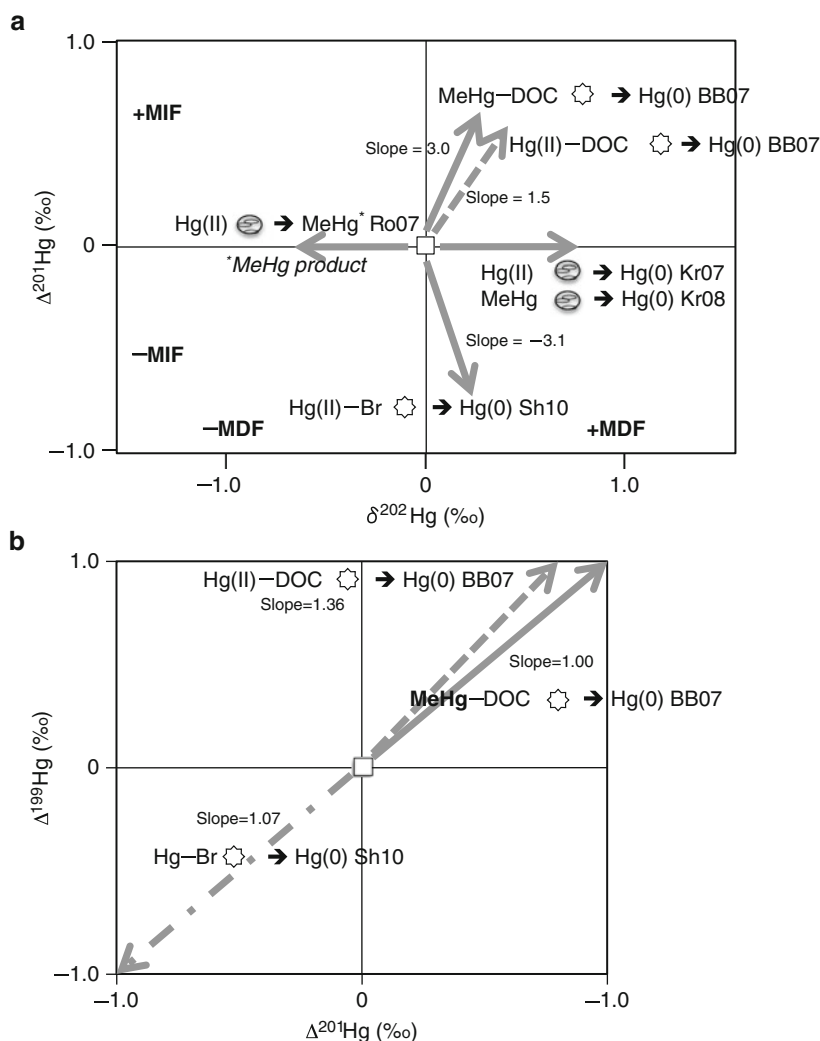


Fig. 12.3 Schematic diagram showing the direction of isotopic evolution of Hg(II) or MeHg beginning with an isotopic composition of NIST SRM-3133 and undergoing photochemical reduction (*sun symbols*), microbial reduction (*microbe symbols*), and microbial methylation (*microbe symbols*). Abbreviations for

references to each study are given in the Fig. 12.1 caption. (a) Slopes of reaction pathways on a plot of $\delta^{202}\text{Hg}$ vs. $\Delta^{201}\text{Hg}$, and (b) slopes of reaction pathways on a plot of $\Delta^{199}\text{Hg}$ vs. $\Delta^{201}\text{Hg}$. “DOC” indicates experiments were carried out in the presence of dissolved organic carbon

precision. In reporting these data, Bergquist and Blum (2007) used an isotopic nomenclature suggested by Blum and Bergquist (2007) that standardized the reporting of Hg isotopic compositions relative to a commonly available standard (NIST SRM-3133). Using fractionation factors determined in the laboratory for photochemical reduction of Hg(II) and MeHg they argued that large variations in $\Delta^{199}\text{Hg}$ and $\Delta^{201}\text{Hg}$ in fish tissues resulted from photochemical degradation of MeHg in the water column prior to its entry into aquatic foodwebs. They also provided

a means of estimating the proportion of MeHg that had been degraded and suggested that the $\Delta^{199}\text{Hg}/\Delta^{201}\text{Hg}$ ratio might be diagnostic of reduction of Hg(II) vs. MeHg. Bergquist and Blum (2007) concluded that MeHg produced in each of three different locations in northern Lake Michigan had experienced differing amounts of photochemical demethylation (up to 76%) and that this was reflected in the $\Delta^{199}\text{Hg}$ and $\Delta^{201}\text{Hg}$ of fish tissues.

Subsequent studies of Hg isotopes in fish tissues have all measured positive MIF, but have come to

conflicting conclusions as to the origin of this fractionation. Jackson et al. (2008) measured Hg isotopes in sediment, crustaceans, forage fish and predator fish from two boreal lakes and Lake Ontario. Based on correlations between MeHg concentration and Hg isotopic composition the authors argued that MIF of Hg occurred during microbial Hg methylation. More recent studies of isotope fractionation during microbial Hg methylation (Rodriguez-Gonzalez et al. 2009) have found no evidence for the occurrence of MIF during methylation. Das et al. (2009) measured Hg isotopes in fish and a zooplankton sample from a Florida lake and based on a correlation of MIF with $\delta^{15}\text{N}$ concluded that in vivo Hg MIF occurring in fish provided the simplest explanation for their data. However, a mechanism for this fractionation has not yet been identified and theoretical arguments have been made that suggest organismal in vivo fractionation is unlikely (Kritee et al. 2009). Laffont et al. (2009) measured Hg isotopes in fish and in human hair from a population eating those fish on a daily basis. They found no evidence for in vivo MIF of Hg in humans, but did find evidence for in vivo MDF of Hg in human hair by $\sim 2\%$ (as measured using $\delta^{202}\text{Hg}$). Finally, Gantner et al. (2009) measured Hg isotopes in sediments, zooplankton, invertebrates and fish from ten Arctic lakes. Each of these organisms displayed MIF and there was no clear pattern of Hg MIF during trophic transfer; in some lakes zooplankton MIF values even exceeded those of fish. The authors concluded that differences in MIF in fish were most likely caused by MeHg photoreduction in the water column and that MDF largely reflected regional differences due to atmospheric and/or terrestrial inputs of Hg to lakes.

12.3.2.2 Marine Sediments and Food Webs

Mercury isotopes were first measured in marine sediments by Gehrke et al. (2009) in a study of mid-Pleistocene (955 kyr) Mediterranean sediment cores. Large fluctuations in Hg concentration were observed in alternating layers of organic rich and organic poor sediments (sapropels) but the Hg isotopic composition of these sediments remained relatively constant at $\delta^{202}\text{Hg} = -0.91\%$ (± 0.15 , 1SD, $n = 5$) and $\Delta^{201}\text{Hg} = 0.04\%$ (± 0.03 , 1SD, $n = 5$). These measurements provided the first estimate of a pre-anthropogenic marine Hg isotope composition. Senn

et al. (2010) measured modern marine sediments in coastal waters in the Gulf of Mexico (GOM) and found Hg isotope ratios of $\delta^{202}\text{Hg} = -1.00\%$ (± 0.11 , 1SD, $n = 6$) and $\Delta^{201}\text{Hg} = -0.04\%$ (± 0.03 , 1SD, $n = 6$). The GOM $\delta^{202}\text{Hg}$ values are indistinguishable from the Mediterranean sapropels and the $\Delta^{201}\text{Hg}$ values are only slightly higher.

To address the question of whether coastal vs. oceanic species of fish in the Gulf of Mexico obtain Hg from the same or different sources, Senn et al. (2010) investigated Hg isotopes and $\delta^{15}\text{N}$ of fish tissues collected in the GOM. Coastal species had distinct and non-overlapping values of $\delta^{202}\text{Hg}$ and $\Delta^{201}\text{Hg}$ compared to oceanic species and this isotopic contrast along with $\delta^{15}\text{N}$ values was used to argue for isotopically distinct MeHg sources. It was proposed that oceanic MeHg was produced in the open ocean and then underwent substantial photodegradation before entering the base of the oceanic food web. This study is described in more detail below as a case study.

12.3.2.3 Point-Source Contamination of Sediments

Several studies have explored the use of Hg isotopes to “fingerprint” point sources of Hg from historic Hg mines and trace them into the surrounding environment. Early studies determined that there was substantial variability in the $\delta^{202}\text{Hg}$ of cinnabar (HgS) ores from various mining districts, ore deposits and volcanic/hydrothermal systems (Hintelmann and Lu 2003; Smith et al. 2005, 2008; Sherman et al. 2009; Zambardi et al. 2009), and explored MDF of Hg isotopes during ore formation. Stetson et al. (2009) showed that the roasting of HgS ore to produce metallic mercury imparted a MDF signature that allows isotopic distinction between roasted ore mine waste (calcine) and un-roasted ore. This provides a means of isotopically differentiating between calcine and background Hg in stream runoff.

Foucher et al. (2009) isotopically characterized cinnabar ores and highly contaminated river sediments from a Hg mining region in Slovenia and then showed that the $\delta^{202}\text{Hg}$ value of Hg in downstream river sediments and in sediments in the Adriatic Sea could be used to determine the proportion of Hg from the mine. Feng et al. (2010) performed a similar study

but used Hg isotopes to fingerprint metallic Hg that was used as a catalyst in industrial acid production. The authors linked Hg in industrial runoff to Hg in contaminated sediments from a downstream reservoir and confirmed this result by showing a contrasting isotopic composition in sediment from an unaffected reservoir.

12.3.2.4 Atmospheric Processes

Mercury is unique as a trace metal pollutant because it has a common volatile form [Hg(0)] with a long (~1 year) atmospheric lifetime, and is thus distributed and deposited globally. There is great interest in understanding sources of mercury to the atmosphere, sources of Hg in wet and dry deposition to the Earth's surface, and the atmospheric redox reactions that lead to the emission and deposition of Hg. These are complex scientific problems that are analytically challenging due to the difficulties of measuring Hg isotope ratios at low atmospheric concentrations. Biswas et al. (2008) measured Hg isotopes in coals, soils and Arctic peat deposits to evaluate sources and sinks for atmospheric Hg. Most coal deposits had negative values of $\delta^{202}\text{Hg}$ and $\Delta^{201}\text{Hg}$ but they varied widely isotopically, offering the possibility that Hg emissions from coal might be distinguishable from global background values in certain coal producing regions. Soils and peat deposits tend to be enriched in Hg concentration near the surface due to deposition from anthropogenic sources and Biswas et al. (2008) found that surface organic soils and peats also had negative values of $\delta^{202}\text{Hg}$ and $\Delta^{199}\text{Hg}$, possibly due to deposition from the atmosphere. Ghosh et al. (2008) reported $\Delta^{201}\text{Hg}$ (but not $\delta^{202}\text{Hg}$) in peat cores and Spanish moss and also found negative (or near 0) values of $\Delta^{201}\text{Hg}$. Carignan et al. (2009) investigated Hg isotopes in tree lichens, which have been widely used as biomonitors of atmospheric metal deposition. This study also found consistently negative values of $\delta^{202}\text{Hg}$ and $\Delta^{201}\text{Hg}$, suggesting that these values might be indicative of atmospheric Hg isotopic composition. This is consistent with the hypothesis that biotic, abiotic, and aqueous photochemical reduction of Hg(II) together produce Hg(0) with negative values of $\delta^{202}\text{Hg}$ and $\Delta^{201}\text{Hg}$ and that this Hg is ultimately deposited to the Earth's surface and sequestered by various forms of organic matter.

Recent measurements of the isotopic composition of Hg in atmospheric samples (Sherman et al. 2010; Gratz et al. 2010) have, however, complicating the view that lichens, peat and organic soils are representative of the isotopic composition of atmospheric Hg. Measurements of Hg(0) in the atmosphere and Hg(II) deposited with snowfall at Barrow, Alaska yielded $\delta^{202}\text{Hg}$ and $\Delta^{201}\text{Hg}$ values close to 0 (Sherman et al. 2010). Measurements of atmospheric Hg(0) and Hg(II) at Dexter, MI showed average $\delta^{202}\text{Hg}$ and $\Delta^{201}\text{Hg}$ values close to 0 for Hg(0) and values that were slightly negative and positive for $\delta^{202}\text{Hg}$ and $\Delta^{201}\text{Hg}$, respectively, in Hg(II) in precipitation (Gratz et al. 2010). These data raise the question of why lichens, mosses and soils have negative $\delta^{202}\text{Hg}$ and $\Delta^{201}\text{Hg}$, whereas atmospheric values are 0 or positive. It appears that either the atmospheric Hg isotopic composition is very heterogeneous and samples of Hg(0) have not captured the same values as organic materials exposed to the atmosphere, or there is isotope fractionation that shifts values for vegetation relative to atmospheric deposition. Recent experiments by Sherman et al. (2010) showed that photochemical reduction of Hg(II) from snow produced Hg(0) with a higher $\Delta^{201}\text{Hg}$ (and $\Delta^{199}\text{Hg}$) than that of the Hg remaining in snow. This fractionation is in the opposite direction of that caused by the photochemical reduction of Hg(II) associated with organic matter in aqueous solution (Bergquist and Blum 2007). Zheng and Hintelmann (2010b) also recently demonstrated experimentally that photochemical reduction of Hg(II) can produce Hg(0) with either positive or negative $\Delta^{201}\text{Hg}$ depending on the ligand to which the Hg(II) was originally attached. Thus, although it remains to be tested rigorously, these data open up the possibility that vegetation acquires negative $\Delta^{201}\text{Hg}$ due to the loss of Hg(0) by photochemical reduction (Gratz et al. 2010).

12.3.2.5 Case Study from Gulf of Mexico Fisheries

The most important pathway for human exposure to Hg is via the consumption of marine fish (Sunderland 2007), yet there is still considerable uncertainty concerning the sources of Hg to different fisheries and the factors that control the concentrations of Hg in these fisheries (e.g., Sunderland et al. 2009). The Gulf of Mexico (GOM) is a highly productive marine region

and a major fishery (Chesney et al. 2000). Fish are harvested in the GOM from both the shallow-water (coastal) region, within tens of kilometers of shore, and from open-ocean (oceanic) regions in deep water hundreds of kilometers from shore. Senn et al. (2010) used N and Hg isotopes in these fisheries to gain insight into the sources and pathways of Hg to these coastal and oceanic fish. This study provides a particularly illustrative example and is used here with some supplementary data to demonstrate how the results of experimental Hg isotope fractionation studies can be linked to environmental data sets to obtain insight into Hg sources and biogeochemical cycling.

Muscle tissue from coastal and oceanic species of fish was collected and additional samples were collected from fish species that are transitional in their habitat (Senn et al. 2010). Samples were analyzed for Hg concentration and the isotopic composition of Hg and N. A plot of $\delta^{15}\text{N}$ vs. Hg concentration revealed two separate, but parallel, trends for coastal vs. oceanic fish indicating disconnected foodwebs based in nitrogen from continental runoff in the coastal areas and open-ocean nitrogen sources for the oceanic fish, with transitional species occupying positions intermediate between these sources (Senn et al. 2010). Figure 12.4a is a plot of $\delta^{202}\text{Hg}$ vs. $\Delta^{201}\text{Hg}$ for the coastal, transitional, and open ocean fish as well as Hg isotope data for the top 2 cm of coastal sediment cores. Sediments have highly negative $\delta^{202}\text{Hg}$ but $\Delta^{201}\text{Hg}$ values close to 0. These values are consistent with geological sources of Hg (Gehrke et al. 2009) as well as with Hg used in industrial applications (Smith et al. 2008), or a combination of these sources. Published Hg isotope values for atmospheric deposition in the GOM are not yet available, but values for the isotopic composition of precipitation from a rural site in Michigan (Dexter, MI; Gratz et al. 2010) that is relatively unaffected by point sources is plotted on Fig. 12.4c, and provides an estimate of the expected isotopic composition of atmospheric Hg in the GOM.

Coastal fish from a variety of species have $\delta^{202}\text{Hg}$ values ranging from the sediment values (-0.82 to -1.11%) up to a much higher value of -0.03% . However, unlike the sediments, the coastal fish display MIF with $\Delta^{201}\text{Hg}$ values of 0.25 – 0.50% . Oceanic fish (yellowfin and bluefin tuna) have much higher, and non-overlapping, values of both $\delta^{202}\text{Hg}$ and $\Delta^{201}\text{Hg}$ compared to coastal fish. Small yellowfin tuna (<16 kg) have the highest $\Delta^{201}\text{Hg}$ values observed in

the GOM. Large yellowfin tuna from the Pacific Ocean near Hawaii, which were collected in 1998 and studied by Kraepiel et al. (2003), also display high $\Delta^{201}\text{Hg}$ values (Blum unpublished; Fig. 12.4). Transitional species of fish in the GOM have both $\delta^{202}\text{Hg}$ and $\Delta^{201}\text{Hg}$ values intermediate between coastal and open ocean species – but with Spanish mackerel displaying more coastal values consistent with their largely coastal range and bluerunner displaying closer to deep water values consistent with their tendency to spend part of their life-cycle in oceanic waters. Because the GOM fish tissues display MIF, it is instructive to also plot the data as $\Delta^{199}\text{Hg}$ vs. $\Delta^{201}\text{Hg}$ (Fig. 12.4b). All of the fish samples from the GOM plot on a single line with slope of 1.20 ± 0.02 . Samples of GOM coastal sediment and yellowfin tuna from the Pacific Ocean also plot very close to this line, although with somewhat greater scatter.

The main purpose of presenting this case study is to demonstrate how one can interpret the trends of biogeochemical data (Fig. 12.4a, b) within the context of the available experiment results. From Fig. 12.4a we know that the Hg in all fish tissues has undergone significant amounts of both MDF and MIF. Based on their experimental results, Bergquist and Blum (2007) argued that a slope of ~ 1.36 in fish tissues would result from photochemical demethylation of MeHg in the water column prior to entering the food web, whereas a slope of ~ 1.00 would result from photochemical reduction of Hg(II) prior to methylation. The authors measured a $\Delta^{199}\text{Hg}/\Delta^{201}\text{Hg}$ slope of 1.28 in burbot fish from Lake Michigan and concluded that photochemical degradation of MeHg was the dominant reaction producing MIF. However, with new experimental data from Zheng and Hintelmann (2009, 2010b) showing that the slope of $\Delta^{199}\text{Hg}/\Delta^{201}\text{Hg}$ varies for photochemical reduction of Hg(II) depending on the Hg/DOC ratio and ligand–Hg binding, it appears that these data may be more complex to interpret than previously realized. Additional data on the $\Delta^{199}\text{Hg}/\Delta^{201}\text{Hg}$ slope during Hg(II) reduction and MeHg degradation under conditions specifically relevant to marine photochemical reactions will be needed to form more definitive conclusions. Nevertheless, empirical observations of $\Delta^{199}\text{Hg}/\Delta^{201}\text{Hg}$ slopes in natural materials show values of ~ 1.0 for processes that involve Hg(II) photoreduction (Biswas et al. 2008; Ghosh et al. 2008; Carignan et al. 2009; Sherman et al. 2010) whereas values in aquatic foodwebs, which

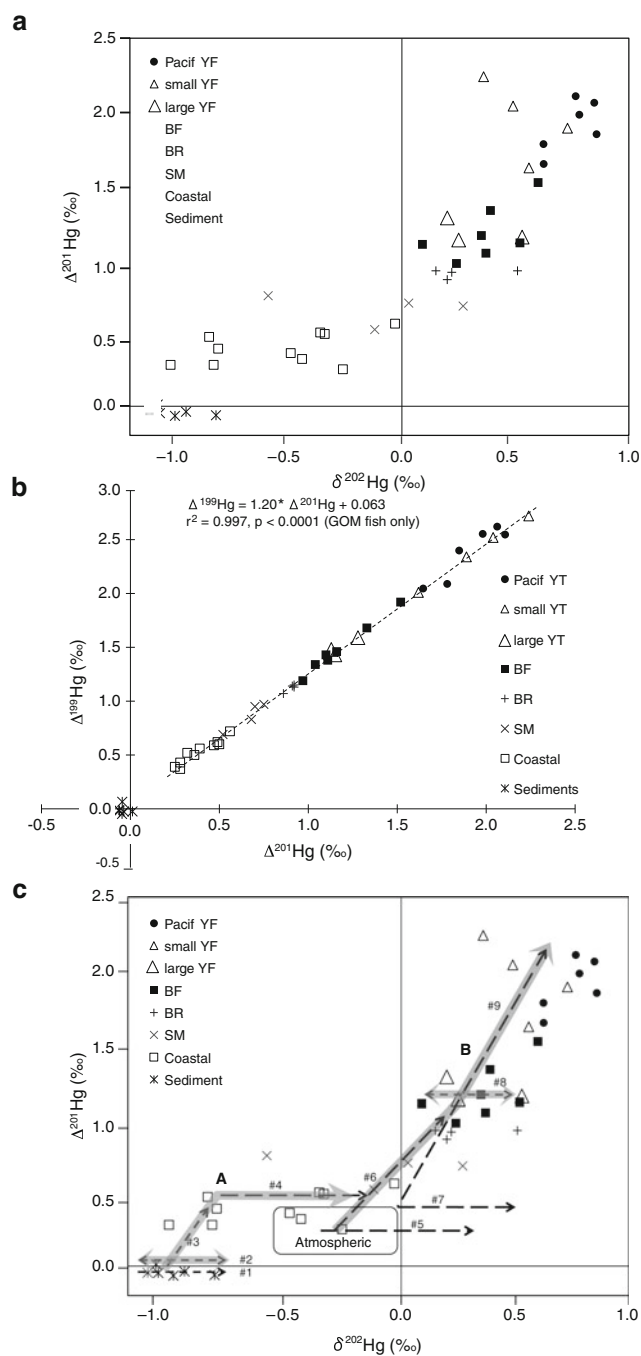


Fig. 12.4 (a) Plot of data for $\delta^{202}\text{Hg}$ vs. $\Delta^{201}\text{Hg}$ for Gulf of Mexico coastal sediments and both coastal and oceanic fish muscle tissues (Senn et al. 2010), as well as Pacific Ocean oceanic fish muscle tissues (Blum, unpublished). YT is yellowfin tuna; BF is blackfin tuna; BR is bluerunner; SM is Spanish mackerel; “coastal” includes red snapper, grey snapper, bay anchovy, speckled trout, red drum, flounder and menhaden (b) Plot of $\Delta^{201}\text{Hg}$ vs. $\Delta^{199}\text{Hg}$ for the same samples as in (a). Linear regression is for all GOM fish samples but excludes Pacific

yellowfin tuna and sediments. (c) Same plot as in (a) but with the addition of a field for regional background precipitation from a remote site (Dexter, MI) from Gratz et al. (2010). *Shaded arrows* indicate inferred isotopic evolution of the MeHg ultimately bio-accumulated in coastal (A) and oceanic (B) fish in the GOM. *Dashed arrows* with numbers represent isotope fractionation pathways expected for nine different processes that are discussed in the text

uniquely involve MeHg, display slopes of ~ 1.2 – 1.3 (Bergquist and Blum 2007; Gantner et al. 2009; Laffont et al. 2009; Senn et al. 2010).

We return now to the relationship between $\delta^{202}\text{Hg}$ and $\Delta^{201}\text{Hg}$ for the GOM samples using Fig. 12.4c, which is a schematic illustration of how various Hg transformations known to occur in the aquatic environment would be expected to affect the isotopic values of the GOM samples. Isotope values for GOM sediments, which contain Hg predominantly in the form of Hg(II), display no MIF and have $\delta^{202}\text{Hg}$ values consistent with eroded geological materials or Hg used in industrial processes. A reasonable assumption based on previous studies of marine systems is that Hg in these reduced sediments is methylated by sulfate reducing bacteria, incorporated into the base of the coastal foodweb and then bioaccumulated in coastal fish (e.g., Fitzgerald and Lamborg 2003). Microbial methylation would drive the produced MeHg to lower $\delta^{202}\text{Hg}$ values and microbial demethylation would increase $\delta^{202}\text{Hg}$ values in remaining MeHg. However, production of significant MIF of Hg isotopes appears to require photochemistry. Because MIF is observed in fish but not in sediments it is most likely that photochemical demethylation produces the observed MIF. This MIF would be accompanied by MDF and might follow the trajectories on Fig. 12.3a. Based on the experimental results of Bergquist and Blum (2007), the MIF observed in coastal fish would represent demethylation of $\sim 15\%$ of the originally produced MeHg prior to incorporation into the food web. Microbial degradation of MeHg before entry into the food web would also drive the residual MeHg to higher values of $\delta^{202}\text{Hg}$ and could account for some of the large variability in the $\delta^{202}\text{Hg}$ values for coastal fish. Although some MDF probably also occurs during trophic transfer of MeHg through the food web, trophic transfer to coastal fish does not appear to be a major driver of the range in $\delta^{202}\text{Hg}$ values in coastal fish for three reasons. First, some fish have $\delta^{202}\text{Hg}$ values that are the same as the sediment values; second, fish of the same species display nearly the full range in coastal fish $\delta^{202}\text{Hg}$ values (Senn et al. 2010); and third, there is no correlation between coastal fish $\delta^{202}\text{Hg}$ values and $\delta^{15}\text{N}$, which is an indicator of trophic position (Senn et al. 2010).

The next question Senn et al. (2010) address is why the Hg isotopic composition of oceanic fish is different

than coastal fish. One possible means by which oceanic fish might acquire Hg is by feeding on coastal fish (Fitzgerald et al. 2007). The higher $\delta^{202}\text{Hg}$ values for oceanic fish could possibly be explained by trophic transfer, but the higher $\Delta^{201}\text{Hg}$ are inconsistent with this hypothesis. Instead MeHg was most likely photochemically demethylated to a greater extent than in the coastal ecosystem, prior to being incorporated into the oceanic food web. Based on the experimental results of Bergquist and Blum (2007) the MIF observed in oceanic fish would represent demethylation of ~ 40 – 60% of the produced MeHg. Microbial demethylation in the open ocean could push $\delta^{202}\text{Hg}$ values in residual MeHg to higher values, and trophic transfer could also push $\delta^{202}\text{Hg}$ values to higher values, but the observed higher $\Delta^{201}\text{Hg}$ values require higher degrees of photochemical MeHg degradation. Thus it is possible that MeHg was produced in the coastal zone and transported to the open ocean with additional photo-demethylation occurring along the way, or that Hg was deposited to the open ocean as Hg(II) through the atmosphere and was methylated and subsequently demethylated in the open ocean.

Several recent studies have argued that open ocean methylation can and does occur (e.g., Sunderland et al. 2009; Monperrus et al. 2007). Based on $\delta^{15}\text{N}$ values, which indicated contrasting N sources to the coastal and oceanic food webs, Senn et al. (2010) argued that the most likely scenario for the pathway of Hg into GOM open ocean fish was deposition of atmospheric Hg and methylation within the open ocean. Although we do not yet know the isotopic composition of Hg deposited from the atmosphere in the GOM, based on atmospheric Hg isotopic composition data from Michigan (Gratz et al. 2010), photochemical demethylation of Hg that was deposited from the atmosphere as Hg(II) and methylated in the open ocean, corresponds well to the range of values observed in oceanic fish (Fig. 12.4c). Senn et al. (2010) also observed that small yellowfin tuna (< 16 kg) from the GOM display higher $\Delta^{201}\text{Hg}$ than large yellowfin tuna, which suggests that they obtain MeHg from a food web in which a higher degree of photochemical demethylation has occurred prior to entry into that food web. Graham et al. (2007) showed that juvenile yellowfin tuna near the Hawaiian Islands feed in the shallow mixed layer and that as they mature they shift to prey in deeper, colder water, which could provide an explanation

of the $\Delta^{201}\text{Hg}$ data for small yellowfin tuna from the GOM. Large yellowfin tuna from near the Hawaiian Islands have higher $\Delta^{201}\text{Hg}$ than large yellowfin tuna from the GOM (Blum, unpublished), suggesting a larger degree of photochemical demethylation of the Hg in the foodweb of the large Hawaiian yellowfin tuna.

As a summary of the GOM fisheries case study, trajectories are plotted for likely Hg speciation transitions on a $\delta^{202}\text{Hg}$ vs. $\Delta^{201}\text{Hg}$ diagram with the GOM data shown in the background (Fig. 12.4c). This conveniently illustrates the possible pathways for the evolution of the Hg isotopic composition within this biogeochemical system. The range of sediment Hg isotope values could be due to contrasting sources of Hg to sediment and could be shifted to higher $\delta^{202}\text{Hg}$, but not higher $\Delta^{201}\text{Hg}$, by microbial reduction (path #1). As Hg in sediments is methylated, MeHg can shift to higher and lower $\delta^{202}\text{Hg}$ by microbial methylation and demethylation (path #2), respectively, and to higher $\delta^{202}\text{Hg}$ and $\Delta^{201}\text{Hg}$ by photochemical demethylation (path #3). Coastal fish show about the same amount of photo-demethylation but a wide range in $\delta^{202}\text{Hg}$; this could be due to varying amounts of microbial demethylation (path #4) or a mixture of MeHg originating from multiple sources such as sediment and atmospheric deposition. The overall pathway that best explains the Hg isotope values of the coastal fish is shown with a gray arrow and labeled "A".

Atmospheric Hg(II) deposited to the ocean surface could be shifted to higher $\delta^{202}\text{Hg}$ by microbial reduction (path #5) or to higher $\delta^{202}\text{Hg}$ and $\Delta^{201}\text{Hg}$ by photochemical reduction (path #6) following the trajectories shown. Transfer of MeHg through the food web could cause an increase in $\delta^{202}\text{Hg}$, but not $\Delta^{201}\text{Hg}$ (path #7). If oceanic fish fed on coastal fish we would expect some increase in $\delta^{202}\text{Hg}$ due to trophic transfer following path #7, but no change in $\Delta^{201}\text{Hg}$. If, however, Hg(II) was deposited to the ocean, photochemically reduced (path #6), microbially methylated and demethylated in the water column (path #8), and then photochemically demethylated (path #9), this could produce the isotopic patterns observed in oceanic fish. This pathway is consistent with the pathway proposed by Monperrus et al. (2007) for production of oceanic MeHg and is shown as the thick gray arrow and labeled "B" on Fig. 12.4c.

12.4 Future Directions

The first set of papers attempting to apply Hg isotope measurements to biogeochemical problems appeared in 2001, and after approximately 6 years of working through the analytical details of how to produce high precision isotope ratio measurements, the field of Hg isotope biogeochemistry began to flourish in 2007. Since that time several research groups have applied Hg isotope measurements to a wide variety of research problems and at last count there were ~20 papers published predominantly on applications of Hg isotopes and another ~30 on experiments and method development related to Hg isotope biogeochemistry. The rate of growth of this field of research has been rapid, and will continue to grow quickly as the Hg biogeochemistry research community realizes the wide utility of this new approach to the study of Hg in the environment. Like all new stable isotope systems the main challenges will be in understanding all of the various fractionation mechanisms and their fractionation factors, and learning how to separate isotopic variation due to different sources of Hg to the environment from isotopic variation imparted by chemical processes occurring in the environment. However, Hg is unique among stable isotopic systems in the multitude of isotope fractionation signals that are built into the isotopic system. In addition to the basic mass-dependent and mass-independent fractionations recorded as $\delta^{202}\text{Hg}$ and $\Delta^{201}\text{Hg}$, there are several other diagnostic ratios that hold important additional information including the $\Delta^{199}\text{Hg}/\Delta^{201}\text{Hg}$ and $\Delta^{199}\text{Hg}/\delta^{202}\text{Hg}$ ratios.

With continued laboratory experimentation to better refine the understanding of Hg fractionation mechanisms and higher precision measurements of Hg isotope ratios in environmental samples, there will be an important place for Hg isotopes in future studies of virtually all aspects of Hg biogeochemistry. The areas where we may see the greatest breakthroughs are perhaps those areas where we have made the least progress using concentration analyses of Hg species alone. These include the detailed understanding of many complex multi-step chemical pathways such as: (1) the atmospheric chemistry that leads to the deposition of Hg(0) from the atmosphere as $\text{Hg(II)}_{\text{gas}}$ and $\text{Hg(II)}_{\text{part}}$, (2) the chemical bonding

environments in sediments that leads to various Hg fractions with chemical behaviors ranging from very recalcitrant to readily bioavailable and (3) the biological pathways that begin with methylation and demethylation and transfer Hg through the food web to top predators. Hg isotopes will undoubtedly also serve as fingerprints of sources of Hg contamination, but it is anticipated that the most significant breakthroughs will come from the insight that Hg isotopes add to our understanding of the chemical processes and pathways of Hg in the environment.

Acknowledgements I wish to thank all of the past and present members of my Hg isotope research group for their persistence, dedication and intellectual contributions to helping develop an important new isotopic system. I also thank J. Sonke and an anonymous reviewer for providing helpful comments that improved the manuscript. This chapter was written while the author was a CIRES visiting fellow at the University of Colorado, and this program is gratefully acknowledged.

References

- Bergquist BA, Blum JD (2007) Mass-dependent and -independent fractionation of Hg isotopes by photo-reduction in aquatic systems. *Science* 318:417–420
- Bergquist BA, Blum JD (2009) Mass dependent and independent fractionation of mercury isotopes. *Elements* 5:353–357
- Biswas A, Blum JD, Bergquist BA et al (2008) Natural mercury isotope variation in coal deposits and organic soils. *Environ Sci Technol* 42:8303–8309
- Blum JD, Bergquist BA (2007) Reporting of variations in the natural isotopic composition of mercury. *Anal Bioanal Chem* 233:353–359
- Buchachenko AL (2009) Mercury isotope effects in the environmental chemistry and biochemistry of mercury-containing compounds. *Russ Chem Rev* 78:319–328
- Carignan J, Estrade N, Sonke JE et al (2009) Odd isotope deficits in atmospheric Hg measured in lichens. *Environ Sci Technol* 43:5660–5664
- Chesney EJ, Baltz DM, Thomas RG (2000) Louisiana estuarine and coastal fisheries and habitats: perspectives from a fish's eye view. *Ecol Appl* 10:350–366
- Das R, Salters VJM, Odom AL (2009) A case for in vivo mass-independent fractionation of mercury isotopes in fish. *Geochem Geophys Geosyst* 10:Q11012
- Douglas TA, Sturm M, Simpson WR, Blum JD, Alvarez-Aviles L, Keeler GJ, Perovich DK, Biswas A, Johnson K (2008) The influence of snow and ice crystal formation and accumulation of mercury deposition to the arctic. *Environ Sci Technol* 42:1542–1551
- Epov VN, Rodriguez-Gonzalez P, Sonke JE et al (2008) Simultaneous determination of species-specific isotopic composition of Hg by gas chromatography coupled to multicollector ICPMS. *Anal Chem* 80:3530–3538
- Estrade N, Carignan J, Sonke JE et al (2009) Mercury isotope fractionation during liquid-vapor evaporation experiments. *Geochim Cosmochim Acta* 73:2693–2711
- Estrade N, Carignan J, Sonke JE et al (2010) Measuring Hg isotopes in bio-geo-environmental reference materials. *Geostandard Geoanal Res* 34:79–93
- Evans RD, Hintelmann H, Dillon PJ (2001) Measurement of high precision isotope ratios for mercury from coals using transient signals. *J Anal At Spectrom* 16:1064–1069
- Evers DC, Han Y-J, Driscoll CT et al (2007) Biological mercury hotspots in the northeastern United States and southeastern Canada. *BioScience* 57:29–43
- Feng XB, Foucher D, Hintelmann H et al (2010) Tracing mercury contamination sources in sediments using mercury isotope compositions. *Environ Sci Technol* 44:3363–3368
- Fitzgerald WF, Lamborg CH (2003) Geochemistry of mercury in the environment. In: Lollar BS (ed) *Treatise on geochemistry*, vol 9. Elsevier, New York, pp 107–148
- Fitzgerald WF, Lamborg CH, Hammerschmidt CR (2007) Marine biogeochemical cycling of mercury. *Chem Rev* 107:641–662
- Foucher D, Hintelmann H (2006) High-precision measurement of mercury isotope ratios in sediments using cold-vapor generation multi-collector inductively coupled plasma mass spectrometry. *Anal Bioanal Chem* 384:1470–1478
- Foucher D, Ogrinc N, Hintelmann H (2009) Tracing mercury contamination from the Idrija mining region (Slovenia) to the Gulf of Trieste using Hg isotope ratio measurements. *Environ Sci Technol* 43:33–39
- Gantner N, Hintelmann H, Zheng W et al (2009) Variations in stable isotope fractionation of Hg in food webs of Arctic lakes. *Environ Sci Technol* 43:9148–9154
- Gehrke GE, Blum JD, Meyers PA (2009) The geochemical behavior and isotopic composition of Hg in a mid-Pleistocene Mediterranean sapropel. *Geochim Cosmochim Acta* 73:1651–1665
- Ghosh S, Xu YF, Humayun M et al (2008) Mass-independent fractionation of mercury isotopes in the environment. *Geochem Geophys Geosyst* 9:Q03004
- Graham BS, Grubbs D, Holland K et al (2007) A rapid ontogenetic shift in the diet of juvenile yellowfin tuna from Hawaii. *Mar Biol* 150:647–658
- Gratz LE, Keeler GJ, Blum JD, Sherman LS (2010) Isotopic composition and fractionation of mercury in Great Lakes precipitation and ambient air. *Environ Sci Technol* 44:7764–7770
- Gustin MS, Lindberg SE, Weisberg PJ (2008) An update on the natural sources and sinks of atmospheric mercury. *Appl Geochem* 23:482–493
- Hintelmann H, Lu SY (2003) High precision isotope ratio measurements of mercury isotopes in cinnabar ores using multi-collector inductively coupled plasma mass spectrometry. *Analyst* 128:635–639
- Hintelmann H, Ogrinc N (2003) Determination of stable mercury isotopes by ICP/MS and their application in environmental studies. *ACS Symp Ser* 835:321–338
- Hintelmann H, Dillon P, Evans RD et al (2001) Comment: variations in the isotope composition of mercury in a freshwater sediment sequence and food web. *Can J Fish Aquat Sci* 58:2309–2311
- Jackson TA (2001a) Variations in the isotope composition of mercury in a freshwater sediment sequence and food web. *Can J Fish Aquat Sci* 58:185–196

- Jackson TA (2001b) Reply: variations in the isotope composition of mercury in a freshwater sediment sequence and food web. *Can J Fish Aquat Sci* 58:2312–2316
- Jackson TA, Muir DCG, Vincent WF (2004) Historical variations in the stable isotope composition of mercury in Arctic lake sediments. *Environ Sci Technol* 38:2813–2821
- Jackson TA, Whittle DM, Evans MS et al (2008) Evidence for mass-independent and mass-dependent fractionation of the stable isotopes of mercury by natural processes in aquatic ecosystems. *Appl Geochem* 23:547–571
- Johnson KP, Blum JD, Keeler GJ et al (2008) A detailed investigation of the deposition and re-emission of mercury in arctic snow during an atmospheric mercury depletion event. *J Geophys Res*. doi:10.1029/2008JD009893
- Klaue B, Blum JD (1999) Trace analysis of arsenic in drinking water by inductively coupled plasma mass spectrometry: high resolution versus hydride generation. *Anal Chem* 71:1408–1414
- Kraepiel AML, Keller K, Chin HB et al (2003) Sources and variations of mercury in tuna. *Environ Sci Technol* 37:5551–5558
- Kritee K, Blum JD, Johnson MW et al (2007) Mercury stable isotope fractionation during reduction of Hg(II) to Hg(0) by mercury resistant bacteria. *Environ Sci Technol* 41:1889–1895
- Kritee K, Blum JD, Barkay T (2008) Constraints on the extent of mercury stable isotope fractionation during reduction of Hg(II) by different microbial species. *Environ Sci Technol* 42:9171–9177
- Kritee K, Barkay T, Blum JD (2009) Mass dependent stable isotope fractionation of mercury during microbial degradation of methylmercury. *Geochim Cosmochim Acta* 73:1285–1296
- Krupp EA, Donard OFX (2005) Isotope ratios on transient signals with GC-MC-ICP-MS. *Int J Mass Spectrom* 242:233–242
- Laffont L, Sonke JE, Maurice L et al (2009) Anomalous mercury isotopic compositions of fish and human hair in the Bolivian Amazon. *Environ Sci Technol* 43:8985–8990
- Lauretta DS, Klaue B, Blum JD et al (2001) Mercury abundances and isotopic composition in the Murchison (CM) and Allende (CV) carbonaceous chondrites. *Geochim Cosmochim Acta* 65:2807–2818
- Lindberg SE, Brooks S, Lin C-J et al (2002) Dynamic oxidation of gaseous mercury in the troposphere at polar sunrise. *Environ Sci Technol* 36:1245–1256
- Mason RP, Fitzgerald WF, Morel FMM (1994) The biogeochemical cycling of elemental mercury – anthropogenic influences. *Geochim Cosmochim Acta* 58:3191–3198
- Meija J, Yang L, Sturgeon RE et al (2010) Certification of natural isotopic abundance inorganic mercury reference material NIMS-1 for absolute isotopic composition and atomic weight. *J Anal At Spectrom* 25:384–389
- Monperrus M, Tessier E, Amouroux D et al (2007) Mercury methylation, demethylation and reduction rates in coastal and marine surface waters of the Mediterranean Sea. *Mar Chem* 107:49–63
- Morel FMM, Kraepiel AML, Amyot M (1998) The chemical cycle and bioaccumulation of mercury. *Annu Rev Ecol Syst* 29:543–566
- Rodriguez-Gonzalez P, Epov VN, Bridou R et al (2009) Species-specific stable isotope fractionation of mercury during Hg(II) methylation by an anaerobic bacteria (*Desulfobulbus propionicus*) under dark conditions. *Environ Sci Technol* 43:9183–9188
- Schauble EA (2007) Role of nuclear volume in driving equilibrium stable isotope fractionation of mercury, thallium, and other very heavy elements. *Geochim Cosmochim Acta* 71:2170–2189
- Schroeder WH, Munthe J (1998) Atmospheric mercury – an overview. *Atmos Environ* 32:809–822
- Senn DB, Chesney EJ, Blum JD et al (2010) Stable isotope (N, C, Hg) study of methylmercury sources and trophic transfer in the northern Gulf of Mexico. *Environ Sci Technol* 44:1630–1637
- Sherman LS, Blum JD, Nordstrom DK et al (2009) Mercury isotopic composition of hydrothermal systems in the Yellowstone Plateau volcanic field and Guaymas Basin sea-floor rift. *Earth Planet Sci Lett* 279:86–96
- Sherman LS, Blum JD, Johnson KP et al (2010) Use of mercury isotopes to understand mercury cycling between Arctic snow and atmosphere. *Nat Geosci* 3:173–177
- Smith CN, Klaue B, Kesler SE et al (2005) Mercury isotope fractionation in fossil hydrothermal systems. *Geology* 33:825–828
- Smith CN, Kesler SE, Blum JD et al (2008) Isotope geochemistry of mercury in source rocks, mineral deposits and spring deposits of the California Coast Range, USA. *Earth Planet Sci Lett* 269:398–406
- Sonke JE, Zambardi T, Toutain JP (2008) Indirect gold trap-MC-ICP-MS coupling for Hg stable isotope analysis using a syringe injection interface. *J Anal At Spectrom* 23:569–573
- Stetson SJ, Gray JE, Wanty RB et al (2009) Isotopic variability of mercury in ore, mine-waste calcine, and leachates of mine-waste calcine from areas mined for mercury. *Environ Sci Technol* 43:7331–7336
- Sunderland EM (2007) Mercury exposure from domestic and imported estuarine and marine fish in the US seafood market. *Environ Health Perspect* 115:235–242
- Sunderland EM, Krabbenhoft DP, Moreau JW et al (2009) Mercury sources, distribution, and bioavailability in the North Pacific Ocean: insights from data and models. *Global Biogeochem Cycles* 23:GB2010. doi:10.1029/2008GB003425
- US Environmental Protection Agency (U.S. EPA) (1997) Mercury study report to congress 2. EPA-452/R-97-003. Office of Air Quality Planning and Standards, Office of Research and Development, Washington, DC
- Xie QL, Lu SY, Evans D et al (2005) High precision Hg isotope analysis of environmental samples using gold trap-MC-ICP-MS. *J Anal At Spectrom* 20:515–522
- Yang L, Sturgeon R (2009) Isotopic fractionation of mercury induced by reduction and ethylation. *Anal Bioanal Chem* 393:377–385
- Zambardi T, Sonke JE, Toutain JP et al (2009) Mercury emissions and stable isotopic compositions at Vulcano Island (Italy). *Earth Planet Sci Lett* 277:236–243
- Zheng W, Hintelmann H (2009) Mercury isotope fractionation during photoreduction in natural water is controlled by its Hg/DOC ratio. *Geochim Cosmochim Acta* 73:6704–6715

- Zheng W, Hintelmann H (2010a) Nuclear field shift effect in isotope fractionation of mercury during abiotic reduction in the absence of light. *J Phys Chem A* 114: 4238–4245
- Zheng W, Hintelmann H (2010b) Isotope fractionation of mercury during its photochemical reduction by low-molecular-weight organic compounds. *J Phys Chem A* 114:4246–4253
- Zheng W, Foucher D, Hintelmann H (2007) Mercury isotope fractionation during volatilization of Hg(0) from solution into the gas phase. *J Anal At Spectrom* 22: 1097–1104

Chapter 13

Thallium Isotopes and Their Application to Problems in Earth and Environmental Science

Sune G. Nielsen and Mark Rehkämper

Abstract This paper presents an account of the advances that have been made to date on the terrestrial stable isotope geochemistry of thallium (Tl). High precision measurements of Tl isotope ratios were only developed in the late 1990s with the advent of MC-ICP-MS and therefore we currently only have limited knowledge of the isotopic behavior of this element. Studies have revealed that Tl isotopes, despite their heavy masses of 203 and 205 atomic mass units, can fractionate substantially, especially in the marine environment. The most fractionated reservoirs identified are ferromanganese sediments and low temperature altered of oceanic crust. These display a total isotope variation of about 35 $\epsilon^{205}\text{Tl}$ -units, which is over 50 times the analytical reproducibility of the measurement technique. The isotopic variation can be explained by invoking a combination of conventional mass dependent equilibrium isotope effects and the nuclear field shift isotope fractionation, but the specific mechanisms are still largely unaccounted for.

Thallium isotopes have been applied to investigate paleoceanographic processes in the Cenozoic and there is some evidence to suggest that Tl isotopes may be utilized as a monitor of Fe and Mn supply to the water column over million year time scales. In addition, Tl isotopes can be used to calculate the magnitude of hydrothermal fluid circulation through ocean crust. Such calculations can be performed both for high and low temperature fluids. Lastly, it has been

shown that marine ferromanganese sediments can be detected in mantle-derived basalts with Tl isotopes (Nature 439:314–317), which confirms that marine sediments subducted at convergent plate margins can be recycled to the surface possibly via mantle plumes.

13.1 Introduction

The element thallium (Tl) was first discovered by William Crookes in 1861 and named after its green spectral line (thallus is latin for budding twig). Historically, the primary use has been as a rodent poison, but it has more recently also been employed as a component in photocells and infrared optical materials. The distribution of Tl in natural environments on Earth is controlled in part by its large ionic radius, which is akin to the alkali metals potassium (K), rubidium (Rb) and cesium (Cs) (Wedepohl 1974; Shannon 1976; Heinrichs et al. 1980). The large ionic radius renders Tl highly incompatible during igneous processing and hence it in the continental crust (Shaw 1952). Another important aspect of Tl chemistry is the ability to take on two different valence states: Tl^+ and Tl^{3+} . The oxidized form makes Tl generally more particle-reactive in solution than the alkali metals, and results in strong adsorption onto authigenic ferromanganese phases and to a lesser extent clay minerals in aqueous environments (Matthews and Riley 1970; McGoldrick et al. 1979; Hein et al. 2000). The higher particle-reactivity means that rivers and particularly the oceans have lower ratios between Tl and the alkali metals compared to the continental crust (Bruland 1983; Flegal and Patterson 1985; Nielsen et al. 2005). Thallium is also concentrated in some sulfide minerals

S.G. Nielsen (✉)
Woods Hole Oceanographic Institution, Dept. Geology and
Geophysics, 02543 Woods Hole, MA, USA
e-mail: snielsen@whoi.edu

M. Rehkämper
Department of Earth Science and Engineering, Imperial
College, London SW7 2AZ, UK

(Shaw 1952; Heinrichs et al. 1980) but it is currently unclear exactly what influence sulfide minerals have on the elemental and isotopic distribution of Tl on Earth.

Thallium has two isotopes with atomic masses 203 and 205 (Table 13.1). This equates to a relative mass difference of <1%. Considering that stable isotope fractionation theory states that the magnitude of isotope fractionation should scale with the relative mass difference of the isotopes (Urey 1947) one would not expect large stable isotope effects for Tl. Hence, it may be considered surprising that stable isotope investigations for Tl were commenced in the first place. However, the first attempts to measure Tl isotope ratios in natural materials were not aimed at terrestrial materials. The main reason behind the first Tl isotope studies was the search for potential radiogenic isotope variations due to decay of the now-extinct radioactive isotope ^{205}Pb (Anders and Stevens 1960; Ostic et al. 1969). Lead-205 decays to ^{205}Tl with a half-life of 15.1 Myr (Pengra et al. 1978), whereas ^{203}Tl is stable and has no radioactive precursor. Therefore, it was believed that variable $^{205}\text{Tl}/^{203}\text{Tl}$ ratios would reveal the former presence of ^{205}Pb when the solar system formed. A number of studies between 1960 and 1994 all failed to register any resolvable Tl isotope variation for some selected terrestrial and a large number of extraterrestrial materials (Anders and Stevens 1960; Ostic et al. 1969; Huey and Kohman 1972; Chen and Wasserburg 1987, 1994). The failure to detect any Tl isotope variation was due to the relatively large errors (>2‰) associated with the thermal ionization mass spectrometry (TIMS) measurements used at that time. The breakthrough came in 1999 when the first high precision Tl isotope measurements by multiple collector inductively coupled plasma mass spectrometry (MC-ICPMS) were published (Rehkämper and Halliday 1999). This technique provided a reduction

in the uncertainty of more than an order of magnitude with errors reported at about 0.1–0.2‰ (Rehkämper and Halliday 1999). As with the previous Tl isotope investigations, Rehkämper and Halliday (1999) were ultimately motivated by the search for ^{205}Pb . However, analyses of a number of terrestrial samples that were meant to define the Tl isotope composition of Earth, which could then be compared to extraterrestrial findings, revealed large Tl isotope variation in excess of 15 times the analytical reproducibility. In principle, it is not possible to distinguish between $^{205}\text{Tl}/^{203}\text{Tl}$ variation caused by decay of ^{205}Pb and stable isotope fractionation because Tl has only two isotopes. However, the observed variation was clearly unrelated to radioactive ^{205}Pb and thus was inferred to be the result of stable isotope fractionation.

In this contribution we summarize the knowledge that has been accumulated since 1999 on the stable isotope geochemistry of Tl in various terrestrial environments. We will divide this into sections covering the continental and marine domains, respectively. We will also review the most notable applications of Tl stable isotopes in geochemical research and outline what future studies are necessary in order to make Tl isotopes a more quantitative tracer in Earth sciences.

13.2 Materials and Methods

13.2.1 Mass Spectrometry

As outlined in the introduction, it was mainly the advent of MC-ICPMS that facilitated the development of high-precision Tl isotope ratio measurements. The principal difference to the previous TIMS measurements was the ability to correct for instrumental isotope fractionation that occurs during the measurement (mass bias or mass discrimination). Stable isotope compositions in general and two-isotope systems in particular are difficult to measure by TIMS because isotope fractionation during volatilization from the filament is mass dependent just like the stable isotope variation that is attempted to be measured. As such, it is very difficult to determine precise stable isotope ratios by TIMS without the use of a double spike (Rudge et al. 2009). However, double spiking can only be performed for elements with four or more

Table 13.1 Physical properties of thallium (Nriagu 1998)

Melting point	577 K
Molar weight	204.38 g
Density	11.85 g/cm ³
Valence states	Tl ⁺ Tl ³⁺
Redox potentials (V)	
Tl _(s) → Tl ⁺ + e ⁻	+0.336
Tl ⁺ → Tl ³⁺ + 2e ⁻	-1.28
Ionic radius (Tl ⁺)	1.50 Å
Ionic radius (Tl ³⁺)	0.89 Å
Isotopes	²⁰³ Tl ²⁰⁵ Tl

isotopes (Rudge et al. 2009) and this is the reason why the early Tl isotope studies by TIMS yielded relatively large uncertainties. The great advantage of MC-ICPMS when measuring Tl isotopes (or any two-isotope system) is that, even though the overall magnitude of instrumental mass discrimination is much larger than for TIMS, it is possible to monitor it independently during a measurement and thus correct for it much more precisely than is possible with TIMS. This mass bias correction can be performed because the sample is introduced into the mass spectrometer as a solution (or a desolvated aerosol). Into this solution can be admixed a separate element with a known isotope composition (for Tl this element is Pb) and by assuming that the mass bias incurred for the two elements are proportional, isotope ratios can be determined very accurately and precisely (Rehkämper and Halliday 1999; Nielsen et al. 2004). In practice (as is the case for all other stable isotope systems) isotope compositions are best determined by referencing to a standard. For Tl this standard is the NIST 997 Tl metal, and isotope compositions are reported as:

$$\varepsilon^{205\text{Tl}} = 10^4 \times \left(\frac{^{205}\text{Tl}/^{203}\text{Tl}_{\text{sample}} - ^{205}\text{Tl}/^{203}\text{Tl}_{\text{NIST997}}}{^{205}\text{Tl}/^{203}\text{Tl}_{\text{NIST997}}} \right)$$

Note that the terminology used for Tl isotope ratios is slightly different to standard stable isotope ratio conventions, which generally use the δ -notation (variations in parts per 1,000). The reason for this is that the Tl isotope system was originally developed as a cosmochemical radiogenic isotope system, which by convention mostly is reported using the ε -notation (variations in parts per 10,000). Hence, it was deemed sensible to keep the original notation in order to make comparisons between cosmochemical and terrestrial data easier. In addition, the analytical uncertainty on and overall variability of stable Tl isotope ratios make the ε -notation very convenient as most data are thereby shown in whole digits and only a single figure behind the decimal point is needed.

13.2.2 Chemical Separation of Thallium

Prerequisites to obtaining precise and accurate stable isotope ratios by MC-ICPMS are the complete separation of the element of interest from the sample matrix

as well as 100% recovery. This is important because residual sample matrix in the purified sample can result in isotope effects either present as instabilities that lead to large uncertainties or as reproducible isotopic offsets leading to precise but inaccurate data (Pietruszka and Reznik 2008; Poirier and Doucelance 2009; Shiel et al. 2009).

The technique for separating Tl from sample matrix when performing isotopic analyses of geologic materials was initially developed by Rehkämper and Halliday (1999). The technique has been modified slightly (Nielsen et al. 2004, 2007; Baker et al. 2009) from the original recipe, but the fundamentals have remained unchanged. Only the elution procedure has been optimized in order to remove matrix elements most efficiently (Fig. 13.1). The separation technique relies on the fact that the trivalent Tl ion produces anionic complexes with the halogens (the technique uses either Cl^- or Br^-) in acidic solutions that partition very strongly to anion exchange resins. Conversely univalent Tl does not form strong anionic complexes and thus does not partition at all to anion exchange resins. Therefore, samples are prepared in oxidizing media by adding small amounts of water saturated in Br_2 to the samples already digested and dissolved in hydrochloric acid. This process ensures that all Tl is in the trivalent state, which will adsorb onto the anion exchange resin prepared in a quartz or teflon column. The sample matrix can then be eluted in various acidic media as long as Br_2 is present. Lastly, Tl is stripped from the resin by elution with a reducing solution that converts Tl to the univalent state. The reducing solution used is 0.1 M hydrochloric acid in which 5% by weight of SO_2 gas has been dissolved. As SO_2 is not stable in solution for long periods of time it is important to make this solution fresh before performing the chemical separation of Tl.

13.2.3 Measurement Uncertainties and Standards

As with most stable isotope measurements by MC-ICPMS, the smallest uncertainties are obtained for pure standard solutions. The most commonly used secondary standard for Tl is a pure 1,000 ppm standard solution for ICP-MS concentration analyses that was originally purchased from Aldrich. Over a period of

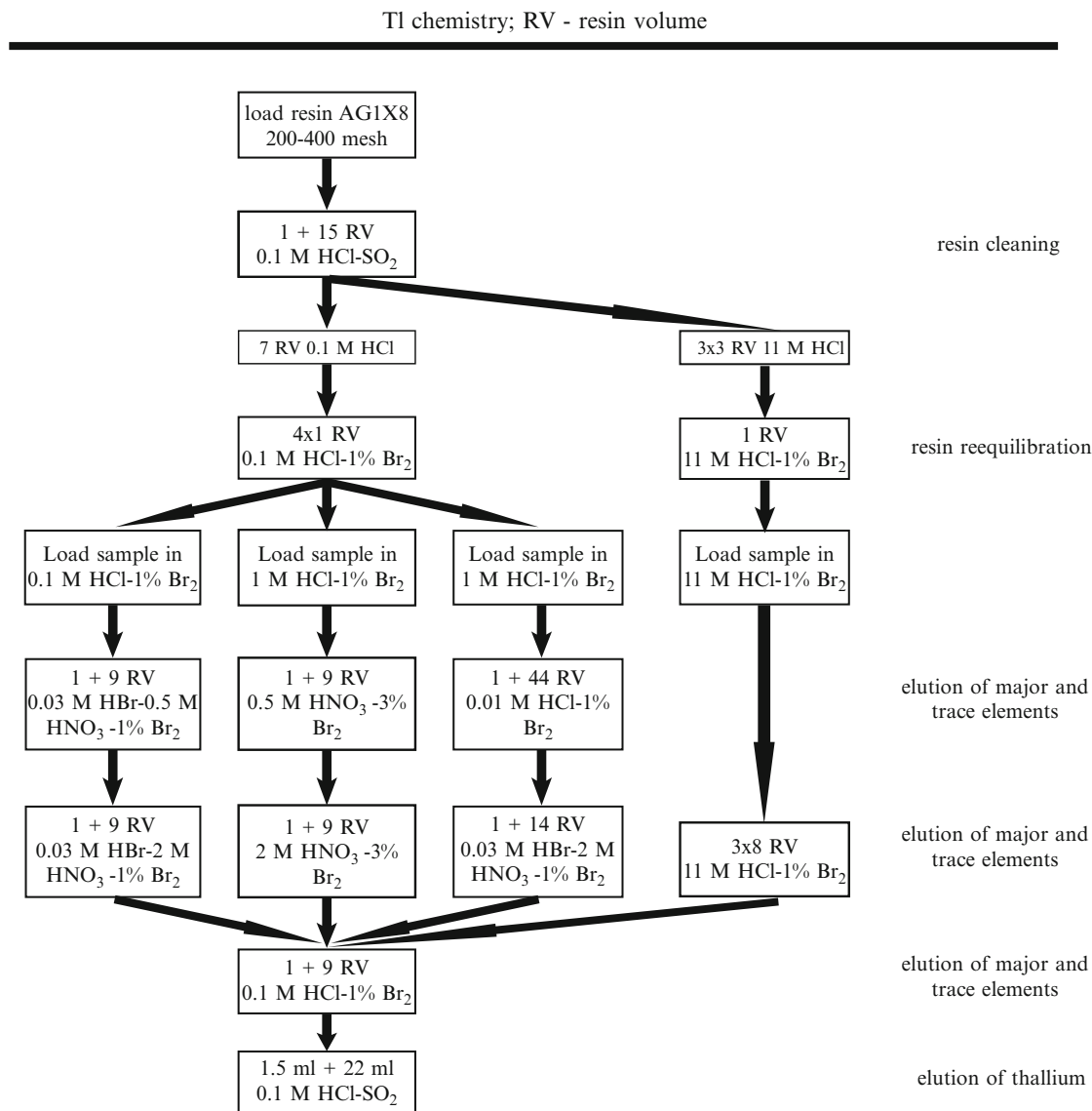


Fig. 13.1 Anion exchange separation procedures for Tl. The recipes can be scaled to any amount of resin (*RV* resin volume) depending on sample size, though large samples require a second 100 μ l resin column to ensure that Tl is sufficiently pure.

Four different elution procedures are outlined here (Rehkämper and Halliday 1999; Nielsen et al. 2004; Baker et al. 2009), where the procedure in dilute HCl and HNO₃ without HBr is the method currently in use in Oxford

more than 10 years this standard has been measured against NIST 997 Tl on six different mass spectrometers with an overall average of $\varepsilon^{205}\text{Tl} = -0.81 \pm 0.33$ (2sd, $n = 133$). This uncertainty, however, is not representative of how well samples can be reproduced mainly because small amounts of sample matrix invariably degrade the measurement precision compared to a pure metal standard even when measuring at the same ion beam intensity. This matrix effect

generally leads to a relationship between sample concentration and measurement uncertainty with the smallest uncertainties obtained for samples with the highest concentrations (Table 13.2, (Nielsen et al. 2004, 2006a, 2007; Baker et al. 2009; Prytulak and Nielsen, unpublished data)).

In cases where the amount of sample is limited it can become an important issue how many ions can be measured for a given amount of Tl. Over the last 10

Table 13.2 Data for geologic reference materials

Standard	Description	$\epsilon^{205}\text{Tl}$	<i>n</i>	Error ^a	Tl concentration (ng/g)	References
Nod P1	Ferromanganese nodule	0.5	1	0.5	146,000	Rehkämper et al. (2002)
Nod A1 ^b	Ferromanganese nodule	10.7	6	0.5	108,000	Rehkämper et al. (2002); Nielsen et al. (2004)
AGV-2	Andesite	-3.0	8	0.6	269	Prytulak and Nielsen, unpublished data; Baker et al. (2009)
BCR-2	Columbia river basalt	-2.5	4	0.4	257	Prytulak and Nielsen, unpublished data
BHVO-2	Hawaii basalt	-1.8	6	0.6	18	Prytulak and Nielsen, unpublished data; Baker et al. (2009)
BIR-1	Iceland basalt	1.1	6	1.2	1.3	Nielsen et al. (2007)
NASS-5	seawater	-5.0	1	1.0	0.0094	Nielsen et al. 2004
TSW ^c	Coastal seawater, Tenerife	-8.7	3	1.0	0.0075	Nielsen et al. (2004)
RRR ^c	Rhine river water	-6.4	4	0.8	0.0036	Nielsen et al. (2004)
Allende	Carbonaceous chondrite	-3.1	8	0.5	55	Baker et al. (2010b)

^aErrors are either 2sd of the population of separate sample splits processed individually ($n \geq 3$) or estimated based on repeat measurements of similar samples ($n = 1$)

^bIsotope composition reported for multiple analyses of one large 300 mg aliquot dissolved in 6 M HCl

^cRRR and TSW are internal laboratory standards that were analyzed multiple times in order to assess reproducibility for samples with such low concentrations of Tl

years MC-ICPMS instruments have been developed to achieve increased transmission (i.e. the fraction of the ions introduced into the machine that reach the collector) and the most recent have values of >1% for Tl and Pb. Although this efficiency may appear low, it enables Tl isotope analyses on samples as small as 1 ng, without compromising counting statistics notably, and an external precision of better than ± 1 ϵ -unit is common (Nielsen et al. 2004, 2006a, 2007; Baker et al. 2009). Smaller sample sizes down to 200 pg can still be analysed on regular Faraday collectors, although precision is significantly degraded to ± 3 ϵ -units (Nielsen et al. 2006a, 2007, 2009b).

13.3 Thallium Isotope Variability in Crustal Environments

13.3.1 Igneous Processes

As discussed previously, Tl generally follows the alkali metals K, Rb and Cs during melting and fractional crystallisation (Shaw 1952; Heinrichs et al. 1980) resulting in higher Tl concentrations in the continental crust (~0.5 ppm) than the mantle (~0.0035 ppm) (Shaw 1952; Wedepohl 1974; Heinrichs et al. 1980; McDonough and Sun 1995; Rudnick and Gao 2003). Though stable isotope fractionation has been documented in igneous systems for relatively

heavy elements such as iron (Williams et al. 2004, 2009), the small relative mass difference between the isotopes of Tl in combination with little or no redox chemistry for Tl in igneous systems, favour the prediction that only very little Tl isotope fractionation may occur during magmatic processing. Several studies found that the isotope composition of the average continental crust, represented by loess, is indistinguishable from the mantle, with both exhibiting a value of $\epsilon^{205}\text{Tl} = -2.0 \pm 0.5$ (Nielsen et al. 2005, 2006b, c, 2007). The uniform isotope composition of the continental crust is further supported by data obtained for an ultrapotassic dike from the Tibetan Plateau ($\epsilon^{205}\text{Tl} = -2.3$; Nielsen and Rehkämper, unpublished results), which represents a melt originating from the sub-continental lithospheric mantle (Williams et al. 2001). Hence, there is no evidence to suggest that melting or fractional crystallisation impart any significant Tl isotope fractionation. Thallium also partitions into some sulphide minerals (Shaw 1952; Heinrichs et al. 1980) and commercial Tl extraction is performed almost exclusively from sulphide ore minerals. So far, there is only one study that investigates Tl isotope fractionation during sulphide ore genesis (Baker et al. 2010a). Here it is shown that the Cu-mineralisation of large porphyry Cu systems in the Collahuasi Formation of Chile is not characterized by Tl enrichments or distinct Tl isotope fingerprints. However, some of the associated hydrothermal processes that mobilised alkali metals also affected Tl concentrations and, to some extent, isotope

compositions ($\epsilon^{205}\text{Tl} = -5$ to 0). This study therefore highlights that Tl may retain its lithophile behaviour even in systems that experience sulphide mineralisation (Baker et al. 2010a). Hence, it is unknown at present exactly under what conditions Tl becomes chalcophile and if Tl isotopes would fractionate substantially under such circumstances. However, it might be expected that at least for magmatic ore formation processes the high temperatures in combination with the small relative mass difference of the Tl isotopes would probably not result in significant isotope fractionation.

13.3.2 Volcanic Degassing

Due to its low boiling point (Table 13.1), Tl is significantly enriched in volcanic gasses and particles compared with the geochemically analogous alkali metals (Patterson and Settle 1987; Hinkley et al. 1994; Gauthier and Le Cloarec 1998; Baker et al. 2009). Consequently, volcanic plumes provide a large Tl flux from igneous to surface environments on Earth, with an estimated flux to the oceans of 370 Mg/year (Rehkämper and Nielsen 2004; Baker et al. 2009). The behaviour of Tl isotopes in volcanic systems was recently investigated by Baker et al. (2009), who identified significant isotope variations. The most likely form of isotope fractionation to occur during degassing is kinetic isotope fractionation, where the light isotope is enriched in the gas phase. The extent of kinetic isotope fractionation between two phases is determined by the relative magnitude of the atomic or molecular velocities, where $\alpha = (m_1/m_2)^\beta$ and β varies from 0.5 (in the case of a vacuum) down to values approaching 0 (Tsuchiyama et al. 1994). Hence, even though the relative mass difference between the two Tl isotopes is small, the maximum kinetic $\alpha_{\text{liq-vap}}$ is 1.0049, or 49 ϵ -units. An isotope composition difference of this magnitude is larger than the entire stable Tl isotope variation recorded on Earth and would hence be readily detectable. However, contrary to the expectation of a gas phase enriched in light isotopes, Baker et al. (2009) found no systematic enrichment of either isotope in volcanic emanations compared with average igneous rocks. Despite large isotopic differences between individual samples, the isotope compositions of 34 samples of gas condensates

and particles from six separate volcanoes showed an overall average of $\epsilon^{205}\text{Tl} = -1.7 \pm 2.0$. This value is indistinguishable from average igneous rocks (Nielsen et al. 2005, 2006b, c, 2007). The Tl isotope variation of volcanic emanations was interpreted to reflect the complex evaporation as well as condensation processes that occur in volcanic edifices (Baker et al. 2009), and which eventually produce no net isotope fractionation between Tl in the magma and the Tl transported into the atmosphere and surface environments on Earth.

13.3.3 Riverine Transport of Tl

Stable isotope fractionation during weathering is often monitored via measurements of isotope ratios in the dissolved and particulate phases in rivers. For example, elements like lithium and molybdenum have been shown to display significant isotope composition variation between different rivers and rocks of the continental crust (Huh et al. 1998; Archer and Vance 2008; Pogge von Strandmann et al. 2010). Numerous kinetic and equilibrium processes can potentially affect the stable isotope budgets of rivers, and as such it is difficult to predict isotope fractionation during weathering. Nielsen et al. (2005) measured the Tl isotope compositions of dissolved and particulate components for a number of major and minor rivers and found that these generally display values similar to those observed for continental crust. The average value for dissolved riverine Tl is $\epsilon^{205}\text{Tl} = -2.5 \pm 1.0$ (Nielsen et al. 2005), with particulate matter ($\epsilon^{205}\text{Tl} = -2.0 \pm 0.5$) being indistinguishable from the dissolved phase (Fig. 13.2, Table 13.3). These data strongly imply that there is little or no Tl isotope fractionation associated with continental weathering processes.

Natural unpolluted Tl abundances in rivers are generally very low and vary between 1 and 10 pg/g (Cheam 2001; Nielsen et al. 2005). An estimated global average riverine concentration of 6 ± 4 pg/g (or 30 ± 20 pmol/l) results in a flux to the oceans of 230 Mg/year. In the study of Nielsen et al. (2005) three rivers exhibited Tl isotope compositions significantly lighter ($\epsilon^{205}\text{Tl} = -6$ to -4) than average continental crust (Fig. 13.2). These lighter compositions were interpreted to reflect the somewhat different Tl isotope composition of marine carbonates that were a main constituent of the drainage areas for these rivers.

Table 13.3 Thallium isotope and concentration data for rivers

Sample	$\epsilon^{205}\text{Tl}$	Tl (ng/kg)
Amazon	-2.3	16.4
Danube	-6.7	16.4
Doubs	-5.5	3.36
Eder	-4.2	1.93
Kalix	-1.6*	1.31
Nahe	-2.5	7.03
Nidda	-2.7	1.67
Nidder	-2.6	2.85
Nile	$\pm 0.0^*$	3.13
Rhine Rueun	-6.4	3.61
Rhine Laufenbg.	-3.0	4.04
Rhine Speyer	-2.8	5.35
Rhine Bingen	-2.9	6.71
Rhone	-2.7	6.54
Volga	-1.1*	1.60

Sample locations are given in Nielsen et al. (2005)

*Uncertainties for these samples were estimated at 1.5 epsilon units due to smaller amounts of Tl available. The remaining samples have uncertainties of about 1 epsilon unit.

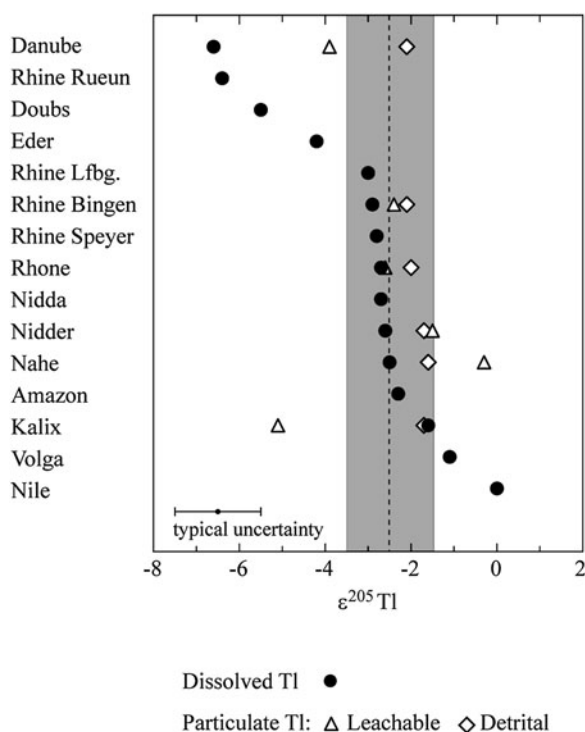


Fig. 13.2 Isotope compositions of riverine dissolved and particulate Tl. The particulate Tl is divided into a labile and detrital fraction. Figure modified from Nielsen et al. (2005)

The more negative $\epsilon^{205}\text{Tl}$ values for marine carbonates were expected, based on the current Tl isotope composition measured for seawater ($\epsilon^{205}\text{Tl} = -5.5 \pm 1.0$;

(Rehkämper et al. 2002; Nielsen et al. 2004, 2006c)). However, marine carbonates including carbonate oozes (Rehkämper et al. 2004), corals (Rehkämper, unpublished data) and foraminifera (Nielsen, unpublished data) exhibit very low Tl concentrations and therefore weathering of marine carbonates will only have a strong influence on rivers predominantly draining such lithologies, and will not strongly affect the total global budget of Tl transported by rivers to the oceans.

13.3.4 Anthropogenic Mobilisation of Tl

To date no study has been carried out to investigate the Tl isotope effects incurred from industrial pollution. Industrial purification of Tl is tightly restricted because of the toxicity of Tl. Therefore, the main emissions of Tl to the environment are not from Tl production but stem from coal burning (Nriagu 1998; Cheam et al. 2000) and zinc smelting (Nriagu 1998). Thallium is present in relatively high concentrations in coal and zinc ore (~1 ppm, (Sager 1993)) and is enriched in the waste products from industrial processing of these resources. There are many examples of adverse environmental effects from Tl pollution caused by industry (Lis et al. 2003; Xiao et al. 2003, 2004; Sasmaz et al. 2007) and hence there may be some potential for using Tl isotopes to monitor industrial pollution. Coal burning and zinc smelting both involve significant heating, during which gases and particulates may escape into the natural environment. One might therefore expect kinetic Tl isotope fractionation to occur and isotopically light Tl could potentially be a signature of Tl pollution, as has been found for volatile Cd (Cloquet et al. 2006). However, if volcanic emissions (see Sect. 13.3.2) can be used as an analogue for these processes, industrial waste pollution may not necessarily carry a very distinct Tl isotope signature.

A secondary issue of potentially tracing Tl pollution using isotope data, is the unknown initial composition of the material. In many cases, it may be reasonable to infer that the isotope composition of continental crust ($\epsilon^{205}\text{Tl} = -2$) will be the dominant “signature” of coal and zinc ore. However, since Tl is mainly associated within these deposits as a result of its affinity to sulfides (Sager 1993; Nriagu 1998), it will be important to investigate Tl isotope variations in sulfides to verify this assumption.

13.4 Thallium Isotopes in the Marine Environment

13.4.1 The Isotope Composition of Seawater

In the oceans, Tl is a conservative low-level trace element with an average dissolved concentration of 13 ± 1 pg/g (64 ± 5 pmol/l) (Flegal and Patterson 1985; Schedlbauer and Heumann 2000; Rehkämper and Nielsen 2004; Nielsen et al. 2006c), which is slightly higher than abundances observed in river water (see Sect. 13.3.3). Based on a thorough review of the marine input and output fluxes of Tl, Rehkämper and Nielsen (2004) concluded that the oceans are currently at steady state and that Tl has a residence time of ~21 kyr, which is consistent with a number of previous studies (Flegal and Patterson 1985; Flegal et al. 1989). With an inferred residence time that is more than an order of magnitude longer than the oceanic mixing time and a conservative distribution, Tl should exhibit an invariant isotope composition in the oceans. Analyses of Arctic, Atlantic and Pacific seawater confirm this prediction (Rehkämper et al. 2002; Nielsen et al. 2004, 2006c) but the current dataset is limited to results for seven samples from only three locations.

It may perhaps be somewhat surprising that the oceans are significantly depleted in ^{203}Tl compared to the continental crust and the mantle (See Chap. 3) with an average value of $\epsilon^{205}\text{Tl} = -5.5 \pm 1.0$ (Rehkämper et al. 2002; Nielsen et al. 2004, 2006c). Hence, it is required either that the marine sources of Tl are isotopically light compared to the crust and mantle or that the outputs are fractionated towards heavy values compared with seawater itself. Rehkämper and Nielsen (2004) showed that the most significant marine inputs for Tl are from rivers, high-temperature hydrothermal fluids, mineral aerosols, volcanic emanations and sediment pore water fluxes at continental margins. In contrast, there are only two important marine Tl sinks, namely Tl adsorption by the authigenic phases of pelagic clays and uptake of Tl during low-temperature alteration of oceanic crust. The relative magnitudes and isotope compositions of these fluxes are summarized in Table 13.4. In the following sections, we outline the main observations that have led to the assessment for these fluxes.

13.4.2 Thallium Isotopes in Marine Input Fluxes

The riverine and volcanic input fluxes have already been discussed in previous sections and hence here we will focus on high-temperature hydrothermal fluids, mineral aerosols and sediment pore water fluxes from continental margins.

13.4.2.1 High Temperature Hydrothermal Fluids

In hydrothermal systems where temperatures exceed $\sim 150^\circ\text{C}$ it has been shown that Tl behaves much like the alkali metals Rb and K (Metz and Trefry 2000), and is leached from the oceanic crust by the circulating fluids. This results in end-member high temperature hydrothermal fluids exhibiting Tl concentrations almost 500 times higher than ambient seawater (Metz and Trefry 2000; Nielsen et al. 2006c) with a best estimate of 4.5 ± 2.2 ppb (22 ± 11 nmol/l) (Nielsen et al. 2006c). Thus hydrothermal fluids represent a significant Tl flux to the oceans with an estimated range of 9–200 Mg/year (Nielsen et al. 2006c). Due to the relatively high temperatures involved ($300\text{--}400^\circ\text{C}$) isotope fractionation is not expected to be significant. This was confirmed by Nielsen et al. (2006c), who determined the Tl isotope composition of hydrothermal fluids from the East Pacific Rise and Juan de Fuca Ridge. All samples had Tl isotope compositions identical to that of average MORB, thus supporting the interpretation that extraction of Tl from the oceanic crust is not associated with isotope fractionation. The chemical and isotopic behavior inferred for Tl from hydrothermal fluids is further in accord with the results of a study of oceanic crust from ODP Hole 504B altered by high temperature hydrothermal fluids. The latter work revealed Tl concentrations for basalts/dikes that were much lower than expected for depleted ocean crust whilst the Tl isotope compositions were identical to average MORB (Nielsen et al. 2006c).

13.4.2.2 Mineral Aerosols

There are no direct investigations of Tl abundances or isotope compositions for mineral aerosols deposited in

the oceans. Based on studies of windborne loess sediments deposited on land, Nielsen et al. (2005) concluded that the average abundance of Tl in dust deposited in the oceans is about 490 ± 130 ng/g. The main uncertainty in determining the Tl flux to the oceans is from estimating the fraction of Tl that is released from the dust into seawater, following deposition and partial dissolution. By comparison with a number of other elements, Rehkämper and Nielsen (2004) concluded that about 5–30% of the Tl transported in aerosol particles would dissolve in seawater, resulting in an annual Tl flux of 10–150 Mg/year.

It may be reasonable to assume that the bulk Tl isotope composition of the material transported to the ocean is identical to loess, and thereby also the continental crust, with $\epsilon^{205}\text{Tl} = -2$ (Nielsen et al. 2005). However, it is unknown whether dust dissolution is associated with any isotope fractionation. Schauble (2007) has shown that significant equilibrium Tl isotope fractionations will be produced primarily by chemical reactions that involve both valence states, Tl^+ and Tl^{3+} . Based on the strongly correlated behaviour of Tl, Rb, Cs and K in the continental crust, univalent Tl should be dominant in mineral aerosols.

Thermodynamic calculations of the valence state of Tl in seawater also predict that all Tl is univalent in this reservoir (Nielsen et al. 2009a). In addition, continental weathering processes, which are ultimately controlled by aqueous dissolution of silicates and are therefore in many ways analogous to the leaching of dust in seawater, induce no detectable Tl isotope fractionations (Nielsen et al. 2005). Hence, we infer that isotope fractionation is unlikely to be significant during the dissolution of mineral aerosols in seawater.

13.4.2.3 Benthic Fluxes from Continental Margins

It has long been known that pore waters, which seep into the oceans from reduced continental margin sediments, are rich in manganese (Elderfield 1976; Sawlan and Murray 1983). Since Tl is strongly associated with Mn oxides (Koschinsky and Hein 2003), Rehkämper and Nielsen (2004) inferred that such pore waters may be an important source of dissolved marine Tl. However, there are currently no data available to constrain either the average Tl concentration or isotope

Table 13.4 The Tl mass balance of the oceans with estimated source and sink fluxes

	Range of Tl flux estimates (Mg/year)	Best estimate (Mg/year)	%	$\epsilon^{205}\text{Tl}$	References
Marine input fluxes					
Rivers	76–380	230	27	–2.5	Rehkämper and Nielsen (2004); Nielsen et al. (2005)
Hydrothermal fluids	9–200	30	4	–2	Nielsen et al. (2006c)
Subaerial volcanism	42–700	370	43	–2	Baker et al. (2009)
Mineral aerosols	10–150	50	6	–2	Rehkämper and Nielsen (2004); Nielsen et al. (2005)
Benthic fluxes from continental margins	5–390	170	19	0	Rehkämper and Nielsen (2004), this study
Total input flux	140–1,820	850	100	–1.8	
Marine output fluxes					
Pelagic clays	240–450	310	36	+10	Rehkämper and Nielsen (2004); Rehkämper et al. (2004), this study
Altered ocean crust	225–1,985	540	64	–8.5	Rehkämper and Nielsen (2004); Nielsen et al. (2006c), this study
Total output flux	430–1,530	850	100	–1.8	
	Mass of Tl (Mg)	Steady-state residence time		$\epsilon^{205}\text{Tl}$	
Global oceans	$1.75 (\pm 0.14) \times 10^7$ ^a	21,000 year		–5.5	Rehkämper and Nielsen (2004); Nielsen et al. (2006c); Rehkämper et al. (2002)

^aFor a global ocean system with 1.348×10^{21} kg, the Tl mass in the oceans is equivalent to an average seawater concentration of 65 ± 5 pmol/kg or 13 ± 1 ng/kg (Rehkämper and Nielsen 2004)

composition of these benthic fluxes. An estimate was therefore derived indirectly, based on (1) Tl/Mn ratios observed in ferromanganese nodules that were known to have precipitated from pore waters (Rehkämper et al. 2002), combined with (2) estimates for benthic Mn fluxes (Sawlan and Murray 1983; Heggie et al. 1987; Johnson et al. 1992). Taken together, these data yield a Tl flux of 5–390 Mg/year, and a best estimate of 170 Mg/year (Rehkämper and Nielsen 2004) which constitutes a substantial fraction of the total Tl flux to the oceans (Table 13.4).

We can use two distinct approaches to estimate the average Tl isotope composition of pore waters. The first utilizes published Tl isotope data for the various components that may supply pore waters with Tl. The second relies on the Tl isotope compositions of sediments that are precipitated from pore waters. The application of these approaches is summarized below.

There are three principle components, which could be mobilized and incorporated into sedimentary pore waters. (1) Labile Tl associated with riverine particles (Nielsen et al. 2005). (2) Thallium adsorbed onto clay minerals from seawater (Matthews and Riley 1970). (3) Thallium bound to authigenic Mn-oxides that precipitated from seawater as part of deep sea red clays (Rehkämper et al. 2004). All three will be present in continental margin sediments in various proportions depending on sedimentation rate and proximity to estuaries, where high sedimentation rates would tend to dilute the Mn-oxides as it is assumed that authigenic precipitation should remain fairly constant. Hence, assuming that there is no isotope fractionation associated with the release of Tl into pore waters, the isotope composition of each component can define bounds on the composition of pore waters.

The labile components in riverine particles have been shown to be isotopically similar to the continental crust and river waters (Fig. 13.2) and thus is characterized by $\epsilon^{205}\text{Tl} = -2$ (Nielsen et al. 2005).

Matthews and Riley (1970) showed that Tl is readily adsorbed onto some clay minerals (in particular illite) where most Tl is exchanged with K. Because of the required charge balance for adsorption reactions, clay adsorption is unlikely to be associated with any Tl reduction/oxidation processes and should thereby exhibit only minimal or no isotope fractionation (Schauble 2007). Since Tl adsorption to clay

minerals would take place primarily within the marine environment, this component should be characterized by $\epsilon^{205}\text{Tl} = -5.5$.

Thallium that is precipitated with Mn oxides onto sedimentary particles has been shown to have a significantly heavier isotope composition than the seawater from which the mineral forms (Rehkämper et al. 2002, 2004). The origin of this isotope fractionation is discussed in Sect. 13.5 below. Theoretically, the pure MnO_2 mineral to which Tl is bound should have approximately the same isotope composition as the surfaces of Fe-Mn crusts, which display $\epsilon^{205}\text{Tl} = +13$ (Fig. 13.4). However, leaching experiments conducted on shelf sediments with HCl and hydroxylamine hydrochloride indicate that the labile Tl on sediment particles features somewhat lower $\epsilon^{205}\text{Tl}$ values of between +3 to +7 (Rehkämper et al. 2004; Nielsen et al. 2005). These lower values could reflect contributions from a component other than Fe-Mn oxides, for example Tl adsorbed to clay minerals that are characterized by negative $\epsilon^{205}\text{Tl}$ -values. Nevertheless, it appears reasonable to infer that the Tl associated with marine authigenic Mn in continental margin sediments exhibits $\epsilon^{205}\text{Tl} \approx +4$ to +10.

In summary, the isotopic data available for these three components indicate that pore waters from continental margin sediments are likely to feature $\epsilon^{205}\text{Tl}$ values of about -4 to $+6$. This range can be compared with the compositions of two different sedimentary archives that form from pore waters. These are diagenetic ferromanganese nodules (which are inferred to originate primarily from pore waters) and early diagenetic pyrite. Rehkämper et al. (2002) analyzed two Mn nodules from the Baltic Sea and these exhibited $\epsilon^{205}\text{Tl} = -0.2$ and -5.2 . Nielsen et al. (2010) measured Tl isotopes in pyrites younger than 10 Myr from continental shelf sediments in the Northeast Pacific and the Caribbean and found $\epsilon^{205}\text{Tl}$ values of between -1 and $+2$. Importantly, both ferromanganese nodules and pyrites thus have Tl isotope compositions that are in accord with the range of values inferred for pore waters based on their constituent components. Taken together (and assuming that there is negligible isotope fractionation between pyrite/Fe-Mn nodules and pore waters) these constraints suggests that benthic fluxes from continental shelf sediments are characterized by $\epsilon^{205}\text{Tl} \sim -3$ to $+3$, with a best estimate of $\epsilon^{205}\text{Tl} \sim 0$.

13.4.3 Thallium Isotope Compositions of Marine Output Fluxes

13.4.3.1 Thallium Adsorption by the Authigenic Phases of Pelagic Clays

There is a significant enrichment of Tl in pelagic clays compared with continental shelf sediments (Matthews and Riley 1970; Heinrichs et al. 1980; Rehkämper et al. 2004). This enrichment is caused by the adsorption of Tl onto hydrogenetic Fe-Mn oxy-hydroxides and clay minerals (Matthews and Riley 1970; McGoldrick et al. 1979; Heinrichs et al. 1980). Two independent methods of calculating the Tl flux associated with these authigenic fluxes agree very well and indicate an annual flux of 200–410 Mg/year, with a best estimate of 270 Mg/year (Rehkämper and Nielsen 2004). Adding the smaller flux of Tl incorporated into pure Fe-Mn deposits of ~40 Mg/year (Rehkämper and Nielsen 2004) yields a total marine authigenic Tl flux of 310 Mg/year (Table 13.4). As discussed in Sect. 13.4.2.3, the isotope composition of the Tl associated with authigenic phases is best characterized by a mixture of Tl bound to Mn oxides that displays $\epsilon^{205}\text{Tl} \sim +13$ and Tl adsorbed onto clay minerals, which likely exhibits $\epsilon^{205}\text{Tl} \sim -5.5$. Due to the strong Mn enrichment of deep sea pelagic clays, it can be assumed that the majority of authigenic Tl in pelagic clays originates from Mn oxides and thus may have an isotope composition more akin to Fe-Mn crusts. We can attempt to quantify this by performing an isotope mass balance calculation for the pelagic clays reported in Rehkämper et al. (2004). The bulk isotope composition of these samples is $\epsilon^{205}\text{Tl} = +3$ to $+5$. About 50% of the Tl in pelagic clays is thought to be of detrital origin (Rehkämper et al. 2004), which is characterized by $\epsilon^{205}\text{Tl} = -2$ (Nielsen et al. 2005). In order to account for the reported bulk isotope compositions, the authigenic component would thus have to display $\epsilon^{205}\text{Tl} \sim +8$ to $+12$, and this implies that the authigenic Tl of pelagic clays features an isotope composition that is slightly lighter than pure Fe-Mn deposits. Based on the above considerations we can calculate that ~75–95% of the authigenic Tl in pelagic clays originates from Mn-oxides, whilst the remainder is bound to clay minerals.

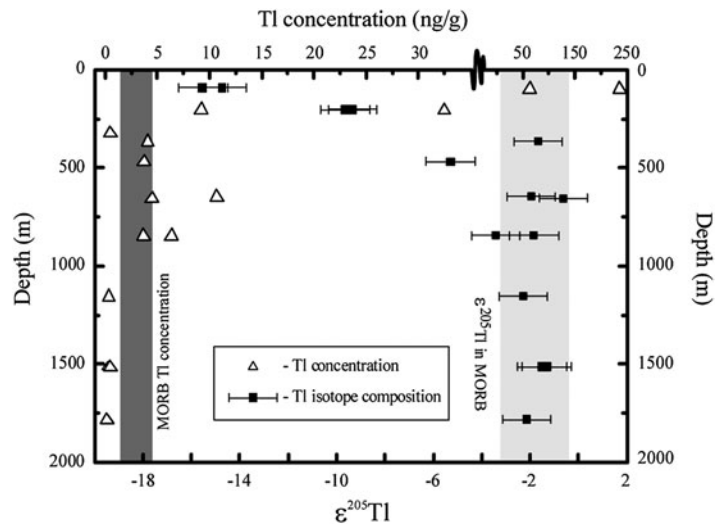
13.4.3.2 Thallium Uptake During Low Temperature Hydrothermal Alteration

It is well-known that alteration minerals produced by interaction between cold ($<100^\circ\text{C}$) seawater and MORB are highly enriched in Tl compared to pristine oceanic crust (McGoldrick et al. 1979; Alt 1995; Jochum and Verma 1996). This process leads to an enrichment of Tl in the volcanic section of oceanic crust (on average the uppermost 500–600 m) that has been shown to be affected by low temperature (low-T) alteration. Estimating an average annual flux of Tl into the oceanic crust would be relatively simple if the average Tl concentration of this material could be determined. This is not a straightforward exercise, however, because of the heterogeneous distribution of alteration minerals in low-T altered crust and the inferred enrichment factors for Tl (compared to its abundance in pristine oceanic crust) therefore vary widely, between values of 1 and 200 (Jochum and Verma 1996; Teagle et al. 1996; Nielsen et al. 2006c). In general, the highest Tl enrichments are detected towards the top of the oceanic crust (Fig. 13.3). Following a conservative approach, based partially on the assumption that Cs and Tl are added to the ocean crust in equal proportions (Rehkämper and Nielsen 2004; Nielsen et al. 2006c), it was proposed that, on average, the upper 600 m of oceanic crust contains 200 ± 150 ng/g of Tl (Nielsen et al. 2006c). This number is equivalent to an element flux of 225–1,985 Mg/year, with a best estimate of ~1,000 Mg/year. The best estimate value, however, is significantly larger than all marine Tl inputs combined (Table 13.4).

Given the uncertainties, it may thus be more reasonable to apply a mass balance approach (which assumes that marine Tl is at steady state) to estimate the Tl flux into low-T altered ocean crust. With a total input flux of 850 Mg/year (Table 13.4) and an authigenic output flux of 310 Mg/year, the marine Tl budget can be balanced with a low-T alteration output of 540 Mg/year, which is well within the range of values estimated based on Tl concentration data available for low-T altered ocean crust (Table 13.4).

The isotope composition of the low-T alteration output is equally difficult to determine. Nielsen et al. (2006c) observed that, in general, the upper oceanic crust is significantly enriched in isotopically light Tl

Fig. 13.3 Thallium concentrations (*triangles*) and isotope compositions (*black squares* with error bars) versus depth for samples from ODP Hole 504B. The *dark* and *light shaded areas* denote the average Tl concentration and isotope composition of MORB. Note the change of scale for Tl concentrations higher than 40 ng/g. Figure modified from Nielsen et al. (2006c)



with the shallowest samples displaying the lightest isotope compositions (Fig. 13.3). This isotopic signature was interpreted to reflect closed system isotope fractionation during uptake of Tl from seawater, which gradually becomes more depleted in Tl as it penetrates deeper into the oceanic crust. As shown by a Rayleigh fractionation model in which an isotope fractionation factor of $\alpha = 0.9985$ was applied (Nielsen et al. 2006c), the isotope composition of the total Tl deposited during low-T alteration depends critically on the fraction of Tl that is extracted from the seawater before it is re-injected into the oceans as a low-T hydrothermal fluid. Stripping the fluid of all the Tl originally present would imply an isotope composition for the low-T alteration flux that is identical to seawater ($\epsilon^{205}\text{Tl} = -5.5$), whilst lower degrees of depletion result in lighter isotope compositions.

Based on the isotope fractionation observed for rocks from ODP Hole 504B, it was estimated that extraction of $\sim 50\%$ of the original seawater Tl by ocean crust alteration would yield an average isotope composition of $\epsilon^{205}\text{Tl} \sim -18$ for the Tl deposited during low-T alteration. The application of this approach to obtain a global estimate for the average Tl isotope composition of the low-T alteration flux is fraught with many uncertainties, however, as the database is currently limited to rocks from just one section of altered ocean crust and Tl concentration measurements for three low-T fluids from the Juan de Fuca ridge (Nielsen et al. 2006c). In principle, average altered upper ocean crust may be characterized by an

$\epsilon^{205}\text{Tl}$ value of between about -18 to -6 . Hence it may again be more appropriate to apply an isotope mass balance approach to obtain a more accurate result. With an isotope composition of $\epsilon^{205}\text{Tl} \sim -1.8$ for the combined marine Tl input fluxes and an authigenic output flux of $\epsilon^{205}\text{Tl} \sim +10$, mass balance dictates that the altered basalt flux is characterized by $\epsilon^{205}\text{Tl} \sim -8.5$ (Table 13.4). This result is certainly within the range of reasonable values but based on Rayleigh fractionation modelling it requires that more than 90% of seawater Tl is removed by alteration processes, which is not entirely supported by the data obtained for ODP Hole 504B (Nielsen et al. 2006c). It is unlikely, however, that the results obtained for Hole 504B are representative for global average ocean crust alteration processes.

13.5 Causes of Thallium Isotope Fractionation

In general, Tl isotope variations on Earth are fairly limited, with only a few select environments displaying significant deviations from the bulk Earth value of $\epsilon^{205}\text{Tl} = -2$ (Nielsen et al. 2005, 2006b, c, 2007). However, the overall magnitude of Tl isotope variation in natural environments on Earth now exceeds 35 $\epsilon^{205}\text{Tl}$ -units (Rehkämper et al. 2002, 2004; Nielsen et al. 2006c; Coggon et al. 2009). This variability is comparable to the extent of fractionation observed for

$^{56}\text{Fe}/^{54}\text{Fe}$ (Anbar 2004), which has a relative mass difference almost four times that of Tl. It would appear that this observation is somewhat contrary to what is predicted from classical stable isotope fractionation theory and it is therefore important to understand the fundamental processes responsible for Tl isotope fractionation.

There are two principle mechanisms by which most stable isotope fractionations are generated – a kinetic route that is associated with unidirectional processes and an equilibrium pathway, which acts during chemical exchange processes. Both mechanisms should scale with the relative mass difference between the two isotopes of interest. As mentioned in Sect. 13.3.2, kinetic isotope fractionation processes are theoretically capable of generating substantial Tl isotope fractionation and there is evidence that such fractionations occur from data acquired for samples from volcanic plumes and some meteorites (Nielsen et al. 2006a; Baker et al. 2009, 2010b). However, the large Tl isotope fractionations observed between seawater and Fe-Mn oxy-hydroxides and for low-T altered oceanic crust are more likely to reflect equilibrium fractionation effects (Rehkämper et al. 2002, Nielsen et al. 2006c).

The larger-than-expected Tl isotope variations for equilibrium reactions were recently shown by Schauble (2007) to be partially caused by the so-called nuclear field shift isotope fractionation mechanism (Bigeleisen 1996). In short, the original equilibrium isotope exchange equation of Bigeleisen and Mayer (1947) had five components, of which four were deemed negligible. However, based on some unusual isotope fractionation effects observed for uranium (Fujii et al. 1989a, b), it was concluded that the nuclear field shift term may be important in some cases (Bigeleisen 1996). Interestingly, nuclear field shift isotope fractionation is not mass dependent but scales positively with the size of the nucleus and hence is also largest for the heavy elements. As Tl has only two isotopes, it is not possible to distinguish nuclear field shift effects from mass dependent isotope fractionation. However, the calculations that were carried out for Tl predict that an equilibrium system with aqueous dissolved Tl^+ and Tl^{3+} will feature both regular mass dependent and nuclear field shift isotope effects, with isotope fractionation factors that act in the same direction (Schauble 2007). When combined, these two components can furthermore reproduce the approxi-

mate magnitude of Tl isotope variation observed on Earth (Schauble 2007). The calculations are particularly relevant for the isotope compositions determined for Fe-Mn crusts and low-T altered basalts as these represent the heaviest and lightest reservoirs, respectively, found to date. The main requirement for substantial equilibrium Tl isotope fractionation to take place, is a chemical exchange reaction that involves two valence states of Tl (Schauble 2007), and these could be Tl^0 , Tl^+ or Tl^{3+} . However, the calculations of Schauble (2007) also imply that the largest isotope effects are expected if Tl^{3+} is present.

Based on these theoretical considerations, experimental work is currently being conducted to investigate the specific mechanism for Tl isotope fractionation during adsorption onto hydrogenetic Fe-Mn crusts (Fig. 13.4) and other Fe-Mn sediments (Nielsen et al. 2008; Peacock et al. 2009). The majority of Tl in these deposits is associated with MnO_2 minerals and the isotope fractionation is therefore likely to occur at or in such phases. Preliminary interpretations of EXAFS/XANES spectra for Tl sorbed onto Mn-oxides have shown that the MnO_2 phase hexagonal birnessite has the capacity to oxidize Tl to Tl^{3+} , following adsorption as a univalent ion (Bidoglio et al. 1993; Peacock et al. 2009). This reaction appears to be associated with isotope fractionation whereas adsorption of Tl onto other MnO_2 mineral structures (Na-birnessite and todorokite), which do not have the same oxidation potential, is not associated with significant isotope effects (Nielsen et al. 2008; Peacock et al. 2009). These results are consistent with the Tl isotope data obtained for natural hydrogenetic and hydrothermal Fe-Mn crusts, which are dominated by H-birnessite and todorokite, respectively (Rehkämper et al. 2002; Nielsen et al. 2008; Peacock et al. 2009). Considering the theoretical predictions (Schauble 2007), these preliminary observations are able to account for at least some of the Tl isotope variability observed in the marine environment. However, the current experiments are still unable to reproduce the magnitude of isotope fractionation observed in nature and it is therefore still unresolved exactly how the large isotope fractionation observed between seawater and Mn-oxides is produced (Rehkämper et al. 2002). Future work will hopefully shed more light on this issue.

Even more enigmatic than the Tl isotope fractionation of Mn oxides are the isotope fractionation effects found in low-T altered ocean crust. In this case, Tl is

extracted from seawater circulating through the rocks with an isotope fractionation factor of about $\alpha = 0.9985$ (Nielsen et al. 2006c; Coggon et al. 2009). It is conceivable that these fractionations reflect kinetic isotope effects, for example as a result of the more rapid diffusion of the light isotopes from the hydrothermal fluid to the alteration minerals that concentrate Tl. However, it is unclear whether diffusion rates can be sufficiently fast, to enable the large isotope effects observed (Nielsen et al. 2006c; Coggon et al. 2009). If an equilibrium reaction is responsible, Tl^{3+} is likely to be involved because large equilibrium isotope fractionations are not expected for reactions without this species (Schauble 2007). Simple models of Tl speciation in seawater predict that only Tl^+ is present (Nielsen et al. 2009a), which implies that the hydrothermal processes that deposit Tl in the oceanic crust produce Tl^{3+} . This inference strongly contradicts observations, which demonstrate that low-T hydrothermal alteration generally occurs at conditions that are more reducing than those prevalent in open ocean seawater (Alt et al. 1996). Additionally, Tl^{3+} has a much lower aqueous solubility than Tl^+ (Nriagu 1998) and this implies that trivalent Tl should be deposited during hydrothermal alteration. However, isotope fractionation calculations indicate that oxidized Tl should be enriched in ^{205}Tl (Schauble 2007), which is at odds with the light Tl isotope signatures observed in altered basalts.

Alternatively, if we ignore the inferred univalent nature of dissolved oceanic Tl, it may be hypothesized that seawater consists of a mixture of uni- and trivalent Tl-species that are isotopically fractionated from each other by $\sim 35 \epsilon^{205}\text{Tl}$ -units (Schauble 2007). This con-

figuration would be consistent with oxidized and isotopically heavy Tl adsorbing onto Mn-oxides whilst reduced and isotopically light Tl would partition into basalt alteration minerals. Together, these fractionated species could thus create the isotope difference observed between these two reservoirs (Rehkämper et al. 2002; Nielsen et al. 2006c; Coggon et al. 2009). In order to reproduce the isotope compositions observed for Fe-Mn crusts ($\epsilon^{205}\text{Tl} \sim +13$, (Rehkämper et al. 2002)) and altered basalts ($\epsilon^{205}\text{Tl} \sim -20$ (Coggon et al. 2009)), mass balance then dictates that seawater with an average isotope composition of $\epsilon^{205}\text{Tl} = -5.5$ would need be characterized by a ratio of $\text{Tl}^{3+}/\text{Tl}^+ \approx 0.8$. Some analytical studies have in fact claimed that significant levels of Tl^{3+} are present in natural waters (Lin and Nriagu 1999), but such results are questionable as the sample preparation procedures may have altered the speciation of Tl. Schedlbauer and Heumann (2000) furthermore identified methylated Tl^{3+} in seawater but these analyses yielded variable $\text{Tl}^{3+}/\text{Tl}^+$ ratios of 1 to <0.05 , which would preclude the globally invariant Tl isotope compositions observed for Fe-Mn crusts (Fig. 13.4).

In summary, the large overall Tl isotope variability observed in the marine environment is most likely produced by a combination of conventional mass dependent and nuclear field shift equilibrium isotope fractionation processes. However, contributions from kinetic isotope effects cannot be ruled out at present. In order to reproduce the magnitude of equilibrium isotope fractionation observed for natural samples, reduction-oxidation processes, in which oxidized Tl^{3+} plays a central role, are predicted to be important. Experimental studies of Tl isotope fractionation are

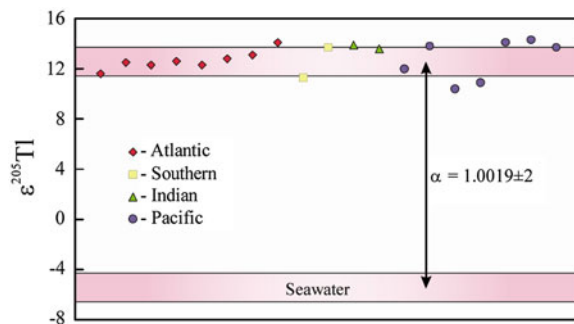


Fig. 13.4 Thallium isotope compositions determined for the growth surfaces of hydrogenetic Fe-Mn crusts and seawater. The Fe-Mn crusts precipitate directly from seawater and hence

there is an isotope fractionation between these two reservoirs of $\sim 19 \epsilon^{205}\text{Tl}$ -units. Data from (Rehkämper et al. 2002; Nielsen et al. 2004, 2006c)

only in their infancy, however, and we still have much to learn about the processes that govern Tl isotope fractionation in natural environments.

13.6 Applications of Tl Isotopes to Problems in Earth Science

13.6.1 Studies of Tl Isotopes in Fe-Mn Crusts

Hydrogenetic Fe-Mn crusts grow on hard substrates that experience little or no regular detrital sedimentation, for example on seamounts where ocean currents prevent gravitational settling of particles (Hein et al. 2000). They precipitate directly from the ambient water mass that surrounds them and feature growth rates of a few mm/Myr (Segl et al. 1984, 1989; Eisenhauer et al. 1992). This implies that sample thicknesses in excess of 10 cm could represent a continuous seawater record through the entire Cenozoic (the last ~65 Myr). Extensive investigations of Fe-Mn crusts over the last 15 years have been conducted to infer changes in the radiogenic isotope compositions of various elements in ocean bottom waters (Lee et al. 1999; Frank 2002). Depending on the marine residence time for the element investigated, the isotopic variability has mainly been interpreted as reflecting changes in either ocean circulation patterns or the marine source and/or sink fluxes (Burton et al. 1997; van de Flierdt et al. 2004).

The globally uniform Tl isotope ratios observed for the surfaces of Fe-Mn crusts (Fig. 13.4), imply that there is a consistent equilibrium isotope fractionation between seawater and Tl incorporated into the Fe-Mn crusts. Time-dependent variations of Tl isotope compositions in Fe-Mn crusts can be interpreted to reflect either changes in the isotope fractionation factor between seawater and Fe-Mn crust or the Tl isotope composition of seawater. In principle, both interpretations are possible, but several lines of reasoning currently favor the latter explanation (Rehkämper et al. 2004; Nielsen et al. 2009a).

Two studies have determined Tl isotope depth profiles for several Fe-Mn crusts, and both identified large systematic changes in Tl isotope compositions (Rehkämper et al. 2004; Nielsen et al. 2009a). The first study produced low-resolution depth profiles for a

number of samples. The largest Tl isotope variations were observed for the early Cenozoic (Rehkämper et al. 2004), but the low sampling density and uncertainties in the models, which were applied to infer the sample growth rates, made it difficult to determine the exact time and duration of this change. It was furthermore argued that the Fe-Mn crusts record variations in the Tl isotope composition of seawater that were caused by changes in the marine input and/or output fluxes of this element (Rehkämper et al. 2004). The second study generated high resolution Tl isotope time series for two Fe-Mn crusts. Improved age models were applied, which resolved a single large shift in Tl isotope composition, which occurred between ~55 and ~45 Ma (Fig. 13.5; (Nielsen et al. 2009a)). Based on an improved understanding of the marine input and output fluxes of Tl and their respective isotope compositions, it was furthermore proposed that the large shift in the $\epsilon^{205}\text{Tl}$ value of seawater reflects a decrease in the amount of authigenic Fe-Mn oxyhydroxides that were deposited with pelagic sediments in the early Eocene (Nielsen et al. 2009a).

It is difficult to assess the underlying mechanism responsible for this global change in Fe-Mn oxyhydroxide precipitation. The strong co-variation of the Tl isotope curve with the sulfur (S) isotope composition of seawater (Fig. 13.5) may imply, however, that the same mechanism is driving the jump in the isotopic evolution of both stable isotope systems, even though S isotopes are known to be unaffected (at least directly) by changes in Fe-Mn oxides precipitation. Baker et al. (2009) proposed that the inferred high Fe-Mn oxyhydroxide precipitation rates for the Paleocene (~65–55 Ma) may be explained by increased deposition of Fe- and Mn-rich volcanic ash particles in the oceans. Such volcanic activity would also supply isotopically light S and this could explain the relatively low $\delta^{34}\text{S}$ value for seawater at this time. The changes in the Tl and S isotope compositions of the oceans between ~55 and ~45 Ma (Fig. 13.5) would then be controlled by diminishing volcanic activity (Wallmann 2001). An alternative model proposes that Fe-Mn precipitation is controlled by biological utilization and burial of Fe and Mn with organic carbon (Nielsen et al. 2009a). High organic carbon burial rates would lead to diminished Fe-Mn precipitation rates as less Fe and Mn are available in the water column. Simultaneously, the increased organic carbon

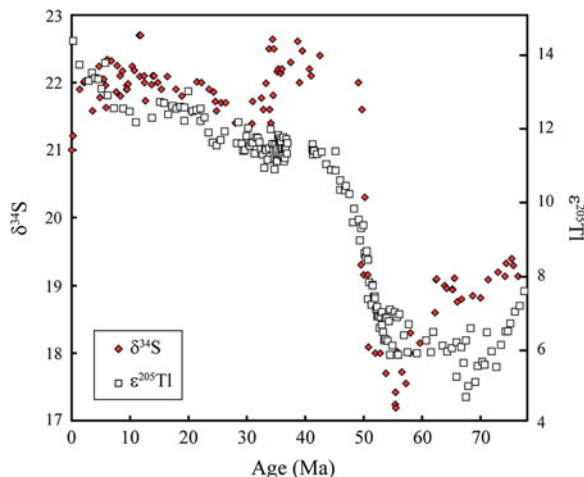


Fig. 13.5 Thallium isotope data for a Fe-Mn crust from the Pacific Ocean and the S isotope seawater curve plotted for the last 75 Myr. The S isotope data are from Paytan et al. (1998; 2004), with ages based on the age model of (Kurtz et al. 2003).

The chronology of the Tl isotope curve was determined based on Os isotope data (Burton 2006). Figure modified from Nielsen et al. (2009a)

burial would result in higher rates of sedimentary pyrite burial, which draws isotopically light S out of seawater (Berner 1984).

In summary, the results of both initial paleoceanographic studies thus indicate that it may be possible to utilize Tl isotopes as a proxy for the Fe and Mn supply to the oceans further back in time. However, much work is still needed to confirm whether these preliminary interpretations are indeed correct.

13.6.2 Calculation of Hydrothermal Fluid Fluxes Using Tl Isotopes in the Ocean Crust

Hydrothermal fluids are expelled from the seafloor (i) at high temperature on mid ocean ridge axes, as fueled by the magmatic energy from the crystallization and cooling of fresh ocean crust to $\sim 300\text{--}400^\circ\text{C}$ and (ii) at lower temperatures on the ridge flanks, as the ocean crust cools slowly over millions of years. These hydrothermal fluxes play pivotal roles in controlling seawater chemistry, but the magnitude of the high temperature water flux at mid-ocean ridge axes remains widely disputed, whilst the volume of low temperature vent fluids expelled at ridge flanks is virtually unconstrained.

As discussed in Sects. 13.4.2.1 and 13.4.3.2, Tl displays distinct behavior during high and low temperature hydrothermal alteration of the ocean crust. High-T fluids effectively leach Tl from the cooling rocks whereas low-T fluids deposit Tl into the upper part of the oceanic crust.

For the high-T hydrothermal fluid flux (F_{hT}), Nielsen et al. (2006c) constructed the following mass balance equation:

$$F_{hT} \times [Tl]_{hT} = F_{oc\ leach} \times [Tl]_{oc} \times f_{Tl\ leach}$$

where $[Tl]_{hT}$ is the average Tl concentration of the vent fluids, $F_{oc\ leach}$ is the mass flux of ocean crust that is leached by high-T fluids, $[Tl]_{oc}$ is the Tl content of the crust prior to leaching, and $f_{Tl\ leach}$ is the fraction of Tl leached from the rocks during alteration. Based on data obtained for samples from ODP Hole 504B (Nielsen et al. 2006c) and high-T hydrothermal fluids (Metz and Trefry 2000; Nielsen et al. 2006c) each of these parameters could be constrained and the equation solved for F_{hT} . This calculation yielded a high temperature hydrothermal water flux of $0.17\text{--}2.93 \times 10^{13}$ kg/year, with a best estimate of 0.72×10^{13} kg/year (Nielsen et al. 2006c). This fluid flux, however, only accounts for about 5–80% of the heat available at mid-ocean ridge axes from the crystallization and cooling of the freshly formed ocean crust. Based on this, it was inferred that some energy at mid ocean ridge axes is

lost via conduction and/or through the circulation of intermediate temperature hydrothermal fluids that do not alter the chemical budgets of Tl in the ocean crust (Nielsen et al. 2006c).

For the low-T hydrothermal fluid circulation (F_{IT}), the following mass balance equation was shown to apply (Nielsen et al. 2006c):

$$F_{VZ} \times ([Tl]_{avz} - [Tl]_{pvz}) = F_{IT} \times [Tl]_{sw} \times f_{upt}$$

where F_{VZ} is the mass flux of ocean crust that is affected by low-T alteration, $[Tl]_{avz}$, $[Tl]_{pvz}$, and $[Tl]_{sw}$ are the Tl concentrations of the altered volcanic zone basalts, their pristine equivalents and seawater, respectively. The fraction of Tl that is removed from seawater by basalt weathering is denoted by f_{upt} . Again, samples from ODP Hole 504B (Nielsen et al. 2006c) combined with literature data (Teagle et al. 1996) enabled an assessment of each parameter and yielded an estimated low-T hydrothermal fluid flux at ridge flanks of $0.2\text{--}5.4 \times 10^{17}$ kg/year (Nielsen et al. 2006c). Using the ridge flank power output of 7.1 TW (Mottl 2003), it was calculated that such fluids have an average temperature anomaly of only about $0.1\text{--}3.6^\circ\text{C}$ relative to ambient seawater, which is lower than most flank fluids sampled to date. It is therefore unclear how representative these fluids are of average low-T ocean crust alteration processes.

In order to improve the utility of Tl mass balance calculations to constrain hydrothermal fluid fluxes it will be essential to obtain more data on altered ocean crust from a number of locations. Such analyses, which are currently in progress, will provide improved constraints on the behavior of Tl during hydrothermal processes and thus ultimately yield more reliable Tl-based estimates of global hydrothermal water fluxes (Coggon et al. 2009).

13.6.3 Thallium Isotopes as a Tracer for Ocean Crust Recycling in the Mantle

One of the central hypotheses of mantle geochemistry over the last 30 years has been the proposed link between ocean crust recycling at convergent plate margins and the upwelling of mantle plumes (Hof-

mann and White 1982) that generate, for example, ocean island basalt (OIB) magmatism. Much work has gone into tracing sediments and altered ocean crust with radiogenic isotopes (e.g. $^{87}\text{Rb}\text{--}^{87}\text{Sr}$, $^{238,235}\text{U}\text{--}^{207,206}\text{Pb}$, $^{147}\text{Sm}\text{--}^{143}\text{Nd}$ and $^{176}\text{Lu}\text{--}^{176}\text{Hf}$) which display variations as a function of time and the fractionation of the parent and daughter elements (Hofmann 1997). Whilst it has become clear that these radiogenic isotope ratios are generally different in OIB compared to the average upper mantle, direct evidence for the presence of marine sediments and/or altered ocean crust in OIB has been elusive. This reflects that the radiogenic isotope and trace element data, which have been used to infer and trace sediment recycling in the mantle, are generally open to alternative interpretations. Stable isotope tracers (e.g. oxygen (O) and lithium (Li)) have therefore been employed as they may trace specific processes such as ocean crust alteration (Alt et al. 1986; Chan et al. 2002; Burton and Vigier 2011). However, light isotopes like O and Li may also fractionate during processes occurring at mantle temperatures (Marschall et al. 2007; Williams et al. 2009) and their mantle concentrations are relatively high, such that the isotope composition of a mantle source would not be readily affected by admixing of sediment and/or ocean crust (Elliott et al. 2004; Thirlwall et al. 2004). Seen in this perspective, Tl isotopes could be a near-perfect tracer of ocean crust recycling for the following reasons:

1. Thallium isotopes do not appear to fractionate during high temperature processing and the isotope composition of (normal) upper mantle material is well defined at $\epsilon^{205}\text{Tl} = -2$ (see Sect. 13.3.2).
2. The isotope composition of low-T altered upper ocean crust and Fe-Mn sediments differ significantly ($\epsilon^{205}\text{Tl} = -8$ and $\epsilon^{205}\text{Tl} = +10$, respectively) from the average upper mantle value (see Sects. 13.4.3.1 and 13.4.3.2).
3. Altered basalts and Fe-Mn sediments have much higher Tl concentrations than average upper mantle material (see Sects. 13.4.3.1 and 13.4.3.2).

Taken together, these characteristics should enable the identification of even very minor contributions of altered basalts and/or Fe-Mn sediments to a mantle source. This inference assumes, of course, that the recycled materials do not lose their distinct Tl signatures during subduction related processes. Bulk addition of $<1\%$ of low-T altered basalt and just a few

parts per million by weight of pure Fe-Mn sediment into a normal mantle material should result in discernible Tl isotope anomalies that are correlated with systematically lower Cs/Tl ratios (Fig. 13.6). The Cs/Tl data can be used to identify admixing of oceanic crust and sediments because this ratio should not be significantly altered by mantle melting or fractional crystallization due to the similar compatibility of the two elements (Nielsen et al. 2006b).

To date, OIB samples from the Azores, Iceland and Hawaii have been investigated (Nielsen et al. 2006b, 2007). As it is unclear whether the Azores basalts were affected by post-eruptional alteration (Nielsen et al. 2007), these data will not be discussed here. Samples from Hawaii exhibit the most convincing Tl isotope evidence for presence of sediments in the mantle source (Fig. 13.6). About 10 ppm of pure Fe-Mn sediment would be sufficient to explain the heavy isotope compositions recorded in these rocks. It is unlikely that the Tl isotope variation originates from anything else than Fe-Mn sediment, but it is uncertain if this component was acquired by the melts during magma ascent via assimilation of modern marine sediments or if it is a feature of the mantle source. The heaviest Tl isotope compositions are, however, also

characterized by the least radiogenic Pb isotope compositions (Nielsen et al. 2006b) which would argue for an old age of the sediment contaminant.

The relatively straightforward interpretation of the Tl isotope data for Hawaii could be considered a “smoking gun” for the presence of recycled ocean crust material in the Hawaiian mantle plume. However, results obtained for a suite of lavas from Iceland strongly indicate that there is some way to go before we can confidently apply Tl isotopes as a unique tracer of crustal recycling processes (Fig. 13.6). The Iceland samples, which include rocks from all major eruption centers, exhibit a complete uniformity of the Tl isotope composition but a large variability in Cs/Tl ratios is apparent. The isotopic invariance is perhaps not so surprising given that the thickness of subducted oceanic lithosphere is >30 km. Thallium isotope anomalies will be situated in only the uppermost ~ 500 – $1,000$ m, whilst the remainder of the oceanic crust is expected to be isotopically identical to the mantle. The mantle-like Tl isotope signatures of the Iceland basalts hence do not argue against the presence of recycled ocean crust in the plume source. Of more concern is that the Iceland samples also display variable Cs/Tl ratios. The large range demonstrates that processes other than the addition of Fe-Mn sediments and

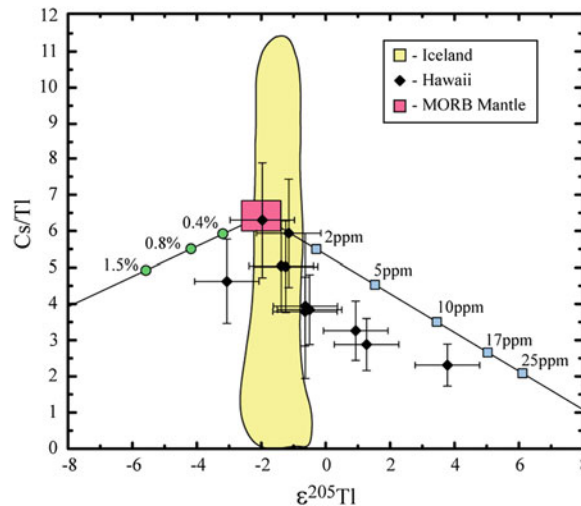


Fig. 13.6 Cs/Tl ratios of primitive basalts from Hawaii (Nielsen et al. 2006b) and Iceland (Nielsen et al. 2007) plotted versus Tl isotope composition. Mixing lines between pristine mantle (large pink square), Fe-Mn oxyhydroxides and low-T altered MORB are also shown. The mantle is assumed to be characterized by $\epsilon^{205}\text{Tl} = -2$ (Nielsen et al. 2006b) and Cs and Tl concentrations of 7.7 ppb (Hofmann and White 1983) and 1.2 ppb (Nielsen et al. 2006b), respectively. For the Fe-Mn

oxyhydroxides, the Tl concentration and isotope composition are assumed to be $100 \mu\text{g/g}$ and $\epsilon^{205}\text{Tl} = +10$, akin to values of modern Fe-Mn crusts and nodules (Hein et al. 2000; Rehkämper et al. 2002). The Cs content of Fe-Mn oxyhydroxides is about 500 ng/g (Ben Othmann et al. 1989). Altered MORB is assumed to be characterized by $\epsilon^{205}\text{Tl} = -15$ and Tl and Cs concentrations of about 200 ng/g (Nielsen et al. 2006c). Error bars denote 2sd uncertainties

low-T altered basalts may alter this ratio. It is conceivable that this could include igneous processes, such as partitioning of Tl and/or Cs into sulfides and/or phyllosilicates as well as mobilization by magmatic fluids (Nielsen et al. 2007).

It is also prudent to consider two other aspects important for the application of Tl isotopes in mantle geochemistry. First, it is likely that the Tl isotope composition of seawater has not remained constant over time and the isotope signatures of altered basalts and Fe-Mn sediments are therefore also expected to exhibit temporal variability. Any such variability will act to obscure the systematic mixing trends, which are produced by contamination of the ambient mantle with these endmember compositions. Second, it is unclear when the oceans became sufficiently oxic to support the precipitation of Fe-Mn oxyhydroxides, but this probably occurred after ~2.4 Ga (Canfield 1998). Sediments that were recycled more than 2.4 billion years ago are therefore unlikely to be enriched in Tl from Fe-Mn sediments and hence would most probably exhibit $\epsilon^{205}\text{Tl} \approx -2$. The isotope fractionation mechanism for altered basalts is yet to be determined, so it is unclear whether such basalts would be isotopically fractionated in ancient environments and thus if ocean crust recycling would be able to alter the Tl isotope composition of the mantle.

13.7 Future Directions and Outlook

High precision measurements of Tl isotope ratios have only been possible for little more than a decade and it is therefore not surprising that our knowledge of the isotopic behavior of this element is limited. To date, studies have revealed that Tl isotopes fractionate substantially in some terrestrial environments, despite their heavy masses. Most of the variation occurs in the marine realm with ferromanganese sediments and low temperature hydrothermal alteration displaying a total isotope variation of about 35 $\epsilon^{205}\text{Tl}$ -units (Rehkämper et al. 2002, 2004; Nielsen et al. 2006c, 2009a; Coggon et al. 2009). The isotopic variation can most likely be accounted for by invoking a combination of conventional mass dependent equilibrium isotope fractionation and nuclear field shift isotope effects (Bigeleisen 1996; Schauble 2007), but the specific mechanisms are still largely unaccounted for.

Thallium isotopes have thus far mainly been applied to investigate past and present marine environments. Firstly, several papers have focused on paleoceanographic processes in the Cenozoic and it appears that Tl isotopes may be utilized as a monitor of Fe and Mn supply to the water column over million year time scales (Rehkämper et al. 2004; Baker et al. 2009; Nielsen et al. 2009a). Secondly, Tl isotopes can be used to calculate the magnitude of hydrothermal fluid circulation through ocean crust. Such calculations can be performed both for high and low temperature fluids (Nielsen et al. 2006c). Thirdly, it has been shown that marine ferromanganese sediments can be detected in mantle-derived basalts (Nielsen et al. 2006b), which confirms that marine sediments subducted at convergent plate margins can be recycled to the surface via mantle plumes (Hofmann and White 1982).

Apart from the obvious overall necessity of expanding the Tl isotope and concentration database for all terrestrial environments in order to gain a better understanding of the geochemical distribution and behavior of this element, there are a few crucial investigations that are needed to advance the utility of Tl isotopes as quantitative tracers of past and present geological processes.

First of all, we must understand the mechanisms that govern the two major Tl isotope effects observed on Earth and which yield highly fractionated Tl in Fe-Mn sediments and low-T altered basalts. This knowledge will not only help expand our appreciation of the physico-chemical processes that cause very heavy isotopes to fractionate, but also enable us to better utilize the Tl isotope system to quantify low-T hydrothermal fluid flow (Nielsen et al. 2006c) and generate more accurate models for the causes of the Tl isotope variations observed in the marine environment over time (Baker et al. 2009; Nielsen et al. 2009a). Efforts are currently in progress that may eventually shed light on the origin of these Tl isotope fractionations (Nielsen et al. 2008; Coggon et al. 2009; Peacock et al. 2009), but there is probably still a long way to go before constraints from experiments and theory can be combined in comprehensive models that are consistent with observations on natural systems.

Secondly, it will be important to refine the three applications outlined in Sect. 13.6. For the paleoceanographic studies this will include a detailed determination of the magnitude and isotope compositions of

the most uncertain marine fluxes. These are benthic pore waters, adsorption processes on pelagic clays and low-T hydrothermal alteration. A complete understanding of the modern marine Tl cycle is a prerequisite for good models of past Tl isotope variations. Another aspect of the oceanic Tl isotope evolution that has yet to be investigated, are short-term fluctuations, for example on glacial-interglacial time-scales. Since the marine residence time of Tl is ~21 kyr (Table 13.4), it should be feasible to observe perturbations of the Tl cycle that happen on geologically rapid time-scales, although it will be vital to identify geological archives that accurately monitor seawater Tl isotope variations with millennial resolution.

The use of Tl isotopes as a tool in mantle geochemistry is currently limited by scant data. Thallium isotope and concentration data are presently available only for a few OIB and we also lack knowledge concerning how Tl is cycled through subduction zones. Two recent studies that attempted to address such questions through Tl isotope analyses of cratonic eclogites (Nielsen et al. 2009b) and island arc lavas (Prytulak and Nielsen, unpublished data) were unable to conclusively constrain the behavior of Tl and further investigations of rocks from subduction related environments are thus necessary. Of particular interest to such studies are the distinct Tl isotope compositions of key arc components, particularly marine sediments and altered basalts. This implies, for example, that Tl isotope data for arc lavas may provide information on the sources of Tl and, more generally, element mobility and transport in subduction zone environments.

Lastly, there are a number of essentially unexplored but potentially useful applications of Tl isotopes. For example, anthropogenic Tl pollution from power plants and zinc smelting might be characterized by distinct Tl isotope fingerprints that reflect kinetic isotope fractionation. The isotope fractionations that may result from the partitioning of chalcophile Tl (Shaw 1952) into sulfide phases has also been largely neglected to date. A Tl isotope study of rocks from the vicinity of a Cu porphyry deposit showed that Tl may retain its lithophile behavior even in sulphide-rich environments (Baker et al. 2010a). Some sulfides, however, are known to be enriched in Tl (Heinrichs et al. 1980), but apart from this, little is known about the association of Tl with sulfide minerals. Hence, it may be of value to investigate Tl isotope fractionation during partitioning into sulfides. Such studies may

yield information about the conditions at which Tl behaves as a lithophile or chalcophile element and, potentially, help improve our understanding of fluid mobility in ore systems.

References

- Alt JC (1995) Subseafloor processes in mid-ocean ridge hydrothermal systems. In: Humphris SE, Lupton JE, Mullineaux LS, Zierenberg RA (eds) *Seafloor hydrothermal systems, physical, chemical, and biological interactions*. AGU, Washington
- Alt JC, Muehlenbachs K, Honnorez J (1986) An oxygen isotopic profile through the upper kilometer of the oceanic crust, DSDP Hole 504B. *Earth Planet Sci Lett* 80:217–229
- Alt JC, Teagle DAH, Bach W et al (1996) Stable and strontium isotopic profiles through hydrothermally altered upper oceanic crust, hole 504B. *Proc ODP Sci Results* 148:57–69
- Anbar AD (2004) Iron stable isotopes: beyond biosignatures. *Earth Planet Sci Lett* 217:223–236
- Anders E, Stevens CM (1960) Search for extinct lead 205 in meteorites. *J Geophys Res* 65:3043–3047
- Archer C, Vance D (2008) The isotopic signature of the global riverine molybdenum flux and anoxia in the ancient oceans. *Nat Geosci* 1(9):597–600
- Baker RGA, Rehkämper M, Hinkley TK et al (2009) Investigation of thallium fluxes from subaerial volcanism-implications for the present and past mass balance of thallium in the oceans. *Geochim Cosmochim Acta* 73(20):6340–6359
- Baker RGA, Rehkämper M, Ihlenfeld C et al (2010a) Thallium isotope variations in an ore-bearing continental igneous setting: Collahuasi Formation, Northern Chile. *Geochim Cosmochim Acta* 74(15):4405–4416
- Baker RGA, Schonbacher M, Rehkämper M et al (2010b) The thallium isotope composition of carbonaceous chondrites – new evidence for live Pb-205 in the early solar system. *Earth Planet Sci Lett* 291(1–4):39–47
- Ben Othmann D, White WM, Patchett J (1989) The geochemistry of marine sediments, island arc magma genesis, and crust-mantle recycling. *Earth Planet Sci Lett* 94:1–21
- Berner RA (1984) Sedimentary pyrite formation – an update. *Geochim Cosmochim Acta* 48(4):605–615
- Bidoglio G, Gibson PN, Ogorman M et al (1993) X-ray-absorption spectroscopy investigation of surface redox transformations of thallium and chromium on colloidal mineral oxides. *Geochim Cosmochim Acta* 57(10):2389–2394
- Bigeleisen J (1996) Nuclear size and shape effects in chemical reactions. Isotope chemistry of the heavy elements. *J Am Chem Soc* 118(15):3676–3680
- Bigeleisen J, Mayer MG (1947) Calculation of equilibrium constants for isotopic exchange reactions. *J Chem Phys* 15(5):261–267
- Bruland KW (1983) Trace elements in seawater. In: Riley JP, Chester R (eds) *Chemical oceanography*. Academic, London
- Burton KW (2006) Global weathering variations inferred from marine radiogenic isotope records. *J Geochem Explor* 88:262–265

- Burton KW, Vigier N (2011) Chapter 4 Lithium Isotopes as Tracers in Marine and Terrestrial Environments. In: Basaran M (ed) Handbook of environmental isotope geochemistry. Springer, Heidelberg
- Burton KW, Ling HF, Onions RK (1997) Closure of the Central American Isthmus and its effect on deep-water formation in the North Atlantic. *Nature* 386(6623):382–385
- Canfield DE (1998) A new model for Proterozoic ocean chemistry. *Nature* 396(6710):450–453
- Chan LH, Alt JC, Teagle DAH (2002) Lithium and lithium isotope profiles through the upper oceanic crust: a study of seawater-basalt exchange at ODP Sites 504B and 896A. *Earth Planet Sci Lett* 201:187–201
- Cheam V (2001) Thallium contamination of water in Canada. *Water Qual Res J Can* 36(4):851–877
- Cheam V, Garbai G, Lechner J et al (2000) Local impacts of coal mines and power plants across Canada. I. Thallium in waters and sediments. *Water Qual Res J Can* 35:581–607
- Chen JH, Wasserburg GJ (1987) A search for evidence of extinct lead 205 in iron meteorites. *LPSC XVIII*:165–166
- Chen JH, Wasserburg GJ (1994) The abundance of thallium and primordial lead in selected meteorites – the search for ²⁰⁵Pb. *LPSC XVV*:245
- Cloquet C, Carignan J, Libourel G et al (2006) Tracing source pollution in soils using cadmium and lead isotopes. *Environ Sci Technol* 40(8):2525–2530
- Coggon RM, Rehkamper M, Atteck C et al (2009) Constraints on hydrothermal fluid fluxes from Tl geochemistry. *Geochim Cosmochim Acta* 73(13):A234–A234
- Eisenhauer A, Gogen K, Pernicka E et al (1992) Climatic influences on the growth-rates of Mn Crusts during the late quaternary. *Earth Planet Sci Lett* 109(1–2):25–36
- Elderfield H (1976) Manganese fluxes to the oceans. *Mar Chem* 4(2):103–132
- Elliott T, Jeffcoate A, Bouman C (2004) The terrestrial Li isotope cycle: light-weight constraints on mantle convection. *Earth Planet Sci Lett* 220:231–245
- Flegal AR, Patterson CC (1985) Thallium concentrations in seawater. *Mar Chem* 15:327–331
- Flegal AR, Sanudo-Wilhelmy S, Fitzwater SE (1989) Particulate thallium fluxes in the northeast Pacific. *Mar Chem* 28:61–75
- Frank M (2002) Radiogenic isotopes: tracers of past ocean circulation and erosional input. *Rev Geophys* 40:art. no.-1001
- Fujii Y, Nomura M, Okamoto M et al (1989a) An anomalous isotope effect of U-235 in U(IV)-U(VI) chemical exchange. *Z Naturforsch* 44(5):395–398
- Fujii Y, Nomura M, Onitsuka H et al (1989b) Anomalous isotope fractionation in uranium enrichment process. *J Nucl Sci Technol* 26(11):1061–1064
- Gauthier PJ, Le Cloarec MF (1998) Variability of alkali and heavy metal fluxes released by Mt. Etna volcano, Sicily, between 1991 and 1995. *J Volcanol Geotherm Res* 81:311–326
- Heggie D, Klinkhammer G, Cullen D (1987) Manganese and copper fluxes from continental margin sediments. *Geochim Cosmochim Acta* 51(5):1059–1070
- Hein JR, Koschinsky A, Bau M et al (2000) Cobalt-rich ferromanganese crusts in the Pacific. In: Cronan DS (ed) Handbook of marine mineral deposits. CRC Press, Boca Raton
- Heinrichs H, Schulz-Dobrick B, Wedepohl KH (1980) Terrestrial geochemistry of Cd, Bi, Tl, Pb, Zn and Rb. *Geochim Cosmochim Acta* 44:1519–1533
- Hinkley TK, Leclourec MF, Lambert G (1994) Fractionation of families of major, minor and trace-metals across the melt vapor interface in volcanic exhalations. *Geochim Cosmochim Acta* 58(15):3255–3263
- Hofmann AW (1997) Mantle geochemistry-the message from oceanic volcanism. *Nature* 385:219–229
- Hofmann AW, White WM (1982) Mantle plumes from ancient oceanic crust. *Earth Planet Sci Lett* 57:421–436
- Hofmann AW, White WM (1983) Ba, Rb and Cs in the Earth's mantle. *Z Naturforsch* 38:256–266
- Huey JM, Kohman TP (1972) Search for extinct natural radioactivity of Pb-205 via thallium-isotope anomalies in chondrites and lunar soil. *Earth Planet Sci Lett* 16:401–412
- Huh Y, Chan LH, Zhang L et al (1998) Lithium and its isotopes in major world rivers: implications for weathering and the oceanic budget. *Geochim Cosmochim Acta* 62:2039–2051
- Jochum KP, Verma SP (1996) Extreme enrichment of Sb, Tl and other trace elements in altered MORB. *Chem Geol* 130:289–299
- Johnson KS, Berelson WM, Coale KH et al (1992) Manganese flux from continental-margin sediments in a transect through the oxygen minimum. *Science* 257(5074):1242–1245
- Koschinsky A, Hein JR (2003) Acquisition of elements from seawater by ferromanganese crusts: solid phase association and seawater speciation. *Mar Geol* 198:331–351
- Kurtz AC, Kump LR, Arthur MA et al (2003) Early Cenozoic decoupling of the global carbon and sulfur cycles. *Paleoceanography* 18(4):14.1–14.14
- Lee D-C, Halliday AN, Hein JR et al (1999) Hafnium isotope stratigraphy of ferromanganese crusts. *Science* 285:1052–1054
- Lin T-S, Nriagu J (1999) Thallium speciation in the Great Lakes. *Environ Sci Technol* 33:3394–3397
- Lis J, Pasieczna A, Karbowska B et al (2003) Thallium in soils and stream sediments of a Zn-Pb mining and smelting area. *Environ Sci Technol* 37(20):4569–4572
- Marschall HR, Pogge von Strandmann PAE, Seitz HM et al (2007) The lithium isotopic composition of orogenic eclogites and deep subducted slabs. *Earth Planet Sci Lett* 262(3–4):563–580
- Matthews AD, Riley JP (1970) The occurrence of thallium in sea water and marine sediments. *Chem Geol* 149:149–152
- McDonough WF, Sun S-S (1995) The composition of the Earth. *Chem Geol* 120:223–253
- McGoldrick PJ, Keays RR, Scott BB (1979) Thallium – sensitive indicator of rock-seawater interaction and of sulfur saturation of silicate melts. *Geochim Cosmochim Acta* 43:1303–1311
- Metz S, Trefry JH (2000) Chemical and mineralogical influences on concentrations of trace metals in hydrothermal fluids. *Geochim Cosmochim Acta* 64:2267–2279
- Mottl MJ (2003) Partitioning of energy and mass fluxes between mid-ocean ridge axes and flanks at high and low temperature. In: Halbach PE, Tunnicliffe V, Hein JR (eds) Energy and mass transfer in marine hydrothermal systems. Dahlem University Press, Berlin

- Nielsen SG, Goff M, Hesselbo SP, et al (2011) Thallium isotopes in early diagenetic pyrite - a paleoredox proxy? *Geochim Cosmochim Acta*, In Press
- Nielsen SG, Rehkämper M, Baker J et al (2004) The precise and accurate determination of thallium isotope compositions and concentrations for water samples by MC-ICPMS. *Chem Geol* 204:109–124
- Nielsen SG, Rehkämper M, Porcelli D et al (2005) The thallium isotope composition of the upper continental crust and rivers – an investigation of the continental sources of dissolved marine thallium. *Geochim Cosmochim Acta* 69:2007–2019
- Nielsen SG, Rehkämper M, Halliday AN (2006a) Large thallium isotopic variations in iron meteorites and evidence for lead-205 in the early solar system. *Geochim Cosmochim Acta* 70:2643–2657
- Nielsen SG, Rehkämper M, Norman MD et al (2006b) Thallium isotopic evidence for ferromanganese sediments in the mantle source of Hawaiian basalts. *Nature* 439:314–317
- Nielsen SG, Rehkämper M, Teagle DAH et al (2006c) Hydrothermal fluid fluxes calculated from the isotopic mass balance of thallium in the ocean crust. *Earth Planet Sci Lett* 251 (1–2):120–133
- Nielsen SG, Rehkämper M, Brandon AD et al (2007) Thallium isotopes in Iceland and Azores lavas – implications for the role of altered crust and mantle geochemistry. *Earth Planet Sci Lett* 264:332–345
- Nielsen SG, Peacock CL, Halliday AN (2008) Investigation of thallium isotope fractionation during sorption to Mn oxides. *Geochim Cosmochim Acta* 72(12):A681
- Nielsen SG, Mar-Gerrison S, Gannoun A et al (2009a) Thallium isotope evidence for increased marine organic carbon export in the early Eocene. *Earth Planet Sci Lett* 278:297–307
- Nielsen SG, Williams HM, Griffin WL et al (2009b) Thallium isotopes as a potential tracer for the origin of cratonic eclogites? *Geochim Cosmochim Acta* 73:7387–7398
- Nriagu J (ed) (1998) *Thallium in the environment*. Wiley, New York
- Ostic RG, Elbadry HM, Kohman TP (1969) Isotopic composition of meteoritic thallium. *Earth Planet Sci Lett* 7(1):72–76
- Patterson CC, Settle DM (1987) Magnitude of lead flux to the atmosphere from volcanos. *Geochim Cosmochim Acta* 51 (3):675–681
- Paytan A, Kastner M, Campbell D et al (1998) Sulfur isotopic composition of Cenozoic seawater sulfate. *Science* 282 (5393):1459–1462
- Paytan A, Kastner M, Campbell D et al (2004) Seawater sulfur isotope fluctuations in the cretaceous. *Science* 304 (5677):1663–1665
- Peacock CL, Moon EM, Nielsen SG et al (2009) Oxidative scavenging of Tl by Mn oxide birnessite: sorption and stable isotope fractionation. *Geochim Cosmochim Acta* 73(13):A1003
- Pengra JG, Genz H, Fink RW (1978) Orbital electron capture ratios in the decay of ²⁰⁵Pb. *Nucl Phys A* 302:1–11
- Pietruszka AJ, Reznik AD (2008) Identification of a matrix effect in the MC-ICP-MS due to sample purification using ion exchange resin: an isotopic case study of molybdenum. *Int J Mass Spectrom* 270(1–2):23–30
- Pogge von Strandmann PAE, Burton KW, James RH et al (2010) Assessing the role of climate on uranium and lithium isotope behaviour in rivers draining a basaltic terrain. *Chem Geol* 270(1–4):227–239
- Poirier A, Doucelance R (2009) Effective correction of mass bias for rhenium measurements by MC-ICP-MS. *Geostand Geoanal Res* 33(2):195–204
- Prytulak J, Nielsen SG (unpublished data) Thallium isotope budget of the Mariana arc and influence of subducted slab components. *Chem Geol*. In Prep
- Rehkämper M, Halliday AN (1999) The precise measurement of Tl isotopic compositions by MC-ICPMS: application to the analysis of geological materials and meteorites. *Geochim Cosmochim Acta* 63:935–944
- Rehkämper M, Nielsen SG (2004) The mass balance of dissolved thallium in the oceans. *Mar Chem* 85:125–139
- Rehkämper M, Frank M, Hein JR et al (2002) Thallium isotope variations in seawater and hydrogenetic, diagenetic, and hydrothermal ferromanganese deposits. *Earth Planet Sci Lett* 197:65–81
- Rehkämper M, Frank M, Hein JR et al (2004) Cenozoic marine geochemistry of thallium deduced from isotopic studies of ferromanganese crusts and pelagic sediments. *Earth Planet Sci Lett* 219:77–91
- Rudge JF, Reynolds BC, Bourdon B (2009) The double spike toolbox. *Chem Geol* 265(3–4):420–431
- Rudnick RL, Gao S (2003) Composition of the continental crust. In: Holland HD, Turekian KK (eds) *Treatise on geochemistry*. Pergamon, Oxford
- Sager M (1993) Determination of arenic, cadmium, mercury, stibium, thallium and zinc in coal and coal fly-ash. *Fuel* 72 (9):1327–1330
- Sasmaz A, Sen O, Kaya G et al (2007) Distribution of thallium in soil and plants growing in the keban mining district of Turkey and determined by ICP-MS. *At Spectrosc* 28 (5):157–163
- Sawlan JJ, Murray JW (1983) Trace-metal remobilisation in the interstitial waters of red clay and hemipelagic marine sediments. *Earth Planet Sci Lett* 64(2):213–230
- Schauble EA (2007) Role of nuclear volume in driving equilibrium stable isotope fractionation of mercury, thallium, and other very heavy elements. *Geochim Cosmochim Acta* 71 (9):2170–2189
- Schedlbauer OF, Heumann KG (2000) Biomethylation of thallium by bacteria and first determination of biogenic dimethylthallium in the ocean. *Appl Organometal Chem* 14:330–340
- Segl M, Mangini A, Bonani G et al (1984) Be-10-Dating of a manganese crust from Central North Pacific and implications for ocean palaeocirculation. *Nature* 309(5968):540–543
- Segl M, Mangini A, Beer J et al (1989) Growth rate variations of manganese nodules and crusts induced by paleoceanographic events. *Paleoceanography* 4(5):511–530
- Shannon RD (1976) Revised effective ionic radii and systematic studies of interatomic distances in halides and chalcogenides. *Acta Crystallogr* A32:751–767
- Shaw DM (1952) The geochemistry of thallium. *Geochim Cosmochim Acta* 2:118–154
- Shiel AE, Barling J, Orians KJ et al (2009) Matrix effects on the multi-collector inductively coupled plasma mass spectrometric analysis of high-precision cadmium and zinc isotope ratios. *Anal Chim Acta* 633(1):29–37
- Teagle DAH, Alt JC, Bach W et al (1996) Alteration of upper ocean crust in a ridge-flank hydrothermal upflow

- zone: mineral, chemical, and isotopic constraints from hole 896A. *Proc ODP Sci Results* 148:119–150
- Thirlwall MF, Gee MAM, Taylor RN et al (2004) Mantle components in Iceland and adjacent ridges investigated using double-spike Pb isotope ratios. *Geochim Cosmochim Acta* 68(2):361–386
- Tsuchiyama A, Kawamura K, Nakao T et al (1994) Isotopic effects on diffusion in MgO melt simulated by the molecular-dynamics (Md) method and implications for isotopic mass fractionation in magmatic systems. *Geochim Cosmochim Acta* 58:3013–3021
- Urey HC (1947) The thermodynamic properties of isotopic substances. *J Chem Soc May*:562–581
- van de Flierdt T, Frank M, Halliday AN et al (2004) Tracing the history of submarine hydrothermal inputs and the significance of hydrothermal hafnium for the seawater budget—a combined Pb-Hf-Nd isotope approach. *Earth Planet Sci Lett* 222:259–273
- Wallmann K (2001) Controls on the Cretaceous and Cenozoic evolution of seawater composition, atmospheric CO₂ and climate. *Geochim Cosmochim Acta* 65(18):3005–3025
- Wedepohl KH (1974) *Handbook of geochemistry*. Springer, Berlin
- Williams H, Turner S, Kelley S et al (2001) Age and composition of dikes in Southern Tibet: new constraints on the timing of east-west extension and its relationship to postcollisional volcanism. *Geology* 29(4):339–342
- Williams HM, McCammon CA, Peslier AH et al (2004) Iron isotope fractionation and the oxygen fugacity of the mantle. *Science* 304:1656–1659
- Williams HM, Nielsen SG, Renac C et al (2009) Fractionation of oxygen and iron isotopes in the mantle: implications for crustal recycling and the source regions of oceanic basalts. *Earth Planet Sci Lett* 283:156–166
- Xiao TF, Boyle D, Guha J et al (2003) Groundwater-related thallium transfer processes and their impacts on the ecosystem: southwest Guizhou Province. *China Appl Geochem* 18(5):675–691
- Xiao TF, Guha J, Boyle D et al (2004) Environmental concerns related to high thallium levels in soils and thallium uptake by plants in southwest Guizhou. *China Sci Total Environ* 318(1–3):223–244

Chapter 14

Po-210 in the Environment: Biogeochemical Cycling and Bioavailability

Guebuem Kim, Tae-Hoon Kim, and Thomas M. Church

Abstract As the heaviest element of Group 6A, ^{210}Po has a unique biogeochemistry in the environment that challenges our understanding. This chapter provides an overview of the research on ^{210}Po in the atmosphere as well as in marine and other aqueous environments. Excess atmospheric ^{210}Po has been attributed to external sources, such as volcanic emissions, resuspension of soil humus, incursion of stratospheric air, sea spray from the oceanic surface micro-layer, plant exudates including evapotranspiration, anthropogenic emissions (e.g., emission from coal combustion), and bio-volatilization through the formation of dimethyl polonide. Most of these sources have been qualitatively identified, yet they remain difficult to quantify. In the aqueous environment, ^{210}Po is efficiently accumulated in plankton and bacteria and is biomagnified through the food webs, relative to its grandparent ^{210}Pb , causing ^{210}Po to be largely deficient in the euphotic zone. Globally, ^{210}Po deficiency increases as ocean productivity decreases in the upper 1,000 m through biological transfer to the upper trophic levels. Smaller ^{210}Po deficiencies in the productive areas of the ocean appear to be related to relatively active bacterial remineralization. Unusually high activities of ^{210}Po are often found in the suboxic and anoxic waters in association with S, Mn, and Fe redox cycles. As many details of these processes remain elusive and under debate, we propose additional studies that should be conducted.

G. Kim (✉) and T.-H. Kim
School of Earth and Environmental Sciences, Seoul National University, Seoul, South Korea

T.M. Church
College of Earth, Ocean, and Environment, University of Delaware, Newark, DE, USA

14.1 Introduction

Naturally occurring ^{210}Po ($t_{1/2} = 138$ days) is the decay product of ^{210}Pb ($t_{1/2} = 22.3$ years) via ^{210}Bi ($t_{1/2} = 5$ days) in the ^{238}U decay series and widely distributed in the earth's crust, rivers, oceans, and the atmosphere. ^{210}Po is highly radioactive, with alpha particle energy of 5.30 MeV. Although alpha particles are not sufficiently energetic to pass through a person's outer skin, they easily penetrate the unprotected lining and pass through living cells when released within the lungs. Thus, ^{210}Po and other radon daughters in the inhaled air may cause lung cancer, especially when individuals are exposed to high activities of point-sources in regions such as confined spaces associated with radioactive materials. In addition, it could pose a risk to human health when it enters the body through food consumption.

The ratios of $^{210}\text{Po}/^{210}\text{Pb}$ vary in the earth's surface, aqueous environment, and atmosphere because of their different chemical reactivity, biological enrichments, and volatility. In the atmosphere, ^{210}Po produced from ^{210}Pb is minor (e.g., $^{210}\text{Po}/^{210}\text{Pb} < 0.1$), as measured in precipitation or fallout particles. However, a large excess (not produced in the troposphere) of ^{210}Po is introduced by a variety of sources, including volcanic emissions, resuspension of top soils, incursion of stratospheric air, sea spray from the oceanic surface micro-layer, bio-volatilization of ^{210}Po from the ocean, and anthropogenic emissions (Vilenskii 1970; Poet et al. 1972; Turekian et al. 1974, 1977; Moore et al. 1976; Bacon and Elzerman 1980; Lambert et al. 1985; Baskaran 2011). In the aquatic environment, ^{210}Po displays a strong biogeochemical cycling, relative to its parent ^{210}Pb , and exhibits a large deficiency in the euphotic zone because of its preferential

removal by biota and rapid regeneration in the subsurface layer because of preferential remineralization from sinking biogenic debris.

Concentration factors for ^{210}Po in the pelagic ecosystem increase through the food web from phytoplankton and finally to fish (15×10^4 , shrimp), although they are only about $12\text{--}23 \times 10^2$ for ^{210}Pb (e.g., Fisher et al. 1983; Stewart and Fisher 2003; Stewart et al. 2005; Waska et al. 2008). Uranium mining operations often result in elevated levels of ^{210}Po in freshwater fish (average 208 mBq g^{-1}), especially in the viscera, while ^{210}Pb concentrates in the bone (Carvalho 1988; Carvalho et al. 2007). Po is effectively taken up by bacteria and dispersed between the cell walls, cytoplasm, and high-molecular-weight proteins in a manner similar to sulfur (Fisher et al. 1983; Cherrier et al. 1995; LaRock et al. 1996; Momoshima et al. 2001; Kim et al. 2005a). Thus, the volatility of Po could be due to the formation of bio-volatile species such as dimethyl polonide (Hussain et al. 1995). Given its high affinity for bacteria, it is not surprising that extremely high and unsupported ^{210}Po activity was found in some sulfide-bearing shallow groundwater in central Florida (Harada et al. 1989).

Thus, studying ^{210}Po in the environment is important in many aspects: (1) it can serve as a tracer for sulfur group elements such as Se and Te in aqueous environments, (2) its bio-accumulation and transfer through terrestrial and marine food chains are of great health concerns for human beings, and (3) the occurrence of excess ^{210}Po in the atmosphere is also important for tracing atmospheric emissions and in enclosed areas for human health. In this chapter, we review recent advances in our understanding of the fate and cycling of ^{210}Po in the atmospheric and aqueous environments.

14.2 Analytical Methods

The analytical methods for measuring ^{210}Po and ^{210}Pb in the same sample are relatively straightforward (e.g., Sarin et al. 1992; Kim et al. 1999; Masque et al. 2002; Stewart et al. 2007; IAEA 2009; Baskaran et al. 2009; GEOTRACES User Manual, Church and Baskaran, <http://www.ldeo.columbia.edu/res/pi/geotraces/documents/GEOTRACESIPYProtocols-Final.pdf>). The source of ^{210}Po is prepared by spontaneous

self-deposition onto a silver disc and following simple pre-concentration procedures to separate ^{210}Pb . Then, ^{210}Pb is measured, via ingrown ^{210}Po , after storing the sample for more than 3 months. Some researchers determine ^{210}Pb activities by beta counting of its daughter, ^{210}Bi , following a specific separation and source preparation in order to obtain ^{210}Pb data without delay (e.g., Nozaki and Tsunogai 1973). Also, some researchers conduct the separation of ^{210}Po from ^{210}Pb via specialized resins before auto-plating in order to eliminate any interference in the alpha counting (e.g., IAEA 2009). However, in this chapter we describe the simplest and most common method for ^{210}Po and ^{210}Pb analyses in water samples. Although we do not include the method for solid samples, the methods after sample dissolution and subsequent $\text{Fe}(\text{OH})_3$ precipitation are the same.

In general, approximately 10–20 L of water is required for the analysis of dissolved or total ^{210}Po and ^{210}Pb in seawater, river water, or lake water. Because the activity of ^{210}Pb in particulate matter is approximately one order of magnitude lower than that in solution, the volume of water required for the analysis of particulate ^{210}Po and ^{210}Pb is approximately 3–5 times higher than that required for the analyses of ^{210}Po and ^{210}Pb in the solution form. Although the uncertainties in measuring the sample volume can easily be reduced in the laboratory, special tools, such as an electronic balance, may be required to weigh the samples in order to reduce the uncertainties onboard ships.

The separation between the dissolved and particulate phases can be performed using the membrane or cartridge filters with a pore size of 0.4–0.8 μm immediately after sample collection. From the GEOTRACE intercalibration results (GEOTRACES User Manual), the difference between the particulate ^{210}Po and ^{210}Pb concentrations using 0.4- or 0.8- μm filters was found to be insignificant, but the choice of the filter materials is important – Supor 0.4–0.8 μm filter cartridges (e.g. Acropak 500) have been found to be reliable. The filtered water samples are stored in acid-cleaned plastic containers with acidification to a pH lower than 2. Because the intercalibration showed higher than 20% uncertainties for 10–20 L water volumes for both nuclides, water volumes of at least 50 L are recommended for particulate ^{210}Po and ^{210}Pb measurements.

The water samples are transferred into plastic buckets or cubitainers, and then spiked with NIST-traceable

^{209}Po , 25 mg of ancient Pb carrier (with a negligible ^{210}Pb activity), and 70 mg of Fe^{3+} carrier for 10–20 L volume. Following stirring with rods or bubbling with N_2 gas for 10–30 min for equilibration of the spikes and carriers, the samples are allowed to stand for an additional hours to ensure complete equilibration (Kim et al. 1999). The Po and Pb are co-precipitated with $\text{Fe}(\text{OH})_3$ at pH 7–8 using ammonia solution, with vigorous stirring during the first 10 min, and the precipitate is then allowed to settle for hours. The supernatant is siphoned off, and the precipitates are collected using a centrifuge or Whatman 54 quantitative-grade paper. The precipitates on the filter paper are dissolved by adding approximately 3 mL of 6 M HCl and are then rinsed thoroughly using about 40 mL of deionized water to bring the samples for plating to approximately 0.5 M HCl. About 200 mg of ascorbic acid is added to reach a colorless solution (Fe is fully reduced). The Po in the solution is spontaneously plated onto a silver disc (the reverse side of which is covered by a neutral cement or plastic film) by swirling the disc in water at temperature at approximately 90°C.

After the self-plating of Po onto the disc, the solution is dried and then dissolved in 5 mL of 9 M HCl. The Pb is separated from Po using a preconditioned 9 M HCl anion-exchange column. The remaining Po is adsorbed onto the column, while Pb passes through the column. To the collected Pb solution, a known amount of ^{209}Po spike is added, and the sample is stored in a clean plastic bottle for more than 3 months. The ^{210}Pb activity is measured by determining the ingrown activity of ^{210}Po . The chemical yield of Pb from all the procedures is determined by measuring the stable Pb recovery for an aliquot of the ^{210}Pb solution. The ^{210}Po activity is determined using alpha spectroscopy.

The time of sampling, anion column separation, and alpha counting should be recorded to conduct the appropriate corrections for the ingrowth and decay of ^{210}Po and ^{210}Pb from sampling to counting (IAEA 2009). The activity of ^{210}Po is calculated by the $^{210}\text{Po}/^{209}\text{Po}$ counting ratios multiplied by the activity of the added ^{209}Po spike. The counts of each Po peak should be carefully corrected for background because Po background builds up easily owing to its volatile nature. The blank activities should be further corrected for the ^{210}Po and ^{210}Pb activities.

14.3 ^{210}Po in the Atmosphere

In the atmosphere, ^{222}Rn daughters, ^{210}Pb , ^{210}Bi , and ^{210}Po , grow in during the residence of aerosols because they are adsorbed readily onto particles. Thus, their disequilibria, $^{210}\text{Pb}/^{222}\text{Rn}$, $^{210}\text{Bi}/^{210}\text{Pb}$, and $^{210}\text{Po}/^{210}\text{Pb}$, have been used to determine the residence times of aerosols (e.g., Turekian et al. 1977; Carvalho 1995a; Church and Sarin 2008). Amongst these pairs, the residence times (10–300 days) of aerosols based on $^{210}\text{Po}/^{210}\text{Pb}$ disequilibria are generally much longer than those based on the other pairs (2–20 days) and aerosol deposition models (e.g., Kim et al. 2005a). Thus, the various possible sources for the excess ^{210}Po (the observed ^{210}Po activity minus the ^{210}Po activity produced from ^{210}Pb in the troposphere) have been reported in many studies. The suggested primary sources include the input of aged aerosols from the stratosphere (residence time of about 1 year) or resuspended dust from topsoil in which the $^{210}\text{Po}/^{210}\text{Pb}$ activity ratios are close to 1. Poet et al. (1972) and Moore et al. (1976) suggested that ^{210}Po mixed down from the stratosphere was 0.2–7% of that in the troposphere. At Lamto, on the west coast of the African continent, soil dusts from Sahara desert contributed to very high $^{210}\text{Po}/^{210}\text{Pb}$ ratios, ranging from 0.30 to 0.54, in the winter atmosphere (Nho et al. 1996). In this chapter, we introduce recent progress in finding the sources of preferential ^{210}Po inputs into the atmosphere via geophysical or biogeochemical processes.

First, high ^{210}Po can be introduced into the atmosphere by volcanic activities because of its high volatility relative to ^{210}Pb . The activity ratios of $^{210}\text{Po}/^{210}\text{Pb}$ were found to be between 5 and 40 in volcanic plumes from Mt. Etna (Lambert et al. 1985) and up to ~600 at the Stromboli volcano (Gauthier et al. 2000). For this reason, the $^{210}\text{Po}/^{210}\text{Pb}$ ratios in freshly erupted pyroclastic or lava flows are close to zero (Bennett et al. 1982; Gill et al. 1985; Rubin et al. 1994). Although quite patchy in space and time, the input of ^{210}Po from volcanic emissions can account for more than one-half of the global budget of ^{210}Po in the atmosphere (Lambert et al. 1979, 1982). In northern Taiwan, Su and Huh (2002) observed higher $^{210}\text{Po}/^{210}\text{Pb}$, derived from pre-eruption gas emission from the Philippines' Mayon volcano. Based on these observational results, they suggested that ^{210}Po might

serve as a precursor of volcano eruptions worldwide if a global network can be properly designed.

Second, the source of excess ^{210}Po activities in the atmosphere can be from sea spray. The sea-surface microlayer has high activity of ^{210}Po relative to ^{210}Pb . The secretion from phytoplankton concentrated in the surface microlayer, where the $^{210}\text{Po}/^{210}\text{Pb}$ activity ratios are as much as 3.8 (Bacon and Elzerman 1980), could increase the $^{210}\text{Po}/^{210}\text{Pb}$ activity ratios in the atmosphere by sea-sprays. Heyraud and Cherry (1983) showed that the $^{210}\text{Po}/^{210}\text{Pb}$ ratios were in the ranges of 1–3 and 2–80 for the surface microlayer and neuston, respectively. Kim et al. (2005a) showed that the seawater fraction of ^{210}Po in aerosol samples from Busan, a harbor city in Korea, explained the unusually high excess of ^{210}Po activities. This suggests that a small fraction of the sea spray can result in a large excess of ^{210}Po in the coastal atmosphere.

Third, bio-volatile ^{210}Po from the eutrophic coastal region could result in high excess ^{210}Po in the atmosphere. Hussain et al. (1995) documented that bio-volatile Po (i.e., dimethylpolonide) can be formed in natural water together with other species, such as DMS, DMSe, and MMHg, through theoretical calculations and laboratory experiments. Similarly, Momoshima et al. (2001) reported that the formation and emission of volatile Po compounds occurred associated with the biological activity of microorganisms in culture medium as well as in natural seawater. Kim et al. (2000) observed that the increase in the excess ^{210}Po in the Chesapeake Bay air was dependent on the wind speed over a threshold of 3 m s^{-1} (mean), similar to other gases (i.e., CO_2 , SF_6 , and DMS) (Fig. 14.1). They showed that the simultaneously measured activity ratios of $^7\text{Be}/^{210}\text{Pb}$ and $^{210}\text{Pb}/^{222}\text{Rn}$ argued against either higher-altitude air or continental soils as the source of this excess. Thus, Kim et al. (2000) suggested that the source of excess ^{210}Po could be from surrounding coastal seawater through the gaseous air-sea exchange of volatile biogenic species (e.g., dimethyl polonide). They found that less than 10% of the total ^{210}Po in the Chesapeake or Delaware Bay was required to be volatile to account for the excess ^{210}Po in the observed air. Hussain et al. (1993) showed nearly threefold higher activity ratios of $^{210}\text{Po}/^{210}\text{Pb}$ in aerosols in and around the mid-Atlantic region in the summer than that in the fall and winter, even through the winter winds are stronger, as an indication

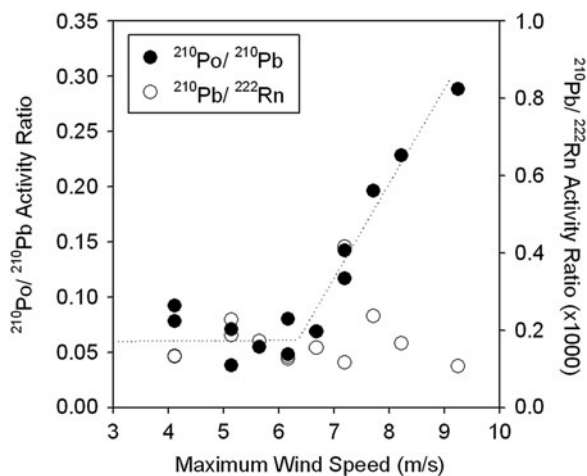


Fig. 14.1 Plots of maximum wind speed vs. $^{210}\text{Po}/^{210}\text{Pb}$ activity ratio for aerosol samples collected in Chesapeake Bay, USA, during 10–24 August 1995 (adapted from Kim et al. 2000). Wind speeds were measured on board hourly

of an additional bio-volatile ^{210}Po source in the marine environment during summer.

Forth, plant exudates, which are submicron particles, can be important sources of excess ^{210}Po in the atmosphere (Moore et al. 1976). Plant exudates are formed by the condensation of volatile organic materials released from the plant surfaces. Stress conditions such as leaf expansion during active growth or by normal weathering due to wind action and abrasion may lead to loss of these exudates (Moore et al. 1976). Moore et al. (1976) predicted that plant exudates contribute to almost 40% of the natural and anthropogenic ^{210}Po fluxes in the atmosphere over the continental USA, on the basis of a weak correlation between submicron aerosols and vegetation density, without actual ^{210}Po data. Since this process seems to be quantitatively important, more direct measurements are necessary in the future.

Fifth, anthropogenic ^{210}Po input can result from its high volatility. Moore et al. (1976) found that up to 7% of the total ^{210}Po flux to the atmosphere in Boulder, Colorado, USA could be from anthropogenic sources. These can be produced from phosphate fertilizer dispersion, a by-product of gypsum or lead refinement, cement and other metal production, and fossil-fuel burning. As such, Carvalho (1995b) reported increased $^{210}\text{Po}/^{210}\text{Pb}$ ratios in precipitation from the industrial emission of ^{210}Po in Lisbon, Portugal. Kim et al. (2005a) documented that excess ^{210}Po in the

metropolitan areas of Seoul, Korea, originates mostly from anthropogenic sources. They observed a strong correlation between non-sea-salt (nss) SO_4^{2-} and excess ^{210}Po , although there was no correlation between nss- SO_4^{2-} and its parent ^{210}Pb , suggesting that both anthropogenic SO_4^{2-} and excess ^{210}Po are controlled mainly by the same factor (Fig. 14.2). Based on this correlation and the $\delta^{34}\text{S}$ values, they concluded that the major source for excess ^{210}Po in Seoul precipi-

tation is anthropogenic, likely from the burning of fossil fuels such as coals and petroleum oils, biomass burning, and/or high-temperature incineration. Gaffney et al. (2004) showed that the contribution of soils or coal-fired power plants to the $^{210}\text{Po}/^{210}\text{Pb}$ activity ratio in aerosols could be successfully evaluated by measuring the activity ratios for both fine ($<1\ \mu\text{m}$) and coarse ($>1\ \mu\text{m}$) fractions.

Nevertheless, $^{210}\text{Po}/^{210}\text{Pb}$ disequilibria have been successfully used for estimating the aerosol residence times in some isolated areas (i.e., Arctic haze). Baskaran and Shaw (2001) observed that the $^{210}\text{Po}/^{210}\text{Pb}$ ratios in Arctic haze aerosols varied between 0 and 0.177; the residence times of the aerosols calculated from these ratios were between 0 and 39 days. In addition, the aerosol residence times calculated from the $^{210}\text{Po}/^{210}\text{Pb}$ ratios at Centerton, New Jersey, USA, were equal to or slightly shorter than those calculated using $^{210}\text{Bi}/^{210}\text{Pb}$ ratios for the same aerosol samples; this indicated the negligible input of excess ^{210}Po in this area. The mean deposition velocity of the aerosols using ^{210}Po was found to be $2.2\ \text{cm s}^{-1}$; this velocity was higher than that reported for ^{210}Pb at the same site (McNeary and Baskaran 2007). The aforementioned difference could be attributed to the difference in the scavenging behaviors of these two nuclides. Thus, to understand the scavenging mechanisms for ^{210}Po - and ^{210}Pb -laden aerosols and to validate the residence time calculation methods using Rn daughters, more extensive measurements must be performed on all Rn daughter pairs under different environmental conditions and for different particle sizes.

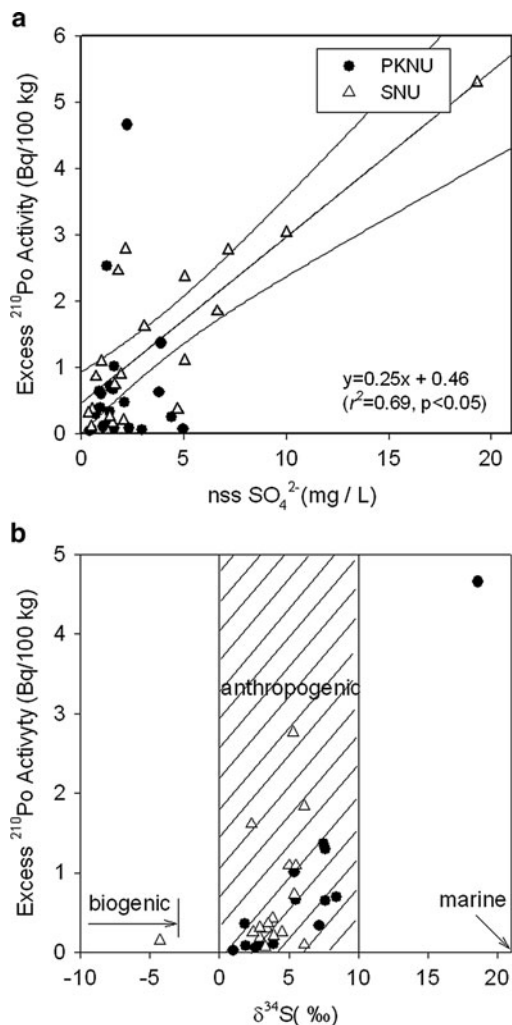


Fig. 14.2 Plots of excess ^{210}Po activities vs. (a) non-sea-salt SO_4^{2-} and (b) $\delta^{34}\text{S}$ in precipitation from Seoul (SNU, Korea) and Busan (PKNU, Korea) stations (adapted from Kim et al. 2005a). A 95% confidence interval is shown for the regression (a). In general, the $\delta^{34}\text{S}$ value is approximately 21‰ for sea spray, 5‰ on average for volcanic emissions, and lower than -4‰ for most of the biogenic emissions (Pichlmayer et al. 1998; Rees 1970). Anthropogenic sulfates exhibit a wide range of values from 0 to 10‰

14.4 ^{210}Po in the Ocean

In the surface ocean, ^{210}Po is generally deficient relative to its parent ^{210}Pb due to preferential removal by biota, where it is in near equilibrium or excess below the surface mixed layer due to rapid regeneration from sinking organic matter (Shannon et al. 1970; Bacon et al. 1976; Thomson and Turekian 1976; Cochran et al. 1983; Chung and Finkel 1988; Bacon et al. 1988). Sarin et al. (1999) showed that the dissolved ^{210}Po activities in the surface waters of the equatorial and South Atlantic Ocean are about a third of the equilibrium concentrations. Based on these

disequilibria, they calculated that the residence times of dissolved ^{210}Po in the surface water at the equatorial and southern sites were about 73 and 130 days, respectively, with longer residence times for the intermediate depths (100–500 m). The observed ^{210}Po - ^{210}Pb disequilibria showed a significant positive correlation ($r^2 = 0.61$) with the POC concentrations, suggesting that the ^{210}Po deficiency in surface water is associated mainly with biological removal from surface waters (Sarin et al. 1999). Therefore, a larger deficiency of ^{210}Po would be expected in the more productive areas of the ocean, where the population of sinking particles is larger. However, Kim (2001) showed that ^{210}Po deficiencies decrease as ocean productivity increases for the globally available ^{210}Po data in the upper 1,000 m (Fig. 14.3). The removal of ^{210}Po through the 500 m depth was about an order of magnitude higher in the oligotrophic ocean than in the productive areas of the ocean.

Nozaki et al. (1990), for the first time, pointed out an unusually large deficiency of Po in the oligotrophic Philippine Sea. They explained this phenomenon with a 2–3-fold larger focusing of atmospheric ^{210}Pb , relative to the model-based estimate, and subsequent ventilation into the deeper ocean. However, Kim (2001) posited that episodic atmospheric focusing could not significantly affect on the large deficiency of ^{210}Po in the upper oligotrophic Sargasso Sea or Philippine Sea due to the following reasons: (1) the effect of a sudden increase in the atmospheric input of ^{210}Pb (with negligible ^{210}Po) cannot be significant because the water

residence times in the upper 500 m are longer than 10 years in the major oceans, allowing almost 100% ^{210}Po ingrowth; (2) the directly measured annual atmospheric deposition of ^{210}Pb during the study period was less than 10% of the deficiency of the ^{210}Po inventory in the 0–700 m layer in the Sargasso-Sea; (3) the largest deficiency of ^{210}Po was found in the subsurface layer (Fig. 14.3) rather than in the surface layer; and (4) the large deficiencies are perennial in the Sargasso Sea based on bimonthly measurements (Kim 2001). Kim (2001) showed that the horizontal transport of waters from the ocean margins also could not be the source of this large ^{210}Po deficiency water because ^{210}Po deficiencies are generally smaller in coastal waters due to rapid remineralization.

Alternatively, Kim (2001) suggested that the large deficiencies of ^{210}Po are likely due to biological removal from the total (dissolved plus particulate) pool by cyanobacteria and subsequent transfer to nekton (via grazing), which is unavailable to normal oceanographic water sampling. He showed the following evidence supporting this hypothesis: (1) the sediment trap based fluxes of ^{210}Po (Bacon et al. 1985) through 3,000 m in the Sargasso Sea were an order of magnitude lower than the calculated ^{210}Po removal flux through 3,000 m; (2) the calculated $^{210}\text{Po}/^{210}\text{Pb}$ export flux ratio in the upper Sargasso Sea (0–500 m) is about 20, which is similar to that in zooplankton (about 20), but much higher than that in sediment trap samples at 500 m in the Sargasso Sea (about 2–3);

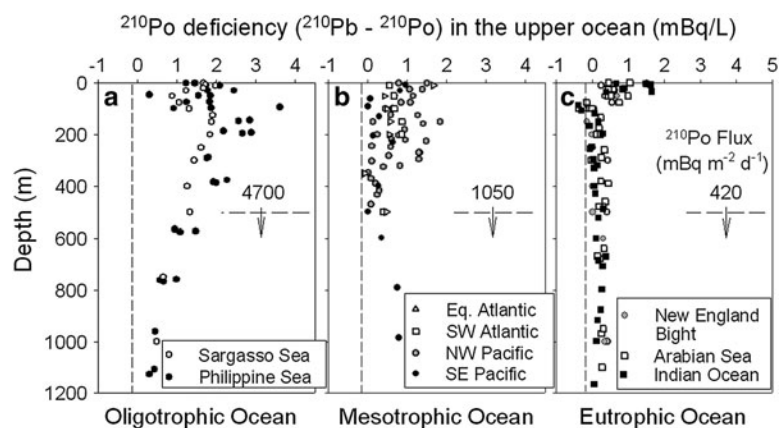


Fig. 14.3 Total (dissolved + particulate) deficiency of ^{210}Po relative to ^{210}Pb in the upper ocean and removal fluxes of ^{210}Po at 500 m (adapted from Kim 2001). The oceanic locations plotted are divided into three categories depending on biological productivity, (a) oligotrophic-very low productive ocean,

(b) mesotrophic-intermediate productive ocean, and (c) eutrophic-relatively high productive ocean. The abbreviations Eq., SW, NW, SE represent equatorial, south western, north western, and south eastern, respectively

(3) in the oligotrophic oceans, such as the Sargasso Sea, bacteria constitute the dominant biomass of the microflora and are partially predated upon by protozoa and higher trophic levels; (4) the particulate fraction (15–75%) in the oligotrophic Sargasso Sea is much higher than that in the productive areas of the ocean (e.g. the Bay of Bengal, <15%); and (5) the largest deficiency of ^{210}Po was found in the subsurface layer, where bacterial production peaks. More evidently, the relative proportion of particulate ^{210}Po was considerably higher during the summer of 1997 in the Sargasso Sea when the maximum nitrogen-fixation occurred, showing a good correlation ($r = 0.85$) between the particulate to dissolved ratios of ^{210}Po and N_2 fixation rates by *Trichodesmium* (size: ~ 0.5 by 3 mm) (Fig. 14.4). Chung and Wu (2005) also found a large deficiency of Po in the northern South China Sea, adjacent to the Philippine Sea. In this region, the mean value of the total and the dissolved ^{210}Po to ^{210}Pb activity ratios was approximately 0.6 for the entire water column. Because this large ^{210}Po deficiency could not be explained by the scavenging of sinking particulates on the basis of sediment trap results, they concluded that the deficiency is associated with biological removal and transfer to the upper trophic levels.

In contrast, in the eutrophic ocean, the ecosystem is supported mainly by macro-phytoplankton (i.e., diatoms), which are less efficient in taking up ^{210}Po relative to bacteria. The enriched Po in diatoms could be rapidly regenerated by attached bacteria and transferred to abundant free-living bacteria, non-sinking fine particles (0.3–0.6 μm diameter), in a manner similar to dissolved organic carbon (Kim 2001). In general, in the eutrophic ocean, the turnover times of bacterial organic carbon (>95% are free-living bacteria) are about fourfold faster, and the amount of free-living bacteria is an order of magnitude larger, relative to the oligotrophic ocean. This suggests that the Po could reside in the non-sinking organic pool for a much longer time in the eutrophic ocean, potentially with other sulfur group elements.

Recent studies have suggested that ^{210}Po is a potentially good tracer for particulate organic carbon (POC) export (Shimmield et al. 1995; Friedrich and Rutgers van der Loeff 2002; Murray et al. 2005; Stewart et al. 2010), similar to ^{234}Th . Friedrich and Rutgers van der Loeff (2002) reported that the observed fractionation of ^{234}Th and ^{210}Po on particles, dependent on particle

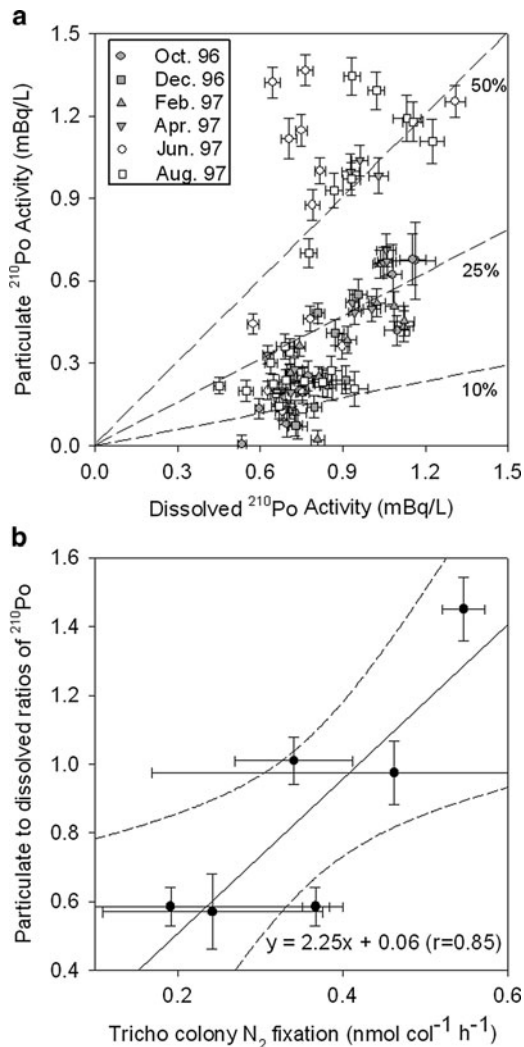


Fig. 14.4 Enrichment of polonium into cyanobacteria (adapted from Kim 2001). (a) A plot of dissolved vs. particulate ^{210}Po in the surface (0–100 m) Sargasso Sea between 1996 and 1997, showing higher enrichment of ^{210}Po to particulate matter during summer (the numbered percentages represent the proportion of particulate ^{210}Po), (b) a correlation between *Trichodesmium* N_2 fixation rates in the surface ocean and relative activities of particulate to dissolved ^{210}Po ratios in surface ocean (upper 20 m). Errors for *Trichodesmium* N_2 fixation rates are from the standard deviation of the average N_2 fixation in Puffs and Tufts for each month, and errors for ^{210}Po are based on 1σ counting error propagation. The dotted lines indicate 95% confidence intervals

composition (POC/biogenic silica ratio), is in accordance with the known preference of ^{210}Po for cytoplasm in the Antarctic Circumpolar Current. On this basis, they suggested that the utilization of the two tracers together would enable a more detailed

interpretation of POC fluxes than would be possible by using ^{234}Th alone. Murray et al. (2005) found that the POC export fluxes calculated from ^{210}Po were much more variable than those calculated from ^{234}Th because of the more variable correction factors for advection in the central equatorial Pacific. Stewart et al. (2010) found a very good correlation (>80%) between the relative fraction of ^{210}Po and POC in size-fractionated particles, with a better relationship during non-bloom conditions at the Bermuda Atlantic Time-series Study (BATS) site. They suggested that ^{210}Po traces POC export fluxes more accurately in low-export seasons than during high-export seasons, such as during a spring bloom. In the Bellingshausen Sea in Antarctica, the export production measured using ^{210}Po was considerably lower than that measured using ^{234}Th , suggesting that a better understanding of radionuclide uptake and recycling in conjunction with POC is necessary to trace export production (Shimield et al. 1995). Careful consideration is thus needed with regard to the use of ^{210}Po as a POC tracer because ^{210}Po uptake rates appear to be largely dependent on ecosystem structures and microbial roles.

14.5 ^{210}Po in Suboxic and Anoxic Waters

The activity of ^{210}Po in oxic waters of major oceans ranges from 1 to 5 mBq L⁻¹. Similarly, in the oligotrophic Crystal Lake in Wisconsin, USA, the mean annual total concentration of ^{210}Po is 1.6 ± 0.7 mBq L⁻¹. However, ^{210}Po activities are higher, up to 17 mBq L⁻¹, in seasonally anoxic ponds such as Pond B in South Carolina, USA (Kim et al. 2005b), and Bickford Pond in Massachusetts, USA (Benoit and Hemond 1990), as well as in permanently anoxic seawater

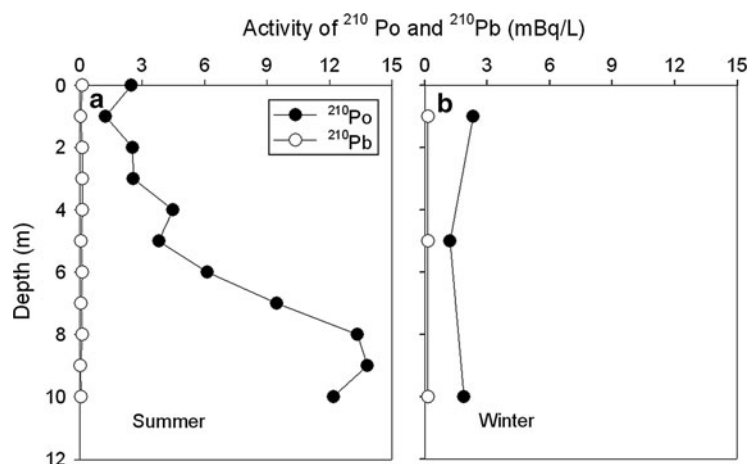
such as Framvaren Fjord in Norway (Swarzenski et al. 1999) (Table 14.1). In the permanently anoxic Jellyfish Lake in Palau, the maximum activity of ^{210}Po was 133 mBq L⁻¹, among the highest found in natural waters, except for some sulfide-bearing shallow groundwater (Harada et al. 1989).

Kim et al. (2005b) showed that, in the seasonally oxic environment, Pond B, the activity of ^{210}Po increases sharply from the surface to the bottom layer, with a maximum activity of 14 mBq L⁻¹, in the summer, while it is vertically uniform and low in winter (Fig. 14.5). In Pond B, the bottom layer becomes anoxic from May to October, and the concentrations of Fe and Mn increase sharply from the surface to the bottom layer during this period, similar to the ^{210}Po pattern, due to the dissolution of metal oxides and oxyhydroxides of Fe and Mn in the reducing bottom sediments (Kim et al. 2005b). It has been reported that Po (IV) is insoluble and is reduced to Po (II) near the potential at which Mn (IV) is reduced to Mn (II) (Benoit and Hemond 1990; Balistrieri et al. 1995). Thus, the summer profile of ^{210}Po resulted from its diffusion from bottom sediments under reducing conditions, together with Fe and Mn, in contrast to its much lower winter patterns as a consequence of efficient co-precipitation with Fe and Mn oxides. However, ^{210}Pb did not show such seasonal variations and was vertically uniform in Pond B, similar to Cs, Al, Na, and Cu, those are not sensitive to redox conditions (Kim et al. 2005b). Based on the seasonal changes in the ^{210}Po budget, Kim et al. (2005b) showed that the actual amount of labile ^{210}Po inputs to the water column is a small fraction (<5%) of the ^{210}Po pool in the surface bottom sediment. However, the activities of total ^{210}Po in the seasonally anoxic Sammamish Lake (0.07–0.47 mBq L⁻¹) in Washington, USA, were much lower than those in Pond B (Balistrieri et al.

Table 14.1 The activity of ^{210}Po in various aquatic environments (after Kim et al. 2005b)

Location	Water type	Depth (m)	^{210}Po (mBq L ⁻¹)	References
Atlantic Ocean	Oxic seawater	0–4,200	1–2	Kim and Church (2001)
Pacific Ocean	Oxic seawater	0–5,420	1–5	Nozaki et al. (1997)
Indian Ocean	Oxic seawater	0–5,587	1–2	Obota et al. (2004)
North Sea	Oxic seawater	5–45	1–5	Zuo and Eisma (1993)
Framvaren Fiord	Permanently anoxic seawater	0–30	0–17	Swarzenski et al. (1999)
Jellyfish Lake	Permanently anoxic seawater	0–30	1–133	Kim et al. (2005b)
Lake Sammamish	Seasonally anoxic freshwater	0–32	0–3	Balistrieri et al. (1995)
Crystal Lake	Seasonally anoxic freshwater	0–20	1–5	Talbot and Andren (1984)
Bickford Pond	Seasonally anoxic freshwater	0–12	1–17	Benoit and Hemond (1990)
Pond B	Seasonally anoxic freshwater	0–12	1–14	Kim et al. (2005b)

Fig. 14.5 Vertical profiles of ^{210}Po and ^{210}Pb activity in the Pond B (South Carolina, USA) water column in the (a) summer and (b) winter



1995). In this pond, the activities of both ^{210}Po and ^{210}Pb increased with depth. The researchers suggested that during oxic periods, ^{210}Pb behavior was linked to Fe cycling, whereas ^{210}Po behavior was more closely linked to the cycling of Mn. In anoxic conditions, both nuclides were influenced by sulfur cycling.

In the permanently anoxic Jellyfish Lake, an order of magnitude higher inventory of ^{210}Po (11 Bq cm^{-2}), compared to Pond B, was observed (Kim et al. 2005b). They showed that this high inventory is associated with an order of magnitude higher ^{210}Pb fluxes to the bottom sediment, compared with the atmospheric input fluxes. In Jellyfish Lake, about 2% of ^{210}Po produced from the ^{210}Pb in the bottom sediments would account for the observed excess in the water column. The benthic fluxes of ^{210}Po to the overlying water column may be controlled either by diffusion or by pore-water advection due to tidal pumping of groundwater and subsequent diffusion upward with the vertical eddy diffusivity of $\sim 0.2 \text{ cm}^2 \text{ s}^{-1}$ between 15 and 30 m.

In the permanently anoxic fjord, Framvaren, in Norway, ^{210}Po and ^{210}Pb were highly enriched at the $\text{O}_2/\text{H}_2\text{S}$ interface layer, where an active community of microbes, such as anoxygenic phototrophs (e.g., Chromatium, Chlorobium sp.), thrives (Swarzenski et al. 1999). The observed dissolved ^{210}Po enrichment at this depth was likely controlled by a phase transformation (particulate \rightarrow dissolved), which could be microbially mediated. They suggested that the dissolved ^{210}Po and ^{210}Pb were sequestered efficiently by particulates in the oxic surface layer, and this process occurred rapidly relative to the kinetics of phase redistribution because enrichment in particulate

^{210}Po did not occur. In anoxic bottom waters, on the other hand, the dissolved ^{210}Po activities were lost from the water column to freshly (co)precipitated sulfide minerals (Swarzenski et al. 1999).

A close link between ^{210}Po and the sulfur cycle has also been observed in anoxic marine sediments (Connan et al. 2009). In the pore waters of anoxic marine sediment from the roads of Cherbourg (France) in the central English Channel, ^{210}Po activity exhibited large excess in the uppermost layer ($\sim 20 \text{ mBq L}^{-1}$) and lower than 3 mBq L^{-1} in the deeper layer, relative to almost constant ^{210}Pb activities ($2.4\text{--}3.8 \text{ mBq L}^{-1}$) over the entire depth (Connan et al. 2009). ^{210}Po and ^{210}Pb activities in the pore water were higher than those in seawater, suggesting that sediments act as a source of both nuclides in seawater. The distributions of ^{210}Po activities in the pore waters correlates well with those obtained for Fe, Mn, and SO_4^{2-} , exhibiting lower ^{210}Po in the deeper pore water by the formation of a metal sulfide (Bangnall 1957; LaRock et al. 1996). Thus, they concluded that early diagenetic process influences the solid-liquid distribution of ^{210}Po in marine sediments.

14.6 ^{210}Po in Groundwater

In groundwater, the ^{210}Po level rarely exceeds 5 mBq L^{-1} since it is rapidly adsorbed onto particles. However, some previous studies (Harada et al. 1989; Neto and Mazzilli 1998; Ruberu et al. 2007; Seiler 2010) have reported unusually high ^{210}Po activities in groundwater. The natural enrichment of ^{210}Po in

groundwater may depend to a large extent on the supply of ^{222}Rn from rocks and sediments, the physicochemical conditions (i.e., pH) of groundwater, and the occurrence of fine particles (i.e., colloids) that can retain Po for a long time in solution. Monitoring of the ^{210}Po levels in groundwater is particularly important for drinking water because Po is highly toxic and it is difficult to predict the exact level of this nuclide on the basis of general geochemical information.

Harada et al. (1989) studied the geochemistry of ^{210}Po in a well containing acidic water (pH < 5) with extraordinarily high ^{210}Po levels ($\sim 17 \text{ Bq L}^{-1}$); in this well water, the activity of ^{210}Po was markedly higher than that of its parents, ^{210}Pb and ^{210}Bi , while the ^{222}Rn activity was moderately high. They found that most of the Po species present in this well was in a form that could not be co-precipitated with iron hydroxide scavenging; during sulfide oxidation, the soluble phase took a few days to convert to the particulate phase. Thus, Harada et al. (1989) speculated that Po cycling in such an extreme environment is related to the sulfur cycle, which in turn may be influenced by sulfur bacteria.

Seiler (2010) found that the activity of ^{210}Po ranged from 0.37 to 6,590 mBq L^{-1} in the groundwater in Lahontan Valley, northern Nevada, USA. In this region, wells with high ^{210}Po activities had low dissolved oxygen concentrations (less than 0.1 mg L^{-1}) and commonly had pH greater than 9. In Lahontan Valley, the ^{210}Po activity varied very slightly over a given period that was several times the half-life of this nuclide, indicating the continuous production of ^{210}Po in the aquifer. In this region, the basin-fill sediments were derived mainly from the erosion of uranium-enriched granite rocks in the Sierra Nevada by streams. Thus, radioactive decay of naturally occurring uranium in the sediments was proposed as the ultimate source of ^{210}Po in this region (Seiler 2010). On the basis of the results obtained for the Lahontan valley and those obtained for Florida and Maryland, Seiler (2010) concluded that natural ^{210}Po enrichment may occur in acidic, neutral, or basic groundwater, irrespective of the presence of ^{222}Rn .

In groundwater wells across the state of California, USA, the ^{210}Po activity ranged from 0.3 to 555 mBq L^{-1} (Ruberu et al. 2007), which was always lower than the ^{210}Pb activity (4–1,500 mBq L^{-1}). According to Ruberu et al. (2007), bacteria may play a role in the preferential removal of ^{210}Po , relative to

^{210}Pb , by bio-volatilization. In the Brazilian springs (Vilela and São Bento), which are fed by sandstone aquifers, the ^{210}Po activity ranged from 120 to 400 mBq L^{-1} , with the $^{210}\text{Po}/^{210}\text{Pb}$ activity ratios ranging from 0.5 to 0.7 (Neto and Mazzilli 1998). Neto and Mazzilli (1998) stated that the high level of ^{210}Po and ^{210}Pb in these spring waters could be attributed to the low pH of the water (4.6–5.4) and the uraniferous nature of the sandstones (0.1–0.2% U_3O_8). Although there was no correlation between ^{210}Po and ^{210}Pb , a weak correlation existed between the ^{210}Po level and the pH. For these spring waters, the calculated radiation doses corresponding to the ingestion of ^{210}Pb and ^{210}Po by the human kidney and bone surface were up to 5.9 and 1.9 mSv year^{-1} , respectively. This is an issue of concern from the viewpoint of human health.

14.7 Enrichment of ^{210}Po in Marine Organisms

^{210}Po has a similar chemical property to Se and Te (Nieboer and Richardson 1980), but ^{210}Po functions differently in living organisms (Carvalho 1988; Carvalho and Fowler 1994; Barceloux 1999; Chasteen and Bentley 2003; Moroder 2005; Waska et al. 2008). Although ^{210}Po is radiotoxic even in small concentrations, ^{210}Po is assimilated preferentially over ^{210}Pb by marine organisms (Heyraud and Cherry 1979; Cherry and Heyraud 1982; Fisher et al. 1983; Carvalho 1988, 1990; Carvalho and Fowler 1994). Thus, the radiation dose from ^{210}Po alone can be very high in human beings who consume seafood. In the ocean, ^{210}Po activities in phytoplankton range from 40 to 450 Bq kg^{-1} (dry wt) (Shannon et al. 1970; Heyraud and Cherry 1979; Cherry et al. 1987), and those in zooplankton range from 100 to 2,000 Bq kg^{-1} (dry wt) (Shannon et al. 1970; Kharkar et al. 1976; Heyraud 1982). For marine fishes and benthic animals, ^{210}Po activities were found to be from 50 to 900 Bq kg^{-1} (dry wt) for the entire body, with exceptionally elevated concentrations in some organs, e.g. the hepatopancreas of crustaceans and in the liver, gonads, and bones of fish (Beasley et al. 1973; Heyraud and Cherry 1979; Carvalho 1988; Cherry et al. 1989). ^{210}Po activities in small mesopelagic fish can reach $\sim 800 \text{ Bq kg}^{-1}$ (wet wt) on a whole-body basis (Carvalho 1988).

Table 14.2 Bioconcentration factors for ^{210}Po , Se, and Te (after Waska et al. 2008)

Sample type	^{210}Po	Se	Te
Phytoplankton	7.6×10^{4a}	1.6×10^{4b}	$600\text{--}4.2 \times 10^{4c}$
Zooplankton	8.3×10^{5a}	3.4×10^{4b}	$8\text{--}20^c$
<i>Loligo</i> sp.			
Muscle	1.9×10^{4d}	2.3×10^{4b}	
Gills	–	7.2×10^{4b}	
Hepatopancreas	2.3×10^{6d}	1.3×10^{5b}	
<i>Todarodes pacificus</i>			
Muscle	6.4×10^{3e}	2.0×10^{4e}	5.8×10^{3e}
Stomach	2.6×10^{4e}	6.2×10^{4e}	5.9×10^{3e}
Gills	2.4×10^{5e}	8.4×10^{4e}	1.6×10^{4e}
Hepatopancreas	1.4×10^{6e}	1.1×10^{5e}	2.2×10^{4e}

^aSuh et al. (1995)^bLiu et al. (1987)^cNolan et al. (1991)^dHeyraud and Cherry (1979)^eWaska et al. (2008)

Concentration factors for ^{210}Po in the pelagic ecosystem increase through the food web from phytoplankton to zooplankton and finally to fish (Table 14.2). The pattern of ^{210}Po accumulation into marine organisms is similar to that for Se (Heyraud and Cherry 1979; Liu et al. 1987; Skwarzec 1988; Chatterjee et al. 2001), which is much more effective than its parent ^{210}Pb (concentration factors from 1.2 to 2.3×10^3 in fish, Cherry and Heyraud 1981, 1982; Carvalho 1988; Stewart and Fisher 2003). The sulfur-group elements may follow the same metabolic pathways, such as biomethylation (Hussain et al. 1995; Chasteen and Bentley 2003; Kim et al. 2000). A ^{210}Po -sulfur covalent bond may be formed in the hepatopancreas of marine invertebrates (Heyraud et al. 1987).

In order to elucidate the relationship between the chemically similar S, Se, Te, and ^{210}Po in marine invertebrates, Waska et al. (2008) measured the distribution patterns of these elements in the pacific flying squid, *Todarodes pacificus*. They found no relationship between chalcogen concentrations and morphological parameters (mantle length, body weight, and sex), but gills showed slightly elevated levels of Se and ^{210}Po , perhaps due to the absorption and uptake of these elements over the gill surface (Table 14.2). All four chalcogens had their highest concentrations in the hepatopancreas and their lowest concentrations in the muscle tissues (Waska et al. 2008). Waska et al. (2008) demonstrated that bioconcentration factors (BCFs), based on reference seawater values and “internal BCFs” based on the enrichment in the hepatopancreas

compared with that in muscle tissues, for ^{210}Po showed a distinct ranking of tissues in the order of muscle < stomach < gills < hepatopancreas, whereas the BCFs for Se and Te in the various tissues were of similar magnitudes. They suggested that the distribution patterns of Se and Te resemble those of essential trace elements such as Zn and Cu, whereas ^{210}Po is partitioned in a manner similar to toxic heavy metals such as Cd and Ag.

14.8 Future Directions

The source of excess ^{210}Po activities in the atmosphere has not been understood thoroughly, especially for plant exudates, anthropogenic sources, and biovolatilization. Thus, more extensive studies are necessary to determine the sources of ^{210}Po , its scavenging mechanisms, and the feasibility of using ^{210}Po as a tracer for aerosol residence time determination. Because the occurrence of radioactive ^{210}Po in air is of great concern, especially when other toxic chemical constituents accompany it in the urban atmosphere, one should determine the detailed sources, mechanisms, and magnitude of anthropogenic ^{210}Po .

In the ocean, Po as a tracer for Se and Te may be taken up efficiently by bacteria (i.e., cyanobacteria) in the oligotrophic ocean and transferred to higher trophic levels (i.e., nekton). In productive areas of the ocean, sulfur group elements seem to reside in the subsurface ocean for much longer periods because they are taken up by abundant free-living bacteria (non-sinking fine particles). Although this hypothesis sheds new light on the global marine biogeochemical cycling of sulfur-group elements in association with microbial activity, more extensive studies are necessary to find direct evidence, together with Se and Te. Although these complicated biogeochemical characteristics hamper the use of ^{210}Po as a tracer for the export of particulate organic matter, it may serve as a tracer of nitrogen fixation in the ocean if a more direct link is demonstrated. In addition, the role of colloids should be investigated in order to fully understand the mechanisms of the biogeochemical cycling of ^{210}Po in the ocean.

In the suboxic and anoxic waters, the direct measurements of ^{210}Po transport from bottom sediments should be conducted using tools such as benthic

chambers. In addition, both microbial and chemical roles for the unusually high enrichment of ^{210}Po in the suboxic and anoxic environments should be further investigated because different regions show different enrichment patterns and biogeochemical cycling. Because ^{210}Po can naturally be highly enriched in anoxic environments to a very high level, studies on the bio-concentrations and bio-magnification of ^{210}Po in these extreme environments are highly recommended. The mechanisms of ^{210}Po enrichment in groundwater has not been elucidated as yet, and the observed results differ with the study region and geochemical conditions. Since high levels of ^{210}Po in drinking groundwater remain a cause of concern from the human-health perspective, extensive studies must be carried out to determine the ^{210}Po level in groundwater as well as the groundwater geochemistry (i.e., Eh, pH, and DO) and health effects of ^{210}Po .

In order to better understand the enrichment of ^{210}Po by marine organisms and to evaluate the human uptake rates of ^{210}Po through marine organisms, we have to quantify the ^{210}Po enrichment for all species for different environmental regions in the future. Many more studies are still needed on the detoxification processes that occur at a molecular level in invertebrates, which could differ depending on the species and its ecological niche.

References

- Bacon MP, Elzerman AW (1980) Enrichment of ^{210}Pb and ^{210}Po in the sea-surface microlayer. *Nature* 284:332–334
- Bacon MP, Spencer DW, Brewer PG (1976) Pb-210/Ra-226 and Po-210/Pb-210 disequilibria in seawater and suspended particulate matter. *Earth Planet Sci Lett* 32:277–296
- Bacon MP, Huh CA, Fleer AP et al (1985) Seasonality in the flux of natural radionuclides and plutonium in the deep Sargasso Sea. *Deep Sea Res* 32:273–286
- Bacon MP, Belastock RA, Tecotzky M et al (1988) Lead-210 and polonium-210 in ocean water profiles of the continental shelf and slope south of New England. *Cont Shelf Res* 8: 841–853
- Balistreri LS, Murray JW, Paul B (1995) The geochemical cycling of stable Pb, ^{210}Pb , and ^{210}Po in seasonally anoxic Lake Sammamish, Washington, USA. *Geochim Cosmochim Acta* 59:4845–4861
- Bangnall KW (1957) Chemistry of the rare radioelements. Academic, New York
- Barceloux DG (1999) Selenium. *Clin Toxicol* 37:145–172
- Baskaran M (2011) Po-210 and Pb-210 as atmospheric tracers and global atmospheric Pb-210 fallout: a review. *J Environ Radioact* 102:500–513
- Baskaran M, Shaw GE (2001) Residence time of arctic haze aerosols using the concentrations and activity ratios of ^{210}Po , ^{210}Pb and ^7Be . *J Aerosol Sci* 32:443–452
- Baskaran M, Hong GH, Santschi PH (2009) Radionuclide analysis in seawater. In: Wurl O (ed) Practical guidelines for the analysis of seawater. CRC Press, Boca Raton, pp 259–304
- Beasley TM, Eagle RJ, Jokela TA (1973) Polonium-210, lead-210 and stable lead in marine organisms. *Q Summ Rep Hlth Saf Lab* 273:2–36
- Bennett JT, Krishnaswami S, Turekian KK et al (1982) The uranium and thorium decay series nuclides in Mt. St. Helens effusive. *Earth Planet Sci Lett* 60:61–69
- Benoit G, Hemond HF (1990) ^{210}Po and ^{210}Pb remobilization from lake sediments in relation to iron and manganese cycling. *Environ Sci Technol* 24:1224–1234
- Carvalho FP (1988) Polonium-210 in marine organisms: a wide range of natural radiation dose domains. *Radiat Prot Dosim* 24:113–117
- Carvalho FP (1990) Contribution a l'étude du cycle du polonium-210 et du plomb-210 dans l'environnement. These de Doctorat, Université de Nice-Sophia Antipolis
- Carvalho FP (1995a) ^{210}Pb and ^{210}Po in sediments and suspended matter in the Tagus estuary, Portugal. Local enhancement of natural levels by wastes from phosphate ore processing industry. *Sci Total Environ* 159:201–214
- Carvalho FP (1995b) Origins and concentrations of ^{222}Rn , ^{210}Pb , ^{210}Bi and ^{210}Po in the surface air at Lisbon, Portugal, at the Atlantic edge of the European continental landmass. *Atmos Environ* 29(15):1809–1819
- Carvalho FP, Fowler SW (1994) A double-tracer technique to determine the relative importance of water and food as sources of polonium-210 to marine prawns and fish. *Mar Ecol Prog Ser* 103:251–264
- Carvalho FP, Oliveira JM, Lopes I et al (2007) Radionuclides from past uranium mining in rivers of Portugal. *J Environ Radioact* 98:298–314
- Chasteen TG, Bentley R (2003) Biomethylation of selenium and tellurium: microorganisms and plants. *Chem Rev* 103:1–25
- Chatterjee A, Bhattacharya B, Das R (2001) Temporal and organ-specific variability of selenium in marine organisms from the eastern coast of India. *Adv Environ Res* 5:167–174
- Cherrier J, Burnett WC, LaRock PA (1995) The uptake of polonium and sulfur by bacteria. *Geomicrobiol J* 13: 103–115
- Cherry RD, Heyraud M (1981) Polonium-210 content of marine shrimp: variation with biological and environmental factors. *Mar Biol* 65:165–175
- Cherry RD, Heyraud M (1982) Evidence of high natural radiation doses in certain mid-water oceanic organisms. *Science* 218:54–56
- Cherry MI, Cherry RD, Heyraud M (1987) Polonium-210 and lead-210 in Antarctic marine biota and sea water. *Mar Biol* 96:441–449
- Cherry RD, Heyraud M, James AG (1989) Diet prediction in common clupeoid fish using polonium-210 data. *J Environ Radioact* 10:47–65
- Chung Y, Finkel R (1988) ^{210}Po in the western Indian Ocean: distributions, disequilibria, and partitioning between

- dissolved and particulate phases. *Earth Planet Sci Lett* 88: 232–240
- Chung Y, Wu T (2005) Large ^{210}Po deficiency in the northern South China Sea. *Cont Shelf Res* 25:1209–1224
- Church TM, Sarin MM (2008) U- and Th-series nuclides in the atmosphere: supply, exchange, scavenging, and applications to aquatic processes. In: Krishnaswami S, Cochran JK (eds) Chapter 2 radioactivity in the environment, Elsevier, Amsterdam, vol 13, p 11–47
- Cochran JK, Bacon MP, Krishnaswami S (1983) Pb-210, Po-210 distributions in the central and eastern Indian Ocean. *Earth Planet Sci Lett* 65:433–452
- Connan O, Boust D, Billon G et al (2009) Solid partitioning and solid–liquid distribution of ^{210}Po and ^{210}Pb in marine anoxic sediments: roads of Cherbourg at the northwestern France. *J Environ Radioact* 100:905–913
- Fisher NS, Burns KA, Cherry RD et al (1983) Accumulation and cellular distribution of ^{241}Am , ^{210}Po , and ^{210}Pb in two marine algae. *Mar Ecol Prog Ser* 11:233–237
- Friedrich J, Rutgers van der Loeff M (2002) A two-tracer (^{210}Po - ^{234}Th) approach to distinguish organic carbon and biogenic silica export flux in the Antarctic circumpolar current. *Deep Sea Res I* 49:101–120
- Gaffney JS, Marley NA, Cunningham MM (2004) Natural radionuclides in fine aerosols in the Pittsburgh area. *Atmos Environ* 38:3191–3200
- Gauthier PJ, Le Gloarec MF, Condomines M (2000) Degassing processes at Stromboli volcano inferred from short-lived disequilibria (^{210}Pb - ^{210}Bi - ^{210}Po) in volcanic gases. *Earth Planet Sci Lett* 102:1–19
- Gill J, Williams R, Bruland K (1985) Eruption of basalt and andesite lava degasses ^{222}Rn and ^{210}Po . *Geophys Res Lett* 12(1):17–20
- Harada K, Burnett WC, LaRock PA et al (1989) Polonium in Florida groundwater and its possible relationship to the sulfur cycle and bacteria. *Geochim Cosmochim Acta* 53: 143–150
- Heyraud M (1982) Contribution a l'etude du polonium-210 et du plomb-210 dans les organismes marins et leur environnement. These de Dotorat d'Etat, Univ, Paris VI
- Heyraud M, Cherry RD (1979) Polonium-210 and Lead-210 in marine food chains. *Mar Biol* 52:227–236
- Heyraud M, Cherry RD (1983) Correlation of ^{210}Po and ^{210}Pb enrichments in the sea-surface microlayer with neuston biomass. *Cont Shelf Res* 1:283–293
- Heyraud M, Cherry RD, Dowdle EB (1987) The subcellular localization of natural ^{210}Po in the hepatopancreas of the rock lobster (*Jasus lalandii*). *J Environ Radioact* 5:249–260
- Hussain N, Church TM, Burnett WC (1993) Volatile polonium in Floridan groundwater. AGU Abstract H22D-5. Fall meeting, San Francisco
- Hussain N, Ferdelman TG, Church TM (1995) Bio-volatilization of polonium: results from laboratory analyses. *Aquat Geom* 1:175–188
- IAEA (2009) A procedure for the determination of Po-210 in water samples by alpha spectrometry. In: IAEA analytical quality in nuclear applications No. IAEA/AQ/12. International Atomic Energy Agency, Vienna
- Kharkar AG, Thomson J, Turekian KK et al (1976) Uranium and thorium decay series nuclides in plankton from the Caribbean. *Limnol Oceanogr* 21:294–299
- Kim G (2001) Large deficiency of polonium in the oligotrophic ocean's interior. *Earth Planet Sci Lett* 192:15–21
- Kim G, Church TM (2001) Seasonal biogeochemical fluxes of ^{234}Th and ^{210}Po in the upper Sargasso Sea: influence from atmospheric iron deposition. *Global Biogeochem Cy* 15(3): 651–661
- Kim G, Hussain N, Church TM et al (1999) A practical and accurate method for the determination of ^{234}Th simultaneously with ^{210}Po and ^{210}Pb in seawater. *Talanta* 49: 851–858
- Kim G, Hussain N, Scudlark JR et al (2000) Factors influencing the atmospheric depositional fluxes of stable Pb, ^{210}Pb , and ^7Be into Chesapeake Bay. *J Atmos Chem* 36:65–79
- Kim G, Hong YL, Jang J et al (2005a) Evidence for anthropogenic ^{210}Po in the urban atmosphere of Seoul, Korea. *Environ Sci Technol* 39:1519–1522
- Kim G, Kim SJ, Harada K et al (2005b) Enrichment of excess ^{210}Po in anoxic ponds. *Environ Sci Technol* 39:4894–4899
- Lambert G, Buisson A, Sanak J (1979) Modification of the atmospheric polonium-210 to lead-210 ratios by volcanic emissions. *J Geophys Res* 84(C11):6980–6986
- Lambert G, Ardouin B, Polian G (1982) Volcanic output of long-lived radon daughter. *J Geophys Res* 87:11103–11108
- Lambert G, Le C, Ardouin MF et al (1985) Volcanic emission of radionuclides and magma dynamics. *Earth Planet Sci Lett* 76:185–192
- LaRock PL, Hyun JH, Boutelle S (1996) Bacterial mobilization of polonium. *Geochim Cosmochim Acta* 60:4321–4328
- Liu DL, Yang YP, Hu MH (1987) Selenium content of marine food chain organisms from the coast of China. *Mar Environ Res* 22:51–165
- Masque P, Sanchez-Cabeza JA, Bruach JM et al (2002) Balance and residence times of ^{210}Pb and ^{210}Po in surface waters of the Northwestern Mediterranean Sea. *Cont Shelf Res* 22: 2127–2146
- McNeary D, Baskaran M (2007) Residence times and temporal variations of ^{210}Po in aerosols and precipitation from southeastern Michigan, United States. *J Geophys Res* 112: D04208. doi:10.1029/2006JD007639
- Momoshima N, Song LX, Osaki S et al (2001) Formation and emission of volatile polonium compound by microbial activity and polonium methylation with methylcobalamin. *Environ Sci Technol* 35:2956–2960
- Moore HE, Martell EA, Poet SE (1976) Source of polonium-210 in atmosphere. *Environ Sci Technol* 10:586–591
- Moroder L (2005) Isosteric replacement of sulfur with other chalcogens in peptides and proteins. *J Peptide Sci* 11: 187–214
- Murray JW, Paul B, Dunne J et al (2005) ^{234}Th , ^{210}Pb , ^{210}Po and stable Pb in the central equatorial Pacific: tracers for particle cycling. *Deep Sea Res I* 52:2109–2139
- Neto AN, Mazzilli B (1998) Evaluation of ^{210}Po and ^{210}Pb in some mineral spring waters in Brazil. *J Environ Radioact* 41: 11–18
- Nho EY, Ardouin B, Le Cloarec MF et al (1996) Origins of ^{210}Po in the atmosphere at Lamto, Ivory coast: biomass burning and Saharan dusts. *Atmos Environ* 30(20):3705–3714
- Nieboer E, Richardson DHS (1980) The replacement of the nondescript term “heavy metals” by a biologically and chemically significant classification of metal ions. *Environ Pollut* 1:3–26

- Nolan C, Whitehead N, Teyssié JL (1991) Tellurium speciation in seawater and accumulation by marine phytoplankton and crustaceans. *J Environ Radioact* 13:217–233
- Nozaki Y, Tsunogai S (1973) A simultaneous determination of lead-210 and polonium-210 in sea water. *Anal Chim Acta* 64:209–216
- Nozaki Y, Ikuta N, Yashima M (1990) Unusually large ^{210}Po deficiency relative to ^{210}Pb in the Kurashio current of the East China and Philippine Seas. *J Geophys Res* 95: 5321–5329
- Nozaki Y, Zhang J, Takeda A (1997) ^{210}Pb and ^{210}Po in the equatorial Pacific and the Bering Sea: the effects of biological productivity and boundary scavenging. *Deep Sea Res II* 44:2203–2220
- Obota H, Nozaki Y, Alibo DS et al (2004) Dissolved Al, In, and Ce in the eastern Indian Ocean and the Southeast Asian Seas in comparison with the radionuclides ^{210}Pb and ^{210}Po . *Geochim Cosmochim Acta* 68:1035–1048
- Pichlmayer F, Schoner W, Seibert P et al (1998) Stable isotope analysis for characterization of pollutants at high elevation alpine sites. *Atmos Environ* 32:4075–4086
- Poet SE, Moore HE, Martell EA (1972) Lead-210, bismuth-210, and polonium-210 in the atmosphere; accurate ratio measurement and application to aerosol residence time determination. *J Geophys Res* 77:6515–6527
- Rees CE (1970) The sulfur-isotope balance of the ocean, an improved model. *Earth Planet Sci Lett* 7:366–370
- Ruberu SR, Liu YG, Perera SK (2007) Occurrence and distribution of ^{210}Pb and ^{210}Po in selected California groundwater wells. *Health Phys* 92:432–441
- Rubin KH, Macdougall JD, Perfit MR (1994) ^{210}Po - ^{210}Pb dating of recent volcanic eruption on the sea floor. *Nature* 368: 841–844
- Sarin MM, Bhushan R, Rengarajan R et al (1992) The simultaneous determination of ^{238}U series nuclides in seawater: results from the Arabian Sea and Bay of Bengal. *Indian J Mar Sci* 21:121–127
- Sarin MM, Kim G, Church TM (1999) ^{210}Po and ^{210}Pb in the South-equatorial Atlantic: distribution and disequilibria in the upper 500 m. *Deep Sea Res II* 46:907–917
- Seiler RL (2010) ^{210}Po in Nevada groundwater and its relation to gross alpha radioactivity. *Ground Water*. doi:10.1111/J.1745-6584.2010.00688
- Shannon LV, Cherry RD, Orren MJ (1970) Polonium-210 and lead-210 in the marine environment. *Geochim Cosmochim Acta* 34:701–711
- Shimmield GB, Ritchie GD, Fileman TW (1995) The impact of marginal ice zone processes on the distribution of ^{210}Pb , ^{210}Po , and ^{234}Th and implications for new production in the Bellingshausen Sea, Antarctica. *Deep Sea Res II* 42: 1313–1335
- Skwarzec B (1988) Accumulation of ^{210}Po in selected species of Baltic fish. *J Environ Radioact* 8:111–118
- Stewart GM, Fisher NS (2003) Experimental studies on the accumulation of polonium-210 by marine phytoplankton. *Limnol Oceanogr* 48:1193–1201
- Stewart GM, Fowler SW, Teyssié JL et al (2005) Contrasting transfer of polonium-210 and lead-210 across three trophic levels in marine plankton. *Mar Ecol Prog Ser* 290:27–33
- Stewart GM, Cochran JK, Xue J et al (2007) Exploring the connection between ^{210}Po and organic matter in the north-western Mediterranean. *Deep Sea Res I* 54:415–427
- Stewart GM, Moran SB, Lomas MW (2010) Seasonal POC fluxes at BATS estimated from ^{210}Po deficits. *Deep Sea Res I* 57:113–124
- Su CC, Huh CA (2002) Atmospheric ^{210}Po anomaly as a precursor of volcano eruptions. *Geophys Res Lett* 29(5). doi:10.1029/2001GL013856
- Suh HL, Kim SS, Go YB et al (1995) ^{210}Po Accumulation in the Pelagic Community of Yongil Bay, Korea (Korean). *J Korean Fish Soc* 28:219–226
- Swarczewski PW, McKee BA, Sørensen K et al (1999) ^{210}Pb and ^{210}Po , manganese and iron cycling across the $\text{O}_2/\text{H}_2\text{S}$ interface of a permanently anoxic fjord: Framvaren, Norway. *Mar Chem* 67:199–217
- Talbot RW, Andren AW (1984) Seasonal variations of ^{210}Pb and ^{210}Po concentrations in an oligotrophic lake. *Geochim Cosmochim Acta* 48:2053–2063
- Thomson J, Turekian KK (1976) ^{210}Po and ^{210}Pb distribution ocean water profiles from the eastern South Pacific. *Earth Planet Sci Lett* 32:297–303
- Turekian KK, Kharkar DP, Thomson J (1974) The fates of ^{210}Pb and ^{210}Po in the ocean surface. *J Rech Atmos* 8:639–646
- Turekian KK, Nozaki Y, Benninger LK (1977) Geochemistry of atmospheric radon and radon products. *Ann Rev Earth Planet Sci* 5:227–255
- Vilenskii VD (1970) The influence of natural radioactive atmospheric dust in determining the mean stay time of lead-210 in the troposphere. *Atmos Ocean Phys* 6:307–310
- Waska H, Kim S, Kim G et al (2008) Distribution patterns of chalogens (S, Se, Te, ^{210}Po) in various tissues of a squid, *Todarodes pacificus*. *Sci Total Environ* 392:218–224
- Zuo Z, Eisma D (1993) ^{210}Pb and ^{210}Po distributions and disequilibrium in the coastal and shelf waters of the southern North Sea. *Cont Shelf Res* 13:999–1022

Chapter 15

Applications of Groundwater Helium

J.T. Kulongoski and D.R. Hilton

Abstract Helium abundance and isotope variations have widespread application in groundwater-related studies. This stems from the inert nature of this noble gas and the fact that its two isotopes – helium-3 and helium-4 – have distinct origins and vary widely in different terrestrial reservoirs. These attributes allow He concentrations and $^3\text{He}/^4\text{He}$ isotope ratios to be used to recognize and quantify the influence of a number of potential contributors to the total He budget of a groundwater sample. These are atmospheric components, such as air-equilibrated and air-entrained He, as well as terrigenous components, including in situ (aquifer) He, deep crustal and/or mantle He and tritogenic ^3He . Each of these components can be exploited to reveal information on a number of topics, from groundwater chronology, through degassing of the Earth's crust to the role of faults in the transfer of mantle-derived volatiles to the surface. In this review, we present a guide to how groundwater He is collected from aquifer systems and quantitatively measured in the laboratory. We then illustrate the approach of resolving the measured He characteristics into its component structures using assumptions of endmember compositions. This is followed by a discussion of the application of groundwater He to the types of topics mentioned above using case studies from aquifers in California and Australia. Finally, we present possible future research directions involving dissolved He in groundwater.

J.T. Kulongoski (✉)
California Water Science Center, U.S. Geological Survey,
San Diego, CA 92101, USA
e-mail: kulongos@usgs.gov

D.R. Hilton
Scripps Institution of Oceanography, University of California
San Diego, La Jolla, CA 92093-0244, USA

15.1 Introduction

Studies of the noble gas characteristics of groundwater have long been used to provide information about climatic conditions during periods of aquifer recharge (e.g. Mazor 1972; Andrews and Lee 1979). In this respect, the key attributes of the noble gases are their inert behavior coupled with their well defined solubility characteristics as a function of temperature and salinity. However, to fully exploit noble gases in this manner, groundwater residence times must also be known in order to place an absolute chronology against climatic variations. Ironically, the least useful noble gas for paleo-climate studies – helium, due to the relative insensitivity of its Henry's Law coefficient to temperature change – is one of the most useful gases for providing chronological information, over both short and long timescales (e.g. Andrews and Lee 1979; Marine 1979; Torgersen 1980; Heaton and Vogel 1981). Thus, helium has often been considered as a stand-alone tracer to the other noble gases as it has found widespread application in groundwater-related research, mostly unrelated to climate studies. This is the approach adopted in this review – we emphasize the role of helium in groundwater – and direct the reader to other publications (e.g. Ballentine et al. 2002; Ballentine and Burnard 2002; Kipfer et al. 2002; Phillips and Castro 2003) which provide background on the utility of the other noble gases in groundwater.

We begin with an overview of the collection and measurement approaches commonly used to produce He data on groundwater samples. We provide details of field and laboratory techniques and protocols for the production of both precise and accurate He isotope and concentration data. By adopting reasonable estimates of potential endmember compositions which

contribute to observed (i.e., measured) values, we show how He variations can be resolved to yield quantitative information on the different sources comprising the He record. Such information can indeed be used to provide chronological information on the residence time of the groundwater since the time of recharge (i.e., since last equilibration with the atmosphere in the unsaturated zone). However, groundwater He data go far beyond this application, and we include discussion on other issues such as degassing fluxes from the crust and the influence of faults on the transfer of mantle-derived volatile to the atmosphere – topics which are amenable to study through exploiting He measurements of groundwater. We end with a section on future prospects of groundwater He studies, particularly in light of the increasing realization that groundwater He concentrations and its isotope composition can vary on both short and long timescales, and that documenting this variability has exciting potential for understanding fluid characteristics and movement through the crust especially in response to external perturbations, including seismic disturbances.

15.2 Materials and Methods

This section gives an overview of the procedures involved in producing helium data on groundwater samples. It includes a brief description of sample collection methods as well as laboratory procedures used to prepare He for isotopic and abundance measurement. It concludes with a note on data quality, nomenclature, and units.

15.2.1 Sample Collection

Collection of groundwaters for dissolved He analysis involves exploiting actively-pumping commercial (i.e., supply) wells, observation wells, natural springs or seeps. In all cases, the essential prerequisite during sampling is to avoid, or at least minimize, air contamination. In the case of wells, it is important that the well volume is purged prior to sampling so that only aquifer water is collected for analysis. This precaution involves sampling only after a given time period equivalent to purging approximately three volumes of

the well. This safeguard is particularly important for observation wells where a pump has to be introduced to sample the groundwater. However, even for apparently continuously-pumping wells, caution must be exercised that sampling does not take place immediately following the start of a new pumping cycle as air can enter the well when the pumping cycle is interrupted or shut-off.

For natural springs and groundwater seeps, air contamination is avoided by inserting sampling tubing as far as possible into the “eye” of the spring, i.e., at the point where water leaves the ground. It must remain submerged and well below the surface level of the water for the entire sampling procedure. The tubing most commonly used is clear and flexible (e.g. PVC or PTFE – polytetrafluoroethylene), and its role is to transfer the groundwater into and out of the sampling vessel. In the case of wells, the same type of tubing can be connected to the well-head directly, usually via a sampling port, or to the outlet of the pump in the case of small, narrow-diameter pumps commonly used for observation wells. In all cases, prolonged flushing with the (water) sample of interest should remove, and can be seen to remove (in the case of transparent plastic tubing), any air bubbles which may have adhered to the sides of the tubing.

There are different types of sampling vessel which are used for the collection and storage of groundwaters for transfer back to the laboratory. The most common type is oxygen-free, annealed copper tubing, which is readily available at plumbers’ supply stores. A length of ~30 cm copper tube with a diameter of ~9–10 mm contains ~12 g water which is more than sufficient for He analysis. The copper tube is connected at each end with the plastic tubing and the system is flushed with the groundwater of interest. Water pressure flowing through the copper tubing can be reduced through innovative use of Y-connectors at the up-flow end of the copper – this can help with sealing of the copper tubes. Capturing the sample in the copper tubing can be achieved by use of two hinged knife-edged clamps (a.k.a. refrigeration clamps) which crimp the copper to form a tight seal – where pressure is maintained on the seal by the clamps, or through cold welding of the copper using specific field-portable welding tools. In the case of particularly gas-rich waters, a pressure release valve can be incorporated at the out-flow end of the plastic tubing to help ensure that any dissolved gases remain in solution.

The alternative type of vessel used in some cases for sample collection is a glass flask, which incorporates either one or two stopcock valves. A single stopcock vessel is evacuated to high vacuum and has a Y-inlet which facilitates flushing of the sample past the stopcock prior to opening the valve and capturing the sample. The other type of glass vessel has a stopcock at both ends and the water is flushed through the entire vessel before the stopcock valves are closed in turn. The essential feature of the glass sample vessels that ensures an accurate measurement of any dissolved helium is the type of glass employed. A number of commercially-available glasses (e.g. Corning-1720, Monax, AR-glass) have low He-permeability characteristics and provide secure sample containers over extended time periods (months to years). Pyrex and Duran glass vessels are not suitable for He work, even over short time periods (days to weeks), due to their high He diffusivity (Norton 1957) although they have been used successfully for gases other than He, including the heavier noble gases.

15.2.2 Sample Extraction and Preparation

Prior to measurement, helium must be purified and isolated from both the water phase and the other dissolved gases. This clean-up procedure usually takes place on a dedicated ultra-high vacuum (UHV) system to which the various sampling devices can be attached. Following opening of the seal or valve of the sample container, the water is captured in a bulb and any water vapor is condensed on a trap through the use of a slurry of dry ice and acetone (approximately -78°C). The remaining gases can be purified further through a combination of exposure of the gas phase to traps both with and without activated charcoal held at liquid nitrogen temperature (to condense CO_2 and Xe and adsorb Ar and Kr, respectively) and active gas reaction, using an active metal getter pump and/or hot titanium sponge. The remaining gas should be dominated by He and Ne. Depending upon the configuration of the line, the gas can be expanded into a glass breakseal for transfer to a mass spectrometer (e.g. Torgersen 1980; Stute et al. 1992; Kulongoski and Hilton 2002) or, if the preparation line is interfaced directly to the mass spectrometer preparation line,

inlet directly for further processing before measurement (e.g. Andrews and Lee 1979; Stute et al. 1995; Beyerle et al. 2000; Furi et al. 2009; Stanley et al. 2009). Further processing usually involves cryogenic separation of He from Ne utilizing an activated charcoal trap attached externally to the cooling stage of a refrigeration unit using He as the coolant. Temperatures ~ 35 K or lower are usually sufficient to adsorb Ne completely onto the trap whilst He remains in the gas phase and thus ready for inlet into the measurement device.

15.2.3 Instrumentation

Most He isotope and He concentration data are produced using magnetic sector noble gas mass spectrometers, incorporating Nier-type ion sources (which use high-sensitivity electron bombardment for ionization) and a sufficiently large radius flight tube (often with extended geometry) to achieve a resolution of 600 or more without undue restriction on the source slit width. In this way, it is possible to completely separate $^3\text{He}^+$ from the interfering HD^+ - T^+ doublet at mass 3 and thus record accurate $^3\text{He}/^4\text{He}$ ratios. With magnetic sector mass spectrometers of lower resolution, a correction is usually applied for the tailing effect of the HD^+ peak into the $^3\text{He}^+$ measurement position. Given the large difference between the relative abundance of ^3He and ^4He in most groundwaters (around six orders of magnitude if $^3\text{He}/^4\text{He}$ ratios are air-like), magnetic sector machines must employ a multiplier device for the small $^3\text{He}^+$ ion beams while $^4\text{He}^+$ can be measured using a conventional Faraday cup collector.

An alternative means of producing He data is to use quadrupole mass spectrometers (a.k.a. residual gas analyzers) which employ a potential field distribution between source and detector to allow transmittance of selected e/m ratios and deflect others to ground. With this type of device, the mass resolution is severely compromised (compared to sector machines) so that it is not possible to separate $^3\text{He}^+$ from interfering species at mass 3: therefore, quadrupole mass spectrometers are useful for measuring ^4He abundances only and $^3\text{He}/^4\text{He}$ ratio information must be gained elsewhere. It is important to note that these instruments do have sufficient resolution to separate peaks at adjacent

masses (e.g. mass 3 and mass 4) so are frequently used to measure the $^3\text{He}/^4\text{He}$ ratio of gases which have been spiked with a known amount of the minor isotope, ^3He . In this way, accurate information on sample ^4He abundances can be gained by the isotope dilution technique which overwhelms natural variations in ^3He (and any HD-T) with spike-derived ^3He (e.g. Poole et al. 1997; Kulongoski and Hilton 2002; Hamme and Emerson 2004; Sano and Takahata 2005). Original (sample) $^3\text{He}/^4\text{He}$ information is not recoverable by this technique.

15.2.4 Measurement Protocols and Standards

Once helium has been purified, the usual measurement protocol upon inlet into the mass spectrometer involves either simultaneous collection of the species of interest, i.e., ^3He and ^4He , or peak jumping whereby masses are measured in sequential fashion by adjustment of a controlling parameter (e.g. magnetic field) allowing greater time to be spent on smaller ion beams, i.e., ^3He . Instrument configuration will determine which mode of measurement is possible. In the case of quadrupole-based instruments, peak jumping (a.k.a. mass scanning) is the only possible mode. Data collected on peaks of interest are normally extrapolated to the time of sample inlet in an attempt to minimize discrimination effects caused by differences in ionization efficiencies of various species and/or mass-dependent collector biases. This approach allows the extrapolated $^3\text{He}/^4\text{He}$ ratio or ^4He abundance to be determined.

An essential prerequisite for the production of accurate $^3\text{He}/^4\text{He}$ and He abundance data is the preparation of standards which are used to calibrate and optimize instrument performance as well as standardize raw sample results. In the first instance, peak shape and peak resolution issues can be resolved through use of standards as well as ensuring that machine sensitivity is adequate for the measurements to be undertaken. Secondly, sample measurements need to be quoted relative to a standard of known isotopic composition and He abundance. In the case of magnetic sector instruments which employ different types of detectors, determining the relative detector gain is an inherent challenge. This is particularly acute for helium isotope measurements because of the

necessity of using a multiplier detector for ^3He , and a Faraday cup for ^4He . In this case, the measured $^3\text{He}/^4\text{He}$ ratio is a purely arbitrary value and specific to the device used and dependent upon source and/or detector conditions operating at the time of measurement. However, knowledge of the multiplier gain is unnecessary as long as measured $^3\text{He}/^4\text{He}$ values are compared to a standard of known He isotopic composition. Air, collected under known conditions of temperature, pressure and relative humidity, is often the standard of choice given its well known (present-day) $^3\text{He}/^4\text{He}$ ratio ($1.399 \pm 0.013 \times 10^{-6}$); Mamyrin et al. 1970) and He abundance (5.24 ± 0.05 ppm volume fraction dry air; Ozima and Podosek 1983). Thus, by measuring aliquots of air He, similar in size to samples and prepared under identical laboratory conditions, and taking account of any variations in collector linearity, it is possible to normalize sample $^3\text{He}/^4\text{He}$ and He abundances to that of the standard giving a measure of the relative enrichment/depletion of ^3He relative to ^4He , or just ^4He , compared to the standard. For example, sample $^3\text{He}/^4\text{He}$ ratios (R) are routinely quoted relative to the air $^3\text{He}/^4\text{He}$ ratio (R_A) with the absolute value known only through multiplying by the $^3\text{He}/^4\text{He}$ of air (1.4×10^{-6}). Thus, if the sample $^3\text{He}/^4\text{He}$ is given as $0.1R_A$, its absolute value is 1.4×10^{-7} .

15.2.5 Data Quality, Nomenclature, and Units

Helium data – isotope ratios and abundances – should be quoted with realistic estimates of the uncertainty on the measurements. The factors that constitute the quoted uncertainty include the measurement statistics on individual measurements of sample and normalizing standard $^3\text{He}/^4\text{He}$ ratios (primarily a measure of the uncertainty on the ^3He measurement), the reproducibility of standard measurements ($^3\text{He}/^4\text{He}$ and He abundance) over the course of the measurement run, and blank contributions. The latter is rarely an issue in groundwater studies provided sufficient volumes of water are used for He extraction (i.e., $> \sim 10 \text{ cm}^3$). Other effects that could contribute to the uncertainty include the linearity of detector response – measurements on standards and samples should be made on approximately the same amounts of

He – and whether He and Ne were separated prior to measurement. Although hardly an issue with the most recent data, there are reports in the older literature (e.g. Rison and Craig 1983) cautioning that the presence of Ne can have an effect on measured $^3\text{He}/^4\text{He}$ ratios.

As stated previously, $^3\text{He}/^4\text{He}$ ratios (R) are usually quoted relative to air (R_A). Occasionally, however, $^3\text{He}/^4\text{He}$ data are reported as absolute values (e.g. 1×10^{-7}). It should be clear from the previous discussion that such values involve selection of the air $^3\text{He}/^4\text{He}$ value – it is worthwhile checking that the air value adopted is explicitly stated to reassure the user when comparing such data to other data quoted in the more conventional manner. We also point out that there are a number of ways that He concentrations are reported. The concentration of He in a groundwater should be reported in stated units (atoms, moles or cm^3 STP) per unit mass (usually gram) of water. For example, the concentration of ^4He in groundwater could be reported as $4.2 \times 10^{-6} \text{ cm}^3$ STP $\text{g}^{-1} \text{ H}_2\text{O}$. Prefixes such as “n” (nano-) – in the form ncm^3 STP – are potentially confusing but are frequently seen: they imply units of 10^{-9} cm^3 STP.

Finally, we note that in addition to He concentration, it is usual to report the Ne concentration in the same sample – in the following section it will become clear why the Ne measurement is so important. Neon concentrations are usually given as either a stand-alone concentration (e.g. atoms Ne $\text{g}^{-1} \text{ H}_2\text{O}$) or as a He/Ne ratio. In the former case, it is worthwhile to check that it is the total Ne concentration that is quoted as opposed to the ^{20}Ne concentration – the major isotope of Ne and one usually selected for measurement. In the latter case of reporting Ne as a He/Ne ratio, it should be explicit in the data table if the value is the absolute ratio or the air-normalized value, i.e., the sample He/Ne ratio divided by the same ratio in air (air He/Ne = 0.288, (Weiss 1971)). Given the means of producing such data by mass spectrometric instrumentation, it is likely to be the latter.

15.3 Applications of Helium Isotopes

Helium is a useful and well-exploited tracer in groundwater-related studies because of its unique isotopic characteristics and inert nature. Helium concentrations in groundwater often exceed the expected solubility

equilibrium values as a result of radiogenic production and release of He from aquifer material into associated pore waters. By measuring the abundance of in situ produced He, it is possible to determine the residence time of the groundwater in the aquifer, over both short and long timescales (Andrews and Lee 1979; Marine 1979; Torgersen 1980; Kipfer et al. 2002).

Complications to He-derived chronologies arise with the introduction of He into the groundwater from extraneous sources. Contributions to the extraneous He content can include (a) release of stored He from aquifer material, either by weathering (Torgersen 1980) or diffusion (Solomon et al. 1996), (b) diffusion of He out of confining strata (Andrews and Lee 1979), (c) a basal flux of He from the deeper crust (Heaton 1984; Torgersen and Clarke 1985; Torgersen and Clarke 1987; Torgersen 2010), and/or (d) a mantle He flux usually associated with faults, volcanic activity, crustal extension, or magmatic intrusion (Torgersen 1993; Kennedy et al. 1997; Kulongoski et al. 2005; Sano and Nakajima 2008; Pik and Marty 2009). In all these cases, He can migrate into the aquifer resulting in observed He excesses. In turn, this can lead to overestimation of groundwater residence times (ages).

Means of resolving and quantifying the extraneous sources of helium rely upon careful scrutiny of the helium isotope and concentration record together with associated properties of the aquifer matrix. The weathering and/or diffusive release of He from aquitards and aquifer minerals generally occurs within ~50 Ma (Solomon et al. 1996), such that sediments >50 Ma will no longer be a significant source of extraneous helium. The basal He flux (J_0) may be identified and quantified if the age structure of the groundwater in the aquifer has been established by alternative techniques (e.g. ^{14}C , ^{36}Cl , or hydrodynamically calculated residence times) (e.g. Andrews and Lee 1979; Torgersen and Clarke 1985; Lehmann et al. 2003; Kulongoski et al. 2008). The subsurface addition of He (^3He or ^4He) will change the $^3\text{He}/^4\text{He}$ ratio from that of air-equilibrated water $\sim 1 R_{\text{eq}}$ (where $R_{\text{eq}} = ^3\text{He}/^4\text{He}$ of air-equilibrated water = $\sim 1.4 \times 10^{-6}$; Clarke et al. 1976), thereby providing a means to identify the source of the extraneous He (e.g. Clarke et al. 1969; Tolstikhin 1975). In the case of mantle helium, its contribution may be identified and quantified based on measured $^3\text{He}/^4\text{He}$ ratios and observed shifts from established crustal production rates (e.g. O’Nions and Oxburgh 1983; Kennedy et al. 1997;

Kulongoski et al. 2003). Consequently, helium isotope ratios have found utility in many areas of contemporary research associated with the occurrence of mantle volatiles in groundwater, including quantifying mantle volatiles fluxes, identifying transport mechanisms, and tracing extant tectonic processes (e.g. Oxburgh et al. 1986; O’Nions and Oxburgh 1988; Torgersen 1993; Kennedy et al. 1997; Kulongoski et al. 2005; Kennedy and Van Soest 2007; Crossey et al. 2009).

15.3.1 Helium Components

In order to effectively use helium as a tracer in groundwater systems, it is first necessary to distinguish the various sources of helium which comprise the total dissolved He content of a water sample. The measured sample He concentration may represent superimposition of several He components, which, upon resolution, can provide insight into the origin of the various He contributions to the system. As described by Kulongoski et al. (2008), the sources of ^3He and ^4He include terrigenous sources, such as in situ production (He_{is}) from the decay of U, Th, and Li in the aquifer material, a mantle flux (He_{m}), a deep crustal flux (He_{dc}), and tritogenic helium-3 ($^3\text{He}_{\text{t}}$) from the decay of tritium in groundwater. Atmospheric sources include air-equilibrated helium (He_{eq}) and dissolved-air bubbles (He_{a}). The He mass-balance equation describing total He dissolved in groundwater (Torgersen 1980; Stute et al. 1992; Castro et al. 2000) resolves the measured $^3\text{He}_s/^4\text{He}_s$ ratio of the sample (R_s) into its components:

$$R_s = \frac{^3\text{He}_s}{^4\text{He}_s} = \frac{^3\text{He}_{\text{eq}} + ^3\text{He}_{\text{a}} + ^3\text{He}_{\text{is}} + ^3\text{He}_{\text{dc}} + ^3\text{He}_{\text{m}} + ^3\text{He}_{\text{t}}}{^4\text{He}_{\text{eq}} + ^4\text{He}_{\text{a}} + ^4\text{He}_{\text{is}} + ^4\text{He}_{\text{dc}} + ^4\text{He}_{\text{m}}} \quad (15.1)$$

In this equation, $^3\text{He}_s$ and $^4\text{He}_s$ are the helium-3 and helium-4 concentrations measured in a groundwater sample.

The different sources of He have distinct $^3\text{He}/^4\text{He}$ ratios. End-member $^3\text{He}/^4\text{He}$ ratio values include air: $R_A = \sim 1.4 \times 10^{-6}$ (Clarke et al. 1976), mantle: $R_m = 1.1 \times 10^{-5} = 8 R_A$ (Graham 2002), and in situ and deep crustal sources: $R_{\text{is}} \sim R_{\text{dc}} \sim 3 \times 10^{-8} = 0.02 R_A$

(Mamyrin and Tolstikhin 1984). These endmembers are used to distinguish between and resolve the various components that comprise the measured $^3\text{He}/^4\text{He}$ ratio of a sample.

15.3.1.1 Atmospheric Helium Components in Groundwater

The atmospheric He components include He_{eq} and He_{a} . The contribution of atmospheric He components to the total (measured) He in a groundwater sample may be calculated using the measured concentrations of Ne, He, and the He/Ne ratio of each sample, along with an estimate of the recharge temperature. The recharge temperature can be derived from the concentration of the noble gases other than He (e.g. Mazor 1972; Stute et al. 1992; Weyhenmeyer et al. 2000; Kipfer et al. 2002; Kulongoski et al. 2009) or from the average temperature measured at the recharge area covering the period of groundwater recharge (e.g. Stute and Schlosser 1993; Kulongoski et al. 2005; Kulongoski et al. 2008).

The amount of air-entrained He in each groundwater sample may be calculated assuming that the dissolved Ne of a sample (Ne_s) represents the sum of the Ne from air-equilibration (Ne_{eq}) and from air-bubble entrainment (Ne_{a}), and that there is no fractionation in the resulting air-entrained He/Ne ratio (Torgersen 1980). The Ne content resulting from air-equilibration can be calculated from knowledge of the temperature at recharge, and is subtracted from the measured Ne concentration to give the amount of Ne due to air-bubble entrainment. The Ne_{a} is then used to calculate the amount of air-entrained He (He_{a}), using the known ratio of He to Ne ratio of air ($\text{He}_{\text{a}}/\text{Ne}_{\text{a}} = 0.288$) (Weiss 1971).

He and Ne oversaturation in groundwater, i.e., relative to air-equilibrated water at a given temperature, may reflect overpressure effects during groundwater infiltration and/or rapid fluctuations in the water table (e.g. Stute and Talma 1998; Beyerle et al. 2003; Kulongoski et al. 2004). This latter possibility is thought to result from large and rapid fluctuations in the water table of shallow aquifers during flood events, resulting in dissolution of trapped air bubbles in the unsaturated zone by increased water pressure (e.g. Kulongoski et al. 2003; Ingram et al. 2007; Kulongoski et al. 2009).

15.3.1.2 Excess (Terrigenous) Helium: Radiogenic, Deep Crustal, Tritogenic, and Mantle Components in Groundwater

The sum of the in situ produced, deep crustal, tritogenic, and mantle He components is often referred to as “excess” or “terrigenous” helium (He_{ex}). Note that although tritium has an atmospheric source, it decays to ^3He ($^3\text{H } t_{1/2} = 12.32$ years) within the groundwater system so the daughter product is included as a terrigenous component. The contribution of each of these components to the total He can be determined using measured ^4He concentrations and assumed $^3\text{He}/^4\text{He}$ ratios which are characteristic of the different sources (endmembers). First, however, excess helium-3 ($^3\text{He}_{\text{ex}}$) and helium-4 ($^4\text{He}_{\text{ex}}$) are calculated by subtracting the concentrations of He due to air equilibration (He_{eq}) and air-bubble entrainment (He_a) from the measured He concentration of the sample (He_s):

$$^4\text{He}_{\text{ex}} = ^4\text{He}_s - ^4\text{He}_{\text{eq}} - ^4\text{He}_a \quad (15.2)$$

Similarly, $^3\text{He}_{\text{ex}}$ is calculated using $^4\text{He}_{\text{eq}}$ and $^4\text{He}_a$ concentrations multiplied by the $^3\text{He}/^4\text{He}$ ratios characteristic of the different sources (endmembers):

$$^3\text{He}_{\text{ex}} = (^4\text{He}_s \times R_s) - (^4\text{He}_{\text{eq}} \times R_{\text{eq}}) - (^4\text{He}_a \times R_a) \quad (15.3)$$

Equations (15.2) and (15.3) can be combined to yield R_{ex} which represents the excess $^3\text{He}_{\text{ex}}/^4\text{He}_{\text{ex}}$ ratio.

15.3.2 Resolution of Helium Components

The total dissolved He of a sample may be separated into its various components by transforming the He mass-balance equation (15.1) (e.g. Torgersen 1980; Stute et al. 1992):

$$\frac{^3\text{He}_s - ^3\text{He}_a}{^4\text{He}_s - ^4\text{He}_a} = \frac{^3\text{He}_{\text{eq}} + ^3\text{He}_{\text{is}} + ^3\text{He}_{\text{dc}} + ^3\text{He}_m + ^3\text{He}_t}{^4\text{He}_{\text{eq}} + ^4\text{He}_{\text{is}} + ^4\text{He}_{\text{dc}} + ^4\text{He}_m} \quad (15.4)$$

R_{ex} may then be defined from (15.2) and (15.3):

$$R_{\text{ex}} = \frac{(^4\text{He}_{\text{is}} \times R_{\text{is}}) + (^4\text{He}_{\text{dc}} \times R_{\text{dc}}) + (^4\text{He}_m \times R_m)}{^4\text{He}_{\text{is}} + ^4\text{He}_{\text{dc}} + ^4\text{He}_m} \quad (15.6)$$

$$= \frac{(^4\text{He}_{\text{is}} \times R_{\text{is}}) + (^4\text{He}_{\text{dc}} \times R_{\text{dc}}) + (^4\text{He}_m \times R_m)}{^4\text{He}_{\text{ex}}} \quad (15.7)$$

Substituting (15.7) into (15.5), gives the linear equation ($Y = mX + b$):

$$\underbrace{\frac{^3\text{He}_s - ^3\text{He}_a}{^4\text{He}_s - ^4\text{He}_a}}_Y = \underbrace{\left(R_{\text{eq}} - R_{\text{ex}} + \frac{^3\text{He}_t}{^4\text{He}_{\text{eq}}} \right)}_m \times \underbrace{\frac{^4\text{He}_{\text{eq}}}{^4\text{He}_s - ^4\text{He}_a}}_X + \underbrace{R_{\text{ex}}}_b \quad (15.8)$$

In (15.8), Y is the measured $^3\text{He}/^4\text{He}$ ratio corrected for air-bubble entrainment (R_c), X is the fraction of ^4He in water resulting from air equilibration with respect to the total ^4He in the sample, corrected for air-bubble entrainment, and $b = R_{\text{ex}}$ is the isotopic ratio of non-atmospheric excess-He (e.g. Weise and Moser 1987; Castro et al. 2000).

In order to identify the addition of extraneous He in a given suite of groundwater samples, it is useful to plot Y vs. X (as defined above) for each groundwater sample. This helium-isotope-evolution plot presents the evolution of the groundwater systems from recharge conditions, where, after correction for air-bubble entrainment, all of the dissolved He is from air-equilibration [$^4\text{He}_{\text{eq}}/(^4\text{He}_s - ^4\text{He}_a) \cong 1$], to conditions dominated by crustal and/or mantle contributions, in which air-equilibrated He is a small fraction of the total He [$^4\text{He}_{\text{eq}}/(^4\text{He}_s - ^4\text{He}_a) < 0.05$]. This Y vs. X plot is used to estimate: (1) R_{ex} (the Y-axis intercept) which is the isotopic ratio of non-atmospheric excess-He (including deep crustal and mantle fluxes), and (2) the possible contribution of

$$= \frac{(^4\text{He}_{\text{eq}} \times R_{\text{eq}}) + (^4\text{He}_{\text{is}} \times R_{\text{is}}) + (^4\text{He}_{\text{dc}} \times R_{\text{dc}}) + (^4\text{He}_m \times R_m) + ^3\text{He}_t}{^4\text{He}_s - ^4\text{He}_a} \quad (15.5)$$

tritogenic ^3He (related to the gradient “m”) which is diagnostic of groundwater recharged since 1953.

A linear regression of the dataset provides the excess-helium ratio (R_{ex}), which is the Y-intercept. The gradient (m) of the regression line represents the decay of tritium and subsequent production of ^3He in the groundwater samples. When using this plot, it is a useful reference to include the evolutionary trajectory representing the addition of radiogenic He (with the $^3\text{He}/^4\text{He}$ ratio of $\sim 0.02 R_A$) to air-saturated water (ASW). If samples plot along the radiogenic He-ASW trajectory, this indicates that the flux of He into such groundwater systems is dominated by radiogenic “crustal” ^4He production, which is typical of stable continental platforms (e.g. Torgersen and Clarke 1985; Torgersen and Clarke 1987; Ballentine et al. 2002; Kulongoski et al. 2008). If samples plot above the radiogenic He-ASW trajectory, then additional ^3He has been added to the groundwater, and may be explained by: (1) a contribution of ^3He from anomalous concentrations of lithium in crustal materials and production of ^3He via the $^6\text{Li}(n, \alpha)^3\text{H}(\beta^-)^3\text{He}$ reaction, (2) mixing of older groundwater with young (nuclear-bomb produced) tritiated water, and/or (3) a contribution from a mantle-derived He flux (Table 15.1).

One or all of these sources of extraneous ^3He , however, may be discounted on the basis of aquifer composition or regional geology. The production of ^3He from the reaction involving thermal neutron capture by lithium ($^6\text{Li}(n, \alpha)^3\text{H}(\beta^-)^3\text{He}$) within the aquifer is negligible if the lithium concentration in the aquifer is low (Andrews 1985). Groundwater that recharged prior to extensive nuclear weapons testing in the 1960s will not contain excess ^3He from the decay of nuclear bomb-derived ^3H . Indeed, relatively young, nuclear-bomb tritiated water with elevated $^3\text{He}/^4\text{He}$ ratios would plot towards the right-hand-side of the helium-isotope-evolution plot (i.e., $^4\text{He}_{\text{eq}}/(^4\text{He}_{\text{s}} - ^4\text{He}_{\text{a}}) \rightarrow 1$). If the sample $^3\text{He}/^4\text{He}$ ratio (R_{s}) reflects radiogenic helium, i.e., no extraneous ^3He is measured, then a mantle-derived He contribution may be discounted.

15.3.2.1 Case Studies: Uluru Basin, Australia and Mojave Desert, USA

An example of the use of the helium-isotope-evolution plot is shown in Fig. 15.1, where helium results from groundwater samples from the Uluru Basin, Northern

Territory, Australia (Kulongoski et al. 2008) and the Eastern Morongo Basin, California, USA (Kulongoski et al. 2005) are plotted together. As a reference, the evolutionary trajectory representing the addition of radiogenic helium ($0.02 R_A$) to air saturated water (ASW) (line labeled “a”) is also included, as is a line representing the addition of 10% mantle helium and $^3\text{He}_{\text{t}}$ from the decay of 4.8 TU of tritium (line labeled “d”).

A linear regression of the Uluru Basin dataset (red squares) gives the equation $Y = 17.5X + 0.07$ ($r^2 = 0.99$) and is labeled as line “b”. The intercept (of line “b”) with the Y-axis is 0.07×10^{-7} ($0.005 R_A$), which is consistent with in situ radiogenic production of He. The Uluru groundwater samples consistently plot along the radiogenic He-ASW trajectory line “a”, from which we conclude that $^3\text{He}_{\text{m}}$, $^3\text{He}_{\text{t}}$, and $^3\text{He}_{\text{is}}$ contribute negligible amounts of helium-3 to the Uluru Basin groundwater system, and the Uluru groundwater basin is dominated by production of radiogenic “crustal” He. Uluru Basin R_{ex} values are also consistent with the He production ratio of between 2.2 and 3.3×10^{-8} (0.016 – $0.024 R_A$) calculated by Torgersen and Clarke (1987) for the Hooray Sandstone in eastern Australia. The gradient ($m = 17.5$) of line “b” reflects the complete decay of approximately 1.8 tritium units (TU) ($1 \text{ TU} = 1 \text{ atom of T in } 10^{18} \text{ atoms of H}$; upon decay, 1 TU yields $2.5 \times 10^{-15} \text{ cm}^3 \text{ STP } ^3\text{He g}^{-1} \text{ H}_2\text{O}$); this represents the background tritium value in the Uluru Basin.

In contrast, all of the Eastern Morongo Basin (EMB) samples (blue circles) plot above the radiogenic He-ASW trajectory (line “a”). A linear regression of the EMB data produces the following equation $Y = 11.8X + 4.4$, ($r^2 = 0.76$), and is labeled line “c” in Fig. 15.1. Significantly, the intercept of line “c” with the Y-axis occurs at $0.32 R_A$. This value (R_{ex}) is considerably greater than expected for in situ radiogenic production of helium. As stated above, there are three possibilities to explain the observation of the apparently high value of the $^3\text{He}/^4\text{He}$ excess: (1) a contribution of ^3He from the $^6\text{Li}(n, \alpha)^3\text{H}(\beta^-)^3\text{He}$ reaction in crustal materials, (2) mixing of older groundwater with younger nuclear-bomb tritiated water, and/or (3) a contribution from a mantle-derived helium flux.

The production of ^3He from the reaction involving thermal neutron capture by lithium ($^6\text{Li}(n, \alpha)^3\text{H}(\beta^-)^3\text{He}$) may be dismissed due to the unrealistically

Table 15.1 Helium-4 and helium-3 fluxes estimated for different regions

Region		$\text{cm}^3 \text{ STP } ^4\text{He cm}^{-2} \text{ a}^{-1} (10^{-6})$	$\text{cm}^3 \text{ STP } ^3\text{He cm}^{-2} \text{ a}^{-1} (10^{-13})$	References
Global flux estimate (including oceans)		0.40	44.8	Torgersen and Clarke (1985)
Continental crust		3.30	0.67	O'Nions and Oxburgh (1983)
Australia	Great Artesian Basin, Australia	3.60	2.24	Torgersen and Clarke (1985)
	Amadeus Basin, Australia	0.30–0.300	nd	Kulongoski et al. (2008)
Africa	Auob sandstone, Namibia	2.20	nd	Heaton (1984)
	Kalahari Desert, Botswana	1.33	nd	Selaolo et al. (2000)
	Lake Nyos, Cameroon	35,212	2,758,285	Sano et al. (1990)
	Central South Africa	1.33	nd	Heaton (1984)
Asia	Northern Taiwan	2.91–3.14	44.8–89.7	Sano et al. (1986)
	South Caspian Sea	2.23	nr	Peeters et al. (2000)
	Central Caspian Sea	6.93	nr	Peeters et al. (2000)
	Black Sea	1.53	nr	Top and Clarke (1983)
	South Lake Bakail	4.26	nr	Hohmann et al. (1998)
	North Lake Bakail	12.8	nr	Hohmann et al. (1998)
Europe	Great Hungarian Plain, Hungary	0.067–0.54	2.0–5.83	Stute et al. (1992)
	Great Hungarian Plain, Hungary	9.41	85.2	Martel et al. (1989)
	Molasse Basin, Austria	0.22	nr	Andrews (1985)
	Lake Laacher See, Switzerland	1,174	87,091	Aeschbach-Hertig et al. (1996)
	Lake Alpnach, Switzerland	1.29	nr	Aeschbach-Hertig et al. (1996)
	Lake Lugano, Switzerland	5.63	Nr	Aeschbach-Hertig et al. (1996)
	Paris Basin, France	0.45	0.45	Marty et al. (1993)
	Paris Basin, France	4.48	4.48	Castro et al. (1998)
North America	Mojave Desert, USA	3.0–10.0	0.20–14.2	Kulongoski et al. (2003)
	Eastern Morongo Basin, USA	0.003–30.0	0.45–135	Kulongoski et al. (2005)
	Crater Lake, USA	64.6	6,397	Collier et al. (1991)
	Pacific Ocean	0.12	46.9	Well et al. (2001)

nd not detected; nr not reported

large concentrations of lithium (>850 ppm Li) which would be necessary in aquifer rock to produce the observed $^3\text{He}/^4\text{He}$ ratio ($0.32 R_A$). Assuming a lithium content of ~50 ppm, an upper limit for a typical sedimentary lithology (Andrews 1985; Ballentine and Burnard 2002), the calculated $^3\text{He}/^4\text{He}$ production ratio in the rock would be 2.59×10^{-8} or $0.02 R_A$ (Kulongoski et al. 2003).

For groundwater residence times >50 years, no excess nuclear-bomb tritium is expected. The groundwaters sampled in this study have helium and/or ^{14}C -derived residence times significantly greater than 50 years. The gradient of the linear-regression of EMB data, 11.8, is consistent with complete decay of 4.8 tritium units (TU); this represents the background tritium value in the EMB. If the background tritium value is taken as 4.8 TU, this would produce $1.2 \times 10^{-14} \text{ cm}^3 \text{ STP } ^3\text{He g}^{-1} \text{ H}_2\text{O}$. For EMB

ground-water samples older than 50 years, ^3He concentrations are significantly higher, ranging from 2 to $1,150 \times 10^{-14} \text{ cm}^3 \text{ STP } ^3\text{He g}^{-1} \text{ H}_2\text{O}$ (Table 15.1): therefore, the decay of nuclear “bomb” produced tritium should represent a negligible contribution to the total measured ^3He .

By default, we conclude that the high R_{ex} in the EMB groundwaters results from an influx of mantle-derived helium-3 ($^3\text{He}_m$). Using the regression value of $0.32 R_A$ we can estimate that the average contribution of mantle He is 4.6% of the total helium, assuming a simple binary mixture of mantle ($R_m \sim 8 R_A$) and crustal ($R_{\text{dc}} \sim 0.02 R_A$) components. Although the sub-continental lithospheric mantle have a lower end-member composition (e.g. $6 R_A$; Dunai and Porcelli 2002), this would make a small difference only to the calculated fraction of mantle-derived He in any given sample.

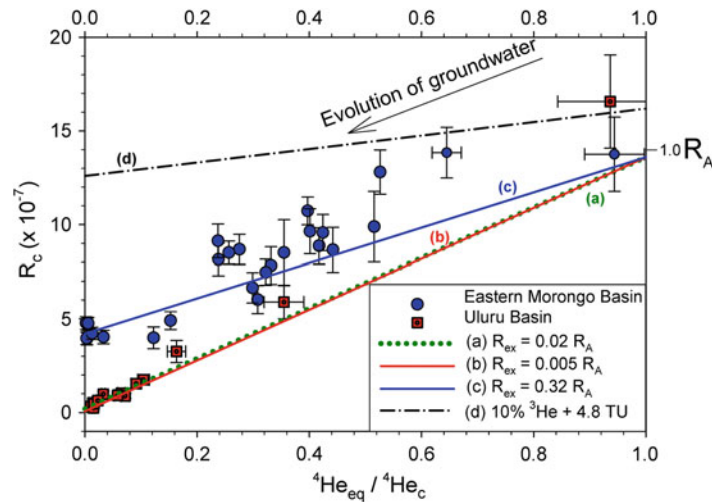


Fig. 15.1 Measured $^3\text{He}/^4\text{He}$ ratios corrected for air-bubble entrapment (R_c), vs. the relative amount of ^4He derived from solubility ($\text{He}_{c,q}$) with respect to total ^4He , corrected for air-bubble entrapment (He_c). Lines (a), (b), and (c) represent the

evolution of the $^3\text{He}/^4\text{He}$ ratio in water samples from atmospheric equilibrium values to excess ratios (see (15.8) in the text). Line (d) represents an addition of 10% mantle helium plus 4.8 TU of tritiogenic ^3He

15.3.3 Excess Helium and the Utility of Helium Isotopes in Groundwaters

In this section, we report on the utility of He studies of groundwater systems. The list is by no means exhaustive but is meant to illustrate recent applications of He geochemistry to issues of groundwater chronology, crustal degassing, and the role of faulting in loss of mantle-derived volatiles to the atmosphere. The approach is predicated on successfully resolving observed He isotope and abundance variations into component structures, as discussed above.

15.3.3.1 Radiogenic Helium Produced In Situ: Chronological Applications

Radiogenic helium is produced by α -decay of U- and Th-series nuclides in crustal minerals, and accumulates in groundwater. The accumulation rate ($^4\text{He}_{\text{sol}}$) of radiogenic ^4He in groundwater can be quantified based on the U and Th content and the porosity of the aquifer (e.g. Andrews and Lee 1979; Torgersen 1980; Stute et al. 1992; Castro et al. 2000):

$$^4\text{He}_{\text{sol}} = \rho \times \Lambda \times \left\{ 1.19 \times 10^{-13} [\text{U}] + 2.88 \times 10^{-14} [\text{Th}] \right\} \times \frac{(1 - \phi)}{\phi} \quad (15.9)$$

In (15.9) $^4\text{He}_{\text{sol}}$ is the rate of ^4He accumulation (the ^4He solution rate in cm^3 STP $\text{He g}^{-1} \text{H}_2\text{O a}^{-1}$); Λ is the fraction of He produced in the rock that is released into the water phase – this is assumed to be unity (Andrews and Lee 1979); and ρ is the bulk density of the aquifer material. The ^4He production rates from U and Th decay are $= 1.19 \times 10^{-13} \text{ cm}^3$ STP $^4\text{He } \mu\text{gU}^{-1} \text{ a}^{-1}$ and $2.88 \times 10^{-14} \text{ cm}^3$ STP $^4\text{He } \mu\text{gTh}^{-1} \text{ a}^{-1}$, respectively (Andrews and Lee 1979). The U and Th concentrations ($[\text{U}]$ and $[\text{Th}]$) in the aquifer material (ppm) and the fractional effective porosity (ϕ) of the aquifer material are measured parameters.

If the accumulation of excess He ($^4\text{He}_{\text{ex}}$) in groundwater can be attributed solely to in situ production, then the He age of the groundwater may be estimated by dividing the excess ^4He ($^4\text{He}_{\text{ex}}$) by the solution rate ($^4\text{He}_{\text{sol}}$) (e.g. Andrews and Lee 1979; Marine 1979). However, we caution that excess He may also be introduced to groundwater reservoirs from a basal flux, in which case it is necessary to account for this He flux in order to calculate realistic groundwater ages (Heaton 1984; Torgersen and Clarke 1985). This topic is considered next. However, we note that in addition to its utility for calibrating He residence times, the flux of He from either continental or mantle degassing also may be used to model constraints on the chemical and thermal evolution of the Earth (e.g. O’Nions

and Oxburgh 1988), and/or examine the transport mechanism of volatiles through the crust (e.g. Torgersen 1993; Kulongoski et al. 2003; 2005).

15.3.3.2 Deep Crustal Helium: Crustal Fluxes

If a basal flux contributes He to a groundwater system, it may be quantified if the groundwater age is known by an independent method (e.g. C-14 chronology). Conversely, the He groundwater age may be determined if the basal flux is known. The corrected groundwater residence time (τ_{corr}) can be calculated from the following equation (e.g. Heaton 1984; Torgersen and Clarke 1985):

$$\tau_{\text{corr}} = \frac{{}^4\text{He}_{\text{ex}}}{\left(\frac{J_0}{\phi z_0 \rho_w} + {}^4\text{He}_{\text{sol}}\right)} \quad (15.10)$$

In (15.10), ${}^4\text{He}_{\text{ex}}$ has units of $\text{cm}^3 \text{STP He g}^{-1} \text{H}_2\text{O}$, J_0 ($\text{cm}^3 \text{STP He cm}^{-2} \text{a}^{-1}$) is the basal flux, ϕ is the effective fractional porosity of the aquifer, z_0 is the depth (cm) at which this flux enters the aquifer, and ρ_w is the density of water ($\sim 1 \text{ g cm}^{-3}$). In many cases, z_0 may be estimated as the distance from the middle of the perforations in the well casing to the interface between the aquifer and the basement formation (Kulongoski et al. 2003; 2005).

In order to determine the basal flux of He (J_0) and improve the sensitivity of the ${}^4\text{He}$ chronometer, it is useful to plot the ${}^4\text{He}$ residence times (age) vs. ages derived by alternative methods (such as ${}^{14}\text{C}$, ${}^{36}\text{Cl}$, or hydrologically derived age). Different values of the basal flux are assumed in order to search for concordance between ${}^4\text{He}$ and other age-dating techniques. Values of $3 \times 10^{-8} \text{ cm}^3 \text{ He STP cm}^{-2} \text{ a}^{-1}$ represent a low basal flux of He, in comparison with fluxes recorded from various aquifers worldwide (see Table 15.1). Groundwater chronometry studies typically investigate aquifers with simple flow systems in which groundwater residence time increases along a confined flow path. Calibration of the flow systems may be made by comparing ${}^4\text{He}$ and ${}^{14}\text{C}$ or ${}^{36}\text{Cl}$ -derived ages.

Observations of high He concentrations in the basal layer of aquifers (e.g. the Great Artesian Basin; Torgersen and Clarke 1985), coupled with numerical models of groundwater flow incorporating advective mass transport (Bethke et al. 1999), indicate that the distribution of helium in aquifer systems must also

have vertical structure, owing to the basal He flux, in addition to horizontal “plug-piston” flow (Zhao et al. 1998). Introduction of the basal flux may occur by diffusion from crystalline basement followed by entrainment and upward migration, particularly as the discharge region is approached (Bethke et al. 2000).

Case Study: Alice Springs, Australia

The following example shows how He can be utilized for groundwater dating purposes. Helium residence times (ages) were calculated for a suite of samples from Alice Springs, Australia assuming $\phi = 0.15$, $\rho = 2.6 \text{ g cm}^{-3}$, $[\text{U}] = 1.7 \text{ ppm}$, $[\text{Th}] = 6.1 \text{ ppm}$ (15.9), and $\text{He}_{\text{sol}} = 3.93 \times 10^{-12} \text{ cm}^3 \text{STP He g}^{-1} \text{H}_2\text{O a}^{-1}$ (Kulongoski et al. 2008). In Fig. 15.2, we plot calculated mean ages derived from ${}^4\text{He}$, ${}^{14}\text{C}$ and ${}^{36}\text{Cl}$ for a range of basal fluxes of ${}^4\text{He}$, from zero to 30×10^{-8} (units of $\text{cm}^3 \text{STP He cm}^{-2} \text{ a}^{-1}$). The straight lines (1:1 reference line) would indicate concordance in ages between the various chronometers.

The He ages of the youngest Alice Springs samples show concordance between ${}^4\text{He}$ - ${}^{14}\text{C}$ - ${}^{36}\text{Cl}$ derived ages when zero or low J_0 -values ($0\text{--}3 \times 10^{-8}$ units of $\text{cm}^3 \text{STP He cm}^{-2} \text{ a}^{-1}$) are adopted (Fig. 15.2). This observation agrees with findings by other workers that relatively young groundwaters ($<50 \text{ ka}$) are dominated by in situ He production, rather than a basal flux (e.g. Torgersen and Clarke 1985). However, a larger basal He flux ($30 \times 10^{-8} \text{ cm}^3 \text{STP He cm}^{-2} \text{ a}^{-1}$) would be required for the ${}^4\text{He}$ ages of the older groundwaters to approximate the ${}^{14}\text{C}$ ages. ${}^{36}\text{Cl}$ -derived ages do not require a larger basal flux for agreement with ${}^4\text{He}$ ages, suggesting that they may also overestimate groundwater ages. The presence of a basal flux in the majority of the groundwater samples suggests that these aquifers accumulate He from a diffusive process rather than from a localized (deep) source, such as faults. It would appear that the stable cratonic continental platform of central Australia, therefore, may limit any trans-crustal flux or mantle-derived volatiles into aquifers of the region.

15.3.3.3 Tritogenic Helium-3: Chronological Applications

The use of tritium (${}^3\text{H}$), combined with its daughter isotope, helium-3 (${}^3\text{He}_t$), to study groundwater flow

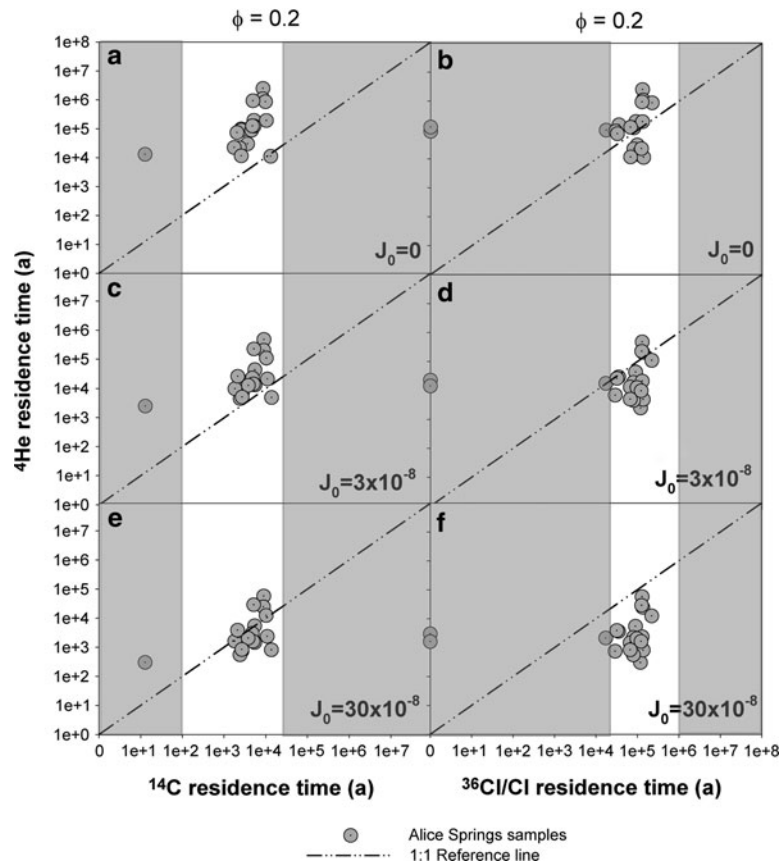


Fig. 15.2 Alice Springs ^4He vs. ^{14}C and $^{36}\text{Cl}/\text{Cl}$ groundwater residence times. Plots of corrected ^4He Alice Springs groundwater residence times (porosity $\phi = 0.2$) vs. ^{14}C derived and $^{36}\text{Cl}/\text{Cl}$ derived residence times, for three basal fluxes ($J_0 = 0$,

3×10^{-8} , and $30 \times 10^{-8} \text{ cm}^3 \text{ STP He cm}^{-2} \text{ a}^{-1}$). Un-shaded areas represent the windows of applicability for ^{14}C (a, c, e) and $^{36}\text{Cl}/\text{Cl}$ (b, d, f). From Kulongoski et al. (2008)

was first proposed by Tolstikhin and Kamenskiy (1969). However, widespread adoption of the ^3H - ^3He method occurred only following the analytical advance of measuring ^3H by the ^3He in-grow method (Clarke et al. 1976). Early studies of marine and lacustrine systems made use of this technique (e.g. Jenkins and Clarke 1976; Kipfer et al. 2002; Schlosser and Winckler 2002). A decade later, the calculation of groundwater residence times (ages) using ^3H - ^3He dating was made possible when the fraction of ^3He derived directly from tritium decay ($^3\text{He}_t$) could be successfully resolved from other sources (e.g. Takaoka and Mizutani 1987; Poreda et al. 1988; Schlosser et al. 1988; Schlosser et al. 1989). Determination of water residence times in lakes and groundwaters by ^3H - ^3He dating is now used extensively to study transport and mixing processes.

The ^3H - ^3He method provides a quantitative determination of groundwater residence time based on the accumulation of the inert gas $^3\text{He}_t$, the β -decay product of tritium decay. As mentioned previously, tritium (^3H) is a short-lived radioactive isotope of hydrogen with a half-life of 12.32 years. ^3H is produced naturally in the atmosphere from the interaction of cosmic radiation with nitrogen (Craig and Lal 1961), by above-ground nuclear explosions, and by the operation of nuclear reactors. Following the release of large amounts of tritium into the atmosphere from nuclear-bomb testing in the 1950s and 1960s, the International Atomic Energy Agency (IAEA) implemented a global monitoring program of tritium in precipitation, with the result that tritium has been used extensively as a tracer in hydrology studies (International Atomic Energy Association 1983; 1986; Hong et al. 2011).

As tritium forms an intrinsic part of a water molecule within a groundwater system, the daughter product (${}^3\text{He}_t$) remains dissolved in solution following decay of the parent. Thus, the tritium-helium clock starts when ${}^3\text{He}_t$ begins accumulating from the decay of ${}^3\text{H}$. The time that the water has resided in the aquifer can be calculated by determining ${}^3\text{He}_t$. This technique, based on the ratio ${}^3\text{H}/{}^3\text{He}_t$, is more precise than using tritium alone because it does not depend on the tritium input function or the atmospheric tritium content at the time of recharge. Instead, the ${}^3\text{H}$ - ${}^3\text{He}$ method is based on the assumption that groundwater is a closed system, and the ${}^3\text{He}_t/{}^3\text{H}$ ratio increases predictably as a function of time. Thus, the calculated ${}^3\text{H}$ - ${}^3\text{He}$ age only depends upon the initial ${}^3\text{H}$ activity and measurement of its daughter product ${}^3\text{He}_t$, which must be resolved from the total ${}^3\text{He}$ dissolved in groundwater (Takaoka and Mizutani 1987; Poreda et al. 1988; Schlosser et al. 1988; Schlosser et al. 1989).

15.3.3.4 Mantle-Derived Helium: Identification, Quantification, and Geologic Significance

The contribution of mantle-derived He to the total He in a groundwater sample may be identified by resolving the measured He concentration into its various components, and then quantified by assuming a binary mantle-crust mixture with end-member compositions (mantle = $8 R_A$, crust = $0.02 R_A$). In this way, it is possible to compute the absolute concentrations of He (${}^3\text{He}$ and ${}^4\text{He}$) contributed by each end-member. The crustal and mantle helium contributions can provide information about the evolution of the groundwater since recharge as well as associated geological processes.

High ${}^3\text{He}/{}^4\text{He}$ ratios (i.e., values greater than crustal production ratios), indicative of a mantle-derived input of He, are often found in close proximity to specific geological features such as volcanic systems and major faults, or associated with regions of high heat flow such as regions of crustal extension or where there is magmatic activity. In such cases, mantle-derived ${}^3\text{He}$ measured in groundwater may be used to explore mantle-crust interaction processes including mechanisms of volatile transfer into and through the crust (Table 15.1). For example, Kennedy et al.

(1997) showed that high ${}^3\text{He}/{}^4\text{He}$ ratios (up to $\sim 4 R_A$) in groundwater proximal to the San Andreas Fault (SAF) in California could be used to estimate the transport rate of mantle fluids through the crust. By assuming that measured values reflect the dilution of mantle helium ($R_m = 8 R_A$) with crustal (radiogenic) helium ($R_{dc} = 0.02 R_A$), they calculated that an upward flow rate of $1\text{--}10 \text{ mm year}^{-1}$ is necessary to maintain observed ratios assuming steady-state production and release of crustal He. This range was considered a lower limit, since hydrodynamic dispersion, the effects of mixing between fault fluids and radiogenic crustal fluids, or episodic flow events were not taken into account. For a crustal thickness of 30 km, and a flow rate of 10 mm year^{-1} , it would require nearly 3 Ma for mantle fluids to reach the surface. Over the same time period, He would be expected to move only $\sim 1 \text{ m}$ by diffusion through bulk granite ($D_{\text{He}} \sim 5 \times 10^{-7} \text{ m}^2 \text{ a}^{-1}$; (Ballentine and Burnard 2002)) or $\sim 300 \text{ m}$ by diffusion through groundwater ($D_{\text{He}} \sim 0.03 \text{ m}^2 \text{ a}^{-1}$; (Ballentine and Burnard 2002)), thus emphasizing the important role of advection in the transport of mantle helium through the crust.

Advective flow of (deep) crustal fluids containing mantle-derived He, particularly in the vicinity of faults, implies that the Eastern California Shear Zone (ECSZ) extends to considerable depths, possibly into the lowermost crust. Episodic fracturing and subsequent fluid flow is a likely mechanism to enable the transfer of mantle volatiles through the brittle-ductile boundary – estimated at a depth between 10 and 15 km for typical crustal thermal gradients – and towards the surface (Nur and Walder 1990; Rice 1992; Kennedy et al. 1997). On the other hand, if faults in the ECSZ are limited to relatively shallow depths, by a mid-crustal decollement for example (e.g. Webb and Kanamori 1985; Jones et al. 1994), then their role would be to transport volatiles from the decollement to the surface. In this case, faults would act as conduits, and fault activity would regulate the release of accumulated ${}^3\text{He}_m$ (and ${}^4\text{He}_{dc}$) into the shallow crust.

Case Study: The Influence of Faults and Seismic Activity in the East Morongo Basin (EMB)

In this section, we review the role of faults – their surface distribution and activity – in controlling the

distribution of $^3\text{He}_m$ and $^4\text{He}_{dc}$ concentrations in groundwaters of the Eastern Morongo Basin (EMB) (Kulongoski et al. 2005).

The presence of faults, particularly if they lead to greater permeability in the fault zone, should act to channel He fluxes to the surface. If this is the case, then wells in close proximity to faults should have groundwater with associated high $^3\text{He}_m$ (and $^4\text{He}_{dc}$) fluxes as a result of relatively rapid transport of helium and other mantle and/or deep-crustal derived volatiles via the fault zone. In the EMB, wells located near the Emerson, Elkins, and Lavic Lake-Bullion Faults have relatively high $^3\text{He}_m$ concentrations; however, wells sampled near the Hidalgo-Surprise Springs Fault Zone (Fig. 3), show no evidence of high concentrations of $^3\text{He}_m$. This leads to the conclusion that the presence of faults alone does not necessarily lead to enhanced transport of deep crustal and mantle fluids.

Intermittent fault activity or episodic fault rupture (Nur and Walder 1990) may be a contributory factor why $^3\text{He}_m$ fluxes vary between sites either close to one another or close to faults. In this scenario, pore fluid pressure in the fault zone could increase until it reaches the level of the least compressive stress in the crust, whereby it would induce hydraulic fracturing and fluid release: this would then be followed by a drop in pore pressure and resealing of the system (Nur and Walder 1990). Local hydro-fracturing, induced by fluid pressure increases (e.g. from porosity reduction, dehydration, vertical fluid fluxes), could create local inter-connected networks allowing fluid flow (Miller and Nur 2000). Such localized networks may explain variations in observed $^3\text{He}_m$ accumulation and mantle flux rates throughout the EMB. It should be noted that significant time periods (Ma) are necessary for advective transport of $^3\text{He}_m$ from the mantle to the shallow crust; therefore, it is unlikely that an individual rupture event would result in instantaneously high $^3\text{He}_m$ groundwater concentrations, unless these faults directly tapped a shallow reservoir containing $^3\text{He}_m$ (Sano 1986; Gulec et al. 2002). However, the cumulative activity (slip) along faults may facilitate transfer and transport of volatiles from the mantle to the crust over geologic time scales, resulting in a heterogeneous distribution of $^3\text{He}_m$, as observed in the EMB. In this respect, it is informative to consider the recent seismic record for the EMB region.

Recent seismic activity in the EMB includes the rupture of the Emerson Fault during the 1992 Landers earthquake, and rupture of the Lavic Lake-Bullion Fault (LLBF) during the 1999 Hector Mine earthquake. Significantly, the highest concentrations of $^3\text{He}_m$ are observed at sites near the terminus of the 1999 rupture of the LLBF and in wells near the Emerson Fault (Fig. 15.3). These observations are consistent with the model of episodic hydrofracture-induced flow enhancing the transfer of mantle volatiles to the shallow crust.

Groundwaters in the EMB that contain relatively high concentrations of $^3\text{He}_m$ are also observed to have high concentrations of crustal (radiogenic) helium ($^4\text{He}_{dc}$). The relation between high $^4\text{He}_{dc}$ and $^3\text{He}_m$ concentrations suggests a similar transport mechanism for the two components through the crust (Ballentine et al. 1991), and may be attributed to increased permeability through the active fault zone. Transmission of mantle and deep crustal fluid/gas through fault zones by episodic fracturing would then represent a plausible mechanism for enhanced helium transport through the crust (Kulongoski et al. 2005).

15.4 Future Prospects

It is becoming increasingly clear that the presence of crustal faulting plays an important role in the transfer of mantle-derived He, and other volatiles through the crust (see discussion in Hilton (2007)). Faults serve as high permeability conduits for fluids as they traverse the crust-mantle transition zone. In turn, this implies that such fluids must exist at extremely high pressures – in order to maintain open pathways during volatile transport. As discussed above, little is known concerning the nature of the flow regime – be it continuous or episodic – so it is difficult to relate spatial variability of groundwater He_m or He_{dc} signals to the location of high permeability zones such as faults. Recent studies have sought to address this issue by adapting or developing instrumentation to collect groundwater and other fluid samples over prolonged time periods to assess temporal variability in the He isotope and abundance record.

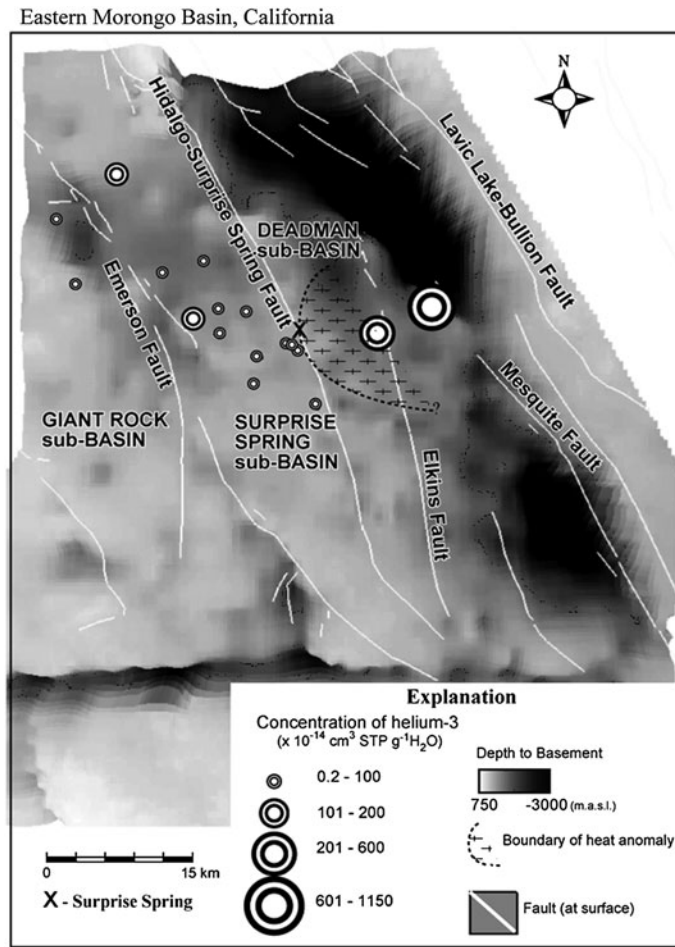


Fig. 15.3 Concentration of excess ^3He measured in Eastern Morongo Basin, California groundwater samples. Also shown is the gravimetric depth to basement in *grey-shading*, regional faults, and region of high thermal anomaly, from Kulongoski et al. (2005)

15.4.1 Submarine Studies Using Fluid Flow Meters

The Extrovert Cliffs site in Monterey Bay, California is situated close to several active strike-slip faults, including the Monterey and San Gregorio fault zones, and has many cold seeps located at $\sim 1,000$ m depth below sea level. By adapting instrumentation designed to measure diffuse fluid fluxes on the seafloor (Tryon et al. 2001), Furi et al. (2009) were able to capture dissolved gases in emanating cold seep fluids over deployment intervals up to 3 weeks.

As illustrated in Fig. 15.4, the measured helium and neon concentrations ($^4\text{He}_m$ and Ne_m) were found to show remarkable fluctuations, on time-scales of only a

few hours. In addition, the isotopic composition of the dissolved He also varied. For example, measured and terrigenic (crust + mantle) $^3\text{He}/^4\text{He}$ ratios increased from 1.2 to 1.5 R_A within just 2.5 h (e.g. at $t = 455$ h). A maximum increase from 0.9 to 1.75 R_A is observed in the data record with the lower time-resolution (at $t = 517$ h). As discussed by Furi et al. (2009), temporal variations in dissolved gas characteristics (isotopes and concentrations) can be influenced by interaction with a hydrocarbon phase within the aquifer. In spite of this complicating process, it was still possible to resolve the He signal into component structures associated with air-equilibration, excess-air entrainment, and terrigenic fluxes (both crustal and mantle-derived). Indeed, the mantle He contribution is mostly 20–30% (up to 2.3 R_A), with a short duration spike of 60% mantle He.

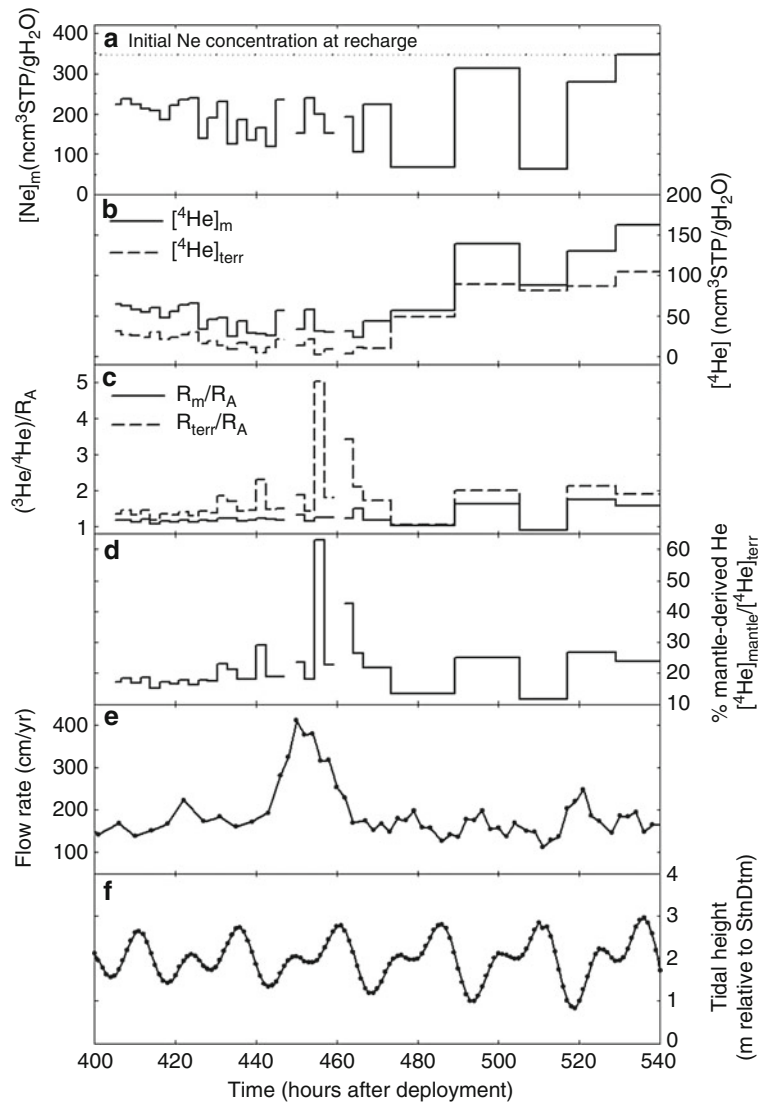


Fig. 15.4 Temporal variation of (a) measured Ne concentration, (b) measured ^4He and calculated terrigenic ^4He concentrations, (c) measured $^3\text{He}/^4\text{He}$ ratio (R_m/R_A) and calculated R_{terr}/R_A ratio, and (d) the fraction of mantle He in seep fluids

Significantly, the correlation of high $^3\text{He}/^4\text{He}$ ratios with a transient pulse in the flow rate at Extrovert Cliff (Fig. 15.4e) indicates that the release of mantle-derived fluids is episodic and cannot be explained solely by hydrostatic pressure changes due to the variable tidal load (Fig. 15.4f). In this respect, the controlling factor is likely episodic fracturing in the San Gregorio or Monterey Bay fault zones. This is consistent with the notion of continuous ascent of mantle-derived fluids through the crust, increasing

collected with CAT meter No. 2. Also shown are (e) the seep flow rate and (f) the tidal height record. Time (in hours) is given relative to the start of sampling on 4 August 2004, at 12 p.m. local time. From Furi et al. (2009)

pore fluid pressure until it overcomes the least principle stress, resulting in hydrofracturing and release of fluids (e.g. Nur and Walder 1990).

15.4.2 On-Land Studies: SPARTAH Instrumentation

Barry et al. (2009) reported a new approach to sampling groundwater from land-based groundwater and

geothermal wells through development of a new instrument for the continuous collection of water samples over prolonged periods, up to ~6 months. The instrument is dubbed SPARTAH (Syringe Pump Apparatus for the Retrieval and Temporal Analysis of Helium). Motivation for the development of SPARTAH came, in part, through He monitoring studies in seismically-active regions of the crust (e.g. Hilton 1996; De Leeuw et al. 2010) whereby collection of samples took place at regular frequencies of ~3 months. However, in some instances (e.g. Italiano et al. 2001), variations in the monitored He record could occur at comparable or shorter frequencies and so would be missed by adoption of a fixed (and regular) sampling regimen.

The SPARTAH device consists of an off-the-shelf programmable syringe pump equipped with a high-power stepper motor capable of extremely accurate and low withdrawal rates (between 0.0001 mL/h and 220 mL/min). The pump is operated in withdrawal mode whereby fluid is accurately and smoothly drawn into the syringe at a user-defined rate. Well water is drawn into the coils at a constant rate set by the syringe pump, and is independent of the pumping rate of the well. The only stipulation is that the well

operates continuously so that air is not entrained into the coils. At any time during a deployment, the tubing can be isolated by closing shut-off valves, and disengaged (for transfer to the laboratory) or replaced to extend the duration of sampling.

SPARTAH was successfully tested at two locations: Selfoss, Iceland and San Bernardino, California (Fig. 15.5). These test deployments demonstrated that well fluids could be drawn smoothly, accurately, and continuously into the Cu-tubing and be time-stamped through user-determined operating parameters. As discussed by Barry et al. (2009), the use of SPARTAH has the potential to revolutionize studies relying on time-series records of dissolved He variations. It has a number of advantages over periodic sampling. Briefly, these include long, maintenance-free deployment times (6 months or more) with continuous sampling, user defined sample resolutions (i.e., sections of coil representing a fixed number of hours or days can be selected for analytical work), and accurate time-stamping of water aliquots due to constant withdrawal rates. Finally, it should be noted that the use of SPARTAH is not restricted to He or any other dissolved gas. The Cu-tubing can be sectioned and processed for various trace elements, stable isotopes or

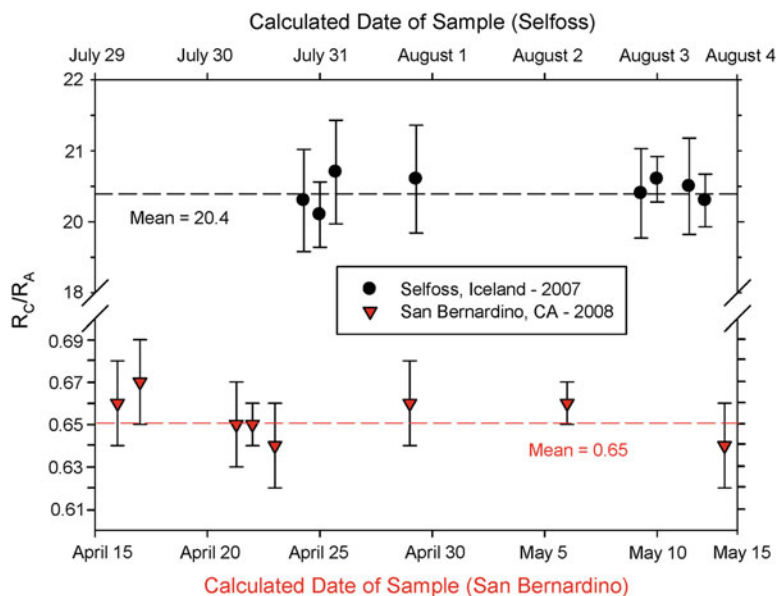


Fig. 15.5 Helium isotope variations captured in the SPARTAH Cu-coils at Selfoss, Iceland (1-week deployment) and San Bernardino, California (1-month deployment). *Note:* helium is mainly mantle-derived in Selfoss but is predominantly crustal

in origin at San Bernardino. Individual error bars are given at the 2σ level. The mean $^3\text{He}/^4\text{He}$ values for Selfoss (*black*) and San Bernardino (*red*) are illustrated by *dashed lines* (Barry et al. 2009)

any other intrinsic water property of interest. Thus, innovative analytical processing could lead to contemporary records of different tracers, enabling assessments of relative sensitivities to external perturbations. Deployment of SPARTAH at strategically-placed locations can lead to more detailed and accurate assessments of the responses of He and other geochemical parameters to external forcing factors, such as earthquakes.

Acknowledgements We thank Mark Baskaran for the invitation to contribute this review chapter. We acknowledge funding from the National Science Foundation, U.S. Geological Survey, and Scripps Institution of Oceanography.

References

- Aeschbach-Hertig W, Kipfer R, Hofer M et al (1996) Quantification of Gas Fluxes From the Subcontinental Mantle - the Example of Laacher See, a Maar Lake in Germany. *Geochim Cosmochim Acta* 60:31–41
- Andrews JN (1985) The isotopic composition of radiogenic helium and its use to study groundwater movement in confined aquifers. *Chem Geol* 49:339–351
- Andrews JN, Lee DJ (1979) Inert gases in groundwater from the Bunter Sandstone of England as indicators of age and paleoclimatic trends. *J Hydrol* 41:233–252
- Ballentine CJ, Burnard P (2002) Production of noble gases in the continental crust. In: Porcelli D et al (eds) *Noble gases in geochemistry and cosmochemistry*. Mineralogical society of America, Washington, 47:481–538
- Ballentine CJ, O’Nions RK, Oxburgh ER et al (1991) Rare gas constraints on hydrocarbon accumulation, crustal degassing and groundwater flow in the Pannonian basin. *Earth Planet Sci Lett* 105:229–246
- Ballentine CJ, Burgess R, Marty B (2002) Tracing fluid origin, transport and interaction in the crust. In: Porcelli D et al (eds) *Noble gases in geochemistry and cosmochemistry*. Mineralogical society of America, Washington, 47:539–614
- Barry PH, Hilton DR, Tryon MD et al (2009) A new syringe pump apparatus for the retrieval and temporal analysis of helium in groundwaters and geothermal fluids. *Geochem Geophys Geosyst* 10:Q05004
- Bethke CM, Zhao X, Torgersen T (1999) Groundwater flow and the ^4He distribution in the Great Artesian Basin of Australia. *J Geophys Res* 104:12999–13011
- Bethke CM, Torgersen T, Park J (2000) The “age” of very old groundwater; insights from reactive transport models. *J Geochem Explor* 69–70:1–4
- Beyerle U, Aeschbach-Hertig W, Imboden DM et al (2000) A mass spectrometric system for the analysis of noble gases and tritium from water samples. *Environ Sci Technol* 34:2042–2050
- Beyerle U, Rueedi J, Leuenberger M et al (2003) Evidence for periods of wetter and cooler climate in the Sahel between 6 and 40 kyr BP derived from groundwater - art. no. 1173. *Geophys Res Lett* 30:1173
- Castro MC, Goblet P, Ledoux E et al (1998) Noble gases as natural tracers of water circulation in the Paris Basin 2. Calibration of a groundwater flow model using noble gas isotope data. *Water Resources Research* 34:2467–2483
- Castro MC, Stute M, Schlosser P (2000) Comparison of ^4He ages and ^{14}C ages in simple aquifer systems: implications for groundwater flow and chronologies. *Appl Geochem* 15:1137–1167
- Clarke WB, Beg MA, Craig H (1969) Evidence for primordial He (super 3) in the earth. *Eos, Transactions, American Geophysical Union* 50:222
- Clarke WB, Jenkins WJ, Top Z (1976) Determination of tritium by mass spectrometric measurement of He-3. *Int J Appl Radiat Isot* 27:515–522
- Collier R, Dymond J, McManus J (1991) Studies of hydrothermal processes in Crater Lake, OR. *College of Oceanography Report #90–7*
- Craig H, Lal D (1961) The production rate of natural tritium. *Tellus* 13:85–105
- Crossey LJ, Karlstrom KE, Springer AE et al (2009) Degassing of mantle-derived CO_2 and He from springs in the southern Colorado Plateau region – neotectonic connections and implications for groundwater systems. *Bull Geol Soc Am* 121:1034–1053
- de Leeuw GAM, Hilton DR, Gulec N et al (2010) Regional and temporal variations in $\text{CO}_2/{}^3\text{He}$, ${}^3\text{He}/{}^4\text{He}$ and d^{13}C along the North Anatolian Fault Zone, Turkey. *Appl Geochem* 25:524–539
- Dunai TJ, Porcelli D (2002) Storage and transport of noble gases in the subcontinental lithosphere. *Rev Mineral Geochem* 47:371–409
- Furi E, Hilton DR, Brown KM et al (2009) Helium systematics of cold seep fluids at Monterey Bay, California, USA: Temporal variations and mantle contributions. *Geochem Geophys Geosyst* 10:Q08013
- Graham DW (2002) Noble gas isotope geochemistry of mid-ocean ridge and ocean island basalts: Characterization of mantle source reservoirs. In: Porcelli D et al. (eds) *Noble gases in geochemistry and cosmochemistry*. Mineralogical Society of America, Washington, 47:247–318
- Gulec N, Hilton DR, Mutlu H (2002) Helium isotope variations in Turkey: relationship to tectonics, volcanism and recent seismic activities. *Chem Geol* 187:129–142
- Hamme RC, Emerson SR (2004) Measurement of dissolved neon by isotope dilution using a quadrupole mass spectrometer. *Mar Chem* 91:53–64
- Heaton THE (1984) Rates and sources of ^4He accumulation in groundwater. *Hydrol Sci J* 29:29–47
- Heaton THE, Vogel JC (1981) “Excess air” in groundwater. *J Hydrol* 50:201–216
- Hilton DR (1996) The helium and carbon isotope systematics of a continental geothermal system – results from monitoring studies at Long Valley caldera (California, USA). *Chem Geol* 127:269–295
- Hilton DR (2007) Geochemistry: the leaking mantle. *Science* 318:1389–1390
- Hohmann R, Hofer M, Kipfer R et al (1998) Distribution of helium and tritium in Lake Baikal. *Journal of Geophysical Research: Oceans* 103:12823–12838

- Hong GH, Hamilton TF, Baskaran M, Kenna TC (2011) Applications of anthropogenic radionuclides as tracers to investigate marine environmental processes. In: Baskaran M (ed) Handbook of environmental isotope geochemistry. Springer, Heidelberg, 47: this volume
- Ingram RGS, Hiscock KM, Dennis PF (2007) Noble gas excess air applied to distinguish groundwater recharge conditions. *Environ Sci Technol* 41:1949–1955
- International Atomic Energy Association (1983) Environmental isotope data No. 7: World survey of isotope concentration in precipitation (1976–1979). Technical Report Series, #206
- International Atomic Energy Association (1986) Environmental isotope data No. 8: World survey of isotope concentration in precipitation (1980–1983). Technical Report Series, #264. 184
- Italiano F, Martinelli G, Nuccio PM (2001) Anomalies of mantle-derived helium during the 1997–1998 seismic swarm of Umbria-Marche, Italy. *Geophys Res Lett* 28:839–842
- Jenkins WJ, Clarke WB (1976) The distribution of ^3He in the western Atlantic Ocean. *Deep-Sea Res* 23:481–494
- Jones DL, Graymer R, Wang C et al (1994) Neogene transpressive evolution of the California coast ranges. *Tectonics* 13:561–574
- Kennedy BM, Van Soest MC (2007) Flow of mantle fluids through the ductile lower crust: helium isotope trends. *Science* 318:1433–1436
- Kennedy BM, Kharaka YK, Evans WC et al (1997) Mantle fluids in the San Andreas fault system, California. *Science* 278:1278–1281
- Kipfer R, Aeschbach-Hertig W, Peeters F et al (2002) Noble gases in lakes and ground waters. In: Porcelli D et al (eds) Noble gases in geochemistry and cosmochemistry. Mineralogical Society of America, Washington, 47:615–700
- Kulongoski JT, Hilton DR (2002) A quadrupole-based mass spectrometric system for the determination of noble gas abundances in fluids. *Geochem Geophys Geosyst* 3:U1–U10
- Kulongoski JT, Hilton DR, Izbicki JA (2003) Helium isotope studies in the Mojave Desert, California: implications for ground-water chronology and regional seismicity. *Chem Geol* 202:95–113
- Kulongoski JT, Hilton DR, Selaolo ET (2004) Climate variability in the Botswana Kalahari from the Late Pleistocene to the present day. *Geophys Res Lett* 31:L10204
- Kulongoski JT, Hilton DR, Izbicki JA (2005) Source and movement of helium in the eastern Morongo groundwater Basin: the influence of regional tectonics on crustal and mantle helium fluxes. *Geochim Cosmochim Acta* 69:3857–3872
- Kulongoski JT, Hilton DR, Cresswell RG et al (2008) Helium-4 characteristics of groundwaters from Central Australia: Comparative chronology with chlorine-36 and carbon-14 dating techniques. *J Hydrol* 348:176–194
- Kulongoski JT, Hilton DR, Izbicki JA et al (2009) Evidence for prolonged El Niño-like conditions in the Pacific during the Late Pleistocene: a 43 ka noble gas record from California groundwaters. *Quatern Sci Rev* 28:2465–2473
- Lehmann BE, Love A, Purtschert R et al (2003) A comparison of groundwater dating with ^{81}Kr , ^{36}Cl and ^4He in four wells of the Great Artesian Basin, Australia. *Earth Planet Sci Lett* 211:237–250
- Mamyrin BA, Anufriev GS, Kamenskiy IL et al (1970) Determination of the isotopic composition of atmospheric helium. *Geochem Int* 7:498–505
- Mamyrin BA, Tolstikhin IN (1984) Helium isotopes in nature. Elsevier, Amsterdam, 274
- Marine IW (1979) The use of naturally occurring helium to estimate groundwater velocities for studies of gologic storage of radioactive waste. *Water Resour Res* 15:1130–1136
- Martel DJ, Deak J, Dovenyi P et al (1989) Leakage of Helium from the Pannonian Basin. *Nature* 342:908–912
- Marty B, Torgersen T, Meynier V et al (1993) Helium isotope fluxes and groundwater ages in the Dogger Aquifer, Paris Basin. *Water Resources Research* 29:1025–1035
- Mazor E (1972) Paleotemperatures and other hydrological parameters deduced from noble gases dissolved in groundwaters; Jordan Rift Valley, Israel. *Geochim Cosmochim Acta* 36:1321–1336
- Miller SA, Nur A (2000) Permeability as a toggle switch in fluid-controlled crustal processes. *Earth Planet Sci Lett* 183:133–146
- Norton FJ (1957) Permeation of Gases through Solids. *J Appl Phys* 28:34–39
- Nur A, Walder J (1990) Time-dependent hydraulics of the Earth's crust. In: The role of fluids in crustal processes. National Academy Press, Washington, 113–127
- O'Nions RK, Oxburgh ER (1983) Heat and helium in the Earth. *Nature* 306:429–431
- O'Nions RK, Oxburgh ER (1988) Helium, volatile fluxes and the development of continental crust. *Earth Planet Sci Lett* 90:331–347
- Oxburgh ER, O'Nions RK, Hill RI (1986) Helium isotopes in sedimentary basins. *Nature* 324:632–635
- Ozima M, Podosek FA (1983) Noble gas geochemistry. Cambridge University Press, Cambridge
- Peeters F, Kipfer R, Achermann D et al (2000) Analysis of deep-water exchange in the Caspian Sea based on environmental tracers. *Deep-Sea Res Pt I-Oceanog Res* 47:621–654
- Phillips FM, Castro MC (2003) Groundwater dating and residence time measurements. In: Holland HD et al. (eds) Treatise on Geochemistry, Surface and Ground Water, Weathering, and Soils. Oxford University Press, Oxford, 5:451–497
- Pik R, Marty B (2009) Helium isotopic signature of modern and fossil fluids associated with the Corinth rift fault zone (Greece): implication for fault connectivity in the lower crust. *Chem Geol* 266:67–75
- Poole JC, McNeill GW, Langman SR et al (1997) Analysis of noble gases in water using a quadrupole mass spectrometer in static mode. *Appl Geochem* 12:707–714
- Poreda RJ, Cerling TE, Salomon DK (1988) Tritium and helium isotopes as hydrologic tracers in a shallow unconfined aquifer. *J Hydrol* 103:1–9
- Rice JR (1992) Fault stress, pore pressure distribution, and the weakness of the San Andreas fault. In: Evans B et al. (eds) Fault mechanics and transport properties of rocks, International Geophysics Series. Academic Press, London, 51:475–503
- Rison W, Craig H (1983) Helium isotopes and mantle volatiles in Loihi Seamount and Hawaiian Islands basalts and xenoliths. *Earth Planet Sci Lett* 66:407–426
- Sano Y (1986) Helium flux from the solid earth. *Geochem J* 20:227–232
- Sano Y, Nakajima J (2008) Geographical distribution of $^3\text{He}/^4\text{He}$ ratios and seismic tomography in Japan. *Geochem J* 42:51–60

- Sano Y, Takahata N (2005) Measurement of noble gas solubility in seawater using a quadrupole mass spectrometer. *J Oceanogr* 61:465–473
- Sano Y, Wakita H, Huang CW (1986) Helium flux in a continental land area estimated from $^3\text{He}/^4\text{He}$ ratio in northern Taiwan. *Nature* 323:55–57
- Schlosser P, Winckler G (2002) Noble gases in ocean waters and sediments. In: Porcelli D et al. (eds) *Noble gases in geochemistry and cosmochemistry*. Mineralogical Society of America, Washington, 47:701–730
- Schlosser P, Stute M, Dorr H et al (1988) Tritium/ ^3He dating of shallow groundwater. *Earth Planet Sci Lett* 89:353–362
- Schlosser P, Stute M, Sonntag C et al (1989) Tritogenic He-3 in shallow groundwater. *Earth Planet Sci Lett* 94:245–256
- Selaolo ET, Hilton DR and Beekman HE (2000) Groundwater recharge deduced from He isotopes in the Botswana Kalahari. In: Sililo O et al. (eds.) *Groundwater: past achievements and future challenges*. Proceedings of the 30th International Association of Hydrogeologists Congress, Cape Town, RSA. A.A. Balkema Publishers, Rotterdam, Netherlands, 313–318
- Solomon DK, Hunt A, Poreda RJ (1996) Source of radiogenic helium 4 in shallow aquifers – implications for dating young groundwater. *Water Resour Res* 32:1805–1813
- Stanley RHR, Baschek B, Lott III DE et al (2009) A new automated method for measuring noble gases and their isotopic ratios in water samples. *Geochem Geophys Geosyst* 10:Q05008
- Stute M, Schlosser P (1993) Principles and applications of the noble gas paleothermometer. In *Climate Change in Continental Isotopic Records* 78:89–100
- Stute M, Talma AS (1998) Glacial temperatures and moisture transport regimes reconstructed from noble gases and O-18, Stampriet aquifer, Namibia. In *Isotope techniques in the study of environmental change*. IAEA, Vienna, 307–318
- Stute M, Sonntag C, Deak J et al (1992) Helium in deep circulating groundwater in the Great Hungarian Plain – flow dynamics and crustal and mantle helium fluxes. *Geochim Cosmochim Acta* 56:2051–2067
- Stute M, Clark JF, Schlosser P et al (1995) A 30,000 yr continental paleotemperature record derived from noble gases dissolved in groundwater from the San Juan Basin, New Mexico. *Quat Res* 43:209–220
- Takaoka N, Mizutani Y (1987) Tritogenic ^3He in groundwater in Takaoka. *Earth Planet Sci Lett* 85:74–78
- Tolstikhin IN (1975) Helium isotopes in the Earth's interior and in the atmosphere; a degassing model of the Earth. *Earth Planet Sci Lett* 26:88–96
- Tolstikhin IN, Kamenskiy IL (1969) Determination of groundwater ages by the T-3He method. *Geochem Intl* 6:810–811
- Top Z, Clarke WB (1983) Helium, neon, and tritium in the Black Sea. *J Mar Res* 41:1–17
- Torgersen T (1980) Controls on pore-fluid concentrations of ^4He and ^{222}Rn and the calculation of $^4\text{He}/^{222}\text{Rn}$ ages. *J Geochem Explor* 13:57–75
- Torgersen T (1993) Defining the role of magmatism in extensional tectonics: He-3 fluxes in extensional basins. *J Geophys Res* 98:16257–16269
- Torgersen T (2010) Continental degassing flux of ^4He and its variability. *Geochem Geophys Geosyst* 11:Q06002
- Torgersen T, Clarke W (1985) Helium accumulation in groundwater: I. An evaluation of sources and continental flux of crustal ^4He in the Great Artesian basin, Australia. *Geochim Cosmochim Acta* 49:1211–1218
- Torgersen T, Clarke WB (1987) Helium accumulation in groundwater; III, limits on helium transfer across the mantle-crust boundary beneath Australia and the magnitude of mantle degassing. *Earth Planet Sci Lett* 84:345–355
- Tryon M, Brown K, Dorman L et al (2001) A new benthic aqueous flux meter for very low to moderate discharge rates. *Deep Sea Res I* 48:2121–2146
- Webb TH, Kanamori H (1985) Earthquake focal mechanisms in the eastern Transverse Ranges and San Emigdio Mountains, southern California and evidence for a regional decollement. *Seismological Soc Am Bull* 75:737–757
- Weise S, Moser H (1987) Groundwater dating with helium isotopes. In: *Techniques in water resources development*. IAEA, Vienna, 105–126
- Weiss RF (1971) Solubility of helium and neon in water and seawater. *J Chem Eng Data* 16:235–241
- Well R, Lupton J, Roether W (2001) Crustal helium in deep Pacific waters. *Journal of Geophysical Research C: Oceans* 106:14165–14177
- Weyhenmeyer CE, Burns SJ, Waber HN et al (2000) Cool glacial temperatures and changes in moisture source recorded in Oman groundwaters. *Science* 287:842–845
- Zhao X, Fritzel TLB, Quinodoz HAM et al (1998) Controls on the distribution and isotopic composition of helium in deep ground-water flows. *Geology* 26:291–294

Chapter 16

Applications of Short-Lived Radionuclides (^7Be , ^{210}Pb , ^{210}Po , ^{137}Cs and ^{234}Th) to Trace the Sources, Transport Pathways and Deposition of Particles/Sediments in Rivers, Estuaries and Coasts

J.Z. Du, J. Zhang, and M. Baskaran

Abstract Natural and anthropogenic radioisotopes can be used to determine not only the mixing and diffusion processes of water masses but also the sources and sedimentary dynamics of particles in aquatic systems such as rivers, estuaries and oceans. Particle-reactive radionuclides that are derived from atmospheric deposition and/or the decay from their parent nuclides in aqueous system, can be used to determine the removal rates of suspended particulate matter, sediment focusing/erosion, sediment resuspension rates and sediment accumulation and mixing rates. They can be also used as analogs for tracing the transport and fates of other particle-reactive contaminants, such as PCBs and PAH. In this chapter, we focus on various applications of short-lived radionuclides (i.e., ^7Be , ^{210}Pb , ^{210}Po , ^{137}Cs and ^{234}Th) as tracers for particle and sediment dynamics to quantify several river, estuary and coastal oceanic processes with their concerned timescales ranging from a few days to about 100 years.

16.1 Introduction

Estuaries and coasts are commonly described as complex reactors at land-sea interface where not only significant transformations of river and stream-borne suspended sediments but also the biogeochemical

cycling of key nutrients take place (Swarzenski et al. 2001; Swarzenski et al. 2003). Whether estuarine and coastal processes of water masses and soluble materials, or of particle/sediment and particle-reactive materials, we can use a suite of applicable radionuclides to trace these processes in different time scales that are comparable to their half-lives. Based on the geochemical behavior, most radionuclides that occur in the environment can be broadly classified into two major categories: (i) the particle-reactive (i.e., non-conservative tracers); and (ii) water soluble (i.e., conservative tracers). The particle-reactive radioactive radionuclides are sorbed onto biogenic and terrigenous particulate matter, including colloidal material and are removed from the water column. In coastal waters, most of the particle-reactive radionuclides are derived either from direct atmospheric fallout (e.g., ^7Be), riverine discharge (e.g., ^{137}Cs), or in situ production from parent nuclides (e.g., ^{234}Th) and are commonly associated with fine particles. The amount of particle-reactive radionuclides discharged through submarine groundwater discharge is likely negligible, compared to other sources (e.g., soluble radionuclides) in the coastal waters. Once-sorbed, the fate of the particle-reactive radionuclides become the fate of the particulate matter, although under some cases, there could be desorption of the radionuclides. In general, the adsorption is faster than the desorption. Owing to irreversible character of solid-water partitioning, particle-reactive radionuclides can serve as a set of powerful tracers to quantify the sedimentary dynamics including removal rates of suspended particulate matter (Baskaran and Swarzenski 2007; Jweda et al. 2008), sediment focusing/erosion, sediment resuspension rates, sediment accumulation and mixing rates, and sediment transport (e.g., Feng et al. 1999a, b; Giffin and Corbett 2003; Lima et al. 2005;

J.Z. Du (✉) and J. Zhang
State Key Laboratory of Estuarine and Coastal Research,
East China Normal University, Shanghai 200062, China
e-mail: jzdu@sklec.ecnu.edu.cn; jzhang@sklec.ecnu.edu.cn

M. Baskaran
Department of Geology, Wayne State University, Detroit,
MI 48202, USA
e-mail: baskaran@wayne.edu

Du et al. 2010). The particle-reactive radionuclides also provide analog information on other particle-reactive organic (e.g., PCBs, PAHs, and other derivatives from petroleum and coal hydrocarbons, synthetic organics, etc. (Gustafsson et al. 1997a, b; Gustafsson and Gschwend 1998)), and inorganic contaminants (e.g., biogenic silica, heavy metals, industrial substrates derived from industrial pollution, etc., Broecker et al. 1973; Buesseler et al. 2001b; Rutgers van der Loeff et al. 2002; Weinstein and Moran, 2005). Organic-rich coastal waters could be ideal sites to investigate the fate of these nuclides and other metals due to metal-organic complexation. The removal rates of particle-reactive radionuclides are also relevant in the use of these radionuclide-based chronologies. Such chronologies are needed to investigate the historical variations on the inputs of organic and inorganic pollutants.

A large number of papers have been published with ^{234}Th as a tracer in aqueous system, with more than 250 papers since the first work by Bhat et al. (1969) and the application and future use are reviewed in Waples et al. (2006). Kaste et al. (2002) reviewed the environment chemistry of ^7Be in the world (also see Kaste and Baskaran 2011). ^7Be and ^{234}Th can be used in the determination of sedimentation rates in short time scale, such as sediment deposition by flood (Sommerfield et al. 1999; Palinkas et al. 2005; Huh et al. 2009). Sediment redistribution parameters such as the settling and resuspension rates can be evaluated using $^7\text{Be}/^{210}\text{Pb}_{\text{xs}}$, and $^{234}\text{Th}_{\text{xs}}/^7\text{Be}$ activity ratios. Moreover, the depth profiles of ^7Be , $^{210}\text{Pb}_{\text{xs}}$ and ^{137}Cs

have been utilized as effective tracers in the study of soil erosion (Walling et al. 1999; also Matisoff and Whiting 2011). In this chapter, we review the utility of particle-reactive radionuclides as tracers for particle and sediment dynamics to quantify several coastal oceanic processes, with special emphasis on the utility of ^7Be , ^{234}Th , ^{210}Po , ^{210}Pb and ^{137}Cs .

16.1.1 Sources of Isotopes: ^7Be , ^{137}Cs , ^{210}Pb , ^{210}Po and ^{234}Th

The nuclear properties of these nuclides are listed in Table 16.1. ^7Be is continuously and globally produced in an endothermic reaction when cosmic-ray-produced neutrons and protons disintegrate the atomic nuclei of atmospheric nitrogen and oxygen at an average rate of $8.1 \times 10^2 \text{ atoms m}^{-2} \text{ s}^{-1}$ (UNSCEAR 1982, 2000). The production rate of ^7Be (and other cosmogenic radionuclides) varies with latitude and altitude. About two thirds of the production takes place in the stratosphere and the remaining one third in the troposphere (Lal and Peters 1967; Lal and Baskaran 2011). The residence time of ^7Be in the stratosphere with respect to removal by scavenging is about 1 year, while that in the troposphere is about 10 days. At the mid-latitudes (about $40\text{--}50^\circ$), there is an intrusion of stratospheric air, primarily during spring, which transfers large amounts of ^7Be and other cosmogenic radionuclides into the troposphere (Lal and Baskaran 2011). Moreover, the high production rate of

Table 16.1 Nuclear properties of ^7Be , ^{137}Cs , ^{210}Pb , ^{210}Po and ^{234}Th ^a

Nuclide	Atomic number	Decay mode	Energy of main peak (MeV)	Intensity (%)	Half-life	Analysis method	Sources
^7Be	4	EC ^b	Gamma-0.4776	10.52	53.3 days	Gamma	Cosmogenic ($810 \text{ atoms m}^{-2} \text{ s}^{-1}$)
		EC	–	89.48			
^{137}Cs	55	Beta	Beta-1.176	94.4	30.0 years	Beta	Human nuclear activity
		Beta	Beta-0.514	5.6			
^{210}Pb	82	Beta	Gamma-0.6617	94.4	22.3 years	Gamma	U-decay series
			Beta-0.0631	16		Beta- ^{210}Bi	
			Beta-0.16	84		Alpha- ^{210}Po	
^{210}Po	84	Alpha	Gamma-0.0465	4.25	138.4 days	Gamma	U-decay series
			Alpha-5.304	100		Alpha- ^{210}Po	
^{234}Th	93	Beta	Beta-0.1985	70.3	24.1 days	Beta	U-decay series
			Beta-0.1035	26.8			
			Beta-0.0833	2.9			
			Gamma-0.0629	4.85			
			Gamma-0.0926	5.58		Gamma	

^aData reproduced from <http://atom.kaeri.re.kr>

^bElectron capture

^7Be in the atmosphere is observed during solar minima during the 11-year sunspot cycle (Masarik and Beer 1999).

Most of the ^{137}Cs present in the oceans was derived from global nuclear fallout, with peak fallout in 1963, riverine input from the erosion of soils and nuclear waste sites, discharge of nuclear effluents from close-in and long-range transport and the Chernobyl accident (more details are given in Hong et al. 2011). Detonation of nuclear weapon tests in the atmosphere starting from 1952 until the cessation of nuclear weapons testing released a large volume of anthropogenic radionuclides to the atmosphere.

There are two components of ^{210}Pb in the Earth's surface. In natural minerals and soils, ^{210}Pb in general is in secular equilibrium with ^{226}Ra , a decay product in the ^{238}U decay series, which is then supplied to rivers along with detrital particles and is termed as the supported ^{210}Pb . An additional source of ^{210}Pb is primarily derived from the atmospheric deposition. ^{222}Rn is constantly released from surface soils, rocks and minerals with a global average rate of $1 \text{ atom cm}^{-2} \text{ s}^{-1}$ from the land surface, while this rate is about two orders of magnitude lower from the ocean (Turekian and Graustein 2003). The atmospheric ^{222}Rn undergoes radioactive decay and eventually produces ^{210}Pb . ^{210}Pb thus formed in the atmosphere is rapidly adsorbed onto aerosol particles, which reach soils and aquatic systems through wet and dry atmospheric depositions. Once delivered at the air-sea interface via wet and dry precipitation, the ^{210}Pb is quickly removed by suspended particulate matter and eventually reaches the sediment-water interface. The concentration of ^{210}Pb in the surface waters thus primarily depends upon the temporally and geographically varying inputs of atmospheric deposition. Subsequently, most of the ^{210}Pb in water column is removed by sorption on to particulate matter.

Polonium, an oxygen-sulfur group element, is used as a tracer of elements fundamental to organic matter. It is a particle-reactive element with a wide range of K_d values, $10^3\text{--}10^5 \text{ cm}^3 \text{ g}^{-1}$ (Carvalho 1997; Nozaki et al. 1997; Hong et al. 1999; Kim and Yang 2004). Most of the dissolved ^{210}Po in the upper waters is from the decay of ^{210}Pb and is ultimately derived from atmospheric fallout with the $^{210}\text{Po}/^{210}\text{Pb}$ activity ratio in depositional flux < 0.1 (e.g., Hussain et al. 1998). More details can be found in Kim and Church (2011).

^{234}Th is a naturally occurring, highly particle-reactive radionuclide produced from the decay of ^{238}U . Due to its high particle-reactivity, Th-sorbed particulate matter eventually reaches the seabed. The sorbed component of ^{234}Th is called excess ^{234}Th ($^{234}\text{Th}_{\text{xs}}$), while the lattice-bound ^{234}Th that is in secular equilibrium with ^{238}U is called parent-supported ^{234}Th . The production rate of ^{234}Th is thus dependent on the concentration of its dissolved parent nuclide ^{238}U . In estuaries and coastal areas, U generally behaves conservatively, although non-conservative behavior has been reported at low salinity waters, and thus, ^{238}U activity increases with salinity and thus production rate of ^{234}Th also increases with salinity.

16.1.2 Factors Affecting the Concentrations and Behavior of ^7Be , ^{137}Cs , ^{210}Pb , ^{210}Po and ^{234}Th in Estuaries and Coasts

The depositional flux of ^7Be to Earth's surface is highly variable, depending upon the amount and frequency of precipitation, latitude, seasons and the nature and height of the cloud cover. The ^7Be specific activity in precipitation has been reported to vary widely. For example, ^7Be in precipitation samples collected over a period of 3 years (1989–1991) in Galveston, TX varied between 0.09 and 20.7 Bq L^{-1} (Baskaran et al. 1993; activities in global precipitation is summarized in Kaste and Baskaran 2011). Most of the ^7Be produced in the stratosphere do not readily reach the troposphere except during spring, when the seasonal thinning of the troposphere occurs at mid-latitudes, resulting in air exchange between the stratosphere and troposphere (e.g., Kim et al. 1998). Therefore, ^7Be flux to the earth surface depends on latitude. Several studies indicated that additional meteorological factors, such as seasonal variability in the amount and frequency of rainfall and the vertical mixing of the lower and upper troposphere, could explain the seasonal variability of ^7Be flux (Baskaran 1995; Benitez-Nelson and Buesseler 1999; Su et al. 2003; Du et al. 2008). During heavy flood events in rivers, ^7Be discharge is very high compared to normal flow periods, and hence, the distribution of particulate ^7Be is affected by the volume of water discharge in estuaries and coastal areas.

At present, there is no global fallout of ^{137}Cs derived from nuclear weapons testing. However, the resuspension of very fine ^{137}Cs -laden dust particles could contribute a very small amount to the ocean surface waters. Rivers discharge ^{137}Cs through suspended particulate and bed load as well as in the dissolved phase. Most of this ^{137}Cs is derived from the erosional input from the watershed (Walling and Quine 1993; Matisoff and Whiting 2011). ^{137}Cs in the oceanic water column behaves as a soluble nuclide and has properties that make it useful as a water mass tracer (Bowen and Roether 1973; Murray et al. 1978; Smith et al. 1990). Note that ^{137}Cs is particle-reactive in freshwater systems due to low potassium (K) concentrations, while in marine systems, the presence of large amounts of K compete with Cs, and hence, the geochemical behavior of Cs is different. Very little of the ^{137}Cs delivered to the ocean has reached the sedimentary column. More details on the sources and distribution of ^{137}Cs in marine environment are given in Hong et al. (2011).

^{210}Pb , similar to ^7Be , is also primarily derived from atmospheric deposition. The atmospheric deposition is also highly variable, depending on the amounts and frequency of precipitation as well as latitude (Baskaran 2011; Kaste and Baskaran 2011). The amount of ^{210}Pb resulting from the decay of ^{226}Ra in coastal areas is negligible compared to the atmospheric depositional flux. After the deposition of ^7Be and ^{210}Pb at the air-sea interface in the coastal waters, these nuclides are quickly removed onto suspended particulate matter. For example, Baskaran and Santschi (1993) reported that about 80% of ^7Be became associated with particulates within an hour after a heavy rainfall event. ^{210}Pb binds irreversibly to soil particles, and is generally immobile in sediments (Koide et al. 1972; Robbins and Edgington 1975; Goldberg et al. 1977). Hawley et al. (1986) reported partition coefficients, K_d for ^7Be and ^{210}Pb greater than 10^4 , indicating that these radionuclides are sufficiently particle-bound that they can be used to trace erosion, particle transport and deposition (Whiting et al. 2005). Annual depositional fluxes of ^{210}Pb are considerably constant over longer periods of time, although they vary with the amounts of precipitation (Baskaran et al. 1993). The removal of ^{210}Pb from the upper ocean is driven by the flux of biogenic material from surface productivity (Fisher et al.

1988; Moore and Dymond, 1988). The atmospheric depositional flux of ^{210}Po is very small compared to ^{210}Pb , with a $^{210}\text{Po}/^{210}\text{Pb}$ activity ratio of <0.1 . One could potentially utilize $^{210}\text{Po}/^{210}\text{Pb}$ ratios in suspended particulate matter to trace the pathways and extent of resuspension of deposited sediment. Polonium has a strong affinity for biogenic material and gets incorporated into organic matter, and thus, Po is expected to trace biogenic organic matter much more closely than Th or Pb (Fisher et al. 1983; Cherrier et al. 1995; LaRock et al. 1996).

The contrasting geochemical difference between insoluble Th and soluble U in the water column and the relatively short residence times of ^{234}Th in surface waters and in the euphotic zone make ^{234}Th a powerful tracer for quantifying spatial and temporal dynamics of particles and other particle-reactive species. Short-lived thorium isotopes are used to examine a large range of water column and seabed processes in estuarine environments (Waples et al. 2006; Rutgers van der Loeff et al. 2006). The earliest observations regarding the disequilibria between ^{234}Th and its parent ^{238}U revealed that the removal rate of ^{234}Th decreased with distance from shore (Bhat et al. 1969). This finding established the particle-reactive nature of thorium and laid the foundation for the use of short-lived thorium isotopes as tracers for geochemical and sedimentary processes in estuarine and coastal environments. The utilization of ^{234}Th as a tracer in estuarine environments is divided into two categories: (1) quantifying the residence time of ^{234}Th (dissolved and particulate, particulate Th is the same as the particulate matter) in the water column, other particle-reactive species with respect to the scavenging and removal from the water column, and (2) quantifying rates of sedimentary processes such as mixing, deposition and transport.

In this chapter, we review the important applications of these short-lived radionuclides in the coastal environments as tracers to quantify the removal rates of suspended particulate matter, particle cycling, sediment dynamics and utility of these tracers as proxies for other contaminants sorbed on to sedimentary particulate matter. These tracers have provided useful information in quantifying the fluxes of particle-sorbed PCBs, PAHs and trace metals (Gustafsson et al. 1997a, b; Weinstein and Moran 2005).

16.2 Methodology for Sample Collection and Laboratory Analysis

Appropriate sampling and analytical methods are all key factors in obtaining high quality data. The sampling and treatment of samples, the laboratory analysis of radioisotopes and quality management are especially important.

16.2.1 Sampling and Treatment

Compared to other chemical analyses (i.e., heavy metals and organic composition), the unintended contamination of samples for the analysis of short-lived radionuclides by material released from the research vessel or by the sampling apparatus is generally negligible. The particle-reactive radionuclides have a strong tendency to sorb onto the walls of the sampling containers, and hence, acidification of the samples immediately after collection is required.

For large-volume surface water sampling, different methods are available. Water samples can be collected either through the seawater supply hose in the ship or through a submersible pump. The seawater hose in the ship tends to accumulate Th and has been reported to release the daughter products of Th (e.g., ^{224}Ra released from the sorbed ^{228}Th). Caution must be exercised for the possible release of radionuclides from the seawater supply hose. Generally, it is necessary to collect large sample volumes (usually 0.02 M^3 to several M^3) to obtain good counting statistics within an acceptable counting time. Sometimes there are few options except having a large volume of water samples (e.g., ^7Be). There are a few methods that can be used for large volume sampling (Rutgers van der Loeff and Moore 1999; Baskaran et al. 2009a).

1. *Rosette sampling* (up to 30 L) is the most convenient method and provides the exact depth profile and for other parameters.
2. *Gerard sampling* (up to 400 L). The bottles must be rinsed using the yo-yo technique to obtain water from the desired depth (Roether 1971). There is a serious risk of exchange of water during recovery (Broecker et al. 1986) due to the loose closure of the lids, which should be checked with indirect

methods (e.g., silicate measurements). Radionuclide sampling with 250-L PVC bottles is described in Nozaki (1993).

3. *In situ pumps* combined with (MnO_2 -coated) absorbers form the only alternative for subsurface sampling volumes of $>400\text{ L}$ for ^{234}Th and ^{210}Pb (Buesseler et al. 1992, 1995; Baskaran et al. 1993; Rutgers van der Loeff and Berger 1993; Rutgers van der Loeff and Moore 1999; Baskaran and Santschi, 2002). This method is ship time-consuming, and there is a risk of loss of particles during the recovery and of particles sticking to the baffles in front of the filters. The simultaneous operation of multiple pumps at multiple depths in the winch will reduce the overall ship time needed for vertical profile sampling. We found a reassuring correspondence between particulate ^{234}Th profiles obtained with Rosette casts and with in situ pumps (Du et al., unpublished data).
4. *Surface seawater supply* is a convenient way to sample surface water. However, there is a risk of artifacts, especially at insufficient throughput through long lines, and clogging inputs, which can affect both the dissolved and particulate phases. Sewage discharge from ship also can pose problems affecting the quality of data.

For volumes less than 30 L, except for the in situ pumps, large-volume filtration normally has to be performed on board. Radionuclides of the dissolved phase (^7Be , ^{210}Pb , ^{210}Po and ^{234}Th) are usually pre-concentrated onboard by coprecipitation with hydroxides and sulfates of Fe, Ba or Mn such as $\text{Fe}(\text{OH})_3$, $\text{Mg}(\text{OH})_2$, MnO_2 , BaSO_4 , PbSO_4 or Co-APDC (Rutgers van der Loeff and Moore 1999; Buesseler et al. 2001a, b; Benitez-Nelson et al. 2001; Elsinger and Moore 1983; details on various sorbents used in literature are summarized in Baskaran et al. 2009a, b). If quantitative recovery cannot be guaranteed, yield tracers must be added such as ^{209}Po for ^{210}Po , stable Pb carrier for ^{210}Pb , stable Be carrier for ^7Be and ^{230}Th or ^{229}Th for ^{234}Th , respectively (Harvey and Lovett 1984).

For the measurements of both dissolved and particulate radionuclides, prefilters followed by MnO_2 -coated fibers connected in series are used to obtain particulate matter (prefilter) and dissolved radionuclides (Th, Pb) from the water column. The prefilter is usually ashed at 550°C for polypropylene fiber

material and can be utilized for the measurements of ${}^7\text{Be}$, ${}^{234}\text{Th}$, ${}^{210}\text{Pb}$ and ${}^{137}\text{Cs}$ but not for particulate ${}^{210}\text{Po}$ because Po is volatile at such high temperatures. The efficiency of extraction, E , for any nuclide can then be calculated from the ratio of the activities A and B measured in the first and second cartridges: $E = 1 - B/A$, (so called the “cartridge formula”). The assumption that both cartridges extract radionuclides uniformly (i.e., constant extraction efficiency by both filters A and B) becomes especially critical at lower efficiencies (Baskaran et al. 1993). Furthermore, a recent study indicates that some of the sorbed Th can desorb during filtration, thus adding uncertainty to the uniform extraction efficiency (Baskaran et al. 2009b). The formula cannot be used if there is a risk of desorption of MnO_2 with associated activity from the first to the second cartridge, either by physical entrainment of MnO_2 particles or by MnO_2 reduction in anoxic water masses. The schematic of the procedures is shown in Fig. 16.1. Detailed methods on the preparation of Mn-fiber and MnO_2 -cartridges can be found in literature (Moore 1976; Buesseler et al. 1992; Rutgers van der Loeff and Moore 1999; Baskaran et al. 1993; 2009a, b). For preconcentrating ${}^{137}\text{Cs}$ from the water sample, a cotton fiber filter impregnated with copper ferrocyanide has been utilized (Buesseler et al. 1990; Baskaran et al. 2009a).

Surface sediments and sediment cores are usually collected by push core from a small boat with a PVC coring device outfitted with a one-way check valve and a 4-in.-diameter clear acrylic tube (core tube).

16.2.2 Laboratory Analysis of Radioisotopes

Alpha spectrometry, beta counting and gamma spectrometry are the commonly used methods for measuring the activity of ${}^7\text{Be}$, ${}^{210}\text{Pb}$, ${}^{210}\text{Po}$, ${}^{137}\text{Cs}$ and ${}^{234}\text{Th}$ (Buesseler et al. 2001a; Rutgers van der Loeff and Moore, 1999; Trimble et al. 2004; Baskaran et al. 2009a). *Gamma spectrometry* allows the simultaneous measurements of ${}^7\text{Be}$, ${}^{210}\text{Pb}$, ${}^{234}\text{Th}$ and ${}^{137}\text{Cs}$ without chemical purification and is the ideal method for non-destructive techniques (Buesseler et al. 1992). However, inherent (Compton) background and self-absorption by the sample, energy- and geometry-dependent detector efficiency and low gamma branching ratios for some of the radionuclides can reduce the sensitivity and accuracy of the method. The overall sensitivity is generally low compared to other techniques (Rutgers van der Loeff and Moore 1999).

Alpha spectrometry is characterized by good isotope separation, uniform (i.e., energy- and isotope-independent) detector efficiency and very low background, typically on the order of 0.001–0.003 counts per minute for the 4–8 MeV energy range of a new surface barrier detector, increasing with time as a result of the accumulation of recoil products from measured samples (Rutgers van der Loeff and Moore 1999). Alpha spectrometry allows precise measurements at low activities and easy calibration with yield tracers. Alpha particles have a very short range. They are absorbed or slowed down by interactions with sample material or by impurities on the source

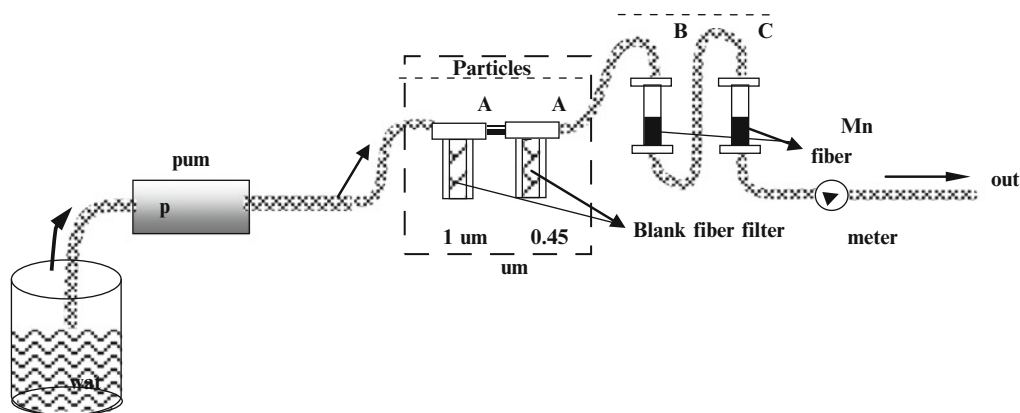


Fig. 16.1 Schematic diagram of the large volume method for ${}^{234}\text{Th}$ collection in the water column (modified from Baskaran et al. 2009a)

which is normally a flat planchet with the purified element plated on it. The best results in terms of efficiency and energy resolution are obtained with clean sources prepared from well-purified samples.

In the case of Beta Spectroscopy, the energy of the beta particles (electrons) has continuous energy distribution and hence identification of beta-emitting radionuclides using beta spectrometer is not possible. Since the beta particles have continuous energy spectrum extending from zero up to the maximum energy, E_{\max} , the thickness of source will affect the beta particles with different energies differently. Thus, in most cases, chemical separation and purification of radionuclides is required.

16.2.2.1 Be-7

The decay of ^7Be can proceed directly to the Li ground state or to the first excited state in ^7Li with the branching ratio of 89.56 and 10.44%, respectively. The latter then proceeds to the ^7Li ground state by emitting gamma rays at 477.6 keV. Because the energy of gamma rays emitted from ^7Be is high, most of the samples are measured by γ -spectrometry (Olsen et al. 1986; Kim et al. 1999; 2000).

16.2.2.2 Po-210 and Pb-210

After a set of chemical procedures, ^{210}Po can be plated on a silver disc and assayed in an alpha spectrometer, more details can be found in Mathews et al. (2007). The ^{210}Pb concentration can be measured using a low-energy (46.3 keV) gamma line of ^{210}Pb . However, the low branching ratio (4.25%; Porcelli and Baskaran 2011) requires that a large volume of water sample be processed for ^{210}Pb (Baskaran and Santschi 2002). ^{210}Po and ^{210}Pb measurements in natural samples are routinely conducted using α -spectrometry, first measuring ^{210}Po (called in situ ^{210}Po) and then keeping the sample for a period of 6 months to 2 years for the in-growth of ^{210}Po from ^{210}Pb . The second ^{210}Po (parent-supported) measurement provides the data on the concentration of ^{210}Pb (Sarin et al., 1992; Church et al., 1994; Radakovitch et al., 1998; Hong et al., 1999; Fridrich and Rutgers van der Loeff 2002; Masque et al., 2002; Stewart et al., 2007). ^{210}Pb can also be measured by the beta counting

method because the beta-ray emitted by ^{210}Pb has lower energy ($\beta_{\max} = 63$ keV); these low energy betas particles need to be suppressed, and ^{210}Bi beta ($\beta_{\max} = 1.16$ MeV) is used to assay ^{210}Pb activity. So when beta counting is used, we can get the concentration of ^{210}Pb through the measurement of ^{210}Bi (half-life: 5.0 days). Multiple counting over a period of 30–35 days (6–7 half-lives of ^{210}Bi) with a beta counter will ensure data quality.

16.2.2.3 Cs-137

^{137}Cs concentrations are most commonly measured using gamma-ray spectrometry when ^{137}Cs decays to the excited state of ^{137}Ba by beta decay and its subsequent transition to ground state. ^{137}Cs can also be directly measured using the beta ($\beta_{\max} = 1.176$ MeV) counting method after separation and purification (Yoshizawa 1958; Baskaran et al. 2009a).

16.2.2.4 Th-234

^{234}Th can be measured by γ -spectrometry. The two suitable peaks for quantifying ^{234}Th are 63.2 keV (branching ratio 4.85%; Porcelli and Baskaran 2011) and 92.4 + 92.8 keV (branching ratio ~5.6%). These low branching ratios result in low gamma counting rates (e.g., Rutgers van der Loeff et al. 2006). Unlike γ -spectrometry, beta counting has an excellent counting efficiency for ^{234}Th . Apparent efficiencies reach almost 100% when the beta emissions for ^{234}Th (weak beta at $E_{\max} = 0.27$ MeV) and its daughter $^{234\text{m}}\text{Pa}$ (strong beta at $E_{\max} = 2.19$ MeV) are combined, and the sample is reduced into a near weightless source via electroplating on a stainless steel disk (Waples et al. 2003). A five-position beta counter manufactured by RISØ National Laboratories (Roskilde, Denmark) with a 10 cm lead shield has been most commonly used at sea and in the laboratory and has background values of 0.15–0.20 cpm for a source of 25-mm diameter. Pates et al. (1996) developed a method for the determination of ^{234}Th in seawater by LSS. A major advantage of using LSS is the avoidance of separate alpha and beta measurements to determine ^{234}Th activities. After the addition of ^{230}Th as a yield tracer, Th is coprecipitated with $\text{Fe}(\text{OH})_3$ and purified through ion exchange chromatography to remove Fe

and U. Details can be seen in a number of published references (Smith et al. 2004; Kersten et al. 1998; Foster and Shimmiel 2002). However, beta counting is not isotope specific. Beta counting is the preferred method for ^{234}Th , and can be used with non-destructive techniques (for particulate samples on filters) and can be used on-board ship. For particulate and sediment samples, chemical separation and purification are required to prevent other beta-emitting radionuclides from interfering with the counting.

Table 16.1 show the nuclear properties of ^7Be , ^{137}Cs , ^{210}Pb , ^{210}Po and ^{234}Th , including decay modes, energies of the main peaks, intensities, half-lives, analytical methods and sources of these nuclides.

16.2.3 Quality Assurance and Quality Control

Each of the collection, handling, storage and preservation steps for samples should be validated to ensure that there are interferences with the measurements of isotopes interest. In cases where there are interferences, they need to be minimized and quantified. This quality control involves evaluation of the blanks and standard reference material (SRMs) containing certified levels of the relevant analytes (to determine analytical precision and/or for calibration of instruments). In general, blank samples should accompany each batch of sample containers to the field sampling site and be subjected to the same handling protocols (e.g., opening, closing, preservation) as the actual sample containers. A list of SRMs commonly utilized is given in Baskaran et al. (2009a). The analysis of natural radionuclides from small-volume water samples, usually less than 20 L, can be collected with CTD rosettes. Sorption to the walls of sample bottles could reduce the dissolved concentration of the nuclide considerably, and thus care must be taken.

To ensure that the analytical results are accurate, quality assurance (QA) measurements are often necessary. Generally, the QA for nuclide analyses include the counting of a known radioactive source in a pre-determined geometry for a specific count time. After data collection, data analysis is performed to determine that the critical parameters such as peak position, resolution and efficiency are within the acceptable

limits. It is noted that the QA measurement is not a substitute for calibration. Moreover, proficiency testing (PT) programs can provide another means for laboratories to assess their ability to perform a particular method and may be an appropriate part of some laboratory approval programs. Currently there are few PT programs for radionuclide analysis, such as GEOTRACES program website (<http://www.usgeotraces.org/>) and “world-wide open proficiency test” of IAEA (<http://nucleus.iaea.org/rpst/index.htm>).

16.2.3.1 Be-7

Getting a certified reference standard for ^7Be measurements is not an easy task due to its short half-life and the expense of producing it. However, calibration of the gamma ray spectrometer can be commonly carried out by establishing the energy vs. absolute efficiency curve. In particular, the two gamma lines with very little interference, 352 keV (^{214}Pb) and 609 keV (^{214}Bi), can be used to evaluate the absolute efficiency of ^7Be at 476 keV (Kaste et al. 2002). The intercalibration of samples collected from natural waters is recommended because it would help to validate the ^7Be measurement. Moreover, in samples with high ^{232}Th concentrations, one should be cautious of the 478.3 keV decay energy of ^{228}Ac (Kaste et al. 2002). To our knowledge, there is no intercalibration attempts have been carried out for this nuclide. It is noted that the efficiency of extracting Be in water onto Fe-coated cartridges (i.e., absolute efficiency in two cartridges connected in series) has been assumed to be constant (Kadko and Olson, 1996). If there is desorption of Be from the first cartridge, then the assumption of constant efficiency might be questionable sometimes.

16.2.3.2 Pb-210

A known amount of primary standards of ^{210}Po and ^{210}Pb (c.f. a list of SRMS is given in Baskaran et al. 2009a) should be used to check the precision of the methodology. In particular, ^{210}Po can be volatile if it is in the reduced state, and hence, its loss during the chemical procedure (if any) needs to be carefully monitored.

16.2.3.3 Po-210

Most of the SRMs for ^{210}Po are the same as ^{210}Pb because ^{210}Po and ^{210}Pb are in secular equilibrium (Baskaran et al. 2009a).

16.2.3.4 Cs-137

Adding a known amount of ^{134}Cs with certified value to standard seawater (e.g., 20 L), following the chemical procedures and comparing the activities to the certified values will ensure that the methodology and counting procedures are working satisfactorily. Meanwhile, for the small-volume seawater samples, it is important to know the background level of ^{137}Cs . The ^{137}Cs activity in CsCl was found to be less than 0.03 mBq g^{-1} based on extremely low-background gamma spectrometry. The ^{137}Cs activity in AMP was found to be less than 0.008 mBq g^{-1} (Hirose et al. 2005).

16.2.3.5 Th-234

The best standard for the intercalibration of ^{234}Th techniques is pristine deep-ocean water (1,000 m), in which the activities are expected to be in equilibrium. Earlier studies, however, have shown that some occasional disequilibrium does occur (c.f. Baskaran et al. 2003), and it is not clear whether some physical and/or biogeochemical processes that lead to this disequilibrium are operating or whether this is due to problems associated with the analytical procedures. To be safe, the best method is to collect a large-volume sample, filter it through a 0.45- μm cartridge filter, acidify the filtrate to $\text{pH} < 1$ and

store it for about 6 months, which will ensure the $^{234}\text{Th}/^{238}\text{U}$ activity ratio of 1.0.

When the small-volume (2–5 L) beta counting method is used, other beta emitters (because beta counting is not isotope specific) of the U-Th decay-series radionuclides (such as betas from the decay of ^{228}Ac , ^{214}Pb , ^{214}Bi , ^{210}Bi , ^{212}Bi , ^{211}Pb , ^{211}Bi , and ^{40}K) could affect the accuracy of the measurements. This problem is more serious when beta counting is conducted without purification of the sample (such as the direct counting of suspended particulate material or MnO_2 precipitates; Rutgers van der Loeff et al. 2006). Beta counting of electroplated sources may be ideal for beta counting (uniform thickness) because non-uniform thickness resulting from uneven loading of particles could alter the self-absorption correction factor. Applying appropriate self-absorption corrections could be challenging because low-energy betas from ^{234}Th ($E_{\text{max}} = 0.27$ MeV) and high-energy betas from its progeny, $^{234\text{m}}\text{Pa}$ ($E_{\text{max}} = 2.19$ MeV), will be absorbed to varying extents (unless a Mylar is used to cut-off all ^{234}Th betas) in different sample thicknesses. More details can be found in Rutgers van der Loeff et al. (2006). Some of the glass fiber filters have been found to contain detectable natural radioactivity within the filter material, and the use of such filters for low-volume water filtration has resulted in relatively high uncertainty in the ^{234}Th data (Buesseler et al. 2001a, b).

16.3 Application

Figure 16.2 shows the conceptual input and output fluxes of ^{234}Th , ^{210}Po , ^{210}Pb , ^{137}Cs and ^7Be in an estuary/coast and its adjacent sea. Note that some

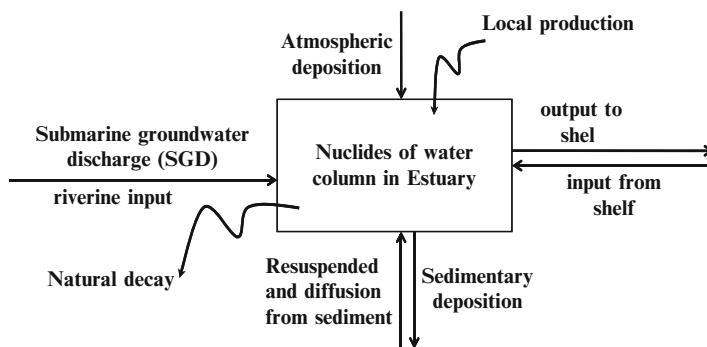


Fig. 16.2 Concept of nuclide material balance in an estuary (modified from Santschi et al. (1979); Feng et al. (1999a, b) and Jweda et al. (2008))

of the input terms for radionuclides are negligible (e.g., submarine groundwater discharge (SGD)-derived ^{137}Cs and ^7Be). The unique sources of ^{234}Th , $^{210}\text{Po}/^{210}\text{Pb}$, ^{137}Cs and ^7Be make them ideal candidates for quantifying particle dynamics and sediment sources and their fate.

16.3.1 Quantifying the Freshly Delivered and Resuspended Sediments in Coastal and Estuarine Zones

Freshly delivered sediments at a given site in the coastal area predominantly contain the $^7\text{Be}/^{210}\text{Pb}$ ratio (A_{Be}^p/A_{Pb}^p) of precipitation, while resuspended sediments will have the ratio similar to the fine particulate matter of the upper layers of the bottom sediments. The specific activity ratio can potentially fingerprint unique particle sources; for example, the A_{Be}^p/A_{Pb}^p ratio may prove particularly useful as a storm-seabed process tracer (Allison et al. 2005). In this case, from the measured $^7\text{Be}/^{210}\text{Pb}$ ratio in the atmospheric deposition and the measured A_{Be}^p/A_{Pb}^p ratio in the particulate matter, bottom sediments and freshly delivered sediments, one can differentiate between resuspension of bed sediments and freshly delivered sediments from the river system. This ratio is also useful for calculating the relative amount of resuspended bed sediments collected in the estuary.

16.3.1.1 $^7\text{Be}/^{210}\text{Pb}_{\text{xs}}$ as Tracer to Identify Sediment Sources and Age

If we assume that the mixtures of suspended sediment in an estuarine system can come from three potential sources: (i) the river system bringing riverine suspended sediment with a finite $^7\text{Be}/^{210}\text{Pb}$ ratio; (ii) suspended sediments brought from the coastal and marine areas; and (iii) sediments from the estuary. Wilson et al. (2007) measured the A_{Be}^p/A_{Pb}^p ratio in each source materials and observed that the riverine $^7\text{Be}/^{210}\text{Pb}_{\text{xs}}$ ratio was greater than the estuarine sediment $^7\text{Be}/^{210}\text{Pb}_{\text{xs}}$. The A_{Be}^p/A_{Pb}^p ratio in resuspended sediments collected in a sediment trap (subscript S) is given by Wilson et al. 2007:

$$(A_{Be}^p/A_{Pb}^p)_s = (A_{Be}^p/A_{Pb}^p)_B \times c + (A_{Be}^p/A_{Pb}^p)_D \times (1 - c), \quad (16.1)$$

where c is the fraction of the resuspension of bed sediments in the efflux, subscript B represents the resuspended bottom sediments and subscript D represents the combined ratio of the recently delivered sediment from both the riverine and adjacent marine system. All of the other terms and symbols used in this equation and the rest of the equations in this article are defined in Appendix. If the suspended sediments in the coastal area and river have the same $^7\text{Be}/^{210}\text{Pb}_{\text{xs}}$ ratio, then both terms can be combined, which results in (16.1). Using (16.1), the efflux of sediments from the bed, c , can be determined.

Furthermore, A_{Be}^p/A_{Pb}^p ratios can also be used as tracers of the “freshness” or “age” of suspended sediments in an estuary. If it is assumed that the suspended sediments in the estuarine water column is from a single riverine source, the decreases in the A_{Be}^p/A_{Pb}^p ratio could arise because of two factors: low A_{Be}^p/A_{Pb}^p ratio due to aging of the sedimentary particulate matter or reduction in this ratio from the dilution of ^7Be -rich sediment by ^7Be -deficient but not $^{210}\text{Pb}_{\text{xs}}$ -dead source. Sometimes, both of these cases can exist (Matisoff et al. 2005).

In the first case, it is possible to calculate the age of the sediment from the $^7\text{Be}/^{210}\text{Pb}_{\text{xs}}$ ratio if the value of that ratio in the precipitation is known (Matisoff et al. 2005; Matisoff and Whiting 2011):

$$\frac{A_{Be}^p}{A_{Pb}^p} = \left(\frac{A_{Be}^p}{A_{Pb}^p} \right)_0 \exp[-(\lambda_{Be} - \lambda_{Pb}) \cdot t] \quad (16.2)$$

where subscript “0” represents the “fresh” and/or original suspended sediment. The age (t) of the sediment is given by

$$t = \frac{1}{\lambda_{Be} - \lambda_{Pb}} \left[\ln \left(\frac{A_{Be}^p}{A_{Pb}^p} \right) - \ln \left(\frac{A_{Be}^p}{A_{Pb}^p} \right)_0 \right]. \quad (16.3)$$

If “new” sediment is defined here as sediment particles that have a A_{Be}^p/A_{Pb}^p ratio equal to that of the precipitation, i.e., “newly tagged sediment”, the sediment particle age is the time since the ^7Be tag was delivered. Most likely, however, soil particles eroded from the landscape and delivered into suspension will have a A_{Be}^p/A_{Pb}^p ratio that is less than that in the

precipitation because of very low ${}^7\text{Be}/{}^{210}\text{Pb}$ ratios in soils (due to differences in the mean-lives of these nuclides). The watershed residence times of ${}^7\text{Be}$ and ${}^{210}\text{Pb}$ are much longer than their mean lives (e.g., Ravichandran et al. 1995), and hence, it is likely that A_{Be}^p/A_{Pb}^p ratio in a river is primarily controlled by the ${}^7\text{Be}/{}^{210}\text{Pb}$ ratio in the precipitation. Equation (16.3) is a simplified case. In the real world, there could be multiple sources of sediments with distinctly different A_{Be}^p/A_{Pb}^p ratios, such as fine particulate matter derived from the offshore region, resuspension of sediments with different activity ratios at the sampling sites, and different activity ratios in the bed load and suspended load of the river, etc. Alternatively, the A_{Be}^p/A_{Pb}^p ratio in suspended sediment can also decrease by the addition of ${}^7\text{Be}$ -deficient sediment from deep soil erosion or the entrainment of old (i.e., ${}^7\text{Be}$ -dead) bottom sediments. In this case, the percentage of new sediment in suspension is directly proportional to the A_{Be}^p/A_{Pb}^p ratio (Matisoff et al. 2005):

$$\% \text{'new' sediment} = 100 \times \left(\frac{A_{Be}^p}{A_{Pb}^p} \right) / \left(\frac{A_{Be}^p}{A_{Pb}^p} \right)_0 \quad (16.4)$$

The percentage of new sediment can also be determined from the age of the sediment:

$$\% \text{'new' sediment} = 100 \times \exp(-(\lambda_{Be} - \lambda_{Pb})t) \quad (16.5)$$

16.3.1.2 ${}^{234}\text{Th}_{xs}/{}^7\text{Be}$ as a Tracer of Particle Dynamics and Sediment Transport in a Partially Mixed Estuary

Using the mass-balance approach for Th and ${}^7\text{Be}$ proposed by Santschi et al. (1979), Feng et al. (1999a, b) elaborated this approach to determine source and dynamics within the turbidity maximum of the Hudson Estuary using the ${}^{234}\text{Th}_{xs}/{}^7\text{Be}$ ratio. In this formulation, the advective transport of particles through the estuary is assumed to be negligible, and transport of particulate ${}^{234}\text{Th}_{xs}/{}^7\text{Be}$ owing to temporal variations of the river flow, tidal mixing and resuspension are also not included in the approach.

In Feng et al. (1999a), local mass balances for dissolved and particulate ${}^{234}\text{Th}$ can be written as below (definitions of each terms are given in Appendix):

$$\frac{\partial A_{Th}^d}{\partial t} = \lambda_{Th} \times A_U - \lambda_{Th} \times A_{Th}^d - k_{Th} \times A_{Th}^d \quad (16.6)$$

and

$$\begin{aligned} \frac{\partial A_{Th}^p}{\partial t} = & k_{Th} \times A_{Th}^d - \lambda_{Th} \times A_{Th}^p - \kappa_{Th}^p \times A_{Th}^p \\ & + \frac{\phi_{Th}^{resus}}{h} \times A_{Th}^{sed} \end{aligned} \quad (16.7)$$

Under steady-state conditions for the dissolved and particulate ${}^{234}\text{Th}$, $\partial A_{Th}^d/\partial t = \partial A_{Th}^p/\partial t = 0$.

$$\lambda_{Th} \times A_U - \lambda_{Th} \times A_{Th}^d - k_{Th} \times A_{Th}^d = 0 \quad (16.8)$$

and

$$k_{Th} \times A_{Th}^d - \lambda_{Th} \times A_{Th}^p - \kappa^p \times A_{Th}^p + \frac{\phi_{Th}^{resus}}{h} \times A_{Th}^{sed} = 0 \quad (16.9)$$

From (16.8) and (16.9), particulate ${}^{234}\text{Th}$ can be expressed as

$$A_{Th}^p = \frac{k_{Th} \times \left(\frac{\lambda_{Th} \times A_U}{\lambda_{Th} + k_{Th}} \right) + \frac{\phi_{Th}^{resus}}{h} \times A_{Th}^{sed}}{\lambda_{Th} + \kappa_{Th}^p} \quad (16.10)$$

Similar to ${}^{234}\text{Th}$, one can set up the mass balance for dissolved and particulate ${}^7\text{Be}$. Assuming steady-state conditions and re-arranging various terms, the particulate ${}^7\text{Be}$ can be calculated from the following formula:

$$A_{Be}^p = \frac{k_{Be} \times \left(\frac{I_{Be}}{h(\lambda_{Be} + k_{Be})} \right) + \frac{\phi_{Be}^{resus}}{h} \times A_{Be}^{sed}}{\lambda_{Be} + \kappa_{Be}^p} \quad (16.11)$$

Combining the particulate ${}^{234}\text{Th}$ and ${}^7\text{Be}$ activities, the particulate ${}^{234}\text{Th}/{}^7\text{Be}$ ratio can be obtained from (16.10) and (16.11):

$$\begin{aligned} \frac{A_{Th}^p}{A_{Be}^p} = & \left(\frac{\lambda_{Be} + \kappa^p}{\lambda_{Th} + \kappa^p} \right) \\ & \times \left[\frac{\left(\frac{k_{Th}}{\lambda_{Th} + k_{Th}} \right) \times \lambda_{Th} \times A_U + \frac{\phi_{Th}^{resus}}{h} \times A_{Th}^{sed}}{\left(\frac{k_{Be}}{\lambda_{Be} + k_{Be}} \right) \times \frac{I_{Be}}{h} + \frac{\phi_{Be}^{resus}}{h} \times A_{Be}^{sed}} \right] \end{aligned} \quad (16.12)$$

Generally, the rather short residence time of Th and Be in the estuaries imply that the scavenging of ^{234}Th and ^7Be onto particles is more rapid than radioactive decay ($k_{\text{Th}} > \lambda_{\text{Th}}$ and $k_{\text{Be}} > \lambda_{\text{Be}}$). Assuming that the resuspension fluxes of Th and Be are negligible relative to ^{234}Th production and ^7Be atmospheric input, we can evaluate (16.12) under two special cases, depending on the residence time of particles in the water column.

In case one, the residence time of particles in the water column is short relative to the half-lives of ^{234}Th and ^7Be (i.e., $k_{\text{P}} > \lambda_{\text{Th}}$ and $k_{\text{P}} > \lambda_{\text{Be}}$). Then (16.12) becomes

$$\frac{A_{\text{Th}}^{\text{P}}}{A_{\text{Be}}^{\text{P}}} = \frac{\lambda_{\text{Th}} \times A_{\text{U}}}{\frac{I_{\text{Be}}}{h}} \quad (16.13)$$

Equation (16.13) states that the $^{234}\text{Th}/^7\text{Be}$ ratio in the particulate matter approaches the ratio of their supply rates if there is rapid scavenging of Th and Be from the dissolved phase with a negligible resuspension contribution from the bottom sediments.

In case two, the residence time of particles is relatively long compared to the half-lives (i.e., $k_{\text{P}} \ll \lambda_{\text{Th}}$, $k_{\text{P}} \ll \lambda_{\text{Be}}$), and the $^{234}\text{Th}_{\text{xs}}/^7\text{Be}$ approaches the inventory ratio. Then (16.12) becomes

$$\frac{A_{\text{Th}}^{\text{P}}}{A_{\text{Be}}^{\text{P}}} = \frac{\lambda_{\text{Be}} \times A_{\text{U}}}{\frac{I_{\text{Be}}}{h}} \quad (16.14)$$

In most of the cases, the A_{U} increases linearly with salinity in estuaries because the ^{238}U concentration in seawater is significantly higher than the average value of ^{238}U in the world rivers.

In the plots of $^{234}\text{Th}_{\text{xs}}/^7\text{Be}$ vs. salinity (Fig. 16.3), Feng et al. (1999a) determined both case one (16.13) and case two (16.14) conditions can be dominant with the seasonal differences in the Hudson Estuary.

16.3.1.3 Quantifying the Advection and Resuspension of Particulate Matter in the Turbidity Maximum Zone Using $^{234}\text{Th}_{\text{xs}}/^7\text{Be}$ as a Tracer

The $^{234}\text{Th}_{\text{xs}}/^7\text{Be}$ ratios can also be applied to quantify the sources of suspended particles in the turbidity maximum of an estuary. In estuaries flood tides result in the transport of suspended particulate matter. This advective component can be quantified using change in $^{234}\text{Th}_{\text{xs}}/^7\text{Be}$ ratios (Feng et al. 1999b). The total fluxes of ^{234}Th and ^7Be in the turbidity maximum are given by (definitions of each terms are given in Appendix):

$$\phi_{\text{Th}}^{\text{total}} = \phi_{\text{Th}}^{\text{prod}} + \phi_{\text{Th}}^{\text{resus}} + \phi_{\text{Th}}^{\text{adv}} \quad (16.15)$$

and

$$\phi_{\text{Be}}^{\text{total}} = \phi_{\text{Be}}^{\text{prod}} + \phi_{\text{Be}}^{\text{resus}} + \phi_{\text{Be}}^{\text{adv}} \quad (16.16)$$

It is assumed that the observed variations in SPM concentrations result both from local bottom resuspension and advective transport and that the observed variation in the SPM flux is the sum of the following:

$$\phi_{\text{part}}^{\text{total}} = \phi_{\text{part}}^{\text{resus}} + \phi_{\text{part}}^{\text{adv}} \quad (16.17)$$

As discussed earlier, $\phi_{\text{part}}^{\text{total}}$ can be calculated from the slope of the increasing portion of the SPM variation with time, and an average value can be used.

$$\phi_{\text{part}}^{\text{resus}} = \phi_{\text{part}}^{\text{total}} - \phi_{\text{part}}^{\text{adv}} \quad (16.18)$$

Then, combining (16.15) and (16.16), we get

$$\frac{\phi_{\text{Th}}^{\text{total}}}{\phi_{\text{Be}}^{\text{total}}} = \frac{\phi_{\text{Th}}^{\text{prod}} + \phi_{\text{Th}}^{\text{resus}} + \phi_{\text{Th}}^{\text{adv}}}{\phi_{\text{Be}}^{\text{prod}} + \phi_{\text{Be}}^{\text{resus}} + \phi_{\text{Be}}^{\text{adv}}} \quad (16.19)$$

Combining (16.17), (16.18) and (16.19), one gets

$$\frac{\phi_{\text{Th}}^{\text{total}}}{\phi_{\text{Be}}^{\text{total}}} = \frac{\lambda_{\text{Th}} A_{\text{U}} + \left(\frac{A_{\text{Th}}^{\text{sed}}}{A_{\text{Be}}^{\text{sed}}} \right) \times (\phi_{\text{part}}^{\text{total}} - \phi_{\text{part}}^{\text{adv}}) \times A_{\text{Be}}^{\text{sed}} + \phi_{\text{Th}}^{\text{prod}} + \left(\frac{A_{\text{Th}}^{\text{adv}}}{A_{\text{Be}}^{\text{adv}}} \right) \times \phi_{\text{part}}^{\text{adv}} \times A_{\text{Be}}^{\text{adv}}}{\frac{I_{\text{Be}}}{h} + (\phi_{\text{part}}^{\text{total}} - \phi_{\text{part}}^{\text{adv}}) \times A_{\text{Be}}^{\text{sed}} + \phi_{\text{part}}^{\text{adv}} \times A_{\text{Be}}^{\text{adv}}} \quad (16.20)$$

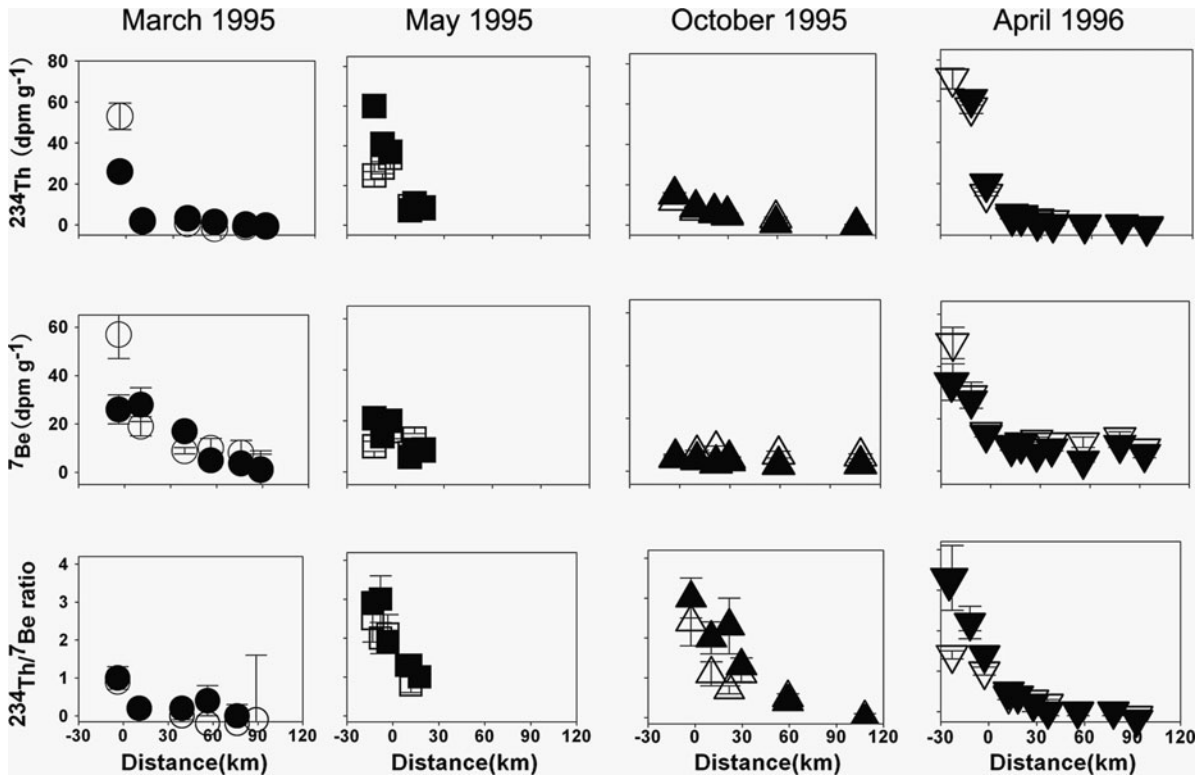


Fig. 16.3 Particulate ^{234}Th and ^7Be specific activities and $^{234}\text{Th}_{\text{xs}}/^7\text{Be}$ activity ratios vs. distance in the Hudson River estuary. Surface and bottom water samples were collected in March, 1995 (circle), May, 1995 (square), October, 1995

(triangle) and April, 1996 (inverted triangle), respectively. The *open symbols* represent surface water and the *filled symbols* represent bottom water (data plotted from Feng et al. (1999a))

The key parameters for (16.20) are the $^{234}\text{Th}/^7\text{Be}$ flux ratio in the turbidity maximum zone ($\phi_{\text{Th}}^{\text{total}}/\phi_{\text{Be}}^{\text{total}}$) and the $^{234}\text{Th}_{\text{xs}}/^7\text{Be}$ activity ratios in the resuspended ($A_{\text{Th}}^{\text{sed}}/A_{\text{Be}}^{\text{sed}}$) and advected ($A_{\text{Th}}^{\text{adv}}/A_{\text{Be}}^{\text{adv}}$) sediments.

In the turbidity maximum zone, ($A_{\text{Th}}^{\text{adv}}/A_{\text{Be}}^{\text{adv}}$) is taken to be the average activity ratio measured from particles collected at the boundary near the estuary. $A_{\text{Th}}^{\text{sed}}/A_{\text{Be}}^{\text{sed}}$ can be obtained from the ratio of the average excess ^{234}Th and ^7Be activities in the bottom sediments. Bottom sediments are initially considered as representative of locally resuspended sediment, and ^{234}Th and ^7Be activities are used in the 0–0.5 cm depth interval of these sediments to estimate the average $^{234}\text{Th}_{\text{xs}}/^7\text{Be}$ activity ratio in resuspended particles (Feng et al. 1999b). Then the parameter $\phi_{\text{part}}^{\text{adv}}$ can be calculated using (16.20). As an example of the application of this model, Feng et al. (1999b) estimated that the lateral advection from the high salinity region corresponded to 31% of the particles, while the

remaining 69% was attributed to the local resuspension from bottom sediments.

16.3.2 Sediment Focusing and Erosion Using ^{210}Pb , ^7Be and ^{234}Th as Tracers

Excess ^{234}Th can be used as a tracer of sediment sources from offshore and higher salinity waters in contrast to ^7Be , which is supplied to the estuary at a higher rate from the discharge of riverine water. Thus, the combined use of ^{234}Th and ^7Be can help to distinguish sediment sources from the supply of new material from the rivers (i.e., high ^7Be) and resuspension and/or mixed sediments from the surface seabed (i.e., high ^{234}Th) (Corbett et al. 2004). In shallow estuaries, where the seabed is disturbed by tidal and

wind-driven resuspension, the ^{234}Th profiles and inventories within the seabed can yield valuable insights about the frequency and intensity of resuspension (Giffin and Corbett, 2003). Moreover, over longer time scales, the sediment focusing and erosion can be investigated using the inventories of ^{210}Pb in the water column and bottom sediments (Cochran et al. 1990; Thomson et al. 1993; Baskaran and Santschi, 2002).

16.3.2.1 The Residence Times and Scavenging Effectiveness for ^{210}Pb

In the box-model (Fig. 16.2), the major inputs (^{210}Pb) to the coastal environment are included of: (i) atmospheric fallout (I_{Pb}) and (ii) the production from its grandparent, ^{226}Ra ($\lambda_{Pb}A_{Ra}$). The major outputs from the box are (i) the decay of ^{210}Pb ($\lambda_{Pb}A_{Pb}$) and (ii) its removal by scavenging ($\kappa_{Pb}A_{Pb}$). In this simple approach, additional sources/sinks (such as lateral advection from and to shelf, diffusion, etc.) have been assumed to be negligible. Evidence for this assumption comes from the measured sediment inventory of ^{210}Pb in several sediment cores. The measured inventory in a large portion of the sediment cores is about the same as that expected from the production rate in the overlying water column, implying that there is no net lateral advective input to the site or net lateral input is offset by sediment erosion (Baskaran and Santschi 2002).

The mass balance of total ^{210}Pb in the water column can be written as (definitions of each terms are given in Appendix):

$$\lambda_{Pb}A_{Ra} + I_{Pb}/h = \lambda_{Pb}A_{Pb} + \kappa_{Pb}A_{Pb} \quad (16.21)$$

From (16.21), the residence times ($\tau_{Pb} = 1/\kappa_{Pb}$ for total ^{210}Pb) with regards to scavenging can be calculated as follows:

$$\begin{aligned} \tau_{Pb} &= 1/\kappa_{Pb} \\ &= A_{Pb}/[\lambda_{Pb}(A_{Ra} + (I_{Pb}/(h\lambda_{Pb})) - A_{Pb})] \end{aligned} \quad (16.22)$$

To determine the residence time of ^{210}Pb in the entire water column, (16.22) can be rewritten in terms of the inventory of ^{210}Pb as

$$\tau_{Pb} = A_{Pb}\lambda_{Pb}/[\lambda_{Pb}A_{Ra} + (I_{Pb}/h) - \lambda_{Pb}A_{Pb}] \quad (16.23)$$

The term $[\lambda_{Pb}A_{Ra} + (I_{Pb}/h)]$ is the total supply of ^{210}Pb . From the mass balance considerations, one can have

$$\begin{aligned} &\text{Total supply } [(\lambda_{Pb}A_{Ra} + (I_{Pb}/h))] \\ &\quad - \text{Measured inventory } [hA_{Pb}\lambda_{Pb}] \\ &= \text{Deficiency } [\lambda_{Pb}hA_{Ra} + (I_{Pb}) - \lambda_{Pb}hA_{Pb}]. \end{aligned} \quad (16.24)$$

Equation (16.23) thus reduces to

$$\tau_c = (\text{Total supply} - \text{Deficiency})/(\lambda_{Pb} \times \text{Deficiency}) \quad (16.25)$$

The scavenging effectiveness (SE) is defined as (Cochran et al. 1990; Thomson et al. 1993; Baskaran and Santschi, 2002) follows:

$$SE = \text{Deficiency}/\text{Total supply} \quad (16.26)$$

$$\tau_c = [(1/SE - 1) \times 1/\lambda_{Pb}]. \quad (16.27)$$

Using (16.26) and (16.27), the residence times and SE for ^{210}Pb for the entire water column can be determined.

16.3.2.2 ^{234}Th as a Tracer of the Fate of Particle-Reactive Species

Using a two-dimensional model, McKee et al. (1984) calculated the residence times of ^{234}Th in the coastal waters. The supply and removal of ^{234}Th are assumed to be in steady state, and the ^{234}Th activity measured in surface waters is assumed to be representative of the average water-column ^{234}Th activity at that station during the ~100 days (i.e., 4–5 times of ^{234}Th 's half life) prior to collection. ^{234}Th sediment inventories reveal that the supply and removal of ^{234}Th are two-dimensional. This result is consistent with the idea of a well-mixed water column during winter. Vertical mixing tends to homogenize (to some extent) the concentrations of suspended sediments and the activities on suspended sediment within the water column. Therefore, the ^{234}Th values measured in surface waters are a reasonable indication of the entire water column ^{234}Th activity during this time of year. Meanwhile, it is assumed that the adsorption of ^{234}Th is irreversible

(negligible desorption) because of the short time scales for scavenging and removal in near-shore environments. In addition, the horizontal ^{234}Th flux is modeled as an advective transport (multiplying the first derivative of ^{234}Th , with respect to x , by an advection coefficient). The horizontal flux can also be modeled as diffusive transport. The governing equations for this model are shown in Table 16.2.

To implement this model, measurements of ^{234}Th were made in surface waters and in the seabed at each station. v and k_{Th} can be evaluated using (16.28–16.30). In the case of the Changjiang Estuary, the residence times of particle-active species from near-shore to offshore areas are around 0.3–4 days with respect to scavenging, and 0.5–11.0 days with respect to the removal to the seabed (McKee et al. 1984). This approach can be extended to other particle-reactive contaminant species that have K_d values similar to that of ^{234}Th .

16.3.3 Tracing the Pathways of ^7Be and ^{210}Pb Following a Heavy Thunderstorm

During rainstorm events, large amounts of ^{210}Pb and ^7Be , along with increase in the river discharge, can be flushed into coastal areas. It was reported that most of the ^7Be (74–86% of the total) as well as ^{210}Pb (80–89%) were associated with particles even less than an hour after the pulse rain input stopped injecting ^7Be and ^{210}Pb into the water. Initial ^7Be and ^{210}Pb concentrations per gram of suspended matter were high when the particle concentration was at a maximum (Fig. 16.4). Meanwhile, there is extensive particle resuspension because of strong winds and high tides. Sommerfield et al. (1999) introduced the application of ^7Be as a tracer

of food sedimentation. At steady state, and assuming no lateral transport, the riverine flux and atmospheric deposition flux are balanced by radioactive decay in the water column (λA_{Be}) and by removal to the sediments (φ_{Be}), i.e., the mass balance of ^7Be in coastal region is expressed as follows:

$$\varphi_{\text{Be}}^{\text{river}} + I_{\text{Be}}/h = \varphi_{\text{Be}} + \lambda_{\text{Be}} A_{\text{Be}} \quad (16.31)$$

Using (16.31), two cases are examined. First, the presence of ^7Be in shelf sediments is expected to undergo rapid removal from the water column through scavenging and deposition prior to radioactive decay (i.e., $\varphi_{\text{Be}} \gg \lambda_{\text{Be}} A_{\text{Be}}$) and/or loss through advective transport (Fig. 16.2). This process is likely facilitated by a lateral (i.e., riverine influx) source of ^7Be and the rapid deposition of ^7Be -laden sediment during floods. In the second case, when rainfall and river runoff are negligible, radioactive decay of ^7Be in the water column (e.g., supported by dry fallout from atmosphere) will generally exceed the removal to the seabed (i.e., $\varphi_{\text{Be}} \ll \lambda_{\text{Be}} A_{\text{Be}}$) due to the much longer residence time of ^7Be in the water column.

16.3.4 ^7Be and ^{210}Pb as Tracers of Particle Dynamics in the River

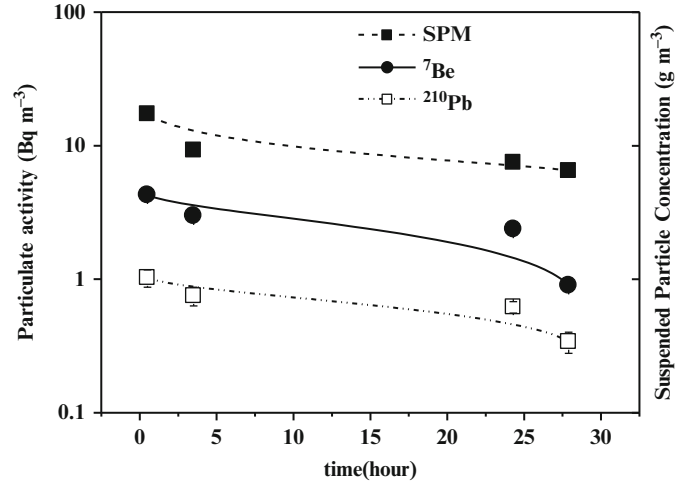
By modeling the distributions of particulate ^7Be and $^{210}\text{Pb}_{\text{xs}}$, the sediment resuspension rate can be quantified. The mass balance equations for the particulate ^7Be and $^{210}\text{Pb}_{\text{xs}}$ can be written as follows (Jweda et al. 2008; definitions of each terms are given in Appendix):

$$\begin{aligned} k_{\text{Be}} A_{\text{Be}}^d + \varphi_{\text{Be}}^{\text{river}} + \phi_{\text{Be}}^{\text{resus}} A_{\text{Be}}^{\text{resus}} / h \\ = \varphi_{\text{Be}}^{\text{out}} + \lambda_{\text{Be}} A_{\text{Be}}^p + \phi_{\text{Be}}^{\text{resus}} A_{\text{Be}}^{\text{trap}} / h \end{aligned} \quad (16.32)$$

Table 16.2 The governing equations for this model (x is the horizontal dimension of the box (in cm); the other horizontal dimension is assumed to have unit length; “in”/“out” are the input/output of ^{234}Th in the box)

Advection-input + Production = Advection-output + Decay + Removal	
Total	$h v A_{\text{Th}}^{\text{in}} + h x \lambda A_{\text{U}}^d = h v A_{\text{Th}}^{\text{out}} + h x \lambda A_{\text{Th}} + h x \varphi_{\text{Th}} \quad (16.28)$
Dissolved	$h v A_{\text{Th}}^{d-\text{in}} + h x \lambda A_{\text{U}}^d = h v A_{\text{Th}}^d + h x \lambda A_{\text{Th}}^d + h x k_{\text{Th}} A_{\text{Th}}^d \quad (16.29)$
Particulate	$h v A_{\text{Th}}^{p-\text{in}} + h x (\lambda A_{\text{U}}^p + k_{\text{Th}} A_{\text{Th}}^d) = h v A_{\text{Th}}^{p-\text{out}} + h x \lambda A_{\text{Th}}^p + h x \varphi_{\text{Th}} \quad (16.30)$

Fig. 16.4 Particulate $^{210}\text{Pb}_{\text{xs}}$, ^7Be and particle concentrations plotted against time after a heavy pulsed rain input into Galveston (Texas) coastal water (data taken from Baskaran and Santschi 1993)



and

$$\begin{aligned} k_{Pb}A_{Pb}^d + \lambda_{Pb}A_{Rn}^p + \varphi_{Pb}^{river} + \phi_{Pb}^{resus}A_{Pb}^{resus}/h \\ = \varphi_{Pb}^{river} + \lambda_{Pb}A_{Pb}^p + \phi_{Pb}^{resus}A_{Pb}^{trap}/h \end{aligned} \quad (16.33)$$

where A_{Rn}^p is the activity of ^{222}Rn (Bq cm^{-3}) adsorbed onto particulate matter.

The activities of the resuspension material are considered to be those of the nuclides in the upper 1 cm of the bottom sediments because this upper layer is likely the most frequently resuspended. The importance of the $\lambda_{Pb}A_{Rn}^p$ term in (16.39) is evaluated by Jweda et al. (2008).

Assuming that the ^7Be and $^{210}\text{Pb}_{\text{xs}}$ activities of the upper layer of the bottom sediment are equal to those of the resuspended sediment, $A_{Be}^{resus} = A_{Be}^{sed}$ and $A_{Pb}^{resus} = A_{Pb}^{sed}$, then the mass balance equations for particulate ^7Be and $^{210}\text{Pb}_{\text{xs}}$ yield sediment resuspension rates ($\text{g cm}^{-2} \text{day}^{-1}$) using ^7Be and $^{210}\text{Pb}_{\text{xs}}$, respectively:

$$\phi_{Be}^{resus} = h \times \frac{k_{Be}A_{Be}^d - \lambda_{Be}A_{Be}^p}{A_{Be}^{trap} - A_{Be}^{resus}} \quad (16.34)$$

and

$$\phi_{Pb}^{resus} = h \times \frac{k_{Pb}A_{Pb}^d - \lambda_{Pb}A_{Pb}^p}{A_{Pb}^{trap} - A_{Pb}^{resus}}. \quad (16.35)$$

As an example, Jweda et al. (2008) reported that the sediment resuspension rates in a river system in southeast Michigan calculated using ^7Be and $^{210}\text{Pb}_{\text{xs}}$

activities to vary between 0.50 and $1.34 \text{ g cm}^{-2} \text{ year}^{-1}$ with average of $0.83 \pm 0.34 \text{ g cm}^{-2} \text{ year}^{-1}$ ($n = 10$) and 0.16 to $1.49 \text{ g cm}^{-2} \text{ year}^{-1}$ with average of $0.38 \pm 0.38 \text{ g cm}^{-2} \text{ year}^{-1}$ ($n = 14$), respectively.

16.3.5 ^{137}Cs and $^{210}\text{Po}/^{210}\text{Pb}$ as Tracers of Historical Records in Sediment Cores

The activity $A_{Pb}^{sed}(0)$ of ^{210}Pb in freshly deposited surface sediments can be expressed by the following equation:

$$A_{Pb}^{sed}(0) = \varphi_{Pb}^{sed}(0)/\phi^{sed}(0) \quad (16.36)$$

where $\varphi_{Pb}^{sed}(0)$ is the sedimentation flux of ^{210}Pb ($\text{Bq cm}^{-2} \text{ year}^{-1}$), and $\phi^{sed}(0)$ is the mass accumulation flux of sediment ($\text{g cm}^{-2} \text{ year}^{-1}$). It is assumed that there is a constant mass and ^{210}Pb flux to the sediment. The activity of $A_{Pb}^{sed}(t)$ at any depth in the core (H) corresponding to any time can be written as a Constant Accumulation (CA) model (Appleby and Oldfield 1978):

$$\begin{aligned} A_{Pb}^{sed}(t) &= \varphi_{Pb}^{sed}(t) \exp(-\lambda_{Pb}t)/\phi^{sed}(t) \\ &= A_{Pb}^{sed}(0)(\exp(-\lambda_{Pb}t)) \end{aligned} \quad (16.37)$$

In the CA model, the sedimentary accumulation rate (v , cm year^{-1}) can be written as

$$v = -\lambda_{Pb}/k_{sl} \quad (16.38)$$

where k_{sl} is the slope in the plot of $\ln A_{Pb}^{sed}(t)$ vs. the core depth (in cm). Then the sediment core age (t, year) corresponding to any depth “H” depth (cm) is as follows:

$$t = \frac{H}{v} = -\frac{H \cdot k_{sl}}{\lambda_{Pb}} \quad (16.39)$$

If there is no physical and/or biological mixing, then the plot of $\ln A_{Pb}^{sed}(t)$ vs. the core depth should show a linear relationship. However, biological and/or physical mixing is very common in riverine and coastal sediments. In such cases, the accumulation rate can be expressed by

$$v = -\lambda_{Pb}/k_{sl} + k_{sl}D, \quad (16.40)$$

where D is the biological mixing coefficient ($\text{cm}^2 \text{year}^{-1}$). Comparing (16.40) to (16.38), it is seen that the deposition rate will be over-estimated if the biological mixing is significant but is ignored. A combination of ^{210}Pb and $^{239,240}\text{Pu}$ or ^{137}Cs can be used to delineate the sediment mixing and accumulation rates (e.g., Zuo et al. 1990).

^{137}Cs has also been used to date sediment cores. The maximum activity of ^{137}Cs in sediment cores is generally observed in the layer of sediment corresponding to 1963 because of the peak nuclear weapon testing were conducted in early 1960s (i.e., 1962–1963; Hong et al. 2011). Hirose et al. (2008) reported

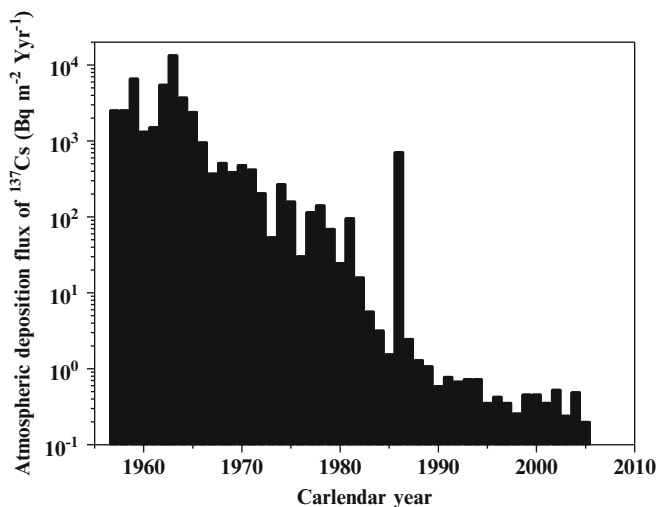
the atmospheric deposition flux of ^{137}Cs in Tsukuba (Japan) during the period 1957–2005 (Fig. 16.5). Two peaks were observed corresponding to calendar years 1963 and 1986. If the peak activity of ^{137}Cs is observed in a layer at the core depth H, the average sedimentation rate v from 1963 to the year the sediment core was collected (y) ($y > 1963$) for sampling can be evaluated as

$$v = \frac{H}{y - 1963} \quad (16.41)$$

It is pertinent to point out two-thirds of the peak activity deposited in 1963 has decayed away by 2010, leaving only one-third of the peak activity. Furthermore, diffusion of ^{137}Cs has led to smearing of this peak, making it more challenging to date sediment cores with this one-layer dating method. In April 1986, the Chernobyl nuclear accident made a secondary peak of ^{137}Cs activity in sediment cores from some regions (e.g., Europe). However, while this activity was very dominant in the Scandinavian Arctic, including countries around Baltic Sea, the Chernobyl-derived fallout was negligible in the Alaskan Arctic and the contiguous United States. In any case, if there is a Chernobyl-derived radiocesium peak (Fig. 16.4), then, the average deposition rate v from 1986 to the calendar year (y) ($y > 1986$) for sampling can be similarly expressed as

$$v = \frac{H}{y - 1986} \quad (16.42)$$

Fig. 16.5 Annual ^{137}Cs deposition (Bq m^{-2}) observed at Tsukuba (Japan) during the period 1957–2005 (data plotted from Hirose et al. (2008))



16.3.6 Case Studies: Utilizing ^7Be as a Tracer to Quantify the Redistribution of PCBs and Other Contaminants

The unique properties of ^7Be , such as particle-reactivity, a relatively short half-life and easily measurable rate of delivery to the surface of the Earth, make this isotope a powerful tracer to quantify seasonal variations and episodic pulses of sediment delivery such as hurricanes, major flood events, etc. in coastal areas (Canuel et al. 1990; Sommerfield et al. 1999; Allison et al. 2000). Furthermore, the K_d of ^7Be ($\sim 10^4$ – 10^5) is comparable to most hydrophobic contaminants, including PCBs, and hence, ^7Be can be used as a surrogate tracer to quantify the rates of processes that affect the cycling of these contaminants (Fitzgerald et al. 2001). As discussed earlier, once ^7Be is introduced into the water column, it is removed quickly onto surface of particles. More than 70% of the ^7Be introduced into the coastal water column by direct atmospheric deposition was removed from the water column in less than 1 day (Baskaran and Santschi 1993), and hence, this tracer is useful for quantifying particle resuspension and deposition. If typically upper 10–15 cm of sediment cores is collected at two different times, T_1 and T_2 , and the inventories of ^7Be at T_1 and T_2 are I_1 and I_2 , respectively, then the residual inventory (I_r) before the second sampling is given by the following equation:

$$I_r = I_1 \exp(-\lambda t) = I_2 - I_d + I_{fe} \quad (16.43)$$

where t is the time elapsed between successive samplings, I_d (Bq cm^{-2}) is the depositional flux between T_1 and T_2 (measured flux) and I_{fe} (Bq cm^{-2}) is the inventory resulting from sediment focusing (+ve) or erosion (-ve). If $I_2 > (I_1 \exp(-\lambda t) + I_d)$, then it represents newly deposited ^7Be -laden sediments. When $I_2 < (I_1 \exp(-\lambda t) + I_d)$, then there is sediment resuspension and removal from that site. The term $I_d + I_{fe}$ corresponds to the new inventory, and the sediment accumulation rate (ϕ^{sed} , $\text{g cm}^{-2} \text{ day}^{-1}$) can be calculated using the terms as follows:

$$\phi^{sed} = (I_d + I_{fe})/A_{Be}^{sed}/(1.44(\ln(2)/\lambda_{Be})) \quad (16.44)$$

The approach presented above is similar to the one proposed by Canuel et al. (1990). The standard

technique for calculating the mass accumulation rate from the slope of the best-fit line of the semi-log plot of ^7Be activity plotted against mass depth assumes that the flux (both mass and ^7Be) is constant, which may be questionable in sediments derived from storm and flood events (Canuel et al. 1990; Sommerfield et al. 1999). It is important to note that the presence of ^7Be indicates sediments deposited in less than ~ 6 months, and hence, this approach cannot be extended for sediments beyond approximately 1 year.

From the I_{fe} calculated as described above and the mean activity of ^7Be in the surficial sediments (A_{Be}^{sed}), one can calculate the depositional or erosional flux (ϕ^{er} , $\text{g cm}^{-2} \text{ day}^{-1}$) as below

$$\phi^{sed}(\phi^{er}) = (I_d + I_{fe})/A_{Be}^{sed}/(1.44(\ln(2)/\lambda_{Be})) \quad (16.45)$$

If C_{PCB} ($\mu\text{g g}^{-1}$ dry wt) is the concentration of PCB in the surficial layer, then the depositional or erosional flux of PCB (ϕ_{PCB} , $\mu\text{g cm}^{-2} \text{ day}^{-1}$) due to resuspension of sediments during episodic events (e.g., storm, flood and other events) can be calculated as

$$\phi_{PCB} = \phi^{sed}(\phi^{er}) \times C_{PCB} \quad (16.46)$$

Knowing the area of the contaminated region, one can calculate the total loading of PCB from the bottom into the water column. Utilizing this approach, Fitzgerald et al. (2001) estimated the total reintroduction of PCBs from sediments to the water column over a period of 40 days to be about 10 kg, which can be compared to the estimated annual flux of PCBs from the Fox River to the Green Bay of 200 kg year^{-1} . This approach can be applied to other contaminants (i.e., both organic and inorganic) that have K_d values similar to that of ^7Be (e.g., Hg, Pb, etc). This approach can also be utilized to quantify the amounts of contaminated sediment resuspension during freight movements in relatively shallow water systems.

Moreover, similar to the application of ^7Be , ^{234}Th is one of the powerful particulate nuclides to trace the PCB and other contaminant transport in aquatic environment. As mentioned above, combination of (16.6) and (16.7), the activity of ^{234}Th in the surface marine water can be a balance between its formation via radioactive decay of ^{238}U , its radioactive decay and removal by particulate matter.

$$\frac{\partial A_{Th}}{\partial t} = \lambda_{Th} \times A_U - \lambda_{Th} \times A_{Th} - \kappa_{Th}^p \times A_{Th}^p \quad (16.47)$$

Based on the assumption of steady state, (16.47) can be rewritten as:

$$\kappa_{Th}^p = \lambda_{Th}(A_U - A_{Th})/A_{Th}^p \quad (16.48)$$

If the concentration of particulate pollutants (e.g., PCBs/PAHs) (mol m^{-3}) in the surface water is known, then, averaged fluxes for PCBs/PAHs can be calculated as follows (definitions of each terms are given in Appendix):

$$\phi_{PCB/PAH} = \kappa_{Th}^p \cdot C_{PCB/PAH} \quad (16.49)$$

Using above equation, Gustafsson et al. (1997a, b) estimated that the vertical fluxes of PCB/PAH in the northwestern Atlantic Ocean in 1993–1994 (Figs. 16.6 and 16.7). It was found that fluxes both of PCB and PAH decreased with distance from coast. But, considering the areal extent, there are only 5% total PCB in the 20-km-wide coastal region closest to the continental source and 20% on the continental shelf. It means that most of PCB would be transported to open sea via lateral particulate matter advection. Similarly, only around 10% of PAH was deposited in coastal waters while the remaining 90% was exported farther offshore on the continental shelf and to the open sea.

Definitely, pollutants with similar properties to PCBs/PAHs can also be evaluated using this approach.

16.4 Future Directions

Although many authors have reported the measurement of particle-active radionuclides (^{210}Pb , ^7Be and ^{234}Th) as one of the useful methods for tracing the sources, transport and deposition of particles/sediments in estuaries and coasts, there are still many interesting questions that are unanswered and many exciting avenues for future research remain unexplored. These applications to quantify dynamic processes in aquatic environment are still complex because there is no generally accepted model for temporal and spatial variations of these nuclides in different areas. For example, even in the same region, the atmospheric deposition fluxes of ^7Be and ^{210}Pb vary spatially and temporally. The watershed erosional input of these nuclides depends on several factors, such as relief, mineralogy, amounts of precipitation, etc. This component is critically needed for constraining the input functions to the coastal and estuarine zones. Colloidal material plays a significant role in the transport of these particle-reactive radionuclides, and their removal rate depends on the complexation capacity of these colloidal materials. The relative importance of colloidal material and suspended particulate material need to be quantified. The behavior of U, whether conservative or non-conservative, plays a key role on the production rates of ^{234}Th in the estuarine and coastal regions, and hence the phases of U that behave as non-conservative components must be determined. For ^{234}Th , there is an

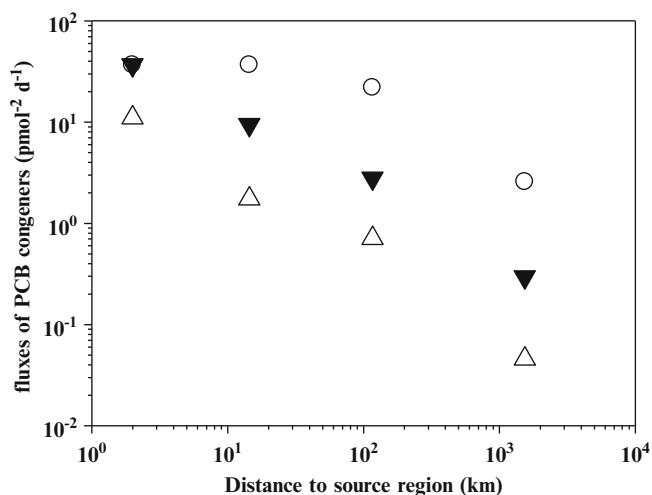
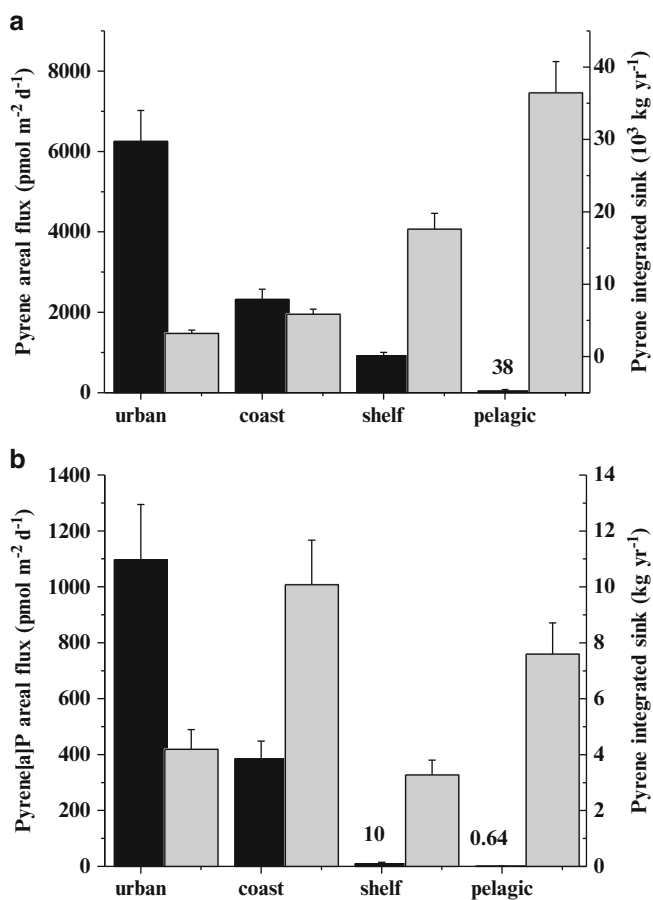


Fig. 16.6 Vertical fluxes into the subsurface ocean of three PCB congeners over coastal to pelagic regimes of the western North Atlantic Ocean (open circles, tetrachlorobiphenyl; filled inverted triangles, hexachlorobiphenyl; open triangles, octachlorobiphenyl) (data plotted from Gustafsson et al. (1997a))

Fig. 16.7 Surface-ocean fluxes and area-integrated mass removal rates of pyrene (a) and benzo[a]pyrene (b) for four marine regimes in the western North Atlantic Ocean. *Dark bars* represent PAH fluxes and *grey bars* denote areally integrated PAH sinks. The uncertainties represent one standard deviation of the propagated analytical variabilities (data plotted from Gustafsson et al. (1997b))



obvious lack of information about the comparisons of ²³⁴Th (and/or ²³⁸U) behavior in the world estuaries.

Higher-frequency sampling would greatly improve our understanding of the fate of these nuclides themselves and the material they trace (suspended particle and particle-reactive chemicals) in dynamic estuarine environments. The distribution of these nuclides in size-fractionated particulate matter (both micro- and macro particulate matter) would provide insight into the scavenging behavior of the particulate matter. Characterizing the particulate matter (organic/inorganic/surface area/charge, etc.) will provide much needed information on the processes that control the removal of particle-reactive radionuclides and other particle-reactive contaminants in coastal and estuarine areas.

Acknowledgments This work was funded by the Natural Science Foundation of China (41021064; 40976054) and the Ministry of Science and Technology of PR China

(2011CB409801). We thank the two reviewers (Chih-An Huh and Brent A. McKee) for their critical reviews of the earlier version of this manuscript.

Appendix: Descriptions of symbols and abbreviation used in this chapter

Symbols	Meaning	Unit
$A_{Th}/A_{Be}/A_{Pb}$	Activity of excess ²³⁴ Th/ ⁷ Be/excess ²¹⁰ Pb in the water column	Bq cm ⁻³
$A_{Th}^p/A_{Be}^p/A_{Pb}^p$	Activity of excess ²³⁴ Th/ ⁷ Be/excess ²¹⁰ Pb in the particulate phase	Bq g ⁻¹ or Bq cm ⁻³
$A_{Th}^d/A_{Be}^d/A_{Pb}^d$	Activity of ²³⁴ Th/ ⁷ Be/ ²¹⁰ Pb in the dissolved phase	Bq cm ⁻³

(continued)

Symbols	Meaning	Unit	Symbols	Meaning	Unit
$A_{Th}^{sed} / A_{Be}^{sed} / A_{Pb}^{sed}$	Activity of excess $^{234}\text{Th}/^{7}\text{Be}/\text{excess}$ ^{210}Pb in surficial bottom sediments subject to resuspension	Bq g^{-1}	$\varphi_{Th}^{adv} / \varphi_{Be}^{adv} / \varphi_{Pb}^{adv}$	Advective flux of particulate excess ^{234}Th and ^{7}Be and excess ^{210}Pb	$\text{Bq cm}^{-3} \text{ day}^{-1}$
$A_{Th}^{adv} / A_{Be}^{adv} / A_{Pb}^{adv}$	Activity of excess $^{234}\text{Th}/^{7}\text{Be}/\text{excess}$ ^{210}Pb on advected particles	Bq g^{-1}	$\varphi_{Th}^{prod} / \varphi_{Be}^{prod} / \varphi_{Pb}^{prod}$	Supply flux of excess ^{234}Th and ^{7}Be and excess ^{210}Pb from ^{238}U decay or the atmosphere (^{7}Be , ^{210}Pb) followed by rapid scavenging fluxes	$\text{Bq cm}^{-3} \text{ day}^{-1}$
$A_{Th}^{resus} / A_{Be}^{resus} / A_{Pb}^{resus}$	Activity of excess $^{234}\text{Th}/^{7}\text{Be}/\text{excess}$ ^{210}Pb on resuspension particles from sea bed	Bq g^{-1}	$\varphi_{Th}^{total} / \varphi_{Be}^{total} / \varphi_{Pb}^{total}$	Total supply flux of particulate excess $^{234}\text{Th}/^{7}\text{Be}/\text{excess}$ ^{210}Pb into turbidity maximum zone	$\text{Bq cm}^{-3} \text{ day}^{-1}$
$A_{Th}^{trap} / A_{Be}^{trap} / A_{Pb}^{trap}$	Activity of excess $^{234}\text{Th}/^{7}\text{Be}/\text{excess}$ ^{210}Pb on settling particles collected by sediment trap	Bq g^{-1}	$\phi_{Th}^{resus} / \phi_{Be}^{resus} / \phi_{Pb}^{resus}$	Sediment resuspension flux by excess ^{234}Th and ^{7}Be and excess ^{210}Pb from the sea bed	$\text{g cm}^{-2} \text{ day}^{-1}$
$\lambda_{Th} / \lambda_{Be} / \lambda_{Pb}$	Decay constant of $^{234}\text{Th}/^{7}\text{Be}/^{210}\text{Pb}$	day^{-1}	$\phi_{part}^{resus} / \phi_{part}^{adv} / \phi_{part}^{total}$	Particle flux from resuspension/advective input/total input	$\text{g cm}^{-3} \text{ day}^{-1}$
$k_{Th} / k_{Be} / k_{Pb}$	Rate constant for the scavenging of dissolved $^{234}\text{Th}/^{7}\text{Be}/^{210}\text{Pb}$ onto particles	day^{-1}	ϕ^{sed} / ϕ^{er}	Sedimentary deposition/erosion flux	$\text{g cm}^{-2} \text{ day}^{-1}$
$\kappa_{Th} / \kappa_{Be} / \kappa_{Pb}$	Removal rate constant of excess $^{234}\text{Th}/^{7}\text{Be}/\text{excess}$ ^{210}Pb in the water column	day^{-1}	$\tau_{Pb} = 1 / \kappa_{Pb}$	Residence times for total ^{210}Pb in the water column	Day
$\varphi_{Th} / \varphi_{Be} / \varphi_{Pb}$	Removal flux of excess ^{234}Th and ^{7}Be and excess ^{210}Pb from water column	$\text{Bq cm}^{-3} \text{ day}^{-1}$	v	Horizontal flux constant	cm day^{-1}
$\varphi_{Th}^p / \varphi_{Be}^p / \varphi_{Pb}^p$	Removal flux of particulate excess ^{234}Th and ^{7}Be and excess ^{210}Pb from water column to the sea bed	$\text{Bq cm}^{-3} \text{ day}^{-1}$	$\varphi_{Be}^{river} / \varphi_{Pb}^{river}$	Riverine input particulate ^{7}Be and excess ^{210}Pb	$\text{Bq cm}^{-3} \text{ day}^{-1}$
$\kappa_{Th}^p / \kappa_{Be}^p / \kappa_{Pb}^p$	Removal rate constant of particulate excess $^{234}\text{Th}/^{7}\text{Be}/\text{excess}$ ^{210}Pb in the water column	day^{-1}	$\varphi_{Be}^{out} / \varphi_{Pb}^{out}$	Riverine output flux of particulate ^{7}Be and excess ^{210}Pb	$\text{Bq cm}^{-3} \text{ day}^{-1}$
I_{Be} / I_{Pb}	$^{7}\text{Be}/^{210}\text{Pb}$ atmospheric deposition flux	$\text{Bq cm}^{-2} \text{ day}^{-1}$	$C_{PCB/PAH}$	Concentration of PCB/PAH in mixing layer of water column	g m^{-3}
A_U / A_{Ra}	Activity of $^{238}\text{U}/^{226}\text{Ra}$ in the water column	Bq cm^{-3}	$\phi_{PCB/PAH}$	Vertical flux of PCB/PAH from mixing layer of water column	$\text{g cm}^{-3} \text{ day}^{-1}$
h	Water depth	cm	AMP	Amaniamolybdenum (III) phosphate	
$\varphi_{Th}^{resus} / \varphi_{Be}^{resus} / \varphi_{Pb}^{resus}$	Resuspension flux of particulate excess ^{234}Th and ^{7}Be and excess ^{210}Pb from the sea bed	$\text{Bq cm}^{-3} \text{ day}^{-1}$	SPM	Suspended particle matter	
			PCB	Polychlorinated biphenyl	
			PAH	Polycyclic aromatic hydrocarbons	
			LSS	Liquid scintillation spectrometry	

(continued)

References

- Allison MA, Kineke GC, Gordon ES et al (2000) Development and reworking of a seasonal flood deposit on the inner continental shelf off the Atchafalaya River. *Cont Shelf Res* 20:2267–2294
- Allison MA, Sheremet A, Goñic MA (2005) Storm layer deposition on the Mississippi–Atchafalaya subaqueous delta generated by Hurricane Lili in 2002. *Cont Shelf Res* 25:2213–2232
- Appleby P, Oldfield F (1978) The calculation of lead-210 dates assuming a constant rate of supply of unsupported lead-210 to the sediment. *Catena* 5:1–8
- Baskaran M (1995) A search for the seasonal variability on the depositional fluxes of ^7Be and ^{210}Pb . *J Geophys Res* 100:2833–2840
- Baskaran M (2011) Po-210 and Pb-210 as atmospheric tracers and global atmospheric Pb-210 fallout: a review. *J Environ Radioactiv* 102:500–513
- Baskaran M, Santschi PH (1993) The role of particles and colloids in the transport of radionuclides in coastal environments of Texas. *Mar Chem* 43:95–114
- Baskaran M, Santschi PH (2002) Particulate and dissolved ^{210}Pb activities in the shelf and slope regions of the Gulf of Mexico waters. *Cont Shelf Res* 22:1493–1510
- Baskaran M, Swarzenski PW (2007) Seasonal variations on the residence times and partitioning of short-lived radionuclides (^{234}Th , ^7Be and ^{210}Pb) and depositional fluxes of ^7Be and ^{210}Pb in Tampa Bay, Florida. *Mar Chem* 104:27–42
- Baskaran M, Coleman CH, Santschi PH (1993) Atmospheric depositional fluxes of ^7Be and ^{210}Pb at Galveston and College Station, Texas. *J Geophys Res* 98:20255–20571
- Baskaran M, Swarzenski PW, Porcelli P (2003) Role of colloidal material in the removal of ^{234}Th in the Canada Basin of the Arctic Ocean. *Deep Sea Res I* 50:1353–1373
- Baskaran M, Hong GH, Santschi PH (2009a) Radionuclide analysis in seawater, Chapter 13. In: Wurl O (ed) *Practical guidelines for the analysis of seawater*. CRC press, Boca Raton
- Baskaran M, Swarzenski PW, Biddanda BA (2009b) Constraints on the utility of MnO_2 cartridge method for the extraction of radionuclides: a case study using ^{234}Th . *Geochem Geophys Geosyst* 10, Q04011, doi:10.1029/2008GC002340
- Benitez-Nelson CR, Buesseler KO (1999) Phosphorus-32, phosphorus-33, beryllium-7 and lead-210: atmospheric fluxes and utility in tracing stratosphere/troposphere exchange. *J Geophys Res* 104:11745–11754
- Benitez-Nelson CR, Buesseler KO, Rutgers van der Loeff M et al (2001) Testing a new small-volume technique for determining ^{234}Th in seawater. *J Radioanal Nucl Chem* 248:795–799
- Bhat SG, Krishnaswami S, Lal D et al (1969) $^{234}\text{Th}/^{238}\text{U}$ ratios in the ocean. *Earth Planet Sci Lett* 5:483–491
- Bowen VT, Roether W (1973) Vertical distributions of strontium-90, cesium-137 and tritium about 45° north latitude in the Atlantic. *J Geophys Res* 78:6277–6285
- Broecker WS, Kaufman A, Trier RM (1973) The residence time of thorium in surface sea water and its implication regarding the fate of reactive pollutants. *Earth Planet Sci Lett* 20:35–44
- Broecker WS, Patzert WC, Toggweiler JR et al (1986) Hydrography, chemistry and radioisotopes in the Southeast-Asian Basins. *J Geophys Res* 91:14345–14354
- Buesseler KO, Casso SA, Hartman MC, Livingston HD (1990) Determination of fission-products and actinides in the Black Sea following the Chernobyl accident. *J Radioanal Nucl Chem* 138:33–47
- Buesseler KO, Cochran JK, Bacon MP et al (1992) Determination of thorium isotopes in seawater by non-destructive and radiochemical procedures. *Deep Sea Res* 39:1103–1114
- Buesseler KO, Andrews JA, Hartman MC et al (1995) Regional estimates of the export flux of particulate organic carbon derived from thorium-234 during the JGOFS EgPac program. *Deep Sea Res II* 42:777–804
- Buesseler KO, Benitez-Nelson CR, Rutgers van der Loeff M et al (2001a) A comparison of methods with a new small-volume technique for thorium-234 in seawater. *Mar Chem* 74:15–28
- Buesseler KO, Ball L, Andrews J et al (2001b) Upper ocean export of particulate organic carbon in the Arabian Sea derived from thorium-234. *Deep Sea Res II* 45:2461–2467
- Canuel EA, Martens CS, Benninger LK (1990) Seasonal variations in ^7Be activity in the sediments of Cape Lookout Bight, North Carolina. *Geochim Cosmochim Acta* 54:237–245
- Carvalho PF (1997) Distribution, cycling and mean residence time of ^{226}Ra , ^{210}Pb and ^{210}Po in the Tagus estuary. *Sci Total Environ* 196:151–161
- Cherrier J, Burnett WC, LaRock PA (1995) Uptake of polonium and sulfur by bacteria. *Geomicrobiol J* 13:103–115
- Church TM, Hussain N, Ferdelman TG et al (1994) An efficient quantitative technique for the simultaneous analyses of radon daughters Pb-210, Bi-210 and Po-210. *Talanta* 41:243–249
- Cochran JK, McKibbin-Vaughan T, Dornblaser MM et al (1990) ^{210}Pb scavenging in the North Atlantic and North Pacific Oceans. *Earth Planet Sci Lett* 97:332–352
- Corbett R, McKee B, Duncan D (2004) An evaluation of mobile mud dynamics in the Mississippi River deltaic region. *Mar Geol* 209:91–112
- Du J, Zhang J, Zhang J et al (2008) Deposition patterns of atmospheric ^7Be and ^{210}Pb in Coast of East China Sea, Shanghai, China. *Atmos Environ* 42:5101–5109
- Du J, Wu Y, Huang D et al (2010) Use of ^7Be , ^{210}Pb and ^{137}Cs tracers to the transport of surface sediments of the Changjiang Estuary, China. *J Mar Syst* 82:286–294
- Elsinger RJ, Moore WS (1983) ^{224}Ra , ^{228}Ra and ^{226}Ra in Winyah Bay and Delaware Bay. *Earth Planet Sci Lett* 64:430–436
- Feng H, Cochran JK, Hirschberg DJ (1999a) ^{234}Th and ^7Be as tracers for the transport and dynamics of suspended particles in a partially mixed estuary. *Geochim Cosmochim Acta* 23:2487–2505
- Feng H, Cochran JK, Hirschberg DJ (1999b) ^{234}Th and ^7Be as tracers for the sources of particles to the turbidity maximum of the Hudson river estuary. *Estuar Coast Shelf Sci* 49:629–645
- Fisher NS, Burns KA, Cherry RD et al (1983) Accumulation and cellular distribution of ^{241}Am , ^{210}Po , and ^{210}Pb in two marine algae. *Mar Eco Prog Ser* 11:233–237
- Fisher NS, Cochran JK, Krishnaswami S et al (1988) Predicting the oceanic flux of radionuclides on sinking biogenic debris. *Nature* 355:622–625

- Fitzgerald SA, Klump JV, Swarzenski PW, Mackenzie RA, Richards KD (2001) Beryllium-7 as a Tracer of Short-Term Sediment Deposition and Resuspension in the Fox River, Wisconsin. *Environ Sci Technol* 35:300–305
- Foster JM, Shimmiel GB (2002) Th-234 as a tracer of particle flux and POC export in the northern North Sea during a coccolithophore bloom. *Deep Sea Res II* 49:2965–2977
- Fridrich J, Rutgers van der Loeff M (2002) A two-tracer (^{210}Po , ^{234}Th) approach to distinguish organic carbon and biogenic silica export flux in the Antarctic circumpolar current. *Deep Sea Res I* 49:101–20
- Giffin D, Corbett R (2003) Evaluation of sediment dynamics in coastal systems via short-lived radioisotopes. *J Mar Syst* 42: 83–96
- Goldberg ED, Gamble E, Griffin JJ et al (1977) Pollution history of Narragansett Bay as recorded in its sediments. *Estuar Coast Mar Sci* 5:549–561
- Gustafsson Ö, Gschwend PM, Buesseler KO (1997a) Settling removal rates of PCBs into the Northwestern Atlantic derived from ^{238}U - ^{234}Th disequilibria. *Environ Sci Technol* 31(12):3544–3550
- Gustafsson Ö, Gschwend PM, Buesseler KO (1997b) Using Th-234 disequilibria to estimate the vertical removal rates of polycyclic aromatic hydrocarbons from the surface ocean. *Mar Chem* 57(1–2):11–23
- Gustafsson Ö, Gschwend PM (1998) The Flux of Black Carbon to Surface Sediments on the New England Continental Shelf. *Geochim Cosmochim Acta* 62:465–472
- Harvey BR, Lovett MB (1984) The use of yield tracers for the determination of alpha emitting actinides in the marine environment. *Nucl Instrum Methods Phys Res* 223:224–234
- Hawley N, Robbins JA, Eadie BJ (1986) The partitioning of beryllium-7 in fresh water. *Geochim Cosmochim Acta* 50: 1127–1131
- Hirose K, Aoyama M, Igarashi Y et al (2005) Extremely low background measurements of ^{137}Cs in seawater samples using an underground facility (Ogoya). *J Radioanal Nucl Chem* 263:349–353
- Hirose K, Igarashi Y, Aoyama M (2008) Analysis of the 50-year records of the atmospheric deposition of long-lived radionuclides in Japan. *Appl Radiat Isot* 66:1675–1678
- Hong GH, Park SK, Baskaran M et al (1999) Lead-210 and Polonium-210 in the winter well-mixed turbid waters in the mouth of the yellow sea. *Cont Shelf Res* 19:1049–1064
- Hong GH, Hamilton TF, Baskaran M, Kenna TC (2011) Applications of anthropogenic radionuclides as tracers to investigate marine environmental processes. In: Baskaran M (ed) *Handbook of environmental isotope geochemistry*. Springer, Heidelberg
- Huh CA, Liu JT, Lin HL et al (2009) Tidal and flood signatures of settling particles in the Gaoping submarine canyon (SW Taiwan) revealed from radionuclide and flow measurements. *Mar Geol* 267:8–17
- Hussain N, Church TM, Veron AJ (1998) Radon daughter disequilibria and lead systematics in the western North Atlantic. *J Geophys Res* 103(D3):16059–16071
- Jweda, J (2007) Short-lived radionuclides (^{210}Pb , ^7Be and ^{137}Cs) as tracers of particle dynamics and chronometers for sediment accumulation and mixing rates in a river system in Southeast Michigan. M.S. Thesis, Department of Geology, Wayne State University, pp 167.
- Jweda J, Baskaran M, van Hees Ed (2008) Short-lived radionuclides (^7Be and ^{210}Pb) as tracers of particle dynamics in a river system in southeast Michigan. *Limnol Oceanogr* 53:1934–1944
- Kadko D, Olson D (1996) Be-7 as a tracer of surface water subduction and mixed layer history. *Deep Sea Res I* 43: 89–116
- Kaste JM, Baskaran M (2011) Meteoric ^7Be and ^{10}Be as process tracers in the environment. In: Baskaran M (ed) *Handbook of environmental isotope geochemistry*. Springer, Heidelberg
- Kaste JM, Norton SA, Hess CT (2002) Environmental chemistry of beryllium-7. *Rev Mineral Geochem* 50:271–289
- Kersten M, Thomsen S, Priebisch W et al (1998) Scavenging and particle residence times determined from $^{234}\text{Th}/^{238}\text{U}$ disequilibria in the coastal waters of Mecklenburg Bay. *Appl Geochem* 13:339–347
- Kim G, Church TM (2011) Po-210 in the environment: biogeochemical cycling and bioavailability. In: Baskaran M (ed) *Handbook of environmental isotope geochemistry*. Springer, Heidelberg
- Kim Y, Yang HS (2004) Scavenging of ^{234}Th and ^{210}Po in surface water of Jinhae Bay, Korea during a red tide. *Geochem J* 38:505–513
- Kim SK, Hong GH, Baskaran M et al (1998) Wet removal of atmospheric ^7Be and ^{210}Pb at the Korean Yellow Sea Coast. *The Yellow Sea* 4:58–68
- Kim G, Alleman LY, Church TM (1999) Atmospheric depositional fluxes of trace element, ^{210}Pb , and ^7Be to the Sargasso sea. *Global Biogeochem Cycle* 13(4):1183–1192
- Kim G, Hussain N, Scudlark JR et al (2000) Factors influencing the atmospheric depositional fluxes of stable Pb, ^{210}Pb , and ^7Be into Chesapeake Bay. *J Atmos Chem* 36:65–79
- Koide M, Soutar A, Goldberg ED (1972) Marine geochronology with ^{210}Pb . *Earth Planet Sci Lett* 14:2–446
- Lal D and Peters B (1967) Cosmic ray produced radioactivity on the Earth. In: *Encyclopedia of physics*. Springer, Berlin
- Lal D, Baskaran M (2011) Applications of cosmogenic-isotopes as atmospheric tracers. In: Baskaran M (ed) *Handbook of environmental isotope geochemistry*. Springer, Heidelberg
- Larock P, Hyun JH, Boutelle S et al (1996) Bacterial mobilization of polonium. *Geochim Cosmochim Acta* 60(22): 4321–4328
- Lima AL, Hudeny JB, Reddy CM et al (2005) High-resolution historical records from Pettaquamscutt River basin sediments: 1. ^{210}Pb and varve chronologies validate record of ^{137}Cs released by the Chernobyl accident. *Geochim Cosmochim Acta* 69:1803–1812
- Masarik J, Beer J (1999) Simulations of particle fluxes and cosmogenic nuclide production in the earth's atmosphere. *J Geophys Res* D104:12099–13012
- Masque P, Sanchez-Cabeza JA, Bruach JM et al (2002) Balance and residence times of ^{210}Pb and ^{210}Po in surface waters of the Northwestern Mediterranean Sea. *Cont Shelf Res* 22: 2127–2146
- Matisoff G, Whiting PJ (2011) Measuring soil erosion rates using natural (^7Be , ^{210}Pb) and anthropogenic (^{137}Cs , $^{239,240}\text{Pu}$) radionuclides. In: Baskaran M (ed) *Handbook of environmental isotope geochemistry*. Springer, Heidelberg

- Matisoff G, Wilson CG, Whiting PJ (2005) The $^7\text{Be}/^{210}\text{Pb}_{\text{xs}}$ ratio as an indicator of suspended sediment age or fraction new sediment in suspension. *Earth Surf Process Landforms* 30:1191–1201
- Matthews KM, Kim CK, Martin P (2007) Determination of ^{210}Po in environmental materials: a review of analytical methodology. *Appl Radiat Isot* 65:267–279
- McKee BA, DeMaster DJ, Nittrouer CA (1984) The use of $^{234}\text{Th}/^{238}\text{U}$ disequilibrium to examine the fate of particle-reactive species on the Yangtze continental shelf. *Earth Planetary Sci Lett* 68:431–442
- Moore WS (1976) Sampling ^{228}Ra in the deep ocean. *Deep Sea Res* 23:647–651
- Moore WS, Dymond J (1988) Correlation of ^{210}Pb removal with organic carbon fluxes in the Pacific Ocean. *Nature* 331:339–341
- Murray CN, Kautsky H, Hoppenheit M (1978) Actinide activities in water entering the northern North Sea. *Nature* 276:225–230
- Nozaki Y (1993) Actinium-227: a steady state tracer for the deep-sea basin-wide circulation and mixing studies. In: Teramoto Y (ed) *Deep ocean circulation: physical and chemical aspects*. Amsterdam, Elsevier
- Nozaki Y, Zhang J, Takeda A (1997) ^{210}Pb and ^{210}Po in the equatorial Pacific and the Bering Sea: the effects of biological productivity and boundary scavenging. *Deep Sea Res II* 44:2203–2220
- Olsen CR, Larsen IL, Lowry PD et al (1986) Geochemistry and deposition of ^7Be in river-estuarine and coastal waters. *J Geophys Res* 91(C1):896–908
- Palinkas CM, Nittrouer CA, Wheatcroft RA et al (2005) The use of ^7Be to identify event and seasonal sedimentation near the Po River delta, Adriatic Sea. *Mar Geol* 222–223:95–112
- Pates JM, Cook GT, MacKenzie AB et al (1996) Determination of ^{234}Th in marine samples by liquid scintillation spectrometry. *Anal Chem* 68:3783–3788
- Porcelli D, Baskaran M (2011) An overview of isotope geochemistry in environmental studies. In: Baskaran M (ed) *Handbook of environmental isotope geochemistry*. Springer, Heidelberg
- Radakovitch O, Cherry RD, Heyraud M et al (1998) Unusual $\text{Po-210}/\text{Pb-210}$ ratio in the surface water of the Gulf of Lions. *Oceanol Acta* 21:459–468
- Ravichandran M, Baskaran M, Santschi PH et al (1995) Geochronology of sediments in the Sabine-Neches estuary, Texas, USA. *Chem Geol* 125:291–306
- Robbins JA, Edgington DN (1975) Determination of recent sedimentation rates in Lake Michigan using ^{210}Pb and ^{137}Cs . *Geochim Cosmochim Acta* 39:285–304
- Roether W (1971) Flushing of the Gerard-Ewing large-volume water sampler. *J Geophys Res* 76:5910–5912
- Rutgers van der Loeff M, Berger GW (1993) Scavenging of ^{230}Th and ^{231}Pa near the Antarctic Polar Front in the South Atlantic. *Deep Sea Res I* 40:339–357
- Rutgers van der Loeff M, Moore WS (1999) The analysis of natural radionuclides in seawater. In: Grasshoff K, Ehrhardt MG, Kremling K (eds) *Methods of seawater analysis*, 3rd edn. Chemie, Weinheim
- Rutgers van der Loeff M, Meyer R, Rudels B, Rachor E (2002) Resuspension and particle export in the benthic nepheloid layer in and near Fram Strait in relation to faunal abundances and Th-234 depletion. *Deep Sea Res I* 49:1941–1958
- Rutgers van der Loeff M, Sarin MM, Baskaran M (2006) A review of present techniques and methodological advances in analyzing ^{234}Th in aquatic systems. *Mar Chem* 100:190–212
- Santschi PH, Li YH, Bell J (1979) Natural radionuclides in the water of Narragansett Bay. *Earth Planet Sci Lett* 45:201–213
- Sarin MM, Bhushan R, Remgarajan R et al (1992) The simultaneous determination of ^{238}U series nuclides in seawater: results from the Arabian Sea and Bay of Bengal. *Indian J Mar Sci* 21:121–127
- Smith JN, Ellis KM, Jones EP (1990) Caesium-137 transport into the Arctic Ocean through Fram Strait. *J Geophys Res* 95(C2):1693–1701
- Smith KJ, Vintro LL, Mitchell PI et al (2004) Uranium-thorium disequilibrium in north-east Atlantic waters. *J Environ Radioact* 74:199–210
- Sommerfield CK, Nittrouer CA, Alexander CR (1999) ^7Be as a tracer of flood sedimentation on the northern California continental margin. *Cont Shelf Res* 19:335–361
- Stewart G, Cochran JK, Xue J et al (2007) Exploring the connection between ^{210}Po and organic matter in the north-western Mediterranean. *Deep Sea Res I* 54:415–427
- Su CC, Huh CA, Lin FJ (2003) Factors controlling atmospheric fluxes of ^7Be and ^{210}Pb in northern Taiwan. *Geophys Res Lett* 30(19):2018. doi:10.1029/2003GL018221
- Swarzenski PW, Reich CD, Spechler RM et al (2001) Using multiple geochemical tracers to characterize the hydrogeology of the submarine spring off Crescent Beach, Florida. *Chem Geol* 179:187–202
- Swarzenski PW, Porcelli D, Andersson Per S et al (2003) The behavior of U- and Th-series nuclides in the Estuarine environment. *Rev Mineral Geochem* 52:577–606
- Thomson J, Colley S, Anderson R et al (1993) ^{210}Pb in the sediments water column of the Northeast Atlantic from 47 to 59°N along 20°W. *Earth Planet Sci Lett* 115:75–87
- Trimble SM, Baskaran M, Porcelli D (2004) Scavenging of thorium isotopes in the Canada Basin of the Arctic Ocean. *Earth Planet Sci Lett* 222:915–932
- Turekian KK, Graustein WC (2003) Natural radionuclide in the atmosphere. *Treatise Geochem* 4:261–279
- UNSCEAR (1982) *Ionizing radiation: sources and biological effects*. United Nations, New York
- UNSCEAR (2000) *Sources and effects of ionizing radiation*. United Nations, New York
- Walling DE, Quine TA (1993) *Use of Cs-137 as a tracer of erosion and sedimentation: handbook for the application of the Cs-137 technique*. University of Exeter, Exeter
- Walling DE, He Q, Blake W (1999) Use of ^7Be and ^{137}Cs measurements to document short- and medium-term rates of water-induced erosion and agricultural land. *Water Resour Res* 35:3865–3874

- Waples JT, Orlandini KA, Weckerly KM et al (2003) Measuring low concentrations of ^{234}Th in water and sediment. *Mar Chem* 80:265–281
- Waples JT, Benitez-Nelson CR, Savoye N et al (2006) An introduction to the application and future use of ^{234}Th in aquatic systems. *Mar Chem* 100:166–189
- Weinstein SE, Moran SB (2005) Vertical flux of particulate Al, Fe, Pb and Ba from the upper ocean determined using $^{234}\text{Th}/^{238}\text{U}$ disequilibrium. *Deep Sea Res I* 52:1477–1488
- Whiting PJ, Matisoff G, Fornes W et al (2005) Suspended sediment sources and transport distances in the Yellowstone River basin. *GSA Bullet* 117:515–529
- Wilson CG, Matisoff G, Whiting PJ (2007) The use of ^7Be and $^{210}\text{Pb}_{\text{ex}}$ to differentiate fine suspended sediment sources in South Slough, Oregon. *Estuar Coast* 30(2):348–358
- Yoshizawa Y (1958) Beta and gamma ray spectroscopy of ^{137}Cs . *Nucl Phys* 5:122–140
- Zuo ZZ, Eisma D, Berger GW (1990) Determination of sediment accumulation and mixing rate in the Gulf of Lion, the Mediterranean Sea. *Water Poll Res Rep* 20:469–499

Chapter 17

Radium Isotope Tracers to Evaluate Coastal Ocean Mixing and Residence Times

L. Zhang, J. Zhang, P.W. Swarzenski, and Z. Liu

Abstract The identification and provenance of unique coastal water masses is essential in near-shore biogeochemical studies. Water mass mixing and residence times impact water quality and can play a role in the evolution of algal blooms. Such information is thus critical for resource managers who have an interest in understanding the source and fate of contaminants and their eventual fate in the coastal ocean. If mixing is important for quantitatively assessing the amount of exchange, the water residence time or water age is important to assess the rate of this exchange. An understanding of water mass residence times is useful to examine time scales of contaminant discharge and to evaluate transport phenomena.

This review summarizes the scientific significance, measurement approaches, and models to evaluate coastal water mixing and residence times using radium isotopes. Each method or model described here is valid, although each has its own advantages and disadvantages. Examples of mixing among different end-members are given as case studies. All approaches presented here demonstrate the utility of radium isotopes for the evaluation of water mass mixing and residence times.

L. Zhang (✉) and J. Zhang
State Key Laboratory of Estuarine and Coastal Research, East China Normal University, 3663 Zhongshan Road North, Shanghai 200062, P.R. China
e-mail: 1979_zhanglei@163.com; jzhang@sklec.ecnu.edu.cn

P.W. Swarzenski
US Geological Survey, 400 Natural Bridges Drive, Santa Cruz, CA 95060, USA
e-mail: pswarzen@usgs.gov

Z. Liu
Key Laboratory of Marine Environment and Ecology (Ocean University of China), Ministry of Education, 238 Songling Road, Qingdao 266003, P.R. China
e-mail: liuzhe_ecnu@yahoo.com.cn

17.1 Introduction

There are four isotopes of radium in the natural environment with a board range of half-lives that extend from 3.66 days to 1,600 years, i.e. ^{226}Ra ($t_{1/2} = 1,600$ year), ^{228}Ra ($t_{1/2} = 5.75$ year), ^{223}Ra ($t_{1/2} = 11.4$ day) and ^{224}Ra ($t_{1/2} = 3.66$ day). Radium is an alkaline earth metal and each isotope is produced by the decay of their radiogenic parents, which belongs to members of the three U/Th decay series (see Fig. 2.2 in Chap. 2). They have different half-lives but similar physicochemical properties. Figure 17.1 is a biogeochemical behavior model for radium isotopes in a coastal environment. In river water, radium isotopes are strongly adsorbed onto particles, but they will rapidly be released into seawater with an increase in ion strength on a short timescale (Moore 1981; Key et al. 1985; Moore and Scott 1986). In dissolved form, radium isotopes move with a water body and are transported in the ocean by advective and diffusive mixing processes, while irreversibly removed from water column via radioactive decay. It has been recently documented that submarine groundwater discharge is an important source of radium in coastal waters (Moore 1999; Krest et al. 1999; Yang et al. 2002; Burnett et al. 2006). Based on their properties and different half-lives, Ra is of particular interest in oceanographic studies because it may lead to an understanding of various mobilization processes in the ocean and has great potential as tracers to evaluate geophysical and environmental processes in the geosphere (Moore 1996; Rama and Moore 1996). Numerous publications have demonstrated the suitability of radium to evaluate mixing dynamics of various water masses and residence time in estuaries, coastal environments, and the

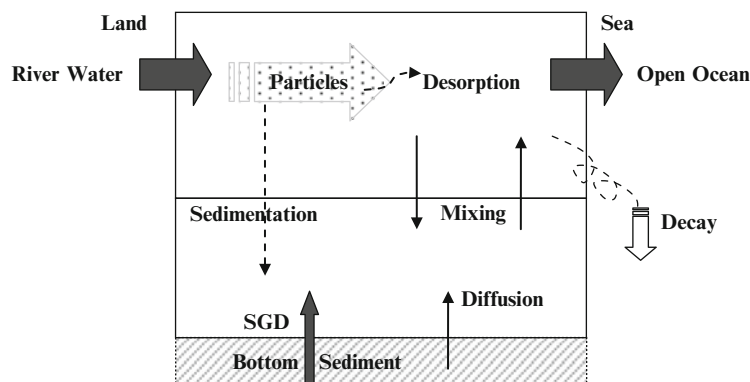


Fig. 17.1 A model budget for radium isotopes in a coastal region. SGD is the abbreviation of submarine groundwater discharge. Assume Ra inputs include river discharge, desorption from riverine particles, diffusion from bottom sediment and

inputs from SGD; Ra outputs include mixing with the open ocean and radioactive decay (Kim et al. 2005; Burnett et al. 2006)

open ocean (Moore et al. 1986; Moore and Todd 1993; Kim et al. 2005; Moore 2006).

17.2 Methods

17.2.1 Gamma Spectrometry

In oceanographic observations, temperature and salinity are measured *in-situ* by a CTD profiler, while for radium isotopes different methods exist for measurements. Gamma spectrometry needs relatively less chemical processing after sample collection, but relative large sample volumes. Large volume (>200 L) water samples can be pumped directly through polypropylene cartridge pre-filters to remove suspended particles followed by two MnO₂ impregnated cartridges connected in a series to concentrate radium (Baskaran et al. 1993, 2009). After the filtration, the MnO₂-fibers are detached from the cartridge and washed with distilled water to remove salts. In the laboratory, the pre-filtered and MnO₂ impregnated cartridges are ashed at 550°C for more than 6 h in a muffle furnace. After cooling, the ashes are weighed and transferred into a plastic vials sealed with epoxy for determination by Gamma-spectrometry. The extraction efficiency of radium from seawater is calculated from relative efficiency of two MnO₂-fibers. Assuming no difference in extraction efficiency exists between two MnO₂-fiber cartridges, the extraction

efficiencies (η) can be calculated by equation $\eta = 1 - A_2/A_1$, where A_1 and A_2 are measured radium isotope activities of the first and second cartridge filters (Hong et al. 2002). However, the extraction of Ra onto MnO₂-fibers at filtration rates of 5–10 L/min is not quantitative. Thus, the large-volume filtration is useful to obtain activity ratios of Ra (such as ²²⁶Ra/²²⁸Ra, ²²⁴Ra/²²⁶Ra and ²²³Ra/²²⁶Ra) and a separate aliquot of 20 L is required for precise ²²⁶Ra measurements. From the precise measurement of ²²⁶Ra and activity ratios of Ra, specific activity of ²²³Ra, ²²⁴Ra and ²²⁸Ra can be determined. Obviously, in most circumstances, the data of short-lived isotopes are difficult to acquire, and the samples volume required for determination are large. So the small volume methods are predominant in near 10 years.

17.2.2 ²²⁶Ra by Alpha Spectrometry

For seawater samples, about 20 L water samples are sufficient for this method. After collection, samples are filtered immediately through a filter (e.g. pore size = 0.45 μm). The resulting pre-filtered waters are stored in pre-cleaned polyethylene containers, and ²²⁹Th-²²⁵Ra yield tracers are added after acidification. Samples are thoroughly mixed for ca. 10 min and then allowed to stand for ca. 6 h for spikes to equilibrate. Briefly, concentrated NH₄OH, KMnO₄ and MnCl₂ solutions are added to form a suspension of MnO₂. The sample is stirred for 30 min, and then allowed to

settle. The precipitate is separated from the supernatant and taken back to the lab for further treatment. In the laboratory, the resultant precipitate is re-dissolved in concentrated HNO_3 and H_2O_2 to make a 0.1-M HNO_3 solution. Detailed procedures for Ra separation and purification are described in Hancock and Martin (1991). The purified Ra is evaporated to a low volume, brought to dryness at low heat, dissolved in 0.5 mL 0.1 M HNO_3 , and finally transferred to a deposition cell with 1 mL 0.05 M HCl and 9 mL ethanol. Ra is electro-deposited onto a stainless steel disc for alpha measurement. One can readily obtain alpha spectrometry data for ^{226}Ra , ^{224}Ra , and ^{223}Ra , but for ^{228}Ra one needs to wait more than 1 year to allow for sufficient ingrowth of ^{228}Th .

17.2.3 Combination of Delayed Coincidence System with Gamma Spectrometry (RaDeCC)

One can obtain short-lived Ra isotope data quickly using a delayed coincidence counting system. Moore and Arnold (1996) used a portable delayed coincidence counter to obtain ^{224}Ra and ^{223}Ra , after which samples were measured using gamma ray spectrometry to assess the activities of ^{226}Ra and ^{228}Ra . The advantage of RaDeCC is the very low detection limit. For example, ^{224}Ra concentrations in the range of 8 mBq m^{-3} will have 1σ uncertainty of $\pm 10\%$ and thus, total number of ^{224}Ra as low as 3,000 atoms can be detected (Moore 2007). For ^{223}Ra , activities as low as 3 mBq m^{-3} can be detected (Moore 2007). Seawater samples sizes are generally 50–100 L, while 20 L groundwater samples are usually sufficient. Radium is extracted from the samples by passing the water through a column filled with about 50 g of manganese-coated acrylic fiber (Moore 1976). Each Mn fiber sample is partially dried with a stream of air and placed in closed loop air circulation system (Moore and Arnold 1996). Using helium as a transport gas, the radiogenic daughters of ^{219}Rn and ^{220}Rn generated by ^{223}Ra and ^{224}Ra decay are used to quantify ^{223}Ra and ^{224}Ra . After the ^{223}Ra and ^{224}Ra measurements, the Mn fibers are leached with HCl to quantitatively remove the long-lived Ra isotopes. The Ra is co-precipitated with BaSO_4 , and the

precipitate is aged for 3 weeks to determine ^{226}Ra and ^{228}Ra in a ultra low background gamma detector.

17.3 Water Mass Mixing and Residence Times Using Radium as Tracers

17.3.1 Study of Water Mixing

The identification of various water masses in the coastal ocean is of critical importance in near-shore oceanography, where oceanographic characteristics are largely determined by the mixing of source water masses (Pickard and Emery 1990; Vilibic and Orlic 2002). The study of water mixing processes can be traced back to the early twentieth century, when the method of classical temperature and salinity data analysis was first established by Helland-Hansen (1916), and later globally applied (e.g. Sverdrup et al. 1946). In 1927, the temperature and salinity (T-S) diagram was used to study the mixing of two water masses by Jacobsen (1927), and later for the analysis of mixing among three water masses at the edge of the continental shelf in the North Atlantic Ocean (Miller 1950; Dulaiova and Burnett 2007). With regards to more complex mixing conditions, for example among four parcels over a shelf, Chen et al. (1995) elaborated a method based on temperature-salinity diagram analysis and series of assumptions, which could give quantitative results at specific conditions and that method had been applied to marginal seas of NW Pacific Ocean. However, this method fails in some circumstances and the intrinsic assumptions are invalid in terms of mathematics and reasonable derivation in oceanography (Zhang et al. 2007). Based on an original theory of equations, in the case when the number of tracers (i.e. in the case of $n = 2$) is less than that of source end-members minus one (i.e. 3) will not produce a definite solution. Other tracers are required ultimately to resolve problems with exact solutions, when the end-members of water mixing are >3 .

In the 1980s, a new water mass analysis technique, the so-called Optimum Multi-parameter (OMP) analysis, with the aid of multiple tracers, was first introduced to characterize water masses in the sea

(Tomczak 1981). Generally, the governing equations describing mixing processes among different water masses can be described by matrix theory:

$$\begin{pmatrix} 1 & 1 & 1 & 1 \\ T_{11} & T_{12} & \cdots & T_{1n} \\ T_{21} & T_{22} & \cdots & T_{2n} \\ \vdots & \vdots & \ddots & \vdots \\ T_{m1} & T_{m2} & \cdots & T_{mn} \end{pmatrix} \begin{pmatrix} f_1 \\ f_2 \\ \vdots \\ f_n \end{pmatrix} = \begin{pmatrix} 1 \\ T_1^{obs} \\ T_2^{obs} \\ \vdots \\ T_m^{obs} \end{pmatrix}, \quad (17.1)$$

where f_i ($i = 1, 2, \dots, n$) is the fraction for the i -th water mass, T_{ij} is the j -th value of tracer for the i -th water mass, T_j^{obs} is the j -th tracer value for a given water sample. By solving these matrix equations, the mixing proportions f_i can be expressed as:

$$\begin{pmatrix} f_1 \\ f_2 \\ \vdots \\ f_n \end{pmatrix} = \begin{pmatrix} 1 & 1 & 1 & 1 \\ T_{11} & T_{12} & \cdots & T_{1n} \\ T_{21} & T_{22} & \cdots & T_{2n} \\ \vdots & \vdots & \ddots & \vdots \\ T_{m1} & T_{m2} & \cdots & T_{mn} \end{pmatrix}^{-1} \begin{pmatrix} 1 \\ T_1^{obs} \\ T_2^{obs} \\ \vdots \\ T_m^{obs} \end{pmatrix}. \quad (17.2)$$

This method solves a set of linear mixing equations with the contribution of the each water type to the given oceanic water as variables and the hydrographic properties as the parameters of the system. OMP analysis has been successfully applied to shelf seas where all hydrographic properties can be considered as a first approximation to be conservative (Maamaatuaiahutapu et al. 1992, 1994; Klein and Tomczak 1994), and is still undergoing further development (Poole and Tomczak 1999; Henry-Edwards and Tomczak 2006).

Stable isotopes, including $\delta^{18}\text{O}$ and $\delta^{13}\text{C}$, nutrient and radioactive isotopes (such as ^{134}Cs , ^{137}Cs and ^{125}Sb) have been used to track mixing of water masses (e.g. Liu et al. 1995; Bailly 1996; Lakey and Krothe 1996; Katz et al. 1997; Lee and Krothe 2001; Zhang 2002; Hong et al. 2011). However, the concentration of $\delta^{18}\text{O}$ in typical marine waters is rather stable with limited variation (e.g. $0 \pm 1\%$), if used as tracer will introduce considerable uncertainty (Chen 1985; Liu et al. 1995). The $\delta^{13}\text{C}$ and nutrients are not strictly conservative because of air-sea exchange and participation in metabolic regulations, and therefore, are

unsuitable in water source discrimination when biological processes are important factors relative to the mixing processes. In order to improve the traceability of the discrimination of source waters, Ra nuclides can be chosen as additional tracers because of its conservative behavior and non-particle reactive nature in the ocean (Moore 2000). In the early 1980s, ^{226}Ra was used as tracer to analyze the mixing between two water parcels in north Pacific (Chung and Craig 1980). Moore (2003) developed a three-end-member mixing model that used radium isotopes to estimate the fractions of ocean water. Furthermore, off western Florida waters from a shallow aquifer and from a deep aquifer were separated using Ra isotopes (Moore et al. 2006). Recently, Zhang et al. (2007) used temperature, salinity and ^{226}Ra as passive tracers to evaluate the mixing proportions among four end-members in the East China Sea.

17.3.2 Study of Residence Time

Trajectory, in terms of a Lagrangian view, is used to describe the path of a moving water parcel through space. Let t denote time, $\vec{r}(t)$ represent the position vector of the fluid parcel at time t , and $\vec{u}(\vec{r}(t), t)$ describe the velocity at the time t and position $\vec{r}(t)$. From the notion of trajectory, the relation between $\vec{r}(t)$ and $\vec{u}(\vec{r}(t), t)$ can be expressed as:

$$\vec{u}(\vec{r}(t), t) = \frac{d\vec{r}(t)}{dt}. \quad (17.3)$$

However, it is rather difficult to understand transport processes by only investigating magnitude and direction of flow (Deleersnijder et al. 2001). Therefore, auxiliary parameters are needed, which are closely related to the flow field and can be used to quantify their functioning of material transport in seawater (Deleersnijder et al. 2001). Water age and residence time are two such variables. Residence time is the complement of age (Takeoka 1984), and provides the timescale available for components to accumulate in the water column (Moore et al. 2006). It should be pointed out that, in some studies, residence time is also taken as the time span of the water parcel (e.g. Bolin and Rodhe 1973), which is different from the above concept. In order to facilitate better understanding, a

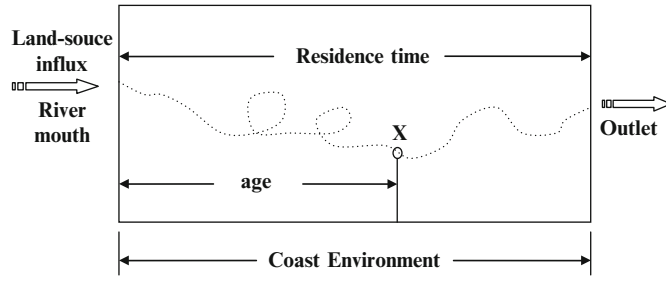


Fig. 17.2 Water age and residence time schematic. The hollow dot represents a water parcel. From river mouth, the water parcel enters the water body, and leaves the water body from outlet.

The point X location means water age of the water parcel and the duration for the water parcel from entering to leaving the water body is residence time (Bolin and Rodhe 1973)

schematic diagram is drawn in Fig. 17.2. In such a view, water age (which is zero when a water parcel enters a water body) and residence time that is the duration for a water parcel from entering to leaving the water body of interest is analogous to that of human age that is zero when people were born and lifespan (i.e. the duration for people from birth to death) (Bolin and Rodhe 1973). Water age is regarded as the time a water parcel has spent since entering the control volume through one of its boundaries, where its age is prescribed to be zero (Delhez et al. 1999). Hence, the age $a[\vec{r}(t), t]$ of water parcel in the domain of interest must progress at the same pace (17.4), since the age is measured by the elapsed time.

$$\frac{dt}{dt} = 1 = \frac{d}{dt} a[\vec{r}(t), t]. \quad (17.4)$$

Residence time is defined as “the time it takes for any water parcel to leave a given water body through its outlet to the sea” (Zimmerman 1976; Mosen et al. 2002). Hence, residence time is the remainder of the life time of a water parcel considered (17.5)

$$RT(\vec{r}(t), t) = a[\vec{r}(t^{out}), t^{out}] - a[\vec{r}(t), t], \quad (17.5)$$

where $RT(\vec{r}(t), t)$ is the residence time, $a[\vec{r}(t), t]$ is the water age at the time of t considered, and $a[\vec{r}(t^{out}), t^{out}]$ is the age the water parcel reaches the outlet and leaves (i.e. life time).

17.3.2.1 Conservative Ra Without Additional Input

This model assumes there is no additional input of radium beyond the nearshore. The coastal ocean is

usually an area for significant radium inputs because radium is released into a water column from riverine particles as well as bottom sediments (Moore 1981; Key et al. 1985; Moore and Scott 1986). In exclusion of the coastal zone, desorption from sediment and pore-water diffusion are the only other inputs (Moore 1969; Li and Chan 1979), and this contribution can be ignored in some circumstances, i.e. strong thermocline will prevent the approach from bottom layer (Moore 2000). If the radioactive isotope with the half-life of $T \log 2$ is contained in a water parcel, where the T is the half-life of the isotope, the concentration within the fluid parcel of this radioactive constituent decreases as:

$$C_r[\vec{r}(t^{end}), t^{end}] = C_r[\vec{r}(t^{ini}), t^{ini}] \exp \frac{t^{ini} - t^{end}}{T}, \quad (17.6)$$

where $C_r[\vec{r}(t^{ini}), t^{ini}]$ and $C_r[\vec{r}(t^{end}), t^{end}]$ is the activity of a radionuclide at initial time t^{ini} in $\vec{r}(t^{ini})$ and arrival time t^{end} in $\vec{r}(t^{end})$, respectively.

Then, combining (17.5) and (17.6) yields

$$\begin{aligned} RT[\vec{r}(t^{end}), t^{end}] &= t^{end} - t^{ini} \\ &= T \log \frac{C_r[\vec{r}(t^{ini}), t^{ini}]}{C_r[\vec{r}(t^{end}), t^{end}]}, \end{aligned} \quad (17.7)$$

or

$$\begin{aligned} RT[\vec{r}(t^{end}), t^{end}] &= t^{end} - t^{ini} \\ &= T \log \frac{C_r[\vec{r}(t^{ini}), t^{ini}] / C_p[\vec{r}(t^{ini}), t^{ini}]}{C_r[\vec{r}(t^{end}), t^{end}] / C_p[\vec{r}(t^{end}), t^{end}]}, \end{aligned} \quad (17.8)$$

where $RT[\vec{r}(t^{end}), t^{end}]$ is the residence time for the water parcel considered, and $C_p[\vec{r}(t), t]$ is the concentration of a passive conservative constituent. The constituent is neither produced nor destroyed. That is to say, the concentration $C_p[\vec{r}(t), t]$ within the fluid parcel remains constant as time progresses (i.e. $C_p[\vec{r}(t^{end}), t^{end}] = C_p[\vec{r}(t^{ini}), t^{ini}]$).

17.3.2.2 Non-Conservative Ra with Additional Input

In estuaries, salt marshes, near-shore coastal waters, and even on the shelf where radium additions are continuous, the above-mentioned activities of a radioactive constituent at some initial time are not constant. The model described in Sect. 17.3.2.1 thus becomes not applicable. Considering the additions and mixing between fresh and ocean water, a different approach has been proposed (Nozaki et al. 1991). Assuming that the decay of isotopes does not measurably affect the activities of long-lived ^{226}Ra and ^{228}Ra on the time-scale of estuarine mixing, and biological uptake/release is negligible, the activity of radium isotopes can be affected by the following three factors: (1) Ra_R ; dissolved radium in the river freshwater end-member, (2) Ra_S ; dissolved radium in saline water end-member, and (3) Ra_{ex} ; “excess” dissolved radium in observed station. The “excess” here means a supply of radium from other sources except the mixture of river water and sea water end-members, including, for example, desorption from particles, diffusion from sediment (e.g. sediment-water exchange) and submarine groundwater (Yang et al. 2002; Moore 2006). Thus, the budget of radium isotopes can be expressed by (Nozaki et al. 1989, 1991)

$$^{226}\text{Ra}_{obs} = f^{226}\text{Ra}_R + (1-f)^{226}\text{Ra}_S + ^{226}\text{Ra}_{ex} \quad (17.9)$$

and

$$^{228}\text{Ra}_{obs} = f^{228}\text{Ra}_R + (1-f)^{228}\text{Ra}_S + ^{228}\text{Ra}_{ex}, \quad (17.10)$$

where f is the fraction of river water, subscript *obs* is the observed activity of radium for a given station.

Assuming that the net effect of evaporation and precipitation is negligible, the surface water at salinity S is the mixture of the river freshwater and the saline water. The f is given by

$$f = (S_S - S)/(S_S - S_R), \quad (17.11)$$

where S_R , S_S , S is the salinity of the river water end-member, sea water end-member, and measured salinity in the sample, respectively. At steady state, the residence time of excess dissolved radium (τ_w) can be expressed using the results of $^{226}\text{Ra}_{ex}$ and $^{228}\text{Ra}_{ex}$.

$$^{226}\text{Ra}_{ex} = F^{226}\text{Ra}\tau_w \quad (17.12)$$

$$^{228}\text{Ra}_{ex} = (F^{228}\text{Ra} - \lambda_{228}^{228}\text{Ra}_{obs})\tau_w, \quad (17.13)$$

where $F^{226}\text{Ra}$ and $F^{228}\text{Ra}$ are the total fluxes of excess radium supplied from particles and sediments, and λ_{228} is the decay constant of ^{228}Ra . The ratio of (17.12) and (17.13) can be expressed as:

$$\left(\frac{^{228}\text{Ra}}{^{226}\text{Ra}}\right)_{ex} = \frac{F^{228}\text{Ra}}{F^{226}\text{Ra}} - \left(\frac{\lambda_{228}}{F^{226}\text{Ra}}\right)^{228}\text{Ra}_{obs}. \quad (17.14)$$

The $(^{228}\text{Ra}/^{226}\text{Ra})_{ex}$ is a linear function of the $^{228}\text{Ra}_{obs}$, and the slope is the ratio of the decay constant of ^{228}Ra and total flux of excess ^{226}Ra (i.e. slope = $\frac{\lambda_{228}}{F^{226}\text{Ra}}$). Then the slope and y-intercept allow us to calculate the absolute values of $F^{226}\text{Ra}$ and $F^{228}\text{Ra}$. In this manner the residence time for each sample can be calculated.

In certain circumstances, the uncertainties are large enough to affect the resulting linear relationship. If that's the case, it is difficult to obtain the available results of the slope mentioned above. Moore et al. (2006) proposed a mass balance approach which assumed a system under steady state conditions. Radium additions, including fluxes from sediment, river and groundwater would be balanced by losses. For short-lived radium isotopes, losses are due to mixing and radioactive decay, but for long-lived radium radioactive decay would be negligible and so affected only by mixing processes.

In the case of ^{224}Ra mass balance, the equation can be expressed as:

$$F^{224}\text{Ra} = I^{224}\text{Ra}(\lambda_{224} + 1/\tau), \quad (17.15)$$

where $F^{224}\text{Ra}$ is the total flux of ^{224}Ra to the system, $I^{224}\text{Ra}$ is the inventory of ^{224}Ra in the system, λ_{224} is the decay constant for ^{224}Ra , and τ is the apparent age of water in the system. A similar equation can be written for ^{226}Ra , with radioactive decay ignored:

$$F^{226}\text{Ra} = I^{226}\text{Ra}(1/\tau). \quad (17.16)$$

Dividing (17.15) by (17.16), we can get:

$$F(^{224}\text{Ra}/^{226}\text{Ra}) = I^{224}\text{Ra}(\lambda_{224} + 1/\tau)/[I^{226}\text{Ra}(1/\tau)]. \quad (17.17)$$

This equation can be rearranged and solved for τ :

$$\tau = [F(^{224}\text{Ra}/^{226}\text{Ra}) - I(^{224}\text{Ra}/^{226}\text{Ra})]/I(^{224}\text{Ra}/^{226}\text{Ra})\lambda_{224}. \quad (17.18)$$

Except for the above-mentioned radiochemical tracers, there have been a number of physical, chemical and modeling techniques used to estimate the residence time of coastal waters, including the tidal prism model, fresh water budgets, dye tracers and numerical models (e.g. Hougham and Moran 2007). Hydrodynamic models are based upon a large number of parameters including tidal range and prism, wind speed and direction, currents and geometry of the reservoir. The acquisition of data has inherent spatio-temporal limitations. Compared with real-time measurements, numerical models can provide information with much higher spatio-temporal resolution. In addition, advection and diffusion processes can be separated in numerical models. However, it can be difficult to separate these two terms from observations alone. All models need observational data for the validation of the model. If real-time measurements are not available, uncertainties associated with the modeled residence time could become quite large, therefore diminishing the utility of the model (Rapaglia et al. 2009). If, for example, the velocity of the current and the turbulent stream are dynamic, the model will yield the correct residence time only if these parameters are known for the period under investigation (Pougatch et al. 2007; Rapaglia et al. 2009). Due to the same chemical properties and different half-lives, the ratio of different radium isotopes could be considered as a good ‘‘inner-clock’’ to study residence time on different time scales. Water flow or separation will result in the variation of the radium activity, while the ratios could thus in effect offset water fractionation and turbulence.

17.3.3 Case Studies: Application of Radium Isotopes

17.3.3.1 Water Mixing

Three-End-Member Mixing

Moore et al. (2006) used ^{228}Ra and salinity as two tracers to analyze the mixing among three end members at Okatee Estuary; namely, (1) water from Port Royal Sound (PRS, here represented by the Colleton River), (2) water from the Okatee River, and (3) groundwater. Equations for water, salt and ^{228}Ra could be expressed as:

$$\begin{pmatrix} 1 & 1 & 1 \\ ^{228}\text{Ra}_S & ^{228}\text{Ra}_R & ^{228}\text{Ra}_{GW} \\ S_S & S_R & S_{GW} \end{pmatrix} \begin{pmatrix} f_S \\ f_R \\ f_{GW} \end{pmatrix} = \begin{pmatrix} 1 \\ ^{228}\text{Ra}_M \\ S_M \end{pmatrix}, \quad (17.19)$$

where f_S , f_R and f_{GW} are the fractions of PRS, Okatee River, and groundwater end-members, respectively; $^{228}\text{Ra}_S$, $^{228}\text{Ra}_R$ and $^{228}\text{Ra}_{GW}$ are the ^{228}Ra activities in PRS, Okatee River and groundwater end-members, respectively; S_S , S_R and S_{GW} are the salinities in the PRS, Okatee and groundwater end-members, respectively. $^{228}\text{Ra}_M$ and S_M are the measured ^{228}Ra concentration and salinity, respectively.

These equations may be solved for the fractions of each end-member (Moore et al. 2006):

$$f_S = \frac{\left(\frac{^{228}\text{Ra}_M - ^{228}\text{Ra}_R}{^{228}\text{Ra}_{GW} - ^{228}\text{Ra}_R}\right) - \left(\frac{S_M - S_R}{S_{GW} - S_R}\right)}{\left(\frac{^{228}\text{Ra}_S - ^{228}\text{Ra}_R}{^{228}\text{Ra}_{GW} - ^{228}\text{Ra}_R}\right) - \left(\frac{S_S - S_R}{S_{GW} - S_R}\right)} \quad (17.20)$$

$$f_{GW} = \frac{S_M - S_R - f_S(S_S - S_R)}{S_{GW} - S_R} \quad (17.21)$$

$$f_R = 1 - f_S - f_{GW}. \quad (17.22)$$

The results of this mixing using data from different dates are shown in Fig. 17.3.

Four-End-Member Mixing

Zhang et al. (2007) used temperature, salinity and ^{226}Ra as tracers to quantify the contribution among four

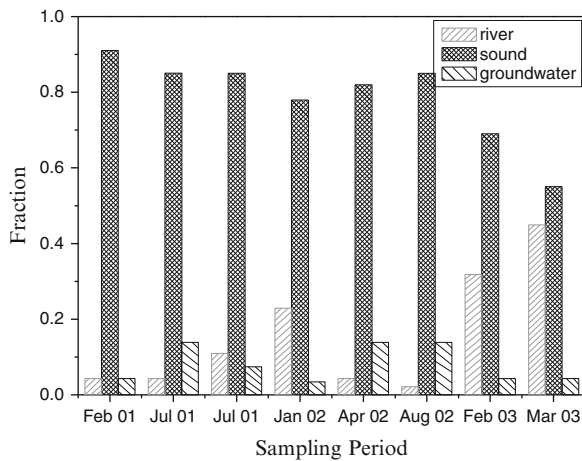


Fig. 17.3 Fraction of river, sound, and groundwater based on a three end-member mixing model (Moore et al. 2006)

end-members mixing in the East China Sea. Figure 17.4 shows the schematic of mixing among the four water masses; namely, Kuroshio Surface Water (KSW), Kuroshio Sub-surface Water (KSSW), Changjiang Diluted Water (CDW), and Taiwan Strait Warm Water (TSWW).

In this example, there were three variables: temperature (T), salinity (S) and radium (Ra) as tracers to analyze the mixing among four end members in that study. Based on the (17.1), the following equations could be obtained:

$$\begin{pmatrix} 1 & 1 & 1 & 1 \\ T_A & T_B & T_C & T_D \\ S_A & S_B & S_C & S_D \\ Ra_A & Ra_B & Ra_C & Ra_D \end{pmatrix} \begin{pmatrix} f_A \\ f_B \\ f_C \\ f_D \end{pmatrix} = \begin{pmatrix} 1 \\ T_{obs} \\ S_{obs} \\ Ra_{obs} \end{pmatrix}, \quad (17.23)$$

where T_i, S_i, Ra_i ($i = A, B, C, D$) are the variable parameters of temperature, salinity and concentrations of Ra isotopes, respectively, for source water type i . Here, A, B, C and D represented the four actual source water masses, namely, the Kuroshio Surface Water, Kuroshio Sub-surface Water, Changjiang Diluted Water and Taiwan Strait Warm Water. $T_{obs}, S_{obs}, Ra_{obs}$ are the measured values of temperature, salinity and Ra concentration, and f_i the corresponding fractions of A, B, C and D for the observed stations, respectively. By solving these equations, the proportions of individual source water components in the ECS water mixed among four end-members could be estimated through exact solutions:

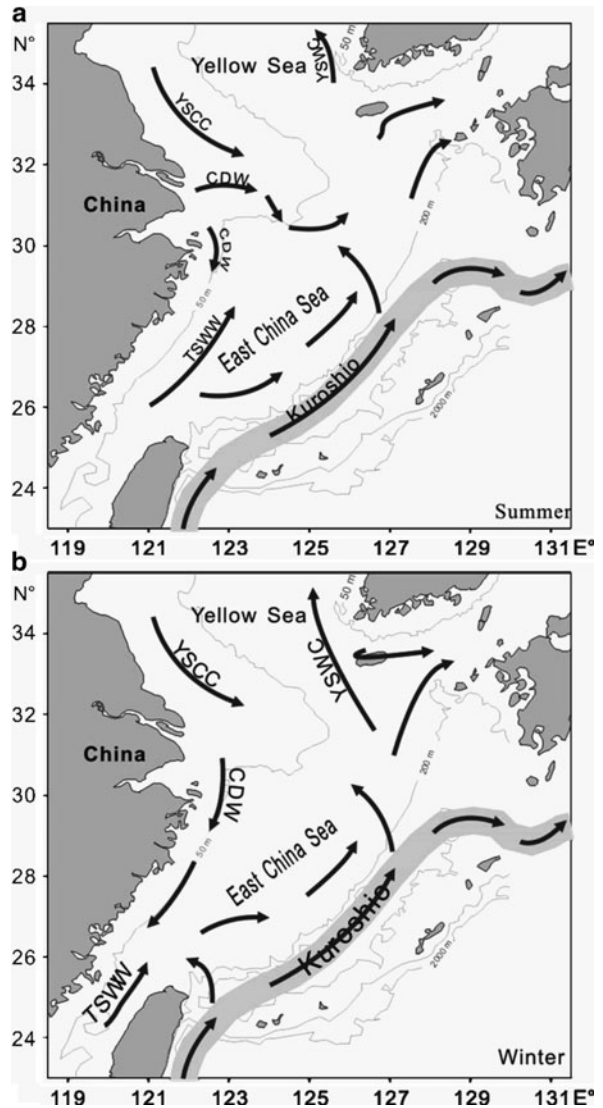


Fig. 17.4 Schematic of mixing among multiple water masses in the East China Sea. The four dominant source waters include: Kuroshio Surface Water (KSW), Kuroshio Sub-surface Water (KSSW), Changjiang Diluted Water (CDW), and Taiwan Strait Warm Water (TSWW) (a) In summer; (b) In winter

$$\begin{pmatrix} f_A \\ f_B \\ f_C \\ f_D \end{pmatrix} = \begin{pmatrix} 1 & 1 & 1 & 1 \\ T_A & T_B & T_C & T_D \\ S_A & S_B & S_C & S_D \\ Ra_A & Ra_B & Ra_C & Ra_D \end{pmatrix}^{-1} \begin{pmatrix} 1 \\ T_{obs} \\ S_{obs} \\ Ra_{obs} \end{pmatrix}. \quad (17.24)$$

Mixing proportions of the four water masses are shown in Fig. 17.5. In this manner, the contribution of each of the source water masses could be evaluated directly.

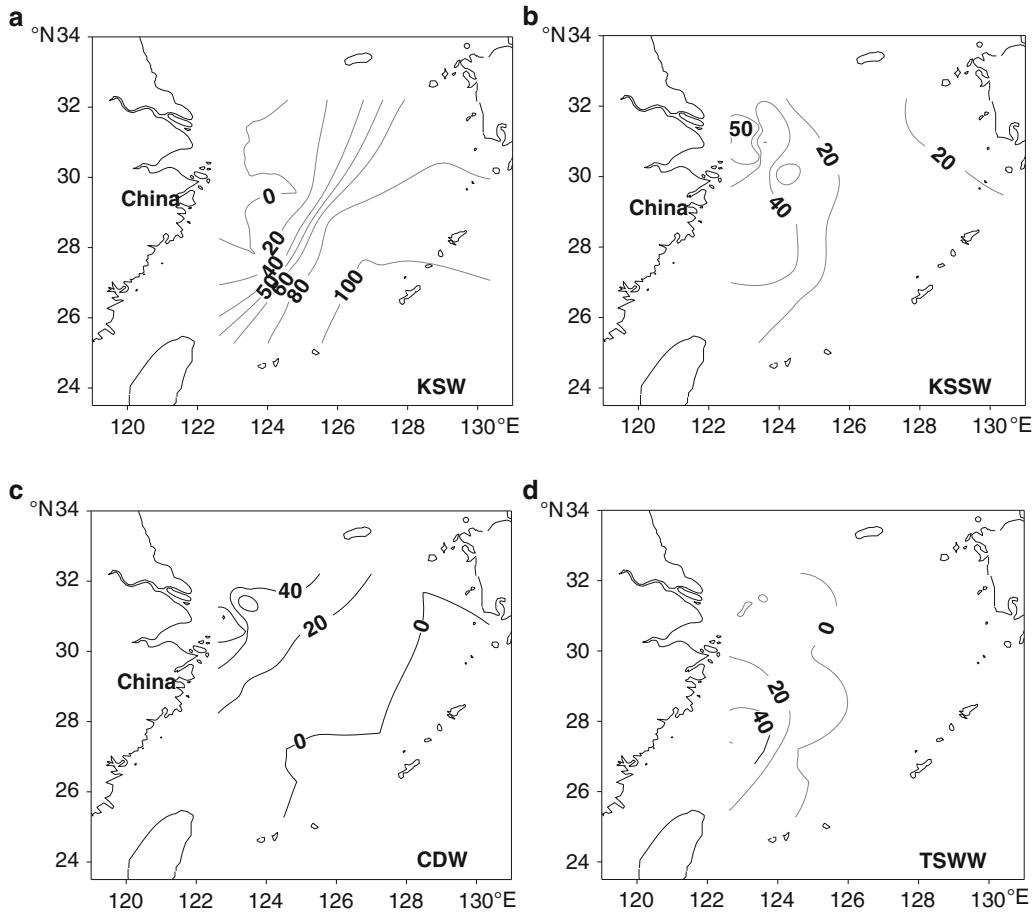


Fig. 17.5 Horizontal distributions of mixing proportion lines of the four water end-members at the surface. (a) Kuroshio surface water (KSW); (b) Kuroshio sub-surface water (KSSW); (c) Changjiang diluted water (CDW); (d) Taiwan strait warm water (TSWW)

17.3.3.2 Residence Time

Conservative Ra Model

^{223}Ra and ^{224}Ra have been used to evaluate near-shore water residence times (Dulaiova et al. 2006; Swarzenski and Izbicki 2009). In a study by Moore (2000) it is assumed that a strong pycnocline isolates the surface water from the bottom water (waters are strongly stratified), and that lateral transport can be ignored. The change in concentration of radium activity (A) with time (t) as a function of distance offshore (Z) may be expressed as a balance of advection and diffusion:

$$\frac{dA}{dt} = K_h \frac{\partial^2 A}{\partial Z^2} - \omega \frac{\partial A}{\partial Z} - \lambda A, \quad (17.25)$$

where K_h is the eddy diffusion coefficient, and ω is the advective velocity. For the long-lived radium isotopes, the decay term again can be neglected. If the offshore distribution is dominated by diffusion with constant K_h , a plot of activity vs. distance will be a straight line connecting the end members. The above equation reduces to

$$\frac{dA}{dt} = K_h \frac{\partial^2 A}{\partial Z^2} - \lambda A. \quad (17.26)$$

Solving the (17.26), we can obtain

$$A = A_1 e^{\sqrt{\frac{\lambda}{K_h}} Z} + A_2 e^{-\sqrt{\frac{\lambda}{K_h}} Z}. \quad (17.27)$$

A_1 and A_2 are constant.

In first case, the boundary conditions are:

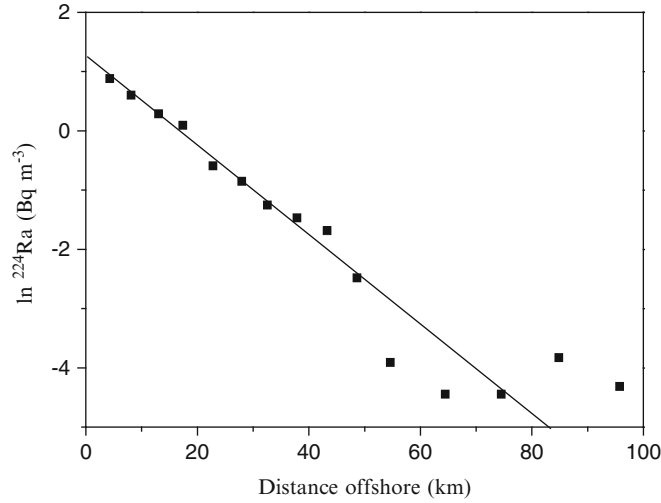


Fig. 17.6 The distance-averaged $\ln^{224}\text{Ra}$ as a function of distance offshore. The lines are based on the best fit to samples collected within 50 km of shore. The slope is $-0.0121 \text{ Bq m}^{-3} \text{ km}^{-1}$ with $R^2 = 0.986$ (Moore 2000)

$$A = A_0 \text{ at } Z = 0,$$

$$A \rightarrow 0 \text{ as } Z \rightarrow \infty.$$

If K_h is constant and the system is in steady state,

$$A_Z = A_0 e^{-\sqrt{\frac{\lambda}{K_h}} Z}, \quad (17.28)$$

where A_Z is the activity at distance Z from the coast, A_0 is the activity at distance 0 from the coast and λ is the decay constant. Based on the above equation, the distance Z can be expressed as:

$$Z = \sqrt{\frac{K_h}{\lambda}} \cdot \ln \frac{A_0}{A_Z}. \quad (17.29)$$

A plot of $\ln^{224}\text{Ra}$ as a function of distance from the coast may be used to estimate K_h , i.e. Fig. 17.6 (Moore 2000). In second case, the boundary conditions are:

$$A = A_0 \text{ at } Z = 0,$$

$$A \rightarrow A_L \text{ as } Z = Z_L$$

Combined with (17.27), we obtain:

$$A_0 = A_1 + A_2$$

and

$$A_L = A_1 e^{\sqrt{\frac{\lambda}{K_h}} Z_L} + A_2 e^{-\sqrt{\frac{\lambda}{K_h}} Z_L}. \quad (17.30)$$

The A_1 and A_2 can be solved as follow

$$A_1 = \frac{A_L - A_0 e^{-\sqrt{\frac{\lambda}{K_h}} Z_L}}{e^{\sqrt{\frac{\lambda}{K_h}} Z_L} - e^{-\sqrt{\frac{\lambda}{K_h}} Z_L}}$$

and

$$A_2 = \frac{A_0 e^{\sqrt{\frac{\lambda}{K_h}} Z_L} - A_L}{e^{\sqrt{\frac{\lambda}{K_h}} Z_L} - e^{-\sqrt{\frac{\lambda}{K_h}} Z_L}}. \quad (17.31)$$

Combined with $\text{Sinh}x = \frac{e^x - e^{-x}}{2}$, the concentration of radium activity (A) is expressed as (Chung and Kim 1980):

$$A = \frac{1}{\text{Sinh}\left(\sqrt{\frac{\lambda}{K_h}} \cdot Z_L\right)} \left(A_L \text{Sinh}\left(\sqrt{\frac{\lambda}{K_h}} \cdot Z\right) + A_0 \text{Sinh}\left[\sqrt{\frac{\lambda}{K_h}} \cdot (Z_L - Z)\right] \right). \quad (17.32)$$

Non-Conservative Ra Model

Kim et al. (2005) used the method (described in Sect. 17.3.2.2) to estimate the average water residence time in Yellow Sea and adjacent ocean. Figure 17.7 shows the $(^{228}\text{Ra}/^{226}\text{Ra})_{ex}$ vs. ^{228}Ra activity; the intercept and slope can be calculated by this relationship. The average water residence times of ~ 4.9 year is obtained using (17.12).

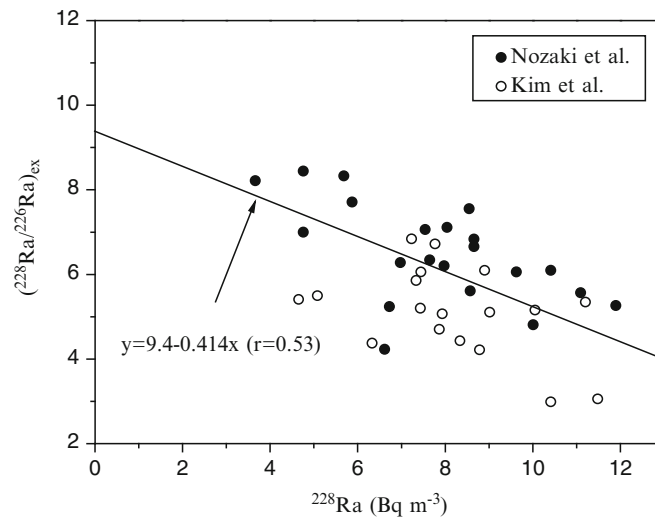


Fig. 17.7 A plot of $(^{228}\text{Ra}/^{226}\text{Ra})_{\text{ex}}$ vs. ^{228}Ra activity. The data for the *closed circles* are from Nozaki et al. (1991) and those for the *open circles* are from Kim et al. (2005). The slope and intercept of this plot are used for calculating Ra fluxes in the study area using (17.14)

17.4 Future Directions

River-dominated coastal waters and the adjacent continental shelf are important marine regions where the continuous exchange of water and chemical constituents bear the geochemical signals entrained between the continent and the open oceans. These waters occupy less than one fifth of the surface area of the world ocean, yet they play a major role in terms of global biogeochemical cycles (Walsh 1991; Iseki et al. 2003). Thus, water mass mixing and exchange rates will continue to be of great interest.

To protect our natural environment, we should resolve to understand the “three-how’s” that define the behavior of a contaminant: “how” many contaminants are flowing into a near-shore, coastal system, “how” long will the contaminants reside there, and “how” far will the impact of the contaminants be? By knowing the source and fate of contaminants in the near-shore, one can more realistically make informed decisions as to their management. For mixing among four unique water masses, a study cannot cease at the relative mixing proportions, but should include an understanding of absolute contributions. That will help evaluate the degree of influence for source contaminants. After establishing the contributions from source water masses, we then can utilize

appropriate tracers to assess the ages of different coastal source waters.

Acknowledgments We thank Willard S. Moore of University of South Carolina for his discussions on this topic. PWS thanks the USGS Coastal and Marine Program for continued support. The application example in the East China Sea was supported by Chinese Ministry of Science and Technology (2006CB400601).

References

- Bailey BP (1996) Mapping of water masses in the North Sea using radioactive tracers. *Endeavour* 20:2–7
- Baskaran M, Murray DJ, Santschi PH et al (1993) A method for rapid in situ extraction and laboratory determination of Th, Pb, and Ra isotopes from large volumes of seawater. *Deep Sea Res* 40:849–865
- Baskaran M, Hong GH, Santschi PH (2009) Radionuclide analyses in seawater. In: Wurl O (ed) *Practical guidelines for the analysis of seawater*. CRC Press, Boca Raton, pp 259–304
- Bolin B, Rodhe H (1973) A note on the concepts of age distribution and transit time in natural reservoirs. *Tellus* 25:58–63
- Burnett WC, Aggarwal PK, Bokuniewicz H et al (2006) Quantifying submarine groundwater discharge in the coastal zone via multiple methods. *Sci Total Environ* 367:498–543
- Chen CT (1985) Preliminary observations of oxygen and carbon dioxide of the winter time Bering Sea marginal ice zone. *Cont Shelf Res* 4:465–483
- Chen CTA, Ruo R, Pai SC et al (1995) Exchange of water masses between the East China Sea and the Kuroshio off northeastern Taiwan. *Cont Shelf Res* 15:19–39

- Chung YC, Craig H (1980) ^{226}Ra in the Pacific Ocean. *Earth Planet Sci Lett* 49:267–292
- Chung YC, Kim K (1980) Excess ^{222}Rn and the benthic boundary layer in the western and southern Indian Ocean. *Earth Planet Sci Lett* 49:351–359
- Deleersnijder E, Campin JM, Delhez EJM (2001) The concept of age in marine modeling. I. I. Theory and preliminary model results. *J Mar Syst* 28:229–267
- Delhez EJM, Campin JM, Hirst AC et al (1999) Toward a general theory of the age in ocean modeling. *Ocean Model* 1:17–27
- Dulaiova H, Burnett WC (2007) Evaluation of the flushing rates of Apalachicola Bay, Florida via natural geochemical tracers. *Mar Chem*. doi:10.1016/j.marchem.2007.09.001
- Dulaiova H, Burnett WC, Wattayakorn G, Sojisuporn P (2006) Are groundwater inputs into river-dominated areas important? The Chao Phraya River – Gulf of Thailand. *Limnol Oceanogr* 51:2232–2247
- Hancock GJ, Martin P (1991) Determination of Ra in environmental samples by alpha-particle spectrometry. *Appl Radiat Isot* 42:63–69
- Helland-Hansen B (1916) Nogen hydrografiske metoder. *Forh Skand Naturf Mote* 16:357–359
- Henry-Edwards A, Tomczak M (2006) Detecting changes in Labrador Sea Water through a water mass analysis of BATS data. *Ocean Sci* 2:19–25
- Hong GH, Zhang J, Chung CS (2002) Impact of interface exchange on the biogeochemical processes of the yellow and East China seas. Bum Shin Press, Korea
- Hong G-H et al (2011) Applications of anthropogenic radionuclides as tracers to investigate marine environmental processes. In: Baskaran M (ed) *Handbook of environmental isotope geochemistry*. Springer, Berlin
- Hougham AL, Moran SB (2007) Water mass ages of coastal ponds estimated using ^{223}Ra and ^{224}Ra as tracers. *Mar Chem* 105:194–207
- Iseki K, Okamura K, Kiyomoto K (2003) Seasonality and composition of downward particulate fluxes at the continental shelf and Okinawa Trough in the East China Sea. *Deep Sea Res* 50:457–473
- Jacobsen JP (1927) Eine graphische Methode zur Bestimmung des Vermischungs-Koeffizienten in Meere. *Gerlands Beitr Geophysik* 16:404
- Katz BG, Coplen TB, Bullen TD et al (1997) Use of chemical and isotopic Tracers to characterize the interactions between ground water and surface water in mantled karst. *Ground Water* 35:1014–1028
- Key RM, Stallard RF, Moore WS et al (1985) Distribution and flux of ^{226}Ra and ^{228}Ra in the Amazon River estuary. *J Geophys Res* 90:6995–7004
- Kim G, Ryu JW, Yang HS et al (2005) Submarine groundwater discharge (SGD) into the Yellow Sea revealed by ^{228}Ra and ^{226}Ra isotopes: implications for global silicate fluxes. *Earth Planet Sci Lett* 237:156–166
- Klein B, Tomczak M (1994) Identification of diapycnal mixing through Optimum Multi-parameter analysis: 2. Evidence for unidirectional diapycnal mixing in the front between North and South Atlantic Central Water. *J Geophys Res* 99:25275–25280
- Krest JM, Moore WS, Rama (1999) ^{226}Ra and ^{228}Ra in the mixing zones of the Mississippi and Atchafalaya Rivers: indicators of groundwater input. *Mar Chem* 64:129–152
- Lakey BL, Krothe NC (1996) Stable isotopic variation of storm discharge from a Perennial karst spring, Indiana. *Water Resour Res* 32:721–731
- Lee ES, Krothe NC (2001) A four-component mixing model for water in a karst terrain in south-central Indiana, USA. Using solute concentration and stable isotopes as tracers. *Chem Geol* 179:129–143
- Li YH, Chan LH (1979) Adsorptions of Ba and ^{226}Ra from river borne sediments in the Hudson estuary. *Earth Planet Sci Lett* 43:343–350
- Liu B, Phillips F, Hoines S et al (1995) Water movement in desert soil traced by hydrogen and oxygen isotopes, chloride, and chlorine-36, southern Arizona. *J Hydrol* 168:91–110
- Maamaatuaiahutapu K, Garcon VC, Provost C et al (1992) Brazil-Malvinas Confluence: water mass composition. *J Geophys Res* 97:9493–9505
- Maamaatuaiahutapu K, Garcon VC, Provost C et al (1994) Spring and winter water mass composition in the Brazil-Malvinas Confluence. *J Mar Res* 52:397–426
- Miller AR (1950) A study of mixing processes over the edge of the continental shelf. *J Mar Res* 9:145–160
- Monsen NE, Cloern JE, Lucas LV (2002) A comment on the use of flushing time, residence time, and age as transport time scales. *Limnol Oceanogr* 47:1545–1553
- Moore WS (1969) The measurements of ^{228}Ra and ^{228}Th in sea water. *J Geophys Res* 74:694–704
- Moore WS (1976) Sampling radium-228 in the deep ocean. *Deep Sea Res* 23:647–651
- Moore WS (1981) Radium isotopes in the Chesapeake Bay. *Estuar Coast Shelf Sci* 12:713–723
- Moore WS (1996) Large ground water inputs to coastal waters revealed by ^{226}Ra enrichments. *Nature* 380:612–614
- Moore WS (1999) The subterranean estuary: a reaction zone of ground water and sea water. *Mar Chem* 65:111–125
- Moore WS (2000) Determining coastal mixing rates using radium isotopes. *Cont Shelf Res* 20:1993–2007
- Moore WS (2003) Sources and fluxes of submarine groundwater discharge delineated by radium isotopes. *Biogeochemistry* 66:75–93
- Moore WS (2006) Radium isotopes as tracers of submarine groundwater discharge in Sicily. *Cont Shelf Res* 26:852–861
- Moore WS, Arnold R (1996) Measurement of ^{223}Ra and ^{224}Ra in coastal waters using a delayed coincidence counter. *J Geophys Res* 101:1321–1329
- Moore WS (2007) Fifteen years experience in measuring ^{224}Ra and ^{223}Ra by delayed-coincidence counting. *Mar Chem*. doi:10.1016/j.marchem.2007.06.015
- Moore DG, Scott MR (1986) Behavior of ^{226}Ra in the Mississippi River mixing zone. *J Geophys Res* 91:14317–14329
- Moore WS, Todd JF (1993) Radium isotopes in the Orinoco estuary and eastern Caribbean Sea. *J Geophys Res* 98:2233–2244
- Moore WS, Sarmiento JL, Key RM (1986) Tracing the Amazon component of surface Atlantic water using ^{228}Ra , salinity and silica. *J Geophys Res* 91:2574–2580
- Moore WS, Blanton JO, Joye SB (2006) Estimates of flushing times, submarine groundwater discharge, and nutrient fluxes to Okatee Estuary, South Carolina. *J Geophys Res* 111:1–14
- Nozaki Y, Kasemuspayya V, Tsubota H (1989) Mean residence time of the shelf water in the East China and Yellow Seas

- determined by $^{228}\text{Ra}/^{226}\text{Ra}$ measurements. *Geophys Res Lett* 16:1297–1300
- Nozaki Y, Tsubota H, Kasempupaya V et al (1991) Residence times of surface water and particle-reactive ^{210}Pb and ^{210}Po in the East China and Yellow seas. *Geochim et Cosmochim Acta* 55:1265–1272
- Pickard GL, Emery WJ (1990) *Descriptive physical oceanography: an introduction*, 5th edn. Pergamon Press, New York
- Poole R, Tomczak M (1999) Optimum multi-parameter analysis of the water mass structure in the Atlantic Ocean thermocline. *Deep Sea Res* 46:1895–1921
- Pougatch K, Salcudean M, Gartshore I et al (2007) Computational modeling of large aerated lagoon hydraulics. *Water Res* 41:2109–2116
- Rama, Moore WS (1996) Using the radium quartet to estimate water exchange and ground water input in salt marshes. *Geochim et Cosmochim Acta* 60:4645–4652
- Rapaglia J, Ferrarin C, Zaggia L et al (2009) Investigation of residence time and groundwater flux in Venice Lagoon: comparing radium isotope and hydrodynamical models. *J Environ Radioact*. doi:10.1016/j.jenvrad.2009.08.010
- Sverdrup HU, Johnson MW, Fleming RH (1946) *The oceans, their physics, chemistry and general biology*. Prentice-Hall, Inc, New York
- Swarzenski PW, Izbicki JA (2009) Examining coastal exchange processes within a sandy beach using geochemical tracers, seepage meters and electrical resistivity. *Estuar Coast Shelf Sci* 83:77–89
- Takeoka H (1984) Fundamental concepts of exchange and transport time scales in a coastal sea. *Cont Shelf Res* 3:322–326
- Tomczak M (1981) A multi-parameter extension of temperature/salinity diagram techniques for the analysis of non-isopycnal mixing. *Prog Oceanogr* 10:147–171
- Vilibic I, Orlic M (2002) Adriatic water masses, their rates of formation and transport through the Otranto Strait. *Deep Sea Res* 49:1321–1340
- Walsh JJ (1991) Importance of continental margins in the marine biogeochemical cycling of carbon and nitrogen. *Nature* 50:53–55
- Yang HS, Hwang DW, Kim G (2002) Factors controlling excess radium in the Nakdong River estuary, Korea: submarine groundwater discharge versus desorption from riverine particles. *Mar Chem* 78:1–8
- Zhang J (2002) Biogeochemistry of Chinese estuaries and coastal waters: nutrients, trace metals and biomarkers. *Reg Environ Change* 3:65–76
- Zhang L, Liu Z, Zhang J et al (2007) Reevaluation of mixing among multiple water masses in the shelf: an example from the East China Sea. *Cont Shelf Res* 27:1969–1979
- Zimmerman JTF (1976) Mixing and flushing of tidal embayments in the Western Dutch Wadden Sea, Part I: distribution of salinity and calculation of mixing time scales. *Nethl J Sea Res* 10:149–191

Chapter 18

Natural Radium and Radon Tracers to Quantify Water Exchange and Movement in Reservoirs

C.G. Smith, P.W. Swarzenski, N.T. Dimova, and J. Zhang

Abstract Radon and radium isotopes are routinely used to quantify exchange rates between different hydrologic reservoirs. Since their recognition as oceanic tracers in the 1960s, both radon and radium have been used to examine processes such as air-sea exchange, deep oceanic mixing, benthic inputs, and many others. Recently, the application of radon-222 and the radium-quartet ($^{223,224,226,228}\text{Ra}$) as coastal tracers has seen a revelation with the growing interest in coastal groundwater dynamics. The enrichment of these isotopes in benthic fluids including groundwater makes both radium and radon ideal tracers of coastal benthic processes (e.g. submarine groundwater discharge). In this chapter we review traditional and recent advances in the application of radon and radium isotopes to understand mixing and exchange between various hydrologic reservoirs, specifically: (1) atmosphere and ocean, (2) deep and shallow oceanic water masses, (3) coastal groundwater/benthic pore waters and surface ocean, and (4) aquifer-lakes. While the isotopes themselves and their distribution in the envi-

ronment provide qualitative information about the exchange processes, it is mixing/exchange and transport models for these isotopes that provide specific quantitative information about these processes. Brief introductions of these models and mixing parameters are provided for both historical and more recent studies.

18.1 Introduction

18.1.1 Hydrologic Cycle

Roughly 97% of the Earth's water resides as salt water in the world's oceans, while the remaining ~3% is sequestered as freshwater in ice caps and glaciers, groundwater, and surface water features such as lakes, rivers, and wetlands (Table 18.1; Fig. 18.1). This water is also the primary transport agent for sediment, solutes, and heat, and the most essential compound for sustaining life on Earth. As a result of human dependencies on these unique characteristics, water and its transfer through the Earth systems has been an active area of human interest for at least 12,000 years (Miller 1982; Hardcastle 1987; Moore et al. 1995). As the Earth is a closed system with respect to water, a global water mass balance (Table 18.1) can be visualized as a group of cyclic processes, such as evaporation and precipitation, that exchange water between three large-scale reservoirs (i.e. ocean, atmosphere, and land). This model represents the water or hydrologic cycle (Fig. 18.2). The purpose of this chapter is to review how the radioisotopes of radium and radon have been utilized as tracers to quantify several hydrologic processes, including water and material exchange across the three main reservoirs and their respective sub-reservoirs. Specific exchange mechanisms addressed in this chapter span

C.G. Smith (✉)
US Geological Survey, 600 4th Street South, St. Petersburg, FL, USA
e-mail: cgsmith@usgs.gov

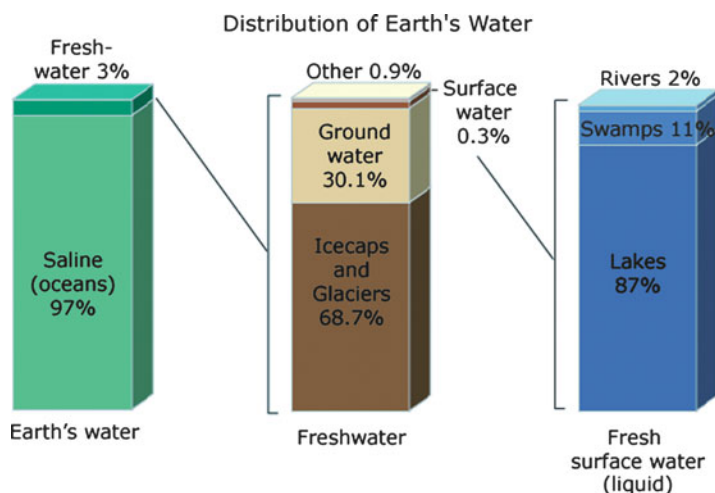
P.W. Swarzenski
US Geological Survey, 400 Natural Bridges Drive, Santa Cruz, CA, USA
e-mail: pswarzen@usgs.gov

N.T. Dimova
UC-Santa Cruz/US Geological Survey, 400 Natural Bridges Drive, Santa Cruz, CA, USA
e-mail: ndimova@usgs.gov

J. Zhang
State Key Laboratory of Estuarine and Coastal Research, East China Normal University, Shanghai 2000062, China
e-mail: jzhang@sklec.ecnu.edu.cn

Table 18.1 List of major reservoirs and sub-reservoirs within the hydrologic cycle and their combined contribution to total water budget and freshwater budget (values obtained from Maidment 1993)

	Volume (km ³)	Percentage of total	Residence time (year)
Water in land areas	47,971,710	3.5	–
Lakes	176,400	0.013	–
Rivers	2,120	0.00015	4
Marshes	11,470	0.00083	–
Groundwater and soil moisture	23,416,500	1.7	20,000
Biological water	1,120	0.00008	–
Icecaps and glaciers	24,364,100	1.8	–
Atmosphere	12,900	0.0009	0.02
Oceans	1,338,000,000	96.5	3,000
Total	1,385,984,610	100	–

**Fig. 18.1** Bar graph showing the two predominant fractions of Earth's water: fresh and saline. The freshwater component is further broken into various fractions or storage (sub)reservoirs. Note, variations in percentages listed in this graph and those

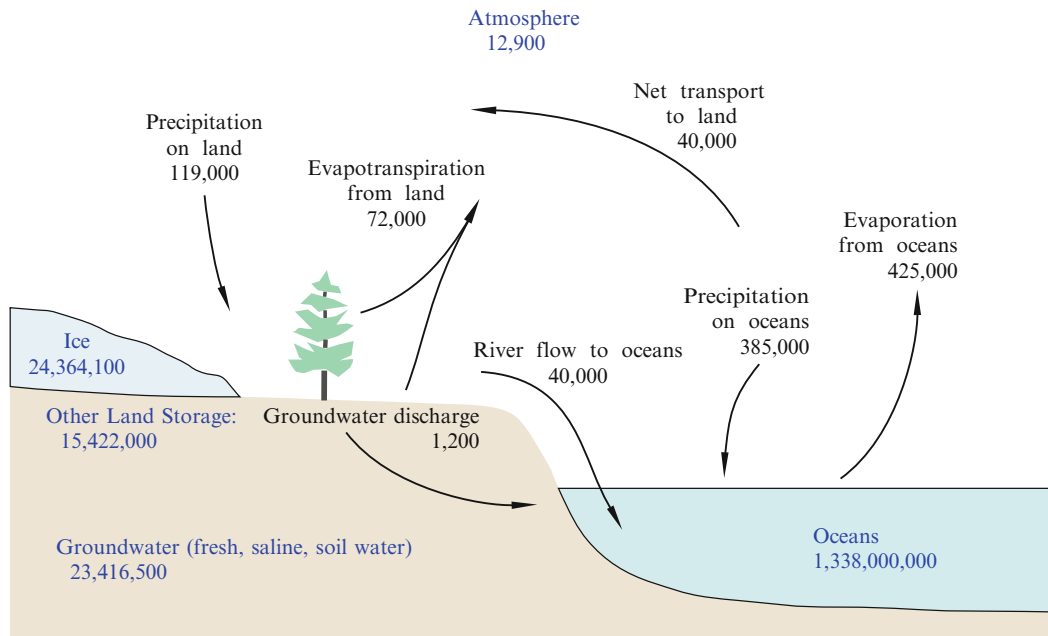
given in Table 18.1 reflect general uncertainty in the division of water into its various forms on Earth. (<http://ga.water.usgs.gov/earthwherewater.html>)

from interstitial fluids to the atmosphere, and include groundwater-coastal water-, riverine-estuarine-, coastal ocean-, and ocean-atmospheric-exchange.

18.1.2 Geochemical and Radiochemical Qualities of Radium-Isotopes

Radium (Ra) is the heaviest (atomic number 88) of the alkaline earth metals, placing it at the base of the second column of the periodic table of elements. Like other alkaline earth metals, radium is a divalent cation (Ra²⁺) and occurs in aquatic environments as either a dissolved cation or as a complex with some anionic ligand. The ionic radius of Ra is 1.40 Å and its ionic potential (Z/r)

is 1.43 (Railsback 2003). In solution, radium behaves very similar to barium (Ba) due to similar ionic potentials ($Ra = 1.43$; $Ba = 1.48$) and substitutes readily for Ba in many minerals (e.g. barite, BaSO₄). The geochemical behavior of Ra and Ba in coastal-marine environments has been studied for over 50 years (e.g. Koczy 1958; Turekian and Johnson 1966; Hanor and Chan 1977; Li and Chan 1979; Key et al. 1985; Moore and Dymond 1991; Webster et al. 1995; Gonnee et al. 2008). In freshwater environments (i.e. ground/surface water), Ra occurs as a dissolved cation that commonly is adsorbed onto negatively-charged clays, mineral coatings, and/or particulate organic matter (Beneš et al. 1984; Langmuir and Riese 1985; Beneš et al. 1986). In contrast, in marine environments Ra remains dissolved (Ra²⁺) or forms complexes with inorganic



Pools are in cubic kilometers

Fluxes are in cubic kilometers per year

Fig. 18.2 Diagrammatic representation of the hydrologic cycle, which shows the predominant (sub) reservoirs (units of km³) and the exchange pathways (units of km³ year⁻¹) among

each. Figure modified from Winter et al. (1998); values obtained from Maidment (1993)

(e.g. RaCl^+ , RaSO_4^0 , RaOH^+) and organic anionic ligands (Lauria et al. 2004). As Ra is transported through estuaries (i.e. mixing between fresh and saline waters) desorption and surface exchange play an important role in its distribution in the water between adsorbed and dissolved phases. This dissimilar behavior in fresh and marine (saline) environments allows Ra to be used to study water mass mixing processes, solute exchange, and fluid exchange between the terrestrial and marine environment (i.e. the land and ocean reservoirs).

There are four naturally occurring isotopes of Ra (^{223}Ra , ^{224}Ra , ^{226}Ra , ^{228}Ra), which have varying half-lives that span from just a few days to over 1,600 year ($t_{1/2}$ ^{223}Ra = 11.4 day, ^{224}Ra = 3.66 day, ^{226}Ra = 1,600 year, and ^{228}Ra = 5.75 year) (Fig. 2.3, Chap. 2). The production of ^{223}Ra , ^{224}Ra , ^{226}Ra , ^{228}Ra is from alpha decay of the strongly particle reactive, sediment-derived, ^{227}Th , ^{228}Th , ^{230}Th , ^{232}Th parents that precede them in the U/Th decay series. The contrasting chemical behavior between Ra and Th generally leads to excess levels of Ra relative to its Th parent in waters in close proximity to sediment sources (i.e. aquifers, estuaries,

pelagic ocean). Also, because the half-life of each Ra isotope is substantially different while each isotope is physicochemically identical, collectively the “Ra-quartet” has been successfully used to examine complex coastal mixing processes and benthic exchange (e.g. Moore 2000a, b).

18.1.3 Geochemical and Radiochemical Qualities of Radon-Isotopes

Radon (Rn) is the heaviest of the noble gases with an atomic number of 86. Because of its balanced outer electron shell, it is chemically inert and behaves conservatively in nearly all chemical reactions in nature (except weak van der Waals bonds). Radon is ubiquitous in the natural environment and found in the atmosphere, trapped in mineral grains, and also dissolved in solution. At standard temperature and atmospheric conditions, the gas solubility constant of Rn in water is $10^{-2.03}$ M ($K = 10^{19.06}$ Bq m⁻³), suggesting that the possibility of saturation is low. There are two

isotopes – radon-222 (^{222}Rn or radon¹) and radon-220 (^{220}Rn or thoron) that are relevant to environmental and hydrologic studies. Both ^{222}Rn and ^{220}Rn are short-lived ($t_{1/2} = 3.82$ days and 55.6 s, respectively), and are produced by the alpha decay of a parent Ra isotope (^{226}Ra and ^{224}Ra , respectively) (Fig. 2.3, Chap. 2). Similar to the Th-Ra parent-daughter relationship, dissimilar geochemical behaviors of Ra and Rn provide for a unique system where the daughter elements can easily decouple, and depending on the environment and processes (turbulent mixing, groundwater flow), either excess or deficiencies of the daughter isotopes relative to their radiogenic parents are likely. To date, ^{222}Rn has been more widely applied to environmental processes than short-lived ^{220}Rn ; however, continued improvements in in situ Rn detection (see Methodology section on Planar silicon detectors) has opened the possibility of using thoron as a powerful hydrologic tracer. Due to its utility more so than its ease of measurement, ^{222}Rn has been used at almost every possible (sub)reservoir interface within the hydrologic cycle (e.g. Broecker et al. 1967; Clements and Wilkening 1974; Hammond et al. 1977; Gruebel and Martens 1984; Hoehn et al. 1992; Bertin and Bourg 1994; Cable et al. 1996a).

18.2 Analysis of Rn and Ra

18.2.1 Radon and Thoron

A variety of analytical techniques exist for quantifying radon and thoron activity; most methods measure particle emission from the Rn isotope (α) and/or daughter isotopes (α/β). For example, ^{222}Rn decay to ^{210}Pb results in three α -particle emissions (Fig. 2.3), all of which are equally detectable. Although other methods exist, the three most commonly used radioanalytical techniques for the measuring Rn in natural waters are the Rn extraction line with Lucas cell system, liquid scintillation counting (LSC) methods, and portable radon-in-air detectors.

One of the earliest and still actively used techniques for measuring Rn and Rn emanation (Ra) is the Rn extraction line with Lucas cell system. The method builds off the closed-vessel experiments by the Curies, Friedrich Ernst Dorn, and Ernest Rutherford that lead to the discovery of a gaseous release from Ra (i.e. radium emanation or radon) and thorium (thorium emanation or thoron) minerals (Rutherford 1906). Detailed procedures are provided in a number of studies and references therein (e.g. Broecker et al. 1967; Key et al. 1979; Mathieu et al. 1988; Cable et al. 1996b; Smith et al. 2008; Peterson et al. 2009b). The system has one of the lowest minimum detection limits/activities (MDL or MDA) and the highest detection efficiencies of all the techniques described in this chapter. Other benefits to this measurement technique are supported ^{222}Rn (^{226}Ra) can be measured on the same sample and the method is non-destructive so that sample can be recovered for additional analysis. However, the sample collection and analysis require substantial preparation and user interaction.

Another common detection method for radon (^{222}Rn) in water is liquid scintillation counting; this technique is widely used in groundwater and pore water studies (e.g. Kitto 1994; Freyer et al. 1997; Purkl and Eisenhauer 2004; Smith et al. 2008) and procedures generally follow Prichard and Gesell (1977). LSC has several advantages that stem from collection to analysis, including rapid and easy sample collection, small sample volumes, high sample throughput (automatic sample changers and pre-set count times), and limited (required) user interaction/involvement during measurements. In addition, modern commercial LSC instruments have a high efficiency (280–340%). Drawbacks of LSC determination of radon are that only total radon is measured, high background can limit MDA, and energy resolution is generally poor. However, improvements to pulse-shape discrimination (PSD) circuitry, coincidence circuitry, and additional high-purity shielding have improved on many of these problems with liquid scintillation analyzers.

More recently, portable radon-in-air monitors coupled with air-water exchangers have been used to provide accurate, near real-time in-situ measurement of Rn dissolved in water (e.g. Burnett and Dulaiova 2003). Commercially available systems are available and are of three general types: (1) portable scintillation or “Lucas” cells and PMTs (e.g. AB-4/AB-4A

¹From this point forward, radon refers to the radionuclide ^{222}Rn unless otherwise indicated.

Portable Radiation Monitors from Pylon Electronics, Inc.); (2) ionization chambers (e.g. TBM-IC-RN by Technical Associates Nuclear Instrumentation); or (3) solid-state (semiconductor) detectors (e.g. RAD7 by Durrige Company, Inc). Critical to these instruments is the extraction of Rn from water into air; this has been accomplished by either sparging a discrete water sample with ambient air (e.g. Lee and Kim 2006) in a closed air loop or by aspirating the water sample into a closed air loop (Burnett et al. 2001; Burnett and Dulaiova 2003; Dulaiova et al. 2005; Dimova et al. 2009). Both techniques have been rigorously tested and verified in both laboratory and field settings (e.g. Burnett et al. 2001; Burnett and Dulaiova 2003; Dulaiova et al. 2005; Lee and Kim 2006). The combined portability of the solid-state detectors and the two quantitative extraction techniques have allowed these systems to be used to map Rn in surface waters (e.g. Dulaiova et al. 2005) as well as provided a more autonomous system for measuring discrete samples, potentially replacing the traditional “radon line” and LSC techniques for discrete samples (Stringer and Burnett 2004; Lee and Kim 2006).

18.2.2 Radium

As with radon and thoron, numerous techniques have been developed to quantify $^{223,224,226,228}\text{Ra}$ isotopes in natural waters (Ivanovich and Murray 1992). Those highlighted in this chapter, which are by no means exhaustive, represent the bulk of the techniques currently used to address the questions concerning fluid and material exchange. Traditional alpha-, beta, or gamma-emissions measurements of appropriate parent or daughter nuclides as well as liquid scintillation (Rutgers van der Loeff and Moore 1999), Rn emanation (Butts et al. 1988), coincidence detection (i.e. α - β , γ - γ) (Antovic and Svrkota 2009), and mass spectrometry (Cohen and O’Nions 1991; Ollivier et al. 2008) have been used for determination of Ra isotopes.

Each of the four Ra isotopes can be very precisely quantified using alpha spectrometry; however, all require antecedent wet-chemistry that is laborious. Thus, indirect ingrowth scintillation methods of Rn-daughters are common. Because of the low activity of $^{223,224,228}\text{Ra}$ in seawater, most of the radioanalytical

techniques require pre-concentration of Ra from large volumes of water. Acrylic fiber impregnated with MnO_2 (i.e. Mn-fiber) or some equivalent (e.g. manufactured MnO_2 cartridge) originally described by Moore and Reid (1973) is the most common pre-concentration media in use today for oceanographic and coastal studies (Bourquin et al. 2008). $^{223,224}\text{Ra}$ isotopes adsorbed on to the Mn-fiber are commonly measured using a delayed coincidence counting method (commonly referred to as RaDeCC) first established by Moore and Arnold (1996). Principles of the RaDeCC system were pioneered by Giffin et al. (1963) who worked on a delayed coincidence method for actinon (^{219}Rn) and thoron (^{220}Rn). Rama et al. (1987) developed a similar recirculating, α -particle measurement system for ^{224}Ra that relied on the ingrowth of ^{220}Rn . However, determination of low-level ^{220}Rn generally required long counting periods and interference from ingrowth ^{222}Rn and its daughter isotopes greatly affected the precision of the instrument. The RaDeCC system can also be used to measure ^{226}Ra on Mn-fiber after an extended 30-day ingrowth period (Waska et al. 2008; Peterson et al. 2009b). Kim et al. (2001) and Dimova et al. (2007) utilized a commercial radon-in-air monitor (RAD7-Durrige Company, Inc) that uses electrostatic attraction to a silicon semiconductor detector to quantify Ra (-224 and -226 specifically) via Rn-ingrowth. One potential problem with these techniques is the reliance on the pre-concentration of Ra onto Mn-fiber. While numerous studies have shown near-quantitative extraction (i.e. nearly 100% adsorption of Ra onto the fiber), a number of other studies have found that the Ra sorption to MnO_2 is sensitive to pH (Bourquin et al. 2008; Dimova et al. 2008), salinity (Moon et al. 2003), and flow-rate (Moon et al. 2003).

Radium-isotopes can also be measured by γ -spectrometry. Each gamma ray photon has a discrete energy, and this energy is characteristic of the source isotope (Michel et al. 1981; Moore 1984; Krishnaswami et al. 1991; Dulaiova and Burnett 2004; van Beek et al. 2010). This measurement technique, while offering the benefit of being minimally destructive and requiring substantially less laboratory time, suffers from usually being less sensitive than standard α - or β -spectrometry methods due to interferences by other gamma-emitting isotopes. As a result, this method is usually applicable to samples containing relatively high activities of $^{226,228}\text{Ra}$.

Measurement of Ra by thermal ionization- and inductively coupled plasma-mass spectrometry (TIMS and ICP-MS, respectively) has increased significantly over the last 20 years (Cohen and O’Nions 1991; Larivière et al. 2003; Ollivier et al. 2008). TIMS has been used to precisely measure the longer-lived $^{226,228}\text{Ra}$ isotopes in a number of field studies where overall activity and/or excess activity were low (Ollivier et al. 2008) and sample volumes were limited (Cohen and O’Nions 1991). However, sample preparation for TIMS is laborious and generally involves the pre-concentration and purification of Ra to remove barium (Ghaleb et al. 2004). Generally speaking, sample preparation times for TIMS are comparable to other radiometric techniques (e.g. α -spectrometry). The advent and progression of high-resolution ICP-MS (HR-ICP-MS) and multiple collector ICP-MS (MC-ICP-MS) have improved the precision and throughput (relative to TIMS) of water samples for Ra analysis (e.g. Varga 2008; Sharabi et al. 2010), often reducing the analytical time for ^{226}Ra to minutes. However, isobaric interferences at the 228 mass often occur with ICP-MS and have limited the detection and quantification of ^{228}Ra via this method (Hou and Roos 2008).

18.3 Application of Radon and Radium to Fluid and Material Exchange Among Hydrologic Reservoirs

18.3.1 Air-Sea Exchange

The exchange of dissolved gases and fluid across the air-sea boundary has been an active area of research for over 60 years (Redfield 1948). However, the importance of the boundary flux has had a substantial revival and progression over the last 20 years due to increased concerns of how the emission of anthropogenic-derived CO_2 and other greenhouse gases will affect global climate and ocean biogeochemistry. While this transfer is not directly facilitated by water (i.e. water is not a “transport agent”), the exchange between two important hydrologic reservoirs (ocean and atmosphere) is the focal point of this globally significant topic, and $^{222}\text{Rn}/^{226}\text{Ra}$ disequilibrium has provided much insight to exchange rates and processes

governing exchange (Peng et al. 1979; Fanning et al. 1982; Kawabata et al. 2003; Schery and Huang 2004; Hirsch 2007). This section provides a brief overview of air-sea exchange and how Rn and Ra isotopes have been used to advance this study. A more comprehensive, updated review of air-sea exchange and its quantification can be found in Liss et al. (1988), Wanninkhof et al. (2009), and references therein.

18.3.1.1 $^{222}\text{Rn}/^{226}\text{Ra}$ Disequilibrium in the Surface Ocean

In 1965, Broecker (1965) suggested that the “discontinuities” (i.e. disequilibrium) between ^{222}Rn and its parent ^{226}Ra in the surface ocean could be used to provide estimates of air-sea exchange, mixing between the surface and deep ocean, and sediment-water (benthic) exchange. Radon’s predictable source/sink terms in the surface ocean, negligible activity in the atmosphere, and its ease of measurement on board ships (using the radon-line and Lucas cell method) made it an attractive tracer to quantify air-sea exchange rates; however, some obstacles for sampling had to be overcome (Peng et al. 1979).

In the surface ocean, the $^{222}\text{Rn}/^{226}\text{Ra}$ disequilibrium originates from the evasion of radon across the air-sea interface. Thus, a near surface water column mass balance of ^{222}Rn ($A_{Rn_{water}}$) can be used to estimate evasion rates or gas transfer velocities (k , m day^{-1}) in the open ocean using (Fig. 18.3)

$$F_{Rn} = k(A_{Rn_{water}} - \alpha A_{Rn_{air}}), \quad (18.1)$$

where F_{Rn} is the flux of radon across air-sea interface ($\text{Bq m}^{-2} \text{day}^{-1}$), α is the Ostwald solubility coefficient (-), and $A_{Rn_{air}}$ is the ^{222}Rn activity in the air (Bq m^{-3}).

Integrating the radon deficit over the thickness of the surface mixed layer provides a deficit inventory of radon (I_{def}) which is proportional to the efflux of radon due to atmospheric evasion (assuming steady-state mixing)

$$F_{^{222}\text{Rn}} = \lambda I_{def} = \lambda \sum_{z=z_{base}}^{z=0} (A_{Rn}(z) - A_{Ra}(z)) \Delta z, \quad (18.2)$$

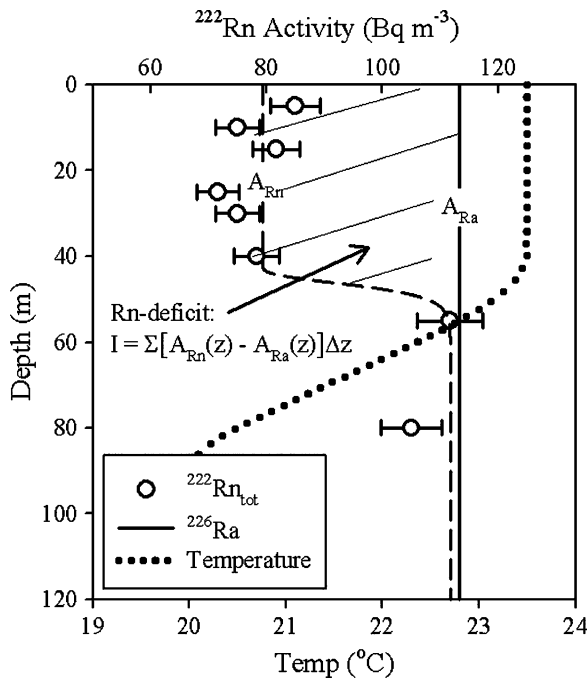


Fig. 18.3 Example of how earlier research where radon was used to evaluate air-sea exchange using a version of the Stagnant Boundary Layer model. The radon deficit is integrated over the upper surface mixed layer (as denoted by both radon and temperature) and used to compute the gas transfer or piston velocity (18.3). Radon data are taken from GEOSECS station number 57 as published by Broecker and Peng (1974) (units were modified from dpm 100 L^{-1} to Bq m^{-3})

where λ is the decay constant of ^{222}Rn (0.181 day^{-1}), $A_{\text{Rn}}(z)$ and $A_{\text{Ra}}(z)$ are the activities (Bq m^{-3}) of ^{222}Rn and ^{226}Ra in the water column, respectively at depth z (m), and Δz is the sample interval (m). Substituting (18.2) into (18.1) and assuming that radon in air is negligible, gas transfer velocity (k) is simply

$$k = \lambda I_{\text{def}} / A_{\text{Rn,water}} \quad (18.3)$$

Broecker et al. (1967) provided a detail proof of concept with data collected from Pacific Ocean (ocean stretch between Hawaii and Japan); however, the data left uncertainties as to the validity of transposing radon based evasion rates to quantifying CO_2 air-sea exchange. Broecker and Peng (1971) used a similar approach at the Bomex site in the Atlantic Ocean; the radon-derived surface boundary layer (SBL) thickness and radon gas transfer velocity were estimated to be

$62 \mu\text{m}$ and 1.9 m day^{-1} , respectively (Table 18.2). Peng et al (1974) followed up with a north Pacific survey at the Papa site; estimates of SBL thickness and radon gas transfer velocity were $20 \mu\text{m}$ and 3.6 m day^{-1} (Table 18.2). Then as part of GEOSECS, Peng et al. (1979) used radon-deficit to quantify gas exchange rates at over 100 sites within the Atlantic and Pacific Oceans, which they used to derive a global gas transfer rate of 2.9 m day^{-1} and a SBL thickness of $36 \mu\text{m}$. The radon-based global gas transfer rate (Peng et al. 1979) agreed favorably well (within 20%) with radiocarbon-based fluxes (Broecker and Peng 1974). Smethie et al. (1985) revisited the transect of Broecker and Peng (1974) and found that radon-estimates of gas exchange rates were within error of those provided by Broecker and Peng (1974) a decade earlier using bomb carbon-14 (^{14}C). Many of these early estimates of radon evasion rates or gas transfer velocities did not specifically address the effects of prolonged storminess or variable wind conditions. In the western North Pacific, Kawabata et al. (2003) estimated gas transfer velocities that ranged from 2.1 to 30.2 m day^{-1} ; which is 1 to $10\times$ the global average proposed by Peng et al. (1979). The higher velocities were related to periods of extended storminess and high apparent wind-speeds, which are not well represented by the steady-state assumption implied in (18.3).

A number of other scientists argued that the gas transfer velocities obtained by Peng et al. (1979) were not consistent with direct estimates of air-sea CO_2 fluxes (e.g. Jones and Smith 1977; Smith and Jones 1985; Liss et al. 1988; Wanninkhof et al. 2009). Peng et al. (1979) admitted to some uncertainty in their own data, as the k values they obtained from the radon-deficit method did not demonstrate a discernible trend with wind speed. The relationship between gas exchange rates and wind speed had already been verified in the laboratory experiments (Broecker et al. 1978). The discrepancy was later shown to reflect the dissimilarity in the time scale of atmospheric forcings (i.e. hours to days) relative to the equilibration of ^{222}Rn in the surface mixed layer (days). That is to say, the ^{222}Rn distributions measured at some point in time in the surface mixed layer is not only a reflection of decay and evasion given the current wind stress, but also had a hysteresis effect from transient atmospheric forcing(s) (Liss et al. 1988; Kawabata et al. 2003; Wanninkhof et al. 2009). If this previous

Table 18.2 Summary table of studies where ^{222}Rn and ^{226}Ra disequilibrium in the surface mixed to determine gas transfer velocities, the general location of each site, temperature (Temp., °C), molecular diffusion coefficient (D_m , $\text{cm}^2 \text{s}^{-1}$), gas transfer velocity (v or k , m day^{-1}), stagnant film thickness (z^* , μm), and gas transfer velocity normalized to 20°C (v_{20} or k_{20} , m day^{-1})

Location	Temp (°C)	D_m ($\text{cm}^2 \text{s}^{-1}$)	k or v (m day^{-1})	z^* (mm)	k_{20} or v_{20} (m day^{-1})	Author
Atlantic Ocean – Bomex	25	1.36E-05	1.91	62	1.6	Broecker and Peng (1971)
North Pacific Ocean – Papa	5	8.10E-06	3.6	20	5.2	Peng et al. (1974)
90-locations Atlantic and Pacific Oceans	20	1.20E-05	2.86	36	2.8	Peng et al. (1979)
18-locations: S. Polar Atlantic, Pacific and Global Oceans	20	1.20E-05	4.1	25	4.0	Peng et al. (1979)
19-locations: S. Temperate Atlantic and Pacific Oceans	20	1.20E-05	2.9	36	2.8	Peng et al. (1979)
24-locations: Equatorial Atlantic and Pacific Oceans	20	1.20E-05	2.1	49	2.0	Peng et al. (1979)
19-locations: N. Temperate Atlantic and Pacific Oceans	20	1.20E-05	2.6	40	2.5	Peng et al. (1979)
10-locations: N. Polar Atlantic and Pacific Oceans	20	1.20E-05	2.6	40	2.5	Peng et al. (1979)
Theoretical for 40 m thick mixed zone	0	7.00E-06	1.5	40	2.5	Broecker and Peng (1982)
Theoretical for 40 m thick mixed zone	24	1.40E-05	3	40	2.5	Broecker and Peng (1982)
Pee Dee River, SC	19.6	1.15E-05	2.7	37	2.8	Elsinger and Moore (1983)
San Francisco Bay – 6 year average	–	–	1.0	–	–	Hartman and Hammond (1984)
26-locations Tropical Atlantic Ocean	26.2	1.42E-05	3.7	34	3.0	Smethie et al. (1985)
Bering Sea*	–	2.74E-07	2.4	42	100.8	Glover and Reeburgh (1987)
Barents Sea – Summer	–	–	1.8	–	3.5	Fanning and Torres (1991)
Barents Sea – Winter	–	–	1.1	–	2.0	Fanning and Torres (1991)
western North Pacific Ocean	20	1.20E-05	9.4	11	9.1	Kawabata et al. (2003)
Upper Gulf of Thailand	–	–	0.38	–	–	Dulaiova and Burnett (2006)

forcing were on different intensity and frequency scales, then the assumption of a steady-state ^{222}Rn distribution would be invalid and likewise the applicability of the model to estimate gaseous transfer.

Kawabata et al. (2003) modified the radon-based gas transfer velocity model to account for sporadic gas exchange. By allowing the radon to exchange with the atmosphere sporadically, (i.e. once or twice per time allotted), the influence of local and regional wind-forcing via storms is more readily represented in a model. Using this approach, the radon activity ($A_{Rn(t)}$; Bq m^{-3}) at any point in time after a sporadic removal and given a prescribed initial gas transfer velocity and mixed layer (i.e. residence time) can be represented by:

$$A_{Rn(t)} = [I_{Rn(t-\Delta t)}e^{-\lambda_{Rn}\Delta t} + A_{Ra}h(e^{-\lambda_{Ra}\Delta t} - e^{-\lambda_{Rn}\Delta t})]/h. \quad (18.4)$$

where; A_{Ra} is the activity of ^{226}Ra in the surface mixed layer (Bq m^{-3}); λ_{Rn} and λ_{Ra} are the decay constants for ^{222}Rn and ^{226}Ra (day^{-1}), respectively; $I_{Rn(t-\Delta t)}$ is the inventory of ^{222}Rn in the surface mixed layer (Bq m^{-2}) for time $t-\Delta t$; h is the thickness of the surface mixed layer (m). The transient gas transfer velocity, $k(t)$ (m day^{-1}) is

$$k(t) = h\lambda_{Rn} \left(\frac{A_{Ra}}{A_{Rn(t)}} - 1 \right). \quad (18.5)$$

This model is not capable of modeling specific wind events but simply addresses how large-scale disturbances influence gas transfer velocities obtained following an event. Kawabata et al. (2003) found that using this approach and assuming a 7-day period between storms, that the steady-state overestimated

gas transfer velocities by less than 20% relative to the sporadic model. Model improvement such as these, which investigate transient impacts to traditionally steady-state assumptions, could represent the next generation of natural tracer estimates of gas transfer between the ocean and atmosphere as well as a means to further refine existing empirical relationships between gas transfer velocities and wind-speed (e.g. MacIntyre et al 1995; Raymond and Cole 2001; Wanninkhof et al. 2009)

Despite the uncertainties and misnomers associated with the radon-derived fluxes, what the radon-deficit method did was start a revelation and progression in air-sea exchange research. For example, Jones and Smith (1977) using eddy correlation technique (i.e. correlation of $p\text{CO}_2$ in the atmosphere and measured wind-speed) to provide some of the first direct measurements of CO_2 flux. Roether and Kromer (1978) and Kromer and Roether (1983) refined atmospheric and aqueous Rn sampling and analyzed the uncertainties with radon-deficit method. While radon is not as widely used to quantify air-sea exchange as it once was; mass balance models are still used, namely the dual-deliberate isotopic methods (e.g. ^3He and SF_6) highlighted by Wanninkhof et al. (1993). Also, the atmospheric radon flux and its parameterization as defined here is one of the key parameters in estimating benthic fluid discharge to the coastal zone as will be described in Sect. 18.3.3 (Cable et al. 1996a, b; Corbett et al. 1997; Burnett and Dulaiova 2003). Modern coastal groundwater studies often use empirical relationships between gas transfer velocities and wind speed (e.g. MacIntyre et al. 1995) and measured radon gradients, temperature, and salinity to estimate atmospheric radon flux. However, re-examination of measured air-sea radon gradients in different coastal

settings and different wind forcing could further refine existing empirical relationships between gas transfer and wind velocities.

18.3.2 Mixing in the Deep and Coastal Ocean

Radium-226 has a mean lifetime, σ , of 2,309 year ($\sigma = \text{decay constant}^{-1}$) that is conveniently in line with the residence time of water in the oceans (~3,200 year; Broecker and Peng 1982; Maidment 1993; Schlesinger 1997). Further, its distribution in the water column is closely tied to the upward diffusion from bottom sediment (Holland and Kulp 1954; Cochran 1980; Cochran et al. 1983; Cochran 1992; Cochran and Kadko 2008) and removal associated with particle scavenging and biological uptake (Broecker and Peng 1982; Ku and Luo 1994; Stewart et al. 2008). Thorium, as the immediate radiogenic parent of Ra, has a very low solubility in seawater that renders the supply of ^{226}Ra from the in situ decay of ^{230}Th mostly negligible. Rivers continuously supply both particulate and dissolved Ra to the ocean and this component usually consists of up to 10% of the total oceanic ^{226}Ra inventory. Global hydrothermal vents contribute another ~5% Ra. As a consequence, ^{226}Ra is ideally suited as a tracer of large scale oceanic mixing, and was used in the seminal work of Koczy (1958) and colleagues in the Baltic Sea. Since then, all the major ocean basins have been examined using ^{226}Ra , and too lesser extent ^{228}Ra , to gain information about water exchange rates across the principal thermoclines and to obtain vertical eddy diffusion coefficients of water mass transport phenomena (Table 18.3).

Table 18.3 Summary of horizontal (K_h) and vertical (K_z) eddy diffusivity coefficients obtained from ^{226}Ra and ^{228}Ra models for various ocean basins

Location	Isotope	K_h ($\text{cm}^2 \text{s}^{-1}$)	K_z ($\text{cm}^2 \text{s}^{-1}$)	Source
Eastern and Central Indian Ocean	^{226}Ra	$10^{4.00}$ – $10^{8.00}$	$10^{-2.00}$ – $10^{1.00}$	Ku and Luo (1994)
Arabian Sea	$^{228}\text{Ra}/^{226}\text{Ra}$	$10^{6.11}$ – $10^{6.49}$	$10^{-0.49}$ – $10^{0.18}$	Somayajulu et al. (1996)
North Pacific	^{226}Ra		$10^{-0.13}$ – $10^{-0.01}$	Chan et al. (1976)
Pacific	^{226}Ra	$10^{5.70}$ – $10^{7.00}$	$\sim 10^{-2.00}$	Chung and Craig (1980)
East Atlantic	^{226}Ra		$10^{-1.00}$ – $10^{1.10}$	Schlitzer (1987), Rhein and Schlitzer (1988)
North Atlantic	^{226}Ra	$10^{7.70}$ – $10^{7.90}$		Sarmiento et al. (1982)
Southern Ocean	$^{226,228}\text{Ra}$		$10^{0.18}$ – $10^{0.75}$	van Beek et al. (2008)
Southern Ocean	$^{223,224}\text{Ra}$; $^{226,228}\text{Ra}$	$10^{0.75}$ – $10^{1.59}$	$10^{0.18}$ – $10^{2.00}$	Charette et al. (2007)

A typical ^{226}Ra profile in the ocean decreases upward through the water column as the distance from sediment/water interface increases. The concave-shape of ^{226}Ra profiles in the open ocean lead to very simple models for vertical exchange across thermoclines and lateral mixing (e.g. Koczy 1958). These simplified models eventually gave way to more sophisticated 2-D advection and diffusion models capable of resolving lateral variations in mixing coefficients (e.g. Ku and Luo 1994) as well as production and consumption associated with particle scavenging and biological uptake (Stewart et al. 2008). A detailed description of the various model types can be found in Ku and Luo (2008). Incorporating results from a variety of model-types, horizontal and vertical diffusivities (K_h and K_z , respectively) estimated by ^{226}Ra and ^{228}Ra for different ocean basins span four orders of magnitude ($K_h = 10^4 - 10^8 \text{ cm}^2 \text{ s}^{-1}$ and $K_z = 10^{-2} - 10^2 \text{ cm}^2 \text{ s}^{-1}$) (Chan et al. 1976; Chung and Craig 1980; Sarmiento et al. 1982; Schlitzer 1987; Rhein and Schlitzer 1988; Ku and Luo 1994; Somayajulu et al. 1996; Charette et al. 2007; van Beek et al. 2008). Overall, despite simplification to a 1-D case, many of the earlier values reported in the literature are still within the uncertainty of the more robust modern models and estimates determined using other radiotracers (e.g. ^3H and ^{14}C) (Ku and Luo 1994). For example, Ra-based K_z values bracket the $0.3 \text{ cm}^2 \text{ s}^{-1}$ vertical mixing coefficient for the global ocean that Toggweiler et al. (1991) derived using a steady-state radiocarbon model.

Lateral transport processes in the water column can result in large discrepancies between diffusive seafloor fluxes and water-column inventories for long-lived ^{226}Ra . In contrast, a reasonable balance between a water-column inventory and a diffusive flux across the sediment/water interface usually is maintained for ^{228}Ra due to its shortened half-life ($t_{1/2} = 5.7$ year). This attribute allows ^{228}Ra to be particularly useful to examine water mixing in regions of the coastal ocean as well as the deep sea, on timescales of up to 30 year. A simple, steady-state 1-D diffusion model has been developed to model the observed seaward exponential decrease of ^{228}Ra in surface waters (Kaufman et al. 1973; Yamada and Nozaki 1986; Moore et al. 1986). Nearshore, ^{228}Ra is often enriched relative to ^{226}Ra and a systematic change in the isotopic ratio of $^{228}\text{Ra}/^{226}\text{Ra}$ as a function of distance away from the shoreline can yield information

on water-mass mixing (horizontal eddy diffusivity) as well as water-mass sources (Moore 1996). Similarly, the two shorter-lived Ra-isotopes ($^{223,224}\text{Ra}$) have also been used to quantify coastal mixing rates (Moore 2000a, b; Burnett et al. 2008; Swarzenski and Izbicki 2009). Moore (2000a) observed that the natural logarithm of the activity of $^{223,224}\text{Ra}$ decreased linearly offshore in the south Atlantic Bight along the southeastern United States coastline. Assuming the water mass becomes isolated from the source and mixes conservatively offshore with losses only by natural radioactive decay, then the slope of the log-linear relationship between Ra-activity and distance offshore could be used to compute a coastal (diffusive) mixing rate (K_h)

$$\ln Ra_x = \ln Ra_0 - xm_1 \quad (18.6a)$$

$$m_1 = \sqrt{\frac{\lambda}{k_h}}, \quad (18.6b)$$

where Ra_x and Ra_0 are the activity of the Ra isotopes at distance x offshore and at the shoreline, respectively and λ is the decay constant of the Ra isotope. Alternatively, Burnett et al. (2008) used the activity ratio of $^{224}\text{Ra}/^{223}\text{Ra}$ to compute an average K_h

$$\ln \left(\frac{^{224}\text{Ra}}{^{223}\text{Ra}} \right)_x = \ln \left(\frac{^{224}\text{Ra}}{^{223}\text{Ra}} \right)_0 - xm_2 \quad (18.7a)$$

$$m_2 = \sqrt{\frac{(\lambda_{224} - \lambda_{223})}{K_h}}. \quad (18.7b)$$

The underlying assumptions of this model are: (1) diffusive-transport dominates, (2) all Ra input occurs at the shoreline (i.e. water mass is disconnected from benthic sources or stratified), and (3) Ra losses are through mixing and/or decay only (Moore 2000a). The activity ratio of $^{224}\text{Ra}/^{223}\text{Ra}$ can also be used to estimate apparent water mass ages in the coastal zone, using an equation similar to (18.8)

$$\left(\frac{^{224}\text{Ra}}{^{223}\text{Ra}} \right)_{\text{sample}} = \left(\frac{^{224}\text{Ra}}{^{223}\text{Ra}} \right)_{\text{source}} \frac{e^{-\lambda_{224}t}}{e^{-\lambda_{223}t}}, \quad (18.8)$$

where the subscripts *sample* and *source* reflect an offshore water column sample and the expected source

of Ra, (e.g. river, estuarine, or groundwater) respectively (Moore 2000b).

As stated earlier, the Ra-quartet has been used in a variety of coastal settings to establish mixing rates and residence times (Table 18.3; also see Zhang et al. 2011). Moore and Todd (1993) used ^{224}Ra and $^{228}\text{Ra}/^{226}\text{Ra}$ to compute apparent ages of water in the Orinoco Estuary and the eastern Caribbean Sea. Based on excess ^{224}Ra data, fresher waters discharged from the Gulf of Paria took anywhere from 0.9 to 9.8 days to thoroughly mix in the Caribbean Sea. Using these apparent ages, current speeds on the order of 15–33 cm s^{-1} were needed to account for the mixing observed (Fig. 18.4). Along the coast of Santa Barbara, CA, USA, Swarzenski and Izbicki (2009) noted much slower mixing rates and current velocities. Based on the short-lived $^{223,224}\text{Ra}$, they estimated mixing rates on the order of $10^{4.12}$ to $10^{4.46} \text{ cm}^2 \text{ s}^{-1}$. Along the west Florida shelf (USA), Smith et al. (2010) reported mixing rates on the order of $10^{5.43}$ – $10^{6.26} \text{ cm}^2 \text{ s}^{-1}$; they noted that the mixing rate was strongly dependent on the offshore extent for which mixing was considered. For example, rates obtained from ^{224}Ra increased an order magnitude when the extent of offshore mixing was extended from 5 to 15 km (Okubo 1971). This distance from shore sensitivity is inevitably tied to the assumptions originally implied when the model was derived (Okubo 1971); namely that the water mass is truly separated from the benthic inputs and completely stratified, such that radioactive decay and mixing must control offshore distribution of Ra. Also in the examples presented (Fig. 18.4b, c), mixing rates derived from ^{224}Ra are larger than those derived from ^{223}Ra . This difference in theory is related to differences in half-lives of the two isotopes and the temporal integration assumed by applying the isotopes to simple mixing equations. Given (18.6b), a similar slope in the natural log of ^{223}Ra and ^{224}Ra would produce mixing rates that differ by a factor of 3 (Charette et al. 2007). The impact of these assumptions on mixing rates is also apparent when considering multiple data sets. For example, mixing rates compiled from 13 different locations incorporating a variety of geologic and hydrodynamic settings vary by over seven orders of magnitude (Table 18.4). While it is not unreasonable that significantly different sites could influence mixing over seven orders of magnitude, it is worth considering

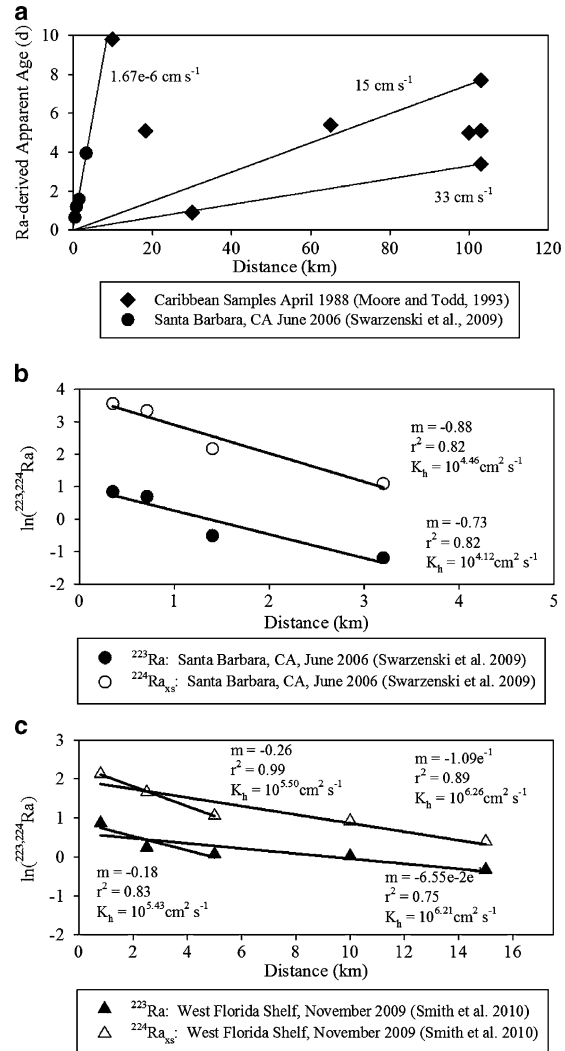


Fig. 18.4 Figure showing various plots of the Ra-derived apparent ages (a) or natural log of the activity of short-lived Ra isotopes ($^{223,224}\text{Ra}$) (b, c) vs. distance offshore compiled from data from Caribbean Sea (Moore and Todd 1993); Santa Barbara, California (Swarzenski and Izbicki 2009); and west Florida shelf (Smith et al. 2010)

how refinement of the model assumptions (i.e. benthic inputs, onshore/offshore advection, etc) might influence the consistency of coastal mixing rates.

Hancock et al. (2006) tested the sensitivity of the Ra-mixing model to benthic inputs with data collected along the Great Barrier Reef and an adjacent lagoon. They found that by including benthic inputs mixing rates decreased by as much as 70% relative to the more

Table 18.4 Summary of horizontal eddy diffusivity coefficients (K_h) obtained from different combinations of $^{223,224,226,228}\text{Ra}$ models for various coastal ocean sites

Location	Isotopes/ratios	K_x ($\text{cm}^2 \text{s}^{-1}$)	Source
Tokyo Bay, Japan and adjacent Shelf	$^{226,228}\text{Ra}$	$10^{5.60} - 10^{7.60}$	Yamada and Nozaki (1986)
Long Island Sound, NY, USA	^{224}Ra	$10^{4.70} - 10^{5.70}$	Torgersen et al. (1996)
South Atlantic Bight, USA	$^{223,224,226,228}\text{Ra}$	$10^{6.56} - 10^{6.62}$	Moore (2000a)
northeastern Gulf of Mexico, USA	^{223}Ra , ^{224}Ra	$10^{4.43}$, $10^{5.08}$	Moore (2003)
Eckernforder Bay, Baltic Sea, Germany	^{224}Ra	$10^{4.0} - 10^{5.70}$	Purkl and Eisenhauer (2004)
Huntington Beach, CA, USA	^{223}Ra , ^{224}Ra	$10^{3.08}$, $10^{3.41}$	Boehm et al. (2006)
West Neck Bay, NY, USA	^{223}Ra	$10^{4.87} - 10^{4.99}$	Dulaiova et al. (2006)
Great Barrier Reef, Australia	$^{223,224}\text{Ra}$	$10^{6.35} - 10^{6.47}$	Hancock et al. (2006)
Ubatuba and Flamengo Bay, Brazil	$^{224}\text{Ra}/^{223}\text{Ra}$	$10^{5.47}$	Burnett et al. (2008)
Drake Passage, Southern Ocean/Antarctic	^{224}Ra	$10^{8.80}$	Dulaiova et al. (2009)
Santa Barbara, California	^{223}Ra , ^{224}Ra	$10^{4.12}$, $10^{4.46}$	Swarzenski and Izbicki (2009)
northeastern Gulf of Mexico, USA	^{223}Ra , ^{224}Ra	$10^{4.99}$, $10^{5.01}$	Santos et al. (2009)
Eastern Gulf of Mexico, USA	$^{223,224}\text{Ra}$	$10^{5.43} - 10^{6.26}$	Smith et al. (2010)

commonly used, simple 1-D mixing model (Hancock et al. 2006). Take for example Fig. 18.4b or c, the slope of radium isotopes offshore remains constant despite the physical process(es) used to model them. For the simple mixing model (Moore 2000a) only mixing (unknown), supply at the shoreline (constant and assumed to be known), and decay (known) are considered, the slope of the offshore gradient implies that turbulent mixing transports the shoreline Ra-signal offshore before it decays away. However, if there were offshore Ra inputs, then turbulent mixing could occur at a slower rate and the same slope could be maintained. Continued refinement of Ra mixing models is occurring, and Zhang et al. (2011) provides derivations for a number of these models. Despite the remaining uncertainties, Ra continues to provide reasonable first-order and sometimes better estimates of coastal mixing that are generally unattainable without sophisticated numerical physical models or large oceanographic surveys.

18.3.3 Benthic Fluxes and Groundwater Discharge

18.3.3.1 Benthic Fluxes and Exchange

Active exchange of fluid across the sediment – water interface is a well-known vector where dissolved constituents in the water column are transported into the sediment and pore water constituents are released into

the water column (e.g. classic textbooks by Berner 1980 and Boudreau 1997). The rate of exchange across the sediment – water interface will ultimately determine the residence time of the fluid in the pore space and influence the transient behavior of chemical reactions that occur between the water and sediment. Quantifying these exchange rates has proven difficult as the size of sediment and pore space vary greatly from one basin to another, and the processes that drive the exchange are numerous (e.g. advection, dispersion, bioturbation, bio-irrigation, etc). Broecker (1965) first suggested radon as a tracer for examining such exchange and interaction. In a symposium note, Broecker (1965) combined the pore water radon data with a simple model of diffusion and a first-order decay equation as a lower boundary condition for water column mass balance of ^{222}Rn in the deep ocean. Numerous other works have built off of this radon pore water profile approach to examine mixing and exchange processes in coastal and marine environments (e.g. Hammond et al. 1977; Hammond and Fuller 1979; Martens et al. 1980; Martin and Sayles 1987; Cable et al. 1996b; Martin et al. 2006, and Smith et al. 2008). In order to quantify rates of exchange, some form of the transient advection-dispersion-reaction equation is used to model the ^{222}Rn pore water distribution:

$$\frac{\partial \varphi C}{\partial t} = \frac{\partial}{\partial z} \left(D_s \varphi \frac{\partial C}{\partial z} \right) - \frac{\partial}{\partial z} (v \varphi C) - \alpha(z) \varphi (C - C_{sw}) + \lambda P - \lambda C, \quad (18.9)$$

where φ is porosity ($-$), C is the pore water concentration of ^{222}Rn (atoms m^{-3}), t is time (day), z is depth (positive downward) (m), D_s is bulk sedimentary diffusion/dispersion coefficient ($\text{m}^2 \text{s}^{-1}$), v is seepage velocity (m s^{-1}), $\alpha(z)$ is a depth-dependant (non-local) mass transfer coefficient (s^{-1}), C_{sw} is the concentration of ^{222}Rn (atoms m^{-3}) in the flushing water of the upper zone, λ is the decay constant for ^{222}Rn ($2.09 \times 10^{-6} \text{s}^{-1}$), and P is the concentration of ^{222}Rn emanated from the sediments and produced by dissolved ^{226}Ra (atoms m^{-3}). On the RHS of (18.9), the first term describes diffusive transport by molecular or dispersive processes; the second term describes advective exchange by pressure gradients (e.g. SGD, wave-induced circulation); the third term describes non-local mixing of porewater with the overlying water column (bioirrigation or non-local advective exchange); the fourth term describes radon production; and the fifth term radon decay. Unknown parameters (e.g. v or $\alpha(x)$) can be estimated by numerically solving (18.9) and minimizing the error between measured and modeled pore water ^{222}Rn (e.g. Meile et al. 2001; Smith et al. 2008).

The above model can be used to evaluate both excess and deficit radon profiles relative to supported fractions. Numerous studies have observed pore water ^{222}Rn deficiencies relative to production from sediment and dissolved ^{226}Ra (e.g. Hammond et al. 1977; Martin and Sayles 1987; Martin et al. 2006; Cable and Martin 2008). In these scenarios (e.g. Martin and Sayles 1987), diffusion or advective exchange occur at time-scale faster than radon production, causing in a radon deficits in the upper 10–20 cm. The rate of advective flow or

biological-processes (i.e. bioturbation or bioirrigation) is quantified using either a numerical or analytical solution to (18.9). In comparison, Smith et al. (2008) found excess radon in shallow pore waters collected along the east coast of Florida. While it was hypothesized that the same shallow mixing processes that cause deficit radon profiles were occurring at this site, additional advective inputs from submarine groundwater discharge delivered radon-enriched groundwater from depth. Smith et al. (2008) reiterated the importance of including non-local processes and more importantly heterogeneous production when considering nearshore pore-water and radon transport.

18.3.3.2 Submarine Groundwater Discharge

The discharge of coastal groundwater is an obvious but hard to quantify pathway for water and associated material transport to the sea (Fig. 18.5). Armed with new geochemical methods for determining submarine groundwater discharge rate measurements, coastal scientists are now assessing the volumetric (Webster et al. 1994; Moore 1996; Burnett et al. 2003, 2006; Cable et al. 1996a, b; Swarzenski and Izbicki 2009) and ecological significance of submarine groundwater discharge (SGD) (Johannes 1980). Observations suggest that the discharge of groundwater into coastal waters may have important environmental consequences because groundwater often carries elevated concentrations of select nutrients, trace elements, radionuclides, and organics. If a coastal groundwater resource has somehow become compromised by salt-water

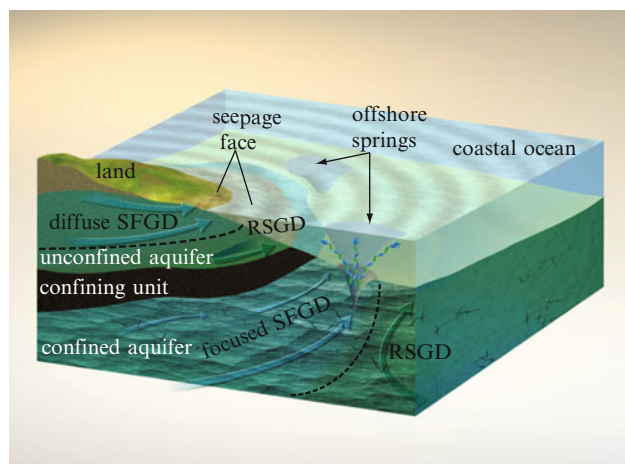


Fig. 18.5 Idealized representation of submarine groundwater discharge, expressed here as discrete springs as well as near-shore diffusive fluxes

intrusion or anthropogenic perturbations, the submarine discharge of this groundwater may directly contribute to the environmental degradation of receiving coastal waters. In this section we briefly explore the unique application of select U/Th series radioisotopes to the study of submarine groundwater discharge.

For almost as long as ^{226}Ra has been utilized as an oceanic water mass tracer, a growing suite of diverse geochemical elements have been explored to quantify rates of fluid exchange across the sediment/water interface. This group of tracers includes: ^{87}Sr , $^{3,4}\text{He}$, ^3H , Fe/Mn, CH_4 , and select U/Th-series isotopes (Cable et al. 1996a, b; Swarzenski 2007; Charette et al. 2008). It is the U/Th-series radionuclides of Ra (e.g. Moore 1996; Rama and Moore 1996; Charette et al. 2001) and Rn (e.g. Cable et al. 1996b; Burnett and Dulaiova 2006; Swarzenski et al. 2007) that have been used extensively to quantify rates of SGD and to identify discharging aquifers. The application of Ra and Rn as SGD tracers is built upon a simple box model that quantifies the removal and supply terms (Fig. 18.6) for a respective radionuclide in a coastal water column (Charette et al. 2008). This balance between supply and removal terms can be expressed as follows:

$$\begin{aligned} \frac{\partial A}{\partial t} = & \left[\frac{A_s - A_0}{T_r} \right] - \left[\frac{QA_r + A_{desorb}}{V} \right] \\ & - \left[\varphi D_s \left(\frac{\partial^2 A_{sed}}{\partial z_{sed}^2} \right) + \omega \left(\frac{\partial A}{\partial z} \right) \right] \\ & + \left[\frac{k(A_s + A_{atm})}{z_{wc}} \right] + \lambda A_s, \end{aligned} \quad (18.10)$$

where the first term on the RHS addresses oceanic exchange (A_s and A_0 = activity of sample and the adjacent ocean, respectively, Bq m^{-3} ; T_r = water residence time, day), the second term quantifies riverine inputs (Q = river discharge, $\text{m}^3 \text{s}^{-1}$; A_r = fresh, riverine activity, Bq m^{-3} ; A_{desorb} = suspended sediment activity available for desorption, Bq m^{-3}), the third addresses benthic flux (φ = sediment porosity, unitless; D_s = molecular diffusion coefficient, $\text{m}^2 \text{s}^{-1}$; ω = advective pore water flux, m s^{-1}), the fourth term accounts for atmospheric evasion (k = piston or gas transfer velocity, m s^{-1} and z_{wc} = depth of the water column, m), and the last term, λA , accounts for radioactive decay. By measuring the radionuclide activity of the discharging groundwater, A_{gw} , and assuming steady-state conditions, one can rearrange the above mass balance equation (after Burnett et al. 2006; Charette et al. 2008) to obtain an SGD rate in terms of $\text{m}^3 \text{m}^{-2} \text{s}^{-1}$ (m s^{-1}):

$$\begin{aligned} SGD = z_w \left(\left[\frac{A_s - A_0}{T_r} \right] - \left[\frac{QA_r + A_{desorb}}{V} \right] \right. \\ \left. - \left[\varphi D_s \left(\frac{\partial^2 A_{sed}}{\partial z_{sed}^2} \right) \right] + \left[\frac{k(A_s + A_{atm})}{z_{wc}} \right] + \lambda A \right) / A_{gw}. \end{aligned} \quad (18.11)$$

Burnett et al. (2007) carefully examined the sensitivity of this ^{222}Rn water column mass balance model for SGD to variations in atmospheric evasion, mixing losses, and groundwater end-member. Of these, the groundwater endmember (A_{gw}) has the most obvious

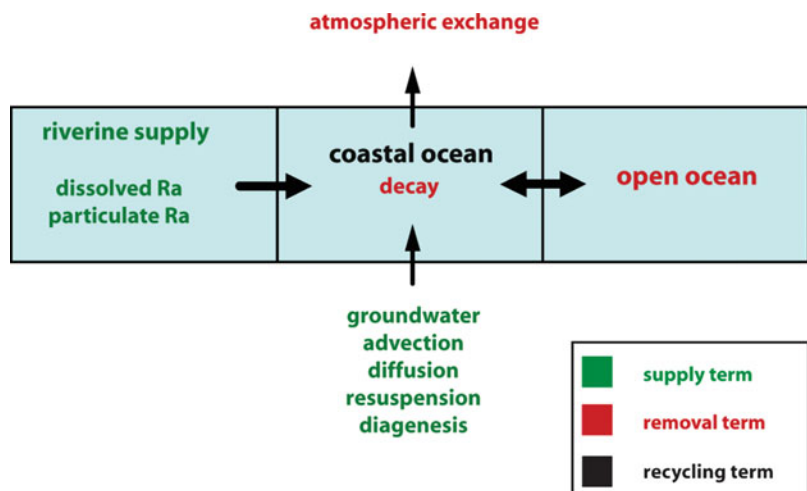


Fig. 18.6 Simplified box model for the application of select U/Th-series isotopes in submarine groundwater discharge studies. Removal and source terms correspond to terms described in (18.11)

influence with a 1:1 inverse relationship with SGD rate. More complicated are the effects of atmospheric evasion (fourth bracketed term on RHS of (18.11)), which generally account for less than 25% of the total radon flux (Burnett et al. 2007). Dulaiova and Burnett (2006) and Burnett et al. (2007) found that for wind speeds less than 10 m s^{-1} , empirical relationships (see section MacIntyre et al. 1995) provide reliable estimates of evasion rates. Import and export of ^{222}Rn into the model via tidal mixing (first bracketed term on RHS of (18.11)) and riverine discharge/offshore mixing (second bracketed term on RHS of (18.11)) are site dependant. Accurate representation of these terms in the model often requires direct or indirect measurements of tidal exchange and/or river discharge. One approach has been to physically instrument the study site with a velocity meter (e.g. ADCP or ADV) and pressure transducer, then compute fluxes using recorded velocity fields, tidal stage, and a representative end-member ^{222}Rn concentration (i.e. ocean, riverine, or estuarine) (Peterson et al. 2009a). When Ra studies are conducted in parallel with Rn studies, $^{223,224}\text{Ra}$ -based mixing coefficients (i.e. (18.4) and (18.5)) can be combined with ^{222}Rn gradients to compute a uni-directional offshore flux (Burnett et al. 2007, 2008). When no other data are available, average negative ^{222}Rn fluxes (i.e. change in inventory over time) are used as representative mixing loss (Burnett et al. 2007). Negative fluxes are generally averaged over a finite time window, usually the local tidal cycle. Refinement in these model parameters will inevitably improve the accuracy of SGD estimates and its role as a coastal vector.

18.3.3.3 Groundwater Discharge into Lakes

Groundwater discharge to a lake can play a major role in its water budget and can also impact its ecological health and general trophic structure (Hayashi and Rosenberry 2002). In the case of seepage lakes, groundwater input is the only substantial source of nutrients besides direct atmospheric deposition. The success of using radon as a groundwater tracer in marine environments in the last few decades has motivated hydrologists to expand its application as a groundwater tracer in fresher water systems, such as, rivers and lakes. While the models developed to interpret radon data for coastal environments can be

complex as corrections for tidal mixing with offshore low-radon waters need to be applied (Burnett and Dulaiova 2003; Burnett et al. 2006), lakes often present a much simpler situation. A single-box model for quantifying groundwater discharge into a lake based on a surface water time-series record of radon inventories was recently developed by Dimova and Burnett (2011). Similar to the coastal SGD radon approach, the lake model for groundwater-surface water interaction is based on a ^{222}Rn water column mass balance. For small seepage lakes, the radon budget is essentially a balance between inflows from groundwater and losses by decay and atmospheric evasion. Thus, this lake radon model requires only equations for radon flux and corrections for radioactive decay. Atmospheric losses through the water-gas interface are evaluated using an empirical relationship for the piston or gas transfer velocity (k ; see Sect. 18.3.1 for background), correlating wind speed and water temperature, as presented in MacIntyre et al. (1995).

$$k(600) = 0.45 \times u_{10}^{1.6} \times (Sc/600)^{-0.5}, \quad (18.12)$$

where u_{10} is the wind speed at 10 m height above the water surface and Sc is the Schmidt number ($Sc = \nu/D_m$). In this case k (i.e. $k(600)$) is normalized to CO_2 at 20°C in freshwater. Although the equation is not strictly derived for radon gas transfer, the relationship could be and has shown to be adequate for evaluating $k(600)$. The diffusion of SF_6 from water surface has similar physics as the diffusion of noble gases, its molecule is non-polar and the molecular weights are not too different. Calculated fluxes based on this equation and another empirical relationship developed specifically for Rn (Hartman and Hammond 1984) showed only 20% difference (Dimova and Burnett 2011). Experience shows that D_m values vary between $10^{-5.086}$ to $10^{-4.824} \text{ cm}^2 \text{ s}^{-1}$ depending on temperature variations. For the same range of temperature and molecular diffusion, Sc calculated were between $10^{2.713}$ and $10^{3.236}$. Main controls include temperature, salinity, and density (respectively kinematic viscosity). Both ν and D_m can be adjusted for temperature changes by well-known relationships. The temperature dependence of the molecular diffusion can be expressed by the equation (Peng et al. 1974; Ullman and Aller 1982):

$$-\log D_m = (980/T_w) + 1.59, \quad (18.13)$$

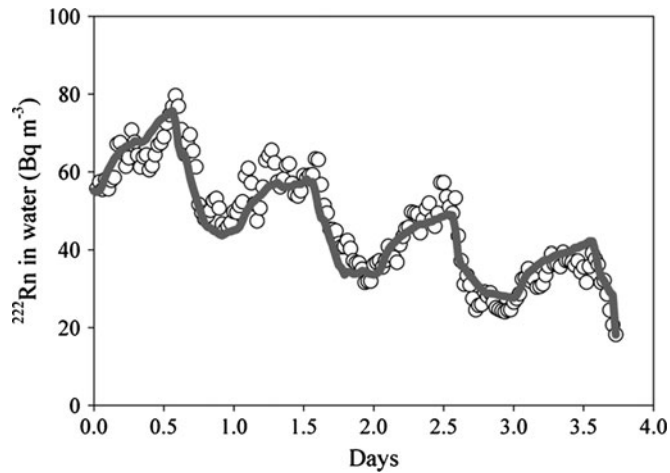


Fig. 18.7 An observed surface-water ^{222}Rn time series in Lake Haines, Florida that can be used to model rates of lacustrine groundwater discharge (modified from Dimova and Burnett 2011)

where T_w is the temperature of the water in K. The kinematic viscosity is a simple ratio of the absolute viscosity, μ , to the density (ρ) of the water at a given temperature:

$$v = \mu/\rho. \quad (18.14)$$

To adjust the absolute viscosity for the differences in the water temperature (T_w in K) the following relationship (Seeton 2006) can be used:

$$\mu = A \times 10^{B(T_w - C)}, \quad (18.15)$$

Where the coefficients in this equation are: $A = 2.414 \times 10^{-5} \text{ kg s}^{-1} \text{ m}^{-1}$ (or Pa s); $B = 247.8 \text{ K}$; and $C = 140 \text{ K}$.

To calculate the water density required in (18.15) as a function of temperature, an empirical relationship for freshwater as derived by Gill (1982) was applied:

$$\begin{aligned} \rho = & 999.842598 + 6.793952 \times 10^{-2} \times T_w \\ & - 9.09529 \times 10^{-3} \times T_w^2 + 1.001685 \\ & \times 10^{-4} \times T_w^3 - 1.120083 \times 10^{-6} \times T_w^4 \\ & + 6.536332 \times 10^{-9} \times T_w^5. \end{aligned} \quad (18.16)$$

Thus, based on information for wind speed and temperature alone, one can model the trends in the radon concentration in the lake by adjusting the radon flux (via groundwater) to balance the observed trends. The minimum root mean square (RMS) error

can be used as a statistical measure to establish best fit between the modeled and observed radon concentration time-series (Fig. 18.7). As in the previously discussed SGD models, one can convert this estimate of the steady-state flux to a water flux by simply dividing by the measured radon-in-groundwater activity. Such a simple, lacustrine groundwater discharge model based solely on Rn offers hydrologists a new tool to easily quantify ground water/surface water exchange.

18.4 Summary and Future Directions

Radium and radon isotopes have proven to be valuable tracers of reservoir exchanges, allowing scientists to quantify fluxes from the ocean to the atmosphere, from land to the ocean, and within the coastal zone. To date, Ra and/or Rn isotopes have been used at almost every hydrological reservoir boundary. Given the diversity of current applied Ra and Rn research, it is difficult to foresee how these radioisotopes will be used to examine additional hydrologic processes. However, improved collection procedures (long-term deployments and in situ measurement) and detection of the short-lived isotopes (i.e. $^{223,224}\text{Ra}$ and $^{219, 220}\text{Rn}$) will inevitably open the door to quantifying processes that occur at much shorter (e.g. advective exchange across rippled bedforms) and longer time-scales (e.g. atmospheric evasion during event and periodic forcing) and smaller spatial-scales (influence of pore-scale diffusion and grain size on current Rn and Ra

source terms) than are currently being examined. These improvements will not only benefit research at new “scales” but also allow scientists to refine current estimates of (hydrologic) reservoir exchange. For example, many of the models that use Rn and Ra to quantify submarine groundwater discharge are relatively young (<15 years) and make various assumptions (e.g. steady-state, uni-directional mixing, isolation of water mass, specific boundary conditions) to simplify the computational aspect of the problem. Thus future research should focus on examining these assumptions in detail, in hopes to removing assumptions outright and having an all-inclusive model. Similarly, the advancement personal computing power over the last 20 years has opened the door to a new application of Ra and Rn data sets, new and old. In some instances this is happening (e.g. Ra in circulation models); however, this approach is not widespread.

Acknowledgments We would like to thank Christopher Conway and Nancy Prouty of the U.S. Geological Survey for reviewing this manuscript prior to publication; their comments and suggestions added greatly to this document. We would also like to thank William Burnett for his comments and suggestions that improved the quality of this manuscript. Any use of trade names is for descriptive purposes only and does not imply endorsement by the U.S. Geological Survey.

References

- Antovic N, Svrkota N (2009) Measuring the radium-226 activity using a multidetector gamma-ray coincidence spectrometer. *J Environ Radioactiv* 100(10):823–830
- Beneš P, Strejc P, Lukavec Z (1984) Interaction of radium with fresh-water sediments and their mineral components. 1 ferric hydroxide and quartz. *J Radioanal Nucl Chem* 82(2):275–285
- Beneš P, Borovec Z, Strejc P (1986) Interaction of radium with fresh-water sediments and their mineral components .3 muscovite and feldspar. *J Radioanal Nucl Chem Art* 98(1):91–103
- Berner RA (1980) *Early diagenesis: a theoretical approach*. Princeton University Press, Princeton
- Bertin C, Bourg CM (1994) Radon-222 and chloride as natural tracers of the infiltration of river water into an alluvial aquifer in which there is significant river/groundwater mixing. *Environ Sci Technol* 28:794–798
- Boehm AB, Paytan A, Shellenbarger GG et al (2006) Composition and flux of groundwater from a California beach aquifer: implications for nutrient supply to the surf zone. *Cont Shelf Res* 26(2):269–282
- Boudreau BP (1997) *Diagenetic models and their implementation: modelling transport and reactions in aquatic sediments*. Springer, New York
- Bourquin M, van Beek P, Reyss JL et al (2008) Comparison of techniques for pre-concentrating radium from seawater. *Mar Chem* 109(3–4):226–237
- Broecker HC, Petermann J, Siems W (1978) The influence of wind on CO₂-exchange in a wind/wave tunnel, including the effects of monolayers. *J Mar Res* 36:595–610
- Broecker WS (1965) An application of natural radon to problems in ocean circulation. In: Ichiye T (ed) *Symposium on diffusion in oceans and fresh waters*. Lamont-Doherty Geological Observatory, Palisades
- Broecker WS, Peng TH (1971) Vertical distribution of radon in Bomex area. *Earth Planet Sci Lett* 11(2):99–108
- Broecker WS, Peng TH (1974) Gas exchange rates between air and sea. *Tellus XXVI*(1–2):21–35
- Broecker WS, Peng TH (1982) *Tracers in the sea*. Lamont-Doherty Geological Observatory, Palisades
- Broecker WS, Li YH, Cromwell J (1967) Radium-226 and Radon-222: concentration in Atlantic and Pacific Oceans. *Science* 158(3806):1307–1310
- Burnett WC, Dulaiova H (2003) Estimating the dynamics of groundwater input into the coastal zone via continuous radon-222 measurements. *J Environ Radioactiv* 69(1–2): 21–35
- Burnett WC, Dulaiova H (2006) Radon as a tracer of submarine groundwater discharge into a boat basin in Donnalucata, Sicily. *Cont Shelf Res* 26:862–873
- Burnett WC, Kim G, Lane-Smith D (2001) A continuous monitor for assessment of Rn-222 in the coastal ocean. *J Radioanal Nucl Chem* 249(1):167–172
- Burnett WC, Bokuniewicz H, Huettel M et al (2003) Groundwater and pore water inputs to the coastal zone. *Biogeochemistry* 66(1–2):3–33
- Burnett WC, Aggarwal PK, Aureli A et al (2006) Quantifying submarine groundwater discharge in the coastal zone via multiple methods. *Sci Total Environ* 367(2–3):498–543
- Burnett WC, Santos IR, Weinstein Y et al (2007) Remaining uncertainties in the use of Rn-222 as a quantitative tracer of submarine groundwater discharge. In: Sanford W, Langevin C, Polemio M, Povinec P (eds) *A new focus on groundwater-seawater interactions*. IAHS Publ, Perugia, 312, pp 125–133
- Burnett WC, Peterson R, Moore WS et al (2008) Radon and radium isotopes as tracers of submarine groundwater discharge – results from the Ubatuba Brazil SGD assessment intercomparison. *Estuar Coast Shelf Sci* 76(3):501–511
- Butts J, Todd JF, Lerche I et al (1988) A simplified method for Ra-226 determinations in natural-waters. *Mar Chem* 25(4):349–357
- Cable JE, Martin JB (2008) In situ evaluation of nearshore marine and fresh pore water transport into Flamengo Bay, Brazil. *Estuar Coast Shelf Sci* 76(3):473–483
- Cable JE, Burnett WC, Chanton JP et al (1996a) Estimating groundwater discharge into the northeastern Gulf of Mexico using Radon-222. *Earth Planet Sci Lett* 144:591–604
- Cable JE, Bugna GC, Burnett WC et al (1996b) Application of ²²²Rn and CH₄ for assessment of groundwater discharge to the coastal ocean. *Limnol Oceanogr* 41(6):1347–1353

- Chan LH, Edmond JM, Stallard RF et al (1976) Radium and barium at GEOSECS stations in the Atlantic and Pacific. *Earth Planet Sci Lett* 32(2):258–267
- Charette MA, Buesseler KO, Andrews JE (2001) Utility of radium isotopes for evaluating the input and transport of groundwater-derived nitrogen to a Cape Cod estuary. *Limnol Oceanogr* 46(2):465–470
- Charette MA, Gonneea ME, Morris PJ et al (2007) Radium isotopes as tracers of iron sources fueling a Southern Ocean phytoplankton bloom. *Deep Sea Res II* 54(18–20):1989–1998
- Charette MA, Moore WS, Burnett WC (2008) Uranium- and thorium-series nuclides as tracers of submarine groundwater discharge. In: Krishnaswami S, Cochran JK (eds) *Radioactivity in the environment*, Vol 13. Elsevier, Oxford
- Chung Y, Craig H (1980) ^{226}Ra in the Pacific Ocean. *Earth Planet Sci Lett* 49(2):267–292
- Clements WE, Wilkening MH (1974) Atmospheric pressure effects on ^{222}Rn transport across the earth-air interface. *J Geophys Res* 79(33):5025–5029
- Cochran JK (1980) The flux of ^{226}Ra from deep-sea sediments. *Earth Planet Sci Lett* 49(2):381–392
- Cochran JK (1992) The oceanic chemistry of the uranium and thorium series nuclides. In: Ivanovich M, Harmon RS (eds) *Uranium series disequilibrium: applications to environmental problems*. Clarendon Press, Oxford
- Cochran JK, Bacon MP, Krishnaswami S et al (1983) ^{210}Po and ^{210}Pb distributions in the central and eastern Indian Ocean. *Earth Planet Sci Lett* 65(2):433–452
- Cochran JK, Kadko DC (2008) Uranium- and thorium-series radionuclides in marine groundwaters. In: Krishnaswami S, Cochran JK (eds) *Radioactivity in the environment*, Vol 13. Elsevier, Oxford
- Cohen AS, O’Nions RK (1991) Precise determination of femto-gram quantities of radium by thermal ionization mass spectrometry. *Anal Chem* 63(23):2705–2708
- Corbett DR, Burnett WC, Cable PH et al (1997) Radon tracing of groundwater input into Par Pond, Savannah River Site. *J Hydrol* 203(1–4):209–227
- Dimova N, Burnett WC, Horwitz EP et al (2007) Automated measurement of ^{224}Ra and ^{226}Ra in water. *Appl Radiat Isot* 65(4):428–434
- Dimova N, Dulaiova H, Kim G et al (2008) Uncertainties in the preparation of ^{224}Ra Mn fiber standards. *Mar Chem* 109(3–4):220–225
- Dimova N, Burnett WC, Lane-Smith D (2009) Improved automated analysis of Radon (^{222}Rn) and Thoron (^{220}Rn) in natural waters. *Environ Sci Technol* 43(22):8599–8603
- Dimova NT, Burnett WC (2011) Evaluation of groundwater discharge into small lakes based on the temporal distribution of radon-222. *Limnol Oceanogr* 56(2):486–494
- Dulaiova H, Burnett WC (2004) An efficient method for γ -spectrometric determination of radium-226,228 via manganese fibers. *Limnol Oceanogr Meth* 2:256–261
- Dulaiova H, Burnett WC (2006) Radon loss across the water-air interface (Gulf of Thailand) estimated experimentally from ^{222}Rn - ^{224}Ra . *Geophys Res Lett* 33(5):L05606
- Dulaiova H, Peterson R, Burnett WC et al (2005) A multi-detector continuous monitor for assessment of Rn-222 in the coastal ocean. *J Radioanal Nucl Chem* 263(2):361–365
- Dulaiova H, Burnett WC, Chanton JP et al (2006) Assessment of groundwater discharges into West Neck Bay, New York, via natural tracers. *Cont Shelf Res* 26(16):1971–1983
- Dulaiova H, Ardelan MV, Henderson PB et al (2009) Shelf-derived iron inputs drive biological productivity in the southern Drake Passage. *Global Biogeochem Cycles* 23:GB4014. doi:10.1029/2008GB003406
- Elsinger RJ, Moore WS (1983) Ra-224, Ra-228, and Ra-226 in Winyah Bay and Delaware Bay. *Earth Planet Sci Lett* 64(3):430–436
- Fanning KA, Torres LM (1991) ^{222}Rn and ^{226}Ra : indicators of sea-ice effects on air-sea gas exchange. *Polar Res* 10(1):51–58
- Fanning KA, Breland JA, Byrne RH (1982) Radium-226 and Radon-222 in the Coastal Waters of West Florida: high concentrations and atmospheric degassing. *Science* 215(4533):667–670
- Freyer K, Treutler HC, Dehnert J et al (1997) Sampling and measurement of radon-222 in water. *J Environ Radioactiv* 37(3):327–337
- Ghaleb B, Pons-Branchu E, Deschamps P (2004) Improved method for radium extraction from environmental samples and its analysis by thermal ionization mass spectrometry. *J Anal At Spectrom* 19(7):906–910
- Giffin C, Kaufman A, Broecker WS (1963) Delayed coincidence counter for the assay of actinon and thoron. *J Geophys Res* 68:1749–1757
- Gill AE (1982) *Atmosphere-ocean dynamics*. Academic, San Diego
- Glover DM, Reeburgh WS (1987) Radon-222 and radium-226 in southeastern Bering Sea shelf waters and sediment. *Cont Shelf Res* 7(5):433–456
- Gonneea ME, Morris PJ, Dulaiova H et al (2008) New perspectives on radium behavior within a subterranean estuary. *Mar Chem* 109(3–4):250–267
- Gruebel KA, Martens CS (1984) Radon-222 tracing of sediment-water chemical transport in an estuarine sediment. *Limnol Oceanogr* 29(3):587–597
- Hammond DE, Fuller C (1979). The use of Radon-222 to estimate benthic exchange and atmospheric exchange rates in San Francisco Bay. *San Francisco Bay: the urbanized estuary* The Pacific Division of the American Association for the Advancement of Science (California Academy of Sciences, San Francisco, CA). pp 213–229
- Hammond DE, Simpson HJ, Mathieu G (1977) Radon-222 distribution and transport across the sediment-water interface in the Hudson River estuary. *J Geophys Res* 82:3913–3920
- Hancock GJ, Webster IT, Stieglitz TC (2006) Horizontal mixing of Great Barrier Reef waters: offshore diffusivity determined from radium isotope distribution. *J Geophys Res* 111(C12):C12019
- Hanor JS, Chan LH (1977) Non-conservative behavior of barium during mixing of Mississippi River and Gulf of Mexico Waters. *Earth Planet Sci Lett* 37(2):242–250
- Hardcastle BJ (1987) Wells ancient and modern; an historical review. *Q J Eng Geol* 20(3):231–238
- Hartman B, Hammond DE (1984) Gas exchange rates across the sediment-water and air-water interfaces in south San Francisco Bay. *J Geophys Res* 89(C3):3593–3603

- Hayashi M, Rosenberry DO (2002) Effects of ground water exchange on the hydrology and ecology of surface water. *Ground Water* 40(3):309–316
- Hirsch AI (2007) On using radon-222 and CO₂ to calculate regional-scale CO₂ fluxes. *Atmos Chem Phys* 7(14):3737–3747
- Hoehn E, von Gunten HR, Stauffer F et al (1992) Radon-222 as a groundwater tracer: a laboratory study. *Environ Sci Technol* 26:734–738
- Holland HD, Kulp LJ (1954) The transport and deposition of uranium, ionium and radium in rivers, oceans and ocean sediments. *Geochim Cosmochim Acta* 5(5):197–213
- Hou X, Roos P (2008) Critical comparison of radiometric and mass spectrometric methods for the determination of radionuclides in environmental, biological and nuclear waste samples. *Anal Chim Acta* 608(2):105–139
- Ivanovich M, Murray A (1992) Spectroscopic methods. In: Ivanovich M, Harmon RS (eds) *Uranium-series disequilibrium: applications to environmental problems*. Clarendon Press, Oxford
- Johannes RE (1980) The ecological significance of the submarine discharge of groundwater. *Mar Ecol-Prog Ser* 3:363–373
- Jones EP, Smith SD (1977) A first measurement of sea-air CO₂ flux by eddy correlation. *J Geophys Res* 82(37):5990–5992
- Kaufman A, Trier RM, Broecker WS et al (1973) Distribution of ²²⁸Ra in the World Ocean. *J Geophys Res* 78(36):8827–8848
- Kawabata H, Narita H, Harada K et al (2003) Air-sea gas transfer velocity in stormy winter estimated from radon deficiency. *J Oceanogr* 59(5):651–661
- Key RM, Brewer RL, Stockwell JH et al (1979) Some improved techniques for measuring radon and radium in marine-sediments and in seawater. *Mar Chem* 7(3):251–264
- Key RM, Stallard RF, Moore WS et al (1985) Distribution and flux of Ra-226 and Ra-228 in the Amazon River Estuary. *J Geophys Res Oceans* 90:6995–7004
- Kim G, Burnett WC, Dulaiova H et al (2001) Measurement of ²²⁴Ra and ²²⁶Ra activities in natural waters using a radon-in-air monitor. *Environ Sci Technol* 35:4680–4683
- Kitto ME (1994) Characteristics of liquid scintillation analysis of radon in water. *J Radioanal Nucl Chem* 185(1):91–99
- Koczy FF (1958) Natural radium as a tracer in the ocean. In: *Proceedings of the second UN international conference on the peaceful uses of atomic energy*. IAEA 18:351–357
- Krishnaswami S, Bhushan R, Baskaran M (1991) Radium isotopes and ²²²Rn in shallow brines, Kharaghoda (India). *Chem Geol* 87(2):125–136
- Kromer B, Roether W (1983). Field measurement of air-sea exchange by the radon deficit method during JASIN 1978 and FGGE 1979. *Meteor Forsch Ergebnisse A/B24:55–75*
- Ku T-L, Luo S (1994) New appraisal of Radium-226 as a large-scale oceanic mixing tracer. *J Geophys Res* 99(C5):10255–10273
- Ku T-L, Luo S (2008) Ocean circulation/mixing studies with decay-series isotopes. In: Krishnaswami S, Cochran JK (eds) *Radioactivity in the environment*, Vol 13. Elsevier, Oxford
- Langmuir D, Riese AC (1985) The thermodynamic properties of radium. *Geochim Cosmochim Acta* 49(7):1593–1601
- Larivière D, Epov VN, Evans RD et al (2003) Determination of radium-226 in environmental samples by inductively coupled plasma mass spectrometry after sequential selective extraction. *J Anal At Spectrom* 18(4):338–343
- Lauria DC, Almeida RMR, Sracek O (2004) Behavior of radium, thorium and uranium in groundwater near the Buena Lagoon in the Coastal Zone of the State of Rio de Janeiro, Brazil. *Environ Geol* 47(1):11–19
- Lee J-M, Kim G (2006) A simple and rapid method for analyzing radon in coastal and ground waters using a radon-in-air monitor. *J Environ Radioactiv* 89(3):219–228
- Li Y-H, Chan L-H (1979) Desorption of Ba and ²²⁶Ra from river-borne sediments in the Hudson estuary. *Earth Planet Sci Lett* 43(3):343–350
- Liss PS, Heimann M, Roether W (1988) Tracers of air-sea gas exchange [and discussion]. *Philos Trans R Soc Lond A* 325 (1583):93–103
- MacIntyre S, Wannikhof R, Chanton JP (1995) Trace gas exchange across the air-water interface in freshwater and coastal marine environments. In: Matson PA, Hariss RC (eds) *Biogenic trace gases: measuring emissions from soil and water*. Blackwell Science, Oxford
- Maidment DR (1993) Hydrology. In: Maidment DR (ed) *Handbook of hydrology*. New York, McGraw-Hill
- Martens CS, Kipphut GW, Klump JV (1980) Sediment-water chemical exchange in the coastal zone traced by in situ Radon-222 flux measurements. *Science* 208(4441):285–288
- Martin JB, Cable JE, Jaeger J et al (2006) Thermal and chemical evidence for rapid water exchange across the sediment-water interface by bioirrigation in the Indian River Lagoon, Florida. *Limnol Oceanogr* 51(3):1332–1341
- Martin WR, Sayles FL (1987) Seasonal cycles of particle and solute transport processes in nearshore sediments: ²²²Rn/²²⁶Ra and ²³⁴Th/²³⁸U disequilibrium at a site in Buzzards Bay, MA. *Geochim Cosmochim Acta* 51:927–943
- Mathieu G, Biscayne P, Lupton R et al (1988) System for measurement of ²²²Rn at low level in natural waters. *Health Phys* 55:989–992
- Meile C, Koretsky CM, Cappellen PV (2001) Quantifying bioirrigation in aquatic sediments: an inverse modeling approach. *Limnol Oceanogr* 46:164–177
- Michel J, Moore WS, King PT (1981) γ -ray spectrometry for determination of radium-228 and radium-226 in natural waters. *Anal Chem* 53(12):1885–1889
- Miller R (1982) Public health lessons from prehistoric times. *World Water* 5:22–25
- Moon DS, Burnett WC, Nour S et al (2003) Preconcentration of radium isotopes from natural waters using MnO₂ Resin. *Appl Radiat Isot* 59(4):255–262
- Moore JE, Zaporozec A, Mercer JW (1995) *Groundwater – a primer*. Childress J (ed) AGI environmental awareness series. American Geological Institute, Arlington
- Moore WS (1984) Radium isotope measurements using germanium detectors. *Nucl Instrum Methods Phys Res* 223:407–411
- Moore WS (1996) Large groundwater inputs to coastal waters revealed by Ra-226 enrichments. *Nature* 380(6575):612–614
- Moore WS (2000a) Determining coastal mixing rates using radium isotopes. *Cont Shelf Res* 20(15):1993–2007
- Moore WS (2000b) Ages of continental shelf waters determined from ²²³Ra and ²²⁴Ra. *J Geophys Res* 105(C9):22117–22122

- Moore WS (2003) Sources and fluxes of submarine groundwater discharge delineated by radium isotopes. *Biogeochemistry* 66:75–93
- Moore WS, Reid DF (1973) Extraction of radium from natural-waters using manganese-impregnated acrylic fibers. *J Geophys Res* 78(36):8880–8886
- Moore WS, Dymond J (1991) Fluxes of Ra-226 and Barium in the Pacific-Ocean - the importance of boundary processes. *Earth Planet Sci Lett* 107(1):55–68
- Moore WS, Todd JF (1993) Radium isotopes in the Orinoco Estuary and eastern Caribbean Sea. *J Geophys Res Oceans* 98(C2):2233–2244
- Moore WS, Arnold R (1996) Measurement of Ra-223 and Ra-224 in coastal waters using a delayed coincidence counter. *J Geophys Res Oceans* 101(C1):1321–1329
- Moore WS, Sarmiento JL, Key RM (1986) Tracing the Amazon component of surface Atlantic Water using Ra-228, salinity and silica. *J Geophys Res Oceans* 91(C2):2574–2580
- Okubo A (1971) Oceanic diffusion diagrams. *Deep Sea Res Oceanogr Abstr* 18(8):789–802
- Ollivier P, Claude C, Radakovitch O et al (2008) TIMS measurements of ^{226}Ra and ^{228}Ra in the Gulf of Lion, an attempt to quantify submarine groundwater discharge. *Mar Chem* 109(3–4):337–354
- Peng TH, Takahashi T, Broecker WS (1974) Surface radon measurements in North Pacific Ocean station Papa. *J Geophys Res* 79(12):1772–1780
- Peng TH, Broecker WS, Mathieu GG et al (1979) Radon evasion rates in the Atlantic and Pacific Oceans as determined during the Geosecs program. *J Geophys Res* 84(C5):2471–2486
- Peterson RN, Santos IR, Burnett WC (2009a) Evaluating groundwater discharge to tidal rivers based on a Rn-222 time-series approach. *Estuar Coast Shelf Sci* 86(2):165–178
- Peterson RN, Burnett WC, Dimova N et al (2009b) Comparison of measurement methods for radium-226 on manganese-fiber. *Limnol Oceanogr Meth* 7:196–205
- Prichard HM, Gesell TF (1977) Rapid measurements of Rn-222 concentration in water with a commercial liquid scintillation counter. *Health Phys* 33:577–581
- Purkl S, Eisenhauer A (2004) Determination of radium isotopes and Rn-222 in a groundwater affected coastal area of the Baltic Sea and the underlying sub-sea floor aquifer. *Mar Chem* 87(3–4):137–149
- Railsback LB (2003) An earth scientist's periodic table of the elements and their ions. *Geology* 31(9):737–740
- Rama, Moore WS (1996) Using the radium quartet for evaluating groundwater input and water exchange in salt marshes. *Geochim Cosmochim Acta* 60(23):4645–4652
- Rama, Todd JF, Butts JL et al (1987) A new method for the rapid measurement of ^{224}Ra in natural waters. *Mar Chem* 22(1):43–54
- Raymond PA, Cole JJ (2001) Gas exchange in rivers and estuaries: choosing a gas transfer velocity. *Estuaries* 24(2):312–317
- Redfield AC (1948) The exchange of oxygen across the sea surface. *J Mar Res* 7:347–361
- Rhein M, Schlitzer R (1988) Radium-266 and barium sources in the deep east atlantic. *Deep Sea Res A* 35(9):1499–1510
- Roether W, Kromer B (1978) Field determination of air-sea gas exchange by continuous measurement of radon-222. *Pure Appl Geophys* 116(2):476–485
- Rutgers van der Loeff MM, Moore WS (1999) Determination of natural radioactive tracers. In: Grasshoff K, Kremling K, Ehrhardt M (eds) *Methods of Seawater Analysis*, 3rd Ed. Wiley-VCH, Weinheim
- Rutherford E (1906) *Radioactive transformation*. Charles Scribner's Sons, New York
- Santos IR, Burnett WC, Dittmar T et al (2009) Tidal pumping drives nutrient and dissolved organic matter dynamics in a Gulf of Mexico subterranean estuary. *Geochim Cosmochim Acta* 73(5):1325–1339
- Sarmiento JL, Rooth C, Broecker W (1982) Radium-228 as a tracer of basin wide processes in the abyssal ocean. *J Geophys Res Oceans* 87:9694–9698
- Seeton CJ (2006) Viscosity-temperature correlation for liquids. *Tribol Lett* 22:67–78
- Schery SD, Huang S (2004) An estimate of the global distribution of radon emissions from the ocean. *Geophys Res Lett* 31(19):L19104
- Schlesinger WH (1997) *Biogeochemistry: an analysis of global change*. Academic Press, Boston
- Schlitzer R (1987) Renewal rates of East-Atlantic Deep-Water estimated by inversion of C-14 data. *J Geophys Res Oceans* 92(C3):2953–2969
- Sharabi G, Lazar B, Kolodny Y et al (2010) High precision determination of Ra-228 and Ra-228/Ra-226 isotope ratio in natural waters by MC-ICPMS. *Int J Mass Spectrom* 294(2–3):112–115
- Smethie WM, Takahashi T, Chipman DW (1985) Gas-exchange and CO_2 flux in the tropical Atlantic Ocean determined from Rn-222 and $p\text{CO}_2$ measurements. *J Geophys Res Oceans* 90(Nc4):7005–7022
- Smith CG, Swarzenski PW, Reich C (2010) Examining the source and magnitude of submarine groundwater discharge along the west Florida shelf, USA. In: *Proceedings of the ASLO/NABS Joint Summer Meeting*, Santa Fe, NM
- Smith CG, Cable JE, Martin JB et al (2008) Evaluating the source and seasonality of submarine groundwater discharge using a Radon-222 pore water transport model. *Earth Planet Sci Lett* 273(3–4):312–322
- Smith SD, Jones EP (1985). Evidence for wind-pumping of air-sea gas-exchange based on direct measurements of CO_2 fluxes. *J Geophys Res Oceans* 90(Nc1):869–875
- Somayajulu BLK, Sarin MM, Ramesh R (1996) Denitrification in the eastern Arabian Sea: evaluation of the role of continental margins using Ra isotopes. *Deep Sea Res II* 43(1):111–117
- Stewart GM, Fowler SW, Fisher NS (2008) The bioaccumulation of U- and Th-series radionuclides in marine organisms. In: Krishnaswami S, Cochran JK (eds) *Radioactivity in the environment*, Vol 13. Elsevier, Oxford
- Stringer C, Burnett WC (2004) Sample bottle design improvements for radon emanation analysis of natural waters. *Health Phys* 87:642–646
- Swarzenski PW (2007) U/Th series radionuclides as coastal groundwater tracers. *Chem Rev* 107(2):663–674
- Swarzenski PW, Izbicki JA (2009) Coastal groundwater dynamics off Santa Barbara, California: combining geochemical tracers, electromagnetic seepmeters, and electrical resistivity. *Estuar Coast Shelf Sci* 83(1):77–89
- Swarzenski PW, Reich C, Kroeger KD et al (2007) Ra and Rn isotopes as natural tracers of submarine groundwater discharge in Tampa Bay, Florida. *Mar Chem* 104(1–2):69–84

- Toggweiler JR, Dixon K, Broecker WS (1991) The Peru upwelling and the ventilation of the South Pacific thermocline. *J Geophys Res* 96:20467–20497
- Torgersen T, Turekian KK, Turekian VC et al (1996) Ra-224 distribution in surface and deep water of Long Island Sound: sources and horizontal transport rates. *Cont Shelf Res* 16 (12):1545–1559
- Turekian KK, Johnson DG (1966) The barium distribution in sea water. *Geochim Cosmochim Acta* 30(11):1153–1174
- Ullman WJ, Aller RC (1982) Diffusion coefficients in nearshore marine sediments. *Limnol Oceanogr* 27(3):552–556
- van Beek P, Souhaut M, Reyss JL (2010) Measuring the radium quartet (^{228}Ra , ^{226}Ra , ^{224}Ra , ^{223}Ra) in seawater samples using gamma spectrometry. *J Environ Radioactiv* 101(7):521–529
- van Beek P, Bourquin M, Reyss JL et al (2008) Radium isotopes to investigate the water mass pathways on the Kerguelen Plateau (Southern Ocean). *Deep Sea Res II* 55(5–7):622–637
- Varga Z (2008) Ultratrace-level radium-226 determination in seawater samples by isotope dilution inductively coupled plasma mass spectrometry. *Anal Bioanal Chem* 390 (2):511–519
- Wanninkhof R, Asher W, Weppernig R et al (1993) Gas transfer experiment on Georges Bank using 2 volatile deliberate tracers. *J Geophys Res Oceans* 98(C11):20237–20248
- Wanninkhof R, Asher WE, Ho DT et al (2009) Advances in quantifying air-sea gas exchange and environmental forcing*. *Ann Rev Mar Sci* 1(1):213–244
- Waska H, Kim S, Kim G et al (2008) An efficient and simple method for measuring Ra-226 using the scintillation cell in a delayed coincidence counting system (RaDeCC). *J Environ Radioactiv* 99(12):1859–1862
- Webster IT, Hancock GJ, Murray AS (1994) Use of radium isotopes to examine pore-water exchange in an estuary. *Limnol Oceanogr* 39:1917–1927
- Webster IT, Hancock GJ, Murray AS (1995) Modelling the effect of salinity on radium desorption from sediments. *Geochim Cosmochim Acta* 59:2469–2476
- Winter TC, Harvey JW, Franke OL et al (1998) Ground water and surface water: a single resource, U.S. Geological Survey Circular 1139. U.S. Geological Survey, Denver
- Yamada M, Nozaki Y (1986) Radium isotopes in coastal and open ocean surface waters of the Western North Pacific. *Mar Chem* 19(4):379–389
- Zhang L, Zhang J, Swarzenski PW, Liu Z (2011) Chapter 19 Radium isotope tracers to evaluate coastal ocean mixing and residence times. In: Baskaran M (ed) *Handbook of environmental isotope geochemistry*. Springer, Berlin

Chapter 19

Applications of Anthropogenic Radionuclides as Tracers to Investigate Marine Environmental Processes

G.-H. Hong, T.F. Hamilton, M. Baskaran, and T.C. Kenna

Abstract Since the 1940, anthropogenic radionuclides have been intentionally and accidentally introduced into the environment through a number of activities including nuclear weapons development, production, and testing, and nuclear power generation. In the ensuing decades, a significant body of research has been conducted that not only addresses the fate and transport of the anthropogenic radionuclides in the marine environment but allows their application as tracers to better understand a variety of marine and oceanic processes. In many cases, the radionuclides are derived entirely from anthropogenic sources and the release histories are well constrained. These attributes, in conjunction with a range of different geochemical characteristics (e.g., half-life, particle affinity, etc.), make the anthropogenic radionuclides extremely useful tools. A number of long-lived and largely soluble radionuclides (e.g., ^3H , ^{14}C , ^{85}Kr , ^{90}Sr , ^{99}Tc , ^{125}Sb , ^{129}I , ^{134}Cs , ^{137}Cs) have been utilized for tracking movement of water parcels in horizontal and vertical directions in the sea, whereas more particle-reactive radionuclides (e.g., ^{54}Mn , ^{55}Fe , ^{103}Ru , ^{106}Ru , Pu isotopes) have been utilized for tracking the movement of particulate matter in the marine environment.

In some cases, pairs of parent-daughter nuclides (e.g., ^3H - ^3He , ^{90}Sr - ^{90}Y and ^{241}Pu - ^{241}Am) have been used to provide temporal constraints on processes such as the dynamics of particles in the water column and sediment deposition at the seafloor. Often information gained from anthropogenic radionuclides provides unique/complementary information to that gained from naturally occurring radionuclides or stable constituents, and leads to improved insight into natural marine processes.

19.1 Introduction

Sustained atmospheric nuclear testings and bomb explosions from 1945 to 1980 in the Equatorial Pacific (Bikini Atoll, Christmas Island, Enewetak Atoll, Johnson Atoll), northern temperate latitudes (Algeria, Japan, Kapustin Yar, Lop Nor, New Mexico, Nevada Test Site, Semipalantinsk, Totsk), polar-north (Nova Zemlya), Southern Hemisphere (Fangatufa Atoll, Malden Island, Maralinga/EMU Test ranges, Monte Bello Islands, Mururoa Atoll) contaminated the entire surface of the earth including the ocean with a suite of anthropogenic radionuclides (Hamilton 2004), ranging from short-lived to long-lived radionuclides (Table 19.1). The oceanic inventory of some selected fallout anthropogenic radionuclides is listed in Table 19.2. Other source terms including effluents from nuclear waste reprocessing plants, nuclear power plants and nuclear weapons production facilities, accidents and losses involving nuclear materials, the burn-up of nuclear powered satellites in the atmosphere have all contributed to the anthropogenic radionuclide contamination (Hong et al. 2004; Linsley et al. 2004). Notably, releases from European nuclear fuel reprocessing facilities (primarily from Sellafield, UK and La Hague, France) have been documented in

G.-H. Hong (✉)
Korea Ocean Research and Development Institute, Ansan
P.O.Box 29 Kyonggi 425–600, South Korea
e-mail: ghhong@kordi.re.kr

T.F. Hamilton
Center for Accelerator Mass Spectrometry, Lawrence Livermore National Laboratory, Livermore, CA 94551–0808, USA

M. Baskaran
Department of Geology, Wayne State University, Detroit, MI 48202, USA

T.C. Kenna
Lamont-Doherty Earth Observatory, Columbia University, Palisades, NY 10964, USA

Table 19.1 List of anthropogenic radionuclides produced and globally dispersed, with their half-lives, decay mode and K_d . (a) Atmospheric nuclear weapon testing and discharge from reprocessing plants. (b) Radionuclides released from nuclear power plants in the United States¹

Radio-nuclide (UNSCEAR 2000)	Half-life (UNSCEAR 2000; Browne and Firestone 1986)	K_d^a	Decay mode (Browne and Firestone 1986)	Daughter (Browne and Firestone 1986)	Dominant form in seawater Byrne (2002) and in the surface of the earth (Bruland 1983; Emsley 1989) (nuclear reactions for the production of radionuclides) (Hou and Roos 2008)
H-3	12.32 a	1×10^0	β	${}^2\text{He-3}$ (stable)	H_2O (gas, liquid, solid), biogenic matter, also produced by the natural process (${}^2\text{H}(\text{n}, \gamma){}^3\text{H}$; ${}^3\text{He}(\text{n}, \text{p}){}^3\text{H}$; ${}^6\text{Li}(\text{n}, \alpha){}^3\text{H}$)
C-14	5730 a	2×10^3	β	${}^7\text{N-14}$ (stable)	Gas CO_2 , liquid, H_2CO_3 , HCO_3^- , CO_3^{2-} , organic matter, biogenic or nonbiogenic (Ca, Mg or other metal) CO_3 , also produced by the natural process
Mn-54	312.5 d	2×10^8	EC, γ	${}^{24}\text{Cr-54}$ (stable)	${}^{14}\text{N}(\text{n}, \text{p}){}^{14}\text{C}$; ${}^{13}\text{C}(\text{n}, \gamma){}^{14}\text{C}$; ${}^{17}\text{O}(\text{n}, \alpha){}^{14}\text{C}$ Ion Mn^{2+} and MnCl^+ , solid MnO_2 , MnCO_3 , earth's crustal material, manganese nodule in the bottom of the sea, ferromanganese oxides (Fe, Mn)Ox, biogenic matter. ($\text{Cr}^{53}(\text{d}, \text{n})\text{Mn}^{54}$) (Kafalas and Irvine 1956)
Fe-55	2.74 a	2×10^8	EC	${}^{25}\text{Mn-54}$ (n, γ), ${}^{25}\text{Mn-55}$ (stable)	$\text{Fe}(\text{OH})_3$, organic complex, contained in the phytoplankton cell, earth's crustal material
Se-79	2.95×10^5 a (Bienvenu et al. 2007)	1×10^3	β	${}^{35}\text{Br-79}$ (stable)	Se, Se^{2+} , SeO_4^{2-} , SeO_3^{2-} , HSeO_3^- , earth's crustal material (${}^{78}\text{Se}(\text{n}, \gamma){}^{79}\text{Se}$; ${}^{235}\text{U}(\text{n}, \text{f}){}^{79}\text{Se}$)
Kr-85	10.72 a	1×10^0	β	${}^{37}\text{Rb-85}$ (stable)	Noble gas, also produced by the natural process
Sr-89	50.55 d	2×10^2	β	${}^{39}\text{Y-91}$	Sr^{2+} , largely soluble in seawater, forms SrSO_4 (celestite) by Acantharia (protozoa) in upper 400 m, earth's crustal material
Sr-90	28.6 a	2×10^2	β	${}^{39}\text{Y-90}$ (2.67 d) to ${}^{40}\text{Zr-90}$ (stable)	${}^{88}\text{Sr}(\text{n}, \gamma){}^{89}\text{Sr}$, (${}^{235}\text{U}(\text{n}, \text{f}){}^{89}\text{Sr}$; ${}^{88}\text{Sr}(\text{n}, \gamma){}^{89}\text{Sr}$, ${}^{235}\text{U}(\text{n}, \text{f}){}^{90}\text{Sr}$)
Y-91	58.51 d	7×10^6	β	${}^{40}\text{Zr-91}$ (stable)	YCO_3^+ , YOH^{2+} , Y^{3+} , particle reactive, earth's crustal material
Zr-93	1.53×10^6 a	7×10^6	β	${}^{41}\text{Nb-93}$	$\text{Zr}(\text{OH})_4^0$, $\text{Zr}(\text{OH})_5^-$, earth's crustal material
Zr-95	64.03 d	7×10^6	β , γ	${}^{41}\text{Nb-95}$ (34.97 d) to ${}^{42}\text{Mo-95}$ (stable)	
Tc-99	2.13×10^5 a	1×10^2	β	${}^{44}\text{Ru-99}$ (stable)	TcO_4^- , earth's crustal material (${}^{235}\text{U}(\text{n}, \text{f}){}^{99}\text{Tc}$; ${}^{98}\text{Mo}(\text{n}, \gamma){}^{99}\text{Mo}(\beta){}^{99}\text{Tc}$)
Ru-103	39.25 d	1×10^3	β , γ	${}^{45}\text{Rh-106}$ (29.8 s) to ${}^{46}\text{Pd-106}$	Earth's crustal material
Sb-125	2.73 a	4×10^3	β , γ	${}^{52}\text{Te-125}$ (stable)	$\text{Sb}(\text{OH})_5^0/\text{Sb}(\text{OH})_6^-$, Earth's crustal material
I-129	1.57×10^7 a	2×10^2	β , γ	${}^{54}\text{Xe-129}$	IO_3^- , I^- Dissolved in the water, incorporated into the seaweeds, lichens, grass, bovine thyroids
I-131	8.02 d	2×10^2	β , γ	${}^{54}\text{Xe-131}$ (stable)	(${}^{129}\text{Xe}(\text{n}, \text{p}){}^{129}\text{I}$; ${}^{235}\text{U}(\text{n}, \text{f}){}^{129}\text{I}$; ${}^{127}\text{I}(\text{n}, \gamma){}^{129}\text{I}$) (${}^{130}\text{Te}(\text{n}, \gamma){}^{131}\text{Te}$ (β^-) ${}^{131}\text{I}$)
Cs-137	30.14 a	2×10^3	β , γ	${}^{56}\text{Ba-137}$ (stable)	Cs^+ , earth's crustal material (${}^{235}\text{U}(\text{n}, \text{f}){}^{137}\text{Cs}$)

(continued)

Table 19.1 (continued)

Radio-nuclide (UNSCEAR 2000)	Half-life (UNSCEAR 2000; Browne and Firestone 1986)	K_d^a	Decay mode (Browne and Firestone 1986)	Daughter (Browne and Firestone 1986)	Dominant form in seawater Byrne (2002) and in the surface of the earth (Bruland 1983; Emsley 1989) (nuclear reactions for the production of radionuclides) (Hou and Roos 2008)
Ba-140	12.75 d	9×10^3	β, γ	$^{57}\text{La-140}$ (1.68 d) to $^{58}\text{Ce-140}$ (stable)	Ba^{2+} , BaSO_4 , earth's crustal material
Ce-141	32.50 d	7×10^7	β, γ	$^{59}\text{Pr-141}$ (stable)	CeCO_3^+ , Ce^{3+} , CeCl^{2+} , earth's crustal material
Ce-144	284.9 d	7×10^7	β, γ	$^{59}\text{Pr-144}$ (7.2 min) to $^{60}\text{Nd-144}$ (2.1×10^5 a) to $^{58}\text{Ce-140}$	
Sm-151	90 a	5×10^5	β	$^{63}\text{Eu-151}$ (stable)	SmCO_3^+ , Sm^{3+} , SmSO_4^+ , earth's crustal material
Eu-155	4.96 a	2×10^6	β, γ	$^{64}\text{Gd-155}$	EuCO_3^+ , Eu^{3+} , EuOH^{2+} , $\text{Eu}(\text{CO}_3)_2^-$, earth's crustal material
Np-237	2.144×10^6 a	1×10^3	α	$^{91}\text{Pa-233}$ (27.01 d)	Trace in uranium mine, $^{238}\text{U}(\text{n}, 2\text{n})^{237}\text{U} \rightarrow ^{237}\text{Np}$; $^{235}\text{U}(\text{n}, \gamma)^{236}\text{U}(\text{n}, \gamma)^{237}\text{U} \rightarrow ^{237}\text{Np}$
Pu-238	87.74 a	1×10^5	α	$^{92}\text{U-234}$	Soluble Pu(V), particulate Pu(IV) $^{235}\text{U}(\text{n}, \gamma)^{236}\text{U}(\text{n}, \gamma)^{237}\text{U}(\beta^-)^{237}\text{Np}(\text{n}, \gamma)^{238}\text{Np}(\beta^-)^{238}\text{Pu}$, $^{238}\text{U}(\text{n}, 2\text{n})^{237}\text{U}(\beta^-)^{237}\text{Np}(\text{n}, \gamma)^{238}\text{Np}(\beta^-)^{238}\text{Pu}$
Pu-239	24,100 a	1×10^5	α, γ	$^{92}\text{U-235}$	$^{238}\text{U}(\text{n}, \gamma)^{239}\text{U}(\beta^-)^{239}\text{Np}(\beta^-)^{239}\text{Pu}$
Pu-240	6560 a	1×10^5	α, γ	$^{92}\text{U-236}$ (2.32×10^7 a)	$^{238}\text{U}(\text{n}, \gamma)^{239}\text{U}(\beta^-)^{239}\text{Np}(\beta^-)^{239}\text{Pu}(\text{n}, \gamma)^{240}\text{Pu}$
Pu-241	14.4 a	1×10^5	β	$^{95}\text{Am-241}$ (432.75 a)	$^{238}\text{U}(\text{n}, \gamma)^{239}\text{U}(\beta^-)^{239}\text{Np}(\beta^-)^{239}\text{Pu}(\text{n}, \gamma)^{240}\text{Pu}(\text{n}, \gamma)^{241}\text{Pu}$
Am-241	432.75 a	2×10^6	α	^{237}Np	$^{241}\text{Pu}(\beta^-)^{241}\text{Am}$
(b)					
Noble gases	^{41}Ar , ^{85}Kr , $^{85\text{m}}\text{Kr}$, ^{87}Kr , $^{131\text{m}}\text{Xe}$, ^{133}Xe , $^{133\text{m}}\text{Xe}$, ^{138}Xe				
Others	^3H , ^{24}Na , ^{51}Cr , ^{54}Mn , ^{55}Fe , ^{56}Mn , ^{57}Co , ^{58}Co , ^{59}Fe , ^{60}Co , ^{65}Zn , ^{89}Sr , ^{90}Sr , ^{92}Sr , ^{95}Nb , ^{95}Zr , ^{97}Nb , ^{97}Zr , ^{99}Mo , $^{99\text{m}}\text{Tc}$, ^{103}Ru , ^{106}Ru , $^{110\text{m}}\text{Ag}$, ^{113}Sn , ^{122}Sb , ^{124}Sb , ^{131}I , ^{132}I , ^{132}Te , ^{133}I , ^{134}Cs , ^{134}I , ^{135}I , ^{136}Cs , ^{137}Cs , ^{138}Cs , ^{139}Ba , ^{140}Ba , ^{140}Pa , ^{141}Ce , ^{143}Ce , ^{144}Ce , ^{187}W , ^{239}Np				

$^a K_d$ (dimensionless) = [concentration per unit mass of particulate (kg/kg or Bq/g dry weight)]/[Concentration per unit mass of water (kg/kg or Bq/kg)]. Value in parenthesis indicate that data area insufficient to calculate K_d s and was chosen to be equal to the K_d s of periodically adjacent elements (IAEA 2004)

Scandinavian waters and the northern portions of the North Atlantic (Irish, North, Norwegian, Barents and Greenland Seas) (Gray et al. 1995; Lindahl et al. 2005). Chernobyl derived contamination has been documented in the Mediterranean Sea and elsewhere (e.g., Buessler and Livingston 1996; Livingston and Povinec 2000; Noureddine et al. 2008; Papucci et al. 1996). Former nuclear weapons program facilities in Siberia (e.g., the Techa and the Tom tributaries of the River Ob, the River Yenisey, Mayak plant explosion in 1957, Karachi Lake in 1967 reported in Vakulovsky 2001) continues to release anthropogenic radionuclides to the Arctic Ocean (e.g., Cooper et al. 1999; Kenna and Sayles

2002). While there is no more direct deposition of fallout to the ocean (ceased since early 1980), a secondary pathway for global fallout nuclides reaching the oceans, such as continental run-off, release of anthropogenic radionuclides from estuarine processes, and atmospheric deposition of continental dust of previously deposited debris, becomes important in some ocean regions.

The anthropogenic radionuclides are the ubiquitous global contaminants as some of them descended from the stratosphere and landed at sea (Tables 19.1 and 19.2). Therefore, they have received great attention from the radiological protection purposes in both the

Table 19.2 Oceanic inventory of fission products and transuranium elements originating from globally dispersed debris, and local and regional deposition from atmospheric nuclear tests, including estimates of regional fallout from Pacific Ocean tests sites and deposition from SNAP-9A decay corrected to 1 January 2000 (reproduced from Hamilton 2004 with some modification, used with permission)

Radio-nuclide	Arctic ocean		Atlantic Ocean		Indian Ocean		Pacific Ocean		Total Oceanic Inventory	
	PBq	Kg	PBq	Kg	PBq	Kg	PBq	Kg	PBq	Kg
³ H									8000 ^a	22
¹⁴ C									130 ^a	3.9
⁹⁰ Sr	2.0	0.40	51	10	22	4	114	23	189	37
⁹⁹ Tc	0.001	1.8	0.03	46	0.01	20	0.07	110	0.11	178
¹²⁹ I	0.000005	0.72	0.0012	18	0.000050	7.7	0.003	43	0.0005	69
¹³⁷ Cs	3.2	1.0	81	25	34	11	182	57	300	93
²³⁷ Np	0.0003	11.3	0.007	263	0.002	94	0.02	888	0.03	1,256
²³⁸ Pu	0.002	0.0032	0.13	0.2	0.11	0.17	0.50	0.78	0.73	1.16
²³⁹ Pu	0.054	23	1.4	591	0.58	250	4.5	2960	6.5	2820
²⁴⁰ Pu	0.036	4.2	0.90	106	0.38	45	4.0	477	5.4	632
²³⁹⁺²⁴⁰ Pu	0.090	28	2.3	697	0.96	295	8.6	2436	12	3,456
²⁴¹ Pu	0.17	0.046	4.3	1.1	1.8	0.48	24	6.2	30	7.9
²⁴² Pu	0.00001	0.091	0.0003	2.3	0.0002	1.0	0.003	22	0.004	26
²⁴¹ Am	0.04	0.29	0.92	7.2	0.39	3.1	3.7	29	5.1	40

^aTaken from Povinec et al. (2010)

terrestrial and marine environment for the past 60 years. As anthropogenic radionuclides are introduced into the sea, they behave almost identical to their stable counterpart (Pu does not have stable nuclide) chemical elements (Table 19.1). Moreover, changes in the level and distribution of specific radionuclides and isotopic ratios in the oceans through radioactive decay and/or transport dynamics provide internal clocks (tracers) of many oceanographic processes including fluxes and input history (e.g., Bowen et al. 1980). The utility of these anthropogenic radionuclides was immediately recognized by the marine science community to apply them to understand the natural marine processes. Often the natural radionuclides present in the earth surface were simultaneously utilized to understand marine biogeochemical processes. The dynamics of water mass movement, biological particle formation, sorption-desorption reactions and decomposition processes, settling rates of particulate matter through the water column, and ultimate deposition of radionuclides onto the seafloor in various ocean basins are of prime interest in ocean geochemistry. In this connection, Broecker (1974) observed that “During the International Geophysical Year (July 1957–December 1958) the atomic technology boom that occurred during the Second World War finally reached the seas. Since then, the field has seen spectacular growth. Great advances have been made in our

understanding of the substances dissolved in the sea and buried in the sediments and their utilization as guides to the nature of both past and present processes within the sea.”

The application of anthropogenic radionuclides has been, however, often limited by the techniques available for sampling and analysis. Earlier analytical methods of most anthropogenic radionuclides required relatively large volumes of seawater (approximately several 100 L), followed by preconcentration and subsequent radiochemical processing and measurements using analysis resulting from radioactive decay using alpha, beta, and gamma ray spectrometers and mass spectrometric atom counting. However, the developments in instrumentation and technology in sample collection, preconcentration, and analysis have reduced the sample size as well as the time involved in processing and measurement of samples for many radionuclides. Readers are advised to consult the sampling and analytical protocols, such as Basakaran et al. (2009), for the individual anthropogenic radionuclide concerned.

A large number of studies of anthropogenic radionuclides in the ocean have contributed either directly or indirectly to the knowledge on the rates, pathways of advection, and physical mixing of ocean water, quantification of marine particle sinking rate and fate in the ocean interior and burial processes in the sea

floor. Numerous studies have applied these man-made tracers to study processes such as velocities of ocean current systems and their mixing rates, particle cycling and transport, sediment accumulation and mixing rates, and pore waters dynamics as well as biological processes (see review articles in Livingston and Povinec 2002; Sholkovitz 1983 and references therein). Here we have collated previous researches that utilize anthropogenic radionuclides to understand processes of circulation and mixing of ocean water, and transport and fate of the particulate matter in the ocean. Application of anthropogenic radionuclides to tracing material transport in the atmosphere, soil, sedimentation dynamics in estuaries, and transuranics are also presented in Chaps. 25 (Matisoff and Whiting), 16 (Du et al.), and 20 (Ketterer et al.), respectively, in this volume.

19.2 Principles of Application

In most cases, the ocean input history of anthropogenic radionuclides is relatively well known; therefore a large number of radionuclides were utilized to trace their carrier phases in the sea as time markers. In particular, a large number of network stations were monitored around the globe by the former Environmental Measurements Laboratory, U.S. Department of Energy and ^{90}Sr fallout were measured over 30 years (from 1952 onwards). Using a constant ratio between ^{90}Sr and other nuclides (such as $^{137}\text{Cs}/^{90}\text{Sr}$, $^{239,240}\text{Pu}/^{90}\text{Sr}$, etc.) in the nuclear-weapons testing-derived fallout, the history of atmospheric fallout of most of anthropogenic radionuclides was documented. Upon reaching the surface of the earth's, each nuclide behaves similar to their stable counterpart chemical elements (except those of plutonium and technetium, as plutonium and ^{99}Tc have no corresponding stable isotopes). The anthropogenic radionuclide carrier phases in the sea are water (dissolved phase), dissolved organic matter, suspended particulate matter, bottom sediments, and biota. The carrier phase of each radionuclide is determined by the chemistry of prevailing redox and acid-base conditions in situ. Chemical forms of radionuclides influence their solubility, cell-membrane transport and bioavailability, adsorptive behavior onto particles, oceanic residence times, and volatility in the sea. In some cases, a pair or multiple anthropogenic radionuclides originated from a particular source could serve to trace the provenance

of the carrier phase material. The daughter products of some of the anthropogenic radionuclides have different particle-affinity than that of their parents and the disequilibrium between the daughters and parents may be used to trace the dynamics of particle formation, sinking rates in the ocean interior and deposition rates on the seafloor. Numerical modeling techniques can be used to improve our understanding of many different environmental processes, and may apply to pollution control on a local, regional and/or planetary scale including climate change predictions. Anthropogenic radionuclides are playing an even important role in helping test the validity of these models by providing ground-truth measurement data on rates and fluxes of carrier phases such as air and water. These measurements are on the input history of radionuclides tracers and their evolution through space and time.

19.2.1 Isotopic Composition of Different Radionuclide Contaminant Sources

The transuranic composition and relative abundance of fission products produced in nuclear explosions are proportional to the duration and intensity of neutron irradiation as well as the isotopic composition of the initial material. More intense the neutron flux (e.g., high versus low burn-up fuels or high versus low explosive yield of an atomic weapon) will lead to a higher proportion of heavier isotopes of transuranics and higher yields of fission products in the irradiated material. For example, fallout debris derived from high yield weapons tests will have a higher $^{240}\text{Pu}/^{239}\text{Pu}$ ratio and contain more ^{137}Cs relative to fallout from a low yield weapons tests. Levels of contamination originating from the reprocessing facilities will differ based on the nature and burn-up characteristics of the fuel (e.g., low burn-up fuel from the production of weapons-grade plutonium or high burn-up fuel resulting from nuclear power generation).

Numerous studies have used the source specific signatures of nuclear contaminants to reconstruct radionuclide time histories and delineate inputs from multiple sources. Much of the available isotopic information documents the isotopic signatures of various sources as they are recorded in different environmental samples (e.g. soils, sediments, biota, ice and water).

Table 19.3 Activity ratios of selected pair of anthropogenic radionuclides useful for marine environmental applications (taken from Hong et al. 2004, used with permission). (a) Activity ratios of selected pair of global fallout radionuclides. (b) Activity and atom ratios of anthropogenic radionuclides originated from various sources other than global fallout. Activity ratios are given at the year 2000

Radionuclides	Activity ratio	Reference
$^3\text{H}/^{90}\text{Sr}$	299	Aarkrog (2003)
$^{14}\text{C}/^{90}\text{Sr}$	0.3424	Aarkrog (2003)
$^{137}\text{Cs}/^{90}\text{Sr}$	1.52	Aarkrog (2003)
$^{238}\text{Pu}/^{239+240}\text{Pu}$	0.030	Baskaran et al. (1995, 2000) ^a
$^{239}\text{Pu}/^{90}\text{Sr}$	0.0105	Aarkrog (2003)
$^{240}\text{Pu}/^{90}\text{Sr}$	0.007	Aarkrog (2003)
$^{241}\text{Pu}/^{90}\text{Sr}$	0.2283	Aarkrog (2003) ^a
$^{241}\text{Pu}/^{239+240}\text{Pu}$	13–14	
$^{240}\text{Pu}/^{239}\text{Pu}$	0.6672 (activity ratio)	Hirose et al. (2001)
$^{239+240}\text{Pu}/^{137}\text{Cs}$	0.182 (atom ratio)	Kelly et al. (1999); Kim et al. (2004)
	0.12 (activity ratio)	Baskaran et al. (1995)

Source	$^{240}\text{Pu}/^{239}\text{Pu}$ (atom ratio)	$^{238}\text{Pu}/^{239+240}\text{Pu}$ (activity ratio)	$^{241}\text{Am}/^{239+240}\text{Pu}$ (activity ratio)	$^{137}\text{Cs}/^{134}\text{Cs}$ (activity ratio)	$^{137}\text{Cs}/^{90}\text{Sr}$ (activity ratio)	$^{239+240}\text{Pu}/^{137}\text{Cs}$ (activity ratio)	$^{238}\text{U}/^{235}\text{U}$ (atom ratio)
Chemobyl	0.40 (Wameke et al. 2002)	0.5 (Hirose et al. 2001)		2 (Aoyama et al. 1991)	12.1 (Aoyama et al. 1991)		
Effluent from Sellafield	0.242 (Lee et al. 2001)	0.27 ± 0.02 (Baskaran et al. 1995)					
dumped reactors in Kara Sea		0.25–0.46 (Baskaran et al. 1995)					
Coral rock and top soil (Mururoa Atoll) (1997)		0.54 ± 0.16 (Irlweck and Hmecek 1999)	1.69 ± 0.51				
Loose coral rocks		30.7 ± 8.6 (Irlweck and Hmecek 1999)	5.0 ± 1.2				
Reactor							
MAGNOX reactor (GCR)		0.23 ^b (Wameke et al. 2002)					15–32 before burn up (Wameke et al. 2002)
Pressurized heavy water reactor (PHWR)		0.41 ^b (Wameke et al. 2002)					
Advanced gas-cooled reactor (AGR)		0.57 ^b (Wameke et al. 2002)					
Pressure tube boiling water reactor (RBMK)		0.67 ^b (Wameke et al. 2002)					

Boiling water reactor (BWR)	0.40 ^b (Warneke et al. 2002)	
Pressurized water reactor (PWR)	0.43 ^b (Warneke et al. 2002)	
Natural uranium		137.88 (Warneke et al. 2002)
Weapon grade uranium		<0.1 (Warneke et al. 2002)
Depleted uranium		250–500 (Warneke et al. 2002)
Weapon production	0.01–0.07 Warneke et al. 2002	
Ivy/Mike shot Eniwetok Island	0.36 (Koide et al. 1985)	
Rongelap atoll	0.276 (Muramatsu et al. 2001)	0.28
Bikini atoll	0.306 (Muramatsu et al. 2001)	0.12
Enewetak atoll (Runit Island)	0.065 (Muramatsu et al. 2001)	34.7
Enewetak atoll (Aej Island)	0.254 (Muramatsu et al. 2001)	1.06
Marshall Island	0.303 (Muramatsu et al. 2001)	0.20
Sempalantinsk, Chenaya Guba, Nevada test sites soils	0.03–0.08 (Muramatsu et al. 2001)	
Nagasaki, Japna	0.037 (Yoshida and Muramatsu 2003)	
Murooa and Fangataufa, sediments	0.035–0.05 (Chiappini et al. 1999)	

^aDecay corrected to the year of 1 January 2000 using Aarkrog (1988) for the northern hemisphere

^bAfter fuel burn-up

A list of useful activity and atom ratios of selected pairs of anthropogenic radionuclides in marine environmental applications are shown in Table 19.3.

19.2.2 Radioactive Fallout from Nuclear Weapons Tests

Atmospheric and aboveground testing of nuclear weapons is significant because it results in the injection of radioactive material into the stratosphere and troposphere; the subsequent deposition of this material on the planet's surface is termed fallout. Fallout can generally be divided into two types: global fallout and local (or close-in) fallout. Global fallout occurs when an explosion of sufficient yield occurs, and the debris is injected into the stratosphere. The deposition pattern of global fallout exhibits a latitudinal dependence with maxima at mid-latitudes and minima at the poles and equator. This is due to the fact that large volumes of air exit the stratosphere via the tropopause discontinuity in the mid-latitudes. Since interhemispheric-stratospheric exchange of materials occurs on longer time scales than materials exchanged between the stratosphere and troposphere, most global fallout is deposited within its hemisphere of origin (Perkins and Thomas 1980).

It is estimated that about 6,500, 4,300, and 40 TBq (4×10^{13} Bq) of ^{239}Pu , ^{240}Pu , and ^{237}Np , respectively have been released globally by the surface and atmospheric weapons tests conducted between 1945 and 1980 (Lindahl et al. 2005). Due to the long half-lives of these radionuclides, these values have not changed substantially. The estimates for ^{137}Cs reached a maximum during the mid to late 1960 of 460 PBq (4.6×10^{17} Bq). Due to its relatively short half-life, this value will have decreased to about 170 PBq by 2010. Of these total, approximately 76% was deposited in the northern hemisphere, nearly all being deposited between 0° N and 70° . Using a value of 55% of oceanic areal coverage, it is estimated that 2,500, 1,600, and 15 TBq and 71 PBq of ^{239}Pu , ^{240}Pu , ^{237}Np , and ^{137}Cs , respectively have been deposited to the marine areas of the Northern Hemisphere (Lindahl et al. 2005; UNSCEAR 2000).

While the initial pathway of fallout nuclides to the marine environment was direct deposition, a secondary pathway for global fallout nuclides reaching the

oceans is continental run-off and related estuarine processes and tropospheric resuspension of previously deposited debris that may serve to modify the global fallout isotopic signatures (e.g., Linsalata et al. 1985; Shlokovitz and Mann 1987; Hamilton et al. 1996; see discussion below about the different geochemical behavior of the radionuclides of interest).

19.2.3 Discharges from the Nuclear Fuel Reprocessing Plant

A number of nuclear fuel reprocessing plants are located at the coast and they discharge radioactive wastes into the sea (Hu et al. 2010). The Sellafield and La Hague in the northern Europe are of global significance in terms of ocean process tracers. The Sellafield Nuclear reprocessing plant has been discharging liquid radioactive wastes containing plutonium isotopes, ^{237}Np , and ^{137}Cs (with some amounts of ^{134}Cs) to the Irish Sea. It has been estimated that 610 and 9.5 TBq (1 TBq = 10^{12} Bq) of $^{239,240}\text{Pu}$ and ^{237}Np , respectively and ~20 PBq (1 PBq = 10^{15} Bq) of ^{137}Cs (decay corrected to 2010) have been released since the plant began operating in 1952 (Assinder 1999; Beasley et al. 1988; Gray et al. 1995; Kuwabara et al. 1996). The reported atom ratios of $^{240}\text{Pu}/^{239}\text{Pu}$ and $^{237}\text{Np}/^{239}\text{Pu}$ in discharges from Sellafield weighted over the operating period of the plant are 0.242 and 1.69, respectively. The La Hague Plant located in the west of Cherbourg, France began operating in 1966. Its radioactive waste discharge peaked in the late 1970 to early 1980. The cumulative discharge from La Hague between 1967 and 1995 was 33, 1,600, 654, 1.3 and 2.5 TBq of ^{60}Co , ^{90}Sr , ^{137}Cs , ^{238}Pu , $^{239+240}\text{Pu}$, respectively (Cundy et al. 2002). The 1997 sample of effluent showed a relatively high $^{240}\text{Pu}/^{239}\text{Pu}$ of 0.34 (Ketterer and Szechenyi 2008). La Hague also discharged ^{129}I as much as 1,640 kg for the period of 1975–1997 (Raisbeck and Yiou 1999).

19.2.4 Chernobyl Derived Contamination

It is estimated that the total activity of $^{239,240}\text{Pu}$ and ^{137}Cs released to the environment as a result of the accident at Chernobyl (April 1986) was 0.055 and 85 PBq (24 PBq in 2010), respectively. Kirchner

and Noack (1988) estimate that the $^{240}\text{Pu}/^{239}\text{Pu}$ and $^{237}\text{Np}/^{239}\text{Pu}$ atom composition in the reactor core at the time of the accident were 0.56 ± 0.16 and 0.023 ± 0.006 , respectively. Although there are no published values for Chernobyl derived ^{237}Np , $^{240}\text{Pu}/^{239}\text{Pu}$ atom ratios of around 0.4 have been determined in soils near the facility (Krey et al. 1986; Muramatsu et al. 2000). Several studies of the Chernobyl accident have shown that the deposition pattern of radioactivity was highly variable over Europe and that the isotopic composition of this material varied throughout the period of the accident (Buesseler and Livingston 1996; Krey et al. 1986; Livingston et al. 1988). Chernobyl-derived ^{137}Cs was estimated to have added 5 and 3 PBq into the Baltic and Black Seas, respectively (Livingston and Povinec 2000) and 3 PBq in the Mediterranean Sea (Papucci et al. 1996).

19.3 Applications of Selected Anthropogenic Radionuclides

19.3.1 Tritium (^3H)

One of the most significant applications of anthropogenic radionuclides to climate studies up to the present is the utilization of the bomb tritium distribution in the North Atlantic (Fig. 19.1). With its presence in intermediate and deep waters, it directly confirmed that the

deep water forms in the North Atlantic as postulated by the box model of global ocean conveyor-belt circulation (Broecker 1974). Before the era of nuclear weapons testing, the world's inventory of cosmic ray-produced tritium was estimated to be ~ 7 kg, however, by the time of the moratorium on widespread testing in 1963 an additional amount of the order of 100 kg had been introduced largely to the northern hemisphere. Both natural and anthropogenic tritium is rapidly transferred to the surface ocean as HTO ($^1\text{H}^3\text{HO}$) via direct precipitation and gas exchange. Tritium decays to ^3He with 12.43 years half-life. Bomb-produced tritium has considerable potential as a tracer for oceanic circulation and for the study of processes with time-scales of less than 100 years due to its short half-life. Tritium is normally reported in Tritium unit (1 TU = 1×10^{-18} atoms of ^3H per atom of hydrogen or 1 tritium atom in 10^{18} hydrogen atoms; 1 TU = 3.19 pCi/L = 118 Bq m^{-3}). In subsurface waters, the ^3He thus formed cannot escape, so that the combined measurements of tritium and the in situ grown ^3He enables tritium– ^3He “dating”, the age is the period since the parcel of water left the surface mixed layer (Roether et al. 1999)

The tritium/ ^3He age, $\tau_{\text{He-3}}$, is calculated using (19.1),

$$\tau_{\text{He-3}} = T_{1/2}/\ln 2 \times \ln(1 + [^3\text{He}_{\text{-tri}}]/[^3\text{H}]) \quad (19.1)$$

where $T_{1/2}$ is a half life of tritium (^3H) and $^3\text{He}_{\text{-tri}}$ is tritogenic ^3He .

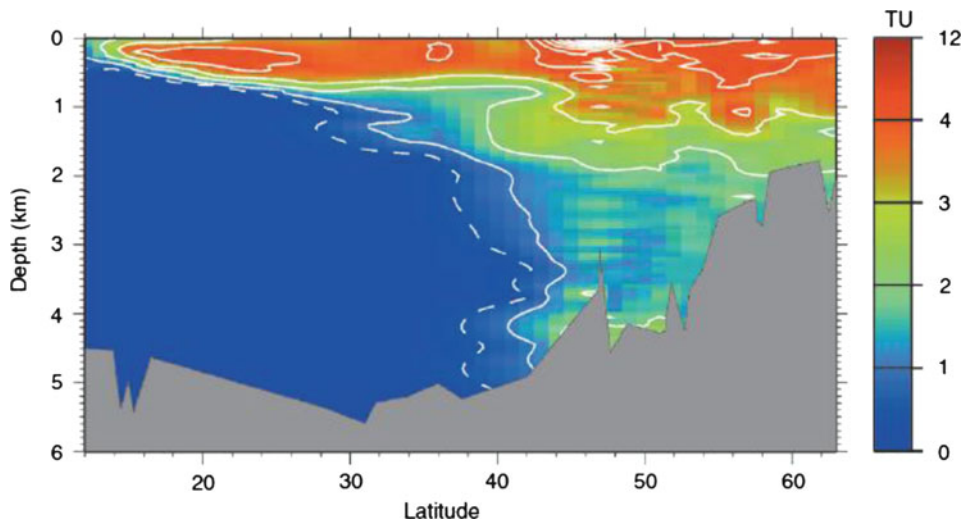


Fig. 19.1 A North Atlantic tritium meridional section in the Denmark Strait to the Central Sargasso Sea taken in the early 1980. The extensive penetration of bomb tritium in the Norwegian Sea (60°N) is clearly visible (Jenkins 2001, used with permission)

Due to radioactive decay, the bomb-produced tritium inventory has reduced from 113,000 PBq at 1963 to 8,000 PBq in 2010 or only about 4 times larger than the natural fallout level. The reprocessing plants-originated ^3H oceanic inventory is estimated to be 45 PBq in 2010 (Povinec et al. 2010). And after cessation of bomb-derived ^3H global fallout in the early 1980, the water circulation and mixing appears to influence ^3H distribution in the ocean more than the atmospheric input in the past.

19.3.2 Radiocarbon (^{14}C)

Radiocarbon is also produced naturally in the atmosphere by nuclear reaction of cosmic ray-produced neutrons with atmospheric nitrogen. The ^{14}C production rate of $2.2 \text{ atoms cm}^{-2} \text{ s}^{-1}$ is balanced by its disintegration by beta decay. During its mean lifetime of 8,200 years radiocarbon can penetrate the active carbon reservoirs through chemical reactions of carbonic acid formation and plant photosynthesis (Fig. 19.2). The production rate of ^{14}C has not been constant with time, and neither have the rates of processes that distribute ^{14}C among various reservoirs. In addition to these natural perturbations, the emission of CO_2 to the atmosphere by fossil fuel combustion has measurably reduced the atmospheric $^{14}\text{C}/^{12}\text{C}$ ratio.

The large input of ^{14}C into the upper atmosphere resulting from nuclear weapon testing became measurable in 1954. At the time of the implementation of the test ban treaty in 1963, the number of nuclear-weapons-derived ^{14}C atoms in the atmosphere was roughly equal to the number of cosmogenic ^{14}C atoms. This excess ^{14}C has decreased to $\sim 10\%$ of the cosmogenic ^{14}C inventory as of the year 2000 (Broecker 2003). This decrease is mainly due to removal of ^{14}C by the exchange with ocean ΣCO_2 and terrestrial biospheric carbon and dilution by the addition of ^{14}C free fossil-fuel-derived CO_2 molecules to the atmosphere (Broecker 2003). And the current atmospheric and biotic mass activities of ^{14}C are close to levels observed prior to atmospheric nuclear weapons testing (Yim and Caron 2006).

As it is difficult to measure absolute ^{14}C concentrations, it is conventional to express ^{14}C determinations as the per mil difference between the specific activity of the sample and 0.95 times the activity of a standard carbon sample ($A_{\text{NBS Std}}$), with the ‘modern’ is defined as the year of 1950. Thus

$$\delta^{14}\text{C} = (A_{\text{sample}} - 0.95A_{\text{NBS Std}}) / (0.95A_{\text{NBS Std}}) \times 1,000 \quad (19.2)$$

The principal modern radiocarbon standard ($A_{\text{NBS Std}}$) is NIST oxalic acid I ($\text{C}_2\text{H}_2\text{O}_4$), made from a crop of 1955 sugar beets. Ninety-five percent of the activity

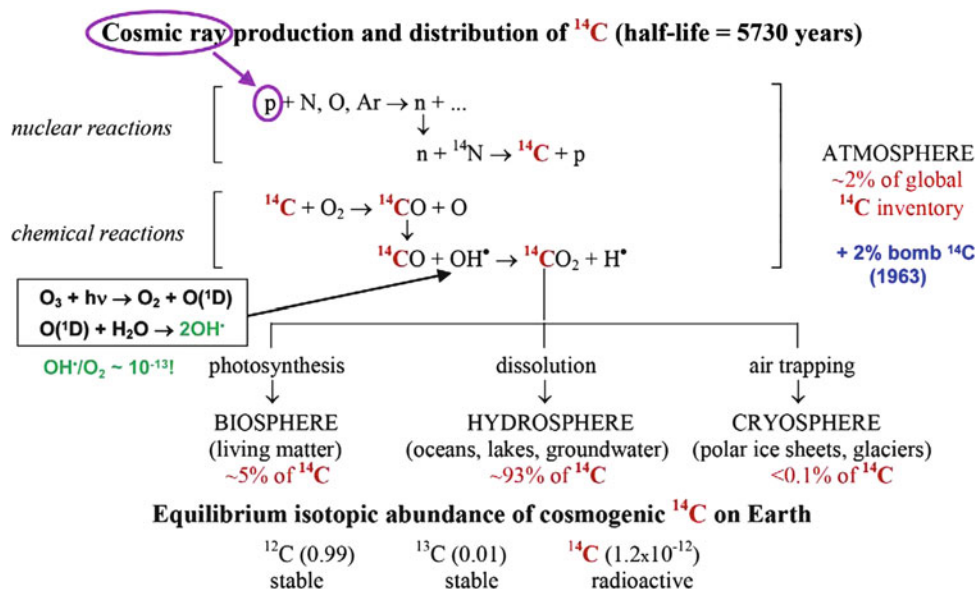


Fig. 19.2 Schematic presentation of the processes leading to the production and distribution of ^{14}C on earth. The sudden increase of ^{14}C in the atmosphere by nuclear weapons testing in the early 1960 is also indicated. (Kutschera 2010, used with permission)

of oxalic acid I from the year 1950 is equal to the measured activity of the absolute radiocarbon standard which is 1890 wood (chosen to represent the pre-industrial atmospheric ^{14}C), corrected for radioactive decay to 1950.

Furthermore, it is necessary to allow for ^{14}C differences produced by isotopic fractionation. This is achieved by use of the $^{13}\text{C}/^{12}\text{C}$ ratio, which is itself also expressed as enrichment:

$$\delta^{13}\text{C}(\text{‰}) = \left[\frac{(^{13}\text{C}/^{12}\text{C})_{\text{sample}} - (^{13}\text{C}/^{12}\text{C})_{\text{standard}}}{(^{13}\text{C}/^{12}\text{C})_{\text{standard}}} \right] \times 1,000 \quad (19.3)$$

Normalized ^{14}C enrichments are then given by the formula:

$$\Delta^{14}\text{C} = \delta^{14}\text{C} - 2(\delta^{13}\text{C} + 25)(1 + \delta^{14}\text{C}/1,000) \text{‰} \quad (19.4)$$

19.3.2.1 Validating Global Ocean Carbon Model

The distribution of bomb-produced ^{14}C in the ocean has been summarized on the basis of radiocarbon measurements made during GEOSECS (Geochemical Ocean Sections Study), TTO (Transient Tracers in the Ocean), and SAVE (South Atlantic Ventilation Experiment) ocean survey programs. The inventory of bomb ^{14}C and the mean penetration depth of this tracer in the water column for the Atlantic (1972–1973), Pacific (1973–1974), and Indian (1977–1978) oceans have been published from the GEOSECS results. To eliminate the time difference, these bomb ^{14}C inventories are normalized to 1 January 1975. This represents the global spatial distribution of bomb ^{14}C tracer, which is required for calibration of ocean models, especially when these models are to be used for estimating the oceanic uptake of CO_2 . In addition, results obtained from expeditions during later years from TTO in the northern and tropical Atlantic (1981–1982), and SAVE in the southern Atlantic (1987–1988) are also published by Broecker et al. (1995). This information depicts the temporal variations of the bomb ^{14}C distribution in the Atlantic Ocean. The evolution of bomb ^{14}C inventory in the ocean with time is another valuable piece of information for verifying the models of the global ocean carbon cycle (Peng et al. 1998).

19.3.2.2 Tracing Dissolved Organic Carbon Sinking in the Sea

According to Beupre and Druffel (2009), dissolved organic carbon (DOC), is largely derived from the autochthonous production in the sun-lit surface ocean, and is the largest reservoir of reduced carbon in the ocean with its magnitude of about 685×10^{15} g C and is comparable to the carbon in the atmosphere in the form of CO_2 . The 4,000–6,000 year ^{14}C ages of deep ocean DOC suggest that a significant portion cycles on longer time scales and ages during deep water transit. The processes that produce these old ages remain unknown. As a tracer of time and carbon sources, the ^{14}C content of marine DOC is a powerful tool for potentially constraining many of these uncertainties. They were able to infer the sinking of DOC from the surface ocean to depths of about 450 m on time scale of months based on the time series observations of $\Delta^{14}\text{C}$ of DOC between 1991 and 2004, and the magnitude and synchronicity of major $\Delta^{14}\text{C}$ anomalies (Beupre and Druffel 2009).

19.3.2.3 Dating Marine Samples for the Recent Past ~60 Years with High Accuracy

Living organisms take up radiocarbon through the food chain and via metabolic processes. This provides a supply of ^{14}C that compensates for the decay of the existing ^{14}C in the organism, establishing equilibrium between the ^{14}C concentration in living organisms and that of the atmosphere. When an organism dies, this supply is cut off and the ^{14}C concentration of the organism starts to decrease by radioactive decay at a rate determined by the radiocarbon half-life. This rate is independent of other physical and environmental factors. The time t elapsed since the organism was originally formed can be determined from (19.5):

$$t = T_{1/2} / \ln 2 \times \ln(N_t/N_o) \quad (19.5)$$

where $T_{1/2}$ is the radiocarbon half-life, N_o is the original ^{14}C concentration in the organism and N_t is its residual ^{14}C concentration at time t (Hua 2009). This method has been utilized extensively for the climate proxies and dating older objects in archaeology. However, we would like to highlight the importance of bomb-derived ^{14}C as the anthropogenic ^{14}C

overwhelmed the naturally produced ^{14}C by masking its natural variability, and thus allowed dating objects of the recent past ~60 years with much greater accuracy than for ^{14}C age-dating conducted during the pre-bomb period, e.g., determination of age-depth model for a salt marsh (Marshall et al. 2007). As another example, accurate measurements of the age of fish provide valuable information for the sustainable management of fish stock in the sea (for dating of fish otoliths, see Chap. 37). Piner et al. (2006) collected otoliths from bocassio rockfish off the coast of Washington State of USA and determined their birth years and inferred that they can live at least 37 years. The age-structured stock assessment is helpful for the fish managers to evaluate the sustainability of the fish populations in the region.

19.3.2.4 Tracing Source of Organic Matter in Estuary

Organic matter is one of the controlling factors determining the fertility and environmental quality of estuaries and coastal oceans. Organic matter may have its origin from in situ primary production, resuspension of the bottom sediment, and terrestrial detritus discharged from surface runoff through rivers and streams. The advantage of ^{14}C determinations over the use of ^{13}C as a marker for the source of organic material is the fact that ^{14}C age of biomass of short living organisms is, unlike $\delta^{13}\text{C}$, the same for all organic constituents, because the effect of isotopic fractionation is removed by the normalization procedure used in ^{14}C age determination as described above. For example, Megens et al. (2001) were able to elucidate that particulate organic matter in the southern North Sea during winter is mainly derived from the resuspension from the bottom sediment by utilizing bomb- ^{14}C signal.

19.3.3 Manganese (^{54}Mn)

^{54}Mn , ^{58}Co , ^{60}Co , ^{134}Cs and ^{137}Cs are among the common beta/gamma emitting radionuclides discharged under normal operating conditions by many nuclear facilities. For instance in 1995, these five isotopes accounted for about 68% of the non-tritium low-level radioactive liquid wastes from French 1,300 MW pressurized reactors. In addition to this radioecological

aspect, the three elements selected present a special interest from a biological standpoint. Cs is biochemically analogous to K while Mn and Co are classified among the ten vital elements for life. Co is vital to many enzymatic systems and to the formation of noble molecules, such as vitamin B-12. Mn is a coactivator of such enzymes as transferases and decarboxylases, and is a constituent of several metalloenzymes, including pyruvate carboxylase and superoxide dismutase. Therefore, these radionuclides could be used to study metal physiology, e.g., trophic transfer factors, in biological organisms in the marine areas adjacent to the nuclear waste discharge facilities (Baudin et al. 2000).

19.3.4 Iron (^{55}Fe)

Introduction, formation, decomposition, dissolution, and sinking of particulate matter is largely responsible for the vertical segregation of biophilic chemical elements in the sea. The main aspects of particulate matter have been the size, settling rate, and physical, chemical and biological compositions. During the 1960, ^{55}Fe constituted one of the major radioactive isotopes present in atmospheric fallout. Although ^{55}Fe , which has a 2.4 year half-life, decays exclusively through electron capture and emits a very weak 5.9 keV X-ray, this isotope is of biological interest because Fe is an essential element for plant growth and is absorbed by red blood cells of animals. ^{55}Fe fallout from atmospheric weapons detonations was largely associated with aerosols as an amorphous oxide or as extremely small particulate species attached to the surfaces of large aerosol particles. The ^{55}Fe contained in these aerosols was more readily solubilized and became available to marine organisms than the stable iron in geological matrix of soil (Weimer and Langford 1978). Massic ^{55}Fe activity was utilized to obtain Fe-laden particle dynamics in the Pacific Ocean. Lal and Somayajulu (1977) found that ^{14}C -laden biogenic calcareous particles (~ 6 μm diameter) sank faster than ^{55}Fe -labeled small particles (~ 1 μm diameter) sinking to the depths of 2,500 m in the Pacific Ocean. And ^{55}Fe -labeled particles sank faster than Pu isotope-labeled particles in the North Pacific Ocean (Livingston et al. 1987). These studies indicated that particulate carrier phase may be specific to each metallic element. Recently the role of iron in the photosynthesis of marine plant,

hence, its influence on the climate change has drawn considerable attention. Its role on the sequestration of atmospheric CO₂ received extensive interests from both scientific and commercial community (e.g., Betram 2010). In this context, biogeochemistry of iron in the sea could be elucidated using ⁵⁵Fe as a tracer at sites where it is released.

19.3.5 Cobalt (⁵⁸Co and ⁶⁰Co)

Controlled low level radioactive waste release from routine operation of nuclear power plants could be monitored using ⁶⁰Co and other radionuclides (¹³⁷Cs, ¹³⁴Cs) and their spatial gradients could be used for estimating the extent of discharge plume in the receiving water body and sediment budget (Olsen et al 1981). Cutshall et al. (1986) used ⁶⁰Co and ¹⁵²Eu to trace the Columbia River derived sediment in Quinault Canyon, Washington, USA by utilizing unusual, once-through, open-loop cooling system at the Hanford nuclear facility. Donoghue et al. (1989) have used ¹³⁴Cs to estimate sediment trapping behind the river dams located below the nuclear reactors as the affinity of cesium for sediment particles, illite mineral in particular, in the fresh-water are very high and desorption does not occur. The presence of ⁶⁰Co in the bottom sediment was used to confirm a nuclear submarine reactor accident occurred in 1985 in Sterlok bay, Peter the Great Bay off Vladivostok (Tkalin and Chaykovskaya 2000).

19.3.6 Krypton (⁸⁵Kr)

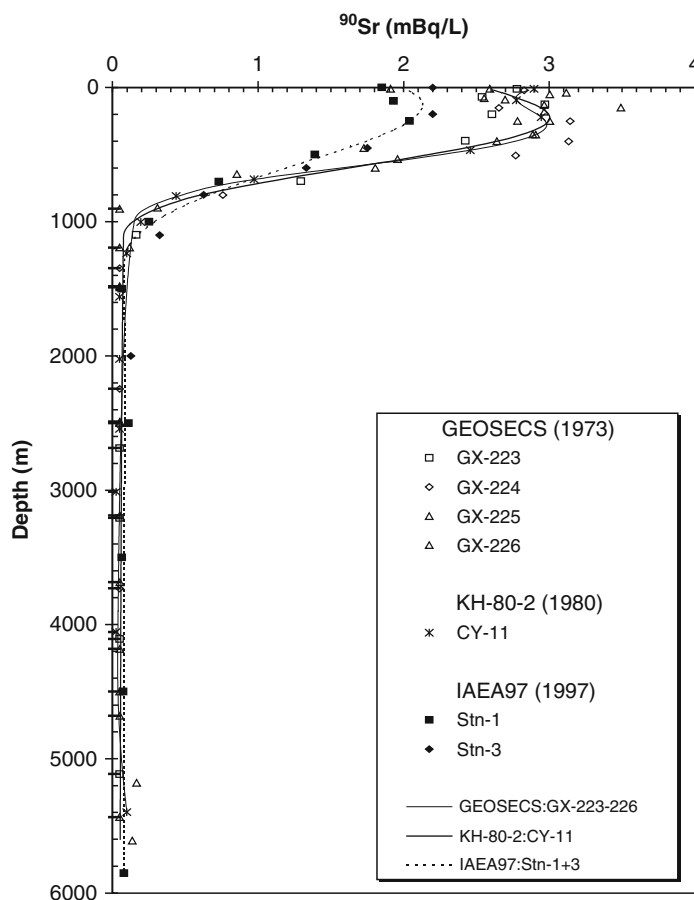
⁸⁵Kr concentrations in the atmosphere and ocean have been increasing steadily since 1945 as a result of atmospheric release from nuclear power plants, plutonium production and nuclear waste processing facilities, and in atmospheric nuclear weapons tests. ⁸⁵Kr has a great potential as a tracer for ocean ventilation and water mass formation. There are two basic reasons for this: (1) ⁸⁵Kr enters the ocean by gas exchange with an equilibration time of 1 month or less. Hence nearly the entire ocean surface will be in equilibrium with the atmosphere, and the surface water concentration as a function of time at any location in the ocean can be accurately calculated from the documented atmospheric history (Winger et al. 2005; Kemp 2008)

and krypton solubility data; and (2) Krypton is an inert gas and ⁸⁵Kr is absolutely conservative in seawater except for its radioactive decay. Smethie et al. (1986) were able to show that Norwegian Sea Deep Water forms from a mixture of Greenland Sea Deep Water and Eurasian Basin Deep Water. They estimated the volume transports for exchange between the surface and deep Greenland Sea and for exchange between the deep Greenland and deep Norwegian seas. They also estimated the residence time of water in the deep Greenland Sea with respect to exchange with surface water. As ⁸⁵Kr is introduced from the air, deep water sample for the gas analysis may be checked with its presence as an indicator of air contamination during sampling (Schlosser et al. 1995).

19.3.7 Strontium (⁸⁹Sr and ⁹⁰Sr)

Most of the ⁹⁰Sr fallout in surface waters is derived from global fallout. The interest in ⁹⁰Sr stems from the following: (1) ⁹⁰Sr is a high-yield product of U and Pu fission; (2) ⁹⁰Sr is a tracer for stable Sr, and Sr has similar properties as Ca; (3) ⁹⁰Sr is the most widely and carefully monitored fallout radionuclide in precipitation, aerosols, and soils. Indeed, the bomb test fallout of ¹³⁷Cs is calculated based on the monitored ⁹⁰Sr fallout, assuming constancy of the ⁹⁰Sr/¹³⁷Cs ratio, and (4) its moderate half-life of 28.9 years (Baskaran et al. 2009). In the year of 2000, total oceanic inventory of ⁹⁰Sr was estimated to be 189 PBq (37 kg) (Hamilton 2004) and it constitutes ca. 0.3×10^{-9} g ⁹⁰Sr/g Sr in the world ocean based on the average Sr concentration (8.7×10^{-5} mole/kg) and world ocean volume (1.37×10^{21} L) (Broecker and Peng 1982). ⁹⁰Sr largely resides in the water column with subsurface peak at ca. 300 m (Fig. 19.6) and very small fractions (0.02–0.04%) are buried in the sediment in the deep Pacific Ocean Basin (Lee et al. 2005). ⁹⁰Sr concentration in the surface 1 km depth decreased approximately 30% over the past 24 years (Fig. 19.3). As the environmental half-life of ⁹⁰Sr in the central NW Pacific Ocean is ca. 15 years (Povinec et al. 2005), ⁹⁰Sr would decrease to 0.1 Bq m⁻³ by 2060 (if there is no additional sources in the future), which would be difficult to measure with 50 L of seawater sample using oxalate precipitation method (Baskaran et al. 2009).

Fig. 19.3 ^{90}Sr concentration profiles in the central NW Pacific Ocean in 1997 (IAEA 1997) along with earlier GEOSECS (1973), KNORR (1978), Hakuho Maru (1980) measurements (Povinec et al. 2003, used with permission)



The residence time of stable Sr is $\sim 5 \times 10^6$ year in the ocean, and several orders of magnitude longer than the global ocean turnover time ($\sim 1,500$ years). The removal from the sea can be made through the formation of SrCO_3 (strontianite), SrSO_4 (celestite), and incorporated into Barite (BaSO_4) as impurities. SrCO_3 is formed when Sr is incorporated into coralline skeletons at sea. The sodium carbonate fortified seawater from which coral skeleton precipitates has a Sr/Ca ratio close to that of seawater ($\sim 0.8 \times 10^{-2}$), but it is depleted in Mg and Ba (Gaetani and Cohen 2006). Recently, it was shown that SrCO_3 mol percentage in coralline algae (rhodoliths) in coastal waters off Scotland closely followed the in situ temperature (Kamenos et al. 2008). Therefore, ^{90}Sr might be utilized as a paleothermometer for corals and other biogenic carbonates proxies.

Celestite is formed as major skeletons and cysts of acantharians, abundant planktonic protists. Settling skeletons of dead acantharians and acantharian cysts are readily dissolved because the ocean is undersaturated with respect to SrSO_4 . Most oceanic water is undersaturated with respect to barite (BaSO_4), yet barite particles are ubiquitous throughout the water column in the ocean. Barite formation in the water column and its accumulation in sediments are closely related to export production of carbon. Sr is incorporated into barite precipitation (average 36.6 mmol Sr/mol Ba) (Paytan et al. 2007). However, the mechanism of barite formation has not been clearly understood yet. Three main hypotheses that have been proposed for barite formation in the oceanic water column include: (1) Barite is formed in microenvironments in which sulfate is enriched due to organic matter oxidation;

(2) A thermodynamically driven barite formation process in which the dissolution of acantharian celestite (SrSO_4), which is enriched in Ba ($\text{BaSO}_4/\text{SrSO}_4$), creates barium rich microenvironments conducive to barite precipitation; and (3) Barite is formed by Ba enrichment rather than SO_4^{2-} enrichments. It is reported that these proposed mechanisms for barite formation are not mutually exclusive. Acantharian dissolution within microenvironments appears to lead to BaSO_4 supersaturation and subsequent barite formation (Bernstein and Byrne 2004).

In case of a relatively fresh fission product mixture, another radiostrontium, ^{89}Sr with a half-life of 50.5 days, can also be present. As the fission yields of both ^{89}Sr and ^{90}Sr are known, their activity ratio can be applied in the dating of the fission product formation. According to UNSCEAR (2000), the $^{89}\text{Sr}/^{90}\text{Sr}$ activity ratio should be 188 just after a nuclear explosion (Paatero et al. 2010)

19.3.7.1 Quantifying Particle Removal

The disequilibrium between the soluble parent isotope ^{90}Sr ($t_{1/2} = 29.1$ years) and its particle-reactive daughter ^{90}Y ($t_{1/2} = 64$ h) has been used to estimate particle settling rates in freshwater systems (Orlandini et al. 2003) and in estuaries and the coastal ocean. Because of the short half-life (64 h) of ^{90}Y , this method could be used to trace faster processes than what is possible using ^{238}U ($t_{1/2} = 4.468 \times 10^9$ years)– ^{234}Th ($t_{1/2} = 24.1$ days) disequilibria. However, in order to utilize ^{90}Y – ^{90}Sr pair as a particle-cycling tracer, the particulate ^{90}Y (^{90}Sr likely negligible) and dissolved ^{90}Y needs to be separated immediately after sample collection and hence immediate filtration is required. The mathematical expressions to relate the measurements of ^{90}Sr – ^{90}Y disequilibrium to the physical dynamics of particles and particle-reactive species are similar to expressions developed and applied to uranium–thorium disequilibria in the sea (19.6).

$$\lambda_p N_p = \lambda_d N_d + k N_d \quad (19.6)$$

Here λ_p and λ_d are the decay constants of the parent (here ^{90}Sr) and the daughter nuclide (^{90}Y), respectively. The N terms are the atom concentrations of the parent and daughter nuclides in the water column. The k term is the first-order net removal rate coefficient

(nonradioactive) for the particle-active daughter nuclide. In (19.6), the advection (horizontal and vertical) and diffusion are neglected. Solving for the removal coefficient (residence time = $1/k$) and converting to activities (A , expressed in Bq m^{-3}) by using the appropriate decay constants gives the following:

$$k = \lambda_d (A_p - A_d) / A_d \quad (19.7)$$

19.3.7.2 Tracing Water Mass Movement

Water column distribution of ^{90}Sr , ^{99}Tc , ^{129}I , ^{137}Cs , ^{238}Pu , ^{239}Pu , and ^{241}Am over time was used to estimate horizontal advection rates of various water masses in various parts of the ocean, for example, in the Arctic Ocean (Livingston et al. 1984), Adriatic Sea (Franić 2005), Norwegian Sea (Yiou et al. 2002), and Sulu Sea (Yamada et al. 2006).

Also, ^{90}Sr activity in the river varies depending upon the watershed soil and denudation characteristics in its watershed, and could serve as a source indicator in the estuary. For example, ^{90}Sr activity in the Danube River was 15–30 times lower than that of Dneiper River in the north-west Black Sea. Based on this information, Stokozov and Buessler (1999) constructed a water mixing model using ^{90}Sr and salinity as water mass tracers for the northwest Black Sea. Present distribution of ^{90}Sr also serves as the benchmark to assess future spreading of radionuclides for specific release scenarios. Gao et al. (2009) modeled the difference between the present-day and the $2 \times$ atmospheric CO_2 -warming scenario runs for the accidental releases of ^{90}Sr in the Ob and Yenisey rivers and indicated that more of the released ^{90}Sr would be confined to the Arctic Ocean in the global warming run, particularly in the coastal, non-European part of the Arctic Ocean.

19.3.8 Ruthenium (^{103}Ru and ^{106}Ru)

^{103}Ru and ^{106}Ru fallout radionuclides released from the Chernobyl accident along with other gamma-emitting fallout radionuclides, ^{134}Cs , ^{137}Cs , $^{110\text{m}}\text{Ag}$, were used to quantify water mass movement in the seas. Carlson and Holm (1992) measured the concentrations of these nuclides in marine plant, *Fucus vesiculosus* L. in the

Baltic Sea area following the Chernobyl accident. The activity ratios of $^{106}\text{Ru}/^{137}\text{Cs}$ and $^{144}\text{Ce}/^{137}\text{Cs}$ in sediment trap and suspended particles were utilized to distinguish the particles laden with Chernobyl Cs ($^{134}\text{Cs}/^{137}\text{Cs} = 0.5$) and earlier global fallout ($^{134}\text{Cs}/^{137}\text{Cs} = 0.0$) in the Black Sea (Buesseler et al. 1990).

19.3.9 Antimony (^{125}Sb)

Antimony-125 is a conservative tracer. A large set of ^{125}Sb data collected from the English Channel and southern North Sea between 1987 and 1994 have been utilized to validate hydrodynamic model in this region (du Bois and Dumas 2005; du Bois et al. 1995). For the field validation with tracers, the coverage of the spatial and temporal tracer concentrations with high accuracy is required. The ideal water mass tracers should show conservative behavior in the water mass, i.e., neither fixed by environmental components (sediment, living species) nor modified during its stay in seawater, and when subsequently diluted, it must be measurable at several hundred or thousand kilometers from its point of discharge. Good tracers must have only one or a set of well-defined and characterized input functions and their flow must be well tracked. In this context, anthropogenic radionuclides released by nuclear fuel reprocessing plants fully meet these specifications if their half-life is long enough compared to the transit-times in the ocean basin. Since 1960, large-scale studies have been chiefly concerned with ^{137}Cs , a point source tracer due to the discharge from the nuclear fuel reprocessing plant at Sellafield on the Irish Sea. Other tracers, namely ^{134}Cs , ^{90}Sr and ^{99}Tc , ^{125}Sb and $^{239+240}\text{Pu}$ have also been used to monitor the transport of water masses. For example, dispersion of a water from the Rhone River into the coastal Mediterranean Sea was modeled using ^{125}Sb , ^{137}Cs and $^{239+240}\text{Pu}$ (Periáñez 2005).

19.3.10 Iodine (^{129}I)

In the terrestrial and marine environment, natural levels of ^{129}I (cosmogenic origin) have been overwhelmed by a build-up of "new" ^{129}I , a product of the nuclear age. Much of this new ^{129}I has entered the

ocean and is now found in its upper layers. Using ^{129}I as a point source tracer due to the discharge from the nuclear fuel reprocessing plants, it has been employed as an oceanographic water mass tracer to determine transit time scale based on the horizontal concentration gradients from the point of discharge. ^{129}I has also been used as a tracer for monitoring nuclear activities, including nuclear safeguard investigations. Furthermore, the differences in the $^{129}\text{I}/^{137}\text{Cs}$ and $^{129}\text{I}/^{99}\text{Tc}$ activity ratios of reprocessed and unprocessed nuclear wastes are also utilized as markers to distinguish water masses because of their unique chemical properties (e.g., solubility, volatility) and high sensitivity of detection. The activity ratio $^{129}\text{I}/^{137}\text{Cs}$ was used to distinguish between accidental or deliberate discharges of these two types of radioactive wastes to the ocean (e.g., Raisbeck and Yiou 1999).

During primary production, iodine is incorporated in marine organic matter and migrates through the food chain. The $^{129}\text{I}/^{127}\text{I}$ atom ratio in marine organics therefore reflects the value found in the ocean's photic zone when the organic matter formed. Because the $^{129}\text{I}/^{127}\text{I}$ atom ratio in any well-mixed marine basin has increased rapidly since the advent of the nuclear age, establishing the buildup pattern of ^{129}I in that basin's surface waters would allow us to "date" the time of formation of any organic matter in the euphotic zone, provided we can obtain an adequate amount of iodine from samples (Schink et al. 1995). Measurement of this ratio currently requires the use of accelerator mass spectrometer (AMS).

19.3.11 Cesium (^{134}Cs and ^{137}Cs)

Cesium is an alkali metal existing as the Cs^+ ion in the oceans. Similar to other alkali metals (e.g., potassium), cesium is conservative in seawater (Brewer et al. 1972). In terrestrial environment, Cs is strongly associated with soil and sediment particles. K_d values for Cs in freshwater environments are large and on the order of $1-5 \times 10^5$. This value decreases substantially as particulate matter is delivered to the oceans via rivers and estuaries. As salinity increases, so too does competition for sediment sorption sites from other cationic species such as K^+ , resulting in desorption of cesium. In pelagic environments, K_d is observed to be significantly lower and has been reported to vary

between 4×10^2 and 2×10^4 L kg⁻¹ (IAEA 2004), with lower end in the Black Sea (Topcuoğlu et al. 2002).

In the year of 2000, total oceanic inventory of ¹³⁷Cs was estimated to be 300 PBq (93 kg) (Hamilton 2004) and it constitutes ca. 0.2×10^{-12} g ¹³⁷Cs/g Cs in the world ocean based on the average Cs concentration of 2.3×10^{-9} mole/kg and world ocean volume of 1.37×10^{21} L (Broecker and Peng 1982). ¹³⁷Cs largely resides in the water column with subsurface peak at ca. 200 m and very small fractions (0.01–0.12%) are buried in the sediment in the deep Pacific Ocean Basin (Lee et al. 2005). ¹³⁷Cs concentration in the surface 1 km depth decreased approximately 40% over the past 24 years (Fig. 19.4). As the environmental half-life of ¹³⁷Cs in the central NW Pacific Ocean is ca. 24 years (Povinec et al. 2005), ¹³⁷Cs would decrease to ca. 0.1 Bq m⁻³ by 2108, which would be difficult to measure with current AMP precipitation method (Baskaran et al. 2009).

19.3.11.1 Utilizing ¹³⁴Cs/¹³⁷Cs Activity Ratios for Estimating Water Transit Time in the Arctic

One of the most significant point source discharges of anthropogenic radionuclides in the ocean is the Sellafield reprocessing plant (formerly Windscale) UK into the Irish Sea since 1952 in the North Atlantic. The reprocessing waste from La Hague, north-west France discharging into the English Channel since 1966 is relatively small compared to Sellafield (Kershaw and Baxter 1995). The contribution of La Hague to the marine inventory of ¹³⁷Cs, ⁹⁰Sr, ⁹⁹Tc and Pu was estimated to be 2.3, 12.2, 12.6 and 0.4%, respectively, of the Sellafield releases (Kershaw and Baxter 1995). The discharge of anthropogenic radionuclides resulted in substantial increase in their inventories in the North Atlantic and its marginal seas. The soluble radionuclides (⁹⁰Sr, ⁹⁹Tc, ¹²⁹I, ¹³⁴Cs, ¹³⁷Cs) released from Sellafield are carried northwards out of the Irish Sea

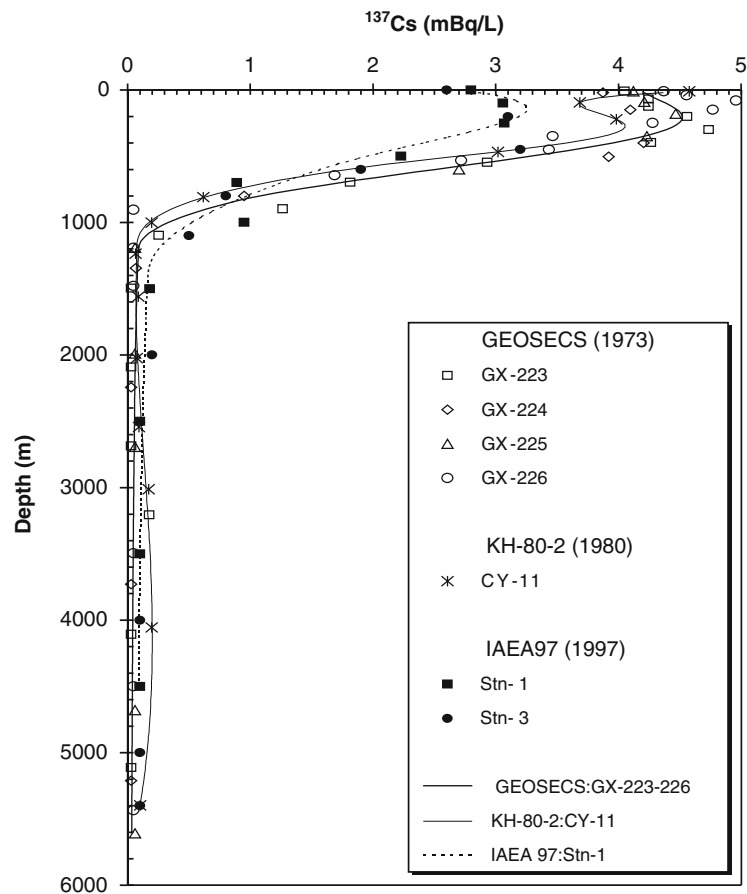


Fig. 19.4 ¹³⁷Cs profiles in the central NW Pacific Ocean in 1997 (IAEA 1997) along with earlier GEOSECS (1973), KNORR (1978), Hakuho Maru (1980) measurements (Povinec et al. 2003, used with permission)

via the North Channel, and flow around the coast of Scotland into the North Sea and then in the Norwegian Coastal Current (NCC). This NCC branches off northwards into the Barents Sea (Vakulovsky 1987) and other current becomes the West Spitzbergen Current, passing through the Fram Strait into the Nansen Basin (Holm et al. 1983; Kautsky 1988; Smith et al. 1990; Kershaw and Baxter 1995). Using $^{134}\text{Cs}/^{137}\text{Cs}$ ratios at the source, one can determine the transit time of water masses from the discharge point to the Arctic Ocean. If R_0 and R_t are the $^{134}\text{Cs}/^{137}\text{Cs}$ activity ratios at the discharge point in Sellafield and at a point in the middle of Nansen Basin, then,

$$R_t = R_0 \exp(\lambda_{137} - \lambda_{134})t \quad (19.8)$$

From this, the transit time (t) can be calculated as follows:

$$\tau = 1/(\lambda_{134} - \lambda_{137}) \times \ln(R_0/R_t) \quad (19.9)$$

λ_{134} and λ_{137} are the decay constants of ^{134}Cs and ^{137}Cs , respectively. There is no other background ^{134}Cs , but there are background ^{137}Cs derived from the global fallout. At the time of sampling (1970), the background ^{137}Cs due to global fallout was in the range of 3–5 Bq m⁻³ at the corresponding latitudes, whereas levels at >120 Bq m⁻³ occurred in the northern Scottish waters. Equation (19.9) assumes the following: (1) the decrease in $^{134}\text{Cs}/^{137}\text{Cs}$ is only due to radioactive decay as the water mass moves; (2) there is no preferential removal of ^{134}Cs or ^{137}Cs ; and (3) the change in $^{134}\text{Cs}/^{137}\text{Cs}$ activity ratio due to mixing with ^{134}Cs depleted water is negligible and the ^{137}Cs contribution from the global fallout to the sample collected is negligible. Using the $^{134}\text{Cs}/^{137}\text{Cs}$ ratios, the transit times were calculated to be 5–6, 7, and 7–9 years in North Cape, Svalbard, East Greenland, respectively (Kautsky 1988). This range of transit time is comparable to the advective time for transport around the perimeter of the Arctic Ocean from the Santa Anna Trough to the southern Canada Basin (~6,000 km) of 7.5 years obtained using H-3-He-3 and chlorofluorocarbon data (Mauldin et al. 2010). These values agree well with the values reported based on ^{137}Cs and ^{99}Tc (summarized in Kershaw and Baxter 1995). The transit time from La Hague to the Arctic is expected to be 3–4 years, about 2 years

shorter than that reported for Sellafield (Kershaw and Baxter 1995).

19.3.11.2 Tracing Deep Water Formation Originated from the Regional Climate Change

The understanding of the deep water formation or intermediate water formation in the ocean is very important to understand the oceanic response due to climate change and vice versa. Sinking of surface water (formation of intermediate and deep water) is largely induced by the intense evaporation and cooling forced by regional climate, and it was generally studied using hydrographic observation such as temperature, salinity and dissolved oxygen. However, these hydrographic variables provide no direct information on the timing and duration of the sinking events. A time series measurement of ^{90}Sr and ^{137}Cs in deep waters could give direct information on the deep water formation. In the Mediterranean Sea, deep water formation occurring in the eastern part of the sea shifted from the southern Adriatic Sea to the Aegean Sea largely during 1989–1995 with exceptional severe winter in 1991–1993, known as Eastern Mediterranean Transient (EMT). The deep water formation in the Aegean Sea was relaxed partially by 1995. The deep penetration of the Aegean surface water was confirmed using time series depth distributions of ^{137}Cs in the water column collected over the period of 1975–1999 by Delfanti et al. (2003). They also utilized the ^{90}Sr -poor water formed during Chernobyl accident in 1986. In the Eastern Mediterranean Sea, ^{137}Cs concentration at 2,000 m depth was found to be ca. 1 and 3 Bq m⁻³ in 1977 and 1995, respectively. The activity ratio of $^{137}\text{Cs}/^{90}\text{Sr}$ in the surface water of the Mediterranean was 1.54 and 12 (in 1986) for the previous global fallout contained water and Chernobyl fallout contained water, respectively. This difference in the $^{137}\text{Cs}/^{90}\text{Sr}$ activity ratio is used to distinguish the water mass laden with ^{90}Sr -poor Chernobyl originated ^{137}Cs (high $^{137}\text{Cs}/^{90}\text{Sr}$ ratio) in 1986 from ^{90}Sr rich previous global fallout ^{137}Cs (low $^{137}\text{Cs}/^{90}\text{Sr}$ ratio) in the early 1960.

Miayo et al. (2000) found the timing of the deep water formation in a large marginal sea in the Northwest Pacific Ocean, East Sea (Sea of Japan) using historical ^{137}Cs profiles collected over the period of

1976–1996. They found that ^{137}Cs concentrations in the upper 200 m layer decreased with time, while those in the deeper layers below 1,500 m depth sharply increased during the period of 1985–1995, accompanied with the increase of the ^{137}Cs inventory. They further identified the area of deep water formation in this period being in the deep Japan Basin off the Peter the Great Bay, Vladivostok, Russia.

19.3.11.3 Tracing Ice Rafted Sediment in the Polar Seas

Sea ice in the polar region is one of the most important transport vectors of terrestrial material to the interior of the ocean. Terrestrial material is incorporated into the sea ice in the coastal areas when it forms and released at farther distances in the Arctic when it melts. In some cases, sea ice melts and the ice-rafted sediments (IRS) are retained in the melt ponds and during early fall, it refreezes. About 15% of the IRS are released during one freeze-melt cycle (details given in Kaste and Baskaran, Chap. 5 in this volume). From the measurements of ^{137}Cs in sea ice sediments, it was found that there is no enrichment of ^{137}Cs or Pu while one to two orders of magnitude enrichment was found for other atmospherically-delivered radionuclides such as ^7Be and ^{210}Pb (Meese et al. 1997; Cooper et al. 1998; Landa et al. 1998; Baskaran 2005; Masque et al. 2007). The $^{239}\text{Pu}/^{240}\text{Pu}$ atom ratios in the IRS were found to be ~ 0.18 , suggesting that most of the Pu were derived from the global fallout (Masque et al. 2007).

19.3.12 Neptunium (^{237}Np)

Np is also an actinide element, but it differs from plutonium in that it is most likely present as the highly soluble Np(V) as NpO_2^+ (Keeney-Kennicutt and Morse 1984). While it can be present as Np(IV), it is proposed that Np (IV) in this form is rapidly oxidized to Np(V) under normal seawater conditions (McCubbin and Leonard 1997; Pentreath et al. 1986). K_d value of $1 \times 10^3 \text{ kg L}^{-1}$ has been reported for Np in coastal sediments. In the open ocean, ^{237}Np is thought to behave conservatively. Livingston et al. (1988) used fallout and Sellafield derived ^{137}Cs and ^{90}Sr to study ventilation and circulation processes in the Mediterranean and the Arc-

tic Seas and documented their input into the North Atlantic Deep Water. ^{237}Np may have similar applications, with added benefits of a significantly longer half-life (2.14×10^6 years) and measurement by ICP-MS which allows lower levels of detection as compared to traditional radio-counting methods for ^{137}Cs and ^{90}Sr (i.e., gamma and beta counting). Furthermore, with the isotopic composition of the main sources of contamination well characterized, water column ^{237}Np inventories and $^{237}\text{Np}/^{239}\text{Pu}$ and $^{237}\text{Np}/^{137}\text{Cs}$ inventory ratios may be useful for identifying non-fallout sources of contamination and providing additional insight into water column scavenging processes.

19.3.13 Plutonium (^{239}Pu and ^{240}Pu)

Plutonium is an actinide element. Although Pu can exist in four oxidation states in natural environment, it is thought to exist in the oceans predominantly in two oxidation states, the particle reactive Pu(IV) as $\text{Pu}(\text{OH})_4$ and the relatively soluble Pu(V) as PuO_2^+ (Sholkovitz 1983; McMahon et al. 2000). In many publications, the Pu(III) and Pu(IV) are grouped together as the reduced forms having average K_d values of $2.5 \times 10^6 \text{ kg L}^{-1}$ and Pu(V) and Pu(VI) are grouped together as the oxidized forms having average K_d values of $1.5 \times 10^4 \text{ kg L}^{-1}$ (Nelson and Lovett 1978).

Much of the published plutonium data is based on alpha spectrometry, which cannot resolve ^{240}Pu (5.168 MeV (73.5%), 5.123 MeV (26.4%)) from ^{239}Pu (5.157 MeV (73.3%), 5.144 MeV (15.1%), 5.106 MeV (11.5%)) and is usually reported as the sum of the ^{239}Pu and ^{240}Pu activity (i.e., $^{239,240}\text{Pu}$). The average $^{239,240}\text{Pu}/^{137}\text{Cs}$ activity ratio of the global fallout is well documented to be 0.026 ± 0.01 (decay corrected to 1 Jan 2010) (Koide et al. 1977; Koide et al. 1975; Krey et al. 1976). More sensitive mass spectrometric techniques (e.g., ICP-MS and TIMS) have the ability to resolve the different isotopes of plutonium (details given in Chap. 18). Kelley et al. (1999) have shown that the atom ratios $^{240}\text{Pu}/^{239}\text{Pu}$, $^{237}\text{Np}/^{239}\text{Pu}$, and $^{241}\text{Pu}/^{239}\text{Pu}$ in soils contaminated by global fallout exhibit relatively little variation globally. Their average ratios in global fallout for the Northern Hemisphere are 0.180 ± 0.014 , 0.480 ± 0.070 , and $(2.44 \pm 0.35) \times 10^{-3}$, respectively (Chap. 20). Several studies have documented

lower plutonium isotopic ratios in debris originating from low-yield nuclear tests conducted at the Nevada Test Site to have an average $^{240}\text{Pu}/^{239}\text{Pu}$ ratio of about 0.035 (Buesseler and Sholkovitz 1987; Krey et al. 1976; Perkins and Thomas 1980).

In the year of 2000, total oceanic inventory of ^{239}Pu and ^{240}Pu are estimated to be 6.5 PBq (2,820 kg) and 5.4 PBq (632 kg), respectively (Hamilton 2004). $^{239+240}\text{Pu}$ largely resides in the water column with subsurface peak at ca. 600 m depth (Fig. 19.5) and substantial fractions (30–112%) are buried in the sediment in the deep Pacific Ocean Basin (Lee et al. 2005). The $^{239+240}\text{Pu}$ profiles in the central NW Pacific Ocean indicate that the subsurface maximum of Pu concentration over the past 24 years decreased by a factor of ca. 4 and the subsurface peaks moved to deeper water from ca. 450 to ca. 800 m and they were getting less sharp and more wide (Fig. 19.6). However, the stations located in the west-ward flowing North Equatorial Current (NEC) with very low biological activity showed no temporal changes in the vertical profiles of $^{239+240}\text{Pu}$ over the last

24 years (Povinec et al. 2003). The persistence of subsurface Pu peak appears to be correlated with the water density gradient (Wong et al. 1992). As the environmental half-life of $^{239+240}\text{Pu}$ in the central NW Pacific Ocean is ca. 7 years (Povinec et al. 2005), $^{239+240}\text{Pu}$ would decrease to less than 1 mBq m^{-3} by 2035, which would be difficult to measure with a conventional 60 L water volume and alpha spectrometry (Baskaran et al. 2009). Similar observation was made for the Santa Monica and San Pedro Basins off California by Wong et al. (1992).

19.3.13.1 Tracing Provenances and Fates of Nuclear Fallout in the Ocean

Buesseler and Sholkovitz (1987) used Pu to document the input of both global stratospheric fallout and tropospheric fallout (derived from tests conducted at the Nevada Test Site) to North Atlantic sediments. They found the $^{240}\text{Pu}/^{239}\text{Pu}$ atom ratios ranged from ~ 0.18 on the shelf to ~ 0.10 at 5,000 m in the solid phase and

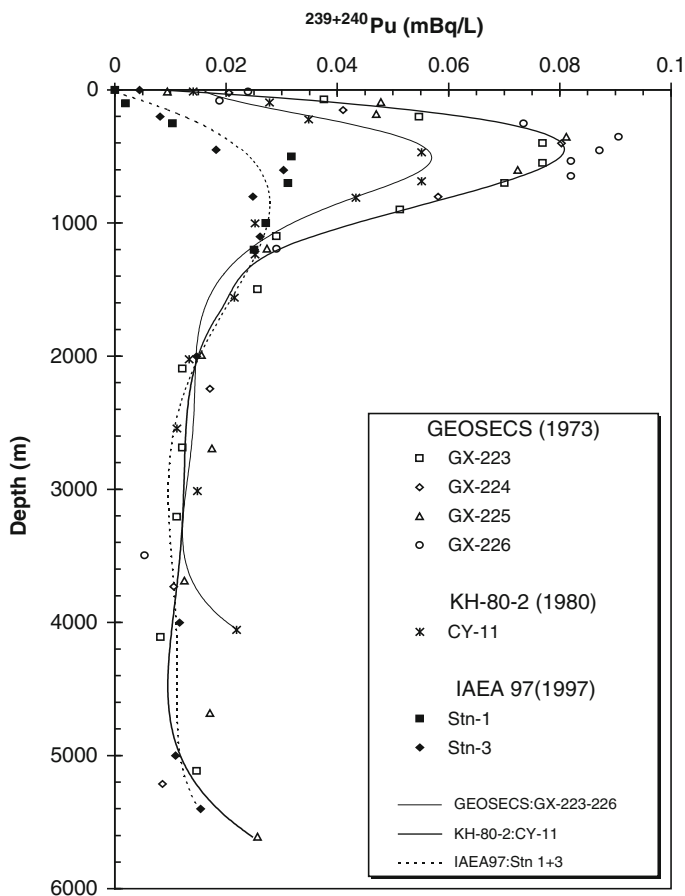
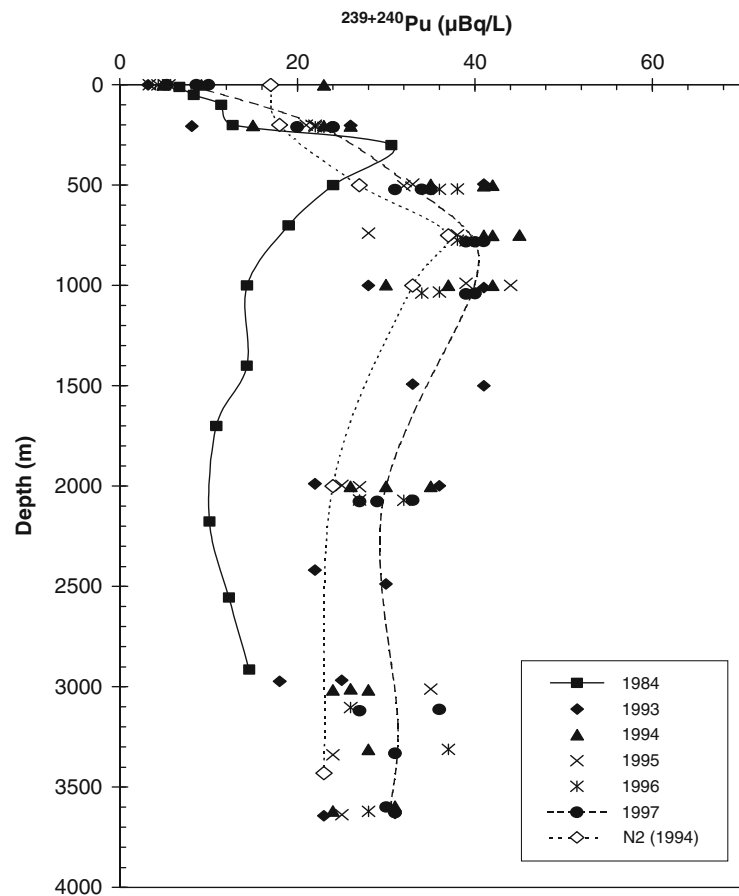


Fig. 19.5 $^{239,240}\text{Pu}$ profiles in the central NW Pacific Ocean in 1997 (IAEA 1997) along with earlier GEOSECS (1973), KNORR (1978), Hakuho Maru (1980) measurements (Povinec et al. 2003, used with permission)

Fig. 19.6 Depth distribution of dissolved $^{239+240}\text{Pu}$ concentrations over 1984–1997 in the Sea of Japan (East Sea) (from IAEA 2005). The time-series measurements were not done in a single fixed station



~ 0.18 in the pore water phases of bottom sediments collected from a transect between Woods Hole and Bermuda in the 1950 and early 1960. Based on the Pu isotopic composition, they were able to infer that there have been at least two distinct sources of fallout Pu in this region: one is global fallout ($^{240}\text{Pu}/^{239}\text{Pu} \sim 0.18$) and another tropospheric fallout from the Nevada Tests ($^{240}\text{Pu}/^{239}\text{Pu} \sim 0.035$), in which Pu derived from the Nevada Tests fallouts have been much more efficiently removed from the water column to deep-sea sediments and they were more refractory relative to Pu from global fallout.

19.3.13.2 Tracing Subtropical Water Movement in the Pacific Ocean

Although the entire surface of the Earth has been contaminated with radioactive fallout due to the atmospheric nuclear weapons tests conducted from 1945

to the early 1980, radioactive contamination in the Pacific Ocean is different from the rest of the world ocean. The earlier nuclear tests were dominated by the U.S. at the Pacific Proving Ground (close-in fallout, atom ratio of $^{240}\text{Pu}/^{239}\text{Pu} > 0.3$) in the 1950, whereas the later tests were largely by the former Soviet Union (stratospheric fallout, atom ratio of $^{240}\text{Pu}/^{239}\text{Pu} \sim 0.18$) in 1961 and 1962. Stratospheric fallout from the atmospheric nuclear tests virtually ceased in the early 1980. Most of the terrestrial Pu contaminations in the world are largely originating from the former USSR nuclear tests. However, the Pu signal in seawater collected in early 2000 from the Pacific Ocean revealed that it was decoupled from that of the adjacent terrestrial environment and the data from the Pacific water has shown that US signal was found even off the Aleutian Chain, several thousand kilometers away from the Proving Ground.

The seawater in the Pacific Ocean had received close-in fallout in the 1950 and the stratospheric

fallout in the 1960. The earlier work (e.g., Noshkin et al. 1975; Buesseler 1997) showed that the $^{239}\text{Pu}/^{240}\text{Pu}$ atom ratios in the Pacific surface seawater had changed from the U.S. signal of >0.3 in the 1950 to a former Soviet signal in the 1960 and returned to the U.S. signal in the early 2000. No observations have been made between the late 1970 and the early 2000, which could be filled using samples from coral skeletons or archived seawater.

The Pu isotopic signature in the region is a potent and unique tracer to distinguish among the different sources of Pu, as well as to understand the variations of $^{239}\text{Pu}/^{240}\text{Pu}$ ratios through time (Ketterer et al., Chap. 20). The US Proving Grounds in the Pacific continue to export Pu with high $^{240}\text{Pu}/^{239}\text{Pu}$ ratio, mainly originated from the nuclear weapons tests in 1950, through the leaching of contaminated carbonate species deposited in the ocean. The massive (dome-shaped) coral *Porites* found throughout the northern tropical Pacific Ocean will allow us to reconstruct the Pu signal in surface waters spanning the last 50 years. By determining atom ratios of $^{240}\text{Pu}/^{239}\text{Pu}$ recorded in coral cores and dating the corals using the $^{210}\text{Pb}/^{226}\text{Ra}$ disequilibria (details on dating of corals is given in Chap. 37), we may be able to accomplish a better understanding of the mixing and circulation of waters between the Warm Pool and adjacent water masses in the Northwest Pacific Ocean. However, this application has not been fully realized yet (Hong et al. 2004).

19.3.13.3 Tracing Material Exchange Between Ocean and its Margins

The dissolved ^{230}Th activity concentration increases with depth in agreement with the balance between the in situ production from the dissolved ^{234}U and the scavenging of ^{230}Th on sinking particles generally in the ocean. However, a significant fraction of dissolved ^{231}Pa (daughter of ^{235}U) and some dissolved ^{230}Th were found to be exported from area of low particle flux to area of high particle flux where ^{230}Th and ^{231}Pa are efficiently scavenged by settling particulate matter to the sea floor. This process became widely known in the early 1980 as “boundary scavenging” because ocean boundaries/margins are generally areas with high biological productivity, high particle flux and high sediment accumulation. The concept of bound-

ary scavenging was first applied to horizontal transport of ^{210}Pb (Spencer et al. 1981; Baskaran and Santchi 2002; Roy-Barman 2009). And enhanced deposition of fallout-derived Pu isotopes in ocean-margin sediments has also been reported (e.g. Koide et al. 1975).

In some ocean margins where large rivers are absent, e.g., East Sea (Sea of Japan), the oceanic $^{239+240}\text{Pu}$ is effectively scavenged through this boundary scavenging process and the deep waters become enriched with $^{239+240}\text{Pu}$ over time (Fig. 19.6) and the marginal sea is destined to continue to serve as a filter for all particle-reactive chemical materials introduced from incoming oceanic waters or atmosphere. This aspect should be investigated more fully in the future.

19.3.13.4 Identifying Subsurface Water Upwelling Areas in the Sea

Although both ^{137}Cs and $^{239+240}\text{Pu}$ radionuclides were injected into the ocean surface by similar processes, the oceanic behavior of plutonium and ^{137}Cs differ from each other. ^{137}Cs , most of which exists in a dissolved form, moves as water mass in the ocean, whereas oceanic behavior of $^{239+240}\text{Pu}$ is controlled both by water movement and adsorption onto the particles formed in situ or introduced and subsequently sinking to the deeper waters. Therefore, in the upper 1,000 m depths, ^{137}Cs concentration decreases exponentially with depth with surface maximum or subsurface maxima where surface water subducts. $^{239+240}\text{Pu}$ has increased with depth toward the subsurface maximum which lies about 500–800 m depth. Hirose et al. (2009) found that activity ratio of $^{239+240}\text{Pu}/^{137}\text{Cs}$ ($R_{\text{Pu}/\text{Cs}}$) increases with depth in the upper 100–1,000 m depth as follows:

$$R_{\text{Pu}/\text{Cs}} = R_{\text{Pu}/\text{Cs},0} \exp(\lambda Z) \quad (19.10)$$

Where λ is the constant related to ocean biogeochemical process of water movement (downwelling and upwelling) and particle formation and destruction and Z is the water depth. They further noted that a half-generation depth of $^{239+240}\text{Pu}$, $Z_h = \ln 2/\lambda$, corresponds to the half-decrease depth of the particulate organic matter in the water column. As the ocean primary productivity depends on the upwelling

intensity of the nutrient-rich deep water, they found that Z_h is deep (~ 300 m) in the eutrophic subarctic Pacific and shallow (~ 100 m) in the subtropical North Pacific.

19.3.13.5 Constraining Sediment Accumulation and Mixing Rates

Particle reactive anthropogenic radionuclides (Table 19.1) has been utilized to determine sediment accumulation and mixing rates in the seafloor based on the input history and their half-lives as they often are adsorbed to the sediment irreversibly in the oceanic environment. Bomb-derived fallout radionuclide (^{137}Cs , $^{239+240}\text{Pu}$) peaks its concentration in 1963 in the Atlantic Ocean. However $^{239+240}\text{Pu}$ peaked in 1954 in the Equatorial-North Pacific Ocean (Hamilton 2004) and the Antarctic Region (Koide et al. 1985) due to the close-in fallout in the Equatorial Pacific. Sediment accumulation rates may be calculated by assuming a fallout maximum in 1963 in the rapid sediment accumulating coastal ocean (e.g., Santschi et al. 2001) or sediment mixing rates may be calculated in the deep ocean basin where sediment accumulation rate is slower than mixing rate (e.g., Pacific Ocean, Cochran 1985).

19.3.14 Americium (^{241}Am)

Measurements of ^{241}Pu ($t_{1/2} = 14.3$ years) and its daughter product, ^{241}Am ($t_{1/2} = 433$ years) in the sediment sample can be used to establish the timing of the source term. Assuming that an initial activity of ^{241}Am in fallout debris is zero, the time elapsed since the Pu was placed, t , can be given by the radioactive decay equation governing the time-dependent activities $A_{\text{Pu-241}}$ and $A_{\text{Am-241}}$, respectively (19.11).

$$t = 1/(\lambda_{\text{Pu-241}} - \lambda_{\text{Am-241}}) \times \ln[1 + (\lambda_{\text{Pu-241}} - \lambda_{\text{Am-241}})A_{\text{Am-241}} / (\lambda_{\text{Am-241}} - \lambda_{\text{Pu-241}})] \quad (19.11)$$

where λ is the radioactive decay constant ($0.693/t_{1/2}$) for a given isotope. In this way, Smith et al. (1995) reaffirmed that the underwater nuclear tests were

conducted in Chernaya Bay to be in 1955 and 1957 (t obtained using (19.11) 36.6 ± 1.2 years can be compared to the time elapsed between 1955 and 1994 (or 1957 and 1994)).

19.4 Future Directions

A major portion of the remaining water soluble radionuclides (such as ^{90}Sr and ^{137}Cs) still exist in the water column with maximum in the surface or subsurface layer and hence these radionuclides can be utilized to study the geochemical pathways of their stable counterparts (e.g., pathways of Sr using ^{90}Sr as a tracer). About 60–70% of the total inventories of these nuclides derived from weapons testing have undergone radioactive decay, but the remaining portions continue to penetrate deeper water column in the ocean. Formation of barite minerals and the chemical reactions linked with such formation can be studied by using ^{90}Sr as a tracer.

Particle reactive anthropogenic radionuclides, e.g., Pu isotopes, continue to be transferred from the water column to the bottom sediments as enhanced in the ocean margins. Therefore, sediment inventories of these radionuclides would provide valuable temporal constraints on the boundary scavenging process occurring between ocean proper and its margins.

Slow movement of waters in the ocean, e.g., downwelling of surface water (deep water formation, draw-down of atmospheric CO_2), upwelling of subsurface water (supplying nutrient rich water to the surface, evasion of CO_2 to the atmosphere), spillover of deep water between basins are generally difficult to address using hydrographic variables such as temperature, salinity and stable isotopes of hydrogen and oxygen, where they have no time information. The current understanding of the spatial and temporal distribution in the sea and marine biogeochemistry of the well-studied anthropogenic radionuclides could serve to detect the slow movement of waters in the ocean. As the changes in slow movement of waters in the ocean are induced by the regional or global climate change, selected anthropogenic radionuclides, reviewed here, warrant a further investigation in a globally coordinated manner. The recently initiated GEOTRACES (an international study of the marine biogeochemical cycles of trace elements and their isotopes) could serve

a useful forum for this purpose (<http://www.ldeo.columbia.edu/res/pi/geotraces/>).

Acknowledgements The authors are grateful to Dr. Katusmi Hirose and an anonymous reviewer for providing valuable comments on the manuscript. This work was partially supported by Korea Ocean Research and Development PM55861 (GHH), was performed under the auspices of the U.S. Department of Energy by Lawrence Livermore National Laboratory in part under Contract W-7405-Eng-48 and in part under Contract DE-AC52-07NA27344 (TFH), Wayne State's Board of Governor's Distinguished Faculty Fellowship (MB). Copyright permission to reproduce here was generously granted for Table 19.2 and Figs. 19.1–19.5 from Elsevier Limited, UK and Table 19.3 from Terra Scientific Publishing Company, Japan.

References

- Aarkrog A (1988) Worldwide data on fluxes of $^{239,240}\text{Pu}$ and ^{238}Pu to the ocean. In Inventories of selected radionuclides in the oceans. IAEA-TECDOC-481, 103–137
- Aarkrog A (2003) Input of anthropogenic radionuclides into the world ocean. *Deep-Sea Res II* 50:2597–2602
- Aoyama M, Hirose K, Sugimura Y (1991) The temporal variation of stratospheric fallout derived from the Chernobyl accident. *J Environ Radioact* 13:103–115
- Assinder DJ (1999) A review of the occurrence and behavior of neptunium in the Irish Sea. *J Environ Radioact* 44:353–347
- Baskaran M (2005) Interaction of sea ice sediment and surface sea water in the Arctic Ocean: evidence from excess ^{210}Pb . *Geophys Res Lett* 32:L12601. doi:10.1029/2004GL022191
- Baskaran M, Asbill S, Santschi PH, Davis T, Brooks JM, Champ MA, Makeyev V, Khlebovich V (1995) Distribution of $^{239,240}\text{Pu}$ and ^{238}Pu concentrations in sediments from the Ob and Yenisey rivers and the Kara Sea. *Appl Radiat Isot* 46:1109–1119
- Baskaran M, Asbill S, Schwantes J, Santschi PH, Champ MA, Brooks JM, Adkins D, Makeyev V (2000) Concentrations of ^{137}Cs , $^{239,240}\text{Pu}$, and ^{210}Pb in sediment samples from the Pechora Sea and biological samples from the Ob, Yenisey Rivers and Kara Sea. *Mar Pollut Bull* 40:830–838
- Baskaran M, Hong GH, Santschi PH (2009) Radionuclide analyses in seawater. In: Wurl O (ed) Practical guidelines for the analysis of seawater. CRC, Boca Raton, pp 259–304
- Baskaran M, Santschi PH (2002) Particulate and dissolved ^{210}Pb activities in the shelf and slope regions of the Gulf of Mexico waters. *Cont Shelf Res* 22:1493–1510
- Baudin JP, Adam C, Garnier-Laplace J (2000) Dietary uptake, retention and tissue distribution of ^{54}Mn , ^{60}Co and ^{137}Cs in the rainbow trout (*Onchoryhynchus Mikiss* Walabaum). *Water Resour* 34:2869–2878
- Beasley TM, Cooper LW, Grebmeier JM, Aagard K, Kelley JM, Kilius LR (1988) $^{237}\text{Np}/^{129}\text{I}$ atom ratios in the Arctic Ocean: has ^{237}Np from western European and Russian fuel reprocessing facilities entered the Arctic Ocean? *J Environ Radioact* 39:255–277
- Beaupre SR, Druffel ERM (2009) Constraining the propagation of bomb-radiocarbon through the dissolved organic carbon (DOC) pool in the northeast Pacific Ocean. *Deep-Sea Res I* 56:1717–1726
- Bernstein RE, Byrne RH (2004) Acantharians and marine barite. *Mar Chem* 86:45–50
- Betram C (2010) Ocean iron fertilization in the context of the Kyoto protocol and the post-Kyoto process. *Energy Policy* 38:1130–1139
- Bienvenu P, Cassette P, Andreoletti G, Be M-M, Comte J, Lepy M-C (2007) A new determination of ^{79}Se half-life. *Appl Radiat Isot* 65:355–364
- Bowen VT, Noshkin VE, Livingston HD, Volchok HL (1980) Fallout radionuclides in the Pacific Ocean: vertical and horizontal distributions, largely from GEOSECS stations. *Earth and Planet Sc Lett* 49:411–434
- Brewer PG, Spencer DW, Robertson DE (1972) Trace element profiles from the GEOSECS-II test station in the Sargasso Sea. *Earth Planet Sci Lett* 16:111–116
- Broecker WS (1974) Chemical oceanography. Harcourt Brace Jovanovich, New York, 214p
- Broecker WS (2003) Radiocarbon. In: Holland HD, Turekian KK (eds) Treatise in geochemistry, the atmosphere, vol. 4. Elsevier-Pergamon, Oxford, pp 245–260
- Broecker WS, Peng TH (1982) Tracers in the sea. Eldigio, New York, p 690
- Broecker WS, Southerland S, Smethie W, Peng TH, Ostlund G (1995) Oceanic radiocarbon: separation of the natural and bomb components. *Global Biogeochem Cycles* 9:263–288
- Browne E, Firestone RB (1986) Table of radioactive isotopes. Wiley-Interscience, New York
- Bruland KW (1983) Trace elements in seawater. In: Riley JP, Chester R (eds) Chemical oceanography, vol 8. Academic, London, pp 157–221
- Buesseler KO (1997) The isotopic signature of allout plutonium in the North Pacific. *J Environ Radioact* 36:69–83
- Buesseler KO, Livingston HD (1996) Natural and man-made radionuclides in the Black Sea. In: Guéguéniat P, Germain P, Métivier H (eds) Radionuclides in the oceans: Inputs and Inventories, Les Editions de physique, Europe Media Duplication S.A. Les Ulis, pp 199–217
- Buesseler KO, Livingston HD, Honjo S, Hay BJ, Konuk T, Kempe S (1990) Scavenging and particle deposition in the southwestern Black Sea – evidence from Chernobyl radionuclides. *Deep-Sea Res* 37:413–430
- Buesseler KO, Sholkovitz ER (1987) The geochemistry of fallout plutonium in the North Atlantic: II. $^{240}\text{Pu}/^{239}\text{Pu}$ ratios and their significance. *Geochim Cosmochim Acta* 51: 2623–2637
- Byrne RH (2002) Inorganic speciation of dissolved elements in seawater: the influence of pH on concentration ratios. *Geochem Trans* 3:11–16
- Carlson L, Holm E (1992) Radioactivity in *Fucus vesiculosus* L. from the Baltic Sea following the Chernobyl accident. *J Environ Radioact* 15:231–248
- Chiappini R, Pointurier R, Milies-Lacroix JC, Lepetit G, Hemet P (1999) $^{240}\text{Pu}/^{239}\text{Pu}$ isotopic ratios and $^{239+240}\text{Pu}$ total measurements in surface and deep waters around Muroroa and Fangataufa atolls compared with Rangiroa atoll (French Polynesia). *Sci Total Environ* 237(238):269–276

- Cochran JK (1985) Particle mixing rates in sediments of the eastern equatorial Pacific: evidence from ^{210}Pb , $^{239,240}\text{Pu}$ and ^{137}Cs distributions at MANOP sites. *Geochim Cosmochim Acta* 49:1195–1210
- Cooper LW, Larsen IL, Beasley TM, Dolvin SS, Grebmeier JM, Kelley JM, Scott M, Johnson-Pyrtle A (1998) The distribution of radiocesium and plutonium in sea ice-entrained Arctic sediments in relation to potential sources and sinks. *J Environ Radioact* 39:279–303
- Cooper LW, Beasley T, Aagaard K, Kelley JM, Larsen IL, Grebmeier JM (1999) Distributions of nuclear fuel-reprocessing tracers in the Arctic Ocean: indications of Russian river influence. *J Mar Res* 57:715–738
- Cundy AB, Croudace IW, Warwick PE, Oh JS, Haslett SK (2002) Accumulation of COGEMA-La Hague-derived reprocessing wastes in French salt marsh sediments. *Environ Sci Technol* 36:4990–4997
- Cutshall NH, Larsen IL, Olsen CR, Nittroter CA, DeMaster DJ (1986) Columbia River sediment in Quinault Canyon, Washington – Evidence from artificial radionuclides. *Mar Geol* 71:125–136
- Delfanti R, Klein B, Papucci C (2003) Distribution of ^{137}Cs and other radioactive tracers in the eastern Mediterranean: relationship to the deepwater transient. *J Geophys Res* 108 (C9):8108. doi:10.1029/2002JC001371
- Donoghue JF, Bricker OP, Oslen CR (1989) Particle-borne radionuclides as tracers for sediment in the Susquehanna River and Chesapeake Bay. *Estuarine Coastal Shelf Sci* 29:341–360
- du Bois PB, Dumas F (2005) Fast hydrodynamic model for medium-and long-term dispersion in seawater in the English Channel and southern North Sea, qualitative and quantitative validation by radionuclide tracers. *Ocean Modell* 9:169–210
- du Bois PB, Salomon JC, Gandon R, Guegueniat P (1995) A quantitative estimate of English Channel water fluxes into the North Sea from 1987 to 1992 based on radiotracer distribution. *J Mar Syst* 6:457–481
- Emley J (1989) The elements. Clarendon, Oxford, p 256
- Franić Z (2005) Estimation of the Adriatic Sea water turnover time using fallout ^{90}Sr as a radioactive tracer. *J Mar Syst* 57:1–12
- Gaetani GA, Cohen AL (2006) Element partitioning during precipitation of aragonite from seawater: a framework for understanding paleoproxies. *Geochim Cosmochim Acta* 70:4617–4634
- Gao Y, Drange H, Johannessen OM, Pettersson LH (2009) Sources and pathways of ^{90}Sr in the North-Arctic region: present day and global warming. *J Environ Radioact* 100:375–395
- Gray J, Jones SR, Smith AD (1995) Discharges to the environment from the Sellafield site, 1951–1992. *J Radiol Prot* 15:99–131
- Hamilton TF, Milliès-Lacroix J-C, Hong GH (1996) ^{137}Cs / ^{90}Sr and Pu isotopes in the Pacific Ocean: sources and trends. In: Guégueniat P, Germain P, Métyvier H (eds) Radionuclides in the oceans. Inputs and Inventories. Les Editions de Physique, Les Ulis, pp 29–58
- Hamilton TF (2004) Linking legacies of the cold war to arrival of anthropogenic radionuclides in the oceans through the 20th century. In: Livingston HD (ed) Marine radioactivity. Elsevier, Amsterdam, pp 23–78
- Hirose K, Aoyama M, Povinec PP (2009) $^{239,240}\text{Pu}/^{137}\text{Cs}$ ratios in the water column of the North Pacific: a proxy of biogeochemical process. *J Environ Radioact* 100:258–262
- Hirose K, Igarashi Y, Aoyama M, Miyao T (2001) Long-term trends of plutonium fallout observed in Japan. In: Kudo A (ed) Plutonium in the environment. Elsevier Science, Amsterdam, pp 251–266
- Holm E, Persson BRR, Hallstadius L, Aarkrog A, Dahlgard H (1983) Radiocesium and transuranium elements in the Greenland and Barents Seas. *Oceanolog Acta* 6:457–462
- Hong GH, Baskaran M, Povinec PP (2004) Artificial radionuclides in the western North Pacific: a review. In: Shiyomi M, Kawahata H, Koizumi H, Tsuda A, Awaya Y (eds) Global environmental change in the ocean and on land. Terrapub, Tokyo, pp 147–172
- Hou X, Roos P (2008) Critical comparison of radiometric and mass spectrometric methods for the determination of radionuclides in environmental, biological and nuclear waste samples. *Anal Chim Acta* 608:105–139
- Hua Q (2009) Radiocarbon: a chronological tool for the recent past. *Quat Geochronol* 4:378–390
- Hu QH, Weng JQ, Wang JS (2010) Sources of anthropogenic radionuclides in the environment: a review. *J Environ Radioact* 101:426–437
- IAEA (2004) Sediment distribution coefficients and concentration factors for biota in the marine environment. Technical reports series No. 422, International Atomic Energy Agency, Vienna, p 93
- IAEA (2005) Worldwide marine radioactivity studies (WOMARS). Radionuclide levels in oceans and seas. IAEA-TECDOC-1429. International Atomic Energy Agency, Vienna, p 187
- Irlweck K, Hrncsek E (1999) ^{241}Am concentration and $^{241}\text{Pu}/^{239,240}\text{Pu}$ ratios in soils contaminated by weapons-grade plutonium. Akademiai Kiado, Budapest, pp 595–599
- Jenkins WJ (2001) Tritium-helium dating. *Encyclopedia of Ocean Sciences* 6:3048–3056
- Kamenos NA, Cusack M, Moore PG (2008) Coralline algae are global paleothermometers with bi-weekly resolution. *Geochim Cosmochim Acta* 72:771–779
- Kafalas P, Irvine J Jr (1956) Nuclear excitation functions and thick target yields: (Cr^{+d}). *Phys Rev* 104:703–705
- Kautsky H (1988) Determination of distribution processes, transport routes and transport times in the North Sea and the northern Atlantic using artificial radionuclides as tracers. In: Guay JC, Guegueniat P, Pentreath RJ (eds) Radionuclides: a tool for oceanography. Elsevier Applied Science, London, pp 271–280
- Kelley JM, Bond LA, Beasley TM (1999) Global distribution of Pu isotopes and ^{237}Np . *The Sci Total Environ* 237(238):483–500
- Keeney-Kennicutt WL, Morse JW (1984) The interaction of $\text{Np}(\text{V})\text{O}_2^+$ with common mineral surfaces in dilute aqueous solutions and seawater. *Mar Chem* 15:133–150
- Kemp RS (2008) A performance estimate for the detection of undecleared nuclear-fuel reprocessing by atmospheric ^{85}Kr . *J Environ Radioact* 99:1341–1348
- Kenna TC, Sayles FL (2002) The distribution and history of nuclear weapons related contamination in sediments from the Ob River, Siberia as determined by isotopic ratios of plutonium and neptunium. *J Environ Radioact* 60:105–137

- Kershaw P, Baxter A (1995) The transfer of reprocessing wastes from north-west Europe to the Arctic. *Deep-Sea Res* 42:1413–1448
- Ketterer ME, Szechenyi SC (2008) Determination of plutonium and other transuranic elements by inductively coupled plasma mass spectrometry: a historical perspective and new frontiers in the environmental sciences. *Spectrochim Acta Part B* 63:719–737
- Kim CK, Kim CS, Chang BU, Choi SW, Chung CS, Hong GH, Hirose K, Igarashi Y (2004) Plutonium isotopes in seas around the Korean Peninsula. *Sci Total Environ* 318:197–209
- Kirchner G, Noack CC (1988) Core history and nuclide inventory of the Chernobyl core at the time of accident. *Nucl Saf* 29:1–5
- Koide M, Berine KK, Chow TJ, Goldberg ED (1985) The $^{240}\text{Pu}/^{239}\text{Pu}$ ratio, a potential geochronometer. *Earth Planet Sci Lett* 72:1–8
- Koide M, Goldberg ED, Herron MM, Langway CC Jr (1977) Transuranic depositional history in South Greenland firn layers. *Nat* 269:137–139
- Koide M, Griffin JJ, Goldberg ED (1975) Records of plutonium fallout in marine and terrestrial samples. *J Geophys Res* 80 (30):4153–4162
- Krey PW, Hardy EP, Pachucki C, Rourke F, Coluzza J, Benson WK (1976) Mass isotopic composition of global fall-out plutonium in soil: Transuranium nuclides in the environment, San Francisco, CA, USA, pp. 671–678
- Kutschera W (2010) AMS and climate change. *Nucl Instrum Methods Phys Res B* 268:693–700
- Kuwabara J, Yamamoto M, Assinder DJ, Komura K, Ueno K (1996) Sediment profiles of ^{237}Np in the Irish Sea: estimation of the total amount of ^{237}Np from Sellafield. *Radiochim Acta* 73:73–81
- Lal D, Somayajulu BLK (1977) Particulate transport of radionuclides ^{14}C and ^{55}Fe to deep waters in the Pacific Ocean. *Limnol Oceanogr* 22:55–59
- Landa E, Reimnitz E, Beals D, Pockowski J, Rigor I (1998) Transport of ^{137}Cs and $^{239,240}\text{Pu}$ by ice rafted debris in the Arctic Ocean. *Arct* 51:27–39
- Lee SH, Gastaud J, La Rosa JJ, Liong Wee Kwong L, Povinec PP, Wyse E, Fitfield LK, Hausladen PA, Di Tada LM, Santos GM (2001) Analysis of plutonium isotopes in marine samples by radiometric, ICP-MS and AMS techniques. *J Radioanal Nucl Chem* 248:757–764
- Lee SH, Povinec PP, Wyse E, Pham MK, Hong GH, Chung CS, Kim SH, Lee HJ (2005) Distribution and inventories of ^{90}Sr , ^{137}Cs , ^{241}Am and Pu isotopes in sediments of the Northwest Pacific Ocean. *Mar Geol* 216:249–263
- Lindahl P, Roos P, Holm E, Dahlgaard H (2005) Studies of Np and Pu in the marine environment of Swedish – Danish waters and the North Atlantic Ocean. *J Environ Radioact* 82:285–301
- Linsalata P, Simpson HJ, Olsen CR, Cohen N, Trier RM (1985) Plutonium and radiocesium in the water column of the Hudson River estuary. *Environ Geol Water Sci* 7:193–204
- Linsley G, Sjoblom K-L, Cabianna T (2004) Overview of point sources of anthropogenic radionuclides in the oceans. In: Livingston HD (ed) *Marine radioactivity*, vol 6, *Radioactivity in the environment*. Elsevier, Amsterdam, pp 109–138
- Livingston HD, Buesseler KO, Izdar E, Konuk T (1988) Characteristics of Chernobyl fallout in the southern Black Sea. In: Guary J, Guegueniat P, Pentreath RJ (eds) *Radionuclides: a tool for oceanography*. Elsevier, Essex, UK, pp 204–216
- Livingston H, Kupferman SL, Bowen VT, Moore RM (1984) Vertical profile of artificial radionuclide concentrations in the Central Arctic Ocean. *Geochim Cosmochim Acta* 48:2195–2203
- Livingston HD, Mann DR, Casso SA, Schneider DL, Surprenant LD, Bowen VT (1987) Particle and solution phase depth distributions of transuranics and ^{55}Fe in the North Pacific. *J Environ Radioact* 5:1–24
- Livingston HD, Povinec PP (2000) Anthropogenic marine radioactivity. *Ocean Coastal Manage* 43:689–712
- Livingston HD, Povinec PP (2002) A millennium perspective on the contribution of global fallout radionuclides to the ocean science. *Health Phys* 82:656–668
- Marshall WA, Gehrels WR, Garnett MH, Freeman SPHT, Maden C, Xu S (2007) The use of ‘bomb spike’ calibration and high-precision AMS ^{14}C analyses to date salt-marsh sediments deposited during the past three centuries. *Quat Res* 68:325–337
- Masque P, Cochran JK, Hirschberg DJ, Dethleff D, Hebbeln D, Winkler A, Pfirman S (2007) Radionuclides in Arctic sea ice: tracers of sources, fates and ice transit time scales. *Deep-Sea Res* 54:1289–1310
- Mauldin A, Schlosser P, Newton R, Smithie WM Jr, Bayer R, Rhein M, Peter JE (2010) The velocity and mixing time scale of the Arctic Ocean Boundary Current estimated with transient tracers. *J Geophys Res* 115:C08002. doi:10.1029/2009JC005965
- McCubbin D, Leonard KS (1997) Laboratory studies to investigate short-term oxidation and sorption behaviour of neptunium in artificial and natural seawater solutions. *Mar Chem* 56:107–121
- McMahon CA, Leon Vintro L, Mitchell PI, Dahlgaard H (2000) Oxidation-state distribution of plutonium in surface and subsurface waters at Thule, northwest Greenland. *Appl Radiat Isot* 52:697–703
- Meese DA, Reimnitz E, Tucker WB III, Gow AJ, Bischoff J, Darby D (1997) Evidence for radionuclide transport by sea ice. *Sci Total Environ* 202:267–278
- Megens L, van der Plight J, de Leeuw JW (2001) Temporal variations in ^{13}C and ^{14}C concentrations in particulate organic matter from the southern North Sea. *Geochim Cosmochim Acta* 65:2899–2911
- Miayo T, Hirose K, Aoyama M, Igarashi Y (2000) Trace of the recent deep water formation in the Japan Sea deduced from historical ^{137}Cs data. *Geophys Res Lett* 27:3731–3734
- Muramatsu Y, Rühm W, Yoshida S, Tagami K, Uchida S, Wirth E (2000) Concentrations of ^{239}Pu and ^{240}Pu and their isotopic ratios determined by ICP-MS in soils collected from the Chernobyl 30-km zone. *Environ Sci Technol* 34:2913–2917
- Muramatsu Y, Hamilton T, Uchida S, Tagami K, Yoshida S, Rosbinson W (2001) Measurement of $^{240}\text{Pu}/^{239}\text{Pu}$ isotopic ratios in soils from the Marshall Islands using ICP-MS. *Sci Total Environ* 278:151–159
- Nelson DM, Lovett MB (1978) Oxidation state of plutonium in the Irish Sea. *Nat* 276:599–601

- Noshkin VE, Wong KM, Eagle RJ, Gatrousis C (1975) Transuranics and other radionuclides in Bikini lagoon. Concentration data retrieved from aged coral sections. *Limnol Oceanogr* 20:729–742
- Noureddine A, Benkrid M, Maoui R, Menacer M, Boudjenoun R, Kadi-Hanifi M, Lee SH, Povinec PP (2008) Radionuclide tracing of water masses and processes in the water column and sediment in the Algerian Basin. *J Environ Radioact* 99(8):1224–1232
- Olsen CT, Larsen IL, Cutshall NH, Donoghue JF, Bricker OP, Simpson HJ (1981) Reactor released radionuclides in Susquehanna River sediments. *Nat* 294:242–245
- Orlandini KA, Bowling JW, Pinder JE III, Penrose WR (2003) ^{90}Y - ^{90}Sr disequilibrium in surface waters: investigating short-term particle dynamics by using a novel isotope pair. *Earth Planet Sci Lett* 207:141–150
- Paatero J, Saxen R, Buyukay M, Outola L (2010) Overview of strontium-89,90 deposition measurements in Finland 1963–2005. *J Environ Radioact* 101:309–316
- Papucci C, Charmasson S, Delfanti R, Gasco C, Mitchell P, Sanchez-Cabeza JA (1996) Time evolution and levels of man-made radioactivity in the Mediterranean Sea. In: Guéguéniat P, Germain P, Métivier H (eds) *Radionuclides in the oceans. Inputs and inventories*. Les Edition de Physique. Institut de Protection et de Surete Nuclaire, Les Ulis cedex A, pp 177–197
- Paytan A, Averyt K, Faul K, Gray E, Thomas E (2007) Barite accumulation, ocean productivity, and Sr/Ba in barite across the Paleocene-Eocene thermal maximum. *Geol* 35:1139–1142
- Peng T-H, Key RM, Ostlund HG (1998) Temporal variations of bomb radiocarbon inventory in the Pacific Ocean. *Mar Chem* 60:3–13
- Pentreath RJ, Harvey BR, Lovett M (1986) Speciation of fission and activation products in the environment. In: Bulman RA, Cooper JR (eds) *Chemical speciation of transuranium nuclides discharged into the marine environment*. Elsevier, London, pp 312–325
- Periáñez R (2005) Modeling the dispersion of radionuclides by a river plume: application to the Rhone River. *Cont Shelf Res* 25:1583–1603
- Perkins RW, Thomas CW (1980) Worldwide fallout. In: Hanson WC (ed) *Transuranic elements in the environment* US DOE/TIC-22800. Office of Health and Environmental Research, Washington DC, pp 53–82
- Piner KR, Wallace JR, Hamel OS, Mikus R (2006) Evaluation of ageing accuracy of bocaccio (*Sebastes paucispinis*) rockfish using bomb radiocarbon. *Fish Res* 77:200–206
- Povinec PP, Aarkrog A, Buesseler KO, Delfanti R, Hirose K, Hong GH, Ito T, Livingston HD, Nies H, Noshkin VE, Shima S, Togawa O (2005) ^{90}Sr , ^{137}Cs and $^{239,240}\text{Pu}$ concentration surface water time series in the Pacific and Indian Oceans – WOMARS results. *J Environ Radioact* 81:63–87
- Povinec PP, Lee SH, Liang Wee Kwong L, Oregioni B, Jull AJT, Kieser WE, Morgenstern U, Top Z (2010) Top Z (2010) Tritium, radiocarbon, ^{90}Sr and ^{129}I in the Pacific and Indian Oceans. *Nucl Instrum Methods Phys Res B* 268:1214–1218
- Povinec PP, Livingston HD, Shima S, Aoyama M, Gastaud J, Goroncy I, Hirose K, Hyunh-Ngoc L, Ikeuchi Y, Ito T, La Rosa J, Kwong LLW, Lee SH, Moriya H, Mulsow S, Oregioni B, Pettersson H, Togawa O (2003) IAEA'97 expedition to the NW Pacific Ocean – results of oceanographic and radionuclide investigations of the water column. *Deep-Sea Res II* 50:2607–2637
- Raisbeck GM, Yiou F (1999) ^{129}I in the oceans: origins and applications. *Sci Total Environ* 237(238):31–41
- Roether W, Beitzel V, Sultenfu J, Putzka A (1999) The eastern Mediterranean tritium distribution in 1987. *J Mar Syst* 20:49–61
- Roy-Barman M (2009) Modelling the effect of boundary scavenging of thorium and protactinium profiles in the ocean. *Biogeosci* 6:3091–3107
- Santschi PH, Presley BJ, Wade TL, Garcia-Romero B, Baskaran M (2001) Historical contamination of PAHs, PCBs, DDTs, and heavy metals in Mississippi River Delta, Galveston Bay and Tampa Bay sediment cores. *Mar Environ Res* 52:51–79
- Schink DR, Santschi PH, Corapcioglu O, Fehn U (1995) Prospects for “iodine-129 dating” of marine organic matter using AMS. *Nucl Instrum Methods Phys Res B* 99:524–527
- Schlosser P, Bonisch G, Kromer B, Loosli HH, Buhler R, Bayer R, Bonani G, Koltermann P (1995) Mid-1980s distribution of tritium, ^3He , ^{14}C and ^{39}Ar in the Greenland/Norwegian Seas and the Nansen Basin of the Arctic Ocean. *Prog Oceanogr* 35:1–28
- Sholkovitz ER (1983) The geochemistry of plutonium in fresh and marine water environments. *Earth Sci Rev* 19:95–161
- Shlokovitz ER, Mann DR (1987) $^{239,240}\text{Pu}$ in estuarine and shelf waters of the north-eastern United States. *Estuarine Coast Shelf Sci* 25:413–434
- Smith JN, Ellis KM, Jones EP (1990) Caesium-137 transport into the Arctic Ocean through Fram Strait. *J Geophys Res* 95 (C2):1693–1701
- Smith JN, Ellis KM, Naes K, Dahle S, Matishov D (1995) Sedimentation and mixing rates of radionuclides in Barents Sea sediments off Novaya Zemlya. *Deep-Sea Res II* 42:1471–1493
- Smethie WM Jr, Ostlund HG, Loosli HH (1986) Ventilation of the deep Greenland and Norwegian seas: evidence from krypton-85, tritium, carbon-14 and argon-39. *Deep-Sea Res* 33:675–703
- Spencer DW, Bacon MP, Brewer PG (1981) Models of the distribution of ^{210}Pb in a section across the north Equatorial Atlantic Ocean. *J Mar Res* 39:119–138
- Stokozov NA, Buesseler KO (1999) Mixing model for the north-west Black Sea using ^{90}Sr and salinity as tracers. *J Environ Radioact* 43:173–186
- Tkalin AV, Chaykovskaya EL (2000) Anthropogenic radionuclides in Peter the Great Bay. *J Environ Radioact* 51:229–238
- Topcuoğlu S, Güngör N, Kirbaşoğlu C (2002) Distribution coefficients (K_d) and desorption rates of ^{137}Cs and ^{241}Am in Black Sea sediments. *Chemos* 49:1367–1373
- UNSCEAR (2000) United Nations Scientific Committee on the Effects of Atomic Radiation (UNSCEAR) Report to the

- general assembly with scientific annexes. Annex C: exposures from man-made sources of radiation. <http://www.unscear.org>. Accessed April 2010
- Vakulovsky S (1987) Determination of distribution processes, transport routes and transport times in the North Sea and the northern North Atlantic using artificial radionuclides as tracers. In: Guary JC, Guegueniat P, Pentreath RJ (eds) *Radionuclides: a tool for oceanography*. Elsevier Applied Science, London, pp 271–280
- Vakulovsky S (2001) Radiation monitoring in Russia at the turn of the millennium. *J Environ Radioact* 55:219–220
- Warneke T, Croudace IW, Warwick PE, Taylor RN (2002) A new ground-level fallout record of uranium and plutonium isotopes for northern temperate latitudes. *Earth Planet Sci Lett* 203:1047–1057
- Weimer W, Langford JC (1978) Iron-55 and stable iron in oceanic aerosols: forms and availability. *Atmos Environ* 12:1201–1205
- Winger K, Feichter J, Kalinowski MB, Sartorius H, Schlosser C (2005) A new compilation of the atmospheric ^{85}Kr inventories from 1945 to 2000 and its evaluation in a global transport model. *J Environ Radioact* 80:183–215
- Wong KM, Jokela TA, Eagle RJ, Brunk JL, Noshkin VE (1992) Radionuclide concentrations, fluxes, and residence times at Santa Monica and San Pedro Basins. *Prog Oceanogr* 30:353–391
- Yamada M, Wang Z-L, Zhen J (2006) The extremely high ^{137}Cs inventory in the Sulu Sea: a possible mechanism. *J Environ Radioact* 90:163–171
- Yim MS, Caron F (2006) Life cycle and management of carbon-14 from nuclear power generation. *Prog Nucl Energy* 48:2–36
- Yiou F, Raisbeck GM, Christensen GC, Holm E (2002) $^{129}\text{I}/^{127}\text{I}$, $^{129}\text{I}/^{137}\text{Cs}$ and $^{129}\text{I}/^{99}\text{Tc}$ in the Norwegian coastal current from 1980 to 1988. *J Environ Radioact* 60:61–71
- Yoshida S, Muramatsu Y (2003) Determination of U and Pu isotopes in environmental samples by inductively coupled plasma mass spectrometry. <http://www.nirs.go.jp/report/nene/h13/05/85.htm>. Accessed April 2010

Chapter 20

Applications of Transuranics as Tracers and Chronometers in the Environment

Michael E. Ketterer, Jian Zheng, and Masatoshi Yamada

Abstract The transuranic elements (TRU) Np, Pu, Am, and Cm have prominently emerged as powerful tracers of earth and environmental processes, applicable to the recent, post nuclear-era timescale. Various long-lived isotopes of these elements are found in the earth's surface environment, almost exclusively as a result of nuclear weapons production, testing, or nuclear fuel cycle activities. A globally recognizable signal, of consistent composition, from stratospheric fallout derived from 1950–1960 above-ground weapons tests is itself useful in tracing applications; in specific local/regional settings, stratospheric fallout is mixed with or dominated by other TRU sources with contrasting isotopic signatures. Both decay-counting and MS approaches have been utilized to measure the concentrations and isotopic ratios of TRU and are useful as discriminators for source characterization, provenance, and apportionment. Examples include the activity ratios $^{238}\text{Pu}/^{239+240}\text{Pu}$, $^{241}\text{Am}/^{239+240}\text{Pu}$, and $^{241}\text{Pu}/^{239+240}\text{Pu}$; atom ratios such as $^{240}\text{Pu}/^{239}\text{Pu}$, $^{237}\text{Np}/^{239}\text{Pu}$, $^{241}\text{Pu}/^{239}\text{Pu}$, and $^{242}\text{Pu}/^{239}\text{Pu}$ are also used in this context. Of the TRU elements, Pu is by far the most widely studied; accordingly, this chapter mainly emphasizes the use of Pu activities and/or atom ratios as tracers and/or chronometers. Nevertheless, Pu is sometimes measured in combination with one or more isotopes of other elements. The TRU elements

offer several prominent applications in environmental/geochemical tracing: (1) chronostratigraphy of sediments and related recent Holocene deposits; (2) using fallout TRU as quantitative probes of soil erosion, transport and deposition; (3) investigating water mass circulation, the transport and scavenging of particulate matter, and tracking the marine geochemical behavior of the TRU elements themselves in the marine environment; and (4) studies of the local/regional transport, deposition and inventories of non-fallout TRU in the surficial environment.

20.1 Introduction

20.1.1 The Elements Np, Pu, Am, and Cm

The transuranic elements (also known as transuranium elements, abbreviated herein as TRU) have atomic numbers (Z) greater than 92. None of these elements are stable; all of their nuclides undergo radioactive decay to form other isotopes, eventually reaching $Z = 82$ (Pb) or $Z = 83$ (Bi). Elements with up to $Z = 103$ (Np–Lw) are members of the $5f$ actinide series, and the named elements with $Z = 104$ – 112 are known as transactinides. The elements with $Z > 98$ (Cf) have not been produced in significant quantities and have never been used other than in limited research settings. Isotopes of the elements Np through Cm ($Z = 93$ – 96 , respectively) are most important in terms of their environmental distribution and occurrence; hence, this chapter focuses upon the elements Np ($Z = 93$), Pu ($Z = 94$), Am ($Z = 95$) and Cm ($Z = 96$). Of these, Pu is by far the most prominent in terms of its importance as an environmental tracer, and in

M.E. Ketterer (✉)

Department of Chemistry and Biochemistry, Box 5698, Northern Arizona University, Flagstaff, AZ 86011-5698, USA
e-mail: Michael.Ketterer@nau.edu

J. Zheng and M. Yamada

Environmental Radiation Effects Research Group, National Institute of Radiological Sciences, 4-9-1 Anagawa, Inage, Chiba 263-8555, Japan

terms of numbers of published studies pertaining to its environmental distribution.

Neptunium has two long-lived, α -emitting isotopes, ^{236}Np ($t_{1/2} = 1.54 \times 10^5$ years) and ^{237}Np ($t_{1/2} = 2.14 \times 10^6$ years). Plutonium has six prominent isotopes: ^{238}Pu ($t_{1/2} = 87.74$ years), ^{239}Pu ($t_{1/2} = 24,110$ years), ^{240}Pu ($t_{1/2} = 6,561$ years), ^{241}Pu ($t_{1/2} = 14.29$ years), ^{242}Pu ($t_{1/2} = 373,000$ years) and ^{244}Pu ($t_{1/2} = 8.3 \times 10^7$ years). The isotopes ^{238}Pu , ^{239}Pu , ^{240}Pu , ^{242}Pu and ^{244}Pu all decay by emission of α particles, while ^{241}Pu undergoes β decay to produce α -emitting ^{241}Am ($t_{1/2} = 432.6$ years). ^{241}Am also generates 59 keV gamma photons coincident with its α decay. In addition to ^{241}Am , Am has a second long-lived α emitting isotope, ^{243}Am ($t_{1/2} = 7,370$ years), and a meta-stable isotope, $^{242\text{m}}\text{Am}$ ($t_{1/2} = 141$ years). The element Cm has seven prominent isotopes: ^{243}Cm , ^{244}Cm , ^{245}Cm , ^{246}Cm , ^{247}Cm , ^{248}Cm , and ^{250}Cm ; these all undergo α decay with respective half-lives of 29.1, 18.1, 8,500, 4,730, 1.56×10^7 , 340,000, and 9,000 years.

The half-lives of the isotopes of Np, Pu, Am, and Cm are too short to have survived decay over the Earth's 4.5 billion year history, though these elements' abundances were probably similar to Th and U at the time of Earth accretion (Taylor 2001). The one exception is ^{244}Pu , of which a few primordial atoms per kg crust are expected to still be present (Taylor 1995; Wallner et al. 2004). The astrophysical r-process is the main production mechanism for ^{244}Pu and other heavy isotopes. ^{244}Pu is also thought to be present in interstellar medium (ISM) grains found in the inner solar system (Ofan et al. 2006). ISM material continuously enters the solar system and the Earth's atmosphere as a source of "live", recently produced ^{244}Pu . The ISM grains are thought to have elemental and isotopic compositions resembling the early Earth; hence, ISM should contain many radionuclides (^{244}Pu and others) with half-lives much less than the age of the Earth. Ofan et al. (2006) estimate that the steady-state flux of ^{244}Pu is about $0.1 \text{ atom cm}^{-2} \text{ year}^{-1}$. In deep-sea sediments with a sedimentation rate of ca. $1 \mu\text{m/year}$, the ^{244}Pu flux would generate a concentration of about 10^5 atoms/kg in young deposits.

The presence of small amounts of ^{237}Np and ^{239}Pu in Nature is well established; these nuclides are continuously produced from ongoing neutron capture processes, and hence natural ^{239}Pu is most abundant in U ores. Curtis et al. (1999) determined $^{239}\text{Pu}/^{238}\text{U}$

atom ratios of 2.4×10^{-12} to 4.4×10^{-11} for ores from the Cigar Lake uranium deposit. In an older study, Myers and Lindner (1971) determined a $^{237}\text{Np}/^{238}\text{U}$ atom ratio of 2.16×10^{-12} in a pitchblende ore. Both ^{237}Np and ^{239}Pu , along with ^{236}U , are produced in Nature by neutron capture on ^{235}U or ^{238}U , with neutrons originating from (α, n) reactions, spontaneous and induced fission, and by cosmic rays (Hotchkis et al. 2000). These neutron capture processes are much less probable in the bulk Earth's crust (ca. $3 \text{ mg } ^{238}\text{U/kg}$) than in U ores but still produce a crustal concentration of $\sim 2 \times 10^{-14} \text{ g } ^{239}\text{Pu/kg}$ (Taylor 1995).

Oxidation-reduction processes are important in determining the environmental behavior of the TRU elements. The elements Am and Cm exist only in the +3 oxidation state under normal environmental conditions (Choppin 2007), while Np and Pu have more complex redox behavior. Np can exist in the +4, +5, and +6 states, with the +5 state being most common in oxic natural waters and sediment- or soil-water-multiphase environments. Pu has analogous behavior with mixtures of the +4 and +5 states being prevalent; under strongly reducing (anoxic) conditions, Pu can also exist in the +3 oxidation state. Given the high charge and small ionic radii of these species, all of the TRU elements tend to be present in colloidal rather than true solute forms in natural waters (Choppin 2007), and all display rather significant propensity to become associated with particle phases (namely, particle reactivity). The sorption coefficient, K_d , is a commonly encountered operational parameter that is used to describe the partitioning of the element between solid-adsorbed and solution phases ($K_d = C_{\text{solid}}/C_{\text{solution}}$) which has units of mL/g. Accordingly, a high value of K_d is indicative of strong tendency towards particle association, and hence, relative immobility as a true solute, while a low K_d indicates significant solubility and the substance's tendency to be transported in solution form. For the TRU elements, a reported K_d is mainly limited to use in the specific environmental circumstances for which it was measured, and may obviously be greatly affected by factors such as the oxidation state/speciation of the element, the environmental temperature, the characteristics of the aqueous phase (pH, ionic strength, and presence of complexants), and the physical and chemical properties of the solid phase (surface area, particle size distribution, mineral composition, etc.).

Despite these limitations, K_d values have been calculated for TRU elements in many different environments. As a case in point, in seawater as the aqueous phase, and with fine-grained clay sediments from the Irish Sea, Nelson and Lovett (1978) determined K_d values in the range of 10^3 – 10^4 for Pu in the +5 and +6 states, while tetravalent Pu exhibited a higher K_d in the range of 10^6 . This result obviously conveys that Pu will be less mobile and more strongly associated with the sediment when present in the reduced +4 state. Hence, calculations and models performed using K_d values should be used as a starting point, or guide for the expected tendencies of the element of interest, and some *a priori* knowledge or actual measurements in the environment of interest is essential. In general, however, most K_d measurements of TRU imply the strong association of these elements with solid phases in many different freshwater and marine environments, which lends well to their use as tracers of particle transport in the environment (*vide infra*).

20.1.2 Sources, Release Histories, and Isotope Compositions

Aside from the above-mentioned natural occurrences of TRU in the Earth surface environment, these elements have become widely distributed in the Earth's surface environment as a result of anthropogenic production in the last six decades. The production mode is again neutron capture in a fission bomb, or a nuclear reactor that is specifically designed to produce electrical power or to transmute ^{238}U into ^{239}Pu for weapons. As a result, essentially all of the TRU in the Earth's surface environment is of anthropogenic origin. The uppermost 30 cm of undisturbed crust, for example, contains ^{237}Np and ^{239}Pu at levels $\sim 10^4$ – 10^5 times greater than the natural concentrations, and no evidence to date has been identified for the natural sources for Am, Cm, or other Pu isotopes besides ^{239}Pu and ^{244}Pu . The main source term for Np, Pu and Am is global fallout from 1950's and 1960's above-ground nuclear weapons tests; chronologies and locations of these tests are described in Carter and Moghissi (1977). Americium (as ^{241}Am) is not itself initially formed in the nuclear tests, but rather it accumulates over time, even during stratospheric residence time-frames, due to its in-growth from the decay of relatively

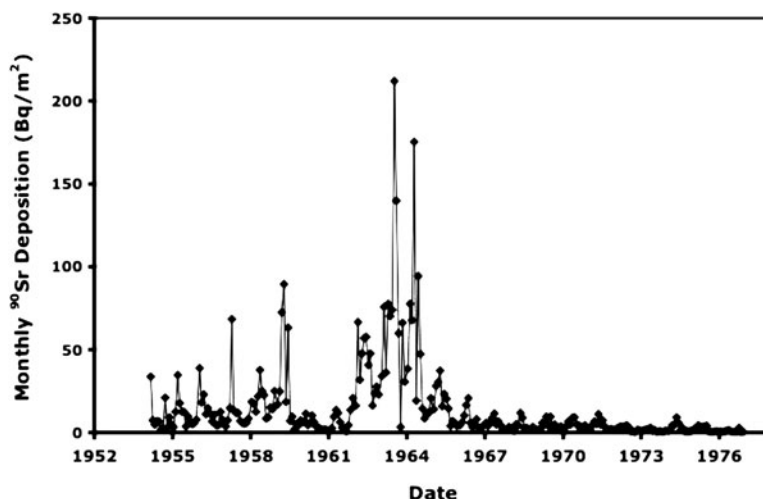
short-lived ^{241}Pu . Curium, however, is neither produced in significant amounts by nuclear tests, nor do any Cm isotopes form by in-growth from fresh testing debris; instead, Cm isotopes are mainly derived from power reactors (Schneider and Livingston 1984; Holm et al. 2002).

In the 30-year span 1945–1975, 801 nuclear detonations were conducted by the United States, former Soviet Union, United Kingdom, Republic of France, People's Republic of China, and India, with a cumulative yield of about 325 Mt TNT (Carter and Moghissi 1977). Several additional Chinese low-yield atmospheric tests were conducted at Lop Nor in the late 1970 (Roy et al. 1981) with the last Chinese atmospheric detonation having occurred in 1980 (Bennett 2002). These tests released $\sim 1.5 \times 10^{16}$ Bq of $^{239+240}\text{Pu}$ into the global environment, corresponding to $\sim 4,000$ kg ^{239}Pu , 700 kg ^{240}Pu , and \geq kg quantities of several other TRU isotopes. After release of these vaporized nuclides into the stratosphere, the TRU and fission products condensed to form very fine aerosols of 10–20 nm diameter (Harley 1980); these fine particles returned to the troposphere and thereafter, became associated with naturally occurring particulate matter, ultimately being removed as wet and dry deposition. In soils, TRU have become associated with specific phases such as iron/manganese oxides and humic acids.

Besides atmospheric weapons tests, other important sources include nuclear reactor accidents (e.g., the 1986 Chernobyl accident), nuclear fuel re-processing facilities (e.g., Sellafield, UK), atmospheric disintegration of satellites with onboard ^{238}Pu -powered thermoelectric generators (e.g., the 1964 SNAP accident), and releases from facilities devoted to the manufacturing or handling of weapons components (e.g., Rocky Flats).

Atmospheric tests can be categorized into two main groups. The first consists of "low-yield" tests that released the bulk of the radionuclide yield into the lower atmosphere, where it was rapidly deposited on a local/regional scale as "tropospheric fallout"; and the second group is "high-yield" tests that injected large amounts of material into the stratosphere, where it was later deposited on a hemispheric scale as "stratospheric" or "global" fallout. The atmospheric deposition of Pu and associated fission products such as ^{137}Cs ($t_{1/2} = 30.07$ years) and ^{90}Sr ($t_{1/2} = 28.78$ years) occurred mainly in the 1950's and 1960's,

Fig. 20.1 Monthly deposition of ^{90}Sr at New York City, USA in the 1954–1976 timeframe. Source: Environmental Measurements Laboratory, US Department of Homeland Security, www.eml.st.dhs.gov/databases/fallout, accessed 19 May 2010



with a pronounced and well-known maximum in 1963, followed by a sharp decrease in deposition. Figure 20.1 depicts the temporal history of ^{90}Sr fallout deposition from atmospheric tests, with prominent 1963 peak, at New York City. A strong seasonality is evident, with the fallout delivery from the stratosphere to the troposphere and surface peaking in the late spring and early summer (Bennett 2002). The decrease in deposition coincided with the 1963 Limited Test Ban Treaty, signed by the USA, former Soviet Union, and United Kingdom. Comparatively minor amounts of fallout are evident in the Fig. 20.1 profile as a result of late 1960's to early 1970's tests conducted by France and China, non-signatories to the Test Ban Treaty. Residence times in the atmosphere are typically less than 1 month for nuclides introduced into the troposphere, while residence times are 0.7–3.4 years for material injected into the stratosphere from different types of tests conducted at different latitudes (Bennett 2002).

In addition to the temporal and seasonal dependencies of fallout deposition, the accumulated inventories of fallout also vary widely versus location on the Earth's surface. The highest inventories are found at mid-latitudes of the Northern Hemisphere, with lower inventories at the Equator and poles; less total fallout deposition occurred in the Southern Hemisphere. The Southern Hemisphere was the location of fewer tests, and the stratospheric air masses are not well-mixed between hemispheres (Bennett 2002); Northern Hemisphere inventories of all fallout nuclides are ~5-fold greater than those in the Southern Hemisphere. Besides its latitude dependency, fallout depositional

inventories also exhibit variation resulting from climate, as atmospheric precipitation is the chief removal mechanism for fallout deposition. For equivalent latitudes, greater fallout inventories are observed in climates with higher mean annual precipitation; consequently, locations with marine climates have larger inventories than desert or humid continental climate patterns (Beck and Bennett 2002). In montane areas with vertical climates, significant local differences in fallout inventory versus altitude can be observed as a result of large differences in annual precipitation (Ulsh et al. 2000).

An authoritative estimate of the isotopic composition of stratospheric fallout Pu is given in Kelley et al. (1999), a study that used samples from 54 worldwide locations. Kelley et al. (1999) reported depositional inventories (10^{12} atoms $^{239}\text{Pu}/\text{m}^2$) and atom ratios ($^{237}\text{Np}/^{239}\text{Pu}$, $^{240}\text{Pu}/^{239}\text{Pu}$, $^{241}\text{Pu}/^{239}\text{Pu}$, and $^{242}\text{Pu}/^{239}\text{Pu}$); several important trends are apparent. First, regional effects, originating from locations such as the USA's Nevada Test Site (NTS), are important in some areas; secondly, slight differences in isotopic composition exist between Northern and Southern Hemisphere deposition. Since Pu is synthetic in origin, its isotope composition varies widely according to its production mechanism; hence, this intrinsic variance serves as the basis for a wide variety of isotopic tracing possibilities in atmospheric, marine, hydrologic, and crustal environments. The atom ratio $^{240}\text{Pu}/^{239}\text{Pu}$ is the most readily measured fingerprint; the $^{237}\text{Np}/^{239}\text{Pu}$ atom ratio and minor Pu isotope ratios provide additional insights and discriminatory power. Figure 20.2

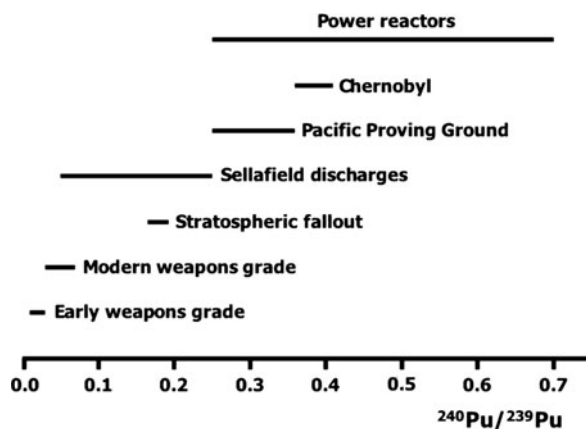


Fig. 20.2 Characteristic ranges for $^{240}\text{Pu}/^{239}\text{Pu}$ in stratospheric fallout and other prominent sources of TRU in the surface environment

depicts $^{240}\text{Pu}/^{239}\text{Pu}$ atom ratios for a number of prominent sources in the global environment. The Pu isotopic composition can therefore provide a “fingerprint” of different sources and is useful in studies of the movement of a specific point or regional source. In these studies, sources other than global fallout are identified and apportioned via their isotopic contrast versus the globally distributed baseline of stratospheric fallout.

In a manner analogous to source provenance with atom ratios, activity ratios are also useful in discrimination between stratospheric fallout and other local/regional sources of TRU. The most important activity ratio in this context is $^{238}\text{Pu}/^{239+240}\text{Pu}$, which is useful in distinguishing many prominent Pu sources (Baskaran et al. 1995). This ratio ranges considerably between relatively low values of <0.05 in both weapons-grade and stratospheric fallout Pu, to much higher values in Pu originating from reactor sources (nuclear fuel reprocessing, Chernobyl, Kara Sea dumped reactor). More details on $^{238}\text{Pu}/^{239+240}\text{Pu}$ source discrimination with reference to the Arctic are given in Baskaran et al. (1995).

“Weapons-grade” Pu consists mainly of ^{239}Pu , with $^{240}\text{Pu}/^{239}\text{Pu} \sim 0.03\text{--}0.07$ being typical for fission weapons and triggers for thermonuclear devices. Releases from low-yield fission tests, such as at the Nevada Test Site, exhibit $^{240}\text{Pu}/^{239}\text{Pu}$ very similar to the Pu present in the original device. The low neutron fluxes in typical kiloton-range fission tests generate only small amounts of neutron capture products such as ^{237}Np , the heavier Pu isotopes, and ^{241}Am . In contrast, the high-yield (thermonuclear) tests, accounting for the

great majority of the worldwide TRU inventory, produced Pu that has undergone significant neutron activation in the high neutron flux environment, thereby accounting for the greater proportions of ^{240}Pu , ^{241}Pu , and ^{242}Pu . For stratospheric fallout in the $31\text{--}70^\circ\text{N}$ latitude band, resulting from the cumulative average of all testing, average atom ratios ($\pm 2\sigma$) are as follows: $^{237}\text{Np}/^{239}\text{Pu} = 0.48 \pm 0.07$; $^{240}\text{Pu}/^{239}\text{Pu} = 0.180 \pm 0.014$; $^{241}\text{Pu}/^{239}\text{Pu} = 0.00194 \pm 0.00028$ (decay-corrected to 1 January 2000); and $^{242}\text{Pu}/^{239}\text{Pu} = 0.00387 \pm 0.00071$. Plutonium that has been subjected to lengthy reactor irradiation (i.e., “burn-up”) also contains relatively larger abundances of the heavier isotopes. As is seen in Fig. 20.2, the Pu isotopic composition from power reactors can vary widely, being characteristic of the neutron flux and reactor conditions.

A specific global source of ^{238}Pu is the 1964 atmospheric burn-up of the radioisotope thermoelectric generator onboard the US satellite SNAP-9A. Upon re-entry to the atmosphere, the satellite incinerated and released $\sim 6 \times 10^{14}$ Bq of ^{238}Pu into the southern Hemisphere stratosphere (Harley 1980). The vast majority of the SNAP-9A ^{238}Pu was subsequently deposited in the southern Hemisphere, since limited mixing occurs between the northern and southern Hemisphere stratospheric air masses. The SNAP ^{238}Pu is now blended with stratospheric fallout Pu, and as a result, the northern and southern Hemispheres exhibit $^{238}\text{Pu}/^{239+240}\text{Pu}$ signatures of ~ 0.025 and 0.25 , respectively (Sam et al. 2000). The 1978 re-entry of the Soviet satellite Cosmos-954 over northern Canada led to its mechanical destruction upon impact; large debris was recovered by clean-up teams; however, high-altitude balloon sampling conducted by the USA demonstrated minimal presence of debris in the atmosphere (Krey et al. 1979).

Another well-known situation where TRU source mixing is observed is in marine systems. Nuclear fuel re-processing facilities such as Sellafield (UK) and La Hague (France) historically released large quantities of TRU and fission products into Northern Hemisphere oceans (Hong et al. 2011); some of these nuclides have remained in the water column, though large amounts have become associated with sediments in coastal areas through particle scavenging processes. In the Pacific Ocean, extensive mixing occurs between directly deposited stratospheric (global) fallout, and close-in regional fallout from the Pacific Proving Ground (PPG). PPG fallout was deposited mainly

from US tests in the 1952–1958 pre-moratorium time-frame (Koide et al. 1985; Hong et al. 2011). As shown in Fig. 20.2, $^{240}\text{Pu}/^{239}\text{Pu}$ is higher in PPG fallout than stratospheric fallout; this isotopic difference is very useful towards tracing the transport of dissolved Pu in the North Pacific (e.g., Zheng and Yamada 2004).

20.2 Techniques for Sample Collection, Processing, and Analysis

20.2.1 Sampling and Sample Size

TRU are commonly determined in environmental media such as soils, sediments, water, atmospheric aerosols, atmospheric deposition, snow pack, ice cores, and biota. Procedures for sampling these media are very similar to methods used in other types of geochemical analysis. TRU are mainly found in surficial soils and sediments; in undisturbed soils, essentially the entire inventory is concentrated in the top 30 cm (Kelley et al. 1999). Grab and composite soil samples are obtained using trowels, augers, and shallow coring tools. Boulyga et al. (2003) collected soil cores to a depth of 20 cm, subsequently sectioned into 1 cm intervals, in order to study the depth distribution of Pu and ^{241}Am in soils from Belarus.

In sediments, the depositional TRU inventory may be focused in a shallow band of <5 cm or distributed across several meters of sediment, depending upon the sedimentation conditions. Coring techniques are best selected based on the water depth and sediment thickness to be recovered. Ketterer et al. (2004a) utilized a “Mini-Mackereth” corer based upon the design of Mackereth (1969) to recover a 120 cm core from 170 m water depth in Loch Ness; detectable levels of ^{239}Pu , ^{240}Pu , and ^{241}Am were found in the top 20 cm of this core. For situations requiring coring to greater depths, other devices such as piston corers (e.g., Nesje 1992) are appropriate.

Determinations of TRU in soil samples require enough mass to isolate and measure (by decay counting or mass spectrometry techniques) a sufficient number of detector events. The sensitivity of a mass spectrometric determination is governed by numbers of analyte atoms; decay-counting analyses are constrained by the numbers of decays that can be recorded during a reasonable counting period. The requisite

sample mass may be in the mg range for high activity soils or sediments, particularly where sensitive techniques such as thermal ionization mass spectrometry (TIMS) are used. Kelley et al. (1999) used TIMS to determine ^{237}Np and Pu isotopes, including low-abundance ^{241}Pu and ^{242}Pu in 1 g of surficial soil. Zheng and Yamada (2006a) used SF-ICP-MS to determine ^{239}Pu and ^{240}Pu in 0.1–1 g samples of settling marine particles. In other cases, sample sizes of 10–100 g are utilized to improve detection of low concentrations of the analyte; Agarande et al. (2001) used sector field inductively coupled plasma mass spectrometry (SF-ICPMS) for ^{241}Am determinations, using up to 100 g for soils and sediments containing <1 Bq/kg (massic activity) of ^{241}Am from stratospheric fallout. For the alpha spectrometric determination of Pu, Am and Cm isotopes, Mietelski and Was (1997) used soil aliquots of 20–40 g.

In other situations, the available amount of analyte is not the basis for determining sample size; rather, one is concerned with analyzing a single aliquot with sufficient mass to contain a statistical representation of high-activity “hot” particles. Maxwell (2008) described the preparation of 100–200 g aliquots to meet this need for determinations of Pu, Am, and Cm in soils.

Preservation is not required for soils and sediments, since the transuranic elements are particle-reactive and non-volatile; however, collection of water samples typically requires preservation by acidification. In a demonstrative example of this methodology, Yamada et al. (2006) collected 250 L seawater samples, which were acidified to pH <2 with HCl and treated with 3 g of Fe^{3+} (aq) carrier before coprecipitation of Pu with $\text{Fe}(\text{OH})_3$. The precipitate was separated aboard ship prior to further processing in a land-based laboratory. The determination of TRU in seawater and other natural waters typically requires very large volume-samples, as the $^{239+240}\text{Pu}$ activity ranges from 1–10 mBq/m³ in the open oceans up to >100 mBq/m³ in semi-enclosed waters near specific sources such as the Irish Sea (Lindahl et al. 2010).

20.2.2 Sample Pre-Treatment Instrumental Methods of Analysis

^{241}Am in solid samples at \geq Bq/kg activity is amenable to direct gamma spectrometric determination

(Warwick et al. 1996); with this exception, most other TRU analytical procedures require destructive radiochemical analyses. The following is a typical sequence of steps: (1) weighing of a homogenous sample aliquot; (2) addition of a spike isotope, also referred to as a yield tracer; (3) sample treatment with reagents suitable to dissolve the entire sample or quantitatively extract the target analyte from the matrix; (4) separation of the analyte from the dissolved sample matrix, and (5) analyte determination by decay-counting or mass spectrometric techniques. A long-lived spike isotope for ^{237}Np is not commercially available, though Kelley et al. (1999) used a reactor-produced ^{236}Np ($t_{1/2} = 1.54 \times 10^5$ years) spike in their TIMS work. Other workers have used freshly prepared ^{239}Np ($t_{1/2} = 2.36$ days) counted separately by gamma spectrometry (Morris et al. 2000), or ^{242}Pu as a pseudo-spike isotope, the latter taking advantage of the rather similar chemical behavior of Np(IV) and Pu(IV) in separations (Chen et al. 2002). Pu determinations entail using 2.86 years half-life ^{236}Pu spike (Mietelski and Was 1995) and in some cases, ^{244}Pu (Kelley et al. 1999), though ^{242}Pu has been most widely used and is available as certified solutions from the US's National Institute of Standards and Technology (NIST) and the European Union's Institute for Reference Materials and Measurements (IRMM). ^{236}Pu and ^{244}Pu would be the ideal spikes to use in alpha spectrometry (AS) and mass spectrometry (MS), respectively, as these isotopes are essentially absent in most samples and their presence does not interfere with analyte isotope measurements. Some tracing studies entail determination of the sample's indigenous $^{242}\text{Pu}/^{239}\text{Pu}$; in this case, the preparation of both ^{242}Pu -spiked and unspiked sub-samples is required. ^{243}Am is widely available as certified solutions and is the routine spike used for determination of ^{241}Am by AS and MS. For measurements of Cm, $^{243+244}\text{Cm}$ is usually measured as a single un-resolved activity peak by AS versus a ^{243}Am pseudo-spike, taking advantage of the very similar separation behavior of Am and Cm (Mietelski and Was 1997).

In many types of solid environmental samples, TRU can be quantitatively extracted by leaching with mineral acids (HNO_3 and/or $\text{HNO}_3\text{-HCl}$) since these elements are not incorporated into the crystal lattices of naturally occurring minerals. TRU from stratospheric fallout origin are readily recovered in this manner, which simplifies chemical pre-treatment.

A representative example is the procedure followed by Liao et al. (2008), in which sediment samples were leached with 8 M HNO_3 on a 200°C hot plate for 4 h. Acid leaching is simplified by first dry-ashing of the samples at $450\text{--}600^\circ\text{C}$ to thoroughly remove organic matter. Nevertheless, some samples contain TRU in physical/chemical forms not recoverable by simple acid leaching; in this event, more rigorous treatment with HF-containing acid mixtures or fusion with alkaline salts is preferred. Sill (1975) first advocated the routine use of high-temperature fusions for complete dissolution of "refractory" TRU contained within fused vitreous silicate particles or in oxide particles previously subjected to high-temperature calcination. Cizdziel et al. (2008) used $\text{HNO}_3\text{-HF-H}_3\text{BO}_3$ dissolutions on ~ 3 g sub-samples to dissolve Pu contained in vitreous silicates originating from the NTS. Kenna (2002) used $\text{HNO}_3\text{-HF}$ dissolutions for determination of Np and Pu isotopes in ~ 10 g environmental samples prior to MS determinations.

In the analysis of water samples, isolation and purification of the TRU elements is generally a multi-stage process. A typical sequence consists of filtration, preservation by acidification, addition of spike isotopes and carriers, precipitation of a carrier such as $\text{Fe}(\text{OH})_3$ or MnO_2 , collection of the TRU-containing precipitate, dissolution of the precipitate, and a subsequent chemical separation of the TRU from the re-dissolved precipitate. Examples of specific procedures for determination of TRU in large-volume water samples are given elsewhere (Chiappini et al. 1999; Yamada et al. 2006; Baskaran et al. 2009).

Following dissolution or leaching, TRU are isolated by preparative separation techniques. In many cases, a targeted TRU element can be separated from other TRU elements, or other more abundant actinides such as Th and U, by taking advantage of differences in redox behavior. For example, U can be maintained as U(VI) under conditions where Pu is stable as Pu(IV); the latter is easily pre-concentrated on anion exchange resins from nitrate solutions while U(VI) is not retained under the same conditions. The preparative steps are intended to remove the sample matrix and any components interfering directly with measurement of the targeted isotope(s), and to enhance the concentration of the target element. Chemical purity (for MS) and obtaining a thin deposit for minimal peak tailing, in AS, are often more paramount considerations than the chemical yield. Co-precipitation with

Fe(OH)₃, MnO₂, or calcium oxalate are typical initial separation steps in analysis of water samples (Yamada et al. 2006; Becker et al. 2004), and sometimes solid samples (Maxwell 2008). Separations are generally based upon ion-exchange schemes with anion or cation resin columns, or selective solid-phase extractants (Ketterer and Szechenyi 2008). The development of commercially available extraction resins for Np, Pu and Am/Cm has greatly simplified TRU separation processes, allowing for the use of small columns and reagent volumes with minimal waste generation (Thakkar 2002).

20.2.3 Instrumental Methods of Analysis

Alpha spectrometry is the classical approach used for decades in the determination of Pu, Am and Cm (for a recent review see Vajda and Kim 2010), though the method is less practical for longer-lived isotopes (e.g., ²³⁷Np and ²⁴⁴Pu). In AS, the element of interest is prepared as a thin-film deposit by microprecipitation with NdF₃, or electrodeposition (Baskaran et al. 2009; Vajda and Kim 2010); the source is placed into an evacuated chamber with a planar Si detector. Equipped with a multi-channel analyzer, the alpha spectrum (Fig. 20.3) is acquired over sufficient counting time to collect adequate counts for the analyte and spike isotopes (typically hours–weeks). The main advantages of AS include its use of relatively simple and inexpensive hardware, the ability to re-measure previously prepared sources, and the ability to determine

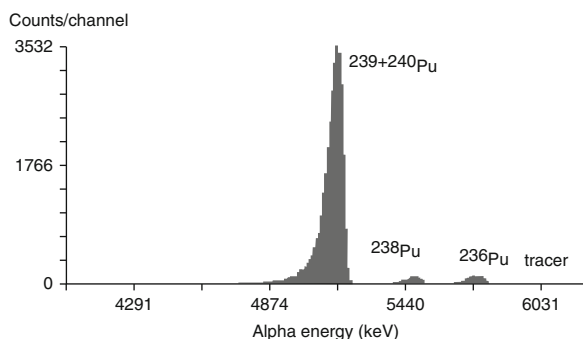


Fig. 20.3 Alpha spectrum of Pu isotopes prepared from 20 g of a surface soil sample from southern Poland; dissolution method per Mietelski and Was (1995). Energy width = 7 keV per channel; measurement time = 1.0 days; 0.0837 Bq ²³⁶Pu tracer was added at the onset of the preparation

selected isotopes such as ²³⁸Pu and ²⁴¹Am that have shorter half-lives or serious isobaric interferences in MS. Besides the long acquisition times, the other major drawback in the AS determination of Pu is its inability to routinely resolve ²³⁹Pu and ²⁴⁰Pu, precluding using ²⁴⁰Pu/²³⁹Pu as a powerful isotopic fingerprint, though this is sometimes possible in high-activity samples by spectral de-convolution methods (Montero and Sanchez 2001). With AS methods, discriminatory activity ratios routinely studied as source tracers include ²³⁸Pu/²³⁹⁺²⁴⁰Pu (Mietelski and Was 1995) and ²⁴¹Am/²³⁹⁺²⁴⁰Pu. AS remains the preferred approach for determinations of ²³⁸Pu, ²⁴¹Am and ²⁴³⁺²⁴⁴Cm, and it appears unlikely that MS will become competitive in the future for measurements of these isotopes.

²⁴¹Pu is a beta-emitting isotope not directly detectable by alpha spectrometry, though it has been measured by alpha-counting the ingrown ²⁴¹Am after a 1–2 year delay (Mietelski et al. 1999). Alternatively, ²⁴¹Pu is directly measured by beta scintillation techniques, enabling source discrimination and mixing calculations using ²⁴¹Pu/²³⁹⁺²⁴⁰Pu activity ratios (Mietelski et al. 1999).

Though it has long had a niche presence in specialized studies (Hardy et al. 1980; Koide et al. 1985), MS has recently enjoyed a tremendous renaissance for low-level measurements of TRU in environmental samples (Lariviere et al. 2006; Ketterer and Szechenyi 2008; Lindahl et al. 2010). Mass spectrometry is inherently advantageous in determinations of long-lived radionuclides having $t_{1/2} \geq 1,000$ years (Lariviere et al. 2006). Several MS techniques have been widely used in TRU determinations, including TIMS, ICPMS, resonance ionization MS (RIMS), accelerator MS (AMS), and secondary ionization MS (SIMS); the role of different MS techniques is discussed in more detail elsewhere (Lariviere et al. 2006; Ketterer and Szechenyi 2008). Though sample preparation is still required, the typical MS determination is performed in a few minutes versus hours–days for decay-counting methods. A mass spectrum depicting the detection of ²³⁷Np, ²³⁹Pu and ²⁴⁰Pu in a stratospheric fallout-containing surface soil is shown in Fig. 20.4.

At this point in time, quadrupole and sector field ICPMS (Q-ICPMS, SF-ICPMS) dominate all the others in numbers of studies, while the remaining MS techniques are nonetheless invaluable in specialized

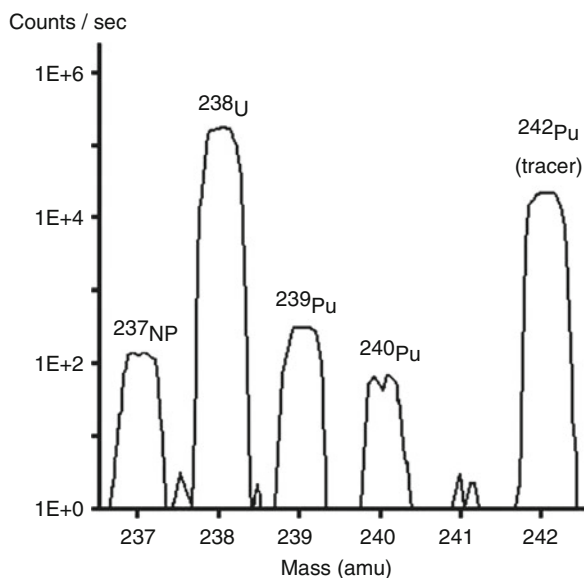


Fig. 20.4 Sector field ICP mass spectrum of Pu extracted from 50 g of a surface soil sample from Chihuahua, Mexico; acid-leaching and Pu separation per Ketterer et al. (2002). Mass spectral data were collected by averaging 50 one-second sweeps in the depicted mass range; the ^{242}Pu peak originates from 50 pg of added yield tracer; ^{238}U is the amount remaining after removal of $>99.999\%$ of the originally leached U content

situations. ICPMS has achieved “workhorse” status because of its widespread availability in labs worldwide; instruments have relatively low capital cost ($<\$150,000$ US for a basic Q-ICPMS). ICPMS is highly compatible with automated introduction of liquid samples, and has modest operator skill requirements. Sample throughput, after preparation of separated sample aliquots, can surpass 100 samples/day. The contrast between ICPMS and AS is apparent by considering the determination of 1 pg of recovered ^{239}Pu , corresponding to 2.5×10^9 atoms and an α decay rate of 2.3 mBq. With an AS counting efficiency of 30% (Vajda and Kim 2010), approximately 17 days are required to collect 1,000 detector events, yielding a relative counting error of 3.1%. However, even with a relatively atom counting efficiency of 0.01% typical of Q-ICPMS, approximately 50,000 atom counts can be registered (in a 20% duty cycle peak-jump experiment with five isotopes sequentially counted) in a matter of several minutes time. Significantly better atom counting efficiencies are routine in SF-ICPMS, and specialized TIMS methods have achieved ionization efficiencies of 2% for ^{237}Np and $\sim 5\%$ for Pu isotopes (Kelley et al. 1999). The main drawbacks of MS

versus decay-counting techniques are permanent contamination of the instrument, high hardware costs, and difficulties with determination of some specific isotopes that have relatively short half-lives, such as ^{238}Pu . Mass spectrometric techniques, particularly ICPMS and SIMS, can be constrained by interfering isobaric polyatomic ions, which are not resolved under low-resolution conditions where sensitivity is optimum. In ICPMS, isobars such as PbCl^+ (Nygren et al. 2003) can generally be removed by suitable preparative separations prior to the determination step; the well-known $^{238}\text{U}^{1}\text{H}$ interference on ^{239}Pu is not problematic if U is sufficiently eliminated beforehand (Ketterer et al. 2004a). In AMS, isobars and abundance sensitivity effects are completely eliminated by high-energy charge-exchange reactions, and definitive detection of transuranic isotopes is performed in an interference-free manner (Fifield 2008). AMS, however, is very capital- and operator skill-intensive, with only a few systems currently in use worldwide for TRU determinations in niche applications. The main advantage of SIMS is its imaging capability and the possibility of performing elemental and isotopic analyses of individual particles, which represents an important capability in nuclear safeguards applications (Pöllänen et al. 2006).

20.2.4 Figures of Merit

Some representative detection limits for MS determinations of Pu in environmental samples are given in Table 20.1. In general, these detection limits are far superior to AS, which affords detection limits of ca. 0.1–1 mBq/sample (Vajda and Kim 2010). Total propagated uncertainties for analytical results of $<5\%$ are achieved relatively easily, and can be better than 1% in some instances. ICPMS or TIMS with multiple ion counting systems (Taylor et al. 2001) potentially offers excellent precision for ratio measurements, both of the sample isotope ratios, and sample-spike atom ratios for isotope dilution determinations. Though these MC-ICPMS systems are expensive and not widely used, they have potential for producing outstanding accuracy if all sources of systematic error (namely isobars, mass discrimination, and detector cross-calibration effects) can be accounted for. Taylor et al. (2001) illustrated the determination of

Table 20.1 Representative detection and performance limits for determination of Pu in environmental samples

Technique	Detection limits	Comments	Reference
TIMS	10 fg $^{239+240}\text{Pu}$	Early TIMS work; ice cores	Koide et al. (1985)
TIMS	~0.01 fg for ^{241}Pu , ^{242}Pu	Precise ratio measurements in ~1 g soils; total dissolution with HNO_3/HF ; ^{244}Pu spike	Kelley et al. (1999)
RIMS	~0.4–4 fg for each isotope	Soil and sediment analysis; alkali fusion for total dissolution	Nunnemann et al. (1998)
AMS	<0.1 fg ^{239}Pu	Ice cores; analysis constrained by 2–5 fg procedural blanks for ^{240}Pu and ^{239}Pu	Olivier et al. (2004)
Q-ICPMS ^a	20 fg $^{239+240}\text{Pu}$	Ratio measurements in Pu solution SRM's, IAEA-135 sediment	Godoy et al. (2007)
SF-ICPMS ^a	5 fg ^{237}Np , ^{239}Pu , ^{240}Pu , ^{241}Pu	10 g samples (LOD 0.5 fg/g); total dissolution with HNO_3/HF ; ^{236}Np and ^{242}Pu spikes; sediments and soils	Kenna (2002)
MC-ICPMS	0.07 fg ^{242}Pu <5 fg ^{242}Pu	Analysis of settling marine particles 0.03–0.50 g <10% RSD achieved for $^{242}\text{Pu}/^{239}\text{Pu}$ ratio measurements with 5 fg ^{242}Pu ; extracts from sediments	Zheng and Yamada (2006a) Taylor et al. (2001)

^aMore discussion and examples of ICPMS detection limits for Pu are given in a review by Kim et al. (2007)

Table 20.2 Standard reference materials with certified activities of TRU in environmental sample matrices

Material ^a	Certified activities	Uncertified (information values)
NIST 4350b, Columbia River Sediment	^{238}Pu , $^{239+240}\text{Pu}$, ^{241}Am	$^{240}\text{Pu}/^{239}\text{Pu}$ atom ratio
NIST 4353a, rocky flats soil #2	^{238}Pu , $^{239+240}\text{Pu}$	^{241}Am , $^{240}\text{Pu}/^{239}\text{Pu}$, $^{241}\text{Pu}/^{239}\text{Pu}$
NIST 4354, lake sediment	^{238}Pu , $^{239+240}\text{Pu}$, ^{241}Am	
NIST 4357, ocean sediment	^{238}Pu , $^{239+240}\text{Pu}$	^{241}Am , ^{237}Np
IAEA 375, soil		^{238}Pu , $^{239+240}\text{Pu}$, ^{241}Am
IAEA 381, Irish sea water	^{237}Np , ^{238}Pu , ^{239}Pu , ^{240}Pu , $^{239+240}\text{Pu}$, ^{241}Am	$^{240}\text{Pu}/^{239}\text{Pu}$ atom ratio ^b
IAEA 384, Fangataufa Sediment	^{238}Pu , $^{239+240}\text{Pu}$, ^{241}Am	^{239}Pu , ^{240}Pu , ^{241}Pu
IAEA 385, Irish Sea Sediment	^{238}Pu , $^{239+240}\text{Pu}$, ^{241}Am	^{239}Pu , ^{240}Pu , ^{241}Pu

^aNIST National Institute of Standards and Technology; IAEA International Atomic Energy Agency (Povinec et al. 2002)

^bA recommended $^{240}\text{Pu}/^{239}\text{Pu}$ value of 0.22 ± 0.03 is given by IAEA. Zheng and Yamada (2007) reported $^{240}\text{Pu}/^{239}\text{Pu} = 0.2315 \pm 0.0008$

$^{240}\text{Pu}/^{239}\text{Pu}$ in 100 fg Pu with 0.7% RSD, and with a precision of better than 0.15% RSD with 3 pg Pu (the latter quantity corresponds to a mixture of 6.1×10^9 atoms ^{239}Pu and 1.4×10^9 atoms ^{240}Pu , or 5.6 mBq ^{239}Pu and 4.7 mBq ^{240}Pu). Clearly, the combination of high transmission efficiency along with simultaneous counting of multiple ion beams at 100% duty cycle is responsible for these outstanding attributes.

Many different standard reference materials are readily available from NIST or IAEA for assay of activities of ^{238}Pu , $^{239+240}\text{Pu}$, and ^{241}Am (a list of reference materials is given in Baskaran et al. 2009). Materials are available that contain nuclides from stratospheric fallout and/or other sources in a range of activities; some examples of commonly used assay standards are given in Table 20.2. Reference materials certified for activities of one or more Cm isotopes are lacking, owing largely to the paucity of environmental

Cm studies. Materials certified for ^{237}Np activity and/or $^{237}\text{Np}/^{239}\text{Pu}$ (along with the availability of ^{236}Np from a commercial or governmental agency source) represent an additional need.

Since many studies are focusing on TRU in seawater, particularly Pu, a standard reference material (IAEA 381, Irish Sea Water) has become available. However, this material contains grossly elevated levels of radionuclides originating from the Sellafield nuclear fuel reprocessing facility; for instance, $^{239+240}\text{Pu}$ is certified at 0.0137 ± 0.0012 Bq/kg, or about 14 Bq/m³, which is 1,000–10,000-fold higher than typical Pu activities in open ocean water. Though the availability of a seawater standard certified for baseline Pu activities, along with atom ratios, would be greatly beneficial to the marine radiochemistry community, the preparation of this material would be exceedingly difficult.

Certified Pu atom ratio standards are available from the US Department of Energy's New Brunswick Labs as CRM 136 and 137 (12 and 18% ^{240}Pu , respectively), though NBL is, at present, unwilling to distribute these CRM's in quantities smaller than 250 mg of Pu metal. The European Union's Institute for Reference Materials and Measurements (IRMM) now sells 1 mg sets of solid Pu nitrate materials certified for $^{239}\text{Pu}/^{242}\text{Pu}$ atom ratios; however, these materials are less useful for evaluating data for the environmentally significant ratios $^{240}\text{Pu}/^{239}\text{Pu}$ and $^{241}\text{Pu}/^{239}\text{Pu}$. Also lacking are natural matrix reference materials certified for Pu atom ratios, though numerous referee analyses of Pu assay SRM's have been published (e.g., Muramatsu et al. 2001; Zheng and Yamada 2007; Ketterer and Szechenyi 2008). In conclusion, critical needs are the development of a spike for mass spectrometric determination of ^{237}Np , and the development of standards for Pu isotopic compositions, in small-quantity solutions, and particularly in actual environmental media.

20.3 Uses of TRU as Tracers and Chronometers

Several prominent areas of applicability exist for using TRU in the context of environmental/geochemical tracing. These may be broadly classified as (1) chronostratigraphy of sediments and related recent Holocene deposits; (2) using fallout TRU as quantitative probes of soil erosion, transport and deposition; (3) investigating water mass circulation, the transport and scavenging of particulate matter, and tracking the marine geochemical behavior of the TRU elements themselves in the marine environment; and (4) studies of the local/regional transport, deposition and inventories of non-fallout TRU in the surficial environment. Each of these is considered separately, again with the perspective that Pu is the most prominent analytical target in all four applications. In some instances, e.g. (1) and (2), one focuses on the globally deposited stratospheric fallout signal, which has a well-known source term. In principle, it should be sufficient to determine activity of one or more TRU nuclides; however, in practice, source provenance with ratios such as $^{240}\text{Pu}/^{239}\text{Pu}$ (Fig. 20.2) is essential.

20.3.1 Chronostratigraphy of Recent Deposits

Layered, cumulative deposits, including aquatic sediments, peats, and ice cores require reliable chronology in studies of phenomena such as anthropogenic pollution and climate change. Th-U dating and ^{14}C ($t_{1/2} = 5,730$ years) are effective for longer time-scales, though the well-known excess ^{210}Pb method is broadly applicable to these deposits for the past 100–200 years (Baskaran and Santschi 2002). ^{210}Pb ($t_{1/2} = 22.2$ years) is a model-dependent dating method that assumes a constant rate of supply or constant initial concentration of the excess (unsupported) ^{210}Pb . In contrast, the delivery of stratospheric fallout has a well-defined history (refer to Fig. 20.1) and a signal recognizable worldwide, even in the Southern Hemisphere. Chronostratigraphic dating pinpoints one or more specific event-associated dates in the layered deposits, and thus is an excellent complement to ^{210}Pb chronology. Chronostratigraphy based upon stratospheric fallout has long been performed using ^{137}Cs ; in freshwater aquatic sediments, Cs is associated with fine-grained clay sediments, intercalating into smectites and illites (Ritchie and McHenry 1990). In an ideal depositional setting, fallout accumulation would precisely coincide with the depositional history (Fig. 20.1); however, in real systems, the fallout nuclides appear in the sediment profile as a result of mixing of direct atmospheric deposition with previously deposited fallout transported in from the catchment basin. These mixing processes, along with time-averaging of material that can remain suspended for long period of times, have the effect of dampening the precise monthly and annual deposition patterns apparent in Fig. 20.1. As a result, one is usually only able to pinpoint three specific dates from the sediment record: (1) fallout onset (1952–1954), (2) maximum activity (1963), and (3) the date of core collection. In most cases, the pre-moratorium and post-moratorium peaks are not separately resolved, and frequently, post-deposition disturbances of the sediment record exact additional loss of resolution or distortion of the record. Post-deposition mixing, whether by physical turbation processes, or by bioturbation, tends to introduce ambiguity in the accurate detection of the onset date marker, although in many of these cases a clear 1963 maximum is still evident. Indeed, an evaluation

of the quality/integrity of the un-disturbed sediment record can be garnered from examining or modeling the sediment activity profile versus the atmospheric deposition source term. Cores exhibiting erratic activity profiles or un-interpretible chronostratigraphies tend to be of limited utility in studies where an accurate timeline is required as part of investigations of other recent phenomena such as pollution or climate histories.

Although ^{137}Cs chronostratigraphy has proven quite successful, it is limited by analytical constraints (i.e., the need to gamma-count many individual samples for hours–days) as well as an appreciable loss of activity due to decay (about two-thirds of the originally deposited fallout ^{137}Cs inventory has decayed away by the year 2010). In regions affected by Chernobyl fallout, including many parts of northern Europe and the former Soviet Union, an additional, larger 1986 ^{137}Cs signal is also present. ^{137}Cs is also less successful as a date marker in marine systems, where K_d for Cs is much lower than in freshwater systems due to competition between Cs and high concentrations of other alkali cations. As alternatives to Cs, any of the TRU similarly associated with stratospheric fallout could be used, and there is now substantial interest in using $^{239+240}\text{Pu}$ in this application. Jaakkola et al. (1983) first used $^{239+240}\text{Pu}$ activities, measured by AS, in a chronostratigraphic study of sediments in Finnish lakes, demonstrating close agreement between the $^{239+240}\text{Pu}$ and ^{137}Cs profiles. The labor involved and the low throughput of AS for $^{239+240}\text{Pu}$ activity measurements render this nuclide less attractive if measured by AS; however, ICPMS-based $^{239+240}\text{Pu}$ activity measurements can be performed rapidly and at low cost. In a proof-of-principle study, Ketterer et al. (2002) used Q-ICPMS to determine a $^{239+240}\text{Pu}$ chronology at Old Woman Creek (Ohio, USA); 20 g samples were leached with 16 M HNO_3 , and the resulting $^{239+240}\text{Pu}$ profile was in excellent agreement with ^{137}Cs . Other studies have used SF-ICPMS (e.g., Ketterer et al. 2004a; Liao et al. 2008; Reynolds et al. 2010), Q-ICPMS (Schiff et al. 2010) or AMS (Tims et al. 2010) and in many cases, excellent results were realized with small sample aliquots of <1 g.

Global inventories of TRU are dominated by stratospheric fallout; nevertheless, it is a pre-condition of chronostratigraphy to be able to demonstrate, unequivocally, that the source term (Fig. 20.1) is precisely what is being measured in a particular setting. This

confirmation of source cannot be performed in conventional ^{137}Cs chronostratigraphy, which is based upon activity measurements of a single radionuclide. Advantageously, mass spectrometric measurements of Pu can confirm or disprove the stratospheric fallout origin of Pu through examining the $^{240}\text{Pu}/^{239}\text{Pu}$ atom ratio (Fig. 20.2). An example of this vetting of the Pu source is shown in Fig. 20.5 for a small arctic lake in southern Alaska (Schiff et al. 2010). The Pu activity record indicates the onset of $^{239+240}\text{Pu}$ detection at 8.50–9.00 cm and a $^{239+240}\text{Pu}$ activity maximum at 5.20–5.40 cm. All depth intervals for which adequate $^{240}\text{Pu}/^{239}\text{Pu}$ ratio counting statistics were realized, in fact, exhibit Pu with atom ratios within measurement error of the stratospheric fallout composition (Kelley et al. 1999).

An important advantage of using $^{239+240}\text{Pu}$ chronostratigraphy in preference to ^{137}Cs is its applicability to marine sediments. Even though ^{210}Pb chronology is applicable in marine settings as well, it is nevertheless very instructive to validate the results using a second, independent tracer such as Pu. In studies of shelf sediments at Poverty Bay (New Zealand), Miller and Kuehl (2009) used $^{239+240}\text{Pu}$ activities, measured in acid-leached samples by SF-ICPMS. Despite the lower inventories of stratospheric fallout in the Southern Hemisphere, Pu was readily measured in these sediments and the resulting $^{239+240}\text{Pu}$ activity profiles validated the ^{210}Pb -inferred chronologies. Sanders et al. (2010) successfully determined sediment accumulation rates and $^{239+240}\text{Pu}$ penetration depths in intertidal mangrove mudflats at a coastal location in southeastern Brazil.

20.3.2 Soil Erosion, Transport, and Deposition

The erosion, transport, and re-deposition of soil are of paramount concern in agriculture as well as the earth sciences. These processes have been studied for decades, and the importance of land-use and tillage practices in minimizing erosion rates is now recognized (Matisoff and Whiting 2011). For obtaining a quantitative understanding of these processes, ^{137}Cs has been used since the 1960's, along with ^{210}Pb and several cosmogenic isotopes (Matisoff and Whiting 2011). Such studies are based upon known source

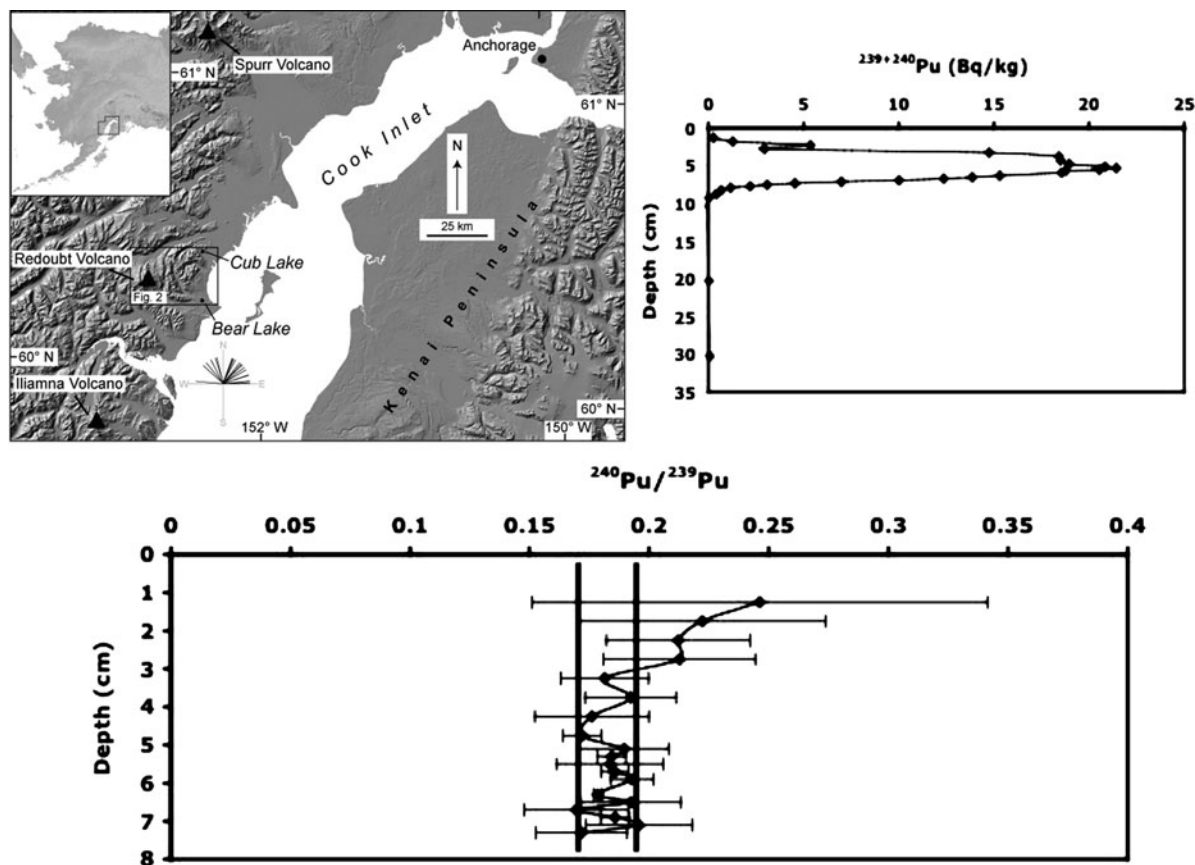


Fig. 20.5 $^{239+240}\text{Pu}$ chronostratigraphy in Bear Lake, Alaska. The location of the lake is shown in the top left panel. $^{239+240}\text{Pu}$ is first detected in the 8.5–9.0 cm depth interval (ca. 1952) and the peak activity is located at 5.2–5.4 cm, ascribed to 1963/

1964. The $^{240}\text{Pu}/^{239}\text{Pu}$ atom ratios, which could be measured in many of the samples with <0.5 g dry sediment, indicate that the Pu is derived from stratospheric fallout

timing with an initially uniform deposition of an isotope within a small-scale experimental area. A “reference inventory” (Bq/m^2) is measured at “undisturbed” locations within or adjoining the study area, and loss or gain of soil by erosion or sedimentation is inferred via comparative measurements of inventories at each specific location versus the reference inventory. ^{137}Cs is well-known in this context, as Cs strongly associates with soil particles (particularly clays) and can be counted using the 661.62 keV gamma photon peak. These studies require an accurate two-dimensional picture of the inventory loss or gain, which is related to the erosion rate via various models (Ritchie and McHenry 1990). As such, a detailed inventory map of even a small field site requires many samples (i.e., hundreds), and the rate of data generation is constrained by numbers of available gamma counters. In Chernobyl-affected locations, the use of stratospheric

fallout ^{137}Cs is complicated by a second 1986 source term that was deposited non-uniformly as tropospheric fallout; gamma spectrometric de-convolution of the 1963 and Chernobyl fallout terms using $^{134}\text{Cs}/^{137}\text{Cs}$ activity ratios is no longer possible now that Chernobyl-produced ^{134}Cs ($t_{1/2} = 2.06$ years) has decayed to non-detectable levels. However, TIMS was used by Lee et al. (1993) to measure $^{137}\text{Cs}/^{135}\text{Cs}$; the long-lived ^{135}Cs isotope ($t_{1/2} = 2.3 \times 10^6$ years) potentially allows for source discrimination between stratospheric fallout and other ^{137}Cs components of the soil.

TRU isotopes, especially $^{239+240}\text{Pu}$, are attractive alternatives to ^{137}Cs , as these isotopes are also associated with soil particles, though they may be present in different soil mineral phases than Cs. Huh and Su (2004) compared the application of ^{137}Cs and $^{239+240}\text{Pu}$ in Taiwan soils, finding that Cs and Pu

conveyed very similar information about soil inventories and transport. When combined with MS (rather than AS) measurements, it is apparent that Pu has significant under-utilized potential as a tracer of soil re-distribution. Further, the distribution of TRU from the Chernobyl accident is much more constrained than is the case with ^{137}Cs ; the TRU isotopes are specifically associated with non-volatile fuel particles (Mietelski and Was 1995, 1997), as opposed to Cs, which was volatilized in the reactor accident and became widespread over Europe and Russia. Once again, MS, through measurements of $^{240}\text{Pu}/^{239}\text{Pu}$ and/or other ratios, routinely allows evaluation of source provenance so that a specific input function (namely, stratospheric fallout) can be confirmed, or de-convoluted if mixed sources are identified.

Kaste et al. (2006) compared ^{137}Cs and $^{239+240}\text{Pu}$ depth profiles in soils from the Konza Prairie site (Kansas, USA), an un-disturbed tall-grass prairie. The activity profiles were very similar, leading to the inference that $^{239+240}\text{Pu}$ could serve the same purpose as a soil erosion tracer. Everett et al. (2008) used AMS to determine $^{239+240}\text{Pu}$ activities in soils from the Herbert River catchment area in northeastern Queensland (Australia); again, $^{239+240}\text{Pu}$ and ^{137}Cs conveyed similar information about erosion and re-distribution of soils in this Southern Hemisphere location. In a study focusing on aeolian transport of surface soils in the steppes of west Texas, Van Pelt et al. (in preparation) compared ^{137}Cs and $^{239+240}\text{Pu}$ activities in soils and transported dusts, again demonstrating the rather similar inferences possible for these two systems (Fig. 20.6).

20.3.3 Transport and Scavenging in Marine Systems

The oceans have received TRU, mainly through global fallout, both as direct atmospheric deposition and as material transported from the continents. Once again, the greatest emphasis in published studies has been on Pu. Sholkovitz (1983) summarized early studies on Pu marine geochemistry. Subsequent to Sholkovitz's review, it is now increasingly apparent that the behavior of Pu in the oceans is very complex. More recent reviews by Skipperud (2004) and Lindahl et al. (2010) describe the behavior of Pu in the arctic marine environment, with prominent mention of the significance of atom ratio data obtained by mass spectrometry.

Classic alpha spectrometric $^{239+240}\text{Pu}$ activity measurements in marine studies often do not provide adequate insight into marine Pu sources. Nevertheless, marine Pu transport depends dramatically upon its source and hence physicochemical speciation, with the oxidation state, size fractionation, and chemical composition of Pu-bearing particles all inevitably determining the resulting behavior. Therefore, MS can play a vital role in these studies, both in terms of measuring activities of very small quantities of Pu, and additionally, in isotopic analysis for source discrimination.

The Pacific Ocean has received significant local/regional fallout from 1946 to 1958 tests at the US's Pacific Proving Grounds and from 1966 to 1974 French tests at Mururoa and Fangataufu. The first ocean-wide study of Pu in the Pacific Ocean originated with the GEOSEC sampling program in the early

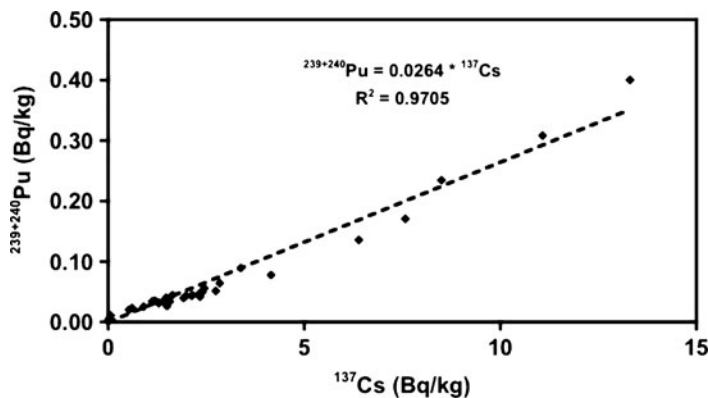


Fig. 20.6 Comparison of $^{239+240}\text{Pu}$ and ^{137}Cs activities in soils from west Texas, USA. ^{137}Cs was determined by gamma spectrometry (24 h counting times); $^{239+240}\text{Pu}$ was determined by SF-ICPMS in 50 g sub-samples leached with 100 mL of 16 M HNO_3 for 16 h at 80°C

1970's, some 10–15 years after the major input of fallout Pu (Bowen et al. 1980). Since then, Pu activities and the element's behavior in the water column and sediments of the Pacific have been intensively studied. In the South Pacific, Chiappini et al. (1999) determined $^{240}\text{Pu}/^{239}\text{Pu}$ atom ratios and $^{239+240}\text{Pu}$ activities in surface and deep waters in the vicinity of Mururoa and Fangataufa atolls. The measurements were obtained using nominal 500 L sample volumes, with a co-precipitation/purification procedure being first used to prepare an alpha spectrometric source; thereafter, the source deposit was dissolved and analyzed by high-sensitivity Q-ICPMS. Evidence for a localized effect from 1966 to 1974 French tests was manifested as $^{240}\text{Pu}/^{239}\text{Pu}$ ratios of 0.07–0.10 in the upper 500 m of the water column. In the North Pacific, a pervasive signal is observed for PPG fallout mixed with stratospheric fallout. The TIMS study of Buesseler (1996) identified $^{240}\text{Pu}/^{239}\text{Pu}$ atom ratios in the range 0.19–0.34 that were ascribed to tropospheric fallout from the PPG; deep water $^{240}\text{Pu}/^{239}\text{Pu}$ atom ratios were systematically higher than global fallout. Buesseler (1996) demonstrated that PPG-derived Pu was more rapidly removed from surface waters than Pu from stratospheric fallout; corals exhibited $^{240}\text{Pu}/^{239}\text{Pu} > 0.20$ for 1955–1961 growth bands, but $^{240}\text{Pu}/^{239}\text{Pu}$ was congruent with stratospheric fallout in 1962–1964 growth. Buesseler (1996) also found evidence for elevated $^{240}\text{Pu}/^{239}\text{Pu}$ ratios in surface sedi-

ments as far north as 40°N . Subsequent work by many groups has confirmed and elaborated upon these findings. Various studies have now documented the presence of PPG fallout in many North Pacific locations, including the Korean Peninsula (Kim et al. 2004), the Southern Okinawa Trench (Lee et al. 2004), the Japan Sea (Zheng and Yamada 2005), the Sea of Okhotsk (Zheng and Yamada 2006b), and the Sulu and South China Seas (Dong et al. 2010). In these cases, it is apparent that Pu is being transported as a solute via ocean currents; in the pelagic zone, particulate matter is present at very low concentrations, and there is little opportunity for particle scavenging. However, once the currents reach near-shore locations, Pu is scavenged from the water column and appears as a sediment-associated component (Zheng and Yamada 2006c). Yamada and Aono (2002) reported large particle-associated fluxes of $^{239+240}\text{Pu}$ on the East China Sea continental margins, which indicated that episodic lateral transport of particles was significant for $^{239+240}\text{Pu}$ delivery on the continental slope in the East China Sea.

The near-shore removal of Pu from the water column is quite apparent in the sediment records from Sagami Bay from the eastern margin of Japan (Zheng and Yamada 2004). This can best be seen by simultaneously evaluating the $^{240}\text{Pu}/^{239}\text{Pu}$ atom ratios alongside the $^{239+240}\text{Pu}$ activity profile (Fig. 20.7). A $^{239+240}\text{Pu}$ activity peak is observed in Core

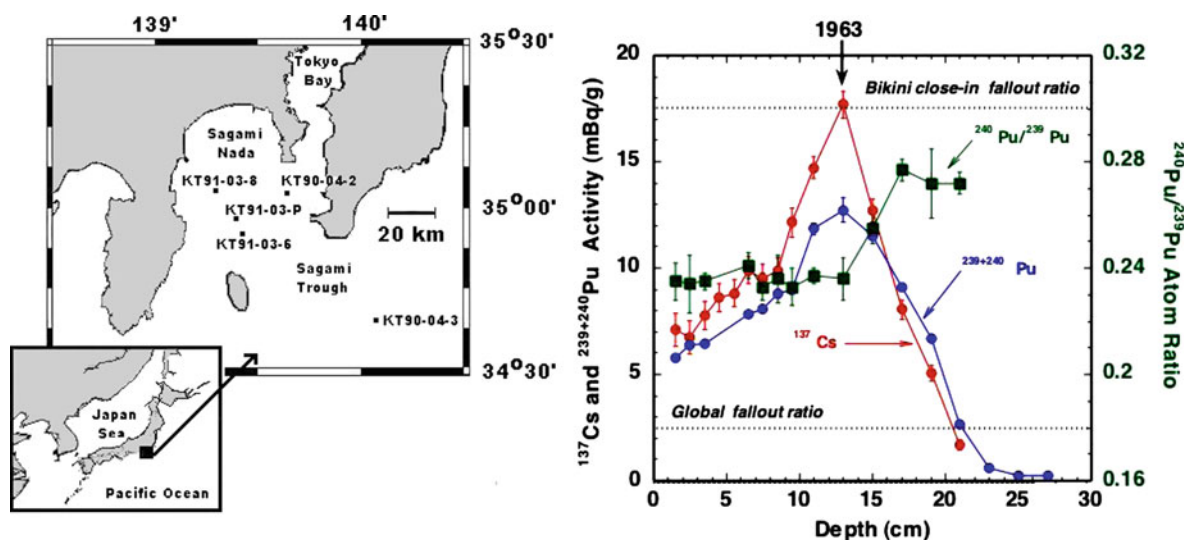


Fig. 20.7 Sediment core location from Sagami Bay near Tokyo, Japan; vertical profiles for $^{239+240}\text{Pu}$ activity, $^{240}\text{Pu}/^{239}\text{Pu}$, and ^{137}Cs activity in Core KT-91-03-8. The vertical

lines shown for comparison versus the $^{240}\text{Pu}/^{239}\text{Pu}$ data are stratospheric fallout (0.18) and Bikini close-in fallout (0.30). Source: Zheng and Yamada (2004)

KT-91-03-8 at a depth of 12–14 cm, which coincides with the ^{137}Cs activity peak; both the $^{239+240}\text{Pu}$ and ^{137}Cs peaks are ascribed to 1963. However, at a depth of 16–18 cm, preceding the 1963 peak and probably reflecting mid-late 1950's sedimentation, a maximum $^{240}\text{Pu}/^{239}\text{Pu}$ ratio of 0.277 ± 0.004 is observed. In post-1963 sediments, a rather uniform $^{240}\text{Pu}/^{239}\text{Pu}$ ratio of ~ 0.23 is observed. These patterns are definitely produced via mixing of stratospheric fallout Pu ($^{240}\text{Pu}/^{239}\text{Pu} \sim 0.18$; Kelley et al. 1999) with higher ratio fallout from the PPG ($^{240}\text{Pu}/^{239}\text{Pu} \sim 0.30$), the latter being transported with the North Equatorial Current and Kuroshio Current. The mixing of PPG source Pu and stratospheric fallout Pu has been observed in the water column by Bertine et al. (1986). They found an average value of $^{240}\text{Pu}/^{239}\text{Pu}$ of 0.23 in two seawater profiles from the North Pacific Ocean; $^{240}\text{Pu}/^{239}\text{Pu}$ was nearly invariant with depth, indicating that Pu has been homogenized in the water column for a time period of the past several decades.

Although the PPG close-in fallout Pu could be removed more rapidly from surface waters than Pu from stratospheric fallout (Buesseler 1996), high contributions of PPG-origin Pu are still observed in the surface waters in the Sulu and Indonesian Seas (39%) and in the South China Sea (42%) after six decades of their input (Yamada et al. 2006). A recent SF-ICP-MS study of Yamada and Zheng (2010) found anomalous increases of $^{239+240}\text{Pu}$ inventory in water columns of Yamato and Tsushima Basins in the Japan Sea; $^{239+240}\text{Pu}$ inventory in the water columns increased almost two times in a 10-year time scale, and constant $^{240}\text{Pu}/^{239}\text{Pu}$ atom ratios of ca. 0.24 were observed in seawaters from surface down to 3,000 m deep, indicating a continuous input and accumulation of Pu with PPG fallout signal in the Japan Sea.

In addition to the Pacific Ocean, other studies have examined the marine transport of Pu from specific point sources. This discrimination is possible using AS data due to the contrast between $^{238}\text{Pu}/^{239+240}\text{Pu}$ in stratospheric fallout (~ 0.025) versus Sellafield emissions (0.20–0.30). Baskaran et al. (1995) summarized the $^{238}\text{Pu}/^{239+240}\text{Pu}$ activity ratios in nuclear effluents from Sellafield and La Hague in dissolved and suspended particulate phases, surficial sediments, and terrestrial samples in the Arctic. Based upon a plot of the ^{238}Pu versus $^{239+240}\text{Pu}$ activities for 82 surface sediments obtained from the Ob and Yenisey River deltas and the Kara Sea, Baskaran et al. (1996)

obtained a slope of 0.034 ± 0.003 , resembling the Northern Hemisphere fallout activity ratio, and concluded that there is virtually no detectable input from either the European effluents nor from the dumped nuclear reactors in the Kara Sea.

Masqué et al. (2003) measured $^{239+240}\text{Pu}$ activities and $^{240}\text{Pu}/^{239}\text{Pu}$ atom ratios in bottom sediments from the Fram Strait of the Arctic Ocean; the low $^{240}\text{Pu}/^{239}\text{Pu}$ atom ratios were ascribed to transport of Pu from sources in the Kara Sea and Novaya Zemlya towards the North Atlantic by sea ice. Kershaw et al. (1999) used AS to demonstrate the transport of Sellafield-derived Pu in seawater samples from the northeast Atlantic. Along the northern Scottish coast, the highest activity sample contained 73 mBq/m^3 $^{239+240}\text{Pu}$ and a Sellafield-dominated $^{238}\text{Pu}/^{239+240}\text{Pu}$ activity ratio of 0.19. Despite the long-range transport of Pu into seas well north of the Arctic Circle, Kershaw et al. (1999) concluded that the vast majority of Sellafield Pu and ^{241}Am reside in Irish Sea sediments.

In marine and coastal estuarine systems, $^{239+240}\text{Pu}$ activities have been widely used to delineate sediment mixing processes, sediment inventories and export, and average sedimentation rates. Ravichandran et al. (1995) used $^{239+240}\text{Pu}$ along with excess ^{210}Pb to investigate sediment deposition processes in the Sabine-Neches estuary of Texas, USA; the sediment mixing coefficients were determined using $^{239+240}\text{Pu}$ activity profiles, which revealed that mixing rates were relatively small. The average sedimentation rates, determined via the location of the 1963 fallout activity maxima, were quite different among four cores, thus indicating substantial differences in sediment deposition processes at different locations within the estuary. Relatively low core inventories of $^{239+240}\text{Pu}$ versus terrestrial deposition indicated the export of substantial quantities of Pu from the estuary to the continental shelf. The $^{239+240}\text{Pu}$ activity profiles yielded better resolution of sedimentation rates than excess ^{210}Pb activity profiles (Ravichandran et al. 1995). Clearly, this and other examples illustrate the utility of Pu as a tracer of marine sedimentation processes in coastal environments.

One overarching conclusion that can be drawn from a synthesis of many different marine studies is that the water column inventories and isotope signatures of TRU in a specific location cannot necessarily be rationalized and anticipated as easily as is the case in the terrestrial environment. While the *initial* deposition at

any given point may have stemmed from stratospheric fallout and/or close-in (tropospheric) debris, it is clear that oceanic currents play a strong role in transport and re-distribution of the initial inventory over vast distances within decadal timescales. Though post-depositional transport complicates the interpretation of spatially resolved data, the results can often be utilized advantageously to obtain new insights into complex marine transport and scavenging processes (Livingston and Povinec 2002).

20.3.4 Studies of Local/Regional TRU Sources in the Surficial Environment

Relatively limited inferences regarding sources and mixing processes can be inferred by solely considering activities, as surficial TRU activities can vary widely depending upon latitude, rainfall, topography, and erosion/deposition processes. It is commonplace to study the characteristics of specific point or local/regional sources and their mixing with ubiquitous stratospheric fallout through use of atom and/or activity ratios. Once again, Pu is the most prominently studied element, though various studies have considered Np and Am, and in some cases, Cm, alongside Pu data. Now that the use of mass spectrometry has become widespread in these studies, the most commonly interpreted discriminatory ratio is $^{240}\text{Pu}/^{239}\text{Pu}$ (refer to Fig. 20.2). Many sources that mix with stratospheric fallout have contrasting values of $^{240}\text{Pu}/^{239}\text{Pu}$ as well as other atom/activity ratios.

TRU with contrasting fingerprints is evident from a large variety of sources, though stratospheric fallout dominates globally. The 1950's US Marshall Islands tests also generated significant higher-ratio close-in fallout, which is prominently evident in the Pacific (refer to Sect. 20.3.3). Table 20.3 lists various prominent additional sources of TRU in the environment; in terms of a global mass balance, stratospheric fallout is by far the largest, accounting for ~4,000 kg of ^{239}Pu along with associated amounts of other TRU isotopes (Harley 1980). Among the other sources, accurate mass balances are not always known, though many of these probably amount to <10 kg ^{239}Pu . While the smaller quantities associated with many different local/regional sources (Table 20.3) may be of minor

significance in the global sense, in local settings, these sources may overwhelm the inventories and surface activities of TRU from stratospheric fallout. Many of the releases shown in Table 20.3 consist of weapons-grade Pu with low $^{240}\text{Pu}/^{239}\text{Pu}$ ratios of 0.02–0.07, originating from low-yield tests (Trinity, NTS, Semipalatinsk-21, Lop Nor, R Greggane, Maralinga, Mururoa/Fangataufa), weapons deployment (Nagasaki), weapons-grade Pu production reactors (Hanford, Savannah River, Mayak, and Sellafield/Windscale), or weapons component fabrication processes (Rocky Flats, Los Alamos, Krasnoyarsk). The low-yield tests produced fallout resembling the starting weapons-grade material because very little production of heavier isotopes occurred in the low neutron fluxes of these kiloton-range fission tests. In contrast, Pu from stratospheric fallout reflects a composite of many high-yield (megaton) tests where intense neutron fluxes generated significant quantities of heavier isotopes by neutron capture processes. Similarly, releases of high burn-up material from re-processing of power reactor fuel (Sellafield, La Hague, West Valley) or from power reactor accidents (Chernobyl) consists of TRU with enhanced abundances of heavier isotopes such as ^{240}Pu , ^{241}Pu , ^{242}Pu , and heavier elements such as Am and Cm not originally present in the fuels.

It is commonplace in isotope geochemistry to investigate mixing processes through a three-isotope, common denominator plot of C/A versus B/A, where A, B and C represent individual isotopes. These atom ratio mixing plots are readily used to pinpoint the mixing of two specific end-members; binary mixtures of the end-members alone plot along a “mixing line” segment, while third sources usually, but do not necessarily have to, appear as deviants from the mixing line. A well-known example is the use of the atom ratios $^{240}\text{Pu}/^{239}\text{Pu}$, $^{241}\text{Pu}/^{239}\text{Pu}$, $^{242}\text{Pu}/^{239}\text{Pu}$, and $^{237}\text{Np}/^{239}\text{Pu}$ in investigations of mixing between stratospheric fallout and low-ratio regional fallout from the NTS (Kelley et al. 1999; Cizdziel et al. 2008). Besides having lower $^{240}\text{Pu}/^{239}\text{Pu}$, the NTS regional source is also characterized by much lower $^{241}\text{Pu}/^{239}\text{Pu}$, $^{242}\text{Pu}/^{239}\text{Pu}$, and $^{237}\text{Np}/^{239}\text{Pu}$. Kelley et al. (1999) used TIMS to measure all four of these ratios in a suite of soils from worldwide locations; for several samples from Nevada and Utah in the western US, mixed ratio fingerprints were evident, though ratios in samples from more distant US locations agreed well with the global stratospheric fallout

Table 20.3 Local/regional sources of TRU in the surficial environment

Source	Location	Type of release
Nevada Test Site	Nevada, USA	1
Trinity Site	New Mexico, USA	1
Semipalatinsk-21	Kurchatov, Kazakhstan	1
Lop Nor	Sinkiang, China	1
Maralinga	South Australia	1
Nagasaki	Nagasaki, Japan	1a
Reggane	French Sahara (now Algeria)	1
Mururoa/Fangataufa	French Polynesia	1
Chernaya Bay	Novaya Zemlya, Siberia, Russia	2
Amchitka Island	Alaska, USA	2
Mayak	Chelyabinsk, Russia	3
Hanford	Washington, USA	3
Savannah River Site	South Carolina, USA	3
Sellafield	Cumbria, UK	3, 4
La Hague	Normandy, France	4
West Valley	New York, USA	4
Los Alamos	New Mexico, USA	5
Krasnoyarsk Complex	Krasnoyarsk, Russia	5
Rocky Flats	Colorado, USA	5
Chernobyl	Chernobyl, Ukraine	6
Palomares	Spain	7
Thule	Greenland	7

1 = Atmospheric releases from above-ground, low-yield nuclear tests; local/regional deposition; resembles weapons-grade Pu. 1a = low-yield deployed weapon; localized deposition resembling weapons-grade Pu. 2 = Underwater, low-yield nuclear tests; local/regional deposition in marine environment; resembles weapons-grade Pu. 3 = Plutonium production reactors for weapons programs; atmospheric and/or aquatic releases resembling weapons-grade Pu. 4 = Atmospheric and/or aquatic releases from re-processing of spent nuclear fuel from commercial or research-grade power reactors; higher burn-up Pu containing heavier isotopes. 5 = Industrial facilities for Pu metallurgy and fabrication of weapons components; atmospheric and/or aquatic releases of material resembling weapons-grade Pu. 6 = Local/regional release of “hot” fuel particles from a 1986 reactor accident; high burn-up Pu with elevated abundances of heavier isotopes. 7 = Aircraft accidents resulting in the mechanical destruction of weapons and local dispersal of particulate Pu in the surface environment

signatures. The inclusion of $^{237}\text{Np}/^{239}\text{Pu}$ provides additional dimensionality in the data, as ^{237}Np is produced through either successive neutron capture of ^{235}U or by (n, 2n) processes of ^{238}U . Moreover, $^{237}\text{Np}/^{239}\text{Pu}$ is more sensitive to subtle differences in nuclear device construction (i.e., how much ^{235}U was used). The $^{237}\text{Np}/^{239}\text{Pu}$ fingerprint could also be influenced by different post-release chemical behavior of Np and Pu in environmental systems, and might be expected to vary significantly in discharges from nuclear fuel re-processing.

The $^{241}\text{Pu}/^{239}\text{Pu}$ ratio also generates interesting possibilities for chronometry; as ^{241}Pu decays with a half-life of 14.29 years, the $^{241}\text{Pu}/^{239}\text{Pu}$ ratio steadily decreases. In a setting where “aged” Pu is mixed with more recently separated Pu, the latter will exhibit much higher $^{241}\text{Pu}/^{239}\text{Pu}$ that is an obvious trend outlier from an established mixing process between two

aged sources. Alternatively, similar inferences could be drawn through activity comparisons of the ^{241}Pu parent with its daughter, ^{241}Am (Pöllänen et al. 2006).

The powerful inferences available from these mixing plots can be seen in Fig. 20.8. Figure 20.8 depicts data from Kelley et al. (1999); all points shown represent samples from the continental US. The Eureka, Nevada location, labeled “1” in the top panel, reasonably approximates the NTS end-member, while the encircled group “5” consists of soils from more distant locations, comprised exclusively of stratospheric fallout. The points labeled 2, 3, and 4 from locations in Utah, California and Texas, respectively, contain binary mixtures of stratospheric fallout and NTS debris. The same inferences result from using any of these three ratios versus $^{240}\text{Pu}/^{239}\text{Pu}$, though in other binary or ternary mixing situations $^{237}\text{Np}/^{239}\text{Pu}$ could behave differently than $^{241}\text{Pu}/^{239}\text{Pu}$ and $^{242}\text{Pu}/^{239}\text{Pu}$.

For $^{241}\text{Pu}/^{239}\text{Pu}$, the ratios are calculated for a reference date of 1 January 2000; a decade later, all of these ratios would plot along a similar line with 62% of the 2000 slope. Kelley et al. (1999) discuss mixing calculations for quantitative apportionment of binary sources using individual or pairs of ratios; obviously, the relative contribution of the two sources is a direct linear function of the position along the mixing line between the two end members.

Other published examples of two-component TRU source mixing have used two-component mixing diagrams in a similar manner. Kenna and Sayles (2002) used $^{237}\text{Np}/^{239}\text{Pu}$ versus $^{240}\text{Pu}/^{239}\text{Pu}$ to investigate mixing of multiple sources of TRU in sediments of the Ob River Delta in Siberia; in this case, ratios were observed that are not solely attributable to simple two-component mixing, as the samples do not all plot along a single line segment. In a study of mixing between stratospheric fallout and Chernobyl fallout

Pu in northeastern Poland, Ketterer et al. (2004b) demonstrated a clear case of two-component mixing between these sources on a plot of $^{241}\text{Pu}/^{239}\text{Pu}$ versus $^{240}\text{Pu}/^{239}\text{Pu}$; the inferences agreed well with source apportionment previously conducted using $^{238}\text{Pu}/^{239+240}\text{Pu}$ activity ratios (Mietelski and Was 1995).

The requisite measurements of $^{237}\text{Np}/^{239}\text{Pu}$, $^{241}\text{Pu}/^{239}\text{Pu}$ and $^{242}\text{Pu}/^{239}\text{Pu}$ by mass spectrometry each present analytical challenges, particularly in small-mass samples and where complete dissolution of all silicates must be performed. For $^{237}\text{Np}/^{239}\text{Pu}$, the atom ratios are reasonably high and present no great difficulty, aside from the limitation that a ^{236}Np spike is not available. As time progresses, more and more ^{241}Pu is decaying away, and $^{241}\text{Pu}/^{239}\text{Pu}$ measurements will become impractical for scenarios such as Fig. 20.8 in succeeding decades. Satisfactory measurements of $^{241}\text{Pu}/^{239}\text{Pu}$ will be possible long into the future, however, for situations like the

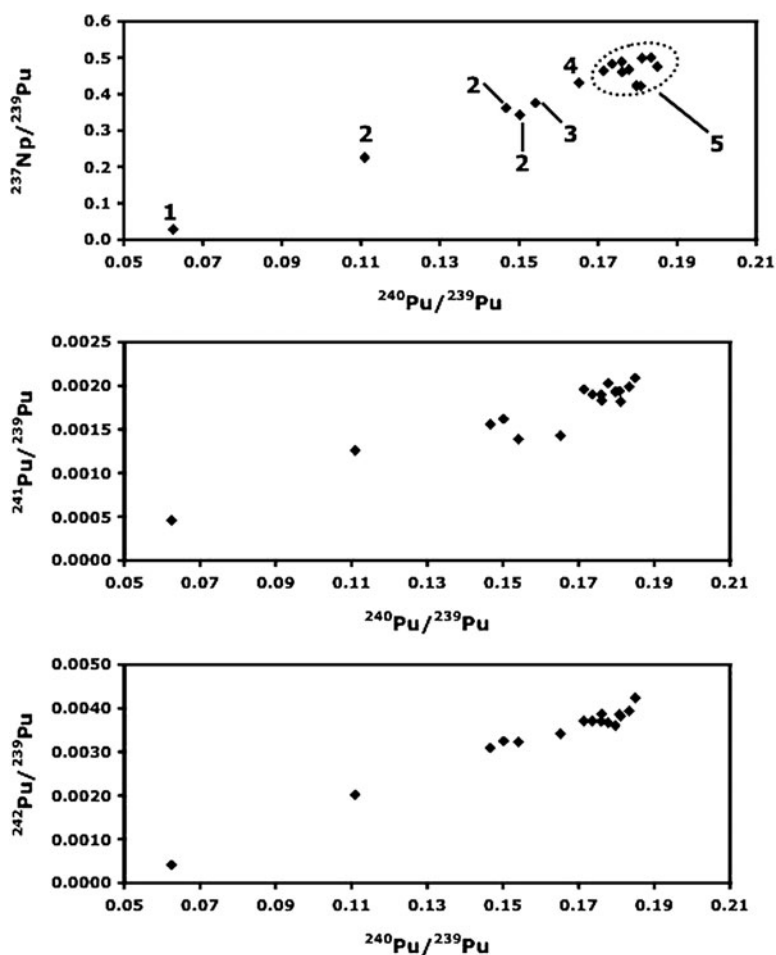


Fig. 20.8 Common-denominator mixing plots of $^{237}\text{Np}/^{239}\text{Pu}$, $^{241}\text{Pu}/^{239}\text{Pu}$, and $^{242}\text{Pu}/^{239}\text{Pu}$ versus $^{240}\text{Pu}/^{239}\text{Pu}$, demonstrating two-component mixing between tropospheric fallout from the NTS, and stratospheric fallout. Point 1 (Eureka, Nevada soil) is a reasonable approximation of the NTS end-member. Group 5 represents soils from distant locations in the continental US lacking any NTS influence; isotope ratios from these samples are congruent with stratospheric fallout in other northern Hemisphere locations. Points 2, 3, and 4 are soils from Utah, California and Texas; these samples are described by two-component mixing between NTS and stratospheric fallout. Source: Kelley et al. (1999)

Chernobyl-stratospheric fallout mixing in Poland (Ketterer et al. 2004b), as the Chernobyl source term presently still contains ~3 atom percent ^{241}Pu .

20.4 Future Directions

The number and scope of studies of environmental TRU has rapidly expanded over the past decade. An important change has been that many more individuals and academic institutions are now involved in a field that has long been studied mainly among government organizations such as the US Department of Energy's National Labs. The widespread availability of MS (particularly ICPMS) has helped to stimulate much of this new interest. The use of $^{239+240}\text{Pu}$ activities and inventories in studies of recent Earth processes, such as erosion and sedimentation, has become routine via MS, while previously the use of Pu in this context would have been totally impractical with AS. In this light, $^{239+240}\text{Pu}$ will probably replace ^{137}Cs as the predominant tracer of these processes.

Most researchers studying TRU sources in the environment will probably favor MS techniques (particularly ICPMS), though AS will remain an important technique for specific measurements such as ^{238}Pu , ^{241}Am , and Cm isotopes. The role of MS in developing a better understanding of Pu distribution and transport in the oceans is quite pronounced (Lindahl et al. 2010). Mass spectrometry already is well-established and an essential tool in nuclear forensics; the role of MS in these endeavors can only be expected to expand. The aforementioned application areas are by no means, fully explored or saturated, and many opportunities for new tracing applications exist that could be tapped with the present well-developed measurement technology. Without question, the upcoming years and decades will generate many exciting and unanticipated new applications of TRU in studies of earth and environmental processes.

Acknowledgments The authors thank J.W. Mietelski for providing the alpha spectrum shown in Fig. 20.3. The authors are indebted to J.W. Mietelski, T.C. Kenna, one anonymous reviewer, and the editorship of M. Baskaran for constructive criticisms of the manuscript. MEK acknowledges ICPMS instrumentation support from Intel Corp., NSF MRI Award No. CHE0118604, and the State of Arizona Technology Research and Innovation Fund. MEK also owes thanks for nearly two

decades of rich and productive interactions with many students and collaborators, and is gratefully indebted to JAK for perspective and inspiration towards facing apparent difficulties in life.

References

- Agarande M, Benzoubir S, Bouisset P et al (2001) Determination of ^{241}Am in sediments by isotope dilution high resolution inductively coupled plasma mass spectrometry (ID HR ICP-MS). *Appl Radiat Isot* 55:161–165
- Baskaran M, Santschi PH (2002) Particulate and dissolved ^{210}Pb activities in the shelf and slope regions of the Gulf of Mexico waters. *Continent Shelf Res* 22:1493–1510
- Baskaran M, Asbill S, Santschi P et al (1995) Distribution of $^{239,240}\text{Pu}$ and ^{238}Pu concentrations in sediments from the Ob and Yenisey Rivers and the Kara Sea. *Appl Radiat Isot* 46:1109–1119
- Baskaran M, Asbill S, Santschi P et al (1996) Pu, ^{137}Cs and excess ^{210}Pb in Russian Arctic sediments. *Earth Planet Sci Lett* 140:243–257
- Baskaran M, Hong G-H, Santschi PH (2009) Radionuclide analysis in seawater. In: Wurl O (ed) *Practical guidelines for the analysis of seawater*. CRC, Boca Raton, FL
- Beck HL, Bennett BG (2002) Historical overview of atmospheric nuclear weapons testing and estimates of fallout in the continental United States. *Health Phys* 82:591–608
- Becker JS, Zoriy M, Halicz L et al (2004) Environmental monitoring of plutonium at ultratrace level in natural water (Sea of Galilee – Israel) by ICP-SFMS and MC-ICP-MS. *J Anal At Spectrom* 19:1–6
- Bennett BG (2002) Worldwide dispersion and deposition of radionuclides produced in atmospheric tests. *Health Phys* 82:644–655
- Bertine KK, Chow TJ, Koide M et al (1986) Plutonium isotopes in the environment: some existing problems and some new ocean results. *J Environ Radioact* 3:189–201
- Boulyga SF, Zoriy M, Ketterer ME et al (2003) Depth profiling of Pu, ^{241}Am and ^{137}Cs in soils from southern Belarus measured by ICP-MS and α and γ spectrometry. *J Environ Monit* 5:661–666
- Bowen VT, Noshkin VE, Livingston HD et al (1980) Fallout radionuclides in the Pacific Ocean: vertical and horizontal distributions, largely from GEOSER stations. *Earth Planet Sci Lett* 49:411–434
- Buesseler KO (1996) The isotopic signature of fallout plutonium in the north Pacific. *J Environ Radioact* 36:69–83
- Carter MW, Moghissi AA (1977) Three decades of nuclear testing. *Health Phys* 33:55–71
- Chen Q, Dahlgaard H, Nielsen SP et al (2002) ^{242}Pu as tracer for simultaneous determination of ^{237}Np and $^{239,240}\text{Pu}$ in environmental samples. *J Radioanal Nucl Chem* 253: 451–458
- Chiappini R, Pointurier F, Millies-Lacroix JC et al (1999) $^{240}\text{Pu}/^{239}\text{Pu}$ isotopic ratios and $^{239+240}\text{Pu}$ total measurements in surface and deep waters around Mururoa and Fangataufa atolls compared with Rangiroa atoll (French Polynesia). *Sci Total Environ* 237(238):269–276

- Choppin GR (2007) Actinide speciation in the environment. *J Radioanal Nucl Chem* 273:695–703
- Cizdziel JV, Ketterer ME, Farmer D et al (2008) $^{239,240,241}\text{Pu}$ fingerprinting of plutonium in western US soils using ICPMS: solution and laser ablation measurements. *Anal Bioanal Chem* 390:521–530
- Curtis D, Fabryka-Martin J, Dixon P et al (1999) Nature's uncommon elements: plutonium and technetium. *Geochim Cosmochim Acta* 63:275–285
- Dong W, Zheng J, Guo QJ et al (2010) Characterization of plutonium in deep-sea sediments of the Sulu and South China Seas. *J Environ Radioact* 101:622–629
- Everett SE, Tims SG, Hancock GJ et al (2008) Comparison of Pu and ^{137}Cs as tracers of soil and sediment transport in a terrestrial environment. *J Environ Radioact* 99:383–393
- Fifield LK (2008) Accelerator mass spectrometry of the actinides. *Quat Geochron* 3:276–290
- Godoy MLDP, Godoy JM, Roldão LA (2007) Application of ICP-QMS for the determination of plutonium in environmental samples for safeguards purposes. *J Environ Radioact* 97:124–136
- Hardy EP, Volchok HL, Livingston HD et al (1980) Time pattern of off-site plutonium deposition from Rocky Flats plant by lake sediment analyses. *Environ Int* 4:21–30
- Harley JH (1980) Plutonium in the environment – a review. *J Radiat Res* 21:83–104
- Holm E, Roos P, Aarkrog A et al (2002) Curium isotopes in Chernobyl fallout. *J Radioanal Nucl Chem* 252:211–214
- Hong G-H (2011) Applications of anthropogenic radionuclides as tracers to investigate marine environmental processes. In: Baskaran M (ed) *Handbook of environmental isotope geochemistry*. Springer, Heidelberg
- Hotchkis MAC, Child D, Fink D et al (2000) Measurement of ^{236}U in environmental media. *Nucl Instrum Meth Phys Res B* 172:659–665
- Huh CA, Su CC (2004) Distribution of fallout radionuclides (^7Be , ^{137}Cs , ^{210}Pb and $^{239,240}\text{Pu}$) in soils of Taiwan. *J Environ Radioact* 77:87–100
- Jaakkola T, Tolonen K, Huttunen P et al (1983) The use of fallout ^{137}Cs and $^{239,240}\text{Pu}$ for dating of lake sediments. *Hydrobiologia* 103:15–19
- Kaste JM, Heimsath AM, Hohmann M (2006) Quantifying sediment transport across an undisturbed prairie landscape using cesium-137 and high resolution topography. *Geomorphology* 76:430–440
- Kelley JM, Bond LA, Beasley TM (1999) Global distribution of Pu isotopes and ^{237}Np . *Sci Total Environ* 237(238):483–500
- Kenna TC (2002) Determination of plutonium isotopes and neptunium-237 in environmental samples by inductively coupled plasma mass spectrometry with total sample dissolution. *J Anal At Spectrom* 17:1471–1479
- Kenna TC, Sayles FL (2002) The distribution and history of nuclear weapons related contamination in sediments from the Ob River, Siberia as determined by isotopic ratios of plutonium and neptunium. *J Environ Radioact* 60:105–137
- Kershaw PJ, McCubbin D, Leonard KS (1999) Continuing contamination of north Atlantic and Arctic waters by Sellafield radionuclides. *Sci Total Environ* 237(238):119–132
- Ketterer ME, Szechenyi SC (2008) Determination of plutonium and other transuranic elements by inductively coupled plasma mass spectrometry: a historical perspective and new frontiers in the environmental sciences. *Spectrochim Acta B* 63:719–737
- Ketterer ME, Watson BR, Matisoff G et al (2002) Rapid dating of recent aquatic sediments using Pu activities and $^{240}\text{Pu}/^{239}\text{Pu}$ as determined by quadrupole inductively coupled plasma mass spectrometry. *Environ Sci Technol* 36:1307–1311
- Ketterer ME, Hafer KM, Jones VJ et al (2004a) Rapid dating of recent sediments in Loch Ness: inductively coupled plasma mass spectrometric measurements of global fallout plutonium. *Sci Total Environ* 322:221–229
- Ketterer ME, Hafer KM, Mieltski JW (2004b) Resolving Chernobyl vs. global fallout contributions in soils from Poland using Plutonium atom ratios measured by inductively coupled plasma mass spectrometry. *J Environ Radioact* 73:183–201
- Kim CK, Kim CS, Chang BU et al (2004) Plutonium isotopes in seas around the Korean Peninsula. *Sci Total Environ* 318:197–209
- Kim CS, Kim CK, Martin P et al (2007) Determination of plutonium concentrations and isotope ratio by inductively coupled plasma mass spectrometry: a review of analytical methodology. *J Anal At Spectrom* 22:827–841
- Koide M, Bertine KK, Chow TJ et al (1985) The $^{240}\text{Pu}/^{239}\text{Pu}$ ratio, a potential geochronometer. *Earth Planet Sci Lett* 72:1–8
- Krey PW, Leifer R, Benson WK et al (1979) Atmospheric burn-up of the Cosmos-954 reactor. *Science* 205:583–585
- Lariviere D, Taylor VF, Evans RD et al (2006) Radionuclide determination in environmental samples by inductively coupled plasma mass spectrometry. *Spectrochim Acta B* 61:877–904
- Lee T, Teh-Lung K, Hsiao-Ling L et al (1993) First detection of fallout Cs-135 and potential applications of $^{137}\text{Cs}/^{135}\text{Cs}$ ratios. *Geochim Cosmochim Acta* 57:3493–3497
- Lee S, Huh C, Su C et al (2004) Sedimentation in the Southern Okinawa Trough: enhanced particle scavenging and teleconnection between the Equatorial Pacific and western Pacific margins. *Deep Sea Res I* 51:1769–1780
- Liao H, Zheng J, Wu F et al (2008) Determination of plutonium isotopes in freshwater lake sediments by sector-field ICP-MS after separation using ion-exchange chromatography. *Appl Radiat Isot* 66:1138–1145
- Lindahl P, Lee S, Worsfold P et al (2010) Plutonium isotopes as tracers for ocean processes: a review. *Mar Environ Res* 69:73–84
- Livingston HD, Povinec PP (2002) A millennium perspective on the contribution of global fallout radionuclides to ocean science. *Health Phys* 82:656–668
- Mackereth FJH (1969) A short core sampler for sub-aqueous deposits. *Limnol Oceanogr* 14:145–151
- Masqué P, Cochran JK, Hebbeln D et al (2003) The role of sea ice in the fate of contaminants in the Arctic Ocean: plutonium atom ratios in the Fram Strait. *Environ Sci Technol* 37:4848–4854
- Matisoff G, Whiting PJ (2011) Measuring soil erosion rates using natural (^7Be , ^{210}Pb) and anthropogenic (^{137}Cs , $^{239,240}\text{Pu}$) radionuclides. In: Baskaran M (ed) *Handbook of environmental isotope geochemistry*. Springer, Heidelberg

- Maxwell SL III (2008) Rapid method for determination of plutonium, americium and curium in large soil samples. *J Radioanal Nucl Chem* 275:395–402
- Mietelski JW, Was B (1995) Plutonium from Chernobyl in Poland. *Appl Radiat Isot* 46:1203–1211
- Mietelski JW, Was B (1997) Americium, curium and rare earths radionuclides in forest litter samples from Poland. *Appl Radiat Isot* 48:705–713
- Mietelski JW, Dorda J, Was B (1999) Pu-241 in samples of forest soil from Poland. *Appl Radiat Isot* 51:435–447
- Miller AJ, Kuehl SA (2009) Shelf sedimentation on a tectonically active margin: a modern sediment budget for poverty continental shelf, New Zealand. *Mar Geol* 270:175–187
- Montero PR, Sanchez AM (2001) Plutonium contamination from accidental release or simply fallout: study of soils at Palomares (Spain). *J Environ Radioact* 55:157–165
- Morris K, Butterworth JC, Livens FR (2000) Evidence for the remobilization of Sellafield waste radionuclides in an intertidal salt marsh, West Cumbria, U.K. *Estuar Coast Shelf Sci* 51:613–625
- Muramatsu Y, Hamilton T, Uchida S et al (2001) Measurement of $^{240}\text{Pu}/^{239}\text{Pu}$ isotopic ratios in soils from the Marshall Islands using ICP-MS. *Sci Total Environ* 278:151–159
- Myers WA, Lindner M (1971) Precise determination of the natural abundance of ^{237}Np and ^{239}Pu in Katanga pitchblende. *J Inorg Nucl Chem* 33:3233–3238
- Nelson DM, Lovett MB (1978) Oxidation state of plutonium in the Irish Sea. *Nature* 276:599–601
- Nesje A (1992) A piston corer for lacustrine and marine sediments. *Arctic Alpine Res* 24:257–259
- Nunnemann M, Erdmann N, Hasse H-U et al (1998) Trace analysis of plutonium in environmental samples by resonance ionization mass spectroscopy (RIMS). *J Alloy Comp* 271–273:45–48
- Nygren U, Rodushkin I, Nilsson C et al (2003) Separation of plutonium from soil and sediment prior to determination by inductively coupled plasma mass spectrometry. *J Anal At Spectrom* 18:1426–1434
- Ofan A, Ahmad I, Greene JP et al (2006) Development of a detection method for ^{244}Pu by resonance ionization mass spectrometry. *New Astron Rev* 50:640–643
- Olivier S, Bajo S, Fifield LK et al (2004) Plutonium from global fallout recorded in an ice core from the Belukha Glacier, Siberian Altai. *Environ Sci Technol* 38:6507–6512
- Pöllänen R, Ketterer ME, Lehto S et al (2006) Multi-technique characterization of a nuclear bomb particle from the Palomares accident. *J Environ Radioact* 90:15–28
- Povinec PP, Badie C, Baeza A et al (2002) Certified reference material for radionuclides in seawater IAEA-381 (Irish Sea Water). *J Radioanal Nucl Chem* 251:369–374
- Ravichandran M, Baskaran M, Santschi PH et al (1995) Geochronology of sediments in the Sabine-Neches estuary, Texas, USA. *Chem Geol* 125:291–306
- Reynolds RL, Mordecai JS, Rosenbaum JG et al (2010) Compositional changes in sediments of subalpine lakes, Uinta Mountains (Utah): evidence for the effects of human activity on atmospheric dust inputs. *J Paleolimnol* 44:161–175
- Ritchie JC, McHenry JR (1990) Application of radioactive fallout cesium-137 for measuring soil erosion and sediment accumulation rates and patterns: a review. *J Environ Qual* 19:215–233
- Roy JC, Turcotte J, Cote JE et al (1981) The detection of the 21st Chinese nuclear explosion in eastern Canada. *Health Phys* 41:449–454
- Sam AK, Ahamed MMO, Khang FE et al (2000) Plutonium isotopes in sediments from the Sudanese coast of the Red Sea. *J Radioanal Nucl Chem* 245:411–414
- Sanders CJ, Smoak JM, Sanders LM et al (2010) Intertidal mangrove mudflat $^{240+239}\text{Pu}$ signatures, confirming a ^{210}Pb geochronology on the southeastern coast of Brazil. *J Radioanal Nucl Chem* 283:593–596
- Schiff CJ, Kaufman DS, Wallace KL et al (2010) An improved proximal tephrochronology for Redoubt Volcano, Alaska. *J Volcanol Geoth Res* 193:203–214
- Schneider DL, Livingston HD (1984) Measurement of curium in marine samples. *Nucl Instrum Meth Phys Res* 223:510–516
- Sholkovitz ER (1983) The geochemistry of Pu in fresh and marine water environments. *Earth Sci Rev* 19:95–161
- Sill CW (1975) Some problems in measuring plutonium in the environment. *Health Phys* 29:619–626
- Skipperud L (2004) Plutonium in the arctic marine environment – a short review. *Sci World J* 4:460–481
- Taylor DM (1995) Environmental plutonium in humans. *Appl Radiat Isot* 46:1245–1252
- Taylor DM (2001) Environmental plutonium – creation of the universe to twenty-first century mankind. In: Kudo A (ed) *Plutonium in the environment*. Elsevier Science, Amsterdam
- Taylor RN, Warneke T, Milton JA et al (2001) Plutonium isotope ratio analysis at femtogram to nanogram levels by multicollector ICP-MS. *J Anal At Spectrom* 16:279–284
- Thakkar AH (2002) A rapid sequential separation of actinides using Eichrom's extraction chromatographic material. *J Radioanal Nucl Chem* 252:215–218
- Tims SG, Pan SM, Zhang R (2010) Plutonium AMS measurements in Yangtze River estuary sediment. *Nucl Instrum Meth Phys Res B* 268:1155–1158
- Ulsh B, Rademacher S, Whicker FW (2000) Variations of ^{137}Cs depositions and soil concentrations between alpine and montane soils in northern Colorado. *J Environ Radioact* 47:57–70
- Vajda N, Kim C (2010) Determination of Pu isotopes by alpha spectrometry: a review of analytical methodology. *J Radioanal Nucl Chem* 283:203–223
- Van Pelt RS, Ketterer ME, Zobeck T et al. Anthropogenic radioisotopes to estimate rates of soil redistribution by wind (manuscript in preparation)
- Wallner C, Faestermann T, Gerstmann U et al (2004) Supernova produced and anthropogenic ^{244}Pu in deep sea manganese encrustations. *New Astron Rev* 48:145–150
- Warwick PE, Croudace IW, Carpenter R (1996) Review of analytical techniques for the determination of americium-241 in soils and sediments. *Appl Radiat Isot* 47:627–642
- Yamada M, Aono T (2002) Large particle flux of $^{239+240}\text{Pu}$ on the continental margin of the East China Sea. *Sci Total Environ* 287:97–105
- Yamada M, Zheng J (2010) Temporal variability of $^{240}\text{Pu}/^{239}\text{Pu}$ atom ratio and $^{239+240}\text{Pu}$ inventory in water columns of the Japan Sea. *Sci Total Environ* 408:5951–5957
- Yamada M, Zheng J, Wang Z (2006) ^{137}Cs , $^{239} + ^{240}\text{Pu}$ and $^{240}\text{Pu} / ^{239}\text{Pu}$ atom ratios in the surface waters of the western

- North Pacific Ocean, eastern Indian Ocean and their adjacent seas. *Sci Total Environ* 366:242–252
- Zheng J, Yamada M (2004) Sediment core record of global fallout and bikini close-in fallout Pu in Sagami Bay, Western North-west Pacific Margin. *Environ Sci Technol* 38:3498–3504
- Zheng J, Yamada M (2005) Vertical distributions of $^{239+240}\text{Pu}$ activities and $^{240}\text{Pu}/^{239}\text{Pu}$ atom ratios in sediment cores: implications for the sources of Pu in the Japan Sea. *Sci Total Environ* 340:199–211
- Zheng J, Yamada M (2006a) Inductively coupled plasma-sector field mass spectrometry with a high-efficiency sample introduction system for the determination of Pu isotopes in settling particles at femtogram levels. *Talanta* 69:1246–1253
- Zheng J, Yamada M (2006b) Determination of Pu isotopes in sediment cores in the Sea of Okhotsk and the NW Pacific by sector field ICP-MS. *J Radioanal Nucl Chem* 267:73–83
- Zheng J, Yamada M (2006c) Plutonium isotopes in settling particles: transport and scavenging of Pu in the western northwest Pacific. *Environ Sci Technol* 40:4103–4108
- Zheng J, Yamada M (2007) Precise determination of Pu isotopes in a seawater reference material using ID-SF-ICP-MS combined with two-stage anion-exchange chromatography. *Anal Sci* 23:611–615

Chapter 21

Tracing the Sources and Biogeochemical Cycling of Phosphorus in Aquatic Systems Using Isotopes of Oxygen in Phosphate

Adina Paytan and Karen McLaughlin

Abstract Phosphorous (P) is an essential nutrient for all living organisms and when available in surplus could cause eutrophication in aquatic systems. While P has only one stable isotope, P in most organic and inorganic P forms is strongly bonded to oxygen (O), which has three stable isotopes, providing a system to track phosphorus cycling and transformations using the stable isotopes of O in phosphate (PO_4), $\delta^{18}\text{O}_p$. This isotope system has only recently been utilized in aquatic environments. Available data obtained from different settings indicate that $\delta^{18}\text{O}_p$ of dissolved phosphate in aquatic systems can be applied successfully for identifying sources and cycling of phosphate in a broad range of environments. Specifically, work to date indicates that $\delta^{18}\text{O}_p$ is useful for deciphering sources of phosphate to aquatic systems if these sources have unique isotopic signatures and if phosphate cycling within the system is limited compared to input fluxes. In addition, because various processes are associated with distinct fractionation effects, the $\delta^{18}\text{O}_p$ tracer can be utilized to determine the degree of phosphorous cycling within the biomass and shed light on the processes imprinting the isotopic signatures. As a better understanding of the systematics of and various controls on $\delta^{18}\text{O}_p$ is gained, it is expected that $\delta^{18}\text{O}_p$ would be extensively applied in research geared to understand phosphorous dynamics in many environments.

A. Paytan (✉)
University of California, Santa Cruz, Santa Cruz, CA 95064,
USA
e-mail: apaytan@ucsc.edu

K. McLaughlin
Southern California Coastal Water Research Project, Costa
Mesa, CA 92626, USA

21.1 Introduction

Phosphorus (P, atomic number 15, relative atomic mass 30,9738) is a multivalent nonmetal element of the nitrogen group. Although 23 isotopes of phosphorus are known (all possibilities from ^{24}P up to ^{46}P), only ^{31}P is stable. Two radioactive isotopes of phosphorus have half-lives which make them useful for scientific experiments. ^{32}P has a half-life of 14.26 days and ^{33}P has a half-life of 25.34 days. Phosphorous compounds (organic and inorganic) are found with phosphorous oxidation states ranging from -3 to $+5$, however the most common oxidation states are $+5$, $+3$ and -3 . Phosphorous abundance in earth's crust is 1,050 ppm by weight (730 ppm by moles) and the abundance in the solar system is 7 ppm by weight (300 ppb by moles) (Emsley 2000). Due to its high reactivity, phosphorus does not occur as a free element in nature, but it is found in many different minerals (e.g. apatite) and organic compounds (e.g. DNA, RNA, ATP, phospholipids) essential for all living cells. It is produced commercially from calcium phosphate (phosphate rock). Large deposits of phosphate rock are located in the Middle East, China, Russia, Morocco and the United States of America. Based on 2010 estimates, at the current rate of consumption, the supply of phosphorus is estimated to run out in about 300 years. Peak P consumption will occur in 30 years and reserves will be depleted in the next 50–100 years (Vaccari 2009).

Phosphorus, being an essential plant nutrient, is predominantly used as a constituent of fertilizers for agriculture. Phosphorus is also used as a precursor for various chemicals, in particular the herbicide glyphosate and to make organophosphorus compounds which have many applications, including in plasticizers,

flame retardants, pesticides, extraction agents, and water treatment. It is an important component in steel production, utilized in the making of special glasses and fine china, a component in some laundry detergents, baking powder, matchbook strikers, flares, and for military use in incendiary bombs and grenades.

Phosphorus is a key element in all known forms of life. Inorganic phosphorus in the form of phosphate (PO_4^{3-}) plays a major role in biological molecules such as DNA and RNA where it forms part of the structural framework of these molecules. Living cells also use phosphate to transport cellular energy in the form of adenosine triphosphate (ATP). Nearly every cellular process that uses energy obtains it in the form of ATP. ATP is also important for phosphorylation, a key regulatory event in cells. Phospholipids are the main structural components of all cellular membranes and calcium phosphate salts assist in stiffening bones. Due to its biological role phosphorus is an essential macromineral (nutrient) for terrestrial plants and for marine phytoplankton, algae, and sea-grasses. In ecological terms, phosphorus is often a limiting nutrient in many environments; i.e. the availability of phosphorus governs the rate of growth of many organisms. Indeed, it has been suggested that phosphorus availability may limit primary productivity in some aquatic systems (Bothwell 1985; Hecky and Kilham 1988; Howarth 1988; Karl and Tien 1997; Karl et al. 2001; Krom et al. 1991; Wu et al. 2000), and may be co-limiting in others (Nicholson et al. 2006; Sundareshwar et al. 2003). However, at times an excess of phosphorus can be problematic causing eutrophication and algal blooms (Sharp 1991; Smith and Kalff 1983; Smith 1984).

Agricultural expansion over the next 50 years is expected to be accompanied by a 2.4- to 2.7-fold increase in nitrogen (N)- and phosphorus (P)-driven eutrophication of terrestrial, freshwater, and near-shore marine environments (Tilman et al. 2001). Much of the P from fertilizer and animal waste enters surface waters and eventually also groundwater (Carpenter et al. 1998) and these nutrient loads can stimulate large scale macroalgal and/or phytoplankton blooms in receiving waters (Beman et al. 2005; Rabalais et al. 2002). Phosphorus enrichment in aquatic systems can cause diverse problems such as harmful algal blooms, anoxia, fish kills, and loss of habitat and biodiversity (Carpenter et al. 1998; Tilman et al. 2001). Thus, identifying and understanding phosphorus input

and cycling and the effects phosphorus limitation or enrichment may have on aquatic ecosystems are of critical importance to management and restoration efforts.

Phosphorus is continuously and rapidly cycled in aquatic environments. Figures 21.1 and 21.2 represent the global biogeochemical cycle of P in the ocean and lakes, respectively and Fig. 21.3 illustrates the various pools and processes involved in the P cycle in aquatic systems.

21.1.1 Stable Isotope Use to Study P Sources and Cycling

Monitoring P sources and transformations in natural environments using stable isotopes has been difficult to do because, in contrast to C, N, O and S, P has only one stable isotope (^{31}P) thus the use of P stable isotope tracing is not an option. Although radioactive P isotopes (^{32}P , ^{33}P) can and have been used for investigation of P transformations in aquatic systems (Benitez-Nelson and Buessler 1998, 1999; Benitez-Nelson and Karl 2002; Lal et al. 1988; Lal and Lee 1988; Lee et al. 1991) there are many complications involved with this procedure. The use of natural stable isotope signatures has advantages as this approach does not perturb the system (e.g. by adding phosphate) and integrates processes over longer time scales. While P has only one stable isotope, P in most organic and inorganic P forms is strongly bonded to oxygen (O), which has three stable isotopes, providing a system to track phosphorus cycling and transformations using the stable isotopes of O in phosphate ($\delta^{18}\text{O}_\text{p}$).

Since the pioneering study of Longinelli and Nuti (1973) and several subsequent publications (Fricke et al. 1998; Longinelli et al. 1976; Longinelli 1984; Luz et al. 1984; Luz and Kolodny 1985; Shemesh et al. 1983, 1988), oxygen isotope ratios of bioapatite in teeth and bones have been widely used as paleoenvironmental proxies. The oxygen isotope paleothermometer is based on an empirical equation that is assumed to represent equilibrium fractionations between phosphate and water as a function of temperature as follows (Longinelli and Nuti 1973):

$$T (^{\circ}\text{C}) = 111.4 - 4.3(\delta^{18}\text{O}_\text{p} - \delta^{18}\text{O}_\text{w}) \quad (21.1)$$

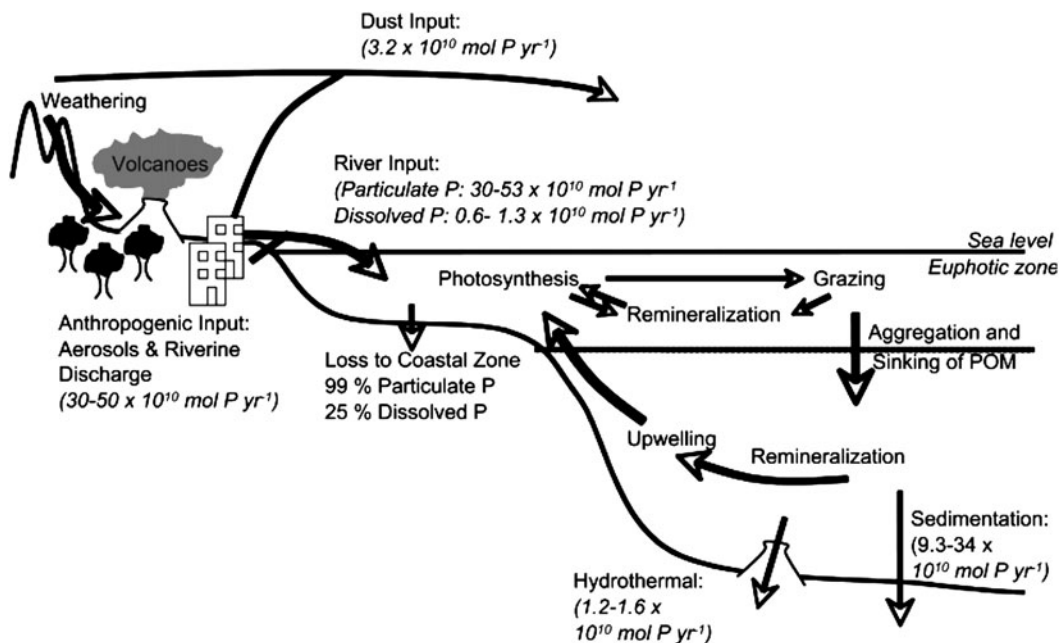


Fig. 21.1 The marine phosphorus cycle. Fluxes are given in italics. Flux data are from Benitez-Nelson (2000) and Follmi (1995). Continental weathering is the primary source of phosphorus to the oceanic phosphorus cycle. Most of this phosphorus is delivered via rivers with a smaller portion delivered via dust deposition. In recent times, anthropogenic sources of phosphorus have become a large fraction of the phosphorus delivered to

the marine environment, effectively doubling the pre-anthropogenic flux. The primary sink for phosphorus in the marine environment is loss to the sediments. Much of the particulate flux from rivers is lost to sediments on the continental shelves, and a smaller portion is lost to deep-sea sediments. Hydrothermal systems constitute an additional small sink for P. Figure modified from Paytan and McLaughlin (2007)

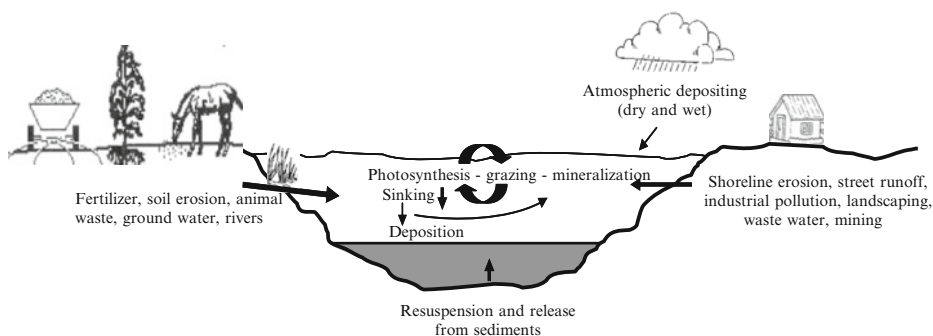


Fig. 21.2 Phosphate sources to lakes include fertilizers, animal waste, soil erosion, industrial and mining waste water input as well as atmospheric deposition. Phosphate enters lakes through rivers, groundwater, direct disposal and runoff. Plants and algae utilize the phosphate as a nutrient. Phosphate is transferred

through the food web and some of this particulate matter is remineralized in the water column. Some phosphate is deposited in the sediment. Under anoxic conditions phosphate from the sediments may be recycled back into the water

where $\delta^{18}\text{O}_\text{P}$ and $\delta^{18}\text{O}_\text{W}$ are the oxygen isotopic composition of phosphate and water, respectively, in equilibrium with environmental temperature T ($^\circ\text{C}$). Importantly, at most earth-surface temperatures ($<80^\circ\text{C}$) and pressures, the P-O bond is resistant to inorganic hydrolysis and does not exchange O with-

out biological mediation (Blake et al. 1997; Lecuyer et al. 1996) preserving the signature of the temperature and water isotope ratio of the solution from which the minerals precipitated.

However, due to the large sample size required for isotope analysis and the low concentrations of

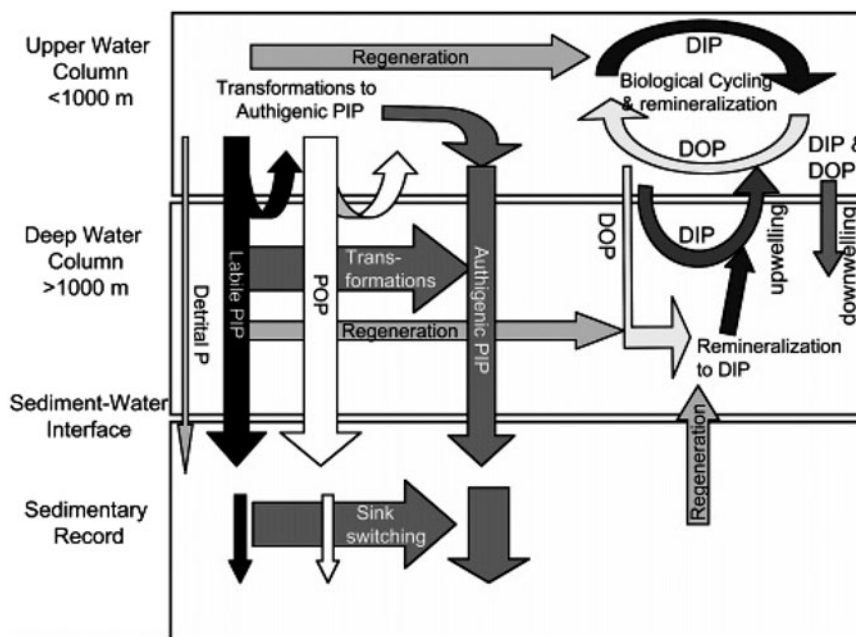


Fig. 21.3 Transformations between P pools in the water column and sediments. Abbreviations are as follows: PIP, particulate inorganic phosphorus; POP, particulate organic phosphorus; DIP, dissolved inorganic phosphorus; DOP, dissolved organic phosphorus. Particulate phosphorus forms can undergo transformations throughout the water column and within sediments. Particulate phosphorus forms may also undergo regeneration into dissolved forms. Particulate phosphorus is lost from surface

waters via sinking. Biological cycling and remineralization are the primary mechanisms of transformations of the dissolved phases and are dominant in surface waters, though microbial remineralization continues at depth. Dissolved phosphorus forms are lost from surface waters via downwelling and biological uptake (into POP) and are returned to surface waters via upwelling and mixing. Regeneration from sediment can add more dissolved phosphate to deep water. Figure modified from Paytan and McLaughlin (2007)

dissolved phosphate in most water bodies, the oxygen isotopic composition of phosphate, $\delta^{18}\text{O}_p$, has only recently been applied systematically for tracking dissolved phosphate in water bodies. Pioneering work by Longinelli et al. (1976) found no variation in the $\delta^{18}\text{O}_p$ of dissolved phosphate in seawater with either depth or latitude in the Atlantic and Pacific Oceans, although there was a significant difference between the two ocean basins. The $\delta^{18}\text{O}_p$ values were thought to reflect kinetic–biological isotopic fractionation. Longinelli et al. (1976) extracted and concentrated P from large volumes of water without pre-filtration using iron-coated fibers that absorb inorganic and organic P indiscriminately. Analysis of mixed organic and inorganic P samples may have confounded interpretation of the results (Blake et al. 2005) and because of the analytical limitations few attempts to follow up on this work have been made for over a decade (Paytan 1989). These complications have been overcome with current technologies, several detailed protocols for isolating, purifying and precipitating small quantities of phos-

phate from complex matrix solutions such as fresh and ocean waters were published and this system has now been applied to various water bodies including oceans (Colman et al. 2005; McLaughlin et al. 2006b, 2011), estuaries (McLaughlin et al. 2006a, d) and lakes (Elsbury et al. 2009; Markel et al. 1994). In addition, extensive and innovative laboratory studies have been conducted to carefully determine the fractionation associated with various biogenic and abiotic transformations of P (Blake et al. 1997, 1998, 2001, 2005; Liang 2005; Liang and Blake 2006a, b, 2007, 2009).

21.1.2 Isotopic Signatures of Potential Phosphate Sources to Aquatic Systems

Identifying point and non-point nutrient sources is important for understanding ecosystem health, and

has implications for designing best management practices, industry regulation and allocation of water discharge permits. P sources can be separated into point sources, such as sewage and industrial discharge sites, and non-point sources like urban and agricultural run-off (Young et al. 2009). Phosphate oxygen isotope tracer studies in natural environments are limited. However, recent field studies have demonstrated the utility of $\delta^{18}\text{O}_p$ as a tracer of various phosphate sources to lakes, rivers, estuaries and the coastal

ocean (Coleman 2002; McLaughlin et al. 2006b, d). A wide range of $\delta^{18}\text{O}_p$ values from 6 to 27‰ has been documented in these various studies (Fig. 21.4a). A significant portion of these samples are not in isotopic equilibrium with the surrounding water, indicating that complete intracellular biological cycling of the orthophosphate had not taken place, and a source signature may have been partially retained. In addition, the $\delta^{18}\text{O}_p$ of some potential end-member sources (wastewater treatment plant effluent, fertilizers, soaps,

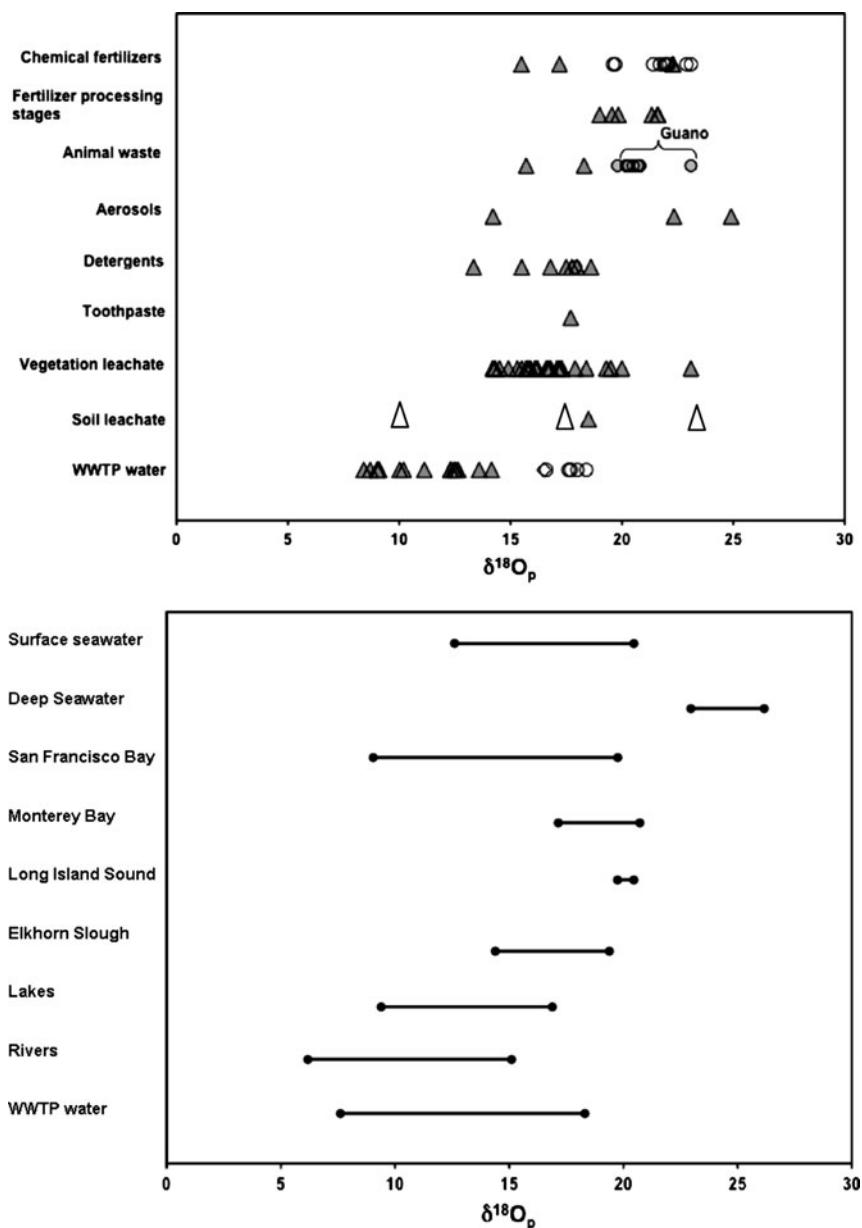


Fig. 21.4 (a) $\delta^{18}\text{O}_p$ of some potential end-member sources. Full triangles from Young et al. (2009); Open circles from Gruau et al. (2005); Full circles from Avliffe et al. (1992); Diamonds from Coleman (2002); Empty triangles from Zohar et al. (2010a, b). Figure modified from Young et al. (2009). (b) Range of $\delta^{18}\text{O}_p$ values observed in different water systems

soil extracts, etc.) has been published (Young et al. 2009) (Fig. 21.4b).

A considerable range of $\delta^{18}\text{O}_p$ values has been measured in various P sources and the differences observed among sources are much larger than the analytical precision ($\pm 0.3\text{‰}$) associated with this technique. Although there is considerable overlap in $\delta^{18}\text{O}_p$ measured in the various groups of samples, these results indicate that in specific geographic regions, different P source types may span a narrower range and have distinct signatures, and in these cases, the $\delta^{18}\text{O}_p$ could be useful for identifying the contribution of the different sources. For example, while the entire range of reported $\delta^{18}\text{O}_p$ values for worldwide wastewater treatment plant effluent overlaps with the values measured for multiple types of detergents, organic fertilizers, and chemical fertilizers, all measured $\delta^{18}\text{O}_p$ values for the Palo Alto Regional Water Quality Control Plant are significantly lower than any of the measured fertilizers and detergents (Young et al. 2009). Thus, if phosphate is not heavily cycled within an ecosystem such that the source signature is reset, $\delta^{18}\text{O}_p$ can be used to identify isotopi-

cally distinct phosphate sources and/or the extent of phosphate cycling in aquatic systems (i.e. the deviation from the isotopic composition of the source towards the expected equilibrium value).

21.1.3 Isotope Fractionations Involved in P Cycling

Isotope fractionations associated with several of the important reactions and transformations operating in the P cycle have been determined in controlled laboratory experiments (Table 21.1). This information provides the basis for interpretation of isotope data ($\delta^{18}\text{O}_p$) obtained from phosphate in the natural environment. In the absence of biological activity at ambient temperatures, pH, and pressure, isotope exchange between phosphate oxygen and water (or other solutions) is slow and can be considered negligible for the time scales of concern of most environmental applications (Blake et al. 1997; Longinelli and Nuti 1973, Longinelli et al. 1976; O'Neil et al. 2003). Studies of precipitation

Table 21.1 Isotope fractionation effects associated with various biogeochemical processes

Process	Fractionation (Δ or ϵ)	Reference
Precipitation/dissolution of P minerals (apatite)	+0.7‰ to +1‰ Heavy isotope in mineral phase	Blake et al. (1997)
Adsorption/desorption of P to/from mineral surfaces	~+1‰ Heavy isotope in mineral phase	Liang and Blake (2007)
Precipitation with sesquioxides and hydroxides	~+1‰ Heavy isotope in mineral phase	Jaisi et al. (2009)
Abiotic hydrolysis of polyphosphate (O:P = 3.33), pyrophosphate (O:P = 3.5), phosphonates (O:P = 3.0), monoesters (O:P = 3.0) and diesters (O:P = 2.0)	No fractionation or temperature effect, however incorporation of oxygen from water during formation of PO_4 (O:P = 4) occurs	McLaughlin et al. (2006a)
Transport by water or air	No fractionation or temperature effect	Longinelli (1965)
Assimilation by phytoplankton	Light isotopes preferentially utilized, enrichment of the residual solution ($\epsilon = -3\text{‰}$)	Blake et al. (2005)
Intracellular processing such as inorganic pyrophosphatase (PPase) catalysis	Equilibrium isotopic exchange T and $\delta^{18}\text{O}_w$ impact (21.2)	Blake et al. (2005)
Alkaline phosphatase (APase) hydrolyzation of phosphomonoesterase (extracellular)	Kinetic isotope effects $\epsilon = -30\text{‰}$ effecting only the newly incorporated oxygen	Liang and Blake (2006a, b)
5'-nucleotidase hydrolyzation (extracellular)	Kinetic isotope effects $\epsilon = -10\text{‰}$ effecting only the newly incorporated oxygen	Liang and Blake (2006a, b)
First step of DNase hydrolyzation	Kinetic isotope effects $\epsilon = -20\text{‰}$ effecting only the newly incorporated oxygen	Liang and Blake (2009)
First step of RNase hydrolyzation	Kinetic isotope effects $\epsilon = +20\text{‰}$ effecting only the newly incorporated oxygen	Liang and Blake (2009)
Transport from roots to leaves (by transporters)	Enrichment in the process foliage heavier than roots	

and dissolution of various P bearing minerals and studies of P adsorption and desorption onto/from mineral surfaces indicate that the fractionation associated with these processes (given equilibration time of more than a few hours) is small – in the range of 1‰ (Jaisi et al. 2009; Liang 2005; Liang and Blake 2006b). Typically the heavier isotopes in these reactions are associated with the mineral phase while the solution retains phosphate with lighter isotopes. Precipitation or dissolution of apatite minerals (inorganically) will be accompanied by a small oxygen isotope fractionation in the range of +0.7‰ to +1‰ (Blake et al. 1997). Similarly, adsorption or precipitation with sesquioxides and hydroxides imprints a small positive isotope effect (Jaisi et al. 2009). In contrast, enzyme mediated biological activity could break the P-O bond in processes that involve large isotopic fractionation. Intracellular as well as extracellular enzymes are expressed by various organisms for the uptake and utilization of P and may play a role in determining the oxygen isotopic composition of phosphate in aquatic systems. Different enzymatic processes induce different isotopic fractionations (Table 21.1). The most dominant enzymatic process controlling $\delta^{18}\text{O}_p$ in the environment is the intracellular activity of pyrophosphatase (PPase) (Blake et al. 2005), which involves equilibrium isotopic exchange. Blake et al. (2005) found that this enzymatic activity results in isotopic equilibrium of oxygen in phosphate similar to that described by Longinelli and Nuti (1973). The equation for phosphate extracted from microbial cultures was described by Blake et al. (1997):

$$T(^{\circ}\text{C}) = 155.8 - 6.4(\delta^{18}\text{O}_p - \delta^{18}\text{O}_w) \quad (21.2)$$

These equilibrium relations have been observed in tissues of a variety of organisms, including fish, mammals (Kolodny et al. 1983), bacteria and algae (Blake et al. 1997, 2005; Paytan et al. 2002). Results of an algae culture experiment indicate that intracellular oxygen isotope exchange between phosphorus compounds and water within cells is very rapid (Paytan et al. 2002). These processes are expected to occur in all organisms and phosphate released from cells to the environment will carry this equilibrium signature and impact dissolved phosphate $\delta^{18}\text{O}_p$ values leading to equilibrium values. Extracellular remineralization and hydrolyzation of organic P (P_o) compounds by phosphohydrolase enzymes such as alkaline phosphatase (APase) and 5'-nucleotidase, involves incorporation of

one or more oxygen atoms from the ambient water with an isotope fractionation of –30 and –10‰, respectively (Liang and Blake 2006b). A summary of published fractionation values to date is given in Table 21.1. The resulting phosphate from such processes will reflect the fractionation and would typically shift $\delta^{18}\text{O}_p$ towards values that are lower than equilibrium. Work by several groups is currently ongoing to determine the isotope fractionation associated with additional enzymes, and will enable better interpretation of field data. Uptake and utilization (assimilation) of phosphate by aquatic plants, algae, and microorganisms is also associated with isotope fractionation. The phosphate with lighter isotopes is preferentially utilized, a process that could enrich the residual solution with phosphate that has heavy isotopes (Blake et al. 2005).

The isotopic composition of dissolved phosphate and particularly the degree of isotope equilibrium or deviation from equilibrium of phosphate in various aquatic systems has been used for deciphering the extent of biological utilization and turnover of phosphate in aquatic systems (Colman et al. 2005; Elsbury et al. 2009; McLaughlin et al. 2006b, d, 2011). This application is based on the assumption that extensive recycling and turnover will lead to isotopic equilibrium while deviation from equilibrium may reflect source signatures or other processes that do not result in isotopic equilibrium such as expression of extracellular enzymes or phosphate uptake (Fig. 21.5). The following sections will describe the methodology (sample preparation and analysis), give examples of application of this system in various settings and address the needs for future progress in this field.

21.2 Materials and Methods

For analysis of $\delta^{18}\text{O}_p$ by isotope ratio mass spectrometry (IRMS), it is necessary to convert the phosphate into a pure solid phase without isotopic alteration. The purification steps are of great importance, since the presence of oxygen sources other than phosphate compromises the results (Weidemann-Bidlack et al. 2008). The final compound analyzed should be non-hygroscopic, stable under laboratory conditions, and should decompose to form carbon monoxide (CO) at temperatures attainable in a lab furnace. Silver phosphate (Ag_3PO_4) has been proven a convenient phase for this purpose

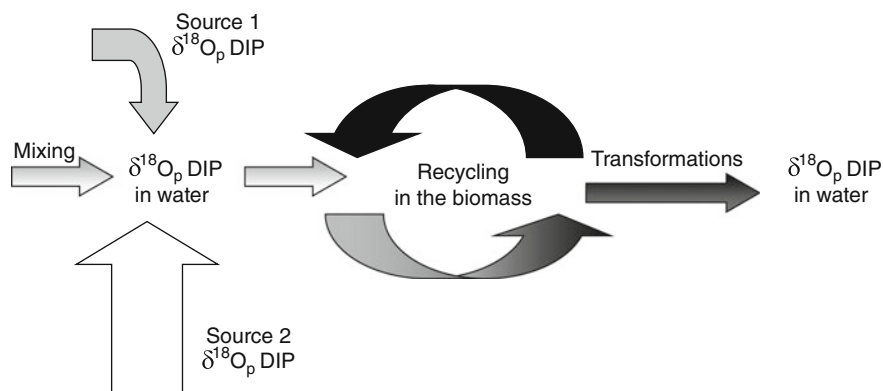


Fig. 21.5 A graphical representation of P mixing and cycling in the water illustrating the utility of $\delta^{18}\text{O}_p$ for identifying sources if biological transformations do not erase the source signatures or

the degree of intracellular biological cycling and turnover by determining the difference between the source signature and expected equilibrium values (see McLaughlin et al. 2006a, b, c, d)

(Firsching 1961; O’Neil et al. 1994) and has gradually substituted the earlier hazardous fluorination technique (Kolodny et al. 1983; Tudge 1960). Ag_3PO_4 is reduced with carbon in an oxygen free atmosphere at high temperature ($>1,300^\circ\text{C}$) using a thermal combustion elemental analyzer (TCEA) to yield carbon monoxide for analysis by IRMS (Coleman 2002, McLaughlin et al. 2004, O’Neil et al. 1994). The TCEA and mass spectrometer are linked via a continuous flow interface, and the CO gas is measured instantaneously after formation (Kornexl et al. 1999). Prior to mass spectrometric analysis phosphate has to be concentrated (phosphate concentrations are low in many environments), isolated, purified, and precipitated as Ag_3PO_4 .

Several detailed protocols for isolating, purifying and precipitating small quantities of phosphate from complex matrix solutions such as fresh and ocean waters have been published (Coleman 2002; Goldhammer et al. 2011; Jaisi and Blake 2010, McLaughlin et al. 2004; Tamburini et al. 2010, Weidemann-Bidlack et al. 2008; Zohar et al. 2010a). Most of these procedures involve a concentration step to collect sufficient amounts of phosphate and remove some of the dissolved organic phosphate and interfering ions from the sample. This is done through a series of precipitations and/or resin treatments followed by a final precipitation as Ag_3PO_4 (Table 21.2). It is important to ensure that the concentration and preparation process does not introduce any isotopic fractionation and all of the above methods report that authentic signatures are preserved. Problems with the final precipitation of silver phosphate have been experienced when working with water samples containing very

high concentrations of dissolved organic matter. Several promising approaches for addressing this problem have been explored, including UV radiation of the sample (Liang and Blake 2006b), passing the sample through phosphate-free activated carbon (Gruau et al. 2005), using resins such as DAX-8 to remove organics (Tamburini et al. 2010), precipitation of humic acids (Zohar et al. 2010a) and treatment with H_2O_2 (Goldhammer et al. 2011; Zohar et al. 2010a). Published procedures report that these methods to remove organic matter retain the original isotopic signature of phosphate.

As mentioned above it is very important that the only source of oxygen analyzed (as Ag_3PO_4) originates from the “authentic” phosphate in the sample. There are however two separate processes that may compromise this requirement. If not all of the organic matter is removed or if other minerals that contain oxygen (such as AgNO_3) precipitate along with the Ag_3PO_4 (e.g. the Ag_3PO_4 is not pure), then the oxygen contributing to the CO gas will not reflect that of phosphate. Data has to be monitored to ensure that this does not occur. This is done by monitoring the oxygen yield (peak area compared to the pure silver phosphate standards) expected based on the weight of the Ag_3PO_4 sample. The oxygen content per unit weight of Ag_3PO_4 is 15.3% and samples which deviate from this value particularly towards higher oxygen yield should be suspected of contamination. Plotting the oxygen yield (or peak area) of analyzed pure Ag_3PO_4 standards along with the samples should yield a linear relation with weight (Fig. 21.6). It is also advised to include a step to remove tightly sorbed

Table 21.2 Published procedures for the concentration and purification of phosphate from water samples and the precipitation of Ag_3PO_4 for analysis of $\delta^{18}\text{O}_\text{p}$

McLaughlin et al. (2004, 2006a, b, c, d); (Elsbury et al. (2009); (Young et al. 2009)	Colman (2002); Colman et al. (2005); Goldhammer et al. (2011)	Tamburini et al. (2010); Tudge (1960); Kolodny et al. (1983); Paytan et al. (2002); Liang and Blake (2007)
Magnesium-induced coprecipitation (MagIC, Karl and Tien 1992)	Magnesium-induced coprecipitation (MagIC, Karl and Tien 1992)	Magnesium-induced coprecipitation (MagIC, Karl and Tien 1992)
Dissolution in acetic and nitric acids and buffering at pH 5.5 with 1M potassium acetate	Dissolution in 0.1 M HNO_3	Dissolution in 1 M HCl
Precipitation as cerium phosphate	Anion removal (AG1X8) in NaHCO_3 form	Precipitation as ammonium phosphomolybdate
Rinses to remove chloride	HCO_3 removal in acid	Dissolution in citric-acid NH_4OH
Dissolution in 0.2 M nitric acid	Cation removal (AG50X8)	Precipitation of magnesium ammonium phosphate
Cation removal (AG50X8)	Volume reduction by evaporation at 60°C	Rinse and dissolve in 0.5 M HNO_3
Ag_3PO_4 fast precipitation	Ag_3PO_4 slow micro precipitation in P:Ag: NO_3 : NH_4OH molar ratios of 1:10:30:75	Cation removal (AG50X8)
		Ag_3PO_4 slow precipitation in P:Ag: NO_3 : NH_4OH molar ratios of 1:100:300:750

Note that in water rich in dissolved organic matter (DOM) a step to remove DOM either from the water before the MagIC step or right after dissolution of the magnesium hydroxide is needed. This could be done by repeat MagIC co-precipitation (Goldhammer et al. 2011), DAX-8 Amberlite resin (Tamburini et al. 2010), activated char (Gruau et al. 2005), or precipitation (Zohar et al. 2010a, b)

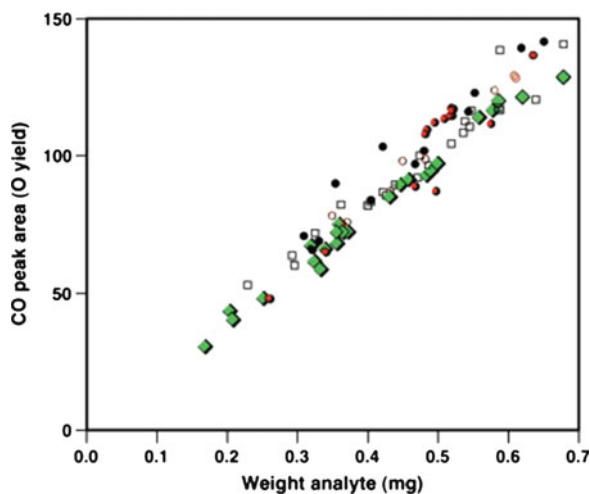


Fig. 21.6 CO peak area for silver phosphate standards (green diamonds) and various samples (other symbols) relative to sample weight introduced into the mass spectrometer. The expected oxygen yield from pure silver phosphate is 15.3%. If samples fall off the line defined by the standards the sample is likely contaminated by an external source of oxygen and might not represent the oxygen isotope ratios in phosphate. Figure modified from Tamburini et al. (2010)

water molecules from silver phosphate. This can be done by heating the silver phosphate samples to $\sim 450^\circ\text{C}$ to get strongly adsorbed water off.

Another potential process by which data could be compromised is contribution of phosphate which is hydrolyzed from condensed forms or organic forms of phosphate for which the O:P ratio is less than 4 during sample processing (this is an analytical artifact) (McLaughlin et al. 2006c). Using ^{18}O -labeled and unlabeled reagents on replicates of the same sample these artifacts could be monitored and corrected. If hydrolysis takes place, oxygen from the acid solution is incorporated into the phosphate group, and because the phosphate in the labeled acid solution will have a higher isotope value than phosphate in the unlabeled solution it could be tracked (McLaughlin et al. 2006c). In this case, the use of a simple equation allows the correction and determination of the isotope value of the extracted phosphate (McLaughlin et al. 2006c).

While all of the concentration, purification, separation and precipitation methods published (Table 21.2) were tested for this potential artifact and report that any

impact, if exists, is below analytical error, it is important to note that because of the vast array of organic P compounds in nature and the huge variability in their concentration and relative abundance in different environmental samples each new set/type of samples should be tested to ensure that such artifacts do not compromise the data.

For mass spectrometric analysis about 200–600 μg of Ag_3PO_4 should be weighed into silver capsules. Some laboratories also add a small amount of finely powdered glassy carbon or nickel-carbide, to improve the reaction between the silver phosphate and carbon during pyrolysis. The samples are introduced into the TCEA via a zero blank autosampler. The TCEA furnace is kept at a constant and consistent temperature (1,375 and 1,450°C have been used). The furnace itself consists of a ceramic tube filled with glassy carbon chips encased in a glassy carbon tube. The produced reaction gases are carried by constantly flushing with a high purity helium stream through a GC column held at fixed temperature (e.g. 80°C) to purify the sample from trace contaminants. The gas is admitted to the mass-spectrometer via a Conflow interface. Some systems also include a copper tube which removes oxygen from the helium carrier gas. The ion currents of masses m/z 28, 29 and 30 are registered on the Faraday cups and converted to $\delta^{18}\text{O}$ values relative to a carbon monoxide standard gas for which $\delta^{18}\text{O}$ has been calculated relative to SMOW. Each sample is run for 300 s with a CO reference peak preceding the sample peak.

Calibration and corrections for instrumental drifts are accomplished by repeated measurements of internal standards. The standard deviation of the analysis based on repeated measures of the standards is typically less than $\pm 0.4\%$. In order to capture instrumental drift with time, delta value linearity, and sample size variability, working standards with known $\delta^{18}\text{O}$ values are weighed out in a range of sizes and analyzed along with the samples during each run (for example at ten sample increments). Raw $\delta^{18}\text{O}$ values are then corrected to the range of standards for drift and off set of the delta values and sample-size linearity.

The oxygen isotopic composition of phosphate is reported in standard delta notation ($\delta^{18}\text{O}$), which is calculated using the following equation:

$$\delta^{18}\text{O} = \left[\frac{R_{\text{sample}}}{R_{\text{VSMOW}}} - 1 \right] \times 1,000 \quad (21.3)$$

where R_{sample} is the ratio of $^{18}\text{O}/^{16}\text{O}$ in a sample and R_{VSMOW} is the ratio of $^{18}\text{O}/^{16}\text{O}$ in the isotopic standard for O, Vienna Standard Mean Ocean Water (VSMOW).

Currently there are no certified international Ag_3PO_4 standards and various laboratories use different “home-made” internal standards for which the $\delta^{18}\text{O}_\text{p}$ has been determined via fluorination (McLaughlin et al. 2004; Vennemann et al. 2002).

21.3 Applications

The use of $\delta^{18}\text{O}_\text{p}$ of dissolved inorganic phosphate (DIP) to study phosphate sources and cycling is relatively new and it is not yet widely used. In the past decade it has been applied in a variety of aquatic systems including estuaries, coastal water, lakes, rivers, and the open ocean. A brief summary of representative examples is given below. These examples demonstrate the great utility of this system and it is likely that now that the methodology has been worked out extensive application of this tool will take place.

21.3.1 Use of $\delta^{18}\text{O}_\text{p}$ as a Tracer for Phosphate Sources in Estuaries

In a study of North San Francisco Bay, McLaughlin et al. (2006d) used $\delta^{18}\text{O}_\text{p}$ to assess mixing of dissolved inorganic phosphate (DIP) sources along an estuarine flow path. Due to different sources of phosphate, temperatures, and $\delta^{18}\text{O}_\text{w}$ the $\delta^{18}\text{O}_\text{p}$ signatures of oceanic and riverine phosphate sources are distinct. Based on salinity and $\delta^{18}\text{O}_\text{w}$, waters in the North San Francisco Bay can be described as a two end-member mixing system between Pacific Ocean waters and the freshwaters of the San Joaquin and Sacramento Rivers (Ingram et al. 1996; McLaughlin et al. 2006d). This mixing can be used to calculate an expected mixing line for $\delta^{18}\text{O}_\text{p}$. Such a trend will be observed if phosphate in the Bay is not being cycled extensively through the biomass or affected by processes that may alter the source $\delta^{18}\text{O}_\text{p}$ signatures. Deviations from the mixing-line are observed and attributed to contribution of phosphate with unique $\delta^{18}\text{O}_\text{p}$ signatures at various locations along the estuary (from point

and non-point sources) such as the discharge points of tributaries or wastewater treatment plants inputs.

The general lack of isotopic equilibrium in DIP throughout the Bay indicates that phosphate cycling is not rapid compared to phosphate input (low utilization rate, short residence time), and that source $\delta^{18}\text{O}_p$ contributed to the observed signature at most, if not all, stations. The deviations from the $\delta^{18}\text{O}_p$ mixing model have been interpreted to represent inputs of phosphate from local point sources within the North Bay (e.g. at the Napa River confluence) (Fig. 21.7).

At another estuary, Elkhorn Slough (McLaughlin et al. 2006a), the phosphate $\delta^{18}\text{O}_p$ within the main channel also indicates variability in phosphate sources throughout the channel, which are related to the surrounding land use. Trends in $\delta^{18}\text{O}_p$ show high values near the mouth reflecting phosphate of an oceanic origin, a minimum value near Hummingbird Island in the central slough reflecting phosphate input from groundwater, and high values near the head of the slough reflecting fertilizer input. A clear change in the relative contribution of these sources is observed and linked to water mixing during changing tidal conations at the mouth of the Slough.

In these studies, McLaughlin et al. (2006a, d) demonstrated that it is possible to use $\delta^{18}\text{O}_p$ to identify

point and non-point source phosphate inputs to aquatic systems and suggest that this may be applied in other impacted systems to identify specific anthropogenic sources, such as fertilizer and sewage phosphate, or to trace natural sources of phosphate. This information is crucial for mitigation of pollution impacts and successful restoration of estuaries and other aquatic systems.

21.3.2 Phosphate Sources and Cycling in Lakes

Phosphorous loading in freshwater lakes has been identified as one of the leading causes for eutrophication and thus linked to hypoxia, harmful algal blooms and other adverse impacts (Schlesinger 1991; Sharp 1991). Despite the clear and wide spread impacts of phosphate loading, relatively few studies have used $\delta^{18}\text{O}_p$ to track sources and learn about P cycling in lakes. A study by Markel et al. (1994) focuses on sediments and suspended matter in Lake Kinneret, Israel. The isotope data show that about 70% of the particulate phosphate come to the lake from a basaltic source ($\delta^{18}\text{O}_p = 6\text{‰}$) with the balance being of sedimentary/anthropogenic origin ($\delta^{18}\text{O}_p = 18\text{--}25\text{‰}$).

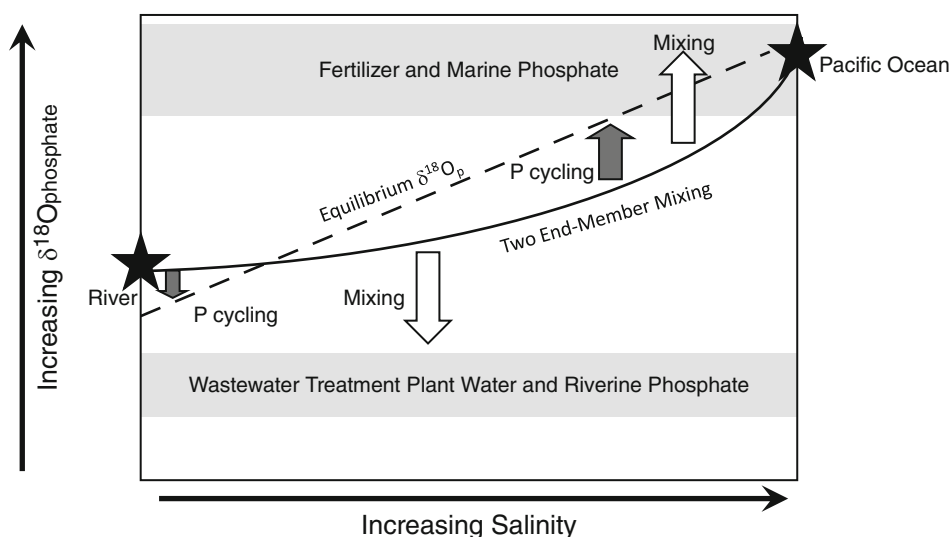


Fig. 21.7 Diagram indicating two end-member mixing (black line) and the expected equilibrium line (dashed line). Values below both the two end-member and the equilibrium line (white down facing arrows) indicate mixing with either riverine or wastewater treatment plant effluent. Deviations which move off the two end-member mixing line in the direction of

equilibrium line be indicative of phosphate cycling, though they may also represent mixing with fertilizer phosphate. Deviations which fall off the two-end member mixing line in the direction of equilibrium, but in excess of equilibrium are indicative of mixing with fertilizer phosphate or treatment plant effluent depending on location along the salinity gradient

This study also alludes to some internal cycling (precipitation and dissolution) of phosphate in the lake. A study by Elsbury et al. (2009) records the distribution of $\delta^{18}\text{O}_p$ in water samples from the western and central basins of Lake Erie along with several potential sources (rivers, waste water treatment plants, atmospheric deposition). $\delta^{18}\text{O}_p$ of lake water is largely out of equilibrium with ambient conditions, indicating that source signatures may be discerned. $\delta^{18}\text{O}_p$ values in the lake range from +10 to +17‰, whereas the equilibrium value is expected to be around +14‰ and riverine weighted average $\delta^{18}\text{O}_p$ value is +11‰ (Fig. 21.8). Therefore, they conclude that some of the lake $\delta^{18}\text{O}_p$ values could not be explained by any known source or process. This indicates that there must be one or more as yet uncharacterized source(s) of phosphate with a high $\delta^{18}\text{O}_p$ value. In this study the authors speculate that a likely source may be the release of phosphate from sediments under reducing conditions that are created during anoxic events in the hypolimnion of the central basin of Lake Erie.

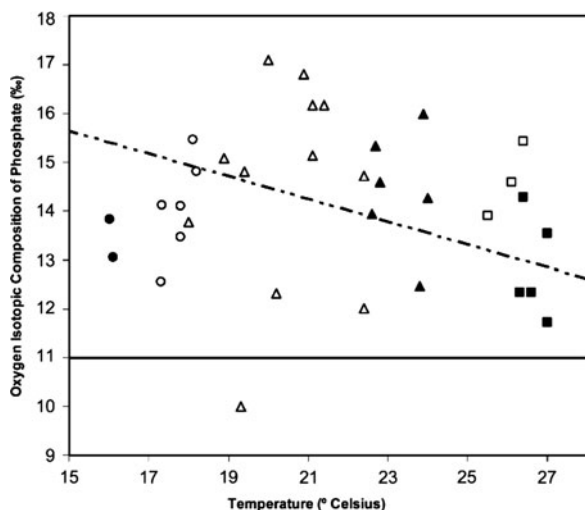


Fig. 21.8 Oxygen isotopic composition of phosphate ($\delta^{18}\text{O}_p$) of Lake Erie surface water. Symbols refer to different sampling trips. The line at +11‰ represents the weighted average riverine $\delta^{18}\text{O}_p$. The dashed line represents the expected $\delta^{18}\text{O}_p$ value calculated based on the temperature for each sample and at the average lake surface $\delta^{18}\text{O}_w$ of -6.78‰ (standard deviation 0.3‰). Samples plotting between the river and equilibrium lines could be explained by P cycling a process that would tend to erase source signature and bring the $\delta^{18}\text{O}_p$ values towards equilibrium. Lines above the equilibrium line suggest a source with $\delta^{18}\text{O}_p$ higher than 17‰ . Figure modified from Elsbury et al. (2009)

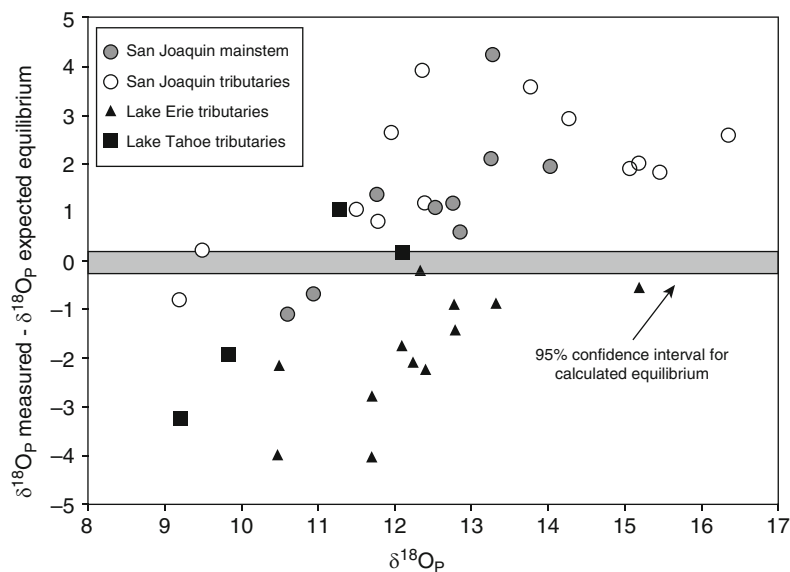
21.3.3 Phosphate Sources and Cycling in Riverine Systems

The range of potential $\delta^{18}\text{O}_p$ values for DIP in riverine systems is much greater than the range expected for open-ocean and coastal waters due to the wider range of temperatures, $\delta^{18}\text{O}$ water values, and phosphate sources found in riverine systems. Furthermore, land use patterns are thought to have a significant impact on nutrient stoichiometry and concentrations in riverine environments (Harris 2001; Lehrter 2006; Neill et al. 2001), thus, differences in land use could provide unique $\delta^{18}\text{O}_p$ signatures with which to trace the relative influence of specific sources to receiving waters. Common phosphate sources for rivers include wastewater treatment effluent, agricultural and urban runoff, manure, leaking septic systems, and natural rock and soil weathering. In addition, river discharge can be viewed as a source of phosphate in relation to other systems; for example, tributaries entering larger rivers, lakes, estuaries, or coastal waters. Although the $\delta^{18}\text{O}_p$ of river water will usually be controlled by a complex combination of source inputs, if the $\delta^{18}\text{O}_p$ of the sources are known, this can be used to trace the phosphate as it moves down the river's flow path. There are not many data sets for $\delta^{18}\text{O}_p$ of rivers but the few that are available report values that do not represent equilibrium and thus most likely reflect changes in source contribution along the river flow path (Fig. 21.9).

Water samples collected from the San Joaquin River (SJR), a hypereutrophic river in the major agricultural region of the California Central Valley, span a range $\delta^{18}\text{O}_p$ values greater than the analytical error, and only one sample fell along the expected equilibrium line. The samples do not show a consistent offset from equilibrium, indicating that the $\delta^{18}\text{O}_p$ at least partially reflects inputs of phosphate sources with different $\delta^{18}\text{O}_p$ signatures, rather than full biological cycling and complete oxygen exchange with water (Young et al. 2009).

Rivers flowing into Lake Erie range in isotope values from +10.5 to +15.2‰. These values range from 4.0‰ lower than the expected isotopic equilibrium to 1.0‰ higher, with two samples falling within range of the expected equilibrium ($\sim 14\text{‰}$) and in general are lower than lake values (Elsbury et al. 2009). Tributaries to Lake Tahoe, CA, are also not at equilibrium with values from 8.2 to 12.2‰ (equilibrium $\sim 11\text{‰}$). While more research is needed, the

Fig. 21.9 Offset from isotopic equilibrium of various river samples. *Gray bar* represents the range of values that would be at equilibrium considering analytical error and calculation errors associated with determining the equilibrium value. Figure modified from Young et al. (2009)



results of river studies in California and the Lake Erie area (Michigan and Ohio) demonstrate two important factors for using $\delta^{18}O_p$ as a source tracer in river systems. The $\delta^{18}O_p$ value of the majority of water samples are not in isotopic equilibrium, indicating that source signatures are not being rapidly overprinted by equilibrium signatures within the river, and in several instances, certain tributaries had $\delta^{18}O_p$ values that are distinct from those of other tributaries, indicating that the contribution of phosphate from specific tributaries to the receiving water body could be identified using this isotope tracing approach.

21.3.4 Phosphorous Cycling in a Coastal Setting

Phosphate in many coastal systems is not the limiting nutrient for productivity, yet is heavily utilized, thus it is expected that the source signature will be at least partially overprinted and that the $\delta^{18}O_p$ will shift towards equilibrium values. If this is indeed the case the degree of deviation from the source signature could be used as a measure of phosphate turnover rate relative to new phosphate input. This principle has been used in California coastal waters (Monterey Bay) (Fig. 21.10). In this system, $\delta^{18}O_p$ tracks seasonal changes in phosphate cycling through the biomass (e.g. phosphate utilization rates) with the greatest

phosphate oxygen isotope exchange occurring during the upwelling season (McLaughlin et al. 2006b). Spatially the greatest percent of phosphate oxygen exchange, and thus the greatest phosphate utilization relative to input, occurs at the locus of upwelling. Episodes of higher phosphate turnover occurs simultaneously throughout the upper 200 m of the water column and on a broad spatial scale. $\delta^{18}O_p$ data also suggest that deep water (~500 m) may be a source of phosphate to the euphotic zone in Monterey Bay.

The degree of P cycling differs among different coastal systems. Colman (2002) concluded that the large deviations in $\delta^{18}O_p$ between riverine and coastal waters in the Long Island Sound reflects extensive equilibration with local coastal water and indicates that in this geographic area rapid microbial cycling overprints source $\delta^{18}O_p$ values on a timescale of weeks.

21.3.5 Phosphorous Cycling in Open Ocean Settings

Dissolved inorganic phosphorus (DIP) concentrations in the open ocean have a typical nutrient profile with low concentrations in surface water due to extensive uptake by primary producers and increasing concentration with depth resulting from regeneration of DIP from sinking particulate matter. The deep Pacific has higher DIP concentration than the deep Atlantic due to

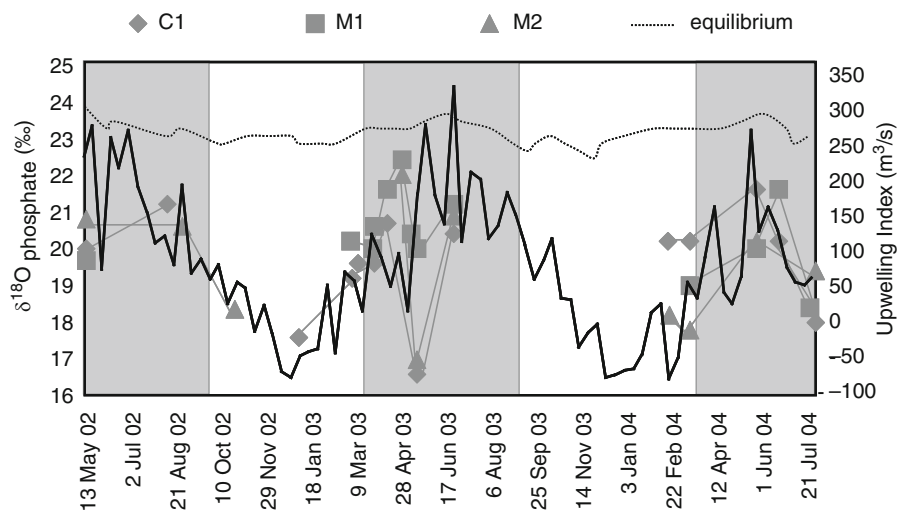


Fig. 21.10 Observed phosphate $\delta^{18}\text{O}_p$ variability from May 2002–August 2004. *Solid line* is the 10-d running mean of the NOAA upwelling index as a function of time; $\delta^{18}\text{O}_p$ is for samples collected at 10-m depth at three monitoring stations

(C1, M1, M2); *dashed line* is the expected equilibrium phosphate $\delta^{18}\text{O}_p$; The $\delta^{18}\text{O}$ of the phosphate source from deep water upwelling is $\sim 17\text{‰}$. Data from McLaughlin et al. (2006a, b, c, d)

aging of the water along the circulation pathway (Broecker and Peng 1982). It would thus be expected that the $\delta^{18}\text{O}_p$ in open ocean waters be primarily a function of biological turnover with potentially some impact of circulation. Colman et al. (2005) measured the $\delta^{18}\text{O}_p$ depth distributions in the Atlantic and Pacific Oceans. At both basins $\delta^{18}\text{O}_p$ values were close to, but slightly offset from, the expected equilibrium values (calculated from equation (21.1) and the seawater temperature and $\delta^{18}\text{O}_w$). Because seawater values at intermediate depths approaches the equilibrium isotopic composition, intracellular cycling at these depths is suggested as the main process affecting the isotopic signatures. The offset at depth is attributed to differences between the deep water temperature and high latitude surface water temperatures, where DIP is equilibrated and transported along the circulation path (Colman et al. 2005) (Fig. 21.11).

In oligotrophic systems, such as the surface waters of the Sargasso Sea, DIP concentrations are extremely low. Consequently, P is thought to limit or co-limit primary productivity in this region. McLaughlin et al. (2011) investigated the biogeochemical cycling of P in the Sargasso Sea, utilizing multiple techniques including $\delta^{18}\text{O}_p$, alkaline phosphatase enzyme-labeled fluorescence (ELF), and ^{33}P uptake derived phosphate turnover rates. Results from these studies indicate that dissolved organic phosphorus (DOP) is utilized by

phytoplankton and bacteria to supplement cellular requirements for this vital nutrient. They show that remineralization of the DOP pool is most extensive above the thermocline, as indicated by a large fraction of eukaryotes producing alkaline phosphatase, rapid phosphorus turnover times, and a large deviation from equilibrium of $\delta^{18}\text{O}_p$ towards lighter values. These data suggest that DOP remineralization by extracellular enzymes is prevalent and that DOP can account for up to 60% of P utilized and support a corresponding amount of primary production. Below the thermocline, alkaline phosphatase expression is reduced, turnover times increase, and $\delta^{18}\text{O}_p$ values approach equilibrium, all of which are indicative of intracellular phosphate cycling and slower turnover of the DOP pool. This study highlights the importance of bioavailable organic P to primary productivity in oligotrophic systems and has implications for the global carbon cycle.

21.4 Future Directions

For a more rigorous interpretation of $\delta^{18}\text{O}_p$ data from environmental samples several gaps in our understanding of how phosphate oxygen is fractionated in aquatic systems must be addressed. Particularly, characterization of the isotopic fractionation of phosphate oxygen associated with additional processes including

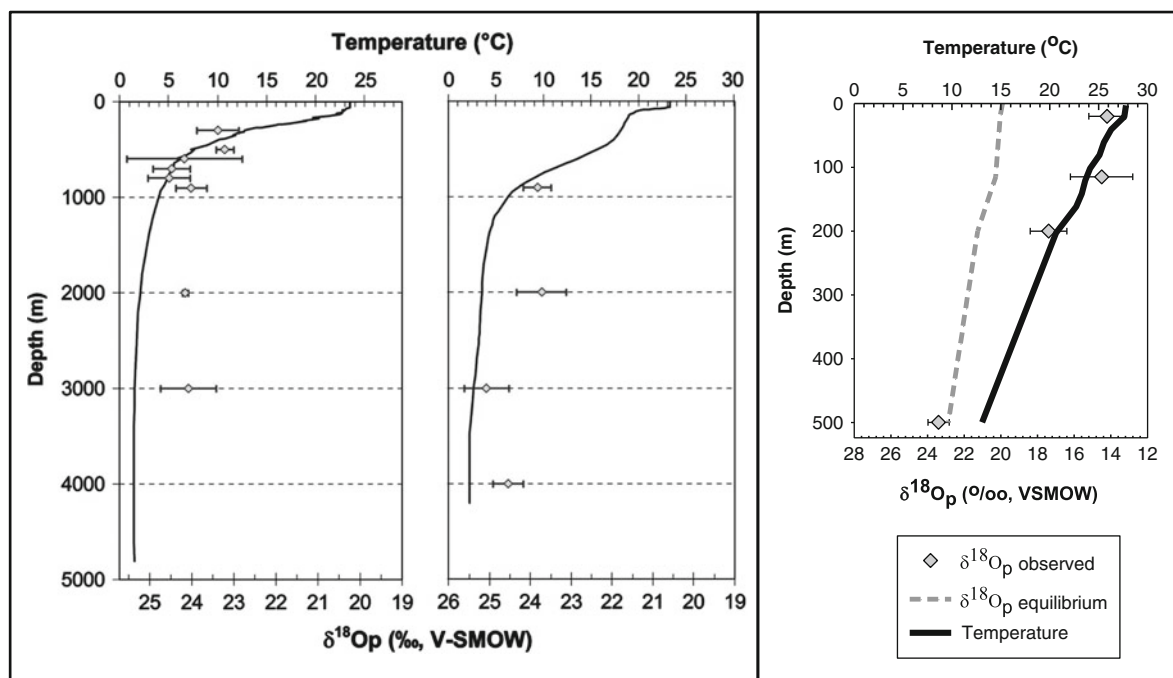


Fig. 21.11 Left panel represented the depth profile of $\delta^{18}\text{O}_p$ in the Pacific (a) and Atlantic (b). Solid lines represent the temperature dependent equilibrium values and open circles are measured values. Error bars represent 95% confidence intervals based on replicate mass spectrometric analyses of single samples. Note the approach to equilibrium values at intermediate depth and off sets in the deep ocean (modified from Colman

et al. 2005). On the right is a depth profile in the upper 500 m of the oligotrophic Sargasso Sea (data from McLaughlin et al. 2011). Circles are measured values and the solid line represents the expected equilibrium $\delta^{18}\text{O}_p$ calculate based on the oxygen isotope value of seawater and the temperature at the respective depth using the equation for equilibrium relation

those associated with different enzymes as well as inorganic processes (desorption from particles and sediment regeneration). Specifically, there is a dearth of data on the fractionation associated with freshwater periphyton (soft algae and diatoms) and freshwater heterotrophic bacteria. Research has suggested that bacteria are superior competitors for phosphate in aquatic systems compared to phytoplankton (Currie and Kalff 1984); however, differences in isotopic fractionation associated with bacterial cycling of phosphorus compared to algal cycling have not been fully defined. More research is needed to understand how various organisms fractionate phosphate oxygen under a variety of temperature and phosphorus concentration regimes.

Isotopic fractionation associated with sorption onto particulate matter and in co-precipitation of phosphate with various minerals must also be further explored. Phosphate interactions with sediments and co-precipitates in lakes and streams have been found

to be an important factor in controlling the dissolved phosphate pool (Fox 1989; House 2003). Such effects are assumed to be negligible in most systems but could potentially play a role in hardwater systems where co-precipitation of phosphate can result in the removal of up to 30% of the dissolved P pool (House 2003). Finally, fractionation associated with remineralization and sedimentary fluxes also needs to be defined.

Procedures for the analysis of oxygen isotopes in organic phosphate compounds have not been fully tested. The only published procedure is of McLaughlin et al. (2006c) in which an $\delta^{18}\text{O}$ enriched isotope spike is used to correct for incorporation of reagent oxygen during hydrolysis of organic phosphate. While data presented in this paper is promising, fractionation effects associated with hydrolysis have not been fully evaluated and work on natural samples is limited. The signatures of dissolved organic phosphate compounds and plant material may be important yet these values are mostly unknown.

The database characterizing source signatures is also relatively limited. Specifically, groundwater, atmospheric deposition and agriculture and urban runoff which are known sources to many aquatic systems have not been measured and only limited information regarding isotope signatures of phosphate regenerated from sediments is available. Similarly the observation that waste water treatment effluents from different locations and treatment plants have different $\delta^{18}\text{O}_p$ values warrants further work to determine how specific treatment protocols impact the isotope ratio. Thus a more extensive data base at a wide range of locations and settings is needed.

In addition, it is vital that a certified international silver phosphate standard be prepared, characterized and distributed to a wider scientific community. This would permit comparison of results among laboratories and will enable laboratories to establish better QA/QC protocols.

Finally, it could be interesting to extend the utility of this isotope system to other areas of environmental research including environmental forensics, climate research, and to study phosphorous cycling in vegetation and soils. Indeed a few attempts to move in that direction have taken place (Jaisi and Blake 2010; Tamburini et al. 2010; Zohar et al. 2010b). The development is rapid and it is expected that this system will see a great expansion in application to a broad range of problems in the near future.

Acknowledgments The authors would like to thank Megan Young, Steve Silva, and Carol Kendall at the USGS Menlo Park, CA, and Federica Tamburini from ETH, Zurich for sharing their experience and knowledge of sample preparation and analyses of oxygen isotopes in phosphate.

References

- Ayliffe LK, Veeh HH, Chivas AR (1992) Oxygen isotopes of phosphate and the origin of island apatite deposits. *Earth Planet Sci Lett* 108(1–3): 119–129
- Beman JM, Arrigo KR, Matson PA (2005) Agricultural runoff fuels large phytoplankton blooms in vulnerable areas of the ocean. *Nature* 434:211–214
- Benitez-Nelson CR (2000) The Biogeochemical Cycling of Phosphorus in Marine Systems. *Earth Sci. Rev.*, 51, 109–135
- Benitez-Nelson CR, Buessler KO (1998) Measurement of cosmogenic ^{32}P and ^{33}P activities in rainwater and seawater. *Analytical Chem* 70:64–72
- Benitez-Nelson CR, Buessler KO (1999) Variability of inorganic and organic phosphorus turnover rates in the coastal ocean. *Nature* 398:502–505
- Benitez-Nelson CR, Karl DM (2002) Phosphorus cycling in the North Pacific Subtropical Gyre using cosmogenic ^{32}P and ^{33}P . *Limnol Oceanogr* 47:762–770
- Blake RE, O'Neil JR, Garcia GA (1997) Oxygen isotope systematics of biologically mediated reactions of phosphate: I. Microbial degradation of organophosphorus compounds. *Geochim Cosmochim Acta* 61:4411–4422
- Blake RE, O'Neil JR, Garcia GA (1998) Effects of microbial activity on the $\delta^{18}\text{O}$ of dissolved inorganic phosphate and textural features of synthetic apatites. *Am Mineralog* 83:1516–1531
- Blake RE, Alt JC, Martin AM (2001) Oxygen isotope ratios of PO_4 : an inorganic indicator of enzymatic activity and P metabolism and a new biomarker in the search for life. *Proc Natl Acad Sci USA* 98:2148–2153
- Blake RE, O'Neil JR, Surkov AV (2005) Biogeochemical cycling of phosphorus: insights from oxygen isotope effects of phosphoenzymes. *Am J Sci* 305:596–620
- Bothwell ML (1985) Phosphorus limitation of lotic periphyton growth rates: an intersite comparison using continuous-flow troughs (Thompson River System, British Columbia). *Limnol Oceanogr* 30:527–542
- Broecker WS, Peng TH (1982) Tracers in the Sea. Columbia University, Lamont-Doherty Geological Observatory
- Carpenter SR, Caraco NF, Correl DL et al (1998) Nonpoint pollution of surface waters with phosphorus and nitrogen. *Ecol Appl* 8:559–568
- Coleman A (2002) The oxygen isotope composition of dissolved inorganic phosphate and the marine phosphorus cycle. *Geology and Geophysics*, Yale
- Colman A (2002) The oxygen isotope composition of dissolved inorganic phosphate and the marine phosphorus cycle. *Geology and Geophysics*, Yale
- Colman AS, Blake RE, Karl DM et al (2005) Marine phosphate oxygen isotopes and organic matter remineralization in the oceans. *Proc Natl Acad Sci USA* 102:13023–13028
- Currie DJ, Kalff J (1984) A comparison of the abilities of freshwater algae and bacteria to acquire and retain phosphorus. *Limnol Oceanogr* 29:298–310
- Elsbury KE, Paytan A, Ostrom NE, Kendall C, Young MB, McLaughlin K, Rollog ME, and Watson S (2009) Using Oxygen Isotopes of Phosphate To Trace Phosphorus Sources and Cycling in Lake Erie. *Environmental Science and Technology* 43:3108–3114
- Emsley J (2000) *The Shocking History of Phosphorus*. Macmillan, London
- Firsching FH (1961) Precipitation of silver phosphate from homogeneous solution. *Analytical Chem* 33:873–874
- Föllmi KB (1995) 160 m.y. record of marine sedimentary phosphorus burial: Coupling of climate and continental weathering under greenhouse and icehouse conditions. *Geology* 23:859–862
- Fox LE (1989) Model for inorganic control of phosphate concentrations in river waters. *Geochim Cosmochim Acta* 53:417–428
- Fricke HC, Clyde WC, O'Neil JR et al (1998) Evidence for rapid climate change in North America during the latest Paleocene thermal maximum: oxygen isotope compositions of biogenic

- phosphate from the Bighorn Basin (Wyoming). *Earth Planet Sci Lett* 160:193–208
- Goldammer T, Max T, Brunner B et al (2011) Marine sediment pore-water profiles of phosphate oxygen isotopes using a refined micro-extraction technique. *Limno. Oceanogr Methods* (submitted)
- Graau G, Legeas M, Riou C et al (2005) The oxygen isotopic composition of dissolved anthropogenic phosphates: a new tool for eutrophication research? *Water Res* 39:232–238
- Harris GP (2001) Biogeochemistry of nitrogen and phosphorus in Australian catchments, rivers and estuaries: effects of land use and flow regulation and comparisons with global patterns. *Mar Freshwater Res* 52:139–149
- Hecky RE, Kilham P (1988) Nutrient limitation of phytoplankton in freshwater and marine environments: a review of recent evidence on the effects of enrichment. *Limnol Oceanogr* 33:796–822
- House WA (2003) Geochemical cycling of phosphorus in rivers. *Appl Geochem* 18:739–748
- Howarth RW (1988) Nutrient limitation of primary production in marine ecosystems. *Annu Rev Ecol Syst* 19:89–110
- Ingram BL, Conrad ME, Ingle JC (1996) Stable isotope and salinity systematics in estuarine waters and carbonates: San Francisco Bay. *Geochim Cosmochim Acta* 60:455–467
- Jaisi DP, Blake RE, Kukkadapu RK (2009) Fractionation of oxygen isotopes in phosphate during its interactions with iron oxides. *Geochim Cosmochim Acta* 74:1309–1319
- Jaisi DP, Blake RE (2010) Tracing sources and cycling of phosphate in Peru Margin sediments using oxygen isotopes in authigenic and detrital phosphates. *Geochim Cosmochim Acta* 74:3199–3212
- Karl DM, Tien G (1992) MAGIC: A sensitive and precise method for measuring dissolved phosphorus in aquatic environments. *Limnol and Oceanogr* 37:105–116
- Karl DM, Tien G (1997) Temporal variability in dissolved phosphorus concentrations in the subtropical North Pacific Ocean. *Mar Chem* 56:77–96
- Karl DM, Bjorkman KM, Dore JE et al (2001) Ecological nitrogen-to-phosphorus stoichiometry at station ALOHA. *Deep-Sea Res II* 48:1529–1566
- Kolodny Y, Luz B, Navon O (1983) Oxygen isotope variations in phosphate of biogenic apatites. I. Fish bone apatite – rechecking the rules of the game. *Earth Planet Sci Lett* 64:398–404
- Kornexl BE, Gehre M, Hofling R et al (1999) On-line $\delta^{18}\text{O}$ measurement of organic and inorganic substances. *Rapid Comm Mass Spect* 13:1685–1693
- Krom MD, Kress N, Brenner S et al (1991) Phosphorus limitation of primary productivity in the eastern Mediterranean Sea. *Limnol Oceanogr* 36:424–432
- Lal D, Chung Y, Platt T et al (1988) Twin cosmogenic radio-tracer studies of phosphorus recycling and chemical fluxes in the upper ocean. *Limnol Oceanogr* 33:1559–1567
- Lal D, Lee T (1988) Cosmogenic ^{32}P and ^{33}P uses as tracers to study phosphorus recycling in the upper ocean. *Nature* 333:752–754
- Lecuyer C, Grandjean P, Emig CC (1996) Determination of oxygen isotope fractionation between water and phosphate from living lingulids: potential application to palaeo-environmental studies. *Paleogeogr Paleoclim Paleocool* 126:101–108
- Lee T, Barg E, Lal D (1991) Studies of vertical mixing in the Southern California Bight with cosmogenic radionuclides ^{32}P and ^{7}Be . *Limnol Oceanogr* 36:1044–1053
- Lehrter JC (2006) Effects of land use and land cover, stream discharge, and interannual climate on the magnitude and timing of nitrogen, phosphorus, and organic carbon concentrations in three coastal plain watersheds. *Water Environ Res* 78:2356–2368
- Liang Y (2005) Oxygen isotope studies of biogeochemical cycling of phosphorus. Ph.D. Thesis. Department of Geology and Geophysics, Yale University, New Haven, CT, USA
- Liang Y, Blake RE (2006a) Oxygen isotope composition of phosphate in organic compounds: isotope effects of extraction methods. *Organic Geochem* 37:1263–1277
- Liang Y, Blake RE (2006b) Oxygen isotope signature of Pi regeneration from organic compounds by phosphomonoesterases and photooxidation. *Geochim Cosmochim Acta* 70:3957–3969
- Liang Y, Blake RE (2007) Oxygen isotope fractionation between apatite and aqueous-phase phosphate: 20–45°C. *Chem Geol* 238:121–133
- Liang Y, Blake RE (2009) Compound- and enzyme-specific phosphodiester hydrolysis mechanisms revealed by $\delta^{18}\text{O}$ of dissolved inorganic phosphate: implications for the marine P cycling. *Geochim Cosmochim Acta* 73:3782–3794
- Longinelli A (1965) Oxygen isotopic composition of orthophosphate from shells of living marine organisms. *Nature* 207:716–719
- Longinelli A (1984) Oxygen isotopes in mammal bone phosphate: a new tool for paleohydrological and paleoclimatological research. *Geochim Cosmochim Acta* 48:385–390
- Longinelli A, Bartelloni M, Cortecci G (1976) The isotopic cycle of oceanic phosphate: I. *Earth Planet Sci Lett* 32:389–392
- Longinelli A, Nuti S (1973) Revised phosphate-water isotopic temperature scale. *Earth Planet Sci Lett* 19:373–376
- Luz B, Kolodny Y, Kovach J (1984) Oxygen isotope variations in phosphate of biogenic apatites III. Conodonts. *Earth Planet Sci Lett* 69:255–262
- Luz B, Kolodny Y (1985) Oxygen isotope variation in phosphate of biogenic apatites IV. Mammal teeth and bones. *Earth Planet Sci Lett* 75:29–36
- Markel D, Kolodny Y, Luz B et al (1994) Phosphorus cycling and phosphorus sources in Lake Kinneret: tracing by oxygen isotopes in phosphate. *Isr J Earth Sci* 43:165–178
- McLaughlin K, Kendall C, Silva S et al (2004) A precise method for the analysis of $\delta^{18}\text{O}$ of dissolved inorganic phosphate in seawater. *Limnol Oceanogr Methods* 2:202–212
- McLaughlin K, Cade-Menun BJ, Paytan A (2006a) The oxygen isotopic composition of phosphate in Elkhorn Slough. A tracer for phosphate sources. *Estuarine, Coastal and Shelf Science*, California. doi:10.1016/j.ecss.2006.06.030
- McLaughlin K, Chavez FP, Pennington JT et al (2006b) A time series investigation of the oxygen isotopic composition of dissolved inorganic phosphate in Monterey Bay. *Limnol Oceanogr* 51:2370–2379
- McLaughlin K, Kendall C, Silva SR et al (2006c) Oxygen isotopes of phosphatic compounds – application for marine

- particulate matter, sediments and soils. *Mar Chem* 98: 148–155
- McLaughlin K, Paytan A, Kendall C et al (2006d) Phosphate oxygen isotopes as a tracer for sources and cycling of phosphate in North San Francisco Bay. *Journal of Geophysical Research-Biogeosciences* 111:G03003. doi:10.1029/2005JG000079
- McLaughlin K, Sohm J, Cutter G et al (2011) Insights into the sources and cycling of phosphate in the Sargasso Sea: a multi-tracer approach. *Global Biogeochemical Cycles* (submitted)
- Neill C, Deegan LA, Thomas SM et al (2001) Deforestation for pasture alters nitrogen and phosphorus in small Amazonian Streams. *Ecol Appl* 11:1817–1828
- Nicholson D, Dyhrman S, Chavez F et al (2006) Alkaline phosphatase activity in the phytoplankton communities of Monterey Bay and San Francisco Bay. *Limnol Oceanogr* 51:874–883
- O'Neil JR, Roe LJ, Reinhard E et al (1994) A rapid and precise method of oxygen isotope analysis of biogenic phosphate. *Isr J Earth Sci* 43:203–212
- O'Neil JR, Vennemann TW, McKenzie WF (2003) Effects of speciation on equilibrium fractionations and rates of oxygen isotope exchange between $(\text{PO}_4)_{\text{aq}}$ and H_2O . *Geochim Cosmochim Acta* 67:3135–3144
- Paytan A (1989) Oxygen isotope variations of phosphate in aquatic systems, Master's Thesis. Hebrew University, Jerusalem
- Paytan A, Kolodny Y, Neori A et al (2002) Rapid biologically mediated oxygen isotope exchange between water and phosphate. *Global Biogeochem Cycles* 16:1013
- Paytan A, McLaughlin K (2007) The Oceanic Phosphorus Cycle. *Chemical Reviews* 107:563–576
- Rabalais NN, Turner RE, Wiseman WJ (2002) Gulf of Mexico hypoxia, a.k.a. "The dead zone". *Annu Rev Ecol Syst* 33:235–263
- Schlesinger WH (1991) *Biogeochemistry*. Academic Press, San Diego, An Analysis of Global Change
- Sharp JH (1991) Review of carbon, nitrogen, and phosphorus biogeochemistry. *Rev Geophys Suppl* 29:648–657
- Shemesh A, Kolodny Y, Luz B (1983) Oxygen isotope variations in phosphate of biogenic apatites. II. Phosphorite rocks. *Earth Planet Sci Lett* 64:405–416
- Shemesh A, Kolodny Y, Luz B (1988) Isotope geochemistry of oxygen and carbon in phosphate and carbonate phosphorite francolite. *Geochim Cosmochim Acta* 52:2565–2572
- Smith REH, Kalff J (1983) Competition for phosphorus among co-occurring freshwater phytoplankton. *Limnol Oceanogr* 28:448–464
- Smith SV (1984) Phosphorus versus nitrogen limitation in the marine environment. *Limnol Oceanogr* 29:1149–1160
- Sundareshwar PV, Morris JT, Koepfler EK et al (2003) Phosphorus limitation of coastal ecosystem processes. *Science* 299:563–565
- Tamburini F, Bernasconi SM, Angert A et al (2010) A method for the analysis of the $\delta^{18}\text{O}$ of inorganic phosphate in soils extracted with HCl. *Eur J Soil Sci* 61:1025–1032
- Tilman D, Fargione J, Wolff B et al (2001) Forecasting agriculturally driven global environmental change. *Science* 292:281–284
- Tudge AP (1960) A method of analysis of oxygen isotopes in orthophosphate – its use in the measurement of paleotemperatures. *Geochim Cosmochim Acta* 18:81–93
- Vaccari DA (2009) Phosphorus famine: the treat to our food supply. *Sci Am* 300:54–59
- Vennemann TW, Fricke HC, Blake RE et al (2002) Oxygen isotope analysis of phosphates: a comparison of techniques for analysis of Ag_3PO_4 . *Chem Geol* 185:321–336
- Weidemann-Bidlack FB, Colman AS, Fogel ML (2008) Stable isotope analyses of phosphate oxygen from biological apatite: a new technique for microsampling, microprecipitation of Ag_3PO_4 , and removal of organic contamination. *Rapid Commun Mass Spectrom* 22:1807–1816
- Wu JF, Sunda W, Boyle EA et al (2000) Phosphate depletion in the western North Atlantic Ocean. *Science* 289:759–762
- Young MB, McLaughlin K, Kendall C et al (2009) Characterizing the oxygen isotopic composition of phosphate sources to aquatic systems. *Environ Sci Tech* 43:5190–5196
- Zohar I, Paytan A, Shaviv A (2010a) A method for the analysis of oxygen isotopic composition of various soil phosphate fractions. *Environ Sci Tech* 44(19):7583–7588
- Zohar I, Shaviv A, Young M et al (2010b) Phosphorus dynamics in soil following irrigation, a study using oxygen isotopic composition of phosphate. *Geoderma* 159:109–121

Chapter 22

Isotopic Tracing of Perchlorate in the Environment

Neil C. Sturchio, John Karl Böhlke, Baohua Gu, Paul B. Hatzinger, and W. Andrew Jackson

Abstract Isotopic measurements can be used for tracing the sources and behavior of environmental contaminants. Perchlorate (ClO_4^-) has been detected widely in groundwater, soils, fertilizers, plants, milk, and human urine since 1997, when improved analytical methods for analyzing ClO_4^- concentration became available for routine use. Perchlorate ingestion poses a risk to human health because of its interference with thyroidal hormone production. Consequently, methods for isotopic analysis of ClO_4^- have been developed and applied to assist evaluation of the origin and migration of this common contaminant. Isotopic data are now available for stable isotopes of oxygen and chlorine, as well as ^{36}Cl isotopic abundances, in ClO_4^- samples from a variety of natural and synthetic sources. These isotopic data provide a basis for distinguishing sources of ClO_4^- found in the environment, and for understanding the origin of natural ClO_4^- . In addition, the isotope effects of microbial ClO_4^- reduction have been measured in laboratory and field experiments, providing a tool for assessing ClO_4^- attenuation in the environment. Iso-

topic data have been used successfully in some areas for identifying major sources of ClO_4^- contamination in drinking water supplies. Questions about the origin and global biogeochemical cycle of natural ClO_4^- remain to be addressed; such work would benefit from the development of methods for preparation and isotopic analysis of ClO_4^- in samples with low concentrations and complex matrices.

22.1 Introduction

Perchlorate (ClO_4^-) is a stable oxyanion consisting of four O^{2-} ions bonded in tetrahedral coordination with a central Cl^{7+} ion. It is ubiquitous in the environment at trace concentrations, and has natural and anthropogenic sources. Natural ClO_4^- is present in precipitation (generally $<0.1 \mu\text{g L}^{-1}$), in soil (generally $<10 \mu\text{g kg}^{-1}$), and in groundwater at concentrations ranging from background levels of about 0.01 to $>100 \mu\text{g L}^{-1}$ in some arid regions where perchlorate has been concentrated by evaporation (Dasgupta et al. 2005; Jackson et al. 2005a; Rao et al. 2007; Rajagopalan et al. 2006, 2009; Parker et al. 2008).

A major production mechanism for natural perchlorate apparently involves reactions of atmospheric Cl species with ozone (O_3) (Simonaitis and Hecklen 1975; Jaegle et al. 1996; Bao and Gu 2004; Dasgupta et al. 2005; Kang et al. 2008; Catling et al. 2010; Rao et al. 2010). Anthropogenic ClO_4^- salts are synthesized by electrolysis of NaCl brines (Schumacher 1960) in quantities on the order of $10^7 \text{ kg year}^{-1}$ (DasGupta et al. 2006) for military, aerospace, and other industrial applications, e.g., solid rocket fuel, explosives, fireworks, road flares, electroplating solutions.

Perchlorate salts (NH_4ClO_4 , KClO_4 , NaClO_4) are soluble in water and some organic solvents. The

N.C. Sturchio (✉)
University of Illinois at Chicago, Chicago, IL 60607, USA
e-mail: sturchio@uic.edu

J.K. Böhlke
U.S. Geological Survey, Reston, VA 20192, USA

B. Gu
Oak Ridge National Laboratory, Oak Ridge, TN 37831, USA

P.B. Hatzinger
Shaw Environmental, Inc., Lawrenceville, NJ 08648, USA

W.A. Jackson
Texas Tech University, Lubbock, TX 79409, USA

ClO_4^- ion in aqueous solution is non-complexing and unreactive at low temperature, resistant to O exchange with H_2O (Hoering et al. 1958), and adsorbs weakly to solids present in soils and aquifers. It is not readily removed by conventional water treatment processes, but special ion exchange resins have been developed to remove ClO_4^- from drinking water (Gu et al. 2007, 2011). Perchlorate can be reduced by microbes under anoxic conditions after available nitrate (NO_3^-) is depleted (Coates and Achenbach 2004), and this biodegradation process has been utilized for both in situ and ex situ treatment of water (Hatzinger 2005). Its chemical properties give ClO_4^- high mobility and general persistence in surface waters, vadose zone environments, and shallow oxic aquifers.

The widespread occurrence of ClO_4^- in drinking water and food supplies (Gullick et al. 2001; Kirk et al. 2003; Jackson et al. 2005b; Sanchez et al. 2005, 2006) has attracted attention because of the potential deleterious health effects of ClO_4^- ingestion caused by interference with human thyroidal hormone production (NRC 2005). Pathways of natural and synthetic perchlorate through the environment, and potential natural attenuation processes, are thus of great interest with respect to human health and the protection of environmental quality.

Stable isotope ratio analyses of oxygen (O) and chlorine (Cl), along with ^{36}Cl abundance measurements, have shown that different ClO_4^- sources have distinct isotopic compositions that provide multiple isotopic tracers of the sources and behavior of ClO_4^- in the environment (Bao and Gu 2004; Böhlke et al. 2005; Sturchio et al. 2006, 2009; Jackson et al. 2010). In this chapter we review the development and current status of sampling and isotopic analytical methods for ClO_4^- , along with a survey of published data. Remaining questions about the origin and behavior of natural ClO_4^- are outlined.

22.1.1 Isotope Abundances and Notation

There are three stable isotopes of O (^{16}O , ^{17}O , and ^{18}O) having natural abundances of approximately 99.76, 0.04, and 0.2%, respectively (Coplen et al. 2002; Hoefs 2009). Variations in O isotope ratios are reported as $\delta^{18}\text{O}$ and $\delta^{17}\text{O}$, defined as the difference between the $^{18}\text{O}/^{16}\text{O}$ or $^{17}\text{O}/^{16}\text{O}$ atom ratio, respec-

tively, of a sample and that of Vienna Standard Mean Ocean Water (VSMOW):

$$\delta^{18}\text{O} = \left[\left(\frac{^{18}\text{O}}{^{16}\text{O}} \right)_{\text{sample}} / \left(\frac{^{18}\text{O}}{^{16}\text{O}} \right)_{\text{VSMOW}} - 1 \right] \quad (22.1)$$

$$\delta^{17}\text{O} = \left[\left(\frac{^{17}\text{O}}{^{16}\text{O}} \right)_{\text{sample}} / \left(\frac{^{17}\text{O}}{^{16}\text{O}} \right)_{\text{VSMOW}} - 1 \right] \quad (22.2)$$

These δ values are normally reported in parts per thousand (‰) following multiplication of both sides of (22.1) and (22.2) by 1,000. In systems where isotopic fractionation is strictly mass-dependent, $\delta^{17}\text{O} \cong 0.52 \cdot \delta^{18}\text{O}$ and is not normally reported. However, natural ClO_4^- commonly has ^{17}O in excess of this relationship (Bao and Gu 2004; Böhlke et al. 2005) and the ^{17}O anomaly commonly is reported as a deviation from the abundance expected for mass-dependent fractionation, according to the approximation (Thiemens 2006):

$$\Delta^{17}\text{O} = \delta^{17}\text{O} - 0.52 \cdot \delta^{18}\text{O} \quad (22.3)$$

Alternatively (Miller 2002), and in this paper:

$$\Delta^{17}\text{O} = \left[(1 + \delta^{17}\text{O}) / (1 + \delta^{18}\text{O})^{0.525} \right] - 1 \quad (22.4)$$

The $\Delta^{17}\text{O}$ value is normally reported in parts per thousand (‰) following multiplication of both sides of (22.3) and (22.4) by 1,000.

There are two stable isotopes of Cl (^{35}Cl and ^{37}Cl) having natural abundances of approximately 75.76 and 24.24%, respectively (Coplen et al. 2002; Hoefs 2009). Chlorine stable isotope ratios are reported as $\delta^{37}\text{Cl}$, defined as the difference between the $^{37}\text{Cl}/^{35}\text{Cl}$ atom ratio of a sample and that of Standard Mean Ocean Chloride (SMOC) (Long et al. 1993; Godon et al. 2004):

$$\delta^{37}\text{Cl} = \left[\left(\frac{^{37}\text{Cl}}{^{35}\text{Cl}} \right)_{\text{sample}} / \left(\frac{^{37}\text{Cl}}{^{35}\text{Cl}} \right)_{\text{SMOC}} - 1 \right] \quad (22.5)$$

Values of $\delta^{37}\text{Cl}$ are normally reported in parts per thousand (‰) following multiplication of both sides of (22.5) by 1,000.

Chlorine-36 is a long-lived radioactive isotope (half-life = 301,000 years) produced largely by cosmic-ray interactions with atmospheric Ar as well as by thermal neutron capture on ^{35}Cl in the terrestrial subsurface environment. Chlorine-36 abundances are measured by accelerator mass spectrometry (AMS) and are expressed as the atom ratio of $^{36}\text{Cl}/\text{Cl}_{\text{total}}$. This ratio ranges from about 10^{-15} to 10^{-11} in terrestrial materials (Phillips 2000).

22.2 Methods

All high-precision stable isotope data ($\delta^{37}\text{Cl}$, $\delta^{18}\text{O}$, $\Delta^{17}\text{O}$) reported for ClO_4^- to date have been measured by isotope-ratio mass spectrometry (IRMS). Methods published by Ader et al. (2001) and Sturchio et al. (2003) are suitable only for determination of Cl isotope ratios in ClO_4^- , and these have been replaced in routine analysis by the methods developed and applied to isotopic analysis of both O and Cl by Böhlke et al. (2005); Sturchio et al. (2006); Hatzinger et al. (2009), and Jackson et al. (2010), which are described below in Sect. 22.2.3. Such measurements begin with a pure alkali- ClO_4^- salt, preferably KClO_4 , RbClO_4 , or CsClO_4 . A typical isotopic analysis of ClO_4^- by IRMS requires at least 0.2 mg of ClO_4^- . Although synthetic ClO_4^- reagents are readily available in large amounts, the concentration of ClO_4^- in most environmental materials is low ($\mu\text{g}/\text{kg}$) and requires elaborate methods of preconcentration, extraction, and purification prior to isotopic analysis (Gu et al. 2011).

22.2.1 Sampling

The most successful and widely used method for isotopic sampling of ClO_4^- from environmental materials has involved the use of a highly ClO_4^- -selective bifunctional ion-exchange resin for preconcentration (Gu et al. 2001, 2007, 2011). This resin was developed initially for large-scale water treatment and is commercially available as Purolite[®] A530E. Its use for preconcentration requires that the ClO_4^- be contained in an aqueous solution. Thus A530E is suitable for preconcentration of ClO_4^- directly from natural

waters or from aqueous solutions obtained by leaching ClO_4^- -bearing solid materials such as soil, caliche, plants, or industrial products.

In practice, the A530E resin (20–30 mesh size) is normally packed into 100-mL size columns fabricated from 38 mm (1.5 in.) diameter clear polyvinyl chloride (PVC) tubing. Water is passed through the column at an optimal rate of 1–2 L per minute to preconcentrate ClO_4^- on the resin, with the objective of obtaining at least 3 mg for isotopic analysis. A prefilter (5–10 μm) may be used to remove particles from the water before passing through the column. Common anions such as Cl^- , NO_3^- , and SO_4^{2-} , along with humic material, if present in sufficient quantities, tend to interfere with uptake of ClO_4^- on the A530E resin. This interference increases with salinity and results in lower efficiency of ClO_4^- adsorption and early breakthrough, thus it is advisable to pass a larger volume of water through the column than that required by the assumption of 100% efficiency. Further details about the performance of A530E resin in ClO_4^- removal are given by Gu et al. (2001, 2007, 2011).

22.2.2 Extraction and Purification

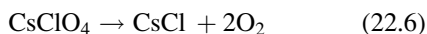
When ClO_4^- has been concentrated on the A530E resin column, there are normally substantial quantities of other common anions present. The first step in recovering ClO_4^- is to flush the column with four to five bed volumes of 4 M HCl. This displaces a large portion of the adsorbed NO_3^- , SO_4^{2-} , carbonates, and organic anions, but adds substantial Cl^- to the resin. The ClO_4^- is then eluted using a solution of 1 M FeCl_3 in 4 M HCl, and the ClO_4^- is displaced from the A530E resin by the FeCl_4^- anion (Gu et al. 2001). After ClO_4^- has been eluted from the column, there are multiple options for Fe^{3+} and Cl^- removal and further purification (Gu et al. 2011). Depending on the bulk sample composition, various issues may arise in ClO_4^- purification, and certain samples are more difficult to purify than others. Generally, lower-concentration samples ($\text{ClO}_4^- < \sim 1 \mu\text{g}/\text{L}$) are more challenging. Ultimately, the purified ClO_4^- is normally precipitated as CsClO_4 , the purity of which is verified by ion chromatography and/or Raman spectroscopy, for isotopic analysis.

22.2.3 Isotopic Analysis

22.2.3.1 Oxygen Isotopes

Oxygen isotope ratios in ClO_4^- may be analyzed by two IRMS methods. First, $\delta^{18}\text{O}$ values may be determined by reaction with glassy carbon at 1,325°C (or higher) to produce CO, which is transferred in a He carrier through a molecular-sieve gas chromatograph to an isotope-ratio mass spectrometer and analyzed in continuous-flow (CF) mode by monitoring peaks at m/z 28 and 30 (this method is referred to as CO-CFIRMS, for CO continuous-flow isotope-ratio mass spectrometry). Yields of O (as CO) typically are $100 \pm 2\%$ for pure ClO_4^- reagents and samples. The 1σ analytical precision of $\delta^{18}\text{O}$ values ranges from ± 0.1 to 0.3‰, based on replicate analyses of samples and isotopic reference materials.

For the second IRMS method, both $\delta^{18}\text{O}$ and $\delta^{17}\text{O}$ values are measured on O_2 produced by in vacuo decomposition of the CsClO_4 at 600–650°C, according to the reaction:



Decomposition can be done in sealed quartz or Pyrex glass tubes (Böhlke et al. 2005; Sturchio et al. 2007) or in a vacuum system equipped with an O_2 trap (Bao and Gu 2004). The O_2 gas is admitted to an isotope-ratio mass spectrometer and analyzed in dual-inlet (DI) mode by measurements at m/z 32, 33, and 34 (this method is referred to as O2-DIIRMS, for O_2 dual-inlet isotope-ratio mass spectrometry). Yields of O (as O_2) by the sealed-tube method are typically within $\pm 5\%$ of those expected from processed sample amounts for pure ClO_4^- reagents and samples and measured aliquots of tank O_2 . Partial exchange of O between O_2 and glass may occur during this decomposition reaction, as a function of sample size, temperature, and time.

Oxygen isotope analyses of ClO_4^- are calibrated using a pair of KClO_4 isotopic reference materials (USGS37, USGS38) with isotopic compositions that differ by more than the samples being analyzed. To monitor drift, analyses include an internal laboratory reference gas (either CO or O_2 , see below), against which all samples and isotopic reference materials are analyzed in the mass spectrometer during a single

batch of analyses in which all samples and reference materials are the same size (in terms of O) and are treated identically. The isotopic reference materials consist of reagent-grade KClO_4 salts (USGS37, USGS38) that were prepared specifically for calibration of ClO_4^- isotopic analyses. The $\delta^{18}\text{O}$ scale is based on CO-CFIRMS analyses of the ClO_4^- isotopic reference materials against international water, nitrate, and sulfate isotopic reference materials as described by Böhlke et al. (2003) and all data are referenced to the conventional VSMOW-SLAP (Standard Light Antarctic Precipitation) scale. The $\Delta^{17}\text{O}$ scale for ClO_4^- is based provisionally on the assumption that the normal reagent KClO_4 reference material (USGS37) has $^{18}\text{O}:^{17}\text{O}:^{16}\text{O}$ ratios that are related to those of VSMOW by normal mass dependent relations ($\Delta^{17}\text{O} = 0.0\text{‰}$) with exponent $\lambda = 0.525$ (see (22.4) above) (Miller 2002; Böhlke et al. 2005). Typical 1σ reproducibility of the $\Delta^{17}\text{O}$ measurements is approximately $\pm 0.1\text{‰}$ after normalization, based on replicate analyses of samples and isotopic reference materials.

22.2.3.2 Chlorine Isotopes

Stable isotope ratios of Cl in purified ClO_4^- samples are analyzed using IRMS techniques, whereas $^{36}\text{Cl}/\text{Cl}$ ratios are determined using AMS (Sturchio et al. 2007, 2009). For $\delta^{37}\text{Cl}$ determinations, ClO_4^- salts are first decomposed at 600–650°C in evacuated glass tubes to produce alkali chloride salts, which are then analyzed according to well established methods (Sturchio et al. 2007). The alkali chloride salts produced by ClO_4^- decomposition are dissolved in warm 18.2 MΩ deionized water, and Cl^- is precipitated as AgCl by addition of AgNO_3 . The resulting AgCl is recovered by centrifugation, washed in dilute HNO_3 , dried, and reacted in a sealed glass tube with excess CH_3I at 300°C for 2 h to produce CH_3Cl . The resulting CH_3Cl is purified using gas chromatography, cryo-concentrated, and then admitted to an isotope-ratio mass spectrometer and analyzed in either continuous-flow or dual-inlet mode (depending on sample size) by measurements at m/z 50 and 52.

Chlorine isotope ratio analyses are normalized using the same ClO_4^- isotopic reference materials described for O analysis in Sect. 22.2.3.1 (USGS37, USGS38). To monitor drift, analyses include an

internal laboratory reference gas (CH_3Cl), against which all samples and reference materials are analyzed in the mass spectrometer during a single batch of analyses. The $\delta^{37}\text{Cl}$ scale is based on isotopic analyses of the USGS ClO_4^- isotopic reference materials against SMOC. After normalization, the 1σ analytical precision of $\delta^{37}\text{Cl}$ values is approximately $\pm 0.2\text{‰}$, based on replicate analyses of samples and isotopic reference materials.

Analysis of ^{36}Cl in ClO_4^- is performed by AMS (Sturchio et al. 2009). Prior to AMS, the CsClO_4 is decomposed in a sealed tube as described above, then the chloride is recovered as CsCl and precipitated as AgCl by addition of excess AgNO_3 solution. The AgCl is dissolved in dilute NH_4OH solution and the Cl^- is purified by anion chromatography on analytical grade 1-X8 resin (using an unpublished protocol provided by the PRIME Lab of Purdue University) to ensure removal of trace amounts of S that might cause isobaric interference (by ^{36}S) at mass 36. An alternative method for purification of Cl^- involves cation-exchange chromatography (Jiang et al. 2004). Purified Cl^- is then precipitated as AgCl for AMS measurement. Analysis of seawater Cl^- provides a reference datum of $^{36}\text{Cl}/\text{Cl} = 0.5 \times 10^{-15}$ (Argento et al. 2010).

22.3 Results and Discussion

22.3.1 Stable Isotopic Composition of Synthetic Perchlorate

Stable isotope data for samples of synthetic ClO_4^- reagents and other commercial ClO_4^- -bearing products have been published by Ader et al. (2001), Bao and Gu (2004), Böhlke et al. (2005), and Sturchio et al. (2006). Data for samples of synthetic ClO_4^- in which both $\delta^{18}\text{O}$ and $\delta^{37}\text{Cl}$ isotope ratios were measured are shown in Fig. 22.1. Published $\delta^{37}\text{Cl}$ values for synthetic ClO_4^- range from -3.1 to $+2.3\text{‰}$ and have a mean value near $+0.6\text{‰}$. This mean value is within the range of common industrial NaCl sources, such as halite from Phanerozoic bedded evaporites having $\delta^{37}\text{Cl}$ values in the range of $0.0 \pm 0.9\text{‰}$ (Eastoe et al. 2007), and indicates that relatively little ($<1\%$) isotopic fractionation of Cl accompanies ClO_4^- syn-

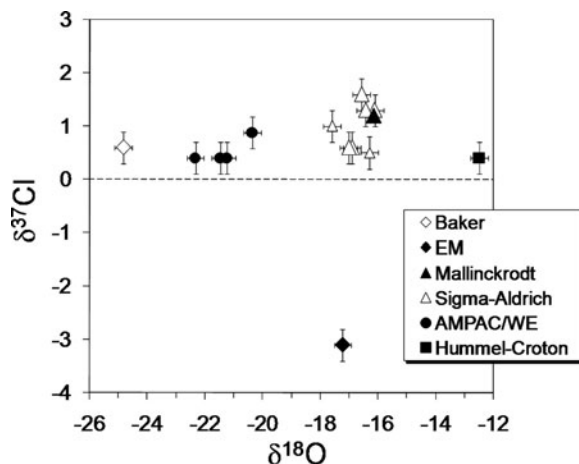


Fig. 22.1 $\delta^{37}\text{Cl}$ (‰) versus $\delta^{18}\text{O}$ (‰) for representative samples of synthetic ClO_4^- grouped by source (see legend). Analytical errors shown at $\pm 0.3\text{‰}$. Dashed line is $\delta^{37}\text{Cl}$ reference value of 0.0‰ for Standard Mean Ocean Chloride. Data from Sturchio et al. (2006)

thesis. Published $\delta^{18}\text{O}$ values of synthetic ClO_4^- range from -24.8 to -12.5‰ , presumably reflecting a range in composition of the local water sources used in production and O isotopic fractionation that occurs during ClO_4^- synthesis (Sturchio et al. 2006). In contrast, $\Delta^{17}\text{O}$ values of synthetic ClO_4^- are consistently $0.0 \pm 0.1\text{‰}$, indicating little or no mass-independent isotopic fractionation in the ClO_4^- synthesis process. All stable isotopic data generated to date for primary synthetic ClO_4^- (as of September, 2010) are within the ranges of $\delta^{18}\text{O}$ and $\delta^{37}\text{Cl}$ shown in Fig. 22.1. Preliminary measurements on ClO_4^- produced by disproportionation reactions in commercial NaOCl (bleach) solutions, however, have indicated some anomalously low values of $\delta^{18}\text{O}$ and anomalously high values of $\delta^{37}\text{Cl}$ (e.g., $\delta^{37}\text{Cl} = +14.0\text{‰}$; (Sturchio et al. 2009)), yielding a potential means by which to distinguish this source of ClO_4^- from that produced by electrochemical synthesis.

22.3.1.1 Isotopic Fractionation of Perchlorate by Microbial Reduction

Kinetic isotopic fractionations are caused by mass dependent differences in reaction rates of different isotopic species during fast, incomplete, or unidirectional reactions such as diffusion, evaporation, and microbial respiration, where reaction products are generally

enriched in the lighter isotopes (Criss 1999). The isotopic fractionation factor, α , is defined as

$$\alpha = R_A/R_B \quad (22.7)$$

where R is an isotope ratio, and A and B are two substances (in the present case, product and reactant, respectively). For O and Cl isotope ratios, R represents $^{18}\text{O}/^{16}\text{O}$ and $^{37}\text{Cl}/^{35}\text{Cl}$, respectively. Values of α can be obtained from the experimental results by assuming the exponential function

$$R/R_0 = f^{\alpha-1} \quad (22.8)$$

where R and R_0 are the O or Cl isotope ratios ($^{18}\text{O}/^{16}\text{O}$ or $^{37}\text{Cl}/^{35}\text{Cl}$) of the residual ClO_4^- and the initial, unreacted ClO_4^- , respectively, and f is the fraction of ClO_4^- remaining. In terms of the δ values of the ClO_4^- , as defined in (22.1), (22.2), and (22.5),

$$(\delta + 1)/(\delta_0 + 1) = f^{\alpha-1} \quad (22.9)$$

where δ is the isotopic composition of the ClO_4^- at any value f , and δ_0 is the isotopic composition at $f = 1$. The value of α can be obtained by fitting data with the natural log of (22.8):

$$\alpha - 1 = \ln(R/R_0)/\ln f \quad (22.10)$$

This describes the mass-dependent Rayleigh-type isotopic fractionation that accompanies a variety of natural processes (Broecker and Oversby 1971). Isotopic fractionation factors are commonly expressed in terms of ε , where

$$\varepsilon = \alpha - 1 \quad (22.11)$$

with ε normally expressed in parts per thousand (‰).

Isotopic fractionation of Cl and O accompanying microbial reduction of ClO_4^- have been investigated in several laboratory experiments and in a field study involving an in situ aquifer push-pull test. Two independent liquid culture experiments published in 2003 used the bacterial species *Azospira suillum* with acetate as the electron donor and ClO_4^- as the sole electron acceptor to investigate the Cl kinetic isotope effect (Coleman et al. 2003; Sturchio et al. 2003). Coleman et al. (2003) maintained the temperature of

their cultures at 37°C, whereas Sturchio et al. (2003) maintained the temperature of their cultures at 22°C, during incubation. Coleman et al. (2003) reported $\varepsilon^{37}\text{Cl}$ values of -15.8 ± 0.4 and -14.8 ± 1.3 ‰ obtained from two separate cultures, both exhibiting nearly complete ClO_4^- reduction in about 90 min. Sturchio et al. (2003) reported comparable $\varepsilon^{37}\text{Cl}$ values of -16.6 and -12.9 ‰ obtained from two separate cultures with complete ClO_4^- reduction times of 18 days and 5.5 h, respectively, noting that less fractionation was observed in the experiment in which ClO_4^- was consumed more rapidly. A subsequent presentation and re-evaluation of the Coleman et al. (2003) data concluded a single and more precise $\varepsilon^{37}\text{Cl}$ value of -14.98 ± 0.15 ‰, following a statistical refinement of the complete experimental data set (Ader et al. 2008).

Further work by Sturchio et al. (2007) produced data on both Cl and O isotope effects of microbial ClO_4^- reduction, this time using two different bacterial genera (*A. suillum* JPLRND and *Dechlorospirillum* sp. FBR2) in liquid cultures at temperatures of 22 and 10°C, and including an experiment using ^{18}O -enriched water to test for O exchange between ClO_4^- and H_2O . This set of experiments resulted in composite $\varepsilon^{37}\text{Cl}$ and $\varepsilon^{18}\text{O}$ values (regressed from the combined data of the five separate experiments, with all points weighted equally) of -13.2 ± 0.5 and -33.1 ± 1.2 ‰, respectively. There was no evidence (within analytical error) for dependence on either bacterial strain or temperature, and no evidence for O exchange between ClO_4^- and H_2O , during ClO_4^- reduction. A key result of this work was the observation that, despite a range in apparent ε values of the individual experiments, the ratio $\varepsilon^{18}\text{O}/\varepsilon^{37}\text{Cl}$ showed a constant value of 2.50 ± 0.04 for the combined experimental results over a range of f from 1.00 to 0.01 (Fig. 22.2).

The applicability of laboratory isotopic fractionation factors in the field was explored by Hatzinger et al. (2009), who performed a push-pull test in 2006 at a site where a soybean oil emulsion had been injected three years earlier in a demonstration of its potential to stimulate ClO_4^- bioremediation (Borden 2007). In the single injection push-pull test, 405 L of contaminated upgradient groundwater (containing 5.5 mg L^{-1} ClO_4^- and 7.7 mg L^{-1} NO_3^-) was amended with NaBr (as a tracer for groundwater mixing) and injected at a rate of 30 L min^{-1} into the zone containing residual emulsified oil (the monitoring well was

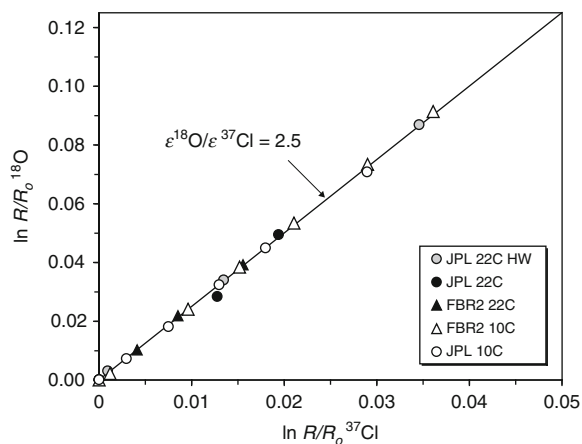


Fig. 22.2 Relation of $\epsilon^{18}\text{O}$ and $\epsilon^{37}\text{Cl}$ in combined results of five liquid culture experiments of microbial ClO_4^- reduction (Sturchio et al. 2007). A constant slope of 2.50 ± 0.04 was observed, independent of bacterial strain and temperature. The experiment labeled “HW” was done in ^{18}O -enriched water ($\delta^{18}\text{O} = +198\text{‰}$) and indicates no measurable O exchange between ClO_4^- and H_2O during microbial reduction under these conditions

screened at depths of 1.8–4.9 m, where total well depth was 5 m below ground surface). Nine water samples of 1–30-L volume (increasing with time) were removed periodically over a period of 30 h for chemical and isotopic analysis. Apparent in situ isotopic fractionation factors for both O and Cl in ClO_4^- were only about 0.3–0.4 times the values reported for pure culture studies (Sturchio et al. 2007; Ader et al. 2008); similarly, apparent fractionation factors for N and O in NO_3^- were only 0.2–0.6 times those reported in laboratory culture studies. The relatively small apparent isotopic fractionation factors observed in the push-pull test may be attributed to physical and chemical heterogeneity in the aquifer, as similar effects have been observed and modeled for NO_3^- reduction in groundwater and surface water (Mariotti et al. 1988; Lehman et al. 2003; Green et al. 2010). Despite the relatively small apparent in situ values of $\epsilon^{18}\text{O}$ and $\epsilon^{37}\text{Cl}$ measured for ClO_4^- in the push-pull test, the ϵ ratio $\epsilon^{18}\text{O}/\epsilon^{37}\text{Cl}$ was 2.63, in excellent agreement with the laboratory-determined value of 2.50 ± 0.04 (Sturchio et al. 2007). This indicates that the fundamental process of ClO_4^- reduction may have been the same in laboratory and field settings, but the heterogeneity of the field setting was such that it caused substantial

underestimation of the extent of ClO_4^- reduction when using an isotopic approach based on laboratory fractionation factors.

22.3.2 Stable Isotopic Composition of Natural Perchlorate

22.3.2.1 Atacama Desert, Chile

The most well-known occurrence of naturally occurring ClO_4^- is in the extensive NO_3^- -rich “caliche”-type salt deposits of the hyperarid Atacama Desert of northern Chile, which contain up to 0.6 wt.% ClO_4^- (Ericksen 1981). The O isotopic composition of Atacama ClO_4^- was first measured by Bao and Gu (2004) who reported $\delta^{18}\text{O}$ values ranging from -24.8 to -4.5‰ and $\Delta^{17}\text{O}$ values ranging from $+4.2$ to $+9.6\text{‰}$. The elevated ^{17}O abundance was interpreted by Bao and Gu (2004) as a reflection of the atmospheric origin of ClO_4^- through photochemical reactions of atmospheric Cl species with O_3 . Additional isotopic data for Atacama ClO_4^- were reported by Böhlke et al. (2005), Sturchio et al. (2006), and Jackson et al. (2010), extending the O isotopic results of Bao and Gu (2004) and, in addition, documenting extreme ^{37}Cl -depletion with $\delta^{37}\text{Cl}$ values ranging from -14.5 to -11.8‰ . An atmospheric origin for ClO_4^- is consistent with N and O isotopic evidence for the atmospheric origin of NO_3^- in the Atacama salt deposits and soils (Böhlke et al. 1997; Michalski et al. 2004; Ewing et al. 2007), where both compounds may have accumulated for millions of years (Ericksen 1981; Rech et al. 2010; Ewing et al. 2006). There is growing interest in the origin and isotopic composition of Atacama ClO_4^- for several reasons: (1) billions of kg of Atacama NO_3^- deposits have been imported to the U.S. for use in agricultural fertilizer (DasGupta et al. 2006), and the distinctive isotopic composition of Atacama ClO_4^- has been found in aquifers across the U.S., indicating past use of Atacama nitrate fertilizer is a source of ClO_4^- in U.S. groundwater (Böhlke et al. 2005, 2009; Sturchio et al. 2011); and (2) the recent discovery of ClO_4^- in Martian and Antarctic soils has led to renewed efforts to understand the mechanism of atmospheric ClO_4^- formation and the planetary geochemical cycles for ClO_4^- on

both Earth and Mars (Hecht et al. 2009; Ming et al. 2010; Catling et al. 2010; Kounaves et al. 2010).

22.3.2.2 Southwestern United States

The occurrence of indigenous natural ClO_4^- (unrelated to imported Atacama ClO_4^-) throughout the United States, especially in the arid southwestern regions, has become increasingly apparent through surveys of ClO_4^- concentrations in precipitation, soil, and groundwater (Plummer et al. 2006; Jackson et al. 2005a; Rajagopalan et al. 2006, 2009; Rao et al. 2007; Parker et al. 2008). The stable isotopic composition of indigenous natural ClO_4^- analyzed to date (hereafter referred to as SW ClO_4^-) is distinct from both Atacama ClO_4^- and synthetic ClO_4^- (Jackson et al. 2010) (Fig. 22.3).

The three types of ClO_4^- shown in Fig. 22.3 can be distinguished completely by their $\delta^{18}\text{O}$ values. Two types of ClO_4^- have overlapping $\delta^{37}\text{Cl}$ values: synthetic ClO_4^- has a range from about -3 to $+2\%$,

whereas SW ClO_4^- has a range from about -3 to $+6\%$. In contrast, Atacama ClO_4^- has a uniquely low range in $\delta^{37}\text{Cl}$ from about -15 to -9% . The reason for such a wide range in $\delta^{37}\text{Cl}$ values for natural ClO_4^- is not yet understood, but may be related to regional or hemispheric differences in the source(s) of atmospheric Cl reactants or the mechanism(s) involved in ClO_4^- production.

The $\Delta^{17}\text{O}$ values of synthetic ClO_4^- are uniformly $0.0 \pm 0.2\%$. Natural ClO_4^- shows a significant ^{17}O excess, with Atacama ClO_4^- showing a relatively narrow range in $\Delta^{17}\text{O}$ values from $+8.1$ to $+10.5\%$, whereas SW ClO_4^- shows a much wider range from about $+0.2\%$ in groundwaters from the Southern High Plains to as high as $+18.4\%$ for an unsaturated zone salt sample from the Zabriskie area (Erickson et al. 1988) near Death Valley, CA. This mass-independent isotopic fractionation effect (Thiemens 2006) is diagnostic of all natural ClO_4^- analyzed to date. The $\Delta^{17}\text{O}$ values of the SW ClO_4^- summarized in Fig. 22.3 display a bimodal distribution, with one group (labeled SHP, for Southern High Plains) having a range from

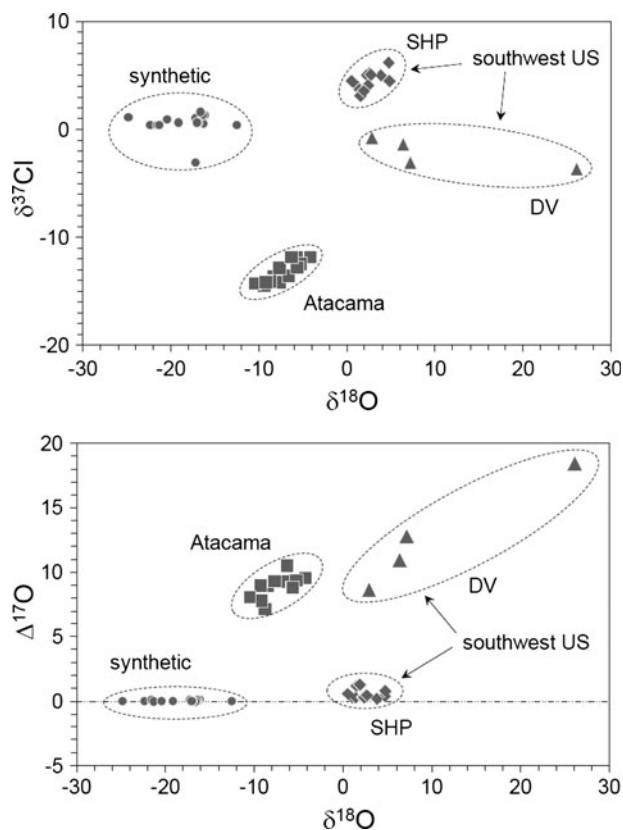


Fig. 22.3 $\delta^{37}\text{Cl}$ (per mil) versus $\delta^{18}\text{O}$ (per mil) values (upper diagram) and $\Delta^{17}\text{O}$ (per mil) versus $\delta^{18}\text{O}$ (per mil) values (lower diagram) for samples of synthetic ClO_4^- , Atacama ClO_4^- , and SW ClO_4^- . Southwest ClO_4^- is subdivided into Southern High Plains (SHP) and Death Valley (DV) as described in text. Data from Böhlke et al. (2005); Sturchio et al. (2006); Jackson et al. (2010)

about +0.2 to +2.6‰, and a second group (labeled DV, for Death Valley) having a range from +8.6 to +18.4‰. This distribution may be related in part with local climate and the mode of ClO_4^- occurrence, as the lower range of values represents ClO_4^- extracted from a number of groundwater samples and an unsaturated zone soil leachate from the Southern High Plains and Middle Rio Grande Basin (Texas and New Mexico), whereas the higher values are from unsaturated zone salts from the vicinity of Death Valley, California. The ranges of O isotopic compositions could imply either (1) there is a primary, high- $\Delta^{17}\text{O}$ atmospheric ClO_4^- signature that is retained for thousands of years in the most arid unsaturated zone profiles (and for millions of years in the hyperarid Atacama Desert) but diminished by slow isotopic exchange with O in slightly wetter environments with time, or (2) there is another production mechanism (e.g., involving UV but not O_3) that results in lower $\Delta^{17}\text{O}$ values for ClO_4^- (Jackson et al. 2010).

22.3.3 Chlorine-36 Abundance in Perchlorate

The radioactive isotope ^{36}Cl (half-life = 301,000 years) provides an additional tracer for ClO_4^- . Chlorine-36 is produced in the atmosphere largely by cosmic-ray interactions with Ar, and also in the subsurface by

thermal neutron capture on ^{35}Cl (Lehmann et al. 1993). The range in measured $^{36}\text{Cl}/\text{Cl}$ ratios of Cl^- in pre-anthropogenic groundwater across the continental U. S. is from $\sim 10 \times 10^{-15}$ near the coasts to as high as $1,670 \times 10^{-15}$ in the central Rocky Mountains (Davis et al. 2003). The lower ratios near the coasts reflect dilution by marine aerosols in which $^{36}\text{Cl}/\text{Cl} = 0.5 \times 10^{-15}$ (Argento et al. 2010). Testing of thermonuclear bombs in the Pacific Ocean during 1952–1958 injected a large amount of ^{36}Cl , produced by neutron irradiation of seawater Cl^- , into the stratosphere, resulting in worldwide ^{36}Cl fallout for several years thereafter (Phillips 2000). The presence of this bomb-pulse Cl^- may be identified from its anomalously high $^{36}\text{Cl}/\text{Cl}$ ratio and its association with relatively high tritium activity. The highest measured $^{36}\text{Cl}/\text{Cl}$ ratio reported for bomb-affected groundwater Cl^- is $12,800 \times 10^{-15}$ (Davis et al. 2003). The $^{36}\text{Cl}/\text{Cl}$ ratio of Cl^- in Long Island (NY) rainwater sampled in 1957 (during the peak of the nuclear bomb testing era in the Pacific) was as high as $127,000 \times 10^{-15}$ (Schaeffer et al. 1960). Arctic deposition in 1957 also had anomalously high $^{36}\text{Cl}/\text{Cl}$ ($28,600 \times 10^{-15}$) as observed in the Dye-3 ice core (Synal et al. 1990).

A reconnaissance survey of ^{36}Cl in ClO_4^- , including a variety of synthetic and natural ClO_4^- samples, showed a range of $^{36}\text{Cl}/\text{Cl}$ ratios exceeding four orders of magnitude (Sturchio et al. 2009) (Fig. 22.4). Synthetic ClO_4^- samples had relatively low $^{36}\text{Cl}/\text{Cl}$ ratios from $\leq 2.5 \times 10^{-15}$ to 40×10^{-15} , reflecting those expected from ancient, marine-derived NaCl sources

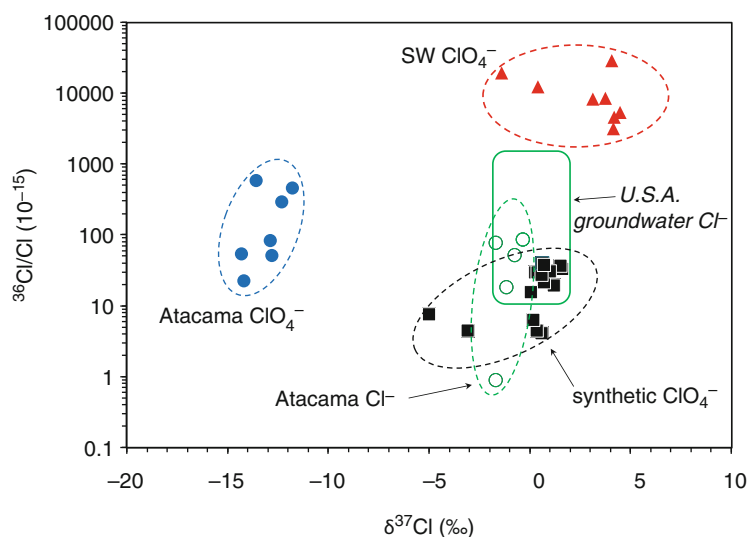


Fig. 22.4 $^{36}\text{Cl}/\text{Cl}$ (atom ratio) versus $\delta^{37}\text{Cl}$ (‰) in representative samples of synthetic ClO_4^- , Atacama ClO_4^- and associated Cl^- , and SW ClO_4^- (adapted from Sturchio et al. 2009)

used in the electrochemical synthesis, such as bedded evaporites and salt domes. Southwest ClO_4^- samples had extremely high $^{36}\text{Cl}/\text{Cl}$ ratios in the range $3,130 \times 10^{-15}$ to $28,800 \times 10^{-15}$. Although the presence of bomb ^{36}Cl could not be ruled out for some of these samples, $^{36}\text{Cl}/\text{Cl}$ ratios of $3,130 \times 10^{-15}$ to $12,300 \times 10^{-15}$ were measured in ClO_4^- extracted from groundwaters having no detectable tritium, indicating groundwater recharge prior to bomb testing and implying that the high $^{36}\text{Cl}/\text{Cl}$ ratios in these ClO_4^- samples are unrelated to the bomb tests. The fact that these ratios are much higher than any others measured for Cl^- from pre-anthropogenic groundwater implies a largely stratospheric source for the ClO_4^- , as any near-surface ClO_4^- production mechanism should yield $^{36}\text{Cl}/\text{Cl}$ ratios in the range of near-surface Cl^- (i.e. $<2,000 \times 10^{-15}$).

Atacama ClO_4^- had an intermediate range of $^{36}\text{Cl}/\text{Cl}$ ratios from 22×10^{-15} to 590×10^{-15} , and Cl^- from two samples of the Atacama caliche and one sample of an Atacama commercial NaNO_3 product had relatively low $^{36}\text{Cl}/\text{Cl}$ ratios identical within error to those of the co-occurring ClO_4^- . The Atacama data could be consistent with initially high $^{36}\text{Cl}/\text{Cl}$ ratios (similar to those of SW ClO_4^- samples) that have decreased by radioactive decay. In those samples where ClO_4^- and Cl^- have identical $^{36}\text{Cl}/\text{Cl}$ ratios, ClO_4^- and Cl^- have apparently approached secular equilibrium with the local radiation environment (i.e., a condition in which the rate of radioactive decay of ^{36}Cl is equal to its rate of production within the sample environment). There has been adequate time for secular equilibrium to be attained, as many of the Atacama caliche deposits began forming at least 9.4 million

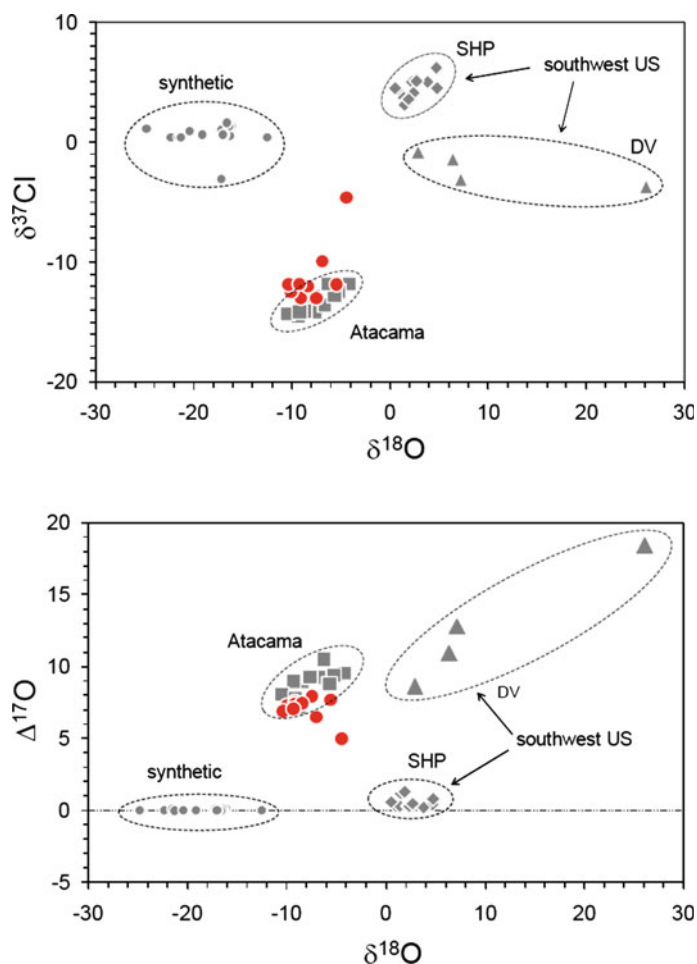


Fig. 22.5 $\delta^{37}\text{Cl}$ (per mil) versus $\delta^{18}\text{O}$ (per mil) values (upper diagram) and $\Delta^{17}\text{O}$ (per mil) versus $\delta^{18}\text{O}$ (per mil) values (lower diagram) showing stable isotope data for ClO_4^- in groundwater samples from the Chino Basin, California (red symbols) in comparison to the principal known ClO_4^- source types in the region as identified in Fig. 22.3. A dominantly Atacama source is inferred for the Chino Basin samples (Sturchio et al. 2008)

years ago (Rech et al. 2006), whereas it takes only about two million years for ^{36}Cl to reach a condition of >99% secular equilibrium.

22.3.4 Tracing Perchlorate in Contaminated Aquifers

The isotopic data accumulated for ClO_4^- during the past decade have created opportunities for tracing ClO_4^- in contaminated aquifers with relatively robust results. The three principal sources of ClO_4^- found in contaminated groundwaters of the US (i.e., synthetic, Atacama, and SW ClO_4^-) are isotopically distinct with respect to stable isotopes of O and Cl (Bao and Gu 2004; Böhlke et al. 2005; Sturchio et al. 2006) (Jackson et al. 2010) as well as ^{36}Cl (Sturchio et al. 2009). Furthermore, the low rate of O exchange

between ClO_4^- and H_2O (Hoering et al. 1958) could maintain the integrity of ClO_4^- source O isotopic ratios over at least several decades under normal groundwater conditions (Böhlke et al. 2009). Biodegradation of ClO_4^- produces systematic stable isotope enrichments that do not significantly affect $\Delta^{17}\text{O}$ values or $^{36}\text{Cl}/\text{Cl}$ ratios, thus potentially allowing detection of the biodegradation without masking the initial source(s) of ClO_4^- (Sturchio et al. 2007; Hatzinger et al. 2009).

Several studies involving the application of stable isotope measurements for tracing ClO_4^- sources in contaminated aquifers have been published with supporting information from other chemical and isotopic tracers. Increasing concentrations of ClO_4^- detected in municipal water supplies of Chino, Ontario, and Pomona, California during 2004 prompted an isotopic investigation to determine the source of this increase. The data showed a dominantly agricultural source

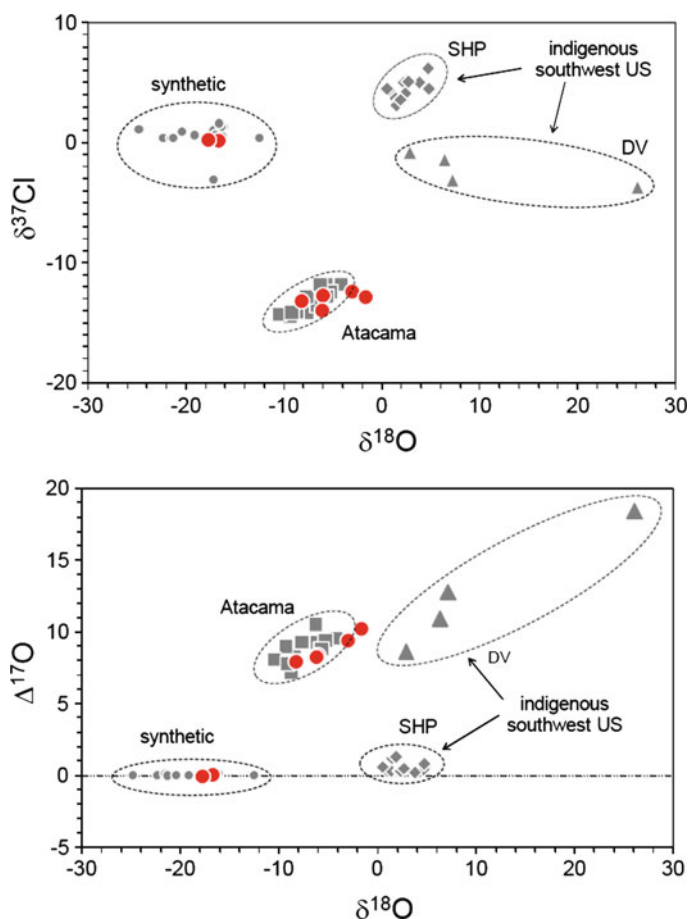


Fig. 22.6 $\delta^{37}\text{Cl}$ (per mil) versus $\delta^{18}\text{O}$ (per mil) values (*upper diagram*) and $\Delta^{17}\text{O}$ (per mil) versus $\delta^{18}\text{O}$ (per mil) values (*lower diagram*) showing stable isotope data for ClO_4^- in groundwater samples (labeled *red symbols*) from Long Island, New York (Böhlke et al. 2009), in comparison to the principal known ClO_4^- source types in the region as identified in Fig. 22.3

with isotopic compositions resembling those of Atacama ClO_4^- , with apparent minor contributions of synthetic and SW ClO_4^- (Fig. 22.5). The northern portion of the Chino Basin was formerly used for citrus cultivation and there is anecdotal evidence for extensive use of Chilean NO_3^- fertilizer (Sturchio et al. 2008).

Böhlke et al. (2009) demonstrated that ClO_4^- originating from known synthetic and agricultural sources in Long Island, New York could be traced from stable isotopic compositions (Fig. 22.6). A history of groundwater contamination by Atacama ClO_4^- in an agricultural area in eastern Long Island was inferred from depth profiles of environmental tracer ages along with concentration and isotopic data for ClO_4^- and NO_3^- (Böhlke et al. 2009). The possible sources of ClO_4^- in the groundwater of Pasadena,

California also were investigated using multiple chemical and isotopic tracers, and evidence was found for at least three distinct sources of ClO_4^- , of which at least two were synthetic (Slaten et al. 2010).

The most intensive local isotopic investigation of ClO_4^- sources in groundwater to date was performed in the southeastern San Bernardino Basin, California. Discrete, intersecting ClO_4^- plumes were found to have distinct sources (Sturchio et al. 2011). One plume containing synthetic ClO_4^- emanated from a former rocket-testing site that had been used subsequently as an artificial recharge basin (labeled “site” at the right side of Fig. 22.7), and another plume containing Atacama-type ClO_4^- emanated from a predominantly agricultural area. Where these plumes intersect, some groundwater wells contain mixtures of synthetic and Atacama ClO_4^- (Figs. 22.7 and 22.8).

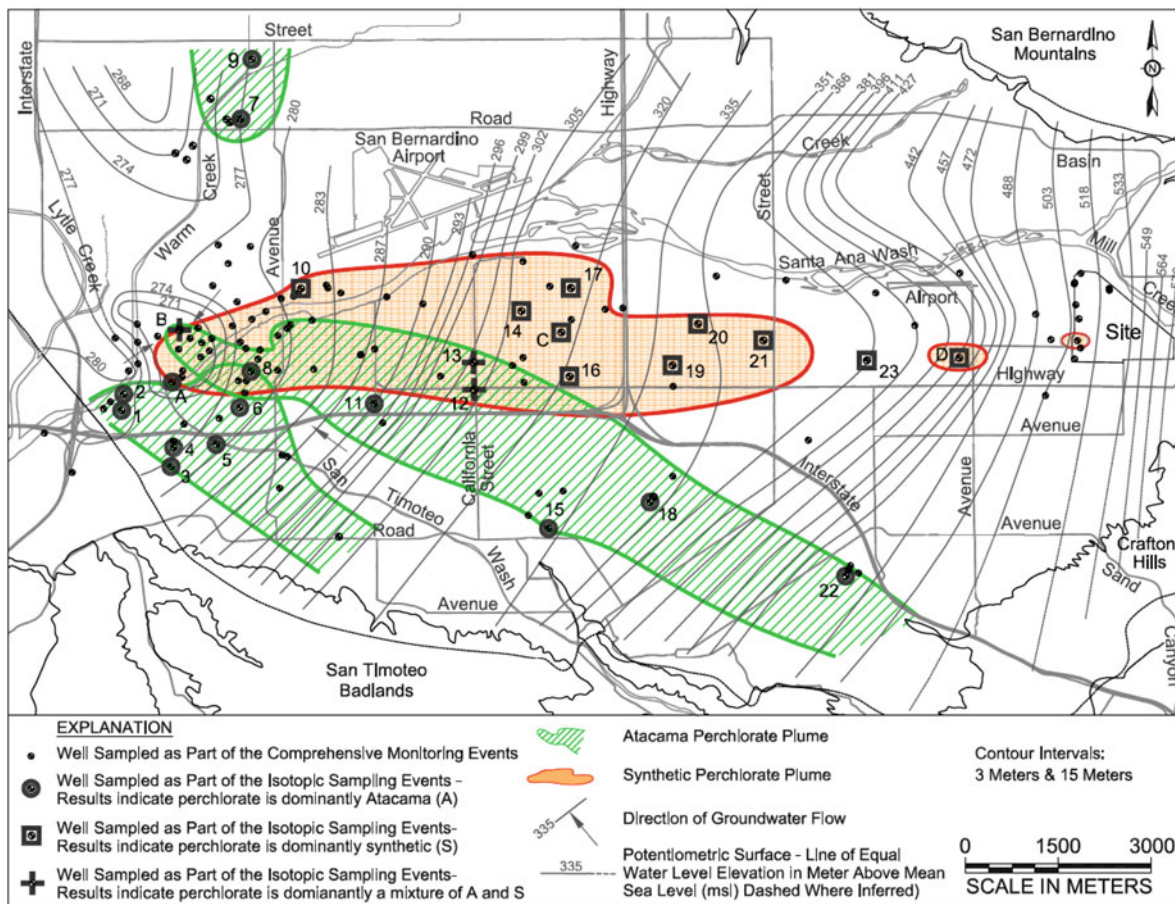
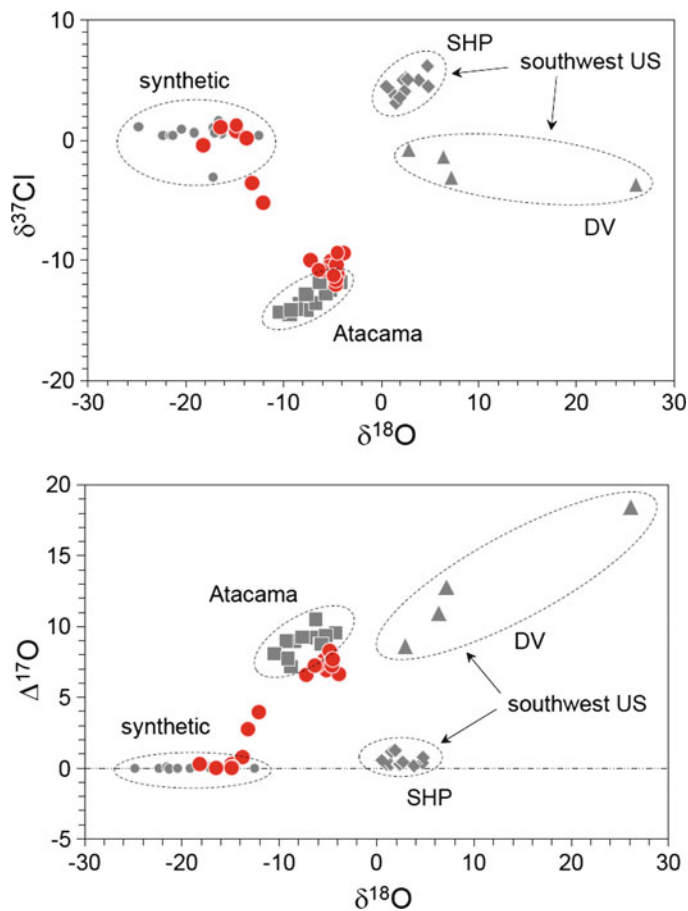


Fig. 22.7 Map showing outlines of discrete groundwater ClO_4^- plumes in Bunker Hill Basin southwest of San Bernardino, California in relation to groundwater potentiometric

surface. Map legend identifies symbols indicating predominant ClO_4^- source type. Adapted from Sturchio et al. (2011)

Fig. 22.8 $\delta^{37}\text{Cl}$ (per mil) versus $\delta^{18}\text{O}$ (per mil) (*upper diagram*) and $\Delta^{17}\text{O}$ (per mil) versus $\delta^{18}\text{O}$ (per mil) (*lower diagram*) for samples of groundwater ClO_4^- plumes in the southeastern San Bernardino Basin, California (*red symbols*) in comparison to the three principal known ClO_4^- source types in the region as identified in Fig. 22.3. One plume has a synthetic source, and the other has a predominantly agricultural (i.e. Atacama-type) source, with some apparent mixing between sources (data from Sturchio et al. 2011)



22.4 Summary and Research Opportunities

Isotopic data can be used for tracing the origin and behavior of ClO_4^- in the environment. Four independently varying parameters have been measured on individual ClO_4^- samples for this purpose: $\delta^{37}\text{Cl}$, $\delta^{18}\text{O}$, $\Delta^{17}\text{O}$, and $^{36}\text{Cl}/\text{Cl}$. At least three distinct types of ClO_4^- have been identified isotopically (i.e., synthetic, Atacama, and SW ClO_4^-), and these distinctions have proven to be useful in forensic applications. Additional data for indigenous, natural ClO_4^- are needed, however, to obtain a global picture of its isotopic variations. Improved methods for sample preparation and isotopic analysis with much better sensitivity would be helpful for measuring ClO_4^- isotopic variations in some sample

types such as aerosols and precipitation as well as foodstuffs and body fluids, which have been precluded by the impracticality of obtaining the currently required milligram amounts of ClO_4^- . Further experimental and theoretical investigations of atmospheric ClO_4^- production mechanisms may lead to improved explanations of observed isotopic variations in natural samples.

Acknowledgements Much of the work reviewed in this chapter was supported by contracts from the Strategic Environmental Research and Development Program and the Environmental Security Technology Certification Program of the U.S. Department of Defense, and by the National Research Program of the U.S. Geological Survey. Use of product or trade names in this paper is for identification purposes only and does not constitute endorsement by the U.S. government. We thank Hans Eggenkamp, Stephanie Ewing, Doug Kent, and an anonymous referee for constructive reviews of the manuscript.

References

- Ader M, Coleman ML, Doyle SP, Stroud M, Wakelin D (2001) Methods for the stable isotopic analysis of chlorine in chlorate and perchlorate compounds. *Anal Chem* 73: 4946–4950
- Ader M, Chaudhuri S, Coates JD, Coleman M (2008) Microbial perchlorate reduction: a precise laboratory determination of the chlorine isotope fractionation and its possible biochemical basis. *Earth Planet Sci Lett* 269:604–612
- Argento DC, Stone JO, Fifield LK, Tims SG (2010) Chlorine-36 in seawater. *Nucl Instr Meth Phys Res B* 268:1226–1228
- Bao H, Gu B (2004) Natural perchlorate has its unique oxygen isotope signature. *Environ Sci Technol* 38:5073–5077
- Böhlke JK, Ericksen GE, Revesz K (1997) Stable isotope evidence for an atmospheric origin of desert nitrate deposits in northern Chile and southern California. *Chem Geol* 136:135–152
- Böhlke JK, Mroczkowski SJ, Coplen TB (2003) Oxygen isotopes in nitrate: new reference materials for ^{18}O : ^{17}O : ^{16}O measurements and observations on nitrate-water equilibration. *Rapid Comm Mass Spec* 17:1835–1846
- Böhlke JK, Sturchio NC, Gu B, Horita J, Brown GM, Jackson WA, Batista JR, Hatzinger PB (2005) Perchlorate isotope forensics. *Anal Chem* 77:7838–7842
- Böhlke JK, Hatzinger PB, Sturchio NC, Gu B, Abbene I, Mroczkowski SJ (2009) Atacama perchlorate as an agricultural contaminant in groundwater: isotopic and chronologic evidence from Long Island, New York. *Environ Sci Technol* 43:5619–5625
- Borden RC (2007) Anaerobic bioremediation of perchlorate and 1,1,1-trichloroethane in an emulsified oil barrier. *J Contam Hydrol* 94:13–33
- Broecker WS, Oversby VM (1971) Chemical equilibrium in the earth. McGraw-Hill, New York
- Catling DC, Clair MW, Zahnle KJ, Quinn RC, Clarc BC, Hecht MH, Kounaves SP (2010) Atmospheric origins of perchlorate on Mars and in the Atacama. *J Geophys Res* 115:E00E11. doi:10.1029/2009JE003425
- Coates JD, Achenbach LA (2004) Microbial perchlorate reduction: rocket-fuelled metabolism. *Nat Rev Microbiol* 2:569–580
- Coleman ML, Ader M, Chaudhuri S, Coates JD (2003) Microbial isotopic fractionation of perchlorate chlorine. *Appl Environ Microbiol* 69:4997–5000
- Coplen TB, Hoppole JA, Böhlke JK, Peiser HS, Rieder SE, Krouse HR, Rosman KJR, DingT, Vocke RD, Jr, Revesz KM, Lamberty A, Taylor P, De Bievre P (2002) Compilation of minimum and maximum isotope ratios of selected elements in naturally occurring terrestrial materials and reagents. U.S. Geology Survey Water Resources Investigation Report 01-4222
- Criss RE (1999) Principles of stable isotope distribution. Oxford University Press, New York
- Dasgupta PK, Martinelango PK, Jackson WA, Anderson TA, Tian K, Tock RW, Rajagopalan S (2005) The origin of naturally occurring perchlorate: the role of atmospheric processes. *Environ Sci Technol* 39:1569–1575
- DasGupta PK, Dyke JV, Kirk AB, Jackson WA (2006) Perchlorate in the United States. Analysis of relative source contributions to the food chain. *Environ Sci Technol* 40:6608–6614
- Davis SN, Moyses S, Cecil LD, Zreda M (2003) Chlorine-36 in groundwater of the United States: empirical data. *Hydrogeol J* 11:217–227
- Eastoe CJ, Peryt TM, Petrychenko OY, Geisler-Cussy D (2007) Stable chlorine isotopes in Phanerozoic evaporites. *Appl Geochem* 22:575–588
- Ericksen GE (1981) Geology and origin of the Chilean nitrate deposits. Professional Paper 1188. U.S. Geological Survey, Washington, DC
- Ericksen GE, Hosterman JW, Amand S (1988) Chemistry, mineralogy, and origin of the clay-hill nitrate deposits Amargosa River Valley, Death Valley region, California, U.S.A. *Chem Geol* 67:85–102
- Ewing SA, Sutter B, Owen J, Nishiizumi K, Sharp W, Cliff SS, Perry K, Dietrich W, McKay CP, Amundsen R (2006) A threshold in soil formation at Earth's arid-hyperarid transition. *Geochim Cosmochim Acta* 70:5293–5322
- Ewing SA, Michalski G, Thiemens M, Quinn RC, Macalady JL, Kohl S, Wankel SD, Kendall C, McKay CP, Amundson R (2007) The rainfall limit of the N cycle on earth. *Glob Biogeochem Cycles* 21:GB3009. doi:10.1029/2006GB002838
- Godon A, Jendrzewski N, Eggenkamp HGM, Banks DA, Ader M, Coleman ML, Pineau F (2004) An international cross calibration over a large range of chlorine isotope compositions. *Chem Geol* 207:1–12
- Green CT, Böhlke JK, Bekins B, Phillips S (2010) Mixing effects on apparent reaction rates and isotope fractionation factors during denitrification in a heterogeneous aquifer. *Water Resour Res* 46:W08525. doi:10.1029/2009WR008903: 1-19
- Gu B, Brown GM, Maya L, Lance MJ, Moyer BA (2001) Regeneration of perchlorate (ClO_4^-)-loaded anion exchange resins by novel tetrachloroferrate (FeCl_4^-) displacement technique. *Environ Sci Technol* 35:3363–3368
- Gu B, Brown GM, Chiang CC (2007) Treatment of perchlorate-contaminated groundwater using highly selective, regenerable ion-exchange technologies. *Environ Sci Technol* 41: 6277–6282
- Gu B, Böhlke JK, Sturchio NC, Hatzinger PB, Jackson WA, Beloso AD Jr, Heraty LJ, Bian Y, Brown GM (2011) Removal, recovery and fingerprinting of perchlorate by ion exchange processes. In: SenGupta AK (ed) Ion exchange and solvent extraction: a series of advances, vol 20. CRC, Boca Raton, FL
- Gullick RW, Barhorst TS, LeChevallier MW (2001) Occurrence of perchlorate in drinking water sources. *J Am Water Works Assoc* 93:66–77
- Hatzinger PB (2005) Perchlorate biodegradation for water treatment. *Environ Sci Technol* 39:239A–247A
- Hatzinger P, Böhlke JK, Sturchio NC, Gu B, Heraty LJ, Borden RC (2009) Fractionation of stable isotopes in perchlorate and nitrate during in situ biodegradation in a sandy aquifer. *Environ Chem* 6:44–52
- Hecht MH, Kounaves SP, Quinn RC, West SJ, Young SMM, Ming DW, Catling DC, Clark BC, Boynton WV, Hoffman J, DeFlores LP, Gospodinova K, Kapit J, Smith PH (2009) Detection of perchlorate and the soluble chemistry of Martian soil at the Phoenix Lander site. *Science* 325:64–67
- Hoefs J (2009) Stable isotope geochemistry, 6th edn. Springer, Berlin

- Hoering TC, Ishimori FT, McDonald HO (1958) The oxygen exchange between oxy-anions and water, 11. Chlorite, chlorate and perchlorate ions. *J Am Chem Soc* 80:3876
- Jackson WA, Anandam SK, Anderson T, Lehman T, Rainwater K, Rajagopalan S, Ridley M, Tock R (2005a) Perchlorate occurrence in the Texas southern high plains aquifer system. *Ground Water Monit Rem* 25:137–149
- Jackson WA, Preethi J, Laxman P, Tian K, Smith PN, Yu L, Anderson TA (2005b) Perchlorate accumulation in forage and edible vegetation. *J Agric Food Chem* 53:369–373
- Jackson WA, Böhlke JK, Gu B, Hatzinger PB, Sturchio NC (2010) Isotopic composition and origin of indigenous perchlorate and co-occurring nitrate in the southwestern United States. *Environ Sci Technol* 44:4869–4876
- Jaegle L, Yung YL, Toon GC, Sen B, Blavier J (1996) Balloon observations of organic and inorganic chlorine in the stratosphere: the role of HClO_4 production on sulfate aerosols. *Geophys Res Lett* 23:1749–1752
- Jiang S, Lin Y, Jiang H (2004) Improvement of the sample preparation method for AMS measurement of ^{36}Cl in natural environment. *Nucl Instr Meth Phys Res B* 223–224: 318–322
- Kang N, Jackson WA, Dasgupta PK, Anderson TA (2008) Perchlorate production by ozone oxidation of chloride in aqueous and dry systems. *Sci Total Environ* 405:301–309
- Kirk AB, Smith EE, Tian K, Anderson TA, Dasgupta PK (2003) Perchlorate in milk. *Environ Sci Technol* 37:4979–4981
- Kounaves SP, Stroble ST, Anderson RM, Moore Q, Catling DC, Douglas S, McKay CP, Ming DW, Smith PH, Tamppari LK, Zent AP (2010) Discovery of natural perchlorate in the Antarctic Dry Valleys and its global implications. *Environ Sci Technol* 44:2360–2364
- Lehman MF, Reichert P, Bernasconi SM, Barbieri A, McKenzie JA (2003) Modeling nitrogen and oxygen isotope fractionation during denitrification in a lacustrine redox-transition zone. *Geochim Cosmochim Acta* 67:2529–2542
- Lehmann BE, Davis SN, Fabryka-Martin JT (1993) Atmospheric and subsurface sources of stable and radioactive nuclides used for groundwater dating. *Water Resour Res* 29:2027–2040
- Long A, Eastoe CJ, Kaufmann RS, Martin JG, Wirt L, Finley JB (1993) High-precision measurement of chlorine stable isotope ratios. *Geochim Cosmochim Acta* 57:2907–2912
- Mariotti A, Simon B, Landreau A (1988) ^{15}N isotope biogeochemistry and natural denitrification process in groundwater: application to the chalk aquifer of northern France. *Geochim Cosmochim Acta* 52:1869–1878
- Michalski G, Böhlke JK, Thiemens M (2004) Long term atmospheric deposition as the source of nitrate and other salts in the Atacama Desert, Chile: new evidence from mass-independent oxygen isotopic compositions. *Geochim Cosmochim Acta* 68:4023–4038
- Miller MF (2002) Isotopic fractionation and the quantification of ^{17}O anomalies in the oxygen three-isotope system: an appraisal and geochemical significance. *Geochim Cosmochim Acta* 66:1881–1889
- Ming DW, Smith PH, Tamppari LK, Zent AP (2010) Discovery of natural perchlorate in the Antarctic Dry Valleys and its global implications. *Environ Sci Technol* 44:2360–2364
- NRC (2005) Committee to Assess the Health Implications of Perchlorate Ingestion, National Research Council. Health implications of perchlorate ingestion. National Academy, Washington, DC. <http://www.nap.edu/catalog/11202.html>
- Parker DR, Seyfferth AL, Reese BK (2008) Perchlorate in groundwater: a synoptic survey of “pristine” sites in the conterminous United States. *Environ Sci Technol* 42:1465–1471
- Phillips FM (2000) Chlorine-36. In: Cook P, Herczeg A (eds) *Environmental tracers in subsurface hydrology*. Kluwer, Boston, pp 299–348
- Plummer LN, Böhlke JK, Doughten MW (2006) Perchlorate in Pleistocene and Holocene groundwater in north-central New Mexico. *Environ Sci Technol* 40:1757–1763
- Rajagopalan S, Anderson TA, Fahlquist L, Rainwater KA, Ridley M, Jackson WA (2006) Widespread presence of naturally occurring perchlorate in high plains of Texas and New Mexico. *Environ Sci Technol* 40:3156–3162
- Rajagopalan S, Anderson TA, Cox S, Harvey G, Cheng Q, Jackson WA (2009) Perchlorate in wet deposition across North America. *Environ Sci Technol* 43:616–622
- Rao B, Anderson TA, Orris GJ, Rainwater KA, Rajagopalan S, Sandvig RM, Scanlon BR, Stonestrom DA, Walvoord MA, Jackson WA (2007) Widespread natural perchlorate in unsaturated zones of the Southwest United States. *Environ Sci Technol* 41:4522–4528
- Rao B, Anderson TA, Redder A, Jackson WA (2010) Perchlorate formation by ozone oxidation of aqueous chlorine/oxy-chlorine species: role of Cl_xO_y radicals. *Environ Sci Technol* 44:2961–2967
- Rech JA, Currie BS, Michalski G, Cowan AM (2006) Neogene climate change and uplift in the Atacama Desert, Chile. *Geology* 34:761–764
- Rech JA, Currie BS, Shullenberger ED, Dunagan SP, Jordan TE, Blanco N, Tomlinson AJ, Rowe HD, Houston J (2010) Evidence for the development of the Andean rain shadow from a Neogene isotopic record in the Atacama Desert, Chile. *Earth Planet Sci Lett* 292:371–382
- Sanchez CA, Crump KS, Krieger RL, Khandaker NR, Gibbs JP (2005) Perchlorate and nitrate in leafy vegetables of North America. *Environ Sci Technol* 39:9391–9397
- Sanchez CA, Krieger RL, Khandaker NR, Valentin-Blasini L, Blount BC (2006) Potential perchlorate exposure from citrus irrigated with contaminated water. *Anal Chim Acta* 567:33–38
- Schaeffer OA, Thompson SO, Lark NL (1960) Chlorine-36 radioactivity in rain. *J Geophys Res* 65:4013–4016
- Schumacher J (1960) Perchlorates: their properties, manufacture, and uses, American Chemical Society Monograph Series 146. Reinhold, New York
- Simonaitis R, Hecklen J (1975) Perchloric acid: possible sink for stratospheric chlorine. *Planet Space Sci* 23: 1567–1569
- Slaten S, Fields KA, Santos S, Barton A, Rectanus HV, Bhargava M (2010) Integrated environmental forensics approach for evaluating the extent of dissolved perchlorate originating from multiple sources. *Environ Forensics* 11:72–93
- Sturchio NC, Hatzinger PB, Arkins MD, Suh C, Heraty LJ (2003) Chlorine isotope fractionation during microbial reduction of perchlorate. *Environ Sci Technol* 37:3859–3863
- Sturchio NC, Böhlke JK, Gu B, Horita J, Brown GM, Beloso AD Jr, Hatzinger PB, Jackson WA, Batista JR (2006) Stable isotopic compositions of chlorine and oxygen in synthetic

- and natural perchlorates. In: Gu B, Coates JD (eds) *Perchlorate environmental occurrences, interactions, and treatment*. Springer, New York, pp 93–109
- Sturchio NC, Böhlke JK, Beloso AD Jr, Streger SH, Heraty LJ, Hatzinger PB (2007) Oxygen and chlorine isotopic fractionation during perchlorate biodegradation: laboratory results and implications for forensics and natural attenuation studies. *Environ Sci Technol* 41:2796–2802
- Sturchio NC, Beloso Jr AD, Heraty LJ, LeClaire J, Rolfe T, Manning KR (2008) Isotopic evidence for agricultural perchlorate in groundwater of the western Chino Basin, California. In: *Sixth international conference on remediation of chlorinated and recalcitrant compounds*, Monterey, CA, 18–22 May 2008
- Sturchio NC, Caffee MR, Beloso AD Jr, Heraty LJ, Böhlke JK, Gu B, Jackson WA, Hatzinger PB, Heikoop JR, Dale M (2009) Chlorine-36 as a tracer of perchlorate origin. *Environ Sci Technol* 43:6934–6938
- Sturchio NC, Hoaglund JR III, Marroquin RJ, Beloso Jr AD, Heraty LJ, Bortz SE, Patterson TL (2011) Isotopic mapping of groundwater perchlorate plumes. *Ground Water*. DOI:10.1111/j.1745-6584.2011.00802.x
- Synal HA, Beer J, Bonani G, Suter M, Wölfli W (1990) Atmospheric transport of bomb-produced ^{36}Cl . *Nucl Meth Instr Phys Res B* 52:483–488
- Thiemens MH (2006) History and applications of mass-independent isotope effects. *Annu Rev Earth Planet Sci* 34:217–262

Chapter 23

The Isotopomers of Nitrous Oxide: Analytical Considerations and Application to Resolution of Microbial Production Pathways

Nathaniel E. Ostrom and Peggy H. Ostrom

Abstract Nitrous oxide (N_2O) is an important greenhouse gas and the most important substance involved in ozone depletion. The N_2O molecule consists of two N atoms that differ in the nature of their covalent bonds and consequently tend to acquire distinct isotopic compositions. Thus, N_2O contains both bulk ($\delta^{15}\text{N}$ and $\delta^{18}\text{O}$) and site specific isotopic information. Site preference (SP) is defined as the difference in $\delta^{15}\text{N}$ between the central (α) and outer (β) N atoms in N_2O . SP has emerged as a potential conservative tracer of microbial N_2O production because (1) it is independent of the isotopologue composition of the substrates of nitrification and denitrification and (2) does not exhibit fractionation during production. In pure microbial culture distinct SP values for N_2O production from bacterial denitrification, including nitrifier denitrification (-10 to 0 ‰), relative to hydroxylamine oxidation and fungal denitrification (33 – 37 ‰) provides a basis to resolve production pathways in the natural environment. Future directions for isotopomer research include (1) improvements in calibration and mass overlap corrections, (2) evaluation of SP signals of microbial production pathways not yet studied including heterotrophic nitrification, codenitrification, and dissimilatory reduction of nitrate to ammonium, and (3) evaluation of the potential for biological production to produce a ^{17}O anomaly in atmospheric N_2O .

23.1 Introduction

Nitrous oxide (N_2O) is a long lived greenhouse gas that is also involved in ozone depletion. Although the atmospheric abundance of N_2O is approximately one thousandth that of CO_2 , relative to CO_2 its radiative efficiency ($\text{Wm}^{-2} \text{ppb}^{-1}$) is 216 times greater. Thus, the contribution of N_2O to atmospheric global warming is substantial (6 %) (Forster et al. 2007). Currently N_2O is the most important ozone depleting substance emitted by human activity but it is not regulated by the Montreal protocol (Ravishankara et al. 2009). The fact that N_2O production is strongly linked to fertilizer application has important implications for management of emissions of this gas (Forster et al. 2007). With expectations of an increase in human population from a current estimate of 7–9 billion by 2050 and the associated escalation in fertilizer production, N_2O emissions are anticipated to rise (Mosier and Kroeze 2000; Tilman et al. 2001; Galloway et al. 2003). While there is compelling need to reduce emissions, we are unable to achieve a lower atmospheric N_2O concentrations simply by controlling anthropogenic sources as the majority of N_2O is not directly derived from human activity. Rather microbial activity produces N_2O and is stimulated upon disturbance of soils, fertilizer application and nitrogen loading to aquatic ecosystems (Seitzinger et al. 2006; Groffman et al. 2006; Forster et al. 2007). Consequently, mitigation of N_2O emissions will not only be dependent upon reducing fertilizer use but also dependent upon measures that regulate microbial activities associated with N_2O production.

Identifying the microbial origin of N_2O in soils and aquatic environments is a long-standing research objective that has remained surprisingly elusive

N. E. Ostrom (✉) and P. H. Ostrom
Department of Zoology, Michigan State University, 204 Natural Sciences Building, East Lansing, MI 48824, USA
e-mail: ostromn@msu.edu

(Mosier et al. 1998a, b; Robertson et al. 2004; Naqvi et al. 2006). A focal point of this objective has been the determination of the importance of nitrification and denitrification in the production of this gas. Nitrification involves oxidation of ammonium to nitrite and/or nitrate in the presence of oxygen. During this process, N_2O is formed as a byproduct of hydroxylamine oxidation. When oxygen is limiting, denitrification invokes the successive reduction of nitrate, nitrite, nitric oxide, and N_2O with dinitrogen gas (N_2) as the most common final product (Firestone and Davidson 1989). Owing to the sensitivity of these reactions to oxygen, the activity of nitrifiers and denitrifiers varies in response to different environmental controls such as changes in pH and the concentration of nitrate and organic carbon (Robertson and Groffman 2006). Thus, microbial controls of N_2O production are expected to depend on management strategies that impact the soil and water environments (Matson et al. 1989; Seitzinger et al. 2006). However, managing soil N_2O emissions is not as simple as regulating nitrification and denitrification. Additional transformation pathways are influential. Nitrifying bacteria produce N_2O by two pathways, hydroxylamine oxidation and reduction of nitrite (Wrage et al. 2001; Fig. 23.1), there is increasing awareness that fungal denitrification is an important mechanism of N_2O production in soils (Laughlin and Stevens 2002; Crenshaw et al. 2008) and other

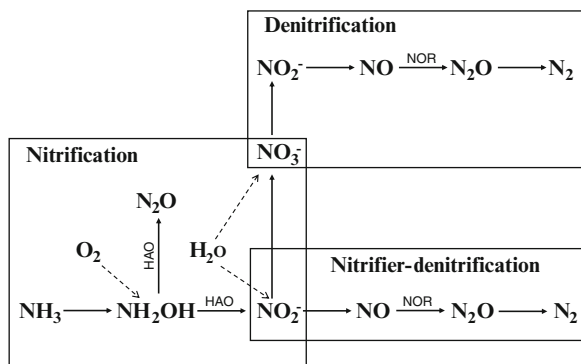


Fig. 23.1 Diagram of microbial N cycling showing pathways leading to N_2O production. The enzyme hydroxylamine oxidoreductase (HAO) is involved in the oxidation of ammonia to hydroxylamine and N_2O with the incorporation of an O atom from O_2 . Nitrous oxide reductase (NOR) is involved in the reduction of nitric oxide to N_2O in both nitrifier-denitrification and denitrification and involves addition of O from water. Adapted from Wrage et al. (2001)

nitrogen cycling pathways such as heterotrophic nitrification, dissimilatory reduction of nitrate to ammonia (DRNA) and anaerobic ammonium oxidation (anammox) may contribute to N_2O production (Scott et al. 2008; Wrage et al. 2001; Kampschreur et al. 2008).

Traditional approaches for apportioning N_2O production to nitrification and denitrification include acetylene inhibition and/or isotope labeling approaches that inherently alter microbial activity (Madsen 1998; Groffman et al. 2006). Acetylene inhibition or ^{15}N tracer approaches have been widely used in both soil and aquatic environments (Groffman et al. 2006). The use of acetylene to define specific production pathways can be problematic owing to the potential for (1) incomplete diffusion of acetylene into the soil and incomplete inhibition of N_2O reduction, (2) alteration of microbial activity as acetylene is a metabolizable source of carbon, (3) inhibition of nitrification and its associated supply of nitrate, and (4) production of N_2O from novel pathways such as fungal denitrification and codenitrification that may not respond to inhibitors (Madsen 1998; Groffman et al. 2006; Wrage et al. 2004, 2005; Laughlin and Stevens 2002; Crenshaw et al. 2008). As a result, there is a strong desire to avoid the use of acetylene and other inhibitors in N cycling studies (Wrage et al. 2004, 2005; Groffman et al. 2006). Application of ^{15}N enriched nitrate or ammonium is a common approach to evaluate N_2O production from nitrification and denitrification, however, this approach may be susceptible to incomplete diffusion of the tracer and stimulation of activity by the addition of the ^{15}N enriched substrates (Groffman et al. 2006). Consequently the challenges to resolving the microbial origins of N_2O are considerable and isotopologue data offer important advantages in the determination of production pathways relative to inhibitor and tracer studies. These include a lack of concern regarding incomplete diffusion of tracers or inhibitors, lack of alteration of microbial activity due to the addition of tracers or inhibitors, and an ability to apply results across broad temporal and spatial scales that is rarely feasible using incubation approaches.

In 1999 two research groups argued that the analysis of the intramolecular distribution of ^{15}N in N_2O could offer additional information regarding the origins of this greenhouse gas relative to the bulk isotope measurements $\delta^{15}N$ and $\delta^{18}O$ (Toyoda and Yoshida

1999; Brenninkmeijer and Röckman 2000; Yoshida and Toyoda 2000). Consequently, distinct terminology is needed to distinguish changes in the average isotopic composition of the N_2O molecule from isotopic variation that is positional dependent. We use the term “isotopomer” to indicate molecules of the same mass in which trace isotopes are arranged differently. “Isotopologue” is a more general term that indicates molecules that differ in their isotopic composition. The N atoms in N_2O have distinct covalent bonds with a central N atom bonded to the terminal N and O atoms. The central and outer N atoms are termed α and β , respectively (Toyoda and Yoshida 1999) or 2 and 1, respectively (Brenninkmeijer and Röckman 2000). Alternatively, Yung and Miller (1997) designate the isotopomers $^{15}\text{N}^{14}\text{N}^{16}\text{O}$ and $^{14}\text{N}^{15}\text{N}^{16}\text{O}$ as 546 and 456. In this chapter, we utilize the α and β terminology as it is common in the biological literature. As the nature of covalent bonds between the α and β positions in N_2O differ there is ample opportunity for equilibrium, photochemical and biological isotope effects. As a result ^{15}N becomes unevenly distributed between the two N atoms within the N_2O molecule (Miller and Yung 2000; Sutka et al. 2006). Consequently, the N_2O molecule contains positional dependent ($\delta^{15}\text{N}^\alpha$ and $\delta^{15}\text{N}^\beta$) in addition to bulk isotopic information $\delta^{15}\text{N}$ and $\delta^{18}\text{O}$. Positional dependent isotope values of N_2O are commonly expressed as site preference (SP) which is the difference in $\delta^{15}\text{N}$ between the α and β positions.

23.2 Analytical Methods

23.2.1 Gas Purification and Mass Spectrometry

The primary instrument used for determining the bulk and positional dependent isotope values of N_2O is the magnetic sector isotope ratio mass spectrometer equipped with 3–5 detectors (collectors). These instruments are commercially available and commonly have one narrow center and two wide axial collectors that enable analysis of the isotopic composition of CO_2 , N_2 and O_2 . Because analysis of the bulk $\delta^{15}\text{N}$ and $\delta^{18}\text{O}$ of N_2O requires monitoring of the same masses as CO_2 (44, 45 and 46 amu), it is

readily accomplished without modification to commercial instruments. A primary challenge for isotopic analysis of N_2O is its low concentration in the atmosphere, 319 ppv (as of 2007; Forster et al. 2007). In comparison, the atmospheric concentration of CO_2 is 1,000 times greater. Because of its low concentration, analysis of the isotope composition of N_2O often required extraction of N_2O from large volumes of air or water. For example, Yoshida and Matsuo (1983) concentrated N_2O from 60 L of air onto molecular sieve 5A. This approach also required the removal of water and CO_2 via a 6 m trap of drierite and a 3 m trap consisting of ascarite, respectively. N_2O was extracted from the molecular sieve by heating and cryogenic purification under vacuum. Quantitative removal of CO_2 is particularly critical owing to the mass overlap with N_2O . Similarly, early analyses of ocean water were accomplished by extracting N_2O from 100 L of seawater using a large stainless steel tank provided from Asahi Breweries, Ltd. (Yoshida et al. 1984).

The use of a gas chromatograph interface to the mass spectrometer has greatly decreased the minimum sample size required for isotope analysis of N_2O . An early approach used vacuum to pass 500 mL of air through ascarite and LiOH traps for removal of CO_2 and water, respectively, and then through a liquid N_2 cooled trap where N_2O was concentrated. Non-condensable gases passed through these traps and were removed by vacuum. The purified N_2O was thawed and separated from remaining traces of CO_2 using a GS-Q gas chromatographic column (J&W Scientific, Inc.) prior to introduction to a mass spectrometer (Bergsma et al. 2001). This approach enabled analysis of samples containing as little as 5 nmol of N_2O . Commercial gas chromatographic systems are currently available from both Elementar Inc. (TraceGas) and Thermo Scientific Inc. (Precon) that transfer the sample to a cryogenic trap via He flow instead of vacuum, utilize a cryofocusing step to further increase sensitivity by approximately a factor of 5, and a gas chromatographic column such as Porapak Q to isolate N_2O from any remaining gases (Brand 1995; Sutka et al. 2003; Röckmann et al. 2003). Röckmann et al. (2003) observed several peaks that eluted well after N_2O and minimized these peaks by optimizing temperature and the column flow rate. Despite this, long eluting peaks carried over from one analysis into the next.

This phenomenon was eliminated by use of a switching valve and by splitting the GC column into pre- and analytical columns. Alternatively, long eluting peaks have been eliminated by preconditioning the column at high temperature (200°C) for several hours after each day of analysis (personal observation).

Estimates of bulk and positional isotope values require monitoring the molecular ion of N_2O^+ with collectors position at m/z 44, 45 and 46 as well as the fragment ion, NO^+ , with collectors positioned at m/z 30 and 31. This enables subsequent determination of ^NR , the ratio of the trace to abundant isotope in which N is the mass of the trace isotope (e.g. the m/z ratios 45/44, 46/44 and 31/30 are denoted ^{45}R , ^{46}R and ^{31}R , respectively). As will be discussed below these ratios are required for determination of bulk and positional isotope values. Although the use of fragment ions in stable isotope analysis was pioneered over 60 years ago, it was not applied to natural samples until the late 1990s (Friedman and Bigeleisen 1950; Brenninkenmeijer and Röckman 2000; Toyoda and Yoshida 1999; Yoshida and Toyoda 2000). Analysis of the five m/z values required for obtaining N_2O isotope values can be conducted on a traditional isotope ratio mass spectrometer with three collectors. The sample, however, must be analyzed twice; initially for ^{45}R and ^{46}R and secondly for ^{31}R . It is now common for instruments to be constructed with five collectors for the simultaneous monitoring of m/z 30, 31, 44, 45 and 46 (Brenninkenmeijer and Röckman 2000; Toyoda and Yoshida 1999; Sutka et al. 2003).

23.2.2 Determining Bulk and Positional Isotope Values

Bulk isotope values are expressed as:

$$\delta^N\text{E} = \left(\left[\frac{^N\text{R}_{\text{sample}}}{^N\text{R}_{\text{standard}}} \right] - 1 \right) \times 1,000 \quad (23.1)$$

$\text{R}_{\text{standard}}$ is V-SMOW and air- N_2 for $\delta^{18}\text{O}$ and $\delta^{15}\text{N}$, respectively. Bulk isotope values derive from the analysis of m/z 44, 45, and 46 associated with the molecular ion, N_2O^+ . $\delta^{15}\text{N}^\alpha$ and $\delta^{15}\text{N}^\beta$ are derived from a series of (23.2)–(23.7) and also require analysis of the fragment ion NO^+ at m/z 30 and 31. Owing to the complexity of the topic, a complete explanation of

the equations required for estimating bulk and positional isotope values is beyond the scope of this chapter. Thus, we provide a foundation with brief explanations of the equations below and refer the reader to Toyoda and Yoshida (1999), Kaiser et al. (2004a) and Westley et al. (2007) where a more expansive discussion can be found.

Determination of the $\delta^{15}\text{N}$, $\delta^{18}\text{O}$, $\delta^{15}\text{N}^\alpha$ and $\delta^{15}\text{N}^\beta$ of N_2O requires an estimate of ^{15}R , $^{15}\text{R}^\alpha$, ^{17}R and ^{18}R that are ultimately derived from analysis of the molecular and fragmentation ions, N_2O^+ and NO^+ . The two stable isotopes of N and three stable isotopes of O in N_2O can combine to produce 12 possible isotopomers (Miller and Yung 2000). Of these, eight isotopomers have m/z values of 44, 45, or 46 and can, therefore, be detected within a triple collector mass spectrometer:

$^{14}\text{N}^{14}\text{N}^{16}\text{O}$	m/z 44
$^{15}\text{N}^{14}\text{N}^{16}\text{O}$	m/z 45
$^{14}\text{N}^{15}\text{N}^{16}\text{O}$	m/z 45
$^{14}\text{N}^{14}\text{N}^{17}\text{O}$	m/z 45
$^{14}\text{N}^{14}\text{N}^{18}\text{O}$	m/z 46
$^{14}\text{N}^{15}\text{N}^{17}\text{O}$	m/z 46
$^{15}\text{N}^{14}\text{N}^{17}\text{O}$	m/z 46
$^{15}\text{N}^{15}\text{N}^{16}\text{O}$	m/z 46

The isotopomers of the fragment ion NO^+ are with m/z values of 30 and 31 are:

$^{14}\text{N}^{16}\text{O}$	m/z 30
$^{15}\text{N}^{16}\text{O}$	m/z 31
$^{14}\text{N}^{17}\text{O}$	m/z 31

In the isotopologue analysis of N_2O m/z 30, 31, 44, 45 and 46 are monitored and therefore the isotopomers shown above will contribute to these collectors. Additional collectors can be added however, isotopomers beyond m/z 32 and 46 for NO^+ and N_2O^+ , respectively, are exceedingly rare and mass 32 suffers from interference from trace levels of O_2 in the mass spectrometer. The goal of monitoring these m/z is to determine ^{15}R , $^{15}\text{R}^\alpha$, $^{15}\text{R}^\beta$ and ^{18}R . As shown above, however, ^{15}R cannot be obtained directly from the ratio of m/z 45 to m/z 44 (^{45}R) because m/z 45 also receives a contribution from the $^{14}\text{N}^{14}\text{N}^{17}\text{O}$ isotopomer. Thus an expression for ^{45}R is:

$$^{45}\text{R} = ^{15}\text{R} + ^{17}\text{R} \quad (23.2)$$

where

$$^{15}\text{R} = (^{15}\text{R}^\alpha + ^{15}\text{R}^\beta)/2 \quad (23.3)$$

Traditional mass spectrometric analysis with three collectors at m/z 44, 45 and 46 can only determine ^{15}R , which (23.3) indicates is the average of $^{15}\text{R}^\alpha + ^{15}\text{R}^\beta$. Thus only bulk $\delta^{15}\text{N}$ can be determined from m/z 44, 45 and 46. Positional isotope abundances require additional monitoring of m/z 30 and 31 as it is the ratio of these masses that contains N from the α position only.

The predominant isotopomer that contributes to m/z 46 is $^{14}\text{N}^{14}\text{N}^{18}\text{O}$. However, m/z 46 also receives a contribution from $^{14}\text{N}^{15}\text{N}^{17}\text{O}$, $^{15}\text{N}^{14}\text{N}^{17}\text{O}$, and $^{15}\text{N}^{15}\text{N}^{16}\text{O}$. Although the probability of N_2O^+ containing two trace isotopes is small, these isotopomers are sufficiently abundant that they cannot be ignored. Consequently, ^{46}R is described as:

$$^{46}\text{R} = ^{18}\text{R} + (^{15}\text{R}^\alpha + ^{15}\text{R}^\beta) * ^{17}\text{R} + ^{15}\text{R}^\alpha + ^{15}\text{R}^\beta \quad (23.4)$$

$\delta^{15}\text{N}^\alpha$ is obtained from the 31 to 30 ion current ratio with a correction for interference from ^{17}O . $\delta^{15}\text{N}$ is the average of $\delta^{15}\text{N}^\alpha$ and $\delta^{15}\text{N}^\beta$ and $\delta^{15}\text{N}^\beta$ is determined by difference. $\delta^{18}\text{O}$ is obtained from the 46:44 ion current ratio. ^{31}R reflects contributions of ^{15}N from the α position and ^{17}O :

$$^{31}\text{R} = ^{15}\text{R}^\alpha + ^{17}\text{R} \quad (23.5)$$

Equations (23.2) through (23.4) are robust given a random or statistical isotope distribution of the N and O isotopes in N_2O . In other words, the presence of one trace isotope does not increase or decrease the probability of the occurrence of a second trace isotope. Theoretical and experimental measurements support this contention (Röckmann et al. 2003; Kaiser et al. 2003); however as we discuss later, this assumption does not extend to the fragmentation and rearrangement processes.

Equations (23.2) and (23.4) can be solved numerically with the assumption of a mass-dependent relationship between $\delta^{17}\text{O}$ and $\delta^{18}\text{O}$ as described by Santrock et al. (1985):

$$\delta^{17}\text{O} = 0.516 * \delta^{18}\text{O} \quad (23.6)$$

Or as presented in Kaiser et al. (2003):

$$^{17}\text{R} = 0.00937035 (^{18}\text{R})^{0.516} \quad (23.7)$$

The mass-dependent relationship between the oxygen isotopes is the fundamental basis for the widely used correction for the overlap of the $^{12}\text{C}^{16}\text{O}^{17}\text{O}$ isotopomer with $^{13}\text{C}^{16}\text{O}^{16}\text{O}$ in determination of $\delta^{13}\text{C}$ that was initially developed by Harmon Craig and has been followed with more recent improvements (Craig 1957; Santrock et al. 1985; Kaiser 2008; Kaiser and Röckmann 2008; Brand et al. 2010). Indeed a simple correction for the interference of ^{17}O with the $\delta^{15}\text{N}$ of N_2O was proposed by Brand (1995) which simply involved applying the CO_2 correction to N_2O multiplied by 0.75. This is convenient as most commercial mass spectrometers are provided with software that includes mass dependent corrections for the $\delta^{13}\text{C}$ of CO_2 but not for N_2O .

23.2.3 Mass-Dependence Between $\delta^{17}\text{O}$ and $\delta^{18}\text{O}$

While the mass dependent relationship between $\delta^{17}\text{O}$ and $\delta^{18}\text{O}$ is robust for the majority of materials on Earth, photochemical reactions in the atmosphere may alter the slope of (23.6) markedly (Thiemens 2006). Most notable is stratospheric ozone that exhibits a $\delta^{17}\text{O}$ to $\delta^{18}\text{O}$ relationship of approximately 0.62 (Lammerzahl et al. 2002). Further, the precise value of the slope for materials on Earth may vary from 0.5000 to 0.5305 (Matsuhisa et al. 1978; Assonov and Brenninkmeijer 2001). The $\delta^{17}\text{O}$ of N_2O is infrequently determined directly and, consequently, corrections for mass overlap depend strongly on the assumption of the mass-dependent relationship between $\delta^{17}\text{O}$ and $\delta^{18}\text{O}$. Tropospheric N_2O , however, is slightly enriched in ^{17}O relative to the mass-dependent line by approximately 0.9 ‰ (Cliff et al. 1999; Cliff and Thiemens 1997; Kaiser et al. 2003, 2004b). As we discuss later, the precise cause of the ^{17}O anomaly in tropospheric N_2O is not known and may reflect an influence from photochemical reactions and/or, possibly, biological production (Kaiser et al. 2004b). At current values of precision commonly obtained in mass spectrometric analysis of N_2O (~0.1–1 ‰) any error introduced to the mass interference correction from the ^{17}O isotopomer at m/z 45 is minor; 0.1 ‰ or less (Toyoda and Yoshida 1999).

Accurate determination of both $\delta^{17}\text{O}$ and $\delta^{18}\text{O}$ values of N_2O is not possible by analysis of the N_2O^+ and NO^+ ions owing to mass overlap and

requires decomposition of N₂O to O₂. One approach for decomposition includes high temperature decomposition of N₂O to both O₂ and N₂ in the presence of a gold catalyst followed by cryogenic purification of each product (Cliff and Thiemens 1994) or under He flow (Kaiser et al. 2007). Alternatively N₂O can be decomposed to O₂ at high temperature in the presence of BrF₅ (Brenninkmeijer and Röckman 2000). While both of these approaches can be used to accurately constrain the presence or absence of a ¹⁷O anomaly, any site specific δ¹⁵N data will be lost.

23.2.4 Isotope Rearrangement

A unique challenge to the isotopic analysis of N₂O is the rearrangement or scrambling of N atoms in the NO⁺ fragment between the α and β positions during ionization. Scrambling was first observed by Friedman and Bigeleisen (1950) and has since been verified in a number of studies based on the analysis of N₂O enriched in ¹⁵N in either the α or β position. These studies have shown that between 7 and 11.7 % of α N atoms may be found in the β position (Friedman and Bigeleisen 1950; Brenninkmeijer and Röckman 2000; Toyoda and Yoshida 1999; Sutka et al. 2004; Westley et al. 2007). The precise causes of scrambling are not certain as the NO⁺ ion may be formed by several pathways from an excited N₂O⁺ molecule. These include collision induced decomposition and decay of metastable ions in transit from the source to collectors (Mark et al. 1981; Westley et al. 2007). As these processes are affected by source conditions (such as acceleration voltage) and are instrument dependent, it is strongly recommended that the degree of scrambling or rearrangement factor be determined on a regular basis and whenever source conditions change markedly (such as filament replacement) (Westley et al. 2007). Nonetheless, the rearrangement factor, γ, is stable under routine operating conditions and provides a basis to correct the observed value for ¹⁵R^α for rearrangement (Toyoda and Yoshida 1999):

$$^{15}\text{R}_{\text{obs}}^{\alpha} = (1 - \gamma)^{15}\text{R}^{\alpha} + \gamma^{15}\text{R}^{\beta} \quad (23.8)$$

In addition to (23.4), (23.5) can be solved to correct ¹⁵R^α for the contribution from ¹⁷O. However, early

correction routines involved two critical assumptions: (1) that different isotopomers of N₂O produce the NO⁺ fragment ion at equal rates and (2) that the fraction of NO⁺ produced from ionization of ¹⁵N¹⁴N¹⁶O is identical to that produced upon ionization of ¹⁴N¹⁴N¹⁶O (Toyoda and Yoshida 1999; Kaiser et al. 2004a). Both of these assumptions have recently been shown to be incorrect (Westley et al. 2007). Differences in bond strength and differences in zero point energies between molecules with and without a trace isotope are the fundamental controls on isotope fractionation. Consequently, it is not surprising that ¹⁵N¹⁴N¹⁶O and ¹⁴N¹⁴N¹⁶O would cleave to produce the NO⁺ fragment at different rates. The mass correction and calibration routine developed by Kaiser et al. (2004a) involved mixtures of isotopically enriched N₂O with a natural abundance standard and was based on the assumption that ¹⁵N¹⁵N¹⁶O yields ¹⁵N¹⁶O at that same rate that ¹⁴N¹⁶O is produced from ¹⁴N¹⁴N¹⁶O. This has been shown to be invalid and calibration based on this assumption yields different results for the same gas analyzed by different mass spectrometers (Westley et al. 2007). The assumption of equal fragmentation rates for different isotopomers in calibration is the likely reason for the nearly 30 ‰ difference in SP reported for tropospheric N₂O by two research groups (Toyoda and Yoshida 1999; Yoshida and Toyoda 2000; Kaiser et al. 2004a). In contrast to mixtures of ¹⁵N enriched and natural abundance standards, calibrations based on the thermal decomposition of ammonium nitrate to produced N₂O are robust (Westley et al. 2007). In thermal decomposition, nitrate and ammonium contribute uniquely to the α and β positions in N₂O, respectively with small and symmetrical fractionation effects (Friedman and Bigeleisen 1950; Toyoda and Yoshida 1999; Westley et al. 2007).

23.2.5 Spectroscopic Analysis of N₂O Isotopomers

An important advantage of spectroscopic approaches in N₂O isotopomer analysis relative to mass spectrometry is that the absorption spectra of each isotopomer are unique and consist of distinct spectral lines such that mass overlap is less of a concern. Thus spectroscopic data provides a truly independent approach to

mass spectrometry. Spectroscopic measurements of N₂O isotopologues in environmental samples are relatively rare (Wahlen and Yoshinari 1985; Yoshinari and Wahlen 1985; Esler et al. 2000; Pérez et al. 2001; Griffith et al. 2000; Turatti et al. 2000). This likely reflects the considerable challenges of spectroscopic approaches for obtaining isotopomer data on N₂O at near atmospheric abundances of approximately 319 ppbv (as of 2007; Forster et al. 2007).

Wahlen and Yoshinari (1985) and Yoshinari and Wahlen (1985) determined the $\delta^{18}\text{O}$ of N₂O in wastewater treatment plants using a high resolution infrared tunable diode laser with a precision better than 1 ‰ for concentrations from ambient to 50 ppmv. Recently, Picarro Instruments (www.picarro.com) reported precision better than 1 ‰ for both $\delta^{15}\text{N}$ and $\delta^{18}\text{O}$ using a cavity ring down spectroscopic instrument with an effective cell path length of 20 km. Determination of site specific isotope values in N₂O have, thus far, been restricted to Fourier Transform Infrared (FT-IR) spectroscopy which may reflect the challenge and time consuming nature of the measurement (Esler et al. 2000; Pérez et al. 2001; Griffith et al. 2000; Turatti et al. 2000). With continued improvements in design broader application of spectroscopic instruments in isotopomer studies will undoubtedly increase. Spectroscopic measurements have proven quite useful in the calibration of internal laboratory standards and in providing accurate data on the SP of tropospheric N₂O (Toyoda and Yoshida 1999; Röckmann et al. 2003; Griffith et al. 2009).

23.2.6 Recommendations for Calibration and Mass Interference Corrections

At the present time, the most accurate approach for calibration and mass overlap corrections of N₂O isotopomers is presented in Westley et al. (2007). Calibration using mixtures of isotopically enriched and natural abundance N₂O standards has not proven successful; however, this approach is essential for determination of the scrambling or rearrangement factor. As the rearrangement factor is dependent upon source conditions it needs to be determined for each instrument and after significant changes to the mass spectrometer ion source (e.g. cleaning and filament

replacement). The isotopomer research community suffers from the lack of an international isotopically characterized N₂O standard. Internal laboratory standards may best be calibrated by thermal decomposition of ammonium nitrate for which the $\delta^{15}\text{N}$ of the ammonium and nitrate are determined by independent approaches (Toyoda and Yoshida 1999; Westley et al. 2007). There is a compelling need for the research community to develop a standard that could be made available from an international agency such as the IAEA.

Recent efforts support a SP of tropospheric N₂O of 18.7 ± 2.2 ‰ (Toyoda and Yoshida 1999; Westley et al. 2007) which is consistent with that obtained by FTIR of 19.8 ± 2.1 ‰ (Griffith et al. 2009). Consequently, all laboratories can analyze the SP of tropospheric N₂O to validate calibrations. Mass interference corrections will undoubtedly continue to be revised. For example, in their corrections, Westley et al. (2007) assumed that $^{14}\text{N}^{14}\text{N}^{17}\text{O}$ has the same rate of fragmentation within the ion source as $^{14}\text{N}^{14}\text{N}^{16}\text{O}$. Yet, they demonstrated that this assumption is not valid for other isotopomers. The impact of this assumption is likely negligible at present levels of precision but could become important in high precision applications or if the sample of N₂O analyzed was far from mass dependence. As the mass interference corrections are not trivial and likely to evolve there is value in using common methods for these corrections (e.g. a downloadable spreadsheet). Similar spreadsheets are currently available for download from the IAEA for spectroscopic analysis of the isotopic composition of waters (<http://www-naweb.iaea.org/napc/ih/index.html>). Because correction routines are complex and changing there may be a need to publish (at least electronically) raw ion current ratios (^{31}R , ^{45}R , and ^{46}R) as well as the isotopomer values of the internal laboratory standard used to enable future revisions of mass interference corrections to be applied to existing data.

A regrettable outcome of the use of mixtures of ^{15}N enriched and natural abundance N₂O for calibration has been the publication of SP values that cannot be considered accurate. These include not only the SP values for tropospheric N₂O but for other natural samples. A simple offset correction cannot be used because the approach based on mixtures of ^{15}N enriched and natural abundance standards will yield different results for the same gas analyzed on different mass spectrometers (Westley et al. 2007).

Consequently, the reader needs to verify the calibration protocol before referencing specific SP values; especially for studies prior to the publication of Westley et al. (2007). It may be possible for the authors of earlier papers to publish corrected values.

23.3 Application of Isotopomers to Resolve Biological Production Pathways

23.3.1 Overview

The isotopologue composition of any material records two kinds of information: its origin and/or process of formation. The former is dependent upon a unique isotopologue signature for the material that is retained during transport or transformation in the environment. This is considered conservative behavior. Non-conservative behavior occurs with isotopic fractionation; the tendency for a molecule with the light isotope to react at a faster rate than the same molecule retaining the heavy isotope. In general, the behaviors of molecules that contain the isotopes of nitrogen are rarely conservative. This is a consequence of (1) the wide range of valence states characteristic of this element and the associated wide range of covalent bonds that can be formed and (2) the fact that N is intimately involved in a large number of different biological reactions and is often a limiting nutrient to primary production and metabolism. In rare circumstances, isotopologue values may retain both source and process information (e.g. Ostrom et al. 2002), but most often source information is lost once fractionation occurs. The behavior of the isotopologies of N₂O is no exception. The observation, however, that during its production in pure culture SP (1) is independent of the substrate's isotopic composition and (2) is constant during the course of production even when $\delta^{15}\text{N}$ and $\delta^{18}\text{O}$ changes markedly, provides strong support for the use of SP as a conservative tracer (Sutka et al. 2003, 2006, 2008; Toyoda et al. 2005). In the remainder of this review, we will discuss the application of isotopologues to resolve microbial N₂O production pathways and how both conservative and non-conservative behavior strengthen or limit interpretations of its origins and processes of formation.

23.3.2 Non-Conservative Behavior of the $\delta^{15}\text{N}$ of N₂O: An Example from Fungal Denitrification

A challenge to the application of bulk isotopes values to resolve origins of N₂O is the wide range of fractionation factors that are associated with production from different pathways. In this paper, we describe fractionation factors as constants that are specific to a single reaction or reaction step. We follow the convention of Mariotti et al. (1981) by defining the magnitude of isotopic fractionation during a single unidirectional reaction as the fractionation factor α ,

$$\alpha = k_2/k_1 \quad (23.9)$$

where k_1 and k_2 are the reaction rates for the light and heavy isotopically substituted compounds, respectively (although some authors use the inverse of this ratio). We further define an isotopic enrichment factor, ε :

$$\varepsilon = (\alpha - 1) * 1,000 \quad (23.10)$$

The value ε is convenient because it is approximately equal to the difference in the isotopic composition of the substrate (δ_s) and product (δ_p) or Δ at any point during the reaction:

$$\varepsilon \approx \Delta = \delta_s - \delta_p \quad (23.11)$$

Values for ε during production of N₂O from nitrification and denitrification vary between -45 and -111 ‰ for nitrification and -13 and -45 ‰ for denitrification (Yoshida 1988; Barford et al. 1999; Pérez et al. 2006). As we explain below, variable isotopic enrichment factors are a consequence of processes in which isotope fractionation may occur at multiple steps. Denitrification, for example, consists of a series of steps that involves diffusion of nitrate into the cell followed by the sequential reduction of nitrate to nitrite to nitric oxide to N₂O and finally N₂ (Davidson 1993). Each step in the denitrification reaction sequence is undoubtedly associated with a unique and constant fractionation factor. Although fractionation occurs at multiple points, it is common to describe fractionation as the difference in the isotope value of the substrate and product (e.g. difference in $\delta^{15}\text{N}$ between nitrate and N₂). This “observed” fractionation is the net

effect of several isotope effects (several cases of fractionation) whose relative importance may vary depending upon environmental conditions. For this reason, we prefer to describe fractionation factors in biological reactions as net isotope effects (NIE) and replace ϵ with η . Following this practice, ϵ is a constant specific to fractionation for a single reaction whereas η is the NIE. We explore this concept below using production of N_2O by fungal denitrification as an example.

Fractionation factors can be determined from a Rayleigh distillation equation that describes fractionation as a function of changes in the abundance and isotopic composition of the substrate and product for a uni-directional reaction within a closed system. The Rayleigh distillation equation has been written in numerous forms, e.g. (23.13), and is amenable to data of Sutka et al. (2008) on N_2O production by fungal denitrification because it allows η to be expressed as a function of the isotopic composition of the accumulating product. This form of the Rayleigh equation is:

$$\delta^{15}N_p = \delta^{15}N_{so} - \eta_{p/s} \left[\frac{f \ln f}{(1-f)} \right] \quad (23.12)$$

where f is defined as the fraction of substrate (NO_2^-) remaining (determined as the ratio of the calculated NO_2^- concentration at any point in time divided by the initial concentration), $\eta_{p/s}$ is the NIE for any substrate (s) converted to a product (p), and (so) refers to the substrate prior to initiation of the reaction (Mariotti et al. 1982). When (23.12) is plotted in coordinates of $-\frac{f \ln f}{1-f}$ vs. $(\delta^{15}N_p - \delta^{15}N_{so})$ the slope of a linear regression equation equates to $\eta_{p/s}$ (Fig. 23.2). Values of η for the change in $\delta^{15}N$ during fungal denitrification are not constant and range from -6.6 to -74.7 ‰ across separate cultures and species (Fig. 23.2).

Evidence for departure from Rayleigh behavior is pronounced for replicate A of *Cylindrocarpon tonkinense*, e.g. in Fig. 23.2 as a curvilinear relationship is observed ($r^2 = 0.97$). The curvilinear nature of the data indicates that η is not constant but variable over the course of fungal denitrification. Therefore, η must be the net result of fractionation during at least two steps.

A frequently cited equation describing η during photosynthesis is (Oleary 1981; Farquhar et al. 1982):

$$\eta = \epsilon_a + (\epsilon_b - \epsilon_a) K_1 / (K_2 + K_3) \quad (23.13)$$

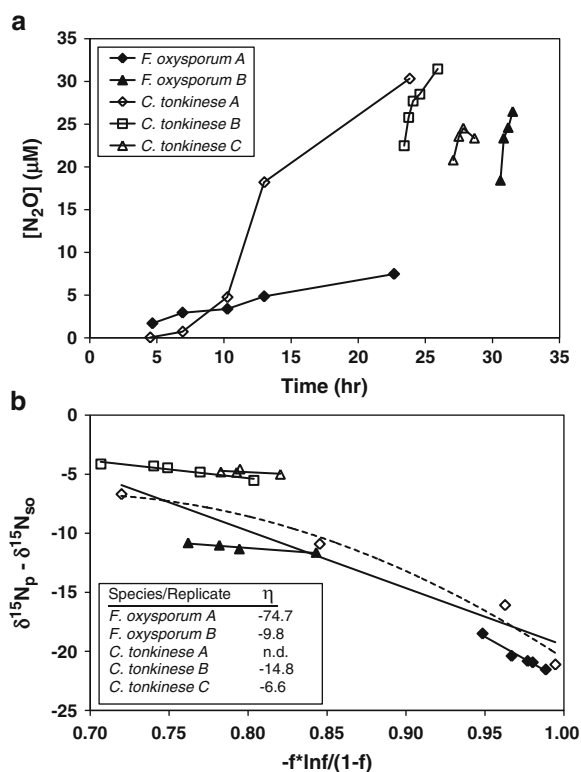


Fig. 23.2 Changes in the concentration (a) and $\delta^{15}N$ (b) of N_2O produced during fungal denitrification for two replicate cultures of *Fusarium oxysporum* (A, B) and three cultures of *Cylindrocarpon tonkinense* (A–C) (data from Sutka et al. 2008). The symbols shown in (a) also apply to (b). The slopes of the regression lines through each culture are equivalent to η as determined by (23.11) and shown for each species within the inset in (b). A curvilinear relationship is evident in the data for *C. tonkinense* A indicating that the net isotope effect is changing over the course of N_2O production

Here the constants ϵ_a and ϵ_b are the isotopic enrichment factors for diffusion of CO_2 in air (-4.4 ‰) and reduction by the enzyme Rubisco (-29.4 ‰), respectively (Guy et al. 1993). Rate constants for diffusion into the cell, out of the cell and for the enzyme activity are given by K_1 , K_2 , and K_3 , respectively. By (23.13), variation in the relative importance of these rate constants determines whether the fractionation factor for diffusion or for enzymatic reduction is the predominant control on η . When $K_1 \ll (K_2 + K_3)$, then $K_1/(K_2 + K_3)$ approaches zero and, η approaches ϵ_a . In this case η is small because it is largely a function of the small fractionation factor for diffusion. In contrast, when diffusion does not limit the supply of N_2O to the enzyme, $K_1/(K_2 + K_3)$

approaches 1 and η approaches ε_b . Enzymatic fractionation factors tend to be quite large relative to those associated with diffusion. Thus (23.13) demonstrates why η associated with many biological reactions tends to be variable while ε is constant and why this is the case even though both η and ε are determined using the same equations. Further, a consideration of the relative magnitude of the rate constants indicates that η should be small when diffusion limits the supply of substrate to the enzyme and large when diffusion is not limiting to the enzymatic process.

Equation (23.13) can be applied to a suite of biological reactions and has been proposed as an explanation for the wide range of NIE values observed during denitrification, N_2O reduction, and consumption of O_2 during respiration (Ostrom et al. 2002, 2005, 2007). Variation in η for fungal denitrification by the same microbial species most likely reflects depletion of the nitrite substrate, over time. A temporal decline in substrate concentration is a common occurrence in “batch” cultures and slows the rate of substrate diffusion into the cell. This then causes $K_1/(K_2 + K_3)$ to shift toward zero and reduces the magnitude of η . Observations of constant fractionation factors during multi-step reactions can be explained as the result of two types of experimental conditions: (1) when depletion of the substrate is minor such that the relationship between $-\frac{f \ln f}{1-f}$ and $(\delta^{15}N_p - \delta^{15}N_{so})$ is approximated by a line or (2) “steady-state” conditions that are offered, for example, by chemostats (Barford et al. 1999). Even within steady-state systems η varies with the relative importance of the reaction rate constants for diffusion and for the enzyme. Ideally, fractionation factors are best constrained by determining the isotope effect associated with each step within a reaction sequence. This can often be accomplished by work with pure enzymes (Guy et al. 1993).

The wide variation in η challenges the use of bulk isotope approaches to resolve the origins of N_2O . The range of published values of η for nitrification, bacterial denitrification, and fungal denitrification, -45 to -111 ‰, -13 to -45 ‰, and -6.6 to -74.7 ‰, respectively, overlap (Yoshida 1988; Barford et al. 1999; Pérez et al. 2006; Sutka et al. 2008). Therefore, $\delta^{15}N$ values cannot be accurately attributed to a specific microbial production pathway. Bulk N isotope values may be insightful if certain processes are known to be inoperative, such as anoxic conditions

that prohibit nitrification, or with the use of inhibitors to isolate specific pathways (but see Sect. 23.1 for challenges associated with inhibitor approaches). While $\delta^{15}N$ values may not provide precise resolution of microbial production pathways they still give insight into sources of N_2O to the atmosphere (e.g. terrestrial vs. oceanic) as well as changes in such sources over time (Kim and Craig 1993; Dore et al. 1998). For example, changes in the $\delta^{15}N$ and $\delta^{18}O$ of ice core N_2O from pre-industrial times to present are consistent with increased emissions from agricultural activities (Stein and Yung 2003; Sowers et al. 2003; Bernard et al. 2006).

23.3.3 The Use of Bulk $\delta^{18}O$ Values in Assessing the Origins of N_2O

$\delta^{18}O$ has been proposed as a tracer of microbial N_2O production in a variety of studies (Ostrom et al. 2000; Mandernack et al. 2000, 2009; Frame and Casciotti 2010). The use of $\delta^{18}O$ requires that different N_2O production pathways have unique fractionation factors or incorporate elemental O from isotopically distinct sources (e.g. water or O_2) (Ostrom et al. 2000).

During nitrification, the first O atom added to ammonium to form hydroxylamine is from O_2 where as those added to form nitrite and nitrate are from water (Dua et al. 1979; Hollocher et al. 1981; Andersson and Hooper 1983; Kumar et al. 1983) (Fig. 23.1). These sources of O in the ocean and soil environments typically differ by greater than 20 ‰ (Kroopnick and Craig 1976). Ostrom et al. (2000) observed that the difference in $\delta^{18}O$ between O_2 and N_2O changed markedly with depth in the water column in the North Pacific Ocean and concluded that these shifts reflected changes in the proportion of N_2O derived from hydroxylamine oxidation or reduction of nitrite. Thus changes in the $\delta^{18}O$ of N_2O and O_2 were used to infer whether N_2O was produced by via hydroxylamine oxidation or by reduction of nitrite (Fig. 23.1). The $\delta^{18}O$ of O_2 is not commonly measured concurrent with that of N_2O particularly in soil environments. Consumption of O_2 during respiration invokes a large isotope effect that can then cause increases in the $\delta^{18}O$ of N_2O upon incorporation of O_2 during nitrification (Mandernack et al. 2009). Consequently, changes in the $\delta^{18}O$ of N_2O may not always reflect

changes in sources but incorporation of a respiration isotope effect from O_2 .

There is ample evidence that elemental O in N_2O exchanges with that in water during the microbial generation of this gas (Kool et al. 2007). Casciotti et al. (2002) found exchange to be low during N_2O production by denitrification in *Pseudomonas aerofaciens* (<10 %) but as high as 78 % in *Pseudomonas chlororaphis*. In incubation of soils with acetylene to inhibit N_2O reduction, Wrage et al. (2005) observed no evidence of exchange, however, in the absence of acetylene exchange was nearly 100 %. Exchange of 1 to 25 % between O in N_2O and water has been shown for a variety of microorganisms during the first step of nitrification, ammonia oxidation (Casciotti et al. 2010). Exchange with water is not expected during N_2O production via hydroxylamine oxidase (HAO) but enzyme studies have shown that exchange occurs during N_2O production by nitrite reductase (NiR) and nitric oxide reductase (NOR) (Ye et al. 1991; Kool et al. 2007). The potential for exchange to occur during microbial N_2O production has led numerous studies to conclude that $\delta^{18}O$ is a poor tracer of microbial origins (Kool et al. 2007, 2009a, b; Ostrom et al. 2007, 2010). Nonetheless, Frame and Casciotti (2010) recently reported a strong relationship between $\delta^{18}O$ and SP in microbial cultures where O_2 levels were

varied to favor production from hydroxylamine oxidation or nitrifier-denitrification and concluded that $\delta^{18}O$ is a potential tracer of these pathways. This observation implies that water exchange must be limited during nitrifier-denitrification and hydroxylamine oxidation. The challenge to studies addressing the origins of N_2O on the basis of $\delta^{18}O$ is to know when exchange of O between N_2O and water occurs and to what extent. In this regard, incubations with ^{18}O -enriched water are a viable approach to resolve this issue.

23.3.4 The Use of SP to Resolve Microbial N_2O Production Pathways

A key advantage of SP in tracing origins of N_2O is that, in contrast to bulk isotope values, SP is independent of the isotopic composition of the substrates of nitrification or denitrification (O_2 , water, nitrate, nitrite or ammonium) (Toyoda et al. 2005; Sutka et al. 2006). Further, in pure microbial cultures the SP of N_2O produced by nitrifying and denitrifying bacteria did not exhibit fractionation ($\eta = 0$ ‰) even though bulk, α and β $\delta^{15}N$ values were characterized by non-zero η values (Fig. 23.3). These characteristics, lack of dependence on the isotopic composition of the substrates and

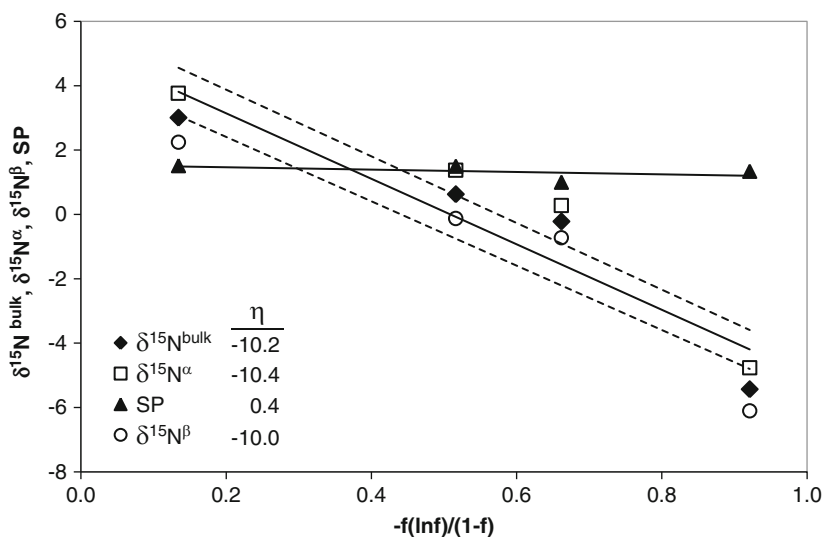


Fig. 23.3 Isotopomer values for N_2O production via bacterial denitrification by *Pseudomonas chlororaphis* as a function of the change in the extent of the reaction, f . Linear regression lines for $\delta^{15}N^{bulk}$ and SP are shown with solid lines and for $\delta^{15}N^{\alpha}$ and $\delta^{15}N^{\beta}$ with dashed lines. Based on (23.3), the slope of the regression equation for each isotopologue data set is

equivalent to η . Values for η are indicated to the left of each isotopologue value in the legend. These data demonstrate that while fractionation is evident during N_2O production by bacterial denitrification for $\delta^{15}N^{bulk}$, $\delta^{15}N^{\alpha}$ and $\delta^{15}N^{\beta}$ fractionation in SP was essentially zero. Data are from Sutka et al. (2006)

lack of fractionation during production, provide strong support for the use of SP as a conservative tracer of microbial production. Critical to this approach, however, is that different sources of N_2O have unique SP values. Recently Sutka et al. (2006) found unique SP values for N_2O derived from hydroxylamine oxidation (nitrification) and nitrite or nitrate reduction (denitrification and nitrifier denitrification) in bacterial cultures and suggested that SP could be used to apportion microbial sources of this gas. Production of N_2O via nitrite or nitrate reduction, whether by nitrifying or denitrifying bacteria, resulted in an average SP values of 0‰ compared to 33‰ for N_2O produced from hydroxylamine oxidation (Sutka et al. 2006). Toyoda et al. (2005) similarly reported a SP value for N_2O produced from one species of denitrifying bacteria of -5.1 ‰. A second species produced N_2O with a SP of 23.3‰; however, this culture occurred with a low growth rate that may have been influenced by inorganic production. Sutka et al. (2008) further demonstrated that fungal denitrification yields N_2O with a SP of 37‰, which is not distinct from that associated with nitrification but clearly distinct from that produced during bacterial denitrification. Collectively these pure culture studies provide compelling evidence that a SP of 0‰ or less is indicative of N_2O produced by denitrifying bacteria whereas values of 33–37‰ indicates production from hydroxylamine oxidation or fungal denitrification.

Soil incubations directed toward defining the SP values associated with nitrification and denitrification have found values distinct from those obtained in pure culture. Although widely cited, the study by Pérez et al. (2006) was based on the calibration approach of Kaiser et al. (2004a) and reported SP values need to be corrected. Well et al. (2008) recently reported a range of 18.3–36.3‰ for N_2O produced by nitrification in soils. The higher values are in agreement with the SP values obtained via hydroxylamine oxidation in pure culture (Sutka et al. 2006). The lower values are consistent with production from a mixture of hydroxylamine oxidation and nitrifier-denitrification which has been shown to have a SP in pure culture near 0‰ (Sutka et al. 2006). Thus the variable SP signals attributed to nitrification are quite readily explained by a mixture of N_2O derived from hydroxylamine oxidation and nitrifier denitrification. Two incubation studies using temperate soils yielded variable SP values for N_2O production from denitrification of 3.1–8.9‰

(Well and Flessa 2009) and 2.3–16‰ (Well et al. 2006). The lower values are similar to those obtained in pure culture (-5 to 0‰; Toyoda et al. 2005; Sutka et al. 2006). The higher values could reflect production from fungal denitrification (Sutka et al. 2008) or, when acetylene was not used, an increase in SP due to reduction of N_2O (Ostrom et al. 2007; Jinuntuya-Nortman et al. 2008). These studies indicate that a significant challenge to soil incubation studies is to isolate specific production pathways in a complex soil community and the results obtained thus far are not inconsistent with SP endmember values obtained in pure culture.

The ultimate control on the SP of N_2O may not be the bacterial species or pathways but the enzymes involved in its production, in particular, NIR and NOR (Stein and Yung 2003; Schmidt et al. 2004). HAO catalyzes the four electron transfer of hydroxylamine to nitrite although N_2O is given off in a branched reaction (Kostera et al. 2008). There are three bacterial and one fungal type of NOR enzymes recognized: CNOR, qNOR, and qCuNor and P450NOR, respectively. cNOR is associated with bacterial denitrification while qNOR and qCuNor are associated with detoxification of NO and may not be environmentally relevant (Hendriks et al. 2000). Traditionally production of N_2O via P450NOR has not been considered important but most fungi lack N_2O reductase and, therefore, all nitrate reduction by fungi yields N_2O whereas most reduction in bacteria yields N_2 (Shoun et al. 1992). Further, recent studies applying antibiotics to soils have implicated fungi as primary sources of N_2O (Crenshaw et al. 2008). The three bacterial NOR mainly differ in electron donors but the active site structures of NOR are considered highly homologous; therefore, they are expected to have identical active sites and behave very similarly (Hendriks et al. 2000; Tavares et al. 2006). The NOR enzymes used in nitrifier-denitrification are nearly identical to those found in denitrifying bacteria and likely were obtained by lateral gene transfer (Garbeva et al. 2007; Kool et al. 2007).

Distinctions and similarities in the SP of N_2O during various production pathways can be understood by consideration of the enzyme pathways in addition to the specific microbial species involved. Sutka et al. (2006) cultured two species of *Pseudomonas* sp. Each species possessed one of the two known types of

dissimilatory NIR. A similar SP was observed in N_2O produced by both species (0 ‰) even though the type of NIR enzyme involved differed. This result provides support for the suggestion that during bacterial denitrification NOR is more important in controlling SP than NIR (Stein and Yung 2003). Highly contrasting SP values have been demonstrated for denitrifying fungi (37 ‰) and bacteria (0 ‰) consistent with a control of NOR on SP (Sutka et al. 2006, 2008). As the NIR and NOR enzymes in denitrifiers and nitrifiers are structurally and genetically related (Casciotti and Ward 2001, 2005; Garbeva et al. 2007) it is not surprising that the SP for N_2O from bacterial denitrification (−2.5 to 1.8 ‰) and nitrifier-denitrification (−4.0 to 1.9 ‰) were found to be similar (Sutka et al. 2006). Bacteria using qNOR have not been cultured to evaluate SP. As this pathway is primarily used in detoxification of environmental NO it likely constitutes a small portion of N_2O production in soils (Hendriks et al. 2000). Thus the SP associated with bacterial denitrification (including nitrifier-denitrification) via cNOR (−5 to 0 ‰) is distinct from other pathways (nitrification via hydroxylamine oxidation and fungal denitrification (33–37 ‰)) and has the potential, therefore, to act as a tracer of its production.

Frame and Casciotti (2010) recently proposed revision of the SP endmember values to −10 and 37 ‰, respectively, for nitrite reduction and hydroxylamine oxidation. Collectively pure culture studies provide compelling evidence that a SP of −10 to 0 ‰ is indicative of N_2O produced by denitrifying bacteria whereas values of 33–37 ‰ indicates production from hydroxylamine oxidation and/or fungal denitrification. These revised ranges of SP values can be used to apportion production of N_2O to (1) bacterial denitrification and (2) hydroxylamine oxidation/fungal denitrification. For example, SP values for soil-derived N_2O were measured throughout a growing season in a temperate agricultural field varied from −12.5 to 17.6 ‰ (Fig. 23.4). The majority of values are consistent with an origin from bacterial denitrification. When each value is weighted by the N_2O flux to the atmosphere at that time, the flux weighted SP for this field is −1.3 ‰. Assuming endmember values of 0 and 33 ‰ or −10 to 37 ‰ for bacterial denitrification and hydroxylamine oxidation/fungal denitrification, respectively, the proportion of N_2O derived from bacterial denitrification is between 73 and 100 %. This result indicates that management activities at this particular location should focus on actions that minimize

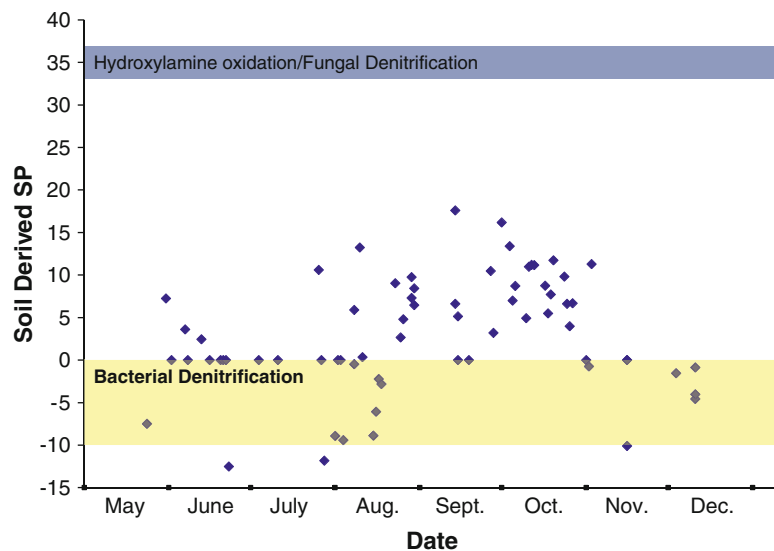


Fig. 23.4 SP values for soil-derived N_2O from an agricultural field planted in wheat in 2007 at the Kellogg Biological Station, Hickory Corners, Michigan. The field received application of urea-ammonium nitrate (28%) fertilizer in the spring at a rate of 246 kg N ha⁻¹. Shown in yellow and blue are the SP values associated with N_2O production from bacterial denitrification and hydroxylamine oxidation/fungal denitrification. Static flux

chambers were used to collect all samples which initially (at time zero) includes N_2O from the atmosphere. Consequently, soil-derived values are calculated by mass balance assuming concentration and isotopomer values for atmospheric N_2O (see Opdyke et al. 2009). N. Ostrom, P. Ostrom, N. Millar, G.P. Robertson, unpublished data

denitrification. Such activities might include, for example, the avoidance of anaerobic conditions resulting from excessive irrigation. Currently, there is not a definitive means on the basis of SP to distinguish the two pathways of N_2O production by nitrifying bacteria; however, some studies have indicated that $\delta^{18}O$ values may hold promise (Mandernack et al. 2000, 2009; Wrage et al. 2005; Frame and Casciotti 2010) and with improvements in precision, $\delta^{17}O$ may be insightful as well (see Sect. 23.3.7).

23.3.5 Isotopomer Effects Associated with Reduction of N_2O

While the SP values of N_2O have the potential to reveal microbial production pathways, consumption (or reduction) of N_2O during denitrification can impart an isotope effect that could bias or obscure source isotope values (Tilsner et al. 2003; Wrage et al. 2004; Yamagishi et al. 2005). Rates of N_2O reduction independent of gross denitrification are rarely determined in soils or in the ocean; hence it is difficult to know the importance of this process a priori (e.g. Bandibas et al. 1994; Cavigelli and Robertson 2001). Denitrification results in cleavage of the N and O covalent bond in N_2O , which based on kinetic isotope theory, is expected to result in an increase in the ^{15}N content of the α position and, therefore, an increase in SP (Popp et al. 2002; Yamagishi et al. 2005). The increase in SP in response to reduction would result in a shift away from values associated with bacterial denitrification (-10 to 0 ‰) towards those associated with hydroxylamine oxidation/fungal denitrification (33 – 37 ‰) (Sutka et al. 2006; Frame and Casciotti 2010) and result in an underestimate of the importance of bacterial denitrification as a source of N_2O . Consequently, the importance of the N_2O reduction isotope effect on SP values should, ideally, be established prior to interpretation of the microbial origins of N_2O .

A number of studies have addressed isotopologue effects associated with N_2O reduction. Ratios of $\delta^{18}O$ to $\delta^{15}N$ and $\eta^{18}O$ to $\eta^{15}N$ are strongly linear during N_2O reduction in pure microbial cultures and soils and to cluster within a narrow range of 2.4 – 2.6 ‰ (Menyailo and Hungate 2006; Ostrom et al. 2007; Vieten et al. 2007; Jinuntuya-Nortman et al. 2008). Similarly, within pure microbial cultures and soil

incubations the relationship between $\eta^{18}O$ and the NIE for SP has been reported to be 1.7 and 1.9 ‰, respectively (Ostrom et al. 2007; Jinuntuya-Nortman et al. 2008). Consequently, these mass dependent relationships between the isotopologues and η values are diagnostic of N_2O reduction. Studies of the η for SP during N_2O reduction have been considerably fewer than those for bulk isotopes. Values for η^{SP} have been reported as -6.4 ‰ from one ocean study, -6.8 to -5.0 ‰ in microbial culture, and -4.5 to -2.9 ‰ in a study of temperate soils (Yamagishi et al. 2005; Ostrom et al. 2007; Jinuntuya-Nortman et al. 2008). Jinuntuya-Nortman et al. (2008) found a strong correlation between η^{SP} and the degree of water filled pore space in soils which was consistent with an increase in the importance of diffusion in controlling η (by (23.13)) as soils become more saturated. Overall the magnitude of the η for SP is small relative to that for bulk $\delta^{15}N$ and $\delta^{18}O$ values but substantial enough that the impact of N_2O reduction on SP should not be ignored. The mass dependent relationships between η for SP and bulk $\delta^{15}N$ and $\delta^{18}O$ for N_2O reduction are strongly diagnostic of this process and unique relative to isotopologue shifts that occur in response to mixing of soil and oceanic N_2O with atmospheric N_2O . Consequently, Ostrom et al. (2007) suggested that the small η for N_2O reduction and observation of a slope of less than 1 for a plot of $\delta^{18}O$ vs. $\delta^{15}N$ indicated that shifts in SP during N_2O reduction were relatively minor whereas those greater than 1 implied that a N_2O reduction had altered SP appreciably. Under the latter condition, a correction to SP is needed before using SP to determine the relative proportion of N_2O derived from bacterial denitrification and hydroxylamine oxidation/fungal denitrification as described in preliminary models (Yamagishi et al. 2005; Ostrom et al. 2007; Opdyke et al. 2009).

23.3.6 Correction of SP Values for N_2O Reduction

All fractionating processes alter the isotopic composition of the substrate and when this occurs the source isotope values are altered and potentially lost. While soils are well established as a source of N_2O to the atmosphere it is also recognized that N_2O is reduced in soils and that reduction alters $\delta^{15}N$, $\delta^{18}O$ and SP (Chapuis-Lardy

et al. 2007; Ostrom et al. 2007; Jinuntuya-Nortman et al. 2008). Once isotopic alteration has occurred the proportion of N_2O derived from bacterial denitrification and hydroxylamine oxidation/fungal denitrification determined from SP will be incorrect unless the isotope effect during reduction can be quantified. Correcting for fractionation during reduction and determining the SP value of N_2O prior to reduction is challenged by the fact that the NIE for reduction is variable. Nonetheless, the mass dependent relationships between $\delta^{15}N$ and $\delta^{18}O$ and $\delta^{15}N$ and SP during N_2O reduction are unique and diagnostic of this process (Menyailo and Hungate 2006; Ostrom et al. 2007; Vieten et al. 2007; Jinuntuya-Nortman et al. 2008). While not quantitative, a simultaneous production and reduction model that describes both isotopologue shifts during production and fractionation during reduction has been developed to estimate the maximum likely

shift in SP due to reduction within soil trace gas flux chambers (Ostrom et al. 2007; Opdyke et al. 2009).

Within soil flux chambers the isotopologue composition of N_2O will change with time owing to (1) mixing of atmospheric and soil derived N_2O and (2) N_2O reduction. The isotopologue shifts due to mixing are described by:

$$\delta_{\text{mix}} = (\delta_{\text{atm}}C_{\text{atm}} + \delta_{\text{SD}}C_{\text{SD}})/C_{\text{mix}} \quad (23.14)$$

where, δ and C refer to the isotopic composition ($\delta^{15}N$, $\delta^{18}O$ or SP) and concentration of N_2O , respectively. The subscripts atm and SD refer to atmospheric and soil derived N_2O , respectively, and mix indicates the resulting mixture of these two sources. Equation (23.14) is shown graphically on a plot of $\delta^{18}O$ vs. $\delta^{15}N$ as the “Atm-Soil N_2O Mixing” line in Fig. 23.5. Once a soil flux chamber is closed and soils release N_2O

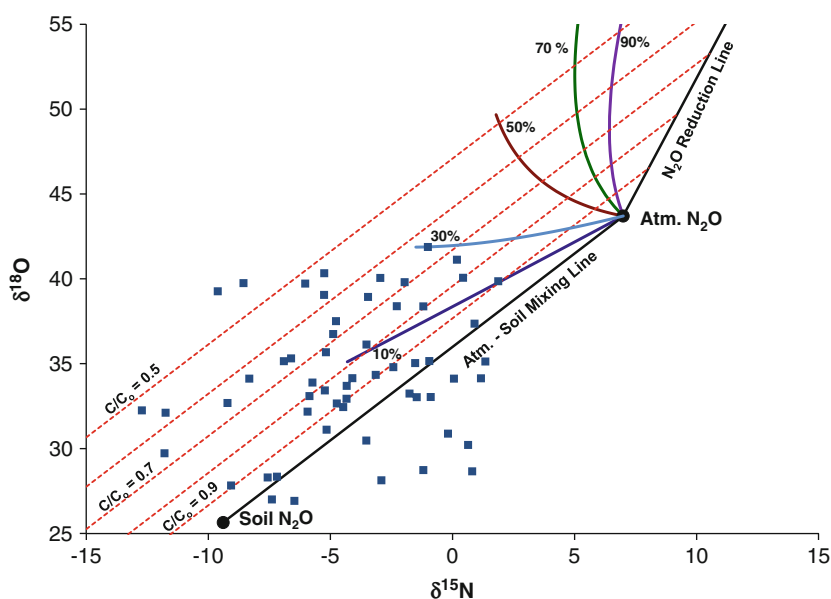


Fig. 23.5 Oxygen and nitrogen isotope data from soil flux chambers in an agricultural field planted in wheat in 2007 at the Kellogg Biological Station, Hickory Corners, Michigan (squares) in comparison to modeled results of simultaneous production and reduction. The isotopic composition of flux weighted “Soil N_2O ” for the entire season is shown as closed circle. In the absence of N_2O reduction, atmospheric N_2O (also shown as a closed circle) mixes with soil derived N_2O and values would lie on a line (Atm. – soil mixing) connecting these two endmembers. The N_2O reduction line indicates where isotope values would lie if reduction was the only process affecting N_2O isotopologues (Ostrom et al. 2007; Jinuntuya-Nortman et al. 2008). The curvilinear lines represent isotopologue

values resulting from simultaneous production (mixing of air and soil N_2O) and reduction at difference percentages of the rate of reduction relative to the rate of production (10, 30, 50, 70 and 90%). The distance along any of the simultaneous production and reduction lines away from atmospheric N_2O values indicates a greater degree of N_2O reduction as described by the observed concentration (C) relative to that which would have been present in the absence of reduction (C_0). The dashed lines connect all points in which the extent of reduction, C/C_0 , is the same. Data points below the mixing line likely represent variation in the isotopologue values of the soil N_2O endmember or non-conservative behavior such as exchange of O with water during production

to the headspace, the isotopologue values will move from those of the atmosphere towards those of soil derived N_2O shown in Fig. 23.5 as the “atm-soil N_2O mixing” line.

The change in isotopologue values resulting from reduction of N_2O can be determined from a Rayleigh fractionation model as the difference between the isotope value of the residual substrate (δ_s) and that prior to any reduction (δ_o) (Mariotti et al. 1981):

$$\Delta = \delta_s - \delta_o = -\eta \ln(C/C_o) \quad (23.15)$$

Here, η is the fractionation factor for N_2O reduction and C/C_o is the ratio of the concentration of the residual N_2O relative to that which was present prior to reduction. Δ is defined as the difference in isotopic composition of N_2O at any point (δ_s) in time and prior to reduction (δ_o). During reduction of N_2O , the ratio of $\eta^{18}O$ and $\eta^{15}N$ has been shown to be constant at a value of 2.6 (Ostrom et al. 2007; Jinuntuya-Nortman et al. 2008). Therefore, if reduction occurred in the absence of production the concentration of N_2O would decline from atmospheric levels and $\delta^{18}O$ and $\delta^{15}N$ values would increase along a slope of 2.6 (shown as the “ N_2O Reduction” line in Fig. 23.5).

The situation in which both production and reduction occur simultaneously can be described by combining (23.14) and (23.15). To effect this we equate the isotopologue and concentration values of the mixture of atmospheric and soil derived N_2O (δ_{mix} and C_{mix} , respectively) in (23.14) to those of the initial substrates in (23.15) (δ_o and C_o , respectively). Thus (23.14) becomes:

$$\delta_o = (\delta_{atm}C_{atm} + \delta_{SD}C_{SD})/C_o \quad (23.16)$$

δ_o from (23.16) is substituted into (23.15) and solved for δ_s

$$\delta_s = (\delta_{atm}C_{atm} + \delta_{SD}C_{SD})/C_o + \eta \ln(C/C_o) \quad (23.17)$$

Equation (23.17) can be written in terms of any isotopologue:

$$\delta^{18}O_s = (\delta^{18}O_{atm}C_{atm} + \delta^{18}O_{SD}C_{SD})/C_o + \eta^{18}O \ln(C/C_o) \quad (23.18)$$

and

$$\delta^{15}N_s = (\delta^{15}N_{atm}C_{atm} + \delta^{15}N_{SD}C_{SD})/C_o + \eta^{15}N \ln(C/C_o) \quad (23.19)$$

Equations (23.18) and (23.19) describe the changes in isotopologue values of N_2O when production occurs simultaneously with consumption as a function of the isotopic composition of soil derived and atmospheric N_2O , the fractionation factors for reduction, and the concentration prior to (C) and after reduction (C_o). A desirable outcome of these equations is the term C/C_o as this would provide a basis to determine the shift in SP (Δ) due to reduction by (23.15). If C/C_o can be determined, Δ for SP can be determined and subtracted from measured SP values to provide a corrected estimate of the fraction of N_2O derived from bacterial denitrification vs. that derived collectively from hydroxylamine oxidation and fungal denitrification. Because C_o appears in both the linear and logarithmic portions of (23.5) and (23.6) an explicit solution is not possible, however, an implicit relationship can be generated graphically using theoretical scenarios of simultaneous production and reduction as shown in Fig. 23.5. An arbitrary production rate is chose and the rate of reduction is set to a percentage of the production rate (10, 30, 50, 70, and 90 % in Fig. 23.5). The following terms are used in (23.18) and (23.19):

$\delta^{15}N_{atm} = 7.0 \text{ ‰}$ (Yoshida and Toyoda 2000)

$\delta^{18}O_{atm} = 43.7 \text{ ‰}$ (Yoshida and Toyoda 2000)

$C_{atm} = 315 \text{ ppbv}$ (Yoshida and Toyoda 2000)

$\delta^{15}N_{SD}$ and $\delta^{18}O_{SD}$ (taken as the flux weighted average for the entire data set)

C_{SD} (difference between the concentration at t_1 and t_0 (C_{atm}))

$\delta^{15}N_s$ and $\delta^{18}O_s$ (measured at t_1)

$\eta^{15}N$ (between -9.2 and -1.8 ‰) (Ostrom et al. 2007)

$\eta^{18}O$ (calculated from $\eta^{18}O$ to $\eta^{15}N$ constant relationship of 2.6) (Jinuntuya-Nortman et al. 2008)

The minimum value for $\eta^{15}N$ observed at this study site (-9.2 ‰) was chosen to create a “worse-case-scenario” in which the greatest Δ SP value can be expected. Production and reduction are allowed to occur for multiple time points over several hours and the results are plotted as simultaneous production and reduction (SPR) curved lines shown in Fig. 23.5. All of the SPR curves originate at the isotope values for atmospheric N_2O (no production or reduction and, therefore, a C/C_o value of 1). As the rate of production outpaces that of reduction the C/C_o term decreases with time. Thus, as the isotope values along any SPR

curve move away from the atmospheric endmember C/C_o decreases. Common C/C_o values between the SPR curves are connected to create the parallel “ C/C_o ” lines shown in Fig. 23.5. Once this theoretical graph is generated field data (from Fig. 23.4) is overlaid. The location of each data point corresponds to a value of C/C_o and a production to reduction ratio. Thus, the data presented has maximum values of the production to reduction ratio of slightly greater than 30 % and C/C_o slightly greater than 0.5. This latter value can be entered into (23.15) to determine the maximum possible Δ value expected. Based on the maximum value for C/C_o and the largest fractionation factor in SP observed during N_2O reduction in soils at this location (-4.5 ‰) (Jinuntuya-Nortman et al. 2008), a maximum shift in SP of 4.0 ‰ can be expected. Given SP values of 0 ‰ for production from denitrification and 37 ‰ from other sources, a shift in SP of 4 ‰ corresponds to an underestimate of production from bacterial denitrification of 10.8 %. Consequently, the maximum expected shifts in SP due to N_2O reduction in this study are small but should not be ignored.

There are limitations to the SPR model that prevent us from determination of Δ values quantitatively. Constant and invariant isotopologue values for the soil derived endmember are assumed (determined as the flux weighted isotope values for the entire data set); however, the soil derived endmember values likely varies in time and space. Further, constant values for $\eta^{15}N$ and $\eta^{18}O$ during reduction are assumed but these values can be expected to vary as well. Thus, the results of the SPR model are considered estimates of the shift in SP during reduction under a “worse-case” scenario. Nonetheless, the results presented in Fig. 23.5 suggest (1) that as the η_{SP} values are small, reduction has to be quite extensive (>50 % the rate of production) to alter SP value substantially and (2) if uncorrected, the shift in SP due to reduction would bias the results in favor of production from hydroxylamine oxidation/fungal denitrification. Thus the observation of a predominance of SP values near the -10 to 0 ‰ endmember for production from bacterial denitrification (Fig. 23.4) is compelling evidence that this process dominates N_2O production as all other processes for which SP is known (hydroxylamine oxidation, fungal denitrification and N_2O reduction) will result in higher SP values.

23.3.7 Resolution of the Causes of the ^{17}O Anomaly in N_2O

It is well known that all biological and most geochemical processes on Earth produce a consistent mass dependent relationship between $\delta^{17}O$ and $\delta^{18}O$ such that the slope of the line relating these terms is constant and equal to 0.516 (Thiemens 2006). Tropospheric N_2O is slightly enriched in ^{17}O relative to the “mass-dependent” line by approximately 0.9 ‰ (Cliff and Thiemens 1997; Cliff et al. 1999; Kaiser et al. 2003, 2004b). Photochemical reactions in the stratosphere are known to produce “mass-independent” relationships and most notable is stratospheric ozone that is defined by $\delta^{17}O$ to $\delta^{18}O$ relationship of approximately 0.62 (Lammerzahl et al. 2002).

The unusual ^{17}O enrichment in tropospheric N_2O has long been assumed to result from photochemical reactions and exchange of N_2O between the stratosphere and troposphere. Prasad and Zipf (2008) recently proposed that the anomaly is a consequence of photochemical production of N_2O . If correct, then the IPCC is overestimating the biological sources of N_2O by approximately 7 % and the global budget of N_2O would be unbalanced. A recent assessment of laboratory experiments and models, however, suggested that only part of the “anomaly” can be explained by photochemical reactions. Biological production has been hypothesized as the cause of the remaining ^{17}O anomaly (Kaiser et al. 2004b; Kaiser and Röckmann 2005). If the anomaly is biological, this would be the first documentation of a biological mass-independent effect. The issue of the ^{17}O anomaly remains unresolved because the $\delta^{17}O$ and $\delta^{18}O$ composition of N_2O produced photochemically has not been determined and by the fact that “no measurements of the oxygen triple isotopic composition [^{16}O , ^{17}O and ^{18}O] of biogenic N_2O exist” (Kaiser and Röckmann 2005). The key limitation has been the size of the anomaly, 0.9 ‰ relative to current analytical precision (0.1–0.5 ‰).

Biological production itself is unlikely to result in mass independence, however, the source of elemental O in N_2O can be either O_2 or water and there is a small but measurable difference in the slopes of the mass-dependent relationships for O_2 and water (Meijer and Li 1998; Angert et al. 2003). Until recently, the relationship between $\delta^{17}O$ and $\delta^{18}O$ was described by a slope

with a value of 0.52 that has been termed the “terrestrial fractionation line” (Young et al. 2002). With this in mind, the ^{17}O anomaly, $\Delta^{17}\text{O}$, can be defined as:

$$\Delta^{17}\text{O} = \delta^{17}\text{O} - 0.52 * \delta^{18}\text{O} \quad (23.20)$$

which describes the magnitude of the enrichment or depletion in ^{17}O relative to what the sample would have if it were in “mass dependence” (Cliff and Thiemens 1997; Kaiser et al. 2004b). A $\Delta^{17}\text{O}$ value of 0 ‰ would normally indicate that the sample followed the terrestrial fractionation line and was mass-dependent. As mentioned, the primary causes of non-zero or “mass-independent” $\Delta^{17}\text{O}$ values are photochemical reactions in the stratosphere and subsequent incorporation into tropospheric materials (Thiemens 2006). As values for the slope are dependent on the isotopic composition of the reference gas, a more accurate way to represent slope values is:

$$\Delta^{17}\text{O} = (\delta^{17}\text{O} + 1) - \lambda * \ln(\delta^{18}\text{O} + 1) \quad (23.21)$$

where λ is the slope of the trend line in a $\ln(\delta^{17}\text{O} + 1)$ vs. $\lambda * \ln(\delta^{18}\text{O} + 1)$ plot and approximately equivalent to the slope from (23.20) (note that values are reported in ‰, however the factor of 1,000 has been omitted for convenience) (Luz and Barkan 2005).

With recent improvements in precision, λ values have been defined to the third decimal and it is now apparent that there are slight variations in the these values between different materials (Luz and Barkan 2005). For example, λ values of 0.518, 0.528 and 0.525 have been reported for respiration, natural waters and rocks, respectively (Meijer and Li 1998; Miller 2002; Angert et al. 2003). For atmospheric N_2O , a slope of 0.516 has been reported (Cliff and Thiemens 1997; Kaiser et al. 2004b). Because different mass-dependent properties may be described by different λ values, it is possible to obtain a non-zero $\Delta^{17}\text{O}$ value for some compounds without invoking mass-independent fractionation. N_2O may be such a compound. Recently it was proposed that if during the biological production of N_2O via denitrification O exchange with water occurred, then N_2O could be produced following the mass-dependent slope of 0.528 for water rather than the value of 0.516 for atmospheric N_2O (Kaiser et al. 2004b). Exchange with water during the production of N_2O by two different species of denitrifying bacteria has

been shown and the extent of exchange was species dependent (Casciotti et al. 2002). With this foundation, Kaiser and Röckmann (2005) proposed that at least 0.4 ‰ of the 0.9 ‰ ^{17}O anomaly present in the atmosphere could be due to biological production. Exchange with water during biological production (Mechanism 1) is only one of three ways that a biological ^{17}O anomaly may become expressed in N_2O .

A second means by which a ^{17}O anomaly may become expressed in N_2O depends upon the pathway of O incorporation during nitrification (Mechanism 2). During nitrification, the first O atom added is derived from O_2 whereas the second is derived from water (Dua et al. 1979; Andersson and Hooper 1983; Kumar et al. 1983) (Fig. 23.1). The $\delta^{18}\text{O}$ of water is generally 20 ‰ greater than that of O_2 (Kroopnick and Craig 1976); therefore, N_2O produced via oxidation of hydroxylamine (in which O is derived from O_2) should be enriched in N_2O relative to that derived from reduction of nitrite (50:50 O_2 and water) and nitrate (1/3 O_2 , 2/3 water). With this foundation shifts in the $\delta^{18}\text{O}$ of N_2O with depth in the ocean have been attributed to shifts in the relative importance of hydroxylamine oxidation or nitrite or nitrate reduction (Ostrom et al. 2000). Since O_2 and water are also characterized by different mass-dependent slopes N_2O derived from oxidation of hydroxylamine or reduction of nitrite or nitrate should acquire distinct ^{17}O anomalies. In fact, as the proportion of elemental O derived from O_2 and water in nitrite and nitrate produced by nitrification differ, the ^{17}O anomaly and measured λ values may enable distinction of N_2O produced by reduction of these two compounds. This would be a significant advance as the SP produced upon reduction of nitrite via nitrifier-denitrification is no different than that produced upon reduction of nitrate by denitrification (Sutka et al. 2006). Consequently, the ^{17}O anomaly may provide a novel tracer of microbial production and may help resolve the importance of nitrifier-denitrification in N_2O reduction relative to other production pathways (Wrage et al. 2001, 2005). Exchange with water may potentially erase the distinction in $\delta^{17}\text{O}$ between N_2O derived from reduction of nitrite or nitrate. Nonetheless exchange with water will result in a distinct ^{17}O anomaly in N_2O relative to N_2O produced from oxidation of hydroxylamine which introduces O from O_2 .

A third means for introduction of a ^{17}O anomaly is a function of the origin of nitrate denitrified to produce

N₂O (Mechanism 3). Atmospheric nitrate has recently been recognized to have a strong ¹⁷O anomaly that ranges between 21 and 35 ‰ and reflects incorporation of a signal from photochemical reactions (Michalski et al. 2003, 2004; Morin et al. 2007, 2009; Kunasek et al. 2008; Michalski et al. 2010; Savarino and Morin 2011). Michalski et al. (2003) proposed that the biological production of N₂O from the denitrification of atmospheric nitrate could be an important source of the ¹⁷O anomaly in atmospheric N₂O. This pathway is not likely to be important in many terrestrial environments in which atmospheric deposition is a small fraction of nitrate inputs relative to that applied as fertilizer or released following soil mineralization/nitrification (e.g. Ostrom et al. 1998) but could be important in organic poor soils (e.g. deserts) and oligotrophic waters. Incorporation of a ¹⁷O anomaly via mechanism 3 would also potentially be moderated to some extent if exchange of water during N₂O production from denitrification is significant. Resolution of which mechanism is predominant is dependent on an improvement in precision beyond 0.1 ‰ and an analytical approach that measures the δ¹⁷O and δ¹⁸O of N₂O without mass interference.

23.4 Synthesis and Future Directions

The pioneering research of Toyoda and Yoshida (1999) and Brenninkmeijer and Röckman (2000) provided strong foundations for the application of SP to evaluate the biogeochemical origins and sinks of N₂O. Because the N₂O molecule contains two elements with a total of 5 stable isotopes a large number of isotopomers of N₂O exist which greatly complicates corrections for mass interference in the mass spectrometer. Refinement of mass interference corrections has been challenging and will undoubtedly continue (e.g. Westley et al. 2007; Frame and Casciotti 2010). The considerable complexity and lack of a consistent correction routine is a serious impediment to the widespread determination of the SP of N₂O even though all modern mass spectrometers are provided with three collectors appropriately configured for its analysis (³¹R, ⁴⁵R and ⁴⁶R can be determined with three collectors by analyzing the same sample twice). Because of this it is recommended that all published manuscripts include (1) the

isotopologue values of the internal laboratory standard used relative to international standards (VSMOW and Air-N₂), (2) the correction routine used, and (3) ³¹R, ⁴⁵R and ⁴⁶R values obtained (perhaps as an electronic annex). In this manner, if revisions to the SP of tropospheric N₂O occur, an international standard is developed, and if improvements to correction routines become available, published data can be corrected and revised to newer scales. Mass interference correction models should be made available to the international community, perhaps posted to a web site, to enable widespread access, consistent reporting of isotopologue data, and improvement to mass correction routines.

There is a current lack of an international standard for calibration and need for the research community to collaborate on its development. At the present time, calibration may be best accomplished by exchange of standards with the laboratory of N. Yoshida at the Tokyo Institute of Technology, analysis of the SP of tropospheric air to obtain a value of 18.7 ‰, and/or by spectroscopic approaches. FT-IR is the only spectroscopic approach to date that has provided data on the SP of tropospheric N₂O and is advantageous given that the analysis avoids the mass interference issues that challenge mass spectrometry (Griffith et al. 2009). Applications of FTIR to obtain field data have been limited but with improvements in methodology and technology spectroscopic approaches (including tunable diode laser and cavity ring down spectroscopy) will undoubtedly increase.

Additional studies are needed using pure microbial cultures, co-cultures, and natural soil and water microbial communities to better understand SP signals and the importance of and extent of water exchange in controlling the δ¹⁸O values of N₂O as well as SP values associated with production by anammox, DNRA and codenitrification. The use of inhibitors may be insightful but results should be interpreted with caution. N₂O production from fungal denitrification, for example, has recently been cited as important based on the use of antibiotics (Laughlin and Stevens 2002), however the inhibitor used does not inhibit archaea and archaea have been implicated in both nitrification and denitrification (Cabello et al. 2004; Leininger et al. 2006). Thus N₂O production in the presence of inhibitors could potentially have been the result of both fungal and archaeal activity. More

research needs to be done to evaluate SP signals from novel N₂O production pathways such as archaeal nitrification and denitrification, codenitrification, anammox and DNRA. Research evaluating isotopologue signals associated with purified enzymes is an important avenue of research for obtaining precise ϵ values in the absence of other isotope effects such as diffusion.

Accurate evaluation of the ¹⁷O anomaly in N₂O is a decisive research direction that will help resolve the global N₂O budget and potentially production pathways, such as nitrifier-denitrification, that cannot be resolved on the basis of SP. Accurate determination of the $\delta^{17}\text{O}$ of N₂O cannot be determined based on the isotopic analysis of the molecular and fragmentation ions with the mass spectrometer as this approach requires assumption of mass dependence. Evaluation of the $\delta^{17}\text{O}$ of N₂O will require decomposition of N₂O to O₂ (e.g. Thiemens 2006; Kaiser et al. 2007) but it also requires an improvement in analytical precision to resolve causes of the small (0.9 ‰) mass independent signal in N₂O. Decomposition of N₂O to O₂ followed by high precision analysis of O₂ (e.g. Barkan and Luz 2003) is potentially a viable approach for obtaining per meg (1/meg = 0.001 ‰) levels of precision for $\delta^{15}\text{N}$, $\delta^{17}\text{O}$ and $\delta^{18}\text{O}$ in N₂O.

Efforts to refine analytical approaches and data interpretation associated with the isotopomers of N₂O have an important payoff in the arena of global climate change. There is a large uncertainty in estimates of N₂O to GWP even though (1) increases in N₂O emissions primarily derive from a single source (agriculture: 70–81 %), (2) estimates for N₂O emissions from fertilized cropland and grasslands have been recently published (3.3 and 1.8 Tg N₂O-N year⁻¹, respectively) and (3) there has been a significant increase in the number of N₂O measurements from agricultural since 2002 (Barton et al. 2008). The magnitude of our uncertainty is illustrated by the large range in the 85 % confidence interval for global N₂O emissions from agricultural soils; -51 to +107 % (Barton et al. 2008). The ability to refine these uncertainties, however, will not reduce global warming. Instead, we need to reduce N₂O emissions. This is where data on N₂O isotopomers and ¹⁷O anomalies will be significant. We know that N₂O emissions primarily derived from soil microbial processes occurring in agricultural soils and that management strategies (e.g. tillage) influence environmental conditions that control microbial N₂O production pathways.

Thus, agriculture is a setting where management practices can be adjusted to minimize N₂O emissions. Effective management strategies will require knowledge of the microbial pathways that control N₂O flux effective. This is, perhaps, the most compelling call for additional and more accurate isotopomer and ¹⁷O anomaly data.

Acknowledgements This manuscript has benefited greatly from conversations over the past decade with a number of researchers and students including Tim Bergsma, Sourendra Bhattacharya, Hasand Gandhi, Eric Hegg, Matthew Opdyke, Malee Jinuntuya-Nortman, Jay Lennon, Adam Pitt, G. Phil Robertson, Robin Sutka, and Joe von Fisher. We greatly appreciate the assistance of Sakae Toyoda, Naohiro Yoshida, David Griffith and Stephen Parkes in the calibration of our internal laboratory standard. We thank two reviewers of this manuscript for their insightful comments. We thank Phil Robertson, Neville Millar, and James Humpala for assistance in the collection and/or analysis of data presented in Figs. 23.4 and 23.5.

References

- Andersson KK, Hooper AB (1983) O₂ and H₂O are each the source of one O in NO₂⁻ produced from NH₃ by nitrosomonas – N-15-NMR evidence. *FEBS Lett* 164:236–240
- Angert A, Barkan E, Barnett B, Brugnoli E, Davidson EA, Fessenden J, Maneepong S, Panapitukkul N, Randerson JT, Savage K, Yakir D, Luz B (2003) Contribution of soil respiration in tropical, temperate, and boreal forests to the ¹⁸O enrichment of atmospheric O₂. *Global Biogeochem Cy* 17:1089. doi:10.1029/2003GB002056
- Assonov SS, Brenninkmeijer CAM (2001) A new method to determine the ¹⁷O isotopic abundance in CO₂ using oxygen isotope exchange with a solid oxide. *Rapid Commun Mass Spectrom* 15:2426–2437
- Bandibas J, Vermoesen A, De Groot CJ, Cleemput OV (1994) The effect of different moisture regimes and soil characteristics on nitrous oxide emission and consumption by different soils. *Soil Sci* 158:106
- Barford CC, Montoya JP, Altabet MA, Mitchell R (1999) Steady-state nitrogen isotope effects of N₂ and N₂O production in *Paracoccus denitrificans*. *Appl Environ Microbiol* 65: 989
- Barkan E, Luz B (2003) High-precision measurements of ¹⁷O/¹⁶O and ¹⁸O/¹⁶O of O₂ and O₂/Ar ratio in air. *Rapid Commun Mass Spectrom* 17:2809–2814
- Barton L, Kiese R, Gatter D, Butterbach-Bahl K, Buck R, Hinz C, Murphy DV (2008) Nitrous oxide emissions from a cropped soil in a semi-arid climate. *Global Change Biol* 14:177–192
- Bergsma TT, Ostrom NE, Emmons M, Robertson GP (2001) Measuring simultaneous fluxes from soil of N₂O and N₂ in the field using the ¹⁵N-Gas “nonequilibrium” technique. *Environ Sci Technol* 35:4307–4312
- Bernard S, Röckmann TR, Kaiser J, Barnola JM, Fischer H, Blunier T, Chappellaz J (2006) Constraints on N₂O budget

- changes since pre-industrial time from new firn air and ice core isotope measurements. *Atmos Chem Phys* 6:493–503
- Brand WA (1995) PreCon: a fully automated interface for the Pre-Gc concentration of trace gases on air for isotopic analysis. *Isot Environ Health Stud* 31:277–284
- Brand WA, Assonov SS, Coplen TB (2010) Correction for the ^{17}O interference in $\delta(^{13}\text{C})$ measurements when analyzing CO_2 with stable isotope mass spectrometry (IUPAC technical report). *Pure Appl Chem* 82:1719–1733
- Brenninkmeijer CAM, Röckman T (2000) Mass spectrometry of the intramolecular nitrogen isotope distribution of environmental nitrous oxide using fragment-ion analysis. *Rapid Commun Mass Spectrom* 13:2028–2033
- Cabello P, Roldan MD, Moreno-Vivian C (2004) Nitrate reduction and the nitrogen cycle in archaea. *Microbiology* 150:3527
- Casciotti KL, Ward BB (2001) Dissimilatory nitrite reductase genes from autotrophic ammonia-oxidizing bacteria. *Appl Environ Microbiol* 67:2213–2221
- Casciotti KL, Ward BB (2005) Phylogenetic analysis of nitric oxide reductase gene homologues from aerobic ammonia-oxidizing bacteria. *FEMS Microbiol Ecol* 52:197–205
- Casciotti KL, Sigman DM, Hastings MG, Bohlke JK, Hilkert A (2002) Measurement of the oxygen isotopic composition of nitrate in seawater and freshwater using the denitrifier method. *Anal Chem* 74:4905–4912
- Casciotti KL, McIlvin M, Buchwald C (2010) Oxygen isotopic exchange and fractionation during bacterial ammonia oxidation. *Limnol Oceanogr* 55:753–762
- Cavigelli MA, Robertson GP (2001) Role of denitrifier diversity in rates of nitrous oxide consumption in a terrestrial ecosystem. *Soil Biol Biochem* 33:297–310
- Chapuis-Lardy L, Wrage N, Metay A, Chotte JL, Bernoux M (2007) Soils, a sink for N_2O ? A review. *Global Change Biol* 13:1–17
- Cliff SS, Thiemens MH (1994) High-precision isotopic determination of the $^{18}\text{O}/^{16}\text{O}$ ratios in nitrous-oxide. *Anal Chem* 66:2791–2793
- Cliff SS, Thiemens MH (1997) The $^{18}\text{O}/^{16}\text{O}$ and $^{17}\text{O}/^{16}\text{O}$ ratios in atmospheric nitrous oxide: a mass-independent anomaly. *Science* 278:1774–1776
- Cliff SS, Brenninkmeijer CAM, Thiemens MH (1999) First measurement of the O-18/O-16 and O-17/O-16 ratios in stratospheric nitrous oxide: a mass-independent anomaly. *J Geophys Res Atmos* 104:16171–16175
- Craig H (1957) Isotopic standards for carbon and oxygen and correction factors for mass-spectrometric analysis of carbon dioxide. *Geochim Cosmochim Acta* 12:133–149
- Crenshaw CL, Lauber C, Sinsabaugh RL, Staveland LK (2008) Fungal control of nitrous oxide production in semiarid grassland. *Biogeochemistry* 87:17–27
- Davidson EA (1993) Soil water content and the ratio of nitrous oxide to nitric oxide emitted from soil. In: Oremland R (ed) *Biogeochemistry of global change*. Chapman Hall, New York, pp 369–386
- Dore JE, Popp BN, Karl DM, Sansone FJ (1998) A large source of atmospheric nitrous oxide from subtropical North Pacific surface waters. *Nature* 396:63–66
- Dua RD, Bhandari B, Nicholas DJD (1979) Stable isotope studies on the oxidation of ammonia to hydroxylamine by *Nitrosomonas europaea*. *FEBS Lett* 106:401–404
- Esler MB, Griffith DWT, Turatti F, Wilson SR, Rahn T, Zhang H (2000) N_2O concentration and flux measurements and complete isotopic analysis by FTIR spectroscopy. *Chemosphere Global Change Sci* 2:445–454
- Farquhar GD, O'Leary MH, Berry JA (1982) On the relationship between carbon isotope discrimination and the intercellular carbon dioxide concentration in leaves. *Aust J Plant Physiol* 9:121–137
- Firestone MK, Davidson EA (1989) Microbiological basis of NO and N_2O production and consumption in soil. In: Andreae MO, Schimel DS (eds) *Exchange of trace gases between terrestrial ecosystems and the atmosphere*. Wiley, New York
- Forster P et al (2007) Changes in atmospheric constituents and in radiative forcing. In: Solomon S (ed) *Climate change 2007: the physical science basis. Contribution of working group I to the fourth assessment report of the intergovernmental panel on climate change*. Cambridge University Press, New York
- Frame C, Casciotti K (2010) Biogeochemical controls and isotopic signatures of nitrous oxide production by a marine ammonia-oxidizing bacterium. *Biogeosci Discuss* 7:3019–3059
- Friedman L, Bigeleisen J (1950) Oxygen and nitrogen isotope effects in the decomposition of ammonium nitrate. *J Chem Phys* 18:1325–1331
- Galloway JN, Aber JD, Erisman JW, Seitzinger SP, Howarth RW, Cowling EB, Cosby BJ (2003) The nitrogen cascade. *Bioscience* 53:341–356
- Garbeva P, Baggs EM, Prosser JI (2007) Phylogeny of nitrite reductase (nirK) and nitric oxide reductase (norB) genes from *Nitrosospora* species isolated from soil. *FEMS Microbiol Lett* 266:83–89
- Griffith DWT, Toon GC, Sen B, Blavier JF, Toth RA (2000) Vertical profiles of nitrous oxide isotopomer fractionation measured in the stratosphere. *Geophys Res Lett* 27:2485–2488
- Griffith DWT, Parkes SD, Haverd V, Paton-Walsh C, Wilson SR (2009) Absolute calibration of the intramolecular site preference of N-15 fractionation in tropospheric N_2O by FT-IR spectroscopy. *Anal Chem* 81:2227–2234
- Groffman PM, Altabet MA, Bohlke JK, Butterbach-Bahl K, David MB, Firestone MA, Giblin AE, Kana TA, Nielsen LP, Voytek MA (2006) Methods for measuring denitrification: diverse approaches to a difficult problem. *Ecol Appl* 16:2091–2122
- Guy RD, Fogel ML, Berry JA (1993) Photosynthetic fractionation of the stable isotopes of oxygen and carbon. *Plant Physiol* 101:37–47
- Hendriks J, Oubrie A, Castresana J, Urbani A, Gemeinhardt S, Saraste M (2000) Nitric oxide reductases in bacteria. *Biochim Biophys Acta* 1459:266–273
- Hollocher TC, Tate ME, Nicholas DJ (1981) Oxidation of ammonia by *Nitrosomonas europaea*. Definite ^{18}O -tracer evidence that hydroxylamine formation involves a monooxygenase. *J Biol Chem* 256:10834
- Jinuntuya-Nortman M, Sutka RL, Ostrom PH, Gandhi H, Ostrom NE (2008) Isotopologue fractionation during microbial reduction of N_2O within soil mesocosms as a function of water-filled pore space. *Soil Biol Biochem* 40:2273–2280

- Kaiser J (2008) Reformulated ^{17}O correction of mass spectrometric stable isotope measurements in carbon dioxide and a critical appraisal of historic "absolute" carbon and oxygen isotope ratios. *Geochim Cosmochim Acta* 72:1312–1334
- Kaiser J, Röckmann T (2005) Absence of isotope exchange in the reaction of $\text{N}_2\text{O} + \text{O}(^1\text{D})$ and the global $\Delta^{17}\text{O}$ budget of nitrous oxide. *Geophys Res Lett* 32. doi:10.1029/2005GL023199
- Kaiser J, Röckmann T (2008) Correction of mass spectrometric isotope ratio measurements for isobaric isotopologues of O_2 , CO , CO_2 , N_2O and SO_2 . *Rapid Commun Mass Spectrom* 22:3997–4008
- Kaiser J, Röckmann T, Brenninkmeijer CAM (2003) Complete and accurate mass spectrometric isotope analysis of tropospheric nitrous oxide. *J Geophys Res Atmos* 108:17
- Kaiser J, Park S, Boering KA, Brenninkmeijer CAM, Hilkert A, Röckmann T (2004a) Mass spectrometric method for the absolute calibration of the intramolecular nitrogen isotope distribution in nitrous oxide. *Anal Bioanal Chem* 378:256–269
- Kaiser J, Röckmann T, Brenninkmeijer CAM (2004b) Contribution of mass-dependent fractionation to the oxygen isotope anomaly of atmospheric nitrous oxide. *J Geophys Res Atmos* 109. doi:10.1029/2003JD003613
- Kaiser J, Hastings MG, Houlton BZ, Röckmann T, Sigman DM (2007) Triple oxygen isotope analysis of nitrate using the denitrifier method and thermal decomposition of N_2O . *Anal Chem* 79:599–607
- Kampschreur MJ, van der Star WRL, Wielders HA, Mulder JW, Jetten SM, van Loosdrecht MCM (2008) Dynamics of nitric oxide and nitrous oxide emission during full-scale reject water treatment. *Water Res* 42:812–826
- Kim KR, Craig H (1993) ^{15}N and ^{18}O characteristics of nitrous oxide – a global perspective. *Science* 262:1855–1857
- Kool DM, Wrage N, Oenema O, Dolfing J, Van Groenigen JW (2007) Oxygen exchange between (de)nitrification intermediates and H_2O and its implications for source determination of NO_3^- and N_2O : a review. *Rapid Commun Mass Spectrom* 21:3569–3578
- Kool DM, Muller C, Wrage N, Oenema O, Van Groenigen JW (2009a) Oxygen exchange between nitrogen oxides and H_2O can occur during nitrifier pathways. *Soil Biol Biochem* 41:1632–1641
- Kool DM, Wrage N, Oenema O, Harris D, Van Groenigen JW (2009b) The ^{18}O signature of biogenic nitrous oxide is determined by O exchange with water. *Rapid Commun Mass Spectrom* 23:104–108
- Kostera J, Youngblut MD, Slosarczyk JM, Pacheco AA (2008) Kinetic and product distribution analysis of NO reductase activity in *Nitrosomonas europaea* hydroxylamine oxidoreductase. *J Biol Inorg Chem* 13:1073–1083
- Kroopnick P, Craig H (1976) Oxygen isotope fractionation in dissolved oxygen in deep-sea. *Earth Planet Sci Lett* 32:375–388
- Kumar S, Nicholas DJD, Williams EH (1983) Definitive ^{15}N -NMR evidence that water serves as a source of O during nitrite oxidation by *Nitrobacter agilis*. *FEBS Lett* 152:71–74
- Kunasek S, Alexander B, Steig E, Hastings MG, Gleason D, Jarvis J (2008) Measurements and modeling of $\Delta^{17}\text{O}$ of nitrate in snowpits from Summit, Greenland. *J Geophys Res* 113. doi:10.1029/2008JD010103
- Lammerzahl P, Röckmann T, Brenninkmeijer CAM, Krankowsky D, Mauersberger K (2002) Oxygen isotope composition of stratospheric carbon dioxide. *Geophys Res Lett* 29. doi:10.1029/2001GL014343
- Laughlin RJ, Stevens R (2002) Evidence for fungal dominance of denitrification and codenitrification in a grassland soil. *Soil Sci Soc Am J* 66:1540–1548
- Leininger S, Urich T, Schloter M, Schwark L, Qi J, Nicol GW, Prosser JI, Schuster SC, Schleper C (2006) Archaea predominate among ammonia-oxidizing prokaryotes in soils. *Nature* 442:806–809
- Luz B, Barkan E (2005) The isotopic ratios $^{17}\text{O}/^{16}\text{O}$ and $^{18}\text{O}/^{16}\text{O}$ in molecular oxygen and their significance in biogeochemistry. *Geochim Cosmochim Acta* 69:1099–1110
- Madsen EL (1998) Epistemology of environmental microbiology. *Environ Sci Technol* 32:429–439
- Mandernack KW, Rahn T, Kinney C, Wahlen M (2000) The biogeochemical controls of the $\delta^{15}\text{N}$ and $\delta^{18}\text{O}$ of N_2O produced in landfill cover soils. *J Geophys Res Atmos* 105:17709–17720
- Mandernack KW, Mills CT, Johnson CA, Rahn T, Kinney C (2009) The $\delta^{15}\text{N}$ and $\delta^{18}\text{O}$ values of N_2O produced during the co-oxidation of ammonia by methanotrophic bacteria. *Chem Geol* 267:96–107
- Mariotti A, Germon JC, Hubert P, Kaiser P, Letolle R, Tardieu A, Tardieu P (1981) Experimental-determination of nitrogen kinetic isotope fractionation – some principles – illustration for the denitrification and nitrification processes. *Plant Soil* 62:413–430
- Mariotti A, Germon JC, Leclerc A (1982) Nitrogen isotope fractionation associated with the NO_2^- to N_2O step of denitrification in soils. *Can J Soil Sci* 62:227–241
- Mark E, Mark TD, Kim YB, Stephan K (1981) Absolute electron impact ionization cross section from threshold up to 180 eV for $\text{N}_2\text{O} + e \rightarrow \text{N}_2\text{O}^+ + 2e$ and the metastable and collision induced dissociation of N_2O^+ . *J Chem Phys* 75:4446–4453
- Matson P, Vitousek P, Schimel D (1989) Regional extrapolation of trace gas flux based on soils and ecosystems. In: Andreae M, Schimel D (eds) Exchange of trace gases between terrestrial ecosystems and the atmosphere. Wiley, New York, pp 97–108
- Matsuhisa Y, Goldsmith JR, Clayton RN (1978) Mechanisms of hydrothermal crystallization of quartz at 250 C and 15 kbar. *Geochim Cosmochim Acta* 42:173–182
- Meijer H, Li W (1998) The use of electrolysis for accurate $\delta^{17}\text{O}$ and $\delta^{18}\text{O}$ isotope measurements in water. *Iso Env Health Stud* 34:349–369
- Menyailo OV, Hungate BA (2006) Stable isotope discrimination during soil denitrification: production and consumption of nitrous oxide. *Global Biogeochem Cy* 20. doi:10.1029/2005GB002527
- Michalski G, Scott Z, Kabling M, Thiemens MH (2003) First measurements and modeling of $\delta^{17}\text{O}$ in atmospheric nitrate. *Geophys Res Lett* 30. doi:10.1029/2003GL017015
- Michalski G, Bohlke JK, Thiemens M (2004) Long term atmospheric deposition as the source of nitrate and other salts in the Atacama Desert, Chile: new evidence from mass-independent oxygen isotopic compositions. *Geochim Cosmochim Acta* 68:4023–4038

- Michalski G, Bhattacharya SK, Mase DF (2010) Oxygen isotopes in atmospheric nitrate. In: Baskaran M (ed) Handbook of environmental isotope geochemistry. Springer, Berlin
- Miller MF (2002) Isotopic fractionation and the quantification of ^{17}O anomalies in the oxygen three-isotope system: an appraisal and geochemical significance. *Geochim Cosmochim Acta* 66:1881–1889
- Miller CE, Yung YL (2000) Photo-induced isotopic fractionation of stratospheric N_2O . *Chemosphere Global Change Sci* 2:255–266
- Morin S, Savarino J, Bekki S, Gong S, Bottenheim JW (2007) Signature of Arctic surface ozone depletion events in the isotope anomaly ($\Delta^{17}\text{O}$) of atmospheric nitrate. *Atmos Chem Phys* 7:1451–1469
- Morin S, Savarino J, Frey MM, Domine F, Jacobi HW, Kaleschke L, Martins JMF (2009) Comprehensive isotopic composition of atmospheric nitrate in the Atlantic Ocean boundary layer from 65 degrees S to 79 degrees N. *J Geophys Res Atmos* 114:19
- Mosier A, Kroeze C (2000) Potential impact on the global atmospheric N_2O budget of the increased nitrogen input required to meet future global food demands. *Chemosphere Global Change Sci* 2:465–473
- Mosier AR, Duxbury JM, Freney JR, Heinemeyer O, Minami K (1998a) Assessing and mitigating N_2O emissions from agricultural soils. *Clim Change* 40:7–38
- Mosier A, Kroeze C, Nevison C, Oenema O, Seitzinger S, van Cleemput O (1998b) Closing the global N_2O budget: nitrous oxide emissions through the agricultural nitrogen cycle – OECD/IPCC/IEA phase II development of IPCC guidelines for national greenhouse gas inventory methodology. *Nutr Cycl Agroecosyst* 52:225–248
- Naqvi SWA, Naik H, Pratihary A, D'Souza W, Narvekar PV, Jayakumar DA, Devol AH, Yoshinari T, Saino T (2006) Coastal versus open-ocean denitrification in the Arabian Sea. *Biogeosciences* 3:621–633
- Oleary MH (1981) Carbon isotope fractionation in plants. *Phytochemistry* 20:553–567
- Opdyke MR, Ostrom NE, Ostrom PH (2009) Evidence for the predominance of denitrification as a source of N_2O in temperate agricultural soils based on isotopologue measurements. *Global Biogeochem Cy* 23. doi:10.1029/2009GB003523
- Ostrom NE, Knoke KE, Hedin LO, Robertson GP, Smucker AJM (1998) Temporal trends in nitrogen isotope values of nitrate leaching from an agricultural soil. *Chem Geol* 146:219–227
- Ostrom NE, Russ ME, Popp BN, Rust TM, Karl D (2000) Mechanisms of nitrous oxide production in the subtropical North Pacific based on determinations of the isotopic abundances of nitrous oxide and di-oxygen. *Chemosphere Global Change Sci* 2:281–290
- Ostrom NE, Hedin LO, von Fischer JC, Robertson GP (2002) Nitrogen transformations and NO_3^- removal at a soil-stream interface: a stable isotope approach. *Ecol Appl* 12:1027–1043
- Ostrom NE, Russ ME, Field A, Piwinski L, Twiss MR, Carrick HJ (2005) Ratios of community respiration to photosynthesis and rates of primary production in Lake Erie via oxygen isotope techniques. *J Great Lakes Res* 31:138–153
- Ostrom NE, Pitt A, Sutka R, Ostrom PH, Grandy AS, Huizinga KM, Robertson GP (2007) Isotopologue effects during N_2O reduction in soils and in pure cultures of denitrifiers. *J Geophys Res Biogeosci* 112. doi:10.1029/2006JG000287
- Ostrom N, Sutka R, Ostrom P, Grandy S, Huizinga K, Gandhi H, von Fischer J, Robertson G (2010) Isotopologue data reveal bacterial denitrification as the primary source of N_2O during a high flux event following cultivation of a native temperate grassland. *Soil Biol Biochem* 42:499–506
- Pérez T, Trumbore SE, Tyler SC, Matson PA, Ortiz-Monasterio I, Rahn T, Griffith DWT (2001) Identifying the agricultural imprint on the global N_2O budget using stable isotopes. *J Geophys Res* 106:9869–9878
- Pérez T, Garcia-Montiel D, Trumbore S, Tyler S, Camargo P, Moreira M, Piccolo M, Cerri C (2006) Nitrous oxide nitrification and denitrification ^{15}N enrichment factors from Amazon forest soils. *Ecol Appl* 16:2153–2167
- Popp BN, Westley MB, Toyoda S, Miwa T, Dore JE, Yoshida N, Rust TM, Sansone FJ, Russ ME, Ostrom NE, Ostrom P (2002) Nitrogen and oxygen isotopomeric constraints on the origins and sea-to-air flux of N_2O in the oligotrophic subtropical North Pacific gyre. *Global Biogeochem Cy* 16. doi:10.1029/2001GB001806
- Prasad SS, Zipf EC (2008) Atmospheric production of nitrous oxide from excited ozone and its potentially important implications for global change studies. *J Geophys Res Atmos* 113. doi:10.1029/2007JD009447
- Ravishankara AR, Daniel JS, Portmann RW (2009) Nitrous oxide (N_2O): the dominant ozone-depleting substance emitted in the 21st century. *Science* 326:123–125
- Robertson G, Groffman P (2006) Nitrogen transformations. In: Paul E, Clark F (eds) Soil microbiology, ecology and biochemistry. Springer, New York, pp 341–364
- Robertson GP, Broome JC, Chornesky EA, Frankenberger JR, Johnson P, Lipson M, Miranowski JA, Owens ED, Pimentel D, Thrupp LA (2004) Rethinking the vision for environmental research in US agriculture. *Bioscience* 54:61–65
- Röckmann T, Kaiser J, Brenninkmeijer CA, Brand WA (2003) Gas chromatography/isotope-ratio mass spectrometry method for high-precision position-dependent ^{15}N and ^{18}O measurements of atmospheric nitrous oxide. *Rapid Commun Mass Spectrom* 17:1897–1908
- Santrock J, Studley SA, Hayes JM (1985) Isotopic analyses based on the mass spectra of carbon dioxide. *Anal Chem* 57:1444–1448
- Savarino J, Morin S (2011) The N, O, S isotopes of oxy-anions in ice cores and polar environments. In: Baskaran M (ed) Handbook of environmental isotope geochemistry. Springer, Berlin
- Schmidt HL, Werner RA, Yoshida N, Well R (2004) Is the isotopic composition of nitrous oxide an indicator for its origin from nitrification or denitrification? A theoretical approach from referred data and microbiological and enzyme kinetic aspects. *Rapid Commun Mass Spectrom* 18:2036–2040
- Scott JT, McCarthy MJ, Gardner WS, Doyle RD (2008) Denitrification, dissimilatory nitrate reduction to ammonium, and nitrogen fixation along a nitrate concentration gradient in a created freshwater wetland. *Biogeochemistry* 87:99–111
- Seitzinger S, Harrison JA, Bohlke JK, Bouwman AF, Lowrance R, Peterson B, Tobias C, Van Drecht G (2006)

- Denitrification across landscapes and waterscapes: a synthesis. *Ecol Appl* 16:2064–2090
- Shoun H, Kim DH, Uchiyama H, Sugiyama J (1992) Denitrification by fungi. *FEMS Microbiol Lett* 94:277–281
- Sowers T, Alley RB, Jubenville J (2003) Ice core records of atmospheric N₂O covering the last 106,000 years. *Science* 301:945–948
- Stein LY, Yung YL (2003) Production, isotopic composition, and atmospheric fate of biologically produced nitrous oxide. *Annu Rev Earth Planet Sci* 31:329–356
- Stuka RL, Ostrom NE, Ostrom PH, Gandhi H, Breznak JA (2003) Nitrogen isotopomer site preference of N₂O produced by *Nitrosomonas europaea* and *Methylococcus capsulatus* Bath. *Rapid Commun Mass Spectrom* 17:738–745
- Stuka RL, Ostrom NE, Ostrom PH, Breznak JA, Gandhi H (2004) Erratum: nitrogen isotopomer site preference of N₂O produced by *Nitrosomonas europaea* and *Methylococcus capsulatus* Bath. *Rapid Commun Mass Spectrom* 18:1–2
- Stuka RL, Ostrom NE, Ostrom PH, Breznak JA, Gandhi H, Pitt AJ, Li F (2006) Distinguishing nitrous oxide production from nitrification and denitrification on the basis of isotopomer abundances. *Appl Environ Microbiol* 72:638–644
- Stuka R, Adams G, Ostrom NE, Ostrom P (2008) Isotopologue fractionation during N₂O production by fungal denitrification. *Rapid Commun Mass Spectrom* 22:3989–3996
- Tavares P, Pereira AS, Moura JJG, Moura I (2006) Metalloenzymes of the denitrification pathway. *J Inorg Biochem* 100:2087–2100
- Thiemens MH (2006) History and applications of mass-independent isotope effects. *Annu Rev Earth Planet Sci* 34:217–262
- Tilman D, Fargione J, Wolff B, D'Antonio C, Dobson A, Howarth R, Schindler D, Schlesinger WH, Simberloff D, Swackhamer D (2001) Forecasting agriculturally driven global environmental change. *Science* 292:281–284
- Tilsner J, Wrage N, Lauf J, Gebauer G (2003) Emission of gaseous nitrogen oxides from an extensively managed grassland in NE Bavaria, Germany II. Stable isotope natural abundance of N₂O. *Biogeochemistry* 63:249–267
- Toyoda S, Yoshida N (1999) Determination of nitrogen isotopomers of nitrous oxide on a modified isotope ratio mass spectrometer. *Anal Chem* 71:4711–4718
- Toyoda S, Mutoke H, Yamagishi H, Yoshida N, Tanji Y (2005) Fractionation of N₂O isotopomers during production by denitrifier. *Soil Biol Biochem* 37:1535–1545
- Turatti F, Griffith DWT, Wilson SR, Esler MB, Rahn T, Zhang H, Blake GA (2000) Positionally dependent ¹⁵N fractionation factors in the UV photolysis of N₂O determined by high resolution FTIR spectroscopy. *Geophys Res Lett* 27:2489–2492
- Vieten B, Blunier T, Neftel A, Alewell C, Conen F (2007) Fractionation factors for stable isotopes of N and O during N₂O reduction in soil depend on reaction rate constant. *Rapid Commun Mass Spectrom* 21:846–850
- Wahlen M, Yoshinari T (1985) Oxygen isotope ratios in N₂O from different environments. *Nature* 313:780–782
- Well R, Flessa H (2009) Isotopologue signatures of N₂O produced by denitrification in soils. *J Geophys Res Biogeosci* 114. doi:10.1029/2008JG000804
- Well R, Kurganova I, de Gerenyu VL, Flessa H (2006) Isotopomer signatures of soil-emitted N₂O under different moisture conditions – a microcosm study with arable loess soil. *Soil Biol Biochem* 38:2923–2933
- Well R, Flessa H, Xing L, Ju XT, Romheld V (2008) Isotopologue ratios of N₂O emitted from microcosms with NH₄⁺ fertilized arable soils under conditions favoring nitrification. *Soil Biol Biochem* 40:2416–2426
- Westley MB, Popp BN, Rust TM (2007) The calibration of the intramolecular nitrogen isotope distribution in nitrous oxide measured by isotope ratio mass spectrometry. *Rapid Commun Mass Spectrom* 21:391–405
- Wrage N, Velthof GL, van Beusichem ML, Oenema O (2001) Role of nitrifier denitrification in the production of nitrous oxide. *Soil Biol Biochem* 33:1723–1732
- Wrage N, Velthof GL, Oenema O, Laanbroek HJ (2004) Acetylene and oxygen as inhibitors of nitrous oxide production in *Nitrosomonas europaea* and *Nitrospira briensis*: a cautionary tale. *FEMS Microbiol Ecol* 47:13–18
- Wrage N, van Groenigen JW, Oenema O, Baggs EM (2005) A novel dual-isotope labelling method for distinguishing between soil sources of N₂O. *Rapid Commun Mass Spectrom* 19:3298–3306
- Yamagishi H, Yoshida N, Toyoda S, Popp BN, Westley MB, Watanabe S (2005) Contributions of denitrification and mixing on the distribution of nitrous oxide in the North Pacific. *Geophys Res Lett* 32. doi:10.1029/2004GL021458
- Ye RW, Torosuarez I, Tiedje JM, Averill BA (1991) H₂O-¹⁸O isotope exchange studies on the mechanism of reduction of nitric oxide and nitrite to nitrous oxide by denitrifying bacteria – evidence for an electrophilic nitrosyl during reduction of nitric oxide. *J Biol Chem* 266:12848–12851
- Yoshida N (1988) ¹⁵N-depleted N₂O as a product of nitrification. *Nature* 335:528–529
- Yoshida N, Matsuo S (1983) Nitrogen isotope ratio of atmospheric N₂O as a key to the global cycle of N₂O. *Geochem J* 17:231–239
- Yoshida N, Toyoda S (2000) Constraining the atmospheric N₂O budget from intramolecular site preference in N₂O isotopomers. *Nature* 405:330–334
- Yoshida N, Hattori A, Saino T, Matsuo S, Wada E (1984) ¹⁵N/¹⁴N ratio of dissolved N₂O in the eastern tropical Pacific Ocean. *Nature* 307:442–444
- Yoshinari T, Wahlen M (1985) Oxygen isotope ratios in N₂O from nitrification at a wastewater treatment facility. *Nature* 317:349–350
- Young ED, Galy A, Nagahara H (2002) Kinetic and equilibrium mass-dependent isotope fractionation laws in nature and their geochemical and cosmochemical significance. *Geochim Cosmochim Acta* 66:1095–1104
- Yung YL, Miller CE (1997) Isotopic fractionation of stratospheric nitrous oxide. *Science* 278:1778–1780

Chapter 24

Using Cosmogenic Radionuclides for the Determination of Effective Surface Exposure Age and Time-Averaged Erosion Rates

D. Lal

Abstract We discuss the cosmogenic method of determining exposure ages and erosion rates of exposed surfaces. This method is recognized to date as the only reliable method of quantifying important processes in geochronology, provided the exposure history of the surfaces can be successfully characterized using two or more cosmogenic nuclides produced in situ in the surfaces of interest. The success of the cosmogenic technique is based on two important characteristics of the secondary cosmic ray beam interacting with the exposed surfaces: (1) cosmic ray labeling is sensitively dependent on the geometry of exposure of the solid, and (2) the mean distance characterizing the absorption of cosmic ray beam in typical rocks is only about 50 cm. These facts make it possible to determine the past exposure history of the exposed surfaces; this task can be put on much firmer ground if information on the exposure history can be constrained based on geological information.

We summarize the early suggestions of Lal (Earth Planet Sci Lett 104:424–439, 1991) for using cosmogenic nuclides in geomorphology, as well as the complex exposure geometries considered subsequently in a paper by Lal and Chen (Earth Planet Sci Lett 236(3–4):797–813, 2005). These methods combined with the ongoing steady improvements in the AMS sensitivity should considerably widen the scope of applications of cosmic ray produced nuclides in geomorphology.

24.1 Introduction

Cosmic ray interactions in the earth's atmosphere produced several radionuclides which are used as tracers to study the motion of the atmospheric gases within the stratosphere and the troposphere, and exchange of gases between the stratosphere and the troposphere (Lal and Baskaran 2011). These tracers also provide valuable data on the movement of the stratospheric aerosols to the troposphere and their removal from the troposphere by wet precipitations and gravitational settling.

Cosmic rays continue to produce radionuclides in situ in the hydrosphere, cryosphere and the lithosphere. In the case of the latter, one can measure cosmogenic effects down to underground depths of ~300 m. They continue to be useful as tracers for studying the movement of fluid in the hydrosphere but they also serve in many different ways, e.g., to date sediments in the hydrosphere and ice layers in the cryosphere. In the lithosphere and in the cryosphere, in-situ produced radionuclides serve to provide valuable information on geomorphologic processes and solar activity, respectively. *In this chapter we would focus on how cosmic ray interactions can be used to delineate geomorphic processes, in particular surface exposure ages and surficial erosion rates* (Lal 1991, 2007; Lal and Chen 2005).

The basis of application of cosmogenic radionuclides in geomorphology is that the continuous rate at which “new” nuclides are “created” in matter, depends on the geometry and duration of irradiation. One of the most remarkable and pervasive natural phenomena which occurs on the Earth, everywhere in the Solar System, and likely in the remotest parts of the Universe, is the occurrence of nuclear interactions produced by energetic particles of the cosmic radiation,

D. Lal (✉)

Geosciences Research Division, Scripps Institution of Oceanography, 9500 Gilman Drive, La Jolla, CA 92093-0244, USA
e-mail: dlal@ucsd.edu

which fill up the galaxies as a result of occasional particle acceleration by type II supernovae. The mean kinetic energies of the primary cosmic ray particles far exceed the binding energy of nucleons in nuclei of ordinary matter, by more than 3 orders of magnitude. The lifetime of cosmic rays in our galaxy is more than 4 orders of magnitude greater than the frequency of occurrence of supernovae in which the cosmic rays are accelerated. These facts translate to a continuous nuclear bombardment of matter in the universe by cosmic ray particles, at an essentially constant rate. Two earlier papers (Lal 1991; Lal and Chen 2005) discuss this essential feature of cosmic ray labeling of erosion surfaces and consider viable models for studying geomorphic processes (Stone 2000; Gosse and Phillips 2001). Lal (1991) discussed the essentials of cosmic ray production rates of several nuclides in *terrestrial solids*, and considered first order models of exposure of surfaces eroding at constant rates, which was followed by more complex exposure models (Lal and Chen 2005).

Before proceeding further, it must be stated that in passage through the atmosphere, the cosmic ray energy and flux are both appreciably reduced at sea level; the rate of production of radioisotopes is also correspondingly appreciably reduced (Fig. 24.1 which gives the rate of nuclear disintegrations in the atmosphere at different geomagnetic latitudes). The field of cosmic ray geomorphology had therefore to wait improvements in the sensitivity of measurement of cosmogenic radioisotopes. This advance occurred with the development of the accelerator mass spectrometry (AMS), which allows direct identification and measurement of the number of atoms of a nuclide in a sample, for several nuclides of interest (Bennett et al. 1977; Nelson et al. 1977; also see reviews by Lal 1988; Tuniz et al. 1998; Gosse and Phillips 2001). Special cases here are the long-lived nuclei, such as ^{14}C (half-life = 5730 years), ^{36}Cl (half-life = 0.3 My), ^{26}Al (half-life = 0.7 My), ^{10}Be (half-life = 1.5 My) and ^{129}I (half-life = 160 My), for which the decay counting method adopted so far required working with large samples, requiring 10^9 – 10^{13} atoms for a measurement. The improvement in sensitivity with the AMS for these nuclides allows convenient study of their atoms in the range of $(10^5$ – $10^6)$ atoms/sample, whereby one can now design studies of cosmogenic effects in the troposphere, and at underground depths, thereby addressing new questions in planetary science,

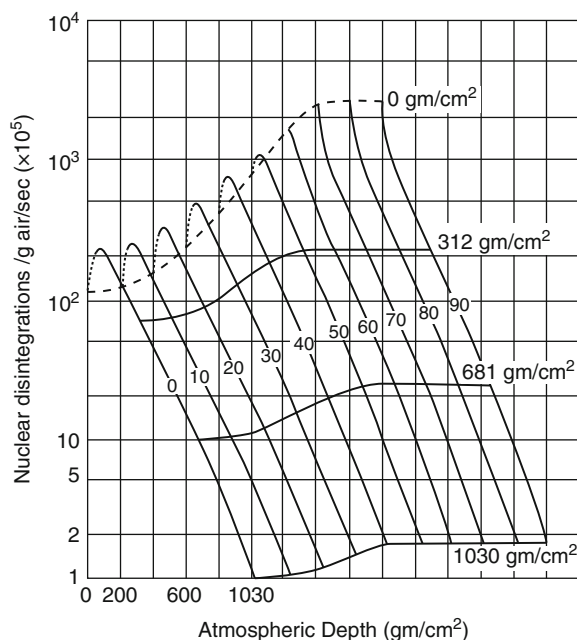


Fig. 24.1 The total rate of nuclear disintegrations in the atmosphere, with energy release of ≥ 40 MeV, is plotted as a function of altitude and geomagnetic latitude in intervals of 10° . Curves for different latitudes have been displaced along the abscissa by 200 g cm^{-2} (based on Lal and Peters 1967)

which could not be addressed earlier. There are two other obvious, highly significant advantages: (1) a reduction in the size of samples (resulting in both economy and simpler chemical processing), and (2) the rapidity with which cosmogenic effects can now be measured. Combination of these improvements allow time-series and/or synoptic measurements of cosmogenic effects in the geospheres.

24.2 Expected Cosmogenic In Situ Radionuclide Concentrations in Solids, for Eroding Surfaces

The time for which a surface has been exposed to cosmic radiation depends on its exposure history and the history of cosmic ray flux during the exposure of the surface. The cosmic ray flux at the top of the Earth's atmosphere is appreciably influenced by two parameters: (1) Geomagnetic field of the Earth, and (2) Solar activity.

1. Cosmic ray flux and nuclide production during different geomagnetic fields

If the past geomagnetic field is known, one can calculate the expected cosmogenic nuclide production rate at different geomagnetic latitudes (Lal et al. 1985; Nishiizumi et al. 1989), basing on the present day field (cf. nuclide production rates for different nuclides as given by Lal and Peters 1967). The vertical cut-off rigidity in the cosmic ray spectrum at the top of the atmosphere, $R_c (=pc/Ze)$, is given by the following relation:

$$R_c = 14.9(M/M_0) \cos^4(\lambda)$$

where p is the particle momentum, c is the speed of light, Z is the particle's atomic number, e is the electronic charge; M and M_0 are the dipole fields during an epoch in the past and during the present time, respectively, for which cosmogenic production rates in the atmosphere have been calculated (Lal and Peters 1967), and λ is the geomagnetic latitude. The corresponding geomagnetic latitude for the past, λ_M , when the dipole field was M , is given by the relation (Lal et al. 1985; Nishiizumi et al. 1989):

$$\cos(\lambda_M) = \left(\frac{M_0}{M}\right)^{1/4} \cos(\lambda_0) \quad (24.1)$$

where λ_0 is the geomagnetic latitude for the present field, M_0 .

2. Cosmic ray flux and nuclide production during periods of different solar activity

The primary galactic cosmic ray (GCR) flux incident at the top of the Earth's atmosphere is anti-correlated with solar activity (with some phase lag). See Gleeson and Axford (1968) for a convection-diffusion theoretical framework for the transport of GCR particles through the heliosphere, and see Castagnoli and Lal (1980) and Papini et al. (1996) for the essential features of the experimental data on solar modulation of primary cosmic ray flux. In terms of the solar modulation formulism (Gleeson and Axford 1968), the effective change in the energy of a charged particle moving from a point P on the boundary along a dynamical trajectory to an interior point Q is $Ze\phi$, irrespective of its path to Q. If the measured kinetic energy of a charged particle at Q is E_k /nucleon,

then it follows (Randall and Van Allen 1986) that its kinetic energy/nucleon at P must have been $(E_k + Ze\phi)$. As shown by Randall and Van Allen (1986), this leads to the following simple equation relating differential fluxes at points P and Q:

$$\frac{j_Q(T)}{T(T+2mc^2)} = \frac{j_P\left(T + \frac{Ze\phi}{A}\right)}{\left(T + \frac{Ze\phi}{A}\right)\left(T + \frac{Ze\phi}{A} + 2mc^2\right)} \quad (24.2)$$

In (24.2), A is the mass number; T is defined as the kinetic energy per nucleon, E_k ; the total kinetic energy = $A E_k$. If the point P is taken at the heliosphere boundary, and the point Q at 1 AU then the charged particle is modulated through a potential difference of ϕ MeV/nucleon.

For more than four decades, the solar modulation of cosmic ray flux has been studied using satellites/spacecraft in orbit around the Earth, and more recently on deep space probes. The range of observed variations in the modulated near-Earth differential flux of GCR protons until the late 1970s are shown in Fig. 24.2 for protons as described by different curves designated by the modulation parameter, ϕ (Randall and Van Allen 1986; Castagnoli and Lal 1980). The hypothetical curve, $\phi = 0$, corresponds to the predicted shape of the interstellar GCR proton flux, i.e. the GCR flux outside the heliosphere. Information about near Earth changes in flux have come largely from the charged particle monitoring experiment (CPME) aboard the IMP 8 satellite since 1973. For a recent summary of these data reference is made to Simunac and Armstrong (2004).

Our knowledge of modulation of GCR through the outer heliosphere comes from deep space probes (Lockwood and Webber 1995) which transmitted in situ cosmic ray data up to distances of more than 70 AU (Pioneers 10 and 11, Voyagers 1 and 2). For details see Lal (2007). Nuclide production rates for different geomagnetic field intensities and modulation parameters, ϕ , have been calculated earlier (cf. Lal 1992).

3. Present day nuclide production rates at different latitudes and at altitudes ≤ 10 km

If the production rate of a nuclide in a rock/soil is known at some latitude and altitude (≤ 10 km), then

Fig. 24.2 Estimated proton spectra for different solar modulation intensities as defined by the parameter, ϕ . The curve labeled $\phi = 0$ corresponds to the unmodulated proton spectra outside the heliosphere

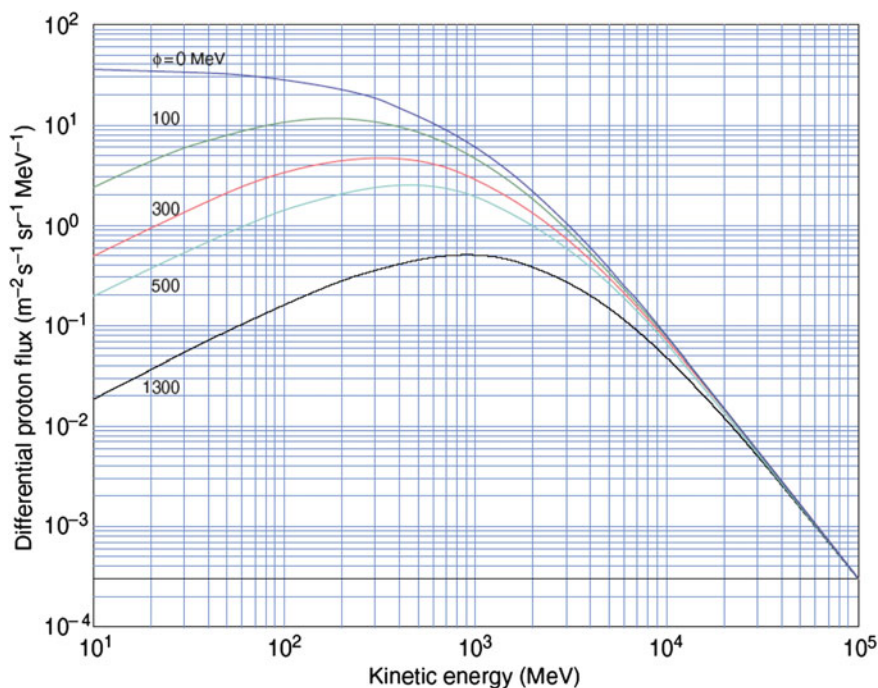


Table 24.1 Nuclear disintegration rates (Lal and Peters 1967) in the atmosphere ($\text{g}^{-1} \text{year}^{-1}$)

Geomagnetic latitude (degrees)	Polynomial coefficients ^a			
	a1	a2	a3	a4
0	3.307×10^2	2.559×10^2	9.843×10^1	2.050×10^1
10	3.379×10^2	2.521×10^2	1.110×10^2	2.073×10^1
20	3.821×10^2	2.721×10^2	1.325×10^2	2.483×10^1
30	4.693×10^2	3.946×10^2	9.776×10^1	4.720×10^1
40	5.256×10^2	5.054×10^2	1.420×10^2	5.887×10^1
50	5.711×10^2	5.881×10^2	1.709×10^2	7.612×10^1
60–90	5.634×10^2	6.218×10^2	1.773×10^2	7.891×10^1

^aThe polynomials (24.3) are valid for 0–10 km altitudes

the production rate at other latitudes and altitudes can be derived using the scaling factors given by Lal and Peters (1967). The scaling factors are primarily based on thermal neutron measurements and take into account the thresholds for nuclide production from the targets of interest (Lal 1958). Third degree polynomials are presented by Lal (1991) for nuclear disintegrations ($\text{g}^{-1} \text{air year}^{-1}$) in the atmosphere in Table 24.1, based on Lal and Peters (1967), and for ^{10}Be and ^{26}Al in quartz ($\text{g}^{-1} \text{year}^{-1}$), based on measurements in quartz from glacially polished rocks (Nishiizumi et al. 1989). The nuclear disintegration rates or the production rates of ^{10}Be , and ^{26}Al in quartz are given by the corresponding polynomial coefficients, P_1 , P_2 , P_3 and P_4 for $q(L, y)$:

$$q(L, y) = P_1(L) + P_2(L)y + P_3(L)y^2 + P_4(L)y^3 \tag{24.3}$$

where $q(L,y)$ is the nuclear disintegration rate in the atmosphere or ^{10}Be or ^{26}Al production rate in quartz ($\text{g}^{-1} \text{SiO}_2 \text{year}^{-1}$) at latitude L , and altitude y (km). The polynomial coefficients are given separately for latitudes: 0, 10, 20, 30, 40, 50, 60–90°, in Tables 24.1 and 24.2.

For completeness we give here the third degree polynomial for converting altitude (y km) to pressure, P (g cm^{-2}), based on the ICAO standard atmosphere (International Civil Aviation Organization 1964):

$$P = p1 + p2 \cdot y + p3 \cdot y^2 + p4 \cdot y^3 \tag{24.4}$$

Table 24.2 Production rates of ^{10}Be and ^{26}Al in quartz ($\text{g}^{-1} \text{SiO}_2 \text{ year}^{-1}$)

Geomagnetic latitude (degrees)	Polynomial coefficients ^a							
	a		b		c		d	
	^{10}Be	^{26}Al	^{10}Be	^{26}Al	^{10}Be	^{26}Al	^{10}Be	^{26}Al
0	3.511	21.47	2.547	15.45	0.9512	5.751	0.18608	1.1154
10	3.596	22.00	2.522	15.32	1.0668	6.444	0.188229	1.1287
20	4.0607	24.84	2.734	16.61	1.2673	7.652	0.2253	1.3504
30	4.994	30.55	3.904	23.67	0.9739	5.911	0.42671	2.5563
40	5.594	34.21	4.946	29.92	1.3817	8.361	0.53176	3.1853
50	6.064	37.08	5.715	34.57	1.6473	9.955	0.68684	4.1138
60–90	5.994	36.67	6.018	36.38	1.7045	10.3	0.71184	4.2634

^aThe polynomials (24.3) are valid for 0–10 km altitudes

where $p_1 = 1032.92$; $p_2 = -121.95$; $p_3 = 5.657$; $p_4 = -0.1095$.

For scaling factors for ^{14}C , reference is made to Miller et al. (2006) and Lifton et al. (2001). Earlier scaling factors for ^3He and $^{20,21,22}\text{Ne}$ are given in Lal (1991) but they have since been considerably improved as a result of efforts made by scientists working jointly in the CRONUS-Earth Project (Cosmic ray produced systematics on Earth Project; Stuart and Dunai 2009).

4. Expected nuclide concentrations in exposed rocks for first order exposure models

As expected, the principal obstacle in determining surface exposure ages or erosion rates is the lack of knowledge regarding the rock's surface exposure history. For example, the rock may have been covered with sediment or have had undergone exfoliation during its prior exposure history. Further, the erosion rate may have varied with climate in the past. Clearly, any evidence from the geologic history of the rock is of paramount importance.

Since the production of cosmogenic nuclides within the rock is a sensitive function of the geometry of the rock, use of two or more cosmogenic nuclides can help constrain the exposure history of the rock. In an earlier paper, Lal (1991) considered the effects of changes in exposure geometry, and also considered first order exposure models. In a subsequent paper, Lal and Chen (2005) considered more complicated exposure geometries and considered possibilities of constraining exposure histories using cosmogenic data alone.

In the following, we will discuss first order exposure models and develop simple equations to bring out salient features of the cosmogenic method, for

instance, the constraints on exposure history that are possible using two or more cosmogenic nuclides.

For simplicity, we will consider a horizontal rock surface; complex rock geometries have been considered by Lal and Chen (2005). As the surface of a rock horizon is exposed, nuclear interactions of cosmic rays produce nuclides at the exposed surface and at depths. The number of atoms of radio-nuclides at time t , $N(x,t)$ within the rock at any depth, $x(t)$ are given by the following differential equation:

$$\frac{dN(x,t)}{dt} = -N(x,t) + P(x,t) \quad (24.5)$$

where λ is the disintegration constant of the nuclide and $P(x,t)$ is the nuclide production rate at depth x (cm), and time t (s). If one considers nuclide production by nucleons, then the nuclide production rate, $P(x,t)$ is fairly well described by the equation:

$$P(x,t) = P(0,t) e^{-\mu \rho x(t)} \quad (24.6)$$

where μ ($\text{cm}^{-2} \text{g}^{-1}$) is the absorption coefficient (inverse of μ is defined as the absorption mean free path (g cm^{-2}) in the rock). The absorption mean free path is altitude and latitude dependant (Table 24.3).

The value of $x(t)$ in (24.2) is given by the integral:

$$x(t) = \int_0^t \varepsilon(t) dt \quad (24.7)$$

- (a) Special case of fixed erosion rate, fixed cosmic ray production rate and uniform erosion history of the surface

If one assumes a constant erosion rate, ε , and constant cosmic ray nuclide production rate, P_0 at the rock

Table 24.3 Absorption mean free paths in the atmosphere for nuclear disintegrations of energy release >40 MeV

Altitude range (km)	Mean free path (g cm ⁻²)		
	0°	30°	60°
0-5	160	150	140
5-10	175	160	150

surface, then the solution of (24.1) nuclide concentration at time t , at depth x can also be written in the integral form:

$$N(x, T) = \int_0^T P_0 e^{-\mu \rho (x+\varepsilon t)} \cdot e^{-\lambda(T-t)} dt \quad (24.8)$$

integrating backwards in time, setting the present time at 0, and $t = T$, when the rock was first exposed to cosmic radiation, as T , the total duration of the exposure.

Solving (24.5) or (24.8) gives the nuclide concentration, $N(x, T)$ in the rock at depth, x :

$$N(x, T) = \frac{P_0}{\lambda + \mu \varepsilon} e^{-\mu x} (1 - e^{-T(\lambda + \mu \varepsilon)}) \quad (24.9)$$

If however, the rock sample had some initial concentration of the radionuclide at the start of the irradiation, $N(x, 0)$, then an additional term, $N(x, 0) \exp(-\lambda T)$ should be added to (24.9).

Equation (24.9) states that if a rock surface undergoes *steady state erosion*, the in situ radionuclides attain secular equilibrium concentration corresponding to an effective disintegration constant, $\lambda + \mu \varepsilon$. The effective irradiation time, T_{eff} for the top surface of the rock is then given by:

$$T_{\text{eff}} = N\left(0, T \gg \frac{1}{\lambda + \mu \varepsilon}\right) / P_0 = \frac{1}{\lambda + \mu \varepsilon} \quad (24.10)$$

The validity of a steady state model can be tested by studying two or more radionuclides of different half-lives in the rock surface. The model steady state erosion at the surface is then given by, based on (24.5):

$$\varepsilon = \frac{1}{\mu} \left[\frac{P(0)}{N(0, T)} - \lambda \right] = \frac{1}{\mu} \left[\frac{1}{T_{\text{eff}}} - \lambda \right] \quad (24.11)$$

If the rock had been undergoing steady state erosion for periods of the order of $\geq(4-5)$ times T_{eff} , it

follows from (24.11) that the quantities below are invariant for different radionuclides:

$$\begin{aligned} \left(\frac{P(0)}{N(0, T)} \right)_1 - \lambda_1 &= \left(\frac{P(0)}{N(0, T)} \right)_2 - \lambda_2 \\ &= \left(\frac{P(0)}{N(0, T)} \right)_3 - \lambda_3 \end{aligned} \quad (24.12)$$

Note that the validity of (24.8) does not necessarily imply that surface has been undergoing erosion on a micro-scale. However it does imply that if the rock has undergone macro-erosion, then the chip-off distances have always been much \ll than the distance $1/\mu$.

The suitability of a radionuclide for determining the erosion rate of a rock horizon is determined by the condition that λ and $\mu \varepsilon$ should be of the same order; in other words T_{eff} and the mean half-life of the radionuclide, λ , should be of the same order. If $\lambda \gg \mu \varepsilon$, the radionuclide would be built to its secular equilibrium value ($T_{\text{eff}} = 1/\lambda$) and no information can be obtained from its study about the erosion rate. Else if $\mu \varepsilon \gg 1$, the nuclide concentrations would build up to the same concentration independent of the half-life of the radionuclide. In this case, the nuclide decay during the build-up period is unimportant and the nuclide behaves similar to a stable nuclide. Also, in this case ($\mu \varepsilon \gg 1$), the apparent surface exposure age, $T_{\text{eff}} = 1/\mu \varepsilon$, i.e. it is the time during which erosion removes a rock depth equivalent to one absorption mean free path for cosmic rays, $1/\mu$, ~ 50 cm in common rocks.

Under steady state, the nuclide build up is shown in Fig. 24.3 for five radionuclides, ³⁹Ar, ¹⁴C, ³⁶Cl, ²⁶Al and ¹⁰Be, and a stable nuclide. These curves are dependent on the values of ε and λ , and provide useful insight if the exposure history of the rock deviates from the assumed steady state erosion (24.10).

If two radionuclides are used, e.g., ¹⁰Be and ²⁶Al, their steady state concentrations are well described for all erosion rates by the shadowed curve in Fig. 24.4, labelled “steady state erosion island”. The temporal evolution of the curves is given by the following:

$$\begin{aligned} \text{Ratio } (^{26}\text{Al}/^{10}\text{Be})_t &= \frac{P(0)_{^{26}\text{Al}}}{P(0)_{^{10}\text{Be}}} \cdot \frac{\lambda_{^{10}\text{Be}} + \mu \varepsilon}{\lambda_{^{26}\text{Al}} + \mu \varepsilon} \frac{(1 - e^{-t(\lambda_{^{26}\text{Al}} + \mu \varepsilon)})}{(1 - e^{-t(\lambda_{^{10}\text{Be}} + \mu \varepsilon)})} \end{aligned} \quad (24.13)$$

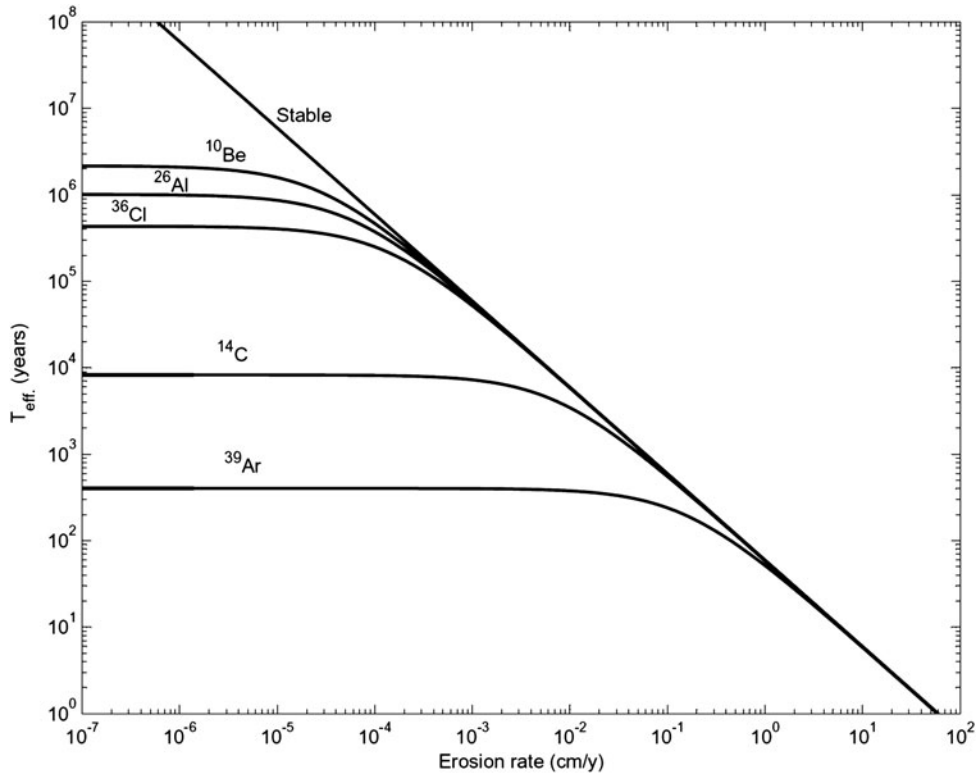


Fig. 24.3 Effective steady state surface exposure ages, T_{eff} (24.6), as a function of erosion rates for five radionuclides, ^{39}Ar , ^{14}C , ^{36}Cl , ^{26}Al and ^{10}Be , and a stable nuclide

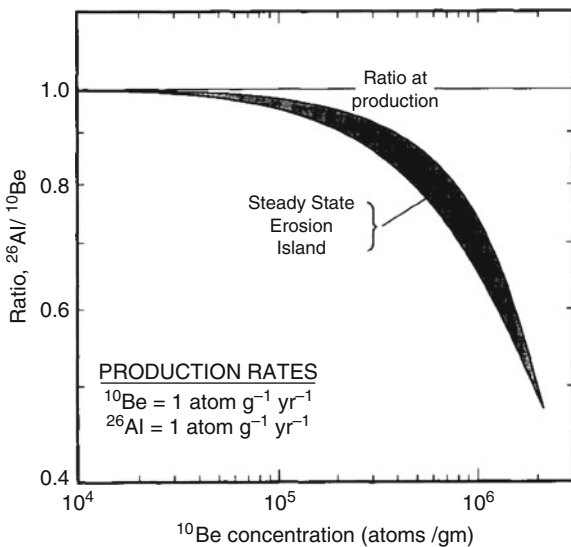


Fig. 24.4 Theoretically calculated steady state build up of $^{26}\text{Al}/^{10}\text{Be}$ ratio and ^{10}Be concentration for hypothetical production rates of $1 \text{ atom g}^{-1} \text{ yr}^{-1}$ for both ^{10}Be and ^{26}Al . The *steady state erosion island* includes the temporal build up of radionuclide concentrations as given by (24.9) for all erosion rates. In steady state all regions above the shaded curve are forbidden

with the ratio lying between two limits:

$$\left[\frac{P(0)_{^{26}\text{Al}}}{P(0)_{^{10}\text{Be}}} \right] \quad \text{and} \quad \left[\frac{P(0)_{^{26}\text{Al}}}{P(0)_{^{10}\text{Be}}} \cdot \frac{\lambda_{^{10}\text{Be}}}{\lambda_{^{26}\text{Al}}} \right] \quad (24.14)$$

corresponding to large and small erosion rates, respectively.

(b) Complex cosmic ray irradiation histories

If the exposure history of the rock is simple as so far considered: a flat rock surface, eroding at a constant rate, curves like that shown in Fig. 24.4 for ^{26}Al and ^{10}Be can be used to ascertain its veracity. One can list a number of complex rock irradiation histories: for instance (1) rock's of different geometrical shapes, (2) the top surface spalls off sometime in the past during irradiation, and (3) the top surface is buried under a layer of sediment. The first case has been considered in some detail by Lal and Chen (2005), who have considered a spheroidal target, a rectangular geometry with a flat top, a sloping surface and a beach terrace with a flat top. The second case of a rock

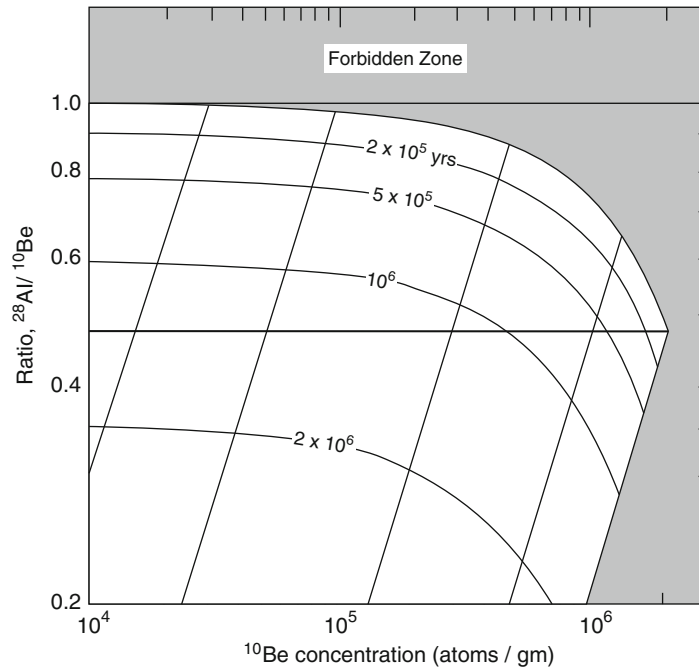


Fig. 24.5 The upper bound of the curve corresponds to temporal evolution for the case of $\varepsilon = 0$, as also in Fig. 24.4. The straight lines denote the path traced by the rock surface after the

top surface was shielded by a thick sediment or rock fragments. The production rates are fixed at 1 atom g^{-1} ^{10}Be and ^{26}Al in the rock

surface spalling of has been considered in detail by Lal (1991), who have considered two cases as examples: the effective exposure age of the rock is (1) small compared to the mean life of the radionuclide, and (2) comparable to the mean life. The third case was in fact discovered in a real case of a soil profile based on studies of ^{14}C and ^{10}Be (Lal et al. 1996). Reference is also made to Miller et al. (2006), who studied ice sheet erosion and complex exposure histories in Bafin Island, Arctic Canada, based on ^{14}C , ^{26}Al and ^{10}Be .

We will not consider here the cases of complex rock geometries since these have been dealt with in detail by Lal and Chen (2005), and also the case (2) of rock spall during cosmic ray exposure (Lal 1991). The third case is an interesting one since in some cases the rock surface may be shielded by a thick sediment or rock layer. In this case, if the shielding of rock surface is substantial, the shorter lived radioisotope would decay much faster than the longer lived radionuclide (Lal 1991), providing an information on the time for which the rock surface was shielded. As a case in point we consider the special case of a rock surface which was exposed under zero erosion rate evolving finally to a ratio, $^{26}\text{Al}/^{10}\text{Be}$:

$$\text{Ratio } (^{26}\text{Al}/^{10}\text{Be})_{\text{Steady State and } \varepsilon=0} = \frac{P(0)_{^{26}\text{Al}}}{P(0)_{^{10}\text{Be}}} \cdot \frac{\lambda_{^{10}\text{Be}}}{\lambda_{^{26}\text{Al}}} \quad (24.15)$$

corresponding to the top curve in Fig. 24.5. If during the evolution of this curve, the rock surface is overlain by a thick deposit of sediment or rock fragments, the ratio $^{26}\text{Al}/^{10}\text{Be}$ and the ^{10}Be concentration will evolve along the example straight lines due to faster decay of ^{26}Al compared to ^{10}Be . These points would generally lie outside the “steady state erosion island” in Fig. 24.4, and can be used to find out if the rock surface was part of the time or continuously shielded on the top surface by a thick sediment layer or rock fragments.

24.3 Future Directions

In this chapter, we have discussed that cosmic ray labeling of erosion surfaces allows one to determine both cosmic ray exposure ages and surface erosion rates. Several radionuclides are produced in situ

rocks/soils from major target elements, e.g., ^{39}Ar , ^{14}C , ^{36}Cl , ^{26}Al and ^{10}Be . This task is accomplished fairly well using two or more radionuclides produced in situ in the rock by cosmic rays.

The single most salient feature of cosmic ray labeling of erosion surfaces is the high sensitivity of the rate of in situ nuclear interactions on the geometry of the irradiation. Note also that the mean absorption distance for cosmic radiation in typical rocks is ~50 cm only. The text in this chapter along with ideas discussed by Lal (1991) and Lal and Chen (2005) cover most of the ideas, which allow one to put severe constraints on the “unknown” exposure history of the rock horizon. As an example: Use of the shorter half-life radionuclides, ^{39}Ar , ^{14}C and ^{36}Cl , in conjunction with ^{10}Be allow one to put severe constraints on the “unknown” rock exposure histories. This task can be put on much firmer ground if information on the exposure history can be constrained based on geological information.

24.4 Conclusion

The cosmogenic nuclear method described in this chapter, bases itself on the fact that several radionuclides are produced in situ in rocks/soils from major target elements. As stated earlier, the single most salient feature of cosmic ray labeling of erosion surfaces is the high sensitivity of the rate of in situ nuclear interactions on the geometry of the irradiation, coupled with the fact that the mean absorption distance for cosmic radiation in typical rocks is ~50 cm.

In the absence of information on the exposure histories of the rock surfaces studied, several ideas to constrain exposure histories were discussed by Lal (1991) and Lal and Chen (2005); these allow one to put severe constraints on the “unknown” exposure history of the rock horizon. As an example, use of the *shorter* half-life radionuclides, ^{39}Ar , ^{14}C and ^{36}Cl , in conjunction with ^{10}Be allow one to put severe constraints on the “unknown” rock exposure histories.

Estimation of exposure ages and erosion requires an accurate knowledge of nuclide production rates. Realizing the importance of determining accurate time scales in earth sciences, several scientists have joined a project “Cosmic ray produced nuclide systematics on Earth project (CRONUS-Earth Project)”

for improving rates of production of cosmogenic nuclides in targets exposed to cosmic radiation under different conditions. These improvements combined with the steady improvements in the AMS sensitivity (cf. Galindo-Uribarri et al. 2007) should considerably widen the scope of applications of cosmic ray produced nuclides in geomorphology.

References

- Bennett CL, Beukens RP, Clover MR, Gove HE et al (1977) Radiocarbon dating using electrostatic accelerators: negative ions provide the key. *Science* 198:508–510
- Castagnoli G, Lal D (1980) Solar modulation effects in terrestrial production of carbon 14. *Radiocarbon* 22:133–158
- Galindo-Uribarri A et al (2007) Pushing the limits of accelerator mass spectrometry. *Nucl Instr Meth Phys Res B* 299:123–130
- Gleeson LJ, Axford WI (1968) Solar modulation of galactic cosmic rays. *Astrophys J* 423:426–431
- Gosse JC, Phillips FM (2001) Terrestrial in situ cosmogenic nuclides: theory and application. *Quat Sci Rev* 20:1475–1560
- International Civil Aviation Organization (1964) Manual of the ICAO standard atmosphere, 2nd edn. International Civil Aviation Organization, Montreal
- Lal D (1958) Investigations of nuclear interactions produced by cosmic rays. Ph.D. Thesis, Bombay University
- Lal D (1988) In-situ produced cosmogenic isotopes in terrestrial rocks. *Ann Rev Earth Planet Sci Lett* 16:355–388
- Lal D (1991) Cosmic ray tagging of erosion surfaces: in situ production rates and erosion models. *Earth Planet Sci Lett* 104:424–439
- Lal D (1992) Expected secular variations in the global terrestrial production rate of radiocarbon. In: Bard E, Broecker WS (eds) *The last deglaciation: absolute and radiocarbon chronologies*. NATO ASI series, vol 12. Springer, Berlin, pp 113–126
- Lal D (2007) Cosmic ray interactions in minerals. In: Elias SA (ed) *Encyclopedia of quaternary science*. Elsevier, Oxford, pp 419–436
- Lal D, Baskaran M (2011) Applications of cosmogenic-isotopes as atmospheric tracers. In: Baskaran M (ed) *Handbook of environmental isotope geochemistry*. Springer, Heidelberg
- Lal D, Chen J (2005) Cosmic ray labeling of erosion surfaces II: special cases of exposure histories of boulders, soils and beach terraces. *Earth Planet Sci Lett* 236(3–4):797–813
- Lal D, Peters B (1967) Cosmic ray produced radioactivity on the earth. In: Flugge S (ed) *Handbook der Physik*, vol 46/2. Springer, Berlin, pp 551–612
- Lal D, Arnold JR, Nishiizumi K (1985) Geophysical records of a tree: new application for studying geomagnetic field and solar activity changes during the past 10^4 years. *Meteoritics* 20(2):403–414
- Lal D, Pavich M, Gu ZY, Jull AJT et al (1996) Recent erosional history of a soil profile based on cosmogenic in-situ radionuclides ^{14}C and ^{10}Be . In: Basu A, Hart S (eds) *Earth processes reading the isotopic code*. Geophysics monograph series, vol 95, pp 371–376

- Lifton NA, Jull AJT, Quade J (2001) A new extraction technique and production rate estimate for in situ cosmogenic ^{14}C in quartz. *Geochim Cosmochim Acta* 65:1953–1969
- Lockwood JA, Webber WR (1995) An estimate of the location of modulation boundary for $E > 70$ MeV galactic cosmic rays using voyager and pioneer spacecraft data. *Astrophys J* 442:852–860
- Miller GH, Briner JP, Lifton NA, Finkel RC (2006) Limited ice-sheet erosion and complex exposure histories derived from in situ cosmogenic ^{10}Be , ^{26}Al and ^{14}C on Baffin Island, Arctic Canada. *Quat Geochronol* 1:74–85
- Nelson DE, Koertling RG, Stott WR (1977) Carbon-14: direct detection at natural concentrations. *Science* 198:507–508
- Nishiizumi K, Winterer EL, Kohl CP, Lal D et al (1989) Cosmic ray production rates of ^{10}Be and ^{26}Al in quartz from glacially polished rocks. *J Geophys Res* 94:17907–17916
- Papini P, Grimani C, Stephens SA (1996) An estimate of the secondary proton spectrum at small atmospheric depths. *Nuovo Cimento* 19C(3):367–388
- Randall BA, Van Allen JA (1986) Heliocentric radius of the cosmic ray modulation boundary. *Geophys Res Lett* 13:628–631
- Simunac KDC, Armstrong TP (2004) Solar cycle variations in solar and interplanetary ions observed with interplanetary monitoring platform. *J Geophys Res* 109:A10101
- Stone JO (2000) Air pressure and cosmogenic isotope production. *J Geophys Res* 105(10):23753–23759
- Stuart GM, Dunai TJ (2009) Advances in cosmogenic isotope research from CRONUS-EU. *Quat Geochronol* 4(6): 435–436
- Tuniz C, Bird JR, Fink D, Herzog GF (1998) Accelerator mass spectrometry. CRC Press, Washington, p 371

Chapter 25

Measuring Soil Erosion Rates Using Natural (^7Be , ^{210}Pb) and Anthropogenic (^{137}Cs , $^{239,240}\text{Pu}$) Radionuclides

Gerald Matisoff and Peter J. Whiting

Abstract This chapter examines the application of natural (^7Be and ^{210}Pb) and anthropogenic fallout radionuclides (^{134}Cs , ^{137}Cs , $^{239,240}\text{Pu}$) to determine soil erosion rates. Particular attention is given to ^{137}Cs because it has been most widely used in geomorphic studies of wind and water erosion. The chapter is organized to cover the formation and sources of these radionuclides; how they are distributed in precipitation and around the globe: their fate and transport in undisturbed and tilled soils; and their time scales of utility. Also discussed are methods for soil collection, sample preparation for ^{137}Cs analysis by gamma spectroscopy, and the selection of standards and instrument calibration. Details are presented on methods for calculating soil erosion, including empirical methods that are related to the Universal Soil Loss Equation (USLE), box models that compare ^{137}Cs activities in a study site to a reference site, and time dependent methods that account for the temporal inputs of ^{137}Cs and precipitation induced erosion. Several examples of recent applications, including the combination of radionuclides with other techniques or measurements, are presented. The chapter concludes with suggestions for future work: the value of new methods and instrumentation to allow for greater spatial resolution of rates and/or greater accuracy; the need to incorporate migration of radionuclides in the time-dependent models; the opportunities to concurrently use the global and Chernobyl signals to better understand temporal variation soil erosion processes and rates; and the importance of the use of these tracers to characterize C storage and cycling.

G. Matisoff (✉) and P.J. Whiting
Department of Geological Sciences, Case Western Reserve
University, Cleveland, OH 44106-7216, USA
e-mail: gerald.matisoff@case.edu; peter.whiting@case.edu

25.1 Introduction

25.1.1 Soil Erosion; Nature of the Problem

Soil is among our most fundamental resources and soil processes help regulate atmospheric composition and climate. Soil anchors and sustains the vegetation that provides sustenance for animals and humans and provides fibers and material used in everything from cotton for clothing to lumber for homes to biomass for energy. The soil itself can be mined for key materials, minerals and metals, and energy. The foundations of most human structures – homes, buildings, and roads – are built on soil. Soil and soil processes filter water, reduce toxicity of airborne pollutants delivered to the land surface, and store carbon and nutrients. The value of soil in terms of ecosystem function and service has been estimated in the hundreds of billions of dollars per year (Pimental et al. 1995).

A comprehensive understanding of material fluxes on the earth surface and its effects on geochemical cycles (hydrologic, C, and N), atmospheric composition and climate, and ocean chemistry depends upon an understanding of soil and soil movement on the landscape including erosion, transport, and deposition. Soils sequester C and N from the atmosphere and retain certain metals during the weathering of rocks, but soil erosion either moves those materials to places of long-term storage or exposes soils to greater reactivity. Soils hold 2,300 Gt of carbon, about four times as much carbon as is in the atmosphere (Lal 2003). It has been suggested that if carbon on the landscape lost by erosion is replaced by new vegetative growth, then intermediate storage in fluvial systems of the eroded carbon represents a net removal of carbon from the atmosphere and

may be the “missing” anthropogenic carbon (Harden et al. 1992; Stallard 1998). Others note that oxidation of a portion of the carbon in transport may produce 0.8–1.2 GtC per year. Thus anthropogenically enhanced soil erosion may reinforce global warming.

Soil is moved by a variety of processes including water (splash, sheetwash, rills), wind, ice (freeze-thaw, glaciers, periglacial), gravity (dry ravel, creep, toppling, debris flows, earthflows), tillage, and bioturbation. Erosion is often accelerated by disturbance (clearing, fire, plowing, overgrazing, compaction, or desiccation) that disrupts soil structure and removes vegetative covering. Oldeman (1994) estimated that 1,094 Mha (1 ha = 10⁴ m²) are affected by water erosion and 549 Mha by wind erosion. These numbers represent 12 and 6% of agricultural land areas, respectively. Total erosion of these areas is approximately 75 billion tons/year (Pimental et al. 1995).

The net loss of soil has both on-site and off-site consequences as summarized by Pimental et al. (1995). In croplands, the diminished fertility due to topsoil erosion requires fertilization or results in diminished yields, creates pressure to deforest new areas as fertility of existing cropland decreases, and results in the loss in water holding capacity of soils. Fertilization, in turn, often has its own consequences. Most fertilizers rely on fossil fuels to create, ship, and apply the material and the applied fertilizer has the potential for creating downstream water quality concerns. The additional water use required because of diminished soil retention taxes another critical resource. In forestlands, soil loss can change species composition, diminish water-holding capacity, and speed desertification. In suburban and urban areas, soil loss can reduce the ability of soils to sustain vegetative cover and trees helpful in addressing air, water, heat, and sound pollution.

Fine sediments derived from erosion of soil are disproportionately responsible for degradation of surface waters (Nelson and Logan 1983; Dong et al. 1984). Eroded soil impairs water quality (Sekely et al. 2002; Sharpley et al. 1994; Pote et al. 1996) to the point that drinking water supplies, aquatic environments, and opportunities for recreation are threatened. Eroded soil often harms aquatic environments by inhibiting light penetration (Yamada and Nakamura 2002), by siltation of rivers (Reiser 1998) and reservoirs (Williams and Wolman 1984), by eutrophication of waterways, lakes, and seas (Rabalais et al.

1999), and by contamination (Tarras-Wahlberg and Lane 2003). In 2000, the US Environmental Protection Agency reported that siltation debilitated 12% of the stream reaches assessed by states and tribes and was responsible for 33% of impairments to beneficial use (USEPA 2000). In areas where wind is an important process of erosion, the transported fine material can be a health problem, foul equipment, and cause abrasion requiring the repainting of structures (Lyles 1985).

History shows that civilization can collapse as the soil resource is depleted (Montgomery 2007; Diamond 2005; Hyams 1952). Plato ascribed the poor soils of his native Attica to erosion after land clearing and his view of the causative factors of poor soil was shared by Aristotle (Montgomery 2007). Loss of production associated with soil loss and degradation ultimately affected the stability of the Greek civilization as it did the Romans later. Lowdermilk (1953) describes a trail of societies from Judea to Syria to China where poor stewardship of the land and resulting erosion led indirectly to conquest or societal discord. More recent examples of societal dislocations (famine and migration) associated with soil erosion and land degradation include the Dustbowl of the 1930s, the Sahel of the 1970s, and Haiti.

25.1.2 Tools for Measuring Soil Erosion

Critical to the understanding and quantification of soil erosion are tools for its measurement. Erosion pins, sediment accumulated in reservoirs, measured sediment concentration in streamflow, photographic techniques, and soil tracers each have their usefulness and limitations. Sediment budgets (Dietrich and Dunne 1978) are often a basis for quantifying the various processes and paths that move soil on the landscape and result in local loss (erosion) and local gain (deposition) of soil.

A particularly useful tool for measuring soil erosion is a conservative tracer of the soil particles, especially when the tracer is relatively easy to measure. Important considerations in the use of a tracer are that the concentration of the tracer is relatively uniform; adsorption of the tracer to soil is strong and quick; variation in adsorption to various sizes or mineralogic/organic constituents is minor or can be accounted for; and methods exist to measure the tracer.

The best known of the tracers for estimating soil erosion are natural and anthropogenic radionuclides. The anthropogenic radionuclides found on the landscape were produced largely by atmospheric nuclear bomb testing and the fallout was distributed globally. The list of fission products is extensive, although many of these radionuclides are too short-lived to be useful tracers of soil erosion. Of the longer-lived fission products, the best known is ^{137}Cs , but the list of other useful tracers includes ^{134}Cs , $^{238,239,240}\text{Pu}$, and ^{241}Am as minute solid particles or sorbed to soil particles; and ^3H and ^{90}Sr as soluble tracers. The naturally-occurring radionuclides are produced by various nuclear reactions, or uranium or thorium decay chains (Porcelli and Baskaran 2011) and include ^7Be , ^{210}Pb and a few others. ^{137}Cs , ^7Be , and ^{210}Pb are each suitable as particle tracers because they have a global distribution, adsorb efficiently to soil particles and thus move with soil, and are relatively easily measured.

^{137}Cs is the most widely used radionuclide tracer for soil erosion (Ritchie and McHenry 1990). For years, Ritchie and Ritchie (2008) maintained a bibliography of publications that utilized ^{137}Cs in the study of soils and sedimentation. Figure 25.1, redrafted from Ritchie and Ritchie (2008) and updated here to include papers published after December 15, 2008, illustrates how widespread the use of ^{137}Cs as a tracer has been. There are a total of about 4,500 Cs references with the vast

majority of the papers following the Chernobyl accident in 1986. In comparison, there are about 2,700 references to the use of ^{210}Pb in studies of soils and sedimentation. The use of ^{210}Pb in such studies now exceeds the use of ^{137}Cs . The use of ^7Be as a tracer in the context of soils and sediment is relatively new and has resulted in about 90 papers to date. It should be noted that substantially less than half of the total number of papers have used the respective tracer to quantify soil erosion.

25.1.3 Summary of Contents of Book Chapter and the Approach Used

This chapter focuses primarily upon the use of anthropogenic and naturally-occurring radionuclides to study soil erosion processes and to quantify rates of soil erosion. Many other processes affect soil and sediment transport and deposition and other radionuclides used in those studies are detailed in other chapters of this collection. Here we devote much of our attention to the anthropogenic radionuclide ^{137}Cs but we also look at other radionuclide tracers in part to show which radionuclides may be the most suitable for given applications. Specifically, we describe the source of the radionuclides; their characteristics, deposition, sorption, and transport; the methods of measurement; the assumptions associated with their use as

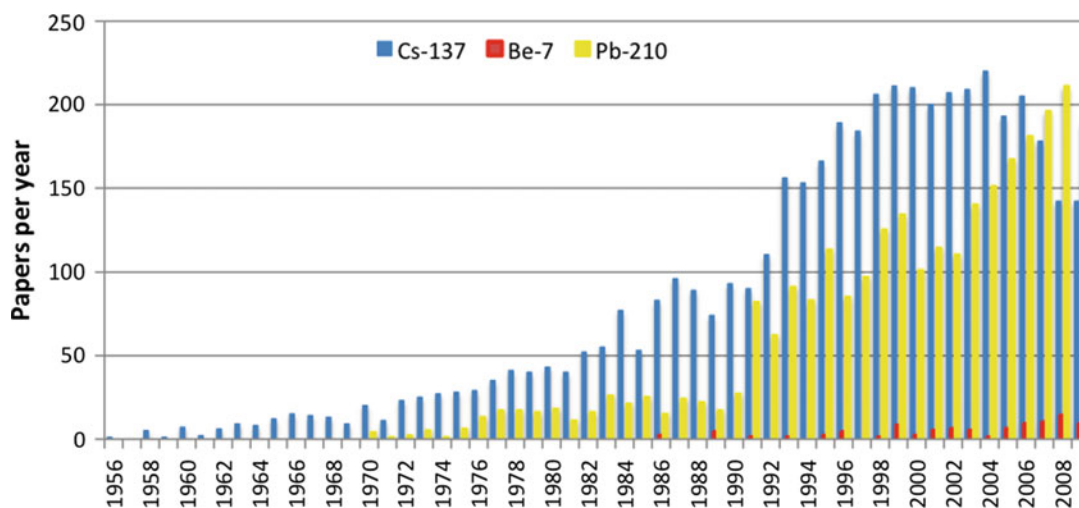


Fig. 25.1 The annual number of papers utilizing ^{137}Cs , ^{210}Pb , and ^7Be in chronologic, geomorphic and sedimentologic studies. The total number of ^{137}Cs papers is now about 4,500. Modified and updated from Ritchie and Ritchie (2008)

tracers; the models used to estimate erosion with the tracers; the relative merits of different models and tracers for investigating soil erosion; recent applications of radionuclides in erosion studies; and foreseeable changes in the use of tracers and the tracers used.

25.2 Background

25.2.1 Radionuclides in the Environment

25.2.1.1 Sources of ^{137}Cs , ^7Be , ^{210}Pb , and $^{239,240}\text{Pu}$

Radionuclides that have been used in studies of soil erosion on decadal time scales or less include ^{134}Cs , ^7Be , ^{210}Pb , and $^{239,240}\text{Pu}$ but the most widely known of these is ^{137}Cs ($t_{1/2} = 30.1$ years). ^{134}Cs ($t_{1/2} = 2.06$ years), ^{137}Cs , ^{239}Pu ($t_{1/2} = 4,110$ years) and ^{240}Pu ($t_{1/2} = 6,537$ years) are present on the global landscape largely as a result of anthropogenic fallout from thermonuclear weapons testing primarily during the period 1954–1968 (Fig. 25.2). In parts of Europe, ^{137}Cs fallout from the nuclear reactor accident at Chernobyl in 1986 is superimposed on the global signal of fallout and the Pu isotopic signatures from stratospheric fallout and from Chernobyl are different from each other (Ketterer et al. 2011; Hong et al. 2011). Other accidental releases of Cs isotopes have created local zones of contamination. ^{210}Pb ($t_{1/2} = 22.3$ years) is delivered to the landscape as a result of the decay of gaseous ^{222}Rn in the ^{238}U decay chain. In that chain, ^{226}Ra in soils and rock decays to ^{222}Rn ($t_{1/2} = 3.8$ days) which is released to the atmo-

sphere and undergoes a series of short-lived decays to ^{210}Pb which, as a particulate, is delivered to the landscape by wet and dry fallout. This ^{210}Pb is termed excess ^{210}Pb ($^{210}\text{Pb}_{\text{xs}}$) (Fig. 25.2). However, some ^{222}Rn that occurs in the soil is trapped in mineral matter or unable to escape to the atmosphere during its 3.8 day half-life, and its decay builds the supported pool of ^{210}Pb in the soil (supported ^{210}Pb). ^7Be ($t_{1/2} = 53.3$ days) is produced by cosmic ray spallation of nitrogen (90%) and oxygen (10%) in the troposphere and stratosphere (Kaste et al. 2002; Kaste and Baskaran 2011) and then it is removed from the atmosphere and is delivered to the landscape often during large thunderstorms (Dibb 1989).

^{137}Cs atmospheric fallout is at present very small and the negligible amount, if any, is due to eolian resuspension of near-surface soil particles with adsorbed ^{137}Cs . ^{210}Pb concentration is highest in air originating over continental regions (Turekian et al. 1983; Paatero and Hatakka 2000) and the activity of ^{210}Pb in the atmosphere decreases with altitude (Kownacka 2002) consistent with the sources of the radionuclide in soil and rock at the earth surface. ^7Be is produced through spallation interactions of atmospheric O and N nuclei and the nucleonic component of the atmospheric cascade induced by galactic cosmic rays (Dorman 2004) (Fig. 25.2). Sugihara et al. (2000) suggest that 70% is produced in the stratosphere. ^7Be is also added to the troposphere from the stratosphere by mixing along the polar front and the subtropical jet and by mixing in large synoptic storms (mid-latitude cyclones and hurricanes). ^7Be concentration increases with altitude given the substantial reservoir in the stratosphere where concentrations may be an order of magnitude higher than in the upper troposphere

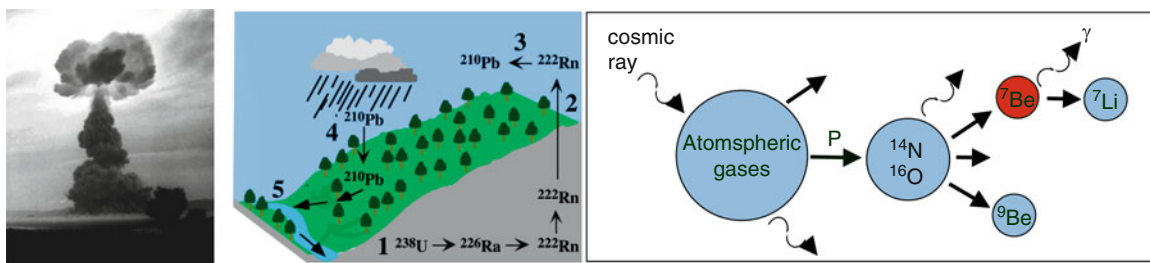


Fig. 25.2 Schematic illustration of fallout radionuclide sources used in erosion studies of decadal or shorter time scales. *Left figure* is a photograph of an atmospheric bomb test, the main source of global radioactive Cs and Pu fallout. Photo from:

<http://www.nv.doe.gov/news&pubs/photos&films/atm.htm>. The *middle figure* illustrates excess ^{210}Pb fallout. The figure on the *right* illustrates the production of ^7Be by cosmic ray spallation of oxygen and nitrogen in the stratosphere

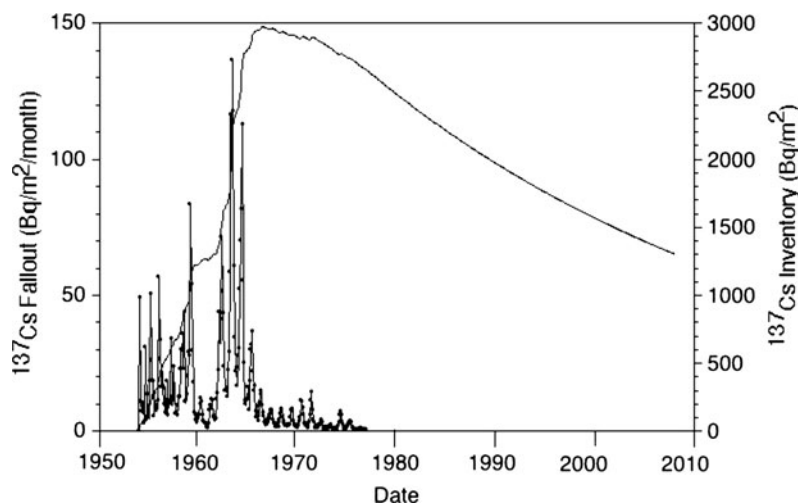


Fig. 25.3 ^{137}Cs fallout ($\text{Bq m}^{-2} \text{ month}^{-1}$) calculated as 1.45 times the average ^{90}Sr monthly fallout at the US DOE monitoring sites (Birmingham, AL; Los Angeles, CA; San Francisco, CA; Denver, CO; Coral Gables/Miami, FL; Argonne, IL; International Falls, MN; Columbia, MO; Helena, MT; New York, NY; Williston, ND; Wooster, OH; Tulsa, OK; Medford, OR;

Columbia, SC; Vermillion, SD; and Green Bay, WI). Data from the Health and Safety Laboratory (1977). Also shown is the calculated ^{137}Cs inventory (Bq m^{-2}) assuming that all the fallout to the soil surface remains in the soil and is subject only to radioactive decay. Chernobyl fallout is not included in this calculation

(Lal and Peters 1967; Dutkiewicz and Husain 1985; Lal and Baskaran 2011). There appears to be some seasonality of the concentrations of ^{210}Pb and ^7Be in the atmosphere with the highest values in late spring and summer (Turekian et al. 1983; Baskaran et al. 1993; Caillet et al. 2001). Valles et al. (2009) show a 2–3-fold variation in monthly concentrations of ^7Be and ^{210}Pb . Greater emissions of ^{222}Rn from snow-free areas and dry soils are thought to increase atmospheric concentrations of ^{210}Pb during summer (Olsen et al. 1985; Caillet et al. 2001). The seasonal peak in ^7Be concentration in late spring and summer (e.g. El-Hussein et al. 2001) is thought to be caused by enhanced mixing of stratospheric air into the troposphere. Longer term fluctuation in ^7Be fallout has been tied to variations in the flux of cosmic galactic primary radiation caused by the 11-year sunspot cycle (Azahra et al. 2003; Kikuchi et al. 2009).

^{137}Cs (+), ^7Be (2+), and ^{210}Pb (2+, 4+) are strongly chemically active, so they rapidly become associated with aerosols and particles (0.7–2 μm ; Ioannidou and Papastefanou 2006) and are delivered from the atmosphere to the earth surface predominantly in precipitation (Olsen et al. 1985). Snow is more efficient than rain at removing radionuclides from air (McNeary and Baskaran 2003; Ioannidou and Papastefanou 2006) and wet precipitation is more efficient than dry precipitation.

Residence times in the troposphere are estimated to be 22–48 days (Durana et al. 1996) for ^7Be and just a few days for the aerosols carrying the ^{210}Pb (Tokieda et al. 1996). ^{137}Cs also has a short residence time partly because the source of the radionuclide is now resuspension of soil particles that are coarser (Papastefanou et al. 1995; Ioannidou and Papastefanou 2006). During the weapons testing era, ^{137}Cs residence time in the atmosphere was longer (~1–10 years) than it is today because of its injection into the stratosphere (Joshi 1987).

Although the first nuclear detonation was in 1945, ^{137}Cs was first detected in fallout in 1951 and over most of the globe it was below detection prior to about 1954, peaked in about 1963, and was effectively below detection by 1983 (Cambray et al. 1985) (Fig. 25.3). The data in Fig. 25.3, for the most part, are not based on actual ^{137}Cs fallout data because ^{137}Cs was not routinely monitored during the 1950–1983 time frame. Instead, ^{90}Sr fallout was usually monitored and ^{137}Cs fallout is inferred by assuming a $^{137}\text{Cs}/^{90}\text{Sr}$ ratio in the bomb fallout (Health and Safety Laboratory 1977; Robbins 1985). This ratio has been estimated to range from 1.4 to 1.65 and is characteristic of production rates of the isotopes and is independent of location. The $^{239+240}\text{Pu}$ depositional fluxes are less well known because certain data (i.e., the ratios of

plutonium to ^{137}Cs , ^{90}Sr) are still classified by the U.S. Government. More recently, for example during the monitoring of Chernobyl fallout, deposition of ^{131}I was monitored and the deposition of all other radionuclides was calculated from the ^{131}I deposition density values using the relationships calculated by Hicks (1982). The overall geographic patterns of ^{90}Sr and $^{239+240}\text{Pu}$ differ slightly from those for ^{137}Cs and ^{131}I primarily due to the differences in the nuclear fuel used in different tests, the size of the particles associated with the radionuclides, and the directions of travel of the clouds of radioactive particles from each test. The overall deposition of ^{90}Sr was very similar to that of ^{137}Cs . For most of the regions in the United States, the activity of ^{137}Cs was 10–20 times the activity of $^{239+240}\text{Pu}$ deposited (Beck 1999; CDC 2006).

Because of the temporal variability with a peak ^{137}Cs fallout activity in 1963, that peak is often used as a time horizon in sediments to indicate the time of deposition of that layer of sediment. Linear sedimentation rates (cm year^{-1}) are then simply calculated as the depth of the layer (cm) divided by the time in years since 1963. The mass flux deposition rates ($\text{g cm}^{-2} \text{ year}^{-1}$) are calculated as the cumulative dry mass of sediment above the 1963 time horizon divided by the cross sectional area of the sediment core divided by the time in years since 1963 until the date of coring (Walling and He 1997a, b; Goodbred and Kuehl 1998).

Inspection of Fig. 25.3 shows that the ^{137}Cs depositional flux was highly variable, reflecting the times of atmospheric testing. There are peaks in fallout observed each year between 1954 and 1959, and much larger peaks in 1962, 1963 and 1964. The maximum global fallout of radioactive nuclides occurred in Spring 1964, but because most field data cannot resolve the 1962 to 1964 fallout peaks, the position of the maximum in ^{137}Cs is often assigned a date of 1963 (1964 in the southern hemisphere). In the late 1960s to mid-1970s, fallout decreased considerably, but the seasonal cycle reflecting precipitation can be seen through the 1970s.

As a result of the nuclear accident at Chernobyl in 1986, additional ^{137}Cs fallout occurred in some areas of Europe. It is estimated that the Chernobyl accident released from 10 to 16% as much ^{137}Cs to the environment as was emitted from all nuclear weapons tests (Flavin 1987). Little Chernobyl fallout occurred over North America (Roy et al. 1988). Note the much

higher levels of ^{137}Cs deposition from Chernobyl than from stratospheric fallout (compare Figs. 25.3–25.5). For example, the *lowest* contours on the Europe map following Chernobyl are $\sim 2 \text{ kBq m}^{-2}$ (light yellow in Fig. 25.4) De Cort et al. (1998) whereas in Fig. 25.3 the *largest* fallout values in the US following bomb testing are $\sim 3,000 \text{ Bq m}^{-2}$ (3 kBq m^{-2}). Monthly deposition values are 20–30 times less than the lowest fluxes deposited from Chernobyl. The highest Chernobyl fluxes are $\sim 1,480 \text{ kBq m}^{-2}$, a value $10,000\times$ larger than the peak monthly fallout from atmospheric weapons testing ($\sim 140 \text{ Bq m}^{-2} \text{ month}^{-1}$) and a value at least $100\times$ larger than the inventory in US soils ($8\text{--}13 \text{ kBq m}^{-2}$, Fig. 25.5). Delivery of ^{137}Cs from the atmosphere is again currently near zero (Quine 1995). The much higher deposition of Chernobyl-derived ^{137}Cs over northern Europe is significant, because in these locations it has swamped the prior global fallout signature and has had the effect of “resetting” the ^{137}Cs soil erosion clock to 1986 because downcore soil inventories and soil activities near the soil surface are now dominated by Chernobyl-derived ^{137}Cs . This is not the case over most of the rest of the world, as the ^{137}Cs fallout from Chernobyl was minimal (Department of National Health and Welfare 1986). Consequently, the current distribution of ^{137}Cs in soils in northern Europe is dominated by Chernobyl fallout and in the US by stratospheric fallout. This resulted because Chernobyl was characterized by the relatively intermittent release of a full range of radionuclides at relatively low temperatures with very heavy local fallout from tropospheric transport. Weapons testing fallout was at a high temperature with more uniform stratospheric transport, longer residence times, and with much less pronounced local fallout (Joshi 1987). Pu atom ratios can be used to distinguish between Chernobyl and stratospheric fallout. The $^{240}\text{Pu}/^{239}\text{Pu}$ atom ratio was about 0.38 in Chernobyl fallout and 0.18 in stratospheric fallout (Ketterer et al. 2011). Further, the distribution of Pu from Chernobyl was much more localized than was ^{137}Cs . Pu isotopes were specifically associated with non-volatile fuel particles (Mietelski and Was 1995) whereas ^{137}Cs volatilized in the reactor accident and was more widely dispersed over much of northern Europe and Russia. ^7Be and ^{210}Pb deposition on the other hand continues as natural processes continue to produce these radionuclides.

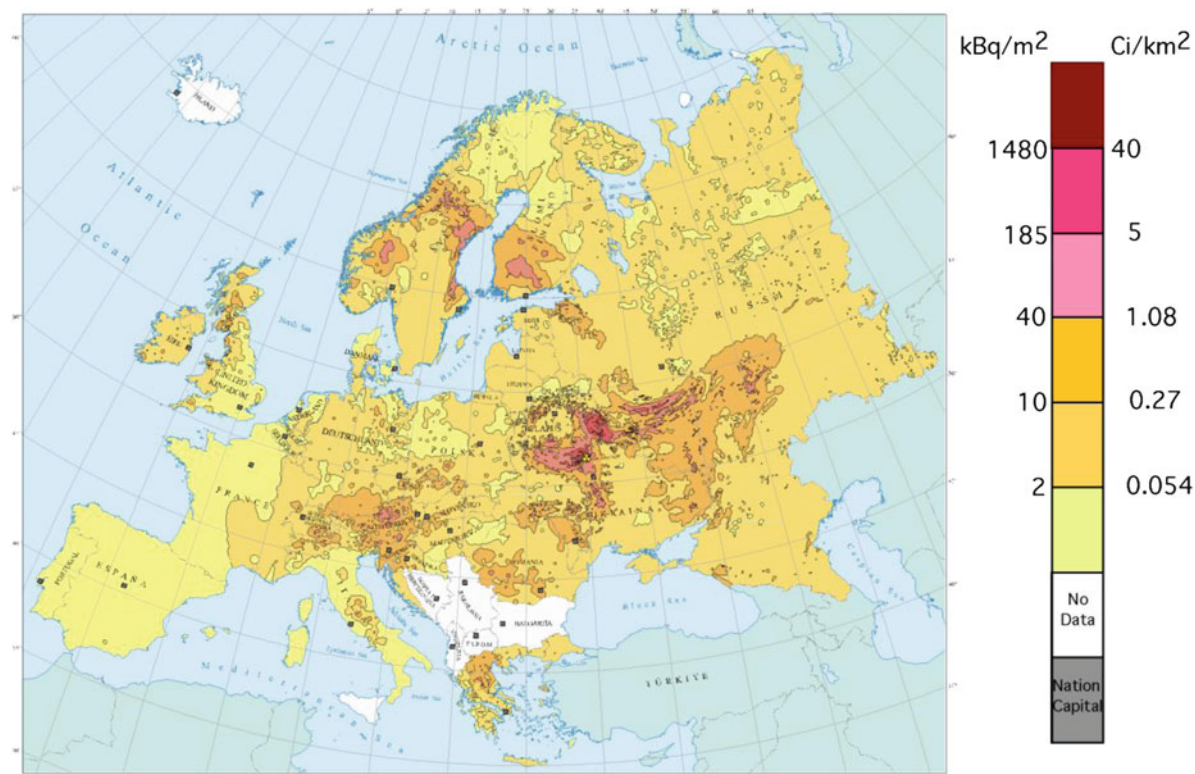


Fig. 25.4 ^{137}Cs fallout deposition over Europe following the Chernobyl accident. Modified from EC/IGCE, Roshydromet (Russia)/Minchernobyl (Ukraine)/Belhydromet (Belarus) (1998)

25.2.1.2 ^{137}Cs , ^7Be and ^{210}Pb in Precipitation

Deposition of radionuclides occurs both by dry and wet fall. The vast majority of ^7Be falls in association with rainfall. Workers have reported dry fall as making up 3–10% of total fallout (Wallbrink and Murray 1994; McNeary and Baskaran 2003; Salisbury and Cartwright 2005; Ioannidou and Papastefanou 2006; Sepulveda et al. 2008). Dry deposition of ^{210}Pb appears to be more variable than ^7Be because of the importance of resuspended soil and dust in contributing to the flux (Todd et al. 1989). The monthly atmospheric depositional flux (wet plus dry) of both ^7Be and ^{210}Pb varies by about a factor of 5 over the course of a year (Matisoff et al. 2005) but exhibits a maximum in the spring (Turekian et al. 1983; Olsen et al. 1985; Dibb 1989; Todd et al. 1989; Robbins and Eadie 1991; Koch et al. 1996; Baskaran et al. 1997) and represents the variability in the quantity of precipitation (Turekian et al. 1983; Koch et al. 1996; Baskaran et al. 1997) and, to a lesser extent, the seasonality

in stratospheric ^7Be production and troposphere-stratosphere exchange (Turekian et al. 1983; Todd et al. 1989; Koch et al. 1996). ^7Be and ^{210}Pb deposition during precipitation events is well correlated to precipitation amount (Cailliet et al. 2001; Ciffroy et al. 2003; Su et al. 2003) reflecting the fact that wet fall is a dominant delivery mechanism. Cailliet et al. (2001) found that ^7Be deposition was slightly better correlated with precipitation than ^{210}Pb deposition ($r^2 = 0.66$ for ^7Be vs. 0.55 for ^{210}Pb). The better correlation with ^7Be is due to the fact that more of the ^{210}Pb comes from dry deposition and ^7Be is often derived from the stratosphere during large thunderstorms. Quine (1995) reported that ^{137}Cs delivery from global fallout was also highest in spring and early summer. Callender and Robbins (1993) observed an annual cycle of ^{137}Cs deposition in the high sedimentation environment of Oahe Reservoir (South Dakota, USA).

Given the correlation between fallout and precipitation amounts during events, it is not surprising that the annual fallout of ^{137}Cs , ^7Be and ^{210}Pb is correlated to

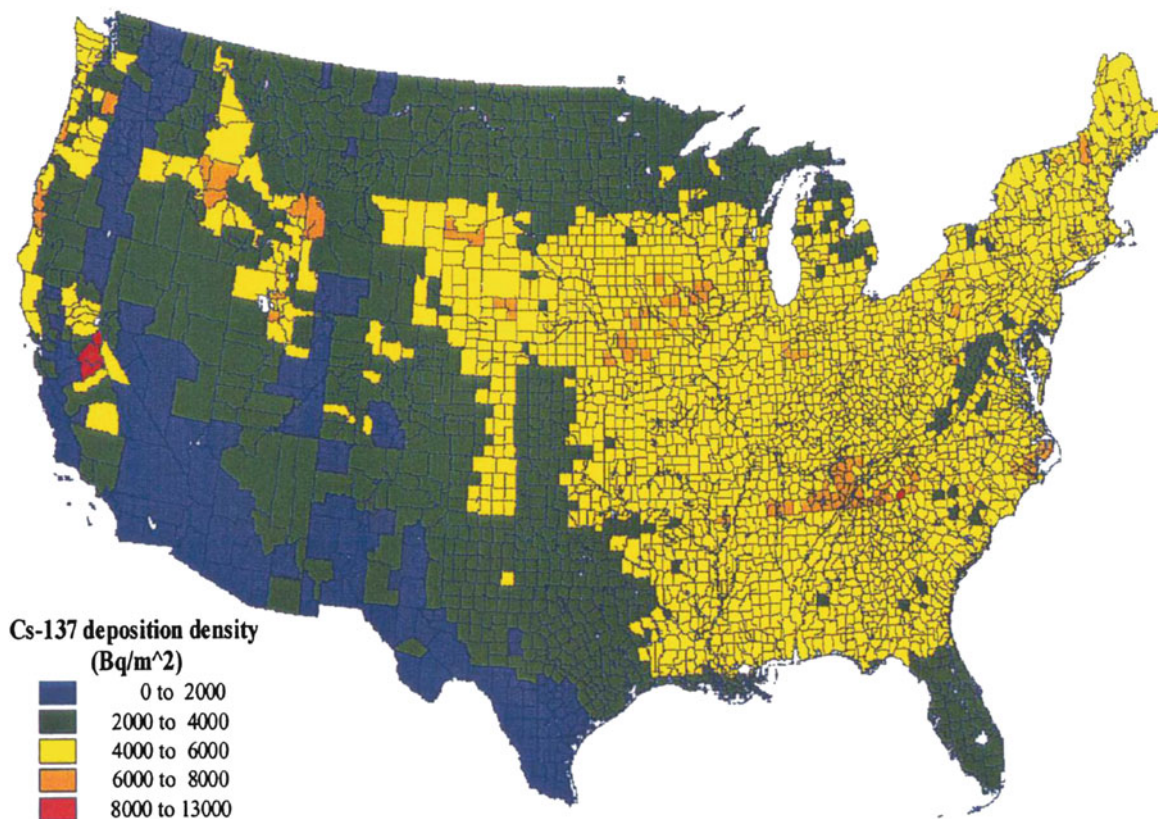


Fig. 25.5 ^{137}Cs depositional flux in the continental United States from global fallout (CDC 2006)

annual precipitation. In most places, the precipitation-normalized annual depositional fluxes have remained constant (Baskaran 1995). Ritchie and McHenry (1978) noted that the variation in ^{137}Cs inventory in the northcentral US was best explained by mean annual precipitation. Rowan (1995) found that variation in mean annual precipitation (900–2,000 mm) explained 75% of the variation in ^{137}Cs inventory in the Exe basin in the United Kingdom. Lance et al. (1986) found a linear relationship between the inventory of ^{137}Cs in soils and average annual precipitation in the southern USA. Baskaran et al. (1993) observed that ^{210}Pb fluxes increased with precipitation and Gallagher et al. (2001) found that ^{210}Pb inventory was significantly higher on the wetter west coast of Ireland than on the east coast. Our survey of annual delivery of ^7Be reported by workers (Turekian et al. 1983; Dibb 1989; Papastefanou and Ionannidou 1991; Baskaran et al. 1993; Caillet et al. 2001; Ayub et al. 2009) as compared to annual

precipitation shows a strong correlation: $r^2 = 0.72$ (Fig. 25.6).

The fallout of ^{137}Cs over the globe as indicated by soil inventories is higher in the mid-latitudes than equatorial areas, and higher in the Northern Hemisphere than in the Southern Hemisphere (Stokes and Walling 2003; Walling et al. 2003). Collins et al. (2001) found inventories that were almost an order of magnitude higher in mid-latitudes of the Northern Hemisphere. Figure 25.7 illustrates the general pattern of inventories by latitude across the globe and Fig. 25.8 illustrates the reconstructed global fallout of ^{137}Cs as of 1970 indicating both the localized fallout from the test sites and the global fallout. McHenry et al. (1973), summarizing several studies, noted that fallout in the USA increased to the north and to the east (Fig. 25.5). Sarmiento and Gwinn (1986) developed a semi-empirical model for the deposition of ^{90}Sr (and hence ^{137}Cs) that is based on latitude, time since 1954, and the monthly precipitation. The distribution

Fig. 25.6 Linear relationship between ^7Be depositional flux and annual precipitation

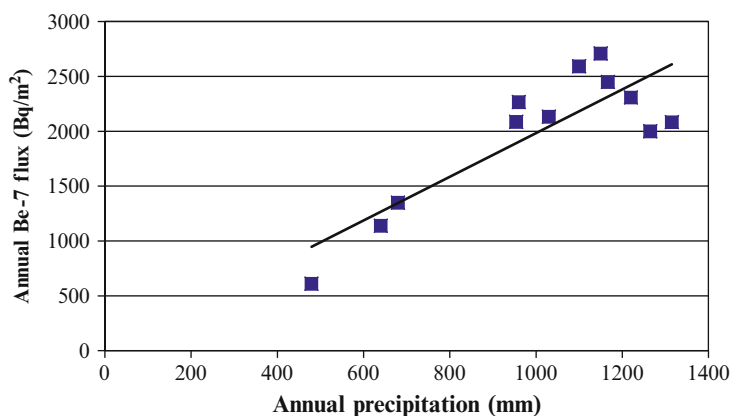
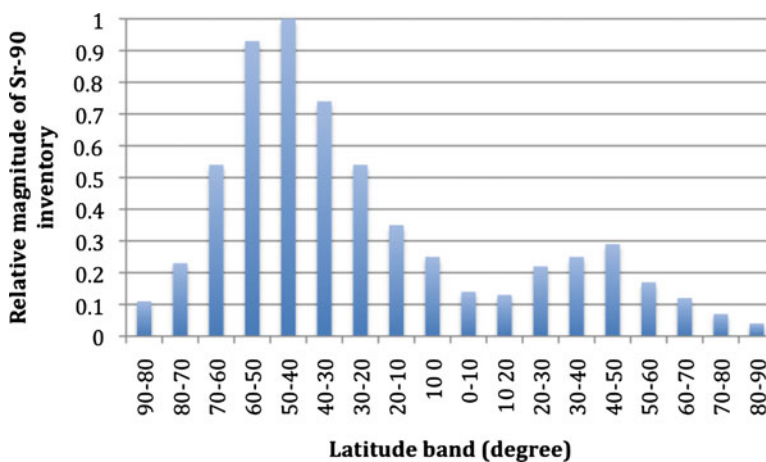


Fig. 25.7 Variation in bomb-derived ^{90}Sr (a surrogate for ^{137}Cs) by latitude band (from Stokes and Walling 2003)



of bomb-derived ^{137}Cs fallout over the globe is relatively smooth in contrast to the Chernobyl fallout (compare Figs. 25.4 and 25.5) because the global fallout signal is due to a series of nuclear explosions that reached into the stratosphere allowing ^{137}Cs to be well mixed in the atmosphere. In contrast, the plume of radioactive debris from Chernobyl did not extend higher than a few km into the atmosphere and thus prevailing winds, and then rainout, determined the pattern of fallout. $^{239,240}\text{Pu}$ was also vaporized during bomb testing and its global distribution is similar to that of ^{137}Cs . However, this did not occur during Chernobyl, so the Pu was delivered as fine particulates and therefore its distribution was not widespread (Mietelski et al. 1996; Ketterer et al. 2004; Brudecki et al. 2009). Global fallout flux of ^{210}Pb is summarized in Baskaran (2011). The inventories of ^{210}Pb are lower in the Southern Hemisphere than the Northern Hemisphere because of the smaller percentage of land area.

The radon flux from the oceans is negligible compared to the continents (Turekian et al. 1977) thus with less continental area in the Southern Hemisphere there will be a lower atmospheric concentration and less deposition of ^{210}Pb . ^7Be inventories should be similar in both hemispheres because of its stratospheric source.

25.2.1.3 ^{137}Cs , ^7Be and ^{210}Pb in Soils

Once the radionuclides ^{137}Cs , ^7Be and ^{210}Pb reach the earth surface, they rapidly sorb to the mineral grains and organic materials of soil particles (Tamura and Jacobs 1960). Cs fixation to soil material depends strongly on soil composition and mineralogy. There is a complicated pattern of preferred sorption of radionuclides to finer particle sizes and to organic materials (He and Walling 1996; Wallbrink and Murray 1996; Motha et al. 2002) and clays (Hawley et al. 1986;

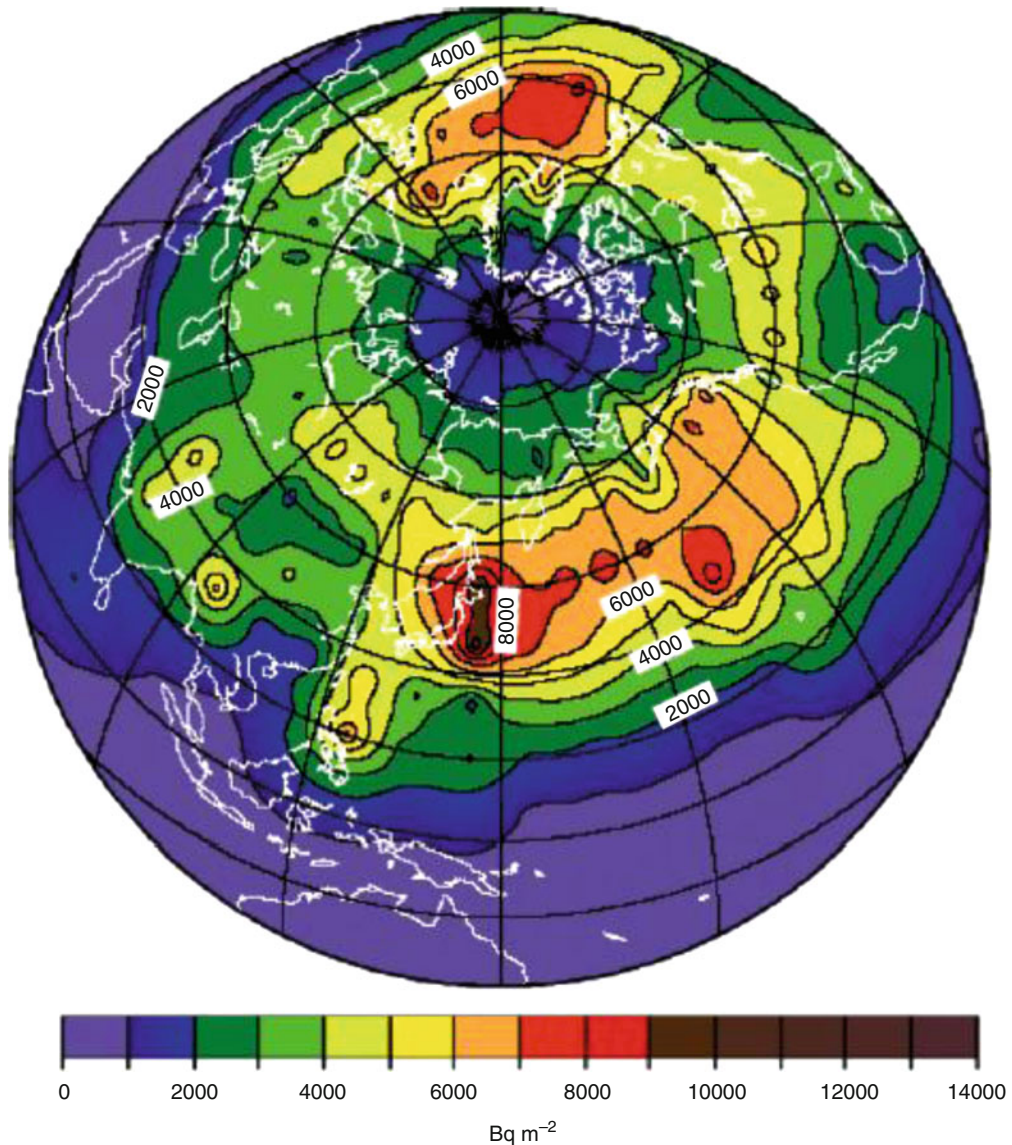


Fig. 25.8 Global distribution of bomb-derived ^{137}Cs fallout illustrating high fallout near testing sites and a strong latitudinal distribution (from Aoyama et al. 2006)

Wang and Cornett 1993; Balistreri and Murray 1984). ^{137}Cs is a 1+ cation and its sorption exceeds that of all other alkali ions (Schultz et al. 1959). Lomenick and Tamura (1965) suggested that the adsorption is almost non-exchangable. Riise et al. (1990) estimated that less than 10% of Cs was leachable. ^7Be reaches the earth surface as a Be^{2+} cation with high charge density which makes it prone to adsorption. ^{210}Pb likewise reaches the surface as a 2+ or 4+ cation and is rapidly adsorbed. Partition coefficients, K_d , for these radionuclides are

$\sim 10^5$ (Olsen et al. 1986; You et al. 1989; Hawley et al. 1986; Steinmann et al. 1999) indicating that these radionuclides are sufficiently particle-bound that they are suitable for tracing erosion, transport, and deposition of soil.

There are, however environments in which ^{137}Cs might fail as a conservative particle tracer. Some previous studies of radiocaesium in soils have failed because K_d values have been derived under conditions very different from those in situ. The partitioning of Cs

in organic-rich soils is reversible and the partition coefficients can be low. Where the soils are peaty or podzolic, the mobility of cesium is considerably greater than in other soils (Sanchez et al. 1999). In acidic soils in coniferous forests in N. Europe Dorr and Munnich (1989) found that Cs migrated faster than ^{210}Pb and suggested that chemical exchange was occurring between the organic and hydrous phases. It is generally believed that radiocaesium retention in soils and sediments is due to the presence of a small number of highly selective sites. Cremers et al. (1988) found that strong Cs adsorption by the solid phase was regulated by the availability of frayed edge sites on illite and is inhibited by the presence of competing poorly hydrated alkali cations (K^+ or NH_4^+). Where geochemical migration of Cs is significant, workers should turn to alternatives such as Pu isotopes.

In soil, cesium has a low mobility; the majority of cesium ions are retained in the upper 20 cm of the soil surface and usually they do not migrate below a depth of 40 cm (Korobova et al. 1998; Matisoff et al. 2002a). For example, vertical migration patterns of ^{137}Cs in four agricultural soils from southern Chile indicated that approximately 90% of the applied cesium was retained in the top 40 cm of soil and as much as 100% was found in the upper 10 cm (Schuller et al. 1997).

^{137}Cs uptake by plants also affects its downcore migration. Clay and zeolite minerals strongly bind cesium cations in interlayer positions of the clay particles and therefore reduce the bioavailability of ^{137}Cs and its uptake by plants (Paasikallio 1999). Plant uptake of ^{134}Cs in a peat soil was decreased by a factor of 8 when zeolites were added (Shenber and Johanson 1992).

The kinetics of sorption are less understood, but Baskaran and Santschi (1993) reported that approximately 80% of ^7Be became associated with particulates within an hour of a rainfall event. In a study where ^{134}Cs was applied in solution to the surface of soils, it was adsorbed in the upper 2.5 cm of the soil (Owens et al. 1996). These results largely mimic the findings of Rogowski and Tamura (1970) who applied ^{137}Cs to the soil surface and also found penetration of only a few cm. This modest penetration during infiltration suggests a timeframe for adsorption of up to 10 min if typical rates of infiltration for these silty sand soils are used.

Some proportion of the radionuclide fallout is retained on vegetation. Doering et al. (2006) observed that 18% of ^7Be was retained on vegetation whereas only about 1% of $^{210}\text{Pb}_{\text{xs}}$ was retained on vegetation. These differences almost surely reflect the much shorter half-life of ^7Be than any differences in affinity for organic material. Very little ^{137}Cs is typically on vegetation today because of the negligible fallout. Plants may also take up radionuclides from soil. Coughtrey and Thorne (1983) supposed that plant uptake could result in a 0.2% loss in ^{137}Cs per year. Numerous studies have shown that radioactive contaminants move through the food chain and can exceed health standards (Davis 1986; Revelle and Revelle 1988). For example, mushrooms have been reported to uptake as much as 50% of the ^{137}Cs inventory in the soil and moose, caribou, sheep and milk consumption have all had radioactive residues that restrict their consumption (Korky and Kowalski 1989).

25.2.1.4 Radionuclide Profiles in Undisturbed Soils

The simplest profile of the set of radionuclides most commonly used in soil erosion studies may be that of ^7Be (Fig. 25.9; see also Kaste and Baskaran 2011). From a peak concentration at the surface, it decreases exponentially down core to non-detectable values below 2–3 cm (Bonniwell et al. 1999; Wilson et al. 2003; Doering et al. 2006). In the case of ^7Be , some fraction is associated with the vegetation growing on the surface (Doering et al. 2006 reported 18%) or associated with organic litter. The half-life of ^7Be is just 53.3 days thus there is a relatively brief period to mix/move the radionuclide downward before the radionuclide decays (Walling et al. 2009). Only very rarely has ^7Be been measured deeper than a couple of cm in the soil. Kaste et al. (1999a, b) noted a second down-profile peak in activity that they hypothesized might be caused by subsurface pipeflow quickly taking the ^7Be cation to depth before sorption.

The next simplest profile may be that of ^{210}Pb (Figs. 25.9 and 25.10). As with ^7Be , $^{210}\text{Pb}_{\text{xs}}$ is delivered by wet and dry fallout to the surface and mixed downward in the soil profile. In the case of ^{210}Pb however, there is both the atmospherically derived $^{210}\text{Pb}_{\text{xs}}$ and the steady background ^{210}Pb activity (called supported ^{210}Pb) maintained by continuous in

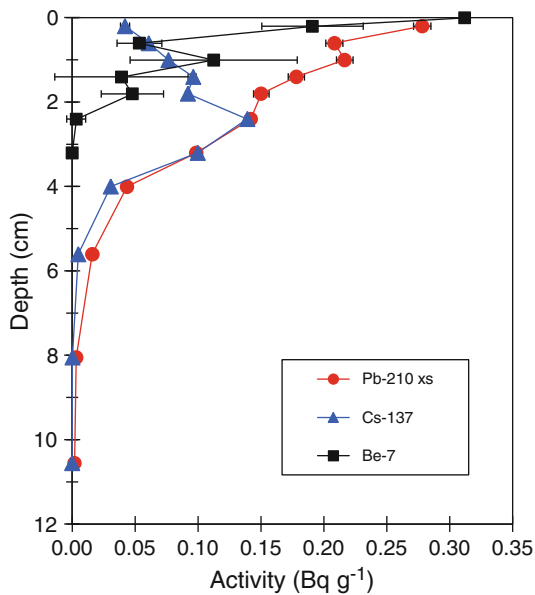


Fig. 25.9 The distribution of radionuclides ^7Be , ^{137}Cs , and $^{210}\text{Pb}_{\text{xs}}$ in this upland soil from near Corwin Springs, Montana, USA is characteristic of undisturbed soils. ^7Be activity is highest at the surface and little is found below 3 cm. ^{137}Cs displays a subsurface peak in activity, in this case between 2 and 3 cm of depth, and no radionuclide activity below 10 cm. $^{210}\text{Pb}_{\text{xs}}$ displays a surface peak in activity. $^{210}\text{Pb}_{\text{xs}}$ activity is negligible below 10 cm (from Whiting et al. 2005)

situ decay of ^{226}Ra in soil and rock (Goldberg and Koide 1962). The surface maximum in activity decreases exponentially downcore to the value of the supported ^{210}Pb . Most $^{210}\text{Pb}_{\text{xs}}$ is found in the upper 10 cm of soil (Bonniwell et al. 1999; Doering et al. 2006). The greater penetration of $^{210}\text{Pb}_{\text{xs}}$ than ^7Be is due to its greater half-life of 22.3 years. With more time to operate, downward migration extends further.

The ^{137}Cs profile is typically more complicated (Figs. 25.9 and 25.10). Over much of the globe, the undisturbed ^{137}Cs profile features a subsurface maximum and then an exponential decrease below that. Very little ^{137}Cs is found below 20 cm (Owens and Walling 1996) in most locales. Unlike the other two radionuclides, the delivery of ^{137}Cs was not steady (Fig. 25.3). It was first detected in fallout in 1951, peaked in about 1963, and was negligible by the early 1980s. In the absence of constant replenishment to the surface, the peak in concentration has migrated below the surface by several cm. In areas receiving significant Chernobyl fallout after the nuclear plant accident in 1986, the distribution of ^{137}Cs from stratospheric fallout is swamped by the Chernobyl fallout so that global fallout can no longer be identified. This interpretation is supported by Pu isotope data which show “hot”

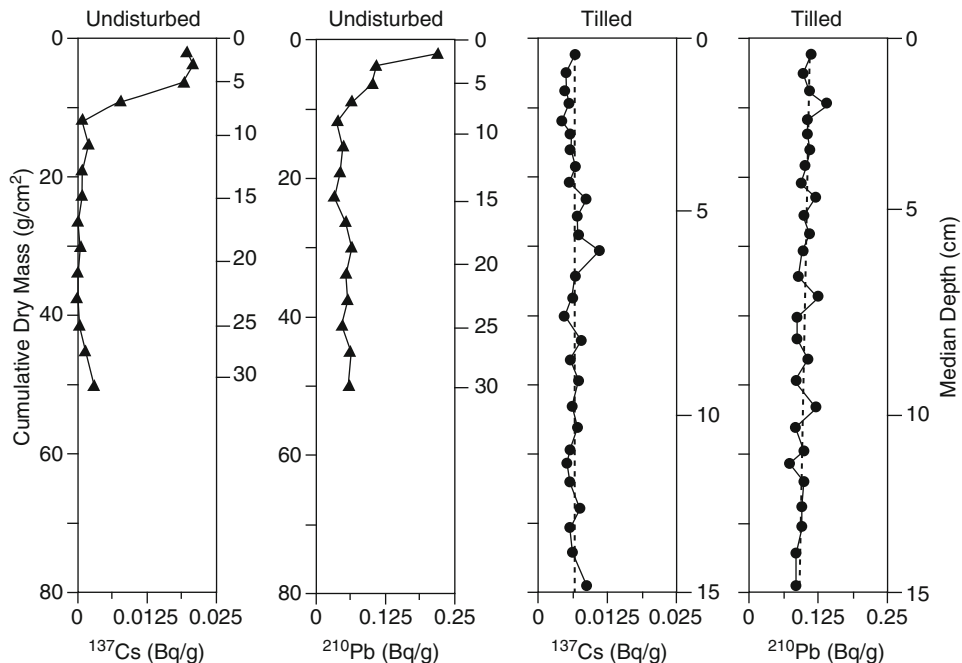


Fig. 25.10 Comparison of ^{137}Cs and ^{210}Pb activities in profiles from undisturbed and tilled soils. Soils collected in Ohio, USA. After Matisoff et al. (2002a, b)

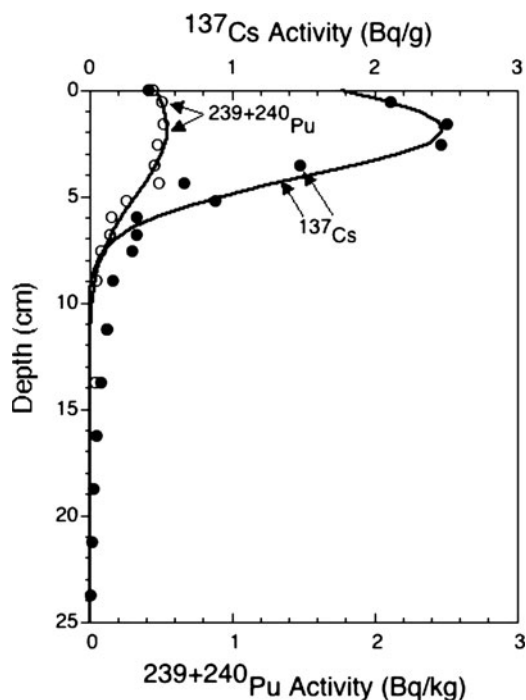


Fig. 25.11 ^{137}Cs and $^{239+240}\text{Pu}$ data from a core collected in 2008 in Skogsvallen, Sweden and a non-local bioturbation model fit to the data. Note that the Pu is derived from global fallout (as determined from Pu isotopes, not shown here), but the ^{137}Cs is derived primarily from Chernobyl fallout (as determined by its relatively high activity)

Chernobyl-derived Pu particles at depth while stratospheric Pu is found both above and below the Chernobyl Pu and the ^{137}Cs profile mimics the Pu profile (Matisoff et al. 2011). Additional support can be seen in Fig. 25.11, where the Pu profile is from global fallout (as determined from Pu isotopes, not shown here), but the ^{137}Cs is derived primarily (as determined by its relatively high activity) from Chernobyl fallout. (Note the much higher activity of ^{137}Cs in Fig. 25.11 compared to that in Figs. 25.9 or 25.10 indicating a Chernobyl source to the soil collected in Sweden in Fig. 25.11 and a global fallout source to the soils collected in the USA shown in Figs. 25.9 and 25.10.)

25.2.1.5 Downcore Migration of Radionuclides in Soils

The radionuclides delivered to the soil surface are moved downward by soil processes including biotur-

bation, leaching, diffusion, and translocation. Movement can be enhanced by disturbance such as plowing. The depth of penetration of each radionuclide into the soil is determined by the rate of this downward movement and the half-life of each radionuclide. DeJong et al. (1986) argue for low leachability of ^{137}Cs but some workers have found substantial mobility, particularly in peaty soils. Kaste et al. (1999a, b) report that as pH increases, ^7Be can be desorbed.

Since the Chernobyl accident there have been a number of studies on the migration of ^{137}Cs and other radionuclides into the soil. Several authors have reported that ^{137}Cs penetration decreases exponentially downcore (Miller et al. 1990; Walling and Woodward 1992; Wallbrink and Murray 1996; Doering et al. 2006). Several studies have described the downcore transport of ^{137}Cs in terms of a diffusion-advection equation for a sorbed radionuclide (Konshin 1992; Bossew and Kirchner 2004; Shimmack et al. 1997; Rosen et al. 1999). These studies have concluded that the model fails to describe the rapid downward migration of the radionuclides shortly after fallout so that a non-linearity or irreversible sorption process leads to a decrease in the migration rate over time. This may help explain why the $^{239,240}\text{Pu}$ and ^{137}Cs profiles match in Fig. 25.11 even though the $^{239,240}\text{Pu}$ was delivered from stratospheric fallout whereas the ^{137}Cs was delivered from Chernobyl fallout.

Recently it has been suggested that ^{137}Cs transport is facilitated by colloidal transport (Flury et al. 2004; Chen et al. 2005), but colloidal transport in a natural, unsaturated media is small (Honeyman and Ranville 2002; Lenhart and Saiers 2002). Février and Martin-Garin (2005) conducted laboratory experiments that demonstrated retention of anionic radionuclides by microbial activity. Bundt et al. (2000) noted enrichment of radionuclides of Pb, Pu, and Cs at depth in preferential flow paths.

The transport of radionuclides in soils also can be facilitated by burrowing organisms such as earthworms, ants, termites and pocket gophers. Some of these bioturbating organisms are present in soils in numbers that can approach tens of millions per square meter and they actively mix the soil to depths ranging from a few centimeters to a few meters (Johnson et al. 1990; Müller-Lemans and van Dorp 1996; Gabet 2000; Gabet et al. 2003). Darwin (1881) first reported the role of earthworms in facilitating the downward migration of objects by ingesting soil and/or plant

matter at depth and depositing it onto the surface as casts. This mixing style incorporates both random (diffusive) and directed (advective) processes and has been termed “conveyor-belt” feeding (Rhoads and Stanley 1964; Rhoads 1974; Powell 1977) or “non-local” mixing (Boudreau 1986a, b; Robbins 1986). Earthworms have been suggested to be the most important factor controlling the vertical transport of radionuclides in central European soils, with the potential to turn over the top layer of soil within 5–20 years (Müller-Lemans and van Dorp 1996). It is possible to model mixing by bioturbation in soils as a diffusive process and burial as an advection velocity. Kaste et al. (2007) used this approach and reported bio-diffusion mixing coefficients of 1–2 cm² year⁻¹ in a grassland in California (USA) and from a forested landscape in Australia, and inferred that the more actively bioturbated soils exhibit higher erosion rates. This approach treats the downward migration as a burial velocity and while it may simulate well the downcore profiles, it does not account for the directed recycling of tracer from depth (non-local mixing) as demonstrated by Robbins et al. (1979) using aquatic oligochaetes. Alternatively it is possible to model mixing by bioturbation as a diffusive process and the downward migration as a burial caused by non-local feeding in which the organisms place soil from depth onto the soil surface (Jarvis et al. 2010). Figure 25.11 is an application of the non-local bioturbation model to Chernobyl fallout at a site in Sweden and yields a bioturbation coefficient of 0.1 cm² year⁻¹ and a feeding rate of 0.002–0.003 year⁻¹ over the top 20 cm. In other words, this bioturbation model can account for the burial of the radionuclides by recycling 0.2–0.3% of the top 20 cm of the soil column each year.

25.2.1.6 Effects of Tillage on Soil Profiles

The radionuclide profiles in tilled soils exhibit considerable differences from the profiles in undisturbed soils (Matisoff et al. 2002b). Undisturbed soils show either a surface maximum (⁷Be, ²¹⁰Pb) or a near surface peak (¹³⁷Cs) followed at depth by a decrease to a constant activity (²¹⁰Pb) or to near zero (⁷Be, ¹³⁷Cs) (Fig. 25.9). Plowing of agricultural soils will mix soils to depths of 10–30 cm creating a relatively uniform

concentration over the plow depth (Wise 1980 in Martz and deJong 1985; Owens et al. 1996). The distribution of radionuclides in the tilled soils is largely homogeneous because plowing mixes surface soils, which are enriched in radionuclides, with deeper soils, which are depleted in both ²¹⁰Pb and ¹³⁷Cs (Fig. 25.10).

Figure 25.12 illustrates a generalized model of the distribution of ⁷Be, ¹³⁷Cs and ²¹⁰Pb in a soil profile. All three isotopes are deposited on the surface through wet and dry fallout. Each radionuclide is distributed differently in the soil because of differences in half-lives, delivery rates, delivery histories, and land use. An undisturbed soil will exhibit higher radionuclide activities near the soil surface, which reflects their surficial input and slow downward transport. The shorter half-life of ⁷Be compared to ²¹⁰Pb results in less downward migration of ⁷Be. Hence ⁷Be is found only at the soil surface but some ²¹⁰Pb will migrate down core. In addition, some ²¹⁰Pb is produced in the soil by in situ decay of ²²²Rn resulting in some ²¹⁰Pb activity at all depths in the soil. Because ¹³⁷Cs had its peak delivery in the early 1960s and almost no delivery before 1951 or since 1975 (or had its peak delivery in 1986 in areas affected by Chernobyl fallout) its activities have a distinct peak at some depth (~10 cm) in the soil. Plowing homogenizes ²¹⁰Pb and ¹³⁷Cs within the plowed layer, but because of its short half-life and constant input, ⁷Be activities are highest at the surface and are homogeneous only immediately after plowing. Because ¹³⁷Cs fallout occurred at a distinct instance of time, its distribution will remain homogeneous within the soil profile, even after the cessation of plowing. On the other hand, ²¹⁰Pb, like ⁷Be, is continuously deposited on the land surface. Its distribution will remain homogeneous if the soil is plowed annually, but it will accumulate at the surface and slowly rebuild a profile with decreasing activity with depth if tillage ceases.

Because ⁷Be, ¹³⁷Cs, and ²¹⁰Pb have different distributions in the soil profile, erosion of the soil to different depths will yield an assemblage of radionuclides in the eroded material that is characteristic of only one depth. Shallow erosion produces proportionally larger amounts of ⁷Be and ²¹⁰Pb because these radionuclides are concentrated near the surface. Deeper incision yields progressively less additional ⁷Be and no additional ⁷Be below about 1 cm. The

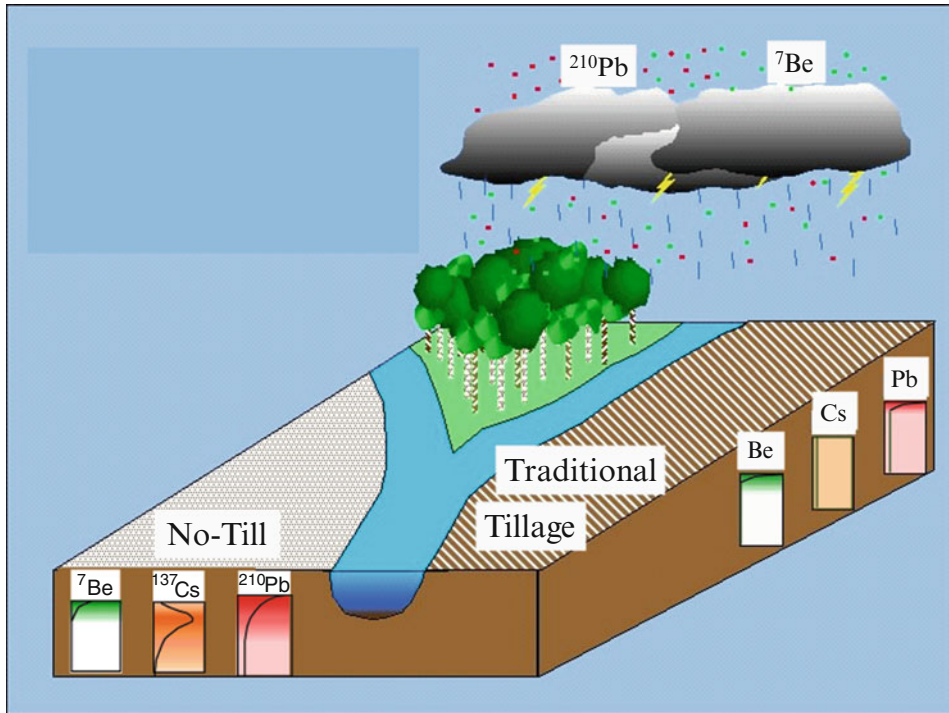


Fig. 25.12 Schematic illustration of soil profiles of ^7Be , ^{137}Cs , and ^{210}Pb in undisturbed soils (no-till) and in soils that have been mixed by plowing (traditional tillage)

proportional contribution of ^{137}Cs increases to the depth of its maximum. Erosion below that depth yields incrementally more ^{210}Pb and ^{137}Cs but at progressively decreasing rates. Below some depth in the soil (~15–30 cm), deeper erosion yields little if any additional ^{137}Cs . ^{210}Pb yield continues to grow in correspondence to the constant supported ^{210}Pb activity.

Sediment eroded from a soil will have a radionuclide signature corresponding to the tillage practice and the depth of erosion. Thus radionuclide signatures in suspended sediments can provide a means of tracing particles eroded from the landscape and can identify soil sources and be used to quantify the erosion (Whiting et al. 2001). The distinct distributions of radionuclides permit in principle the use of multiple mass balances to quantitatively estimate the areal extent of rill and sheet erosion and the characteristic depth of erosion associated with each mechanism (Wallbrink et al. 1999; Whiting et al. 1999, 2001). In essence, it is possible to infer the “recipe” for erosion – for example, 1 part sheet erosion to 10 parts rill erosion – on the basis of the total yield of radionuclides and sediment.

25.2.2 Concept of Inventory

The inventory, or standing stock, of a radionuclide represents the total amount of a radionuclide per unit area and is determined by atmospheric delivery, radioactive decay, gain, and loss. Gain typically reflects deposition and loss typically reflects erosion or leaching. In the case of ^{137}Cs , local inventories at stable locations (neither eroding or depositing) are steadily dropping because contemporary fallout to replenish the stock is essentially zero (Fig. 25.3). In 2010, ^{137}Cs inventories are less than half of what they were in 1974, except in areas affected by Chernobyl fallout. ^{210}Pb inventories at stable sites are more or less steady because annual contributions (fallout) to the stock and variation in the delivery from year-to-year are both small compared to the total inventory. For instance, fallout of ^{210}Pb in a typical year represents no more than 3% of the stock of $^{210}\text{Pb}_{\text{xs}}$. ^7Be inventories at stable sites tend to vary over the year due to the variation in delivery with the seasons and the short half-life of 53 days. Individual storms can deliver

>50% of the ^7Be inventory particularly when the precipitation event arrives after a period of drought lasting weeks to months.

To use these tracers to quantify erosion or deposition, the amount of the radionuclides in a vertical column of soil (the measured inventory) is compared to the expected amount in the soil profile based upon fallout (the expected inventory). The fundamental idea is that the inventory (stock) of radionuclides will be changed only by additions of radionuclides as wet- and dry-fallout or by sediment deposition or by losses by decay and soil erosion. If the measured inventory is less than the expected inventory, then erosion has occurred and the soil loss is proportional to the ratio of the inventories. If the inventory is greater than the expected inventory, deposition has occurred.

25.2.2.1 The Spatial Variability of Inventory

Erosion and deposition are the primary causes of variation in radionuclide inventory. But other factors also influence the inventory and these include: (1) random spatial variability, (2) systematic spatial variability, (3) sampling variability, and (4) precision in measurement (Owens and Walling 1996). Random spatial variability can be tied to local soil properties, microtopography (i.e. Lance et al. 1986), and localized vegetation distributions. Systematic variation is caused by gradients in precipitation, slope, aspect, windfields, and soil types. Sampling variability is tied to the area of collection with large areas of collection featuring lower variability (Loughran et al. 1988). Owens and Walling (1996) and Foster et al. (1994) estimate variation associated with sampling area is approximately 5%. Finally, measurement precision is an important source of variability and is typically about 10%. Owens and Walling (1996) concluded that local variation in ^{137}Cs inventory was relatively large thus single measurements were unlikely to be appropriate measures of activity. Their summary of their own work and the work of others showed a range in coefficient of variation in Cs inventories of 5–47% with an average value of 29%. For ^7Be , Wilson et al. (2003) found a coefficient of variation of 33% in inventories. It might be expected that with the shorter half-life that local variation might add substantially to variability, but that does not appear to be the case.

The change in the inventory of a radionuclide tracer is the basis for estimating soil erosion. In using a radionuclide to quantify erosion, one assumes that the erosion that removes soil also removes the radionuclide tracer. Ideally there is equivalence between the mass loss relative to the potentially erodible material and the radionuclide loss relative to the potentially lost material (inventory). However, radionuclides can still be used to quantify erosion in the absence of equivalence if the tracer loss:soil loss relationship can be quantified. For instance, preferential erosion of certain sized particles enriched in radionuclides might appear to invalidate the assumption of equivalence, but the ability to describe this enrichment will permit determination of erosion.

25.2.3 Time Scales of Utility

Fundamental to the use of tracers to measure rates of soil erosion is the time span over which the loss is calculated. In other words, to determine the rate of erosion using radionuclides, the denominator – time in this case – must be established. Using ^{137}Cs as an example, delivery to the earth surface began around about 1954, peaked in about 1963, and was effectively below detection by 1983 (except in parts of Europe). If we ignore for the moment various other issues, we might reasonably calculate the amount of erosion by measuring the amount of Cs in the soil lost relative to the amount we would expect based upon fallout (accounting for decay). To determine a rate, we do not know anything about the timing of erosion in this interval since deposition so we will assume that the erosion occurred over the period since 1954 when deposition began. In such a scenario, the erosion rate is determined for a period of 56 years (assuming 2010 as the measurement date).

What sets the shortest and longest scales for the use of a radionuclide to estimate erosion? If erosion rate is being determined retrospectively, these are the considerations for the timescale of utility. In the case of a retrospective analysis, the scientist is typically measuring one time the inventory of the radionuclide at a site where erosion occurred and comparing this inventory to the inventory at a reference site without erosion or to the inventory expected given the estimated fallout. The changes in inventory are converted

to soil loss and the rate is determined by the time since deposition.

If repeated measurements of inventory are made and made sufficiently far apart in time, the erosion of soil over shorter time periods can be examined. What is “sufficiently far apart in time?” To estimate erosion a difference in inventory must be measurable. It is typical that analytical errors in activity are at least 10%. In the case of ^{137}Cs , a 10% uncertainty in measured activity when compared to the decay rate, corresponds to a resolution in time no finer than 5 years (~10% of the mean life of the ^{137}Cs). Longer time scales, at least a decade (Walling and Quine 1990), are typically needed to produce measurable changes in ^{137}Cs inventories. In the case of Pb, this finest resolution is about 3 years (~10% of the mean life of ^{210}Pb). For ^7Be , the variable flux means that under certain circumstances, the finest resolution is a matter of days or at the scale of individual precipitation events. One factor influencing the timeframe over which changes in inventory can be recognized is the distribution of the tracer in the soil. If the bulk of the tracer is at the surface, significant amounts of the tracer can be removed with a given amount of erosion. Less of the tracer will be removed by the same amount of erosion if the same inventory is distributed more deeply in the soil. In summary, the amount of erosion; the half-life; the history of deposition, erosion, and mixing of the surface fallout into the soil profile; and the precision in measurement are the keys to the timescale of utility for the various radionuclides. Section 25.4, which summarizes the major classes of models for estimating erosion rates using ^{137}Cs and their assumptions, will treat this subject further.

25.3 Collection and Measurement of Samples

25.3.1 Soil Collection

In order to determine soil radioactivity inventories it is necessary to collect intact soil cores and measure vertical profiles of the radioactivity. Since the radioactivity of ^{137}Cs has often migrated downcore to depths of 20 cm or more, push cores, for example the

types used by golf courses to examine turf quality, are too short. Accordingly, hammer-driven cores and soil pits are used to obtain deeper cores. If high resolution profiling of the cores is desired, for example to obtain a ^7Be profile, then the diameter of the tube needs to be large enough to collect sufficient sample to measure the radionuclide activities in a reasonable counting time. Typical push or hammer cores obtain a 1-in. diameter tube, and by using extension rods the tubes can be collected to a depth of 60-cm or more. However, this type of coring method causes significant (often ~20–30%) compaction of the soil, so that the true depths are poorly known even if they are compaction corrected. Compaction can be minimized by using a larger diameter tube, but it is more difficult to obtain deeper cores with a larger diameter tube. High-resolution soil profiles are easier to obtain from soil pits (Wilson et al. 2003) but the digging and sampling of soil pits is tedious and slower. Alternatively, thin layers of soil may be scraped from the surface of a large area to obtain high resolution vertical profiles (Walling et al. 1999a, b) – a method that is also quite tedious to construct. Regardless of the sampling technique used, it is necessary to know the surface area sampled since radionuclide inventories are expressed as activity per unit area.

After collection, the soil samples need to be dried, ground with a mortar and pestle to a fine texture, placed in standardized geometries, and analyzed by gamma spectroscopy for their radionuclide activities.

25.3.2 ^{137}Cs Measurement

The measurement of ^{137}Cs is accomplished by gamma spectroscopy. ^{137}Cs undergoes β^- (negatron) decay and emits gamma energies at 31.82 keV (relative intensity = 1.96%), 32.19 keV (relative intensity = 3.61%), 36.40 keV (relative intensity = 1.31%), and 661.66 keV (relative intensity = 85.21%). The two lowest energy photopeaks usually cannot be baseline resolved, so they are not used. The photopeak at 36.40 keV has been used, but it is not an ideal choice for measurement because the weak gamma in that energy range undergoes significant sample self absorption for which a large correction is necessary (Cutshall et al. 1983), its relative intensity is fairly small, and, depending on what other isotopes are

being analyzed in the same spectrum, that portion of the spectrum may not have good photopeak separation. The photopeak at 661.66 keV is usually used because the relative intensity is much larger, the spectrum background and the efficiency are relatively constant in that part of the spectrum, and there are no other peaks that overlap or interfere. However, the detector efficiency for solid-state detectors is low at that energy requiring large sample sizes or long counting times to acquire a suitable peak for quantitation.

There are several different types of detectors capable of measuring ^{137}Cs . While Si detectors are commonly used for X-ray analyses, their efficiencies are too low at the higher energies needed for ^{137}Cs detection. The most common detectors that can measure the 661.66 keV photopeak of ^{137}Cs include NaI and Germanium (HPGe) semiconductors, although it is possible to use other detectors, such as Cd-Te, Cd-Zn-Te, and Hg-I. These other detectors have an advantage of reasonably good photopeak resolution and peak to Compton ratio while not require liquid nitrogen cooling. Their disadvantage is that for most applications they are too small and have a very low efficiency at 661.66 keV and therefore require counting times that are too long for practical applications. However, larger crystals are being developed and they may eventually replace NaI and HPGe detectors. NaI detectors have the advantages of being relatively inexpensive, have the highest efficiency of all the detectors discussed here, and requiring no liquid nitrogen for cooling. However, the photopeak energy resolution for NaI detectors is very poor and in most samples the ^{137}Cs photopeak is not visually detectable. Quantitation of a non-visual photopeak requires complex peak separation software, and since the peaks are not visually obvious, the use of NaI detectors to measure ^{137}Cs in soils and sediments seems a “bit like magic” or at the very least results in a lack of confidence in the results. High purity germanium detectors (HPGe) provide the easiest, and most accurate quantitation of the 661.66 keV photopeak of ^{137}Cs . These detectors provide excellent energy resolution and peak to Compton ratios over most of the applicable gamma-ray spectrum, so that ^{210}Pb , ^7Be , ^{134}Cs , ^{137}Cs and ^{40}K and other gamma-emitting isotopes may all be determined at the same time from a single spectrum. However, they are more expensive than the other types of semiconductors discussed here and they require liquid nitrogen cooling. Other analytical techniques, such as

alpha and beta spectroscopy for the determination of ^{210}Pb and ICP-MS for the determination $^{239,240}\text{Pu}$ are discussed in more detail in other chapters (Ketterer et al. 2011).

25.3.3 Calibration and Standards

Calibration of a detector for ^{137}Cs analyses consists of both an energy calibration and an efficiency calibration. The purpose of the energy calibration is to assign the correct photopeak to its appropriate energy. This is accomplished by counting a series of known radionuclides (energies) to determine their channel positions on the energy spectrum. The efficiency calibration is required to relate measured counts to the absolute values of the sample activities and it depends on kind and size of the detector, instrument settings, sample geometry (i.e., the size and shape of the container), sample volume, and shielding (background activities). Consequently, it is necessary to calibrate the energy and efficiency of each machine for every amplifier setting and sample geometry that will be used. Typical efficiencies for the low energy ^{210}Pb photopeak (46.52 keV) are ~0.5% and the efficiencies are about a factor of 3–5 less at the higher energies of ^7Be (477.59 keV) and ^{137}Cs (661.66 keV). Because of these low efficiencies and the low activities in most samples (some Chernobyl samples are an exception) counting times of about 1 day are needed to obtain enough counts to reduce the counting error to <10%. Typical self-absorption correction factors (Cutshall et al. 1983) at the low energy of ^{210}Pb can range from 10 to 80% depending on the size and shape of the sample while the self-absorption correction factor at the higher energy of ^{137}Cs is negligible.

Determining the efficiency requires the use of a standard for which the activity is known. Unfortunately there are no commercially available standards of soils or sediments that are suitable for the efficiency determination of the entire suite of radionuclides commonly measured (^{210}Pb , ^7Be , ^{137}Cs , ^{40}K) although there are a couple of samples that can be used as Quality Assurance samples or as a laboratory standard for efficiency calibration for ^{137}Cs , such as NIST 4350B Columbia River Sediment and International Atomic Energy Agency Reference Material IAEA-375. A list of primary standards available for the

calibration of instruments and chemical procedures is given in Baskaran et al. (2009). In particular, RGU-1 (IAEA – 400 $\mu\text{g g}^{-1}$ with ^{238}U concentration with all its daughter products in secular equilibrium) is a suitable standard for the calibration of ^{210}Pb . Alternatively, it is possible to prepare a standard by spiking a “clean” soil or sediment with the appropriate radionuclides of known activities (for example, Amersham plc QCY44 or NG4 Mixed Radionuclide Solutions) and then placing those prepared soils in the appropriate container for the efficiency calibration of that geometry.

25.4 Methods for Calculating Soil Erosion

Soil erosion can be calculated by the change in the inventory of radionuclides. While the same basic approaches can be used with any of the radionuclides, we detail the use of ^{137}Cs in erosion studies because it was for ^{137}Cs that the methods were originally developed.

Estimation of the erosion rate using ^{137}Cs inventories is typically addressed as an inverse problem with known ^{137}Cs inventories, cultivation and precipitation histories. The simplest method to estimate erosion rates is by a comparison of the ^{137}Cs inventory in soil cores with a reference value from a nearby non-eroded site. The non-eroded site represents the expected baseline fallout to the local geographic area, so that an eroded site would be expected to have less inventory compared to the non-eroded site. Various models have been applied to ^{137}Cs inventories where the erosion rate is assumed to be correlated to the percent of the ^{137}Cs inventory lost from a site (Ritchie et al. 1974; Spomer et al. 1985; Brown et al. 1981; Kachanoski and deJong 1984; DeJong et al. 1986; Lowrance et al. 1988; Soileau et al. 1990; Montgomery et al. 1997; Walling et al. 1999a, b; Fornes et al. 2005). These methods have been recently reviewed (Walling et al. 2002; Poreba 2006) in more detail than we present below and an analysis of these methods led Zapata et al. (2002) to conclude that there are uncertainties associated with the model selection used to estimate erosion rates, that most of the models do not address short-term changes in erosion rates

such as those related to changes in land use and management practices, and that the methodology needs further standardization of the protocols for its general application worldwide.

25.4.1 Empirical, Non-Linear Model

Studies conducted in the 1960s and early 1970s in which ^{137}Cs inventory loss was compared with soil loss estimated using the Universal Soil Loss Equation (Wischmeier and Smith 1978) showed a strong, non-linear empirical relationship at several sites following the equation

$$E = 0.0087P^{1.18} \quad (25.1)$$

where E is erosion rate ($\text{g cm}^{-2} \text{ year}^{-1}$) and P is the percent ^{137}Cs inventory lost from the study site (Ritchie et al. 1974). Percent radionuclide inventory lost is defined as

$$P = (I_{\text{ref}} - I_{\text{site}})/I_{\text{ref}} * 100 \quad (25.2)$$

where I_{ref} is the ^{137}Cs inventory from an undisturbed reference site (Bq m^{-2}) and I_{site} is the ^{137}Cs inventory for the study site. This led to the development of a number of models to calculate erosion rate on the basis of percent inventory lost. In essence, the model assumes a uniform distribution of ^{137}Cs throughout the soil profile so that erosion removes a proportional fraction of the inventory. This approach can result in significant error in the estimation of erosion rate in areas where land use, conservation practices, precipitation or other environmental conditions are not constant throughout the sampling period. For example, if atmospheric ^{137}Cs fallout were confined to the upper layer of soil prior to being eroded or distributed within the cultivation layer, a singular erosion event occurring just after the atmospheric fallout peak in 1964 (following the peak in stratospheric fallout) or in 1986 (following Chernobyl fallout in Europe) would remove a disproportionate amount of ^{137}Cs inventory and result in an overestimate of the soil erosion rate throughout the sampling period. Conversely, a major erosion event today will remove only a small fraction of the inventory because of the downward migration of ^{137}Cs in the

intervening time period and may result in an underestimate of the erosion rate. The use of a reference site does not solve this problem.

25.4.2 Linear Box Model Methods

There are two major classes of models that linearly correlate the percent ^{137}Cs inventory lost with erosion rate. One approach assumes that the total ^{137}Cs inventory is eligible for erosion (Linear 1-Box model; Brown et al. 1981; Spomer et al. 1985) and those in which only the ^{137}Cs inventory within a surface or tillage layer is eligible for erosion (Linear-2Box model; DeJong et al. 1986; Lowrance et al. 1988; Soileau et al. 1990; Montgomery et al. 1997). The key difference between the Linear-1Box and Linear-2Box models lies in the vertical distribution of ^{137}Cs . The Linear-1Box model assumes (sometimes incorrectly) that the entire ^{137}Cs inventory is confined to the tillage layer, whereas the Linear-2Box model allows for some portion of the inventory to reside beneath the tillage layer where it is unavailable for erosion. Spomer et al. (1985) used the Linear-1Box model to describe soil erosion during the period 1954–1974, so that

$$E = DP_L K/T \quad (25.3)$$

where D is the average tillage mixing depth (cm), K is the dry bulk density of the soil (g cm^{-3}), and T is the time since the onset of ^{137}Cs deposition (y). P_L is defined as

$$P_L = (I_{\text{ref}} - I_{\text{site}})/I_{\text{ref}} \quad (25.4)$$

The Linear-2Box model (i.e., tillage depth $<$ ^{137}Cs penetration depth) described soil erosion with the relationship

$$E = DP_{\text{till}} K/T \quad (25.5)$$

P_{till} is analogous to P_L , but the inventory is confined to the tillage layer or to the same depth as the tillage layer at reference sites. Comparisons of results obtained with both the Linear 1-Box and Linear 2-box models indicate little differences in derived erosion rates at Spomer et al.'s (1985) field site (Fornes et al. 2005).

25.4.3 Time-Dependent Model Methods

Some approaches (detailed in Ritchie et al. 1974) are limited in their use because the relationship between erosion rate and ^{137}Cs inventory is incorrectly assumed to be independent of time or cultivation, even failing to account for the radioactive decay of ^{137}Cs (Kachanoski and deJong 1984). These various approaches produced a wide range of erosion rates at a single site (Fornes et al. 2000) confirming that model assumptions significantly influence ^{137}Cs -derived soil erosion rates. Thus, these models are limited because they are single time-step models that do not consider the time-dependent nature of ^{137}Cs fallout (Kachanoski and deJong 1984; Spomer et al. 1985; Walling et al. 1999a, b) or the downcore migration of ^{137}Cs (Figs. 25.9–25.11).

It is possible to obtain improved estimates of soil erosion rates based upon changes in ^{137}Cs inventories by addressing issues associated with model assumptions and changes in soil conservation practices by modeling the time-dependent ^{137}Cs fallout, precipitation and soil cultivation (Kachanoski and deJong 1984; Walling and He 1997a, b; Zhang et al. 1999; Fornes et al. 2005). Using this approach, the equation describing the rate of change of total ^{137}Cs inventory is

$$\partial I/\partial t = F(t) - EC(t) - \lambda I \quad (25.6)$$

where I is ^{137}Cs inventory (Bq cm^{-2}), E is erosion rate ($\text{g cm}^{-2} \text{ year}^{-1}$), $C(t)$ is the concentration of ^{137}Cs (Bq g^{-1}), $F(t)$ is the time-dependent atmospheric fallout of ^{137}Cs (Bq cm^{-2}), and λ is the radioactive decay constant (year^{-1}). Temporal variation of ^{137}Cs fallout, $F(t)$, can be derived from the measured fallout data (Fig. 25.3) with the magnitude adjusted to the local ^{137}Cs reference inventory (Health and Safety Laboratory 1977; Cambray et al. 1989). This model can be kept compatible with the Linear-1Box and Linear-2Box models, by assuming steady-state erosion and cultivation. Soil erosion rates can also be calculated under more detailed constraints such as precipitation-dependent erosion and ephemeral homogenization of the cultivated layer (Walling and He 1997a, b; Zhang et al. 1999; Fornes et al. 2005) for more accurate and realistic erosion rates.

Figure 25.13 illustrates the differences in calculated erosion rates that model assumptions governing the

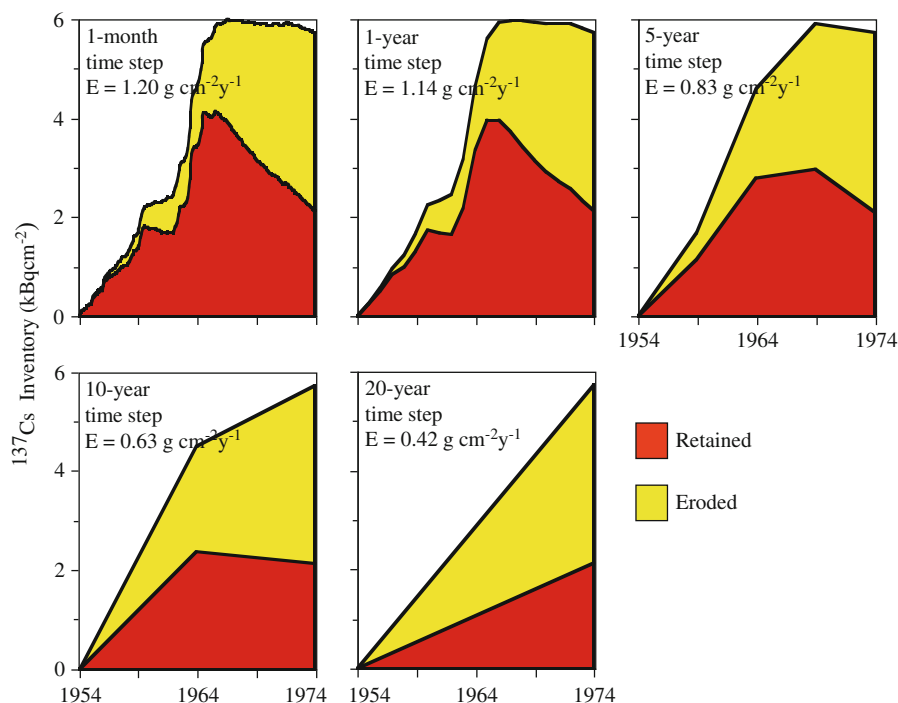


Fig. 25.13 Calculated ^{137}Cs inventories in a soil subject to atmospheric deposition of ^{137}Cs , periodic (annual) cultivation, and erosion over the time period 1954–1974. Note that inclusion

of monthly data results in an erosion rate about 3 times larger than that calculated from the soil inventory only at the end of the 20-year time period. After Fornes et al. (2005)

choice of time step exert on the calculated erosion rates. In these simulations of Fornes et al. (2005), the erosion rate decreased by a factor of three as the model time step was increased from 1 month to 20 years. With a single 20-year time step, erosion rates are virtually the same as those estimated by Spomer et al. (1985) because Spomer et al. (1985) used a Linear-1Box model to describe soil erosion during a single time interval of 1954–1974. The modest differences between the 20-year time step and those reported by Spomer et al. (1985) can be explained by noting that the cultivation depth used in the Fornes et al. (2005) simulations was 10 cm, but Spomer et al. (1985) used a 15 cm cultivation depth. Deposition, cultivation, and erosion in the Spomer et al. (1985) model occur in a single step beginning c. 1954 and ending when the core was collected in 1974. The Fornes et al. (2005) model incorporates a monthly time step (Fig. 25.13) so the 20-year interval is approximated by 240 monthly time steps of deposition and erosion. These results indicate that ^{137}Cs -derived erosion rates are highly sensitive to the length of the time step used in the model because of the combina-

tion of the timing of the fallout, cultivation, and erosion. These results suggest that models that fail to account for temporal variations in atmospheric deposition and/or cultivation practices can grossly miscalculate erosion rates.

25.4.4 Tillage Erosion

While the radionuclide inventory in a core and/or the downcore profile of a radionuclide in that core may indicate erosion, the models described above do not necessarily inform the cause of that erosion. The pattern of radionuclide inventories in a field may be strongly influenced by tillage translocation rather than water erosion. For example, poor agreement has been reported between spatially-distributed ^{137}Cs -derived soil redistribution rates with those derived from water erosion (Quine 1999). Reduced inventories on hillslope convexities and deposition in hollows have been attributed to soil loss caused by tillage redistribution rather than by water erosion

(DeJong et al. 1983; Lobb et al. 1995). Consequently, several workers have developed models which attempt to distinguish the two drivers of radionuclide redistribution and thereby obtain an estimate of the erosion caused solely by water erosion (Govers et al. 1994, 1996; Lobb and Kachanoski 1999). Van Oost et al. (2006) provide a review of the literature on tillage erosion and conclude that based on a global data set tillage erosion rates are comparable to or higher than water erosion rates. They note that because of the widespread use of tillage practices, the high translocation rates resulting from tillage, and the effects of tillage on soil properties, that tillage erosion should be considered in soil landscape studies.

The most widespread used tillage model treats tillage erosion as a diffusion-type process (Govers et al. 1994). The model of Govers et al. (1994) relates the rate of soil translocation to the soil bulk density, the average soil translocation distance in the direction of tillage, and the depth of tillage. They treat translocation distances resulting from a single tillage pass to be linearly and inversely related to slope and that multiple passes in opposing directions results in a net downslope transport. Additional assumptions are that the tillage depth and soil bulk density do not vary in space, tillage soil translocation can be expressed as a linear function of the slope gradient, and tillage is conducted in opposing directions. Using the continuity equation they determine that the tillage erosion may be written as

$$E = -\frac{\partial Q_s}{\partial x} = -D\rho_b b \frac{\partial h}{\partial x} = k_{til} \frac{\delta^2 h}{\delta x^2} \quad (25.7)$$

where E is the tillage erosion rate ($\text{kg m}^{-2} \text{a}^{-1}$); Q_s is the rate of soil translocation in the direction of tillage ($\text{kg m}^{-1} \text{a}^{-1}$); D is the tillage depth (m); ρ_b is the soil bulk density (kg m^{-3}); x is the distance (positive downslope) (m); d is the average soil translocation distance in the direction of tillage (m a^{-1}) ($=a + bS$ where a and b are regression constants (m a^{-1}) and S is the slope tangent (positive upslope; negative downslope) (dimensionless)); h is the height at a given point of the hillslope (m); and k_{til} ($=-D\rho_b b$) is the tillage transport coefficient ($\text{kg m}^{-2} \text{a}^{-1}$).

This model has been applied to a number of studies to compare different plowing directions (Van Muysen et al. 2002; St Gerontidis et al. 2001; De Alba 2001;

Quine and Zhang 2004; Heckrath et al. 2006), and erodability of the landscape (Lobb et al. 1999) as affected by implement characteristics (tool shape, width, length) and operational parameters (tillage depth, speed, tillage direction). Reported implement erosivities as characterized by the tillage transport coefficient are fairly consistent and range from 400 to 800 $\text{kg m}^{-2} \text{year}^{-1}$ for mechanized plowing and from 70 to 260 $\text{kg m}^{-2} \text{year}^{-1}$ for non-mechanized agriculture (Van Oost et al. 2006). Van Oost et al. (2006) also report that decreasing tillage depth and plowing along contour lines substantially reduce tillage erosion rates and can be considered as effective soil conservation strategies.

25.4.5 Wind Erosion

Compared to water there has been relatively little work using ^{137}Cs to study aeolian processes of erosion and deposition. Recently, however, the application of ^{137}Cs to study wind erosion has received some attention (Sutherland and deJong 1990; Sutherland et al. 1991; Chappell 1996, 1998; Yan and Zhang 1998; Yan et al. 2001; Yan and Shi 2004; Hu et al. 2005). The determination of the wind erosion rate is important in assessing the extent and intensity of desertification and the effectiveness of counter-measures.

Calculation of wind erosion rates has been based on the same proportional inventory models that are sometimes used to estimate erosion by water (Sutherland and deJong 1990; Walling and Quine 1993), although it is recognized that these models sometimes suffer from the same issues affecting their use to quantify water erosion – failure to account for surface enrichment of ^{137}Cs and ^{137}Cs dilution by tillage. Mass balance models (Kachanoski and deJong 1984; Zhang et al. 1990) are more suitable for assessing soil erosion in soils where ^{137}Cs is distributed uniformly, such as croplands. In settings where the ^{137}Cs profile is not homogeneous, such as grasslands, the profile distribution model is more appropriate. The calculation of wind erosion loss in these models (Yan et al. 2001; Hu et al. 2005) is estimated by

$$E = \text{CPR} * \text{Bd} * \text{DI} * 10^4 / T \quad (25.8)$$

where E is the net wind erosion rate of the sample site ($\text{Mg ha}^{-1} \text{ a}^{-1}$); B_d is the bulk density of the soil (Mg m^{-3}); DI is the sampling depth increment (assumed = plow depth in farmlands, Sutherland and deJong 1990; Walling and Quine 1993) and in undisturbed soils it is approximately the depth over which ^{137}Cs is found ($\sim 0.1\text{--}0.3$ m); T is the time period between the year of initial ^{137}Cs fallout (assumed to be the year of maximum fallout, 1963) and the sampling year of the study; CPR is the percentage residual at a sampling point in the field relative to the native control area (%):

$$CPR = (CPI - k * CRI) * 100 / (k * CRI) \quad (25.9)$$

where CPI is the ^{137}Cs inventory at the sampling site (Bq m^{-2}); k is a coefficient of ^{137}Cs redistribution caused by snow-blown and vegetation removal (sometimes set =1; =0.95 in Yan et al. 2001); and CRI is the ^{137}Cs inventory at the reference site (Bq m^{-2}).

Studies using this model to quantify wind erosion yield rates that range from 300 to 8,400 $\text{Mg m}^{-2} \text{ a}^{-1}$ depending on the vegetative cover (Yan et al. 2001; Yan and Shi 2004; Hu et al. 2005) where grasslands exhibit the least erosional loss and croplands and dunelands the highest. In one study (Li et al. 2005), an attempt was made to estimate the relative magnitudes of both wind and water erosion in the same study area, and the authors report that wind erosion can account for at least 18% of the total soil loss.

25.5 Recent Applications

In this section, we describe new applications of ^{137}Cs and other radionuclides in studies of surface erosion and deposition.

25.5.1 Single Event Erosion Measurement

One limitation of the longer-lived radionuclides ^{137}Cs and ^{210}Pb is their inability to quantify erosion over short time periods; for instance, the erosion occurring during a single storm. ^{137}Cs and ^{210}Pb are unsuitable for such studies because the change in inventory due to erosion during a single event is small compared to the

total inventory. Walling and Quine (1990) estimated that at least a decade of erosion is necessary to produce a large enough change in ^{137}Cs inventory ($t_{1/2} = 30.1$ years) that the difference is measurable. Following this reasoning, at least 5–8 years of erosion would be required to recognize erosion using changes in $^{210}\text{Pb}_{\text{xs}}$ inventory ($t_{1/2} = 22.3$ years). ^7Be has a sufficiently short half-life ($t_{1/2} = 53$ days) that Blake et al. (1999), Walling et al. (1999a, b) and Wilson et al. (2003) used the radionuclide to estimate erosion occurring during single rainfall events. The workers determined the pre-storm and post-storm inventory of ^7Be as well as the delivery with precipitation. The erosion during the single event studied by Wilson et al. (2003) corresponded to 23% of the average annual erosion rate determined by ^{137}Cs and the mass-balance approach yielded an erosion amount that matched the erosion determined from sediment flux off the field.

Vitko (2007) used ^7Be to recognize redistribution of plowed soil from ridges into adjacent furrows finding that fields plowed along contour had greater retention of ^7Be than fields plowed up-down the slope presumably due to less soil erosion and/or greater deposition.

25.5.2 Sediment Sources

The radionuclides ^7Be , ^{137}Cs , and ^{210}Pb have been used individually and in tandem to quantify the relative contributions of different processes of erosion to sediment. Nagle et al. (2007) used the activity of ^{137}Cs in suspended sediments to determine the provenance of sediment. Collins and Walling (2007) utilized ^{137}Cs and several other constituents in a multivariate sediment mixing model to identify principle sources of fine sediment. He and Owens (1995) used ^{137}Cs , $^{210}\text{Pb}_{\text{xs}}$, and ^{226}Ra in tandem to provide radionuclide fingerprints of cultivated land, uncultivated land, and stream banks and their contributions to the sediment pool. Walling and Woodward (1992) used ^7Be , ^{137}Cs , $^{210}\text{Pb}_{\text{xs}}$ to distinguish sediment from surficial and channel sources and the trend in ^7Be during the studied event allowed them to recognize changing sources. Brigham et al. (2001) used $^{210}\text{Pb}_{\text{xs}}$, ^7Be , and ^{137}Cs as separate tracers to determine the relative importance of surficial and streambank erosion. There was

substantial variation in the estimated percentage of sediment from surface soil erosion – $^{137}\text{Cs} = 34\%$, $^{210}\text{Pb}_{\text{xs}} = 71\%$, $^7\text{Be} = 91\%$. Gellis and Landwehr (2006) used ^{137}Cs and unsupported ^{210}Pb , stable isotopes (del ^{13}C and del ^{15}N), total carbon, nitrogen, and phosphorus to successfully partition sources of fine-grained suspended sediment in the Pocomoke River watershed from cropland, forest, channel and ditch banks, and ditch beds. Devereux et al. (2010) used concentrations of 63 elements and two radionuclides to fingerprint fine sediment sources by both physiographic province (Piedmont and Coastal Plain) and source locale (streambanks, upland and street residue).

Here we consider several specific examples of the use of tracers in source identification. Whiting et al. (2005) established the contribution of streambanks to the suspended sediment flux with a two-component mixing model that used the distinctive radionuclide signatures of the streambanks and of the landscape soils to define the end members of the mixing model (Fig. 25.14). Sediment delivered to the channel by erosion of the soil surface has relatively high activities of ^7Be and ^{210}Pb because of the atmospheric delivery of the radionuclides to the soil surface (Fig. 25.12). Sediment delivered to the channel by bank erosion (largely toppling) has much lower radionuclide activities because the low-activity material from deeper in the bank dilutes the high activity material from atop the

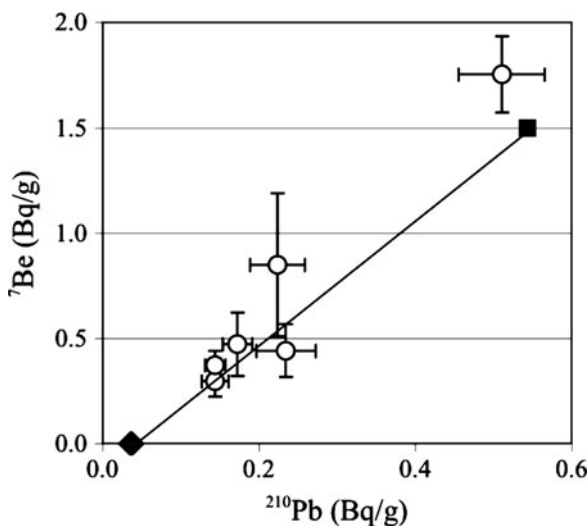


Fig. 25.14 The suspended sediment samples (o) along Soda Butte Creek in Yellowstone National Park, Wyoming, USA, are intermediate between two endmember sources for fine sediment: bank material (diamond) and surficial soils (square)

bank. The height of the collapsed bank is so much larger than the depth of penetration of ^7Be into the soil that the activity of ^7Be in the eroded bank material is effectively zero. The depth to which the bank material is removed corresponds to that part of the soil profile where only the low-activity supported ^{210}Pb is found. Consequently, the ^{210}Pb activity of the bank material is much lower than the surface activity and is similar to the constant value that reflects in situ decay of soil minerals.

In another study, Whiting et al. (2001) used the distinct distribution of ^7Be , ^{137}Cs , and ^{210}Pb with depth in soils on an agricultural plot (Fig. 25.12) and the measured radionuclide flux in runoff in multiple mass balances to quantitatively estimate the areal extent of rill and sheet erosion and the characteristic depth of erosion associated with each mechanism. They examined 15.5 million possible combinations of the depth and areal extent of rill and sheet erosion and found that the best solution to the mass balances corresponded to rills eroding 0.38% of the basin to a depth of 35 mm and sheetwash eroding 37% of the basin to a depth of 0.012 mm. Rill erosion produced 29 times more sediment than sheet erosion.

The identification of sources and depositional locations identified by the radionuclide ratios as discussed herein can be the basis for quantifying a sediment budget. Blake et al. (2002) used ^7Be and ^{137}Cs to quantify various elements of a sediment budget – soil erosion and remobilization from hillslopes, erosion and deposition in river channels, and floodplain deposition. ^{137}Cs has been a common tool for characterizing soil redistribution on landscapes (Walling and Quine 1992; Owens et al. 1997; Walling et al. 2003; Kaste et al. 2006).

25.5.3 Pu as a Tracer

$^{239,240}\text{Pu}$ may be a promising substitute for ^{137}Cs measurements. Stratospheric $^{239,240}\text{Pu}$ is also bomb-derived, behaves similarly once delivered to the earth surface, and gives equivalent information. In fact, Figs. 25.11 and 25.15 show how similar the profiles for the two radionuclides can be and Fig. 25.16 illustrates the strong correlation between ^{137}Cs and $^{239,240}\text{Pu}$ inventories. There are several reasons why $^{239,240}\text{Pu}$ may become used more often than ^{137}Cs . With the development of a method for using inductively coupled plasma mass spectrometry (ICPMS)

Fig. 25.15 Comparison of ^{137}Cs and $^{239+240}\text{Pu}$ profiles in undisturbed prairie soils from Konza Prairie, KS. Plutonium data courtesy of Michael Ketterer

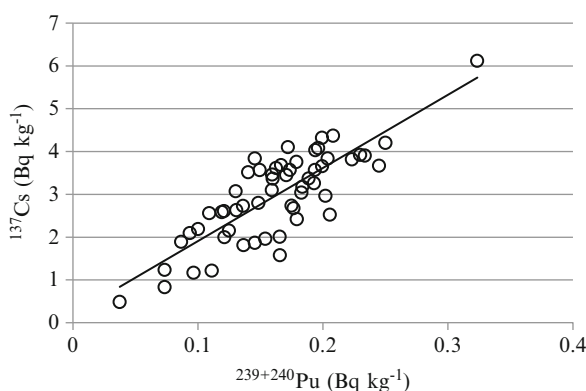
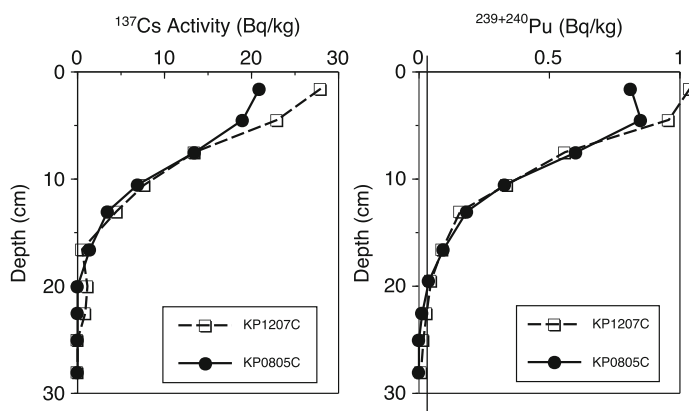


Fig. 25.16 ^{137}Cs inventory vs. $^{239,240}\text{Pu}$ inventory for soil auger samples from 54 sites in the Murder Creek, Georgia USA watershed (from Stubblefield et al. ms)

and high sample through-put, the use of $^{239,240}\text{Pu}$ may be more cost effective (Ketterer and Szechenyi 2008). Moreover, ^{137}Cs half-life ($t_{1/2} = 30.1$ years) is such that peak inventories were observed in the mid- to late-1960s, and by 2010 inventories are only $\sim 40\%$ of original values and dropping. The half-life of both Pu isotopes is several thousand years. Finally, the $^{240}\text{Pu}/^{239}\text{Pu}$ values in fallout in the 1950s and after 1965 differ which may allow partial differentiation of the time frame of erosion.

25.5.4 Use with Other Techniques and in Other Settings

Recently we have seen the use of the fallout radionuclides in conjunction with other erosion measure-

ment techniques. Fondran (2007) combined the use of multiple mass-balances of radionuclides and a laser line scanner with sub-millimeter vertical resolution. With the laser line scanner, Lorimor was able to measure changes in topography (erosion and deposition) and compare these results to the estimates of the depth and areal extent of rills and sheetwash as determined from the multiple mass balances. In the same study, rare earth element tagged soils were deployed to provide information on the proportion of sediment delivered from the top of the slope compared to the middle and bottom of the slope (Stubblefield et al. 2006). O'Farrell et al. (2007) used pond sediment volumes, ^{137}Cs and ^{210}Pb activities, and ^{10}Be and ^{26}Al activities to examine different approaches and timeframes for estimating landscape denudation. Walling et al. (1999a, b) used ^7Be and ^{137}Cs respectively to evaluate event and decadal erosion rates. The conjunctive use of fallout radionuclides (Mabit et al. 2008) especially with other radionuclides, promises to provide key information on variation in denudation rates over time driven by changes in climate and landuse.

Yet other applications include using radionuclide based sedimentation estimates to test predictions of floodplain sedimentation (Siggars et al. 1999) and to compare aerial photography-derived and radionuclide-derived meander migration rates (Black et al. 2010) or accretion rates (Provansal et al. 2010). Various workers have used ^7Be and/or ^{210}Pb to investigate resuspension in rivers and estuaries (Fitzgerald et al. 2001; Wilson et al. 2003, 2005, 2007; Jweda et al. 2008), erosion after forest harvesting (Schuller et al. 2006), and wildfire (Blake et al. 2009).

While the use of radionuclides in surficial studies has focused on tracing fine materials, Salant et al. (2006) used ^7Be to recognize and track medium and coarse sand released from an impoundment. Fisher et al. (2010) likewise used ^7Be to constrain the timescales of sediment storage associated with large woody debris.

25.6 Future Directions

Although there are about 5,000 papers in the literature devoted to the radionuclides discussed in this chapter there is still room for improvement in the methodologies and applications. From a technological perspective, improvements in instrumentation and detection and lowering of costs should enable greater numbers of samples to be collected and analyzed. For example, the development of larger, low cost gamma detectors that do not require liquid nitrogen cooling will enable a more routine use of the equipment, field deployment and more detailed spatial resolution. This could lead to watershed scale or even landscape scale studies. Another technological improvement could be the development of ICP-MS methods for the measurement of ^{137}Cs and ^{210}Pb . Measurement of gamma decays is inefficient because it measures only those atoms that undergo decay during the counting period. But the vast majority of the atoms of interest do not undergo decay during the counting period, especially for the longer lived isotopes. Instead, mass measurements have the advantage of measuring all the atoms that are present in the sample. While ICP-MS methods have been developed for Pu isotopes (Ketterer et al. 2002) it appears that natural levels of ^{137}Cs and ^{210}Pb cannot be detected by current instrumentation. However, with improvements in ICP-MS technology this may change and permit cost-effective analyses of much larger numbers of samples. As with the development of larger low cost gamma detectors, the development of these techniques could enable much higher spatial resolution studies. For example studies comparing $^{239,240}\text{Pu}$ -derived erosion rates as a surrogate for ^{137}Cs -derived erosion rates can be done now, since there are already ICP-MS methods for $^{239,240}\text{Pu}$ and larger numbers of samples can be run for $^{239,240}\text{Pu}$ than for ^{137}Cs .

Earlier in this chapter we demonstrated that the derived erosion rate is model dependent, and in partic-

ular, also depends on the time interval used to evaluate erosion. But these models do not account for the steady, downward migration of the radionuclides. Further progress will require the incorporation of the downward migration into the time dependent erosion models. Furthermore, these models will need to be more comprehensive in their treatment of the downward migration process. Particle mixing by bioturbation as well as solute transport with adsorption will both need to be included in models to enable a better description of the vertical profiles as a function of time. Furthermore, there is evidence that the downward migration process is not steady, and may be affected by non-linear adsorption and/or flow through macropores or channels. A more rigorous evaluation and treatment of these processes needs investigation and incorporation into the models.

It may be possible to use the much better ^{137}Cs soil data sets collected following Chernobyl than the older soil profiles collected a couple of decades after stratospheric fallout to constrain erosion models, quantify soil properties, and improve estimates of soil transport and sources. Even more intriguing is the possibility of combining from the same soil column ^{137}Cs profiles that are dominated by Chernobyl fallout with $^{239,240}\text{Pu}$ profiles derived from global fallout because this will enable comparison of two different tracers over two different time periods within the same soil profile. Furthermore, it may be possible to find locations where the ^{137}Cs signal from stratospheric fallout is comparable in magnitude to the ^{137}Cs fallout from Chernobyl. In such a situation it may be possible to identify and separate the two overlapping signals which will help constrain soil processes and model coefficients.

Finally, soil fertility and C sequestration in soils remain global issues. Thus, accurately determining soil erosion rates, which clearly impacts soil fertility and affects estimates of C sequestration and C removal, remains an important component in research on these topics. Similar studies could also be done to relate past and current erosion rates to land usage to provide both estimates of the historical impacts of land usage on erosion and also future impacts of land usage on C storage and cycling.

Acknowledgements This chapter is dedicated to the memory of Jerry Ritchie.

We would like to thank our former students for their contributions to our research, some of which is highlighted in this chapter: undergraduates Rita Cabral, Joel Saylor, Derek Smith,

Natalie Vajda, and Lauren Vitko; graduate students Chris Bonniwell, Travis Bukach, Carol Fondran, and Chris Wilson; post-doctoral research associates Bill Fornes and Andrew Stubblefield; and colleagues Michael Ketterer, J. Wojciech Mietelski, Klas Rosén, Fred Soster, Louis Thibodeaux, and their students. James Kaste and an anonymous reviewer provided comments that improved the manuscript.

References

- Aoyama M, Hirose K, Igarashi Y (2006) Re-construction and updating our understanding on the global weapons tests ^{137}Cs fallout. *J Environ Monitor* 8:431–438
- Ayub JJ, Di Gregorio DE, Velasco H, Huck H, Rizzotto LF (2009) Short-term seasonal variability in Be-7 wet deposition in a semiarid ecosystem of central Argentina. *J Environ Radioact* 100:977–981
- Azahra M, Camacho-Garcia A, Gonzalez-Gomez C, Lopez-Penalver JJ, El Bardouni T (2003) Seasonal Be-7 concentrations in near-surface air of Granada (Spain) in the period 1993–2001. *Appl Radiat Isot* 59:159–164
- Balistreri LS, Murray JW (1984) Marine scavenging: trace metal adsorption by interfacial sediment from MANOP site H1. *Geochim Cosmochim Acta* 48:921–929
- Baskaran M (1995) A search for the seasonal variability on the depositional fluxes of ^7Be and ^{210}Pb . *J Geophys Res* 100:2833–2840
- Baskaran M (2011) Po-210 and Pb-210 as atmospheric tracers and global atmospheric Pb-210 fallout: a review. *J Environ Radioact* 102:500–513
- Baskaran M, Santschi PH (1993) The role of particles and colloids in the transport of radionuclides in coastal environments of Texas. *Mar Chem* 43:95–114
- Baskaran M, Coleman CH, Santschi PH (1993) Atmospheric depositional fluxes of Be-7 and Pb-210 at Galveston and College Station, Texas. *J Geophys Res* 98:20555–20571
- Baskaran M, Ravichandran M, Bianchi TS (1997) Cycling of ^7Be and ^{210}Pb in a high DOC, shallow, turbid estuary of southeast Texas. *Estuar Coast Shelf Sci* 45:165–176
- Baskaran M, Hong G-H, Santschi PH (2009) Radionuclide analysis in seawater. In: Wurl O (ed) *Practical guidelines for the analysis of seawater*. CRC Press, Boca Raton, pp 259–304
- Beck HL (1999) External radiation exposure to the population of the continental U.S. from Nevada weapons tests and estimates of deposition density of radionuclides that could significantly contribute to internal radiation exposure via ingestion. Report to the National Cancer Institute, P.O. #263-MQ-909853. New York
- Black E, Renshaw CE, Magilligan FJ, Kaste JM, Dade WB, Landis JD (2010) Determining lateral migration rates using fallout radionuclides. *Geomorphology* 123:364–369
- Blake WH, Walling DE, He Q (1999) Fallout beryllium-7 as a tracer in soil erosion investigations. *Appl Radiat Isot* 51:599–605
- Blake WH, Walling DE, He Q (2002) Using cosmogenic Beryllium-7 as a tracer in sediment budget investigations. *Geogr Ann* 84:89–102
- Blake WH, Wallbink PJ, Wilkinson SN, Humphreys GS, Doerr SH, Shakesby RA, Tomkins KM (2009) Deriving hillslope sediment budgets in wildfire affected forests using fallout radionuclide tracers. *Geomorphology* 104:105–116
- Bonniwell EC, Matisoff G, Whiting PJ (1999) Fine sediment residence times in rivers determined using fallout radionuclides (^7Be , ^{137}Cs , ^{210}Pb). *Geomorphology* 27:75–92
- Bossew P, Kirchner G (2004) Modeling the vertical distribution of radionuclides in soil. Part 1. The convection-dispersion equation revisited. *J Environ Radioact* 73:127–150
- Boudreau BP (1986a) Mathematics of tracer mixing in sediments: I. Spatially-dependent, diffusive mixing. *Am J Sci* 286:161–198
- Boudreau BP (1986b) Mathematics of tracer mixing in sediments: II. Nonlocal mixing and biological conveyor-belt phenomena. *Am J Sci* 286:199–238
- Brigham ME, McCullough CJ, Wilkinson P (2001) Analysis of suspended-sediment concentrations and radioisotope levels in the Wild Rice River basin, northwestern Minnesota, 1973–98. US Geological Survey Water Resources Investigation Report 2001-4192
- Brown RB, Kling GF, Cutshall NH (1981) Agricultural erosion indicated by ^{137}Cs redistribution: II. Estimates of erosion rates. *Soil Sci Soc Am J* 45:1191–1197
- Brudecki K, Suwaj J, Mietelski JW (2009) Plutonium and ^{137}Cs in forest litter: the approximate map of plutonium from Chernobyl deposition in Northeastern and Eastern Poland. *Nukleonika* 54(3):199–209
- Bundt M, Albrecht A, Froidevaux BP, Fluhler H (2000) Impact of preferential flow on radionuclide distribution in soil. *Environ Sci Technol* 34:3895–3899
- Cailliet S, Arpagaus P, Monna F, Dominik J (2001) Factors controlling Be-7 and Pb-210 atmospheric deposition as revealed by sampling individual rain events in the region of Geneva, Switzerland. *J Environ Radioact* 53:241–256
- Callender E, Robbins JA (1993) Transport and accumulation of radionuclides and stable elements in a Missouri River reservoir. *Water Resour Res* 29:1787–1804
- Cambay RS, Playford K, Lewis GNJ (1985) Radioactive fallout in air and rain: results to the end of 1984. In: Report *AERE-R11915*, Harwell
- Cambay RS, Playford K, Carpenter RC (1989) Radioactive fallout in air and rain: results to the end of 1988. Report no. AERE-R 10155, U.K. Atomic Energy Authority
- CDC (2006) Report on the feasibility of a study of the health consequences to the American population from nuclear weapons tests conducted by the United States and Other Nations. <http://www.cdc.gov/nceh/radiation/fallout/>. Accessed date: March 17, 2010
- Chappell A (1996) Modelling the spatial variation of processes in redistribution of soil: digital models and ^{137}Cs in the south-west Niger. *Geomorphology* 17:249–261
- Chappell A (1998) Using remote sensing and geostatistics to map ^{137}Cs -derived net soil flux in the south-west Niger. *J Arid Environ* 39:441–455
- Chen G, Flury M, Harsh JB, Lichtner PC (2005) Colloid-facilitated transport of cesium in variably saturated Hanford sediments. *Environ Sci Technol* 39:3435–3442
- Ciffroy P, Reyss J, Siclet F (2003) Determination of the residence time of suspended particles in the turbidity maximum

- of the Loire estuary by ^7Be analysis. *Estuar Coast Shelf Sci* 57:553–568
- Collins AL, Walling DE (2007) The storage and provenance of fine sediment on the channel bed of two contrasting lowland permeable catchments, UK. *River Res Appl* 23: 429–450
- Collins AL, Walling DE, Sickingabula HM, Leeks GJL (2001) Using ^{137}Cs measurements to quantify soil erosion and redistribution rates for areas under different land use in the Upper Kaleya River basin, southern Zambia. *Geoderma* 104:229–323
- Coughtrey PJ, Thorne MC (1983) Radionuclide distribution and transport in terrestrial and aquatic ecosystems: a critical review. A.A. Balkema, Rotterdam
- Cremers AE, De Preter P, Maes A (1988) Quantitative analysis of radiocaesium retention in soils. *Nature* 335:247–249
- Cutshall NH, Larsen IL, Olsen CR (1983) Direct analysis of ^{210}Pb in sediment samples; self adsorption correction. *Nucl Instr Meth* 206:309–312
- Darwin C (1881) The formation of vegetable mould through the action of worms. London: J. Murray (Facsimilies republished in 1982 and 1985, University of Chicago Press, Chicago)
- Davis L (1986) Concern over Chernobyl-tainted birds. *Sci News* 130:54
- de Alba S (2001) Modeling the effects of complex topography and patterns of tillage on soil translocation by tillage with mouldboard plough. *J Soil Water Conserv* 56:335–345
- De Cort M, Dubois G, Fridman SD, Germenchuk MG, Izrael YA, Janssens A, Jones AR, Kelly GN, Kvasnikova EV, Matveenko IL, Nazarov IM, Pokumeiko YuM, Sitak VA, Stukin ED, Tabachny LY, Tsaturov YS, Avdyushin SI (1998) Atlas of caesium deposition on Europe after the Chernobyl accident, EUR 16733 EC. Office for Official Publications of the European Communities, Luxembourg
- DeJong E, Begg CBM, Kachanoski RG (1983) Estimates of soil-erosion and deposition for some Saskatchewan soils. *Can J Soil Sci* 63:607–617
- DeJong E, Wang C, Rees HW (1986) Soil redistribution on three cultivated New Brunswick hillslopes calculated from ^{137}Cs measurement, solum data and the USLE. *Can J Soil Sci* 66:721–730
- Department of National Health and Welfare (1986) Environmental radioactivity in Canada (Radiological monitoring annual report). Department of National Health and Welfare, Ottawa
- Devereux OH, Prestegaard KL, Needleman BA, Gellis AC (2010) Suspended-sediment sources in an urban watershed, Northeast Branch Anacostia River, Maryland. *Hydrol Process* (www.interscience.wiley.com). doi:10.1002/hyp.7604
- Diamond J (2005) Collapse: how societies choose to fail or succeed. Viking, New York
- Dibb JE (1989) Atmospheric deposition of beryllium-7 in the Chesapeake Bay region. *J Geophys Res* 94:2261–2265
- Dietrich WE, Dunne T (1978) Sediment budget for a small catchment in mountainous terrain. *Z Geomorphol Suppl Bd* 29:191–206
- Doering C, Akber R, Heijnis H (2006) Vertical distributions of Pb-210 excess, Be-7 and Cs-137 in selected grass covered soils in Southeast Queensland, Australia. *J Environ Radioact* 87:135–147
- Dong A, Chesters G, Simsman GV (1984) Metal composition of soil, sediments, and urban dust and dirt samples from the Menomonee River watershed, Wisconsin, USA. *Water Air Soil Pollut* 22:257–275
- Dorman L (2004) Cosmic rays in the Earth's atmosphere and underground. Kluwer Academic, Dordrecht
- Dorr H, Munnich KO (1989) Downward movement of soil organic matter and its influence on trace-element transport (^{210}Pb , ^{137}Cs) in the soil. *Radiocarbon* 31:655–663
- Durana L, Chudy M, Masarik J (1996) Investigations of Be-7 in the Bratislava atmosphere. *J Radioanal Nucl Chem* 207:345–356
- Dutkiewicz VA, Husain L (1985) Stratospheric and tropospheric components of ^7Be in surface air. *J Geophys Res* 90:5783–5788
- EC/IGCE (1998) Roshydromet (Russia)/Minchernobyl (Ukraine)/Belhydromet (Belarus)
- El-Hussein A, Mohamemed A, Abd El-Hady M, Ahmed AA, Ali AE, Barakat A (2001) Diurnal and seasonal variation of short-lived radon progeny concentration and atmospheric temporal variations of Pb-210 and Be-7 in Egypt. *Atmos Environ* 35:4305–4313
- Environmental Protection Agency (2000) National water quality inventory, 2000 report. URL:<http://www.epa.gov/305b/2000report/>. Accessed date: March 19, 2010
- Février L, Martin-Garin A (2005) Biogeochemical behaviour of anionic radionuclides in soil: evidence for biotic interactions. *Radioprotection* 40:S79–S86
- Fisher GB, Magilligan FJ, Kaste JM, Nislow KH (2010) Constraining the timescales of sediment sequestration with large woody debris using cosmogenic ^7Be . *J Geophys Res* 115: doi:10.129/2009JF001352
- Fitzgerald SA, Klump JV, Swarzenski PW, Mackenzie RA, Richards KD (2001) Beryllium-7 as a tracer of short-term sediment deposition and resuspension in the Fox River, Wisconsin. *Environ Sci Technol* 35:300–305
- Flavin C (1987) Reassessing nuclear power: the fallout from Chernobyl. *Worldwatch* paper 75, Washington
- Flury MS, Czigany S, Chen G, Harsh JB (2004) Cesium migration in saturated silica sand and Hanford sediments as impacted by ionic strength. *J Contam Hydrol* 71:111–126
- Fondran CL (2007) Characterizing erosion by laser scanning. M.A. Thesis, Case Western Reserve University, 60 pp
- Fornes WL, Matisoff G, Wilson CG, Whiting PJ (2000) Cs-137-derived soil erosion rates under changing tillage practices. *EOS Transactions, Amer. Geophys. Union Fall Meeting*, San Francisco, CA
- Fornes WL, Matisoff G, Wilson CG, Whiting PJ (2005) Erosion rates using Cs-137; the effects of model assumptions and management practices. *Earth Surf Process Landforms* 30:1181–1189
- Foster IDL, Dalglish H, Deargin JA, Jones ED (1994) Quantifying soil erosion and sediment transport in drainage basins; some observations on the use of ^{137}Cs . In: Variability in stream erosion and sediment transport. IAHS Press, Wallingford
- Gabet EJ (2000) Gopher bioturbation: field evidence for non-linear hillslope diffusion. *Earth Surf Process Landforms* 25:1419–1428
- Gabet EJ, Reichman OJ, Seabloom EW (2003) The effects of bioturbation on soil processes and sediment transport. *Ann Rev Earth Planet Sci* 31:249–273

- Gallagher D, McGee EJ, Mitchell PI (2001) A recent history of C-14, Cs-137 and Pb-210 accumulation in Irish peat bogs: an east versus west coast comparison. In: RadioCarbon conference, Jerusalem, June 2000
- Gellis AC, Landwehr JM (2006) Identifying sources of fine-grained suspended-sediment for the Pocomoke River, an Eastern Shore tributary to the Chesapeake Bay. In: Proceedings of the 8th federal interagency sedimentation conference, Reno, Nevada, 2–6 April 2006, Reno, NV, Paper 5C-1 in CD_ROM file ISBN 0-9779007-1-1, 9
- Goldberg ED, Koide M (1962) Geochronological studies of deep sea sediments by the ionium/thorium method. *Geochim Cosmochim Acta* 26:417–450
- Goodbred SL, Kuehl SA (1998) Floodplain processes in the Bengal Basin and the storage of Ganges-Brahmaputra river sediment: an accretion study using ^{137}Cs and ^{210}Pb geochronology. *Sediment Geol* 121:239–258
- Govers G, Vandaele K, Desmet P, Poesen J, Bunte K (1994) The role of tillage in soil redistribution on hillslopes. *Eur J Soil Sci* 45:469–478
- Govers G, Quine TA, Desmet PJ, Walling DE (1996) The relative contribution of soil tillage and overland flow erosion to soil redistribution on agricultural land. *Earth Surf Process Landforms* 21:929–946
- Harden JW, Sundquist ET, Stallard RF, Mark RK (1992) Dynamics of soil carbon during deglaciation of the Laurentide ice sheet. *Science* 258:1921–1924
- Hawley N, Robbins JA, Eadie BJ (1986) The partitioning of $^7\text{beryllium}$ in fresh water. *Geochim Cosmochim Acta* 50:1127–1131
- He Q, Owens P (1995) Determination of suspended sediment provenance using caesium-137, unsupported lead-210 and radium-226; a numerical mixing model approach. In: Gurnell A, Webb B, Foster I (eds) *Sediment and water quality in river catchments*. London, Wiley, pp 207–227
- He Q, Walling DE (1996) Interpreting particle size effects in the adsorption of ^{137}Cs and unsupported ^{210}Pb by mineral soils and sediments. *J Environ Radioact* 30:117–137
- Health and Safety Laboratory (1977) Final tabulation of monthly ^{90}Sr fallout data: 1954–1976. *USERDA Report HASL-329*
- Heckrath G, Halekoh U, Djurhuus J, Govers G (2006) The effect of tillage direction on soil redistribution by mouldboard ploughing on complex slopes. *Soil Tillage Res* 88:225–241
- Hicks HG (1982) Calculation of the concentration of any radionuclide deposited on the ground by off-site fallout from a nuclear detonation. *Health Phys* 42:585–600
- Honeyman BD, Ranville JF (2002) Colloid properties and their effects on radionuclide transport through soils and groundwater. In: Zhang P-C, Brady PV (eds.) *Geochemistry of soil radionuclides*. SSSA special publication 59; Soil Science Society of America, Madison, pp 131–163
- Hong G-H, Hamilton TF, Baskaran M, Kenna TC (2011) Applications of anthropogenic radionuclides as tracers to investigate marine environmental processes. In: Baskaran M (ed) *Handbook of environmental isotope geochemistry*. Springer, Heidelberg
- Hu Y, Liu J, Zhuang D, Cao H, Yan H, Yang F (2005) Distribution characteristics of ^{137}Cs in wind-eroded soil profile and its use in estimating wind erosion modulus. *Chin Sci Bull* 50:1155–1159
- Hyams E (1952) *Soil and civilization*. Thames and Hudson, London
- Ioannidou A, Papastefanou C (2006) Precipitation scavenging of Be-7 and Cs-137 radionuclides in air. *J Environ Radioact* 85:121–136
- Jarvis NJ, Taylor A, Larsbo M (2010) Modeling the effects of bioturbation on the re-distribution of ^{137}Cs in an undisturbed grassland soil. *Eur J Soil Sci* 61:24–34
- Johnson DL, Keller EA, Rockwell TK (1990) Dynamic pedogenesis – new views on some key soil concepts, and a model for interpreting quaternary soils. *Quat Res* 33:306–319
- Joshi SR (1987) Early Canadian results on the long-range transport of chernobyl radioactivity. *Sci Total Environ* 63:125–137
- Jweda J, Baskaran M, van Hees E, Schweitzer L (2008) Short-lived radionuclides (Be-7 and Pb-210) as tracers of particle dynamics in a river system in southeast Michigan. *Limnol Oceanogr* 53:1934–1944
- Kachanoski RG, deJong E (1984) Predicting the temporal relationship between soil cesium-137 and erosion rate. *J Environ Qual* 13:301–304
- Kaste JM, Baskaran M (2011) Meteoric ^7Be and ^{10}Be as process tracers in the environment. In: Baskaran M (ed) *Handbook of environmental isotope geochemistry*. Springer, Heidelberg
- Kaste JM, Fernandez IJ, Hess CT, Norton SA, Pillerin BA (1999a) Sinks and mobilization of cosmogenic beryllium-7 and bedrock-derived beryllium-9 in forested watersheds in Maine, USA. *Geol Soc Am Abst Prog* 31:305
- Kaste JM, Fernandez IJ, Hess CT, Norton SA (1999b) Delivery of cosmogenic beryllium-7 to forested watersheds in Maine, USA. *Geol Soc Am Abst Progr* 31:305
- Kaste JM, Norton SA, Hess CT (2002) Environmental chemistry of beryllium-7. *Rev Mineral Geochem* 50:271–289
- Kaste JM, Heimsath AM, Hohmann M (2006) Quantifying sediment transport across an undisturbed prairie landscape using cesium-137 and high resolution topography. *Geomorphology* 76:430–440
- Kaste JM, Heimseth AM, Bostick BC (2007) Short-term soil mixing quantified with fallout radionuclides. *Geology* 35:243–246
- Ketterer ME, Szechenyi SC (2008) Determination of plutonium and other transuranic elements by inductively coupled plasma mass spectrometry: a historical perspective and new frontier in the environmental sciences. *Spectrochim Acta* 63:719–737
- Ketterer ME, Watson BR, Matisoff G, Wilson CG (2002) Rapid dating of recent aquatic sediments using Pu activities and $^{240}\text{Pu}/^{239}\text{Pu}$ as determined by quadrupole inductively coupled plasma mass spectrometry. *Environ Sci Technol* 36:1307–1311
- Ketterer ME, Hafer KM, Mietelski JW (2004) Resolving Chernobyl vs. global fallout contributions in soils from Poland using plutonium atom ratios measured by inductively coupled plasma mass spectrometry. *J Environ Radioact* 73:183–201
- Ketterer ME, Zheng J, Yamada M (2011) Source tracking of transuranics using their isotopes. In: Baskaran M (ed) *Handbook of environmental isotope geochemistry*. Springer, Heidelberg
- Kikuchi S, Sakurai H, Gunji S, Tokanai F (2009) Temporal variation of Be-7 concentrations in atmosphere for 8 y

- from 2000 at Yamagata, Japan: solar influence on the Be-7 time series. *J Environ Radioact* 100:515–521
- Koch DM, Jacob DJ, Graustein WC (1996) Vertical transport of tropospheric aerosols as indicated by ^7Be and ^{210}Pb in a chemical tracer model. *J Geophys Res* 101:18651–18666
- Konshin OV (1992) Mathematical model of ^{137}Cs migration in soil: analysis of observations following the Chernobyl accident. *Health Phys* 63:301–306
- Korky JK, Kowalski L (1989) Radioactive cesium in edible mushrooms. *J Agric Food Chem* 37:568–569
- Korobova E, Ermakov A, Linnak V (1998) ^{137}Cs and ^{90}Sr mobility in soils and transfer in soil-plant systems in the Novozybkov district affected by the Chernobyl accident. *Appl Geochem* 13:803–814
- Kownacka L (2002) Vertical distributions of beryllium-7 and lead-210 in the tropospheric and lower stratospheric air. *Nukleonika* 47:79–82
- Lal D, Baskaran M (2011) Applications of cosmogenic isotopes as atmospheric tracers. In: Baskaran M (ed) *Handbook of environmental isotope geochemistry*. Springer, Heidelberg
- Lal D, Peters B (1967) Cosmic ray produced radioactivity on the Earth, p. 551–612. In *Encyclopedia of physics*. V. 46/2. Springer
- Lal R (2003) Soil erosion and the global carbon budget. *Environ Internat* 29:437–450
- Lance J, McIntyre SC, Naney JW, Rousseva SS (1986) Measuring sediment movement at low erosion rates using cesium 137. *Soil Sci Soc Am J* 50:1303–1309
- Lenhart JJ, Saiers JE (2002) Transport of silica colloids through unsaturated porous media: experimental results and model comparisons. *Environ Sci Technol* 36:769–777
- Li M, Li ZB, Liu PL, Yao WY (2005) Using Cesium-137 technique to study the characteristics of different aspect of soil erosion in the wind-water erosion crisscross region on Loess Plateau of China. *Appl Radiat Isot* 62:109–113
- Lobb DA, Kachanoski RG (1999) Modeling tillage translocation using step, linear-plateau and exponential functions. *Soil Till Res* 51:317–330
- Lobb DA, Kachanoski RG, Miller MH (1995) Tillage translocation and tillage erosion on shoulder slope landscape positions measured using Cs-137 as a tracer. *Can J Soil Sci* 75:211–218
- Lobb DA, Kachanoski RG, Miller MH (1999) Tillage translocation and tillage erosion in the complex upland landscapes of southwestern Ontario, Canada. *Soil Tillage Res* 51:189–209
- Lomenick TF, Tamura T (1965) Naturally occurring fixation of cesium-137 on sediments of lacustrine origin. *Soil Sci Soc Am Proc* 29:383–386
- Loughran J, Elliott GL, Campbell BL, Shelly DJ (1988) Estimation of soil erosion from caesium-137 measurements in a small, cultivated catchment in Australia. *Applied Radiation and Isotopes* A39, pp. 1153–1157
- Lowdermilk WC (1953) Conquest of the land through 7000 years. *Agricultural Info Bull* No. 99
- Lowrance R, McIntyre S, Lance C (1988) Erosion and deposition in a field/forest system estimated using cesium-137 activity. *J Soil Water Conserv* 43:195–199
- Lyles L (1985) Predicting and controlling wind erosion. *Agric Hist Soc* 59:205–214
- Mabit L, Benmansour M, Walling DE (2008) Comparative advantages and limitations of the fallout radionuclides Cs-137, Pb-210(ex) and Be-7 for assessing soil erosion and sedimentation. *J Environ Radioact* 99:1799–1807
- Martz LW, de Jong E (1985) The relationship between land surface morphology and soil erosion-deposition rates in a small Saskatchewan basin. *Proceedings of the Canadian Society for Civil Engineering, Annual Conference, Hydro-technical Division, July 1985, Saskatoon, Sask., 1–19*
- Matisoff G, Bonniwell EC, Whiting PJ (2002a) Soil erosion and sediment sources in an Ohio watershed using Beryllium-7, Cesium-137, and Lead-210. *J Environ Qual* 31:54–61
- Matisoff G, Bonniwell EC, Whiting PJ (2002b) Radionuclides as indicators of sediment transport in agricultural watersheds that drain to Lake Erie. *J Environ Qual* 31:62–72
- Matisoff G, Wilson GC, Whiting PJ (2005) $^7\text{Be}/^{210}\text{Pb}$ ratio as an indicator of suspended sediment age or fraction new sediment in suspension. *Earth Surf Process Landforms* 30:1191–1201
- Matisoff G, Ketterer ME, Rosén K, Mielowski JW, Vitko LF, Persson H, Lokas E (2011) Downward Migration of Chernobyl-derived Radionuclides in Soils in Poland and Sweden. *Applied Geochemistry* 26:105–115
- McHenry JR, Ritchie JC, Gill AC (1973) Accumulation of fallout cesium 137 in soils and sediments in selected watersheds. *Water Resour Res* 9:676–686
- McNeary D, Baskaran M (2003) Depositional characteristics of Be-7 and Pb-210 in southeastern Michigan. *J Geophys Res Atmos* 108:4210
- Mielowski JW, Was B (1995) Plutonium from Chernobyl in Poland. *Appl Radiat Isot* 46:1203–1211
- Mielowski JW, Jasińska M, Kozak K, Ochab E (1996) The method of measurements used in the investigation of radioactive contamination of forests in Poland. *Appl Radiat Isot* 47:1089–1095
- Miller KM, Kuiper JL, Helfer IK (1990) ^{137}Cs fallout depth distributions in forest versus field sites: implications for external gamma dose rates. *J Environ Radioact* 12:23–47
- Montgomery DR (2007) *Dirt: the erosion of civilizations*. University of California Press, California
- Montgomery JA, Busacca AJ, Frazier BE, McCool DK (1997) Evaluating soil movement using cesium-137 and the revised universal soil loss equation. *Soil Sci Soc Am J* 61:571–579
- Motha JA, Walbrink PJ, Hairsine PB, Grayson RB (2002) Tracer properties of eroded sediment and source material. *Hydrol Process* 16:1983–2000
- Müller-Lemans H, van Dorp F (1996) Bioturbation as a mechanism for radionuclide transport in soils: relevance of earthworms. *J Environ Radioact* 31:7–20
- Nagle GN, Fahey T, Ritchie JC, Woodbury PB (2007) Variations in sediment sources in the Finger Lakes and Western Catskills regions of New York. *Hydrol Process* 21:828–838
- Nelson DW, Logan TJ (1983) Chemical processes and transport of phosphorus. In: Schaller FW, Bailey GW (eds) *Agricultural management and water quality*. Iowa State University Press, Iowa
- O'Farrell CR, Heimsath AM, Kaste JM (2007) Quantifying hillslope erosion rates and processes for a coastal California landscape over varying timescales. *Earth Surf Process Landforms* 32:544–560

- Oldeman LR (1994) The global extent of soil degradation. In: Grelaud DJ, Szabolcs I (eds) Soil resilience and sustainable land use. CAB International, Wallingford, pp 99–118
- Olsen CR, Larsen IL, Lowry PD, Cutshall NH, Todd JF, Wong GTF, Casey WH (1985) Atmospheric fluxes and marsh-soil inventories of ^7Be and ^{210}Pb . *J Geophys Res* 90:10487–10495
- Olsen CR, Larsen IL, Lowry PD, Cutshall NH (1986) Atmospheric fluxes and marsh-soil inventories of ^7Be and ^{210}Pb . *J Geophys Res* 90:10487–10495
- Owens PN, Walling DE (1996) Spatial variability of caesium-137 inventories at reference sites: an example from two contrasting sites in England and Zimbabwe. *Appl Radiat Isot* 47:699–707
- Owens PN, Walling DE, He Q (1996) The behavior of bomb-derived caesium-137 fallout in catchment soils. *J Environ Radioact* 32:169–191
- Owens PN, Walling DE, He Q, Shanahan J, Foster I (1997) The use of caesium-137 measurements to establish a sediment budget for the Start catchment, Devon, UK. *Hydrol Sci* 42:405–423
- Paasikallio A (1999) Effect of biotite, zeolite, heavy clay, bentonite and apatite on the uptake of radiocaesium by grass from peat soil. *Plant Soil* 206:213–222
- Paatero J, Hatakka J (2000) Source areas of airborne Be-7 and Pb-210 measured in Northern Finland. *Health Phys* 79:691–696
- Papastefanou C, Ioannidou A (1991) Depositional fluxes and other physical characteristics of atmospheric Beryllium-7 in the temperate zones (40N) with a dry (precipitation free) climate. *Atmos Environ* 25:2335–2343
- Papastefanou C, Ioannidou A, Stoulos S, Manolopoulou M (1995) Atmospheric deposition of cosmogenic ^7Be and ^{137}Cs from fallout of the Chernobyl accident. *Sci Total Environ* 170:151–156
- Pimental D, Harvey C, Resosuarmo P, Sinclair K, Kurz D, McNair M, Crist S, Shpritz L, Fitton L, Saffourni R, Blair R (1995) Environmental and economic costs of soil erosion and conservation benefits. *Science* 267:1117–1123
- Porcelli D, Baskaran M (2011) An overview of isotope geochemistry in environmental studies. In: Baskaran M (ed) *Handbook of environmental isotope geochemistry*. Springer, Heidelberg
- Poreba GJ (2006) Caesium-137 as a soil erosion tracer: a review. *Geochronometria* 25:37–46
- Pote DH, Daniel TC, Sharpley AN, Moore PA, Edwards DR, Nichols DJ (1996) Relating extractable soil phosphorus to phosphorus losses in runoff. *Soil Sci Soc Am J* 60:855–859
- Powell EN (1977) Particle size selection and sediment reworking in a funnel feeder, *Leptosynapta benvis* (Holothuroidea, Synaptidae). *Int Rev Gesamten Hydrobiol* 62:385–408
- Provansal M, Villiet J, Eyrolle F, Raccasi G, Gurriaran R, Antonelli C (2010) High-resolution evaluation of recent bank accretion rate of the managed Rhone: a case study by multi-proxy approach. *Geomorphology* 117:287–297
- Quine TA (1995) Estimation of erosion rates from Caesium-137 data: the calibration question. In: Foster IDL et al (eds) *Sediment and water quality in river catchments*. Chichester, Wiley, pp 307–329
- Quine TA (1999) Use of caesium-137 data for validation of spatially distributed erosion models: the implications of tillage erosion. *Catena* 37:415–430
- Quine TA, Zhang Y (2004) Re-defining tillage erosion: quantifying intensity – direction relationships for complex terrain. (1) Derivation of an adirectional soil transport coefficient. *Soil Use and Management* 20(2):114–123
- Rabalais NN, Turner RE, Dubravko J, Dortsch Q, Wisman WJ (1999) Characterization of hypoxia: topic 1 report for the integrated assessment on hypoxia in the Gulf of Mexico. NOAA Coastal Ocean Program Decision Analysis Series No. 17, NOAA Coastal Ocean Office, Silver Spring
- Reiser DW (1998) Sediment in gravel bed rivers. In: Klingeman PC, Beschta RL, Komar PD, Bradley JB (eds) *Ecological and biological considerations*. Water Resource Publications, Highland Ranch
- Revelle P, Revelle C (1988) *The environment*. Jones and Bartlett, Boston
- Rhoads DC (1974) Organism-sediment relations on the muddy sea floor. *Oceanogr Mar Biol Annu Rev* 12:263–300
- Rhoads DC, Stanley DJ (1964) Biogenic graded bedding. *J Sediment Petrol* 35:956–963
- Riise G, Bjornstad HE, Lien HN, Oughton DH, Saibu B (1990) A study on radionuclide association with soil components using a sequential extraction procedure. *J Radioanal Nucl Chem* 142:531–538
- Ritchie JC, McHenry JR (1978) Fallout Cs-137 in cultivated and noncultivated North Central United States watersheds. *J Environ Qual* 7:40–44
- Ritchie JC, McHenry JR (1990) Application of radioactive fallout Cesium-137 for measuring soil erosion and sediment accumulation rates and patterns – a review. *J Environ Qual* 19:215–233
- Ritchie JC, Ritchie CA (2008) Bibliography of publications of $^{137}\text{cesium}$ studies related to erosion and sediment deposition. <http://web.cena.usp.br/apostilas/Osny/BiblioCs137December2008.pdf>. Accessed 21 Jan 2010
- Ritchie JC, Spraberry JA, McHenry JR (1974) Estimating soil erosion for the redistribution of fallout ^{137}Cs . *Soil Sci Soc Am J* 38:137–139
- Robbins JA (1985) Great Lakes regional fallout source functions. NOAA Technical Memorandum ERL GLERL-56, Ann Arbor, MI
- Robbins JA (1986) A model for particle-selective transport of tracers in sediments with conveyor-belt deposit feeders. *J Geophys Res* 91(C7):8542–8558
- Robbins JA, Eadie BJ (1991) Seasonal cycling of trace elements ^{137}Cs , ^7Be , and $^{239+240}\text{Pu}$ in Lake Michigan. *J Geophys Res* 96:17081–17104
- Robbins JA, McCall PL, Fisher JB, Krezoski JR (1979) Effect of deposit feeders on migration of ^{137}Cs in lake sediment. *Earth Planet Lett* 42:277–287
- Rogowski AS, Tamura T (1970) Environmental mobility of cesium-137. *Radiat Bot* 10:35–45
- Rosen K, Oborn L, Lonsjo H (1999) Migration of radiocaesium in Swedish soil profiles after the Chernobyl accident, 1987–1995. *J Environ Radioact* 46:45–66
- Rowan JS (1995) The erosional transport of radiocaesium in catchment systems: a case study of the Exe basin, Devon. In: Foster IDL et al (eds) *Sediment and water quality in river catchments*. Wiley, Chichester
- Roy JC, Cote JE, Mahfoud A, Villeneuve S, Turcotte J (1988) On the transport of Chernobyl radioactivity to eastern Canada. *J Environ Radioact* 6:121–130

- Salant NL, Renshaw CE, Magilligan FJ, Kaste JM, Nislow KH, Heimsath AM (2006) The use of short-lived radionuclides to quantify transitional bed material transport in a regulated river. *Earth Surf Process Landforms* 32:509–524
- Salisbury RT, Cartwright J (2005) Cosmogenic Be-7 deposition in North Wales: Be-7 concentrations in sheep faeces in relation to altitude and precipitation. *J Environ Radioact* 78:353–361
- Sanchez AL, Wright SM, Smolders E, Naylor C, Stevens PA, Kennedy VH, Dodd BA, Singleton DL, Barnett CL (1999) High plant uptake of radiocesium from organic soils due to Cs mobility and low soil K content. *Environ Sci Technol* 33:2752–2757
- Sarmiento JL, Gwinn E (1986) Strontium-90 fallout prediction. *J Geophys Res* 91:7631–7646
- Schuller P, Eilers A, Kirchner G (1997) Vertical migration of fallout ^{137}Cs in agricultural soils from Southern Chile. *Sci Total Environ* 193:197–205
- Schuller P, Iroume A, Walling DE, Mancilla HB, Castillo A, Trumper RE (2006) Use of beryllium-7 to document soil redistribution following forest harvest operations. *J Environ Qual* 35:1756–1763
- Schultz RK, Overstreet R, Barshad I (1959) On the soil chemistry of cesium-137. *Soil Sci* 89:19–27
- Sekely AC, Bauer DW, Mulla DJ (2002) Streambank slumping and its contribution to the phosphorus and suspended sediment loads of the Blue Earth River, Minnesota. *J Soil Water Conserv* 57:243–250
- Sepulveda A, Schuller P, Walling DE, Castillo A (2008) Use of Be-7 to document soil erosion associated with a short period of extreme rainfall. *J Environ Radioact* 99:35–49
- Sharpley AN, Daniel TC, Edwards DR (1994) Phosphorus movement in the landscape. *J Product Agric* 6:492–500
- Shenber MA, Johanson KJ (1992) Influence of zeolite on the availability of radiocaesium in soil to plants. *Sci Total Environ* 113:287–295
- Shimmack W, Flessa H, Bunzl K (1997) Vertical migration of Chernobyl-derived radiocesium in Bavarian Grassland soils. *Naturwissenschaften* 84:204–207
- Siggars GB, Bates PD, Anderson MG, Walling DE, He Q (1999) A preliminary investigation of the integration of modeled floodplain hydraulics with estimates of overbank floodplain sedimentation derived from Pb-210 and Cs-137 measurements. *Earth Surf Process Landforms* 24:211–231
- Soileau JM, Hajek BF, Touchton JT (1990) Soil erosion and deposition evidence in a small watershed using fallout cesium-137. *Soil Sci Soc Am J* 54:1712–1719
- Spomer RG, McHenry JR, Piest RF (1985) Sediment movement and deposition using cesium-137 tracer. *Trans Am Soc Agric Eng* 28:767–772
- St Gerontidis DV, Kosmas G, Detsis G, Marathianou M, Zafirios T, Tsara M (2001) The effect of mouldboard plow on tillage erosion along a hillslope. *J Soil Water Conserv* 56:147–152
- Stallard RF (1998) Terrestrial sedimentation and the carbon cycle: coupling weathering and erosion to carbon burial. *Global Biogeochem Cy* 12:231–257
- Steinmann P, Billen T, Loizeau J-L, Dominik J (1999) Beryllium-7 as a tracer to study mechanisms and rates of metal scavenging from lake surface waters. *Geochim Cosmochim Acta* 63:1621–1633
- Stokes S, Walling DE (2003) Radiogenic and isotopic methods for the direct dating of fluvial sediments. In: Kondolf GM, Piegay H (eds) *Tools in fluvial geomorphology*. Wiley, Chichester
- Stubblefield AP, Fondran C, Ketterer ME, Matisoff G, Whiting PJ (2006) Radionuclide and rare earth element tracers of erosional processes on the plot scale. In: Joint Eighth Federal Interagency Sedimentation Conference and Third Federal Interagency Modeling Conference, Reno, Nevada
- Stubblefield AP, Whiting PJ, Matisoff G, Fondran C, Wilson C, Calhoun FC, ms. Delivery of nutrients by rill and sheet erosion in agricultural settings. In preparation
- Su CC, Huh CA, Lin FJ (2003) Factors controlling atmospheric fluxes of Be-7 and Pb-210 in northern Taiwan. *Geophys Res Lett* 30:2018
- Sugihara S, Momoshima N, Maeda Y, Osaki S (2000) Variation of atmospheric ^7Be and ^{210}Pb depositions at Fukuoka, Japan. In: 10th international congress of the international radiation protection association. Hiroshima, Japan 10–19 May 2000
- Sutherland RA, deJong E (1990) Estimation of sediment redistribution within agricultural fields using caesium-137. Crystal Springs, Saskatchewan, Canada. *Appl Geograph* 10:205–213
- Sutherland RA, Kowalchuk T, deJong E (1991) Caesium-137 estimates of sediment redistribution by wind. *Soil Sci* 151:387–396
- Tamura T, Jacobs DG (1960) Structural implications in cesium sorption. *Health Phys* 2:391–398
- Tarras-Wahlberg NH, Lane SN (2003) Suspended sediment yield and metal contamination in a river catchment affected by El Nino events and gold mining activities; the Puyango River Basin, Southern Ecuador. *Hydrol Process* 17:3101–3123
- Todd JF, Wong GRF, Olsen CR, Larsen IL (1989) Atmospheric depositional characteristics of Beryllium 7 and Lead 210 along the southeastern Virginia Coast. *J Geophys Res* 94:11106–11116
- Tokieda T, Yamanaka K, Harada K, Tsunogai S (1996) Seasonal variation of residence time and upper atmospheric contribution of aerosols studied with Pb-210, Po-210 and Be-7. *Tellus* 48:690–702
- Turekian KK, Nozaki Y, Benninger LK (1977) Geochemistry of atmospheric radon and radon products. *Ann Rev Earth Planet Sci* 5:227–255
- Turekian KK, Benninger LK, Dion EP (1983) ^7Be and ^{210}Pb total deposition fluxes at New Haven, Connecticut and at Bermuda. *J Geophys Res* 88:5411–5415
- Valles I, Camacho A, Ortega X (2009) Natural and anthropogenic radionuclides in airborne particulate samples collected in Barcelona (Spain). *J Environ Radioact* 100:102–107
- Van Muysen W, Govers G, Van Oost K (2002) Identification of important factors in the process of tillage erosion: the case of mouldboard tillage. *Soil Till Res* 65:77–93
- Van Oost K, Govers G, de Albe S, Quine TA (2006) Tillage erosion: a review of controlling factors and implications for soil quality. *Progr Phys Geog* 4:443–466
- Vitko L (2007) Evaluating soil erosion on agricultural plots using radionuclides. BA Thesis, Case Western Reserve University
- Wallbrink PJ, Murray AS (1994) Fallout of ^7Be in south Eastern Australia. *J Environ Radioact* 25:213–228

- Wallbrink PJ, Murray AS (1996) Distribution and variability of Be-7 in soils under different surface cover conditions and its potential for describing soil redistribution processes. *Water Resour Res* 32:467–476
- Wallbrink PJ, Murray AS, Olley JM (1999) Relating suspended sediment to its original soil depth using fallout radionuclides. *Soil Science Society of America Journal* 63:369–378
- Walling DE, He Q (1997a) Investigating spatial patterns of overbank sedimentation on river floodplains. *Water Air Soil Pollut* 99:9–20
- Walling DE, He Q (1997b) Models for converting ^{137}Cs measurements to estimates for soil redistribution on cultivated and uncultivated soils (including software for model implementation). In: International Atomic Energy Agency (IAEA) coordinated research programmes on soil erosion (D1.50.05) and sedimentation (F3.10.01). University of Exeter, Exeter
- Walling DE, Quine TA (1990) Calibration of cesium-137 measurements to provide quantitative erosion rate data. *Land Degrad Rehab* 2:161–175
- Walling DE, Quine TA (1992) The use of caesium-137 measurements in soil erosion surveys. In: Erosion and sediment transport monitoring programmes in River Basins, IAHS publications 210, Wallingford
- Walling DE, Quine TA (1993) Use of caesium-137 as a tracer of erosion and sedimentation: Handbook for the application of the caesium-137 technique. U.K Overseas Development Administration Research Scheme R4579, Department of Geography, University of Exeter, Exeter, United Kingdom, 196 p
- Walling DE, Woodward JC (1992) Use of radiometric fingerprints to derive information on suspended sediment sources. In: Erosion and sediment transport monitoring programmes in River Basins, IAHS publications 210, Wallingford
- Walling DE, He Q, Blake W (1999a) Use of Be-7 and Cs-137 measurements to document short- and medium term rates of water-induced soil erosion on agricultural land. *Water Resour Res* 35:3865–3874
- Walling DE, Owens PN, Leeks GJL (1999b) Fingerprinting suspended sediment sources in the catchment of the River Ouse, Yorkshire, UK. *Hydrol Process* 13:955–975
- Walling DE, He Q, Appleby PG (2002) Conversion models for use in soil-erosion, soil-redistribution and sedimentation investigations. In: Zapata F (ed) Handbook for the assessment of soil erosion and sedimentation using environmental radionuclides. Kluwer Academic Publishers, Dordrecht, pp 111–164
- Walling DE, Collins AL, Sickingabula HM (2003) Using unsupported lead-210 measurements to investigate erosion and sediment delivery in a small Zambian catchment. *Geomorphology* 52:193–213
- Walling DE, Schuller P, Zhang Y, Iroume A (2009) Extending the timescale for using beryllium 7 measurements to document soil redistribution by erosion. *Water Resour Res* 45: W02418
- Wang K, Cornett RJ (1993) Distribution coefficients of ^{210}Pb and ^{210}Po in laboratory and natural aquatic systems. *J Paleolimnol* 9:179–188
- Whiting PJ, Bonniwell EC, Matisoff G (1999) A Mass Balance Method for Determining the Depth and Area of Rill and Sheetwash Erosion of Soils using Fallout Radionuclides (^7Be , ^{137}Cs , ^{210}Pb): EOS Transactions, American Geophysical Union Fall Meeting, v. 80. p. F445
- Whiting PJ, Bonniwell EC, Matisoff G (2001) Depth and areal extent of sheet wash and rill erosion from radionuclides in soils and suspended sediment. *Geology* 29:1131–1134
- Whiting PJ, Matisoff G, Fornes W, Soster F (2005) Suspended sediment sources and transport distances in the Yellowstone basin. *Geol Soc Am Bull* 117:515–529
- Williams GP, Wolman MG (1984) Downstream effects of dams on alluvial rivers. US Geological Survey Professional Paper 1286, p 83
- Wilson CG, Matisoff G, Whiting PJ (2003) Short-term erosion rates from a Be-7 inventory balance. *Earth Surf Process Landforms* 28:967–977
- Wilson CG, Matisoff G, Whiting PJ (2005) Transport of fine sediment through the Old Woman Creek, OH, wetland using radionuclide tracers. *J Great Lakes Res* 31:56–67
- Wilson CG, Matisoff G, Whiting PJ (2007) The use of ^7Be and $^{210}\text{Pb}_{\text{xs}}$ to differentiate suspended sediment sources in South Slough, OR. *Estuar Coasts* 30:348–358
- Wischmeier WH, Smith DD (1978) Predicting rainfall erosion losses – a guide to conservation planning. In: Agricultural handbook No. 537. US Department of Agricultural Science and Education Administration, Washington
- Wise SW (1980) Caesium-137 and lead-210: a review of the technique and application to geomorphology, pp. 109–127. In: Cullingford RA, Davidson RA, Lewin J (eds) Timescales in geomorphology, John Wiley and Sons, New York
- Yamada H, Nakamura F (2002) Effect of fine sediment deposition and channel works on periphyton biomass in the Makoanai River, Northern Japan. *River Res Appl* 18:481–493
- Yan P, Shi P (2004) Using the ^{137}Cs technique to estimate wind erosion in Gonghe Basin, Qinghai Province, China. *China Soil Sci* 169:295–305
- Yan P, Zhang XB (1998) Prospects of caesium-137 used in the study of aeolian processes. *J Desert Res* 18:182–187
- Yan P, Dong Z, Dong G, Zhang X, Zhang Y (2001) Preliminary results of using ^{137}Cs to study wind erosion in the Qinghai-Tibet plateau. *J Arid Environ* 47:443–452
- You CF, Lee T, Li YH (1989) The partition of Be between soil and water. *Chem Geol* 77:105–118
- Zapata F, Garcia-Agudo E, Ritchie JC, Appleby PG (2002) Introduction. In: Zapata F (ed) Handbook for the assessment of soil erosion and sedimentation using environmental radionuclides. Kluwer Academic Publishers, Dordrecht, pp 1–14
- Zhang XB, Higgitt DL, Walling DE (1990) A preliminary assessment of the potential for using cesium-137 to estimate rates of soil-erosion in the Loess Plateau of China. *Hydrol Sci* 35:243–252
- Zhang XB, Walling DE, He Q (1999) Simplified mass balance models for assessing soil erosion rates and cultivated land using cesium-137 measurements. *Hydrol Sci* 44:33–45

Chapter 26

Sr and Nd Isotopes as Tracers of Chemical and Physical Erosion

Gyana Ranjan Tripathy, Sunil Kumar Singh, and S. Krishnaswami

Abstract The applications of radiogenic isotopes to investigate chemical and physical erosion processes, particularly in river basins of the Himalaya, have led to interesting inferences on the relationship between tectonics, weathering and climate. The chemical weathering studies rely more on Sr isotopes because of their widely different ratios in various end members, their uniform distribution in the oceans and the availability of continuous and robust record of marine $^{87}\text{Sr}/^{86}\text{Sr}$ through much of the geological past. The record for the Cenozoic shows steady increase in $^{87}\text{Sr}/^{86}\text{Sr}$; one of the hypotheses suggested to explain this is enhanced continental silicate weathering due to the uplift of the Himalaya. This hypothesis linking tectonics-weathering-climate, based on $^{87}\text{Sr}/^{86}\text{Sr}$ as an index of silicate weathering, however, is being challenged by the recent observations that there are a variety of carbonates in the river basins of the Himalaya with $^{87}\text{Sr}/^{86}\text{Sr}$ similar to that of silicates which have the potential to contribute significantly to the high $^{87}\text{Sr}/^{86}\text{Sr}$ of rivers such as the Ganga-Brahmaputra. Further, the non-stoichiometric release of Sr isotopes during chemical weathering of minerals and rocks, the imbalance of Sr isotope budget in the oceans and temporal variations in riverine fluxes due to impact of glaciations all have compounded the problem.

Studies on the provenance of sediments and physical erosion pattern employ both Sr and Nd isotopes under the assumption that their source signatures are preserved in sediments. Though there are concerns on

how well this assumption is satisfied especially by the Sr isotope system, both Sr and Nd systems are being used to learn about physical erosion in the Himalaya, its variability and causative factors. The results show that at present the major source of sediments to the Ganga plain and the Bay of Bengal is the Higher Himalayan Crystallines and that physical erosion among the various sub-basins is very heterogeneous with maximum rates in regions of intense precipitation and high relief. There are three such “hot-spots”, one each in the basins of the Ganga, Brahmaputra and the Indus, which unload huge amount of sediments promoting rapid uplift of regions surrounding them and enhance chemical weathering by exposing fresh rock surfaces. The pattern of physical erosion and its temporal variations shows that it is influenced by climate change both on ky and My time scales though during the latter periods the erosion regime has been by and large stable. This article reviews investigations on the present and past chemical and physical erosion in river basins of the Himalaya using Sr and Nd isotope systematics in water and sediments.

26.1 Introduction

The Earth's continental surface is subject to continuous physical and chemical weathering and erosion by wind, water and glaciers. Physical weathering is the process of breakdown of rocks into finer fragments without affecting their composition, whereas chemical weathering is a complex process of conversion of rocks into its soluble and insoluble secondary products through water-rock interactions. The process of removal of soluble and particulate weathering

G.R. Tripathy, S.K. Singh, and S. Krishnaswami (✉)
Geosciences Division, Physical Research Laboratory,
Ahmedabad 380009, India
e-mail: swami@prl.res.in

products from the site of their formation to their final repository is erosion, though weathering and erosion are often used interchangeably. Erosion therefore plays an important role in exposing “fresh” rock and mineral surfaces in a drainage basin for weathering, a key factor regulating their chemical weathering rates (Stallard and Edmond 1983; Kump et al. 2000). A major driver of chemical weathering is carbonic acid formed by the solution of CO₂ in natural waters. Therefore, studies of chemical weathering are intimately linked to global carbon cycle. In recent years there have been several studies to determine the chemical erosion rates of major global river basins and the various factors regulating it, especially the role of tectonics and climate (Negrel et al. 1993; Derry and France-Lanord 1997; Edmond and Huh 1997; Gaillardet et al. 1997, 1999; Galy and France-Lanord 1999; Huh and Edmond 1999; Krishnaswami et al. 1999; Kump et al. 2000; Millot et al. 2002; Blum and Erel 2003; Dessert et al. 2003; Bickle et al. 2005; Das et al. 2005; Singh et al. 2005; West et al. 2005; Wu et al. 2005; Moon et al. 2007; Peucker-Ehrenbrink et al. 2010; Tripathy and Singh 2010). One of the key topics of interest in this area is silicate weathering of river basins, a major sink for atmospheric CO₂ on million year time scales. This makes the determination of silicate erosion rates (SER) of river basins and its temporal variations an important component of studies on atmospheric CO₂ balance through time and its impact on long term global change, the tectonics-weathering-climate link (Walker et al. 1981; Berner et al. 1983; Raymo et al. 1988; Raymo and Ruddiman 1992; Ruddiman 1997; Kump et al. 2000). These studies though rely primarily on the chemical composition of dissolved phase of rivers, radiogenic isotopes, particularly ⁸⁷Sr/⁸⁶Sr and ¹⁴³Nd/¹⁴⁴Nd, have provided important additional insights into mineral and rock weathering processes that have implications to isotope geochemistry of rivers and oceans and contemporary and paleo-silicate erosion of continents. The unique radiogenic isotope composition of minerals and rocks and the near conservative behavior of the isotope ratios in solution (unlike major elements which are prone to removal from solution by precipitation, ion-exchange and biological cycling) make these isotope techniques very useful to investigate kinetics of rock-water interactions in natural systems where the reactions often

proceed at very slow rates (Blum and Erel 2003; Gaillardet 2008).

In contrast to studies on chemical erosion which rely mainly on the chemical and isotopic composition of dissolved phases, investigations on physical erosion (e.g. provenance studies) depend on chemical and isotopic signatures of sediments. Construction of the physical erosion pattern of sedimentary basins and its controlling factors requires tracking the source of sediments. Sr and Nd isotopes have been extensively used as provenance indicators of river and ocean sediments (Dia et al. 1992; Allegre et al. 1996; Pierson-Wickmann et al. 2001; Singh and France-Lanord 2002; Clift 2006; Colin et al. 2006; Singh et al. 2008; Viers et al. 2008) ever since the pioneering study of Dasch (1969) on tracing the source of deep-sea surface sediments of the Atlantic using Sr isotopes. These isotope systems have become increasingly popular in such studies because their signatures among the various sources (end members) are often markedly different and easily distinguishable. Further, the application of these isotopes as provenance tracers is promoted by the property of the sediments to preserve in them the isotope composition of sources. There have been a number of Sr and Nd isotopic studies in river and ocean sediments from different basins to tag their provenances (e.g. Derry and France-Lanord 1997; Colin et al. 1999; Tutken et al. 2002; Clift et al. 2008; Singh et al. 2008) and their temporal variations to infer about factors controlling physical erosion in the past, particularly its link to regional changes in climate and/or tectonics (France-Lanord et al. 1993; Walter et al. 2000; Li et al. 2003; Clift et al. 2008; Rahaman et al. 2009; Galy et al. 2010). During the past decade, in addition to Sr-Nd, the applications of other isotope systems such as U series disequilibrium (Chabaux et al. 2008, Vigier and Bourdon 2011), Lu-Hf (Ma et al. 2010) and some of the non-traditional isotopes, e.g. Si, Mg and Ca (Tipper et al. 2008; Reynolds 2011) are also being explored to investigate chemical and physical erosion.

This chapter reviews selected studies on the applications of Sr and Nd isotopes as tracers to investigate chemical and physical erosion with emphasis on river basins of the Himalaya. The topics addressed include chemical weathering of minerals and rocks,

silicate erosion in river basins and sediment provenance studies and the relation among erosion, tectonics and climate.

26.2 Chemical Weathering in River Basins

26.2.1 Overview of Sr, Nd in Rocks and Their Isotope Systematics

Strontium is an alkaline earth element with chemical properties similar to that of Ca. It occurs as a minor constituent in rock-forming minerals often replacing Ca or K. Sr has four naturally occurring isotopes, of these ^{87}Sr is radiogenic, produced from the radioactive decay of ^{87}Rb ($t_{1/2} = 4.88 \times 10^{10}$ years). Rb is an alkali element with properties similar to K, therefore it is more abundant in K-rich minerals. As a result, minerals with high K/Ca (\sim Rb/Sr) ratio develop more radiogenic Sr with time. Thus in a rock suite with minerals of the same age, those with high Rb and low Sr (e.g. biotite, muscovite) will have higher $^{87}\text{Sr}/^{86}\text{Sr}$ (refers to $^{87}\text{Sr}/^{86}\text{Sr}$ ratio) compared to minerals with low Rb and high Sr (e.g. plagioclase, apatite). During chemical weathering, Sr is generally more mobile than Rb; therefore, the Rb/Sr ratio of weathered residues is higher than that in parent rocks. The results of Dasch (1969) and subsequent studies on Rb/Sr abundances in weathering profiles developed on basalts and granites confirm this behavior with the weathered residues having higher Rb/Sr than the parent rocks. Preferential adsorption of Rb on clays can also contribute to the higher Rb/Sr in the weathered residues.

The rare earth elements (REEs) occur as trace elements in major rock forming minerals and in higher concentrations in the accessory minerals, e.g. zircon, apatite, monazite and allanite. The concentrations of REEs vary widely in accessory minerals; they are often a minor constituent in zircon and apatite, but are a major component of REE bearing minerals such as monazite and allanite. The REEs are classified broadly into two groups, the light rare earth elements (LREE; La-Sm) and the heavy rare earth elements (HREE; Eu-Lu). Major rock forming minerals are relatively

enriched in one of these two groups, for example feldspars and apatite are more abundant in LREE whereas pyroxenes and garnet prefer HREE. The concentrations of Sm and Nd in rock-forming minerals increase in the sequence in which they crystallize from magma, however due to the close similarity in the chemical properties between Sm and Nd their fractionation during geological processes is limited. As a result, the Sm/Nd abundance ratio in terrestrial rocks and minerals is within a narrow range (0.1–0.5), in contrast to Rb/Sr which varies widely, from 0.005 to 3 (Faure 1986).

Neodymium is a light rare-earth element having seven naturally occurring isotopes. Among these, ^{142}Nd and ^{143}Nd are radiogenic produced by the α -decay of ^{146}Sm ($t_{1/2} = 1.03 \times 10^8$ years) and ^{147}Sm ($t_{1/2} = 1.06 \times 10^{11}$ years), respectively. ^{146}Sm , because of its short half-life is now an extinct radionuclide; its signature however has been detected in meteorites through measurements of ^{142}Nd (Amelin and Rotenberg 2004; Anderasen and Sharma 2006). The $^{143}\text{Nd}/^{144}\text{Nd}$ ratio of minerals and rocks increases with time due to production of ^{143}Nd from ^{147}Sm , their $^{143}\text{Nd}/^{144}\text{Nd}$, therefore depends on their Sm/Nd ratios and ages. The isotopic composition of Nd ($^{143}\text{Nd}/^{144}\text{Nd}$) is expressed in epsilon units (ϵ , DePaolo and Wasserburg 1976), which represents the relative deviation of $^{143}\text{Nd}/^{144}\text{Nd}$ in the sample from $^{143}\text{Nd}/^{144}\text{Nd}$ of the chondritic uniform reservoir (CHUR) in units of 10^4 . ϵ is expressed as,

$$\epsilon_{Nd}(0) = \left(\frac{\left(\frac{{}^{143}\text{Nd}}{{}^{144}\text{Nd}} \right)_{\text{sample}}(0)}{\left(\frac{{}^{143}\text{Nd}}{{}^{144}\text{Nd}} \right)_{\text{CHUR}}(0)} - 1 \right) \times 10^4$$

where $(^{143}\text{Nd}/^{144}\text{Nd})_{\text{CHUR}}(0)$ and $(^{143}\text{Nd}/^{144}\text{Nd})_{\text{sample}}(0)$ are the present day $^{143}\text{Nd}/^{144}\text{Nd}$ ratio of CHUR ($= 0.512638$; Jacobsen and Wasserburg 1980) and the sample, respectively. The normalization of Nd isotopic ratios of rocks with chondritic value provides information on the relative Sm/Nd ratio of their sources. For example, a negative epsilon value indicates that the rock is derived from sources lower in Sm/Nd than CHUR (Faure 1986). Further, as the Nd isotopic variations in natural systems are quite small, the ϵ notation provides a convenient approach to express and appreciate these small variations.

26.2.2 Behavior of Sr and Nd Isotopes During Chemical Weathering of rocks and Mineral Weathering Kinetics

26.2.2.1 $^{87}\text{Sr}/^{86}\text{Sr}$ Release During Mineral and Rock Weathering: Laboratory and Field Studies

The major source of dissolved Sr to rivers is chemical weathering of silicates and carbonates in their drainage basins, with minor contribution from other lithologies such as evaporites. The silicates of bed rocks are an assemblage of minerals, which have different chemical and mineralogical composition and weathering properties. Each of these minerals has their own distinct $^{87}\text{Sr}/^{86}\text{Sr}$ corresponding to their age and Rb and Sr concentrations. During chemical weathering of silicate rocks, Sr isotopes from various minerals are released depending on their weathering rates and accessibility to weathering. As a result, Sr from easily weatherable minerals is expected to be released to solution initially from freshly exposed rock surfaces. The exposure of fresh rock surfaces is facilitated by physical erosion, tectonics and glaciations.

Studies on the release of Sr and $^{87}\text{Sr}/^{86}\text{Sr}$ during weathering of continental rocks and their subsequent behavior are being carried out (1) to determine their release pattern from minerals in the parent rock and its implications to mineral weathering rates and $^{87}\text{Sr}/^{86}\text{Sr}$ of rivers, (2) to assess the relative roles of silicate and carbonate sources to their budget in river/ground water systems and to explore the possibility of using $^{87}\text{Sr}/^{86}\text{Sr}$ in rivers as a proxy for silicate weathering and (3) to interpret Sr isotope records in marine archives. The $^{87}\text{Sr}/^{86}\text{Sr}$ of the oceans, as recorded in carbonate shells of marine sediments, is known to be steadily increasing since the Cenozoic (Burke et al. 1982; Veizer 1989; Richter et al. 1992). Delineating the sources responsible for this increase in terms of silicate/carbonate weathering can prove useful in deciphering the weathering history of continents and its role in atmospheric CO_2 drawdown.

Erel et al. (2004) conducted laboratory studies of granitoid weathering to determine trends in Sr isotope release with time and its implications to mineral weathering. These authors based on combined studies

of major elements and Sr isotopes in minerals of a granitoid rock from Elat, Israel and in the solution from its weathering observed that during initial stages the granitoid dissolution is dominated by contributions from easily weatherable trace phases, calcites/apatites, followed by biotites in the intermediate stages and plagioclase during the later stages of weathering (Fig. 26.1). By comparing these laboratory experimental data with Sr isotope distribution in soil chronosequences from the Wind River and Sierra Nevada mountains, Erel et al. (2004) were able to deduce the temporal pattern of Sr release during granitoid weathering under natural conditions and from it the mineral dissolution sequence for the granite. The results showed that the easily weatherable trace phases in the granitoid, calcites and apatites are the major source of elements to solution from rock weathering during the initial few hundred years, biotites determining the supply from rock surfaces exposed to weathering a few hundreds to ~10,000 years and plagioclase accounting for much of the cations from surfaces that have been weathered for more than ~100,000 years.

The distribution of Sr isotopes in different components of soil chronosequences provided independent evidences for the non-stoichiometric release of Sr during rock weathering. Measurements of Sr isotopes

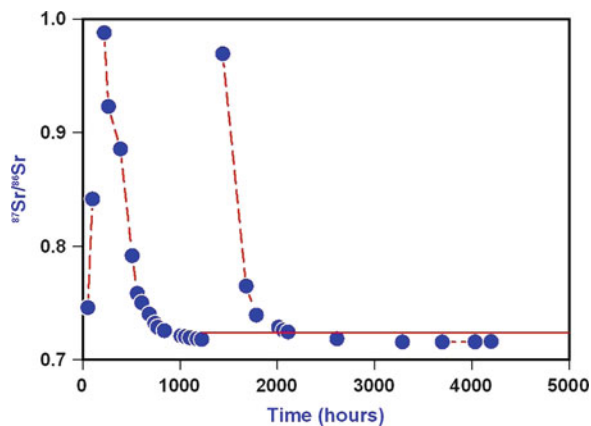


Fig. 26.1 The release pattern of $^{87}\text{Sr}/^{86}\text{Sr}$ during dissolution of a granitoid rock with time. The low $^{87}\text{Sr}/^{86}\text{Sr}$ during the early stage of dissolution is a result of preferential weathering of calcites; this is followed by a sharp peak in Sr isotopic ratio due to weathering of biotites. The straight line parallel to the x-axis is the $^{87}\text{Sr}/^{86}\text{Sr}$ of the whole rock. The weathered residue of the granitoid rock after ~1,200 h of experiment was dried and subjected to further dissolution; this resulted in the second $^{87}\text{Sr}/^{86}\text{Sr}$ peak. Figure replotted from Erel et al. (2004)

(Blum and Erel 1995, 1997) in the exchangeable fractions and bulk soils from a granitic soil chronosequence developed on the Wind River Mountains (0.4–300 ky) showed very significant and systematic decrease in $^{87}\text{Sr}/^{86}\text{Sr}$ of the exchangeable pool with soil age (Fig. 26.2). The primary source of exchangeable Sr in the soil profile is that released during chemical weathering of rocks. This Sr, retained in the exchangeable sites of soils, can be released to solution by ion exchange with suitable reagents. Therefore the decrease in $^{87}\text{Sr}/^{86}\text{Sr}$ (from 0.7947 to 0.7114; Fig. 26.2) of the exchangeable pool with age suggests that $^{87}\text{Sr}/^{86}\text{Sr}$ released during the early stages of weathering was far more radiogenic than that released during the later stages. This was interpreted in terms of preferential weathering of biotites from freshly exposed rock surfaces (<20 ky), underscoring its importance as a source of highly radiogenic Sr to waters draining young rocks rich in biotite. These granites/gneisses were devoid of even trace amounts of calcite (Blum and Erel 1995) precluding it as a source for Sr in the early stages of weathering (c.f. Erel et al. 2004). The data also suggested that biotites weather much faster relative to plagioclase in young soils (~8 times) and that the impact of its (biotite) weathering becomes less as the soil gets older, primarily due to depletion in the abundances of unweathered

biotites (Blum and Erel 1995). More importantly, the non-stoichiometric release of $^{87}\text{Sr}/^{86}\text{Sr}$ due to differences in mineral weathering rates led to the suggestion that exposure of new weathering surfaces (e.g. by glaciation and/or mountain uplift) can make the $^{87}\text{Sr}/^{86}\text{Sr}$ of rivers significantly more radiogenic for periods of ~20 ky following their exposure and thus elevate the riverine $^{87}\text{Sr}/^{86}\text{Sr}$ input to the oceans during such periods. This result also provides a mechanism to link global glaciations with Sr isotope evolution of the oceans (Armstrong 1971; Blum and Erel 1995, 1997; Zachos et al. 1999). More studies on Sr isotopes in granitic soil chronosequence from other locations however showed that the composition of the exchangeable Sr depended on the history of the profile. For example, in a profile from central Sierra Nevada (Bullen et al. 1997), developed on granitic alluvium the exchangeable $^{87}\text{Sr}/^{86}\text{Sr}$ was dominated by supply from plagioclase and K-feldspars and not biotite as was observed by Blum and Erel (1997). This difference was attributed to the absence of fresh biotites in the soil profile of Sierra Nevada, further attesting to the importance of biotite weathering from freshly exposed rock surfaces in contributing to highly radiogenic Sr to solutions.

Analogous to field studies of rock weathering, mineral weathering experiments also brought out the role of non-stoichiometric release of Sr isotope ratios during their early stages of dissolution. Brantley et al. (1998) in their dissolution experiments of feldspars observed that in the initial stages the release of Sr was not stoichiometric and its isotope composition was different from that of the host mineral. This difference was explained in terms of contribution of Sr either from fluorite and zeolites, trace secondary phases in the feldspars and/or to preferential leaching of Sr from more easily weatherable sites of the primary mineral. The isotopic composition of the solution attained steady-state and became close to that of the host mineral with progressive dissolution. These results have led to the suggestion that non-stoichiometric release of Sr and $^{87}\text{Sr}/^{86}\text{Sr}$ can also occur in natural systems, but only for short time periods (<10³ years) following the exposure of fresh mineral/rock surfaces for weathering. Taylor et al. (2000) also have reported similar non-stoichiometric release of Sr and $^{87}\text{Sr}/^{86}\text{Sr}$ during early stages of dissolution of biotites and phlogopites (Fig. 26.3). These results were interpreted in terms of preferential dissolution of trace

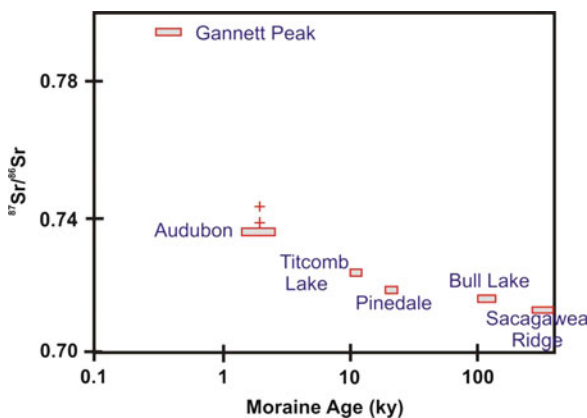


Fig. 26.2 Variations in the Sr isotopic ratio in the exchangeable fractions of a granitoid soil chronosequence developed on glacial moraines in the Wind River Range. The negative correlation between exchangeable $^{87}\text{Sr}/^{86}\text{Sr}$ and moraine age indicates release of more radiogenic $^{87}\text{Sr}/^{86}\text{Sr}$ from biotites during the early stage of weathering. The $^{87}\text{Sr}/^{86}\text{Sr}$ values for two stream water samples (marked as +) draining the Audubon till are also shown in the figure. Figure redrawn from Blum and Erel (1995)

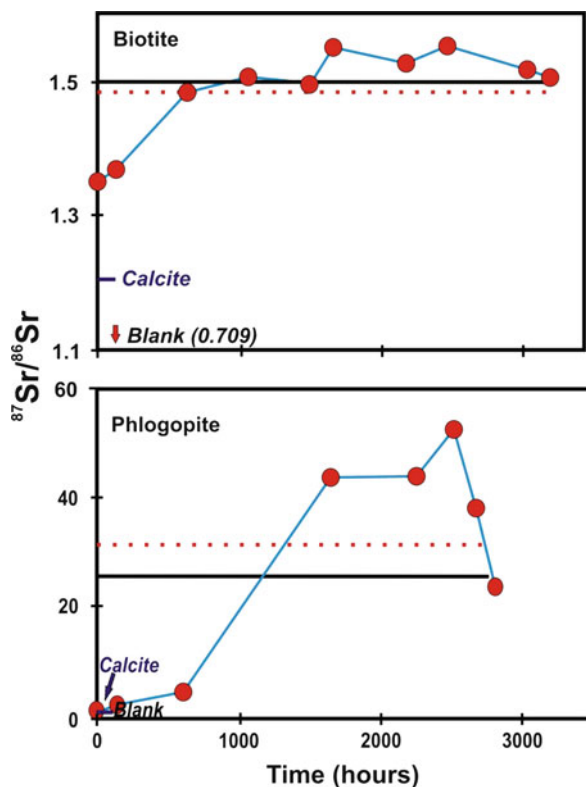


Fig. 26.3 The release pattern of $^{87}\text{Sr}/^{86}\text{Sr}$ in laboratory leaching experiments of biotite and phlogopite. The low Sr isotopic ratio during the initial stages of the experiment is a result of Sr release from trace calcite contained in the minerals. The solid (black) and dotted (red) lines in the figure represent the pre-experiment and post-experiment values of the minerals respectively. Figure redrawn from Taylor et al. (2000)

calcite in the primary minerals and materials from their interlayer sites, the later being more radiogenic as they concentrate Rb. Based on the results of these experiments the authors calculated the dissolution rate of ^{87}Sr to be marginally higher than that of ^{86}Sr in biotites and that steady state with respect to release of Sr isotopes would be reached in a few thousand years.

The importance of trace calcic phases (e.g. calcite, apatite, and bytownite) in dominating the supply of Ca, Sr and Sr isotopes during granite weathering has also been demonstrated through field studies (Blum et al. 1998; Jacobson et al. 2002; Oliva et al. 2004). Results of Sr isotope measurements in rivers draining small catchments of the Himalaya suggest that vein calcites in granites of the basin can be an important source of Ca and Sr with high $^{87}\text{Sr}/^{86}\text{Sr}$ (Blum et al. 1998). The researches of Oliva et al. (2004) on chemical weathering of high elevation Estibere granitic

watershed showed that trace calcic phases, epidote, bytownite, prehnite and apatite, contributed significantly to the Ca, Sr and Sr isotope fluxes. However, unlike in the crystallines of the Himalaya, the majority of trace calcic phases in the Estibere watershed is silicates and therefore contributes to silicate weathering and atmospheric CO_2 drawdown. Similarly, the studies of Aubert et al. (2001) in the Strengbach watershed (France) showed that the Sr and Nd isotope composition of streams and spring waters of the region can be interpreted in terms of two end member mixing, apatite and plagioclase. The authors also inferred that biotites and K-feldspars only have a “weak influence” on the Sr isotope budget of these waters (c.f. Blum and Erel 1995; Bullen et al. 1997). All these field and laboratory studies bring out the important role of trace calcic inclusions such as calcites, apatites and silicates (epidote, bytownite, prehnite) often contained in silicate rocks in supplying Ca and Sr and $^{87}\text{Sr}/^{86}\text{Sr}$ to streams during rock weathering. These results have vital implications on the use of Sr isotopes to track silicate weathering (see Sect. 26.2.4).

The impact of mineral weathering kinetics is also evident in the seasonal variations of $^{87}\text{Sr}/^{86}\text{Sr}$ of rivers. Tipper et al. (2006a) observed that during the monsoon season the $^{87}\text{Sr}/^{86}\text{Sr}$ of the headwater tributaries of the Marsyandi, a sub-tributary of the Ganga was less radiogenic compared to that during non-monsoon periods (Fig. 26.4) similar to that noted earlier by Krishnaswami et al. (1999) and Bickle et al. (2003) for the headwaters of the Ganga. The Sr isotopic composition of rivers in the Himalaya is determined by the mixing proportion of contributions from two major sources, marginally radiogenic sedimentary carbonates ($^{87}\text{Sr}/^{86}\text{Sr} \sim 0.715$; Singh et al. 1998) and radiogenic silicates (with associated trace phases; $^{87}\text{Sr}/^{86}\text{Sr} \sim 0.75\text{--}0.80$, Krishnaswami et al. 1999). The difference in weathering kinetics of silicates and carbonates and its climatic dependence is an important cause contributing to the seasonal variations in $^{87}\text{Sr}/^{86}\text{Sr}$ of rivers. The weathering rates of carbonates are significantly higher than silicates, this enhances their relative contribution to rivers during high runoff. Considering that Sr in sedimentary carbonates is generally far less radiogenic relative to Sr in silicates, higher proportion of Sr from such carbonates to rivers during monsoon would make the riverine Sr lower in $^{87}\text{Sr}/^{86}\text{Sr}$. In contrast during dry periods when more time becomes

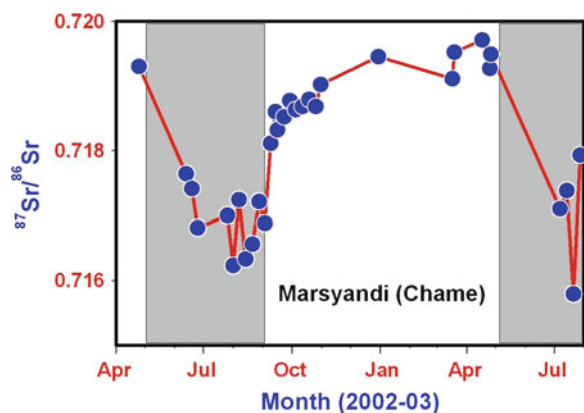


Fig. 26.4 Seasonal variations in $^{87}\text{Sr}/^{86}\text{Sr}$ of the Marsyandi River, Nepal, a sub-tributary of the Ganga river. The data show significantly lower $^{87}\text{Sr}/^{86}\text{Sr}$ ratio during monsoon (*shaded zone*) due to relatively more contribution of unradiogenic Sr from carbonates. Figure replotted from Tipper et al. (2006a)

available for water–rock interactions the contribution from silicates is relatively more than that during monsoon. Similar seasonal trends in riverine silicate cations and $^{87}\text{Sr}/^{86}\text{Sr}$ have been documented in a few other rivers (Moon et al. 2007; Rai and Singh 2007; Tripathy et al. 2010).

Thus the laboratory experiments and field data provide evidences to suggest that during weathering, particularly in early stages, Sr isotope composition of the solution can be significantly different from that of the parent material primarily due to differences in mineral weathering kinetics. Such non-stoichiometric release of Sr isotopes can result in increasing $^{87}\text{Sr}/^{86}\text{Sr}$ of rivers, if minerals with highly radiogenic Sr isotope composition (e.g. biotite) are freshly exposed for weathering. These studies also establishes a link between dissolved fluxes of rivers and glaciation/mountain uplift as the exposure of fresh rock surfaces for weathering is promoted by tectonics, glaciation and intense physical erosion. Two other consequences of non-stoichiometric release of Sr isotopes pertain to their applications in weathering and provenances studies. The finding that trace calcites and apatites can be important sources of Ca, Sr and radiogenic $^{87}\text{Sr}/^{86}\text{Sr}$ to rivers can constrain the use of $^{87}\text{Sr}/^{86}\text{Sr}$ as a proxy of silicate weathering if such contributions are major on a basin wide scale. Similarly the non-stoichiometric release of $^{87}\text{Sr}/^{86}\text{Sr}$ to solution, if significant on a basin scale, it can result in the formation of sediments with $^{87}\text{Sr}/^{86}\text{Sr}$ different from that of parent material, a

result that can challenge the use of $^{87}\text{Sr}/^{86}\text{Sr}$ as a provenance tracer.

26.2.2.2 REE (Sm/Nd) and $^{143}\text{Nd}/^{144}\text{Nd}$ Release During Mineral and Rock Weathering: Laboratory and Field Studies

Compared to Rb–Sr and $^{87}\text{Sr}/^{86}\text{Sr}$, there are only a few investigations on the behavior of Sm–Nd and $^{143}\text{Nd}/^{144}\text{Nd}$ during progressive weathering of rocks. Generally, most of the REEs in rocks, ~70–90%, is present in accessory minerals (e.g. allanite, monazite, sphene, zircon and apatite) and the remainder distributed among the primary rock forming minerals (Barun et al. 1993; Harlavan et al. 2009). Therefore studies on the release of REEs during rock weathering serve as a probe to investigate their fractionation and to infer the weathering characteristics of the accessory minerals. Early investigations (Nesbitt 1979) based on the abundances and distribution of LREEs and HREEs in soil profiles developed on granodiorite demonstrated that during chemical weathering they are leached from the upper layers of soil depleting their concentrations relative to parent rocks. During their downward transport they get sequestered in the weathering products in the deeper layers enriching their abundances. The mobilization and fractionation behavior of the two groups of REEs during chemical weathering however, was found to be different and that it was determined by (1) the chemistry of soil water, pH and dissolved organic matter concentration. This is consistent with the subsequent studies that these two properties of water play an important role in regulating the concentration and mobilization of dissolved Nd in rivers (Sect. 26.2.3.2), (2) the abundance and weathering pattern of different accessory minerals in rocks hosting the REEs and (3) the formation of secondary phases in the soil that sequester the REEs.

Subsequent studies based on different components of soil profiles and laboratory leaching experiments on granitoid weathering have by and large attested to the above findings (Nesbitt and Markovics 1997; Aubert et al. 2001; Harlavan and Erel 2002; Ma et al. 2007; Harlavan et al. 2009); solubilization of REEs from accessory minerals in the upper layers of the soil and their uptake in secondary phases in the deeper layers causing their redistribution within the soil column.

The solubilization and transport of REEs was linked to the availability of organic matter.

The accessory minerals involved in the REE release were identified and their weathering sequence determined through inter-element/isotope association. For example, in the soil profile from Vosges Mountains, France (Aubert et al. 2001), the correlation of REEs with P and Th suggested apatite and monazite to be the main phases determining the mobilization and budget of REEs. Similarly, Harlavan and Erel (2002) in their laboratory experiments on the release of Pb isotopes, REEs and major elements during granitoid weathering observed that dissolution of allanite dominated REEs supply to solution initially, followed by weathering of allanite, apatite and sphene in the later stages and contributions from dissolution of feldspar becoming prominent during the final stages. These results also provided weathering sequences for the accessory minerals as allanite > apatite > sphene. These findings were independently confirmed by Harlavan et al. (2009) based on their studies on REE abundances and Pb isotopes in the labile pool of soil chronosequences. These latter studies, as they were based on soil

chronosequences, also provided time constraints on the processes governing REEs mobilization and distribution in soils. Investigations on the mobilization and redistribution of REEs during intense weathering of basalts (Ma et al. 2007) also reveal similar pattern with extensive removal from the upper layers of soil and uptake in the deeper layers. The mobilization results in fractionation of LREEs from HREEs, the former group being relatively less mobile. As in earlier studies, the availability of organic matter was found to be a key factor in the mobilization of REEs and the formation of secondary phases such as phosphates and Fe-Mn oxy/hydroxides for their sequestration in deeper layers.

Information on the behavior of Sm/Nd during weathering is derived mainly from studies of their distribution in soil profiles (Fig. 26.5). These results however do not show any consistent pattern on their relative mobilities. For example, Nesbitt and Markovics (1997) did not observe significant fractionation between Sm and Nd as a function of weathering intensity in the Toorango soil profile, Australia (Fig. 26.5a) relative to the parent granitoid rock though both elements were mobilized by chemical weathering. These results led to

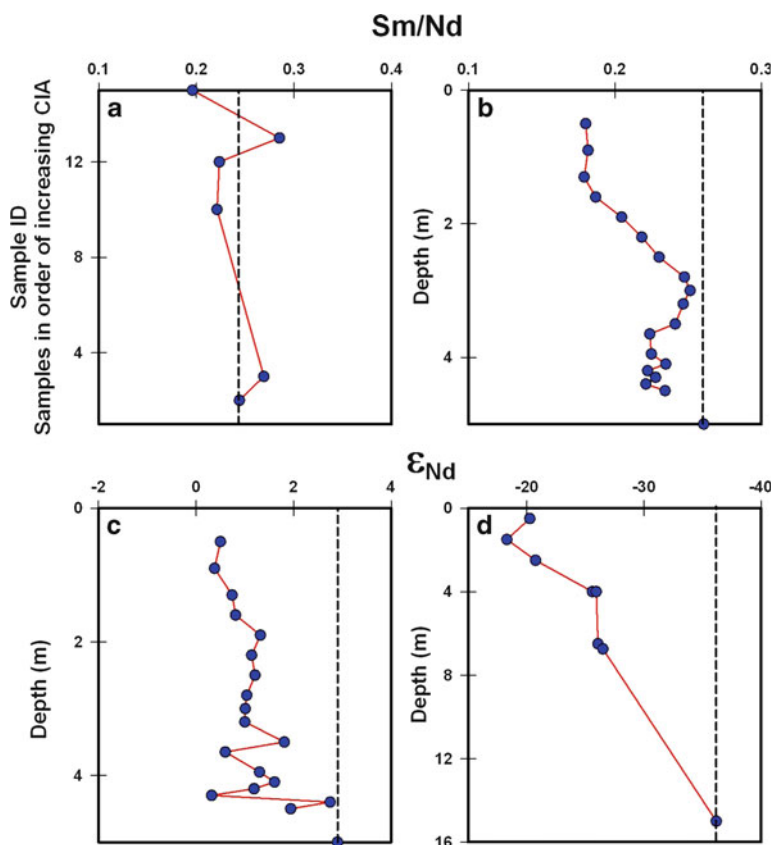


Fig. 26.5 The behavior of Sm/Nd and ϵ_{Nd} during chemical weathering as recorded in soil profiles. The results show different patterns. (a) (Toorango granodiorite, Australia; Nesbitt and Markovics 1997) indicates Sm/Nd remain nearly constant during weathering; whereas (b, c) (Neogene basalts from South China; Ma et al. 2010) and (d) (granodiorite from southern Cameroon; Viers and Wasserburg 2004) depict effects of preferential mobilization of Sm. The bottom and top sides of the figures show the least and most weathered rocks; the dashed straight line in the figure represents the bed rock value

the conclusion that in this profile chemical weathering has not affected the Sm-Nd chronology. In contrast, a number of studies (e.g. MacFarlane et al. 1994; Ohlander et al. 2000; Ma et al. 2010) report significant fractionation in Sm/Nd during chemical weathering. Ohlander et al. (2000) observed that during weathering of till, Nd is preferentially released over Sm from minerals with lower Sm/Nd (allanite, monazite) than the bulk soil leading to enhancement in the ϵ_{Nd} value, by up to four units (~ -22 to -18), in the weathered till. MacFarlane et al. (1994) also observed preferential release of LREEs and fractionation of Nd isotopes and $^{147}\text{Sm}/^{144}\text{Nd}$ in two weathering profiles preserved between flows of the Mt. Roe basalts in Western Australia. Investigations of Sm/Nd and ϵ_{Nd} in soil profiles formed by intensive weathering of basalts (Ma et al. 2010) also showed effects of Sm/Nd fractionation with corresponding changes in ϵ_{Nd} values (Fig. 26.5b, c). Viers and Wasserburg (2004) investigated the behavior of Sm/Nd and Nd isotope composition during weathering of granite by analyzing a lateritic soil profile in a tropical watershed from Cameroon along with surface waters collected from the region. The results showed major changes in ϵ_{Nd} , from ~ -36 in the parent rock to -18 near the top of the soil profile (Fig. 26.5d), without any major shifts in Sm/Nd. These results were attributed to preferential dissolution of minerals such as feldspars and apatite with least radiogenic Nd.

The above studies thus suggest that an important source of REEs to solution during chemical weathering of rocks is dissolution of accessory minerals. The differences in mineral weathering rates can cause the Nd isotope composition of the solution and residual solids to be different from that of the parent rock. However, the changes observed in Nd isotopic ratios due to chemical weathering in the basins are often less compared to the variations observed among global sediments (Ma et al. 2010).

26.2.3 Dissolved Sr, $^{87}\text{Sr}/^{86}\text{Sr}$, Nd and ϵ_{Nd} in Rivers

26.2.3.1 Sr and $^{87}\text{Sr}/^{86}\text{Sr}$

The concentration of dissolved Sr and its isotopic composition have been measured in a large number of global rivers to learn about its behavior during

weathering and transport, its flux to the oceans and its marine budget (Goldstein and Jacobsen 1987; Palmer and Edmond 1989; Trivedi et al. 1995; Gaillardet et al. 1999; Vance et al. 2009; Peucker-Ehrenbrink et al. 2010). The dissolved Sr concentration of major global rivers varies widely, by more than an order of magnitude, from ~ 0.21 to ~ 7.46 μM (Table 26.1). Among the major rivers (Table 26.1) Sr concentration is the highest for the Yellow and the lowest for the Orinoco, with the Yangtze delivering the maximum amount of Sr to the ocean, $\sim 7\%$ of the global riverine Sr flux compared to its contribution of $\sim 2.5\%$ to water discharge. The global discharge-weighted average concentration of Sr based on data in Table 26.1 (which make up $\sim 44\%$ of global water discharge and $\sim 33\%$ of drainage area) is ~ 0.94 μM ; this corresponds to an annual flux of 36.5×10^9 mol/y consistent with some of the earlier estimates (Palmer and Edmond 1989; Vance et al. 2009; Table 26.1). This is expected considering that much of the data in Table 26.1 are from earlier compilations. More recently, Peucker-Ehrenbrink et al. (2010) have calculated following a different approach (by averaging Sr concentration on the basis of large scale drainage regions and extrapolating them) the contemporary supply of dissolved Sr to the ocean to be 47×10^9 mol/y, $\sim 30\%$ higher than the present and some of the earlier estimates (Table 26.1).

The major uncertainty in the flux estimates arises from the use of the available Sr data (Table 26.1) which are often based on a single or a few measurements in a river during a year, as the annual mean Sr concentration. Such an approach can be subject to significant errors because of short-term/seasonal variations in Sr abundance of rivers, in general it seems to show a decreasing trend with increasing water discharge. For example, Sr in the Brahmaputra measured at biweekly intervals over a period of ~ 10 months shows that it varies by a factor of ~ 2 (Rai and Singh 2007), similar to the range reported by Galy et al. (1999) and for some of the other major global rivers such as the Orinoco, Yukon, Mississippi and the Ganga (Palmer and Edmond 1989; Xu and Marcantonio 2007; Rai et al. 2010; Table 26.2). It is apparent from these data that the determination of Sr flux based on a single measurement in a river can differ from the annual average value by as much as $\pm 50\%$. Other potential sources of uncertainty in the flux estimates are (1) inter-annual variation in water discharge. The

Table 26.1 Dissolved Sr concentration and $^{87}\text{Sr}/^{86}\text{Sr}$ ratios of global rivers

River	Water discharge (km ³ /y)	Drainage area (10 ⁶ km ²)	Sr (nM)	Sr flux (10 ⁹ mol/y)	$^{87}\text{Sr}/^{86}\text{Sr}$	Reference
Amazon	6,590	6.112	310	2.04	0.71165	Peucker-Ehrenbrink et al. (2010)
Zaire (Congo)	1,200	3.698	313	0.38	0.71550	Palmer and Edmond (1989)
Orinoco	1,135	1.1	210	0.24	0.71830	Palmer and Edmond (1989)
Mississippi	580	2.98	2,130	1.24	0.70957	Xu and Marcantonio (2007)
Parana	568	2.783	520	0.30	0.71390	Gaillardet et al. (1999)
Lena	525	2.49	1,100	0.58	0.71048	Peucker-Ehrenbrink et al. (2010)
Tocantins	372	0.757	380	0.14	0.72067	Gaillardet et al. (1999)
Amur	344	1.855	500	0.17	0.70923	Moon et al. (2009)
St. Lawrence	337	1.02	1,200	0.40	0.70962	Yang et al. (1996)
Mackenzie	308	1.787	2,740	0.84	0.71138	Millot et al. (2003)
Columbia	236	0.669	982	0.23	0.71210	Goldstein and Jacobsen (1987)
Danube	207	0.817	2,760	0.57	0.70890	Gaillardet et al. (1999)
Yukon	200	0.849	1,590	0.32	0.7137	Gaillardet et al. (1999)
Niger	154	1.2	250	0.04	0.71400	Palmer and Edmond (1989)
Fraser	112	0.22	913	0.10	0.71200	Palmer and Edmond (1989)
Rhine	69	0.224	6,227	0.43	0.70920	Palmer and Edmond (1989)
<i>HT rivers</i>						
Yangtze (Chang Jiang)	928	1.808	2,830	2.63	0.71032	Noh et al. (2009)
Brahmaputra	510	0.58	730	0.37	0.71920	Krishnaswami et al. (1992)
Ganga	493	1.05	560	0.28	0.72910	Galy et al. (1999)
Irrawaddy ^a	486	0.41	-	-	0.71010	Tipper et al. (2006b)
Mekong	467	0.795	3,080	1.44	0.71035	Noh et al. (2009)
Pearl	363	0.437	767	0.28	0.71190	Palmer and Edmond (1989)
Indus	238	0.47	3,689	0.88	0.71110	Pande et al. (1994)
Salween	211	0.325	1,330	0.28	0.71405	Noh et al. (2009)
Hong (Red)	123	0.12	1,158	0.14	0.71284	Moon et al. (2007)
Huang He (Yellow)	41	0.752	7,458	0.31	0.71110	Palmer and Edmond (1989)
<i>Peninsular Indian rivers</i>						
Godavari	105	0.313	1,375	0.14	0.7152	Trivedi et al. (1995)
Mahanadi	66	0.132	704	0.05	0.71930	Trivedi et al. (1995)
Narmada	39	0.102	2,156	0.08	0.71140	Trivedi et al. (1995)
Krishna	30	0.259	3,742	0.11	0.71420	Trivedi et al. (1995)
Kaveri (Cauvery)	21	0.088	2,690	0.06	0.71498	Pattanaik et al. (2007)
<i>Discharge-weighted Sr concentration and $^{87}\text{Sr}/^{86}\text{Sr}$</i>						
HT Rivers	3,860	6.75	1,956	7.55	0.71179	
Non-HT rivers	1,3199	29.5	641	-	0.71163	
Global river	3,8857	110	939	36.5	0.71171	
<i>Earlier estimates of global river Sr and $^{87}\text{Sr}/^{86}\text{Sr}$</i>						
Goldstein and Jacobsen (1987)			705	-	0.7101	
Palmer and Edmond (1989)			890	33.3	0.7119	
Vance et al. (2009)			-	33.7	0.7114	
Peucker-Ehrenbrink et al. (2010)			1,220	47	0.7111	

Average discharge-weighted Sr and $^{87}\text{Sr}/^{86}\text{Sr}$ values for global river are estimated based on the data in the table. The discharge-weighted average Sr for rivers listed in the table is taken to be the same for the mean global river, this value is multiplied by global water discharge to estimate global riverine Sr flux.

^aFor flux calculations, the Sr concentration of Irrawaddy is assumed to be the same as the mean of HT rivers.

Hydrological parameters are from Pande et al. (1994); Gaillardet et al. (1999); Peucker-Ehrenbrink (2009). For the HT and Non-HT rivers, average Sr and $^{87}\text{Sr}/^{86}\text{Sr}$ are estimated based on the data compiled in this study from the citations in the table.

Table 26.2 Temporal variations in Sr and $^{87}\text{Sr}/^{86}\text{Sr}$ in rivers

River	Location	Sr, nM	$^{87}\text{Sr}/^{86}\text{Sr}$	Reference
Ganga	Patna	1,017–2,270	0.7224–0.7249	Krishnaswami et al. (1992)
	Rajshahi	560–2,710	0.7235–0.7291	Galy et al. (1999)
	Rajmahal	1,122–2,157	–	Rai et al. (2010)
Brahmaputra	Goalpara	670–1,082	0.7187–0.7197	Krishnaswami et al. (1992)
	Chilmari	320–900	0.7218–0.7413	Galy et al. (1999)
	Guwahati	604–1,392	0.7159–0.7180	Rai and Singh (2007)
Mekong	Da Hai	3,080–5,770	0.7098–0.7104	Noh et al. (2009)
Orinoco	–	132–312	0.7175–0.7199	Palmer and Edmond (1989)
Yukon	–	1,116–2,390	0.7136–0.7139	Palmer and Edmond (1989)
Red	Phu Tho	1158–1413	0.7121–0.7128	Moon et al. (2007)

Ganga, for example shows a spread of $\pm 20\%$ in water discharge during decadal time scales (1950–1960; 1965–1973; <http://www.grdc.sr.unh.edu>). This variation however is much higher, a factor of ~ 2 on a year to year basis and (2) validity of calculating global flux by extrapolating Sr data from available measurements (Table 26.1) which represents only 40–50% of global river discharge and about a third of drainage area. Such a calculation requires that the measured data is globally representative in terms of different factors that include discharge (climate), areal coverage and lithological distribution of the river basins. In this context, the available data (Table 26.1) may not have adequate representation of rivers from volcanic islands and island arcs.

The concentration of dissolved Sr in rivers is determined largely by the lithology of the drainage basin and the intensity of chemical weathering. In general, silicate and carbonates are the major lithologies of river basins with minor occurrence of evaporites and sulfides. The weathering kinetics of carbonates is much faster than that of silicates (Drever 1997); this can make carbonates an important source of Sr to rivers even if their areal exposure in river basins is relatively less and their Sr abundances comparable to that in silicates. The role of carbonates and silicates in determining the budget of Sr in rivers is borne out from the linear co-variation of dissolved Sr/Na with Ca/Na in several large and medium size global rivers (Gaillardet et al. 1999), attributable to mixing between a high Ca/Na, Sr/Na end member (carbonates) and a low Ca/Na, Sr/Na end member (silicates). Model calculations to constrain the silicate and carbonate derived Sr in rivers have met with challenges due to large variations in elemental ratios of end members and precipitation of calcite from water (e.g. Galy et al.

1999; Krishnaswami et al. 1999; Bickle et al. 2005). Some of these challenges, particularly those pertaining to end member values have been addressed through the use of inverse model (Negrel et al. 1993; Gaillardet et al. 1999; Moon et al. 2007; Tripathy and Singh 2010). The application of such a model (Tripathy and Singh 2010) to the headwaters of the Ganga system rivers in the Himalaya show that $\sim 70\%$ of dissolved Sr in them is derived from carbonates and $\sim 20\%$ from silicates, despite relatively low aerial exposure of carbonates in the catchment (Amiotte Suchet et al. 2003; Tripathy and Singh 2010). The uncertainties in the estimates of Sr supply from silicates and carbonates and insufficient knowledge on the release ratios of Sr to (Na, K, Mg and Ca) from the major lithologies of the basin restricts the use of dissolved Sr concentration in rivers as an index to derive silicate and carbonate erosion rates of their basins.

The $^{87}\text{Sr}/^{86}\text{Sr}$ of the major rivers ranges from 0.7089 to 0.7291 (Table 26.1) with the highest value for the Ganga and the lowest for the Danube. The $^{87}\text{Sr}/^{86}\text{Sr}$ of rivers is determined by the mixing proportion of Sr contributed predominantly by silicates and carbonates in the catchment. The Sr isotopic composition of sedimentary carbonates is fairly well established and is generally unradiogenic, in the range of 0.705–0.709 (Veizer 1989; Allegre et al. 2010). Metamorphic alteration of carbonates however, can make their $^{87}\text{Sr}/^{86}\text{Sr}$ far more radiogenic, as has been observed in some of the carbonates from the Himalaya (Singh et al. 1998; Bickle et al. 2001). The limited range in $^{87}\text{Sr}/^{86}\text{Sr}$ of carbonates is in contrast to the Sr isotope composition of silicates which show a very wide range, from unradiogenic volcanic rocks to highly radiogenic granites and gneisses such as those from the Himalaya (Singh et al. 1998, 2008; Dalai

et al. 2003). The $^{87}\text{Sr}/^{86}\text{Sr}$ of silicates in the drainage basin is often reflected in the isotopic composition of dissolved Sr in rivers draining them. The recent compilation of $^{87}\text{Sr}/^{86}\text{Sr}$ of dissolved Sr from large scale drainage regions (Peucker-Ehrenbrink et al. 2010) shows an overall increasing trend with bed rock ages of the region.

The Sr flux weighted $^{87}\text{Sr}/^{86}\text{Sr}$ for the global river is 0.7117 (based on data in Table 26.1), close to the value of 0.7119 (Palmer and Edmond 1989) and is marginally more radiogenic than the values of 0.7114 and 0.7111 reported by Vance et al. (2009) and Peucker-Ehrenbrink et al. (2010). Analogous to Sr concentration, $^{87}\text{Sr}/^{86}\text{Sr}$ of rivers also show significant seasonal variations (Table 26.2). This can result from variations in the relative contribution of Sr from silicates and carbonates and/or from different tributaries. Whatever may be the cause for such variations, they highlight the need for long term monitoring of rivers along with their discharge to obtain representative global riverine Sr concentration and $^{87}\text{Sr}/^{86}\text{Sr}$.

The Sr elemental and isotopic data for the major rivers listed in Table 26.1 show distinctly high $^{87}\text{Sr}/^{86}\text{Sr}$ with moderate Sr concentration in the Ganga-Brahmaputra rivers compared to the others. Identifying the source for the high $^{87}\text{Sr}/^{86}\text{Sr}$ in these rivers has been a topic of investigation and debate over the last few decades (Sect. “Can $^{87}\text{Sr}/^{86}\text{Sr}$ be a Proxy for Silicate Erosion?”). The discharge weighted Sr concentration for the nine Himalayan-Tibetan rivers listed in Table 26.1 is 1.96 μM with a flux weighted $^{87}\text{Sr}/^{86}\text{Sr}$ of 0.7118. These rivers account for $\sim 21\%$ of global riverine Sr flux, disproportionately higher compared to their contribution to water discharge ($\sim 10\%$).

26.2.3.2 Nd and ϵ_{Nd}

Studies on the concentration of dissolved Nd in rivers (0.20–0.45 μM filtered) and its isotopic geochemistry are limited compared to those of Sr. Initial studies of Nd concentration in river waters showed that it varies widely, from 0.02 to 21.8 nM, with a discharge-weighted average value of 0.28 nM for the global river (Goldstein and Jacobsen 1987). The concentration of Nd in these rivers was found to be inversely correlated with their pH and (Na + Ca) abundances; relationships that underscore the importance of water chemistry in determining the Nd concentration of

rivers. Further, the measurements of Sm in these rivers indicated that its geochemical behavior is similar to that of Nd, though there was a minor fractionation between them. The Sm/Nd in solution was marginally higher ($\sim 10\%$) compared to that in suspended phases, suggestive of preferential release of Sm to solution. There was also a hint that the fractionation increased with pH, likely due to greater stability of Sm-carbonate complexes. The importance of pH in determining the abundances and fractionation of REEs in the dissolved load of rivers was also brought out in the studies of Gaillardet et al. (1997) in rivers of the Amazon basin and Tricca et al. (1999) for mature rivers of the Rhine valley. Some of the subsequent studies have provided an alternative explanation for the pH–REE relationship. Ingri et al. (2000) in their investigations of Kalix River observed that La concentrations are strongly correlated with DOC (dissolved organic carbon) and that high La and DOC abundances are associated with lower pH. These results led to the suggestion that DOC is the primary factor governing REE abundances in filtered river waters and that the REE–pH relation is a result of pH–DOC correlation. Subsequent studies have both supported (e.g. Johannesson et al. 2004; Shiller 2010) and challenged (e.g. Steinmann and Stille 2008) the REE–DOC relationship.

The role of colloids in contributing to REE abundances in filtered river water and its impact on REE behavior in rivers and estuaries became a topic of investigation following advances in analytical techniques for the study of colloids. Measurement of REEs in filtered river waters and their colloidal fractions (Ingri et al. 2000; Andersson et al. 2001) suggest that REEs are largely associated with colloids, with less than 5% in dissolved phase (< 3 kD fraction). Both organic rich and inorganic (Fe oxyhydroxides) colloids have been suggested as potential “carriers” of REEs. Barroux et al. (2006) and Steinmann and Stille (2008) have invoked the important role of REE–colloid interactions in determining the concentrations and fractionation of REEs in rivers. The observation that the Nd concentration in the Amazon increases linearly with water discharge led Barroux et al. (2006) to suggest that enhanced mobilization of particles and colloids during rain events can be a cause for the discharge–REE relationship. More recently, Steinmann and Stille (2008) have explained the steady increase in LREE depletion along the course of small rivers in Massif Central (France) in terms of

precipitation of colloidal Fe-oxyhydroxides that preferentially scavenge LREEs.

The behavior of dissolved Nd in estuaries determines the significance of rivers in contributing to the budget of Nd and its isotopes in the ocean. Investigations on the abundance and distribution of dissolved REEs in estuaries show their widespread removal in the low salinity regions due to coagulation and settling of colloids, the major carrier phase of dissolved Nd (Sholkovitz 1995; Sholkovitz and Szymczak 2000; Frank 2002; Jeandel et al. 2007; Porcelli et al. 2009). The budget of dissolved Nd and its isotopic composition in the oceans, therefore has to be supported by input from other sources such as desorption from river particulates and atmospheric dust and boundary exchange at the continental margins, among these the boundary exchange has been suggested as the dominant mode of supply (Tachikawa et al. 2003; Jeandel et al. 2007).

The ϵ_{Nd} values for rivers also show a wide range (−44 to +7) with a global Nd flux weighted riverine average of −8.4 (Goldstein and Jacobsen 1987). The ϵ_{Nd} of river water is often found to be similar to that of the bedrocks in their basin, and therefore correlates with the age of the rocks (Goldstein and Jacobsen 1987; Peucker-Ehrenbrink et al. 2010). There are however, minor differences in the ϵ_{Nd} values of dissolved and suspended loads of rivers, most likely a result of preferential weathering of phases with different Sm/Nd and ϵ_{Nd} . The ϵ_{Nd} of rivers shows an inverse relation with $^{87}Sr/^{86}Sr$ resulting from Nd and Sr isotope composition of rocks being weathered and mixing of various end members with different ϵ_{Nd} and $^{87}Sr/^{86}Sr$.

26.2.4 Silicate Erosion in River Basins

26.2.4.1 Contemporary Silicate Erosion in the Ganga-Brahmaputra System

Silicate weathering on land is a fundamental process that determines the supply of materials derived from crustal silicates to the oceans. This process is driven primarily by CO_2 , making silicate weathering an important regulator of CO_2 budget over million year time scales and a key component of global carbon cycle. Therefore, changes in silicate weathering rates on long time scales can affect the atmospheric CO_2

budget and hence global climate. Recognizing the importance of silicate weathering on the exogenic cycles of elements, global carbon cycle and climate, there have been a number of investigations to determine silicate erosion rates (SER) and the factors regulating it. These investigations have been based both on small streams which by and large drain monolithologic terrains and large river systems which integrate contributions from their tributaries draining different lithologies. The studies on small streams are an approach to derive mineral weathering rates in natural settings, whereas larger river basins provide estimates of regional silicate erosion. The studies on large river basins, particularly those draining young orogenic belts such as the Himalaya have also been motivated by the hypothesis (Raymo et al. 1988; Raymo and Ruddiman 1992; Ruddiman 1997) that enhanced silicate weathering in this mountain belt can be the driver of global cooling during the Cenozoic, as the conducive monsoon climate, high relief and intense physical erosion of the region all can significantly enhance silicate weathering and associated atmospheric CO_2 drawdown. The steady increase in the Sr isotope composition of the oceans during the Cenozoic (Fig. 26.6) has been suggested as a major support for the tectonics-weathering-climate hypothesis (Raymo and Ruddiman 1992; Richter et al. 1992). Based on the present day Sr concentration and its isotopic composition of rivers draining the

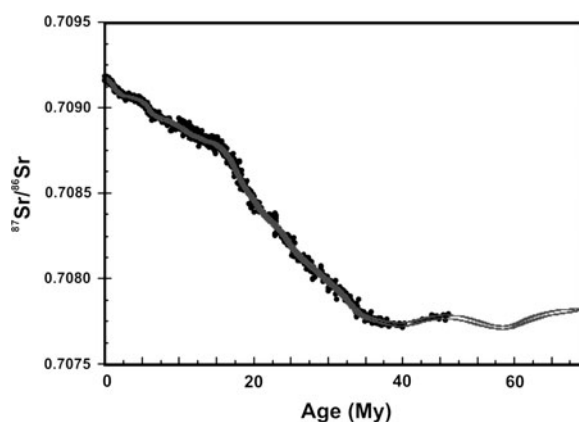


Fig. 26.6 Evolution of seawater $^{87}Sr/^{86}Sr$ since the last 70 My. Intense chemical weathering in the Himalaya is suggested as a potential cause for the steady increase in $^{87}Sr/^{86}Sr$ since 40 My (Raymo and Ruddiman 1992). Figure modified from Ravizza and Zachos (2003)

Himalayan-Tibet region, it is argued that the observed steady increase in the marine $^{87}\text{Sr}/^{86}\text{Sr}$ can result from silicate weathering in this region. This hypothesis invokes the use of Sr isotope composition of seawater as a proxy of silicate weathering on the continents. This suggestion has been a topic of debate as diverse and at times controversial sources have been proposed for Sr and its isotopes in rivers of the Himalaya (Edmond 1992; Krishnaswami et al. 1992; Palmer and Edmond 1992; Blum et al. 1998; Jacobson and Blum 2000; Bickle et al. 2001). If, however, the use of Sr isotopes as a proxy of silicate weathering is validated, it would also serve as a tool to investigate its past variations which are difficult to determine using other approaches.

The determination of contemporary SER relies mainly on the chemical composition of rivers. The chemistry of rivers is dominated by contributions from various lithologies of river basins and the kinetics of rock–water interaction. From the measured concentrations, the contributions from silicates, carbonates and evaporites are deduced using either the forward or the inverse model (Negrel et al. 1993; Singh et al. 1998; Gaillardet et al. 1999; Galy and France-Lanord 1999; Krishnaswami et al. 1999; Bickle et al. 2005; Singh et al. 2005; Wu et al. 2005; Hren et al. 2007; Tripathy and Singh 2010). In the forward model, Na^* (Na corrected for Cl ; $\text{Na}^* = \text{Na}_{\text{riv}} - \text{Cl}_{\text{riv}}$, where “riv” refers to measured concentration in rivers) is used as an index of silicate weathering. This coupled with knowledge of release ratios of $(\text{K} + \text{Mg} + \text{Ca})$ to Na^* from silicates in the basin to rivers is used to derive SER. The release ratios would depend on the silicate lithology of the basin and the nature of weathering (mineral specific/stoichiometric) and therefore can have a wide range. In contrast, in the inverse model likely elemental ratios for various end members contributing to major cation abundances to rivers is assigned a priori and following the method of iteration and material balance considerations the best end member ratios that can generate the measured river water composition is derived. The removal of Ca from rivers by calcite precipitation can be a source of uncertainty in this approach. Both the forward and inverse methods have been widely used to derive contemporary SER and associated CO_2 consumption rates for various major rivers including the Ganga-Brahmaputra. The contemporary SER (calculated from the sum of cations derived from silicates

and SiO_2) for the headwaters of the Ganga, Bhagirathi and Alaknanda range between 10 and 15 $\text{tons km}^{-2} \text{y}^{-1}$ (Krishnaswami and Singh 2005), a factor of $\sim 2\text{--}3$ higher than the global average value of $\sim 5.5 \text{ tons km}^{-2} \text{y}^{-1}$ (Gaillardet et al. 1999). The higher SER in the headwater basins of the Ganga suggests more intense silicate erosion in these Himalayan basins (Galy and France-Lanord 1999; Krishnaswami et al. 1999). Independent estimates of SER have been obtained by France-Lanord and Derry (1997) and McCauley and DePaolo (1997) based on the deficiency in Na , K , Ca , and Mg in the Bay of Bengal sediments relative to that in crystallines of the Himalaya; these estimates generally are time-averaged values, unlike that based on river water data which are based on snap shot sampling.

Can $^{87}\text{Sr}/^{86}\text{Sr}$ be a Proxy for Silicate Erosion?

Generally rivers draining old silicate rocks have lower Sr with higher $^{87}\text{Sr}/^{86}\text{Sr}$ compared to rivers weathering marine limestones/evaporites. The large difference in the $^{87}\text{Sr}/^{86}\text{Sr}$ among the different lithologies in the drainage basin promotes the use of Sr isotopes as a natural tracer to determine Sr contribution to rivers from various end members.

Figures 26.7 (a, b) are examples of mixing plots for Sr isotopes in two river systems, the Orinoco and the Yamuna headwaters. The plots show an overall linear trend albeit some scatter, suggestive of two component mixing (Palmer and Edmond 1992; Dalai et al. 2003). From the mixing array, the Sr contribution to the rivers from the two end members can be determined if their Sr isotope composition are known and from it the SER of the basin if $(\text{Na} + \text{K} + \text{Ca} + \text{Mg})/\text{Sr}$ release ratios are known. Estimates of these release ratios are available based on different approaches and models (e.g. Krishnaswami et al. 1999), however as mentioned earlier they are not well constrained. More importantly, such calculations generally assume that the high $^{87}\text{Sr}/^{86}\text{Sr}$ end member is silicates; ascertaining the validity of this assumption is critical to the application of $^{87}\text{Sr}/^{86}\text{Sr}$ as proxy for silicate weathering. Krishnaswami et al. (1992) and Dalai et al. (2003) based on the widespread occurrence of crystallines with highly radiogenic Sr isotope composition ($\sim 0.75\text{--}1.0$) in the drainage basins of the headwaters of the Yamuna and the Ganga and the strong correlation between “silicate indices” and $^{87}\text{Sr}/^{86}\text{Sr}$ of these

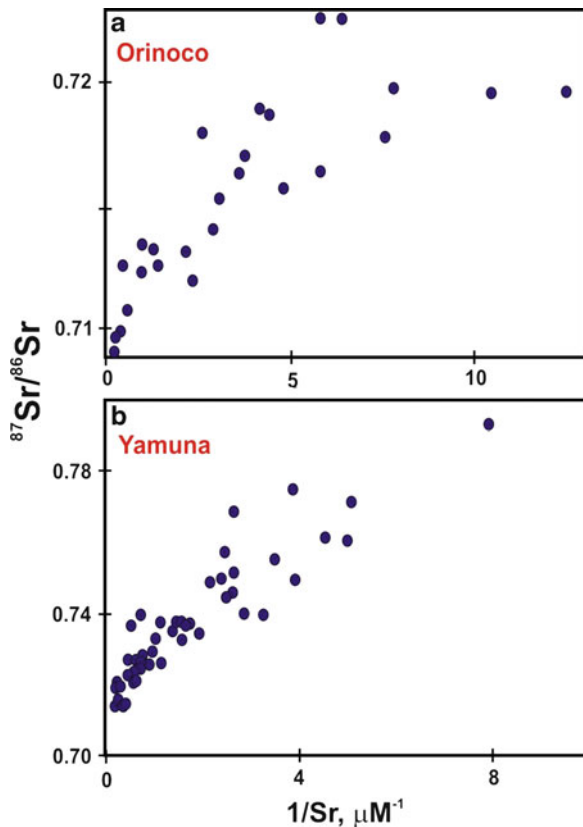


Fig. 26.7 Sr mixing plots for two major rivers, the Orinoco and the Yamuna headwaters. The near linear trend is suggestive of a two component mixing, the high $^{87}\text{Sr}/^{86}\text{Sr}$ and low Sr silicates with the low $^{87}\text{Sr}/^{86}\text{Sr}$ and high Sr carbonates. Figure redrawn from Palmer and Edmond (1989) and Dalai et al. (2003)

ivers (Fig. 26.8) suggested that the high $^{87}\text{Sr}/^{86}\text{Sr}$ end member is indeed silicates of the drainage basin. However, the occurrence of metamorphic carbonates and vein calcites in these river basins with highly radiogenic $^{87}\text{Sr}/^{86}\text{Sr}$ similar to that of the crystallines and considering that carbonates are more easily weatherable compared to silicates has challenged the assignment of high $^{87}\text{Sr}/^{86}\text{Sr}$ end member to silicates. These studies instead suggest that the metamorphosed carbonates and vein calcites to be the dominant sources of high $^{87}\text{Sr}/^{86}\text{Sr}$ to the rivers in the Himalaya (Palmer and Edmond 1992; Blum et al. 1998; Quade et al. 1997; Harris et al. 1998; Jacobson and Blum 2000; Oliver et al. 2003). Attempts to test the different components of this hypothesis have resulted in contrasting conclusions. Singh et al. (1998) measured Sr isotopic composition of Pre-Cambrian carbonates from the Lesser Himalaya to assess their role in contributing to the high $^{87}\text{Sr}/^{86}\text{Sr}$ of the Ganga-Yamuna source waters. Their results, though brought out the important role of metamorphism in considerably elevating the $^{87}\text{Sr}/^{86}\text{Sr}$ of these sedimentary carbonates locally, suggested that their weathering is unlikely to be a major source for the high $^{87}\text{Sr}/^{86}\text{Sr}$ to the headwaters of the Ganga on a basin wide scale. The results of Bickle et al. (2005) on the Sr isotopic composition of the Ganga headwater basins also show that it is dominated by contribution from weathering of silicates (~50% of total Sr) with the balance from trace calcites (~10%) and sedimentary carbonates (~35%). In contrast, the

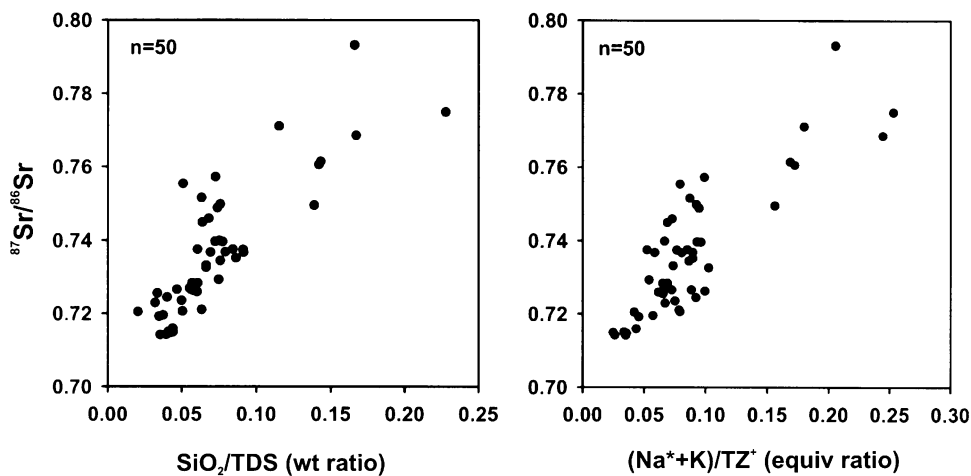


Fig. 26.8 Scatter diagrams of $^{87}\text{Sr}/^{86}\text{Sr}$ with other “silicate indices” (SiO_2/TDS and $(\text{Na}^* + \text{K})/\text{TZ}^+$) in the Yamuna headwaters. The good correlation between them has been interpreted

to suggest that the high $^{87}\text{Sr}/^{86}\text{Sr}$ end member in these rivers is of silicate origin and that $^{87}\text{Sr}/^{86}\text{Sr}$ can serve as a proxy of silicate weathering. Figure from Dalai et al. (2003)

work of Oliver et al. (2003) brought out the major role of metasedimentary carbonates as the source of elevated $^{87}\text{Sr}/^{86}\text{Sr}$ to the sub-tributaries of the Ganga (Bhote Kosi-Sun Kosi, Nepal). Their work based on downstream variations in the chemistry and $^{87}\text{Sr}/^{86}\text{Sr}$ of rivers and mass balance considerations led to infer that the Paleo-Proterozoic impure carbonates with highly radiogenic Sr isotope composition can be significant contributor to the high $^{87}\text{Sr}/^{86}\text{Sr}$ of the Ganga river, accounting for a major fraction of their supply to the marine $^{87}\text{Sr}/^{86}\text{Sr}$. Thus, the available results on Sr isotope composition of metamorphosed carbonates from the Himalaya and their interpretation have led to diverging views on their role as a major source of high $^{87}\text{Sr}/^{86}\text{Sr}$ to the Ganga river on a basin wide scale.

In addition to metamorphosed carbonates, the significance of disseminated carbonates and vein calcites as sources of highly radiogenic Sr to the Ganga river also have been investigated. For example, Sr isotope studies (Jacobson et al. 2002) on glacial moraine chronosequences from the Himalaya containing trace carbonates demonstrated that their weathering can be a significant source of Ca, Sr and radiogenic Sr to rivers for thousands of years subsequent to their exposure. In addition, as mentioned earlier, there are also results which suggest that vein calcites in granites of the Himalaya can be an important source of Ca and Sr with high $^{87}\text{Sr}/^{86}\text{Sr}$ (Blum et al. 1998).

It is thus evident from the available results and interpretation that both silicates and carbonates can contribute to the high $^{87}\text{Sr}/^{86}\text{Sr}$ of the Ganga-Brahmaputra rivers. However, their relative significance to the Sr isotope budget remains to be established quantitatively. This information is essential to decide on the applicability of Sr isotopes as a proxy of silicate erosion, one of the basis of the tectonics-weathering-climate hypothesis.

26.2.4.2 Seawater $^{87}\text{Sr}/^{86}\text{Sr}$ Record During the Cenozoic: Impact of Weathering in the Himalaya and Deccan Traps

Chemical weathering of continental crust and the supply of its products to the ocean is a key process regulating its chemical and isotopic evolution through time. The chemical and isotopic composition of the authigenic and biogenic components of marine

sediments hold clues to temporal variations in continental inputs to the sea. Among these the Sr isotope records hold promise to retrieve continental weathering history.

The evolution of seawater Sr isotopic composition can be expressed using a balance equation involving the various Sr supply and removal terms. Early attempt in this direction was made by Brass (1976) to explain the variations in the oceanic $^{87}\text{Sr}/^{86}\text{Sr}$ over the past ~400 My based on changes in $^{87}\text{Sr}/^{86}\text{Sr}$ input from weathering of silicates and carbonates on continents. These mass balance calculations showed that the variations in seawater $^{87}\text{Sr}/^{86}\text{Sr}$ since the last 200 My can be attributed to changes in the $^{87}\text{Sr}/^{86}\text{Sr}$ supplied to the ocean from weathering of silicates on land; the ratio being dependent on the proportion of radiogenic Sr from old acidic rocks and unradiogenic Sr from young basic rocks. The mixing proportion of Sr from these two silicate lithologies can vary depending on their exposure to weathering which in turn is governed by processes such as tectonics/glaciation.

The Sr isotope evolution of the ocean was investigated in great detail during 1970–1990 which resulted in a robust and dense record of $^{87}\text{Sr}/^{86}\text{Sr}$ in marine carbonates since the Cenozoic (Fig. 26.6; Veizer 1989). Richter et al. (1992) based on these data developed a model to test the hypothesis (Raymo et al. 1988; Raymo and Ruddiman 1992) that silicate weathering in the Himalaya-Tibet (HT) is the primary factor contributing to the steady increase in the Sr isotope composition of the oceans during this period. In this model, the marine budget of Sr and its isotopes are determined by their supply from rivers, hydrothermal sources and diagenetic alteration/dissolution of carbonates from sediments and their removal to ocean floor *via* calcareous skeletons. Among the three input sources, Sr flux from diagenetic alteration/dissolution of carbonates is much less than the fluxes from the other two sources (Richter et al. 1992; Banner 2004) and therefore as an approximation this term is often neglected from the budget calculations. The mass balance equation for the rate of change of marine Sr isotope ratio is:

$$N \frac{dR_{SW}}{dt} = J_r(R_r - R_{SW}) + J_h(R_h - R_{SW}) \quad (26.1)$$

where N is total Sr (in moles) in the ocean. J_r and J_h are the flux (moles/y) of Sr from the riverine and

hydrothermal sources. R_{sw} , R_r and R_h are the $^{87}\text{Sr}/^{86}\text{Sr}$ of seawater, river and hydrothermal sources respectively. Equation (26.1) suggests that the $^{87}\text{Sr}/^{86}\text{Sr}$ of seawater is governed by the balance between supply of radiogenic Sr from rivers and unradiogenic mantle like Sr derived from hydrothermal sources. In the above equation the temporal changes in J_r , R_r and J_h are not known, though J_h is often assumed to be proportional to ocean floor production (Richter et al. 1992). The variations in either J_r or R_r or both can bring about changes in R_{sw} (Edmond 1992; Krishnaswami et al. 1992; Richter et al. 1992; Derry and France-Lanord 1997; McCauley and DePaolo 1997; Kump et al. 2000; Gaillardet 2008). Increase in J_r (riverine flux) would imply more intense continental weathering (Raymo et al. 1988) whereas increasing R_r would suggest change in the source material being weathered (Edmond 1992; Derry and France-Lanord 1997; Kump et al. 2000). Therefore to determine variations in the intensity of continental weathering, information on changes in R_r is required. These data are generally unavailable and therefore the equation is solved using reasonable assumptions. Richter et al. (1992) by solving equation (26.1) with the then available data on contemporary fluxes and ratios (Table 26.3) showed that the increase in the $^{87}\text{Sr}/^{86}\text{Sr}$ of seawater since the past ~40 My is due to enhanced supply of Sr and $^{87}\text{Sr}/^{86}\text{Sr}$ by rivers and that increase in both J_r and R_r are required to balance the evolution of R_{sw} . In their calculations they also evaluated the impact of temporal variations in J_h on the evolution of seawater $^{87}\text{Sr}/^{86}\text{Sr}$ and concluded that though changes in J_h could explain about half the change in R_{sw} , the evolutionary trend was not consistent with the observations.

Table 26.3 Numerical (present day) values of various parameters used in seawater Sr budget model (Richter et al. 1992)

Parameter		
J_r	Riverine flux	3.3×10^{10} mol/y
J_h	Hydrothermal alteration flux	0.82×10^{10} mol/y
J_d	Digenetic flux	~0
J_{r0}	Riverine flux excluding HT rivers	2.2×10^{10} mol/y
J_{r1}	HT riverine flux	7.7×10^9 mol/y
N	Total Sr in ocean	1.25×10^{17} mol
R_r	Riverine $^{87}\text{Sr}/^{86}\text{Sr}$	0.711
R_h	Hydrothermal $^{87}\text{Sr}/^{86}\text{Sr}$	0.7030
R_d	Digenetic $^{87}\text{Sr}/^{86}\text{Sr}$	0.7084
R_{r0}	$^{87}\text{Sr}/^{86}\text{Sr}$ global rivers excluding HT rivers	0.710
R_{r1}	$^{87}\text{Sr}/^{86}\text{Sr}$ of HT rivers	0.7127

To further evaluate the role of Himalayan-Tibetan (HT) rivers on $^{87}\text{Sr}/^{86}\text{Sr}$ of oceans, the river water flux and Sr isotopic ratio terms in the above equation is split into two parts, one representing global rivers excluding those from HT and the other representing the extra flux (J_{r1}) with $^{87}\text{Sr}/^{86}\text{Sr}$, R_{r1} required to explain the observed variation in seawater Sr evolution (Richter et al. 1992). The modified equation is:

$$N \frac{dR_{SW}}{dt} = J_{r0}(R_{r0} - R_{SW}) + J_{r1}(R_{r1} - R_{SW}) + J_h(R_h - R_{SW}) \quad (26.2)$$

where, J_{r0} and R_{r0} are the Sr flux and $^{87}\text{Sr}/^{86}\text{Sr}$ from the global rivers excluding those from the HT. The calculations showed that the Sr flux (J_{r1}) required to reproduce the sea water $^{87}\text{Sr}/^{86}\text{Sr}$ curve using present day value of R_{r1} is roughly consistent with that measured indicating that the HT rivers can be a dominant source to account for the marine Sr isotope evolution during the past ~40 My. These calculations and inferences derived from them rely on the compilation of riverine Sr flux and $^{87}\text{Sr}/^{86}\text{Sr}$ (c.f. Table 26.1), which as mentioned earlier can be subject to uncertainties arising from intra and inter-annual variations in Sr concentration and $^{87}\text{Sr}/^{86}\text{Sr}$ of rivers, water discharge and inadequate sampling of rivers from various major lithologies. These results and therefore the conclusions based on them maybe subject to revision as more robust data on Sr concentration of rivers and its isotopic composition become available. For example, subsequent to the work of Richter et al. (1992) there have been more measurements of Sr and $^{87}\text{Sr}/^{86}\text{Sr}$ in the HT rivers, particularly in the Ganga and the Brahmaputra during various seasons including peak discharge. These results show that the dissolved Sr concentration of the Ganga is much lower during peak discharge (0.56 μM ; Galy et al. 1999) than the value used by Richter et al. (1992) in their model (1.58 μM), the corresponding $^{87}\text{Sr}/^{86}\text{Sr}$ values also being significantly different (0.7257–0.7291). The Brahmaputra at its mouth also exhibits a similar difference in its Sr concentration with a value of 0.32 μM (Galy et al. 1999) during peak flow compared to 0.93 μM used in the model (Richter et al. 1992). Considering that much of the annual water discharge of the Ganga (~75%) is during its peak flow, the Sr concentration measured during this period is likely to be more representative of its annual average

concentration. This value for the Sr concentration of the Ganga yields a Sr flux weighted $^{87}\text{Sr}/^{86}\text{Sr}$ ratio of 0.7118 for the HT rivers, very close to $^{87}\text{Sr}/^{86}\text{Sr}$ of global rivers 0.7117 and lower than 0.7127, used in the model calculations (Richter et al. 1992). The use of the revised $^{87}\text{Sr}/^{86}\text{Sr}$ of the HT rivers in the model calculation suggest that the Sr flux (J_r) required from the HT rivers would be significantly higher than the estimates of Richter et al. (1992) and their contemporary measured flux (Table 26.1). These observations underscore the importance of regular monitoring of rivers to obtain representative values for the annual average Sr concentration and $^{87}\text{Sr}/^{86}\text{Sr}$.

The inferences of Richter et al. (1992) can be used to deduce the weathering history of continents if data on temporal variations of either J_r or R_r are available. Derry and France-Lanord (1996) obtained $^{87}\text{Sr}/^{86}\text{Sr}$ data for the Ganga during the past ~20 My based on Sr isotope record of the Ganga floodplain as preserved in the pedogenic clays of the Bay of Bengal sediments. The results showed significant temporal changes in the Sr isotopic ratio of the Ganga with highly radiogenic ratios during 1–7 My (~0.74) compared to ~0.72 during 0–1 and 7–20 My periods. The higher $^{87}\text{Sr}/^{86}\text{Sr}$ during 1–7 My requires a decrease in the riverine Sr flux during this period to balance the Sr isotope data of the oceans. This led to the suggestion that increase in $^{87}\text{Sr}/^{86}\text{Sr}$ of oceans need not be driven by a concomitant increase in riverine Sr flux and therefore continental weathering. Quade et al. (1997) also observed that the Sr isotopic composition of Himalayan rivers (Ganga, Indus) had varied with time based on $^{87}\text{Sr}/^{86}\text{Sr}$ of shells and paleosol carbonates from the Siwaliks, further attesting to the idea that the Sr isotope evolution of the oceans can be a result of variations in source composition.

Another recent development on Sr budget in the oceans is the finding that its hydrothermal flux is much less than that estimated earlier ($\sim 1.0 \times 10^{10}$ mol/y; Palmer and Edmond 1989) and that the current estimate can support only about a third or less of Sr required to balance its budget in the oceans (Davis et al. 2003). This imbalance in the marine Sr budget therefore, requires that there has to be additional major source (s) of unradiogenic Sr to the oceans. Investigations on chemical weathering rates, Sr concentration and $^{87}\text{Sr}/^{86}\text{Sr}$ of rivers, groundwater and hydrothermal sources in volcanic islands and island arcs (Rad et al. 2007; Allegre et al. 2010) suggest that supply from

these regions can be the “missing source” of unradiogenic Sr to the oceans. Budget model for present day oceanic $^{87}\text{Sr}/^{86}\text{Sr}$ shows that hydrothermal sources contribute only ~27% of mantle-like unradiogenic Sr to the sea compared to ~73% from island arcs and volcanic islands (Allegre et al. 2010). Temporal variation in the Sr concentration from these sources to the sea can also impact the Sr isotope evolution of the ocean; however there is no data to evaluate this.

Analogous to the studies on the role of HT rivers on the $^{87}\text{Sr}/^{86}\text{Sr}$ of the oceans, the impact of weathering Deccan trap basalts was also assessed using data from rivers flowing through them and suitable models (Dessert et al. 2001; Das et al. 2006). The results of Dessert et al. (2001) showed an increase in seawater $^{87}\text{Sr}/^{86}\text{Sr}$ from 0.70782 to 0.70789 over a period of a few My after the Deccan eruption followed by a steady decrease. The initial increase was explained in terms of enhanced continental weathering by CO_2 (and hence temperature) released during the emplacement of the Deccan basalts. The subsequent decrease in the seawater $^{87}\text{Sr}/^{86}\text{Sr}$ is attributed to a combined effect of contribution of unradiogenic Sr from the weathering of Deccan basalts and decrease in atmospheric CO_2 which decreases continental weathering. Das et al. (2005, 2006) carried out major ion and Sr isotope studies on several rivers exclusively draining the Deccan traps to investigate the role of their weathering on the evolution of marine $^{87}\text{Sr}/^{86}\text{Sr}$ at around K-T boundary and early Tertiary. Their results and model calculations showed that the supply of unradiogenic Sr from the Deccan basalt weathering caused the decline in seawater $^{87}\text{Sr}/^{86}\text{Sr}$ during the early Tertiary. As basalts are a source of unradiogenic Sr to the oceans, changes in their Sr contribution relative to that from old sialic rocks can modify the riverine $^{87}\text{Sr}/^{86}\text{Sr}$ which in turn can affect the Sr isotope composition of the oceans (Brass 1976; Taylor and Lasaga 1999). Such a relative change in weathering of silicate lithology can also bring about changes in oceanic $^{87}\text{Sr}/^{86}\text{Sr}$ without invoking changes in the intensity of chemical weathering on continents (Taylor and Lasaga 1999).

Thus, many of the above studies bring out the potential of Sr isotopes in oceans and rivers to provide information on contemporary and past global chemical weathering patterns and the role of weathering in the Himalaya and Deccan traps in contributing to the Sr isotope evolution of the oceans since the Cenozoic. The potential of Sr isotopes as a proxy of silicate

weathering in the Himalaya however awaits quantitative information on the role of radiogenic carbonates as a source riverine $^{87}\text{Sr}/^{86}\text{Sr}$ and temporal variations in riverine $^{87}\text{Sr}/^{86}\text{Sr}$.

26.3 Physical Erosion in River Basins

Physical erosion is a key process that determines the geomorphology of the earth surface and promotes chemical weathering intensity of river basins. The records of physical erosion contained in sediments hold clues to the spatial and temporal erosion pattern of the source region and its dependence on climatic and tectonic factors (e.g., Dia et al. 1992; Asahara et al. 1999; Burbank et al. 2003; Singh et al. 2008; Rahaman et al. 2009; Galy et al. 2010). Over the years there have been a number of studies both in river and marine basins to decipher these patterns by tracking the sediment provenances through their geochemical, mineralogical and isotopic composition. The successful application of these proxies require their source signatures to be well preserved in the sediments, a requirement that has met with challenges because of chemical weathering of source rocks and size sorting of sediments. Many of the initial studies on sediment provenances were based on clay mineralogy. The clay minerals provide information more on their weathering provenances than their geological provenances (Dasch 1969) as they are the end products of chemical weathering of minerals present in source rocks.

Historically, the use of Sr isotopes as a proxy for sediment provenance was recognized and demonstrated during the 1960's (Dasch 1969). The detailed study of spatial distribution of $^{87}\text{Sr}/^{86}\text{Sr}$ in surface sediments of the Atlantic (Dasch 1969; Fig. 26.9) showed large variations which were interpreted in terms of differences in their provenances. During the last few decades, radiogenic isotope ratios particularly $^{87}\text{Sr}/^{86}\text{Sr}$ and ϵ_{Nd} of sediments have often found applications as tracers to track the provenance of sediments (Goldstein and O'Nions 1981; France-Lanord et al. 1993; Winter et al. 1997; Pierson-Wickmann et al. 2001; Banner 2004; Yang et al. 2007; Singh et al. 2008; Viers et al. 2008; Ahmad et al. 2005, 2009; Galy et al. 2010). These isotope systems serve as reliable proxies for sediment provenance

studies because of their distinctly different isotopic composition in different sources and the near preservation of the source isotope composition during weathering and transport. Processes that can affect the preservation of source isotope composition in sediments are chemical weathering and sediment transport. These processes are likely to influence the preservation of $^{87}\text{Sr}/^{86}\text{Sr}$ more than that of $^{143}\text{Nd}/^{144}\text{Nd}$ because (1) generally the isotopic composition of Nd is relatively more uniform among the minerals in the parent rock compared to $^{87}\text{Sr}/^{86}\text{Sr}$ as the fractionation between Sm and Nd is significantly less compared to Rb and Sr during mineral formation. Therefore, preferential dissolution of specific minerals during chemical weathering though can influence the preservation of source isotope composition of both Sr and Nd, the impact is likely to be more on $^{87}\text{Sr}/^{86}\text{Sr}$ and (2) during transportation of sediments size sorting is common; if this results in mineralogical differences in the various size fractions, then the isotope composition of the sediment may differ from that of the source rock. Here again, the influence is likely to be more on $^{87}\text{Sr}/^{86}\text{Sr}$ because of its wider range among various minerals present in a parent rock compared to ϵ_{Nd} . Studies of soil profiles (c.f. Sect. 26.2.2) and sediments (Tutken et al. 2002) have provided evidences for alteration of isotopic composition of source rock during weathering and transport (Fig. 26.10). These data indicate that between $^{87}\text{Sr}/^{86}\text{Sr}$ and ϵ_{Nd} , the later is less susceptible for alteration during weathering and transportation making it a more robust tracer for fingerprinting the provenance of sediments (Walter et al. 2000). Such differences in the behavior of Sr and Nd isotopes during weathering and transport have led to combine studies of Sr-Nd isotope systematics in sediments to derive more detailed information on sediment provenances and related sedimentary processes (e.g. Colin et al. 1999; Walter et al. 2000; Tutken et al. 2002; Singh et al. 2008).

Sr and Nd isotope compositions of riverine and marine sediments though are being used often to track their provenances, there are lingering questions about how well the source isotope signatures are preserved in them. Therefore to make the interpretation more robust preference should be for the use of multi-tracer approaches involving isotopic and chemical/mineralogical composition of sediments. Such approaches can also help in determining the factors contributing to the changes in the isotopic,

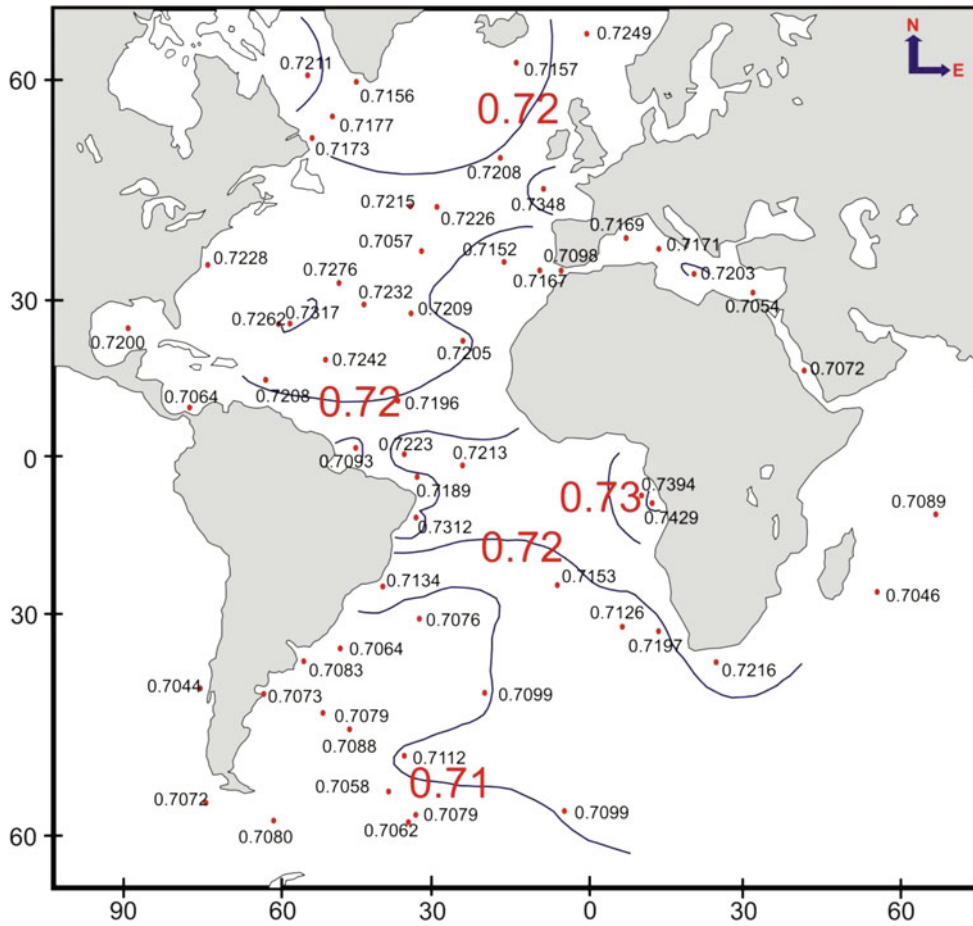


Fig. 26.9 $^{87}\text{Sr}/^{86}\text{Sr}$ of Atlantic surface sediments. The ratio shows significant spatial variations which has been used to infer their provenances. Figure redrawn from Dasch (1969)

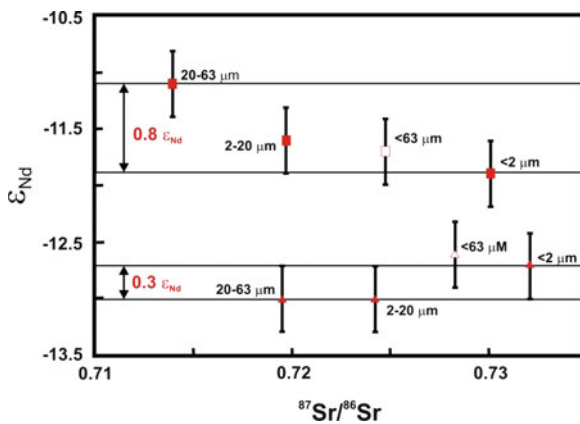


Fig. 26.10 Sr and Nd isotopic ratios in different size fractions of two sections from an Arctic sediment core. The $^{87}\text{Sr}/^{86}\text{Sr}$ shows significant variation with size whereas ϵ_{Nd} is relatively constant. Figure modified from Tutken et al. (2002).

chemical and mineralogical composition of sediments (France-Lanord et al. 1993; Colin et al. 1999; Singh and France-Lanord 2002; Viers et al. 2008).

26.3.1 Contemporary Physical Erosion Pattern of River Basins in the Himalaya

The rate of physical erosion of river basins of the Himalaya, particularly the Ganga and the Brahmaputra is a topic of investigation in recent years because of their importance to the sediment budget of the ocean, the global carbon and geochemical cycles of various elements and to understand the physical erosion pattern of their sub-basins and their controlling factors.

Singh and France-Lanord (2002) and Singh et al. (2008) investigated the Sr-Nd isotopic composition of bank and suspended sediments of the Brahmaputra and the Ganga plain along with those of their tributaries to determine the sources of sediments to the mainstream and their relative contributions. The Brahmaputra mainstream receives sediments from three sources, the Trans-Himalayan plutonic belt, the Lesser and the Higher Himalaya. The Sr-Nd isotopic composition of the Brahmaputra sediments is nearly uniform all along its course in the plain downstream Pasighat, in spite of contributions from the Himalayan tributaries with a wide range of Sr and Nd isotope composition (Fig. 26.11). This uniformity in ϵ_{Nd} and $^{87}\text{Sr}/^{86}\text{Sr}$ suggests that the sediment contributions from the Siang, draining the Eastern Syntaxis of the Himalaya and southern Tibet (Tsangpo) overwhelm that from other sources. Material balance calculations based on isotope data show that about half of the sediments of

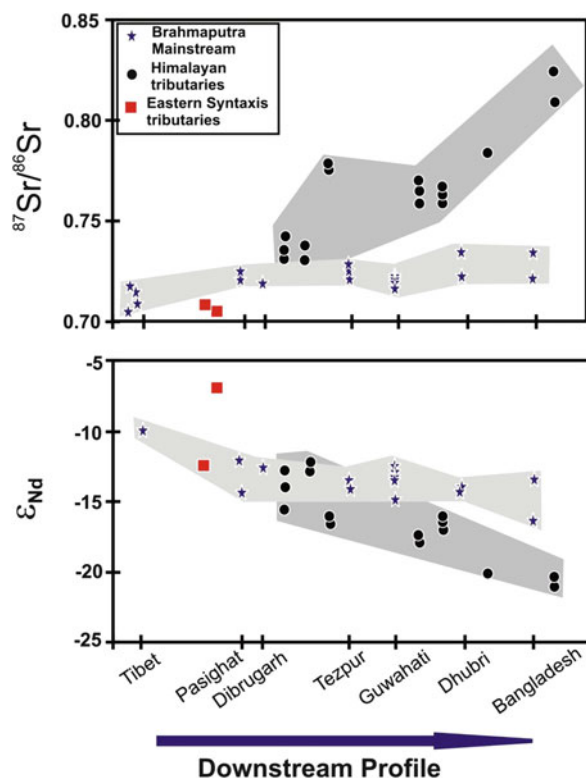


Fig. 26.11 Spatial variations in $^{87}\text{Sr}/^{86}\text{Sr}$ and ϵ_{Nd} of sediments of the Brahmaputra river system. The Sr-Nd isotopic signatures of the Brahmaputra mainstream sediments downstream Pasighat remains nearly uniform. Figure redrawn from Singh and France-Lanord (2002)

the Brahmaputra at its outflow are from the Siang resulting from intense localised erosion. Thus the sediment flux of the Brahmaputra is dominated by the Eastern Syntaxis “hot spot” where the physical erosion is controlled by runoff and relief (Singh and France-Lanord 2002; Singh 2006, 2007).

Similar studies in the Ganga mainstream sediments and its tributaries show that their $^{87}\text{Sr}/^{86}\text{Sr}$ and ϵ_{Nd} values are close to or by and large within the range reported for the Higher Himalayan Crystallines (HH, Fig. 26.12). The Sr and Nd isotope mass balance of these sediments on the basis of a two component (Higher and Lesser Himalayan Crystallines) mixing suggests that the HH account for more than two thirds of the contemporary Ganga Plain sediments (Fig. 26.12), consistent with the results from sediments of the Bay of Bengal (France-Lanord et al. 1993; Derry and France-Lanord 1997; Galy et al. 2010). More interestingly, the Sr isotopic composition of the Ganga sediments showed significant spatial variation along the plain with a drastic decrease from 0.768 to 0.755 immediately following the confluence of the Ganga with the Gandak (Fig. 26.13). A similar feature was also recorded in the spatial distribution of ϵ_{Nd} . Budget calculations based on the isotopic composition of these sediments show that the Gandak sub-basin which occupies only $\sim 5\%$ of the total drainage

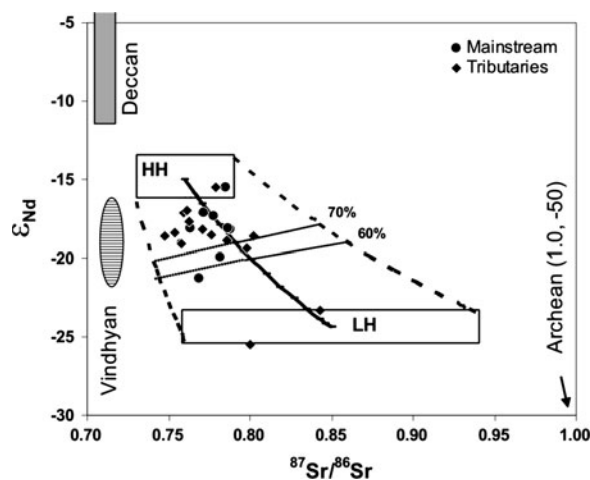


Fig. 26.12 Sr-Nd isotope mixing plot of river sediments from the Ganga plain. The isotopic composition of these sediments is interpreted in terms of a two component mixing, HH and LH. The isotopic compositions of various other end members which can contribute to the Ganga sediments are also shown. Figure modified from Singh et al. (2008)

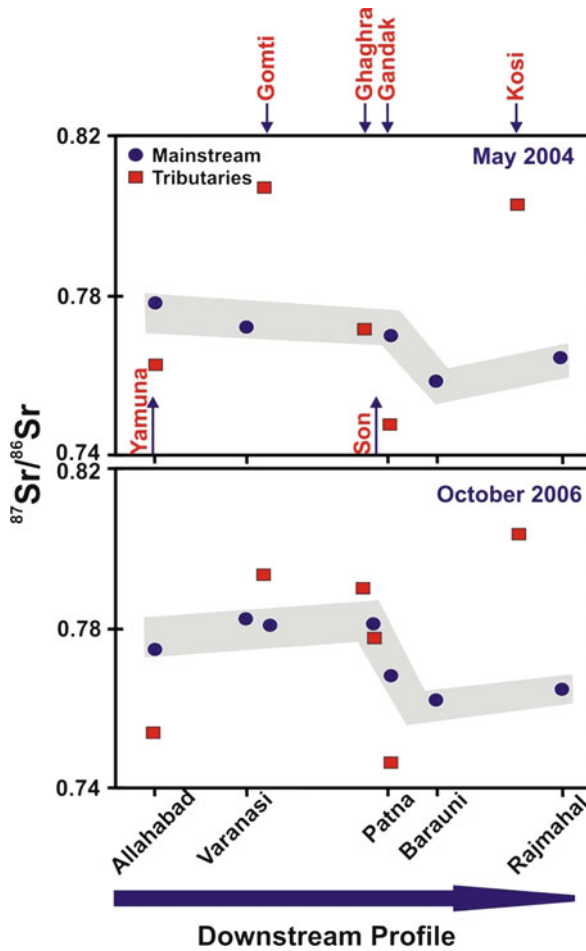


Fig. 26.13 Spatial variations (along the Ganga mainstream) in $^{87}\text{Sr}/^{86}\text{Sr}$ and ε_{Nd} of sediments from the Ganga and its tributaries. A major dip in the Sr isotopic ratio of the Ganga sediments is seen after the confluence of the Gandak, suggesting dominant supply of sediments to the Ganga mainstream from this tributary. Figure modified from Singh et al. (2008)

area of the Ganga, accounts for about half of the Ganga sediments at its outflow. These results bring out the intense physical erosion of the Gandak basin due to the high relief and focused precipitation over its headwater basins in the Himalaya (Singh et al. 2008). This observation highlights the coupling between high rainfall and relief with high physical erosion rate of river basins, linking climate (rainfall) and tectonics (relief) with contemporary erosion pattern of the Himalaya.

The Sr and Nd isotope studies of sediments from various sub-basins of the three major global rivers draining the Himalaya, the Brahmaputra, the Ganga and the Indus show that physical erosion rates are

quite high in sub-basins characterized by intense precipitation over regions of high relief, the Gandak, the Siang, and the Nanga Parbat (Leland et al. 1998; Clift et al. 2002; Singh and France-Lanord 2002; Singh 2006; Singh et al. 2008) and that the sediment fluxes of these major rivers are dominated by contributions from these “hot spots” of physical erosion. Such high and focused erosion in these hot spots is unloading huge amount of sediments from the Himalaya causing regions around them to uplift more rapidly compared to other regions (Molnar and England 1990; Montgomery 1994; Zeitler et al. 2001). Importantly, these results underscore the coupling among tectonics, climate and physical erosion. Further as physical and chemical erosion are linked (Bluth and Kump 1994; Edmond and Huh 1997; Gaillardet et al. 1999; Millot et al. 2002; Singh et al. 2005) these hot-spots could also facilitate intense chemical weathering by continuously exposing “fresh” rock surfaces.

26.3.2 Paleo-Erosion in Selected River Basins of the Himalaya and Its Controlling Factors

26.3.2.1 Shorter Time (ky) Scales

One of the key topics of interest in studies of physical erosion is its temporal variations and factors contributing to it. In this regard there have been a number of investigations in recent years to decipher the physical erosion history of the Himalaya and its link to tectonics and climate using river and marine sediments of Himalayan origin.

Rahaman et al. (2009) derived temporal variations in the physical erosion pattern of the Ganga basin from depth profiles of Sr and Nd isotopes in the silicate fraction of a dated sediment core from the Ganga Plain. Both $^{87}\text{Sr}/^{86}\text{Sr}$ and ε_{Nd} exhibited significant variations with depth in the core, the range in their values, however, were bound by those for the Higher and the Lesser Himalayan Crystallines, the two major sediment sources to the Ganga plain. This led to the suggestion that the observed depth variations were due to differences in the mixing proportion of sediments from the Higher and Lesser Himalaya. Furthermore, the results also showed two major excursions in the

Sr-Nd isotope composition at approximately 20 and 70 ky (Fig. 26.14), which were attributed to a decrease in the proportion of sediments from the Higher Himalaya caused by decrease in monsoon precipitation and an

increase in glacial cover both of which result from lower solar insolation. Thus, the temporal variations in the relative sediment flux from the Higher and Lesser Himalaya were attributed to climate variability.

Colin et al. (1999, 2006) used Sr and Nd isotope composition along with clay mineralogy to constrain sediment sources to the Bay of Bengal and the Andaman Sea, to reconstruct the erosional history of the Indo–Burman ranges and to assess the role of climate changes (monsoon rainfall variations) on erosion. The geographical (spatial) distribution of Nd and Sr isotope composition in the Bay of Bengal and the Andaman Sea suggest that these basins receive sediments from several sources; the Ganga-Brahmaputra rivers dominating the supply to the western Bay of Bengal, the Himalayan and Indo-Burman ranges to the eastern Bay and the Irrawaddy River to the Andaman Basin. The sediments of the Andaman Sea and the Bay of Bengal deposited during the last glacial maximum (LGM) are characterized by more radiogenic $^{87}\text{Sr}/^{86}\text{Sr}$ compared to interglacial sediments with roughly the same ϵ_{Nd} (Fig. 26.15). The lack of concomitant changes in the Sr and Nd isotope composition led to interpret the $^{87}\text{Sr}/^{86}\text{Sr}$ results in terms of variations in chemical weathering intensity rather than to provenance changes (see Sect. 26.2.2). The more radiogenic $^{87}\text{Sr}/^{86}\text{Sr}$ during glacial periods at the core site was attributed to efficient transport of unaltered Rb-rich

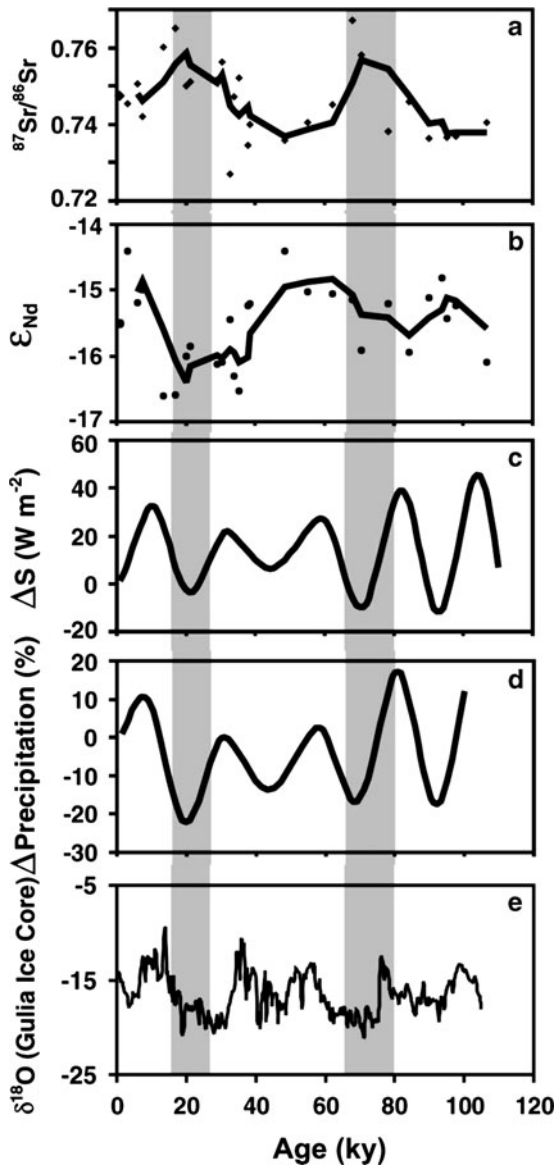


Fig. 26.14 Temporal variations in Sr and Nd isotopic ratios (panel a and b) of sediments from the Ganga plain during the past ~100 ky. These variations suggest relative changes in provenances (HH and LH) of the sediments and coincide with regional climatic changes (panel c: Solar insolation, panel d: Monsoon precipitation and panel e: Oxygen isotopic record of a Tibetan ice core), bringing out the role of climate on physical erosion of the Himalaya. Figure modified from Rahaman et al. (2009)

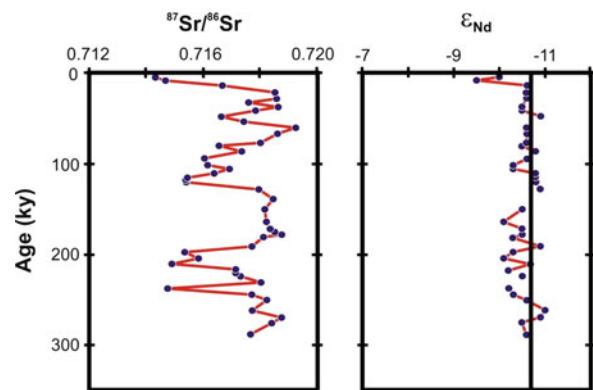


Fig. 26.15 Glacial-interglacial variations in Sr and Nd isotopic ratios of Andaman sea sediments. $^{87}\text{Sr}/^{86}\text{Sr}$ data show significant temporal variations, whereas ϵ_{Nd} is nearly uniform with depth. The straight line through ϵ_{Nd} data is the present-day ϵ_{Nd} value of the Irrawaddy river sediment. The lack of concomitant changes in $^{87}\text{Sr}/^{86}\text{Sr}$ and ϵ_{Nd} suggests that the variations in $^{87}\text{Sr}/^{86}\text{Sr}$ are a result of fractionation during weathering and transport rather than changes in provenance. Data Source: Colin et al. (2006)

minerals exposed in the headwater basin of the Irrawaddy river by glacier grinding.

The impact of climate variations on physical erosion in the Irrawaddy Basin was also brought out in the Sr-Nd isotope composition of sediments from a core raised from the Ninety East Ridge of the Bay of Bengal (Ahmad et al. 2005). The results showed concomitant temporal changes in $^{87}\text{Sr}/^{86}\text{Sr}$ and ϵ_{Nd} and that these changes overlapped with the records of Heinrich events. This led to suggest that these fluctuations in the isotope records are probably a result of relatively higher sediment contribution from the Irrawaddy river caused by intensification of NE monsoon in response to the cold events of the North Atlantic via an atmospheric teleconnection.

Analogous to the studies in the Bay of Bengal which receives sediments predominantly from the central and eastern Himalaya, there have also been investigations in the Indus delta and the Arabian Sea to decipher the erosional history of the western Himalaya. In one such study, Clift et al. (2008) observed significant temporal variations in the Nd isotope composition of sediments from the Indus delta with lesser radiogenic Nd in sediments younger than 14 ky. This suggested relatively increased sediment flux to these regions from sources with less radiogenic Nd, the Lesser and/or Greater (Higher) Himalaya compared to other sources (e.g. primitive arc rocks of the Indus suture and Trans-Himalaya) with LH dominating the contribution. This change in provenance of Indus sediments is attributed to change in the monsoon strength during these periods highlighting the importance of climate in regulating the erosion over western Himalaya on millennial time scales.

26.3.2.2 Longer Time (My) Scales

The Himalaya is one of the young and active mountain ranges and ranks first in the supply of sediments to the ocean (Milliman and Meade 1983; Milliman and Syvitski 1992). The temporal variation in the sediment supply from the Himalaya on million year time scales, particularly from its different sub-basins (e.g. Higher and Lesser Himalaya) and the factors regulating it have implications to global carbon cycle and therefore to climate. This has prompted studies on the pattern of physical erosion in the Himalaya and its variations over My time scales based mainly on Sr and Nd

isotopic composition of sedimentary archives preserved in the Bay of Bengal and the Arabian Sea. In one such study, France-Lanord et al. (1993) investigated variations in the Sr and Nd isotopic ratios, together with stable isotopes and clay mineral abundances in a sediment core from the Bay of Bengal spanning 17 My time period. The results showed that the dominant source of these sediments is the Higher Himalayan Crystallines. The narrow range in Sr-Nd isotopic values of these sediments over their 17 My depositional history further suggested that their source remained nearly invariant despite significant changes in sedimentation rate, tectonic history and climate. In a more recent study, Galy et al. (2010) observed from the Sr and Nd isotopic composition of sediments deposited in the deep Bengal Fan that they were mainly derived from the High Himalaya Crystallines with sub-ordinate contributions from the Lesser Himalaya and Trans-Himalayan batholiths. Further, it was observed that the isotopic composition of sediments deposited during the recent 20 ky was very similar to that deposited during the past 12 My confirming the generally stable erosion regime of the Himalaya during this long time period. This stable erosion regime argues against any major impact on Himalayan erosion by glacier advance and retreat. The overall covariation between Sr and Nd isotope data further suggested that the isotope systematics were by and large, controlled by sediment provenances and not by changes in chemical weathering intensity. The near synchronicity between minor changes in erosion pattern during late Miocene and at the Plio-Pleistocene transition and climate parameters, precipitation and glacier development, brought out yet another example of climate-erosion link.

Clift and Blusztajn (2005) reconstructed the long-term erosional history of the Indus river system based on Nd isotope composition of the Arabian Sea sediments deposited during 30 My to present. The ϵ_{Nd} values showed a range from $\sim(-11)$ to $\sim(-9.5)$ during the period 30–5 My ago. These values suggest a provenance dominated by Karakoram (ϵ_{Nd} : -10 to -11), in contrast to a Himalayan source which is characterized by less radiogenic ϵ_{Nd} (~-25 to ~-15). The ϵ_{Nd} values during 5 My to Late Pleistocene (~ 300 ky ago) showed a trend towards more negative values, from $\sim(-10)$ to $\sim(-13)$ that require enhanced relative contribution from the Himalayan source at the expense of supply from the Karakoram or the Indus suture zone.

The negative shift in ϵ_{Nd} has been explained in terms of capture of the ancestral Himalayan tributaries of the Ganga by the Indus. Currently much of the Himalayan sediments of the Indus river is supplied by its four large tributaries, the Sutlej, Ravi, Chennab and Jellum. It is suggested that ~5 My ago these rivers were part of the Ganga river system and not of the Indus drainage.

The above examples demonstrate the successful applications of Sr-Nd isotopes to reconstruct the erosion patterns of different sediment basins at various spatial and temporal scales. These studies also have brought out the links between the patterns of physical erosion and tectonic/climate changes.

26.4 Future Directions

This review addressed the applications of Sr and Nd isotope systems for investigating contemporary and past chemical (silicate) and physical erosion in river basins, particularly those from the Himalaya. Available results show that both these isotope systems, especially $^{143}Nd/^{144}Nd$, have been successfully used to track sediment sources and characterize physical erosion patterns, which have brought out the coupling between tectonics, erosion and climate. The use of Sr isotopes as a proxy for silicate weathering in the Himalaya has been controversial because of the presence of carbonates with highly radiogenic Sr similar to that of silicates, which makes it difficult to clearly identify the sources of radiogenic Sr to the rivers; resolving this issue would be an important challenge for the future. An approach to pursue this problem could be through a multi-tracer systematic study of rivers (major ions, Sr isotopes and other potential proxies of silicate/carbonate weathering, e.g. Ge, $^{234}U/^{238}U$, Ca and Mg isotopes) draining small and medium sized watersheds of the Himalaya with well characterized basin properties, lithology, mineralogy and temporal variations in water discharge. There have been a few investigations in this direction. For example, Chabaux et al. (2001) through measurements of U, Sr isotopes and major ions in selected Himalayan rivers concluded that “U activity ratios, in association with Sr isotope ratios, can be used to trace the sources of dissolved fluxes carried by these rivers”. However, analogous to Sr isotopes, the role of trace phases in rocks in contributing to dissolved U in rivers can

frustrate the interpretation of results. Another group of isotope tracers that may help in quantification of sources of alkaline earth elements to rivers is Ca and Mg isotopes (Tipper et al. 2008). Studies of these isotopes in rivers of the Himalayan-Tibetan Plateau indicate that in small rivers these isotopes hold promise to provide information on the sources of Ca and Mg whereas in large rivers the lithological control on the isotopic composition seem obscured by isotope fractionation during weathering and calcite precipitation. Better characterization of the impact of these processes on the isotope composition of Ca and Mg may provide a way forward for their application to quantify their sources to rivers.

Additional complexities on the use of Sr isotopes as silicate weathering proxy arise from their supply to rivers via hot springs. Studies on the role of hot springs in regulating river water chemistry and on the Sr isotopic budget of the Marsyandi river, a sub-tributary of the Ganga (Evans et al. 2001, 2004) have shown that they can be an important source of dissolved major ions and Sr with highly radiogenic $^{87}Sr/^{86}Sr$ to this river. An interesting aspect of this study has been the application of Ge/Si as a tracer to evaluate the hot spring contribution to the water flux and alkalinity of river. More detailed studies are required to quantitatively evaluate the role of hot springs in determining the budget of major ions and Sr isotopes on basin-wide and global scales.

The marine budget of strontium shows an imbalance between its supply and removal (Davis et al. 2003; Vance et al. 2009). Uncertainties in the estimates of hydrothermal and riverine fluxes and recent enhancement in riverine flux due to weathering of finely ground rock left behind by glaciers (Vance et al. 2009) can all contribute to this imbalance. Therefore, obtaining better estimates of mean Sr flux and $^{87}Sr/^{86}Sr$ to the ocean through temporally and spatially (lithology based) representative sampling of rivers from basins with different climate and physical features should provide better understanding of the Sr isotope budget of the oceans and their potential to yield information on continental weathering history. In this context, the roles of island arcs and ocean islands in contributing unradiogenic Sr to the oceans and the release of Sr during enhanced chemical weathering of fresh and finely ground rocks produced by glaciers are being increasingly recognized. Similarly, ascertaining the relative variation in riverine

fluxes between glacial and interglacial periods through investigations of weathering indices in dated sediments from selected basins can also contribute to better understanding of the marine geochemistry and budget of Sr.

Another source of dissolved Sr to the oceans which is not included in its marine budget calculations is sub-marine groundwater discharge (SGD), though its importance is getting increasingly recognized. For example, available results for the Bay of Bengal (Basu et al. 2001) indicate that SGD can be a very significant source of Sr to the bay, with moderately radiogenic Sr ($^{87}\text{Sr}/^{86}\text{Sr} \sim 0.715\text{--}0.720$). More data for other coastal regions are needed to quantify the global significance of this input and its role in Sr isotope evolution of the oceans.

Recently, questions have been raised about the uplift-erosion-climate hypothesis based on depositional trends of dissolved $^{10}\text{Be}/^9\text{Be}$ in ocean sediments and Fe-Mn crusts during the past 12 My (Willenbring and Blanckenburg 2010). These trends do not show any significant temporal variation leading to infer that global weathering fluxes have not been interrupted by mountain building pulses during the late-Cenozoic era. A topic for future study could be reconciliation of these findings with the marine Sr isotope record which shows a steady increase during this period.

26.5 Summary

Continental erosion, both physical and chemical, regulates global geochemical cycles, shapes Earth's surface morphology and influences its climate pattern. The global significance of erosion processes has led to several studies on them and their variations in space and time to learn about the evolutionary history of our planet. A topic of considerable interest in recent years in this field has been to understand the coupling between tectonics-erosion-climate. Radiogenic isotopes, particularly $^{87}\text{Sr}/^{86}\text{Sr}$ has proven to be a powerful tool in these investigations.

Chemical weathering of silicate minerals on continents is an important process that serves as a major sink for atmospheric CO_2 on My time scales. An important development on this topic has been the suggestion that enhanced silicate weathering in young orogenic belts such as the Himalaya is the

driver of global cooling during the Cenozoic. This led to detailed investigations on silicate weathering, both present and past, particularly its relation with tectonics and climate. One of the key requirements in these studies is the availability of suitable proxies that can track changes in silicate weathering in the past. Sr isotope ratios recorded in carbonates of deep sea sediments hold clues to these variations, however deciphering them is challenging because of multiple sources supplying Sr to the sea and the assumptions required to interpret the Sr isotope record. For example, the Cenozoic increase in marine $^{87}\text{Sr}/^{86}\text{Sr}$ can result either from enhanced riverine Sr flux of constant $^{87}\text{Sr}/^{86}\text{Sr}$ or changes in its $^{87}\text{Sr}/^{86}\text{Sr}$ or both. Earlier studies argued in favor of increasing the riverine Sr flux and therefore intensity of silicate weathering to reproduce the marine Sr isotope record, whereas some of the later work suggested changing the riverine $^{87}\text{Sr}/^{86}\text{Sr}$ and therefore the source composition rather than the intensity of silicate weathering to explain the increase in seawater $^{87}\text{Sr}/^{86}\text{Sr}$. Sr isotope studies of clays and river carbonates formed during the past several My seem to support the later view, thereby challenging the proposition of enhanced silicate weathering during the Cenozoic. Another issue pertaining to the Sr isotope problem is the source of highly radiogenic Sr in rivers of the Himalaya; there have been both laboratory and field studies which demonstrate that trace calcites contained in granites and metamorphosed sedimentary carbonates dispersed in the drainage basins can also supply high radiogenic Sr to rivers. If the major source of radiogenic Sr to the Himalayan rivers is indeed trace calcites and metamorphosed carbonates, it would have serious repercussions on the use of Sr isotopes as a silicate proxy. Thus the multiple variables associated with the supply of Sr and $^{87}\text{Sr}/^{86}\text{Sr}$ to rivers and oceans have raised new challenges on the use of Sr isotopes to determine silicate weathering rates.

Physical erosion is another key process that influences climate by regulating the transport and burial of organic carbon and determining chemical erosion rates. This has led to a number of studies on the physical erosion pattern of river basins, their variability in space and time and the factors controlling them. These studies rely mainly on Sr and Nd isotopes to determine the sediment provenances, under the assumption that the isotope signatures of sources are well preserved in the sediments. This assumption

though is generally valid, there are evidences based both on laboratory and field studies that suggest non-stoichiometric release of Sr and Nd isotopes during different stages of rock weathering; the release being governed by the weathering sequence of minerals in the rock. For example, it has been demonstrated that during early stages of granite weathering Sr isotopes are released preferentially from minerals such as calcites, apatites, bytownite and biotite contained in them.

The non-stoichiometric release of Sr isotopes from rocks during their weathering though has raised concerns about its application as a provenance tracer, it has been used extensively often with Nd isotopes to investigate spatial and temporal variations in physical erosion pattern of river basins and factors controlling them. Nd being less mobile than Sr during weathering and transport its source composition is expected to be preserved better in sediments, therefore concomitant changes in both Sr and Nd isotopic composition of sediments is generally interpreted in terms of source variations. In recent years there have been many studies, using Sr and Nd isotope proxies, on the physical erosion pattern of river basins from the Himalaya because of their dominance in sediment flux to the ocean and major role in global carbon cycle. These studies identified HH to be the major source of sediments depositing at present and over the past several My in the Ganga Plain and the Bay of Bengal and that the erosional regime has been generally stable during this period. The primary factors controlling contemporary physical erosion in the Himalaya are relief and climate and that most of the erosion occurs in “hot spots” characterized by intense precipitation over regions of high relief. These hot spots unload huge amounts of sediments promoting more rapid uplift of regions around them thereby coupling tectonics and erosion. The past erosion pattern of the Himalaya deduced from the Sr and Nd isotope records in sediments from the Ganga Plain, the Bay of Bengal and the Arabian Sea all show that it was linked to climate changes both on ky and My time scales, however there was only limited impact of glacier advance and retreat on erosion. There are also evidences to demonstrate that capture of Ganga tributaries by the Indus contributed to changes in its erosion pattern during the past ~5 My. It is evident from the above examples that Sr and Nd isotope studies of contemporary and ancient sediments hold valuable information on their sources and controlling agents of physical erosion in

respective basins. These studies also have underscored the importance of climate and tectonics in regulating continental erosion.

Acknowledgements SK thanks the Indian National Science Academy, New Delhi for Senior Scientistship and the Director, PRL for logistical support. Reviews and comments from Prof. M. Baskaran and two anonymous reviewers have helped improve the article.

References

- Ahmad S, Babu G, Padmakumari V et al (2005) Sr, Nd isotopic evidence of terrigenous flux variations in the Bay of Bengal: implications of monsoons during the last 34,000 years. *Geophys Res Lett* 32:1–4
- Ahmad S, Padmakumari V, Babu G (2009) Strontium and neodymium isotopic compositions in sediments from Godavari, Krishna and Pennar rivers. *Curr Sci* 97:1766–1769
- Allegre C, Dupre B, Negrel P et al (1996) Sr–Nd–Pb isotope systematics in Amazon and Congo River systems: constraints about erosion processes. *Chem Geol* 131:93–112
- Allegre C, Louvat P, Gaillardet J et al (2010) The fundamental role of island arc weathering in the oceanic Sr isotope budget. *Earth Planet Sci Lett* 292:51–56
- Amelin Y, Rotenberg E (2004) Sm–Nd systematics of chondrites. *Earth Planet Sci Lett* 223:267–282
- Amiotte Suchet P, Probst J, Ludwig W (2003) Worldwide distribution of continental rock lithology: implications for the atmospheric/soil CO₂ uptake by continental weathering and alkalinity river transport to the oceans. *Glob Biogeochem Cycles* 17:1038. doi:10.1029/2002GB001891
- Anderasen R, Sharma M (2006) Solar Nebula heterogeneity in p-process Samarium and Neodymium isotopes. *Science* 314:806–809
- Andersson P, Dahlqvist R, Ingri J et al (2001) The isotopic composition of Nd in a boreal river: a reflection of selective weathering and colloidal transport. *Geochim Cosmochim Acta* 65:521–527
- Armstrong RL (1971) Glacial erosion and the variable isotopic composition of strontium in seawater. *Nature* 230:132–134
- Asahara Y, Tanaka T, Kamioka H et al (1999) Provenance of the north Pacific sediments and process of source material transport as derived from Rb–Sr isotopic systematics. *Chem Geol* 158:271–291
- Aubert D, Stille P, Probst A (2001) REE fractionation during granite weathering and removal by waters and suspended loads: Sr and Nd isotopic evidence. *Geochim Cosmochim Acta* 65:387–406
- Banner J (2004) Radiogenic isotopes: systematics and applications to earth surface processes and chemical stratigraphy. *Earth Sci Rev* 65:141–194
- Barroux G, Sonke J, Boaventura G et al (2006) Seasonal dissolved rare earth element dynamics of the Amazon River main stem, its tributaries, and the Curuaí floodplain. *Geochim Geophys Geosyst* 7:Q12005. doi:10.1029/2006GC001244

- Barun JJ, Pagel M, Herbillon A et al (1993) Mobilization and redistribution of REEs and thorium in a syenitic lateritic profile: a mass balance study. *Geochim Cosmochim Acta* 57:4419–4434
- Basu A, Jacobsen S, Poreda R et al (2001) Large groundwater strontium flux to the oceans from the Bengal basin and the marine strontium isotope record. *Science* 293:1470–1473
- Berner R, Lasaga A, Garrels R (1983) The carbonate–silicate geochemical cycle and its effect on atmospheric carbon dioxide over the past 100 million years. *Am J Sci* 283: 641–683
- Bickle M, Harris N, Bunbury J et al (2001) Controls on the $^{87}\text{Sr}/^{86}\text{Sr}$ ratio of carbonates in the Garhwal Himalaya, Headwaters of the Ganges. *J Geol* 109:737–753
- Bickle M, Bunbury J, Chapman H et al (2003) Fluxes of Sr into the headwaters of the Ganges. *Geochim Cosmochim Acta* 67:2567–2584
- Bickle M, Chapman H, Bunbury J et al (2005) Relative contributions of silicate and carbonate rocks to riverine Sr fluxes in the headwaters of the Ganges. *Geochim Cosmochim Acta* 69:2221–2240
- Blum JD, Erel Y (1995) A silicate weathering mechanism linking increases in marine Sr-87/Sr-86 with global glaciation. *Nature* 373:415–418
- Blum JD, Erel Y (1997) Rb-Sr isotope systematics of a granitic soil chronosequence: the importance of biotite weathering. *Geochim Cosmochim Acta* 61:3193–3204
- Blum JD, Erel Y (2003) Radiogenic isotopes in weathering and hydrology. In: Holland HD, Turekian KK (eds) *Surface and ground water, weathering and soils*, vol. 5, Treatise on geochemistry. Elsevier-Pergamon, Oxford, pp 365–392
- Blum JD, Gazis CA, Jacobson A et al (1998) Carbonate versus silicate weathering rates in the Raikot watershed within the High Himalayan crystalline series. *Geology* 26:411–414
- Bluth G, Kump L (1994) Lithologic and climatologic controls of river chemistry. *Geochim Cosmochim Acta* 58:2341–2359
- Brantley S, Chesley J, Stillings L (1998) Isotopic ratios and release rates of strontium measured from weathering feldspars. *Geochim Cosmochim Acta* 62:1493–1500
- Brass GW (1976) The variation of the marine $^{87}\text{Sr}/^{86}\text{Sr}$ ratio during Phanerozoic time; interpretation using a flux model. *Geochim Cosmochim Acta* 40:721–730
- Bullen T, White A, Blum A et al (1997) Chemical weathering of a soil chronosequence on granitoid alluvium: II mineralogical and isotopic constraints on the behavior of strontium. *Geochim Cosmochim Acta* 61:291–306
- Burbank D, Blythe A, Putkonen J et al (2003) Decoupling of erosion and precipitation in the Himalayas. *Nature* 426:652–655
- Burke W, Denison R, Hetherington E et al (1982) Variation of seawater $^{87}\text{Sr}/^{86}\text{Sr}$ throughout Phanerozoic time. *Geology* 10:516–519
- Chabaux F, Riotte J, Clauer N et al (2001) Isotopic tracing of the dissolved U fluxes of Himalayan rivers: implications for present and past U budgets of the Ganges-Brahmaputra system. *Geochim Cosmochim Acta* 65:3201–3217
- Chabaux F, Bourdon B, Riotte J (2008) U-series geochemistry in weathering profiles, river waters and lakes. In: Krishnaswami S, Cochran JK (eds) *U/Th series radionuclides in aquatic systems*, vol 13, Radioactivity in the environment. Elsevier, New York, NY, pp 49–104
- Clift P (2006) Controls on the erosion of Cenozoic Asia and the flux of clastic sediment to the ocean. *Earth Planet Sci Lett* 241:571–590
- Clift P, Blusztajn J (2005) Reorganization of the western Himalayan river system after five million years ago. *Nature* 438:1001–1003
- Clift P, Lee J, Hildebrand P et al (2002) Nd and Pb isotope variability in the Indus river system: implications for crustal heterogeneity in the western Himalaya. *Earth Planet Sci Lett* 200:91–106
- Clift P, Giosan L, Blusztajn J et al (2008) Holocene erosion of the Lesser Himalaya triggered by intensified summer monsoon. *Geology* 36:79–82
- Colin C, Turpin L, Bertaux J et al (1999) Erosional history of the Himalayan and Burman ranges during the last two glacial-interglacial cycles. *Earth Planet Sci Lett* 171: 647–660
- Colin C, Turpin L, Blamart D et al (2006) Evolution of weathering patterns in the Indo-Burman ranges over 280 kyr: effects of sediment provenance on $^{87}\text{Sr}/^{86}\text{Sr}$ ratios tracer. *Geochem Geophys Geosyst* 7:Q03007. doi:10.1029/2005GC000962
- Dalai T, Krishnaswami S, Kumar A (2003) Sr and $^{87}\text{Sr}/^{86}\text{Sr}$ in the Yamuna River System in the Himalaya: sources, fluxes, and controls on Sr isotope composition. *Geochim Cosmochim Acta* 67:2931–2948
- Das A, Krishnaswami S, Sarin M et al (2005) Chemical weathering in the Krishna Basin and Western Ghats of the Deccan Traps, India: rates of basalt weathering and their controls. *Geochim Cosmochim Acta* 69:2067–2084
- Das A, Krishnaswami S, Kumar A (2006) Sr and $^{87}\text{Sr}/^{86}\text{Sr}$ in rivers draining the Deccan Traps (India): implications to weathering, Sr fluxes and marine $^{87}\text{Sr}/^{86}\text{Sr}$ record around K/T. *Geochem Geophys Geosyst* 7:Q06014. doi:10.1029/2005GC001081
- Dasch E (1969) Strontium isotopes in weathering profiles, deep-sea sediments, and sedimentary rocks. *Geochim Cosmochim Acta* 33:1521–1552
- Davis A, Bickle M, Teagle D (2003) Imbalance in the oceanic strontium budget. *Earth Planet Sci Lett* 211:173–187
- DePaolo D, Wasserburg G (1976) Nd isotopic variations and petrogenetic models. *Geophys Res Lett* 3:249–252
- Derry L, France-Lanord C (1996) Neogene Himalayan weathering history and river $^{87}\text{Sr}/^{86}\text{Sr}$: impact on the marine Sr record. *Earth Planet Sci Lett* 142:59–74
- Derry L, France-Lanord C (1997) Himalayan weathering and erosion fluxes: climate and tectonic controls. In: Ruddiman WF (ed) *Tectonic uplift and climate change*. Plenum, New York, pp 290–312
- Dessert C, Dupre B, Francois L et al (2001) Erosion of Deccan Traps determined by river geochemistry: impact on the global climate and the $^{87}\text{Sr}/^{86}\text{Sr}$ ratio of sea water. *Earth Planet Sci Lett* 188:459–474
- Dessert C, Dupre B, Gaillardet J et al (2003) Basalt weathering laws and the impact of basalt weathering on the global carbon cycle. *Chem Geol* 20:1–17
- Dia A, Dupré B, Allègre C (1992) Nd isotopes in Indian Ocean sediments used as a tracer of supply to the ocean and circulation paths. *Mar Geol* 103:349–359
- Drever J (1997) *The geochemistry of natural waters*, 3rd edn. Prentice Hall, NJ, p 436

- Edmond JM (1992) Himalayan tectonics, weathering processes, and the strontium isotope record in marine limestone. *Science* 258:1594–1597
- Edmond J, Huh Y (1997) Chemical weathering yields from basement and orogenic terrains in hot and cold climates. In: Ruddiman WF (ed) *Tectonic Uplift and Climate Change*. Plenum Press, New York, pp 330–351
- Erel Y, Blum JD, Roueff E et al (2004) Lead and strontium isotopes as monitors of experimental granitoid mineral dissolution. *Geochim Cosmochim Acta* 68:4649–4663
- Evans M, Derry L, Anderson S et al (2001) Hydrothermal source of radiogenic Sr to Himalayan rivers. *Geology* 29:803–806
- Evans M, Derry L, France-Lanord C (2004) Geothermal fluxes of alkalinity in the Narayani river system of central Nepal. *Geochim Geophys Geosyst* 5:Q08011. doi:10.1029/2004GC000719
- Faure G (1986) *Principles of Isotope Geology*, 2nd edn. Wiley, Hoboken, N.J.
- France-Lanord C, Derry L (1997) Organic carbon burial forcing of the carbon cycle from Himalayan erosion. *Nature* 390:65–67
- France-Lanord C, Derry L, Michard A (1993) Evolution of the Himalaya since Miocene time: isotopic and sedimentologic evidence from the Bengal Fan. In: Treloar PJ, Searle M (eds) *Himalayan tectonics*, vol 74, Geological Society of London Special Publication. Geological Society of London, London, pp 603–621
- Frank M (2002) Radiogenic isotopes: tracers of past ocean circulation and erosional input. *Rev Geophys* 40(1):1001. doi:10.1029/2000RG000094
- Gaillardet J (2008) Isotope geochemistry as a tool for deciphering kinetics of water-rock interaction. In: Brantley S, Kubicki J, White A (eds) *Kinetics of water-rock interaction*, Chap. 12. Springer, New York, pp 611–674
- Gaillardet J, Dupre B, Allegre C (1997) Chemical and physical denudation in the Amazon river basin. *Chem Geol* 142:141–173
- Gaillardet J, Dupre B, Louvat P et al (1999) Global silicate weathering and CO₂ consumption rates deduced from the chemistry of large rivers. *Chem Geol* 159:3–30
- Galy A, France-Lanord C (1999) Weathering processes in the Ganges-Brahmaputra basin and the riverine alkalinity budget. *Chem Geol* 159:31–60
- Galy A, France-Lanord C, Derry L (1999) The strontium isotopic budget of Himalayan Rivers in Nepal and Bangladesh. *Geochim Cosmochim Acta* 63:1905–1925
- Galy V, France-Lanord C, Peucker-Ehrenbrink B et al (2010) Sr–Nd–Os evidence for a stable erosion regime in the Himalaya during the past 12 Myr. *Earth Planet Sci Lett* 290:474–480
- Goldstein SL, Jacobsen SB (1987) The Nd and Sr isotopic systematics of river-water dissolved material: implications for the sources of Nd and Sr in the seawater. *Chem Geol* 66:245–272
- Goldstein SL, O’Nions RK (1981) Nd and Sr isotopic relationships in pelagic clays and ferromanganese deposits. *Nature* 292:324–327
- Harlavan Y, Erel Y (2002) The release of Pb and REE from granitoids by the dissolution of accessory phases. *Geochim Cosmochim Acta* 66:837–848
- Harlavan Y, Erel Y, Blum JD (2009) The coupled release of REE and Pb to the soil labile pool with time by weathering of accessory phases, Wind River Mountains, WY. *Geochim Cosmochim Acta* 73:320–336
- Harris N, Bickle M, Chapman H et al (1998) The significance of Himalayan rivers for silicate weathering rates: evidence from the Bote Kosi tributary. *Chem Geol* 144:205–220
- Hren M, Chamberlain C, Hilley G et al (2007) Major ion chemistry of the Yarlung Tsangpo-Brahmaputra river: chemical weathering, erosion, and CO₂ consumption in the southern Tibetan Plateau and eastern syntaxis of the Himalaya. *Geochim Cosmochim Acta* 71:2907–2935
- Huh Y, Edmond J (1999) The fluvial geochemistry of the rivers of Eastern Siberia: III Tributaries of the Lena and Anbar draining the basement terrain of the Siberian Craton and the Trans-Baikal Highlands. *Geochim Cosmochim Acta* 63:967–987
- Ingrì J, Widerlund A, Land M et al (2000) Temporal variations in the fractionation of the rare earth elements in a boreal river; the role of colloidal particles. *Chem Geol* 166:23–45
- Jacobsen S, Wasserburg G (1980) Sm–Nd isotopic evolution of chondrites. *Earth Planet Sci Lett* 50:139–155
- Jacobson AD, Blum JD (2000) The Ca/Sr and ⁸⁷Sr/⁸⁶Sr geochemistry of disseminated calcite in Himalayan silicate rocks from Nanga Parbat: influence on river water chemistry. *Geology* 28:463–466
- Jacobson AD, Blum JD, Chamberlain CP et al (2002) The Ca/Sr and Sr isotope systematics of a Himalayan glacial chronosequence: carbonate versus silicate weathering rates as a function of landscape surface age. *Geochim Cosmochim Acta* 66:13–27
- Jeandel C, Arsouze T, Lacan F et al (2007) Isotopic Nd compositions and concentrations of the lithogenic inputs into the ocean: a compilation, with an emphasis on the margins. *Chem Geol* 239:156–164
- Johannesson K, Tang J, Daniels J et al (2004) Rare earth element concentrations and speciation in organic-rich blackwaters of the Great Dismal Swamp, Virginia. *USA Chem Geol* 209:271–294
- Krishnaswami S, Singh SK (2005) Chemical weathering in the river basins of the Himalaya. *India Curr Sci* 89:841–849
- Krishnaswami S, Trivedi JR, Sarin MM et al (1992) Strontium isotopes and rubidium in the Ganga-Brahmaputra river system: weathering in the Himalaya, fluxes to the Bay of Bengal and contributions to the evolution of oceanic ⁸⁷Sr/⁸⁶Sr. *Earth Planet Sci Lett* 109:243–253
- Krishnaswami S, Singh SK, Dalai TK (1999) Silicate weathering in the Himalaya: role in contributing to major ions and radiogenic Sr to the Bay of Bengal. In: Somayajulu BLK (ed) *Ocean science, trends and future directions*. Indian National Science Academy and Akademia International, New Delhi, pp 23–51
- Kump LR, Brantley SL, Arthur MA (2000) Chemical weathering, atmospheric CO₂ and climate. *Annu Rev Earth Planet Sci* 28:611–667
- Leland J, Reid MR, Burbank DW et al (1998) Incision and differential bedrock uplift along the Indus River near Nanga Parbat, Pakistan Himalaya, from ¹⁰Be and ²⁶Al exposure age dating of bedrock straths. *Earth Planet Sci Lett* 154:93–107

- Li XH, Wei GJ, Shao L et al (2003) Geochemical and Nd isotopic variations in sediments of the South China Sea: a response to Cenozoic tectonism in SE Asia. *Earth Planet Sci Lett* 211:207–220
- Ma J, Wei G, Xu Y et al (2007) Mobilization and re-distribution of major and trace elements during extreme weathering of basalt in Hainan Island, South China. *Geochim Cosmochim Acta* 71:3223–3237
- Ma J, Wei G, Xu Y et al (2010) Variations of Sr–Nd–Hf isotopic systematics in basalt during intensive weathering. *Chem Geol* 269:376–385
- MacFarlane A, Danielson A, Holland H et al (1994) REE chemistry and Sm–Nd systematics of late Archean weathering profiles in the Fortescue Group, Western Australia. *Geochim Cosmochim Acta* 58:1777–1794
- McCauley S, DePaolo D (1997) The marine $^{87}\text{Sr}/^{86}\text{Sr}$ and $\delta^{18}\text{O}$ records, Himalayan alkalinity fluxes and Cenozoic climate records. In: Ruddiman W (ed) *Tectonics uplift and climate change*. Plenum, New York, pp 428–467
- Milliman J, Meade R (1983) World-wide delivery of river sediment to the oceans. *J Geol* 91:1–21
- Milliman JD, Syvitski PM (1992) Geomorphic/Tectonic control of sediment discharge to the ocean: the importance of small mountainous rivers. *J Geol* 100:525–544
- Millot R, Gaillardet J, Dupre B et al (2002) The global control of silicate weathering rates and the coupling with physical erosion: new insights from rivers of the Canadian Shield. *Earth Planet Sci Lett* 196:83–98
- Millot R, Gaillardet J, Dupre B et al (2003) Northern latitude chemical weathering rates: clues from the Mackenzie River basin, Canada. *Geochim Cosmochim Acta* 67:1305–1329
- Molnar P, England P (1990) Late Cenozoic uplift of mountain ranges and global climate change: chicken or egg? *Nature* 346:29–34
- Montgomery DR (1994) Valley incision and the uplift of mountain peaks. *J Geophys Res* 99:913–921
- Moon S, Huh Y, Qin J et al (2007) Chemical weathering in the Hong (Red) River basin: rates of silicate weathering and their controlling factors. *Geochim Cosmochim Acta* 71:1411–1430
- Moon S, Huh Y, Zitsev A (2009) Hydrochemistry of the Amur River: weathering in a northern temperate basin. *Aquat Geochem* 15:497–527
- Negrel P, Allegre CJ, Dupre B et al (1993) Erosion sources determined by inversion of major and trace element ratios and strontium isotopic ratios in river water: the Congo Basin case. *Earth Planet Sci Lett* 120:59–76
- Nesbitt H (1979) Mobility and fractionation of rare earth elements during weathering of a granodiorite. *Nature* 279:206–210
- Nesbitt HW, Markovics G (1997) Weathering of granodioritic crust, long-term storage of elements in weathering profiles, and petrogenesis of silicate minerals. *Geochim Cosmochim Acta* 61:1653–1670
- Noh H, Huh Y, Qin J et al (2009) Chemical weathering in the three rivers region of Eastern Tibet. *Geochim Cosmochim Acta* 73:1857–1877
- Ohlander B, Ingri J, Land M et al (2000) Change of Sm–Nd isotope composition during weathering of till. *Geochim Cosmochim Acta* 64:813–820
- Oliva P, Dupre B, Martin F et al (2004) The role of trace minerals in chemical weathering in a high-elevation granitic watershed (Estibere, France): chemical and mineralogical evidence. *Geochim Cosmochim Acta* 68:2223–2243
- Oliver L, Harris N, Bickle M et al (2003) Silicate weathering rates decoupled from the $^{87}\text{Sr}/^{86}\text{Sr}$ ratio of the dissolved load during Himalayan erosion. *Chem Geol* 201:119–139
- Palmer M, Edmond J (1989) The strontium isotope budget of the modern ocean. *Earth Planet Sci Lett* 92:11–26
- Palmer MR, Edmond JM (1992) Controls over the strontium isotope composition of river water. *Geochim Cosmochim Acta* 56:2099–2111
- Pande K, Sarin MM, Trivedi JR et al (1994) The Indus river system (India-Pakistan): major-ion chemistry, uranium and strontium isotopes. *Chem Geol* 116:245–259
- Pattanaik J, Balakrishnan S, Bhutani R et al (2007) Chemical and strontium isotopic composition of Kaveri, Palar and Ponnaiyar rivers: significance to weathering of granulites and granitic gneisses of southern Peninsular India. *Curr Sci* 93:523–531
- Peucker-Ehrenbrink B (2009) Land2Sea database of river drainage basin sizes, annual water discharges, and suspended sediment fluxes. *Geochem Geophys Geosyst* 10:Q06014. doi:10.1029/2008GC002356
- Peucker-Ehrenbrink B, Miller MW, Arsouze T et al (2010) Continental bedrock and riverine fluxes of strontium and neodymium isotopes to the oceans. *Geochem Geophys Geosyst* 11:Q03016. doi:10.1029/2009GC002869
- Pierson-Wickmann AC, Reisberg L, France-Lanord C et al (2001) Os–Sr–Nd results from sediments in the Bay of Bengal: implications for sediment transport and the marine Os record. *Paleoceanography* 16:435–444
- Porcelli D, Anderson P, Baskaran M et al (2009) The distribution of neodymium isotopes in Arctic Ocean basins. *Geochim Cosmochim Acta* 73:2645–2659
- Quade J, Roe L, DeCelles P et al (1997) The late neogene $^{87}\text{Sr}/^{86}\text{Sr}$ record of lowland Himalayan rivers. *Science* 276:1828–1831
- Rad S, Allegre C, Lovat P (2007) Hidden erosion on volcanic islands. *Earth Planet Sci Lett* 262:109–124
- Rahaman W, Singh SK, Sinha R et al (2009) Climate control on erosion distribution over the Himalaya during the past 100 ka. *Geology* 37:559–562
- Rai SK, Singh SK (2007) Temporal variation in Sr and $^{87}\text{Sr}/^{86}\text{Sr}$ of the Brahmaputra: implications for annual fluxes and tracking flash floods through chemical and isotope composition. *Geochem Geophys Geosyst* 8:Q08008
- Rai SK, Singh SK, Krishnaswami S (2010) Chemical weathering in the plain and peninsular sub-basins of the Ganga: impact on major ion chemistry and elemental fluxes. *Geochim Cosmochim Acta* 74:2340–2355
- Ravizza G, Zachos J (2003) Records of Cenozoic chemistry. In: Holland HD, Turekian KK (eds) *The oceans and marine chemistry*, vol. 6, Treatise on geochemistry. Elsevier-Pergamon, Oxford, pp 551–582
- Raymo ME, Ruddiman WF (1992) Tectonic forcing of late Cenozoic climate. *Nature* 359:117–122
- Raymo ME, Ruddiman WF, Froelich PN (1988) Influence of late Cenozoic mountain building on ocean geochemical cycles. *Geology* 16:649–653

- Reynolds B (2011) Silicon isotopes as tracers of terrestrial processes. In: Baskaran M (ed) Handbook of environmental isotope geochemistry. Chapter 6. Springer, Heidelberg
- Richter FM, Rowley DB, DePaolo DJ (1992) Sr isotope evolution of seawater: the role of tectonics. *Earth Planet Sci Lett* 109:11–23
- Ruddiman W (1997) *Tectonic Uplift and Climate Change*. Plenum, New York, p 535
- Shiller A (2010) Dissolved rare earth elements in a seasonally snow-covered, alpine/subalpine watershed, Loch Vale, Colorado. *Geochim Cosmochim Acta* 74:2040–2052
- Sholkovitz E (1995) The aquatic chemistry of rare earth elements in rivers and estuaries. *Aquat Geochem* 1:1–34
- Sholkovitz E, Szymczak R (2000) The estuarine chemistry of rare earth elements: comparison of the Amazon, Fly, Sepik and the Gulf of Papua systems. *Earth Planet Sci Lett* 179:299–309
- Singh SK (2006) Spatial variability in erosion in the Brahmaputra basin: causes and impacts. *Curr Sci* 90:1271–1276
- Singh SK (2007) Erosion and weathering in the Brahmaputra river system. In: Gupta A (ed) *Large rivers*. Wiley, Chichester, pp 373–393
- Singh SK, France-Lanord C (2002) Tracing the distribution of erosion in the Brahmaputra watershed from isotopic compositions of stream sediments. *Earth Planet Sci Lett* 202:645–662
- Singh SK, Trivedi JR, Pande K et al (1998) Chemical and strontium, oxygen, and carbon isotopic compositions of carbonates from the Lesser Himalaya: implications to the strontium isotope composition of the source waters of the Ganga, Ghaghara, and the Indus Rivers. *Geochim Cosmochim Acta* 62:743–755
- Singh SK, Sarin MM, France-Lanord C (2005) Chemical erosion in the eastern Himalaya: major ion composition of the Brahmaputra and $\delta^{13}\text{C}$ of dissolved inorganic carbon. *Geochim Cosmochim Acta* 69:3573–3588
- Singh SK, Rai SK, Krishnaswami S (2008) Sr and Nd isotopes in river sediments from the Ganga basin: sediment provenance and spatial variability in physical erosion. *J Geophys Res* 113:F03006. doi:10.1029/2007JF000909
- Stallard RF, Edmond JM (1983) Geochemistry of the Amazon 2. *J Geophys Res* 88:9671–9688
- Steinmann M, Stille P (2008) Controls on transport and fractionation of the rare earth elements in stream water of a mixed basaltic-granitic catchment basin (Massif Central, France). *Chem Geol* 254:1–18
- Tachikawa K, Athias V, Jeandel C (2003) Neodymium budget in the modern ocean and paleo-oceanographic implications. *J Geophys Res* 108:3254. doi:10.1029/1999JC000285
- Taylor AS, Lasaga AC (1999) The role of basalt weathering in the Sr isotope budget of the oceans. *Chem Geol* 161:199–214
- Taylor AS, Blum JD, Lasaga AC et al (2000) Kinetics of dissolution and Sr release during biotite and phlogopite weathering. *Geochim Cosmochim Acta* 64:1191–1208
- Tipper E, Bickle M, Galy A et al (2006a) The short term climatic sensitivity of carbonate and silicate weathering fluxes: insight from seasonal variations in river chemistry. *Geochim Cosmochim Acta* 70:2737–2754
- Tipper E, Galy A, Gaillardet J et al (2006b) The magnesium isotope budget of the modern ocean: constraints from riverine magnesium isotope ratios. *Earth Planet Sci Lett* 250:241–253
- Tipper E, Galy A, Bickle M (2008) Calcium and magnesium isotope systematics in rivers draining the Himalaya-Tibetan-Plateau region: lithological or fractionation control? *Geochim Cosmochim Acta* 72:1057–1075
- Tricca A, Stille P, Steinmann M et al (1999) Rare earth elements and Sr and Nd isotopic compositions of dissolved and suspended loads from small river systems in the Vosges mountains (France), the river Rhine and groundwater. *Chem Geol* 160:139–158
- Tripathy GR, Singh SK (2010) Chemical erosion rates of river basins of the Ganga system in the Himalaya: reanalysis based on inversion of dissolved major ions, Sr, and $^{87}\text{Sr}/^{86}\text{Sr}$. *Geochem Geophys Geosyst* 11:Q03013. doi:10.1029/2009GC002862
- Tripathy GR, Goswami V, Singh SK et al (2010) Temporal variations in Sr and $^{87}\text{Sr}/^{86}\text{Sr}$ of the Ganga headwaters: estimate of dissolved Sr flux to the mainstream. *Hydrol Process* 24:1159–1171. doi:10.1002/hyp.7572
- Trivedi J, Pande K, Krishnaswami S et al (1995) Sr isotopes in rivers of India and Pakistan: a reconnaissance study. *Curr Sci* 69:171–178
- Tutken T, Eisenhauer A, Wiegand B et al (2002) Glacial-interglacial cycles in Sr and Nd isotopic composition of Arctic marine sediments triggered by the Svalbard/Barents Sea ice sheet. *Mar Geol* 182:351–372
- Vance D, Teagle D, Foster G (2009) Variable Quaternary chemical weathering fluxes and imbalances in marine geochemical budgets. *Nature* 458:493–496
- Veizer J (1989) Strontium isotopes in sea water through time. *Annu Rev Earth Planet Sci* 17:141–168
- Viers J, Wasserburg GJ (2004) Behavior of Sm and Nd in a lateritic soil profile. *Geochim Cosmochim Acta* 68:2043–2054
- Viers J, Roddaz M, Filizola N et al (2008) Seasonal and provenance controls on Nd–Sr isotopic compositions of Amazon river suspended sediments and implications for Nd and Sr fluxes exported to the Atlantic Ocean. *Earth Planet Sci Lett* 274:511–523
- Vigier N, Bourdon B (2011) Constraining rates of chemical and physical erosion using U-series radionuclides. In: Baskaran M (ed) *Handbook of environmental isotope geochemistry*, Chapter 27. Springer, Heidelberg
- Walker J, Hays P, Kasting J (1981) A negative feedback mechanism for the long-term stabilization of Earth's surface temperature. *J Geophys Res* 86:9776–9782
- Walter HJ, Hegner E, Diekmann B et al (2000) Provenance and transport of terrigenous sediment in the south Atlantic Ocean and their relations to glacial and interglacial cycles: Nd and Sr isotopic evidence. *Geochim Cosmochim Acta* 64:3813–3827
- West AJ, Galy A, Bickle M (2005) Tectonic and climatic controls on silicate weathering. *Earth Planet Sci Lett* 235:211–228
- Willenbring JK, Blanckenburg FV (2010) Long-term stability of global erosion rates and weathering during late-Cenozoic cooling. *Nature* 465:211–214
- Winter B, Johnson C, Clark D (1997) Strontium, neodymium and lead isotope variations of authigenic and silicate sediment components from the Late Cenozoic Arctic Ocean:

- implications for sediment provenance and source of trace metals in sea water. *Geochim Cosmochim Acta* 61: 4181–4200
- Wu L, Huh Y, Qin J et al (2005) Chemical weathering in the Upper Huang He (Yellow River) draining the eastern Qinghai-Tibet Plateau. *Geochim Cosmochim Acta* 69:5279–5294
- Xu Y, Marcantonio F (2007) Strontium isotope variations in the lower Mississippi River and its estuarine mixing zone. *Mar Chem* 105:118–128
- Yang C, Telmer K, Veizer J (1996) Chemical dynamics of the “St. Lawrence” riverine system: δD_{H_2O} , $\delta^{18}O_{H_2O}$, $\delta^{13}C_{DIC}$, $\delta^{34}S_{sulfate}$, and dissolved $^{87}Sr/^{86}Sr$. *Geochim Cosmochim Acta* 60:851–866
- Yang S, Jiang S, Ling H et al (2007) Sr-Nd isotopic compositions of the Changjiang sediments: implications for tracing sediment sources. *Sci China Ser D-Earth Sci* 50:1556–1565
- Zachos J, Opdyke B, Quinn T et al (1999) Early Cenozoic glaciation, Antarctic weathering, and seawater $^{87}Sr/^{86}Sr$: is there a link? *Chem Geol* 161:165–180
- Zeitler P, Koons P, Bishop M et al (2001) Erosion, Himalayan geodynamics, and the geomorphology of metamorphism. *GSA Today* 11:4–9

Chapter 27

Constraining Rates of Chemical and Physical Erosion Using U-Series Radionuclides

Nathalie Vigier and Bernard Bourdon

Abstract This chapter relates recent developments concerning the use of several U-series nuclides, in particular ^{234}U - ^{238}U and ^{230}Th - ^{238}U disequilibria, for constraining physical and chemical erosion rates and sediment age. Indeed, the ability to measure these disequilibria with an extremely high precision, even in samples with low concentrations such as natural waters, has opened new avenues for investigating erosional processes. This chapter is articulated in three main parts: a brief introduction and presentation of modern technical methods is followed by a description of how ^{234}U - ^{238}U and ^{230}Th - ^{238}U disequilibria measured in dissolved (water) and solid (sediment) river phases can be used to provide quantitative constraints on physical and chemical erosion rates at the basin scale. In parallel, recoil effects occurring during sediment formation can now be modelled and used to estimate the residence time of a sediment within a basin. Finally, the last part of this chapter presents the latest findings concerning the study of weathering profiles and the modelling of U and Th migration within an aquifer system.

27.1 Introduction

27.1.1 U-Series as a Tool for Studying Environmental Processes

Across a broad range of fields within the Earth sciences, U-series nuclides have emerged as a set of powerful tools to constrain the rates and timescales of geological processes. Following the discovery of radioactivity by Becquerel (1896), it was soon realized that the radioactivity of natural uranium was due to other elements contained in minute quantities. The most famous decay product was radium, discovered in 1898 by the Curies. In the following years many other elements were identified and the concept of a decay chain was elaborated by Rutherford and Soddy (1903). In the Earth sciences, it took many decades before the applications of these nuclides to Earth processes would flourish. As fully summarized in Ivanovich and Harmon (1992), there have been some pioneering applications of U-series nuclides to understand weathering processes based on α -counting measurements (Plater et al. 1992, 1994; Rosholt et al. 1966; Latham and Schwarz 1987) but the expansion of the field was somewhat limited by the precision of measurements, as well as the relatively large quantities of samples needed for analysis. With the advent of mass spectrometric techniques in the 1990 (Edwards et al. 1987; Goldstein and Stirling 2003), the variations of the longer lived U-series nuclides could then be fully investigated. Recent reviews of U-series applications to studying environmental processes can be found in Chabaux et al. (2003a); Dosseto et al. (2008a); Chabaux et al. (2008).

N. Vigier (✉)
CRPG-CNRS, Nancy Université, 15 rue Notre Dame des
Pauvres, 54500 Vandoeuvre les Nancy, France
e-mail: nvigier@crpg.cnrs-nancy.fr

B. Bourdon
Institute of Geochemistry and Petrology, Clausiusstrasse 25,
ETH Zurich, Zurich 8092, Switzerland

27.1.2 Properties of U-Series Nuclides in the Weathering Environment

In what follows we summarize the geochemical and nuclear properties of U-series nuclides that are relevant to the weathering environment. First, these nuclides are radioactive with half lives that range between 1,600 yr and 244 kyr, therefore providing a range of timescales relevant for the study of chemical weathering. Second, the geochemical properties of U-Th-Ra and Pa are not identical. During the dissolution of minerals and water-rock interaction, U and Ra are considered as mobile elements ($U > Ra$) while Th and Pa are considered as immobile elements. The geochemical properties of these elements have been reviewed in detail in Ivanovich and Harmon (1992); Bourdon et al. (2003); or Chabaux et al. (2008). Essentially the fractionation of U-series nuclides in the weathering environment is controlled by their speciation in aqueous solution, their nuclear properties and their interaction with mineral surfaces and with organic material present as solid load or as dissolved load. In oxidized environments, U^{6+} reacts with the water molecule and is in the form of UO_2^{2+} , which is a dissolved cation that is often complexed by carbonates or possibly other ligands if they are present in solution. The adsorption of U onto mineral surfaces has been studied rather extensively and shows that uranium can interact with carbonates, iron oxides or clay minerals (e.g., Duff et al. 2002; Bruno et al. 1995; Giammar and Hering 2001; Singer et al. 2009; Ames et al. 1983).

In contrast, Th is far more insoluble and reacts readily with mineral surfaces and with organic substances to a greater extent (Chen and Wang 2007). Thorium will easily adsorb to many mineral surfaces and its own solubility is extremely low (Dähn et al. 2002; Degueldre and Kline 2007; Geibert and Usbeck 2004; Rojo et al. 2009). Thus, it is expected that under weathering conditions, U concentrations in waters will be greatly enhanced relative to that of Th.

In comparison, there have been fewer studies on the relative mobility of Ra. As an alkali earth, Ra is more mobile than Th although its intrinsic solubility in aqueous solutions is low. In general, the complexation of Ra in solution is more limited than that of Th, but one should not underestimate the ability of Ra to interact with negatively charged surfaces of clay minerals in

mildly acidic to neutral conditions (Lazar et al. 2008; Hidaka et al. 2007; Willett and Bond 1995).

In summary, upon congruent dissolution of silicate minerals, all U-series nuclides should be released into solution. In general, their concentrations in solution is not high enough to allow direct precipitation of $Th(OH)_4$, UO_2 or $RaSO_4$ but they will definitely interact to a variable degree with mineral surfaces. A complete database of sorption behavior in the presence of relevant ligands is currently not available. However, it can be predicted that the level of interaction of U-Th-Ra-Pa with minerals under oxic conditions follows the order: $Th \approx Pa > U > Ra$. For the purpose of this review, it suffices to mention that in general natural river waters will show a larger abundance of U and Ra relative to Th and Pa. There could be an exception to this case if waters are organic rich (dissolved or colloidal organic matter), which enhances the solubility of Th in waters (Dosseto et al. 2006c). As the affinity of Th for organic acids is extremely high, the presence of dissolved organic matter can result in a lower adsorption of Th to solids and hence a higher effective concentration in solutions (Reiller et al. 2002).

The second property of the U-series nuclides that must be considered is the effect of recoil. As detailed in Bourdon et al. (2003), radioactive decay inside minerals leads to the emission of α -particles with a high energy (4–8 MeV) (Fleischer 1980; Fleischer and Raabe 1978; Huang and Walker 1967; Kigoshi 1971). A non-negligible part of this energy is given to the daughter nuclide upon decay (e.g. ^{234}U , ^{230}Th or ^{226}Ra). This energy termed “recoil energy” is in the form of kinetic energy, which means that the daughter nuclide will be displaced from its original site by a distance that depends on the magnitude of this energy and the properties of the mineral. The theoretical recoil distance is around 30 nm for silicate and carbonate minerals with the consequence that, depending on the grain size of minerals, and how far from the grain boundary the parent nuclides are located, a variable fraction of the daughter nuclides is ejected from minerals into surrounding solutions. The recoil effect can significantly contribute to the fractionation between ^{234}U - ^{238}U observed during erosion processes, or perhaps, in some cases, be the dominant cause of this fractionation. As the geochemical contrast between U and Th or Ra and Th is large, it is generally considered that the main cause for fractionation between these

nuclides is chemical rather than being due to recoil effects (e.g. Bourdon et al. 2003; DePaolo et al. 2006).

27.2 Material and Methods

The measurement of U-series nuclides, and in particular of U and Th isotopes, in weathering products (sediments and soil samples), as well as in river and ground waters, requires specific procedures. The main reasons are: (1) solid phases sampled in soils may contain U or Th rich accessory phases particularly resistant to dissolution procedures (2) natural waters are often characterized by very low levels of U and Th, and the precise measurement of their isotope composition requires the use of highly sensitive mass spectrometers, as well as a specific chemical separation allowing negligible external contamination.

Soil and regolith samples are usually collected using drilling techniques and hand augers (Ma et al. 2010; Hubert et al. 2006; Bourdon et al. 2009). Soil and river sediments are generally sieved before being crushed, in order to remove pebbles and gravels (greater than sand-sized particles). In order to avoid contamination, the crushing is generally done using agate material. Powders are then dissolved in mixtures of concentrated acids (generally HF, HNO₃ and HCl, with HClO₄ in the case of organic matter) (e.g. Ma et al. 2010; Granet et al. 2007). In some cases, samples are ashed at 550°C overnight before dissolution (Dossseto et al. 2008a, b). In order to ensure complete dissolution and to avoid fluoride precipitation that may easily retain elements such as thorium, boric acid may be added (e.g. Vigier et al. 2001).

Since most natural water samples have very low levels in U-series nuclides, it is often necessary to perform a pre-concentration procedure. This can be done through the evaporation of a significant volume of water, but evaporation of large volumes of water may result in substantial external contamination. As a consequence, another pre-concentration technique has been developed (Chen et al. 1986; Vigier et al. 2001), which consists of co-precipitating radionuclides with Fe hydroxides from 15–20 L of filtered water.

Filtration is usually performed in the field, the same day of the sampling, using 0.2 or 0.45 µm filters (e.g. Hubert et al. 2006, Vigier et al. 2001). Sampling techniques specific for aquifer environments

are given in Hubert et al. (2006) and in Maher et al. (2006a).

Before isotope composition measurements, U and Th need to be fully separated from the rest of the sample matrix. This is classically performed by ion chromatography, using anion exchange resin columns, in a clean laboratory (Manhès 1981; Luo et al. 1997; Turner et al. 1997; Aciego et al. 2009).

Over the past few years, U and Th isotope compositions (²³⁴U, ²³⁸U, ²³⁰Th and ²³²Th) have typically been measured using new generation mass spectrometers, either by thermal ionisation mass spectrometer (TIMS) (e.g. TRITON) or by multicollector-inductively coupled plasma mass spectrometer (MC-ICP-MS) (e.g. Nu Instruments, Neptune or Isoprobe) (Ma et al. 2010; Granet et al. 2007, 2010; Pelt et al. 2008; Dossseto et al. 2008a, b; Hubert et al. 2006; Bourdon et al. 2009; Maher et al. 2006a, b; Vigier et al. 2006; Andersen et al. 2004, 2008; Ball et al. 2008; Fietzke et al. 2005; Hellstrom 2003). For U isotopes, both types of mass spectrometers require a quantity of 10–100 ng of uranium, depending on the sensitivity of the instrument. Both ²³⁴U/²³⁸U and ²³⁰Th/²³²Th ratios are very low in nature (usually of the order of 10⁻⁵ to 10⁻⁶ respectively), which requires first that they cannot be measured with the same type of collector, and second that the abundance sensitivity of the mass spectrometer is highly optimized (it typically needs to be below 0.1 ppm). The measured isotope ratio needs to be corrected for instrumental mass bias (more significant with MC-ICP-MS), and for the relative gain between the ion counting system (IC) used for the low abundance isotope, and Faraday cup, used for the high abundance isotope. Bourdon et al. (2009) report specific procedures used to perform both types of corrections. The most recent internal precision and published reproducibility (at the 2σ level) for ²³⁴U/²³⁸U ranges between 1 and 3‰. The accuracy is checked using uranium reference materials, either synthetic solutions (e.g. NBS 960, now CRM-145 or NBL 112a) or rocks (HU1, BeN, AthO, UB-N, BHVO-1).

For Th isotope measurements, the amount of Th used is highly variable and mostly depends on the Th concentration of the sample. Solids are generally enriched in Th, and isotope analyses require sample size that generally contain 100–500 ng Th. In that case, similar corrections as for uranium isotopes are made (see e.g. Turner et al. 2001; Sims et al. 2008),

and both published internal and external errors are around 5‰ ($\pm 2\%$). For samples with much lower concentrations, such as natural waters, highly sensitive MC-ICP-MS are preferred. In that specific case, errors obtained are directly correlated to the amount of available Th for isotope analyses (see Vigier et al. 2006 for more details). The accuracy of Th isotope measurements is checked using Th synthetic solutions (e.g. Th-105, Th-S1, IRMM 35 and 36), and rock standards (generally TML and BeN).

27.3 Chemical and Physical Erosion Dynamics at Large Scale

The application of U-series nuclides to study the dynamics of chemical and physical erosion in large river basins is relatively recent although some earlier work by Plater et al. (1992) had hinted at some potential applications. More recently, the studies of Porcelli et al. (1997, 2001) highlighted the behaviour of U-series nuclides in organic-rich northern-high-latitude waters. Following the study of Vigier et al. (2001) many studies have exemplified how U-series can be used to constrain the timescales of physical and chemical erosion in large rivers. Recent reviews of the approach are given in Chabaux et al. (2003b, 2008); Dosseto et al. (2008a) In this section we review critically the most recent literature and further examine the great potential of U-series for constraining chemical and physical erosion rate and timescales.

27.3.1 Rates of Chemical and Physical Erosion

As explained in the Introduction, the different chemical and nuclear properties of U-series nuclides leads to fractionation in the U-series decay chain. First, the greater mobility of U and Ra relative to Th leads to enhancement of U and Ra in the dissolved fraction while Th is enriched in solids. Overall, river waters show $^{230}\text{Th}/^{238}\text{U}$ and $^{230}\text{Th}/^{226}\text{Ra}$ activity ratios in the dissolved loads smaller than 1, while in the suspended loads these activity ratios are greater than 1 (Fig. 27.1). Part of the fractionation can be related to adsorption of U-series nuclides either in the soil environment or

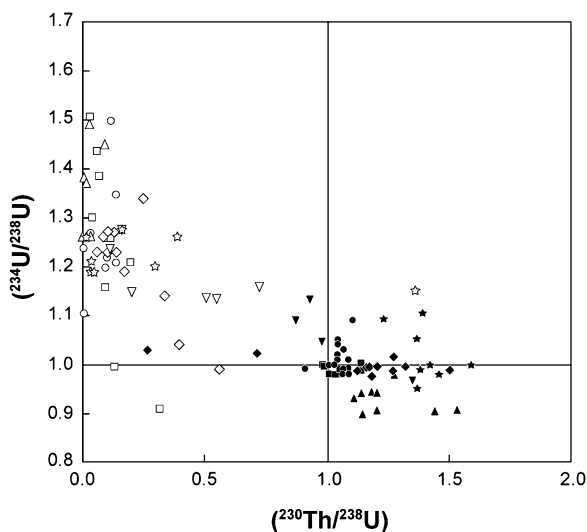


Fig. 27.1 Compilation of literature data of ^{234}U - ^{238}U and ^{230}Th - ^{238}U disequilibria measured in river filtered waters (*open symbols*) and corresponding river sediments (*black symbols*). *Triangles*: Mackenzie Basin rivers (Vigier et al. 2001). *Squares*: Bolivian Andes rivers (Dosseto et al. 2006b). *Stars*: Deccan Traps rivers (Vigier et al. 2005). *Inverse triangles*: Murray-Darling River (Dosseto et al. 2006c). *Circles*: Icelandic rivers (Vigier et al. 2006). *Diamonds*: Amazon rivers (Dosseto et al. 2006a)

during transport in rivers. In principle, adsorption of Th onto solids would be greater than that of U and Ra, leading to even greater $^{230}\text{Th}/^{238}\text{U}$ and $^{230}\text{Th}/^{226}\text{Ra}$ activity ratios. If the fractionation in $^{230}\text{Th}/^{238}\text{U}$ and $^{226}\text{Ra}/^{230}\text{Th}$ activity ratios is related to the degree of mineral alteration, then, in principle, the measurements of these ratios can be used to estimate the timescales and the rates of chemical weathering.

Another important type of fractionation that has been widely observed is the fractionation between ^{234}U and ^{238}U . There can be two distinct processes for creating ^{234}U - ^{238}U fractionation. First, the α -decay of ^{238}U to ^{234}Th and then to ^{234}U leads to direct ejection of the daughter nuclide from its current site by a distance that depends on the properties of the surrounding medium. In minerals, this distance should be approximately 30 nm. For grain that are smaller than 10 μm , the recoil can lead to measurable depletion of the solids over timescales of the order of magnitude of the half life of ^{234}U (Fig. 27.2). Another possibility is the preferential leaching of minerals leading to the enhancement of ^{234}U in the solution, as was first documented by Kigoshi (1971). This effect has been further documented in a number of laboratory

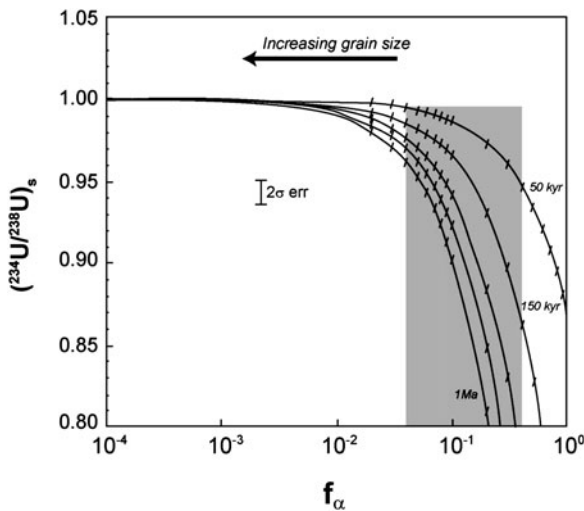


Fig. 27.2 Evolution of $(^{234}\text{U}/^{238}\text{U})_s$ activity ratio in a sediment as a function of the fraction of recoiled ^{234}Th (f_α , see text for more details). Each curve correspond to a specific comminution age. If f_α can be estimated independently for a size fraction of sediment, a corresponding precise measurement of $(^{234}\text{U}/^{238}\text{U})_s$ can lead to an estimation of the comminution age. The grey shadow corresponds to published range for f_α (DePaolo et al. 2006; Maher et al. 2006a, b; Hubert et al. 2006; Dosseto et al. 2010; Bourdon et al. 2009)

experiments (Hussain and Lal 1986; Andersen et al. 2009; Bourdon et al. 2009) for silicate and carbonate lithologies. In both cases, significant ^{234}U - ^{238}U fractionation can be observed. More specifically, it is likely that the degree of ^{234}U - ^{238}U fractionation actually depends on the nature of mineral phases. In what follows, we describe a number of applications of U-series nuclides for understanding the dynamics of weathering, rates and timescales of chemical weathering.

27.3.1.1 Dynamics of Erosion

An intrinsic property of landscape evolution is that it is in general a slow process, relative to human timescales, such that the direct measurement of erosion rates or soil formation rates is difficult. For dynamic systems that evolve slowly it is tempting to assume steady-state erosion. In this particular context, “steady-state” implies that the “weathering zone” in a given basin has reached a constant mass (M_w) or in other words that the output fluxes (mass being exported per unit of time as solid and dissolved loads in rivers, ϕ_{out}) is

balanced by the input fluxes (new bedrock material being weathered per unit of time, ϕ_{in}). The equation describing steady-state of erosion can be written as:

$$\frac{dM_w}{dt} = \phi_{in} - \phi_{out} = 0 \quad (27.1)$$

One can then write a similar equation for each of the nuclides of the U-series decay chain (e.g. C_i):

$$\frac{dM_w C_i}{dt} = \phi_{in} C_i^{in} - \phi_{out} C_i^{out} = 0 \quad (27.2)$$

The output flux can be estimated based on both the dissolved (d) and the suspended solids or particles (sol) exported by rivers:

$$\frac{dM_w C_i}{dt} = \phi_{in} C_i^{in} - \phi_{sol} C_i^{sol} - \phi_d C_i^d = 0 \quad (27.3)$$

After rearranging the equations, it can be shown that (Vigier et al. 2001):

$$\left(\frac{^{234}\text{U}}{^{238}\text{U}}\right)_d X_d + \left(\frac{^{234}\text{U}}{^{238}\text{U}}\right)_{sol} (1 - X_d) = 1 \quad (27.4)$$

where X_d represents the mass fraction of dissolved uranium relative to the total U export flux. Thus, using measured U activity ratios in the dissolved and suspended load of a basin river, one can evaluate if erosion operates in steady-state or not at the basin scale. This can be done by comparing the value of X_d deduced from U isotopes with that estimated based on direct measurements of U content in the dissolved and solid load (U_w and U_s), and of the total suspended solids (TSS), thereby providing an important constraint on the dynamics of erosion. Indeed, X_d is an inverse function of TSS ($X_d = U_w/(U_w + \text{TSS} \cdot U_s)$), and therefore of the physical erosion rate ($\Phi = \text{TSS} \times \text{discharge/area}$). In the end, this approach can be used to assess whether soils are being destroyed or be constructed at the scale of a watershed or a large basin. When the physical erosion rate (or sediment yield) based on U-series is slower than the observed erosion rate, it would indicate that the soils are being destroyed, while if it is faster, then the soils should be building up (Fig. 27.3). Thus, the U-series can provide important constraints on the dynamics of soils in river basins.

In principle, the attainment of steady-state erosion should be observed when the forcing parameters that

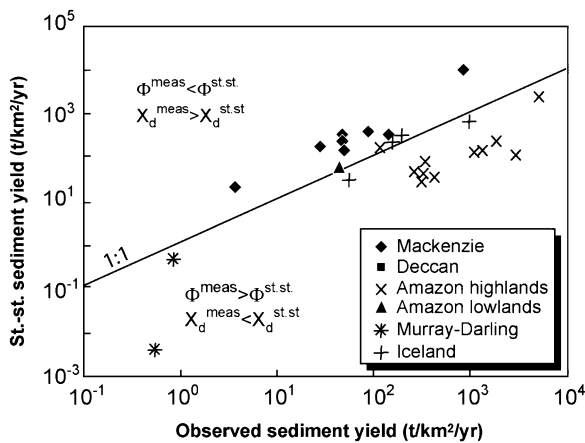


Fig. 27.3 Comparison of erosion rates (sediment yield or $\Phi = \text{TSS} \times \text{discharge/area}$) based on direct measurements of suspended load in rivers, and that inferred from U-series measurements (assuming a steady-state of erosion at the scale of the basin). See text for details. If the measured sediment yield is lower than the steady-state one, this can result either from a recent decrease of physical erosion rates, or alternatively from a recent increase of the proportion of dissolved uranium (X_d , see (27.4)), which is expected to be related to an increase of chemical erosion rate. The Mackenzie Basin (Canada) and the Amazon highlands are the regions the furthest from steady-state. Corresponding references are (Dosseto et al. 2006a, b, c; Vigier et al. 2001, 2005, 2006). Graph modified from Dosseto et al. (2008a)

affect the rates of erosion (due to climate, tectonic activity and/or human activity) have been varying slowly enough to allow the rate of soil production to adjust to new conditions. The parameters that control the rate of soil production are not precisely known and it is even more difficult to constrain the rate at which soil productions can adjust to new conditions. However it has been shown that the rate of soil production is lower when soils are thicker (Heimsath et al. 1997). The study of several large river basins has revealed that the erosion process in such basins is not always at steady-state (Vigier et al. 2001, 2005; Dosseto et al. (2006a, 2008a) (Fig. 27.3). In most cases, the absence of steady-state can be explained by recent changes in natural or human forcing parameters. For example, in the case of the Mackenzie river basins, this was attributed to recent deglaciation after the LGM. This concept has been further utilized by Vance et al. (2009) to explain variations in Sr isotopes in the marine record. Studies of rivers draining the Deccan trap (Vigier et al. 2005) have shown that agriculture was likely responsible for the destruction of soils in this region of India,

which is characterized by intense deforestation. In the Andes, Dosseto et al. (2008a, b) have shown that accelerated erosion rates due to increased rainfall during the Holocene led to destruction of soils. However, in contrast, in Iceland, where chemical and physical erosion rates display a large range, erosion processes were found to operate at steady-state at the scale of the island, although this region was strongly affected by the last glaciation, and maximum soil age was estimated to be 10 kyr (Vigier et al. 2006).

There have been criticisms of this approach (e.g. Granet et al. 2007) and it is quite clear that these studies have to be refined to accommodate them. Indeed, although equation (27.4) may seem rather simple, it hides some complexities that need to be assessed. In order to have a robust mass balance, one needs to make sure that there is no additional flux of dissolved uranium that is coming from another weathering zone, in particular from deep groundwaters. It is possible that in some cases, there is a significant contribution of uranium from deep aquifers, as suggested by Durand et al. (2005). This aspect was also studied by Bourdon et al. (2009) who have analyzed surface and groundwater samples in a small chalk river basin. This study showed that up to 40% of the uranium budget could be coming from aquifers in this carbonate environment. This might be an extreme case because the dissolution of carbonate is relatively fast. In the Amazon river basin, even by considering a contribution of up to 20% uranium from aquifers, the conclusion that erosion is not at steady-state is not affected. Given that the degree of disequilibrium of erosion processes is high for the Amazon basins, the conclusions are overall robust. Second, the potential for U or Th redistribution during transport also needs to be examined carefully. These questions have been discussed at some length in Dosseto et al. (2006a, b, 2008a) and it was shown that in most cases, the consideration of these effects did not greatly affect the conclusions, although they should not be neglected. For example, the adsorption of Th onto particles could decrease the $^{230}\text{Th}/^{238}\text{U}$ ratio measured in the dissolved load while the $^{230}\text{Th}/^{238}\text{U}$ ratio in the suspended load would increase. In fact it has been shown in several studies that the Th in the dissolved load of rivers is mostly associated with colloids (Viers et al. 1997; Dosseto et al. 2006c) and that its abundance in river waters is generally much higher than what the solubility would predict. Thus, given the

association of Th with colloids it is not clear that adsorption of Th onto suspended particles (size $>0.2 \mu\text{m}$) is taking place during transport.

Another important pitfall of this approach (that is in fact not specific to the U-series) is the representativeness of the analysis with respect to the possibility that the composition of the suspended load is not homogeneous or that the bedload also needs to be taken into account. The study of Granet et al. (2010) shows that there is sometimes a significant variability in the $^{230}\text{Th}/^{238}\text{U}$ ratios of the suspended load of rivers (2–50% in the most extreme case). Similarly, Dosseto et al. (2006c) have shown that the $^{230}\text{Th}/^{238}\text{U}$ and $^{234}\text{U}/^{238}\text{U}$ ratios of various size fractions in rivers is highly variable and that these size fractions can be represented by a mixture of a true dissolved load and suspended loads. However, the technique that consists of filtering samples at $0.2 \mu\text{m}$ rather than determining the true endmember of the dissolved load yielded similar results in terms of mass balance.

In the end, the study of erosion dynamics based on U-series will need some refinement and a careful assessment of the pitfalls and potential complexities need to be made to assess the robustness of conclusions. In particular, further detailed sampling will certainly be needed in the future.

27.3.1.2 Rates and Timescale of Chemical Weathering

In principle, U-series nuclides should be one of the best suited tools to determine the rates and timescales of chemical weathering in river basins. In comparison, the ^{10}Be method has been used to determine physical erosion rates by analyzing ^{10}Be production in quartz transported in rivers (Hewawasam et al. 2003; von Blanckenburg 2006). Physical and chemical erosion rates using Nd and Sr isotopes are discussed in Tripathy et al. (2011).

The basic principles for deriving the rates and timescales of chemical weathering are based on some simple assumptions about the origin of U-series fractionation. Upon mineral alteration, the U-series nuclides are fractionated due either to differences in chemical behaviour or due to recoil effects. If one can estimate the degree of fractionation based on some simple laws, it is then possible to derive a timescale by measuring the fractionation between ^{234}U - ^{238}U or

^{230}Th - ^{238}U in the weathered solids (as in river suspended particles) and in solutions (river waters). Furthermore, if we can make the additional assumption regarding the initial state of the system prior to the inception of chemical weathering, one can derive the rates of chemical and physical weathering. For the U-series nuclides, one can write the following equations. The equation of decay for a given number of atoms, N , of a given nuclide can be written as follows:

For the parent nuclide (N_1):

$$\frac{dN_1}{dt} = -\lambda_1 N_1 \quad (27.5)$$

For all the intermediate nuclides i of interest:

$$\frac{dN_i}{dt} = -\lambda_i N_i + \lambda_{i-1} N_{i-1} \quad (27.6)$$

where the decay constant, λ is related to the half-life by $\lambda = \ln 2/t_{1/2}$ and subscript $i-1$ refers to the next nuclide higher up in the decay chain (i.e. parent nuclide). For timescales greater than 5–6 times the half life of the longest lived daughter, the decay chain can be shown to be in secular equilibrium, i.e. all activities are equal:

$$\lambda_{i-1} N_{i-1} = \lambda_i N_i \quad (27.7)$$

We assume that the U-series decay chain is initially in secular equilibrium in minerals, i.e. the U decay chain has not been disturbed over the past million year and all activities are equal. The main consequence of this assumption is that the net effect of chemical weathering can be assessed by considering the measured activity ratios in weathering products. However, it is arguable whether this assumption is completely valid. This can be assessed by considering measurements of U-series nuclides in boreholes that extend below the typical weathering zone in order to examine to what extent U-series nuclides are disturbed in the underground, below the regolith. Several studies suggest that where there is no large crustal fluid flow, the U-series decay chain is generally in secular equilibrium at least for the ^{234}U - ^{238}U or ^{230}Th - ^{238}U systems. This has been checked in the case of carbonates (Bourdon et al. 2009) or in the case of granites (Noseck et al. 2008), or even in the case of clays (Pekala et al. 2009). It turns out that for a number of

lithologies, although there are small deviations from secular equilibrium, overall the assumption of initial secular equilibrium for bulk rocks can be considered as valid.

The second condition for deriving the rates and timescale of weathering concerns the assumption that one can make about the laws describing chemical weathering. This has been the subject of some discussion for a number of reasons. Following the early study of Plater et al. (1992), a number of authors have assumed that the release of U-series nuclides follow first order kinetics (Plater et al. 1992; Vigier et al. 2001; Dosseto et al. 2006a, b, c; Chabaux et al. 2003a, b). There are a number of obvious reasons for which such a law is likely to be incorrect, simply because U-series nuclides are prone to redistribution rather than simple release. As U, Th and Ra often interact with mineral surfaces or with organic matter, it is not unreasonable to consider that these elements can be redistributed in weathering profiles (see e.g. Dequincey et al. 2002). Such a redistribution is particularly likely in climate where iron oxides or hydroxides form due to iron oxidation and transport. In such a context, the adsorption of U or Th is likely and the first order law for chemical weathering is probably inadequate and an additional term for describing the evolution of U-series nuclides fractionation is justified (e.g. Granet et al. 2010). However, in other cases, as argued by Chabaux et al. (2008), for systems that are largely undersaturated, first-order kinetics are justified. If the system reaches saturation in a secondary phase, then it is expected that the rates of chemical weathering will be different (Ganor et al. 2007; Maher et al. 2009).

By analyzing the dissolved and suspended load in rivers it is possible to infer both the rate of U release and the time over which this release has taken place. If the timescale of transport is relatively short, then the timescale over which U release has taken place should be equivalent to the residence time of U in soils (Dosseto et al. 2008a, b). As described in Vigier et al. (2001), the process of chemical weathering for the U-series decay chain in the solid (p) can be described by the following equation:

$$\frac{d^{238}U_p}{dt} = -k_8^{238}U_p \quad (27.8)$$

Where $^{238}U_p$ is the number of atoms of ^{238}U in river or soil particles. For ^{234}U , the equation can be written as:

$$\frac{d^{234}U_p}{dt} = \lambda_8^{238}U_p - (k_4 + \lambda_4)^{234}U_p \quad (27.9)$$

Where $^{234}U_p$ represents the number of ^{234}U atoms, λ_4 the decay constant of ^{234}U and k_4 the rate of release of ^{234}U into water of nuclide i. For the dissolved load, it is possible to integrate over the soil thickness, or in other words over the timescale since the inception of weathering in the soils:

$$^{238}U_d = \int_0^\tau k_8^{238}U_p(t)dt \quad (27.10)$$

In the case of ^{238}U - ^{234}U - ^{230}Th system, a system of four non-linear equations with four unknowns (time, k_8 , k_4 and k_0) can be solved. Some more complex forms of this equations have been used in the literature to derive timescales (Dequincey et al. 2002; Vigier et al. 2005; Granet et al. 2007) although the introduction of more complex models is not always warranted. For example, based on the earlier models of Ghaleb et al. (1990), Dequincey et al. (2002) have proposed that the release of U can be described by the following equation:

$$\frac{d^{234}U_p}{dt} = \lambda_8^{238}U_p - (k_4 + \lambda_4)^{234}U_p + F_4 - F_8 \quad (27.11)$$

Where F_i represent a zeroth order additional flux due to input of U per unit of time. This form of model adds an additional level of complexity, thereby providing additional degrees of freedom without having an obvious external constraint to solve the equations. Nevertheless, in some cases, a reasonable solution, albeit non unique can be derived (Granet et al. 2007).

If dissolution is congruent, then the constant k_i should be directly related to the dissolution rate (Maher et al. 2004). Here the dissolution rate is reported in yr^{-1} , while the usual unit for dissolution rates are in $mol\ m^{-2}\ y^{-1}$ (r_{diss}). The relationship between the two dissolution rates can be described by the following equations:

$$r_{diss} = \frac{k_i}{M.S_{BET}} \quad (27.12)$$

Where S_{BET} is the BET surface area in m^2/g , and M the molar mass of the minerals. A compilation of dissolution rates obtained for large river basins based on U-series showed that there is a negative correlation between the rate of dissolution and the timescale of weathering (Fig. 27.4). A similar correlation has also been reported by Maher et al. (2004) and White and Brantley (2003), although the trend based on U-series was offset from that based on dissolution experiments for silicate minerals. The general explanation for this trend is still unclear although several explanations have been proposed. Over long timescales, it could be that the nature of weathering changes due to modification of mineral surface area or composition. For example, the soils with older ages could be characterized by a greater proportion of secondary clay minerals that should dissolve slower. Alternatively, longer soil residence times are expected to correspond to greater soil thickness, which could ultimately lead to slower weathering rates. In principle, the presence of thicker soils is in general an indicator of areas with stable tectonics that should be characterized by a transport-limited erosion regime. Thermodynamic effects (i.e. fluids equilibrating with the solids) and the potential change in hydraulic properties (e.g. reduced permeability) may also play key roles (e.g. Maher 2010).

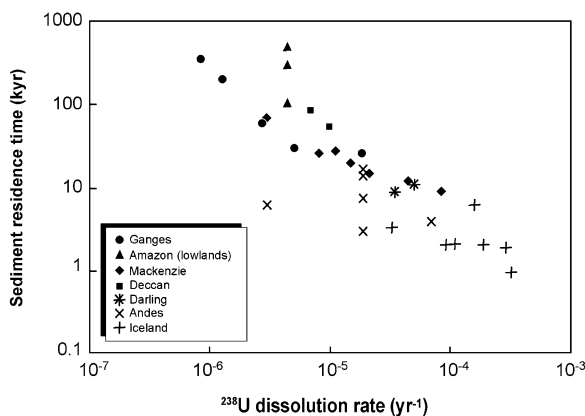


Fig. 27.4 ^{238}U dissolution or leaching rate as a function of the timescale of weathering deduced from U-series disequilibria measured in river waters and/or sediments. The negative trend is close to the one obtained based on the comparison of field and laboratory experiments (White and Brantley 2003). Corresponding references are: Ganges (Granet et al. 2007, 2010); Amazon (Dosseto et al. 2006a, b, c); Mackenzie (Vigier et al. 2001); Deccan (Vigier et al. 2005); Andes (Dosseto et al. 2006a, b, c); Iceland (Vigier et al. 2006). Modified from Dosseto et al. (2008a, b)

In such a regime it is expected that the soil production is actually inversely correlated with soil thickness. Thus, the negative correlation shown in Fig. 27.4 could simply reflect the slower weathering rates expected from thicker soils.

The U-series nuclide data for large river basin can also be used to infer the timescale of chemical weathering, i.e. the average soil residence time at the scale of the whole basin (if the following transport time is short). Although there could be some pitfalls in this approach (see above), a compilation of the data reported so far in the literature lends some confidence in their reliability. First, the soil residence times are positively correlated with independent estimations of soil thickness (not shown here), which would make sense because one would expect that the time spent by a given solid particle in a soil should scale directly with soil thickness. Furthermore, a consideration of several large river basins shows that the sediment residence time is often directly related to the past climates or geological history: mountain areas are generally characterized by short timescale, while stable cratons with constant climatic conditions show long residence time (Dosseto et al. 2006a). The recently glaciated basin of the Mackenzie river (Vigier et al. 2001) is perhaps an exception as it shows relatively short soil residence time. In this particular case, it is expected that the Laurentian ice sheet that covered this area removed existing soils and prevented soil formation until the onset of deglaciation.

27.3.2 Sediment Residence Time and Transport Time

The timescales over which sediments can be transported from their source region to the oceans and the possible implications on the evolution of landscapes is still a key question in geomorphology, despite recent theoretical or analytical developments (e.g. von Blanckenburg 2006). Based on U-series radionuclide measurements, new approaches to derive timescales of sediment production and transport have been proposed and the principles are based again on the fractionation of the U-series decay chain. There have been two main approaches used recently to derive the timescale of sediment production and transport.

27.3.2.1 Comminution Ages of Sediment

The grain size of sediment is in general variable with a generally decreasing size away from the source region. Starting from a massive bedrock, physical and chemical erosion processes will lead to the destruction of the cohesive structure of rocks, thereby leading to the observed grain size distribution (Turcotte 1986). As the grain size approaches micrometers, the fraction of recoiled ^{234}U increases so as to yield a measurable depletion in the grain (more than a few permil). If one is able to estimate reliably the fraction of ^{234}Th ejected due to recoil (f_α), then one can estimate the time since the grains reached their current size, provided uranium in the mineral is uniformly distributed. DePaolo et al. (2006) have coined this time the “comminution age” of the sediment. The methodology has been applied to a number of sediments and shown to yield reasonable estimates for the age of comminution (DePaolo et al. 2006; Dosseto et al. 2010; Lee et al. 2010). For example, Dosseto et al. (2010) have shown that the comminution age of sediments in a semi-arid Australian catchment has been variable over the past 120 kyr and could be explained by variations in the source of sediments, ultimately due to climatic change.

One key aspect of this methodology is to obtain a reliable estimate of the parameter f_α (the fraction of recoiled nuclide), in order to calculate an age. The various approaches have been summarized for example in Maher et al. (2006a, b). One can use the ratio of surface to volume with the equation:

$$f_\alpha = \frac{3\lambda_r L}{2d_p} \quad (27.13)$$

L is the recoil distance of ^{234}Th , d_p is the diameter of the particle, and λ_r is a correction for surface roughness. An alternative is to use the surface area based on BET surface area measurements:

$$f_\alpha = \frac{1}{4} L \cdot S \cdot \lambda_r n \rho_s \quad (27.14)$$

(S being for the specific surface area, and ρ_s is the density, and similar symbols as for 27.13).

This method overestimates the value of f_α because the lengthscale of recoil is much greater than the size of individual N_2 molecules used in the BET experi-

ments. As shown by Bourdon et al. (2009), this effect can be corrected for by using the fractal dimension of the surface and the theoretical model of Semkow (1991). In this case:

$$f_\alpha = \frac{1}{4} \left[\frac{2^{D-1}}{4-D} \left[\frac{a}{R} \right]^{D-2} \right] R \cdot S_{\text{BET}} \rho_s \quad (27.15)$$

where D is the fractal dimension of the surface, a the diameter of the adsorbate molecule (N_2), R the recoil length, ρ_s the density of the solid, and S_{BET} the measured BET surface area.

This latter approach has been further validated by the calculated f_α values used for the dating of ice-core samples (Aciego et al. 2009).

Another aspect of this methodology is that the sediment often needs to be leached prior to U-series analysis and this leaching could lead to some spurious ^{234}U - ^{238}U fractionation in the grain. It is known that leaching can produce excess of ^{234}U in the solution (see above), therefore the leaching procedure needs to be more thoroughly evaluated. It is currently not known whether the leaching with HCl produces spurious fractionation or only removes carbonates or nuclides adsorbed at the mineral surfaces. Last, the determination of comminution ages neglects the possible effect of preferential release of ^{234}U into solution during alteration/dissolution, as highlighted experimentally. If there is preferential release of ^{234}U , the comminution ages probably need to be adjusted (DePaolo et al. 2006; Lee et al. 2010).

Overall, this new method for deriving comminution ages looks very promising and should be further developed and calibrated while paying specific attention to its analytical methodology.

27.3.2.2 Sediment Transport Time

As suggested by Dosseto et al. (2006b), it is possible to investigate the transport time of sediments in rivers based on U-series nuclide fractionation. By measuring ^{238}U - ^{230}Th in the suspended or bed load in rivers along a given river, it is possible to determine the timescale of transport since the ^{238}U - ^{230}Th fractionation is time-dependent. However, some assumptions are required in order to apply this methodology. First, one needs to ascertain the origin of particles; ideally they should

come from the same source region, as particles from multiple sources with various chemical compositions would make this method untractable. Second, one needs to show that the observed ^{238}U - ^{230}Th variation is indeed due to transport or weathering during transport. If this is the case, then a sediment transport time can be calculated. For example Dosseto et al. (2006b) investigated the suspended load of the Amazon river and were able to show that there was a negligible contribution of particles from the plain river while most of the suspended load was derived from the Andes. They also showed that the variation in ^{238}U - ^{230}Th was directly correlated with the depletion in Na relative to Sm as particles were being transported to the river mouth, and that the transport time was increasing up to approximately 20 kyr along the river. This was interpreted as a result of mixing of suspended and remobilized particles. Granet et al. (2007, 2010) also investigated the time scale of sediment transport in Himalayan rivers both on the suspended and bedload fractions and found that the transport time of the bedload was on the order of several 100 kyrs while that of the suspended load was less than 20–25 kyr, which was consistent with the results found by Dosseto et al. (2006b). However, there might be some additional inherent complexities and further tests in other basins would be useful. A complete characterization of the sediments could probably help to ensure that all the conditions for obtaining reliable timescale are fulfilled.

27.4 Small Scale Studies

27.4.1 Soil Age and Production Rate

At a smaller scale, at the scale of a soil or a weathering profile, it is also possible to use U-series disequilibria for estimating the timescale and rate of chemical weathering. Over the last couple of years, this tool has even been investigated for estimating soil production rate.

The pioneering work of Rosholt et al. (1966, 1983) have early established the following observations, based on a systematic study of ^{234}U - ^{238}U and ^{230}Th - ^{238}U in soil samples developed on loess, shales and trachytes, and also by comparing fresh and weathered granites. First, in petrologically fresh granites, U-series nuclides

of concern are in secular equilibrium, within analytical uncertainties. Second, the preferential leaching of ^{234}U occurs before soil development, in the first step of rock alteration. In the following stages of weathering, there is a significant leaching of U relative to Th at the beginning of soil formation, associated with little ^{234}U - ^{238}U fractionation. In contrast, significant ^{234}U - ^{238}U fractionation can be observed in soil horizons where the most mobile U has already been leached away. Third, there can also be uptake of U in the upper soil horizons, that seems to be linked to the occurrence of organic matter and sometimes iron oxides, and that has been interpreted as adsorption of dissolved U which is often enriched in ^{234}U (Fig. 27.1).

From these first set of studies, two main results already emerged: the time dependence of ^{234}U - ^{238}U and ^{230}Th - ^{238}U disequilibria systematics found in solid weathered products, and the relationship between ^{234}U - ^{238}U fractionation and the degree of chemical erosion, responsible for U release from soils. These fundamental observations are the basis for the modelling of U-series in soils that were developed more recently, and which were aimed at constraining (1) the age of the soil and (2) soil or saprolite production rates.

Most U-Th data for soils developed on silicate lithologies lie very near the equiline in the classical ^{238}U - ^{230}Th isochron diagram (e.g. Fig. 27.5a). This implies that, in order to constrain timescales as precisely as possible from U-series disequilibria, isotope ratios need to be measured with high precision techniques, which has been made possible only with the advent of mass spectrometric techniques (see Sect. 27.2).

Various sets of soils developed on granites and granodiorites yield positive correlations passing through the secular equilibrium point in a ^{234}U - ^{238}U versus ^{230}Th - ^{238}U diagram (Fig. 27.5b). This pattern is similar for a series of weathering profiles developed in different climatic and geographical contexts: for example the Kaya laterite, located in Northern Burkina Faso (Dequincey et al. 2002), and soils from the Bega River Basin (SE Australia, Dosseto et al. 2008b). In contrast, various regoliths developed on US shales display a negative trend in the same diagram (Ma et al. 2010).

The model presently used for determining the soil age, or the age of the most recent U mobilisation in a weathering profile is based on equations detailed in Dequincey et al. (2002), and are partly summarized by equation (27.11). In this model, in addition to U release from the soils, U inputs are also taken

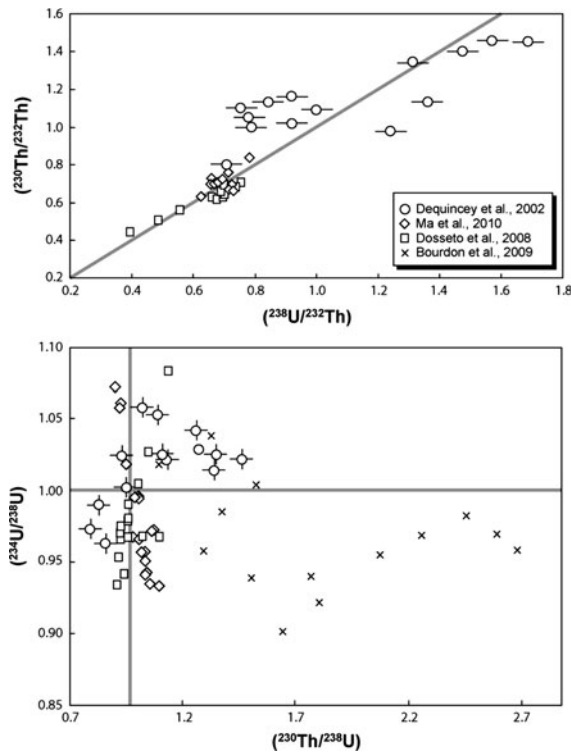


Fig. 27.5 Compilation of recent literature data of U-series disequilibria measured in soil profiles (a) reported in a isochron-type diagram (b) reported in the diagram of $(^{234}\text{U}/^{238}\text{U})$ versus $(^{230}\text{Th}/^{238}\text{U})$ diagram, often used in soil studies (see Chabaux et al. 2003b for a review). Data from Dequincey et al. (2002), Ma et al. (2010) and Dosseto et al. (2008b) correspond to soils developed on silicate lithologies. The Bourdon et al. (2009) data is a profile developed on carbonates

into account. These inputs may come either from atmospheric deposition (Hirose 2011), from soils located upslope, or simply from vertical transfer within a profile. Ages for the African Kaya laterites (Dequincey et al. 2002), regoliths developed on shales (Ma et al. 2010) and saprolite and soils developed on Australian granodiorite (Dosseto et al. 2008a, b) could be determined, using the following equation, describing the time variation of a nuclide j in a soil sample (N_j):

$$\frac{dN_j}{dt} = \lambda_i N_i - \lambda_j N_j + f_j N_{j,0} - k_j N_j \quad (27.16)$$

where λ_i is the decay constant of the parent nuclide, N_i the abundance of the parent nuclide in the sample, λ_j the decay constant of nuclide j , f_j an input coefficient for nuclide j (in yr^{-1}), $N_{j,0}$ the initial nuclide abundance

and k_j for the rate of release into the water of nuclide j (in yr^{-1}) (for simplifying we use k_4 , k_8 , k_0 , k_2 and f_4 , f_8 , f_0 and f_2 for k and f coefficients of ^{234}U , ^{238}U , ^{230}Th and ^{232}Th respectively). In this model, the f_j coefficient represents the rate at which nuclide addition occurs, through chemical illuviation in saprolite, or in soils through dust deposition and from soils located upslope. In all cases, there are more unknowns than input parameters (usually measured activity ratios and U and Th concentrations). Consequently, some or several simplifications need to be made for solving the entire set of equations: (1) no leaching of ^{230}Th (Dequincey et al. 2002); (2) identical k_4/k_8 and f_4/f_8 for several saprolites located along a single slope (Dosseto et al. 2008b); (3) $k_0/k_2 = 1$ and $f_0/f_2 = 1$, i.e. there is no differential fractionation of thorium isotopes during leaching and input (Dosseto et al. 2008b); and (4) constant input and output coefficients (f_8 , f_4 , f_0 , k_8 , k_4 , k_0) for all samples of a single soil profile (Ma et al. 2010).

Soil ages that could be calculated with this method cover a large range, between 7 ka (± 1) and more than 6 Ma (± 0.9) (for the Australian saprolite). The two studies concerning a series of profiles located along a (~ 300 m) hillslope display roughly the same systematics: small residence time close to the ridge and an increase of the soil and saprolite age as a function of the distance from the ridge top (Fig. 27.6). For a saprolite developed from granodiorite, Dosseto et al. (2008b) interpreted these results as an increase in the duration of weathering with distance from the ridge.

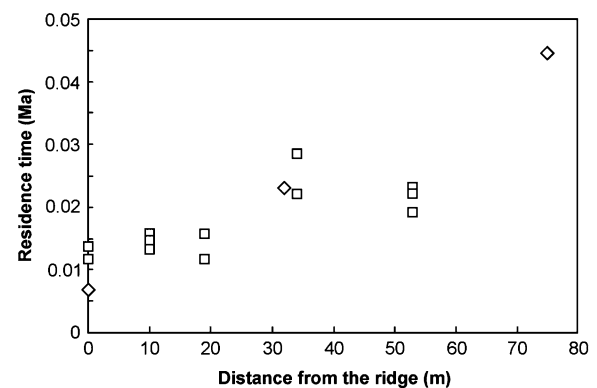


Fig. 27.6 Soil residence time as a function of the distance from the ridge for soils of two different locations (in Australia, Dosseto et al. 2008a, b, squares), and in central Pennsylvania (USA, Ma et al. 2010, diamonds). Both series of profiles show the same trend

In addition, U dissolution rates (k_g) were also found to decrease with increasing distance from the ridge. Two laterites of similar thickness located in the Amazonian craton, and in Northern Burkina Faso respectively yielded ages greater than 300 ka.

With this methodology, the formation rate of saprolite and soils (ε_s) could also be estimated. Indeed, using the age calculated from U-series measurements (τ_s) and the height of a sample, either above the bedrock-saprolite boundary or above the soil-saprolite boundary respectively (h_s), the production rate is:

$$\varepsilon_s = h_s / \tau_s \quad (27.17)$$

By considering the parameter h_s , (i.e. the difference between the sample depth and the bottom limit of the profile), the production rate is found to be independent of physical erosion rate that removes material from the top of the profile. Consequently, the production rate estimated with this methodology corresponds to the rate at which the profile deepens within the bedrock, and there is no need of assuming a balance between physical and chemical erosion (such as for a soil in steady-state which would have remained at a constant thickness during its estimated age). If instead of h_s , the whole profile thickness is considered, then calculated production rates are valid only if the soil rapidly reached a steady-state since the onset of its formation, i.e. only if the integrated soil production has counterbalanced the integrated denudation rates, over the lifetime of the profile.

The few recent studies using U-series for determining profile production rate have shown that soils, saprolite and regolith all display a range of production rate that is relatively large and relatively similar (from a few mm/kyr to ~60 mm/kyr). This is surprising since the various profiles also have significantly different thicknesses and weathering timescales. However, soils, regoliths – as well as saprolites and laterites – are characterized by a systematic inverse trend as a function of the profile age: more “recent” weathering profiles exhibit the largest production rates, in soils and also within saprolite (Fig. 27.7). This is consistent with larger scale studies, where it is found that dissolution rate or uranium leaching coefficient is decreasing as a function of time, or of the sediment age (Fig. 27.4). Chemical erosion is thus thought to be more intensive at the beginning of a profile formation, when the proportion of fresh minerals is still high. These deductions are in agreement with initial observations of Rosholt et al. (1966), although more

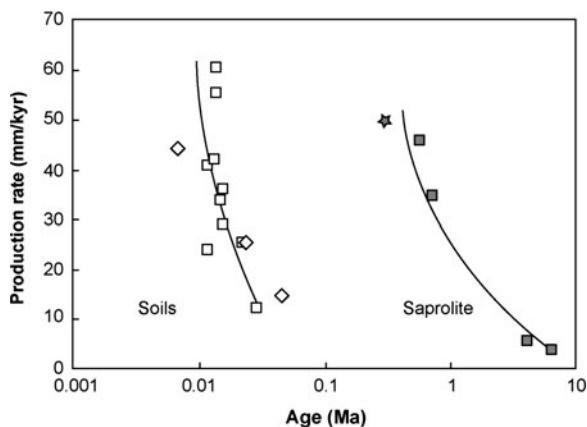


Fig. 27.7 Compilation of production rate and age of soil and saprolite profiles, both determined using U-series disequilibria. White symbols correspond to soil samples (Dosseto et al. 2008b; Ma et al. 2010), and saprolite data are displayed in grey (Mathieu et al. 1995; Dosseto et al. 2008b)

studies of weathering profile are now needed, that should benefit from recent advances in the field.

27.4.2 Weathering in Aquifers

Over the past few years, an effort has also been made to use U-series nuclides for determining weathering rates and fluid flow within aquifers. Groundwaters are characterized by U-series activity ratios that are generally distinct from river water signatures. For example, ($^{234}\text{U}/^{238}\text{U}$) ratios can be extremely high in some aquifers (see review in Ivanovich and Harmon 1992; Osmond and Coward 2000), and this can help their contribution to river waters to be quantified (e.g. Durand et al. 2005; Riotte and Chabaux 1999; Chabaux et al. 2001; Riotte et al. 2003). This was the case in a systematic study of river and ground waters of the Rhine graben (Durand et al. 2005). The coupling of ^{234}U - ^{238}U disequilibria and $^{87}\text{Sr}/^{86}\text{Sr}$ show that all the stream samples can be explained by a mixing of three types of waters (deep, shallow and alluvial).

In parallel with these studies focusing on the origin of elements carried in river waters, transport modelling has been developed and applied in more complete and sophisticated ways to single aquifer systems (see for a detailed review Porcelli and Swarzenski 2003; Porcelli 2008). Since the early 1980, simple mathematical treatments of aquifer models have been

developed for constraining rates of weathering, adsorption/desorption, and migration of some specific radionuclides (e.g. Krishnaswami et al. 1982; Davidson and Dickson 1986; Ku et al. 1992; Luo et al. 2000). These modelling approaches could recently be further constrained due to improved precision on isotope ratios, and the ability to measure substantial number of low level samples – using MC-ICP-MS. Indeed, until a decade ago, most of the data of U-series nuclides in aquifers were obtained using counting techniques, and were associated with significant uncertainties. High precision measurements were developed over the past ten years, and only a few aquifer systems have been studied thus far. These studies have shown that it was possible to provide, for a few case studies, some quantitative constraints on weathering rates within the aquifer or the vadose zone, and/or other parameters such as fluid flow and the age of the system. For example, based on the distribution of U-Th series radionuclides in an unconfined aquifer, Tricca et al. (2001) proposed that the source of ^{222}Rn is mainly derived from the precipitation of ^{232}Th and ^{230}Th on surface coating since the formation of the aquifer. This surface coating is found to account for $\sim 10\%$ of the total Th content of the rock.

In summary, different approaches have been developed, based on the same general equation, of a one dimensional advective transport along a groundwater flow path:

$$\left(\frac{\partial C_w^i}{\partial t}\right) + v\left(\frac{\partial C_w^i}{\partial x}\right) = R_\alpha + R_{diss} + R_{des} - R_{ads} + \lambda_p C_w^p - \lambda_i C_w^i \quad (27.18)$$

In this equation, C_w^i represents the concentration of a nuclide i in water, and C_w^p the concentration of its direct parent within its U-decay series. R_α represents the α -recoil loss rate. It is therefore a function of C_s^p , i. e. the concentration of the parent nuclide in the solid, and f_α (see Sect. 27.3.2.1). R_{diss} is the dissolution term, and is function of the dissolution coefficient for the nuclide (i) and C_s^i , the concentration of (i) in the solid. In Tricca et al. (2000, 2001) and Reynolds et al. (2003), for simplification purposes, the coefficient of dissolution is assumed to be the same for various nuclides such as ^{234}U , ^{238}U and ^{232}Th . The desorption term (R_{des}) is a function of a desorption coefficient and C_s^i , and, similarly, the adsorption term (R_{ads}) is a function of an adsorption coefficient (and C_w^i). The

two other terms in the right hand side of equation (27.18) represent input from decay of the radioactive parent present in water, and output due the radioactive decay of nuclide (i) of concern.

The differences between the various published models reside first in the number of aquifer phases taken into account. In most cases, except in Hubert et al. (2006), the solid phase is not analysed. However, a fine layer located at the grain surface is now included in the modelling. This surface layer is considered to “collect” the nuclides ejected by the solid phase due to α -recoil, and the dissolved nuclides that get adsorbed. Tricca et al. (2001) estimated the residence time of Th in the surface coating to be $\sim 3,000$ yr while in the water it is ~ 1 h. The second key point is the modelling of the recoil fraction, as described in detail in Sect. 27.3.2.1.

Even when considering the three aquifer phases (solid, surface layer and water), the number of unknowns always exceeds the number of measured parameters (i.e. activity ratios and nuclide concentrations). As a consequence, the resolution of such models necessarily requires some basic assumptions, and/or, as recently developed by Maher et al. (2006a, b), the coupling with other isotope systems (i.e. Sr isotopes). The first set of studies assumed a steady-state: it was supposed that no evolution of the nuclide concentration as a function of time occurs at the time of the water sampling (Tricca et al. 2000; Reynolds et al. 2003). The number of unknowns was also reduced by considering that all nuclides were released into water at the same rate (w). In other words, no ^{234}U - ^{238}U fractionation occurred due to leaching/dissolution. Finally, it was assumed that all the isotope and chemical signatures of the waters are the result of in-situ weathering, with no significant input from the vadose zone for example. Under these conditions, $(^{234}\text{U}/^{238}\text{U})_w$ activity ratio in the water is directly related to the ratio of uranium dissolution coefficient (w_8) and the α -recoil degree ($f_\alpha =$ fraction of rock ^{234}Th ejected into the water). If f_α can be estimated independently (from geometrical consideration for example, see Sect. 27.3.2.1), then w_8 can be determined:

$$\left(^{234}\text{U}/^{238}\text{U}\right)_w = 1 + f_\alpha \lambda_4 / w_8 \quad (27.19)$$

From this equation, it appears that particularly high $(^{234}\text{U}/^{238}\text{U})_w$ ratios, such as those found in the aquifer of Ojo Alamo Aquifer (New Mexico), located in an

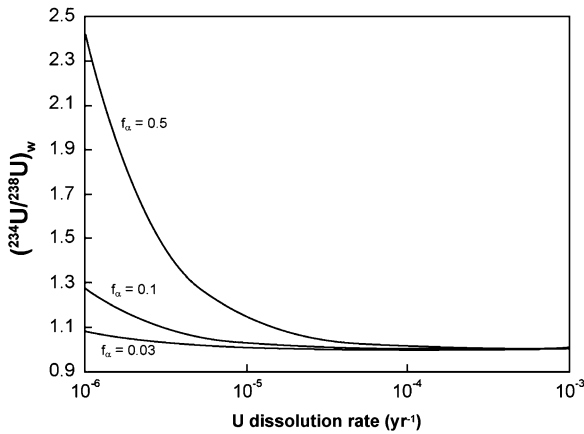


Fig. 27.8 Theoretical dependence of groundwater ($^{234}\text{U}/^{238}\text{U}$)_w as a function of the U dissolution rate assuming a steady-state and no ^{234}U - ^{238}U fractionation during dissolution (see equation 19). High ($^{234}\text{U}/^{238}\text{U}$) in old aquifer waters can thus be explained by low dissolution rates and high recoil effects (high f_{α} values)

arid environment (Reynolds et al. 2003), can result from low weathering rates (resulting in low w_8), and strong α -recoil effects (Fig. 27.8).

However, over short distances, ($^{234}\text{U}/^{238}\text{U}$)_w is expected to evolve as a function of the distance from the recharge zone. In that case, if one still assumes a steady-state, ($^{234}\text{U}/^{238}\text{U}$)_w is found to be a function of w_i/v (the dissolution rate over the water velocity ratio). Thus, further constraints on the dissolution rate can be obtained either by a direct estimation of the water infiltration flux, or by coupling with other isotope systems, such as Sr isotopes (see Maher et al. 2006a, b; Singleton et al. 2006). Here, the high ($^{234}\text{U}/^{238}\text{U}$)_w values found in aquifers were explained by low infiltration rates. When the water velocity increases, the ($^{234}\text{U}/^{238}\text{U}$) of the pore water is expected to decrease.

In the case of a non steady-state approach, such as developed in Hubert et al. (2006), ($^{234}\text{U}/^{238}\text{U}$)_w is found to vary as a function of the water velocity and f_{α} , but also as a function of time, the initial activity ratio of the solid (at $t = 0$, $x = 0$), the distance from catchment divide, and the uranium distribution coefficient (resulting from adsorption and desorption processes). It can be seen that activity ratios measured in aquifer waters are not significantly affected by the activity of nuclides in the surface layer. Indeed, this layer is in steady-state regardless of adsorption and desorption processes (see Hubert et al. 2006 for more details), having therefore no influence on the water composition.

The study of the aquifer solid phase can provide important constraints on the modelling of the U-series nuclides. First, considering that the solid phase has also reached a steady-state, Maher et al. (2006a, b) have shown that its ($^{234}\text{U}/^{238}\text{U}$)_s is roughly equal to $(1-f_{\alpha})$, assuming no ^{234}U - ^{238}U fractionation linked to dissolution. Consequently, for old sediments (typically >1 Ma), a measurement of their ($^{234}\text{U}/^{238}\text{U}$)_s leads to a direct estimation of f_{α} . However, this technique is applicable only if f_{α} is significantly different from 1 (within uncertainties), i.e. for grains lower than a certain size (estimated by the authors to be $\sim 100\mu\text{m}$). If steady-state has not been reached, ($^{234}\text{U}/^{238}\text{U}$)_s of the solid is simply a function of time and of the α -recoil term (f_{α}):

$$\left(\frac{^{234}\text{U}}{^{238}\text{U}}\right)_s = (1 - f_{\alpha})(1 - e^{-\lambda_4 t}) + e^{-\lambda_4 t} \quad (27.20)$$

assuming that no uranium isotope fractionation occurs during dissolution, and that the initial solid (at $t = 0$) was in secular equilibrium (Hubert et al. 2006). Again, the role of the surface layer is negligible, since the fraction of this surface is very small compared to the typical grain size. Equation (27.20) shows that, if an independent estimation of f_{α} can be obtained, the age of the aquifer can be determined (Fig. 27.9).

Overall, recent studies of aquifers in carbonate (Bourdon et al. 2009) and silicate lithologies show that, with a few assumptions, it is possible to estimate

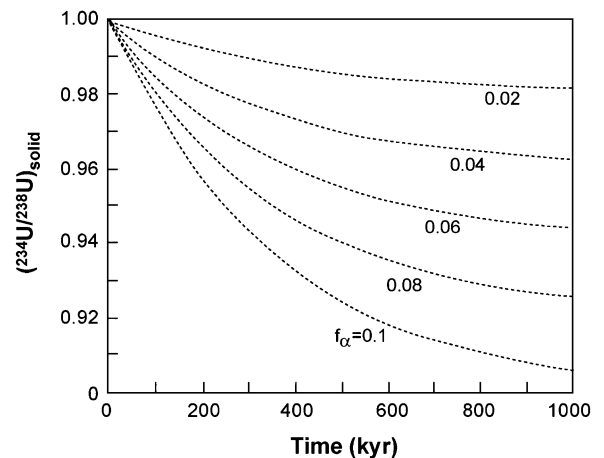


Fig. 27.9 Theoretical evolution of ($^{234}\text{U}/^{238}\text{U}$)_s in an aquifer rock matrix versus the age of the rock since the beginning of water percolation. Model curves are labeled with f_{α} values. Modified from Hubert et al. (2006)

the chemical erosion rate, based on U-series nuclides measured in water and solid samples, even in the case of a non steady-state system. It appears that, as well as for all studies concerning U-series nuclides in surficial environment, there is now a strong need for independent and precise estimates of the α -recoil term (f_α), and for a better understanding of nuclide fractionation during chemical erosion and leaching of minerals.

27.5 Conclusion and Future Directions

Over the past few years, several nuclides of the U-series have emerged as powerful tracers of chemical erosion at various scales, including those pertinent to continents, basins, soils and aquifers. This is essentially due to new mass spectrometric developments permitting high precision measurements of low concentration samples (typically water samples). Furthermore, these analytical methods have triggered the development of new and more sophisticated transport and erosion models. It must be pointed out, however, that recent studies all highlight that in the future it will be necessary to have a better determination of recoil effects at the mineral scale, and to have a better knowledge of nuclide fractionation and redistribution during chemical alteration and transport. To this end, experimental studies should help to quantify key parameters such as the leaching coefficients. In natural systems, coupling of U-series disequilibria with other tools such as ^{10}Be , or Sr and Nd isotopes for example, has been little investigated thus far, nevertheless this is a promising approach in the sense that both methods provide independent and complementary quantitative information.

Despite the uncertainties highlighted, some systematics are already apparent, such as the major role of recent climatic variations and land use on physical erosion rates presently estimated for some basins. This has been observed in North American cratons, but also in mountainous areas such as the Andes. Another concept that has emerged is the link between the age of a profile and its production rate. Chemical erosion rates are high at the beginning of soil formation. A similar relationship is found for sediments carried by rivers: old sediments are located in areas where chemical erosion rates (and therefore U dissolution rates) are lower. Since high precision data are still quite limited, these trends must of course be

refined. Nevertheless, if they are confirmed they could greatly improve our understanding/modelling of the recent evolution of continental chemical erosion and its effect on the transfer of weathered material to the sea, and in consequence on ocean chemistry.

Acknowledgements We thank the two reviewers, Kate Maher and Anthony Dosseto, for their helpful comments on this chapter. We are also grateful for the constructive comments of the Editor, Mark Baskaran.

References

- Aciego SM, Bourdon B, Lupker M, Rickli J (2009) A new procedure for separating and measuring radiogenic isotopes (U, Th, Pa, Ra, Sr, Nd, Hf) in ice cores. *Chem Geol* 266:194–204
- Ames LL, McGarrah JE, Walker BA, Salter PF (1983) Uranium and radium sorption on amorphous ferric oxyhydroxide. *Chem Geol* 40:135–148
- Andersen MB, Stirling CH, Potter EK, Halliday AN (2004) Toward epsilon levels of measurement precision on U-234/U-238 by using MC-ICPMS. *Int J Mass Spec* 237:107–118
- Andersen MB, Stirling CH, Potter EK, Halliday AN, Blake SG, McCulloch MT, Ayling BF, O'Leary M (2008) High-precision U-series measurements of more than 500,000 year old fossil corals. *Earth Planet Sci Lett* 265:229–245
- Andersen MB, Erel Y, Bourdon B (2009) Experimental evidence for ^{234}U - ^{238}U fractionation during granite weathering with implications for $^{234}\text{U}/^{238}\text{U}$ in natural waters. *Geochim Cosmochim Acta* 73:4124–4141
- Ball L, Sims KWW, Schwieters J (2008) Measurements of $^{234}\text{U}/^{238}\text{U}$ and $^{230}\text{Th}/^{232}\text{Th}$ in volcanic rocks using the Neptune MC-ICP-MS. *JAAS* 23:173–180
- Becquerel AH (1896) On the invisible rays emitted by phosphorescent bodies. *CR Séances Acad Sci* 122:501–503
- Bourdon B, Turner S, Henderson GM, Lundstrom CC (2003) Introduction to U-series geochemistry. In: Bourdon B, Henderson GM, Lundstrom CC, Turner SP (eds) Uranium-series geochemistry, vol 52. Geochemical Society – Mineralogical Society of America, Washington, DC, pp 1–21
- Bourdon B, Bureau S, Andersen MB, Pili E, Hubert A (2009) Weathering rates from top to bottom in a carbonate environment. *Chem Geol* 258:275–287
- Bruno J, de Pablo J, Duro L, Figuerola E (1995) Experimental study and modeling of the U(VI)-Fe(OH)₃ surface precipitation/coprecipitation equilibria. *Geochim Cosmochim Acta* 59:4113–4123
- Chabaux F, Riotte J, Clauer N, France-Lanord C (2001) Isotopic tracing of the dissolved U fluxes of Himalayan rivers: implications for present and past U budgets of the Ganges-Brahmaputra system. *Geochim Cosmochim Acta* 65(19):3201–3217
- Chabaux F, Dequincey O, Leveque JJ, Leprun JC, Clauer N, Riotte J, Paquet H (2003a) Tracing and dating recent chemical transfers in weathering profiles by trace-element geochemistry and U-238-U-234-Th-230 disequilibria: the

- example of the Kaya lateritic toposequence (Burkina-Faso). *CR Geosci* 335:1219–1231
- Chabaux F, Riotte J, Dequincey O (2003b) U-Th-Ra fractionation during weathering and river transport. In: Bourdon B, Henderson GM, Lundstrom CC, Turner SP (eds) *Uranium-series geochemistry*, vol 52. Geochemical Society – Mineralogical Society of America, Washington, DC, pp 533–576
- Chabaux F, Bourdon B, Riotte J (2008) U-series geochemistry in weathering profiles, river waters and lakes. In: Krishnaswami S, Cochran JK (eds) *U/Th series radionuclides in aquatic systems*, vol 13, Radioactivity in the environment. Elsevier, New York, NY, pp 49–104
- Chen JH, Edwards RL, Wasserburg GJ (1986) ^{238}U , ^{234}U and ^{232}Th in seawater. *Earth Planet Sci Lett* 80:241–251
- Chen C, Wang X (2007) Sorption of Th (IV) to silica as a function of pH, humic/fulvic acid, ionic strength, electrolyte type. *Appl Radiat Isot* 65:155–163
- Dähn R, Scheidegger AM, Manceau A, Curti E, Baeyens B, Bradbury MH, Chateigner D (2002) Th uptake on montmorillonite: a powder and polarized extended X-ray absorption fine structure (EXAFS) study. *J Colloid Interface Sci* 249:8–21
- Davidson MR, Dickson BL (1986) A porous flow model for steady-state transport of radium in ground waters. *Water Resour Res* 22:34–44
- DePaolo DJ, Maher K, Christensen JN, McManus J (2006) Sediment transport time measured with U-series isotopes: results from ODP North Atlantic drift site 984. *Earth Planet Sci Lett* 248:394–410
- Degueldre C, Kline A (2007) Study of thorium association and surface precipitation on colloids. *Earth Planet Sci Lett* 264:104–113
- Dequincey O, Chabaux F, Clauer N, Sigmarsson O, Liewig N, Leprun JC (2002) Chemical mobilizations in laterites: evidence from trace elements and ^{238}U - ^{234}U - ^{230}Th disequilibrium. *Geochim Cosmochim Acta* 66:1197–1210
- Dosseto A, Hesse PP, Maher K, Fryirs K, Turner S (2010) Climatic and vegetation control on sediment dynamics during the last glacial cycle. *Geology* 38:395–398
- Dosseto A, Bourdon B, Turner S (2008a) Uranium-series isotopes in river materials: Insights into the timescales of erosion and sediment transport. *Earth Planet Sci Lett* 265:1–17
- Dosseto A, Turner SP, Chappell J (2008b) The evolution of weathering profiles through time: new insights from uranium-series isotopes. *Earth Planet Sci Lett* 274:359–371
- Dosseto A, Bourdon B, Gaillardet J, Allègre CJ, Filizola N (2006a) Timescale and conditions of chemical weathering under tropical climate: study of the Amazon basin with U-series. *Geochim Cosmochim Acta* 70:71–89
- Dosseto A, Bourdon B, Gaillardet J, Maurice-Bourgoin L, Allègre CJ (2006b) Weathering and transport of sediments in the Bolivian Andes: time constraints from uranium-series isotopes. *Earth Planet Sci Lett* 248(3–4):759–771
- Dosseto A, Turner S, Douglas GB (2006c) Uranium-series isotopes in colloids and suspended sediments: timescale for sediment production and transport in the Murray-Darling River system. *Earth Planet Sci Lett* 246:418–431
- Durand S, Chabaux F, Rihs S, Düringer P, Elsass P (2005) U isotope ratios as tracers of groundwater inputs into surface waters: Example of the Upper Rhine hydrosystem. *Chem Geol* 220:1–19
- Duff MC, Coughlin JU, Hunter DB (2002) Uranium co-precipitation with iron oxide minerals. *Geochim Cosmochim Acta* 66:3533–3547
- Edwards RL, Chen JH, Wasserburg GJ (1987) ^{238}U - ^{234}U - ^{230}Th - ^{232}Th systematics and the precise measurement of time over the past 500,000 years. *Earth Planet Sci Lett* 81:175–192
- Fietzke J, Liebtrau V, Eisenhauer A, Dullo C (2005) Determination of uranium isotope ratios by multi-static MIC-ICP-MS: method and implementation for precise U- and Th-series isotope measurements. *JAAS* 20:395–401
- Fleischer RL (1980) Isotopic disequilibrium of uranium – alpha-recoil damage and preferential solution effects. *Science* 207(4434):979–981
- Fleischer RL, Raabe OG (1978) Recoiling alpha-emitting nuclei – mechanisms for uranium-series disequilibrium. *Geochim Cosmochim Acta* 42(7):973–978
- Giammar DE, Hering JG (2001) Timescale for sorption-desorption and surface precipitation of uranyl on goethite. *Environ Sci Technol* 35:3332–3337
- Goldstein SJ, Stirling CH (2003) Techniques for measuring uranium series nuclides: 1992–2002. In: Bourdon B, Henderson GM, Lundstrom CC, Turner SP (eds) *Uranium-series geochemistry*, vol 52. Geochemical Society – Mineralogical Society of America, Washington, DC, pp 23–57
- Ganor J, Lu P, Zheng Z, Zhu C (2007) Bridging the gap between laboratory measurements and field estimations of weathering using simple calculations. *Environ Geol* 53:599–610
- Geibert W, Usbeck R (2004) Adsorption of thorium and protactinium onto different particle types: experimental findings. *Geochim Cosmochim Acta* 68:1489–1501
- Ghaleb B, Hillaire-Marcel C, Causse C, Gariépy C, Vallières S (1990) Fractionation and recycling of U and Th isotopes in a semiarid endoreic depression of central Syria. *Geochim Cosmochim Acta* 54:1025–1035
- Granet M, Chabaux F, Stille P, France-Lanord C, Pelt E (2007) Time-scales of sedimentary transfer and weathering processes from U-series nuclides: clues from the Himalayan rivers. *Earth Planet Sci Lett* 261:389–406
- Granet M, Chabaux F, Stille P, Dosseto A, France-Lanord C, Blaes E (2010) U-series disequilibria in suspended river sediments and implication for sediment transfer time in alluvial plains: the case of the Himalayan rivers. *Geochim Cosmochim Acta* 74:2851–2865
- Heimsath AM, Dietrich WE, Nishizumi K, et al. (1997) The soil production function and landscape equilibrium. *Nature* 388:358–361
- Hellstrom H (2003) Rapid and accurate U/Th dating using parallel ion-counting multi-collector ICP-MS. *JAAS* 18:1346–1351
- Hewawasam T, von Blanckenburg F, Schaller M, Kubik PW (2003) Increase of human over natural erosion rates in tropical highlands constrained by cosmogenic nuclides. *Geology* 31:597–600
- Hidaka H, Horie K, Gauthier-Lafaye F (2007) Transport and selective uptake of radium into natural clay minerals. *Earth Planet Sci Lett* 264:167–176

- Huang WH, Walker RM (1967) Fossil alpha-particle recoil tracks: a new method of age determination. *Science* 155: 1103–1106
- Hubert A, Bourdon B, Pili E, Meynadier L (2006) Transport of radionuclides in an unconfined chalk aquifer inferred from U-series disequilibria. *Geochim Cosmochim Acta* 70:5437–5454
- Hussain N, Lal D (1986) Preferential solution of ^{234}U from recoil tracks and $^{234}\text{U}/^{238}\text{U}$ radioactive disequilibrium in natural waters. *Proc Ind Acad Sci (Earth Planet Sci)* 95:245–263
- Ivanovich M, Harmon RS (1992) Uranium-series disequilibrium: applications to earth, marine, and environmental sciences. Oxford University Press, Oxford, p 910
- Kigoshi K (1971) Alpha recoil thorium-234: dissolution into water and uranium-234/uranium-238 disequilibrium in nature. *Science* 173:47–49
- Krishnaswami S, Graustein WC, Turekian KK, Dowd JF (1982) Radium, thorium and radioactive lead isotopes in groundwaters: application to in situ determination of adsorption-desorption rate constants and retardation factors. *Water Res* 18:1663–1675
- Ku T-L, Luo S, Leslie BW, Hammond DE (1992) Decay-series disequilibrium applied to the study of rock-water interaction and geothermal system. In: Ivanovich M, Harmon RS (eds) Uranium-series disequilibrium: applications to earth, marine, and environmental sciences. Clarendon, Oxford, pp 631–668
- Latham AG, Schwarz HP (1987) On the possibility of determining rates of removal of uranium from crystalline igneous rocks using U-series disequilibria-I: a U-leach model and its applicability to whole-rock data. *App Geochem* 2:55–65
- Lazar B, Weinstein Y, Paytan A, Magal E, Bruce B, Kolodny Y (2008) Ra and Th adsorption coefficients in lakes – Lake Kinneret (Sea of Galilee) “natural experiment. *Geochim Cosmochim Acta* 72:3446–3459
- Lee VE, DePaolo DJ, Christensen JN (2010) Uranium-series comminution ages of continental sediments: case study of a Pleistocene alluvial fan. *Earth Planet Sci Lett* 296:244–254
- Luo SD, Ku T-L, Roback R, Murrell M, McLing TL (2000) In-situ radionuclide transport and preferential groundwater flows at INEEL (Idaho): decay-series disequilibrium studies. *Geochim Cosmochim Acta* 64:867–881
- Luo X, Rehkamper M, Lee DC, Halliday AN (1997) High precision $^{230}\text{Th}/^{232}\text{Th}$ and $^{234}\text{U}/^{238}\text{U}$ measurements using energy-filtered ICP magnetic sector multiple collector mass spectrometry. *Int J Mass Spectrom Ion Process* 171:105–117
- Ma L, Chabaux F, Pelt E, Blaes E, Jin L, Brantley S (2010) Regolith production rates calculated with uranium-series isotopes at Susquehanna/Shale Hills Critical Zone Observatory. *Earth Planet Sci Lett* 297:211–225
- Maher K, DePaolo DJ, Lin C-F (2004) Rates of silicate dissolution in deep-sea sediment: in situ measurement using $^{234}\text{U}/^{238}\text{U}$ of pore fluids. *Geochim Cosmochim Acta* 68: 4629–4648
- Maher K, DePaolo DJ, Christensen JN (2006a) U-Sr isotopic speedometer: fluid flow and chemical weathering rates in aquifers. *Geochim Cosmochim Acta* 70:4417–4435
- Maher K, Steefel CI, DePaolo DJ, Viani BE (2006b) The mineral dissolution rate conundrum: insights from reactive transport modeling of U isotopes and pore fluid chemistry in marine sediments. *Geochim Cosmochim Acta* 70: 337–363
- Maher K, Steefel CI, White AF et al. (2009) The role of reaction affinity and secondary minerals in regulating chemical weathering rates at the Santa Cruz soil chronosequence, California. *Geochim Cosmochim Acta* 73:1804–2831
- Maher K (2010) The dependence of chemical weathering rates on fluid residence time. *Earth Planet Sci Lett* 294:101–110
- Manhès G (1981) Développement de l'ensemble chronométrique U-Th-Pb: contribution à la chronologie initiale du système solaire Thèse d'état, Université Paris 6, Paris
- Mathieu D, Bernat M, Nahon D (1995) Short-lived U and Th isotope distribution in a tropical laterite derived from granite (Pitinga river basin, Amazonia, Brazil): application to assessment of weathering rate. *Earth Planet Sci Lett* 136: 703–714
- Noseck U, Brassler T, Suksi J, Havlová V, Hercik M, Denecke MA, Förster H-J (2008) Identification of uranium enrichment scenarios by multi-method characterisation of immobile uranium phases *Phys. Chem Earth* 33:969–977
- Osmond JK, Coward JB (2000) U-series nuclides as tracers in groundwater hydrology. In: Cook P, Herczeg A (eds) Environmental tracers in subsurface hydrology. Kluwer, Boston, pp 290–333
- Pekala M, Kramers JD, Waber HN, Gimmi T, Alt-Epping P (2009) Transport of ^{234}U in the Opalinus Clay on centimetre to decimetre scales. *App Geochem* 24:138–152
- Pelt E, Chabaux F, Innocent C, Navarre-Sitcher A, Sak PB, Brantley SL (2008) Uranium-Thorium chronometry of weathering rinds: rock alteration rate and paleo-isotopic record of weathering fluids. *Earth Planet Sci Lett* 276:98–105
- Plater AJ, Ivanovich M, Dugdale RE (1992) Uranium series disequilibrium in river sediments and waters: the significance of anomalous activity ratios. *Appl Geochem* 7: 101–110
- Plater AJ, Dugdale RE, Ivanovich M (1994) Sediment yield determination using uranium-series radionuclides: the case of The Wash and Fenland drainage basin, eastern England. *Geomorphology* 11(1):41–56
- Porcelli D, Andersson PS, Baskaran M, Wasserburg GJ (2001) Transport of U- and Th-series nuclides in a Baltic Shield watershed and the Baltic Sea. *Geochim Cosmochim Acta* 65:2439–2459
- Porcelli D, Andersson PS, Wasserburg GJ, Ingri J, Baskaran M (1997) The importance of colloids and mires for the transport of uranium isotopes through the Kalix River watershed and Baltic Sea. *Geochim Cosmochim Acta* 61:4095–4113
- Porcelli D, Swarzenski PW (2003) The behavior of U- and Th-series nuclides in groundwater. In: Bourdon B, Henderson GM, Lundstrom CC, Turner SP (eds) Uranium-series geochemistry, vol 52. Mineralogical Society of America – Geochemical Society, Washington, DC, pp 317–361
- Porcelli D (2008) Investigating groundwater processes using U- and Th-series nuclides. In: Krishnaswami S, Cochran JK (eds) U-Th series nuclides in aquatic systems, vol 13. Elsevier, New York, NY, pp 105–154
- Reiller P, Moulin V, Casanova F, Dautel C (2002) Retention behaviour of humic substances onto mineral surfaces and consequences upon thorium (IV) mobility: case of iron oxides. *Appl Geochem* 17:1551–1562
- Reynolds BC, Wasserburg GJ, Baskaran M (2003) The transport of U- and Th-series nuclides in sandy confined aquifers. *Geochim Cosmochim Acta* 67:1955–1972

- Riotte J, Chabaux F (1999) $^{234}\text{U}/^{238}\text{U}$ Activity ratios in freshwaters as tracers of hydrological processes: the Strengbach watershed (Vosges, France). *Geochim Cosmochim Acta* 63:1263–1275
- Riotte J, Chabaux F, Benedetti M, Dia A, Gerard M, Boulegue J, Etame J (2003) Uranium colloidal transport and origin of the U-234-U-238 fractionation in surface waters: new insights from Mount Cameroon. *Chem Geol* 202:365–381
- Rojo I, Seco F, Rovira M, Giménez J, Cervantes G, Martí V, de Pablo J (2009) Thorium sorption onto magnetite and ferrihydrite in acidic conditions. *J Nucl Mater* 385:474–478
- Rosholt JN, Doe BR, Tastumoto M (1966) Evolution of the isotopic composition of uranium and thorium in soil profiles. *Geol Soc Am Bull* 77:987–1004
- Rosholt JN (1983) Isotopic composition of uranium and thorium in crystalline rocks. *J Geophys Res* 88:7315–7330
- Rutherford E, Soddy F (1903) The radioactivity of uranium. *Philosoph Mag* 5:441–445
- Semkow TM (1991) Fractal model of radon emanation from solids. *Phys Rev Lett* 66:3012–3015
- Sims KW, Gill JB, Dossato A, Hoffmann DL, Lundstrom CC, Williams RW, Ball L, Tollstrup D, Turner S, Prytulak J, Glessner JJ, Standish J, Elliott T (2008) An Inter-Laboratory Assessment of the Thorium Isotopic Composition of Synthetic and Rock Reference Materials. *Geostand Geoanal Res* 32:65–91
- Singer DM, Maher K, Brown GE Jr (2009) Uranyl-chlorite sorption/desorption: evaluation of different U(VI) sequestration processes. *Geochim Cosmochim Acta* 73:5989–6007
- Singleton MJ, Maher K, DePaolo DJ, Conrad ME, Dresel PE (2006) Dissolution rates and vadose zone drainage from strontium isotope measurements of groundwater in the Pasco Basin, WA unconfined aquifer. *J Hydrol* 321:39–58
- Tricca A, Porcelli D, Wasserburg GJ (2000) Factors controlling the groundwater transport of U, Th, Ra and Rn. *Proc Ind Acad Sci (Earth Planet Sci)* 109:95–108
- Tricca A, Wasserburg GJ, Porcelli D, Baskaran M (2001) The transport of U- and Th-series nuclides in a sandy unconfined aquifer. *Geochim Cosmochim Acta* 65:1187–1210
- Tripathy GR, Singh SK, Krishnaswami S (2011) Sr and Nd Isotopes as Tracers of Chemical and Physical Erosion, *Handbook of environmental Isotope Geochemistry*, Springer, Ed: M. Baskaran, ch. 26, this book.
- Turcotte DL (1986) Fractals and fragmentation. *J Geophys Res* 91:1921–1926
- Turner S, Van Calsteren P, Vigier N, Thomas L (2001) Determination of thorium and uranium isotope ratios in low-concentration geological materials using a fixed multi-collector-ICP-MS. *JAAAS* 16:612–615
- Turner S, Hawkesworth C, Rogers N, Bartlett J, Worthington T, Hergt J, Pearce J, Smith I (1997) ^{238}U - ^{230}Th disequilibria, magma petrogenesis, and flux rates beneath the depleted Tonga-Kermadec, island arc. *Geochim Cosmochim Acta* 61:4855–4884
- Vance D, Teagle DAH, Foster GL (2009) Variable Quaternary chemical weathering fluxes and imbalances in marine geochemical budgets. *Nature* 458:493–496
- Viers J, Dupre B, Polve M, Schott J, Dandurand JL, Braun JJ (1997) Chemical weathering in the drainage basin of a tropical watershed (Nsimi-Zoetele site, Cameroon): comparison between organic-poor and organic-rich waters. *Chem Geol* 140:181–206
- Vigier N, Bourdon B, Turner S, Allègre CJ (2001) Erosion timescales derived from U-decay series measurements in rivers. *Earth Planet Sci Lett* 193:549–563
- Vigier N, Bourdon B, Turner S, Van Calsteren P, Subramanian V, Dupré B, Allègre CJ (2005) Parameters influencing the duration and rates of weathering deduced from U-series measured in rivers: the Deccan Trap region (India). *Chem Geol* 219:69–91
- Vigier N, Burton KW, Gislason SR, Rogers NW, Duchene S, Thomas L, Hodge E, Schaefer B (2006) The relationship between riverine U-series disequilibria and erosion rates in a basaltic terrain. *Earth Planet Sci Lett* 249(3–4):258–273
- Von Blanckenburg F (2006) The control mechanisms of erosion and weathering at basin scale from cosmogenic nuclides in river sediment. *Earth Planet Sci Lett* 242:224–239
- White AF, Brantley SL (2003) The effect of time on the weathering of silicate minerals: why do weathering rates differ in the laboratory and field? *Chem Geol* 202:479–506
- Willett IR, Bond WJ (1995) Sorption of manganese, uranium, and radium by highly weathered. *Soils J Environ Qual* 24:834–845
- Hirose K (2011) Uranium, thorium and anthropogenic radionuclides as atmospheric tracers. In: Baskaran M (ed) *Handbook of environmental isotope geochemistry*. Springer, Heidelberg
- Tripathy GR, Singh SK, Krishnaswami S (2011) Sr and Nd Isotopes as tracers of chemical and physical erosion. In: Baskaran M (ed) *Handbook of environmental isotope geochemistry*. Springer, Heidelberg

Part III
Isotopes as Tracers of Atmospheric Processes

Chapter 28

Applications of Cosmogenic Isotopes as Atmospheric Tracers

D. Lal and M. Baskaran

Abstract Earth's atmosphere is constantly bombarded by cosmic-ray particles and the interaction of these cosmic-ray particles with the target nuclei continuously produce a suite of radionuclides which serve as powerful tracers to identify and quantify several atmospheric processes. These include sources and transport and mixing of air masses, exchange of air-masses between various layers of the atmosphere (e.g., stratosphere–troposphere exchange, STE), residence times of atmospheric gases, removal rates and residence times of atmospheric pollutants to name a few. Combining the cosmogenic radionuclides with other naturally-occurring (primarily daughter products of ^{222}Rn) and anthropogenic (mainly derived from nuclear weapons testing) radionuclides, have significantly aided to improve our understanding of the time scales involved with the interhemispheric exchange, meridional mixing and cross-Equator mixing as well as residence time of tropospheric aerosols. In this article, we review some of the key applications of cosmogenic radionuclides tracers in the atmosphere.

28.1 Introduction

28.1.1 Atmosphere

The science of the Earth's atmosphere is indeed a vast field: how it was formed in the first place; is it growing or decreasing in mass with time; how does it control Earth's climate, what are its layers that serve as important controllers of physical processes; how it shields inhabitants of the Earth from harmful radiations and fast particles of matter, etc. Over the past six decades, we have obtained large amount of information on which part of the atmosphere controls Earth's climate. In dealing with vast subjects, we generally deal with a very narrow subset of problems, meaning that we *generally* look at the panorama through a narrow long tube, because that is all that one can do to remain confined.

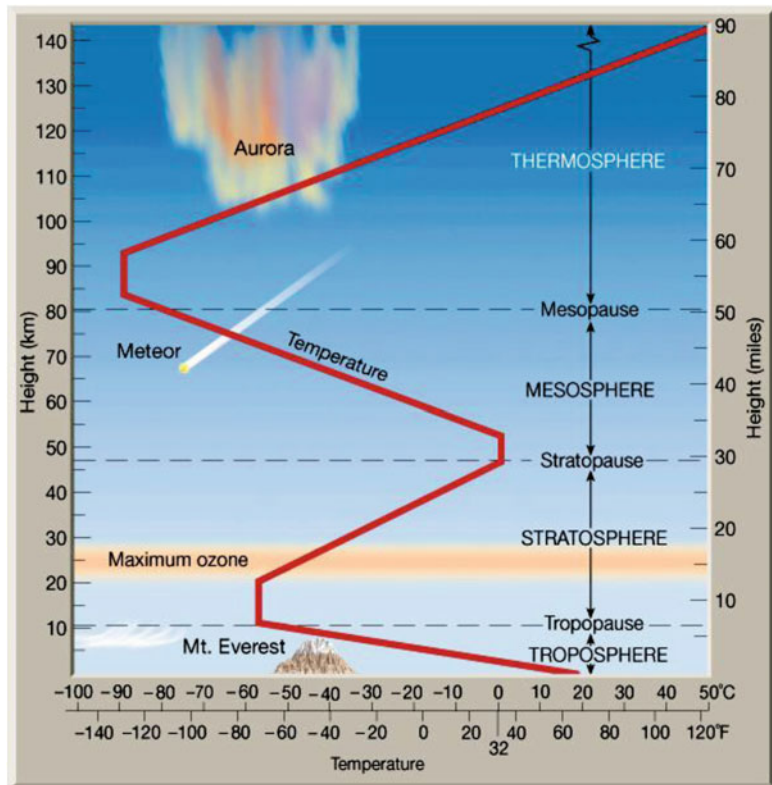
This purpose of this chapter is to discuss what atmospheric processes we can learn using radioactive tracers, which are naturally or artificially injected in the atmosphere. Even this is a large field but we will try to constrain our discussions to cosmic ray produced nuclides, supplementing the discussions with two other types of tracers: (1) naturally occurring tracers belonging to the U-Th series, and (2) radionuclides artificially injected in to the atmosphere by nuclear weapon's testing.

It is important to consider at first the structure of the Earth's atmosphere with respect to its density, temperature and thermal stability (Fig. 28.1). Starting from the sea level, we first encounter a region of the atmosphere where temperature decreases by about 6.5°C per km (known as the *lapse rate*) as one goes up in altitude, up to the top of the troposphere. By its

D. Lal (✉)
Scripps Institution of Oceanography, University of California,
San Diego, CA 92093, USA
e-mail: dlal@ucsd.edu

M. Baskaran
Department of Geology, Wayne State University, Detroit,
MI 48202, USA
e-mail: Baskaran@wayne.edu

Fig. 28.1 Vertical profile of temperature in the atmosphere



temperature structure, the troposphere promotes vertical mixing; its name in the Greek word “τροπή”, *trope*, meaning turn or overturn. The troposphere contains roughly ~83% of the mass of the atmosphere, and ~99% of global water vapor. The boundary between the top of the troposphere and the bottom of the stratosphere is the tropopause, where the temperature remains invariant with height. Above the tropopause lies the stratosphere, a layer in which the temperature increases with altitude above the tropopause; the stratosphere gets its name from the Greek meaning “stratified layer”. The temperature increase with altitude in stratosphere is a result of solar ultraviolet light interacting with the ozone also produced by ultraviolet light causing the temperature increase. The boundary between the stratosphere and the next layer, mesosphere, is called the stratopause. The total mass of the atmosphere in the stratosphere is about 16%; and above the stratopause, ~0.1%.

There are exchanges of air molecules between the troposphere and the stratosphere. The principal mechanisms of exchange between the troposphere and the stratosphere are two: (1) the Brewer–Dobson

model which has been proposed for the “equator to poles” troposphere–stratosphere–troposphere” circulation (Brewer 1949), and (2) the seasonal downward transport of stratospheric air masses at extra-tropical latitudes (Danielsen and Mohnen 1977; Danielsen et al. 1987), linked to large scale cyclogenesis in the winter and early spring. These have been verified using both nuclear weapon transient tracers (e.g., ^{90}Sr) and cosmic ray produced isotopes (cf. Lal and Peters 1967; Lal and Suess 1968; Lal 2002).

28.1.2 Radionuclides as Atmospheric Tracers

There are three groups of radionuclides that have been widely used as atmospheric tracers: (1) naturally-occurring radionuclides, mainly ^{222}Rn and its daughter products; (2) anthropogenic radionuclides, mainly derived from nuclear weapons testing; and (3) cosmogenic isotopes produced by cosmic rays from interaction with the gaseous components of the atmosphere (N_2 , O_2 , Ar, etc.).

Radon-222 and its progenies (mainly ^{210}Pb , ^{210}Bi , ^{210}Po) have provided a wealth of information on the sources of aerosols and airmasses, stability and vertical movements of airmasses, removal rate constants and residence times of aerosols, and deposition velocities of aerosols in the planetary boundary layer (e.g., review paper by Baskaran 2011). Due to three orders of magnitude higher concentrations of ^{226}Ra in rocks and minerals ($\sim 31 \text{ mBq g}^{-1}$, assuming ^{238}U and ^{226}Ra are in secular equilibrium; ^{238}U concentration in the upper crust = 2.5 ppm; Wedepohl 1995) compared to water ($1.2 \times 10^{-3} \text{ mBq g}^{-1}$; details given in Baskaran (2011), the ^{222}Rn emanation rates from land is ~ 2 orders of magnitude higher than that of the oceans ($1,300\text{--}1,800 \text{ Bq m}^{-2} \text{ d}^{-1}$ from continents as opposed to $\sim 17 \text{ Bq m}^{-2} \text{ d}^{-1}$ from oceanic areas (Samuelsson et al. 1986; Nazaroff 1992). Thus, the continental and maritime air masses have distinctly different concentrations of ^{222}Rn and their progenies, and the gradients in the concentration and activity ratios are used to quantify atmospheric processes.

The anthropogenic radionuclides in the atmosphere (termed as transient tracers) from the detonation of nuclear weapon tests were introduced in the atmosphere starting from 1952 (although two nuclear tests were conducted in 1945 at Nagasaki and Hiroshima). The uneven deposition and temporal variations in the atmosphere and of the fallout of radionuclides, such as ^{90}Sr , ^3H , and ^{14}C , at different latitude belts (heaviest fallout in the northern hemisphere with the peak between 30 and 60°N and lowest in the polar and equatorial regions) provided deeper insight on the time scales of interhemispheric exchange in the troposphere, rates of meridional transport within the two hemispheres, mixing times scales of air masses within Hadley and Polar cells, and also on time scales of meridional mixing in the Northern hemisphere, and cross-Equator mixing time scale in the troposphere (Lal and Rama 1966; reviewed in Lal 2002). A very brief historical background is given below.

The 1954 spring Castle thermonuclear test introduced a large amount of artificial ^3H (tritium: half-life = 12.3 years) in the atmosphere. Studies of its concentrations in rains clearly showed that it was removed from the atmospheric layers below cloud cover in periods as short as weeks. Similarly the injections of the fission radionuclide, ^{90}Sr , in the atmosphere in stratospheric tests of nuclear weapons, led to the first insight into time scales of removal of

aerosols from the stratosphere to the troposphere and finally on to the surface of the Earth, within periods of the order of 1–2 years. These were remarkable observations indeed, since conventional physical meteorological studies did not provide even rough estimates of the time scales involved in circulation and self-purging of the atmosphere, although enough was known about the physical state of the atmosphere. The nuclear weapons-test derived ^{14}C in the atmosphere provided better insight on the residence time of CO_2 in the atmosphere. At the time of nuclear test ban treaty went into effect on 1 January 1963, the amount of ^{14}C activity in the atmosphere was roughly equal to the activity produced by cosmogenic nuclear reaction. Within the next 40 years, the bomb-produced ^{14}C inventory in the atmosphere constituted $\sim 10\%$ of the total ^{14}C inventory (Broecker 2003). More details on the sources, fate and transport of anthropogenic radionuclides in the environment are discussed in texts by Hong (2011) and Ketterer et al. (2011).

The field of cosmogenic nuclides as tracers of large-scale atmospheric circulation and mixing took its root in the fifties, which was a period when detonation of nuclear weapon were started (1952) in the atmosphere. This was a period when new information about space-time integrals of large-scale motion in the atmosphere emerged from studies of both transient nuclear weapon and cosmogenic tracers. The power of tracers in fluids undergoing complex, space-time dependant motions cannot be underestimated.

The cosmogenic nuclide production within the stratosphere and the troposphere depends on their masses, and the development of the secondary cosmic ray component whose flux decreases steadily with atmospheric pressure (Lal and Peters 1967). In the case of ^{14}C , which is primarily produced by thermal neutron capture in ^{14}N , $\sim 56\%$ is produced in the stratosphere. In the case of all other nuclides, which are produced by energetic neutrons, $\sim 67\%$ is produced in the stratosphere. Note here that since negligible production of cosmogenic nuclides occurs above the stratosphere, due to very low abundances of target nuclei, cosmogenic nuclides are useful mainly as tracers for large-scale circulation in the stratosphere and the troposphere.

In contrast to the transient tracers, the *cosmogenic nuclides* continually inject nuclides, which serve as *tracers* for studying the nature of large-scale motions of the atmosphere. The unique features of these tracers

are: (1) the source functions of the tracers in all parts of the atmosphere can be determined precisely as a function of time, and (2) several radionuclides with different chemical properties and half-lives varying in the range of less than an hour to more than million years, are produced by cosmic rays. Consequently, air transport/mixing and aerosol scavenging processes by wet precipitation can be studied quantitatively, on time scales ranging from hours to years (Lal and Peters 1967). Their distribution in the atmosphere allows one to assess the nature of the large-scale air mass circulation as well as time scales of their mixing within the stratosphere, between the stratosphere and the troposphere, and finally, their removal from the lower atmosphere by wet precipitation and dry deposition (details on the deposition of ^7Be and ^{10}Be to the Earth's surface are discussed in Kaste and Baskaran (2011)).

Combining the concentrations of cosmogenic radionuclides (e.g., ^7Be) that are primarily derived from upper atmosphere with the radionuclides that are derived from Earth's surface (e.g., ^{210}Pb , ^{210}Po), the sources of airmasses (continent versus oceanic) and their horizontal and vertical transport can be quantified. The concentration of ^{210}Pb in the air, since its source is at the ground level, decreases with elevation from the ground due to decreases in the concentration of ^{222}Rn . On the other hand, the concentration of ^7Be in air increases with increasing altitude from the surface of the Earth. Beryllium-7 is mixed downward while ^{210}Pb mixed upwards and both are primarily removed by precipitation. This ratio has been reported to be the highest over continents during the summer due to increased dry convective mixing (e.g., Baskaran et al. 1993; McNeary and Baskaran 2003; Turekian and Graustein 2003). Therefore, the $^7\text{Be}/^{210}\text{Pb}$ ratio is a potential tracer for large-scale transport such as Hadley circulation and for vertical mixing in the mid-troposphere. On the other hand, the delivery of high-altitude ^7Be -rich air to the surface is primarily through convective transport (Koch et al. 1996). More details on the applications of U-Th series radionuclides as atmospheric tracers is given in Hirose (2011).

28.1.3 Historical Background for Cosmogenic Radionuclides

The discovery in late forties of the cosmic ray produced radionuclide, ^{14}C , in the earth's atmosphere

(Libby 1946) marked the onset for the search for other cosmic ray produced (cosmogenic) nuclides. During the next four decades since Libby's discovery of ^{14}C , about four dozen and two dozen stable and radioactive nuclides were discovered in extra-terrestrial samples (Reedy et al. 1983) and on the Earth (Lal and Peters 1967). The cosmogenic nuclides found large number of applications in planetary and earth sciences.

Interconnection between cosmic rays and geophysics was established with Libby's discovery of ^{14}C . Other developments soon established the fact that cosmic rays are indeed a very powerful tool in astronomy, astrophysics and geophysics. The galaxy has been continuously filled with cosmic rays, up to energies of $\sim 10^{20}$ eV. Nuclear effects of cosmic rays in objects without an appreciable atmosphere, go down to $\sim 1,000$ g cm^{-2} . On the Earth however, the effects are measurable up to depths of 10^6 g cm^{-2} , since charged pions produced in nuclear interactions in the atmosphere decay, giving rise to the penetrating muons.

Today the field of cosmogenic nuclides in extra-terrestrial and terrestrial samples is a large field which grew, and is still growing since Libby's discovery of ^{14}C , pushed to new dimensions with the development of new techniques in detection and measurement of cosmogenic nuclides; see Lal (1988) for historical development of ideas in this field. An important technical development was the accelerator mass spectrometry (AMS) technique in 1970s for detecting and measuring small sample of long-lived radionuclides.

The AMS technique is based on acceleration of nuclides to MeV energies in electrostatic tandem accelerators and then identifying the nuclide (pioneering studies were carried out by Nelson et al. 1977 and Bennett et al. 1977), without having to wait for the nuclide to decay. The AMS technique works efficiently for several nuclides (^{14}C , ^{41}Ca , ^{36}Cl , ^{26}Al , ^{10}Be and ^{129}I), permitting detection of $\leq 10^6$ atoms in each case (cf. Elmore and Phillips 1987), provided the isotope/element ratio is $> 5 \times 10^{-15}$. This gave a gain factor of 10^6 over isotope detection by the decay-counting method. The 4–6 orders of magnitude higher isotope measurement sensitivity meant a large reduction in sample sizes, from (10–100) g to (1–10) mg, and in turn re-opening a host of investigations carried out earlier using the decay-counting method, for a more detailed study of biogeochemical processes. The decrease in the sample size meant:

1. Economy on precious samples, both extraterrestrial and terrestrial samples.
2. Making measurements not possible earlier with the sample sizes available, e.g. Nuclide time series in ice cores.
3. Making adequate number of measurements to characterize geochemical entities, e.g., marine sediments and weathered soil profiles; and
4. Measuring concentrations of cosmogenic nuclides produced in situ in terrestrial solids.

28.1.4 Production of Cosmogenic Nuclides in the Atmosphere

Cosmic rays are accelerated in shocks in Type II Supernova and are composed of high-energy particles of nuclear matter. Typical energies of nuclei in the primary cosmic ray beam lie in the range of 1–10 GeV; the total energy range is of course much greater, 10^{-1} – 10^{11} GeV. Most of the cosmic ray particles have velocities comparable to that of light, and have energies sufficient to break nuclei into fragments. Note that typical binding energies of nucleons in nuclei are of the order of 10 MeV. During their passage through the earth's atmosphere, a nucleonic cascade develops

because of nuclear interactions of cosmic rays with the atmospheric nuclei. As a result, the cosmic ray beam is composed of greater number of secondary cosmic ray particles at depths, which are capable of inducing further nuclear reactions. A variety of stable and radioactive nuclei is produced in the nuclear interactions of primary and secondary cosmic rays with the atmospheric nuclei, N, O, Ar, Kr and Xe. In Tables 28.1 and 28.2, we list cosmogenic nuclides produced in the earth's atmosphere, with half-lives exceeding 30 min, which find varied applications as tracers in earth sciences.

The cosmogenic nuclide production rates are severely dependant on latitude and altitude in the atmosphere. These have been estimated rather accurately, and further attempts are underway to improve these estimates. Estimates have been made of the intensities of slow neutrons in the atmosphere, which allow one to estimate the altitude-latitude dependence in the rate of production of ^{14}C and ^{81}Kr in the atmosphere in the capture of a slow neutron by ^{14}N and ^{80}Kr , respectively. Most other isotopes are produced in *high-energy spallation (fragmentation)* of nuclei; their rates are approximately proportional to the rates of nuclear disintegrations, and have been estimated accurately based on measurements of slow neutrons in the atmosphere. Figure 28.2 shows the latitude-altitude dependence in

Table 28.1 Cosmogenic nuclides produced in the atmosphere (with half-lives^a greater than 1 day) and their applications. Arranged in order of increasing atomic number

Nuclide	Half-life	Main target nuclide	Production rate (atoms $\text{cm}^{-2} \text{s}^{-1}$)	
			Troposphere	Total atmosphere
^3H	12.3 years	N, O	No data	No data
^3He	Stable	N, O	6.7×10^{-2}	0.2
^7Be	53 days	N, O	2.7×10^{-2}	8.1×10^{-2}
^{10}Be	1.5×10^6 years	N, O	1.5×10^{-2}	4.5×10^{-2}
^{14}C	5,730 years	N, O	1.1	2.5
$^{20,21,22}\text{Ne}$	Stable	Ar	No data	No data
^{22}Na	2.6 years	Ar	2.4×10^{-5}	8.6×10^{-5}
^{26}Al	7.1×10^5 years	Ar	0.38×10^{-4}	1.4×10^{-4}
^{32}Si	150 years	Ar	0.54×10^{-4}	1.6×10^{-4}
^{32}P	14.3 days	Ar	2.7×10^{-4}	8.1×10^{-4}
^{33}P	25.3 days	Ar	2.2×10^{-4}	6.8×10^{-4}
^{35}S	87 days	Ar	0.49×10^{-3}	1.4×10^{-3}
^{36}Cl	3.0×10^5 years	Ar	0.40×10^{-3}	1.1×10^{-3}
^{37}Ar	35 days	Ar	2.8×10^{-4}	8.3×10^{-4}
^{39}Ar	268 years	Ar	0.45×10^{-2}	1.3×10^{-2}
^{81}Kr	2.3×10^5 years	Kr	0.52×10^{-6}	1.2×10^{-6}
^{129}I	1.6×10^7 years	Xe	No data	No data

^aArranged in order of increasing mass numbers

Table 28.2 Cosmogenic radionuclides produced in the atmosphere (with half-lives^a greater than 30 min to less than a day) and their applications

Nuclide	Half-life	Main target Nuclide	Production rate (atoms cm ⁻² s ⁻¹)	
			Troposphere	Total atmosphere
²⁴ Na	15.0 h	Ar	0.82×10^{-4}	3.0×10^{-4}
²⁸ Mg	21.2 h	Ar	0.46×10^{-4}	1.7×10^{-4}
³¹ Si	2.6 h	Ar	1.5×10^{-4}	4.4×10^{-4}
³⁸ S	2.9 h	Ar	1.7×10^{-5}	4.9×10^{-5}
^{34m} Cl	32.0 min	Ar	1.1×10^{-4}	2.0×10^{-4}
³⁸ Cl	37.3 min	Ar	7.7×10^{-4}	2.0×10^{-4}
³⁹ Cl	55.5 min	Ar	0.49×10^{-3}	1.4×10^{-3}

^aArranged in order of increasing mass numbers

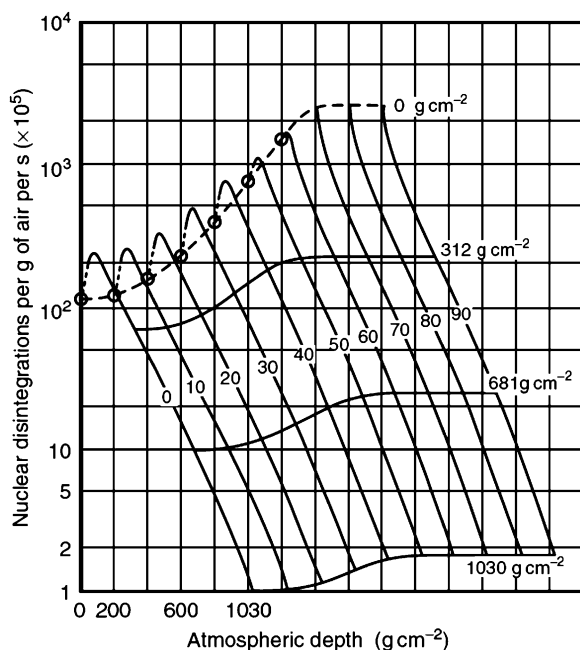


Fig. 28.2 The rate of production of nuclear disintegrations, with energy release above 40 MeV, is plotted as a function of atmospheric pressure (from Lal and Peters 1967). To avoid overlapping, curves for different latitudes have been displaced with respect to each other successively by 200 gm. cm⁻² along the abscissa

the rate of *nuclear disintegrations* in the atmosphere. For deviations in the altitude–latitude dependence of nuclide yields from nuclear disintegration rates; reference is made to Lal and Peters (1967). Note that Fig. 28.2 shows the approximate relative latitude–altitude dependence of all nuclides, except for ¹⁴C and ⁸¹Kr; reference is made to Lal and Peters (1967) for their latitude–altitude dependence.

Cosmogenic nuclides, except for ³He, ^{37,39}Ar and ⁸¹Kr, get oxidized shortly after their production (Table 28.3). The nuclides that do not form compounds (noble gases) are useful to investigate air-sea exchange, temporal variations of cosmic radiation, atmospheric circulation, dating of groundwater and vertical mixing of water masses in the oceans and lakes (Table 28.3). A list of nuclides that attach to aerosols are given in Table 28.3. Attachment occurs primarily on small size particles, <1 μm (Junge 1963). Some of the short-lived radionuclides (³⁹Cl, ³⁸S, ³⁸Cl, ^{34m}Cl, ³¹Si, ²⁸Mg, ²⁴Mg) are useful for cloud formation and dissipation studies and to quantify aerosol scavenging processes by wet precipitation. Their half-lives are of the same order of magnitude as the time scale on which precipitation processes occur. Except for CO₂, which is a permanent gas, all other oxides get attached to aerosols within a short time. Consequently, these nuclides do not settle gravitationally and follow the mass motion of the molecules in the stratosphere. In the troposphere, however, the aerosols are effectively removed by condensation of vapor at and below cloud cover.

28.1.5 Distributions of Cosmogenic Nuclides in the Stratosphere and Troposphere and their Implications

As stated earlier, in the stratosphere, the temperature increases with altitude as a result of solar ultraviolet light interacting with the ozone, causing the temperature increase. Consequently, since the stratosphere is stable against vertical mixing, air molecules primarily mix

Table 28.3 Important characteristics and principal applications of selected cosmogenic nuclides produced in the atmosphere

<i>Isotopes which do not form compounds</i>		
³ He	Stable	Air-sea exchange; escape of helium from the atmosphere
³⁷ Ar	35 days	Atmospheric circulation and air-sea exchange
³⁹ Ar	268 years	Atmospheric circulation; vertical mixing in oceans
⁸¹ Kr	2.3×10^5 years	Ground water ages, and constancy of cosmic radiation
<i>Isotopes which attach to aerosols/particles</i>		
⁷ Be	53 days	Atmospheric circulation, vertical mixing in surface ocean waters
¹⁰ Be	1.5×10^6 years	Atmospheric circulation; role of particle scavenging in the coastal and open oceans; dating of sediments and accretions
²⁶ Al	7.1×10^5 years	Role of particle scavenging in the coastal and open oceans; dating of marine sediments and accretions
³² Si (HSiO ₃ , SiO ₂)	~150 years	Atmospheric circulation; labeling the dissolved oceanic silicon pool; atmospheric circulation
³³ P, ³² P	14.3, 25.3 days	Atmospheric circulation; labeling the dissolved oceanic phosphorus pool; tropospheric circulation
³⁹ Cl, ³⁸ S, ³⁸ Cl, ^{34m} Cl, ³¹ Si, ²⁸ Mg, ²⁴ Mg	0.5–21 h	Cloud formation and dissipation, and aerosol scavenging processes by wet precipitation
<i>Isotopes, of half-lives >2 weeks, which label constituent molecules in the atmosphere and the hydrosphere</i>		
³ H (H ₂ O)	12.3 years	Atmospheric circulation; characterizing water molecules in the atmosphere, hydrosphere and cryosphere
¹⁴ C (CO ₂ , CO ₃ , HCO ₃)	5,730 years	Atmospheric circulation; characterization of the carbon cycle reservoirs
³² Si (HSiO ₃ , SiO ₂)	~150 years	Atmospheric circulation; biogeochemical cycle of silicon
³³ P, ³² P (DIP, DOP)	14.3, 25.3 days	Atmospheric circulation; biogeochemical cycle of phosphorous

horizontally. In the troposphere, several processes affect the distribution of cosmogenic radionuclides: meridional and vertical transport, sedimentation and precipitation scavenging. However, in the stratosphere, the deposition velocities are very low (~100 m/month; Junge 1963) and also there occurs no precipitation. Thus, the concentrations of cosmogenic radionuclides in the stratosphere are governed by local production, meridional and vertical downward transport, and radioactive decay.

Air motions are conveniently expressed by the conservation relation (Lal and Peters 1967);

$$\frac{dc^*}{dt} = q - \lambda c^* - v \cdot \nabla c^* \quad (28.1)$$

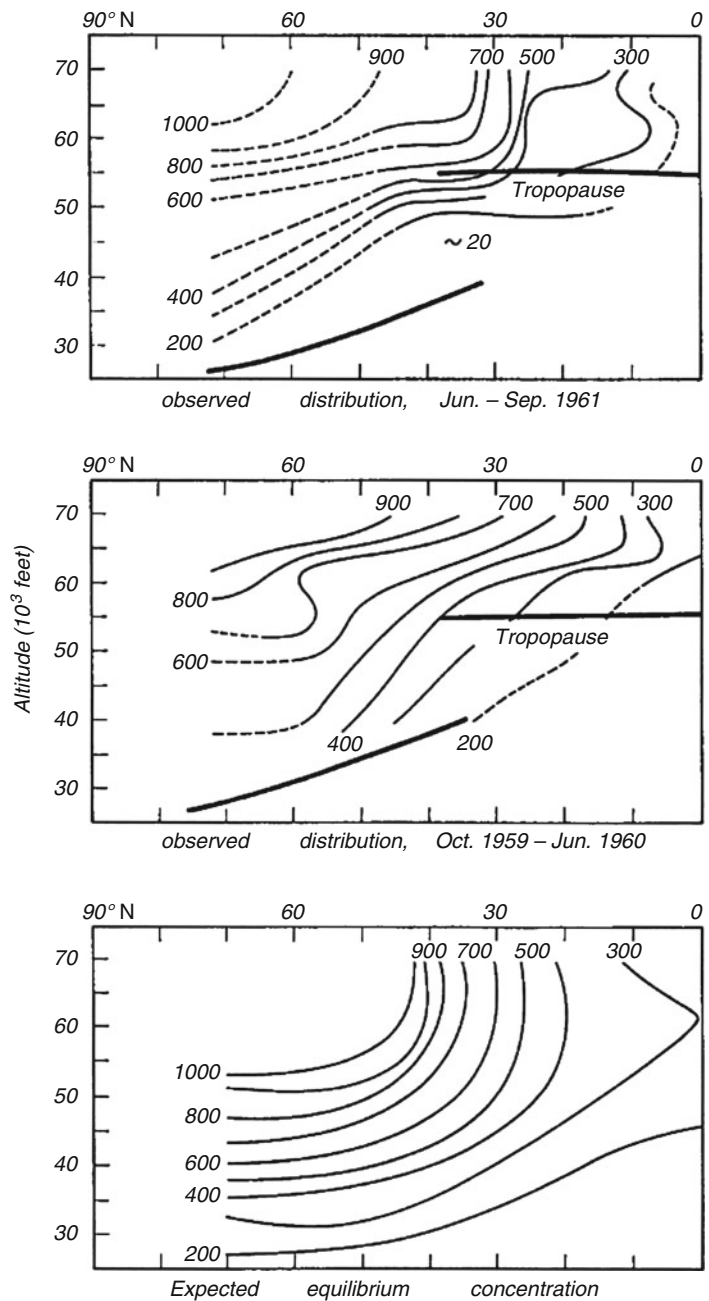
where v is the velocity vector, λ is the nuclide disintegration constant, c^* is the nuclide concentration and q is its production rate by cosmic rays. If the velocity field of stratospheric winds is stable for long periods compared to the nuclide half-life, a steady state is set up, and (28.1) reduces to:

$$v \cdot \nabla c^* = q - \lambda c^* \quad (28.2)$$

Since in the case of cosmogenic nuclides, q is known everywhere, non-parallel velocity gradients are given by nuclides of different half-lives. An important feature of (28.2) is the fact that even in the presence of strong zonal winds that prevail in the stratosphere, the velocity vector remains sensitive to both slow vertical drifts and small meridional components of the motion. As shown by Lal and Peters (1967), a deviation in ⁷Be concentration from its equilibrium value by about 20 % corresponds to vertical air-drifts of $0.4 < v_{\text{vert.}} < 0.8$ m per hour and meridional wind speeds of $4.5 < v_{\text{merid.}} < 9$ cm per second.

In Fig. 28.3, we show the measured concentration profiles of ⁷Be during two seasons, along with the expected equilibrium ⁷Be concentration profile, and in Fig. 28.4, the measured ²²Na/⁷Be ratios in the atmosphere. These data clearly show that the transport/mixing characteristics show altitude and latitude as well as seasonal dependence. For detailed measurements of ³²P, ⁷Be and ²²Na in the same air filters, reference is made to Bhandari et al. (1966). Ratios of isotope concentrations are particularly valuable since they are independent of any uncertainties in the volume of air filtered. The observed degree of under saturation in ²²Na concentrations indicates that the

Fig. 28.3 Measured concentrations of ^7Be (in $\text{dpm}/10^3$ cu. ft. S. T. P.; $1 \text{ dpm}/10^3$ cu. ft. = $0.589 \text{ mBq}/\text{m}^3$), in air during two periods of observation in the northern hemisphere. The contour lines of equal production rates of ^7Be are given in the bottom panel of Fig. 28.3, (in $\text{dpm}/10^3$ cu. ft. S. T. P.), corresponding to the expected ^7Be concentrations for a motionless atmosphere. *Thick lines* show the position of the tropopause. For details see Lal and Peters 1967 and Bhandari et al. (1966b)



apparent irradiation age of stratospheric air ranges from a few months in the lower layer just above the tropopause at high latitudes to ~ 1 – 2 years at low latitudes; see also similar inferences based on Fig. 28.3.

28.2 Materials and Methods

Of the list of cosmogenic radionuclides listed in Tables 28.1 and 28.2, only a few have been measured continuously over the past five decades. For example,

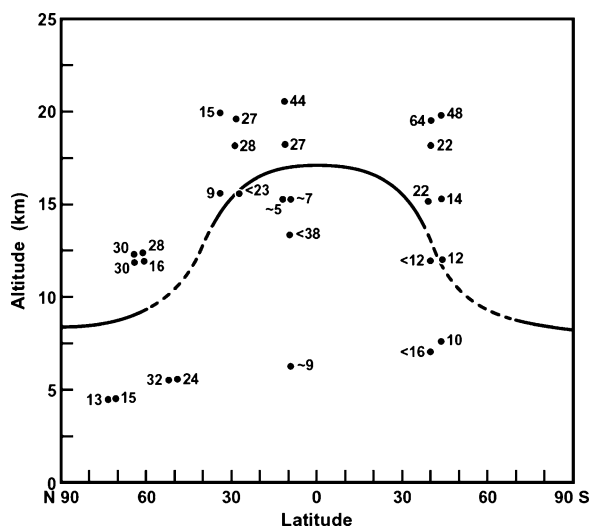


Fig. 28.4 Measured ratios of activities (dpm/10³ cu. ft. S. T. P.; 1 dpm/10³ cu. ft. = 0.589 mBq/m³) of ²²Na and ⁷Be in the atmosphere in a N–S section of the atmosphere. The numbers shown in the figure should be multiplied by 10⁻⁵ to obtain the absolute activity ratios. For details, see Bhandari and Rama (1963) and Lal and Peters 1967

from the initial method of measurement of ⁷Be with γ counting (NaI or Ge(Li) or pure Ge-well detectors) to the new AMS method the detection limit decreased over two orders of magnitude (detection limit of $\sim 10^6$ atoms by gamma-ray spectrometric methods versus $\sim 10^4$ atoms by AMS; see Kaste and Baskaran (2011)). Most of the short-lived cosmogenic radionuclides (Tables 28.1 and 28.2) were measured by counting methods, and extensive chemical separation and purification were conducted for those radionuclides whose activities were measured with beta counting method, since beta counting is not isotope-specific; also note that beta energy spectrum is continuous (0– E_{\max}). Interferences from other beta-emitting radionuclides need to be separated and hence rigorous chemical separation and purification is required. Detailed chemical separation and purification of Mg (for ²⁸Mg), Na (for ²⁴Na), S (for ³⁸S), Si (for ³¹Si) and Cl (for ^{34m}Cl, ³⁸Cl, ³⁹Cl) and radiochemical assay are given in Bhandari et al. (1966). A summary of the methods used, sample size, and references are given in Table 28.4.

28.3 Specific Applications of Cosmogenic Isotopes as Tracers

Discovery of a suite of short-lived cosmogenic radionuclides (³⁹Cl, ²⁴Na, ³⁸Cl, ³⁸S, ²⁸Mg, ³¹Si, ^{34m}Cl; Table 28.2; Winsberg (1956); Rodell (1963); Perkins

et al. (1965); Bhandari et al. (1966)) produced from the spallation of ⁴⁰Ar with cosmic rays have provided a basis for studying precipitation formation processes and thus serve as tracers of in-cloud scavenging. Inference on the mechanisms of cloud condensation, coalescence versus condensation, has been made based on the variations of the concentrations of short-lived radionuclides (Perkins et al. 1970). Measurements of these cosmogenic radionuclides in precipitation yielded information on in-cloud and below-cloud scavenging as well as on the scavenging efficiency and the altitude from which the precipitation occurred. The activity ratios of short-lived cosmogenic radionuclides in precipitation provide insight into the condensation processes and air movements within a storm system (Wogman et al. 1968). For example, high concentrations of ³⁶Cl and high ³⁹Cl/³⁸Cl activity ratios in precipitation is interpreted to have composed of small raindrops that have spent longer periods in their in-cloud development from coalescence of cloud droplets rather than growth of raindrops from condensation (Perkins et al. 1970). The updrafts within a cloud can, in principle, be studied using short-lived radionuclides, and thus, any measurements of these radionuclides in major hailstorms is expected to yield information linking the extent of updraft and concentrations and activity ratios of these short-lived cosmogenic radionuclides. Comparison of the ratios of various cosmogenic radionuclides in precipitation to the ratios at production in the atmosphere aid in constraining the time period required for the development of a precipitation episode. In addition, ratios of long-lived to short-lived isotopes (e.g., ²⁴Na/³⁸Cl) in precipitation can help to constrain the period between previous atmospheric removal due to precipitation scavenging. In this section, we specifically discuss some of the key applications of cosmogenic tracers to quantify some of the atmosphere processes.

28.3.1 Residence Times in the Stratosphere and Troposphere and Stratosphere–Troposphere Exchange Using ⁷Be/¹⁰Be Ratios

The factors and processes that control the stratospheric-tropospheric exchange are of interest for a number of reasons that include atmospheric cycling of natural and anthropogenically introduced trace species (such as CFCs, VOCs) and their potential impact on the stratospheric O₃, and residence times of stratospheric aerosols and their ultimate removal.

Table 28.4 Sampling and analysis of cosmogenic radionuclides produced in the atmosphere

Nuclide	Volume of air (m ³)	Volume of precipitation (L)	Analytical method	References
³ H	10 ¹ –10 ²	1–10	LSC	Lewis et al. (1986)
⁷ Be	10 ³	1–5	γ	McNeary and Baskaran (2003)
	10 ²	0.1–1.0	AMS	Raisbeck and Yiou (1988)
¹⁰ Be	10	1–10	AMS	Raisbeck et al. (1978)
¹⁴ C	0.010	10–50	AMS	Suter et al. (1984)
²² Na	10 ³ –10 ⁴	5–50	γ, LSC	Bhandari (1965)
²⁴ Na	NA	200	β ⁻ , γ	Rodel (1963); Bhandari et al. (1966)
²⁶ Al	10 ¹ –10 ²	10–50	AMS	Kubik and Christl (2010)
²⁸ Mg	NA	200	β ⁻	Bhandari et al. 1966
³¹ Si	NA	2–100	β ⁻	Bhandari et al. 1966; Wogman et al. (1968)
³² Si	–	10 ⁴	β ⁻	Nijampurkar and Somayajulu 1974
³² P	–	5–20	LSC	Benitez-Nelson and Buesseler (1998)
³³ P	–	5–20	LSC	Benitez-Nelson and Buesseler (1998)
³⁵ S	1	1–5		Tanaka and Turekian (1991)
³⁸ S	NA	50	β ⁻ , γ	Perkins et al. (1965); Bhandari et al. (1966)
^{34m} Cl	NA	2–100	β ⁺ , γ	Bhandari (1965); Wogman et al. (1968)
³⁶ Cl	10 ³	1–5	AMS	Galindo-Uribarri et al. (2007)
³⁸ Cl	NA	50	β ⁻ , γ	Perkins et al. (1965); Bhandari et al. (1966)
³⁹ Cl	NA	50	β ⁻ , γ	Winsberg (1956); Bhandari et al. (1966)
¹²⁹ I	–	1–5	AMS	Elmore et al. (1980)

Tropopause folds in mid-latitudes near the jet stream and changing seasonal structure of the stratosphere also can facilitate the exchange of air masses (Danielson 1968). Although the ratio of the production rates of ⁷Be/¹⁰Be has remained constant, a large range of values at various layers in the atmosphere have been reported (Dibb et al. 1994; Jordan et al. 2003).

Although time-series measurements have shown that the ⁷Be concentrations in aerosols and precipitation vary over an order of magnitude, the ⁷Be/¹⁰Be ratios has remained constant within a factor of 2. The ⁷Be/¹⁰Be ratios in precipitation samples varied between 0.67 and 0.85 in the Northern hemisphere and between 0.47 and 0.61 in the Southern hemisphere (summarized in Graham et al. 2003). Using a simple box-model approach, the residence time of Be-bearing aerosols in the stratosphere can be evaluated.

$$N_7^m = (P_7 + Q_7)[1 - \exp(-(\lambda_r + \lambda_7)t)] / (\lambda_r + \lambda_7) \quad (28.3)$$

$$N_{10}^m = (P_{10} + Q_{10})[1 - \exp(-(\lambda_r + \lambda_{10})t)] / (\lambda_r + \lambda_{10}) \quad (28.4)$$

where N_7^m and N_{10}^m are the measured concentrations of ⁷Be and ¹⁰Be; P_i and Q_i are the in-situ production

and injection of ‘*i*’ (⁷Be or ¹⁰Be), respectively. λ_r , λ_7 , λ_{10} are the removal rate constant (=1/residence time of Be) of Be (which is the same for both ⁷Be and ¹⁰Be), and decay constants of ⁷Be and ¹⁰Be respectively. In the stratosphere, Q_i (both ⁷Be = ¹⁰Be = 0) can be assumed to be zero at $t \rightarrow \infty$ and this condition represents equilibrium. Also, $\lambda_7 \gg \lambda_{10}$, and hence combining (28.3) and (28.4) and simplifying, we get

$$(N_7/N_{10})^m = (P_7/P_{10}) \lambda_7 / (\lambda_r + \lambda_7) \quad (28.5)$$

From (28.5) and from the established value of P_7/P_{10} , one can calculate λ_r and the residence time ($\tau = 1/\lambda_r$). A number of values for P_7/P_{10} have been reported in the literature. For a specific average Solar activity and present geomagnetic field intensity, Masarik and Beer (1999) calculated an average global average value of 1.9. Nishihizumi et al. (1996) measured production ratio in oxygen (P_7/P_{10}) to be 1.9 ± 0.1 at Echo Lake and 1.8 ± 0.2 at La Jolla. Raisbeck et al. (1981) reported a value of 0.42 for $(N_7/N_{10})^m$ from a set of samples collected at altitudes of 13.7, 16.8 and 19.2 km at 65°N. Assuming a production ratio of 2.0, a stratospheric residence time of ~350 days (28.5) is obtained. This value is in general agreement with values reported earlier (e.g., Reiter 1975).

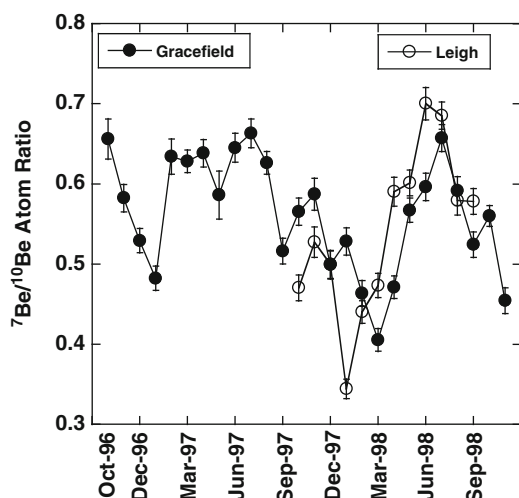


Fig. 28.5 Temporal monthly variations of ${}^7\text{Be}/{}^{10}\text{Be}$ ratios in two sites in New Zealand (Gracefield near Wellington: $41^\circ 15'\text{S}$, $174^\circ 55'\text{E}$ and Leigh, 50 km N of Auckland: $36^\circ 17'\text{S}$, $174^\circ 48'\text{E}$). Data for the plot are taken from Graham et al. 2003

From the ground-based measurements of ${}^7\text{Be}/{}^{10}\text{Be}$ ratios in aerosols, we can determine the residence times of Be-bearing aerosols in the stratosphere. Temporal variations of ${}^7\text{Be}/{}^{10}\text{Be}$ ratios for two stations from New Zealand over a period of 12 and 26 months are shown in Fig. 28.4. This ratio in monthly samples varied between 0.34 and 0.70, with the highest values in the summer months. This higher value is partly attributed to the higher contributions of atmospheric dust (Graham et al. 2003). In long-term precipitation samples (1 year or more), this ratio has been found to vary between 0.67 and 0.85 in the Northern Hemisphere ($n = 3$) and 0.47–0.61 in the Southern Hemisphere (data summarized in Graham et al. 2003). The corresponding residence time of Be-bearing aerosols in the troposphere was estimated to vary between 60 and 120 days (100–120 days based on the data from Dübendorf (440 m) and Jungfrauoch (3,580 m) in Switzerland (Heikkilä et al. 2008); 77–109 days in New Zealand, Graham et al. 2003). Although this ratio varied within a factor of 2, the concentrations of ${}^7\text{Be}$ or ${}^{10}\text{Be}$ in air have been observed to vary by larger factors. For example, in a mid-latitude station in Southeast Michigan (Detroit, $42^\circ 25'\text{N}$; $83^\circ 1'\text{W}$, 175 m amsl), ${}^7\text{Be}$ concentrations in aerosols varied by a factor of 6.3 (0.16–9.8 mBq m^{-3}) over a period of 17 months (McNeary and Baskaran 2003).

It has been shown that simultaneous measurements of O_3 and ${}^7\text{Be}$ in tropospheric air can be used to quantify the amount of O_3 derived from stratosphere (e.g., Dibb et al. 1994, 2003). Turekian and Graustein (2003) showed that much of the tropospheric ozone in the Canaries free troposphere is made in the upper troposphere and very little from the stratosphere. Dibb et al. (1994) estimated the portion of surface O_3 at Alert, Northwest Territories, Canada using Be isotopes as tracers, with a maximum stratospheric influence during spring accounting for 10–15% of the surface concentrations. The contribution of O_3 from stratosphere to troposphere during Arctic winter remains unknown. Raisbeck et al. (1981) showed that even 5% air intrusion from stratosphere into the troposphere can be determined using the ${}^7\text{Be}/{}^{10}\text{Be}$ ratios.

28.3.2 Applications of ${}^{35}\text{S}$ as a Tracer of SO_2 in the Atmosphere

The increase in anthropogenic emissions of SO_2 has resulted in the perturbation of sulfur cycle on regional and global scales (Solomon et al. 2007) including increase in acid rain and particulate SO_4^{2-} concentrations in the air. The aerosol sulfate (SO_4^{2-}) can serve as a cloud condensation nuclei affecting cloud formation and thereby affecting the heat balance of the lower troposphere. Since sulfur exists both as a solid and gas simultaneously, ${}^{35}\text{S}$ can be used as a tracer of gas and aerosol sulfate residence times and turnover kinetics of both sulfate phases (Tanaka and Turekian 1991; Igarashi et al. 1998; Brothers et al. 2010). Furthermore, sulfuric acid and sulfate salts are the dominant aerosol particles in the stratosphere and much of the upper troposphere (Buseck and Schwartz 2003). In a pioneering study, Tanaka and Turekian (1991) measured ${}^{35}\text{S}$ in gaseous SO_2 , aerosol sulfate and precipitation to determine time constants of oxidation, in-cloud scavenging and aerosol deposition. Turekian and Tanaka (1992) explored the use of ${}^{35}\text{S}$ and ${}^7\text{Be}$ as tracers of gaseous SO_2 and aerosol SO_4 , and Be removal processes to the Earth's surface.

Measurements of ${}^{35}\text{S}$ are commonly done at the Earth's surface (planetary boundary layer) and assuming a box model for the particulate and gaseous phase

separately, the mass balance equations are given as follows:

For the gas phase:

$$d[{}^{35}\text{SO}_2^g/\text{dt}] = P - k_{\text{ox}}[{}^{35}\text{SO}_2^g] - k_d[{}^{35}\text{SO}_2^g] - k_w[{}^{35}\text{SO}_2^g] - \lambda[{}^{35}\text{SO}_2^g] \quad (28.6)$$

where ${}^{35}\text{SO}_2^g$ is the concentration of SO_2 in the air (gas phase), P is the effective tropospheric production rate (= in-situ tropospheric production rate + fraction of ${}^{35}\text{S}$ injected into the troposphere from the stratospheric reservoir), k_{ox} , k_d , and k_w are the oxidation rate constant, removal rate constant due to dry deposition and wet deposition, respectively and λ is the decay constant of ${}^{35}\text{S}$ ($= 7.94 \times 10^{-3} \text{ d}^{-1}$). The total removal rate constant, k_{total} , is given by:

$$k_{\text{total}} = k_{\text{ox}} + k_d + k_w + \lambda \quad (28.7)$$

The mass balance for the aerosol (particulate) sulfate is given by:

$$d[{}^{35}\text{SO}_2^p/\text{dt}] = k_{\text{ox}}[{}^{35}\text{SO}_2^p] - k[{}^{35}\text{SO}_2^p] - \lambda[{}^{35}\text{SO}_2^p] \quad (28.8)$$

where ${}^{35}\text{SO}_2^p$ is the concentration of SO_2 in the aerosols (particulate phase) and k is the scavenging constant of removal of aerosols by precipitation.

Assuming steady-state conditions within the box ($d[{}^{35}\text{SO}_2^g/\text{dt}] = 0$), then (28.6) reduces to

$$P = (k_{\text{ox}} + k_d + k_w + \lambda)[{}^{35}\text{SO}_2^g] = k_{\text{total}}[{}^{35}\text{SO}_2^g]$$

or

$$\tau_{\text{total}} = [{}^{35}\text{SO}_2^g]/P \quad (28.9)$$

A comparison of the total residence time calculated using (28.9) on simultaneously collected samples from San Fernando Valley, CA (34.212°N, 118.061°W) and San Diego, CA (32.867°N, 117.257°W) indicates that the residence times is about 3–53 times longer in San Fernando Valley compared to San Diego, assuming that the production rate in both places to be the same ($4.75 \times 10^{-4} \text{ atoms m}^{-3} \text{ s}^{-1}$, Brothers et al. 2010). The $[{}^{35}\text{SO}_2^g]$ was calculated from the measured concentrations of ${}^{35}\text{SO}_2$ in the precipitation and assuming a deposition velocity of aerosols.

The average rate of in-cloud and raindrop scavenging of SO_2 relative to precipitation of $\text{SO}_4^{2-}/{}^{210}\text{Pb}$ can be calculated from the measurements of ${}^{210}\text{Pb}$ and sulfate in aerosols and in precipitation. A comparison of the ($\text{SO}_4^{2-}/{}^{210}\text{Pb}$) ratio in precipitation to that in aerosols yield information on the fraction of sulfate that is not associated with aerosol ${}^{210}\text{Pb}$ measured on filters (Tanaka and Turekian 1991). It was estimated that ~30% of the total SO_2 flux was removed by in-cloud scavenging (Tanaka and Turekian 1991). From the measured concentrations of ${}^{35}\text{SO}_2$ in the aerosols and gaseous phase, oxidation rate constant, aerosol removal rate constant and removal rate constant by precipitation, were reported to be 0.142, 0.084 and 0.056 d^{-1} respectively, corresponding to a mean SO_2 oxidation time of 7 days and an aerosol mean residence time of 12 days, and in-cloud mean scavenging time of 18 days (Tanaka and Turekian 1991). Based on 1-year sampling in New Haven, Connecticut, Tanaka and Turekian (1995) showed that about 25% of SO_2 in the air is removed by oxidative conversion of SO_2 to sulfate on surfaces. There are two distinct pathways by which SO_2 is converted to SO_4^{2-} (Tanaka et al. 1994): (1) homogenous pathway involving gas reaction with hydroxyl radicals ($\text{SO}_2 + \bullet\text{OH} \rightarrow \bullet\text{HOSO}_2 + \text{O}_2 \rightarrow \text{SO}_3 + \bullet\text{HOH} \rightarrow \text{H}_2\text{SO}_4$) and (2) a heterogeneous oxidation pathway involving oxidation in solution ($\text{SO}_2(\text{g}) \rightarrow \text{SO}_2(\text{aq}) + \text{H}_2\text{O} \rightarrow \text{HSO}_3^- + \text{H}^+$; $\text{HSO}_3^- + \text{H}_2\text{O}_2 \rightarrow \text{SO}_4^{2-} + \text{H}^+ + \text{H}_2\text{O}$). The oxidation pathways involving solution is likely dominant in the lower troposphere below cloud height and hence the relative importance of these two pathways at different heights from planetary boundary layer can be investigated using ${}^{35}\text{S}$. Turekian et al. (1989) used the $\text{SO}_4^{2-}/{}^{210}\text{Pb}$ ratios in aerosols collected from a network of stations across the Pacific for identifying possible sources of aerosols (continental, both industrial and non-industrial and oceanic) as well as efficiency of conversion of gaseous sulfur species to SO_4^{2-} .

28.3.3 ${}^{10}\text{Be}$ as a Tracer of Atmospheric Dust

In the determination of the tropospheric residence times of aerosols (and aerosol-laden Be), it is assumed that ${}^7\text{Be}$ and ${}^{10}\text{Be}$ are contributed from their cosmogenic production and the contribution from atmospheric

dust is not included. Due to its half-life, the amount of ^7Be contribution from terrestrial-derived atmospheric dust is expected to be negligible. However, the fine dust is likely to contribute a significant portion of the ^{10}Be to the rain (Monaghan et al. 1986). Finer particulate matter ($<10\ \mu\text{m}$) that can be carried by wind to longer distances likely will have significantly higher concentrations partly due to scavenging of Be-10 from the air. Also, since sorption is a surface area effect and hence finer particles will have higher specific concentrations (concentration per unit mass). Graham et al. (2003) reported that $^7\text{Be}/^{10}\text{Be}$ ratios in New Zealand increased from 0.47–0.61 to 0.50–0.70 after correcting for the dust input in the rain collector. Heikkilä et al. (2008) estimated that recycled ^{10}Be from atmospheric dust could contribute up to 10–20% of the concentration. Monaghan et al. (1986) estimated the recycled component of ^{10}Be to vary between 8 and 35% of the measured ^{10}Be in precipitation from seven stations around the continental United States. The recycling of ^{10}Be from continents to the atmosphere has resulted in significant variations in the concentrations of ^{10}Be (atoms/g aerosol). In aerosol dust collected from Miami, FL, the ^{10}Be concentration was reported to be $(2.12 \pm 0.04) \times 10^9$ ^{10}Be atoms/g dust (Lal 2007). Lal (2007) estimated a global average value for the aeolian dust to be $(6.5 \pm 3.5) \times 10^9$ ^{10}Be atoms/g aeolian dust. The ^{10}Be flux in the polar region during 20–35 kyr B.P. was appreciably lower than during Holocene and this was attributed to the major reorganization of the air circulation pattern in the polar region during this time period (Lal 2007). It is important to quantify the amount of ^{10}Be contributed from atmospheric dust which will vary depending on the air trajectory and season. Index elements such as Al or Ti can be used to quantify the terrigenous dust. Then, by direct measurements of ^{10}Be on aerosols, one can determine the concentrations of $^{10}\text{Be}/\text{g}$ and of Al in the aerosol. It is likely that this value is relatively constant and one can use this value along with measured Al value to quantify the amount of ^{10}Be derived from terrigenous dust.

28.4 Concluding Remarks and Future Directions

One of the prerequisite for the utility of tracers is that their source functions are well characterized along with

their chemical properties. The wide range of half-lives, chemical properties and their applications as proxies for their counterparts make the cosmogenic isotopes as ideal candidates for investigating spatial and temporal atmospheric processes. Some of the cosmogenic radionuclides such as ^7Be have been measured extensively in precipitation and aerosols, but combining with naturally-occurring radionuclides (such as daughter products of ^{222}Rn , ^{210}Pb , ^{210}Po , ^{210}Bi) that have a predominantly earth-surface origin, will be useful to trace species that originate both from earth's surface (such as Hg, SO_4^{2-} , NO_3^- ; Lamborg et al. 2000) and those that originate in the upper atmosphere (e.g., O_3). Except a few cosmogenic isotopes (^{10}Be , ^7Be , ^{36}Cl) very few studies have been conducted since their discovery in the 1950 and 1960 and any dedicated synoptic effort in the collection and analysis of aerosols at various altitudes, from planetary boundary layer to the lower stratosphere, as well in precipitation will provide insight on the scavenging mechanisms by precipitation and particle-reactive aerosols. Combining ^{129}I and ^{36}Cl , they could serve as tracers of atmospheric halides and chlorinated hydrocarbons. When CFCs reach the stratosphere, release of atomic chlorine will accelerate the destruction of stratospheric O_3 , and ^{36}Cl could be used as a tracer for this atomic chlorine. ^{36}Cl and ^{22}Na can be used as effective tracers of atmospheric chloride in the atmosphere and can be utilized to quantify the extent of recycling of seawater in the atmosphere.

Acknowledgements We thank two reviewers (Karl Turekian and an anonymous) for several useful suggestions to extend the scope of the text.

References

- Baskaran M (2011) Po-210 and Pb-210 as atmospheric tracers and global atmospheric Pb-210 fallout: a review. *J Environ Radioact.* 102:500–513
- Baskaran M, Coleman CH, Santschi PH (1993) Atmospheric depositional fluxes of ^7Be and ^{210}Pb at Galveston and College Station, Texas. *J Geophys Res* 98:20555–20571
- Benitez-Nelson CR, Buesseler KO (1998) Measurement of cosmogenic ^{32}P and ^{33}P activities in rainwater and seawater. *Anal Chem* 70:64–72
- Bennett CL, Beukens RP, Clover M, Grove HE et al (1977) Radiocarbon dating using electrostatic accelerators: negative ions provide the key. *Science* 198:508–510
- Bhandari N (1965) Studies of some physical processes occurring in the atmosphere based on radionuclides of natural and artificial origin, Ph.D. Thesis, University of Bombay, India, pp. 164

- Bhandari N, Rama T (1963) Atmospheric circulation from observations of ^{22}Na and other short-lived natural radioactivities. *J Geophys Res* 68:1959–1966
- Bhandari N, Lal D, Rama T (1966) Stratospheric circulation studies based on natural and artificial radioactive trace elements. *Tellus* 18:391–406
- Brewer AW (1949) Evidence for a world circulation provided by the measurements of helium and water vapor distribution in the stratosphere. *Q J Roy Meteorol Soc* 75:351–363
- Broecker WS (2003) Radiocarbon. In: Turekian KK, Holland D, Turekian KK, Holland D (eds) *Treatise on geochemistry*, vol 4. Elsevier, Oxford, pp 245–260
- Brothers LA, Dominguez G, Abramian A, Corbin A et al (2010) Optimized low-level liquid scintillation spectroscopy of ^{35}S for atmospheric and biogeochemical chemistry applications. *Proc Natl Acad Sci USA* 107(12):5311–5316
- Buseck PR, Schwartz SE (2003) Tropospheric aerosols. In: Turekian KK, Holland D (eds) *Treatise in geochemistry*, 4.04. Elsevier, Amsterdam, pp 91–109
- Danielsen EF (1968) Stratospheric-tropospheric exchange based on radioactivity, ozone, and potential vorticity. *J Atmos Sci* 25:502–518
- Danielsen EF, Mohnen VA (1977) Project Dustorm report: ozone transport, in situ measurements, and meteorological analyses of tropopause folding. *J Geophys Res* 82:5867–5877
- Danielsen EF, Hipskind RS, Gaines SE et al (1987) Three dimensional analysis of potential vorticity associated with tropopause folds and observed variations of ozone and carbon monoxide. *J Geophys Res* 92:2103–2111
- Dibb JE, Meeker LD, Finkel RC, Southon JR et al (1994) Estimation of stratospheric input to the Arctic troposphere: ^7Be and ^{10}Be in aerosols at Alert, Canada. *J Geophys Res* 99:12855–12864
- Dibb JE, Talbot RW, Scheuer E, Seid G, DeBell L (2003) Stratospheric influence on the northern American free troposphere during TOPSE: ^7Be as a stratospheric tracer. *J Geophys Res* 108:8363. doi:10.1029/2001JD001347
- Elmore D, Gove HE, Ferraro R et al (1980) Determination of I-129 using tandem accelerator mass-spectrometry. *Nature* 286:138–140
- Elmore D, Phillips FM (1987) Mass spectrometry for measurement of long-lived radioisotopes. *Science* 236:543–550
- Galindo-Uribarri A, Beene JR, Danchev M et al (2007) Pushing the limits of accelerator mass spectrometry. *Nucl Instrum Meth Phys Res B* 259B:123–130
- Graham I, Ditchburn R, Barry B (2003) Atmospheric deposition of ^7Be and ^{10}Be in New Zealand rain (1996–98). *Geochim Cosmochim Acta* 67(3):361–373
- Heikkilä U, Beer J, Alfimov V (2008) Beryllium-10 and beryllium-7 in precipitation in Dubendorf (440 m) and at Jungfraujoch (3580 m), Switzerland (1998–2005). *J Geophys Res* 113:D11104. doi:10.1029/2007JD0091960, 2008
- Hirose K (2011) Uranium, thorium and anthropogenic radionuclides as atmospheric tracers. In: Baskaran M (ed) *Handbook of environmental isotope geochemistry*. Springer, Heidelberg
- Hong G-H (2011) Applications of anthropogenic radionuclides as tracers to investigate marine environmental processes. In: Baskaran M (ed) *Handbook of environmental isotope geochemistry*. Springer, Heidelberg
- Igarashi Y, Hirose K, Otsuji-Hatori M (1998) Beryllium-7 deposition and its relation to sulfate deposition. *J Atmos Chem* 29:217–231
- Jordan CE, Dibb JE, Finkel RC (2003) $^{10}\text{Be}/^7\text{Be}$ tracer of atmospheric transport and stratosphere-troposphere exchange. *J Geophys Res* 108:4234. doi:10.1029/2002JD002395
- Junge CE (1963) *Air chemistry and radioactivity*. Academic, San Diego
- Kaste JM, Baskaran M (2011) Meteoric ^7Be and ^{10}Be as process tracers in the environment. In: Baskaran M (ed) *Handbook of environmental isotope geochemistry*. Springer, Heidelberg
- Ketterer ME (2011) Applications of transuranics as tracers and chronometers in the environment. In: Baskaran M (ed) *Handbook of environmental isotope geochemistry*. Springer, Heidelberg
- Koch DM, Jacob DJ, Graustein WC (1996) Vertical transport of tropospheric aerosols as indicated by ^7Be and ^{210}Pb in a chemical tracer model. *J Geophys Res* 101:18651–18666
- Kubik PW, Christl M (2010) Be-10 and Al-26 measurements at the Zurich 6 MV Tandem AMS facility. *Nucl Instrum Meth Phys Res B* 268:880–883
- Lal D (1988) In-situ produced cosmogenic isotopes in terrestrial rocks. *Ann Rev Earth Planet Sci Lett* 16:355–388
- Lal D, Rama T (1966) Characteristics of global tropospheric mixing based on man-made C^{14} , H^3 , and Sr^{90} . *J Geophys Res* 71:2865–2874
- Lal D, Peters B (1967) Cosmic-ray produced radioactivities on the earth. In: *Handbuch der Physik*, vol 46. Springer, Berlin, p 551
- Lal D, Suess HE (1968) The radioactivity of the atmosphere and hydrosphere. *Annu Rev Nucl Sci* 18:407–434
- Lal D (2002) Cosmogenic radionuclides. In: Holton JR, Pyle J, Curry JA (eds) *Encyclopedia of atmospheric sciences*. Academic, London, pp 1891–1900
- Lal D (2007) Recycling of cosmogenic nuclides after their removal from the atmosphere; special case of appreciable transport of Be-10 to polar regions by Aeolian dust. *Earth Planet Sci Lett* 264:177–187
- Lamborg CH, Fitzgerald WF, Graustein WC, Turekian KK (2000) An examination of the atmospheric chemistry of mercury using ^{210}Pb and ^7Be . *J Atmos Chem* 36:325–338
- Lewis R, Fröhlich K, Hebert D (1986) Measurements of specific tritium activities of precipitation and air humidity samples – methods and application. *Isotopenpraxis* 22:269–272
- Libby WF (1946) Atmospheric helium-three and radiocarbon from cosmic radiation. *Phys Rev* 69:671–672
- Masarik J, Beer J (1999) Simulation of particle fluxes and cosmogenic nuclide production in the Earth's atmosphere. *J Geophys Res* 104(D14):12009–12111
- McNeary D, Baskaran M (2003) Depositonal characteristics of ^7Be and ^{210}Pb in southeastern Michigan. *J Geophys Res* 108:4210. doi:10.1029/2002JD003021
- Monaghan M, Krishnaswami S, Turekian KK (1986) The global-average production of ^{10}Be . *Earth Planet Sci Lett* 76:279–287
- Nazaroff WW (1992) Radon transport from soil to air. *Rev Geophys* 30:137–160
- Nelson DE, Korteling RG, Stott WR (1977) Carbon-14: direct detection at natural accelerations. *Science* 198:507–508

- Nijampurkar VN, Somayajulu BLK (1974) An improved method of Silicon-32 measurement of groundwater. *Proc Ind Acad Sci* 80:289–298.
- Nishihizumi K, Finkel RC, Klein J, Middleton R (1996) Cosmogenic production of ^7Be and ^{10}Be in water targets. *J Geophys Res* 101(B10):22,225–22,232
- Perkins RW, Thomas CW, Hill MW, Nielsen JM (1965) Chlorine-38 and sulphur-38 produced by cosmic radiation. *Nature* 205:790–791
- Perkins RW, Thomas CW, Young JA (1970) Application of short-lived cosmogenic radionuclides as tracers of in-cloud scavenging processes. *J Geophys Res* 75:3076–3087
- Raisbeck GM, Yiou F, Fruneau M, Loiseaux JM, Lieuvain M, Ravel JC (1981) Cosmogenic $^{10}\text{Be}/^7\text{Be}$ as a probe of atmospheric transport processes. *Geophys Res Lett* 8(9): 1015–1018
- Reedy RC, Arnold JR, Lal D (1983) Cosmic ray record in solar system matter. *Annu Rev Nucl Part Sci* 35:505–537
- Raisbeck GM, Yiou F, Fruneau F, Loiseaux JM (1978) Be-10 mass spectrometry with a cyclotron. *Science* 202:215–217
- Raisbeck GM, Yiou F (1988) Measurement of Be-7 by accelerator mass-spectrometry. *Earth Planet Sci Lett* 89:103–108
- Reiter R (1975) Stratospheric-tropospheric exchange processes. *Rev Geophys Space Phys* 13:459
- Rodel W (1963) Sodium-24 produced by cosmic radiation. *Nature* 200:999–1000
- Samuelsson C, Hallstadius L, Persson B, Hedvall R, Holm E (1986) ^{222}Rn and ^{210}Pb in the Arctic summer air. *J Environ Radioact* 3:35–54
- Solomon S et al (2007) Climate change 2007: the physical science basis. Contribution of Working Group I to the Fourth Assessment Report of the Intergovernmental Panel on Climate Change. Cambridge University Press, Cambridge), p 996
- Suter M, Balzer R, Bonani G et al (1984) Precision-measurements of C-14 in AMS – some results and prospects. *Nucl Instrum Meth Phys Res B* 5:117–122
- Tanaka N, Turekian KK (1991) Use of cosmogenic ^{35}S to determine the rates of removal of atmospheric SO_2 . *Nature* 352:226–228
- Tanaka N, Turekian KK (1995) Determination of the dry depositional flux of SO_2 using cosmogenic ^{35}S and ^7Be measurements. *J Geophys Res* 100:2841–2848
- Tanaka N, Rye DM, Xiao Y, Lasaga AC (1994) Use of stable sulfur isotope systematic for evaluating oxidation reaction pathways and in-cloud-scavenging of sulfur dioxide in the atmosphere. *Geophys Res Lett* 21(4):1519–1522
- Turekian KK, Tanaka N (1992) The use of atmospheric cosmogenic ^{35}S and ^7Be in determining depositional fluxes of SO_2 . *Geophys Res Lett* 19(17):1767–1770
- Turekian KK, Graustein WC, Cochran JK (1989) Lead-210 in the SEAREX Program: an aerosol tracer across the Pacific. In: Riley JP, Chester R, Duce RA (eds) *Chemical oceanography*, vol 10. Academic, London, pp 51–81
- Turekian KK, Graustein WC (2003) Natural radionuclides in the atmosphere. In: *Treatise in geochemistry*, 4. Elsevier, Amsterdam, pp 261–279
- Winsberg L (1956) The production of chlorine-39 in the lower atmosphere by cosmic radiation. *Geochim Cosmochim Acta* 9:183
- Wogman NA, Thomas CW, Cooper JA, Engelmann RJ, Perkins RW (1968) Cosmic-ray produced radionuclides as tracers of atmospheric precipitation processes. *Science* 159:189–192
- Wedepohl KH (1995) The composition of the continental crust. *Geochim Cosmochim Acta* 59:1217–1232

Chapter 29

Uranium, Thorium and Anthropogenic Radionuclides as Atmospheric Tracers

K. Hirose

Abstract Anthropogenic radionuclides (^{137}Cs , ^{90}Sr , Pu isotopes and others) and uranium and thorium in rainwater and airborne dust are useful tracers for better understanding of atmospheric transport processes, micrometeorological processes, and natural and human induced environmental changes. Typically, analyses on spatial and temporal changes of anthropogenic radionuclides have aided to constrain the time scale of atmospheric transport of aerosols, such as stratosphere and troposphere residence times of aerosols. Although uranium and thorium in the atmosphere are used primarily as tracers of soil dust, their levels and isotope ratios have been significantly perturbed by anthropogenic sources, (e.g., fly ash and accidental releases of uranium). Therefore, uranium, thorium and their isotope ratios in airborne dust and rainwater reflect environmental changes caused by human activities and climate change. Taking into account that rates of anthropogenic radioactive fallout have recently been boosted by the resuspension of radionuclides in deposited particles, recent variations of anthropogenic radionuclides in rainwater and surface air, as well as thorium and uranium isotopes, is important tracers to study ongoing terrestrial environmental changes due to human activities.

29.1 Introduction

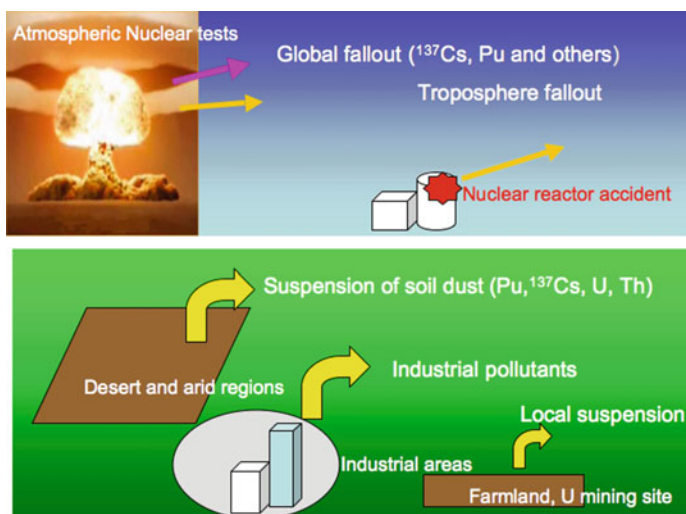
Radioactive elements have been released in the atmosphere by natural and anthropogenic processes as shown in Fig. 29.1, which have been extensively

cycling in the earth environment. Especially anthropogenic radionuclides (e.g., fission products such as ^{137}Cs (half-life: 30.07 years), ^{90}Sr (half-life: 28.78 years) and others, and fissile materials (e.g., ^{239}Pu , half-life: 2.411×10^4 years)), are unique tracers because the depositional input both spatially and temporally have been well documented. Anthropogenic radionuclides were initially injected into the atmosphere by atmospheric nuclear explosions at Alamogordo (New Mexico, USA), Hiroshima and Nagasaki (Japan) in 1945. Anthropogenic radionuclides released from atmospheric nuclear tests, serious nuclear reactor accidents, and other sources (e.g., atmospheric burn-up of nuclear satellites) are spread over the globe and are almost globally detectable in the environment (Harley 1980; UNSCEAR 2000). Peaks in the annual deposition of anthropogenic radionuclides occurred in 1963 in the northern hemisphere stations, just after the 1961–1962 large-scale atmospheric nuclear testing conducted by the US and the former USSR, whereas maximum deposition in the southern hemisphere stations appeared in 1964. Maximum annual depositions of ^{137}Cs , ^{90}Sr , and $^{239,240}\text{Pu}$ in 1963 observed at Meteorological Research Institute (MRI), Japan were $1.94 \times 10^3 \text{ Bq m}^{-2}$, $0.71 \times 10^3 \text{ Bq m}^{-2}$, and 7.4 Bq m^{-2} , respectively (Hirose et al. 1987, 2001).

As a result, most of the presently observed anthropogenic radionuclides on the Earth's surface have originated from atmospheric nuclear-weapons testing: the cumulative depositions of ^{137}Cs , ^{90}Sr , and $^{239,240}\text{Pu}$ on the Earth's surface are estimated to be 948×10^{15} , 622×10^{15} , and $11 \times 10^{15} \text{ Bq}$, respectively (UNSCEAR 2000). Another source of atmospheric anthropogenic radionuclides, the Chernobyl nuclear reactor accident, which occurred on April 1986, resulted in global release of anthropogenic

K. Hirose
Department of Materials and Life Sciences, Sophia University,
7-1 Kioicho, Chiyodaku, Tokyo 102-8554, Japan
e-mail: hirose45037@mail2.accsnet.ne.jp

Fig. 29.1 A schematic diagram on the sources and cycling of anthropogenic radionuclides, U and Th in the environment



radionuclides: 38×10^{15} , 8×10^{15} , and 0.06×10^{15} Bq of ^{137}Cs , ^{90}Sr , and $^{239,240}\text{Pu}$ in about 10 days after the explosion (IAEA 1986; also Hong et al. 2011). The anthropogenic radionuclides released from these sources have been cycling and redistributed on the Earth's surface.

In order to apply anthropogenic radionuclides as effective tracers, it is important to obtain long-term data of continuous measurements of anthropogenic radionuclides in air and rainwater under global network (Hardy 1977; Cambrey et al. 1968). Database of anthropogenic radioactivity depositions obtained from global and regional radioactivity observation networks has been constructed (Aoyama et al. 2006; NUSTL Database: www.eml.st.ahs.gov/database/). Analyses of the time series data on the deposition of radionuclides (^{137}Cs , ^{90}Sr , and Pu isotopes) have allowed us to investigate the processes of transport and removal of aerosols in the atmosphere, the processes of exchange between the stratosphere and troposphere (Krey and Krajewski 1970; Hirose et al. 1987), and environmental change (Hirose et al. 2003).

Uranium and thorium are typical fissile materials. Major isotopes of uranium (^{238}U , half-life: 4.47×10^9 years) and thorium (^{232}Th , half-life: 1.41×10^{10} years) in airborne dust and rainwater are of lithogenic origin; especially uranium mine operation sites are sources of uranium and thorium bearing particles (Martin 2003). Therefore, uranium and thorium in rainwater and airborne dust are primarily tracers of soil dust and contaminated soil particles due to human

activities. On the other hand, significant amounts of uranium and thorium are also released to the atmosphere by industrial activities such as coal burning. Fly ash particles are considerably enriched in several radionuclides (Kolb 1989; Tadmor 1986). In addition to major isotopes of uranium and thorium, several long-lived isotopes of uranium- and thorium-series (Chap. 2) have also been observed in rainwater and airborne particles; for uranium, ^{235}U (half-life: 7.04×10^8 years), ^{234}U (half-life: 2.45×10^5 years), a progeny of ^{234}Th (half-life: 24.1 days) belonging to U-238 series and for thorium, ^{230}Th (half-life: 7.54×10^4 years), a progeny of ^{234}U belonging to U-238 series and ^{228}Th (half-life: 1.91 years), a progeny of ^{228}Ra (half-life: 5.75 years) belonging to Th-232 series. Anthropogenic processes such as ^{235}U release from atmospheric burn-up of nuclear satellites (Krey et al. 1979) and nuclear explosions of ^{235}U (Matsunami and Mamuro 1975), cause perturbation of isotope ratios of uranium, whereas natural fractionation processes in the course of erosion of rocks may occur between progenies of uranium and thorium; e.g., $^{238}\text{U} - ^{234}\text{U}$, $^{232}\text{Th} - ^{228}\text{Th}$. Therefore, the isotope ratios of uranium and thorium can provide important information on sources of airborne particles and transport processes.

Here, we review studies on the atmospheric behavior of anthropogenic (typically, ^{137}Cs , ^{90}Sr , and Pu isotopes) and natural radionuclides (uranium and thorium isotopes). We discuss to usefulness of these radionuclides as atmospheric tracers.

29.2 Method

29.2.1 Sampling

29.2.1.1 Airborne Particle Sampling

A high volume sampler installed into a precipitation shelter is generally used to collect samples of airborne particulate materials on dense cellulose, glass fiber, or membrane filters at flow rates of $0.5\text{--}2\text{ m}^3\text{ min}^{-1}$ (e.g., glass fiber filter (GB-100R) with a nominal collection efficiency of 99.9% for larger than $0.3\text{ }\mu\text{m}$ of aerodynamic particle diameter at a flow rate of $1\text{ m}^3\text{ min}^{-1}$; cellulose filters (Whatman 41) with a collection efficiency of the range of 70–80% for ^{210}Pb (Turekian and Cochran 1981; Turekian et al. 1989)). The sampler is generally set at the observation field at least 1 meter above the ground. The filter is changed at time spans from a day to a week to avoid lowering of collection efficiency. High-volume cascade impactors (HVCI) are used to determine the size distribution of radionuclide-bearing particles in surface air (e.g., Shibata-type HVCI, Five stages: I $>7\text{ }\mu\text{m}$, II $3.3\text{--}7.0\text{ }\mu\text{m}$, III $2.0\text{--}3.3\text{ }\mu\text{m}$, IV $1.1\text{--}2.0\text{ }\mu\text{m}$, V $<1.1\text{ }\mu\text{m}$ of aerodynamic diameter with a flow rate of 600 L min^{-1} (Hirose 2000); a modified Harvard HVCI, four stages: I $2.5\text{--}10\text{ }\mu\text{m}$, II $1.0\text{--}2.5\text{ }\mu\text{m}$, III $0.2\text{--}1.0\text{ }\mu\text{m}$, IV $<0.2\text{ }\mu\text{m}$ of aerodynamic diameter with a flow rate of 800 L min^{-1} (Pennannen et al. 2007)). A glass fiber filter is commonly used as a backup filter to collect airborne particles in each stage. The particulate mass agrees with 10% of sum of multi-stage size distribution of the HVCI. The sampling period for the collection of size-fractionated airborne particle samples is 1–10 days. Time span for aerosol sampling depends on the research purpose; short time sampling is required to investigate local and micrometeorological processes, whereas monthly sampling is adequate to elucidate seasonal change and long-term variability. Filter samples are subjected to radiochemical analysis for radionuclides (Sect. 2.2).

29.2.1.2 Dry Deposition Sampling

Dry deposition samples of natural and anthropogenic radionuclides have been collected in a plastic-made sampler of a smooth surface of known area (e.g.,

1 m^2), which is installed at 1 m above the ground level. Dry deposition sampling periods are one to several days, which typically correspond to the time span between passing troughs accompanied with rain events in certain areas. Dry deposition samples on the sampler are gathered using distilled water and transferred into a plastic container. Usually, acid cleaning is routinely done to prevent the wall adsorption of radionuclides. Dry deposition samples are subjected to radiochemical analysis for radionuclides (Sect. 2.2).

29.2.1.3 Rainwater Sampling

Each rainwater sample is collected in a plastic sampler with smooth surface of known area (e.g., 1 m^2), installed at 1 m height above the ground level. To study removal processes of aerosols, serial sampling is commonly performed. In general, the collector is changed after approximately equal amounts of rainfall. However, the activity of radionuclides in a sample collected after the initial 0.5 or 1.0 mm of precipitation amount is usually higher than the following samples, because the early part of a rainfall is expected to be the period of most rapid change in dust loadings. Rainwater samples are subjected to radiochemical analysis for radionuclides (Sect. 2.2).

29.2.1.4 Total or Bulk Deposition Sampling

Monthly deposition samples including rainwater and falling dust are collected by using plastic open-surface collectors with surface areas of 1 m^2 (sometimes using samplers with wider surface area of $>2\text{ m}^2$). The 1-m^2 collector is installed at about 1 m height above the ground level on the observation field.

29.2.2 Analytical Method

A composite of air filters corresponding to several days to 1 month is usually subjected for radionuclide analysis. A portion of filter samples is pressurized to make a disk for γ -spectrometry. Another portion of filter samples is digested by concentrated nitric acid to extract ^{90}Sr , $^{239,240}\text{Pu}$, uranium and thorium. Radiochemical separation and purification for these radionuclides are similar to the chemical analysis for dry and bulk deposition samples described below.

Monthly total (wet + dry) deposition samples (rain-water between 10 and 100 L) are evaporated to dryness in an evaporation dish, or in a glass flask in a rotary vacuum evaporator. Residue samples in the monthly deposition are weighed after being dried in an oven at 110°C. In our study, the mean weight of the residue in the monthly deposition during the period 1990–2005 was in a range from 0.8 to 9.4 g m⁻² (Hirose et al. 2007). The monthly residue sample is transferred to a plastic container. The residue samples are subjected to quantification of γ -emitting radionuclides (e.g., ¹³⁷Cs photo peak at 661 keV) by γ -spectrometry with a Ge detector. After γ ray measurements, the residue samples are digested with concentrated nitric acid and small amounts of perchloric acid on a hotplate. This process is expected to decompose most of the organic matter. The solution obtained is subjected to radiochemical separation to quantify ⁹⁰Sr, ^{239,240}Pu, uranium and thorium.

After the radiochemical separation from α -emitters, ⁹⁰Sr is quantified by β -counting with a low-background 2 π gas-flow β -counter (described in detail by Otsuji-Hatori et al. 1996). α -emitters (^{239,240}Pu, uranium, thorium) in deposition and air filter samples are quantified using α -spectrometer comprising of semiconductor detectors and multichannel pulse-height analyzer after chemical separation and purification with an anion exchange resin and/or extraction chromatography techniques (Berne 1995; Hirose et al. 2010; IAEA/AQ/11 2009; Kim et al. 2000; Martin 2003). For plutonium analysis by α -spectrometry, the sum of ²³⁹Pu (E_a : 5.15 MeV) and ²⁴⁰Pu (E_a : 5.17 MeV) activities are measured because the alpha spectrometry cannot resolve 20 keV energy difference between ²³⁹Pu and ²⁴⁰Pu. On the other hand, uranium (²³⁸U (E_a : 4.18 MeV) and ²³⁴U (E_a : 4.77 MeV)) and thorium isotopes (²³²Th (E_a : 3.99 MeV), ²³⁰Th (E_a : 4.68 MeV) and ²²⁸Th (E_a : 5.42 MeV)) can be separately determined by α -spectrometry. Chemical yields of plutonium, uranium and thorium are determined with ²⁴²Pu (E_a : 4.90 MeV), ²³²U (E_a : 5.23 MeV) and ²²⁹Th (E_a : 4.85 MeV) yield tracers, respectively.

Mass spectrometry is a powerful tool to gain information on precious isotope ratios (e.g., ²⁴⁰Pu/²³⁹Pu, ²³⁵U/²³⁸U and others) and to do ultra low-level trace measurements. Especially, thermal ionization mass spectrometer (TIMES) has been used as the only reliable tool to measure ²³⁴U/²³⁸U and ²³⁰Th/²³²Th atom ratios in the geological field for many years (Faure

1986). Recent development of mass spectrometry techniques (accelerator mass spectrometry (AMS) and inductively coupled plasma mass spectrometry (ICPMS)) allows us to do high sensitive isotope determination of long-lived α -emitters (Chamizo et al. 2008; Kikawada et al. 2009; Kim et al. 2000, 2007; Roos 2008).

In order to ensure high precision and accuracy of the ¹³⁷Cs, ⁹⁰Sr, and Pu isotope analyses in environmental samples, it is important to establish standard analytical procedures with standard/reference materials. The quality of the ¹³⁷Cs, ⁹⁰Sr, and Pu isotope analyses of the deposition samples was assured by checking against a reference material made by a composite of deposition samples collected in 12 stations of Japan (Otsuji-Hatori et al. 1996; Zhang et al. 2010). A list of Standard Reference Materials for these nuclides is listed in Baskran et al. (2009).

29.3 Atmospheric Tracers

29.3.1 Anthropogenic Radionuclides

29.3.1.1 Tracers of Global Transport Including Stratosphere and Troposphere Exchange

Anthropogenic radionuclides originating from the atmospheric nuclear explosions were injected into stratosphere and upper troposphere; injection altitude is dependent on the scale and height of nuclear explosion (Reiter and Bauer 1975). Anthropogenic radionuclides produced by the nuclear explosion immediately attach to sub-micrometer aerosols, although several fission products initially are present in gaseous forms (e.g., ¹³⁷Xe (half-life: 3.818 min) → ¹³⁷Cs). Therefore, anthropogenic radionuclides are good tracers of air motion within and between the upper troposphere and stratosphere. In order to assess the environmental effects of anthropogenic radioactivity originating from the atmospheric nuclear tests, atmospheric monitoring networks of radioactivity were established in 1958 (e.g., the Global Fallout Program (EML) (Hardy 1977); UKAEA (Cambray et al. 1968); recent CTBTO network: www.ctbto.org). In these network stations, atmospheric dust and

dry and wet deposition samples were collected in upper atmosphere and ground level. The radioactivity fallout data is provided in some databases (NUSTL Database: www.eml.st.ahs.gov/database/; IGFD Database: Aoyama et al. 2006). Figure 29.2 shows the deposition history of ^{137}Cs and $^{239,240}\text{Pu}$ observed in Meteorological Research Institute (MRI) at Tsukuba, Japan (Hirose et al. 2008). The long-term monitoring of anthropogenic radioactivity allowed us to have information on transport processes and residence times of aerosols in the upper troposphere and the stratosphere (Hirose et al. 1987; Igarashi et al. 1996; Katsuragi 1983; Katsuragi et al. 1982; Reiter and Bauer 1975). The stratospheric residence time of radioactive aerosols was estimated to be about 1 year from the temporal change of the stratospheric radionuclide inventory and radionuclide deposition. However, the temporal change of the annual deposition of anthropogenic radionuclides after the 1961–1962 nuclear testing did not follow a simple exponential curve. Furthermore, the calculated apparent stratospheric residence times depended on the nuclear explosions (the magnitude of the explosion, its location and others) and anthropogenic radionuclides derived from nuclear explosions.

To explain the temporal variation of the radioactive deposition, a two-compartment model of the strato-

sphere, which comprises of the upper and lower stratosphere with half residence times of 0.5 and 0.7 years, respectively, was introduced (Krey and Krajewski 1970). The two compartments model, however, failed to reproduce the temporal variations of radionuclide deposition resulting from smaller scale nuclear explosion such as the 26th Chinese atmospheric nuclear test, conducted on 16 Oct 1980. A three compartment model, which includes an active mixing layer just above tropopause with a half residence time of 0.3 years in addition to upper and lower stratosphere, has been successful to explain all the observed stratospheric injection (Hirose et al. 1987). The monthly radioactivity depositions in the 1960s and 1970s in the mid-latitudes exhibited a typical seasonal change, with a maximum in spring, which is related to the stratosphere–troposphere exchange of radioactive aerosols in the mid-latitude regions (Katsuragi 1983; Katsuragi and Aoyama 1986). A schematic diagram of air motion in the troposphere and stratosphere is shown in Fig. 29.3.

The cumulative deposition of anthropogenic radionuclides shows a typical latitudinal distribution, with high levels in the mid-latitude regions of the Northern Hemisphere (UNSCEAR 2000), reflecting active stratosphere–troposphere exchange of air mass in the mid-latitude region. However, the water column

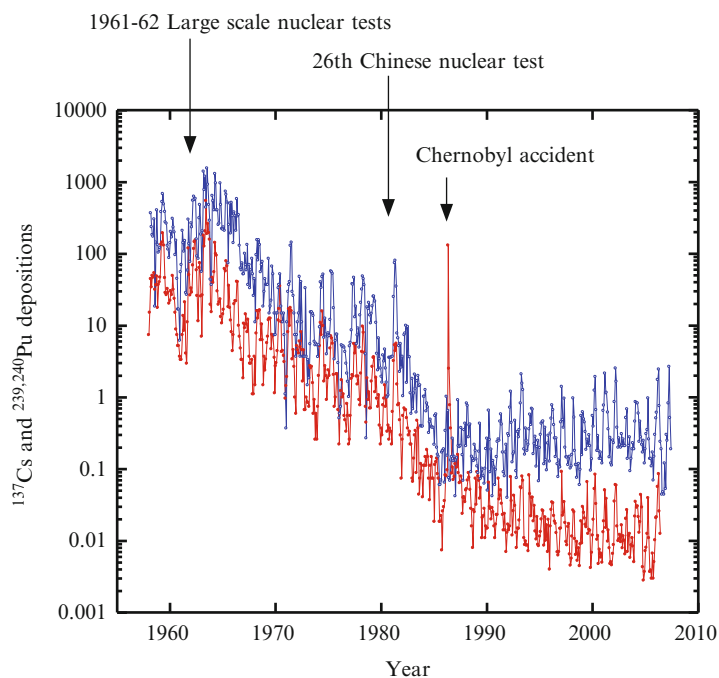


Fig. 29.2 Annual ^{137}Cs and $^{239,240}\text{Pu}$ depositions observed at Tsukuba during the period 1957–2006. Closed circles and open circles are ^{137}Cs (Bq m^{-2}) and $^{239,240}\text{Pu}$ (mBq m^{-2}), respectively

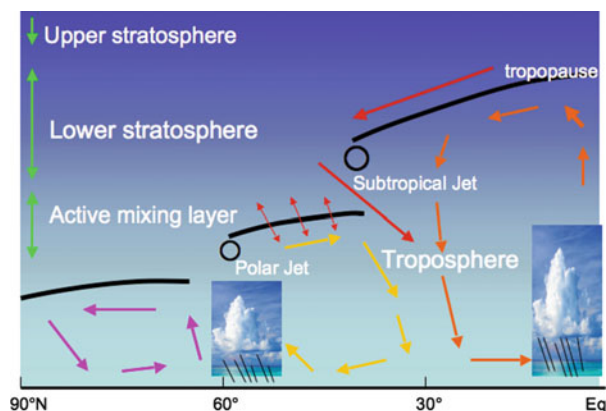


Fig. 29.3 Schematic diagram of air motion in the troposphere and stratosphere. The tropopause height changes from polar region (about 8 km) to equatorial region (about 17 km). Occurrence of polar jet depends on meteorological conditions. As a major pathway of stratosphere and troposphere exchange,

stratospheric air is transported into troposphere via tropopause gap in midlatitude. The active air exchange between stratosphere and troposphere occurs over the mid-latitude tropopause accompanied with strong turbulences. *Orange arrow*: Hadley Cell, *yellow arrow*: Ferrel Cell, *pink arrow*: Polar Cell

inventories of ^{137}Cs in the North Pacific Ocean were 2–3 times higher than the cumulative decay-corrected ^{137}Cs fallout at the same latitude as stated in the UNSCEAR Reports (Hong et al. 2011). Recently, the global total deposition pattern of ^{137}Cs was reconstructed from a comprehensive dataset, which consists of the cumulative ^{137}Cs depositions and ^{137}Cs inventories of soil columns and water columns in each site (Aoyama et al. 2006; Hong et al. 2011). The reconstructed geographical distribution of the total ^{137}Cs deposition (Fig. 29.4) suggests that the markedly higher cumulative ^{137}Cs deposition regions appeared in the western North Pacific near Japan and the western North Atlantic near Canada whereas the low total ^{137}Cs deposition occurred in the desert and arid regions of the mid-latitude zone. These high total deposition regions correspond to areas of high precipitation amounts in addition to location of the active stratosphere–troposphere exchange. Therefore, any particles introduced into the stratosphere, such as volcanic ash, could spill over largely in those two regions compared to the rest of the northern hemisphere.

29.3.1.2 Tracers of Troposphere Transport: Chernobyl-Derived Radionuclides

Large amounts of anthropogenic radionuclides were injected from the Chernobyl accident (from 28 April

1986 through 6 May 1986) into the lower troposphere. As a result, several anthropogenic radionuclides were observed in air and rainwater of the Northern Hemisphere, mainly in the Scandinavian region. ^{137}Cs and ^{134}Cs (half-life: 2.046 years) in surface air and rainwater collected at MRI, Japan in May 1986 as well as volatile short-lived radionuclides (^{131}I (half-life: 8.02 day), ^{103}Ru (half-life: 39.26 day) and others) increased markedly compared to those in the previous years (Aoyama et al. 1986) (Fig. 29.2), whereas plutonium did not show any marked increase in Japan, although higher depositions of the Chernobyl-derived transuranics were observed in the eastern Europe (IAEA 2006). The Chernobyl radioactivity in surface air (Fig. 29.5), which was characterized by volatile short-lived radionuclides, decreased in accordance with the tropospheric residence time of about 25 days (^{137}Cs) (Aoyama 1999). The $^{134}\text{Cs}/^{137}\text{Cs}$ activity ratio in surface air (0.5) was constant during the period from May to June 1986, whereas the $^{131}\text{I}/^{137}\text{Cs}$ activity ratio increased exponentially, and the $^{103}\text{Ru}/^{137}\text{Cs}$ activity ratio showed higher values from 20 May to June 10 (Fig. 29.6). The differences in the atmospheric behavior between different Chernobyl-derived radionuclides are attributable to the differences in chemical properties (e.g., gas – particle exchange for radioiodine) and method of release of the radioactive-plume (larger amounts of ^{103}Ru was released in the secondary stage rather than the initial explosion at Chernobyl). Although the Chernobyl radioactivity was

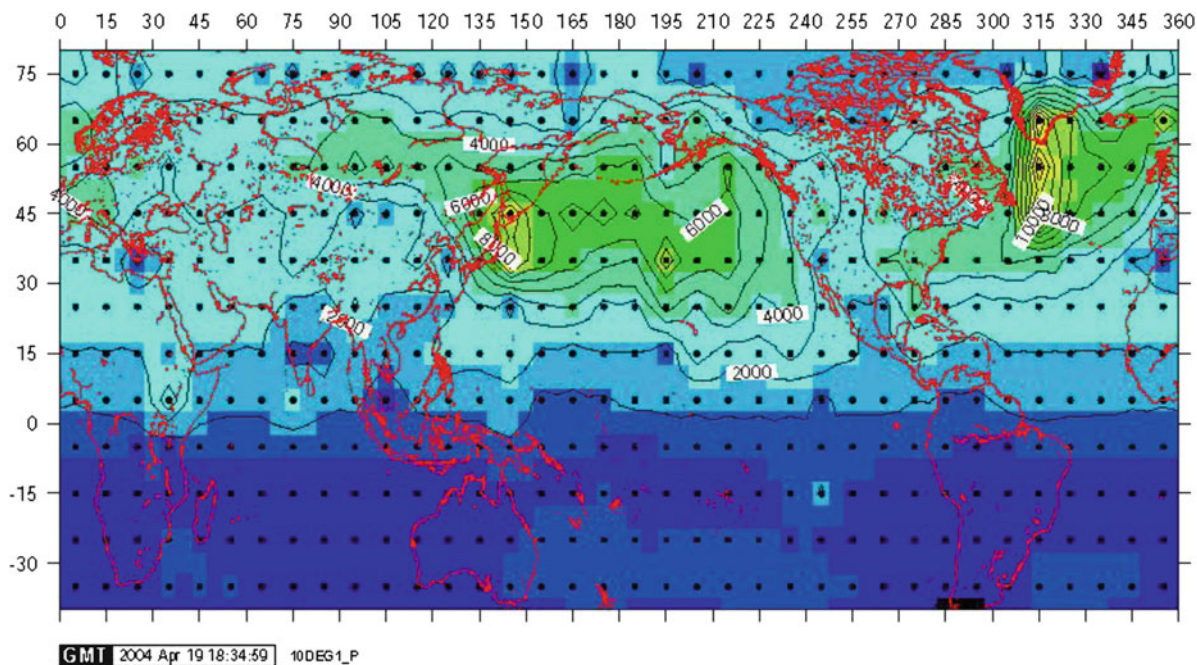
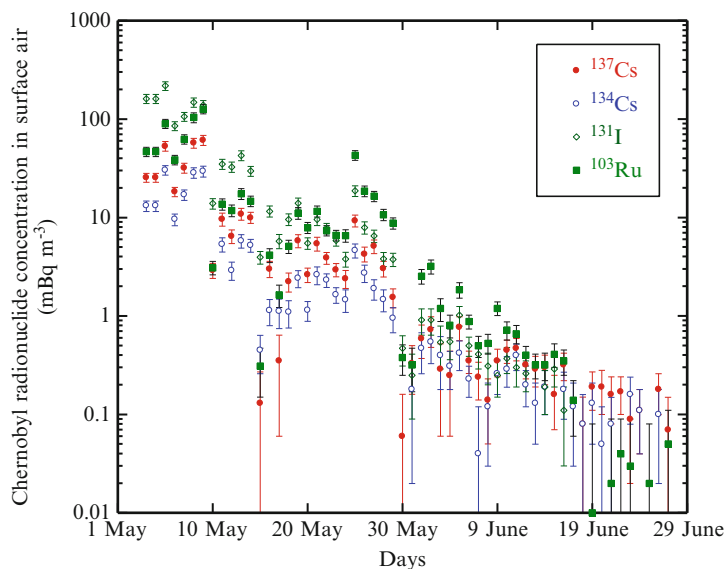


Fig. 29.4 Geographical distribution of ^{137}Cs inventory due to global fallout as of 1970, from Aoyama et al. (2006)

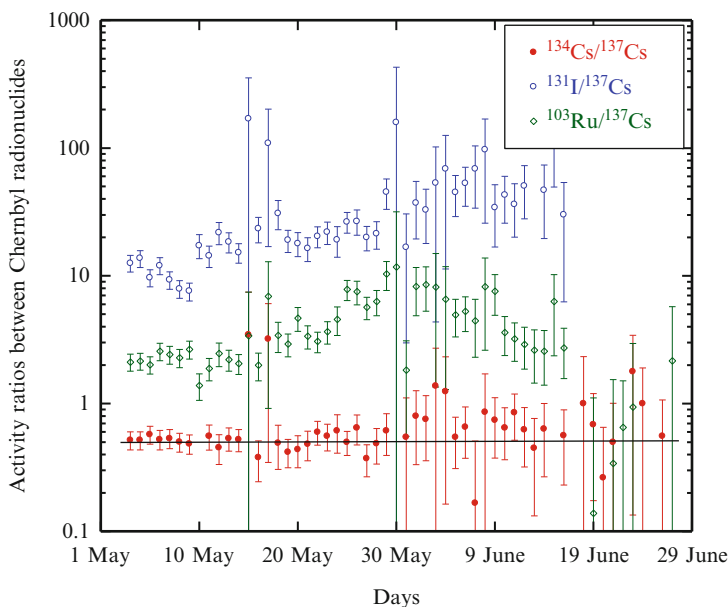
Fig. 29.5 Temporal trends of the Chernobyl radionuclides in surface air observed at the MRI, Tsukuba, Japan during May and June 1986. The data are taken from Aoyama (1999)



injected into the lower troposphere, small amounts of the Chernobyl ^{137}Cs (about 0.5% of total release) were transported to the stratosphere (Aoyama 1988; Aoyama et al. 1991). The effect of the Chernobyl radioactivity on the total deposition in Japan depended on the kind

of radionuclide: the relative contributions (F) of the Chernobyl-derived ^{90}Sr and $^{239,240}\text{Pu}$ to the Chernobyl-derived ^{137}Cs ($F = (D_R/D_{\text{Cs}}) \cdot (I_R/I_{\text{Cs}})^{-1}$, where D_R and D_{Cs} are the depositions of the Chernobyl-derived radionuclide and ^{137}Cs , respectively, and I_R and I_{Cs} are

Fig. 29.6 Temporal trends of radionuclide ratios derived from the Chernobyl accident. Radioactive decay of ^{131}I and ^{103}Ru concentrations in surface air was corrected to the first day of the accident. The data are taken from Aoyama (1999)



the total released amounts of the Chernobyl-derived radionuclide and ^{137}Cs , respectively) were only 1.5 and 0.18%, respectively – much smaller than the contribution of the Chernobyl-derived ^{137}Cs (Hirose 1995). The difference in deposition behavior among the Chernobyl-derived radionuclides is mainly attributable to the difference in size of the radionuclide-bearing particles (size order $^{137}\text{Cs} < ^{90}\text{Sr} < ^{239,240}\text{Pu}$): larger particles are more easily removed from the atmosphere by wet and dry deposition (Aoyama et al. 1992; Hirose 1995; Hirose et al. 1993, 2001).

29.3.1.3 Tracers of Regional Transport: Anthropogenic Radionuclides-Bearing Soil Dust

The anthropogenic radionuclides observed presently in surface air and rainwater are considered to have been derived from the resuspension of radionuclides deposited on the land surface (Arimoto et al. 2005; Karlsson et al. 2008; Nicholson 1988; Rosner and Winkler 2001). After more than 10 years since the cessation of atmospheric nuclear testing, the atmospheric deposition of ^{137}Cs , ^{90}Sr and $^{239,240}\text{Pu}$ derived from nuclear tests are negligible (UNSEAR 2000). It is likely that the anthropogenic radionuclides and their activity ratios in surface air and rainwater reflect their redistri-

bution processes on the land surface. Especially, regional transport of soil dust from the desert and arid region (e.g., the Sahara dust in Europe and the Asian dust in East Asia) is an important factor for the resuspension of anthropogenic radionuclides (Fujiwara et al. 2007; Igarashi et al. 2001, 2003, 2009; Hirose et al. 2003, 2004; Lee et al. 2002; Lee et al. 2006). In addition to the resuspension, biomass burning such as forest fires is another potential source of several anthropogenic radionuclides in the air and rainwater (e.g., in highly contaminated areas near the Chernobyl accident site), although the radioactivity emitted by biomass burning depends on the radionuclides ($^{137}\text{Cs} \gg \text{Pu}$) (Lujaniené et al. 2009). In fact, sporadic high ^{137}Cs concentrations in surface air were observed near the region heavily contaminated with the Chernobyl fallout (Grabowska et al. 2003; Yoschenko et al. 2006). Atmospheric behavior, therefore, differs among anthropogenic radionuclides. In fact, ^{90}Sr and ^{137}Cs deposition fluxes observed in Japan since 1990 have been decreasing slowly, whereas $^{239,240}\text{Pu}$ deposition has been almost constant since 1985, although there is inter-annual variability of the $^{239,240}\text{Pu}$ deposition (Fig. 29.2). In the 2000s, levels of the annual deposition rates of ^{137}Cs , ^{90}Sr , and $^{239,240}\text{Pu}$ observed at MRI, Japan were $110\text{--}260 \text{ mBq m}^{-2} \text{ y}^{-1}$, $50\text{--}100 \text{ mBq m}^{-2} \text{ y}^{-1}$, and $3\text{--}7 \text{ mBq m}^{-2} \text{ y}^{-1}$, respectively. The monthly anthropogenic radionuclide depositions in East Asia

exhibited seasonal changes, with a maximum in spring (Hirose et al. 2003, 2008; Igarashi et al. 2001, 2003); especially, $^{239,240}\text{Pu}$ deposition showed the most typical seasonal change among ^{137}Cs , ^{90}Sr , and $^{239,240}\text{Pu}$ (Hirose et al. 2003, 2008). The annual and seasonal changes in $^{239,240}\text{Pu}$ deposition coincide with the occurrence of the Kosa (Asian dust) event observed in spring (typically, March and April) in Japan (Hirose et al. 2007). These findings suggest that the major source of the recent anthropogenic radioactive depositions in Japan is aeolian dust produced in the East

Asian deserts and arid areas (Hirose et al. 2003; Igarashi et al. 2001).

To gain a better understanding of the differences in the recent deposition behaviors of the anthropogenic radionuclides, the temporal variations in the specific activities of anthropogenic radionuclides in depositions (activity in residue, in Bq g^{-1}) were examined (Fig. 29.7) (Hirose et al. 2003, 2008); these approximately correspond to the specific activities in soil (Hirose et al. 2003). The $^{239,240}\text{Pu}$ specific activities, which were high in the dust season (January to May) and low in the nondust season (Fig. 29.7a), showed no

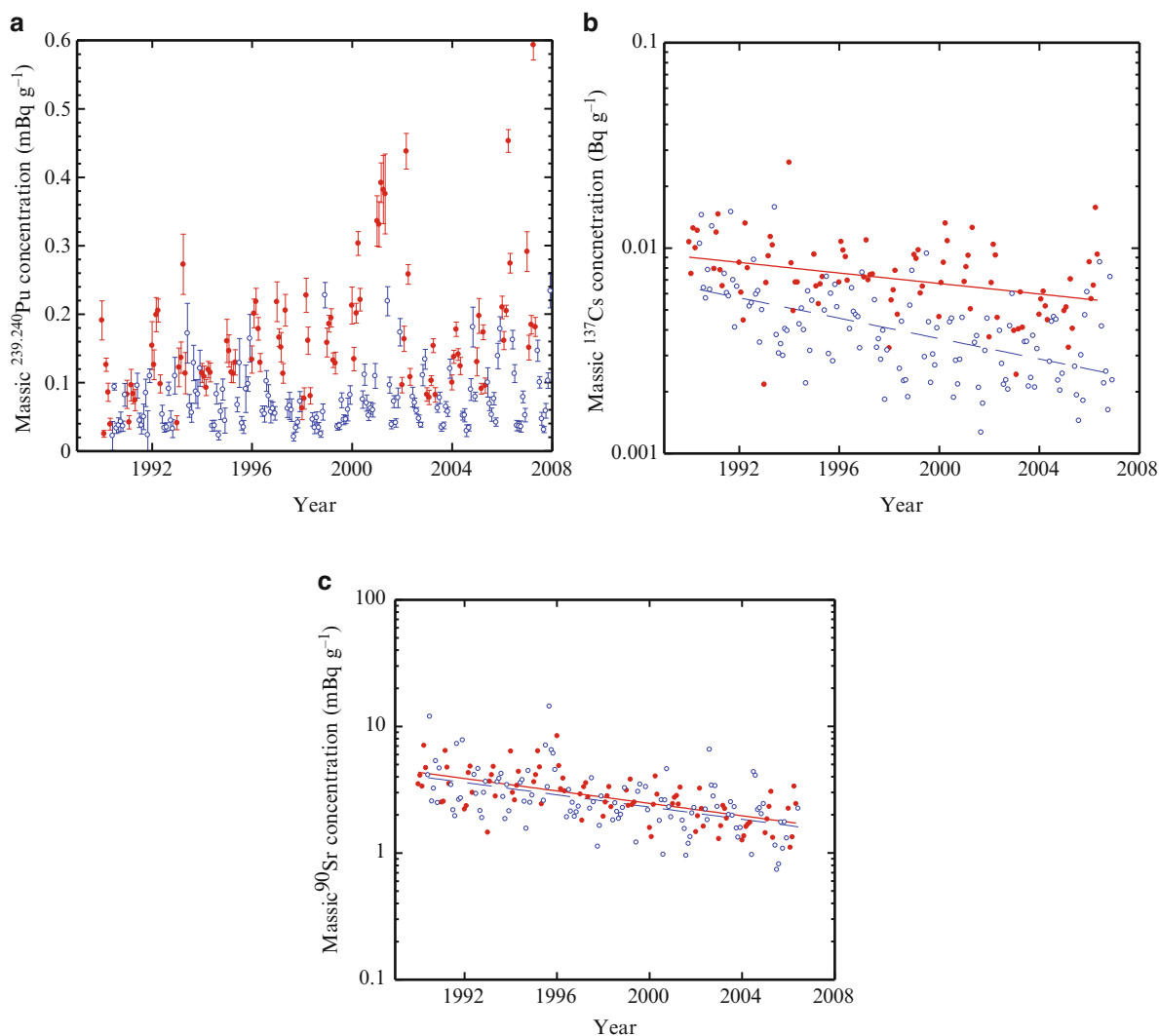
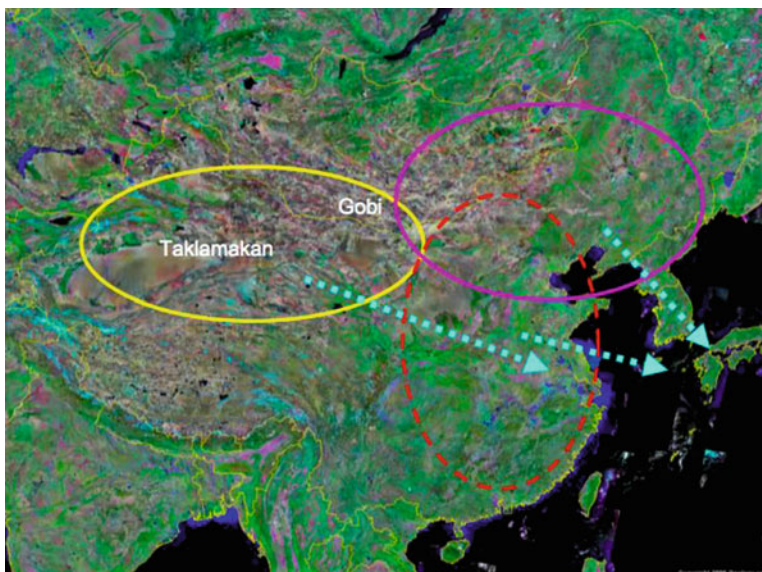


Fig. 29.7 Specific activity concentrations of $^{239,240}\text{Pu}$ (a), ^{137}Cs (b), and ^{90}Sr (c) in monthly depositions observed at Tsukuba during the period 1990–2007. Closed circles are

measurements taken in the dust period (January to May) and open circles are those taken in the nondust period (June to December)

Fig. 29.8 Geographical distributions of source areas of Kosa (yellow), new type of Kosa (purple) and brown cloud derived from Chinese industrial areas (red). Soil dust and pollutants are transported over the North Pacific and US via Korean Peninsula and Japan by prevailing wind system



overall decrease during the period 1990–2007. High $^{239,240}\text{Pu}$ specific activities occurred in the dust season (March or April) of 2000, 2001, 2002, 2006 and 2007 compared to other years. In this connection, Kurosaki and Mikami (2003) reported that from 2000 to 2002 there were marked dust storms around the North China Plain, northeastern China, and the Korean Peninsula, rather than in the Chinese deserts such as Gobi and Taklamakan (Fig. 29.8). Furthermore, plutonium isotope ($^{240}\text{Pu}/^{239}\text{Pu}$) ratios (Hirose et al. 2004) suggest that the plutonium in the recent deposition samples originated from nuclear weapons testing. The change of deposition signal such as $^{137}\text{Cs}/^{90}\text{Sr}$ ratios was observed in the 2000s (Igarashi et al. 2009). These findings suggest that the change of deposition signal of anthropogenic radionuclides in the 2000s reflect recent desertification in the North China Plain, northeastern China, and the Korean Peninsula due to over-cropping and climate change. The ^{137}Cs specific activities, which, like those of plutonium, were high in the dust season and low in the nondust season (Fig. 29.7b), gradually decreased during the period 1990–2006 (Hirose et al. 2008). The apparent half-residence times (HRTs) of the ^{137}Cs specific activity in the dust and nondust seasons were calculated to be 30 ± 10 and 16 ± 4 years, respectively, during the period 1992–2006, taking into account the effect of the Chernobyl ^{137}Cs . The apparent HRT of the ^{137}Cs specific activity in the dust season almost coincided

with the half-life of ^{137}Cs , suggesting that ^{137}Cs did not migrate into the surface soils of the East Asian continent, whereas the apparent HRT of the ^{137}Cs specific activity in the nondust season was consistent with that in Japanese surface soils (14.4 years) (Igarashi et al. 2003). The ^{90}Sr specific activities, which showed no difference between the dust and nondust seasons in contrast to ^{137}Cs and plutonium, gradually decreased (Fig. 29.7c). The apparent HRT of the ^{90}Sr specific activity was calculated to be 12 ± 2 years during the period 1990–2005, which coincides with previous estimates of HRTs in annual depositions (10 years) and surface soil (11 years) (Igarashi et al. 2003). This finding suggests that in spite of the environmental conditions of the sources of ^{90}Sr , it gradually migrates from the soil surface layer by processes such as downward movement with percolating water flow in the soil column and/or incorporation onto larger soil particles from small particles.

Although these three long-lived anthropogenic radionuclides in recent deposition samples originate from atmospheric nuclear testing, now they are derived from the resuspension of radionuclide-bearing surface soil particles and their deposition behaviors differed from each other; in particular, higher $^{239,240}\text{Pu}$ deposition with higher specific activity occurred in the 2000s, whereas ^{90}Sr deposition gradually decreased, as did specific ^{90}Sr activity. In the nondust season, anthropogenic radionuclides in

surface soil derived from atmospheric dust migrate in the order given by: $^{239,240}\text{Pu} < ^{137}\text{Cs} < ^{90}\text{Sr}$. These findings suggest that this set of radionuclides in deposition are useful tools for monitoring ongoing environmental changes in the terrestrial environment.

29.3.2 Uranium and Thorium

29.3.2.1 Tracers of Regional and Local Atmospheric Processes: Uranium Isotopes

Uranium and thorium in atmospheric dust are considered to be derived from suspended soil particles. Contribution from volcanic eruption was pointed out as another natural source of atmospheric uranium (Sakuragi et al. 1983). Anthropogenic sources from atmospheric nuclear tests (Matsunami and Mamuro 1975) and other human activities (e.g., fly ash from coal burning, and locally, uranium mining and milling sites) have significantly perturbed atmospheric dust composition. Especially, coal burning is an important anthropogenic source in Far East Asia because of increasing coal consumption in China. China's coal production in 2007 is estimated to be 2.6×10^{15} gC year⁻¹, which corresponds to atmospheric emission of about 0.8×10^{12} Bq U (6×10^7 g U), if 1% of uranium in China's coal (0.03 Bq g⁻¹; Yang 2007) is released to the atmosphere from coal burning (Papastefanou 2010) (so-called Asian brown cloud: the source region is shown in Fig. 29.8).

To elucidate removal processes of dust including uranium sequential intra-storm samples were analyzed for uranium concentration (Martin 2003). The uranium concentrations in sequential rainwater, as did thorium isotopes, were positively correlated with corresponding filterable solid concentrations. This result is consistent with the finding that uranium in the air is present as forms associated with larger and insoluble particles rather than soluble particles such as sea salts or sulfate particles similar to thorium. The highest uranium concentration was observed at the first stage (the first 0.5 mm of precipitation amount) of the course of a storm and the uranium concentration decreased over the course of a storm, whereas ^{210}Pb concentration, a progeny of ^{222}Rn , showed no decrease over the course of a storm. However, it is

noteworthy that in many cases, ^{210}Pb concentrations in rainwater decreased with increasing precipitation amount (Baskaran et al. 1993; McNeary and Baskaran 2003). The uranium concentration change along the course of a storm is a typical feature of the removal process due to below-cloud washout.

Uranium isotope ratios in atmospheric samples ($^{234}\text{U}/^{238}\text{U}$ and $^{235}\text{U}/^{238}\text{U}$) are a useful tool to identify sources of atmospheric uranium. Uranium isotope ratios, in particular the $^{235}\text{U}/^{238}\text{U}$ ratio, does not change substantially (within ca. $\pm 1\%$) under natural conditions (Weyer et al. 2008). However, atmospheric nuclear tests and accidental releases from nuclear reactor satellites such as atmospheric burn-up of the former USSR satellite Cosmos-954 in January 1978 and Cosmos 1402 in February 1984 (Krey et al. 1979; Sakuragi et al. 1983) caused changes in the uranium isotope ratios ($^{234}\text{U}/^{238}\text{U}$ and $^{235}\text{U}/^{238}\text{U}$) in the air and rainwater. On the other hand, use of depleted uranium is another factor to perturb uranium isotope ratios. Although there is no information on the long term variability of uranium in surface air and rainwater, the uranium isotope ratios recorded in the archived herbage samples in UK and the Alpine ice core samples demonstrated that enriched uranium resulting from nuclear explosions had fallen between 1950s and 1960s (Warneke et al. 2002). Recent analysis of archived deposition samples suggests that enriched uranium has fallen in Japan continuously since the 1960s until today (Kikawada et al. 2009). In addition, significant amounts of the deposition of depleted uranium (DU) in Japan in the past have also been reported.

29.3.2.2 Tracers of Regional and Local Atmospheric Processes: Thorium

Although thorium is one of fissile materials, there is no significant amount of thorium release from nuclear industry and nuclear explosions. A major source of thorium isotopes in atmosphere is dust originating from surface soil. Thorium in air and rainwater primarily reflects chemical constituents on the land surface corresponding to the source regions of the atmospheric dust. Especially thorium isotopic compositions ($^{230}\text{Th}/^{232}\text{Th}$ and $^{228}\text{Th}/^{232}\text{Th}$) in airborne dust are affected by selective dissolution of uranium and radium isotopes in soil erosion processes

and uranium contamination of surface soils due to fertilizer and other industrial materials (Hirose 2000). Therefore, thorium isotopes are considered to be a useful probe to identify sources of atmospheric dust. Furthermore, the temporal change of atmospheric thorium and its isotope ratios would reflect the ongoing environmental change due to human activities on the land surface. In fact, comparison between surface and higher altitude thorium deposition (Hirose et al. 2010) revealed that the deposition of ^{232}Th was markedly lower at a high altitude site (Mt. Haruna: 1,370 m asl) than at a low altitude site (Tsukuba: 28 m asl), in contrast to the mostly similar rates of deposition of $^{239,240}\text{Pu}$ at these two sites. This finding suggests that a significant amount of thorium in deposition samples is originating from local suspension. However, it is noteworthy that coal burning is a potential important source of atmospheric thorium in East Asia; for example, about 0.78×10^{12} Bq of thorium is estimated to be released into the atmosphere due to China's coal burning in 2007 (2.6×10^{15} gC), assuming thorium content of 0.03 Bq g^{-1} in coal (Lu et al. 2006; Tadmor 1986), and 1% of the thorium in coal is released to the atmosphere from coal burning (Papastefanou 2010).

To understand the characteristics of seasonal change of radionuclides in surface air and deposition, it is important to identify their potential sources (Kolb 1989) and to know what kind of environmental changes are taking place. A time series data set of monthly ^{232}Th depositions at Tsukuba (MRI, Japan) during the period

1990–2007 were analyzed. The monthly ^{232}Th depositions at Tsukuba ranged from 4.2 to 73.4 mBq m^{-2} with an average of 23.4 mBq m^{-2} . The monthly ^{232}Th depositions at Tsukuba showed marked seasonal changes, with high values in spring (Hirose et al. 2004, 2007, 2010). Figure 29.9 shows the long-term variation of the monthly ^{232}Th depositions observed at Tsukuba during the period 1990–2007. Most of the higher monthly ^{232}Th depositions at Tsukuba in this period occurred in March and April, which corresponded with high dust (Kosa) events period in the East Asia. This pattern is similar to that for $^{239,240}\text{Pu}$, although it is a typical feature of anthropogenic radionuclide deposition in Japan in the 1990s and 2000s (Hirose et al. 2004, 2007). The higher ^{232}Th deposition in spring implies a greater soil dust load in East Asian air because ^{232}Th is essentially of terrestrial origin. Hirose et al. (2007) showed that the inter-annual differences in the ^{232}Th deposition in spring appear to roughly correspond to the frequency of the Kosa events; in fact, the ^{232}Th deposition in spring (Mar and Apr) in 2001 (more Kosa events) was greater than that in 2003 (fewer Kosa events). Hirose et al. (2007) also reasoned that the source of $^{239,240}\text{Pu}$ in the deposition samples differed from that of ^{232}Th because the peak in the monthly ^{232}Th deposition does not always coincide with that of $^{239,240}\text{Pu}$ deposition, even though both are primarily supported by the atmospheric dust particles derived from soil. This could be due to agricultural activity. Tilling will result in diluting the atmospherically

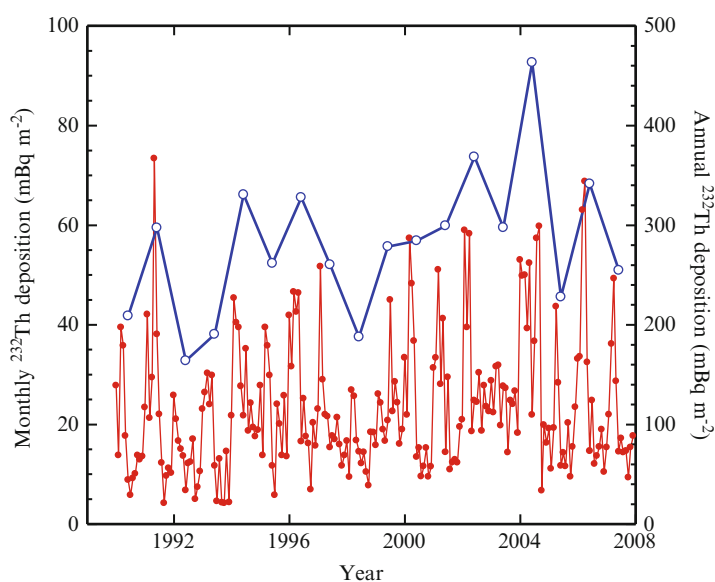


Fig. 29.9 Temporal variation of monthly ^{232}Th deposition observed at Tsukuba, Japan during the period 1990–2007. Closed circle (red): monthly ^{232}Th deposition, open circle (blue): annual ^{232}Th deposition

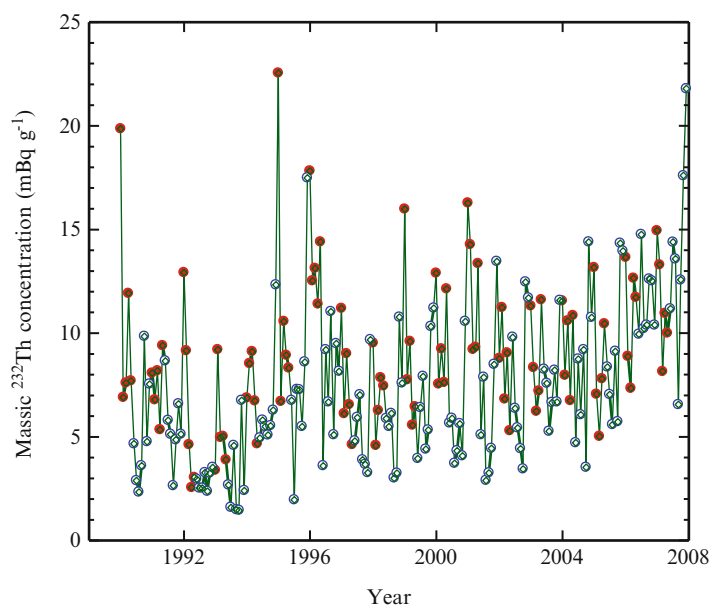


Fig. 29.10 Temporal variation of the ^{232}Th specific activity concentrations at Tsukuba, Japan during the period 1990–2007. Closed circles are measurements taken in the dust period

(January to May) and open circles are those taken in the nondust period (June to December)

delivered Pu in the surface soil, while ^{232}Th will not significantly change in the area tilled soil (Chap. 23). Hirose et al' study (2010) revealed that the monthly ^{232}Th deposition at a higher altitude station (Mt. Haruna) was generally lower than that at the lower altitude station (Tsukuba), except in May and June 2007, and was less than half of that at Tsukuba in Nov 2006, Dec 2006, Jan 2007 and Mar 2007. This suggests that a considerable portion of the atmospheric dust at Tsukuba consists of suspended soil particles derived from local farmland, a source that would be less pronounced at Mt. Haruna.

The annual ^{232}Th depositions observed at Tsukuba during the period 1990–2007 ranged from 164 to 463 mBq m^{-2} (average = 280 mBq m^{-2}). The annual ^{232}Th deposition exhibited a long-term variability as shown Fig. 29.9. In contrast to the monthly ^{232}Th deposition in spring, the annual ^{232}Th deposition did not correspond to frequency of the Kosa events. Factors controlling the long-term variability of the annual ^{232}Th deposition need further investigation.

Specific activity of ^{232}Th in the monthly deposition samples is calculated from the weight of the corresponding monthly residue (Fig. 29.10). The ^{232}Th specific activities during 1990–2007 at Tsukuba

ranged from 1.5 to 22.5 Bq kg^{-1} and exhibited seasonal variations with high values in winter and low values in summer and fall, which is different from that of $^{239,240}\text{Pu}$. A similar seasonal change of the ^{232}Th specific activities at Mt. Haruna with a larger range of values (1.7–19 Bq kg^{-1}) compared to the values at Tsukuba was observed, possibly suggesting that higher specific activity values occurred in winter and lower values in summer and fall (Hirose et al. 2010). The ^{232}Th concentrations in cultivated soils at Tsukuba were in the range 4.4–28.6 Bq kg^{-1} with an average of 13.9 Bq kg^{-1} . The ^{232}Th specific activities in deposition samples were in the same order of magnitude as the concentrations observed in local soil. This suggests that mineral dust originating from soil represents a significant proportion of the deposition residue at Tsukuba, although other possible constituents of deposition could include fly ash, sulfate, sea salt, and other aerosols. The winter peak of the ^{232}Th specific activities observed at Tsukuba is difficult to explain by dust load due to soil suspension. The enhanced ^{232}Th specific activity observed in winter in an urban area such as Tsukuba may be attributed to the contribution from fly ash. The ^{232}Th specific activity seems to increase during the period

1990–2007, with this tendency more remarkable in nondust period. Although causes of this long-term trend at present are unknown, ^{232}Th in fly ash produced by increasing coal burning in China may affect increasing trend of the ^{232}Th specific activities in Japan.

29.3.2.3 Thorium Isotopes as Tracers of Provenance of Soil Dust

The $^{230}\text{Th}/^{232}\text{Th}$ activity ratios in surface air and rain-water in Japan exhibit larger variations than that observed in natural soils, rocks and minerals (Hirose 2000). For example, the $^{230}\text{Th}/^{232}\text{Th}$ activity ratios in monthly deposition samples varied from 0.65 to 1.53 during the period 1990–2007 at Tsukuba (MRI), whereas it varied from 0.75 to 1.03 at the high altitude site (Mt. Haruna) in 2007 (Hirose et al. 2010). High $^{230}\text{Th}/^{232}\text{Th}$ activity ratios occurred at Tsukuba in early spring (February and March), whereas there were no marked peaks in the $^{230}\text{Th}/^{232}\text{Th}$ activity ratios at Mt. Haruna. Although there is no information on the $^{230}\text{Th}/^{232}\text{Th}$ activity ratios in samples collected in China during Kosa events, we can estimate that from the uranium/thorium activity ratios because ^{230}Th is a progeny in the decay series of ^{238}U . Feng et al. (2008) measured the chemical composition of heavy dust falls observed in Beijing in April 2006; the U/Th activity ratio in the dust was found to be 0.45, very different from the $^{230}\text{Th}/^{232}\text{Th}$ ratios in the deposition in Japan. The $^{230}\text{Th}/^{232}\text{Th}$ ratios in surface soils (<53 μm particle size) around Tsukuba are relatively high (2.1–2.6 from 9 samples in cultivated fields near the MRI; Hirose et al. 2007), which may be attributed to ^{230}Th contribution from traces of uranium in fertilizer (assuming that ^{230}Th are also elevated in fertilizers, similar to ^{238}U , ^{234}U and ^{226}Ra). In contrast, the $^{230}\text{Th}/^{232}\text{Th}$ ratios of Chinese soils (<53 μm particle size) have lower values (0.47–0.65; 7 samples from the Taklamakan desert; Hirose et al. 2007), which reflect the absence of fertilizers. The $^{230}\text{Th}/^{232}\text{Th}$ activity ratios in deposition samples from Tsukuba, which were systematically higher than those from Nagasaki (Hirose et al. 2007), were approximately midway between the $^{230}\text{Th}/^{232}\text{Th}$ activity ratios of soils from Tsukuba and the Taklamakan desert. This reveals that the dust with high $^{230}\text{Th}/^{232}\text{Th}$ activity ratios at Tsukuba could not be derived entirely from Asian dust

such as Kosa; there must be another source with a higher $^{230}\text{Th}/^{232}\text{Th}$ activity ratio involved. A high ^{232}Th deposition and high $^{230}\text{Th}/^{232}\text{Th}$ activity ratio observed in February 2002 did not coincide with the Pu peak (Hirose et al. 2007), strongly suggesting that a substantial amount of the dust load in early spring at Tsukuba originated from local sources of suspended soil particles with higher $^{230}\text{Th}/^{232}\text{Th}$ and lower Pu/Th ratios than those of Kosa. The deposition samples at Mt. Haruna showed no peak in the $^{230}\text{Th}/^{232}\text{Th}$ activity ratios in spring, suggesting that fewer suspended soil particles derived from local cultivated fields occur at the Mt. Haruna site because it is located in the boundary layer (Hirose et al. 2010).

29.3.2.4 Two End-Members Mixing Model: Local and Remote Source Fractions in Soil-Derived Dust

Because the $^{230}\text{Th}/^{232}\text{Th}$ activity ratios in local soil (Kanto plain including Tsukuba) differ from those in remote soil (China and Mongolia), Hirose et al. (2010) proposed that the $^{230}\text{Th}/^{232}\text{Th}$ activity ratio in deposition residues can be used to estimate contributions of locally suspended and remotely transported dust for thorium in deposition residues at Tsukuba and Mt. Haruna. Assuming that the ^{232}Th deposition observed at Tsukuba arises from a two-end member mixing of remote and local fractions, the remote fraction in the ^{232}Th deposition, $D(\text{Remote Th})$, is calculated from the observed ^{232}Th deposition, $D_{\text{Th,obs}}$, and observed $^{230}\text{Th}/^{232}\text{Th}$ activity ratio in deposition, R_{obs} , by the following equation:

$$D(\text{Remote Th}) = D_{\text{Th,obs}}(R_L - R_{\text{obs}})/(R_L - R_R), \quad (29.1)$$

where R_L and R_R are the $^{230}\text{Th}/^{232}\text{Th}$ activity ratios in the local and remote fractions of dust, respectively. In this calculation, the $^{230}\text{Th}/^{232}\text{Th}$ activity ratios of 2.3 for the local fraction and 0.65 for the remote fraction from mean values of local soils and East Asian continental soils are assumed. The result of our partitioning calculations is shown in Fig. 29.11. The local ^{232}Th fraction in deposition at Tsukuba varied seasonally, with a maximum in early spring, whereas the local ^{232}Th fraction at a higher altitude site (Mt. Haruna) did

Fig. 29.11 Fractions of ^{232}Th deposition from remote and local sources observed at Tsukuba, Japan during the period 1990–2007. Remote and local fractions at Tsukuba are shown in closed and open circles, respectively

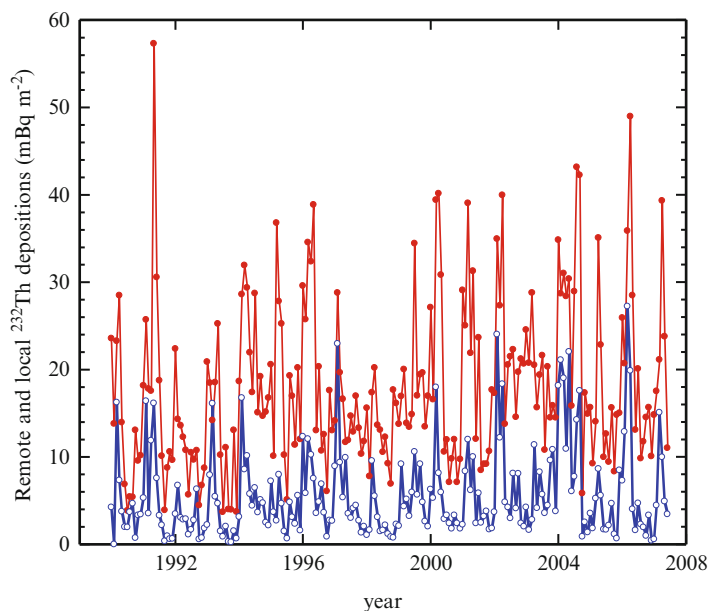
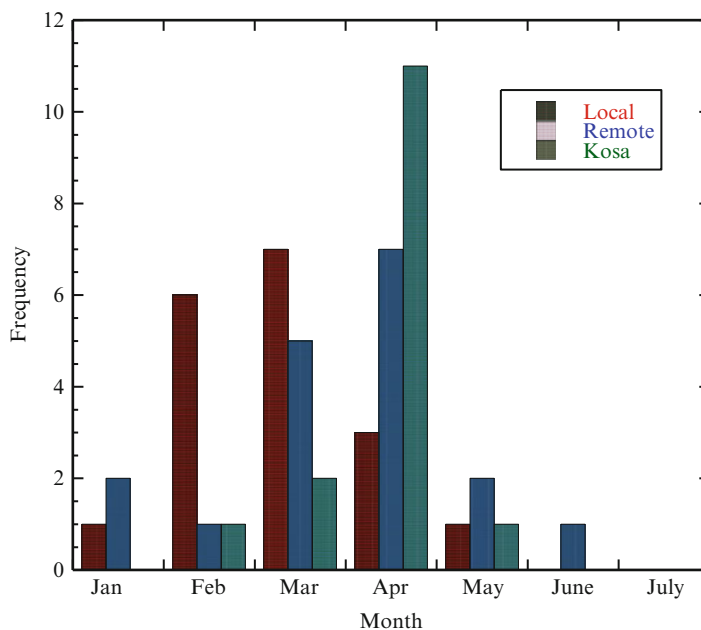


Fig. 29.12 Frequency of month occurring peak ^{232}Th deposition for the remote and local fractions and maximum frequency of Kosa events in Japan during the period 1990–2007



not display pronounced seasonal variation (Hirose et al. 2010). When the peaks in the local ^{232}Th fraction at Tsukuba is compared with the occurrence of local dust storms on the Kanto plain in early spring (Feb and Mar), the ^{232}Th peak was found at about 1 month earlier than those in the remote ^{232}Th fraction as shown in Fig. 29.12. Similarly, the ^{232}Th peaks in

the remote study site in April coincided with that of the maximum frequency of the Kosa events observed in Japan (Fig. 29.12). Contribution of the local ^{232}Th fraction to the total deposition ranged from 0.1 to 53% with an average of 21% at Tsukuba and 6–22% at Mt. Haruna. This may suggest that the remote fraction dominates the ^{232}Th deposition in the Far East Asia

through all seasons. It is noteworthy that partitioning of the remote and local fractions is only a first approximation because the ^{232}Th and $^{230}\text{Th}/^{232}\text{Th}$ activity ratios in air and rainwater are affected by anthropogenic sources such as coal burning. The other factors that can affect the calculation are: (1) variations in the concentrations of ^{238}U and ^{232}Th in the mineral grains between these two sites; (2) variations in the amount of phosphate fertilizer used in these two regions; and (3) variations in the ^{238}U and ^{232}Th concentrations caused by anthropogenic activities.

If the amount of $^{239,240}\text{Pu}$ in the atmospheric deposition derived from local resuspended dust can be evaluated, then, the amount of Pu derived from remote areas (mainly due to Kosa events) can be estimated. Such an estimate is useful for a better understanding of other contaminants borne by long-range atmospheric dust. Hirose et al. (2010) estimated the contribution of the local resuspended $^{239,240}\text{Pu}$ from the $^{239,240}\text{Pu}/^{232}\text{Th}$ ratio in local soil and the local fraction in the ^{232}Th deposition, assuming that the local fraction of $^{239,240}\text{Pu}$ deposition is derived from the suspension of local cultivated soil particles that have a constant $^{239,240}\text{Pu}/^{232}\text{Th}$ activity ratio of 0.025 (Fig. 29.13). The remote fraction in $^{239,240}\text{Pu}$ deposition at Tsukuba usually peaked in April, corresponding to the monthly maximum frequency of the Kosa events in Japan, whereas the local fraction peaked in early spring (Feb and Mar). At a high altitude site (Mt. Haruna),

the local fraction in the $^{239,240}\text{Pu}$ deposition, which showed no marked peak, was lower than that at Tsukuba in early spring (Hirose et al. 2010). This suggests there is less local presence of resuspended $^{239,240}\text{Pu}$ in the deposition at Mt. Haruna than in that at Tsukuba. In spring, most of the $^{239,240}\text{Pu}$ deposition was derived from remote sites, i.e., originating from Kosa events, whereas in summer and fall the major fraction in the $^{239,240}\text{Pu}$ deposition was attributable to the local suspension of soil particles, the reverse of the situation for ^{232}Th deposition. This suggests that the remote fraction of dust particles contains a greater proportion of $^{239,240}\text{Pu}$ -enriched particles in winter and spring and smaller proportion of $^{239,240}\text{Pu}$ particles in summer and fall, which might reflect different source regions of dust particles in different seasons.

29.3.3 Atmospheric Removal Processes of Radionuclides

In the utility of uranium, thorium, and anthropogenic radionuclides as tracers, it is important to have better understanding of the atmospheric removal processes of these radionuclides. Airborne particles containing these radionuclides are deposited on land surface via dry and wet deposition processes.

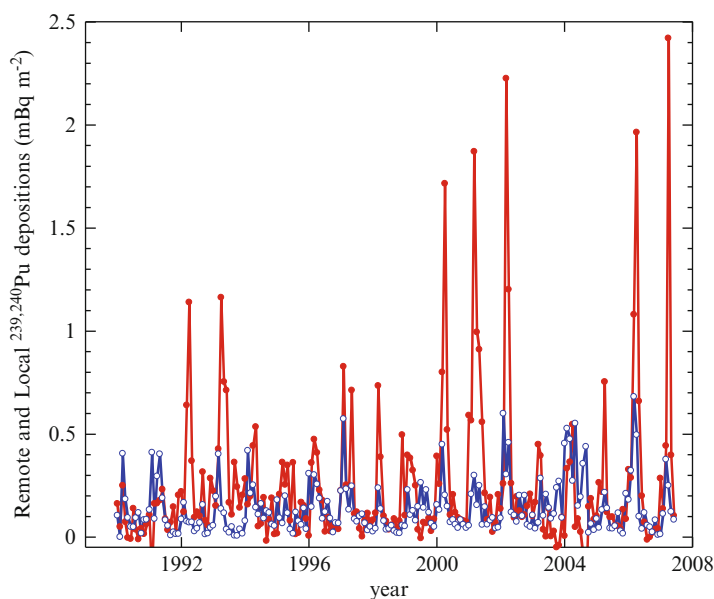


Fig. 29.13 Remote and local fractions of $^{239,240}\text{Pu}$ deposition observed at Tsukuba, Japan during the period 1990–2007. Remote and local fractions at Tsukuba are shown in closed and open circles, respectively

29.3.3.1 Dry Deposition

The dry removal process of radionuclide isotopes-bearing particles is characterized by dry deposition velocities of each radionuclide. The dry deposition velocity ($V_{dry,R}$: m s^{-1}) is written as follows:

$$V_{dry,R} = D_{d,R}/C_{a,R}, \quad (29.2)$$

where $D_{d,R}$ and $C_{a,R}$ are dry deposition flux ($\text{Bq m}^{-2}\text{s}^{-1}$) and surface air concentration (Bq m^{-3}) of the radionuclide, respectively. The dry deposition velocity depends on kind of radionuclides and isotopes. The dry deposition velocities of thorium isotopes ranged from 0.0038 to 0.040 m s^{-1} (Hirose 2000) and from 0.002 to 0.064 m s^{-1} (Crecelius et al. 1978). On the other hand, the dry deposition velocities of the Chernobyl radioactivity (a range from 0.000035 to 0.0006 m s^{-1} for ^{137}Cs , ^{103}Ru and ^{90}Sr) (Aoyama et al. 1992) were more than an order of magnitude smaller than that of thorium. According to studies of dry deposition processes (Schmel 1980), a major process controlling the dry deposition velocity of aerosols is the gravitational settling, which is related to particle size and density of airborne particles. The gravitational settling rate of soil particles is calculated to be around 0.001 m s^{-1} for a mean particle size of 7 μm and a particle density of about 1.5 g cm^{-3} , which is the minimum value because the dry deposition velocity increases due to friction velocity and surface conditions (Schmel 1980). A reason for the higher dry deposition velocities of thorium-bearing particles is attributable to the fact that most of the thorium isotopes are found in relatively large particles, which may originate from the resuspension of soils.

29.3.3.2 Wet Deposition

The major pathway of deposition of the natural radioactivity in the atmosphere is precipitation scavenging. In order to elucidate the wet removal processes of radionuclides, wet deposition velocity ($V_{wet,R}$) of the radionuclides is a useful tool, which is calculated from wet deposition flux (D_R : $\text{Bq m}^{-2}\text{s}^{-1}$) and surface air concentration ($C_{a,R}$: Bq m^{-3}) of radionuclides using a equation ($V_{wet,R} = D_R/C_{a,R}$). The wet deposition velo-

cities of thorium and anthropogenic radionuclides varied considerably and depended on the type of radionuclides and rainfall events (Hirose 2000). The washout ratios are usually used to describe the wet removal processes of atmospheric pollutants (Barrie 1985; Englemann 1971). The wet deposition velocity can be calculated from:

$$V_{wet,R} = WI_R, \quad (29.3)$$

where I_R is rainfall rate (mm h^{-1}), and W the washout ratio (or scavenging ratio). Washout ratio is given by a ratio of the concentration in bulk precipitation (C_{rain} : Bq m^{-3}) to the concentration in surface air (C_{air} : Bq m^{-3}): C_{rain}/C_{air} . It must be noted that as another definition of washout ratio, W' is equal to $\rho C_{rain}/C_{air}$ where C_{rain} and C_{air} are the concentration in bulk precipitation (Bq kg^{-1}) and surface air (Bq m^{-3}) and ρ is the density of air at standard conditions 1.2 kg m^{-3} at 20°C and 0.76 m Hg (McNeary and Baskaran 2003). The following relationship is established between different defined washout ratios: $W = 10^3 W'/\rho$.

The washout ratios of natural and anthropogenic radionuclides for individual rainfall events are usually on the order of 10^6 ; the washout ratios of ^{232}Th , ^{230}Th and ^{228}Th ranged from 0.13×10^6 to 3.2×10^6 , from 0.087×10^6 to 1.9×10^6 and from 0.16×10^6 to 4.6×10^6 , respectively (Hirose 2000), it was 0.92×10^6 for ^7Be (Harvey and Matthews 1989), from 0.18×10^6 to 1.7×10^6 with an average of 0.79×10^6 for ^7Be and from 0.046×10^6 to 1.9×10^6 with an average of 0.53×10^6 for ^{210}Pb (McNeary and Baskaran 2003); for anthropogenic radionuclides (1×10^6) derived from atmospheric nuclear tests (Slinn 1978) and the Chernobyl radioactivity (^{137}Cs : 0.19×10^6 – 0.53×10^6 , ^{103}Ru : 0.16×10^6 – 0.37×10^6 and ^{90}Sr : 0.50×10^6 – 1.4×10^6) (Hirose et al. 1993).

The washout ratio of atmospheric aerosols depends on meteorological, physical and chemical factors. From a theoretical stand point (Harvey and Matthews 1989; Slinn 1978), the weak dependence of washout ratio on the rainfall rate is predicted, as given in equation (4):

$$W = \alpha I_R^{-\beta}, \quad (29.4)$$

where α and β are constants. For thorium isotopes, the washout ratios were correlated with rainfall rate; values of α and β for ^{232}Th , ^{230}Th and ^{228}Th were estimated to be 0.67×10^6 and 0.69, 0.43×10^6 and 0.72, and 0.88×10^6 and 0.81, respectively (Hirose 2000). The washout ratio of Chernobyl ^{90}Sr , whose AMAD was about $1 \mu\text{m}$, seems to be dependent on the rainfall rate with $\beta = 0.22$ (Hirose et al. 1993). On the other hand, the washout ratios for ^{137}Cs and ^{103}Ru in the Chernobyl radioactivity were nearly independent on the rainfall rate. The constancy of the washout ratio was observed for ^7Be (Harvey and Matthews 1989). It is noteworthy that ^{137}Cs and ^{103}Ru in the Chernobyl radioactivity and cosmogenic ^7Be attach to primarily submicrometer particles. A theoretical model suggests that β is expected to be in the range of 1/4 (for frontal storms) to 1/2 (for convective storms) (Harvey and Matthews 1989). However, these findings suggest that β values of chemical components, reflecting different physical and chemical types of aerosols, may be related to particle sizes of corresponding chemical component-bearing particles instead of rainfall type; in other words, β values seem to increase with particle sizes.

The result indicates that the factors that control the wet deposition flux of airborne particles in individual rainfall events are their concentration in air, particle diameter, and rainfall rate rather than precipitation amount, although the wet deposition flux of radionuclides in larger particles is relatively weakly dependent on rainfall rate in comparison with that of submicrometer particles such as the particles that carried Chernobyl radioactivity.

29.4 Future Directions

The anthropogenic radionuclides in air and rainwater have been measured for more than 5 decades. These data, provided as database, reveal that the anthropogenic radionuclides deposited on the earth surface from the atmospheric nuclear testing and the Chernobyl accident have continuously been redistributed in each geochemical compartment and among compartments due to natural processes and human activities. Environmental changes preferentially reflect concentrations of these radionuclides in the atmosphere. Therefore, these radionuclides in air and rainwater have a great potential to be

utilized to trace ongoing environmental changes occurring in the global and regional scale. Since large-scale release of the anthropogenic radionuclides such as atmospheric nuclear tests and nuclear reactor accidents did not happen in the past 2–3 decades and is not foreseeable in the immediate future, use of anthropogenic radionuclides as atmospheric tracers have declined. However, increasing nuclear power activities in the world could result in the great production of radioactive noble and other gases, which may be useful as tracers (Hirota et al. 2004; Weiss et al. 1983), and increase the possibilities of routine and accidental releases of anthropogenic radionuclides such as ^{137}Cs , ^{90}Sr and Pu. In such events, there will be increasing concern to measure anthropogenic radionuclides in the atmosphere. Although the present levels of anthropogenic radionuclides in surface air and deposition (rainwater) are very low, they are more effective tracers to quantify the environmental changes because high sensitive techniques (ICP-MS and AMS) are available for precise measurements of these radionuclides. Although thorium and uranium in air and rainwater are primarily tracers of soil dynamics in the earth surface, temporal and spatial variations of these isotopes are sometimes caused by perturbation of human activities; especially, current increase in the industrial activities in East Asia causes atmospheric release of huge amounts of pollutants, which may affect natural radioactivity in the atmosphere. High precision measurements of U and Th isotopes using analytical instruments such as MC-ICPMS, TIMS will enable to quantify the changes in the U and Th (and other members in the U-Th series), which can be related to environmental and climatic changes. Furthermore, high precision measurements of Pu along with ^{232}Th measurements will help to quantify the amounts of soil particles derived from tilled areas, as Pu concentration is expected to be very low in surface soil while ^{232}Th concentration is expected to be the same, both in tilled and untilled soil particles. In conclusion, long-lived anthropogenic radionuclides, thorium and uranium isotopes along with the daughter products in the atmosphere will be useful tracers not only to elucidate the atmospheric behaviors of aerosols but also to evaluate ongoing environmental changes, such as desertification and erosion in the terrestrial regions.

Acknowledgements We thank Pavel P. Povinec of Comenius University and Michio Aoyama and Yasuhito Igarashi of the Geochemical Research Department, MRI, for their help in

preparing the manuscript. We also thank two reviewers (Gi-Hoon Hong and Paul Martin) and the editor (Mark Baskaran) for their constructive comments and suggestions.

References

- Aoyama M (1988) Evidence of stratospheric fallout of caesium isotopes from the Chernobyl accident. *Geophys Res Lett* 15:327–330
- Aoyama M (1999) Geochemical studies on behavior of anthropogenic radionuclides in the atmosphere, PhD Thesis, Kanazawa University
- Aoyama M, Hirose K, Suzuki Y, Inoue H, Sugimura Y (1986) High level radioactive nuclides in Japan in May. *Nature* 321:819–820
- Aoyama M, Hirose K, Sugimura Y (1991) The temporal variation of stratospheric fallout derived from the Chernobyl accident. *J Environ Radioact* 13:103–115
- Aoyama M, Hirose K, Takatani S (1992) Particle size dependent dry deposition velocity of the Chernobyl radioactivity. In: Schwartz SE, Slinn WGN (eds) *Precipitation scavenging and atmospheric-surface exchange processes: fifth international conference, hemisphere, vol 3.*, pp 1581–1593
- Aoyama M, Hirose K, Igarashi Y (2006) Re-construction and updating our understanding on the global weapons tests ^{137}Cs fallout. *J Environ Monitor* 8:431–438
- Arimoto R, Webb JL, Conley M (2005) Radioactive contamination of atmospheric dust over southeastern New Mexico. *Atmos Environ* 39:4745–4754
- Barrie LA (1985) Scavenging ratios, wet deposition, and in-cloud oxidation: an application to the oxides of sulphur and nitrogen. *J Geophys Res* 90:5789–5799
- Baskaran M, Coleman CH, Santschi PH (1993) Atmospheric depositional fluxes of ^7Be and ^{210}Pb at Galveston and College Station, Texas. *J Geophys Res* 98:20, 555–520, 571
- Baskaran M, Hong GH, Santschi PH (2009) Radionuclide analysis in seawater. In: Wurl O (ed) *Practical guidelines for the analysis of seawater*. CRC Press, Boca Raton, pp 259–304
- Berne A (1995) Use of EICRoM TRU RESIN in the determination of americium, plutonium and uranium in air filter and water samples. USDOE Report EML-575
- Cambray RS, Fisher EMR et al (1968) Radioactive fallout in air and rain: Result to the middle of 1968. AERE-R 5899 HMSO, London
- Chamizo E, Jimenez-Romos MC et al (2008) Isolation of Pu isotopes from environmental samples using ion chromatography for accelerator mass spectrometry and alpha spectrometry. *Anal Chim Acta* 606:239–245
- Creclius EA, Robertson DE et al (1978) Atmospheric deposition of ^7Be and other elements on the Washington coast. Pacific Northwest Laboratory Annual Report for 1977 to the DOE Assistant Secretary for Environment: Ecological Sciences, PNL-2500 PT-2, Battelle, Pacific Northwest Laboratory, pp 7.25–7.26
- Englemann RJ (1971) Scavenging prediction using ratios of concentrations in air and precipitation. *J Appl Meteorol* 10:493–497
- Faure G (1986) *Principles of isotope geology*, 2nd edn. Wiley, New York
- Feng J-L, Zhu L-P et al (2008) Heavy dust fall in Beijing, on April 16–17, 2006: geochemical properties and indications of the dust provenance. *Geochem J* 42:221–236
- Fujiwara H, Fukuyama T et al (2007) Deposition of atmospheric ^{137}Cs in Japan associated with the Asian dust event of March 2002. *Sci Total Environ* 384:306–315
- Grabowska S, Mietelski JW et al (2003) Gamma emitters on micro-Becquerel activity level in air at Krakow (Poland). *J Atmos Chem* 46:103–116
- Hardy EPJr (1977) Final tabulation of monthly ^{90}Sr data, 1954–1976. USERDE Report HASL-329
- Harley JH (1980) Plutonium in the environment— a review. *J Radiat Res* 21:83–104
- Harvey MJ, Matthews KM (1989) ^7Be deposition in a high-rainfall area of New Zealand. *J Atmos Chem* 8:299–306
- Hirose K (1995) Geochemical studies on the Chernobyl radioactivity in environment. *J Radioanal Nucl Chem Articles* 197:315–335
- Hirose K (2000) Dry and wet deposition behaviors of thorium isotopes. *J Aerosol Res Jpn* 15:256–263
- Hirose K, Aoyama M et al (1987) Annual deposition of Sr-90, Cs-137 and Pu-239,240 from the 1961–1980 nuclear explosions: a simple model. *J Meteor Soc Japan* 65:259–277
- Hirose K, Takatani S, Aoyama M (1993) Wet deposition of radionuclides derived from the Chernobyl accident. *J Atmos Chem* 17:61–71
- Hirose K, Igarashi Y et al (2001) Long-term trends of plutonium fallout observed in Japan. In: Kudo A (ed) *Plutonium in the environment*. Elsevier Science, Amsterdam, pp 251–266
- Hirose K, Igarashi Y et al (2003) Recent trends of plutonium fallout observed in Japan: plutonium as a proxy for desertification. *J Environ Monitor* 5:1–7
- Hirose K, Kim CK et al (2004) Plutonium deposition observed in Daejeon, Korea: wet and dry depositions of plutonium. *Sci Total Environ* 332:243–252
- Hirose K, Igarashi Y, Aoyama M (2007) Recent trends of plutonium fallout observed in Japan: comparison with natural lithogenic radionuclides, thorium isotopes. *J Radioanal Nucl Chem* 273:115–118
- Hirose K, Igarashi Y, Aoyama M (2008) Analysis of 50 years records of atmospheric deposition of long-lived radionuclides in Japan. *Appl Radiat Isot* 66:1675–1678
- Hirose K, Igarashi Y et al (2010) Depositional behaviors of plutonium and thorium at Tsukuba and Mt Haruna in Japan indicate the sources of atmospheric dust. *J Environ Radioact* 101:106–112
- Hirota M, Nemoto K et al (2004) Spatial and temporal variations of atmospheric ^{85}Kr observing during 1995–2001 in Japan: estimation of atmospheric ^{85}Kr inventory in the northern hemisphere. *J Rad Res* 45:405–413
- Hong G-H et al (2011) Applications of anthropogenic radionuclides as tracers to investigate marine environmental processes. In: Baskaran M (ed) *Handbook of environmental isotope geochemistry*. Springer, Heidelberg
- IAEA (1986) Summary Report on the Post-Accident Review Meeting on the Chernobyl Accident. Safety Series No. 75-INSAG-1, International Atomic Energy Agency, Vienna

- IAEA (2006) Experimental consequences of Chernobyl accident and their mediation: twenty years of experience. Report of the Chernobyl Forum Expert Group 'Environment', Radiological assessment reports series, International Atomic Energy Agency, Vienna
- IAEA/AQ/11 (2009) A procedure for the rapid determination of Pu isotopes and Am-241 in soil and sediment samples by alpha spectrometry, IAEA Analytical Quality in Nuclear Application Series No. 11, International Atomic Energy Agency, Vienna
- Igarashi Y, Otsuji-Hatori M, Hirose K (1996) Recent deposition of ^{90}Sr and ^{137}Cs observed in Tsukuba. *J Environ Radioact* 31:157–169
- Igarashi Y, Aoyama M et al (2001) Is it possible to use ^{90}Sr and ^{137}Cs as tracers for the aeolian transport? *Water Air Soil Poll* 130:349–354
- Igarashi Y, Aoyama M et al (2003) Resuspension: decadal monitoring time series of the anthropogenic radioactivity deposition in Japan. *J Rad Res* 44:319–328
- Igarashi Y, Inomata Y et al (2009) Possible change in Asian dust source suggested by atmospheric anthropogenic radionuclides during the 2000s. *Atmos Environ* 43:2971–2980
- Karlsson L, Hernandez F et al (2008) Using ^{137}Cs and ^{40}K to identify natural Saharan dust contributions to PM_{10} concentrations and air quality impairment in the Canary Islands. *Atmos Environ* 42:7034–7042
- Katsuragi Y (1983) A study of ^{90}Sr fallout in Japan. *Papers Meteor Geophys* 33:277–291
- Katsuragi Y, Aoyama M (1986) Seasonal variation of Sr-90 fallout in Japan through the end of 1983. *Pap Meteor Geophys* 37:15–36
- Katsuragi Y, Hirose K, Sugimura Y (1982) A study of plutonium fallout in Tokyo through the end of 1966. *Papers Meteor Geophys* 33:85–93
- Kikawada Y, Oda K et al (2009) Anomalous uranium isotope ratio in atmospheric deposits in Japan. *J Nucl Sci Tech* 46:1094–1098
- Kim CS, Kim CK et al (2000) Rapid determination of Pu isotopes and atom ratios in small amounts of environmental samples by an on-line sample pre-treatment system and isotope dilution high resolution inductively coupled plasma spectrometry. *J Anal At Spectrom* 15:247–255
- Kim CS, Kim CK et al (2007) Determination of Pu isotope concentrations and isotope ratio by inductively coupled plasma mass spectrometry: a review of analytical methodology. *J Anal At Spectrom* 22:827–841
- Kolb W (1989) Seasonal fluctuations of the uranium and thorium contents of aerosols in ground-level air. *J Environ Radioact* 9:61–75
- Krey PW, Krajewski BT (1970) Comparison of atmospheric transport model calculations with observations of radioactive debris. *J Geophys Res* 75:2901–2908
- Krey PW, Leifer R et al (1979) Atmospheric burn-up of the Cosmos-954 reactor. *Science* 205:583–585
- Kurosaki Y, Mikami M (2003) Recent frequent dust events and their relation to surface wind in East Asia. *Geophys Res Lett* 30:1736. doi:10.1029/2003GL017261
- Lee SH, Pham MK, Povinec PP (2002) Radionuclide variations in the air over Monaco. *J Radioanal Nucl Chem* 254:445–453
- Lee HN, Igarashi Y et al (2006) Global model simulations of the transport of Asian and Sahara dust: total deposition of dust mass in Japan. *Water Air Soil Poll* 169:137–166
- Lu X, Jia X, Wang F (2006) Natural radioactivity of coal and its by-products in the Baoji coal-fire power plant, China. *Cur Sci* 91:1508–1511
- Lujanienė G, Aninkevicius V, Lujanas V (2009) Artificial radionuclides in the atmosphere over Lithuania. *J Environ Radioact* 100:108–119
- Martin P (2003) Uranium and thorium series radionuclides in rainwater over several tropical storms. *J Environ Radioact* 65:1–18
- Matsunami T, Mamuro T (1975) Study of uranium deposition by basin method. *Ann Rep Radiat Cen Osaka Pref* 16:22–24
- McNeary D, Baskaran M (2003) Depositional characteristics of ^7Be and ^{210}Pb in southeastern Michigan. *J Geophys Res* 108: D7, 4201, doi:10.1029/2002JD003021.
- Nicholson KW (1988) A review of particle resuspension. *Atmos Environ* 22:2639–2651
- Otsuji-Hatori M, Igarashi Y, Hirose K (1996) Preparation of a reference fallout material for activity measurements. *J Environ Radioact* 31:143–155
- Papastefanou C (2010) Escaping radioactivity from coal-fired plants (CPPs) due to coal burning and associated hazards: a review. *J Environ Radioact* 101:191–200
- Pennanen AS, Sillanpää M et al (2007) Performance of a high-volume cascade impactor in six European urban environments: mass measurement and chemical characterization of size segregated particulate samples. *Sci Total Environ* 15:297–310
- Reiter ER, Bauer E (1975) Residence times of atmospheric pollutant. CIAP Monogr.1, US Department of Transportation, Washington DC
- Roos P (2008) Analysis of radionuclides using ICP-MS. In: Povinec PP (ed) Analysis of environmental radionuclides, Elsevier Science, Amsterdam, pp 295–330
- Rosner G, Winkler R (2001) Long-term variation (1986–1998) of post-Chernobyl ^{90}Sr , ^{137}Cs , ^{238}Pu and $^{239,240}\text{Pu}$ concentrations in air, depositions to ground, resuspension factors and resuspension rates in south Germany. *Sci Total Environ* 273:11–25
- Sakuragi Y, Meason JL, Kuroda PK (1983) Uranium and plutonium isotopes in the atmosphere. *J Geophys Res* 88: 3718–3724
- Schmel GA (1980) Particle and gas dry deposition: a review. *Atmos Environ* 14:983–1011
- Slinn WGN (1978) Parametrizations for resuspension and for wet and dry deposition of particles and gases for use in radiation dose calculations. *Nucl Saf* 19:205–219
- Tadmor J (1986) Radioactivity from coal-fired plants. A review. *J Environ Radioact* 4:177–204
- Turekian KK, Cochran JK (1981) ^{210}Pb in surface air at Enewetak and the Asian dust to the Pacific. *Nature* 292:522–524
- Turekian KK, Graustein WC, Cochran JK (1989) Lead-210 in the SEAREX Program: an aerosol tracer across the Pacific. In: Duce RA (ed) Chemical oceanography, vol 10. Academic, San Diego, pp 51–80
- UNSCEAR (2000) Sources and effects of ionizing radiation, vol. 1: Sources, United Nations Scientific Committee on the Effects of Atomic Radiation, United Nations, New York

- Warneke T, Croudace IW et al (2002) A new ground-level fallout record of uranium and plutonium isotopes for northern temperate latitudes. *Earth Planet Sci Lett* 203:1047–1057
- Weiss W, Sittkus A et al (1983) Large-scale atmospheric mixing derived from meridional profiles of krypton 85. *J Geophys Res* 88:8574–8578
- Weyer S, Anbar AD et al (2008) Natural fractionation of $^{238}\text{U}/^{235}\text{U}$. *Geochim Cosmochim Acta* 72:345–359
- Yang J (2007) Concentration and distribution of uranium in Chinese coals. *Energy* 32:203–212
- Yoschenko VI, Kashparov AV et al (2006) Resuspension and redistribution of radionuclides during grassland and forest fires in the Chernobyl exclusion zone: part I, Fire experiments. *J Environ Radioact* 86:143–163
- Zhang Y, Zheng J et al (2010) Characterization of Pu concentration and its isotopic composition in a reference fallout material. *Sci Total Environ* 408:1139–1144

Chapter 30

Oxygen Isotope Dynamics of Atmospheric Nitrate and Its Precursor Molecules

Greg Michalski, S.K. Bhattacharya, and David F. Mase

Abstract The stable oxygen isotopic composition of atmospheric nitrate is a powerful proxy for assessing what oxidation pathways are important for converting nitrogen oxides into nitrate. Large ^{18}O enrichments and excess ^{17}O (i.e. mass independent composition) are observed in atmospheric nitrate collected across the globe. These isotope enrichments and their variability in space and time have been linked to the magnitude of ozone oxidation. Attempts to model the oxygen isotope enrichments using simplified isotope mass balance assumptions and photochemical models have yielded reasonably good agreement between observations and simulations. However, there is a lack of atmospheric nitrate isotope measurements across a range of different atmospheric environments. Isotopes of oxygen in atmospheric nitrate can be utilized to assess changes in atmospheric chemistry, applied as tracers in nitrate deposition studies, and used to assess the atmosphere's chemical response to environmental change over time using ice core nitrate.

30.1 Introduction

The oxidation of nitrogen compounds into nitrate in the atmosphere is an important mechanism in atmospheric chemistry that controls the transport of this biogeochemically important element. Oxides of nitrogen ($\text{NO}_x = \text{NO} + \text{NO}_2$) are emitted as a by-product

of combustion processes, with anthropogenic emissions from coal burning power plants and automobiles dominating global atmospheric inputs (Galloway et al. 2004; Galloway 1998). However, NO_x is also formed by natural processes such as biogenic nitrification or denitrification (Mosier et al. 1998) and lightning (Martin et al. 2007). A major fraction of NO_x is oxidized in the atmosphere to nitric acid, which is a strong acid that can dramatically lower the pH of precipitation (Rodhe et al. 2002; Galloway 1995). Nitric acid can also react with NH_3 or alkaline dust, generating new aerosols or altering the chemical composition and size of existing particles (Zhang et al. 2000). Atmospheric nitrate ($\text{HNO}_{3(\text{g})}$, $\text{NO}_{3(\text{s})}^-$, $\text{NO}_{3(\text{aq})}^-$) that is removed from the atmosphere by dry and wet deposition is an important new source of N to surface waters, soils, and plant canopies that in turn can impact the function of many ecosystems (Bobbink et al. 2010). Therefore, identifying the mechanisms that transform NO_x into nitrate is key to understanding the natural and human impacted nitrogen cycles from local to regional and global scales.

The use of multiple oxygen isotopes to understand NO_x oxidation in the atmosphere is a recent development. Oxygen has three stable isotopes with approximate mole fractions of: ^{16}O (0.9976), ^{17}O (0.0004) and ^{18}O (0.0020). The international reference material for oxygen is Vienna Standard Mean Ocean Water (V-SMOW) with accepted ratios of 2.0052×10^{-3} for $^{18}\text{O}/^{16}\text{O}$ and 3.827×10^{-4} for $^{17}\text{O}/^{16}\text{O}$ (Kaiser 2009).

The three stable oxygen isotopes normally fractionate in a mass dependant manner, therefore an approximately linear relationship exists between changes in $\delta^{18}\text{O}$ and $\delta^{17}\text{O}$ (Miller 2002). This linearity can be expressed as (Matsuhisa et al. 1978)

G. Michalski (✉) and D.F. Mase
Purdue University, 550 Stadium Mall Drive, West Lafayette,
IN 47907-1210, USA
e-mail: gmichals@purdue.edu; dmase@purdue.edu

S.K. Bhattacharya
Physical Research Laboratory, Navrangpura, Ahmedabad, India
e-mail: bhatta@prl.res.in

$$\delta^{17}\text{O} = 0.52 \cdot \delta^{18}\text{O} \quad (30.1)$$

A plot of $\delta^{17}\text{O}$ vs. $\delta^{18}\text{O}$ (dual isotope ratio plot) values of the main oxygen reservoirs on Earth, including silicate and carbonate rocks (Miller 2002), waters (Meijer and Li 1998), and oxygen in air (Luz and Barkan 2005) confirms this theoretical relationship, and the resulting line is referred to as the oxygen isotope terrestrial fractionation line (TFL – Fig. 30.1).

One notable exception to this mass dependence rule is the isotopic fractionation that occurs during ozone formation (Thiemens et al. 2001; Thiemens and Heidenreich 1983), when the $^{18}\text{O}/^{16}\text{O}$ and $^{17}\text{O}/^{16}\text{O}$ ratios become equally elevated ($\sim 60\text{--}100\text{‰}$ relative to initial O_2). Since the enrichment is nearly the same in both minor isotopes, independent of their mass difference, this process has been termed a mass independent fractionation (MIF) and is quantified approximately by (Miller 2002).

$$\Delta^{17}\text{O} \sim \delta^{17}\text{O} - 0.52 \cdot \delta^{18}\text{O} \quad (30.2)$$

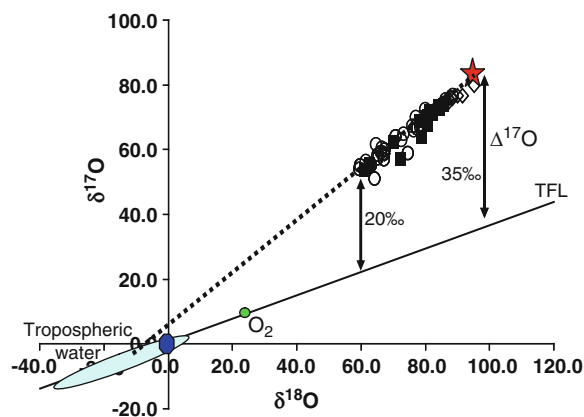


Fig. 30.1 The terrestrial fractionation line (TFL) of oxygen based on the mass dependence of isotope kinetic and equilibrium fractionations that follow $\delta^{17}\text{O} = 0.52 \delta^{18}\text{O}$. The 0.52 coefficient is an average of values that range from 0.5 to 0.53 depending on temperature and the thermodynamics of many reactions (Matsuhisa et al. 1978). The data points show the range of $\Delta^{17}\text{O}$ ($\Delta^{17}\text{O} \sim \delta^{17}\text{O} - 0.52 \cdot \delta^{18}\text{O}$) in atmospheric nitrate from mid-latitudes (Michalski et al. 2003; Kaiser et al. 2007; Morin et al. 2009; Patris et al. 2007). The red star is the approximate triple isotope composition of tropospheric ozone (Johnston and Thiemens 1997; Krankowsky et al. 1995), the blue oval is the range of tropospheric water, and atmospheric O_2 and V-SMOW are the green and blue dots respectively. The atmospheric nitrate data suggest a mixing line between tropospheric ozone and water, in agreement with our mass balance model

Here, MIF has a specific meaning: reactants, whose isotopic compositions lie on the TFL, react and generate products that are offset from the TFL resulting in positive (or negative) $\Delta^{17}\text{O}$ values. In other words, MIF is a chemical process. On the other hand, non-zero $\Delta^{17}\text{O}$ values can be produced either by MIF or by isotope mass balance. For example, when ozone, a powerful oxidizer, transfers O atoms to products during chemical reactions the resulting products have positive $\Delta^{17}\text{O}$ values (Lyons 2001; Michalski and Bhattacharya 2009; Savarino et al. 2000, 2008).

Oxygen isotope compositions in atmospheric nitrate are due to the mixing of oxygen sources (e.g. O_3 , H_2O , O_2) and kinetic and/or equilibrium effects occurring when NO_x is photochemically converted into nitrate. Large $\Delta^{17}\text{O}$ values (23–31‰) observed in atmospheric nitrate (Sect. 30.3) suggest ozone plays an important role as an oxygen source. Tropospheric ozone is also known to have high $\delta^{18}\text{O}$ values ($\sim 80\text{--}130\text{‰}$ V-SMOW) (Sect. 30.5.1) that can be transferred to nitrate and this transfer may partially explain the elevated $\delta^{18}\text{O}$ values observed in atmospheric nitrate (Sect. 30.3). There are other sources of oxygen, however, that are also important during NO_x oxidation, as are the kinetic/equilibrium isotope fractionations that occur during the multiple steps of oxidation. Unfortunately there is currently limited data and little discussion on their importance in controlling the $\delta^{18}\text{O}$ values of atmospheric nitrate. This review will present the current state of knowledge on the chemistry that controls the oxygen isotope composition of atmospheric nitrate, their potential to increase our understanding of NO_x oxidation in the atmosphere, and what future research is needed to maximize this potential.

30.2 Methods for Oxygen Isotope Analysis of Nitrate

The initial analytical approaches for $\delta^{18}\text{O}$ and $\Delta^{17}\text{O}$ analysis of nitrate were pyrolysis techniques. The first reported nitrate pyrolysis technique used a mixture of KNO_3 and $\text{Hg}(\text{CN})_2$ heated to 550°C and isotopic analysis was carried out on the product CO_2 after offline purification (Amberger and Schmidt 1987). Similar offline pyrolysis methods were developed

using a mixture of nitrate salts and graphite, sealed in quartz tubes and heated to 800°C (Revesz et al. 1997; Silva et al. 2000; Wassenaar 1995). This became the preferred method due to the toxicity risks associated with handling cyanide and mercury compounds. Later it was reported that at 800°C the silicate in the quartz reaction vessels would exchange oxygen, to varying degrees, with the product gases. This introduced analytical biases and high uncertainties in data generated using this method (Michalski et al. 2002; Revesz and Böhlke 2002). Kornexl et al. (1999) converted KNO₃ to CO₂ using a high temperature pyrolysis (1,400°C) with a graphite/glassy carbon reaction tube that resolved the exchange problem. In addition, this technique utilized thermal conversion elemental analyzer (TC/EA) devices that could be automated when interfaced with continuous flow isotope ratio mass spectrometer (CF-IRMS) systems. The precision using the TC/EA techniques for nitrate isotopic analysis is ±0.7 per mil for δ¹⁸O. The first technique for Δ¹⁷O analysis in nitrate was the thermal decomposition of AgNO₃ (520°C) followed by IRMS analysis of the product O₂ (Michalski et al. 2002). The relatively low decomposition temperature limited the amount of oxygen exchange with the pre-treated quartz reaction tubes and resulted in highly precise Δ¹⁷O determination (±0.3‰). One drawback of the various pyrolysis techniques is the need for rather large amounts of nitrate (~10⁻⁵–10⁻⁶ mol), which is usually found only in trace amounts in the environment, and makes it difficult to obtain sufficient sample size. In addition, the steps needed to purify environmental samples, such as removing other anions and organic matter, can be inefficient and time consuming (Chang et al. 1999; Michalski 2009).

The size and purification limitations of the pyrolysis methods were largely overcome by the development of the bacterial nitrate reduction technique. The technique is suitable for isotopic analysis of nanomolar amounts of nitrate and requires limited sample preparation. Casciotti et al. (2002) developed the technique, which uses *Pseudomonas aureofaciens* bacteria to produce N₂O that is then analyzed for δ¹⁸O using CF-IRMS. The key is finding suitable bacteria that lack nitrous oxide reductase activity and do not initiate exchange between nitrogen oxide intermediates and cellular water during the reduction. The reported precision of δ¹⁸O using the bacteria technique is ±0.5‰. This technique was modified to analyze Δ¹⁷O by

Kaiser et al. (2007) who reacted the product N₂O over gold (Cliff and Thiemens 1994) to produce N₂ and O₂ and determined the Δ¹⁷O on the product O₂ by CF-IRMS with a precision of ±0.6‰.

A third method for measuring δ¹⁸O in nitrate is the reduction-azide technique (McIlvin and Altabet 2005). This approach first reduces nitrate to nitrite using spongy cadmium. Nitrite is then converted to N₂O by reaction with hydrazoic acid and isotopic analysis is carried out on the N₂O using headspace extraction and CF-IRMS. During the azide-nitrite reaction, roughly 20% of the oxygen in the product N₂O is derived from water in the reactant solution, requiring a significant correction to the data. The δ¹⁸O precision using the reduction-azide technique is ±0.5‰. The azide technique was recently modified to determine Δ¹⁷O using CF-IRMS by converting the product N₂O into O₂ and N₂ over heated gold (Komatsu et al. 2008) with a precision in Δ¹⁷O of ±0.2, and 0.2‰ for δ¹⁸O.

All of the above methods require standardization of the analysis using nitrate reference materials in order to attain accurate nitrate Δ¹⁷O and/or δ¹⁸O values. This is particularly true for Δ¹⁷O analysis which is very sensitive to oxygen blanks arising from exchange reactions or air O₂. The only available Δ¹⁷O reference material to date is USGS-35, a NaNO₃ from the Atacama Desert, which was developed for nitrate Δ¹⁷O analysis (Michalski et al. 2002). Additional nitrate reference salts have been developed to span a range of δ¹⁸O and δ¹⁵N values as discussed by Böhlke et al. (2003) and are available through the National Institute of Science and Technology (NIST).

30.3 Observations of Δ¹⁷O and δ¹⁸O in Atmospheric Nitrate

There are a number of studies on the spatial and seasonal variation of oxygen isotopes in atmospheric nitrate. The first study measuring δ¹⁸O in precipitation nitrate showed that the atmospheric nitrate δ¹⁸O values were very elevated relative to V-SMOW ranging from +55 to +72‰ (Durka et al. 1994; Kendall 1998). Subsequent studies extended the range of values from +25 to +115‰ (Fig. 30.2). Notable annual variations were observed, with higher atmospheric nitrate δ¹⁸O values being found in the colder months and

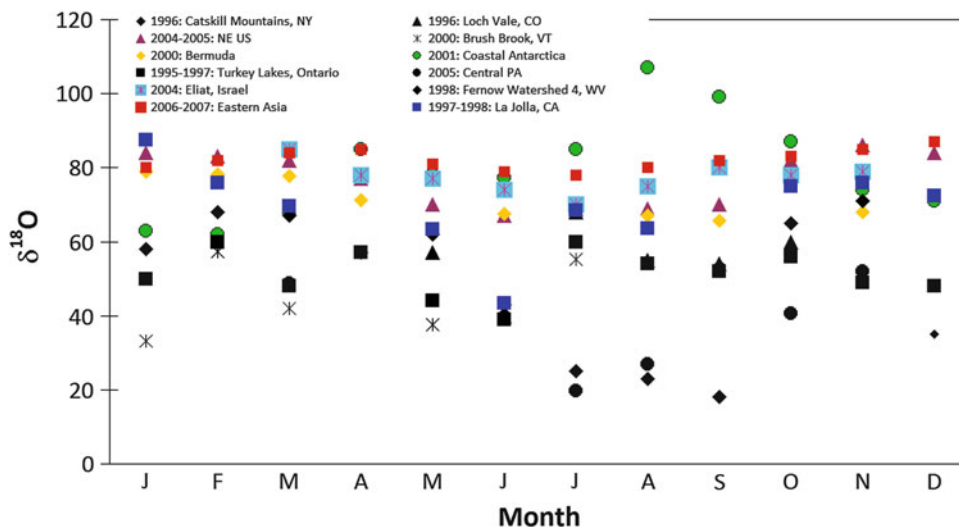


Fig. 30.2 Seasonal variation in $\delta^{18}\text{O}$ values of atmospheric nitrate collected from mid latitude and polar region sites. Individual data sets show that atmospheric nitrate $\delta^{18}\text{O}$ values are usually elevated in the winter months relative to summer. Note data from Savarino et al. data (green colored circle) is from Antarctica, where the seasons are out of phase relative to the northern hemisphere. Black symbols are data produced using the thermal reduction of nitrate by graphite in quartz tube. Color

symbol data was obtained either by the silver nitrate decomposition or bacterial reduction methods. Uncertainty for any given measurement (± 0.4) is the size of the data symbols. Data is from Durka et al. (1994), Morin et al. (2007), Savarino et al. (2006), Spoelstra et al. (2001), Burns and Kendall (2002), Campbell et al. (2002), Hales et al. (2007), Hastings et al. (2003), Michalski et al. (2003), Elliott et al. (2009), Patris et al. (2007), Morin et al. (2009), and Buda and DeWalle (2009)

lower values in the warmer months. Studies conducted at high latitudes (Morin et al. 2007; Savarino et al. 2006; Spoelstra et al. 2001) also show that atmospheric nitrate had elevated $\delta^{18}\text{O}$ values relative to the mid-latitudes. Nitrate $\delta^{18}\text{O}$ values (Fig. 30.2) in precipitation collected in the Catskill Mountains of New York (Burns and Kendall 2002), the Loch Vale watershed, Colorado (Campbell et al. 2002), and Brush Brook, Vermont (Hales et al. 2007), tended to be lower than the $\delta^{18}\text{O}$ values at other mid-latitude sites including Bermuda (Hastings et al. 2003), La Jolla, California, (Michalski et al. 2003), the North-eastern United States (Elliott et al. 2009), coastal sites (Michalski et al. 2003; Patris et al. 2007) and from aerosols over the Atlantic ocean (Morin et al. 2009). The former studies utilized the graphite reduction method (Silva et al. 2000) whereas the latter studies used either the denitrifier (Casciotti et al. 2002) or the AgNO_3 thermal decomposition method (Michalski et al. 2002). It is probable that the studies with lower $\delta^{18}\text{O}$ values suffer from the oxygen exchange analytical bias that leads to a decrease in the nitrate's $\delta^{18}\text{O}$

value (Michalski et al. 2002; Revesz and Böhlke 2002). However, Xue et al. (2010) demonstrated that the graphite- AgNO_3 method produces $\delta^{18}\text{O}$ results that compare well with those obtained using the denitrifier method, suggesting that these low $\delta^{18}\text{O}$ values may be valid.

The first $\Delta^{17}\text{O}$ measurement in atmospheric nitrate was reported by Michalski et al. (2003). This study analyzed aerosols collected over a 1 year period from a coastal urban site in southern California. A seasonal oscillation in the atmospheric nitrate $\Delta^{17}\text{O}$ values was observed, ranging from 23‰ during the summer/spring to 31‰ in the winter months. This was attributed to ozone oxidation chemistry during the conversion of NO_x into HNO_3 (see Sects. 30.5 and 30.6). Subsequent studies of $\Delta^{17}\text{O}$ variation in precipitation and aerosols (Fig. 30.3) from several mid-latitude locations showed similar ranges of values (see Fig. 30.3 and references). There are also seasonal trends in atmospheric nitrate $\Delta^{17}\text{O}$ values. They vary between a low of 22 and a high 44‰, with the higher values occurring during colder months, and the low values

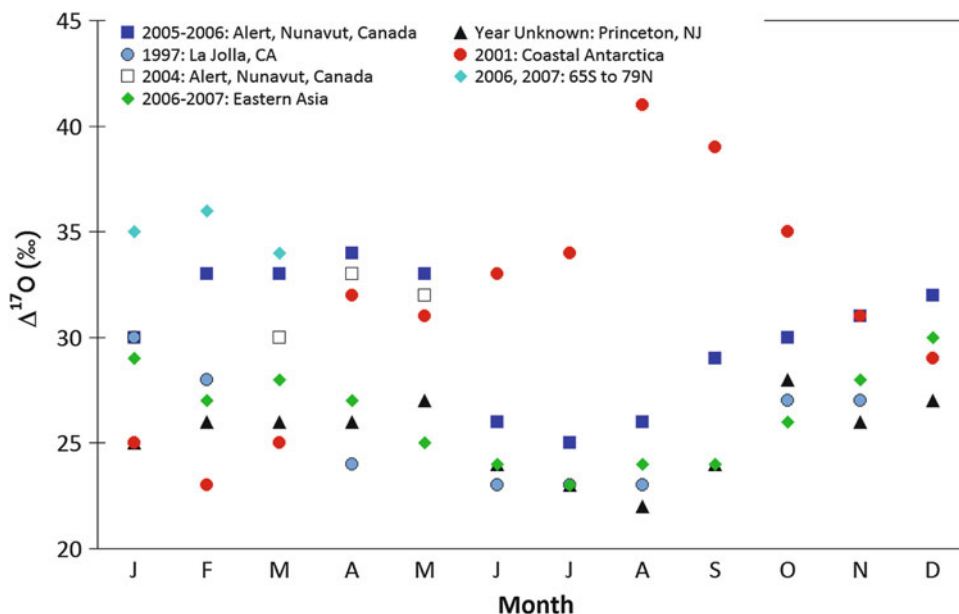


Fig. 30.3 Seasonal trends in the $\Delta^{17}\text{O}$ values of atmospheric nitrate. Nitrate collected in the southern hemisphere (McCabe et al. 2007; Savarino et al. 2007) have the opposite phase relative to northern hemisphere nitrate. Mid-latitude locations have atmospheric nitrate $\Delta^{17}\text{O}$ values that span 20–30‰

(Michalski et al. 2003; Morin et al. 2007; Kaiser et al. 2007; Patris et al. 2007), while polar regions tend to have higher $\delta^{18}\text{O}$ values and more pronounced seasonal trends. Uncertainty for any given $\Delta^{17}\text{O}$ measurement (± 0.4) is the size of the data symbols

occurring during warmer periods, similar to the $\delta^{18}\text{O}$ seasonal trends (Fig. 30.3). Atmospheric nitrate $\Delta^{17}\text{O}$ values also vary with latitude: Summit, Greenland (Kunasek et al. 2008), Alert, Canada (Morin et al. 2008), Dumont d’Urville, Antarctica (Savarino et al. 2006), Northern Ellesmere Island, Canada (Morin et al. 2007), and the South Pole (McCabe et al. 2007) all tend to have higher $\Delta^{17}\text{O}$ values relative to the mid-latitude sites (Michalski et al. 2003; Kaiser et al. 2007; Morin et al. 2009; Patris et al. 2007). The preponderance of studies in polar regions is due to an abundance of interest in using isotopes in ice core nitrate as a proxy for past chemistry/climate change (see Chap. 39 and 40).

The seasonal and spatial trends in atmospheric nitrate $\Delta^{17}\text{O}$ and $\delta^{18}\text{O}$ values are intriguing and suggest that there may be some utility in understanding the underlying mechanisms that cause these trends. The oxidation of NO_x into nitrate is tightly controlled by reactions with ozone (Sect. 30.4), which is also known to have high $\Delta^{17}\text{O}$ and $\delta^{18}\text{O}$ values

(Krankowsky et al. 1995; Johnston and Thiemens 1997). Theoretical models have tried to explain the atmospheric nitrate isotope trends in terms of isotope mass balance mixing models (Michalski et al. 2003; Morin et al. 2007; Alexander et al. 2009; see Sect. 30.6), where different oxidation pathways utilized unique oxygen sources, including ozone. These models suggested that oxygen isotopes in atmospheric nitrate might be used to trace the relative importance of different oxidation pathways (gas phase vs. aerosol reactions) under changing environmental conditions (e.g. polluted, volcanic events, climate change). In addition, since atmospheric nitrate can be incorporated into polar ice caps, nitrate oxygen isotopes might be a new proxy for studying the past oxidation state of the atmosphere (paleo-atmospheric chemistry; see Chap. 39). The theory behind these isotope mass balance models and their ability to reproduce observed isotopic trends in atmospheric nitrate are discussed in the remaining sections of this review.

30.4 Mass Balance Approach to Oxygen Isotope Variation in Atmospheric Nitrate

30.4.1 Isotope Mass Balance During Nitrate Production

When a compound is formed, its isotopic composition is determined by the isotopic composition of the reactants and kinetic or equilibrium fractionation effects that occur during the formation process. For oxygen isotopes, this can be formulated as

$$\delta^{18}\text{O}_{\text{prod}} = \sum a_i \delta^{18}\text{O}_{\text{react } i} + \sum \varepsilon_{\text{rxn } i} \quad (30.3)$$

$$\delta^{17}\text{O}_{\text{prod}} = \sum a_i \delta^{17}\text{O}_{\text{react } i} + \sum \varepsilon_{\text{rxn } i} \quad (30.4)$$

where $\varepsilon_{\text{rxn } i}$ is the temperature dependent kinetic isotope effect (KIE) or equilibrium enrichment factor (in ‰) for the reaction (i), and a_i is the mole fraction of oxygen in the product attained from a given reactant (i). The sums arise when more than one reactant contributes oxygen to the system ($\sum a_i = 1$) and multiple kinetic steps exist in the reaction mechanism. When using an isotope mass balance model, for simplification, the $\varepsilon_{\text{rxn } i}$ of the reactions are ignored. This simplification is used in modeling atmospheric nitrate production because few of the oxygen $\varepsilon_{\text{rxn } i}$ relevant to nitrate production have been measured. This is a limitation, but as experimental or theoretical determinations of these KIE and equilibrium enrichment factors become available they can be incorporated into, and improve, the models.

A similar isotope composition equation can be derived for $\Delta^{17}\text{O}$ values

$$\Delta^{17}\text{O}_{\text{prod}} = \sum a_i \Delta^{17}\text{O}_{\text{react } i} + \sum \Delta \varepsilon_{\text{rxn } i} \quad (30.5)$$

There are relatively few reactions that generate $\Delta^{17}\text{O}$ values in products from reactants that have isotopic compositions on the TFL (Fig. 30.1) i.e. MIF. The MIF enrichment factor for a given reaction (i) is noted as $\Delta \varepsilon_{\text{rxn } i}$ in (30.5). Indeed, ozone formation is the only known tropospheric reaction that has a major MIF (Sect. 30.5.1). This leads to the approximation that, other than ozone production, the $\sum \Delta \varepsilon_{\text{rxn } i} = 0$ for

other atmospheric nitrate production processes and this approximation has been used in models that predict the evolution of $\Delta^{17}\text{O}$ signatures in atmospheric nitrate (Sect. 30.6).

30.4.2 Isotope Mass Balance During Nitrate Removal

Processes that remove a compound through transport or reactivity can also change the isotopic composition of the residual compound. For oxygen isotopes this can be formulated as

$$\delta^{18}\text{O}_{\text{residual}} = \delta^{18}\text{O}_{\text{initial}} - \sum \varepsilon_{\text{rxn } i} \quad (30.6)$$

$$\Delta^{17}\text{O}_{\text{residual}} = \Delta^{17}\text{O}_{\text{initial}} - \sum \Delta \varepsilon_{\text{rxn } i} \quad (30.7)$$

where $\varepsilon_{\text{rxn } i}$ is the temperature dependent, kinetic or equilibrium fractionation factor of a loss process (i). The loss processes change the isotopic composition of the initial reservoir in a mass dependent manner and they often exhibit Rayleigh distillation-type behavior, where the isotope ratios in the residual reactant change exponentially as a function of the fraction (f) of the compound remaining, which is usually a function of time.

$$\delta^{18}\text{O}_{\text{residual}} = \delta^{18}\text{O}_{\text{initial}} - \varepsilon_{\text{rxn}} \ln[f(t)] \quad (30.8)$$

$$\Delta^{17}\text{O}_{\text{residual}} = \Delta^{17}\text{O}_{\text{initial}} - \Delta \varepsilon_{\text{rxn}} \ln[f(t)] \quad (30.9)$$

The main loss process for atmospheric nitrate is removal by wet and dry deposition. To the best of our knowledge there is no data that has measured the ε_{rxn} for either depositional process, which is a serious limitation when interpreting $\delta^{18}\text{O}$ variations observed in atmospheric nitrate. The $\Delta \varepsilon_{\text{rxn}}$ of wet and dry deposition, however, should follow mass dependent isotope fractionation rules, so $\Delta \varepsilon_{\text{rxn}} \sim 0$ can be assumed. This assumption dictates that nitrate $\Delta^{17}\text{O}$ values are not impacted by the loss process itself. However, in time-dependent models, the loss process can influence the $\Delta^{17}\text{O}$ values of nitrate depending on environmental conditions. This is because evaluating $\Delta^{17}\text{O}$ values in nitrate during each time step requires incorporating the nitrate $\Delta^{17}\text{O}$ values from the previous time step. In

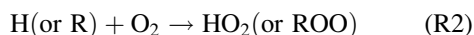
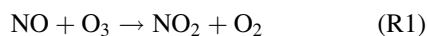
other words, the $\Delta^{17}\text{O}_{\text{residual}}$ term in the loss equation (30.9) must be carried over into the isotope mass balance in the production equation (30.5) at the next time step:

$$\Delta^{17}\text{O}_{(\text{total})} = x(\Delta^{17}\text{O}_{\text{prod}})_t + (1-x)(\Delta^{17}\text{O})_i \quad (30.10)$$

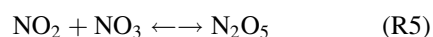
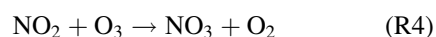
where x is the mole fraction of nitrate produced in the current time step (t) relative to the total amount of nitrate in the atmosphere. In cases where the loss processes are ignored, nitrate builds up in the atmosphere and the instantaneous $\Delta^{17}\text{O}$ value produced in the current time step ($\Delta^{17}\text{O}_{\text{prod}})_t$ becomes less important as x becomes smaller. Such a situation might arise during dry periods in areas below temperature inversions where both deposition mechanisms are minimized. Conversely, if removal is rapid then the nitrate $\Delta^{17}\text{O}$ values will more closely reflect the current chemistry because x is large. This situation might occur during periods of regular precipitation that would scrub nitrate from the atmosphere. The loss processes must also be considered in one, two or three dimensional models. In these models, nitrate produced in an adjacent grid cell with different chemistry and isotopic ratios can be transported into the grid cell under consideration, changing the isotopic composition of the nitrate depending on nitrate production/transport ratio.

30.4.3 Oxygen Isotope Mass Balance During Nitrate Production

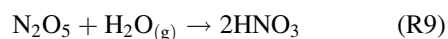
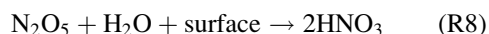
Nitrate production is initiated by the oxidation of NO. The first step is the conversion of NO into NO_2 , which can occur by oxidation by either ozone (R1) or peroxy radicals (R3). The majority of peroxy radicals are produced when radical species such as H, CH_3 , and R (where R is an organic radical), combine with atmospheric O_2 (R2).



Therefore, in order to use the isotope mass balance simplification in the NO oxidation step, the $\delta^{18}\text{O}$ and $\Delta^{17}\text{O}$ values of tropospheric O_3 and O_2 need to be known, which is discussed in Sects. 30.5.1 and 30.5.4, respectively. More oxidized forms of nitrogen, NO_3 and N_2O_5 , are produced by NO_2 oxidation via ozone (R4 and R5). Again, the isotopic mass balance approximation can be used by assuming no KIE during the oxidation and having measured or modeled the isotopic composition of tropospheric ozone (Sect. 30.5.1)



In the final steps of nitric acid formation, two other oxygen sources enter into the equation, OH radicals and liquid water. The primary oxidation pathway for the production of nitric acid is the third body (M) mediated OH oxidation of NO_2 (R6). An important alternative pathway that forms nitric acid is the heterogeneous hydrolysis of N_2O_5 on wet aerosol surfaces (R8). Finally, a minor but non-trivial pathway to nitric acid is through hydrogen abstraction by nitrate radicals (R7). Again, to use an isotope mass balance approach for predicting isotope variation in nitric acid, one needs to know how $\delta^{18}\text{O}$ and $\Delta^{17}\text{O}$ values in tropospheric water (Sect. 30.5.2) and OH radicals (Sect. 30.5.3) vary in space and time.

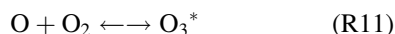
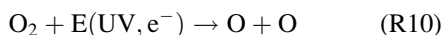


To summarize, in order to predict the isotope composition of atmospheric nitrate using a simple isotope mass balance model, the isotopic composition of tropospheric O_3 , H_2O , OH, and O_2 need to be known (measured) or approximated (modeled).

30.5 Isotopic Composition of Oxygen Sources that Contribute to Nitrate

30.5.1 Oxygen Isotope Composition of Tropospheric O₃

There is a tremendous amount of published research on isotope effects that occur during the formation of ozone (Thiemens et al. 2001; Mauersberger et al. 2003). Ozone formation is initiated when oxygen atoms are produced either by high energy (E) photons/electrons (R10) or through NO₂ photodissociation (see R16 below). O₂ molecules react with ground state oxygen atoms to form an excited ozone complex (R11) that can either decompose or be stabilized to ground state O₃ (R12) by a third body (M):



The isotopic composition of the product ozone is characterized by a large enrichment in the heavy isotopes ¹⁷O and ¹⁸O (relative to ¹⁶O), when compared to the O₂ reactant (Thiemens and Heidenreich 1983; Mauersberger et al. 2001). As mentioned before, not only are the heavy isotopes more abundant, but there is a large MIF (Thiemens and Heidenreich 1983).

Many theoretical attempts have been made to understand the basic principle behind the large MIF associated with ozone formation (Heidenreich and Thiemens 1983; Valentini 1987; Gellene 1996; Gao and Marcus 2001). The most successful is the theory of Hathorn, Gao and Marcus, which uses a modified version of the Rice–Ramsperger–Kassel–Marcus (RRKM) theory of unimolecular decomposition to treat reaction R11 (Gao and Marcus 2001; Hathorn and Marcus 1999; Hathorn and Marcus 2000). Ozone formation is visualized to be a time-dependent competition between unimolecular decomposition (R11) and the collisional stabilization of O₃* (R12). If energy can be shared among the vibrational-rotational modes of the O₃* complex, its lifetime is extended and therefore more O₃ is formed. It has been suggested that the asymmetric ozone isotopomers, with heavy isotopes

at the terminal position, dissociate (R11) slower than symmetric isotopomers due to a larger number of symmetry-allowed mode couplings. Therefore asymmetric ozone, regardless which minor isotope breaks the symmetry, have higher formation rates relative to symmetric species (i.e. ¹⁶O¹⁶O¹⁶O). This leads to the equal enrichment of ¹⁷O and ¹⁸O in the product ozone.

This theoretical model implies that the MIF is driven by a symmetry effect. This would suggest that the non-zero Δ¹⁷O resides only in the molecules of type OOQ (asymmetric) and not in type OQO (symmetric), where Q is either ¹⁷O or ¹⁸O. Any enrichment observed in the symmetrical molecules (like OQO) should follow the mass dependent fractionation relationship. Three experiments have been conducted to test this hypothesis by studying chemical systems where ozone reacts through its terminal position atom: ozone reacting on solid silver foil (Bhattacharya et al. 2008), with NO_(g) (Savarino et al. 2008), and nitrite in solution (Michalski and Bhattacharya 2009). If the bulk ozone Δ¹⁷O anomaly resides only in the terminal position then by mass balance:

$$\Delta^{17}\text{O}(\text{terminal}) = 1.5 \cdot \Delta^{17}\text{O}(\text{bulk}) \quad (30.11)$$

as the central atom would only dilute the anomaly. The isotopic composition of the oxygen atom transferred during these reactions would therefore have Δ¹⁷O 1.5 times the initial ozone if this hypothesis is true. In all three experiments the expected factor of 1.5 is observed (Fig. 30.4) within the uncertainty of the experiments. There are some small discrepancies that need additional investigation, but in general the hypothesis of the anomalous ¹⁷O enrichment residing in the terminal atoms appears to be valid. This is important in the nitrate mass balance models because NO oxidation by O₃ via its terminal atom (R1) would be different if the anomaly were evenly distributed across all oxygen atoms in ozone.

The isotope effects generated during ozone formation have been investigated under a number of conditions. Experiments using either electrical discharge or UV radiation generate product ozone with δ¹⁸O and Δ¹⁷O values in the range of 70–120‰ and 32–45‰ respectively (relative to the initial O₂). This variation is the result of different pressure and temperature conditions under which the ozone is formed. Experiments examining the pressure dependency (Guenther

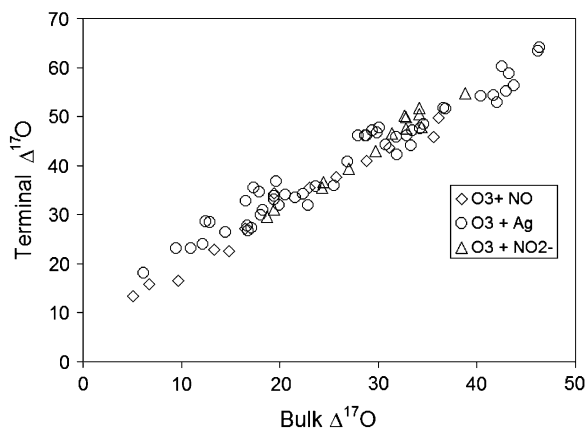


Fig. 30.4 Experiments that assess the terminal atom enrichment in ozone. If the symmetry hypothesis is correct then the terminal atoms should be enriched by a factor of 1.5 relative to the bulk. The terminal enrichment coefficients are 1.63 ± 0.33 (Bhattacharya et al. 2008), 1.59 ± 0.39 (Savarino et al. 2008), and 1.49 ± 0.06 (Michalski and Bhattacharya 2009)

et al. 2000; Thieme and Jackson 1990) showed that both the $\delta^{18}\text{O}$ and the $\Delta^{17}\text{O}$ enrichments in ozone decrease with increasing pressure (Fig. 30.5) and disappear at very high pressures (Thieme and Jackson 1990). The experimental pressure dependence of ozone's $\delta^{18}\text{O}$ and $\Delta^{17}\text{O}$ values (at 321 K) can be fitted to an equation in P (pressure in the range 50–800 torr). For pressures typical of the troposphere (500–800 torr), a regression of data reported in Morton et al. (1990) yields the pressure-dependency equation ($\delta^{18}\text{O}_{(\text{ozone})}$ relative to the initial O_2):

$$\delta^{18}\text{O}_{(\text{ozone})} = -0.03P_{\text{torr}} + 112.4 \quad (30.12)$$

The ozone $\delta^{18}\text{O}$ temperature dependency (at 50 torr), can also be found by regressing Morton et al.'s data:

$$\delta^{18}\text{O}_{(\text{ozone})} = 0.52T(\text{K}) - 45 \quad (30.13)$$

Calculating the expected $\delta^{18}\text{O}$ value for ozone in the troposphere, which has variable temperature and pressure, requires corrections based on these equations. Since the reference temperature for the pressure experiments in Morton et al. was 321 K (far higher than the average surface temperature), (30.12) is modified for the temperature difference using $0.52 \cdot (T(\text{K}) - 321)$. In addition, the enrichments determined by

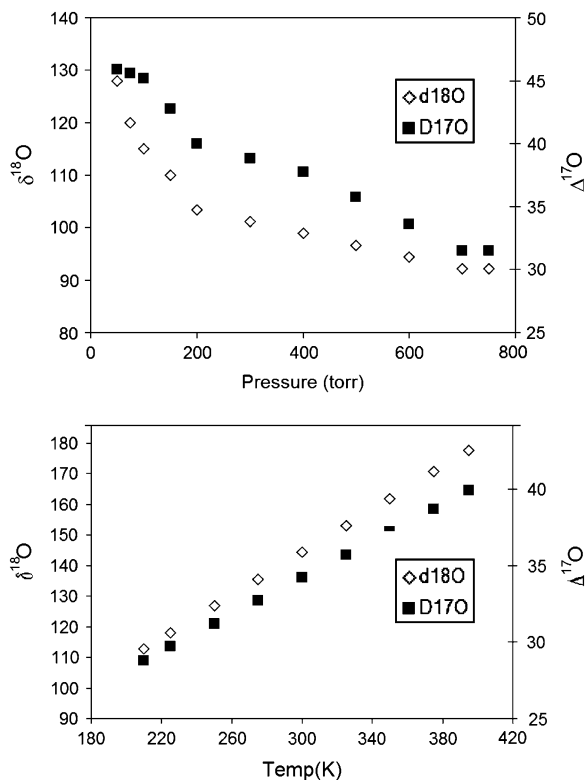


Fig. 30.5 Temperature and pressure dependence of $\Delta^{17}\text{O}$ (solid square) and $\delta^{18}\text{O}$ (open diamond) values generated during ozone production. Data was reproduced by averaging data from Guenther et al. (2000), Thieme and Jackson (1990), and Morton et al. (1990)

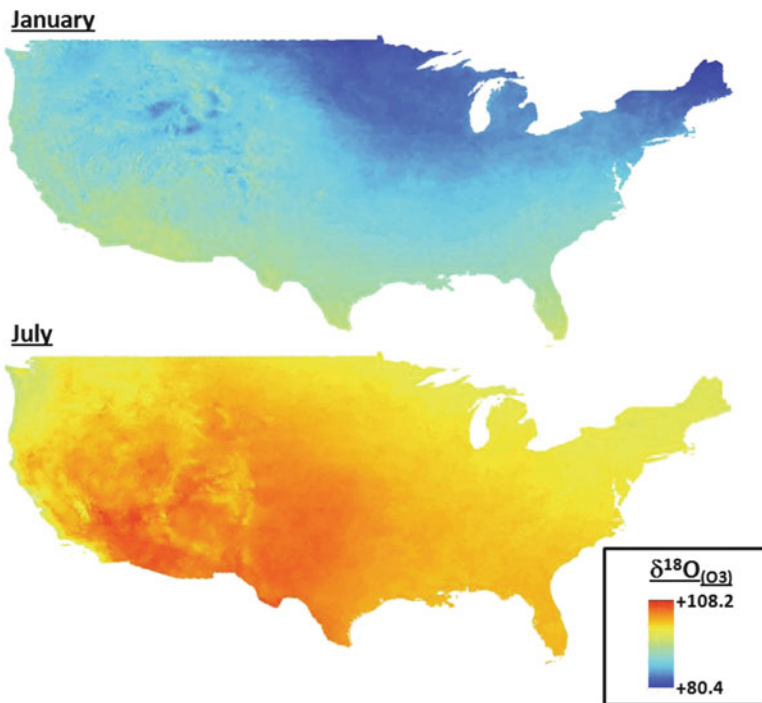
Morton et al. were relative to the initial O_2 composition. In the atmosphere where air O_2 is +23.4‰ relative to V-SMOW (Barkan and Luz 2003), an additional standard correction factor ($\delta_{\text{O}_3-\text{VSMOW}} = \delta_{\text{O}_3-\text{air}} + \delta_{\text{air-VSMOW}} + \delta\delta^1/1,000$) is applied to the fitted data when using V-SMOW as the reference point yielding:

$$\delta^{18}\text{O}_{(\text{ozone})} = (-0.028P_{\text{torr}} + 134.8) + [0.52 \cdot (T(\text{k}) - 321)] \quad (30.14)$$

Using (30.14) and pressure/temperature estimates from the North American Regional Reanalysis (NARR) dataset (Kalnay et al. 1996), we calculated the spatial variability of the predicted $\delta^{18}\text{O}$ values of ozone over the continental US (Fig. 30.6). The predicted $\delta^{18}\text{O}$ values (80–108‰) span the same range as those observed in tropospheric ozone collected in southern California (95–115‰V-SMOW) by Johnston

Fig. 30.6 Spatial and seasonal variation of ozone $\delta^{18}\text{O}$ variation across the continental US for January 1 and July 1 of 2001.

The values are calculated using (30.14) and the NARR temperature and pressure data. The predicted range of ozone $\delta^{18}\text{O}$ values is $\sim 28\text{‰}$ and tracks with temperature in regions with minimal topography and pressure in mountainous regions



and Thiemens (1997). However, the observed ozone $\delta^{18}\text{O}$ values are always higher ($\sim 3 - 18\text{‰}$) relative to those predicted by our P/T model when using temperature and pressures at the California site during collection times. The other tropospheric ozone $\delta^{18}\text{O}$ dataset collected in Germany (Krankowsky et al. 1995) has ozone values spanning $100 - 130\text{‰}$, again higher than our model predictions. One factor for this discrepancy is that the average surface temperature and pressure are used to calculate the $\delta^{18}\text{O}$ values in Fig. 30.6, when average boundary layer temperatures and pressures may be more appropriate. Another possibility for the discrepancy is KIE associated with O_3 dry deposition or photolysis reactions that may leave the residual O_3 enriched (Liang et al 2006). The ozone $\delta^{18}\text{O}$ observations were limited in their spatial and temporal scope, therefore it is difficult to evaluate whether extrapolating the laboratory based data to atmospheric conditions is rigorously reflecting ozone $\delta^{18}\text{O}$ value or if the ozone $\delta^{18}\text{O}$ measurements are inaccurate, but in general there is relatively good agreement between model estimated and observed tropospheric ozone $\delta^{18}\text{O}$ values.

Temperature (Morton et al. 1990) and pressure data (Thiemens and Jackson 1990; Guenther et al. 2000)

was also fitted to assess how $\Delta^{17}\text{O}$ values might vary in the atmosphere. Fitting these data sets yields pressure (P at constant 321 K) and temperature (T at constant 50 torr) $\Delta^{17}\text{O}$ equations

$$\Delta^{17}\text{O} = 78.8P^{-0.122} \quad (30.15)$$

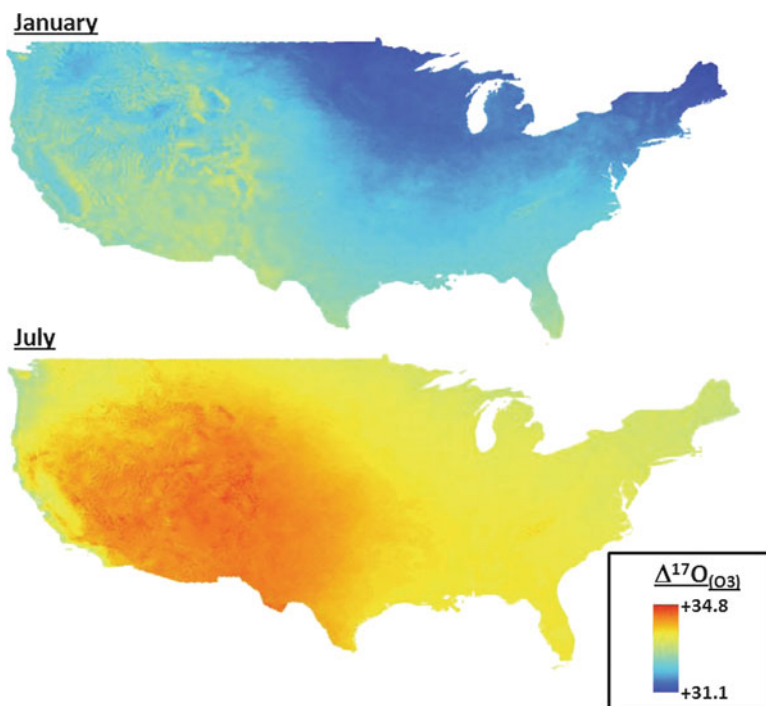
$$\Delta^{17}\text{O} = 16.2 + 0.06 \cdot T(\text{K}) \quad (30.16)$$

Normalizing to the experimental temperature (i.e. as in (30.14)) gives

$$\Delta^{17}\text{O} = (78.8P^{-0.122}) + 0.06 \cdot (T(\text{K}) - 321) \quad (30.17)$$

Using NARR temperature and pressure data and (30.17) we have estimated the winter and summer ozone $\Delta^{17}\text{O}$ values over the continental US (Fig. 30.7). The predicted ozone $\Delta^{17}\text{O}$ values span a relatively narrow range, from 31 to 35‰, and they generally follow the seasonal change in temperature, but low pressure at high altitudes is also a factor (Fig. 30.7). These predicted values are close to observed $\Delta^{17}\text{O}$ values of ozone collected at the White Mountain Research Station (27–35.8‰) but higher

Fig. 30.7 Modeled ozone $\Delta^{17}\text{O}$ values across the US for January 1 and July 1, 2001. Total variation is less than 5‰ and mainly correlates with temperature, with lower ozone $\Delta^{17}\text{O}$ values in flat regions and cooler climates, where surface pressure varies by only tens of millibars. However, pressure is clearly a factor in mountainous regions in the western US, where the $\Delta^{17}\text{O}$ increases with decreasing pressure. The data is generated using (30.17) and the mean daily temperature and pressure from the NARR dataset



than $\Delta^{17}\text{O}$ values of tropospheric ozone sampled from coastal (20–35.8‰; average 26.4‰, $n = 29$) and urban (19–22‰; average 21.2‰, $n = 7$) sites in Southern California (Johnston and Thiemens 1997). The discrepancy between the modeled $\Delta^{17}\text{O}$ values (Fig. 30.7) and the observations is likely due to the difficulties encountered using the ozone collection system, which may lead to isotopic fractionation, exchange, or contamination. Resolving this discrepancy between predicted $\delta^{18}\text{O}$ and $\Delta^{17}\text{O}$ values of tropospheric ozone at a given pressure and temperature is an area of active research.

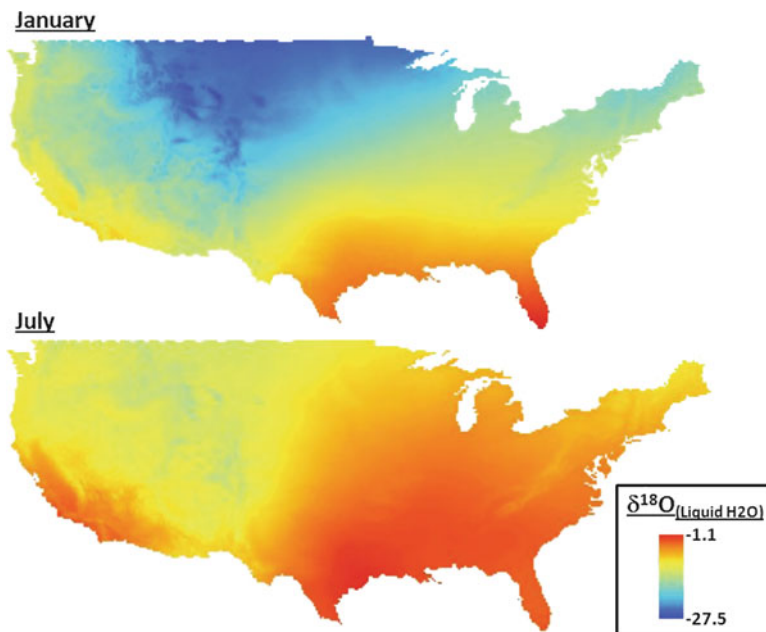
30.5.2 Oxygen Isotopic Composition of Tropospheric Water

There is a tremendous amount of data on the isotopic composition of water in the troposphere, stemming largely from the efforts of the Global Network of Isotopes in Precipitation (GNIP) (IAEA/WMO 2006). GNIP and other organizations at various local levels have compiled $\delta^{18}\text{O}$ and δD values in precipitation across many sites over the past 40 years (Araguas-Araguas et al.

2000; Vuille et al. 2005). The GNIP data and spatial interpolation techniques have been used to model continuous global spatial variations of water $\delta^{18}\text{O}$ values (Bowen and Revenaugh 2003). The interpolated data is available in a number of formats but the Waterisotopes.org web site (<http://wateriso.eas.purdue.edu/waterisotopes/>) is a very user-friendly resource. Complete details of water isotope variations and their use are detailed in Chap. 33).

Water does not act as an oxidant during the conversion of NO_x into nitrate, but it does act as an oxygen source during several steps in the oxidation scheme. Therefore, understanding its variation is important for understanding the variability of $\Delta^{17}\text{O}$ and $\delta^{18}\text{O}$ in nitrate. Water in the troposphere has a $\Delta^{17}\text{O}$ value of approximately 0 (Meijer and Li 1998), though small variations of up to 0.08‰ have been detected using high precision techniques (Barkan and Luz 2005; Uemura et al. 2010). Conversely, tropospheric water $\delta^{18}\text{O}$ values are highly variable and are a function of the source of the water (i.e. oceanic, lake, evapotranspiration) and the temperature of evaporation and condensation (Gat 1996). The lowest precipitation $\delta^{18}\text{O}$ values are found at the poles (−70‰) and highs (+10‰) are usually found in arid environments.

Fig. 30.8 Estimated $\delta^{18}\text{O}$ values for precipitation water across the contiguous United States for January and July of 2001, based on interpolation (from <http://www.waterisotopes.org>)



Spatial trends in water isotopes are often addressed in terms of latitudinal effects, longitudinal effects and altitude effects (Gat 1996). The interpolated model of variations in the $\delta^{18}\text{O}$ of precipitation across the continental US for January and June of 2001 is shown in Fig. 30.8.

Water can be incorporated into nitrate during NO_x oxidation from both the liquid and gas phase. Liquid water is incorporated into nitrate when N_2O_5 is converted to HNO_3 on wetted aerosol surfaces (R8). Since N_2O_5 is nitric acid anhydride, this occurs fairly rapidly (Hallquist et al. 2000; Mentel et al. 1999), although there are still some uncertainties concerning what role aerosol composition plays in the efficiency of N_2O_5 uptake (Brown et al. 2003). Current models (Alexander et al. 2009; Michalski et al. 2003) assume that there is no additional exchange between aerosol water and N_2O_5 during the hydrolysis but this has yet to be shown experimentally. Once formed, the exchange between water and nitrate is negligible except under extremely low pH conditions (Böhlke et al. 2003; Bunton et al. 1952). The gas phase reaction between $\text{H}_2\text{O}_{(\text{g})}$ and N_2O_5 (R9) is believed to be too slow to be a significant source of HNO_3 (Tuazon et al. 1983; Wahner et al. 1998).

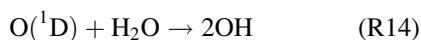
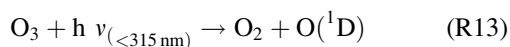
Water in the gas phase can also be incorporated into nitrate via the NO_2 reaction with OH (R6). OH can

exchange with gas phase water (Dubey et al. 1997) and the $\delta^{18}\text{O}$ of OH will ultimately be dependent on the $\delta^{18}\text{O}$ of water vapor with which it exchanges. Temperature dependent variations in water vapor enrichment factors, relative to the liquid water, can be fitted by inverting the experimental data for the temperature dependent $\text{H}_2\text{O}_{(\text{g})} \leftrightarrow \text{H}_2\text{O}_{(\text{l})}$ equilibrium (Horita and Wesolowski 1994; Majoube 1971)

$$\varepsilon_{\text{g-l}} = 1,000 \ln \alpha_{(\text{g})} = -7.685 + 6.7123(1,000/T) - 1.6664(10^6/T^2) + 0.35041(10^9/T^3) \quad (30.18)$$

30.5.3 Oxygen Isotope Composition of Tropospheric OH

The OH radical is the dominant oxidizer in the atmosphere and is a key oxidizer of NO_2 because of the gas phase reaction that leads to nitric acid (R6) with a rate constant of $2.8 \times 10^{-11} \text{ cm}^3 \text{ molecule}^{-1} \text{ s}^{-1}$ (at 300 K, 101 kPa). OH is formed by the production of $\text{O}(^1\text{D})$ atoms via ozone photolysis that react with water vapor



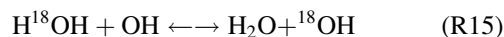
Because of OH's high reactivity and low steady state concentration (10^5 – 10^6 molecules cm^{-3}) there are, however, no direct measurements of its isotopic composition in the troposphere. By isotope mass conservation (R13 and R14) the isotopic composition of OH should be a mixture of ozone and tropospheric water vapor. However, the OH radical is capable of exchanging with water vapor (R15) with a Arrhenius rate constant of $2.3 \times 10^{-13} \exp[(2,100(\pm 250))/T] \text{ cm}^3 \text{ molecule}^{-1} \text{ s}^{-1}$ (Dubey et al. 1997). At 300 K this is a relatively slow reaction ($3 \times 10^{-16} \text{ cm}^3 \text{ molecule}^{-1} \text{ s}^{-1}$). However, if the ratio (ρ) of the rate of exchange relative to the rate of reaction with NO_2 (R6) is high (>10) the exchange would dominate and equilibrium be essentially achieved:

$$\rho = k_{\text{R15}}[\text{H}_2\text{O}]/k_{\text{R6}}[\text{NO}_2] \quad (30.19)$$

Under most NO_x scenarios ($\text{NO}_2 < 1$ ppbv) and water mixing ratios (~ 0.01), ρ is on the order of 10^1 – 10^3 . However, under high NO_x (10 ppbv) and/or low water mixing ratios (5×10^{-3} and $\sim 50\%$ relative humidity at 275 K) the isotope exchange can become comparable to reactivity rates. But these cases are rare (Morin et al. 2008); so under most circumstances it can be approximated that OH achieves equilibrium with water vapor. This exchange would eliminate any $\Delta^{17}\text{O}$ transfer during reaction R14. This is not true for the stratosphere or polar regions, where water is at ppmv levels, and OH may retain its ozone $\Delta^{17}\text{O}$ signature (Lyons 2001).

Because of this exchange reaction, the $\delta^{18}\text{O}$ values of OH in the troposphere will be a function of the $\delta^{18}\text{O}$

of the water vapor in the air mass and the fractionation factor for the equilibrium reaction



Using observed water isotopologue vibrational frequencies (Herzberg 1966), the OH vibrational frequency (Dieke and Crosswhite 2010), and the reduced mass, simple harmonic oscillator approximation, the reduced partition functions of OH and water isotopologues can be determined as a function of temperature (Urey 1947). Calculating the isotope enrichment factor over a tropospheric temperature range of 250–310 K and fitting the data yields a temperature dependent fractionation factor for OH given by:

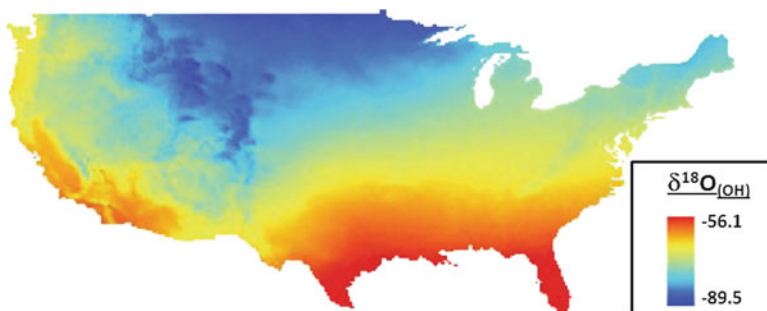
$$\varepsilon = 1,000 \ln \alpha = 0.188T - 99.3 \quad (30.20)$$

This equation predicts that OH should be depleted by roughly 44‰ relative to atmospheric water vapor at 298 K. Using the $\delta^{18}\text{O}$ of tropospheric water (Fig. 30.8) and (30.18) and (30.20), the $\delta^{18}\text{O}$ of OH over the continental US was modeled (Fig. 30.9). This estimate of the $\delta^{18}\text{O}$ of OH does not consider any of the KIE arising during the reactions between OH and the numerous organic compounds in the atmosphere and should only be taken as a first order approximation.

30.5.4 Oxygen Isotope Composition of Tropospheric O_2

Atmospheric O_2 is incorporated into nitrate via the oxidation of NO by peroxy radicals (R3) formed from O_2 reactions with H and organic radicals (R2).

Fig. 30.9 Modeled $\delta^{18}\text{O}$ values of OH for January 1, 2001. The values are determined using modeled water vapor $\delta^{18}\text{O}$ assuming equilibrium with liquid water (30.18) and the calculated OH-water equilibrium fractionation factor (30.20)

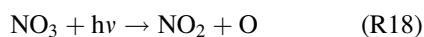
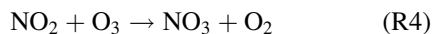
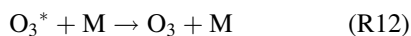
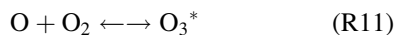
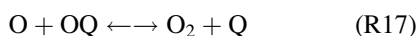
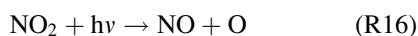
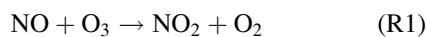


The $\delta^{18}\text{O}$ value of atmospheric oxygen is $\sim 23\%$ relative to V-SMOW, a value that is controlled by the balance between photosynthesis and respiration isotope effects, known as the Dole effect (Dole et al. 1954). Because of its huge abundance and the well-mixed nature of the troposphere, there is essentially no spatial or temporal variation in tropospheric O_2 $\delta^{18}\text{O}$ values. Measurement of the $\delta^{17}\text{O}$ value of atmospheric O_2 relative to V-SMOW indicates a small negative $\Delta^{17}\text{O}$ value for O_2 (Luz et al. 2005; Barkan and Luz 2003). This negative anomaly can be explained by isotopic mass balance when stratospheric oxygen atoms derived from ozone impart MIF to CO_2 (Thiemens et al 1991; Yung et al. 1991).

30.6 Modeling Oxygen Isotope Variation in Atmospheric Nitrate

30.6.1 Oxygen Isotope Variation in NO_x

Atmospheric nitrate is derived from NO_x and its oxygen isotope composition is dependent on isotope effects associated with the NO_x cycle. The NO_x cycle is initiated by NO oxidation by ozone, which is then followed by photolysis of NO_2 by solar actinic flux and the subsequent reformation of O_3



During this cycling, isotope exchange between oxygen atoms and O_2 is rapid (R17) and this equilibration erases any isotope effect that might have carried over from NO_2 formation or photolysis. During the O_3 formation process, however, large $\delta^{18}\text{O}$ and

$\Delta^{17}\text{O}$ values are generated during the recombination reaction (Sect. 30.5.1). The transfer of heavy isotopes from ozone to NO_2 during R1 leads to a NO_x - O_3 equilibrium as a quasi steady state balance of these reactions develops. This has recently been demonstrated experimentally (Michalski et al. in preparation).

The dynamics of the NO - O_3 reaction system and the internal distribution of isotopes in ozone are important controls on the isotopic composition of the product NO_2 . As discussed in Sect. 30.5.1 the isotope anomaly ($\Delta^{17}\text{O}$) and some of the ^{18}O enrichment is found in the terminal atom of O_3 , via the so-called symmetry effect. If NO reacts with ozone through a terminal atom transition state, as shown by ab initio calculations (Peiro-Garcia and Nebot-Gil 2002), then the heavy isotope transfer will be larger than if all three oxygen atoms in ozone reacted with equal probability. Savarino et al. (2008) evaluated the fractionation between ozone and NO_2 during NO oxidation, a combination of the internal distribution of ^{18}O in ozone and the KIE of the reaction itself. The experiments conducted at pressures and temperatures typical of the troposphere showed a $\delta^{18}\text{O}$ correction factor of 0.83 (Savarino et al. 2008). We applied this correction factor to (30.14), which yields a T-P equation that predicts the $\delta^{18}\text{O}$ value (V-SMOW) of the oxygen atom transferred to NO_2 during NO oxidation:

$$\delta^{18}\text{O}_{(\text{trans})} = 0.83 * \{(-0.028P_{\text{torr}} + 134.8) + [0.52 * (T(\text{k}) - 321)]\} \quad (30.21)$$

The same experiment examined the $\Delta^{17}\text{O}$ transfer during the oxidation via R1 and showed that the branching ratio of the reaction for the central atom in ozone is only 0.08 suggesting that the terminal abstraction pathway is dominant (Savarino et al. 2008). Using this branching ratio and the terminal only enrichment hypothesis (30.11) yields a $\Delta^{17}\text{O}$ value of the oxygen atom transferred from ozone to NO_2 during NO oxidation as:

$$\Delta^{17}\text{O}_{\text{NO}+\text{O}_3} = 1.5 * 0.92 * \Delta^{17}\text{O}_{\text{O}_3(\text{bulk})} \quad (30.22)$$

Using the modeled $\Delta^{17}\text{O}_{\text{O}_3(\text{bulk})}$ for the continental US (Fig. 30.7) would yield a typical NO_x - O_3 equilibrium value of $\sim 46\%$. A more realistic experiment recently examined the isotope effect during the full

NO_x equilibrium (Michalski et al. in preparation), and generated $\Delta^{17}\text{O}$ value in NO_2 of $\sim 45\text{‰}$, in excellent agreement with Savarino et al. (2008).

30.6.2 Box Model Evaluation of $\Delta^{17}\text{O}$ Variations in Atmospheric Nitrate

Several zero dimensional photochemical box models have been used to simulate $\Delta^{17}\text{O}$ variations in atmospheric nitrate (Michalski et al. 2003; Morin et al. 2008; Michalski and Xu 2010). The models calculate how much atmospheric nitrate is produced by reactions R6, R7, and R8. In each of these pathways the main reactant is NO_2 , or higher oxides of nitrogen derived from NO_2 ; therefore, the first step is to assess NO_2 $\Delta^{17}\text{O}$ either directly (see Sect. 30.6.1) or calculate it based on the $\Delta^{17}\text{O}$ of ozone and the reaction dynamics. However, under natural conditions peroxy radical (ROO) oxidation of NO (R3) is an alternative mechanism for generating NO_2 . This pathway can be significant depending on local concentrations of organic compounds and NO_x (Jaegle et al. 2000). In the case of ROO, the oxygen atom transferred to NO_2 is derived from reactions of organic radicals with O_2 (R2) which has a $\Delta^{17}\text{O} \sim 0\text{‰}$ (Sect. 30.5.4). Therefore, one can define an oxidation parameter, ϕ , which is the mole fraction of NO oxidation by ozone relative to total NO oxidation: $\phi = \text{R1}/(\text{R1} + \Sigma\text{R3's})$. The term ΣR3 arises because a number of organo-peroxy and HO_x radicals are capable of oxidizing NO to NO_2 . Based on this, the $\Delta^{17}\text{O}$ of NO_2 (Δ^{NO_2}) in the troposphere is estimated to be

$$\Delta^{\text{NO}_2}(\text{trop}) = \phi \Delta^{\text{NO}_2}(\text{exp}) = \phi \Delta^{\text{O}_3\text{trans}} \quad (30.23)$$

where $\Delta^{\text{NO}_2}(\text{exp})$ is the experimental $\Delta^{17}\text{O}$ of NO_2 in the NO_x - O_3 equilibrium experiment (Michalski et al. in preparation) or the $\Delta^{17}\text{O}$ value of the terminal oxygen atom (P,T dependent) that equilibrates with NO_x (Savarino et al. 2008).

Based on the inspection of reactions R6, R7, and R8 and using the approximation that H_2O , O_2 , and OH all have $\Delta^{17}\text{O}$ values of $\sim 0\text{‰}$ (see Sect. 30.5), a set of $\Delta^{17}\text{O}$ mass balance equations can be derived (Michalski et al. 2003):

$$\Delta^{\text{HNO}_3}(\gamma) = \Delta^{\text{O}_3} \cdot (2\phi/3), \quad (30.24)$$

$$\Delta^{\text{HNO}_3}(\eta) = \Delta^{\text{O}_3} \cdot (2\phi + 1)/3, \quad (30.25)$$

$$\Delta^{\text{HNO}_3}(\phi) = \Delta^{\text{O}_3} \cdot (4\phi + 1)/6, \quad (30.26)$$

where ϕ is the mole fraction of NO oxidized by O_3 , and γ , η , and ϕ are the mole fractions of HNO_3 produced by the reaction pathways R6, R7, and R8 respectively. Predicting $\Delta^{17}\text{O}$ anomalies in atmospheric nitrate (Δ^{HNO_3}) is then a matter of estimating the $\Delta^{17}\text{O}$ value of O_3 (or NO_2) and calculating the mole fractions (ϕ, γ, η, ϕ) using a photochemical kinetics model. $\Delta^{17}\text{O}$ values are calculated in each time step and normalized to the total nitrate produced during the simulation.

Several box model systems have been used to simulate atmospheric nitrate $\Delta^{17}\text{O}$ data. The first study (Michalski et al 2003) utilized a box model for simulating nitrate production in a polluted marine boundary layer (Yvon et al. 1996). There was reasonably good agreement between the observed $\Delta^{17}\text{O}$ values of atmospheric nitrate and the predicted values, but during the spring there were predicted-observed differences of up to 5‰. This was attributed to the model's inability to account for transport of atmospheric nitrate from neighboring regions by advective flow. Morin et al. (2008) estimated atmospheric nitrate $\Delta^{17}\text{O}$ values by adapting CiTTyCAT (Cambridge Transport Trajectory model of Chemistry And Transport), a photochemical box model previously used to examine the origin of polluted layer in the North Atlantic (Wild et al. 1996). This model's predictions agreed reasonably well with observed $\Delta^{17}\text{O}$ variations in the Arctic (Morin et al. 2008). Michalski and Xu (2010) used the regional atmospheric chemical mechanism (RACM) (Stockwell et al. 1997) and the $\Delta^{17}\text{O}$ mass balance approximation (ISO-RACM = isotope RACM) to assess changes in $\Delta^{17}\text{O}$ over a wide range of atmospheric parameters (Fig. 30.10). Using the terminal atom $\text{O}_3 + \text{NO}$ reaction mechanism, ISO-RACM predicts a range $\Delta^{17}\text{O}$ values that is similar to that observed in the atmosphere (Figs. 30.3 and 30.10). The simulations also tested the sensitivity of atmospheric nitrate $\Delta^{17}\text{O}$ predictions to a range of atmospheric parameters including temperature, relative humidity, trace gas concentrations, and surface solar radiation (actinic flux). Atmospheric nitrate $\Delta^{17}\text{O}$

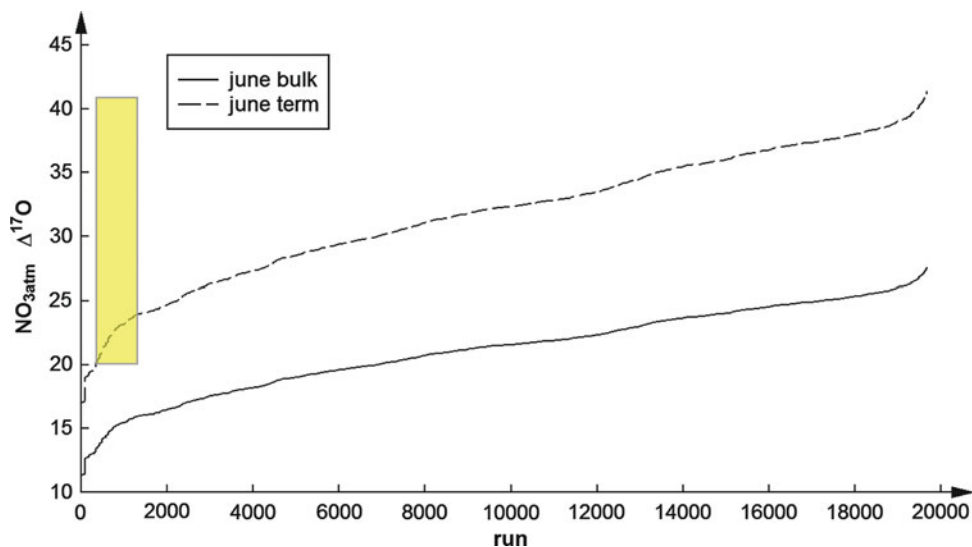


Fig. 30.10 Simulated $\Delta^{17}\text{O}$ values of atmospheric nitrate under a wide range of simulated atmospheric conditions (NO_x , organic compounds, temperature, humidity, etc.) for June (each run is a different set of conditions). Recent experiments have

provided new evidence that the “bulk transfer” mechanism is not likely to be valid but rather it is the terminal mechanism (Savarino et al. 2008). All observed data (yellow box) fall within the predicted range when using the terminal mechanism

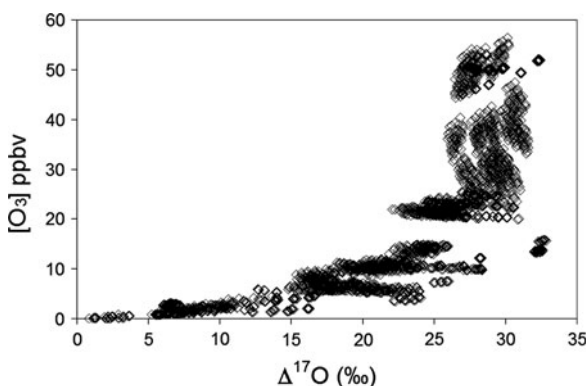


Fig. 30.11 Variation of atmospheric nitrate $\Delta^{17}\text{O}$ values as a function of O_3 mixing ratios. The graph highlights that by observing atmospheric nitrate, inferences can be made about the oxidation state of the atmosphere (i.e. importance of ozone or peroxy radicals). This highlights the potential for using atmospheric nitrate contained in ice cores as a proxy for changes in oxidative potential

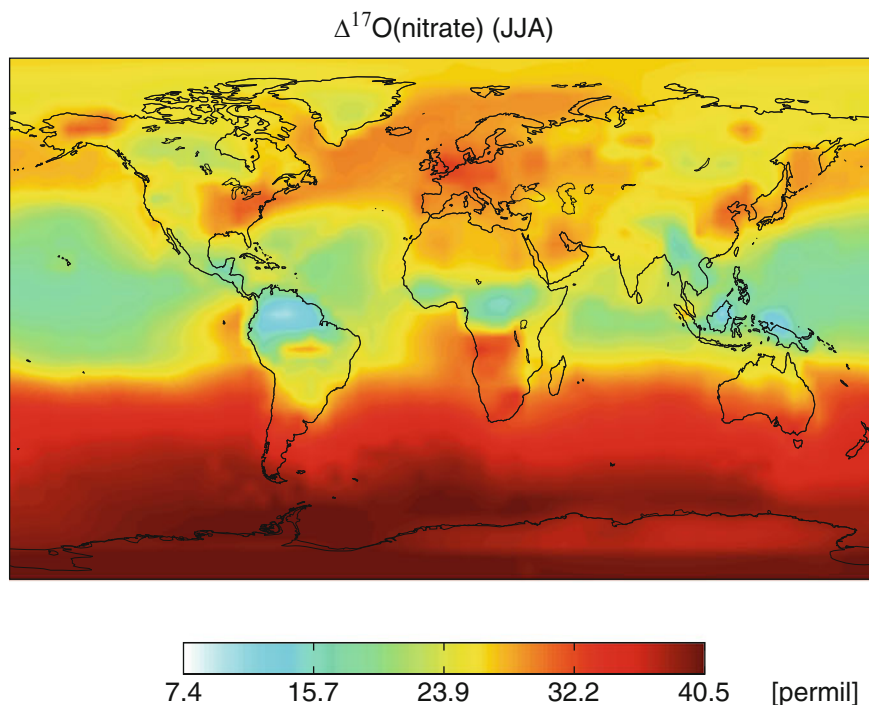
values were found to be sensitive to actinic flux, with increased fluxes (longer days during spring/summer) generating lower $\Delta^{17}\text{O}$ values in agreement with observed seasonal trends (Fig. 30.3). This effect is derived from smaller ϕ values with increased sunlight through increased production of peroxy radicals and higher γ values driven by the increase of NO_2 oxidation by OH during sunlight conditions. Atmospheric

nitrate $\Delta^{17}\text{O}$ values were also sensitive to concentration of certain trace gases. While variations in methane and carbon monoxide mixing ratios had little influence on predicted $\Delta^{17}\text{O}$ values, the trace gases such as NO_x , volatile organic compounds, and ozone clearly influenced the predicted $\Delta^{17}\text{O}$ values by shifting nitrate production pathways. For example, higher $\Delta^{17}\text{O}$ values were predicted at higher O_3 mixing ratios relative to low levels (Fig. 30.11).

30.6.3 3D Modeling of Nitrate $\Delta^{17}\text{O}$ Values

Global variations in atmospheric nitrate $\Delta^{17}\text{O}$ values were recently modeled using a 3D chemical transport model GEOS-Chem (Alexander et al. 2009). The model uses the same simple mass balance approach discussed above. The GEOS-Chem model does have the advantage of being able to include vertical and horizontal transport, and incorporates spatial variations in surface fluxes of important primary pollutants such as NO_x and VOC's, which is a serious limitation in the box models. Full details of the model resolution, fluxes, chemistry, etc. can be found in Alexander et al. (2009).

Fig. 30.12 Predicted global $\Delta^{17}\text{O}$ values in atmospheric nitrate for boreal summer using GEOS-Chem 3D chemical transport model (Alexander et al. 2009). Clear latitudinal $\Delta^{17}\text{O}$ variations are simulated and are the result of a combination of daylight hours, peroxy radical oxidation, and shifts in the relative importance of nitrate production pathways R6–R8. Such spatial heterogeneity of atmospheric nitrate $\Delta^{17}\text{O}$ values have not been verified by measurements



The GEOS-Chem model predicts atmospheric nitrate $\Delta^{17}\text{O}$ values that generally fall within the range of observations (Fig. 30.12). Globally, $\Delta^{17}\text{O}$ values range from a low of $\sim 7\text{‰}$ up to a maximum of 41‰ and exhibit a similar seasonal variation (high in winter, low in summer) as observations (Sect. 30.3). The model tends to over predict $\Delta^{17}\text{O}$ values in the mid to high latitudes in winter and underestimates them in polar regions during the spring and summer. The model attributes the seasonal $\Delta^{17}\text{O}$ variation in atmospheric nitrate to changes in the relative amount of NO oxidized by O_3 (ϕ) and seasonal changes in the relative importance of the N_2O_5 hydrolysis (φ). This study also supports the hypothesis that change in the oxygen isotopes in atmospheric nitrate reflects changes in oxidation chemistry in the atmosphere.

The purpose of both the box model and 3D simulations is to try and rationalize the atmospheric nitrate $\Delta^{17}\text{O}$ measurements in the context of changes in atmospheric chemistry. Shifts to peroxy radical (R3) and OH (R6) oxidation will lead to lower $\Delta^{17}\text{O}$ values. This will tend to happen in regions with high volatile organic carbon emissions and abundant sunlight (Alexander et al. 2009; Michalski and Xu 2010) such as the tropics. Conversely, N_2O_5 (R8) and O_3 (R1)

oxidation push atmospheric nitrate $\Delta^{17}\text{O}$ values higher. The N_2O_5 reaction is a strong function of aerosol surface area, aerosol type, limited sunlight and temperature (at cold temperature the R5 equilibrium favors N_2O_5). This reaction would be favored in the high latitude during winter when it is cold and dark. Therefore, the objective is to use the isotopes to understand the chemistry and how that might change under anthropogenic and natural environmental perturbations.

Two things are required for the predictions of atmospheric nitrate $\Delta^{17}\text{O}$ models to converge with observations (1) A detailed understanding of the isotope effects arising during different steps of NO_x oxidation (2) Confidence in the chemical and biogeochemical mechanisms in the model itself (i.e. reaction rates, uptake coefficients, emission inventories, meteorology etc.). This review has focused on the former rather than the latter. This is because the model mechanisms have been extensively dealt with by the larger atmospheric chemistry community. Conversely, research on the isotopic effects in the NO_x – NO_y system has only recently been developed and the largest error in the predictions is likely to come from the unknowns in these effects. If these uncertainties in the

isotope mechanisms can be significantly reduced, then atmospheric nitrate $\Delta^{17}\text{O}$ values may be a new way of validating the chemical models themselves.

30.6.4 Modeling $\delta^{18}\text{O}$ Values in Atmospheric Nitrate

Modeling $\delta^{18}\text{O}$ values in atmospheric nitrate is more challenging relative to $\Delta^{17}\text{O}$ models for two reasons. First, unlike $\Delta\epsilon$ in the $\Delta^{17}\text{O}$ case, the KIE/equilibrium enrichment factors (ϵ) may be significant for the mass dependent reactions occurring during NO_x oxidation (i.e. R1–R6), but they are largely unknown. Second, the other oxygen sources (water, OH) that contribute to atmospheric nitrate have variable $\delta^{18}\text{O}$ values. This is unlike the $\Delta^{17}\text{O}$ modeling where all oxygen sources other than ozone are assumed to have a $\Delta^{17}\text{O}$ value ~ 0 . Variability of the $\delta^{18}\text{O}$ of water affects atmospheric nitrate isotopic composition both directly (R8) and indirectly (R6), adding complexity, because water $\delta^{18}\text{O}$ values vary significantly in time and space. Global 3D models simulating $\delta^{18}\text{O}$ of precipitation from first principles (i.e. Rayleigh distillations, temperature effects, equilibrium fractionations) are challenging tasks in and of themselves.

Recently, however, a relatively simple modeling approach has been used to predict $\delta^{18}\text{O}$ values in atmospheric nitrate (Mase 2010). Similar to the $\Delta^{17}\text{O}$ model, the isotope mass balance simplification was used and the unknown ϵ 's were ignored. However, the equilibrium enrichment factors between liquid water and vapor (30.18) and OH and water vapor (30.20) were taken into account. The atmospheric nitrate $\delta^{18}\text{O}$ mass balance equations, which are analogous to the $\Delta^{17}\text{O}$ mass balance, are given as:

$$\delta^{18}\text{ONO}_2 = \phi \delta^{18}\text{OO}_3 + (1 - \phi) \delta^{18}\text{OO}_2 \quad (30.27)$$

$$\delta^{18}\text{ONO}_3(\gamma) = \delta^{18}\text{ONO}_2(2/3) + 1/3 \delta^{18}\text{OOH} \quad (30.28)$$

$$\delta^{18}\text{OHNO}_3(\eta) = 2/3 \delta^{18}\text{ONO}_2 + 1/3 \delta^{18}\text{OO}_3 \quad (30.29)$$

$$\delta^{18}\text{O HNO}_3(\varphi) = 4/6 \delta^{18}\text{O NO}_2 + 1/6 \delta^{18}\text{O O}_3 + 1/6 \delta^{18}\text{O H}_2\text{O}_{\text{liq}} \quad (30.30)$$

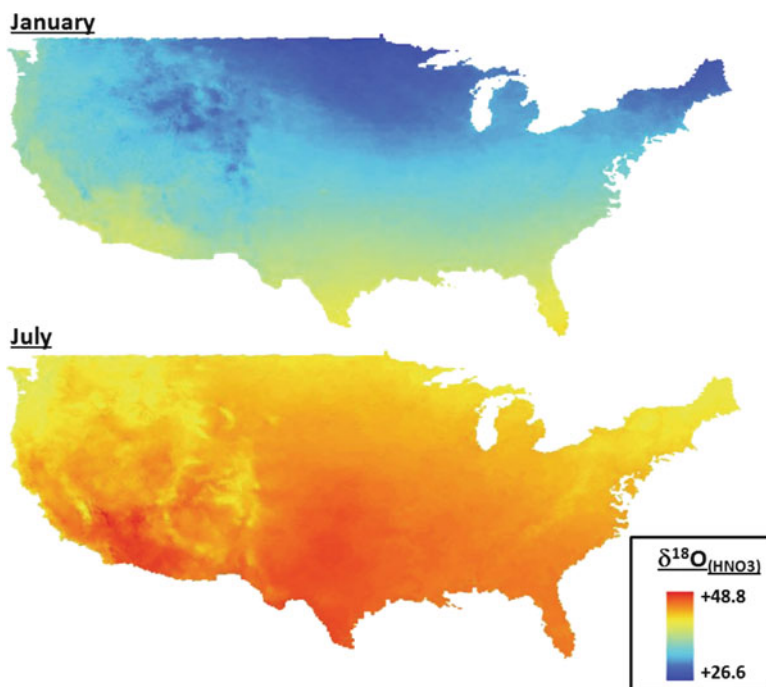
The $\delta^{18}\text{O}$ of liquid water was taken from interpolation of the GNIP data set (Fig. 30.5). The derivation of the $\delta^{18}\text{O}$ of O_3 and OH is discussed in Sects. 30.5.1 and 30.5.3 respectively. The temperature and pressure data was obtained from the NARR data set. For a given location, the daily average ϕ , γ , η , and φ are calculated using ISO-RACM.

As an example, Fig. 30.13 shows the $\delta^{18}\text{O}$ values of atmospheric nitrate for January and June, 2001. In these two cases, we fixed parameters ϕ , γ , η , and φ at values of 0.95, 0.65, 0.3, and 0.05 respectively. This shows that $\delta^{18}\text{O}$ variations are driven by factors other than simply the changes in NO_x oxidation pathways. These factors are spatial changes in $\delta^{18}\text{O}$ of the water and temperature that impact the $\delta^{18}\text{O}$ of the equilibrium water, and thus OH $\delta^{18}\text{O}$ (Figs. 30.8 and 30.9), and the $\delta^{18}\text{O}$ of ozone (Fig. 30.6). Clearly this isotope mass balance approach has some limitations, primarily through the use of daily average oxidation parameters (instead of an hourly time step), average temperatures, monthly resolution on the $\delta^{18}\text{O}$ of water and ignoring KIEs. The model predicts that atmospheric nitrate $\delta^{18}\text{O}$ values over North America would seasonally span $\sim 25\%$, with lower values occurring in the winter. This agrees with the seasonal trends for a given dataset in Fig. 30.2, but the absolute values are lower than observations by $\sim 10\text{--}20\%$. This is primarily due to the very negative $\delta^{18}\text{O}$ values assigned to OH that is based for $\text{H}_2\text{O}\text{--OH}$ equilibrium (Fig. 30.9). It is likely that the highly reactive OH is isotopically enriched by KIE during the oxidation of reduced compounds in the atmosphere.

In addition, exchange reactions between NO_x and OH (Zahn et al. 2006) may be important and increases OH's $\delta^{18}\text{O}$ and $\Delta^{17}\text{O}$ values over what would be expected based on water-OH equilibrium.

This approach to modeling atmospheric nitrate $\delta^{18}\text{O}$ values is crude, but it is also a first step. The model show that while the variations in atmospheric nitrate $\Delta^{17}\text{O}$ values are driven almost exclusively by shifts in chemical pathways, the $\delta^{18}\text{O}$ variability is likely a function of both chemistry, the $\delta^{18}\text{O}$ of local water in the atmosphere, and temperature. Why might

Fig. 30.13 Simulated $\delta^{18}\text{O}$ values of atmospheric nitrate for January and July 1, 2001 for the continental US. Values are calculated using methods described in the text



modeling $\delta^{18}\text{O}$ values in atmospheric nitrate be useful? If this can be done accurately it can be a way of estimating the $\delta^{18}\text{O}$ in atmospheric nitrate deposition over extended areas and timeframes. This data could be used as the atmospheric nitrate component in end member isotopic mixing models that try to use nitrate $\delta^{18}\text{O}$ values as a tracer of different N sources in watersheds (see Burns and Kendall 2002; Campbell et al. 2002). In addition, it might be a secondary constraint on oxidation chemistry that could be used in conjunction with the $\Delta^{17}\text{O}$ values. In particular, the incorporation of water, whose $\delta^{18}\text{O}$ values are highly variable in space and time, may be a way of tracing the importance of the N_2O_5 oxidation pathway.

30.7 Future Directions

There is a tremendous amount of science still needed for interpreting isotopic variation in atmospheric nitrate, but the potential outcomes will be well worth the effort. The first and foremost need is an expanded observational data set. Given the potential use of oxygen isotopes in the atmospheric nitrate system (understanding chemical pathways, the feedbacks between

climate and chemistry), the lack of data is surprising. This is largely due to limitations of the dual inlet methods that require relatively large amount of nitrate (Sect. 30.2). With new continuous flow techniques, this limitation has been lifted, which opens the way for wider spatial and better temporal measurements of both $\delta^{18}\text{O}$ and $\Delta^{17}\text{O}$ in atmospheric nitrate. Since the models predict strong $\Delta^{17}\text{O}$ variations under different chemical and meteorological conditions, the potential for verifying and improving the predictive capability of the models relies on observations from a wide range of environments. Data that compares urban vs. rural, high aerosol vs. low aerosol environments, different forested ecosystems where volatile organic emissions are high (deciduous, evergreen, tropical rainforest), latitudinal and longitudinal gradients, ocean vs. continental, and diurnal/hourly variability are just a few examples. Assessing isotope variation in the different phases (Elliott et al. 2009) of atmospheric nitrate ($\text{HNO}_{3(\text{g})}$, particulate nitrate and dissolved NO_3^-) and in different aerosol sizes would also be helpful for both understanding the fundamental chemical processes that form atmospheric nitrate and its isotopic variability.

Additional experiments investigating isotope effects in the NO_x -nitrate system are also needed.

Assessing the dependence of ozone's $\Delta^{17}\text{O}$ and $\delta^{18}\text{O}$ values on changes in temperature and pressure are primary in this regard. Direct determination of isotope effects in NO_x through experiments, instead of inferences using ozone data and reaction dynamics, would help to reduce uncertainties. Whether water contributes only one oxygen atom during N_2O_5 hydrolysis or if additional exchange occurs also needs to be addressed. An experimental investigation of the isotope effect of HO_2 formation and subsequent NO oxidation is important because current models assume any associated $\Delta^{17}\text{O}$ effect to be negligible. In order to interpret polar region data, the transfer coefficients and gas phase exchange reactions of oxidized halogens (BrO_x , ClO_x) need to be determined. There is almost no experimental data on some of the key mass dependent processes that might influence $\delta^{18}\text{O}$ and $\delta^{15}\text{N}$ in atmospheric nitrate. It is likely that the temperature sensitive $\text{NH}_4\text{NO}_3 \leftrightarrow \text{HNO}_3 + \text{NH}_3$ equilibrium will have a significant mass dependent effect, which should be determined experimentally.

A number of advances in the modeling approaches that try to simulate atmospheric nitrate oxygen isotope variations are also possible. Nitrate's short atmospheric lifetime and sensitivity to local scale trace gas concentrations would suggest that higher resolution 3D regional models would do a better job of simulating data. Adapting regional modeling platforms such as CMAQ or WRF-Chem to the atmospheric nitrate problem would be very beneficial. The models also must be kept up to date with new data from experimental work as discussed above. Incorporating equilibrium and KIE into model chemistry mechanisms for a more robust simulation of $\delta^{18}\text{O}$ and $\delta^{15}\text{N}$ variability would be an ambitious, long-term goal. This would require experimental and theoretical determination of a large number of KIE and photolysis effects that are quite challenging.

References

- Alexander B, Hastings MG, Allman DJ et al (2009) Quantifying atmospheric nitrate formation pathways based on a global model of the oxygen isotopic composition ($\Delta^{17}\text{O}$) of atmospheric nitrate. *Atmos Chem Phys* 9:5043–5056
- Amberger A, Schmidt HL (1987) Natural isotope content of nitrate as an indicator of its origin. *Geochim Cosmochim Acta* 51:2699–2705
- Araguas-Araguas L, Froehlich K, Rozanski K (2000) Deuterium and oxygen-18 isotope composition of precipitation and atmospheric moisture. *Hydrol Process* 14:1341–1355
- Barkan E, Luz B (2003) High-precision measurements of $^{17}\text{O}/^{16}\text{O}$ and $^{18}\text{O}/^{16}\text{O}$ of O_2 and O_2/Ar ratio in air. *Rapid Commun Mass Spectrom* 17:2809–2814
- Barkan E, Luz B (2005) High precision measurements of $^{17}\text{O}/^{16}\text{O}$ and $^{18}\text{O}/^{16}\text{O}$ ratios in H_2O . *Rapid Commun Mass Spectrom* 19:3737–3742
- Bhattacharya SK, Pandey A, Savarino J (2008) Determination of intramolecular isotope distribution of ozone by oxidation reaction with silver metal. *J Geophys Res* 113. doi:10.1029/2006JD008309
- Bobbink R, Hicks K, Galloway J et al (2010) Global assessment of nitrogen deposition effects on terrestrial plant diversity: a synthesis. *Ecol Appl* 20:30–59
- Böhlke JK, Mroczkowski SJ, Coplen TB (2003) Oxygen isotopes in nitrate: new reference materials for $^{18}\text{O}:^{17}\text{O}:^{16}\text{O}$ measurements and observations on nitrate-water equilibration. *Rapid Commun Mass Spectrom* 17:1835–1846
- Bowen GJ, Revenaugh J (2003) Interpolating the isotopic composition of modern meteoric precipitation. *Water Resour Res* 39. doi:10.1029/2003WR002086
- Brown SS, Stark H, Ryerson TB et al (2003) Nitrogen oxides in the nocturnal boundary layer: simultaneous in situ measurements of NO_3 , N_2O_5 , NO_2 , NO , and O_3 . *J Geophys Res* 108. doi:10.1029/2002JD002917
- Buda AR, DeWalle DR (2009) Using atmospheric chemistry and storm track information to explain the variation of nitrate stable isotopes in precipitation at a site in central Pennsylvania, USA. *Atmos Environ* 43:4453–4464
- Bunton CA, Halevi EA, Llewellyn DR (1952) Oxygen exchange between nitric acid and water. Part 1. *J Chem Soc*: 4913–4916
- Burns DA, Kendall C (2002) Analysis of $\delta^{15}\text{N}$ and $\delta^{18}\text{O}$ to differentiate NO_3^- sources at two watersheds in the Catskill Mountains of New York. *Water Resour Res* 38. doi:10.1029/2001WR000292
- Campbell DH, Kendall C, Chang CCY et al (2002) Pathways for nitrate release from an alpine watershed: determination using $\delta^{15}\text{N}$ and $\delta^{18}\text{O}$. *Water Resour Res* 38. doi:10.1029/2001WR000294
- Casciotti KL, Sigman DM, Hastings MG et al (2002) Measurement of the oxygen isotopic composition of nitrate in seawater and freshwater using the denitrifier method. *Anal Chem* 74:4905–4912
- Chang CCY, Langston J, Riggs M et al (1999) A method for nitrate collection for $\delta^{15}\text{N}$ and $\delta^{18}\text{O}$ analysis from waters with low nitrate concentrations. *Can J Fish Aquat Sci* 56:1856–1864
- Cliff SS, Thiemens MH (1994) High precision isotopic determination of the $^{18}\text{O}/^{16}\text{O}$ and $^{17}\text{O}/^{16}\text{O}$ ratio in nitrous oxide. *Anal Chem* 66:2791–2793
- Dieke GH, Crosswhite HM (2010) The ultraviolet bands of OH fundamental data. *J Quant Spectrosc Radiat Transfer* 111: 1516–1542
- Dole M, Lane GA, Rudd DP et al (1954) Isotopic composition of atmospheric oxygen and nitrogen. *Geochim Cosmochim Acta* 6:65–78
- Dubey MK, Mohrshchladt R, Donahue NM, Anderson JG (1997) Isotope-specific kinetics of hydroxyl radical (OH) with water

- (H₂O): testing models of reactivity and atmospheric fractionation. *J Phys Chem A* 101:1494–1500
- Durka W, Schulze ED, Gebauer G et al (1994) Effects of forest decline on uptake and leaching of deposited nitrate determined from ¹⁵N and ¹⁸O measurements. *Nature* 372: 765–767
- Elliott EM, Kendall C, Boyer EW et al (2009) Dual nitrate isotopes in dry deposition: utility for partitioning NO_x source contributions to landscape nitrogen deposition. *J Geophys Res* 114. doi:[10.1029/2008JG000889](https://doi.org/10.1029/2008JG000889)
- Freyer HD (1991) Seasonal-variation of ¹⁵N/¹⁴N ratios in atmospheric nitrate species. *Tellus Ser B* 43:30–44
- Galloway JN (1995) Acid deposition: perspectives in time and space. *Water Air Soil Pollut* 85:15–24
- Galloway JN (1998) The global nitrogen cycle: changes and consequences. *Environ Pollut* 102:15–24
- Galloway JN, Dentener FJ, Capone DG et al (2004) Nitrogen cycles: past, present, and future. *Biogeochemistry* 70: 153–226
- Gao YQ, Marcus RA (2001) Strange and unconventional isotope effects in ozone formation. *Science* 293:259–263
- Gat JR (1996) Oxygen and hydrogen isotopes in the hydrologic cycle. *Annu Rev Earth Planet Sci* 24:225–262
- Gellene GI (1996) An explanation for symmetry-induced isotopic fractionation in ozone. *Science* 274:1344–1346
- Guenther J, Krankowsky D, Mauersberger K (2000) Third-body dependence of rate coefficients for ozone formation in ¹⁶O/¹⁸O mixtures. *Chem Phys Lett* 324:31–36
- Hales HC, Ross DS, Lini A (2007) Isotopic signature of nitrate in two contrasting watersheds of Brush Brook, Vermont, USA. *Biogeochemistry* 84:51–66
- Hallquist M, Stewart DJ, Baker J et al (2000) Hydrolysis of N₂O₅ on submicron sulfuric acid aerosols. *J Phys Chem A* 104:3984–3990
- Hastings MG, Sigman DM, Lipschultz F (2003) Isotopic evidence for source changes of nitrate in rain at Bermuda. *J Geophys Res* 108. doi:[10.1029/2003JD003789](https://doi.org/10.1029/2003JD003789)
- Hathorn BC, Marcus RA (1999) An intramolecular theory of the mass-independent isotope effect for ozone. I. *J Chem Phys* 111:4087–4100
- Hathorn BC, Marcus RA (2000) An intramolecular theory of the mass-independent isotope effect for ozone II. Numerical implementation at low pressures using a loose transition state. *J Chem Phys* 113:9497–9509
- Heidenreich JE III, Thiemens MH (1983) A non-mass-dependent isotope effect in the production of ozone from molecular oxygen. *J Chem Phys* 78:892–895
- Herzberg G (1966) *Infrared and Raman spectra of polyatomic molecules*, 2nd edn. Krieger, Malabar
- Horita J, Wesolowski DJ (1994) Liquid-vapor fractionation of oxygen and hydrogen isotopes of water from the freezing to the critical-temperature. *Geochim Cosmochim Acta* 58: 3425–3437
- Jaegle L, Jacob DJ, Brune WH et al (2000) Photochemistry of HO_x in the upper troposphere at northern midlatitudes. *J Geophys Res* 105:3877–3892
- Johnston JC, Thiemens MH (1997) The isotopic composition of tropospheric ozone in three environments. *J Geophys Res* 102:25395–25404
- Kaiser J (2009) Reformulated ¹⁷O correction of mass spectrometric stable isotope measurements in carbon dioxide and a critical appraisal of historic absolute carbon and oxygen isotope ratios. *Geochim Cosmochim Acta* 72:1312–1334
- Kaiser J, Hastings MG, Houlton BZ et al (2007) Triple oxygen isotope analysis of nitrate using the denitrifier method and thermal decomposition of N₂O. *Anal Chem* 79:599–607
- Kalnay E, Kanamitsu M, Kistler R et al (1996) The NCEP/NCAR 40-year reanalysis project. *Bull Am Meteorol Soc* 77:437–471
- Kendall C (1998) Tracing nitrogen sources and cycling in catchments. Elsevier Science B.V, Amsterdam, pp 519–576
- Komatsu DD, Ishimura T, Nakagawa F et al (2008) Determination of the ¹⁵N/¹⁴N, ¹⁷O/¹⁶O, and ¹⁸O/¹⁶O ratios of nitrous oxide by using continuous-flow isotope-ratio mass spectrometry. *Rapid Commun Mass Spectrom* 22:1587–1596
- Kornel BE, Gehre M, Hoffling R et al (1999) On-line δ¹⁸O measurement of organic and inorganic substances. *Rapid Commun Mass Spectrom* 13:1685–1693
- Krankowsky D, Bartecki F, Klees GG et al (1995) Measurement of heavy isotope enrichment in tropospheric ozone. *Geophys Res Lett* 22:1713–1716
- Krankowsky D, Lammerzahl P, Mauersberger K (2000) Isotopic measurements of stratospheric ozone. *Geophys Res Lett* 27:2593–2595
- Kunasek SA, Alexander B, Steig EJ et al (2008) Measurements and modeling of Δ¹⁷O of nitrate in snowpits from Summit, Greenland. *J Geophys Res* 113. doi:[10.1029/2008JD010103](https://doi.org/10.1029/2008JD010103)
- Liang MC, Irion FW, Weibel JD et al (2006) Isotopic composition of stratospheric ozone. *J Geophys Res* 111. doi:[10.1029/2005JD006342](https://doi.org/10.1029/2005JD006342)
- Luz B, Barkan E (2005) The isotopic ratios ¹⁷O/¹⁶O and ¹⁸O/¹⁶O in molecular oxygen and their significance in biogeochemistry. *Geochim Cosmochim Acta* 69:1099–1110
- Lyons JR (2001) Transfer of mass-independent fractionation in ozone to other oxygen-containing radicals in the atmosphere. *Geophys Res Lett* 28:3231–3234
- Majoube M (1971) Oxygen-18 and deuterium fractionation between water and steam. *J Chim Phys Physicochim Biol* 68:1423–1436
- Martin RV, Sauvage B, Folkens I et al (2007) Space-based constraints on the production of nitric oxide by lightning. *J Geophys Res* 112. doi:[10.1029/2006JD007831](https://doi.org/10.1029/2006JD007831)
- Mase D (2010) A coupled modeling and observational approach to understanding the ¹⁵N and ¹⁸O of atmospheric nitrate. M.S. Thesis, Purdue University
- Matsuhisa Y, Goldsmith JR, Clayton RN (1978) Mechanisms of hydrothermal crystallization of quartz at 250°C and 15 kbar. *Geochim Cosmochim Acta* 42:173–182
- Mauersberger K, Lammerzahl P, Krankowsky D (2001) Stratospheric ozone isotope enrichments-revisited. *Geophys Res Lett* 28:3155–3158
- Mauersberger K, Krankowsky D, Janssen C (2003) Oxygen isotope processes and transfer reactions. *Space Sci Rev* 106:265–279
- McCabe JR, Thiemens MH, Savarino J (2007) A record of ozone variability in South Pole Antarctic snow: role of

- nitrate oxygen isotopes. *J Geophys Res* 112. doi:[10.1029/2006JD007822](https://doi.org/10.1029/2006JD007822)
- McIlvin MR, Altabet MA (2005) Chemical conversion of nitrate and nitrite to nitrous oxide for nitrogen and oxygen isotopic analysis in freshwater and seawater. *Anal Chem* 77: 5589–5595
- Meijer HAJ, Li WJ (1998) The use of electrolysis for accurate $\delta^{17}\text{O}$ and $\delta^{18}\text{O}$ isotope measurements in water. *Isotopes Environ Health Stud* 34:349–369
- Mentel TF, Sohn M, Wahner A (1999) Nitrate effect in the heterogeneous hydrolysis of dinitrogen pentoxide on aqueous aerosols. *Phys Chem Chem Phys* 1:5451–5457
- Michalski G (2009) Purification procedure for $\delta^{15}\text{N}$, $\delta^{18}\text{O}$, $\Delta^{17}\text{O}$ analysis of nitrate. *Int J Environ Anal Chem* 90:586–590
- Michalski G, Bhattacharya SK (2009) The role of symmetry in the mass independent isotope effect in ozone. *Proc Natl Acad Sci U S A* 106:11496–11501
- Michalski G, Xu F (2010) Isotope modeling of nitric acid formation in the atmosphere using ISO-RACM: testing the importance of nitric oxide oxidation, heterogeneous reactions, and trace gas chemistry. *Atmos Chem Phys* (in review)
- Michalski G, Savarino J, Böhlke JK et al (2002) Determination of the total oxygen isotopic composition of nitrate and the calibration of a $\Delta^{17}\text{O}$ nitrate reference material. *Anal Chem* 74:4989–4993
- Michalski G, Scott Z, Kabling M et al (2003) First measurements and modeling of $\Delta^{17}\text{O}$ in atmospheric nitrate. *Geophys Res Lett* 30:1870. doi:[10.1029/2003GL017015](https://doi.org/10.1029/2003GL017015)
- Michalski G, Bhattacharya SK, Girsch G (In preparation) Isotope effects occurring during the NO_x cycle
- Miller MF (2002) Isotopic fractionation and the quantification of ^{17}O anomalies in the oxygen three-isotope system: an appraisal and geochemical significance. *Geochim Cosmochim Acta* 66:1881–1889
- Morin S, Savarino J, Bekki S et al (2007) Signature of Arctic surface ozone depletion events in the isotope anomaly ($\Delta^{17}\text{O}$) of atmospheric nitrate. *Atmos Chem Phys* 7: 1451–1469
- Morin S, Savarino J, Frey MM et al (2008) Tracing the origin and fate of NO_x in the Arctic atmosphere using stable isotopes in nitrate. *Science* 322:730–732
- Morin S, Savarino J, Frey MM et al (2009) Comprehensive isotopic composition of atmospheric nitrate in the Atlantic Ocean boundary layer from 65°S to 79°N . *J Geophys Res* 114. doi:[10.1029/2008JD010696](https://doi.org/10.1029/2008JD010696)
- Morton J, Barnes J, Schueler B et al (1990) Laboratory studies of heavy ozone. *J Geophys Res* 95:901–907
- Mosier A, Kroeze C, Nevison C et al (1998) Closing the global N_2O budget: nitrous oxide emissions through the agricultural nitrogen cycle. *Nutr Cycl Agroecosyst* 52:225–248
- Patris N, Cliff SS, Quinn PK et al (2007) Isotopic analysis of aerosol sulfate and nitrate during ITCT-2k2: determination of different formation pathways as a function of particle size. *J Geophys Res* 112:D23301. doi:[10.1029/2005JD006214](https://doi.org/10.1029/2005JD006214)
- Peiro-Garcia J, Nebot-Gil I (2002) Ab initio study of the mechanism and thermochemistry of the atmospheric reaction $\text{NO} + \text{O}_3 \rightarrow \text{NO}_2 + \text{O}_2$. *J Phys Chem A* 106:10302–10310
- Revesz K, Böhlke JK (2002) Comparison of $\delta^{18}\text{O}$ in nitrate by different combustion techniques. *Anal Chem* 74: 5410–5413
- Revesz K, Böhlke JK, Yoshinari T (1997) Determination of $\delta^{18}\text{O}$ and $\delta^{15}\text{N}$ in nitrate. *Anal Chem* 69:4375–4380
- Rodhe H, Dentener F, Schulz M (2002) The global distribution of acidifying wet deposition. *Environ Sci Technol* 36: 4382–4388
- Savarino J, Lee CCW, Thiemens MH (2000) Laboratory oxygen isotopic study of sulfur (IV) oxidation: origin of the mass-independent oxygen isotopic anomaly in atmospheric sulfates and sulfate mineral deposits on Earth. *J Geophys Res* 105:29079–29088
- Savarino J, Kaiser J, Morin S et al (2007) Nitrogen and oxygen isotopic constraints on the origin of atmospheric nitrate in coastal Antarctica. *Atmos Chem Phys* 7:1925–1945
- Savarino J, Bhattacharya SK, Morin S et al (2008) The $\text{NO} + \text{O}_3$ reaction: a triple oxygen isotope perspective on the reaction dynamics and atmospheric implications for the transfer of the ozone isotope anomaly. *J Chem Phys* 128. doi:[10.1063/1.2917581](https://doi.org/10.1063/1.2917581)
- Silva SR, Kendall C, Wilkison DH et al (2000) A new method for collection of nitrate from fresh water and the analysis of nitrogen and oxygen isotope ratios. *J Hydrol* 228:22–36
- Spoelstra J, Schiff SL, Elgood RJ et al (2001) Tracing the sources of exported nitrate in the Turkey Lakes Watershed using $^{15}\text{N}/^{14}\text{N}$ and $^{18}\text{O}/^{16}\text{O}$ isotopic ratios. *Ecosystems* 4: 536–544
- Stockwell WR, Kirchner F, Kuhn M et al (1997) A new mechanism for regional atmospheric chemistry modeling. *J Geophys Res* 102:25847–25879
- Thiemens MH, Heidenreich JE III (1983) The mass-independent fractionation of oxygen: a novel isotope effect and its possible cosmochemical implications. *Science* 219:1073–1075
- Thiemens MH, Jackson T (1990) Pressure dependency for heavy isotope enhancement in ozone formation. *Geophys Res Lett* 17:717–719
- Thiemens MH, Jackson T, Mauersberger K, Schueler B, Morton J (1991) Oxygen isotope fractionation in stratospheric CO_2 . *Geophys Res Lett* 18:669–672
- Thiemens MH, Savarino J, Farquhar J et al (2001) Mass-independent isotopic compositions in terrestrial and extraterrestrial solids and their applications. *Acc Chem Res* 34: 645–652
- Tuazon EC, Atkinson R, Plum CN et al (1983) The reaction of gas-phase N_2O_5 with water-vapor. *Geophys Res Lett* 10: 953–956
- Uemura R, Barkan E, Abe O et al (2010) Triple isotope composition of oxygen in atmospheric water vapor. *Geophys Res Lett* 37. doi:[10.1029/2009GL041960](https://doi.org/10.1029/2009GL041960)
- Urey HC (1947) Thermodynamic properties of isotopic substances. *J Chem Soc*:562–581
- Valentini JJ (1987) Mass-independent isotopic fractionation in nonadiabatic molecular-collisions. *J Chem Phys* 86: 6757–6765
- Vuille M, Werner M, Bradley RS et al (2005) Stable isotopes in precipitation in the Asian monsoon region. *J Geophys Res* 110:D23108. doi:[10.1029/2005JD006022](https://doi.org/10.1029/2005JD006022)
- Wahner A, Mentel TF, Sohn M (1998) Gas-phase reaction of N_2O_5 with water vapor: importance of heterogeneous hydrolysis of N_2O_5 and surface desorption of HNO_3 in a large teflon chamber. *Geophys Res Lett* 25:2169–2172

- Wassenaar LI (1995) Evaluation of the origin and fate of nitrate in the Abbotsford Aquifer using the isotopes of ^{15}N and ^{18}O in NO_3^- . *Appl Geochem* 10:391–405
- Wild O, Law KS, McKenna DS et al (1996) Photochemical trajectory modeling studies of the North Atlantic region during August 1993. *J Geophys Res* 101:29269–29288
- Williard KWJ, DeWalle DR, Edwards PJ, Sharpe WE (2001) ^{18}O isotopic separation of stream nitrate sources in mid-Appalachian forested watersheds. *J Hydrol* 252:174–188
- Yung YL, DeMore WB, Pinto JP (1991) Isotopic exchange between carbon dioxide and ozone via $\text{O}(^1\text{D})$ in the stratosphere. *Geophys Res Lett* 18:13–16
- Yvon SA, Plane JMC, Nien CF et al (1996) Interaction between nitrogen and sulfur cycles in the polluted marine boundary layer. *J Geophys Res* 101:1379–1386
- Zahn A, Franz P, Bechtel C, Grooß JU, Röckmann T (2006) Modelling the budget of middle atmospheric water vapour isotopes. *Atmos Chem Phys* 6:2073–2090
- Zhang Y, Seigneur C, Seinfeld JH et al (2000) A comparative review of inorganic aerosol thermodynamic equilibrium modules: similarities, differences, and their likely causes. *Atmos Environ* 34:117–137

Part IV
Isotopes as Tracers of Environmental Forensics

Chapter 31

Applications of Stable Isotopes in Hydrocarbon Exploration and Environmental Forensics

R. Paul Philp and Guillermo Lo Monaco

Abstract Hydrocarbon exploration and environmental forensics may appear to be two unrelated topics but in many ways are closely related. Techniques that have been developed and utilized in the hydrocarbon exploration and exploitation industry for many decades have found their way to the forefront of environmental forensics area over the past decade. Whereas hydrocarbon exploration is geared towards finding new resources, environmental forensics is directed to looking at what happens to those resources as they, or products derived from them, are spilled into the environment. In the former one uses sophisticated techniques to correlate oils, or gases, with their suspected sources and in the later, one is trying to correlate the spilled product with its suspected source. The source may be a tanker, pipeline, underground storage tank or something similar. The most widely used techniques in both of these areas for many years have been gas chromatography (GC) and gas chromatography mass spectrometry (GCMS) but recent years have seen an exponential increase in the utilization of stable isotopes. There is nothing new about applying stable isotopes to exploration problems but the majority of the older applications utilized bulk isotope numbers for crude oil correlation studies. The availability of the combined gas chromatography-isotope ratio mass spectrometer systems (GCIRMS) over the past 10–20 years, has played an important role in the increased number of applications where stable isotopes have to be used to investigate problems in both of these areas.

In this chapter, we examine developments and applications in hydrocarbon exploration and environmental

forensics. In addition areas that are currently just starting to emerge particularly in the area of environmental forensics will also be discussed.

31.1 Introduction

Hydrocarbon exploration has become more and more sophisticated over the years with many new techniques being developed and applied to improve exploration success rates. These techniques maybe in areas such as geophysics and seismic acquisition and interpretation; or in geology where constantly evolving concepts such as sequence stratigraphy provide a far more comprehensive understanding of the ways in which source rocks were deposited (Slatt 2006); or geochemistry where a variety of novel analytical techniques permit a detailed understanding of the different types of organic matter deposited in a variety of depositional environments, hundreds of millions of years ago, and ultimately converted to oil and/or gas (Peters et al. 2005). Understanding organic matter types and depositional environments provides a far better understanding of the quality and quantity of oil and gas that may be produced from a certain type of source material (Killops and Killops 2005). In the first part of this chapter it is proposed to review the evolution of these various geochemical techniques applied to hydrocarbon exploration with specific emphasis on the utilization of stable isotopes and the type of information that can be provided and then the second part will show how stable isotopes are becoming widely used in the field of environmental forensics.

Hydrocarbon exploration, in one form or another, has been going on for many hundreds of years although commercial production is a more recent phenomena

R.P. Philp (✉) and G.L. Monaco
School of Geology and Geophysics, University of Oklahoma,
Norman, OK 73019, USA
e-mail: pphilp@ov.edu

dating back only a 100 years or more. Early exploration simply looked for surface expressions, or seeps, indicating that there was an oil accumulation in the area and wells that were drilled were normally quite shallow and right on top of the seep (Philp and Crisp 1982). Attempts to correlate any discovered oil with its suspected source rock depended on simple properties like color, density, API (American Petroleum Institute) gravity and various other bulk parameters. However in the 1950s and 1960s with the development of gas chromatography (GC), the major oil companies started to use this technique to characterize their oils and it was recognized that the distributions of the various n-alkanes detected by gas chromatography could give information about source and maturity of the oil and associated source rock (Bray and Evans 1964). An even more significant breakthrough came in the 1970s with the development of gas chromatograph-mass spectrometer (GCMS) systems. Crude oils, being such complex mixtures, were perfect candidates for analysis by GCMS and at the same time the concept of biomarkers was being developed and quickly applied to the characterization of crude oils (Eglinton and Calvin 1967). A biomarker can be defined as a compound in the geologic record with a carbon skeleton essentially identical to the carbon skeleton of its functional precursor molecule (Calvin 1969). An example would be cholesterol, a widely occurring natural product, which upon being deposited into a natural environment over an extended period of geologic time will be converted into cholestane. The carbon skeleton of cholestane is identical to that of cholesterol so the presence of cholestane in a crude oil tells us the ancient source material for that oil included cholesterol. The presence of that biomarker and many others helps the petroleum geochemist reconstruct the origin and history of the oil, providing useful information in the search for new accumulations of crude oil.

The concept of biomarkers had its origin in early studies on the origin of life and the search for earliest life forms in Precambrian rocks and organic compounds in the returned lunar samples of the 1970s (Eglinton and Calvin 1967; Calvin 1969). The Precambrian studies identified compounds in these extremely old rocks that could be associated with blue green algae and other early life forms (Han et al. 1968). In the early 1970s attention switched to the characterization of organic matter in very recent lake sediments, following the old adage that the key to

the past lies in the present (Brooks et al. 1976, 1977). These studies led to the identification of numerous compounds that could be associated with specific inputs of organic matter to lacustrine environments.

The recognition by Wolfgang Seifert (Seifert and Moldowan 1978, 1981; Seifert et al. 1978), a geochemist with Chevron, in the mid 1970s, that the stereochemistry of biomarkers, previously observed by Kimble (1972) in various shales, could be used to evaluate changes in the maturity of source rocks responsible for crude oil generation had a major impact on their use in petroleum exploration studies. Today the biomarker approach is a routine, mature science used by major and minor oil companies alike in exploration, reservoir and production chemistry. By quantifying a wide range of biomarkers in a crude oil or source rock extract, it is possible to build up a picture of the type of organic material responsible for a crude oil and the environment in which it was deposited as well as the geological age of the oil (Moldowan et al. 1993). Biomarkers, such as steranes and terpanes, are typically present in crude oils in relatively low concentrations but readily determined by GC-MS and multiple ion detection (MID). The sterane and terpane fingerprints can be used as correlation tools to determine whether two oils are derived from the same or different source rocks. These applications are used extensively in the petroleum industry and are well documented in the literature. This chapter is not intended to review the history of biomarkers and an excellent and relatively recent comprehensive review of this topic can be found in the Biomarker Guide by Peters et al. (2005). At the same time as developments in GC and GCMS were taking place, a number of the major oil companies, particularly Shell and Chevron, were starting to exploit the use of stable isotopes in their exploration activities. In general any crude oil correlation or characterization study depends upon the use of a multitude of parameters. These may be bulk parameters such as API gravity, elemental ratios such as Ni/V ratios, stable isotopes, or more specific biomarker parameters. In general the more parameters used for this purpose the more confident one can be of the outcome. In large studies when a significant number of oils are being compared, the data are best treated through some form of statistical treatment as described by Peters and Fowler (2002).

The utilization of stable isotopes in environmental forensics is a more recent phenomenon and primarily

evolved as a result of the development of the GCIRMS system (Matthews and Hayes 1978; Hayes et al. 1987, 1990; Freeman et al. 1990). While it is true that bulk stable isotopes of certain environmental contaminants such as crude oils and refined hydrocarbon products had been used prior to this development, GCIRMS became particularly useful for the characterization of ground water contaminants. Two major applications in environmental forensics have developed, namely source/contaminant correlation and monitoring the onset of natural attenuation. Both of these applications can be utilized in groundwater studies. Many groundwater samples are contaminated with a single contaminant rendering GC and GCMS virtually useless when trying to correlate or discriminate potential sources. However variations in isotopic composition of the contaminant may provide an additional parameter that can be used to differentiate the sources. Utilization of 2 or 3 isotope values (C, H, Cl) provide an even more powerful discriminatory tool (Kuder et al. 2005). In the case of semi-volatile contaminants, the isotopic fingerprint of the individual components in the sample provide another tool that can be used for correlation purposes in conjunction with the GC and GCMS fingerprints (Philp et al. 2002).

In terms of monitoring the onset and extent of natural attenuation, the application here is primarily directed at groundwater contaminants such as MTBE, PCE, BTEX and the typical VOC groundwater contaminants. As explained in more detail below, natural attenuation leads to isotopic enrichment of the residual contaminant and the extent of enrichment can be related to the extent of natural attenuation. Such an application is becoming an extremely powerful tool for regulators who need multiple lines of evidence, in addition to decreasing concentration, to verify that degradation is taking place (USA EPA Report 2008). Very recent developments in this area are starting to see incorporation of isotope data into fate and transport models leading to more accurate predictions of time required to degrade groundwater contaminants (van Breukelen et al. 2005).

In the following sections the basic concepts of stable isotopes that are applicable to both hydrocarbon exploration and environmental forensics will be discussed. This will be followed by a review of isotope applications to hydrocarbon exploration problems and examples of the integration of the isotope data and finally an overview on the utilization of stable isotopes

in environmental studies will be provided. These two areas, hydrocarbon exploration and environmental forensics, are grouped together in this chapter since there are many similarities in the types of problems being dealt with in these areas.

31.1.1 Stable Isotopes

There are many excellent monographs and papers that have been published over the years that provide a comprehensive introduction to stable isotope geochemistry and the reader is advised to consult such sources for additional information in this area. For example Hoeffs (2004) and Faure and Mensing (2005) are two textbooks related to stable isotope geochemistry, while Melander and Saunders (1980), Galimov (1985) and Cook (1991) focus on chemical and biochemical aspects of stable isotopes. Two review papers published several years ago by Stahl (1977) and Fuex (1977) provide a good background primarily on applications of bulk isotope in petroleum exploration up until that time. Schoell (1983, 1984a, b, 1988) provided a good coverage of stable isotopes in natural gas exploration and then in more recent times there have been numerous articles by Whiticar and others that have discussed the use of stable isotopes in natural gas exploration (Whiticar 1990, 1996; Whiticar and Faber 1986; Whiticar et al. 1985). In environmental forensics a number of review articles have been published in the past few years that provide a fairly comprehensive coverage of isotope applications in that area (Slater 2003; Schimmelmann et al. 2006; Philp and Kuder 2008).

The two most commonly used stable isotopes in both hydrocarbon exploration and environmental forensics are those of carbon and hydrogen. In hydrocarbon exploration there have been occasions where stable sulfur isotopes have been used and in environmental forensics we are seeing increasing interest and use of the stable isotopes of chlorine and nitrogen (Sakaguchi-Söder et al. 2007; Shouakar-Stash et al. 2007, 2009). In general there are two approaches used to determine the stable isotope composition of a particular compound or product. The isotope values can either be determined as bulk isotope values or the isotopic composition of individual compounds (compound specific isotope analysis-CSIA) may be

determined through the use of gas chromatography-isotope ratio mass spectrometry (GCIRMS) as described below. Both approaches are discussed since they are both used extensively in exploration studies and environmental forensics.

31.1.1.1 Basic Methodology Overview for the Determination of C Isotopes

Carbon exists as three isotopes, ^{12}C , ^{13}C , and ^{14}C , which in terms of their atomic structure have the same number of protons and electrons but differ in the number of neutrons which increase from 6 to 8 respectively. ^{12}C and ^{13}C are stable isotopes and ^{14}C is a radioactive isotope with a half life of 5,730 years. ^{14}C has been used extensively in recent years for archeological dating purposes and in a number of biofuel studies where there is also recent carbon (Reddy et al. 2008) but not extensively in environmental forensics at this time. The principle behind the determination of either bulk stable isotope values of complex mixtures or the isotopic composition of individual compounds is very similar. Each method requires complete combustion of the sample, regardless of its origin, and conversion to CO_2 and water. For bulk determinations, the combustion is undertaken in a sealed tube in the presence of CuO or alternatively the sample can be converted to CO_2 using an elemental analyzer interfaced directly to an isotope ratio mass spectrometer. The CO_2 , comprised of both $^{13}\text{CO}_2$ and $^{12}\text{CO}_2$, is transferred and analyzed in a stable isotope ratio mass spectrometer. The relative proportions of the $^{13}\text{CO}_2$ and $^{12}\text{CO}_2$, are measured relative to that of a standard material Vienna Pee Dee Belemnite (VPDB) whose carbon isotope value, expressed in the δ notation (see below) has a value of 0. Virtually all samples will contain less ^{13}C than the standard, and being depleted in ^{13}C , have negative $\delta^{13}\text{C}$ values. Stable

carbon-isotope ratios ($R = ^{13}\text{C}/^{12}\text{C}$) are expressed relative to the VPDB standard using the “delta” notation, where: $\delta^{13}\text{C} = (R_{\text{sample}}/R_{\text{standard}} - 1) \times 1,000$ (units are ‰ or per mil or parts per thousand). Although this refers specifically to carbon isotopes, the ratios for the other elements such as O, H, Cl, S or N are expressed in the same way relative to their specific standard. The natural abundance of the stable isotopes commonly utilized in these two areas and the international standards used in the calculation of their δ values is given in Table 31.1.

To determine the isotopic composition of individual compounds by GCIRMS, the components pass through a combustion reactor after they are eluted from the GC column and are combusted to CO_2 and water (Fig. 31.1). The water is removed and the CO_2 moves into the isotope ratio mass spectrometer where the relative proportions of the $^{13}\text{CO}_2$ and $^{12}\text{CO}_2$ are determined and $\delta^{13}\text{C}$ values calculated for each individual compound. It is extremely important to point out that despite the seemingly simplistic nature of this technique, it is far from being as universal as GCMS. The main reason being that it is absolutely essential to get optimum chromatographic separation of the complex mixture of components. Basically the components have to be visible on the gas chromatogram and the peaks of interest resolved as far as possible from any co-eluting or partially co-eluting components. In the case of GCMS, there are ancillary techniques available, such as multiple ion detection, that permit one to delve into the baseline components in the chromatograms and detect trace components. There is no such luxury in GCIRMS and if isotopic values are required on trace components in the crude oils or source rock extracts then one either needs extensive separation of the compounds of interest or characterize less mature samples where the biomarkers are often present in relatively higher concentrations and can be observed in the chromatograms (Hayes et al. 1987).

Table 31.1 Isotope ratios of stable isotopes

Element	Notation	Ratio	Standard	Absolute ratio
Hydrogen	δD	$\text{D}/\text{H} (^2\text{H}/^1\text{H})$	SMOW	1.557×10^{-4}
Carbon	$\delta^{13}\text{C}$	$^{13}\text{C}/^{12}\text{C}$	PDB	1.122×10^{-2}
Nitrogen	$\delta^{15}\text{N}$	$^{15}\text{N}/^{14}\text{N}$	Atmosphere	3.613×10^{-3}
Oxygen	$\delta^{18}\text{O}$	$^{18}\text{O}/^{16}\text{O}$	SMOW, PDB	2.0052×10^{-3}
Chlorine	$\delta^{37}\text{Cl}$	$^{37}\text{Cl}/^{35}\text{Cl}$	Seawater	~ 0.31978
Sulfur	$\delta^{34}\text{S}$	$^{34}\text{S}/^{32}\text{S}$	CDT	4.43×10^{-2}

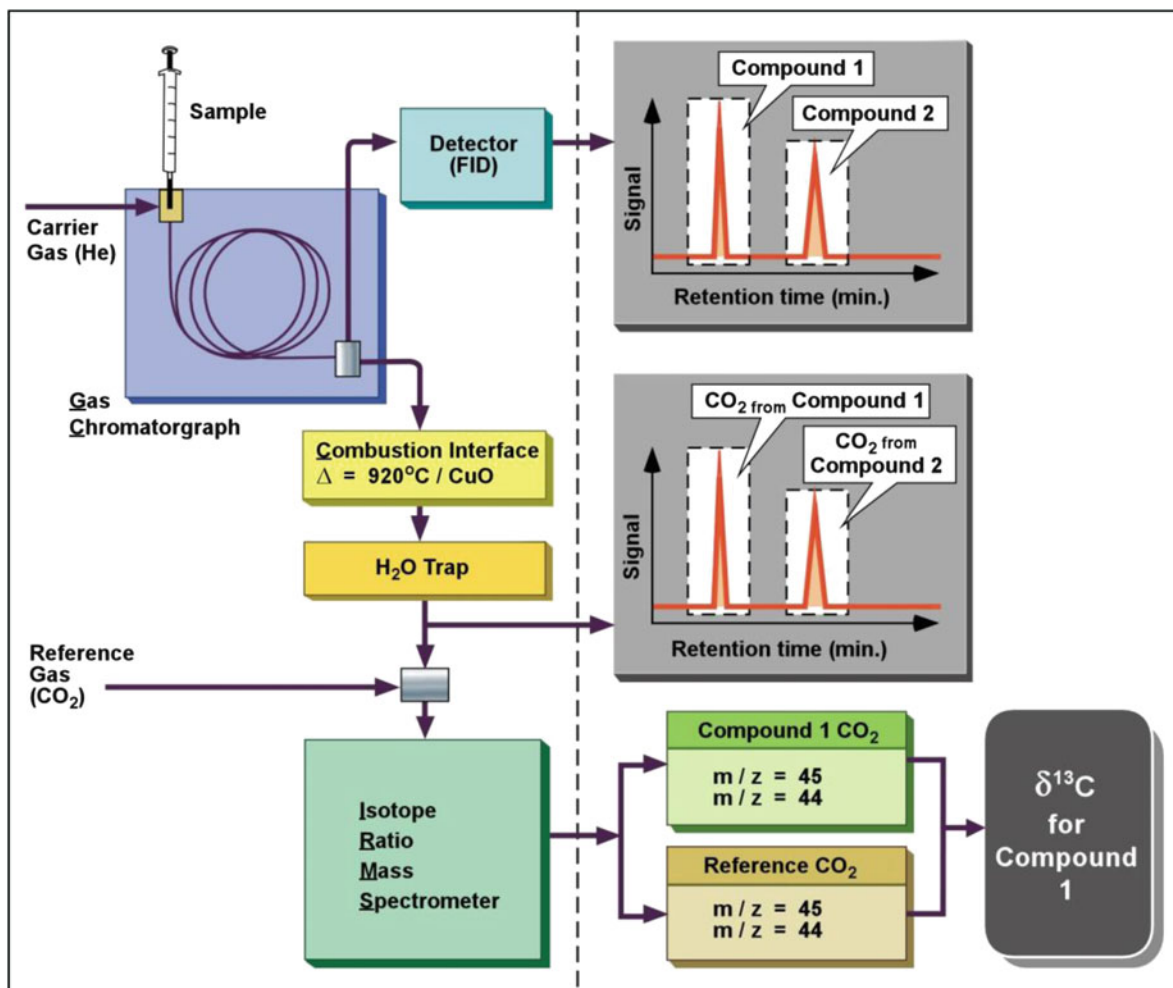


Fig. 31.1 Schematic representation of a GCIRMS system for continuous flow determination of isotopic compositions of individual compounds

31.1.1.2 Variations in the Isotopic Composition of Source Materials

The key to the successful application of stable isotopes in exploration and environmental applications is based on variations in the isotopic compositions of the compounds being monitored. The question to be addressed in this section is why do we see these variations? The answer to that question can be traced back to photosynthesis and the formation of the original source material for crude oils.

Source rocks for crude oils are initially formed from a variety of source materials deposited in various types of depositional environments (Hunt 1996). When these source materials such as plants, phytoplankton,

and bacteria are initially being formed through the process of photosynthesis, a number of factors, discussed below, will determine their isotopic compositions. As this organic material is buried, degraded, and ultimately heated to form crude oils or natural gas, all of the original isotopic source signatures will be homogenized and change somewhat as a result of maturation. However the key factor here is that since different crude oils are derived from different mixtures of source materials, it is reasonable to expect some variations in the ultimate isotopic composition of the resulting crude oils. Hence the utilization of the isotopic composition of differentiate crude oils from different sources. However this can also be taken a step further since virtually all environmental contaminants

have their source in feedstocks that are derived from crude oils. Therefore in turn one may expect that the same contaminant derived from two different feedstocks may have different isotopic compositions. It is important to emphasize that not every single crude oil or every contaminant will have a unique isotopic signature permitting differentiation of every oil or contaminant, since there is a limited range of isotopic signatures. In the following section an overview of the process of photosynthesis will be provided along with information on variations that may be expected in the different types of source materials and products.

In order to understand why stable isotopes can be used for correlation of crude oils in hydrocarbon exploration or contaminants in environmental forensics, it is first necessary to review how crude oils are formed. Basically the starting point in the formation of a crude oil is atmospheric CO₂ through the process of photosynthesis, which leads to the incorporation of that C into cell wall materials, providing energy promoting plant growth, as summarized by the simple reaction below:



Once the living plants and aquatic organisms die, the organic material from these sources is deposited in various types of environments. A large amount of this material will be degraded depending on the environment, but a relatively small percentage will be incorporated into the sedimentary record, undergo diagenetic changes, followed by thermal alteration of the residual organic matter to ultimately produce oil and/or gas (Hunt 1996). During the process of photosynthesis the extent of fractionation between the atmospheric ¹³CO₂ and ¹²CO₂ will vary depending on whether the source material is land plant or marine organisms and within land plants there are different photosynthetic cycles that will further determine the extent of fractionation.

Isotopic compositions of plants were first determined by Craig (1953) who, in an extensive survey on the carbon isotopic composition of natural materials, noted that in the sample set examined at that time most of the plant materials had a relatively constant δ¹³C value near -27‰. He observed there seemed to be no important species or geographical effects although he reported one grass with a δ¹³C value of -12‰, later recognized as a C₄ plant. The plants

studied by Craig (1953) and later by Park and Epstein (1960) were C₃ plants, which incorporate CO₂ from the atmosphere by carboxylation of ribulose biphosphate. C₄ plants incorporate CO₂ by the carboxylation of phosphoenolpyruvate. The carboxylation product is transported from the outer layer of photosynthetic cells (mesophyll cells) to the inner layer (the bundle sheath), where decarboxylation and refixation by ribulose biphosphate carboxylase occur. Isotope studies demonstrated that C₄ plants show less negative δ¹³C values than C₃ plants. C₃ plants generally grow in cooler wetter climates and include trees, shrubs and have isotope values in the -26 to -30 per mil range, plants with the C₄ cycle, including grasses, corn, maize, grow under dryer, hotter conditions and have isotope values in the -10 to -14‰ range. The difference in the isotopic composition of C₃ and C₄ plants has become one of the standard methods to distinguish these plant types (O'Leary 1981) and provides an important diagnostic tool in differentiating specific source materials.

Numerous studies of marine and continental (terrestrial and freshwater) plants have revealed a depletion of ¹³C in land plants compared with marine plants due to the differences in the isotopic composition of carbon sources (Craig 1953; Galimov 1968). Analogous isotopic differences have been observed in recent sediments (Stuermer et al. 1978; Schoell 1984a, b; Sofer 1984). The organic matter in recent marine sediments is typically depleted in ¹³C relative to local marine fauna and flora (Aizenshtat et al. 1973; Sackett et al. 1974; Gormley and Sackett 1977). This ¹³C depletion may be attributed to diagenetic effects. The diagenetic loss of δ¹³C-enriched carboxyl carbon has been proposed to account for the ¹³C depletion (Brown et al. 1972; Peters et al. 1981). Alternatively, Gormley and Sackett (1977) suggested that maturation of ¹³C-depleted lipids leads to the formation of the ¹³C-depleted organic matter in marine sediments. However, the ¹³C depletion of marine sedimentary carbon could also be explained by selective preservation, where ¹³C-depleted refractory components of algae are selectively concentrated in sediment and the ¹³C-enriched components are microbially degraded and lost (Hatcher et al. 1983).

The situation becomes far more complicated, and much less specific, in the case of source rocks since source rocks are very heterogeneous mixtures of many different types of organic material and the resulting

isotopic composition of the source rock will be a weighted average of the isotopic compositions of all the different preserved and residual source materials. As a result there will be variations in the bulk isotopic compositions of the source rocks, and subsequently the oils, dependent upon the original mixture of source materials. It has been commonly assumed that the relative depletion in ^{13}C of some marine sediments samples can be explained by significant contribution of terrestrial organic debris to the organic precursors of marine organic matter (Silverman and Epstein 1958; Eckelmann et al. 1962; Hunt 1970).

Isotopic variations in the original source materials are one reason for variations in the resulting crude oils. These variations in turn will determine the isotopic composition of environmental contaminants since these are primarily derived from crude oil feedstocks. However isotopic fractionation through a number of processes may also impact the resulting isotopic values but prior to discussing these processes a brief discussion of the concept of isotopic fractionation is given below.

31.1.1.3 Isotopic Fractionation

In addition to variations in isotopic source signatures, processes such as maturation and biodegradation can affect the isotopic composition of a crude oil, or environmental contaminants, and their individual constituents as a result of isotopic fractionation associated with these processes (Fuex 1977; Stahl 1977). There are basically two fractionation processes responsible for these isotopic changes, namely the kinetic isotope effect and the equilibrium isotope effect. While both processes may be active, in most hydrocarbon exploration studies it is primarily the kinetic isotope effect that is most important and this is most evident in natural gas exploration studies (Schoell 1983, 1984a, b) In environmental studies while the kinetic effect is most prevalent, particularly in cases where natural attenuation is underway, there are examples where equilibrium isotopic fractionation has also been observed. In the following section a brief description of the kinetic isotope is provided, with specific reference to environmental applications, it is generally utilized to a far greater extent in that area than in the hydrocarbon exploration applications.

Kinetic isotope effects associated with degradation and maturation processes occur as a result of different reaction rates for the heavy vs. light isotopes (e.g. ^{13}C vs. ^{12}C). The presence of a “heavy” species (e.g. ^{13}C) in the bond targeted by the degradation increases the bond cleavage activation energy and, in consequence, reduces their rate of degradation. During the progress of degradation, the residual substrate becomes progressively enriched in the “heavier” isotope species (*i.e.* $^{13}\text{C}/^{12}\text{C}$ increases). Degradation-related isotope effects are strong for the atoms included at the chemical bond being broken (primary isotope effects), while weak secondary isotope effects affect the remaining atoms. At the normal precision of CSIA (compound specific isotopic analysis), only secondary isotope effects of hydrogen are significant. In molecules where only a selected atomic position (or positions) is targeted by a biodegradation process (e.g. oxidation of a methyl group of toluene), the overall expression of isotope fractionation, as measured by CSIA, is “diluted”. The intrinsic isotope effect (the isotope effect affecting the atoms directly participating in the reaction) is not affected by the size of the molecule and can be calculated from CSIA data (Elsner et al. 2005). Isotope effects upon biodegradation reflect the first rate-limiting step of the reaction sequence. In certain cases, the slow step may not be a bond cleavage but a phenomenon that does not cause isotope fractionation, e.g. formation of substrate-enzyme complex. If the latter is completely rate limiting, no isotope fractionation will be observed. The rule of thumb is that observable biodegradation isotope effects are limited to small molecules, readily permeating cell membranes of degraders. So in environmental studies this would include chlorinated ethenes and ethanes, MTBE and mono-aromatic compounds that have been widely studied and where isotope fractionation has been typically observed (Sherwood Lollar et al. 2001; McKelvie et al. 2007). In exploration studies, fractionation has been observed to occur in the lighter hydrocarbons in the C_5 to C_{10} range (George et al. 2002). Biodegradation of semi-volatile environmental contaminants, such as long chain n-alkanes, multi-ring PAHs and PCBs typically does not result in a detectable isotopic fractionation. It is also important to note that in larger molecules with more than approximately 10–12 carbon atoms the isotopic changes occurring to the one carbon atom being attacked are diluted by the presence of the

other unaffected carbon atoms. Therefore when the isotope values are measured the overall changes in the isotopic composition of these larger molecules are generally not detectable.

Physical processes such as phase transitions, sorption and diffusion can also cause isotope fractionation (Schuth et al. 2003; Kopinke et al. 2005; Kuder et al. 2009). The mass difference between isotope species result in different kinetic energies of gaseous phase molecules leading to differential rates of vapor migration and different bond energies of light isotope- vs. heavy isotope-substituted molecules which will affect phase partitioning equilibria and evaporation-condensation. While isotope fractionation due to physical processes is general negligible in environmental science applications, it cannot be completely ignored, especially in the case of systems dominated by gas/vapor phase migration. Various laboratory studies of isotope effects upon VOC volatilization show, in general, small carbon isotope fractionation, more pronounced chlorine isotope fractionation and in select cases, strong hydrogen fractionation (*e.g.* Poulson and Drever 1999; Wang and Huang 2003 and references therein). Open-system progressive evaporation, more relevant to environmental conditions, has not been extensively studied. It appears that in experimental conditions where the NAPL-vapor equilibrium element is significant, the residual NAPL tends to become enriched in the lighter ^{12}C and H which is the reverse of the direction of fractionation upon degradation (Wang and Huang 2003). If the kinetic fractionation element (diffusion of vapor) is more significant, the residual NAPL may become enriched in the heavier carbon isotope ^{13}C (Kuder et al. 2009). In a study of a controlled kerosene release in a soil column, Kjeldsen et al. (2003) reported that molecules of VOC with lighter isotope (^{12}C) migrated faster through the vadose zone, resulting with $\delta^{13}\text{C}$ reduction by several units over the distance of three meters of sand (eventually, after the onset of biodegradation, the transport-related isotope effects were obliterated). Isotope effects have been identified in laboratory experiments or proposed to result from sorption phenomena (*e.g.* Schuth et al. 2003; Kopinke et al. 2005), in particular for VOC compounds, however, at the scale of a contaminant plume sorption is not supposed to cause a detectable extent of isotope fractionation (Kopinke et al. 2005).

Following this basic introduction to stable isotopes applicable to both hydrocarbon exploration and

environmental forensics a number of applications will be discussed. This will not necessarily be a comprehensive review but rather examples illustrating the applications of stable isotopes in both of these areas. At the same time as mentioned above it is also important to recognize that isotopes are only part of the total analytical tool box available in both of these areas.

31.1.2 Applications of Stable Isotopes to Hydrocarbon Exploration

There are numerous questions that have to be addressed in any petroleum exploration program and many of these issues are summarized in monographs by Tissot and Welte (1984) and Hunt (1996) but primary among those issues are questions related to the source and quality of the organic matter in the source rocks. Characterization of the organic matter in a source rock is very important in determining whether a particular formation will generate oil or gas or both. The organic matter can be characterized by a variety of techniques, including visual characterization, extraction and identification of specific biomarkers, and also stable isotopes. In the following section an overview as to why the isotopes are an important part of characterizing the organic matter will be discussed (Peters et al. 2005).

In the earliest investigations of stable isotopes in hydrocarbon exploration, Craig (1953), Silverman and Epstein (1958) and Silverman (1965) observed that oils from terrigenous sources were depleted in ^{13}C relative to oils from marine sources. Such a trend appeared to follow that observed for living systems, with land plants generally being depleted in ^{13}C relative to aquatic plants and marine heterotrophs. It has also been observed that organic matter in recent sediments becomes depleted in ^{13}C as the depositional facies changes from marine to terrigenous (Andrusevich et al. 1998). Carbon isotopes are often used to distinguish between oils derived from marine and nonmarine organic matter. The differences between marine and nonmarine oils are also manifested in the relationships between the isotopic composition of the saturate and aromatic fractions (Sofer 1991). Odden et al. (2002) evaluated the source influence on the stable carbon isotope ratios and noted that the $\delta^{13}\text{C}$ values become less negative with increasing

terrestrial input. Kvenvolden and Squires (1967) successfully used isotopic age trends to relate and distinguish crude oils on a regional basis in west Texas. A general trend of enrichment of the lighter isotope with increasing geological age of oils was observed by Welte et al. (1975) and Stahl (1977), possibly caused by variations in intensity of photosynthesis and changes in the isotopic composition of the atmospheric CO_2 and more recently this observation formed the basis for isotopic age-dating methods developed by Andrushevich et al. (1998).

Stable carbon isotope ratios are useful for providing one parameter that can be obtained relatively quickly to provide a preliminary assessment between oils and their suspected source rocks or with other oils thought to be derived from the same source. There are numerous papers in the literature where isotopes have been used as a routine correlation parameter and a number of references are provided here but in general it is simply a matter of obtaining the bulk carbon isotope values and if the values are different it is strong evidence to suggest the oils are derived from different sources. If they are similar the result is somewhat more difficult to interpret since it may mean a common source or it could simply be coincidence and require greater use of supporting data from the biomarkers to establish the relationship between the samples (Galimov and Frick 1985; Peters et al. 1989, 1993; Fildani et al. 2005).

Use of the bulk isotopes can be taken a step further and provide a little more specificity by fractionating the oil into saturates, aromatics, NSO (nitrogen, sulfur, oxygen) and asphaltene fractions. Isotope data from the individual fractions can then be plotted in a number of ways. A plot of saturates vs. aromatics can be extremely useful in grouping oils derived from similar source materials or distinguishing those from different depositional environments as illustrated in the following Fig. 31.2. The isotope values can also be used to construct the so-called Stahl-type curves (Stahl 1978). If the suspected source rock is available, the stable isotope value for the kerogen can be incorporated into this plot. If the appropriate source rock is selected, it will show a direct relationship with the individual fractions as illustrated below (Fig. 31.3a). The advantage of this approach is that $\delta^{13}\text{C}$ values differentiates the carbon in the different fractions and provides a more powerful correlation tool, although one has to be vigilant in distinguishing the effects of increasing maturity (Chung et al. 1981), phase effects, and subsequent alteration in

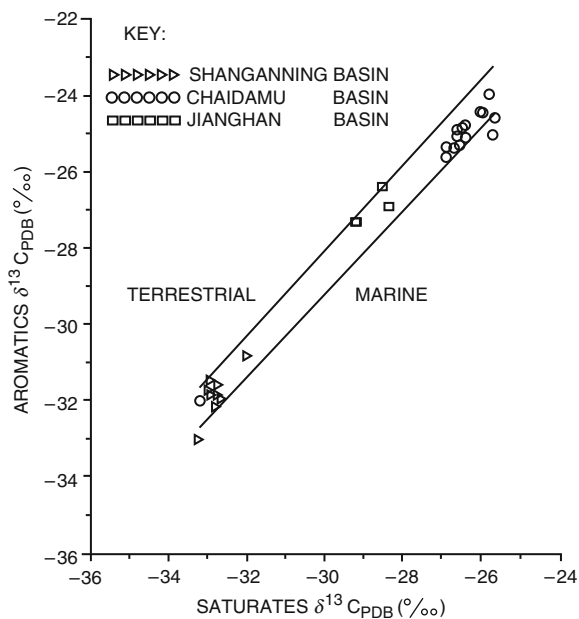


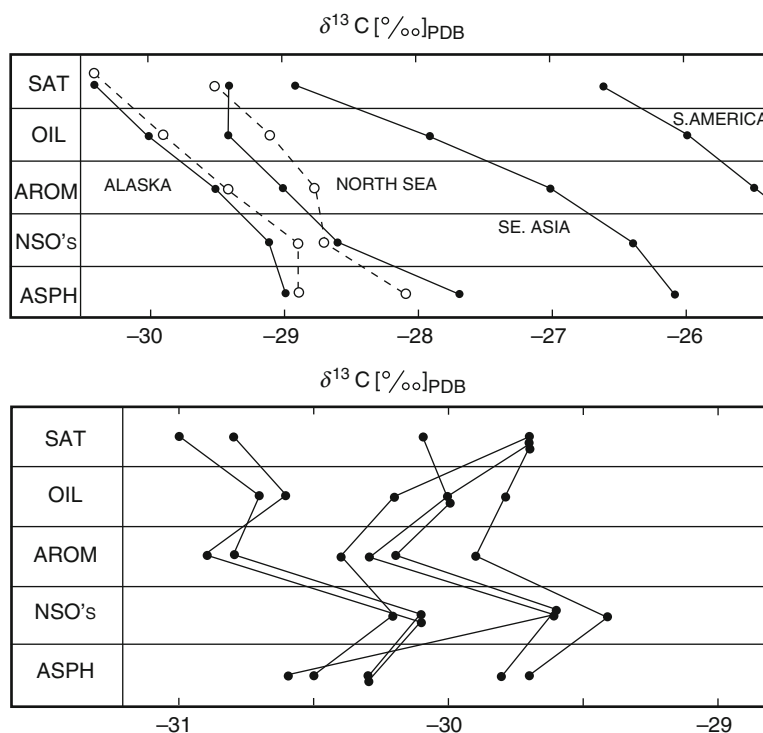
Fig. 31.2 A plot of the $\delta^{13}\text{C}$ values for saturates vs. aromatics provide a means of correlating samples of similar origin (Reproduced from Philp and Jarde 2007 with permission of Elsevier)

the reservoir such as water washing (Palmer 1993) or biodegradation (Stahl 1980). The reliability of isotopic correlation therefore hinges on being able to understand and quantify these effects (Clayton 1991a, b). Therefore in the following sections the factors that can affect the isotopic composition of the crude oils in addition to source variations will be described.

31.1.2.1 Biodegradation of Hydrocarbons

In order to understand the isotope changes resulting from biodegradation one needs to understand the impact of biodegradation on a crude oil. The effects of biodegradation are fairly well understood with well defined set of changes occurring during the degradation processes (Peters et al. 2005). However the major changes affecting the isotopic composition will be related to bulk changes in the oil and not changes occurring to individual molecules. For example as illustrated below the most obvious change to a crude oil with biodegradation is the removal of the n-alkanes (Fig. 31.4). In general the lower carbon number compounds are removed initially and then higher carbon numbers. The extent of alteration to the aromatic and

Fig. 31.3 Stahl plots for the representation of the isotopic relationship between the carbon isotope values of the various fractions and the source rock extracts. *SAT* saturate hydrocarbons; *OIL* whole oil; *AROM* aromatic hydrocarbons; *NSO's* nitrogen, sulfur, oxygen compounds; *ASPH* asphaltenes (Reproduced from Stahl 1977 with permission from Elsevier)



polar fractions is much less significant apart from cases of extreme biodegradation (Sofer 1984, 1991). However the impact on the isotopic composition of the saturate fraction can be much more significant since the n-alkanes comprise a significant fraction of the saturate fraction and their removal has an impact on the isotopic composition, and in general the saturate fraction will become isotopically heavier as illustrated in the Stahl diagram below (Fig. 31.3b).

31.1.2.2 Maturity of Hydrocarbons

Unlike biodegradation, maturity can have an impact on the isotopic composition of all the fractions, since maturity will basically result in the cracking of carbon-carbon bonds in all fractions to generate relatively higher concentrations of the lighter hydrocarbons. The formation of crude oils also involves burial and maturation and there will be some variation in isotope composition as a result of thermal maturation. Changes in the $\delta^{13}\text{C}$ values of kerogens in the natural system as a result of maturation have been well documented (Hoeffs and Frey 1976; Lewan 1983). During the maturation process the kinetic isotope

effect, as described above in Sect. 31.1.1.3, predominates and leads to preferential cleavage of the bonds containing the lighter isotope. As a result the residual fractions will become enriched in the heavier isotope and hence the general trend will be one of isotopic enrichment with increasing maturity. The extent of the enrichment will vary from oil to oil and will also depend on the level of maturation. Oil to gas cracking in a reservoir destroys oil by converting it to low molecular weight compounds. Isotopic effects in this case are more likely to reflect kinetic isotope fractionation due to preferential cleavage of $^{12}\text{C}-^{12}\text{C}$ bonds over the $^{13}\text{C}-^{12}\text{C}$ bonds, leaving the residual oil enriched in ^{13}C (Clayton 1991a, b). Increasing maturity of source rocks and cracking of the kerogen within the source rock to generate oil will have similar effects with the residual kerogen becoming isotopically heavier with increasing maturity. Initially the products that are generated from the kerogen will be isotopically light but as the maturity level increases and the more isotopically enriched kerogen is thermally degraded so the resulting products will become isotopically heavier. In general, reactions involving compounds with six or more carbon atoms will show negligible kinetic isotopic fractionation (Clayton 1991a, b).

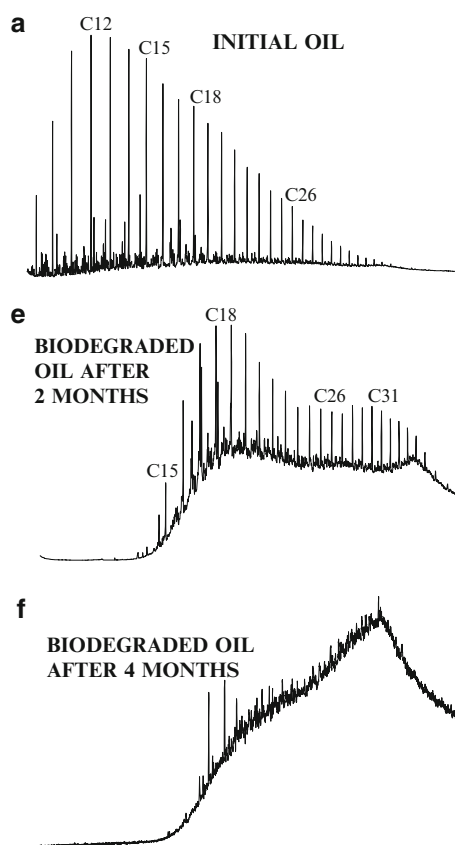


Fig. 31.4 Biodegradation of crude oils initially leads to the removal of the lighter n-alkanes and then progressive removal of the longer chain n-alkanes (peaks labels refer to carbon number of n-alkanes i.e. C12 = n-alkane with 12 carbons in chain)

For condensates, or light oils, an additional isotopic fractionation step has to be taken into account. Condensates (typically C_{6+} compounds) condense from the subsurface gas phase (“gas condensate”) as it is brought to the surface and temperature and pressure decrease. Isotope effects during this process will be minimal because we are concerned with the transition between a compound in the liquid state (“oil”) and the same compound in the vapour state (“condensate”). Any isotope effect here will result from equilibrium isotope effects and not the kinetic isotope effect. However, condensates will preferentially accumulate lower molecular weight compounds relative to the oil from which they formed. Any difference in bulk $\delta^{13}C$ between low and high molecular weight compounds will be reflected in differences between the bulk $\delta^{13}C$ values for the oil and condensate (Clayton 1991a, b).

There are two approaches for investigating isotopic effects resulting from the maturation and generation process. First, reservoir oils generated from a single source rock, but at different levels of maturity based on biomarker maturity parameters, can be characterized isotopically and differences in the $\delta^{13}C$ values ascribed to maturity differences. This also assumes no other in-reservoir alteration processes have occurred. An alternative approach is to perform laboratory maturation experiments such as hydrous pyrolysis experiments as described by Lewan et al. (1979) where an immature source rock sample is heated in the presence of liquid water at subcritical temperatures ($< 374^{\circ}C$). Although relatively high temperatures ($300\text{--}365^{\circ}C$) are used in these experiments to offset the long time requirements necessary to generate oil in the natural system ($10^6\text{--}10^9$ years), the expelled pyrolysates from potential source rocks are similar to natural crude oil (Lewan et al. 1979). Measured parameters of the resulting matured source rocks, such as vitrinite reflectance and atomic H/C ratio of pyrolysates, showed similar changes to those observed in the natural system (Lewan 1983; Lewan and Williams 1987). In terms of the influence of thermal maturation on $\delta^{13}C$ values of the kerogen, bitumen, and crude oil, immature source rock samples from the Woodford Shale were artificially matured and it was observed that the expelled oil became enriched in ^{13}C with increasing thermal maturation (Fig. 31.5). As described above this ^{13}C enrichment can be attributed to kinetic isotope effect and increasing cleavage of $^{13}C\text{--}^{12}C$ bands in the bitumen as it continues to decompose into expelled oil and preferential cleavage of $^{12}C\text{--}^{12}C$ bonds in the expelled pyrolysate as it decomposes into gases and pyrobitumen.

31.1.2.3 Migration of Hydrocarbons

Silverman (1965) was among the first to recognize isotopic changes during oil migration by noting a slight depletion in ^{13}C in the bulk carbon isotope values with increasing migration distance in the Quiriquire field in Venezuela. The whole oil $\delta^{13}C$ values decrease slightly with migration as a result of changes in chemical composition of the oils during migration. The ratio of saturates to aromatics increases during migration and the preferential removal of the more polar and water soluble aromatic compounds, which

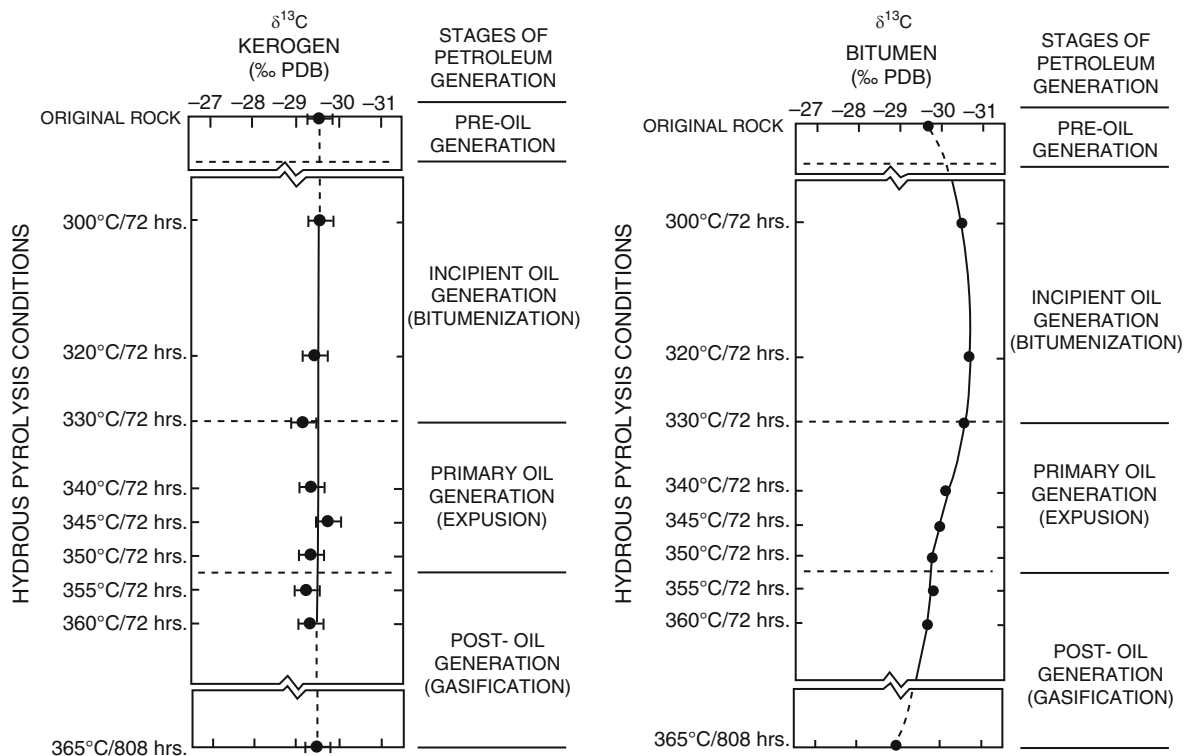


Fig. 31.5 Maturation of kerogens and crude oils can also lead to changes in their isotopic compositions. These changes can be monitored by laboratory hydrous pyrolysis studies as described

by Lewan (1983) (Reproduced from Lewan 1983 with permission from Elsevier)

are commonly richer in ^{13}C than the saturates, result in a slight decrease of the $\delta^{13}\text{C}$ of the whole oil.

The effects of migration on the isotope values, can be evaluated by looking directly at bitumen in the source rock, thus eliminating any effects related to biodegradation and water washing. Migration, or expulsion from the source rock, is still potentially a problem in that saturate and aromatic compounds are expelled preferentially over the NSO and asphaltene fractions (Clayton 1991a, b). Variability of stable carbon isotopes in kerogens and bitumens may be evaluated in the natural system by acquiring samples of the same rock unit at different levels of thermal maturity. Unfortunately, acquiring samples of crude oils that have been expelled from the same rock unit at different levels of thermal maturation is not as practical but can be simulated in the laboratory through hydrous pyrolysis experiments. In these experiments, the variability of stable carbon isotopes of indigenous and expelled organic phases of a rock unit may be directly correlated with level of thermal maturation (Lewan 1983).

Table 31.2 Isotope ratios for pristane and phytane used to determine source relationships between the isoprenoids. In the case of the Messel shale the pristane and phytane have significantly different isotope values suggesting they are derived from different sources, hence negating the use of the Pr/Ph ratio as an indicator of oxicity

Sample	Pristane	Phytane
Barracouta	-28.1	-28.6
Turrum	-26.6	-26.9
Messel shale	-25.4	-31.8

31.1.2.4 Depositional Environments

Mello et al. (1988) undertook an extensive geochemical study of oils from offshore Brazil and used a number of parameters to differentiate oils coming from different depositional environments. The oils were divided into five groups (I to V) based on a wide range of parameters including the $\delta^{13}\text{C}$ values. A summary of some of the bulk parameters including bulk isotope analyses, elemental analyses, and alkane distributions for each group of oils are summarized in

Table 31.3. The higher sulphur contents and V/Ni elemental ratios relative to the group I oils, may reflect the more saline character (with high Eh) of the depositional environment of the source rocks of the group II oils. Enhanced salinity might also explain why the oils from group II are isotopically heavy ($\delta^{13}\text{C}$ values around -25‰). Plants from saline environments can preferentially utilize carbonate complexes as their carbon source for photosynthesis. These are richer in ^{13}C than atmospheric carbon dioxide, which is enhanced in ^{12}C (Tissot and Welte 1984). The bulk geochemical properties of the group II oils are, in most respects, similar to those of the group III oils. The $\delta^{13}\text{C}$ (‰) values of the whole oils range from -26.8 to -27.6 ,

around -27.5 for the saturate and -26.7 to -27.1 for the aromatic fraction. The geochemical characteristics of group III oils include high sulphur contents (0.5–1.5%), medium V/Ni elemental ratios (~ 0.2), and $\delta^{13}\text{C}$ (‰) values within the narrow range of -25.4 to -26.6 for whole oil, -26.4 to -27.3 for saturates and -25.4 to -26.4 for the aromatic fraction (Fig. 31.6). Group III and IV show a predominance of low molecular weight n-alkanes (around C_{18} – C_{20}) with a slight predominance of even numbered homologues and a predominance of phytane over pristane. The isotopically light values of $\delta^{13}\text{C}$ (always $< -28\text{‰}$ for the whole oils) also indicate their freshwater origin, since the principal lipid constituents, originating from

Table 31.3 Bulk and elemental properties of Brazilian offshore oils (Reproduced from Mello et al. 1988 with permission of Elsevier)

Property	Group I	Group II	Group III	Group IV	Group V
$\delta^{13}\text{C}$ ‰	< -28.0	-23.0 to -25.6	-25.4 to -26.6	-26.8 to 27.6	-24.4 , -25.1
% Sulphur	Low	Medium	High	High	Medium
V/Ni ³	Low	High/medium	Medium	High	High
% Saturates	High	High	Low/medium	Low/medium	High
n-Alkanes dominance	C_{23} – C_{25}	C_{17} – C_{21}	C_{17} – C_{19}	C_{18} – C_{20}	C_{20} – C_{22}
Odd/even	High	High	Low	Low	Low
Pristane/phytane	High	High	Low	Low	Low
Inferred depositional environment	Lacustrine/fresh water	Lacustrine/saline water	Marine evaporitic	Marine carbonate	Marine deltaic

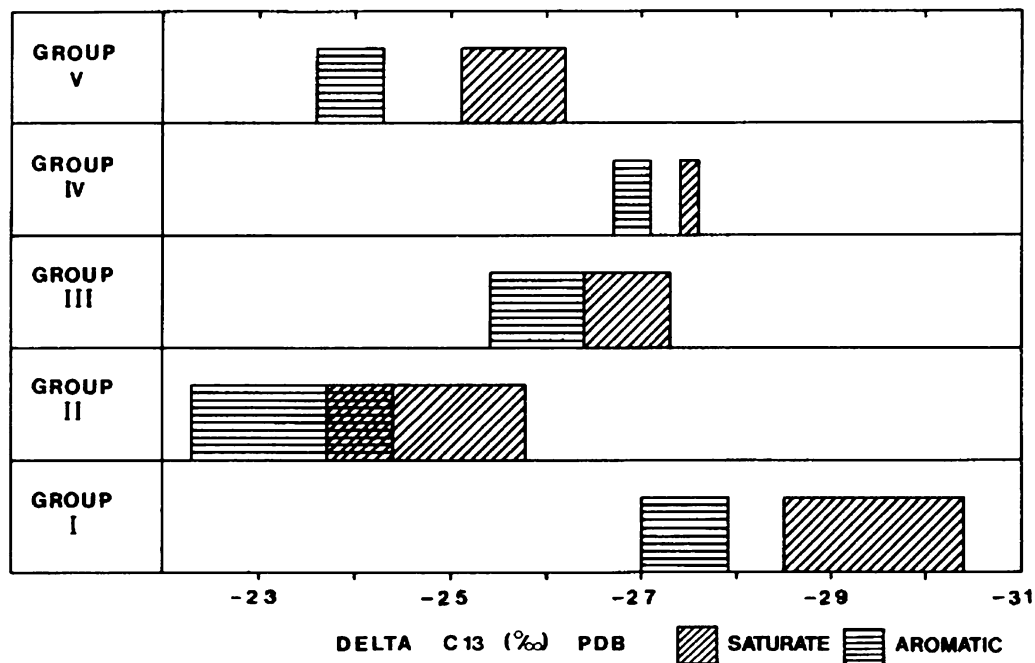
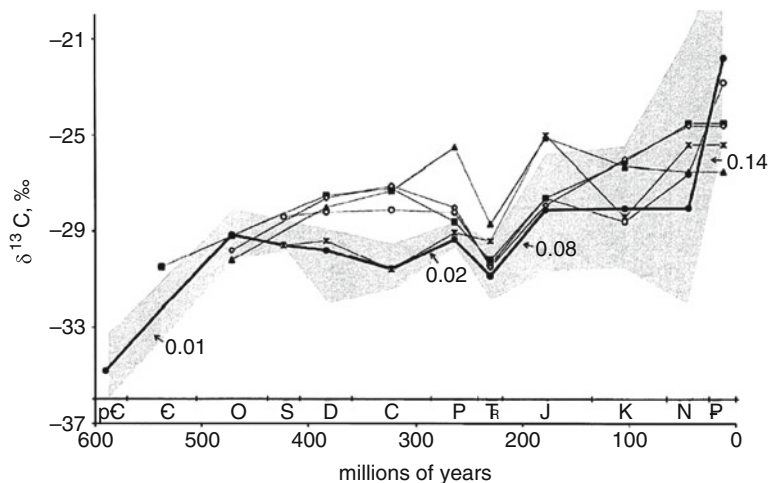


Fig. 31.6 Saturate and aromatic carbon isotopic data of oils from Brazilian offshore basins (Reproduced from Mello et al. 1988 with permission from Elsevier)

Fig. 31.7 Stable carbon isotope composition of crude oils vs. geologic age (Reproduced from Andrushevich et al. 1998 with permission from Elsevier)



terrestrial plants and freshwater algae, are depleted in ^{13}C relative to those of marine or saline plants (Galimov 1973; Tissot and Welte 1984). Moldowan et al. (1985) found that, individually, carbon isotopes and pristane/phytane ratios were ineffective in distinguishing non-marine and marine environments on a global basis. Taken together, the carbon isotope values ($\delta^{13}\text{C}$) and pristane/phytane ratios, however, discriminate between these distinct groups and can be considered a useful geochemical measure for the differentiation of non-marine and marine related oils found in the Brazilian offshore basins (Table 31.3).

31.1.2.5 Utilization of Stable Isotopes of Hydrogen and Carbon for Age Dating

Exploration studies have used a variety of biomarker parameters that can be related to specific evolutionary events in order to age-date oil samples (Moldowan et al. 1993). The interest in the age dating is based on the fact that in many exploration cases only oil samples are recovered and in order to determine the source formation responsible for the generation of a specific oil, it is very valuable to be able to predict the age of the source rock from the crude oil parameters.

Andrushevich et al. (1998) investigated the potential of age dating crude oils using stable carbon isotopic compositions of different fractions of oil samples and noted that the oils became enriched in ^{13}C with decreasing geologic age (Fig. 31.7). In particular, changes in $\delta^{13}\text{C}$ apparently occur in concert with

global fluctuation of the $\delta^{13}\text{C}$ carbonate carbon (Andrushevich et al. 1998). Earlier investigations of the stable carbon isotopic composition of oils ($\delta^{13}\text{C}$) over geologic time are generally consistent and documented a trend of ^{13}C enrichment with decreasing age (Stahl 1977, Chung et al. 1992). In general, the $\delta^{13}\text{C}$ value of oil is dependent upon the $\delta^{13}\text{C}$ value of the kerogen in the source rock from which it was derived. The $\delta^{13}\text{C}$ value of kerogen depends, in turn, on the types of organisms preserved and the $\delta^{13}\text{C}$ values of its substrate, which in turn goes back to the original conditions of photosynthesis as described above. Assuming that the present is the key to the past, the stable isotope composition of carbon in ancient biospheres was likely affected by conditions known to be important in the modern biosphere such as, temperature, pCO_2 , and depositional environments. Changes in these conditions would have affected organic carbon and carbonate carbon production as well as their respective $\delta^{13}\text{C}$ values (Knoll 1991). The geologic record reflects fluctuations in the $\delta^{13}\text{C}$ values of organic and carbonate carbon, and changes in the relative concentrations of atmospheric gases such as CO_2 and O_2 (Andrushevich et al. 1998).

Variations in the carbon isotope values with time are relatively easily rationalized. The original CO_2 in the atmosphere was derived from outgassing of the core and had a fixed isotopic composition. With time and evolution of more complex forms of photosynthetic organisms and plants, the CO_2 content of the atmosphere decreased and in general became isotopically heavier. At times there were isotopic excursions where as a result of significant increases in

productivity, the CO₂ became even heavier and in turn the primary photosynthesizers also assumed a heavier isotopic signature. At the present time with the increased burning of fossil fuels, the isotopic composition of the atmospheric CO₂ is becoming isotopically lighter since most fossil fuels and their combustion products have isotopic values in the range of -25 to -35 per mil.

31.1.2.6 Isotopic Determination of Individual Compounds in Crude Oils and Source Rock Extracts

As mentioned in the introduction, the capability to measure the isotopic composition of individual compounds became available almost two decades ago. Gas chromatography–isotope ratio mass spectrometry (GC–IRMS) permits continuous flow determination of carbon isotope values of individual components in complex mixtures of geochemical interest (Matthews and Hayes 1978; Hayes et al. 1987, 1990; Freeman et al. 1990). As discussed above, before the development of GC–IRMS, only bulk isotopic data were available (Sofer 1984) which lack a lot of specificity as a result of the heterogeneous nature of the original source material (Philp 1996). Consequently, the interpretation of the isotopic data of crude oils and source rock extracts must be integrated along with other available geochemical information (Cortes et al. 2010). Utilization of GCIRMS now permits determination of the isotopic composition of individual compounds in the crude oils and source rock extracts. For the most part investigations have focused on the n-alkanes and isoprenoids since they are generally well resolved in the chromatograms (Liu et al. 2006). The $\delta^{13}\text{C}$ values of individual n-alkanes have been widely used in making oil/oil and oil/source rock correlations (Bjørøy et al. 1992; Karlsen et al. 1995; Stoddart et al. 1995) and reconstructing paleoenvironment and paleoclimate (Hayes et al. 1990; Schoell 1994). δD values of individual organic compounds have also been used in a number of petroleum exploration and production studies (Liu et al. 2006).

The isotopes of individual compounds provide an additional correlation parameter, and in addition can be used to evaluate whether or not individual compounds are derived from the same precursor molecule. This is particularly important for one of the most

widely used geochemical parameters in exploration studies, namely the ratio of pristane/phytane (Peters et al. 2005). This ratio is widely used for correlation and also to provide an indication of the oxicity of the depositional environment. However this latter application assumes both compounds are derived from the side chain of chlorophyll and if they are not then the use of this ratio is not valid. The only way to determine if they are indeed from the same source is to measure the carbon isotope value of these compounds. In the Table 31.2, the carbon isotope values are given for two oils and the Messel shale. Note that in the oils the values are very similar suggesting a common source but in the Messel extract the values are significantly different indicating that the pristane and phytane are derived from different sources (Hayes et al. 1987; Table 31.2).

The isotopic composition of individual compounds have also been successfully applied to the characterization of specific components in the saturate hydrocarbon fraction and used as a parameter to establish oil–oil and oil–source rock correlations (Schoell 1984a, b; Bjørøy et al. 1992; Rooney et al. 1998; Li et al. 2001; Inaba and Suzuki 2003). Several researchers have applied this technique to evaluate the presence of unusual polycyclic alkanes in extracts of source rocks and crude oils where hopanoids and steranes were either absent or present in extremely low abundance (Riediger et al. 1997; Schaeffer et al. 1994; Li et al. 1997; Cuishan et al. 2003).

The correlation of oil to source rock is based on the assumption that the oil and the corresponding source rock have similar $\delta^{13}\text{C}$ values. In order to use isotopic compositions from crude oils and source rock extracts for direct oil/oil and oil/source correlations, two preconditions must be satisfied: the first is that the maturity level of the oil and corresponding source rock is similar; and secondly, secondary alterations such as hydrocarbon expulsion, migration, biodegradation and water washing etc., have had no significant effect on the isotopic composition of either the oil or potential source rock (Xiong and Geng 2000; Liao et al. 2004). These conditions need to be satisfied regardless of whether bulk or individual compound isotopes are being determined.

The carbon isotope profiles of n-alkanes can readily differentiate source rock samples from different areas in a basin such as that described by Xiong et al. (2005) where $\delta^{13}\text{C}$ values of individual n-alkanes were

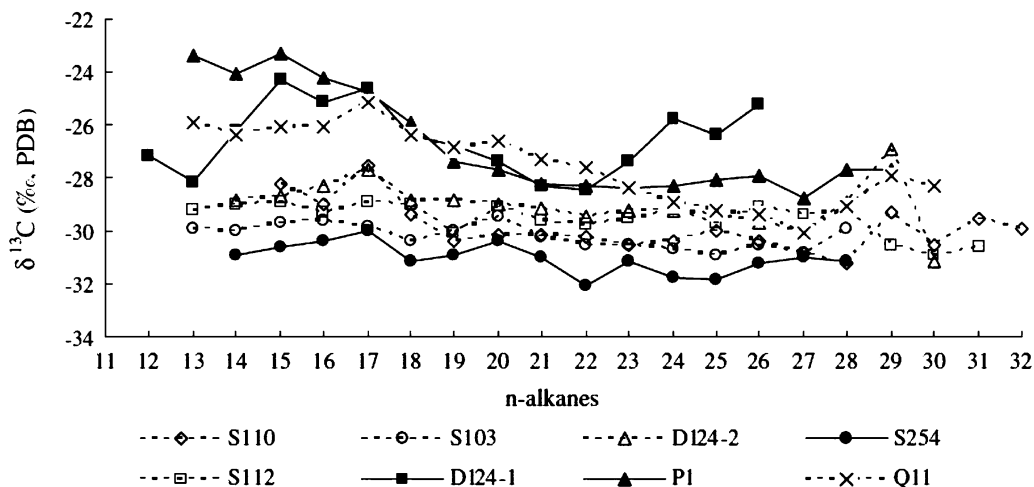


Fig. 31.8 Carbon isotopic compositions of individual n-alkanes in source rocks of the Western depression of the Liaohe Basin (Reproduced from Xiong et al. 2005 with permission from Elsevier)

measured for different formations within the Liaohe Basin China. The n-alkanes of one of the Es4 members displays a relatively constant isotopic profile, with $\delta^{13}\text{C}$ values in the range from -28 to -32‰ , while the n-alkane $\delta^{13}\text{C}$ values for the other Es3 source rocks vary from -23 to -28‰ , and show a trend toward isotopically lighter values with increasing n-alkane chain length, the range being typically 2–5‰ (Li et al. 1995; Xiong et al. 2003). The n-alkanes from the samples analyzed are typical of the Es4 source rocks, suggesting a relatively closed saline lacustrine environment (Fig. 31.8; Xiong et al. 2005).

In recent years, it has become possible to measure the hydrogen isotope compositions of individual organic compounds (Burgoyne and Hayes 1998; Hilker et al. 1999). Deuterium (D) and hydrogen (H) have the largest percent of relative mass difference of any stable isotope pair, and therefore hydrogen isotopes exhibit the greatest fractionation in natural systems (Bigeleisen 1965). The greater range of δD values and distinct chemical reactivity of hydrogen make compound-specific hydrogen isotope data a valuable complement to $\delta^{13}\text{C}$ values in petroleum systems (Li et al. 2001). Measured δD values in hydrocarbons in petroleum systems result from a combination of the isotopic composition of the source organic matter (Hoeffs 2004), hydrogen exchange processes that involve D/H in water (Sessions et al. 2004) and/or clay minerals (Alexander et al. 1982), and thermal maturation processes (Schimmelmann et al. 2001). Additionally, water washing, biodegradation, and

migration all have the potential to alter δD values; the magnitude of these effects are still being evaluated (Schimmelmann et al. 2006).

For the stable hydrogen isotopic composition (δD) of sedimentary hydrocarbons to reflect that of their biosynthetic precursors, the δD signature of the precursor must be preserved throughout sedimentation, burial, diagenesis and catagenesis (Dawson et al. 2007). Thermal maturation in particular has been found to play a significant role in the alteration of indigenous δD signatures, where a general enrichment of D in hydrocarbon fractions and individual hydrocarbons is observed with increasing maturity (Dawson et al. 2007). This is thought to be a result of the hydrocarbons exchanging hydrogen with relatively D-rich formation waters (Stalker et al. 1998; Schimmelmann et al. 1999).

Biodegradation of crude oil in the reservoir is an important process of secondary alteration with major economic consequences. Although the actual processes involved (e.g. site and rate of degradation, nutrient supply and nature of by-products) during in-reservoir biodegradation of crude oil are still being evaluated, their effects on the composition and physical properties are well known (Sun et al. 2005). In most cases, the components of crude oils are removed sequentially in the order of n-alkanes > monocyclic alkanes > alkyl benzenes > isoprenoid alkanes > alkyl naphthalenes > bicyclic alkanes > steranes > hopanes. Based on this sequence, many compound-related indicators have been proposed for

the characterization of the level of biodegradation of crude oil (Peters et al. 2005). The effects of biodegradation on the isotopic composition of individual compounds have been investigated recently for potential applications in petroleum and environmental science (Boreham et al. 1995; Mansuy et al. 1997; Huang et al. 1997; Wilkes et al. 2000; Hunkeler et al. 2001; Masterson et al. 2001; Mazeas et al. 2002; Pond et al. 2002; George et al. 2002; Mancini et al. 2003).

Studies by Masterson et al. (2001) and George et al. (2002) showed that the effects of slight and moderate biodegradation on light hydrocarbons (C_5 – C_9) also consistently lead to enrichment in ^{13}C for each remaining compound. However, Boreham et al. (1995) and Sun et al. (2005) observed that slight and moderate biodegradation caused insignificant enrichment in residual C_{10} – C_{14} n-alkanes, with a maximum $\delta^{13}C$ increase of 0.5‰. It has long been recognized that the stable carbon isotopic compositions of natural gas components (C_2 – C_5) are highly fractionated during biodegradation (Pallasser 2000).

It is also of interest to investigate the effect of biodegradation on the stable hydrogen isotopic compositions of individual compounds. Because of the larger relative mass difference between deuterium and hydrogen than for ^{13}C and ^{12}C , hydrogen isotopes become fractionated significantly more during natural processes (Faure 1986). Previous aerobic laboratory experiments on moderately degraded oils showed that the C_{15} – C_{18} n-alkanes that were degraded at the fastest rates had the largest overall isotopic fractionation (<12–25‰ deuterium enrichment). On the other hand, the hydrogen isotopic compositions of the longer chain n-alkanes (C_{19} – C_{27}) were relatively stable during slight to moderate biodegradation (<5‰ overall deuterium enrichment), indicating that these compounds might be effective tracers for oil–source correlation (Pond et al. 2002). This is an important result with respect to laboratory investigations, but it is more important for petroleum geochemists to know if any fractionation takes place during natural biodegradation in subsurface petroleum reservoirs (Sun et al. 2005).

31.1.3 Natural Gas Isotope Analyses

Unlike crude oils, natural gas are relatively simple mixtures limiting the number of parameters that are

available for correlation purposes or distinguishing gases from different sources. Most natural gas samples will be dominated by hydrocarbons in the C_1 to C_5 range and possibly varying amounts of CO_2 , H_2S , and N_2 . The amounts of various components will, to a large extent, vary as a result of maturity of the source rock or oil from which the gas was generated. Gases that are dominated by methane are generally formed at high levels of thermal maturity or may result from biogenic activity at low levels of thermal maturity. One of the more extensive applications of stable isotopes is in differentiating biogenic from thermogenic methane. Biogenic gas is generally isotopically very light, typically around -70 per mil whereas thermogenic methane will range from -30 to -50 per mil approximately. This was recognized many years ago and lead to one of the earliest correlation or source discrimination diagrams by Bernard et al. (1976). Basically this is a cross plot of $\delta^{13}C$ of methane vs. the ratio of C_1/C_{2+} and as shown below the biogenic samples are distinguished by the isotopically light methane and the high value for the C_1/C_{2+} ratio (Fig. 31.9). Thermogenic gas samples will be isotopically heavier and have lower values for the compositional ratio. There is also an area of mixed gas where it is a little more difficult to assign a specific source to the gases in that region. The reason for the variation in these isotopic ratios is a result of the kinetic isotope effect. Preferential cleavage of ^{12}C – ^{12}C bonds by the bacteria will lead to the production of isotopically light biogenic gas. From a thermogenic perspective at low levels of maturity again these bonds require less energy to be broken than a ^{12}C – ^{13}C bond. As the maturity level increases more of the bonds that include the heavier isotope will be broken and the methane produced will become isotopically heavier.

As mentioned above in terms of correlation or discrimination of natural gas samples, options are more limited than with crude oils. These correlations have to be undertaken using the isotopic composition of the individual compounds in the gas samples plus variations in the relative proportions of the individual compounds. The development of the GCIRMS system has been exceedingly useful and made it relatively easy to obtain the isotopic compositions of individual compounds in complex mixtures. Prior to the advent of the GCIRMS it was necessary to physically isolate each individual compound in order to measure its isotopic composition. With the GCIRMS system it is

Fig. 31.9 Bernard et al. (1976) diagram showing the relationship between carbon isotope values in methane and the $C_1/(C_2 + C_3)$ compositional ratios of natural gas samples. (Reproduced from Bernard et al. 1976 with permission from Elsevier)

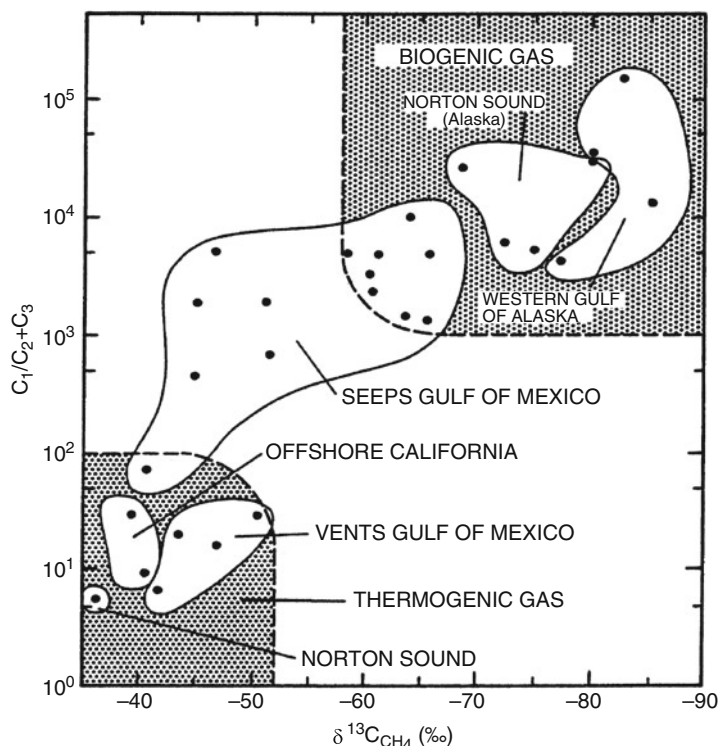
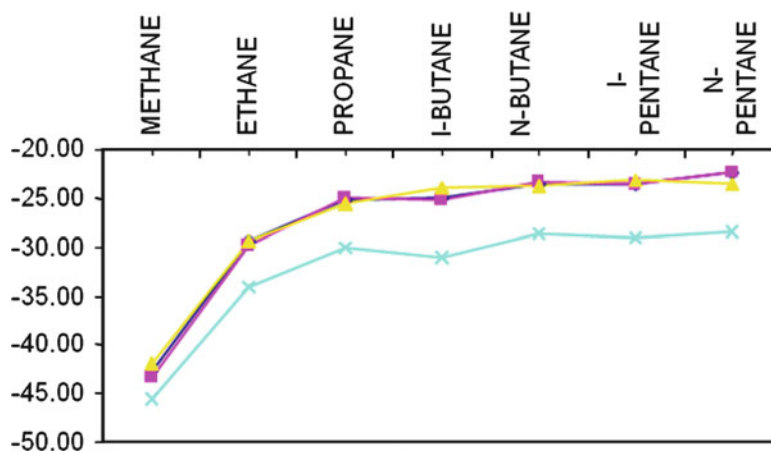


Fig. 31.10 The stable isotope ratios of what (specify the y-axis) can be plotted as shown in this diagram to establish relationships between families of gases within a specific basin. In this example those samples whose values do not coincide differ as a result of differences in maturity or source differences



of course possible to simply introduce the sample into the GC and obtain the isotopic composition of each component in a relatively short period of time. It should also be mentioned that it is possible to obtain both carbon and hydrogen isotope values on these individual compounds and a combination of the two isotopes provides an additional correlation parameter.

The most useful application of the isotopes for correlation purposes is to simply plot the isotope

values of the individual compounds against their carbon number. Then with a large number of gas samples from the same basin those that are related to each other will group relatively closely whereas those coming from different sources or generated at different levels of maturity will plot separately as shown below (Fig. 31.10).

There are a number of interesting extensions to this plot which can provide a significant amount of

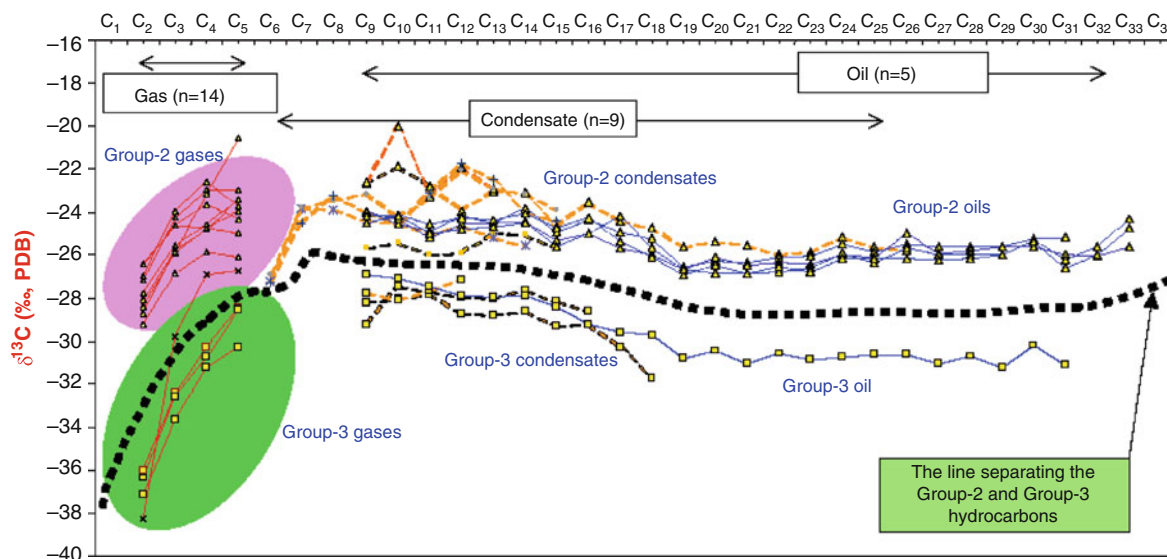


Fig. 31.11 The above plot developed by Gürgey et al. (2005) is used to establish relationships between gases and condensates produced from the same formation. The condensates can then be

correlated using compounds such as the diamondoids (Reproduced from Gürgey et al. 2005 with permission from Elsevier)

additional information. As mentioned above we are somewhat limited in being able to differentiate the sources of the natural gases. However it has been shown that for wells that produce condensates as well as gas it is possible to extend the plots shown above into the condensate range after measuring the isotopic composition of the individual compounds in the condensates. Then if the condensate and gas are derived from the same source and at the same level of maturity, the isotope values for the individual compounds in the condensate will simply be an extension of the related gas sample as shown (Fig. 31.11). The advantage of obtaining these extended plots is that not only can we use the isotopes to establish the relationship between gas and condensate but also with the condensates there are biomarkers, such as diamondoids, that can be used to correlate or differentiate samples.

Establishing the exact source of natural gas is far more complicated than establishing the source of a crude oil. One cannot simply undertake the correlation between the source rock extract and the gas sample. It is possible to undertake hydrous pyrolysis as with the oils and analyse the gases that are produced during the hydrous pyrolysis reactions. These gases can be characterized isotopically and compared with the produced gas. In an alternative approach it is possible to use the isotope data of the individual compounds to construct a

Chung plot (Chung et al. 1988), which is basically a plot of the isotope values plotted against the reciprocal of the carbon number of the component (Fig. 31.12). The extension of this plot to the y axis in the way it is plotted below provides an estimate of the isotopic composition of the source rock responsible for generating the gas. This in itself is quite important since it may be possible from this information to eliminate certain formations as possible sources for the gas. Another important part of any gas exploration study is evaluating the maturity level at which a gas was generated since that provides further information on possible sources, depth of burial, migration distances. If the $\delta^{13}\text{C}$ value of the suspected kerogen can be obtained, then it is possible to model suspected isotope values of the gases generated at different levels of maturity through the use of the Berner model as described below.

There have been numerous attempts to relate isotope values with the maturity level of gas generation. The carbon isotopic composition ($\delta^{13}\text{C}$) of individual compounds in hydrocarbon gases depends not only on the isotopic composition of the source, but also on the level of maturity to which the source has been subjected (Schoell 1984a, b; Hunt 1996). Several empirical models have been developed over the past 30 years that relate isotopic composition and maturity of different source rocks from around the world (Stahl 1977;

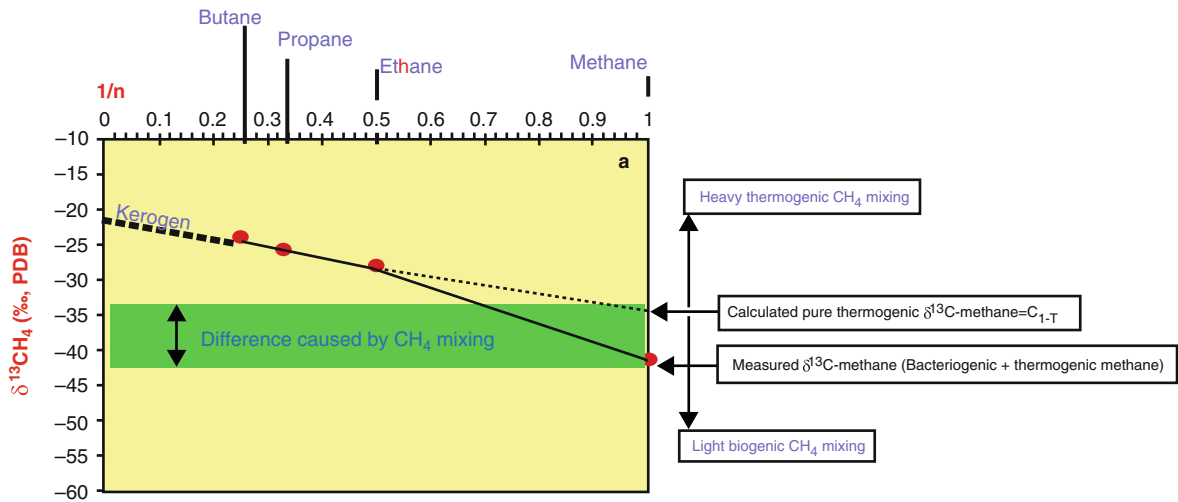
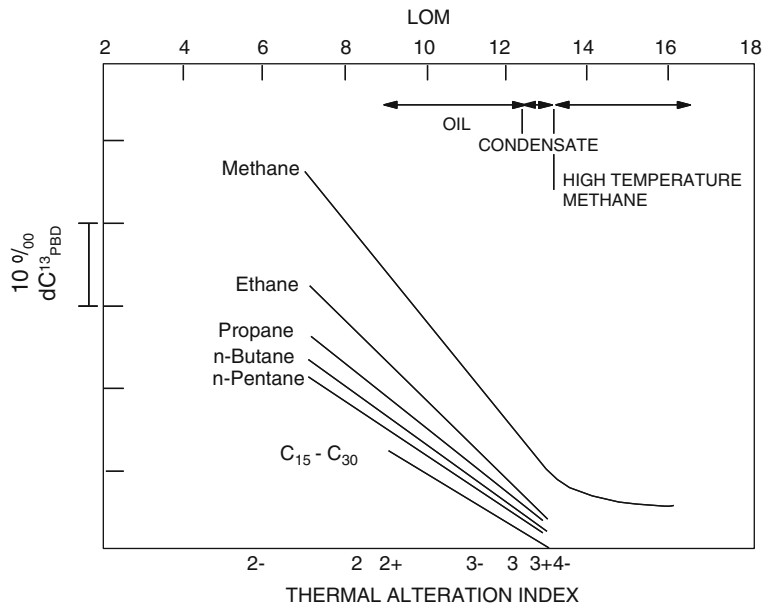


Fig. 31.12 The Chung plot shown, the reciprocal of the carbon number plotted against the carbon isotope values, can be used to determine the carbon isotope value of the kerogen responsible

for generation of the gases (Reproduced from Chung et al. 1988 with permission from Elsevier)

Fig. 31.13 Theoretical maturation diagram showing calculated carbon isotopic separations between gas components plotted against source rock LOM. For reference, Thermal Alteration Index is also shown (Reproduced from James 1983 and reprinted by permission of AAPE and whose permission is required for further use)



Clayton 1991a, b; Berner and Faber 1996). More recently, general models combining maturity predictions with mixing and secondary cracking have been published (Ellis et al. 2003). One of the first attempts to relate isotopic composition and maturity was made by Stahl (1977) who published quantitative relationships between $\delta^{13}\text{C}$ of methane and vitrinite reflectance for gases from northwest Germany. Stahl noticed that the relationship was different for gases derived from marine sources and gases from coal beds.

This early observation already indicated that maturity models were dependant on source rock type.

James (1983) suggested that uncertainties can arise from the sole use of methane for maturity prediction and suggested that the difference of carbon isotope ratio between hydrocarbon components has more advantages and no prior knowledge of the source of the gas was required. James’s theoretical maturation diagram showing the calculated isotopic separation between gas components is illustrated in Fig. 31.13.

This approach, although useful in some cases, relates isotopic composition to level of organic metamorphism (LOM) and thermal alteration index (TAI), which are not as widely used as vitrinite reflectance because of the uncertainties associated with them. Level of organic metamorphism was defined by Hood et al. (1975) who created a continuous numerical scale equivalent to Suggate's (1959) coal-rank column, which covers the entire range of petroleum generation and destruction. The thermal alteration index on the other hand, is a scale that uses the color changes in organic debris to determine the severity of organic thermal metamorphism (Staplin 1969).

There have been a number of attempts to model and predict the isotopic composition of gases derived from various sources at different levels of maturity. For example Clayton (1991a, b) modeled the $\delta^{13}\text{C}$ of a hydrocarbon gas as a function of the gas precursor in a refractory (humic) kerogen using a parameter he defined as the gas generation index (GGI):

$$\text{GGI} = \text{total gas generated/total gas potential}$$

Although it requires an independent estimate of the $\delta^{13}\text{C}$ of the source of the kerogen, his model allowed determination of the source and its maturity for gases generated from labile (sapropelic) and refractory kerogens. Summary diagrams of Clayton's model are shown in Fig. 31.14a, b.

In another example, Berner et al. (1995) modeled the isotopic fractionation between organic matter and single gas compounds. Their model, based on primary cracking simulation using open system pyrolysis, showed that with increasing maturity of algal-rich kerogen, an increase of the isotope ratios of pyrolytic ethane, ethane and propane is observed (Fig. 31.15). Berner and Faber (1996) used the empirical data generated by Berner et al. (1995) to develop a model using a statistical evaluation of the data to generate equations that correlate vitrinite reflectance equivalent values with the isotopic compositions of methane, ethane and propane. One of the greatest advantages of the Berner and Faber model over the previous ones is that isotopic composition is related directly to vitrinite reflectance which is the most commonly used maturity parameter by organic geochemists. The graphic relationship between $\delta^{13}\text{C}$ of methane, ethane and propane and vitrinite reflectance (%Ro) is illustrated in Fig. 31.16. The model of Berner and Faber (1996) is a simple and

flexible model that can be easily applied to different types of source rocks, nevertheless one should keep in mind that any attempt at maturity prediction should take into account the intrinsic variability of the source rock that generated the gases under evaluation.

Ellis et al. (2003) presented a new model that can be used to predict gas thermal maturity and bacterial gas contribution from the isotopic composition of methane, ethane and propane. The application of this maturity-mixing model to Barnett shale data is illustrated in Fig. 31.17. This relationship extrapolates well to geological data as shown by Hill et al. (2007) and can be used in conjunction with other models to corroborate maturity predictions.

In addition to investigating the maturity levels at which gases were generated, hence providing depths of burial, there are numerous correlation plots that have been developed over time and used routinely in this field. A number of these plots will be summarized here. The first by Schoell (1983) is based on a large set of empirical data and is a plot of the $\delta^{13}\text{C}$ values against the δD values for methane in the gas samples. As can be seen from this plot this provides information, primarily derived from maturity differences, as to the source of the gas and whether it is oil associated or deep dry gas etc. This can also be very useful for grouping families of gases within a basin (Fig. 31.18).

In a relatively recent modification of the Bernard diagram, Gürgey et al. (2005) modified the diagram such that it incorporates trends expected in the gases based on whether the gases are derived from a Type II or Type III kerogen. (Kerogen is the insoluble organic matter in organic rich source rocks that is primarily responsible for the generation of oil and/or gas. It is formed from dead organic matter deposited in various depositional environments, that undergoes diagenesis and thermal alteration and is ultimately converted into an insoluble matrix called kerogen. The structure of the kerogen will vary depending on the types of original source material responsible for its formation. Tissot and Welte (1984) developed a classification scheme for kerogen types initially based on their elemental compositions. In summary Type I kerogens are predominantly formed from lacustrine source materials and are generally oil prone. Type II kerogens are derived from marine organic matter and produce primarily oil along with some gas. Type III kerogens are typically derived from terrigenous source materials and are generally gas prone.) Such information can

Fig. 31.14

(a) Summary diagram of methane isotope ratios and fraction of methane in gas. All four sources of gas are clearly differentiated, and source-rock maturity can be determined. $C_1/\Sigma C_{1-5}$ is the fraction of methane in total C_1-C_5 hydrocarbon fraction (derived empirically from field data, and $\Delta^{13}C$ is the modeled per-mil difference between methane and total source kerogen. Error bars are $2 \times$ standard error of the mean for calibration data set (Clayton 1991a, b)).

(b) Modeled maturity variations in $\Delta^{13}C$ of methane through butane, relative to $\delta^{13}C$ of total source kerogen. "Pure" gases plot parallel to these trends; mixing of gases leads to cross-cutting relationships. Error bars are $2 \times$ standard error of the mean for calibration data sets (Reproduced from Clayton 1991a, b by permission of Elsevier)

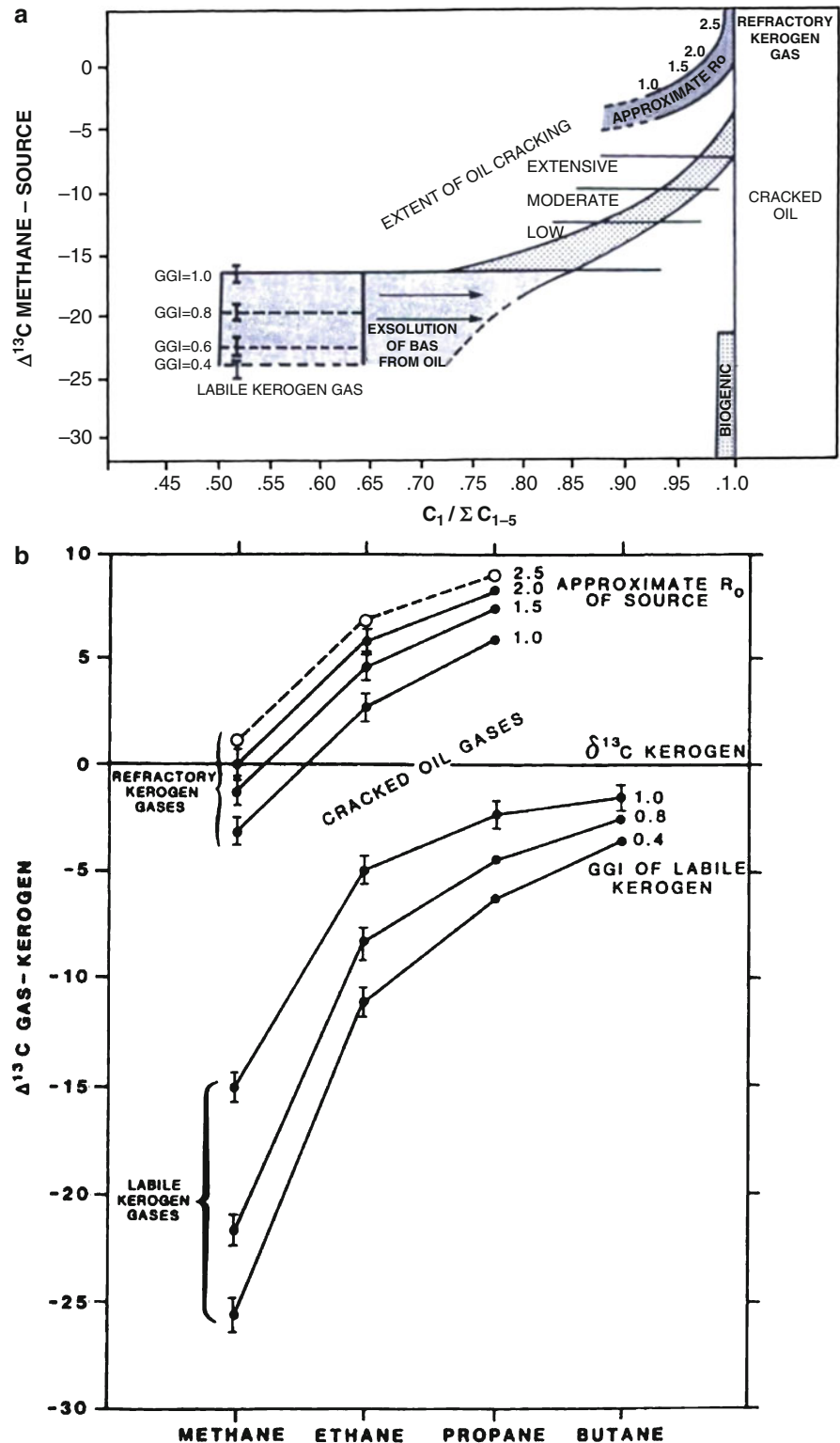


Fig. 31.15 Comparison between measured and calculated carbon isotope ratios of methane, ethane and propane generated during pyrolysis of (a) Kukersite and (b) xylite (Reproduced from Berner et al. 1995 with permission of Elsevier)

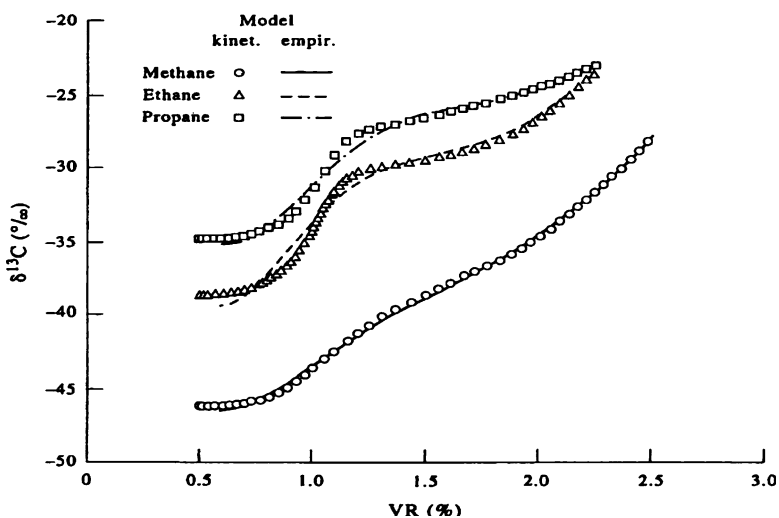
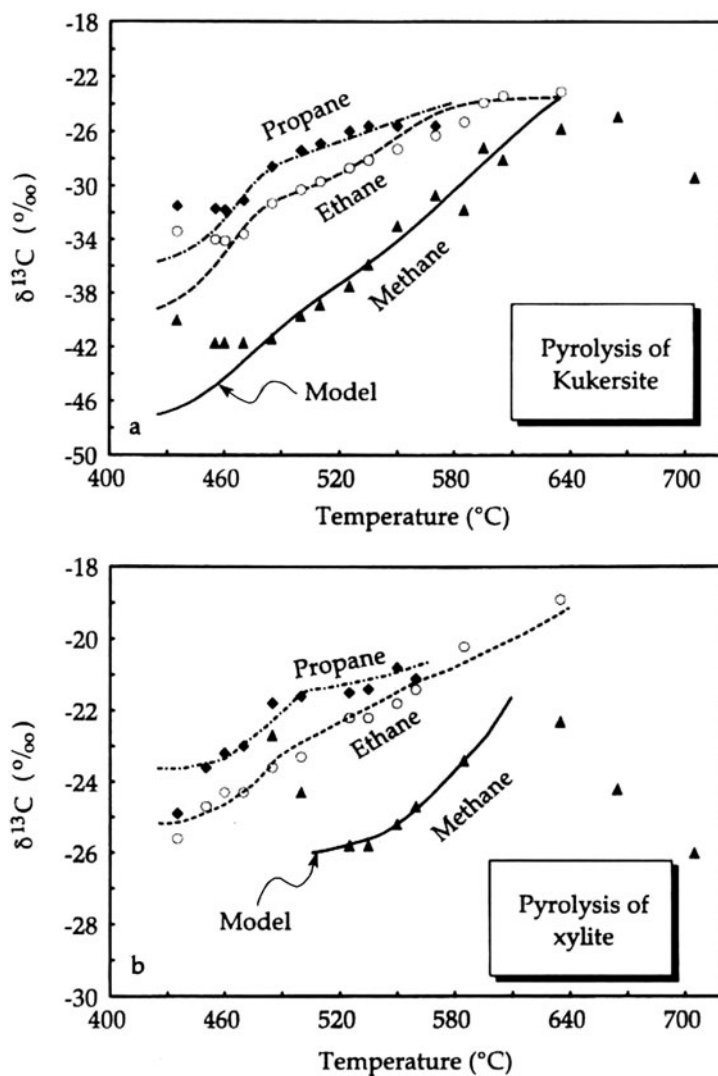


Fig. 31.16 Empirical models that describe instantaneous gas generation from algal kerogens derived through statistical evaluation of kinetic models of Berner et al. (1995); (Reproduced from Berner and Faber 1996 with permission of Elsevier)

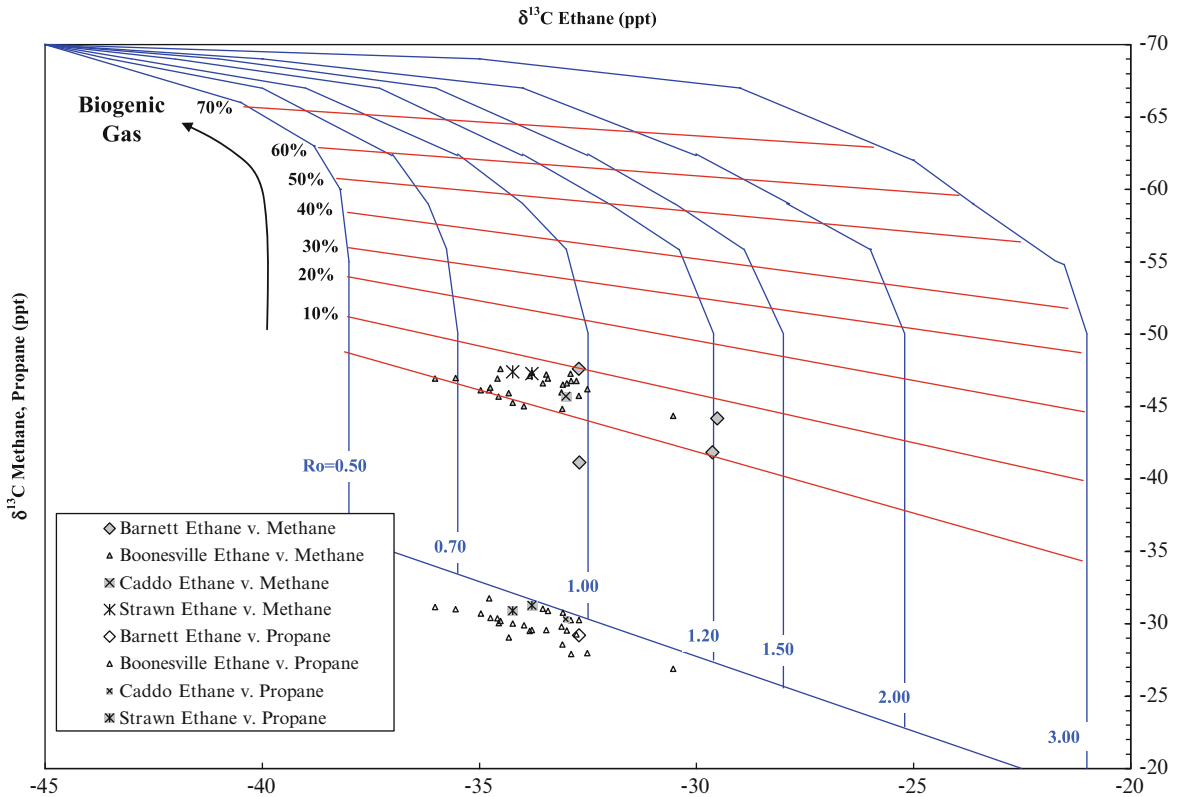
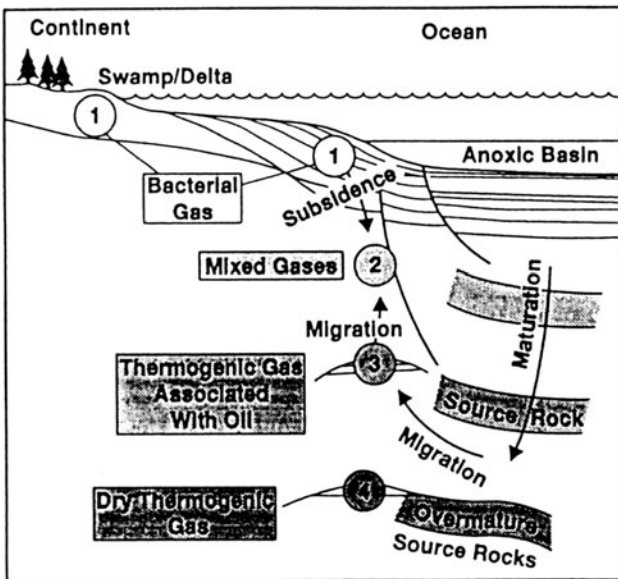


Fig. 31.17 $\delta^{13}\text{C}$ ethane vs. $\delta^{13}\text{C}$ methane and $\delta^{13}\text{C}$ propane for estimating gas maturity and biogenic gas content. Gas maturity is expressed as equivalent vitrinite reflectance (Reproduced

from Hill et al. 2007 with permission of AAPG & whose permission is required for further use)

a



b

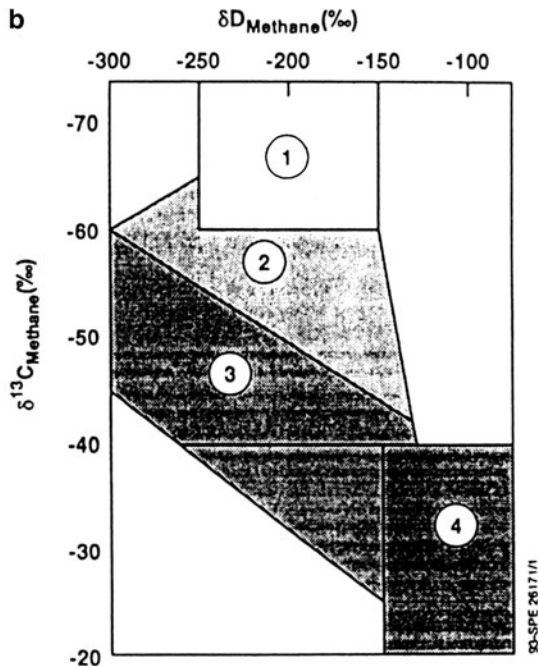


Fig. 31.18 Schoell plot showing relationship between C and H isotope ratios of natural gas samples and depth of generation (Reproduced from Schoell 1983 with permission of AAPG & whose permission is required for further use)

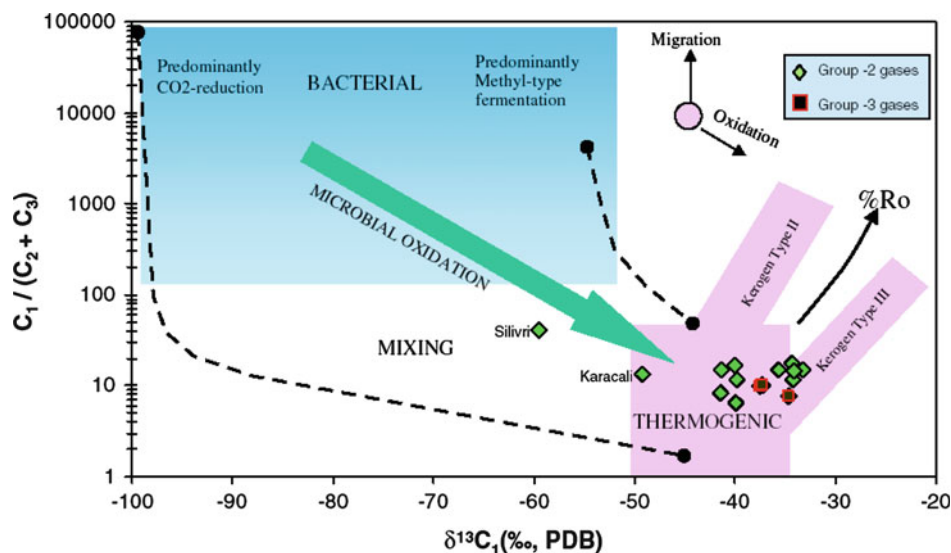


Fig. 31.19 Modification of the Bernard et al. (1977) plot illustrating how this plot can be extended to provide information on the kerogen type responsible for the gas generation (Reproduced from Gürgey et al. 2005 with permission of Elsevier)

again be extremely useful when trying to determine the particular source rock in a basin that may have been responsible for generating the gas (Fig. 31.19).

Finally in terms of gas exploration another important application of the isotopes is their use for undertaking correlation studies within a reservoir. As with crude oil reservoirs, a knowledge of continuity within a reservoir is extremely important for production purposes (Schoell and Jenden 1993). Once again the concept is relatively simple and based on the concept that if samples in two different blocks of the same reservoir have different isotopic fingerprints then it can be assumed that they are not in communication with each other. If they were then they would homogenize and have the same isotope signatures. However if they have the same isotope values, this result is a little more ambiguous and more difficult to interpret. It may imply that the samples are homogenized and in communication but it may simply be a coincidence. However it is still a relatively cheap and convenient way of monitoring communication. In addition comingling of production can be monitored through the use of the isotopes. If samples of the original products are available, then a mixing curve can be developed such that the comingled samples that are produced can be characterized isotopically and then using the calibration curve the relative proportions of the two end members determined.

31.1.4 Environmental Forensics

The preceding sections have dealt with the utilization of stable isotopes in hydrocarbon exploration and the remainder of the chapter will focus on applications of stable isotopes to environmental problems. Environmental forensics has developed rapidly over the past decade and has greatly benefitted from the development of the GCIRMS systems (Matthews and Hayes 1978; Hayes et al. 1987, 1990; Freeman et al. 1990). The study of organic pollutants or contaminants in the environment has been an active field for 50 years or more. In the early 1970s the commercial availability of gas chromatograph-mass spectrometer (GCMS) systems and the evolution of the biomarker concept in the oil industry lead to the extensive use of the same techniques a few years later in environmental problems related to oil spills (Philp 2003). These early studies formed the foundation for what today has expanded into a very sophisticated area of research and applications directed towards extensive characterization of fossil fuel derived products, and their degradation products, in the environment. While early efforts were limited towards obtaining fingerprints of spilled product and suspected source, this has now been taken to a much higher level where, for example in the case of gasolines, even the nature of the catalytic cracking

catalyst used in the refinery can be determined through ratios of specific compounds in the gasoline (Murphy and Morrison 2002). Age dating of spilled products has become another extensive area of study. Determination of when a spill occurred is clearly important since if one can show a spill occurred at a site 20 years ago and a person only owned the site for 5 years, clearly that person is not responsible for the spill. Applications have also diversified from crude oils and refined products into a large variety of groundwater contaminants such as BTEX, PCE, TCE, MTBE, 1,4-dioxane; coal tars and other sources of PAHs; pesticides; explosive residues; and many other sources of organic compounds too extensive to describe here (Wang and Stout 2007). In the past decade there has been an exponential increase in the application of stable isotopes to environmental problems primarily catalyzed by the commercial availability of combined gas chromatograph-isotope ratio mass spectrometers (GCIRMS) (Sherwood Lollar et al. 2001; Lesser et al. 2008; Philp and Kuder 2008; USEPA 2008). Such systems permit the almost routine determination of carbon, hydrogen and nitrogen isotopes of individual compounds present in complex mixtures. Methods for the determination of chlorine isotopes are currently being developed and will be discussed below.

There is of course nothing new about utilizing stable isotopes in a wide variety of problems and as discussed above isotopes have been used extensively in hydrocarbon exploration for more than 50 years as careful examination of the petroleum literature will reveal (Silverman 1965). Bulk isotopes have been used in a number of environmental studies, particularly those involved with crude oil spills (Kvenvolden et al. 1993, 1995). While bulk isotopes are useful in environmental problems related to crude oils, contaminated ground water samples with a wide variety of contaminants requires the use of GCIRMS to discriminate sources and monitor the onset and extent of natural attenuation or degradation of these compounds. GCIRMS is also used extensively to characterize a wide range of less volatile products such as PAHs or PCBs but with those types of samples more emphasis is placed on using the isotope fingerprints as a correlation tool since any changes to these types of compounds resulting from degradation are not typically discernable when measured by GCIRMS.

The only modification of the GCIRMS system necessary for the analysis of groundwater samples is the

addition of a purge and trap system to extract the compounds of interest and facilitate their introduction into the GCIRMS system. The use of purge and trap provides a far more reproducible method for extracting the compounds compared to techniques such as heated headspace or SPIME extraction techniques. Purge and trap permits detection of groundwater contaminants down to levels of 1–5 ppb for many common groundwater contaminants for carbon and slightly higher for hydrogen (Hunkeler et al. 2008; USA EPA 2008).

31.1.4.1 Recent Developments in Determination of Chlorine Isotopes

There is currently a great deal of interest in developing the capability to determine the Cl isotopic ratios of the chlorinated compounds at contaminated sites (e.g. Sturchio et al. 2011). It is thought in many areas that this may provide an additional line of evidence that will permit differentiation of sources for chlorinated contaminants that may not be distinguishable on the basis of carbon isotopes alone. Chlorine isotope data published to date on common groundwater contaminants have, to a large degree, been based on pure compounds, or isolated from microcosm experiments, and not compounds actually isolated from groundwater (Shouakar-Stash et al. 2003). The reason is that the current method developed by Holt et al. (1997) some years ago is a very long complex process which requires conversion of the chlorinated compound into CH_3Cl , a process requiring multiple offline conversions. However most groundwater samples are contaminated at low ppb levels with a mixture of compounds and therefore to use this conversion method would first require isolation of the mixture of chlorinated species from the groundwater, which would require large volumes of water, and then physically separating each component prior to converting each compound into CH_3Cl .

The determination of the chlorine isotopic composition is based on the mass 52/50 of methyl chloride ($\text{CH}_3^{37}\text{Cl}/\text{CH}_3^{35}\text{Cl}$) and several studies in dual inlet measurements for pure chlorinated solvents have been reported. Measured $\delta^{37}\text{Cl}$ values for the chlorinated compounds are in the range of -3.54 to 4.08% (Shouakar-Stash et al. 2003, 2006). $\delta^{37}\text{Cl}$ analysis has also been used in the investigation of

reductive dechlorination of chlorinated ethylenes (Sturchio et al. 1998; Heraty et al. 1999; Numata et al. 2002) and the anaerobic degradation of PCE and TCE by testing various bacteria (Numata et al. 2002). Heraty et al. (1999) reported smaller chlorine isotope effects for the aerobic degradation of DCM and TCE and noted the $\delta^{37}\text{Cl}$ values of the residual DCM increased as a function of biodegradation.

Recently an alternative approach to the off-line method has started to emerge involving the use GCMS instead of GCIRMS. Due to the relatively high abundance of the ^{37}Cl isotope relative to ^{35}Cl isotope, it is possible to measure the $^{37}\text{Cl}/^{35}\text{Cl}$ ratio with greater precision on a conventional GCMS system and with the appropriate standard of known isotopic composition calibrated to the Cl standard (SMOW-standard mean ocean water) these values can also be calculated with a high degree of accuracy. This method lends itself to the Cl isotope determination of individual compounds in groundwater samples and will also permit detection down to the low ppb levels. A few papers have been published on this approach in the past few years but one can also expect to see many more papers appearing in the next few years once it is applied to actual problems (Sakaguchi-Söder et al. 2007).

31.1.4.2 Rayleigh Fractionation Model

The two major uses of stable isotopes in environmental forensics are: (i) as a tool to determine the onset and extent of natural attenuation and (ii) a tool for source discrimination or correlation. In the following sections examples of the use of isotopes in both of these applications will be described but prior to that it is important to introduce the Rayleigh equation and describe why this is important in attenuation studies. It should also be noted that in terms of the natural attenuation, the use of the isotopes for this purpose is primarily useful for molecules with less than approximately 10 carbon atoms. While any molecule will experience an intrinsic isotope effect at a specific carbon atom upon attenuation, what is measured in the routine GCIRMS analyses is the intrinsic isotope effect at that specific carbon diluted over all the carbon atoms in the molecule. Therefore in molecules with 10 carbons or less even when this effect is distributed over all 10 carbons it can be measured but if distributed over say 20

carbons it cannot be determined directly. As mentioned previously the dilution effect resulting from the presence of non-reactive carbon atoms and the precision of the instrument means that the overall isotopic shift may not be observable. The positive side of that is that in the larger molecules such as PAHs, the isotope fingerprint provides a strong correlation tool and if samples have different isotope fingerprints, these result from source differences and not attenuation.

The Rayleigh fractionation model provides a mathematical framework for interpretation of isotope fractionation and is a particularly important application in natural attenuation studies, since it basically establishes the relationship between isotopic fractionation and changes in concentration of the contaminant. The model is valid for fractionation occurring in unidirectional, irreversible reactions (kinetic isotope fractionation) and was originally developed for distillation of mixed liquids (Rayleigh 1896) and is based on the principle of a constant relationship between reaction rates of the elements in the reacting mixture. If ^{13}k is the rate constant of degradation of a ^{13}C -substituted bond, and ^{12}k is the rate constant of degradation of a ^{12}C -substituted bond, the constant ratio of $^{12}\text{k}/^{13}\text{k}$ is referred to as fractionation factor (α). The same can be expressed if instantaneous isotope ratios ($R = ^{13}\text{C}/^{12}\text{C}$) are substituted for reaction rates:

$$\alpha = R_{\text{product}}/R_{\text{substrate}} \quad (31.1)$$

Modification of (31.1) to substitute the instantaneous isotope ratios with the readily measurable isotope ratio and concentration of remaining reaction substrate yields (31.2). R_t is R of substrate at time t; $R_{t=0}$ is R of substrate at time t = 0 (at the beginning of the reaction); F represents the remaining ratio of substrate remaining at time = t to concentration at t = 0 (concentration_t/concentration_{t=0}); ϵ (ϵ = enrichment factor) is the isotopic enrichment factor ($\epsilon = 1,000 * (\alpha - 1)$).

$$1000 * \ln(R_t/R_{t=0}) = \epsilon * \ln F \quad (31.2)$$

A simplified variant of (31.2), reasonably accurate for ϵ between 0 and -20, is shown below as (31.3) where F is the remaining fraction of the substrate.

$$\delta^{13}\text{C}_t = \delta^{13}\text{C}_{t=0} + \epsilon * \ln F \quad (31.3)$$

With this equation it is possible to monitor the progress of natural attenuation by measuring the change in the isotopic composition of a particular contaminant for which the enrichment factor has already been determined. A number of tables summarizing enrichment factors that have been measured for many common groundwater contaminants have been published elsewhere (Hunkeler et al. 2008; USA EPA 2008)

31.1.4.3 Applications to Environmental Problems

Natural Attenuation

In one of the first applications of stable isotopes to investigate attenuation of ground water contaminants, Sherwood Lollar et al. (2001) demonstrated that attenuation of PCE and TCE in a groundwater plume at Dover AFB produced a significant enrichment in the carbon isotope compositions of PCE and TCE. This has led to a number of studies where changes in both carbon and hydrogen isotope compositions of a number of groundwater contaminants, including MTBE, BTEX, PCE and TCE have been used as a tool to monitor the onset of natural attenuation (Slater et al. 2001; Sherwood Lollar et al. 2001; Gray et al. 2002; Kolhatkar et al. 2002; Griebler et al. 2004; Kuder et al. 2005). Utilization of changes in the isotopic compositions in this manner has attracted the attention of the regulators and this approach is now being utilized at many contaminated sites to monitor progress of natural attenuation in conjunction with concentration changes (USEPA 2008).

Methyl *tert*-butyl ether (MTBE) is a major ground water contaminant that was used extensively as an oxygenate from 1990 to approximately 2004 when it was phased out in California and many other states followed their lead. It has been a known carcinogen since 1979 but was thought to be less of a health risk than many of the other constituents of gasoline (Hanson 1999). Determining the precise origin of MTBE in groundwater can be an extremely difficult question since a site may have contributions of MTBE from multiple gas stations in the area. Early studies indicating the recalcitrant nature of MTBE were initially thought to provide an opportunity for the source/spill correlation of MTBE using isotope-ratio mass

spectrometry (Smallwood et al. 2001). GCIRMS can provide accurate and precise carbon isotope values for MTBE at concentrations levels of around 1 ppb. The threshold for taste and odor of MTBE in drinking water in USA is between 15 and 20 ppb. This is also the limit set by most states, within the United States, for the maximum concentration of MTBE allowed before remediation is enforced or drinking water wells are shut down. However following the initial source correlation studies it was recognized that there were sites where isotopically enriched MTBE was observed and such enrichment could only occur if the MTBE was degrading. As a result of these observations the major interest in utilization of isotopes in the study of MTBE moved away from source determination to the use of the isotopes as a tool for evaluating the onset of natural attenuation. Remediation of contaminated sites is always an expensive proposition but natural attenuation can greatly reduce clean up costs. Concentration changes may result from dilution and dispersion and therefore a combination of concentration changes and isotopic enrichment can be used as evidence for the onset of natural attenuation (Gray et al. 2002; Kuder et al. 2005; Mancini et al. 2003; Chartrand et al. 2005). Methyl *tert*-butyl ether (MTBE) is rapidly mineralized by a variety of aerobic bacteria but from a practical point of view, the bulk of MTBE plumes are anaerobic and anaerobic biodegradation will be the more significant mechanism for natural attenuation (Bradley et al. 1999; Finneran and Lovley 2001). Degradation under anaerobic conditions (Somsamak et al. 2001) is slower and in most cases restricted to biotransformation of MTBE to *tert*-butyl alcohol (TBA). As a consequence, natural attenuation of anaerobic plumes tends to be relatively slow, resulting in the accumulation of *tert*-butyl alcohol (TBA) as MTBE disappears.

Anaerobic biodegradation of MTBE using stable carbon and hydrogen isotopes was documented by the work of Kuder et al. (2005). An initial study reported enrichment of carbon isotopes during anaerobic biodegradation of MTBE (Kolhatkar et al. 2002), but progress in method optimization also allowed determination of hydrogen isotope ratios of MTBE in aqueous samples at environmentally relevant concentrations. Having data on both carbon and hydrogen isotopes is particularly powerful, since the concurrent fractionation of C and H can prove that a field sample was degraded through the anaerobic pathway. If the

pathway was anaerobic, then the isotope data can also be used to calculate the extent of biodegradation using the Rayleigh equation described above. The calculated extent of biodegradation can be compared to overall attenuation in concentrations to evaluate the relative contribution of biodegradation.

Similar isotopic changes have also been observed for other compounds undergoing biodegradation, particularly in laboratory studies. In a study of the degradation of C₁–C₅ alkylbenzenes in crude oils, Wilkes et al. (2000) observed a shift in $\delta^{13}\text{C}$ of 4‰ for *o*-xylene after loss of 70% of the original material whereas a shift of 6‰ was observed for *o*-ethyltoluene. Similar results were obtained for sites contaminated with benzene, toluene, ethylbenzene and xylenes (BTEX) from a tanker truck accident (Meckenstock et al. 2002), a landfill leachate plume (Richnow et al. 2003), and a former gas works site (Griebler et al. 2004). Calculation of the residual substrate concentrations along such monitoring transects relies on knowing, or estimating R₀, the isotope ratio of the substrate in the source. This parent value (usually the most depleted in ¹³C) may be replaced by the isotope ratio of the substrate in the most upstream monitoring well near the source, if the source itself is not available, without changing the result of the calculation. A similar approach has been successfully used to estimate the extent of biodegradation for benzene at a contaminated site based on laboratory-derived carbon and hydrogen fractionation factors with good agreement between findings from the two elements (Mancini et al. 2002). At a former gas works site, carbon isotope fractionation of BTEX and naphthalenes during anaerobic degradation was observed (Griebler et al. 2004). The observed fractionation factors for naphthalenes were much smaller than for BTEX. It is not known yet if this is due to different rate-limiting steps during degradation or to larger number of carbon atoms in the naphthalene structure that “dilute” the measured isotope fractionation.

Chlorinated solvents, such as PCE, TCE and associated degradation products have received extensive coverage since the early work of Sherwood Lollar et al. (2001) mentioned above. Numerous studies have reported enrichment factors for the various degradation steps involved in the pathways for PCE to ethene (Song et al. 2002; Chu et al. 2004; Brungard et al. 2003). Latest developments relate to the incorporation of this information into fate and transport

models to more accurately quantify degradation of these compounds at contaminated sites (Van Breukelen and Prommer 2005).

Source Discrimination or Correlation

There are many situations in environmental forensics where GC and GCMS data may be ambiguous, or inconclusive, primarily as a result of weathering processes such as evaporation, photooxidation, water-washing, and biodegradation changing the distribution of components in the spilled material vs. the original sample (Palmer 1993). With the possibility of incorporating the isotopic data, primarily carbon or hydrogen isotopic data (Macko and Parker 1983; Wang et al. 2004; Glaser et al. 2005; Wen et al. 2005) and, in selected cases, chlorine, nitrogen, oxygen or sulfur isotopes (Sturchio et al. 1998; Beneteau et al. 1999; Reddy et al. 2000; Coffin et al. 2001; Shouakar-Stash et al. 2003) many of these ambiguities can be eliminated.

The isotopic composition of a specific compound, or the spilled material, will play little, if any, role in the task of actually identifying individual components in the contaminant. The power of stable isotopes is their ability to permit correlations between source samples and spilled samples even if the samples are weathered. Chemical fingerprinting of the n-alkane fraction in crude oils and refined products in combination with isotopic characterization of carbon in the individual homologues has been successfully used to allocate sources of sediment contamination (Rogers and Savard 1999; Smallwood et al. 2002) and bird feather oiling (Mansuy et al. 1997; Mazeas and Budzinski 2002). Hough et al. (2006) used the $\delta^{13}\text{C}$ values of individual n-alkanes to identify the source of hydrocarbons in soils contaminated with residual heavy or weathered petroleum wastes. A comprehensive review of the subject can be found in papers presented by Meier-Augenstein (1999) and Schmidt et al. (2004).

A study of gasolines from different retailers from the East Coast and Southwestern USA has showed different $\delta^{13}\text{C}$ fingerprints permitting discrimination between the samples (Smallwood et al. 2002). A combined 2-dimensional (carbon-hydrogen or carbon-chlorine) isotope analysis should provide the most robust fingerprinting tool. An example of 2D bulk isotope fingerprinting was shown by Davis et al.

(2005), who applied the technique as one of the lines of evidence to delineate hydrocarbon plumes at a former refinery site at Yukon Territory, Canada.

Determination of the origin of polycyclic aromatic hydrocarbons (PAHs) provides another challenging environmental problem. PAHs in the environment may be derived from sources such as coal tar, crude oils, to name a few. In many cases the chromatographic distributions of these compounds for different sources may be very similar and of little use in terms of distinguishing one source from another. On a regional scale, source apportionment of polycyclic aromatic hydrocarbons (PAHs) both in the atmosphere and in sediment records has been studied intensely using $\delta^{13}\text{C}$ analysis. A combination of concentration measurements and $\delta^{13}\text{C}$ isotopic analysis of individual PAHs in sediments from Lake Erie permitted three areas with different contamination histories to be distinguished. Furthermore, it could be shown that the main emission pathway for PAHs was fluvial input (Smirnov et al. 1998). A significant study to evaluate the use of stable isotopes to differentiate PAHs derived from urban backgrounds vs. those derived from coal gasification plants has been published (Saber et al. 2003, 2005; Craig et al. 2005). Coal-derived PAHs released during different thermal conversion processes (combustion, pyrolysis, gasification) could be distinguished on the basis of their isotopic compositions conserved in soil (McRae et al. 1999, 2000). Extremely isotopically light PAHs ($\delta^{13}\text{C}$ from -31 to -62‰) in lagoon sediments near Ravenna (Italy) indicated that the primary source of these PAHs was a nearby plant using biogenic methane as a feedstock ($\delta^{13}\text{C}$ from -69 to -73‰) rather than a plant using isotopically heavier petrogenic feedstocks (McRae et al. 2000). $\delta^{13}\text{C}$ composition of perylene was used to substantiate the hypothesis that in tropical environments recent biological sources of PAHs related to termites are important, whereas pyrolytic sources dominate in temperate climate (Wilcke et al. 2002). PAHs in atmospheric particles resulting from natural burning processes have been distinguished from those stemming from various anthropogenic combustion processes by fingerprinting and $\delta^{13}\text{C}$ analysis of individual compounds (Norman et al. 1999; Okuda et al. 2002a, b). In Chinese urban areas, PAH $\delta^{13}\text{C}$ analysis was successfully used to identify either vehicle exhaust or coal combustion as major PAH source (Okuda et al. 2002a, b). In contrast, PAH fingerprinting did not yield

equivalent information. Many of these studies show the necessity of combining chemical fingerprinting techniques and with compound-specific isotope analysis.

The use of $\delta^{13}\text{C}$ and $\delta^{15}\text{N}$ isotope analyses in field and laboratory experiments to trace the sources of TNT in contaminated soils and groundwater has been evaluated by Coffin et al. (2001). Their results allowed them to distinguish five different sources of TNT on the basis of the carbon and nitrogen isotope ratios, highlighting the potential of this approach. Once again it should be noted that with the capability of determining the N isotope composition of individual compounds, in the near future one could expect to see an increase in the use of the N isotopes to study the fate of N-containing pesticides and sources (animal waste, fertilizer, sewage) of excess nitrate (the standard being 10 mg/L) in groundwater.

The widespread occurrence, and stability, of chlorinated contaminants in the environment, PCBs, dioxins, DDT, and a wide variety of other compounds, has led to an increased interest in the possible use of the chlorine isotope ratios as a means of studying the origin, transport, and fate of these compounds in the environment. A paper by Reddy et al. (2000) described the study of a number of PCBs from a variety of sources and noted that the $\delta^{37}\text{Cl}$ values fell within a narrow range from -3.4 to 2.1‰ but found no correlation between the mass percent of chlorine and $\delta^{37}\text{Cl}$ values. It should be noted that the samples used in this particular study were obtained from environmental standard suppliers who in turn had obtained the materials from Bayer (Germany) and Caffaro (Italy). In the US there was only one manufacturer of PCBs, namely Monsanto. The variability observed in the standards was suggested to arise from differences in the starting materials, synthetic methods, purification, or postproduction storage and handling of these products or some combination of all these factors. PCBs extracted from sediments ranged from -4.54 to -2.25‰ . These isotopic variations suggest that $\delta^{37}\text{Cl}$ could be a useful tool for tracing the sources and fate of PCBs. In a limited number of experiments there did not appear to be any significant differences between the $\delta^{37}\text{Cl}$ values for individual congeners. It can be anticipated that with the development of methods that permit routine on-line measurements of Cl isotopes, described above, that there will more publications describing the use of Cl isotopes in environmental forensics.

Jarman et al. (1998) examined the carbon isotope variations on individual PCB congeners in a variety of commercial PCBs. The bulk carbon isotope values for individual PCBs varied from -22.34 to -26.95% , whereas individual congeners showed values ranging from -18.65 to -27.98% . Large differences were observed for individual congeners between mixtures and the $\delta^{13}\text{C}$ values for individual congeners showed a depletion of ^{13}C with increasing chlorine content probably as result of a kinetic isotope effect caused by the position of the chlorine atom on the biphenyl molecule. Such a wide diversity of carbon isotope values may prove to be very powerful in source determination of PCBs in the environment.

In the past few years attention has turned to the more volatile chlorinated compounds such as PCE, TCE, and related degradation products. These chlorinated hydrocarbons have been used in a variety of industries since the 1940s including electronic and instrument manufacturing, aerospace, machine, printing and dry cleaning industries (Beneteau et al. 1999; Hunkeler et al. 1999; Jendrzewski et al. 2001). They have been, and continue to be, the cause of major environmental contaminants in water as a result of spills, leaks, or improper disposal. As these compounds are DNAPLs (dense non-aqueous phase liquids), they tend to persist for a long time in groundwater systems (Feenstra and Cherry 1988). For example, TCE is detected in approximately 19% of groundwater samples worldwide, at mean concentrations of 27.3 ppb (IARC 1995). At contaminated sites, the complex dispersal of these compounds, the presence of different contaminants sources and their ability to migrate long distances often leads to complex plumes of dissolved chlorinated solvents and related degradation products, which are difficult to trace to source (Huang et al. 1999). As with some other organic groundwater contaminants like MTBE, GCIRMS has been recognized as a valuable technique in the investigation of the sources and behavior of chlorinated compounds. Most of the work to date with the chlorinated compounds has been related to utilization of the carbon isotopes and, to a lesser extent, hydrogen isotopes (Shouakar-Stash et al. 2006). With the abundance of chlorinated hydrocarbons in the environment there is a growing interest in utilizing chlorine isotopes as an additional tool for source apportionment (Sakaguchi-Söder et al. 2007).

The availability of online $\delta^{37}\text{Cl}$ measurements will be an asset in the degradation studies of chlorinated solvents that, with the few exceptions mentioned above have been limited to online $\delta^{13}\text{C}$ measurements (Hunkeler et al. 1999; Bloom et al. 2000; Sherwood Lollar et al. 2001; Slater et al. 2001). Some studies have investigated continuous GCIRMS measurements of $\delta^{37}\text{Cl}$ of inorganic chlorine in environmental samples (Wassenaar and Koehler 2004; Shouakar-Stash et al. 2005a, b). Their results on inorganic species, particularly perchlorate (Shouakar-Stash et al. 2005a, b; Sturchio et al. 2003, 2011), are promising and illustrate the potential of on-line chlorine assays in environmental samples.

31.2 Summary and Future Directions

This chapter has discussed the evolution of stable isotopes in applications related to both hydrocarbon exploration and environmental forensics. Applications in hydrocarbon exploration have a much longer history than environmental forensics. The early applications in hydrocarbon exploration utilized bulk isotopes, primarily carbon, but by the time environmental forensics started to evolve two decades ago, a significant analytical development had occurred, namely combined gas chromatograph-isotope ratio mass spectrometry. As a result it is now possible to obtain the carbon and hydrogen isotope compositions of individual compounds within complex mixtures. Even more important is the ability to obtain isotopic compositions of trace amounts of groundwater contaminants down to the low ppb levels. This has proven to be exceedingly valuable both in determining the source of contaminants and also the onset and extent of natural attenuation. In both of these areas, stable isotopes are one piece of the analytical tool box, which on their own may not provide a unique answer, but one integrated into the rest of the analytical data can assist in providing a comprehensive solution to the problem at hand.

In terms of future developments in both of these areas, they are many and varied, and a number of future applications are possible in both areas. First in the case of crude oils, the biomarker concept has been established for many years and in both of the topics discussed in this paper, biomarkers are used

extensively for correlation purposes. These correlations are undertaken by GCMS and ancillary techniques such as multiple ion detection. However there are few papers in the literature that discuss the isotopic compositions of individual biomarkers in crude oils. The reason being that these compounds are present in relatively low concentrations and generally cannot be seen on a regular gas chromatogram, hence it is not possible to get isotopic compositions of individual biomarkers on a routine basis. The need here is to develop more routine molecular sieving methods that can be used to isolate concentrates of the biomarkers and then determine the isotopic composition of these compounds and provide another fingerprinting tool for correlation purposes.

Secondly in the area of environmental forensics, there is undoubtedly a need to continue the development of routine methods for the determination of stable chlorine isotopes of individual compounds, particularly groundwater contaminants. These values can then be used in conjunction with the carbon and hydrogen isotopes to provide a more comprehensive set of isotope fingerprints for correlation purposes and also in natural attenuation studies. In another area of environmental forensics, continued development of fate and transport models that can be used to quantify the extent of degradation using isotope data will be extremely beneficial to environmental forensic investigators.

In both areas, it is now possible to routinely determine carbon and hydrogen isotopes of individual compounds. As mentioned above, methods are being developed for the determination of the chlorine isotopes. There are numerous potential applications for the utilization of nitrogen isotopes, particularly in the area of environmental forensics where it will be very useful for investigations involving explosive residues. The methods are in place and it is possible to do this but it still requires a great deal of method development before it can be considered to be a routine application.

Many of the applications in environmental forensics have been directed towards studies of natural attenuation. However in recent years, more attention has been directed to investigating degradation mechanisms for individual compounds based on enrichment factors. This is particularly important in the attenuation studies since most plumes are not homogeneous and some parts of the plume may be aerobic and other parts anaerobic. Degradation rates are different in the

different parts of the plume and it is necessary to understand rates and mechanisms of individual compounds in order to quantify degradation rates.

In hydrocarbon exploration, it is a little more difficult to see additional areas where novel applications may occur apart from those mentioned above. There is definitely room for more studies directed towards using the isotopes to determine the origin of individual compounds. However there is a need to develop better separation methods since that is the more significant problem.

In summary utilization of stable isotopes has been extremely beneficial for both of these areas. While they do not necessarily provide the silver bullet that answers all problems, when integrated with other geochemical data, it provides a powerful package of information that can be applied to many different problems.

References

- Aizenshtat Z, Baedeker MJ, Kaplan IR (1973) Distribution and diagenesis of organic compounds in JOIDES sediment from Gulf of Mexico and Western Atlantic. *Geochim Cosmochim Acta* 37:1881–1898
- Alexander R, Kagi RI, Larcher AV (1982) Clay catalysis of aromatic hydrogen-exchange reactions. *Geochim Cosmochim Acta* 46:219–222
- Andrusevich VE, Engel MH, Zumberge JE, Brothers LA (1998) Secular, episodic changes in stable carbon isotope composition of crude oils. *Chem Geol* 152:59–72
- Beneteau KM, Aravena R, Frapce SK (1999) Isotopic characterization of chlorinated solvents-laboratory and field results. *Org Geochem* 30(8):739–753
- Bernard BB, Brooks JM, Sackett WM (1976) Natural gas seepage in the Gulf of Mexico. *Earth Planet Sci Lett* 31:48–54
- Berner U, Faber E (1996) Empirical carbon isotope/maturity relationships for gases from algal kerogens and terrigenous organic matter, based on dry, open-system pyrolysis. *Org Geochem* 24:947–955
- Berner U, Faber E, Scheeder G, Panten D (1995) Primary cracking of algal and landplant kerogens; kinetic models of isotope variations in methane, ethane and propane; processes of natural gas formation. *Chem Geol* 126:233–245
- Bigeleisen J (1965) Chemistry of isotopes. *Science* 147: 463–471
- Bjørøy M, Hall K, Gillyon P, Jumeau J (1992) Carbon isotope variations in n-alkanes and isoprenoids in whole oils. *Chem Geol* 93:13–20
- Bloom Y, Aravena R, Hunkeler D, Edwards E, Frapce SK (2000) Carbon isotope fractionation during microbial dechlorination of trichloroethene, cis-1,2-dichloroethene, and vinyl chloride: implications for assessment of natural attenuation. *Environ Sci Technol* 34(13):2768–2772

- Boreham CJ, Dowling LM, Murray AP (1995) Biodegradation and maturity influences on n-alkane isotopic profiles in terrigenous sequences. In: Abstracts of 17th International Meeting on Organic Geochemistry, San Sebastian, Spain, pp 539–541
- Bradley PM, Landmeyer JE, Chapelle FH (1999) Aerobic mineralization of MTBE and tert-butyl alcohol by stream-bed sediment micro-organisms. *Environ Sci Technol* 33(11): 1877–1879
- Bray EE, Evans ED (1964) Distribution of n-paraffins as a clue to recognition of source beds. *Geochim Cosmochim Acta* 22:2–15
- Brooks PW, Eglinton G, Gaskell SJ, Maxwell JR, McHugh DJ, Philp RP (1976) Lipids of recent sediments part I: straight-chain hydrocarbons and carboxylic acids of some temperate lacustrine and sub-tropical lagoonal/tidal flat sediments. *Chem Geol* 18:21–38
- Brooks PW, Eglinton G, Gaskell SJ, Maxwell JR, McHugh DJ, Philp RP (1977) Lipids of recent sediments. Part II: branched and cyclic alkanes and alkanolic acids of some temperate lacustrine and subtropical lagoonal/tidal flat sediments. *Chem Geol* 20:189–204
- Brown FS, Baedeker MJ, Nissenbaum A, Kaplan IA (1972) Early diagenesis in a reducing fjord, Saanch Inlet, British Columbia—III. Changes in organic constituents of sediment. *Geochim Cosmochim Acta* 36:1185–1203
- Brungard KL, Munakata-Marr J, Johnson CA, Mandernack KW (2003) Stable carbon isotope fractionation of trans 1,2-dichloroethylene during co-metabolic degradation by methanotrophic bacteria. *Chem Geol* 195:59–67
- Burgoyne TW, Hayes JM (1998) Quantitative production of H₂ by pyrolysis of gas chromatographic effluents. *Anal Chem* 70:5136–5141
- Calvin M (1969) *Chemical evolution*. Oxford University Press, Oxford, p 278
- Chartrand MMG, Morrill PL, Lacrampe-Couloume G, Sherwood Lollar B (2005) Stable isotope evidence for biodegradation of chlorinated ethenes at a fractured bedrock site. *Environ Sci Technol* 39(13):4848–4856
- Chu K-H, Mahendra S, Song DL, Conrad ME, Alvarez-Cohen L (2004) Stable carbon isotope fractionation during aerobic biodegradation of chlorinated ethenes. *Environ Sci Technol* 38:3126–3130
- Chung HM, Brand SW, Grizzle PL (1981) Carbon isotope geochemistry of Paleozoic oils from Big Horn Basin. *Geochim Cosmochim Acta* 45:1803–1815
- Chung HM, Gormly JR, Squires RM (1988) Origin of gaseous hydrocarbons in subsurface environments: theoretical considerations of carbon isotope distribution. *Chem Geol* 71:97–103
- Chung HM, Rooney MA, Toon MB, Claypool GE (1992) Carbon isotope composition of marine crude oils. *Bull Am Assoc Petrol Geol* 76:1000–1007
- Clayton CJ (1991a) Carbon isotope fractionation during natural-gas generation from kerogen. *Mar Petrol Geol* 8:232–240
- Clayton CJ (1991b) Effect of maturity on carbon isotope ratios of oils and condensates. *Org Geochem* 17:887–899
- Coffin RB, Miyares PH, Kelley CA, Cifuentes LA, Reynolds CM (2001) $\delta^{13}\text{C}$ and $\delta^{15}\text{N}$ isotope analysis of TNT; two dimensional source identification. *Environ Toxicol Chem* 20 (12):2676–2680
- Cook PF (1991) *Enzyme mechanism from isotope effects*. CRC Press, Boca Raton
- Cortes J, Rincon J, Jaramillo J, Philp R, Allen J (2010) Biomarkers and compound-specific stable carbon isotope of n-alkanes in crude oils from Eastern Llanos Basin, Colombia. *J S Am Earth Sci* 29:198–213
- Craig H (1953) The geochemistry of the stable carbon isotopes. *Geochim Cosmochim Acta* 3:53–92
- Craig DR, Mauro D, Saber D, Sirivedhin T, Philp RP, Allen JA (2005) Carbon isotope ratios of PAHs in urban background soil. In: *Third International Conference on Remediation of Contaminated Sediments*. 57th Annual Meeting American Academy of Forensic Sciences, New Orleans, 21–26 Feb 2005
- Cuishan Z, Hong Z, Peirong W, Zebo Z, Anding C (2003) The distribution and carbon isotopic composition of unusual polycyclic alkanes in the Cretaceous Lengshuiwu Formation, China. *Org Geochem* 34:1027–1035
- Davis A, Howe B, Nicholson A, McCaffery S, Hoenke KA (2005) Use of geochemical forensics to determine release eras of petrochemicals to groundwater, Whitehorse, Yukon. *Environ Forensic* 6:253–271
- Dawson D, Grice K, Alexander R, Edwards D (2007) The effect of source and maturity on the stable isotopic compositions of individual hydrocarbons in sediments and crude oils from the Vulcan Sub-basin, Timor Sea, Northern Australia. *Org Geochem* 38:1015–1038
- Eckelmann W, Broecker W, Whitlock D, Allsup J (1962) Implications of carbon isotopic composition of total organic carbon of some recent sediments and ancient oils. *Am Assoc Pet Geol Bull* 46:699–704
- Eglinton G, Calvin M (1967) Chemical fossils. *Sci Am* 261:23–32
- Ellis L, Brown A, Schoell M, Uchytel Y (2003) Mud gas isotope logging (MGIL) assists in oil and gas drilling operations. *Oil Gas J* 101:32–34
- Elsner N, Zwank L, Hunkeler D, Schwarzenbach RP (2005) A new concept linking observable stable isotope fractionation to transformation pathways of organic pollutants. *Environ Sci Technol* 39:6896–6916
- Faure G (1986) *Principles of isotope geology*. Wiley, New York
- Faure G, Mensing TM (2005) *Isotopes: principles and applications*. Wiley, Hoboken
- Feenstra S, Cherry JA (1988) Subsurface contamination by dense non-aqueous phase liquid (DNAPL) chemicals. In: *International Groundwater Symposium*. International Association of Hydrology, Halifax, Nova Scotia
- Fildani A, Hanson AD, Chen Z, Moldowan JM, Graham SA, Arriola PP (2005) Geochemical characteristics of oil and source rocks and implications for petroleum systems, Talara Basin, northwest Peru. *Am Assoc Pet Geol Bull* 89:1519–1545
- Finneran KT, Lovley DR (2001) Anaerobic degradation of methyl tert-butyl ether (MTBE) and tert-butyl alcohol (TBA). *Environ Sci Technol* 35(9):1785–1790
- Freeman KH, Hayes JM, Trendel JM, Albrecht P (1990) Evidence from carbon isotope measurements for diverse origins of sedimentary hydrocarbons. *Nature* 343:254–256
- Fuex A (1977) The use of stable carbon isotopes in hydrocarbon exploration. *J Geochem Explor* 7:155–188
- Galimov E (1968) *Geochemistry of stable isotopes*. Nedra, Moscow

- Galimov E (1973) Carbon isotopes in oil–gas geology. Nedra, Moscow
- Galimov EM (1985) The biological fractionation of isotopes. Academic, Orlando
- Galimov E, Frick M (1985) Isotopic method of source-rocks diagnostic. *Geochemistry* 10:1474–1486
- George SC, Boreham CJ, Minifie SA, Teerman SC (2002) The effect of minor to moderate biodegradation on C₅ to C₉ hydrocarbons in crude oils. *Org Geochem* 33:1293–1317
- Glaser B, Dreyer A, Bock M, Fiedler S, Mehring M, Heitmann T (2005) Source apportionment of organic pollutants of a highway-traffic-influenced urban area in Bayreuth (Germany) using biomarker and stable carbon isotope signatures. *Environ Sci Technol* 39:3911–3917
- Gormley JR, Sackett WM (1977) Carbon isotope evidence for the maturation of marine lipids. In: Campos R, Goni J (eds) *Advances in organic geochemistry 1975*. Enadisma, Madrid, pp 321–339
- Gray R, Lacrampe-Couloume G, Gandhi D, Scow KM, Wilson RD, Mackay DM, Sherwood Lollar B (2002) Carbon and hydrogen isotopic fractionation during biodegradation of methyl tert-butyl ether. *Environ Sci Technol* 36(9):1931–1938
- Griebler C, Safinowski M, Vieth A, Richnow HH, Meckenstock RU (2004) Combined application of stable carbon isotope analysis and specific metabolites determination for assessing in situ degradation of aromatic hydrocarbons in a tar oil-contaminated aquifer. *Environ Sci Technol* 38(2):617–631
- Gürgey K, Philp P, Clayton C, Emiroglu H, Siyako M (2005) Geochemical and isotopic approach to maturity/source/mixing estimations for natural gas and associated condensates in the Thrace Basin, NW Turkey. *Appl Geochem* 20:2017–2037
- Han J, McCarthy ED, van Hoesen W, Calvin M, Bradley WH (1968) Organic geochemical studies. II-preliminary report on the distribution of aliphatic hydrocarbons in algae, in bacteria and in recent lake sediments. *Proc Nat Acad Sci USA* 59:29–33
- Hanson D (1999) MTBE-villain or victim. *Chem Eng News* 19 October, p 49
- Hatcher PG, Spiker EC, Szeverenyi NM, Maciel GE (1983) Selective preservation and origin of petroleum-forming aquatic kerogen. *Nature* 305:498–501
- Hayes JM, Takigiku R, Ocampo R, Callot HJ, Albrecht P (1987) Isotopic composition and probable origins of organic molecules in the Eocene Messel Shale. *Nature* 329:48–51
- Hayes JM, Freeman KH, Popp BN, Hoham CH (1990) Compound-specific isotopic analysis: a novel tool for reconstruction of ancient biogeochemical processes. *Org Geochem* 16(4–6):1115–1128
- Heraty LJ, Fuller ME, Huang L, Abrajano T, Sturchio NC (1999) Isotopic fractionation of carbon and chlorine by microbial degradation of dichloromethane. *Org Geochem* 30(8):739–753
- Hilkert AW, Douthitt CB, Schluter HJ, Brand WA (1999) Isotope ratio monitoring gas chromatography/mass spectrometry of D/H by high temperature conversion isotope ratio mass spectrometry. *Rapid Commun Mass Spectrom* 13:1226–1230
- Hill R, Jarvie D, Zumberge J, Henry M, Pollastro R (2007) Oil and gas geochemistry and petroleum systems of the Fort Worth Basin. *Am Assoc Pet Geol Bull* 91:445–473
- Hoeffs J (2004) *Stable isotope geochemistry*. Springer, Berlin
- Hoeffs J, Frey M (1976) The isotopic composition of carbonaceous matter in metamorphic profile from the Swiss Alps. *Geochim Cosmochim Acta* 40:945–951
- Holt BD, Sturchio NC, Abrajano T, Heraty LJ (1997) Conversion of chlorinated volatile compounds to carbon dioxide and methyl chloride for isotopic analysis of carbon and chlorine. *Anal Chem* 69(14):2727–2733
- Hood A, Gutjahr CCM, Heacock RL (1975) Organic metamorphism and the generation of petroleum. *Am Assoc Pet Geol Bull* 59:986–996
- Hough RL, Whittaker M, Fallick AE, Preston T, Farmer JG, Pollard SJ (2006) Identifying source correlation parameters for hydrocarbon wastes using compound-specific isotope analysis. *Environ Pollut* 143:489–498
- Huang Y, Eglinton G, Ineson P, Latter PM, Bol R, Harkness DD (1997) Absence of carbon isotope fractionation of individual n-alkanes in a 23-year field decomposition experiment with *Calluna vulgaris*. *Org Geochem* 26:497–501
- Huang L, Sturchio NC, Abrajano T, Heraty LJ, Holt BD (1999) Carbon and chlorine isotope fractionation of chlorinated aliphatic hydrocarbons by evaporation. *Org Geochem* 30:777–785
- Hunkeler D, Aravena R, Butler BJ (1999) Monitoring microbial dechlorination of tetrachloroethene (PCE) in groundwater using compound-specific stable carbon isotope ratios: microcosm and field studies. *Environ Sci Technol* 33(16):2733–2738
- Hunkeler D, Andersen N, Aravena R, Bernasconi SM, Butler BJ (2001) Hydrogen and carbon isotope fractionation during aerobic biodegradation of benzene. *Environ Sci Technol* 35:3462–3467
- Hunkeler D, Meckenstock RU, Sherwood Lollar B, Schmidt CT, Wilson JT (2008) A guide for assessing biodegradation and source identification of organic ground water contaminants using compound specific isotope analysis (CSIA). Office of Research and Development, Ada, OK: EPA 600/R-08/148
- Hunt J (1970) The significance of carbon isotope variations in marine sediments. In: Hobson GD, Speers GC (eds) *Advances in organic geochemistry*. Pergamon, Oxford
- Hunt JM (1996) *Petroleum geochemistry and geology*. W.H. Freeman, New York
- IARC (1995) Dry cleaning, some chlorinated solvents and other industrial chemicals. IARC Monographs on the evaluation of carcinogenic risk of chemicals to humans:63. International Agency for Research on Cancer, Lyon
- Inaba T, Suzuki N (2003) Gel permeation chromatography for fractionation and isotope ratio analysis of steranes and triterpanes in oils. *Org Geochem* 34:635–641
- James AT (1983) Correlation of natural-gas by use of carbon isotopic distribution between hydrocarbon components. *Am Assoc Pet Geol Bull* 67:1176–1191
- Jarman WM, Hilkert A, Bacon CE, Collister JW, Ballschmitter P, Risebrough RW (1998) Compound specific carbon isotope analysis of Aroclors, Clophens, Kaneclors, and Phenoclor. *Environ Sci Technol* 32(6):833–836
- Jendrzewski N, Eggenkamp HG, Coleman ML (2001) Characterization of chlorinated hydrocarbons from chlorine and carbon isotopic compositions: scope of application to environmental problems. *Appl Geochem* 16(9–10):1021–1031

- Karlsen DA, Nyland B, Flood B, Ohm SE, Brekke T, Olsen S, Backer-Owe K (1995) In: Cubbit JM, England WA (eds) Petroleum geochemistry of the Haltenbanken, Norwegian Continental Shelf. The Geochemistry of Reservoirs Geological Society:86. Special Publication, London
- Killops S, Killops V (2005) Introduction to organic geochemistry. Blackwell, Oxford
- Kimble BJ (1972) The Geochemistry of Tertiary Hydrocarbons Ph.D. Thesis, University of Bristol pp. 302
- Kjeldsen P, Christophersen M, Broholm P, Höhener R, Aravena R, Hunkeler D (2003) Biodegradation of fuel vapours in the vadose zone at Airbase Værløse, Denmark. In: D. Halm and P. Grathwohl (eds), Second International Workshop on Groundwater Risk Assessment at Contaminated sites and Integrated Soil and Water Protection, Tuebingen, 20–21 March 2003. *Tübinger Geowissenschaftliche Arbeiten* 69: 31–39
- Knoll AN (1991) End of proterozoic eon. *Sci Am* 265:64–73
- Kolhatkar R, Kuder T, Philp P, Allen J, Wilson JT (2002) Use of compound-specific stable carbon isotope analyses to demonstrate anaerobic biodegradation of MTBE in groundwater at a gasoline release site. *Environ Sci Technol* 36(23): 5139–5146
- Kopinke F, Georgi A, Voskamp M, Richnow HH (2005) Carbon isotope fractionation of organic contaminants due to retardation on humic substances: implications for natural attenuation studies in aquifers. *Environ Sci Technol* 39:6052–6062
- Kuder T, Wilson J, Kaiser P, Kolhatkar R, Philp P, Allen J (2005) Enrichment of stable carbon and hydrogen isotopes during anaerobic biodegradation of MTBE: microcosm and field evidence. *Environ Sci Technol* 39(1):213–220
- Kuder T, Philp RP, Allen J (2009) Effects of volatilization on carbon and hydrogen isotope ratios of MTBE. *Environ Sci Technol* 43(6):1763–1768
- Kvenvolden K, Squires R (1967) Carbon isotopic composition of crude oils from Ellenburger Group (Lower Ordovician), Permian basin, West Texas and eastern New Mexico. *Am Assoc Pet Geol Bull* 51:1293–1303
- Kvenvolden KA, Hostettler FD, Rapp JB, Carlson PR (1993) Hydrocarbons in oil residues on beaches of islands of Prince William Sound, Alaska. *Mar Pollut Bull* 26:24–29
- Kvenvolden KA, Hostettler FD, Carlson PR, Bapp JB, Threlkeld CN, Warden A (1995) Ubiquitous tar balls with a California-source signature on shorelines of Prince William Sound, Alaska. *Environ Sci Technol* 29(10):2684–2694
- Lesser EL, Johnson PC, Aravena R, Spinnler GE, Bruce CL, Salanitro JP (2008) An evaluation of compound specific isotope analyses for assessing the biodegradation of MTBE at Port Hueneme, CA. *Environ Sci Technol* 42:6637–6643
- Lewan M (1983) Effects of thermal maturation on stable organic carbon isotopes as determined by hydrous pyrolysis of Woodford Shale. *Geochim Cosmochim Acta* 47:1471–1479
- Lewan M, Williams J (1987) Evaluation of petroleum generation from resinites by hydrous pyrolysis. *Am Assoc Pet Geol Bull* 71:207–214
- Lewan M, Winters J, McDonald J (1979) Generation of oil-like pyrolysates from organic-rich shales. *Science* 203:896–899
- Li M, Larter S, Mei B, Bjorøy M (1995) Compound specific isotopic compositions for end members of crude oils and related source rocks from the Liaohai Basin: paleoenvironmental implications. In: Grimalt JO, Dorronsoro C (eds) Organic geochemistry: developments and application to energy, climate and human history (selected papers from the 17th International Meeting on Organic Geochemistry). A.I.G.O.A., Spain, pp 38–40
- Li M, Riediger CL, Fowler MG, Snowdon LR (1997) Unusual polycyclic aromatic hydrocarbons in the Lower Cretaceous Ostracode Zone sedimentary and related oils of the Western Canada Sedimentary Basin. *Org Geochem* 27:439–448
- Li M, Huang YS, Obermajer M, Jiang CQ, Snowdon LR, Fowler MG (2001) Hydrogen isotopic compositions of individual alkanes as a new approach to petroleum correlation: case studies from the Western Canada Sedimentary Basin. *Org Geochem* 32:1387–1399
- Liao Y, Geng A, Xiong Y, Liu D, Lu J, Liu J, Zhang H, Geng X (2004) The influence of hydrocarbon expulsion on carbon isotopic compositions of individual n-alkanes in pyrolysates of selected terrestrial kerogens. *Org Geochem* 35:1479–1488
- Liu J, Geng A, Xiong Y (2006) The application of stable carbon and hydrogen isotopic compositions of individual n-alkanes to Paleozoic oil/source rock correlation enigmas in the Huanghua depression, China. *J Petrol Sci Eng* 54:70–78
- Macko SA, Parker PL (1983) Stable nitrogen and carbon isotope ratios of beach tars on south Texas barrier islands. *Mar Environ Res* 10:93–103
- Mancini SA, Lacrampe-Couloume G, Jonker H, van Breukelen BN, Groen J, Volkering F, Sherwood Lollar B (2002) Hydrogen isotopic enrichment: an indicator of biodegradation at a petroleum hydrocarbon contaminated field site. *Environ Sci Technol* 36(11):2464–2470
- Mancini SA, Ulrich A, Lacrampe-Couloume G, Sleep B, Edwards E, Sherwood Lollar B (2003) Carbon and hydrogen isotopic fractionation during anaerobic biodegradation of benzene. *Appl Environ Microbiol* 69:191–198
- Mansuy L, Philp RP, Allen J (1997) Source identification of oil spills based on the isotopic composition of individual components in weathered oil samples. *Environ Sci Technol* 31(12):3417–3425
- Masterson WD, Dzou LIP, Holba AG, Fincannon AL, Ellis L (2001) Evidence for biodegradation and evaporative fractionation in West Sak, Kuparuk and Prudhoe Bay field areas, North Slope, Alaska. *Org Geochem* 32:411–441
- Matthews DE, Hayes JM (1978) Isotope-ratio-monitoring gas chromatography mass spectrometry. *Anal Chem* 50:1465–1473
- Mazeas L, Budzinski H (2002) Molecular and stable carbon isotopic source identification of oil residues and oiled bird feathers sampled along the Atlantic Coast of France after the Erika oil spill. *Environ Sci Technol* 36(2):130–137
- Mazeas L, Budzinski H, Raymond N (2002) Absence of stable carbon isotopic fractionation of saturated and polycyclic aromatic hydrocarbons during aerobic bacterial biodegradation. *Org Geochem* 33:1259–1272
- McKelvie JR, Mackay DM, de Sieyes NR, Lacrampe-Couloume G, Sherwood Lollar B (2007) Quantifying MTBE degradation in the Vandenberg Air Force Base ethanol release study using stable carbon isotopes. *J Contam Hydrol* 94:157–165
- McRae C, Sun C, Snape CE, Fallick AE, Taylor D (1999) $\delta^{13}\text{C}$ values of coal-derived PAHs from different processes and their application to source apportionment. *Org Geochem* 30:881–889

- McRae C, Snape CE, Sun C, Fabbri D, Tartari D, Trombini C, Fallick AE (2000) Use of compound-specific stable isotope analysis to source anthropogenic natural gas-derived polycyclic aromatic hydrocarbons in a Lagoon sediment. *Environ Sci Technol* 34:4684–4686
- Meckenstock RU, Morasch B, Kastner M, Vieth A, Richnow HH (2002) Assessment of bacterial degradation of aromatic hydrocarbons in the environment by analysis of stable carbon isotope fractionation. *Water Air Soil Pollut Focus* 2:141–152
- Meier-Augenstein W (1999) Applied gas chromatography coupled to isotope ratio mass spectrometry. *J Chromatogr A* 842 (1–2):351–371
- Melander L, Saunders WH (1980) Reaction rates of isotopic molecules. Wiley, New York
- Mello MR, Telnaes N, Gaglianone PC, Chicarelli MI, Brassell SC, Maxwell JR (1988) Organic geochemical characterization of depositional palaeoenvironments of source rocks and oils in Brazilian marginal basins. *Org Geochem* 13:31–45
- Moldowan JM, Seifert W, Gallegos E (1985) Relationship between petroleum composition and depositional environment of petroleum source rocks. *Am Assoc Pet Geol Bull* 69:1255–1268
- Moldowan JM, Dahl JE, Huizinga BJ, Jacobson SR, Taylor DW (1993) The relationship of angiosperms and oleanane in petroleum through geologic time. *Am Assoc Pet Geol Bull* 77:334–335
- Murphy BL, Morrison RD (2002) Introduction to environmental forensics. Academic, New York
- Norman AL, Hopper JF, Blanchard P, Ernst D, Brice K, Alexandrovi N, Klouda G (1999) The stable carbon isotope composition of atmospheric PAHs. *Atmos Environ* 33(17): 2807–2814
- Numata M, Nakamura N, Koshikawa H, Terashima Y (2002) Chlorine isotope fractionation during reductive dechlorination of chlorinated ethenes by anaerobic bacteria. *Environ Sci Technol* 36(20):4389–4394
- O'Leary M (1981) Carbon isotope fractionation in plants. *Phytochemistry* 20(553):567
- Odden W, Barth T, Talbot M (2002) Compound-specific carbon isotope analysis of natural and artificially generated hydrocarbons in source rocks and petroleum fluids from offshore Mid-Norway. *Org Geochem* 33:47–65
- Okuda T, Kumata H, Zakaria MP, Naraoka H, Ishiwatari R, Takada H (2002a) Source identification of Malaysian atmospheric polycyclic aromatic hydrocarbons nearby forest fires using molecular and isotopic compositions. *Atmos Environ* 36:611–618
- Okuda T, Kumata H, Naraoka H, Ishiwatari R, Takada H (2002b) Vertical distributions and $\delta^{13}\text{C}$ isotopic compositions of PAHs in Chidorigafuchi Moat sediment, Japan. *Org Geochem* 33(7):843–848
- Pallasser RJ (2000) Recognizing biodegradation in gas/oil accumulations through the $\delta^{13}\text{C}$ compositions of gas components. *Org Geochem* 31:1363–1373
- Palmer SE (1993) Effect of biodegradation and water-washing on crude oil composition. In: Engel MH, Macko SE (eds) *Organic geochemistry*. Plenum, New York, pp 511–534
- Park R, Epstein S (1960) Carbon isotope fractionation during photosynthesis. *Geochim Cosmochim Acta* 21:110–126
- Peters KE, Fowler MG (2002) Applications of petroleum geochemistry to exploration and reservoir management. *Org Geochem* 33(1):5–36
- Peters KE, Rohrback BG, Kaplan IR (1981) Carbon and hydrogen stable isotope variations in kerogen during laboratory-simulated thermal maturation. *Am Assoc Pet Geol Bull* 65:501–508
- Peters K, Moldowan JM, Driscoll AR, Demaison GJ (1989) Origin of Beatrice oil by co-sourcing from Devonian and Middle Jurassic source rocks, Inner Moray Firth, United Kingdom. *Am Assoc Pet Geol Bull* 73:454–471
- Peters K, Kontorovich AEh, Moldowan JM, Andrushevich VE, Huizinga BJ, Demaison GJ, Stasova OF (1993) Geochemistry of selected oil and rocks from the Central Portion of the West Siberian Basin Russia. *Am Assoc Pet Geol Bull* 77:863–887
- Peters KE, Walters CC, Moldowan JM (2005) *The biomarker guide*. Cambridge University Press, Cambridge
- Philp RP (1996) *Reservoir geochemistry*. The University of Oklahoma, Norman
- Philp RP (2003) Formation and geochemistry of oil and gas. In: McKenzie F (vol ed), Holland HD, Turekian K (Ex. eds), *Treatise on geochemistry*, vol. 7, Ch 10. Elsevier, New York, pp 223–256
- Philp RP, Crisp PT (1982) Surface geochemical methods used for oil and gas prospecting. A review. *J Geochem Explor* 17:1–34
- Philp RP, Jarde E (2007) Application of stable and radioisotopes. In: Murphy B, Morrison R (eds) *Introduction to environmental forensics*. Elsevier, New York, pp 455–512
- Philp RP, Kuder T (2008) Biomarkers and stable isotopes in environmental forensic studies. In: Mudge SM (ed) *Methods in environmental forensics*. CRC Press, Boca Raton, pp 113–171
- Philp RP, Allen J, Kuder T (2002) The use of the isotopic composition of individual compounds for correlating spilled oils and refined products in the environment with suspected sources. *Environ Forensics* 3(3–4):341–348
- Pond KL, Huang Y, Wang Y, Kulpa CF (2002) Hydrogen isotopic composition of individual n-alkanes as an intrinsic tracer for bioremediation and source identification of petroleum contamination. *Environ Sci Technol* 36:724–728
- Poulson SR, Drever JI (1999) Stable isotope (C, Cl, and H) fractionation during vaporization of trichloroethylene. *Environ Sci Technol* 33:3689–3694
- Rayleigh JWS (1896) Theoretical considerations respecting the separation of gases by diffusion and similar processes. *Philos Mag* 42:493–498
- Reddy CM, Heraty LJ, Holt BD, Sturchio NC, Eglinton TI, Drenzek NJ, Xu L, Lake JL, Maruya KA (2000) Stable carbon isotope compositions of Aroclors and Aroclor contaminated sediments. *Environ Sci Technol* 34(13):2866–2870
- Reddy CM, DeMello A, Carmichael CA, Peacock EA, Xu L, Arey JS (2008) Determination of biodiesel blending percentages using natural abundance radiocarbon analysis: testing the accuracy of retail biodiesel blends. *Environ Sci Technol* 42(7):2476–2482
- Richnow HH, Meckenstock RU, Reitzel LA, Baun A, Ledin A, Christensen TH (2003) In situ biodegradation determined by carbon isotope fractionation of aromatic hydrocarbons in an

- anaerobic landfill leachate plume (Vejen, Denmark). *J Contam Hydrol* 64(1–2):59–72
- Riediger C, Fowler M, Snowdon L (1997) Organic geochemistry of the Lower Cretaceous Ostracode Zone, a brackish/non-marine source for some lower Manville oils in southeastern Alberta. *Can Soc Petrol Geol Mem* 18:93–102
- Rogers KM, Savard MM (1999) Detection of petroleum contamination in river sediments from Quebec City region using GC-IRMS. *Org Geochem* 30(12):1559–1569
- Rooney MA, Vuletich AK, Griffith CE (1998) Compound-specific isotope analysis as a tool for characterizing mixed oils: an example from the west of Shetlands area. *Org Geochem* 29:241–254
- Saber D, Mauro D, Philp RP, Allen J, Kuder T (2003) Carbon isotope ratios of PAHs in urban background soil. Battelle Meeting, Orlando, June 2003
- Saber D, Mauro D, Philp RP, Allen JA (2005) Chemical fingerprinting of sediments and soils near a former MPG site. In: Third International Conference on Remediation of Contaminated Sediments, New Orleans, January 2005 Abstract only
- Sackett WM, Eadie BJ, Exner ME (1974) Stable isotope composition of organic carbon in recent Antarctic sediments. In: Tissot B, Bienner F (eds) *Advances in organic geochemistry 1973*. Technip, Paris, pp 661–671
- Sakaguchi-Söder K, Jäger J, Grund H, Matthäus F, Schüth C (2007) Monitoring and evaluation of dechlorination processes using compound-specific chlorine isotope analysis. *Rapid Commun Mass Spectrom* 21:3077–3084
- Schaeffer P, Poinot J, Hauke V, Adam P, Wehrung P, Trendel JM, Albrecht P, Dessort D, Connan J (1994) Novel optically active hydrocarbons in sediments: evidence for an extensive biological cyclization of higher regular polyphenols. *Angew Chem Int* 33:1166–1169
- Schimmelmann A, Lewan MD, Wintsch RP (1999) D/H isotope ratios of kerogen, bitumen, oil, and water in hydrous pyrolysis of source rocks containing kerogen types I, II, IIS, and III. *Geochim Cosmochim Acta* 63:3751–3766
- Schimmelmann A, Boudou JP, Lewan MD, Wintsch RP (2001) Experimental controls on D/H and $^{13}\text{C}/^{12}\text{C}$ ratios of kerogen, bitumen and oil during hydrous pyrolysis. *Org Geochem* 32:1009–1018
- Schimmelmann A, Sessions A, Mastalerz M (2006) Hydrogen isotopic (D/H) composition of organic matter during diagenesis and thermal maturation. *Annu Rev Earth Planet Sci* 34:501–533
- Schmidt TC, Zwank L, Elsner M, Berg M, Meckenstock RU, Haderlein SB (2004) Compound-specific stable isotope analysis of organic contaminants in natural environments: a critical review of the state of the art, prospects, and future challenges. *Anal Bioanal Chem* 378:283–300
- Schoell M (1983) Genetic characterization of natural gases. *Am Assoc Pet Geol Bull* 67:2225–2238
- Schoell M (1984a) Recent advances in petroleum isotope geochemistry. *Org Geochem* 6:645–663
- Schoell M (1984b) Stable isotopes in petroleum research. In: Brooks J, Welte D (eds) *Advances in petroleum geochemistry*, vol 1. Academic, London, pp 215–245
- Schoell M (1988) Multiple origins of methane in the Earth. *Chem Geol* 71:1–10
- Schoell M (1994) Carbon isotopic composition of individual biomarkers in gilsonites (Utah). *Org Geochem* 21:673–683
- Schoell M, Jenden PD (1993) Isotope analysis of gases in gas field and gas storage. SPE Paper 26171, 337–344. SPE Gas Technology Symposium, Calgary, Alberta, Canada, June 1993
- Schuth C, Taubald H, Bolano N, Maciejczyk K (2003) Carbon and hydrogen isotope effects during sorption of organic contaminants on carbonaceous materials. *J Contam Hydrol* 64:269–281
- Shouakar-Stash O, Alexeev SV, Frape SK, Alexeeva LP, Drimmie RJ (2007) Geochemistry and stable isotopic signatures, including chlorine and bromine isotopes, of the deep groundwaters of the Siberian Platform, Russia. *Appl Geochem* 22(3):589–605
- Seifert WK, Moldowan JM (1978) Applications of steranes, terpanes and monoaromatics to the maturation, migration and source of crude oils. *Geochim Cosmochim Acta* 42:77–95
- Seifert WK, Moldowan JM (1981) Paleoreconstruction by biological markers. *Geochim Cosmochim Acta* 45:783–794
- Seifert WK, Moldowan JM, Smith GW, Whitehead EV (1978) First proof of a C_{28} pentacyclic triterpane in petroleum. *Nature* 271:436–437
- Sessions AL, Sylva SP, Summons RE, Hayes JM (2004) Isotopic exchange of carbon-bound hydrogen over geologic time-scales. *Geochim Cosmochim Acta* 68:1545–1559
- Sherwood Lollar B, Slater GF, Sleep B, Witt M, Kledka GM, Harkness M, Spivack J (2001) Stable carbon isotope evidence for intrinsic bioremediation of tetrachloroethene and trichloroethene at area 6, Dover Air Force Base. *Environ Sci Technol* 35(2):261–269
- Shouakar-Stash O, Frape SK, Drimmie RJ (2003) Stable hydrogen, carbon and chlorine isotope measurements of selected chlorinated organic solvents. *J Contam Hydrol* 60(3–4):211–228
- Shouakar-Stash O, Frape SK, Drimmie RJ (2005a) Determination of bromine stable isotopes using continuous-flow isotope ratio mass spectrometry. *Anal Chem* 77:4027–4033
- Shouakar-Stash O, Drimmie RJ, Frape SK (2005b) Determination of inorganic chlorine stable isotopes by conditions flow isotope ratio mass spectrometry. *Rapid Commun Mass Spectrom* 19:121–127
- Shouakar-Stash O, Drimmie RJ, Zhang M, Frape SK (2006) Compound specific chlorine isotope ratio of TCE, PCE, and DCE isomers by direct injection using CF-IRM. *Appl Geochem* 21:766–781
- Shouakar-Stash O, Frape SK, Aravena R (2009) Analysis of compound-specific chlorine stable isotopes of vinyl chloride by continuous flow-isotope ratio mass spectrometry (FC-IRMS). *Environ Forensics* 10:299–306
- Silverman SR (1965) Migration and segregation of oil and gas. In Young A, Galley GE (eds) *Fluids in subsurface environments*. *Am Assoc Petrol Geol Memoir* 4:54–65
- Silverman S, Epstein S (1958) Carbon isotopic compositions of petroleum and other sedimentary organic materials. *Am Assoc Petrol Geol Bull* 42:998–1012
- Slater GF (2003) Stable isotope forensics – when isotopes work. *Environ Forensics* 4:13–23
- Slater GF, Sherwood Lollar B, Sleep BE, Edwards EA (2001) Variability in carbon isotopic fractionation during biodegradation of chlorinated ethenes: implications for field applications. *Environ Sci Technol* 35(5):901–907

- Slatt R (2006) Stratigraphic reservoir characterization for petroleum geologists, geophysicists, and engineers. In: Handbook of petroleum exploration and production, vol 6. Elsevier, New York
- Smallwood BJ, Philp RP, Burgoyne TW, Allen JD (2001) The use of stable isotopes to differentiate specific source markers for MTBE. *Environ Forensics* 2:215–221
- Smallwood BJ, Philp RP, Allen J (2002) Stable carbon isotopic composition of gasolines determined by isotope ratio monitoring gas chromatography mass spectrometry. *Org Geochem* 33(2):149–159
- Smirnov A, Abrajano TA, Smirnov A, Stark A (1998) Distribution and sources of polycyclic aromatic hydrocarbons in the sediments of Lake Erie, Part 1. Spatial distribution, transport, and deposition. *Org Geochem* 29(5–7):1813–1828
- Sofer Z (1984) Stable carbon isotope compositions of crude oils: application to source depositional environments and petroleum alteration. *Am Assoc Petrol Geol Bull* 68:31–49
- Sofer Z (1991) Stable isotopes in petroleum exploration. Source and migration process and evaluation techniques. Amoco Production, Tulsa, pp 103–106
- Somsamak P, Cowan RM, Haggblom MM (2001) Anaerobic biotransformation of fuel oxygenates under different anoxic conditions. *FEMS Microbiol Ecol* 37:259–264
- Song DL, Conrad ME, Sorenson KS, Alvarez-Cohen L (2002) Stable carbon isotope fractionation during enhanced in-situ bioremediation of trichloroethene. *Environ Sci Technol* 36:2262–2268
- Stahl W (1977) Carbon and nitrogen isotopes in hydrocarbon research and exploration. *Chem Geol* 20:121–149
- Stahl W (1978) Source rock-crude oil correlation by isotope type curves. *Geochim Cosmochim Acta* 43:1573–1577
- Stahl W (1980) Compositional changes and $^{13}\text{C}/^{12}\text{C}$ fractionations during the degradation of hydrocarbons by bacteria. *Geochim Cosmochim Acta* 44:1903–1907
- Stalker L, Larter SR, Farrimond P (1998) Biomarker binding into keogens: evidence from hydrous pyrolysis using heavy water (D_2O). *Org Geochem* 28:239–253
- Staplin F (1969) Sedimentary organic matter, organic metamorphism, and oil and gas occurrences. *Bull Can Petrol Geol* 17:47–66
- Stoddart DP, Hall PB, Larter SR, Brasher J, Li M, Bjørøy M (1995) In: Cubitt JM, England WA (eds) The reservoir geochemistry of the Eldfish field, Norwegian North Sea. The Geochemistry of Reservoirs Geological Society 86:257–279 Special Publication, London
- Stuermer DH, Peters KE, Kaplan IR (1978) Source indicators of humic substances and proto-kerogen: Stable isotope ratios, elemental composition, and electron spin resonance spectra. *Geochim Cosmochim Acta* 42:989–997
- Sturchio NC, Clausen JL, Heraty L, Huang L, Holt BD, Abrajano T (1998) Chlorine isotope investigation of natural attenuation of trichloroethene in an aerobic aquifer. *Environ Sci Technol* 32(20):3037–3042
- Sturchio NC, Hatzinger PB, Arkins MD, Suh C, Heraty LJ (2003) Chlorine isotope fractionation during microbial reduction of perchlorate. *Environ Sci Technol* 37(17):3859–3863
- Sturchio NC, Bohlke JK, Gu B, Hatzinger PB, Jackson WA (2011) Isotopic tracing of perchlorate in the environment. In: Baskaran M (ed) Handbook of environmental isotope geochemistry. Springer, Heidelberg
- Suggate RP (1959) Paparoa mine area. Greymouth coalfield; swelling properties and reserves of coal. *NZ J Geol Geophys* 2:355–367
- Sun Y, Chen Z, Xu S, Cai S (2005) Stable carbon and hydrogen isotopic fractionation of individual n-alkanes accompanying biodegradation: evidence from a group of progressively biodegraded oils. *Org Geochem* 36:225–238
- Tissot B, Welte D (1984) Petroleum formation and occurrence, 2nd edn. Springer, Berlin
- USA EPA (2008) A guide for assessing biodegradation and source identification of organic ground water contaminants using compound specific isotope analysis (CSIA). EPA 600/R-08/148, December 2008
- Van Breukelen BM, Prommer H (2005) Beyond the Rayleigh equation: reactive transport modeling of isotope fractionation effects to improve quantification of biodegradation. *Environ Sci Technol* 42:2457–2463
- van Breukelen BM, Hunkeler D, Volkering F (2005) Quantification of sequential chlorinated ethene degradation by use of a reactive transport model incorporating isotope fractionation. *Environ Sci Technol* 39:4189–4197
- Wang Y, Huang Y (2003) Hydrogen isotopic fractionation of petroleum hydrocarbons during vaporization: implications for assessing artificial and natural remediation of petroleum contamination. *Appl Geochem* 18:1641–1651
- Wang Z, Stout SA (2007) Oil spill environmental forensics: fingerprinting and source identification. Academic, New York
- Wang Y, Huang Y, Huckins JN, Petty JD (2004) Compound-specific carbon and hydrogen isotope analysis of sub-parts per billion level waterborne petroleum hydrocarbons. *Environ Sci Technol* 38:3689–3697
- Wassenaar L, Koehler G (2004) On-line technique for the determination of the ^{37}Cl of inorganic and total organic Cl in environmental samples. *Anal Chem* 76:6384–6388
- Welte D, Hagemann H, Hollerbach A, Leythausen D, Stahl W (1975) Correlation between petroleum and source rock. Proceedings of Ninth World Petroleum Congress. Applied Science Publishers II, London, pp 179–191
- Wen S, Feng Y, Yu Y, Bi X, Wang X, Sheng G, Fu J, Peng P (2005) Development of a compound-specific isotope analysis method for atmospheric formaldehyde and acetaldehyde. *Environ Sci Technol* 39(16):6202–6207
- Whiticar M (1990) A geochemical perspective of natural gas and atmospheric methane. *Org Geochem* 16:531–547
- Whiticar M (1996) Stable isotope geochemistry of coals, humic kerogens and related natural gases. *Int J Coal Geol* 32:191–215
- Whiticar M, Faber E (1986) Methane oxidation in sediment and water column environments-isotope evidence. *Org Geochem* 10:759–768
- Whiticar M, Faber E, Schoell M (1985) Hydrogen and carbon isotopes of C1 to C5 alkanes in natural gases. *Am Assoc Pet Geol Bull* 69:316
- Wilcke W, Krauss M, Amelung W (2002) Carbon isotope signature of polycyclic aromatic hydrocarbons (PAHs): evidence for different sources in tropical and temperate environments. *Environ Sci Technol* 36(16):3530–3535
- Wilkes H, Boreham C, Harms G, Zengler K, Rabus R (2000) Anaerobic degradation and carbon isotopic fractionation of alkylbenzenes in crude oil by sulphate-reducing bacteria. *Org Geochem* 31(1):101–115

- Xiong Y, Geng A (2000) Carbon isotopic composition of individual n-alkanes in asphaltene pyrolysates of biodegraded crude oils from the Liaohe basin, China. *Org Geochem* 31:1441–1449
- Xiong Y, Geng A, Wang C, Sheng G, Fu J (2003) The origin of crude oils from the Shuguang-Huanxiling buried hills in the Liaohe Basin, China: evidences from chemical and isotopic compositions. *Appl Geochem* 18:445–456
- Xiong Y, Geng A, Pan C, Liu D, Peng P (2005) Characterization of the hydrogen isotopic composition of individual n-alkanes in terrestrial source rocks. *Appl Geochem* 20:455–464

Chapter 32

Utility of Stable Isotopes of Hydrogen and Carbon as Tracers of POPs and Related Polyhalogenated Compounds in the Environment

W. Vetter

Abstract Polyhalogenated persistent organic pollutants (POPs) belong to the most hazardous environmental pollutants of our days. The concentrations of compounds such as PCBs, PCDD/Fs, chloropesticides, and brominated flame retardants in the environment are well-documented. In order to determine the origins and fate of the POPs, however, the concentrations in the environment must be related to the processes that redistribute these pollutants. A suitable tool for such a purpose is stable isotope analysis. This chapter describes the techniques used for the determination of stable carbon and hydrogen isotopes of POPs. Element analyzer-isotope ratio mass spectrometry (EA-IRMS) was used for the determination of bulk $\delta^{13}\text{C}$ values and bulk $\delta^2\text{H}$ values. Linking of a gas chromatograph to IRMS enabled the compound-specific isotope analysis (CSIA) of $\delta^{13}\text{C}$ values. Moreover, theoretical aspects as to the intramolecular deuterium distribution can be explored by means of quantitative ^2H -NMR. The knowledge of published applications in stable isotope analysis of POP is presented. On several occasions IRMS data was suited to distinguish technical products from different producers, metabolites from native POPs, and to address kinetic isotope effects (KIE) during the transformation of POPs. Problems and limitations of the current state of the art in stable isotope analysis of POPs are presented as well.

32.1 Introduction

Polyhalogenated persistent organic pollutants (POPs) are a group of compound classes used for decades by mankind in diverse industrial and agriculture areas.

W. Vetter
University of Hohenheim, Institute of Food Chemistry,
Garbenstrasse 28, 70599 Stuttgart, Germany
e-mail: walter.vetter@uni-hohenheim.de

Unintended leaching of POPs and related compounds into the environment since the 1930s has polluted the globe. The high persistency and their semi-volatile nature led to a widespread distribution and transport of particularly recalcitrant pollutants to remote areas. Cold condensation resulted in a transfer from the areas of application of POPs to the Arctic, the Antarctic, and also mountain areas. The given toxicity attributed to these compounds made them to a serious environmental problem and a hot topic for the consumers of food. To better understand the fate of these compounds national monitoring programs have been established worldwide and the distribution of POPs in different environmental compartments has been modelled. In this context, knowledge of the history of the POPs detected in the environment is of central interest. Some of the key questions include: Are POP residues in a given sample the result of long-range transport? Has biodegradation been involved and, if so, to what extent? Are some of these compounds metabolites of others? Is there one source or are there multiple ones? Some of these questions can be answered by means of stable isotope analysis.

Stable isotope analyses of POPs mainly take advantage of the ratio of the carbon isotopes (^{13}C , ^{12}C) and hydrogen (^2H , ^1H) isotopes in samples by means of isotope ratio mass spectrometry (IRMS). For instance, in food authentication it is possible by IRMS to determine the country in which the "sample" was harvested or produced, or if a natural product (e.g. a flavor compound) is authentic or synthetic. In food authentication such measurements are standard for about two decades. However, the application of IRMS in the field of research on POPs is a relatively young and scarcely used technique. The reason for this is that it appears that these measurements are rather complicated. There is a lack of suitable reference standards for a proper

and straight forward isotope determination of POPs. The compounds are diverse in structure and concentration and the respective gas chromatograms of sample extracts are full of peaks which may interfere with each other. Moreover, any remainders of the sample matrix will also hamper the correct determination, and isotope fractionation during sample preparation may be a point of concern. The conversion of polyhalogenated organic material into CO₂ is accompanied with the formation of aggressive halogenated compounds which are detrimental to the system. The high masses of Cl and Br reduce the mass percentage of carbon in a POP. Moreover, kinetic isotope effects (KIE) may take place under the chemical POP synthesis. This in turn was suggested to be useful to identify the producer of a given POP by means of stable isotope analysis of both the standard and its residues in the environment. Like all compounds, POPs are degraded in the environment albeit at very low rate. These environmental processes are usually linked with KIE, and it has been suggested that stable isotope data of POPs might add valuable knowledge to the fate of the pollutants. The techniques useful for this approach are element analyzer-isotope ratio mass spectrometry (EA-IRMS), gas chromatography interfaced with isotope ratio mass spectrometry (GC-IRMS), and from a theoretical point of view, deuterium isotopomer analysis by nuclear magnetic resonance spectroscopy (NMR).

32.2 Materials and Methods

In contrast to conventional mass spectrometers that yield structural information by screening of a wide mass range for characteristic fragment ions, IRMS achieves highly accurate and precise measurements of the isotopic abundance of simple gases at the expense of the flexibility of scanning MS (Meier-Augenstein 1999, 2002). In IRMS, the polyhalogenated compound has to be converted into an element-specific gas (i.e. CO₂ in the case of carbon and H₂ for hydrogen isotopes) which is then analyzed in relation to a gas obtained from a standard compound of known isotope composition. The pre-requisite is that this conversion is quantitative and reproducible. However, this is much more complicated in the case of POPs (see below). A second problem is that any compound converted into the measured gas can falsify the result.

Hence, only standards or isolated compounds can be analyzed by conventional element analyzer isotope mass spectrometry (EA-IRMS, Sect. 32.2.1). The scope can be broadened when the IRMS inlet is linked to a chromatographic system which is typically a gas chromatograph (Sect. 32.2.2). Due to the chromatographic peak resolution, the different sample compounds can be analyzed individually, and this technique is usually termed compound-specific isotope analysis (CSIA). Still the problem exists that co-eluting compounds will be measured together and the interference will falsify the result obtained. Therefore, different quality control measures have been introduced (see below).

In IRMS (Sect. 32.2.1) conversion of all carbon into CO₂ is a prerequisite for the measurements of carbon isotopes. In that, the isotope information on individual atoms (i.e. the isotopomer distribution) gets lost. The best strategy to obtain site-specific isotope data is currently achievable with NMR. Isotopomer distributions (i.e. the differences in the abundances on individual nuclei of the same type) can then be studied if all signals are resolved. In this field it is of particular disadvantage that ¹²C has no nuclear spin. Thus, application of NMR is currently limited to determine ²H/¹H distributions (Sect. 32.2.2). Noteworthy, Philp and Monaco (2011) deal with stable isotopes in hydrocarbon exploration in the present book. This chapter adds some valuable additional information the reader may take advantage of.

32.2.1 Isotope Ratio Mass Spectrometry

The standard IRMS method is based on the conversion of organic materials into gases like CO₂ and H₂. For this purpose any covalent bond in the molecule hosting the target element has to be cleaved. This is obtained in an oxidative furnace for carbon to produce CO₂ and in a reductive furnace to produce H₂ (for typical settings see below). Owing to instrumental limitations with regard to long-term stability and lab-to-lab comparability, the use of reference standards compared to which the analytes are measured was mandatory for the success story of IRMS. The worldwide accepted reference standard for carbon isotopes to give standard CO₂ is Pee Dee Belemnite, a carbonate which has received the name from its origin, i.e. the habitat of

the Pee Dee American native tribe in South Carolina. Likewise standard mean ocean water is used for the generation of standard H_2 for hydrogen isotope measurements. Both references can be obtained from the International Atomic Energy Agency (IAEA) in Vienna (<http://www.iaea.org>). For this reason, these primary reference standards are labelled Vienna Pee-Dee Belemnite (V_{PDB}) and Vienna standard mean ocean water (V_{SMOW}). Current EA-IRMS configurations take advantage of a dual inlet system which allows for the alternating measurement of reference gas and sample while GC-IRMS is performed in continuous flow mode. The setup of a modern GC-IRMS instrument is shown in Fig. 32.1. Owing to the small differences, the result is multiplied by 1,000 and thus generally expressed in ‰. The resulting δ -value (in ‰)

expresses the isotope measurements as ratio between sample and standard (32.1):

$$\delta^{13}C = \left(\frac{\left(\frac{^{13}C}{^{12}C} \right)_{\text{sample}}}{\left(\frac{^{13}C}{^{12}C} \right)_{\text{standard}}} - 1 \right) \times 1,000\text{‰} \quad (32.1)$$

The relation between sample and standard becomes more explicit in (32.2) where the term “1” was substituted with $^{13}C/^{12}C_{\text{standard}}/^{13}C/^{12}C_{\text{standard}}$.

$$\delta^{13}C = \left(\frac{\left(\frac{^{13}C}{^{12}C} \right)_{\text{sample}} - \left(\frac{^{13}C}{^{12}C} \right)_{\text{standard}}}{\left(\frac{^{13}C}{^{12}C} \right)_{\text{standard}}} \right) \times 1,000\text{‰} \quad (32.2)$$

As can be gathered from (32.2), the richer a sample is in ^{12}C the smaller the $^{13}C/^{12}C$ fraction. Thus, a sample richer in ^{12}C (or depleted in ^{13}C) than the reference standard has a $\delta^{13}C$ value $<0\text{‰}$. The $\delta^{13}C$ value of the reference standard can also be depicted from (32.2). If the sample is substituted by the reference standard, the numerator in (32.2) is zero, and thus the $\delta^{13}C$ value is per definition 0‰ . Noteworthy, the accepted $^{13}C/^{12}C$ ratio of the reference standard V_{PDB} according to Chang and Li is 0.0111802 (Werner and Brand 2001), and this would give the opportunity to calculate the exact $^{13}C/^{12}C$ ratio in samples (Fig. 32.2), but this is scarcely done. Usually, the $\delta^{13}C$ value is reported in papers dealing with IRMS determinations of stable isotopes. However, to give an impression of the quantities involved in isotope effects, a depletion of the $\delta^{13}C$ value by 1‰ will

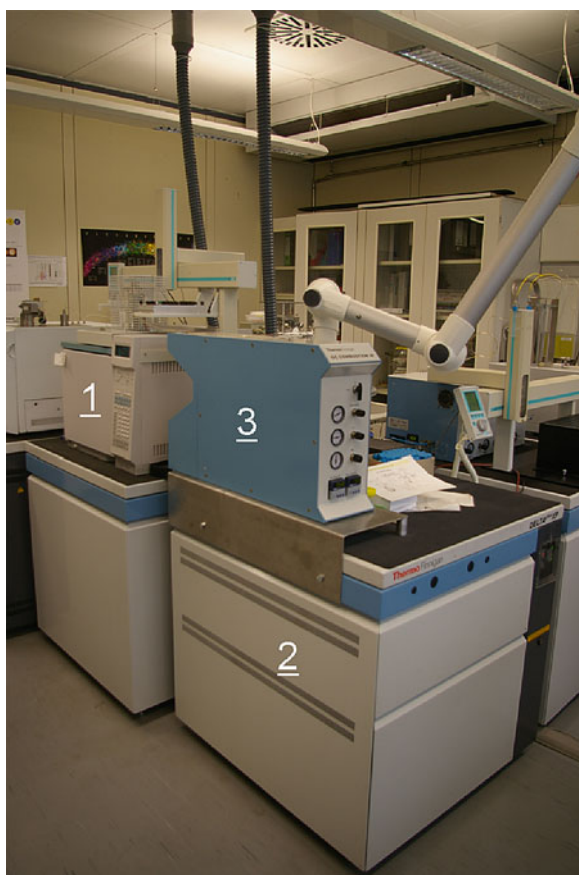


Fig. 32.1 Photo of a typical GC-IRMS system with (1) the gas chromatograph, (2) the mass spectrometer unit and (3) the combustion interface (photo by Natalie Rosenfelder)

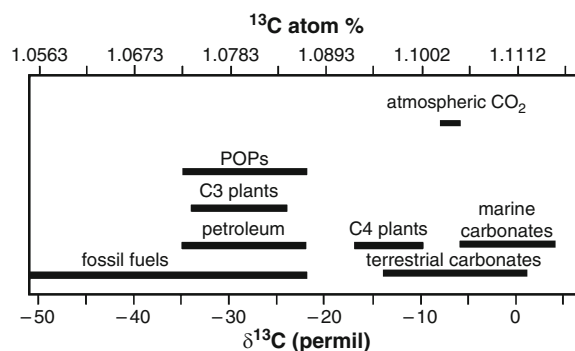


Fig. 32.2 Ranges of $\delta^{13}C$ values (vs. V_{PDB}) of relevant groups of compounds and the corresponding ^{13}C atom percentages (modified from Meier-Augenstein 1999)

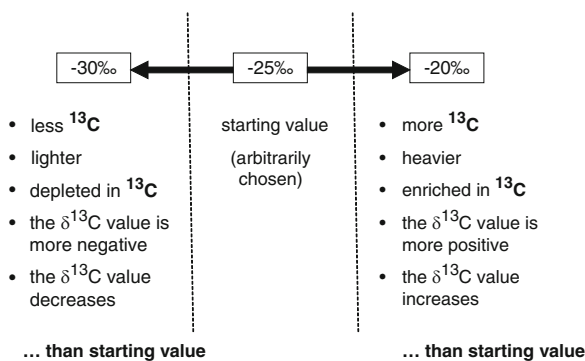


Fig. 32.3 Schematic presentation of changes in $\delta^{13}\text{C}$ values

decrease the ^{13}C weight percent by 0.0011‰ or 11 parts per million (Fig. 32.2).

Owing to the extraordinary high proportion of ^{13}C in Pee Dee Belemite, more or less all other compounds and all the POPs dealt in this chapter have negative $\delta^{13}\text{C}$ values. The more negative a $\delta^{13}\text{C}$ value is, the less ^{13}C the compound contains (or the “lighter” it is) compared to the reference standard V_{PDB} . Especially for scientists new in the field, these relationships cumbersome to remember are summarized in Fig. 32.3.

Major differences in the $\delta^{13}\text{C}$ values of organic compounds originate from the biosynthesis pathways of organic materials, namely in the fixation of CO_2 in photosynthesis. Atmospheric CO_2 has currently a $\delta^{13}\text{C}$ value of -8‰ (Whiticar 1996). Over the past decades, this $\delta^{13}\text{C}$ value has gradually shifted towards lighter carbon ($\sim 1\text{‰}$) due to the human impact via fossil biofuel and biomass (Whiticar 1996). C_3 plants pass through the Calvin circle. In Rubisco, ^{13}C is particularly discriminated so that all C_3 plants have $\delta^{13}\text{C}$ values between -30 and -20‰ . The discrimination of ^{13}C relative to atmospheric CO_2 is more moderate in C_4 plants which typically have $\delta^{13}\text{C}$ values between -20 and -10‰ . Petroleum is the primary source of industrial organic chemistry and thus the production of polyhalogenated compounds. The $\delta^{13}\text{C}$ value of the carbon source of crude oil aligns with that of C_3 plants (Whiticar 1996).

The hydrogen isotope signature of a molecule is also expressed via the δ -scale with Vienna standard mean ocean water (V_{SMOW}) being the reference standard. Owing to the relationship given above, samples depleted in ^2H relative to the reference standard have negative $\delta^2\text{H}$ values. The effect between ^1H and ^2H in

a molecule is much more pronounced compared to ^{12}C and ^{13}C due to percentage mass difference.

The “weight” of hydrogen in a compound and sample is mainly governed by climatic factors, especially in the form of evaporation and condensation effects in the natural water cycle. Evaporation of water supports the release of water lighter in hydrogen, while condensation favours the precipitation of water enriched in ^2H . Thus, the farther water vapour is transported from the ocean over the landmass, the lighter it gets in hydrogen (and oxygen). Due to the enormous ocean water reservoir, the permanent evaporation of water does not change the $\delta^2\text{H}$ value within the lifespan of isotope research. Thus, the reference standard (standard mean) ocean water is among the most heavy natural compounds with regard to the hydrogen content so that virtually all compounds are depleted in ^2H and thus have negative $\delta^2\text{H}$ value. C_3 plants and petroleum have $\delta^2\text{H}$ values in the range -175 to -75‰ (Whiticar 1996). As can be seen from these numbers, the variations and effects of hydrogen isotope abundances are more pronounced compared to carbon isotopes. The origins are primarily due to variations in the $\delta^2\text{H}$ value of the groundwater used in plant growth (Whiticar 1996).

However, the conversion of the analyte into CO_2 or H_2 might not be as straight forward as that of the reference standard which is only available for limited series of measurements. Therefore, the use of a secondary reference standard (laboratory standard) of known isotopic composition is the rule in virtually all laboratories (Werner and Brand 2001). The laboratory standard is first calibrated against the IAEA reference standard. Thereafter, the laboratory standard is used to determine the samples and the measured $\delta^{13}\text{C}$ value is corrected by the difference between laboratory and reference standard to obtain values on the δ -scale.

Difficulties also exist in the conversion of the laboratory standard into CO_2 . Consequently, the laboratory standard should be as similar as possible to the analyte (s). That is where the key-problem arises with POPs. Currently, there are no suitable laboratory standards available that are suited for the referencing of semi-volatile polyhalogenated compounds. Individual researchers are pursued to choose their own laboratory standard. Typically, the laboratory standard should be structurally and, for CSIA, chromatographically related to the analytes. Application of a structurally-

related laboratory standard provides a good precision of the measurements because systematic errors by insufficient combustion efficiency are minimized. With a proper laboratory standard, variations and drift of $\delta^{13}\text{C}$ values may be limited to $\sim 0.1\%$ (Drenzek et al. 2001). While the precision obtainable by using a suitable laboratory standard can be optimized it does not necessarily mean that the $\delta^{13}\text{C}$ values are correct. Consequently, $\delta^{13}\text{C}$ value determined in different laboratories for a given POP may not be identical (see below). Accuracy would require a laboratory POP standard with known $\delta^{13}\text{C}$ value. A further key-problem with polyhalogenated compounds is that they include carbon-halogen bonds from which the reactive halogens are released upon combustion. Two problems are linked to this, i.e. that the oxidation/reduction unit might get destroyed and that there is no standard reference material available which is similar to the properties of the analytes. Thus, specific precautions have to be undertaken in order to produce valuable data. Unfortunately, the problems associated with the isotope measurements of polyhalogenated compounds are not well documented. It might seem odd that the measurement technique for POPs is not more frequently used. It should be said at this point that reliable and reproducible stable isotope measurements are far more difficult in the case of polyhalogenated compounds compared to other organic compounds. Those starting in the field should be aware of such problems and it might take some time to obtain reliable and satisfactory results in the laboratory.

In the case of CO_2 , three different isotopomers (i.e. isomers having the same number of each isotopic atom but differing in their positions, <http://www.iupac.org/goldbook/I03352.pdf>) – $^{12}\text{C}^{16}\text{O}_2$ (m/z 44), $^{13}\text{C}^{16}\text{O}_2$ (m/z 45) and $^{12}\text{C}^{16}\text{O}^{18}\text{O}$ (m/z 46) – are formed and measured when organic material is converted into CO_2 . In addition, the instrument software performs the so-called Craig-correction by 7% for eliminating the impact of $^{12}\text{C}^{16}\text{O}^{17}\text{O}$ on m/z 45 (Werner and Brand 2001). The three m/z values are registered simultaneously by three Faraday cups. The resulting ion currents are continuously monitored, and leveled to obtain a more proportional visualization. The relative abundances – also known as sensitivity factors – (in parentheses) at which these ions are displayed in standard mode are m/z 44 (1), m/z 45 (100), and m/z 46 (300) (Werner and Brand 2001). The corresponding peak areas are quantified and isotope ratios are calculated. Because ^{13}C is only of low abundance in natural

materials, the IRMS system has to be very sensitive for low amounts of ^{13}C . It is thus essential for the measurements that no isotope-labelled internal standards are added to the sample. Thus, isotope dilution method taking advantage of ^{13}C marked internal standards is not possible in the measurement of native POPs.

Finally, it should be noted that “CSIA” and “bulk δ -values” are terms which have non-uniformly been used in different IRMS applications. In this article, “bulk $\delta^{13}\text{C}$ values” and “bulk $\delta^2\text{H}$ values” is used when the measurement was performed in combination with EA-IRMS, even when reliable POP standards or isolated POPs were measured, while CSIA is exclusively used when δ -values were determined using GC-IRMS.

32.2.1.1 Bulk Carbon Isotope Ratios by EA-IRMS

As mentioned above, the determination of polyhalogenated compounds is more difficult compared to other compounds. Consequently, it is more complicated to generate and verify stable (precise) and correct (accurate) δ -values. A large part of the problem is related to the movement of the halogens upon CO_2 generation. Jarman et al. (1998) predicted that the lifetime of the furnace used for PCB oxidation would be reduced due to the Cl buildup. Although no degradation of the reactor was observed, a re-oxidation was performed once a day for ~ 15 min (Jarman et al. 1998). Such measures are highly recommended in practice although they have not been distilled into general rules, yet.

$\delta^{13}\text{C}$ value evaluations cannot be based on single measurements. Despite the use of a dual inlet system for calibration, individual measurements are very sensitive to changes. Therefore, samples need to be analyzed repeatedly in order to eliminate outliers. A suitable measurement scheme as reported by Werner and Brand (2001) may serve as a blueprint for the setup within individual laboratories. For bulk $\delta^{13}\text{C}$ values, the temperature and time of the combustion process were typically set at 850°C and 4 or 5 h (Jarman et al. 1998; Drenzek et al. 2002). A higher temperature of 940 – $1,020^\circ\text{C}$ was used by Vetter et al. (2005, 2006a, b). High quality crystalline standards (0.5–2 mg) were weighed in tin capsules (Vetter et al. 2005, 2006a) or sample solutions (in the volatile pentane) were weighed in pre-combusted quartz tubes

at amounts to yield 5–30 μmol carbon (Drenzek et al. 2002). Jarman et al. (1998) evaporated PCB solutions in isooctane in sealed tubes and added silver foil for chlorine uptake.

32.2.1.2 GC-IRMS for Carbon Isotopes

The coupling of GC with IRMS is not as straightforward as with conventional mass spectrometers. Any analyte leaving the GC column has to be converted on line into the measured gas (e.g. CO_2) in order to provide analytes amenable to high-precision isotopic analysis (Ricci et al. 1994). Thus, the GC cannot be directly connected with the IRMS but is connected through the oxidation/reduction platform. GC-IRMS was introduced in the 1970s (Sano et al. 1976; Matthews and Hayes 1978) and further developed in the 1980s (Barrie et al. 1984; Freedman et al. 1988) for routine use (Ricci et al. 1994). The GC effluent is interfaced to the combustion reactor filled with CuO/Pt or CuO/NiO/Pt . Water vapour generated during combustion is separated by means of a water trap because it would protonate CO_2 and thus falsify the measurements (Meier-Augenstein 1999).

In GC-IRMS we must additionally take into account that compounds labeled with ^{13}C or ^2H elute prior to the native compounds. This so-called gas chromatographic isotope effect or inverse isotope effect is due to the higher volatility of isotopically heavier organic compounds. Due to the chromatographic isotope effect, isotope distribution within a peak is not symmetrical, and in the combustion unit, the m/z 45 signal ($^{13}\text{CO}_2$) precedes the m/z 44 signal ($^{12}\text{CO}_2$) by 150 ms on average (Meier-Augenstein 1999). As a consequence the sensitivity-corrected ratio of m/z 45 to m/z 44 is not a constant parallel line but a curve starting positive (relatively higher abundance of the earlier eluting $^{13}\text{CO}_2$) and gets negative in the end of the peak (relatively higher proportion of $^{12}\text{CO}_2$) (Werner and Brand 2001). For this reason, it is essential that the entire GC peak is converted into CO_2 . Incomplete analysis of a partially collected and integrated peak will severely compromise the quality of the isotope ratio measurement by GC-IRMS. In addition, the analyte has to be baseline separated from other compounds in the sample because traces of an interfering peak eluting in close proximity to the analyte will make accurate peak integration virtually

impossible. These circumstances must be born in mind when complex mixtures and environmental sample extracts are analyzed. In GC-IRMS, a true baseline separation for adjacent peaks is of paramount importance for high-precision CSIA (Meier-Augenstein 1999). Problems due to co-elutions can be overcome by multidimensional- or heart-cut 2D-GC (MDGC) in which (only) the analyte is trapped from one column onto the second column on which it is analyzed free from interferences. This technique has been used by Horii et al. (2005, 2008) for the analysis of PCB mixtures and octachlorodibenzo-*p*-dioxin (OCDD). These authors also received a better sensitivity when MDGC was used as a prelude to isotope analysis.

In polyhalogenated compounds, carbon typically contributes <50% to the molecular weight. The carbon produced from the analyte should be in the range of 25 ng in order to produce signals that can be precisely integrated and reproduced. This would require injections of solutions containing 50 ng or more of an organic substance onto the column. Transferred to a molar level it is the low or even sub-nM range. For instance, the molecular weight of the hexachlorobiphenyl PCB 153 is 360.9 g/mol, the carbon content is ~40% (144.1 g/mol) so that 1 nM will provide ~144 ng carbon. To increase confidence levels, ~0.33 nM PCB 153 should be injected onto the GC column. However, the amount available for a study should be higher because replicate analyses are required to determine and verify the required precision. Since the injection medium is a solution which can hardly be reduced to <30 μL , a good starting point for POPs would be 30–100 nM. Using MDGC the amount of carbon required for precise measurements could be reduced to 24 ng OCDD or ~7.6 ng carbon (Horii et al. 2008).

Since the IRMS signal is a direct response to CO_2 any co-eluting peak cannot be distinguished from the signal. Thus, an effluent split leading to ~10% of the gas flow to a conventional ion trap mass spectrometer are partly in use for quality control (for instance in the BGC-Jena-lab, Vetter and Gleixner 2006; Vetter et al. 2006b). However, such systems are not standard in IRMS laboratories, so that other quality controls should be established. Suitable techniques could be previous analysis with the same chromatographic setup. Vetter et al. (2007) used derivative chromatography for monitoring peak purity.

All essential details on the method were not reported in all studies. In the following, typical

GC-IRMS settings are listed: Solutions with POPs were usually injected in splitless mode into hot injector ports (280°C) (Jarman et al. 1998). In virtually all studies with POPs a capillary column coated with 95% methyl 5% phenyl polysiloxane was used. The column dimensions were between 30 and 60 m length, 0.25 or 0.32 mm i.d. and a film thickness of 0.17–0.25 μm . Longer columns were especially used for the analysis of multicomponent mixtures (Jarman et al. 1998; Drenzek et al. 2001; Yanik et al. 2003) which is also recommended at this point. When shorter columns were used, this was done in combination with additional features such as an effluent split to a conventional MS (see above) or with MDGC (Horii et al. 2005). The setup for MDGC took advantage of a GC combination of 30 m \times 0.25 mm i.d. \times 0.25 μm film thickness DB5 followed by an RTX-200 (25 m \times 0.32 mm i.d. \times 0.25 μm d_f) column. Details on the reference gas were not reported in all earlier studies. Jarman et al. (1998) used reference gas with a $\delta^{13}\text{C}$ value of -34.42‰ vs. V_{PDB} whereas Vetter and Gleixner (2006) used NBS 19 and V_{PDB} as isotope standards.

The oxidation reactor/combustion furnace usually consisted of CuO and was heated at 850°C (Yanik et al. 2003), 940°C (Horii et al. 2005; Vetter and Gleixner 2006) or 960°C (Jarman et al. 1998). The reduction reactor was typically set at 650°C (Jarman et al. 1998).

Water was removed by an ethanol/ CO_2 cryogenic trap (-80°C ; Yanik et al. 2003) or via a Nafion tube (Horii et al. 2005). The later is the typical design used in most instruments. Nafion is a fluorinated polymer that acts as a semi-permeable membrane through which water passes freely while all the other combustion products are retained in the carrier gas stream (Meier-Augenstein 1999).

For POPs, CSIA (for PCBs) precision was reported to be $\sim 0.5\text{‰}$ (Jarman et al. 1998). This is the typical precision reported for GC-IRMS of POPs and agrees with values reported for volatile halogenated compounds (Sherwood Lollar et al. 2001). Using an internal standard eluting between two PCBs studied, Drenzek et al. (2001) noted that the $\delta^{13}\text{C}$ values of individual PCBs (in CSIA) were determined relative to a co-injected PCB standard rather than the reference gas. They stated that this type of measurement minimized any bias associated with GC inlet or combustion unit. The drift of internal standard and reference gas was 0.10%. This method is however limited to

scenarios with sufficient separation in the gas chromatogram between the individual analytes. This is difficult to obtain in the case of multicomponent mixtures or environmental samples.

32.2.1.3 IRMS Determination of Hydrogen Isotopes

Clearly, the determination of $\delta^2\text{H}$ values would provide additional and valuable insights into the fate of POPs (see also the paper by Philp and Monaco (2011)). While GC-IRMS was used to determine $\delta^2\text{H}$ value of other nonhalogenated pollutants such as benzene (Mancini et al. 2003), in the case of polyhalogenated compounds, only $\delta^{13}\text{C}$ values can currently be obtained with standard instruments equipped with a high-temperature pyrolysis (HTP) unit. HTP of polyhalogenated compounds fails to deliver significant signals for H_2 due to the formation of HCl (Armbruster et al. 2006). Only 5–20% of the theoretical hydrogen content in the polyhalogenated compounds was picked up by the detector. The resulting hydrogen peaks generated were very small and non-reproducible (Armbruster et al. 2006). This drawback was overcome in a two-step method by transformation of hydrogen from organohalogen compounds first into H_2O followed by reduction to H_2 with Zn at 500°C (Poulsen and Drever 1999). However, this two-step method cannot be used in the continuous flow mode (Chartrand et al. 2007). Morrison et al. (2001) developed a chromium reactor for the on-line determination of $\delta^2\text{H}$ value of nL-water samples size. A similar chromium-loaded reactor was used by Armbruster et al. (2006) to determine bulk $\delta^2\text{H}$ value of POPs. This system consisted of a self-made chromium reduction reactor (1,000°C) in the form of a quartz tube filled with 10 cm quartz chips and 6 cm Cr reagent and quartz chips (4:1, w/w). Problems associated with this technique have been reported by Armbruster et al. (2006). This approach was simple but restricted to analyze bulk $\delta^2\text{H}$ values of POPs (Armbruster et al. 2006; Vetter et al. 2006a). Although a similar design could be used in combination with a GC interface to generate CSIA, this has not been achieved, yet.

Chartrand et al. (2007) presented the first working system for GC-IRMS method for the determination of $\delta^2\text{H}$ values of halogenated volatile organic compounds

(VOCs), and this system seems to be appropriate for POPs as well. They added a trap filled with liquid N₂ for the elimination of HCl from gas flow after the pyrolysis oven. This system was used to determine the $\delta^2\text{H}$ values of 1,2-dichloromethane from different producers. Application of this technique would be an excellent starting point for the generation of $\delta^2\text{H}$ values of POPs in environmental samples. Thus, it could be interesting to follow these trends in future.

32.2.2 Deuterium Isotopomer Determination by Quantitative ^2H -NMR

Most molecules exhibit nonstatistical hydrogen isotope distribution, and the true mole fraction of the monodeuterated isotopomers can be directly determined by quantitative ^2H -NMR (Martin et al. 2008). This technique is also referred to as site-specific natural isotope fractionation (SNIF) NMR (maybe intramolecular isotope fractionation would have been a better term). These isotope abundances in non-symmetrical molecules depend on physical and (bio)chemical isotope fractionations (Augusti et al. 2009). A prerequisite for such measurements is that the hydrogen is fixed in the molecule and does not equilibrate with its surrounding. For this reason, hydrogen in hydroxyl or carboxyl groups cannot be evaluated because they rather reflect the medium in which they were produced or stored. Further drawbacks of SNIF-NMR are the high amounts required for the measurements: ~50 mg of good quality compounds are required making it difficult to apply this technique to environmental samples. Moreover, only simple molecules in which the NMR resonances are resolved can be studied. Excluded from measurements are POPs which do not form stable conformations. For instance, hexachlorocyclohexanes (HCHs) cannot be determined by ^2H -NMR because of the ring flipping which permanently changes between chair and boat conformations. Despite these drawbacks, ^2H -NMR may add valuable information to isotope distribution of POPs and three studies on SNIF-NMR experiments with POPs have been published to date (Nikiforov et al. 2005; Vetter et al. 2006a; Augusti et al. 2009).

The SNIF-NMR spectrum of 2,4-dibromoanisole as determined by the group of J. Schleucher is shown in

Fig. 32.4 (Vetter et al. 2006a). The abundances of H_B and H_C slightly exceeded H_A. In turn, the three aromatic hydrogens exceeded the intensity of the methoxy-hydrogens (whose signal area must be divided by three due to the three individual H contributing to this moiety). Deuterium isotope data of individual isotopomers is usually described relative to the average deuterium abundance of the whole molecule set to 1.00 or 100%. In the example given in Fig. 32.4, the area of proton signals H_A, H_B, H_C, and CH₃ is summed up and set to 600%. Thus, each signal in the spectrum has an average intensity of 100% (the three equivalent methyl protons count three). Consequently, individual signals with abundances >100% are obtained for a deuterium content above average while signals (<100%) are depleted in deuterium relative to the mean deuterium content of the molecule. In the example of Fig. 32.4, signals H_A, H_B and H_C are 1.8, 9.7, and 8.5%, respectively, richer in deuterium (together by 20%) than the average molecule while the methyl group is poorer in deuterium by 6.7% (with three equivalent protons this group is 20% lighter in deuterium than the average molecule). Interestingly, the results of the SNIF-NMR measurements can be related to the bulk $\delta^2\text{H}$ value determined with EA-IRMS (Vetter et al. 2006a; Augusti et al. 2009). If the bulk $\delta^2\text{H}$ value (in ‰) is known, the individual isotopomer distributions as determined with SNIF-NMR will directly lead to the isotope abundances of the individual nuclei.

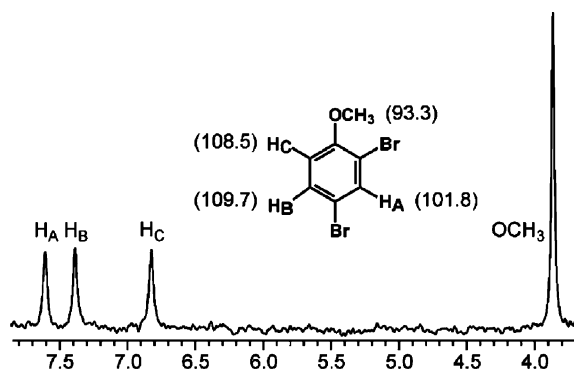


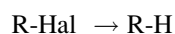
Fig. 32.4 Deuterium NMR spectrum of 2,4-dibromoanisole (Vetter et al. 2006a). Integrals of the signals are proportional to ^2H isotopomer abundance (values relative to the average deuterium abundance of the whole molecule, which was set to 100)

32.2.3 Carbon Isotopomer Distributions, Kinetic Isotope Effects (KIE), and the Rayleigh Model

While deuterium isotopomer distributions can be determined by SNIF- ^2H -NMR, it is difficult to obtain isotopomer-specific data for carbons. However, carbon isotope abundances are also not symmetrically distributed in the molecule. The origins for these intramolecular nonstatistical isotope distributions are governed by statistical mechanics (Schmidt 2003). As reported above, in IRMS all carbons are converted into CO_2 and information on the isotope composition on individual atoms – the so-called isotopomer distribution – is lost. Still the determination of $\delta^{13}\text{C}$ values by IRMS is a valuable tool to study the underlying principles and mechanisms of isotope fractionation processes.

Many studies have unequivocally shown that kinetic isotope effects (KIE) determine the isotopic abundance in many defined molecule positions (Schmidt 2003). Most of these studies were based on biosynthesis of organic material (Hayes 2001). However, KIE must essentially contribute to the formation of intramolecular isotope distributions in irreversible or unidirectional reactions (Schmidt 2003). In biosynthesis, the isotope discriminating effect at particular positions can be severe. For instance, C-1 of natural glycerol from plant fat may be depleted by up to -14% relative to the corresponding C-3 and C-4 positions of its precursor glucose (Weber et al. 1997).

An impact of these effects can be assessed by a look at the $\delta^{13}\text{C}$ value of individual carbons of fructose with a $\delta^{13}\text{C}$ value of -25.3% . However, selective step-by-step elimination of carbons (Rossmann et al. 1990) allowed one to determine that the $\delta^{13}\text{C}$ values (in parenthesis) at C-1 (-26.5%), C-2 (-26.1%), C-3 (-23.4%), C-4 (-18.8%), C-5 (-26.3%), and C-6 (-30.4%) differed significantly (Weber et al. 1997; Schmidt 2003). Results from measurements on individual carbons are very difficult and complicated to obtain. In order to better understand the meaning of carbon isotopomer distributions, let us consider a single polyhalogenated compound (reactant or substrate) that is converted into metabolite with one halogen less by reductive dehalogenation:



According to the data discussed for glycerol and fructose, an effect of -14% on one individual carbon can be categorized as a severe event. We must assume that the effect is frequently lower. However, PCBs, for instance, contain 12 carbons, and the reductive dechlorination will almost exclusively affect the carbon from which the halogen is removed. When the PCB is combusted to CO_2 , the overall effect would be $-14\%/12 \approx -1.2\%$. Thus, a process which changes the $\delta^{13}\text{C}$ value of POPs by $\sim 1\%$ must be taken for one accompanied with a severe isotope effect. Still changes in the $\delta^{13}\text{C}$ value in the range of 0.5% may weigh high in the case of POPs. This is where the problem arises with POPs, because the typical precision of $\delta^{13}\text{C}$ values for polyhalogenated compounds is 0.5% and is in the same range as large isotope effects. Therefore, caution has to be undertaken when $\delta^{13}\text{C}$ value in reactions are going to be interpreted. This makes POPs completely different than VOC (such as CHCl_3 and CCl_4). In these light molecules all carbons are involved in the bond that is dechlorinated and the full effect can be measured without dilution by non-involved carbons.

The isotopic compositions of organic compounds differ because of mass-dependent isotopic fractionation effects where one isotope may react faster or be incorporated preferentially (Melander and Saunders 1980). Isotope fractionation may occur during production, post-production, handling and storage, and hence have the potential to be used in identifying different sources as was shown for VOCs (van Warmerdam et al. 1995; Beneteau et al. 1999).

Although IRMS measurements provide only bulk $\delta^{13}\text{C}$ values and the isotope information on the individual nuclei gets lost, the evaluation of $\delta^{13}\text{C}$ values of POPs still can provide valuable insights into kinetics, mechanisms and even the history of pollution. Partitioning of isotopes between two compounds containing the same element (or between two phases) with different isotopic ratios is called isotope fractionation (Mariotti et al. 1981). In a simple reactant-product (two component) scheme, the kinetic isotope fractionation factor α can be dealt using the mathematical description developed by Rayleigh (1896) for the fractional distillation of mixed liquids. This classical relationship originally derived for fractionation in the diffusion of gases was later used to describe kinetic isotope fractionation in different disciplines of natural science

(Elsner et al. 2005). For isotope analysis, the Rayleigh equation was transferred by taking advantage of the δ notation (Mariotti et al. 1981). Initially developed for nitrogen isotopes, this model has been used to determine the isotopic fractionation and the amount of transformation of contaminants in single step unidirectional reactions (32.3):

$$\ln R_t/R_0 = \ln[(1,000 + \delta^{13}\text{C}_0 + \Delta \delta^{13}\text{C}) / (1,000 + \delta^{13}\text{C}_t)] = (\alpha - 1) \ln f = \varepsilon 10^{-3} \ln f \quad (32.3)$$

with

R_0 and R_t being the $^{13}\text{C}/^{12}\text{C}$ ratios at start (0) and after the transformation (t)

α : fractionation factor of the reaction

f : fraction of parent compound remaining

$\delta^{13}\text{C}_0$: initial isotopic signature of the parent compound

$\delta^{13}\text{C}_t$: isotopic signature of the compound after transformation

$\Delta\delta^{13}\text{C}$: difference in the isotopic signature between after transformation (C_t) and before transformation (C_0)

ε : is the enrichment factor in ‰ with $\varepsilon = 1,000(\alpha - 1)$

Using $\delta^{13}\text{C}_0$, $\delta^{13}\text{C}_t$ and α , the extent of transformation can be calculated (Hirschorn et al. 2007). Non-degradative processes such as volatilization, dissolution and sorption were found to be relatively non-fractionating in terms of isotope distributions while degradation processes usually produce significant isotopic enrichments in (volatile) chlorinated aliphatics (Hirschorn et al. 2007). Quantitative estimates of the extent of biotransformation using the Rayleigh model provide conservative estimates of the extent of biotransformation (Hirschorn et al. 2007). In a wider, more general scope, it is a chemical reaction with cleavage of covalent bonds that has the highest contribution to isotope fractionation (Elsner et al. 2005). Significant isotope fractionation can only be expected at positions where covalent bonds (and to a lesser degree adjacent positions with impact on the nucleus studied) are broken or formed during the rate-limiting step(s) of a given process. Processes that act on the compound as a whole such as advective-dispersive transport, volatilization, sorption/desorption or binding to an enzyme cause much smaller changes in the

overall isotope composition, which are often not detectable within the precision of the analytical method (Elsner et al. 2005).

As pointed out, the heavier isotopes will react more slowly than the lighter normal isotope effect. This results in the known normal kinetic isotope effect (KIE).

$$\text{KIE} = \frac{\text{rate constant of light isotope/}}{\text{rate constant of heavy isotope } (k_L/k_H)}$$

Inverse isotope effects are scarce. All isotope effects are mass-dependent. The mass is related to vibrational and not electronic energies (i.e. the determining factors for activation energies in reactions). Therefore, KIEs are not directly correlated with reaction rates. Degradation of POPs is mostly dependent on the cleavage of C–Hal bonds, and this can be assumed to have the following major consequences. Briefly, the KIE will be higher if:

1. The relative mass difference is higher (so that it is higher for H than C isotopes)
2. The mass of the bonded partner is higher (for instance Br > Cl)
3. The bond strength is changed between ground and transition state of a reaction

The type of reaction (S_N1 or S_N2) has an effect, too (Elsner et al. 2005). An in-depth evaluation of this topic is beyond the scope of this review, and readers are recommended to refer to the original textbooks or the review of Elsner et al. (2005) as valuable introductions to this topic. Typical KIE for reactions involving cleavage of C–Cl bonds are in the range $\text{KIE} = 1.00 - 1.03$ (S_N1) and $\text{KIE} = 1.03 - 1.09$ (S_N2) (Elsner et al. 2005). The effect will be greater for C–Br bonds (see (2), above). Oxidative processes such as epoxidation are in the range 1.01–1.02. The values and ranges might appear small especially for POPs where the dilution effect mentioned above overlay the measurements due to the multiple carbons that remain unaltered.

Elsner et al. (2005) pointed out that the current use of the Rayleigh model has some limitations. Its merits are undisputed for simple situation (one compound transferred into another) but it is unclear if it will be valid for more complex situations which are found when POPs and other pollutants are investigated in

natural systems. For instance let a compound be transformed to another with a change in the $\delta^{13}\text{C}$ value. Elsner et al. (2005) pointed out that under environmental conditions, permanent input of a reactant into the system being studied will dilute the isotope effect which may become hard to measure (due to small changes in the $\delta^{13}\text{C}$ value) and to interpret (if transformation effect on $\delta^{13}\text{C}$ value is not exactly known). Thus, the measured KIE usually referred to as the apparent KIE (AKIE) and may not be identical with the intrinsic KIE.

A procedure on how to use experimental IRMS data to determine the KIE, was shown by Elsner et al. (2005) for CCl_4 dehalogenation. Linear regression of plots of ϵ over $\ln f$ according to (32.3) results in a straight line with the slope (here: -0.0262) being the $\delta^{13}\text{C}$ value of -26.2‰ (Fig. 32.5). Insertion of the $\delta^{13}\text{C}$ value (in form of -0.0262) gives the fractionation factor $\alpha = 1.000 - 0.0262 = 0.9738$. The KIE is the reciprocal value of this measurement, i.e. ~ 1.027 (Elsner et al. 2005). This means that over the whole reaction time, $^{12}\text{CCl}_4$ molecules reacted 1.027-fold more than $^{13}\text{CCl}_4$ molecules. As a consequence, the remaining reactant CCl_4 (S_t) at a given time will be relatively enriched in ^{13}C (i.e. a less negative $\delta^{13}\text{C}$ value compared to S_0).

However, this relation is only valid for the conversion of one reactant S into one product P (which does not undergo degradation). This situation is hardly found for POPs because the P with one halogen less

will be transformed into product P' with two halogens less (and so on). Therefore, the transformation/dehalogenation rate of such intermediate products cannot be simply determined by the Rayleigh model (Hirschhorn et al. 2007). In such scenarios the real amount of degradation will likely be higher than those calculated by means of the Rayleigh model (compare AKIE with KIE). Different models have been developed for calculations in such situations (Elsner et al. 2005; van Breukelen 2007). However, the database for POPs is currently too small to warrant adoption of these models to the compounds dealt in this chapter.

32.3 Applications of Stable Isotope Analyses of POPs

32.3.1 Bulk $\delta^{13}\text{C}$ Values of Polyhalogenated POPs

Most POPs and VOCs are synthesized from raw materials from the petroleum industry. Petroleum $\delta^{13}\text{C}$ values (typical starting materials from crude oil/coal: -33 to -19‰) (Whiticar 1996) usually match those of POPs (Drenzek et al. 2002) but some halogenated VOCs (e.g. chloroform and carbon tetrachloride) had $\delta^{13}\text{C}$ values of ~ -38 and -45‰ , respectively, and were isotopically lighter in carbon (Zwank et al. 2003). Consequently, the carbon signature of the raw materials is occasionally retained by the product during the synthesis of POPs in contrast to some VOCs. Because of the given wide range of $\delta^{13}\text{C}$ values for petroleum, and hence petrochemicals, the isotope signature of the starting materials might constitute the key factor for the bulk $\delta^{13}\text{C}$ values of POPs. This would mean that the same polyhalogenated compound or mixture produced by different companies could be distinguished by their $\delta^{13}\text{C}$ values if they were made from starting materials with different $\delta^{13}\text{C}$ values, and to a lesser degree because of the reaction pathways and/or post-reaction procedures such as precipitation/crystallization, separation/purification, or any other fractionation step. If the same product of a multicomponent mixture with different degrees of halogenation such as PCBs, is produced from the same quality of raw material from the same source at a given period, then, the reactant (e.g. biphenyl in the case of PCBs),

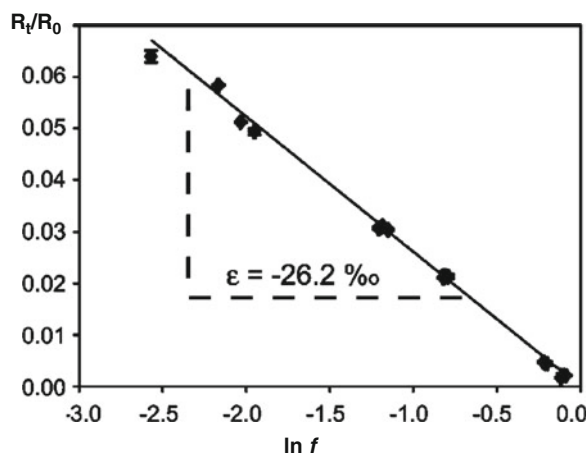


Fig. 32.5 Rayleigh plot of the reductive dechlorination of CCl_4 by a reduced porphyrin (Elsner et al. 2005), with $R_t/R_0 = [(1,000 + \delta^{13}\text{C}_0 + \Delta \delta^{13}\text{C}) / (1,000 + \delta^{13}\text{C}_t)]$ and $\ln f = \ln[(\text{CCl}_4)_t / (\text{CCl}_4)_0]$ according to (32.3)

is expected to have constant $\delta^{13}\text{C}$ values within the range of petrochemicals. If we further assume that no carbon is lost during the synthesis and that the biphenyl quantitatively reacted to a technical PCB mixture, it is likely that the $\delta^{13}\text{C}$ value of the product will match that of the reactant. Moreover, PCB products of the same manufacturer halogenated to different degrees (processed from the same raw material) would have the same $\delta^{13}\text{C}$ value. This is the situation described for closed two-component systems (Mariotti et al. 1981):

$$P_t + S_t = S_0 \quad (32.4)$$

with

S_0 = isotope composition of the reactant at start

S_t = isotope composition of the reactant at any point t of the reaction

P_t = isotope composition of the product at any point t of the reaction

Expressed for a closed multicomponent system we obtain (32.5):

$$\sum P_t + S_t = S_0 \quad (32.5)$$

In (32.5), all reaction products are summed up by taking into account the molar proportions of the individual compounds that contribute to the reaction mixture. In a closed system, the bulk $\delta^{13}\text{C}$ value before and after a reaction will be unaltered. The pre-requisite is that no reactant (or product) is lost (so that all products are determined with the bulk value), and this is independent of the amount of reactant consumed. Likewise, the number of products will not play a role but it is essential that all products produced are registered. A reaction in which all reactant is converted into one or more products, can be expressed as follows:

$$\sum P_t = S_0 \quad (32.6)$$

with $S_t = 0$; S_0 = isotope composition of the reactant at start and P_t = isotope composition of the product at anytime t of the reaction.

In this context a lab-experiment was carried out with camphene (i.e. the starting material of toxaphene) by Vetter et al. (2006a). The reactant camphene had a

bulk $\delta^{13}\text{C}$ value of -30.5‰ , and low, medium, and high chlorinated toxaphene produced by the three chlorination products of this camphene gave bulk $\delta^{13}\text{C}$ values of -30.5 , -30.5 , and -30.1‰ , respectively. It was assumed that the slight difference observed for the high-chlorinated toxaphene was due to analytical problems rather than the course of the chemical reaction (Vetter et al. 2006a). For instance the uncertainty in the $\delta^{13}\text{C}$ value determination of volatile polyhalogenated compounds (i.e. the precision) usually reported is $\sim 0.5\text{‰}$ (Hirschorn et al. 2007). We must also take into account that the higher the degree of chlorination of a compound or mixture, the less the carbon contributes to its mass. A PCB (mixture) with three chlorine substituents (on average) has a carbon content of $\sim 56\%$ while the perchlorinated PCB 209 has a carbon content of $\sim 29\%$ only. Consequently, determination of the $\delta^{13}\text{C}$ value will be more difficult the higher the degree of halogenation is. Typically, the deviations in the $\delta^{13}\text{C}$ values increase with increasing degree of halogenation. The synthesis experiment with camphene confirmed predictions made by Drenzek et al. (2001) who analyzed different PCB mixtures produced in the same plant and found rather narrow bulk $\delta^{13}\text{C}$ values ($-26.17 \pm 0.37\text{‰}$, $n = 10$). The authors reported an excellent precision of 0.10‰ for the measurements (but it is still difficult to conclude that the accuracy was on the same level for all products, although there are no concerns). Changes in the $\delta^{13}\text{C}$ value by 0.4‰ during the reductive dechlorination of a PCB congener were not considered to be an isotopic effect. Based on these evaluations the variations observed in technical PCBs by Drenzek et al. (2001) and that in the chlorination of camphene (Vetter et al. 2006a) represent no isotope effect.

In their ground-breaking paper, Jarman et al. (1998) studied bulk $\delta^{13}\text{C}$ values of technical PCB mixtures from four manufacturers (for more information on PCBs see Sect. 32.3.1.1). They reported an increased depletion in ^{13}C with increasing average chlorine content of the technical PCBs. However, this statement was not fully justified by the data shown in the paper: the Clophen products did not consistently follow this trend (Table 32.1) and five Kanechlors showed only slightly more negative $\delta^{13}\text{C}$ values. Finally, only the heaviest Phenoclor mixture was depleted in ^{13}C compared to the other Phenoclors. Furthermore, the $\delta^{13}\text{C}$ value reported by Drenzek et al. (2002) for the same type of (heavy) product was $\sim 2\text{‰}$ less depleted in ^{13}C

Table 32.1 Bulk $\delta^{13}\text{C}$ values (‰) of different commercial PCB products (data from Jarman et al. 1998, except where noted)

Technical PCB product (number of products analyzed)	$\delta^{13}\text{C}$ values (‰)
Clophen ($n = 3$)	-26.95/-25.46/-26.26 ^a
Kanechlor ($n = 5$)	-25.00/-25.31/-25.69/-25.39/-25.67 ^a
Aroclor ($n = 1$)($n = 12$) ^b	-26.13/-26.17 ^b
Phenoclor ($n = 4$)($n = 1$) ^b	-22.34/-22.67/-22.50/-25.63 ^c or -23.55 ^b

^aProducts listed with increasing chlorine content

^bData from Drenzek et al. (2002)

^cPotential outlier

and closer to the $\delta^{13}\text{C}$ value observed for other Phenoclor (Table 32.1). If we re-evaluate the bulk $\delta^{13}\text{C}$ of PCBs, one may come to the conclusion that the $\delta^{13}\text{C}$ values of products from the same producer were rather constant. In this context it will be valuable to study bulk $\delta^{13}\text{C}$ values of other polyhalogenated compounds.

The relationship between the reactants and products discussed above may be used to get access to secondary standards of POPs with known $\delta^{13}\text{C}$ values. Suitable laboratory standards of polyhalogenated compounds could be obtained by the halogenation of a non-halogenated reactant with known isotope composition. In a closed system reaction where only one product is obtained, the bulk $\delta^{13}\text{C}$ value of reactant and product will be the same (see (32.6) with only one product formed). Thus, the bulk $\delta^{13}\text{C}$ value of the unhalogenated reactant may be used to verify the accuracy of the halogenated product.

32.3.1.1 Bulk $\delta^{13}\text{C}$ Values of Polychlorinated Biphenyls (PCBs)

The commercial production of PCBs started in 1929 (Tanabe 1988). Technical PCB mixtures with different chlorine content were produced worldwide for use in a wide field of industrial applications (DFG 1988). Major producing countries/products were USA/Aroclor (61.4%), Germany/Clophen (12.4%), France/Phenoclor (9.6%), UK (6.3%), Japan/Kanechlor (5.6%), Spain (2.4%) and Italy (2.2%) while detailed data from Eastern Europe (e.g. former CSSR/Delcor and USSR/Sovol) is not available (Kannan et al. 1991). In 1966, PCB residues were discovered (Jensen 1966) and since then have been found in every environmental compartment throughout the world. Although the application range has been stepwise reduced since the 1970s and finally a global ban was declared in the Stockholm convention. PCB residues are still a major environmental

problem and PCBs research is still very active after more than 40 years. In theory, 209 PCB congeners can exist and about 130 of them have been identified in different technical products (Frame 1996a, b). Individual PCB mixtures still contain 60–70 different PCB congeners which are difficult to separate by GC. In fact, a range of co-elutions have been reported irrespective of the column type and conditions used (Frame 1996a, b).

As mentioned above, it is likely that different products produced within one plant at a given time have more or less identical bulk $\delta^{13}\text{C}$ values. In the following, published bulk $\delta^{13}\text{C}$ values of such products were rounded to the mean after elimination of potential outliers. Based on this data treatment, different Clophens ($\delta^{13}\text{C}$ value -26.3‰), Kanechlors ($\delta^{13}\text{C}$ value -25.4‰), Phenoclor ($\delta^{13}\text{C}$ value -22.5‰) and one Aroclor ($\delta^{13}\text{C}$ value -26.1‰) showed some distinct differences (Jarman et al. 1998). Similar results can also be extracted from data provided by Drenzek et al. (2002) who studied 12 Aroclor samples (according to the data available all Aroclor was generated in the only PCB-producing plant in North America located in Alabama) and determined the $\delta^{13}\text{C}$ value to be $-26.17 \pm 0.37\text{‰}$ (Table 32.1). This value is in excellent agreement with the sample studied by Jarman et al. (1998). These analyses also covered the same (labeled) Aroclor products which spanned over 0.4 and 0.6‰. Since the same technique was used this range could represent different periods or more generally batches. It appears that Phenoclor has distinct bulk $\delta^{13}\text{C}$ value in that they were heavier in carbon than the other PCB products.

32.3.1.2 Bulk $\delta^{13}\text{C}$ Values of Chloropesticides

DDT was the most frequently used pesticide in the 1950s and is one of the most controversial chemicals ever synthesized. On one hand, its use as an insecticide

in the control of Malaria saved the life of millions of humans. On the other hand, the massive use in agriculture led to severe environmental pollution and the detection of DDT in animals and its investigation may be seen as the starting point of environmental chemistry. DDT is synthesized by the condensation of chloral hydrate ($\text{Cl}_3\text{C}-\text{CH}(\text{OH})_2$) with chlorobenzene. The process not only yielded the desired *p,p'*-DDT but also *o,p'*-DDT along with many other minor products (WHO 1989). Technical DDT (Aldrich, technical grade) and a sample of neat *p,p'*-DDT (Ultra Scientific) had bulk $\delta^{13}\text{C}$ values of -28.3% (Drenzek et al. 2002). Less depleted in ^{13}C were several DDT-related standards from other sources ($\delta^{13}\text{C}$ values -27.5 to -22.9% , Vetter et al. 2006a). Some of these standard compounds were of analytical and some of technical grade, and thus difficult to compare because the procedures for purification may alter the isotope composition (Vetter et al. 2006a). The range of $\delta^{13}\text{C}$ values was comparable with the PCBs despite the very different routes of production. PCBs are obtained by the chlorination of biphenyl and – as discussed above – should resemble the $\delta^{13}\text{C}$ value of the starting material. In the case of DDT, already the technical production of the volatile chloral could have been accompanied with a stronger depletion of ^{13}C (as found e.g. for CHCl_3 , see above), the starting material and the reaction, and finally, the purification in order to obtain standards could have added some isotope fractionation effects, too.

Toxaphene is special in that it is produced from young carbon (and not from petrochemicals) by chlorination of waste from tree production (Saleh 1991). The multicomponent mixture consists of $\sim 1,000$ compounds (Korytár et al. 2003). However, only a few of the compounds of technical toxaphene are recalcitrant and thus accumulate in environmental samples (Vetter and Oehme 2000). Toxaphene was mainly produced in the USA along with lower amounts in Eastern Germany and Russia (Saleh 1991). Drenzek et al. (2002) combusted three samples of toxaphene and found bulk $\delta^{13}\text{C}$ values of -27.9 , -28.7 , and -28.2% , respectively. An authentic Hercules toxaphene (USA) had a bulk $\delta^{13}\text{C}$ value of -28.4% whereas the East-German product Melipax had a bulk $\delta^{13}\text{C}$ value of -27.6% and thus was slightly less depleted in ^{13}C (Vetter et al. 2006a).

Hexachlorocyclohexanes (HCHs) were produced for the first time in 1825 by M. Faraday. In 1912 van

der Linden succeeded in the isolation of α -, β -, γ - and δ -HCH from the reaction mixture. Technical HCH was used since the early 1940s as an insecticide. Later it was shown that γ -HCH (lindane) is the only active HCH isomer. Since 1950, technical HCH was gradually substituted with lindane (i.e. a product consisting of $>99\%$ γ -HCH, DFG 1983). Lindane is not specifically synthesized but has to be obtained from technical HCH by crystallization and/or extraction. This is important to note because this specific production procedure includes different steps that could be associated with isotope fractionation. However, the bulk $\delta^{13}\text{C}$ values of three samples of lindane (-26.3 , -25.6 , and -25.9%) were in a narrow range (Drenzek et al. 2002; Vetter et al. 2006a). Compared to lindane, other HCH isomers were lighter, with α -HCH being most depleted in ^{13}C (bulk $\delta^{13}\text{C}$ value -31.7% , Vetter et al. 2006a).

Technical grade chlordane and heptachlor are classic (hexachloro)cyclodiene chloropesticides. Two products differed by almost 9% in their bulk $\delta^{13}\text{C}$ values (Drenzek et al. 2002). This was surprising given the fact that the principal compounds in both products are identical except for one hydrogen on heptachlor substituted with chlorine in the case of chlordane. The bulk $\delta^{13}\text{C}$ values of two further cyclodiene pesticides (Aldrin and Dieldrin) were similar to heptachlor, and these three products were from the same source (Drenzek et al. 2002). Hence, it is almost impossible that the chlordane was produced with the same reactant. Further research would be useful if this difference can be generalized and if the origin of the residues of selected cyclodiene pesticides in environmental samples can be identified.

Two synthesized standards of pentachlorophenol (PCP) had bulk $\delta^{13}\text{C}$ values of -31.7 ± 0.1 and $-30.9 \pm 0.7\%$ (Horii et al. 2008).

32.3.1.3 Bulk $\delta^{13}\text{C}$ Values of Further POPs and Related Compounds

Brominated flame retardants (BFR) are a group of novel POPs. BFRs are routinely added to industrial products for several decades to reduce fire-related injury and property damage. The major compound classes with POP-like properties are polybrominated diphenyl ethers (PBDEs, see Sect. 32.3.2.3), polybrominated biphenyls (PBBs), and hexabromocyclododecane (HBCD).

PBDEs were produced with an average content of five, eight, and ten bromine substituents. The average carbon content in these products is only ~15–25%. A sample of technical pentabromodiphenyl ether (Bromkal 70-5DE, produced in Germany) had a bulk $\delta^{13}\text{C}$ value of -26.7‰ (Reddy et al. 2002a) and a sample of technical octabromodiphenyl ether from North America (DE-79) had a bulk $\delta^{13}\text{C}$ value of -27.9‰ (Rosenfelder et al. 2010). A sample of HBCD had a bulk $\delta^{13}\text{C}$ value of -25.9‰ (Vetter et al. 2006a). The BFR dibromopropyltribromophenyl ether (DPTE) is synthesized from bromoallyltribromophenyl ether (ATE) by addition of bromine (von der Recke and Vetter 2007). Since the bromination reaction of ATE can be performed quantitatively, the bulk $\delta^{13}\text{C}$ value should be unaltered, and this was in fact observed in terms of bulk $\delta^{13}\text{C}$ values of -28.70‰ (DPTE) (Rosenfelder et al. 2010) and -28.67‰ (ATE) (Rosenfelder et al. 2010, unpublished results).

Polychlorinated dibenzo-*p*-dioxins (PCDDs) and dibenzofurans (PCDFs) are a group of toxic POPs that occur as (unintended) by-products in various processes. The synthesized perchlorinated congeners octachlorodibenzo-*p*-dioxin (OCDD) and octachlorodibenzofuran (OCDF) were analyzed by Horii et al. (2008). The bulk $\delta^{13}\text{C}$ value of OCDD ($n = 4$) ranged from -30.7 to -28.6‰ and was lighter than that of OCDF (bulk $\delta^{13}\text{C}$ values: -25.8 to -24.1‰) (Horii et al. 2008).

While the bulk $\delta^{13}\text{C}$ values of all POPs shown so far fell into the range of petroleum values (Fig. 32.2), that of different brominated phenols, anisoles, and a guaiacol were frequently much lighter in carbon (Vetter et al. 2006a). Some of these compounds are also used in the synthesis of BFRs. 2,4,6-Tribromoanisole and a sample of pentachloroanisole were most depleted in ^{13}C with bulk $\delta^{13}\text{C}$ values of -38.2 and -36.1‰ , respectively (Vetter et al. 2006a).

Halogenated natural products (HNPs) are a further class of polyhalogenated compounds detected in the environment. Over 4,500 structural varieties are produced by algae, sponges and bacteria (Gribble 1998), some of these HNPs have been detected in organisms that were not the producers but received them in a similar way as anthropogenic POPs (Vetter 2006). A synthesized sample of the HNP 1'-methyl-2,3,3', 4,4',5,5'-heptachloro-1,2'-bipyrrole (Q1) had a bulk $\delta^{13}\text{C}$ value of -34.78‰ (Vetter and Gleixner 2006).

The only bulk $\delta^{13}\text{C}$ value of a non-commercially synthesized polyhalogenated compound that did not originate from the laboratory but was isolated by natural products chemists from a biological sample is that reported for the HNP 3,5-dibromo-2-(2',4'-dibromo)phenoxyanisole (BC-3). BC-3 isolated from its natural producer, the sponge *Phyllospongia foliascens*, was strongly depleted in ^{13}C and had a bulk $\delta^{13}\text{C}$ value of -35.9‰ (Drenzek et al. 2002). This value was unexpected because marine higher plants and organisms tend to be heavier than crude oil which resembles the range of cellulose (Whiticar 1996). Likewise marine plankton is isotopically heavier in carbon than freshwater plankton. Thus, the authors concluded that isotope fractionation might have occurred during isolation of the target compound from the sponge (Teuten et al. 2005). This was further evidenced by CSIA measurements of the $\delta^{13}\text{C}$ value of this compound and a further isomer isolated from whale blubber which was in the range -22‰ (Teuten et al. 2005). This example underscores the difficulties and limitations of EA-IRMS and some advantages in using GC-IRMS.

32.3.2 Compound-Specific Isotope Analysis (CSIA) of POPs by GC-IRMS

A reliable standard compound should give the same $\delta^{13}\text{C}$ value when analyzed by EA-IRMS and GC-IRMS (CSIA). However, this is not always the case with POPs. For instance, the $\delta^{13}\text{C}$ value of the heptahalogenated natural product Q1 differed by $\sim 0.6\text{‰}$ between EA-IRMS and CSIA (Vetter and Gleixner 2006). Similar results were also obtained in our laboratory for some other POP standards (unpublished results). This problem has been identified in the literature. For instance, bulk δ -values of PCBs presented by Jarman et al. (1998) were significantly heavier than mean value of the PCB congeners determined with CSIA. There are many possible sources of error in the CSIA system (e.g. caused by the GC part) so it might be plausible that $\delta^{13}\text{C}$ values determined with EA-IRMS are more accurate although this cannot be verified unequivocally at this point. However, since all isotope measurements are relative to a reference, the difference between individual isotope data obtained within a study ($\Delta\delta^{13}\text{C}$ values) can be evaluated and

easily transferred to other studies. Difficulties may arise with regard to the reported numbers (i.e. the $\delta^{13}\text{C}$ values measured in different labs) which may not be absolutely the same.

32.3.2.1 CSIA of Polychlorinated Biphenyls (PCBs)

While the bulk $\delta^{13}\text{C}$ values of technical PCB mixtures seem to represent the $\delta^{13}\text{C}$ value of the reactant biphenyl, this does not mean that the individual PCB congeners in these mixtures have identical $\delta^{13}\text{C}$ values. In fact, it was already shown in the first CSIA study by Jarman et al. (1998) that individual PCB congeners become more depleted in ^{13}C with higher chlorine content is. This is due to the fact that chemical bonds between heavy isotopes are less easily formed. Thus, halogens preferably add to the lighter isotope, ^{12}C . Considering the closed system already introduced in Sect. 32.3.1, the following scheme can be explained when the overlaying processes are separated: in the beginning of the reaction the reactant biphenyl (S_0 , $\delta^{13}\text{C}$ value $\equiv 0\text{‰}$) is chlorinated. Owing to the reactivity, addition of one Cl will result in a monochlorobiphenyl (P_1) which is lighter in carbon (negative $\delta^{13}\text{C}$ value relative to $S_0 \equiv 0\text{‰}$) while the remaining biphenyl (S_1) would become heavier (positive $\delta^{13}\text{C}$ value relative to S_0) in order to fulfill (32.4).

The same scheme can be applied again when the monochlorobiphenyl is converted into a dichlorobiphenyl (and a dichlorobiphenyl in a trichlorobiphenyl a.s.o). However, in this step the monochlorobiphenyl is the reactant which gets enriched in ^{13}C in this reaction. As a consequence, intermediate products will not permanently become depleted in ^{13}C , but eventually may drop back in direction $\delta^{13}\text{C}$ value of S_0 and even below. Consequently, the individual congeners in a mixture will be more depleted in carbon the higher chlorinated they are, and all $\delta^{13}\text{C}$ values of individual compounds will be spread around the bulk $\delta^{13}\text{C}$ value of the product, irrespective of the degree of halogenation. Indeed, such a gradient from low to high chlorinated can be tentatively extracted from the data compiled in Table 32.2. Within one product, low chlorinated congeners (those appearing at the top of the columns in Table 32.2) are heavier in carbon than the high-chlorinated congeners listed at the bottom of the respective column.

The data in Table 32.2 points us to another problem associated with CSIA of complex samples. Partly, the same technical PCB products were studied by different groups and it is likely that the isotope composition was very similar if not identical on all occasions. However, the individual $\delta^{13}\text{C}$ values varied widely. For instance, the $\delta^{13}\text{C}$ value of PCB 18 in Aroclor 1242 was reported to be -25.7 , -27.5 , and -26.9‰ and clearly extended beyond the accepted uncertainty of 0.5‰ associated with $\delta^{13}\text{C}$ value determinations of POPs. Different co-elutions were noted for PCB congeners (Frame 1996a, b) and it is likely that at least some of the deviations in these measurements have their origins in GC separation problems and for this purpose an in-depth evaluation of $\delta^{13}\text{C}$ values of individual PCB congeners needs to be carried out.

32.3.2.2 CSIA of Polychlorinated Naphthalenes (PCNs)

Technical PCN products with varied weight% of chlorine were produced mainly in the 1930s–1950s for various industrial applications (Jakobsson and Asplund 2000). In theory, 75 congeners may exist and each technical product contains various PCN congeners. Horii et al. (2005) determined $\delta^{13}\text{C}$ values of individual congeners in six technical PCN products by application of MDGC. The weight percentage of chlorine in the products ranged from 23 (~ 2 Cl atoms/molecule on average) to 60% (~ 5 Cl atoms/molecule on average). The $\delta^{13}\text{C}$ values of individual PCN congeners spanned from -26.3 to -21.7‰ . Average $\delta^{13}\text{C}$ values presented by Horii et al. (2005) were a little misleading because they did not take into account the quantities of individual PCNs but just calculated the mean value of the individual $\delta^{13}\text{C}$ values. Nevertheless, the results are in clear support of the principles demonstrated above with technical PCB mixtures. The congeners within a given technical product became depleted in ^{13}C with increasing Cl content. The technical PCN products (Halowax) were from the same source and it was apparent that the bulk $\delta^{13}\text{C}$ values were similar. The results also show that PCN congeners present in technical mixtures with different Cl content were heaviest in the highly-chlorinated product (Horii et al. 2005).

32.3.2.3 CSIA of Polybrominated Diphenyl Ethers (PBDEs)

From an environmental point of view, (poly)brominated diphenyl ethers (PBDEs) are the most relevant BFR. As with PCBs, 209 PBDE congeners can exist and the IUPAC numbers correspond with the PCB congeners. Technical PBDEs were available as penta-, octa-, and decabromo mixtures which all contain only a few congeners. The major congeners of technical PentaBDE are BDE 47 (ca. 38%), BDE 99 (ca. 49%), and BDE 100 (ca. 13%). Technical OctaBDE mainly consists of BDE 197 (ca. 22%) and BDE 183 (ca. 42%), while technical DecaBDE predominantly consists of BDE 209 (>90%) (La Guardia et al. 2006). While technical DecaBDE was used in the highest amounts, the main residues in the environment originate from BDE 47, BDE 99, and BDE 100, i.e. the major congeners of PentaBDE (although this product was used the least). Reductive debromination is thought to be a key-process in explaining the high amounts of low-brominated diphenyl ethers in environmental samples.

Technical PBDE mixtures composed of about ten PBDEs and a good GC separation of mixtures is much easier to achieve compared to PCBs (see above). On the other hand, the mass contribution of Br is higher than that of Cl and this reduces the amount of carbon in the molecule. For instance, carbon accounts for 44.0% of the molecular weight to DiBDEs, 25.5% to PentaBDEs (e.g. BDE 99) and only 15.0% to DecaBDE (BDE 209).

The $\delta^{13}\text{C}$ values of individual PBDE congeners in the technical PentaBDE product DE-71 followed the trend shown for PCBs (see above), i.e. they became depleted in ^{13}C with increasing degree of bromination, and the same tendency was also observed for the technical OctaBDE product DE-79 (Vetter et al. 2008; Rosenfelder et al. 2010). A closer look at the BDEs in both products shows that the three hexaBDEs (BDE 153, BDE 154, and BDE 138) present in both products had significantly different $\delta^{13}\text{C}$ values in both products. DE-71 was the highest brominated and thus were depleted in ^{13}C . The opposite was valid for the congeners in DE-79 where they represent low degrees of brominating and thus belong to the heaviest congeners (Vetter et al. 2008). Altogether, the $\delta^{13}\text{C}$ values of the three hexaBDEs differed by 3–6‰ in the two products (Vetter et al. 2008).

32.3.3 Stable Isotope Analysis of POPs in Environmental Samples and Lab Reactions (Case Studies)

A number of studies with POPs in environmental samples or in reactions that simulate environmental processes (application of standards to anaerobic solutions, UV-irradiation) have been evaluated by taking advantage of isotope data. Most of these studies focused on the transformation of individual POPs by dehalogenation reactions. A brief summary of issues associated with the $\delta^{13}\text{C}$ values is presented here. Isotopomer fractionation of 14‰ was considered severe (see Sect. 32.2.3). The POPs discussed below have 6–12 carbons and the non-reacting carbons will thus dilute the result because they are combusted as well. Thus, effects measured in such reactions with POPs can change the $\delta^{13}\text{C}$ value by 1‰ and are considered to be quite significant. Noteworthy, this is the range of isotope fractionation observed in the chemical reaction leading to the POP mixtures. Still changes in the range of 0.3–0.5‰ can be interpreted as relevant isotope effects, and this is within the range of the precision of $\delta^{13}\text{C}$ value measurements. Therefore, it is difficult to unequivocally identify isotope effects with POPs. The following studies are also examined in this regard.

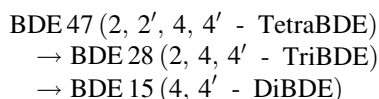
32.3.3.1 Anaerobic Transformation of a PCB Congener

Drenzek et al. (2001) studied the transformation of 2,3,4,5-tetrachlorobiphenyl (PCB 61) by dehalogenating bacteria. PCB 61 is not present in any technical PCB mixture, and errors (e.g. from lab background) can be excluded. After 90 days, approximately 90% of the PCB 61 was converted into 2,3,5-trichlorobiphenyl (PCB 23) with no other products being detected (Drenzek et al. 2001). The $\delta^{13}\text{C}$ value of reactant and product were relatively constant throughout the reaction. For the reactant PCB 61 a $\delta^{13}\text{C}$ value of -28.2‰ was observed while the product PCB 23 had a $\delta^{13}\text{C}$ value of -27.8‰ (Drenzek et al. 2001). The average difference in the $\delta^{13}\text{C}$ value of reactant and product was 0.3‰ and significant at 95% but not at 98% confidence level (Drenzek et al. 2001). As pointed out by Drenzek et al. (2001), the $\delta^{13}\text{C}$ value was in

the range of the uncertainty of $\delta^{13}\text{C}$ value determinations of 0.5‰ for polyhalogenated compounds. This assessment by the authors is further underscored by the direction of the potential development of the $\delta^{13}\text{C}$ value. In reactions of the type shown in (32.4), the $\delta^{13}\text{C}$ value of the reactant should become heavier than that of the product due to the higher strength of the bonds with heavy isotopes.

32.3.3.2 Light-Induced Transformation of Polybrominated Diphenyl Ethers (PBDEs)

Rosenfelder et al. (2010) irradiated BDE 47 and technical DE-79 by means of a sunlight simulator. In either case, remarkable isotope effects were observed for both the reactants and the products. BDE 47 was irradiated for 110 and 160 min, respectively, and the reactant (BDE 47) and the predominant products (BDE 28, BDE 15) were monitored:



After 110 and 160 min of irradiation, BDE 47 became enriched in ^{13}C by 1.8 and 3.1‰, respectively. After 110 min, BDE 28 and BDE 15 became depleted in ^{13}C by 0.1 and 2.2‰, respectively, compared to the initial value for BDE 47. After 160 min, BDE 28 became heavier by 0.3‰ and BDE 15 by 0.5‰ (Rosenfelder et al. 2010). This course of the reaction can be explained as follows: The average $\delta^{13}\text{C}$ value (i.e. the bulk $\delta^{13}\text{C}$ value) has to be retained in this closed system. Because of the stronger bonds between heavier isotopes, BDE 47 must become permanently

heavier, and this was observed. At the start, when only BDE 28 was formed, this product (BDE 28) compensated for this by becoming lighter. However, BDE 28 was not only formed from BDE 47 but also converted into BDE 15. In turn, the heavier isotope will react less, so that BDE 28 became heavier in carbon while the resulting BDE 15 became lighter. Between 110 and 160 min, BDE 15 became heavier in carbon (but still was much lighter than BDE 47 at start) which may look odd. However, we must take into account that BDE 15 is much more persistent than BDE 28 (and BDE 47). Thus, comparably more BDE 28 will be converted into BDE 15, and BDE 28 became heavier between 110 and 160 min (Rosenfelder et al. 2010). The strong isotope effect observed in both reactant and products is remarkable because it completely differed from the anaerobic transformation of PCBs (see Sect. 32.3.3.1). Between start and 110 min of irradiation, BDE 47 became heavier in carbon by 1.8‰. This effect must solely go back to changes on C-2 from which the bromine is removed. Due to the symmetrical substitution of BDE 47, this carbon represents 1/6 of the molecule carbon. Thus, the isotope effect at C-2 would be $1.8 \times 6 = 10.6\%$, by which this isotopomer became heavier compared to its starting value. This can be considered as a severe isotope effect (see above). This was mostly at the cost of BDE 15, whose C-2 carbon(s) became depleted in ^{13}C to the same extend.

More complex interactions were observed when DE-79 was UV-irradiated for 80 min (Table 32.3) (Rosenfelder et al. 2010). During UV/vis-irradiation with simulated sunlight, the $\delta^{13}\text{C}$ values of the major compounds BDE 183 and BDE 197 became enriched in ^{13}C . By contrast, the newly formed Tri- to PentabDEs became depleted in ^{13}C . As a consequence, in the solution at start (i.e. the technical product), the

Table 32.3 $\delta^{13}\text{C}$ (‰) values of different BDE congeners (mean and standard deviation) in the technical products DE-71 and DE-79 as well as during the UV/vis-irradiation of DE-79 (Rosenfelder et al. 2010)

	BDE 28	BDE 47	BDE 100	BDE 99	BDE 154	BDE 153	BDE 183	BDE 197
DE-71	n.d.	-27.1 (±0.3) (n = 8)	-28.9 (±0.3) (n = 9)	-29.8 (±0.2) (n = 8)	-30.4 (±1.1) (n = 9)	-32.4 (±1.1) (n = 2)	n.d.	-
DE-79	-	-	-	-	-26.8 (±0.4) (n = 2)	-26.6 (±0.1) (n = 6)	-29.8 (±0.2) (n = 6)	-30.8 (±0.1) (n = 4)
DE-79 (UV/vis, 80 min)	-30.0 (±0.1) (n = 4)	-28.6 (±0.5) (n = 4)	-29.0 (±0.1) (n = 3)	-27.6 (±0.6) (n = 4)	-28.1 (±1.0) (n = 4)	-25.5 (±0.3) (n = 4)	-25.6 (±0.4) (n = 4)	n.d.

n Repetitive injections (Nalimov outliers were eliminated); *n.d.* not detected

$\delta^{13}\text{C}$ values *decreased* with increasing degree of bromination from -26.8 to -30.8‰ while after the irradiation they *increased* with increasing degree of bromination from -30.0 to -25.6‰ (Table 32.3). If the decisive reactions of the reductive debromination of high-brominated BDE congeners are accompanied with similar isotope effects, the $\delta^{13}\text{C}$ values of BDE 47, BDE 99, and BDE 153 in environmental samples can be used to elucidate their origins: if these $\delta^{13}\text{C}$ values become lighter in this order, the BDE residues would originate mainly from DE-71, if they become heavier in this order, they would originate from the transformation of higher brominated BDE congeners (Rosenfelder et al. 2010).

32.3.3.3 Isotope Analysis of Polychlorinated Dibenzo-*p*-Dioxins (PCDDs)

Ewald et al. (2007) studied the microbial degradation of two PCDD standards (1,2,4-TriCDD and 1,2,3-TriCDD) with *Dehalococcoides*. In both occasions chlorine was removed at the position flanked by the most electronegative substituents (i.e. position 1 in 1,2,4-TriCDD and position 2 in 1,2,3-TriCDD). For both reactants, the product is 1,3-DiCDD. The same principle led to the next dehalogenation product in form of 2-MonoCDD. The latter, 2-MonoCDD, was trapped by headspace SPME (Ewald et al. 2007). This process is not quantitative but simplified the sample clean-up (Ewald et al. 2007). Tests with standard compounds verified that the headspace SPME procedure had only a minor effect on the $\delta^{13}\text{C}$ value. The sterile control showed no alteration in concentration or $\delta^{13}\text{C}$ value. In addition, 1,2,3-TriCDD was enriched in $\delta^{13}\text{C}$ by 1.6‰. In the case of 1,2,3-TriCDD the alteration must go back to C-2, which is only one out of eight carbons. Consequently, the C-2 carbon would have become heavier by 12.8‰ (see discussion above on dilution effects). This has to be considered as a severe isotope effect at this position. This interpretation differs from that given by Ewald et al. (2007). No isotope effect could be identified for 1,2,4-TriCDD. However, the end product 2-MCDD was lighter in carbon once it was formed but became gradually enriched in ^{13}C throughout the reaction. This would point towards a much higher stability compared to the TriCDDs and 1,3-DiCDD.

The Rayleigh model (Sect. 32.2.3) was applied to 1,2,3-TriCDD. The fractionation factor α (see (32.3), Sect. 32.2.3) of the reaction was 1.00092 and thus one order of magnitude lower than in the case of TCE (Nijenhuis et al. 2005). However, when the dilution effect (Ewald et al. 2007) is eliminated, the actual effect on the carbon involved was almost comparable to that observed in the transformation of TCE (Nijenhuis et al. 2005). In fact, the authors concluded that isotope data will be a suitable parameter to study the PCDD degradation in field (Ewald et al. 2007). The approach was further expanded by transformation experiments with 1,2,3,4-tetrachlorodibenzo-*p*-dioxin which was converted into 1,2,4-TrCDD and 1,3-DCDD (Liu et al. 2010). The results confirmed carbon isotope fractionation during sequential reductive dechlorination of PCDDs (Liu et al. 2010).

Horii et al. (2008) measured OCDD from different sources and found discrete ranges in the $\delta^{13}\text{C}$ value (Fig. 32.6). Compared to the standards analyzed ($\delta^{13}\text{C}$ value $\sim -30\text{‰}$), OCDD was enriched in ^{13}C in fly ash and ball clay samples while it was lighter in OCDD from PCP. The $\delta^{13}\text{C}$ values of OCDD in sediment and soil spanned over a wider range than the standards measured (Fig. 32.6). The difference between the classic OCDD sources (PCP and fly ash) was about 10‰. The sample size was not suited to generalize these values in a global content, and, as stated by Horii et al. (2008), further OCDD sources have to be taken into account in future. However, the observed

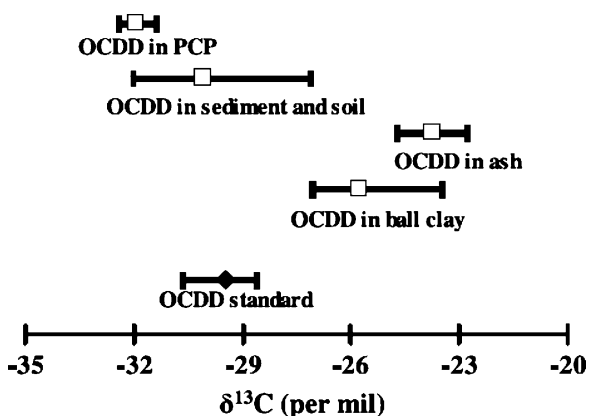


Fig. 32.6 Mean and range of $\delta^{13}\text{C}$ values of OCDD in ball clay and anthropogenic source materials, along with OCDD standards. The $\delta^{13}\text{C}$ value of OCDD in each matrix were 25.8‰ for clay, 30.1‰ for soil and sediment, 23.7‰ for fly ash, 31.9‰ for PCP, and 29.5‰ for OCDD standard (Horii et al. 2008)

differences in the $\delta^{13}\text{C}$ value are very promising especially also with regard to different modes new formation and degradation reactions which permanently may change or dilute isotope effects. Again it may be re-called that transformation of the reactant OCDD would lead to a permanent enrichment of ^{13}C (e.g. in soil or sediment). Consequently, the authors also suggested that there is a chance to distinguish naturally produced OCDD from anthropogenic OCDD (Horii et al. 2008). Natural formation of OCDD in kaolin clay has been suggested by Rappe et al. (2001) and Gaus et al. (2002).

32.3.3.4 Isotope Analysis of the Bacterial Degradation of Lindane

Badea et al. (2009) studied the degradation of lindane by sulphate-reducing bacteria (*Desulfococcus multivorans* and *Desulfovibrio gigas*) using the Rayleigh model approach in combination with stable carbon isotope analysis. The bacteria were found to transform lindane as follows: lindane \rightarrow 3,4,5,6-tetrachlorocyclohexene \rightarrow 5,6-dichlorocyclohexa-1,3-diene \rightarrow benzene/chlorobenzene (Badea et al. 2009). In all experiments with living cells the $\delta^{13}\text{C}$ value of lindane was changed during the dehalogenation (Badea et al. 2009). With *D. gigas*, lindane became enriched in ^{13}C with time (from -27.6‰ at start to -16.4‰). In this period, 95% of the lindane was consumed. After 6 days, chlorobenzene was detected with an initial $\delta^{13}\text{C}$ value of -29.6‰ . At the end of the experiment the chlorobenzene became heavier and it ended with a $\delta^{13}\text{C}$ value of -26‰ which is slightly heavier than the starting material. The results obtained with *D. multivorans* were similar (Badea et al. 2009). Unfortunately, further intermediate or dead-end metabolites could not be studied, so that a mass balance could not be established. However, the data was used to calculate the isotope enrichment factor ϵ (Fig. 32.7).

32.3.3.5 CSIA of Toxaphene Congeners in Technical Mixtures and Antarctic Seals

The multicomponent mixture toxaphene (Sect. 32.3.1.2) cannot be separated even by MDGC. Therefore, the $\delta^{13}\text{C}$ value of individual compounds in the technical

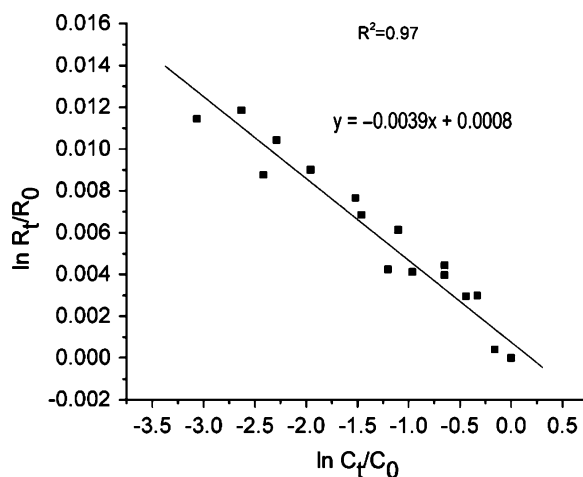


Fig. 32.7 Quantitative assessment of isotope fractionation of lindane in dechlorination experiments with *D. gigas* using the Rayleigh model using the bulk enrichment factor $\epsilon = -3.9$ (Badea et al. 2009)

product cannot be determined by GC-IRMS but have to be isolated and enriched. Vetter et al. (2006b) used HPLC to isolate the main toxaphene pollutants 2-endo,3-exo,5-endo,6-exo,8,8,10,10-octachlorobornane (B8-1413) and 2-endo,3-exo,5-endo,6-exo,8,8,10,10-octachlorobornane (B9-1679) from two technical products and an extract of Antarctic Weddell seal (*Leptonychotes weddelli*). The $\delta^{13}\text{C}$ value of B8-1413 isolate from Melipax varied by 2‰ in the replicates, and only one isolate from Toxaphene could be analyzed, the uncertainty was rather high. The latter was lighter and this agreed with determinations of the bulk value (see above). The value of B8-1413 in the Weddell seal sample fell between the two technical products (Vetter et al. 2006b). Still, the $\delta^{13}\text{C}$ value of the compounds in the seal was in proximity to the technical products. This is interesting because the toxaphene congeners were likely long-range transported to Antarctica (which could be associated with isotope fractionation due to different volatilities and with UV transformation). In addition, they were bioaccumulated in the food chain and potentially transformed in these bodies since Weddell seals are top predators mainly feeding on fish. Although it is possible that these effects averaged out each other (distribution due to volatilization should result in depletion of ^{13}C), the rather unaltered $\delta^{13}\text{C}$ value points to rather little changes in the $\delta^{13}\text{C}$ values of the persistent toxaphene congeners in the environment (Vetter et al. 2006b). The absence of measureable

isotope effects was also reported for PCBs (Reddy et al. 2002a) whereas lindane (Badea et al. 2009) and BDEs (Rosenfelder et al. 2010) showed such an isotope effect.

32.3.4 Hydrogen Isotope Analysis of POPs

Armbruster et al. (2006) and Vetter et al. (2006a) published bulk $\delta^2\text{H}$ values of about 50 POPs. The bulk $\delta^2\text{H}$ values ranged from -230 to $+75\text{‰}$. These values clearly exceeded the range reported for petrol compounds at both ends. The positive $\delta^2\text{H}$ values were particularly surprising. The chlorination of camphene gave first indications as to how such values are generated. Starting from camphene ($\delta^2\text{H}$ value -325‰), ^2H was enriched with the increase in the product chlorination (bulk $\delta^2\text{H}$ values -233‰ for low-chlorinated camphene $\rightarrow -184\text{‰}$ for medium-chlorinated camphene $\rightarrow -96\text{‰}$ for high-chlorinated camphene) (Vetter et al. 2006a). In agreement with the theory, the heavier deuterium reacted slower and more ^1H was substituted with chlorine. SNIF-NMR was used to study the synthesis of toxaphene in the laboratory (Nikiforov et al. 2005). Starting from α -pinene, the different positions involved in the rearrangement to bornylchloride and the subsequent halogenation was studied. KIE of two were found during the chlorination accompanied with an enrichment of deuterium in the products (Nikiforov et al. 2005).

The bulk $\delta^2\text{H}$ values of the North American and the East German toxaphenes differed by 80‰ . This has most likely its origin in the monoterpene(s) used for the chlorination. An explanation could be that the US toxaphene plant is closer to the ocean and this would acquire a higher deuterium content in the reactant from this site (Armbruster et al. 2006). Aside from these samples mainly analytical standards were determined so far and it is difficult to evaluate these samples results because lack of experimental background data. However, two lindane samples showed bulk $\delta^2\text{H}$ values of -70 and -110‰ while the $\delta^{13}\text{C}$ values were almost identical (Armbruster et al. 2006). From these results it may be concluded that the combination of carbon and hydrogen isotope data will be more effective in tracking sources and pathways of POPs.

The $\delta^2\text{H}$ values 2,4-dibromophenol and 2,4-dibromoanisole are difficult to compare, since the phenolic

H is arbitrarily in the molecule. Since this OH is also determined by IRMS, the bulk $\delta^2\text{H}$ value of both compounds cannot be compared. By contrast, using SNIF-NMR the proportions of isotopomers can be determined (Vetter et al. 2006a). Evaluation of only the aromatic hydrogens demonstrated that deuterium of H-6 was enriched relative to H-5 and H-3 in 2,4-dibromophenol but not in 2,4-dibromoanisole (Fig. 32.4) (Vetter et al. 2006a). The isotopomer abundances can be linked to $\delta^2\text{H}$ values (only for the aromatic system), the $\delta^2\text{H}$ values of the individual isotopomers in 2,4-dibromophenol ranged from -122 to $+220\text{‰}$ while they ranged from -46 to $+17\text{‰}$ in 2,4-dibromoanisole (Augusti et al. 2009). These ratios helped to verify that the anisole was not formed from the present phenol. Furthermore, they clearly show how much the $\delta^2\text{H}$ value of a reactant can be changed by the substitution of just one hydrogen atom with chlorine.

32.4 Current Limitations and Future Perspectives

It is the concentrations of POPs in the environment that are of major concern since the days of Paracelsus, as higher concentrations hazardous to humans and the environment. For understanding the fate of pollutants (transport, metabolism, accumulation etc.), a second, independent parameter has to be evaluated as well. Suitable options for this purpose are physico-chemical data and models that take advantage of them. Other options are enantioselective data if the pollutant is chiral. Another, particularly promising tool in the field of POPs is stable isotope analysis. Several interesting findings have been elaborated so far but the benefits IRMS and SNIF-NMR may add to the field have not been exhaustively exploited. The major reason for this is that applications in POP research are still far from being a routine method. A range of instrumental and theoretical unknowns should be explored in order to bring also IRMS full to fruition in POP research.

Based on existing equipment, a better lab-to-lab intercalibration of the protocols for EA-IRMS to CSIA-IRMS for the measurements of $\delta^{13}\text{C}$ values of POPs would be a large step forward for the usefulness of this technique. The generation of a widely available

standard reference material (SRM) for polyhalogenated compounds would be useful in order to verify inter-comparability of $\delta^{13}\text{C}$ values. Currently, only a few groups are involved in stable isotope research of POPs, and a better precision would attract more researchers into the field.

It is very likely that the combination of multiple isotopic data will improve the quality of the assessment of POPs. Clearly, bulk isotope data were important in the beginning of IRMS research on POPs and still may add important aspects to the field. However, real progress can only be made when IRMS is coupled with a chromatographic separation system. In POP research, the choice will be GC given the complexity of the samples. In addition to $\delta^{13}\text{C}$ values it would be required to study the $\delta^2\text{H}$ values of POPs by GC-IRMS. A step forward in this direction was made by Chartrand et al. (2007) in the field of VOCs. Generally, the state of the art in the use of stable isotope analysis of water contaminants (VOCs) is much more developed compared to POPs and the articles published in this field (see Sherwood Lollar et al. 2001; Schmidt et al. 2004; Elsner et al. 2005) should be reviewed as well by those who wish to switch to IRMS in POP research. Moreover, it would be valuable to have $\delta^{37}\text{Cl}$ values and $\delta^{81}\text{Br}$ values at hand. Very promising bulk $\delta^{37}\text{Cl}$ value analyses (see the paper of Sturchio et al. (2011) for general aspects of chlorine isotopes) of technical PCB mixtures, PCB extracted from sediment, and of DDT transformation experiments have been carried out by Reddy et al. (2000, 2002b). These methods cannot be linked with a GC interface but, very recently, Aeppli et al. (2010) presented a method for the direct determination of $\delta^{37}\text{Cl}$ values of organochlorines by using benchtop gas chromatography-quadrupole mass spectrometry instruments. Moreover, Holmstrand et al. (2010) used GC interfaced to inductively coupled plasma mass spectrometry (GC/ICP-MS) for the compound-specific determination of $\delta^{81}\text{Br}$ values which was used for the analysis of PBDEs. Stable halogen isotope analysis will for certain add valuable facets to the field. Likewise, it would be important to generate more data on isotopomer distributions. Currently, only quantitative ^2H NMR is suited for such investigations with POPs. However, it would be desirable that quantitative isotopomer analysis ^{13}C NMR would become available as well. There is a chance that suitable methods will be introduced within this decade,

and it is evident that they will be suited to bring the theoretical understanding of carbon isotopomer distributions of POPs and many other compounds on a higher level. This will surely improve the theoretical understanding with regard to the interpretation of KIE of POPs. Even without isotopomer distributions, IRMS data can be used to model the transformation rates of pollutants.

Finally, the *polluter pays* principle is getting more and more relevant in the field of POPs. A producer will faster reconsider the usefulness of products when analysts are able to trace back residues in an environmental or food sample to a specific product manufactured in a specific plant. Again, IRMS will be the most suited technique to provide such proof. The future has begun.

Acknowledgment I wish to acknowledge valuable input by the external reviewers and the editor on an earlier draft of this paper.

References

- Aeppli C, Holmstrand H, Andersson P, Gustafsson Ö (2010) Direct compound-specific stable chlorine isotope analysis of organic compounds with quadrupole GC/MS using standard isotope bracketing. *Anal Chem* 82:420–426
- Armbruster W, Lehnert K, Vetter W (2006) Establishing a chromium-reactor design for measuring $\delta^2\text{H}$ values of solid polyhalogenated compounds using direct elemental analysis and stable isotope ratio mass spectrometry. *Anal Bioanal Chem* 384:237–243
- Augusti A, Betson T, Gebrekirstos A, Vetter W, Schleucher J (2009) NMR quantification of isotopomers as tool in environmental sciences. In: Yoshida N, Thieme MH (eds) *Proceedings of the 3rd international symposium on isotopomers*, San Diego, USA, 27–31 August 2006, pp 93–103
- Badea S-L, Vogt C, Weber S, Danet A-F, Richnow H-H (2009) Stable isotope fractionation of γ -hexachlorocyclohexane (lindane) during reductive dechlorination by two strains of sulfate-reducing bacteria. *Environ Sci Technol* 43: 3155–3161
- Barrie A, Bricout J, Koziol J (1984) Gas chromatography-stable isotope ratio analysis at natural abundance levels. *Biomed Environ Mass Spectrom* 11:583–588
- Beneteau KM, Aravena R, Frapet SK (1999) Isotopic characterization of chlorinated solvents – laboratory and field results. *Org Geochem* 30:739–753
- Chartrand MMG, Hirschorn SK, Lacrampe-Couloume G, Sherwood Lollar B (2007) Compound-specific hydrogen isotope analysis of 1,2-dichloroethane: potential for delineating source and fate of chlorinated hydrocarbon contaminants in groundwater. *Rapid Commun Mass Spectrom* 21:1841–1847
- DFG (1983) DFG-Forschungsbericht: Hexachlorocyclohexan als Schadstoff in Lebensmitteln. Verlag Chemie, Weinheim

- DFG (1988) Polychlorierte Biphenyle. Mitteilung XIII der Senatskommission zur Prüfung von Rückständen in Lebensmitteln. VCH, Weinheim
- Drenzek NJ, Eglinton TI, Wirsen CO, May HD, Wu Q, Sowers KR, Reddy CM (2001) The absence and application of stable carbon isotopic fractionation during the reductive dechlorination of polychlorinated biphenyls. *Environ Sci Technol* 35:3310–3313
- Drenzek NJ, Tarr CH, Eglinton TI, Heraty LJ, Sturchio NC, Shiner VJ, Reddy CM (2002) Stable chlorine and carbon isotopic compositions of selected semi-volatile organochlorine compounds. *Org Geochem* 33:437–444
- Elsner M, Zwank L, Hunkeler D, Schwarzenbach R (2005) A new concept linking observable stable isotope fractionation to transformation pathways of organic pollutants. *Environ Sci Technol* 39:6896–6916
- Ewald E-M, Wagner A, Nijenhuis I, Richnow H-H, Lerchner U (2007) Microbial dehalogenation of trichlorinated dibenzo-*p*-dioxins by a *Dehalococcoides*-containing mixed culture is coupled to carbon isotope fractionation. *Environ Sci Technol* 41:7744–7751
- Frame GM (1996a) A collaborative study of 209 PCB congeners and 6 Aroclors on 20 different HRGC columns. 1. Retention and coelution database. *Fresenius J Anal Chem* 357:701–713
- Frame GM (1996b) A collaborative study of 209 PCB congeners and 6 Aroclors on 20 different HRGC columns: 2. Semi-quantitative Aroclor congener distributions. *Fresenius J Anal Chem* 357:714–722
- Freedman PA, Gillyon ECP, Jumeau EJ (1988) Design and application of a new instrument for GC-isotope ratio MS. *Am Lab* 20:114–119
- Gaus C, Brunskill GJ, Connell DW, Prange J, Mueller JF, Pöpke O, Weber R (2002) Transformation processes, pathways, and possible sources of distinctive polychlorinated dibenzo-*p*-dioxin signatures in sink environments. *Environ Sci Technol* 36:3542–3549
- Gribble GW (1998) Naturally occurring organohalogen compounds. *Acc Chem Res* 31:141–152
- Hayes JM (2001) Fractionation of the isotopes of carbon and hydrogen in biosynthetic processes. *Rev Mineral Geochem* 43:225–277
- Hirschorn SK, Grostern A, Lacrampe-Couloume G, Edwards EA, MacKinnon L, Repta C, Major DW, Sherwood Lollar B (2007) Quantification of biotransformation of chlorinated hydrocarbons in a biostimulation study: added value via stable carbon isotope analysis. *J Contam Hydrol* 94:249–260
- Holmstrand H, Unger M, Carrizo D, Andersson P, Gustafsson Ö (2010) Compound-specific bromine isotope analysis of brominated diphenyl ethers using gas chromatography multiple collector/inductively coupled plasma mass spectrometry. *Rapid Commun Mass Spectrom* 24:2135–2142
- Horii Y, Kannan K, Petrick G, Gamo T, Falandysz J, Yamashita N (2005) Congener-specific carbon isotopic analysis of technical PCB and PCN mixtures using two-dimensional gas chromatography-isotope ratio mass spectrometry. *Environ Sci Technol* 39:4206–4212
- Horii Y, van Bavel B, Kannan K, Petrick G, Nachtigall K, Yamashita N (2008) Novel evidence for natural formation of dioxins in ball clay. *Chemosphere* 70:1280–1289
- Jakobsson E, Asplund L (2000) Polychlorinated naphthalenes (PCNs). In: Paasivirta J (ed) *Handbook of environmental chemistry*, vol 3, part K. Springer, Heidelberg, pp 97–126
- Jarman WM, Hilkert A, Bacon CE, Collister JW, Ballschmiter K, Risebrough RW (1998) Compound-specific carbon isotopic analysis of Aroclors Clophens, Kanelcors, and Phenocors. *Environ Sci Technol* 32:833–836
- Jensen S (1966) Report of a new chemical hazard. *New Sci* 32:612
- Kannan N, Schulz-Bull DE, Petrick G, Duinker JC (1991) High resolution PCB analysis of Kanechlor, Phenoclor and Sovol mixtures using multidimensional gas chromatography. *Int J Environ Anal Chem* 47:201–215
- Korytár P, Van Stee LLP, Leonards PEG, de Boer J, Brinkman UAT (2003) Attempt to unravel the composition of toxaphene by comprehensive two-dimensional gas chromatography with selective detection. *J Chromatogr A* 994:179–189
- La Guardia MJ, Hale RC, Harvey E (2006) Detailed polybrominated diphenyl ether (PBDE) congener composition of the widely used penta-, octa-, and deca-PBDE technical flame-retardant mixtures. *Environ Sci Technol* 40:6247–6254
- Liu F, Cichocka D, Nijenhuis I, Richnow H-H, Fennel DE (2010) Carbon isotope fractionation during dechlorination of 1,2,3,4-tetrachlorodibenzo-*p*-dioxin by a *Dehalococcoides*-containing culture. *Chemosphere* 80:1113–1119
- Mancini SA, Ulrich AC, Lacrampe-Couloume G, Sleep B, Edwards EA, Sherwood Lollar B (2003) Carbon and hydrogen isotopic fractionation during anaerobic biodegradation of benzene. *Appl Environ Microbiol* 69:191–198
- Mariotti A, Germon JC, Hubert P, Kaiser P, Letolle R, Tardieux A, Tardieux P (1981) Experimental determination of nitrogen kinetic isotope fractionation: some principles; illustration for the denitrification and nitrification processes. *Plant Soil* 62:413–430
- Martin GJ, Akoda S, Martin ML (2008) SNIF-NMR – part 1: principles. In: Webb GA (ed) *Modern magnetic resonance*. Springer, Dordrecht, pp 1651–1658
- Matthews DE, Hayes JM (1978) Isotope-monitoring gas chromatography-mass spectrometry. *Anal Chem* 50:1465–1473
- Meier-Augenstein W (1999) Applied gas chromatography coupled to isotope ratio mass spectrometry. *J Chromatogr A* 842:351–371
- Meier-Augenstein W (2002) Stable isotope analysis of fatty acids by gas chromatography-isotope ratio mass spectrometry. *Anal Chim Acta* 465:63–79
- Melander L, Saunders WH (1980) *Reaction rates of isotopic molecules*. Wiley, New York
- Morrison J, Brockwell T, Merren T, Fourel F, Phillips AM (2001) On-line high-precision stable hydrogen isotopic analyses on nanoliter water samples. *Anal Chem* 73:3570–3575
- Nijenhuis I, Andert J, Beck K, Kastern M, Diekert G, Richnow HH (2005) Stable isotope fractionation of tetrachloroethene during reductive dechlorination of *Sulfurospirillum multivorans* and *Desulfotobacterium* sp. strain PCE-S and abiotic reactions with cyanocobalamin. *Appl Environ Microbiol* 71:3413–3419
- Nikiforov VA, Selivanov SI, Podkorytov IS (2005) Kinetic isotope effects in environmental chemistry: natural distribution of deuterium in different positions of pinene and theoretical analysis of isotopic distribution in polychlorobornanes. *Organohalogen Compd* 67:1374–1376
- Philp RP, Monaco GL (2011) Applications of stable isotopes in hydrocarbon exploration and environmental forensics. In: Baskaran M (ed) *Handbook of environmental isotope geochemistry*, Chapter 31, Springer, Heidelberg

- Poulsen SR, Drever JI (1999) Stable isotope (C, Cl, H) fractionation during vaporization of trichloroethylene. *Environ Sci Technol* 33:3689–3694
- Rappe C, Tysklind M, Andersson R, Bruns PC, Irvine RL (2001) Dioxin in ball clay and kaolin. *Organohalogen Compd* 51:259–263
- Rayleigh JWS (1896) Theoretical considerations respecting the separation of gases by diffusion and similar processes. *Philos Mag* 42:493–498
- Reddy CM, Heraty LJ, Holt BD, Sturchio NC, Eglinton TI, Drenzek NJ, Xu L, Lake JL, Maruya KA (2000) Stable chlorine isotopic compositions of Aroclors and Aroclor-contaminated sediments. *Environ Sci Technol* 34:2866–2870
- Reddy CM, Xu L, Eglinton TI, Boon JP, Faulkner DJ (2002a) Radiocarbon content of synthetic and natural semi-volatile halogenated organic compounds. *Environ Pollut* 120:163–168
- Reddy CM, Drenzek NJ, Eglinton TI, Heraty LJ, Sturchio NC, Shiner VJ (2002b) Stable chlorine intramolecular isotope effects from the abiotic dehydrochlorination of DDT. *Environ Sci Pollut Res* 9:183–186
- Ricci MP, Merritt DA, Freeman KH, Hayes JM (1994) Acquisition and processing of data for isotope-ratio-monitoring mass spectrometry. *Org Geochem* 21:561–571
- Rosenfelder N, Bendig P, Vetter W (2010) $\delta^{13}\text{C}$ values of polybrominated diphenyl ethers and their UV-transformation products. *Organohalogen Compd* 1423. <http://www.xcdtech.com/dioxin2010/pdf/1423.pdf>
- Rossmann A, Butzenlechner M, Schmidt H-L (1990) Evidence for a nonstatistical carbon isotope distribution in natural glucose. *Plant Physiol* 96:609–614
- Saleh MA (1991) Toxaphene: chemistry, biochemistry, toxicity and environmental fate. *Rev Environ Contam Toxicol* 118:1–85
- Sano M, Yotsui Y, Abe H, Sasaki S (1976) A new technique for the detection of metabolites labeled by the isotope ^{13}C using mass fragmentography. *Biomed Mass Spectrom* 3:1–3
- Schmidt H-L (2003) Fundamental and systematics of the non-statistical distributions of isotopes in natural compounds. *Naturwissenschaften* 90:537–552
- Schmidt TC, Zwank L, Elsner M, Berg M, Meckenstock RU, Haderlein SB (2004) Compound-specific stable isotope analysis of organic contaminants in natural environments: a critical review of the state of the art, prospects, and future challenges. *Anal Bioanal Chem* 378:283–300
- Sherwood Lollar B, Slater GF, Sleep B, Witt M, Klecka GM, Harkness M, Spivack J (2001) Stable carbon isotope evidence for intrinsic bioremediation of tetrachloroethene and trichloroethene at Area 6, Dover Air Force Base. *Environ Sci Technol* 35:261–269
- Sturchio NC, Böhlke JK, Gu B, Hatzinger PB, Jackson WA (2011) Isotopic tracing of perchlorate in the environment. In: Baskaran M (ed) *Handbook of environmental isotope geochemistry*, Chapter 22, Springer, Heidelberg
- Tanabe S (1988) PCB problems in the future: foresight from current knowledge. *Environ Pollut* 50:5–28
- Teuten EL, Xu L, Reddy CM (2005) Two abundant bioaccumulated halogenated compounds are natural products. *Science* 307:917–920
- van Breukelen BM (2007) Extending the Rayleigh equation to allow competing isotope fractionating pathways to improve quantification of biodegradation. *Environ Sci Technol* 41:4004–4010
- van Warmerdam EM, Frapce SK, Aravena R, Drimmie RJ, Flatt H, Cherry JA (1995) Stable chlorine and carbon isotope measurements of selected chlorinated organic solvents. *Appl Geochem* 10:547–552
- Vetter W (2006) Marine halogenated natural products of environmental and food relevance. *Rev Environ Contam Toxicol* 188:1–57
- Vetter W, Gleixner G (2006) Compound-specific stable carbon isotope ratios ($\delta^{13}\text{C}$ values) of the halogenated natural product 2,3,3',4,4',5,5'-heptachloro-1'-methyl-1,2'-bipyrrrole (Q1). *Rapid Commun Mass Spectrom* 20:3018–3022
- Vetter W, Oehme M (2000) Toxaphene. Analysis and environmental fate of congeners. In: Paasivirta J (ed) *Handbook of environmental chemistry*, vol 3, part K. Springer, Heidelberg, pp 237–287
- Vetter W, Gleixner G, Armbruster W, Ruppe S, Stern GA, Braekevelt E (2005) Congener-specific concentrations and carbon stable isotope ratios ($\delta^{13}\text{C}$) of two technical toxaphene products (Toxaphene® and Melipax®). *Chemosphere* 58:235–241
- Vetter W, Armbruster W, Betson TR, Schleucher J, Kapp T, Lehnert K (2006a) Baseline isotopic data of polyhalogenated compounds. *Anal Chim Acta* 577:250–255
- Vetter W, Schlatterer J, Gleixner G (2006b) Experiments directed to the compound-specific determination of the stable carbon isotope ratios of the Toxaphene congener B8-1413 in two technical mixtures and Antarctic Weddell seal. *J Chromatogr A* 1110:165–170
- Vetter W, Gaul S, Melcher J (2007) Improved quality control in gas chromatography interfaced to stable isotope ratio mass spectrometry by application of derivative chromatography. *Anal Chim Acta* 590:49–54
- Vetter W, Gaul S, Armbruster W (2008) Stable carbon isotope ratios of POPs – a tracer that can lead to the origins of pollution. *Environ Int* 34:357–362
- von der Recke R, Vetter W (2007) Synthesis and characterization of 2,3-dibromopropyl-2,4,6-tribromophenyl ether (DPTE) and structurally related compounds evidenced in seal blubber and brain. *Environ Sci Technol* 41:1590–1595
- Weber D, Kexel H, Schmidt H-L (1997) ^{13}C pattern of natural glycerol: origins and practical importance. *J Agric Food Chem* 45:2042–2046
- Werner RA, Brand WA (2001) Referencing strategies and techniques in stable isotope ratio analysis. *Rapid Commun Mass Spectrom* 15:501–519
- Whitaker MJ (1996) Stable isotope geochemistry of coals, humic kerogens and related natural gases. *Int J Coal Geol* 32: 191–215
- WHO (1989) DDT and its Derivatives – Environmental Aspects. *Environmental Health Criteria* 83
- Yanik PJ, O'Donnell TH, Macko SA, Qian Y, Kennicutt MC II (2003) Source apportionment of polychlorinated biphenyls using compound specific isotope analysis. *Org Geochem* 34:239–251
- Zwank L, Berg M, Schmidt TC, Haderlein SB (2003) Compound-specific carbon isotope analysis of volatile organic compounds in the low-microgram per liter range. *Anal Chem* 75:5575–5583

Part V
Isotopes as Tracers in Archaeology
and Anthropology

Chapter 33

Light-Element Isotopes (H, C, N, and O) as Tracers of Human Diet: A Case Study on Fast Food Meals

Lesley A. Chesson, James R. Ehleringer, and Thure E. Cerling

Abstract Tracking the production and movement of foods from farm to fork has become increasingly complex in recent years due to changes in modern food markets, including the globalization of food sources and their distribution. Dietary habits have changed as well, with meals eaten outside of the home representing an ever-increasing fraction of the modern human diet. Stable isotope analysis has proven to be a reliable technique for characterizing biological substances, such as food, because stable isotopes record aspects of photosynthesis, nutrition, and source water. Here we present stable isotope ratios ($\delta^{13}\text{C}$, $\delta^{15}\text{N}$, $\delta^2\text{H}$, and $\delta^{18}\text{O}$) measured for one ubiquitous example of modern convenience food, the fast food meal. In a series of paired observations among cities in the U.S., we compared the isotopic composition of components of a fast food meal to similar foods purchased from grocery stores. Isotope analyses revealed several interesting patterns in both food production and food origin within the modern American food market. Carbon isotope ratio analysis of proteins highlighted the impact of consumer choice: patrons in a fast food restaurant consumed beef containing a lower proportion of C_4 plants than beef purchased from a grocery store. The relative trophic-level position of beef avail-

able in both fast food restaurants and grocery stores was similar based on $\delta^{15}\text{N}$ values. The $\delta^2\text{H}$ and $\delta^{18}\text{O}$ values of the beef, bread, and milk samples were independently and positively correlated, suggesting that both plants and animals recorded the isotopic composition of local environmental water and, therefore, geographic source. Overall, these results demonstrated the promise and potential of food stable isotope analyses to broad areas of societal interest: food safety, food authenticity, and food traceability.

33.1 Introduction

Food sources and eating habits are changing rapidly in our increasingly globalized societies. Tracing the production and movement of food from farm to fork is not necessarily an easy task in the modern food market because the diet of today's global citizen often includes foods from other countries or continents. Maintaining tracking records as foods are moved across the globe is difficult and poor or lost records often prevent investigators from easily tracing food source. Despite the globalization of food markets, there is an emerging interest in buying local foods. Even so consumers lack a method to verify that foods labeled as locally grown are truly produced locally. Stable isotope analysis can be useful for food tracing and has proven to be a powerful tool for investigations into the diet of both ancient (Macko et al. 1999a, b; O'Connell and Hedges 1999a; Sponheimer and Lee-Thorp 1999; White et al. 2004) and modern (O'Connell and Hedges 1999b; O'Connell et al. 2001; Nardoto et al. 2006) man.

Historically, applications of stable isotope analysis in dietary studies have focused on understanding the

L.A. Chesson (✉) and J.R. Ehleringer
IsoForensics Inc, Salt Lake City, UT 84108, USA
Department of Biology, University of Utah, Salt Lake City,
UT 84112, USA
e-mail: lesley@isoforensics.com; jim@isoforensics.com

T.E. Cerling
IsoForensics Inc, Salt Lake City, UT 84108, USA
Department of Biology, University of Utah, Salt Lake City,
UT 84112, USA
Department of Geology and Geophysics, University of Utah,
Salt Lake City, UT 84112, USA
e-mail: thure.cerling@utah.edu

impact of different inputs on the final isotopic composition of the consumer's tissue(s) [e.g., (Nardoto et al. 2006; O'Brien and Wooller 2007; Ehleringer et al. 2008)]. However, stable isotope analysis can also be used to trace the origin of and determine the production method for individual food items (Rossmann 2001; Kelly et al. 2005). To date, most food tracer studies have focused on the analysis of specialty items, such as cheese (Pillonel et al. 2003; Camin et al. 2004; Manca et al. 2006), olive oil (Bontempo et al. 2009; Camin et al. 2010) or wine (West et al. 2007) that have relatively few and well understood origins and methods of production. Stable isotope analyses can be applied more broadly to the protein, carbohydrate, and lipid components of human diets.

Stable isotopes act as natural recorders of the biological, chemical, environmental, and physiological processes at work on organic materials (West et al. 2006b). The analysis of a plant or animal samples for a suite of elemental isotope concentrations can therefore provide information on the previous conditions experienced by those tissues. The information provided by each of the elements hydrogen (H), carbon (C), nitrogen (N), and oxygen (O) varies; together, the analysis and interpretation of these light-element isotopes often provides unambiguous information in tracing studies of human dietary food items.

33.1.1 Carbon Isotope Ratios Are Ultimately Linked to Photosynthesis

The measured $\delta^{13}\text{C}$ value of a food is ultimately linked to plant photosynthesis because plants discriminate against $^{13}\text{CO}_2$ in the atmosphere during carbon assimilation (Ehleringer et al. 1993). The carbon isotopic composition of atmospheric CO_2 is relatively constant across the globe, with an approximate average value of -8‰ (Keeling et al. 2005), but see (Peck and Tubman 2010) for a discussion of changing carbon dioxide $\delta^{13}\text{C}$ values. Discrimination against ^{13}C in carbon dioxide is larger in plants that use the C_3 (Calvin cycle) photosynthetic pathway than in plants that use the C_4 (Hatch-Slack cycle) pathway. Thus, C_3 plants, which include temperate grasses (e.g., wheat, barley, rye, rice) and most fruit and vegetables as important human dietary components, are characterized by $\delta^{13}\text{C}$ values ranging from -30 to -22‰ (Cerling et al.

1997). On the other hand, C_4 plants are characterized by relatively higher $\delta^{13}\text{C}$ values, ranging from -14 to -10‰ (Cerling et al. 1997). Examples of C_4 plants important in human diet include corn (maize), sugar cane, and other tropical grains such as millet, teff, and fonio.

Due to the large differences in the $\delta^{13}\text{C}$ values of C_3 and C_4 plants, it is possible to develop two-source mixing models to calculate the relative proportions of different plant sources to a mixture (Phillips and Gregg 2001). For example, a two-source mixing model can be used to detect the introduction of a C_4 -plant derived adulterant (cane sugar; $\delta^{13}\text{C} = -12.5\text{‰}$) to C_3 -plant derived food item (maple syrup; $\delta^{13}\text{C} = -23.6\text{‰}$) (Martin et al. 1996). This approach has also been used to detect the adulteration of wildflower honey, a C_3 plant-based food, with C_4 sugars (White et al. 1998).

The $\delta^{13}\text{C}$ values of animal-derived food items like beef, chicken, or milk will reflect the carbon stable isotope ratios of the animal's dietary inputs (Bahar et al. 2005; Schmidt et al. 2005; Camin et al. 2008; Rhodes et al. 2010). Similar to the adulteration detection examples, mixing models can also be used to calculate the fraction of C_3 - or C_4 -plants fed to an animal during its growth (Schwarcz and Schoeninger 2011). However, because of a small fractionation during the incorporation of carbon atoms from diet to tissue, the $\delta^{13}\text{C}$ value of the carbon source may not exactly match that of the tissue (Peterson and Fry 1987).

33.1.2 Nitrogen Isotopes Trace the Flow of Organic Matter Through Food Webs

Ecosystem nitrogen influxes and effluxes influence soil and plant baseline $\delta^{15}\text{N}$ values. The nitrogen cycle – and its impact on soils and plants – has been previously reviewed (Högberg 1997; Amundson et al. 2003; Pardo and Nadelhoffer 2010), so we present only a summary here. Inputs to the ecosystem include atmospheric N deposition (soils) and N fixation (plants). Nitrogen outputs include gaseous losses and hydrologic leaching from soils. Examples of internal fluxes and transformation within the ecosystem are N taken up from soil by plants via nitrogen fixation or mycorrhizae; alterations within plants via transport,

assimilation, and translocation; and then deposited to soil via litter fall.

In general, nitrogen stable isotope ratios are increased ~3.2‰ per trophic step in a food web (Peterson and Fry 1987). It is therefore possible to broadly estimate the functional trophic level (TL) of many consumers within a food web as

$$TL_{\text{consumer}} = TL_{\text{base}} + (\delta^{15}\text{N}_{\text{SC}} - \delta^{15}\text{N}_{\text{base}})/3.2,$$

where TL_{base} is the assumed TL of the organism used to estimate the food web's baseline nitrogen isotope ratio (for a primary consumer, $TL_{\text{base}} = 1$) and $\delta^{15}\text{N}_{\text{base}}$ and $\delta^{15}\text{N}_{\text{SC}}$ are the measured nitrogen isotope ratios of the web's baseline and a secondary consumer, respectively [equation modified from (Post 2002)]. However, nitrogen discrimination between diet and consumer can vary about the value of 3.2‰ due to many factors, including the amount of nitrogen (as protein) in the diet and the quality of the protein source (Robbins et al. 2005, 2010). For example, nitrogen discrimination factors published in the literature range from 1.4‰ for nursing coyote offspring (Jenkins et al. 2001) to 5.8‰ for grizzly bears on controlled diets fed apples [(Felicetti et al. 2003); see also (Robbins et al. 2005)].

Despite the multiple pathways for N movement in an ecosystem, nitrogen isotope ratios can be used to construct food web assemblages by estimating organisms' trophic levels (Cabana and Rasmussen 1996; Hansson et al. 1997; Bösl et al. 2006). Nitrogen stable isotope analysis is also a powerful tool for investigations into the flow of organic matter and energy through a food web (Peterson et al. 1985; Vander Zanden et al. 1999). The nitrogen isotope analysis of human hair has been used to successfully trace the source (animal vs. plant) of protein in the consumer's diet (O'Connell and Hedges 1999b; Petzke et al. 2005a, b).

33.1.3 Hydrogen and Oxygen Isotope Ratios Record Geolocation Information

The majority of water in the Earth's water cycle is found in the oceans, which have defined hydrogen and oxygen stable isotope ratios of 0‰ for each (Gat

1996). As water from the surface of the ocean is evaporated into the atmosphere, the water vapor in clouds is depleted in ^2H and ^{18}O relative to the ocean. In turn, water condensation from the cloud mass is enriched in ^2H and ^{18}O relative to the cloud. After a precipitation event the residual cloud mass is further depleted in ^2H and ^{18}O relative to both the original cloud and the ocean. The systematic fractionation within a cloud mass during successive precipitation events results in a predictable depletion of ^2H and ^{18}O across landscapes (Gat 1996). This simplified model does not capture all the processes taking place in the hydrologic cycle, but it explains a large portion of the isotope gradients observed across the Earth's surface that are related to the isotope ratios of meteoric water.

The predictable geographic pattern in meteoric water $\delta^2\text{H}$ and $\delta^{18}\text{O}$ values can be spatially presented in an isotopic landscape, or *isoscape* (West et al. 2010b). In general, higher $\delta^2\text{H}$ and $\delta^{18}\text{O}$ water values are measured near coasts and in low latitudes or low elevation regions. Lower $\delta^2\text{H}$ and $\delta^{18}\text{O}$ values are measured in high latitude, high altitude, and inland regions. The tissues of both plants and animals record the stable isotope ratios of local environmental water (West et al. 2006a, 2008, 2010b). Thus, the stable isotope ratios of a plant- or animal-derived food item will vary with geography and these values can be used to investigate its region-of-origin.

Two concepts serve as the basis for understanding the relationship between animal or plant tissue and water. First, (Craig 1961) described the relationship between the $\delta^2\text{H}$ and $\delta^{18}\text{O}$ values of meteoric water collected across the globe. Known as the Global Meteoric Water Line (GMWL), it is described as

$$\delta^2\text{H} = 8 * \delta^{18}\text{O} + 10\text{‰}.$$

Because the hydrogen and oxygen isotope ratios of meteoric water are correlated, we expect that the $\delta^2\text{H}$ and $\delta^{18}\text{O}$ values of animal and plant tissues will also be related and mimic the spatial distribution of water isotopes. However, the water in organisms is subject to evaporation, which differentially impacts the abundance of ^2H and ^{18}O in tissues. In animals, metabolic water will additionally influence the $\delta^2\text{H}$ and $\delta^{18}\text{O}$ values of body water. The foundation for understanding the isotopic enrichment measured in animal and plant tissue $\delta^2\text{H}$ and $\delta^{18}\text{O}$ values associated with

evaporation is the Craig-Gordon model (Craig and Gordon 1965). Mechanistic studies on the $\delta^2\text{H}$ and $\delta^{18}\text{O}$ values of animal and plant tissues for food tracing are all necessarily based on these two fundamental concepts.

33.1.4 Fast Food Stable Isotope Analysis Characterizes the Average American Diet

One defining characteristic of today's American diet is the inclusion of prepared foods obtained away from the home. In 1970, the average US citizen spent 26% of his total yearly food budget on food prepared away from home (Lin and Frazão 1999). By 1999, the proportion had roughly doubled to ~50% (Clauson 2000). Fast food restaurants are the single largest supplier of away-from-home food for the average American, accounting for approximately 12% of daily caloric (i.e., energy) intake (Guthrie et al. 2002). The "meat and potatoes" fast food meal leads sales, with consumers eating hamburgers and French fries more often than any other restaurant menu item offered (Jekaniowski 1999; French et al. 2000).

Americans increased spending on foods prepared outside the home from \$263 billion in 1992 to \$415 billion in 2002, an increase of 23% when corrected for inflation (Stewart et al. 2004). In an effort to continue increasing profit margins, the food industry has begun to change the face of agriculture in the USA. Key to this change is consolidation of supply chains, allowing a company to control all aspects of food production from feedlot to meat counter and thereby cutting costs in the process. Between 1975 and 2000, there was increased geographic concentration in the cattle, hog, and poultry industries (Drabenstott et al. 1999; Herath et al. 2004). By 1999, approximately 60% of all cattle were raised in three states, while two-thirds of chickens were raised in five (Drabenstott et al. 1999), creating the most concentrated manufacturing sector in the USA (Herath et al. 2004).

Ongoing consolidation in the food industry should reduce isotopic variation for different food items. We investigated patterns in meat production methods through the stable isotope analysis of carbon and nitrogen. We used hydrogen and oxygen stable isotope ratios to investigate the potential relationship between

local environmental conditions at food growing regions and the measured $\delta^2\text{H}$ and $\delta^{18}\text{O}$ values of food. Because of its importance to the modern American diet, we concentrated our survey on the most ubiquitous example of food prepared away-from-home: the fast food meal.

We focused on the three basic components of a fast food meal: (a) protein (beef patty), (b) carbohydrates (hamburger bun and French fries), and (c) beverage (milk). Dietary protein is the source of essential amino acids used for protein synthesis in the consumer and thus, the analysis of proteinaceous tissues can be used to infer something of a consumer's protein intake. Carbohydrates (and, though not discussed in this text, fat) represent the energy source for metabolism. For example, the stable isotope analysis of breath CO_2 is used to indicate the carbohydrate fuel of a consumer (Ayliffe et al. 2004). The liquid intake of a consumer will impact his body water pool, which in turn influences the isotopic composition of amino acids and proteins in the consumer's other tissues.

33.2 Materials and Methods

We collected the hamburger (beef) patty, hamburger bun, French fries, and milk drink from Hamburger Happy Meals™ purchased from McDonald's® restaurants in 36 cities distributed across the contiguous USA in February 2008 (Fig. 33.1). To allow food choice comparisons, ground beef (and chicken), loaf bread, and milk were also purchased in a supermarket in each city. Details of sample collection, preparation, and analysis can be found in (Chesson et al. 2008, 2010a, b).

In stable isotope analysis of foods to calculate dietary inputs or for region-of-origin assignment, it is important that samples are lipid-free as the carbon and hydrogen isotope ratios of lipids are typically light and inconsistent amounts of lipids in samples can differentially affect measured $\delta^{13}\text{C}$ and $\delta^2\text{H}$ values. Thus, all meat samples and French fries were delipidified prior to analysis to remove fat and cooking oils. In order to assure sample homogeneity, delipidified samples were then ground to a fine powder to minimize heterogeneity. No special procedures were required to process the hamburgers buns or loaf breads prior to grinding. We extracted the water from milk

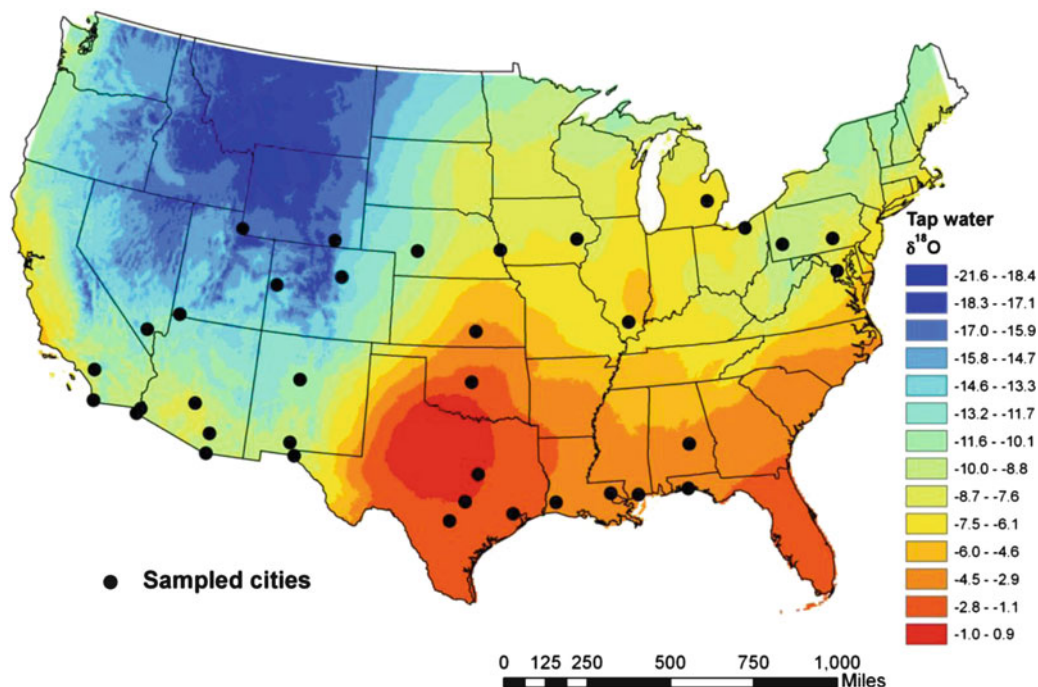


Fig. 33.1 Locations of fast food restaurants (McDonald's®) and supermarkets visited in this American food survey, shown on a predicted tap water oxygen isoscape for the USA (Bowen et al. 2007)

samples for stable isotope ratio analysis (West et al. 2006a).

Measured H, C, N, and O isotope ratios are reported vs. Vienna Standard Mean Ocean Water (VSMOW), Pee Dee Belemnite (PDB), atmospheric air, and VSMOW, respectively. We recognized that some proportion of the H atoms in organic molecules is exchangeable (DeNiro 1981). Therefore, the H exchange factors were controlled for meats during sample preparation and analysis (Bowen et al. 2005; Chesson et al. 2009). Atom exchange with the environment was not a concern for C, N, or O stable isotope ratio measurements.

33.3 Results and Discussion

33.3.1 Supermarket Beef Cattle Eat More Corn than Fast Food Cattle in the USA

As a result of consolidation in meat production and supply chains in the USA, we hypothesized that beef cattle raised for the fast food and for the grocery retail

markets would be fed similar feed and thus display similar $\delta^{13}\text{C}$ values. As expected, we found that the mean carbon isotope ratios of beef were similar, whether purchased as McDonald's hamburgers or as ground beef from supermarkets. However, the distributions of measured $\delta^{13}\text{C}$ values within each dataset were markedly different, as seen in a comparison of the cumulative frequency distributions for hamburger and ground beef carbon isotope ratios (Fig. 33.2). The supermarket dataset contained samples with (on average) higher measured $\delta^{13}\text{C}$ values than the hamburger dataset; yet it also contained the two lowest measured $\delta^{13}\text{C}$ values. As shown in Fig. 33.2, the distribution of carbon isotope ratios in the supermarket beef dataset was not normal, as compared to the $\delta^{13}\text{C}$ values of restaurant hamburgers.

Several recent studies have investigated the impact of diet on the carbon isotope ratios of ruminants (De Smet et al. 2004; Bahar et al. 2005; Schmidt et al. 2005; Bahar et al. 2008). Two of these present two-source mixing models for calculating the incorporation of C_4 -based diet into cow tissue (De Smet et al. 2004; Bahar et al. 2005). Using a similar approach as that presented by De Smet et al. (2004) and Bahar et al. (2005), we calculated the percentage of C_4 -based plant

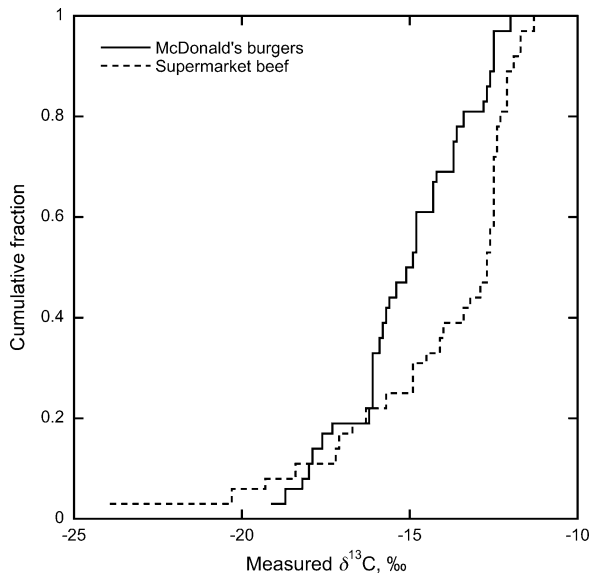


Fig. 33.2 The distribution of measured carbon isotope ratios in the fast food hamburger (*solid line*) and supermarket ground beef (*dashed line*) samples collected in this survey. Data are presented as cumulative fractions to highlight the different distribution in measured $\delta^{13}\text{C}$ values of each dataset

material in the diets of the cows that served as the source of beef for McDonald's restaurants and supermarkets. (We assume that mostly corn and not C_4 grass represents this dietary biomass.)

In the mixing model we used a value of -24.0‰ to represent cattle eating only C_3 biomass, which was calculated from the analysis of beef from a ranch raising grass-fed cattle in Idaho ($1\sigma = 0.4\text{‰}$, $n = 8$; unpublished data). We used a carbon isotope ratio of -11.4‰ to represent cattle eating solely C_4 biomass, which was calculated using hamburgers collected from McDonald's restaurants in Brazil ($1\sigma = 0.8\text{‰}$, $n = 10$; unpublished data.) The calculated proportion of corn in the diet of cattle that served as the source of meat for McDonald's hamburgers ranged from 0.39 to 0.95. The range for fractional contribution of corn in the diet calculated for supermarket beef was larger and spanned from 0.01 to 1.0.

From the available beef datasets and the dietary corn proportion calculations we observed a previously undocumented difference between the measured $\delta^{13}\text{C}$ values of lipid-free beef samples collected in the same location but from different sources: fast food restaurants and supermarkets. In addition, the proportional contribution of C_4 plants to the diets of beef cattle

sourced by supermarkets spanned a larger range than the contribution of C_4 plants to cattle sourced by restaurants. Based on this observation, a consumer choosing to eat dinner at McDonald's could incorporate a significantly different carbon isotope ratio from his hamburger patty than a consumer who chose to grill her own burger at home using beef from the supermarket meat counter. Interestingly, it appears beef cattle from American supermarkets were generally fed more corn prior to slaughter than beef cattle served by McDonald's restaurants, contrary to popular perception (Dotinga 2008; Pickert 2008).

33.3.2 There Are No Trophic Level Differences Between Restaurant and Supermarket Beef

Beef cattle are primary consumers and in the USA are likely consuming mostly corn prior to slaughter (see Sect. 33.3.1, above). Thus, we expected that the measured $\delta^{15}\text{N}$ values of beef cattle collected from fast food restaurants and supermarkets would be similar. If we knew or could estimate the $\delta^{15}\text{N}$ value of the baseline for the beef food web, we hypothesize that we would be able to calculate the functional trophic level of beef cattle.

There was no difference between the mean $\delta^{15}\text{N}$ values of beef in the two datasets (Fig. 33.3). All beef appear to occupy the same relative trophic level. While this is not surprising since these animals are primary consumers, it does suggest that the nitrogen isotope values of the feed available to beef stock (e.g., corn, grasses) were grown on nitrogen sources that had generally the same nitrogen isotope ratio value. The measured $\delta^{15}\text{N}$ values of all the beef samples covered a small range, from 5.1 to 7.8‰ for hamburgers and from 5.3 to 7.9‰ for ground beef from supermarkets.

We observed a difference in the mean measured $\delta^{15}\text{N}$ values of beef and chicken available to the modern American consumer (Fig. 33.3); nitrogen stable isotope ratios were significantly lower for chicken than for McDonald's hamburgers or supermarket ground beef (ANOVA with Tukey's post-hoc test; $F_{2,104} = 814.9$, $P < 0.0001$). The range in $\delta^{15}\text{N}$ values for chicken samples was 1.6–3.5‰. Our fast food meat nitrogen isotope data agreed well with a survey of fast food meals purchased from different

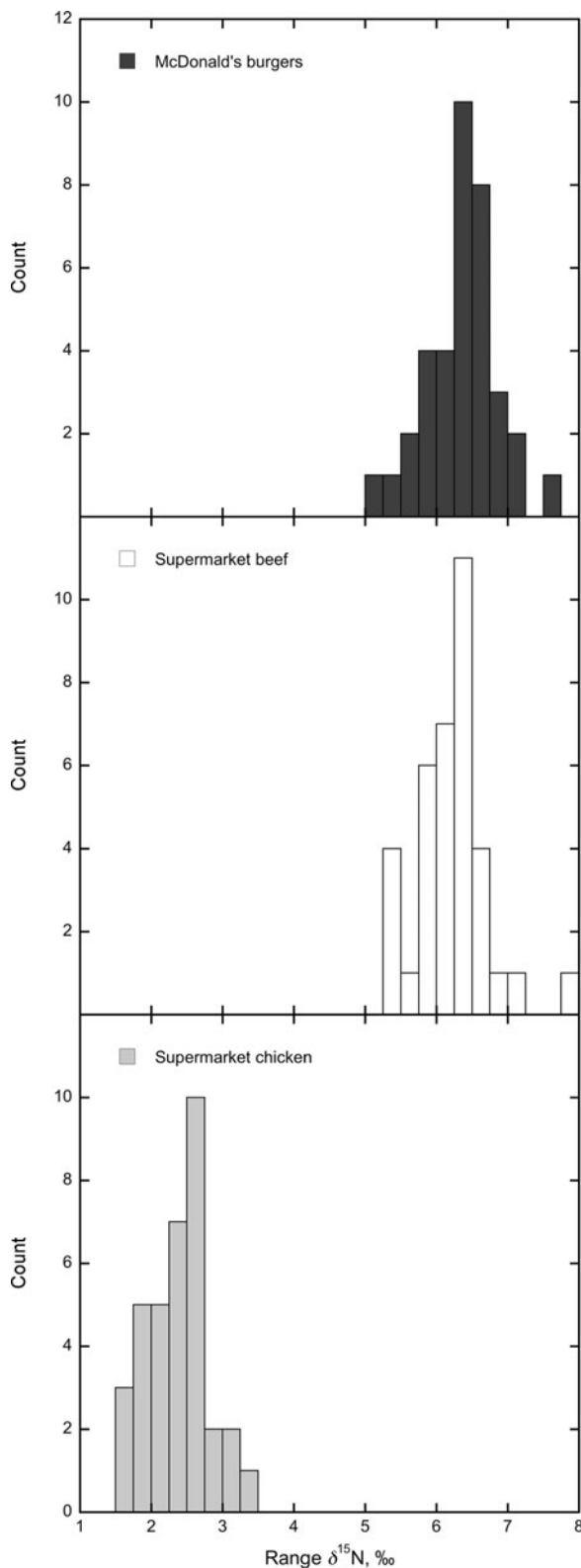


Fig. 33.3 The distribution of measured nitrogen isotope ratios of collected fast food hamburgers (*top*), supermarket ground beef (*middle*), and supermarket chicken (*bottom*)

restaurant chains in selected cities in the USA by Jahren and Kraft (2008).

In this survey of American fast food items we assumed, as did Jahren and Kraft (2008), that the majority of feed for animals raised for sale to the food industry is corn. We therefore used a $\delta^{15}\text{N}$ values for the nitrogen input of corn fed to both chickens and cows of $\sim 3\text{‰}$ (Schoeller et al. 1986; Masud et al. 1999; Bahar et al. 2005). Using the modified equation of Post (2002) and a diet-consumer nitrogen discrimination factor of 3.2‰, we calculated the mean functional TL of beef cattle and chickens where corn was the food web baseline so that $\text{TL}_{\text{base}} = 0$ and $\delta^{15}\text{N}_{\text{base}} = 3\text{‰}$. We calculated mean TL for beef purchased at both McDonald's restaurants and supermarkets as 1.0; the calculated TL of chicken from supermarkets was 0.0.

While a calculated TL of ~ 1 was expected for beef cattle, we did not expect to find that the calculated trophic level of chickens was the same as that of plants (i.e., $\text{TL} = 0$). Chickens are omnivorous and would naturally occupy a functional trophic level greater than one. We present two possibilities to explain the low calculated TL of chickens. First, our estimates of feed $\delta^{15}\text{N}$ values may be incorrect for chicken. In other words, chickens raised for distribution to fast food restaurants are fed a nitrogen source with a $\delta^{15}\text{N}$ value near 0‰. Alternatively, the fractionation between diet and tissue nitrogen isotope ratios, assumed to be 3.2‰ here, is not the same for beef cattle and chickens, leading us to underestimate the functional TL of chickens. For commercially raised chicken that cannot forage, pre-mixed feeds include nitrogen in the form of fish or feather meals. A chicken consuming a diet with large quantities of crude protein – protein from an animal-derived source – may have a dietary nitrogen discrimination factor much lower than an average value of 3.2‰ (Robbins et al. 2005, 2010).

33.3.3 Beef Hydrogen and Oxygen Ratios May Be Useful for Region-of-Origin Assignment

If cattle production is consolidated in the USA, the range in measured $\delta^2\text{H}$ and $\delta^{18}\text{O}$ values observed in beef samples may be limited due to the limited geographic (and thus, isotopic) variation of the production regions. Independent of the amount of beef isotopic

variation the relationship between $\delta^2\text{H}$ and $\delta^{18}\text{O}$ values of beef tissue should mimic the GMWL because beef cattle incorporate environmental water during growth. We expected to see a positive correlation between measured beef hydrogen and oxygen isotope ratios. However, due to the impact of metabolic water on an organism's body water pool and/or the evaporation of water within an organism's tissues we did not necessarily expect to find that the slope or intercept of the relationship between beef $\delta^2\text{H}$ and $\delta^{18}\text{O}$ values would exactly match those of the meteoric water line.

The measured $\delta^2\text{H}$ and $\delta^{18}\text{O}$ values of beef purchased from McDonald's restaurants and supermarket meat counters spanned a large range, from -157 to -98‰ for hydrogen and from 9.2 to 18.1‰ for oxygen. The hydrogen and oxygen isotope ratios of beef co-varied (Fig. 33.4) and the ordinary least squares regression (OLS) lines fitted to the separate beef datasets were described by the equations

$$\delta^2\text{H} = 6.4 * \delta^{18}\text{O} - 211\text{‰} \quad (r^2 = 0.91)$$

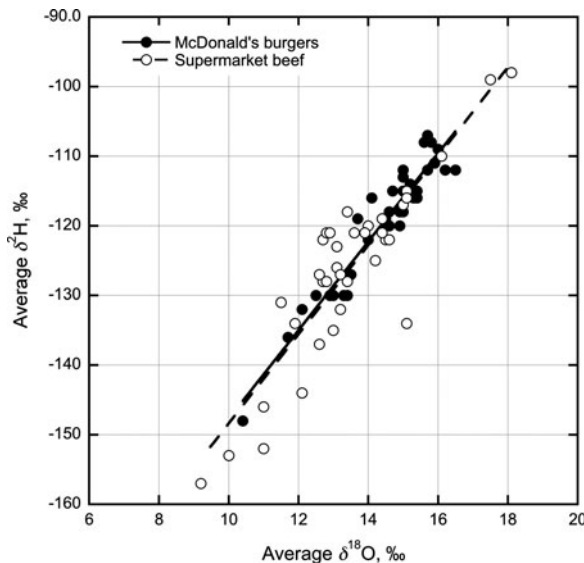


Fig. 33.4 A bi-plot of the measured hydrogen and oxygen isotope ratios of fast food hamburgers (*closed circles*) and supermarket ground beef (*open circles*). The measured $\delta^2\text{H}$ and $\delta^{18}\text{O}$ values for each data set were correlated. Ordinary least squares regression lines fitted to the data are shown in *solid black* for burgers and *dashed black* for ground beef and described by the equations $\delta^2\text{H} = 6.4 * \delta^{18}\text{O} - 211\text{‰}$ ($r^2 = 0.91$) and $\delta^2\text{H} = 6.4 * \delta^{18}\text{O} - 213\text{‰}$ ($r^2 = 0.80$), respectively

for fast food restaurant hamburgers and

$$\delta^2\text{H} = 6.4 * \delta^{18}\text{O} - 213\text{‰} \quad (r^2 = 0.80)$$

for ground beef from supermarket meat counters. Both the lines were different from the GMWL. However, neither of the slopes were different from the slope of a regression line describing the relationship between hydrogen and oxygen isotope ratios of human hair collected throughout the USA [$m = 5.7$; (Ehleringer et al. 2008)].

The congruence between the slopes of the OLS regression lines fitted to measured $\delta^2\text{H}$ and $\delta^{18}\text{O}$ values of beef protein and human hair keratin suggests that the incorporation of H and O atoms from the cow's diet, drinking water, and O_2 inputs is similar to the incorporation of H and O from various dietary and fluid inputs to human hair. A semi-mechanistic model developed to describe the relationship between the stable isotope ratios of inputs to human hair $\delta^2\text{H}$ and $\delta^{18}\text{O}$ values (Ehleringer et al. 2008) may therefore also be useful – after some modification – to understand the incorporation of hydrogen and oxygen atoms to beef cattle muscle tissue because both hair and muscle are proteins. Using the Ehleringer et al. (2008) publication for reference, we attempted to adapt the model as follows to predict the measured oxygen stable isotope ratios of beef protein.

We assumed that the O atoms of amino acids are exposed to isotopic exchange within the animal's body water pool when proteins from the diet are cleaved in the stomach and small intestine during digestion at low pH. After absorption across the gut wall, the oxygen isotope ratio of an amino acid is, in essence, fixed. Thus, the oxygen isotopic composition of protein in cow muscle is related to that of water in the cow's gut ($\delta^{18}\text{O}_{\text{wg}}$) during digestion such that

$$\delta^{18}\text{O}_{\text{muscle}} = \alpha_o \bullet (1,000 + \delta^{18}\text{O}_{\text{wg}}) - 1,000, \quad (33.1)$$

where α_o is the fractionation in oxygen isotope ratio associated with protein synthesis and is assigned a value of 1.0164 (Kreuzer-Martin et al. 2003). Note that (33.1) presented here is the same as Equation (1) in Ehleringer et al. (2008) and Equation (19) in Podlesak et al. (2008). For cows that eat dry feed, gut water is a mixture of gastric fluids from the body water pool ($\delta^{18}\text{O}_{\text{wb}}$) and possibly drinking water ($\delta^{18}\text{O}_{\text{we}}$):

$$\delta^{18}O_{wg} = g_1 \cdot \delta^{18}O_{wb} + g_2 \cdot \delta^{18}O_{we}, \quad (33.2)$$

where g_1 and g_2 represent the fraction of water in the gut from body water and drinking water, respectively. Unlike the human hair keratin model, we do not consider water contained within food as a contributor to gut water. We initially assume that the contribution of drinking water to gut water is insignificant ($g_2 = 0$) and thus the oxygen isotopic composition of water in the gut is the same as that of body water ($g_1 = 1$ and $\delta^{18}O_{wg} = \delta^{18}O_{wb}$).

The body water pool does not have the same isotope ratio as drinking water because of the contribution of metabolic water (Gretebeck et al. 1997). The oxygen isotopic composition of body water is described as

$$\delta^{18}O_{wb} = \frac{a \cdot \delta^{18}O_{we} + b \cdot \delta^{18}O_d + c \cdot [\alpha_{O_2}(1,000 + \delta^{18}O_{O_2}) - 1,000]}{h \cdot \alpha_{fwo} + j \cdot \alpha_{CO_2} + k}, \quad (33.3)$$

where $\delta^{18}O_d$ and $\delta^{18}O_{O_2}$ are the stable isotope ratios of food and inhaled oxygen, respectively; a , b , and c are the fractional contributions of drinking water, food, and atmospheric oxygen, respectively, to body water; h , j , and k are the proportions of O lost as fractionated water, exhaled CO_2 , and unfractionated water, respectively, from the body water pool; and α_{O_2} , α_{fwo} , and α_{CO_2} are the isotopic fractionation factors for the absorption of O_2 , loss of oxygen through breathing and transcutaneous evaporation, and loss of oxygen in exhaled CO_2 . Equation (33.3) is unchanged from the Ehleringer et al. (2008) model, presented by the authors as Equation (6). This is also essentially the same model for body water oxygen isotope ratios as Equation (24) in Podlesak et al. (2008), though the authors used experimentally derived values for the proportion of drinking water, food, and O_2 contributing to wood rat body water $\delta^{18}O$ values while we have used values from Gretebeck et al. (1997), which were originally derived for humans.

We previously collected and analyzed a sample of grass-fed beef collected in Soda Springs, ID. Using the predicted tap water oxygen isotope ratio ($\delta^{18}O_{we}$) of the location (Bowen et al. 2007), we attempted to use the modified model described above to calculate a predicted beef meat $\delta^{18}O_{muscle}$ value. We used a

value of 21.0‰ for $\delta^{18}O_d$, which was measured for locally grown hay in the Salt Lake City, UT area (unpublished data). Using the predicted $\delta^{18}O_{we}$ value of -17.0 ‰, the modified protein model predicted a $\delta^{18}O_{muscle}$ value of 12.0‰ for beef cattle raised in Soda Springs. The predicted $\delta^{18}O_{muscle}$ value was greater than the measured oxygen isotope ratio 9.2‰, a difference of 2.8‰. However, the variation (calculated as 1σ) in measured $\delta^{18}O$ values of several samples of beef collected from different individual animals within the same herd of cattle in ID ($n = 8$) was 1.2‰. Indeed, one sample of meat collected from the ID herd had a measured $\delta^{18}O$ value of 12.3‰, very near the theoretical predicted value of 12.0‰.

Tracing the geographical origin of beef has recently been recognized as a food-safety concern in Europe and Asia. Preliminary data suggest the stable isotope analysis of beef may be useful to answer questions of region-of-origin (Nakashita et al. 2008; Bong et al. 2010; Horacek and Min 2010). A recent survey of beef raised in Japan published by Nakashita et al. (2008) observed a relationship between the oxygen isotope ratio of water available to beef cattle and the measured $\delta^{18}O$ value of delipidified beef, described by:

$$\delta^{18}O_{muscle} = 0.59 * \delta^{18}O_{we} + 15.56\text{‰}. \quad (33.4)$$

We also tested the Nakashita et al. (2008) model using the predicted tap water $\delta^{18}O$ value of -17.0 ‰ for Soda Springs, ID. Equation (33.4) predicted a muscle tissue oxygen isotope ratio of beef raised in ID of 5.5‰, much lower than the measured $\delta^{18}O_{muscle}$ value of 9.2 and 3‰ lower than any value measured for cattle in the ID herd (minimum = 8.6‰).

33.3.4 Bread Hydrogen and Oxygen Isotope Ratios Are Positively Correlated

Following a similar water-based dependence, the hydrogen and oxygen isotope ratio of both beef and bread should be positively correlated. We expected to see a correlation between the measured δ^2H and $\delta^{18}O$ values of breads collected from McDonald's restaurants as hamburger buns and from supermarkets as loaves because the source of H and O atoms in wheat

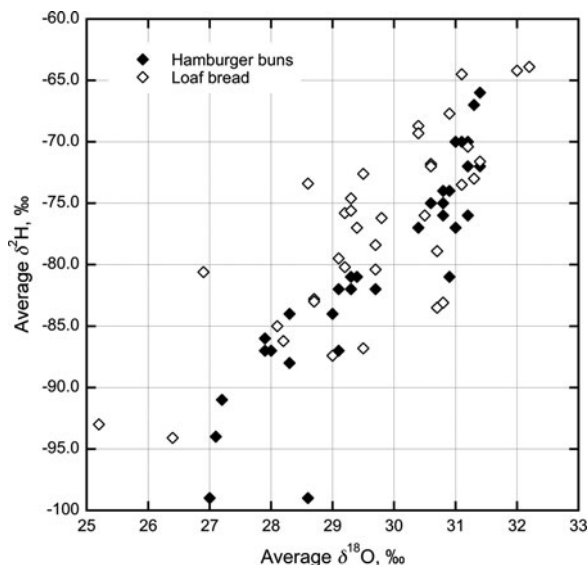


Fig. 33.5 A bi-plot of the measured hydrogen and oxygen isotope ratios of fast food hamburger buns (*closed diamonds*) and supermarket loaf bread (*open diamonds*). The measured $\delta^2\text{H}$ and $\delta^{18}\text{O}$ values for each data set were correlated ($r = 0.90$ for hamburger buns and $r = 0.77$ for loaf bread)

are derived from meteoric water. The ranges in $\delta^2\text{H}$ and $\delta^{18}\text{O}$ values of hamburger buns spanned from -99 to -66‰ and from 27.0 to 31.4‰ , respectively (Fig. 33.5). The ranges in hydrogen and oxygen isotope ratios of bread samples spanned from -94 to -64‰ and from 25.2 to 32.2‰ , respectively (Fig. 33.5). Hydrogen and oxygen isotope ratios of the two bread datasets were significantly correlated at the $\alpha = 0.05$ level (two-tailed Pearson correlation; $r = 0.90$ for buns and $r = 0.77$ for loaf bread).

A model of the hydrogen and oxygen isotope ratios of plants carbohydrate (cellulose) has been developed and tested in the past decade (Roden et al. 2000). Recently the hydrogen and oxygen isotope ratios of materials of forensics interest, plant-based poisons and counterfeit money (West et al. 2010a), have also been examined and modeled. Based on the extent of variation in bread $\delta^2\text{H}$ and $\delta^{18}\text{O}$ values – and the correlation between the two isotopes – we propose that similar tracing and geolocating approaches could be used for food items like the hamburger buns and loaves of bread collected in the survey.

Models exist to provide a theoretical foundation for predicting the isotopic composition of leaf water (West et al. 2008) based on the distribution of water isotope globally. Other models that use the

Craig-Gordon evaporation model as a foundation can be used to interpret the transformation of leaf water $\delta^2\text{H}$ and $\delta^{18}\text{O}$ values to plant cellulose $\delta^2\text{H}$ and $\delta^{18}\text{O}$ values (Roden and Ehleringer 1999; Roden et al. 2000). With some work, these models may be adapted to model the hydrogen and oxygen isotope ratios of wheat-based carbohydrates like hamburger buns and bread.

In addition to hydrogen and oxygen isotope ratios, we also compared the measured $\delta^{13}\text{C}$ values of hamburger buns and loaf breads. We found the mean measured $\delta^{13}\text{C}$ values of the datasets were statistically different (unpaired t test; $t_{69} = 3.8$, $P < 0.001$); the mean carbon isotope ratio for hamburger buns (-23.6‰) was higher than that of loaf bread samples (-24.1‰). This difference is likely due to the ingredients used to make hamburger buns, which include high fructose corn syrup, a C_4 -based sweetener. These measured carbon isotope ratios highlight the need for caution when adapting models to trace wheat-based food like bread. Developed models must recognize the potential confounding impact of other ingredients (with other origins) in the bulk bread sample submitted for stable isotope analysis.

33.3.5 Interpreting Potato Hydrogen and Oxygen Isotopes is Challenging at the Moment

We expected the measured hydrogen and oxygen isotope ratios of potatoes and potato products (i.e., French fries) would be significantly correlated because the $\delta^2\text{H}$ and $\delta^{18}\text{O}$ values of meteoric water are related (Gat 1996). The ranges in measured $\delta^2\text{H}$ and $\delta^{18}\text{O}$ values for delipidified French fries and baking potatoes are shown in Fig. 33.6. We found that the hydrogen and oxygen stable isotope values of French fries and baking potatoes collected in this American food survey were significantly and positively correlated at the $\alpha = 0.05$ level, when tested using the two-tailed Pearson correlation. However, the amount of variation in H explained by O was very low for both fries and potatoes ($r^2 = 0.15$ and 0.26 , respectively).

There may be multiple explanations why $\delta^2\text{H}$ and $\delta^{18}\text{O}$ values in potatoes are not as tightly correlated as they are in the GMWL. One possibility is that starch, the main storage molecule of the potato tuber and

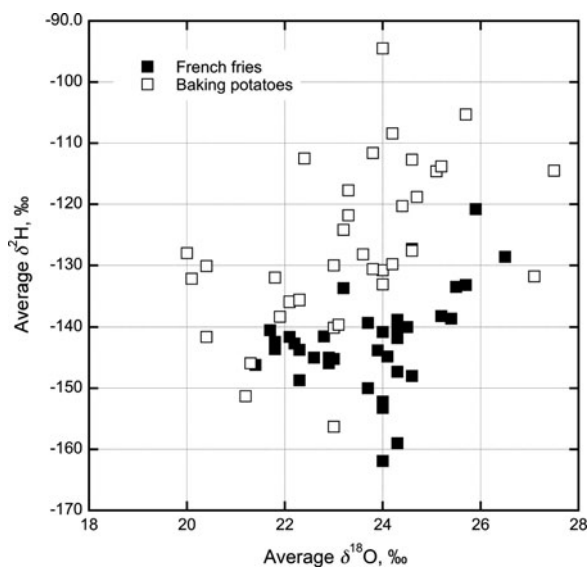


Fig. 33.6 A bi-plot of the measured hydrogen and oxygen isotope ratios of fast food French fries (*closed squares*) and baking potatoes purchased from supermarkets (*open squares*). The measured $\delta^2\text{H}$ and $\delta^{18}\text{O}$ values for each data set were correlated though the amount of variance in measured $\delta^2\text{H}$ values explained by $\delta^{18}\text{O}$ values was low ($r^2 = 0.15$ for French fries and $r^2 = 0.26$ for potatoes)

containing exchangeable hydroxyl groups, has opportunities for H atoms to interact with different water sources between the time a potato is harvested in the field and sold to the consumer. Despite the protective effects of the potato skin, tubers gain or lose weight according to the relative humidity of the surrounding environment (DeNiro and Cooper 1989). Hydrogen atoms may also have the opportunity for exchange during potato processing post harvest. For example, potatoes for French fries are commonly steam cleaned to remove the skin and any attached debris (Lisińska and Gołubowska 2005). During this process, hydrogen atoms in the hydroxyl groups are subject to exchange with ambient water surrounding the potato tuber. Lisińska and Gołubowska (2005) have shown change in both carbohydrate characteristics and water content during the production of pre-frozen French fries. Thus, the isotopic composition of the water vapor at the storage location and the method of processing post-harvest potatoes could contribute to the decoupling of French fry and potato $\delta^2\text{H}$ and $\delta^{18}\text{O}$ values.

In addition, a French fry is not simply a sliced potato. A second possibility is the conversion of carbohydrates during French fry production and/or

cooking that were composed of different $\delta^2\text{H}$ and/or $\delta^{18}\text{O}$ values, because the local water environment is different than that of the original tuber. For instance, while the delipidation step should have removed any fats introduced during the production-cooking processes, conversion of starches to sugars may have altered the overall $\delta^2\text{H}$ and $\delta^{18}\text{O}$ values from that originally characterizing the potato. Supporting this argument, a comparison of the mean measured hydrogen and oxygen isotope ratios of French fries and baking potatoes found a significant difference between $\delta^2\text{H}$ values (unpaired t test; $t_{69} = 6.0$, $P < 0.0001$) but no difference between $\delta^{18}\text{O}$ values.

33.3.6 Milk Water Isotope Ratios Show Promise for Tracing the Origin of Dairy Products

Chesson et al. (2010a) recently presented a model to predict the isotope ratios of drinking water for cows based on the $\delta^2\text{H}$ and $\delta^{18}\text{O}$ values of water extracted from milk. The authors used the OLS regression line describing the relationship between the oxygen isotope ratios of paired cow drinking water and milk water samples as an approximation of a semi-mechanistic model accounting for the proportional contributions of drinking water and meteoric water to body water (i.e., milk water). The relationship is

$$\delta^{18}\text{O}_{\text{milk}} = 0.86 * \delta^{18}\text{O}_{\text{we}} + 1.1\text{‰}, \quad (33.5)$$

where $\delta^{18}\text{O}_{\text{milk}}$ and $\delta^{18}\text{O}_{\text{we}}$ are the oxygen isotope ratios of water extracted from milk and water in the environment, respectively (Chesson et al. 2010a). The study then examined the predicted drinking water $\delta^{18}\text{O}$ values for a number of McDonald's milk samples purchased from different cities, which grouped into three distinct data clusters. Predicted water for the three groups of restaurant samples overlapped with known regions of high dairy cow concentration in the US. That study could not go further given the lack of information on the original source of the purchased restaurant samples.

The authors noted that the generally high total water flux (TWF) in dairy cows should drive body water stable isotope ratio values closer to those of

drinking water. This is because a high water input rate has the potential to reduce the impacts of metabolic water on body water isotope values. Thus milk water $\delta^{18}\text{O}$ values (which are equivalent to body water $\delta^{18}\text{O}$ values) should be closer to drinking water oxygen isotope ratios in dairy cows than non-lactating cows (e.g., beef cattle). With that assumption in mind, we modified (33.3) to predict the oxygen isotope ratio of milk water ($\delta^{18}\text{O}_{\text{milk}} = \delta^{18}\text{O}_{\text{wb}}$). Constrained by the lack of information in the literature, we made estimates of how lactating and non-lactating cows might differ. We increased the relative contribution of drinking water to body water from 0.62 to 0.90 to reflect a lactating condition and decreased the proportional contributions of O atoms in food and inhaled O_2 from 0.14 and 0.24, respectively, to 0.05 and 0.05, respectively.

Using cow drinking water ($\delta^{18}\text{O}_{\text{we}}$) values from the dairy farm collection of Chesson et al. (2010a), $\delta^{18}\text{O}_{\text{wb}}$ values were predicted for the dairy cows and then compared to the original $\delta^{18}\text{O}_{\text{milk}}$ values. The slope of the OLS regression line describing the relationship between drinking water and $\delta^{18}\text{O}_{\text{milk}}$ values ($m = 0.86$; data not shown) was not significantly different from the slope of the line describing the relationship between drinking water and predicted $\delta^{18}\text{O}_{\text{wb}}$ values ($m = 0.89$; data not shown). On the other hand, the y-intercept of the measured milk water line (1.1) was significantly different from the predicted body water line y-intercept (1.8; $F_{1,13} = 12.6$, $P < 0.01$).

It appears the regression-based model presented as (33.5) and the process-based model modified from (33.3) may represent equally valid methods for predicting cow drinking water from the oxygen stable isotope analysis of water extracted from milk. Using both model approaches, we predicted the $\delta^{18}\text{O}_{\text{we}}$ value for a sample of milk collected in Salt Lake City, UT and distributed by local dairy, Winder Farms (www.winderfarms.com). The $\delta^{18}\text{O}_{\text{milk}}$ value measured for the water extracted from the milk sample was -13.8‰ . The predicted value for $\delta^{18}\text{O}_{\text{we}}$ using modified (33.3) was -17.5‰ and using (33.5) was -17.4‰ . Because the two models predicted nearly identical cow drinking water values, we used only the value predicted using (33.5) to then generate a predicted region-of-origin for the cow(s) that produced the milk (Fig. 33.7), using a tap water isoscape for the continental USA (Bowen et al. 2007) and an error estimate of $3\sigma = 1.2\text{‰}$ (Chesson et al. 2010a).

The predicted regions-of-origin included the purported site of the dairy farm operation, West Valley City, UT. The predicted regions also included portions of several states north of Utah (Idaho, Montana, and Wyoming). While not normally considered centers of dairy milk production, northern Utah and states to the north are home to several regional milk production facilities. Those regions are characterized by relatively low measured tap water $\delta^2\text{H}$ and $\delta^{18}\text{O}$ values (Bowen et al. 2007) and thus all predicted regions shown in Fig. 33.7 would be consistent with predicted sources of the milk sold under the local Winder Farms label. Despite the fact stable isotope analysis alone is not enough to predict regions with a smaller margin of the error the possible source of the milk sample, the predicted regions are relatively local to the purchase location in Salt Lake City, UT.

33.3.7 Stable Isotope Analyses Reveal Several Patterns in the Modern American Diet

From this case study on the stable isotope analysis of fast food meals for questions of food tracking we have revealed several patterns in the modern American's diet. First, the carbon stable isotope analysis of beef and breads from McDonald's restaurants and supermarkets has shown the impact of a consumer's food choice. The $\delta^{13}\text{C}$ value of beef from a restaurant can be markedly different from that of beef purchased from a supermarket in the same town, with consequences for the carbon isotope ratio of dietary inputs incorporated by a consumer. Similarly, the prevalence of C_4 -based sweeteners in breads available to fast food diners means the $\delta^{13}\text{C}$ value of the hamburger bun input is generally higher than the loaf bread input of a consumer eating bread from the store. Thus, "where you eat matters" when calculating the carbon isotope ratios of inputs in your diet.

Next, the hydrogen and oxygen stable isotope analysis of all components of the fast food meal – and the supermarket correlates – demonstrated the existence of significant isotopic, and thus geographic, variation in the foods available to consumers eating out or dining in at mealtimes. However, our current ability to interpret these isotope ratios varies. For example,

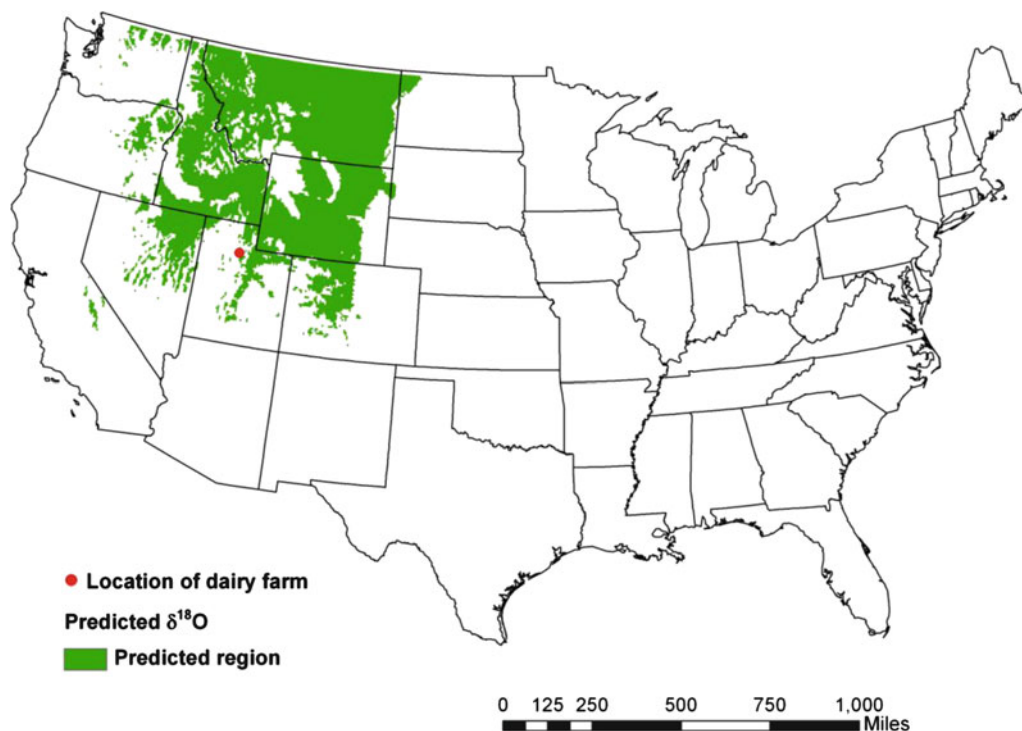


Fig. 33.7 The predicted regions-of-origin for cows that could have produced the Winder Farms milk collected in Salt Lake City, UT. Predictions were generated using the Chesson et al. (2010b) model, (33.5) in the text. The location of the purported

dairy farm source is shown by the red point. Predicted regions were generated using a tap water oxygen isoscape for the USA (Bowen et al. 2007) and include an error estimate of 1.2‰ around the predicted $\delta^{18}\text{O}$ dairy cow drinking water value

the analysis of beef and milk water for $\delta^2\text{H}$ and $\delta^{18}\text{O}$ values may be very useful for food tracing applications and possible origin assignment of individual samples, as demonstrated for samples of beef and milk collected local to Salt Lake City, UT. The interpretation of bread and potato $\delta^2\text{H}$ and $\delta^{18}\text{O}$ values was not as straightforward but could prove useful in the future as we understand more about the impacts between origin and hydrogen and oxygen isotope ratios of those foods.

Finally, the stable isotope analysis of four elements (H, C, N, and O) provides investigators complimentary information on both the source and production of food. Consider the beef samples collected in this survey. Carbon isotope ratios revealed the different diets of cattle used by fast food restaurants and supermarkets. Despite the dietary differences, the trophic levels of all cattle were similar, as revealed by nitrogen isotope analysis. Contrary to trends in agricultural consolidation, the measured $\delta^2\text{H}$ and $\delta^{18}\text{O}$ values of beef revealed that cattle come from many isotopic regions. These individual pieces of information together show that an aggregated analysis of stable

isotope ratio food values can be useful for tracing both the production and origin of food as it travels to a consumer's plate.

33.4 Future Directions

In the second volume of the *Handbook of Environmental Isotope Geochemistry* Hillaire-Marcel predicted that stable isotope chemistry had a promising future in the field of food tracing (Hillaire-Marcel 1986). Here two decades later in the *Handbook's* fourth volume we have highlighted an application of stable isotope analysis for tracing the origins of and production methods for a select group of food items in arguably the most consumed meal in the US today: the fast food restaurant meal. Isotope applications in foods are now approached as including both process and region-of-origin information. This is an active area of international research and one likely to significantly advance in the next two decades as biochemistry,

geography, economics, and stable isotopes find more common ground.

The stable isotope ratios of food items are ultimately linked to two processes: natural environmental variation in stable isotope ratios and processes associated with animal and plant physiology. Pioneering stable isotope research focused on the environmental patterns associated with meteoric water hydrogen and oxygen stable isotopes (Craig 1961) and atmospheric $^{13}\text{CO}_2$ (Keeling 1961) laid the foundation for today's advances. Theoretical advances in understanding carbon isotopes (Ehleringer et al. 1993), hydrogen and oxygen in carbohydrates (Roden et al. 2000), and in animal proteins (Ehleringer et al. 2008), to name a few, have laid the foundation for interpreting isotope ratio variations among foods. The exciting area of *isoscapes* has now emerged, advancing our understanding of geospatial isotope patterns (West et al. 2010b).

In order to scale environmental patterns in atmospheric, plant, and water isotopes to animal-derived food items, we believe more fundamental mechanistic research is needed before we can fully understand the isotope physiology of common domesticated animals. Key among the unknowns are relationships related to turnover of protein, carbohydrates, and fats, especially in growing animals and animals shifting diets in the last phases of animal production (e.g., feedlots). This need includes controlled diet studies for food-providing animals like that of Bahar et al. (2005) with beef cattle. It also includes an understanding of between-tissue variation in animals (Bahar et al. 2009) as well as seasonal variation caused by variable environmental conditions or feed changes (Boner and Förstel 2004). For example, consider the prediction of dairy cow drinking water from the measured $\delta^{18}\text{O}$ values of milk. Predictions would likely be much improved if we understood more fully the physiology of the cow and how respiration rates, water flux, and the isotopic composition of diet affected final milk isotope ratios.

Second, food traceability should be critically tested to evaluate its potential relative to other technologies. While discussions of food authenticity and potential regulations are discussed globally today verification approaches, such as stable isotope analyses, have not yet been approached with the depth and rigor needed to apply to a global food network. Examples such as the European TRACE Project (www.trace.eu.org) provide a framework for future studies.

Finally, stable isotope analyses are part of a larger, integrated analytical approach to food safety, food authenticity, and food traceability. Stable isotope analyses can complement other approaches, including trace element analysis (Heaton et al. 2008), trace metal analysis (Anderson et al. 1999), radioactive element analysis (Pillonel et al. 2003), and compound characterization [e.g., gas chromatography-mass spectrometry or high pressure liquid chromatography (Földházi 1994; Aichholz and Lorbeer 1999; Cotte et al. 2004)].

Acknowledgments Janet Barnette, David Podlesak, and Ben Quigley helped collect fast food and supermarket samples. The Salt Lake City hay sample was provided by Dawn Roper. Grass-fed Idaho beef samples were provided by John and Lori Anne Lau, Lau Family Farms. Brazil hamburger carbon isotope data were provided by Gabriela Nardoto and Luiz Martinelli. Extracted water from the Winder Farms milk samples was collected by Jordan Denos. Luciano Valenzuela produced the GIS-based maps presented in Figs. 33.1 and 33.7. Brad Erkkila provided preparation and analytical assistance. We thank Shannon O'Grady and Luciano Valenzuela for providing feedback on an early draft of this text. Funding for this study was provided by IsoForensics, Inc.

References

- Aichholz R, Lorbeer E (1999) Investigation of combwax of honeybees with high-temperature gas chromatography and high-temperature gas chromatography-chemical ionization mass spectrometry I. High temperature gas chromatography. *J Chromatogr A* 855:601–615
- Amundson R, Austin A, Shuur E et al (2003) Global patterns of the isotopic composition of soil and plant nitrogen. *Glob Biogeochem Cycles* 17:1031
- Anderson KA, Magnuson BA, Tschirgi ML et al (1999) Determining the geographic origin of potatoes with trace metal analysis using statistical and neural network classifiers. *J Agr Food Chem* 47:1568–1575
- Ayliffe LK, Cerling TE, Robinson T et al (2004) Turnover of carbon isotopes in tail hair and breath CO_2 of horses fed an isotopically varied diet. *Oecologia* 139:11–22
- Bahar B, Monahan FJ, Moloney AP et al (2005) Alteration of the carbon and nitrogen stable isotope composition of beef by substitution of grass silage with maize silage. *Rapid Commun Mass Spectrom* 19:1937–1942
- Bahar B, Schmidt O, Moloney A et al (2008) Seasonal variation in the C, N and S stable isotope composition of retail organic and conventional Irish beef. *Food Chem* 106: 1299–1305
- Bahar B, Moloney AP, Monahan FJ et al (2009) Turnover of carbon, nitrogen, and sulfur in bovine longissimus dorsi and psoas major muscles: implications for isotopic authentication of meat. *J Anim Sci* 87:905–913

- Boner M, Förstel H (2004) Stable isotope variation as a tool to trace the authenticity of beef. *Anal Bioanal Chem* 378: 301–310
- Bong Y-S, Shin W-J, Lee A-R et al (2010) Tracking the geographical origin of beefs being circulated in Korean markets based on stable isotopes. *Rapid Commun Mass Spectrom* 24:155–159
- Bontempo L, Camin F, Larcher R et al (2009) Coast and year effect on H, O and C stable isotope ratios of Tyrrhenian and Adriatic Italian olive oils. *Rapid Commun Mass Spectrom* 23:1043–1048
- Bösl C, Grupe G, Peters J (2006) A late Neolithic vertebrate food web based on stable isotope analyses. *Int J Osteoarchaeol* 16:296–315
- Bowen GJ, Chesson L, Nielson K et al (2005) Treatment methods for the determination of $\delta^2\text{H}$ and TM^{18}O of hair keratin by continuous-flow isotope-ratio mass spectrometry. *Rapid Commun Mass Spectrom* 19:2371–2378
- Bowen GJ, Ehleringer JR, Chesson LA et al (2007) Stable isotope ratios of tap water in the contiguous United States. *Water Resour Res* 43:W03419
- Cabana G, Rasmussen JB (1996) Comparison of aquatic food chains using nitrogen isotopes. *Proc Natl Acad Sci* 93: 10844–10847
- Camin F, Wietzerbin K, Cortes A et al (2004) Application of multielement stable isotope ratio analysis to the characterization of French, Italian, and Spanish cheeses. *J Agric Food Chem* 52:6592–6601
- Camin F, Perini M, Colombari G et al (2008) Influence of dietary composition on the carbon, nitrogen, oxygen and hydrogen stable isotope ratios of milk. *Rapid Commun Mass Spectrom* 22:1690–1696
- Camin F, Larcher R, Nicolini G et al (2010) Isotopic and elemental data for tracing the origin of European olive oils. *J Agric Food Chem*. doi:10.1021/jf902814s
- Cerling TE, Harris JM, MacFadden BJ et al (1997) Global vegetation change through the Miocene/Pliocene boundary. *Nature* 389:153–158
- Chesson LA, Podlesak DW, Thompson AH et al (2008) Variation of hydrogen, carbon, nitrogen, and oxygen stable isotope ratios in an American diet: fast food meals. *J Agric Food Chem* 56:4084–4091
- Chesson LA, Podlesak DW, Cerling TE et al (2009) Evaluating uncertainty in the calculation of non-exchangeable hydrogen fractions within organic materials. *Rapid Commun Mass Spectrom* 23:1275–1280
- Chesson LA, Valenzuela LO, O'Grady SP et al (2010a) Hydrogen and oxygen stable isotope ratios of milk in the USA. *J Agric Food Chem*. doi:10.1021/jf904151c
- Chesson LA, Podlesak DW, Erkkila BR et al (2010b) Isotopic consequences of consumer food choice: hydrogen and oxygen stable isotope ratios in foods from fast food restaurants versus supermarkets. *Food Chem* 119:1250–1256
- Clauson A (2000) Spotlight on national food spending. *Food Rev* 23:15–17
- Cotte JF, Casabianca H, Giroud B et al (2004) Characterization of honey amino acid profiles using high-pressure liquid chromatography to control authenticity. *Anal Bioanal Chem* 378:1342–1350
- Craig H (1961) Isotopic variations in meteoric waters. *Science* 133:1702–1703
- Craig H, Gordon LI (1965) Deuterium and oxygen-18 variations in the ocean and the marine atmosphere. In: Tongiorgi E (ed) *Proceedings of a conference on stable isotopes in oceanographic studies and paleotemperatures*. Italy, Spoleto
- De Smet S, Balcaen A, Claeys E et al (2004) Stable carbon isotope analysis of different tissues of beef animals in relation to their diet. *Rapid Commun Mass Spectrom* 18: 1227–1232
- DeNiro MJ (1981) The effects of different methods of preparing cellulose nitrate on the determination of the D/H ratios of non-exchangeable hydrogen of cellulose. *Earth Planet Sci Lett* 54:177–185
- DeNiro MJ, Cooper LW (1989) Post-photosynthetic modification of oxygen isotope ratios of carbohydrates in the potato: implications for paleoclimatic reconstruction based upon isotopic analysis of wood cellulose. *Geochim Cosmochim Acta* 53:2573–2580
- Dotinga R (2008) Traces of corn found in almost all fast food. U.S. News & World Report available: <http://www.usnews.com/health/diet-fitness/diet/articles/2008/11/13/traces-of-corn-found-in-almost-all-fast-food.html>, accessed 3/26/2010
- Drabenstott M, Henry M, Mitchell K (1999) Where have all the packing plants gone? The new meat geography in rural America. *Econ Rev* III:65–82
- Ehleringer JR, Hall AE, Farquhar GD (1993) Stable isotopes and plant carbon-water relations. Academic, San Diego
- Ehleringer JR, Bowen GJ, Chesson LA et al (2008) Hydrogen and oxygen isotope ratios in human hair are related to geography. *Proc Natl Acad Sci* 105:2788–2793
- Felicetti LA, Schwartz CC, Rye RO et al (2003) Use of sulfur and nitrogen stable isotopes to determine the importance of whitebark pine nuts to Yellowstone grizzly bears. *Can J Zool* 81:763–770
- Földházi G (1994) Analysis and quantification of sugars in honey of different botanical origin using high performance liquid chromatography. *Acta Alimentaria* 23:299–311
- French SA, Harnack L, Jeffery RW (2000) Fast food restaurant use among women in the Pound of Prevention study: dietary, behavioral and demographic correlates. *Int J Obes* 24: 1353–1359
- Gat JR (1996) Oxygen and hydrogen isotopes in the hydrological cycle. *Annu Rev Earth Planet Sci* 24:225–262
- Gretebeck RJ, Schoeller DA, Socki RA et al (1997) Adaptation of the doubly labeled water method for subjects consuming isotopically enriched water. *J Appl Physiol* 82:563–570
- Guthrie JF, Lin BH, Frazao E (2002) Role of food prepared away from home in the American diet, 1977–78 versus 1994–96: changes and consequences. *J Nutr Educ Behav* 34:140–150
- Hansson S, Hobbie JE, Elmgren R et al (1997) The stable nitrogen isotope ratio as a marker of food-web interactions and fish migration. *Ecology* 78:2249–2257
- Heaton K, Kelly SD, Hoogewerf J et al (2008) Verifying the geographical origin of beef: the application of multi-element isotope and trace element analysis. *Food Chem* 107:506–515
- Herath DP, Weersink AJ, Carpentier CL (2004) Spatial and temporal changes in the U.S. hog, dairy, and fed-cattle sectors, 1975–2000. *Rev Agric Econ* 27:49–69
- Hillaire-Marcel G (1986) Isotopes and food. In: Fritz P, Fontes JC (eds) *Handbook of environmental isotope geochemistry*. Elsevier, Amsterdam

- Högberg P (1997) Tansley Review No. 95 ^{15}N natural abundance in soil-plant systems. *New Phytol* 137:179–203
- Horacek M, Min J-S (2010) Discrimination of Korean beef from beef of other origin by stable isotope measurements. *Food Chem*. doi:10.1016/j.foodchem.2009.12.018
- Jahren AH, Kraft RA (2008) Carbon and nitrogen stable isotopes in fast food: signatures of corn and confinement. *Proc Natl Acad Sci* 105:17855–17860
- Jekanowski MD (1999) Causes and consequences of fast food sales growth. *Food Rev* 22:11–16
- Jenkins SG, Partridge ST, Stephenson TR et al (2001) Nitrogen and carbon isotope fractionation between mothers, neonates, and nursing offspring. *Oecologia* 129:336–341
- Keeling CD (1961) The concentration and isotopic abundances of carbon dioxide in rural and marine air. *Geochim Cosmochim Acta* 24:277–298
- Keeling CD, Piper SC, Bacastow RB et al (2005) Atmospheric CO_2 and ^{13}C exchange with the terrestrial biosphere and oceans from 1978 to 2000: observations and carbon cycle implications. In: Ehleringer JR, Cerling TE, Dearing MD (eds) A history of atmospheric CO_2 and its effects on plants, animals, and ecosystems. Springer, New York
- Kelly S, Heaton K, Hoogewerf J (2005) Tracing the geographical origin of food: the application of multi-element and multi-isotope analysis. *Trends Food Sci Technol* 16:555–567
- Kreuzer-Martin HW, Lott MJ, Dorigan J et al (2003) Microbe forensics: oxygen and hydrogen stable isotope ratios in *Bacillus subtilis* cells and spores. *Proc Natl Acad Sci* 100:815–819
- Lin BH, Frazão E (1999) Away-from-home foods increasingly important to quality of American diet. *Agriculture Information Bulletin No. 749*, U.S. Department of Agriculture
- Lisińska G, Gołubowska G (2005) Structural changes of potato tissue during French fries production. *Food Chem* 93:681–687
- Macko SA, Lubec G, Teschler-Nicola M et al (1999a) The Ice Man's diet as reflected by the stable nitrogen and carbon isotopic composition of his hair. *FASEB J* 13:559–562
- Macko SA, Engel MH, Andrushevich V et al (1999b) Documenting the diet in ancient human populations through stable isotope analysis of hair. *Philos Trans R Soc Lond B Biol Sci* 354:65–75
- Manca G, Franco M, Versini G et al (2006) Correlation between multielement stable isotope ratio and geographical origin in Peretta cows' milk cheese. *J Dairy Sci* 89:831–839
- Martin GG, Martin Y-L, Nault N et al (1996) Application of ^2H SNIF-NMR and ^{13}C SIRA-MS analyses to maple syrup: detection of added sugars. *J Agric Food Chem* 44:3206–3213
- Masud Z, Vallet C, Martin G (1999) Stable isotope characterization of milk components and whey ethanol. *J Agric Food Chem* 47:4693–4699
- Nakashita R, Suzuki Y, Akamatsu F et al (2008) Stable carbon, nitrogen, and oxygen isotope analysis as a potential tool for verifying geographical origin of beef. *Anal Chim Acta* 617:148–152
- Nardoto G, Silva S, Kendall C et al (2006) Geographical patterns of human diet derived from stable-isotope analysis of fingernails. *Am J Phys Anthropol* 131:137–146
- O'Brien D, Wooller M (2007) Tracking human travel using stable oxygen and hydrogen isotope analyses of hair and urine. *Rapid Commun Mass Spectrom* 21:2422–2430
- O'Connell TC, Hedges REM (1999a) Isotopic comparison of hair and bone: archaeological analyses. *J Archaeol Sci* 26:661–665
- O'Connell TC, Hedges REM (1999b) Investigations into the effect of diet on modern human hair isotopic values. *Am J Phys Anthropol* 108:409–425
- O'Connell TC, Hedges REM, Healey MA et al (2001) Isotopic comparison of hair, nail and bone: modern analyses. *J Archaeol Sci* 28:1247–1255
- Pardo LH, Nadelhoffer KJ (2010) Using nitrogen isotope ratios to assess terrestrial ecosystems at regional and global scales. In: West JB, Bowen GJ, Dawson TE et al (eds) *Isoscapes: understanding movement, pattern, and process on Earth through isotope mapping*. Springer, New York
- Peck WH, Tubman SC (2010) Changing carbon isotope ratio of atmospheric carbon dioxide: implications for food authentication. *J Agric Food Chem*. doi:10.1021/jf100104s
- Peterson BJ, Fry B (1987) Stable isotopes in ecosystem studies. *Annu Rev Ecol Syst* 18:293–320
- Peterson BJ, Howarth RW, Garritt RH (1985) Multiple stable isotopes used to trace the flow of organic matter in estuarine food webs. *Science* 227:1361–1363
- Petzke KJ, Boeing H, Metzges CC (2005a) Choice of dietary protein of vegetarians and omnivores is reflected in their hair protein ^{13}C and ^{15}N abundance. *Rapid Commun Mass Spectrom* 19:1392–1400
- Petzke KJ, Boeing H, Klaus S et al (2005b) Carbon and nitrogen stable isotopic composition of hair protein and amino acids can be used as biomarkers for animal-derived dietary protein intake in humans. *J Nutr* 135:1515–1520
- Phillips DL, Gregg JW (2001) Uncertainty in source partitioning using stable isotopes. *Oecologia* 127:171–179
- Pickert K (2008) Fast food's secret ingredient: corn. Time available: <http://www.time.com/time/health/article/0,8599,1859018,00.html>, accessed 3/26/2010
- Pillonel L, Badertscher R, Froidevaux P et al (2003) Stable isotope ratios, major, trace and radioactive elements in Emmental cheeses of different origin. *Lebensm Wiss u Technol* 36:615–623
- Podlesak DW, Torregrossa A-M, Ehleringer JR, Dearing MD, Passey BH, Cerling TE (2008) Turnover of oxygen and hydrogen isotopes in the body water, CO_2 , hair, and enamel of a small mammal. *Geochim Cosmochim Acta* 72:19–35
- Post DM (2002) Using stable isotopes to estimate trophic position: models, methods and assumptions. *Ecology* 83:702–718
- Rhodes CN, Lofthouse JH, Hird S et al (2010) The use of stable carbon isotopes to authenticate claims that poultry have been corn-fed. *Food Chem* 118:927–932
- Robbins CT, Felicetti LA, Sponheimer M (2005) The effect of dietary protein quality on nitrogen isotope discrimination in mammals and birds. *Oecologia* 144:534–540
- Robbins CT, Felicetti LA, Florin ST (2010) The impact of protein quality on stable nitrogen isotope ratio discrimination and assimilated diet estimation. *Oecologia* 162:571–579
- Roden JS, Ehleringer JR (1999) Observations of hydrogen and oxygen isotopes in leaf water confirm the Craig-Gordon

- model under wide-ranging environmental conditions. *Plant Physiol* 120:1165–1173
- Roden J, Lin G, Ehleringer J (2000) A mechanistic model for interpretation of hydrogen and oxygen isotope ratios in tree-ring cellulose. *Geochim Cosmochim Acta* 64:21–35
- Rossmann A (2001) Determination of stable isotope ratios in food analysis. *Food Rev Int* 17:347–381
- Schmidt O, Quilter J, Bahar B et al (2005) Inferring the origin and dietary history of beef from C, N and S stable isotope ratio analysis. *Food Chem* 91:545–549
- Schoeller DA, Minagawa M, Slater R et al (1986) Stable isotopes of carbon, nitrogen and hydrogen in the contemporary North American human food web. *Ecol Food Nutr* 18:159–170
- Schwarcz HP, Schoeninger MJ (2011) Stable isotopes of carbon and nitrogen as tracers for paleo-diet reconstruction. In: Baskaran M (ed) *Handbook of environmental isotope geochemistry*. Springer, Berlin
- Sponheimer M, Lee-Thorp JA (1999) Isotopic evidence for the diet of an early hominid, *Australopithecus africanus*. *Science* 283:368–370
- Stewart H, Blisard N, Bhuyan S, Nayga Jr RM (2004) The demand for food away from home. Agricultural Economic Report No. 829, U.S. Department of Agriculture
- Vander Zanden MJ, Casselman JM, Rasmussen JB (1999) Stable isotope evidence for the web consequences of species invasions in lakes. *Nature* 401:464–467
- West AG, Patrickson SJ, Ehleringer JR (2006a) Water extraction times for plant and soil materials used in stable isotope analysis. *Rapid Commun Mass Spectrom* 20:1317–1321
- West JB, Bowen GJ, Cerling TE et al (2006b) Stable isotopes as one of nature's ecological recorders. *Trends Ecol Evol* 21:408–414
- West JB, Ehleringer JR, Cerling TE (2007) Geography and vintage predicted by a novel GIS model of wine $\delta^{18}\text{O}$. *J Agric Food Chem* 55:7075–7083
- West JB, Sobek A, Ehleringer JR (2008) A simplified GIS approach to modeling global leaf water isoscapes. *PLoS ONE* 3:1–8
- West JB, Kreuzer HW, Ehleringer JR (2010a) Approaches to plant hydrogen and oxygen isoscapes generation. In: West JB, Bowen GJ, Dawson TE et al (eds) *Isoscapes: understanding movement, pattern, and process on Earth through isotope mapping*. Springer, Dordrecht
- West JB, Bowen GJ, Dawson TE et al (2010b) *Isoscapes: understanding movement, pattern, and process on Earth through isotope mapping*. Springer, Dordrecht
- White JW, Winters K, Martin P et al (1998) Stable carbon isotopic analysis of honey: validation of internal standard procedure for worldwide application. *J AOAC Int* 81:610–619
- White C, Longstaffe FJ, Law KR (2004) Exploring the effects of environment, physiology and diet on oxygen isotope ratios in ancient Nubian bones and teeth. *J Archaeol Sci* 31:233–250

Chapter 34

Stable Isotopes of Carbon and Nitrogen as Tracers for Paleo-Diet Reconstruction

H.P. Schwarcz and M.J. Schoeninger

Abstract The isotopic compositions of the tissues of animals and humans are determined by the proportions of the various nutrients which they consume. This allows us to determine how much of each of their available foods were actually consumed over various parts of their lifetime. We apply this to ancient humans by analysis of bones, teeth and, rarely desiccated softer tissues (hair, skin). We review variations in $\delta^{13}\text{C}$ and $\delta^{15}\text{N}$ of known classes of nutrients (plants and animals), and discuss the chemical species whose isotopic composition can be analysed: collagen, bone-mineral, and lipids (cholesterol, etc.). Some variation in $\delta^{15}\text{N}$ also arises from variations in $\delta^{15}\text{N}$ of soil, particulate matter in the sea, and effect of aridity on N balance in terrestrial animals. Examples are presented of variation in $\delta^{13}\text{C}$ due to consumption of maize (a C_4 plant) and in $\delta^{15}\text{N}$ due to trophic level effects in prehistoric hunter-gatherers.

34.1 Introduction

34.1.1 The Concept of Isotopic Paleodiet Analysis

Beginning in the 1970s, scientists recognized that natural variation in $\delta^{13}\text{C}$ and $\delta^{15}\text{N}$ of human tissues could be used to learn something about past human diet. This

H.P. Schwarcz (✉)
School of Geography and Earth Sciences, McMaster University,
Hamilton ON L8S 4K1, Canada
e-mail: schwarcz@mcmaster.ca

M.J. Schoeninger
University of California at San Diego, 9500 Gillman Drive,
La Jolla, CA 92093, USA
e-mail: mjschoen@ucsd.edu

concept was almost simultaneously introduced by two groups of researchers: DeNiro and Epstein (1978, 1981) who carried out animal feeding experiments to show that “you are what you eat plus a few per mille”; and Vogel and van der Merwe (1977) who used $\delta^{13}\text{C}$ values of bone collagen to show the use of maize by American native people. Shortly afterwards Chisholm et al. (1982) used $\delta^{13}\text{C}$ values to estimate the dependence on marine foods of natives of the Canadian Pacific Coast. Since then the number of papers describing the use of stable isotopes to investigate past human diet has steadily increased. In this chapter we shall review these techniques and some of the main conclusions from current and past research.

34.1.2 Isotopic Labeling of Biological Materials

The tissues of all plants and animals are composed of molecules, which have been absorbed or ingested from the environment or have been synthesized by the organism. These molecules are generally labeled with stable isotopes whose relative abundances vary in nature. As a consequence the isotopic compositions of the corresponding elements vary to an extent, which is generally well within the range of analytical detection. Therefore, by analysis of tissues of plants and animals, it is possible to learn something about the environmental isotope ratios that were present during their lifetimes. In the case of plants these isotopic abundances are also influenced by environmental parameters (relative humidity, temperature, nutrient levels, etc.) whereas in animals, isotopes in tissues are almost entirely controlled by the diet of the animal.

Although this chapter is focused on the analysis and interpretation of isotope ratios in animals, it is necessary to consider to some extent variations in plants as these will have a direct effect on the animals which consume them.

We will be concerned here principally with isotopes of the light elements nitrogen and carbon. The paleodietary implications of other light elements (hydrogen, oxygen, and sulfur) have been studied but will not be discussed here. While other heavy elements (e.g., Fe, Zn, Se) are essential in animal metabolism, there have been no concerted attempts as yet to use these to trace diet of animals or humans.

We will now itemize the isotopic ratios which we will be reviewing. For each ratio there is a corresponding δ value defined to be

$$\delta^n E_x = \left[\left(\frac{[{}^n E / {}^m E]_x}{[{}^n E / {}^m E]_{\text{std}}} \right) - 1 \right] \times 1,000, \quad (34.1)$$

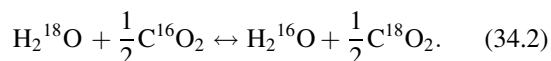
where E is the element in question (C, N), n, m are the mass numbers of the less- and more-abundant isotope respectively, x = sample and std = the isotopic ratio standard material (Table 34.1). The units of $\delta^n E_x$ are per mille (‰).

Using conventional analytical methods (see Sect. "34.2"), the precision for each of these δ values is about 0.1 ‰, throughout this paper all δ values will be given with respect to the standards listed in Table 34.1.

Natural variations in δ values were first discovered in the early twentieth C. and eventually attributed by Urey (1947) to differences in the quantum-mechanical thermodynamic partition functions for isotopically labeled species. As a result we expect to see differences arising in these ratios as a result of two discrete types of phenomena:

Equilibrium fractionation: where two isotopically labeled molecules or chemical species are in contact and where a mechanism exists for them to exchange isotopes, then there exists some equilibrium distribu-

tion of isotopes between these species through an *isotopic exchange reaction*. For example



The equilibrium partitioning of O isotopes between these species is represented by the isotopic equilibrium constant

$$K^{18}_{\text{H}_2\text{O}-\text{CO}_2} = \left(\frac{{}^{18}\text{O}/{}^{16}\text{O}}{\text{CO}_2} \right) / \left(\frac{{}^{18}\text{O}/{}^{16}\text{O}}{\text{H}_2\text{O}} \right). \quad (34.3)$$

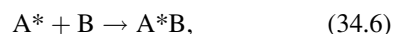
Urey (1947) showed that K was dependent only on the temperature (T) of equilibrium; as $T \rightarrow \infty$, $K \rightarrow 1.0$. Over some part of the T range, we observe that

$$\ln K = AT^{-2}. \quad (34.4)$$

Also, to a good approximation

$$1,000 \ln K_{a-b} = \delta_a - \delta_b. \quad (34.5)$$

Kinetic isotope effects (KIE's): In any reaction which involves isotopically labeled species, the rate of the reaction depends on the isotopic mass of the reacting species. That is, in a reaction of the form



where * represents an isotopic label, the forward rate of the reaction is generally faster for the lighter isotope. As a result, when the reaction has progressed only part way, the product will generally have a higher abundance of the light isotope than the substrate. An example of this is the rapid evaporation of water (in such a way that the vapor and liquid cannot equilibrate). Here the ${}^{18}\text{O}/{}^{16}\text{O}$ ratio of the vapor will be lower than that of remaining liquid.

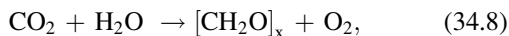
Diffusion of isotopes through membranes or any other medium also results in a kinetic separation of isotopes; in general the diffusion coefficients of isotopically labeled molecules depend on the molecular reduced masses as follows:

$$D^*/D = \sqrt{(M/M^*)}. \quad (34.7)$$

Table 34.1 Isotope ratios and δ values reviewed in this chapter

Element	Isotope ratio	Delta value	Standard
Carbon	${}^{13}\text{C}/{}^{12}\text{C}$	$\delta^{13}\text{C}$	VPDB
Nitrogen	${}^{15}\text{N}/{}^{14}\text{N}$	$\delta^{15}\text{N}$	AIR

In most biochemical reactions such as the enzymatic synthesis of molecules, it is assumed that KIE's control the isotopic composition of the product since the substrate and product are not expected to be isotopic equilibrium. For example in the photosynthetic reaction



where $[\text{CH}_2\text{O}]_x$ represents a carbohydrate, there is a KIE for carbon isotopes such that the product carbohydrate is depleted by ~17 % with respect to the substrate CO_2 .

34.1.3 Paleodiet

The study of the subsistence of past humans is a rich and complex subject which has traditionally mainly focused on the study of the traces of consumed foods: bones, shells, seeds, pollen, etc. (Ungar and Teaford 2002; Miracle and Milner 2008). Isotopic paleodiet cannot provide such specific information about the foods consumed. Rather, the approach should be to determine the isotopic compositions of the foods known to have been in the diet of a given population, and use these data to interpret the compositions of the preserved tissues of members of that population as well as food residues from cookware and storage vessels. In rare cases, it is possible, using analyses of tissues, to recognize that specific foods had been consumed, because of the unique isotopic compositions of those foods. More generally, it is necessary to use some sort of multicomponent data analysis procedure to estimate the relative proportions of multiple foods (Phillips and Gregg 2003; Schwarcz 1991). Other earlier reviews of these methods include Schwarcz and Schoeninger (1991), Schoeninger and Moore (1992); Katzenberg (2000); Ambrose and Katzenberg (2000).

34.2 Methods

34.2.1 Sample Preparation

In the study of humans from the past, we are generally limited to analyzing bones and teeth since "soft tissues" are usually lost through biologically driven decay. Rarely, when working in arctic or hyper-arid

regions, soft tissues such as hair, skin, are also preserved. Even in temperate regions, we cannot assume perfect preservation of skeletal materials.

34.2.1.1 Collagen

The main target of paleodietary study is collagen which makes up about 40 wt% of living bone. The best-preserved fossil (archaeological) bone yields about 22 wt% collagen, a difference which is attributable to dehydration during burial. At some archaeological sites, however, the collagen content recoverable from bone drops to as low as 1% or less, with the result that the bone is essentially unusable for this purpose. Also, we observe changes in the composition of the collagen recovered, which suggest that it is unrepresentative of the native material. DeNiro (1985) recommends that if the atomic C:N ratio lies outside the range 2.9–3.2, the sample should be rejected even if the yield is high. For a more detailed discussion of collagen preservation see DeNiro et al. (1985), DeNiro and Weiner (1988), Schoeninger et al. (1989) and Ambrose (1990).

Bone collagen is obtained by demineralizing the bone using weak acid (usually 0.2 N HCl) at room temperature over a period of several days. Alternately the Ca chelating agent EDTA (ethylene diamine tetraacetic acid) can be used although there is some risk that traces of this compound may be adsorbed onto the collagen (Weiner, pers comm.). If bone is well-preserved, this procedure yields a *pseudomorph* of the bone fragments used, composed of gelatinous collagen. This material is then dissolved in very dilute acid (HCl) at 60°C to produce a gelatin solution, which is then filtered, lyophilized and stored until analysis. If more finely powdered bone is used, it is impossible to observe pseudomorphs, the presence of which provide a useful indication of collagen preservation. Ambrose (1990) also emphasizes the need to determine the percent C and N in the bone as independent indicators of collagen preservation; these data are readily obtained using the CF method.

Analysis is by direct combustion with O_2 in a continuous-flow (CF) IRMS; the product CO_2 and N_2 are analyzed for $\delta^{13}\text{C}$ and $\delta^{15}\text{N}$ respectively. Older methods included reacting collagen with cupric oxide (CuO) in an evacuated pyrex tube at 550°C, which produced quantitative yields of C as CO_2 and N as N_2 .

The $\delta^{13}\text{C}$ value of collagen is generally observed to be higher than that of the bulk tissue of the diet. In free-ranging animals an offset of 5 ‰ is observed (Lee-Thorp et al. 1989; Schwarcz and Schoeninger 1991) although experimentally fed animals display smaller offsets, $\sim 2\text{--}3$ ‰ (DeNiro and Epstein 1978; Ambrose and Norr 1993; Kellner and Schoeninger 2007). The $\delta^{15}\text{N}$ offset between collagen and diet is mainly due to the trophic level effect, discussed below.

34.2.1.2 Other Components of Bones and Teeth

Bone contains many other molecular species some of which may survive prolonged periods of burial. These include proteins such as osteopontin (Masters 1987), osteocalcin; proteoglycans such as glycosaminoglycan; and lipids and related molecules such as cholesterol. While the initial concentrations of most of these species are too low to permit their eventual recovery from fossil bone, cholesterol has shown some promise in this regard. It is a component of the plasma membrane of all animal cells and can be recovered from fossil bones using simple chemical extraction procedures, followed by chromatographic separation from other lipids (Evershed 2008). The use of cholesterol as a tracer of paleodiet has been elaborated by Stott et al. (1999), Jim et al. (2004) and Corr et al. (2008). The latter authors showed how, in exceptionally well preserved human remains other lipids indicative of dietary source can be isolated and isotopically analyzed.

Bone, Tooth Carbonate

The mineral phase of bone, hydroxyapatite (HA), contains a few mol% of CO_3 in its crystal lattice, substituting for either OH or PO_4 . This can be extracted from the bone by reacting it with phosphoric acid in the same manner (and same equipment) as is used for the analysis of the isotopic composition of CaCO_3 in shells, etc. The reaction is usually carried out at an elevated temperature ($85\text{--}95^\circ\text{C}$) and both $\delta^{13}\text{C}$ and $\delta^{18}\text{O}$ are obtained for the bone or tooth material. A sample of CaCO_3 of known isotopic composition is analysed at the same time to serve as a reference material. Archaeological materials are pretreated with a buffered ($\text{pH} = 5.5$) solution of acetic acid

before analysis to remove traces of CaCO_3 that may have been deposited in or on the bone during burial.

The $\delta^{13}\text{C}$ value of CO_2 liberated in this way is offset from that of the diet. The amount of this offset in humans is not precisely known, although it has been studied in animals where it is found to vary widely (Passey et al. 2005). Some but not all of the variation in this offset in animals is due to the effect of excretion of waste C in the form of ^{13}C -depleted methane, especially in ruminants (Hedges and van Klinken 2000). This effect is not likely to be significant in humans. Prowse et al. (2003) noted that assuming an offset of 13 ‰ leads to an average diet for terrestrial C_3 consumers of -25 ‰. In the absence of well controlled experimental data comparable to those used by Passey et al. an objective determination is as yet unknown.

Testing for Diagenesis

During their burial history, both bone and tooth may have been subject to alteration by soil water, resulting in changes in the δ values of the tissues. It has generally been a practice of archaeological scientists to test bone for diagenesis, usually by measuring change in the degree of crystallinity of the HA using Fourier-transform infrared spectrometry (FTIR). The separation between a pair of FTIR peaks at $\sim 600\text{ cm}^{-1}$ is measured; this increases as the bone is recrystallized, and is much larger in tooth enamel than in bone (Fig. 34.1). The separation is quantified using the so-called crystallinity index

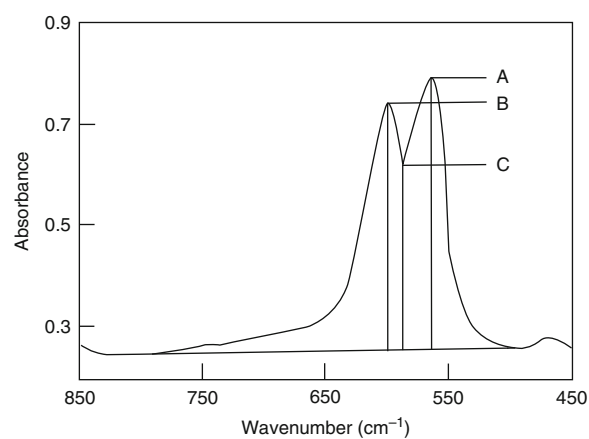


Fig. 34.1 Splitting of 600 cm^{-1} peak in FTIR spectrum of bone. Peaks shown are: 565 cm^{-1} (A), 595 cm^{-1} (C) and 605 cm^{-1} (B)

$$CI = \{A_{565} + A_{605}\} / A_{595}, \quad (34.9)$$

Where A_x = absorbance at frequency x . Various studies have shown that CI is of limited value in predicting the reliability of isotopic analyses (e.g., Stuart-Williams et al. 1996; Trueman et al. 2008). Recent studies (Lebon et al. 2010) have suggested that CI is a rather insensitive measurement of the degree of recrystallization and only begins to change significantly after major reconstitution of the structure; they propose the use of indices based on features within the $1,150 \text{ cm}^{-1}$ PO_4 absorption peak.

34.2.2 Analysis of Soft Tissues

Where hair, skin or other soft tissues are preserved in mummified or frozen human remains, these can be analysed in the same way as collagen, that is, by direct combustion in a CF/IRMS. It is advisable to clean the samples before analysis following appropriate protocols. For hair, see O'Connell and Hedges (1999).

34.2.3 Analysis of Individual Molecules

Most animal and plant tissues are composed of biopolymers which were synthesized (assembled) from multiple molecular species. These can be isolated from the tissues and in some cases extracted from artifacts to yield additional isotopic information about paleodiet. Specifically, we see $\delta^{13}\text{C}$ analyses of: individual amino acids isolated from bone collagen (Fogel and Tuross 2003; Smith et al. 2009); individual fatty acids extracted from potsherds (Evershed 2008); cholesterol extracted from bone (Jim et al. (2004); and $\delta^{15}\text{N}$ analyses of amino acids (Naito et al. 2010). Some amino acids cannot be synthesized by animals and therefore their carbon skeletons are transferred from plants to herbivores and thence to carnivores, preserving the $\delta^{13}\text{C}$ value of the plant (C_3 or C_4). Likewise, some amino acids are not transaminated after ingestion and therefore conserve the $\delta^{15}\text{N}$ value of the food from which they were derived; the high $\delta^{15}\text{N}$ of proteins derived from marine foods can be recognized this way (see below).

34.3 Natural Variation in Isotopic Composition of Human Nutrients

A fundamental principle in isotopic paleodiet studies is that the analysis of the δ values of human tissues can only be interpreted in terms of the possible range of composition available in the foods that were consumed. Therefore, before considering the variation in isotopic composition of human tissues, it is necessary to consider the variation present in foods.

Humans entirely depend on plant foods for their nutrition, either through herbivory or through consumption of the flesh of terrestrial animals (largely herbivorous), aquatic fish and marine animals both herbivorous and carnivorous. Therefore variation in the isotopic composition of plants accounts for a large part of the variation in both $\delta^{13}\text{C}$ and some of the variation in $\delta^{15}\text{N}$ observed in humans. We shall first consider carbon isotopic variation in plants, focusing on primary producers (as heterotrophic plants [fungi] are a usually minor component of human or animal diet).

34.3.1 Plant Foods

34.3.1.1 Carbon Isotopes ($\delta^{13}\text{C}$)

Almost all plants (except fungi) obtain their food energy through photosynthesis (34.8), but plants use one of three photosynthetic pathways, each of which has different isotopic consequences. In the C_3 or Calvin cycle, the first product of CO_2 reduction is a three-carbon molecule, 3-phosphoglycerate. C_3 plants have $\delta^{13}\text{C}$ values averaging around -25 ‰ although they can vary for reasons to be discussed. Most wild and cultivated plants of temperate, tropical or subarctic regions are C_3 . In the C_4 or Hatch-Slack cycle, the initial product of CO_2 reduction is a four-carbon molecule oxaloacetate. Most C_4 plants are grasses and have typical $\delta^{13}\text{C}$ values near -12 ‰ . Wild C_4 plants are principally found in warm, arid to subarid regions although some C_4 grasses exist in temperate regions along with C_3 grasses. Some important cultigens are C_4 plants: maize ("corn" in America), millet and sorghum. Plants using crassulacean acid metabolism (CAM) are all succulents, living in hot, arid

environments, and include cacti, some of which produce edible fruits. Carbon fixed by the CAM cycle has $\delta^{13}\text{C}$ values that range between those of C_3 and C_4 plants.

Besides the variation in photosynthetic pathways, $\delta^{13}\text{C}$ values of plant tissues can vary for a number of other reasons:

Water use efficiency: All plants transpire water through stomata in their leaves; when under water stress (insufficient supply through the roots) or under arid conditions, these stomata are partially closed, resulting in limited circulation of CO_2 through them. As a result, CO_2 reduction to carbohydrates is more complete and isotopic fractionation is less strongly expressed, resulting in higher $\delta^{13}\text{C}$ values (Farquhar et al. 1989). Although C_4 plants are considered to be less responsive to aridity, there is a significant negative relationship between average rainfall and the $\delta^{13}\text{C}$ values in C_4 grasses as well (Murphy and Bowman 2009).

Canopy effect: when plants grow under dense cover of trees, the CO_2 which they take up through their stomata is partly derived from the decomposition of leaves from the trees, and is therefore depleted in ^{13}C compared to the global atmospheric value (-7‰) (van der Merwe and Medina 1991). Plants can be shifted to values as low as -35‰ by this means. C_4 plants do not appear to be affected by the canopy effect; those growing under trees do not display lower $\delta^{13}\text{C}$ values (Murphy and Bowman 2009).

Marine plants: The CO_2 used in primary production by algae and plankton in the sea is derived from dissolved inorganic carbon (DIC) in seawater, which is mainly hydrogen carbonate ions (HCO_3^-). These are enriched with respect to atmospheric CO_2 by about 7‰ ; therefore all marine flora and low trophic-level fauna are enriched by about this amount with respect to terrestrial plants and animals.

Suess effect: Since the beginning of the Industrial Revolution in the eighteenth C., CO_2 derived from burning of fossil fuels has been entering the atmosphere, resulting in a gradual lowering of the $\delta^{13}\text{C}$ of atmospheric CO_2 (Suess 1955; Marino and McElroy 1991). Pre-1800s plants and faunal materials should be corrected for this effect with the magnitude of the effect gradually rising through the nineteenth c. to its present value of -1.5‰ . It is most clearly seen in C_4 plants whose $\delta^{13}\text{C}$ values are less strongly affected by relative humidity effects.

34.3.1.2 Nitrogen Isotopes ($\delta^{15}\text{N}$)

Plants uptake nitrogen from the soil either as ammonium (NH_4^+) or as nitrate (NO_3^-) ions. These are fixed from atmospheric nitrogen (N_2) principally by bacteria, either rhizobacteria attached to roots of plants (especially legumes) or as cyanobacteria in the upper layers of the soil. By definition, $\delta^{15}\text{N}$ of atmospheric $\text{N}_2 = 0\text{‰}$ (AIR), and bacterially fixed N has $\delta^{15}\text{N}$ values close to zero or less. Plants, however, can process N in their roots and stems, leading to isotopic fractionation (Evans 2007) with the result that leaves can be enriched by several ‰ with respect to soil N. Environmental conditions, and especially availability of N in the soil can influence the degree of fractionation. Soil N can also be isotopically fractionated through the combined process of denitrification (conversion to N_2) and mineralization (conversion of organic N into ammonium and nitrate) (Evans 2008). In general, ammonia (NH_3), one of the intermediate products in mineralization, is highly depleted in ^{15}N , and is volatile and therefore capable of migrating upward in the soil and even escaping. As a result, $\delta^{15}\text{N}$ may decrease upward in soils, so that plants with more shallow root systems display lower $\delta^{15}\text{N}$ values.

Generally, non-leguminous plants have $\delta^{15}\text{N}$ values ranging from ~ 2 to 6‰ . Legumes, as a result of their association with N-fixing rhizobacteria, can have significantly lower values, ranging to -5‰ although the overall difference in $\delta^{15}\text{N}$ between legumes and non-legumes is generally smaller. In arid regions, we observe higher $\delta^{15}\text{N}$ of soil and plants, partly as a result of the enhanced loss of NH_3 . This amplifies the effect of lowered rainfall on $\delta^{15}\text{N}$ of herbivores (see below). The primary source of fixed nitrogen in marine and aquatic ecosystems is largely cyanobacteria which fix dissolved atmospheric N_2 ($\delta^{15}\text{N} = 0$), without significant fractionation (Sachs et al. 1999).

34.3.2 Animal Foods

34.3.2.1 Herbivores

In general, animals conform to the principle that “you are what you eat plus some ‰ ”. If we consider an animal as a “black box” with inputs, outputs and storage then the net isotopic composition of the animal

(=stored component) will be determined by the isotopic mass balance between the inputs and outputs. As a consequence, the isotopic compositions (δ values) of herbivorous animals represent the weighted average of the isotopic compositions of all the plant foods which they consume. The average δ value will also depend on the local availability of plants of a given δ value. For wild animals, specific effects are expected for each isotope as listed below. For domesticated animals, these effects will depend on the fodder provided.

Carbon

Animals living in hotter, drier environments exhibit higher $\delta^{13}\text{C}$ values, partly due to the higher abundance of C_4 grasses and also as a result of water-use efficiency effects. These effects may occur seasonally at a given locale, resulting in interseasonal changes recorded in serial sections of teeth or hair (Schwarcz and White 2004; Balasse et al. 2002). A smaller shift to lower $\delta^{13}\text{C}$ with increasing RH occurs. The canopy effect lowers $\delta^{13}\text{C}$ values of the tissues of animals living in a forest (Schoeninger et al. 1999). These $\delta^{13}\text{C}$ effects are recorded both in bone collagen and in bone/tooth carbonate (Cerling et al. 2003).

Marine herbivores including filter-feeders are generally enriched by about 7 ‰ with respect to terrestrial herbivores (Schoeninger and DeNiro 1984), due to the corresponding enrichment in phytoplankton and other marine plants which derive their C from DIC of sea-water.

Nitrogen

The $\delta^{15}\text{N}$ of most wild forage ranges between 0 and 7 ‰; in warm, arid regions, ^{15}N of soil is higher due to ammonia loss although there is a large range of effects reported in the literature (Murphy and Bowman 2009). These effects are recorded in bone collagen. $\delta^{15}\text{N}$ values of marine animals are significantly higher than those of terrestrial animals (Schoeninger and DeNiro 1985). This is partly due to the generally high $\delta^{15}\text{N}$ of nitrate and particulate organic matter in sea-water (Guo et al. 2004) which form the nutrient for the base of the food chain. This effect is amplified by the longer trophic systems in the marine system (Peterson and Fry 1987; Fry 2006). In addition, there is

some evidence from Atlantic and Pacific turtles that the $\delta^{15}\text{N}$ values of fauna within the Atlantic system are lower than those within the Pacific system (Wallace et al. 2006).

34.3.2.2 Trophic Level Effects

As a result of the isotopic balance between dietary inputs and outputs, the δ values of herbivores (and higher trophic level organisms) are offset with respect to the diet, and generally enriched in the heavy isotope. We refer to this as a “trophic level effect” (TLE)

$$\text{TLE} = f_{\text{tissue-diet}} = \delta^x_{\text{tissue}} - \delta^x_{\text{diet}}$$

In addition to this fractionation between bulk composition of the animal and its diet, specific edible tissues in the animal may be isotopically fractionated with respect to the bulk organism. Also, it is possible to analyze single amino acids, which are differentially fractionated with respect to diet for both ^{13}C (Fogel and Tuross 2003) and ^{15}N (Naito et al. 2010).

For carbon, there is a small TLE of approximately 1 ‰, which is barely detectable in herbivores, but more apparent in systems with many trophic levels such as marine vertebrate ecosystems (Schoeninger and DeNiro 1984). No specific mechanism has yet been proposed for the origin of this effect. The TLE for nitrogen is known from animal populations to be approximately 2–3 ‰ (Minagawa and Wada 1984; Schoeninger and DeNiro 1984; Schwarcz and Schoeninger 1992) although Hedges and Reynard (2007) suggest values as high as 6 ‰ (see also Richards and Trinkaus 2009). A possible cause of this effect is that when nitrogenous molecules are oxidized in the body, the product species (mainly urea) are strongly depleted in ^{15}N ; the residual amine (NH_2) pool in the plasma is therefore enriched in ^{15}N . Almost all amino acids in the plasma are transaminated before being used to make proteins and therefore are labeled with the ^{15}N -enriched amino groups (Steele and Daniel 1978; Yoneyama et al. 1983).

A specific example of the TLE in humans is seen in the weaning effect, first recognized by Fogel and Tuross (see Fogel et al. 1997). Since the only source of nutrient of most nursing babies is the milk of their mothers, the infants are one trophic level higher than their mothers. This was first seen by Fogel and Tuross in the $\delta^{15}\text{N}$ values of hair and nails of pre-weaning

infants and was also clearly detectable in the skeletons of infants. This method has been used to determine the age of weaning in several archaeological populations (e.g., Katzenberg et al. 1996; Wright and Schwarcz 1998; Schurr 1998). As noted above, the TLE can be seen in both $\delta^{15}\text{N}$ and $\delta^{13}\text{C}$ values. The small (about 1 ‰) TLE for $\delta^{13}\text{C}$ is most clearly seen in cross-plots of $\delta^{15}\text{N}$ vs. $\delta^{13}\text{C}$ for bone collagen extracted from infants, which generate correlations with a slope around 3.0 (Fuller et al. 2006).

34.3.2.3 Aridity Effect on $\delta^{15}\text{N}$

Heaton et al. (1986) showed that $\delta^{15}\text{N}$ of herbivore tissues increased with decreasing rainfall. They attributed this to two effects: (a) loss of ammonia from the soil in hot, arid conditions; and (b) increased storage of urea in urine used by animals (and humans) which experience water shortage in order to decrease loss of water as urine (see Sponheimer et al. 2003). A single relationship between $\delta^{15}\text{N}$ and rainfall appears to be valid globally (Schwarcz et al. 1999).

34.3.2.4 Carnivores and Omnivores

Animals (including humans) which consume other animal tissues will inherit the δ values of these animal derived foods (largely protein and fat); omnivores have isotopic characteristics intermediate between herbivores and carnivores. In both types, the TLE results in enrichment of heavy isotopes of C and N in the consumer's tissues. In terrestrial environments, we generally expect to observe only three levels of enrichment: from plants to herbivores and thence to carnivores, whereas omnivores (with mixed plant- and animal-based diets) would be expected to exhibit intermediate TLE's. Marine and aquatic realms have many more trophic levels, with the result that the total enrichment in ^{15}N and ^{13}C can be much larger for top-feeders (Fig. 34.2).

The range of $\delta^{15}\text{N}$ and $\delta^{13}\text{C}$ values expected in the tissues of carnivores depends on their dietary base. For terrestrial carnivores who are not also consuming aquatic fish, the highest values expected would be about one TLE above that of herbivores, that is, $\delta^{15}\text{N}$ ~8–12 ‰ and $\delta^{13}\text{C}$ values near -25 ‰ except where the herbivore sources have been consuming C₄ grasses (Fig. 34.2).

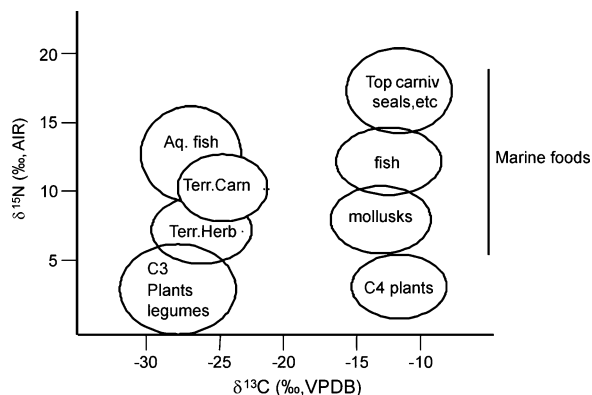


Fig. 34.2 $\delta^{13}\text{C}$ vs. $\delta^{15}\text{N}$ for animals, plants

The $\delta^{15}\text{N}$ values of marine carnivores can be much higher than any encountered on land, due to the multiple trophic levels in the marine realm. Therefore, high $\delta^{15}\text{N}$ values in human (and animal) tissues are useful indicators of consumption of marine foods, except where the diet has focused on low-TL foods (e.g., mollusks). The $\delta^{13}\text{C}$ values of marine consumers are shifted up by at least 7 ‰ relative to terrestrial feeders, plus approximately 1 ‰ per trophic level (Fry et al. 1978).

34.4 Paleodietary Analyses of Ancient Human Populations

34.4.1 General Principles

Based on the various techniques described above it is possible to interpret the isotopic compositions of tissues obtained from ancient or modern animals and humans in terms of the proportions of various foods that were consumed through their lifetime. We should not assume, however, that there is a simple correspondence between diet and isotopic composition since many specific factors limit the resolution of these methods, as follows.

34.4.1.1 Chronology of Individual Isotopic Records

As the body of an animal grows from infancy to maturity and senescence, matter is constantly being

transferred into and out of its tissues, so that any particular sample of an animal possesses an isotopic record of some part of the life history of ingestion by the animal. The earliest recorded part of the life of any vertebrate is found in the teeth, both in the enamel (which contains negligible protein but traps a $\delta^{13}\text{C}$ dietary signal in CO_3 ions in hydroxyapatite) and the dentine which is a bone-like tissue containing collagen formed in infancy or adolescence. Bones are constantly being remodeled by the action of specialized cells within Haversian systems (Bilezikian et al. 2008) at a rate which depends on the skeletal element and the age. The average residence time of C and N atoms in bone collagen is about 10 y but can be longer than 20 y in older individuals (Manolagas 2000; Hedges et al. 2007). Generally, the turnover rate is greater in trabecular bone than in cortical bone. The shortest-lived records (days to months) are found in soft tissues including hair and skin.

Serial records of diet, showing change in diet through life, are preserved in dentine (Fuller et al. 2003), in enamel (Balasse et al. 2002) and in hair (Schwarcz and White 2004). Bone is not macroscopically laminated in such a way to permit serial sections that display the growth history.

34.4.1.2 Mixing of Multiple Dietary Inputs

In any given tissue sample (e.g., bone collagen), the δ values represent a mixture of the various ingested sources of atoms. Schwarcz (1991) suggested using a simple graphical, algebraic method to estimate the relative proportions of the various dietary components and also to characterize the homogeneity or lack thereof in ancient populations. He noted that in general we cannot use δ values to deduce paleodiet; rather, these data must be used in conjunction with known or inferred δ values of the available foods to estimate the relative proportions of these foods. This method, which is sometimes referred to as the “scrambled” paleodiet model, assumes that all foods contribute in proportion to their atom fraction in the diet. An alternative approach is that proposed by Krueger and Sullivan (1984), namely that the amino acids of bone collagen are derived exclusively from dietary protein (“routing”). This model was partially supported by experimental studies using isotopically labeled (C_3 or C_4) protein and non-protein foods fed to rats by

Ambrose and Norr (1993) and to mice by Tieszen and Fagre (1993). Schwarcz (2000) noted that all but 22% of the C atoms in the amino acids of collagen are in non-essential amino acids that could have been synthesized from the total C pool in the body; in the absence of abundant external sources of protein, such endosynthesis will incorporate C isotopic signals from carbohydrates and fats as well as protein. Howland et al. (2003) show how endosynthesis contributes to the C isotopic label of non-essential amino acids.

More recently, Kellner and Schoeninger (2007) and Froehle et al. (in press, JAS) undertook meta-analyses of all the experimental data on the $\delta^{13}\text{C}$ of bone carbonate ($\delta^{13}\text{C}_{\text{apatite}}$) and collagen ($\delta^{13}\text{C}_{\text{collagen}}$) from rats, mice and swine (Hare et al. 1991; Ambrose and Norr 1993; Tieszen and Fagre 1993; Howland et al. 2003; Jim et al. 2004; Warinner and Tuross 2009) to assess the relationship between animal diet and $\delta^{13}\text{C}_{\text{collagen}}$ and $\delta^{13}\text{C}_{\text{apatite}}$. When controlled for the source of protein (C_3 -protein, C_4 /marine-protein), regression relationships between $\delta^{13}\text{C}_{\text{collagen}}$ and $\delta^{13}\text{C}_{\text{diet}}$ reached significance within each protein-specific group. As a group, swine tended to fall slightly above the rodent C_3 line, consistent with the 5–35% C_4 protein included in many of their diets (Fig. 34.3a). High- and low-protein diet data did not diverge systematically from the regression lines. In spite of body size differences, then, when protein sources are controlled, swine and rodents do not differ in the way $\delta^{13}\text{C}_{\text{collagen}}$ relates to $\delta^{13}\text{C}_{\text{diet}}$ for animals on experimental diets and the offsets suggest that about 60% of the carbon in collagen originates in dietary protein. The $\delta^{13}\text{C}_{\text{apatite}}$ in contrast to $\delta^{13}\text{C}_{\text{collagen}}$ correlates strongly with $\delta^{13}\text{C}_{\text{diet}}$ for animals on experimental diets (Fig. 34.3b). As with $\delta^{13}\text{C}_{\text{collagen}}$ all animals showed similar correlation with $\delta^{13}\text{C}_{\text{diet}}$ irrespective of body size.

In addition to these basic relationships, dietary information is also assumed to reside in the offset between $\delta^{13}\text{C}_{\text{collagen}}$ and $\delta^{13}\text{C}_{\text{apatite}}$ (i.e., $\Delta^{13}\text{C}_{\text{CO-AP}}$). Data from a large study of wild South African fauna appeared to support Kruger and Sullivan’s 1984 model that the offset varies according to whether an animal is herbivorous, omnivorous or carnivorous (Lee-Thorp et al. 1989). Using archaeological data, Harrison and Katzenberg (2003) found that maize agriculturists who ate fauna with a C_3 signature had larger $\Delta^{13}\text{C}_{\text{CO-AP}}$ than did human foragers who ate C_3 plants along with marine fish even though both groups were clearly omnivorous. The recent meta-analysis of all

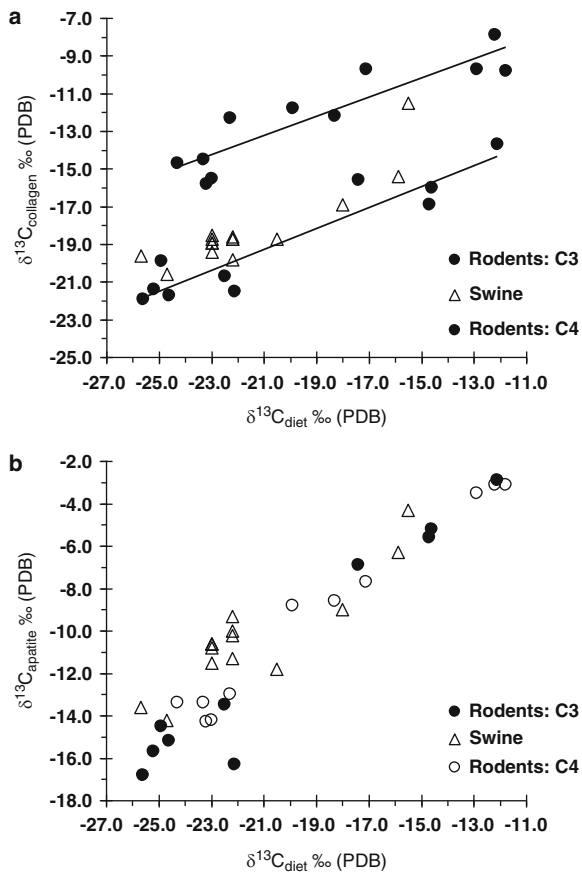


Fig. 34.3 Isotopic data from feeding experiments: (a) $\delta^{13}\text{C}$ of collagen vs. $\delta^{13}\text{C}$ of diet; (b) $\delta^{13}\text{C}$ of collagen vs. $\delta^{13}\text{C}$ of bone apatite; collagen-apatite relationship, controlled for diet types

experimental fauna showed that when controlled for diet protein (Fig. 34.3c), regressions showed a tight correlation between $\delta^{13}\text{C}_{\text{apatite}}$ and $\delta^{13}\text{C}_{\text{collagen}}$ (both $P < 0.001$; C_3 : $R^2 = 0.921$; C_4/marine $R^2 = 0.814$). Slopes did not differ, but vertical intercepts and adjusted group means did. When both values are available in prehistoric bone and they are plotted on the graph generated by the experimental fauna, they provide a detailed picture of diet composition (both diet and diet protein).

Phillips and Gregg (2003) refined the mixing model by also considering the relative weight percent of C and N in different foods, which would modify the estimates of their proportions in the diet. Software based on their model has been developed by the U.S. Environmental Protection Agency (2009) for use in interpretation of analyses of animals in relation to

their ecosystem. Moore and Semmens (2008) have incorporated Bayesian analysis into the procedure to produce another software package, MixSIR 1.0 (Semmens and Moore 2008). These models have so far had limited use: Bocherens et al. (2005) attempted to quantify the relative proportions of multiple sources of herbivore flesh. Newsome et al. (2004) estimated the relative contribution of multiple marine and terrestrial food sources to coastal populations from central California. Note that these methods assume that C isotopes from all food sources are “scrambled”. Also, at present the models have not attempted to include $\delta^{13}\text{C}$ data from bone carbonate.

34.4.1.3 Goals of Paleodiet Analysis

The isotopic analysis of human remains and food-related materials is used by archaeologists to examine a number of issues in prehistory and the historic past. Amongst these are the following:

- Relationships between diet, age (including infancy), sex, social status, and health-related descriptors.
- Relationship between isotopic indicators of diet and other indicators such as tooth wear, dental caries, food remains, written texts (where present).
- Historic changes in diet of populations at a given site (e.g., an ancient city or shell-midden).
- Historic shifts in diet over long distances and time scales, such as the transition from the Mesolithic to the Neolithic, or the collapse of the Maya.

Paleodiet analysis is considered to be complementary to other indicators of ancient behavior, such as destruction levels at sites representing warfare, size of settlements, use of advanced farming techniques such as terraces and irrigation. As much as possible, isotopic analyses should be interpreted in the context of the entire reconstructed record of a site and the people who inhabited it.

34.4.2 Application to Ancient Populations

We will conclude this chapter by presenting a number of examples of the application of isotopic paleodiet analysis that demonstrate its potential to provide

answers to some of the questions just noted. Given the space limitations of the chapter, this can only be a cursory glance at this rich field. Selected references to other examples of the same types of studies are also included.

34.4.2.1 Maize as a Cultigen in the Americas

Maize is a C_4 plant derived from a grass (*teosinte*) that grows wild in the Valley of Mexico. It was domesticated sometime in the sixth millennium BCE, and its use spread gradually throughout Central and South America in the period before 1000 CE. Subsequently a hardier version of this plant expanded into N. America reaching as far north as central Ontario. The first use of isotopic paleodiet analysis was applied to the spread of maize into the northeastern US by van der Merwe and Vogel (1978), almost concurrent with DeNiro and Epstein's (1978) first demonstration of the use of isotopic indicators of diet.

Within southern Ontario, first Schwarcz et al. (1985) and then Katzenberg et al. (1995) analyzed collagen from the bones of aboriginal natives. The $\delta^{13}C$ values increased from levels typical of pure C_3 consumers (c. -21 ‰) prior to c. 700 AD, to values suggesting ingestion of large amounts of maize around 1200 AD (Fig. 34.4). At the same time, the $\delta^{15}N$ values of collagen remained essentially constant, and much higher than expected for a diet based on the flesh of C_3 -consuming herbivores (e.g., white-tailed deer). This suggested that aquatic fish were a significant

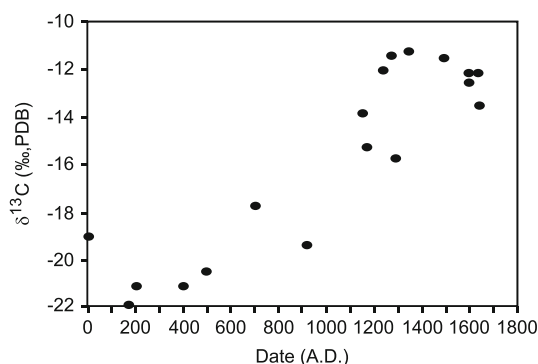


Fig. 34.4 Variation in $\delta^{13}C$ (collagen) of human bones vs. age, through the period of adoption of maize as a cultigen in Southern Ontario (from Katzenberg et al. 1995)

source of protein to these people. Throughout North America there was significant variation in the amount of maize in human diet. In the southwestern U.S., prehistoric Pecos Pueblo relied more heavily on maize when compared to Grasshopper Pueblo (Kellner et al. 2010). Both Pueblo groups used more maize than the Ontario agriculturists (Katzenberg et al. 1995) and those on the coast of today's Georgia (Kellner and Schoeninger 2007). Figure 34.5 shows $\delta^{13}C$ and $\delta^{15}N$ data for these sites as well as non-agricultural coastal people of S. California; much of the variation in $\delta^{15}N$ for both inland and coastal people reflects variation in dependence on fish and other marine foods.

34.4.2.2 Coastal Populations and Marine Food Consumption

Because of the large differences observed in both $\delta^{13}C$ and $\delta^{15}N$ between terrestrial and marine food sources (Fig. 34.2), many studies of isotopic paleodiet have focused on human populations living on or near the sea. An early study by Chisholm et al. (1982) used $\delta^{13}C$ values of coastal human populations in British Columbia, Canada to show a surprisingly high degree of dependence of these people on marine foods (mostly salmon) in spite of the presence of abundant terrestrial nutrients. Schoeninger et al. (1983) showed that $\delta^{15}N$ and $\delta^{13}C$ both discriminate marine from terrestrial human consumers. In regions where prehistoric human populations had access to both marine and maize, which confound the use of $\delta^{13}C$ values, bone collagen $\delta^{15}N$ values distinguish between dependence on marine foods or maize (Schoeninger et al. 1990). For example, the Nasca people of coastal southern Peru ate little marine food even though whales and fish are commonly depicted on their ceramics (Kellner and Schoeninger 2007 and Fig. 34.3b).

Covariation between $\delta^{15}N$ and $\delta^{13}C$ of bone collagen allows us to see more clearly the dependence of coastal and island populations on mixtures of terrestrial and marine foods. A study by Walker and DeNiro (1986) of coastal and island populations from the Santa Barbara Islands (Fig. 34.6) showed that people living on the islands displayed higher $\delta^{15}N$ and $\delta^{13}C$ values than those on the coast. In addition, marine diets high in secondary carnivores (e.g., toothed whales, seals and carnivorous fish) have higher $\delta^{15}N$ values than do diets with marine invertebrates due to trophic

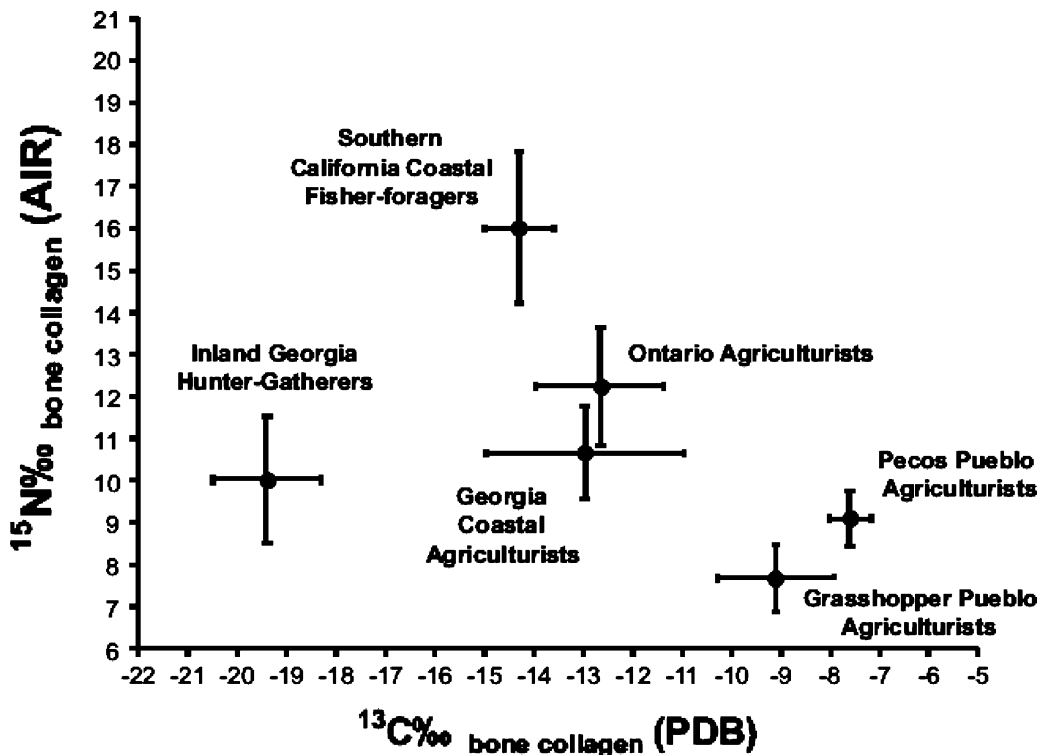


Fig. 34.5 $\delta^{13}\text{C}$ vs. $\delta^{15}\text{N}$ for bone collagen of N. American indigenous people before European contact. See text for explanation

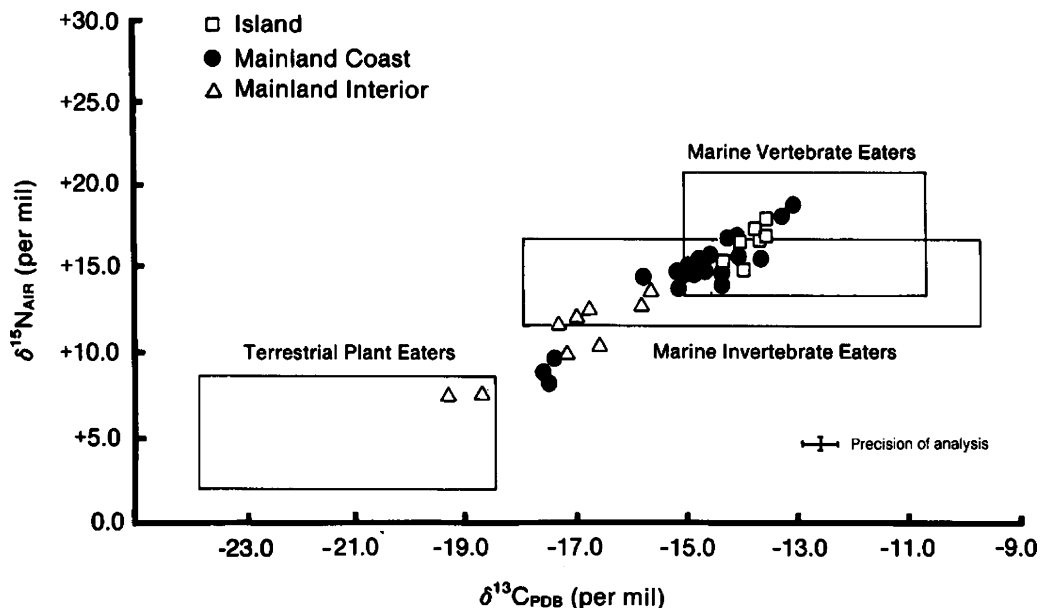


Fig. 34.6 Correlation between $\delta^{13}\text{C}$ and $\delta^{15}\text{N}$ for prehistoric people from Channel Islands, S. California (Walker and DeNiro 1986)

level effects. Several studies distinguish between open ocean fishing on seals and carnivorous fish (e.g., Schoeninger et al. 1983; Pfeiffer and Sealy 2006;

Barrett and Richards 2004; Keenleyside et al. 2008; Prowse et al. 2003) vs. nearshore collection of mussels, lobsters, and clams (Little and Schoeninger 1995).

Some sites are found on coastlines in arid regions where the use of enriched ^{15}N in collagen is compromised by the effect of aridity on human $\delta^{15}\text{N}$ values. Corr et al. (2005) found that people who had consumed marine foods could also be identified through analysis of the difference in $\delta^{13}\text{C}$ between two amino acids, glycine and phenylalanine. Marine consumers displayed higher values of $\Delta_{\text{glycine-phenylalanine}}$ than terrestrial consumers of either C_3 or C_4 foods.

34.4.2.3 Mesolithic-Neolithic Transition

Tauber (1981), studying $\delta^{13}\text{C}$ in collagen of coastal Mesolithic and Neolithic people from Denmark, showed that the earlier Mesolithic people were significantly enriched in ^{13}C whereas the Neolithic population was uniformly depleted, lying in the range expected for terrestrial C_3 consumers. In 1994, Lubell et al. showed that Mesolithic people from coastal Portugal displayed a linear trend on a plot of $\delta^{13}\text{C}$ vs. $\delta^{15}\text{N}$, which extended between terrestrial and a marine dietary regimes. These authors also noted that the marine component appeared to represent high trophic-level consumers. By contrast, Neolithic people from the same region lay entirely within the terrestrial end of this distribution (low $\delta^{13}\text{C}$, $\delta^{15}\text{N}$), suggesting that there was an abrupt shift in the food economy shortly after 8,000 cal BP away from marine resources. Richards et al. (2003) showed a similar sharp shift in diet at the end of the British Mesolithic.

Away from the coastline, the cultural transition from hunting-gathering to farming and domestication of animals is less readily identifiable by isotopic analysis of human bone collagen. Alternatively, specific subsistence strategies may be recognized through analysis of lipid residues in ceramics. For example, dairying can be recognized through the presence of lipids with diagnostic distributions of $\delta^{13}\text{C}$ values in lipids adsorbed in ceramic sherds. These are presumed to date to when the pot was used for the preparation of milk products (Spangenberg et al. 2006; Dudd and Evershed 1998).

34.4.2.4 Millet and Sorghum

The presence of millet (*Panicum* sp., *Pennisetum* sp.), a group of C_4 cultivated grasses, can also serve as an

indicator of the inception of agriculture. Millets were introduced into human diet in the Far East (China, Korea) in the early Neolithic but eventually spread through Asia and eventually became a major food-crop in northern, sub-Saharan Africa (e.g., Nubia). The distinctive increase in the $\delta^{13}\text{C}$ of bone collagen in humans and animals is attributable to the presence of this crop (Pechenkina et al. 2005). Millet grows optimally during hot, dry weather and may, in some locations, be harvested at the end of summer, while other C_3 plants (wheat, barley, oats) are planted and harvested in the cooler months. Hairs recovered from mummified remains in lower Nubia were shown to preserve this seasonal cycle of millet/ C_3 grains (Schwarz and White 2004). During the Iron Age in Europe, records indicate that millet was solely animal food; but isotope analysis of human skeletal remains from the period show a strong C_4 signal (Murray and Schoeninger 1988).

Sorghum (*Sorghum bicolor*) is another C_4 grain that grows in warm, dry environments. Its use has not yet been detected in human diet but could be disguised by the presence of millet whose habitat preferences are similar.

34.4.2.5 Diet of Prehistoric Hominins

The oldest prehistoric hominin species for which paleodiet data exist are specimens found in limestone caves of S. Africa. While their skeletons do not contain measurable amounts of collagen, their tooth enamel can be analysed for $\delta^{13}\text{C}$. A 3 My *Australopithecus africanus* individual from the cave of Makapansgat in S. Africa has been shown to have had a diet enriched in ^{13}C compared to contemporaneous herbivores (Sponheimer and Lee-Thorpe 1999) while similar enrichment was found in specimens of *Paranthropus* (formerly *Australopithecus*) *robustus* from the cave of Swartkrans (Lee-Thorpe et al. 1994).

Collagen is sufficiently well preserved in the skeletons of some Paleolithic humans to permit carrying out $\delta^{13}\text{C}$ and $\delta^{15}\text{N}$ analysis in order to learn about their diet (Richards et al. 2009; Hu et al. 2009; Richards et al. 2000). Earlier, Aiello and Wheeler (1995) had suggested that, due to the energy demands of their larger brains, the genus *Homo* had become more carnivorous than ancestral hominins. This has been generally supported by analyses of $\delta^{15}\text{N}$ in Neanderthals.

Surprisingly, the bone collagen of early anatomically modern humans (AMH'S) displayed even higher $\delta^{15}\text{N}$ values (Richards and Trinkaus 2009), from which it is inferred that these people became adept at capturing fresh-water fish (Fig. 34.6). In addition, Richards and Trinkaus conclude that some AMH's also included marine foods in their diet base.

34.4.3 Ethical and Cultural Limitations of Paleodiet Analysis

In many parts of the world we are now seeing limitations placed on the use of human remains for paleodiet (as well as other anthropological) studies. Early studies of paleodiet were focused on analysis of collagen extracted from human bone. Many of the studies carried out in North America, involved the analysis of the remains of people who were recognized to be ancestral to living populations in the same area. In more recent years such research programs have been curtailed out of respect for the cultural and religious traditions of these people, as defined by the Native American Graves Protection and Repatriation Act (U.S Federal Register 2010). A similar agreement now exists in Canada. Some studies have continued under special

agreements with local tribal councils. In some regions outside North America anthropologists currently encounter fewer restrictions on access to human remains for analysis, with the notable exceptions of Australia and Israel where study of human remains from historic sites is also proscribed.

Alternative strategies have been devised. For example, it has been shown that the diet of domesticated dogs is very close to that of the associated humans (Cannon et al. 1999). Analysis of charred food remains adhering to pot-sherds preserves the C, N isotopic compositions of the foods (Hastorf and DeNiro 1985; Morton and Schwarcz 2004) as do adsorbed residues (Evershed 2008).

34.5 Conclusions

The recognition that some foods differ significantly in their stable isotopic compositions has allowed us to recognize past variations in human diet. By analysis of the tissues remaining in buried remains of ancient human populations, archaeological scientists have added a new dimension to the study of past human subsistence. Most of the studies in this field have been through the analysis of the carbon and nitrogen isotopic composition of collagen extracted from bone. These data are believed to present us with rough estimates of the sources of protein in diet, although we have seen that some of the carbon skeleton of the amino acids of collagen is also derived from other nutrient sources (carbohydrates and lipids). Complementary information about the carbon isotopic composition of total diet can be gleaned from $\delta^{13}\text{C}$ analyses of the carbonate component of bone and tooth enamel. The combination of these two approaches (C isotopes from collagen and carbonate) adds a further dimension to the characterization of diet.

An essential "theorem" of this discipline is that isotopic analyses should only be used to estimate the dietary proportions of known nutrients, and cannot by themselves be used to tell the archaeologist what people were eating in the past. In most cases these reference δ values for the proposed foods can be obtained by analysis of modern exemplars, but we must be aware that conditions may have changed. Aside from the well known Suess effect shifting global $\delta^{13}\text{C}$ values downward by c. 1.5 ‰, there may be local

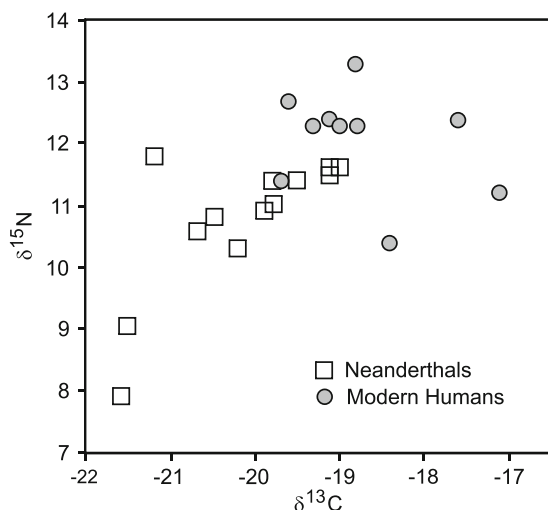


Fig. 34.7 Carbon and nitrogen isotopic variation in collagen from Neanderthal and anatomically modern humans (from Richards and Trinkaus 2009). Errors in both isotope ratios are typically $\pm 0.2\%$

effects that are harder to evaluate. For example, many areas that are now open treeless fields were once densely forested and agriculture was carried out in small clearings where the $\delta^{13}\text{C}$ of atmospheric CO_2 would have been distinctly lower. Similar effects on $\delta^{15}\text{N}$ in the soil may have occurred as a result of world-wide depletion of soil N, compounded by the use of fertilizers.

As we noted almost 20 years ago (Schoeninger et al. 1990; Schwarcz 1991), the optimal use of stable isotopic paleodiet data is the simultaneous analysis of multiple isotope ratios to see if and how they co-vary. Essentially, this allows us to learn not only about the proportions of foods in the diet of one individual, but also about the dispersion and isotopic covariation within populations. For example, in some coastal populations we see extended collinear variation in $\delta^{13}\text{C}$ and $\delta^{15}\text{N}$ which bespeaks varying degrees of dependence on terrestrial as well as marine resources. Where the population clusters tightly around a narrow range of intermediate values (i.e., mixtures of two food sources) one might be tempted to interpret that as dietary behavior restricted by social norms.

34.6 Future Directions

The prospects for continued advancement in isotopic paleodiet look bright but partly hinge on technical innovations that may challenge some researchers in this field. Specifically, more attention should be directed to the analysis of single amino acids, both for $\delta^{15}\text{N}$ and $\delta^{13}\text{C}$. The latter is now feasible using high-performance liquid chromatography (HPLC) (Smith et al. 2009; Fogel and Tuross 2003). This approach can provide analysis of $\delta^{13}\text{C}$ of all the amino acids in a single cycle, and in principle could allow researchers to untangle some of the problems associated with routing of C atoms from specific food sources. A similar approach to $\delta^{15}\text{N}$ is possible using GC/IRMS methods and should be further developed (Naito et al. 2010). Although most amino acids are transaminated intracellularly and thus lose their diet signal, a few have secondary amine sites which are conserved and record trophic level effects. The combined use of these two techniques promises to add further dimensions to the analysis of paleodiet. At the same time, we look forward to further

breakthroughs in the analysis of lipids some of which are surprisingly well preserved in human bones and can be used to identify specific nutrients including milk, animal flesh, fish, etc. (Evershed 2008). Both C and H isotopic analyses can contribute useful information. Another area of potential development is the search for better-preserved isotopic markers in more ancient hominin skeletons. The barrier of diagenetic loss of information may yet be pushed further back in time and allow analysis of samples from even older specimens from a wider range of localities. Thanks to the more sensitive methods of continuous-flow mass spectrometry, we can use techniques of collagen extraction that were developed for ^{14}C dating purposes (Stafford et al. 1988) in order to look at older hominin skeletons as well as the more poorly preserved skeletal samples from later periods of prehistory (Richards et al. 2000).

References

- Aiello LC, Wheeler P (1995) The expensive-tissue hypothesis: the brain and the digestive system in human and primate evolution. *Curr Anthropol* 36:199–221
- Ambrose SH (1990) Preparation and characterization of bone and tooth collagen for isotopic analysis. *J Archaeol Sci* 17:431–451
- Ambrose S, Katzenberg MA (eds) (2000) Biogeochemical approaches to paleodietary analysis. Kluwer Academic, New York, p 269
- Ambrose SH, Norr L (1993) Experimental evidence for the relation of the carbon isotope ratios of whole diet and dietary protein to those of collagen and carbonate. In: Lambert JB, Grupe G (eds) Prehistoric human bone-archaeology at the molecular level. Springer, Berlin, pp 1–37
- Balasse M, Ambrose SH, Smith AB, Price TD (2002) The seasonal mobility model for prehistoric herders in the south-western Cape of South Africa assessed by isotopic analysis of sheep tooth enamel. *J Archaeol Sci* 29:917–932
- Barrett JH, Richards MP (2004) Evidence for marine resource intensification in identity, gender, religion and economy: new isotope and radiocarbon evidence in early historic Orkney, Scotland UK. *Eur J Archaeol* 7:249
- Bilezikian, John P, Raisz, Lawrence G, Martin T. John (eds) (2008) Principles of bone biology. 3rd ed. Elsevier, Boston
- Bocherens H, Drucker DG, Billiou D, Patou-Mathis M, Vandermeersch B (2005) Isotopic evidence for diet and subsistence pattern of the Saint-Césaire I Neanderthal: review and use of a multi-source mixing model. *J Hum Evol* 49:71–87
- Cannon A, Schwarcz HP, Knyf M (1999) Marine-based subsistence trends and the stable-isotope analysis of dog bones from Namu, British Columbia. *J Archaeol Sci* 26:399–408

- Cerling TE, Harris J, Passey B (2003) Diets of East African bovidae based on stable isotope analyses. *J Mammal* 84:456–470
- Chisholm BS, Nelson DE, Schwarcz HP (1982) Stable carbon isotope ratios as a measure of marine versus terrestrial protein in ancient diets. *Science* 216:1131–1132
- Corr LT, Sealy JC, Horton MC, Evershed RP (2005) A novel marine dietary indicator utilizing compound-specific bone collagen amino acid $\delta^{13}\text{C}$ values of ancient humans. *J Archaeol Sci* 32:321–330
- Corr LT, Richards MP, Jim S, Ambrose SH, Mackie A, Beattie O, Evershed RP (2008) Probing dietary change of the Kwaday Dan Ts'inci individual, an ancient glacier body from British Columbia: I. Complementary use of marine lipid biomarker and carbon isotope signatures as novel indicators of a marine diet. *J Archaeol Sci* 35:2102–2110
- DeNiro MJ, Epstein S (1978) Influence of diet on the distribution of carbon isotopes in animals. *Geochim Cosmochim Acta* 42:495–506
- DeNiro MJ, Epstein S (1981) Influence of diet on the distribution of nitrogen isotopes in animals. *Geochim Cosmochim Acta* 45:341–351
- DeNiro MJ, Weiner S (1988) Organic matter within crystalline aggregates of hydroxyapatite: A new substrate for stable isotopic and possibly other biochemical analyses of bone. *Geochim. Cosmochim Acta* 52:2415–2423
- DeNiro MJ (1985) Postmortem preservation and alteration of in vivo bone collagen isotope ratios in relation to palaeodietary reconstruction. *Nature* 317:806–809
- DeNiro MJ, Schoeninger MJ, Hastorf CA (1985) Effect of heating on the stable carbon and nitrogen isotope ratios of bone collagen. *J Archaeol Sci* 12:1–7
- Dudd SN, Evershed RP (1998) Direct demonstration of milk as an element of archaeological economies. *Science* 282:1478–1481
- Evans RD (2007) Soil nitrogen isotope composition. In: Mitchener R, Lajtha, K (eds) *Stable Isotopes in Ecology and Environmental Science*. 2nd Ed. Blackwell, Oxford, 83–98
- Evans RD (2008) Soil nitrogen isotope composition. In: Michener RH, Lajtha K (eds) *Stable isotopes in ecology and environmental science*, 2nd edn. Wiley, Chichester, pp 83–98
- Evershed RP (2008) Organic residue analysis in archaeology: the archaeological biomarker revolution. *Archaeometry* 50:895–924
- Farquhar GD, Ehleringer JR, Hubick KT (1989) Carbon isotope discrimination and photosynthesis. *Annu Rev Plant Physiol Plant Mol Biol* 40:503–537
- Fogel ML, Tuross N, Johnson BJ, Miller GH (1997) Biogeochemical record of ancient humans. *Org Geochem* 27:275–287
- Fogel ML, Tuross N (2003) Extending the limits of paleodietary studies of humans with compound specific carbon isotope analysis of amino acids. *J Archaeol Sci* 30:535–545
- Fry B, Jeng WL, Scalani RS, Parker PL, Baccus J (1978) $\delta^{13}\text{C}$ food web analysis of a Texas sand community. *Geochim Cosmochim Acta* 42:1299–1302
- Fry B (2006) *Stable isotope ecology*. Springer, New York
- Fuller BT, Richards MP, Mays SA (2003) Stable carbon and nitrogen isotope variation in tooth dentine serial sectionals from Wharram Percy. *J Archaeol Sci* 30:1673–1684
- Guo L, Tanaka T, Wang D, Tanaka N, Murata A (2004) Distributions, speciation and stable isotope composition of organic matter in the southeastern Bering Sea. *Mar Chem* 91:211–226
- Harrison RG, Katzenberg MA (2003) Paleodiet studies using stable carbon isotopes from bone apatite and collagen: examples from Southern Ontario and San Nicolas Island, California. *J Anthropol Arch* 22:227–244
- Hastorf CA, DeNiro MJ (1985) Reconstruction of prehistoric plant production and cooking practices by a new isotopic method. *Nature* 315:489–491
- Heaton JHE, Vogel JC, von la Chevallerie G, Collet G (1986) Climatic influence on the isotopic composition of bone nitrogen. *Nature* 322:822–823
- Hedges REH, van Klinken G (2000) “Consider a spherical cow . . .” – on modeling and diet. In: Ambrose S, Katzenberg MA (eds) *Biogeochemical approaches to paleodietary analysis*. Kluwer Academic, New York, pp 211–241
- Hedges REM, Reynard L (2007) Nitrogen isotopes and the trophic level of humans in archaeology. *J Archaeol Sci* 34:1240–1251
- Hedges REM, Clement JG, Thomas CDL, O’Connell TC (2007) Collagen turnover in the adult femoral mid-shaft: modeled from anthropogenic radiocarbon tracer measurements. *Am J Phys Anthropol* 133(2):808–816
- Howland MR, Corr LT, Young SM, Jones V, Jim S, van der Merwe NJ, Mitchell AD, Evershed RP (2003) Expression of the dietary isotope signal in the compound-specific $\delta^{13}\text{C}$ values of pig bone lipids and amino acids. *Int J Osteoarch* 13:54–65
- Hu Y, Shang H, Tong H, Nehlich O, Liu W, Zhao C, Yu J, Wang C, Trinkaus E, Richards M (2009) Stable isotope dietary analysis of the Tianyuan 1 early modern human. *Proc Natl Acad Sci (USA)* 106:10971–10974
- Jim S, Ambrose SH, Evershed RP (2004) Stable carbon isotopic evidence for differences in the dietary origin of bone cholesterol, collagen and apatite: implications for their use in palaeodietary reconstruction. *Geochim Cosmochim Acta* 68:61–72
- Katzenberg MS (2000) Stable isotope analysis: a tool for studying past diet, demography and life history. In: Katzenberg MA, Saunders SR (eds) *The biological anthropology of the human skeleton*. Wiley, New York, pp 305–327
- Katzenberg MA, Schwarcz HP, Knyf M, Melbye FJ (1995) Stable isotope evidence for maize horticulture and paleodiet in southern Ontario, Canada. *Am Antiquity* 60:335–350
- Katzenberg MA, Herring DA, Saunders SR (1996) Weaning and infant mortality: evaluating the skeletal evidence. *Yrbk Phys Anthropol* 39:177–199
- Keenleyside A, Schwarcz HP, Stirling L, Lazreg NB (2008) Stable isotopic evidence for diet in a Roman and late Roman population from Leptiminus, Tunisia. *J Archaeol Sci* 36:51–63
- Kellner CM, Schoeninger MJ (2007) A simple carbon isotope model for reconstructing human diet. *Am J Phys Anthropol* 133:1112–1127
- Kellner CM, Schoeninger M, Spielmann KA, Moore K (2010) Stable isotope data show temporal stability in diet at Pecos

- Pueblo and diet variation among southwest Pueblos. In: Morgan ME (ed) *Pecos revisited*. Harvard University Press, Cambridge, pp 79–91
- Krueger HW, Sullivan CH (1984) Models for carbon isotope fractionation between diet and bone. In: Turnlund JE, Johnson PE (eds) *Stable isotopes in nutrition*. American Chemical Society Symposium Series 258. American Chemical Society, Washington, pp 205–222
- Lebon M, Reiche I, Bahain J-J, Chadeaux C, Moigne A-M, Fröhlich F, Sémah F, Schwarcz H, Falguères C (2010) New parameters for the characterization of diagenetic alterations and heat-induced changes of fossil bone mineral using Fourier Transform Infrared Spectrometry. *J Archaeol Sci* 37:2265–2276
- Lee-Thorp JA, Sealy JC, van der Merwe NJ (1989) Stable carbon isotope ratio differences between bone collagen and bone apatite, and their relationship to diet. *J Archaeol Sci* 16:585–599
- Lee-Thorp JA, van der Merwe NJ, Brain CK (1994) Diet of *Australopithecus robustus* at Swartkrans from stable carbon isotope analysis. *J Hum Evol* 27:361
- Little EA, Schoeninger MJ (1995) The late Woodland diet on Nantucket Island and the problem of maize in coastal New England. *Am Antiquity* 60:351–368
- Manolagas S (2000) Birth and death of bone cells: basic regulatory mechanisms and implications for the pathogenesis and treatment of osteoporosis. *Endocr Rev* 21:115–137
- Marino BD, McElroy JB (1991) Isotopic composition of atmospheric CO₂ inferred from carbon in C₄ plant cellulose. *Nature* 349:127–131
- Masters PM (1987) Preferential preservation of noncollagenous protein during bone diagenesis: implications for chronometric and stable isotopic measurements. *Geochim Cosmochim Acta* 51:3209–3214
- Minagawa M, Wada E (1984) Stepwise enrichment of ¹⁵N along food chains: further evidences and the relation between δ¹⁵N and animal age. *Geochim Cosmochim Acta* 48:1135–1140
- Miracle P, Milner N (2008) *Consuming Passions and Patterns of Consumption*. [electronic resource] Cambridge UK, McDonald for Archaeological Research, Institute, Ebooks Corporation
- Moore JW, Semmens BX (2008) Incorporating uncertainty and prior information into stable isotope mixing models. *Ecol Lett* 11:470–480
- Morton J, Schwarcz HP (2004) Paleodietary implications from isotopic analysis of food residues on prehistoric Ontario ceramics. *J Archaeol Sci* 31:503–517
- Murphy BP, Bowman DMJS (2009) The carbon and nitrogen isotope composition of Australian grasses in relation to climate. *Funct Ecol* 23:1040–1049
- Murray M, Schoeninger MJ (1988) Diet, status, and complex social structure in Iron Age Central Europe: some contributions of bone chemistry. In: Gibson B, Geselowitz M (eds) *Tribe and polity in late prehistoric Europe*. Plenum Press, New York, pp 157–178
- Naito YI, Honch NV, Chikaraishi Y, Ohkouchi N, Yoneda M (2010) Quantitative evaluation of marine protein contribution in ancient diets based on nitrogen isotope ratios of individual amino acids in bone collagen: an investigation at the Kitakogane Jomon site. *Am J Phys Anth* 143:31–40
- Newsome SD, Phillips DL, Culleton BJ, Guilderson TP, Koch PL (2004) Dietary reconstruction of an early to middle Holocene human population from the central California coast: insights from advanced stable isotope mixing models. *J Archaeol Sci* 31:1101–1115
- O'Connell TC, Hedges REM (1999) Isotopic composition of hair and bone: archaeological analyses. *J Archaeol Sci* 26:661–665
- Passey B, Robinson TF, Ayliffe LK, Cerling TE, Sponheimer MM, Dearing D, Roeder BL, Ehleringer JR (2005) Carbon isotope fractionation between diet, breath CO₂, and bioapatite in different mammals. *J Archaeol Sci* 32:1459–1470
- Pechenkina EA, Ambrose SH, Xiaolin M, Benfer RA Jr (2005) Reconstructing northern Chinese Neolithic subsistence practices by isotopic analysis. *J Archaeol Sci* 32:1176–1189
- Peterson BJ, Fry B (1987) Stable isotopes in ecosystem studies. *Ann Rev Ecol Syst* 18:293–320
- Pfeiffer S, Sealy J (2006) Body size among Holocene foragers of the Cape Ecozone, southern Africa. *Am J Phys Anth* 129:1–11
- Phillips DL, Gregg JW (2003) Source partitioning using stable isotopes: coping with too many sources. *Oecologia* 136:261–269
- Prowse T, Schwarcz HP, Saunders S, Macchiarelli R, Bondioli L (2003) Isotopic paleodiet studies of skeletons from the Imperial Roman-age cemetery of Isola Sacra, Rome, Italy. *J Archaeol Sci* 31:259–272
- Richards MP (2009) Stable isotope evidence for European Upper Paleolithic human diets. In: Hublin J-J, Richards MP. *The Evolution of Hominin Diets*, Springer, Berlin, 251–258
- Richards MP, Trinkaus E (2009) Isotopic evidence for the diets of European Neanderthals and early modern humans. *PNAS* 106:16034–16039
- Richards MP, Schulting RJ, Hedges REM (2003) Sharp shift in diet at the onset of the Neolithic. *Nature* 425:366
- Richards MP, Pettitt PB, Trinkaus E, Smith FE, Paunovic M, Karavanic I (2000) Neanderthal diet at Vindija and Neanderthal predation: the evidence from stable isotopes. *Proc Nat Acad Sci USA* 97:7663–7666
- Sachs JP, Repeta DJ, Goericke R (1999) Nitrogen and carbon isotopic ratios of chlorophyll from marine phytoplankton. *Geochim Cosmochim Acta* 63:1431–1441
- Schoeninger MJ, DeNiro MJ (1984) Nitrogen and carbon stable isotope ratios of bone collagen reflect marine and terrestrial components of prehistoric human diet. *Geochim Cosmochim Acta* 48:625–639
- Schoeninger MJ, DeNiro MJ, Tauber H (1983) Stable nitrogen isotope ratios of bone collagen reflect marine and terrestrial components of prehistoric human diet. *Science* 220:1381–1383
- Schoeninger MJ, Moore K (1992) Bone stable isotope studies in archaeology. *J World Prehistory* 6:247–296
- Schoeninger MJ, Moore KM, Murray ML (1989) Detection of bone preservation in archaeological and fossil samples. *J Appl Geochem* 4:281–292
- Schoeninger MJ, Moore J, Sept JM (1999) Subsistence strategies of two 'savanna' chimpanzee populations: the stable isotope evidence. *Am J Primatol* 47:297–314
- Schoeninger MJ, van der Merwe NJ, Moore K, Lee-Thorp J, Larsen CS (1990) Decrease in diet quality between the prehistoric and contact periods. In: Larsen CS (ed) *The*

- Archaeology of Mission Santa Catalina de Guale: 2. Biocultural Interpretations of a Population in Transition. *Anthropological Papers of the American Museum of Natural History* 68, pp 78–93, American Museum of Natural History, New York
- Schurr MR (1998) Using stable nitrogen isotopes to study weaning behavior in past populations. *World Archaeol* 30:327–342
- Schwarcz HP (1991) Some theoretical aspects of isotope paleodiet studies. *J Archaeol Sci* 18:261–275
- Schwarcz HP, Melbye J, Katzenberg MA, Knyf M (1985) Stable isotopes in human skeletons of southern Ontario: reconstructing paleodiet. *J Archaeol Sci* 12:187–206
- Schwarcz HP, Schoeninger M (1991) Stable isotope analyses in human nutritional ecology. *Yearb Phys Anthropol* 34:283–321
- Schwarcz HP, White CD (2004) The grasshopper or the ant? Cultigen-use strategies in ancient Nubia from C-13 analyses of human hair. *J Archaeol Sci* 31:753–762
- Schwarcz HP, Dupras T, Fairgrieve SI (1999) ^{15}N enrichment in the Sahara: in search of a global relationship. *J Archaeol Sci* 26:629–636
- Semmens BX, Moore JW (2008) MixSIR (Version 1.0) <http://conserver.iugo-cafe.org/node/870/download> (accessed June 3 2011)
- Smith CI, Fuller BT, Choy K, Richards MP (2009) A three-phase liquid chromatographic method for $\delta^{13}\text{C}$ analysis of amino acids from biological protein hydrolysates using liquid chromatography–isotope ratio mass spectrometry. *Anal Biochem* 390:165–172
- Spangenberg JE, Jacomet S, Schibler J (2006) Chemical analyses of organic residues in archaeological pottery from Arbon Bleiche 3, Switzerland – evidence for dairying in the late Neolithic. *J Archaeol Sci* 33:1–13
- Sponheimer M, Lee-Thorp JA (1999) Isotopic evidence for the diet of an early hominid, *Australopithecus africanus*. *Science* 283:368–370
- Sponheimer M, Robinson TF, Roeder BL, Passey BH, Ayliffe LK, Cerling TE, Dearing MD, Ehleringer JR (2003) An experimental study of nitrogen flux in llamas: is ^{14}N preferentially excreted? *J Archaeol Sci* 30:1649–1655
- Stafford TW Jr, Brendel K, Duhamel RC (1988) Radiocarbon, ^{13}C and ^{15}N analysis of fossil bone: removal of humates with XAD-2 resin. *Geochim Cosmochim Acta* 52:2257–2267
- Stott AW, Evershed RP, Jim S, Jones V RJM, Tuross N, Ambrose S (1999) Cholesterol as a new source of palaeodietary information: experimental approaches and archaeological applications. *J Archaeol Sci* 26:705–16
- Steele KW, Daniel RMJ (1978) Fractionation of nitrogen isotopes by animals: a further complication to the use of variations in the natural abundance of ^{15}N for tracer studies. *J Agric Sci* 90:7–9
- Stuart-Williams H, Schwarcz HP, White C, Spence M (1996) The isotopic composition and diagenesis of human bone at Teotihuacan and Oaxaca, Mexico. *Paleogeogr Paleoclimatol* 126:1–14
- Suess HE (1955) Radiocarbon concentration in modern wood. *Science* 122:415–417
- Tauber H (1981) ^{13}C evidence for dietary habits of prehistoric man in Denmark. *Nature* 292:332–333
- Tieszen L, Fagre T (1993) Effect of diet quality and composition on the isotopic composition of respiratory CO_2 , bone collagen, bioapatite, and soft tissues. In: Lambert JB, Grupe G (eds) *Prehistoric human bone: archaeology at the molecular level*. Springer, Berlin
- Trueman CN, Privat K, Field J (2008) Why do crystallinity values fail to predict the extent of diagenetic alteration of bone mineral? *Paleogeogr Paleoclimatol* 266:160–167
- Ungar PS, Teaford M (2002) Human diet: its origin and evolution. Bergin & Garvey, Westport, p 206
- Urey HC (1947) The thermodynamic properties of isotopic substances. *J Chem Soc* 1947, 562–581
- U.S. Federal Register (2010) Department of the Interior, National Park Service, Native American Graves Protection and Repatriation Review Committee, Findings Related to the Identity of Cultural Items in the Possession of the American Museum of Natural History, New York, NY, Federal Register, Notices, Vol. 75, No. 67/Thursday, April 8, 2010
- van der Merwe NJ, Medina E (1991) The canopy effect, carbon isotope ratios and foodwebs in Amazonia. *J Archaeol Sci* 18:249–259
- van der Merwe NJ, Vogel JC (1978) ^{13}C content of human collagen as a measure of prehistoric diet in woodland North America. *Nature* 276:815–816
- Vogel J, van der Merwe N (1977) Isotopic evidence for early maize cultivation in New York State. *Am Antiquity* 42:238–242
- Walker PL, DeNiro M (1986) Stable nitrogen and carbon isotope ratios in bone collagen as indices of prehistoric dietary dependence on marine and terrestrial resources in Southern California. *Am J Phys Anthropol* 71:51–61
- Wallace BP, Seminoff JA, Kilham SS, Spotila JR, Dutton PH (2006) Leatherback turtles as oceanographic indicators: stable isotope analyses reveal a trophic dichotomy between ocean basins. *Mar Biol* 149:953–960
- Warinner C, Tuross N (2009) Alkaline cooking and stable isotope tissue-diet spacing in swine: archaeological implications. *J Archaeol Sci* 36(8):1690–1697
- Wright LE, Schwarcz HP (1998) Stable carbon and oxygen isotopes in human tooth enamel: identifying breast-feeding in prehistory. *Am J Phys Anthropol* 106:1–18
- Yoneyama T, Ohta Y, Ohtani T (1983) Variations of natural $\delta^{13}\text{C}$ and $\delta^{15}\text{N}$ abundances in the rat tissues and their correlation. *Radioisotopes* 32:330–332

Chapter 35

Applications of Sr Isotopes in Archaeology

N.M. Slovak and A. Paytan

Abstract The inclusion of radiogenic strontium isotope ($^{87}\text{Sr}/^{86}\text{Sr}$) analysis in archaeological and bioarchaeological research has resulted in the creation of new data by which to evaluate models of migration, culture change, colonization, trade, and exchange. Overwhelmingly, archaeologists have used radiogenic strontium isotope signatures in human enamel and bone apatite to reconstruct ancient mobility patterns and to distinguish between individuals of local and non-local origins at archaeological sites. The method also has been employed to establish the provenience of artifacts, ancient building materials, and foodstuffs as well as to track the origins and migratory patterns of prehistoric animals. The present chapter provides an introduction to the fundamental principles, approaches, applications, and future directions of radiogenic strontium isotope analysis in archaeology.

35.1 Introduction

The application of radiogenic strontium isotope ($^{87}\text{Sr}/^{86}\text{Sr}$) analysis¹ in archaeology has revolutionized paleomobility studies. Whereas traditional archaeo-

logical investigations relied on artifactual and architectural evidence as proxies for population movement, the retrieval of radiogenic strontium isotope signatures from human and faunal skeletal material allows archaeologists to directly examine past residential mobility and related phenomena. The present chapter provides an introduction to the principles, methods, and applications of radiogenic strontium isotope analysis in archaeology, beginning with a general discussion of the properties of strontium isotopes.

Strontium (Sr) is a trace element that is found in most igneous, metamorphic, and sedimentary rock, as well as in river water, groundwater, seawater, soil, plants, and animals. Strontium has four naturally occurring stable isotopes (^{84}Sr , ^{86}Sr , ^{87}Sr , and ^{88}Sr), three of which are non-radiogenic: ^{84}Sr (0.560%), ^{86}Sr (9.870%), and ^{88}Sr (82.53%). The remaining isotope, ^{87}Sr (7.040%), is radiogenic and is formed by the radioactive decay of ^{87}Rb , with a half life of approximately 4.88×10^{10} years (Faure and Mensing 2005). The amount of ^{87}Sr in a mineral or rock containing Rb depends upon two things: the age of the rock or mineral and its Rb/Sr ratio (Faure and Mensing 2005). The highest $^{87}\text{Sr}/^{86}\text{Sr}$ values are found in very old rocks with high Rb/Sr ratios such as granites and shales, while younger rocks and minerals with low Rb/Sr ratios have correspondingly low $^{87}\text{Sr}/^{86}\text{Sr}$ ratios (Faure 1977).

Because of their large atomic mass, $^{87}\text{Sr}/^{86}\text{Sr}$ values change little as they pass from weathered rocks through soils to the food chain (Hurst and Davis 1981; Beard and Johnson 2000; but see Fietzke and Eisenhauer 2006; De Souza et al. 2007; Wakabayashi et al. 2007; Halicz et al. 2008; Ruggeberg et al. 2008). Importantly, variations in $^{87}\text{Sr}/^{86}\text{Sr}$ values that occur along biogeochemical pathways are corrected for during mass spectrometry, at which time $^{87}\text{Sr}/^{86}\text{Sr}$ signatures are normalized to the constant value of $^{86}\text{Sr}/^{88}\text{Sr}$ in natural

¹Traditionally, many scholars have used the expression “stable strontium isotopes” when referring to $^{87}\text{Sr}/^{86}\text{Sr}$ signatures. In the present chapter, we prefer to employ the phrase “radiogenic strontium isotopes” in reference to $^{87}\text{Sr}/^{86}\text{Sr}$ values so as to distinguish this kind of data from recent paleodietary research (Knudson et al. 2010) that utilizes stable $\delta^{88}\text{Sr}/^{86}\text{Sr}$ signatures.

N.M. Slovak (✉)
Department of Behavioral Sciences, Santa Rosa Junior College,
1501 Mendocino Avenue, Santa Rosa, CA, USA
e-mail: nmslovak@yahoo.com

A. Paytan
University of California, Santa Cruz, CA 95064, USA
e-mail: apaytan@ucsc.edu

rocks (Beard and Johnson 2000). Accordingly, $^{87}\text{Sr}/^{86}\text{Sr}$ ratios in soil, groundwater, vegetation, and fauna largely reflect underlying $^{87}\text{Sr}/^{86}\text{Sr}$ bedrock values (Capo et al. 1998), with some input from atmospheric sources (see discussion in Bentley 2006 and references therein). A similar principle applies to the marine environment where the isotopic composition of modern seawater, characterized as $^{87}\text{Sr}/^{86}\text{Sr} = 0.7092$ (Veizer 1989), is derived from $^{87}\text{Sr}/^{86}\text{Sr}$ signatures of the input sources of strontium to the ocean and strontium deposition into sediments (Faure 1977).

Building off of the principles of strontium isotope geochemistry, Ericson (1985) first demonstrated that $^{87}\text{Sr}/^{86}\text{Sr}$ in human bones and teeth could be used to study aspects of ancient human behavior. Strontium substitutes for calcium in the foodweb, and is deposited in hydroxyapatite crystal in human tooth enamel and bones (Comar et al. 1957). Given that any mass-dependent fractionation is corrected for, reported $^{87}\text{Sr}/^{86}\text{Sr}$ signatures in human tissue should reflect the $^{87}\text{Sr}/^{86}\text{Sr}$ composition of water, plants, and animals consumed, which in turn should reflect $^{87}\text{Sr}/^{86}\text{Sr}$ bedrock signatures in a given region (Ericson 1985).

Tooth enamel forms during infancy and childhood, after which its chemical composition does not change (Hillson 1996). Conversely, human bone remodels continuously (Parfitt 1983). Assuming that an individual consumed only locally grown foods during his or her

lifetime, $^{87}\text{Sr}/^{86}\text{Sr}$ values in tooth enamel should reflect childhood diet and, by extension, childhood locale, while $^{87}\text{Sr}/^{86}\text{Sr}$ signatures in bone will reflect adult diet and, ideally, adult locale (Ericson 1985; Sealy et al. 1991). Different $^{87}\text{Sr}/^{86}\text{Sr}$ values in enamel and bone from a single individual may indicate dietary changes over time, which in turn, may indicate residence change (Ericson 1985) (Fig. 35.1).

As originally noted by Ericson (1985), the ability to trace prehistoric mobility using $^{87}\text{Sr}/^{86}\text{Sr}$ in human tissue is constrained by several factors. First, there must be sufficient geologic variability between the different residence areas under study such that variations in $^{87}\text{Sr}/^{86}\text{Sr}$ values can be detected. Conversely, there must be sufficient geologic homogeneity within a region if one is relying primarily on geologic data to reconstruct the $^{87}\text{Sr}/^{86}\text{Sr}$ range for a locale, although it should be noted that archaeologists regularly incorporate other classes of data (e.g. faunal and human isotopic values) when determining local $^{87}\text{Sr}/^{86}\text{Sr}$ signatures for a region (see Sect. 35.2.1). Second, radiogenic strontium isotope analysis may not be as effective at tracking movement between coastal areas if the inhabitants of those areas relied solely on marine foods. In such instances, individuals' $^{87}\text{Sr}/^{86}\text{Sr}$ values will reflect the marine $^{87}\text{Sr}/^{86}\text{Sr}$ signature ($^{87}\text{Sr}/^{86}\text{Sr} = 0.7092$, Veizer 1989), rather than terrestrial $^{87}\text{Sr}/^{86}\text{Sr}$ values. Third, $^{87}\text{Sr}/^{86}\text{Sr}$ values among human populations can

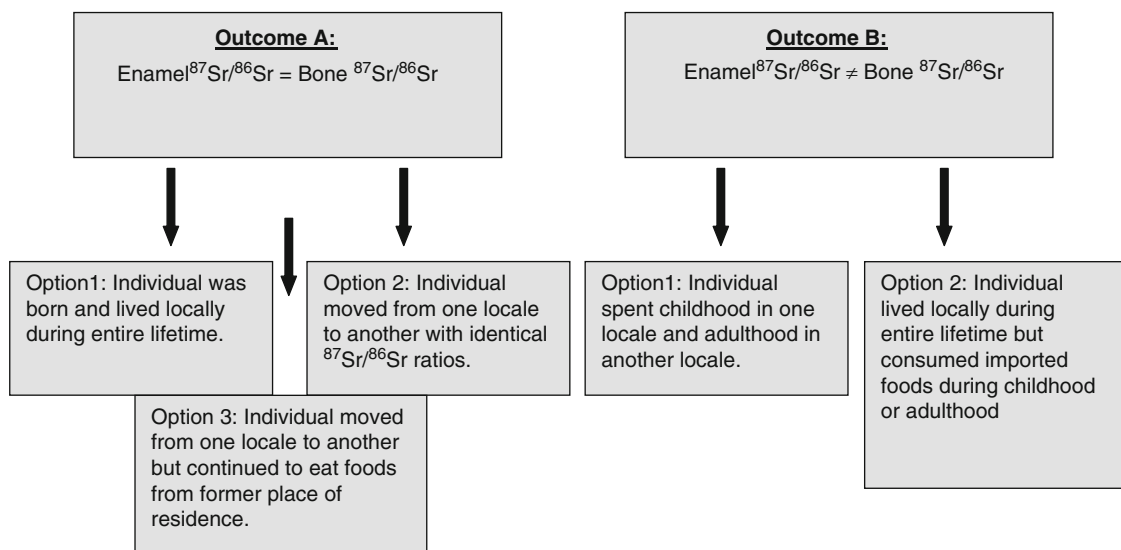


Fig. 35.1 Potential outcomes and interpretations involved in strontium isotope analysis of human tooth enamel and bone. Although option 1 is the most frequent interpretation in either outcome, the remaining options should be ruled out (or at least considered) in strontium isotope studies

serve as accurate markers of prehistoric mobility only if a dependency on imported foods can be ruled out. The consumption of foreign foods, particularly those high in Ca and Sr (e.g., dairy products, leafy greens, legumes, and fish), and Sr-rich food additives such as sea salt (Wright 2005) can significantly alter $^{87}\text{Sr}/^{86}\text{Sr}$ signatures in human bones and teeth, even when consumed in small amounts (Burton and Wright 1995); thus a consideration of total dietary intake is necessary when interpreting $^{87}\text{Sr}/^{86}\text{Sr}$ results.

35.2 Materials and Methods

35.2.1 Determining Local $^{87}\text{Sr}/^{86}\text{Sr}$ Signatures for a Region

The first step in conducting radiogenic strontium isotope analysis in archaeology is establishing local $^{87}\text{Sr}/^{86}\text{Sr}$ values for the regions or sites under study. A broad range of $^{87}\text{Sr}/^{86}\text{Sr}$ signatures for an area can be estimated from geological maps and later refined by measuring $^{87}\text{Sr}/^{86}\text{Sr}$ values in local, exposed bedrock and whole soil. Very old rocks with high Rb/Sr ratios generally exhibit $^{87}\text{Sr}/^{86}\text{Sr}$ signatures above 0.710 while younger rocks will have $^{87}\text{Sr}/^{86}\text{Sr}$ values less than 0.704. Although these types of data will provide a reliable estimate of geologic $^{87}\text{Sr}/^{86}\text{Sr}$ values for a region, they may not be indicative of human $^{87}\text{Sr}/^{86}\text{Sr}$ values. As initially noted by Sillen et al. (1998) and subsequently demonstrated and discussed by others (Price et al. 2002; Poszwa et al. 2004; Bentley 2006; Hedman et al. 2009), $^{87}\text{Sr}/^{86}\text{Sr}$ signatures in geologic substrate can deviate significantly from bioavailable $^{87}\text{Sr}/^{86}\text{Sr}$ values in the food chain. In order to best capture biologically available $^{87}\text{Sr}/^{86}\text{Sr}$ values for a region, it is recommended that researchers measure $^{87}\text{Sr}/^{86}\text{Sr}$ signatures from small, local animals whose diets have been shown to reflect average $^{87}\text{Sr}/^{86}\text{Sr}$ regional values (Price et al. 2002).

Scholars have relied on a variety of fauna to calculate biologically available strontium isotope levels including cattle (Montgomery et al. 2003; Buzon et al. 2007), guinea pig (Knudson et al. 2004; Slovak et al. 2009), pigs (Bentley et al. 2004), and rabbit (Price et al. 2000). There is some debate over whether archaeological or modern fauna should be used to calculate bio-

logically available $^{87}\text{Sr}/^{86}\text{Sr}$ signatures, largely because modern animal diets often include imported foods and fertilizers that may skew $^{87}\text{Sr}/^{86}\text{Sr}$ faunal values (Price et al. 2002; Bentley 2006). On the other hand, archaeological bone, and to a lesser extent tooth enamel, is susceptible to diagenetic contamination. Given that $^{87}\text{Sr}/^{86}\text{Sr}$ signatures in modern and archaeological fauna are subject to potential alteration, it is advisable to incorporate both types of data (preferably archaeological tooth enamel rather than bone) when establishing biologically available strontium isotope levels. Additionally comparative $^{87}\text{Sr}/^{86}\text{Sr}$ measurements from multiple species of local fauna likely will yield the most accurate representations of biologically available $^{87}\text{Sr}/^{86}\text{Sr}$ values (Price et al. 2002).

The bioavailable $^{87}\text{Sr}/^{86}\text{Sr}$ signature for a region generally is represented as a range of values, which is calculated using the mean of biologically available strontium isotope levels (as determined by local fauna) ± 2 s.d. (Price et al. 2002). These confidence limits, while admittedly arbitrary, have allowed researchers to differentiate between individuals of local and non-local origins at various archaeological sites. In some cases, however, biologically available strontium isotope ranges are inadequate proxies for human dietary Sr.

In her study of human skeletons from the archaeological site of Tikal, Guatemala, for example, Wright (2005) noted that approximately half of her human sample exhibited $^{87}\text{Sr}/^{86}\text{Sr}$ signatures higher than the $^{87}\text{Sr}/^{86}\text{Sr}$ range established for local fauna, plants, and water. Wright attributed these elevated human $^{87}\text{Sr}/^{86}\text{Sr}$ values to the consumption of imported sea salt, whose $^{87}\text{Sr}/^{86}\text{Sr}$ of 0.7092 was significantly higher than the local Tikal signature ($^{87}\text{Sr}/^{86}\text{Sr} = 0.7078\text{--}0.7081$) (Wright 2005). A similar trend was noted at the archaeological site of Ancón, Peru (Slovak et al. 2009) where 34 of 35 human skeletons exhibited $^{87}\text{Sr}/^{86}\text{Sr}$ values notably higher than the biologically available $^{87}\text{Sr}/^{86}\text{Sr}$ range for the region (Fig. 35.2). Based on carbon and nitrogen isotope data from a subset of the Ancón skeletal sample, Slovak et al. (2009) and Slovak and Paytan (2009) demonstrated that marine resources comprised nearly half of ancient Ancóneros' diets. The authors argue that the regular consumption of seafood likely raised inhabitants' $^{87}\text{Sr}/^{86}\text{Sr}$ values from the local range ($^{87}\text{Sr}/^{86}\text{Sr} = 0.7063\text{--}0.7068$) toward the $^{87}\text{Sr}/^{86}\text{Sr}$ of seawater.

In both of these case studies, local $^{87}\text{Sr}/^{86}\text{Sr}$ values for a human population would be better determined by

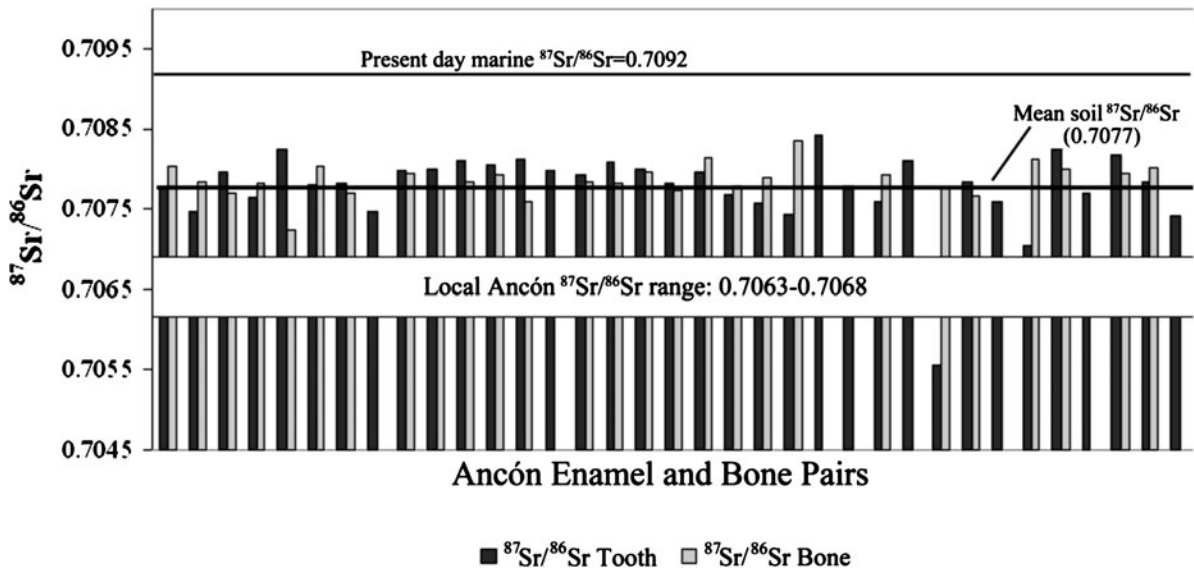


Fig. 35.2 $^{87}\text{Sr}/^{86}\text{Sr}$ ratios in human tooth enamel and bone from 35 skeletons buried at the coastal site of Ancón. Note that almost all $^{87}\text{Sr}/^{86}\text{Sr}$ values fall between Ancón's biologically available $^{87}\text{Sr}/^{86}\text{Sr}$ range and the present day marine $^{87}\text{Sr}/^{86}\text{Sr}$ signature, indicating that the majority of site inhabitants consumed a

mixed diet of marine and terrestrial foods. Figure adapted from Slovak et al. (2009). Seawater $^{87}\text{Sr}/^{86}\text{Sr}$ is based on Veizer (1989). Reprinted from Slovak et al. (2009), with permission from Elsevier

referencing the human $^{87}\text{Sr}/^{86}\text{Sr}$ data rather than using a $^{87}\text{Sr}/^{86}\text{Sr}$ range based on fauna and/or plants. This method, originally proposed by Wright (2005), removes individuals with outlying $^{87}\text{Sr}/^{86}\text{Sr}$ values from the data set, such that the revised body of data conforms to a normal distribution and more accurately reflects a local $^{87}\text{Sr}/^{86}\text{Sr}$ signature.

Ultimately, and perhaps frustratingly, there is no one method that best establishes a local $^{87}\text{Sr}/^{86}\text{Sr}$ signature for all sites and all individuals. In instances where archaeologists suspect that most of the human study population is locally born and most individuals consumed local, terrestrial foods, biologically available strontium isotope levels based on fauna or plants likely can identify prehistoric migration. On the other hand, if residential mobility is suspected or if imported or marine foods were consumed by some or all of the population, then statistical analyses of the human data is probably more effective at differentiating between local and non-local individuals.

Finally, the incorporation of additional isotopic tracers, particularly carbon ($\delta^{13}\text{C}$), nitrogen ($\delta^{15}\text{N}$), and oxygen ($\delta^{18}\text{O}$), also may help to clarify ambiguous $^{87}\text{Sr}/^{86}\text{Sr}$ data. Briefly, $\delta^{13}\text{C}$ and $\delta^{15}\text{N}$ values in

human tissue reflect $\delta^{13}\text{C}$ and $\delta^{15}\text{N}$ signatures in different classes of plants and animals consumed and can be used to assess the relative amounts of marine and terrestrial foods in paleodiets (DeNiro and Epstein 1978, 1981; Schoeninger and DeNiro 1984). While neither carbon nor nitrogen isotope analysis can differentiate between individuals of local and non-local origin, they are important to migration studies because they can identify potential dietary biases that would affect strontium isotope signatures such as the ingestion of marine foods (for a more detailed discussion of carbon and nitrogen isotope applications in archaeology, see also Schwarcz and Schoeninger 2011).

Oxygen isotope signatures ($\delta^{18}\text{O}$), on the other hand, can detect prehistoric migration and have been used independent of, and in tandem with, strontium isotope signatures to identify paleomobility (White et al. 1998; Dupras and Schwarcz 2001; Müller et al. 2003; Bentley and Knipper 2005; Knudson and Price 2007). $\delta^{18}\text{O}$ values in human tissue ultimately reflect the $\delta^{18}\text{O}$ in drinking water (Longinelli 1984; Koch et al. 1989), which in turn depends on a number of factors including temperature, distance from the sea, and elevation (Gat 1980; Yurtsever and Gat 1981; White et al. 1998). Oxygen isotope data, therefore,

provides an alternative line of evidence by which to track migration and monitor $^{87}\text{Sr}/^{86}\text{Sr}$ results.

35.2.2 Sample Selection and Sampling Techniques for Human Remains

35.2.2.1 The Potential for Diagenesis

Diagenesis, or the molecular alteration of skeletal material after interment, is one of the major obstacles facing applications of radiogenic strontium isotope analysis in archaeology. Both physical and chemical changes to bones and teeth can occur in the post-depositional environment, including loss of biogenic $^{87}\text{Sr}/^{86}\text{Sr}$ signatures (Nelson et al. 1986; Sillen 1986; Price et al. 1992; Sillen and Sealy 1995; Hoppe et al. 2003). The degree of diagenetic contamination in any skeletal element is variable and depends on a number of factors including the length of interment, burial environment, and climate (Price et al. 1992; Nielsen-Marsh and Hedges 2000a, b). The type of material (tooth enamel vs. bone) and chemical element (strontium vs. carbon) analyzed also can affect the degree and rate of diagenetic processes over time (Schoeninger 1995).

Fortunately for strontium isotope studies, tooth enamel is largely resistant to diagenesis owing to its highly crystalline nature, low organic matter content, and lack of porosity (Koch et al. 1997; Hillson 2005). Numerous studies have demonstrated that biogenic enamel isotope signatures are retrievable from prehistoric samples with minimal treatment (Quade et al. 1992; Wang and Cerling 1994; Koch et al. 1997; Budd et al. 2000; Hoppe et al. 2003; Trickett et al. 2003). Bone, on the other hand, is much more prone to diagenetic alteration than tooth enamel, largely because of its high organic matter content (~30%), high porosity, and poorly crystalline structure. Upon interment, physical contaminants from the surrounding soil such as quartz, calcite, and clay can seep into the pore spaces of bone (Kyle 1986). Additionally, the post-mortem dissolution and recrystallization of bone mineral can affect strontium isotope levels in bone as well as the ratio of strontium to other elements such as calcium (Ca) and phosphorus (P) (Sillen 1981, 1989; Nelson et al. 1986; Price et al. 1992; Sandford 1992).

Over the last few decades, a number of studies have documented ways of measuring and monitoring diage-

netic contamination in prehistoric materials and have established protocols to counteract diagenetic contamination in teeth and bone (Nelson et al. 1986; Sillen 1986; Price et al. 1992; Sillen and Sealy 1995; Nielsen-Marsh and Hedges 2000a, b; Hoppe et al. 2003). While the loss of biogenic isotope signatures in archaeological samples is at times unavoidable, the degree and effects of diagenetic contamination can be monitored and often ameliorated by appropriate sampling and cleaning procedures. (A more thorough discussion of these techniques can be found in Sects. 35.2.3.2 and 35.2.3.5.)

35.2.2.2 Selecting a Sample: Human Teeth and Bone

Tooth enamel of the permanent dentition is laid down as a series of layers beginning just before birth, as is the case with the first molar crown, and continuing to approximately 14 years of age with the completion of the third molar crown (Table 35.1). Once formed, chemical signatures in teeth do not alter. $^{87}\text{Sr}/^{86}\text{Sr}$ values in different teeth, therefore, represent discrete growth periods in an individual's childhood and adolescence.

Scholars generally select enamel samples from the first, second, and third permanent molars, as well as premolars, for radiogenic strontium isotope analysis. First molars begin their initial formation in utero (about 28–32 weeks after fertilization) (Hillson 1996) and are completed by around 3 years of age, while

Table 35.1 Approximate timing of dental crown and root formation of human permanent dentition

Permanent tooth type	Approximate timing of dental crown formation	Approximate timing of dental root formation
First incisor	3 months to 5 years old	5–9½ years old
Second incisor	3 months to 5 years old	5–10½ years old
Canine	6 months to 4 years old	4–12 years old
First premolar	2–5 years old	5–12½ years old
Second premolar	3–6 years old	6–14 years old
First molar	0–2½ years old	2½–9 years old
Second molar	3½–6½ years old	6½–14½ years old
Third molar	9½–12 years old	12–20 years old

Note that the age ranges here are approximate and that actual values may vary. Data compiled from Schour and Massler (1940) and Smith (1991)

second molars initially begin to form in an individual's second or third year and crown completion takes place at 7 or 8 years (Schour and Massler 1940; Smith 1991). Premolars have fairly identical formation rates as second molars with the initiation of first and second premolar crowns beginning towards the end of the second year and continuing into the third year (Schour and Massler 1940; Smith 1991). First premolar crowns generally are completed by 6 years, followed closely by second premolar crowns at 7 years (Schour and Massler 1940; Smith 1991). Third molars are the most variable tooth in terms of their development (Hillson 1996), initially forming sometime between 7 and 13 years of age and crown completion occurring between 12 and 16 years. Third molars form well after the period of weaning and therefore are the least likely of all teeth to be affected by maternal strontium isotope signatures. On the other hand, not all individuals develop third molars (Garn et al. 1962) and therefore these teeth may not always be available for study. Additionally, by analyzing $^{87}\text{Sr}/^{86}\text{Sr}$ values in third molars in lieu of earlier forming teeth, archaeologists might overlook evidence for residential mobility that occurred earlier in childhood and adolescence.

Mandibular and maxillary dentitions have comparable development rates (Hillson 1996) such that isotope ratios from upper and lower teeth in the same dental position should be expected to yield highly similar isotope ratios. Similarly, chemical signatures are not expected to vary significantly among the different crown side surfaces (i.e., lingual, buccal, mesial, and distal) (Dolphin et al. 2005).

In compiling enamel samples for radiogenic strontium isotope analysis most researchers collect material from a single tooth rather than multiple teeth for any one individual. By doing so, archaeologists minimize their impact on the skeleton. At the same time, however, they likely underestimate the amount of mobility in prehistoric populations (Schweissing and Grupe 2003). A small number of researchers have addressed this problem by serially sampling teeth from a single individual. Schweissing and Grupe (2003), for example, collected enamel from each permanent tooth type from seven adult skeletons buried at the archaeological site of Neuburg/Donau in Bavaria. Their analysis revealed that six of the seven individuals migrated to the site at various stages in their childhoods, including one individual who appeared to have moved between

at least two different regions in his life: once during childhood and another after 14 years of age. Importantly, in the case of this latter individual, evidence for multiple migrations would have remained undetected had the authors not sampled several teeth from the same skeleton. Similarly, Buikstra et al. (2004) documented several examples of early life migrations among skeletons from the Copan Acropolis. By comparing $^{87}\text{Sr}/^{86}\text{Sr}$ values from multiple teeth from single individuals the authors were able to determine around what age migrant individuals settled at Copan and, in at least one instance, detect multiple residence changes during an individual's childhood (Fig. 35.3). Ultimately, the number of teeth analyzed from any one individual is subject to access and approval by curators and governmental agencies, and is likely to be guided by several factors including availability and integrity of dental material, cost of analysis, and the research question(s).

While it is feasible to differentiate between individuals of local and non-local origin using tooth enamel alone, many archaeological studies incorporate comparisons of strontium isotope signatures in tooth *and* bone from the same individual. Unlike tooth enamel, which forms early and does not chemically alter once laid down, human bone remodels throughout an individual's lifetime (Tetelbaum 2000). The rate at which bones remodel depends upon the skeletal element and the type of bone analyzed. The diaphyses of long bones such as the tibia and femur take decades to remodel, while ribs replace their chemical constituents after only a few years (Jowsey 1961; Jowsey et al. 1965; Parfitt 1983; Eriksen 1986; Hill 1998). Similarly, different types of bone mineralize at different rates, such that dense cortical bone remodels slowly while trabecular bone remodels relatively rapidly (Mulhern and Van Gerven 1997, 2000).

Rates of turnover for different bones have significant consequences for migration studies and should be taken into account when selecting bone samples for analysis (Price et al. 2002). In instances where migrants relocated to an area within months or a few years prior to death, $^{87}\text{Sr}/^{86}\text{Sr}$ values in their skeletons, particularly among those bones with long turnover rates, likely will reflect their last place of residence rather than their new locale simply because strontium turnover in bone takes time. On the other hand, individuals who have resided in a place for multiple years and who have eaten locally-grown foods during that

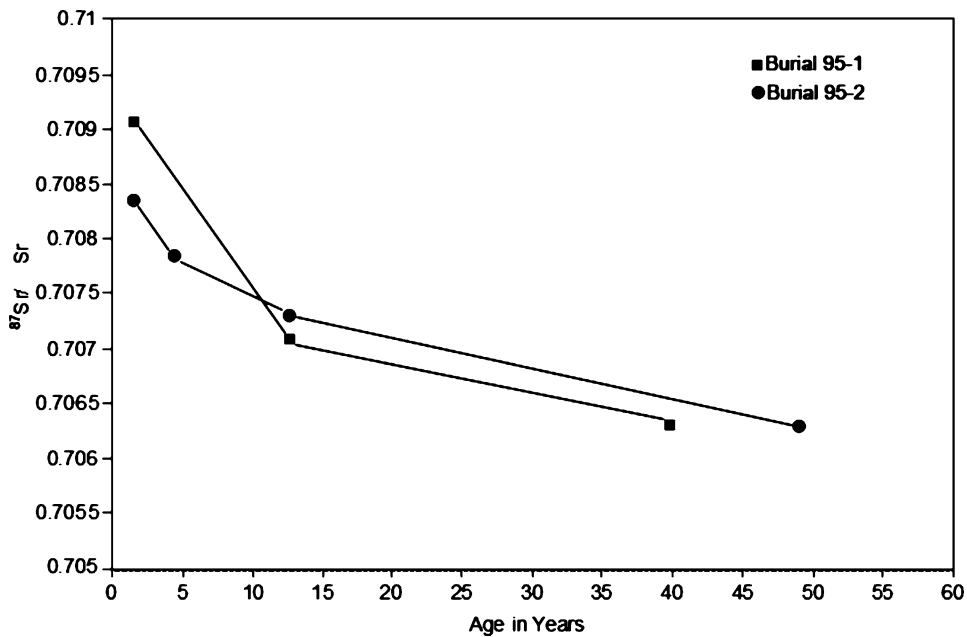


Fig. 35.3 $^{87}\text{Sr}/^{86}\text{Sr}$ ratios from tooth enamel and bone for two adult individuals buried at the site of Copan. Based on data from Buikstra et al. (2004), this figure illustrates that neither individual was born locally although $^{87}\text{Sr}/^{86}\text{Sr}$ values from their bones (plotted at 40 and 50 years respectively) indicate that they lived at Copan several years prior to their death. Note that residence

change for Burial 95-1 likely would not have been detected using the third molar (M3) only. Similarly, potential evidence for multiple childhood migrations for Burial 95-2 is detectable only by sampling several of the individual's teeth (i.e., M1, I2, and M3)

time will exhibit skeletal $^{87}\text{Sr}/^{86}\text{Sr}$ values closer to, or within, the local $^{87}\text{Sr}/^{86}\text{Sr}$ range. In cases where individuals have resided at a new location for a period of a few years, $^{87}\text{Sr}/^{86}\text{Sr}$ values among bones with rapid turnover likely will approximate local values while $^{87}\text{Sr}/^{86}\text{Sr}$ signatures from bones with prolonged remodeling rates probably will fall somewhere between the $^{87}\text{Sr}/^{86}\text{Sr}$ range of their previous locale and that of their current place of residence. A small number of studies have analyzed multiple bones from a single individual with interesting results. For example, in their study of the Tyrolean Iceman colloquially known as "Ötzi," Hoogewerff et al. (2001) documented different $^{87}\text{Sr}/^{86}\text{Sr}$ values in the Iceman's rib and femur, potentially indicating that Ötzi travelled to multiple locales during the last years of his life.

While it may be tempting to select those bones with fairly rapid turnovers such as ribs or the ends of long bones for radiogenic strontium isotope analysis, these bones are composed primarily of trabecular bone, which is much more susceptible to diagenesis than compact, cortical bone (Lambert et al. 1982; Buikstra et al. 1989). Ultimately the selection of bone(s) for

sampling should be guided not only by the research question and scope, but also by the integrity of the specimen and the overall risk of diagenetic contamination as assessed from the burial environment.

35.2.2.3 Sampling Strategies for Human Tooth Enamel and Bone

Tooth Enamel

Most strontium isotope analyses of archaeological human tooth enamel rely on the bulk sampling method, in which enamel is collected across a tooth's buccal, lingual, mesial, or distal crown surface from the occlusal margin to the cemento-enamel junction (CEJ), indiscriminate of enamel growth phases. By collecting samples in this manner, scientists average out potential fluctuations in $^{87}\text{Sr}/^{86}\text{Sr}$ that may have accumulated over the course of a tooth's mineralization, which as discussed in the previous section occurs at different times and rates in an individual's life. The resulting $^{87}\text{Sr}/^{86}\text{Sr}$ enamel value, therefore, represents

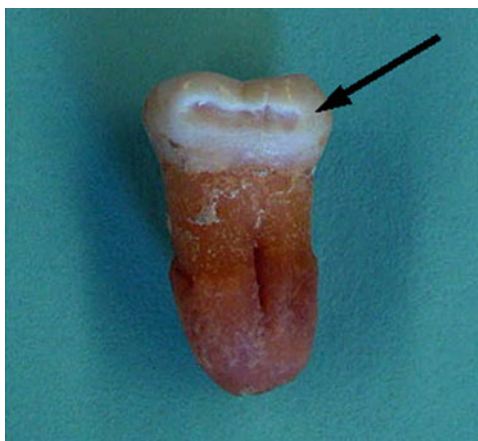


Fig. 35.4 Bulk sampling of enamel for $^{87}\text{Sr}/^{86}\text{Sr}$ isotope analysis from a human skeleton buried at the site of Ancón, Peru. The *arrow* points to the region of the tooth from which enamel was drilled

a bulk signature formed over a period of several months or years in an individual's childhood or adolescence (Fig. 35.4).

The collection of enamel bulk samples for isotope analysis is relatively straightforward. The enamel surface of the tooth selected for sampling should be abraded using either a Dremel tool or dental drill fitted with a carbide burr to eliminate adhering materials and to remove surface enamel that is most susceptible to diagenetic alteration (Hillson 1996). Enamel samples then can be drilled into a fine powder or chunked and later ground to a powder using a sterilized mortar and pestle. Researchers should aim to collect approximately 5–20 mg of tooth enamel if possible. Although only a small amount of enamel is needed for actual analysis, some material may be lost during sample preparation.

As an alternative to collecting samples in bulk, some consideration has been given to the possibility of microsampling enamel growth layers using either microdrilling or laser ablation. Laser ablation, and to a lesser extent microdrilling, requires far smaller samples than the bulk method, making it well-suited for isotopic analyses of rare materials such as fossil specimens or extremely small faunal teeth (Copeland et al. 2008). Furthermore, microsamples from a single human tooth potentially can capture seasonal fluctuations in enamel isotope values in strontium and other elements, as has been demonstrated in isotope studies of non-human animals (Koch et al. 1995; Fricke and O'Neil 1996; Stuart-Williams and Schwarcz 1997).

Despite these proposed benefits, microsampling remains largely untested on human archaeological samples. In part, this is due to the fact that microsampling via microdrilling remains technically difficult and fairly specialized (Richards et al. 2009). In addition, comparisons of laser ablation (LA)- and traditional solution mode-multi-collector inductively coupled plasma mass spectrometry (MC-ICP-MS) $^{87}\text{Sr}/^{86}\text{Sr}$ measurements from tooth enamel have shown that the former method is generally more inaccurate and imprecise than solution-based techniques, owing to potential isobaric interferences during laser analysis (Simonetti et al. 2008; Nowell and Horstwood 2009). In recent years, however, a small number of studies have addressed these deficiencies and demonstrated that LA-MC-ICP-MS data may be appropriate in some archaeological cases. Research by Horstwood et al. (2008), for example, indicates that with proper on-line interference correction routines and additional calibration against a set of reference materials, reliable LA-MC-ICP-MS-based $^{87}\text{Sr}/^{86}\text{Sr}$ signatures from archaeological specimens potentially can be produced. While Horstwood et al. (2008) acknowledge that their analytical protocol appears to work well on samples with concentrations >300 ppm Sr, the authors note that laser ablation data from samples with concentrations ≤ 200 ppm Sr exhibit a much greater degree of inaccuracy and should be used cautiously. Copeland et al. (2008, 2010) analyzed modern and fossil rodent teeth from the Sterkfontein Valley of South Africa using both LA-MC-ICP-MS and TIMS. While their LA-MC-ICP-MS-based enamel $^{87}\text{Sr}/^{86}\text{Sr}$ values were less precise than the corresponding TIMS values, the authors do argue that LA-MC-ICP-MS is sufficiently accurate to investigate geographic origins and residential mobility *if* the geologic units under study are considerably variable from one another.

Finally, it is still somewhat unclear whether the analysis of microsamples from different human enamel growth layers can actually capture seasonal variations in $^{87}\text{Sr}/^{86}\text{Sr}$. As noted by Montgomery and Evans (2006), enamel mineralization in human teeth occurs in a multidirectional pattern such that $^{87}\text{Sr}/^{86}\text{Sr}$ values likely are averaged out across a tooth's surface rather than occurring in a well-ordered, sequential fashion across growth layers. Recent research (Dolphin et al. 2005; Richards et al. 2008), however, indicates that incremental shifts in $^{87}\text{Sr}/^{86}\text{Sr}$ values within a single human tooth may be detectable using laser ablation

techniques. In their study of deciduous dentition from modern children living in the Solís Valley of Mexico, Dolphin et al. (2005) illustrated that significant intra-tooth variations in trace element concentrations between prenatally- and postnatally-formed enamel were detectable using LA-ICP-MS. Similarly Richards et al. (2008) used laser ablation plasma ionization mass spectrometry (LA-PIMMS) to document three distinct clusters of $^{87}\text{Sr}/^{86}\text{Sr}$ values from a single Neanderthal third molar, which appeared to correspond to distinct phases of enamel secretion (Fig. 35.5). Richards et al. (2008) interpret the variation in

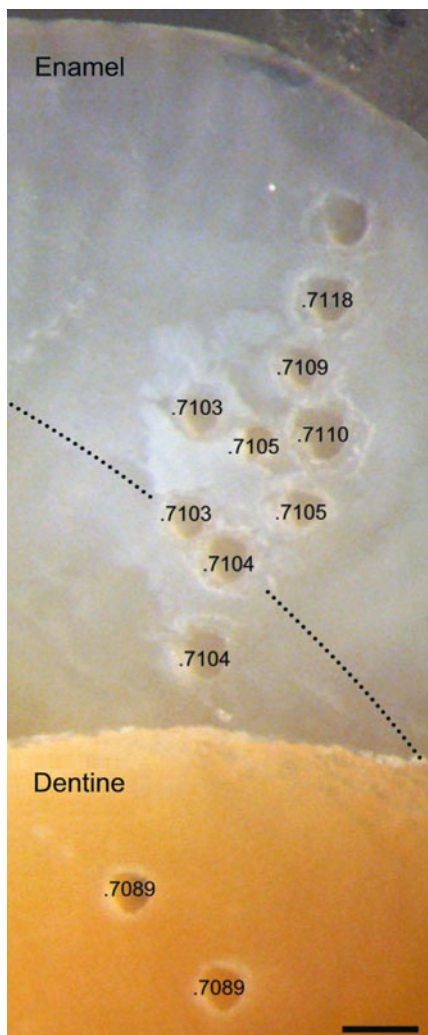


Fig. 35.5 Sequential sampling of a Neanderthal tooth using laser ablation. Numerical values represent the $^{87}\text{Sr}/^{86}\text{Sr}$ ratios for the individual laser-ablation pits. Reprinted from Richards et al. (2008), with permission from Elsevier

$^{87}\text{Sr}/^{86}\text{Sr}$ signatures over time as evidence for Neanderthal mobility. Assuming the results of Dolphin et al.'s (2005) and Richards et al.'s (2008) study are applicable to archaeological samples more broadly, then laser ablation ICP-MS methods potentially can capture variation in enamel $^{87}\text{Sr}/^{86}\text{Sr}$ at much finer temporal resolutions than previously achieved using the bulk sampling technique.

Bone

The collection of bone for radiogenic strontium isotope analysis also can be performed using a Dremel Multipro drill, generally outfitted with an inverted cone tip to remove bone powder or a diamond disk saw to remove bone chunks. Prior to removing the sample, the sample area should be gently abraded to remove surface contamination. Samples should be taken from cortical bone, if possible, as this type of bone is less susceptible to diagenetic alteration than trabecular bone. It is suggested that at least 50 mg to 1 g of bone be collected since some preparation protocols for bone are quite rigorous and can result in a partial loss of sample (Hoppe et al. 2003).

A Cautionary Note

We conclude our discussion on sample selection with a note of caution. It should be remembered that collecting samples for radiogenic strontium isotope analysis involves the permanent removal of enamel and bone from archaeological specimens, samples which are entirely consumed during purification and mass spectrometry. Although the amount of enamel and bone needed for isotopic analysis is quite small (less than 20 mg for traditional bulk sampling methods and even less for laser ablation techniques), there are ways of minimizing one's impact on archaeological materials when selecting specimens for sampling. In the case of tooth enamel, researchers should attempt to sample teeth that are no longer embedded in the alveolar bone if possible as this reduces the risk of damage to the surrounding alveolus and bones of the skull. When selecting bone for analysis, researchers should avoid sampling intact bone if fragmentary bone is available for study, so as to minimize impact to the skeleton. Additionally, scientists should try to avoid removing

enamel or bone samples from those teeth or parts of the skeleton that exhibit pathological lesions, cultural modifications, or other diagnostic markers as these features potentially can be used to reconstruct aspects of health, diet, growth, and socio-cultural practices among ancient populations (see e.g., Larsen 1997; Katzenberg and Saunders 2008). Finally, since multiple isotopic signatures can be retrieved from a single dental or bony element, scientists should formulate hypotheses and devise their sampling strategy so as to maximize the kinds of chemical information that can be retrieved from their samples while minimizing damage to the skeleton.

35.2.3 Laboratory Analysis

Radiogenic strontium isotope analysis is a well established procedure and has long been used by geologists. Accordingly laboratory sample preparation procedures and analytical techniques have been thoroughly studied and routinely applied (see e.g. Faure and Mensing 2005). Here we briefly summarize preparation protocols relevant for archeological studies and provide some information on mass spectrometric analyses.

35.2.3.1 Preparation Protocols for Isotopic Analysis of Bedrock, Soil, and Groundwater

To determine the strontium isotopic composition of environmental samples that represent the local provenance signature, care must be given to collect relevant and representative samples. As discussed earlier, such samples may include bedrock, soil, groundwater, river/lake water or vegetation, as well as archaeozoological and archaeobotanical materials (the seawater signature is well established and does not need to be analyzed). Several sub-samples from different, randomly spread locations relevant to the study should be collected and homogenized. Archaeobotanical remains should be carefully cleaned of dust by ultrasonication in milliQ water and acetone several times, while archaeozoological materials should be prepared for analysis following the protocols outlined for human samples below.

Homogenized samples are dissolved in preparation for strontium separation for mass spectrometry. Many sample dissolution methods have been used ranging from an acid pre-leach followed by partial dissolution in weak acid (McArthur et al. 1993) to a total dissolution in mixed strong acids (Hein et al. 1993). The main purpose of the pre-leaching is to minimize contamination by non-target components which may adhere to the sample surface. Such cleaning should be included if diagenetic contamination is expected (Bailey et al. 2000). The pristine, clean, representative target samples should then be fully dissolved. The exact procedure for sample dissolution will depend on the properties of the sample. For example, pure carbonate rocks may be digested by relatively dilute acetic acid (Montanez et al. 1996), while bulk silicate rocks and soil are typically dissolved in a mixture of hot concentrated HNO_3 and HF acids followed by drying and repeat treatment with HCl and HNO_3 (Billings and Adams 1964). Organic substances like vegetation are either oxidized in hot HNO_3 or ashed for 4 h in a muffle furnace at 550°C and then dissolved in a mixture of 6 N HNO_3 and HCl (Porder et al. 2003), followed by removal of any residue through filtration. After dissolution, samples are dried down and then re-constituted in a minimal amount of acid (typically HCl or HNO_3) in preparation for strontium separation by ion chromatography. Water or other fluids containing strontium are filters and the appropriate volume containing enough strontium for analysis is dried down and re-constituted as above. All reagents used for dissolution must be trace metal clean or distilled to lower strontium blanks.

35.2.3.2 Preparation Protocols for Isotopic Analysis of Archaeological Human Remains and Modern Fauna

Pretreatment protocols for archaeological specimens will vary depending on the element analyzed. As discussed earlier, tooth enamel is largely resistant to diagenetic contamination while archaeological bone is highly susceptible to post-mortem alteration. As a result, pretreatment protocols for tooth enamel are relatively straightforward and less intensive than that required for archaeological bone specimens.

While various preparation methods exist for archaeological tooth enamel, the general consensus is that

sequential rinses or an overnight bath in weak (≤ 1.0 N) acetic acid remove most diagenetic carbonates in enamel (Sillen 1986; Hoppe et al. 2003). It should be noted that samples can lose up to 70% of their weight depending on the specific preparation protocol followed (Hoppe et al. 2003); thus, care should be taken in determining the number of rinses enamel powder should be subjected to. Once acetic acid has been removed from enamel samples, the residual powder should be rinsed with distilled/deionized water and sonicated three times for at least 5 min. Samples can be left overnight to dry or dried down using a desiccator, hot plate, or oven (below 50°C).

Archaeological bone samples should be subjected to more rigorous preparation procedures than those established for enamel, although it should be emphasized that no one pretreatment protocol has been found that completely separates biogenic and diagenetic strontium in bone (Koch et al. 1997; Hoppe et al. 2003; Trickett et al. 2003). Many studies have adopted Sillen's (1986) solubility profile method (or a version thereof), in which powdered bone is subjected to a series of washes in 0.1 N buffered acetic acid ($\text{pH} = 4.5$). Following acid treatment, bone samples should be rinsed and sonicated three or more times using distilled/deionized water for several minutes. Given the large number of rinses (Sillen's original 1986 study consisted of 24 acid washes), it is recommended that powdered bone samples initially weigh between 30 and 50 mg, as significant amounts of sample can be lost during preparation. As an alternative to Sillen's method, Knudson et al. (2004) recommend sonication of chunked bone in deionized water for 30 min, followed by sonication in 5% acetic acid for 30 min, and a second aliquot of 5% acetic acid for 5 min. Once rinsed, bone samples can be ashed and powdered.

Since diagenesis is not an issue when analyzing bones and teeth from modern fauna, enamel and/or bone from these specimens require minimal pretreatment prior to analysis. Mechanical cleaning is recommended for all modern samples, and if necessary, samples can be left overnight in H_2O_2 (30%) to remove organics. Cleaned samples should then be sonicated with distilled water and dried down. All dried samples (both archaeological and modern tooth enamel and bone) can then be dissolved in either HCl or HNO_3 in preparation for strontium separation by ion chromatography.

35.2.3.3 Strontium Separation

Prior to mass spectrometric analysis strontium has to be purified to reduce mass interference (isobaric interference) by other elements and compounds (specifically ^{87}Rb) and to maximize ionization efficiency (residual Ca decreases the ionization efficiency of strontium and the stability of the ion beam). This is done using ion chromatography by passing the sample solution through columns filed with cation exchange resin (Hart and Brooks 1974). About $1\ \mu\text{g}$ of strontium is typically prepared for isotope analysis. The most commonly used separation technique involves cation-exchange chromatography using resin (AG 50W-X8) in HCl medium. This resin retains strontium more strongly than singly charged alkali metals including major elements such as Mg and trace elements such as Rb (Hart et al. 1974). However the separation from Ca and Al can be compromised when these are present in higher concentrations relative to Sr. Use of longer columns can alleviate some of these problems (Birck 1986). Columns are conditioned with 3–5 column volumes of 0.75 N HCl and the sample (dissolved in a small amount of 0.75 N HCl) is loaded. The cations are eluted with 1.8 or 2 N HCl (depending on the acid strength used for calibration). The strontium fraction is collected and this fraction is dried down in preparation for mass spectrometry. Columns should be calibrated routinely to ensure clean separation and efficient recovery of Sr.

Strontium can also be extracted from nitric acid media using crown ether in octanol, sorbed on an inert substrate (Sr-Spec, Eichrom[®] non-ionic ester polymer resin, 100–150 mesh) (Horwitz et al. 1991, 1992). This method is more selective for strontium and strontium does not break through from the columns until about 30 column volumes of 3 M HNO_3 . Strontium is eluted using 0.05 M HNO_3 . Using Sr-Spec is very effective in separating rubidium and calcium from Sr, although barium is not as easily removed and longer columns or stronger acid should be used for barium-rich samples (Pin and Bassin 1992). Strontium blanks of the Sr-Spec columns are typically higher than those of the AG 50W-X8 resin, particularly when using columns repeatedly, thus care should be taken to monitor blanks or to avoid re-use of columns (Pin and Bassin 1992). All reagents used for strontium separation should be trace metal grade or

distilled to ensure low blanks, and procedural blanks should be monitored routinely.

35.2.3.4 Instrumentation

Several options are available for mass spectrometric analysis including solid-source thermal ionization mass spectrometry (TIMS), solution quadrupole-based ICP-mass spectrometry (ICP-QMS) (Vanhaecke et al. 1999), or multi collector ICP-mass spectrometry (MC-ICPMS) (Waight et al. 2002). The MC-ICPMS could also be coupled to laser ablation (LA-MC-ICPMS) (Christensen et al. 1995; Vroon et al. 2008). TIMS has been used for longer than the other instruments and is the most routinely used procedure for strontium isotope analyses. Although using the TIMS is time consuming (each analysis could take 1–2 h) it requires less strontium compared to other solution-based analyses and has the highest reproducibility and precision.

For TIMS, following strontium purification, the samples are dried down, re-dissolved in 1% HNO₃, and loaded with 0.1 M H₃PO₄ on degassed Re or Ta filaments. Samples as small as 20 ng of strontium can be routinely analyzed using TIMS although larger samples are desirable if sample is available. The isobaric interferences of ⁸⁷Rb are determined by monitoring ⁸⁵Rb and applying corrections as needed. All ⁸⁷Sr/⁸⁶Sr values are corrected for mass fractionation in the instrument using ⁸⁶Sr/⁸⁸Sr = 0.1194 (this correction is also referred to as normalization). NIST SRM 987 strontium carbonate standard is always analyzed along with samples, and the value of this standard is used to determine long-term external precision as well as for comparison of data between laboratories. The accepted value of the SRM 987 standard is 0.71024 and data is either corrected for offset from this value or the value obtained for SRM 987 is reported along with the data. Typical internal precision on the mass spectrometer is around 0.000010, and the external precision is approximately ±0.000020 (Oslick et al. 1994) (2σ standard deviation).

Techniques for radiogenic strontium isotope analysis on a double-focusing multiple collector inductively coupled plasma mass spectrometer (MC-ICPMS) can be done on unspiked or spiked samples (Fortunato et al. 2004). Measurement protocol includes standard–sample–standard bracketing methods using the

isotopic reference material (SRM 987) with wash solutions between sample or standard introductions. This permits internal correction of the isotope ratios ⁸⁷Sr/⁸⁶Sr and ⁸⁴Sr/⁸⁶Sr with ⁸⁸Sr/⁸⁶Sr and lowering of memory effects from preceding samples. Using MC-ICPMS can yield accurate and precise results similar to those obtainable by TIMS and the procedure is faster (about four samples per hour). This procedure, however, requires a larger amount of strontium (at least 300 ng per sample) in comparison to TIMS. Moreover, backgrounds should be measured to correct for interferences on masses 84 and 86 derived from small amounts of krypton in the argon supply in the plasma, and stable, residual memory strontium and rubidium signals from sample material on the torch and cones. Simultaneous ionization of all elements during plasma-based ionization also proves to be a disadvantage during radiogenic strontium isotope analysis as extra chemical clean-up steps, beyond those necessary for TIMS analyses, are required to remove potential isobaric interference. LA-MC-ICPMS strontium isotope ratio measurements of various geological and biological samples allow analyses of small samples and fine spatial resolution with minimal preparation. However significant deviations in the ⁸⁴Sr/⁸⁶Sr ratio and the radiogenic ⁸⁷Sr/⁸⁶Sr ratio from values obtained by analysis of strontium chemically separated from the sample matrix have been reported (Vroon et al. 2008). The precise reasons for this remain unclear but likely reflect a combination of isobaric interferences from Ca dimers and Ca argides and doubly charged REE, as well as disruption of mass bias effects due to differential loading of the plasma.

It is also unclear whether this is an instrument- or technique-specific problem and great care should be taken when attempting strontium isotope analyses by in situ LA-MC-ICPMS techniques (García-Ruiz et al. 2008; see also Section “Tooth Enamel,” this chapter, for a related discussion).

35.2.3.5 Monitoring for Diagenesis

The identification and removal of diagenetic contamination are crucial steps in radiogenic strontium isotope analysis of archaeological materials. As discussed above, the elimination of post-depositional contaminants from bone and enamel can be achieved through mechanical cleaning at the time of sample collection

and through chemical cleaning prior to sample dissolution. Even with these pretreatment procedures in place, however, it is difficult to be sure that all diagenetic contamination has been successfully removed. Several methods for monitoring diagenetic contamination have been established (Sillen 1989; Price et al. 1992; Nielsen-Marsh and Hedges 2000a, b), and a few techniques are briefly summarized here.

Changes to the mineralogy and crystallinity of enamel and bone can be monitored using either X-Ray Diffraction (XRD) or Fourier Transform Infrared Spectroscopy (FTIR). In general, crystallinity is higher in altered apatite than in pristine apatite (Sillen 1989; Shemesh 1990). The degree of crystallinity can be measured by calculating the crystallinity index (CI). On an infrared spectrum, the CI is the extent of phosphate peak splitting at 565–605 cm^{-1} and is measured by calculating the relative depth of the valley between the two peaks (Shemesh 1990). Samples that exhibit CI's above the range established for fresh bone, 2.8–3.1 (Weiner and Bar-Yosef 1990; Wright and Schwarcz 1996; White et al. 1998; Garvie-Lok et al. 2004), likely have been altered.

Diagenetic contamination in enamel and bone also can be detected by comparing levels of trace elements in archaeological samples with those in modern specimens (Kohn et al. 1999; Hoogewerff et al. 2001; Price et al. 2002). The ratio of calcium to phosphorus (Ca/P), for example, commonly is used to monitor potential alteration in archaeological materials. Modern, unaltered bone contains approximately 37% Ca by weight and 17% P, with a Ca/P ratio of about 2 (Kyle 1986). Ca/P ratios much greater than 2, therefore, indicate contamination. Additionally, scientists have measured carbonate/phosphate ratios (C/P) in archaeological specimens (Nielsen-Marsh and Hedges 2000a), as well as the concentration of uranium (U) in archaeological bone samples (Kohn et al. 1999; Knudson and Price 2007; Conlee et al. 2009) in order to monitor diagenetic contamination.

35.3 Applications

The number and diversity of strontium isotope studies in archaeology have increased dramatically over the last two decades. The technique primarily has been used to differentiate between individuals and fauna of

local and non-local origin, although a few studies have adopted the method as a means of identifying and sourcing non-local building materials, artifacts, and foodstuffs. While not exhaustive, the present section highlights some of the major applications of radiogenic strontium isotope analysis in archaeology to date (Table 35.2).

35.3.1 $^{87}\text{Sr}/^{86}\text{Sr}$ Analyses of Archaeological Humans

The majority of strontium isotope applications have focused on analyses of human skeletons from archaeological sites. While $^{87}\text{Sr}/^{86}\text{Sr}$ values in human bones and teeth have been used primarily to identify immigrants and track the degree of residential mobility in the past, archaeologists have applied $^{87}\text{Sr}/^{86}\text{Sr}$ data to address broader socio-cultural questions pertaining to imperial strategies and colonization, marital residence patterns, ethnicity and identity, and violence and warfare.

Ancient complex societies adopted various political strategies to manage their vast territories, including the establishment of colonies. Traditionally, archaeologists have used the presence of foreign, imperial-style ceramics, textiles, architecture, and burial practices as proxies for population movement and imperial control. With the introduction of radiogenic strontium isotope analysis to archaeology, scientists have been able to directly document the presence of foreigners at ancient sites and, thus, explore colonization models more effectively.

A number of such studies has been conducted in the Andean region of South America, including Kelly Knudson and colleagues' work (Knudson et al. 2004; Knudson and Price 2007; Knudson 2008) on residential mobility within the Tiwanaku polity during the Middle Horizon (550–1000 AD). In a pioneering study, Knudson et al. (2004) identified a number of migrants at the eponymous capital of Tiwanaku in Bolivia, as well as two immigrants, likely from Tiwanaku, at the site of Chen Chen in Peru. The latter site had been interpreted as a Tiwanaku colony based on the presence of Tiwanaku-style artifacts, but prior to Knudson et al.'s work, no definitive evidence for Tiwanaku migration was available.

Similar research has been carried out by Slovak (2007) and Slovak et al. (2009) on the nature of Wari

Table 35.2 Summary of major radiogenic strontium isotope studies mentioned in text organized by geographic region

Region	References	Primary organism(s) or materials analyzed	Site(s), country	Time period	Additional isotopes used
Europe	Grupe et al. (1997)	Human	Bavaria	Bell Beaker period	—
Europe	Price et al. (1998)	Human	Bavaria	Bell Beaker period	—
Europe	Bentley et al. (2003)	Human	Vaihingen, Germany	Neolithic	—
Europe	Montgomery et al. (2003)	Human	Isle of Lewis, Scotland	Early Norse period	—
Europe	Schweissing and Grupe (2003)	Human	Neuburg/Donau, Bavaria	Roman period	—
Europe	Bentley et al. (2004)	Human	Germany	Neolithic	—
Europe	Price et al. (2004)	Human	SE Europe	Bell Beaker period	—
Europe	Vanhaeren et al. (2004)	Shell (<i>Dentalium</i> sp.)	La Madeleine, France	Upper paleolithic	—
Europe	Montgomery et al. (2005)	Human	West Heslerton, England	Fifth to seventh centuries AD	Several Pb variants
Europe	Price et al. (2006a, b)	Human	Talheim, Germany	Neolithic	—
Europe	Richards et al. (2008)	Neanderthal	Lakonis, Greece	40,000 ya	—
Europe	Frei et al. (2009)	Sheep (<i>Ovis aries</i>)	Scandinavia; Shetland Islands; Faroe Islands; New Zealand	Modern/archaeological (eighth century BC to fifth century AD)	—
Europe	Nehlich et al. (2009)	Human	Nieder-Mörlen, Germany	Neolithic	$\delta^{15}\text{N}$, $\delta^{13}\text{C}$
Europe	Towers et al. (2009)	Cattle (<i>Bos Taurus</i>), Auroch (<i>Bos primigenius</i>)	England	Bronze age	—
Mediterranean/ Near East	Gale et al. (1988)	Gypsum	Mediterranean	Bronze age	$\delta^{34}\text{S}$
Mediterranean/ Near East	Freestone et al. (2003)	Glass	Eastern Mediterranean	Sixth to eleventh centuries AD	—
Mediterranean/ Near East	Brilli et al. (2005)	Marble	Mediterranean	—	—
Mediterranean/ Near East	Henderson et al. (2005)	Glass	Al-Raqq, Syria	Eighth to ninth centuries AD	$\delta^{18}\text{O}$, Pb
Mediterranean/ Near East	Buzon et al. (2007)	Human	Tombo, ancient Nubia	New Kingdom period	—
North America	Price et al. (1994)	Human	Grasshopper Pueblo and Walnut Creek, Arizona	Fourteenth century AD	—
North America	Hoppe et al. (1999)	Mammoths (<i>Mammuthus</i> sp.), Mastodons (<i>Mammot americanum</i>)	Florida	Late pleistocene	—
North America	Ezzo and Price (2002)	Human	Grasshopper Pueblo, Arizona	Thirteenth to fourteenth centuries AD	—
North America	Porder et al. (2003)	Several small mammal species	Yellowstone National Park, Wyoming	Holocene	—
North America	Hoppe (2004)	Mammoths (<i>Mammuthus</i> sp.)	Texas, New Mexico, Colorado	Late pleistocene	$\delta^{18}\text{O}$, $\delta^{13}\text{C}$
North America	Reynolds et al. (2005)	Ponderosa pine (<i>Pinus ponderosa</i>)	Chaco Canyon, New Mexico	Tenth to twelfth centuries AD	—
North America	Benson et al. (2006)	Willow (<i>Salix</i> sp.), Tule (<i>Schoenoplectus</i> sp.)	Great Basin	Lovelock cultural period	$\delta^{18}\text{O}$
North America	Feranec et al. (2007)	Several species of mammals	Yellowstone National Park, Wyoming	Holocene	—

North America	Benson et al. (2009)	Maize (<i>Zea mays</i>)	Chaco Canyon and Aztec Ruin, New Mexico	Twelfth to thirteenth centuries AD	—
North America	Benson (2010)	Maize (<i>Zea mays</i>)	Chaco Canyon, New Mexico	Twelfth century AD	—
Mesoamerica	Price et al. (2000)	Humans	Teotihuacan, Mexico	First millennium AD	—
Mesoamerica	Wright (2005)	Human	Tikal, Guatemala	Early through late classic periods	—
Mesoamerica	Price et al. (2006a, b)	Human	Campeche, Mexico	Colonial period	—
South America	Knudson et al. (2004)	Human	Tiwanaku, Bolivia; Chen Chen, Peru	Middle horizon	—
South America	Knudson and Price (2007)	Human	Chiribaya/Tiwanaku-affiliated sites, South Central Andes	Middle horizon	$\delta^{18}\text{O}$
South America	Knudson (2008)	Human	South Central Andes	Middle horizon	—
South America	Tung and Knudson (2008)	Human	Conchopata, Peru	Middle horizon	—
South America	Andrushko et al. (2009)	Human	Chokepukio, Peru	Late horizon	—
South America	Conlee et al. (2009)	Human	La Tiza and Pajonal Alto, Peru	Middle horizon, late intermediate period	—
South America	Knudson and Torres-Rouff (2009)	Human	Caspana, Chile	Late intermediate period	$\delta^{18}\text{O}$
South America	Knudson et al. (2009)	Human	Nasca, Peru	Early intermediate period	$\delta^{18}\text{O}$, $\delta^{13}\text{C}$
South America	Slovak et al. (2009)	Human	Ancón, Peru	Middle horizon	$\delta^{15}\text{N}$, $\delta^{13}\text{C}$
South America	Turner et al. (2009)	Human	Machu Picchu, Peru	Late horizon	$\delta^{18}\text{O}$, several Pb variants
South America	Thornton et al. (2010)	Llama (<i>Lama glama</i>), Alpaca (<i>Lama paca</i>)	Osmore Valley, Peru	Middle horizon through colonial period	$\delta^{15}\text{N}$, $\delta^{13}\text{C}$
South Africa	Sillen et al. (1995)	<i>Australopithecus robustus</i> , <i>Homo</i> sp.	Swartkrans, South Africa	Pleistocene	—
South Africa	Balasse et al. (2002)	Sheep (<i>Ovis aries</i>), Cow (<i>Bos taurus</i>)	Kasteelberg, South Africa	Late stone age	$\delta^{18}\text{O}$, $\delta^{13}\text{C}$

imperial influence at the site of Ancón on Peru's Central Coast. While some scholars have suggested that the site functioned as an important Wari outpost, other researchers have argued that Ancón remained free of Wari political and economic control. While the results of Slovak et al.'s (2009) radiogenic strontium isotope study do not resolve the debate entirely, the presence of a migrant, likely from the Wari heartland, coupled with Wari-style objects at the site suggests that the identification of Ancón as a Wari colony is at the very least plausible.

Radiogenic strontium isotope research on Late Horizon (1400–1532 AD) sites in the Andes has shed light on Inka political strategies as well, including the state-mandated resettlement of individuals into *mitima* communities (D'Altroy 2005). Andrushko et al. (2009), for example, noted a dramatic increase in the number of migrants at the Inka site of Chokepukio, Peru during the Late Horizon, which the authors partially attribute to coerced migrations resulting from Inka imperial labor policies. On the other hand, a multi-isotopic study by Turner et al. (2009) has shown that the famed site of Machu Picchu likely did *not* function as a *mitima* colony composed of relocated colonists from a common geographic area or areas, but rather was maintained as a private estate for the Inka emperor by elite retainers whose geographic origins were widely dispersed.

In the Old World, strontium isotope data also has been used to investigate colonization. Buzon et al. (2007), for example, examined radiogenic strontium isotope signatures among individuals buried at the site of Tombos in ancient Nubia during the Egyptian New Kingdom Period – a time when the Nubian Kingdom was subsumed under Egyptian rule. As noted by the Buzon et al. (2007), the nature and extent of Egyptian control over Nubia remains unclear; however, strontium isotope data indicates that colonial rule at Tombos may have been administered not only by individuals of foreign origin (i.e., Egyptians) but by local Nubians as well.

Montgomery et al. (2005) used both strontium and lead isotopes to explore the origins of potential immigrants at an Anglian cemetery in England during the fifth to seventh centuries AD, a time period that partially overlaps with the mass migration of Anglo-Saxons into Britain. While the geographic origins of the individuals identified as non-local based on their $^{87}\text{Sr}/^{86}\text{Sr}$ signatures in Montgomery et al.'s (2005)

study could not be assigned definitively to Angeln, the authors' results highlight the potential of strontium isotope applications to elucidate the nature and extent of colonization and mass migrations in the archaeological record.

Finally, extensive evidence for human migration has been documented via radiogenic strontium isotope analysis during the early and late Neolithic periods of Europe (see e.g., Bentley et al. 2003, 2004; Price et al. 2004, 2006a, b; Nehlich et al. 2009). Price et al. (2004), for example, employed radiogenic strontium isotope analysis to determine whether the spread of Bell Beaker culture throughout many parts of Europe during the Neolithic/Bronze Age transition resulted from the migration of foreign peoples into these areas, or from the importation of Bell Beaker-style artifacts into communities by local peoples. The results of their study, which included skeletons from Bell Beaker graves in Austria, the Czech Republic, Germany, and Hungary, demonstrate that 51 of 81 individuals analyzed (61.7%) were born elsewhere. While Price et al.'s (2004) data does not entirely resolve the question of whether migration or diffusion was responsible for the rapid and widespread expansion of the Bell Beaker culture at this time, their work underscores the considerable degree of human mobility that did occur during the Neolithic and provides an alternative line of evidence for evaluating the Bell Beaker phenomenon.

Radiogenic strontium isotope analysis also has yielded potential evidence for exogamous marriage practices in the past, particularly among females. Grupe et al. (1997) and Price et al. (1998) documented a disproportionate number of migrant females at Bell Beaker period (2500–1900 BC) sites in Bavaria, which they interpret as tentative evidence for exogamy. Similarly Schweissing and Grupe (2003) noted a similar trend among southern Bavarian populations during the Roman-period occupation. In this latter case study, approximately 56% of females analyzed (or 10 out of 18 women) yielded non-local $^{87}\text{Sr}/^{86}\text{Sr}$ enamel signatures compared to 37% of males (or 15 of 41 men). These results potentially suggest that females were married into the community at a greater rate than men. Elsewhere in Europe, Bentley et al. (2004) documented significantly more female immigrants than male immigrants at Early Neolithic cemeteries in Germany, which may indicate that larger number of females married into low-lying agricultural communities during this time period.

In some cases, strontium isotope data from human skeletons has been used to elucidate the relationship between ethnic identity and geographic origin. Price et al. (2000), for example, analyzed $^{87}\text{Sr}/^{86}\text{Sr}$ values from a sample of individuals buried in various ethnic enclaves or *barrios* at the site of Teotihuacan in Mexico and discovered that the majority of people appear to have been born non-locally. In this instance, then, the presence of foreign cultural elements such as architecture, pottery, burial practices, and food preparation techniques within the *barrios* appear to have resulted (at least in part) from foreign peoples living there. In a similar vein, Bentley et al. (2003) noted a significant correlation between burial location and $^{87}\text{Sr}/^{86}\text{Sr}$ signatures at the site of Vaihingen, Germany. A greater percentage of non-local individuals (14 of 24), as determined by their $^{87}\text{Sr}/^{86}\text{Sr}$ values, were buried in the Neolithic ditch encircling Vaihingen than in the settlement itself (5 of 22 individuals) (Bentley et al. 2004). These findings potentially suggest that non-local individuals were viewed as socially and/or ethnically different and buried distinctly (Bentley et al. 2003). Finally, in an innovative study by Price et al. (2006a, b), $^{87}\text{Sr}/^{86}\text{Sr}$ signatures from five individuals buried at a colonial cemetery in Campeche, Mexico indicate that they likely were born in West Africa. Importantly, four of these individuals appeared ethnically distinct prior to isotope analysis based on the type of dental modification they exhibited. Price et al.'s (2006a, b) study not only documents some of the earliest representatives of the pre-eighteenth century slave trade, but also highlights a correlation between biological indicators of identity, i.e., place of origin, and sociocultural indicators of identity, i.e., dental modification practices.

On the other hand, radiogenic strontium isotope data may not always accord well with sociocultural data. Expanding on research produced in an earlier pilot study (Price et al. 1994; Ezzo et al. 1997), Ezzo and Price (2002), noted that ethnic identities among individuals buried at Grasshopper Pueblo, Arizona often were blurred and not necessarily correlated with strontium isotope signatures. Similarly, Knudson and Torres-Rouff (2009) documented a complex relationship between isotope signatures and cultural identity among individuals buried at the site of Caspana in northern Chile during the Late Intermediate Period (1100–1400 AD). Based on potential ethnic markers such as cranial modification and burial styles, the

Caspana individuals were distinct from neighboring groups in the region, as might be expected among a migrant community; however all but one of the individuals at Caspana was born and raised locally.

Finally, the use of strontium isotope data has been applied to investigations of violence and warfare in the archaeological record. The identity of trauma victims has long been of interest to archaeologists and physical anthropologists but has been relatively difficult to ascertain; radiogenic strontium isotope analysis has the potential to provide archaeologists with data regarding the geographic origins of these individuals in the past. Price et al. (2006a, b) analyzed $^{87}\text{Sr}/^{86}\text{Sr}$ signatures from 22 of the 34 human skeletons uncovered in a Neolithic-period mass grave in Talheim, Germany. The results of their study indicate that the majority of the individuals were born locally, and lend support to the authors' (Price et al. 2006a, b) interpretation that the burials probably represent members of a single community who were killed by another group. In a similar vein, recent applications of radiogenic strontium isotope analysis to victims of trophy head taking in the Andes, a practice in which the skull of an individual was obtained either through decapitation or by its removal from a corpse, has produced interesting and exciting results. In a study by Tung and Knudson (2008), 3 of 5 trophy heads found at the Wari site of Conchopata in Peru were identified as non-local using radiogenic strontium isotope analysis. The authors suggest that one possible interpretation for these results is that the non-local trophy heads were foreign enemies who had been taken captive and subsequently decapitated. On the other hand, strontium isotope data from Conlee et al. (2009) and Knudson et al. (2009) have established that trophy head taking among the ancient Nasca of southern Peru was a localized phenomena, in which trophy head victims likely were culled from local populations in the region.

35.3.2 $^{87}\text{Sr}/^{86}\text{Sr}$ Analyses of Archaeological Fauna

In addition to examining human mobility in the past, scholars have analyzed strontium isotope data from fauna to better understand animal migration patterns. While the technique has been widely applied to extant animal populations (van der Merwe et al. 1990; Koch

et al. 1992, 1995; Chamberlain et al. 1997), the present section highlights radiogenic strontium isotope studies of archaeological fauna.

Hoppe et al.'s (1999) investigation of mammoth and mastodon mobility in the American Southeast during the late Pleistocene was one of the earliest applications of $^{87}\text{Sr}/^{86}\text{Sr}$ to prehistoric faunal populations. Hoppe et al.'s (1999) research demonstrated that neither mammoth nor mastodons engaged in large-scale migrations (>700 km), and highlighted significant variability in the extent and frequency of mobility between the two animal species. Subsequent radiogenic strontium isotope studies on the origins and migration patterns of Pleistocene- and Holocene-era North American fauna have been carried out by other scholars, including Porder et al. (2003), Hoppe (2004), and Feranec et al. (2007).

While the above investigations have improved researchers' understanding of prehistoric animal behavior, radiogenic strontium isotope ratios from ancient fauna also have been used to elucidate *human* activity in the past. Towers et al. (2009), for example, recently investigated the origins of cattle and aurochs buried in two Bronze Age barrows in England. Hundreds of cattle remains had been found associated with human burials within the barrows, but little was known about the animals' origins or the purpose(s) of their placement in the tombs. Radiogenic strontium isotope data from a sub-sample of the archaeological fauna indicated that while most animals were raised locally, two individuals had been born elsewhere, suggesting that long-distance exchange was undertaken by human populations at the time (Towers et al. 2009).

Radiogenic strontium isotope analyses of archaeological fauna also can shed light on ancient animal husbandry practices. Balasse et al. (2002) determined strontium isotope ratios from two archaeological sheep and one archaeological cow (along with C and N isotope ratios from these and other archaeological fauna) to investigate the plausibility of a seasonal mobility model for Late Stone Age pastoralists in South Africa. Their findings suggest that ancient fauna were not herded between the coast and hinterland seasonally, but rather stayed within one region for their entire lives or migrated at some point (rather than seasonally) during their lifetimes. In a more recent multi-isotopic study of ancient herding practices, Thornton et al. (2010) tentatively reconstructed prehistoric herding practices among human groups in the

Osmore Valley, Peru using $^{87}\text{Sr}/^{86}\text{Sr}$ signatures (along with $\delta^{13}\text{C}$ and $\delta^{15}\text{N}$ values) from archaeological camelid bone. Although radiogenic strontium isotopes were unable to differentiate between camelids potentially herded in mid- to lower-elevation zones, $^{87}\text{Sr}/^{86}\text{Sr}$ values were sufficiently different to distinguish between camelids pastured in the highland *puna* region and those herded in middle and lower elevation habitats.

35.3.3 $^{87}\text{Sr}/^{86}\text{Sr}$ Analyses of Building Materials, Artifacts, and Food

Similar to radiogenic strontium isotope studies of human and faunal remains, the origins of artifacts, archaeological building materials, and ancient food stuffs have been traced using $^{87}\text{Sr}/^{86}\text{Sr}$ analysis. For example, Freestone et al. (2003) reconstructed the potential origins and raw materials used to create sixth to eleventh century AD glass found in the Eastern Mediterranean region by determining $^{87}\text{Sr}/^{86}\text{Sr}$ values from four production sites in Israel and Egypt. Similarly, Henderson et al. (2005) utilized radiogenic strontium isotopes (along with oxygen and lead isotopes) to trace the potential geologic sources of Syrian glass from the eighth to ninth centuries AD. Elsewhere in the Old World, radiogenic strontium isotope analysis has been applied to shell beads from the Paleolithic La Madeleine child burial in France to determine their origin (Vanhaeren et al. 2004). $^{87}\text{Sr}/^{86}\text{Sr}$ results indicate that at least some of the shells were collected from faraway beaches rather than nearby outcrops. The authors (Vanhaeren et al. 2004) argue that prehistoric artisans likely preferred beach shells to shells found in neighboring Miocene outcrops because the former type was morphologically more compatible with Paleolithic bone needle technology.

The origins of textiles, particularly those made from plant materials, can be elucidated using radiogenic strontium isotope analysis. Benson et al. (2006), for example, employed $^{87}\text{Sr}/^{86}\text{Sr}$ analysis (as well as oxygen isotopes) to successfully trace the origins of raw materials used in textile manufacture in the American Southwest. In a more recent study, the feasibility of radiogenic strontium isotope analysis to track the origins of ancient woolen textiles was recently tested by Frei et al. (2009) using modern sheep hair from Scandinavian specimens. The authors determined that

with appropriate pretreatment procedures, $^{87}\text{Sr}/^{86}\text{Sr}$ values from hair potentially can be used to source woolen materials in the archaeological record (Frei et al. 2009).

In addition to artifacts, the sources of various building materials have been identified via radiogenic strontium isotope analysis. At various archaeological sites in the Mediterranean, Gale et al. (1988) used sulfur and strontium isotopes to trace the geologic sources of gypsum – a material used in internal construction during Mycenaean times. Similarly, Brilli et al. (2005) determined $^{87}\text{Sr}/^{86}\text{Sr}$ values for eight Mediterranean quarry areas which were in use during classical times. While some of the quarries exhibited overlapping $^{87}\text{Sr}/^{86}\text{Sr}$ values, the authors demonstrate that radiogenic strontium isotope data, in tandem with other geochemical and petrographic applications, can be used to determine the potential provenance of architectural and sculptural marble artifacts (Brilli et al. 2005). At Chaco Canyon, New Mexico, Reynolds et al. (2005) determined $^{87}\text{Sr}/^{86}\text{Sr}$ data for multiple specimens of ponderosa pine used in the construction of buildings at various Great Houses. Reynolds et al.'s (2005) results indicate that Chaco's ancient inhabitants sourced their timber from a number of different outcrops, many of which were located at considerable distances from archaeological sites.

Finally, radiogenic strontium isotope analysis has been used to investigate the origins of food stuffs in the archaeological record. Recently, Benson et al. (2009) and Benson (2010) have determined $^{87}\text{Sr}/^{86}\text{Sr}$ values for maize found at sites in Chaco Canyon and Aztec Ruin, New Mexico, which in turn have allowed the authors (Benson et al. 2009; Benson 2010) to speculate on changing trade relationships in the ancient American Southwest.

35.4 Future Directions

Radiogenic strontium isotope analysis in archaeology has come a long way in the last 25 years, but more work remains to be done. The distribution of radiogenic strontium isotope applications thus far has been limited to several key areas in space and time, including the Neolithic in central Europe, Great Britain, and Southeast Asia; the Late Stone age in South Africa; early colonization of the Pacific; the Pleistocene/Holocene

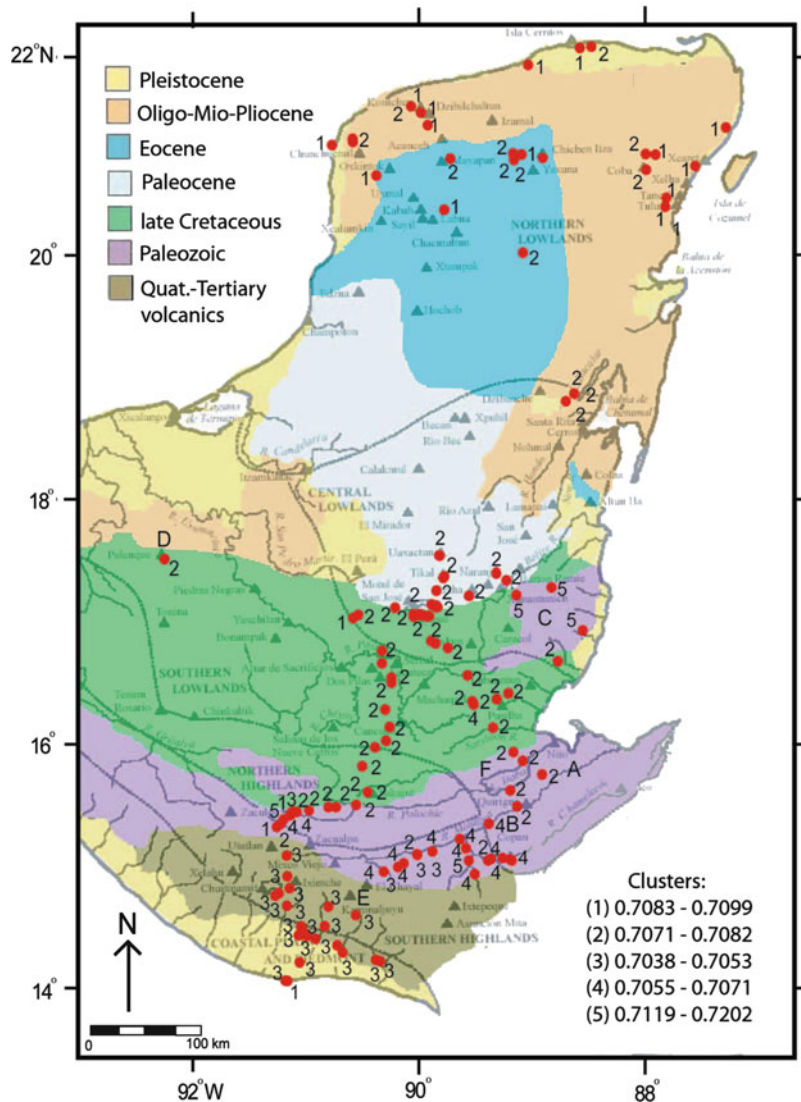
transition in the central and Southeastern U.S.; and the development of complex societies in the American Southwest, Mesoamerica, and the Middle through Late Horizons in the Andes of South America. Many areas and time periods, including the hominid fossil record, remain relatively unexplored using radiogenic strontium isotope analysis, although the few studies that have been conducted indicate enormous promise.

Sillen et al. (1995), for example, measured $^{87}\text{Sr}/^{86}\text{Sr}$ values from ~1.8 ma *Homo* sp. and *Australopithecus robustus* skeletons at the site of Swartkrans in South Africa, and (as discussed earlier) Richards et al. (2008) determined $^{87}\text{Sr}/^{86}\text{Sr}$ signatures from a 40,000 ya Neanderthal tooth found in Greece. Additionally, Sillen et al. (1998) compiled $^{87}\text{Sr}/^{86}\text{Sr}$ isotope data for the Sterkfontein Valley of South Africa using water, soil, and plant samples and compared these values to $^{87}\text{Sr}/^{86}\text{Sr}$ from Pleistocene-era vertebrates. All three studies have shed light on hominid diet and potential mobility patterns, although future applications of radiogenic strontium isotope analysis to fossil hominids may be hindered by the rare nature of the specimens and the potential for diagenetic contamination. To this end, the recent work by Copeland et al. (2008, 2010) that demonstrates the non-destructive nature of sampling via laser-ablation should prove critical.

In those regions of the world where radiogenic strontium isotope analysis has been applied, more work should be done to define local $^{87}\text{Sr}/^{86}\text{Sr}$ signatures. Ideally, such reconstructions would entail the collection of samples from exposed bedrock, soil, plants, and water along with small fauna and archaeological human remains from the region. Hodell et al.'s (2004) study of the Maya region, which involved the collection of 216 samples of rock, soil, water, and plants from Mexico, Honduras, and Guatemala, provides a good model for other researchers to follow (Fig. 35.6), as does Hedman et al.'s (2009) recent research on bioavailable $^{87}\text{Sr}/^{86}\text{Sr}$ values for the Midwestern United States. In this latter study, local $^{87}\text{Sr}/^{86}\text{Sr}$ signatures were established using the remains of nearly 50 ancient fauna from 14 archaeological sites in Illinois, Iowa, Indiana, and Missouri (Fig. 35.7). Both Hodell et al. (2004) and Hedman et al.'s (2009) research demonstrate the effectiveness and utility of collecting numerous and varied environmental samples from broad geographic regions and major geologic zones.

As discussed in the previous section, the ability of radiogenic strontium isotope analysis to source food

Fig. 35.6 Simplified geologic map of the Maya region indicating the age of regional bedrock and the results of Hodell et al.'s (2004) cluster analysis. $^{87}\text{Sr}/^{86}\text{Sr}$ values for the region were calculated using water, bedrock, soils, and plants. Reprinted from Hodell et al. (2004), with permission from Elsevier



stuffs at ancient sites primarily has been used to examine archaeological models of prehistoric trade, exchange, and technology. Radiogenic strontium isotopes from ancient foodstuffs, however, also can be used to monitor the reliability of archaeological human $^{87}\text{Sr}/^{86}\text{Sr}$ values. The effectiveness of $^{87}\text{Sr}/^{86}\text{Sr}$ data as an indicator of migration depends upon the premise that ancient humans primarily ate locally-grown foods; however even foods that appear to have been cultivated locally may have been brought in from elsewhere or treated with foreign additives during food preparation (see e.g. Wright 2005). Analyzing $^{87}\text{Sr}/^{86}\text{Sr}$ values from food found in archaeological contexts (including those resources presumed

to have been grown or raised locally), would better refine archaeological and isotopic interpretations.

The inclusion of additional isotopic tracers to radiogenic strontium isotope applications in archaeology also can facilitate interpretation of trends observed, and already has been alluded to in this chapter. Briefly, carbon ($\delta^{13}\text{C}$) and nitrogen ($\delta^{15}\text{N}$) isotope analyses of human remains can trace the relative contributions of C_4 -, C_3 -, and marine-based foods in an individual's overall diet (DeNiro and Epstein 1978, 1981; Schoeninger and DeNiro 1984; Schwarcz and Schoeninger 2011) and thus can be used to identify potential dietary biases that might affect strontium isotope signatures. Similarly, oxygen isotope data in human tissue ($\delta^{18}\text{O}$),

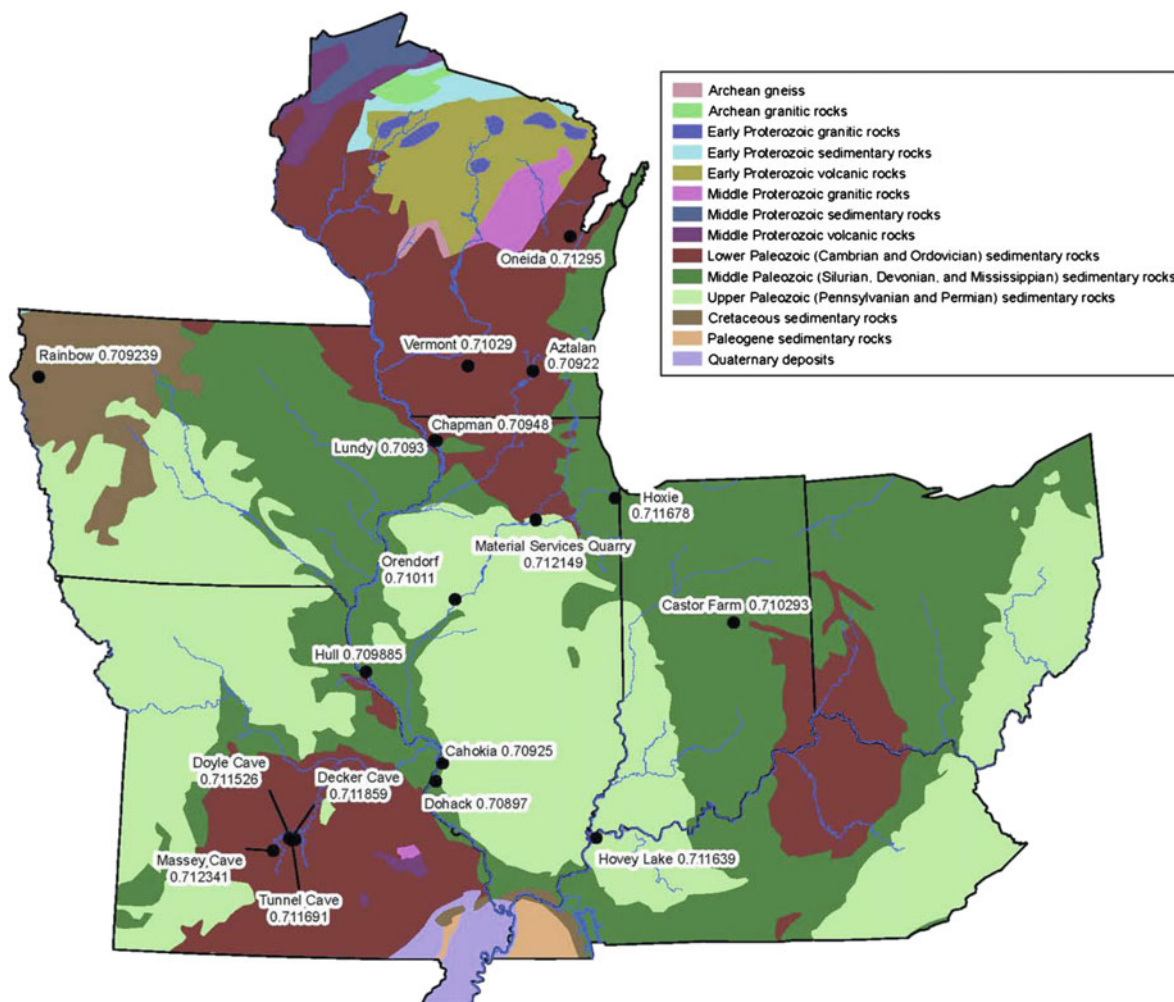


Fig. 35.7 Geologic map of Midwestern U.S. with mean $^{87}\text{Sr}/^{86}\text{Sr}$ values for various archaeological sites as determined

by tooth enamel from local archaeological fauna. Reprinted from Hedman et al. (2009), with permission from Elsevier

which is dependent on a variety of climatic factors (Gat 1980; Yurtsever and Gat 1981; White et al. 1998), provides an alternative, independent marker of migration.

Finally, new research by Knudson et al. (2010) demonstrates that the relationship between ^{88}Sr and ^{86}Sr (expressed as $\delta^{88}\text{Sr}/^{86}\text{Sr}$ and reflecting mass dependent fractionation) also can be significant to archaeological studies. According to Knudson et al. (2010), $\delta^{88}\text{Sr}/^{86}\text{Sr}$ varies by trophic level, such that in terrestrial ecosystems $\delta^{88}\text{Sr}/^{86}\text{Sr}$ decreases as one moves from bedrock and soils to points further along the food web, while in marine environments $\delta^{88}\text{Sr}/^{86}\text{Sr}$ is highest in seawater and lowest in carnivorous fish and marine mammals. Ideally, then, it should be

possible to distinguish among different components in ancient diets by examining $\delta^{88}\text{Sr}/^{86}\text{Sr}$ data in human bone and tooth mineral. While still in its incipient stages, Knudson et al.'s research using $\delta^{88}\text{Sr}/^{86}\text{Sr}$ data revealed dietary variability among archaeological Andean populations, and holds enormous promise for future archaeological studies.

35.5 Conclusion

The contributions of radiogenic strontium isotope analysis to archaeology thus far have been many. The provenience of artifacts, architectural elements,

and food stuffs can be sourced using this method, and the social and cultural implications of such findings explored more readily and reliably by archaeologists. Similarly, $^{87}\text{Sr}/^{86}\text{Sr}$ data from the human skeleton potentially provides researchers with direct evidence for an individual's geographic origin and a means to measure the degree of residential mobility within his or her lifetime. These results, in turn, have been used to reexamine models of migration, colonization, marital patterns, warfare, ethnicity, and cultural identity in past societies.

Despite these successes, however, the interpretation of $^{87}\text{Sr}/^{86}\text{Sr}$ data is hardly straightforward. While the technique is often employed as a way of differentiating between migration and diffusion in the archaeological record (see e.g., Knudson et al. 2004; Price et al. 2004; Slovak et al. 2009), the presence of foreign individuals at sites, even when accompanied by foreign-style artifacts, should be viewed cautiously. In most cases, even with evidence for migration, scholars cannot rule out the possibility that other social processes such as trade and exchange or competition between elites in a local community for exotic goods may have played an equally significant part in instigating widespread cultural change. Similarly, there may be any number of reasons to explain why an individual relocated to a site during his or her lifetime. Simple radiogenic strontium isotope models that would equate foreigners with colonizers, for example, can be just as problematic as earlier archaeological approaches that equated archaeological cultures with peoples (see e.g., critique in Jones 1997).

In addition to these theoretical challenges, various aspects of strontium isotope methodology remain problematic. For example, no single pretreatment protocol (or series of protocols) is used exclusively to prepare archaeological samples for analysis (see Sects. 35.2.3.1 and 35.2.3.2 and references therein), nor is there a consensus as to whether biogenic $^{87}\text{Sr}/^{86}\text{Sr}$ values can be retrieved from archaeological bone (Sillen 1986; Koch et al. 1997; Hoppe et al. 2003; Trickett et al. 2003). Similarly, no one method appears to be universally adequate for establishing a "local" $^{87}\text{Sr}/^{86}\text{Sr}$ signature (Price et al. 2002; Wright 2005), nor is there absolute agreement on the reliability and comparability of LA-MS-ICP-MS-based $^{87}\text{Sr}/^{86}\text{Sr}$ data and traditional solution-based TIMS data (see e.g., Horstwood et al. 2008; Simonetti et al. 2008; Nowell and Horstwood 2009; Copeland et al. 2010).

Current and future radiogenic strontium isotope research surely will help to resolve some of these issues; in the interim, $^{87}\text{Sr}/^{86}\text{Sr}$ analysis remains a powerful tool with which to critically examine the archaeological record.

Acknowledgments The authors are grateful to Dr. Mark Basaran (Wayne State University) for inviting us to contribute to this volume. We also thank the various grant agencies, especially the National Science Foundation, for their continued financial support of isotopic studies in archaeology. Thanks as well to Elsevier for granting permission to reprint various figures from the *Journal of Archaeological Science* free of charge. We appreciate Kelly Knudson and colleagues' willingness to share their then unpublished $\delta^{88}\text{Sr}/^{86}\text{Sr}$ data and methodology with us for inclusion in this chapter. Finally, we thank two anonymous reviewers for their thoughtful comments and suggestions.

References

- Andrushko VA, Buzon MR, Simonetti A et al (2009) Strontium isotope evidence for prehistoric migration at Choquepukio, valley of Cuzco, Peru. *Lat Am Antiq* 20:57–75
- Bailey TR, McArthur JM, Prince H et al (2000) Dissolution methods for strontium isotope stratigraphy: whole rock analysis. *Chem Geol* 167:313–319
- Balasse M, Ambrose SH, Smith A et al (2002) The seasonal mobility model for prehistoric herders in the South-western cape of South Africa assessed by isotopic analysis of sheep tooth enamel. *J Archaeol Sci* 29:917–932
- Beard BL, Johnson CM (2000) Strontium isotope compositions of skeletal material can determine the birth place and geographic mobility of animals and humans. *J Forensic Sci* 45(5):1049–1061
- Benson LV (2010) Who provided maize to Chaco Canyon after the mid-12th-century drought? *J Archaeol Sci* 37:621–629
- Benson LV, Hattori EM, Taylor HE et al (2006) Isotope sourcing of prehistoric willow and tulle textiles recovered from western great basin rock shelters and caves: proof of concept. *J Archaeol Sci* 33:1588–1599
- Benson LV, Stein JR, Taylor HE (2009) Possible sources of archaeological maize found in Chaco Canyon and Aztec Ruin. *New Mexico J Archaeol Sci* 36:387–407
- Bentley RA (2006) Strontium isotopes from the earth to the archaeological skeleton: a review. *J Archaeol Meth Theor* 13:135–187
- Bentley RA, Knipper C (2005) Geographical patterns in biologically available strontium, carbon and oxygen isotope signatures in prehistoric SW Germany. *Archaeometry* 47:629–644
- Bentley RA, Krause R, Price TD et al (2003) Human mobility at the early neolithic settlement of Vaihingen, Germany: evidence from strontium isotope analysis. *Archaeometry* 45:471–486
- Bentley RA, Price TD, Stephan E (2004) Determining the "local" $^{87}\text{Sr}/^{86}\text{Sr}$ range for archaeological skeletons: a case study from neolithic Europe. *J Archaeol Sci* 31:365–375

- Billings GK, Adams JAS (1964) The analysis of geological materials by atomic absorption spectrometry. *At Absorpt News* 23:1–7
- Birck JL (1986) Precision K–Rb–Sr isotopic analysis – application to Rb–Sr chronology. *Chem Geol* 56:73–83
- Brilli M, Cavazzini G, Turi B (2005) New data of $^{87}\text{Sr}/^{86}\text{Sr}$ ratio in classical marble: an initial database for marble provenance determination. *J Archaeol Sci* 32:1543–1551
- Budd P, Montgomery M, Barreiro B et al (2000) Differential diagenesis of strontium in archaeological human dental tissues. *Appl Geochem* 15:687–694
- Buikstra JE, Frankenberg S, Lambert JB et al (1989) Multiple elements: multiple expectations. In: Price TD (ed) *The chemistry of prehistoric bone*. Cambridge University Press, Cambridge
- Buikstra JE, Price TD, Wright LE et al (2004) Tombs from the Copan acropolis: a life-history approach. In: Bell EE, Canuto MA, Sharer RJ (eds) *Understanding early classic Copan*. University of Pennsylvania Museum of Archaeology and Anthropology, Philadelphia
- Burton J, Wright L (1995) Nonlinearity in the relationship between bone Sr/Ca and diet: paleodietary implications. *Am J Phys Anthropol* 96:273–282
- Buzon MR, Simonetti A, Creaser RA (2007) Migration in the Nile valley during the new kingdom period: a preliminary strontium isotope study. *J Archaeol Sci* 9:1391–1401
- Capo RC, Stewart BW, Chadwick OA (1998) Strontium isotopes as tracers of ecosystems processes: theory and methods. *Geoderma* 82:197–225
- Chamberlain CP, Blum JD, Holmes RT et al (1997) The use of isotope tracers for identifying populations of migratory birds. *Oecologia* 109:132–141
- Christensen JN, Halliday AN, Lee DC et al (1995) In situ Sr isotope analysis by laser ablation. *Earth Planet Sci Lett* 136:79–85
- Comar CL, Russell RS, Wasserman RH (1957) Strontium-calcium movement from soil to man. *Science* 126:485–492
- Conlee CA, Buzon MR, Gutierrez AN et al (2009) Identifying foreigners versus locals in a burial population from Nasca, Peru: an investigation using strontium isotope analysis. *J Archaeol Sci* 36:2755–2764
- Copeland SR, Sponheimer M, Roux PJI et al (2008) Strontium isotope ratios ($^{87}\text{Sr}/^{86}\text{Sr}$) of tooth enamel: a comparison of solution and laser ablation multicollector inductively coupled plasma mass spectrometry methods. *Rapid Commun Mass Spectrom* 22:3187–3194
- Copeland SR, Sponheimer M, Lee-Thorp JA et al (2010) Strontium isotope ratios in fossil teeth from South Africa: assessing laser ablation MC-ICP-MS analysis and the extent of diagenesis. *J Archaeol Sci* 37:1437–1446
- D'Altroy TN (2005) Remaking the social landscape: Colonization in the Inka empire. In: Stein GJ (ed) *The archaeology of colonial encounters*. School of American Research Press, Santa Fe
- De Souza GF, Reynolds BC, Bourdon B (2007) Evidence for stable strontium isotope fractionation during chemical weathering. *Geochim Cosmochim Acta* 71:A220
- DeNiro MJ, Epstein S (1978) Influence of diet on the distribution of carbon isotopes in animals. *Geochim Cosmochim Acta* 42:495–506
- DeNiro MJ, Epstein S (1981) Influence of diet on the distribution of nitrogen isotopes in animals. *Geochim Cosmochim Acta* 45:341–351
- Dolphin AE, Goodman AH, Amarasiriwardena DD (2005) Variations in elemental intensities among teeth and between pre- and postnatal regions of enamel. *Am J Phys Anthropol* 128:878–888
- Dupras TL, Schwarcz HP (2001) Strangers in a strange land: stable isotope evidence for human migration in the Dakhleh oasis, Egypt. *J Archaeol Sci* 28:1199–1208
- Ericson JE (1985) Strontium isotope characterization in the study of prehistoric human ecology. *J Hum Evol* 14:503–514
- Eriksen B (1986) Normal and pathological remodeling of human trabecular bone: three dimensional reconstruction of the remodeling sequence in normal and in metabolic bone disease. *Endocr Rev* 7:379
- Ezzo JA, Price TD (2002) Migration, regional reorganization, and spatial group composition at Grasshopper Pueblo, Arizona. *J Archaeol Sci* 29:499–520
- Ezzo J, Johnson CM, Price TD (1997) Analytical perspectives on prehistoric migration: a case study from east-central Arizona. *J Archaeol Sci* 24:447–466
- Faure G (1977) *Principles of isotope geology*. Wiley, New York
- Faure G, Mensing TM (2005) *Isotopes: principles and applications*. Wiley, Hoboken
- Feranec R, Hadly E, Paytan A (2007) Determining landscape use of Holocene mammals using strontium isotopes. *Oecologia* 153(4):943–950
- Fietzke J, Eisenhauer A (2006) Determination of temperature-dependent stable strontium isotope ($^{88}\text{Sr}/^{86}\text{Sr}$) fractionation via bracketing standard MC-ICP-MS. *Geochim Geophys Geosyst*. doi:10.1029/2006GC001243
- Fortunato G, Mumic K, Wunderli S et al (2004) Application of strontium isotope abundance ratios measured by MC-ICP-MS for food authentication. *J Anal At Spectrom* 19:227–234
- Freestone IC, Leslie KA, Thirlwall M et al (2003) Strontium isotopes in the investigation of early glass production: byzantine and early Islamic glass from the near east. *Archaeometry* 45:19–32
- Frei KM, Frei R, Mannering U et al (2009) Provenance of ancient textiles – a pilot study evaluating the strontium isotope system in wool. *Archaeometry* 51:252–276
- Fricke HC, O'Neil JR (1996) Inter- and intra-tooth variation in the oxygen isotope composition of mammalian tooth enamel phosphate: implications for palaeoclimatological and palaeobiological research. *Palaeogeogr Palaeoclimatol Palaeoecol* 126:91–99
- Gale NH, Einfalt HC, Hubberten HW et al (1988) The sources of Mycenaean gypsum. *J Archaeol Sci* 15:57–72
- García-Ruiz S, Moldovan M, García Alonso JI (2008) Measurement of strontium isotope ratios by MC-ICP-MS after on-line Rb–Sr ion chromatography separation. *J Anal At Spectrom* 23:84–93
- Garn SM, Lewis AB, Vicinus JH (1962) Third molar agenesis and reduction in the number of other teeth. *J Dent Res* 46:963–972
- Garvie-Lok SJ, Varney TL, Katzenberg MA (2004) Preparation of bone carbonate for stable isotope analysis: the effects of treatment time and acid concentration. *J Archaeol Sci* 31:763–776

- Gat JR (1980) The isotopes of hydrogen and oxygen in precipitation. In: Fritz P, Fontes JC (eds) *Handbook of environmental isotope geochemistry*. Elsevier, Amsterdam
- Grupe G, Price TD, Schröter P et al (1997) Mobility of bell beaker people revealed by strontium isotope ratios of tooth and bone: a study of southern Bavarian skeletal remains. *Appl Geochem* 12:517–525
- Halicz L, Segal I, Fruchter N et al (2008) Strontium stable isotopes fractionate in the soil environments? *Earth Planet Sci Lett* 272:406–411
- Hart SR, Brooks C (1974) Clinopyroxene-matrix partitioning of K, Rb, Cs, Sr and Ba. *Geochim Cosmochim Acta* 38:1799–1806
- Hart SR, Erlank AJ, Kable EJD (1974) Sea floor basalt alteration: some chemical and Sr isotopic effects. *Contr Miner Petrol* 44:219–230
- Hedman KM, Curry BB, Johnson TM et al (2009) Variation in strontium isotope ratios of archaeological fauna in the Midwestern United States: a preliminary study. *J Archaeol Sci* 36:64–73
- Hein JR, Yeh HW, Gunn SH et al (1993) Two major Cenozoic episodes of phosphogenesis recorded in equatorial Pacific seamount deposits. *Paleoceanography* 8:293–311
- Henderson J, Evans JA, Sloane HJ et al (2005) The use of oxygen, strontium and lead isotopes to provenance ancient glasses in the middle east. *J Archaeol Sci* 32:665–673
- Hill PA (1998) Bone remodeling. *Br J Orthop* 25:101–107
- Hillson S (1996) *Dental anthropology*. Cambridge University Press, Cambridge
- Hillson S (2005) *Teeth*. Cambridge University Press, Cambridge
- Hodell DA, Quinn RL, Brenner M et al (2004) Spatial variation of strontium isotopes ($^{87}\text{Sr}/^{86}\text{Sr}$) in the Maya region: a tool for tracking ancient human migration. *J Archaeol Sci* 31:585–601
- Hoogewerff J, Papesch W, Kralik M et al (2001) The last domicile of the iceman from Hauslabjoch: a geochemical approach using Sr, C and O isotopes and trace element signatures. *J Archaeol Sci* 28:983–989
- Hoppe KA (2004) Late pleistocene mammoth herd structure, migration patterns, and Clovis hunting strategies inferred from isotopic analyses of multiple death assemblages. *Paleobiology* 30:129–145
- Hoppe KA, Koch PL, Carlson RW et al (1999) Tracking mammoths and mastodons: reconstruction of migratory behavior using strontium isotope ratios. *Geology* 27:439–442
- Hoppe KA, Koch PL, Furutani TT (2003) Assessing the preservation of biogenic strontium in fossil bones and tooth enamel. *Int J Osteoarchaeol* 13:20–28
- Horstwood MSA, Evans JA, Montgomery J (2008) Determination of Sr isotopes in calcium phosphates using laser ablation inductively coupled plasma mass spectrometry and their application to archaeological tooth enamel. *Geochim Cosmochim Acta* 72:5659–5674
- Horwitz EP, Dietz ML, Fischer DE (1991) Separation and pre-concentration of strontium from biological, environmental, and nuclear waste samples by extraction chromatography using a crown ether. *Anal Chem* 63:522–525
- Horwitz EP, Chiarizia R, Dietz ML (1992) A novel strontium-selective extraction chromatographic resin. *Solvent Extr Ion Exchange* 10:313–336
- Hurst RW, Davis TE (1981) Strontium isotopes as tracers of airborne fly ash from coal-fired power plants. *Environ Geol* 3:363–367
- Jones S (1997) *The archaeology of ethnicity: constructing identities in the past and present*. Routledge, London
- Jowsey J (1961) Age changes in human bone. *Clin Orthop* 17:210–218
- Jowsey J, Kelley PJ, Riggs DL et al (1965) Quantitative micro-radiographic studies of normal and osteoporotic bone. *J Jt Bone Surg* 47a:785–806
- Katzenberg MA, Saunders SR (eds) (2008) *Biological anthropology of the human skeleton*, 2nd edn. Wiley, New York
- Knudson KJ (2008) Tiwanaku influence in the south central Andes: strontium isotope analysis and Middle Horizon migration. *Lat Am Antiq* 19:3–24
- Knudson KJ, Price TD (2007) Utility of multiple chemical techniques in archaeological residence mobility studies: case studies from Tiwanaku- and Chiribaya-affiliated sites in the Andes. *Am J Phys Anthropol* 132:25–39
- Knudson KJ, Torres-Rouff C (2009) Investigating cultural heterogeneity in San Pedro de Atacama, northern Chile, through biogeochemistry and bioarchaeology. *Am J Phys Anthropol* 138:473–485
- Knudson KJ, Price TD, Buikstra JE et al (2004) The use of strontium isotope analysis to investigate Tiwanaku migration and mortuary ritual in Bolivia and Peru. *Archaeometry* 46:5–18
- Knudson KJ, Williams SR, Osborn R et al (2009) The geographic origins of Nasca trophy heads using strontium, oxygen, and carbon isotope data. *J Anthropol Archaeol* 28:244–257
- Knudson KJ, Williams HM, Buikstra JE et al (2010) Introducing $\delta^{88}\text{Sr}/^{86}\text{Sr}$ analysis in archaeology: a demonstration of the utility of strontium isotope fractionation in paleodietary studies. *J Archaeol Sci* 39(9):2352–2364
- Koch PL, Fisher D, Dettman D (1989) Oxygen isotope variation in the tusks of extinct proboscideans: a measure of season of death and seasonality. *Geology* 17:515–519
- Koch PL, Halliday AN, Walter LM et al (1992) Sr isotopic composition of hydroxyapatite from recent and fossil salmon: the record of lifetime migration and diagenesis. *Earth Planet Sci Lett* 108:277–287
- Koch PL, Heisinger J, Moss C et al (1995) Isotopic tracking of change in diet and habitat use in African elephants. *Science* 267:1340–1343
- Koch PL, Tuross N, Fogel M (1997) The effects of sample treatment and diagenesis on the isotopic integrity of carbonate in biogenic hydroxylapatite. *J Archaeol Sci* 24:417–429
- Kohn MJ, Schoeninger MJ, Barker WW (1999) Altered states: effects of diagenesis on fossil tooth chemistry. *Geochim Cosmochim Acta* 63:2737–2747
- Kyle JH (1986) Effect of post-burial contamination on the concentrations of major and minor elements in human bones and teeth – the implications for paleodietary research. *J Archaeol Sci* 13:403–416
- Lambert JB, Simpson SV, Szpunar CB et al (1982) A comparative study of the chemical analysis of ribs and femurs in woodland populations. *Am J Phys Anthropol* 59:289–294
- Larsen CS (1997) *Bioarchaeology: interpreting behavior from the human skeleton*. Cambridge University Press, Cambridge

- Longinelli A (1984) Oxygen isotopes in mammal bone phosphate: a new tool for paleohydrological and paleoclimatological research? *Geochim Cosmochim Acta* 48:385–390
- McArthur JM, Thirlwall MF, Gale AS et al (1993) Strontium isotope stratigraphy for the Late Cretaceous: a new curve, based on the English chalk. In: Hailwood EA, Kidd RB (eds) *High resolution stratigraphy*. Geological Society Special Publication 70, pp 195–209
- Montanez IP, Banner JL, Osleger DA et al (1996) Integrated Sr isotope variations and sea-level history of Middle to Upper Cambrian platform carbonates: implications for the evolution of Cambrian seawater $^{87}\text{Sr}/^{86}\text{Sr}$. *Geologia* 24:917–920
- Montgomery J, Evans JA (2006) Immigrants on the Isle of Lewis – combining traditional funerary and modern isotope evidence to investigate social differentiation, migration and dietary change in the Outer Hebrides of Scotland. In: Gowland R, Knusel C (eds) *The social archaeology of funerary remains*. Oxbow Books, Oxford
- Montgomery J, Evans JA, Neighbour T (2003) Sr isotope evidence for population movement within the Hebridean Norse community of NW Scotland. *J Geol Soc Lond* 160:649–653
- Montgomery J, Evans JA, Powlesland D et al (2005) Continuity or colonization in Anglo-Saxon England? Isotope evidence for mobility, subsistence practice and status at West Heslerton. *Am J Phys Anthropol* 126:123–138
- Mulhern DM, Van Gerven DP (1997) Patterns of femoral bone remodeling dynamics in a Medieval Nubian population. *Am J Phys Anthropol* 104:133–146
- Mulhern DM, Van Gerven DP (2000) Rib remodeling dynamics in a skeletal population from Kulubnarti, Nubia. *Am J Phys Anthropol* 111:519–530
- Müller W, Fricke H, Halliday AN et al (2003) Origin and migration of the alpine iceman. *Science* 203:862–866
- Nehlich O, Montgomery J, Evans J et al (2009) Mobility or migration: a case study from the Neolithic settlement of Nieder-Mörlen (Hessen, Germany). *J Archaeol Sci* 36:1791–1799
- Nelson BK, DeNiro MJ, Schoeninger MJ et al (1986) Effects of diagenesis on strontium, carbon, nitrogen and oxygen concentration and isotopic composition of bone. *Geochim Cosmochim Acta* 50:1941–1949
- Nielsen-Marsh CM, Hedges REM (2000a) Patterns of diagenesis in bone I: the effects of site environments. *J Archaeol Sci* 27:1139–1150
- Nielsen-Marsh CM, Hedges REM (2000b) Patterns of diagenesis in bone II: effects of acetic acid treatment of the removal of diagenetic CO_3^{2-} . *J Archaeol Sci* 27:1151–1159
- Nowell GM, Horstwood MSA (2009) Comments on Richards et al., *Journal of Archaeological Science* 35, 2008 “strontium isotope evidence of Neanderthal mobility at the site of Lakonis, Greece using laser-ablation PIMMS”. *J Archaeol Sci* 36:1334–1341
- Oslett JS, Miller KG, Feigenson MD (1994) Oligocene-Miocene strontium isotopes: stratigraphic revisions and correlations to an inferred glacioeustatic record. *Paleoceanography* 9:427–443
- Parfitt AM (1983) The physiologic and clinical significance of bone histomorphometric data. In: Recker RR (ed) *Bone histomorphometry: techniques and interpretation*. CRC Press, Boca Raton
- Pin C, Bassin C (1992) Evaluation of the strontium-specific extraction chromatography method for isotopic analysis in geological materials. *Anal Chim Acta* 269:249–255
- Porder S, Paytan A, Hadly E (2003) Mapping the origin of faunal assemblages using strontium isotopes. *Paleobiology* 29(2):197–204
- Poszwa A, Ferry B, Dambrine E et al (2004) Variations of bioavailable Sr concentration and $^{87}\text{Sr}/^{86}\text{Sr}$ ratio in boreal forest ecosystems: role of biocycling, mineral weathering and depth of root uptake. *Biogeochemistry* 67:1–20
- Price TD, Blitz J, Burton J et al (1992) Diagenesis in prehistoric bone: problems and solutions. *J Archaeol Sci* 19:513–529
- Price TD, Johnson CM, Ezzo JA et al (1994) Residential mobility in the prehistoric Southwest United States: a preliminary study using strontium isotope analysis. *J Archaeol Sci* 21:315–330
- Price TD, Grupe G, Schröter P (1998) Migration in the bell beaker period of central Europe. *Antiquity* 72:405–411
- Price TD, Manzanilla L, Middleton WD (2000) Immigration and the ancient city of Teotihuacan in Mexico: a study using strontium isotope ratios in human bone and teeth. *J Archaeol Sci* 27:903–913
- Price TD, Burton JH, Bentley RA (2002) The characterization of biologically available strontium isotope ratios for the study of prehistoric migration. *Archaeometry* 44:117–135
- Price TD, Knipper C, Grupe G et al (2004) Strontium isotopes and prehistoric migration: the Bell Beaker Period in central Europe. *Eur J Archaeol* 7:9–40
- Price TD, Tiesler V, Burton JH (2006a) Early African diaspora in colonial Campeche, Mexico: strontium isotopic evidence. *Am J Phys Anthropol* 130:485–490
- Price TD, Wahl J, Bentley RA (2006b) Isotopic evidence for mobility and group organization among Neolithic farmers at the Talheim, Germany, 5000 BC. *Eur J Archaeol* 9(2):259–284
- Quade J, Cerling TE, Barry JC et al (1992) A 16ma record of paleodiet using carbon and oxygen isotopes in fossil teeth from Pakistan. *Chem Geol* 94:183–192
- Reynolds AC, Betancourt JL, Quade J et al (2005) $^{87}\text{Sr}/^{86}\text{Sr}$ sourcing of ponderosa pine used in Anasazi great house construction at Chaco Canyon, New Mexico. *J Archaeol Sci* 32:1061–1075
- Richards M, Harvati K, Grimes V et al (2008) Strontium isotope evidence of Neanderthal mobility at the site of Lakonis, Greece using laser-ablation PIMMS. *J Archaeol Sci* 35:1251–1256
- Richards M, Grimes V, Smith C et al (2009) Response to Nowell and Horstwood. *J Archaeol Sci* 36:1657–1658
- Ruggeberg A, Fietzke J, Liebetrau V et al (2008) Stable strontium isotopes ($\delta^{88}\text{Sr}/^{86}\text{Sr}$) in cold-water corals – a new proxy for reconstruction of intermediate ocean water temperatures. *Earth Planet Sci Lett* 269:570–575
- Sandford MK (1992) A reconsideration of trace element analysis in prehistoric bone. In: Saunders SR, Katzenberg MA (eds) *Skeletal biology and past peoples: research methods*. Wiley-Liss, New York
- Schoeninger MJ (1995) Stable isotope studies in human evolution. *Evol Anthropol* 4:83–98
- Schoeninger MJ, DeNiro MJ (1984) Nitrogen and carbon isotopic composition of bone collagen from marine and terrestrial animals. *Geochim Cosmochim Acta* 48:625–639

- Schour I, Massler M (1940) Studies in tooth development: the growth pattern of human teeth. *J Am Dent Assoc* 27 (1778–1792):1918–1931
- Schwarcz HP, Schoeninger MJ (2011) Stable isotopes of carbon and nitrogen as tracers for paleo-diet reconstruction. In: Baskaran M (ed) *Handbook of environmental isotope geochemistry*. Springer, Heidelberg
- Schweissing M, Grupe G (2003) Stable strontium isotopes in human teeth and bone: a key to migration events of the late Roman period in Bavaria. *J Archaeol Sci* 30:1373–1383
- Sealy JC, van der Merwe NJ, Sillen A et al (1991) $^{87}\text{Sr}/^{86}\text{Sr}$ as a dietary indicator in modern and archaeological bone. *J Archaeol Sci* 18:399–416
- Shemesh A (1990) Crystallinity and diagenesis of sedimentary apatites. *Geochim Cosmochim Acta* 54:2433–2438
- Sillen A (1981) Strontium and diet at Hayonim Cave. *Am J Phys Anthropol* 56:131–138
- Sillen A (1986) Biogenic and diagenic Sr/Ca in plio-pleistocene fossils of the Omo Shungura formation. *Paleobiology* 12:311–323
- Sillen A (1989) Diagenesis of the inorganic phase of cortical bone. In: Price TD (ed) *The chemistry of prehistoric bone*. Cambridge University Press, Cambridge
- Sillen A, Sealy JC (1995) Diagenesis of strontium in fossil bone: a reconsideration of Nelson et al. (1986). *J Archaeol Sci* 22:313–320
- Sillen A, Hall G, Armstrong R (1995) Strontium calcium ratios (Sr/Ca) and strontium isotopic ratios ($^{87}\text{Sr}/^{86}\text{Sr}$) of *Australopithecus robustus* and *Homo* sp. from Swartkrans. *J Hum Evol* 28:277–285
- Sillen A, Hall G, Richardson S et al (1998) $^{87}\text{Sr}/^{86}\text{Sr}$ ratios in modern and fossil food-webs of the Sterkfontein valley: implications for early hominid habitat preference. *Geochim Cosmochim Acta* 62:2463–2478
- Simonetti A, Buzon MR, Creaser RA (2008) In-situ elemental and Sr isotope investigation of human tooth enamel by laser ablation-(MC)-ICP-MS: successes and pitfalls. *Archaeometry* 50:371–385
- Slovak NM (2007) Examining imperial influence on Peru's central coast: isotopic and cultural analyses of Middle Horizon burials at Ancón. PhD Dissertation Thesis, Stanford University, Stanford
- Slovak NM, Paytan A (2009) Fisherfolk and farmers: carbon and nitrogen isotope evidence from Middle Horizon Ancón, Peru. *Int J Osteoarchaeol*. doi:10.1002/oa.1128
- Slovak NM, Paytan A, Wiegand BA (2009) Reconstructing middle horizon mobility patterns on the coast of Peru through strontium isotope analysis. *J Archaeol Sci* 36:157–165
- Smith BH (1991) Standards of human tooth formation and dental age assessment. In: Kelley MA, Larsen CS (eds) *Advances in dental anthropology*. Wiley-Liss, New York
- Stuart-Williams HLQ, Schwarcz HP (1997) Oxygen isotopic determination of climatic variation using phosphate from beaver bone, tooth enamel and dentine. *Geochim Cosmochim Acta* 61:2539–2550
- Tetelbaum SL (2000) Bone resorption by osteoclasts. *Science* 289:1504
- Thornton EK, Defrance SD, Krigbaum J et al (2010) Isotopic evidence for Middle Horizon to 16th century camelid herding in the Osmore valley, Peru. *Int J Osteoarchaeol*. doi:10.1002/oa.1157
- Towers J, Montgomery J, Evans J et al (2009) An investigation of the origins of cattle and aurochs deposited in the early Bronze Age barrows at Gayhurst and Irthlingborough. *J Archaeol Sci* 37:508–515
- Trickett MA, Budd P, Montgomery J et al (2003) An assessment of solubility profiling as a decontamination procedure for the $^{87}\text{Sr}/^{86}\text{Sr}$ analysis of archaeological human tissue. *Appl Geochem* 18:653–658
- Tung TA, Knudson KJ (2008) Social identities and geographical origins of Wari trophy heads from Conchopata, Peru. *Curr Anthropol* 49:915–925
- Turner BL, Kamenov GD, Kingston JD et al (2009) Insights into immigration and social class at Machu Picchu, Peru based on oxygen, strontium, and lead isotopic analysis. *J Archaeol Sci* 36:317–332
- van der Merwe NJ, Lee-Thorp JA, Thackeray JF et al (1990) Source-area determination of elephant ivory by isotopic analysis. *Nature* 346:744–746
- Vanhaecke F, De Wannemacker G, Moens L et al (1999) The determination of strontium isotope ratios by means of quadrupole-based ICP-mass spectrometry: a geochronological case study. *J Anal At Spectrom* 14:1691–1696
- Vanhaeren M, d'Errico F, Billy I et al (2004) Tracing the source of upper palaeolithic shell beads by strontium isotope dating. *J Archaeol Sci* 31:1481–1488
- Veizer J (1989) Strontium isotopes in seawater through time. *Annu Rev Earth Planet Sci* 1:141–167
- Vroon PZ, van der Wagt B, Koornneef JM et al (2008) Problems in obtaining precise and accurate Sr isotope analysis from geological materials using laser ablation MC-ICPMS. *Anal Bioanal Chem* 390:465–476
- Waight T, Baker J, Peate D (2002) Sr isotope ratio measurements by doublefocusing MC-ICP-MS: techniques, observations and pitfalls. *Int J Mass Spectrom* 221:229–244
- Wakabayashi T, Ohno T, Fukushi Y et al (2007) Simultaneous determination of mass-dependent isotopic fractionation and radiogenic isotope variation of Sr in geochemical samples. *Geochim Cosmochim Acta* 71:A1079
- Wang Y, Cerling TE (1994) A model of fossil tooth and bone diagenesis: implications for paleodiet reconstruction from stable isotopes. *Palaeogeogr Palaeoclimatol Palaeoecol* 107:281–289
- Weiner S, Bar-Yosef O (1990) States of preservation of bones from prehistoric sites in the Near East: a survey. *J Archaeol Sci* 17:187–196
- White CD, Spence MW, Stuart-Williams HLQ et al (1998) Oxygen isotopes and the identification of geographical origins: the valley of Oaxaca versus the valley of Mexico. *J Archaeol Sci* 25:643–655
- Wright LE (2005) Identifying immigrants to Tikal, Guatemala: defining local variability in strontium isotope ratios of human tooth enamel. *J Archaeol Sci* 32:555–566
- Wright LE, Schwarcz HP (1996) Infrared and isotopic evidence for diagenesis of bone apatite at Dos Pilas, Guatemala: palaeodietary implications. *J Archaeol Sci* 23:933–944
- Yurtsever Y, Gat JR (1981) Atmospheric waters. In: Gat JR, Gonflantini R (eds) *Stable isotope hydrology: deuterium and oxygen-18 in the water cycle*. Technical report series no. 210. International Atomic Energy Agency, Vienna

Chapter 36

Sources of Lead and Its Mobility in the Human Body Inferred from Lead Isotopes

Brian L. Gulson

Abstract Compared with studies applying the lead isotope method to environmental questions, those involving humans (and animals) are small in number. This brief review outlines some of the applications of the method, especially to those focussed on pregnancy, a time during which increased bone turnover associated with calcium requirements results in release of lead from the maternal skeleton and the lead can also be transferred to the infant. Thus, sources of lead to blood can be considered as external (environmental) and internal (skeletal).

36.1 Introduction

Lead (Pb) is a highly toxic element, causing a variety of detrimental effects at low dose levels. It is the most studied toxic metal but actual mechanisms to account for neurological damage are still not understood. Comprehensive reviews of Pb have been undertaken by the International Agency for Research on Cancer (IARC 2006), the US Agency for Toxic Substances Disease Registry (ATSDR 2007) and the US Environmental Protection Agency (EPA 2006). Acute or short-term exposure to high levels of Pb in humans can cause brain damage, kidney damage, and gastrointestinal distress. Chronic or long-term exposure to Pb in humans results in effects on the blood, central nervous system, blood pressure, kidneys, and Vitamin D metabolism. Children are particularly sensitive to the

chronic effects of Pb, with diminished cognitive development, reduced growth and other effects reported. Reproductive effects, such as decreased sperm count in men and spontaneous abortions in women, have been associated with high Pb exposure. The developing fetus is at particular risk from maternal Pb exposure, with low birth weight and slowed postnatal neurobehavioral development noted. Human studies are inconclusive regarding Pb exposure and cancer (US EPA 2007).

36.2 Potential Exposure

Humans may be exposed to Pb from several sources and via several pathways (Fig. 36.1). Industrial exposure arises from mining and smelting, battery manufacture, recycling of products such as batteries and electronic waste (e.g., Zheng et al. 2008), and ship repair and demolition. Exposure from environmental activities that can generate Pb dust and/or fumes include: restoration of homes, boats, cars and furniture coated with lead-based paints; pottery; soldering; Pb casting; and burning of Pb-stabilised plastics or materials coated with lead-based paints. Other potential sources of Pb include: ceramic ware, PVC blinds, toys, seasonal decorations, some “traditional” medicines and supplements (Cooper et al. 2007), some cosmetics and hair dyes, and jewellery (Weidenhamer and Clement 2007).

Although Pb from gasoline additives and paint were major sources of direct exposure in the past, they may now be indirect sources of exposure as the Pb could still be present in soil and house dust and be resuspended by wind action (Laidlaw and Filippelli 2008). Lead from food may contribute variable

B.L. Gulson (✉)
Graduate School of the Environment, Macquarie University,
Sydney, NSW 2109, Australia

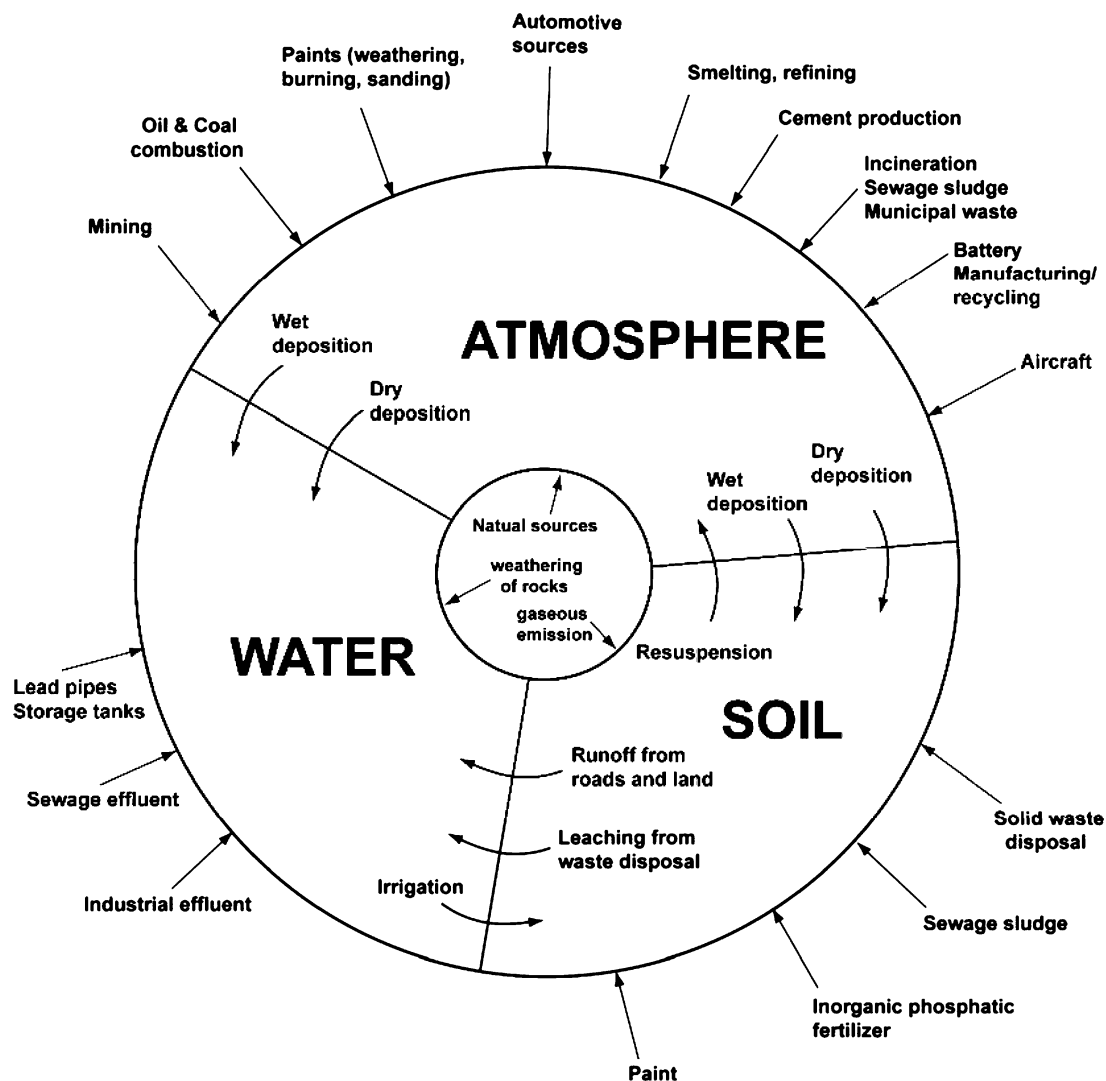


Fig. 36.1 Transport pathways for Pb in the environment [amended from US Environmental Protection Agency 2006 and Zabel 1993; with permission from US EPA]

amounts of Pb to blood lead (PbB), the currently accepted biomarker of exposure, depending on both amounts of Pb and age of the individual. Lead in drinking water is commonly included in dietary intakes but may be a significant contributor of Pb by itself (Renner 2010). Phasing out of gasoline Pb, removal of Pb from canned foods, and increased public awareness of the hazards and health effects of Pb has resulted in a decline in PbB levels in U.S. children aged 1–5 years from a geometric mean of ~ 15 $\mu\text{g}/\text{dL}$ in 1976–1980 to ~ 1 – 2 $\mu\text{g}/\text{dL}$ (2 $\mu\text{g}/100$ mL) in the 2000–2004 period shown by the National Health and Nutrition Examination Surveys (NHANES; ATSDR

2007). Similar declines in PbB levels have been observed in several countries.

Although recognised as a critical source of exposure in the 1980s, house dust has emerged as an important contributor to PbB, especially in children (Lanphear and Roghmann 1997; Lanphear et al. 1998, 2002, 2005a, b). Several new studies have shown a strong association between PbB of children and interior dust Pb loading and this association will be reflected in hand Pb (Manton et al. 2000). The mouthing behaviour of young children, coupled with the ease with which they absorb and retain Pb, make children more vulnerable to Pb exposure than adults.

36.3 Biomarkers of Exposure

Lead may enter the body via inhalation, ingestion or dermal pathways. Once in the body it is distributed to various organs via blood (Fig. 36.2). Lead leaves the body primarily through faeces and urine. Lead in blood is primarily in the red blood cells (~99%) rather

than the plasma (US EPA 2006). In adults, more than 90% of the total body burden of Pb is found in the skeleton whereas bone Pb accounts for ~70% of the body burden in children (US EPA 2006). Approximately 15% of circulating Pb per day is incorporated into bone (Rabinowitz 1991) where it substitutes for calcium in hydroxyapatite. Lead is not distributed uniformly in bone.

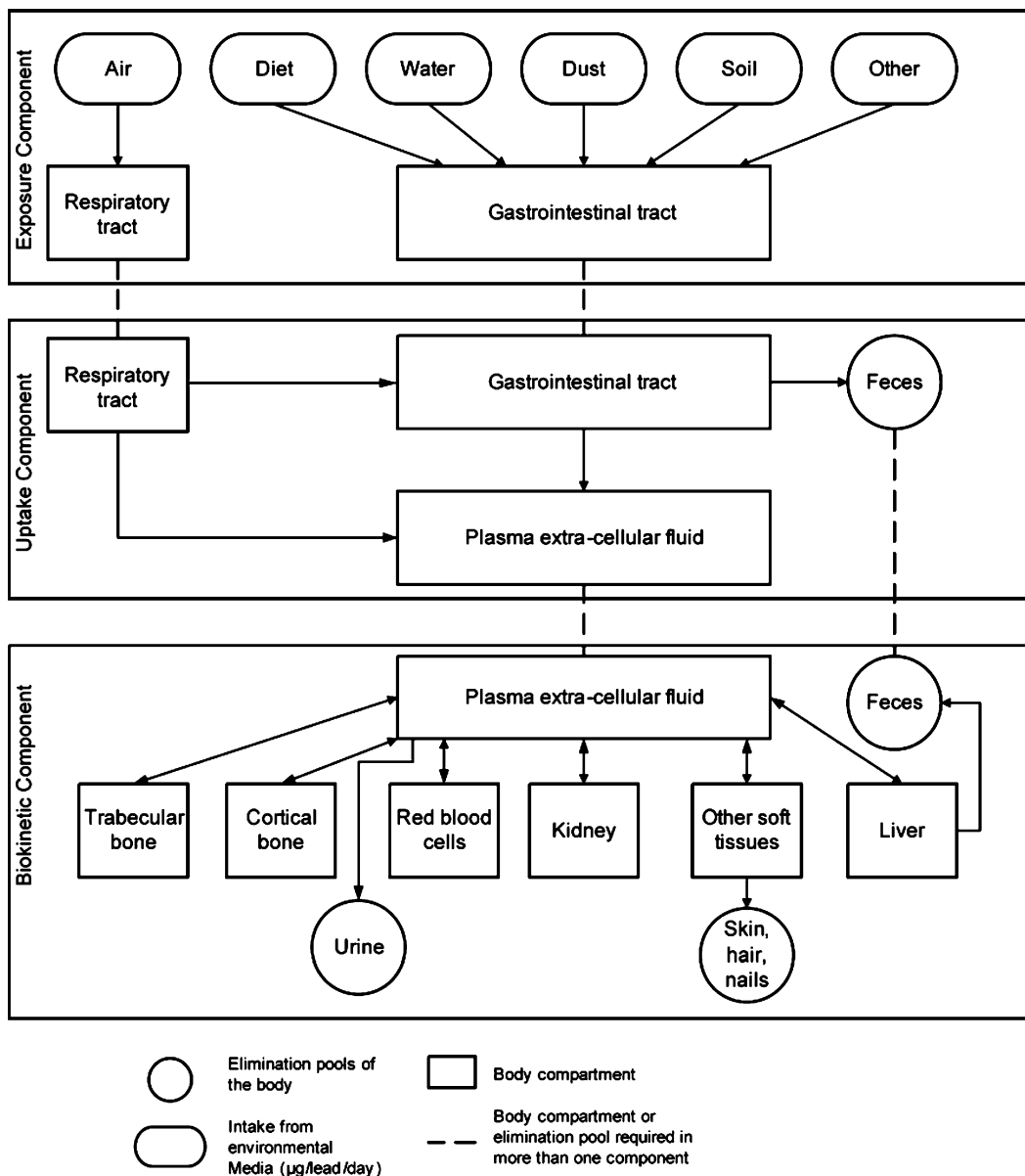


Fig. 36.2 Structure of the integrated exposure uptake biokinetics model for lead in children (amended from the US Environmental Protection Agency 2006, with permission from US EPA)

Table 36.1 Common biomarkers of Pb exposure (with permission from Ayres et al. (2010))

Medium	Methods of analysis	Parameter	Advantages	Disadvantages
Blood Pb	GFAAS/ICP-MS/TIMS	µg/dL	Accepted biomarker; easily collected (venous recommended); 10 µg/dL is considered to be the “level of concern”	Indicator of short term exposure (<100 days)
Urine	GFAAS/ICP-MS/TIMS	µg/L	Non-invasive; about 10% of PbB value; indicator of very short term exposure although used in chelation provocation testing	No value guidelines; potential for contamination especially in young children
Plasma/serum	GFAAS/LA-ICP-MS/TIMS	µg/L	Potentially more interesting toxicologically; <0.3% of PbB value	No guidelines; easily contaminated during analysis; problems of hemolysis
Bone	K α -XRF	µg/g bone mineral	Non-invasive; indicator of long-term exposure; can measure trabecular and cortical bone to provide data on different exposures	No guidelines; limited access to XRF units; problems at low bone Pb levels; length of time of measurement (~30 min), potential movement of patient
Teeth	GFAAS/ICP-MS/TIMS	µg/g	Non-invasive; indicator of long-term exposure; can measure enamel and dentine to provide data on different exposures, especially in deciduous teeth	No guidelines; different tooth types can have different Pb concentrations
Nails	GFAAS/ICP-MS/TIMS	µg/g	Potential longer period of exposure (months)	No guidelines; easily contaminated from exogenous sources
Hair	GFAAS/ICP-MS/TIMS	µg/g	Potential longer period of exposure (months)	No guidelines; easily contaminated from exogenous sources
Sweat	GFAAS/ICP-MS/TIMS	µg/g	Potential indicator of short term exposure	No guidelines; limited data; easily contaminated in collection
Breast milk	GFAAS/ICP-MS/TIMS	µg/L	Potential indicator of body burden and short term exposure	No guidelines; limited data; easily contaminated in collection and analysis

GFAAS graphite furnace atomic absorption spectroscopy; *LA-ICP-MS* Laser ablation inductively coupled plasma mass spectrometry; *TIMS* thermal ionization mass spectrometry; *XRF* X-ray fluorescence

Various biomarkers are listed in Table 36.1 and some discussion of half lives (or residence time) of Pb in these media is given in the Sect. 36.6.8. The currently accepted biomarker of exposure is PbB. At present a value of 10 µg/dL (0.48 µm/L) is taken as a so called “level of concern” but it is recognized that PbB may only reflect primarily recent exposure (e.g., <30 days; Rabinowitz et al. 1976). In spite of the concerns about PbB reflecting recent (acute) exposure, stable isotope studies show that 40–70% of Pb in blood is derived from endogenous sources such as the skeleton (Manton 1985; Gulson et al. 1995a; Smith et al. 1996) and for environmentally exposed subjects, an equilibrium between skeletal Pb and PbB is reached in a matter of months (Gulson et al. 1995a) (Fig. 36.5, this paper).

The use of lead isotopes in teeth are described in more detail in Sect. 36.6.2 although tooth Pb measurements have declined in popularity in recent years as

there is some uncertainty in the interpretation of the results (Gulson et al. 2004a).

Evaluation of the use of urine instead of blood as an indicator of Pb exposure, especially in infants, showed a high correlation (R^2 0.98) between the blood and “spot” and 24-h urine collections, indicating rapid isotopic equilibrium between blood and urine (Gulson et al. 1998a). Spot urines can reflect Pb from the most recent meal or from doses of tracer (Rabinowitz et al. 1980). Similar conclusions were reached earlier by Rabinowitz et al. (1976) and in the Omaha study by Angle et al. (1995) and confirmed later in Omaha by Manton et al. (2003). Urine can be considered filtered blood plasma. However, Pb concentrations in blood and in urine are only weakly related and concentrations of Pb in urine cannot be used to predict concentrations of Pb in blood, particularly at the lower range of exposures, for example, at PbB concentrations less than 10 µg/dL.

36.4 The Pb Isotope Method in Environmental Health Investigations

In contrast to the widespread use of Pb isotopes in the earth sciences for more than 40 years and their increased application in more recent decades for environmental investigations, the number of environmental health studies focussed on humans is limited. This is in spite of the demonstrated utility of the approach in the pioneering studies of Rabinowitz et al. (1973, 1974, 1976, 1977, 1980) and Manton (1973) in the 1970s. Some of the possible reasons for this are the cost and expertise required for the analyses, the reluctance of researchers to work on human samples, and limited collaboration between the medical fraternity and other disciplines.

This brief review will be restricted to an outline of the use of Pb isotopes in “modern-day” humans as a more detailed review of this topic has been described in Gulson (2008). Here a summary of some of the different areas of application will be mentioned and examples especially focussed on mobilisation of Pb in the body will be provided.

The Pb isotope method makes use of the natural variations, arising from radioactive decay throughout geological time, in abundances of three of four Pb isotopes and relative concentrations of Pb, Th and U and the time when the ore was formed. Lead has four naturally-occurring isotopes three of which are the stable end products of radioactive decay of uranium and thorium: ^{206}Pb is derived by radioactive decay from ^{238}U , ^{207}Pb from ^{235}U , and ^{208}Pb from ^{232}Th . The other low abundance isotope, ^{204}Pb (approximately 1%), has no known radioactive parent and is used as a reference isotope. The data are presented as ratios of abundance of one to the other, such as $^{208}\text{Pb}/^{204}\text{Pb}$, $^{207}\text{Pb}/^{204}\text{Pb}$, and $^{206}\text{Pb}/^{204}\text{Pb}$, or any combinations of these. In the earlier days of use of Pb isotopes, because of the difficulty in measurement of the low abundance ^{204}Pb isotope, the data were reported as $^{206}\text{Pb}/^{207}\text{Pb}$ ratios and this is the case for isotopic analyses by ICP-MS (see below).

Because of radioactive decay, Pb mineral accumulations (mines, deposits) of different geological age have different isotope ratios. For example, the geologically-ancient massive sulphide Pb-Zn-Ag Broken Hill and Mt Isa deposits in Australia formed about

1,800 million years ago and have a $^{206}\text{Pb}/^{204}\text{Pb}$ ratio of 16.0 or 16.1 respectively. In contrast, geologically younger deposits of similar composition in eastern Australia, western Tasmania and many countries around the world that were formed 300–500 million years ago have much higher $^{206}\text{Pb}/^{204}\text{Pb}$ ratios (e.g., 18.1). These large isotopic differences between Australia and many other countries allow for definitive studies to be undertaken.

36.5 Analytical Methods

Current methods for high precision Pb isotope analyses employ either thermal ionization mass spectrometry (TIMS) or multi-collector inductively coupled plasma mass spectrometry (MC-ICP-MS). The relative standard deviations for isotopic ratios obtained by these methods are usually better than 0.0X% (Komárek et al. 2008); ICP-QMS is routinely employed in environmental studies but interpretations are constrained by the poorer precision compared with TIMS or MC-ICP-MS, including inability to obtain reliable data for the ^{204}Pb isotope. Accuracy and precision for isotope ratios measured by ICP-QMS range from 0.1 to 0.5% (Komárek et al. 2008). Although the high temperature conditions in the plasma of the ICP-MS approach theoretically allows analysis without chemical separation, under real conditions, to obtain high precision data, it is necessary to undertake a limited sample treatment (Chillrud et al. 2005). In low resolution mode, ICP sector-based or sector field (ICP-SFMS) and time-of-flight ICP-MS (TOF-ICP-MS) can obtain isotope ratio precision of <0.05% (Komárek et al. 2008).

36.6 Examples of Use of Pb Isotopes in Environmental Health

The successful application of Pb isotopes in environmental investigations requires a number of conditions to be satisfied which include (i) knowledge (data) of relevant potential sources, (ii) the sources need to be isotopically distinct (i.e., the isotopic separation between the sources needs to be significantly larger than the observed variability within a source), with the

larger the separation the more advantageous to obtain meaningful results, and (iii) isotopic data with precision significantly higher than differences between sources. For example, the use of Pb isotopes has seen limited application in human studies in the U.S. because of overlapping sources especially from paint samples, and difficulties in assigning sources at PbB concentrations below 5 µg/dL. Thus Manton et al. (2003) suggested that the success of source apportionment studies using Pb isotopes in humans in the US is about 1 in 5.

Potential sources of Pb in many studies are rarely simple to identify and characterize and are usually a mixture. There is always the concern that an important major source has been overlooked and hence characterizing source(s) needs to be site/person specific. The most common method of identifying sources is to use isotopic data from ore deposits but significant contributions of Pb may also derive from materials such as coal. There is also the problem that even within one country, Pb ore used in products may have quite different isotopic signatures, as noted above, and result in complex mixtures. Use of air particulate data, such as that collected by Bollhöfer and Rosman (2001), are an important data set to consider in source and pathways investigations.

36.6.1 Sources and Pathways of Pb in Urban Environments

Investigations of sources and pathways in urban and mining/smelting environments represent the bulk of applications of the Pb isotope method. With respect to urban environments, the largest isotopic study undertaken so far was The Isotopic Lead Experiment carried out in Turin and surrounding areas (Facchetti 1990). In this study, Pb in gasoline with isotopes characteristic of those from a geologically-younger European-type source was replaced with tetraethyl Pb manufactured from the geologically-old Broken Hill mine in Australia.

Other isotopic measurements of blood and environmental samples include those from California (Yaffe et al. 1983; Gwiazda and Smith 2000), Washington D.C. (Tera et al. 1985), Boston (Rabinowitz 1987), U.K. (Campbell and Delves 1989; Viczian et al. 1990; Delves and Campbell 1993), Saudi Arabia (al-Saleh et al. 1993), Mexico City (Chaudhary-Webb et al.

1998), Ecuador (Counter et al. 2000), Armenia (Kurkjian and Flegal 2003), Paris (Glorennec et al. 2010), Shanghai (Liang et al. 2010) and Australia (Gulson et al. 1995a, b, 1996a, 1997b, 1998b, 2003; James and Gulson 1999). Isotopic measurements of hair from Japanese women collected over the twentieth century were correlated with differing and changing sources of contamination (Matsumoto and Yoshinaga 2010).

Keinonen (1992) found the Pb isotope ratios in human liver, lung, and bone from individuals who died between 1976 and 1979 reflected the large Pb emissions from the incinerators and Pb smelters in the Helsinki area in the 1960s and 1970s.

36.6.2 Sources and Pathways of Pb in Mining and Smelting Communities

Investigations of blood and environmental samples from mining and smelting communities include those of mine concentrates in Lima Peru (Naeher et al. 2003), of smelter emissions in Omaha Nebraska (Angle et al. 1995; Manton et al. 2000), of mining contamination in Broken Hill NSW Australia (Gulson et al. 1994a, b, 1996b, c, d), of mining contamination in Woodlawn NSW Australia (Chiaradia et al. 1997a), of smelting contamination in Port Pirie South Australia (Gulson et al. 1996a) and the Illawarra region NSW (Chiaradia et al. 1997b), and uranium mining in the Northern Territory Australia (Gulson et al. 2005).

Lead isotopic analyses of teeth can provide exposure information in mining and smelting environments and in contrast to blood analyses which generally reflect recent exposure to Pb, isotopic analyses of teeth (and bone) provide a longer term integration of exposure. For example, in children from the Broken Hill Pb mining community, Gulson and Wilson (1994) and Gulson (1996a) showed that the source of Pb from the incisal (enamel) sections was different from the source of Pb in the cervical (dentine) sections of deciduous teeth reflecting the change in Pb from in utero exposure to early childhood (Fig. 36.3). Based on changes in the isotopic composition of enamel and dentine in deciduous teeth sections from the Broken Hill mining community children, Gulson (1996a) estimated that approximately 2–3% Pb is added to dentine per year. A follow-up study of teeth from Broken Hill

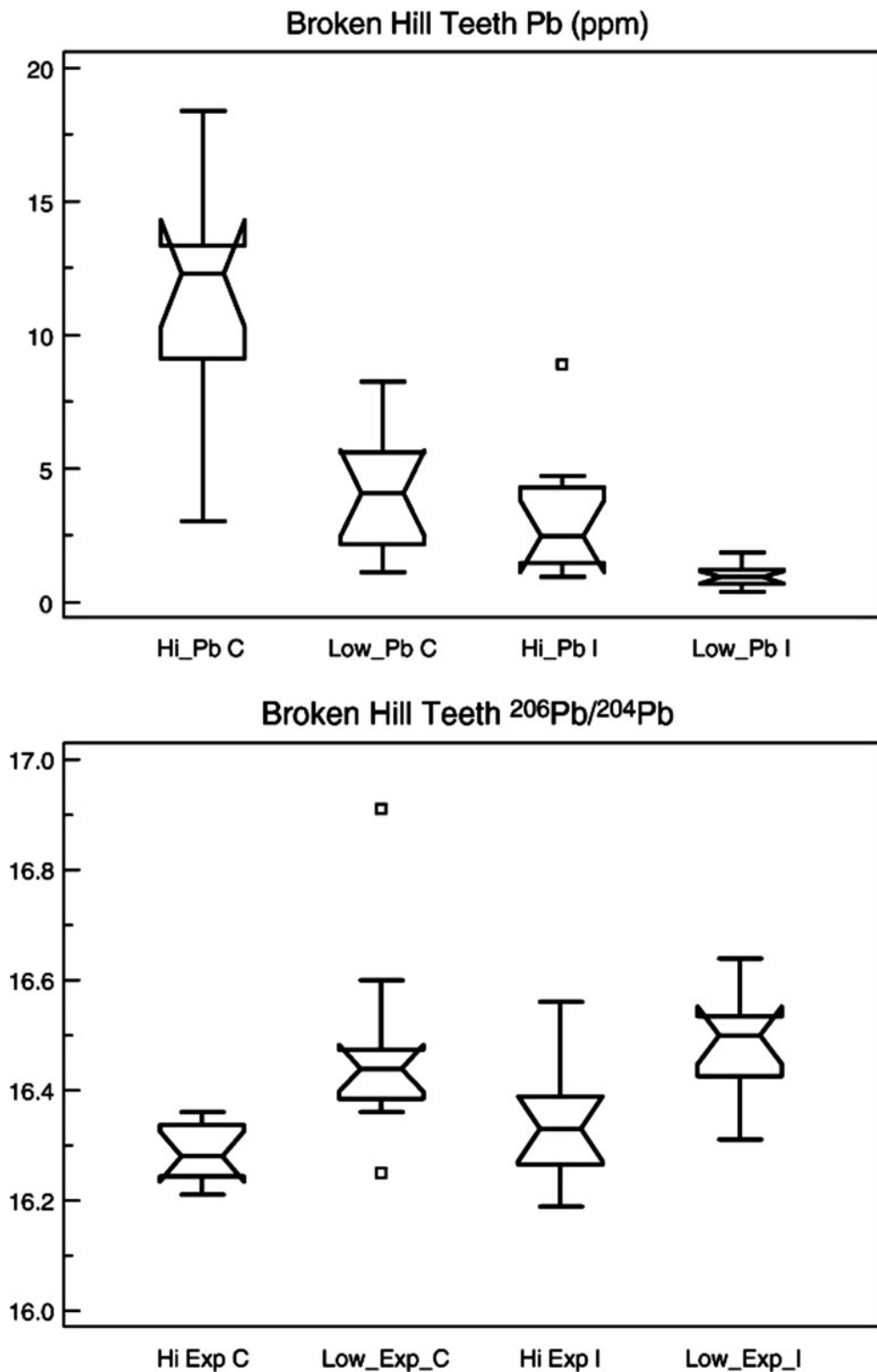


Fig. 36.3 Notched box plots for deciduous teeth from Broken Hill children who had suffered differing lead exposure (Exp). I denotes incisal (enamel) and C cervical (dentine-rich) parts of the teeth. (a) Pb concentrations in the teeth showing the large differences between exposed (Hi Exp) and less exposed children

(Low_Exp). (b) Isotopic analyses of the teeth with the most exposed sections showing the highest amount of lead coming from the Broken Hill ore the value of which is 16.0 (redrawn from Gulson 1996a; with permission from Elsevier)

children has been undertaken using MC-ICP-MS by Arora et al. (2006). Other investigations using Pb isotopes in teeth include those at a primary zinc-Pb smelter community at North Lake Macquarie, New South Wales, Australia (Gulson et al. 2004a) and to evaluate delayed visual maturation of the optic nerve (blindness) in children (Gulson et al. 1998d). Lead isotopes can be used to estimate exchanges in Pb in teeth from adults and for forensic investigations (Gulson et al. 1997a).

36.6.3 Biokinetics of Pb

The most significant contributions of Pb isotopes to human studies were the early work of Rabinowitz and Manton. The stable isotope investigations of Rabinowitz and colleagues in the early 1970s provided the basis of pharmacokinetic models for Pb and complemented the earlier work of, for example, Kehoe (1969), using radioactive isotopes.

In the Rabinowitz investigations (1973, 1974, 1976, 1977, 1980), 5 healthy male volunteers were studied in the metabolic unit of the Veterans Administration Wadsworth Hospital Centre in Los Angeles for periods from 10 to 210 days. Enriched stable isotopes of Pb (^{204}Pb and/or ^{207}Pb) were added to the diet (68–204 $\mu\text{g}/\text{day}$ of tracer) and administered over 10–121 days; they were further monitored for up to 285 days. This was done in an effort to distinguish ingested, dietary Pb, from inhaled aerosol Pb. During this whole time they ate a constant diet in a metabolic balance ward. Their diets were designed to be relatively low in Pb, so that with the addition of the tracer, their total Pb intake was close to their pre-study levels. There was concern at that time of some unknown homeostasis for Pb, so the men were kept in steady state, with minimal change in total PbB, while Pb fluxes were measured. Their total intake was considered representative at the time, but nowadays would be thought excessive. Indeed, their PbB levels, all above 17 $\mu\text{g}/\text{dL}$ and averaging 19 $\mu\text{g}/\text{dL}$, reflected the prevalence then of leaded fuels and Pb-soldered canned foods in the US. Comprehensive sampling and isotopic analysis of air, duplicate diets, total urine and faeces, blood, hair, and nails was undertaken on regular basis and occasionally bone, bile and sweat. From these data, Rabinowitz and colleagues proposed a parsimonious 3-compartment model for

Pb (Rabinowitz 1998; Fig. 36.2 of this paper) which has been gradually refined over the decades as more information has become available.

The meticulous investigations of Manton (1973, 1977, 1985, 1992) approached biokinetics of lead in a different way by carefully monitoring the isotopic composition of blood (and urine) of 1 male adult and 2 females over several years. Several bone biopsies from the male were also measured. Besides illustrating the changes in PbB over time and the importance of careful laboratory practice, Manton's work pointed to the potential mobilisation of lead from bone during times of physiological stress, such as pregnancy, rather than the bone acting as a stable repository of lead.

36.6.4 Contribution of Bone Pb to Blood Pb

Knowledge of the contribution of bone Pb to PbB is essential in pharmacokinetic studies and where subjects may have been exposed to past elevated Pb levels as this Pb may be mobilised during times of physiological stress, discussed below. "Isotope ratios detect shifts in the sites where bone is being resorbed. As such they are unique and can detect processes that are invisible to biomarkers and bone mineral density measurements" (Manton et al. 2003). Data for estimates of skeletal contribution to PbB are limited to stable and radiogenic isotopic studies and, in more recent times, bone XRF measurements.

Earlier estimations of bone Pb to PbB were about 45% (Rabinowitz et al. 1976) and about 70% (Manton 1985). In a study of 5 patients who underwent total hip or knee joint replacement, Smith et al. (1996) determined that the skeleton contributed 40–70% of the Pb in the blood of these subjects. In a study of 3 children whose houses were undergoing remediation, Gwiazda et al. (2005) estimated bone Pb contribution to PbB concentration in 2 children was about 40–65% and in the other child the contribution was >90%. In the studies of Gulson et al. (1995a, 1997b, 1998b, 1999a, b, 2001, 2003, 2004b) participants were female immigrants to Australia of child-bearing age (18–35 years) and their children (5–11 years) whose skeletal Pb isotopic composition was determined to be different from that in their current Australian environment (Fig. 36.4). The estimation of skeletal Pb isotopic composition was based

on analysis of a blood sample as soon as possible after the subject arrived in Australia and/or tooth analyses (Gulson and Gillings 1997). The mean contribution of skeletal Pb to PbB was the same for the female adults and children at about 50% with a range from 40 to 70%.

36.6.5 Mobilisation of Pb from the Maternal Skeleton

More than 90% of the Pb stored in bones has a very slow turnover and there is potential for this seques-

tered Pb to be mobilised at an accelerated rate during times of physiological stress associated with enhanced bone remodelling such as pregnancy and lactation, menopause, extended bed rest, hyperparathyroidism, and weightlessness. This large pool of Pb in adults can serve to maintain elevated PbB levels long after exposure has ended.

Investigations carried out in Australia were based on the fact that the Pb isotopic composition or “fingerprint” in long-term Australian residents was markedly different from that in subjects from most other countries (Fig. 36.4). When people moved to Australia there was an exchange in the Pb isotopic composition from their home countries, reflected by the Pb in their skeletons, and that prevailing in Australia. The isotopic changes were exponential and they gradually reached an equilibrium generally after about 3 months residence in Australia, which is the mean life of red blood cells in the body (Fig. 36.5). The changes with time were consistent for female adults and their children and allowed the rate of clearance from blood (half-life of Pb in blood) to be estimated (as described below). If a woman conceived and Pb was released from her skeleton, the isotopic composition of this Pb would reflect that from her country of origin and, in most cases, this would be an increase in $^{206}\text{Pb}/^{204}\text{Pb}$ ratio (Fig. 36.6). Hence, by monitoring migrant subjects who conceived after arrival in Australia, it was possible to detect changes in isotopic composition and PbB during pregnancy and the post-partum period arising from increased mobilization of skeletal Pb, an approach suggested earlier by Manton (1977, 1985) and later by Rabinowitz (1991).

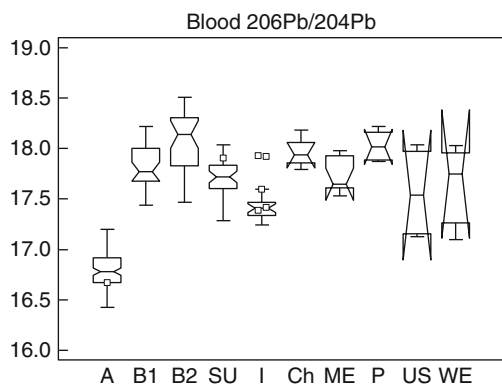


Fig. 36.4 Notched box plots of the $^{206}\text{Pb}/^{204}\text{Pb}$ ratios for blood samples from female subjects of child-bearing age from different countries showing significant differences between subjects from these countries and Australian subjects. A Australia; B1 Albania, Bulgaria, Romania, Slovakia; B2 Bosnia, Croatia, Serbia; SU former Soviet Union; I Bangladesh, India, Pakistan; Ch China; ME Iran, Iraq, Lebanon, and Turkey; US USA, Mexico, Chile and Colombia; WE Western Europe U.K

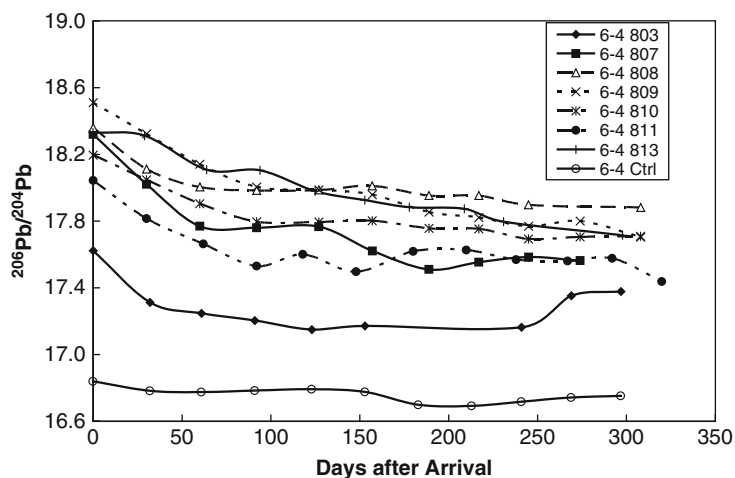
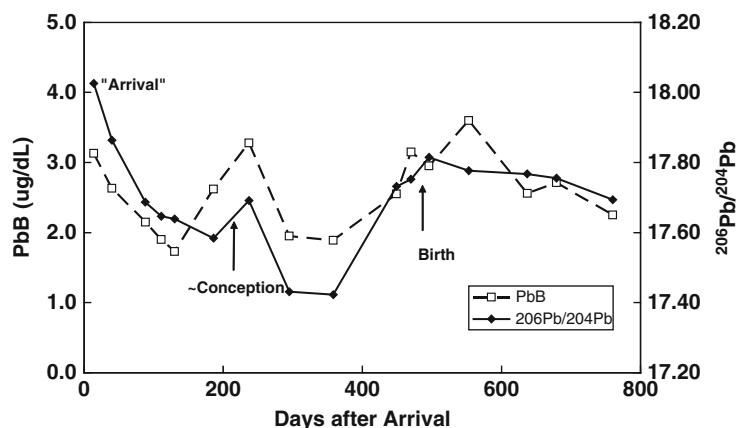


Fig. 36.5 Changes in blood $^{206}\text{Pb}/^{204}\text{Pb}$ ratio over time in for non-pregnant female adult migrants from Europe to Australia compared with an Australian control subject. The day 0 values reflect the isotopic composition of Pb prevailing in the skeleton and the decreasing values for migrants, the exchange of skeletal Pb with Australian Pb. An equilibrium is reached usually after about 3 months, the life of the red blood cell, host to most of the Pb in blood

Fig. 36.6 Lead in blood concentration (PbB $\mu\text{g}/\text{dL}$) and $^{206}\text{Pb}/^{204}\text{Pb}$ ratio for a new arrival in Australia from Eastern Europe who conceived approximately 7 months after arrival. There are the decreases reflecting exchange between skeletal Pb and that prevailing in the Australian environment until the subject conceived. Thereafter the increases are attributed to extra Pb being remobilised from the skeleton during pregnancy and lactation



In the Australian studies, Gulson and colleagues monitored two immigrant cohorts with the same design and monitoring protocols longitudinally during pregnancy and 6 months postpartum over a 10-year period. The first cohort (Gulson et al. 1997b, 1998b) comprised 16 immigrant, 6 long-term Australian subjects, and 8 non-pregnant immigrant controls. Blood and urine samples were collected monthly and environmental samples including 6-day duplicate diets were collected quarterly. Changes for an individual monitored for over 2 years are shown in Fig. 36.6. Skeletal contribution to PbB, based on the isotopic composition for the immigrant subjects, increased in an approximately linear manner during pregnancy with mean increases in skeletal contribution for each individual during pregnancy varying from 26 to 99%. Skeletal Pb contribution to PbB was significantly greater ($p < 0.001$) during the post-pregnancy period than during the 2nd and 3rd trimesters. The contribution of skeletal Pb to PbB during the post-pregnancy period remained essentially constant at the increased level of Pb mobilization, although the duration of breastfeeding varied from 1 week to more than 6 months. The increased contribution of skeletal Pb to PbB during the post-pregnancy period was attributed to increased mobilization of Pb from maternal skeletal stores during lactation, possibly related to the low mean calcium intake (approximately 500 mg Ca/day) of most of their subjects.

In a follow-up study with a different immigrant cohort of 12 women supplied with calcium supplementation at the recommended level of approximately 1,000 mg Ca/day, Gulson et al. (2004b) found increased mobilization of Pb occurred in the 3rd

trimester rather than in the 2nd trimester observed with first cohort. In addition, the extra flux released from bone during late pregnancy and postpartum varied from 50 to 380 μg Pb (geometric mean, 145 μg Pb) compared with 330 μg Pb in the previous cohort (Gulson et al. 1999a, b). Gulson et al. (2004b) suggested that for subjects whose intake of calcium was sufficient, the delay in increase in PbB and halving of the extra flux released from bone during late pregnancy and postpartum may provide less Pb exposure to the developing fetus and newly born infant.

In a study of 12 women from the 2nd trimester of pregnancy until at least 8 months after delivery, Manton et al. (2003) concluded that bone resorption rather than dietary absorption controlled changes in PbB; PbB concentrations decreased in early pregnancy and rose during late pregnancy which they attributed to changes in bone resorption with decoupling of trabecular and cortical bone sites. The authors proposed that during lactation the whole skeleton underwent resorption and the PbB of nursing mothers continued to rise, reaching a maximum 6–8 months after delivery.

36.6.6 Transplacental Transfer of Pb

Isotopic analyses also provide information on the maternal-to-foetal transfer of Pb and this process appears to be related partly to the mobilization of Pb from the maternal skeleton. Besides direct evidence from cynomolgus monkeys (Inskip et al. 1996; Franklin et al. 1997; O'Flaherty et al. 1998), a 0.99

correlation in Pb isotopic ratios for maternal and cord blood (Manton 1985; Gulson et al. 1997b, 1998b) and similarity of isotopic ratios in maternal blood and that in blood and urine of newly-born infants provide strong evidence of the placental transfer (Gulson et al. 1999a, b). Using ICP-MS, Levesque et al. (2003) reported that cord blood $^{206}\text{Pb}/^{207}\text{Pb}$ ratios of Inuit and southern Quebec newborn infants was different and Pb shot used for game hunting was an important source of Pb exposure in the Inuit population. Patel et al. (2008) found the isotopic profiles in blood of Alaskan Native women significantly different from those in lead shot but the source of the lead in the shot was probably not from the manufacturer that they tested.

36.6.7 Lead in Breast Milk to Pb in Blood, Urine and Diet of the Infant and Mother

Breast milk can also be a pathway of maternal excretion of Pb. However, given the very low Pb concentrations and analytical difficulties arising from high fat contents in breast milk, such analyses require careful attention (Gulson et al. 1998c). Newly-born infants and their mothers from the migrant study monitored for 6 months postpartum showed that the major sources of Pb in breast milk were from the maternal bone and diet (Gulson et al. 1998c).

36.6.8 Rates of Exchange of Pb in Blood of Newly-Born Infants and Mothers

As mentioned above, the changes in Pb isotopic composition of blood over time for migrant mother and their newly-born infants can be used to determine the clearance rates of Pb from blood (Gulson et al. 1999a, b). The rate of exchange ($t/2$) for the migrant infants, of Pb in blood derived from the mother during pregnancy and the Pb from the current environment, was calculated using a linear function and ranged from 65 to 131 (mean and standard deviation, 91 ± 19) days. The half lives for the exchange of skeletal and

environmental Pb for 7 of the 8 female adults prior to significant mobilization of Pb from the maternal skeleton, ranged from 50 to 66 (59 ± 6) days.

36.6.9 Bone Turnover in the Elderly Using Bisphosphonate Treatment

As bone resorption is of major concern in the elderly and markers of bone turnover not always diagnostic, Pb isotopic analyses and PbB changes offer a potential to monitor changes in bone turnover. In a longitudinal pilot study of elderly immigrant subjects over a 30 month period, Gulson et al. (2002b) found a decrease in PbB concentrations and changing Pb isotopic composition for nine subjects treated for 6 months with a popular anti bone resorptive bisphosphonate drug. Upon cessation of treatment, the PbB concentrations increased and the isotopic composition changed, consistent with changes in bone remodeling associated with bisphosphonate use.

36.6.10 "Forensic" Capabilities of Pb Isotopes

Although the Pb isotope method has been used in forensic investigations involving firearms (Gulson et al. 2002a, c) it can also be used in less violent cases such as teeth analyses for identifying missing persons (Gulson et al. 1997a). The following are two cases arising from the migrant study described above where there were unexpected changes in the Pb isotopic compositions and PbB of subjects. Because of the delay in obtaining isotopic analyses after sampling these cases were not discovered for several months.

The first case involved a Russian mother and daughter. As mentioned earlier, the $^{206}\text{Pb}/^{204}\text{Pb}$ ratio in most migrants to Australia is higher than that in Australian subjects or the environment and there is a steady decrease after they arrive in Australia reflecting a changing equilibrium between Pb in their skeleton and the Australian Pb (Fig. 36.7). There were sudden changes in the $^{206}\text{Pb}/^{204}\text{Pb}$ of both subjects and then a decrease and it eventuated that the couple had returned to Russia without informing the cohort co-ordinator.

Fig. 36.7 Changes in lead in blood concentration (PbB $\mu\text{g}/\text{dL}$) and $^{206}\text{Pb}/^{204}\text{Pb}$ ratio for a mother and child who returned to Russia for a holiday. Changes in PbB are not diagnostic compared with the increases in the $^{206}\text{Pb}/^{204}\text{Pb}$ ratio reflecting renewed exposure to Russian Pb

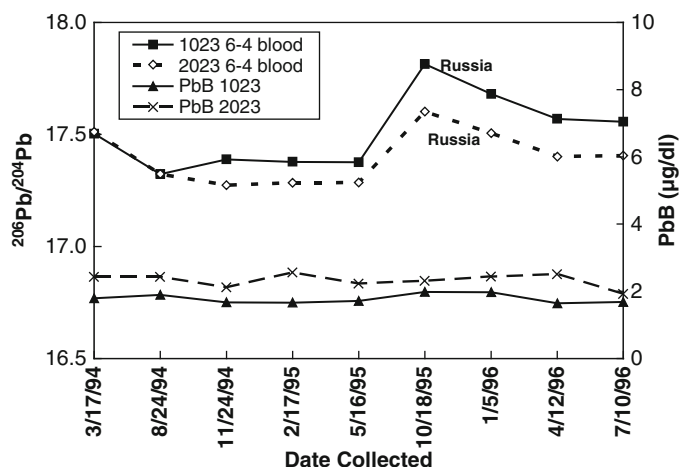
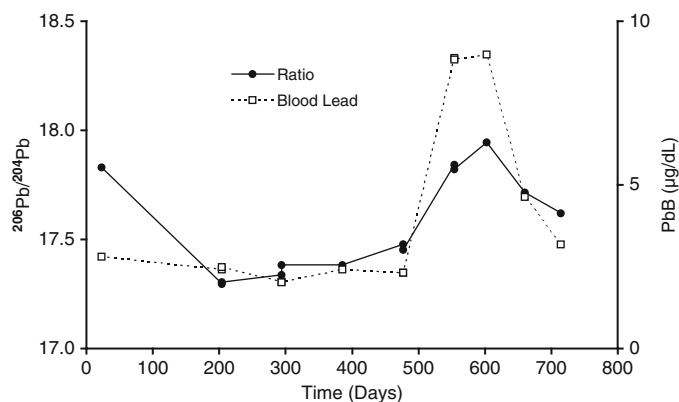


Fig. 36.8 Changes in the $^{206}\text{Pb}/^{204}\text{Pb}$ ratio PbB for a subject from the former Soviet Union. The marked increase in $^{206}\text{Pb}/^{204}\text{Pb}$ ratio and PbB was traced to consumption of water from a Russian samovar. Multiple points are separate analyses of the same samples (redrawn from Gulson 1996b; with permission from John de Laeter)



The second case also involved an increase in $^{206}\text{Pb}/^{204}\text{Pb}$ and PbB for a Russian mother (Fig. 36.8). In this case, her mother had visited from Russia and brought out a Samovar used for heating water. This water was used for beverages as well as cooking. Once the isotopic and PbB data were shown to the mother, further use of the Samovar was discontinued and her blood returned to normal.

Other examples of the “forensic” application of Pb isotopes include ingestion of soft solder (Manton and Malloy 1983), and changes in isotopic composition of a recreational shooter who made his own ammunition (Gulson et al. 2002a). Lead ammunition was identified as a source of lead exposure for First Nations people by Tsuji et al. (2008).

36.6.11 Lead in Wine

Lead isotopes have made useful contributions to the wine and spirit industry, especially where the use of Pb is involved such as storage in Pb-crystal glass containers or contribution of Pb to wine from the previous use of Pb capsules (Gulson et al. 1992). For example, Graziano et al. (1996) showed using sherry stored in a Pb-crystal decanter manufactured with Pb from Australia, that on average about 70% of the ingested dose of Pb was absorbed and could cause elevated PbB levels. In a similar study, Gulson et al. (1998d, e) evaluated the contribution to PbB from wine when a normal quantity of wine was consumed with a meal and compared the changes under fasting conditions.

In the initial phase, white wine dosed with a ^{207}Pb tracer was consumed by an adult male with a meal and under fasting conditions and isotope ratios in blood, urine and faeces were monitored for up to 4 months. Approximately equal proportions of unspiked red and white wine were consumed over the 4 months by the male and his spouse residing in the same household. No detectable increase in PbB was observed when wine was consumed with the meal but a 6% increase was detected when wine was consumed during fasting. Over the 4 months of the trial there was no measurable change in the isotopic ratios in both subject and control confirming the minimal uptake of Pb from wine when consumed with food.

36.6.12 Chelation

Evaluation of the chelating agent Succimer (meso-2,3-dimercaptosuccinic acid) to determine if it increased the absorption of Pb from the gastrointestinal tract during treatment, Smith et al. (1994) administered a single dose of ^{204}Pb (200 μg) by ingestion followed by a single oral dose of placebo or Succimer

to 12 male subjects. The authors suggested that gastrointestinal absorption was enhanced by Succimer and mediated the redistribution of Pb from the circulation to other tissues. However, because of the large within-group variability, none of the differences between groups were statistically significant. Similar chelation studies in humans could be undertaken where there was significant difference in the Pb isotopic composition of the skeleton and prevailing environmental Pb.

36.6.13 Esperance and Bird Kills

A recent example of the use of Pb isotopes in human, animal and environmental investigations is from the seaside community of Esperance in Western Australia. In late 2006, this community was alerted to thousands of native bird species dying. The source of the Pb was thought to derive from the handling of Pb carbonate concentrate through the port, begun in July 2005. It was known from earlier isotopic investigations associated with mineral exploration that this Pb ore had a unique isotopic composition for Australia (Fig. 36.9). This uniqueness allowed for a high degree of certainty

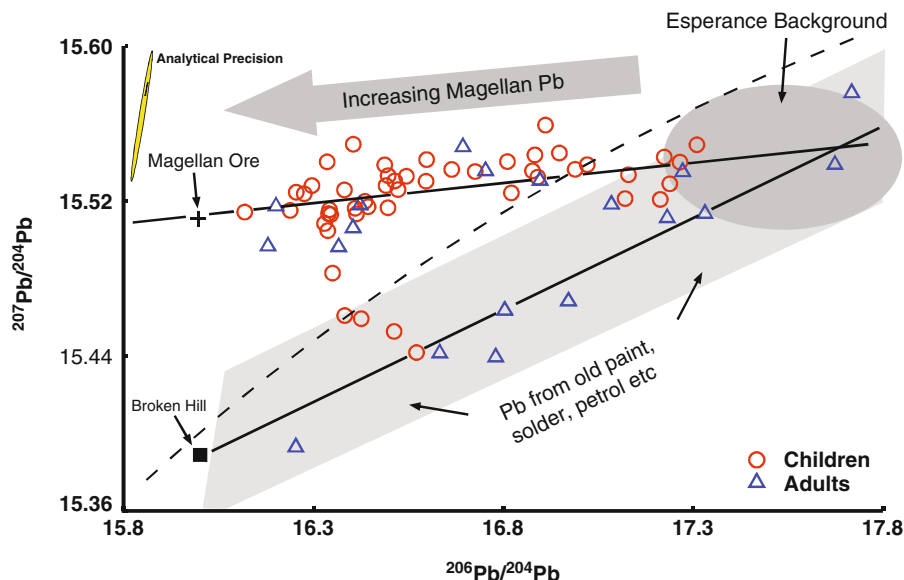


Fig. 36.9 Conventional isotope ratio plot for uranium-derived Pb isotopes. The *dashed line* is the growth curve or Pb evolution curve along which most massive sulfide deposits lie, such as Broken Hill (95% confidence ellipse for samples from the deposits is shown). The 95% confidence ellipse in the *upper left hand corner* represents the measuring precision. The isoto-

pic value of the Pb concentrate (Magellan ore) is unique in the Australian environment and allows simple two-component mixing to estimate the contributions of the carbonate to PbB and environmental samples (data not shown) (redrawn from Gulson et al. 2008, with permission from Environmental Health Perspectives)

in source apportionment for Pb in blood from adults and children, bird organs, and environmental samples including rainwater, soil, vegetation, harbour sediments, and air particulates (Gulson et al. 2009).

In addition, Pb isotopes have been used in monitoring workers handling the ore concentrate and in decontamination of the residences.

36.7 Summary and Future Research

Source apportionment in biological or environmental samples, where there are diverse sources of Pb, using the Pb isotope method relies on a significant difference between the isotopic composition in the target media and the sources. Although the unique isotopic composition of Australian Pb has meant that source apportionment has been relatively successful in the past, Gulson et al. (2006) pointed out that the same might not apply in the future either in Australia or in other countries because of globalization. Furthermore, the increases in blood $^{206}\text{Pb}/^{204}\text{Pb}$ ratio in Australian subjects, combined with globalization, which has resulted in the increases in $^{206}\text{Pb}/^{204}\text{Pb}$ ratio for diet, means that diagnostic isotopic studies undertaken over a decade ago, are now considerably more difficult, not only in Australia but also in other countries where the isotopic differences are even less than in Australia.

Rabinowitz (written communication 2010) has suggested that perhaps it is time to re-visit the currently accepted biokinetic values, which are still based on only five adult males from several decades ago. Ambient Pb levels have dropped to less than one tenth

of what they were in the 1970s. Also, recent advances in rapid mass spectrometry have made the enterprise easier. Furthermore, long term, in-patient studies lasting months are not necessary. Most of the coefficients of interest (gut absorption rate, central pool size and turnover, fractional excretion to urine, and into deeper body stores) and the daily dietary lead intake could be measured with a single dose of Pb tracer of less than 10 μg , with urine and feces collections for only a few days, and a small number of blood samples. Return of Pb from deeper body stores such as bone could not be estimated, but all of the most important biokinetic parameters could be determined. With such an approach, emphasis could be placed on measuring more subjects, allowing for estimates of variability among individuals according to age, gender, genetic factors, geography or metabolic state, thus gaining a broader picture of lead biokinetics.

Increasingly Pb from paint has gained notoriety, as Pb from gasoline and diet have decreased. This is true not only for children but also adults, especially where building renovations may be undertaken. Lead isotopes in paint, however, have been measured over the decades, but because of the isotopic variability, even within a single dwelling, any results need to be treated with caution. Using Pb isotopes and microscopy, Gulson et al. (1995b) showed that houses can contain up to 13 layers of lead-bearing paint of different isotopic compositions. A single layer of house paint reflects the isotope ratios of the commercial sources of its Pb pigment, which was made from refined Pb metal, and whose ratios depend on the mines which provide their feedstock ores. Some of the problems in using Pb isotopes in paint have been illustrated by recent US studies

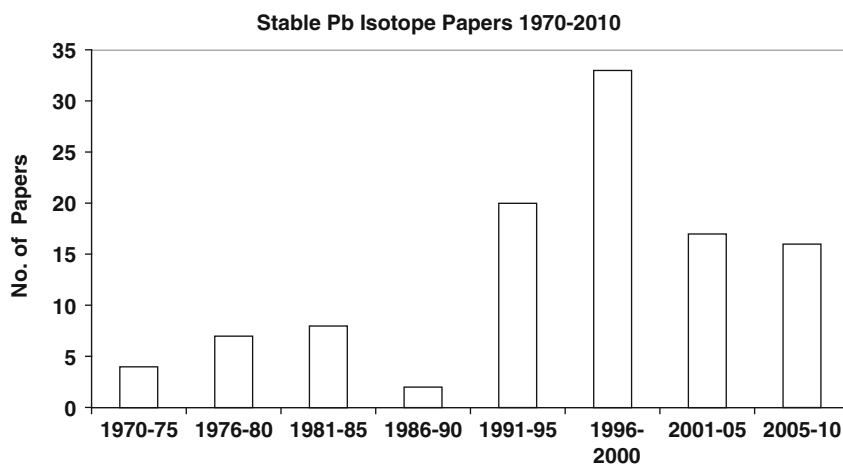


Fig. 36.10 Changes over time in the number of publications using stable Pb isotopes for studies of humans

by Gwiazda and Smith (2000) and Rabinowitz and Hall (2003) and Rabinowitz (2005).

Lead isotopes still have a very important role to play in evaluating sources and pathways given the advocacy of preventative measures to minimise Pb exposure, the associated pressure to lower the guidance level of PbB (e.g., Lanphear et al. 2005a) especially in the USA, and the controversy over Pb in, for example, toys and other items especially those deriving from Asia.

Unfortunately the number of laboratories undertaking high precision Pb isotopic measurements of biological samples is small and diminishing as shown by the decreasing number of publications using Pb isotopes in humans in Fig. 36.10; these include archeological papers on teeth and bone. (Data from PubMed with a search of Lead AND Human AND isotope). Furthermore, with declining PbB levels internationally, high precision isotope measurements will be essential in any investigation, a problem already enunciated by Manton et al. (2000) and Gulson et al. (1996a).

Acknowledgements I dedicate this paper to Kathryn Mahaffey who unfortunately passed away in 2009. She initiated and provided guidance in the Biokinetics of Lead in Human Pregnancy study and was a great friend to a novice in the toxicology field. There are too many people to thank individually who have contributed to our Pb isotope investigations over the years but mention has to be made of Karen Mizon for a superb role in recruitment and retention of cohorts from several studies, and Michael Korsch for maintaining the mass spectrometers in peak condition and feedback; Tony McMichael who began the Biokinetics study and went to greener pastures but which forced me to change fields, something I have never regretted; participants in the studies; Massimo Chiaradia, Matt James, Alistair Law, Karen Mizon, Jackie Palmer, Nicole Patison and Monserrat Vidal for technical assistance and running some of the projects; Mary Salter for phlebotomy; financial support from NIEHS through NOI-ES-05292 and for various expert peer review panels; NSW EPA for financial assistance; Bill Jameson, Jim Fouts, Beth Ragan, and Bob Goyer from NIEHS for continued support and consultation over the years of the study; and Paul Mushak provided ongoing guidance, encouragement and constructive criticism.

References

- al-Saleh IA, Fellows C, Delves T, Taylor A (1993) Identification of sources of lead exposure among children in Arar, Saudi Arabia. *Ann Clin Biochem* 30:142–145
- Angle CR, Manton WI, Stanek KL (1995) Stable isotope identification of lead sources in preschool children—the Omaha Study. *J Toxicol Clin Toxicol* 33:657–662
- Arora M, Kennedy BJ, Elhlou S et al (2006) Spatial distribution of lead in human primary teeth as a biomarker of pre- and neonatal lead exposure. *Sci Total Environ* 371:55–62
- ATSDR (2007) Agency for Toxic Substances and Disease Registry. Toxicological profile for lead. U.S. Department of Health and Human Services, Public Health Service, Atlanta
- Ayres J, Harrison R, Nichols G, Maynard R (eds) (2010) *Environmental medicine*. Hodder Arnold, London
- Bollhöfer A, Rosman K (2001) Isotopic source signatures for atmospheric lead; the Northern hemisphere. *Geochim Cosmochim Acta* 65:1727–1740
- Campbell MJ, Delves HT (1989) Accurate and precise determination of lead isotopic ratios in clinical and environmental samples using inductively coupled plasma mass spectrometry. *J Anal At Spectrom* 4:235–256
- Chaudhary-Webb M, Paschal D, Ellion C et al (1998) Determination of lead isotope ratios in whole blood, pottery, and leaded gasoline; lead sources in Mexico City. *At Spectrosc* 19:156–163
- Chiaradia M, Gulson BL, MacDonald K (1997a) Contamination of houses by workers occupationally exposed in a lead-zinc-copper mine and impact on blood lead concentrations in the families. *Occup Environ Med* 54:117–124
- Chiaradia M, Chenhall BE, Depers AM et al (1997b) Identification of historical lead sources in roof dusts and recent lake sediments from an industrialized area: indications from lead isotopes. *Sci Total Environ* 205:107–128
- Chillrud SN, Hemming NG, Ross JM et al (2005) A rapid and precise procedure for Pb isotopes in whole blood by Fe coprecipitation and MC-ICPMS analysis. *Appl Geochem* 20:807–813
- Cooper K, Noller B, Connell D et al (2007) Public health risks from heavy metals and metalloids present in traditional Chinese medicines. *J Toxicol Environ Health A* 70:1694–1699
- Counter SA, Buchanan LH, Ortega F et al (2000) Environmental lead contamination and pediatric lead intoxication in an Andean Ecuadorian village. *Int J Occup Environ Health* 30:169–176
- Delves HT, Campbell MJ (1993) Identification and source apportionment of sources of lead in human tissue. *Environ Geochem Health* 15:75–84
- U.S. EPA (2006) Air quality criteria for lead. October 2006 EPA/600/R-5/144aF
- U.S. EPA (2007) Technology transfer network air toxics web site. Lead compounds. <http://www.epa.gov/ttn/atw/hlthef/lead.html>. Accessed 20 March 2010
- Facchetti S (1990) Isotopic lead experiment. *Sci Total Environ* 93:537–538
- Franklin CA, Inskip MJ, Bacchanale CL et al (1997) Use of sequentially administered stable lead isotopes to investigate changes in blood lead during pregnancy in a nonhuman primate (*Macaca fascicularis*). *Fundam Appl Toxicol* 39:109–119
- Glorennec P, Peyr C, Poupon J et al (2010) Identifying sources of lead exposure for children, with lead concentrations and isotope ratios. *J Occup Environ Hyg* 7:253–260
- Graziano JH, Blum CB, Lolocono NJ et al (1996) A human in vivo model for the determination of lead bioavailability using stable isotope dilution. *Environ Health Perspect* 104:176–179
- Gulson BL (1996a) Tooth analyses of sources and intensity of lead exposure in children. *Environ Health Perspect* 104:306–312
- Gulson BL (1996b) Stable heavy isotopes in human health. *J R Soc West Aust* 79:83–88

- Gulson BL (2008) Stable lead isotopes in environmental health with emphasis on human investigations. *Sci Total Environ* 400:75–92
- Gulson BL, Gillings BR (1997) Lead exchange in teeth and bone—a pilot study using stable lead isotopes. *Environ Health Perspect* 105:820–824
- Gulson B, Wilson D (1994) History of lead exposure in children revealed from isotopic analyses of teeth. *Arch Environ Health* 49:279–283
- Gulson BL, Lee TW, Mizon KJ, Eschnauer H (1992) The application of lead isotope ratios to determine the contribution of the tin-lead capsule to the lead content of wine. *Am J Enol Vitic* 43:180–190
- Gulson BL, Davis JJ, Mizon KJ et al (1994a) Lead bioavailability in the environment of children: blood lead levels in children can be elevated in a mining community. *Arch Environ Health* 49:326–331
- Gulson BL, Mizon KJ, Law AJ et al (1994b) Source and pathways of lead in humans from broken hill mining community – an alternative use of exploration methods. *Econ Geol* 89:889–908
- Gulson BL, Davis JJ, Bawden-Smith J (1995a) Paint as a source of recontamination of houses in urban environments and its role in maintaining elevated blood leads in children. *Sci Total Environ* 164:221–235
- Gulson BL, Mahaffey KR, Mizon KJ et al (1995b) Contribution of tissue lead to blood lead in adult female subjects based on stable lead isotope methods. *J Lab Clin Med* 125:703–712
- Gulson BL, Mizon KJ, Korsch MJ et al (1996a) Impact on blood lead in children and adults following relocation from their source of exposure and contribution of skeletal tissue to blood lead. *Bull Environ Contam Toxicol* 56:543–550
- Gulson BL, Mizon KJ, Korsch MJ et al (1996b) Importance of monitoring family members in establishing sources and pathways of lead in blood. *Sci Total Environ* 188:173–182
- Gulson BL, Mizon KJ, Korsch MJ et al (1996c) Non-orebody sources are significant contributors to blood lead of some children with low to moderate lead exposure in a major lead mining community. *Sci Total Environ* 181:223–230
- Gulson BL, Pisaniello D, McMichael AJ et al (1996d) Stable lead isotope profiles in smelter and general urban communities. Comparison of biological and environmental measures. *Environ Geochem Health* 18:147–163
- Gulson BL, Jameson CW, Gillings BR (1997a) Stable lead isotopes in teeth as indicators of past domicile—a potential new tool in forensic science? *J Forensic Sci* 42:787–791
- Gulson BL, Jameson CW, Mahaffey KR et al (1997b) Pregnancy increases mobilization of lead from maternal skeleton. *J Lab Clin Med* 130:51–62
- Gulson BL, Cameron MA, Smith AJ et al (1998a) Blood lead-urine lead relationships in adults and children. *Environ Res* 78:152–160
- Gulson BL, Jameson CW, Mahaffey KR et al (1998b) Relationships of lead in breast milk to lead in blood, urine, and diet of the infant and mother. *Environ Health Perspect* 106:667–674
- Gulson BL, Mahaffey KR, Jameson CW et al (1998c) Mobilization of lead from the skeleton during the postnatal period is larger than during pregnancy. *J Lab Clin Med* 131:324–329
- Gulson BL, Yui LA, Howarth D (1998d) Delayed visual maturation and lead pollution. *Sci Total Environ* 224:215–219
- Gulson BL, Stockley CS, Lee TH et al (1998e) Contribution of lead in wine to the total dietary intake of lead in humans with and without a meal: a pilot study. *J Wine Res* 9:5–14
- Gulson BL, Gray B, Mahaffey KR et al (1999a) Comparison of the rates of exchange of lead in the blood of newly born infants and their mothers with lead from their current environment. *J Lab Clin Med* 133:171–178
- Gulson BL, Pounds JG, Mushak P et al (1999b) Estimation of cumulative lead releases (lead flux) from the maternal skeleton during pregnancy and lactation. *J Lab Clin Med* 134:631–640
- Gulson BL, Mizon KJ, Palmer JM et al (2001) Contribution of lead from calcium supplements to blood lead. *Environ Health Perspect* 109:283–288
- Gulson BL, Eames JC, Davis JD (2002a) Evaluation of exhibits from a murder case using the lead isotope method and scanning electron microscopy. *J Forensic Sci* 47:1015–1021
- Gulson B, Mizon K, Smith H et al (2002b) Skeletal lead release during bone resorption: effect of bisphosphonate treatment in a pilot study. *Environ Health Perspect* 110:1017–1023
- Gulson BL, Palmer JM, Bryce A (2002c) Changes in blood lead of a recreational shooter. *Sci Total Environ* 293:143–150
- Gulson BL, Mizon KJ, Korsch MJ et al (2003) Mobilization of lead from human bone tissue during pregnancy and lactation—a summary of long-term research. *Sci Total Environ* 303:79–104
- Gulson BL, Mizon KJ, Davis JD et al (2004a) Identification of sources of lead in children in a primary zinc-lead smelter environment. *Environ Health Perspect* 112:52–60
- Gulson BL, Mizon KJ, Palmer JM et al (2004b) Blood lead changes during pregnancy and postpartum with calcium supplementation. *Environ Health Perspect* 112:1499–1507
- Gulson BL, Mizon KJ, Dickson BL et al (2005) Detection of exposure of employees to mining and millings operations in a uranium mine using lead isotopes – a pilot study. *Sci Total Environ* 339:269–272
- Gulson B, Mizon K, Korsch M et al (2006) Changes in the lead isotopic composition of blood, diet and air in Australia over a decade: globalization and implications for future isotopic studies. *Environ Res* 100:130–138
- Gulson BL, Korsch MJ, Matison M et al (2009) Windblown lead carbonate as the main source of lead in blood of children from a seaside community: an example of local birds as “canaries in the mine”. *Environ Health Perspect* 117:148–154
- Gwiazda RH, Smith DR (2000) Lead isotopes as a supplementary tool in the routine evaluation of household lead hazards. *Environ Health Perspect* 108:1091–1097
- Gwiazda R, Campbell C, Smith D (2005) A noninvasive isotopic approach to estimate the bone lead contribution to blood in children: implications for assessing the efficacy of lead abatement. *Environ Health Perspect* 113:104–110
- IARC (2006) Inorganic and organic lead compounds, vol 87. International Agency for Research on Cancer, Lyon
- Inskip MJ, Franklin CA, Bacchanale CL et al (1996) Measurement of the flux of lead from bone to blood in a nonhuman primate (*Macaca fascicularis*) by sequential administration of stable lead isotopes. *Fundam Appl Toxicol* 33:235–245
- James MG, Gulson BL (1999) Engine reconditioning workshops: lead contamination and the potential risk for workers: a pilot study. *Occup Environ Med* 56:429–431

- Kehoe RA (1969) Toxicological appraisal of lead in relation to the tolerable concentration in the ambient air. *J Air Pollut Control Assoc* 19:690–700
- Keinonen M (1992) The isotopic composition of lead in man and the environment in Finland 1966–1987: isotope ratios of lead as indicators of pollutant source. *Sci Total Environ* 113:251–268
- Komárek M, Ettler V, Chrastný V, Mihaljevič M (2008) Lead isotopes in environmental sciences: a review. *Environ Int* 34:562–577
- Kurkjian R, Flegal AR (2003) Isotopic evidence of the persistent dominance of blood lead concentrations by previous gasoline lead emissions in Yerevan, Armenia. *Environ Res* 93:308–315
- Laidlaw MAS, Filippelli GM (2008) Resuspension of urban soils as a persistent source of lead poisoning in children: a review and new directions. *Appl Geochem* 23:2021–2039
- Lanphear BP, Roghmann KJ (1997) Pathways of lead exposure in urban children. *Environ Res* 74:67–73
- Lanphear BP, Burgoon DA, Rust SW (1998) Environmental exposures to lead and urban children's blood lead levels. *Environ Res* 76:120–130
- Lanphear BP, Hornung R, Ho M (2002) Environmental lead exposure during early childhood. *J Pediatr* 140:40–47
- Lanphear BP, Hornung R, Ho M (2005a) Screening housing to prevent lead toxicity in children. *Public Health Rep* 120:305–310
- Lanphear BP, Hornung R, Houry J et al (2005b) Low-level environmental lead exposure and children's intellectual function: an international pooled analysis. *Environ Health Perspect* 113:894–899
- Levesque B, Duchesne JF, Gariépy C et al (2003) Monitoring of umbilical cord blood lead levels and sources assessment among the Inuit. *Occup Environ Med* 60:693–695
- Liang F, Zhang G, Tan M et al (2010) Lead in children's blood is mainly caused by coal-fired ash after phasing out of leaded gasoline in Shanghai. *Environ Sci Technol* 44:4760–4765
- Manton WI (1973) Significance of lead isotope composition in blood. *Nature* 244:165–167
- Manton WI (1977) Sources of lead in blood. Identification by stable isotopes. *Arch Environ Health* 32:149–159
- Manton WI (1985) Total contribution of airborne lead to blood lead. *Br J Ind Med* 42:168–172
- Manton WI (1992) Postpartum changes to maternal blood lead concentrations. *Br J Ind Med* 49:671–672
- Manton WI, Malloy CR (1983) Distribution of lead in body fluids after ingestion of soft solder. *Br J Ind Med* 40:51–57
- Manton WI, Angle CR, Stanek KL et al (2000) Acquisition and retention of lead by young children. *Environ Res* 82:60–80
- Manton WI, Angle CR, Stanek KL et al (2003) Release of lead from bone in pregnancy and lactation. *Environ Res* 92:139–151
- Matsumoto M, Yoshinaga J (2010) Isotope ratios of lead in Japanese women's hair of the twentieth century. *Environ Sci Pollut Res Int* 17:643–649
- Naeher LP, Rubin CS, Hernandez-Avila M et al (2003) Use of isotope ratios to identify sources contributing to pediatric lead poisoning in Peru. *Arch Environ Health* 58:579–589
- O'Flaherty EJ, Inskip MJ, Franklin CA et al (1998) Evaluation and modification of a physiologically based model of lead kinetics using data from a sequential isotope study in cynomolgus monkeys. *Toxicol Appl Pharmacol* 149:1–16
- Patel MM, Adrienne H, Jones R et al (2008) Use of lead isotope ratios to identify sources of lead exposure in Alaska Natives. *Int J Circumpolar Health* 67:261–268
- Rabinowitz MB (1987) Stable isotope mass spectrometry in childhood lead poisoning. *Biol Trace Elem Res* 12:223–229
- Rabinowitz M (1991) Toxicokinetics of bone lead. *Environ Health Perspect* 91:33–37
- Rabinowitz M (1998) Historical perspective on lead biokinetic models. *Environ Health Perspect* 106(suppl 6):1461–1465
- Rabinowitz M (2005) Lead isotopes in soils near five historic American lead smelters and refineries. *Sci Total Environ* 346:138–148
- Rabinowitz M, Hall GS (2003) Isotopic characterization of six major brands of white basic lead carbonate paint pigments. *Bull Environ Contam Toxicol* 69:617–623
- Rabinowitz MB, Wetherill GW, Kopple JD (1973) Lead metabolism in the normal human: stable isotope studies. *Science* 182:725–727
- Rabinowitz M, Wetherill GW, Kopple JD (1974) Studies of human lead metabolism by use of stable isotope tracers. *Environ Health Perspect* 7:145–153
- Rabinowitz MB, Wetherill GW, Kopple JD (1976) Kinetic analysis of lead metabolism in healthy humans. *J Clin Invest* 58:260–270
- Rabinowitz MB, Wetherill GW, Kopple JD (1977) Magnitude of lead intake from respiration by normal man. *J Lab Clin Med* 90:238–248
- Rabinowitz MB, Kopple JD, Wetherill GW (1980) Effect of food intake and fasting on gastrointestinal lead absorption in humans. *Am J Clin Nutr* 33:1784–1788
- Renner R (2010) Exposure on tap: drinking water as an overlooked source of lead. *Environ Health Perspect* 118:a68–a72
- Smith DR, Markowitz ME, Crick J et al (1994) The effects of succimer on the absorption of lead in adults determined by using the stable isotope ^{204}Pb . *Environ Res* 67:39–53
- Smith DR, Osterloh JD, Flegal AR (1996) Use of endogenous stable lead isotopes to determine release of lead from the skeleton. *Environ Health Perspect* 104:60–66
- Tera O, Schwartzman DW, Watkins TR (1985) Identification of gasoline lead in children's blood using isotopic analysis. *Arch Environ Health* 40:120–123
- Tsuji LJ, Wainman BC, Martin ID et al (2008) The identification of lead ammunition as a source of lead exposure in First Nations: the use of lead isotope ratios. *Sci Total Environ* 393:291–298
- Viczian M, Lasztity A, Barnes RM (1990) Identification of potential environmental sources of childhood lead poisoning by inductively coupled plasma mass spectrometry. *J Anal At Spectrom* 5:293–300
- Weidenhamer JD, Clement ML (2007) Evidence of recycling of lead battery waste into highly leaded jewellery. *Chemosphere* 69:1670–1672
- Yaffe Y, Flessel CP, Wesolowski JJ et al (1983) Identification of lead sources in California children using the stable isotope ratio technique. *Arch Environ Health* 38:237–245
- Zabel TF (1993) Diffuse sources of pollution by heavy metals. *J Inst Water Environ Manage* 7:513–520
- Zheng L, Wu K, Li Y et al (2008) Blood lead and cadmium levels and relevant factors among children from an e-waste recycling town in China. *Environ Res* 108:15–20

Part VI
**Isotopes as Tracers of Paleoclimate
and Paleoenvironments**

Chapter 37

Dating of Biogenic and Inorganic Carbonates Using ^{210}Pb - ^{226}Ra Disequilibrium Method: A Review

Mark Baskaran

Abstract The uniqueness of the recent (<100–150 years) carbonate proxies is that the archived paleoclimatological and paleoenvironmental parameters inscribed in them at the time of their formation can be calibrated in most cases with existing hard data and thus, provides an excellent opportunity to verify their utility to retrieve long-term paleorecords. Determination of precise chronology of these proxies such as corals (both shallow and deep-sea), fish bones (otoliths), mollusks, speleothems, and inorganic carbonates that precipitate from natural reservoirs and man-made structures therefore becomes very important. The chronological retrieval of the archived records in these proxies are relevant to several important issues that include development of fisheries management strategies, reconstruction of environmental and geochemical changes that are taking place in coastal, estuarine and lacustrine waters and time frames of the initiation of degradation of engineering structures such as bridges. Several recent developments have contributed to high-precision dating of these carbonates. For example, with the advent of mass spectrometry (both TIMS and ICPMS), it has become possible to make high precision measurements of ^{226}Ra measurements which has significantly reduced uncertainties of $^{210}\text{Pb}/^{226}\text{Ra}$ ages. In this article, the current status of the $^{210}\text{Pb}/^{226}\text{Ra}$ dating method of biogenic and inorganic carbonates is reviewed and the gaps in this field are discussed.

37.1 Introduction

Recent (<150 years old) carbonates (both biogenic and inorganic including corals, mollusk shells, otoliths, fish bones, speleothems, inorganic carbonates formed under concrete bridges and whale falls) hold signatures of the past history of climatological, environmental and chemical changes that have taken place in various earth systems from which they form such as lakes, rivers, oceans, karsts, and other terrestrial environments. Corals are excellent proxies in marine environment as post-depositional changes, such as bioturbation and to a large extent diagenesis will not affect the preserved paleo-record. Recently growing deep-sea corals in particular could be used for understanding the penetration of anthropogenic substances into the ocean including transient tracers (such as Pu), as well as paleocirculation changes in the deep sea on decadal and subdecadal time scales (Druffel et al. 1990). Surface water corals could be utilized as archives to retrieve seasonal and interannual variations of temperature and salinity. Molluskan shells are ubiquitous and are common in freshwater and marine systems. Reliable dating of these shells coupled with measurements of geochemical parameters (e.g., stable isotopes, concentrations of minor and trace elements) will aid in the reconstruction of paleo-environmental changes and pollution over the past 100–150 years. Cave deposits are also ubiquitous and have been widely utilized as proxies for reconstructing paleoclimate and paleoenvironmental changes. Recent cave deposits (<150 years) have the potential to reconstruct climate such as temperature and amount of precipitation (Baskaran and Krishnamurthy 1993; Tanahara et al. 1997; Ku and Li 1998; Woo et al. 2005). Retrieval of these records requires precise chronology.

M. Baskaran
Department of Geology, Wayne State University, Detroit, MI
48202, USA
e-mail: Baskaran@wayne.edu

In general, dating of biological organisms relies on the identification of annual growth increments of ear bones (otoliths), teeth, vertebrae, scales, and other bony tissues. There are uncertainties with the regularity of the growth increments and sometimes identification of those markers is difficult. The most common isotope pairs that are used to date <150 years-old carbonates are: $^{228}\text{Th}/^{228}\text{Ra}$ and $^{210}\text{Pb}/^{226}\text{Ra}$ (Campana et al. 1993; recent review by Schmidt and Cochran 2010). As a general rule (or a thumb rule), the useful time range for dating with a particular isotope is about 5 half-lives (corresponding to Daughter/Parent activity ratio of 0.97, if there is no initial daughter activity at the time of formation or 97% of the excess activity decays).

^{226}Ra and ^{210}Pb are the decay products in the ^{238}U series. In the decay sequence, the noble gas daughter ^{222}Rn (half-life = 3.82 day) diffuses out of earth's surface from rocks and minerals (and relatively minor amount from surface waters, Baskaran 2011) and are subsequently transported by turbulence and advection through the atmosphere. The decay products of ^{222}Rn are heavy metal and metal atoms (e.g., ^{210}Pb , ^{214}Pb) and thus, upon production they rapidly become attached to atmospheric aerosols. These ^{210}Pb -laden aerosols are returned to earth through atmospheric scavenging processes via rain, snow and dry fallout. Thus, most of the ^{210}Pb in surface waters is derived from atmospheric deposition. Most of the ^{226}Ra in the ocean is derived from diffusion of bottom sediments.

$^{210}\text{Pb}/^{226}\text{Ra}$ dating method can be grouped into two categories: (i) method based on decay of unsupported ^{210}Pb (also called excess ^{210}Pb dating method; e.g., dating of speleothems, corals). In this case, the excess ^{210}Pb undergoes radioactive decay to the parent-supported level; and (ii) method based on growth of ^{210}Pb from the decay of ^{226}Ra (also called daughter deficient method, e.g., dating of otoliths, fish bones, mollusk shells, inorganic carbonates in concrete structures). In this case, the knowledge of initial ^{210}Pb (at $t = 0$) is needed, very often this is ~ 0 . Disequilibrium between ^{210}Pb and ^{226}Ra is caused by biological discrimination and geochemical fractionation due to differences in their mobility. ^{210}Pb is depleted with respect to ^{226}Ra in coastal and deep ocean environments due to its highly particle-reactive nature (Rama et al. 1961; Craig et al. 1973; McKee 2008; Van der Loeff and Geibert 2008). Biogenic carbonates (corals, mollusks and fish otoliths) preferentially incorporate either ^{226}Ra (fish otoliths and mollusks) or ^{210}Pb (in corals, although

it may be adsorbed on to organic films, details in Sect. 37.3.4.1) in them causing disequilibrium between these two nuclides. In the case of corals, some amount of ^{210}Pb is also sorbed onto the symbiotic algae growing on their surface that contributes to excess ^{210}Pb . In speleothems, excess ^{210}Pb is produced from the decay of ^{222}Rn in the drip water from the ceiling of the cave (Baskaran and Iliffe 1993; Tanahara et al. 1997; Ku and Li 1998; Woo et al. 2005). This ^{210}Pb - ^{226}Ra disequilibrium will diminish with time either through the decay of excess ^{210}Pb (speleothems and corals) or growth of ^{210}Pb towards ^{226}Ra (in mollusks, fish otoliths and inorganic carbonates). The restoration of secular equilibrium between the daughter (^{210}Pb) and parent (^{226}Ra) isotopes in the carbonate material is the basis of the $^{210}\text{Pb}/^{226}\text{Ra}$ dating technique. Most of the ^{210}Pb in coastal and lacustrine sedimentary layers as well as ice cores corresponding to ages < 150 years is predominantly derived from atmospheric deposition (Goldberg 1963; Crozaz et al. 1964; Krishnaswamy et al. 1971).

The purpose of this article is to critically review the current status of $^{210}\text{Pb}/^{226}\text{Ra}$ dating method of recent biogenic and inorganic carbonates and assess the gaps in our knowledge to establish reliable chronology. The time scale involved is recent (<100–150 years) and a relatively large body of data exists on the environmental/climatic parameters from various regions making it possible to calibrate these carbonate proxies with “hard data” that have been recorded during the anthropocene. Such an exercise would pave the way for the use of these proxies to retrieve paleo records stored in them beyond the anthropocene. A key requirement for this is a very reliable chronology of these carbonates.

37.2 Materials and Methods

37.2.1 Analytical Methods

^{210}Pb analysis can be conducted by alpha, beta or gamma spectrometric methods. The alpha method involves determination of ^{210}Pb via its grand-daughter, ^{210}Po ($t_{1/2} = 138$ days). A known amount of carbonate sample (100 mg to ~ 2 g, depending on the activity in the sample) is dissolved in 25 mL 6 M HCl, after adding a known amount of ^{209}Po (or ^{208}Po) yield monitor. ^{209}Po is a primary reference material

(obtained from NIST in the United States) and is certified. In the case of pure corals, otoliths and pure speleothems, often there is very little residue in the solution. In some of the mollusk shells, there could be some impurities and the solution may have to be filtered. One of the most widely accepted method of preparing the polonium source is by spontaneous deposition. The amounts of iron, manganese, chromium and other oxidants in the solution are very low and usually does not interfere with plating. However, as a precaution, addition of small amounts of oxidants such as ascorbic acid (50–200 mg) or hydroxylamine hydrochloride (2 mL of 20% (w/v)) to reduce the oxidation state (e.g., Fe^{3+} to Fe^{2+}) will prevent any oxidant from plating on to the Ag plachets. A small amount of citric acid (2 mL of 20% (w/v)) in the form of sodium citrate is also added to prevent competition of other ions that may be present in the solution. To prevent ^{210}Bi from plating, hold-back carrier of stable Bi (~ 2 mg/mL of the solution of stable Bi) is also commonly added. This ascorbic acid/hydroxylamine hydrochloride, citric acid and hold-back carriers are not commonly used in the analysis of most carbonates. The solution is continuously stirred during plating with a magnetic stirrer on a hot plate, with the temperature of the bottom solution in the Teflon beaker being between 70 and 90°C. The plating time for carbonates is usually about ~ 2 h, but a wide range of temperatures and plating times have been utilized (1.5–24 h and 60–95°C; summarized in Mathews et al. 2007).

The advantage of alpha spectrometry is the high-energy resolution (18 keV for an active area of 450 mm², with a typical background of 6 counts per day; 0.8–2 counts per day in the 200 keV envelope area for ^{209}Po and ^{210}Po peaks), low background (less than 0.05 counts/h/cm²) in the energy range of 3–8 MeV. Many of the currently used solid-state detectors (such as PIPS detectors, Canberra Inc) have a minimum active thickness of greater than 140 μm which is sufficient for full absorption of alpha particles of up to 15 MeV, with a background of 3–10 counts per day in the ^{210}Po or ^{209}Po envelope region (in an envelope area of ~ 200 keV, corresponding to 0.038–0.115 mBq), and relatively high absolute efficiency ($\sim 30\%$) and these features make α -spectrometric technique attractive for ^{210}Po assay. When Fe^{3+} , Cr^{6+} , and other oxidants are not reduced to lower valence states, they often get plated and result in thick sources with poor plating efficiency and low resolution. Often in such cases,

^{210}Po (5.304 MeV) and ^{209}Po (4.881 MeV) cannot be resolved (or ^{210}Po and ^{208}Po (5.115 MeV)).

The minimum detectable activity for ^{210}Pb via ^{210}Po by alpha spectrometry is affected by the level of the chemical (or reagent) blank which arises from contamination from reagents, and sample and source preparation steps. For relatively new alpha detectors, the background of 0.03–0.09 counts per hour (cph) corresponds to 0.03–0.08 mBq (assuming detector efficiency of 30% and all the counts are coming from inside or outside the detector). Based on the past 30 years of research experience with ^{210}Po measurements in a variety of matrices (tissues of animals, bone samples, carbonates, sediments), it is our experience that the reagent blanks are typically less than 0.05 mBq and hence a detection limit of 0.1 mBq ($=0.035$ fg ^{210}Pb , 1 mBq = 3.54×10^{-16} g for ^{210}Pb) for a counting time of about 6,000 min (mainly due to very low background alpha detectors, with background ranging between 0.03 and 0.09 cph) is achievable.

^{210}Pb measurements can also be made via its beta-emitting daughter, ^{210}Bi . Beta counting is not isotopic-specific and hence other beta emitting radionuclides can interfere. Multiple counting will ensure the reliability of the data. For example, the gas-flow anti-coincidence counter with 10 cm lead shielding Risø Counter (manufactured by Risø National Laboratory, Roskilde, Denmark), gives a background value of 0.15–0.20 count per minute (cpm) for a source of 25 mm diameter. The absolute efficiency is $\sim 40\%$. A 0.20 cpm background will correspond to ~ 8 mBq (assuming counting efficiency of 40%) compared to 0.1 mBq by alpha spectrometry and hence the detection limit by beta counting method is more than an order of magnitude higher than that of alpha spectrometry.

The radiochemical procedure for beta counting method is as follows: To the dissolved solution, a known amount of iron (25 mg of Fe in the form of FeCl_3) is added. Lead is precipitated as a mixed ferric hydroxide/lead chromate by adding ammonia (Craig et al. 1973). The precipitate and the solution are separated by decanting and centrifugation. The precipitate is then dissolved in acetic acid and the lead is reprecipitated as the chromate. The lead chromate is dissolved in 1.5 mL HCl and passed through an anion exchange resin (DOWEX-1-X8-100-200 mesh) column. The Pb is retained in the column and is eluted with warm water, the Pb fraction is precipitated as the sulphate and mounted on a sample holder and counted with a

0.9 mg/cm² Mylar window. The source is counted at regular intervals over a period of 30–35 days until ²¹⁰Pb and ²¹⁰Bi attain secular equilibrium. The temporal evolution of ²¹⁰Bi is plotted and the $t = 0$ activity of ²¹⁰Pb is calculated. During beta assay of ²¹⁰Pb–²¹⁰Bi, the low energy betas of ²¹⁰Pb (²¹⁰Pb β_{\max} = 0.063 Mev) are cut-off using suitable absorbers.

Gamma-ray spectrometry has been utilized to measure ²¹⁰Pb using its 46.5 keV energy photons (e.g., Baskaran and Santschi 2002; McNeary and Baskaran 2007; Jweda et al. 2008). The sensitivity of gamma counting is significantly lower than that of the alpha and beta counting methods, mainly due to its low branching ratio (4.65%). The distinct advantage of the gamma counting method, however, is that it is non-destructive (and least labor-intensive) and thus there is no need for a spike and chemical processing. Sample preparation is straight forward and many other nuclides including ²²⁶Ra (via its progenies, such as ²¹⁴Bi and ²¹⁴Pb) can be simultaneously measured. The absolute efficiency of the gamma detector depends on its geometry (planar, closed-end coaxial and well-type). In a well detector, the sample in low volume (well-depth of 40 mm corresponds to ~4 mL) is surrounded by germanium crystal and hence the geometrical counting efficiency is high. Overall, for small samples, the well detectors provide the best overall sensitivity compared to all the existing gamma-ray detectors. Attempts have been made to measure ²¹⁰Pb by ICPMS, but isobaric and molecular ionic interferences (²⁰⁹Bi¹H, ²⁰⁸Bi¹H₂, ¹⁹⁴Pt¹⁶O, ¹⁹⁸Hg¹²C, etc) are major impediments that need to be overcome. Furthermore, the atomic abundances of ²¹⁰Pb are very low (detection limit in alpha spectrometry is 0.1 mBq = 1.02×10^5 atoms).

Radium-226 can be measured by several methods: (i) gamma-ray spectrometry; (ii) α -spectrometry; (iii) radon emanation method; and (iv) mass spectrometry. Of these, the gamma-ray spectrometric method is the least sensitive. Usually, it is measured via one or more its daughter products (e.g., ²¹⁴Pb, 352 keV, branching ratio = 35.9%; ²¹⁴Bi, 609.3 keV, branching ratio = 46.1%) because these lines have very little interference from other gamma lines and have higher branching ratios. For solid samples, such as corals, otoliths, mollusks, speleothems, etc the radon emanation is only from the outer ~200 Å and hence the effect on the activity due to ²²²Rn loss is generally negligible. We have measured RGU-1 standard (IAEA SRM) repeatedly on our gamma-ray spectrometers and

found that ²³⁴Th, ²²⁶Ra and ²¹⁰Pb all are in secular equilibrium ($\pm 5\%$), as expected, indicating that the ²²²Rn loss is negligible. Counting of a 10-g sample with ~10 mBq/g ²²⁶Ra (total of 100 mBq = 2.77 pg of ²²⁶Ra; 1 mBq = 2.77×10^{-14} g for ²²⁶Ra), the 1 σ propagated error on the final activity is ~10% in a Ge-well detector, when the sample is counted in a well geometry for ~24 h (Baskaran et al. 2005). When the sample size is small and/or the ²²⁶Ra activity is lower, then, the associated propagated error will be higher. ²²⁶Ra has a gamma line at 186.2 keV, but it has a branching ratio of only 3.51%. Further, this energy has interference from ²³⁵U and Compton background due to other radionuclides present in the sample making this method less sensitive (Hou and Roos 2008).

In alpha spectrometry ²²⁶Ra is co-precipitated with barium, using a ¹³³Ba yield tracer followed by chemical separation and purification of Ra. The chemical yields for Ba and Ra are assumed to be the same. Following the purification of Ra, it is electroplated and assayed in a α -spectrometer. Since the alpha detectors have very low background, and therefore lower detection limits, this method can be utilized to measure samples with very low ²²⁶Ra concentration (as low 0.1–0.2 mBq, 2.7–5.4 fg; Hou and Roos 2008).

The radon emanation method involves the measurement of ²²⁶Ra via its gaseous daughter, ²²²Rn. The carbonate sample is brought into solution and stored in glass gas bottle for about 20 days for ²²²Rn to grow towards secular equilibrium with ²²⁶Ra. The ²²²Rn is stripped quantitatively from the bottle and transferred into a Lucas cell (coated with scintillating material such as ZnS). The daughter products of ²²²Rn, ²¹⁸Po and ²¹⁴Po, are allowed to reach secular equilibrium (intermediate daughter products, ²¹⁴Pb, half-life = 26.8 min and ²¹⁴Bi, half-life = 19.7 min which takes about 3 h for ²²²Rn, ²¹⁴Pb and ²¹⁴Bi to reach secular equilibrium). The precision of the ²²⁶Ra activity determination depends on errors associated with the efficiency of the scintillation counter, background corrections of the Lucas cell, and the efficiency of ²²²Rn transfer from the graphite column (where ²²²Rn is trapped) to the Lucas cell. In samples with very low ²²⁶Ra activities, the propagated errors could result in relatively large analytical uncertainties (>100%, Bennett et al. 1982; Kastle et al. 1994). The detection limit for this method for ²²⁶Ra is ~8 mBq (=218 fg).

Instead of measuring the decay events (either by α -, or β - or γ -counting methods), ²²⁶Ra can be directly

measured by counting the ionized atoms with lower detection limits and higher analytical precision (Volpe et al. 1991; Cohen and O’Nions 1991; Andrews et al. 1999a, b). In deepwater fish otoliths, ^{226}Ra concentrations were reported to be 10–100 times lower than that of the coastal species, due to much lower concentrations of ^{226}Ra in the deep sea, and hence precise measurements in the deep-sea species requires the utility of TIMS. Radium-228 (free from ^{226}Ra) spike is added as a yield tracer in the isotope-dilution TIMS method (Andrews et al. 1999a). The detection limit by TIMS method is significantly lower than that of ICPMS (Hou and Roos 2008). Often the Ca content in biogenic and inorganic carbonate is about 35–40% and hence separation of radium from calcium and barium is essential to obtain good radium ionization efficiency in thermal ionization mass spectrometry (TIMS). For the separation of Ca and Ba from Ra, ion-exchange separation techniques have been employed (Chabaux et al. 1994; Andrews et al. 1999a). With TIMS, in about 1.1–1.3 g of otolith sample with ~ 0.5 mBq/g, the analytical uncertainty was reported to be 1.4–2.3% while about 15 times more material was required in the radon emanation method to obtain an analytical uncertainty of 3.4–5.2% (Andrews et al. 1999a). The alpha spectrometry yielded comparable analytical uncertainty to that of TIMS (Andrews et al. 1999a). The detection limit for ^{226}Ra by ICP-MS ranges from 0.1 to 0.5 mBq while with TIMS, it is reported to be 37 μBq (summarized in Hou and Roos 2008).

37.2.2 Precleaning of Carbonate Samples

There are impurities in many of the carbonate specimens. The extraneous material is commonly removed to obtain reliable ages/growth rates. A rigorous sequence of cleaning protocols involving oxidative, reductive and dilute acid treatments have been effectively utilized to eliminate detrital and adsorbed organic phases for trace metals in corals (Shen and Boyle 1988). There are two components of ^{210}Pb in corals: (i) ^{210}Pb derived from the decay of ^{226}Ra incorporated in the lattice structure and (ii) adsorbed ^{210}Pb (either by sorption or occlusion) in the coral surface (which is mostly unsupported or excess ^{210}Pb). The adsorbed component could be added any-time after the initial aragonite growth so long as the

growth layer is exposed to the surrounding environment and should be removed for reliable age determination. In areas where the growth rate is slower, the sorption of dissolved ^{210}Pb from the water column onto the organic tissue is likely higher and thus an inverse correlation between growth rate and excess ^{210}Pb concentration is expected, although no such relationship has been reported so far in literature. In mollusk shells and corals, chemical and mechanical precleaning procedures are routinely followed (to remove exterior contamination and loosely attached detritus). Briefly, the shell or coral fragments are mechanically brushed and rinsed with deionized water followed by rinsing in H_2O_2 and acetone. Repeated 15-min ultrasonication of the marine mollusk shells in H_2O_2 over several days resulted in the loss of up to 5% of the initial sample weight and the debris removed from such a cleaning was comprised of fragments of organic rich surface layer, and other unidentified minerals (Staubwasser et al. 2004). Adkins et al. (2004) reported a loss of $\sim 10\%$ of the coral mass when the samples were precleaned with a mixture of $\text{H}_2\text{O}_2/\text{NaOH}$ and $\text{H}_2\text{O}_2/\text{HClO}_4$. Such a treatment not only removed adsorbed radionuclides from the coral’s exterior but also dissolved some of the sample. For example, one *Desmophyllum cristagalli* coral sample was cut into three sections (Fig. 37.1) and two of those three sections (A and B) were both mechanically and chemically cleaned while the third one, C, was only mechanically cleaned. The top section that underwent mechanical cleaning only had 3–5 times higher ^{210}Pb activity than that was chemically-cleaned (Fig. 37.2, data taken from Adkins et al. 2004 online data). Since a major fraction of ^{226}Ra is lattice-bound while significant amount of excess ^{210}Pb is sorbed onto the coral, it is likely that chemical precleaning procedures preferentially remove the sorbed ^{210}Pb compared to ^{226}Ra . This topic needs further study. The near-equal activity of ^{226}Ra in both chemically-cleaned and only mechanically-cleaned samples (Adkins et al. 2004) supports the hypothesis that ^{226}Ra is lattice-bound. It is not known if sorbed ^{210}Pb is associated with one or more phases or multiple phases of organic matter and whether only selective phases are removed by the chemical cleaning. More work needs to be done with a number of leachants to quantify nature and extent of the ^{210}Pb removal and their association with organic components.

Andrews et al. (1999a, b) have provided rigorous cleaning procedure for otoliths. However, details on

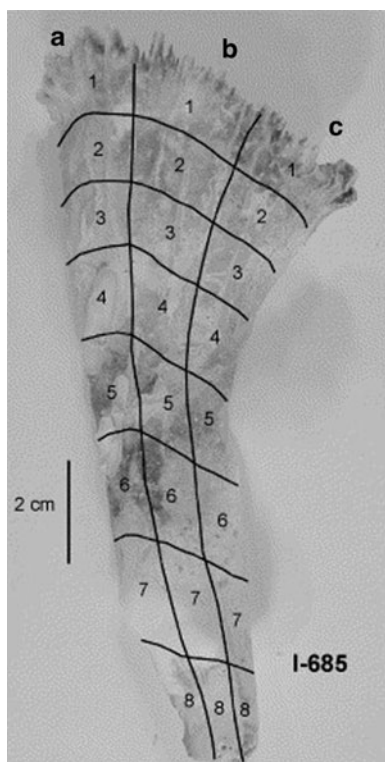


Fig. 37.1 Vertical sampling (A–C) of a deep-sea coral *D. cristagalli* sample I-685 (48°19.5'S; 179°29.5'W, 722 m). A and B were chemically cleaned and C was only mechanically cleaned. Concentrations of ^{210}Pb and ^{226}Ra in these three sections are shown in Fig. 37.2 (taken from Adkins et al. 2004). With permission from Elsevier

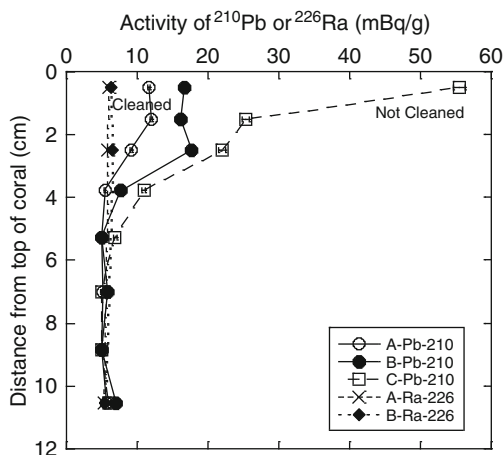


Fig. 37.2 Activities of $^{210}\text{Pb}_{\text{xs}}$ and ^{226}Ra of three transects of *D. cristagalli* coral. Subsamples in lines A and B were mechanically and chemically cleaned while in line C they were only mechanically cleaned. The importance of chemical cleaning is illustrated by the differences in the activities of ^{210}Pb in A–C. The data is taken from Adkins et al. (2004) and replotted

cleaning procedures of otoliths are sparse (in particular where ^{226}Ra was measured using scintillation or alpha counting methods), hence it is not clear if any rigorous cleaning procedure was followed or not in these studies. A brief outline of the cleaning procedures are as follows: the otoliths were cleaned in de-ionized water followed by ultrasonication sequentially in dilute Micro solution, de-ionized water and MQ water for at least 5 min in each of dilute Micro solution, de-ionized water and MQ water. Fine cleaning was followed with four cleaning solutions in sonicator in the following sequence: MQ water (10 min), 0.15 N HNO_3 (1 min), basic 1:1 mixture of 30% H_2O_2 :0.4 N NaOH (10 min), MQ water (10 min), and 0.001 N HNO_3 (3 times at 1 min). Extraneous material in speleothems is removed by mechanically brushing and rinsing with deionized water followed by rinsing in H_2O_2 and acetone. There is no information on rigorous cleaning protocols involving oxidative, reductive and dilute acid treatments for speleothems.

37.3 Age Determination of Carbonates

37.3.1 Basics of Age Determination from ^{210}Pb - ^{226}Ra Disequilibrium

37.3.1.1 Age Determination Based on Excess ^{210}Pb Method (Corals and Speleothems)

The excess ^{210}Pb activity in speleothems decreases from top to interior (Figs. 37.2 and 37.4; or bottom to top in the case of soda-straw stalactites). The activity of $^{210}\text{Pb}_{\text{xs}}$ at any depth z ($^{210}\text{Pb}_{\text{xs}}$) is given by:

$$^{210}\text{Pb}_{\text{xs}} = ^{210}\text{Pb}_{\text{xs}}^0 \exp(-\lambda z/S) \quad (37.1)$$

where $^{210}\text{Pb}_{\text{xs}}$ is the measured excess ^{210}Pb ($=^{210}\text{Pb}_{\text{total}} - ^{226}\text{Ra}$), $^{210}\text{Pb}_{\text{xs}}^0$ is the initial activity at the time of incorporation, z is the distance from the growing surface, S is the linear growth rate, and λ is the decay constant of ^{210}Pb ($=0.03067/\text{year}$). Implicit assumptions in (37.1) are: (i) the initial activity have remained constant throughout its growth period; (ii) the growth rate has remained constant (Sect. 37.3.1.2); and (iii) the system has remained $^{210}\text{Pb}_{\text{xs}}^0$ closed with respect to ^{226}Ra and ^{210}Pb after its formation (Sect. 37.3.2).

37.3.1.2 Modeling Variable Growth Rates of Corals or Speleothems

In the calculation of growth rates of speleothems or corals, it is assumed that the growth rate and the amount of excess ^{210}Pb incorporated are constant. When the $\ln ^{210}\text{Pb}_{\text{xs}}$ activities are plotted against the mean linear depth (from (37.1)), the resultant least squares best fit $^{210}\text{Pb}_{\text{xs}}$ slope is used to calculate the linear growth rate (S , in cm/year):

$$S = \text{slope} \times (-\lambda_{\text{Pb}}) \quad (37.2)$$

where λ_{Pb} is the decay constant of ^{210}Pb . Equation (37.2) is obtained from (37.1). The mass accumulation rates (ω_{Pb} in g/cm year) using $^{210}\text{Pb}_{\text{xs}}$ is calculated by plotting $\ln ^{210}\text{Pb}_{\text{xs}}$ activities against the cumulative mass depth and substituting ω_{Pb} for S in (37.2). The ages (year) of any layer can be determined from the equation:

$$t = \frac{M}{\omega_{\text{Pb}}} \quad (37.3)$$

where M is the cumulative mass depth (g/cm).

If mass accumulation rates are variable, then ages of various layers can be calculated using either: (i) the constant rate of supply (production (in speleothems) or accumulation (corals)) of ^{210}Pb model or (ii) the constant initial concentration (both corals and speleothems) model. The constant rate of supply model assumes that there is a constant production or accumulation resulting in a constant rate of supply to the accreting carbonate layer even if the growth rate varies over time. In the constant rate of supply model, the initial $^{210}\text{Pb}_{\text{xs}}$ activity varies inversely with the accumulation rate and is given by:

$$\sum A_m = \left(\sum A_\infty \right) (1 - e^{-\lambda_{\text{Pb}}t}) \quad (37.4)$$

where $\sum A_m$ is the $^{210}\text{Pb}_{\text{xs}}$ inventory to a mass depth m_i (Bq/cm) and $\sum A_\infty$ is the total $^{210}\text{Pb}_{\text{xs}}$ inventory of the carbonate sample. The age (year) of the carbonate layer is calculated from the following equation:

$$t = - \frac{\ln \left(1 - \frac{\sum A_m}{\sum A_\infty} \right)}{\lambda_{\text{Pb}}} \quad (37.5)$$

The constant initial concentration model assumes a constant initial activity at the top of the carbonate layer regardless of changes in net growth. Growth layer ages (year) based on this model can be calculated from:

$$t = - \frac{\ln \left(\frac{A_M}{A_0} \right)}{\lambda_{\text{Pb}}} \quad (37.6)$$

where A_0 is the initial $^{210}\text{Pb}_{\text{xs}}$ activity at the top of the carbonate layer (Bq/g) and A_M is the $^{210}\text{Pb}_{\text{xs}}$ activity at the cumulative mass depth “ M ”. Equations (37.2), (37.3), (37.5) and (37.6) can be employed to determine the ages under different model setting. So far, (37.2) and (37.3) have been employed, but (37.5) and (37.6) have not been used in dating carbonates with $^{210}\text{Pb}_{\text{xs}}$ method.

37.3.1.3 Age Determination Based on Daughter-Deficient Method (Mollusk Shells, Clams, Otoliths, Inorganic Carbonates in Concrete Structures)

In mollusk shells, clams, fish bones, and other inorganic carbonates where ^{226}Ra gets incorporated and ^{210}Pb is discriminated, the in-growth of ^{210}Pb from the decay of ^{226}Ra can be employed to determine the age of the specimen. The assumptions on this method dating are discussed in: (i) closed system (Sect. 37.3.2); and (ii) there is no initial ^{210}Pb (Sect. 37.3.5).

If $[^{210}\text{A}_0]$ and $[^{210}\text{A}_t]$ are the initial activity of ^{210}Pb and at the time of its death (or when it was caught alive) respectively, and $[^{226}\text{Ra}]$ is the activity of ^{226}Ra in the bivalve at that time, then:

$$\begin{aligned} [^{210}\text{A}_t] &= [^{210}\text{A}_0] \times \exp(-\lambda_{\text{Pb}}t) \\ &+ [\lambda_{\text{Pb}}/(\lambda_{\text{Pb}} - \lambda_{\text{Ra}})] [^{226}\text{Ra}] \times \{1 - \exp(-\lambda_{\text{Pb}}t)\} \end{aligned} \quad (37.7)$$

where λ_{Pb} is the decay constant of ^{210}Pb . When $t \gg$ half-life of ^{210}Pb , the $^{210}\text{Pb}/^{226}\text{Ra}$ ratio tends towards the equilibrium value of 1.014 ($=\lambda_{\text{Pb}}/(\lambda_{\text{Pb}} - \lambda_{\text{Ra}})$). Since $\lambda_{\text{Pb}} \gg \lambda_{\text{Ra}}$, if $^{210}\text{A}_0 = 0$, then, the age of the shell t can be calculated as follows:

$$t(\text{yr}) = \tau \ln\left(\frac{[^{226}\text{Ra}]}{\{[^{226}\text{Ra}] - [^{210}\text{At}]\}}\right) \quad (37.8)$$

Equation (37.7) assumes that the “clock” starts ticking at the time of the death of the organism. If the shell grew with a constant mass per unit time, then, its age is calculated from the equation:

$$[^{210}\text{At}] = [^{226}\text{Ra}] \times \{1 - \exp(-\lambda_{\text{Pb}}t)\} / \lambda_{\text{Pb}}t \quad (37.9)$$

The choice between (37.7) and (37.9) depends on the mass growth rate of the shell. In shallow waters, the clam generally starts with an initial slow growth followed by quasi-linear mass increase with time and then, a slowing down at old age. During this life time, some amount of ^{210}Pb would have been produced making the shell to have some amount of initial ^{210}Pb at the time of its death. If there is significant initial ^{210}Pb , then, ages calculated using (37.8) would be over estimates.

37.3.1.4 Mass-Growth Model for Dating Otoliths in Fish

Bennett et al. (1982) developed a mass-growth model, with the assumption of continuous addition of ^{210}Pb to the core. This model involves the assumption of the initial age of the redfish (*Sebastes diploproa*). Campana et al. (1990) determined the age of the central core of the otolith which was formed near the time of hatch, thus yielding the age of the fish.

Models have been developed that address the relationship between $^{210}\text{Pb}/^{226}\text{Ra}$ activity ratio in an otolith and age (Bennett et al. 1982; Smith et al. 1991; Francis 1995). The activity of ^{226}Ra at any time (A_{Ra}) in terms of its initial activity A_{Ra}^0 is given by (note: all activities are in Bq/g):

$$A_{\text{Ra}} = A_{\text{Ra}}^0 e^{-\lambda_{\text{Ra}}t} \quad (37.10)$$

The activity of ^{210}Pb (A_{Pb}) at any time from the production of ^{226}Ra and initial activity A_{Pb}^0 is given by:

$$A_{\text{Pb}} = A_{\text{Ra}}^0 \frac{(\lambda_{\text{Pb}})}{(\lambda_{\text{Pb}} - \lambda_{\text{Ra}})} \{e^{-\lambda_{\text{Ra}}t} - e^{-\lambda_{\text{Pb}}t}\} + A_{\text{Pb}}^0 e^{-\lambda_{\text{Pb}}t} \quad (37.11)$$

When the otolith grows, new material will accrete at the outer surface with an initial activity ratio of

$R^0 = A_{\text{Pb}}^0/A_{\text{Ra}}^0$. The core of the nucleus will have an activity ratio of $A_{\text{Pb}}/A_{\text{Ra}}$. The total activity of ^{226}Ra (S_{Ra}) and ^{210}Pb (S_{Pb}) in the otolith is calculated by integrating the product of the mass-growth rate ($G(t)$) and (37.10) for ^{226}Ra and $G(t)$ and (37.11) for ^{210}Pb (the formulation given below is adapted from Smith et al. 1991).

$$S_{\text{Ra}}(T) = \int_0^T G(t)A_{\text{Ra}} dt = \frac{M}{T} \int_0^T A_{\text{Ra}}^0 e^{-\lambda_{\text{Ra}}t} dt \quad (37.12)$$

$$S_{\text{Pb}}(T) = \int_0^T G(t)A_{\text{Pb}} dt = \frac{M}{T} \int_0^T A_{\text{Ra}}^0 \frac{(\lambda_{\text{Pb}})}{(\lambda_{\text{Pb}} - \lambda_{\text{Ra}})} \times \{e^{-\lambda_{\text{Ra}}t} - e^{-\lambda_{\text{Pb}}t}\} dt + \frac{M}{T} \int_0^T A_{\text{Pb}}^0 \{e^{-\lambda_{\text{Pb}}t}\} dt \quad (37.13)$$

where A_{Pb} and A_{Ra} and λ_{Pb} and λ_{Ra} are the activities and decay constants of ^{210}Pb and ^{226}Ra , respectively; t is the time since from the formation of otolith; $R^0 = A_{\text{Pb}}^0/A_{\text{Ra}}^0$; S_{Pb} and S_{Ra} are the total activities of ^{210}Pb and ^{226}Ra , respectively; $G(t)$, M and T are the mass growth rate, total mass, and age, respectively.

Integration of (37.12) and (37.13) and dividing S_{Pb} by S_{Ra} and simplifying we get

$$\frac{A_{\text{Pb}}(T)}{A_{\text{Ra}}(T)} = \frac{S_{\text{Pb}}}{S_{\text{Ra}}} = \frac{(\lambda_{\text{Pb}})}{(\lambda_{\text{Pb}} - \lambda_{\text{Ra}})} + \left\{ R^0 - \frac{(\lambda_{\text{Pb}})}{(\lambda_{\text{Pb}} - \lambda_{\text{Ra}})} \right\} \frac{\lambda_{\text{Ra}}(1 - e^{-\lambda_{\text{Pb}}T})}{\lambda_{\text{Pb}}(1 - e^{-\lambda_{\text{Ra}}T})} \quad (37.14)$$

The age of the otolith core is T years and variation of its activity with time is governed by the radioactive decay equation. The activity ratio of the $^{210}\text{Pb}/^{226}\text{Ra}$ in the otolith core at any future time is given by combining (37.10), (37.11) and (37.14), we get

$$\frac{A_{\text{Pb}}(t)}{A_{\text{Ra}}(t)} = \frac{(\lambda_{\text{Pb}})}{(\lambda_{\text{Pb}} - \lambda_{\text{Ra}})} \{1 - e^{-(\lambda_{\text{Pb}} - \lambda_{\text{Ra}})(t-T)}\} + \left[\frac{(\lambda_{\text{Pb}})}{(\lambda_{\text{Pb}} - \lambda_{\text{Ra}})} \right] \left\{ R^0 - \frac{(\lambda_{\text{Pb}})}{(\lambda_{\text{Pb}} - \lambda_{\text{Ra}})} \right\} \times \frac{\lambda_{\text{Ra}}(1 - e^{-\lambda_{\text{Pb}}t})}{\lambda_{\text{Pb}}(1 - e^{-\lambda_{\text{Ra}}t})} e^{-(\lambda_{\text{Pb}} - \lambda_{\text{Ra}})(t-T)} \quad (37.15)$$

Since $\lambda_{\text{Pb}} \gg \lambda_{\text{Ra}}$ and the decay of ^{226}Ra in 100 years is only 4.3%, (37.14) and (37.15) simplify to:

$$\frac{A_{pb-210}}{A_{Ra-226}} = 1 - (1 - R^0) \frac{(1 - e^{-\lambda t})}{\lambda t} \quad \text{when } 0 < t < \leq T \quad (37.16)$$

$$\frac{A_{pb-210}}{A_{Ra-226}} = (1 - e^{-\lambda(t-T)}) + \frac{\{1 - (1 - R^0)(1 - e^{-\lambda T})\}}{\lambda T} \times e^{-\lambda(t-T)} \quad \text{when } T < t \quad (37.17)$$

From the measured values of $^{210}\text{Pb}/^{226}\text{Ra}$, the age can be calculated using (37.11) (when $0 < t \leq T$) and (37.17) (when $T < t$).

37.3.2 Validity of Closed System Assumption

The ages of the carbonates rely on the measured $^{210}\text{Pb}/^{226}\text{Ra}$ disequilibrium and assumptions regarding the behavior of Pb and Ra in the carbonate matrix. The accuracy and reliability of age determination and/or growth rates critically depends on the fundamental assumptions upon which the dating method is based. One of the critical assumptions is that the system remains closed with respect to transport of the parent and the daughter. In the case of $^{210}\text{Pb}/^{226}\text{Ra}$, all the daughter products of ^{226}Ra (mainly ^{222}Rn and its short-lived daughter products including ^{210}Pb (^{210}Bi and ^{210}Po in case if we measure ^{210}Pb via ^{210}Po)) must remain as a closed system (no exchange with the surrounding). The carbonate sample that is being analyzed must be pure without any detritus or coating of Fe/Mn oxides or organic material. A detailed discussion is given below.

Different geochemical processes such as recrystallization, diffusion of ions through growth surfaces or porous grains, and differences in geochemical affinities between members of the daughter products from ^{226}Ra to ^{210}Po in the ^{238}U decay chain can result in disequilibrium between ^{210}Pb and ^{226}Ra in carbonates. Unaltered corals are generally free of recrystallization and have consistently yielded reliable concordant ages obtained from at least two pairs in the three pairs ($^{234}\text{U}/^{238}\text{U}$, $^{231}\text{Pa}/^{235}\text{U}$ and $^{230}\text{Th}/^{234}\text{U}$) in the ^{238}U and ^{235}U series (Ku 1976; Latham and Schwarcz 1992). However, when aragonite corals

undergo recrystallization and become calcite, some of the U has been reported to be lost (Ku 1976; Latham and Schwarcz 1992). It is not clear if there is any Ra loss during such recrystallization. However, as the dating range of $^{210}\text{Pb}/^{226}\text{Ra}$ pair is recent <150 years compared to the $^{231}\text{Pa}/^{235}\text{U}$ or $^{230}\text{Th}/^{234}\text{U}$ dating range, which are generally $>10,000$ years, recrystallization over such short periods is likely to be negligible. Growth of speleothems (stalactite, stalagmite and flowstone) takes place by slow precipitation of CaCO_3 . Such deposits are generally microcrystalline and compact and are not subject to post-depositional leaching and drip water from cave ceiling pass through them (Ku 1976). Speleothems with well-preserved internal stratigraphy have been successfully dated with $^{230}\text{Th}/^{234}\text{U}$ and $^{234}\text{U}/^{238}\text{U}$ methods going back to ~ 500 kyr, and therefore it seems unlikely that there is post-depositional mobility of ^{210}Pb or ^{226}Ra and its daughter products, particularly considering the short time periods involved. Note that the loss of U does not guarantee close system for Ra and Pb, as their geochemistries are different. Mollusk shells have been reported to have postmortem uranium uptake, with the fossil mollusks having about an order of magnitude higher U than their live counterparts (Kaufman et al. 1971, 1996). While living mollusk shell discriminates against U uptake resulting in very low concentrations of ^{238}U (0.05–0.10 ppm; Broecker 1963; Kaufman et al. 1971), the presence of higher amounts of U in fossil shells is attributed to diffusion along growth surfaces. ^{226}Ra is incorporated into carbonates (aragonite) from freshwater and seawater at the Ra/Ca ratio present in the water. Although no observation has been reported on the post formation migration of the daughter products of ^{226}Ra from bivalves, loss of ^{222}Rn through diffusion from fish otoliths has been reported (Whitehead and Ditchburn 1995). In contrast, Andrews et al. (1999b) observed that there is no minor loss of ^{222}Rn from fish otolith if measurements are made after precleaning the samples and using isotope-dilution TIMS. Baker et al. (2001) observed that an average of $\sim 1.8\%$ of ^{222}Rn from fish otoliths escapes. The recoil range of ^{222}Rn when ^{226}Ra undergoes alpha decay is typically $0.04 \mu\text{m}$ and hence only a small fraction of the ^{222}Rn produced from the decay of ^{226}Ra atoms that are in the outer $0.04 \mu\text{m}$ layer can recoil and escape the mineral, assuming that ^{226}Ra is uniformly distributed within the carbonate sample.

37.3.3 Distribution Factor for Pb (D_{Pb}) and Ra (D_{Ra})

The distribution factor (also commonly called *discrimination factor*, *concentration factor*, *empirical partition coefficient* or *distribution coefficient*) compares the concentration of an element in the specimen (mollusk, coral, speleothem, otolith or other specimen) to that in the surrounding water from which the element is drawn, (e. g., coastal or deep-sea water, lakes, rivers, etc) and is commonly normalized with respect to Ca. It is defined as:

$$\text{Distribution Factor} = \frac{[\text{Element/Ca}]_{\text{specimen}}}{[\text{Element/Ca}]_{\text{water}}}$$

where the terms in brackets represent concentrations of the element divided by the concentration of calcium in the specimen and water, respectively. The factors that can affect the values of distribution factor include thermodynamics of seawater, crystal chemistry of the specimen, biological differences between the species, temperature and growth rate of the specimen (e.g., Kelley et al. 2009). The distribution factor for Pb (D_{Pb}) varies between 2 and 20 for corals (Table 37.1). This relatively large variation is due to the varying amount of ^{210}Pb adsorbed on the organic film at the growing surface of the corals. There is no data on D_{Pb} for inorganic carbonates (such as speleothems and flowstones). D_{Ra} values for corals vary between 1.3 and 4, significantly higher than the values reported for other elements in the same group, such as Sr and Ba.

Table 37.1 D_{Pb} and D_{Ra} ^a values in organic and inorganic carbonates

Sample	D_{Pb}	D_{Ra}	References
Corals			
<i>D. cristagalli</i>	3–20	4	Adkins et al. (2004)
Atlantic coral	8	1.3–2.7	Druffel et al. (1990)
Bermuda	2.3	–	Shen and Boyle (1987)
North Atlantic	2.8–3.6	–	Kelley et al. (2009)
Hydrothermal carbonates	–	0.47–0.80	Rihs et al. (2000)
Aragonitic travertines	–	0.33	Sturchio (1990)
Calcitic travertines	–	0.40	Caboi et al. (1991)

The distribution coefficient (D) is defined as: $D_{Pb/Ra} = \frac{(^{210}\text{Pb} \text{ or } ^{226}\text{Ra})/\text{Ca}_{\text{coral}}}{(^{210}\text{Pb} \text{ or } ^{226}\text{Ra})/\text{Ca}_{\text{seawater}}}$

^aEquilibrium value of 0.013 for D_{Ra} in calcite at 25°C was proposed by Gnanapragasam and Lewis (1995)

The values >1 in corals are due to Ra adsorbed onto the organic films at the growing layers of aragonite. In other carbonates (hydrothermal carbonates, aragonitic and calcitic travertines) the D_{Ra} values are <1.0 (Table 37.1). One other possible factor for the variations in the uptake of Ra in corals follows that proposed to explain the variations of Sr (Weber 1973). There are three possible domains of Ra consisting of: (i) seawater surrounding the growing coral; (ii) a layer of organic soft tissue (symbiotic algae) of unspecified but finite thickness and (iii) skeletal CaCO_3 underlying the soft organic layer. During calcification, Ca^{2+} and Ra^{2+} dissolved in seawater diffuse through the surface layer of organic soft tissue to the site of skeletogenesis where these ions are incorporated into the growing calcitic layer (Weber 1973). Since Ra is heavier than that of Ca, it is expected to diffuse less rapidly through a given medium than would Ca and hence this could cause differences in the Ra concentration from coral to coral, even though Ra concentrations in the ambient waters could remain constant.

37.3.4 Excess ^{210}Pb Dating Method

37.3.4.1 Dating of Recent Corals

Most of the surface water corals are confined to shallow tropical seas while recent deep-ocean exploration using advanced acoustics and submersibles indicate that the deep sea corals are widespread. Diverse coral ecosystems exist in deep waters on continental shelves, slopes, seamounts and ridge systems around the world (Roberts et al. 2006).

The first dating of surface water corals based on $^{210}\text{Pb}/^{226}\text{Ra}$ disequilibrium method was reported for samples from the Discovery Bay, Jamaica and Onslow Bay, North Carolina (Moore and Krishnaswami 1972). They reported that the $^{210}\text{Pb}/^{226}\text{Ra}$ ratio did not obey the ideal ^{210}Pb decay suggesting that this ratio cannot be used to date coral growth rates though gross changes in the ratio can yield information on the nature of coral growth over time. These authors also observed that the bands in corals need not represent annual growth layers, but are response of coral growth to environmental changes. Subsequent studies by Moore et al. (1973) assumed that the ($^{210}\text{Pb}/^{226}\text{Ra}$) initial activity ratio in corals is constant and after

incorporation into skeletons, the system is closed with respect to ^{210}Pb and ^{226}Ra . They also reported high concentrations of ^{226}Ra in organic material associated with the coral skeleton. The first set of researchers did not report chemical cleaning of the coral specimens and hence it is likely that the excess ^{210}Pb profile ($^{210}\text{Pb}_{\text{xs}}$) reflected both adsorbed and lattice-bound $^{210}\text{Pb}_{\text{xs}}$ (Moore and Krishnaswami 1972; Moore et al. 1973; Dodge and Thomson 1974). The reported growth rates for deep-sea corals vary over two orders of magnitude, from 0.11 to 26 mm/year, although all these determinations did not all employ radiometric dating methods (Bell and Smith 1999; Druffel et al. 1990). Details on the calculation of growth rates of corals are given in Sect. 37.3.1.1.

A comparison of the $^{210}\text{Pb}/\text{Ca}$ ratio in corals with that in the surrounding seawater showed that the $^{210}\text{Pb}/\text{Ca}$ ratio in a coral is about 2 times higher than that of seawater (Dodge and Thomson 1974). They reported that the $^{210}\text{Pb}_{\text{initial}}$ activity in *D. labyrinthiformis* coral collected from Castle Harbor, Bermuda varied between 2.7 and 4.4 mBq/g, again suggesting variable initial ^{210}Pb values. Similarly, vertical profile of ^{226}Ra from a trunk of *Corallium niobe* at 600 m depth off the Little Bahama Banks showed that the activities varied between 1.7 and 3.6 mBq/g which was attributed to the presence of living tissue at outer edge and less rigorous precleaning (Druffel et al. 1990) (Fig. 37.3).

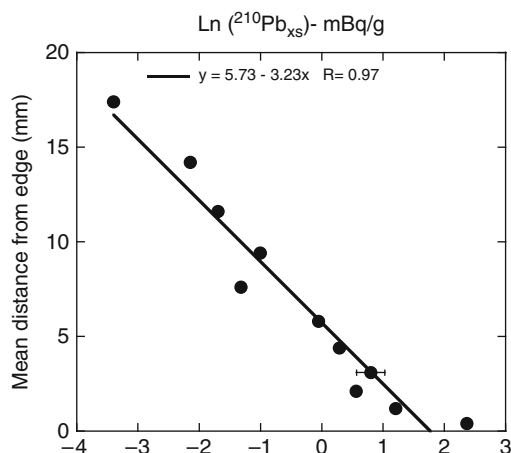


Fig. 37.3 $\text{Ln}(^{210}\text{Pb}_{\text{xs}})$ plotted against the mean distance from edge of the coral *Corallium niobe* (primarily calcite; data from Druffel et al. 1990). The calculated growth rate of 0.11 ± 0.02 mm/year agrees with the growth rate of 0.11 ± 0.03 mm/year calculated using ^{14}C ages (Druffel et al. 1990)

Recent studies after extensive cleaning of coral samples showed that $^{210}\text{Pb}_{\text{xs}}$ in their tips varied by a factor of 2, suggesting that either the tips are not growing at the same rate and/or the tips are growing with different distribution coefficients (D_{Pb}) (Adkins et al. 2004). Note that the D_{Pb} values depend on the $^{210}\text{Pb}_{\text{xs}}$ on coral, assuming that the deep-water ^{210}Pb concentration remains constant. The temporal variations in the atmospheric depositional flux will only affect the upper waters (<100 m or so) and deeper waters are expected to be in steady-state with respect to ^{210}Pb removal. Due to differences in the physiological, biological and biochemical characteristics of different species of corals, some species of aragonitic coral species, genus, or family can be enriched or depleted in Sr relative to the skeletal aragonite of other species, despite the ambient conditions for both being the same (Weber 1973). It is likely that this is also true for Ra. Variations in growth rates could determine the sorbed-component of ^{210}Pb in the coral and the D_{Pb} values. Inter- and intra species growth rate variations also have also been reported (Andrews et al. 2009). For example, *D. cristagalli* exhibited the slowest vertical extension rates of 0.5–2 mm/year, while *Lophelia* sp. and *E. rostrata* extended at rates (>5 mm/year) that were much faster (Cheng et al. 2000; Adkins et al. 2004). However, Houlbreque et al. (2010) reported that *E. rostrata* and *D. cristagalli* had comparable vertical extension rates, but *L. pertusa* had a higher vertical extension rate. Andrews et al. (2009) reported vertical extension rates (axial growth rate) of 7–14 mm/year for three different species of bamboo corals (*Keratoisis* sp.) from the northeastern Pacific Ocean while the corresponding radial growth rate varied between 0.055 and 0.10 mm/year. The radial growth rates are generally much lower, 0.01–0.08 mm/year (Adkins et al. 2004; Houlbreque et al. 2010). Druffel et al. (1990) reported very good agreement between the $^{210}\text{Pb}_{\text{xs}}$ based average growth rate (0.11 ± 0.02 mm/year) and ^{14}C -based growth rate (0.11 ± 0.03 mm/year). The faster growing species offer the potential of obtaining annual records. Furthermore, in *E. rostrata*, ^{210}Pb -based dating showed that each banding corresponds to 10 years suggesting that the assumption of annual banding is erroneous, as observed earlier by Moore and Krishnaswami (1972). Using $^{230}\text{Th}/^{234}\text{U}$ -ages, Houlbreque et al. (2010) also confirmed that the discordancy between growth-ring based ages and radiometric ages, emphasizing the

importance of absolute radiometric dating methods to constrain growth rates. In *Paragorgia* sp. there was no correlation between the ^{210}Pb -based growth rate and growth zone counts, as the skeletal structure is a spongy matrix and is highly organic with tissue present throughout the skeleton (Andrews et al. 2005). In a *Lepidisis* sp. colony the ^{210}Pb -based ages did not match with the zone counts (Tracy et al. 2007). The ^{210}Pb -based age data on *Keratoisis* sp. were significantly lower than those estimated from ^{14}C ages (Tracy et al. 2007). In two other specimens, *Keratoisis* sp. and *Corallium* sp. the ^{210}Pb dating method was successful to differing degrees. In the coral skeleton, there are fibrous aragonitic/calcitic bundles in which organic material could be trapped which may exhibit strong organic complexation with Pb. Similar observations have been reported for Ba by Hart and Cohen (1996). Moore et al. (1973) and Flor and Moore (1977) reported that the surface organic materials of living corals contained at least 10 times more ^{226}Ra than the carbonate matrix. Dodge and Thomson (1974) suggested the possibility that boring algae in Bermuda coral may play a role in fixing Ra. It is likely that this excess Ra decreases in older skeletal material due to the time-dependent degradation of trapped organic matter. These observations seem to indicate that the discordancy between ^{210}Pb -based growth rates and other methods (such as ^{14}C) could be due to lack of rigorous cleaning by oxidative, reductive and acid treatments to remove adsorbed ^{210}Pb . It is also not clear if the discordancy between $^{210}\text{Pb}_{\text{xs}}$ -based and growth-ring-based methods is due to inadequate cleaning protocols or if there are problems associated with the growth-ring counting method or a combination of both. To summarize, precleaning of corals (details given in Sect. 37.2.2) is a prerequisite to obtain reliable age information and comparisons of growth rates can only be reliably made for samples that have undergone rigorous chemical precleaning.

37.3.4.2 Dating of Speleothems

Speleothems (*Spelaion* means cave and *thema* means deposit in Greek) are CaCO_3 minerals (primarily calcite and aragonite) deposited in a cave environment, the common forms being stalactites, stalagmites and flowstones. These minerals are formed when groundwater supersaturated with respect to CaCO_3 drips from

ceiling of caves. During this process, part of soil-derived CO_2 dissolved in the water escapes resulting in precipitation of CaCO_3 . ^{222}Rn concentrations in groundwater are generally high. The ^{222}Rn contained in the groundwater droplets decays to ^{210}Pb which gets incorporated into the precipitating CaCO_3 . Dripping water from the cave roof deposits CaCO_3 on the ceiling roof and gradually constructs a hollow tube stalactite (also called “soda-straw”) which starts with a diameter of ~5 mm, equivalent to the size of a water droplet. Growth of the soda-straw stalactites occurs longitudinally as new rings of calcite form at the tip from where water drops are suspended before falling. During the finite time that the water droplets hang in the tip of the soda-straw, decay of ^{222}Rn results in ^{210}Pb and thus, ^{210}Pb is incorporated at different layers of the stalactite. The bottom-most layer from the cave ceiling is the most recent deposit and the age of the soda-straw stalactite gets older from the base to the top. If the central canal of the straw becomes plugged, water begins to run down the exterior producing lateral growth that results in characteristic icicle shapes. ^{222}Rn containing water flowing over the icicle stalactite produces ^{210}Pb and CaCO_3 precipitates layer by layer and in each layer $^{210}\text{Pb}_{\text{xs}}$ is incorporated. In this case, the outmost layer is the youngest, similar to Mn-nodules that grow at the bottom of the ocean floor. When the dripping water falls on the ground, some of the remaining CO_2 from the water escapes and CaCO_3 precipitate on the floor forming stalagmites. They grow upwards from the floor toward the drip source. Here again the ^{222}Rn remaining in the drip water is in contact with the calcite layer producing ^{210}Pb and hence there is also excess ^{210}Pb in the stalagmite. A fossil stalagmite in a cave where there was no actively growing stalactite was observed to have no $^{210}\text{Pb}_{\text{xs}}$, ruling out the possibility of adsorption of ^{210}Pb being derived from the decay of ^{222}Rn in air. The ^{222}Rn in the air could contribute to the ^{210}Pb on speleothems, but this is likely negligible. Tanahara et al. (1997) reported ^{222}Rn concentration in Gyokusen-do limestone cave in Okinawa (Japan) varying between 10 and 3,000 Bq/m^3 and being controlled by the exchange of air between the cave and external environment. The ^{226}Ra concentrations in sediments, speleothems and limestone within that particular cave were very low (1.8–41.8 mBq/g) suggesting that most of the elevated ^{222}Rn levels in air are derived from the degassing of ^{222}Rn during the dripping of water from the ceiling.

The ^{210}Pb in the outer most layer of icicle-shaped currently-growing stalactite was reported to be as high as 1.64 Bq/g. In the case of a soda-straw stalactite, the bottom-most segment had values as high as 1.68 Bq/g while the parent-supported ^{210}Pb ($=^{226}\text{Ra}$) activity was <8.3 mBq/g (Baskaran and Iliffe 1993; Fig. 37.4). If the growth-rate and production of ^{210}Pb are constant, then, the exponential decrease of the activity from outer layer to inner layer (for icicle stalactite and stalagmite) or longitudinal distance from bottom (for soda-straw) can be utilized to obtain the average growth-rate (Baskaran and Iliffe 1993;

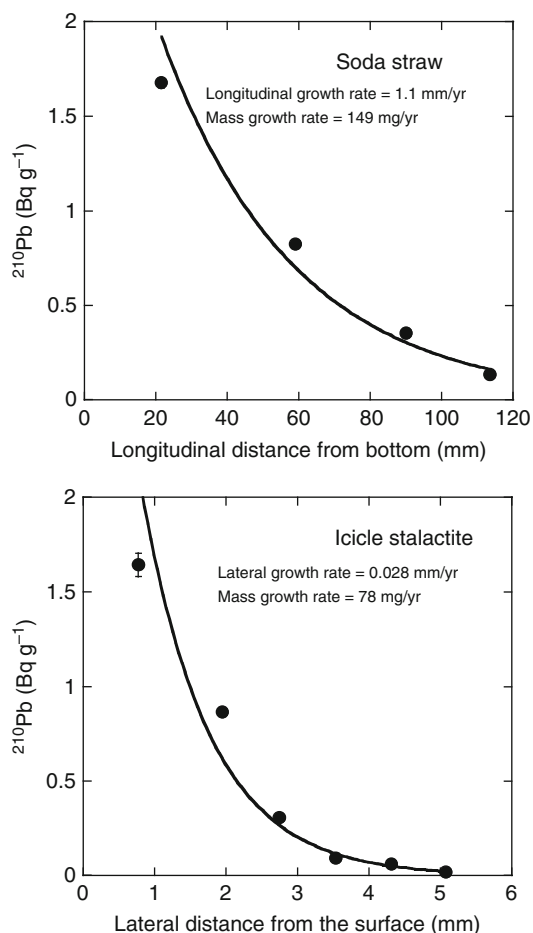


Fig. 37.4 ^{210}Pb contents of a soda straw and icicle shaped stalactite from central Texas. Concentration of ^{210}Pb exhibits an exponential decrease with distance from the bottom of the soda straw, the most recently deposited carbonate. In icicle shaped stalactite, the outer layer is the most recently deposited layer. Since all the data points fall very close to the curve fit indicating incorporation of excess ^{210}Pb had been constant with time (replotted the data from Baskaran and Iliffe 1993)

equations to calculate growth rates are given in Sects. 37.3.1.1 and 37.3.1.2). The factors that can affect the average growth-rate determination rate are: (i) non-uniform growth rate on the time-scale of interest (<150 years); (ii) hiatus in the continuous growth; (iii) variations in the groundwater concentrations of ^{222}Rn that discharges in the cave that can affect the production rates of $^{210}\text{Pb}_{\text{xs}}$; and (iv) variations in the discharge rate of groundwater, that can result in variations in the contact time of ^{222}Rn atom at the tip of the soda-straw stalactite or at the outermost layer of the icicle stalactite. The data is limited and hence we do not know how these factors listed above affect the growth rates of speleothems and this needs further investigation. Some of the speleothems are porous ($\sim 10\%$ porosity in white calcite fabrics of stalagmites which is attributed to the weaker crystalline coalescence, Baker et al. 1998). Such high porosity values will not affect the dating method using excess ^{210}Pb .

The longitudinal growth rates of soda-straw stalactites that are <100 year old have been reported to vary between 1 and 6 mm/year (linear: 1.1 mm/year, mass-growth rate: 149 mg/year from a central Texas cave; Baskaran and Iliffe 1993; 2.2 and 5.9 mm/year in southern Okinawa Island, Japan; Tanahara et al. 1998; 1.7 mm/year in Daeya cave, S. Korea; Woo et al. 2005). Paulsen et al. (2003) reported relatively low excess ^{210}Pb (13 mBq/g) in a stalagmite sample from Buddha Cave ($33^{\circ}40'\text{N}$; $109^{\circ}05'\text{E}$) in central China, with the excess ^{210}Pb found in the upper 9 mm of the stalagmite. The growth rate obtained using $^{210}\text{Pb}_{\text{xs}}$ of 0.089 ± 0.007 mm/year for the upper 14 mm is about 5.5 times faster than the growth rate reported for 1.4–16.5 cm using the $^{230}\text{Th}/^{234}\text{U}$ disequilibrium dating method and such a difference was attributed to change in deposition rate of CaCO_3 (Paulsen et al. 2003).

While the cave speleothems derived from groundwater have excess ^{210}Pb from the decay of ^{222}Rn , the carbonates precipitated from CO_2 -rich thermal waters in caves contain high concentrations of ^{226}Ra , with virtually no ^{210}Pb (Rihs et al. 1997; Condomines and Rihs 2006). Loss of ^{222}Rn from the hydrothermal stalagmites has not been documented. However, stalagmites that are >150 years yielding $^{210}\text{Pb}/^{226}\text{Ra}$ equilibrium value of 1.014 [$=\lambda_{\text{Pb}}/(\lambda_{\text{Pb}}-\lambda_{\text{Ra}})$] will ensure no loss of ^{222}Rn . Any loss of ^{222}Rn will result in a younger age estimate of the stalagmite. Condomines and Rihs (2006) analyzed a 3-mm thick layer of a stalagmite and reported a $^{210}\text{Pb}/^{226}\text{Ra}$ ratio

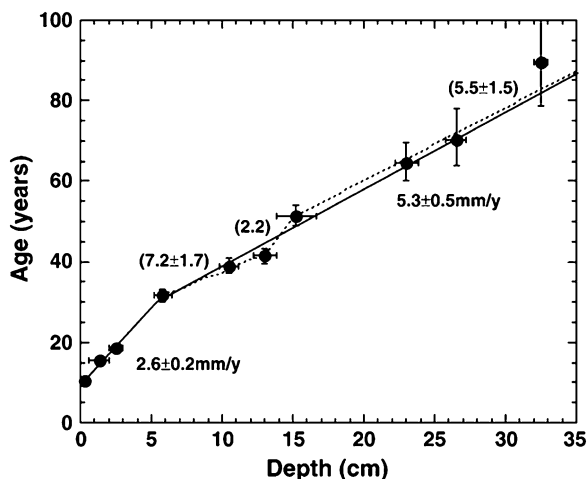


Fig. 37.5 Calculated $^{210}\text{Pb}/^{226}\text{Ra}$ -ages versus depth in the stalagmite. The data can be explained in two ways: (i) by two growth periods with axial growth rates of 5.3 and 2.6 mm/year; or (ii) the oldest one is subdivided in three episodes with respective growth rates of 5.5, 2.2 and 7.2 mm/year (*dashed lines*). Figure is from Condomines and Rihs (2006) with permission from Elsevier

of 0.029, yielding an average age of 0.8 year (corresponding to a growth rate of 1.8 mm/year), confirming that there is no significant initial ^{210}Pb incorporated in the stalagmite. The ^{226}Ra concentrations in the hydrothermal stalagmite varied almost by a factor of 3, from 0.42 to 1.27 Bq/g, and were attributed to the variations in Ra content of the thermal water and short-term fluctuations in Ra content resulting from the mixing of thermal waters with groundwater (Condomines and Rihs 2006). A plot the $^{210}\text{Pb}/^{226}\text{Ra}$ -based ages plotted against depth from the surface of the Mt. Cornadore (St. Nectaire, French Massif Central) stalagmite shows there is some scatter in the data, possibly due to variations in growth rates with two or three possible growth rates (Fig. 37.5; Condomines and Rihs 2006). A finer scale sampling will provide better insight into possible variations in growth-rates, if any.

37.3.5 Dating of Recent Carbonates by Daughter-Deficient Method

37.3.5.1 Mollusk Shells and Clams

Mollusk shells have been utilized to retrieve information such as changes in productivity, temperature and

salinity as well as chemical composition and the status of pollution in bays, estuaries and other coastal water bodies (e.g., Fritz and Poplawski 1974; Phillips 1976; Killingley and Berger 1979; Muhs and Kyser 1987; Klein et al. 1996; Vander Putten et al. 2000; Wanamaker et al. 2007; Lartaud et al. 2010). Mollusk shells are commonly found in a variety of environments that include raised sea coasts, former lake shores, paleosols, etc. During the skeletal formation, divalent cations (e.g., Sr, Ba, and Ra) are incorporated into the carbonate matrix by isomorphic substitution. At the same time, mollusk shells discriminate against many elements including Pb, as observed on two live bivalve samples (Clam *Corbicula* and Unionid mussel shells) from a shallow Florida lake with negligible initial ^{210}Pb concentration (Brenner et al. 1994). There is very limited data in the open literature that evaluates the initial activity of ^{210}Pb in mollusk shells. Although there appears to be no evidence that Pb gets incorporated into the calcite/aragonite crystal structure, it can be adsorbed on to the skeletal organic matrix (Lingard et al. 1992). Stable Pb/Ca ratios in surface water coral samples (corresponding to the last ~200 years) in the North Atlantic varied from 4 to 80 nmol/mol and such variations were primarily due varying inputs of atmospheric Pb in the surface waters (Kelley et al. 2009). Variations in the abundance and composition of the absorbed organic matrix could affect the amount of Pb incorporated during skeleton growth (Vander Putten et al. 2000). The total concentration of ^{210}Pb in the coastal/estuarine waters are low (of which bioavailable Pb is much lower) and hence it is likely that this contribution is likely very small. Also, it remains unknown if the organic layers in mollusks play any role at all in the removal of ^{210}Pb or ^{226}Ra , as was reported in corals. Based on trace metal studies on *Mytilus edulis* shells, Vander Putten et al.'s study (2000) indicates that the overall skeletal Pb trends may not be related to variations in aquatic Pb concentrations and skeletal Pb concentrations cannot be used to infer the past changes in the water. Fossil shells (~ 10^5 years old) have been reported to have higher U concentrations and $^{234}\text{U}/^{238}\text{U}$ activity ratios than live shells and this was attributed to postmortem U uptake, although interiors of shells up to 130 kyr have generally been closed to U uptake for the vast majority of their existence (Kaufman et al. 1971, 1996). Since U is not lattice-bound and the shells discriminate against U while Ra is taken-up along

with other divalent cations (Ca, Sr, Ba), the closed-system assumption with respect to Ra is very reasonable. Equations (37.7) and (37.9) assume that the system is closed with respect to ^{210}Pb and ^{226}Ra . While it is highly unlikely that ^{210}Pb will move out or move into the system, the only noble gas in the ^{238}U -decay chain, ^{222}Rn , could escape when it undergoes recoil, resulting in loss of ^{210}Pb and hence, a younger age estimate. The recoil range of ^{222}Rn when ^{226}Ra undergoes alpha decay is $\sim 0.04\ \mu\text{m}$ (e.g., Rama and Moore 1984) and hence only a small fraction (upper 40 nm) of Rn produced can escape due to recoil out of the mineral, assuming that ^{226}Ra is incorporated uniformly in the lattice structure. However, if there is large amounts of nanocracks (as was proposed by Rama and Moore 1984 for various natural minerals) or extensive radiation damage due to nuclei-, alpha, and fission-recoil tracks (e.g., Garver and Baskaran 2004) in bivalves, then, these cracks/tracks could serve as conduits for the leakage of ^{222}Rn and hence leakage from $>40\ \text{nm}$ from the surface could be significant, although the radiation damage is expected to be extremely low due to the relatively low U content and younger age of the samples. However, the role of nanopores from mineral has been challenged (Krishnaswami and Seidemann 1988).

Ages obtained using (37.8) are compared to the ages calculated from the collection record for 17 samples comprising of 9 different species collected in the Gulf and Atlantic coasts of US in Fig. 37.6. The ^{226}Ra concentrations in those 9 species varied between 2.0 and 15.9 Bq/kg. The concentrations of ^{226}Ra in one species collected from different bays as well species collected from one bay vary widely and are attributed to the differences in the mineralogy of the species and the concentrations in source waters. For example, ^{226}Ra concentrations in 9 mollusk shells from Tampa Bay varied between 20 and 168 Bq/kg (average = 57 Bq/kg; Baskaran, unpublished data) which is about an order of magnitude higher than those reported from 11 other estuarine and coastal waters (Baskaran et al. 2005) along the Gulf and Atlantic coasts. This is primarily due to the very high dissolved ^{226}Ra (1.5–4.9 Bq/100 L, Swarzenski et al. 2007) in Tampa Bay derived from phospho-gypsum deposits, compared to shelf waters (typically 0.3 Bq/100 L).

Clams from hydrothermal vents have been dated using U-Th-series radionuclides (Turekian et al. 1979, 1981, 1983). The vesicomysid clams (*Catyoptogena*

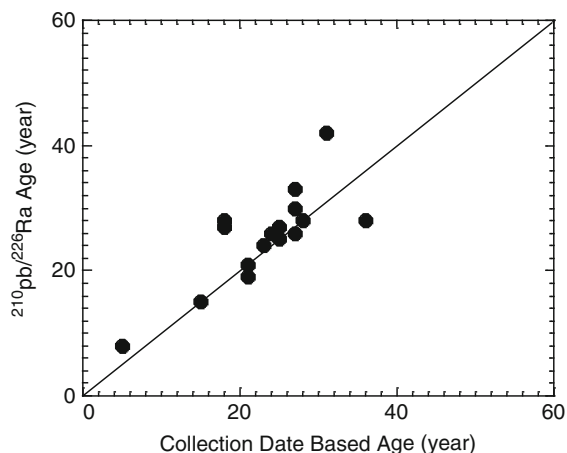


Fig. 37.6 Comparison of the ages of bivalves (9 different species from the Gulf and Atlantic coasts along the US; $n = 17$) obtained using $^{210}\text{Pb}/^{226}\text{Ra}$ activity ratios with those calculated from the collection record (taken from Baskaran et al. 2005). The error associated with $^{210}\text{Pb}/^{226}\text{Ra}$ -based method is relatively high mainly due to low levels of ^{226}Ra in the samples and the analytical method used (gamma-ray spectrometry). Diagonal line is the ideal line. All the data points fall on this diagonal line within $\pm 1\sigma$ as shown in Baskaran et al. (2005)

magnifica) are considered to be typical members of the deep-sea biological communities supported by sulfide-oxidizing chemoautotrophic bacteria (Karl et al. 1980; Felbeck et al. 1981). Turekian et al. (1979) showed that there is excess ^{210}Pb , with $^{210}\text{Pb}/^{226}\text{Ra}$ activity ratio of 3.79 ± 0.20 in dead vesicomysid clam from the Galapagos Rift. Growth rates between clams collected at different sites in deep ocean have been found to differ by a factor of ~ 500 and growth rates appear to be primarily controlled by the rate of supply of food (Turekian et al. 1975, 1979). A live clam collected from the Galapagos Spreading Center had $^{210}\text{Pb}/^{226}\text{Ra}$ ratios varying between 2.85 and 4.78 along the growth layers of a vesicomysid shell, while ^{226}Ra concentrations varied within 15% ($n = 4$, between 1.4 and 1.7 mBq/g of CaCO_3 ; Turekian and Turekian 1981). Although the live clam sample was cleaned by a series of washings with dilute HCl and chips of each sample were cleaned in 30% H_2O_2 , yet, a plot of the $^{228}\text{Th}/^{228}\text{Ra}$ ratio versus age indicated an initial $^{228}\text{Th}/^{228}\text{Ra}$ activity ratio of 0.4. Since uptake of Th has been assumed to be discriminated by clam, the presence of initial ^{228}Th ($t = 0$) was attributed either to trapped ^{228}Th in the lattice site of the growing aragonite or association of ^{228}Th with organic matrices within the shell which was not

removed by the cleaning procedure (Turekian et al. 1975, 1979; Turekian and Cochran 1981). The $^{210}\text{Pb}/^{226}\text{Ra}$ activity ratios in a live vesicomid clam from the 21°N East Pacific Rise hydrothermal area varied between 3.4 and 13.4, again suggesting excess ^{210}Pb , although ^{226}Ra concentrations remained constant within a factor of ~2 (1.1–1.7 mBq/g; Turekian et al. 1983), suggesting incorporation and/or sorption of variable ^{210}Pb in the shell. Thus, the origin of the excess ^{210}Pb found in vesicomid clams from the vicinity of hydrothermal vents, either incorporation in the lattice structure of aragonite or sorption of Pb on to the organic film at the growth zones or sorption on to oxyhydroxides of Fe/Mn, remains unknown. Absence of initial ^{210}Pb in other mollusks suggests that either sorption of ^{210}Pb on to Fe/Mn oxyhydroxides or on to organic film seems to be the cause for the presence of excess ^{210}Pb . Further study on the microstructural properties of different species of mollusks (both aragonitic and calcitic species) could provide insight into the mechanism(s) of Pb incorporation.

37.3.5.2 Dating of Fish Bones

Since the pioneering work on age determination of fish otoliths using $^{210}\text{Pb}/^{226}\text{Ra}$ by Bennett et al. (1982), a large number of studies have been conducted. Age distribution of a fish population is critically needed for fishery management. The total number of growth-zones is normally determined either by the whole otolith technique (counting external growth-zones) or otolith section technique (examination of otolith cross-sections). One of the fundamental questions is whether the growth-zones are yearly bands or not. The growth increment age determination method has limited applicability to deep-water or long-lived fishes (Mace et al. 1990; McFarlane and Beamish 1995). In cases such as shortraker fish, the growth zones in the otoliths are difficult to interpret, as light and dark growth zones may have irregular spatial patterns that bring into question whether they are annual marks (Hutchinson et al. 2007). The $^{210}\text{Pb}/^{226}\text{Ra}$ disequilibria method has been successfully employed to date otoliths in about a dozen different species (deep sea rock fish (*Sebastolobus altivelis* and *S. alascanus*, Kline 1996); *S. diploproa* (Bennett et al. 1982); redfish (*Sebastes mentella*, Campana et al. 1990); Orange roughy (*Hoplostethus atlanticus*, Fenton

et al. 1991; Smith et al. 1995); Sable fish (*Anoplopoma fimbria*, Kastle et al. 1994); blue grenadier (*Macruronus novaezelandiae*, Fenton and Short 1995); tropical snapper (Lutjanidae, Milton et al. 1995); warty oreo (*Allocyttus verrucosus*, Stewart et al. 1995); bank rockfish (*Sebastes rufus*); Pacific grenadier (*Coryphaenoides acrolepis*, Andrews et al. 1999b)).

There are two assumptions involved with the dating of the otoliths: (i) closed system (see Sect. 37.3.2) with respect to ^{210}Pb and ^{226}Ra and its daughter products, which implies that all ^{210}Pb produced from the decay of ^{226}Ra is retained within the system (no leakage of ^{222}Rn ; and ii) the initial activity of $^{210}\text{Pb} = 0$ or it is precisely known). In the case of otoliths, the core is generally considered to have formed near the time of hatch. Subsequent to that, the otolith accretes forming a new outer sheath of material having $^{210}\text{Pb}/^{226}\text{Ra}$ ratio of ~0 while the layers below it have produced some amounts of ^{210}Pb from the decay of ^{226}Ra . Thus, it is anticipated that there will be some gradient in the $^{210}\text{Pb}/^{226}\text{Ra}$ activity ratio from the center of otolith to the surface at the time when the outermost sheath is formed, resulting in age range between 0 year (corresponding to the outermost layer) to a finite year (corresponding to the center of the core and, the year of hatch). Analysis of the bulk otolith sample will thus yield an average value which will be an underestimate of the true age. A mass-growth model to obtain ages of otoliths is given in Sect. 37.3.1.4 and the $^{210}\text{Pb}/^{226}\text{Ra}$ -based ages of otoliths can be obtained using (37.11) and (37.17).

37.3.5.3 Dating of Whale Bones

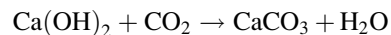
For the study of whale population dynamics, key information such as population structure, growth rates, age at sexual maturity and maximum age are needed. George et al. (1999) reported a wide range of ages (1 ± 6 to 211 ± 35 year) on a total of 48 eye globes of bowhead whales using the aspartic acid racemization technique. This method involves several assumptions affecting the age determination. Those assumptions include presence of possible cataract disease in the eye, presence of more asparagines residues in the eye globe, differential racemization between different aspartic residues, lower internal eye globe temperature than the deep body temperature, and possible

contamination of the eye globe with surrounding tissue or blood during dissection (George et al. 1999), and thus, validation of these ages by isotope-based method is needed. A few attempts to date whale bones (tympanic bullae and whale falls) have been made with limited success (Kastelle et al. 2003; Schuller et al. 2004). In the first attempt using radiometric dating on marine mammals, Kastelle et al. (2003) reported $^{210}\text{Pb}/^{226}\text{Ra}$ ratio to be <1 in the tympanic bullae of four gray whales, possibly providing age information, under the assumption that there was no initial ^{210}Pb and there was no metabolic turnover of Pb in the bone. The growth zones or laminae were not readily visible in the bullae which will be useful to validate the age obtained by $^{210}\text{Pb}/^{226}\text{Ra}$ method (Kastelle et al. 2003). In one gray whale the $^{210}\text{Pb}/^{226}\text{Ra}$ AR varied between 1.7 and 3.0, with the ^{226}Ra concentration range of 0.3–0.5 mBq/g, much lower than the other 4 samples (3.2–13.4 mBq/g). The $^{210}\text{Pb}/^{226}\text{Ra}$ AR varied between 1.6 and 8.8 in two bowhead whales, suggesting excess ^{210}Pb is present in the sample. It is widely known that bones have a strong affinity for Pb and excess ^{210}Pb has been reported in many other bones (e.g., sea otter bones, Baskaran et al. 2003; Caribou and Musk Ox bone, Hong et al. 2011). Schuller et al. (2004) assumed that only ^{226}Ra is retained by the bone and that the retention of ^{210}Pb takes place only after the whale's death. This assumption is highly questionable for two reasons: First from the time ^{226}Ra is incorporated, it will start producing ^{210}Pb and hence the assumption that initial ^{210}Pb (at the time of death) is negligible is likely flawed. Second, Pb is a bone seeking element and hence high levels of Pb (including ^{210}Pb) in mammalian bones have been reported (Baskaran et al. 2003; Hong et al. 2010). It has been shown that bone metabolism results in ~10% of bone remodeling in adults for humans, unlike otoliths in fish. Some of the factors that can affect this dating method include: (i) species effect which depends on the physiology or bone metabolism affecting the turnover of ^{210}Pb ; (ii) a remodeling process throughout their life that results in constant incorporation and release of bone ^{210}Pb ; and (iii) differences in feeding behavior and prey type between species. It has been shown that bowhead and gray whales grow very fast in the first year (~4.5 m at birth, ~8 m in 1 year and then at 0.5–1.0 m/year thereafter; Sumich 1986; Schell and Saupe 1993). During bone (bullae) growth, it is not clear what per-

centage of the mass is turned over since the first deposition and whether ^{210}Pb is incorporated during that period. Aggressive cleaning of the bullae resulted in low activity in the cleaning solution, indicating sorbed ^{210}Pb and/or ^{226}Ra were negligible (Kastelle et al. 2003). Assuming that the oldest original material was formed during fetal development and the system has remained closed (these are considered to be the densest bones in any mammal; Ketten 1992) with respect to mobility of Pb and Ra, then, sampling the interior portion of the bullae will yield the age since the whale was born. Clearly, more systematic work needs to be done to make this method robust for whale bones. All the inherent assumptions and uncertainties (such as initial $^{210}\text{Pb} = 0$, close system assumption (e.g., bone turnover resulting in release of ^{210}Pb)) need to be thoroughly investigated.

37.3.5.4 Dating of Inorganic Carbonates in Concrete Structures

Secondary carbonate mineral growth occurs primarily in the form of stalactites, stalagmites, flowstones and pedogenic carbonates. Formation of secondary carbonate mineral growths on concrete structures is widely believed to initiate and accelerate the degradation of the structures below which it is formed. Much of the Ca needed for the formation of CaCO_3 under concrete structures is derived from the concrete, as there is no soil cover above the structures (Troxell et al. 1968; Lea 1970). The suggested overall chemical reaction that drives the formation of carbonates in environments associated with concrete is given by (e.g., Krishnamurthy et al. 2003):



When surface water containing Ca and ^{226}Ra infiltrates through the cracks in the bridge, Ra gets incorporated into the carbonate that precipitates from the flowing water. Since Pb is highly particle-reactive, it is likely that the initial ^{210}Pb is 0 and it grows towards equilibrium from ^{226}Ra and thus, the ^{210}Pb - ^{226}Ra disequilibrium can be utilized to date the age of concrete-derived carbonate mineral collected under the bridge.

If the formation of the carbonate takes place shortly after the formation of the bridge, then, the oldest age obtained can be compared to the age of the bridge. The

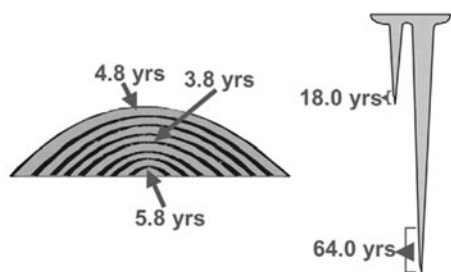


Fig. 37.7 Cross sectional views of the flowstones and stalactite specimens from the Michigan site along with their ^{210}Pb dates. The arrows indicate the spots of sampling for radionuclide analysis. Figure is taken from Krishnamurthy et al. (2003)

ages of 5 samples from flowstones and stalactite samples collected from a bridge in Michigan is given in Fig. 37.7. The dates were obtained on composite sample and hence the date is an average age and thus can be considered as a minimum age (Krishnamurthy et al. 2003). The age of the longer stalactite yielded an age of 64 ± 23 years (Fig. 37.7). The time elapsed between the collection of sample (1998) and construction of the bridge (1931) is 67 years, the age seems to suggest the stalactite started forming within a few years after the bridge construction. The ages of flowstones are much younger than the stalactites suggesting that the flowstone was formed much later in the degradation process. Although there is only one study and the scope was limited, more thorough study from other bridges are needed. This study holds the promise of providing valuable information on the timing of the onset of degradation of the concrete structures.

37.4 Future Directions

From the studies conducted so far, there are several outstanding issues that need further investigation. Although a number of researchers have dated recent corals based on excess ^{210}Pb method, it is not clear if the ^{210}Pb is incorporated into the lattice or it is adsorbed on to the organic tissue which is present in the outermost layers in corals. There is no data on how the concentration and composition of these organic layers affects the adsorption of ^{210}Pb . The temporal variations of organic tissue decomposition on corals also remain unknown. Recent (<150 years) clams

collected in the hydrothermal vent areas have been reported to have $^{210}\text{Pb}/^{226}\text{Ra}$ activity ratios of 3.4–13.4 while mollusks collected near coastal areas and lakes have ratios <1.0 . It is not clear what causes the former high values. They may result, for example, from sorption of ^{210}Pb onto the organic film at the growth zones and/or sorption on to oxyhydroxides of Fe/Mn. There are very limited studies on the growth rate/age determination of recently growing speleothems. The factors that can affect these ages include: non-uniform growth rate over the time-scales of interest, a hiatus in the growth rate, variations in the ^{222}Rn concentrations of the groundwater that discharges via stalactites in the cave ceiling and variations in the discharge rates of groundwater, resulting in variations of the contact time of ^{222}Rn atoms at the tip of the soda-straw stalactite or at the outmost layer of the icicle stalactite. Calibration of the historical data on temperature, amount of precipitation, and vegetation changes with proxy data obtained from speleothems that are <100–150 years old will put this branch of earth science on a firmer footing in the use of speleothems for much longer time scales. Dating of whale bones is still in its infancy and it is not clear how ^{210}Pb is deficient (i.e., $^{210}\text{Pb}_{\text{initial}} \text{ activity} = 0$) in bones compared to ^{226}Ra when bones have a high tendency to accumulate Pb. More systematic studies are needed to determine if the $^{210}\text{Pb}/^{226}\text{Ra}$ disequilibrium method can be employed at all to date mammalian bones. Indeed, if there is excess ^{210}Pb and the activity is known in bones at the time of death, we can utilize that bone by excess ^{210}Pb dating method (assuming that bone remains as a closed system after the animal's death) to determine the time elapsed since the death of the animal. So far, no attempts have been made in this direction. Secondary carbonate minerals occurring below bridges could serve as a powerful proxy to provide information on when the structure has begun to degrade, but more studies linking the age of the bridge (time elapsed from time when it was built to present) to the present condition of the bridge and the age of CaCO_3 formed under the bridge need to be conducted.

Acknowledgements The work synthesized in this manuscript was partially supported by NSF Grant (OCE-0851032). The author is grateful for a thorough review of four reviewers (S. Krishnaswami, John Smith, Allen Andrews and Kirk Cochran) of the earlier version of this manuscript.

References

- Adkins JF, Henderson GM, Wang SL et al (2004) Growth rates of the deep-sea scleractinia *Desmophyllum cristagalli* and *Enallpsammia rostrata*. *Earth Planet Sci Lett* 227: 481–490
- Andrews AH, Coale KH, Nowicki JL, Lundstrom C et al (1999a) Application of an ion-exchange separation technique and thermal ionization mass spectrometry to ^{226}Ra determination in otoliths for radiometric age determination of long-lived fishes. *Can J Fish Aquat Sci* 56:1329–1338
- Andrews AH, Cailliet GM, Coale KH (1999b) Age and growth of the Pacific grenadier (*Coryphaenoides acrolepsis*) with age estimate validation using an improved radiometric ageing technique. *Can J Fish Aquat Sci* 56:1339–1350
- Andrews AH, Cailliet GM, Kerr LA et al (2005) Investigations of age and growth for three deep-sea corals from the Davidson Seamount off central California. In: Freiwald A, Roberts JM (eds) *Cold-water corals and ecosystems*. Springer, Berlin, pp 1021–1038
- Andrews AH, Stone RP, Lundstrom CC, DeVogelaere AP (2009) Growth rate and age determination of bamboo corals from the northeastern Pacific Ocean using refined Pb-210 dating. *Mar Ecol Prog Ser* 397:173–185
- Baker MS, Wilson CA, VanGent DL (2001) Testing assumptions of otolith radiometric aging with two long-lived fishes from the northern Gulf of Mexico. *Can J Fish Aquat Sci* 58:1244–1252
- Baker A, Gentry D, Dreybrodt W, Barnes WL et al (1998) Testing theoretically predicted stalagmite growth rate with recent annually laminated samples: implications for past stalagmite deposition. *Geochim Cosmochim Acta* 62 (3):393–404
- Baskaran M (2011) Po-210 and Pb-210 as atmospheric tracers and global atmospheric Pb-210 fallout: a Review. *J Environ Radioact* 102:500–513
- Baskaran M, Iliffe TM (1993) Age determination of recent cave deposits using excess ^{210}Pb – a new technique. *Geophys Res Lett* 20(7):603–606
- Baskaran M, Krishnamurthy RV (1993) Speleothems as proxy for the carbon isotope composition of atmospheric CO_2 . *Geophys Res Lett* 20(24):2905–2908
- Baskaran M, Santschi PH (2002) Particulate and dissolved ^{210}Pb activities in the shelf and slope regions of the Gulf of Mexico waters. *Continent Shelf Res* 22:1493–1510
- Baskaran M, Hong GH, Dayton S, Bodkin JL, Kelley JJ (2003) Temporal variations of natural and anthropogenic radionuclides in sea otter skull tissue in the North Pacific Ocean. *J Environ Radioact* 64:1–18
- Baskaran M, Hong GH, Kim SH, Wardle WJ (2005) Reconstructing seawater and column ^{90}Sr based upon $^{210}\text{Pb}/^{226}\text{Ra}$ disequilibrium dating of mollusk shells. *Appl Geochem* 20:1965–1973
- Bell N, Smith J (1999) Coral growing on North Sea oil rigs. *Nature* 402:601
- Bennett JT, Boehlert GW, Turekian KK (1982) Confirmation of longevity in *Sebastes dipoproa* from Pb-210/Ra-226 measurements in otoliths. *Mar Biol* 71:209–215
- Brenner M, Peplow AJ, Schelske CL (1994) Disequilibrium between ^{226}Ra and supported ^{210}Pb in a sediment core from a shallow Florida lake. *Limnol Oceanog* 39:1222–1227
- Broecker WS (1963) A preliminary evaluation of uranium series inequilibrium as a tool for absolute age measurement on marine carbonates. *J Geophys Res* 68:2817–2834
- Caboi R, Cidu R, Fanfani L, Zuddas P, Zuddas PP (1991) Geochemistry of Funtana Maore travertines (central Sardinia, Italy). *Miner Petrogr Acta* 34:77–93
- Campana S, Zwanenburg KCT, Smith JN (1990) Pb-210/Ra-226 determination of longevity in redfish. *Can J Fish Aquat Sci* 47(1):163–165
- Campana SE, Oxenford HA, Smith JN (1993) Radiochemical determination of longevity in flyingfish *Hirundichthys affinis* using Th-228/Ra-228. *Mar Ecol Prog Ser* 100:211–219
- Chabaux F, Ben Othman D, Birck JL (1994) A new Ra-Ba chromatographic separation and its application to Ra mass spectrometric measurement in volcanic rocks. *Chem Geol* 114:191–197
- Cheng H, Adkins J, Edwards RL, Boyle EA (2000) U-Th dating of deep-sea corals. *Geochim Cosmochim Acta* 64:2401–2416
- Cohen AS, O’Nions RK (1991) Precise determination of femto-gram quantities of radium by thermal ionization mass spectrometry. *Anal Chem* 63:2705–2708
- Condomines M, Rihs S (2006) First ^{226}Ra - ^{210}Pb dating of a young speleothem. *Earth Planet Sci Lett* 250:4–10
- Craig H, Krishnaswami S, Somayajulu BLK (1973) Pb-210, Ra-226: radioactive disequilibrium in the deep sea. *Earth Planet Sci Lett* 17:295–305
- Crozaz G, Picciotto E, De Brueck W (1964) Antarctic snow chronology with Pb-210. *J Geophys Res* 69:2597
- Dodge RE, Thomson J (1974) The natural radiochemical and growth records in contemporary hermatypic corals from the Atlantic and Caribbean. *Earth Planet Sci Lett* 23:313–322
- Druffel ERM, King LL, Belostock RA, Buesseler KO (1990) Growth rate of a deep-sea coral using ^{210}Pb and other isotopes. *Geochim Cosmochim Acta* 54:1493–1500
- Felbeck H, Childress JJ, Somero GN (1981) Calvin-Benson cycle and sulphide oxidation enzymes in animals from sulphide-rich habitats. *Nature* 289:291–293
- Fenton GE, Short SA (1995) Radiometric analysis of blue grenadier, *Macruronus novaezelandiae*, otolith cores. *Fish Bull* 93:391–396
- Fenton GE, Short SA, Ritz DA (1991) Age determination of orange roughy, *Hoplostethus atlanticus* (Pisces: Trachichthyidae) using ^{210}Pb : ^{226}Ra disequilibria. *Mar Biol* 109:197–202
- Flor TH, Moore WS (1977) Radium/calcium and uranium/calcium determinations for Western Atlantic reef corals. In: *Proceedings of Third International Coral Reef Symposium*, Miami, pp 555–561
- Francis RICC (1995) The problem of specifying otolith-mass growth parameters in the radiometric estimation of fish age using whole otoliths. *Mar Biol* 124:169–176
- Fritz P, Poplawski S (1974) ^{18}O and ^{13}C in the shells of freshwater mollusks and their environments. *Earth Planet Sci Lett* 24:91–98
- Garver E, Baskaran M (2004) Effects of heating on the emanation rates of radon-222 from a suite of natural minerals. *Appl Radiat Isot* 61:1477–1485

- George JC, Bada J, Zeh J, Scott L, Brown SE, O'Hara T, Suydam R (1999) Age and growth estimates of bowhead whales (*Balaena mysticetus*) via aspartic acid racemization. *Can J Zool* 77(4):571–580
- Gnanapragasam E, Lewis BA (1995) Elastic strain energy and the distribution coefficient of radium in solid solutions with calcium salts. *Geochim Cosmochim Acta* 59:5103–5111
- Goldberg ED (1963) Geochronology with Pb-210. In: Radioactive dating. IAEA, Vienna, pp 121–131
- Hart SR, Cohen AL (1996) An ion probe study of annual cycles of Sr/Ca and other trace elements in corals. *Geochim Cosmochim Acta* 60:3075–3084
- Hong G-H, Baskaran M, Molaroni SM, Burger J (2011) Anthropogenic and Natural Radionuclides in Caribou and Muskoxen in the Western Alaskan Arctic and Marine Fish in the Aleutian Islands in the First Half of 2000. *Sci Total Environ* (in press)
- Hou X, Roos P (2008) Critical comparison of radiometric and mass spectrometric methods for the determination of radionuclides in environmental, biological and nuclear waste samples. *Anal Chim Acta* 608:105–139
- Houlbreque F, McCulloch M, Roark B, Guilderson T et al (2010) Uranium-series dating and growth characteristics of the deep-sea scleractinian coral: *Enallopsammia rostrata* from the Equatorial Pacific. *Geochim Cosmochim Acta* 74:2380–2395
- Hutchinson CE, Kastle CR, Kimura DK (2007) Using radiometric ages to develop conventional ageing methods for shortraker rockfish (*Sebastes borealis*). In: Biology, assessment, and management of North Pacific Rockfishes, Alaska Sea Grant College Program, AK-SG-07-01, pp 237–249
- Jweda J, Baskaran M, Van Hees E, Schweitzer L (2008) Short-lived radionuclides (^7Be and ^{210}Pb) as tracers of particle dynamics in a river system in southeast Michigan. *Limnol Oceanogr* 53(5):1934–1944
- Karl D, Wirsén C, Jannasch H (1980) Deep-sea primary production at the Galapagos hydrothermal vents. *Science* 207:1345–1347
- Kastelle CR, Kimura DK, Nevissi AE, Gunderson DR (1994) Using Pb-210/Ra-226 disequilibria for sablefish, *Anoplopoma fimbria*, age validation. *Fish Bull* 92:292–301
- Kastelle CR, Shelden KEW, Kimura DK (2003) Age determination of mysticete whales using $^{210}\text{Pb}/^{226}\text{Ra}$ disequilibria. *Can J Zool* 81:21–32
- Kaufman A, Broecker WS, Ku T-L, Thurber DL (1971) The status of U-series methods of mollusk dating. *Geochim Cosmochim Acta* 35:1155–1183
- Kaufman A, Ghaleb B, Wehmiller JF, Hillaire-Marcel C (1996) Uranium concentration and isotope ratio profiles within *Mercenaria* shells: geochronological implications. *Geochim Cosmochim Acta* 60:3735–3746
- Kelley AE, Reuer MK, Goodkin NF, Boyle ED (2009) Lead concentrations and isotopes in corals and water near Bermuda, 1780–2000. *Earth Planet Sci Lett* 283:93–100
- Ketten DR (1992) The cetacean ear: form, frequency, and evolution. In: Thomas JA, Kastelein RA, Supin AY (eds) Marine mammal sensory systems. Plenum, New York, pp 53–75
- Killingley JS, Berger WH (1979) Stable isotopes in a mollusk shell: detection of upwelling events. *Science* 205:186
- Klein RT, Lohmann KC, Thayer CW (1996) Bivalve skeletons record sea-surface temperature and $\delta^{18}\text{O}$ via Mg/Ca and $^{18}\text{O}/^{16}\text{O}$ ratios. *Geology* 24:415–418
- Krishnamurthy RV, Schmitt D, Atekwana EA, Baskaran M (2003) Isotopic investigations of carbonate growth on concrete structures. *Appl Geochem* 18:435–444
- Krishnaswami S, Seidemann DE (1988) Comparative study of Rn-222, Ar-40 and Ar-37 leakage from rocks and minerals – implications for the role of nanopores in gas transport through natural silicates. *Geochim Cosmochim Acta* 52:655–658
- Krishnaswamy S, Lal D, Martin JM, Meybeck M (1971) Geochronology of lake sediments. *Earth Planet Sci Lett* 11:407–414
- Ku T-L (1976) The uranium-series methods of age determination. *Annu Rev Earth Planet Sci* 4:347–379
- Ku T-L, Li HC (1998) Speleothems as high-resolution paleoenvironmental archives: records from northeastern China. *Proc Indian Acad Sci (Earth Planet Sci)* 107(4):321–330
- Lartaud F, Emmanuel L, de Rafelis M, Pouvreau S, Renard R (2010) Influence of food supply on the delta C-13 signature of mollusk shells: implications for palaeoenvironmental reconstructions. *Geo Mar Lett* 30(1):23–24
- Latham AG, Schwarcz HP (1992) Carbonate and sulphate precipitates. In: Ivanovich M, Harmon RS (eds) Uranium-series disequilibrium: applications to earth, marine, and environmental sciences. Clarendon, Oxford, pp 423–459
- Lea FM (1970) The chemistry of cement and concrete, 3rd edn. Edward Arnold, Glasgow
- Lingard SM, Evans RD, Bourgoin BP (1992) Method for the estimation of organic-bound and crystal-bound metal concentrations in bivalve shells. *Bull Environ Contam Toxicol* 48:179–184
- Mace PM, Fenaughty JM, Coburn RP, Doonasn IJ (1990) Growth and productivity of orange roughy (*Hoplostethus atlanticus*) on the north Chatham Rise, N.Z. *J Mar Freshw Res* 24:105–109
- Mathews KM, Kim CK, Martin P (2007) Determination of ^{210}Po in environmental materials: a review of analytical methodology. *Appl Radiat Isot* 65:267–279
- McFarlane GA, Beamish RJ (1995) Validation of the otolith cross-section method of age determination for sablefish (*Anoplopoma fimbria*) using oxytetracycline. In: Secor DH, Dean JM, Campana SE (eds) Recent developments in fish otolith research. The Belle W. Baruch Library in Marine Science, No. 19, University of South Carolina Press, Columbia, South Carolina, pp 319–329
- McKee B (2008) U-Th Series Nuclides in Estuarine Environments. In: Krishnaswami S, Cochran JK (eds) U and Th Series Radionuclides in Aquatic Systems. Krishnaswami S, Cochran JK (eds) Elsevier Press. pp. 193–226
- McNeary D, Baskaran M (2007) Residence times and temporal variations of ^{210}Po in aerosols and precipitation from Southeastern Michigan, USA. *J Geophys Res* 112:D04208. doi:10.1029/2006JD007639
- Milton DA, Short SA, O'Neill MF, Blaber SJM (1995) Ageing of three species of tropical snapper (Lutjanidae) from the Gulf of Carpentaria, Australia, using radiometry and otolith ring counts. *Fish Bull* 93:103–115
- Moore WS, Krishnaswami S (1972) Coral growth rates using ^{228}Ra and ^{210}Pb . *Earth Planet Sci Lett* 15:187–190

- Moore WS, Krishnaswami S, Bhat SG (1973) Radiometric determinations of coral growth rates. *Bull Mar Sci* 23: 157–176
- Muhs DR, Kyser TK (1987) Stable isotope compositions of fossil mollusks from Southern California: evidence for a cool last interglacial ocean. *Geology* 15(2):119–122
- Paulsen DE, Li H-C, Ku T-L (2003) Climate variability in central China over the last 1270 years revealed by high-resolution stalagmite records. *Quat Sci Rev* 22:691–701
- Phillips DJH (1976) The common mussel *Mytilus edulis* as an indicator of pollution by zinc, lead and copper, I: effects on environmental variables on uptake of metals. *Mar Biol* 38:59–69
- Rama, Moore WS (1984) Mechanism of transport of U-Th series radioisotopes from solids into groundwater. *Geochim Cosmochim Acta* 48:393–399
- Rama MK, Koide M, Goldberg ED (1961) Lead-210 in natural waters. *Science* 134:98–99
- Rihs S, Condomines F, Sigmarsson O (2000) U, Ra and Ba incorporation during precipitation of hydrothermal carbonates: implications for Ra-226-Ba dating of impure carbonates. *Geochim Cosmochim Acta* 64:661–671
- Rihs S, Condomines M, Fouillac C (1997) Uranium and thorium series radionuclides in CO₂ rich-geothermal systems from the French Massif Central. *J Radioanal Nucl Chem* 226:149–157
- Roberts JM, Wheeler AJ, Freiwald A (2006) Reefs of the deep: the biology and geology of cold-water coral ecosystems. *Science* 312:543–546
- Rutgers van der Loeff MM, Geibert W (2008) U- and Th-series nuclides as tracers of particle dynamics, scavenging, and biogeochemical cycles in the oceans. In: Krishnaswami S, Cochran JK (eds) *U and Th Series Radionuclides in Aquatic Systems*. Elsevier Press. pp. 227–268
- Schell DM, Saupe SM (1993) Feeding and growth as indicated by stable isotopes. In: Burns JJ, Montague JJ, Cowles CJ (eds) *The bowhead whale*. Soc Mar Mammal Spec Publ 2. Allen, Lawrence, pp 491–509
- Schmidt S, Cochran JK (2010) Radium and radium-daughter nuclides in carbonates: a brief overview of strategies for determining chronologies. *J Environ Radioact* 101:530–537
- Schuller D, Kadko D, Smith CR (2004) Use of ²¹⁰Pb/²²⁶Ra disequilibria in the dating of deep-sea whale falls. *Earth Planet Sci Lett* 218:277–289
- Shen GT, Boyle EA (1988) Determination of lead, cadmium, and other trace metals in annually-banded corals. *Chem Geol* 67:47–62
- Smith JN, Nelson R, Campana SE (1991) The use of Pb-210/Ra-226 and Th-228/Ra-228 dis-equilibria in the ageing of otoliths of marine fish. In: Kershaw PH, Woodhead DS (eds) *Radionuclides in the study of marine processes*. Elsevier Applied Science, New York, pp 350–359
- Smith DC, Fenton GE, Robertson SG, Short SA (1995) Age determination and growth of orange roughy (*Hoplostethus atlanticus*): a comparison of annulus counts with radiometric ageing. *Can J Fish Aquat* 52:391–401
- Staubwasser M, Henderson GM, Berkman PA, Hall BL (2004) Ba, Ra, Th and U in marine mollusk shells and the potential of ²²⁶Ra/Ba dating of Holocene marine carbonate shells. *Geochim Cosmochim Acta* 68:89–100
- Stewart BD, Fenton GE, Smith DC, Short SA (1995) Validation of otolith-increment age estimates for a deepwater fish species, the warty oreo *Allocyttus verrucosus*, by radiometric analysis. *Mar Biol* 123:29–38
- Sturchio NC (1990) Radium isotopes, alkaline earth diagenesis, and age determination of travertine from Mammoth Hot Springs, Wyoming, U.S.A. *Appl Geochem* 5:631–640
- Sumich JL (1986) Growth in young gray whales (*Eschrichtius robustus*). *Mar Mamm Sci* 2:145–152
- Swarzenski PW, Reich C, Kroeger KD, Baskaran M (2007) Ra and Rn isotopes as natural tracers of submarine groundwater discharge in Tampa Bay, Florida. *Mar Chem* 104:69–84
- Tanahara A, Taira H, Takemura M (1997) Radon distribution and the ventilation of a limestone cave on Okinawa. *Geochem J* 31:49–56
- Tanahara AH, Taira H, Yamakawa K, Tsuha A (1998) Application of excess Pb-210 dating method to stalactites. *Geochem J* 32(3):183–187
- Tracy DM, Neil HP, Marriott PAH, Andrews AH et al (2007) Age and growth of two genera of deep-sea bamboo corals (family *isididae*) in New Zealand waters. *Bull Mar Sci* 81(3):393–408
- Troxell GE, Davis HE, Kelley J (1968) *Composition and properties of concrete*, 2nd edn. McGraw-Hill Civil Engineering Series, McGraw Hill, New York
- Turekian KK, Cochran JK (1981) Growth rate of a Vesicomylid Clam from the Galapagos Spreading Center. *Science* 214:909–911
- Turekian KK, Cochran JK, Kharkar DP, Cerrato RM et al (1975) Slow growth rate of a deep-sea clam determined by ²²⁸Ra chronology. *Proc Natl Acad Sci USA* 72(7):2829–2832
- Turekian KK, Cochran JK, Nozaki Y (1979) Growth rate of a clam from the Galapagos Rise hot spring field using natural radionuclide ratios. *Nature* 280:385–387
- Turekian KK, Cochran JK, Bennett JT (1983) Growth rate of a vesicomylid clam from the 21°N East Pacific Rise hydrothermal area. *Nature* 303:55–56
- Vander Putten E, Dehairs F, Keppens E, Baeyens W (2000) High resolution distribution of trace elements in the calcite shell layer of modern *Mytilus edulis*: environmental and biological controls. *Geochim Cosmochim Acta* 64:997–1011
- Volpe AM, Olivares JA, Murrell MT (1991) Determination of radium isotope ratios and abundances in geologic samples by thermal ionization mass spectrometry. *Anal Chem* 63:913–916
- Wanamaker AD, Kreutz KJ, Borns HW, Introne DS et al (2007) Experimental determination of salinity, temperature, growth, and metabolic effects on shell isotope chemistry of *Mytilus edulis* collected from Maine and Greenland. *Paleoceanography* 22(2):PA2217
- Whitehead NE, Ditchburn RG (1995) Two new methods of determining radon diffusion in fish otoliths. *J Radioanal Nucl Chem* 198:399–408
- Weber JN (1973) Incorporation of strontium into reef coral skeletal carbonate. *Geochim Cosmochim Acta* 37:2172–2190
- Woo KS, Hong G-H, Choi DW, Jo KN et al (2005) A reconnaissance on the use of the speleothems in Korean limestone caves to retrospective study on the regional climate change for the recent and geologic past. *Geosci J* 9:243–247

Chapter 38

Isotope Dendroclimatology: A Review with a Special Emphasis on Tropics

S.R. Managave and R. Ramesh

Abstract Isotope dendroclimatological investigations have yielded crucial high-resolution climatic data spanning the past few centuries. The success of using stable isotope ratios of oxygen ($\delta^{18}\text{O}$) and hydrogen (δD) of tree cellulose for reconstructing past climate depends to a large extent upon the strength of the correlation between $\delta^{18}\text{O}$ (and δD) of rainfall and the amount of precipitation (in the tropics) or ambient temperature (mid to high latitudes). The usefulness of carbon isotope ratios ($\delta^{13}\text{C}$) on the other hand, depends upon the extent to which stomatal conductance is influenced by relative humidity and soil moisture, and the dependence of photosynthetic rate on light intensity. Temperature indirectly affects the $\delta^{13}\text{C}$ values of tree cellulose through its association with relative humidity and/or irradiance. These conditions put geographical constraints on suitable locations for isotope dendroclimatological investigations.

The composition of tree cellulose is affected by various isotopic fractionation processes occurring during and post photosynthesis. A reasonable mechanistic understanding of the former has been achieved while that of the latter is still inadequate. Improved quantitative understanding of various eco-physiological processes affecting isotopic fractionation and faster cellulose extraction techniques developed recently have made intra-annual isotopic studies increasingly valuable. Intra-molecular isotopic techniques too are being developed for resolving the stem cellulose iso-

topic ratio into signals associated with the source water (related to temperature/precipitation) and leaf water (relative humidity).

Issues related to temporally and spatially varying correlations between the isotopic composition of precipitation and climatic parameters (e.g. temperature and amount of precipitation) and the influence of post-photosynthetic effects of plant physiological factors on the isotopic composition of tree cellulose need to be resolved for the optimization of past climatic reconstruction using the stable isotopic compositions of tree cellulose.

38.1 Introduction

Among the proxies (e.g. ice cores, lake sediments, corals and speleothems) suitable for reconstruction of past climate, tree rings have unique advantages: they have a wide geographic distribution, preserve a continuous record, are annually resolved, and thus easily dated by ring-counting. Seasonality in the growth of trees driven by the ambient environment can result in discernible annual growth rings in trees. Individual tree rings faithfully record contemporary environmental signatures, and hence help decipher climatic variations over the life-span of the tree. In dendrochronology, cross-dating, a method of matching ring patterns of live trees with that of dead trees and wood fragments derived from archeological sites and historical buildings (e.g. Fritts 1976), is used to extend back the tree-ring record for the past several 1,000 years. Some of the longest records are the bristlecone pine (*Pinus aristata* and *Pinus longaeva*) chronology from the White Mountains, California, USA, spanning a period over 8,700 years (Ferguson and Graybill 1983) and the oak (*Quercus robur* and *Quercus petraea*)

S.R. Managave (✉)

Presently at Department of Earth Sciences, Pondicherry University, R.V. Nagar, Kalapet, Puducherry 605014
e-mail: shreyasman@gmail.com

R. Ramesh

Geosciences Division, Physical Research Laboratory, Navrangpura, Ahmedabad 380009, India

chronology from Germany, now going back to approximately 9,200 years (Becker and Schmidt 1989). In the early years of dendroclimatology, mostly variations in the ring-width were used for climate reconstruction. For example, in the trees from high latitude/altitude regions, wider (narrower) rings corresponded to higher (lower) temperature/precipitation. However, this simple relationship between width and climate is confounded by a variety of site specific non-climatic factors such as light availability, topography, soil type and forest thinning, ecological parameters (pest/insect infestations) and also genetic variability among trees of the same species (e.g. Fritts 1976; Cook 1990; Kress et al. 2009).

During the synthesis of plant biomass, various eco-physiological and climatological processes affect its stable isotope ratios of carbon ($\delta^{13}\text{C}$), hydrogen (δD) and oxygen ($\delta^{18}\text{O}$). The isotopic composition of tree rings is believed to be less influenced by biological and ecological parameters relative to ring-widths and could be more effective in climate reconstruction. For example, Rowell et al. (2009) observed a significant genetic variability in ring-width but not in $\delta^{13}\text{C}$ of cellulose of *P. radiata* growing in water-stressed conditions. Sano et al. (2010) observed that tree cellulose $\delta^{18}\text{O}$ was much more sensitive to rainfall fluctuations than ring-width and ring-density, the typical dendroclimatological parameters. Further, the isotopic records of tree rings can preserve low-frequency variations in climate (Gagen et al. 2007), difficult to discern from the ring-width record due to the “segment length curse” (the loss of low-frequency climate information as a result of detrending methods used to remove the age trend). It has been shown by previous studies (Schiegl 1974; Gray and Thompson 1976; Epstein and Yapp 1977; Burk and Stuiver 1981; Ramesh et al. 1985; Lipp et al. 1991; Feng and Epstein 1994; McCarroll and Loader 2004 and references therein; Treydte et al. 2006; Loader et al. 2008) that the isotopic records of oxygen and hydrogen of cellulose from individual growth rings can be successfully used as proxies for climatic parameters such as rainfall, humidity and temperature.

Some of the earlier reviews dealing with this subject were written by Ramesh et al. (1986a), Farquhar et al. (1989), Dawson et al. (2002), McCarroll and Loader (2004), Hobbie and Werner (2004), McCarroll and Loader (2006), Barbour (2007), Robertson et al. (2008), Sternberg (2009). Several chapters in Griffiths

(1998) and Dawson and Siegwolf (2007) deal with the climatic and plant physiological aspects of isotope dendroclimatology. In this review, we highlight some of the recent developments pertinent to the interpretation of isotopic composition of tree cellulose, a preferred component of wood for isotope studies, for reconstructing past climate with a special emphasis on the monsoon tropics. The studies related to the interpretations of $\delta^{18}\text{O}$ and $\delta^{13}\text{C}$ of tree cellulose are dealt with separately. As $\delta^{18}\text{O}$ and δD variations in tree cellulose carry similar information, δD variations are not discussed.

Isotopic compositions of oxygen and carbon in a sample are conventionally reported in the delta (δ) notation as deviations in parts per mil from the isotopic ratios of an internationally accepted standard:

$$\delta = \left(\frac{R_{\text{sample}}}{R_{\text{standard}}} - 1 \right) * 1,000, \quad (38.1)$$

where R is ratio of abundances of heavy and light isotopes (e.g. $^{18}\text{O}/^{16}\text{O}$, $^{13}\text{C}/^{12}\text{C}$). $\delta^{18}\text{O}$ of the sample are reported relative to VSMOW (Vienna Standard Mean Ocean Water, $^{18}\text{O}/^{16}\text{O} = 0.0020052$) while $\delta^{13}\text{C}$ values are reported with respect to VPDB (Vienna Pee Dee Belemnite, $^{13}\text{C}/^{12}\text{C} = 0.0112372$) (Mook 2006).

38.2 Oxygen Isotope Studies: Factors Influencing $\delta^{18}\text{O}$ of Tree Cellulose

The oxygen isotope composition ($\delta^{18}\text{O}$) of plants is affected by various physiological and environmental/climatic processes (Fig. 38.1). It mainly depends upon $\delta^{18}\text{O}$ of the source water, the level of evaporative enrichment of the source water in the leaf during transpiration, biochemical fractionation associated with the synthesis of sucrose in the leaf and the extent of exchange between carbohydrate and xylem water during cellulose synthesis. Since $\delta^{18}\text{O}$ of precipitation is directly related to temperature at mid to high latitudes (Dansgaard 1964) and the amount of precipitation in the tropics (Dansgaard 1964; Rozanski et al. 1993; Yadava et al. 2007; Schmidt et al. 2007; Bowen 2008), it is possible to use tree cellulose $\delta^{18}\text{O}$ as a powerful tool to reconstruct past climate. A brief description of processes that govern the above factors follows.

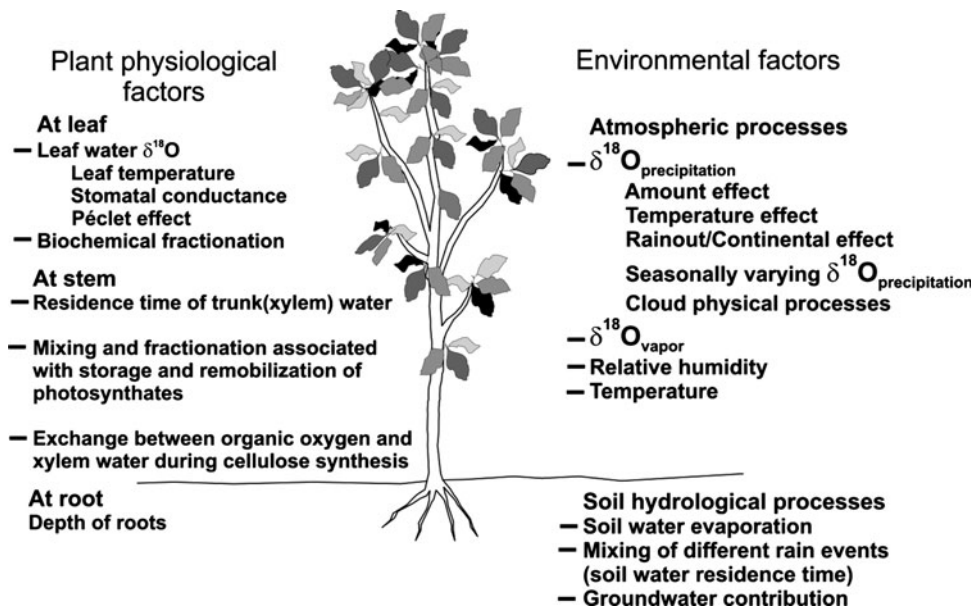


Fig. 38.1 Plant physiological and environmental/climatic factors influencing oxygen isotope ratios of plant cellulose

38.2.1 Atmospheric/Environmental Processes

This section describes atmospheric and environmental factors influencing plant cellulose $\delta^{18}\text{O}$. Among these, $\delta^{18}\text{O}$ of precipitation and atmospheric water vapor, and relative humidity are important atmospheric factors whereas soil hydrological processes are crucial environmental factors. $\delta^{18}\text{O}$ of precipitation and its subsequent evolution during various soil hydrological processes determine $\delta^{18}\text{O}$ of water trees take up through roots and use for photosynthesis. $\delta^{18}\text{O}$ of water vapor and relative humidity modify the source water $\delta^{18}\text{O}$ during transpiration. As this modified water is actually used for photosynthesis, a good knowledge of what decides $\delta^{18}\text{O}$ of local precipitation and atmospheric water vapor, and changes in relative humidity during the growing season are required to interpret the tree cellulose $\delta^{18}\text{O}$ record.

38.2.1.1 $\delta^{18}\text{O}$ of Precipitation

A detailed account of world-wide variation in the $\delta^{18}\text{O}$ and δD of rainfall since 1961 is maintained by the Global Network “Isotopes in Precipitation” (GNIP)

(IAEA/WMO 2006: <http://isohis.iaea.org>). On the global scale, $\delta^{18}\text{O}$ of precipitation is largely governed by ambient temperature. Decreasing temperature results in reducing saturation vapor pressure of air and drives the rainout process. As a result, the progressive precipitation associated with still lower temperatures becomes increasingly depleted in ^{18}O . Dansgaard (1964) demonstrated a linear relationship between surface air temperature (T_{annual}) and $\delta^{18}\text{O}$ of mean annual precipitation ($\delta^{18}\text{O}_a$) on the global scale as

$$\delta^{18}\text{O}_a = 0.695T_{\text{annual}} - 13.6. \quad (38.2)$$

In the tropics, the typical relationship between $\delta^{18}\text{O}$ of rainfall and surface air temperature is overshadowed by the amount effect, an inverse relationship between $\delta^{18}\text{O}$ of rainfall and amount of precipitation on the monthly (Dansgaard 1964; Rozanski et al. 1993) or individual rain event (Miyake et al. 1968; Yadava et al. 2007) scale. Dansgaard (1964) explained the amount effect in terms of (1) fractional removal of heavy isotopes in the rain; (2) equilibration of light rain (smaller drops) with enriched vapor below the cloud base; and (3) higher relative loss of light isotopes when raindrops evaporate below the cloud base in arid region. A recent model by Risi et al. (2008) suggests reevaporation of the falling rain, and

diffusive exchange with the surrounding vapor, and recycling of the subcloud layer vapor feeding the convective system as the likely causes for the amount effect. Yurtsever and Gat (1981) analyzed rainfall and its isotopic composition at 14 island stations in the equatorial belt, and found a linear relationship (linear correlation coefficient $r = 0.87$) between mean monthly $\delta^{18}\text{O}$ of rainfall ($\delta^{18}\text{O}_m$) and mean monthly rainfall amount (P_m)

$$\delta^{18}\text{O}_m = (-0.015 \pm 0.002)P_m - (0.47 \pm 0.42). \quad (38.3)$$

The average rate of depletion in $\delta^{18}\text{O}$ of rainfall with increase in monthly rain amount was $-1.5 \pm 0.2\%$ for 100 mm. This amount effect prevails in the precipitation in south and south-east Asia (Araguás-Araguás et al. 1998). Yadava and Ramesh (2005) measured rainfall amount and its $\delta^{18}\text{O}$ for all monsoon rain events in 1999 at Jharsuguda (22°N , 84°E), central India, and found a depletion rate of $-9.2 \pm 1.1\%$ per 100 mm rain for individual rain events and $-2.2 \pm 0.8\%$ per 100 mm of rain for monthly total rainfall. The correlation of $\delta^{18}\text{O}$ of precipitation with air temperature (amount of precipitation) is mostly prevalent poleward (equatorward) of 30°N/S (Fig. 38.2, Bowen 2008). More than 66% of the total stations with recorded isotope data of precipitation, and more than 80% of the earth's land surface exhibit relationships between climate variables (temperature and precipitation amount) and the isotopic composition of precipitation (Bowen 2008). Figure 38.2 exhibits regions where temperature and amount of precipitation correlate with $\delta^{18}\text{O}$ of precipitation. Trees growing in such areas are likely to preserve information on past precipitation/temperature, and are most suited for isotope dendroclimatology.

Rainout is a process by which a moving air mass loses its water vapor through precipitation and the remaining vapor becomes progressively depleted in ^{18}O . If at each stage within the cloud there is isotopic equilibrium between rain and vapor, $\delta^{18}\text{O}$ (and δD) of a moving air parcel can be modeled by Rayleigh fractionation (Clark and Fritz 1997)

$$\delta^{18}\text{O}_{V(f)} = \delta_0^{18}\text{O}_v + \epsilon^{18}\text{O}_{l-v} \cdot \ln f, \quad (38.4)$$

where $\delta^{18}\text{O}_{V(f)}$ and $\delta_0^{18}\text{O}_v$ are $\delta^{18}\text{O}$ of the residual fraction f of water vapor and the initial water vapor,

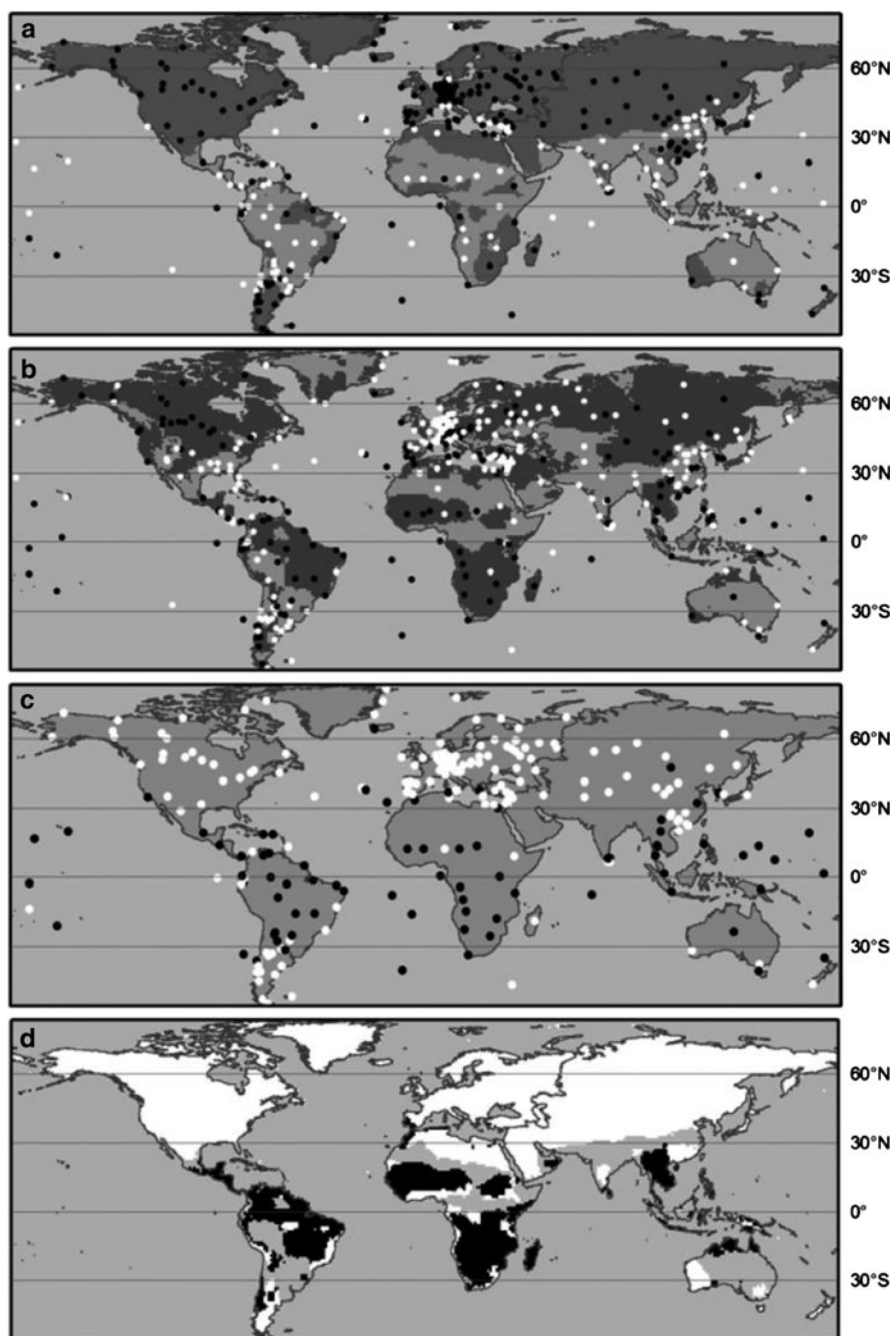
respectively; $\epsilon^{18}\text{O}_{l-v}$ the oxygen isotopic fractionation factor between the rain and vapor expressed in per mil (‰) units. At about 25°C , $\delta^{18}\text{O}$ of accompanying rainfall is about 9‰ higher relative to the vapor. An example of rainout effect in the Asian region is illustrated by Araguás-Araguás et al. (1998), who showed a progressive depletion of $\delta^{18}\text{O}$ of rainfall along the trajectory of Pacific monsoon from Haikou and Hong Kong (south of China) to Lhasa (Tibetan plateau) where $\delta^{18}\text{O}$ of rainwater changed from -7.2 to -18.3% , demonstrating the “continental” effect.

In addition to the amount and rainout (continental) effects, $\delta^{18}\text{O}$ of precipitation also changes with season (Fig. 38.3), plausibly implying different sources of vapor. In India, the southwest (SW) and northeast (NE) monsoons have different isotopic signatures (Geeta Rajagopalan 1996). Yadava et al. (2007) analyzed $\delta^{18}\text{O}$ of daily rains for 2 years at Mangalore (12.53°N and 74.52°E), which receives both the monsoons and showed that the NE monsoon precipitation is relatively more depleted in ^{18}O . This contrasts with observations elsewhere in Southeast Asia, where summer rains are depleted in ^{18}O relative to winter rains (Fig. 38.3, Araguás-Araguás et al. 1998).

38.2.1.2 $\delta^{18}\text{O}$ of Atmospheric Vapor

$\delta^{18}\text{O}$ of atmospheric water vapor is one of the factors that decide the $\delta^{18}\text{O}$ of leaf water and its effectiveness increases with relative humidity (Roden et al. 2000). Higher relative humidity facilitates towards achieving isotopic equilibration of atmospheric water vapor with leaf water. Unfortunately, the isotopic composition of the atmospheric water vapor has not been monitored as extensively as that of precipitation. In general, atmospheric vapor is assumed to be in isotopic equilibrium with local rainwater and its isotopic composition calculated using the corresponding equilibrium fractionation factor. It is known that $\delta^{18}\text{O}$ of atmospheric water vapor depends upon the moisture source and its interaction with the surface (Gat 1996; Tian et al. 2007). Further, mixing of water vapor from ocean and local evaporation is likely to affect $\delta^{18}\text{O}$ of local atmospheric water vapor. Srivastava (2009) found the atmospheric water vapor, in general, to be in equilibrium with ambient rain during the Indian monsoon.

Fig. 38.2 Significance level of correlation between long-term monthly average precipitation $\delta^{18}\text{O}$ and climatological parameters. (a, b) Stations and grid area with significant ($p < 0.05$; black dots and dark gray shading) and no significant (white dots, light gray shading) correlation between temperature (a) or precipitation amount (b) and $\delta^{18}\text{O}$. (c, d) Mode (white indicates temperature; black indicates precipitation) of the strongest climatological correlation at all stations (c) or grid points with one or more significant correlation (d) (from Bowen 2008)



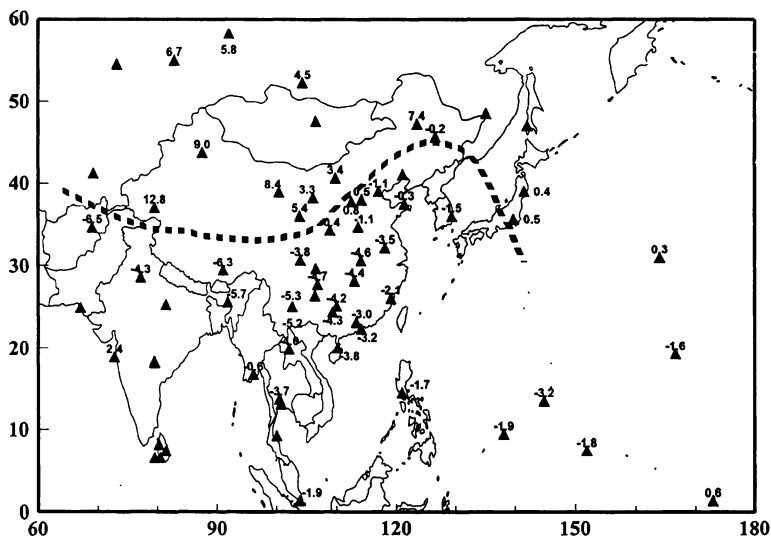
38.2.1.3 Relative Humidity

Atmospheric relative humidity too plays an important role in governing $\delta^{18}\text{O}$ of cellulose. During transpiration, lower ambient relative humidity increases the evaporative enrichment of ^{18}O in leaf water, which,

in turn leads to the synthesis of cellulose enriched in ^{18}O . It has been shown that in drier locations soil moisture deficit affects the $\delta^{18}\text{O}$ of cellulose (Saurer et al. 1997; Roden et al. 2005) as well.

In the tropics, quite often there might be a correlation between rainfall and relative humidity. If so, past

Fig. 38.3 Spatial distribution of the difference ($\delta^{18}\text{O}_{\text{summer}} - \delta^{18}\text{O}_{\text{winter}}$) at Asian stations. The *dashed line* separates the area of positive and negative values of the difference, and coincides with the maximum northward extent of the Intertropical Convergence Zone (ITCZ) in the region during summer (from Araguás-Araguás et al. 1998)



rainfall could be reconstructed even in the case when the amount effect is absent or only weakly present; higher rainfall, through its effect on relative humidity, would result in lower enrichment of the leaf water $\delta^{18}\text{O}$ and that of the subsequently formed cellulose. Further, changes in the atmospheric circulation pattern, especially with the movement of the Inter Tropical Convergence Zone (ITCZ), can induce seasonal variation in relative humidity in some parts of the tropics (Managave et al. 2010d).

38.2.1.4 Soil Hydrological Processes

While rain water is the source water for plants, various subsequent soil hydrological processes operating on the percolated rain water decide the $\delta^{18}\text{O}$ of water available to plant. Understanding and quantification of soil hydrological processes (viz. water percolation in soil and its evaporation), however, is yet to receive sufficient attention in dendroclimatology.

The isotopic composition of soil water primarily depends upon the isotopic composition of precipitation and ground water. In addition, environmental factors (viz. relative humidity, solar irradiance), through their effect on evaporation of soil water, also affect the isotopic composition of soil water. Spatial and temporal heterogeneity in the isotopic composition of soil water has been reported. Barnes and Allison (1989) showed that an isotopic gradient exists in soil water due to evaporation in the upper part of the soil. The

shape of this profile depends upon soil moisture content, soil texture, and changing isotopic composition and amount of precipitation; the maximum heterogeneity in $\delta^{18}\text{O}$ and δD of soil water is observed at the soil surface and it gradually decreases with depth.

Tang and Feng (2001) conducted a detailed field investigation of these effects in Hanover, NH, USA, where precipitation is more evenly distributed throughout the year, with isotopically enriched summer and depleted winter rainfall. By measuring the temporal variation in the isotopic composition of rainwater, soil water at different depths and twig water from a maple tree, they demonstrated that (1) soil water isotopic composition is much less variable than that of precipitation, implying mixing of water from various precipitation events; (2) evaporation isotopically enriches the surface soil water; (3) water from summer rains gradually replaces water of winter precipitation, the extent of which depends upon the intensity and frequency of summer precipitation; its influence decreases with depth; and (4) $\delta^{18}\text{O}$ of twig water reflects that of the soil water that has experienced evaporation.

Tsuji et al. (2006), in their study of $\delta^{18}\text{O}$ of co-existing tree species in Hokkaido, Japan, have shown the importance of the rooting system of plants in controlling the plant's isotopic composition: water uptake characteristics of plants in the rhizosphere (a part of soil affected by root system), in addition to the soil water processes, ultimately decide the tree cellulose isotopic composition. They found that shallow-rooted tree species (spruce) responded to $\delta^{18}\text{O}$ of summer

precipitation unlike deep-rooted (oak) trees, which may not sample summer precipitation.

Isotopic analysis of xylem water in conjunction with those of rain and ground water helps study water utilization by plants. White et al. (1985) have shown that a single white pine (*Pinus Strobus*) tree could rapidly (within 3 days) switch its uptake from shallower surface rain water to deeper groundwater. Dawson and Ehleringer (1991), on the contrary, showed that mature riparian trees growing close to perennial streams use little or no stream water, but instead prefer ground water. They explained this behavior in terms of mature trees preferring reliable ground water instead of unreliable surface or rain water. The source water for the tree may change with its age. Dawson (1996) showed that older (larger) *Acer saccharum* trees had access to both shallow soil and ground water while younger (smaller) trees of the species depended on shallow soil water. Such results are important as different sources of water often have different isotopic compositions and decide the isotopic composition of tree cellulose.

38.2.2 Modeling Plant Physiological Processes Affecting Cellulose $\delta^{18}\text{O}$

Trees take up the soil water through roots with little isotopic fractionation (White et al. 1985) and transport it to the leaf through the xylem. Analysis of xylem water/cellulose shows (Ehleringer and Dawson 1992; Lin et al. 1996; Schwinning et al. 2002; Evans and Schrag 2004) that plants do preserve the isotopic composition of precipitation. The extent of isotopic enrichment of the leaf water depends primarily upon vapor pressure difference between the intercellular air space of the leaf and ambient air, which in turn depends upon the leaf and air temperature, and relative humidity. Effect of relative humidity on the evaporative isotopic enrichment of the leaf water is lower at higher ambient humidity (e.g. monsoon), a condition often characteristic of the main growing season in the tropics. But at higher ambient humidity, the isotopic composition of atmospheric water vapor through its exchange with the leaf water becomes important. During the drier late growing season (e.g. post-monsoon), lower humidity creates higher vapor pressure gradients across the leaf, which results in a higher evaporative isotopic

enrichment of the leaf water. Variation in the isotopic composition of the leaf water (and hence that of cellulose synthesized from it) depends upon the isotopic composition of source water (therefore a function of ambient temperature or amount of precipitation) and the extent of isotopic enrichment of leaf water due to evaporation (therefore a function of ambient relative humidity).

Plant physiological models (e.g. Flanagan et al. 1991; Saurer et al. 1997; Farquhar et al. 1998; Barbour and Farquhar 2000; Roden et al. 2000; Barbour et al. 2004; Ogée et al. 2009) are useful for the quantitative interpretation of the isotopic composition of plant cellulose.

Various models have been proposed to calculate the isotopic composition of the leaf water. Such models are based on detailed theoretical as well as laboratory experiments. Based on the model of Craig and Gordon (1965) describing isotopic fractionation during evaporation from an open surface and then incorporating leaf boundary layer effects and diffusion through stomata, Dongmann et al. (1974) and Flanagan et al. (1991) expressed the isotopic composition of the leaf water (R_{wl}) as

$$R_{wl} = \alpha^* \left[\alpha_k R_{wx} \left(\frac{e_i - e_s}{e_i} \right) + \alpha_{kb} R_{wx} \left(\frac{e_s - e_a}{e_i} \right) + R_a \left(\frac{e_a}{e_i} \right) \right], \quad (38.5)$$

where R_{wl} , R_{wx} and R_a refer to isotopic ratios ($^{18}\text{O}/^{16}\text{O}$) of leaf water, xylem water and bulk air, respectively; water vapor pressure of intercellular leaf space is e_i , of leaf surface is e_s and of bulk air is e_a ; α^* , α_k , and α_{kb} are respectively liquid-vapor equilibrium and kinetic fractionation factors associated with the leaf, and leaf-air boundary layer.

Alternatively, $\delta^{18}\text{O}$ of the leaf water at the site of evaporation ($\Delta^{18}\text{O}_e$) with respect to that of the source water was written by Farquhar and Lloyd (1993) as

$$\Delta^{18}\text{O}_e = \varepsilon^* + \varepsilon_k + (\Delta^{18}\text{O}_v - \varepsilon_k)e_a/e_i, \quad (38.6)$$

where ε^* and ε_k are equilibrium and kinetic fractionation factors, respectively. $\Delta^{18}\text{O}_v$ is $\delta^{18}\text{O}$ of atmospheric water vapor relative to the source water. e_a and e_i are the same as described earlier.

In (38.5) and (38.6), e_i depends upon the leaf temperature, generally assumed to be the same or linearly related to the ambient temperature. However, Helliker and Richter (2008), based on tree-ring $\delta^{18}\text{O}$ data across the latitudinal range of 50° , demonstrated the possible role of plant physiology in moderating leaf temperature with respect to ambient temperature, wherein a constant value of the leaf temperature ($21.4 \pm 2.2^\circ\text{C}$) was observed across a range 50° of latitude from boreal to subtropical biomes.

The isotopic composition of the leaf water calculated using the above (38.5) and (38.6) is more enriched than that of the observed bulk leaf water due to the Péclet effect – transpirational advection of ^{18}O depleted (xylem) water to the evaporating site opposed by the backward diffusion of ^{18}O enriched water from the leaf (Farquhar and Lloyd 1993). The model of Barbour et al. (2004) includes the Péclet effect. Determining the Péclet number for different tree species involves the measurement of effective path length; a model parameter that accounts for the discrepancy between the $\delta^{18}\text{O}$ values predicted by the Craig-Gordon model and measured bulk leaf water. Generally, a detailed knowledge of the Péclet number for a given species and for any part of the growing season is unavailable. This difficulty is usually circumvented by either assuming a reasonable value of the effective path length (and Péclet number) or by using models (e.g. Roden et al. 2000) that ignore the Péclet effect. The results of the latter option are interpreted keeping in mind that the leaf water in such models could be somewhat enriched in ^{18}O relative to actual values. This might be preferable until the Péclet number for more species of trees during various times of the growing season are carefully measured.

Sucrose formed by photosynthesis in the leaf carries the isotopic composition of the leaf water, modified by the Péclet effect. Subsequent biochemical pathways leading to formation of cellulose are described by Farquhar et al. (1998). Based on review of available data in literature, Sternberg (1989) reported a value of $27 \pm 3\%$ as the enrichment for cellulose $\delta^{18}\text{O}$ of exchangeable oxygen in carbohydrate relative to the water at site of synthesis. Further, it has been shown (Sternberg et al. 1986; Saurer et al. 1997) that 45% of oxygen in cellulose is expected to exchange with (xylem) water during synthesis of cellulose from sucrose. This implies that $\sim 55\%$ of oxygen atoms in

cellulose carry the signature of evaporation (and hence relative humidity conditions) taking place in the leaf.

Roden et al. (2000) outlined a mechanistic model for interpreting $\delta^{18}\text{O}$ and δD of tree cellulose. Their model considers exchange of oxygen atoms of sucrose with the medium (xylem) water during synthesis of cellulose. In their model, the final isotope composition of tree cellulose ($\delta^{18}\text{O}_{\text{cx}}$) is given by

$$\delta^{18}\text{O}_{\text{cx}} = f_{\text{O}} \cdot (\delta^{18}\text{O}_{\text{wx}} + \varepsilon_{\text{O}}) + (1-f_{\text{O}}) \cdot (\delta^{18}\text{O}_{\text{wl}} + \varepsilon_{\text{O}}), \quad (38.7)$$

Where f_{O} is the fraction of oxygen that undergoes exchange with medium water, $\delta^{18}\text{O}_{\text{wx}}$ is xylem water, $\delta^{18}\text{O}_{\text{wl}}$ refers to $\delta^{18}\text{O}$ of leaf water at the site of sucrose synthesis and ε_{O} , the biochemical fractionation factor. The authors estimated f_{O} to be ~ 0.42 based on model and experimental results.

It can be seen from (38.5) to (38.7) that the e_a/e_i ratio, hence atmospheric relative humidity, and $\delta^{18}\text{O}$ of precipitation play a crucial role deciding $\delta^{18}\text{O}$ of cellulose. The importance of relative humidity in deciding plant $\delta^{18}\text{O}$ is highlighted by Sheshshayee et al. (2005). In the tropics, there is enough variation in relative humidity during growing season to leave its imprint on the isotopic composition of cellulose (Geeta Rajagopalan et al. 1999). Likewise, as a result of the amount effect, precipitation amount is also expected to affect tree cellulose $\delta^{18}\text{O}$.

The interpretation of cellulose $\delta^{18}\text{O}$ data from tropics, however, may not be straight-forward; factors such as the duration of the growing season in relation to seasonal changes in relative humidity, and the strength of the amount effect in rainfall are likely to influence $\delta^{18}\text{O}$ values of trees. Managave et al. (2010d) showed varying response of cellulose $\delta^{18}\text{O}$ of teak trees in differing monsoon environments to monsoon rainfall. Their work underscored the importance of considering movement of the ITCZ and associated changes in relative humidity and isotopic composition of rainfall while interpreting isotopic record of tropical trees. Teak from southern India shows a significant negative correlation with the amount of rainfall, plausibly because of a more pronounced amount effect in the region. Cellulose $\delta^{18}\text{O}$ of teak trees from western and central India show a significant positive correlation with the amount of rainfall, contrary to expectation. The positive correlation between teak cellulose

δD and local rainfall record has been also demonstrated for teak from western India by Ramesh et al. (1989). This is possibly a result of rainfall-induced changes in the length of growing season in relation to the movement of the ITCZ. In India, the movement of the ITCZ divides the growing season into two parts: the humid monsoon period when the southwesterly oceanic air mass brings moisture to the continent and the (relatively) dry post-monsoon period dominated by northeasterly flowing continental air mass. Higher rainfall leads to lengthening of the growing season and teak grows until a period of the lower relative humidity (post-monsoon season) leading to more evaporative enrichment of the leaf water in ^{18}O and hence higher cellulose $\delta^{18}O$ values.

38.3 Carbon Isotopes in Trees

Isotopic composition of carbon fixed during photosynthesis of C_3 plant material ($\delta^{13}C_{Plant}$) depends mainly upon factors that control the CO_2 concentration inside the leaf and $\delta^{13}C$ of atmospheric air. Figure 38.4 illustrates various factors influencing $\delta^{13}C$ of plant cellulose. Farquhar et al. (1982) proposed an equation for the $\delta^{13}C$ of plant material ($\delta^{13}C_{Plant}$) as

$$\delta^{13}C_{Plant} = \delta^{13}C_{Air} - a - (b-a)(c_i/c_a), \quad (38.8)$$

where a and b are constants and represent respectively the carbon isotope fractionations during the diffusion of CO_2 through stomata (4.4‰), and during enzymatic CO_2 fixation (27‰); c_i/c_a is the ratio of the intercellular to atmospheric CO_2 concentration; $\delta^{13}C_{Air}$ is $\delta^{13}C$ of atmospheric CO_2 ; c_i is further related to the (photosynthetic) assimilation rate of CO_2 (A) and stomatal conductance (g_s) in the following way.

$$c_i = c_a - A/g_s. \quad (38.9)$$

Thus the main climatic parameters influencing $\delta^{13}C$ of carbon fixed during photosynthesis are those controlling g_s and A . Dominant factors controlling g_s are relative humidity, temperature and soil moisture content whereas A depends on the photon flux as well. In the moist, high altitude environments $\delta^{13}C_{Plant}$ is governed by photosynthetic rate (Gagen et al. 2007) whereas g_s controls $\delta^{13}C_{Plant}$ at drier environment. Seasonal soil moisture status is shown to affect seasonal variations in $\delta^{13}C$ of tree rings (Leavitt 2002, 2007). Cloud amount can modulate photon flux thereby affecting A and hence c_i and $\delta^{13}C_{plant}$. This was illustrated by Ramesh et al. (1986b) who observed a negative correlation between cellulose $\delta^{13}C$ and cloud cover. The effect of cloud cover over the tropics in limiting light availability for photosynthesis is illustrated by Graham et al. (2003), who showed that the heavy cloud cover associated with La Niña in the

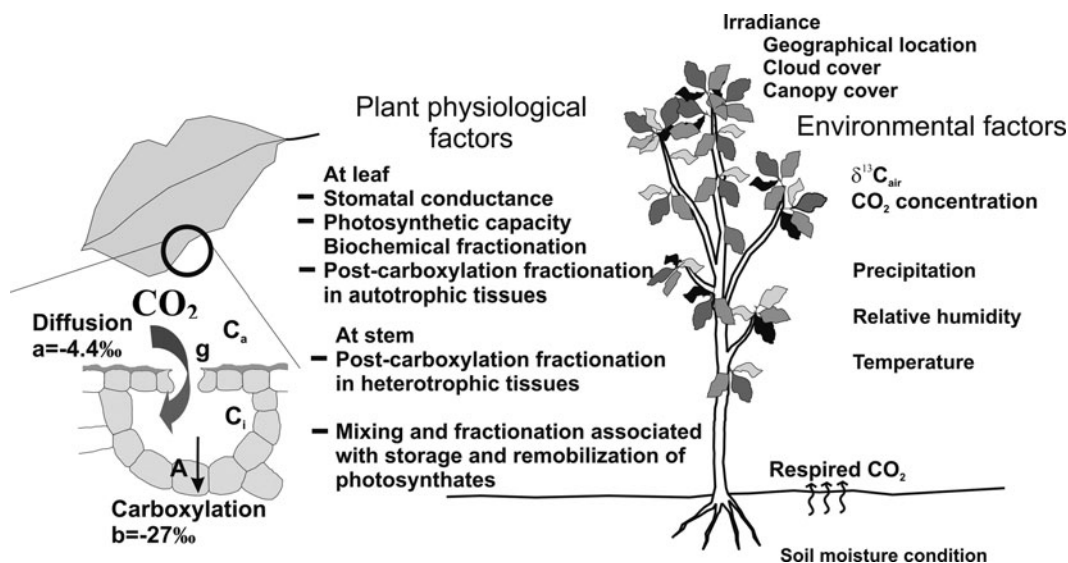


Fig. 38.4 Plant physiological and environmental/climatic factors influencing carbon isotope ratios of tree

Republic of Panama resulted in the reduction of photosynthesis and vegetation growth. It was also reported that at a given site both the net radiation and vapor pressure deficit could affect $\delta^{13}\text{C}$ variations of tree cellulose (Vaganov et al. 2009). Diefendorf (2010) found that on the global scale carbon isotope fractionation during assimilation by plants is correlated with mean annual precipitation indicating water-supply-mediated stomatal control on the leaf-gas exchange processes as a dominant factor.

38.3.1 Non-Climatic Factors Influencing $\delta^{13}\text{C}$ of Tree Rings

In addition to plant physiological responses, $\delta^{13}\text{C}_{\text{plant}}$ values are affected by $\delta^{13}\text{C}_{\text{atm}}$ and its concentration (c_a), both changing over the industrial period. Addition of fossil fuel carbon to the atmosphere has decreased the $\delta^{13}\text{C}_{\text{atm}}$ throughout the industrial period (Suess effect), with the decrease of 1.52‰ during AD 1850–1998 (McCarroll and Loader 2004). A calibration of the $\delta^{13}\text{C}$ record of tree rings with ambient climatic parameters, without due attention to increasing c_a and depleting $\delta^{13}\text{C}_{\text{atm}}$ is likely to lead to an erroneous reconstruction of past climate.

The post-AD 1850 decline observed in $\delta^{13}\text{C}$ record of trees cannot be fully accounted by the decrease in $\delta^{13}\text{C}_{\text{atm}}$ alone (Waterhouse et al. 2004; Gagen et al. 2007; Loader et al. 2007). Changes in the plant physiological response of trees to the increased CO_2 concentration could also be a likely reason. Before relating the observed tree ring $\delta^{13}\text{C}$ variations to meteorological data, it is necessary to remove the changes in tree ring $\delta^{13}\text{C}$ values induced by both the declining $\delta^{13}\text{C}_{\text{atm}}$ values and increasing c_a . A correction for the decrease in $\delta^{13}\text{C}_{\text{atm}}$ due to the Suess effect is made either by fitting a smooth curve to tree ring $\delta^{13}\text{C}$ variation and then subtracting the fitted values (Freyer 1986) or by subtracting the $\delta^{13}\text{C}_{\text{atm}}$ as obtained from ice cores and instrumental data from tree ring $\delta^{13}\text{C}$ values (McCarroll and Loader 2004). Any remaining decreasing trend in corrected tree ring $\delta^{13}\text{C}$ ($\delta^{13}\text{C}_{\text{corr}}$) could partly be due to increasing c_a . This is accounted by (1) considering potential linear discrimination from -0.05 to 0.1% per ppm change in CO_2 concentration (Treydte et al. 2009) (2) by non-linear de-trending of low frequency $\delta^{13}\text{C}_{\text{corr}}$ (e.g. McCarroll et al. 2009).

A “juvenile effect” (depleted and gradually increasing $\delta^{13}\text{C}$ in the first few decades of trees) is another non-climatic cause influencing $\delta^{13}\text{C}$ of tree rings (Freyer and Belacy 1983; McCarroll and Pawellek 2001; Gagen et al. 2004; Anderson et al. 2005). The explanations given for this effect are (1) trees grow in shade during early years of growth (Francey and Farquhar 1982) (2) trees ingest soil respired CO_2 , depleted in $\delta^{13}\text{C}$, during early age and the intake reduces as tree gains height, and (3) reducing stomatal conductance with age as trees gain height (McDowell et al. 2002). It is not possible to detect the juvenile effect of individual trees when the samples are pooled before extraction of cellulose. If individual trees are to be considered for $\delta^{13}\text{C}$ measurements, then the rings corresponding to the juvenile effect are best avoided (McCarroll and Loader 2004). This provides an advantage of using non-detrended $\delta^{13}\text{C}$ series and hence no climatic signal is lost. Alternatively, the “regional curve standardization” technique (e.g. Briffa et al. 2001) could be used to correct for the juvenile effect (Gagen et al. 2008). Here tree ring series are aligned according to their cambial age and a standardized juvenile growth trend is obtained. This trend is then used to remove juvenile effect.

38.4 Recent Developments in Isotope Dendroclimatology

38.4.1 Post-Photosynthetic Processes and Isotopic Composition of Tree Rings

In addition to the processes occurring during photosynthesis, post-photosynthetic processes also modify $\delta^{18}\text{O}$ and $\delta^{13}\text{C}$ of tree cellulose. A good mechanistic understanding has been gained on isotopic fractionation during the formation of photosynthates (Farquhar et al. 1982; Roden et al. 2000; Barbour et al. 2004) (see (38.5), (38.6) and (38.8)). However, understanding of the post-photosynthetic processes is limited. Evolution of the isotopic composition of photosynthates while being transported from the leaf to the tree trunk needs to be quantitatively explored for better interpretation of isotopic composition of tree rings.

It has been observed that $\delta^{13}\text{C}$ and $\delta^{18}\text{O}$ of newly assimilated sugar is correlated with photosynthesis-weighted c_i/c_a (Brandes et al. 2006) and photosynthesis-weighted $\delta^{18}\text{O}$ of mean lamina mesophyll water (Cernusak et al. 2005), respectively. The latter have shown correspondence between phloem sap sugar exported from leaves of *E. globules* and observed leaf water enrichment when diurnal variation in photosynthesis was taken into account. During the night or early morning, enrichment in $\delta^{13}\text{C}$ values of soluble organic matter has been reported (Brandes et al. 2006; Gessler et al. 2007a; Kodama et al. 2008). This necessitates consideration of diel biochemical processes fractionating isotopes of exported sugar from the leaf. Further, Gessler et al. (2008) have shown that $\delta^{13}\text{C}$ of leaf-exported carbon, integrated over the day (24 h), is enriched with respect to the primary assimilate, possibly explaining the enrichment in $\delta^{13}\text{C}$ of tissues in C_3 plants produced by non-photosynthetic processes compared to that produced by photosynthetic processes (Cernusak et al. 2009 and references therein).

Diel variations in $\delta^{13}\text{C}$ have also been observed in phloem sap sugar (Gessler et al. 2008). Comparative studies of diel variations in $\delta^{13}\text{C}$ of water soluble organic matter of leaf, twig phloem sap and trunk phloem of *Pinus sylvestris* (Kodama et al. 2008) showed a progressive dampening of variations during transport from the leaf to the trunk. Similar observations have been reported by Betson et al. (2007) for *Picea abies* and by Gessler et al. (2007a), for *Eucalyptus delegatensis*. Mixing of the different carbon pools having different metabolic histories could be the likely reason for this (Brandes et al. 2007). By monitoring modifications of the isotopic signals of $\delta^{13}\text{C}$ and $\delta^{18}\text{O}$ from the leaf to phloem and to tree ring in *Pinus sylvestris*, Gessler et al. (2009) have reported the uncoupling of $\delta^{13}\text{C}$ in the tree cellulose and the c_i/c_a ratio at the leaf level, implying variable enrichment in ^{13}C of sugar due to phloem loading and transport. The authors could trace time-lagged transfer of $\delta^{18}\text{O}$ signal from the leaf water to the tree cellulose. Damesin and Lelarge (2003) have demonstrated that the $\delta^{13}\text{C}$ of stem of *Fagus sylvatica* is affected by isotopic fractionation during transfer of sugar from leaves to stems and during stem respiration. They further cautioned that these processes may partially mask the climatic signal inherited during photosynthesis. As freshly developing xylem tissue carries the isotopic signature of phloem sugars (Cernusak et al. 2005; Gessler et al. 2007b),

the dampened climate signal observed in phloem sap is likely preserved in tree cellulose.

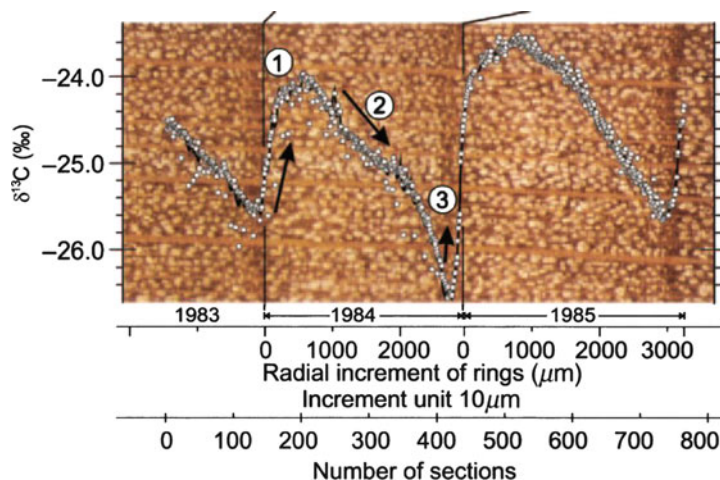
Further dampening of the climate signal could occur during synthesis of cellulose in the stem where 45% of oxygen in cellulose is expected to exchange with (xylem) water (Sternberg et al. 1986, and Saurer et al. 1997). Meinzer et al. (2006) gave an account of whole-tree water transport and storage properties in coniferous trees *Pseudotsuga menziesii* (Mirb.) and *Tsuga heterophylla* (Raf.) Sarg. They observed the transit times for D_2O labeled water from the tree base to the upper crown ranged from 2.5 to 21 days, and the residence times of labeled water in tree ranged from 36 to 79 days, with the values increasing with the diameter of trees. This entails water from a given precipitation event being taken up by roots continuously exchanging oxygen isotopes with starch during cellulose synthesis, thereby further dampening the temporal climate signal preserved in the bark phloem starch.

38.4.1.1 Inter-Annual Transfer of Photosynthates

Helle and Schleser (2004) invoked post-photosynthetic fractionation during carbohydrate metabolism as a likely reason for the observed seasonally persistent intra-annual $\delta^{13}\text{C}$ pattern in broad-leaved deciduous species *Fagus sylvatica*, *Populus nigra*, *Quercus petraea* and *Morus alba*. In their highly resolved intra-annual isotopic measurements (40–100 measurements within each ring), a tri-phase $\delta^{13}\text{C}$ pattern (Fig. 38.5) was found with (1) values showing increasing trend during the early growing season (2) a subsequent declining trend up to the late wood (3) an increasing trend at the end of each ring. Inconsistency between the observed pattern and modeled carbon isotope fractionations during photosynthesis was found and it was suggested that the isotopic fractionation during the storage and remobilization of plant organic matter could be the likely cause. The earlywood and the end of the latewood appear to be affected by post-photosynthetic metabolic processes while the mid-section is most probably affected by climatic influences on leaf carbon isotope discrimination, making it more suited for past climate studies.

The importance of storage and remobilization of carbon pools in the tree has been experimentally demonstrated by Kagawa et al. (2006a). The authors

Fig. 38.5 Seasonal carbon isotope behavior in total organic matter of tree rings from *Fagus sylvatica* (beech) (from Helle and Schleser 2004)



pulse labeled *Larix gmelinii* with $^{13}\text{CO}_2$ for understanding the transfer of photoassimilates from 1 year to the next. The earlywood of the current year was seen to get contributions from previous summer, autumn as well as the current spring, whereas the latewood mainly contained photoassimilates from the current summer/autumn. In another study, Kagawa et al. (2006b) showed the non-needle starch pool gets approximately 43% of carbon from previous year's storage. As the non-needle starch pool can be used for xylem tissues, the interannual transfer of photoassimilates could be the likely reason for the autocorrelation observed in isotope dendroclimatological studies (Kagawa et al. 2006b). This could seriously limit the resolution of climate reconstruction at intra-annual time scales.

38.4.2 Plant Physiological Models and the Interpretation of Cellulose $\delta^{18}\text{O}$

The plant physiological models discussed earlier have greatly helped quantifying the relationship between climatic (and plant physiological) parameters and cellulose $\delta^{18}\text{O}$. Anderson et al. (2002) calibrated a tree cellulose $\delta^{18}\text{O}$ series from central Switzerland with $\delta^{18}\text{O}$ of precipitation (from the Swiss Network for Isotopes in the Hydrological Cycle station), temperature, relative humidity and ring-width. With a modified leaf-water model of Dongmann et al.

(1974) they found variations in the dampening factor (f_0) from 0.27 to 0.49 and to be dependent on the relative humidity. This factor accounts for the degree of dampening of leaf water $\delta^{18}\text{O}$ enrichment as reflected in the stem cellulose, which is likely a result of the leaf water isotopic inhomogeneity and exchange between sucrose and stem water during cellulose synthesis (Saurer et al. 1997). A comparison of observed and modeled $\delta^{18}\text{O}$ of oak (*Quercus robur* L.) from Norfolk, UK enabled Waterhouse et al. (2002) to deduce that the trees used a constant mixture of precipitation and groundwater. Berkelhammer and Stott (2009) used a modeling approach to infer the insignificant role of $\delta^{18}\text{O}$ of the source water pool and the important role of the length of the growing season in determining intra-annual $\delta^{18}\text{O}$ cycles of bristlecone pine tree rings.

Importance of the forward modeling approach in interpreting tree-ring isotope data has been demonstrated by Evans (2007) and Anchukaitis et al. (2008). Given site-specific climate data, forward modeling can be used to quantify the dominant control of and expected variability in the isotopic composition of tree cellulose. The expected variability in the isotopic record can be estimated using Monte Carlo simulations to randomly varying input parameters in the plant physiological model (Evans 2007; Berkelhammer and Stott 2009; Managave et al. 2010a, c). Managave et al. (2010a) used this approach for detecting the record of seasonally varying isotopic composition of rains in teak trees from southern India.

38.4.3 Response to Global Climate Change

Duquesnay et al. (1998) have reported increased water-use efficiency (a ratio of net photosynthesis A to conductance for water vapor g_{H_2O}) from 23 to 44% during the past century in beech (*Fagus sylvatica* L.) as a consequence of increasing CO_2 concentration. Saurer et al. (2004) studied the effect of increasing c_a on $\delta^{13}C$ record of *Larix*, *Pinus* and *Picea* trees growing in northern Eurasia, from Norway to Eastern Siberia. They observed constant discrimination ($\delta^{13}C_{\text{plant}} - \delta^{13}C_{\text{atm}}$) values of two periods, 1861–1890 and 1961–1990 CE, despite average increase in c_a by about 43 ppm. Constant discrimination values yielded constant c_i/c_a ratio for the given duration indicating, the authors explained, increased intrinsic water-use efficiency of trees by acclimatization to increased c_a through decreasing stomatal conductance. Increase in the water-use efficiency by 34 and 52% for tropical species *Cedrela ordata* L. (tropical cedar) and *Swietenia macrophylla* King (big leaf mahogany) respectively as a result of increase in c_a has also been reported (Hietz et al. 2005).

Treydte et al. (2006) using $\delta^{18}O$ variations of juniper tree-ring cellulose from northern Pakistan reconstructed precipitation history back to 828 CE. One of their important results was the detection of unprecedented twentieth-century intensification of the hydrological cycle in western Central Asia, perhaps an effect of global climate change due to anthropogenic forcing of climate.

38.4.4 Inferences from Combined Carbon and Oxygen Isotope Studies

$\delta^{13}C_{\text{plant}}$ is mainly controlled by intercellular concentration of CO_2 , c_i , which in turn depends on stomatal conductance, g_s , and photosynthetic capacity, A (38.9). Both lower g_s and higher A result in the reduction of c_i . Thus higher $\delta^{13}C_{\text{plant}}$ values observed in the plant cellulose could be because of lower g_s and/or higher A . $\delta^{18}O$ measurements of plant cellulose can potentially help ascertain relative importance of g_s and A in influencing $\delta^{13}C_{\text{plant}}$ (Saurer et al. 1997; Scheidegger et al. 2000). Equations (38.5), (38.6) and (38.7)

indicate that one of the factors influencing $\delta^{18}O$ of plant cellulose is relative humidity. It affects the degree of evaporative enrichment of the leaf water in ^{18}O and subsequently synthesized cellulose i.e. lower relative humidity induces higher cellulose $\delta^{18}O$. Thus it follows that if the relative humidity is the dominant control over stomatal behavior, there should be a positive correlation between $\delta^{18}O_{\text{plant}}$ and $\delta^{13}C_{\text{plant}}$. This approach assumes that the variance in $\delta^{18}O_{\text{plant}}$ introduced by changes in $\delta^{18}O$ of source water and atmospheric water vapor is minor compared to that introduced by stomatal behavior controlled by relative humidity. In other words, the correlated variations in $\delta^{18}O_{\text{plant}}$ and $\delta^{13}C_{\text{plant}}$ can be considered as indicative of dominance of relative humidity in controlling stomatal behavior.

Saurer et al. (1997) highlighted the importance of drier conditions in deciding $\delta^{18}O$ and $\delta^{13}C$ of tree cellulose from Switzerland using plant physiological models. Further, combining plant physiological models for interpreting $\delta^{18}O$ and $\delta^{13}C$ of cellulose, the authors showed relation between the slope of the cellulose $\delta^{18}O - \delta^{13}C$ curve and the sensitivity of the c_i/c_a (ratio of intercellular and atmospheric CO_2 concentrations) of a plant to changing relative humidity.

A positive correlation between $\delta^{18}O$ and $\delta^{13}C$ of plant cellulose in several studies support this. Saurer et al. (1997) found that $\delta^{18}O_{\text{cellulose}}$ and $\delta^{13}C_{\text{cellulose}}$ of beech, pine and spruce trees growing at a site with differing soil moisture conditions are positively correlated for each species (r^2 varying from 0.87 to 0.98). Barbour et al. (2002) have also reported positive correlation between the $\delta^{18}O_{\text{cellulose}}$ and $\delta^{13}C_{\text{cellulose}}$ records of *Pinus radiata* from tree sites with different water balance in New Zealand. Within these sites, the slope of the $\delta^{18}O_{\text{cellulose}} - \delta^{13}C_{\text{cellulose}}$ curve, i.e. change in $\delta^{18}O_{\text{cellulose}}$ per unit change in $\delta^{13}C_{\text{cellulose}}$, was found to increase with increasing vapor pressure deficit of the individual sites. A positive correlation between $\delta^{13}C$ and $\delta^{18}O$ of the organic matter of the phloem sap of European beech (*Fagus sylvatica* L.) was reported by Keitel et al. (2003). The authors attributed the observed correlation to stomatal control as a common driving force. Roden et al. (2005) found similar response in deviations in $\delta^{18}O_{\text{cellulose}}$ from stem water $\delta^{18}O$ ($\delta^{18}O_{\text{cellulose}} - \delta^{18}O_{\text{stem water}}$) and $\delta^{13}C_{\text{cellulose}}$ along a precipitation gradient in western Oregon, United States. If photosynthetic capacity controls $\delta^{13}C_{\text{plant}}$, i.e. light-limiting conditions, there

should not be any correlation between $\delta^{18}\text{O}_{\text{plant}}$ and $\delta^{13}\text{C}_{\text{plant}}$, as photosynthetic capacity affects only $\delta^{13}\text{C}_{\text{plant}}$. A negative correlation between $\delta^{18}\text{O}_{\text{plant}}$ and $\delta^{13}\text{C}_{\text{plant}}$ is also reported for plants subjected to higher changes in A with relatively constant g_s (Scheidegger et al. 2000).

38.4.4.1 Insect Outbreak and Isotope Studies

Knowledge of the past variations in the insect outbreaks and their correlation with climate would help assess the impact of global climate change on forest dynamics. Insect outbreaks are known to affect tree-ring widths/growth (Swetnam and Lynch 1993; Boulanger and Arseneault 2004; Sudheendrakumar et al. 1993). However, no conclusive evidences exist supporting stable isotopes for identifying past insect outbreaks (Weidner et al. 2006; Simard et al. 2008; Haavik et al. 2008; Kress et al. 2009). Whereas $\delta^{13}\text{C}_{\text{plant}}$ depends upon both A and g_s (38.9), $\delta^{18}\text{O}_{\text{plant}}$ is related mainly to g_s (cf. discussion made in Sect. 38.3). Therefore, in principle, any process that affects A but not g_s could be deciphered by the combined $\delta^{13}\text{C}$ and $\delta^{18}\text{O}$ data. It has been observed that plant defoliation induces higher A (Little et al. 2003; Lavigne et al. 2001). Simard et al. (2008), compared $\delta^{13}\text{C}$ and $\delta^{18}\text{O}$ record of host and non-host species to show the potential of detecting spruce budworm outbreaks. Kress et al. (2009), however, found isotopes were unable to detect larch budmoth infection.

38.4.5 Intra-Annual Isotopic Studies

A few studies have referred to intra-annual sampling as intra-ring sampling. But the term “intra-ring sampling” could also imply sampling within a growth ring but along different radial directions. Hence we recommend using the term “intra-annual” or “sub-annual” for this type of high resolution sampling.

Traditional isotope dendroclimatological investigations have employed analysis of the latewood or whole ring and reconstructed past climate with an annual resolution. Climate reconstructions on intra-annual timescales were not considered feasible until recently partly due to the laborious and time consuming methods involved in cellulose extraction and its isoto-

pic measurement. Recently developed rapid cellulose extraction techniques (e.g. Brendel et al. 2000; Gaudinski et al. 2005; Anchukaitis et al. 2008) aided by faster isotopic measurements by continuous flow mass spectrometry have, however, increased the sample throughput, making it feasible. The possibility of using plant physiological models (e.g. Roden et al. 2000; Barbour et al. 2004) developed for the interpretation of cellulose $\delta^{18}\text{O}$ and δD has also given impetus to intra-annual isotope studies. The potential of intra-annual resolution isotope studies in reconstructing past climatic has been demonstrated (Loader et al. 1995; Barbour et al. 2002; Poussart et al. 2004; Evans and Schrag 2004; Helle and Schleser 2004; Verheyden et al. 2004; Poussart and Schrag 2005; Miller et al. 2006; Skomarkova et al. 2006; Leavitt 2007; Jahren and Sternberg 2008; Anchukaitis et al. 2008; Roden et al. 2009; Berkelhammer and Stott 2009; Managave 2009; Managave et al. 2010a–c).

To successfully reconstruct past climate on intra-annual time scales, a precise dating of the intra-annual sections of the rings is required. For this, exact data on their growth pattern is needed. It is known that the length of growing season could vary interannually. Further, as the tree growth rates are not uniform throughout the growing season, intra-annual segments of equal widths may not necessarily represent equal spans of time. Therefore, some approximations are usually made while assigning time to the different intra-annual segments as in high resolution coral studies (Chakraborty and Ramesh 1993, 1997). Barbour et al. (2002) employed actual dendrometric growth observations corresponding to the years assigned to the rings analyzed for intra-annual isotopic studies. Berkelhammer and Stott (2009) assigned time to different intra-annual sections based of dendrographic growth patterns of bristlecone pine monitored by Fritts (1969). Managave et al. (2010a–c) used radial growth increment and cambial activity data for assigning time to various intra-annual segments of teak.

As extensive diameter growth measurements are not available for most tree species, some additional criteria are needed for identifying seasonal growth within a ring. Leavitt et al. (2002) used false rings occurring within each annual growth rings of ponderosa pine from southwestern United States to assign time to intra-annual segments. They attributed the false rings to hyper-arid conditions during May and June, and assigned winter-spring vs. summer times

to parts of the ring developed before and after the false-latewood band. Another approach could be the age model hypothesis of Evans and Schrag (2004)

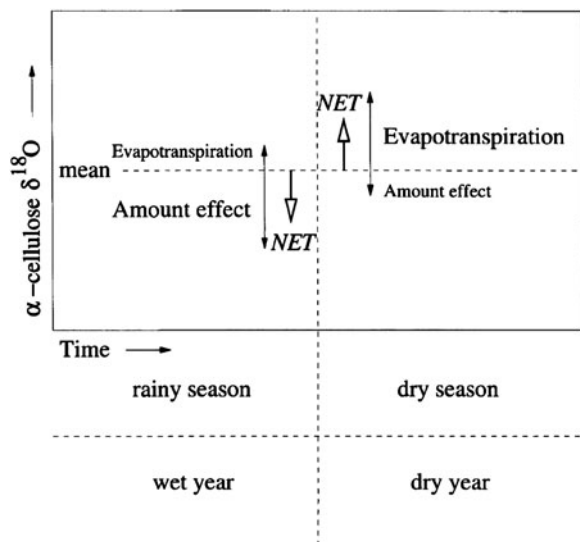


Fig. 38.6 Conceptual model of expected isotopic effects in tropical tree cellulose as a function of the annual cycle and interannual variations of tropical convective rainfall and evapotranspiration (from Evans and Schrag 2004)

(Fig. 38.6) wherein the segments exhibiting the lowest intra-annual $\delta^{18}\text{O}$ value is assigned the month of highest rainfall. This approach is useful in the tropics where the amount effect and higher relative humidity associated with the higher rainfall lead to production of photosynthates with lower $\delta^{18}\text{O}$ values (see Sect. 38.2.2 for explanation). This approach, however, cannot be used where the amount effect is absent in the rainfall. For example, studies made at Mumbai and Meghalaya clearly lack the amount effect (Ramesh et al. 1989; Breitenbach et al. 2010). Trees from regions with seasonally changing $\delta^{18}\text{O}$ of rainwater (due different sources of moisture) may not produce cellulose with the lowest $\delta^{18}\text{O}$ in the month of highest rainfall (Managave et al. 2010a). It thus follows that site-specific age models might need to be developed after giving due consideration to the climate and tree growth relationship.

It has been shown that under favorable conditions the environmental and/or tree physiological forcing could produce annual cycles in the intra-annual isotope variations (Evans and Schrag 2004; Poussart et al. 2004; Helle and Schleser 2004; Verheyden et al. 2004; Anchukaitis et al. 2008; Managave et al. 2010b, c). Figure 38.7 displays intra-annual teak cellulose $\delta^{18}\text{O}$

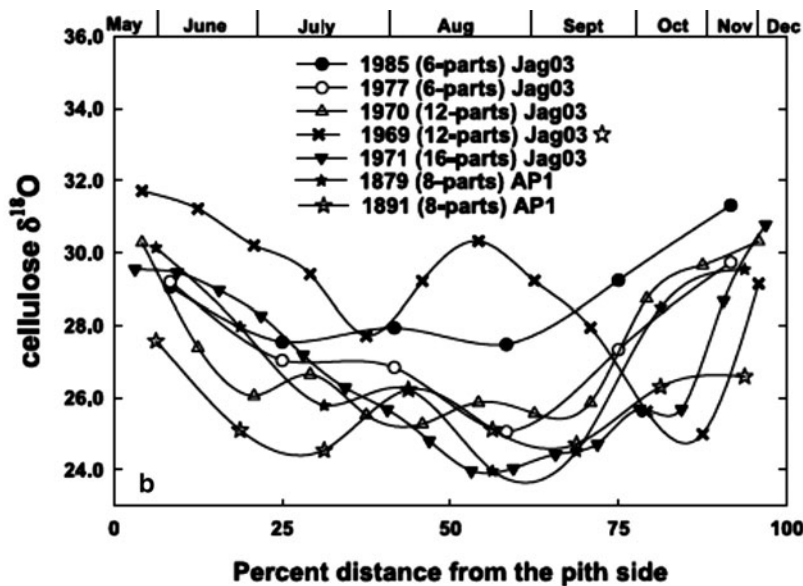
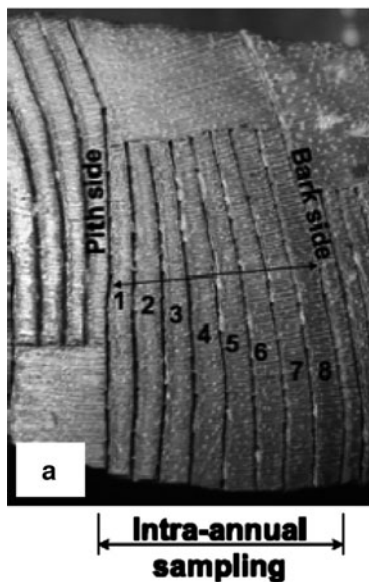


Fig. 38.7 (a) Photograph illustrating intra-annual sampling. Arrows marks the full annual ring. (b) Intra-annual $\delta^{18}\text{O}$ variations as a function of time of growth (top) in teak from Jagdalpur (Jag03) and Hanamkonda (AP1), central India. Legend

represents years (AD) corresponding to the rings analyzed, the number of sub-samples and sample name (from Managave et al. 2010b)

variations observed by Managave et al. (2010b). The tree species from such locales which do not exhibit discernable growth rings are also likely to show seasonal cycles in their isotopic record. This could be used to establish a chronology in the trees lacking growth rings. In their approach of “tropical isotope dendrochronology” Evans and Schrag (2004) suggested wood corresponding to one $\delta^{18}\text{O}$ cycle can be considered as a “ring” and routine tree ring dating methods could be used to assign calendar years to various parts within the trees lacking growth rings. Based on this approach, Poussart and Schrag (2005) established a chronology of trees lacking growth rings from Thailand and used these data to measure past growth rates of trees. However, the number of subsamples that can be taken in a ring depends on its width and this might limit the detection of the full cycle, as demonstrated for corals (Chakraborty and Ramesh 1998).

Ogé et al. (2009) developed a single substrate model for explaining seasonal/intra-annual variations in $\delta^{18}\text{O}$ and $\delta^{13}\text{C}$ of plant cellulose, taking into account post-photosynthetic processes. They considered the mixing of recent photoassimilates during translocation and the time taken for cellulose deposition during wood formation. This could explain seasonal variations in cellulose $\delta^{18}\text{O}$ and $\delta^{13}\text{C}$ of *Pinus pinaster*.

Past climate reconstructions using isotopic studies of trees could also be used to decipher role of climate and other factors in the extinction of fauna. Based on high-resolution sub-annual isotopic studies, Anchukaitis and Evans (2010) established a chronology in trees lacking growth rings of the montane cloud forest of Costa Rica. The reconstructed hydroclimatology of the region revealed coincidence of the exceptionally dry interval generated by El Niño events and extinction of the Montverde golden toad, implying possible role of climate in extinction.

38.4.6 Components of Wood Other than Whole Cellulose

Progress has been made in the direction of using oxygen/hydrogen isotopic composition of atoms having specific positions in the cellulose structure rather than using whole cellulose for climate reconstruction. Sternberg et al. (2007) used the cellulose-derived

phenylglucosazone, a compound which lacks the oxygen attached to the second carbon of the cellulose-glucose moieties, instead of bulk cellulose. They showed that it may be a better proxy for the $\delta^{18}\text{O}$ of stem water and relative humidity, as the oxygen attached to the second carbon atom in cellulose can introduce isotopic “noise” in the climate signal. Betson et al. (2006) and Augusti et al. (2008) used the nuclear magnetic resonance (NMR) method for studying deuterium isotopomer distribution (DID) within glucose moieties of tree cellulose. Betson et al. (2006) showed DID was non-random and carried information about isotopic effects during photosynthesis. Augusti et al. (2008) formulated an approach wherein combination of δD and DID can be used to simultaneously reconstruct climate and a signal related to tree physiology. In their approach the relative D isotope abundance of C2-H group appears to be better than the whole-molecule δD of tree-ring cellulose for paleoclimate reconstruction.

38.5 Future Research Direction

38.5.1 Autocorrelation in Tree Ring Isotope Record

One of the factors that could introduce noise in the climate reconstruction from tree-ring studies on annual and intra-annual timescales is autocorrelation, correlation of the isotopic composition of tree rings with the environmental conditions of the previous year/years. The autocorrelation observed in tree ring-width and isotopic data series is thought to be the result of storage of starches produced in the later growing season of the previous year and used in the early current year growth (Helle and Schleser 2004; Kagawa et al. 2006a). Unfortunately, a quantitative understanding of the process is still lacking. The questions that need to be answered are (1) to what extent stem cellulose $\delta^{13}\text{C}$ and $\delta^{18}\text{O}$ values get simultaneously modified in this process (2) how environmental factors (e.g. drought) would affect the amount of storage and transfer of starch, and (3) are there any age related variations in these processes? A better understanding of these issues would help devise improved sampling strategy so that optimum climate could be retrieved.

38.5.2 Relationship Between Climatic Parameters and $\delta^{18}\text{O}$ of Rainfall

The dependence of isotopic composition of rainfall on temperature and amount of rainfall needs to be examined in more detail for successfully exploiting the isotope dendroclimatological potential of trees. Although the regions exhibiting correlation of isotopic composition of precipitation with surface temperature and amount of rainfall fall in well-defined geographical zones, the strength of correlation within these zones varies significantly (Bowen 2008). Thus there could be an error in the reconstructed local temperature/amount of precipitation if a regional relationship between climate- $\delta^{18}\text{O}_{\text{precipitation}}$ is used for reconstruction (Bowen 2008). Further, there could be temporal variations in the strength of the climate- $\delta^{18}\text{O}_{\text{precipitation}}$ relationship following variations in the forcing factors (Schmidt et al. 2007).

38.5.3 Light Availability and $\delta^{13}\text{C}$ of Tree Rings in Tropics

In the high latitude regions, the growth and $\delta^{13}\text{C}$ of trees are affected by light availability (i.e. photon flux, Gagen et al. 2007). Its role in the tropics is not fully explored as it is generally assumed that there is no dearth of sunlight in the tropics. However, during the tropical rainy season, cloud cover reduces light intensity and thereby reduces CO_2 uptake and tree growth (Graham et al. 2003). The region between $\sim 10^\circ\text{N}$ and $\sim 10^\circ\text{S}$ is characterized by highly reflective clouds associated with the movement of the ITCZ (Waliser and Gautier 1999). The $\delta^{13}\text{C}$ record of tree cellulose from such regions is likely affected by the light limiting conditions. Thus, the level of photosaturation for different tree species needs to be documented.

38.5.4 Varying Strength of Correlation Between Tree Ring Isotope Record and Climatic Parameters

Tree-ring based paleoclimatic reconstructions assume that the observed correlation between climatic parameter (e.g. precipitation/temperature) and tree-ring isotope record is constant in the past, which may be too simplistic an assumption. Within the calibration period, the strength of correlation between the proxy and climatic parameter can vary, probably indicating varying strength of the forcing factors (Fig. 38.8) associated with the epochal changes in the ENSO activity. Schmidt et al. (2007), by including water isotope tracers in the hydrological cycle of coupled ocean-atmospheric models, have shown that the correlation between the $\delta^{18}\text{O}$ of precipitation and a specific climatic parameter (e.g. precipitation) may vary over different timescales and in response to different forcing mechanisms. This variation was reported to be more in the precipitation-dominated tropics than in the temperature-dominated high latitude regions. Kumar et al. (1999) have shown the epochal changes in the strength of the ENSO: the ENSO and its precursors were of decreased amplitude and 5–7 year periods during AD 1911–1950 and they were of higher amplitudes and 3–5 year periods during AD 1951–1990. It is highly likely that these epochal changes in the strength of ENSO would also affect the tree-ring records. This adds to the uncertainty associated with the reconstructed past climate: a climate reconstruction based on the calibration of tree-ring and climatic parameters during a weaker ENSO phase might not accurately reconstruct variations in the climatic parameter during a stronger ENSO phase. Thus, ideally, to minimize the uncertainties on the reconstructed climate, a calibration with weaker (stronger) ENSO epochs should be used to reconstruct past weaker (stronger) ENSO epochs only, identified by an independent proxy (e.g. corals).

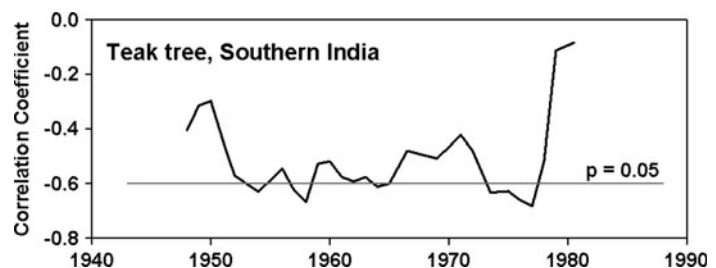


Fig. 38.8 Eleven year centered moving correlation between cellulose $\delta^{18}\text{O}$ record of teak from southern India and the local rainfall record (Managave et al. 2010d)

38.6 Concluding Remarks

Over the last few decades, the efficacy of isotopic composition of tree rings in reconstructing past climate has been improved significantly. Better understanding of various eco-physiological processes affecting isotopic composition of tree cellulose has yielded quantitative relationships of biochemical and environmental factors with the isotopic composition of tree cellulose. The causal link thus established helps to address a variety of environmental and climatic questions using isotope dendroclimatological techniques.

Intra-annual isotope studies combined with plant physiological modeling has given crucial insights into identifying factors governing isotopic composition of tree rings during various phases of the growing season. Identification of parts within the rings possibly affected by isotopic fractionation associated with storage and transfer of photosynthates from a year to the next can help decide the sampling strategy for the optimum retrieval of past climate from tree cellulose. Several studies demonstrate the usefulness of intra-annual isotopic studies in reconstructing past climate, establishing chronology in trees lacking growth rings, identifying past tropical cyclones and growth associated with seasonally varying isotopic compositions of rainfall.

In addition to reconstructing past rainfall/temperature, the combined use of $\delta^{18}\text{O}$ and $\delta^{13}\text{C}$ gives additional information about past variations in relative humidity, sunlight availability and occurrences of insect outbreaks. Further, issues related to the response of plants to the global climate change (e.g. change in the plant water-use efficiency due to increased atmospheric CO_2 concentration) could be quantitatively addressed using $\delta^{13}\text{C}$ of tree cellulose.

The new developments in using intra-molecular and intra-annual isotopic techniques combined with a better understanding of modification of the isotopic composition of photosynthates during translocation offers a promising future for isotope dendroclimatology.

Acknowledgments We thank M. Baskaran for the invitation to write this review, collaborators H.P. Borgaonkar and A. Bhattacharyya for samples and ISRO-GBP for funding. We are grateful to the two anonymous reviewers for an in-depth review, which helped to improve the presentation.

References

- Anchukaitis KJ, Evans MN, Wheelwright NT, Schrag DP (2008) Stable isotope chronology and climate signal calibration in neotropical montane cloud forest trees. *J Geophys Res* 113:G03030. doi:10.1029/2007JG000613
- Anchukaitis KJ, Evans MN (2010) Tropical cloud forest climate variability and the demise of the Monteverde golden toad. *PNAS* 107(11):5036–5040. doi:10.1073/pnas.0908572107
- Anderson WT, Bernasconi SM, McKenzie JA, Saurer M, Schweingruber F (2002) Model evaluation for reconstructing the oxygen isotopic composition in precipitation from tree ring cellulose over the last century. *Chem Geol* 182:121–137
- Anderson WT, Sternberg L, Pinzon MC, Gann-Troxler T, Childers DL, Duever M (2005) Carbon isotope composition of cypress trees from South Florida and changing hydrologic conditions. *Dendrochronologia* 23:1–10
- Araguás-Araguás L, Froehlich K, Rozanski K (1998) Stable isotope composition of precipitation over southeast Asia. *J Geophys Res* 103(22):28721–28742
- Augusti A, Betson TR, Schleucher J (2008) Deriving correlated climate and physiological signals from deuterium isotopomers in tree rings. *Chem Geol* 252:1–8
- Barbour MM, Farquhar GD (2000) Relative humidity – and ABA-induced variation in carbon and oxygen isotope ratios of cotton leaves. *Plant Cell Environ* 23:473–485
- Barbour MM (2007) Stable oxygen isotope composition of plant tissue: a review. *Funct Plant Biol* 34:83–94
- Barbour MM, Roden JS, Farquhar GD, Ehleringer JR (2004) Expressing leaf water and cellulose oxygen isotope ratios as enrichment above source water reveals evidence of a Péclet effect. *Oecologia* 138:426–435
- Barbour MM, Walcroft AS, Farquhar GD (2002) Seasonal variation in $\delta^{13}\text{C}$ and $\delta^{18}\text{O}$ of cellulose from growth rings of *Pinus radiata*. *Plant Cell Environ* 25:1483–1499
- Barnes CJ, Allison GB (1989) Temperature gradient effects on stable isotope and chloride profiles in dry soils. *J Hydrol* 100:143–176
- Becker B, Schmidt B (1989) Extension of the European oak chronology to the past 9224 years. *PACT* 29:1–10
- Berkelhammer M, Stott LD (2009) Modeled and observed intraring $\delta^{18}\text{O}$ cycle within the late Holocene bristlecone pine tree samples. *Chem Geol* 264:13–23
- Betson NR, Göttlicher SG, Hall M, Wallin G, Richter A, Högberg P (2007) No diurnal variation in rate or carbon isotope composition of soil respiration in a boreal forest. *Tree Physiol* 27:749–756
- Betson TR, Augusti A, Schleucher J (2006) Quantification of deuterium isotopomers of tree-Ring cellulose using nuclear magnetic resonance. *Anal Chem* 78:8406–8411
- Boulanger Y, Arseneault D (2004) Spruce budworm outbreaks in eastern Quebec over the last 450 years. *Can J Forest Res* 34:1035–1043. doi:10.1139/x03-269
- Bowen GJ (2008) Spatial analysis of the intra-annual variation of precipitation isotope ratios and its climatological corollaries. *J Geophys Res* 113:D05113
- Brandes E, Wenninger J, Koeniger P, Schindler D, Rennenberg H, Leibundgut C, Mayer H, Gessler A (2007) Assessing environmental and physiological controls over water relations

- in a Scots pine (*Pinus sylvestris* L.) stand through analyses of stable isotope composition of water and organic matter. *Plant Cell Environ* 30:113–127
- Brandes E, Kodama N, Whittaker K, Weston C, Rennenberg H, Keitel C, Adams MA, Gessler A (2006) Short-term variation in the isotopic composition of organic matter allocated from the leaves to the stem of *Pinus sylvestris*: effects of photosynthetic and postphotosynthetic carbon isotope fractionation. *Glob Change Biol* 12:1922–1939
- Brendel O, Iannetta PPM, Stewart D (2000) A rapid and simple method to isolate pure alpha-cellulose. *Phytochem Anal* 11:7–10
- Breitenbach SFM, Adkins JF, Meyer H, Marwan N, Kumar KK, Haug GH (2010) Strong influence of water vapor source dynamics on stable isotopes in precipitation observed in Southern Meghalaya, NE India. *Earth Planet Sci Lett* 292:212–220
- Briffa KR, Osborn TJ, Schweingruber FH, Harris IC, Jones PD, Shiyatov SG, Vaganov EA (2001) Low frequency temperature variations from a northern tree-ring density network. *J Geophys Res* 106:2929–41
- Burk RL, Stuiver M (1981) Oxygen isotope ratios in trees reflect mean annual temperature and humidity. *Science* 211:1417–1419
- Cernusak LA, Farquhar GD, Pate JS (2005) Environmental and physiological controls over carbon and oxygen isotope composition of Tasmanian blue gum, *Eucalyptus globulus*. *Tree Physiol* 25:129–146
- Cernusak LA, Tcherkez G, Keitel C, Cornwell WK, Santiago LS, Knohl A, Barbour MM, Williams DG, Reich PB, Ellsworth DS, Dawson TE, Griffiths HG, Farquhar GD, Wright IJ (2009) Why are non-photosynthetic tissues generally ^{13}C enriched compared with leaves in C_3 plants? Review and synthesis of current hypotheses. *Funct Plant Biol* 36:199–213
- Chakraborty S, Ramesh R (1998) Stable isotope variations in a coral (*Favia speciosa*) from the Gulf of Kutch during 1948–1989 A.D.: environmental implications. *Proc Ind Acad Sci (Earth Planet Sci)* 107(4):331–341
- Chakraborty S, Ramesh R (1997) Environmental significance of carbon and oxygen isotope ratios of banded corals from Lakshadweep, India. *Quatern Int* 37(1):55–65
- Chakraborty S, Ramesh R (1993) Monsoon induced sea surface temperature changes recorded in Indian corals. *Terra Nova* 5:545–551
- Clark ID, Fritz P (1997) *In environmental isotopes in hydrogeology*. Lewis Publisher, Boca Raton, p 328
- Cook ER (1990) A conceptual linear aggregate model for tree rings. In: Cook ER, Kairiukstis LA (eds) *Methods of dendrochronology*. Kluwer, Boston, pp 98–104
- Craig H, Gordon L (1965) Deuterium and oxygen 18 variations in the ocean and marine atmosphere. In: Tongiorgi E (ed) *Third Spoleto Conference, Stable Isotopes in Oceanographic Studies and Paleotemperatures*. Lischi & Figli, Pisa, pp 1–22
- Damesin C, Lelarge C (2003) Carbon isotope composition of current-year shoots from *Fagus sylvatica* in relation to growth, respiration and use of reserves. *Plant Cell Environ* 26:207–219
- Dansgaard W (1964) Stable isotopes in precipitation. *Tellus* 16:436–468
- Dawson TE (1996) Determining water use by trees and forests from isotopic, energy balance and transpiration analyses: the roles of tree size and hydraulic lift. *Tree Physiol* 16:263–272
- Dawson TE, Ehleringer JR (1991) Streamside trees do not use stream water: evidence from hydrogen isotope ratios. *Nature* 350:335–337
- Dawson TE, Mambelli S, Plamboeck AH, Templer PH, Tu KP (2002) Stable isotopes in plant ecology. *Annu Rev Ecol Syst* 33:507–559
- Dawson TE, Siegwolf RTW (2007) *Isotopes as indicators of ecological change*. Elsevier, San Diego, pp 1–417
- Diefendorf AF, Mueller KE, Wing SL, Koch PL, Freeman KH (2010) Global patterns in leaf ^{13}C discrimination and implications for studies of past and future climate. *PNAS* 107:5738–5743. doi:10.1029/2005JG000033
- Dongmann G, Nurnberg HW, Forstel H, Wagoner K (1974) On the enrichment of H_2^{18}O in the leaves of transpiring plants. *Radiat Environ Biophys* 11:41–52
- Duquesnay A, Breda N, Stievenard M (1998) Changes of tree-ring $\delta^{13}\text{C}$ and water-use efficiency of beech (*Fagus sylvatica* L.) in north-eastern France during the past century. *Plant Cell Environ* 21:565–572
- Ehleringer JR, Dawson TE (1992) Water uptake by plants: perspectives from stable isotope composition. *Plant Cell Environ* 15:1073–1082
- Epstein S, Yapp CJ (1977) Isotope tree thermometers. *Nature* 266:477–478
- Evans MN (2007) Toward forward modeling for paleoclimatic proxy signal calibration: a case study with oxygen isotopic composition of tropical woods. *Geochem Geophys Geosyst* 8:Q07008. doi:10.1029/2006GC001406
- Evans MN, Schrag DP (2004) A stable isotope-based approach to tropical dendroclimatology. *Geochim Cosmochim Acta* 68(16):3295–3305
- Farquhar GD, Lloyd J (1993) Carbon and oxygen isotope effects in the exchange of carbon dioxide between terrestrial plants and the atmosphere. In: Ehleringer JE et al (eds) *Stable isotopes and plant carbon-water relations*. Academic, New York, pp 47–70
- Farquhar GD, O'Leary MH, Berry JA (1982) On the relationship between carbon isotope discrimination and the intercellular carbon dioxide concentration in leaves. *Aust J Plant Physiol* 9:121–137
- Farquhar GD, Ehleringer JR, Hubick KT (1989) Carbon isotope discrimination and photosynthesis. *Annu Rev Plant Physiol Plant Mol Biol* 40:503–537
- Farquhar GD, Barbour MM, Henry BK (1998) Interpretation of oxygen isotopic composition of leaf material. In: Griffiths H (ed) *Stable isotopes: integration of biological, ecological, and geochemical processes*. BIOS Scientific Publishers, Oxford, pp 27–48
- Feng X, Epstein S (1994) Climatic implications of an 8000-year hydrogen isotope time series from bristlecone pine trees. *Science* 265:1079–1081
- Ferguson CW, Graybill DA (1983) Dendrochronology of bristlecone pine: a progress report. *Radiocarbon* 25:287–288
- Flanagan LB, Comstock JP, Ehleringer JR (1991) Comparison of modeled and observed environmental influences on the stable oxygen and hydrogen isotope composition of leaf water in *Phaseolus vulgaris* L. *Plant Physiol* 96:588–596

- Francey RJ, Farquhar GD (1982) An explanation of $^{13}\text{C}/^{12}\text{C}$ variations in tree rings. *Nature* 297:28–31
- Freyer HD, Belacy N (1983) $^{13}\text{C}/^{12}\text{C}$ records in Northern Hemispheric trees during the past 500 years – anthropogenic impact and climate superpositions. *JGR* 88(C11):6844–6852
- Freyer HD (1986) Interpretation of the northern hemispheric record of $^{13}\text{C}/^{12}\text{C}$ trends of atmospheric CO_2 in tree rings. In: Trabalka JR, Reichle DE (eds) *The global carbon cycle*. Springer, London
- Fritts HC (1976) *Tree rings and climate*. Academic, London
- Fritts HC (1969) *Bristlecone Pine in the White Mountains of California, Growth and Ring-Width Characteristics*. Tucson, Arizona, The University of Arizona Press, 1069. 44pp. Papers of the Laboratory of Tree-ring Research, No. 4.
- Gagen M, Danny McCarroll D, Iain Robertson I, Neil J, Loader NJ, Jalkanen R (2008) Do tree ring $\delta^{13}\text{C}$ series from *Pinus sylvestris* in northern Fennoscandia contain long-term non-climatic trends? *Chem Geol* 252:42–51
- Gagen MH, McCarroll D, Loader NJ, Robertson I, Jalkanen R, Anchukaitis KJ (2007) Exorcising the “segment length curse”: summer temperature reconstruction since AD 1640 using non de-trended stable carbon isotope ratios from pine trees in northern Finland. *Holocene* 17:433–444
- Gagen M, McCarroll D, Edouard J-L (2004) The effect of site conditions on pine tree ring width, density and $\delta^{13}\text{C}$ series. *Arct Antarct Alpine Res* 36(2):166–171
- Gat JR (1996) Oxygen and hydrogen isotopes in the hydrological cycle. *Annu Rev Earth Planet Sci* 24:225–262
- Gaudinski JB, Dawson TE, Quideau S, Schuur EAG, Roden JS, Trumbore SE, Sandquist DR, Oh S, Wasylishen RE (2005) Comparative analysis of cellulose preparation techniques for use with ^{13}C , ^{14}C , and ^{18}O isotopic measurements. *Anal Chem* 77:7212–7224
- Geeta Rajagopalan (1996) *Stable isotope paleoclimatology based on tropical peat deposits in Nilgiri hills, southern India*. Unpublished thesis. M.S. University of Baroda, Vadodara, 119 p
- Rajagopalan G, Ramesh R, Sukumar R (1999) Climatic implications of $\delta^{13}\text{C}$ and $\delta^{18}\text{O}$ ratios from C3 and C4 plants growing in a tropical montane habitat in southern India. *J Biosci* 24:491–498
- Gessler A, Brandes E, Buchmann N, Helle G, Rennenberg H, Barnard RL (2009) Tracing carbon and oxygen isotope signals from newly assimilated sugars in the leaves to the tree-ring archive. *Plant Cell Environ* 32:780–795
- Gessler A, Keitel C, Kodama N, Weston C, Winters AJ, Keith H, Grice K, Leuning R, Farquhar GD (2007a) $\delta^{13}\text{C}$ of organic matter transported from the leaves to the roots in *Eucalyptus delegatensis*: short-term variations and relation to respired CO_2 . *Funct Plant Biol* 34:692–706
- Gessler A, Peuke AD, Keitel C, Farquhar GD (2007b) Oxygen isotope enrichment of organic matter in *Ricinus communis* during the diel course and as affected by assimilate transport. *New Phytol* 174:600–613
- Gessler A, Tcherkez G, Peuke AD, Ghashghaie J, Farquhar GD (2008) Experimental evidence for diel variations of the carbon isotope composition in leaf, stem and phloem sap organic matter in *Ricinus communis*. *Plant Cell Environ* 31:941–953
- Graham EA, Mulkey SS, Kitajima K, Phillips NG, Wright SJ (2003) Cloud cover limits net CO_2 uptake and growth of a rainforest tree during tropical rainy seasons. *PNAS* 100:572–576
- Gray J, Thompson P (1976) Climatic information from $^{18}\text{O}/^{16}\text{O}$ ratios of cellulose in tree rings. *Nature* 262:481–482
- Griffiths H (1998) *Stable isotopes: integration of biological, ecological, and geochemical processes*. BIOS Scientific Publishers, Oxford, p 438
- Haavik LJ, Stephen FM, Fierke MK, Salisbury VB, Leavitt SW, Billings SA (2008) Dendrochronological parameters of northern red oak (*Quercus rubra* L. (Fagaceae)) infested with red oak borer (*Enaphalodes rufulus* (Haldeman) (Coleoptera: Cerambycidae)). *For Ecol Manage* 255:1501–1509. doi:10.1016/j.foreco.2007.11.005
- Helle G, Schleser GH (2004) Beyond CO_2 -fixation by Rubisco – an interpretation of C-13/C-12 variations in tree rings from novel intra-seasonal studies on broad-leaf trees. *Plant Cell Environ* 27:367–380
- Helliker BR, Richter SL (2008) Subtropical to boreal convergence of tree-leaf temperatures. *Nature* 454:511–514
- Hietz P, Wanek W, Dunisch O (2005) Long-term trends in cellulose $\delta^{13}\text{C}$ and water-use efficiency of tropical *Cedrela* and *Swietenia* from Brazil. *Tree Physiol* 25:745–752
- Hobbie EA, Werner RA (2004) Intramolecular, compound-specific, and bulk carbon isotope patterns in C₃ and C₄ plants: a review and synthesis. *New Phytol* 161:371–385
- IAEA/WMO (2006) *Global Network of Isotopes in Precipitation*. The GNIP Database. Accessible at: <http://isohis.iaea.org>, accessed on 1 July 2010
- Jahren AH, Sternberg LSL (2008) Annual patterns within tree rings of the Arctic middle Eocene (ca. 45 Ma): isotopic signatures of precipitation, relative humidity, and deciduousness. *Geology* 36:99–102
- Kagawa A, Sugimoto A, Maximov TC (2006a) $^{13}\text{C}\text{O}_2$ pulse-labelling of photoassimilates reveals carbon allocation within and between tree rings. *Plant Cell Environ* 29:1571–1584
- Kagawa A, Sugimoto A, Maximov TC (2006b) Seasonal course of translocation, storage and remobilization of ^{13}C pulse-labeled photoassimilate in naturally growing *Larix gmelinii* saplings. *New Phytol* 171:793–804
- Keitel C, Adams MA, Holst T, Matzarakis A, Mayer H, Rennenberg H, Gessler A (2003) Carbon and oxygen isotope composition of organic compounds in the phloem sap provides a short-term measure for stomatal conductance of European beech (*Fagus sylvatica* L.). *Plant Cell Environ* 26:1157–1168
- Kodama N, Barnard RL, Salmon Y et al (2008) Temporal dynamics of the carbon isotope composition in a *Pinus sylvestris* stand: from newly assimilated organic carbon to respired carbon dioxide. *Oecologia* 156:737–750
- Kress A, Saurer M, Büntgen U, Treydte KS, Bugmann H, Siegwolf RTW (2009) Summer temperature dependency of larch budmoth outbreaks revealed by Alpine tree-ring isotope chronologies. *Oecologia* 160:253–265
- Kumar KK, Kleeman R, Cane MA, Rajagopalan B (1999) Epochal changes in Indian monsoon-ENSO precursors. *Geophys Res Lett* 26:75–78
- Lavigne MB, Little CHA, Major JE (2001) Increasing the sink: source balance enhances photosynthetic rate of 1-year-old balsam fir foliage by increasing allocation of mineral nutrients. *Tree Physiol* 21:417–426

- Leavitt SW (2002) Prospects for reconstruction of seasonal environment from tree-ring $\delta^{13}\text{C}$: baseline findings from the Great Lakes area, USA. *Chem Geol* 192:47–58
- Leavitt SW, Wright WE, Long A (2002) Spatial expression of ENSO, drought and summer monsoon in seasonal $\delta^{13}\text{C}$ of ponderosa pine tree rings in southern Arizona and New Mexico. *J Geophys Res* 107(D18):4349. doi:10.1029/2001JD001312
- Leavitt SW (2007) Regional expression of the 1988 U.S. Midwest drought in seasonal $\delta^{13}\text{C}$ of tree rings. *J Geophys Res* 112:D06107. doi:10.1029/2006JD007081
- Lin G, Phillips SL, Ehleringer JR (1996) Monsoonal precipitation responses of shrubs in a cold desert community on the Colorado Plateau. *Oecologia* 106:8–17
- Lipp J, Trimborn P, Fritz P, Moser H, Becker B, Franzel B (1991) Stable isotopes in tree ring cellulose and climatic change. *Tellus* 43B:322–330
- Little CHA, Lavigne MB, Ostaff DP (2003) Impact of old foliage removal, simulating defoliation by the balsam fir sawfly, on balsam fir tree growth and photosynthesis of current-year shoots. *For Ecol Manag* 186:261–269
- Loader NJ, Switsur VR, Field EM (1995) High-resolution stable isotope analysis of tree rings: implications of “microdendroclimatology” for palaeoenvironmental research. *Holocene* 1(5):457–460
- Loader NJ, McCarroll D, Gagen MH, Robertson I, Jalkanen R (2007) Extracting climate information from stable isotopes in tree rings. In: Dawson TE, Siegwolf RTW (eds) *Isotopes as indicators of ecological change*. Elsevier, Amsterdam pp 27–48
- Loader NJ, Santillo PM, Woodman-Ralph JP, Rolfe JE, Hall MA, Gagen M, Robertson I, Wilson R, Froyd CA, McCarroll D (2008) Multiple stable isotopes from oak trees in south-western Scotland and the potential for stable isotope dendroclimatology in maritime climatic regions. *Chem Geol* 252:62–71
- Managave SR (2009) High resolution monsoon reconstruction using oxygen isotopes in teak trees. Unpublished thesis. M.S. University of Baroda, Vadodara, 98 p
- Managave SR, Sheshshayee MS, Bhattacharyya A, Ramesh R (2010a) Intra-annual variations of cellulose $\delta^{18}\text{O}$ of teak from Kerala, India: implications to reconstruction of past summer and winter monsoon rains. *Clim Dyn* in press. doi:10.1007/s00382-010-0917-9
- Managave SR, Sheshshayee MS, Borgaonkar HP, Ramesh R (2010b) Past break-monsoon conditions detectable by high resolution intra-annual $\delta^{18}\text{O}$ analysis of teak rings. *Geophys Res Lett* 37:L05702. doi:10.1029/2009GL041172
- Managave SR, Sheshshayee MS, Borgaonkar HP, Ramesh R (2010c) Intra-annual oxygen isotope variations in central Indian teak cellulose: possibility of improved resolution for past monsoon reconstruction. *Curr Sci* 98:930–937
- Managave SR, Sheshshayee MS, Ramesh R, Borgaonkar HP, Shah SK, Bhattacharyya A (2010d) Response of cellulose oxygen isotope values of teak trees in differing monsoon environments to monsoon rainfall. *Dendrochronologia* 29: 89–97
- McCarroll D, Pawellek F (2001) Stable carbon isotope ratios of *Pinus sylvestris* from northern Finland and the potential for extracting a climate signal from long Fennoscandian chronologies. *Holocene* 11:517–526
- McCarroll D, Loader NJ (2004) Stable isotopes in tree rings. *Quatern Sci Rev* 23:771–801
- McCarroll D, Loader NJ (2006) Isotope in tree rings. In: Melanie Leng J (ed) *Isotopes in palaeoenvironmental research*. Springer, Dordrecht, The Netherlands 67–106
- McCarroll D, Gagen MH, Loader NJ, Robertson I, Anchukaitis KJ, Los S, Young GHF, Jalkanen R, Kirchhefer A, Waterhouse JS (2009) Correction of tree ring stable carbon isotope chronologies for changes in the carbon dioxide content of the atmosphere. *Geochim Cosmochim Acta* 73:1539–1547
- McDowell N, Phillips N, Lunch C, Bond BJ, Ryan MG (2002) An investigation of hydraulic limitation and compensation in large, old Douglas-fir trees. *Tree Physiol* 22:763–774
- Meinzer FC, Brooks JR, Domec JC, Gartner BL, Warren JM, Woodruff DR, Bible K, Shaw DC (2006) Dynamics of water transport and storage in conifers studied with deuterium and heat tracing techniques. *Plant Cell Environ* 29:105–114
- Miller DL, Mora CI, Grissino-Mayer HD, Mock CJ, Uhle ME, Sharp Z (2006) Tree ring isotope record of tropical cyclone activity. *PNAS* 103(39):14294–14297
- Miyake Y, Matsubaya O, Nishihara C (1968) An isotopic study on meteoric precipitation. *Pap Meteorol Geophys* 19:243–266
- Mook WG (2006) Introduction to isotope hydrology stable and radioactive isotopes of hydrogen, oxygen and carbon. Taylor and Francis, London, p 226
- Ogée J, Barbour MM, Wingate L, Bert D, Bosc A, Stievenard M, Lambrot C, Pierre M, Bariac T, Loustau D, Dewar RC (2009) A single-substrate model to interpret intra-annual stable isotope signals in tree-ring cellulose. *Plant Cell Environ* 32: 1071–1090
- Poussart PF, Schrag DP (2005) Seasonally resolved stable isotope chronologies from northern Thailand deciduous trees. *Earth Planet Sci Lett* 235:752–765
- Poussart PF, Evans MN, Schrag DP (2004) Resolving seasonality in tropical trees: multi-decade, high-resolution oxygen and carbon isotope records from Indonesia and Thailand. *Earth Planet Sci Lett* 218:301–316
- Ramesh R, Bhattacharya SK, Gopalan K (1985) Dendrochronological implications of isotope coherence in trees from Kashmir Valley, India. *Nature* 317:802–804
- Ramesh R, Bhattacharya SK, Gopalan K (1986a) Stable isotope systematics in tree cellulose as palaeoenvironmental indicators – a review. *J Geol Soc India* 27:154–167
- Ramesh R, Bhattacharya SK, Gopalan K (1986b) Climatic correlations in the stable isotope records of silver fir (*Abies pindrow*) trees from Kashmir, India. *Earth Planet Sci Lett* 79:66–74
- Ramesh R, Bhattacharya SK, Pant GB (1989) Climatic significance of δD variations in a tropical tree species from India. *Nature* 337:149–150
- Risi C, Bony S, Vimeux F (2008) Influence of convective processes on the isotopic composition ($\delta^{18}\text{O}$ and δD) of precipitation and water vapor in the tropics: 2. Physical interpretation of the amount effect. *J Geophys Res* 113: D19306. doi:10.1029/2008JD009943
- Robertson I, Leavitt S, Loader N, Buhay W (2008) Progress in isotope dendroclimatology. *Chem Geol* 252:EX1–EX4
- Roden JS, Lin G, Ehleringer JR (2000) A mechanistic model for interpretation of hydrogen and oxygen isotope ratios in tree-ring cellulose. *Geochim Cosmochim Acta* 64(1):21–35

- Roden JS, Johnstone JA, Dawson TE (2009) Intra-annual variation in the oxygen and carbon ratios of cellulose in tree rings of coastal redwood (*Sequoia sempervirens*). *Holocene* 19: 189–197
- Roden JS, Bowling DR, McDowell NG, Bond BJ, Ehleringer JR (2005) Carbon and oxygen isotope ratios of tree ring cellulose along a precipitation transect in Oregon, United States. *J Geophys Res* 110:G02003
- Rowell DM, Ades PK, Tausz M, Arndt SK, Adams MA (2009) Lack of genetic variation in tree ring $\delta^{13}\text{C}$ suggests a uniform, stomatal-driven response to drought stress across *Pinus radiata* genotypes. *Tree Physiol* 29:191–198
- Rozanski K, Araguas-Araguas L, Giofanti R (1993) Isotopic patterns in modern global precipitation. *Geophys Monogr* 78: 1–36
- Sano M, Sheshshayee MS, Managave S, Ramesh R, Sukumar R, Sweda T (2010) Climatic potential of $\delta^{18}\text{O}$ of *Abies spectabilis* from the Nepal Himalaya. *Dendrochronologia* 28: 93–98
- Saurer M, Aellen K, Siegwolf R (1997) Correlating $\delta^{13}\text{C}$ and $\delta^{18}\text{O}$ in cellulose of trees. *Plant Cell Environ* 20: 1543–1550
- Saurer M, Siegwolf RTW, Schweingruber FH (2004) Carbon isotope discrimination indicates improving water-use efficiency of trees in northern Eurasia over the last 100 years. *Glob Change Biol* 10:2109–2120
- Scheidegger Y, Saurer M, Bahn M, Siegwolf R (2000) Linking stable oxygen and carbon isotopes with stomatal conductance and photosynthetic capacity: a conceptual model. *Oecologia* 125:350–357
- Schiegl WE (1974) Climatic significance of deuterium abundance in growth rings of *Picea*. *Nature* 251:582–584
- Schmidt GA, LeGrande AN, Hoffmann G (2007) Water isotope expressions of intrinsic and forced variability in a coupled ocean-atmosphere model. *J Geophys Res* 112:D10103. doi:10.1029/2006JD007781
- Schwinning S, Davis K, Richardson L, Ehleringer JR (2002) Deuterium enriched irrigation indicates different forms of rain use in shrub/grass species of the Colorado Plateau. *Oecologia* 130:345–355
- Sheshshayee MS, Bindumadhava H, Ramesh R, Prasad TG, Lakshminarayana MR, Udaykumar M (2005) Oxygen isotope enrichment ($\Delta - \text{O}-18$) as a measure of time-averaged transpiration rate. *J Exp Bot* 56:3033–3039
- Simard S, Elhani S, Morin H, Krause C, Cherubini P (2008) Carbon and oxygen stable isotopes from tree rings to identify spruce budworm outbreaks in the boreal forest of Quebec. *Chem Geol* 252:80–87. doi:10.1016/j.chemgeo.2008.01.018
- Skomarkova MV, Vaganov EA, Mund M, Knohl A, Linke P, Boerner A, Schulze E-D (2006) Inter-annual and seasonal variability of radial growth, wood density and carbon isotope ratios in tree rings of beech (*Fagus sylvatica*) growing in Germany and Italy. *Trees* 20:571–586
- Srivastava (2009) Stable isotope studies of Atmospheric water vapour and clouds. Unpublished thesis. M.S. University, Udaipur, 114 p
- Sternberg LDL (2009) Oxygen stable isotope ratio of tree-ring cellulose: the next phase of understanding. *New Phytol* 181:553–562
- Sternberg LDL, DeNiro MJ, Savidge RA (1986) Oxygen isotope exchange between metabolites and water during biochemical reactions leading to cellulose synthesis. *Plant Physiol* 82: 423–427
- Sternberg LDL, Pinzon MC, Vendramini PF, Anderson WT, Jahren AH, Beuning K (2007) Oxygen isotope ratios of cellulose-derived phenylglucosazone: an improved paleoclimate indicator of environmental water and relative humidity. *Geochim Cosmochim Acta* 71:2463–2473
- Sternberg LDL (1989) Oxygen and hydrogen isotope measurements in plant cellulose analysis. In: Linskens HF, Jackson JF (eds) *Plant fibres. Modern methods of plant analysis*, Vol 10. Springer, Berlin, pp 89–99
- Sudheendrakumar VV, Nair KSS, Chacko KC (1993) Phenology and seasonal growth trend of teak at Nilambur (Kerala), India. *Ann For* 1(1):42–46
- Swetnam TW, Lynch AM (1993) Multi-century, regional-scale patterns of western spruce budworm history. *Ecol Monogr* 63:399–424. doi:10.2307/2937153
- Tang K, Feng X (2001) The effect of soil hydrology on the oxygen and hydrogen isotopic compositions of plants' source water. *Earth Planet Sci Lett* 185:355–367
- Tian L, Yao T, MacClune K, White JWC, Schilla A, Vaughn B, Vachon R, Ichiyanagi K (2007) Stable isotopic variations in west China: a consideration of moisture sources. *J Geophys Res* 112:D10112. doi:10.1029/2006JD007718
- Treydte KS, Schleser GH, Helle G, Frank DC, Winiger M, Haug GH, Esper J (2006) The twentieth century was the wettest period in northern Pakistan over the past millennium. *Nature* 440:1179–1182. doi:10.1038/nature04743
- Treydte KS, Frank DC, Saurer M, Helle G, Schleser GH, Esper J (2009) Impact of climate and CO_2 on a millennium-long tree-ring carbon isotope record. *Geochim Cosmochim Acta* 73:4635–4647
- Tsuji H, Nakatsuka T, Takagi K (2006) $\delta^{18}\text{O}$ of tree-ring cellulose in two species (spruce and oak) as proxies of precipitation amount and relative humidity in northern Japan. *Chem Geol* 231:67–76
- Vaganov EA, Schulze E-D, Skomarkova MV, Knohl A, Brand WA, Roscher C (2009) Intra-annual variability of anatomical structure and $\delta^{13}\text{C}$ values within tree rings of spruce and pine in alpine, temperate and boreal Europe. *Oecologia* 161:729–745. doi:10.1007/s00442-009-1421-y
- Verheyden A, Helle G, Schleser GH, Dehairs F, Beeckman H, Koedam N (2004) Annual cyclicity in high-resolution stable carbon and oxygen isotope ratios in the wood of the mangrove tree *Rhizophora mucronata*. *Plant Cell Environ* 27: 1525–1536
- Waliser DE, Gautier C (1999) A satellite derived climatology of the ITCZ. *J Clim* 6:2162–2174
- Waterhouse JS, Switsur VR, Barker AC, Carter AHC, Hemming DL, Loader NJ, Robertson I (2004) Northern European trees show a progressively diminishing response to increasing atmospheric carbon dioxide concentrations. *Quatern Sci Rev* 23:803–810
- Waterhouse JS, Switsur VR, Barker AC, Carter AHC, Robertson I (2002) Oxygen and hydrogen isotope ratios in tree rings: how well do models predict observed values? *Earth Planet Sci Lett* 201:421–430
- Weidner K, Helle G, Löffler J, Neuwirth B, Schleser GH (2006) Stable isotope and tree-ring width variations of larch affected by larch budmoth outbreaks. In: Haneca K, Verheyden A, Beeckman H, Gärtner H, Helle G, Schleser GH (eds)

- TRACE – tree rings in archaeology, climatology and ecology, vol 5. FZ Jülich, Jülich, pp 148–153
- White JWC, Cook ER, Lawrence JR, Broecker WS (1985) D/H ratios of sap in trees: implication for water source and tree ring D/H ratios. *Geochim Cosmochim Acta* 49:237–246
- Yadava MG, Ramesh R (2005) Monsoon reconstruction from radiocarbon dated tropical speleothems. *Holocene* 15:48–59
- Yadava MG, Ramesh R, Pandarinath K (2007) A positive amount effect in the Sahayadri (Western Ghats) rainfall. *Curr Sci* 93(2):560–564
- Yurtsever Y, Gat JR (1981) Atmospheric waters. In: Gat JR, Gonfiantini R (eds) *Stable isotope hydrology*. Technical Report Series No. 210, IAEA, Vienna. 103–142

Chapter 39

The N, O, S Isotopes of Oxy-Anions in Ice Cores and Polar Environments

Joël Savarino and Samuel Morin

Abstract For more than 60 years, ice from the polar caps has been used to unravel the evolution of our past climate and environment. Throughout technological improvements, climate researchers have gradually adapted their scientific tools to study the isotope content of the impurities present in it, with the hope to gather more and better information of the Earth's shattered history. In this chapter, we present an overview of the techniques and studies which use stable isotope analysis to gain new insight. This domain has become so vast that we have limited our presentation to the recent analysis of the two major oxy-anions present in snow: sulfate and nitrate. These species are characteristic of the sulfur and nitrogen cycles. Describing the results obtained on ice without discussing the present atmosphere make little sense as ice is precisely used as a proxy for our past atmosphere. Consequently, beyond the analytical methods to measure the sulfur, nitrogen and oxygen isotopes of sulfate and nitrate, this chapter presents the results obtained at the interface between atmosphere, snow and ice with a focus on polar regions. The current state-of-the-art is presented for these two oxy-anions, including their non-mass-dependent isotope effects.

J. Savarino (✉)
Laboratoire de Glaciologie et Géophysique de l'Environnement,
Université Joseph Fourier, St Martin d'Hères, France
and
Institut National des Sciences de l'Univers, CNRS, Grenoble,
France
e-mail: jsavarino@lgge.obs.ujf-grenoble.fr

S. Morin
Météo-France, CNRM-GAME, Centre d'Études de la Neige,
St Martin d'Hères, France
and
Institut National des Sciences de l'Univers, CNRS, Grenoble,
France

39.1 Introduction

39.1.1 General Context

The stable isotopes of the light elements, that is to say H, C, N, O and S, are the backbone of isotope geochemistry. In the seminal work of Urey (1947), considered as the birth of quantitative isotope geochemistry, isotopes of H, C, N, O were dealt with great detail and occupied a central position, allowing the calculation of the position of equilibrium for isotopic substituted molecules in a exchange reaction. The revision of Urey's work, 30 years later by Richet et al. (1977), now including the sulfur stable isotopes, has reinforced the primacy of stable isotopes of the light elements in geochemistry. Despite the revolution of new techniques and methods (e.g. continuous flow injection, GC-IRMS couplings, ICP-MS, Ion Probe, Cavity Ring Down Spectroscopy (CRDS)) which are cheaper, faster and better, stable isotopes of light elements are still today the main activity of the majority of stable isotope laboratories worldwide.

Among oxy-anions, only sulfate and nitrate play a significant role in the chemical activity of the atmosphere. Their atmospheric formation ensues from the volatility of their precursors, sulfur dioxide (SO₂) and nitrogen oxides (NO_x = NO + NO₂), respectively. These gas precursors, emitted by natural and anthropogenic sources, are oxidized owing to the strong oxidative capacity of the atmosphere and thus transformed to their main final products, sulfuric and nitric acids. With an atmospheric lifetime of about a week for these species, prevailing winds and the general circulations of air masses transport these oxy-anions to polar ice caps where they can be stored for hundreds of thousands of years.

Glaciochemistry, the science which focuses on the chemical impurities present in ice cores, has proved to be a valuable approach to decipher the evolution of past climate and environment (Bender et al. 1997; Legrand and Mayewski 1997). Dansgaard et al. (1969) were the first to use the potential of old ice to reveal past temperature evolutions starting from the last thousand centuries to glacial-interglacial cycles but it is only recently that isotopic studies spread into the trace species buried in ice and snow, starting with the carbon isotopes of carbon dioxide (Friedli et al. 1984) and methane a few years later (Craig et al. 1988). Regarding the sulfate and nitrate oxy-anions, isotopic analysis had to wait another decade to see the first data published (Freyer et al. 1996; Patris et al. 2000), due to their lower abundance and sensitivity limitations of the analytical methods.

39.1.2 Definitions, Mass Dependent and Non-Mass Dependent Compositions and Rational

With two, three and four stable isotopes for N, O, S respectively, a total of six atomic isotope ratios can be considered: ^{15}R ($=^{15}\text{N}/^{14}\text{N}$), ^{17}R ($=^{17}\text{O}/^{16}\text{O}$), ^{18}R ($=^{18}\text{O}/^{16}\text{O}$), ^{33}R ($=^{33}\text{S}/^{32}\text{S}$), ^{34}R ($=^{34}\text{S}/^{32}\text{S}$), ^{36}R ($=^{36}\text{S}/^{32}\text{S}$), with the most abundant isotope conventionally taken as the denominator. Due to minute variations and comparison considerations, atomic isotope ratios are reported on the delta scale (McKinney et al. 1950) where variations of atomic isotope ratios are scaled against an international reference taken as the standard. Using this notation, ^xR for sulfur is expressed by:

$$\delta^x\text{S} = \frac{{}^xR_{\text{spl}}}{{}^xR_{\text{ref}}} - 1 \quad \text{with } x = 33, 34 \text{ or } 36$$

The same is true for the N and O systems making the logical substitutions. R_{ref} is the isotopic ratio of the reference material and it follows from the definition that variations of the sample isotopic ratio (R_{spl}) are measured as enrichments ($\delta > 0$) or depletions ($\delta < 0$) with respect to the isotope ratio of the international reference standard, R_{ref} . Thus it can readily be deduced that nitrate and sulfate are isotopically fully defined by three ($\delta^{15}\text{N}$, $\delta^{17}\text{O}$ and $\delta^{18}\text{O}$) and five ($\delta^{17}\text{O}$,

$\delta^{18}\text{O}$, $\delta^{33}\text{S}$, $\delta^{34}\text{S}$ and $\delta^{36}\text{S}$) δ values, respectively. However, for years, only the dominant isotopic ratios for oxygen and sulfur (i.e. $\delta^{18}\text{O}$ and $\delta^{34}\text{S}$) were reported in the literature. The laws of quantum and classical mechanics and thermodynamics which are at the base of most of the isotopic fractionation processes dictate that multiple isotope ratios of the same element are strongly correlated by mass dependent laws (Young et al. 2002). For more information, readers are referred to Chap. 30 (Michalski et al.) of this book which exposes in greater details the basic phenomena explaining the mass laws. We note here that the following relationships hold for the oxygen and sulfur isotope systems:

$$\delta^{17}\text{O} \approx 0.52 \delta^{18}\text{O}$$

$$\delta^{33}\text{S} \approx 0.52 \delta^{34}\text{S} \quad \text{and} \quad \delta^{36}\text{S} \approx 1.91 \delta^{34}\text{S}$$

A simple and elegant while not totally correct way to explain these coefficients is to remember that isotopic fractionations are primarily driven by mass difference so $0.52 \approx (m_{17} - m_{16}) / (m_{18} - m_{16})$ with m the atomic mass of the oxygen isotope considered, the same holding for the sulfur. These mass-dependent relationships are robust in the nature and thus, it has been concluded unnecessary to measure all possible isotope ratios as they were providing redundant information.

This vision was challenged radically when Thiemens' laboratory at the University of California in San Diego (USA) discovered deviations from these mass laws for both the oxygen and sulfur systems (Thiemens and Heidenreich 1983; Heidenreich and Thiemens 1986; Farquhar et al. 2000a, 2001) that were directly applicable to the Earth's atmosphere. First, laboratory-made ozone was found to display a radical deviation from the mass law. This deviation or anomaly is quantified using $\Delta^{17}\text{O}$ (isotope anomaly or ^{17}O excess):

$$\Delta^{17}\text{O} \approx \delta^{17}\text{O} - 0.52 \delta^{18}\text{O}$$

and the processes at the origin of this anomaly are referred to as non-mass dependent fractionation (NMD) or mass-independent fractionation (MIF).

Measurements of atmospheric ozone later confirmed the existence of this isotopic anomaly in the atmosphere (Mauersberger 1987; Krankowsky et al. 1995, 2000;

Johnston and Thiemens 1997; Mauersberger et al. 2001). A similar story emerged for sulfur isotopes with first the discovery of a sulfur anomaly in ancient rocks (Farquhar et al. 2000a), later reproduced in the laboratory (Farquhar et al. 2001). These anomalies are generated in the gas-phase on species too unstable to be preserved in any natural archives. Nevertheless they leave fingerprints on the end-members of the oxidation chains, such as nitrate and sulfate. These signatures are specific to a few reactions in the atmosphere. For instance, in a series of papers, Greg Michalski and Huming Bao took advantage of this specific and unique atmospheric isotope signature to determine the origin of the massive salt deposits found in hyper-arid environments and quantify the influence of atmospheric depositions (Bao et al. 2000, 2001; Michalski et al. 2004a, b, 2005a, b; Bao and Marchant 2006). In Table 39.1, we list the species for which an isotope anomaly has been found and their probable origin.

For polar environments and ice cores, only sulfate and nitrate have been studied for their oxygen and sulfur isotopic anomalies, enhanced by new analytical methods and relative ease in extraction. While sulfur and nitrogen isotopes can provide information about source apportionment, oxygen isotopes are fully controlled by the interaction of the precursors with the chemical activity of the atmosphere. Indeed, as a first approximation, one can consider that during the inevitable transformation of reduced sulfur and nitrogen species emitted by different continental or oceanic

sources (e.g. dimethyl sulfite (CH_3SCH_3), hydrogen sulfite (H_2S), ammonia (NH_3) etc) to their final oxidized forms (i.e. sulfate and nitrate, respectively), the sulfur and the nitrogen isotopes of these end-products represent a mass-weighted mixture of the individual sources. Thus, analysis of sulfur and nitrogen isotopes of sulfate and nitrate can be a valuable tool in constraining the flux emission of individual continental/oceanic sources. On the other hand, the transformation of precursors to end-oxidation products results in the incorporation of oxygen atom from different oxidation agents. Oxygen isotopes of sulfate and nitrate are thus integrators of the oxidative capacity of the atmosphere, a fundamental notion in atmospheric chemistry that describes the natural property of the atmosphere to cleanse itself by production of radicals and oxidative species. Aided by the unique and strange isotopic composition of ozone, it was realized that such end-oxidation products archive this fundamental chemical property of the atmosphere, otherwise inaccessible by any other means. With the exception of modeling exercises (Thompson 1992; Thompson et al. 1993; Karol et al. 1995; Martinerie et al. 1995; Wang and Jacob 1998; Valdes et al. 2005; Shindell et al. 2006), the chemical activity of the pre industrial atmosphere has never been determined and thus the climate–chemistry interplay is currently unconstrained. As we will see, the discovery of the isotope anomaly has opened new ways to tackle this difficult issue using the glaciological archives.

Table 39.1 Species presenting an isotope anomaly measured in the Earth's environment

Species	Environments	Origin	Mechanism	Range
O_3	Atmosphere	$\text{O} + \text{O}_2$	Symmetry effect	$\Delta^{17}\text{O} \approx 20\text{--}40\text{‰}$
CO_2	Stratosphere	$\text{O}(^1\text{D}) + \text{CO}_2$	Transfer from ozone and possible symmetry effect	$\Delta^{17}\text{O} \approx 0\text{--}2\text{‰}$
N_2O	Atmosphere	Unknown, possible $\text{NH}_2 + \text{NO}_2$	Transfer from ozone	$\Delta^{17}\text{O} \approx 1\text{‰}$
CO	Atmosphere	$\text{CO} + \text{OH}$	Symmetry effect?	$\Delta^{17}\text{O} \approx 0.2\text{--}8\text{‰}$
H_2O_2	Atmosphere	$\text{H} + \text{O}_2$	Unknown	$\Delta^{17}\text{O} \approx 1\text{--}2.5\text{‰}$
NO_3^-	Atmosphere, ice cores, salt deposits	$\text{NO} + \text{O}_3, \text{NO}_x + \text{O}_3$	Transfer from ozone	$\Delta^{17}\text{O} \approx 10\text{--}40\text{‰}$
SO_4^{2-}	Oxygen Atmosphere, ice cores, salt deposits	$\text{HSO}_3^{2-} + \text{O}_3$ in liquid phase	Transfer from ozone	$\Delta^{17}\text{O} \approx 0\text{--}7\text{‰}$
	Sulfur Archean rocks, volcanic sulfate	UV photolysis of SO_2	Self shielding, symmetry?	$\Delta^{33}\text{S} \approx -2$ to 10‰
ClO_4^-	Salt deposits	$\text{Cl} + \text{O}_3, \text{ClO} + \text{O}_3?$	Transfer from ozone	$\Delta^{17}\text{O} \approx 5\text{--}11\text{‰}$
Hg(II)	Atmosphere, deposits, food web	Photoreduction of Hg, gas–liquid equilibrium	Nuclear magnetic effect or nuclear volume effect	$\Delta^{201}\text{Hg} \approx 0.2\text{--}4\text{‰}$

Due to the reactivity of ozone with many other short-live species, the atmosphere contains certainly more compounds possessing an isotope anomaly

39.2 Materials and Methods

39.2.1 A Short Description of Methods for Isotopic Ratio Measurements

Gas isotope ratio mass spectrometer (G-IRMS) is still the favored instrument for measuring isotopic ratios of light elements for highest precision. Despite being invented in the 1940s (Nier 1936, 1940, 1947), this instrument continues today to follow the original concept of its designers. The dual-inlet, the concept of introducing with adjustable volumes reference and sample gases, was the first method to free the analysis from instrumental bias (Murphey 1947; McKinney et al. 1950). Sano et al. (1976) and subsequently Matthews and Hayes (1978) changed the principle of introducing the reference and sample by coupling a Gas Chromatography (GC) with the IRMS. This method combines the GC selectivity (i.e. its capacity to separate complex gas mixture) and sensitivity of the IRMS to measure isotopic ratios and is becoming the most popular IRMS technique.

G-IRMS, however, is not the only instrument designed to measure isotope ratios despite its usefulness. Thermal Ionization Mass Spectrometer (TIMS) has been used since WWII for solid samples and low volatility elements. The sample is deposited directly on the filament and upon fast heating, vaporization and ionization is accomplished (Mann and Kelly 2005). The ion probe is a method based on sputtering solid samples with a primary ion beam (Chabala et al. 1995). Secondary ions produced from the sample are collimated and mass filtered. Inductively Coupled Plasma Mass Spectrometry (ICPMS) allows liquid samples to be sprayed and introduced in a plasma to the source (Halliday et al. 1998; Yang 2009). Matrix effects limit this technique to heavy elements and require high mass resolution to avoid isobaric interferences. Finally, optical spectroscopy coupled with high reflectivity cell has made a staggering entrance on the isotope geochemistry marketplace (Cavity RingDown Spectroscopy – CRDS). Small molecules with a dipole moment (e.g. CO₂, H₂O, H₂S, N₂O, CO, CH₄, etc) possess well-defined infrared absorption band lines that are shifted upon isotopic substitution. If bands from different isotopologues overlap in the wavelength range of a given laser diode then isotopic ratios can be obtained (Ding et al. 2004). Instruments measuring CO₂, H₂O

isotopologues are now sold off-the-shelf. In theory, this new technology presents many advantages such as light weight, portability and low power requirement. This allows continuous monitoring with a high sensitivity, in a specific and non-destructive manner, involving little sample manipulation and with site-specific isotope analytical capabilities (e.g. ¹⁵N¹⁴NO vs. ¹⁴N¹⁵NO). In practice, CRDS techniques are currently limited by the narrow range of infrared laser diode available on the market, lack of high resolution infrared spectra database for major and minor isotopologues and precise line assignment. Nevertheless, recent commercialization of instruments for water and CO₂ isotopes shakes the foundation of light elements isotope geochemistry and is becoming a serious competitor for the traditional G-IRMS.

39.2.2 Sulfur and Oxygen Isotopes of Sulfate

Since both sulfur and oxygen isotopes of sulfate possess geochemical interest, techniques were developed with the objective of extracting this dual atomic information. Starting with the major isotope ratios ($\delta^{34}\text{S}$ and $\delta^{18}\text{O}$), methods progressively expanded to the minor isotope ratios ($\delta^{33}\text{S}$, $\delta^{36}\text{S}$ and $\delta^{17}\text{O}$) when it was realized that the latter ratios are also of geochemical interest.

39.2.2.1 Preparation of Samples for Sulfur Isotopes

Conventionally, measurements of sulfur isotope ratios are performed using G-IRMS in which sulfur is introduced as gaseous SO₂ or SF₆ (Thode et al. 1961; Hulston and Thode 1965; Bailey and Smith 1972; Robinson and Kusakabe 1975; Coleman and Moore 1978; Matthews and Hayes 1978; Ueda and Krouse 1986; Giesemann et al. 1994). The latter is preferred for high precision S analysis because SF₆ is an inert gas and has no mass interference (Rees 1978). The general scheme follows the conversion of sulfate ions to barium sulfate precipitate (BaSO₄), conversion of BaSO₄ to H₂S (Pepkowitz and Shirley 1951; Kiba et al. 1955) and finally precipitating H₂S as CdS and Ag₂S before

the fluorination step (Thode et al. 1961; Hulston and Thode 1965; Rees 1978; Rai et al. 2005). The analytical technique using SO_2 presents the net advantage of being a on-line method with high throughput when O isotope interferences can be minimized by careful control of the oxygen atom sources (Pichlmayer and Blochberger 1988; Giesemann et al. 1994; Grassineau et al. 2001; Grassineau 2006). In this case, BaSO_4 is mixed with V_2O_5 and O_2 and flash combusted in a $1,020^\circ\text{C}$ oven containing pure copper to reduce SO_3 . Precisions of $\pm 0.2\text{‰}$ for sample sizes in the several tens of nanomole range are achievable (Giesemann et al. 1994; Fritzsche and Tichomirowa 2006).

The recent discovery of anomalous sulfur isotopic composition in archean environments (Farquhar et al. 2000a, 2001, 2002; Farquhar and Wing 2003) and volcanic sulfates (Savarino et al. 2003; Baroni et al. 2007, 2008; Martin and Bindeman 2009) has reinvigorated the necessity to measure minor sulfur isotopic ratios. While Ag_2S fluorination in heated nickel tubes (Hulston and Thode 1965; Gao and Thiemens 1993a, b; Farquhar et al. 2000b; Rai et al. 2005) has been the favored method to measure the $\delta^{33}\text{S}$ and $\delta^{36}\text{S}$ isotope ratios, IR laser heating (Beaudoin and Taylor 1994) or UV laser sputtering (Hu et al. 2003; Ono et al. 2006) is proposed to simplify the production of SF_6 , with precisions reaching 0.2‰ for 100–200 nmol of sulfur. Others are also now proposing to use directly SO_2 and/or its SO fragment with appropriate corrections to measure $\delta^{33}\text{S}$ (Baublys et al. 2004; Poulson 2005), with encouraging precisions and accuracy ($\pm 0.3\text{‰}$ for $\delta^{33}\text{S}$ for few micromole of sulfite). Alternatively, solid samples can be analyzed for the entire sulfur isotope spectrum by ion probe at nanomole level but with degraded precision for δ values (± 0.5 and $\pm 0.25\text{‰}$ at 1σ for $\delta^{34}\text{S}$ and $\delta^{33}\text{S}$, respectively) but acceptable $\Delta^{33}\text{S}$ ($\pm 0.1\text{‰}$) (Mojzsis et al. 2003; Papineau et al. 2005, 2007; Kamber and Whitehouse 2007). Given the sample sizes in ice cores, we note that none of these techniques are really adapted for ice cores analysis. We still lack of a SF_6 analytical method to deal with the minute sulfate quantities found in ice.

39.2.2.2 Preparation of Samples for Oxygen Isotopes

Fewer techniques are available for the analysis of oxygen isotopes of sulfate. Rafter (1967) was the

first to propose a methodology. Soluble sulfate is precipitated as barium sulfate, mixed with pure carbon graphite and combusted at high temperature, producing CO/CO_2 gas and solid BaS . CO is further converted to CO_2 in a glow discharge chamber. BaS is eventually recovered and oxidized back to sulfate for sulfur isotopes while CO_2 is directly used for $\delta^{18}\text{O}$ or further fluorinated in a high temperature nickel tube to quantitatively obtain O_2 (Bhattacharya and Thiemens 1989), enabling the measurement of $\delta^{18}\text{O}$ and $\delta^{17}\text{O}$ (Lee and Thiemens 2001; Lee et al. 2002). Good precision for both $\delta^{18}\text{O}$ and $\Delta^{17}\text{O}$ are obtained (± 0.2 and $\pm 0.1\text{‰}$, respectively for 3–6 μmol of sulfur). However, this method is long, difficult and time-consuming, limiting its use.

High temperature Conversion/Elemental Analyzer (TC/EA), a standard technique dated back to the 1970s, can also be used to convert BaSO_4 to CO in a glassy carbon oven (Kornexl et al. 1999; Böhlke et al. 2003; Boschetti and Iacumin 2005; Brand et al. 2009). Good reproducibility is found between the different laboratories but with lower accuracy (Boschetti and Iacumin 2005). The drawback is that the production of CO prohibits the measurement of the $\delta^{17}\text{O}$, masked by the mass interference with ^{13}C .

For atmospheric chemistry and ice core sciences, there is a strong interest to measure all sulfur and oxygen isotope ratios. Considering the limited amount of sulfate available in remote atmospheres and ice sheets, none of the former methods are appropriate. Savarino et al. (2001) developed a pyrolysis method, interfaced with a GC where silver sulfate (Ag_2SO_4) is thermally decomposed in a He flow to produce SO_2 and O_2 . The main advantage of this method is the direct production of O_2 , suitable for the dual oxygen ratio analysis while SO_2 can be used as it is for $\delta^{34}\text{S}$ or be reoxidized to sulfate for sulfur isotopic analysis using the SF_6 method. Pure sulfate is obtained by a semi-preparative ion chromatography (Alexander et al. 2004; Kunasek et al. 2010) and conversion to silver sulfate is achieved with a cation exchange membrane (De Angelis et al. 2004; Kunasek et al. 2010). This method allows the separation, purification and processing of a few micromole of sulfate for $\delta^{17}\text{O}$ and $\delta^{18}\text{O}$ typically contained in aerosols or ice while maintaining the precision ($\pm 0.5\text{‰}$ for $\delta^{18}\text{O}$ and $\pm 0.1\text{‰}$ for $\Delta^{17}\text{O}$). Furthermore, SO_2 of the same sample is still available for sulfur isotope analysis.

39.2.3 Nitrogen and Oxygen Isotopes of Nitrate

Nitrate in the environment is as ubiquitous as sulfate. Its formation in the atmosphere derives from nitrogen oxides, which are the compounds controlling ozone formation. Nitrate is also a major component of the food web, and its acid form (HNO_3) a major component of acid rain. Heavily used as a fertilizer, excess soil nitrate, surface waters and in ecosystems in general is a serious environmental issue. Nitrogen and oxygen isotopic analysis of nitrate is therefore used as a fundamental diagnostic tool to understand the nitrogen cycle (Kendall 1998). Below we briefly review the methods used to analyze its stable isotopes.

39.2.3.1 Methods for the Analysis of Nitrogen Isotopes in Nitrate

Sprinson and Rittenberg (1949) presented methodology where organic nitrogen is transformed to ammonium by Kjeldahl digestion (hot, concentrated sulfuric acid/potassium sulfate) followed by the decomposition of ammonium to N_2 . After a few purification steps, N_2 is introduced to the mass spectrometer and measured against air N_2 (Mariotti 1983). Parwel et al. (1957) expanded this method to nitrate ions and was further used by Hoering (1955, 1957). Alternative wet chemistry methods have also been proposed to expand and simplify laboratory manipulations (Bremner and Keeney 1965, 1966; Cheng and Bremner 1966; Keeney and Bremner 1966; Silva and Bremner 1966). However, these wet chemistry methods are now replaced by a simpler solid/combustion method (Gunther et al. 1966), avoiding the long preparation time intrinsic to wet chemistry and more adapted for online analysis (Fiedler and Proksch 1975; Metzger 1978; Preston and Owens 1983; Nevins et al. 1985; Owens 1988; Pichlmayer and Blochberger 1988; Owens and Rees 1989). The wet and dry methods have been intensively used and comparisons have yielded satisfactory results, although new recommendations have also been proposed (Fiedler and Proksch 1972, 1975; Minagawa et al. 1984; Kendall and Grim 1990). Current online analyses reach internal precisions of $\pm 0.1\%$ for submicromole amounts of nitrogen (Werner et al. 1999). This technique was the

first to be used for ice core ^{15}N -nitrate analysis, using an ion chromatography preconcentration method (Bordat et al. 1992). Despite still being in use for ^{15}N -nitrate of natural water with methodology improvement (Ogawa et al. 2001), EA-IRMS has been in the most recent years supplanted by a completely new approach that uses the generation of N_2O after nitrate reduction, allowing the measurement of all possible isotope ratios of N and O of nitrate in the same sample. This new approach will be detailed in the next paragraph dealing with oxygen isotopes of nitrate.

39.2.3.2 Methods for the Analysis of Oxygen Isotopes in Nitrate

^{18}O analysis (and even later for ^{17}O) of nitrate were performed much later than ^{15}N , mainly due to the difficulty of maintaining the integrity of the oxygen isotope during combustion/oxidation/reduction steps. Furthermore, it was recognized only recently that the oxygen atoms could provide a more reliable indicator of the origin of the nitrate considering the large difference in isotopic composition of the O-atom pools that composed the nitrate. The origin of the three oxygen atoms composing nitrate can be tracked back to three different sources with distinctive $\delta^{18}\text{O}$ oxygen isotopic compositions: water (-10%), O_2 -air ($+23.5\%$) and ozone ($+90\%$), for instance allowing the identification of large pools of atmospherically-made nitrate in arid environments (Bao et al. 2000, 2001; Michalski et al. 2004a, b, 2005a, b; Bao and Marchant 2006). Amberger and Schmidt (1987) proposed a CO/CO_2 method based on the combustion of KNO_3 with $\text{Hg}(\text{CN})_2$ at 550°C which was adapted from a method for organic compounds (Rittenberg and Ponticorvo 1956). To avoid the toxicity of $\text{Hg}(\text{CN})_2$, alternative chemicals were proposed such as graphite (Kornexl et al. 1994) or graphite-gold-palladium combined catalyst (Revesz et al. 1997). Low yields inherent of these methods were eventually overcome using guanidine hydrochloride (Brauer and Strauch 2000). Silva et al. (2000) proposed both a new method to collect and preserve nitrate from groundwater and advocated the use of AgNO_3 instead of KNO_3 . Silver nitrate is obtained by purifying the sample with ion exchange resin, BaCl_2 and Ag_2O in an acid medium. Pure silver nitrate solution is finally freeze-dried and mixed with graphite (Chang et al. 1999; Silva et al. 2000) or

AgCN (Wassenaar 1995) before combustion. With this method CO₂ yields approach 100% and a precision for 6–10 μmol of N to be ±0.2‰. The potassium/silver nitrate were turned into an on-line method using TC/EA-IRMS, first by producing CO₂ (Kornexl et al. 1994) and then CO to increase yield and chromatographic properties (Kornexl et al. 1999), with precisions of ±0.5 for few micromole range of material but limited to the δ¹⁸O ratio only. To access both δ¹⁷O and δ¹⁸O, the silver nitrate technique was eventually modified. AgNO₃ is directly pyrolyzed in a vacuum line, producing among others O₂, a suitable gas to measure all oxygen isotopic ratios (Michalski et al. 2002, 2003; Morin et al. 2007). The major drawbacks of these nitrate methods are their cost and potential interferences with dissolved organic carbon (Haberhauer and Blochberger 1999; Michalski 2010).

Nitrate and nitrite isotope analysis gained new momentum when the Sigman's group in Princeton published a series of papers (Sigman et al. 2001; Casciotti et al. 2002, 2007) describing the adaptation of a denitrifying bacteria method for natural isotope abundances originally developed for nitrate concentration determination and as ¹⁵N tracer in saline samples (Christensen and Tiedje 1988; Hojberg et al. 1994). This method makes use of specific strains of denitrifying bacteria which lack a gene to encode the N₂O reductase, the enzyme that reduces N₂O to N₂. With this method, nitrate contained in any solution – with the exception of bactericide matrix – is directly added to the bacteria solution which under anaerobic conditions uses nitrate/nitrite as an electron acceptor to produce N₂O. The latter is an inert gas with good chromatographic properties, having the same isotopic masses than CO₂. N₂O can therefore be used to measure the O and N isotopic ratios of nitrate with a IRMS configured for CO₂. This method surpasses all other methods published so far for being specific to nitrate/nitrite (no need to purify and isolate nitrate from its solution), independent of the organic and saline loading of the sample, highly sensitive (down to 20 nmol of N₂O), allowing both nitrogen and oxygen isotope analysis during the same run, being precise enough (±0.3 and ±0.4‰ for δ¹⁵N and δ¹⁸O respectively) and easily portable to on-line analysis. This method has now been both compared with the silver nitrate (Xue et al. 2010) and graphite combustion (Chmura et al. 2009). Results show that the bacteria method is highly correlated and statistically interchangeable with the

inorganic methods. Bacteria can either use nitrate or nitrite for their metabolism and thus nitrite can interfere with the analysis of nitrate. For samples containing significant nitrite levels, the samples can be either pre-treated to remove nitrite (Granger et al. 2006; Granger and Sigman 2009) or sequentially analyzed by combining different strains of bacteria (Böhlke et al. 2007). McIlvin and Altabet (2005) proposed an alternative approach of the bacteria method with identical performance. Nitrate is first reduced to nitrite with a Cd catalyst, followed by sodium azide treatment in acid medium to quantitatively reduce nitrite to N₂O. This method also allows sequential analysis of nitrite and nitrate. Growing bacteria is avoided with this method, azide is nevertheless a toxic chemical that needs to be handled with extreme care in a fume hood. For both methods, extensions are now available to complement the isotopic analysis δ¹⁷O but at the expense of a slight decrease in sensitivity (50 nmol of N₂O). To obtain the δ¹⁷O, a dual bacterial denitrification technique can be used (Coplen et al. 2004) or more simply by the catalytic thermal decomposition of N₂O into N₂ and O₂ products (Kaiser et al. 2007; Komatsu et al. 2008) using gold heated at ~800–900°C (Cliff and Thiemens 1994) (see also Chapter 23 of this book, Ostrom and Ostrom, 2011). Since all nitrogen-bearing compounds can potentially be converted to nitrate, the bacteria or azide methods have the potential to become the reference method for the isotopic analysis of nitrogen-containing compounds. In the near future, these methods might gain even more momentum as measurements of isotope ratios by optical spectroscopy progress towards N₂O as the analyte gas (Mohn et al. 2010).

39.3 Application and Synthesis

With the exception of water stable isotopes, the isotope analysis of natural impurities contained in trace amount (i.e. nmol/g of ice and below) in ice cores is still in its infancy. The cost, logistical difficulty and drilling technology limits the amount of ice material that can be recovered during field operations taking place in the most desolated regions of the Earth. Moreover, high latitude or altitude icy terrains receive little material from the main surface source emissions. Impurities are thus found at trace levels in ice. Limited

amounts of ice combined with trace levels of impurities have made any stable isotope studies challenging. It is not until recently that progress in mass spectrometry has allowed stable isotope analysis of trace species trapped in ice. In the following, we will limit the discussion to the main oxy-anions found in ice, namely sulfate and nitrate.

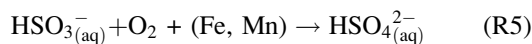
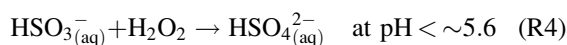
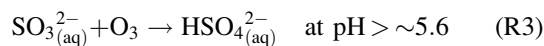
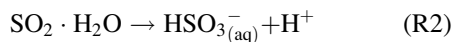
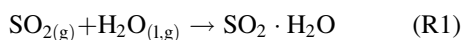
39.3.1 Stable Isotopes of Sulfate Found in Polar Environments

Sulfate deposition on ice sheets is predominantly regulated by the tropospheric oxidation of biogenic marine emissions of reduced sulfur species (dimethylsulfide or DMS) and sea-salt sulfate input, the latter representing generally less than 10% of the total sulfate. Sporadic, large volcanic eruptions in the mid and low latitudes emit copious amounts of SO₂. This sulfur dioxide is oxidized and transported through the atmosphere to the polar regions where it may dominate the atmospheric sulfur budget for short time periods with significant climatic consequences (Zielinski et al. 1994). It is thus generally accepted that sulfate in ice results from the combination of three distinctive sources: sea salt, biogenic sulfur and volcanoes.

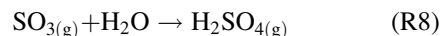
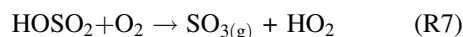
39.3.1.1 Interpreting δ¹⁸O of Sulfate

The measurement of oxygen isotope ratios in meteoric waters and atmospheric sulfates is a useful analytical method for studying formation mechanisms of sulfates from the precursor sulfur dioxide (Holt et al. 1981). Contrary to sulfur, oxygen is not conserved between the sulfur dioxide precursor and sulfate. Extensive studies conducted by Holt and his colleagues in the 1970s (reviewed in Holt and Kumar (1991)) lead to the conclusion that oxygen isotopes of sulfate could be a method to determine the different oxidation pathways leading to the formation of sulfate. Formation of sulfate in the atmosphere can be summarized as follows (Seinfeld and Pandis 1998):

Heterogeneous oxidation reactions:



Homogeneous oxidation reactions:

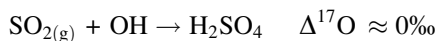
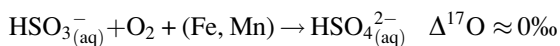


Rapid equilibration occurs between SO_{2(g)} and associated atmospheric water (liquid or vapour) so that SO_{2(g)} retains none of its initial oxygen isotopic signature. During subsequent oxidation steps, the isotopic composition is determined by the particular pathway utilized. Since the oxidants involved in the possible pathways have different isotopic compositions, they produce sulfate with different δ¹⁸O compositions, but still with up to ¾ of the oxygen atoms of sulfate controlled by isotopic exchange with water (Holt and Kumar 1991). Once formed, the sulfate retains the oxygen isotopic signature of its formation mechanism since sulfate is very stable isotopically and undergoes little or no secondary isotopic exchange under normal atmospheric conditions. An important result which emerged from the extensive investigations into sulfur oxidation by Holt and his colleagues is the finding that primary sulfates (formed at high temperatures in combustion sources, e.g. power plants, smelters, etc.) can be differentiated from secondary sulfates (formed in the atmosphere at lower temperatures by heterogeneous and homogeneous oxidation of SO₂) on the basis of their δ¹⁸O values. These primary sulfates are substantially enriched in ¹⁸O (δ¹⁸O = +40 to +45‰) as a result of the reactions that occur between atmospheric oxygen, water vapor, and SO_{3(g)} at high temperatures. Thus under the assumptions that oxidants carry a significant ¹⁸O composition, Holt and collaborators hypothesized that primary and secondary sulfate emissions as well as oxidation mechanisms could be decoupled on the basis of ¹⁸O measurements

of atmospheric sulfate. While there is evidence that ^{18}O alone, or in association with ^{34}S can provide useful information on the origin (Corcecci and Longinel 1970), transport history of sulfate (Wadleigh et al. 1996, 2001) and source apportionment between primary and secondary atmospheric sources (Jamieson and Wadleigh 1999, 2000) depending on the location of the collected sample, it should be recognized that ^{18}O alone has given poor information about the oxidation processes itself (Holt et al. 1981). The domination of the oxygen exchange with water in the control of the oxygen content of sulfate, associated with kinetic and equilibrium isotopic fractionations render any interpretation of the ^{18}O in term of oxidation pathways very speculative if not impossible.

39.3.1.2 Interpreting $\Delta^{17}\text{O}$ of Sulfate

The breakthrough in sulfate isotopic analysis came with the association of the ^{17}O measurements enabling to quantify the $\Delta^{17}\text{O}$ of sulfate. In a series of papers (Savarino and Thiemens 1999a, b; Savarino et al. 2000), authors have established the framework for the interpretation of the transfer of isotope anomaly between S(IV) ($=\text{SO}_2$, HSO_3^- , SO_3^{2-}) and S(VI) ($=\text{SO}_4^{2-}$, H_2SO_4) for the homogeneous and heterogeneous oxidation pathways. These results can be summarized as follows considering the oxygen anomaly of the different atmospheric oxidation (assuming $\Delta^{17}\text{O}(\text{O}_3) \approx 27\text{‰}$ and $\Delta^{17}\text{O}(\text{H}_2\text{O}_2) \approx 1.9\text{‰}$):



Using this framework, new insight into the origin, and most importantly the formation of sulfate has emerged, ranging from hyper arid deserts (Bao et al. 2000, 2001), groundwater sulfate (Johnson et al. 2001), coastal and high elevation sites (Lee and Thiemens 2001; Lee et al. 2001; Dominguez et al. 2008), primary sulfate combustion (Lee et al. 2002), oceanic boundary layers (Alexander et al. 2005) to

global sulfur cycle model improvement (Alexander et al. 2009a). For an atmospheric point of view, models can now integrate an isotope anomaly continuity equation (like they do routinely for concentration) that describes the time variation of the $\Delta^{17}\text{O}$:

$$\frac{d}{dt}(\Delta^{17}\text{O}_{\text{SO}_4} \times [\text{SO}_4]) = \sum P_i \times \Delta^{17}\text{O}_i - L \times \Delta^{17}\text{O}_{\text{SO}_4} \quad (39.1)$$

where P_i is the production rate of reaction i with the specific anomaly $\Delta^{17}\text{O}_i$, L the sum of all sinks (wet/dry depositions producing no specific isotope anomalies) and $\Delta^{17}\text{O}_{\text{SO}_4}$ and $[\text{SO}_4]$ the oxygen anomaly and sulfate concentration of the atmospheric reservoir, respectively. Depending on environmental conditions, this equation can be simplified using the steady state approximation where:

$$\frac{d}{dt}([\text{SO}_4]) \approx 0 \quad (39.2)$$

which assumes that concentrations vary slowly enough with time so that production and sink terms are almost equal, leading to the well-established relation:

$$\tau \times \sum P_i \times \Delta^{17}\text{O}_i = \Delta^{17}\text{O}_{\text{SO}_4} \times [\text{SO}_4] \quad (39.3)$$

where τ is the atmospheric lifetime of sulfate in the atmosphere under consideration. In the absence of sufficiently-developed chemistry models, such an equation can be further simplified as:

$$f_i = \frac{P_i}{P} \quad (39.4)$$

with P is the overall production rate and thus f_i the relative production rate and recognizing that:

$$\tau \times P = [\text{SO}_4] \quad (39.5)$$

so that (39.3) simplifies to

$$\sum f_i \times \Delta^{17}\text{O}_i = \Delta^{17}\text{O}_{\text{SO}_4} \quad (39.6)$$

with (39.7)

$$\sum f_i = 1 \quad (39.7)$$

Equation (39.6) is actually the one given in many publications utilizing the oxygen anomaly of nitrate and/or sulfate without giving the mathematical development shown above (originally (39.6) was given in Lee and Thiemens (2001)). Considering the specificity of sulfur chemistry (R1–R8), (39.6) can eventually be simplified as H_2O_2 dominates the aqueous oxidation at $\text{pH} < 5$ while at $\text{pH} > 6$ O_3 prevails and because O_2 (Luz and Barkan 2005) and OH (Dubey et al. 1997) have negligible $\Delta^{17}\text{O}$. The important point is that $\Delta^{17}\text{O}$ mass balance puts supplemental constraints on the relative importance of individual oxidation pathways with finer details than just bulk concentration when models and observations are confronted. Furthermore, $\Delta^{17}\text{O}$ opens new opportunities to probe the present and past atmosphere as sulfate is ubiquitously found in the atmosphere, ground surface and ice.

39.3.1.3 $\Delta^{17}\text{O}$ of Atmospheric Sulfate

The first analysis of $\Delta^{17}\text{O}$ of sulfate was carried out at low latitudes. Lee and Thiemens (2001) measured $\Delta^{17}\text{O}$ sulfate ranging from 0.2 to 1.6‰ in Southern California and using the (39.6) approach, one could determine the relative contribution of the aqueous and gas phase secondary sulfate production, being

approximately equal in this environment. Jenkins and Bao (2006) found no correlation between $\Delta^{17}\text{O}$ and $\delta^{18}\text{O}$ or $\delta^{34}\text{S}$ in Baton Rouge (Louisiana), with values ranging from +0.25 to +1.43‰, consistent with an oxidation pathway dominated by aqueous oxidation by H_2O_2 . Alexander et al. (2005) compared remote oceanic sulfate observation during the Indian Ocean Experiment (INDOEX) with a global chemistry model. $\Delta^{17}\text{O}$ values of up to 6.7‰ were observed and they used to test different schemes for the titration of sea-salt alkalinity, excluding the regeneration of the sea-salt aerosol alkalinity by OH uptake.

McCabe et al. (2006) measured the oxygen isotopic composition ($\Delta^{17}\text{O}$) of non-sea-salt sulfate (nss sulfate) aerosol in samples from the High Arctic (Alert, Canada) over 1 year (July 1999–June 2000). Measurements of $\Delta^{17}\text{O}$ of nss sulfate were used to evaluate the relative contributions of O_3 , H_2O_2 , and OH oxidation leading to the formation of SO_4^{2-} and were compared to a chemistry model. Figure 39.1 reproduces their original observations. Clearly, the model was unable to reproduce the sulfate oxygen isotope anomaly, systematically overestimating the $\Delta^{17}\text{O}$ in the dark polar winter. Based on this comparison and the tendency for the model to give too much importance to ozone oxidation pathways, the authors claimed that the isotopic composition was consistent with a 10–18%

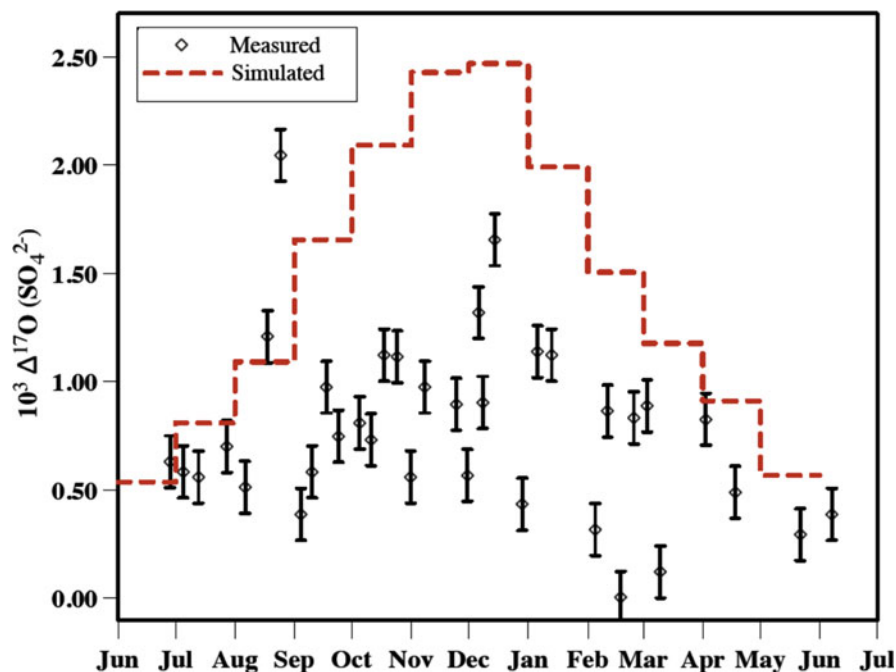


Fig. 39.1 $\Delta^{17}\text{O}$ of non-sea-salt sulfate aerosols collected at Alert (Canada) and comparison with monthly estimates $\Delta^{17}\text{O}$ based on model prediction of the sulfate formation (McCabe et al. 2006). The discrepancy points to a different mode of formation than what the model codes

contribution from a non-photochemical oxidation pathway, likely $\text{Fe}^{3+}/\text{Mn}^{2+}$ -catalyzed O_2 oxidation, during the dark Arctic winter, illustrating the contribution of oxygen isotope anomalies to understand sulfate formation. The tendency for models to overestimate the ozone oxidation contribution in the Arctic winter was further tested by Alexander et al. (2009a). Including the metal catalyzed O_2 oxidation in a three dimensional transport/chemistry model (GEOS-CHEM), these authors were able to reconcile the observed and calculated $\Delta^{17}\text{O}$ values of sulfate.

39.3.1.4 $\Delta^{17}\text{O}$ of Ice Core Sulfate

The first sulfate ice core study was performed by Alexander et al. (2002). The oxygen isotopic composition of sulfate in eight samples from the Vostok, Antarctica ice core, covering one full climate cycle, was presented. Through a limited dataset, higher $\Delta^{17}\text{O}$ values of sulfate were systematically observed during the warm periods (Fig. 39.2). A good correlation was observed when $\delta^{17}\text{O}$ data were compared to $\delta^{18}\text{O}$, displaying a mixing line between end-members of OH- and O_3 -dominated oxidation pathways. Assuming tropospheric-derived sulfate only and applying the mixing line model, the authors concluded that the ratio of gas-phase over aqueous-phase oxidation of S(IV)

species was greater during the last glacial than the surrounding interglacial periods. If this interpretation is correct, $\Delta^{17}\text{O}$ measurements provide a means of distinguishing variations in the oxidation pathways and their connection to climate evolution. More data covering the same time period is necessary to firmly establish the validity of this interpretation.

Part of this validation effort has been recently undertaken due to the new West Antarctic Ice Sheet (WAIS) Divide deep ice core drilling (expect to be achieved in 2011), an experiment designed to recover at least two warm periods (~120,000 years of climate record) in a relatively high accumulation Antarctic site for time-resolution optimization. Kunasek et al. (2010) presented a $\Delta^{17}\text{O}$ record from the early 1800s to early 2000s. $\Delta^{17}\text{O}$ of non-sea salt sulfate shows a small, but significant increase between the late 1700s ($1.8 \pm 0.2\text{‰}$) and late 1800s ($2.6 \pm 0.2\text{‰}$), although one lower than the Holocene values observed in the Vostok ice core (Fig. 39.2). The lack of change in $\Delta^{17}\text{O}$ of non-sea-salt sulfate from the mid-1800s to early 2000s ($2.4\text{--}2.6 \pm 0.2\text{‰}$) is consistent with atmospheric chemistry model estimates, indicating preindustrial to industrial increases in O_3 as high as 50% and decreases in OH of 20% in the southern polar troposphere, provided H_2O_2 concentrations also increase by over 50%; the latter increase is at least qualitatively supported by the H_2O_2 concentrations

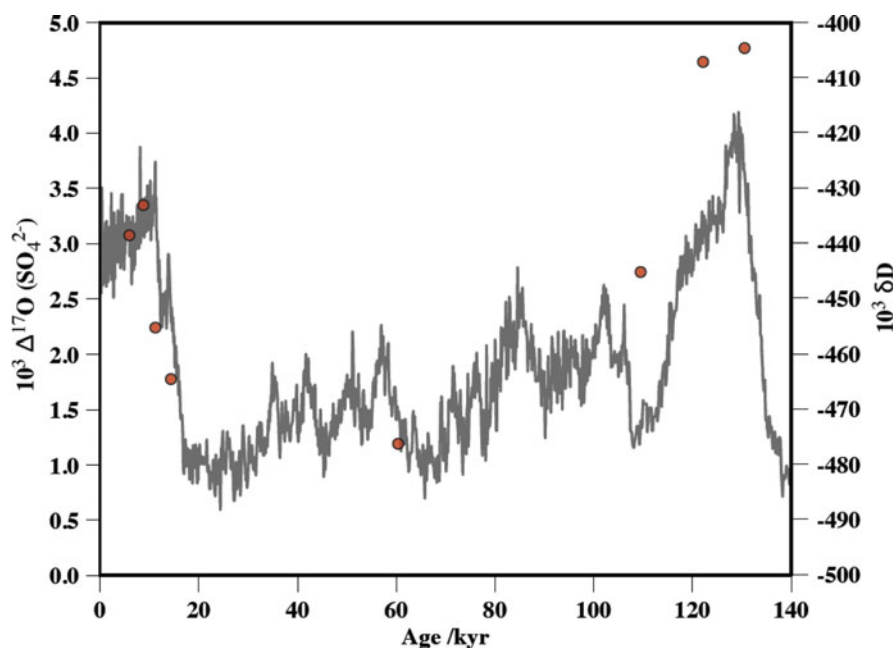
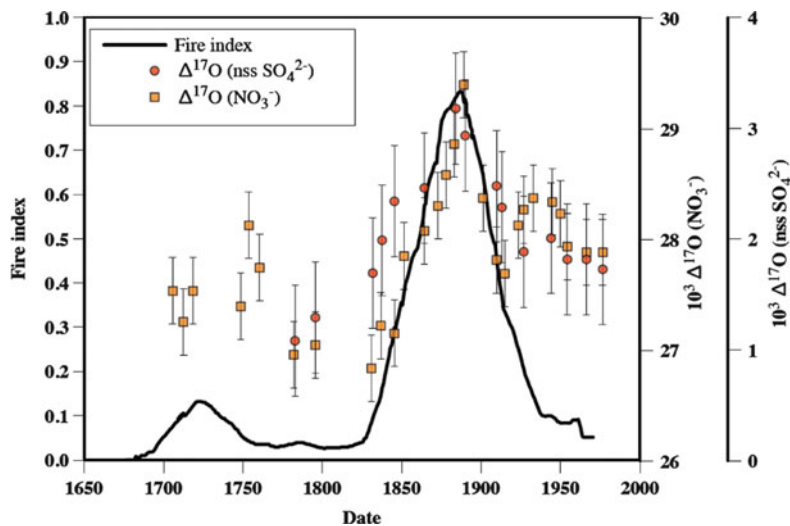


Fig. 39.2 Glacial and interglacial variation of $\Delta^{17}\text{O}$ of sulfate in the Vostok ice core. This limited dataset suggests that sulfur oxidation between glacial and interglacial times differs significantly, favoring OH and O_3 oxidation, respectively (adapted from Alexander et al. (2002))

Fig. 39.3 Time variation during the last ca. 300 years of $\Delta^{17}\text{O}$ of nitrate and sulfate observed in Greenland ice cores and comparison with a fire index transcribing the frequency of biomass burning events recorded in ice. The perfect match between peaks of these proxies strongly supports the idea that forest fires have strongly perturbed the atmospheric ozone concentration at those times. Industrialization of the Northern hemisphere is not imprinted in the $\Delta^{17}\text{O}$ (adapted from Alexander et al. (2004))



archived during the past century in the southern polar region (Frey et al. 2005).

In a different use of the sulfate oxygen isotopic anomalies, De Angelis et al. (2004) measured the $\Delta^{17}\text{O}$ of sulfate from accreted ice of the Vostok ice core. The bottom of the Vostok ice core is made of refrozen water from the underlying lake. Unlike the sulfate of the glacier ice, which shows a significant $\Delta^{17}\text{O}$, no such isotope anomaly was found in the accreted ice. Based on this consideration and other trace chemical information, the authors concluded that the dissolved sulfate present in the lake originated probably from ancient evaporites or sedimentary formations accumulated at the bottom of the lake before the building of the ice sheet and not the result of inputs of atmospheric sulfate from the melt of the glacier ice.

The chemical composition of the ice cores and modeling studies indicate a significant change in the oxidation capacity of the atmosphere at the onset of the Industrial Revolution due to increase of fossil fuel emissions, mainly in the Northern hemisphere where emissions are at their maximum. Alexander et al. (2004) analyzed the oxygen isotopes of sulfate and nitrate trapped in a Greenland ice core to see if such changes in the chemical activity of the atmosphere could be imprinted in the $\Delta^{17}\text{O}$. The data revealed that both $\Delta^{17}\text{O}$ of sulfate and nitrate show little difference between the industrialization period of the Northern hemisphere and the 1700s. Instead, both species display a significant peak, centered around 1880 AD (Fig. 39.3) and in perfect phase with biomass-burning marker found in Greenland ice. The end of the

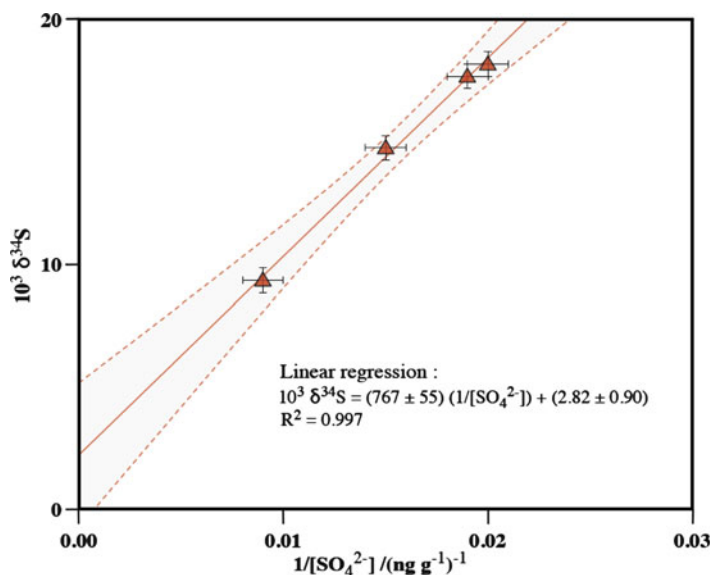
nineteenth century is known as the Pioneer Agricultural Revolution, corresponding to new settlements of North America which were accompanied by forest clearing and burning. The authors asserted that high emissions of volatile organic carbon and NO_x by forest fires led to a regional increase in O_3 concentration during this period which in turn contributed to increase $\Delta^{17}\text{O}$ of sulfate and nitrate by favoring ozone oxidation pathways.

39.3.1.5 Sulfur Isotopes of Background Sulfate in Ice Cores

Patris et al. (2000) were the first to successfully adapt modern sulfur isotopic analysis to ice core geochemistry. Focusing on South Pole shallow ice cores centered on the Mt Agung eruption (Indonesia, 1963), they were able to demonstrate the significant volcanic contribution to sulfate deposition on the central Antarctic ice cap during volcanic events and also confirmed the dominance of a marine biogenic origin for present background sulfate. Figure 39.4 displays their main result where $\delta^{34}\text{S}$ is plotted vs. the inverse concentration. The straight line obtained indicates the presence of a mixture of two sources influencing the sites. Extrapolations allowed them to establish the sulfur isotopic signatures of the marine biogenic sulfate and volcanic sulfate of the Mt Agung to be $+18.6 \pm 0.9\%$ and $+2.7 \pm 1.1\%$, respectively.

In a site closer to the West Antarctic coast, covering the same timeframe as Patris' study, sulfur isotopes of

Fig. 39.4 $\delta^{34}\text{S}$ vs. inverse of sulfate concentration found in shallow ice cores from South Pole. The straight line suggests a mixing between two end-member sources of sulfate, marine biogenic emissions at ca. 18‰ and volcanic emissions at ca. 2.8‰ (adapted from Patris et al. (2000))



sulfate revealed a different picture (Pruett et al. 2004). At this site $\delta^{34}\text{S}$ values are significantly lower than those found at South Pole, both for the background and Agung sulfate, ranging from 3.1 to 9.9‰. These low values were later confirmed by Kunasek et al. (2010). At first glance, these observed values appear odd considering the larger influence of marine biogenic and abiogenic sulfur at this site and the well-established sulfur composition of these sources: 18‰ (Calhoun et al. 1991) and 21‰ (Rees et al. 1978), respectively. To reconcile the findings, the authors claimed that their site is probably influenced by depleted ^{34}S of stratospheric sulfate and/or by local volcanoes such as the Erebus. Comparison between coastal and central sites of the East Antarctica shows relative homogeneous $\delta^{34}\text{S}$ values of $+14.6 \pm 0.3\text{‰}$ and $+14.7 \pm 0.3\text{‰}$ for Holocene samples (Jonsell et al. 2005). When the influence of sporadic volcanic eruptions is subtracted, the isotopic composition of sulfate reaches a value of $+15.4 \pm 0.6\text{‰}$, significantly lower than the prescribed values for marine biogenic sulfur, suggesting additional sources contributing to the sulfate budget.

A different interpretation of $\delta^{34}\text{S}$ is proposed by Alexander et al. (2003). By studying the sulfur isotope ratios of sulfate trapped in the deep Dome C and Vostok ice cores (central eastern Antarctic plateau) covering a full glacial/interglacial cycle, the authors propose that fractionations related to the chemical conversion of SO_2 to sulfate during transport is the main process responsible for the $\delta^{34}\text{S}$ values of ice

core sulfate. This suggestion is fueled by an observed 6‰ lower difference in average $\delta^{34}\text{S}$ of the Eastern ice compared to the South Pole that could not be explained by volcanic inputs. Non-sea-salt sulfate ranges from 7.5 to 15.1‰ with glacial period displaying systematic lower values than interglacial times (Fig. 39.5). Chemical transformation during transport is attributed to be the main process responsible for the $\delta^{34}\text{S}$ variation and is supported by the correlation observed between $\delta^{34}\text{S}$ and $\Delta^{17}\text{O}$ of the same samples, the latter being a direct fingerprint of the different oxidation pathways producing sulfate (see Sect. 39.3.1.4). This interpretation nevertheless remains controversial. Jonsell et al. (2005) challenged this idea on the premise that in their study, coast and central sites displayed the same sulfur isotopic composition. Recently, Kunasek et al. (2010) also refuted this idea based on spatial variability in $\delta^{34}\text{S}$, including West Antarctic $\delta^{34}\text{S}$ data. However, comparison of reduced and oxidized sulfur species concentration between coastal and inland sites (Cosme et al. 2005; Preunkert et al. 2008) as well as evolution of isotopic composition of sulfate during oxidation and transport (Castleman et al. 1974) suggests that interpreting sulfur isotopes based solely on source apportionment is probably a too simplistic approach.

Turning now to the Greenland ice sheet, Patris et al. (2002) presented a detailed study of the Greenland sulfate covering preindustrial and industrial periods. Figure 39.6 shows the most significant result of this

Fig. 39.5 Evolution of sulfate $\delta^{34}\text{S}$ extracted from Vostok and Dome C ice core during a full glacial/interglacial cycle. Temperature variation are expressed by the D/H ratio of the water (Alexander et al. 2003)

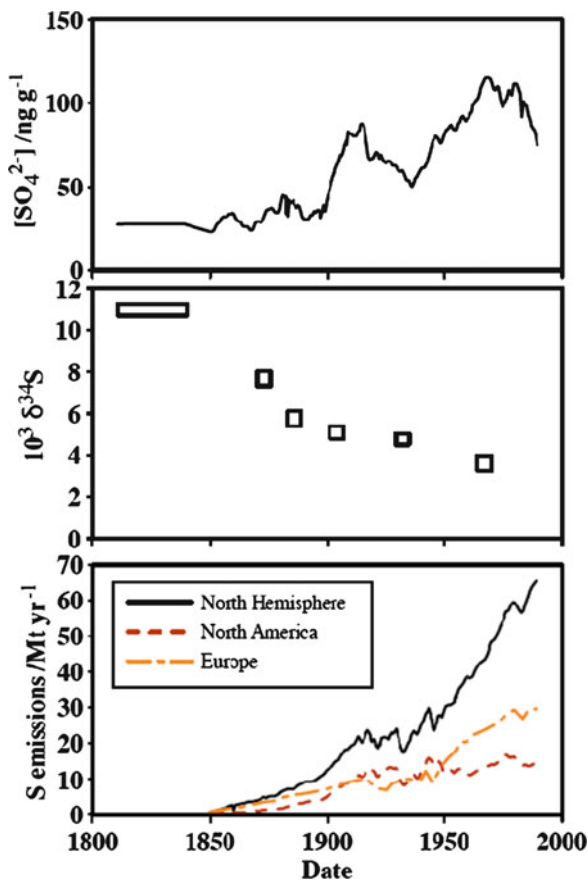
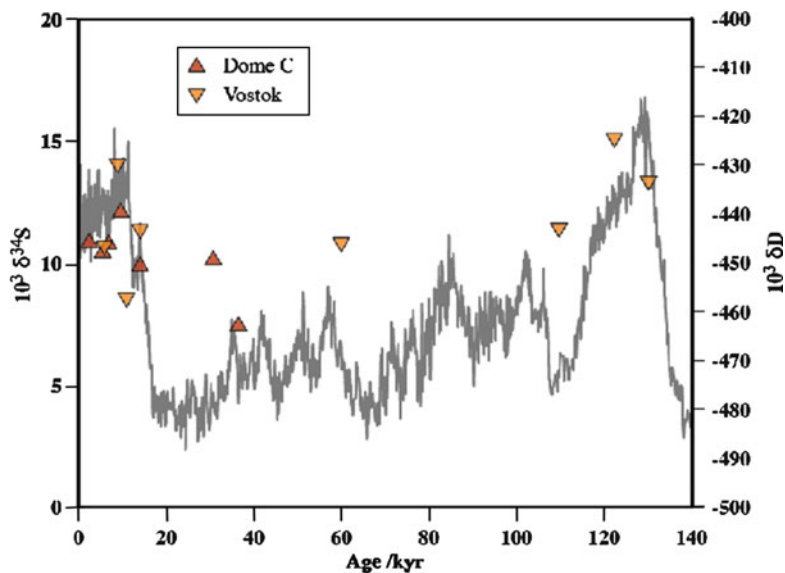


Fig. 39.6 Time-evolution of the $\delta^{34}\text{S}$ of sulfate in a Greenland ice core along with the evolution of its concentration and global sulfur emissions of in Northern hemisphere (adapted from Patris et al. (2002))

study. Contrary to Antarctica, which is not impacted by anthropogenic emissions of sulfur, concentrations of sulfate in Greenland ice follow closely the increase of industrial sulfur emissions due to its proximity to industrialized countries. The $\delta^{34}\text{S}$ of sulfate shows a pronounced decrease in phase with the increased input of anthropogenic sulfur. The impact of human-driven emissions on the sulfate deposited in central Greenland ice is visible in isotope data as early as 1870 AD and dominates all other natural sources. The isotopic signature of anthropogenic sulfur deposited during the twentieth century is found to be constant ($\delta^{34}\text{S} = +3.0 \pm 1.5\%$), regardless of the changes of source regions and emission processes, a value significantly different than the Antarctic background. During the preindustrial period, sulfur isotopes indicate that the preindustrial background sulfate budget is shared by marine biogenic emissions (49%) and by continental sources, including background volcanism (44%). Sulfur emitted by relatively weak eruptions is found to be largely depleted in ^{34}S compared to bulk volcanic S, suggesting an efficient washout of the heavier isotope during tropospheric transport (Patris et al. 2002).

39.3.1.6 Tracing the Large Volcanic Eruptions with the Multiple Sulfur Isotope Array

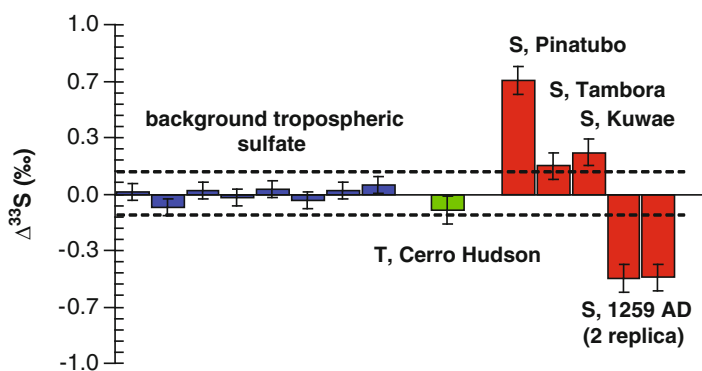
Ice cores are well-known proxies to provide a precise record of the Earth's volcanic activity, a major player

of the Earth's climate system. Volcanic activity is recorded in the ice in the form of a sulfuric acid peak (Hammer 1977). However, not all recorded events have a large scale climatic impact, capable of significantly reducing ground surface temperatures for several years. The volcanism recorded in the ice can be divided into two groups according to their climatic effect. Small eruptions that inject their debris principally into the troposphere have no climatic effect because of the short lifetime of the debris in this part of the atmosphere, but can be recorded in the ice if they are close enough to ice sheets. In contrast, powerful and catastrophic volcanic eruptions injecting their debris directly into the stratosphere where the stability and dryness of this section of the atmosphere can maintain volcanic sulfuric acid aerosols for years and globalize their radiative effect (Robock 2000).

Savarino et al. (2003) introduced the analysis of the three sulfur isotope ratios, i.e. $\delta^{33}\text{S}$, $\delta^{34}\text{S}$ and $\delta^{36}\text{S}$ in the field of ice cores to study paleo-volcanism. The interest resides in the fact that combining the three isotopes allows the distinction in the nature of the volcanic eruption recorded, discriminating significant climatic events vs. regional events. In a pioneering work, Farquhar et al. (2000a, 2001) discovered that when SO_2 is subject to intense UV, reduced and oxidized sulfur products carry non-zero $\Delta^{33}\text{S}$ and $\Delta^{36}\text{S}$ sulfur isotope anomalies, a strong support for a deoxygenated early archaean atmosphere. Today, only in the stratosphere is SO_2 subjected to UV radiation, thus, sulfuric acid produced in this part of the atmosphere should possess a sulfur isotope anomaly while tropospheric-produced sulfate should not. This difference in sulfur isotopic composition could provide an elegant way to distinguish the two types of volcanism recorded in ice. Figure 39.7 shows the result obtained

for different origins of sulfate and demonstrates that only stratospheric-produced sulfate displays a significant sulfur isotope anomaly, albeit with variable sign. This was later explained by Baroni et al. (2007) in a detailed snow pit study of the shallow volcanic events of the Pinatubo (1991, Philippines) and Mt Agung (1963, Indonesia). Time-resolved analysis of the volcanic sulfate deposits showed an inversion of sign between the start and the end of the sulfate peak, demonstrating that the sulfur isotope anomalies of volcanic sulfate is a time-dependent process, first displaying a positive $\Delta^{33}\text{S}$ followed by a negative $\Delta^{33}\text{S}$ at the end of the volcanic plume depositional process. It was concluded that the mass-independent process occurred on a monthly time scale before SO_2 is fully converted to H_2SO_4 . Such observations also provided a scenario to close the budget of the sulfur isotopic anomaly (Pavlov et al. 2005) as anomalies are observed neither at the point source of volcanic emissions (Mather et al. 2006; Bindeman et al. 2007; Martin and Bindeman 2009) nor for background ice core sulfate (Alexander et al. 2003; Kunasek et al. 2010). The photochemical conversion of SO_2 to sulfuric acid in the stratosphere creates two reservoirs of sulfur with anomalies of opposite signs that should be physically separated in space and time during sedimentation. It should be noted however that even if UV photolysis triggers the process, the detailed understanding of the chain reaction is still uncertain despite speculative considerations such as self-shielding (Lyons 2007) or heterogeneous chemistry (Lasaga et al. 2008; Watanabe et al. 2009) to explain the observations. We note that the heterogeneous chemistry is incompatible with the volcanic S isotopic anomaly observations as sulfate is formed by homogeneous gas-phase reaction in the stratosphere, as well as part

Fig. 39.7 Sulfur isotopic anomalies of stratospheric and tropospheric sulfate. From this limited data set, stratospheric volcanic sulfates are clearly seen by the $\Delta^{33}\text{S}$ they carry. This isotopic fingerprint is used to classify the nature of any volcanic eruption recorded in ice, independently of its depositional flux. The two dashed lines represent the two standard deviations ($\pm 0.1\%$) of the isotopic standards. S and T stand for stratosphere and troposphere (Savarino et al. 2003)



of it in the troposphere. Self-shielding is a photochemical process where specific lines of a broadband incident light are optically tick at some depth for the most abundant isotopologue, thus stopping its photodissociation further deep in the light path while still allowing the photodissociation of the minor isotopologues, thus creating an isotope-selective photolysis process at the opposite side of the incident light. Lyons (2007) claimed that such process could explain the volcanic sulfur anomalies. However, such process implicitly assumes no mixing of the SO₂ cloud and the radiative transfer model was not tested for the 260–340 nm range where photolysis of SO₂ occurs today, thus leaving still unresolved the mechanism responsible for the sulfur isotope anomaly of volcanic sulfate. Nevertheless, sulfur isotope anomalies provide a new opportunity to revisit the climatic forcing of volcanoes by providing information about the stratospheric or tropospheric nature of an unknown eruption. At present, the past climatic forcing of volcanoes rely on concentration measurements which make identification of unknown stratospheric events difficult and hypothetical. A concrete application of this new isotopic tool is presented by Cole-Dai et al. (2009). The unknown 1809 volcanic event preceding the massive explosion of the Tambora (1815, Indonesia) shows a significant sulfur isotope anomaly and thus can be classified as stratospheric. This characterization provides a rational explanation for the coldest decade observed for the past 500 years, a decade that started few years before the Tambora eruption. A reexamination of the nature of some volcanoes recorded in ice is also presented in Baroni et al. (2008) and as expected, no correlation was found between the concentrations in the ice and the climatic importance of the events.

39.3.2 Stable Isotopes of Nitrate Found in Polar Environments

Nitrate exists in the atmosphere in several forms including gaseous nitric acid (HNO₃) and various chemical assemblages of the nitrate ion (NO₃⁻) in aerosols. Because primary sources of nitrate are extremely scarce (Finlayson-Pitts and Pitts 2000), most of the nitrate found in the atmosphere results from the chemical transformation of gaseous precursors, in particular nitrogen oxides (NO_x = NO + NO₂). Atmospheric

deposition constitutes the major contributor to the budget of nitrate in snow (Wolff 1995), despite recent findings that biological activity can lead to in situ production of nitrate within the snowpack (Wadham et al. 2006; Amoroso et al. 2010). The isotopic composition of atmospheric nitrate thus depends on (1) the isotopic composition of NO_x, (2) the isotopic fractionation associated with the chemical oxidation of NO_x to nitrate, and (3) isotopic fractionation associated with nitrate transport within the atmosphere. The oxygen and nitrogen isotopic fractionation constants associated with processes (1) and (2) are currently poorly known besides a few experimental studies (Chakraborty and Chakraborty 2003). The use of δ¹⁸O as the only oxygen isotopic composition of atmospheric nitrate to extract atmospheric reaction mechanisms is thus discouraged by some authors (Morin et al. 2008, 2009) as too many kinetic isotope fractionations are currently unknown. In contrast, the use of Δ¹⁷O levies this weakness pertaining to the interpretation of δ¹⁵N and δ¹⁸O data since Δ¹⁷O is a conservative quantity not affected by isotopic fractionation processes. Readers are referred to Chap. 30 (Michalski et al.) of this handbook for an extensive discussion about the origin and benefits of using Δ¹⁷O of nitrate.

39.3.2.1 Δ¹⁷O of Atmospheric Nitrate

Up to now, much emphasis has been put on the interpretation of seasonal variations of Δ¹⁷O of atmospheric nitrate at Earth's surface. The recent emergence of bacteria and silver nitrate techniques suited for Δ¹⁷O analysis of nitrate (Michalski et al. 2002; Kaiser et al. 2007) has lead to the build-up of a small number of datasets, which are key to test our ability to interpret variations of Δ¹⁷O of nitrate in the atmosphere. This constitutes a logical prerequisite to interpreting its variations in snow and ice matrices. Several measurement-based modeling studies (Michalski et al. 2003; Kunasek et al. 2008a; Morin et al. 2008) have substantiated the idea that variations of Δ¹⁷O of nitrate mostly stem from variations in the relative contribution of different NO_x oxidation pathways (see Chap. 30). Oxygen atoms bearing a non-zero Δ¹⁷O signature, initially originating from ozone, are propagated throughout the photochemical cycling of NO_x, NO₂ oxidation and diluted with other oxygen atom sources (H₂O, O₂) that do not bear a significant Δ¹⁷O

signature. Different NO_x oxidation pathways induce different dilution factors, thus leading to differing $\Delta^{17}\text{O}$ values in nitrate produced through these pathways. For instance, the daytime production of atmospheric nitrate through the reaction between NO_2 and OH leads to a smaller $\Delta^{17}\text{O}$ than the nighttime reactions involving the nitrate radical (Michalski et al. 2003; Kunasek et al. 2008a; Morin et al. 2009). This explains why in summer $\Delta^{17}\text{O}$ of nitrate is generally lower than winter, as the relative proportion between daytime and nighttime nitrate production pathways undergoes seasonal changes due to seasonal variations in day length (or daily integrated actinic flux). Such seasonal variations are maximized in polar regions, where extended periods of absence or presence of sunlight occur. Thus locally produced nitrate is expected to display large seasonal variations of $\Delta^{17}\text{O}$. Mid-latitude summertime $\Delta^{17}\text{O}$ values are on the order of 10–25‰, while wintertime 25–35‰ (Michalski et al. 2003). Alexander et al. (2009b) implemented the basic mass balance of $\Delta^{17}\text{O}$ for nitrate in the 3D GEOS-Chem chemical transport model to produce a global view of the nitrate ^{17}O anomaly (Fig. 39.8), showing a strong seasonal

amplitude with values ranging from 7‰ in the tropics to 41‰ in polar regions. At present $\Delta^{17}\text{O}$ is viewed as an indicator of the average proportion between nitrate production channels (Alexander et al. 2009b). It suffers, however, from several shortcomings, including:

- Large uncertainties in the $\Delta^{17}\text{O}$ of tropospheric ozone (value and seasonal variations, see Morin et al. (2007), Bhattacharya et al. (2008), Michalski and Bhattacharya (2009))
- Unknown $\Delta^{17}\text{O}$ transfer rate through many chemical reactions (with the notable exception of $\text{NO} + \text{O}_3$ (Savarino et al. 2008))
- The absence of a fully fledged modeling framework to fully interpret intra-seasonal (up to diurnal) variations
- The overlap between the signature of different nitrate production channels (see Kunasek et al. (2008a), Morin et al. (2009))

With the exception of the latter, all others shortcomings can be resolved with dedicated efforts and experiments. Measuring the isotopic composition of ozone in the troposphere should be a first priority to better constrain its natural variations. Recently, Michalski and Bhattacharya (2009) proposed a chemical method where ozone is allowed to react with nitrite, forming nitrate. They have demonstrated that from the isotopic analysis of the produced molecular oxygen, one can reconstruct the ozone original isotopic composition, thus avoiding the complex and difficult cryogenic method used in the past to measure its atmospheric isotopic composition. Designing specific experiments in atmospheric simulation chambers can solve the quantification of the anomaly transfer between reactants and products, in a similar fashion as proposed in Savarino et al. (2008). Finally, incorporating all this information in a chemistry model calculating explicitly the progress and propagation of the oxygen isotopic anomaly among atmospheric species should be relatively easy considering the current maturity of chemistry models and the power of today desktop computers.

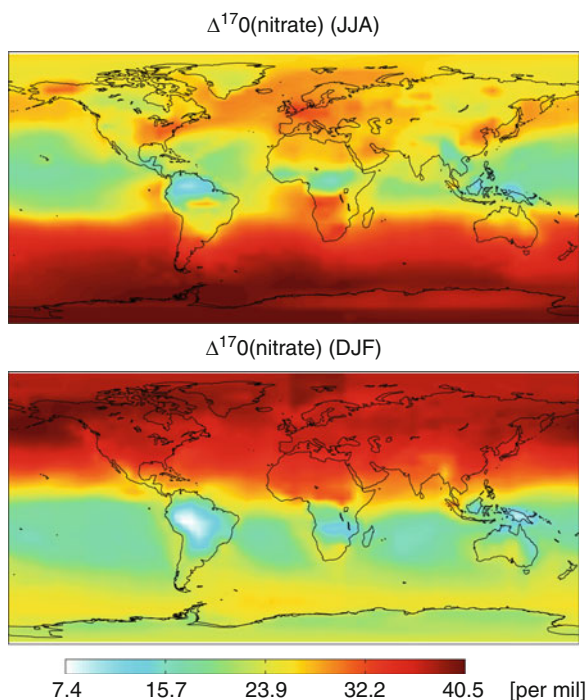


Fig. 39.8 Global seasonality view of nitrate $\Delta^{17}\text{O}$ as generated by the GEOS-CHEM model (Alexander et al. 2009b) (Copyright under Creative Common Licence)

39.3.2.2 Impact of Reactive Halogens on $\Delta^{17}\text{O}$

The presence of reactive halogens in the production pathway of nitrate was hypothesized by Morin et al. (2007) and Patris et al. (2007) as they have a significantly influence on the $\Delta^{17}\text{O}$ of atmospheric

nitrate. It is known in marine polar regions that reactive halogens are particularly chemically active in springtime, leading to spectacular ozone depletion from the lower atmosphere in relationship to the presence of reactive radicals such as BrO, which are emitted from sea-salt through a mechanism that remains elusive (Simpson et al. 2007). BrO not only depletes ozone catalytically; it also reacts with NO₂ to yield BrONO₂, which undergoes hydrolysis on frozen aqueous surfaces leading to nitrate formation (Sander et al. 1999). This reaction induces a low $\Delta^{17}\text{O}$ dilution factor, and was considered responsible for high (ca. 32‰) $\Delta^{17}\text{O}$ values in atmospheric nitrate during the Arctic springtime at Alert, Nunavut (Morin et al. 2008). Reactive halogens are also hypothesized to play a role at Summit, Greenland, which could explain why higher than anticipated $\Delta^{17}\text{O}$ values were measured there (Kunasek et al. 2008a).

39.3.2.3 Stratospheric $\Delta^{17}\text{O}$ Signature

Of particular relevance to studies in the polar atmosphere is the $\Delta^{17}\text{O}$ signature of stratospheric nitrate. Stratospheric ozone possesses a higher $\Delta^{17}\text{O}$ than in the troposphere (Mauersberger et al. 2001; Thiemens 2006). Since stratospheric nitrate production proceeds through heterogeneous reactions hypothesized to possess a low $\Delta^{17}\text{O}$ dilution rate (thus leading to high $\Delta^{17}\text{O}$ values in the final nitrate), the $\Delta^{17}\text{O}$ of stratospheric nitrate is generally assumed to be higher than tropospheric nitrate. This property has been used to place new constraints on the origin of nitrate in the Antarctic troposphere. Indeed, it was long debated whether the stratosphere was a significant direct contributor of nitrate to the lower atmosphere, following its denitrification in the late austral winter (Legrand and Kirchner 1990). The measurement of $\Delta^{17}\text{O}$ values of tropospheric nitrate higher than 40‰ in tropospheric nitrate samples collected in August/September in coastal (Savarino et al. 2007) and central (Frey et al. 2009) Antarctica is independent evidence that the stratosphere is a major contributor to the budget of tropospheric nitrate at this period of the year. Tropospheric reactive halogens are excluded here since ozone depletion episodes are absent from both this coastal Antarctica monitoring station and in central Antarctica (Legrand et al. 2009).

39.3.2.4 Biological Processes

Until recently, atmospheric wet and dry deposition was considered the only source of nitrate to polar environments. In recent years isotopic evidence accumulated to indicate that in situ production of nitrate can operate in glacial environments, including dry snowpacks (Wadham et al. 2006; Wynn et al. 2007). Amoroso et al. (2010) recently reported isotopic data for snowpack nitrate showing $\Delta^{17}\text{O}$ values very close to 0‰, which clearly cannot be accounted for by atmospheric deposition (concurrent $\Delta^{17}\text{O}$ values in atmospheric nitrate were on the order of 30‰ on the days when snow deposited on the ground). Combining such observations with detailed investigations of the outgoing flux of reactive nitrogen from the snowpack in the absence of sunlight and the chemical composition of the snow, they concluded that microbial nitrification and denitrification was most likely operating in the snowpack and responsible for the production of nitrate with a zero $\Delta^{17}\text{O}$: only biologically mediated production of nitrate from water or atmospheric oxygen can lead to such a low signature as ice cores demonstrate that nitrate can keep its oxygen anomaly in ice for hundreds thousand of years. This finding is consistent with the measurements by Sowers (2001), who found isotopic evidence for in situ production of N₂O in polar ice through biological processes (for a detailed discussion about the N₂O cycle and its isotopic system, readers can refer to the article of Ostrom and Ostrom, Chapter 23, of this book) even in places where the mean annual temperature is lower than -50°C . Thus, biologically-mediated nitrate production can occur in virtually all snow-covered areas; taking into account its impact on the isotopic composition of nitrate in glaciological archives is necessary, although this has not been carried out in studies published hitherto.

39.3.2.5 $\Delta^{17}\text{O}$ of Nitrate in Snow and Ice Cores

As briefly discussed in Sect. 39.3.1.4, Alexander et al. (2004) were the first to use the $\Delta^{17}\text{O}$ of nitrate in association with sulfate $\Delta^{17}\text{O}$ in an ice core study. Both isotope tracers follow the same pattern, displaying a remarkable peak around 1880 in phase with a biomass burning index. Interpreting their isotope profiles in term of more or less ozone activity, they suggested that the intense fire activity recorded at that time

was responsible for a significant increase of tropospheric ozone, leading to an enhancement of $\Delta^{17}\text{O}$ in both species. Hastings et al. (2004) and Hastings et al. (2005) also present nitrate results of Greenland snow, although limited to ^{18}O . Both seasonal (snowpits) and climate-scale (ice cores) ^{18}O variations were interpreted in terms of relative contributions between $\text{NO}_2 + \text{OH}$ (lowering $^{18}\text{O}/^{16}\text{O}$) vs. N_2O_5 hydrolysis (raising $^{18}\text{O}/^{16}\text{O}$) with winter and cold climates favouring the latter. As pointed out previously, caution should be exercised when interpreting $^{18}\text{O}/^{16}\text{O}$ ratios solely in terms of chemical reactions, ignoring de facto fractionations due to kinetic, transport, sedimentation or post-depositional effects. This weakness was raised in two recent studies (Jarvis et al. 2008, 2009). In the first paper, they observed that the range in $\delta^{18}\text{O}$ of nitrate is smaller than that modelled from HNO_3 production pathways, suggesting that other processes may also be required to explain the seasonality in snow nitrate $\delta^{18}\text{O}$. The second study compares gas-phase HNO_3 isotopic composition with surface snow NO_3^- . A systematic depletion of the $\delta^{18}\text{O} \approx 40\%$ of the air samples with respect to snow is observed. Reconciliation is obtained with a photochemical box modelling if local post depositional effects are considered. The same conclusion is reached by Kunasek et al. (2008b) when the $\Delta^{17}\text{O}$ of nitrate of a Greenland snowpit is compared with a box model with boundary conditions constrained by the 3D GEOS-Chem model. Measured values of $\Delta^{17}\text{O} \text{NO}_3^-$ covering three seasonal cycles range from 22.4‰ in summertime to 33.7‰ in wintertime, while model results show a larger range (18.9–31.5%). The discrepancy, especially in summertime, is suspected to result from processes not taken into account by the model (e.g. transport, stratospheric influences, halogen chemistry).

McCabe et al. (2007) presented a detailed snow pit study of nitrate $\Delta^{17}\text{O}$ at South Pole. The analysis of trends in $\Delta^{17}\text{O}$ of the 6 m excavated snowpit covering the last 25 years revealed a strong 2.7 years cycle that correlated negatively ($R = 0.77$) with the October–November–December stratospheric ozone column. The mechanism proposed by the authors to explain this negative correlation invokes the increase of UV radiation at ground during low levels of stratospheric ozone, leading to a more intense nitrate recycling in the boundary layer and thus erasing the original high $\Delta^{17}\text{O}$ of the stratospheric nitrate injection (Savarino et al. 2007; Frey et al. 2009) in favor of the lower $\Delta^{17}\text{O}$ of

tropospheric-made nitrate. Finally, in a detailed survey of post processing of nitrate in central Antarctica, Frey et al. (2009) reassert the very good preservation of atmospheric $\Delta^{17}\text{O} \text{NO}_3^-$ in snow, despite a small tendency for decrease possibly due to exchange with water during photolysis. A periodic oscillation with a mean periodicity of 2.3–3.0 years, similar to the one reported by McCabe et al. (2007), is also preserved in Dome C snow. It therefore seems conceivable to reconstruct past shifts in tropospheric oxidation pathways from the $\Delta^{17}\text{O} \text{NO}_3^-$ record preserved in ice cores. Such work is currently underway in different laboratories.

39.3.2.6 $\delta^{15}\text{N}$ in Tropospheric Nitrate in Mid-Latitudes

In contrast to $\delta^{18}\text{O}$ and $\Delta^{17}\text{O}$, $\delta^{15}\text{N}$ has been measured in atmospheric nitrate samples for a half century. Hoering (1957) reported the first measurements of $\delta^{15}\text{N}$ of atmospheric nitrate samples, followed by Moore (1974, 1977). More recently, studies by Freyer (1978, 1991) and Heaton (1987) have increased knowledge regarding the range of variations of $\delta^{15}\text{N}$ in atmospheric nitrate. Despite many measurement-based studies devoted to $\delta^{15}\text{N}$ of atmospheric nitrate, it is still debated whether $\delta^{15}\text{N}$ of atmospheric nitrate primarily reflects $\delta^{15}\text{N}$ of NO_x sources (Hastings et al. 2003) or results from isotopic fractionation within NO_x (Freyer et al. 1993) or during transport (see Morin et al. 2009), for an overview). In addition, many studies have focused on rainwater nitrate samples (e.g. Hastings et al. 2003) or Elliott et al. (2007)), which were shown by Freyer (1991) to display a marked offset from aerosol nitrate. As discussed in Morin et al. (2009), the sign of such offset apparently depends on environmental conditions so that interpreting $\delta^{15}\text{N}$ data from rainwater in terms of $\delta^{15}\text{N}$ of atmospheric nitrate may be misleading. Nevertheless, it has been recurrently observed that $\delta^{15}\text{N}$ of atmospheric nitrate in mid-latitudes undergoes weak seasonal variations between -10 and 10% (Freyer 1991; Morin et al. 2009). The seasonal cycle is not understood at present, since some areas seem to display a seasonal cycle with a maximum in hemispheric summer (Morin et al. 2008) while others display an opposite seasonal cycle with maximum values in hemispheric winter (Freyer 1991; Yeatman et al. 2001). Proposed mechanisms to explain ^{15}N variations in

nitrate aerosols include thermodynamically driven equilibrium between HNO_3 , NH_3 gases and NH_4NO_3 particles (Yeaman et al. 2001) or temperature driven isotopic exchange between NO_x species (Freyer et al. 1993). More in situ laboratory and observations are clearly needed to fully interpret these contrasting observations.

39.3.2.7 $\delta^{15}\text{N}$ in Tropospheric Nitrate in Polar Regions

The most striking feature of atmospheric nitrate $\delta^{15}\text{N}$ data from polar regions is the extremely low values encountered in spring and summer in snow-covered areas. These were first noticed by Freyer et al. (1996), when values as low as -38 to -63‰ were measured in samples collected in coastal Antarctica but remained unexplained. Wagenbach et al. (1998) also reported such low values and attributed them to stratospheric denitrification, although both the timing and the isotopic composition of nitrate did not match. Similarly low $\delta^{15}\text{N}$ values were again reported by Savarino et al. (2007), who attempted to explain the low values as a consequence of snowpack photodenitrification featuring a strongly negative fractionation constant, leading to the emission of isotopically light NO_x and thus atmospheric nitrate (see Sect. 39.3.2.8). Since then, low $\delta^{15}\text{N}$ values in atmospheric nitrate were reported from the Arctic atmosphere (Morin et al. 2008), the Antarctic sea ice (Morin et al. 2009), Antarctic plateau at Dome C (Frey et al. 2009) and Dronning Maud Land station (Floch 2006). Low $\delta^{15}\text{N}$ values were also observed in soils downwind from the Antarctic plateau (Michalski et al. 2005b). Figure 39.9 shows the results of Morin et al. (2008) in coastal Arctic where the drop in atmospheric nitrate $\delta^{15}\text{N}$ is observed to be in phase with a snow illumination index built as the product of actinic flux and snow cover, strongly suggesting the influence of NO_x emission by the snowpack at the onset of polar sunrise. However, Jarvis et al. (2009) did not observe such low $\delta^{15}\text{N}$ signatures in gaseous HNO_3 samples collected at Summit, Greenland, with authors suggesting that either the effective fractionation of local NO_x cycling and transformation to HNO_3 counteract the photolysis fractionation or that export of photolyzed nitrate products occurs such that the local photolysis effect is erased. Nevertheless, considering the environmental simi-

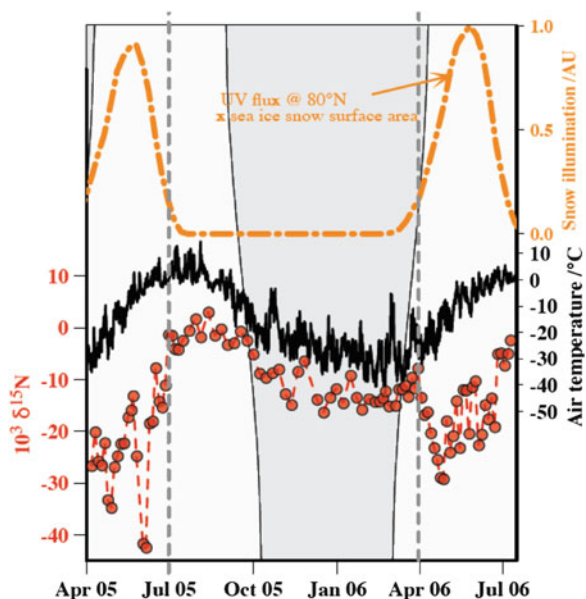


Fig. 39.9 Seasonal variation of $\delta^{15}\text{N}$ of atmospheric nitrate at Alert, Canada showing the brutal depletion of ^{15}N at the onset of the polar sunrise. The simultaneity between the depletion and the product of snow cover area by the actinic solar flux strongly advocates for a snowpack source of the depleted ^{15}N nitrate most probably via the photolysis of snow nitrate followed by local emissions of NO_x (Morin et al. 2008)

tude between Antarctic, Arctic and Greenland icy terrains, the lack of significant depleted ^{15}N in atmospheric nitrate above the Summit snowpack seems odd.

39.3.2.8 Isotopic Impact of Processes Operating in Snow

It has long been recognized that nitrate deposited on snow (following wet or dry deposition) is chemically labile. The sharp vertical profile of the concentration of nitrate found in shallow snow pits in Antarctic, displaying high concentrations of nitrate towards the surface, was soon interpreted as a consequence of the remobilization of nitrate from the snow to the surface (Neubauer and Heumann 1988; Dibb and Whitlow 1996; Mulvaney et al. 1998; Wagon et al. 1999; Röthlisberger et al. 2002; Udisti et al. 2004). Observations soon followed which showed that nitrate is photochemically active in the polar snowpack (Honrath et al. 1999) and that its photolysis leads to the emissions of reactive nitrogen species into the overlying

atmosphere (Jacobi et al. 2000; Jones et al. 2000; Grannas et al. 2007). It is noteworthy that Freyer et al. (1996) recognized a few years earlier that nitrate from Antarctic and Greenland snow and ice cores features elevated $\delta^{15}\text{N}$ values, which they attributed to “glaciological processes” found to correlate negatively with snow accumulation rates (the lower the accumulation, the higher the $\delta^{15}\text{N}$). A quantitative explanation for this process was not given. Blunier et al. (2005) demonstrated both experimentally and in the field at Dome C, Antarctica, that the depletion of nitrate was accompanied by an increase of its $\delta^{15}\text{N}$. They concluded that the photolysis of nitrate can be represented as a Rayleigh-type mechanism with a negative fractionation constant $^{15}\epsilon$. Their experimental determination of $^{15}\epsilon$ (-12%) differed from the field estimate ($-54 \pm 9\%$). Frey et al. (2009) re-analyzed the experimental data and identified an experimental bias in the choice of the UV lamp used to perform the experiments of Blunier et al. (2005). Taking into account the spectral signature of the UV lamp used for the experiments leads to reconciliation of the two approaches. The present state of knowledge is that photolysis of nitrate in snow leads to the emission of isotopically-depleted NO_x species and the accumulation of isotopically-enriched nitrate remaining in the snow, especially at low accumulation sites. The compilation of data from various snow pits excavated in Dome C, Antarctica, and theoretical considerations on the impact of isotopic substitutions on the shift in UV light absorption Miller and Yung (2000) convolved with the solar spectrum in the near UV, lead to an estimated $^{15}\epsilon$ value on the order of $-60 \pm 10\%$ (Frey et al. 2009). Figure 39.10 shows typical snow pit profiles found in central Antarctica, making apparent the strong denitrification of the snow accompanied by the strong ^{15}N enrichment of nitrate. More work is currently underway regarding a clearer understanding of the time scales of the photolytical recycling of nitrate in the uppermost snowpack in low accumulation sites. Nevertheless, this process explains the occurrence of low $\delta^{15}\text{N}$ values found in atmospheric nitrate in polar regions, provided snow and UV light are simultaneously present (see Morin et al. (2008) and Fig. 39.9).

In higher accumulation sites such as Summit, Greenland, the identification of recycling by means of isotopic methods is less obvious, since higher snow accumulation rates than on the Antarctic plateau

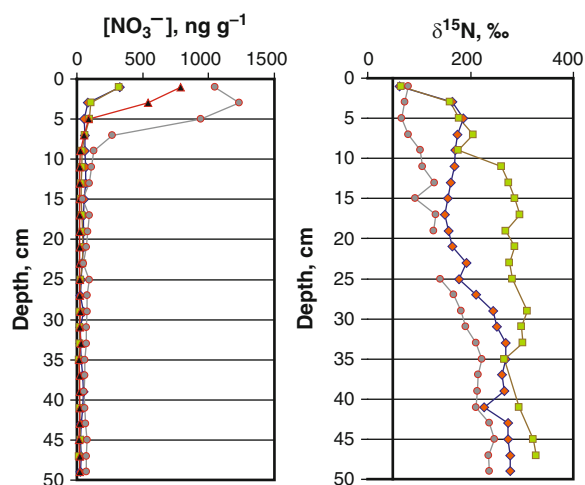


Fig. 39.10 Typical snow pit profiles in central Antarctica (Dome C) showing the strong denitrification of the snow in a very short depth accompanied by a strong ^{15}N enrichment of nitrate (Savarino, unpublished data)

make photochemistry a smaller net player on the budget of snow nitrate. Nitrate loss through post-depositional processes range between 5 and 25% (Burkhart et al. 2004; Dibb et al. 2007). This explains why small deviations from atmospheric $\delta^{15}\text{N}$ values are typically found in the snowpack in Summit, Greenland (Hastings et al. 2004; Jarvis et al. 2008, 2009). Heaton et al. (2004) also found negative $\delta^{15}\text{N}$ values in snow in Svalbard, consistent with the annual cycle of $\delta^{15}\text{N}$ in Arctic air (Morin et al. 2008) but displaying no specific enrichment in the snow.

39.3.2.9 $\delta^{15}\text{N}$ of Nitrate in Firn and Ice-Core Records

Few papers have been published on the $\delta^{15}\text{N}$ of nitrate archived in ice cores. As discussed, Freyer et al. (1996) were the first to notice that ice core nitrate features a peculiar isotopic composition. They analyzed selected samples from ice cores from Summit, Greenland and several places on the Antarctic plateau, and systematically measured $\delta^{15}\text{N}$ values higher than atmospheric ranges (up to 150‰ in a Dome C ice core). The set of measurements presented by Freyer et al. (1996) were complemented by two recent studies by Hastings et al. (2005) and Hastings et al. (2009) at Summit, Greenland. Regarding the last century, results by Freyer et al. (1996) and Hastings et al. (2009) are

extremely similar, as shown in Fig. 39.11. Hastings et al. (2009) assert that changes in $\delta^{15}\text{N}$ are associated with a source change in terms of NO_x emissions, although it remains challenging to interpret a drop of ca. 10‰ of $\delta^{15}\text{N}$ in the last 100 years (from values on the order of 10–15‰ to values slightly lower than 0‰), since $\delta^{15}\text{N}$ values as high as 10‰ have so far not been

measured for any atmospheric source. The same applies to the interpretation of Hastings et al. (2005) of an ice core spanning the last 35,000 years, displaying $\delta^{15}\text{N}$ values as high as 35‰ during the last interglacial. At present, no identified atmospheric source can explain such high $\delta^{15}\text{N}$ values in snow and ice nitrate (see details in Morin et al. (2009)). Figure 39.12 summarizes the ^{15}N variations of nitrate in snow and polar environments.

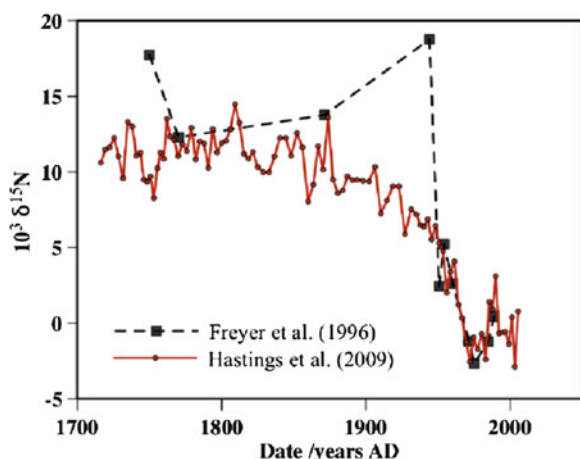


Fig. 39.11 Variations of ^{15}N of nitrate in Greenland ice for the preindustrial and industrial periods showing the decreasing of $\delta^{15}\text{N}$ linked with anthropogenic NO_x emissions (Freyer et al. 1996; Hastings et al. 2009)

39.4 Future Directions

Application of stable isotope composition variations of light elements in polar regions, with the notable exception of water isotopes, is still in its infancy. Access to deep old ice will always be a difficult and expensive task, even with new technological developments such as fast drilling, lateral drilling or in situ borehole measurements. Advancement and expansion of stable isotope analysis are thus confined to the improvement of laboratory procedures and increased sensitivities of the analytical methods. Isotopic analysis of sulfate and nitrate is on a good track and should produce better resolved isotopic signals covering all possible time frame accessible by the ice in the future.

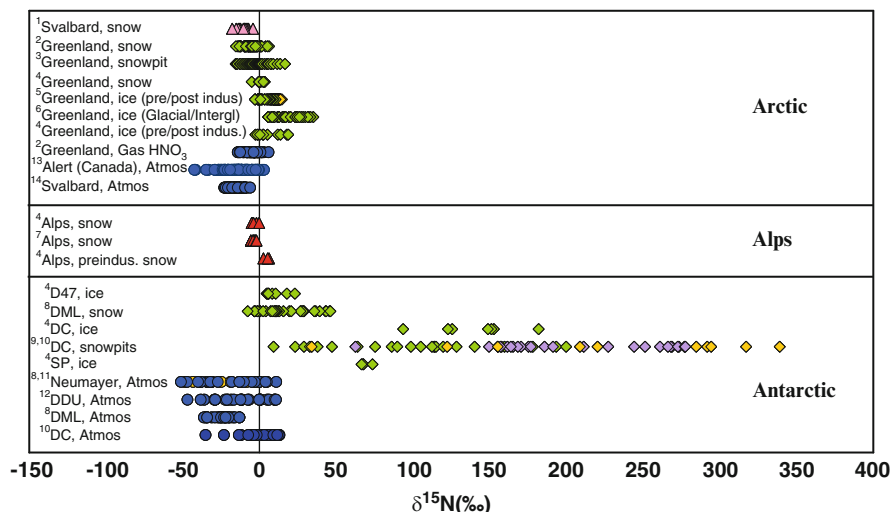
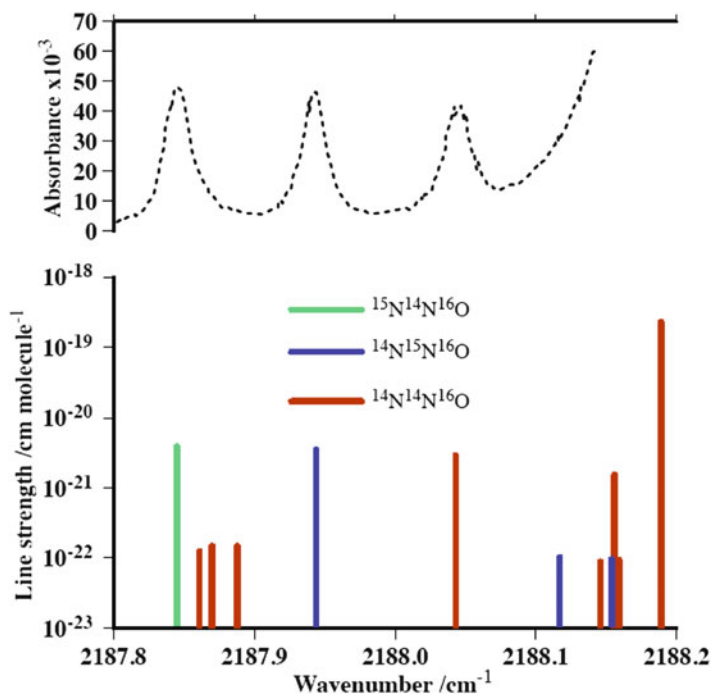


Fig. 39.12 Overview of $\delta^{15}\text{N}$ of nitrate in snow and polar environments. The singularity of the polar regions is evidenced by the low and very high $\delta^{15}\text{N}$ of atmospheric and snow/ice nitrate, respectively. 1(Heaton et al. 2004), 2(Jarvis et al. 2009), 3(Hastings et al. 2004), 4(Freyer et al. 1996), 5(Hastings et al. 2009), 6(Hastings et al. 2005), 7(Pichlmayer et al. 1998), 8(Floch 2006), 9(Blunier et al. 2005), 10(Frey et al. 2009), 11(Wagenbach et al. 1998), 12(Savarino et al. 2007), 13 (Morin et al. 2008), 14(Morin et al. 2009)

Fig. 39.13 Portion of the infrared spectrum suitable for the measurement of isotopic ratios of N_2O , including ^{15}N positioning by optical spectroscopy using the CRDS technique. This technology under development has the potential to replace in the near future the traditional G-IRMS (Mohn et al. 2010)



CO and organic compounds have great potential to also improve our understanding of the atmospheric chemistry and its interplay with climate. CO possesses a non-zero $\Delta^{17}\text{O}$ produced by a mass-independent fraction coming from the $\text{CO} + \text{OH}$ reaction (Huff and Thiemens 1998; Röckmann et al. 1998). This system is in direct link with the OH radicals, the most reactive radical in the atmosphere. Gaining information of its past isotopic variations would be a crucial and central step for our understanding of not only the oxidative capacity of the atmosphere under different climate regimes but also for important greenhouse gas cycles like methane (Chappellaz et al. 1993). The organic matter studies could also become an interesting target for future analysis. Ozonolysis is a well-known cleavage reaction on unsaturated organic compounds (alkenes and alkynes), breaking carbon double bonds and incorporating oxygen atoms into products. Bulk or specific compounds analysis of organic carbon $\Delta^{17}\text{O}$ might therefore provide another proxy of the ozone chemical activity and be a gauge to estimate the aging of organic matter during transport. Unfortunately, even with the latest advances in continuous flow development, such measurements are beyond the analytical capacities of the current G-IRMS. In preindustrial ice, the mixing ratio of CO

is on the order of 50 nmol mol^{-1} (or 2.2 pmol cm^{-3}) in trapped air bubbles (Haan et al. 1996). One kilogram of ice contains $\sim 100 \text{ mL}$ of air STP, so that 1 kg of ice contains only 0.22 nmol of CO . This amount is at best an order of magnitude lower than the current sensitivity – without taking into account the manipulation necessary to extract the ^{17}O information. Without a radical technological leap, such an analysis will stay inaccessible for years to come. There might be however some hope with the recent development of optical spectroscopy using long path cavity of high reflectivity. Mohn et al. (2010) recently presented a technique that makes use of this new technology for N_2O gas where a windows covering the laser mid IR emission allows the simultaneous measurement of the positioning of ^{15}N and ^{18}O (Fig. 39.13). Such technology may become the future of isotope ratios analysis in the next decade (see also Ostrom and Ostrom, Chapter 23 in this book).

Acknowledgements The authors are grateful to Becky Alexander and Mark Thiemens for their exhaustive review which significantly improved the reading and the clarity of the manuscript. We also thank the Institut National des Sciences de l'Univers (CNRS/INSU) and the LEFE program for their continuous funding support. Equally, the strong support for the logistic operations in the difficult environment of Antarctica and through the funding program 1011 NITEDC of the Institut

Polaire Paul Emile Victor (IPEV) is deeply acknowledged. JS acknowledges the support of the French Agence Nationale de la Recherche (ANR), under grants VOLSOL (NT09_431976) “Forçages climatiques naturels volcanique et solaire” and OPALE (NT09-451281) “Oxidant Production over Antarctica Land and its Export”. And last but not least, JS deeply wants to thank all undergraduates, PhD students and post-docs who spent countless hours to develop, measure and discuss data, always with enthusiasm and motivation. Some of the work presented here would not have been possible without their spirit.

References

- Alexander B, Savarino J, Barkov NI et al (2002) Climate driven changes in the oxidation pathways of atmospheric sulfur. *Geophys Res Lett*. doi:10.1029/2002gl014879
- Alexander B, Thiemens MH, Farquhar J et al (2003) East Antarctic ice core sulfur isotope measurements over a complete glacial-interglacial cycle. *J Geophys Res*. doi:10.1029/2003jd003513
- Alexander B, Savarino J, Kreutz KJ et al (2004) Impact of preindustrial biomass-burning emissions on the oxidation pathways of tropospheric sulfur and nitrogen. *J Geophys Res*. doi:10.1029/2003jd004218
- Alexander B, Park RJ, Jacob DJ et al (2005) Sulfate formation in sea-salt aerosols: constraints from oxygen isotopes. *J Geophys Res*. doi:10.1029/2004jd005659
- Alexander B, Park RJ, Jacob DJ et al (2009a) Transition metal-catalyzed oxidation of atmospheric sulfur: global implications for the sulfur budget. *J Geophys Res*. doi:10.1029/2008jd010486
- Alexander B, Hastings MG, Allman DJ et al (2009b) Quantifying atmospheric nitrate formation pathways based on a global model of the oxygen isotopic composition ($\delta O-17$) of atmospheric nitrate. *Atmos Chem Phys*. doi:10.5194/acp-9-5043-2010
- Amberger A, Schmidt HL (1987) The natural isotope content of nitrate as an indicator of its origin. *Geochim Cosmochim Acta* 51:2699–2705
- Amoroso A, Domine F, Esposito G et al (2010) Microorganisms in dry polar snow are involved in the exchanges of reactive nitrogen species with the atmosphere. *Environ Sci Technol*. doi:10.1021/es9027309
- Bailey SA, Smith JW (1972) Improved method for preparation of sulfur-dioxide from barium sulfate for isotope ratio studies. *Anal Chem* 44:1542–1543
- Bao HM, Marchant DR (2006) Quantifying sulfate components and their variations in soils of the McMurdo Dry Valleys, Antarctica. *J Geophys Res*. doi:10.1029/2005jd006669
- Bao HM, Thiemens MH, Farquhar J et al (2000) Anomalous O-17 compositions in massive sulphate deposits on the Earth. *Nature* 406:176–178
- Bao HM, Michalski GM, Thiemens MH (2001) Sulfate oxygen-17 anomalies in desert varnishes. *Geochim Cosmochim Acta* 65:2029–2036
- Baroni M, Thiemens MH, Delmas RJ et al (2007) Mass-independent sulfur isotopic compositions in stratospheric volcanic eruptions. *Science* 315:84–87
- Baroni M, Savarino J, Cole-Dai JH et al (2008) Anomalous sulfur isotope compositions of volcanic sulfate over the last millennium in Antarctic ice cores. *J Geophys Res*. doi:10.1029/2008jd010185
- Baublys KA, Golding SD, Young E et al (2004) Simultaneous determination of $\delta(33)SV-CDT$ and $\delta S-34(V-CDT)$ using masses 48, 49 and 50 on a continuous flow isotope ratio mass spectrometer. *Rapid Commun Mass Spectrom*. doi:10.1002/rcm.1681
- Beaudoin G, Taylor BE (1994) High-precision and spatial-resolution sulfur isotope analysis using miles laser microprobe. *Geochim Cosmochim Acta* 58:5055–5063
- Bender M, Sowers T, Brook E (1997) Gases in ice cores. *Proc Natl Acad Sci U S A* 94:8343–8349
- Bhattacharya SK, Thiemens MH (1989) New evidence for symmetry dependent isotope effect: O + CO reaction. *Z Naturforsch* 44A:435–444
- Bhattacharya SK, Pandey A, Savarino J (2008) Determination of intramolecular isotope distribution of ozone by oxidation reaction with silver metal. *J Geophys Res*. doi:10.1029/2006JD008309
- Bindeman IN, Eiler JM, Wing BA et al (2007) Rare sulfur and triple oxygen isotope geochemistry of volcanogenic sulfate aerosols. *Geochim Cosmochim Acta*. doi:10.1016/j.gca.2007.01.026
- Blunier T, Floch GL, Jacobi HW et al (2005) Isotopic view on nitrate loss in Antarctic surface snow. *Geophys Res Lett*. doi:10.1029/2005gl023011
- Böhlke JK, Mroczkowski SJ, Coplen TB (2003) Oxygen isotopes in nitrate: new reference materials for ^{18}O : ^{17}O : ^{16}O measurements and observations on nitrate-water equilibration. *Rapid Commun Mass Spectrom* 17:1835–1846
- Böhlke JK, Smith RL, Hannon JE (2007) Isotopic analysis of N and O in nitrite and nitrate by sequential selective bacterial reduction to N_2O . *Anal Chem*. doi:10.1021/ac070176k
- Bordat P, Freyer HD, Kobel K et al (1992) HPLC preparation of nitrate from ice cores for mass spectrometric N-15/N-14 measurements. *Fresenius J Anal Chem* 344:279–282
- Boschetti T, Iacumin P (2005) Continuous-flow $\delta O-18$ measurements: new approach to standardization, high-temperature thermodynamic and sulfate analysis. *Rapid Commun Mass Spectrom*. doi:10.1002/rcm.2161
- Brand WA, Coplen TB, Aerts-Bijma AT et al (2009) Comprehensive inter-laboratory calibration of reference materials for $\delta O-18$ versus VSMOW using various on-line high-temperature conversion techniques. *Rapid Commun Mass Spectrom*. doi:10.1002/rcm.3958
- Brauer K, Strauch G (2000) An alternative procedure for the O-18 measurement of nitrate oxygen. *Chem Geol* 168:283–290
- Bremner JM, Keeney DR (1965) Steam distillation methods for determination of ammonium nitrate and nitrite. *Anal Chim Acta* 32:485–490
- Bremner JM, Keeney DR (1966) Determination and isotope-ratio analysis of different forms of nitrogen in soils.3. Exchangeable ammonium nitrate and nitrite by extraction-distillation methods. *Soil Sci Soc Am Proc* 30:577–587
- Burkhart JF, Hutterli M, Bales RC et al (2004) Seasonal accumulation timing and preservation of nitrate in firn at Summit, Greenland. *J Geophys Res*. doi:10.1029/2004JD004658

- Calhoun JA, Bates TS, Charlson RJ (1991) Sulfur isotope measurements of submicrometer sulfate aerosol particles over the Pacific Ocean. *Geophys Res Lett* 18:1877–1880
- Casciotti KL, Sigman DM, Hastings MG et al (2002) Measurement of the oxygen isotopic composition of nitrate in seawater and freshwater using the denitrifier method. *Anal Chem*. doi:10.1021/ac020113w
- Casciotti KL, Böhlke JK, McIlvin MR et al (2007) Oxygen isotopes in nitrite: analysis, calibration, and equilibration. *Anal Chem*. doi:10.1021/ac061598h
- Castleman AWJ, Munkelwitz HR, Manowitz B (1974) Isotopic studies of the sulfur component of the stratospheric aerosol layer. *Tellus* 26:222–234
- Chabala JM, Soni KK, Li J et al (1995) High-resolution chemical imaging with scanning ion probe SIMS. *Int J Mass Spectrom Ion Process* 143:191–212
- Chakraborty S, Chakraborty S (2003) Isotopic fractionation of the O-3-nitric oxide reaction. *Curr Sci* 85:1210–1212
- Chang CCY, Langston J, Riggs M et al (1999) A method for nitrate collection for delta N-15 and delta O-18 analysis from waters with low nitrate concentrations. *Can J Fish Aquat Sci* 56:1856–1864
- Chappellaz J, Fung IY, Thompson AM (1993) The atmospheric methane increase since the Last Glacial Maximum 1. Source estimates. *Tellus* 45B:228–241
- Cheng HH, Bremner JM (1966) Determination and isotope-ratio analysis of different forms of nitrogen in soils 2. A simplified procedure for isotope-ratio analysis of soil nitrogen. *Soil Sci Soc Am Proc* 30:450–454
- Chmura WM, Rozanski K, Kuc T et al (2009) Comparison of two methods for the determination of nitrogen and oxygen isotope composition of dissolved nitrates. *Nukleonika* 54:17–23
- Christensen S, Tiedje JM (1988) Sub-parts-per-billion nitrate method – use of an N₂O-producing denitrifier to convert NO₃⁻ or (NO₃⁻)-N-15 to N₂O. *Appl Environ Microbiol* 54:1409–1413
- Cliff SS, Thieme M (1994) High-precision isotopic determination of the ¹⁸O/¹⁶O and ¹⁷O/¹⁶O ratios in nitrous oxide. *Anal Chem* 17:2791–2793
- Cole-Dai J, Ferris D, Lanciki A et al (2009) Cold decade (AD 1810–1819) caused by Tambora (1815) and another (1809) stratospheric volcanic eruption. *Geophys Res Lett*. doi:10.1029/2009gl040882
- Coleman ML, Moore MP (1978) Direct reduction of sulfates to sulfur-dioxide for isotopic analysis. *Anal Chem* 50:1594–1595
- Coplen TB, Böhlke JK, Casciotti KL (2004) Using dual-bacterial denitrification to improve delta N-15 determinations of nitrates containing mass-independent ¹⁷O. *Rapid Commun Mass Spectrom* 18:245–250
- Cortecci G, Longinel A (1970) Isotopic composition of sulfate in rain water, Pisa, Italy. *Earth Planet Sci Lett* 8:36–40
- Cosme E, Hourdin F, Genthon C et al (2005) Origin of dimethylsulfide, non-sea-salt sulfate, and methanesulfonic acid in eastern Antarctica. *J Geophys Res*. doi:10.1029/2004jd004881
- Craig H, Chou CC, Welhan JA et al (1988) The isotopic composition of methane in polar ice cores. *Science* 242:1535–1539
- Dansgaard W, Johnsen SJ, Moller J et al (1969) One thousand centuries of climatic record from camp century on Greenland ice sheet. *Science* 166:377–381
- De Angelis M, Petit JR, Savarino J et al (2004) Contributions of an ancient evaporitic-type reservoir to subglacial Lake Vostok chemistry. *Earth Planet Sci Lett* 222:751–765
- Dibb JE, Whitlow S (1996) Recent climate anomalies and their impact on snow chemistry at South Pole, 1987–1994. *Geophys Res Lett* 23:1115–1118
- Dibb JE, Whitlow SI, Arsenault M (2007) Seasonal variations in the soluble ion content of snow at Summit, Greenland: constraints from three years of daily surface snow samples. *Atmos Environ*. doi:10.1016/j.atmosenv.2006.12.010
- Ding Y, Macko P, Romanini D et al (2004) High sensitivity cw-cavity ringdown and Fourier transform absorption spectroscopies of (CO₂)-C-13. *J Mol Spectrosc*. doi:10.1016/j.jms.2004.03.009
- Dominguez G, Jackson T, Brothers L et al (2008) Discovery and measurement of an isotopically distinct source of sulfate in Earth's atmosphere. *Proc Natl Acad Sci U S A*. doi:10.1073/pnas.0805255105
- Dubey MK, Mohrschladt R, Donahue NM et al (1997) Isotope specific kinetics of hydroxyl radical (OH) with water (H₂O): testing models of reactivity and atmospheric fractionation. *J Phys Chem* 101:1494–1500
- Elliott EM, Kendall C, Wankel SD et al (2007) Nitrogen isotopes as indicators of NO_x source contributions to atmospheric nitrate deposition across the Midwestern and northeastern United States. *Environ Sci Technol*. doi:10.1021/es070898t
- Farquhar J, Wing BA (2003) Multiple sulfur isotopes and the evolution of the atmosphere. *Earth Planet Sci Lett*. doi:10.1016/s0012-821x(03)00296-6
- Farquhar J, Bao HM, Thieme M (2000a) Atmospheric influence of Earth's earliest sulfur cycle. *Science* 289:756–758
- Farquhar J, Savarino J, Jackson TL et al (2000b) Evidence of atmospheric sulfur in the Martian regolith from sulfur isotopes in meteorites. *Nature* 404:50–52
- Farquhar J, Savarino J, Airieau S et al (2001) Observation of wavelength-sensitive mass-independent sulfur isotope effects during SO₂ photolysis: implications for the early atmosphere. *J Geophys Res* 106:32829–32839
- Farquhar J, Wing BA, McKeegan KD et al (2002) Mass-independent sulfur of inclusions in diamond and sulfur recycling on early earth. *Science* 298:2369–2372
- Fiedler R, Proksch G (1972) Determination of nitrogen content and nitrogen-15 abundance by means of nitrogen gas generated from inorganic and organic materials. *Anal Chim Acta* 60:277–285
- Fiedler R, Proksch G (1975) Determination of nitrogen-15 by emission and mass-spectrometry in biochemical analysis – review. *Anal Chim Acta* 78:1–62
- Finlayson-Pitts BJ, Pitts JN (2000) Chemistry of the upper and lower atmosphere: theory, experiments and applications. Academic, San Diego
- Floch GL (2006) Composition isotopique du nitrate dans le névé Antarctique: Avancées et nouvelles perspectives sur les phénomènes post-dépôts. PhD dissertation, University of Bern, Bern
- Frey MM, Stewart RW, McConnell JR, Bales RC (2005) Atmospheric hydroperoxides in West Antarctica: Links to stratospheric ozone and atmospheric oxidation capacity. *Journal*

- of Geophysical Research 110(D23), D23301, doi: 10.1029/2005jd006110
- Frey MM, Savarino J, Morin S et al (2009) Photolysis imprint in the nitrate stable isotope signal in snow and atmosphere of East Antarctica and implications for reactive nitrogen cycling. *Atmos Chem Phys*. doi:10.5194/acp-9-8681-2009
- Freyer HD (1978) Seasonal trends of NH_4^+ and NO_3^- nitrogen isotope composition in rain collected at Julich, Germany. *Tellus* 30:83–92
- Freyer HD (1991) Seasonal-variation of N-15/N-14 ratios in atmospheric nitrate species. *Tellus* 43B:30–44
- Freyer HD, Kley D, Volzthomas A et al (1993) On the interaction of isotopic exchange processes with photochemical-reactions in atmospheric oxides of nitrogen. *J Geophys Res* 98:14791–14796
- Freyer HD, Kobel K, Delmas RJ et al (1996) First results of N-15/N-14 ratios in nitrate from alpine and polar ice cores. *Tellus* 48B:93–105
- Friedli H, Moor E, Oeschger H et al (1984) C-13/C-12 ratios in CO_2 extracted from Antarctic ice. *Geophys Res Lett* 11:1145–1148
- Fritzsche F, Tichomirowa M (2006) Signal improvement in elemental analyzer/continuous flow isotope ratio mass spectrometry for samples with low sulfur contents using a pre-concentration technique for on-line concentration adjustment. *Rapid Commun Mass Spectrom*. doi:10.1002/rcm.2488
- Gao X, Thiemens MH (1993a) Variations of the isotopic composition of sulfur in enstatite and ordinary chondrites. *Geochim Cosmochim Acta* 57:3171–3176
- Gao X, Thiemens MH (1993b) Isotopic composition and concentration of sulfur in carbonaceous chondrites. *Geochim Cosmochim Acta* 57:3159–3169
- Gieseemann A, Jager HJ, Norman AL et al (1994) Online sulfur-isotope determination using an elemental analyzer coupled to a mass-spectrometer. *Anal Chem* 66:2816–2819
- Granger J, Sigman DM (2009) Removal of nitrite with sulfamic acid for nitrate N and O isotope analysis with the denitrifier method. *Rapid Commun Mass Spectrom*. doi:10.1002/rcm.4307
- Granger J, Sigman DM, Prokopenko MG et al (2006) A method for nitrite removal in nitrate N and O isotope analyses. *Limnol Oceanogr Methods* 4:205–212
- Grannas AM, Jones AE, Dibb J et al (2007) An overview of snow photochemistry: evidence, mechanisms and impacts. *Atmos Chem Phys*. doi:10.5194/acp-7-4329-2007
- Grassineau NV (2006) High-precision EA-IRMS analysis of S and C isotopes in geological materials. *Appl Chem*. doi:10.1016/j.apgeochem.2006.02.015
- Grassineau NV, Matthey DP, Lowry D (2001) Sulfur isotope analysis of sulfide and sulfate minerals by continuous flow-isotope ratio mass spectrometry. *Anal Chem* 73:220–225. doi:10.1021/ac000550f
- Gunther H, Floss HG, Simon H (1966) Ein vereinfachtes verfahren zur ^{15}N -bestimmung. *Fresenius Z Anal Chem* 218:401–408
- Haan D, Martinerie P, Raynaud D (1996) Ice core data of atmospheric carbon monoxide over Antarctica and Greenland during the last 200 years. *Geophys Res Lett* 23:2235–2238
- Haberhauer G, Blochberger K (1999) A simple cleanup method for the isolation of nitrate from natural water samples for O isotope analysis. *Anal Chem* 71:3587–3590
- Halliday AN, Lee DC, Christensen JN et al (1998) Applications of multiple collector-ICPMS to cosmochemistry, geochemistry, and paleoceanography. *Geochim Cosmochim Acta* 62:919–940
- Hammer CU (1977) Past volcanism revealed by Greenland ice sheet impurities. *Nature* 270:482–486
- Hastings MG, Sigman DM, Lipschultz F (2003) Isotopic evidence for source changes of nitrate in rain at Bermuda. *J Geophys Res*. doi:10.1029/2003JD003789
- Hastings MG, Steig EJ, Sigman DM (2004) Seasonal variations in N and O isotopes of nitrate in snow at Summit, Greenland: implications for the study of nitrate in snow and ice cores. *J Geophys Res*. doi:10.1029/2004jd004991
- Hastings MG, Sigman DM, Steig EJ (2005) Glacial/interglacial changes in the isotopes of nitrate from the Greenland Ice Sheet Project 2 (GISP2) ice core. *Glob Biogeochem Cycles*. doi:Gb4024, 10.1029/2005gb002502
- Hastings MG, Jarvis JC, Steig EJ (2009) Anthropogenic impacts on nitrogen isotopes of ice-core nitrate. *Science* 324:1288. doi:10.1126/science.1170510
- Heaton THE (1987) N-15/N-14 ratios of nitrate and ammonium in rain at Pretoria, South-Africa. *Atmos Environ* 21:843–852
- Heaton THE, Wynn P, Tye AM (2004) Low N-15/N-14 ratios for nitrate in snow in the High Arctic (79 degrees N). *Atmos Environ*. doi:10.1016/j.atmosphere.2004.06.028
- Heidenreich JE III, Thiemens MH (1986) A non-mass-dependent oxygen isotope effect in the production of ozone from molecular oxygen: the role of symmetry in isotope chemistry. *J Chem Phys* 84:2129–2136
- Hoering T (1955) Variations of nitrogen-15 abundance in naturally occurring substances. *Science* 122:1233–1234
- Hoering T (1957) The isotopic composition of the ammonia and the nitrate ion in rain. *Geochim Cosmochim Acta* 12: 97–102
- Hojberg O, Johansen HS, Sorensen J (1994) Determination of N-15 abundance in nanogram pools of NO_3^- and NO_2^- by denitrification bioassay and mass-spectrometry. *Appl Environ Microbiol* 60:2467–2472
- Holt BD, Kumar R (1991) Oxygen isotope fractionation for understanding the sulphur cycle. In: Krouse HR, Grinenko VA (eds) *Stable isotopes: natural and anthropogenic sulphur in the environment*, vol 43, SCOPE. Wiley, New York
- Holt BD, Cunningham PT, Kumar R (1981) Oxygen isotopy of atmospheric sulfates. *Environ Sci Technol* 15:804–808
- Honrath RE, Peterson MC, Guo S et al (1999) Evidence of NO_x production within or upon ice particles in the Greenland snowpack. *Geophys Res Lett* 26:695–698
- Hu GX, Rumble D, Wang PL (2003) An ultraviolet laser microprobe for the in situ analysis of multisulfur isotopes and its use in measuring Archean sulfur isotope mass-independent anomalies. *Geochim Cosmochim Acta* 67:3101–3118
- Huff AK, Thiemens MH (1998) O-17/O-16 and O-18/O-16 isotope measurements of atmospheric carbon monoxide and its sources. *Geophys Res Lett* 25:3509–3512
- Hulston JR, Thode HG (1965) Variations in S33 S34 and S36 contents of meteorites and their relation to chemical and nuclear effects. *J Geophys Res* 70:3475–3480

- Jacobi HW, Weller R, Jones AE et al (2000) Peroxyacetyl nitrate (PAN) concentrations in the Antarctic troposphere measured during the photochemical experiment at Neumayer (PEAN'99). *Atmos Environ* 34:5235–5247
- Jamieson RE, Wadleigh MA (1999) A study of the oxygen isotopic composition of precipitation sulphate in eastern Newfoundland. *Water Air Soil Pollut* 110:405–420
- Jamieson RE, Wadleigh MA (2000) Tracing sources of precipitation sulfate in eastern Canada using stable isotopes and trace metals. *J Geophys Res* 105:20549–20556
- Jarvis JC, Steig EJ, Hastings MG et al (2008) Influence of local photochemistry on isotopes of nitrate in Greenland snow. *Geophys Res Lett*. doi:10.1029/2008gl035551
- Jarvis JC, Hastings MG, Steig EJ et al (2009) Isotopic ratios in gas-phase HNO₃ and snow nitrate at Summit, Greenland. *J Geophys Res*. doi:10.1029/2009jd012134
- Jenkins KA, Bao HM (2006) Multiple oxygen and sulfur isotope compositions of atmospheric sulfate in Baton Rouge, LA, USA. *Atmos Environ*. doi:10.1016/j.atmosenv.2006.04.010
- Johnson CA, Mast MA, Kester CL (2001) Use of O-17/O-16 to trace atmospherically-deposited sulfate in surface waters: a case study in alpine watersheds in the Rocky Mountains. *Geophys Res Lett* 28:4483–4486
- Johnston JC, Thiemens MH (1997) The isotopic composition of tropospheric ozone in three environments. *J Geophys Res* 102:25395–25404
- Jones AE, Weller R, Wolff EW et al (2000) Speciation and rate of photochemical NO and NO₂ production in Antarctic snow. *Geophys Res Lett* 27:345–348
- Jonsell U, Hansson ME, Morth CM et al (2005) Sulfur isotopic signals in two shallow ice cores from Dronning Maud Land, Antarctica. *Tellus* 57B:341–350
- Kaiser J, Hastings MG, Houlton BZ et al (2007) Triple oxygen isotope analysis of nitrate using the denitrifier method and thermal decomposition of N₂O. *Anal Chem*. doi:10.1021/ac061022s
- Kamber BS, Whitehouse MJ (2007) Micro-scale sulphur isotope evidence for sulphur cycling in the late Archean shallow ocean. *Geobiology*. doi:10.1111/j.1472-4669.2006.00091.x
- Karol IL, Frolkis VA, Kiselev AA (1995) Radiative-photochemical modeling of the annually averaged composition and temperature of the global atmosphere during the last glacial and interglacial periods. *J Geophys Res* 100:7291–7301
- Keeney DR, Bremner JM (1966) Determination and isotope-ratio analysis of different forms of nitrogen in soils.4. Exchangeable ammonium nitrate and nitrite by direct-distillation methods. *Soil Sci Soc Am Proc* 30:583–589
- Kendall C (1998) Tracing nitrogen sources and cycling in catchments. In: Kendall C, McDonnell JJ (eds) *Tracers in catchment hydrology*. Elsevier Science, Amsterdam
- Kendall C, Grim E (1990) Combustion tube method for measurement of nitrogen isotope ratios using calcium-oxide for total removal of carbon-dioxide and water. *Anal Chem* 62:526–529
- Kiba T, Takagi T, Yoshimura Y et al (1955) Tin (II)-strong phosphoric acid – a new reagent for the determination of sulfate by reduction of hydrogen sulfide. *Bull Chem Soc Jpn* 28:641–644
- Komatsu DD, Ishimura T, Nakagawa F et al (2008) Determination of the N-15/N-14, O-17/O-16, and O-18/O-16 ratios of nitrous oxide by using continuous-flow isotope-ratio mass spectrometry. *Rapid Commun Mass Spectrom*. doi:10.1002/rcm.3493
- Kornelx B, Medina R, Schmidt HL (1994) A sensitive method for the fast and simultaneous determination of delta-N-15-values and delta-O-18-values in nitrate. *Isotopenpraxis* 30:215–218
- Kornelx BE, Gehre M, Hofling R et al (1999) On-line delta O-18 measurement of organic and inorganic substances. *Rapid Commun Mass Spectrom* 13:1685–1693
- Krankowsky D, Bartecki F, Klees GG et al (1995) Measurement of heavy isotope enrichment in tropospheric ozone. *Geophys Res Lett* 22:1713–1716
- Krankowsky D, Lammerzähl P, Mauersberger E (2000) Isotopic measurements of stratospheric ozone. *Geophys Res Lett* 27:2593–2595
- Kunasek SA, Alexander B, Steig EJ et al (2008a) Measurements and modeling of Delta O-17 of nitrate in snowpits from Summit, Greenland. *J Geophys Res*. doi:10.1029/2008jd010103
- Kunasek SA, Alexander B, Steig EJ et al (2008b) Reinterpreting Delta O-17 of nitrate in ice cores at high accumulation sites. *Geochim Cosmochim Acta* 72:A502
- Kunasek SA, Alexander B, Steig EJ et al (2010) Sulfate sources and oxidation chemistry over the past 1230 years from sulfur and oxygen isotopes of sulfate in a West Antarctic ice core. *J Geophys Res*. doi:10.1029/2010JD013846
- Lasaga AC, Otake T, Watanabe Y et al (2008) Anomalous fractionation of sulfur isotopes during heterogeneous reactions. *Earth Planet Sci Lett*. doi:10.1016/j.epsl.2008.01.016
- Lee CCW, Thiemens MH (2001) δ¹⁷O and δ¹⁸O measurement of atmospheric sulfate from a coastal and high alpine region: a mass independent isotopic anomaly. *J Geophys Res* 106:17359–17374
- Lee CW, Savarino J, Thiemens MH (2001) Mass independent isotopic composition of atmospheric sulfate: origin and implications for the present and past atmosphere of Earth and Mars. *Geophys Res Lett* 28:1783–1786
- Lee CCW, Savarino J, Cachier H et al (2002) Sulfur (S-32, S-33, S-34, S-36) and oxygen (O-16, O-17, O-18) isotopic ratios of primary sulfate produced from combustion processes. *Tellus* 54B:193–200
- Legrand MR, Kirchner S (1990) Origins and variations of nitrate in south polar precipitation. *J Geophys Res* 95:3493–3507
- Legrand M, Mayewski P (1997) Glaciochemistry of polar ice cores: a review. *Rev Geophys* 35:219–243
- Legrand M, Preunkert S, Jourdain B et al (2009) Year-round record of surface ozone at coastal (Dumont d'Urville) and inland (Concordia) sites in East Antarctica. *J Geophys Res*. doi:10.1029/2008jd011667
- Luz B, Barkan E (2005) The isotopic ratios O-17/O-16 and O-18/O-16 in molecular oxygen and their significance in biogeochemistry. *Geochim Cosmochim Acta*. doi:10.1016/j.gca.2004.09.001
- Lyons JR (2007) Mass-independent fractionation of sulfur isotopes by isotope-selective photodissociation of SO₂. *Geophys Res Lett*. doi:22810.21029/22007GL031031
- Mann JL, Kelly WR (2005) Measurement of sulfur isotope composition (delta S-34) by multiple-collector thermal ionization mass spectrometry using a S-33-S-36 double spike. *Rapid Commun Mass Spectrom*. doi:10.1002/rcm.2213

- Mariotti A (1983) Atmospheric nitrogen is a reliable standard for natural N-15 abundance measurements. *Nature* 303:685–687
- Martin E, Bindeman I (2009) Mass-independent isotopic signatures of volcanic sulfate from three supereruption ash deposits in Lake Tecopa, California. *Earth Planet Sci Lett.* doi:10.1016/j.epsl.2009.03.005
- Martinerie P, Brasseur GP, Granier C (1995) The chemical composition of ancient atmospheres: a model study constrained by ice core data. *J Geophys Res* 100:14, 291–214, 304
- Mather TA, McCabe JR, Rai VK et al (2006) Oxygen and sulphur isotope composition of volcanic sulphate aerosol at the point of emission. *J Geophys Res.* doi:10.1029/2005JD006584
- Matthews DE, Hayes JM (1978) Isotope-ratio-monitoring gas chromatography-mass spectrometry. *Anal Chem* 50: 1465–1473
- Mauersberger K (1987) Ozone isotope measurement in the stratosphere. *Geophys Res Lett* 14:80–83
- Mauersberger K, Lammerzahl P, Krankowsky D (2001) Stratospheric ozone isotope enrichments – revisited. *Geophys Res Lett* 28:3155–3158
- McCabe JR, Savarino J, Alexander B et al (2006) Isotopic constraints on non-photochemical sulfate production in the Arctic winter. *Geophys Res Lett.* doi:10.1029/2005gl025164
- McCabe JR, Thiemens MH, Savarino J (2007) A record of ozone variability in South Pole Antarctic snow: role of nitrate oxygen isotopes. *J Geophys Res.* doi:10.1029/2006jd007822
- McIlvin MR, Altabet MA (2005) Chemical conversion of nitrate and nitrite to nitrous oxide for nitrogen and oxygen isotopic analysis in freshwater and seawater. *Anal Chem.* doi:10.1021/ac050528s
- McKinney CR, McCrea JM, Epstein S et al (1950) Improvements in mass spectrometers for the measurement of small differences in isotope abundance ratios. *Rev Sci Instrum* 21:724–730
- Metzger J (1978) Rapid simultaneous determination of N-15 and total nitrogen by direct coupling of mass-spectrometer and automatic elemental analyzer. *Fresenius Z Anal Chem* 292:44–45
- Michalski G (2010) Purification procedure for delta N-15, delta O-18, Delta O-17 analysis of nitrate. *Int J Environ Anal Chem.* doi:10.1080/03067310902783593
- Michalski G, Bhattacharya SK (2009) The role of symmetry in the mass independent isotope effect in ozone. *Proc Natl Acad Sci U S A.* doi:10.1073/pnas.0812755106
- Michalski G, Savarino J, Bohlke JK et al (2002) Determination of the total oxygen isotopic composition of nitrate and the calibration of a Delta O-17 nitrate reference material. *Anal Chem.* doi:10.1021/ac0256282
- Michalski G, Scott Z, Kabling M et al (2003) First measurements and modeling of Delta O-17 in atmospheric nitrate. *Geophys Res Lett.* doi:10.1029/2003gl017015
- Michalski G, Böhlke JK, Thiemens M (2004a) Long term atmospheric deposition as the source of nitrate and other salts in the Atacama Desert, Chile: new evidence from mass-independent oxygen isotopic compositions. *Geochim Cosmochim Acta.* doi:10.1016/j.gca.2004.04.009
- Michalski G, Meixner T, Fenn M et al (2004b) Tracing atmospheric nitrate deposition in a complex semi-arid ecosystem using $\Delta^{17}\text{O}$. *Environ Sci Technol.* doi:10.1021/es034980
- Michalski G, Rech J, Thiemens M (2005a) The onset of hyperaridity in the Atacama Desert: nitrate $\Delta\text{O-17}$ as a tracer of soil moisture. *Geochim Cosmochim Acta* 69:A444
- Michalski G, Bockheim JG, Kendall C et al (2005b) Isotopic composition of Antarctic Dry Valley nitrate: implications for NO_y sources and cycling in Antarctica. *Geophys Res Lett.* doi:10.1029/2004gl022121
- Miller CE, Yung YL (2000) Photo-induced isotopic fractionation. *J Geophys Res* 105:29039–29051
- Minagawa M, Winter DA, Kaplan IR (1984) Comparison of Kjeldahl and combustion methods for measurement of nitrogen isotope ratios in organic-matter. *Anal Chem* 56:1859–1861
- Mohn J, Guggenheim C, Tuzson B et al (2010) A liquid nitrogen-free preconcentration unit for measurements of ambient N₂O isotopomers by QCLAS. *Atmos Meas Tech* 3:609–618
- Mojzsis SJ, Coath CD, Greenwood JP et al (2003) Mass-independent isotope effects in Archean (2.5 to 3.8 Ga) sedimentary sulfides determined by ion microprobe analysis. *Geochim Cosmochim Acta.* doi:10.1016/s0016-7037(00)00059-0
- Moore H (1974) Isotopic measurement of atmospheric nitrogen-compounds. *Tellus* 26:169–174
- Moore H (1977) The isotopic composition of ammonia, nitrogen dioxide and nitrate in the atmosphere. *Atmos Environ* 11: 1239–1243
- Morin S, Savarino J, Bekki S et al (2007) Signature of Arctic surface ozone depletion events in the isotope anomaly ($\Delta^{17}\text{O}$) of atmospheric nitrate. *Atmos Chem Phys.* doi: 10.5194/acp-7-1451-2007
- Morin S, Savarino J, Frey MM et al (2008) Tracing the origin and fate of NO_x in the Arctic atmosphere using stable isotopes in nitrate. *Science.* doi:10.1126/science.1161910
- Morin S, Savarino J, Frey MM et al (2009) Comprehensive isotopic composition of atmospheric nitrate in the Atlantic Ocean boundary layer from 65° S to 79° N. *J Geophys Res.* doi:10.1029/2008jd010696
- Mulvaney R, Wagenbach D, Wolff EW (1998) Postdepositional change in snowpack nitrate from observation of year-round near-surface snow in coastal Antarctica. *J Geophys Res* 103:11021–11031
- Murphey BF (1947) The temperature variation of the thermal diffusion factors for binary mixtures of hydrogen, deuterium, and helium. *Phys Rev* 72:834–837
- Neubauer J, Heumann KG (1988) Determination of nitrate at the ng/g level in Antarctic snow samples with ion chromatography and isotope-dilution mass-spectrometry. *Fresenius Z Anal Chem.* doi:10.1007/BF01105161
- Nevins JL, Altabet MA, McCarthy JJ (1985) Nitrogen isotope ratio analysis of small samples – sample preparation and calibration. *Anal Chem* 57:2143–2145
- Nier AO (1936) A mass-spectrographic study of the isotopes of argon, potassium, rubidium, zinc and cadmium. *Phys Rev* 50:1041–1045
- Nier AO (1940) A mass spectrometer for routine isotope abundance measurements. *Rev Sci Instrum* 11:212–216
- Nier AO (1947) A mass spectrometer for isotope and gas analysis. *Rev Sci Instrum* 18:398–411

- Ogawa Y, Nishikawa M, Nakasugi O et al (2001) Determination of the abundance of delta N-15 in nitrate ion in contaminated groundwater samples using an elemental analyzer coupled to a mass spectrometer. *Analyst* 126:1051–1054
- Ono S, Wing B, Rumble D et al (2006) High precision analysis of all four stable isotopes of sulfur (S-32, S-33, S-34 and S-36) at nanomole levels using a laser fluorination isotope-ratio-monitoring gas chromatography-mass spectrometry. *Chem Geol.* doi:10.1016/j.chemgeo.2005.08.005
- Owens NJP (1988) Rapid and total automation of shipboard N-15 analysis – examples from the North-Sea. *J Exp Mar Biol Ecol* 122:163–171
- Owens NJP, Rees AP (1989) Determination of N-15 at submicrogram levels of nitrogen using automated continuous-flow isotope ratio mass-spectrometry. *Analyst* 114:1655–1657
- Papineau D, Mojzsis SJ, Coath CD et al (2005) Multiple sulfur isotopes of sulfides from sediments in the aftermath of Paleoproterozoic glaciations. *Geochim Cosmochim Acta.* doi:10.1016/j.gca.2005.07.005
- Papineau D, Mojzsis SJ, Schmitt AK (2007) Multiple sulfur isotopes from Paleoproterozoic Huronian interglacial sediments and the rise of atmospheric oxygen. *Earth Planet Sci Lett.* doi:10.1016/j.epsl.2006.12.015
- Parwel A, Ryhage R, Wickman FE (1957) Natural variations in the relative abundances of the nitrogen isotopes. *Geochim Cosmochim Acta* 11:165–170
- Patris N, Delmas RJ, Jouzel J (2000) Isotopic signatures of sulfur in shallow Antarctic ice cores. *J Geophys Res* 105:7071–7078
- Patris N, Delmas RJ, Legrand M et al (2002) First sulfur isotope measurements in central Greenland ice cores along the pre-industrial and industrial periods. *J Geophys Res.* doi:4115, 10.1029/2001jd000672
- Patris N, Cliff SS, Quinn PK et al (2007) Isotopic analysis of aerosol sulfate and nitrate during ITCT-2k2: determination of different formation pathways as a function of particle size. *J Geophys Res.* doi:23310.21029/22005JD006214
- Pavlov AA, Mills MJ, Toon OB (2005) Mystery of the volcanic mass-independent sulfur isotope fractionation signature in the Antarctic ice core. *Geophys Res Lett* 32. doi:10.1029/2005gl022784
- Pepkowitz LP, Shirley EL (1951) Microdetection of sulfur. *Anal Chem* 23:1709–1710
- Pichlmayer F, Blochberger K (1988) Isotopic abundance analysis of carbon, nitrogen and sulfur with a combined elemental analyzer-mass spectrometer system. *Fresenius Z Anal Chem* 331:196–201
- Pichlmayer F, Schonher W, Seibert P et al (1998) Stable isotope analysis for characterization of pollutants at high elevation alpine sites. *Atmos Environ* 32:4075–4085
- Poulson SR (2005) The effect of sulfate-delta O-18 upon on-line sulfate-delta S-34 analysis, and implications for measurements of delta S-33 and Delta S-33. *Rapid Commun Mass Spectrom.* doi:10.1002/rcm.1754
- Preston T, Owens NJP (1983) Interfacing an automatic elemental analyzer with an isotope ratio mass-spectrometer – the potential for fully automated total nitrogen and N-15 analysis. *Analyst* 108:971–977
- Preunkert S, Jourdain B, Legrand M et al (2008) Seasonality of sulfur species (dimethyl sulfide, sulfate, and methanesulfonate) in Antarctica: inland versus coastal regions. *J Geophys Res-Atmospheres.* doi:10.1029/2008jd009937
- Pruett LE, Kreutz KJ, Wadleigh M et al (2004) Sulfur isotopic measurements from a West Antarctic ice core: implications for sulfate source and transport. *Ann Glaciol* 39:161–168
- Rafter TA (1967) Oxygen isotopic composition of sulphates. I. A method for extraction of oxygen and its quantitative conversion to carbon dioxide for isotope radiation measurements. *N Z J Sci* 10:493–510
- Rai VK, Jackson TL, Thiemens MH (2005) Photochemical mass-independent sulfur isotopes in achondritic meteorites. *Science* 309:1062–1065
- Rees CE (1978) Sulfur isotope measurements using SO₂ and SF₆. *Geochim Cosmochim Acta* 42:383–389
- Rees CE, Jenkins WJ, Monster J (1978) Sulfur isotopic composition of ocean water sulfate. *Geochim Cosmochim Acta* 42:377–381
- Revesz K, Böhlke JK, Yoshinari T (1997) Determination of delta O-18 and delta N-15 in nitrate. *Anal Chem* 69:4375–4380
- Richet P, Bottinga Y, Javoy M (1977) A review of hydrogen, carbon, nitrogen, oxygen, sulphur, and chlorine fractionation among gaseous molecules. *Annu Rev Earth Planet Sci* 5:65–110
- Rittenberg D, Ponticorvo L (1956) A method for the determination of the ¹⁸O is concentration of the oxygen of organic compounds. *Int J Appl Radiat Isot* 1:208–214
- Robinson BW, Kusakabe M (1975) Quantitative preparation of sulfur-dioxide, for S-34-S-32 analyses, from sulfides by combustion with cuprous-oxide. *Anal Chem* 47:1179–1181
- Robock A (2000) Volcanic eruptions and climate. *Rev Geophys* 38:191–219
- Röckmann T, Brenninkmeijer CAM, Saueressig G et al (1998) Mass-independent oxygen isotope fractionation in atmospheric CO as a result of the reaction CO + OH. *Science* 281:544–546
- Röthlisberger R, Hutterli MA, Wolff EW et al (2002) Nitrate in Greenland and Antarctic ice cores: a detailed description of post-depositional processes. *Ann Glaciol* 35:209–216
- Sander R, Rudich Y, von Glasow R et al (1999) The role of BrNO₃ in marine tropospheric chemistry: a model study. *Geophys Res Lett* 26:2857–2860
- Sano M, Yotsui Y, Abe H et al (1976) New technique for detection of metabolites labeled by isotope C-13 using mass fragmentography. *Biomed Mass Spectrom* 3:1–3
- Savarino J, Thiemens MH (1999a) Analytical procedure to determine both δ¹⁸O and δ¹⁷O of H₂O₂ in natural water and first measurements. *Atmos Environ* 33:3683–3690
- Savarino J, Thiemens MH (1999b) Mass-independent oxygen isotope (¹⁶O, ¹⁷O, ¹⁸O) fractionation found in H_x, O_x reactions. *J Phys Chem* 103:9221–9229
- Savarino J, Lee CW, Thiemens MH (2000) Laboratory oxygen isotopic study of sulfur (IV) oxidation: origin of the mass independent oxygen isotopic anomaly in atmospheric sulfates and other sulfate mineral deposits. *J Geophys Res* 15:29079–29089
- Savarino J, Alexander B, Darmohusodo V et al (2001) Sulfur and oxygen isotope analysis of sulfate at micromole levels using a pyrolysis technique in a continuous flow system. *Anal Chem.* doi:10.1021/ac010017f
- Savarino J, Romero A, Cole-Dai J et al (2003) UV induced mass-independent sulfur isotope fractionation in

- stratospheric volcanic sulfate. *Geophys Res Lett.* doi:10.1029/2003gl018134
- Savarino J, Kaiser J, Morin S et al (2007) Nitrogen and oxygen isotopic constraints on the origin of atmospheric nitrate in coastal Antarctica. *Atmos Chem Phys.* doi:10.5194/acp-7-1925-2007
- Savarino J, Bhattacharya SK, Morin S et al (2008) The NO + O₃ reaction: a triple oxygen isotope perspective on the reaction dynamics and atmospheric implications for the transfer of the ozone isotope anomaly. *J Chem Phys.* doi:10.1063/1.2917581
- Seinfeld JH, Pandis SN (1998) *Atmospheric chemistry and physics*, 1st edn. Wiley, New York
- Shindell DT, Faluvegi G, Unger N et al (2006) Simulations of preindustrial, present-day, and 2100 conditions in the NASA GISS composition and climate model G-PUCCINI. *Atmos Chem Phys.* doi:10.5194/acp-6-4427-2006
- Sigman DM, Casciotti KL, Andreani M et al (2001) A bacterial method for the nitrogen isotopic analysis of nitrate in seawater and freshwater. *Anal Chem* 73:4145–4153
- Silva JA, Bremner JM (1966) Determination and isotope-ratio analysis of different forms of nitrogen in soils.5. Fixed ammonium. *Soil Sci Soc Am Proc* 30:587–592
- Silva SR, Kendall C, Wilkison DH et al (2000) A new method for collection of nitrate from fresh water and the analysis of nitrogen and oxygen isotope ratios. *J Hydrol* 228:22–36
- Simpson WR, von Glasow R, Riedel K et al (2007) Halogens and their role in polar boundary-layer ozone depletion. *Atmos Chem Phys.* doi:10.5194/acp-7-4375-2007
- Sowers T (2001) N₂O record spanning the penultimate deglaciation from the Vostok ice core. *J Geophys Res* 106:31903–31914
- Sprinson DB, Rittenberg D (1949) The rate of utilization of ammonia for protein synthesis. *J Biol Chem* 180:707–714
- Thiemens MH (2006) History and applications of mass-independent isotope effects. *Annu Rev Earth Planet Sci.* doi:10.1146/annurev.earth.34.031405.125026
- Thiemens MH, Heidenreich JE III (1983) The mass-independent fractionation of oxygen: a novel isotope effect and its possible cosmochemical implications. *Science* 219:1073–1075
- Thode HG, Monster J, Dunford HB (1961) Sulphur isotope geochemistry. *Geochim Cosmochim Acta* 25:159–174
- Thompson AM (1992) The oxidizing capacity of the Earth's atmosphere – probable past and future changes. *Science* 256:1157–1165
- Thompson AM, Chappellaz JA, Fung IY et al (1993) The atmospheric CH₄ increase since the last glacial maximum.2. Interactions with oxidants. *Tellus* 45B:242–257
- Udisti R, Becagli S, Benassai S et al (2004) Atmosphere-snow interaction by a comparison between aerosol and uppermost snow-layers composition at Dome C, East Antarctica. *Ann Glaciol* 39:53–61
- Ueda A, Krouse HR (1986) Direct conversion of sulfide and sulfate minerals to SO₂ for isotope analyses. *Geochem J* 20:209–212
- Urey HC (1947) The thermodynamic properties of isotopic substances. *J Chem Soc*:562–581
- Valdes PJ, Beerling DJ, Johnson CE (2005) The ice age methane budget. *Geophys Res Lett.* doi:02710.01029/02004GL021004
- Wadhwa JL, Hallam KR, Hawkins J et al (2006) Enhancement of snowpack inorganic nitrogen by aerosol debris. *Tellus Series.* doi:10.1111/j.1600-0889.2006.00180.x
- Wadleigh MA, Schwarcz HP, Kramer JR (1996) Isotopic evidence for the origin of sulphate in coastal rain. *Tellus* 48B:44–59
- Wadleigh MA, Schwarcz HP, Kramer JR (2001) A real distribution of sulphur and oxygen isotopes in sulphate of rain over eastern North America. *J Geophys Res* 106:20883–20895
- Wagenbach D, Legrand M, Fischer H et al (1998) Atmospheric near-surface nitrate at coastal Antarctic sites. *J Geophys Res* 103:11007–11020
- Wagnon P, Delmas RJ, Legrand M (1999) Loss of volatile acid species from the upper firn layers at Vostok, Antarctica. *J Geophys Res* 104:3423–3431
- Wang YH, Jacob DJ (1998) Anthropogenic forcing on tropospheric ozone and OH since preindustrial times. *J Geophys Res* 103:31123–31135
- Wassenaar LI (1995) Evaluation of the origin and fate of nitrate in the Abbotsford aquifer using the isotopes of N-15 and O-18 in NO₃. *Appl Chem* 10:391–405
- Watanabe Y, Farquhar J, Ohmoto H (2009) Anomalous fractionations of sulfur isotopes during thermochemical sulfate reduction. *Science.* doi:10.1126/science.1169289
- Werner RA, Bruch BA, Brand WA (1999) ConFlo III – an interface for high precision delta C-13 and delta N-15 analysis with an extended dynamic range. *Rapid Commun Mass Spectrom* 13:1237–1241
- Wolff E (1995) Nitrate in polar ice. In: Delmas R (ed) *Ice core studies of global biogeochemical cycles*, vol 30. Springer, New York
- Wynn PM, Hodson AJ, Heaton THE et al (2007) Nitrate production beneath a high Arctic glacier, Svalbard. *Chem Geol.* doi:10.1016/j.chemgeo.2007.06.008
- Xue DM, De Baets B, Botte J et al (2010) Comparison of the silver nitrate and bacterial denitrification methods for the determination of nitrogen and oxygen isotope ratios of nitrate in surface water. *Rapid Commun Mass Spectrom.* doi:10.1002/rm.4445
- Yang L (2009) Accurate and precise determination of isotopic ratios by MC-ICP-MS: a review. *Mass Spectrom Rev.* doi:10.1002/mas.20251
- Yeatman SG, Spokes LJ, Dennis PF et al (2001) Comparisons of aerosol nitrogen isotopic composition at two polluted coastal sites. *Atmos Environ* 35:1307–1320
- Young E, Galy A, Nagahara H (2002) Kinetic and equilibrium mass-dependent isotope fractionation laws in nature and their geochemical and cosmochemical significance. *Geochim Cosmochim Acta* 66:1095–1104
- Zielinski GA, Mayewski PA, Meeker LD et al (1994) Record of volcanism since 7000-BC from the GISP2 Greenland ice core and implications for the volcano-climate system. *Science* 264:948–952

Chapter 40

Stable Isotopes of N and Ar as Tracers to Retrieve Past Air Temperature from Air Trapped in Ice Cores

A. Landais

Abstract Ice cores are paleoclimatic archives that permit the reconstruction of past local precipitation temperature (from the measurements of water isotopes) and past atmospheric gas concentration (from the analysis of the air trapped in the ice) over the past 800,000 years. However, water isotopes are not a quantitative tracer for past temperature in Greenland ice cores. Moreover, because of the entrapment process, air is always younger than the surrounding ice so that the temporal phasing between temperature and atmospheric concentration changes is difficult to estimate.

Here, we present a recently developed method that permits us to infer the amplitude of past abrupt temperature changes from the air trapped in an ice core. This method is based on very accurate measurements of $\delta^{15}\text{N}$ of N_2 and $\delta^{40}\text{Ar}$ of Ar in the air trapped in ice cores. Abrupt temperature changes at the surface of the ice-sheets create a transient temperature gradient in the firn (unconsolidated snow in the top 100 m of the ice sheet), which leads to isotopic fractionation of nitrogen and argon. The variations of $\delta^{15}\text{N}$ and $\delta^{40}\text{Ar}$ arising from surface temperature change are then trapped at the bottom of the firn as air bubbles close off. Then, combining the isotopic measurements with a firnification model including heat diffusion permits us to determine the amplitude of the past temperature change with an accuracy of $\pm 2.5^\circ\text{C}$. This method has demonstrated in particular that the Dansgaard Oeschger events that punctuated the last glacial period had an associated amplitude of up to 16°C in less than 100

years and that methane and Greenland temperature increases were synchronous (within 50 years).

Finally, there is hope that such a method may be used in Antarctic ice cores to constrain the phasing between changes in local temperature and in atmospheric concentration. This is however still an ongoing task, because in Antarctica, the temperature changes are too slow to induce a strong thermal gradient in the firn and the measured evolution of $\delta^{15}\text{N}$ and $\delta^{40}\text{Ar}$ is only partly understood. Still, promising first results using $\delta^{15}\text{N}$ and $\delta^{40}\text{Ar}$ measurements in the air trapped in an Antarctic ice core have shown that over a glacial to interglacial transition, CO_2 was lagging East-Antarctic temperature by 800 ± 200 years.

40.1 Introduction

Polar ice cores are essential archives for reconstructing the past climate and environment. Records of past local temperature are classically retrieved from the isotopic composition of ice. Indeed, measurements along transects in Greenland and Antarctica have shown that the present isotopic composition of surface snow (δD and $\delta^{18}\text{O}$ of H_2O) in the polar region is linearly related to the surface temperature. This well-known fact is the result of progressive distillation of the water mass toward the coldest regions (Dansgaard 1954, 1964; Picciotto et al. 1960). Then, by making the critical assumption that such a spatial slope between surface temperature and isotopic composition of the ice can also be used for linking temporal variations of $\delta^{18}\text{O}$ and δD of ice and temperature, past temperature of the polar regions is reconstructed from the depth profile of $\delta^{18}\text{O}$ or δD of H_2O in the ice cores.

Polar ice cores are also unique in providing direct records of past atmospheric composition (i.e. CO_2 ,

A. Landais
Institut Pierre Simon Laplace/Laboratoire des Sciences du Climat et de l'Environnement, CEA/CNRS/UVSQ, Orme des Merisiers, 91191 Gif sur Yvette, France
e-mail: amaelle.landais@lscce.ipsl.fr

CH₄, N₂O concentrations). Although surface snow is a porous media, it is transformed to ice (impermeable to most gas species) because of the snow load at around 100 m depth under the ice sheet surface. The snow-ice transition is associated with air bubble entrapment. These tiny bubbles record the atmospheric composition at the time of their formation.

Despite the high quality and high resolution of measurements of water isotopic composition and greenhouse gas concentrations, the interpretation of ice core records is not always straightforward. First, although the use of the spatial slope to reconstruct past temperature in East Antarctica was shown to be valid (Jouzel et al. 2003), it can lead to an error of up to a factor of 2 in the reconstruction of past temperature variations in Greenland. As a concrete example, the temperature variation between the last glacial maximum (21 kiloyears Before Present, hereafter kyr BP, where Present is 1950 CE) and the early Holocene (10 kyr BP) inferred from the water isotopic record and the spatial slope for the NorthGRIP drilling site in Greenland summit (Fig. 40.1) is around 10°C while the same surface temperature change inferred from borehole temperature measurements has been estimated as 23°C (Dahl-Jensen et al. 1998). Such large errors can be explained by a change of the seasonality of the precipitation over Greenland with time (i.e. mainly summer precipitation during the glacial period and precipitation throughout the year during the interglacial period) and/or by change in the origin of the moisture between glacial and interglacial periods, which modifies the distillation history of the water precipitating over Greenland (Boyle 1997; Krinner et al. 1997; Fawcett et al. 1997). Such effects would bias the link between $\delta^{18}\text{O}$ or δD and local temperature predicted from the observed spatial slope.

The second problem is related to the sequence of events involving changes in temperature inferred from $\delta^{18}\text{O}$ or δD of ice and changes in atmospheric composition. In particular, when air is trapped at the bottom of the firm (unconsolidated snow at the surface of the ice sheet), its composition is similar to the current atmosphere. This snow-ice transition occurs at around 100 m depth, so that the ice enclosing the air is already older by several centuries to millennia depending on the surface accumulation rate and temperature. As a consequence, at the same depth in the ice core, there is an age difference (called Δage) between the ice records (i.e. temperature inferred from $\delta^{18}\text{O}$ or δD) and the gas records. This Δage value has strong spatial and temporal variations (100–7,000 years) since the firnification process is mainly affected by surface temperature and accumulation rate, which display strong variations in Greenland and Antarctica. Numerical firnification models have been developed to estimate Δage , but despite many decades of work still have an accuracy no better than 10–20% (Goujon et al. 2003). This obscures precise determination of the phasing between changes in greenhouse gases and changes in temperature inferred from ice isotopic measurements.

Isotopes measurements of nitrogen and argon in the air trapped in ice cores are a powerful tool to make progress on the two aforementioned problems. Indeed, they can be used to reconstruct the amplitude of the abrupt temperature changes at the surface of the ice-sheet directly in the gas phase. Because nitrogen and argon are gases, they permit the direct comparison of the evolution of local temperature and of greenhouse gas concentration on a depth scale, without any calculation of the Δage and without its associated uncertainties.

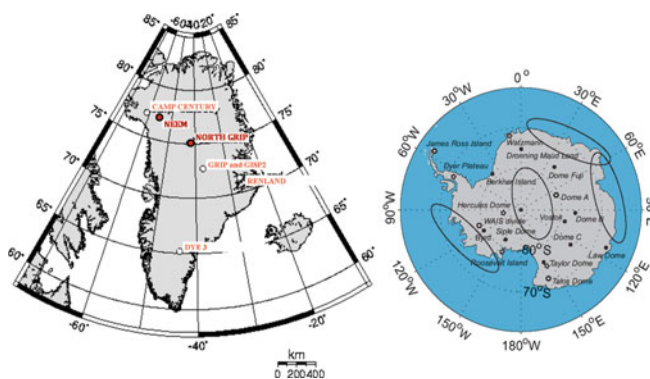
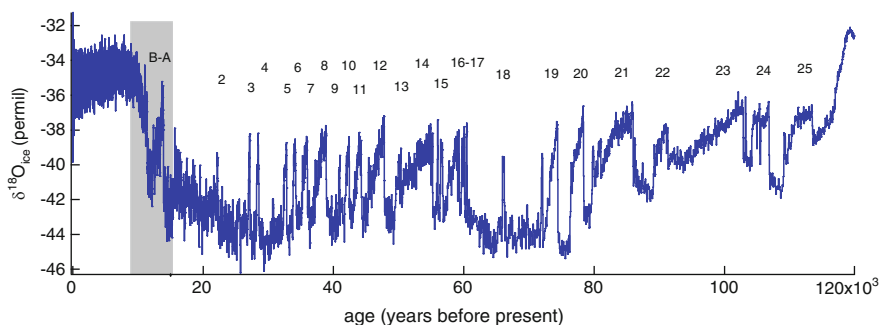


Fig. 40.1 Maps of Greenland and Antarctica with the location of the different drilling sites

Fig. 40.2 Record of $\delta^{18}\text{O}$ of the ice from the NorthGRIP ice core (NorthGRIP Community Members 2004). The Dansgaard-Oeschger events are labeled from number 2–25. B-A Bølling-Allerød



It is important to note here that this method is limited at present to large-amplitude rapid events, associated with mean annual surface temperature changes of several degrees over less than 100 years. Until now, it has thus been mainly applied to the study of the so-called Dansgaard-Oeschger events (hereafter DO events) recorded in the Greenland ice cores (Fig. 40.2). These climatic events are the most prominent warm events punctuating the last glacial period (~115–18 kyr BP). These events are characterized in Greenland by a transition from a cold stage (Greenland Stadial, GS) to a warm stage (Greenland Interstadial, GIS) within 10–150 years. These events are not limited to Greenland and are associated with significant changes in oceanic circulation (McManus et al. 2004), vegetation and temperature in low and middle latitudes (Voelker 2002), as well as smaller and slower (~1,000 year duration) surface temperature changes in Antarctica.

In this chapter, we present in the first section the material and methods needed to measure with the necessary accuracy the isotopic composition of nitrogen and argon in the air trapped in bubbles. We will then detail the different effects that have to be taken into account to isolate the isotopic fractionation related to temperature changes from other effects. In the second section, we will describe various original results that have been obtained to quantify (1) the past changes of surface temperature at the surface of the Greenland ice-sheet and (2) the relationship between changes in surface temperature and atmospheric concentration over the sequence of 25 DO events of the last glacial period, and one example during the Holocene. Finally, we will present future directions for the use of isotopic composition of nitrogen and argon in the air trapped in polar ice cores, focusing on Antarctica where past climate changes were much slower than in Greenland.

40.2 Materials and Methods

40.2.1 Isotopic Ratios

The aim is to measure the isotopic composition of nitrogen and of argon in atmospheric air. For nitrogen, we consider the ratio between ^{15}N and the most abundant isotope ^{14}N in N_2 . The measured ratio is thus $^{29}\text{N}_2/^{28}\text{N}_2$. We use the conventional δ -notation for expressing the isotopic ratio in the air with respect to a standard:

$$\delta^{15}\text{N} = 1,000 * \left(\frac{\left(\frac{^{29}\text{N}_2}{^{28}\text{N}_2} \right)_{\text{sample}}}{\left(\frac{^{29}\text{N}_2}{^{28}\text{N}_2} \right)_{\text{standard}}} - 1 \right) \quad (40.1)$$

where $(^{29}\text{N}_2/^{28}\text{N}_2)_{\text{sample}}$ is the ratio between the concentration of N_2 of mass 29 and the concentration of N_2 of mass 28 in the sample; $(^{29}\text{N}_2/^{28}\text{N}_2)_{\text{standard}}$ is the same ratio of concentrations but measured in the standard. $\delta^{15}\text{N}$ is finally expressed in per mil (‰). For our purpose, the standard is dry atmospheric air sampled around the laboratory. Such a standard is well adapted to this use and can be sampled at any place around the world because of the long residence time of nitrogen (10^7 years).

As for the temporal evolution of the isotopic composition of nitrogen, the anthropogenic effects of nitrogen fixation for fertilizer production is negligible on timescales of hundreds of years (Sowers et al. 1992). Moreover, natural (non-anthropogenic) processes such as nitrification and denitrification are thought to have negligible effects on $\delta^{15}\text{N}$ of N_2 on timescales of hundreds of thousands years, the relevant timescales for ice core reconstructions of past temperature (Mariotti 1983). The underlying reason

for this is that the entire denitrifiable inventory of fixed nitrogen represents less than 0.01% of the enormous inventory of N₂ in atmospheric air (Schlesinger 1997), combined with the small observed δ¹⁵N deviations in fixed nitrogen. δ¹⁵N of N₂ in atmospheric air is thus the same at the Earth's surface all around the world and does not display significant temporal evolution at timescales less than 100 kyr.

For argon, the relevant isotopic ratio for our study is the ratio between the most abundant isotope ⁴⁰Ar, and ³⁶Ar. As for nitrogen, the results are expressed in per mil with respect to the standard, which is dry atmospheric air:

$$\delta^{40}\text{Ar} = 1,000 * \left(\frac{\left(\frac{^{40}\text{Ar}}{^{36}\text{Ar}} \right)_{\text{sample}}}{\left(\frac{^{40}\text{Ar}}{^{36}\text{Ar}} \right)_{\text{standard}}} - 1 \right) \quad (40.2)$$

As for δ¹⁵N, δ⁴⁰Ar is constant at the Earth's surface for timescales less than 100 kyr (Bender et al. 2008).

In contrast to the measurements of δ¹⁵N, which are performed directly on dry air, δ⁴⁰Ar is usually measured after a purification step (see details later) so that the measured sample and standard contain only nitrogen, argon and the other rare gases.

The measurements are usually performed on a mass spectrometer with a dual inlet. For δ¹⁵N, 3 series of 8 dual inlet measurements (8 s pumping, 8 s measuring) are run consecutively and the resulting standard deviation given by the mass spectrometer is typically 0.01‰ for one run. For δ⁴⁰Ar, 3 series of 16 dual inlet measurements (16 s pumping, 16 s measuring) are run consecutively and the resulting standard deviation given by the mass spectrometer is 0.04‰ for one run. Longer integration times allow ultimate precision of 0.01‰ on replicate samples (Severinghaus et al. 2003).

40.2.2 Preparation of the Samples

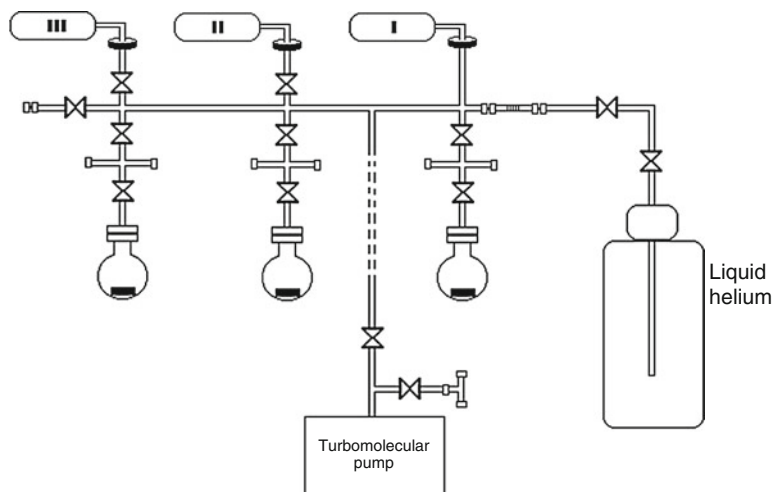
Several methods have been developed to extract air from ice core bubbles and obtain high precision δ¹⁵N and δ⁴⁰Ar measurements. The first one dedicated to simultaneous δ¹⁵N and δ¹⁸O measurements in air bubbles was developed by Sowers et al. (1989) and applied with slight improvements in different institutes (Scripps, LSCE). The melt-refreeze method used at the Scripps Institution of Oceanography (e.g. Severinghaus et al.

1998) and at LSCE (e.g. Landais et al. 2004a; details in Landais et al. 2003a) requires 10–15g of ice sample with 3 mm removed from all surfaces to eliminate contamination with the modern atmosphere. The ice is placed in vessels and headspaces are evacuated for 40 min (Fig. 40.3). The samples are then melted at ambient temperature and slowly refrozen from the bottom by immersing the bottom part of a copper heat sink in contact with the vessel in liquid nitrogen, reaching a temperature of –100°C to immobilize water. The Scripps method was modified in 2002 to remove CO₂ by passing the air sample through a glass trap at –196°C, which improved precision of both δ¹⁵N and δ¹⁸O (Petrenko et al. 2006). The liberated dry air is then trapped in a stainless steel tube immersed in liquid helium. After 40 min at room temperature for homogenization of the gas mixture, the sample air can be expanded into the mass spectrometer bellows.

At Princeton, the method is slightly different. It was inspired by the headspace equilibration method of Emerson et al. (1995) used for extracting dissolved gas in ocean water. This method (Dreyfus et al. 2010) requires 15–25g samples with 3 mm trimmed from the surface that are placed in sealed bottles (using Viton O-ring of 34 mm). The first step consists of evacuating the bottles for 20 min while the samples are kept in a –25°C bath. Once evacuated, the bottles are isolated from the pumping line and ice melts. Sample bottles are then attached to a rotator and the dissolved gases equilibrate with the headspace for 3 h. Then, excess water is removed from the bottles to an evacuated vacuum flask. The samples are then transferred to stainless steel tubes immersed in liquid helium as in the previous method and the sample can then be transferred into the mass spectrometer.

More recently, Huber and Leuenberger (2005) developed an “on-line” method for the simultaneous measurements of δ¹⁵N of N₂ and δ¹⁸O of O₂ in the air trapped in an ice core. This method consists of continuously melting a long ice stick and degassing the water in a helium flow for continuous flow analysis of δ¹⁵N and δ¹⁸O in the air. The ice stick has a cross section of 2*2 cm and is placed on a heated melting device in a freezer (–20°C). The melting device was designed at the University of Bern initially for chemical continuous flow analysis (see details in Sigg et al. 1994). The ice is melted continuously and meltwater with gases is permanently drained off by a peristaltic pump at low flow. The ice sample cannot be

Fig. 40.3 Manual extraction line used for $\delta^{15}\text{N}$ measurements at LSCE (Landais et al. 2003a)



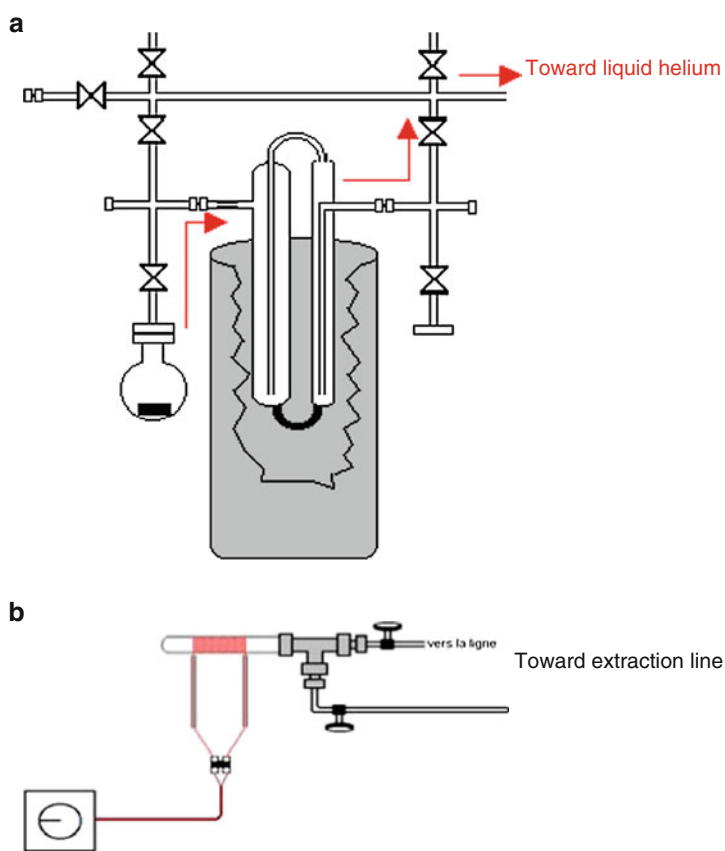
contaminated by the outside atmosphere because only the innermost part of the core section is used for the analyses (1 cm^3 section). The air is then separated from the water through a gas-permeable hydrophobic membrane and the air is carried by helium to a mass spectrometer. On its way to the mass spectrometer, helium flow carrying extracted air passes through a Nafion tube and a cold trap immersed in liquid nitrogen to remove water and CO_2 . The samples are then analyzed by the continuous flow method on the mass spectrometer (the flow of sample gas in the mass spectrometer is 0.35 mL min^{-1}) for 4–20 min depending on the sample length. Reference air standard is introduced online to the mass spectrometer before and after each sample.

The first method for accurately measuring $\delta^{40}\text{Ar}$ in the air trapped in ice cores was developed by Severinghaus et al. (2003). This method requires ice samples of 45 g after 3–5 mm have been removed from the surface before air extraction. Ice samples are then placed in vessels with a glass-coated magnetic stirrer bar. The vessels are connected through a copper gasket and Conflat flange to an extraction line similar to the one used for the first melt-refreeze method detailed above. They are then maintained at -20°C in an ethanol bath for 40 min while the headspaces are evacuated. After evacuation, the valves over the vessels are closed, the ethanol bath is removed and the ice slowly melts. The water is then agitated vigorously and the extracted gases are trapped in a stainless steel tube immersed in liquid helium over the course of 15 min. On its way, the gases pass through a glass water trap at -90°C (Fig. 40.4). The tube with the sample is then connected

to a quartz tube wrapped with heating wire containing Zr/Al getter. The glass tube is first evacuated and the getter is activated by heating to 900°C under vacuum for 5 min (Fig. 40.4). The sample is then gettered for 10 min at 900°C to absorb N_2 , O_2 , CO_2 and other reactive gases followed by 2 min at 300°C to absorb H_2 . The remaining is then again trapped in a stainless steel tube immersed in liquid helium. Because the final sample size is too small to be introduced into the mass spectrometer, pure nitrogen is added to the tube in a quantity of 10:1. After 40 min at room temperature for homogenization the sample can then be transferred to the mass spectrometer bellows. Note that this method also permits one to obtain with a high accuracy the concentration and isotopic composition of other rare gases (e.g. Xe and Kr).

Finally, Kobashi et al. (2008a) developed a method enabling the combined analyses of $\delta^{15}\text{N}$ and $\delta^{40}\text{Ar}$ on the same sample with a high accuracy. This method gives the best results when 150 g of ice are used for each sample. As for the previous methods, 3–5 mm of ice should be removed from the surface. The samples are then placed at -20°C in extraction vessels with two magnetic stirrers in each. The vessels are connected to the extraction line with copper gaskets on Conflat seats and evacuated for 40 min while immersed in an ethanol bath. Vessels are then isolated, the ethanol bath removed, and the ice is allowed to melt at room temperature. The melted water is then vigorously agitated and air is transferred to a stainless steel tube immersed in liquid helium through two cryotrap (T1 and T2), heated copper and a third cryotrap. T1 is at -90°C to remove water vapor, and T2 is

Fig. 40.4 (a) Set up used to dry and extract the air from melted ice (first step of sample preparation for $\delta^{40}\text{Ar}$ measurements) (Severinghaus et al. 2003). (b) Set up used to purify the extracted air (second step of sample preparation for $\delta^{40}\text{Ar}$ measurements) (Severinghaus et al. 2003). Zr/Al sheets are inside the quartz tubes wrapped with heating wires (in red)



at -196°C (liquid nitrogen) to remove CO_2 . The sample then passes through a 5 cm length of heated copper wool warmed to 500°C , and the final cryotrap at -196°C removes CO_2 produced by the reaction with copper. The copper enables the absorption of O_2 so that the final sample contains mainly N_2 , Ar and other rare gases. This eliminates an isobaric interference at mass 36 from the $^{18}\text{O}^{18}\text{O}$ isotopologue. The copper must be regenerated after several uses by passing H_2 gas through it at 500°C . After 40 min at room temperature, the stainless steel tube can be connected to the mass spectrometer and sample transferred to the bellows. Typical precision for $\delta^{15}\text{N}$ of N_2 on replicate analyses is 0.004 per mil, and for $\delta^{40}\text{Ar}$ the typical precision is 0.016 per mil. Note that a similar technique has recently been developed for purifying N_2 and thus measuring only $\delta^{15}\text{N}$ of N_2 in air trapped in an ice core (Mani et al. 2008) on 20 g ice samples with a precision similar to the first melt-refreeze method.

All the methods presented above have advantages and drawbacks. The first melt and refreeze method

(Severinghaus et al. 1998; Landais et al. 2003a) has the advantage of consuming little ice (<10 g per sample) and leads to a rather good analytical precision for simultaneous measurements of $\delta^{15}\text{N}$, $\delta^{18}\text{O}$, $\delta\text{O}_2/\text{N}_2$ and $\delta\text{Ar}/\text{N}_2$ (respectively pooled standard deviations of 0.005, 0.015, 1 and 1‰). The two drawbacks are time consumption (6–9 samples a day) and the inability to measure $\delta^{15}\text{N}$ and $\delta^{40}\text{Ar}$ simultaneously. The second method (Dreyfus et al. 2010) has the advantage of being semi-automated and thus less time consuming. Still, only eight samples can be processed a day, $\delta^{40}\text{Ar}$ cannot be measured with high precision, and the amount of ice consumed is larger than for the first method (20 g). The analytical precision is comparable to the first method. The online method (Huber and Leuenberger 2005) has the advantage of producing data very rapidly but ice consumption is higher (around 150 g per ice stick), the analytical precision is lower (0.02 and 0.05‰ for $\delta^{15}\text{N}$ and $\delta^{18}\text{O}$ respectively), and again $\delta^{40}\text{Ar}$ cannot be measured simultaneously. From the two methods enabling the high precision

measurements of $\delta^{40}\text{Ar}$ (pooled standard deviation better than 0.02‰), the second one (Kobashi et al. 2008a) is certainly preferable since it permits the simultaneous measurement of $\delta^{15}\text{N}$ and $\delta^{40}\text{Ar}$. However, $\delta^{18}\text{O}$ cannot be measured at the same time, while simultaneous $\delta^{18}\text{O}$ and $\delta^{15}\text{N}$ measurements are often needed for dating and the study of the biosphere and hydrological cycle (Bender et al. 1994a, b; Landais et al. 2010; Severinghaus et al. 2009). Moreover, this method is time and ice consuming (150 g per sample) while the first method (Severinghaus et al. 2003) requires only 40 g of ice per sample.

40.2.3 Calibration and Corrections

40.2.3.1 Calibration with Atmospheric Air

For each method and each lab, a working standard is used for performing the isotopic measurements. For the dual inlet methods, this standard is connected to the standard side of the mass spectrometer and for the on-line system, the standard is introduced to the mass spectrometer between two samples. However, the isotopic ratios of ice core samples are ultimately referenced to the isotopic ratios of atmospheric air in the δ notation. As a consequence, the working standard must be calibrated with respect to atmospheric air. This is done by sampling atmospheric air in an empty glass flask without fractionation, usually done by pumping cryogenically-dried air through a flask with two valves to flush it thoroughly. This flask is then connected to the extraction line and the same purification procedure of the air is followed as with ice core samples. For the melt-refreeze method, the air is simply dried through a glass trap immersed in an ethanol-liquid nitrogen mixture at -80°C . For high precision $\delta^{40}\text{Ar}$ and $\delta^{15}\text{N}$ measurements, the atmospheric air is also gettered. Such a procedure is done once a week to check for any trend in the isotopic composition of the working standard.

40.2.3.2 Standard Corrections, Interfering Masses

After mass spectrometer measurements of the ratios M29/M28 ($^{15}\text{N}/^{14}\text{N}$ of N_2), M34/M32 ($^{18}\text{O}/^{16}\text{O}$ of O_2),

M32/M28 (O_2/N_2), M40/M36 ($^{40}\text{Ar}/^{36}\text{Ar}$) and M40/M28 (Ar/N_2) in the sample and standard, small routine corrections are performed. In particular, $\delta^{15}\text{N}$ is sensitive to the amount of CO^+ in the mass spectrometer source since CO has a mass of 28 also. This is the reason why we also measure M44 (CO_2) on the mass spectrometer and experimentally determine the relationship between $\delta^{15}\text{N}$ and M44 for standard samples artificially enriched in CO_2 . This relationship varies with the tuning of the mass spectrometer source. The order of magnitude of such correction can be as high as 0.02‰ on $\delta^{15}\text{N}$. Then, we also have to take into account the so-called “chemical slope”. Owing to ion-molecule reactions in the mass spectrometer source, and associated changes in the relative ionization efficiencies of isotopologues, the variations of $\delta\text{O}_2/\text{N}_2$ and of $\delta\text{Ar}/\text{N}_2$ respectively influence the measured $\delta^{15}\text{N}$ and $\delta^{40}\text{Ar}$ values. These slopes are determined by progressive enrichment of O_2 in a dry air standard for the influence of $\delta\text{O}_2/\text{N}_2$ on $\delta^{15}\text{N}$ and by progressive enrichment of N_2 in a Ar/N_2 standard mixture for the influence of $\delta\text{Ar}/\text{N}_2$ on $\delta^{40}\text{Ar}$. The orders of magnitude of these corrections are 0.006‰ for $\delta^{15}\text{N}$ and 0.02‰ for $\delta^{40}\text{Ar}$.

40.2.3.3 Gas Loss Correction

An important problem to consider for the analyses of gas in trapped ice is gas loss through the ice matrix. This effect was first noted from anomalously low O_2/N_2 and Ar/N_2 ratios in ice cores compared to atmospheric air (Bender et al. 1994c), and was interpreted as artifactual gas loss during coring and storage, the smaller molecules (O_2 , Ar) being more easily lost than the larger ones (N_2). Then, Ikeda-Fukazawa et al. (2005) found a drift in the O_2/N_2 ratio correlated with the duration of storage in a freezer at -25°C . To explain this size dependent effect, two mechanisms have been proposed: diffusion through the ice lattice by breaking of hydrogen bonds (Ikeda-Fukazawa et al. 2005) or diffusion through small channels in the ice lattice with a threshold dimension of 3.6 Å (i.e. molecules with a diameter larger than 3.6 Å, like N_2 , will not escape the bubbles) (Huber et al. 2006a). A related size-dependent effect was noted by measuring air pumped from the firm in polar sites, in which O_2/N_2 , Ar/N_2 , and Ne/N_2 are altered by the preferential

exclusion of smaller molecules (O_2 , Ar, Ne) from over-pressured air bubbles (Severinghaus and Battle 2006).

This effect has important consequences when looking at the isotopic composition of $\delta^{18}O$ and $\delta^{40}Ar$ in air trapped in ice cores. It has indeed been shown that the storage effect leads to a 0.1‰ increase of $\delta^{18}O$ for a 10‰ decrease in $\delta O_2/N_2$ (e.g. Landais et al. 2003b; Severinghaus et al. 2009). The typical variations in $\delta O_2/N_2$ in air trapped in ice cores are 10–20‰. As for $\delta^{40}Ar$, the effect is also significant, even if it is less important. Kobashi et al. (2008a) plotted the difference in $\delta^{40}Ar$ for two replicate samples taken from the same depth vs. the difference in $\delta Ar/N_2$ for the same samples. They infer a 0.05‰ decrease of $\delta^{40}Ar$ for a 10‰ increase of $\delta Ar/N_2$. The typical variations of $\delta Ar/N_2$ in ice core samples are within 10‰. Fortunately, it has been shown that $\delta^{15}N$ is only very slightly affected by this process: using very poorly stored samples, Caillon et al. (2001) have shown no deviation of the $\delta^{15}N$ from well stored samples; more recently, Kobashi et al. (2008a) have shown only a 0.003‰ decrease in $\delta^{15}N$ for a 1% increase in the Ar/ N_2 ratio. Finally, it is especially important to correct for the gas loss effect on $\delta^{40}Ar$. To this end, $\delta Ar/N_2$ should be measured at the same time as $\delta^{40}Ar$, and this can only be done when using the copper method presented by Kobashi et al. (2008a).

40.2.4 Extraction of the Temperature Signal from the Combined Measurements of $\delta^{15}N$ and $\delta^{40}Ar$

40.2.4.1 Two Fractionation Signals

$\delta^{15}N$ and $\delta^{40}Ar$ are constant in the atmosphere on timescales of <100,000 years (Bender et al. 2006; Mariotti 1983; Sowers et al. 1992). Therefore the variations of $\delta^{15}N$ and $\delta^{40}Ar$ recorded in the air bubbles are only the results of fractionation in the firm. After bubble close-off has occurred, $\delta^{15}N$ and $\delta^{40}Ar$ remain stable except for the tiny gas loss effect (see above). The firm can be divided into three zones from the surface of the ice-sheet to the close-off depth (Fig. 40.5): (1) the convective zone (0–40 m) where air is mixed with the atmosphere, (2) the diffusive zone where fractionation occurs in response to tem-

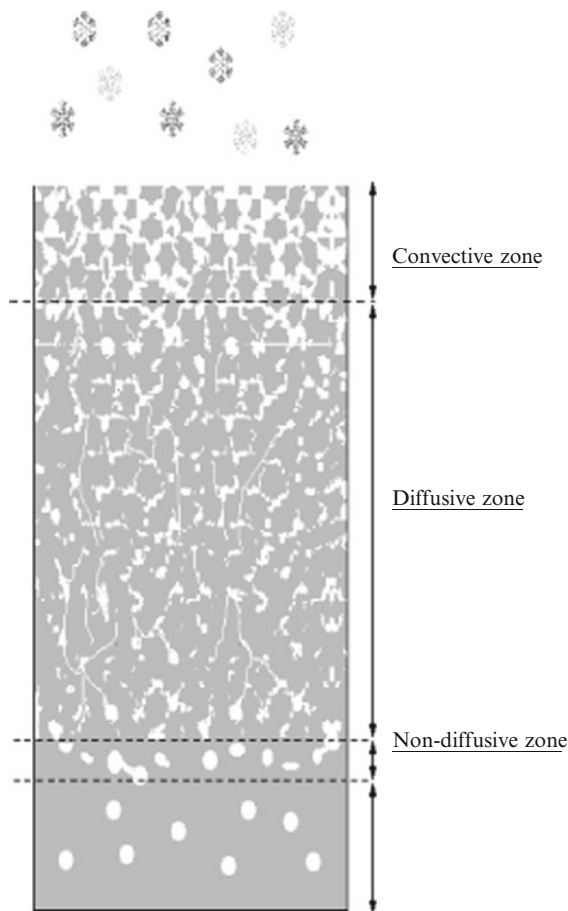


Fig. 40.5 Schematic of the firm with the division between convective, diffusive and non-diffusive zones. The close-off depth is at the bottom of the non-diffusive zone

perature gradients and the gravity field, and (3) the non-diffusive zone (~10 m above the close-off) where air composition does not change due to the existence of horizontal impermeable ice layers.

In the diffusive zone, two fractionation processes modify the elemental and isotopic composition of air with depth. First, equilibrium between a flux driven by gravity and a flux driven by concentration gradient leads to a steady-state isotopic enrichment with depth that can be expressed using the barometric equation (Craig et al. 1988; Sowers et al. 1989; Schwander 1989):

$$\begin{aligned} \delta &= 1,000 \times (\exp(\Delta mgz/RT) - 1) \\ &\cong 1,000 \times \Delta mgz/RT \end{aligned} \quad (40.3)$$

where Δm is the mass difference between the isotope species (1 g mol⁻¹ for $^{15}N/^{14}N$, 4 g mol⁻¹ for

$^{40}\text{Ar}/^{36}\text{Ar}$), T is the mean firn temperature, z is the firn depth, g the Earth gravitational acceleration and R the ideal gas constant. This gravitational effect drives the heaviest species toward the deepest levels.

Second, when a temperature gradient exists in the firn, thermal diffusion has to be considered. The process of thermal diffusion has been described in the framework of gas kinetic theory by number of researchers (Chapman 1917; Enskog 1917; Chapman and Dootson 1917). The effect is to unmix the molecules as a function of the mass difference between them among other properties: the greater the mass difference, the greater the tendency of the two molecules to separate by thermal diffusion. The effect on the isotopic ratio can be expressed as follows:

$$\delta = 1,000 \times \left(\left(\frac{T_t}{T_b} \right)^{\alpha_T} - 1 \right) \cong \Omega \times \Delta T \quad (40.4)$$

where ΔT is the temperature difference between the temperature at the top (T_t) and at the bottom (T_b) of the diffusive column, α_T is the thermal diffusion factor (unitless), and Ω the thermal diffusion sensitivity ($\% \text{K}^{-1}$). The thermal diffusion factor α_T (and thus Ω) depends on the composition of the gas mixture, on the pressure and on the temperature (Mason et al. 1966), although Ω has the advantage that it is much less dependent on temperature than α_T within the typical firn temperature range. For most gases including $\delta^{15}\text{N}$ and $\delta^{40}\text{Ar}$, the general effect of thermal fractionation is to drive the heaviest isotopes toward the coldest end.

These fractionation effects can be seen on the $\delta^{15}\text{N}$ and $\delta^{40}\text{Ar}$ profiles down in the firn (Fig. 40.6). Below 30 m, $\delta^{15}\text{N}$ and $\delta^{40}\text{Ar}$ have a linear evolution with depth; this reflects gravitational fractionation. As expected, $\delta^{40}\text{Ar}/4$ is similar to $\delta^{15}\text{N}$ because of the quasi-linear dependence with mass differences between the two isotopes. Above 20 m depth, the bell-shaped bump reflects thermal fractionation induced by the seasonal temperature gradient (Fig. 40.6). This reflects the fact that the gas sampling was performed in summer, so that there was a temperature gradient between the surface (summer temperature) and the temperature at ~10 m depth (corresponding almost to mean temperature of the firn). Hence, heavier isotopes preferentially migrate toward the cold 10 m level. For this thermal effect, $\delta^{40}\text{Ar}/4$ is not the same as $\delta^{15}\text{N}$. The difference in

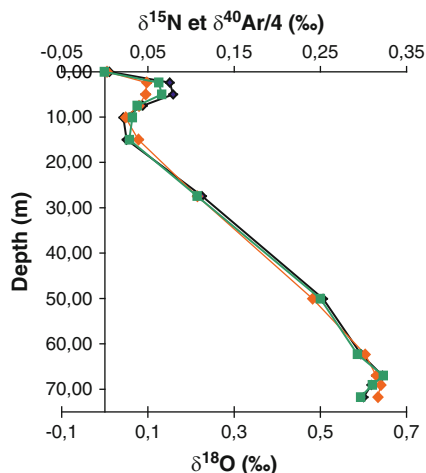


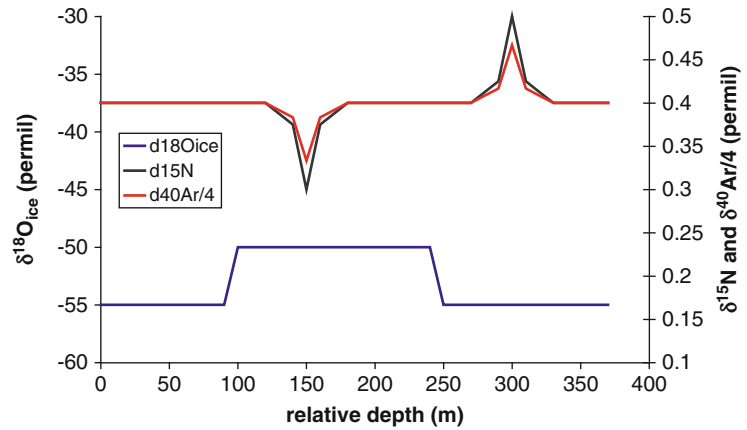
Fig. 40.6 Depth evolution of $\delta^{15}\text{N}$, $\delta^{40}\text{Ar}/4$ and $\delta^{18}\text{O}$ in the firn at NorthGRIP (Landais et al. 2006)

the behavior between the two isotopic ratios is explained by the different value of Ω for $^{15}\text{N}/^{14}\text{N}$ and $^{40}\text{Ar}/^{36}\text{Ar}$ in atmospheric air.

In Fig. 40.6, the effect of seasonal temperature change is recorded at the top of the firn but no thermal fractionation affects the bottom of the firn near the close-off depth, so that the $\delta^{15}\text{N}$ and $\delta^{40}\text{Ar}$ recorded in the air bubbles will only bear the gravitational effect. This is because the mean annual surface temperature is not experiencing significant changes recently over Greenland and Antarctica. On the contrary, over the succession of DO events during the last glacial period, mean surface temperature has varied by more than 10°C in a decade. Such temperature changes induced large temperature gradients affecting the whole firn over the course of about 100 years (i.e. the time needed for heat to diffuse through the snow). Such temperature gradients affect the divergent patterns of $\delta^{15}\text{N}$ and $\delta^{40}\text{Ar}$ over the whole firn. When surface warms rapidly, the temperature gradient in the firn drives the heaviest isotopes toward the cold bottom end of the firn: the $\delta^{15}\text{N}$ at pore close-off will thus be higher than pure gravitational $\delta^{15}\text{N}$. On the contrary, during a rapid cooling, the surface is relatively cold so that the heaviest isotopes migrate toward the top of the firn, hence counterbalancing the gravitational fractionation: the $\delta^{15}\text{N}$ at the pore close-off depth will thus be lower than pure gravitational $\delta^{15}\text{N}$.

We show in Fig. 40.7 the expected evolution with depth of $\delta^{15}\text{N}$ and $\delta^{40}\text{Ar}$ over an idealized DO event

Fig. 40.7 Idealized DO event recorded in the ice phase ($\delta^{18}\text{O}_{\text{ice}}$) and in the gas phase ($\delta^{15}\text{N}$ and $\delta^{40}\text{Ar}/4$)



with respect to the temperature evolution classically retrieved by the water isotopes ($\delta^{18}\text{O}_{\text{ice}}$). At the onset of the DO event, temperature increases abruptly as marked by the abrupt $\delta^{18}\text{O}_{\text{ice}}$ rise. At the same time, $\delta^{15}\text{N}$ and $\delta^{40}\text{Ar}$ at the bottom of the firm increases from a pure gravitational fractionation value to higher values because of thermal fractionation during the surface warming. The signature of the thermal effect can thus be seen in the rapid increases of $\delta^{15}\text{N}$ and $\delta^{40}\text{Ar}/4$ with different amplitudes during this warming. It should be noted that the $\delta^{15}\text{N}$ and $\delta^{40}\text{Ar}$ increases are recorded deeper in the ice core than the $\delta^{18}\text{O}_{\text{ice}}$ increase. This shift corresponds to the paleo-firm depth: while the temperature change modifies the $\delta^{18}\text{O}_{\text{ice}}$ at the surface of the firm, it influences the whole firm temperature gradient and then $\delta^{15}\text{N}$ and $\delta^{40}\text{Ar}$ at close-off depth, i.e. much deeper than the change in $\delta^{18}\text{O}_{\text{ice}}$. The $\delta^{15}\text{N}$ and $\delta^{40}\text{Ar}$ changes permit the recording of the temperature change directly in the gas phase, which has important consequences for determining the sequence of events between changes in temperature and changes in atmospheric concentration. After this abrupt temperature increase, the firm is homogenized in temperature during the GIS so that $\delta^{15}\text{N}$ and $\delta^{40}\text{Ar}$ only reflect gravitational fractionation with a similar value of $\delta^{15}\text{N}$ and $\delta^{40}\text{Ar}/4$. Finally, the rapid cooling toward the GS is marked by a transient decrease of $\delta^{15}\text{N}$ and $\delta^{40}\text{Ar}/4$ with different amplitudes because of the thermal effect. Again, the cooling is recorded deeper in the ice core in the gas phase than in the ice phase. This depth difference between the same abrupt event, recorded in the $\delta^{18}\text{O}_{\text{ice}}$ and in the $\delta^{15}\text{N}$, varies with depth in the ice core as a function of

initial firm depth and the typical ice thinning due to glacier flow that increases with depth.

In order to quantitatively estimate temperature changes from $\delta^{15}\text{N}$ and $\delta^{40}\text{Ar}$ measurements, it is necessary to disentangle the thermal and the gravitational signals. This is done by introducing $\delta^{15}\text{N}_{\text{excess}}$ as:

$$\delta^{15}\text{N}_{\text{excess}} = \delta^{15}\text{N} - \delta^{40}\text{Ar}/4 \quad (40.5)$$

$\delta^{15}\text{N}$ and $\delta^{40}\text{Ar}/4$ displays the same gravitational signal so that $\delta^{15}\text{N}_{\text{excess}}$ depends only on thermal fractionation.

From the thermal fractionation effect on $\delta^{15}\text{N}$ and $\delta^{40}\text{Ar}$ (40.4), we can write $\delta^{15}\text{N}_{\text{excess}}$ as:

$$\delta^{15}\text{N}_{\text{excess}} = (\Omega_{15\text{N}/14\text{N}} - \Omega_{40\text{Ar}/36\text{Ar}}) * \Delta T \quad (40.6)$$

Actually, to be fully correct and because gases do not diffuse instantaneously, a disequilibrium term γ should be incorporated in (40.6) so that $\delta^{15}\text{N}_{\text{excess}} = (\Omega_{15\text{N}/14\text{N}} - \Omega_{40\text{Ar}/36\text{Ar}}) * \Delta T * \gamma$ during transient evolution of the gas composition in response to an imposed temperature gradient.

As a consequence of (40.6), the combined measurements of $\delta^{15}\text{N}$ and $\delta^{40}\text{Ar}$ lead to the determination of ΔT , the temperature gradient in the firm. This requires however the precise determination of $\Omega_{15\text{N}/14\text{N}}$ and $\Omega_{40\text{Ar}/36\text{Ar}}$ in atmospheric air (see next section). Then, it should be noted that ΔT does not correspond to the surface temperature change but is the temperature difference between the top and the bottom of the diffusive column. In order to reconstruct the amplitude

of the past temperature change, we need a firm model including heat diffusion as detailed in Sect. 40.2.4.3.

40.2.4.2 Calibration

Theoretical calculations are not accurate enough for determining Ω for $^{15}\text{N}/^{14}\text{N}$ and $^{40}\text{Ar}/^{36}\text{Ar}$ in the atmospheric air (Mason et al. 1966). As a consequence, the best way is to make experimental measurements. Grachev and Severinghaus (2003a) designed laboratory experiments to measure thermal diffusion of $^{29}\text{N}_2/^{28}\text{N}_2$ in air for small, tightly controlled temperature differences in the range -60 to 0°C . Such a temperature range spans the different conditions that can be encountered when studying ice core paleothermometry in Greenland and Antarctica. They found omega varying as:

$$\Omega_{^{15}\text{N}/^{14}\text{N}} = (8.656/T - 1,232/T^2) \pm 3 \text{ K}^{-1} \quad (40.7)$$

with T the mean temperature expressed in Kelvin.

The same experimental designed has been used to measure α_T associated with $^{40}\text{Ar}/^{36}\text{Ar}$ thermal diffusion in air in the temperature range -60 to -10°C (Grachev and Severinghaus 2003b) and they reported:

$$\alpha_{T,^{40}\text{Ar}/^{36}\text{Ar}} * 1,000 = 26.08 - 3,952/T \pm 1 \quad (40.8)$$

where T is the mean temperature expressed in Kelvin.

40.2.4.3 Firnification and Heat Diffusion Model

The first empirical steady state firn densification model was proposed by Herron and Langway (1980). A refined model based on ice deformation has been developed by Pimienta (1987) and Barnola et al. (1991). Schwander et al. (1997) then incorporated heat transfer in this model so that this model is well adapted to the reconstruction of the amplitude of abrupt temperature changes in the past. In parallel, Arnaud et al. (2000) developed a more mechanistic firn model; they included the physical process of pressure sintering to depict the firn densification. At the top of the firn, densification is described as grain boundary sliding (model from Alley 1987); then, when firn density is higher than 0.6 g cm^{-3} , the snow densification is assumed to occur through plastic deformation

(Arzt 1982; Arzt et al. 1983). Goujon et al. (2003) then added heat diffusion to the Arnaud et al. (2000) model from a simplified model of heat diffusion in ice sheets given by Ritz (1989).

We do not further detail the densification and heat diffusion model here but instead describe its application to reconstruct past surface temperature changes from $\delta^{15}\text{N}$ and $\delta^{40}\text{Ar}$ data as depicted by Landais et al. (2004a). In order to run the model of Goujon et al. (2003), the following inputs are needed: the correspondence between depth levels and ice ages, and the temporal evolution of past surface temperature and accumulation rate. Then, the temporal evolution of ice-sheet temperature with depth is computed as well as the past firn depth evolution. These two parameters permit us to deduce the gas age scale of the ice core and the $\delta^{15}\text{N}$, $\delta^{40}\text{Ar}$ and hence $\delta^{15}\text{N}_{\text{excess}}$ profiles along the ice cores using the values of Ω or α_T determined by Grachev and Severinghaus (2003a, b) (previous section). The goal is then to find the best agreement between modeled and measured $\delta^{15}\text{N}$ and $\delta^{40}\text{Ar}$ for the different Dansgaard-Oeschger events. It should be noted that past surface temperature is not the sole input that modifies the calculated $\delta^{15}\text{N}$ and $\delta^{40}\text{Ar}$ profiles; accumulation rate has a great influence too because it affects the firn depth. This will modify $\delta^{15}\text{N}$ and $\delta^{40}\text{Ar}$ mainly because of gravitational fractionation but also $\delta^{15}\text{N}_{\text{excess}}$ because heat diffusion will be different for different firn depth. This is especially true for DO events because abrupt warmings are also accompanied by abrupt increases in surface accumulation rate. As a consequence, the uncertainty in the amplitude of the temperature change determined by this model should take into account the uncertainty in the associated change in accumulation rate. Finally, the different uncertainties that should be considered when estimating the amplitude of the temperature increase are the following: uncertainty associated with the model, dating uncertainty (i.e. on the duration of the rapid warming), uncertainty in the change in accumulation rate, and analytical uncertainties on $\delta^{15}\text{N}$ and $\delta^{40}\text{Ar}$ measurements. At the end, we could show that the amplitude of the rapid warming can be determined with an associated total uncertainty of 2.5°C (Landais et al. 2004a).

It should be noted that similar but slightly less sophisticated methods have also been developed in parallel to estimate the amplitudes of the surface warmings. On the one hand, Huber et al. (2006b)

used a high resolution $\delta^{15}\text{N}$ profile combined with the Schwander et al. (1997) model; they modify the past temperature input in the Schwander et al. (1997) model to reproduce their $\delta^{15}\text{N}$ profile. However, this method does not separate the thermal from the gravitational signals since no $\delta^{40}\text{Ar}$ measurements are used. On the other hand, Grachev and Severinghaus (2005) simply assumed that the temperature gradient retrieved from the $\delta^{15}\text{N}_{\text{excess}}$ signal relates to the past temperature change with a heat-model-based transfer correction of 2°C , but this heat transfer correction and associated uncertainties would be better estimated using a firn densification and heat diffusion model since it can be highly variable (e.g. with surface accumulation rate or duration of the warming transition)

40.3 Applications/Results/Discussion/Synthesis

40.3.1 Two Abrupt Warmings During the Last Deglaciation

Severinghaus et al. (1998), Severinghaus and Brook (1999) first presented high resolution and high precision $\delta^{15}\text{N}$ and $\delta^{40}\text{Ar}$ measurements over the two abrupt events that punctuated the last deglaciation on

the GISP2 ice core located at the Greenland summit. Each of these events (onset of the Bølling-Allerød 14.6–14.7 kyr BP, end of the Younger Dryas 11.6–11.7 kyr BP) are recorded as abrupt shifts in $\delta^{18}\text{O}$ of the ice (Fig. 40.8). The $\delta^{15}\text{N}$ and $\delta^{40}\text{Ar}$ records show as well abrupt increases by more than 0.15 and 0.4‰ respectively for each event as a result of thermal fractionation. Note that the $\delta^{15}\text{N}$ and $\delta^{40}\text{Ar}$ increases are recorded ~ 20 m deeper than the $\delta^{18}\text{O}_{\text{ice}}$ increases. This depth shift (Δdepth) is expected because of firn processes: during an abrupt warming, $\delta^{18}\text{O}$ of the ice increases at the top of the firn while the modification of gaseous $\delta^{15}\text{N}$ because of the thermal gradient in the firn will be recorded at the bottom of the firn during pore close-off. Because of ice thinning, the firn depth that is around 70 m today at the surface in GISP2 represents only 20 m at around 1,700 m.

The $\delta^{15}\text{N}$ and $\delta^{40}\text{Ar}$ increases are markers for the temperature increase in the gas phase and can be directly compared with the methane curve on the same depth scale (Fig. 40.8). Such a comparison leads to the conclusion that temperature and methane increases were synchronous within ± 10 years during these two events (Severinghaus et al. 1998).

The combined measurements of $\delta^{15}\text{N}$ and $\delta^{40}\text{Ar}$ in $\delta^{15}\text{N}_{\text{excess}}$ were then used to determine the amplitude of the two abrupt warmings punctuating the last deglaciation. The first temperature change estimates were

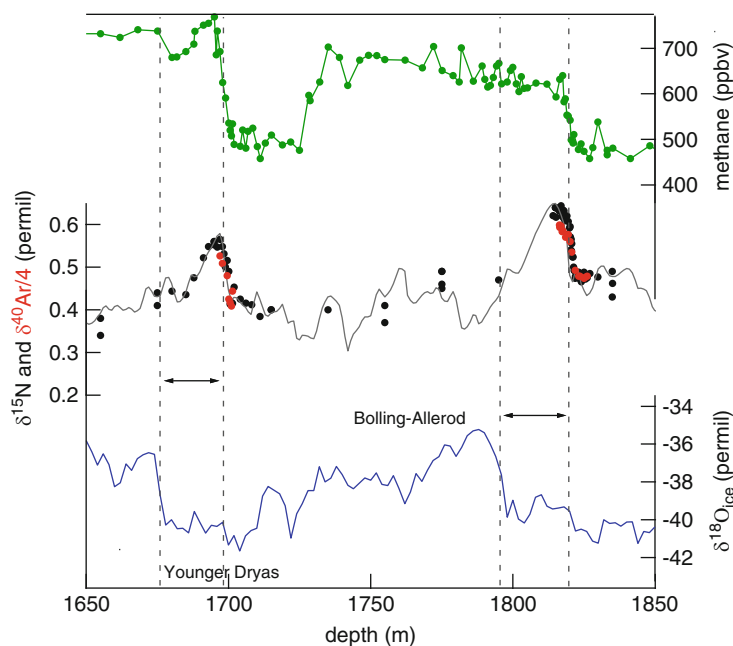


Fig. 40.8 Gas data inspired from the results obtained by Severinghaus et al. (1998) and Severinghaus and Brook (1999) on the GISP2 ice core. From top to bottom: CH_4 (green), $\delta^{15}\text{N}$ (black) and $\delta^{40}\text{Ar}/4$ (red), $\delta^{18}\text{O}_{\text{ice}}$ (blue). The double arrows display the depth difference (Δdepth) between the same event recorded in the ice and in the gas phases

given by Severinghaus et al. (1998) for the end of the Younger Dryas ($5\text{--}10^\circ\text{C}$) and Severinghaus et al. (2003) for the onset of the Bølling-Allerød ($11 \pm 3^\circ\text{C}$). Unfortunately, at the time of these earlier determinations, no proper determination of the fractionation coefficients associated with thermal diffusion had been performed for $\delta^{15}\text{N}$ and $\delta^{40}\text{Ar}$. Moreover, the firm densification and heat diffusion models were still very basic (only steady state models that did not account for heat diffusion over the whole ice sheet). More recently, Grachev and Severinghaus (2005) revisited the magnitude of the abrupt change in Greenland temperature at the Younger Dryas termination using the results of thermal diffusion experiments for $\delta^{15}\text{N}$ and $\delta^{40}\text{Ar}$ (Grachev and Severinghaus 2003a, b). In the absence of a dynamical firm model including heat diffusion, they assumed a heat transfer correction of 2°C and ended up with an amplitude of $10 \pm 4^\circ\text{C}$ for the warming at the end of the Younger Dryas. In parallel, Goujon et al. (2003) combined their model of firm densification and heat diffusion and the experimental determination of thermal fractionation coefficients for $\delta^{15}\text{N}$ and $\delta^{40}\text{Ar}$. They found that the onset of the Bølling-Allerød should be associated with an increase of 16°C and the end of the Younger Dryas with an increase of 12°C , in agreement with the Grachev and Severinghaus (2005) determination. Unfortunately, the determination of the associated uncertainties could not be accurately estimated.

40.3.2 Uncertainty on the Amplitude of the Rapid Warming: The Example of DO Event 12

A difficulty associated with the paleothermometry method using $\delta^{15}\text{N}$ and $\delta^{40}\text{Ar}$ of air trapped in ice cores is to correctly assess the uncertainty attached to the amplitude of the temperature change. We illustrate this problem on the determination of the amplitude of temperature change at the onset of DO event 12 from the study of Landais et al. (2004a).

Figure 40.9 shows the measurements of $\delta^{15}\text{N}$ and $\delta^{40}\text{Ar}$ performed over DO event 12 on the GRIP ice core. As expected both $\delta^{15}\text{N}$ and $\delta^{40}\text{Ar}$ increase at the onset of DO event 12 as a result of the surface temperature change. The amplitude of $\delta^{15}\text{N}$ change is larger than the corresponding $\delta^{40}\text{Ar}/4$ amplitude since most

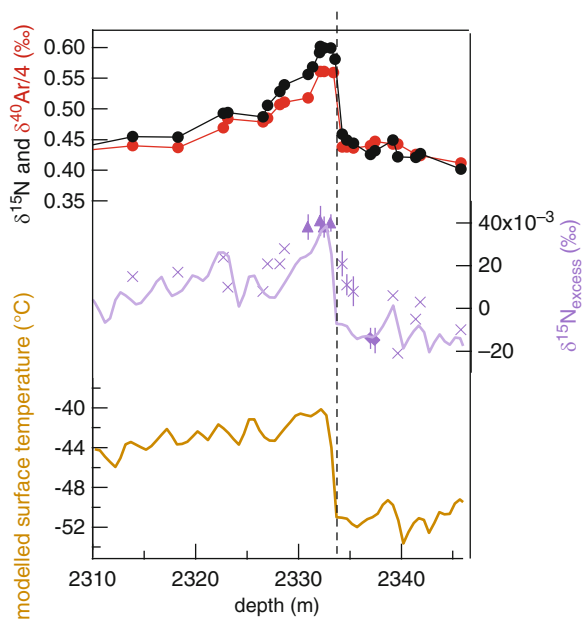


Fig. 40.9 Gas data inspired from air isotopic measurements performed for DO event 12 on the GRIP ice core (Landais et al. 2004a). From top to bottom: $\delta^{15}\text{N}$ (black) and $\delta^{40}\text{Ar}/4$ (red), calculated $\delta^{15}\text{N}_{\text{excess}}$ (purple triangle and crosses) and modeled $\delta^{15}\text{N}_{\text{excess}}$ (purple continuous line), modeled surface temperature (brown line) corresponding to the modeled $\delta^{15}\text{N}_{\text{excess}}$ above

of this increase is due to thermal fractionation. However, a significant part of the $\delta^{15}\text{N}$ and $\delta^{40}\text{Ar}$ increases can also be due to an increase in the gravitational signal. Indeed, at the onset of a DO event, the accumulation rate and temperature increases lead to a transient firm depth increase, hence an increase in the gravitational $\delta^{15}\text{N}$ and $\delta^{40}\text{Ar}$. To disentangle the gravitational and thermal signals, $\delta^{15}\text{N}_{\text{excess}}$ has been calculated as depicted in Sect. 40.2.4. It shows a 54 permeg increase at the DO event 12 onset (Fig. 40.9). The individual $\delta^{15}\text{N}_{\text{excess}}$ uncertainty is directly related to the $\delta^{15}\text{N}$ and $\delta^{40}\text{Ar}$ analytical errors (Fig. 40.9) and the resulting uncertainty on the $\delta^{15}\text{N}_{\text{excess}}$ variation has been calculated to be 8 permeg (1σ).

In order to infer the temperature change from the measured $\delta^{15}\text{N}_{\text{excess}}$ change, the firmification and heat diffusion model of Goujon et al. (2003) has been adapted to the GRIP site. It has first been tuned so that it can reproduce the whole temperature profile over 3,200 m deep in the ice sheet as measured in the GRIP borehole after ice core retrieval. Then, this model has been forced with different surface temperature scenarios so that it can reproduce the measured

$\delta^{15}\text{N}_{\text{excess}}$ variation. In a first attempt, it has been assumed that the $\delta^{18}\text{O}_{\text{ice}}$ record on the official GRIP chronology (ss09sea, Johnsen et al. 2001) gives the correct timing for the temperature increase at the onset of DO event 12, i.e. that the abrupt temperature change occurred in 75 years. In this case, the temperature increase that best fits the measured $\delta^{15}\text{N}_{\text{excess}}$ is of $+12^\circ\text{C}$.

However, because of large uncertainties on the accumulation rate changes at the onset of a DO event, an increase of surface temperature in 75 years can be challenged. This has important implications for interpretation of the $\delta^{15}\text{N}$ and $\delta^{40}\text{Ar}$ signals. Indeed, if the temperature change is more abrupt, the instantaneous temperature gradient in the firm will be larger (less time to allow heat diffusion) and thus the $\delta^{15}\text{N}_{\text{excess}}$ variation will be larger. To explore such an effect, different timings for the abrupt surface temperature increase have been tested as inputs of the Goujon et al. (2003) model. The results of the different tests are presented in Fig. 40.10: it clearly shows that for a shorter duration of the same 12°C temperature increase, the $\delta^{15}\text{N}_{\text{excess}}$ change will be larger.

Finally, Fig. 40.10 combines the uncertainty on the $\delta^{15}\text{N}_{\text{excess}}$ increase (± 8 permeg) as well as the uncertainty on the duration of the rapid temperature increase (30–150 years). It thus permits us to determine the range of possible amplitudes of the warming at the onset of DO event 12 as $9.5\text{--}14.5^\circ\text{C}$. This is significantly larger than the 7°C change that would result for a simple interpretation of the $\delta^{18}\text{O}_{\text{ice}}$ profile assuming

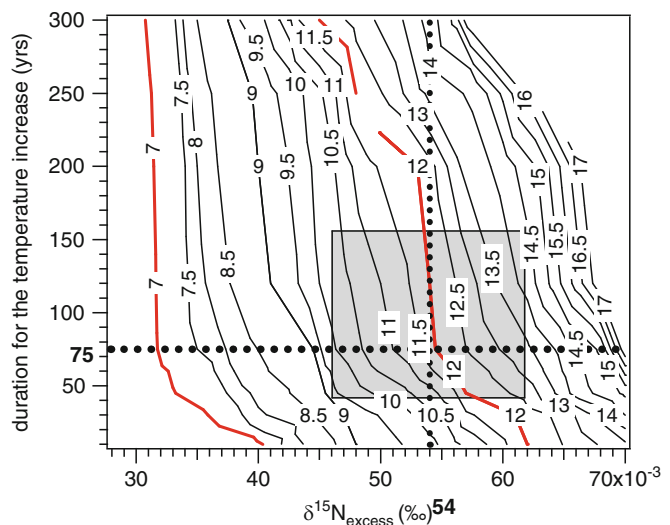
that past temperature can be reconstructed using the present-day relationship between surface temperature and isotopic composition of the surface snow.

40.3.3 Characterization of DO Events During MIS 3 and MIS 5

The characterization of DO events during the last glacial period has been widely studied. Many studies first focused on the MIS 3 period. Indeed, this time period is associated with two “pseudo-regular” DO events sequences called Bond cycles (Bond et al. 1997) (one long DO event – DO events 12 or 8 – followed by three small DO events – DO events 9, 10, 11 or DO 5, 6, 7; see Figs. 40.2 and 40.11). The pacing between two DO events is around 1,500 years during that period. This time period is often used by climate modelers as a target for simulating abrupt shifts of the climate system (i.e. Ganopolski and Rahmstorf 2001). However, more recently, studies have been also dedicated to older periods like MIS 4 (75–60 kyr BP) and MIS 5 (130–75 kyr BP). During these periods, no periodicity can be observed for the occurrence of DO events. Moreover, each DO event of these periods shows different patterns so that a simple description of the “typical” DO event is very difficult.

From this observation, it follows that a complete characterization of every DO event is important to draw. The paleothermometry method derived from

Fig. 40.10 Sensitivity of modelled $\delta^{15}\text{N}_{\text{excess}}$ (X axis) to different scenarios of surface temperature increase for DO event 12: different durations for the warming (Y axis) and amplitudes of the warming (“isotherms”) were imposed over a large range of values (duration: 10–300 years; temperature: $6.6\text{--}17.2^\circ\text{C}$). The value of the observed $\delta^{15}\text{N}_{\text{excess}}$ variation ($0.054 \pm 0.008\text{‰}$) is reported (solid line and shaded area) and we restrained the possible surface temperature change duration between 30 and 150 years. The best fit is obtained for a $12 \pm 2.5^\circ\text{C}$ temperature change. For reference, the indication of the 6.8°C temperature change as deduced from the spatial relationship between water isotopes and surface temperature is shown in bold red line



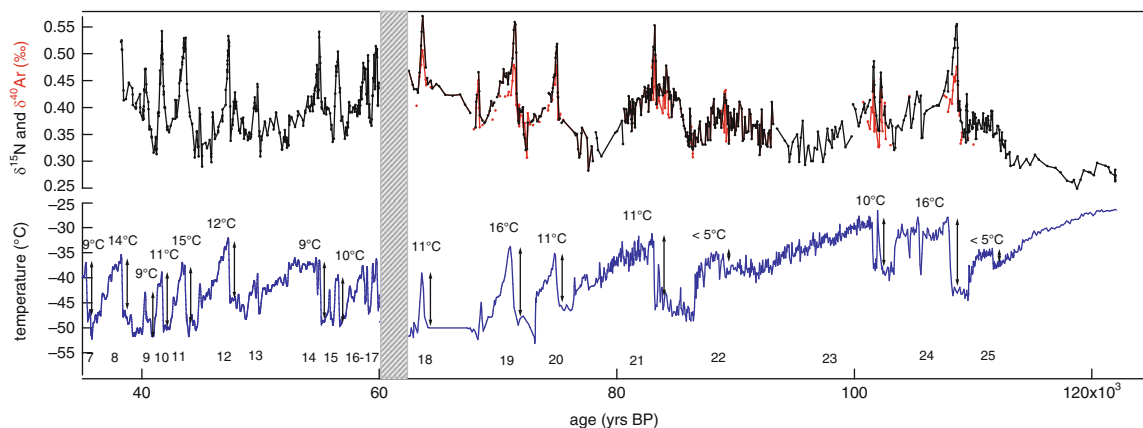


Fig. 40.11 Determination of the amplitudes of temperature increase for the different DO events of MIS 3, 4 and 5 on the NorthGRIP ice core (Huber et al. 2006a, b; Landais et al. 2004b, 2005; Capron et al. 2010b). *Top:* $\delta^{15}\text{N}$ (black) and $\delta^{40}\text{Ar}/4$ (red); *Bottom:* $\delta^{18}\text{O}$ of the ice (blue)

combined $\delta^{15}\text{N}$ and $\delta^{40}\text{Ar}$ of air in the ice core is an important component of such an effort. The first quantifications of the temperature increase at DO event onsets from Greenland ice cores were undertaken on the GRIP ice core for DO events 19 and 12 (Lang et al. 1999; Landais et al. 2004a). However, this ice core was retrieved in 1992 so little ice was available for these analyses. Moreover, the long duration of storage affects the isotopic composition of the trapped ice.

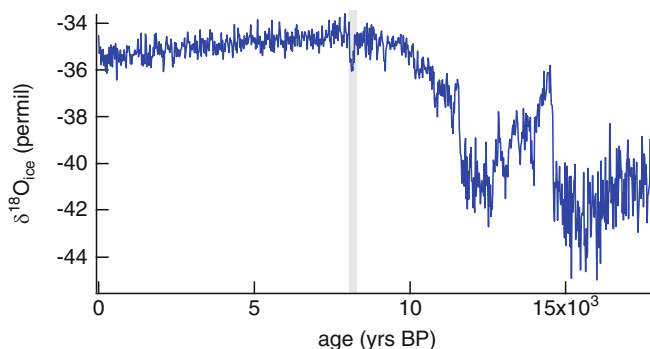
The drilling of the northern Greenlandic NorthGRIP ice core ended in 2003 and extended back to 123 kyr BP (NorthGRIP Community Members 2004). It offered new possibilities for $\delta^{15}\text{N}$ and $\delta^{40}\text{Ar}$ of air analyses on fresh ice. As a consequence, very high resolution (0.5–1 m) measurements of $\delta^{15}\text{N}$ could be performed on the series of DO events of the last glacial period. Additional $\delta^{40}\text{Ar}$ measurements were also performed at the onset of some DO events. The older DO events were analyzed at LSCE using a melt-refreeze manual technique for DO events 18, 19, 20 (Landais et al. 2004b), 23, 24, 25 (Landais et al. 2005; Capron et al. 2010b) and an automated wet extraction technique for DO events 21 and 22 (Capron et al. 2010a). The younger DO events (7–15) were analyzed at the Oeschger Center for Climate Science in Bern using the online method described in Sect. 40.2.2 (Huber et al. 2006a, b).

Figure 40.11 shows the whole $\delta^{15}\text{N}$ record over MIS 3 (60–30 kyr BP), 4 and 5 with additional $\delta^{40}\text{Ar}$ data over the older DO events. The amplitude of the surface temperature changes was inferred from the comparison of outputs of the firnification and heat

diffusion model of Goujon et al. (2003) to the $\delta^{15}\text{N}_{\text{excess}}$ data for the older DO events (MIS 4 and 5), as described in the previous section. For the younger DO events (MIS 3), the amplitude is inferred from the comparison of the firnification and heat diffusion model of Schwander et al. (1997) and the $\delta^{15}\text{N}$ record. The uncertainty on the amplitude of temperature changes was calculated as 2.5°C for the older DO events and 3°C for the younger ones. From these determinations, the lower part of Fig. 40.11 presents the reconstruction of surface temperature for the NorthGRIP site.

When comparing the amplitudes of the rapid warming at the onset of two DO events at GRIP and NorthGRIP, at 367 km distance, it appears that the temperature change was homogeneous at the regional scale: (1) the onset of DO event 12 is characterized by a warming of 12°C both at GRIP (Landais et al. 2004a) and at NorthGRIP (Huber et al. 2006a, b) and (2) the onset of DO event 19 is characterized by a warming of 16°C both at GRIP (Lang et al. 1999) and at NorthGRIP (Landais et al. 2004b). However, things are more complicated when looking on a larger scale. Sánchez Goñi et al. (2008) compared the amplitude of DO event onsets over MIS 3, 4 and 5 as inferred from the $\delta^{15}\text{N}$ -based temperature reconstruction in the NorthGRIP ice core, with pollen-based vegetation reconstructions at low latitudes in the Atlantic (37–45°N). Some coherency can be found at the beginning of MIS 5: as an example, the onset of DO event 24 is marked by both a large increase in NorthGRIP temperature (16°C) and a strong increase in

Fig. 40.12 Location of the 8.2 ka BP event in the Holocene (grey shaded area) on the $\delta^{18}\text{O}_{\text{ice}}$ profile of the NorthGRIP ice core



Mediterranean vegetation at 37°N (+45%). For more recent DO events, the amplitudes of high- and low-latitude changes are no longer correlated: while DO event 19 is marked by a strong 16°C warming, it is only showing a less than 5% change in Mediterranean vegetation at 37°N ; similarly, DO event 21 is associated with a strong +36% change in Mediterranean vegetation but only an $+11^\circ\text{C}$ temperature increase at NorthGRIP. The differing amplitudes for DO event onsets in Greenland and subtropical latitudes are not unexpected. Indeed, because of the large Laurentide and Fennoscandian ice-sheets during the last glacial period, Greenland was strongly isolated from lower latitude, so that Greenland climate was modulated by the waning and waxing of these ice-sheets in addition to the succession of DO events.

Finally, the $\delta^{15}\text{N}$ record over the succession of DO events has also been used to infer the phasing between surface temperature change in Greenland and variations in atmospheric methane concentration. This comparison shows that CH_4 and surface temperature were basically synchronous at the onset of every DO events within 100 years.

40.3.4 Studies on the Holocene

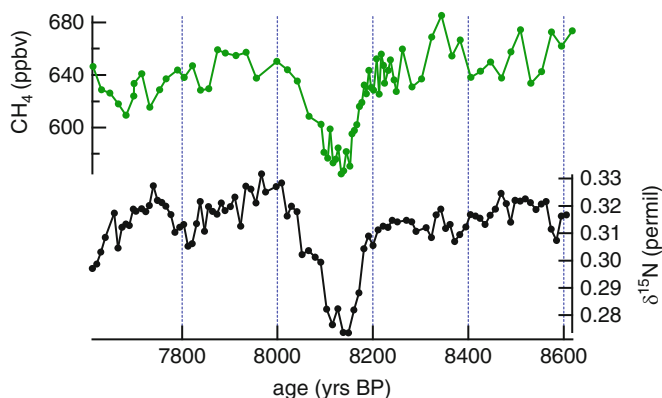
The main application of $\delta^{15}\text{N}$ and $\delta^{40}\text{Ar}$ measurements is to determine the amplitude of the warming at the onset of the DO events. However, efforts also have been recently devoted to use $\delta^{15}\text{N}$ and $\delta^{40}\text{Ar}$ to reconstruct smaller and smoother temperature changes. In particular, Kobashi et al. (2007, 2008a, b, 2010) devoted several studies to the reconstruction of temperature change during the Holocene warm

period extending over the last 11,600 years (i.e. since the end of the Younger Dryas).

We will focus only on the studies that were dedicated to the 8.2 ka event. This event is characterized by a drop of 1–2‰ in $\delta^{18}\text{O}_{\text{ice}}$ on a very short timescale (less than 200 years) in the Greenland ice core records about 8.2 kyr BP (Fig. 40.12). This is logically interpreted as a rapid cooling during a warm period, and this event is of high importance since it is the only prominent rapid event occurring during an interglacial period, in contrast to the numerous DO events occurring during a glacial period. Leuenberger et al. (1999) first measured $\delta^{15}\text{N}$ over this event on the GRIP ice core with a rather high resolution and could detect a small drop in $\delta^{15}\text{N}$ located deeper than the $\delta^{18}\text{O}_{\text{ice}}$ drop, hence confirming that a strong temperature change affected Greenland at that time. However, the accuracy on their $\delta^{15}\text{N}$ measurements was still rather poor ($1\sigma = 0.03\text{‰}$) and they did not have $\delta^{40}\text{Ar}$ measurements, so they gave a rather large range for the associated temperature change between 5.4 and 11.7°C .

Kobashi et al. (2007) recently revisited this estimate using a more accurate technique for $\delta^{15}\text{N}$ and $\delta^{40}\text{Ar}$ measurements in the air extracted from the ice (copper method, see Sect. 40.2). They obtained high resolution $\delta^{15}\text{N}$ and $\delta^{40}\text{Ar}$ measurements over the 8.2 ka event (Fig. 40.13 for $\delta^{15}\text{N}$), and using the firnification and heat diffusion model of Goujon et al. (2003) proposed that this event was associated with a $3.3 \pm 1.1^\circ\text{C}$ cooling on a decadal average. Moreover, due to the very high $\delta^{15}\text{N}$ resolution, they were able to show that the surface temperature pattern explaining the shape of the $\delta^{15}\text{N}$ record was in agreement with the $\delta^{18}\text{O}_{\text{ice}}$ record on a decadal average. This result is important: while the large $\delta^{18}\text{O}_{\text{ice}}$ variations in Greenland observed over the

Fig. 40.13 Record of CH₄ (top, green) and δ¹⁵N (bottom, black) on the GISP2 ice core for the 8.2 kyr BP event (Kobashi et al. 2007)



glacial-interglacial transition and at the onset of DO events are clearly mainly due to surface temperature change, the smaller changes can be questioned since modifications of the hydrological cycle (location of the source regions, seasonality of the precipitation) can also lead to significant $\delta^{18}\text{O}_{\text{ice}}$ variations. For the 8.2 ka BP event, Greenland $\delta^{18}\text{O}_{\text{ice}}$ variations thus mainly reflect local temperature.

In parallel to the temperature reconstruction, Kobashi et al. (2007) also presented high resolution methane data. The methane profile shows a drop by ~ 40 ppbv associated with the 8.2 ka BP event, thus suggesting that this event was not confined to Greenland but also affected lower latitudes. Doing a careful comparison of $\delta^{15}\text{N}$ and CH₄ data sets on the common depth scale (Fig. 40.13), Kobashi et al. (2007) suggested that the methane concentration lagged temperature very slightly (7.6 ± 4 years) over this event. Because the methane atmospheric lifetime is about 8 year, changes in methane source fluxes to the atmosphere are expected to lead methane concentration changes by about 8 year. Therefore, the observed lag is consistent with a synchronous change in methane source fluxes and Greenland temperature to within an uncertainty of about ± 4 year. This near synchronicity between changes in Greenland temperature and atmospheric CH₄ concentration could only be determined through the high resolution $\delta^{15}\text{N}$ data, hence highlighting the importance of this method.

40.4 Future Directions

Combined measurements of $\delta^{15}\text{N}$ and $\delta^{40}\text{Ar}$ in the air trapped in ice core will be performed in the future on

the different Greenland ice cores. This should provide the amplitude of temperature changes for the different DO events in the spatial dimension from the coast to the Greenland summit, and hence permit us to better understand the regional pattern of climatic response in Greenland to these abrupt events.

More challenging is the use of $\delta^{15}\text{N}$ and $\delta^{40}\text{Ar}$ in the trapped air of Antarctic ice cores. In Antarctica, no major thermal fractionation signal is expected because temperature changes are slow (less than 2°C in 1,000 years). Thus, $\delta^{15}\text{N}$ and $\delta^{40}\text{Ar}$ trapped in air bubbles should reflect the gravitational signal only and thus the depth of the firn diffusive column. Since no large convective zone has been observed in the firn of the different drilling sites over Antarctica today (Landais et al. 2006), it has been assumed as a first approximation that the convective zone is negligible and thus that $\delta^{15}\text{N}$ and $\delta^{40}\text{Ar}$ in air trapped in Antarctic ice core can be used to retrieve the evolution of close-off depth with time. If true, $\delta^{15}\text{N}$ and $\delta^{40}\text{Ar}$ or air in Antarctica would add important value to paleoclimatology since it would permit a constraint on the evolution of the age difference between gas and ice at the same depth level, and hence the phasing between change in atmospheric composition and change in local temperature.

Many $\delta^{15}\text{N}$ and $\delta^{40}\text{Ar}$ measurements in Antarctic ice cores have been performed during the last 20 years (e.g. Sowers et al. 1989; Caillon et al. 2003; Landais et al. 2006; Dreyfus et al. 2010). However, the interpretation of such records is still incomplete. This is mainly due to the inability of the different firn models to reproduce the observed evolution of $\delta^{15}\text{N}$ and $\delta^{40}\text{Ar}$. Indeed, while firn models are able to reproduce the Holocene $\delta^{15}\text{N}$ value in the tops of various ice cores, thus predicting the correct close-off depth for the large ranges of temperature and accumulation rate

measured in the different regions of Antarctica, then they fail to predict the $\delta^{15}\text{N}$ value observed for LGM trapped air. Whereas the model predicts a larger close-off depth during glacial periods because of lower temperature compared to interglacial periods, the measurements display an increase of $\delta^{15}\text{N}$ or $\delta^{40}\text{Ar}$ during terminations (i.e. the transitions from glacial to interglacial periods) (Fig. 40.14).

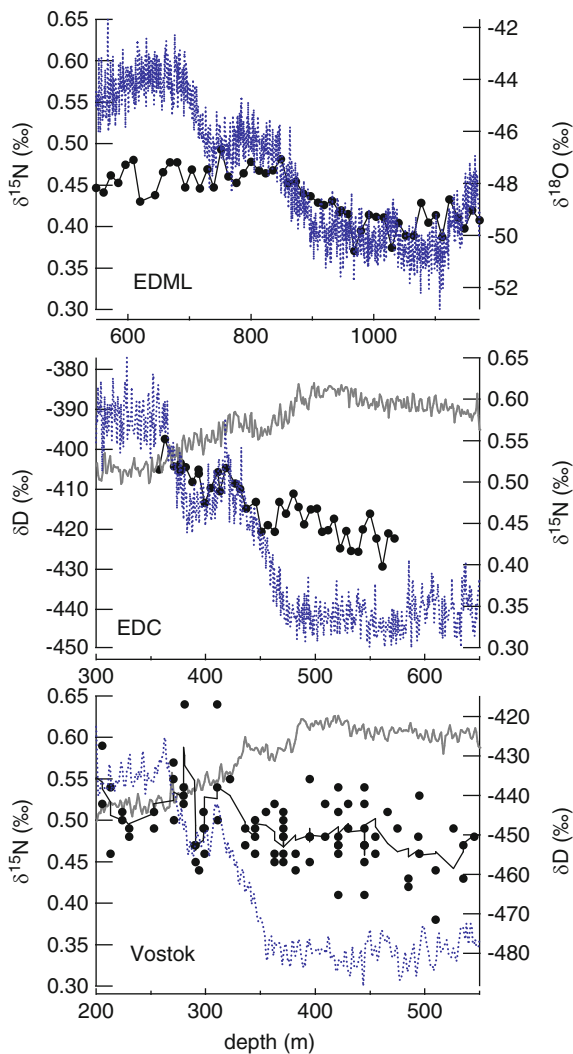
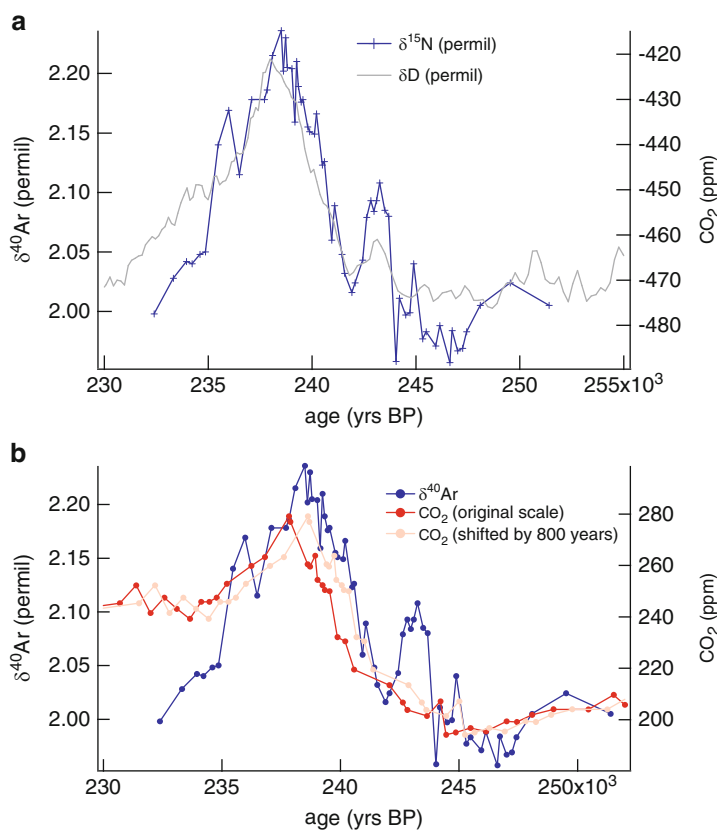


Fig. 40.14 Comparison of the evolution with depth of δD or $\delta^{18}\text{O}_{\text{ice}}$ (dashed blue line) for the local temperature evolution, measured $\delta^{15}\text{N}$ (black dots and lines) and modeled $\delta^{15}\text{N}$ assuming that no convective zone existed (grey continuous line) for three sites (from top to bottom: EPICA Dronning Maud Land; EPICA Dome C, Vostok)

Several hypotheses have been proposed to explain this discrepancy (Landais et al. 2006; Dreyfus et al. 2010):

- Firm models do not have the correct physics to predict the evolution of close-off depth with time. They are however able to reproduce the correct evolution of $\delta^{15}\text{N}$ in Greenland and to reproduce the large variety of close-off depths for the large range of temperature and accumulation rate observed at the surface of Greenland and Antarctica today.
- A unexpected thermal signal would explain why $\delta^{15}\text{N}$ and $\delta^{40}\text{Ar}$ do not reflect a pure gravitational signal and hence cannot be simply related to the close-off depth. However, combined measurements of $\delta^{15}\text{N}$ and $\delta^{40}\text{Ar}$ on some terminations do not support this hypothesis (e.g. Dreyfus et al. 2010).
- The accumulation rate and temperature reconstructed for the glacial period and inferred from water isotopes are not correct, hence the forcing of firm models is not correct. This hypothesis has indeed been confirmed for one Antarctic coastal site (Law Dome) but cannot explain the large discrepancy between models and measurements in inland sites (Landais et al. 2006).
- During glacial periods, a large convective zone develops in the firm so that the diffusive column depth is no longer equal to the firm close-off depth. This hypothesis is supported by the existence of 20 m deep convective zones observed today in a megadunes region with almost no accumulation rate (Severinghaus et al. 2010). This explanation would be satisfactory to explain the up to 40 m discrepancy (Caillon et al. 2003; Dreyfus et al. 2010) between diffusive column depth inferred from $\delta^{15}\text{N}$ or $\delta^{40}\text{Ar}$ and modeled firm close-off depth at cold drilling sites of East Antarctica (Dome C, Vostok, Dome F). This is also supported by the fact that glacial surface conditions are expected to be extreme (mean surface temperature below -60°C ; annual surface accumulation rate around $1\text{ cm water year}^{-1}$) with no present-day equivalent in central East Antarctica. However, this explanation is probably not sufficient enough to reconcile the large discrepancy between models and measurements recently observed in sites characterized by intermediate accumulation rate and temperature during the glacial period, for which present-day analogues do exist (Capron et al. 2008).

Fig. 40.15 (a) Evolution of δD (dashed grey) and $\delta^{40}Ar$ (blue) on the Vostok ice core for termination 3 (Caillon et al. 2003). (b) Evolution on the same gas age scale of CO_2 (red) and $\delta^{40}Ar$ (blue) on the Vostok ice core for termination 3 (Caillon et al. 2003). The pink line indicates the CO_2 curve shifted by 800 years, which gives the best agreement with the $\delta^{40}Ar$ evolution over the warming phase



Despite this disappointing observation, important results can still be inferred from $\delta^{15}N$ and $\delta^{40}Ar$ measured in the air of Antarctic ice cores. In particular, for East Antarctic ice cores with very low accumulation rate (Dome C, Vostok, Dome F), $\delta^{15}N$ and $\delta^{40}Ar$ histories seem to closely follow the water δD evolution (Dreyfus et al. 2010; Caillon et al. 2003; Kamawura 2000, Figs. 40.14 and 40.15a). Even if this evolution is opposite to the one predicted by firnification models, one can explain such a discrepancy by the development of a large convective zone when accumulation rate is very low (Albert et al. 2004; Dreyfus et al. 2010). As accumulation rate is probably related to the condensation temperature (which is linearly related to water δD in central East Antarctica), it is thus expected that $\delta^{15}N$ ($\delta^{40}Ar$) will record the evolution of local temperature in the air trapped in ice core through the evolution of the convective zone depth. As a consequence, the direct comparison of $\delta^{15}N$ ($\delta^{40}Ar$) and greenhouse gas concentration on the same gas timescale should permit one to directly infer the phasing between local temperature and CO_2 .

A first application of such a technique was performed by Caillon et al. (2003) on the Vostok ice core for the termination that occurred 240 kyr BP (Termination III). High resolution measurements of $\delta^{40}Ar$ were performed and compared to the CO_2 profile on the same gas age scale. The comparison clearly shows that the CO_2 increase occurred later than the $\delta^{40}Ar$ one by about 800 years (Fig. 40.15b). This led to the conclusion that during the deglaciation, Antarctic temperature or the closely-associated southern ocean temperature was driving the initial CO_2 increase which then subsequently contributed to the global warming as a positive feedback mechanism.

As a conclusion, $\delta^{15}N$ and $\delta^{40}Ar$ measurements in Antarctica are a very promising future direction to better constrain the phasing between atmospheric concentration and temperature changes. However, a lot of work should be done in order to properly understand the mechanism leading to an increase of $\delta^{15}N$ ($\delta^{40}Ar$) over the terminations despite the firnification models' prediction of a decrease of the close-off depth. The existence of a large convective zone in glacial periods

is a satisfactory explanation for $\delta^{15}\text{N}$ evolution at central East Antarctic sites with exceptionally low surface accumulation rate, but such an explanation is still unable to reconcile model and measurements at intermediate-accumulation sites where glacial conditions have present day analogs without observed convective zones.

40.5 Conclusion

The combination of $\delta^{15}\text{N}$ of N_2 and $\delta^{40}\text{Ar}$ measurements in the air trapped in Greenland ice cores is a powerful tool to quantitatively determine the amplitude of the abrupt temperature changes, as well as the phasing between greenhouse gas concentration and temperature over the abrupt events. Such a method has revealed that the DO events characterizing the last glacial period were associated with increases in temperature with an amplitude of up to $+16^\circ\text{C}$ in less than a century and that methane and temperature were increasing synchronously (within sampling resolution of ~ 50 years).

This paleothermometry method is now developed in several ice core laboratories and the aim is to systematically measure $\delta^{15}\text{N}$ and $\delta^{40}\text{Ar}$ on new Greenland ice cores. This especially will be done as a collaborative effort in the framework of the NEEM drilling project in Greenland.

Finally, such high precision measurements can also be applied to Antarctica. In this case, $\delta^{15}\text{N}$ and $\delta^{40}\text{Ar}$ give information on the phasing of changes between atmospheric concentration and local temperature. However, if the $\delta^{15}\text{N}$ and $\delta^{40}\text{Ar}$ evolution in Antarctic ice cores seems to be closely related to surface temperature and accumulation rate, the exact mechanism linking the surface characteristics to the isotopic composition of the air trapped in ice cores is still not fully understood and much work remains to be done in this direction, notably $\delta^{15}\text{N}$ and $\delta^{40}\text{Ar}$ measurements on shallow cores and firn at various locations in Antarctica.

References

- Albert M, Shuman C, Courville Z et al (2004) Extreme firn metamorphism: impacts of decades of vapor transport on near surface firn at a low-accumulation glazed site on the East Antarctic Plateau. *Ann Glaciol* 39:73–78
- Alley RB (1987) Firn densification by grain boundary sliding: a first model. *J Phys* 48(C1):249–256
- Arnaud L, Barnola JM, Duval P (2000) Physical modeling of the densification of snow/firn and ice in the upper part of polar ice sheets. In: Hondoh T (ed) *Physics of ice core records*. Hokkaido University Press, Sapporo, pp 285–305
- Arzt E (1982) The influence of an increasing particle coordination on the densification of spherical powders. *Acta Metall* 30(10):1883–1890
- Arzt E, Ashby MF, Easterling KE (1983) Practical applications of hotisostatic pressing diagrams: four case studies. *Metall Trans A* 14:211–221
- Barnola JM, Pimienta P, Raynaud D et al (1991) CO_2 climate relationship as deduced from the Vostok ice core: a re-examination based on new measurements and on a re-evaluation of the air dating. *Tellus* 43B:83–91
- Bender ML, Floch G, Chappellaz J, Suwa M, Barnola J-M, Blunier T, Dreyfus G, Jouzel J, Parrenin F (2006) Gas age-ice age differences and the chronology of the Vostok ice core, 0–100 ka. *J Geophys Res*, vol. 111, D21115, doi:10.1029/2005JD006488
- Bender ML, Sowers TA, Labeyrie LD (1994a) The Dole effect and its variation during the last 130,000 years as measured in the Vostok core. *Global Biogeochem Cy* 8(3):363–376
- Bender ML, Sowers TA, Dickson ML et al (1994b) Climate correlations between Greenland and Antarctica during the last 100,000 years. *Nature* 372:663–666
- Bender ML, Sowers TA, Barnola JM et al (1994c) Changes in the O_2/N_2 ratio of the atmosphere during recent decades reflected in the composition of air in the firn at Vostok station. *Antarct Geophys Res Lett* 21:189–192
- Bender ML, Barnett B, Dreyfus G et al (2008) The contemporary degassing rate of ^{40}Ar from the solid Earth. *PNAS* 105(24):8232–8237
- Bond G, Showers W, Cheseby M et al (1997) A pervasive millennial-scale cycle in North Atlantic holocene and glacial climate. *Science* 278:1257–1266
- Boyle EA (1997) Cool tropical temperatures shift the global $\delta^{18}\text{O}$ -T relationship: an explanation for the ice core $\delta^{18}\text{O}$ -borehole thermometry conflict. *Geophys Res Lett* 24:273–276
- Caillon N, Severinghaus JP, Chappellaz J et al (2001) Impact of refrigeration temperature history on isotopic composition of air bubbles trapped in polar ice samples. *Notes des Activités Instrumentales de l'IPSL* 14
- Caillon N, Severinghaus JP, Jouzel J et al (2003) Timing of CO_2 and temperature changes across termination – III. *Science* 299:1728–1731
- Capron E, Landais A, Masson-Delmotte V et al (2008) Isotopic composition of the air trapped in the EDML Ice Core ($\delta^{15}\text{N}$, $\delta^{18}\text{Oatm}$, $\delta^{40}\text{Ar}$, dO_2/N_2) over the last 140 kyr. *EGU2008-A-03049*, Vienna
- Capron E, Landais A, Lemieux-Dudon B et al (2010a) Synchronising EDML and NorthGRIP ice cores using $\delta^{18}\text{O}$ of atmospheric oxygen ($\delta^{18}\text{Oatm}$) and CH_4 measurements over MIS 5 (80–123 ka). *Quat Sci Rev* 29(1–2):235–246
- Capron E, Landais A, Chappellaz J et al (2010b) Millennial and sub-millennial scale climatic variations recorded in polar ice cores over the last glacial period. *Clim Past* 6:345–365
- Chapman S (1917) The kinetic theory of simple and composite monatomic gases: VISCOSITY thermal conduction, and

- diffusion. Reprinted in: Brush SG (1972) *Kinetic theory*, vol 3, p 102. Pergamon, New York
- Chapman S, Dootson FW (1917) A note on thermal diffusion. *Philos Mag* 33:248–253
- Craig H, Horibe Y, Sowers T (1988) Gravitational separation of gases and isotopes in polar ice caps. *Science* 242:1675–1678
- Dahl-Jensen D, Mosegaard K, Gundestrup GD et al (1998) Past temperatures directly from the Greenland ice sheet. *Science* 282:268–271
- Dansgaard W (1954) The O18-abundance in fresh water. *Geochim Cosmochim Acta* 6:241–260
- Dansgaard W (1964) Stable isotopes in precipitation. *Tellus* 16(4):436–468
- Dreyfus GB, Jouzel J, Bender ML et al (2010) Firn processes and $\delta^{15}\text{N}$: potential for a gas-phase climate proxy. *Quatern Sci Rev* 29(1–2):28–42
- Emerson S, Quay P, Stump C et al (1995) Chemical tracers of productivity and respiration in the subtropical Pacific Ocean. *J Geophys Res* 100:15873–15887
- Enskog D (1917) *Kinetic theory of processes in dilute gases*. Reprinted in: Brush SG (1972) *Kinetic theory*, vol 3. Pergamon, New York
- Fawcett PJ, Aguttsdottir AM, Alley RB et al (1997) The Younger Dryas termination and North Atlantic deepwater formation: insights from climate model simulations and Greenland ice core data. *Paleoceanography* 12(1):23–38
- Ganopolski A, Rahmstorf S (2001) Rapid changes of glacial climate simulated in a coupled climate model. *Nature* 409:153–158
- Grachev AM, Severinghaus JP (2003a) Determining the thermal diffusion factor for $^{40}\text{Ar}/^{36}\text{Ar}$ in air to aid paleoreconstruction of abrupt climate change. *J Phys Chem* 107:4636–4642
- Grachev AM, Severinghaus JP (2003b) Laboratory determination of thermal diffusion constants for $^{29}\text{N}_2/^{28}\text{N}_2$ in air at temperature from -60 to 0°C for reconstruction of magnitudes of abrupt climatic changes using the ice core fossil-air paleothermometer. *Geochim Cosmochim Acta* 67:345–360
- Grachev A, Severinghaus JP (2005) A revised $+10\pm 4$ C magnitude of the abrupt change in Greenland temperature at the Younger Dryas termination using published GISP2 gas isotope data and air thermal diffusion constants. *Quat Sci Rev* 24:513–519
- Goujon C, Barnola J-M, Ritz C (2003) Modeling the densification of firn including heat diffusion: application to close-off characteristics and gas isotopic fractionation for Antarctic and Greenland sites. *Journal of Geophysical Research* 108:4792
- Herron M, Langway C (1980) Firn densification: an empirical model. *J Glaciol* 25:373–385
- Huber C, Leuenberger M (2005) On-line systems for continuous water and gas isotope ratio measurements. *Isot Environ Health Stud* 41(3):189–205
- Huber C, Beyerle U, Leuenberger M et al (2006a) Evidence for molecular size dependent gas fractionation in firn air derived from noble gases, oxygen, and nitrogen measurements. *Earth Planet Sci Lett* 243:61–73
- Huber C, Leuenberger M, Spahni R et al (2006b) Isotope calibrated Greenland temperature record over marine isotope stage 3 and its relation to CH_4 . *Earth Planet Sci Lett* 243:504–519
- Ikeda-Fukazawa T, Fukumizu K, Kawamura K (2005) Effects of molecular diffusion on trapped gas composition in polar ice cores. *Earth Planet Sci Lett* 229(3–4):183–192
- Johnsen SJ, Dahl-Jensen D, Gundestrup N et al (2001) Oxygen isotope and palaeotemperature records from six Greenland ice-core stations: Camp Century, Dye 3, GRIP, GISP2, Renland and NorthGRIP. *J Quat Sci* 16(4):299–307
- Jouzel J, Vimeux F, Caillon C et al (2003) Temperature reconstruction from antarctic ice cores. *J Geophys Res* 108(6):1–10
- Kamawura K (2000) Variations of atmospheric components over the past 340000 years from Dome Fuji deep ice core, Antarctica. PhD Thesis, Tohoku
- Kobashi T, Severinghaus JP, Brook EJ et al (2007) Precise timing and characterization of abrupt climate change 8,200 years ago from air trapped in polar ice. *Quatern Sci Rev* 26:1212–1222
- Kobashi T, Severinghaus JP, Kawamura K (2008a) Argon and nitrogen isotopes of trapped air in the GISP2 ice core during the Holocene epoch (0–11,500 B.P.): methodology and implications for gas loss processes. *Geochim Cosmochim Acta* 72:4675–4686
- Kobashi T, Severinghaus JP, Barnola JM (2008b) $4\pm 1.5^\circ\text{C}$ abrupt warming 11,270 years ago identified from trapped air in Greenland ice. *Earth Planet Sci Lett* 268:397–407
- Kobashi T, Severinghaus JP, Barnola JM et al (2010) Persistent multi-decadal Greenland temperature fluctuation through the last millennium. *Clim Change* 100:733–756
- Krinner G, Genthon C, Jouzel J (1997) GCM analysis of local influences on ice core δ signals. *Geophys Res Lett* 24:2825–2828
- Landais A, Caillon N, Severinghaus JP et al (2003a) Analyses isotopiques à haute précision de l'air piégé dans les glaces polaires pour la quantification des variations rapides de température: méthode et limites. *Notes des Activités Instrumentales de l'IPSL* 39
- Landais A, Chappellaz J, Delmotte M et al (2003b) A tentative reconstruction of the last interglacial and glacial inception in Greenland based on new gas measurements in the Greenland Ice Core Project (GRIP) ice core. *J Geophys Res* 108. doi:10.1029/2002JD003147
- Landais A, Caillon N, Jouzel J et al (2004a) Quantification of rapid temperature change during DO event 12 and phasing with methane inferred from air isotopic measurements. *Earth Planet Sci Lett* 225:221–232
- Landais A, Barnola JM, Masson-Delmotte V et al (2004b) A continuous record of temperature evolution over a whole sequence of Dansgaard-Oeschger during Marine Isotopic Stage 4 (76 to 62 kyr BP). *Geophys Res Lett* 31. doi:10.1029/2004GL021193
- Landais A, Masson-Delmotte V, Jouzel J et al (2005) The glacial inception recorded in the NorthGRIP Greenland ice core: information from air isotopic measurements. *Clim Dyn*. doi:10.1007/ss00382-005-0063-y
- Landais A, Barnola JM, Kawamura K et al (2006) Firn-air d^{15}N in modern polar sites and glacial-interglacial ice: a model-data mismatch during glacial periods in Antarctica? *Quatern Sci Rev* 25(1–2):49–62
- Landais A, Dreyfus G, Capron E et al (2010) What drives the orbital and millennial variations of $\text{d}^{18}\text{O}_{\text{atm}}$? *Quatern Sci Rev* 29(1–2):235–246

- Lang C, Leuenberger M, Schwander J et al (1999) 16°C rapid temperature variation in central Greenland 70,000 years ago. *Science* 286:934–937
- Leuenberger M, Lang C, Schwander J (1999) Delta15N measurements as a calibration tool for the paleothermometer and gas-ice age differences: a case study for the 8200 B.P. event on GRIP ice. *J Geophys Res* 104:22163–22170
- Mani FP, Dennis P, Sturges WT et al (2008) An improved method for delta 15N measurements in ice cores. *Clim Past Discuss* 4:149–171
- Mariotti A (1983) Atmospheric nitrogen is a reliable standard for natural 15N abundance measurements. *Nature* 303: 685–687
- Mason EA, Munn RJ, Smith FJ (1966) Thermal diffusion in gases. *J Adv At Mol Phys* 2:33–91
- McManus JF, Francois R, Gherardi JM et al (2004) Collapse and rapid resumption of atlantic meridional circulation linked to deglacial climate changes. *Nature* 428:834–837
- NorthGRIP-Community-Members (2004) High resolution climate record of the northern hemisphere reaching into the last interglacial period. *Nature* 431:147–151
- Petrenko VV, Severinghaus JP, Brook EJ et al (2006) Gas records from the west Greenland ice margin covering the last glacial termination: a horizontal ice core. *Quatern Sci Rev* 25:865–875
- Picciotto E, deMaere X, Friedmann I (1960) Isotope composition and temperature of formation of Antarctic snows. *Nature* 187(4740):857–859
- Pimienta P (1987) Etude du comportement mécanique des glaces polycristallines aux faibles contraintes; application aux glaces de calottes polaires. Université Joseph Fourier, Grenoble
- Ritz C (1989) Interpretation of the temperature profile measured at Vostok, East Antarctica. *Ann Glaciol* 12:138–144
- Sánchez Goñi MF, Landais A, Fletcher WJ et al (2008) Contrasting impacts of Dansgaard–Oeschger events over a western European latitudinal transect modulated by orbital parameters. *Quatern Sci Rev* 27(11–12):1136–1151
- Schlesinger WH (1997) Biogeochemistry. *Geotimes* 42(2):44
- Schwander J (1989) The transformation of snow to ice and the occlusion of gases. In: Oeschger H, Langway CC Jr (eds) *Environmental record in glaciers and ice sheets*. Wiley, New York
- Schwander J, Sowers T, Barnola JM et al (1997) Age scale of the air in the summit ice: implication for glacial-interglacial temperature change. *J Geophys Res* 102:19483–19493
- Severinghaus JP, Battle M (2006) Fractionation of gases in polar ice during bubble close-off: new constraints from firm air Ne, Kr, and Xe observations. *Earth Planet Sci Lett* 244:474–500
- Severinghaus JP, Brook E (1999) Abrupt climate change at the end of the last glacial period inferred from trapped air in polar ice. *Science* 286:930–934
- Severinghaus J, Sowers T, Brook E et al (1998) Timing of abrupt climate change at the end of the Younger Dryas interval from thermally fractionated gases in polar ice. *Nature* 391:141–146
- Severinghaus JP, Grachev A, Battle M (2001) Thermal fractionation of air in polar firm by seasonal temperature gradients. *Geochem Geophys Geosyst* 2(7):1048
- Severinghaus JP, Grachev A, Luz B et al (2003) A method for precise measurement of argon 40/36 and krypton/argon ratios in trapped air in polar ice with application to past firm thickness and abrupt climate change in Greenland and at Siple Dome, Antarctica. *Geochim Cosmochim Acta* 67: 325–343
- Severinghaus JP, Beaudette RA, Headly M et al (2009) Oxygen-18 of O2 records the impact of abrupt climate change on the terrestrial biosphere. *Science* 324:1431–1434
- Severinghaus JP, Albert MR, Courville ZR et al (2010) Deep air convection in the firm at a zero-accumulation site, central Antarctica. *Earth Planet Sci Lett* 293:359–367
- Sigg A, Fuhrer K, Anklin M et al (1994) A continuous analysis technique for chemical trace species in polar ice cores. *Environ Sci Technol* 28:204–209
- Sowers TA, Bender ML, Raynaud D (1989) Elemental and isotopic composition of occluded O2 and N2 in polar ice. *J Geophys Res* 94:5137–5150
- Sowers TA, Bender ML, Raynaud D et al (1992) The d15N of N2 in air trapped in polar ice: a tracer of gas transport in the firm and a possible constraint on Ice age-Gas age differences. *J Geophys Res* 97:15683–15697
- Voelker A (2002) Global distribution of centennial-scale records for Marine Isotope Stage (MIS) 3: a database. *Quatern Sci Rev* 21:1185–1212

Author Index

A

- Aagaard, K., 367
Aagard, K., 372
Aarkrog, A., 370, 371, 377, 382
Abbene, I., 441, 445, 446, 449
Abdel-Aziz, Y.M., 212, 213
Abe, H., 680, 834
Abe, O., 621
Abe, Y., 165
Abelson, P.H., 3
Aber, J.D., 451
Abisheva, Z.S., 220
Abouchami, W., 128–136, 141, 143, 145–147, 149–151, 181, 186
Abraham, K., 95
Abrajano, A. Jr., 22
Abrajano, T.A., 662, 663, 665–667
Abramian, A., 583, 584
Achenbach, L.A., 178, 436
Aciego, S.M., 553, 560
Adam, C., 376
Adam, P., 651
Adams, J.A.S., 748
Adams, M.A., 808, 817, 819
Adelson, J.M., 219
Ader, M., 436, 437, 439–441
Ades, P.K., 808
Adkins, D., 370
Adkins, J.F., 789, 790, 794, 795, 821
Adrienne, H., 775
Aellen, K., 811, 813, 814, 817–819
Aeppli, C., 697
Aerts-Bijma, A.T., 835
Aeschbach-Hertig, W., 285, 289, 290, 296
Agarande, M., 398
Agemian, H., 159
Aggarwal, J.K., 89, 90, 93, 96, 186
Aggarwal, P.K., 329, 330, 350, 355–357
Aguilar, C., 179, 187, 198
Agustsdottir, A.M., 868
Ahmad, S., 537, 542
Ahmed, A.H., 212, 213
Aichholz, R., 716
Aiello, L.C., 733
Airieau, S., 832, 833, 835, 845
Aizenshtat, Z., 642
Akamatsu, F., 211
Akber, R., 495–497
Akoda, S., 682
Albarède, F., 5, 26, 27, 137, 147, 159, 160, 180, 186, 188, 197, 198
Albert, M.R., 878, 879
Albrech, P., 639, 640, 651, 661
Albrecht, A., 497
Albrecht, P., 639, 651, 661
Aldahan, A.A., 78
Alewell, C., 464, 465
Alexander, B., 469, 615, 622, 626, 627, 835, 839–845, 847, 848
Alexander, C.M.O., 219
Alexander, C.R., 63, 309, 319, 322
Alexander, R., 652
Alexandre, A., 93
Alexandri, N., 666
Alfimov, V., 78, 583, 585
Ali, A., 184
Alibo, D.S., 278
Allegre, C.J., 207–209, 212–215, 520, 529, 532, 533, 536, 537, 554–556
Alleman, L.Y., 90, 91, 93, 98, 311
Allemand, D., 113
Allen, D.E., 52, 53
Allen, H.E., 75
Allen, J., 639, 644, 645, 651, 653, 664–666
Allen, J.A., 666
Allen, J.D., 644
Allenby, R.J., 90, 92
Aller, R.C., 76
Alley, R.B., 460, 868, 871
Allison, G.B., 812
Allison, M.A., 314, 322
Allman, D.J., 615, 622, 626, 627, 847
Allsup, J., 643
Almeida, R.M.R., 345
al-Saleh, I.A., 770
Al-Salih, H., 71
Alt, J.C., 51–53, 257, 260, 263, 419, 420, 422–425, 432
Altabet, M.A., 451, 452, 458, 460, 613, 836, 837
Alt-Epping, P., 558
Alvarez, L.W., 206, 210
Alvarez, W., 206
Alvarez-Aviles, L., 229
Alvarez-Cohen, L., 665

- Amacher, M.C., 157
 Amand, S., 442
 Amarasiriwardena, D.D., 744, 746, 747
 Ambe, S., 63, 65, 80
 Amberger, A., 612, 836
 Ambrose, S.H., 723–725, 727, 729, 733, 753, 756
 Amelin, Y., 521
 Amelung, W., 666
 Ames, L.L., 552
 Amini, M., 106
 Amiotte Suchet, P., 529
 Amoroso, A., 846, 848
 Amouroux, D., 241, 242
 Amtmann, A., 109
 Amundsen, R., 441
 Amundson, R., 186, 704
 Amyot, M., 229
 An, Z.S., 216
 Anandam, S.K., 435, 442
 Anbar, A.D., 116, 117, 146, 160, 179, 180, 184, 186, 189, 190,
 196, 198, 199, 207, 211–217, 259, 599
 Anchukaitis, K.J., 808, 815, 816, 818, 820–823
 Anderasen, R., 521
 Anders, E., 205, 207, 248
 Andersen, A.B., 553–556, 558, 560, 565
 Andersen, K.K., 216
 Andersen, M.B., 8, 20
 Andersen, N., 653
 Andersen, T., 128
 Anderson, E.C., 6
 Anderson, J.G., 622, 623
 Anderson, K.A., 716
 Anderson, M.A., 46
 Anderson, M.G., 509
 Anderson, P., 531
 Anderson, R., 318
 Anderson, R.F., 69, 79
 Anderson, R.M., 442
 Anderson, S., 543
 Anderson, T.A., 435, 436, 442
 Anderson, W.T., 816, 818, 822
 Andersson, K.K., 460, 468
 Andersson, P.S., 17, 69–71, 99, 530, 554, 697
 Andersson, R., 695
 Andersson, S., 305
 Andert, J., 694
 Anding, C., 651
 Andre', L., 89–91, 93–99, 101
 Andreani, M., 837, 851
 Andren, A.W., 278
 Andreoletti, G., 366
 Andrews, A.H., 789, 793, 795, 796, 800
 Andrews, J., 306, 313
 Andrews, J.E., 356
 Andrews, J.N., 262, 285, 287, 289, 293, 294
 Andrusevich, V.E., 644, 645, 650, 703
 Andrushko, V.A., 753, 754
 Angeli, I., 147, 148
 Angert, A., 424, 425, 432, 467, 468
 Anghel, I., 47
 Angle, C.R., 766, 768, 770, 779
 Aninkevicius, V., 596
 Anklin, M., 864
 Antonelli, C., 509
 Antovic, N., 347
 Aono, T., 407
 Aoyama, M., 313, 321, 370, 371, 381, 382, 384, 386, 494, 589,
 590, 592–598, 600, 602, 605, 606
 Appleby, P.G., 320, 503
 Araguás-Araguás, L., 621, 808–810, 812
 Arai, S., 212, 213
 Aravena, R., 22, 639, 644, 653, 662, 665, 667, 683
 Archer, C., 179, 184, 198, 199, 252
 Ardelan, M.V., 354
 Ardisson, G., 71
 Ardouin, B., 273
 Ardouin, M.F., 271, 273
 Argento, D.C., 439, 443
 Arimoto, R., 596
 Arkins, M.D., 437, 440, 667
 Armbruster, T., 45
 Armbruster, W., 679, 681, 682, 686, 688, 689, 692, 696
 Armstrong, R.L., 523, 753, 757
 Armstrong, T.P., 477
 Armytage, R.M.G., 90, 93, 96
 Arnaud, L., 871
 Arndt, S.K., 808
 Arnold, G.L., 146, 180, 184, 186, 196
 Arnold, J.R., 71, 477, 576
 Arnold, R., 347, 352, 355, 356
 Arnold, T., 180, 190, 194
 Arora, M., 772
 Arpagaus, P., 64, 489, 491, 492
 Arrigo, K.R., 418
 Arriola, P.P., 645
 Arseneault, D., 820
 Arsouze, T., 531
 Arthur, M.A., 262, 520, 535
 Arzt, E., 871
 Asael, D., 164, 196
 Asahara, Y., 537
 Asaro, F., 206
 Asbill, S., 370
 Ashby, M.F., 871
 Asher, W.E., 348, 349, 351
 Asplund, L., 690
 Assinder, D.J., 372
 Assonov, S.S., 455
 Aston, F.W., 126
 Atekwana, E.A., 801, 802
 Athias, V., 531
 Atkinson, R., 622
 Atteck, C., 258, 260, 263, 265
 Aubert, D., 524–526
 Audry, S., 180, 194
 Augusti, A., 682, 696, 822
 Aureli, A., 350, 355–357
 Austin, A., 704
 Averill, B.A., 461
 Averyt, K., 378
 Axford, W.I., 477
 Aylett, B.J., 125, 126

- Ayliffe, L.K., 706, 724, 728
 Ayres, J., 768
 Ayub, J.J., 492
 Azahra, M., 489
- B**
- Babu, G., 537, 542
 Bacastow, R.B., 704
 Baccanale, C.L., 774
 Baccus, J., 728
 Bach, R.O., 42
 Bach, W., 43, 257, 260, 263
 Backer-Owe, K., 651
 Bacon, C.E., 667, 679–681, 686, 687, 689, 690
 Bacon, M.P., 271, 274–276, 309, 310, 351, 386
 Bada, J., 800
 Badea, S-L., 695, 696
 Badertscher, R., 704, 716
 Baedecker, M.J., 642
 Baeyens, B., 552
 Baeyens, W., 798
 Baggs, E.M., 452, 462, 463, 468
 Bahar, B., 704, 707, 709, 716
 Bahn, M., 819, 820
 Bailey, S.A., 834
 Bailey, T.R., 748
 Bailly, B.P., 332
 Bain, D.J., 163, 164
 Baker, A., 797
 Baker, E.T., 215
 Baker, J., 249–257, 260, 622, 750
 Baker, R.G.A., 132, 134, 140, 249–252, 255, 259, 261, 265, 266
 Balakrishna, K., 212, 216
 Balakrishnan, S., 528
 Balan, E., 98
 Balasse, M., 727, 729, 753, 756
 Balcaen, A., 707
 Balci, N., 179
 Bales, R.C., 851
 Balistrieri, L., 151
 Balistrieri, L.S., 146, 157, 199, 278, 494
 Ball, J.W., 156, 157, 162–164, 166, 178, 191
 Ball, L., 43, 306, 313, 553
 Ballentine, C.J., 285, 292, 293, 297, 298
 Ballschmitter, K., 679–681, 686, 687, 689, 690
 Ballschmitter, P., 667
 Balsiger, H., 184
 Balter, V., 197, 198
 Baltz, D.M., 239
 Balzer, R., 582
 Bandibas, J., 455
 Bangnall, K.W., 279
 Banks, D.A., 436
 Banner, J.L., 534, 537, 748
 Bao, H.M., 22, 435, 436, 438, 439, 441, 445, 832, 833, 835, 836, 839, 840, 845
 Bapp, J.B., 662
 Barbante, C., 206, 207, 211, 212, 217
 Barbieri, A., 441
 Barbour, M.M., 808, 813, 814, 816, 817, 819, 820, 822
 Barceloux, D.G., 280
 Barefoot, R.R., 207
 Barford, C.C., 458, 460
 Barg, E., 65, 66, 71, 73, 418
 Bariac, T., 813, 822
 Barkan, E., 467, 468, 470, 612, 619, 621, 624, 840
 Barkay, T., 230, 234, 237
 Barker, A.C., 816, 818
 Barker, J.L., 205, 207
 Barker, M., 250, 251, 266
 Barker, W.W., 751
 Barklem, P.S., 41
 Barkov, N.I., 847
 Barling, J., 146, 160, 180, 184, 186, 196, 198, 249
 Bar-Matthews, M., 164
 Barnard, R.L., 817
 Barnes, C.J., 812
 Barnes, J., 619, 620
 Barnes, P.W., 77
 Barnes, R.M., 770
 Barnes, W.L., 797
 Barnett, B., 467, 468, 864
 Barnett, C.L., 495
 Barnett, M.O., 88
 Barnola, J.M., 460, 856–869, 875–878
 Baroni, M., 835, 845, 846
 Barreiro, B., 743
 Barrett, J.H., 732
 Barrie, A., 680
 Barrie, L.A., 605
 Barroux, G., 530
 Barroux, J., 534, 537
 Barry, B., 62, 78, 582, 583, 585
 Barry, J.C., 743
 Barry, P.H., 300, 301
 Barshad, I., 494
 Bartecki, F., 612, 615, 620, 832
 Bartelloni, M., 418, 420, 422
 Barth, T., 644
 Bartlett, J., 553
 Barton, A., 446
 Barton, L., 470
 Barun, J.J., 525
 Bar-Yosef, O., 751
 Baschek, B., 287
 Basile-Doelsch, I., 90, 93, 100, 101
 Baskaran, M., 4, 7, 13, 14, 17, 18, 22, 28, 62–64, 67–72, 75, 76, 78, 79, 271, 272, 275, 296, 305–313, 315, 319–322, 330, 347, 365, 368, 370, 377, 381, 383, 384, 386, 387, 397, 399, 400, 402, 403, 408, 475, 485, 487–489, 491, 493, 495, 503, 509, 531, 554, 564, 565, 575, 576, 581–583, 592, 599, 605, 785, 786, 788, 797, 799, 801, 802
 Bassett, R.L., 162
 Bassin, C., 749
 Basu, A.R., 100, 160, 161, 164–166, 192, 544
 Batanova, V.G., 212, 213
 Bate, G.L., 207
 Bates, P.D., 509
 Bates, T.S., 843
 Batista, J.R., 436–439, 441, 442, 445
 Battle, M., 864, 867
 Bau, M., 247, 261, 264

- Baublys, K.A., 835
 Baudin, J.P., 376
 Bauer, D.W., 486
 Bauer, E., 592, 593
 Baum, B.R., 119
 Baun, A., 665
 Bavel, B., 680, 688, 689, 694
 Bawden-Smith, J., 768, 770, 772
 Baxter, A., 381, 382
 Baxter, D.C., 89–93, 96, 98, 99, 101
 Bayer, R., 377, 382
 Bayon, G., 45
 Bazan, J.M., 208
 Be, M-M., 366
 Beals, D., 383
 Beamish, R.J., 800
 Beard, B.L., 26, 27, 159–161, 164, 168, 170, 179, 184, 186, 187, 189, 190, 197, 198, 739
 Beary, E.S., 206
 Beasley, T.M., 280, 367, 372, 383
 Beattie, O., 724
 Beaudette, R.A., 867
 Beaudoin, G., 835
 Beaupre, S.R., 375
 Becagli, S., 833
 Beck, H.L., 79, 396
 Beck, K., 694
 Becker, B., 807, 808
 Becker, J.S., 400
 Becquerel, A.H., 3, 551
 Beckman, H., 820, 821
 Beene, J.R., 582
 Beer, J., 61, 62, 69, 70, 78, 261, 443, 582, 583, 585
 Beerling, D.J., 831
 Beg, M.A., 289
 Begg, C.B.M., 506
 Begun, G.M., 42
 Beitzel, V., 373
 Bekins, B., 441
 Bekki, S., 469, 615, 623, 625, 837, 847
 Belacy, N., 816
 Be' langer, N., 109, 117–119
 Belastock, R.A., 275, 785, 794, 795
 Bell, J., 313, 315
 Bell, N., 795
 Beloso, A.D. Jr., 436–439, 441, 445–447
 Belshaw, N.S., 43, 53, 54, 69, 110, 111, 113, 115, 116, 160, 198
 Beman, J., 418
 Ben Othmann, D., 264, 789
 Benassai, S., 833
 Bencs, L., 217, 221
 Bender, M.L., 142, 172, 832, 863–868, 877–879
 Bendig, P., 689, 692–694, 696
 Benedetti, M., 564
 Benes, P., 63, 65, 80, 344
 Beneteau, K.M., 665, 667, 683
 Benfer, R.A. Jr., 733
 Benitez-Nelson, C.R., 307, 309, 310, 313, 418, 419, 582
 Benkrid, M., 367
 Benmansour, M., 509
 Bennett, B.G., 395, 396
 Bennett, C.L., 476, 576
 Bennett, J.T., 273, 788, 792, 799, 800
 Bennett, R.P., 6
 Benning, L.G., 49
 Benninger, L.K., 35, 63, 64, 76, 271, 273, 322, 488, 489, 491–493
 Benoit, G., 278
 Benson, L.V., 752, 753, 756, 757
 Benson, S.M., 168
 Benson, W.K., 383, 384
 Bentley, R.A., 280, 281, 740–742, 744, 751–755, 760
 Benton, L.D., 51
 Bentov, S., 114
 Berelson, W.M., 180, 196, 256
 Berg, H.L., 90, 92
 Berg, M., 665, 685
 Berger, G.W., 321
 Berger, W.H., 798
 Berggren, A.M., 62
 Bergquist, B.A., 178, 181, 186, 189, 230–236, 238, 239, 241
 Bergsma, T.T., 453
 Berine, K.K., 371, 387
 Berkelhammer, M., 818, 820
 Berkman, P.A., 789
 Bermin, J., 146, 179, 198
 Bern, C.R., 95
 Berna, E.C., 160, 161, 164–166, 192
 Bernard, B.B., 653, 654, 657, 661
 Bernard, S., 460
 Bernasconi, S.M., 424, 425, 432, 441, 653, 818
 Bernat, M., 563
 Berne, A., 592
 Berner, R.A., 106, 107, 262, 354, 520
 Berner, U., 656, 657, 659
 Bernoux, M., 464
 Bernstein, R.E., 379
 Berry, J.A., 459, 460, 815, 816
 Bert, D., 813, 822
 Bertaux, J., 520, 537
 Bertin, C., 346
 Bertine, K.K., 408
 Bertsch, P.M., 46
 Berzina, A.N., 213
 Betancourt, J.L., 752, 757
 Bethke, C.M., 295
 Betram, C., 377
 Betson, N.R., 817
 Betson, T.R., 679, 681, 682, 686, 688, 689, 696, 822
 Beucher, C.P., 89, 90, 92, 93, 95–97
 Beukens, R.P., 6, 476, 576
 Beukes, N.J., 190
 Beuning, K., 822
 Beyerle, U., 287, 290, 867, 875
 Bhandari, B., 460, 468
 Bhandari, N., 579–582
 Bhargava, M., 446
 Bhat, S.G., 306, 308, 794–796
 Bhattacharya, B., 281

- Bhattacharya, S.K., 469, 612, 618, 619, 624–626, 808, 815, 821, 835, 847
 Bhattacharyya, A., 812, 814, 818, 820, 821, 823
 Bhushan, R., 272, 311, 347
 Bhutani, R., 528
 Bi, X., 665
 Bian, Y., 437
 Bianchi, T.S., 491
 Bible, K., 817
 Bice, A., 196
 Bickle, M.J., 87, 100, 106, 108, 111, 520, 524, 529, 532–534, 536, 543
 Biddanda, B.A., 71, 310, 311
 Bidoglio, G., 259
 Biegeleisen, J., 147
 Bienvenu, P., 366
 Bierman, P.R., 66, 73
 Bigeleisen, J., 4, 156, 259, 265, 454, 456, 652
 Bilezikian, J.P., 729
 Billen, T., 74, 80, 494
 Billings, G.K., 46, 748
 Billings, S.A., 820
 Billiou, D., 730
 Billon, G., 279
 Billy, I., 752, 756
 Bindeman, I.N., 835, 845
 Bindi, A.B., 167
 Bindumadhava, H., 814
 Birck, J.L., 207–209, 212–215, 749, 789
 Bird, D.K., 157, 163
 Bird, J.R., 476
 Biscaye, P.E., 19
 Biscayne, P., 346
 Bischoff, J., 383
 Bishop, M., 540
 Biswas, A., 229, 232, 238, 239
 Bjorkman, K.M., 418, 425
 Bjornstad, H.G., 494
 Bjorøy, M., 651, 652
 Blaber, S.J.M., 800
 Black, E., 509
 Blaes, E., 553, 561–563, 565
 Blake, G.A., 457
 Blake, R.E., 419, 420, 422–426, 432
 Blake, W.H., 63, 64, 73, 75, 81, 306, 504, 507, 508
 Blamart, D., 43, 55, 541
 Blanc, G., 180, 194
 Blanchard, P., 666
 Blanckenburg, F.V., 544
 Blanco, N., 441
 Blanton, J.O., 330, 332–336
 Blatt, M., 109
 Blavier, J.F., 435, 457, 469
 Blenkinsop, J., 87
 Blitz, J., 743, 751
 Blochberger, K., 837
 Bloom, N., 65, 82
 Bloom, Y., 667
 Blount, B.C., 436
 Blowes, D.W., 157, 165
 Blum, A.E., 95, 523, 524
 Blum, C.B., 776
 Blum, J., 22
 Blum, J.D., 6, 19, 45, 147, 178, 181, 184, 186, 189, 191, 229–241, 520, 522–526, 756
 Blum, J.S., 167
 Blunier, T., 460, 851
 Blusztajn, J., 43, 542
 Blusztjan, J., 90
 Bluth, G., 540
 Blythe, A., 537
 Boaventura, G., 530
 Bobbink, R., 611
 Bocca, B., 207
 Bocherens, H., 730
 Bock, M., 665
 Bockheim, J.G., 833, 836, 840
 Bodkin, J.L., 801
 Boehlert, G.W., 788, 792, 800
 Boehm, A.B., 354
 Boeing, H., 705
 Boering, K.A., 454, 456, 462
 Boerner, A., 820
 Bohlert, R., 66
 Böhlke, J.K., 22, 89, 126, 127, 435–446, 451, 452, 461, 468, 469, 613, 614, 622, 662, 667, 697, 833, 835–837, 846
 Böhm, F., 87, 105–108, 112–116, 121, 185, 198
 Bokuniewicz, H., 329, 330, 346, 347, 351, 355, 357
 Bol, R., 653
 Bolano, N., 644
 Bolin, B., 332, 333
 Bollhöfer, A., 770
 Boltwood, B.B., 3
 Boltz, D.F., 88
 Bonani, G., 78, 261, 377, 443, 582
 Bond, A., 111
 Bond, B.J., 811, 816, 819
 Bond, G., 874
 Bond, L.A., 383
 Bond, W.J., 552
 Bondioli, L., 724, 732
 Boner, M., 716
 Bong, Y.-S., 711
 Bonisch, G., 377
 Bonniwell, E.C., 63–66, 75, 495, 496
 Bonniwell, E.G., 492
 Bonte, P., 193
 Bontempo, L., 704
 Bony, S., 809
 Boon, J.P., 689, 696
 Bordat, P., 836
 Borden, R.C., 437, 440, 445
 Boreham, C.J., 643, 653, 665
 Borgeonkar, H.P., 812, 814, 818, 820, 821, 823
 Borge, G., 157
 Borgoul, P.V., 207, 210, 211, 220
 Borns, H.W., 798
 Borovec, Z., 344
 Borrok, D.M., 179, 180, 184, 199
 Bortz, S.E., 441, 446, 447
 Bosc, A., 813, 822
 Boschetti, T., 835

- Bösl, C., 705
 Bossew, P., 497
 Bostick, B.C., 63, 72, 212, 498
 Bothner, M.H., 206, 208, 218
 Bothwell, M.L., 418
 Böttcher, M.E., 180, 196
 Botte, J., 834
 Bottenheim, J.W., 469
 Bottinga, Y., 831
 Boudjenoun, R., 367
 Boudou, J.P., 652
 Boudreau, B.P., 354, 498
 Boulanger, Y., 820
 Boulegue, J., 564
 Boulyga, S.F., 398
 Bouman, C., 43, 44, 263
 Bourdon, B., 3, 17, 29, 90, 111, 131, 132, 187, 197, 198, 248, 249, 520, 551–566, 739
 Bourg, C.M., 346
 Bourgoïn, B.P., 798
 Bourles, D., 65, 81
 Bourquin, M., 347, 351, 352
 Boust, D., 279
 Boutelle, S., 272, 279, 308
 Boutron, C.F., 212
 Bouville, A., 79
 Bouwman, A.F., 451, 452
 Bowen, G.J., 621, 704, 705, 707, 710, 711, 714–716, 808, 810, 811, 823
 Bowen, V.T., 308, 368, 376, 379
 Bowling, D.R., 811, 819
 Bowling, J.W., 379
 Bowman, D.M.J.S., 726, 727
 Boyd, R., 212, 213
 Boyer, E.W., 614, 629
 Boyle, D., 253
 Boyle, E.A., 54, 134, 141–143, 147, 150, 151, 180, 181, 189, 194, 207, 210, 215, 418, 789, 795, 862
 Boyle, E.D., 794, 798
 Boynton, W.V., 441
 Bracke, G., 112
 Bradbury, M.H., 552
 Bradley, P.M., 664
 Bradley, R.S., 621
 Bradley, W.H., 638
 Bradshaw, J.S., 45
 Braekevelt, E., 679
 Brain, C.K., 733
 Brand, S.W., 645
 Brand, W.A., 453, 455, 652, 677–680, 816, 835, 836
 Brandes, E., 817
 Brandes, J.A., 172
 Brandon, A.D., 206, 249–252, 258, 264, 265
 Brandova, D., 66
 Brantley, S.L., 88, 179, 520, 523, 535, 553, 556, 558, 561–563, 565
 Brasher, J., 651
 Brass, G.W., 534, 536
 Brassell, S.C., 648–650
 Brasser, T., 558
 Brasseur, G.P., 833
 Braterman, P.S., 179, 189
 Brauer, K., 836
 Braun, J.J., 97, 557
 Bray, E.E., 638
 Breda, N., 819
 Breitenbach, S.F.M., 821
 Brekke, T., 651
 Breland, J.A., 348
 Bremner, J.M., 835, 836
 Bremond, L., 96, 97
 Brendel, K., 735
 Brendel, O., 820
 Brenner, M., 757, 758
 Brenner, S., 418
 Brenninkenmeijer, C.A.M., 453–455, 462, 467–469
 Brenninkmeijer, C.A.M., 853
 Brenot, A., 45
 Breuer, J., 92, 93, 95, 96
 Brewer, P.G., 151, 275, 380, 386
 Brewer, R.L., 346
 Briat, J.F., 197
 Brice, K., 666
 Bricker, O.P., 377
 Bricout, J., 680
 Bridou, R., 230, 234, 237
 Briffa, K.R., 816
 Brigham, M.E., 507
 Brill, M., 752, 757
 Briner, J.P., 479, 483
 Brinkman, U.A.T., 688
 Broadley, M., 109
 Brockwell, T., 681
 Broecker, H.C., 349
 Broecker, W.S., 69, 79, 106, 306, 309, 346–354, 357, 368, 373–375, 377, 381, 430, 440, 575, 643, 793, 798, 813
 Broholm, P., 644
 Brook, E.J., 832, 864, 865, 867, 872, 876, 877
 Brooker, R., 43
 Brooks, C., 749
 Brooks, J.M., 370, 653, 654, 657, 661
 Brooks, J.R., 817
 Brooks, P.W., 638
 Brooks, S., 229
 Broome, J.C., 452, 463, 464, 470
 Brothers, L.A., 583, 584, 644, 645, 650, 839
 Brown, A., 656, 657
 Brown, E.T., 63, 66, 69
 Brown, F.S., 642
 Brown, G.E. Jr., 168, 552
 Brown, G.M., 436–439, 441, 442, 445
 Brown, K., 299
 Brown, K.M., 287, 299, 300
 Brown, L., 62, 63, 65, 67, 73, 75, 76, 78
 Brown, R.B., 503, 504
 Brown, S.E., 800
 Brown, S.S., 622
 Browne, E., 366, 367
 Brownlee, D.E., 212
 Bruach, J.M., 272, 311
 Bruce, B., 552
 Bruce, C.L., 662, 667

- Bruch, B.A., 836
 Brüchert, V., 156
 Brudecki, K., 493
 Brugmann, G., 212, 213
 Brugnoli, E., 467, 468
 Bruland, K.W., 134, 141, 142, 247, 273, 366–367
 Brune, W.H., 625
 Brunet, F., 43, 53, 55
 Brungard, K.L., 665
 Brunk, J.L., 384
 Brunner, B., 424, 425
 Bruno, J., 552
 Brunskill, G.J., 45, 212, 695
 Bruns, P.C., 695
 Bryce, A., 775
 Brzezinski, M.A., 89–93, 95–98, 101
 Buchachenko, A.L., 147, 234
 Buchanan, L.H., 770
 Buchanan, R.F., 128
 Büchl, A., 212, 213
 Buchmann, N., 817
 Buchwald, C., 460, 461, 463, 464
 Buck, R., 470
 Buda, A.R., 614
 Budd, P., 743, 749, 760
 Budzinski, H., 653, 665
 Buesseler, K.O., 306–310, 313, 323, 324, 356, 367, 373, 377, 379, 380, 383, 384, 386, 407, 408, 418, 419, 582, 785, 794, 795
 Bugmann, H., 808, 820
 Bugna, G.C., 346, 351, 354–356
 Buhay, W., 808
 Buhl, D., 107, 115
 Buhler, R., 377
 Buikstra, J.E., 739, 741, 744, 745, 749, 751, 753, 759, 760
 Buisson, A., 273
 Bukurov, T.N., 220
 Bullen, T.D., 22, 109, 110, 116–118, 120, 157, 160–166, 168–172, 178, 179, 184–187, 189, 191, 192, 194–196, 198, 199, 332, 523, 524
 Bunbury, J., 529, 532
 Bundt, M., 497
 Bunte, K., 506
 Büntgen, U., 808, 820
 Bunton, C.A., 622
 Bunzl, K., 497
 Bureau, R.G., 156
 Burbank, D.W., 537, 540
 Bureau, S., 553–556, 558, 560, 565
 Burg, A., 160–162
 Burger, J., 801
 Burgess, B.K., 198
 Burgess, R., 285, 292, 293, 297, 298
 Burgmann, H., 195
 Burgoon, D.A., 766
 Burgoyne, T.W., 644, 652
 Burk, R.L., 808
 Burke, T., 219
 Burke, W., 522
 Burkhart, J.F., 851
 Burles, S., 50
 Burnard, P., 285, 293, 297
 Burnett, W.C., 272, 274, 278–280, 308, 329–331, 337, 346, 347, 350–352, 354–358
 Burns, D.A., 614
 Burns, K.A., 272, 280, 308
 Burns, S.J., 290
 Burrus, D., 64, 67
 Burton, J., 741, 743, 751
 Burton, J.H., 741, 744, 751–755, 760
 Burton, K.W., 22, 42, 44–47, 49–51, 55, 87, 98, 99, 101, 206, 212, 215, 216, 252, 261–263
 Busacca, A.J., 503
 Buseck, P.R., 583
 Buss, H., 179
 Butler, B.J., 653, 667
 Buttefield, D.A., 215–217
 Butterbach-Bahl, K., 451, 452, 470
 Butts, J.L., 347
 Butzenlechner, M., 683
 Buyukay, M., 379
 Buzon, M.R., 741, 746, 751–755, 760
 Buzzelli, J., 167
 Byrne, R.H., 213, 348, 366, 367, 379
- C**
- Cabana, G., 705
 Cabello, P., 469
 Cabianca, T., 365
 Cable, J.E., 346, 351, 354–356
 Cable, P.H., 351
 Caboi, R., 794
 Cachier, H., 835, 839
 Cade-Menun, B.J., 420, 422, 424, 425, 427, 430
 Caffee, M.R., 436, 438, 439, 443, 445
 Caffee, M.W., 61
 Caffrey, P.F., 207, 220, 221
 Cai, S., 652, 653
 Cailliet, S., 64, 489, 491, 492
 Cailliet, G.M., 789, 793, 796, 800
 Caillon, C., 862
 Caillon, N., 864, 865, 867, 871, 873, 875, 877–879
 Caldeira, K., 107, 108
 Calhoun, J.A., 843
 Callender, E., 491
 Callot, H.J., 639, 640, 651, 661
 Calvin, M., 638
 Camacho-Garcia, A., 489
 Camargo, P., 458, 462
 Cambier, P., 193
 Cambray, R.S., 504, 590, 592
 Cameron, M.A., 768
 Cameron, V., 179, 184, 199
 Camin, F., 704
 Campana, S., 792, 800
 Campana, S.E., 786, 792
 Campbell, C., 772
 Campbell, D.H., 262, 614
 Campbell, J.A., 322
 Campbell, M.J., 770
 Campin, J.M., 332, 333
 Canard, E., 194, 195

- Cane, M.A., 823
 Canfield, D.E., 156, 158, 163, 164, 169, 170, 265
 Cannon, A., 734
 Canters, G.W., 198
 Canuel, E.A., 63, 322
 Cao, H., 506, 507
 Capmas, F., 207–209
 Capo, R.C., 740
 Capone, D.G., 611
 Capron, E., 866, 875, 878
 Caraco, N.F., 418
 Cardinal, D., 43, 89–91, 93–99, 101
 Carelli, G., 207
 Carignan, J., 42–46, 51, 138, 160–162, 170, 180, 181, 188, 189, 194, 232, 233, 235, 238, 239, 253
 Carlson, L., 379
 Carlson, P.R., 662
 Carlson, R.W., 752, 756
 Carmichael, C.A., 640
 Caron, F., 374
 Carpenter, R.C., 399, 504
 Carpenter, S.R., 115, 418
 Carpentier, C.L., 706
 Carrick, H.J., 460
 Carrizo, D., 697
 Carson, B.L., 221
 Carter, A.H.C., 816, 818
 Carter, M.W., 395
 Cartwright, J., 63, 79, 491
 Carvalho, F.P., 272–274, 280, 281
 Carvalho, P.F., 307
 Casabianca, H., 716
 Casanova, F., 552
 Casciotti, K.L., 460, 461, 463, 464, 468, 469, 613, 614, 837
 Casselman, J.M., 705
 Cassette, P., 366
 Casso, S.A., 310, 376
 Castagnoli, G., 477
 Castillo, A., 491, 509
 Castresana, J., 462, 463
 Castro, M.C., 14, 19, 285, 290, 291, 294
 Catling, D.C., 435, 441, 442
 Causse, C., 558
 Cavagna, A.J., 95
 Cavazzini, G., 752, 757
 Cavigelli, M.A., 464
 Cecil, L.D., 443
 Celso, V., 182, 184
 Cenko-Tok, B., 109, 117, 118
 Cerling, T.E., 22, 296, 297, 621, 704, 706, 707, 724, 727, 728, 743
 Cernusak, L.A., 817
 Cerrato, R.M., 799, 800
 Cerri, C., 458, 462
 Cervantes, G., 552
 Chabala, J.M., 834
 Chabaux, F., 17, 46–48, 106–109, 117, 118, 520, 543, 551, 553, 556, 558, 561–565, 789
 Chacko, K.C., 820
 Chacko, T., 155
 Chadwick, O.A., 47, 90, 95–98, 101, 109, 117, 118, 740
 Chai, Z.F., 207, 211, 216
 Chakraborty, S., 820, 822, 846
 Chamberlain, C.P., 19, 532, 756
 Chamizo, E., 592
 Champ, M.A., 370
 Chan, L.-H., 43–48, 50–54, 252, 263, 333, 344, 351, 352
 Chang, B.U., 370, 371
 Chang, C.C.Y., 613, 614, 837
 Chang, V., 112, 113
 Chang, Z., 179
 Chanton, J.P., 346, 351, 354–357
 Chapelle, F.H., 664
 Chapman, H., 533
 Chapman, S., 868
 Chappell, A., 506
 Chappell, B.W., 43, 44
 Chappellaz, J.A., 460, 833, 853, 867, 875
 Chapis-Lardy, L., 464
 Charette, M.A., 351–353, 356
 Charlson, D.V., 198
 Charlson, R.J., 843
 Charmasson, S., 367, 373
 Chartrand, M.M.G., 664, 681, 697
 Chasteen, T.G., 280, 281
 Chateigner, D., 552
 Chatterjee, A., 281
 Chaudhary-Webb, M., 770
 Chaudhuri, S., 440, 441
 Chaussidon, M., 43
 Chavez, F.P., 418, 420, 421, 423–425, 430
 Chaykovskaya, E.L., 377
 Cheam, V., 159, 252, 253
 Chen, C.T.A., 205–207, 209, 212–216, 218, 220, 331, 332, 552
 Chen, G., 497
 Chen, H.W., 53
 Chen, J., 475, 476, 479, 481–483
 Chen, J.B., 186, 192, 193
 Chen, J.H., 4, 6, 248, 551, 553
 Chen, Q., 399
 Chen, X., 52
 Chen, Z.Y., 94, 95, 645, 652, 653
 Cheng, H.H., 35, 795, 836
 Cheng, Q., 442
 Chenhall, B.E., 770
 Cherdyntsev, V.V., 4
 Cherrier, J., 272, 308
 Cherry, J.A., 22, 667, 683
 Cherry, M.I., 280
 Cherry, R.D., 272, 274, 280, 281, 308, 311
 Cherubini, P., 820
 Cheseby, M., 874
 Chesley, J., 523
 Chesney, E.J., 237, 239–241
 Chesson, L.A., 22, 621, 704, 706, 707, 710, 711, 713–716
 Chesters, G., 486
 Cheung, Y.Y., 210
 Chiappini, R., 309, 371, 407
 Chiaradia, M., 770
 Chiarizia, R., 749
 Chicarelli, M.I., 648–650
 Chikaraishi, Y., 725, 727, 735

- Child-ers, D.L., 816
 Childers, S.E., 168, 169, 173
 Childress, J.J., 799
 Childs, C.W., 179, 198
 Chillrud, S.N., 769
 Chin, H.B., 239
 Chipman, D.W., 349, 350
 Chisholm, B.S., 721, 731
 Chiu, T.-C., 35
 Chizhikov, D.M., 125, 126, 137
 Chmura, W.M., 837
 Choi, D.W., 785, 786, 797
 Choi, S.W., 370, 371
 Choppin, G.R., 394
 Choquette, C.E., 63
 Chornesky, E.A., 452, 463, 464, 470
 Chotte, J.L., 464
 Chou, C.C., 832
 Chow, T.J., 371, 387
 Choy, K., 725, 735
 Chrastný, V., 769
 Christensen, G.C., 379
 Christensen, J.N., 552, 555, 560, 750, 834
 Christensen, S., 837
 Christensen, T.H., 665
 Christl, M., 582
 Christophersen, M., 644
 Chruch, M., 48
 Chu, K.-H., 665
 Chu, N.-C., 45, 110, 116
 Chudy, M., 489
 Chung, C.S., 330, 370, 371, 377, 381, 384
 Chung, H.M., 645, 650, 655
 Chung, Y.C., 275, 277, 332, 338, 351, 352, 418
 Church, T., 17
 Church, T.M., 14, 17, 272–276, 278, 281, 307, 311
 Cichočka, D., 692
 Cidu, R., 794
 Ciffroy, P., 491
 Cifuentes, L.A., 665, 666
 Cizdziel, J.V., 399, 409
 Claeys, E., 707
 Clair, M.W., 435, 442
 Clark, B.C., 441
 Clark, D., 537
 Clark, I.D., 189, 810
 Clark, J.F., 287
 Clark, S.K., 157, 160–162, 168–173
 Clarke, W.B., 289, 290, 296
 Claude, C., 347, 348
 Clauer, N., 543, 558, 561, 562, 564
 Clausen, J.L., 22, 663, 665
 Clauson, A., 706
 Claypool, G.E., 650
 Clayton, C.J., 645–648, 655–658
 Clayton, D.D., 206
 Clayton, R.N., 6, 455, 611, 612
 Cleemput, O.V., 455
 Clement, J.G., 727, 729
 Clement, M.L., 765
 Clements, W.E., 346
 Clementz, M., 109, 110, 116
 Cliff, S.S., 441, 455, 456, 467, 468, 612–615, 837, 847
 Clift, P., 520, 540, 542
 Clifton, R.J., 76
 Clode, P., 113
 Cloern, J.E., 333
 Cloquet, C., 128–130, 135, 138, 149, 180, 181, 188, 189, 194, 253
 Clover, H.E., 6
 Clover, M.R., 476, 576
 Clyde, W.C., 418
 Coale, K.H., 90, 256, 789, 793, 800
 Coates, J.D., 178, 436, 440, 441
 Coath, C.D., 835
 Coburn, R.P., 800
 Coccioni, R., 206
 Cochran, J.K., 3, 5, 35, 68, 70, 72, 77, 78, 272, 275, 305, 308–311, 313, 315–318, 351, 383, 387, 576, 583, 591, 786, 799, 800
 Cockburn, H.A.P., 16
 Cocquyt, C., 90, 98
 Coffey, P.E., 62
 Coffin, R.B., 665, 666
 Coggon, R.M., 258, 260, 263, 265
 Cohen, A., 114
 Cohen, A.L., 378, 796
 Cohen, A.S., 6, 207, 208, 789
 Cohen, N., 372
 Cole, D.R., 155
 Cole, J.J., 351
 Cole-Dai, J.H., 835, 845, 846
 Coleman, A., 421, 424
 Coleman, C.H., 62, 63, 79, 308–310, 320, 322, 489, 492, 495, 576, 599
 Coleman, M.L., 436, 437, 439–441, 667, 834
 Coles, B.J., 180, 190, 194, 197, 198
 Colin, C., 520, 537, 541
 Colin, F., 93
 Colin, J.L., 193
 Collet, G., 728
 Collet, R., 41
 Colley, S., 318
 Collier, R., 142
 Collins, A.L., 492, 493, 507
 Collister, J.W., 667, 679–681, 686, 687, 689, 690
 Colman, A.S., 423, 424
 Colodner, D.C., 207, 210, 215
 Colombari, G., 704
 Colten, V.A., 50
 Coluzza, J., 383, 384
 Comans, R.N.J., 46
 Comar, C.L., 740
 Comstock, J.P., 813
 Comte, J., 366
 Condomines, M., 273, 797, 798
 Conen, F., 464, 465
 Coney, L., 206
 Conlee, C.A., 751, 753, 755
 Conley, D.J., 92, 96, 97, 101
 Conley, M., 596
 Connan, J., 651

- Connan, O., 279
 Connell, D.W., 695, 765
 Connelly, D.P., 53
 Conrad, M.E., 426, 565, 665
 Cook, D.L., 206
 Cook, E.R., 808, 813
 Cook, G.T., 311
 Cook, P.F., 639
 Cooper, J.A., 581, 582
 Cooper, K., 43, 765
 Cooper, L.W., 66, 72, 77, 367, 372, 383, 713
 Copeland, S.R., 746, 757, 760
 Coplen, T.B., 42, 89, 332, 436, 438, 455, 613, 622, 835, 837
 Corapcioglu, O., 380
 Corbett, D.R., 76, 351
 Corbett, R., 305, 317, 318
 Corbin, A., 583, 584
 Cornelis, J.T., 94, 97
 Cornett, R.J., 497
 Cornu, S., 73
 Cornwell, W.K., 817
 Corr, L.T., 724, 729, 733
 Correl, D.L., 418
 Cortecchi, G., 418, 420, 422, 839
 Cortes, A., 704
 Cortes, J., 651
 Cosby, B.J., 451
 Cosme, E., 843
 Cotte, J.F., 716
 Cotton, F.A., 125, 126
 Coughlin, J.U., 552
 Coughtrey, P.J., 495
 Counter, S.A., 770
 Courville, Z.R., 878, 879
 Cowan, A.M., 445
 Cowan, R.M., 664
 Coward, J.B., 564
 Cowling, E.B., 451
 Cox, L., 179, 187, 198
 Cox, S., 442
 Craig, D.R., 666
 Craig, H., 289, 296, 299, 332, 351, 352, 455, 460, 468, 642, 644, 705, 706, 716, 786, 787, 813, 832, 868
 Creaser, R.A., 6, 208, 211, 741, 746, 752, 754, 760
 Crecelius, E.A., 64, 65, 82, 605
 Cremers, A.E., 495
 Crenshaw, C.L., 452, 462
 Cresswell, R.G., 292, 293, 295, 296
 Crick, J., 777
 Crisp, P.T., 638
 Criss, R.E., 136, 137, 155, 156, 440
 Croke, J., 75
 Crompton, R., 53, 54
 Cromwell, J., 346, 349
 Crossey, L.J., 290
 Crosswhite, H.M., 623
 Croudace, I.W., 370–372, 399, 599
 Crowley, D.E., 197
 Crozaz, G., 786
 Crump, K.S., 436
 Cuif, J-P., 113
 Cuishan, Z., 651
 Cullen, D., 256
 Cullen, J.T., 142
 Cundy, A.B., 372
 Cunningham, M.M., 275
 Cunningham, P.T., 838, 839
 Curie, C., 197
 Curie, M., 3
 Currie, B.S., 441, 445
 Currie, D.J., 431
 Curry, B.B., 741, 757, 759
 Curti, E., 552
 Curtis, D., 413
 Cusack, M., 378
 Cutshall, N.H., 71, 377, 501–504
 Cutter, G.A., 157, 420, 423
 Cutter, L.S., 157
 Czaja, A.D., 179, 190
 Czigany, S., 497
- D**
 Dabek-Zlotorzynska, E., 182, 184
 Dade, W.B., 509
 Dahl, J.E., 638, 649
 Dahle, S., 387
 Dahlgaard, H., 367, 372, 382, 383
 Dahl-Jensen, D., 862, 874
 Dahlqvist, R., 530
 Dähn, R., 552
 Dail, M., 76
 Dalai, T.K., 206, 212, 216, 530, 532, 533
 Dale, M., 436, 438, 439, 443, 445
 Dalglish, H., 500
 Dalley, N.K., 45
 Dalmasso, J., 71
 Dalpé, C., 43, 44
 D'Altroy, T.N., 754
 Dambrine, E., 741
 Damesin, C., 817
 Damon, P.E., 67
 Danchev, M., 582
 Dandurand, J-L., 97, 557
 Danet, A-F., 695, 696
 Daniel, J.S., 451
 Daniel, R.M.J., 727
 Daniel, T.C., 486
 Daniels, J., 530
 Danielsen, E.F., 574, 582
 Danielson, A., 527
 Danny McCarroll, D., 816
 Dansgaard, W., 832
 Dansgaard, W., 808, 809, 861, 863, 871
 D'Antonio, C., 451
 D'Antonio, M., 51
 Darby, D., 383
 Darling, K., 105, 111
 Darwin, C., 497
 Das, A., 520, 536
 Das, J., 184
 Das, R., 230, 237, 281
 Dasch, E., 520, 521, 537, 538

- Dasgupta, P.K., 435, 436, 441
 daSilva, J., 65
 Date, A.R., 210
 Dauphas, N., 189
 Dauphin, Y., 113
 Dautel, C., 552
 Davey, J.T., 76
 David, M.B., 451, 452
 Davidson, E.A., 452, 458, 467, 468
 Davidson, M.R., 564
 Davis, A.E., 108, 156, 210, 536, 543, 665
 Davis, A.M., 137
 Davis, H.E., 801
 Davis, J.D., 768, 772, 775, 776
 Davis, J.J., 768, 770, 772
 Davis, K., 813
 Davis, L., 495
 Davis, S.N., 443
 Davis, T.E., 370, 739
 Dawson, D., 652
 Dawson, T.E., 705, 808, 813, 817, 820
 Dayton, S., 801
 De Alba, S., 504, 508
 de Albe, S., 518
 De Angelis, M., 835, 842
 de Baar, H.J.W., 134, 142, 146
 De Baets, B., 837
 de Bievre, P., 3, 89, 436
 de Boer, J., 688
 de Bourmonville, G., 95, 96, 99
 De Brueck, W., 786
 de Flores, L.P., 441
 de Gerenyu, V.L., 462
 de Groot, C.J., 455
 De Jong, E., 79
 de Jong, J.T.M., 90, 91, 95
 De La Rocha, C.L., 90–93, 98, 100, 106–108, 112, 115, 144
 de Laeter, J.R., 126, 129, 132, 133, 140, 149
 de Leeuw, G.A.M., 301
 de Leeuw, J.W., 376
 de Maere, X., 861
 de Pablo, J., 552
 de Ponteves, C., 193
 de Preter, P., 46, 495
 de Rafelis, M., 798
 de Sieyes, N.R., 643
 De Smet, S., 707
 de Souza, G.F., 87, 739
 De Wannemacker, G., 750
 Deak, J., 287, 290, 291, 293, 294
 Deargin, J.A., 500
 Dearing, D., 724
 Dearing, M.D., 728
 Déath, R., 49
 DeBell, L., 583
 Debievre, P., 92
 Deboudt, K., 180, 194
 Decarreau, A., 42, 46, 51
 DeCelles, P., 533, 536
 Decitre, S., 51
 Deegan, L.A., 428
 Defrance, S.D., 753, 756
 deGregori, I., 159
 Degueldre, C., 552
 Dehairs, F., 90, 798, 820, 821
 Dehnert, J., 346
 deJong, E., 497, 503, 504, 506
 Delaney, M.L., 54
 DeLange, G.J., 53
 DelaRocha, C.L., 100
 Delbos, E., 93
 Deleersnijder, E., 332
 Delfanti, R., 367, 373, 377, 382
 Delhez, E.J.M., 332, 333
 Delmas, R.J., 832, 835, 842–845, 850–852
 Deloule, E., 51
 Delstanche, S., 95, 96, 99, 101
 Delvaux, B., 90, 94–97, 99, 101
 Delves, H.T., 770
 Delves, T., 770
 Delvigne, C., 96, 97
 Demaison, G.J., 645
 Demarest, M.S., 90, 92, 95, 97
 DeMaster, D.J., 318, 319, 377
 DeMello, A., 640
 DeMore, W.B., 624
 Denecke, M.A., 558
 DeNiro, M.J., 90–93, 98, 707, 713, 721, 723, 724, 727, 731, 732, 734, 742, 743, 758, 814, 817
 Denison, R., 522
 Dennis, P.F., 290, 849, 865
 Dentener, F.J., 611
 DePaolo, D.J., 105–112, 114–116, 119, 521, 522, 531, 532, 534–536, 552, 553, 555, 556, 559, 560, 565
 Depers, A.M., 770
 Dequincey, O., 17, 551, 558, 561, 562
 d'Errico, F., 752, 756
 Derry, L.A., 97, 520, 535–537, 543
 Deschamps, P., 348
 Descy, J-P., 90, 98
 Desmet, P.J., 506
 Dessert, C., 520, 536
 Dessort, D., 651
 Dethleff, D., 77, 383
 Detmers, J., 156
 Detsis, G., 506
 Dettman, D., 742
 DeVogelaere, A.P., 795
 Devol, A.H., 172, 452
 deWaal, E.C., 198
 DeWalle, D.R., 614
 Dewar, R.C., 813, 822
 Di Gregorio, D.E., 492
 Di Tada, L.M., 370
 Dia, A., 520, 537, 564
 Diamond, J., 486
 Dibb, J.E., 64, 65, 67, 68, 70, 488, 491, 492, 582, 583, 850, 851
 Dickson, B.L., 564, 770
 Dickson, M.L., 866, 867
 Diefendorf, A.F., 816
 Dieke, G.H., 623
 Diekert, G., 694

- Diekmann, B., 520, 537
 Dietrich, W.E., 66, 73, 441, 486
 Dietz, M.L., 749
 Dietzel, M., 99, 113, 115, 116
 Dillon, P.J., 232, 235
 Dimova, N.T., 346, 347, 357, 358
 Ding, T.P., 89, 90, 92, 94, 95, 97, 98, 436
 Ding, Y., 834
 Dion, E.P., 64, 488, 489, 491, 492
 Ditchburn, R., 62, 78, 582, 583, 585
 Dittmar, T., 354
 Dixon, J.L., 142
 Djurhuus, J., 506
 Dobson, A., 451
 Dodd, B.A., 495
 Dodge, R.E., 795, 796
 Dodson, M.H., 131
 Doe, B.R., 551, 561, 563
 Doering, C., 495–497
 Doerr, S.H., 507, 508
 Dole, M., 4, 624
 Dolfig, J., 461, 462
 Dolphin, A.E., 744, 746, 747
 Dolvin, S.S., 383
 Domec, J.C., 817
 Domine, F., 469, 846, 848
 Dominguez, G., 583, 584, 839
 Dominik, J., 64, 67, 74, 80, 489, 491, 492, 494
 Donahue, N.M., 622, 623, 840
 Donard, O.F.X., 157, 189, 194, 232
 Donat, J.R., 142
 Dong, A., 486
 Dong, G., 506
 Dong, W., 407
 Dong, Z., 506
 Dongmann, G., 813, 818
 Donoghue, J.F., 377
 Doonasn, I.J., 800
 Dootson, F.W., 868
 Dore, J.E., 418, 425, 460, 464
 Dorigan, J., 36, 710
 Dorman, L., 299, 488
 Dornblaser, M.M., 318
 Dorr, H., 296, 297, 495
 Dortsch, Q., 486
 Dosseto, A., 551–554, 556, 558–563
 Dotinga, R., 708
 Doucelance, R., 147, 249
 Doughten, M.W., 442
 Douglas, G.B., 552, 554, 556, 558–560
 Douglas, S., 442
 Douglas, T.A., 229
 Douthitt, C.B., 90, 92–94, 652
 Dowd, J.F., 564
 Dowd, J.W., 35
 Dowdle, E.B., 281
 Dowling, L.M., 653
 Doyle, S.P., 437, 439
 Drabenstott, M., 706
 Drange, H., 379
 Draye, X., 90, 95
 Drenzek, N.J., 665, 666, 679–681, 685–689, 692, 697
 Dresel, P.E., 565
 Drever, J.I., 529, 644, 681
 Dreybrodt, W., 797
 Dreyer, A., 665
 Dreyfus, G., 864, 866
 Dreyfus, G.B., 864, 865, 877–879
 Drimmie, R.J., 22, 639, 662, 665, 667, 683
 Driscole, A.R., 645
 Driscoll, C.T., 230
 Drucker, D.G., 730
 Druffel, E.R.M., 375, 785, 794, 795
 Drury, J.S., 42
 D'Souza, W., 452
 du Bois, P.B., 380
 Du, J.Z., 14, 76, 306, 307
 Dua, R.D., 460, 468
 Dubey, M.K., 622, 623, 840
 Dubravko, J., 486
 Duchesne, J.F., 775
 Dudd, S.N., 733
 Duever, M., 816
 Duff, M.C., 552
 Dugdale, R.E., 551, 554, 558
 Duhamel, R.C., 735
 Duinker, J.C., 687
 Dulaiova, H., 331, 337, 344, 346, 347, 350, 351, 354–357
 Dullo, C., 553
 Dumas, F., 380
 Dunagan, S.P., 441
 Dunai, T.J., 16, 293, 479
 Duncan, D., 317
 Dunford, H.B., 834
 Dunisch, O., 819
 Dunne, J., 277, 278
 Dunne, T., 486
 Duprá, B., 554–556
 Dupras, T.L., 728, 742
 Dupré, B., 97, 99, 180, 194, 197, 198, 520, 524, 529, 532, 536, 537, 540, 557
 Duquesnay, A., 819
 Durana, L., 489
 Durand, S., 556, 564
 Durringer, P., 556, 564
 Durka, W., 613, 614
 Duro, L., 552
 Dutkiewicz, V.A., 489
 Dutton, P.H., 727
 Duval, P., 871
 Duxbury, J.M., 452
 Dyhrman, S., 418
 Dyke, J.V., 435, 441
 Dymond, J., 308, 344
 Dzou, L.I.P., 653
- E**
 Eadie, B.J., 65, 74, 308, 491, 493, 494, 642
 Eagle, R.J., 280, 384, 385
 Eames, J.C., 775, 776
 Easterling, K.E., 871
 Eastoe, C.J., 436, 443

- Eberl, D., 95
 Ebihara, M., 207, 208
 Ecke, F., 98, 99
 Eckelmann, W., 643
 Economou-Eliopoulos, M., 212, 213
 Edgington, D.N., 308
 Edmond, J.M., 44, 46, 48, 50–53, 63, 66, 69, 141, 142, 207, 210,
 215, 351, 352, 520, 527, 532, 533, 535, 536, 540
 Edmonds, H.N., 37, 215
 Edouard, J.-L., 816
 Edwards, D.R., 486, 652
 Edwards, E.A., 653, 664, 667, 681, 684–686
 Edwards, R.L., 4, 6, 35, 551, 553, 795
 Eggenkamp, H.G.M., 436, 667
 Egli, M., 66
 Eglinton, G., 638, 653
 Eglinton, T.I., 665, 666, 679–681, 685–689, 692, 696, 697
 Ehleringer, J.R., 22, 36, 621, 704, 705, 707, 710–712, 714–716,
 724, 726, 728, 808, 810, 811, 813, 814, 816, 819, 820
 Eicken, H., 77
 Eiler, J.M., 845
 Einfalt, H.C., 752, 757
 Eisenhauer, A.E., 43, 78, 87, 106, 107, 110–117, 185, 187, 189,
 198, 261, 346, 354, 520, 537, 538, 553, 739
 Eisma, D., 278, 321
 El Bardouni, T., 489
 Elbadry, H.M., 248
 Elderfield, H., 51, 53, 142–144, 149–151, 255
 Elgood, R.J., 614
 Elhani, S., 820
 Elhlou, S., 772
 Elis, K.M., 382, 387
 Elliers, A., 495
 Ellion, C., 770
 Elliott, E.M., 614, 629, 849
 Elliott, T., 43, 44, 263
 Ellis, A.S., 22, 160–165, 168–170, 178, 184, 186, 190–192
 Ellis, K.M., 308
 Ellis, L., 653, 656, 657
 Ellsworth, D.S., 817
 Elmgren, R., 705
 Elmore, A.J., 64, 79
 Elmore, D., 18, 62, 208, 576, 582
 Elsass, F., 99, 101
 Elsass, P., 556, 564
 Elsbury, K.E., 420, 423, 428
 Elsinger, R.J., 309, 350
 Elsner, M., 643, 665, 684, 685, 697
 Elwood, M.J., 179
 Elzerman, A.W., 271, 274
 Emerson, S.R., 288, 864
 Emery, K.O., 170
 Emery, W.J., 331
 Emig, C.C., 419
 Emiroglu, H., 655, 657
 Emmanuel, L., 798
 Emmons, M., 453
 Emsley, J., 366, 367, 420
 Engel, M.H., 644, 645, 650, 703
 Engelmann, R.J., 581, 582
 England, P., 540
 Englemann, R.J., 605
 Engström, E., 89, 90, 93, 96, 98, 99, 206, 219
 Enskog, D., 868
 Entwistle, A., 3
 Enzweiler, J., 207, 210
 Epov, V.N., 230, 232, 234, 237
 Epstein, E., 94
 Epstein, S., 90, 642–644, 721, 724, 731, 742, 758, 808, 832, 834
 Erel, Y., 45, 520, 522, 523, 525, 526, 554
 Erez, J., 113–115
 Ericksen, G.E., 441, 442
 Ericson, J.E., 740
 Eriksen, B., 744
 Erisman, J.W., 451
 Erkkila, B.R., 706, 715
 Erlank, A.J., 749
 Ermakov, A., 495
 Ernst, D., 666
 Erzinger, J., 43, 210
 Eschnauer, H., 776
 Esler, M.B., 457
 Esper, J., 808, 816, 819
 Esposito, G., 846, 848
 Esser, B.K., 205, 206, 212, 218
 Estrade, N., 147, 148, 189, 194, 232, 233, 235, 238, 239
 Etame, J., 564
 Etoubleau, J., 45
 Ettler, V., 769
 Evans, D., 232
 Evans, E.D., 638
 Evans, J.A., 741, 746, 752, 754, 756, 760
 Evans, M.N., 543, 813, 818, 820–822
 Evans, M.S., 237
 Evans, R.D., 232, 235, 726, 798
 Evans, W.C., 195, 289–290, 297
 Everett, S.E., 406
 Evers, D.C., 230
 Evershed, R.P., 724, 725, 729, 733–735
 Ewald, E.-M., 694
 Ewing, S.A., 111, 119, 441, 447
 Exner, M.E., 642
 Eyrolle, F., 509
 Ezzo, J.A., 752, 755
- F**
 Fabbri, D., 666
 Faber, E., 639, 656, 657, 659
 Fabryka-Martin, J.T., 443
 Facchetti, S., 770
 Faestermann, T., 394
 Fagliano, J., 219
 Fagre, T., 729
 Fahey, T., 507
 Fahlquist, L., 435, 442
 Fairbanks, R.G., 35
 Fairgrieve, S.I., 728
 Fajans, K., 3, 9
 Falandysz, J., 680, 681, 690
 Falkner, K.K., 48, 213
 Fallick, A.E., 665, 666
 Falvarez, W.A., 210

- Fanfani, L., 794
 Fang, S.L., 63
 Fanning, K.A., 348, 350
 Fantle, M., 107, 108, 110, 111, 115
 Fantle, M.S., 187
 Fargione, J., 418, 451
 Faris, J.P., 128
 Farkaš, J., 87, 105–108, 112, 121
 Farley, K.A., 206
 Farmer, J.G., 665
 Farmer, V.C., 93
 Farquhar, G.D., 459, 704, 716, 726, 808, 813–817, 819, 820
 Farquhar, J., 612, 618, 832, 833, 835, 836, 839, 845
 Farquhar, J.B., 22
 Farrimond, P., 652
 Fassett, J.D., 208
 Faul, K., 378
 Faulkner, D.J., 689, 696
 Faure, G., 521, 592, 639, 653, 739, 740, 748
 Fawcett, P.J., 868
 Feenstra, S., 667
 Fehn, U., 208
 Feichter, J., 377
 Feigenson, M.D., 750
 Fein, J., 142
 Felbeck, H., 799
 Felicetti, L.A., 705, 709
 Fellows, C., 770
 Fenaughty, J.M., 800
 Fendorf, S.E., 156, 157, 163
 Feng, H., 68, 70, 305, 313, 315–317
 Feng, J-L., 602
 Feng, X.B., 19, 237, 808, 812
 Feng, Y., 665
 Fennel, D.E., 692
 Fenton, G.E., 800
 Feranec, R., 752, 756
 Ferdelman, T.G., 272, 274, 281, 311
 Ferguson, C.W., 807
 Ferguson, T.L., 221
 Fernandez, I.J., 495, 497
 Ferrari, C., 217
 Ferrarin, C., 335
 Ferraro, R., 582
 Ferrier-Pagès, C., 113
 Ferris, D., 846
 Ferry, B., 741
 Fershtater, G.B., 212, 213
 Fessenden, J., 467, 468
 Février, L., 497
 Fiani, E., 194, 195
 Fiedler, R., 836
 Fiedler, S., 665
 Field, A., 460
 Field, E.M., 820
 Field, J., 725
 Fields, K.A., 446
 Fierke, M.K., 820
 Fietzke, J., 110, 111, 553, 739
 Fifield, L.K., 66, 439, 443
 Figueiredo, A.M.G., 207, 210
 Figuerola, E., 552
 Fike, D., 197, 198
 Fildani, A., 645
 Fileman, T.W., 277, 278
 Filippelli, G.M., 765
 Filizola, N., 537, 538
 Fincannon, A.L., 653
 Fink, D., 476
 Fink, R.W., 248
 Finkel, R.C., 62, 73, 275, 479, 483, 582, 583
 Finlayson-Pitts, B.J., 846
 Finley, J.B., 436
 Finneran, K.T., 664
 Firestone, M.A., 451, 452
 Firestone, M.K., 459
 Firestone, R.B., 28, 29, 366, 367
 Firsching, F.H., 423
 Fischer, D.E., 749
 Fischer, H., 460, 850
 Fisher, D., 742
 Fisher, E.M.R., 590, 592
 Fisher, G.B., 510
 Fisher, J.B., 498
 Fisher, N.S., 272, 280, 281, 308, 351, 352
 Fisher, P.C., 212, 213
 Fisher, R.E., 53
 Fitfield, L.K., 370
 Fitoussi, C., 90
 Fitzgerald, S.A.Q., 75, 322, 509
 Fitzgerald, W.F., 229, 230, 241, 585
 Fitzwater, S.E., 178, 254
 Flament, P., 180, 194
 Flanagan, L.B., 813
 Flatt, H., 22, 683
 Flavin, C., 490
 Fleer, A.P., 276
 Legal, A.R., 247, 254, 768, 770, 772
 Fleischer, R.L., 552
 Fleisher, M., 79
 Fleming, R.H., 331
 Flessa, H., 462, 497
 Flessel, C.P., 770
 Fletcher, I., 110
 Fletcher, W.J., 871
 Flexser, S., 168
 Floch, G.L., 850–852
 Flood, B., 651
 Flor, T.H., 796
 Florin, S.T., 705, 709
 Floss, H.G., 835
 Fluhler, H., 497
 Flury, M., 497
 Flury, M.S., 497
 Fogarty, P., 75
 Fogel, M.L., 423, 424, 459, 460, 725, 727, 735, 743, 749, 760
 Földházi, G., 716
 Foley, S.F., 95
 Folkins, I., 611
 Folt, C.L., 19
 Fondran, C., 509

- Fontana, L., 221
 Fornes, W.L., 62–64, 308, 503, 505
 Förstel, H., 716, 813, 818
 Forster, P., 451, 453, 457
 Forti, L., 194, 195
 Fortunato, G., 750
 Foster, G.L., 527, 528, 530, 543, 556
 Foster, I.D.L., 500, 508
 Foster, J.M., 312
 Foucher, D., 230, 232, 235, 237
 Fouillac, C., 797
 Fouquet, Y., 160–162, 170
 Fourel, F., 681
 Fournier, R.O., 88
 Fowler, M.G., 638, 651
 Fowler, S.W., 272, 280, 351, 352
 Fox, D., 77
 Fox, L.E., 431
 Frame, C., 460, 461, 463, 464, 469
 Frame, G.M., 687, 690
 France-Lanord, C., 42, 46, 51, 520, 527, 529, 532, 535–537,
 539, 542, 543, 553, 556, 558, 561, 564
 Francey, R.J., 816
 Francis, R.I.C.C., 792
 Franck, V.M., 90
 Franco, M., 704
 Francois, L., 536
 Francois, R., 863
 Frani' Z, 379
 Frank, D.C., 808, 816, 819
 Frank, M., 69–71, 78, 90, 91, 98, 146, 251, 253–261, 264,
 265, 531
 Franke, O.L., 345
 Frankenberg, S., 745
 Frankenberger, J.R., 452, 463, 464, 470
 Franklin, C.A., 774
 Franzel, B., 808
 Frape, S.K., 22, 639, 662, 665, 667, 683
 Frazao, E., 706
 Frazier, B.E., 503
 Freedman, P.A., 680
 Freeman, K.H., 639, 650, 651, 661, 680, 816
 Freeman, S.P.H.T., 376
 Freestone, I.C., 752, 756
 Frei, K.M., 206, 752, 756, 757
 Frei, R., 164, 206, 752, 756, 757
 Freiwald, A., 794
 French, S.A., 706
 Freney, J.R., 452
 Fresco, J., 211, 214
 Frew, R.D., 142
 Frey, F.A., 45
 Frey, M.M., 469, 615, 623, 625, 646, 846, 848–852
 Freydier, R., 146, 180, 194, 197, 198
 Freyer, H.D., 816, 832, 836, 849–852
 Freyer, K., 346
 Frick, M., 639
 Fricke, H., 742
 Fricke, H.C., 418, 426, 746
 Fridrich, J., 311
 Friedli, H., 832
 Friedman, L., 454, 456
 Friedmann, I., 861
 Friedrich, J., 277
 Fries, T.L., 73
 Frignani, M., 35
 Fripiat, F., 95
 Fritts, H.C., 807, 808, 820
 Fritz, P., 170, 189, 808, 810
 Fritzel, T.L.B., 295
 Fritzsche, F., 835
 Froehlich, K., 621, 810, 812
 Froelich, P., 48
 Frohlich, K., 582
 Froidevaux, B.P., 497
 Froidevaux, P., 704, 716
 Frolkis, V.A., 833
 Froyd, C.A., 808
 Fruchter, N., 739
 Fruneau, F., 582
 Fruneau, M., 68, 69, 71, 72, 582
 Fry, B., 168, 169, 704, 705, 727, 728
 Fryer, B.J., 188, 210
 Fryirs, K., 551, 553, 554, 556, 558, 560–563
 Fu, J., 652, 665
 Fuex, A., 639, 643
 Fuhrer, K., 864
 Fujii, T., 147, 148
 Fujii, Y., 259
 Fujiwara, H., 596
 Fukumizu, K., 866, 867
 Fukushi, Y., 739
 Fukuyama, T., 596
 Fuller, B.T., 725, 729, 735
 Fuller, C., 354
 Fuller, M.E., 663
 Fung, I.Y., 833, 853
 Furi, E., 287, 299, 300
 Furla, P., 113
 Furutani, T.T., 743, 747, 749, 760
- G**
 Gabet, E.J., 497
 Gabitov, R., 114
 Gabrielli, P., 206, 207, 211, 212
 Gaetani, G.A., 378
 Gaffney, J.S., 275
 Gagen, M.H., 808, 815, 816, 823
 Gaglianone, P.C., 648–650
 Gagner, C.L., 142
 Gaillardet, J., 43, 44, 97, 186, 192, 193, 520, 528, 529, 535, 536,
 540, 543
 Gaines, S.E., 574
 Gainville, R., 197, 198
 Gale, A.S., 748
 Gale, N.H., 752, 757
 Galer, S.J.G., 128–135, 141, 145–147, 149–151, 181, 186
 Galimov, E.M., 639, 642, 645, 649
 Galindo-Uribarri, A., 483, 582
 Gallagher, D., 492
 Gallegos, E., 649
 Galloway, J.N., 451, 611, 619

- Galy, A., 43, 54, 87, 89, 106, 108, 110–112, 115, 135, 137, 468, 520, 524, 527–529, 532, 535, 537, 539, 542, 832
- Gamble, E., 308
- Gamo, T., 680, 681, 690
- Ganapath, R., 210
- Gandhi, D., 664
- Gandhi, H., 461, 462, 464–467, 470
- Gandon, R., 380
- Gannoun, A., 46, 47, 49, 51, 206, 212, 215, 216, 255, 260–262, 265
- Gann-Troxler, T., 816
- Ganopolski, A., 874
- Ganor, J., 558
- Gantner, N., 237, 241
- Gao, B., 129, 130, 134, 135, 138–140
- Gao, S., 43, 44, 134, 140, 168, 170–172, 251
- Gao, X., 835
- Gao, Y.Q., 22, 379, 618
- Garbai, G., 253
- Garbeva, P., 462, 463
- García Alonso, J.I., 750
- Garcia, G.A., 419, 420, 422–425, 432
- Garcia-Agudo, E., 503
- Garcia-Montiel, D., 458, 462
- Garcia-Romero, B., 387
- García-Ruiz, S., 750
- Garcon, V.C., 332
- Gardner, L.R., 47
- Gariepy, C., 206, 558, 775
- Garn, S.M., 744
- Garnett, M.H., 376
- Garnier-Laplace, J., 376
- Garrels, R., 106, 107, 520
- Garritt, R.H., 705
- Gartner, B.L., 817
- Gartshore, I., 335
- Garver, E., 799
- Garvie-Lok, S.J., 751
- Gasco, C., 367, 373
- Gaskell, S.J., 638
- Gaspar, M., 179
- Gastaud, J., 370, 381, 384
- Gat, J.R., 621, 622, 705, 712, 742, 759, 810
- Gatrousis, C., 385
- Gatter, D., 470
- Gaucher, C., 164
- Gaudinski, J.B., 820
- Gaul, S., 680, 689, 692
- Gault-Ringold, M., 143
- Gaus, C., 695
- Gauthier, P.J., 252, 273
- Gauthier-Lafaye, F., 552
- Gautier, C., 823
- Gay, A., 10
- Gaymard, F., 197
- Gebauer, G., 464, 613, 614, 629
- Gebrekirstos, A., 682, 696
- Gee, M.A.M., 263
- Geeta Rajagopalan, 810, 814
- Gehre, M., 424, 613, 835, 837
- Gehrels, W.R., 376
- Gehrke, G.E., 237, 239
- Geibert, W., 552
- Geisler-cussy, D., 443
- Gélabert, A., 197, 198
- Gelinas, A., 206
- Gellene, G.I., 618
- Gellis, A.C., 508
- Gelting, J., 196
- Gemeinhardt, S., 462, 463
- Geng, A., 651, 652
- Geng, X., 651
- Genthon, C., 843, 862
- Gentry, D., 797
- Genz, H., 248
- Georg, R.B., 87, 89–91, 93, 96–101
- George, J.C., 800
- George, S.C., 643, 653
- Georgi, A., 644
- Gerard, M., 564
- Gerlach, R., 168, 169, 173
- Germon, J.C., 458, 460, 466, 683, 684, 686
- Gerstmann, U., 394
- Gesell, T.F., 346
- Gessler, A., 817, 819
- Ghaleb, B., 348, 558, 793, 798
- Ghashghaie, J., 817
- Gherardi, J.M., 863
- Ghosh, S., 238, 239
- Giammar, D.E., 552
- Gibbs, J.P., 436
- Giblin, A.E., 451, 452
- Gibson, P.N., 259
- Giesemann, A., 834, 835
- Gieskes, J.M., 51–53
- Giffaut, E., 157
- Giffin, C., 347
- Giffin, D., 305, 318
- Gill, A.C., 492
- Gill, A.E., 358
- Gill, G.A., 48
- Gill, J.B., 273, 553
- Gillings, B.R., 772, 773, 775
- Gillis, K., 48, 50–52
- Gillyon, E.C.P., 680
- Gillyon, P., 651
- Giménez, J., 552
- Gimmi, T., 558
- Giofiantini, R., 808, 809
- Giroud, B., 716
- Gisalason, S.R., 42, 44, 46, 47, 49–51, 87
- Glaser, B., 665
- Gleason, D., 469
- Gleeson, L.J., 477
- Gleixner, G., 679–682, 686, 688, 689, 695, 696
- Glessner, J.J., 163, 164
- Glorennec, P., 770
- Glover, D.M., 350
- Gnanapragasam, E., 794
- Go, Y.B., 281
- Gobeil, C., 215
- Goderis, S., 206, 212

- Godon, A., 436
 Godoy, M.L.D.P., 402
 Goericke, R., 726
 Goff, M., 256
 Gogen, K., 261
 Goldberg, E.D., 209, 212, 308, 371, 383, 386, 387, 496, 786
 Goldhammer, T., 424, 425
 Golding, S.D., 835
 Goldoft, M., 219
 Goldsmith, J.R., 455, 611, 612
 Goldstein, S.J., 6, 551
 Goldstein, S.L., 216, 527, 528, 537
 Golubowska, G., 713
 Gong, S., 469
 Goñic, M.A., 314
 Gonneea, M.E., 344, 351–353
 Gonzalez-Gomez, C., 489
 Goodbred, S.L., 490
 Goodkin, N.F., 794, 798
 Goodman, A.H., 744, 746, 747
 Goonan, T.G., 220
 Gopalan, K., 808
 Göpel, C., 132, 147
 Gordon, E.S., 322
 Gordon, G.W., 199, 206, 212, 215, 219
 Gordon, L.I., 706, 813
 Gormley, J.R., 642
 Gormly, J.R., 645
 Goroncy, I., 381, 384
 Gospodinova, K., 441
 Gosse, J.C., 16, 476
 Gosse, W., 210
 Goswami, V., 520
 Göttlicher, S.G., 817
 Gove, H.E., 476, 582
 Gove, R.B., 6
 Govers, G., 506
 Gow, A.J., 383
 Graber, B.E., 75
 Grabowska, S., 596
 Grachev, A.M., 864–866, 868, 871–873
 Graham, B.S., 241
 Graham, D.W., 290
 Graham, E.A., 815, 823
 Graham, I., 62, 78, 582, 583, 585
 Graham, S.A., 645
 Grandjean, P., 419
 Grandy, A.S., 460–462, 464–466
 Grandy, S., 461
 Granet, M., 553, 556, 558, 561
 Granger, D.E., 18
 Granier, C., 833
 Grannas, A.M., 851
 Grassineau, N.V., 835
 Gratz, L.E., 238–241
 Graustein, W.C., 34, 35, 307, 491, 564, 576, 583, 585, 591
 Gray, B., 772, 774, 775
 Gray, E., 378
 Gray, J.E., 237, 367, 372, 808
 Gray, R., 664
 Graybill, D.A., 807
 Graymer, R., 297
 Grayson, R.B., 493
 Graziano, J.H., 776
 Grebmeier, J.M., 77, 367, 372, 383
 Green, C.T., 441
 Greenwood, J.P., 835
 Gregg, J.W., 704, 723, 730
 Gregoire, D.C., 210
 Gretebeck, R.J., 711
 Gribble, G.W., 689
 Grice, K., 652, 817
 Griebler, C., 664, 665
 Griffin, J.J., 308, 383, 386
 Griffin, W.L., 251, 266
 Griffith, C.E., 651
 Griffith, D.W.T., 457, 469
 Griffith, E., 106–108, 112, 115
 Griffiths, H.G., 808, 817
 Grim, E., 836
 Grimani, C., 477
 Grimes, V., 746, 747, 752, 757
 Grissino-Mayer, H.D., 820
 Grizzle, P.L., 645
 Groen, J., 665
 Groffman, P., 451, 452, 463, 464, 470
 Gromaire, M.C., 193
 Groning, M., 611
 Gros, M., 210
 Grossman, L., 6
 Grostern, A., 684–686
 Grousset, F.E., 19
 Grove, D.B., 159
 Grove, H.E., 576
 Gruau, G., 421, 424, 425
 Grubbs, D., 241
 Gruber, N., 90
 Gruebel, K.A., 346
 Grund, H., 639, 663, 667
 Grundahl, F., 41
 Grupe, G., 705, 744, 752, 754, 760
 Gschwend, P.M., 306, 308, 323, 324
 Gu, B., 22, 435–439, 441–443, 445, 446, 449, 697
 Gu, Z.Y., 63, 477, 482
 Guegueniat, P., 380
 Guelke, M., 109, 196–199
 Guenther, J., 618–620
 Guerrot, C., 43, 44
 Guggenheim, C., 837, 853
 Guha, J., 253
 Guilderson, T., 795
 Gulbransen, E.A., 4
 Gulec, N., 298, 301
 Gulson, B.L., 19, 768–779
 Gunderson, D.R., 788, 800
 Gunderstrup, G.D., 862
 Gundestrup, N., 874
 Güngör, N., 381
 Gunji, S., 489
 Gunn, S.H., 748
 Gunther, H., 835
 Guo, L., 727

- Guo, S., 850
 Guo, W., 55
 Guo, Y., 160, 198
 Gürgey, K., 655, 657
 Gurriaran, R., 509
 Gussone, M., 112
 Gussone, N., 105, 106, 110–116
 Gustafsson, Ö., 306, 308, 323, 324, 697
 Gustin, M.S., 229
 Guthrie, J.F., 706
 Gutierrez, A.N., 751, 753, 755
 Gutjahr, C.C.M., 657
 Guy, R.D., 459, 460
 Gwiazda, R.H., 770, 772, 779
 Gwinn, E., 492
- H**
- Haan, D., 853
 Haavik, L.J., 820
 Haba, H., 213
 Haberhauer, G., 837
 Habicht, K.S., 156
 Haderlein, S.B., 665, 685
 Hadly, E., 748, 752, 756
 Haeckel, M., 53
 Hafer, K.M., 493
 Hagemann, H., 645
 Haggblom, M.M., 664
 Hagiwara, Y., 168, 170
 Hairsine, P., 75
 Hairsine, P.B., 493
 Hajek, B.F., 503, 504
 Hale, R.C., 692
 Halekoh, U., 506
 Hales, H.C., 614
 Halevi, E.A., 622
 Halicz, L., 110, 111, 160–162, 164, 196, 739
 Hall, A.E., 704, 716
 Hall, B.L., 789
 Hall, G.S., 741, 753, 757, 779
 Hall, J.M., 43, 53, 54
 Hall, K., 651
 Hall, M., 817
 Hall, M.A., 808
 Hall, P.B., 651
 Hallam, K.R., 846, 848
 Haller, M., 46
 Halliday, A.N., 7, 8, 20, 87, 90, 91, 93, 96, 98–101, 195, 207, 211, 248–251, 259, 261, 265, 553, 742, 750, 756, 834
 Hallquist, M., 622
 Hallstadius, L., 382, 575
 Hamel, O.S., 376
 Hamilton, T.F., 18, 296, 308, 321, 365, 368, 370–373, 377, 381, 384, 387, 488
 Hammarlund, D., 196
 Hamme, R.C., 288
 Hammer, C.U., 845
 Hammerschmidt, C.R., 241
 Hammond, D.E., 346, 350, 354, 355, 357, 564
 Han, J., 638
 Han, Y.-J., 230
 Hancock, G.J., 331, 344, 353–355
 Handler, R.M., 179, 190
 Hanikenne, M., 198
 Hannon, J.E., 837
 Hanor, J.S., 50, 344
 Hanson, A.D., 645
 Hanson, D., 664
 Hansson, M.E., 843
 Hansson, S., 705
 Harada, K., 272, 278–280, 348–350, 489
 Hardcastle, B.J., 343
 Harden, J.W., 73, 486
 Hardy, E.P. Jr., 383, 384, 400, 590, 592
 Harkness, D.D., 653
 Harkness, M., 643, 662, 664, 665, 667, 681, 697
 Harlavan, Y., 525, 526
 Harley, J.H., 395, 397, 409, 589
 Harmon, R.S., 3, 5, 551, 552, 564
 Harms, G., 653, 665
 Harnack, L., 706
 Harris, D., 461
 Harris, G.P., 428
 Harris, I.C., 816
 Harris, J.M., 704, 727
 Harris, N.B.W., 42, 44, 48, 529, 532–534
 Harrison, J.A., 451, 452
 Harrison, R., 768
 Harsh, J.B., 497
 Hart, S.R., 141, 749, 796
 Hartman, B., 350, 357
 Hartman, M.C., 310
 Harvati, K., 746, 747, 752, 757
 Harvey, B.R., 383
 Harvey, C., 485, 486
 Harvey, E., 692
 Harvey, G., 442
 Harvey, J.W., 345
 Harvey, M.J., 62, 605, 606
 Hasegawa, Y., 42
 Haslett, S.K., 372
 Hassler, D.R., 208
 Hastings, J.L., 849–852
 Hastings, M.G., 456, 461, 468–470, 612–615, 622, 626, 627, 837, 846, 847, 849–852
 Hastorf, C.A., 727, 734
 Hatakka, J., 488
 Hatcher, P.G., 642
 Hathorn, B.C., 618
 Hathorne, E.C., 43, 53, 54
 Hattori, E.M., 752, 756
 Hatzinger, P.B., 22, 436–443, 445, 446, 449, 662, 667, 697
 Haug, G.H., 808, 819, 821
 Hauke, V., 651
 Hausladen, P.A., 370
 Haverd, V., 457, 469
 Havlová, V., 558
 Hawkesworth, C., 108, 553
 Hawkins, J., 846, 848
 Hawley, N., 65, 308, 493, 494
 Hay, B.J., 380
 Hayashi, M., 357

- Hayes, J.M., 156, 158, 164, 455, 639, 640, 651, 652, 661, 680, 683, 834
- Hays, P., 520
- He, P.N., 508
- He, Q., 63, 64, 73, 75, 81, 306, 490, 493, 495, 496, 498, 500, 504, 507–509
- Heacock, R.L., 657
- Headly, M., 867
- Healey, M.A., 703
- Heaney, P.J., 88
- Heaton, J.H.E., 728
- Heaton, K., 704, 716
- Heaton, T.H.E., 289, 293–295, 848, 849, 851, 852
- Hebbeln, D., 383
- Hebert, D., 582
- Hecht, M.H., 435, 441, 442
- Heckrath, G., 506
- Hecky, R.E., 428
- Hedges, R.E.H., 109, 110, 116, 117, 724
- Hedges, R.E.M., 703, 705, 725, 727, 729, 733, 743, 751
- Hedin, L.O., 458, 460, 469
- Hedman, K.M., 741, 757, 759
- Hedvall, R., 575
- Heeschen, K., 53
- Heggie, D., 256
- Hegner, E., 520, 537
- Heicklen, J., 435
- Heidenreich, B.C. III., 6
- Heidenreich, J.E. III., 612, 618, 832
- Heier, K.S., 46
- Heijnis, H., 495–497
- Heikkilä, U., 78, 583, 585
- Heikkoop, J.R., 436, 438, 439, 443, 445
- Heimann, A., 179, 190
- Heimann, M., 348, 349
- Heimsath, A.M., 63, 72, 498, 508–510
- Hein, J.R., 52, 53, 134, 135, 145, 247, 251, 253–261, 264, 265, 748
- Heinemeyer, O., 452
- Heinrich, W., 52
- Heinrichs, H., 134, 140, 151, 247, 248, 251, 257, 266
- Heisinger, J., 746, 756
- Heitmann, T., 665
- Hel, J.V., 195
- Helfer, I.K., 497
- Helland-Hansen, B., 331
- Helle, G., 808, 816–822
- Heller-Zeisler, S.F., 207, 210
- Helliker, B.R., 814
- Hellstrom, H., 553
- Helz, G.R., 219
- Helz, R.T., 43–45
- Hemet, P., 371
- Hemming, D.L., 816
- Hemming, N.G., 769
- Hemming, S.R., 206
- Hemond, H.F., 206, 218, 278
- Hendershot, W., 75
- Henderson, G.M., 3, 29, 42, 43, 46, 47, 51, 53–55, 109, 110, 113, 115–117, 142, 552, 789, 790, 794, 795
- Henderson, J., 752, 756
- Henderson, P.B., 354
- Hendriks, J., 462, 463
- Hendry, K.R., 90, 142
- Heninger, I., 159
- Henriet, C., 90, 95
- Henry, B.K., 813, 814
- Henry, M., 657, 660, 706
- Henry-Edwards, A., 332
- Hensen, C., 53
- Herath, D.P., 706
- Heraty, L.J., 22, 436–441, 443, 445–447, 662, 663, 665–667, 679, 680, 685–689, 697
- Heraty, L.J. Jr., 437
- Herbel, M.J., 160, 161, 168–172
- Herbillon, A., 525
- Hercik, M., 558
- Hergt, J., 553
- Hering, J.G., 552
- Hernandez, F., 596
- Hernandez-Avila, M., 770
- Herr, W., 206
- Herring, D.A., 728
- Herron, M.M., 383, 871
- Hervig, R.L., 46
- Herzberg, G., 623
- Herzog, G.F., 476
- Hess, C.T., 63, 68, 302, 312, 488, 495, 497
- Hesse, P.P., 551, 553, 554, 556, 558, 560–563
- Hesselbo, S.P., 256
- Hetherington, E., 522
- Heumann, K.G., 208, 211, 254, 260, 850
- Heuser, A.E., 106, 107, 110–113, 115, 117
- Hewawasam, T., 557
- Heyraud, M., 274, 280, 281, 311
- Hickman, R.E., 73
- Hicks, H.G., 490
- Hicks, K., 611
- Hidaka, H., 552
- Hiemstra, T., 88
- Hietz, P., 819
- Higgins, S., 206
- Higgitt, D.L., 506
- Hildebrand, P., 540
- Hilkert, A.W., 454, 456, 461, 462, 468, 652, 667, 679–681, 686, 687, 689, 690
- Hill, M.W., 581, 582
- Hill, P.A., 744
- Hill, R.I., 290, 657, 660
- Hillaire-Marcel, C., 558, 793, 798
- Hillaire-Marcel, G., 715
- Hilley, G., 532
- Hillson, S., 740, 743, 744, 746
- Hilton, D.R., 14, 19, 287–288, 290, 292, 293, 295, 296, 298–301
- Hinkley, T.K., 249–252, 255, 259, 261, 265
- Hintelmann, H., 230, 232–235, 237–239, 241
- Hintenberger, H., 206
- Hinz, C., 470
- Hippler, D., 105, 106, 110–112, 115
- Hipskind, R.S., 574

- Hirata, T., 110, 117, 182
Hird, S., 704
Hirose, K., 17, 313, 321, 370, 371, 377, 381, 382, 384, 386, 494, 561, 576, 583, 589–602, 604–606
Hirota, M., 606
Hirotzu, T., 46
Hirsch, A.I., 348
Hirschberg, D.J., 68, 70, 77, 305, 313, 315–317, 383
Hirschorn, S.K., 681, 684–686, 697
Hirst, A.C., 333
Hirt, B., 206
Hiscock, K.M., 290
Ho, D.T., 348, 349, 351
Ho, M., 766
Hoaglund, J.R., 441, 446, 447
Hobbie, E.A., 808
Hobbie, J.E., 705
Hodell, D.A., 757, 758
Hodge, V., 207, 210, 211, 214
Hodson, A.J., 848
Hodson, M.J., 94
Hoeffs, J., 639, 646, 652
Hoefs, J., 43, 53, 436
Hoehn, E., 346
Hoenke, K.A., 665
Hoering, T.C., 436, 445, 836, 849
Hoffman, E.L., 208, 210
Hoffman, J., 441
Hoffmann, D.L., 553
Hoffmann, G., 808, 823
Hoffmeister, W., 206
Hofling, R., 424, 613, 835, 837
Hofmann, A.W., 131, 206, 209, 212, 216, 263–265
Högberg, P., 704, 817
Hoham, C.H., 639, 650
Höhener, R., 644
Hohmann, M., 508
Hoines, S., 332
Hojberg, O., 837
Holba, A.G., 653
Holbrèque, F., 113
Holcomb, M., 114
Holden, N.E., 89
Holden, P., 109, 110, 116
Holland, H., 527
Holland, H.D., 351
Holland, K., 241
Holleman, A.F., 125, 126
Hollerbach, A., 645
Hollocher, T.C., 460
Holm, E., 367, 372, 379, 382, 395, 575
Holman, E.S., 160
Holmden, C., 106, 109, 110, 117–119
Holmes, R.T., 19, 756
Holmstrand, H., 697
Holst, T., 819
Holt, B.D., 22, 662, 663, 665–667, 697, 838, 839
Honch, N.V., 725, 727, 735
Honda, M., 65, 68
Honesto, J., 212
Honeyman, B.D., 74, 497
Hong, G.-H., 7, 18, 28, 70–72, 272, 307–313, 321, 330, 332, 365, 368, 370–372, 377, 381, 384, 386, 397, 398, 488, 503, 575, 590, 592, 594, 785, 786, 788, 797, 799, 801
Hong, Y.L., 272–275, 278
Hong, Z., 651
Hönisch, B., 115
Honjo, S., 380
Honnorez, J., 263
Honrath, R.E., 850
Hood, A., 657
Hoogewerff, J., 704, 716, 745, 751
Hooper, A.B., 460, 468
Hoppe, K.A., 743, 747, 749, 752, 756, 760
Hoppenheit, M., 308
Hopper, J.F., 666
Hopple, J.A., 89, 436
Horacek, M., 711
Horan, M.F., 205, 206, 212
Horibe, Y., 868
Horie, K., 552
Horii, Y., 680, 681, 688–690, 694
Horita, J., 155, 436–439, 441, 442, 445, 622
Horner, T.J., 20, 129, 130, 132, 134, 145, 146, 150, 151, 181
Hornung, R., 766
Horstwood, M.S.A., 197, 198, 746, 760
Horton, J.W., 206
Horton, M.C., 733
Horwitz, E.P., 111, 347, 749
Hosterman, J.W., 442
Hostettler, F.D., 662
Hotchkis, M.A.C., 394
Hou, X., 348, 366, 367, 788, 789
Hough, R.L., 665
Hougham, A.L., 335
Houlbreque, F., 795
Houlton, B.Z., 456, 470, 612, 613, 615, 837, 846
Hourdin, F., 843
House, C., 179, 184, 199
House, W.A., 428
Houston, J., 441
Hovius, N., 32
Howarth, D., 772, 776
Howarth, R.W., 418, 451, 705
Howe, B., 665
Howland, M.R., 729
Hren, M., 532
Hrnecek, E., 370
Hseu, Z.Y., 73
Hu, G.X., 835
Hu, M.H., 281
Hu, Q.H., 372
Hu, Y., 506, 507, 733
Hu, Z., 140
Huang, D., 306
Huang, L., 22, 663, 665, 667
Huang, M., 184
Huang, S., 112, 348
Huang, W.H., 552
Huang, Y., 644, 653, 665
Huang, Z.Y., 78
Huang, Y.S., 651, 652

Hubberten, H.W., 752, 757
 Huber, C., 864, 866, 867, 871, 875
 Hubert, A., 553–556, 558, 560, 564–566
 Hubert, P., 458, 466, 683, 684, 686
 Hubick, K.T., 726, 808
 Huck, H., 492
 Huckins, J.N., 665
 Hudeny, J.B., 305
 Huettel, M., 346, 347, 351, 355, 357
 Huey, J.M., 248
 Huff, A.K., 853
 Hughes, H.J., 97
 Huh, C.A., 273, 276, 306, 307, 405, 491
 Huh, Y., 44, 46–48, 53, 252, 520, 525, 528, 529, 532, 540
 Huizenga, J.R., 207
 Huizinga, B.J., 638, 645, 649
 Huizinga, K.M., 460–462, 464–466
 Hulston, J.R., 88, 137, 834, 835
 Humayun, M., 238, 239
 Humphreys, G.S., 507, 508
 Hungate, B.A., 464, 465
 Hunkeler, D., 165, 639, 643, 644, 653, 662, 664, 667, 684, 685, 697
 Hunt, A., 289
 Hunt, J., 643
 Hunt, J.M., 641, 642, 644, 655
 Hunter, D.B., 552
 Hunter, K.A., 142
 Huntsman, S.A., 142
 Huon, S., 192, 193
 Hure, A., 194, 195
 Hurst, R.W., 739
 Husain, L., 62, 489
 Hussain, N., 272–274, 281, 307, 311, 554
 Hutchinson, C.E., 800
 Hutterli, M.A., 850, 851
 Hutton, R.C., 6
 Huybrechts, P., 49
 Hwang, D.W., 329, 334
 Hyams, E., 486
 Hyun, J.H., 272, 279, 308
 Hyunh-Ngoc, L., 381, 384

I

Iacumin, P., 835
 Iain Robertson, I., 816
 Iannetta, P.P.M., 820
 Iavicoli, I., 207, 221
 Ichiyanagi, K., 810
 Icopini, G.A., 88
 Igarashi, Y., 313, 321, 370, 371, 382, 494, 583, 589, 590, 592–598, 600–602, 604
 Ihlenfeld, C., 251, 252, 266
 Ikeda-Fukazawa, T., 866, 867
 Ikeuchi, Y., 381, 384
 Ikuta, N., 276
 Iler, R.K., 88
 Iliffe, T.M., 786, 797
 Ilyashuk, B., 196
 Imamura, M., 61
 Imboden, D.M., 287

Inaba, T., 651
 Ineson, P., 653
 Ingle, J.C., 426
 Ingram, B.L., 426
 Ingram, R.G.S., 290
 Ingri, J., 98, 99, 527, 530, 564
 Innocent, C., 558
 Inomata, Y., 596, 598
 Inoue, H., 590
 Inoue, M., 184
 Inoue, T., 78
 Inskip, M.J., 774
 Introne, D.S., 798
 Ioannidou, A., 64, 489, 491, 492
 Ionov, D., 43
 Irion, F.W., 620
 Irisawa, K., 182
 Irlweck, K., 370
 Iroume, A., 64, 503, 509
 Irvine, J. Jr., 366
 Irvine, R.L., 695
 Iseki, K., 339
 Ishikawa, T., 43
 Ishikawa, Y., 62, 64, 79
 Ishimori, F.T., 436, 445
 Ishimura, T., 613, 837
 Ishiwatari, A., 213
 Ishiwatari, R., 666
 Italiano, F., 301
 Ito, T., 377, 381, 384
 Ivanovich, M., 3, 5, 347, 551, 552, 554, 558, 564
 Iwashita, T., 94
 Izatt, R.M., 45
 Izbicki, J.A., 157, 163, 164, 166, 178, 191, 290, 292, 293, 295, 298, 299, 337, 352–355
 Izdar, E., 373, 383

J

Jaakkola, T., 404
 Jackson, S.E., 210
 Jackson, T., 619, 620, 624
 Jackson, T.A., 232, 235, 237
 Jackson, T.L., 835, 839
 Jackson, W.A., 22, 435–439, 441–443, 445, 662, 667, 697
 Jacob, D.J., 491, 576, 625, 833, 839–841
 Jacobi, H.W., 469, 851
 Jacobs, D.G., 493
 Jacobsen, J.P., 331
 Jacobsen, S., 112, 521, 544
 Jacobson, S.R., 638, 649
 Jacomet, S., 733
 Jaeger, J., 354, 355
 Jaegle, L., 435, 625
 Jager, H.J., 834, 835
 Jager, J., 639, 663, 667
 Jahn, B.M., 205, 206, 212, 215, 218
 Jahren, A.H., 820, 822
 Jaisi, D.P., 422–424, 432
 Jakobsson, E., 690
 Jalkanen, R., 808, 815, 816, 823
 James, A.G., 280

- James, A.T., 656
 James, M.G., 770
 James, R.H., 42–44, 46–54, 252
 Jameson, C.W., 770, 772, 774, 775
 Jamieson, R.E., 839
 Jang, J., 272–275, 278
 Jannasch, H., 799
 Janssen, C., 618
 Jaramillo, J., 651
 Jarde, E., 645
 Jarman, W.M., 667, 679–681, 686, 687, 689, 690
 Jarvie, D., 657, 660
 Jarvis, J.C., 469, 849–852
 Jarvis, K.E., 207, 210
 Jarvis, N.J., 489
 Jarzecki, A.A., 179
 Jasińska, M., 493
 Javoy, M., 831
 Jayakumar, D.A., 452
 Jeandel, C., 48, 531
 Jeffcoate, A., 43, 44, 263
 Jeffcoate, A.B., 43, 44
 Jeffery, R.W., 706
 Jekanowski, M.D., 706
 Jenden, P.D., 661
 Jendrzewski, N., 436, 667
 Jeng, W.L., 728
 Jenkins, K.A., 840
 Jenkins, S.G., 705
 Jenkins, W.J., 35, 289, 290, 296, 373, 843
 Jensen, S., 687
 Jetten, S.M., 456, 470
 Jia, X., 600
 Jiang, C.Q., 651, 652
 Jiang, H., 435
 Jiang, S.Y., 212, 435, 537
 Jiang, X., 55
 Jickells, T.D., 216
 Jim, S., 724, 725, 729
 Jimenez-Romos, M.C., 592
 Jin, L., 553, 561–563, 565
 Jinuntuya-Nortman, M., 462, 464–467, 470
 Jo, K.N., 785, 786, 797
 Jochum, K.P., 257
 Johannesen, G.M., 212, 213
 Johannessen, O.M., 379
 Johannesson, K., 530
 Johansen, H.S., 837
 Johanson, K.J., 495
 John, S.G., 146, 180, 181, 189, 194
 Johnsen, S.J., 832, 874
 Johnson, B.J., 727
 Johnson, C., 537
 Johnson, C.A., 460, 665, 839
 Johnson, C.E., 831
 Johnson, C.M., 159–161, 164, 168, 170, 179, 184, 187, 189, 190, 197, 198, 739, 752, 755
 Johnson, D.G., 344
 Johnson, D.L., 497
 Johnson, K., 229
 Johnson, K.P., 230, 232, 234, 235, 237–239
 Johnson, K.S., 256
 Johnson, M.W., 230, 234, 331
 Johnson, P.C., 452, 463, 464, 470, 662, 667
 Johnson, T.M., 22, 157, 160–166, 168–173, 178, 184, 186, 191, 192, 194, 195, 741, 757, 759
 Johnson-Pyrtle, A., 383
 Johnston, A., 71
 Johnston, J.C., 612, 615, 619, 621, 833
 Johnstone, J.A., 820
 Jokela, T.A., 280, 384
 Jones, A.E., 851
 Jones, D.L., 297
 Jones, E.D., 500
 Jones, E.P., 308, 349, 351, 382
 Jones, J.L., 90, 92
 Jones, P.D., 816
 Jones, R.T., 213, 218, 220, 775
 Jones, S.R., 367, 372, 760
 Jones, V., 729
 JonesV, R.J.M., 724
 Jonker, H., 665
 Jonsell, U., 843
 Joos, E., 194, 195
 Jordan, C.E., 582
 Jordan, T.E., 441
 Joshi, S.R., 489, 490
 Jourdain, B., 843, 848
 Jouzel, J., 832, 842, 843, 862, 864, 865, 871, 873, 875, 877–879
 Jowsey, J., 744
 Joye, S.B., 330, 332–336
 Ju, X.T., 462
 Jubenville, J., 460
 Juillot, F., 146
 Jull, A.J.T., 212, 368, 374, 477, 482
 Jumeau, E.J., 680
 Jumeau, J., 651
 Jung, M., 67, 74
 Junge, C.E., 578, 579
 Jungers, M.C., 66, 73
 Jweda, J., 68, 72, 75, 305, 312, 313, 319, 320, 509, 788
- K**
 Kabling, M., 452, 469, 612, 614, 615, 622, 624, 837, 846, 847
 Kable, E.J.D., 749
 Kachanoski, R.G., 503, 504, 506
 Kaczorek, D., 92, 93, 95, 96
 Kadi-Hanifi, M., 367
 Kadko, D.C., 76, 77, 312, 351, 801
 Kafalas, P., 366
 Kagawa, A., 818, 822
 Kagi, R.I., 652
 Kaiser, J., 454–456, 460, 462, 467, 468, 612, 613, 615, 837, 846, 848, 850, 852
 Kaiser, P., 458, 466, 639, 683, 684, 686
 Kaleschke, L., 469
 Kalf, J., 418, 431
 Kalinowski, M.B., 377
 Kallemeyn, G.W., 134
 Kalnay, E., 619
 Kalt, A., 51
 Kamawura, K., 879

- Kamber, B.S., 835
 Kamenos, N.A., 378
 Kamenov, G.D., 753, 754
 Kamenskiy, I.L., 296
 Kamioka, H., 537
 Kampschreur, M.J., 456, 470
 Kana, T.A., 451, 452
 Kanamitsu, M., 619
 Kanamori, H., 297
 Kang, N., 435
 Kannan, K., 680, 681, 688–690, 694
 Kannan, N., 687
 Kanoh, H., 46
 Kapit, J., 441
 Kaplan, I.A., 642
 Kaplan, I.R., 156, 170, 642, 836
 Kapp, T., 679, 681, 682, 686, 688, 689, 696
 Karavanic, I., 733, 735
 Karbowska, B., 253
 Karl, D.M., 418, 460, 468, 799
 Karlsen, D.A., 651
 Karlsson, L., 596
 Karlstrom, K.E., 290
 Karner, D.B., 206, 207, 210
 Karol, I.L., 833
 Kasemann, S.A., 43, 108, 111, 114, 121
 Kasemuspayaya, V., 334, 339
 Kashparov, A.V., 596
 Kaste, J.M., 22, 63, 64, 68, 72, 79, 302, 306–308, 312, 406, 488, 495, 497, 498, 508–510, 576, 581
 Kastle, C.R., 788, 800, 801
 Kastern, M., 694
 Kasting, J., 520
 Kastner, M., 262, 665
 Katsuragi, Y., 593
 Katz, B.G., 332
 Katz, S.A., 157
 Katzenberg, M.A., 723, 728, 731, 748, 751
 Katzenberg, M.S., 723
 Kaufman, A., 306, 347, 352, 793, 798
 Kaufmann, R.S., 436
 Kautsky, H., 308, 382
 Kavner, A., 180, 181, 189, 194
 Kawabata, H., 348–350
 Kawamura, H., 42
 Kawamura, K., 252, 865–867, 876–878
 Kaya, G., 253
 Keys, R.R., 210, 247, 257
 Keeler, G.J., 229, 232, 238–241
 Keeling, C.D., 704, 716
 Keeney, D.R., 835
 Keeney-Kennicutt, W.L., 383
 Keenleyside, A., 732
 Kehoe, R.A., 772
 Keigwin, L.D., 147, 150
 Keinonen, M., 770
 Keisch, B., 36
 Keitel, C., 817, 819
 Keith, H., 817
 Keller, E.A., 497
 Keller, K., 19, 239
 Kelley, A.E., 794, 798
 Kelley, C.A., 665, 666
 Kelley, J., 801
 Kelley, J.J., 801
 Kelley, J.M., 367, 372, 383, 396, 398, 399, 401, 402, 404, 408–411
 Kelley, K., 51
 Kelley, P.J., 744
 Kelley, S., 251
 Kellner, C.M., 724, 729, 731
 Kelly, E.F., 90, 95–98, 101
 Kelly, S.D., 704, 716
 Kelly, W.R., 834
 Kelly-Gerreyn, B.A., 53
 Kemp, R.S., 377
 Kempe, S., 380
 Kendall, C., 22, 164, 189, 420, 421, 423–426, 430, 431, 441, 613, 614, 703, 833, 836, 837, 840, 849
 Kenison-Falkner, K., 207, 209, 214
 Kenna, T.C., 18, 296, 308, 321, 367, 399, 402, 411, 412, 488
 Kennedy, B.J., 772
 Kennedy, B.M., 289–290, 297
 Kennedy, B.P., 19
 Kennedy, V.H., 495
 Kennicutt, M.C. II., 681
 Keppens, E., 798
 Kerr, L.A., 796
 Kershaw, P.J., 381, 382, 408
 Kersten, M., 312
 Kesler, S.E., 232, 235, 237, 239
 Kester, C.L., 839
 Ketten, D.R., 801
 Ketterer, M.E., 18, 372, 393, 398, 400, 401, 403, 404, 411, 412, 509, 510, 575
 Kexel, H., 683
 Key, R.M., 329, 330, 333, 344, 346, 352, 375
 Khandaker, N.R., 436
 Kharaka, Y.K., 289–290, 297
 Kharkar, A.G., 280
 Kharkar, D.P., 271, 799, 800
 Khlebovich, V., 370
 Houry, J., 766
 Kiba, T., 834
 Kiczka, M., 197, 198
 Kiese, R., 470
 Kieser, W.E., 368, 374
 Kigoshi, K., 552, 554
 Kikawada, Y., 592, 599
 Kikuchi, S., 489
 Kilham, P., 428
 Kilham, S.S., 727
 Kilius, L.R., 372
 Killingley, J.S., 798
 Killups, S., 637
 Killups, V., 637
 Kim, C., 400, 401
 Kim, C.K., 370, 371, 407, 592, 596, 598, 600, 787
 Kim, C.S., 370, 371, 407, 592
 Kim, D.H., 462
 Kim, G., 14, 17, 272–281, 307, 311, 329, 330, 334, 338, 339, 347

- Kim, K.R., 338, 460
 Kim, S., 272, 280, 281, 347
 Kim, S.H., 377, 381, 384, 788, 799
 Kim, S.J., 278, 279
 Kim, S.K., 307
 Kim, S.S., 281
 Kim, T.-H., 14, 17
 Kim, Y.B., 307, 456
 Kimble, B.J., 638
 Kimirei, I., 90, 98
 Kimura, D.K., 788, 800, 801
 Kineke, G.C., 322
 King, L.L., 785, 794, 795
 King, P.T., 347, 355
 Kingston, J.D., 753, 754
 Kinney, C., 460, 464
 Kipfer, R., 285, 289, 290, 296
 Kipphut, G.W., 354
 Kirbasaoğlu, C., 381
 Kirchhefer, A., 816
 Kirchner, F., 625
 Kirchner, G., 372, 495, 497
 Kirchner, S., 848
 Kirk, A.B., 435, 436, 441
 Kirk, G.J.D., 197, 198
 Kirk, L.B., 168, 169, 173
 Kisakurek, B., 42, 44, 47, 48, 112, 116, 185, 198
 Kiselev, A.A., 833
 Kiss, J.J., 79
 Kistler, R., 619
 Kitajima, K., 815, 823
 Kitchen, J.W., 164
 Kitto, M.E., 346
 Kiyomoto, K., 339
 Kjeldsen, P., 644
 Klaue, B., 232, 235, 237
 Klaus, S., 705
 Klecka, G.M., 681, 697
 Kledka, G.M., 643, 662, 664, 665, 667
 Kleeman, R., 823
 Klees, G.G., 612, 615, 620, 832
 Klein, B., 332, 382
 Klein, C., 190
 Klein, J., 62, 63, 76, 78, 582
 Klein, R.T., 798
 Kleine, T., 90
 Klewe-Nebenius, H., 126
 Kley, D., 849, 850
 Kline, A., 552
 Kling, G.F., 503, 504
 Kling, G.W., 19, 195
 Klinkhammer, G., 256
 Klouda, G., 666
 Klump, J.V., 75, 354, 509
 Knies, D.L., 62
 Knipper, C., 742, 752, 754, 760
 Knohl, A., 816, 817, 820
 Knoke, K.E., 469
 Knoll, A.N., 650
 Knudson, K.J., 739, 741, 749, 751, 753, 755, 759, 760
 Knutsen, A.B., 128
 Knyazev, D.A., 147, 148
 Knyf, M., 731, 734
 Kobashi, T., 865–867, 876, 877
 Kobel, K., 832, 836, 850–852
 Koch, D.M., 62, 491, 576
 Koch, P.L., 109, 110, 116, 742, 743, 746, 747, 749, 752, 756, 760, 816
 Koczy, F.F., 344, 351, 352
 Kodama, N., 817
 Koeberl, C., 206
 Koedam, N., 820, 821
 Koehler, G., 667
 Koeniger, P., 817
 Koepfler, E.K., 418
 Koertling, R.G., 6, 476
 Kohl, C.P., 477, 478
 Kohl, S., 441
 Kohman, T.P., 248
 Kohn, M.J., 751
 Koide, M., 207, 209–212, 214, 308, 371, 383, 386, 387, 398, 400, 402, 496
 Kolb, W., 590, 600
 Kolhatkar, R., 639, 664
 Koller, D., 6
 Kolodny, Y., 160–162, 348, 418, 423–425, 552
 Koltermann, P., 367, 377
 Komárek, M., 769
 Komatsu, D.D., 613, 837
 Komiya, T., 116
 Komura, K., 372
 Konishi, S., 94
 Konshin, O.V., 497
 Konuk, T., 373, 380, 383
 Koons, P., 540
 Koornneef, J.M., 750
 Kopinke, F., 644
 Kopple, J.D., 768, 769, 772
 Korkisch, J., 128
 Korky, J.K., 495
 Korn, A.J., 41
 Kornexl, B.E., 424, 613, 835–837, 839
 Korobova, E., 495
 Korsch, M.J., 770, 771, 778, 779
 Korteling, R.G., 576
 Korytár, P., 688
 Koschinsky, A., 247, 255, 261, 264
 Koshikawa, H., 663
 Kosler, J., 42, 53
 Kosmas, G., 506
 Kostera, J., 462
 Koud, J.-M., 93
 Kounaves, S.P., 435, 442
 Kovach, J., 418
 Kowalchuk, T., 506
 Kowalski, L., 495
 Kownacka, L., 488
 Kozak, K., 493
 Kozdon, R., 105–108, 111, 112, 115
 Koziet, J., 680
 Krabbenhoft, D.P., 238, 241
 Kraemer, S.M., 197, 198

- Kraepiel, A.M.L., 229, 239
 Krahenbuhl, U., 206
 Krajewski, B.T., 590, 593
 Kralik, M., 745, 751
 Kramer, J.R., 839
 Kramer, U., 198
 Kramers, J.D., 180, 188, 558
 Krankowsky, D., 455, 467, 612, 615, 618–620, 832, 833, 848
 Krause, C., 820
 Krause, R., 752, 754, 755
 Krauss, M., 666
 Kress, A., 808, 820
 Kress, N., 418
 Krest, J.M., 329
 Kretzschmar, R., 197, 198
 Kreutz, K.J., 798, 835, 842, 843, 848
 Kreuzer, H.W., 712
 Kreuzer-Martin, H.W., 36, 710
 Krey, P.W., 383, 384, 397, 590, 593, 599
 Krezoski, J.R., 498
 Krieger, R.L., 436
 Krigbaum, J., 753, 756
 Kring, D.A., 206
 Krinner, G., 862
 Krishnamurthy, R.V., 785, 801, 802
 Krishnaswami, S., 3–5, 19, 35, 62–64, 71–73, 76, 78, 206, 273,
 275, 306, 308, 347, 351, 520, 527, 530, 532, 533, 536,
 557, 564, 585, 786, 787, 794–796, 799
 Kritee, K., 230, 234, 237
 Kroeger, K.D., 356, 799
 Kroeze, C., 451, 452, 611
 Krom, M.D., 418
 Kromer, B., 351, 377
 Kroopnick, P., 460, 468
 Krothe, N.C., 332
 Krouse, H.R., 77, 89, 109, 119, 120, 161, 168, 169, 436, 834
 Krueger, H.W., 729
 Krupp, E.A., 232
 Ku, T.-L., 65–71, 78, 80, 351, 352, 564, 785, 786, 793, 797, 798
 Kubik, P.W., 32, 69, 557, 582
 Kuc, T., 837
 Kucera, M., 42, 53
 Kuder, T., 639, 644, 662, 664, 666
 Kudrass, H., 78
 Kudryavtzev, D.I., 99
 Kuehl, S.A., 404, 490
 Kuever, J., 156
 Kuhn, M., 625
 Kuhnert, H., 112
 Kuiper, J.L., 497
 Kukkadapu, R.K., 422–424, 432
 Kulongoski, J.T., 14, 19, 287–288, 290, 292, 293, 295, 296,
 298, 299
 Kulp, J.L., 34
 Kulp, L.J., 351
 Kulpa, C.F., 653
 Kumar, A., 530, 532, 533, 536
 Kumar, K.K., 821, 823
 Kumar, R., 838, 839
 Kumar, S., 460, 468
 Kumata, H., 666
 Kump, L.R., 262, 520, 535, 540
 Kunasek, S.A., 469, 615, 835, 841, 843, 845–848
 Kupferman, S.L., 379
 Kurganova, I., 462
 Kurkjian, R., 770
 Kuroda, P.K., 599
 Kurosaki, Y., 598
 Kurtz, A.C., 97, 262
 Kurz, D.R., 485, 486
 Kusakabe, M., 65, 67–71, 78, 80, 195, 834
 Kutschera, W., 374
 Kuwabara, J., 372
 Kuzyakov, Y., 92, 93, 95, 96
 Kvenvolden, K.A., 645, 662
 Kwong, L.L.W., 381, 384
 Kylander, M.E., 206
 Kyle, J.H., 743, 751
 Kyser, T.K., 798
 Kyte, F.T., 206
- L**
 La Guardia, M.J., 692
 La Roche, J., 146
 La Rosa, J.J., 370, 381, 384
 Laanbroek, H.J., 452, 468
 Labeyrie, L.D., 866, 867
 Lacan, F., 129–131, 133, 134, 143, 144, 149, 531
 Lacrampe-Couloume, G., 643, 653, 664, 665, 681,
 684–686, 697
 Laffont, L., 230, 237, 241
 Lagos, M., 141
 Laidlaw, M.A.S., 765
 Lake, J.L., 665, 666, 697
 Lakey, B.L., 332
 Lakshminarayana, M.R., 814
 Lal, D., 4, 13, 14, 16, 61, 63–67, 71–73, 212, 296, 306, 308, 376,
 418, 475–483, 489, 554, 573–585, 786
 Lal, R., 485
 Lambert, G., 252, 271, 273
 Lambert, J.B., 745
 Lamberty, A., 89, 436
 Lamborg, C.H., 230, 241, 585
 Lambrot, C., 813, 822
 Lammertzahl, P., 455, 467, 618, 832, 833, 848
 Lamothe, P.J., 184
 Lampitt, R.S., 53
 Lance, C., 503, 504
 Lance, J., 492, 500
 Lance, M.J., 436, 437
 Lanciki, A., 846
 Land, M., 89, 90, 93, 96, 99, 527, 530
 Landa, E., 383
 Landais, A., 615, 861, 864–867, 869, 871, 873, 875, 877, 878
 Landis, J.D., 509
 Landmeyer, J.E., 664
 Landreau, A., 441
 Landwehr, J.M., 508
 Lane, G.A., 624
 Lane, S.N., 486
 Lane, T.W., 142
 Lane-Smith, D., 347

- Lang, C., 864, 866, 875, 876
 Lange, H.J., 61
 Langer, G., 114
 Langford, J.C., 376
 Langman, S.R., 288
 Langmuir, C.H., 43, 44
 Langmuir, D., 344
 Langston, J., 613, 837
 Langway, C., 871
 Langway, C.C. Jr., 383
 Lanphear, B.P., 766, 779
 Lao, Y., 69, 76, 79
 Larcher, A.V., 652
 Larcher, R., 704
 Larieve, D., 400
 Larimer, J.W., 150
 Larivière, D., 348
 Lark, N.L., 443
 LaRock, P.A., 272, 278–280, 308
 LaRock, P.L., 272, 279
 Larsbo, A., 489
 Larsen, C.S., 731, 735, 748
 Larsen, I.L., 62–64, 71, 75, 77, 311, 367, 377, 383, 491, 494, 501, 502
 Larsen, M.C., 63
 Larson, P.B., 179
 Lartaud, F., 798
 Larter, S.R., 651, 652
 Lasaga, A.C., 106, 107, 520, 524, 536, 584, 845
 Laszity, A., 770
 Latham, A.G., 551, 793
 Latter, P.M., 653
 Lauber, C., 452, 462
 Lauf, J., 464
 Laughlin, R.J., 452, 469
 Laul, J.C., 210
 Lauretta, D.S., 232
 Lauria, D.C., 345
 Lavigne, M.B., 820
 Law, A.J., 770
 Law, K.R., 703
 Law, K.S., 625
 Lawrence, A.E., 69
 Lawrence, J.R., 813
 Laxman, P., 436
 Lazar, B., 348, 552
 Lazreg, N.B., 732
 Lazzeri, M., 98
 Le, C., 271, 273
 Le Cloarec, M.F., 252, 273
 Le Gloarec, M.F., 273
 Le Roux, P., 43, 44
 Lea, D.W., 147
 Lea, F.M., 801
 Lear, C.H., 54
 Leavitt, S.W., 808, 815, 820
 LeBaron, G., 48
 LeBihan, O., 194, 195
 Lechner, J., 253
 LeClaire, J., 444, 446
 Leclerc, A., 460
 Lecloarec, M.F., 252
 Lecuyer, C., 419
 Ledin, A., 665
 Lee, A-R., 711
 Lee, C.C.W., 612, 835, 839, 840
 Lee, C.T.A., 206
 Lee, C.W., 835, 839
 Lee, D-C., 261, 553, 750, 834
 Lee, D.J., 285, 287, 289, 294
 Lee, E.S., 332
 Lee, H.J., 377, 381, 384
 Lee, J-M., 347, 540
 Lee, S., 407
 Lee, S.H., 367, 368, 370, 374, 377, 381, 384, 596
 Lee, S.R., 206
 Lee, T., 53, 61, 65, 71, 405, 418, 494
 Lee, T.H., 772, 776
 Lee, T.W., 776
 Lee, V.E., 560
 Leeks, G.J.L., 504
 Leeman, W.P., 53, 54
 Lee-Thorp, J.A., 703, 724, 729, 731, 733, 735, 746, 755, 757, 760
 Legeas, M., 421, 424, 425
 Legrand, M.R., 832, 843, 844, 848, 850
 LeGrande, A.N., 808, 823
 Lehman, M.F., 441
 Lehman, T., 435, 442
 Lehmann, B.E., 289, 443
 Lehmann, M.F., 180
 Lehnert, K., 679, 681, 682, 686, 688, 689, 696
 Lehrter, J.C., 428
 Leibundgut, C., 817
 Leifer, R., 590, 599
 Leininger, S., 469
 Leland, J., 540
 Leland, W.T., 126
 Lelarge, C., 817
 Lemarchand, D., 109, 113, 115–118
 Lemarchand, E., 46–48
 Lemieux-Dudon, B., 875
 Lemly, A.D., 157
 LeMoulllec, Y., 194, 195
 Lenaers, G., 92
 Leng, M.J., 89, 90, 93, 96
 Lenhart, J.J., 497
 Leon Vintro, L., 383
 Leonard, K.S., 383
 Leonards, P.E.G., 688
 Lepetit, G., 371
 Leprun, J.C., 558, 561, 562
 Lepy, M-C., 366
 Lerche, I., 347
 Lerchner, U., 694
 Leslie, B.W., 564
 Leslie, K.A., 752, 756
 Lesser, E.L., 662, 667
 Lestel, L., 193
 Letolle, R., 458, 466, 683, 684, 686
 Leuenberger, M., 290, 864, 866, 867, 871, 875, 876
 Leuning, R., 817

- Levasseur, S., 207, 209, 212–215
 Levesque, B., 775
 Levine, J., 206, 207, 210
 Lewan, M.D., 646–648, 652
 Lewis, A.B., 744
 Lewis, B.A., 794
 Lewis, R., 582
 Leya, I., 61
 Leythausen, D., 645
 Li, H-C., 785, 786, 797
 Li, J., 834
 Li, M., 507, 651, 652
 Li, R.H., 90, 95
 Li, S.H., 157, 172, 207, 211, 216
 Li, W.J., 467, 468, 612, 621
 Li, X.H., 520
 Li, Y-H., 61, 65, 80, 135, 313, 315, 333, 344, 346, 349, 494, 765
 Li, Z.B., 507
 Liang, F., 770
 Liang, M.C., 620
 Liang, X., 157, 172
 Liang, Y., 420, 422–425
 Liao, H., 398, 404
 Liao, Y., 651
 Libby, W.F., 6, 576
 Libourel, G., 138, 181, 189, 194, 253
 Lichtner, P.C., 497
 Liebetrau, V., 53, 553, 739
 Lien, H.N., 494
 Liermann, L., 179
 Lieuvain, M., 582
 Liewig, N., 558, 561, 562
 Lifton, N.A., 479, 483
 Lima, A.L., 305
 Lin, B.H., 706
 Lin, C-F., 559
 Lin, C-J., 229
 Lin, F.J., 307, 491
 Lin, G., 712, 716, 810, 813, 814, 816, 820
 Lin, H.L., 306
 Lin, T-S., 260
 Lin, X., 55
 Lin, Y., 435, 611
 Lin, Z.B., 207, 220, 221
 Lindahl, P., 367, 372, 398, 400, 406, 412
 Lindberg, S.E., 229
 Lindner, M., 394
 Ling, H.F., 212, 261, 537
 Lingard, S.M., 798
 Lini, A., 614
 Linke, P., 820
 Linnak, V., 495
 Linsalata, P., 372
 Linsley, G., 365
 Liong Wee Kwong, L., 368, 370, 374
 Lipp, J., 808
 Lipschultz, F., 614, 849
 Lipschutz, M.E., 150, 184
 Lipson, M., 452, 463, 464, 470
 Lis, J., 253
 Lisińska, G., 713
 Liss, P.S., 348, 349
 Little, C.H.A., 820
 Little, E.A., 732
 Liu, B., 332
 Liu, D.L., 281, 651, 652
 Liu, F., 692
 Liu, J.T., 306, 506, 507, 651
 Liu, P.L., 507
 Liu, T.S., 63
 Liu, T.Z., 79
 Liu, W., 733
 Liu, Y.G., 43, 44, 184, 279, 280
 Liu, Z., 331, 332, 335
 Livingston, H.D., 5, 310, 367–369, 373, 376, 377, 379–381, 383, 384, 409
 Llewellyn, D.R., 622
 Lloyd, J., 813, 814
 Loader, N., 808
 Loader, N.J., 808, 815, 816, 820, 823
 Lobb, D.A., 506
 Lockwood, J.A., 477
 Lodders, K., 134
 Löffler, J., 820
 Lofthouse, J.H., 704
 Logan, T.J., 486
 Lohan, M.C., 179
 Lohmann, K.C., 115, 798
 Loiseaux, J.M., 582
 Loizeau, J.I., 74, 80
 Loizeau, J-L., 494
 Lolacono, N.J., 776
 Lomas, M.W., 277, 278
 Lomenick, T.F., 494
 Long, A., 436, 820
 Longerich, H.P., 188
 Longinel, A., 839
 Longinelli, A., 418, 420, 422, 423, 742
 Longstaffe, F.J., 703
 Lonsjo, H., 497
 Loosli, H.H., 377
 Lopes, I., 272
 Lopez-Penalver, J.J., 489
 Lorand, J.P., 210
 Lorbeer, E., 716
 Lord, R.A., 212, 213
 Los, S., 816
 Lott Iii, D.E., 287
 Lott, M.J., 36, 710
 Loustau, D., 813, 822
 Louvat, P., 186, 192, 193, 520, 529, 536
 Lovat, P., 533, 536
 Love, A., 289
 Love, S.G., 212
 Lovett, M.B., 383, 395
 Lovley, D.R., 664
 Lowdermilk, W.C., 486
 Lowrance, R., 451, 452, 503, 504
 Lowry, P.D., 62–64, 75, 311, 494
 Lu, J., 651
 Lu, P., 558
 Lu, S.Y., 232, 237

- Lu, X., 600
 Lubec, G., 703
 Lucas, L.V., 333
 Lucas, Y., 96, 97
 Luck, J.M., 206, 208
 Ludden, J., 160–162, 170
 Ludwig, W., 529
 Luguët, A., 210
 Lujanas, V., 596
 Lujaniené, G., 596
 Lukavec, Z., 344
 Lunch, C., 816
 Lundstrom, C.C., 3, 29, 552, 553, 789, 793, 795, 800
 Luo, S.D., 66, 69, 351, 352, 564
 Luo, X., 553
 Luo, Y., 182, 184
 Lupker, M., 553, 560
 Lupton, R., 346
 Lux, B., 468, 470
 Luz, B., 418, 423–425, 467, 468, 612, 619, 621, 624, 840,
 864–866, 868, 871, 873
 Lyden, E.F.X., 65, 68
 Lyles, L., 486
 Lynch, A.M., 820
 Lynch-Stieglitz, J., 142, 147
 Lyons, J.R., 612, 623, 845, 846
 Lyons, T.W., 170, 180, 186, 199
 Lyons, W.B., 42, 43
- M**
- Ma, G.R., 90, 95
 Ma, J.F., 94, 525, 527
 Ma, L., 553, 561–563, 565
 Maamaatuaiahutapu, K., 332
 Mabit, L., 509
 Macalady, J.L., 441
 Macchiarelli, R., 724, 732
 MacClune, K., 810
 MacDonald, K., 770
 Macdonald, R.W., 215
 Macdougall, J.D., 105, 106, 110, 112, 273
 Mace, P.M., 800
 MacFadden, B.J., 704
 MacFarlane, A., 527
 Machado, A., 65
 Maciejczyk, K., 644
 Maciel, G.E., 642
 MacIntyre, S., 351, 357
 Mackay, D.M., 643, 664
 MacKenzie, A.B., 311
 Mackenzie, F.T., 44, 53
 Mackenzie, R.A., 509
 Mackereth, F.J.H., 398
 Mackie, A., 724
 MacKinnon, L., 684–686
 Macko, P., 834
 Macko, S.A., 665, 681, 703
 Maden, C., 376
 Madsen, E.L., 452
 Maeda, Y., 488
 Maejima, Y., 73
- Maes, A., 495
 Magal, E., 552
 Maggi, A., 110
 Magilligan, F.J., 75, 509, 510
 Magini, A., 69, 70
 Magnuson, B.A., 716
 Maguire, D., 109, 118
 Mahaffey, K.R., 770, 772, 774, 775, 778
 Mahannah, R., 76, 77, 80
 Mahendra, S., 665
 Maher, K., 179, 551–556, 558–563, 565
 Maidment, D.R., 344, 345, 351
 Maier-Reimer, E., 100
 Major, D.W., 684–686
 Major, J.E., 820
 Majoube, M., 623
 Makdisi, R.S., 160, 161, 164–166, 192
 Makeyev, V., 370
 Makishima, A., 112, 113
 Makita, Y., 46
 Malhotra, P.K., 61
 Malinovsky, D., 196
 Malloy, C.R., 776
 Mambelli, S., 808
 Mamuro, T., 590, 599
 Mamyryn, B.A., 290
 Managave, S.R., 808, 812, 814, 818, 820, 821, 823
 Manca, G., 704
 Manceau, A., 552
 Mancilla, H.B., 509
 Mancini, S.A., 653, 664, 665, 681
 Mandernack, K.W., 179, 460, 464, 665
 Manepong, S., 467, 468
 Mangini, A., 67, 71, 74, 78, 261
 Manhès, G., 132, 147, 553
 Mani, F.P., 865
 Mann, D.R., 376
 Mann, J.L., 834
 Mann, M.E., 62
 Mannering, U., 752, 756, 757
 Manning, K.R., 444, 446
 Manolagas, S., 729
 Manowitz, B., 843
 Mansuy, L., 653, 665
 Manton, W.I., 766, 768–770, 772–776, 779
 Manzanilla, L., 741, 753, 755
 Mao, X.Y., 207, 211, 216
 Maoui, R., 367
 Marathianou, M., 506
 Marcantonio, F., 206, 219, 527, 528
 Marchant, D.R., 833, 836, 840
 Marcus, R.A., 22, 618
 Maréchal, C.N., 5, 137, 146, 180, 188
 Mar-Gerrison, S., 255, 260–262, 265
 Maria, H., 71
 Marin, L., 160–162, 170
 Marinaccio, A., 221
 Marincovich, L., 77
 Marine, I.W., 285, 289
 Marino, B.D., 726
 Mariotti, A., 441, 683, 684, 686, 836, 863, 867

- Mark, E., 456
 Mark, T.D., 456
 Markel, D., 420, 427
 Markovics, G., 525, 526
 Markowitz, M.E., 777
 Marley, N.A., 275
 Marriott, C.S., 43, 53, 54, 113, 115
 Marriott, P.A.H., 796
 Marroquin, R.J., 441, 446, 447
 Marschall, H.R., 263
 Marschner, H., 94, 108, 196–198
 Marshall, A., 113
 Marshall, W.A., 376
 Martell, E.A., 34, 271, 273, 274
 Marten, R., 71
 Martens, C.S., 63, 322, 346, 354
 Martí, V., 552
 Martin, A.M., 419, 420, 422–425, 432
 Martin, C.E., 212
 Martin, E., 835, 845
 Martin, F., 524
 Martin, G., 709
 Martin, G.G., 704
 Martin, G.J., 682
 Martin, I.D., 776
 Martin, J.B., 346, 354, 355
 Martin, J.G., 436
 Martin, J.H., 178
 Martin, J.M., 151, 214, 786
 Martin, M.L., 682
 Martin, P., 331, 590, 592, 599, 704, 787
 Martin, R.V., 611
 Martin, S., 43, 55
 Martin, T.J., 729
 Martin, W.R., 354, 355
 Martin, Y-L., 704
 Martinelango, P.K., 435
 Martinelli, G., 301
 Martinerie, P., 833, 853
 Martinez, C.E., 75
 Martin-Garin, A., 497
 Martins, J.M.F., 469
 Martinsson, O., 196
 Marty, B., 289
 Marty, B., 285, 292, 293, 297, 298
 Martz, L.W., 79
 Maruya, K.A., 665, 666, 697
 Marwan, N., 821
 Masarik, J., 61, 62, 489, 582
 Mase, D., 628
 Mase, D.F., 469
 Mashonkina, L., 41
 Mason, E.A., 868, 871
 Mason, P.R.D., 170
 Mason, R.P., 229
 Mason, T.F.D., 180, 190, 194, 197, 198
 Masque, P., 77, 272, 311, 383, 408
 Massler, M., 743, 744
 Masson-Delmotte, V., 875, 878
 Mast, M.A., 839
 Mastalerz, M., 652
 Masters, P.M., 724
 Masterson, W.D., 653
 Masud, Z., 709
 Masuda, A., 184, 211
 Mather, T.A., 845
 Mathews, K.M., 787
 Mathieu, D., 563
 Mathieu, G.G., 346, 349, 350, 354, 355
 Mathur, R., 179
 Matishov, D., 387
 Matisoff, G., 18, 62–66, 72, 75, 306, 308, 314, 315, 404, 485–511
 Matmon, A., 66, 73
 Matson, P., 452
 Matson, P.A., 418, 457
 Matsubaya, O., 809
 Matsuhisa, Y., 455, 611, 612
 Matsumoto, K., 90
 Matsumoto, M., 770
 Matsumura, H., 78
 Matsunami, T., 590, 599
 Matthäus, F., 639, 663, 667
 Matthews, A.D., 164, 198, 247, 256, 257
 Matthews Bar-Matthews, M., 196
 Matthews, D.E., 639, 651, 661, 680, 834
 Matthews, K.M., 62, 605, 606
 Mattie, P., 51
 Mattielli, N., 180, 194
 Matzarakis, A., 819
 Mauersberger, E., 832
 Mauersberger, K., 455, 467, 618–620, 624, 832, 833, 848
 Mauldin, A., 382
 Mauri, F., 98
 Maurice, L., 230, 237, 241
 Mauro, D., 666
 Max, T., 424, 425
 Maximov, T.C., 818, 822
 Maxwell, J.R., 638, 648–650
 Maxwell, S.L., 398, 400
 May, H.D., 679, 681, 686, 692
 Maya, L., 436, 437
 Maybeck, M., 193
 Mayeda, T.K., 6
 Mayer, H., 817, 819
 Mayer, M.G., 259
 Mayewski, P.A., 832, 838
 Maynard, R., 768
 Mays, S.A., 729
 Mazeas, L., 653, 665
 Mazor, E., 285, 290
 Mazzilli, B., 279, 280
 McAlister, D., 111
 McArthur, J.M., 748
 McBride, M., 75
 McCabe, J.R., 615, 840, 845, 849
 McCaffery, S., 665
 McCaffrey, R.J., 35
 McCall, P.L., 498
 McCammon, C.A., 251
 McCarroll, D., 808, 815, 816, 823
 McCarthy, E.D., 638

- McCarthy, J.J., 836
 McCauley, S., 532, 535
 McCool, D.K., 503
 McCormick, M., 77
 McCrea, J.M., 832, 834
 McCubbin, D., 383
 McCulloch, M., 795
 McCullough, C.J., 507
 McDaniel, D.K., 206
 McDermott, T., 168, 169, 173
 McDonald, H.O., 436, 445
 McDonald, I., 140, 206
 McDonald, J., 647
 McDonnell, J.J., 22, 189
 McDonough, W.F., 43, 44, 53, 134, 141, 212, 251
 McDowell, N.G., 811, 816, 819
 McElroy, J.B., 726
 McFarlane, G.A., 800
 McGarrah, J.E., 552
 McGee, E.J., 492
 McGoldrick, P.J., 247, 257
 McHargue, L.R., 67
 McHenry, J.R., 492, 503–505
 McHenry, M.C., 403, 405
 McHugh, D.J., 638
 McIlvin, M.R., 460, 461, 463, 464, 613, 837
 McIntyre, S.C., 492, 500, 503, 504
 McKay, C.P., 441, 442
 McKean, J.A., 66, 73
 McKee, B.A., 76, 278, 279, 317–319
 McKeegan, K.D., 835
 McKelvie, J.R., 643
 McKenna, D.S., 625
 McKenzie, J.A., 441, 818
 McKenzie, W.F., 422
 McKibbin-Vaughan, T., 318
 McKinney, C.R., 832, 834
 McLaughlin, K., 417, 419–430
 McLaughlin, M., 8
 McLennan, S.M., 134
 McLing, T.L., 164, 166, 564
 McMahan, C.A., 383
 McManus, J.F., 180, 196, 199, 552, 555, 560, 863
 McNeal, J.M., 157
 McNear, D., 62, 64, 275, 489, 491, 576, 582, 583, 599, 605, 788
 McNeill, G.W., 288
 McRae, C., 666
 Meade, R., 542
 Meason, J.L., 599
 Measures, C.I., 48, 66, 69–71, 150
 Meckenstock, R.U., 662, 664, 665
 Medina, E., 726
 Medina, R., 836, 839
 Meeker, L.D., 582, 583, 838
 Meese, D.A., 383
 Megens, L., 376
 Méheut, M., 98
 Mehring, M., 665
 Mei, B., 652
 Meibom, A., 43, 55, 113
 Meier-Augenstein, W., 665, 676, 677, 680, 681
 Meija, J., 230
 Meijer, H., 467, 468
 Meijer, H.A.J., 612, 621
 Meile, C., 355
 Meinert, L.D., 179
 Meinzer, F.C., 817
 Meire, P., 92, 101
 Meisel, T., 206, 207, 209–212
 Meixner, A., 52, 53
 Melander, L., 639, 683
 Melbye, F.J., 731
 Melbye, J., 731
 Melcher, J., 680, 689
 Melieres, M.A., 69
 Mellars, P., 35
 Mello, M.R., 648–650
 Menacer, M., 367
 Mensing, T.M., 739, 748
 Mentel, T.F., 622
 Menyailo, O.V., 464, 465
 Mercer, J.W., 343
 Merren, T., 681
 Merrill, J.R., 65, 68
 Merritt, D.A., 680
 Metay, A., 464
 Metges, C.C., 705
 Metz, S., 254, 262
 Metzger, J., 836
 Meunier, J.-D., 90, 93, 100, 101
 Mével, C., 51
 Meybeck, M., 214, 786
 Meyer, H., 821
 Meyer, R., 306, 311
 Meyers, P.A., 237, 239
 Meyers, R.E., 62
 Meynadier, L., 553, 555, 564–566
 Mezger, K., 184
 Miayo, T., 382
 Michael, P.J., 215
 Michalski, G.M., 441, 445, 452, 469, 612–619, 622, 624, 625, 627, 833, 836, 837, 839, 840, 846, 847
 Michel, H.V., 210
 Michel, J., 347
 Middleton, R., 76, 582
 Middleton, W.D., 741, 753, 755
 Mietelski, J.W., 398–400, 406, 411, 412, 490, 493, 596
 Mietelski, M.E., 488, 490, 502
 Mihaljevič, M., 769
 Mikami, M., 598
 Mikus, R., 376
 Milies-Lacroix, J.C., 371
 Miller, A.J., 404
 Miller, A.R., 331
 Miller, C.E., 453, 454, 460, 462, 463, 851
 Miller, C.V., 219
 Miller, D.L., 820
 Miller, G.H., 479, 483, 727
 Miller, J.D., 93
 Miller, K.G., 750
 Miller, K.M., 497
 Miller, M.F., 88, 436, 448, 611, 612

- Miller, M.H., 506
 Miller, R., 343
 Miller, S.A., 298
 Miller, W.P., 46
 Millero, F., 115
 Milliés-Lacroix, J-C., 372
 Milliman, J.D., 542
 Millot, R., 42–44, 46–49, 51, 52, 87
 Mills, C.T., 460
 Mills, M.J., 845
 Mills, R.A., 53, 179
 Milner, N., 723
 Milton, D.A., 800
 Min, J-S., 711
 Minagawa, M., 216, 709, 727, 836
 Minai, Y., 63, 65, 80
 Minami, K., 452
 Mineev, S.D., 190
 Ming, D.W., 441, 442
 Minifie, S.A., 643, 653
 Miracle, P., 723
 Miranowski, J.A., 452, 463, 464, 470
 Mitani, N., 94
 Mitchell, A.D., 729
 Mitchell, K., 170, 706
 Mitchell, M., 117, 118, 120
 Mitchell, P.I., 312, 367, 373, 383, 492
 Mitchell, R., 458, 460
 Miwa, T., 464
 Miyada, M., 209
 Miyake, Y., 809
 Miyao, T., 370, 371
 Miyares, P.H., 665, 666
 Mizon, K.J., 768, 770–772, 774–776, 778, 779
 Mizutani, Y., 296, 297
 Mock, C.J., 820
 Moens, L., 750
 Moghissi, A.A., 395
 Mohn, J., 837, 853
 Mohnen, V.A., 582
 Mohrschladt, R., 622, 623, 840
 Moilleron, R., 193
 Mojzsis, S.J., 835
 Mokadem, F., 42, 44, 47, 49, 51, 87
 Molaroni, S.M., 801
 Moldovan, M., 750
 Moldowan, J.M., 637, 638, 644, 645, 649, 651, 653
 Moller, J., 832
 Molnar, P., 540
 Moloney, A.P., 704, 707, 709, 716
 Momoshima, N., 272, 274, 488
 Monaco, G.L., 676, 681
 Monaghan, M.C., 62–64, 66, 73, 585
 Monahan, F.J., 704, 707, 709, 716
 Monna, F., 64, 489, 491, 492
 Monperrus, M., 241, 242
 Monsen, N.E., 333
 Monster, J., 834, 843
 Montagne, D., 73
 Montanez, I.P., 748
 Montero, P.R., 400
 Montgomery, D.R., 486, 540
 Montgomery, J.A., 503, 741, 746, 752, 754, 756, 760
 Montgomery, M., 743
 Montomery, J., 743, 749, 760
 Montoya, J.P., 458, 460
 Mook, W.G., 808
 Moon, D.S., 347
 Moon, E.M., 259, 265
 Moon, S., 520, 525, 528, 529
 Moor, E., 832
 Moorbath, S., 90, 93
 Moore, D.G., 333
 Moore, H.E., 271, 273, 274, 849
 Moore, J., 727
 Moore, J.E., 343
 Moore, J.W., 730
 Moore, K., 723, 724, 727, 731, 735
 Moore, M.P., 834
 Moore, P.A., 486
 Moore, P.G., 378
 Moore, Q., 442
 Moore, R.M., 379
 Moore, R.R., 207, 210
 Moore, W.S., 7, 76, 77, 79, 80, 308–310, 329–338, 344, 345, 347, 350, 352–357, 794–796, 799
 Mora, C.I., 820
 Moran, S.B., 277, 278, 306, 308, 335
 Morasch, B., 665
 Morcelli, C.P.R., 207, 210
 Moreau, J.W., 238, 241
 Moreira, M., 458, 462
 Morel, F.M.M., 142, 229
 Morel, J., 71
 Moreno-Vivian, C., 469
 Morey, G.W., 88
 Morgan, J.W., 205, 206, 208, 212
 Morgenstern, U., 368, 374
 Morin, H., 820
 Morin, S., 469, 612, 614, 615, 618, 619, 623–626, 837, 846–852
 Moriya, H., 381, 384
 Moroder, L., 280
 Morrill, P.L., 664
 Morris, J.T., 418
 Morris, K., 399
 Morris, P.J., 344, 351–353
 Morrison, J., 681
 Morrison, R.D., 662
 Morse, J.W., 383
 Morth, C.M., 843
 Mortlock, R.A., 35, 48
 Morton, J., 619, 620, 734
 Mosegaard, K., 862
 Moser, H., 291, 808
 Moser, J., 207, 209–211
 Mosier, A.R., 451, 452, 611
 Moss, C., 746, 756
 Motelica, M., 179
 Motha, J.A., 493
 Mottl, M.J., 263
 Moulin, V., 552
 Moura, I., 462

- Moura, J.J.G., 462
 Moyer, B.A., 436, 437
 Moynier, F., 147, 197, 198
 Moysey, S., 443
 Mroczkowski, S.J., 438, 441, 445, 446, 449, 613, 622, 835
 Muehlenbachs, K., 263
 Mueller, J.F., 695
 Mueller, K.E., 816
 Muhs, D.R., 798
 Muir, D.C.G., 182, 184, 232
 Mulder, J.W., 456, 470
 Mulhern, D.M., 744
 Mulkey, S.S., 815, 823
 Mulla, D.J., 486
 Müller, A., 106, 110–112, 115
 Muller, B., 195
 Muller, R.A., 6, 206, 207, 210
 Müller, W., 742
 Müller-Lemans, H., 497, 498
 Mulsow, S., 381, 384
 Mulvaney, R., 850
 Mumic, K., 750
 Munakata-Marr, J., 665
 Mund, M., 820
 Munkelwitz, H.R., 843
 Munker, C., 184
 Munn, R.J., 868, 871
 Munnecke, A., 87
 Munnich, K.O., 495
 Munthe, J., 181, 229
 Murakami, H., 62, 64, 79
 Muramatsu, Y., 370, 371, 373, 403
 Murata, A., 727
 Murphey, B.F., 834
 Murphy, B.L., 662
 Murphy, B.P., 726, 727
 Murphy, D.V., 470
 Murphy, G.M., 4, 7
 Murphy, S.F., 95
 Murphy, T.J., 92
 Murray, A., 347
 Murray, A.P., 653
 Murray, A.S., 62–66, 71, 75, 344, 355, 491, 493
 Murray, C.N., 308
 Murray, D.J., 330
 Murray, J.W., 151, 255, 256, 277, 278, 494
 Murray, M., 733
 Murrell, M.T., 6, 564, 789
 Muscheler, R., 61, 62
 Mushak, P., 772, 774, 775
 Mutlu, H., 298
 Muzikar, P., 18
 Myasoedov, N.F., 147, 148
 Myers, W.A., 394
 Myneni, S.C.B., 168
- N**
- Nachtigall, K., 680, 688, 689, 694
 Nadelhoffer, K.J., 704
 Naeyer, L.P., 770
 Naes, K., 382, 387
 Nagahara, H., 89, 135, 137, 468, 832
 Nagai, H., 72
 Nagao, S., 94
 Nagle, G.N., 507
 Nägler, T.F., 106, 110–112, 115, 180, 188, 196
 Nahon, D., 563
 Naik, H., 452
 Nair, K.S.S., 820
 Naito, Y.I., 725, 727, 735
 Nakagawa, F., 613, 837
 Nakai, S., 184
 Nakajima, J., 289
 Nakamura, F., 486
 Nakamura, N., 663
 Nakao, T., 252
 Nakashita, R., 211
 Nakasugi, O., 836
 Nakatsuka, T., 812
 Naldrett, A.J., 208, 210, 212, 213
 Naney, J.W., 492, 500
 Nanjo, Y., 42
 Naqvi, S.W.A., 452
 Naraoka, H., 666
 Nardoto, G., 703
 Narita, H., 348–350
 Narvekar, P.V., 452
 Nathan, Y., 107
 Naulet, N., 704
 Navarre-Sitcher, A., 558
 Navon, O., 418, 423–425
 Naylor, C., 495
 Nazaroff, W.W., 575
 Nazarov, M.A., 206
 Nealson, K.H., 160, 179, 184, 187, 189, 197, 198
 Neary, C.R., 212, 213
 Nebot-Gil, I., 624
 Negrel, C., 529, 536
 Negrel, P., 43, 44, 520, 529, 532
 Nehlich, O., 733, 752, 754
 Neighbour, T., 741, 752
 Neil, H.P., 796
 Neil, J., 816
 Neill, C., 428
 Nelson, B.K., 743
 Nelson, D.E., 6, 78, 476, 576, 721, 731
 Nelson, D.M., 383, 395
 Nelson, D.W., 486
 Nelson, R., 792
 Nemoto, K., 606
 Neori, A., 423, 425
 Nesbitt, H.W., 525, 526
 Nesje, A., 398
 Neto, A.N., 279, 280
 Neubauer, J., 850
 Neubert, N., 180, 196
 Neumann, S., 61
 Neuwirth, B., 820
 Nevins, J.L., 836
 Nevison, C., 452, 611
 Nevissi, A.E., 788, 800
 Newman, D.K., 197

- Newton, R., 382
 Nho, E.Y., 273
 Nicholas, D.J.D., 460, 468
 Nichols, G., 768
 Nicholson, A., 665
 Nicholson, D., 418
 Nicholson, K.W., 596
 Nicol, G.W., 469
 Nicolini, G., 704
 Nieboer, E., 280
 Niedermann, S., 16
 Nielsen, J.M., 581, 582
 Nielsen, L.P., 451, 452
 Nielsen, S.G., 22, 147, 247, 249–266
 Nielsen-Marsh, C.M., 743, 751
 Nielson, K., 707
 Niemeyer, S., 212
 Nieminen, T.M., 180, 190, 194
 Nien, C.F., 625
 Nier, A.O., 4, 126, 834
 Nies, H., 377
 Nijenhuis, I., 692, 694
 Nikiforov, V.A., 682, 696
 Nimickm, D.A., 179, 180, 199
 Ning, S., 78
 Nishihara, C., 809
 Nishiizumi, K., 61, 62, 441, 477, 478, 582
 Nishikawa, M., 836
 Nishio, Y., 43
 Nislow, K.H., 75, 510
 Nissenbaum, A., 642
 Nittrouer, C.A., 63, 306, 309, 318, 319, 322, 377
 Niu, Y., 43, 44
 Njo, H.B., 47
 Noack, C.C., 372
 Nogueira, C.A., 210
 Noh, H., 528, 529
 Nolan, C., 281
 Noller, B., 765
 Nolleth, K.M., 50
 Nomura, M., 259
 Nonell, A., 197, 198
 Nordstrom, D.K., 156, 230, 235, 237
 Norman, A.L., 666, 834, 835
 Norman, M.D., 251, 252, 258, 264, 265
 Norr, L., 724, 729
 Norton, F.J., 287
 Norton, S.A., 63, 68, 302, 312, 488, 495, 497
 Noseck, U., 558
 Noshkin, V.E., 368, 377, 384, 385
 Nour, S., 347
 Noureddine, A., 367
 Nowell, G.M., 746, 760
 Nowicki, J.L., 789, 793, 800
 Nozaki, Y., 271–273, 276, 278, 307, 309, 334, 339, 352, 354, 493, 799, 800
 Nriagu, J.O., 138, 248, 253, 260
 Nuccio, P.M., 301
 Numata, M., 663
 Nunnemann, M., 402
 Nur, A., 297, 298, 300
 Nurnberg, D., 77
 Nurnberg, H.W., 813, 818
 Nuti, S., 418, 422, 423
 Nyffeler, U.P., 65, 80
 Nygren, U., 401
 Nyland, B., 651
- O**
 Oberli, F., 87, 90, 91
 Obermajer, M., 651, 652
 Oborn, L., 497
 Obota, H., 278
 O'Brien, D., 704
 Ocampo, R., 639, 640, 651, 661
 Ochab, E., 493
 O'Connell, T.C., 703, 705, 725, 727, 729
 Oda, K., 592, 599
 Odden, W., 644
 Odom, A.L., 230, 237
 O'Donnell, T.H., 681
 Oehme, M., 688
 Oenema, O., 452, 461, 462, 464, 468
 Oeschger, H., 832
 Ofan, A., 396
 O'Farrell, C.R., 509
 O'Flaherty, E.J., 774
 Ogawa, Y., 836
 Ogée, J., 813, 822
 Ogorman, M., 259
 O'Grady, S.P., 706, 713, 714
 Ogrinc, N., 232, 237
 Oh, J.S., 372
 Oh, S., 820
 O'Hara, T., 800
 Ohba, T., 195
 Ohkouchi, N., 725, 727, 735
 Ohlander, B., 90–92, 98, 99, 101, 527
 Ohm, S.E., 651
 Ohmoto, H., 845
 Ohno, T., 116, 739
 Ohta, K., 209
 Ohta, Y., 727
 Ohtani, T., 727
 Okamoto, M., 42, 259
 Okamura, K., 43, 339
 Okin, G.S., 64, 79
 Okubo, A., 353
 Okuda, T., 666
 Oldeman, L.R., 486
 Oldfield, F., 320
 O'Leary, J.M., 190
 O'Leary, M.H., 459, 642, 815, 816
 Oliva, P., 197, 198, 524
 Olivares, J.A., 6, 789
 Olive, K.A., 42
 Oliveira, J.M., 272
 Oliver, L., 533, 534
 Olivier, S., 402
 Olley, J.M., 75

- Ollivier, P., 347, 348
 Olsen, C.R., 62–64, 66, 68, 72, 75, 77, 311, 372, 377, 491, 494, 501, 502
 Olsen, C.T., 377
 Olsen, R.L., 156
 Olsen, S., 651
 Olsher, U., 45
 Olson, D., 71, 76, 312
 O'Neil, J.R., 4, 45, 46, 418–420, 422–425, 432, 746
 O'Neill, H.S.C., 134, 140
 O'Neill, M.F., 800
 O'Nions, R.K., 6, 69, 160, 198, 289, 290, 293–295, 298, 789
 Onions, R.K., 261
 Onitsuka, H., 259
 Ono, S., 835
 Ooi, K., 46
 Opdyke, B., 523
 Opdyke, M.R., 463–465, 470
 Opfergelt, S., 89, 90, 93–97, 99, 101
 Oregioni, B., 368, 374, 381, 384
 Oremland, R.S., 167–169
 Orians, K.J., 134, 135, 138, 139, 181, 249
 Orlandini, K.A., 311, 379
 Orlic, M., 331
 Orren, M.J., 280
 Orris, G.J., 435
 Ortega, F., 770
 Ortega, X., 489
 Ortiz-Monasterio, I., 457
 Osaki, S., 272, 274, 488
 Osborn, R., 753, 755
 Osborn, T.J., 816
 Osleger, D.A., 748
 Oslén, C.R., 377
 Oslick, J.S., 750
 Osmond, J.K., 564
 Ostaff, D.P., 820
 Osterloh, J.D., 768, 772
 Osterlund, H., 98, 99
 Ostic, R.G., 248
 Ostlund, G., 375
 Ostlund, H.G., 375, 377
 Ostrom, N.E., 420, 423, 428, 451, 458, 460–470
 Ostrom, P.H., 460–467, 470
 Oszczepalskim, S., 164
 Otake, T., 845
 Otsuji-Hatori, M., 583, 592
 Oubrie, A., 462, 463
 Oughton, D.H., 494
 Oura, Y., 207, 208
 Oversby, V.M., 440
 Overstreet, R., 494
 Owen, J., 441
 Owens, E.D., 452, 463, 464, 470
 Owens, N.J.P., 836
 Owens, P.N., 495, 496, 498, 500, 504, 507
 Owens, T., 106, 109–112, 115, 116
 Oxburgh, E.R., 289, 290, 293–295, 298
 Oxburgh, R., 206, 216
 Oxenford, H.A., 786
 Oze, C., 157, 163
 Ozima, M., 288
- P**
 Paasikallio, A., 495
 Paatero, J., 379, 488
 Pacheco, A.A., 462
 Pachucki, C., 383, 384
 Pacyna, J.M., 138
 Padmakumari, V., 237, 542
 Page, B., 117, 118, 120
 Pagel, M., 525
 Pai, S.C., 331
 Palinkas, C.M., 306
 Palko, A.A., 42
 Pallasser, R.J., 653
 Palme, H., 134, 140, 150
 Palmer, J.M., 772, 774, 775
 Palmer, M.R., 42, 43, 46, 51, 52, 208, 213, 527, 532, 533, 536
 Palmer, S.E., 645
 Pan, C., 651, 652
 Panapitukkul, N., 467, 468
 Pandarinath, K., 808–810
 Pande, K., 527, 528
 Pandey, A., 618, 619, 847
 Pandis, S.N., 838
 Pant, G.B., 815, 821
 Panten, D., 657, 659
 Papanastassiou, D.A., 6, 110, 111, 113, 115, 116, 207–209, 211–217
 Papastefanou, C., 64, 489, 491, 492, 599, 600
 Papesch, W., 745, 751
 Papineau, D., 835
 Papini, P., 477
 Pöpke, O., 695
 Papucci, C., 367, 373, 382
 Paquay, F.S., 206, 212
 Pardo, L.H., 704
 Parfitt, A.M., 740, 744
 Park, J., 295
 Park, R.J., 642, 839–841
 Park, S.K., 307, 311, 454, 456, 462
 Parker, D.R., 435, 442
 Parker, P.L., 665, 728
 Parkes, S.D., 457, 469
 Parkinson, I.J., 206, 215, 216
 Parron, C., 90, 93, 100, 101
 Partridge, S.T., 705
 Parwel, A., 836
 Pasava, J., 212
 Paschal, D., 770
 Pasiieczna, A., 253
 Passey, B.H., 724, 727, 728
 Patchett, J., 264
 Pate, J.S., 817
 Patel, M.M., 775
 Pates, J.M., 311
 Paton-Walsh, C., 457, 469
 Patou-Mathis, M., 730
 Patrick, R., 801
 Patrickson, S.J., 707
 Patris, N., 612, 614, 615, 832, 842–844, 847

- Pattanaik, J., 528
 Patterson, C.C., 247, 252, 254
 Patterson, T.L., 441, 446, 447
 Patzert, W.C., 309
 Paul, B., 277, 278
 Paul, M., 207, 209, 212, 213
 Paulsen, D.E., 797
 Paunovic, M., 733, 735
 Pavich, M.J., 63, 65–67, 73, 75, 477, 482
 Pavlov, A.A., 845
 Pawellek, F., 816
 Payne, J., 108, 121
 Payne, T., 49
 Paytan, A., 19, 106–108, 112, 115, 121, 262, 354, 378, 417–420, 423, 425, 552, 741, 742, 748, 751–754, 756, 760
 Peacock, C.L., 259, 265
 Peacock, E.A., 640
 Pearce, J., 553
 Pearson, D.G., 207, 211
 Pearson, P., 111, 114, 121
 Peate, D., 750
 Pechenkina, E.A., 733
 Peck, W.H., 704
 Pedersen, R.B., 212, 213
 Peeters, F., 285, 289, 290, 296
 Pegram, W.J., 206
 Peiro-Garcia, J., 624
 Peirong, W., 651
 Peiser, H.S., 89, 92, 436
 Pekala, M., 558
 Pelly, I.Z., 184
 Pelt, E., 553, 556, 558, 561–563, 565
 Peng, P., 651, 652, 665
 Peng, T.-H., 106, 349–351, 353, 357, 375, 377, 381, 430
 Pengra, J.G., 248
 Pennannen, A.S., 591
 Pennington, J.T., 420, 421, 423–425, 430
 Penrose, W.R., 379
 Pentreath, R.J., 383
 Pepkowitz, L.P., 835, 836
 Perakis, S., 109, 118
 Perdrix, E., 180, 181, 189, 194
 Pereira, A.S., 462
 Perera, S.K., 279, 280
 Pérez, T., 457, 458, 460, 462
 Perfit, M.R., 273
 Perriñez, R., 380
 Perini, M., 704
 Perkinas, R.W., 581, 582
 Perkins, J., 179
 Perkins, R.W., 372, 384, 581, 582
 Pernicka, E., 261
 Perovich, D.K., 229
 Perry, K., 441
 Persson, B., 575
 Persson, B.R.R., 382
 Peryt, T.M., 443
 Peslier, A.H., 251
 Petelet-Giraud, E., 43, 44, 194, 195
 Peter, J.E., 382
 Petermann, J., 349
 Peters, B., 4, 61, 306, 476–478, 575, 576, 578–581
 Peters, J., 705
 Peters, K.E., 637, 638, 642, 644, 645, 651, 653
 Peterson, B.J., 451, 452, 704, 705
 Peterson, M.C., 850
 Peterson, R.N., 346, 347, 352, 354, 357
 Petit, J.C.J., 180, 194
 Petit, J.R., 835, 842
 Petit, S., 42, 46, 51
 Petrenko, V.V., 864
 Petrick, G., 680, 681, 687–690, 694
 Petrychenko, O.Y., 443
 Pettersson, H., 381, 384
 Pettersson, L.H., 379
 Pettitt, P.B., 733, 735
 Petty, J.D., 665
 Petzke, K.J., 705
 Peucker-Ehrenbrink, B., 43, 205, 206, 208, 212, 213, 215, 218
 Peuke, A.D., 817
 Peyr, C., 770
 Peyton, B., 168, 169, 173
 Pfeiffer, S., 732
 Pfennig, G., 126
 Pfirman, S., 383
 Pfitzner, J., 50
 Pham, M.K., 377, 381, 384, 596
 Phillips, A.M., 681
 Phillips, D.J.H., 798
 Phillips, D.L., 704, 723, 730
 Phillips, F.M., 14, 16, 19, 285, 332, 437, 443, 476, 576
 Phillips, N.G., 815, 816, 823
 Phillips, R.B., 211, 214
 Phillips, S.L., 441, 813
 Philp, P., 639, 644, 655, 657, 664
 Philp, R.P., 638, 639, 644, 645, 651, 653, 661, 662, 665, 666, 676, 681
 Picciotto, E., 786, 861
 Piccolo, M., 458, 462
 Pichat, S., 197, 198
 Pichlmayer, F., 275, 852
 Pickard, G.L., 331
 Pickert, K., 708
 Pickett, D.A., 6
 Pierre, M., 813, 822
 Pierret, M.-C., 46–48
 Pierson-Wickmann, A.C., 206
 Piest, R.F., 503–505
 Pietruszka, A.J., 249
 Pik, R., 289
 Pili, E., 553–556, 558, 560, 564–566
 Pillans, B., 66
 Pillerin, B.A., 495, 497
 Pillonel, L., 704, 716
 Pimentel, D., 452, 463, 464, 470, 485, 486
 Pimienta, P., 871
 Pin, C., 749
 Pinder, J.E.III., 379
 Pineau, F., 436
 Piner, K.R., 376
 Pinochet, H., 159
 Pinto, J.P., 624

- Pinzon, M.C., 816, 822
 Piper, S.C., 704
 Piskunov, N., 41
 Pistiner, J.S., 46, 47, 51
 Pitt, A., 460–462, 464–466
 Pitts, J.N., 846
 Piwinski, L., 460
 Plamboeck, A.H., 808
 Plane, J.M.C., 206, 207, 211, 212, 625
 Plank, T., 53, 54
 Plater, A.J., 551, 554, 558
 Platt, T., 418
 Playford, K., 504
 Plessen, H.G., 210
 Plisnier, P-D., 90, 98
 Plum, C.N., 622
 Plummer, L.N., 442
 Pobi, M., 184
 Pockowski, J., 383
 Podkorytov, I.S., 682, 696
 Podlesak, D.W., 706, 707, 715
 Podosek, F.A., 288
 Poesen, J., 506
 Poet, S.E., 271, 273, 274
 Pogge von Strandmann, P.A.E., 46, 47, 49–51, 252, 263
 Poincot, J., 651
 Pointurier, R., 371
 Poirier, A., 206, 249
 Pokrovsky, O.S., 99, 146
 Polian, G., 273
 Polizzotto, M., 217
 Pöllänen, R., 401, 410
 Pollard, S.J., 665
 Pollastro, R., 657, 660
 Polve, M., 557
 Polvé, M., 97
 Polyakov, V.B., 190
 Pond, K.L., 653
 Pons, M-L., 197, 198
 Pons-Branchu, E., 348
 Ponticorvo, L., 836
 Poole, J.C., 288
 Poole, R., 332
 Popp, B.N., 452, 460, 464, 468, 639, 650
 Porcelli, D., 17, 69–71, 247, 251–253, 255–258, 293, 305, 310, 311, 487, 531, 554, 564, 565
 Porcelli, P., 313
 Porder, S., 748, 752, 756
 Poreba, G.J., 503
 Poreda, R., 544
 Poreda, R.J., 289, 296, 297
 Portmann, R.W., 451
 Possnert, G., 62, 78
 Post, D.M., 705, 709
 Poszwa, A., 741
 Pote, D.H., 486
 Potin-Gautier, M., 157, 159
 Potter, E-K., 8, 20, 553
 Potter, G.V., 88
 Potts, P.J., 207, 210
 Pougatch, K., 335
 Poulsen, S.R., 681
 Poulson, R.L., 180, 196
 Poulson, S.R., 644, 835
 Poulton, S.W., 164
 Pounds, J.G., 772, 774, 775
 Poupon, J., 770
 Pourchet, M., 69
 Poussart, P.F., 820–822
 Pouvreau, S., 798
 Povinec, P.P., 365, 367–370, 373, 374, 377, 381, 384, 386, 403, 596
 Powell, E.N., 498
 Powlesland, D., 752, 754
 Prange, J., 695
 Prasad, S.S., 464
 Prasad, T.G., 814
 Pratihary, A., 452
 Pravec, A., 108
 Preethi, J., 436
 Preiss, N., 69
 Presley, B.J., 387
 Presser, T.S., 157, 171
 Preston, T., 665, 836
 Preunkert, S., 843, 848
 Price, N.M., 142
 Price, T.D., 727, 729, 741, 743–745, 749, 751–755, 760
 Prichard, H.M., 212, 213, 346
 Pride, C.J., 90
 Priebisch, W., 312
 Prince, H., 748
 Privat, K., 725
 Prizkow, W., 127
 Probst, A., 524–526
 Probst, J., 529
 Prokopenko, M.G., 837
 Proksch, G., 836
 Prommer, H., 639
 Prosser, J.I., 462, 463, 469
 Provansal, M., 509
 Provost, C., 332
 Prowse, T., 724, 732
 Pruett, L.E., 843
 Prytulak, J., 250, 251, 266
 Puchtel, I.S., 206
 Purkl, S., 346, 354
 Purtschert, R., 289
 Pushkarev, E.V., 212, 213
 Putkonen, J., 537
 Putzka, A., 373
 Pyle, D., 207, 210–211
- Q**
 Qi, H.P., 42
 Qi, J., 469
 Qian, Y., 681
 Qin, J., 520, 525, 528, 529, 532
 Quade, J., 479, 533, 536, 743, 752, 757
 Quay, P., 864
 Quétel, C., 194, 195
 Quideau, S., 820
 Quilter, J., 704, 707

- Quine, T.A., 308, 490, 491, 501, 505, 506
 Quinn, P.K., 612, 614, 615, 847
 Quinn, R.C., 435, 441, 442
 Quinn, R.L., 757, 758
 Quinn, T., 523
 Quinodoz, H.A.M., 295
- R**
- Raabe, O.G., 552
 Rabalais, N.N., 418, 486
 Rabinowitz, M.B., 767–770, 772, 773, 779
 Rabus, R., 653, 665
 Raccasi, G., 509
 Rachor, E., 306, 311
 Rad, S., 533, 536
 Radakovitch, O., 311, 347, 348
 Raddatz, A.L., 164, 166
 Rafter, T.A., 835
 Rahaman, W., 520, 537, 541
 Rahmstorf, S., 874
 Rahn, T., 457, 460, 464
 Rai, S.K., 525, 527
 Rai, V.K., 835, 845
 Railsback, L.B., 344
 Rainwater, K.A., 435, 442
 Raisbeck, G.M., 37, 63, 65, 66, 68, 69, 71, 72, 78, 81, 372, 379, 380, 582
 Raiswell, R., 49
 Raisz, L.G., 729
 Rajagopalan, B., 823
 Rajagopalan, S., 435, 442
 Rama, 329, 347, 356, 799
 Rama, Moore, WS, 329
 Rama, T., 575, 579–582
 Rama, Todd, J.F., 347
 Ramesh, R.R., 351, 352, 808–810, 812, 814, 815, 818, 820, 821, 823
 Ramos, F.C., 179
 Ramos, M.A., 65
 Randall, B.A., 477
 Randerson, J.T., 467, 468
 Ranger, J., 94, 97
 Ranville, J.F., 497
 Rao, B., 435, 442
 Rapaglia, J., 335
 Rapp, J.B., 662
 Rappe, C., 695
 Rashid, K., 168, 169
 Rasko, M., 71
 Rasmussen, J.B., 705
 Rau, G.H., 90
 Rauch, S., 206, 218
 Rausch, N., 180, 190, 194
 Ravel, J.C., 582
 Raven, J.A., 94
 Ravichandran, M., 315, 408, 491
 Ravindra, K., 217, 221
 Ravishankara, A.R., 451
 Ravizza, G.E., 206–216, 218, 527
 Rayleigh, J.W.S., 663, 683
 Raymo, M.E., 87, 520, 534
 Raymond, N., 653, 665
 Raymond, P.A., 351
 Raynaud, D., 853, 863, 864, 867, 868, 871, 877
 Reardon, E.J., 170
 Rech, J.A., 441, 445, 833, 836
 Rectanus, H.V., 446
 Redder, A., 435
 Reddy, C.M., 305, 640, 665, 666, 679–681, 685–689, 692, 696, 697
 Redfield, A.C., 348
 Reeburgh, W.S., 350
 Reed, N.M., 6
 Reedy, R.C., 576
 Rees, A.P., 836
 Rees, C.B., 168, 169
 Rees, C.E., 275, 834, 835, 843
 Rees, H.W., 497, 503, 504
 Reese, B.K., 435, 442
 Rehkämper, M., 7, 8, 20, 22, 43, 127–135, 137–141, 143–149, 151, 181, 184, 186, 207, 211, 247–266, 553
 Reich, C.D., 305, 353, 354, 356, 799
 Reich, P.B., 817
 Reichert, P., 441
 Reichman, O.J., 497
 Reid, A.F., 6
 Reid, D.F., 347
 Reid, M.R., 540
 Reiller, P., 552
 Reimnitz, E., 77, 383
 Reimold, W.U., 206
 Reimus, P.W., 47
 Reinhard, E., 423
 Reisberg, L., 206, 207, 209, 212, 213
 Reiser, D.W., 486
 Reiter, E.R., 592, 593
 Reiter, R., 582
 Reitz, A., 53
 Reitzel, L.A., 665
 Remgarajan, R., 311
 Renac, C., 263
 Renard, R., 798
 Rengarajan, R., 272
 Rennenberg, H., 817, 819
 Renner, R., 766
 Renshaw, C.E., 75, 509, 510
 Repeta, D.J., 726
 Repta, C., 684–686
 Resiberg, L., 51
 Resosuarmono, P., 485, 486
 Reuer, M.K., 794, 798
 Revelle, C., 495
 Revelle, P., 495
 Revenaugh, J., 621
 Revesz, K., 89, 441, 613, 614, 836
 Revesz, K.M. Jr., 436
 Reynard, L., 109, 110, 116, 117
 Reynaud, S., 43, 55
 Reynolds, A.C., 752, 757
 Reynolds, B.C., 22, 89–91, 93, 96, 98–101, 131, 132, 187, 248, 249, 520, 564, 565, 739
 Reynolds, C.M., 665, 666

- Reynolds, J.H., 92
 Reynolds, R.L., 404
 Reyss, J.L., 347, 351, 352, 491
 Reznik, A.D., 249
 Rhein, M., 351, 352, 382
 Rhoads, D.C., 498
 Rhodes, C.N., 704
 Ricci, M.P., 680
 Rice, D.L., 64
 Rice, J.R., 297
 Richard, O., 41
 Richards, M.P., 724, 725, 727, 729, 732–735, 746, 747, 752, 757
 Richardson, D.H.S., 280
 Richardson, L., 813
 Richardson, S., 741, 757
 Richet, P., 831
 Richnow, H.H., 644, 664, 665, 692, 694–696
 Richter, A., 817
 Richter, F.M., 108, 137, 189, 522, 531, 534–536
 Richter, S.L., 814
 Rickaby, R.E.M., 90, 142–144, 149–151
 Rickli, J., 553, 560
 Ridley, M., 435, 442
 Ridley, W.I., 179, 180, 184, 199
 Rieck, H.G., 67, 80
 Riedel, K., 848
 Rieder, S.E., 89, 436
 Riediger, C.L., 651
 Riese, A.C., 344
 Riggs, D.L., 744
 Riggs, M., 613, 837
 Rigor, I., 383
 Rihs, S., 556, 564, 797, 798
 Riise, G., 494
 Riley, J.P., 247, 256, 257
 Rimetz-Planchon, J., 180, 194
 Rincon, J., 651
 Riotte, J., 17, 180, 194, 520, 543, 551, 558, 564
 Riou, C., 421, 424, 425
 Ripperger, S., 129–135, 142–146, 149, 181
 Risebrough, R.W., 667, 679–681, 686, 687, 689, 690
 Risi, C., 809
 Rison, W., 299
 Ritchie, C.A., 487
 Ritchie, G.D., 277, 278
 Ritchie, J.C., 403, 405, 487, 492, 503, 507
 Rittenberg, D., 836
 Rittenberg, S.C., 156, 170
 Ritz, C., 871
 Ritz, D.A., 800
 Rizzotto, L.F., 492
 Roark, B., 795
 Roback, R., 564
 Robbins, C.T., 705, 709
 Robbins, J.A., 65, 74, 308, 491, 493, 494, 498
 Robert, F., 43
 Roberts, J.M., 794
 Robertson, D.E., 67, 80, 380, 605
 Robertson, G.P., 452, 453, 458, 460–466, 469, 470
 Robertson, I., 808, 815, 816, 818, 823
 Robertson, S.G., 800
 Robinson, B.W., 834
 Robinson, L.F., 90
 Robinson, N., 206
 Robinson, T.F., 119, 706, 724, 728
 Robock, A., 845
 Rocher, V., 193
 Rockman, M., 206
 Röckmann, T.R., 453–456, 460, 462, 467–469, 853
 Rockwell, T.K., 497
 Roddaz, M., 537, 538
 Rodel, W., 582
 Roden, E.E., 197, 198
 Roden, J.S., 712, 716, 810, 811, 813, 814, 816, 819, 820
 Rodhe, H., 332, 333, 611
 Rodolfo-Metalp, R., 43, 55
 Rodriguez-Gonzalez, P., 230, 232, 234, 237
 Rodushkin, I., 89–93, 96, 98, 99, 101, 206, 219
 Roe, J.E., 160, 184, 198
 Roe, L.J., 423, 533, 536
 Roeder, B.L., 724, 728
 Roether, W., 308, 309, 348, 349, 351, 373
 Rogers, K.M., 665
 Rogers, N., 553
 Roghmann, K.J., 766
 Rogowski, A.S., 495
 Rohrback, B.G., 642
 Rojo, I., 552
 Roldan, M.D., 469
 Rolfe, B.A., 190, 196
 Rolfe, J.E., 808
 Rolfe, T., 444, 446
 Rollion-Bard, C., 43, 53, 55, 110, 111, 114, 115, 121
 Romanini, D., 834
 Romer, R.L., 52, 53
 Romero, A., 835, 845
 Romheld, V., 197, 462
 Rooney, M.A., 650, 651
 Roos, P., 348, 366, 367, 372, 592, 788, 789
 Rooth, C., 351, 352
 Rosbinson, W., 370, 371, 373
 Roscher, C., 816
 Rosen, K., 497
 Rosenberg, E.J., 215–217
 Rosenberry, D.O., 357
 Rosenfelder, N., 689, 692–694, 696
 Rosenthal, Y., 54
 Rosholt, J.N., 551, 561, 563
 Rosman, K., 110, 770
 Rosman, K.J.R., 6, 89, 126, 127, 129, 132, 133, 140, 149, 436
 Rosner, G., 596
 Rosner, M., 43
 Ross, D.S., 614
 Ross, J.M., 769
 Rossmann, G.R., 155, 163
 Rossmann, A., 683, 704
 Rotenberg, E., 521
 Roth, E., 89
 Röthlisberger, R., 850
 Roueff, E., 522, 525, 526
 Rourke, F., 383, 384

- Rousseva, S.S., 492, 500
 Roux, P.Jl., 746, 757
 Rouxel, O., 160–162, 170
 Rovira, M., 552
 Rowan, J.S., 592
 Rowe, H.D., 441
 Rowe, J.J., 88
 Rowell, D.M., 808
 Rowley, D.B., 522, 531, 534–536
 Roy Barman, M., 207–209
 Roy, J.C., 395
 Roy-Barman, M., 386
 Rozanski, K., 621, 808–810, 812
 Ruberu, S.R., 279, 280
 Rubin, C.S., 770
 Rubin, K.H., 273
 Rudd, D.P., 624
 Ruddiman, W., 520, 531
 Ruddiman, W.F., 87, 520, 534
 Rudels, B., 306, 311
 Rudge, J.F., 111, 131, 132, 187, 248, 249
 Rudich, Y., 848
 Rudnick, R.L., 43, 44, 47, 134, 251
 Rudnicki, M.D., 51, 52
 Rueedi, J., 290
 Ruggeberg, A., 739
 Ruiz, J., 179
 Rumble, D., 835
 Ruo, R., 331
 Ruppe, S., 679
 Russ, G.P., 208
 Russ, M.E., 460, 464, 468
 Russell, I.J., 63
 Russell, R.S., 740
 Russell, W., 110, 111
 Rust, S.W., 766
 Rust, T.M., 460, 464, 468
 Rutgers van der Loeff, M.M., 277, 306, 308–311, 313, 347
 Rutherford, E., 3, 346, 551
 Ryan, J.G., 51
 Ryan, M.G., 816
 Rye, D.M., 584
 Rye, R.O., 705
 Ryerson, T.B., 622
 Ryhage, R., 836
 Ryu, J.W., 330, 338, 339
- S**
 Saber, D., 666
 Sachs, J.P., 726
 Sackett, W.M., 642, 653, 654, 657, 661
 Safinowski, M., 664, 665
 Sager, M., 253
 Sahoo, Y.V., 184
 Saibu, B., 494
 Saiers, J.E., 497
 Saino, T., 452
 Sak, P.B., 558
 Sakaguchi-Söder, K., 639, 663, 667
 Sakuragi, Y., 599
 Sakurai, H., 489
 Salamanca, M., 35
 Salanitro, J.P., 662, 667
 Salant, N.L., 75, 510
 Salcudean, M., 335
 Saleh, M.A., 688
 Salem, H., 157
 Salisbury, R.T., 63, 79, 491
 Salisbury, V.B., 820
 Salmon, Y., 817
 Salomon, D.K., 296, 297
 Salomon, J.C., 380
 Salter, P.F., 552
 Salters, V.J.M., 230, 237
 Salvato, B., 198
 Sam, A.K., 397
 Samuelsson, C., 575
 Sanak, J., 273
 Sanchez, A.L., 495
 Sanchez, A.M., 400
 Sanchez, C.A., 436
 Sánchez Goñi, M.F., 871
 Sanchez-Cabeza, J.A., 272, 311, 367, 373
 Sander, R., 848
 Sanders, C.J., 404
 Sandford, M.K., 743
 Sandquist, D.R., 820
 Sands, D.G., 126, 132
 Sandvig, R.M., 435
 Sangster, A.G., 94
 Sanjuan, B., 43, 44, 52
 Sano, M., 680, 808, 834
 Sano, Y., 43, 288, 289, 293, 298
 Sansone, F.J., 460, 464
 Santiago, L.S., 817
 Santillo, P.M., 808
 Santos, G.M., 370
 Santos, I.R., 354, 356, 357
 Santos, S., 446
 Santrock, J., 455
 Santschi, P.H., 7, 28, 62–65, 70–72, 74, 78–80, 272, 307–313, 315, 318, 320, 322, 330, 368, 370, 377, 380, 381, 384, 386, 387, 403, 495, 503, 576, 592, 599, 788
 Sanudo-Wilhelmy, S., 254
 Saraste, M., 462, 463
 Sarin, M.M., 17, 272, 273, 275, 276, 308, 311, 313, 351, 352, 520, 528
 Sarmiento, J.L., 90, 329, 330, 351, 352, 492
 Sartorius, H., 377
 Sasaki, S., 680
 Sasmaz, A., 253
 Sass, S., 180, 181, 189, 194
 Saueressig, G., 853
 Saunders, S.R., 724, 728, 732, 748
 Saunders, W.H., 639, 683
 Saupe, S.M., 801
 Saurer, M., 808, 811, 813, 814, 816–820
 Sauvage, B., 611
 Sauve, S., 75
 Savage, K., 467, 468
 Savage, P.S., 90, 93, 96
 Savard, M.M., 665

- Savarino, J., 469, 612–619, 623–626, 832, 833, 835, 837, 839, 840, 842, 845–852
- Savidge, R.A., 814, 817
- Savov, I.P., 51
- Savoie, N., 90
- Sawlan, J.J., 255, 256
- Saxen, R., 379
- Sayles, F.L., 354, 355, 367, 412
- Scaillet, B., 43, 44, 52
- Scalan, R.S., 728
- Scanlon, B.R., 435
- Schaeffer, O.A., 443
- Schaeffer, P., 651
- Schäfer, J., 180, 194
- Schaller, M., 32, 557
- Schauble, E.A., 20, 90, 147, 148, 155, 163, 178, 190, 233, 255, 256, 259, 260, 265
- Schediwy, S., 126, 129, 132, 133, 140
- Schedlbauer, O.F., 254, 260
- Scheeder, G., 657, 659
- Scheidegger, A.M., 552
- Scheidegger, Y., 819, 820
- Schell, D.M., 801
- Scherer, M.M., 179, 190
- Schery, S.D., 348
- Scheuer, E., 583
- Schibler, J., 733
- Schiegl, W.E., 808
- Schiff, C.J., 404
- Schiff, S.L., 614
- Schilla, A., 810
- Schilling, K., 168, 170
- Schimel, D., 452
- Schimmelmann, A., 652
- Schindler, D., 451, 817
- Schink, D.R., 380
- Schlatterer, J., 679, 680, 695
- Schleper, C., 469
- Schleser, G.H., 808, 816–822
- Schlesinger, W.H., 427, 451, 864
- Schleucher, J., 679, 681, 682, 686, 688, 689, 696, 822
- Schlitzer, R., 351, 352
- Schlusser, C., 377
- Schlusser, P., 287, 290, 291, 294, 296, 297, 377, 382
- Schlöter, M., 469
- Schluter, H.J., 652
- Schmel, G.A., 607, 610
- Schmid, M., 195
- Schmidt, B., 807
- Schmidt, C.T., 662, 664
- Schmidt, D., 111, 114, 121
- Schmidt, G.A., 808, 823
- Schmidt, H-L., 462, 612, 683, 697, 836, 839
- Schmidt, O., 704, 707
- Schmidt, S., 786
- Schmidt, T.C., 665, 685
- Schmitt, A-D., 105–112, 117, 128–135, 141, 145–147, 149–151, 181, 186
- Schmitt, A.K., 835
- Schmitt, D., 801, 802
- Schmitz, B., 206
- Schneider, D.L., 376, 395
- Schoell, M., 639, 642, 643, 651, 655–657, 660, 661
- Schoeller, D.A., 709, 711
- Schoenberg, R., 8, 160–162, 164, 178, 191
- Schoeninger, M.J., 3, 22, 704, 723, 724, 727, 729, 731–735, 742, 743, 751, 758
- Scholz, F., 53
- Schönbächler, M., 130, 131, 141, 150, 251, 259
- Schoner, W., 275, 852
- Schoonmaker, J.E., 135
- Schott, J., 97, 99, 557
- Schou, M., 42
- Schour, I., 743, 744
- Schrag, D.P., 813, 818, 820–822
- Schramm, D.N., 42
- Schroeder, W.H., 181, 229
- Schröter, P., 752, 754
- Schueler, B., 619, 620, 624
- Schuler, C., 64, 74, 80
- Schuller, D., 801
- Schuller, P., 63–65, 491, 495, 503, 509
- Schulting, R.J., 733
- Schultz, A., 51, 53
- Schultz, R.K., 494
- Schulz, M., 611
- Schulz, M.S., 95, 179, 198
- Schulz-Bull, D.E., 687
- Schulz-Dobrick, B., 134, 140, 151, 247, 248, 251, 257, 266
- Schulze, E.D., 613, 614, 629, 816, 820
- Schumacher, J., 435
- Schuraytz, B.C., 206
- Schurr, M.R., 728
- Schuster, S.C., 469
- Schüth, C., 639, 644, 663, 667
- Schuur, E.A.G., 820
- Schwander, J., 864, 866, 868, 871, 872, 875, 876
- Schwantes, J., 370
- Schwarcz, H.P., 3, 22, 704, 721, 723–725, 727–729, 731–735, 742, 746, 751, 758, 793, 839
- Schwark, L., 469
- Schwartz, C.C., 705
- Schwartz, S.E., 583
- Schwartzman, D.W., 770
- Schwarz, H.P., 551
- Schwarzenbach, R.P., 643, 684, 685, 697
- Schweingruber, F.H., 816, 818, 819
- Schweissing, M., 744, 752, 754
- Schweitzer, L., 509, 788
- Schwieters, J.B., 160, 186, 553
- Schwinning, S., 813
- Sclater, F., 141, 142
- Scott, B.B., 247, 257
- Scott, L., 800
- Scott, M.R., 333, 383
- Scott, Z., 452, 469, 612, 614, 615, 622, 624, 837, 846, 847
- Scow, K.M., 664
- Scudlark, J.R., 274, 281, 311
- Seabloom, E.W., 497
- Sealy, J.C., 724, 729, 732, 733, 740, 743
- Seby, F., 157
- Seco, F., 552

- Sedwick, P.N., 206, 212–214, 216, 218, 220
 Seelmann-Eggebert, W., 126
 Segal, I., 107, 739
 Segl, M., 69, 70, 78, 261
 Seibert, P., 275, 852
 Seid, G., 583
 Seidemann, D.E., 799
 Seifert, W.K., 638, 649
 Seigneur, C., 611
 Seiler, R.L., 279, 280
 Seinfeld, J.H., 611
 Seitz, H.M., 51, 263
 Seitzinger, S.P., 451, 452
 Sekely, A.C., 486
 Sekine, T., 62, 64, 79
 Selaolo, E.T., 290
 Selivanov, S.I., 682, 696
 Seminoff, J.A., 727
 Semkow, T.M., 560
 Semmens, B.X., 730
 Sen, B., 435, 457, 469
 Sen, O., 253
 Sengupta, J.G., 210
 Senn, D.B., 237, 239–241
 Sepman, S., 71
 Sept, J.M., 727
 Sepulveda, A., 491
 Sessions, A.L., 652
 Seth, B., 464, 465
 Settle, D.M., 252
 Sevcik, K., 63, 65, 80
 Severinghaus, J.P., 864–868, 871–873, 876–879
 Severmann, S., 179, 189, 199
 Seyffferth, A.L., 435, 442
 Seyfried, W.E. Jr., 52, 53
 Shah, S.K., 812, 814, 823
 Shakesby, R.A., 507, 508
 Shanahan, J., 508
 Shang, H., 733
 Shanks, W.C., 179
 Shannon, L.V., 280
 Shannon, R.D., 45, 126, 247
 Shao, L., 520
 Sharabi, G., 348
 Sharma, M., 205–207, 209, 212–220, 521
 Sharma, P., 62, 76, 77, 80
 Sharp, J.H., 418, 427
 Sharp, W., 441
 Sharp, Z., 820
 Sharpley, A.N., 486
 Sharpton, V.L., 206
 Shaviv, A., 421, 424, 425, 432
 Shaw, D.C., 817
 Shaw, D.M., 247, 248, 251, 266
 Shaw, G.E., 71, 275
 Shaw, S., 53, 54
 Sheets, R.W., 69
 Sheldon, K.E.W., 801
 Shellenbarger, G.G., 354
 Shemesh, A., 418, 751
 Shen, G.J., 35
 Shen, G.T., 789
 Shen, J.J., 208
 Shenber, M.A., 495
 Sheng, G., 652, 665
 Sheremet, A., 314
 Sherman, L.S., 230, 234, 235, 237–241
 Sherwood Lollar, B., 8, 643, 653, 662, 664, 665, 667, 681, 684–686, 697
 Sheshshayee, M.S., 808, 812, 814, 818, 820, 821, 823
 Shi, P., 506
 Shiel, A.E., 128–131, 134, 135, 138, 139, 181, 249
 Shiller, A., 530
 Shima, S., 377, 381, 384
 Shimmack, W., 497
 Shimmield, G.B., 277, 278, 312
 Shin, W.-J., 711
 Shindell, D.T., 833
 Shiner, V.J., 679, 680, 685–689, 697
 Shinotsuka, K., 211
 Shirey, S.B., 43, 44, 206, 208, 211
 Shirley, E.L., 834
 Shirley, V.S., 28, 29
 Shiyatov, S.G., 816
 Shoemaker, R.C., 198
 Sholkovitz, E.R., 369, 383, 384, 531
 Short, S.A., 800
 Shouakar-Stash, O., 639, 662, 665, 667
 Shoun, H., 462
 Showers, W., 874
 Shui, M.X., 90, 95
 Shullenberger, E.D., 441
 Shuman, C., 879
 Shuur, E., 704
 Sichingabula, H.M., 492, 493
 Siclet, F., 491
 Siebert, C., 146, 180, 188, 196
 Siegert, M., 49
 Siegwolf, R., 811, 813, 814, 817–820
 Siegwolf, R.T.W., 808, 819, 820
 Siems, W., 349
 Sievers, A.J., 322
 Sigg, A., 864
 Siggars, G.B., 509
 Sigman, D.M., 90, 143, 150, 456, 461, 468, 470, 613, 614, 837, 849, 851, 852
 Sigmarsson, O., 558, 561, 562
 Sikora, E.R., 164, 178, 191, 192
 Silker, W.B., 67, 70, 71, 76, 80
 Sill, C.W., 399
 Sillanpää, M., 591
 Sillen, A., 740, 741, 743, 749, 751, 753, 757, 760
 Silva, J.A., 836
 Silva, S.R., 424–426, 430, 431, 613, 614, 703, 836, 837
 Silverman, S.R., 643, 644, 647, 662
 Simard, S., 820
 Simberloff, D., 451
 Sime, N., 107, 112, 115
 Simon, B., 441
 Simon, H., 835
 Simon, J.I., 106, 112, 137
 Simon, S.L., 79

- Simonaitis, R., 435
 Simonetti, A., 741, 746, 752–754, 760
 Simpson, H.J., 346, 354, 355, 372, 377
 Simpson, S.V., 745
 Simpson, W.R., 229, 848
 Sims, K.W.W., 553
 Simsiman, G.V., 486
 Simunac, K.D.C., 477
 Sinclair, K., 485, 486
 Singer, D.M., 552
 Singh, S.K., 19, 520, 525, 527, 532, 536, 537, 541, 557
 Singleton, D.L., 495
 Singleton, M.J., 565
 Sinha, R., 520, 537, 541
 Sinsabaugh, R.L., 452, 462
 Sinyinza, D., 90, 98
 Sirivedhin, T., 666
 Sittkus, A., 606
 Sivry, Y., 180, 194
 Siyako, M., 655, 657
 Sjoblom, K-L., 365
 Skipperud, L., 406
 Skomarkova, M.V., 816, 820
 Skorupa, J.P., 157
 Skulan, J.L., 106, 109–112, 115–117, 179, 189
 Skwarzec, B., 281
 Slaten, S., 446
 Slater, G.F., 8, 639, 643, 662, 664, 665, 667, 681, 697
 Slater, J.C., 126
 Slater, R., 709
 Slatt, R., 637
 Sleep, B.E., 8, 643, 653, 662, 664, 665, 667, 681, 697
 Slinn, W.G.N., 605
 Sloane, H.J., 89, 90, 93, 96, 752, 756
 Slobod, R.L., 4
 Slosarczyk, J.M., 462
 Slovak, N.M., 19, 741, 742, 751, 753, 754, 760
 Smallwood, B.J., 644, 665
 Smethie, W.M., 349, 350, 375
 Smethie, W.M. Jr., 377
 Smirnov, A., 666
 Smis, A., 92, 101
 Smith, A., 753, 756
 Smith, A.B., 727, 729
 Smith, A.D., 367, 372
 Smith, A.J., 768
 Smith, B.H., 743, 744
 Smith, C., 746
 Smith, C.G., 346, 353–355
 Smith, C.I., 725, 735
 Smith, C.N., 147, 232, 235, 237, 239
 Smith, C.R., 801
 Smith, D., 772
 Smith, D.C., 800
 Smith, D.D., 503
 Smith, D.R., 768, 770, 772, 777, 779
 Smith, E.E., 436
 Smith, F.E., 733, 735
 Smith, F.J., 868, 871
 Smith, G.W., 638
 Smith, H., 775
 Smith, I.C., 221, 553
 Smith, J., 795
 Smith, J.N., 308, 382, 387, 786, 792, 800
 Smith, J.W., 834
 Smith, K.J., 312
 Smith, P.H., 441, 442
 Smith, P.N., 436
 Smith, R., 837
 Smith, R.E.H., 418
 Smith, S.D., 349, 351
 Smith, S.V., 418
 Smithie, W.M. Jr., 382
 Smoak, J.M., 17
 Smolders, E., 495
 Smucker, A.J.M., 469
 Snape, C.E., 666
 Snell, J., 194, 195
 Snowdon, L.R., 651, 652
 Sobek, A., 705, 712
 Socki, R.A., 711
 Soddy, F., 3
 Sofer, Z., 642, 644, 646, 651
 Sohm, J., 420, 423
 Sohn, M., 622
 Soileau, J.M., 503, 504
 Sojisuporn, P., 337
 Solomon, D.K., 66, 72, 77, 289
 Solomon, S., 583
 Somayajulu, B.L.K., 77, 78, 351, 352, 376, 786, 787
 Somero, G.N., 799
 Sommer, M., 92, 93, 95, 96
 Sommerfield, C.K., 63, 309, 319, 322
 Somsamak, P., 664
 Song, D.L., 665
 Song, L.X., 272, 274
 Sonke, J.E., 180, 189, 194, 197, 198, 230, 232, 233, 235, 237–239, 241, 530
 Sonntag, C., 287, 290, 291, 293, 294, 296, 297
 Sonoda, A., 46
 Soody, F., 551
 Sorensen, J., 837
 Sørensen, K., 278, 279
 Sorenson, K.S., 665
 Sorlin, D., 206, 219
 Sotnikov, V.I., 213
 Soudry, D., 107
 Souhaut, M., 347
 Soutar, A., 308
 Southerland, S., 375
 Southon, J.R., 65, 70, 78, 80, 582, 583
 Sowers, K.R., 679, 681, 686, 692
 Sowers, T.A., 460, 832, 848, 863–868, 871, 872, 875, 877
 Spahni, R., 875
 Spangenberg, J.E., 733
 Spechler, R.M., 305
 Spence, M.W., 725, 742, 751, 759
 Spencer, D.W., 275, 380, 386
 Spencer, R., 109, 119, 120
 Spezzaferri, S., 43, 53, 55, 110, 111, 114, 115, 121
 Spielhagen, R.F., 78
 Spielmann, K.A., 731

- Spiker, E.C., 642
 Spinnler, G.E., 662, 667
 Spiro, T.G., 179, 190, 196
 Spite, F., 41
 Spite, M., 41
 Spivack, A.J., 51, 53
 Spivack, J., 643, 662, 664, 665, 667, 681, 697
 Spoelstra, J., 614
 Spokes, L.J., 849
 Spomer, R.G., 503–505
 Sponheimer, M.M., 703, 705, 709, 724, 728, 746, 757, 760
 Spotila, J.R., 727
 Spraberry, J.A., 503
 Springer, A.E., 290
 Sprinsson, D.B., 836
 Squires, R., 645
 Sracek, O., 345
 Srivastava, 810
 St Gerontidis, D.V., 506
 Stafford, T.W. Jr., 735
 Stahl, W., 639, 643, 645, 646, 655, 656
 Stalker, L., 652
 Stallard, M., 207, 210, 211, 214
 Stallard, R.F., 63, 329, 333, 344, 351, 352, 486, 520
 Stanek, K.L., 766, 768, 770, 779
 Stanley, D.J., 498
 Stanley, R.H.R., 287
 Staplin, F., 657
 Stark, A., 666
 Stark, H., 622
 Stasova, O.F., 645
 Statham, P.J., 179, 198
 Staubwasser, M., 53, 54, 160–162, 164, 178, 191, 789
 Stauffer, F., 346
 Stavely, L.K., 452, 462
 Steefel, C.I., 553, 556, 560
 Steele, K.W., 727
 Steig, E.J., 469, 615, 835, 841, 843, 845, 849–852
 Stein, J.R., 753, 757
 Stein, L.Y., 460, 462, 463
 Steinmann, M., 530
 Steinmann, P., 74, 80, 494
 Stensland, G.J., 62, 63, 78
 Stephan, E., 741, 752, 754, 755
 Stephan, K., 456
 Stephen, F.M., 820
 Stephens, S.A., 477
 Stephenson, T.R., 705
 Sterckeman, T., 181, 189, 194
 Stern, G.A., 679
 Sternberg, L., 816
 Sternberg, L.D.L., 808, 814, 817, 822
 Sternberg, L.S.L., 820
 Stetson, S.J., 237
 Steuber, T., 107, 115
 Stevens, C.M., 248
 Stevens, P.A., 495
 Stevens, R., 452, 469
 Stewart, B.D., 800
 Stewart, B.W., 740
 Stewart, D.J., 622, 820
 Stewart, G.M., 272, 277, 278, 281, 311, 351, 352
 Stieglitz, T.C., 353, 354
 Stevenard, M., 813, 819, 822
 Stille, P., 106–109, 111, 112, 117, 524–526, 530, 553, 556, 558, 561
 Stilling, L.L., 157
 Stillings, L., 523
 Stirling, C.H., 6, 8, 20, 130, 131, 147, 551, 553
 Stirling, L., 732
 Stockley, C.S., 772, 776
 Stockwell, J.H., 346
 Stockwell, W.R., 625
 Stoddart, D.P., 651
 Stoffyn-Egli, P., 44, 50, 53
 Stokes, P.E., 42
 Stokes, S., 492, 493
 Stokozov, N.A., 379
 Stoll, P.M., 42
 Stollenwerk, K.G., 159
 Stolz, J., 167
 Stone, J.O., 439, 443, 476
 Stone, R.P., 795
 Stonestrom, D.A., 95, 435
 Stott, A.W., 724
 Stott, L.D., 818, 820
 Stott, W.R., 6, 476, 576
 Stout, S.A., 662
 Strauch, G., 836
 Streger, S.H., 438, 440, 441, 445
 Strejc, P., 344
 Strelow, F.W.E., 128
 Strickland, J.D.H., 88
 Stringer, C., 347
 Stroble, S.T., 442
 Strodal, M.C., 48
 Strong, D.F., 188
 Stroud, M., 437, 439
 Strutt, R.J., 3
 Struyf, E., 92, 101
 Stuart, G.M., 479
 Stuart-Williams, H., 725
 Stuart-Williams, H.L.Q., 742, 746, 751, 759
 Stubblefield, A.P., 509
 Studley, S.A., 455
 Stuermer, D.H., 642
 Stuver, M., 808
 Stump, C., 864
 Sturchio, N.C., 22, 435–447, 449, 662, 663, 665–667, 679, 680, 685–689, 697, 794
 Sturgeon, R.E., 160–162, 230, 234, 235
 Sturges, W.T., 865
 Sturm, M., 229
 Stute, M., 287, 290, 291, 293, 294, 296, 297
 Su, C.C., 273, 307, 405, 491
 Suarez, A.E., 207, 220, 221
 Subramanian, V., 556
 Sudheendrakumar, V.V., 820
 Suess, H.E., 574, 726
 Suga, A., 110, 116, 117
 Suggate, R.P., 657
 Sugihara, S., 488

- Sugimoto, A., 818, 822
 Sugimura, Y., 370, 595
 Sugiyama, J., 462
 Suh, C., 437, 440, 667
 Suh, H.L., 281
 Suksi, J., 558
 Sukumar, R., 808, 814
 Sullivan, C.H., 729
 Sultenfu, J., 373
 Sumich, J.L., 801
 Summerfield, M.A., 16
 Summons, R.E., 652
 Sun, C., 666
 Sun, H., 179, 187, 189, 198
 Sun, L., 94, 95
 Sun, S-S., 134, 212, 251
 Sun, Y., 652, 653
 Sunda, W.G., 142, 418
 Sundareshwar, P.V., 418
 Sundby, B., 215
 Sunderland, E.M., 230, 238, 241
 Sundquist, E.T., 486
 Surkov, A.V., 419, 420, 422–425, 432
 Surprenant, L.D., 376
 Suter, M., 443, 582
 Sutherland, R.A., 506
 Sutka, R.L., 453–456, 458–468, 470
 Sutley, S.J., 157, 163, 164, 166, 178, 191
 Sutter, B., 441
 Suwaj, J., 493
 Suydam, R., 800
 Suzuki, K., 211, 216
 Suzuki, M., 198
 Suzuki, N., 651
 Suzuki, T., 209
 Suzuki, Y., 211
 Svendsen, K.M., 75
 Sverdrup, H.U., 331
 Svrkota, N., 347
 Swackhamer, D., 451
 Swart, P., 77
 Swarzenski, P.W., 17, 67, 68, 70, 71, 75, 78, 278, 279, 305,
 307, 310, 311, 313, 337, 352–356, 509, 564, 799
 Sweda, T., 808
 Swetnam, T.W., 820
 Switsur, V.R., 816, 818, 820
 Sylva, S.P., 652
 Sylvester, P., 42, 53
 Symons, E.A., 42
 Synal, H-A., 3, 443
 Syvitski, P.M., 542
 Sywall, M., 43, 53
 Szechenyi, M.E., 493
 Szechenyi, S.C., 372, 403, 509
 Szeverenyi, N.M., 642
 Szpunar, C.B., 745
 Szymczak, R., 531
- T**
- Tachikawa, K., 531
 Tada, W., 78
 Tadmor, J., 590, 600
 Tagami, K., 370, 371, 373
 Tailleux, A., 180, 194
 Taira, H., 785, 786, 796, 797
 Takada, H., 666
 Takagi, K., 812
 Takagi, T., 834
 Takahashi, T., 349, 350, 357
 Takahashi, Y., 63, 65, 80, 213
 Takahata, N., 288
 Takaoka, N., 296, 297
 Takatani, S., 596, 605, 606
 Takeda, A., 278
 Takemura, M., 785, 786, 796
 Takeoka, H., 332
 Takigiku, R., 639, 640, 651, 661
 Talbot, M., 644
 Talbot, R.W., 278, 583
 Talke, I.N., 198
 Talma, A.S., 290
 Tamai, K., 94
 Tamburini, F., 424, 425, 432
 Tambutté, E., 113
 Tampari, L.K., 442
 Tamura, T., 493–495
 Tan, M., 770
 Tanabe, S., 687
 Tanahara, A.H., 785, 786, 796, 797
 Tanaka, N., 207, 208, 576, 582–584, 727
 Tanaka, S., 78
 Tanaka, T., 537, 727
 Tang, J., 113, 115, 116, 530
 Tang, K., 812
 Tanimizu, M., 43
 Tanji, K.K., 168, 170–172
 Tanji, Y., 458, 461
 Tanoshima, M., 110, 117
 Tanyileke, G., 195
 Tardieux, A., 458, 466, 683, 684, 686
 Tardieux, P., 458, 466, 683, 684, 686
 Tarr, C.H., 679, 680, 685–689
 Tarras-Wahlberg, N.H., 486
 Tartari, D., 666
 Tassinari, M., 206
 Tastumoto, M., 551, 561, 563
 Tate, M.E., 460
 Taubald, H., 644
 Tauber, H., 731–733
 Tausz, M., 808
 Tavares, P., 462
 Taylor, A.S., 489, 524, 536, 770
 Taylor, B.E., 92, 835
 Taylor, D., 666
 Taylor, D.M., 394, 401, 402
 Taylor, D.W., 638, 649
 Taylor, H.E., 752, 753, 756, 757
 Taylor, H.P., 155, 163
 Taylor, H.P. Jr., 90
 Taylor, P., 436
 Taylor, P.D.P., 3, 89
 Taylor, R.N., 263, 370, 371, 401

- Taylor, S.R., 134, 205
Taylor, T.I., 41, 46
Tcherkez, G., 817
Teaford, M., 723
Teagle, D., 527, 528, 530, 536, 543
Teagle, D.A.H., 51–53, 253–255, 257–260, 262–265, 556
Teczotzky, M., 275
Teerman, S.C., 643, 653
Telmer, K., 537
Telnaes, N., 648–650
Télouk, P., 5, 137, 180, 188
Templer, P.H., 808
Teng, F.-Z., 43, 44, 189
Teng, R., 208
Teng, R.T.D., 208
Teplyakov, N., 160–162
Tera, F., 43–45
Tera, O., 770
Terashima, Y., 663
Teschler-Nicola, M., 703
Tessier, E., 241, 242
Tettelbaum, S.L., 744
Teuten, E.L., 689
Teutsch, N., 195
Teyssié, J.L., 272, 281
Thackeray, J.F., 755
Thakkar, A.H., 400
Thayer, C.W., 798
Thevenot, D.R., 193
Thiemens, M.H., 5, 6, 22, 147, 436, 441, 442, 452, 455, 456, 467–469, 612, 613, 615, 618–621, 624, 832, 833, 835–837, 839, 840, 843–845, 848, 849, 853
Thirlwall, M.F., 147, 263, 748, 752, 756
Thode, H.C., 161, 168, 169
Thode, H.G., 88, 137, 168, 169, 834, 835
Thomas, A., 43, 44
Thomas, C.D.L., 727, 729
Thomas, C.W., 372, 384, 581, 582
Thomas, E., 378
Thomas, J.H., 63, 64, 71, 73
Thomas, R.G., 239
Thomas, S.M., 428
Thompson, A.H., 706
Thompson, A.M., 833, 853
Thompson, G., 48, 50–53
Thompson, P., 808
Thompson, S.O., 443
Thoms, S., 114
Thomsen, S., 312
Thomson, J., 35, 271, 275, 280, 318, 795, 796
Thorne, M.C., 495
Thornton, E.K., 753, 756
Thouron, D., 48
Thrupp, L.A., 452, 463, 464, 470
Thurber, D.L., 4, 793, 798
Tian, K., 435, 436
Tian, L., 810
Tian, S.H., 94, 95
Tichomirowa, M., 835
Tiedemann, R., 112
Tiedje, J.M., 461, 837
Tien, G., 418, 425
Tiesler, V., 752–755
Tieszen, L., 729
Tilman, D., 418, 451
Tilsner, J., 464
Tims, S.G., 439, 443
Tipper, E.T., 87, 106–108, 111, 115, 524
Tissot, B., 644, 649, 657
Titley, S., 179
Tkalin, A.V., 377
Tobias, C., 451, 452
Tock, R.W., 435, 442
Todd, J.F., 62, 64, 330, 347, 353, 491
Togawa, O., 377, 381, 384
Togawa, P.P., 381, 384
Toggweiler, J.R., 309
Tokanai, F., 489
Tokieda, T., 489
Tokunaga, T.K., 168
Tolstikhin, I.N., 289, 290, 296
Tomascak, P.B., 43–45, 47
Tombrello, T., 110, 111
Tomczak, M., 332
Tomkins, K.M., 507, 508
Tomlinson, A.J., 441
Tonarini, S., 51
Tong, H., 733
Toon, G.C., 435, 457, 469
Toon, M.B., 650
Toon, O.B., 845
Top, Z., 289, 290, 296, 368, 374
Topcuoğlu, S., 381
Torgersen, T., 285, 287, 289–295, 354
Torosuares, I., 461
Torres, L.M., 350
Torres-Rouff, C., 753, 755
Toth, R.A., 457, 469
Touchton, J.T., 503, 504
Toutain, J.P., 232, 237
Towers, J., 752, 756
Toyoda, S., 452–458, 461, 462, 464, 466, 468–470
Tracy, D.M., 796
Tranter, M., 49
Trefry, J.H., 254, 262
Trendel, J.M., 639, 651, 661
Treutler, H.C., 346
Treydte, K.S., 808, 816, 819, 820
Tricca, A., 530, 564, 565
Trickett, M.A., 743, 749, 760
Trier, R.M., 306, 352, 372
Trimble, S.M., 69, 310
Trimborn, P., 808
Trinkaus, E., 727, 733–735
Tripathy, G.R., 19, 520, 557
Trivedi, J.R., 527, 528
Trombini, C., 666
Troxell, G.E., 801
Trudell, L.A., 88
Trueman, C.N., 725
Trull, T.W., 90
Trumbore, S.E., 6, 457, 458, 462, 820

- Trumper, R.E., 509
 Truran, J.W., 206
 Trust, B.A., 168, 169
 Tryon, M., 299
 Tryon, M.D., 300, 301
 Tsai, H., 73
 Tsara, M., 506
 Tschirgi, M.L., 716
 Tsubota, H., 334, 339
 Tsuchiyama, A., 252
 Tsuha, A., 797
 Tsuji, H., 812
 Tsuji, L.J., 776
 Tsunogai, S., 272, 489
 Tu, K.P., 808
 Tuazon, E.C., 622
 Tubman, S.C., 704
 Tuchiya, K., 42
 Tucker, W.B. III., 383
 Tudge, A.P., 168, 424, 425
 Tudhope, A.W., 43, 53, 54
 Tung, T.A., 753, 755
 Tuniz, C., 476
 Turatti, F., 457
 Turchyn, A., 108, 121
 Turcotte, D.L., 559
 Turekian, K.K., 34–36, 43, 53, 62, 64, 72, 78, 205, 206, 208,
 212, 213, 215, 216, 218, 219, 271, 273, 275, 280, 307,
 344, 354, 488, 489, 491–493, 564, 576, 582–585, 591,
 788, 792, 799, 800
 Turekian, V.C., 354
 Turi, B., 752, 757
 Turin, H.J., 47
 Turner, B.L., 753, 754
 Turner, M.S., 50
 Turner, R.E., 418, 486
 Turner, S.P., 3, 29, 251, 551–554, 556, 558–563
 Tuross, N., 724, 725, 727, 735, 743, 749, 760
 Turpin, L., 520, 537, 541
 Tutken, 520, 537, 538
 Tuzson, B., 837, 853
 Twiss, M.R., 460
 Tyler, S.C., 457, 458, 462
 Tysklind, M., 695
- U**
- Uchida, S., 370, 371, 373
 Uchiyama, H., 462
 Uchytill, Y., 656, 657
 Udaykumar, M., 814
 Udisti, R., 833
 Ueda, A., 834
 Uemura, R., 621
 Ueno, K., 372
 Uhle, M.E., 820
 Ukonmaanaho, L., 180, 190, 194
 Ullman, W.J., 359, 365
 Ulrich, A.C., 653, 664, 681
 Ulsh, B., 396
 Umeda, M., 42
 Ungar, P.S., 723
- Unger, M., 697
 Unger, N., 833
 Urbani, A., 462, 463
 Urey, H.C., 4, 7, 41, 46, 248, 623, 831
 Urich, T., 469
 Usbeck, R., 552
- V**
- Vaccari, D.A., 417
 Vachon, R., 810
 Vaganov, E.A., 816, 820
 Vajda, N., 400, 401
 Vakulovsky, S., 382
 Valdes, P.J., 833
 Valentin-Blasini, L., 436
 Valentini, J.J., 618
 Valenzuela, L.O., 706, 713, 714
 Valettesilver, N., 63, 65, 67, 75
 Valkiers, S., 92
 Valles, I., 489
 Vallet, C., 709
 Valley, J.W., 155
 Vallières, S., 558
 Van Allen, J.A., 477
 van Beek, P., 347, 351, 352
 van Belle, C.C., 90
 van Bergen, M.J., 90, 101
 van Beusichem, M.L., 452, 461, 464, 468
 Van Bocxstaele, M., 194, 195
 van Breukelen, B.M., 639, 685
 van Breukelen, B.N., 665
 van Calsteren, P., 46, 49–51, 556
 Van Cappellen, P., 170
 van Cleemput, O., 452
 Van Damme, S., 92, 101
 van de Fliedrt, T., 261
 van den Boom, S., 89, 90, 93, 96
 van den Boom, S.H.J.M., 90, 101
 van der Loeff, M.M.R., 69
 van der Merwe, N.J., 36, 724, 726, 729, 731, 733, 735, 740, 755
 van der Plight, J., 376
 van der Star, W.R.L., 456, 470
 van der Wagt, B., 90, 750
 van Dorp, F., 497, 498
 van Drecht, G., 451, 452
 van Geldern, R., 87
 Van Gerven, D.P., 744
 Van Grieken, R., 217, 221
 van Groenigen, J.W., 431, 462
 van Hees, E., 68, 72, 75, 305, 313, 319, 320, 509, 788
 van Hoeven, W., 638
 van Klinken, G., 724
 Van Loon, J.C., 207
 van Loosdrecht, M.C.M., 456, 470
 Van Muysen, W., 506
 Van Oos, K., 506
 van Riemsdijk, W.H., 88
 Van Soest, M.C., 290
 Van Stee, L.L.P., 688
 Van Stempvoort, D.R., 170
 van Warmerdam, E.M., 22, 683

- Vance, D., 179, 184, 198, 199, 252, 527, 528, 530, 543, 556
 Vandaele, K., 506
 Vander Putten, E., 798
 Vander Zanden, M.J., 705
 Vander-meersch, B., 730
 Vanhaecke, F., 180, 750
 Vanhaeren, M., 752, 756
 Vanloon, J.C., 208, 210
 Vanneste, H., 53
 Varela, D.E., 90
 Varga, A., 207, 211
 Varga, Z., 348
 Varney, T.L., 751
 Vasconcelos, P.M., 73
 Vaughn, B., 810
 Veizer, J., 87, 522, 529, 534, 537, 740, 742
 Velasco, H., 492
 Velthof, G.L., 452, 461, 464, 468
 Vendramini, P.F., 822
 Vennemann, T., 106, 107
 Vennemann, T.W., 422, 426
 Verheyden, A., 820, 821
 Verhoogen, J., 92
 Verma, S.P., 257
 Vermoesen, A., 455
 Vernet, J-P., 64, 67
 Veron, A.J., 307
 Versini, G., 704
 Vesely, J., 63, 65, 80
 Vetter, W., 679–682, 686–689, 692–696
 Veysseyre, A., 217
 Vicinus, J.H., 744
 Viczian, M., 770
 Viers, J., 97, 146, 180, 194, 197, 198, 526, 527, 537, 538, 557
 Vieten, B., 464, 465
 Vieth, A., 664, 665
 Vigier, N., 17, 22, 42–44, 46–51, 53, 55, 87, 110, 111, 114, 115, 121, 207, 209, 212, 213, 263, 520, 551–566
 Vilenskii, V.D., 271
 Vilibic, I., 331
 Villalobos-Aragon, A., 163, 164
 Villiet, J., 509
 Vils, F., 51
 Vimeux, F., 809, 862
 Vincent, W.F., 232
 Vintro, L.L., 312
 Vitko, L., 507
 Vitousek, P., 109, 117, 118, 452
 Vivit, D.V., 95, 179, 198
 Vocke, R.D., 89, 436
 Voelker, A., 863
 Vogel, J.C., 67–71, 80, 728, 731
 Vogler, S., 67, 74
 Vogt, C., 695, 696
 Voigt, S., 87
 Volchock, H.L., 368
 Volkening, J., 208
 Volkering, F., 639, 665
 Volpe, A.M., 6, 789
 Volzthomas, A., 849, 850
 von Blanckenburg, F., 16, 32, 62, 65, 69, 73, 79, 109, 160–162, 164, 178, 180, 191, 196–199, 557, 559
 Von Damm, K.L., 35
 von der Recke, R., 689
 von Fischer, J.C., 458, 460, 461
 von Glasow, R., 848
 von Gunten, H.R., 346
 von la Chevalerie, G., 728
 von Wirén, N., 196, 198, 199
 Vonmoos, M., 61, 62
 Voshage, H., 206
 Voskamp, M., 644
 Voytek, M.A., 451, 452
 Vroon, P.Z., 89, 90, 93, 96, 101, 750
 Vuille, M., 621
 Vuletich, A.K., 651
- W**
 Waber, H.N., 290, 558
 Wacker, L., 3
 Wada, E., 727
 Wade, T.L., 387
 Wadhams, J.L., 846, 848
 Wadleigh, M.A., 839, 843
 Wagenbach, D., 850
 Wagener, K., 813, 818
 Wagner, A., 694
 Wagnon, P., 850
 Wahl, J., 752–755
 Wahlen, M., 457, 460, 464
 Wahner, A., 622
 Waight, T., 750
 Wainman, B.C., 776
 Wakabayashi, T., 739
 Wakelin, D., 437, 439
 Walbrink, P.J., 493
 Walcroft, A.S., 819, 820
 Walczyk, T., 110, 185, 187, 189, 208, 211
 Walder, A.J., 3, 6
 Walder, J., 297, 298, 300
 Waliser, D.E., 823
 Walker, B.A., 552
 Walker, J., 520
 Walker, P.L., 731, 732
 Walker, R., 209
 Walker, R.J., 43–45, 205–208, 211–213, 219
 Walker, R.M., 552
 Wallace, B.P., 727
 Wallace, J.R., 376
 Wallbink, P.J., 507, 508
 Wallbrink, P.J., 62–66, 75, 491, 493
 Wallin, G., 817
 Walling, D.E., 63–65, 73, 75, 81, 306, 308, 490–493, 495–498, 500, 501, 503, 504, 506–509
 Walling, X.B., 504
 Wallmann, K., 87, 105–108, 121, 261
 Wallner, C., 394
 Walsh, J.J., 339
 Walter, H.J., 520, 537
 Walter, L.M., 756
 Walters, C.C., 637, 638, 644, 645, 651, 653

- Walvoord, M.A., 435
 Wan, D.F., 90, 92, 95, 97, 98
 Wanamaker, A.D., 798
 Wanek, W., 819
 Wang, C.Y., 90, 92, 95, 97, 98, 297, 497, 503, 504, 652, 733
 Wang, D., 727
 Wang, F., 600
 Wang, J.S., 372
 Wang, P.L., 835
 Wang, Q.Z., 42
 Wang, S.L., 789, 790, 794, 795
 Wang, W., 35
 Wang, X., 552, 665
 Wang, Y.H., 42, 644, 653, 665, 743, 833
 Wang, Z.-L., 379
 Wankel, S.D., 441, 849
 Wanninkhof, R., 348, 349, 351, 357
 Wanty, R.B., 179, 180, 184, 199, 237
 Waples, J.T., 311
 Ward, B.B., 463, 465
 Wardle, W.J., 788, 799
 Warneke, T., 370, 371, 599
 Warren, J.M., 817
 Warwick, P.E., 370–372, 399
 Was, B., 398–400, 406, 411, 490
 Waska, H., 272, 280, 281, 347
 Wassenaar, L.L., 613, 667, 837
 Wasserburg, G.J., 4, 6, 113, 115, 116, 206, 208, 209, 211–217,
 248, 521, 526, 527, 537, 538, 551, 553, 554, 564, 565
 Wasserman, R.H., 740
 Wasson, J.T., 134, 206
 Wasson, R.J., 66
 Wasylenki, L.E., 190, 196
 Wasylishen, R.E., 820
 Watanabe, H., 46
 Watanabe, S., 452, 468
 Watanabe, Y., 845
 Waterhouse, J.S., 816, 818
 Waters, F.G., 207, 208
 Watkins, T.R., 770
 Watson, B.R., 510
 Watson, P.G., 76
 Wattayakorn, G., 337
 Webb, J.L., 596
 Webb, T.H., 297
 Webber, W.R., 477
 Weber, D., 683
 Weber, J.N., 794, 795
 Weber, K.A., 178
 Weber, R., 695
 Weber, S., 695, 696
 Webster, C.L., 168
 Webster, I.T., 344, 353–355
 Weckerly, K.M., 311
 Wedepohl, K.H., 134, 140, 151, 247, 248, 251, 257, 266, 575
 Weeks, C.L., 190, 196
 Weersink, A.J., 706
 Wehmiller, J.F., 793, 798
 Wehrli, B., 195
 Wehrung, P., 651
 Wei, G.J., 520, 525, 527
 Weibel, J.D., 620
 Weidemann-Bidlack, F.B., 423, 424
 Weidenhamer, J.D., 765
 Weidner, K., 820
 Weimer, W., 376
 Weiner, S., 751
 Weinhouse, S., 6
 Weinstein, S.E., 306, 308
 Weinstein, Y., 356, 357, 552
 Weis, D., 180, 194
 Weisberg, P.J., 229
 Weise, S.M., 53, 291
 Weiss, D.J., 8, 134, 135, 138, 139, 159, 180, 181, 190,
 194, 196–199
 Weiss, H.V., 211, 214
 Weiss, R.F., 289, 290
 Weiss, Z., 606
 Welhan, J.A., 832
 Well, R., 462
 Weller, R., 851
 Welte, D., 644, 645, 649, 657
 Wen, H.J., 161, 170, 172, 173, 188
 Wen, S., 665
 Weng, J.Q., 372
 Wenger, M., 45
 Wenninger, J., 817
 Wentz, R.F., 207, 211
 Weppernig, R., 351
 Werner, M., 621
 Werner, R.A., 462, 677–680, 808, 836
 Weser, U., 198
 Wesolowski, D.J., 622
 Wesolowski, J.J., 770
 West, A.G., 707
 West, A.J., 98–101, 520
 West, J.B., 704, 705, 712
 West, S.J., 441
 Westley, M.B., 452, 464, 468
 Weston, C., 817
 Wetherill, G.W., 131, 768, 769, 772
 Weyer, S., 147, 160, 599
 Weyhenmeyer, C.E., 290
 Wheatcroft, R.A., 306
 Wheeler, A.J., 794
 Wheeler, P., 733
 Wheelwright, N.T., 818, 820, 821
 White, A.F., 90, 95, 96, 168, 179, 198, 523, 524, 556
 White, C.D., 703, 725, 727, 729, 733, 734, 742, 751, 759
 White, J.W.C., 704, 810, 813
 White, P., 109
 White, W.M., 263–265
 Whitehead, E.V., 638
 Whitehead, N., 281
 Whitehouse, M.J., 835
 Whitfield, M., 151
 Whitar, M.J., 639, 678, 685, 689
 Whiting, J., 404
 Whiting, P.J., 18, 62–66, 72, 75, 306, 308, 314, 315, 491,
 495–497, 500, 501, 503, 505, 507, 509
 Whitlock, D., 643
 Whitlow, S.I., 850, 851

- Whittaker, K., 817
 Whittaker, M., 665
 Whittle, D.M., 237
 Wiberg, E., 125, 126
 Wiberg, N., 125, 126
 Wickman, F.E., 836
 Widdowson, M., 47
 Widerlund, A., 530
 Widory, D., 194, 195
 Wiechert, U.H., 87, 90, 91
 Wiederhold, J.G., 197, 198
 Wiegand, B.A., 109, 117, 118, 520, 537, 538, 741, 742, 751, 753, 754, 760
 Wieland, E., 64, 74
 Wielders, H.A., 456, 470
 Wieser, M.E., 126, 186
 Wiesli, R.A., 190
 Wietzerbin, K., 704
 Wilcke, W., 168, 170, 666
 Wild, O., 625
 Wilkening, M.H., 346
 Wilkes, H., 653, 665
 Wilkinson, G., 125, 126
 Wilkinson, J.J., 180, 190, 194
 Wilkinson, P., 507
 Wilkinson, S.N., 507, 508
 Wilkison, D.H., 613, 614, 836, 837
 Willenbring, J.K., 16, 62, 65, 73, 78, 79, 544
 Willett, I.R., 552
 Williams, D.G., 817
 Williams, E.H., 460, 468
 Williams, G.A., 206, 216, 219
 Williams, H.M., 90, 93, 96, 251, 263, 266, 739, 759
 Williams, J., 646, 647
 Williams, L.B., 46
 Williams, R., 112, 113, 273
 Williams, R.J.P., 198
 Williams, R.W., 6
 Williams, S.R., 753, 755
 Wilson, C.G., 63, 75, 314, 315, 491, 495, 500, 501, 503, 505, 507, 509, 510
 Wilson, D., 770
 Wilson, J.T., 639, 664
 Wilson, R.D., 664, 808
 Wilson, S.R., 457, 469
 Wimpenny, J., 46, 47, 49, 51
 Winckler, G., 296
 Wing, B.A., 835, 845
 Wing, S.L., 816
 Wingate, L., 813, 822
 Winger, K., 377
 Winiger, M., 808, 819
 Winkler, A., 383
 Winkler, R., 596
 Winsberg, L., 581, 582
 Winter, B., 537
 Winter, D.A., 836
 Winter, T.C., 345
 Winterer, E.L., 477, 478
 Winters, A.J., 817
 Winters, K., 704
 Wintsch, R.P., 652
 Wiren, N., 109
 Wirsen, C.O., 679, 681, 686, 692, 799
 Wirt, L., 436
 Wischmeier, W.H., 503
 Wischmeyer, A., 100
 Wiseman, C.L.S., 217, 221
 Wiseman, W.J., 418
 Wisman, W.J., 486
 Witherow, R.A., 42, 43
 Witt, M., 8, 643, 662, 664, 665, 667, 681, 697
 Witt-Eickschen, G., 134, 140
 Witte-Lien, K., 179
 Wogman, N.A., 581, 582
 Wolf, R., 184
 Wolff, B., 418, 451
 Wolff, E.W., 846, 850, 851
 Wolf-Gladrow, D.A., 100
 Wölfli, W., 443
 Wollenberg, H.A., 168
 Wollenburg, I., 77
 Wombacher, F., 20, 44, 126–135, 137–141, 148–151, 181, 184, 186
 Wong, G.R.F., 491
 Wong, G.T.F., 62, 64
 Wong, K.M., 384, 385
 Woo, K.S., 785, 786, 797
 Woodbury, P.B., 507
 Woodhouse, O.B., 207, 209, 214
 Woodland, S.J., 207, 211
 Woodman-Ralph, J.P., 808
 Woodruff, D.R., 817
 Woodward, J.C., 497
 Wooller, M., 704
 Workman, R.K., 141
 Worthington, T., 553
 Wrage, N., 452, 461, 462, 464, 468
 Wright, I.J., 817
 Wright, L., 741
 Wright, L.E., 728, 741, 742, 744, 745, 751, 753, 758, 760
 Wright, S.J., 815, 823
 Wright, S.M., 495
 Wright, W.E., 820
 Wu, C.C., 207, 220, 221
 Wu, F-Y., 43, 44
 Wu, J.F., 418
 Wu, K., 765
 Wu, L., 94, 179, 190, 520, 532
 Wu, L.H., 94, 95
 Wu, Q., 679, 681, 686, 692
 Wu, T., 277
 Wu, Y., 306
 Wunder, B., 52
 Wunderli, S., 750
 Wynn, P.M., 848
 Wyse, E., 370, 377, 381, 384

X
 Xiao, T.F., 253
 Xiao, Y.K., 89, 584
 Xiaolin, M., 733

- Xie, Q.L., 147, 232
 Xing, L., 462
 Xiong, Y., 651, 652
 Xu, F., 625, 627
 Xu, L., 640, 665, 666, 689, 696, 697
 Xu, S., 376, 652, 653
 Xu, Y.F., 142, 238, 239, 525, 527, 528
 Xue, D.M., 837
 Xue, J., 272, 311
 Xue, Z., 20, 143, 181
- Y**
- Yadava, M.G., 808–810
 Yaffe, Y., 770
 Yakir, D., 467, 468
 Yamada, H., 486
 Yamada, M., 18, 352, 354, 379, 393, 398–400, 402, 403, 407, 408, 488, 490, 502
 Yamagishi, H., 452, 458, 461, 468
 Yamaji, K., 46
 Yamakawa, K., 797
 Yamamoto, M., 372
 Yamanaka, K., 489
 Yamashita, N., 680, 681, 688–690, 694
 Yamashita, Y., 213
 Yan, H., 506, 507
 Yan, P., 506
 Yang, F., 506, 507
 Yang, H.S., 307, 329, 330, 334, 338, 339
 Yang, J.H., 212, 599
 Yang, L., 160–162, 182, 184, 230, 234, 235, 834
 Yang, S., 537
 Yang, W., 109, 111, 119, 120
 Yang, Y.P., 281
 Yanik, P.J., 681
 Yano, M., 94
 Yao, D., 55
 Yao, T., 810
 Yao, W.Y., 507
 Yapp, C.J., 808
 Yashima, M., 276
 Ye, R.W., 461
 Yeatman, S.G., 849
 Yee, A.W., 168
 Yee, N., 142
 Yeh, H.W., 748
 Yi, W., 134, 140
 Yi, Y.V., 211
 Yim, M.S., 374
 Yiou, F., 65, 68, 69, 71, 72, 78, 81, 372, 379, 380, 582
 Yokoyama, T., 219
 Yoneda, M., 725, 727, 735
 Yoneyama, T., 727
 Yoschenko, V.I., 596
 Yoshida, N., 452–458, 461, 462, 464, 466, 468–470
 Yoshida, S., 370, 371, 373
 Yoshida, Y., 195
 Yoshimura, Y., 834
 Yoshinaga, J., 770
 Yoshinari, T., 452, 457, 613, 614, 836
 Yoshizawa, Y., 311
- Yotsui, Y., 680, 834
 You, C-F., 43, 51–53, 61, 65, 494
 Young, E., 832, 835
 Young, E.D., 89, 135, 137, 468
 Young, G.H.F., 816
 Young, J.A., 581
 Young, M.B., 421–423, 428, 429
 Young, S.M.M., 441, 729
 Youngblut, M.D., 462
 Yu, J., 733
 Yu, L., 436
 Yu, Y., 665
 Yui, L.A., 772, 776
 Yui, T.F., 53
 Yung, Y.L., 435, 453, 454, 460, 462, 463, 624, 851
 Yurtsever, Y., 742, 759, 810
 Yvon, S.A., 625
- Z**
- Zabel, T.F., 766
 Zaccarini, F., 212, 213
 Zachos, J., 523, 527
 Zafirios, T., 506
 Zaggia, L., 335
 Zagorognyaya, A.N., 220
 Zahnle, K.J., 435, 442
 Zakaria, M.P., 666
 Zambardi, T., 232, 237
 Zapata, F., 503
 Zaporozec, A., 343
 Zasoski, R.J., 156
 Zawislanski, P.T., 160, 161, 168, 170–172, 178
 Zebo, Z., 651
 Zeh, J., 800
 Zeitler, P., 540
 Zengler, K., 653, 665
 Zent, A.P., 442
 Zereini, F., 217, 221
 Zhai, S., 55
 Zhang, F., 90, 92, 95, 97, 98
 Zhang, G., 770
 Zhang, H., 457, 651
 Zhang, J., 14, 76, 278, 307, 330–332, 335
 Zhang, L., 44, 46, 48, 51–53, 252, 331, 332, 335, 353, 354
 Zhang, M., 662, 667
 Zhang, X.B., 506
 Zhang, Y., 63–65, 188, 503, 506, 592, 611
 Zhao, C., 733
 Zhao, F.J., 197, 198
 Zhao, X., 295
 Zhen, J., 379
 Zheng, B., 157, 172
 Zheng, J., 18, 393, 398, 402, 403, 407, 408, 488, 490, 502, 592
 Zheng, L., 765
 Zheng, W., 230, 232–235, 237, 239, 241
 Zheng, Z., 558
 Zhou, J.X., 94, 95
 Zhou, Z.Q., 37
 Zhu, C., 100, 558
 Zhu, J.M., 62, 157, 170, 172, 173

- Zhu, L-P., 602
Zhu, P., 105, 106, 110, 112
Zhu, X.K., 160, 188, 198
Zhuang, D., 506, 507
Ziegler, K., 90, 91, 95–98, 101
Zielinski, G.A., 838
Zimmerman, J.T.F., 333
Zink, S., 160–162, 164, 178, 191
Zipf, E.C., 464
Zobeck, T., 406
Zoccola, D., 113
Zohar, I., 421, 424, 425, 432
Zonneveld, K., 112
Zreda, M., 443
Zuddas, P.P., 794
Zumberge, J.E., 644, 645, 650, 657, 660
Zuo, W., 157, 172
Zuo, Z.Z., 278, 321
Zurcher, L., 206
Zwanenburg, K.C.T., 792, 800
Zwank, L., 643, 665, 684, 685, 697
Zylberberg, D.R., 216

Subject Index

A

Abrupt temperature changes, 862, 871, 874, 880
Absorption
 coefficient, 479
 of cosmic ray, 483
Abyssal peridotite, 51, 216
Accelerator mass spectrometry (AMS), 27–28, 439, 576, 581, 582
Accessory minerals, 525–526
Accumulation, 76–77, 320–321, 369, 387, 791, 851, 871, 878–880
Adenosine triphosphate (ATP), 417, 418
Adsorption, 23, 46, 47, 50, 51, 65, 163–164, 169–170, 257, 265–266, 422
Advection, 165, 316–319
 of particulate matter, 316–317
Aegean Sea, 382
A530E resin, 437
Aerobic degradation, 663
Aerosols, 18, 34, 207, 212, 221, 254–255, 273, 275, 376, 575, 578, 579, 583–585, 840
A-horizon,
Airborne particle sampling, 590
Air bubble, 290, 291, 294
Air-sea exchange, 348–351, 579
Air trapped in ice, 861–880
Alice Springs, 295, 296
Alkaline phosphatase (APase), 422, 423, 440
Alkyl benzenes, 652, 665
Alkyl naphthalenes, 652
Allanite, 521, 526
Alpha particle, 23–24
Alpha spectrometry (AS), 23–24, 27–28, 310, 330–331
Am–241, 367, 387
American Petroleum Institute (API) gravity, 638
Americium (^{241}Am), 18, 365, 367, 368, 387, 394, 398, 400, 402
AMH'S. *See* Anatomically modern humans
Amino acids, 725, 729, 735
Ammonia oxidation, 461
AMS. *See* Accelerator mass spectrometry
Anaerobic degradation, 663, 665, 668
Analysis of oxygen isotopes in nitrate, 836–837
Anatomically modern humans (AMH'S), 733–734
Ancient human population, 728–734
Ancient mobility patterns, 739
Ancient Nasca, 755

Ancón, 741, 742, 746, 753, 754
Andaman Sea, 541
Anomalous sulfur isotopic composition, 835
Anoxic condition, 279, 394, 419, 436, 460
Anoxic events, 428
Anthropocene, 5, 97, 101, 786
Anthropogenic Cd isotope fractionation, 149–150
Anthropogenic emissions, 138–140, 229, 271, 583
Anthropogenic isotopes, 17–19
Anthropogenic lithium, 44
Anthropogenic radioisotopes, 355–356
Anthropogenic radionuclides, 365–388, 487, 589–606
Antimony (^{125}Sb), 380
Apatites, 422, 521, 522, 524–527, 730, 751
Applications of Ra isotopes, 336
Arctic, 69, 77, 144, 145, 215, 368, 379, 381–382, 408, 538
Atacama ClO_4^- , 441–443, 446
Atmospheric Cl, 435, 442
Atmospheric CO_2 , 65, 143, 520, 531, 726, 815
Atmospheric deposition, 119, 307, 308, 325, 419, 505, 786
Atmospheric life of $[\text{Hg}(0)]$, 229, 238
Atmospheric lifetime of sulfuric and nitric acids, 831
Atmospheric nitrate, 611–630, 846–850
Atmospheric removal of radionuclides, 13
Atmospheric tracers, 573–585, 589–606
Atmospheric transport, 72, 79
Atomic chlorine, 585
ATP. *See* Adenosine triphosphate
Authigenic Tl, 257
Autocorrelation, 818, 822

B

Bacterial denitrification, 460–467
Bacteria method, 837
BAM–1012 reference material, 130, 132, 133, 136
Barium (Ba), 208, 309, 311, 344, 378
Barometric equation, 868
Basaltic weathering, 95
Bay of Bengal, 100, 277, 519, 532, 536, 539, 541, 542, 545
 ^7Be , 61–81, 305–325, 485–511, 576, 577, 579–585
 and ^{10}Be in freshwater, 66–67
 and ^{10}Be in marine environment, 61, 65, 67–69
 as a tracer to quantify the redistribution of PCBs and other contaminants, 322–323
 Be –7, 311, 312

- ¹⁰Be, 61–81, 478–483, 581–585
 in continental dust, 62–63
 in groundwater, 67
 inventory, 63, 65, 70, 73, 79
- ⁷Be/¹⁰Be ratios, 78, 80, 581–583
- Bedrock signatures, 740
- Beef hydrogen and oxygen ratios, 709–711
- Benthic fluxes, 255–256, 354–358
- Benzene, toluene, ethylbenzene and xylenes (BTEX), 665
- ⁷Be/²¹⁰Pb ratios
 in sediments, 75, 314–315
 as tracer of particle dynamics, 319–320
- Beta particle, 24, 25, 311
- Beta spectrometry, 24–25, 310, 311
- Bichromate, 178
- Bicyclic alkanes, 652
- Bioaccumulation of ²¹⁰Po, 229, 272
- Biodegradation, 7, 436, 445, 643–648, 651–653, 663–665
- Biogenic carbonates, 43, 54, 106, 115, 116
- Biogenic enamel isotope signatures, 743
- Biogenic methane, 653, 666
- Biogeochemical cycle, 100–101, 579
- Biogeochemical cycling of phosphorus, 417–432
- Biokinetics of lead, 772, 778
- Biological fractionation, 8
- Biological mass-independent effect, 467
- Biological pathways of calcification, biocalcification pathway, 112
- Biological production pathways, 458–469
- Biomagnification, 282
- Biomarker, 179, 190, 638, 667–668, 767–768
- Biomass burning index, 848
- Biomineralization, marine biomineralization, 112–116
- Biosignatures, 198–199
- Biotites, 42, 96, 140, 522–524
- Bioturbation, 497–498
- Biovolatilization of ²¹⁰Po, 271
- Bisphosphonate treatment, 775
- Bolling-Allerod, 872
- Bonding energies, 155
- Bone
 apatite, 730
 diagenetic alteration, 743, 747
 remodel, 744, 755, 773, 801
 turnover, 775
- Boundary scavenging, 76–77, 386, 387
- Box model, 356, 504, 625–626
- Brahmaputra, 519, 527–529, 531–535, 538–541
- Bulk silicate Earth (BSE), 93, 105, 112, 133, 134, 140–141, 146, 150
 standard, 105, 112
- C**
- ¹⁴C, 4–6, 12–14, 374–376
- $\delta^{42/40}\text{Ca}$,
 $\delta^{44/40}\text{Ca}$, 105–120
 of Ca fluxes in seawater, 106
 on ecosystem calcium fractionation, 117
 in rivers, 108
 temperature dependence in calcite and aragonite, 54
 variation
 with time in tree rings, 120
 in tree rings, 119–120
- CaCO₃ fractionation
 as a function of mineralogy, 107, 108
 as a function of precipitation rate, 115–116
- Cadmium (Cd) isotopes, 126–133, 136–149
 in marine environment, 150–151
 stable, fractionation during evaporation, 136–137
 variation, 125–151
- Calcic phases, 524
- Calcification mechanism, 114
- Calcium (Ca)
 availability in vertebrates, 110
 biogeochemistry, 105–121
 isotopes, 105–121
 in bones, 116–117
 in corals, 113–114
 in food chains, 109–110
 fractionation, 106, 108, 110, 113–116
 isotopic variation, 109
 residence time in oceans, 105–108
 transport during biomineralization, 108
 transport in corals, 113
- Calvin cycle, 704, 725
- Canopy effect, 726, 727
- Carbohydrate, 196, 704, 706, 712, 713, 716, 722, 726, 729, 734, 808, 814, 817
- Carbonates, 16, 18, 43, 48, 53–55, 106, 107, 111, 115, 116, 147, 212, 524–525, 529–534, 663, 724, 785–802
- Carbonic acid, 88, 108, 115, 374, 520
- Carbon isotopes, 644–646, 649–656, 659, 666–667, 679–680, 683–685, 704, 725–726
 in cellulose, 815–816
 composition of atmospheric CO₂, 704
 ratios of beef, 707
 tracer for food adulteration, 704
 in trees, 815–816
- Carnivores, 728
- Catchments, 48, 97–99, 117
- Cave deposits, 785
- Cavity Ring Down Spectroscopy (CRDS), 469, 831, 834, 853
- ¹¹³Cd, 126
- ¹¹⁴Cd, 126, 147, 181
- ¹¹⁶Cd, 126, 132, 147–148, 181
- Cd/Ca, 134, 142, 147, 150, 151
- ¹¹⁰Cd/¹¹¹Cd, 135
- ¹¹²Cd/¹¹⁰Cd, 23, 135
- ¹¹³Cd/¹¹⁴Cd, 126, 135, 148
- ¹¹⁴Cd/¹¹⁰Cd, 23, 126, 128, 133–138, 181
- ¹¹⁴Cd/¹¹²Cd, 135
- CDW. *See* Changjiang diluted water
- Cellulose, 808–815, 818–823
 $\delta^{18}\text{O}$, 813–815, 818, 819, 823
 synthesis, 808, 817, 818
- Cesium (¹³⁷Cs and ¹³⁴Cs), 380–383
- Chalcophile, 140, 205, 206, 208, 211, 252, 266
- Changes in $\delta^{15}\text{N}$ per trophic step, 709, 733
- Changes in isotopic composition of a recreational shooter, 776
- Changjiang diluted water (CDW), 336, 337
- Chelation, 777

- Chemical erosion, 49, 555–556
 Chemical signatures, 51, 142, 565, 744
 in teeth, 743
 Chemical weathering, 521–537, 557–559
 Chernobyl, 372–373, 489, 491, 497, 594–596
 Chlorinated ethenes, 643
 Chlorine–36, 443–445
 abundance in perchlorate, 443–445
 Chlorine (Cl)
 isotopes in environmental forensics, 666
 isotopic ratio, $\delta^{37}\text{Cl}$, 436, 439
 Chlorofluorocarbon (CFCs), 232, 581–582
 Cholesterol, 638, 724, 725
 Chondritic uniform reservoir (CHUR), 521
 C-horizon, 65, 73
 Chromate (CrO_4^{2-}), 178, 180
 Chromium (Cr)
 contamination in groundwater, 164
 isotopes, 156–157, 160, 162–167
 Chronosequences, 95, 522–523, 526, 534
 CHUR. *See* Chondritic uniform reservoir
 CI. *See* Crystallinity index
 ^{36}Cl , 15, 296
 Climate change, 382–383, 615, 819
 Climate parameters, 542
 Closed system, 73, 99, 144, 165, 208, 258, 297, 343, 459,
 686, 687, 690, 693, 791, 793, 799, 800
 assumption, 793
 cNOR, 462, 463
 CO_2 , 87–88, 219, 374–375, 453, 531, 579, 640, 642,
 676–678, 815
 Coastal ocean mixing, 329–339
 Cobalt (^{58}Co and ^{60}Co), 210, 367, 376
 CO continuous-flow isotope-ratio mass spectrometry
 (CO-CFIRMS), 438
 Cold vapor introduction system, 232
 Collagen, 723–724, 727, 729–735
 Colloidal transport, 497
 Colloids, 74, 80, 323, 530–531, 552
 Colonization, 751, 754
 3-Compartmental model for Pb, 772
 Compound specific isotope analysis (CSIA), 639–640, 666,
 676, 689–690
 Concentration of Pb in urine, 768
 Condensates, 647, 655
 Condensation, 581, 688, 978
 Conflat seats, 865
 Congruent weathering, 407, 411
 Conservative radium (Ra) model, 337–338
 Conservative tracer, 380, 458, 462, 486
 Contaminants, 164–167, 190–195, 322–323, 369–372
 Continental weathering, 45–50, 54, 106, 206, 252, 255,
 419, 534–536, 543
 Continuous flow isotope ratio mass spectrometer
 (CF-IRMS), 438, 613, 723, 725
 Continuous flow method, 232, 865
 Contribution of bone Pb to blood Pb, 772–773
 Copper isotopes, 179, 180
 Corals, 55, 113–114, 370, 386, 786, 789–791, 794–796
 Cosmic irradiation history, 481–482
 Cosmic ray produced nuclide systematics on Earth project
 (CRONUS-Earth Project), 479, 483
 Cosmic rays, 306, 475, 479–481, 488, 576, 577
 flux, 126, 476–477
 Cosmogenic isotopes, 573–585
 Cosmogenic nuclides, 14–16, 477–479, 575–580
 Cosmogenic production rate, 477
 Cosmogenic radionuclides, 475–483, 576–582
 Cosmos-954, 397, 599
 Counting methods, 22–25, 27, 72, 78, 311, 788
 C_4 (Hatch-Slack cycle) pathway, 704
 C_3 (Calvin cycle) photosynthetic pathway, 704
 C_3 plants, 36, 642, 678, 817
 C_4 plants, 36, 642, 678, 704, 708, 725, 726
 Cr(III), 162, 163
 oxidation, 163, 164
 Cr(VI), 156–157, 162, 164
 reduction, 163, 165–167, 191–192
 Craig-Gordon model, 704–705, 814
 Crassulacean acid metabolism (CAM) cycle, 725–726
 $^{53}\text{Cr}/^{52}\text{Cr}$, 23, 157, 159, 163–164
 CRDS. *See* Cavity Ring Down Spectroscopy
 CRM, 403, 553
 Crude oil-isotopic composition, 638, 641, 643, 645, 647–648,
 650–653
 Crustal flux, 41
 Crystallinity index (CI), 724–725, 751
 ^{137}Cs
 and $^{210}\text{Po}/^{210}\text{Pb}$ as tracers of historical records in river
 basin sediments, 305–325
 profile, 381–383, 404, 496, 497, 506
 transport, 497
 CSIA. *See* Compound specific isotope analysis
 Cu(I), 179, 196
 Cu(II), 179, 196
 $^{65}\text{Cu}/^{63}\text{Cu}$, 23, 179
 Culture change, 36
 Curium, 395
- D**
 Dansgaard-Oeschger events, 863, 871
 Dating, 14, 16, 18, 20, 35, 73, 78, 80, 206, 295, 321, 373,
 375–376, 403, 579, 649–651, 785–802, 822
 of particulate matter, 78, 80
 Daughter deficient method, 786, 791–792, 798–802
 DCM. *See* Dichloromethane
 DDT. *See* Dichlorodiphenyltrichloroethane
 Decay series nuclides, 16–17
 Deccan basalts, 47, 536
 Deep crustal helium, 295
 Deep-sea corals, 55, 790, 795
 Deep water formation, 382–383, 387
 Degree of crystallinity, 724, 751
 Degree of isotope equilibrium, 423
 Degree of weathering, 48
 Dehydration kinetics, 114
 Delayed coincidence system, 331
 Deleterious health effects of ClO_4^- , 436
 Denitrification, 452, 458–469, 726, 837, 848, 851
 Denitrifier method, 614

- Denitrifying bacteria method, 837
 Dense non-aqueous phase liquid (DNAPL), 667
 Dentine, 729, 768, 770
 Depleted MORB source mantle (DMM), 140–141
 Deposition, 61–63, 79–80, 305–325, 404–406, 591, 604–606, 648–649
 environment, 648–650, 657, 743
 flux of ⁷Be, 61–63, 323, 325
 flux of ¹⁰Be, 13, 61–63, 77
 velocity, 14, 584, 605
 Depth shift, 872
 Desorption from riverine particles, 330
 Deuterium enrichment, 653
 Deuterium isotopomer distribution (DID), 683, 822
 Diagenesis, 51–52, 724–725, 743, 750–751
 in teeth and bone, 749
 Diagenetic contamination, 741, 743, 745, 750–751
 in enamel and bone, 748, 751
 Dichlorodiphenyltrichloroethane (DDT), 666, 687–688
 Dichloromethane (DCM), 663
 DID. *See* Deuterium isotopomer distribution
 Dietary protein, 706, 729
 Diffusion, 43–44, 55, 76, 165, 172, 260, 279, 289, 321, 330, 335, 337, 350, 352, 355, 357–358, 452, 458–460, 477, 506, 683–684, 722, 754, 786, 793, 868, 871–873
 from bottom sediments, 278, 786
 coefficient, 76, 350, 351, 722
 through the ice, 866–867
 Diffusive seafloor flux, 352
 Dioxins, 666
 Discharge-weighted, 527, 528, 530
 Dispersion, 165, 166, 186, 274, 297, 380, 735
 Dissolution, 45, 46, 73, 88, 96, 97, 100, 179, 198, 208, 216, 255, 278, 379, 399, 400, 402, 422, 425, 522, 523, 534, 552, 556, 559, 564, 565, 599, 748
 experiments, 523, 529
 kinetics, 144, 198
 Dissolved inorganic phosphate (DIP), 420, 426, 427
 Dissolved oceanic Tl, 260
 Dissolved organic carbon (DOC), 234, 236, 375, 530
 Dissolved organic matter (DOM), 424, 425, 525, 552
 Dissolved Sr in rivers, 529, 530
 DNAPL. *See* Dense non-aqueous phase liquid
 Dole effect, 624
 Double spike, 26, 110, 129, 131–132, 149, 159–161, 187, 188
 Downwelling, 386, 387, 420
 Drinking water and δ¹⁸O values, 713–716
 Dual oxygen ratio analysis, 835
- E**
 EA-IRMS. *See* Element analyzer-isotope ratio mass spectrometry
 Early life migrations, 744
 Early tertiary, 536
 East Antarctica, 843, 862, 878
 East Asian dust, 597, 600
 East China Sea, 336
 Eastern California Shear Zone (ECSZ), 297
 East Morongo Basin (EMB), 292, 293, 297–298
 East Pacific Rise (EPR), 44, 216, 800
 ECSZ. *See* Eastern California Shear Zone
 Eddy diffusion coefficient, 76, 351
 Effective fractionation factor, 172
 Efficiency of the detectors, 72
 Eichrom TRU resins, 129
 Element analyzer-isotope ratio mass spectrometry (EA-IRMS), 676, 677, 679–680, 689, 696
 Elkhorn Slough, 427
 EMB. *See* East Morongo Basin
 Endogenous sources of lead, 768
 Enrichment of Tl, 257
 Environmental forensics, 7, 23, 637–668
 Environmental half-life, 377, 381, 384
 Environmental tracer, 34–35, 446
 Enzyme cofactor, 179, 180
 EPR. *See* East Pacific Rise
 Equilibrium fractionation, 5, 94, 137, 612, 616, 722
 factors, 115, 163, 168, 623, 810
 Tl isotope, 255, 259
 Erosion, 317–319, 404–406, 475–483, 485–510, 519–545, 551–566
 rates, 17, 20, 49, 73, 405, 475–483, 485–511, 540, 544, 555–557, 563, 566
 Estuaries and coasts, 305–325
 Estuarine behaviour of lithium, 49–50
 Estuary, 50, 68, 164, 313, 315–317, 335, 376, 379, 408, 427
 Ethanes, 643
 Ethylbenzene, 665
 Eutrophication, 418, 427
 Evaporation, 70, 128, 136–138, 148, 149, 211, 252, 425, 553, 644, 678, 705–706, 712, 810, 812, 813
 Evaporites, 439, 529, 532
 EXAFS/XANES spectra. *See* Extended x-ray absorption fine structure spectra
 Excess helium, 292, 294–298
 Excess Pb–210 dating method, 786, 794–798
 Exchangeable Sr, 523
 Exchanges of Pb in teeth, 772
 Exposure age, 16, 475–483
 Exposure history, 476, 479, 481–483
 Extended x-ray absorption fine structure (EXAFS/XANES) spectra, 259
 External doping, 91
- F**
 Fallout, 372, 382, 384–385, 396, 403, 404, 407–409, 490, 497
 Faraday collectors, 91, 159, 251, 287
 Fast food stable isotopes, 706
 Fate and cycling of ²¹⁰Po, 272
 Fatty acids, 725
 Fe(II), 162, 178–179, 190, 195, 197, 199
 Fe(III), 162, 178–179, 189, 195, 197–199
 Ferromanganese (Fe-Mn)
 crust, 145
 deposit, 55
 sediment, 216, 263–265
 Fingerprint, 12, 167, 199, 217, 233, 237–238, 243, 251, 266, 314, 397, 409–410, 507, 537, 638, 639, 661–663, 665–666, 773, 843, 845
 Firm densification, 871–873

- Firnification model, 862, 871–873, 875, 876, 879
 First-order kinetics, 11, 558
 Fishbones, 786, 791, 800
 Fission products, 5, 368, 369, 379, 395–396, 487
 Food web, 235–237, 239–243, 281, 419, 704–705, 709, 740, 759, 833, 836
 assemblages, 705
 Formation of sulfate, 838, 839
 Forward model, 532, 818
 Fossil fuel emission, 842
 Four-end-member mixing, 332, 335–337
 Fourier-transform infrared spectrometry (FTIR), 457, 469, 724, 751
 Fractionation, 5–6, 52, 115–116, 136–137, 147–149, 157–159, 162–163, 167–168, 189–190, 233–234, 258–261, 422–423, 439–441, 643–644, 663–664, 867–871
 coefficients, 873
 factors, 20, 46–47, 51, 89, 94, 95, 98, 107, 112, 115, 137, 138, 144, 151, 156, 158, 163, 167–169, 234, 236, 259, 440–441, 458–460, 466, 623, 683, 810
 mechanisms, 7, 113, 149, 242, 259
 signals, 867–871
 in Sm/Nd, 521, 527
 Functional trophic level (TL), 705, 708, 709
 Fungal denitrification, 458–460, 462, 463, 465, 467, 469
- G**
- Galactic cosmic ray (GCR), 370, 477
 Gamma-ray spectrometry, 311, 312, 331, 368, 581, 788, 799
 Gamma spectrometry, 23, 25, 310, 313, 330, 331, 405, 406, 786
 Gamma spectroscopy, 501
 Gandak, 539–540
 Ganga-Brahmaputra river system, 531–534
 Ganga plain, 539–541, 545
 Ganga tributaries, 545
 Garden variety, 61
 Gas age scale, 871, 879
 Gas chromatography (GC), 8, 438, 638, 665, 697, 834
 Gas chromatography-isotope ratio mass spectrometer (GCIRMS), 638–641, 651, 653–654, 662–664, 667, 677, 680–682, 689–670
 Gas chromatography mass spectrometry (GCMS), 639–640, 661, 663, 665, 668, 716
 Gas generation index (GGI), 657
 Gas isotope ratio mass spectrometer (G-IRMS), 834
 Gas loss correction, 866–867
 Gas solubility constant of radon, 345
 Gas source mass spectrometry, 27, 92
 GC. *See* Gas chromatography
 GCIRMS. *See* Gas chromatography-isotope ratio mass spectrometer
 GCMS. *See* Gas chromatography mass spectrometry
 GCR. *See* Galactic cosmic ray
 Geiger-Müller (GM) counter, 24–25
 Geochemical behavior
 of Ra, 344, 346
 of Rn, 346
 Geochemical fractionation, 786
 Geochemical Ocean Sections Study (GEOSECS), 349, 375, 378, 381, 384
 Geochronology, 16–17
 Geological provenance, 537
 Geomagnetic field, 476–477, 582
 Geomagnetic latitude, 476–479
 Geomorphology, 475–476, 537
 GEOSECS. *See* Geochemical Ocean Sections Study
 Ge/Si, 97, 543
 Gettered sample, 865
 GF-AAS. *See* Graphite Furnace Atomic absorption Spectrometry
 GGI. *See* Gas generation index
 G-IRMS. *See* Gas isotope ratio mass spectrometer
 GIS. *See* Greenland Interstadial
 Glaciological processes, 851
 Global average concentration of Tl, 252
 Global budget of Tl, 253
 Global carbon cycle, 87, 520, 531, 542, 545
 Global fallout, 367, 370, 372, 374, 377, 382, 383, 385, 395, 397, 406, 407, 490–493, 497, 510, 595
 Global homogeneity of Tl isotopes,
 Global marine Ca budget, 108
 Global meteoric water line (GMWL), 705, 709–710, 712
 Global Network of Isotopes in Precipitation (GNIP), 621, 628, 809
 Global rivers, 520, 527–530, 535, 536, 540
 Global Si isotopic balance, 93
 Global Sr flux, 527, 528, 530, 535
 GM counter. *See* Geiger-Müller counter
 GMWL. *See* Global meteoric water line
 GNIP. *See* Global Network of Isotopes in Precipitation
 Gobi, 215–216, 598
 Granitic soil chronosequence, 522–523
 Granitoid weathering, 522, 525, 526
 Graphite furnace atomic absorption spectrometry (GF-AAS), 209–211, 768
 Grasshopper Pueblo, 731, 752, 755
 Gravitational effects, 868, 869
 Greenhouse gases, 348, 451–453, 853, 862, 879
 Greenland, 211, 217, 377, 410, 843, 849–851, 862, 863, 869, 871–873, 876–878, 880
 ice, 842, 844, 852
 ice cores, 842, 844, 851, 863, 875–877
 Greenland Interstadial (GIS), 863, 870
 Greenland Stadial (GS), 863, 870
 Greenockite (CdS), 125, 140
 GRIP drilling site, 862
 Groundwater, 99–100, 191–192, 279–280, 285–302, 354–358, 748
 discharge into lakes, 357–358
 GS. *See* Greenland Stadial
- H**
- HA. *See* Hydroxyapatite
 Half-residence time (HRT), 593, 598
 Hanford, 18, 410
 HAO. *See* Hydroxylamine oxidate
 Harmful algal blooms, 8, 418
 Hatch-Slack cycle, 704, 725
 Headspace
 equilibration method, 864
 extraction, 613

- Headwaters, 529, 532–533, 541–542
 Heavy rare earth elements (HREE), 521, 525
 Helium (He), 285–302, 331, 864, 865
 components, 290–294
 flux, 289, 292, 295
 isotope, 289–298, 301
 Herbivores, 116, 117, 726–728
 Heterogeneous hydrolysis, 617
 Heterogeneous oxidation reactions, 838
 $^{202}\text{Hg}/^{198}\text{Hg}$, 21, 23, 230
 ^{196}Hg , ^{198}Hg , ^{199}Hg , ^{200}Hg , ^{201}Hg , ^{202}Hg , ^{204}Hg , 181, 230
 Higher Himalaya, 539, 541, 542
 High mobility, 436
 Hill slope hydrology,
 Himalayan-Tibetan region, 530, 535
 Himalayan tributaries, 539
 Himalaya-Tibet (HT), 534
 rivers, 528, 535, 536
 Homogenous oxidation reactions, 584
 Hopanes, 652
 Horizontal eddy diffusivity, 352, 354
 Hot spot, 539, 540
 Hot springs, 543
 HREE. *See* Heavy rare earth elements
 HRT. *See* Half-residence time
 HT. *See* Himalaya-Tibet
 Human diet, 36, 703–716, 733
 Human enamel, 746
 Hummingbird Island, 427
 Hydrocarbon exploration, 637–668
 Hydrochromate (HCrO_4^-), 156
 Hydrogen
 bonds, 866–867
 and oxygen ratios record glaciations, 709–711
 Hydrogen isotopic composition (δD), 36, 652
 Hydrolysis
 constant, 65
 product, 65
 Hydrothermal, 50–53, 135, 145–146, 235, 254, 260, 262–263,
 419, 535, 798, 800, 802
 alteration, 35, 216, 257–258, 265
 deposits, 146
 Hydroxyapatite (HA), 724, 740
 Hydroxylamine oxidate (HAO), 452, 461, 462
 Hydroxylamine oxidation, 452, 462, 463, 465, 467, 468
 Hydroxyl (OH) radical, 584, 617, 622, 623, 853
 Hydroxyl radicals (OH), 584
- I**
 Institute Reference Materials and Measurements (IRMM),
 188, 399, 403
 Iron (^{55}Fe), 376–377
- J**
 Juan de Fuca ridge, 216, 254, 258
 Juvenile effect, 816
- K**
 K_d , 65, 68, 307, 366–367, 383, 394–395
 Kerogen, type II, type III, 657–658
 KIE. *See* Kinetic isotope effect
- Kinetic and equilibrium
 fractionation, 5, 21, 94, 115, 163, 168, 233–234, 418, 616,
 644, 722, 813
 provenance,
 Kinetic fractionation, 21, 233–234, 644
 Kinetic isotope effect (KIE), 156, 158, 189, 422, 643, 676,
 683–685, 722–723
 Kinetic isotope fractionation, 137, 156, 252, 683–684
 Kjeldahl digestion, 836
 Kosa, Kosa events, 597, 600, 602, 604
 K-rich minerals, 521
 Krypton (^{85}Kr), 18, 377
 K-T boundary, 536
 Kuroshio sub-surface water (KSSW), 336–337
 Kuroshio surface water (KSW), 336
- L**
 Labile Tl, 256
 Lake Erie, 428–429
 Large deficiency of ^{210}Po , 276
 Laser ablation multi-collector inductively coupled plasma mass
 spectrometry (LA-MC-ICPMS), 746, 750
 Last glacial maximum (LGM), 541
 Late horizon, 754
 Late intermediate period, 753, 755
 Lead (Pb)
 in blood, 767, 774
 in breast milk to Pb in blood, 775
 from food, 765–766
 isotopes
 in environmental health, 769–778
 in human studies, 769
 in teeth, 768
 isotopic analyses of teeth, 770
 isotopic composition, 770
 levels in humans, 765
 in mining and smelting communities, 770–772
 Leaf boundary layer effects, 813
 Lesser Himalaya, 533, 540
 LGM. *See* Last glacial maximum
 Li/Ca ratio, 54
 Light rare earth elements (LREE), 521, 525, 526
 Lipids, 642, 706, 733
 Liquid scintillation counting (LSC), 25, 346, 582
 Lithium (Li)
 abundances in mantle rocks, 42
 deuteride, 42
 fluoride, 42
 in foraminiferal records, 53
 isotopes
 composition of seawater, 48, 55
 fractionation, 46–47, 54–55
 as tracers of continental weathering, 45–50
 as tracers of hydrothermal processes, 50–52
 in marine records, 52–55
 Lithology, 44, 529
 Local and regional transuranic sources, 409–412
 Loess, 134, 141, 251
 Long-term exposure to Pb, 765
 Loss of biogenic ($^{87}\text{Sr}/^{86}\text{Sr}$) signatures, 743
 Low-frequency climate, 808

- Low-frequency variations in climate, 808
 LREE. *See* Light rare earth elements
 LSC. *See* Liquid scintillation counting
- M**
- Machu Picchu, 754
 Magnetic isotope effect (MIE), 147–148, 233–234
 Manganese (^{54}Mn), 376
 Mantle flux, 290
 Mantle helium, 289, 297
 Margin, 76, 191, 255–256, 386
 Marine biogenic sulfate, 842
 Marine calcium cycle, 105–108
 Marine environment, 67–69, 75–78, 134, 141–147, 254–258
 processes, 365–387
 Marine Hg isotope composition, 237
 Marine output fluxes, 255, 257–258
 Markers of prehistoric mobility, 740–741
 Mass balance, 97, 215–217, 262, 290, 315, 318, 334, 356, 506,
 584, 616–617, 628
 equation, 262, 263, 290, 291, 319, 320, 356, 534, 583,
 625, 628
 Mass bias, 43, 91, 130, 131, 159–161, 187, 233, 249
 correction, 91, 127, 130, 161, 233, 249
 shifts, 161
 Mass burials, 261–262
 Mass conservation, 623
 Mass dependent fractionation (MDF), 5–6, 89, 157, 181, 188,
 230–231, 233–235, 436, 740
 Mass dependent isotope fractionation, 5, 132, 137, 148, 616
 Mass dependent Rayleigh-type isotope fractionation, 440
 Mass discrimination, 27
 Mass fractionation, 91, 95, 96, 106, 129, 131, 135, 750
 correction, 110, 129, 131
 Mass-growth model, 792–793, 800
 Mass independent composition, 611
 Mass independent fractionation (MIF), 5–6, 147, 181, 230–231,
 233–235, 237, 241, 242, 612, 616, 832
 Mass independent isotope fractionation, 230
 Mass interference, 457–458, 469
 corrections, 457–458, 469
 Mass laws, 832
 Mass spectrometry (MS), 6, 25–28, 90, 129–131, 159–162, 184,
 185, 188, 248–249, 400, 453–454, 592, 676–682,
 834, 865, 866
 Maternal Pb exposure, 765
 Matrix effects, 90, 91, 101, 834
 Maturity, 646–647, 657, 660
 MC-ICPMS. *See* Multi-collector inductively coupled plasma
 mass spectrometry
 MDF. *See* Mass dependent fractionation
 Mean free path, 479, 480
 Mechanisms of Hg isotope fractionation, 233–234
 Mediterranean, 35, 382, 752
 Melt ponds, 77, 383
 Melt-refreeze method, 864–866
 Mercury (Hg)
 bioaccumulation, 229
 biogeochemistry, 229
 isotopes, 229–243
 in fish tissues, 236–237
 in food webs, 235, 237
 in marine sediments, 237
 in tree lichens, 238
 Meridional mixing, 575
 Metal redox cycles, 195–196
 Metal scavenging, 74
 Metal toxicity, 196
 Metamorphism, 140, 533, 657
 Meteoric, 61–81, 212, 705
 Meteorites, 16, 134, 206, 211–213
 Methane, 653, 657, 658, 660, 877
 Methylated Tl, 260
 Methyl *tert*-butyl ether (MTBE), 643, 664
 Microbes, 168, 169, 179, 279
 Microbial ClO_4 reduction, 440, 441
 Microbial degradation of MeHg, 241
 Microbial Hg methylation, 235, 237, 241, 242
 Microbial redox reactions, 159
 Microbial reduction, 163, 169, 179, 234, 242, 439–441
 Microbial Se(VI) reduction, 169, 171
 MID. *See* Multiple ion detection
 Mid-ocean ridge basalts (MORB), 43–44, 134
 MIE. *See* Magnetic isotope effect
 MIF. *See* Mass independent fractionation
 Migration
 of hydrocarbon, 647–648
 of radionuclides, 497–498
 Migratory patterns prehistoric animals, 739
 Milk isotope ratios, 713–714
 Milk water line, 714
 Mineralization, 112–116
 Mineralogical composition, 522, 537–538
 Mineral weathering kinetics, 522–527
 Mineral weathering rates, 522, 524, 563
 Minimum detectable activity, 787
 Missing anthropogenic carbon, 485–486
 Mixing, 76, 144, 166, 191, 192, 329–339, 351–354, 387, 427,
 602–604, 657, 660, 729–730, 817
 of air masses, 397
 in the coastal ocean, 351–354
 in the deep ocean, 351–354
 dynamics, 329
 models, 167, 353–354, 602–604, 704, 730
 rates, 76, 352–354, 387
 ^{54}Mn , 18, 376
 Mobilisation
 of lead from bone, 772
 of Pb from the maternal skeleton, 773–774
 of Pb in the body, 769, 773–774
 of skeletal Pb, 773–774
 Mobility of lead in human body, 765–779
 Modulation parameter, 477
 Mojave desert, 164, 166, 292–294
 Molecular interference, 27, 127–129, 132
 Mollusk shells, 787, 789, 791–793, 798–800
 Molybdenum isotopes, 180
 Monazite, 521, 526
 Monochromatic compounds, 643
 Monocyclic alkanes, 652
 Monomethylmercury (MeHg), 181
 Monsoon, 63, 524–525

- Monte Carlo simulation, 818
 MORB. *See* Mid-ocean ridge basalts
 MS. *See* Mass spectrometry
 Mt. Agung, 842
 MTBE. *See* Methyl *tert*-butyl ether
 MTBX,
 Multi-collector inductively coupled plasma mass spectrometry (MC-ICPMS), 42–43, 91, 110–111, 129–131, 159–161, 184–187, 232
 Multiple ion detection (MID), 638, 640, 668
- N**
 NAA. *See* Neutron activation analysis
 n-alkanes, 638, 645–647, 650–653
 N and Ar as tracers, 861–880
 Naphthalene, 652, 665
 National Institute of Standards and Technology (NIST), 107, 189, 230, 272–273, 402
 Natural and anthropogenic sources of perchlorate, 435
 Natural attenuation, 166, 639, 643, 662–665, 667, 668
 Natural ClO₄⁻, 435, 436, 441–443, 447
 Natural gas isotope analyses, 653–661
¹⁴³Nd/¹⁴⁴Nd release, 525–527
 Neanderthal, 733–734, 747, 752
 Negative thermal ionization mass spectrometry (N-TIMS), 5, 207–209, 215
 Neodymium (Nd), 521
 isotopes, 519, 523, 527, 537, 539–543, 545
 Neogene, 108, 526
 Neolithic, 733, 752, 754, 757
 Net isotope effects (NIE), 459, 460
 Neutron activation analysis (NAA), 207–209, 211, 215, 221
 Neutron capture, 14, 16, 126, 394, 397, 409, 410
 Nevada Test Site (NTS), 18, 371, 383–384, 396, 409–411
⁶⁰Ni/⁵⁸Ni, 23, 179
 NiR. *See* Nitrite reductase
 NIST. *See* National Institute of Standards and Technology
 NIST SRM–997, 230, 233
 NIST SRM–3133, 230, 236
 Nitrate (NO₃⁻), 611–630, 836–837, 846–852
 Nitric oxide reductase (NOR), 452, 461–463
 Nitrification, 452, 460–463, 468–470, 863
 Nitrite reductase (NiR), 461–463
 Nitrogen
 cycle, 704
 isotopes ($\delta^{15}\text{N}$), 465, 666, 668, 704–705, 708, 709, 715, 726, 742, 833, 836
 analysis of human hair, 705
 ratios of a secondary consumer, 705
 ratios of the web's baseline, 705
 trace the flow of organic matter, 704–705
 Nitrogen oxides (NO_x), 611, 612, 615, 621, 622, 624–627, 629–630, 836, 842, 846–847, 850, 852
 Nitrous oxide (N₂O), 451–470
 Ni/V elemental ratio, 638
 NMD. *See* Non-mass dependent fractionation
 Noble gas, 5, 17, 27, 285, 345, 357, 366–367, 578
 Non-climatic factors, 808, 816
 Non-linear model, 503–504
 Non-local trophy heads, 755
 Non-mass dependent fractionation (NMD), 832
 Non-mass-dependent isotope effects, 148
 Non-photochemical oxidation pathway, 840–841
 Non-sea-salt (nss) sulfate, 275, 840, 841, 843
 Non-spectral interferences, 130–131
 Non-stoichiometric release of Sr, 522–523, 525, 544, 545
 NOR. *See* Nitric oxide reductase; N₂O reductase
 N₂O reductase (NOR), 452, 460–468, 613, 837
 North Atlantic, 35, 44, 323, 324, 331, 351, 373, 383, 794, 798
 Northern hemisphere deposition, 372, 396, 575, 589, 593
 North San Francisco Bay, 426
 Norwegian sea, 373, 377, 379
 Nova Zemlya, 365
²³⁷Np, 283, 367, 368, 372, 383, 394–402, 409–411
 NTBT. *See* Nuclear test ban treaty
 N-TIMS. *See* Negative thermal ionization mass spectrometry
 NTS. *See* Nevada Test Site
 Nubians, 733, 754
 Nuclear field shift effects, 147, 148
 Nuclear fuel reprocessing plant, 372, 380
 Nuclear power plants, 34, 365, 366, 377
 Nuclear test ban treaty (NTBT), 4, 575
 Nuclear testing, 385, 387, 395, 410, 575, 589, 593, 599, 605, 606
 Nuclear volume effects (NVE), 147, 148, 233, 235, 833
 Nuclide production rate, 61–62, 477, 479–480, 577
 Nutrient pathways, 120
 NW Pacific Ocean, 331, 377, 378, 381, 384
- O**
¹⁷O anomaly, 436, 455, 467–470, 618, 625, 847
 Ocean circulation tracers, 36
 Ocean-floor weathering, 50–52
 Ocean island basalt (OIB), 134, 141, 263, 264, 266
 Oceanographic Si cycle, 101
 Ocean sediments, 402, 520, 544
 Octahedral coordination, 45–46, 190
O-ethyltoluene, 665
 OH radical. *See* Hydroxyl radical
 OIB. *See* Ocean island basalt
 Omnivores, 709, 728, 729
 Open ocean methylation, 241
 Optical spectroscopy, 834, 837, 853
 Optimum multi-parameter (OMP), 331–332
 Organic fertilizers, 422
 Organophosphorous compounds, 417–418
 Origins, 382–383, 460–461, 709–711, 713–714
 Orinoco, 48, 66, 67, 353, 527–529, 532, 533
 Orthophosphate, 421
 Os/Ir in marine sediments, 206, 208, 211–213
 Os/Ir ratios, 212, 213, 215, 217
 Osmium (Os), 6, 20, 23, 205–221, 262
 isotopes, 206, 208, 209, 212, 214, 218–220, 262
 mass balance in oceans, 215–217, 221
 residence time in oceans, 216
 Osteopontin, 724
 Otliths,
 Otolith, 786, 789–793, 800
 Ötzi, 745
 Oxidation
 capacity of the atmosphere, 842, 853
 pathways, 23, 584, 615, 617, 838–841, 843, 846–847

- pathways using $\delta^{18}\text{O}$ in sulfate, 617, 628
 - of S(IV) species, 841
- Oxidative species, 833
- Oxidative stress, 179
- Oxidized Tl, 256, 260
- Oxyanions, 435, 831–853
- Oxygen isotopic composition of protein, 710
- O*-xylene, 665
- Ozone (O_3), 6, 34, 435, 467, 583, 612, 616–626, 628, 629, 832, 833, 836, 839, 841, 842, 847–849, 853
 - formation, 612, 616, 618, 624, 835
 - oxidation pathways, 840–842
- P**
- Pacific ocean test sites, 368
- Pacific proving ground (PPG), 385, 397, 406
- PAH. *See* Polycyclic aromatic hydrocarbon
- Paleodiet, 23, 110, 721–735, 742
- Paleomobility studies, 739
- Paleo-silicate erosion, 520
- Paleo-volcanism, 845
- Particle, 4, 11, 13, 16, 23–25, 45, 61, 68, 72–78, 183, 194, 217–221, 229, 247, 256, 271, 274–281, 305–325, 329, 330, 345, 351, 366, 368, 376, 379, 386, 387, 394, 397–399, 402, 405–407, 477, 493, 557, 558, 560, 577, 585, 594, 604, 611, 666, 787, 850
 - dynamics in a river, 319–320
- Particulate dynamics, 72, 74
- Particulate organic matter, 281, 324, 344, 376, 386, 727
- Partition coefficients, 308, 494, 495
- Past air temperature, 861–880
- Past temperature, 832, 861–863, 871, 872, 874
- Patterns in the modern American diet using stable isotopes, 714–715
- ^{210}Pb , 14, 16, 28, 30, 34, 75, 218, 271–281, 305–325, 346, 386, 403, 485–510, 576, 584, 591, 605, 785–802
 - inventories in Northern Hemisphere, 493
 - ^{226}Ra disequilibrium, 785–802
 - Southern hemisphere, 493
- PbB during pregnancy and the postpartum period, 773
- PCE, 639, 662–665, 667
- Péclet effect, 814
- Péclet number, 814
- Pelagic sediments, 146, 150, 212, 214, 261
- Peninsular indian rivers, 528
- Perchlorate, 435–447, 667
- Permanent molars, 743
- Perylene, 666
- Pharmacokinetic models for Pb, 772
- Pharmacokinetic studies, 772
- Phosphate
 - in the ocean, 418
 - sources, 419–422, 426–429
- Phosphohydrolase enzymes, 423
- Phospholipids, 417, 418
- Phosphorous (P)
 - abundance, 417
 - cycling, 429–430, 432
 - dynamics, 417
 - oxidation states, 417
- Phosphorylation, 418
- Photochemical box modeling, 625, 849
- Photochemical degradation of MeHg, 236, 239, 241
- Photochemical reduction of Hg(II), 234–236, 238, 239
- Photolysis, 620, 622, 624, 630, 833, 845, 846, 849–851
- Photoreduction, 234, 237, 239, 833
- Photosynthesis, 119, 374, 376, 459, 624, 641, 642, 645, 649, 650, 678, 704, 725, 809, 814–817, 819, 822
- Phreatophytes in Death Valley, California, 109
- Physical erosion, 519–545, 551–566
- Physical weathering, 519, 557
- Physiological models, 813, 818–820
- Phytoliths, 88, 93, 95, 97, 99, 101
- Pinatubo, 845
- Pioneer agricultural revolution, 842
- Plants
 - nutrition, 190, 196–198
 - physiological models, 813, 818–820
 - physiological processes, 813–815
 - uptake, 94, 97, 118, 168, 171, 495, 812
- Platinum group elements (PGE), 6, 206–208, 210–213, 217–221
 - magmatic sulfide ores, 212, 213
- Plutonium, 36, 369, 372, 377, 383–387, 397, 410, 490, 509, 592, 594, 598
- P450NOR, 462
- ^{210}Po , 14, 16, 23, 28, 34, 271–282, 306–314, 320–321, 786, 787, 793
- P-O bond, 419, 423
- Podiform chomitiite deposits, 213
- ^{210}Po in sulfide-bearing shallow groundwater, 272, 278
- Polar ice cores, 861, 863
- Polyatomic interferences, 91, 92
- Polychlorinated biphenyls (PCBs), 75, 308, 322–323, 643, 662, 666, 667, 680, 681, 683, 685–690, 692, 696
- Polycyclic aromatic hydrocarbon (PAH), 220, 308, 323–325, 643, 662, 663, 666
- Pore waters, 42, 47, 48, 51, 52, 172, 255, 256, 266, 279, 289, 346, 355, 369
- Post-photosynthetic processes, 816–818, 822
- Potato hydrogen and oxygen isotopes, 712–713
- PPG. *See* Pacific proving ground
- Preconcentration methods, 69–71, 836
- Prehistoric mobility, 740
- Primary use of thallium, 247
- Pristine/phytane ratio, 649
- Production method of food items and stable isotopes, 704, 706, 715
- Production of cosmogenic radionuclides, 479, 577
- Production rate, 4, 15, 16, 61, 62, 73, 179, 189, 219, 289, 294, 323, 476–478, 481, 482, 561, 563, 577, 580, 582, 797
 - of Be–7, 312
- Progressive dissolution, 523
- Progressive distillation, 861
- Protein synthesis, 706, 710
- Provenance studies, 520, 521, 525, 537
- Provenance tracers, 520, 525, 545
- Provenience of artifacts, 759
- Proxies, 308, 375, 378, 418, 537, 543–545, 739, 741, 751, 785, 786, 807, 808, 842, 844
- Proxy of silicate weathering, 525, 532, 533

- Pseudomorph, 723
²³⁸Pu, 367, 368, 370, 372, 379, 394, 395, 397, 400–402, 408, 411
²³⁹Pu, 18, 367–370, 379, 383–387, 394–411, 488, 509, 589, 592, 598
²⁴⁰Pu, 18, 321, 367–370, 372, 380, 383–387, 394–398, 395, 400, 402–412, 485–510, 589–593, 600, 604
²⁴¹Pu, 18, 367, 368, 370, 383, 387, 394–398, 402, 409–412
^{239,240}Pu, 18, 321, 372, 384, 485–510, 589–593, 595–598, 600, 604
 Pyrolysis, 426, 612, 613, 647, 648, 655, 657, 659, 666, 681, 835
 method, 612, 613, 835
 Pyrophosphatase, 422, 423
- Q**
 qCuNOR, 462
 qNOR, 462, 463
 QUAD-ICP-MS, 42
 Quadrupole ICP-MS, 235
- R**
 Radiative effect, 845
 Radicals, 6, 179, 584, 617, 623, 625, 627, 832, 848, 853
 ions, 179
 pair reactions, 6, 234
 Radioactive decay law, 11
 Radiocarbon (¹⁴C), 35, 374–376
 Radiogenic carbonates, 537
 Radiogenic isotopes, 19, 20, 44, 87, 131, 248, 261, 263, 520, 537
 Radiogenic Sr isotopes in archaeology, 741, 743, 750, 751, 756–758
 Radiogenic strontium isotope analysis (⁸⁷Sr/⁸⁶Sr), 739
 Radionuclide profiles, 495–498
 Radium isotope, 329–339, 344–348, 353, 599
 Radon–222, 346, 575
 Radon daughters, 271
 Radon emanation method, 788, 789
 Radon extraction, 346
 Rainwater sampling, 591
 Rare earth elements (REE), 521
 Rate of diagenetic processes, 743
 Rates of exchange of Pb in blood, 775
 Ratio of calcium to phosphorus (Ca/P), 751
 Rayleigh denitrification equation,
 Rayleigh distillation, 21, 158, 459, 616, 628
 Rayleigh fractionation model, 165, 166, 258, 466, 663–664
 Rayleigh-type mechanism, 851
 Rb/Sr, 19, 739, 741
 fractionation, 521
 Reactive halogens, 679, 847–848
 Recoil, 4, 17, 35, 310, 552, 555, 560, 564–566, 793, 799
 Reconstruction of past climate, 807, 816
 Record of oceanic Ca isotopes, 107
 Records of seawater isotope composition, 150
 Redox
 cycles, 195–196, 271
 dynamics, 189
 processes, 22, 155–173, 190, 196
 sensitive metals, 189
 Reduction-azide technique, 613
 REE. *See* Rare earth elements
- Relationship between coral skeletal $\delta^{44/40}\text{Ca}$ and
 temperature, 114
 Relative humidity, 288, 623, 625, 713, 809, 811–815, 818, 822
 Remediation of contaminated site, 664
 Remineralization, 16, 144, 271, 272, 276, 420, 430, 431
 Reservoirs, 3, 4, 13, 14, 41, 76, 93, 118, 134, 140–141, 196, 259, 260, 294, 343–359, 373, 486, 579, 645, 661, 845
 effect, 172
 Residence time, 3, 14, 18, 67–69, 74, 216, 217, 275, 285, 289, 293–296, 308, 318, 325, 329–339, 396, 489, 559, 575, 581–583, 598, 817
 of Cs, Be, 489–490
 of Th, Po, 34, 273, 276, 318, 565
 of Tl, 266
 Resonance ionization mass spectrometer (RIMS), 208, 209, 400, 402
 Resuspension, 16, 67, 74–75, 271, 305, 308, 314–320, 322, 325, 372, 376, 419, 488, 509, 596, 598, 605
 of particulate matter, 316–317
 of top soils, 271
 Rhenium (Re), 182
 RIMS. *See* Resonance ionization mass spectrometer
 Ring-width, 808, 816, 818, 822
 Riverine input, 106, 216, 230, 307, 325, 356
 River, 16, 19, 44, 48–49, 53, 65, 74–75, 95, 98–101, 106, 138, 214–216, 247, 252–255, 271, 305–325, 343, 344, 351, 386, 402, 410, 419, 426, 428, 429, 520, 522–525, 527–543, 554–558, 560, 785, 794
 sediments, 75, 138, 139, 237, 539, 553, 554
 water, 44, 45, 54, 98, 100, 180, 192–193, 211, 212, 254, 329, 334, 344, 428, 508, 528, 530, 543, 554, 556, 564, 739, 748
 RNAA, 207, 214
 Rock-water interaction, 3, 520
 Rock weathering, 55, 118, 520, 522–527
 Rocky flats, 402, 409, 410
 Ruthenium (¹⁰³Ru and ¹⁰⁶Ru), 379–380
- S**
³⁵S, 14, 577, 582–584
 Samarium/Neodymium (Sm/Nd), 521, 525–527, 530, 531
 San Bernardino, 301, 446, 447
 San Joaquin River (SJR), 428
 Sargasso Sea, 214, 215, 276–277, 373, 430, 431
¹²⁵Sb, 332, 380
 Scavenging effectiveness (SE), 66, 276, 318, 516, 752
 Scavenging ratio, 605
 SE. *See* Scavenging effectiveness
 Se(IV), 159, 161, 162, 168–173
 Se(VI), 159, 162, 168–173
 Sea ice sediments, 80, 383
 Sea of Japan (East Sea), 382–383, 385, 386
 Seasonal variations in (⁸⁷Sr/⁸⁶Sr), 524, 525, 746
 Seawater, 207, 213–215, 254, 278, 534–537
 Secondary ion mass spectrometry (SIMS), 6, 110, 207, 208, 400, 401
 Secondary minerals, 45–49, 52, 55, 65, 73, 88, 93, 95, 98
 Sector field inductively coupled plasma mass spectrometry (SF-ICP-MS), 398, 401, 402, 406, 408, 769
 Sediment, 74–78, 141–143, 145–147, 235–238, 305–325, 383, 387, 507–508, 559–561

- accumulation, 14, 76, 305, 322, 369, 387, 404
 erosion and focusing using ^{210}Pb , ^7Be and ^{234}Th , 76, 317–319
 focusing, 14, 76, 78, 317–319, 322
 provenance, 537, 542, 544
 transport, 73, 75, 315–316, 369, 487, 537, 560–561, 849
 transport in estuary, 315–316
 traps, 76, 77, 80, 276–277, 314, 325, 377, 380
 Sedimentary carbonates, 524, 529, 533, 544
 Sedimentary diffusion coefficient, 355
 Seepage velocity, 355
 Segment length curve, 808
 Se isotopes, 155, 159, 161, 167–173
 Selenate, 157, 168–172
 Selenium (Se)
 isotope, 167–173
 oxidation, 169–170
 Selfoss Iceland, 301
 Sellafield, 18, 372, 380–383, 395, 397, 402, 408–410
 Se(IV) oxidation, 159, 169–170
 SER. *See* Silicate erosion rates
 Se(VI) reduction, 168–173
 $^{80}\text{Se}/^{76}\text{Se}$, 23, 167, 170
 $^{82}\text{Se}/^{76}\text{Se}$, 157, 161, 167
 SF-ICP-MS. *See* Sector field inductively coupled plasma mass spectrometry
 SGD. *See* Submarine groundwater discharge
 Short-lived radionuclides, 7, 305–325, 578, 581, 594
 Siang, 539–540
 Sierra Nevada, 280, 522, 523
 Silcretes, 100–101
 Silicate erosion rates (SER), 520, 531, 532
 Silicates, 12, 43, 48, 55, 65, 88, 90, 93, 101, 112, 128, 134, 140–141, 150, 208, 211, 265, 399, 520, 522, 524–525, 529–537, 543, 544, 552, 554, 561, 562, 613, 748
 proxies, 544
 Silicic acid, 88, 91, 94, 96–98, 101
 Silicon (Si), 15, 23, 24, 87–101, 346, 347, 400, 502, 543, 579
 isotopes, 87–101
 Siltation, 486
 Silver (Ag), 182, 272, 273, 311, 423–426, 432, 618, 835–837
 Silver phosphate (Ag_3PO_4), 423–426, 432
 SIMS. *See* Secondary ion mass spectrometry
 Site preference (SP), 453, 456–458, 461–470
 Siwaliks, 536
 SJR. *See* San Joaquin River
 Skeletal contribution to PbB, 772, 774
 Skeletal Pb contribution to PbB, 774
 Skeletal Pb to PbB during the post-pregnancy, 774
 Smelter, 139, 194, 220, 770, 772
 Sm/Nd. *See* Samarium/Neodymium
 SMOC. *See* Standard Mean Ocean Chloride
 SNAP. *See* Systems Nuclear Auxiliary Power Program
 SNAP-9A, 368, 397
 Soil, 47–48, 72–73, 95–97, 561–563, 596–599, 748
 erosion, 404–406, 485–511
 hydrological processes, 809, 812–813
 profiles, 62, 498–499, 526, 527, 562
 Solar activity, 62, 476, 477, 582
 Solid-solution partitioning, 394
 Solubility coefficient, 348
 Soot particles, 220, 221
 Source apportionment studies using Pb isotopes in humans, 770
 Source discrimination, 665–667
 Source of Pb–210, 307
 Sources and pathways of Pb in urban environments, 770
 Sources of lead using lead isotopes, 765–779
 Sources of radionuclides, 305–325
 Source tracking, 20, 23
 South America, 731, 751, 753
 Southern hemisphere, 397, 404, 406, 493, 615
 deposition, 396
 SP. *See* Site preference
 Spallation, 16, 61, 488, 577
 SPARTAH. *See* Syringe pump apparatus for the retrieval and temporal analysis of helium
 Spatial variability, 500
 Species effect, 54
 Speleothems, 790, 791, 793, 796–798
 Sphalerite (ZnS), 125, 140
 SPIME extraction, 662
 SRM-979, 161, 165
 SRM-3149, 161, 170
 SRM for calcium measurements, 111
 Stable isotopes, 19–22, 36–37, 136–137, 155–173, 177–199, 418–420, 637–668, 675–697, 706, 714–715, 721–735, 838–846, 861–880
 of Cl, 436
 of Cr and Se, 155–173
 fractionation, 4, 21, 22, 113, 126, 136–137, 147, 148, 178, 179, 248, 252, 259
 processes, 189–190, 192, 198
 of nitrate, 846–852
 of O, 436, 445, 454
 of post-transition metals, 177–199
 of transition metals, 177–199
 Stable mercury isotopes, 229–243
 Stable Tl, 249, 252
 Standard Mean Ocean Chloride (SMOC), 436, 439
 Standards, 710–712, 187–189, 249–251, 288, 502–503, 866
 corrections, 866
 Stratospheric $\Delta^{17}\text{O}$ signature, 846–848
 STE. *See* Stratosphere-troposphere exchange
 Steady state erosion island, 480, 481
 Stem water, 818, 819, 822
 Steranes, 638, 651
 Stoichiometric release of Sr, 544–545
 Stomata, 726, 819
 Strains of denitrifying bacteria, 837
 Stratosphere, 34, 306, 372, 395, 396, 467, 468, 488–489, 493, 574, 575, 578–583, 592–594, 845–846, 848
 Stratosphere-troposphere exchange (STE), 581–583, 593
 Stratospheric, 34, 306–307, 490, 491, 508, 575, 581–582, 593, 594, 843, 845, 846, 848
 fallout, 395–398, 400, 403–405, 407–411, 490, 510
 nitrate, 848, 849
 Strengbach watershed, 524
 Strontium (^{89}Sr and ^{90}Sr), 377–379
 Strontium (Sr)
 flux, 527, 528, 530, 534–536, 543
 isotopes, 519–545, 739–760
 origins of food stuffs, 757
 signatures in tooth and bone, 744

- to trace woolen textiles, 756
 - to track silicate weathering, 524
 - Subduction zones, 266
 - Submarine groundwater discharge (SGD), 305, 314, 330, 355–357, 355–359, 544
 - Sucrose, 814
 - Suess effect, 726, 734, 816
 - Sulfate, 378, 584, 831, 834–835, 838–846
 - in ice, 842–844
 - Sulfur and nitrogen cycles, 831
 - Sulfur dioxide (SO₂), 831, 838
 - Sulfur isotopes, 639, 838–835, 842–846
 - Sulfur isotopic anomalies, 833, 845
 - Sulfur isotopic signature, 842
 - Sulphur dioxide (SO₂), 220, 583
 - oxidation, 584
 - Supernovae, 475–476
 - Surface exposure age, 475–483
 - Symbiotic algae, 786, 794
 - Symmetry effect, 618, 624, 833
 - Synthetic ClO₄⁻, 437
 - Synthetic perchlorate, 439–441
 - Syringe pump apparatus for the retrieval and temporal analysis of helium (SPARTAH), 300–302
 - Systems Nuclear Auxiliary Power Program (SNAP), 368, 397
 - accident, 395
- T**
- Taiwan strait warm water (TSWW), 336, 337
 - Taklamakan, 598, 602
 - Tambora, 846
 - ⁹⁹Tc, 368, 369, 379–382
 - TCE, 7, 662–665, 667, 694
 - TCEA. *See* Thermal combustion elemental analyzer
 - Tectonics, 520, 522, 525, 531, 540, 543–545, 559
 - activity, 107, 555
 - weathering-climate, 520, 531, 534
 - Temperature sensitivity of Ca isotopic composition, 115
 - Teotihuacan, 753, 755
 - Terrestrial biogenic Ca fractionation, 108
 - Terrestrial calcium cycle, 108–109
 - Terrestrial fractionation line, 467–468, 612
 - Terrestrial Si cycle, 88, 101
 - Thallium (Tl)
 - absorbed onto clay minerals, 256, 257
 - in authigenic Mn-oxides, 257
 - in continental crust, 251, 252
 - enrichment factors, 257
 - flux, 252, 254–257, 298
 - isotopes, 247–266
 - change, 645
 - composition, 248, 252–256, 258, 261, 264–266
 - compositon of seawater, 253, 254, 258
 - fractionation, 251–253, 255, 258–261, 259–261, 265, 266
 - in hydrothermal systems, 265
 - mobility, 253, 264, 266
 - in volcanic systems, 252
 - isotopic variation, 22
 - loss,
 - in mineral aerosols, 255
 - in Mn nodules, 256
 - reduction/oxidation processes, 256
 - as a tracer of ocean crust recycling, 263
 - Th–234 as a tracer of particle-reactive species, 308, 318–319
 - Thermal combustion elemental analyzer (TCEA), 424
 - Thermal diffusion, 868, 871, 873
 - Thermal fractionation, 869, 870, 872, 873, 877
 - Thermal ionization mass spectrometry (TIMS), 5–7, 26, 42, 53, 110, 111, 129–132, 147–149, 159, 161, 184, 186, 248, 348, 398, 401, 402, 606, 750, 769, 789, 793, 834
 - Thermal maturation, 646–648, 652
 - Thermodynamic law, 832
 - Thorium, 17, 35, 308, 346, 379, 552, 589–606, 769
 - Thoron, 346–347
 - Three-end-member mixing, 332, 335
 - Thyroidal hormone, 436
 - Tillage, 404, 486, 498–499, 504–506
 - Time-averaged erosion rates, 475–483
 - TIMS. *See* Thermal ionization mass spectrometry
 - Titanium (Ti), 182, 183, 287
 - ²⁰⁵Ti, 248–258, 260, 261, 263–265
 - Tl speciation, 260
 - ²⁰⁵Tl/²⁰³Tl, 23, 230, 233, 248
 - TNT, 395, 666
 - Tombo, 752, 754
 - Tooth enamel, 724, 733, 734, 740–750, 759
 - Topsoil erosion, 63, 72, 486
 - Total body burden of Pb, 767
 - Total deposition sampling, 591–593
 - Total water flux in dairy cows, 713
 - Trace minerals, 523–524
 - Tracers, 3, 7, 13, 33–37, 41–55, 61–81, 87–101, 105–121, 149, 155–173, 177–199, 205–222, 263–265, 277, 285, 296, 305, 314–323, 329–339, 343–359, 365–388, 393–412, 426–427, 443, 452, 468, 475, 486, 501, 508–509, 519–545, 573–585, 589–606, 629, 675–697, 703–716, 721–735, 777, 788, 848, 861–880
 - of human diet, 22, 703–716
 - for paleo-diet reconstruction, 721–735
 - studies on cheese, 704
 - studies on olive oil, 704
 - studies on wine, 704
 - Tracing food source, 703
 - Tracing perchlorate in contaminated aquifer, 445–447
 - Tracing the origin of dairy products, 713–714
 - Tracing the pathways of ⁷Be and ²¹⁰Pb after a heavy thunderstorm, 319
 - Trade and exchange, 758
 - Transfer of isotope anomaly, 839
 - Trans-Himalayan plutonic belt, 539
 - Transient tracers, 375, 574, 575, 785
 - Transient Tracers in the Ocean (TTO), 375
 - Transport, 3, 20, 35, 72–77, 97, 108, 113, 120, 195, 220, 252–255, 281, 298, 305–325, 332, 351, 369, 404–409, 422, 485, 526, 559–561, 590–594, 596–599, 666, 766, 817, 839, 847
 - in rivers, 74–75, 554
 - Transuranics, 18, 369, 393–412, 594
 - elements, 393, 398

- Trap, 76, 77, 80, 186, 215, 219, 232, 276, 287, 453, 536, 554, 662, 866
- Tree physiology, 822
- Tritogenic helium, 290, 295–297
- Tritium (^3H), 18, 295–297, 296, 368, 373–374, 575, 577
- Trophic level effect, 724, 727–728
- Trophic transfer of MeHg, 241
- Tropical isotope dendroclimatology, 822
- Troposphere, 14, 33, 62, 306, 307, 372, 467, 475, 489, 574–580, 583, 592–596, 623, 841, 848
- Troposphere-stratospheric exchange, 593, 594
- Tropospheric fallout, 384, 385, 395, 405, 407, 411
- Tropospheric O₃, 617–621
- Tropospheric OH, 617, 622–623
- TSWW. *See* Taiwan strait warm water
- TTO. *See* Transient Tracers in the Ocean
- Tungsten, 180, 182
- Turnover rates of bones, 744
- Tyrolean Iceman, 745
- U**
- Uluru Basin, 292–294
- UNSCEAR, 366, 367, 379, 589, 594
- Upwelling, 51, 52, 144, 263, 386–387, 420, 429, 430
- Uranium, 17, 23, 33, 35, 42, 259, 272, 280, 367, 371, 394, 487, 551, 553, 555, 560, 565, 589–606, 769, 770, 777, 793
- Urine measurements of the isotopic ratios, 768
- U-Th series, 3, 5–7, 17, 24, 73, 564, 573, 576, 799
- V**
- Valence states of Tl, 247, 248, 255, 259
- Vanadium, 182
- Variability of $\epsilon^{114}\text{Cd}/^{110}\text{Cd}$, 138, 141
- Variations of $\delta^{44/40}\text{Ca}$ with trophic level, 108, 116
- Vein calcites, 524, 533, 534
- Vienna Pee Dee Belemnite (VPDB), 119, 640, 722, 808
- Vienna Standard Mean Ocean Water (VSMOW), 426, 436, 454, 611–613, 619, 624, 677, 678, 707, 808
- Violence/warfare, 751, 755
- Vital effects in tree rings, 109, 119–120
- Volcanic sulfate, 833, 835, 845, 846, 872
- VSMOW-SLAP scale, 438
- W**
- Wari, 751, 754, 755
- Washout ratio, 605, 606
- Water exchange, 343–359, 468, 469
rate, 351
- Water mass, 14, 16, 142, 144, 305, 310, 329, 331, 332, 336, 339, 379, 380, 386, 578
analysis technique, 331
mixing, 144, 331–339, 345, 352
- Water mixing tracers, 331, 379
- Water parcel, 332, 333
- Watershed, 63, 66, 67, 99, 106, 308, 315, 379, 508, 509, 524, 527, 555, 629
residence time, 315
- Weapons testing, 292, 307, 308, 369, 374, 387, 488, 489, 574, 589, 598
- Weathering, 19, 20, 23, 45–50, 55, 78, 87, 93, 95, 99, 108, 119, 157, 164, 170, 206, 252, 263, 419, 485, 519, 521–537, 541, 551–552, 555, 557–559, 563–566
kinetics, 522–527, 529
properties, 522
provenance, 537
tracer, 46
and transport, 48, 527, 537, 541
- Wind erosion, 486, 506–507
- Wine, 704, 776–777
- X**
- Xylem water, 808, 813, 814, 817
- Y**
- ^{90}Y , 365, 379
- Yamuna, 532, 533
- Young orogenic belts, 531, 544
- Z**
- Zinc isotopes, 180
- $^{66}\text{Zn}/^{64}\text{Zn}$, 23, 146, 180